CODEN: JASMAN 4966

THE JOURNAL of the Acoustical Society of America

Vol. 105, No. 2, Pt. 1 February 1999

SOUNDINGS SECTION

(Continued)

CONTENTS—*Continued from preceding page*

(Continued)

CONTENTS—*Continued from preceding page*

BIOACOUSTICS [80]

LETTERS TO THE EDITOR

CUMULATIVE AUTHOR INDEX

NOTES CONCERNING ARTICLE ABSTRACTS

1. The number following the abstract copyright notice is a Publisher Item Identifier (PII) code that provides a unique and concise identification of each individual published document. This PII number should be included in all document delivery requests for copies of the article.
2. PACS numbers are for subject classification and indexing. See June and December issues for detailed listing of acoustical classes and subclasses.
3. The initials in brackets following the PACS numbers are the initials of the JASA Associate Editor who accepted the paper for publication.

CONTENTS

SOUNDINGS

Section Editor: Richard Stern

This front section of the *Journal* includes acoustical news, views, reviews, and general tutorial or selected research articles chosen for wide acoustical interest and written for broad acoustical readership.

ACOUSTICAL NEWS—USA

Elaine Moran
Acoustical Society of America, 500 Sunnyside Boulevard, Woodbury, New York 11797

Editor's Note: *Readers of this Journal are asked to submit news items on awards, appointments, and other activities about themselves or their colleagues. Deadline dates for news items and notices are 2 months prior to publication.*

New Fellows of the Acoustical Society of America

Christopher W. Clark—For contributions to whale acoustics.

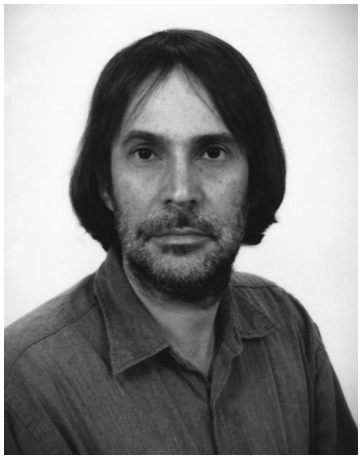

Rudolph Martinez—For contributions linking fluid mechanics and acoustics.

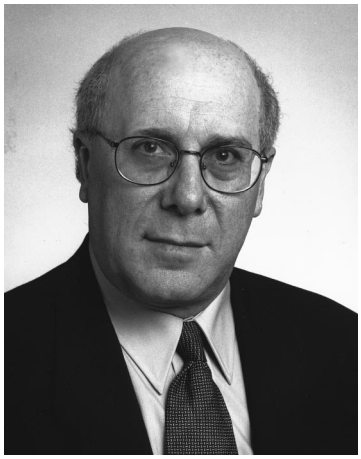

Philip Rubin—For contributions to modeling speech production.

Sid P. Bacon becomes new Associate Editor of the *Journal*

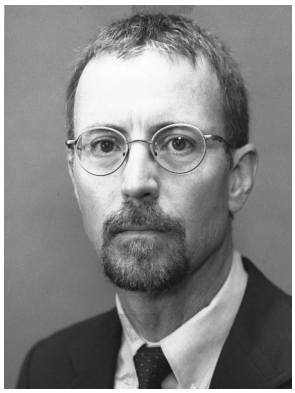

Sid P. Bacon

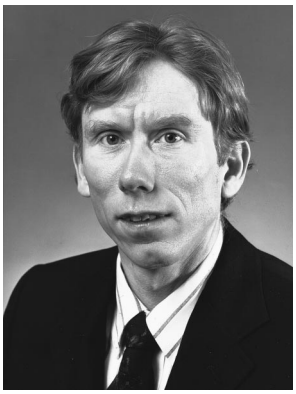

Joseph W. Hall

In January 1999 Professor Sid P. Bacon of the Department of Speech and Hearing Science at the Arizona State University, Tempe, Arizona, became a new Associate Editor of the *Journal* for papers in Psychological Acoustics (PACS 43.66). He succeeded Professor Joseph W. Hall of the Division of Otology at the University of North Carolina, who requested replacement after a three-year term of faithful and effective service. The Editor-in-Chief expresses his deep appreciation to Professor Hall and to his institution for support.

Sid P. Bacon received a B.G.S. degree in Speech Pathology and audiology from University of Kansas in 1977. He also received there the M.A. degree in Audiology in 1979. After his Ph.D. in Experimental Psychology in 1985 from University of Minnesota he spent postdoctoral periods in Psychophysics at University of Cambridge in UK and at Boys Town National Institute. From 1986 to 1988 Sid Bacon was at Vanderbilt University as assistant professor of Hearing and Speech Sciences and director of research at the Bill Wilkerson Hearing and Speech Center. In 1988 he moved to the Department of Speech and Hearing Science at Arizona State University where he is a Professor and the Director of the Interdisciplinary Ph.D. program.

Sid Bacon's psychoacoustical research interests have been in temporal effects, in forward masking, and modulation detection. He has published widely, including over 30 articles in our *Journal.* Sid has served on the ASA Education Committee and on the Technical Committee for Psychological and Physiological Acoustics. He has also served as an Associate Editor for the *Journal of Speech, Language, and Hearing Research.*

The Editor-in-Chief and his colleagues welcome Professor Bacon to membership on the Editorial Board.

DANIEL W. MARTIN
Editor-in-Chief

Semi J. Begun elected to National Inventors Hall of Fame

Semi J. Begun (1905–1995), past Fellow of the Acoustical Society of America, was inducted into the National Inventors Hall of Fame on 19 September 1998, in recognition of his inventions in magnetic recording. Much of his early magnetic recording was in labs at the Society for the Blind in New York City. In 1938, Begun joined the Brush Development Company located in Cleveland, Ohio. One of his applications there was the ''Black Box'' aircraft recorder used in investigating aircraft incidents. Thirty of his patents were reviewed in the Acoustical Patent Review section of our *Journal.*

Each year since 1973, the National Inventors Hall of Fame has honored the top inventors that have made a significant contribution to society. The nominations are open to any individual with at least one invention covered by a U.S. patent. ASA is represented on the NIHF selection committee along with about 40 national scientific and technical organizations. The 135 past inductees include Thomas Edison, Alexander Graham Bell, and Marvin Camras.

The NIHF highlights, through interesting displays, video, and patent application models, the lives and inventions of its inductees. The Hall of Fame was founded by the National Council of Intellectual Property Law Associations and the United States Patent and Trademark Office. In 1987 Akron, Ohio was selected as the permanent home for the National Inventors Hall of Fame and opened in 1995 as part of Inventure Place, an interactive museum that allows development of creativity and the exploration of invention. To learn more about the National Inventors Hall of Fame, or to nominate an inventor, visit the web site at ⟨http://www.invent.org⟩.

Position Open

Stanford University: Faculty Opening. Stanford University's Departments of Linguistics and Computer Science seek applicants for a tenure-track faculty position in areas combining linguistics and computation. Candidates will be expected to show breadth and depth in both areas and to demonstrate the ability to make an intellectual contribution to both linguistics and computer science. Example topics of interest include, but are not limited to, natural language dialogue processing and understanding, development and evaluation of linguistic methods using large speech and text databases, speech recognition, computational modeling of cognitive processing of language, lexical knowledge bases, symbolic and statistical methods of language processing, and linguistic knowledge representation. Interest in an application area, such as information retrieval, data mining, or web services is desirable. Higher priority will be given to the innovation and promise of the candidate's work than to any of these specific topics and applications.

Applicants should have a Ph.D. in a relevant field. Evidence of the ability to pursue a research program and a strong commitment to graduate and undergraduate teaching are required. The successful candidate will be expected to teach courses, both in the candidate's specialty area and in related subjects, at the graduate and undergraduate levels, and to build and lead a team of graduate students in Ph.D. research.

The appointment will be made at the level of an Assistant Professor. The position is available beginning Autumn 1999 and is offered jointly in the Linguistics and Computer Science Departments. Further information about these departments can be found at http://www-linguistics.stanford.edu and http://www-cs.stanford.edu, respectively.

Applications should include a curriculum vita, statements of research and teaching interests, and the names of five references. The application should be sent to: Professor John Mitchell, Search Committee Chair c/o Laura Kenny-Carlson Computer Science Department, Stanford University, Gates 2B, Stanford, CA 94305-9025.

The interview process will begin on 15 January 1999, but applications will be accepted until 15 February 1999. Stanford University is an equal opportunity employer and welcomes applications from women and minority candidates.

USA Meetings Calendar

Listed below is a summary of meetings related to acoustics to be held in the U.S. in the near future. The month/year notation refers to the issue in which a complete meeting announcement appeared.

1999

25–27 Feb.	24th Annual Conference, National Hearing Conservation Association, Atlanta, GA [National Hearing Conservation Association, 9101 E. Kenyon Ave., Suite 3000, Denver, CO 80237, Tel.: 303-224-9022; Fax: 303-770-1812; E-mail: nhca@gwami.com].
15–19 March	Joint meeting: 137th meeting of the Acoustical Society of America/2nd Convention of the European Acoustics Association: Forum Acusticum, integrating the 25th Anniversary DAGA conference, Berlin, Germany [Acoustical Society of America, 500 Sunnyside Blvd., Woodbury, NY 11797, Tel.: 516-576-2360; Fax: 516-576-2377; E-mail: asa@aip.org; WWW: asa.aip.org].
10–12 May	AIAA/CEAS Aeroacoustics Conference, Bellevue, WA [Belur Shivashankara, The Boeing Company, P.O. Box 3707, MS 67-ML, Seattle, WA 98124-2207; Tel.: 425-234-9551; Fax: 425-237-5247; E-mail: belun.n.shivashankara@boeing.com].
6–7 June	1999 SEM Spring Conference, Cincinnati, OH [Katherine M. Ramsay, Conference Manager, Society for Experimental Mechanics, Inc., 7 School St., Bethel, CT 06801; Tel.: 203-790-6373; Fax: 203-790-4472; E-mail: meetings@sem1.com].
27–30 June	ASME Mechanics and Materials Conference, Blacksburg, VA [Mrs. Norma Guynn, Dept. of Engineering Science and Mechanics, Virginia Tech, Blacksburg, VA 24061-0219; Fax: 540-231-4574; E-mail: nguynn@vt.edu; WWW: www.esm.vt.edu/mmconf/].
6–11 July	1999 Clarinetfest, Ostend, Belgium [International Clarinet Association, Keith Koons, Music Dept., Univ. of Central Florida, P.O. Box 161354, Orlando, FL 32816-1354].
7–10 Oct.	Symposium on Occupational Hearing Loss, Philadelphia, PA [American Institute for Voice and Ear Research, Attn: Barbara-Ruth Roberts, 1721 Pine St., Philadelphia, PA 19103, Tel.: 215-545-2068; Fax: 215-735-2725].
1–5 Nov.	138th meeting of the Acoustical Society of America, Columbus, OH [Acoustical Society of America, 500 Sunnyside Blvd., Woodbury, NY 11797, Tel.: 516-576-2360; Fax: 516-576-2377; E-mail: asa@aip.org; WWW:asa.aip.org].
2–4 Dec.	ACTIVE 99, Fort Lauderdale, FL [Institute of Noise Control Engineering, P.O. Box 3206, Arlington Branch, Poughkeepsie, NY 12603, Tel.: 914-462-4006; Fax: 914-463-020; E-mail: INCEUSA@aol.com; WWW:users.aol.com/inceusa/ince.html].
6–8 Dec.	INTER-NOISE 99, Fort Lauderdale, FL [Institute of Noise Control Engineering, P.O. Box 3206, Arlington Branch, Poughkeepsie, NY 12603, Tel.: 914-462-4006; Fax: 914-463-020; E-mail: INCEUSA@aol.com; WWW:users.aol.com/inceusa/ince.html].

ACOUSTICAL NEWS—INTERNATIONAL

Walter G. Mayer
Physics Department, Georgetown University, Washington, DC 20057

Websites—An update

Several national acoustical societies have established or changed addresses of homepages which contain information about various aspects of the organization, meeting announcements, and other items of interest. Below are the most recent new or updated listings:

Canadian Acoustical Association	www.uwo.ca/hhcru/caa/
Institute of Acoustics (UK)	ioa.essex.ac.uk/ioa/
French Acoustical Society	www.loa.espci.fr/sfa/
German Acoustical Society	www.dega.itap.de
Brazilian Acoustical Society	www.sobrac.ufsc.br
European Acoustics Association	wrangler.essex.ac.uk/eaa/
International Commission on Acoustics	gold.sao.nrc.ca/ims/ica/

Papers published in JASJ(E)

A listing of Invited Papers and Regular Papers appearing in the latest issue of the English language version of the *Journal of the Acoustical Society of Japan*, JASJ(E), was published for the first time in the January 1995 issue of the Journal. This listing is continued below.

The November issue of JASJ(E), Vol. 19, No. 6 (1998) contains the following papers:

M. G. S. Ali and A. R. Mohamed ''Numerical calculation of the frequency response of the radiation coupling in lossy medium''
T. Taniguchi, S. Kajita, K. Takeda, and F. Itakura ''Blind signal separation for recognizing overlapped speech''
N. Nakasako, Y. Mitani, and M. Ohta ''A practical and probabilistic evaluation method of sound insulation systems based on the extended regression analysis for roughly observed data''
H. Kamata, T. Endo, and Y. Ishida ''Practical private speech communication system with chaos using digital signal processor''

International Meetings Calendar

Below are announcements of meetings to be held abroad. Entries preceded by an * are new or updated listings with contact addresses given in parentheses. Month/year listings following other entries refer to issues of the *Journal* which contain full calendar listings or meeting announcements.

March 1999

10–12 *__Acoustical Society of Japan Spring Meeting__, Tokyo, Japan. (ASJ, Ikeda Building, 2-7-7, Yoyogi, Shibuya-ku, Tokyo 151-0053, Japan; Fax: +81 3 3379 1456; e-mail: kym05145@niftyserve.or.jp)

15–19 **Joint Meeting of EAA Forum Acusticum, and 137th meeting of the Acoustical Society of America**, Berlin. *6/97*

April 1999

27–29 **International Conference on Vibration, Noise, and Structural Dynamics**, Venice. *8/98*

May 1999

10–14 **4th International Conference on Theoretical and Computational Acoustics**, Trieste. *6/98*

24–26 **2nd International Conference on Emerging Technologies in NDT**, Athens. *8/98*

24–27 *__2nd EAA International Symposium on Hydroacoustics__, Gdańsk-Jurata, Poland. (EAA Symposium, Department of Acoustics, Technical University of Gdańsk, ul. G. Narutowicza 11/12, 80-952 Gdańsk, Poland; Fax: +48 58 347 1535; Web: www.hydro.eti.pg.gda.pl)

30–3 **16th International Evoked Response Audiometry Study Group Symposium**, Tromsø. *12/98*

June 1999

28–30 **1st International Congress of the East European Acoustical Association**, St. Petersburg. *10/97*

28–1 **Joint Conference of Ultrasonics International '99 and World Congress on Ultrasonics '99 (UI99/WCU99)**, Lyngby. *6/98*

July 1999

4–9 **10th British Academic Conference in Otolaryngology**, London. *10/97*

5–8 **6th International Congress on Sound and Vibrations**, Copenhagen. *2/98*

August 1999

2–6 *__International Symposium on High-Power Ultrasonics__, Vitebsk, Belarus. (Institute of Technical Acoustics, National Academy of Sciences of Belarus, Ludnikov av. 13, Vitebsk 210717, Belarus; Fax: +375 212 24 39 53; e-mail: 1pm@ita.belpak.vitebsk.by)

September 1999

1–4 **15th International Symposium on Nonlinear Acoustics (ISNA-15)**, Göttingen. *10/97*

15–17 **British Society of Audiology Annual Conference**, Buxton. *8/98*

October 1999

20–22 **Iberian Meeting of the Spanish Acoustical Society and the Portuguese Acoustical Society**, Avila. *12/98*

March 2000

20–24 **Meeting of the German Acoustical Society (DAGA)**, Oldenburg. *10/98*

July 2000

4–7 **7th International Congress on Sound and Vibration**, Garmisch-Partenkirchen. *12/98*

October 2000

3–5 **WESTPRAC VII**, Kumamoto. *6/98* *(new Web: cogni.eecs.kumamoto-u.ac.jp/others/westprac7)

16–18 **2nd Iberoamerican Congress on Acoustics, 31st National Meeting of the Spanish Acoustical Society, and EAA Symposium**, Madrid. *12/98*

16–20 **6th International Conference on Spoken Language Processing**, Beijing. *10/98*

September 2001

2–7 **17th International Congress on Acoustics (ICA)**, Rome. *10/98*

BOOK REVIEWS

James F. Bartram
94 Kane Avenue, Middletown, Rhode Island 02842

These reviews of books and other forms of information express the opinions of the individual reviewers and are not necessarily endorsed by the Editorial Board of this Journal.

Editorial Policy: *If there is a negative review, the author of the book will be given a chance to respond to the review in this section of the Journal and the reviewer will be allowed to respond to the author's comments. [See ''Book Reviews Editor's Note,'' J. Acoust. Soc. Am.* ***81****, 1651 (May 1987).]*

Nonlinear Acoustics

Mark F. Hamilton and David T. Blackstock, Editors

Academic Press, San Diego, 1998.
xviii+455 pp. Price: $95.00.

Contemporary nonlinear acoustics is essentially an interdisciplinary area. Historically, it is closely associated with classical fluid and solid mechanics, and in recent decades it also has become a branch of nonlinear wave theory. After World War II, the subject of nonlinear acoustics developed much faster but in a rather nonuniform manner. After a boom during the 1960s and 1970s due to a new type of antenna, namely parametric arrays, it kept a relatively low profile. A new wave of interest, associated with applications in biology and material diagnostics arose during the 1990s. An indicator of this interest is the appearance of new books on nonlinear acoustics.

Nonlinear Acoustics is a very good collection of 15 chapters written by many leading scientists in this area and carefully edited by Mark Hamilton and David Blackstock. It covers a wide spectrum of problems, from classical to brand-new. I read many of its sections with intense interest. This interest was stimulated by the opening historical Chapter 1 entitled ''History of nonlinear acoustics: 1750s–1930s,'' written by D. Blackstock. This is a brilliantly written history of relevant hydrodynamics and of a transition to the modern nonlinear acoustics of fluids. (I'd like to see an equally interesting outline of the history of nonlinear acoustics of solids.) The following chapter, ''The parameter B/A,'' written by R. Beyer, one of the founders of contemporary nonlinear acoustics, gives a good tutorial explanation and outline of methods for measuring a fundamental parameter of quadratic nonlinearity in fluids.

The next few chapters deal with approximate equations used in nonlinear acoustics, and their typical solutions. Chapter 3, ''Model equations,'' written by M. Hamilton and C. Morfey, summarizes different simplifications of basic nonlinear equations by using smallness of local effects of nonlinearity, dissipation, and diffraction. In particular, the most usable Burgers equation and Khokhlov–Zabolotskaya–Kuznetsov (KZK) equation are derived to describe progressive waves and wave beams. These equations are utilized in Chapter 4, ''Progressive waves in lossless and lossy fluids,'' by D. Blackstock, M. Hamilton, and A. Pierce. They consider, for the most part, classical aspects of nonlinear acoustics: simple wave propagation and shock waves in plane, cylindrical, and spherical geometry. This topic is continued in Chapter 5, ''Dispersion,'' in which M. Hamilton, Yu. Il'inskii, and E. Zabolotskaya consider waves in relaxing media, where dispersion is weak and is of a dissipative nature, and in waveguides and bubbles, where it can play a dominant role in wave interactions. Two subsequent chapters, 6, ''Radiation pressure and acoustic levitation'' by T. Wang and C. Lee, and 7, ''Acoustic streaming,'' deal not with the sound propagation, but rather with the action of sound on small bodies and inducement of the hydrodynamic motion of the medium itself.

As the editors state, these first seven chapters of the book are largely self-contained and can be used as a course text, while the remaining eight chapters cover more special topics. I found that the separation of these two parts of the book is not very distinct. Chapter 8, ''Sound beams,'' written by M. Hamilton, is based on the parabolic KZK equations and treats both perturbations of the linear diffraction theory results and the theory of strongly distorted wave beams. Chapter 9, ''Finite-amplitude waves in solids,'' by A. Norris, is a good summary of mostly classical results. Still, I find it unfortunate that this chapter is the only ''non-fluid'' piece in the book. The next two chapters, 10, ''Perturbation methods,'' by J. Ginsberg, and 11, ''Computational methods,'' by J. Ginsberg and M. Hamilton, discuss some analytical and computational aspects of nonlinear acoustics; the latter seems particularly useful; it contains an accessible explanation of numerical problems.

The rather lengthy chapters 12 and 13 deal with very general problems. The former, ''Propagation in inhomogeneous media (Ray theory),'' by C. Morfey and F. Cotaras, gives a clear and comprehensive narrative of nonlinear geometrical acoustics. To have a complete picture of this large area, it would be desirable to include more information on self-refraction problems and to discuss the relationship between ray theory and the theory of diffracting sound beams. The latter, ''Statistical phenomena,'' by S. Gurbatov and O. Rudenko, describes some results of the theory of nonlinear propagation of random acoustic waves and their interaction with regular signals.

The last two chapters are about two relatively new topics in nonlinear acoustics. In Chapter 14, ''Parametric layers, four-wave mixing, and wavefront reversal,'' H. Simpson and P. Marston discuss some ''four-wave'' processes associated mainly with cubic nonlinearity of the medium. Similar processes have long been commonplace in optics. I would have liked to see a brief discussion of this in the chapter. Also, since the early 1980s, these problems have been penetrating into nonlinear acoustics. They include, in particular, the different phase-conjugating processes, such as wavefront reversal, and some experiments in this area are also mentioned. The last chapter, 12, ''Biomedical applications,'' written by E. Carstensen and D. Bacon, gives an outline of one of the most important applications of intensive ultrasound. These applications, such as lithotripsy and ultrasonic surgery, have been known for a relatively long time, but actually, the theoretical approach based in principle on the nonlinear acoustics equations, has a rather short history in biological problems.

In general, this is a very good and useful book. The chapter-to-chapter inhomogeneity inevitable in books composed of a collection of essays, has been successfully minimized by the editors, and most of the materials are presented clearly and systematically. The book could be recommended both for scientists and for students. The only critical note I could have is that the book concentrates almost completely on acoustics of fluids (with the exception of chapter 9, which is rather short), somewhat ignoring recent progress in nonlinear acoustics of solids, including such ''nonclassical'' media as rocks and construction materials.

Coincidentally, only slightly later, a monograph entitled ''Nonlinear wave processes in acoustics'' by N. Naugolnykh and L. Ostrovsky was published by Cambridge University Press. Luckily, as a coauthor, I do not feel any conflict of interest regarding the reviewed book, or vice versa. Notwithstanding the natural overlap of a part of the topics, the books are rather complementary: while the first book gives detailed derivations of the main equations and their solutions and explains almost all the main effects of classical nonlinear acoustics of fluids and such important applications as biomedical acoustics, the second one gives a more compact, monographic outline of the problems of nonlinear acoustics. It includes more about solid state acoustics, the acoustics of dispersive media, and the problems relevant to nonlinear material characterization. As I mentioned earlier, the appearance of new books can be considered as an indicator of growing interest in nonlinear acoustics, which is stimulated by new and developing applications.

LEV A. OSTROVSKY
University of Colorado/NOAA Environmental Technology Laboratory, Boulder, Colorado 80303

Signals, Sound, and Sensation

William M. Hartmann

AIP Press, Woodbury, NY, 1997.
xvii+647 pp. Price: $80.00.

When I first saw this book, I was struck by the apparent similarity to another one that I reviewed in the December 1993 issue of *JASA: Signals and Systems for Speech and Hearing*, by Stuart Rosen and Peter Howell. Certainly the title is quite similar, and so is the intended readership. To quote Hartmann, ''*Signals, Sound, and Sensation* is a book for people who are actively interested in the perception of sound.'' Rosen and Howell target ''people working in the speech and hearing sciences.'' Both books seek to teach ''the mathematics of the signal'' to this audience in a friendly fashion.

Further reading soon reveals that the books have important differences: Hartmann's has twice as many pages as Rosen and Howell's (and costs twice as much). Whereas Rosen and Howell ''tell the entire story in words and pictures, with only minimal mathematics,'' Hartmann ''assumes that the reader is comfortable with the concepts and the practice of differential and integral calculus.''

What sort of book is this? Let me quote from the jacket: ''This is a unique book on the mathematics of signals written for hearing science researchers. Designed to follow an introductory text on psychoacoustics, *Signals, Sound, and Sensation* takes the reader through the mathematics of signal processing from its beginnings in the Fourier transform to advanced topics in modulation, dispersion relations, minimum phase systems, sampled data, and nonlinear distortion.''

To quote further, this time from the Preface, ''...*SS&S* resembles an engineering text, though it is friendlier than most of that genre.'' Well, with my background in electrical engineering, I regard such texts as old friends! On the other hand, I am delighted that Hartmann is so friendly in his exposition of concepts with which my knowledge is not so intimate: loudness, pitch, timbre, auditory filters, etc. In other words, I find that I can use the book to learn about psychoacoustics, already knowing about signals. This seems to be an inversion of what Hartmann intended, but it works for me.

Another feature I like about this book is the inclusion of biographical sketches of prominent workers in the field over the years: Hertz, Lord Reyleigh, Fletcher, Fourier, Barkhausen, Helmholtz, Von Békésy, Stevens, Hilbert, Fechner. I am concerned, however, about the biographical sketch of Hilbert. The author states that ''he invented the word 'spectrum.' '' I would venture to say that this gives short shrift to Isaac Newton, who used the word ''spectrum'' in *Phil. Trans. VI, 1671*.

This bit of ''nitpicking'' aside, I like Hartmann's book, and I recommend it, not only for those wishing to teach signal theory to students of psychoacoustics, but also for those wishing to teach basic psychoacoustic concepts to students already familiar with signal theory.

JAMES F. BARTRAM
JFB Consultants
94 Kane Avenue
Middletown, Rhode Island 02842

Signals, Sound, and Sensation

William M. Hartmann

AIP Press, Woodbury, NY, 1997.
xvii+647 pp. Price: $80.00.

When I first saw this book, I was struck by the apparent similarity to another one that I reviewed in the December 1993 issue of *JASA: Signals and Systems for Speech and Hearing*, by Stuart Rosen and Peter Howell. Certainly the title is quite similar, and so is the intended readership. To quote Hartmann, ''*Signals, Sound, and Sensation* is a book for people who are actively interested in the perception of sound.'' Rosen and Howell target ''people working in the speech and hearing sciences.'' Both books seek to teach ''the mathematics of the signal'' to this audience in a friendly fashion.

Further reading soon reveals that the books have important differences: Hartmann's has twice as many pages as Rosen and Howell's (and costs twice as much). Whereas Rosen and Howell ''tell the entire story in words and pictures, with only minimal mathematics,'' Hartmann ''assumes that the reader is comfortable with the concepts and the practice of differential and integral calculus.''

What sort of book is this? Let me quote from the jacket: ''This is a unique book on the mathematics of signals written for hearing science researchers. Designed to follow an introductory text on psychoacoustics, *Signals, Sound, and Sensation* takes the reader through the mathematics of signal processing from its beginnings in the Fourier transform to advanced topics in modulation, dispersion relations, minimum phase systems, sampled data, and nonlinear distortion.''

To quote further, this time from the Preface, ''...*SS&S* resembles an engineering text, though it is friendlier than most of that genre.'' Well, with my background in electrical engineering, I regard such texts as old friends! On the other hand, I am delighted that Hartmann is so friendly in his exposition of concepts with which my knowledge is not so intimate: loudness, pitch, timbre, auditory filters, etc. In other words, I find that I can use the book to learn about psychoacoustics, already knowing about signals. This seems to be an inversion of what Hartmann intended, but it works for me.

Another feature I like about this book is the inclusion of biographical sketches of prominent workers in the field over the years: Hertz, Lord Reyleigh, Fletcher, Fourier, Barkhausen, Helmholtz, Von Békésy, Stevens, Hilbert, Fechner. I am concerned, however, about the biographical sketch of Hilbert. The author states that ''he invented the word 'spectrum.' '' I would venture to say that this gives short shrift to Isaac Newton, who used the word ''spectrum'' in *Phil. Trans. VI, 1671*.

This bit of ''nitpicking'' aside, I like Hartmann's book, and I recommend it, not only for those wishing to teach signal theory to students of psychoacoustics, but also for those wishing to teach basic psychoacoustic concepts to students already familiar with signal theory.

JAMES F. BARTRAM
JFB Consultants
94 Kane Avenue
Middletown, Rhode Island 02842

REVIEWS OF ACOUSTICAL PATENTS

Daniel W. Martin
7349 Clough Pike, Cincinnati, Ohio 45244

The purpose of these acoustical patent reviews is to provide enough information for a Journal reader to decide whether to seek more information from the patent itself. Any opinions expressed here are those of reviewers as individuals and are not legal opinions. Printed copies of United States Patents may be ordered at $3.00 each from the Commissioner of Patents and Trademarks, Washington, DC 20231.

Reviewers for this issue:

GEORGE L. AUGSPURGER, *Perception Incorporated, Box 39536, Los Angeles, California 90039*
DAVID A. PREVES, *Micro-Tech, 3500 Holly Lane N., Plymouth, Minnesota 55447*
D. LLOYD RICE, *11222 Flatiron Drive, Lafayette, Colorado 80026*
CARL J. ROSENBERG, *Acentech Incorporated, 33 Moulton Street, Cambridge, Massachusetts 02138*
ROBERT C. WAAG, *University of Rochester Medical Center, 601 Elmwood Avenue, Rochester, New York 14642*

5,739,432

43.35.Yb ULTRASONIC CHARACTERIZATION OF SINGLE DROPS OF LIQUIDS

Dipen N. Sinha, assignor to the University of California
14 April 1998 (Class 73/579), filed 30 May 1996

This is a diagnostic system for characterizing the ultrasonic properties of a single drop of liquid. An excitation transducer **24** mounted on holder **10** rests lightly on droplet **18**, transmitting a pulse from surface **40** to the opposite surface **38** in contact with receiver transducer **26**. Examples of samples for which the apparatus and method can be used are tear drops, blood, and other body fluid samples and snake and bee venom, especially for forensic investigations.—DWM

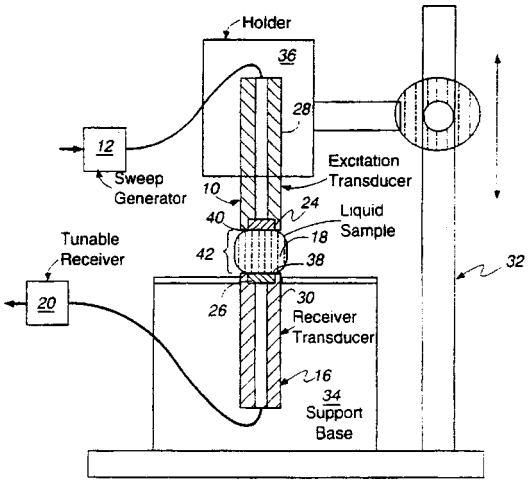

5,764,784

43.38.Ja ELECTROACOUSTIC TRANSDUCER

Hiroshi Sato and Akira Yoshino, assignors to Sanyo Electric Company
9 June 1998 (Class 381/199); filed in Japan 12 September 1994

If a cylindrical voice coil is located close to a disk-shaped magnet, it will drive a cone or diaphragm without the need for a pot structure or pole pieces. The basic idea of a gapless dynamic loudspeaker has already been implemented in a number of patented designs. The variant described here is simple, inexpensive, and allows very thin assemblies. Whether it is really ''highly efficient'' is a question of semantics.—GLA

5,778,084

43.38.Ja LOUDSPEAKER WITH PHASE CORRECTION

Martin Kling and Jurgen Freitag, Hannover, Germany
7 July 1998 (Class 381/156); filed in Germany 27 January 1996

The patent explains that the function of a phasing plug is to transmit sound from all parts of the diaphragm to the horn throat with near-equal path lengths. The assertion is correct. The patent also implies that the insight is new. In fact, basic design criteria and practical implementations of multi-element phasing plugs were described by various researchers more than 60 years ago.—GLA

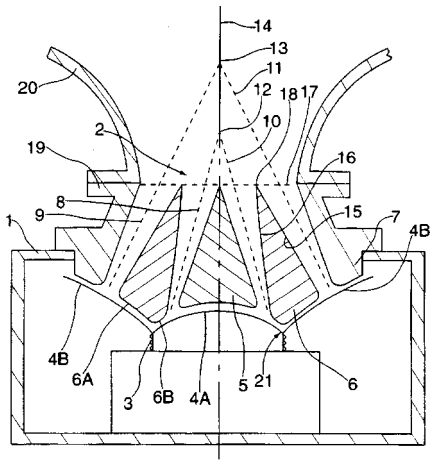

5,771,296

43.38.Lc AUDIO CIRCUIT

Toyoaki Unemura, assignor to Matsushita Electric Industrial Company
23 June 1998 (Class 381/28); filed in Japan 17 November 1994

Many pipe organs include ''synthetic'' ranks which fool the listener into hearing fundamental tones that do not exist. In the 1940s some radio receivers achieved a similar effect by adding controlled low-frequency distortion. The patented circuit is designed to process the output of a full-wave rectifier, and thereby deliver subjectively strong bass from a conventional TV set.—GLA

5,774,560

43.38.Lc DIGITAL ACOUSTIC REVERBERATION FILTER NETWORK

Alvin Wen-Yu Su and Li-Wei Wang, assignors to Industrial Technology Research Institute
30 June 1998 (Class 381/63); filed 30 May 1996

The filter network is a ''good sounding'' digital reverberator intended for use in recording studios. Digital wave-ladder filters and distribution matrices are used to model the response of an imaginary room. Reverberation effects are obtained by using a finite impulse response filter to mimic early reflections, then feeding the signal to the filter network for late reflections. The patent is interesting and easy to follow.—GLA

5,809,158

43.38.Si TRANSDUCER

Aart van Halteren and Onno Geschiere, assignors to Microtronic Nederland, B.V.
15 September 1998 (Class 381/200); filed 24 July 1996

An output transducer is described that is intended for use as a hearing aid receiver. The device includes a means for limiting the maximum output SPL produced via a connecting piece attached to the armature or by projections on the armature or coil.—DAP

5,742,687

43.38.Vk SIGNAL PROCESSING CIRCUIT INCLUDING A SIGNAL COMBINING CIRCUIT STEREOPHONIC AUDIO REPRODUCTION SYSTEM INCLUDING THE SIGNAL PROCESSING CIRCUIT AND AN AUDIO-VISUAL REPRODUCTION SYSTEM INCLUDING THE STEREOPHONIC AUDIO REPRODUCTION SYSTEM

Ronaldus M. Aarts, assignor to U.S. Philips Corporation
21 April 1998 (Class 381/1); filed in Belgium 17 January 1994

By processing and cross feeding left and right stereo signals, the perceived sound stage can be made wider than the distance between the two loudspeakers, and there are numerous patents to prove it. This patent describes ''...means by which the stereo image is enhanced without appreciable signal colouring occurring when mono signals are reproduced.''—GLA

5,751,817

43.38.Vk SIMPLIFIED ANALOG VIRTUAL EXTERNALIZATION FOR STEREOPHONIC AUDIO

Douglas S. Brungart, Salem, NH
12 May 1998 (Class 381/25); filed 30 December 1997

Active analog filter circuitry is used to simulate pinnae functions and to provide delay. When the circuit was designed, this approach could be described as ''simplified, low-cost'' in contrast to digital implementation. Only 2 years later the opposite is probably true.—GLA

5,768,393

43.38.Vk THREE-DIMENSIONAL SOUND SYSTEM

Masahiro Mukojima and Shigemitsu Yamaoka, assignors to Yamaha Corporation
16 June 1998 (Class 381/17); filed in Japan 18 November 1994

The patent document is short, clear, and interesting. It describes an improved method for coordinating sound image localization with three-dimensional computer graphics. High-quality sound generation can be achieved with relatively little processing load on the host computer.—GLA

5,768,394

43.38.Vk SURROUND AUDIO SIGNAL REPRODUCING APPARATUS HAVING A SUB-WOOFER MIXING FUNCTION

Jae-hoon Heo, assignor to Samsung Electronics Company
16 June 1998 (Class 381/18); filed in Rep. of Korea 18 August 1995

The public relations bandwagon for 5:1 consumer stereo is picking up speed, apparently fueled by the conviction that a variety of program material in one format or another will be available soon. The patent describes a method of eliminating one of the six power amplifiers by mixing the subwoofer channel into the left and right surround channels. High-level dividing networks extract the three signals and drive appropriate loudspeakers.—GLA

5,771,041

43.38.Vk SYSTEM FOR PRODUCING DIRECTIONAL SOUND IN COMPUTER BASED VIRTUAL ENVIRONMENT

Ian S. Small, assignor to Apple Computer, Incorporated
23 June 1998 (Class 345/326); filed 3 December 1996

Many graphics-intensive computer programs allow the user to move anywhere within a virtual environment. Ideally, the accompanying sound field should change accordingly. The system allows the user to create a sound map that establishes relative levels of individual sound sources at various locations. At run time, when a particular view is selected, a hearing area corresponding to that view is calculated, and various stored sound sources are mixed to provide the desired sound output.—GLA

5,771,295

43.38.Vk 5-2-5 MATRIX SYSTEM

James K. Walker, Jr., assignor to Rocktron Corporation
23 June 1998 (Class 381/18); filed 18 December 1996

The system attempts to provide discrete five-channel audio signals anywhere, any time, from any two-channel program source. ''The matrix system is compatible with all existing stereo materials and material encoded for use with other existing surround systems. Material specifically encoded for this system can be played back through any other existing decoding systems without producing undesirable results.''—GLA

5,778,087

43.38.Vk METHODS FOR STEREO LOUDSPEAKER PLACEMENT

John Harold Dunlavy, Colorado Springs, CO
7 July 1998 (Class 381/303); filed 24 March 1995

The patent argues that accurate two-channel stereophonic reproduction requires identical acoustic path lengths from the two loudspeakers to the listening location. Since slight variations between loudspeakers are likely, a tape measure does not necessarily serve as an accurate indicator. A better method is to feed the signal from a random noise generator (optionally band-limited) to both channels, and then move a sound level meter back and forth across the center line to find the location where the level peaks. Conversely, the two channels can be connected in reverse polarity and the sound level meter used to pinpoint the resulting null location. Both of these tricks have long been used by installers of professional playback systems.—GLA

5,771,300

43.50.Ki LOUDSPEAKER PHASE DISTORTION CONTROL USING VELOCITY FEEDBACK

Mark A. Daniels, assignor to Carrier Corporation
23 June 1998 (Class 381/71.5); filed 25 September 1996

Active noise reduction in chimneys and ducts utilizes at least one loudspeaker to cancel unwanted sound, and a microphone (located downstream from the loudspeaker) to sense the result and provide a feedback signal. The basis for the patent lies in two axioms. The first is that optimum performance and minimum physical separation require an undistorted electroacoustic transfer function. Ideally, the microphone, amplifier, and loudspeaker would all have flat response and negligible phase shift through the frequency range of interest. However, faced with the limitations of an im-

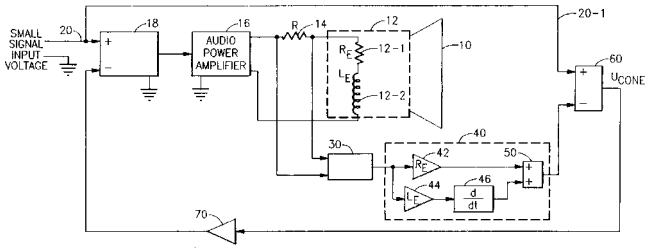

perfect loudspeaker, one can incorporate appropriate equalization in the amplifier circuitry. The second axiom states that a loudspeaker driving a long duct should act as a constant velocity piston all the way down to the lowest frequency of interest. This apparently has led to a number of questionable assumptions about loudspeakers in general, and then to design of a current feedback equalization scheme which involves deriving a voltage signal that mimics theoretical cone velocity. All of this is strongly reminiscent of several ''servo control'' high-fidelity loudspeaker patents. It can be made to work, but there are easier ways to achieve the desired results.—GLA

5,750,944

43.55.Ev FOIL SOUND ABSORBERS

Helmut Fuchs, assignor to Fraunhofer-Gesellschaft zur Foerderung der angewandten Forschung e.V.
12 May 1998 (Class 181/290); filed in Germany 15 March 1994

This foil absorber has at least two, preferably three, smooth air-impermeable foils spaced at varying distances from each other and from a reverberant (hard) back-up wall. The surface weight of the foils is approximately 0.05 to 1.0 kg/m^2, and the distance between the foils can be from 5 to 100 mm. The absorber is said to be simple to fabricate and easy to clean.—CJR

5,780,785

43.55.Ev ACOUSTIC ABSORPTION DEVICE AND AN ASSEMBLY OF SUCH DEVICES

Alan Eckel, Westford, MA
14 July 1998 (Class 181/295); filed 12 March 1997

This patent discloses a variation on acoustical treatments for use in an anechoic chamber. The device has spires with flat sides protruding from a

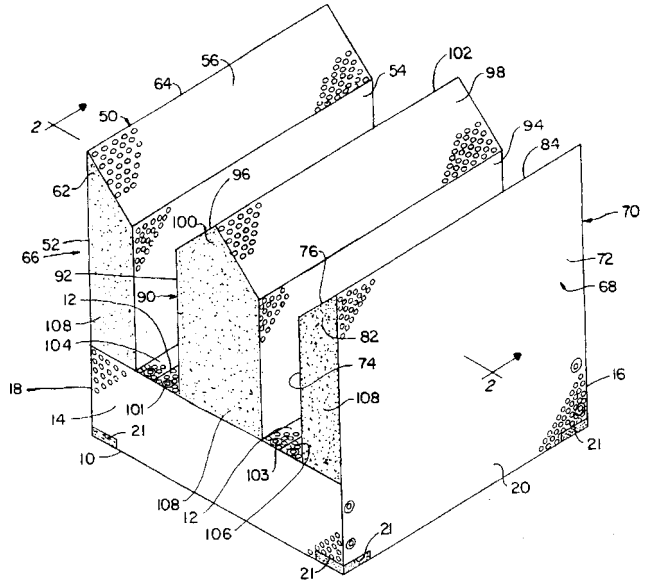

rectangular base instead of traditional wedges, and the device could be made of perforated metal to protect the glass fiber absorption material. The device can be arranged in an array with alignment at alternating right angles.—CJR

5,782,551

43.55.Ev ACOUSTICAL LIGHTING FIXTURE

Raymond W. Capaul, Aurora, IL
21 July 1998 (Class 362/148); filed 19 January 1996

The lighting fixture incorporates an absorptive material, such as glass fiber, directly into the fixture behind the light source. The bottom of the

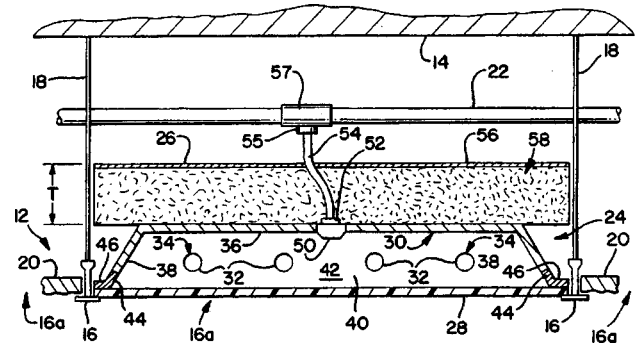

fixture can be a louver which allows sound to not be reflected. The result is said to be a light fixture that is as effective as an acoustical tile at both absorbing sound and at blocking sound.—CJR

5,796,055

43.55.Ev SOUND ABSORBING ARTICLE AND METHOD OF MAKING SAME

Vernon C. Benson, Jr. and Glenn E. Freeman, assignors to PPG Industries, Incorporated
18 August 1998 (Class 181/208); filed 13 January 1997

The patent describes improvements on construction of sound damping glazing, with variations on the thickness and the number of interlayers between sheets of glass. The product is envisioned for use in the automotive industry, but would perhaps have applications in regular building construction as well.—CJR

5,787,187

43.58.Bh SYSTEMS AND METHODS FOR BIOMETRIC IDENTIFICATION USING THE ACOUSTIC PROPERTIES OF THE EAR CANAL

Ann Marie Bouchard and Gordon Osborne, assignors to Sandia Corporation
28 July 1998 (Class 382/115); filed 1 April 1996

This system is said to verify a person's identity based on differences in acoustic properties of ear canals. Acoustic signals are transmitted into the ear canal, and the resulting acoustic response signals are detected and compared against stored reference features for the individual. Several feature extraction, analysis, and pattern recognition techniques are employed.—DAP

5,792,072

43.58.Bh SYSTEM AND METHOD FOR MEASURING ACOUSTIC REFLECTANCE

Douglas H. Keefe, assignor to University of Washington
1 August 1998 (Class 600/559); filed 8 April 1996

A small probe assembly containing a sound source and microphone is inserted into the ear canal. The system measures at different stimulus levels the reflectance, admittance, and impedance as a function of static pressure applied to the ear. These are used to calculate the sound power absorbed by the ear and to develop level-dependent transfer functions.—DAP

5,809,149

43.66.Pn APPARATUS FOR CREATING 3D AUDIO IMAGING OVER HEADPHONES USING BINAURAL SYNTHESIS

Terry Cashion and Simon Williams, assignors to Qsound Labs, Incorporated
15 September 1998 (Class 381/17); filed 25 September 1996

A sound image processing system is described that can produce large, smooth movements in the apparent sound source location for a listener wearing headphones.—DAP

5,784,471

43.66.Ts HEARING AID WITH AN ELECTRODYNAMIC ACOUSTIC TRANSDUCER

Wolf-Dietrich Bebenroth, assignor to Sennheiser electronic GmbH
21 July 1998 (Class 381/69); filed 11 July 1996

A mass-produced, modular two-piece hearing aid having a movable, foam-filled eartube to adapt to individual ear canals is described. The construction of an electrodynamic output transducer that provides wider bandwidth amplification than those in conventional hearing aids is disclosed. The replaceable foam transmits sound without attenuation while preventing dirt and cerumen from entering the hearing aid.—DAP

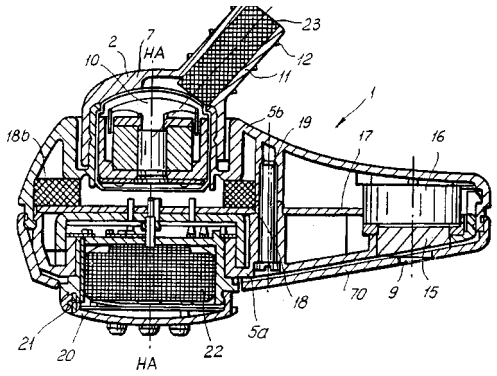

5,785,661

43.66.Ts HIGHLY CONFIGURABLE HEARING AID

Adnan Shennib, assignor to Decibel Instruments, Incorporated
28 July 1998 (Class 600/559); filed 17 August 1994

A binaural system using intracanal transducers is described that includes an SPL audiometer, a simulated hearing aid, and a real-ear measurement system. Acoustic test signals representative of real world listening environments are produced by the system. Individualized acoustic transfer functions in three-dimensional space are used to create virtual acoustic conditions and to set up the hearing aid specifications.—DAP

5,793,875

43.66.Ts DIRECTIONAL HEARING SYSTEM

Michael Lehr and Bernard Widrow, assignors to Cardinal Sound Labs, Incorporated
11 August 1998 (Class 381/684); filed 22 April 1996

A necklace housing an array of two or more microphones is disclosed. The system is made directional by processing the microphone output signals, and the amplified output signal drives a conducting loop encircling the

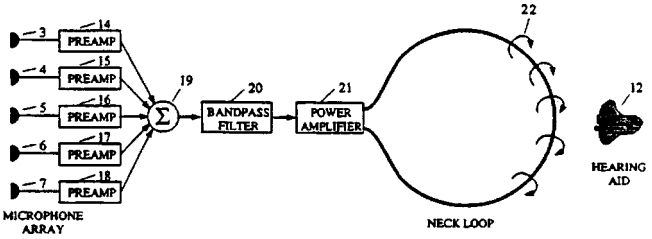

wearer's neck to produce a representative magnetic field. An induction pickup coil is housed on or in the wearer's ear and drives an electroacoustic transducer that produces an acoustic signal emphasizing sounds arriving from the frontal direction.—DAP

5,794,187

43.66.Ts METHOD AND APPARATUS FOR IMPROVING EFFECTIVE SIGNAL TO NOISE RATIOS IN HEARING AIDS AND OTHER COMMUNICATION SYSTEMS USED IN NOISY ENVIRONMENTS WITHOUT LOSS OF SPECTRAL INFORMATION

David Franklin and Michael Steele, assignors to Audiological Engineering Corporation
11 August 1988 (Class 704/225); filed 16 July 1996

A system is described that improves signal-to-noise ratio by a small automatic and rapid downward expansion (attenuation) of the signal by up

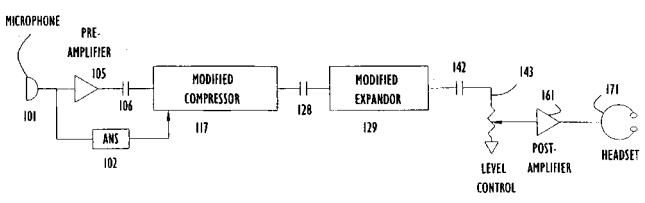

to a factor of three times when it determines that noise is present without speech. The noise-sensing algorithm assumes that signal amplitudes below a predetermined level constitute noise alone.—DAP

5,796,848

43.66.Ts DIGITAL HEARING AID

Raimund Martin, assignor to Siemens Audiologische Technik GmbH
18 August 1998 (Class 381/68); filed 6 December 1996

The digital hearing aid described is said to be relatively insensitive to electromagnetic interference. The hearing aid microphone and analog-to-digital converter are integrated together inside the microphone housing, thus eliminating long, low-level analog signal lines. Electromagnetic shielding is derived from the microphone housing.—DAP

5,765,135

43.70.Dn SPEECH THERAPY SYSTEM

Arye Friedman *et al.*, assignors to Speech Therapy Systems Limited
9 June 1998 (Class 704/276); filed in Israel 9 March 1994

This therapeutic speech training device is intended for use with stutterers and patients with respiratory-related speech problems. It records the respiratory state along with the speech, sound and displays both, allowing a patient to learn the breathing patterns related to normal and his or her own speech.—DLR

5,768,473

43.72.Ar ADAPTIVE SPEECH FILTER

Graham P. Eatwell and Kenneth P. Davis, assignors to Noise Cancellation Technologies, Incorporated
16 June 1998 (Class 395/2.35); filed 30 January 1995

Wiener and Kalman filtering, as applied to speech processing, are similar to LPC except that computations are typically done on a sample-by-sample basis. This adaptive filter uses Kalman techniques to estimate the spectra of mixed speech and noise signals. The method is said to allow improved detection of voice presence.—DLR

5,774,850

43.72.Ar SOUND CHARACTERISTIC ANALYZER WITH A VOICE CHARACTERISTIC CLASSIFYING TABLE, FOR ANALYZING THE VOICES OF UNSPECIFIED PERSONS

Ichiro Hattori and Akira Suzuki, assignors to Fujitsu Limited & Animo Limited
30 June 1998 (Class 704/250); filed in Japan 26 April 1995

A typical karaoke system, during use, provides a voice channel relatively free of music, of an unknown speaker speaking (or singing) known words. This voice analyzer uses that information to extract vowel duration,

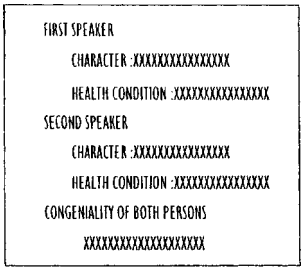

ANALYSIS RESULT OUTPUT SCREEN (B)

vowel spectra, and pitch range features and compares these to the features of stored reference words in an attempt to determine the health and stress level of the user.—DLR

5,771,306

43.72.Bs METHOD AND APPARATUS FOR EXTRACTING SPEECH RELATED FACIAL FEATURES FOR USE IN SPEECH RECOGNITION SYSTEMS

David G. Stork *et al.*, assignors to Ricoh Corporation
23 June 1998 (Class 382/100); filed 26 May 1992

This speech recognizer uses both acoustic and visual inputs to form analysis feature vectors. The sound is transformed to mel cepstral features while LED indicators attached to the face are tracked to provide point-to-

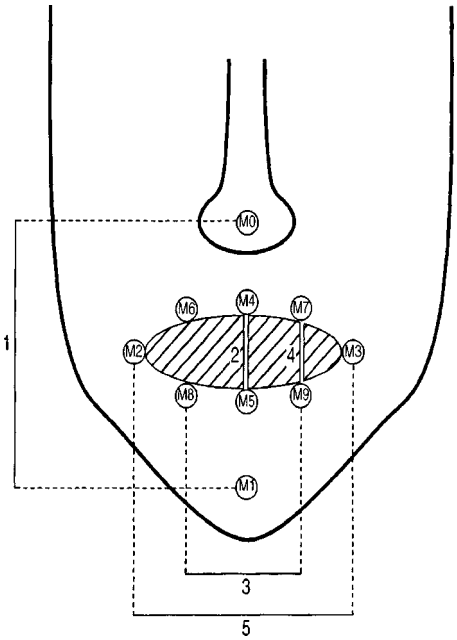

point distances from a video facial image. Visual and acoustic features are processed by separate time-delay neural networks that feed a classifier able to recognize one of ten utterances.—DLR

5,768,474

43.72.Dv METHOD AND SYSTEM FOR NOISE-ROBUST SPEECH PROCESSING WITH COCHLEA FILTERS IN AN AUDITORY MODEL

Chalapathy V. Neti, assignor to International Business Machines Corporation
16 June 1998 (Class 395/2.44); filed 29 December 1995

The patent begins by stating that auditory-based models are superior to standard spectral analysis techniques in extraction of the speech signal from noise. In the model presented here, the mechanisms of the ear are simulated by taking derivatives in both time and frequency of the output of a set of cochlealike bandpass filters. After negative clipping, frequency-scaled features are extracted from the time domain signals.—DLR

5,771,486

43.72.Dv METHOD FOR REDUCING NOISE IN SPEECH SIGNAL AND METHOD FOR DETECTING NOISE DOMAIN

Joseph Chan and Masayuki Nishiguchi, assignors to Sony Corporation
23 June 1998 (Class 704/200); filed in Japan 13 May 1994

This noise reduction system is based on computation of the frame-by-frame rms as a measure of the signal energy. The frame energy is compared

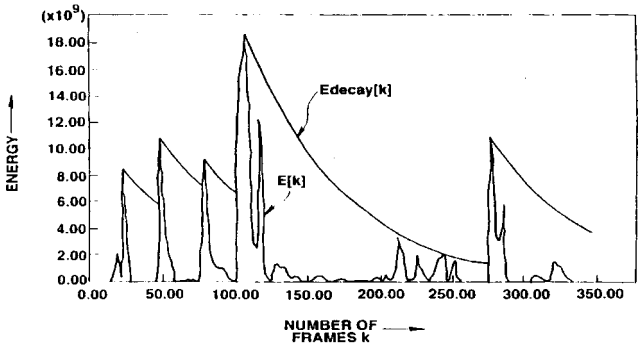

to a threshold to detect speech. Speech and nonspeech energies are adapted over time and subtracted to determine a signal-to-noise ratio. Speech is filtered by a maximum likelihood filter to reduce noise effects.—DLR

5,771,299

43.72.Ew SPECTRAL TRANSPOSITION OF A DIGITAL AUDIO SIGNAL

John Laurence Melanson, assignor to AudioLogic, Incorporated
23 June 1998 (Class 381/68.2); filed 20 June 1996

The patent describes a speech processing filter in which the spectral characteristics are removed and then reinserted by complementary zero and pole configurations. However, in the synthesis step, unit delays are replaced

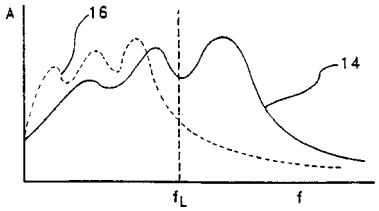

by non-unity-delay all-pass filters, resulting in controllable spectral compression, expansion, or inversion. In the figure, compression has lowered frequency f to frequency fL. The degree of shift may be frequency dependent.—DLR

5,781,885

43.72.Ew COMPRESSION/EXPANSION METHOD OF TIME-SCALE OF SOUND SIGNAL

Takeo Inoue and Shozo Sugishita, assignors to Sanyo Electric Company
14 July 1998 (Class 704/267); filed in Japan 9 September 1993

Many schemes have been proposed for varying a speech playback rate by adding or deleting pitch periods. In this variation, adjacent periods in the input waveform are averaged. For time scale compression, the average forms a single output period replacing the two originals, while, for expansion, the average period is inserted between the original two periods.—DLR

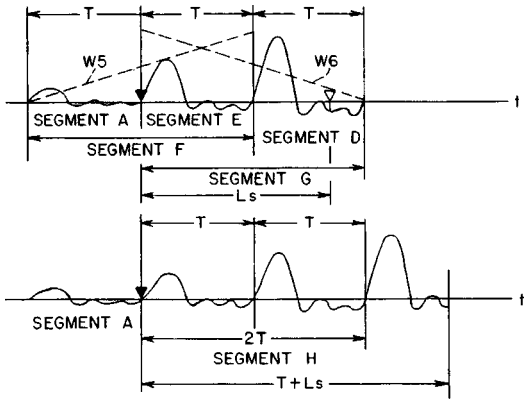

5,774,837

43.72.Gy SPEECH CODING SYSTEM AND METHOD USING VOICING PROBABILITY DETERMINATION

Suat Yeldener and Joseph Gerard Aguilar, assignors to Voxware, Incorporated
30 June 1998 (Class 704/208); filed 13 September 1995

This harmonic amplitude vocoder divides the speech spectrum into voiced and unvoiced portions. Based on an initial pitch estimate, a frequency point is determined below which the frame is considered voiced.

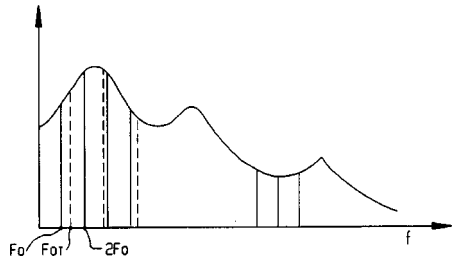

The voiced portion is analyzed for harmonic amplitude and phase information, while the unvoiced portion of the spectrum is analyzed by linear prediction.—DLR

5,778,335

43.72.Gy METHOD AND APPARATUS FOR EFFICIENT MULTIBAND CELP WIDEBAND SPEECH AND MUSIC CODING AND DECODING

Anil Wamanrao Ubale and Allen Gersho, assignors to The Regents of the University of California
7 July 1998 (Class 704/219); filed 26 February 1996

This wideband audio signal coder uses a single, 38th-order LPC analysis for the spectrum representation, but uses multiple codebooks dividing the excitation into multiple frequency bands. The input signal energy, short-term gain, and spectral flatness are analyzed to classify the input as speech or music and the excitation reconstruction is adjusted accordingly.—DLR

5,778,336

43.72.Gy SPEECH CODING AND JOINT DATA/CHANNEL BIAS ESTIMATION USING FINITE STATE VECTOR QUANTIZER DERIVED FROM SEQUENTIAL CONSTRAINTS

Wu Chou and Nambirajan Seshadri, assignors to Lucent Technologies, Incorporated
7 July 1998 (Class 704/222); filed 1 October 1996

This vocoder uses a trellis-encoded vector quantizer and decoder similar to that used in modem technology to estimate speech and transmission channel conditions. Similar decoders previously proposed were memoryless in that no use was made of the sequential spectral constraints in the speech signal. This system does use such constraints, helping to reduce channel bias and noise.—DLR

5,781,888

43.72.Gy PERCEPTUAL NOISE SHAPING IN THE TIME DOMAIN VIA LPC PREDICTION IN THE FREQUENCY DOMAIN

Juergen Heinrich Herre, assignor to Lucent Technologies, Incorporated
14 July 1998 (Class 704/219); filed 16 January 1996

The patent describes a ''pre-echo'' problem often heard in previous perceptual coders when sending rapid-transient nonspeech sounds. The problem is caused by the temporal blurring of transient conditions throughout the frame. This solution avoids the ''pre-echo'' problem by using differential coding (DPCM) to encode the filter band outputs after the perceptual masking levels have been computed.—DLR

5,774,855

43.72.Ja METHOD OF SPEECH SYNTHESIS BY MEANS OF CONCENTRATION AND PARTIAL OVERLAPPING OF WAVEFORMS

Enzo Foti *et al.*, assignors to CSELT-Centro Studi e Laboratori Tellecomunicazioni S.p.A.
30 June 1998 (Class 704/267); filed in Italy 29 September 1994

This time-domain speech synthesizer creates the output speech waveform by adding overlapped segments of stored model waveforms. A fading

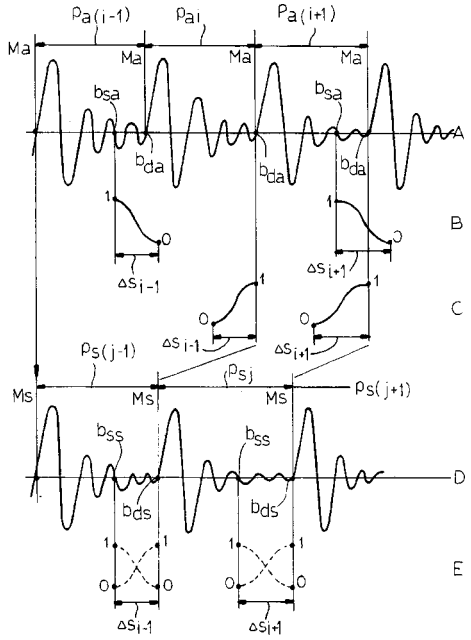

function controls the relative amplitudes of the overlapped segments during the addition process.—DLR

5,781,884

43.72.Ja GRAPHEME-TO-PHONEME CONVERSION OF DIGIT STRINGS USING WEIGHTED FINITE STATE TRANSDUCERS TO APPLY GRAMMAR TO POWERS OF A NUMBER BASIS

Fernando Carlos Neves Pereira *et al.*, assignors to Lucent Technologies, Incorporated
14 July 1998 (Class 704/260); filed 24 March 1995

This text-to-speech system for digit strings codes each digit according to its power-of-10 numerical value and uses a finite state grammar of number syntax patterns to generate an appropriate prosodic sequence for pronouncing the number. The pronunciation system is easily adaptable to languages other than English.—DLR

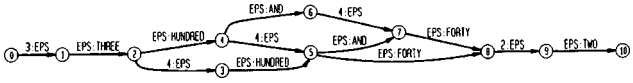

5,774,848

43.72.Ne REFERENCE PATTERN TRAINING SYSTEM AND SPEECH RECOGNITION SYSTEM USING THE SAME

Hiroaki Hattori, assignor to NEC Corporation
30 June 1998 (Class 704/244); filed in Japan 9 March 1995

This speech recognition training system uses separate dictionaries of training words and recognition words. During training, phonetic context representations are built up from the training words and stored in such a way that reference patterns can be built for each phonetic context during recognition.—DLR

5,777,255

43.75.Mn EFFICIENT SYNTHESIS OF MUSICAL TONES HAVING NONLINEAR EXCITATIONS

Julius O. Smith III and Scott A. Van Duyne, assignors to Stanford University
7 July 1998 (Class 84/661); originally filed 10 May 1995

This patent discloses ''an efficient digital waveguide synthesizer for simulating the tones produced by a non-linearly excited vibrational element coupled to a resonator, such as in a piano.... The synthesizer creates an excitation pulse from a table containing the impulse response of a piano soundboard and enclosure.... The excitation pulse is fed into a filter that

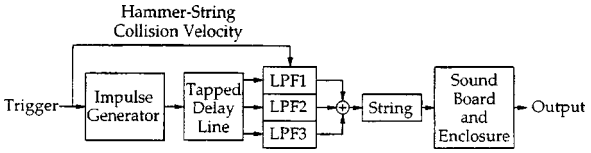

simulates the collision of the piano hammer and string. Because the hammer-string interaction is nonlinear, the characteristics of this filter vary with the amplitude of the tone produced. The filtered excitation pulse is then fed into a filtered delay line loop which models the vibration of a piano string.''—DWM

5,747,715

43.75.Rs ELECTRONIC MUSICAL APPARATUS USING VOCALIZED SOUNDS TO SING A SONG AUTOMATICALLY

Shinichi Ohta and Masashi Hirano, assignors to Yamaha Corporation
5 May 1998 (Class 84/609); filed in Japan 4 August 1995

According to the patent this computerized electronic musical apparatus synthesizes successive syllables of vocal singing sounds at frequencies and times determined by operating a computer keyboard, which generates consonant sounds at times and vowel formant patterns at times and for durations corresponding to a melody designated by stored text and performance data. The production of a naturally sung song is said to be possible.—DWM

5,760,325

43.75.Tv CHORD DETECTION METHOD AND APPARATUS FOR DETECTING A CHORD PROGRESSION OF AN INPUT MELODY

Eiichiro Aoki, assignor to Yamaha Corporation
2 June 1998 (Class 84/613); filed in Japan 15 June 1995

This musical chord detection system automatically chooses appropriate chords in accordance with the progression of a melody, by comparing the frequencies of sequential tones with the frequencies in an existing chord and effecting appropriate transitions as the melody progresses.—DWM

5,763,802

43.75.Tv APPARATUS FOR CHORD ANALYSIS BASED ON HARMONIC TONE INFORMATION DERIVED FROM SOUND PATTERN AND TONE PITCH RELATIONSHIPS

Eiichiro Aoki and Kazunori Maruyama, assignors to Yamaha Corporation
9 June 1998 (Class 84/613); filed in Japan 27 September 1995

This is another chord analysis patent issued to the same inventor (and a coinventor) as 5,760,325 (reviewed above) in which the analysis uses tone frequency difference patterns compared to program memory tables.—DWM

5,744,742

43.75.Wx PARAMETRIC SIGNAL MODELING MUSICAL SYNTHESIZER

Eric Lindemann and Jeffrey Barish, assignors to EuPhonics, Incorporated
28 April 1998 (Class 84/623); originally filed 7 November 1995

Analog musical synthesizers and electronic musical instruments have long used formant filters to control the timbre of complex musical tone wave input signals of varying frequency. The relative efficiency of this method, in comparison to the digital storage of individual musical waveforms, is

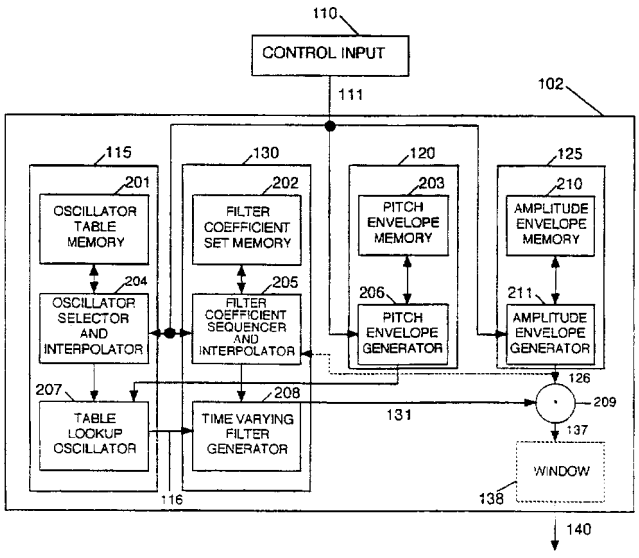

achieved in this digital musical synthesizer by providing multidimensional filters for which the filter coefficients can be programmed for smooth interpolation over fundamental frequency, intensity, and time. The noise components and tonal attacks are modeled separately.—DWM

5,779,484

43.80.Qf APPARATUS AND METHOD OF SIMULATING BREATHING SOUNDS

Samsun Lampotang *et al.*, assignors to University of Florida
14 July 1998 (Class 434/266); filed 17 December 1996

For training medical students about medical procedures (e.g., anaesthesia) a manikin **4** is provided having a pneumatically operated lung bel-

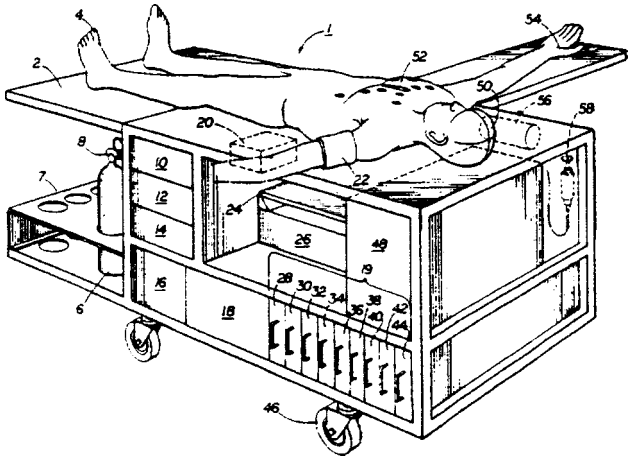

lows and a loudspeaker near the mouth for reproducing prerecorded audible breathing sounds corresponding to appropriate physiological sounds for various circumstances.—DWM

5,782,240

43.80.Qf METHOD OF CLASSIFYING RESPIRATORY SOUNDS

Gil Raviv and Charles A. Weingarten, assignors to SNAP Laboratories
21 July 1998 (Class 128/671); filed 22 December 1994

The respiratory sounds of this patent pertain to sleep apnea and snoring. Recording microphones mounted in a tubular structure worn by the sleeper provide signals to a data encoder for analysis along with other physiological signals for subsequent classification of the sound analyses in connection with respiratory events. Although apparatus is described in the patent, this is a method patent having to do with comparison of a second set of data to thresholds based on a standard or reference set of data.—DWM

5,788,636

43.80.Vj METHOD AND SYSTEM FOR FORMING AN ULTRASOUND IMAGE OF A TISSUE WHILE SIMULTANEOUSLY ABLATING THE TISSUE

Michael G. Curley, assignor to Acuson Corporation
4 August 1998 (Class 600/439); filed 25 February 1997

Imaging is accomplished by interlacing the times of the pulse-echo part of the ultrasonic imaging process and the times during which the current performing ablation is applied.—RCW

5,797,397

43.80.Vj ULTRASOUND IMAGING SYSTEM AND METHOD USING INTENSITY HIGHLIGHTING TO FACILITATE TISSUE DIFFERENTIATION

Mark Rosenberg, assignor to Hewlett-Packard Company
25 August 1998 (Class 128/660.04); filed 25 November 1996

An ultrasonic intensity range of interest is selected and ultrasonic image areas that contain these intensities are highlighted, typically with a distinctive color.—RCW

5,797,845

43.80.Vj ULTRASOUND APPARATUS FOR THREE DIMENSIONAL IMAGE RECONSTRUCTION

Leonid S. Barabash, Phoenix, AZ *et al.*
25 August 1998 (Class 600/443); filed 4 November 1996

This apparatus employs a phased transducer to produce flat transmit beams and flat receive beams that cross in space and are scanned to form a pencil beam from the product of the beams. A fast acquisition method that uses dynamic focusing of a scanned flat beam and synthetic receive apertures from stored amplitude information is included.—RCW

5,797,849

43.80.Vj METHOD FOR CARRYING OUT A MEDICAL PROCEDURE USING A THREE-DIMENSIONAL TRACKING AND IMAGING SYSTEM

Ivan Vesely and Wayne Smith, assignors to Sonometrics Corporation
25 August 1998 (Class 600/461); filed 7 March 1997

This method tracks the position of a surgical instrument within the body. The location of the instrument relative to its immediate surroundings is displayed. Procedures during which this method may be used include biopsy, amniocentesis, and transmyocardial myocardial revascularization.—RCW

5,806,521

43.80.Vj COMPOSITE ULTRASOUND IMAGING APPARATUS AND METHOD

Alan K. Morimoto *et al.*, assignors to Sandia Corporation
15 September 1998 (Class 128/661.01); filed 26 March 1996

Composite two- and three-dimensional images are produced from individual ultrasonic frames. The reconstruction uses transducer orientation and a known center. Motion compensation, rank value filtering, noise suppression, and tissue classification are included to optimize the composite image.—RCW

5,807,258

43.80.Vj ULTRASONIC SENSORS FOR MONITORING THE CONDITION OF A VASCULAR GRAFT

George E. Cimochowski, Dallas, PA and George W. Keilman, Woodinville, WA
15 September 1998 (Class 600/454); filed 14 October 1997

Flow through a graft or vessel is monitored by a conformal array transducer or a tilted element using either transit time or Doppler measurements. Implantable electronic circuits are connected to excite and to receive ultrasonic signals. A radio frequency coil is connected to the electronic circuits and also implanted. An external coil connected to a power supply and console is used to convey power and receive data from the implanted apparatus.—RCW

Capped ceramic underwater sound projector: The "cymbal" transducer[a),b)]

James F. Tressler[c)] and Robert E. Newnham
Materials Research Laboratory, The Pennsylvania State University, University Park, Pennsylvania 16802

W. Jack Hughes
Applied Research Laboratory, The Pennsylvania State University, University Park, Pennsylvania 16802

(Received 11 February 1998; accepted for publication 26 September 1998)

A new type of transducer has been developed for use as a shallow-water sound projector at frequencies below 50 kHz. Dubbed the ''cymbal,'' it is similar to the more commonly known ''moonie'' and class V ring/shell flextensional designs. Prototype cymbal arrays 2 mm thick with a radiating area of 11.4 cm^2 have been developed and calibrated. Two mounting schemes have been examined: unpotted (oil-filled) and potted in a 5-mm thick layer of stiff polyurethane. In both cases, a transmitting response comparable to the more widely used Tonpilz transducer (with an equivalent radiating area) is attainable. When tested under hydrostatic pressures, a standard cymbal configuration has been shown to withstand exposures of 2.5 MPa (which corresponds to 250 m of water depth) before failure. © *1999 Acoustical Society of America.* [S0001-4966(99)02801-5]

PACS numbers: 43.10.Ln, 43.38.Fx, 43.30.Yj [SLE]

INTRODUCTION

Sound transmission is the single most effective means of directing energy transfer over large distances underwater.[1] The acoustic frequency range for various types of underwater transducer applications spans seven decades, from 10 Hz to 100 MHz.[2] There is currently a great interest in the development of shallow-water (<250 m) acoustic projectors that operate in the frequency range from 1 kHz to 100 kHz.[3] Potential applications include seabed penetration for buried mines as well as underwater surveillance, navigation, target detection and classification. Ideally, these transducers should be thin, lightweight, exhibit medium to high acoustic-output power, be able to conform to a curved surface, and be of simple design such that they are easy and inexpensive to mass produce.

Currently, the predominant underwater projector systems that operate in the 1 kHz to 100-kHz frequency band are Tonpilz transducers and 1-3 type piezoelectric composites. The Tonpilz transducer consists of a stack of piezoelectric ceramic (typically lead zirconate titanate-PZT) rings connected mechanically in series and electrically in parallel. The ring stack is sandwiched between two metal masses: a heavy tailmass and a light, flared headmass which serves to transmit the generated acoustic energy into the surrounding medium. Tonpilz transducers are characterized by their very large acoustic-output power, are typically tens of centimeters in thickness, weigh up to several kilograms, and are designed to operate at frequencies up to 100 kHz.

The 1-3 type piezoelectric composites consist of a number of piezoelectric ceramic rods separated by a 3-D interconnected polymer matrix. These composites have been manufactured in a number of ways.[4] The current state-of-the-art fabrication technique is injection molding.[5] The performance of 1-3 piezoelectric composites is strongly affected by the elastic properties of both the ceramic and polymer phases as well as the aspect ratio, the volume fraction, and the arrangement of the piezoelectric ceramic rods.[6] These types of composites can be conformed to a curved surface and acoustically matched with water. The 1-3 piezoelectric composites designed for use below 100 kHz are at least 10 mm thick.

Polyvinylidene fluoride (PVDF) and its chemically related copolymers are piezoelectric polymers that are readily available from a number of commercial manufacturers in material thicknesses ranging from 5 to at least 600 μm.[7] The high compliance and low density of these piezoelectric polymers allow them to be easily shaped to conform to curved surfaces and to acoustically match to water. The large piezoelectric voltage coefficient, g_h, of PVDF renders it an excellent acoustic receiver material. However, its low piezoelectric strain coefficient, d_h, makes it a rather poor sound projector. A low permittivity also requires the use of expensive built-in electronics packaging because of the large electrical impedance mismatch between the piezoelectric polymer and the circuitry.[8]

A third type of underwater projector that is seeing a resurgence in interest is the flextensional transducer. Flextensionals have been in existence since the 1920s and have seen use as underwater projectors since the late 1950s.[9] Flextensionals consist of a piezoelectric ceramic drive element or assembly encapsulated by a metal shell. The metal shell acts as a mechanical transformer to convert the large generative force of the piezoelectric ceramic into increased displacement. The shape of the shell has become quite diverse over the years, and so a classification system has been established to group the common designs together.[10] Flextensional trans-

[a)]''Selected research articles'' are ones chosen occasionally by the Editor-in-Chief that are judged (a) to have a subject of wide acoustical interest, and (b) to be written for understanding by broad acoustical readership.

[b)]Presented at the 133rd meeting of the Acoustical Society of America held at The Pennsylvania State University, June 1997 [J. Acoust. Soc. Am. **101**, 3094(A) (1997)].

[c)]Present address: Naval Research Laboratory, 4555 Overlook Avenue, Washington, DC 20375-5350.

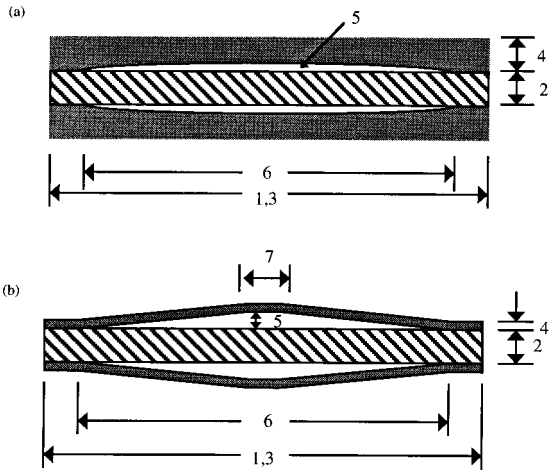

FIG. 1. Cross-sectional views of the (a) moonie-type, and (b) cymbal-type transducers. The dark areas represent the caps and the cross-hatched areas the PZT disks. The dimensions designated by the numerals shown are listed in Table I.

ducers typically range in size from several centimeters to several meters in length and can weigh up to several hundreds of kilograms.

A miniaturized version of the class V flextensional transducer was developed in the late 1980s at the Materials Research Laboratory at The Pennsylvania State University for use as a hydrophone.[11,12] This transducer is named the moonie due to the crescent moon-shaped cavity on the inner surface of the caps. A second generation moonie-type transducer, which consists of a thinner cap with a slightly different shape, has recently been developed for use as a micropositioning actuator.[13,14] This transducer has been dubbed the cymbal due to the similarity in the shape of its caps to that of the musical instrument of the same name. The cymbal cap shape is also more conducive to mass production than the moonie. A comparison of the moonie and cymbal designs is shown in Fig. 1.

The moonie and cymbal transducers consist of a piezoelectric ceramic (usually PZT) disk poled in the thickness direction which is sandwiched between and mechanically coupled to two metal caps, each of which contains a shallow, air-filled cavity on its inner surface. When used as a sound projector, the caps convert and amplify the small radial displacement and vibration velocity of the piezoelectric ceramic disk into a much larger axial displacement and vibration velocity normal to the surface of the caps. This enhanced displacement and vibration velocity from the caps contribute to a much larger acoustic-pressure output than would occur in the uncapped ceramic. The principle of using the cymbal as a hydrophone has been explained previously.[15] The dimensions of the standard-size moonie and cymbal transducers are presented in Table I.

The cymbal cap design was an outgrowth of results obtained via finite element analysis (using SAP90, MARK, and ANSYS®) on transducers with the moonie-style cap. Large stress concentrations were calculated in the moonie cap in the region above the bonding area.[14,16] In order to reduce this stress concentration, ring-shaped grooves of varying size were introduced into the moonie-type caps. This design

TABLE I. Dimensions of the standard moonie and cymbal transducers.

Moonie parameter	Dimension (mm)
1—PZT diameter	12.7
2—PZT thickness	1.0
3—cap diameter	12.7
4—cap thickness	1.0
5—cavity depth	0.25
6—cavity diameter	9.0
Cymbal parameter	**Dimension (mm)**
1—PZT diameter	12.7
2—PZT thickness	1.0
3—cap diameter	12.7
4—cap thickness	0.25
5—cavity depth	0.32
6—base cavity diameter	9.0
7—dimple diameter	3.0

modification was found to not only reduce the stress concentration in the metal, but also enhanced the axial displacement at the center of the caps.[17,18] Onitsuka's results showed that the optimum groove size extended from the edge of the inner air cavity to the outer edge of the cap.[18] Dogan extended this concept and devised the cymbal cap design along with a fabrication technique applicable to mass produce the caps.[19] The effects of materials properties and cap geometry on the actuator performance of the cymbals have been modeled both analytically[20] and using finite element analysis.[21] Finite element modeling to ascertain underwater acoustic performance is ongoing.

I. PARAMETERS TO MEASURE

Among the relevant parameters required to fully characterize an underwater projector, the most important are resonance frequency, mechanical $Q(Q_m)$, electroacoustic efficiency, electromechanical coupling coefficient (k_{eff}), transmitting voltage response (TVR), source level (SL), and acoustic directivity (beam) patterns. Transmitting voltage response is equal to the ratio of the sound pressure produced by the projector, referenced (*re*:) to a distance of one meter from its acoustic center, to unit voltage applied across the electrical terminals of the transducer.[22] It is reported in terms of dB *re*: 1 μPa/V @1 m, or as 1 μPa·m/V. Source level is the intensity of the radiated sound field relative to the intensity of a plane wave of rms pressure 1 μPa referred to a point one meter from the acoustic center of the projector.[23] Source level is related to the transmitting voltage response through the applied input rms voltage as:

$$\text{SL} = \text{TVR} + 20 \cdot \log V_{\text{in,rms}}. \tag{1}$$

In general, a source level of greater than 200 dB *re*: 1 μPa @1 m is desirable. The beam pattern describes the response of the transducer relative to its main acoustic axis.

II. EXPERIMENTAL PROCEDURE

Single-element cymbal transducers were fabricated by first punching 12.7-mm-diam blanks from a sheet of metal foil. These blanks were then molded into caps of the desired

TABLE II. Relevant materials properties of the caps[a] and PZT.[b]

Cap material	Young's modulus	Density	Poisson's ratio
brass	100.6 GPa	8550 kg/m^3	0.35
titanium	120.2 GPa	4500 kg/m^3	0.361
molybdenum	324.8 GPa	10 200 kg/m^3	0.28

PZT type	d_{31}	d_{33}	Dielectric constant $(\varepsilon_{33}^T/\varepsilon_0)$
552 (5H)	−274 pC/N	593 pC/N	3400
5A	−171 pC/N	374 pC/N	1700
4	−123 pC/N	289 pC/N	1300
8	−93 pC/N	218 pC/N	1000

[a]*Smithell's Metals Reference Book*, edited by E. A. Brandes (Butterworth, New York, 1983), 6th ed., Table 15.1.
[b]H. Jaffe and D. A. Berlincourt, ''Piezoelectric Transducer Materials,'' Proc. IEEE **53**(10), 1372–1386 (1965).

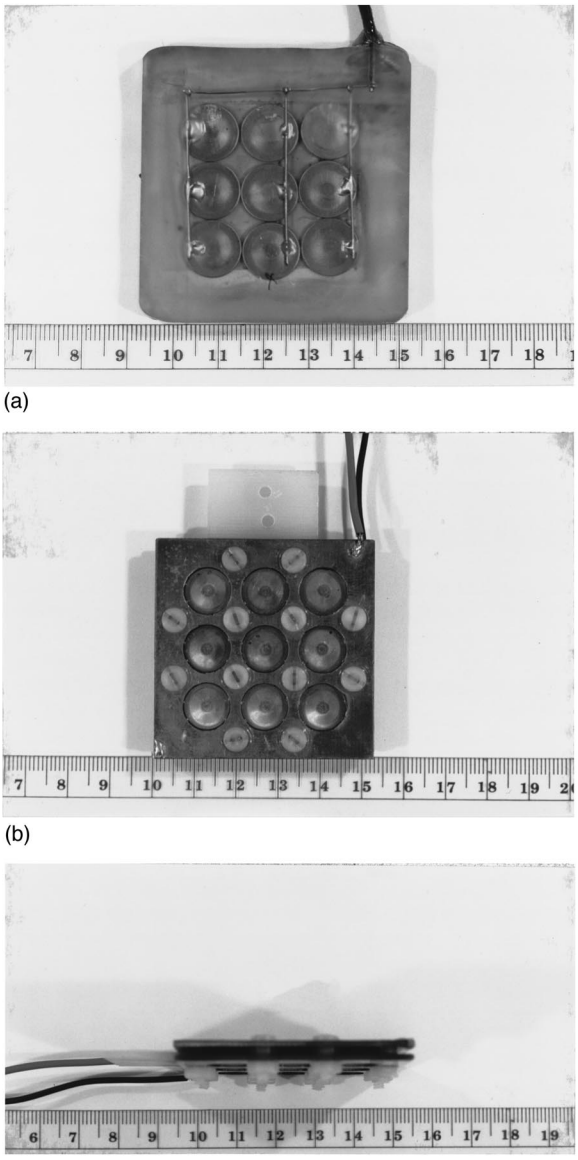

FIG. 2. Top views of the 9-element cymbal arrays (a) potted in polyurethane and (b) unpotted; (c) unpotted cymbal array viewed from the side. The scale is ruled in centimeters.

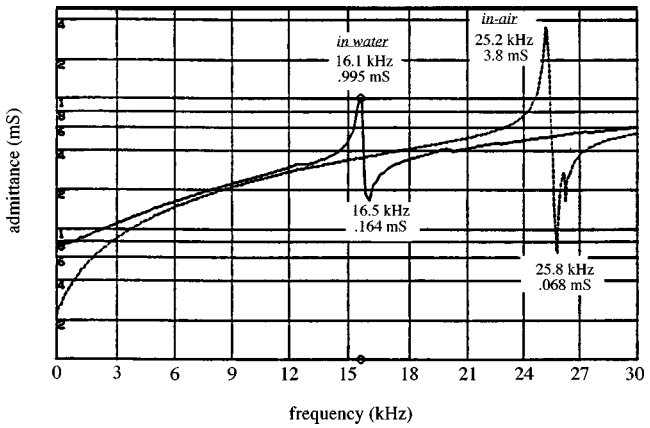

FIG. 3. Measured admittance spectra of a standard-size brass-capped cymbal both in air and in water. Resonance is associated with the fundamental flexural vibration mode of the caps.[21]

shape using a die press. Since there is no machining involved, this process is relatively inexpensive and hospitable to mass production. The flanges of the caps were bonded to a poled PZT-552 disk (Piezo Kinetics, Inc., Bellefonte, PA) using a very thin ($\approx$20 μm) layer of insulating epoxy (Eccobond® 45LV/Catalyst 15LV; Emerson and Cuming, Inc., Woburn, MA). The entire assembly was allowed to cure at room temperature for at least 24 h while under moderate pressure. The relevant properties of the cap materials and piezoelectric ceramics used are given in Table II.

The quality of the bonding layer after curing was characterized by measuring the in-air admittance spectra of the transducer using an HP 4194A impedance/gain phase analyzer. Spurious vibration modes are indicative of a poorly bonded transducer.[24] Admittance characteristics, both in air and in water, were also used to determine resonance frequency, k_{eff}, Q_m, and electroacoustic efficiency. Charge amplification on the PZT electrodes (due to the presence of the caps) was measured using a modified Berlincourt d_{33} meter. The water depths to which the cymbal transducers can be taken before failure was ascertained by measuring their effective hydrostatic piezoelectric charge coefficient (d_h^{eff}) as a function of hydrostatic pressure. A thorough explanation of this procedure has been previously provided.[15]

Single-element transducers utilizing the PZT-552 composition as the active component were incorporated into 9-element square arrays. Two mounting schemes were investigated: unpotted (i.e., oil-filled boot) and potted in approximately 5 mm of water-impedance-matching polyurethane

TABLE III. Typical air- and water-loaded characteristics of the standard-size brass-capped cymbal transducer.

	Air-loading	Water-loading
Resonance frequency	25.2 kHz	16.1 kHz
k_{eff}	0.214	0.219
Q_m	200	20
electroacoustic efficiency		90%
d_{33}^{eff} (PZT-552)	12 000 pC/N	
d_{33}^{eff} (PZT-5A)	8 000 pC/N	
d_{33}^{eff} (PZT-4)	6 000 pC/N	
d_{33}^{eff} (PZT-8)	5 000 pC/N	

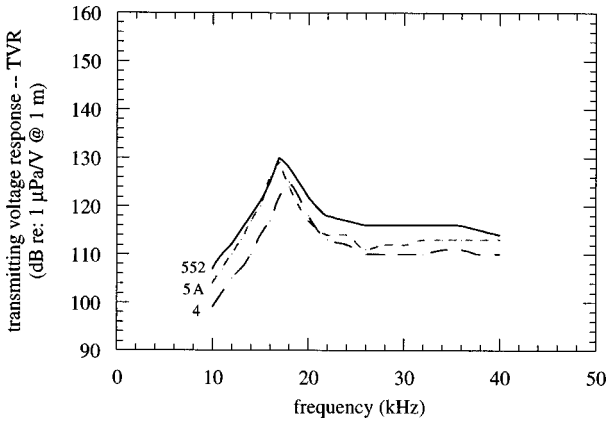

FIG. 4. Transmitting voltage response in the neighborhood of the fundamental resonance frequency of single-element, standard-size brass-capped cymbals utilizing PZT-552, 5A, or 4.

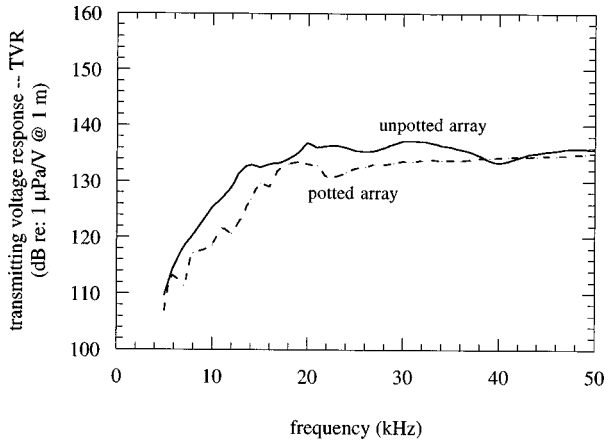

FIG. 6. Comparison of the transmitting voltage response of the potted and unpotted (oil-filled) 9-element cymbal arrays.

with hardness Shore-A90. In both cases, the center-to-center spacing between the elements was about 13.4 mm. For the potted array, electrical leads were attached to the caps on the positive side on each of the nine cymbals in the array using silver epoxy, and the assembly was wired together in parallel. The other surface of the array was attached to a kapton backing with conductive transfer tape, which served as the ground electrode.

The single elements in the unpotted array were sandwiched between two copper-clad printed circuit boards, each 1.5 mm thick. Holes 11.2 mm in diameter were drilled equidistant from one another through the boards which then housed the elements, thus allowing the dome of the cymbal caps to flex freely. Plastic spacers 1.5 mm thick were used to maintain a uniform distance between the upper and lower panels, which were screwed together tightly, as well as to keep the cymbal elements in place. Pictures of the two mounting configurations are shown in Fig. 2.

Underwater calibration tests were performed in the anechoic water tank at the Applied Research Laboratory at Penn State. The tank measured 7.9 m in length, 5.3 m in width, and 5.5 m in depth. A pure-tone sinusoidal pulse signal of 2 ms duration was applied to the test transducer, and its acoustic output was subsequently measured by a standard $F33$ recalibrated as a hydrophone. The test transducer and the standard were positioned so that they were at a depth of 2.74 m and separated by a distance of 3.16 m.

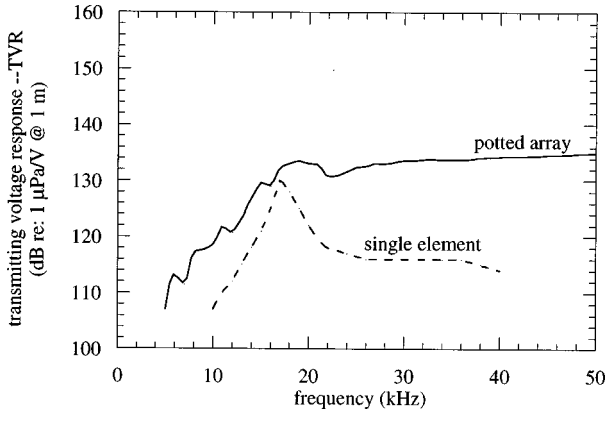

FIG. 5. Comparison of the transmitting voltage response of a single-element brass-capped cymbal with that of the potted 9-element array.

III. RESULTS AND DISCUSSION

Figure 3 shows the measured admittance spectra of a well-bonded, standard-size brass-capped cymbal transducer in the neighborhood of its fundamental resonance frequency both in air and in water. The downward shift in the resonance frequency is due to the acoustic mass-loading effect of the water. The resonance frequency of the cymbal transducer is controlled by the elastic properties of the cap material, the cap shape, and the overall diameter of the device.[21] Table III provides typical measured data for the parameters described in Sec. I. These are all values for standard-size, single-element brass-capped cymbals. The reported d_{33} coefficient is actually an effective d_{33} coefficient (since it is reported for a device) and will hereafter be designated as d_{33}^{eff}. The PZT type in parentheses is the type used as the active element in the transducer.

The transmitting voltage response in the neighborhood of the first resonance frequency for same-size, single-element brass-capped cymbal transducers utilizing different PZT types is shown in Fig. 4. The peak value of the transmitting response correlates with the d_{33}^{eff} coefficient of the device, as seen from Table III. The higher d_{33} (and thus d_{31}) coefficient of the piezoelectric ceramic results in a larger axial displacement in the caps; hence, a larger volume velocity which

TABLE IV. The calculated increase in TVR (in the neighborhood of the fundamental resonance of the single element) for unpotted oil-filled brass-capped cymbal arrays of different radiating area. The measured TVR at this frequency is shown for comparison. Active element is PZT-552.

Radiating area	Number of cymbals in the array	Expected increase in TVR at 18 kHz[a]	Measured TVR at 18 kHz
1.27 cm^2	1	0 dB	130 dB
11.4 cm^2	9	4 dB	134 dB
127 cm^2	100	23 dB	153 dB[b]
507 cm^2	400	35 dB	···

[a]As compared to the single element, includes mutual acoustic interactions between elements.

[b]J. Zhang and W. J. Hughes, The Pennsylvania State University, unpublished data, 1998.

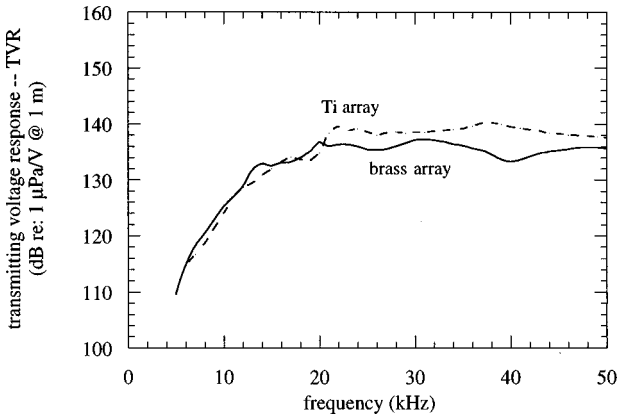

FIG. 7. Comparison of the transmitting voltage response of unpotted 9-element cymbal arrays with either brass caps or titanium caps.

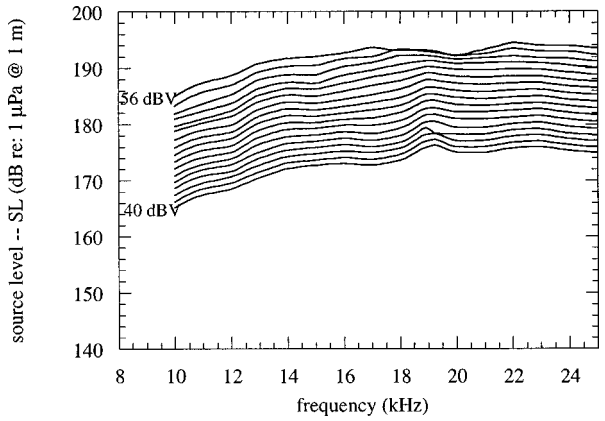

FIG. 8. Source level curves for the 9-element unpotted brass-capped array for drive levels starting at 40 dB *re*: 1 V and ending at 56 dB *re*: 1 V in increments of 1 dB *re*: 1 V.

leads to a higher acoustic-output pressure and subsequently, a higher TVR at resonance. Single-element cymbals are characterized by a relatively high $Q_m(\approx 20)$, low k_{eff} (≈ 0.22) and consequently, a narrow bandwidth.

If the acoustic impedance loading of a single cymbal were purely real (i.e., no mass loading), then incorporating the single-cymbal elements into a 9-element square array should theoretically enhance the transmitting voltage response by a factor of about 19 dB($=20\cdot\log 9$). A single cymbal, however, is mass loaded. Increasing the radiating area of the projector should serve to increase its radiation resistance and hence boost its acoustic-output power. Figure 5 compares the TVR of the single-element cymbal transducer to that of the 9-element potted array. When the single elements were potted in an array, the fundamental resonance was strongly damped, and there was only about a 4-dB enhancement in the TVR. The damping of the resonance was attributed to two detrimental effects: the shear components of the polyurethane potting layer acting to damp the resonance, and array element interactions. Interestingly, though, a more broadband transmitting response was observed. The larger radiating area also means that the array begins to approach ''ρc'' loading conditions as compared to the ''mass'' radiation loaded single element. The array resonance, therefore, does not shift down in frequency from the in-air measurement as much as does the single element. No significant difference in projector performance was observed when comparing results with the polyurethane layer (front) or the kapton layer (back) facing the standard receiver. The phasing of the displacements of the single-element cymbals relative to one another in the array was measured using a fiber-optic interferometer. When the array was driven at 100 V (peak) at 10 kHz, all the transducers were found to vibrate in phase within one deg.

In order to further examine the effect the potting layer had on the performance of the cymbal array, a second array was built and tested. This array was unpotted (i.e., oil filled). The TVR curves for the potted and unpotted arrays are compared in Fig. 6. Even in the case of the oil-filled array, the resonance frequency is again strongly damped. The mutual acoustic impedance between the individual radiators in the array was then estimated using a technique described by Pritchard.[25] In his analysis of same-size circular disks vibrating (all with the same velocity) in an infinite rigid plane, the mutual radiation impedance (Z_{12}) can be expressed as:

$$Z_{12}=(R_{12}+jX_{12})\cong\left\{\rho c\,\pi a^2\cdot\frac{(ka)^2}{2}\right\}\cdot\left[\frac{\sin(kd_i)}{kd_i}+j\,\frac{\cos(kd_i)}{kd_i}\right],\qquad(2)$$

when $(ka)^2\ll 1$ and $(a/d)\ll 1$ and where R_{12} is the mutual radiation resistance, X_{12} is the mutual radiation reactance, ρc is the characteristic impedance of the medium, a is the radius of the disk, d_i is the respective center-to-center spacing between the disks, and k is the wave number. Since the ka for the nine element array (≈ 2 at 18 kHz) is sufficiently large such that $R\gg X$, the mutual radiation impedance can be taken as simply the real part of Z_{12} at this frequency. The term in braces { } in Eq. (2) is equal to the self-radiation resistance (R_s) of a single radiator in the array. Ultimately, the mutual radiation resistance (R_m) seen by the array is equal to nine times the self-radiation resistance (due to the ninefold increase in area) multiplied by a factor representing the inter-element interactions, R_i [i.e., the bracketed term [ ] in Eq. (2)]. Taking the radiating frequency as 18 kHz and the closest center-to-center spacing between two adjacent elements in the array as 13.4 mm, the real part of the bracketed term, R_i, is equal to 5.714. The expected increase in TVR in an array as compared to a single element at a given frequency is therefore actually equal to $(20\cdot\log N-20\cdot\log R_i)$, where N is the increase in radiating area (or number of elements in the array). In the case of the nine-element arrays used in this analysis, the calculated increase in TVR (taking into account the mutual radiation impedance) at 18 kHz as compared to the single element should be 4 dB, which is what was experimentally observed in the case of the unpotted array (see Table IV). The slightly lower TVR seen in the case of the potted array can then be attributed to additional damping effects due to the stiff polymer. At frequencies beyond the resonance, mutual radiation impedance becomes less significant, and the approximate 19-dB increase in TVR as expected in the case of the unloaded array is observed.

Figure 7 compares the TVR curves for unpotted

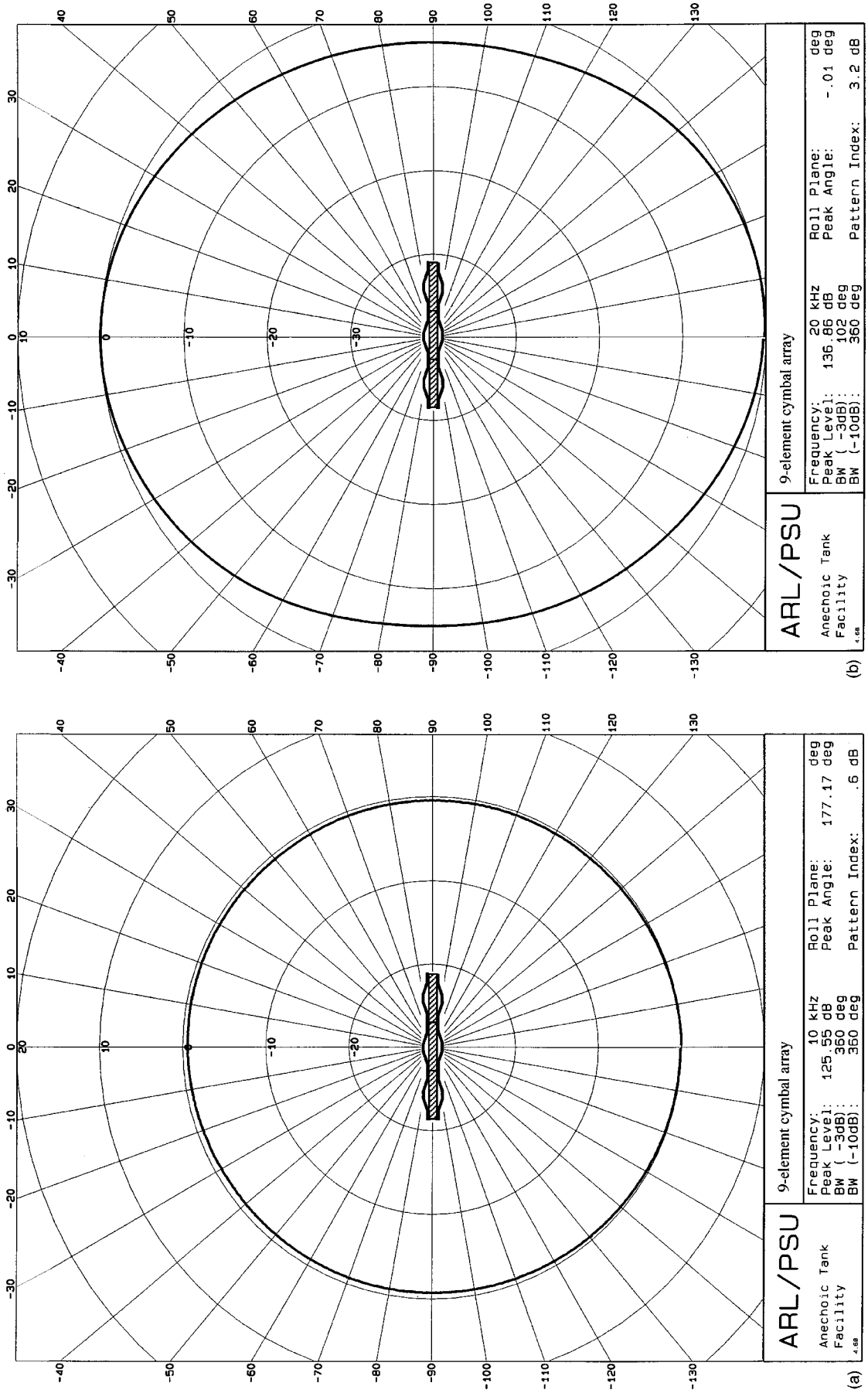

FIG. 9. Transmit-beam patterns for the cymbal arrays at (a) 10 kHz, (b) 20 kHz, (c) 30 kHz, (d) 50 kHz, and (e) 130 kHz.

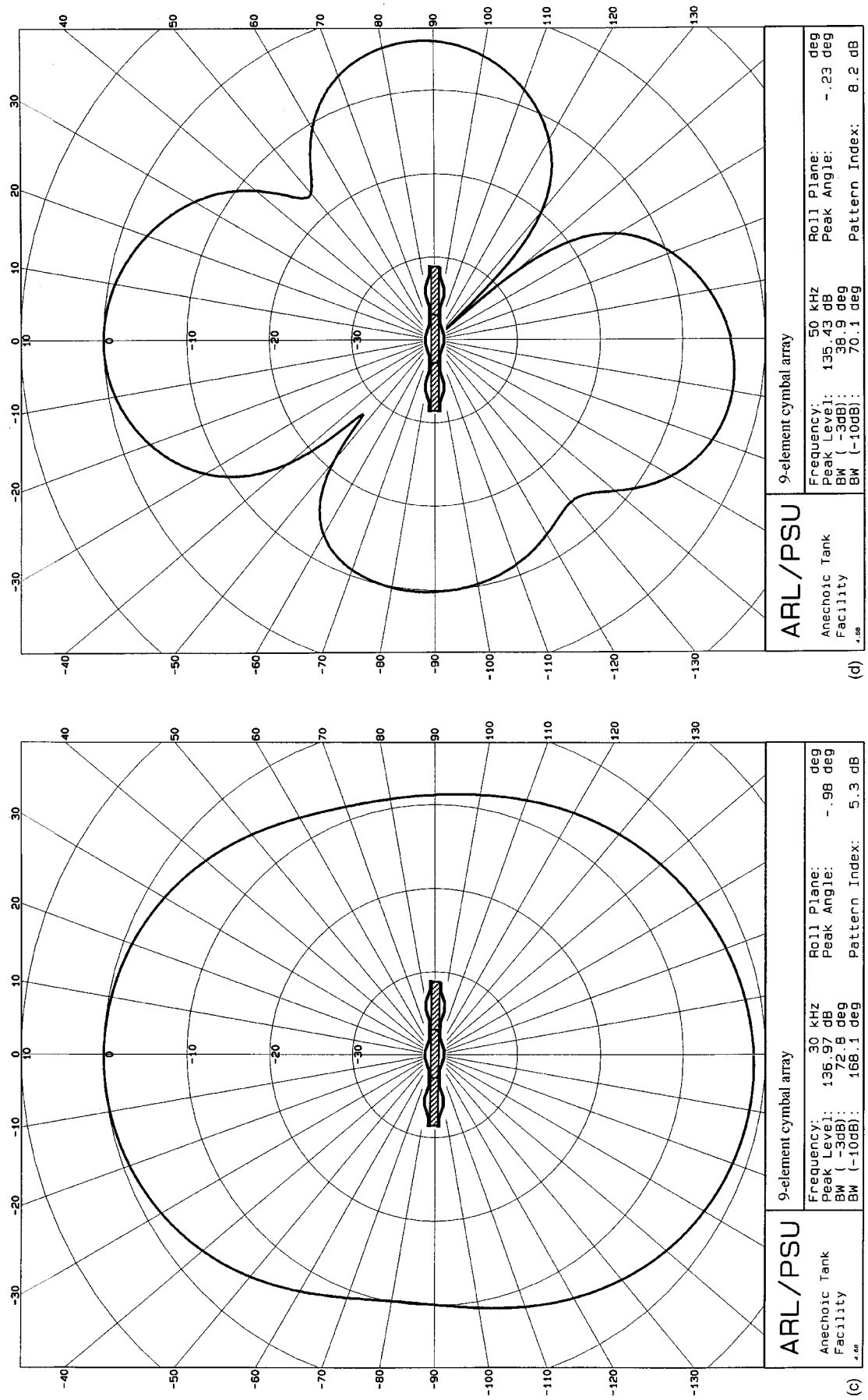

FIG. 9. (*Continued.*)

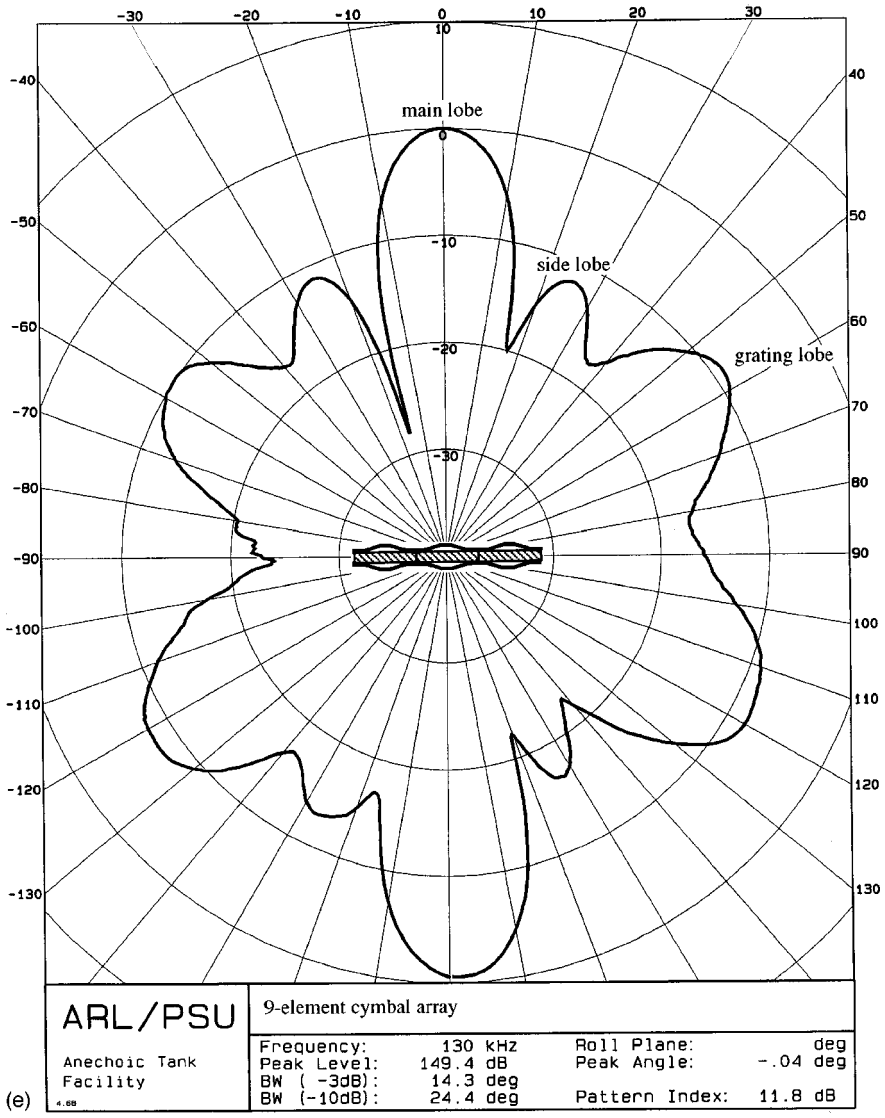

FIG. 9. (*Continued.*)

9-element cymbal arrays consisting of either brass or titanium caps. Below 20 kHz, the curves are practically identical. At higher frequencies, however, the titanium-capped cymbal array exhibits about a 3-dB higher TVR than the brass-capped cymbal array. The specific acoustic impedance ($z=\rho c$) of brass, titanium, and water are 40.4, 27.3, and 1.5 MPa·s/m, respectively.[26] Since the ratio of the characteristic impedance of brass to water is approximately $\sqrt{2}$ times the ratio of the characteristic impedance of titanium to water, and $20\cdot\log\sqrt{2}$ is 3 dB, the increase in TVR may be due to the better acoustic match of titanium to the water environment.

Figure 8 shows the measured source-level curves for the unpotted brass-capped array. The curves correspond to drive levels ranging from 40 dB *re*: 1 V to 56 dB *re*: 1 V in increments of 1 dB *re*: 1 V. At a drive level of 57 dB *re*: 1 V, the array failed and hence no measurement was recorded. The cause of failure was cracking in the caps due to work hardening.[27] The primary resonance is evident at 18.5 kHz, when the drive level is 40 dB *re*: 1 V and is present up to a drive level of 54 dB *re*: 1 V, above which it is suppressed and nonlinear behavior becomes apparent. When driven slightly below its failure level (e.g., 52 dB *re*: 1 V), a source level of 180 dB *re*: 1 μPa·m or greater is generated between 10 and at least 25 kHz. However, this is for a radiating area of only 11.4 cm^2. A simple way to enhance the source level is by increasing the number of elements in the array and hence increase the radiating area.

The beam patterns at various frequencies for the cymbal array are shown in Fig. 9. At low frequency (half-wavelength aperture or less), the array exhibits near-omnidirectionality. Interference between the signals generated by the individual elements in the array leads to more complex beam patterns seen at higher frequencies. Nonsymmetry in the patterns is a result of individual elements in the array not being matched in phase. It is important to be able to determine the theoretical patterns to know what to expect from the measured array. In order to calculate the patterns in this 3×3 array, simple line theory was used. The patterns in the horizontal plane can be calculated by using a line array consisting of N ($=3$ in this case) equally spaced, equally phased, equal strength sources. The relative strength, P, at any incident

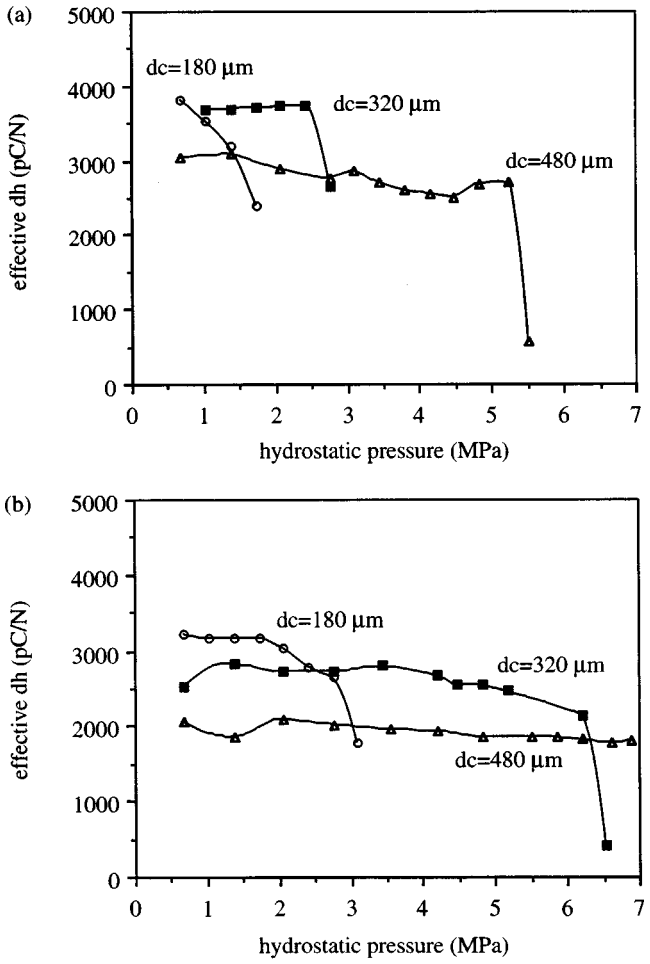

FIG. 10. Pressure dependence of the effective d_h coefficient for standard-size single-element cymbal transducers with (a) brass caps and (b) molybdenum caps of varying cavity depth.

angle, $\varnothing$, normal to the face of the projector can be calculated from the expression:[28]

$$P = \frac{\sin\left(\frac{Nkd \cdot \sin \varnothing}{2}\right)}{N \cdot \sin\left(\frac{kd \cdot \sin \varnothing}{2}\right)}, \tag{3}$$

where d is the center-to-center spacing between the elements and k is the wave number. The nulls are found by calculating the angles which make $P=0$. From Eq. (3), the appearance of the first null is predicted to occur at 37 kHz when $\varnothing$ is 90 deg. Nulls in the pattern occur at angles where the radiated waves from each cymbal are separated by a distance of one half-wavelength. Grating lobes, which are secondary major lobes, will appear at higher frequencies. The number of side lobes present between the main and grating lobes is equal to the number of cymbal elements along a side in the array less two. As seen at 130 kHz [Fig. 9(e)], there is one side lobe between the main lobe and the grating lobe. In Fig. 9(d), 50 kHz, the side lobes becomes significant. The only null in the first quadrant at 50 kHz was calculated to be about 48 deg, which compares well to the null seen in the pattern in Fig. 9(d). The first quadrant nulls at 130 kHz were calculated to be at about 17, 35, and 59 deg. The first two correlate well with those seen in the pattern [Fig. 9(e)]. However, the null at 59 deg is masked by the grating lobe.

Figure 10 shows the measured pressure dependence of the d_h^{eff} coefficients of single-element brass-capped and molybdenum-capped cymbal transducers with different cavity depths (dc). The standard brass-capped cymbal can withstand hydrostatic pressures of up to 2.5 MPa (250 m water depth) before failing. Failure was found to be due to the caps being deformed beyond their elastic limits, hence eliminating the effective stress-transfer mechanism between the piezoelectric ceramic and the caps.[27] As can be seen, the pressure tolerance of the transducer is dependent upon the stiffness of the cap material as well as the cap shape. With the stiff molybdenum caps, cymbals with deep cavities can withstand at least 7 MPa of pressure. Unfortunately, the stiff molybdenum caps cannot flex as readily as the softer brass caps, hence their displacement (and ultimately the TVR) is expected to be lower than that of the brass-capped cymbals.

IV. CONCLUSIONS

The cymbal transducer array appears to be a viable candidate for medium- to high-power shallow-water acoustic projector applications at frequencies below 50 kHz. Preliminary results indicate that it compares quite favorably with both the Tonpilz and 1-3 composites, at least in terms of output power. Its thin profile when incorporated into arrays makes it ideal for conforming to a curved surface. In addition, its simple design and uncomplicated construction method should render it easy and hence inexpensive to mass produce.

ACKNOWLEDGMENTS

The authors would like to thank Robert Dashem and Greg Granville of the Applied Research Laboratory, the Center for Acoustics and Vibration at Penn State, as well as Ender Kuntsal of International Transducer Corporation in Santa Barbara, CA, for their contributions. The authors would also like to acknowledge the Office of Naval Research and the Defense Advanced Research Projects Agency (DARPA) for their financial support.

[1] R. F. W. Coates, *Underwater Acoustic Systems* (Macmillan, Hong Kong, 1990), p. 2.
[2] W. J. Hughes, ''Transducers, Underwater Acoustic,'' in *Encyclopedia of Applied Physics, Vol. 22*, edited by G. L. Trigg, W. Greulich, and E. S. Vera (Wiley-VCH GmbH, Weinheim, Germany, 1998), pp. 67–84.
[3] T. R. Howarth, ''A Multilayer 1-3 Piezoelectric Composite Underwater Projector,'' presented at the 133rd meeting of the Acoustical Society of America, The Pennsylvania State University, June 1997 [J. Acoust. Soc. Am. **101**, 3095(A) (1997)].
[4] V. F. Janas and A. Safari, ''Overview of Fine-Scale Piezoelectric Ceramic/Polymer Composite Processing,'' J. Am. Ceram. Soc. **78**(11), 2945–2955 (1995).
[5] L. Bowen, R. Gentilman, D. Fiore, H. Pham, W. Serwatka, C. Near, and B. Pazol, ''Design, Fabrication, and Properties of Sonopanel™ 1-3 Piezocomposite Transducers,'' Ferroelectrics **187**, 109–120 (1996).
[6] W. Cao, Q. M. Zhang, and L. E. Cross, ''Theoretical Study on the Static Performance of Piezoelectric Ceramic-Polymer Composites with 1-3 Connectivity,'' J. Appl. Phys. **72**, 5814–5821 (1992).
[7] Q. X. Chen and P. A. Payne, ''Industrial Applications of Piezoelectric

Polymer Transducers,'' Meas. Sci. Technol. **6**(3), 249–267 (1995).
[8] R. Y. Ting, ''Composite Piezoelectric Materials for Transduction,'' Appl. Acoust. **41**, 325–335 (1994).
[9] K. D. Rolt, ''History of the Flextensional Electroacoustic Transducer,'' J. Acoust. Soc. Am. **87**, 1340–1349 (1990).
[10] E. F. Rynne, ''Innovative Approaches for Generating High Power, Low Frequency Sound,'' in *Transducers for Sonics and Ultrasonics*, edited by M. D. McCollum, B. F. Hamonic, and O. B. Wilson (Technomic, Lancaster, PA, 1993), Chap. 3, pp. 38–49.
[11] Q. C. Xu, S. Yoshikawa, J. R. Belsick, and R. E. Newnham, ''Piezoelectric Composites with High Sensitivity and High Capacitance for Use at High Pressures,'' IEEE Trans. Ultrason. Ferroelectr. Freq. Control **38**, 634–639 (1991).
[12] R. E. Newnham, Q. C. Xu, and S. Yoshikawa, ''Transformed Stress Direction Acoustic Transducer,'' U.S. Patent 4,999,819 (1991).
[13] R. E. Newnham and A. Dogan, ''Metal-Electroactive Ceramic Composite Transducer,'' U.S. Patent 5,729,077 (1998).
[14] A. Dogan, K. Uchino, and R. E. Newnham, ''Composite Piezoelectric Transducer with Truncated Conical Endcaps 'Cymbal','' IEEE Trans. Ultrason. Ferroelectr. Freq. Control **44**, 597–605 (1997).
[15] J. F. Tressler, A. Dogan, J. F. Fernandez, J. T. Fielding Jr., K. Uchino, and R. E. Newnham, ''Capped Ceramic Hydrophones,'' in *1995 IEEE Ultrasonics Symposium Proceedings*, edited by M. Levy, S. C. Schneider, and B. R. McAvoy (IEEE, Piscataway, NJ, 1995), pp. 897–900.
[16] K. Onitsuka, A. Dogan, J. F. Tressler, Q. Xu, S. Yoshikawa, and R. E. Newnham, ''Metal-Ceramic Composite Transducer, the 'Moonie','' J. Intell. Mater. Syst. Struct. **6**, 447–455 (1995).
[17] K. Onitsuka, A. Dogan, Q. Xu, S. Yoshikawa, and R. E. Newnham, ''Design Optimization for Metal-Ceramic Composite Actuator, 'Moonie','' Ferroelectrics **156**, 37–42 (1994).
[18] K. Onitsuka, ''Effects of Bonding and Geometry on the Flextensional Transducer, 'Moonie','' Ph.D. thesis, The Pennsylvania State University, 1993, Chap. 3, pp. 30–139.
[19] A. Dogan, ''Flextensional 'Moonie and Cymbal' Actuators,'' Ph.D. thesis, The Pennsylvania State University, 1994, Chap. 3, p. 42.
[20] J. F. Fernandez, A. Dogan, J. T. Fielding, K. Uchino, and R. E. Newnham, ''Tailoring the Performance of Ceramic-Metal Piezocomposite Actuators, 'Cymbals','' Sens. Actuators A **65**, 228–237 (1998).
[21] J. F. Tressler, W. Cao, K. Uchino, and R. E. Newnham, ''Finite Element Analysis of the Cymbal-Type Flextensional Transducer,'' IEEE Trans. Ultrason. Ferroelectr. Freq. Control **45**, 1363–1369 (1998).
[22] R. J. Bobber, *Underwater Electroacoustic Measurements* (Naval Research Laboratory, Washington, DC, 1970), p. 6.
[23] R. J. Urick, *Principles of Underwater Sound* (McGraw-Hill, New York, 1983), 3rd ed., p. 71.
[24] A. Dogan, ''Flextensional 'Moonie and Cymbal' Actuators,'' Ph.D. thesis, The Pennsylvania State University, 1994, Chap. 8, pp. 144–171.
[25] R. L. Pritchard, ''Mutual Acoustic Impedance between Radiators in an Infinite Rigid Plane,'' J. Acoust. Soc. Am. **32**, 730–737 (1960).
[26] C. T. Lynch, editor, *CRC Handbook of Materials Science, Vol. I: General Properties* (CRC Press, Cleveland, OH, 1974), Table 3–47, pp. 405–407.
[27] J. F. Tressler, ''Capped Ceramic Underwater Sound Projector, the 'Cymbal' ,'' Ph.D. thesis, The Pennsylvania State University, 1997, Chap. 8, pp. 209–228.
[28] O. B. Wilson, *Introduction to Theory and Design of Sonar Transducers* (Peninsula, Los Altos, CA, 1988), p. 169.

Modeling of borehole Stoneley waves in the presence of skin effects[a)]

Bart W. Tichelaar[b)]
Shell International Exploration & Production B. V., Volmerlaan 8, 2288 GD Rijswijk, The Netherlands

Hsui-Lin Liu and David L. Johnson
Schlumberger-Doll Research, Old Quarry Road, Ridgefield, Connecticut 06877-4108

(Received 30 October 1997; revised 20 August 1998; accepted 9 September 1998)

An important aspect of oil production from a geological formation is the process of flow into a well penetrating the formation. Recent laboratory experiments indicate that well-inflow can be significantly reduced by a skin effect caused by the presence of a thin layer of low permeability around the wellbore. This impairment layer is drilling induced and differs from the mudcake that is usually encountered when logging a well. Whereas a mudcake may have built up on the borehole wall during drilling, the drawdown pressure often removes it when oil is produced from the well. In contrast with such a temporary mudcake, the impairment layer is believed to form a permanent flow impedance throughout the lifetime of a well unless extensive cleaning measures are taken. A simple poro-elastic model is constructed to investigate the propagation of Stoneley waves in a borehole with a thin impairment layer. If the impairment layer affects Stoneley wave propagation, it may be possible to acoustically detect this layer with sonic logging tools. Using realistic values for the impairment flow impedance, model calculations for a typical sandstone reservoir of 20% porosity indicate that the impairment layer changes the dispersion characteristics of borehole Stoneley waves. The magnitude of these changes increases with increasing mobility of the reservoir pore fluid. [S0001-4966(99)00101-0]

PACS numbers: 43.10.Ln, 43.20.Jr [ANN]

INTRODUCTION

The advent of full-waveform sonic logging tools such as the dipole sonic imager or DSI (trademark of Schlumberger) (Harrison *et al.*, 1990) has made it possible to record a variety of waveforms excited by various types of borehole acoustic sources. In addition to the compressional and shear head wave, which travel along the borehole wall at the formation compressional and shear wave velocity, a number of borehole modes can be excited. The most well known modes are the borehole Stoneley wave, or tube wave, which is efficiently excited by a low-frequency monopole source, and the borehole flexural wave excited by a dipole source. In general, the phase velocity of such modes propagating along the borehole wall varies with frequency. A theoretical overview of acoustic wave propagation in fluid-filled boreholes is given in Tsang and Rader (1979), Cheng and Toksöz (1981), Kurkjian and Chang (1986), and Winbow (1988).

In the oil industry, the primary measurements from full-waveform borehole sonic tools are the elastic wave velocities of the formation in which the logging tool is employed. The formation compressional and shear wave velocities are obtained from the waveform data in a direct way through first motion detection or semblance processing (Kimball and Marzetta, 1984). Other important measurements, such as permeability (Rosenbaum, 1974; Williams *et al.*, 1984; Chang *et al.*, 1987; Schmitt *et al.*, 1988; Winkler *et al.*, 1989; Tang *et al.*, 1991), formation mechanical properties (Sinha *et al.*, 1996) and anisotropy (Mueller, 1991; Hatchell and Cowles, 1992; Esmersoy *et al.*, 1994; Sinha *et al.*, 1994; Tichelaar and Hatchell, 1997) are obtained in a more indirect way and require extensive processing of the recorded waveforms. Furthermore, a borehole sonic tool has recently been used to image reservoir structure from a horizontal well (Esmersoy *et al.*, 1998).

An important aspect of oil production from a geological formation is the process of flow into a well penetrating the formation. Obviously this process is in part controlled by the permeability of the formation (the reservoir). In addition to reservoir permeability, however, well-inflow is also controlled by the permeability of a zone around the borehole that is altered by the drilling process. Such alteration is due to the interaction between the borehole fluid, which is a carefully designed drilling mud, and the porous reservoir. During drilling operations it is common practice to have the pressure of the drilling mud exceed the reservoir pore fluid pressure with a few hundred psi. Because of this overbalance in pressure, the drilling mud invades into the reservoir. One product of mud invasion that is well known in the logging industry is the build-up of a mudcake on the borehole wall which complicates acoustic log interpretation (e.g., Tang, 1994; Liu and Johnson, 1997). From the perspective of optimization of oil production rates, the mudcake is often not of major concern since it is designed to be removed by the drawdown pressure after a well has been producing for a certain amount of time.

A more serious problem encountered in production technology is caused by the invasion of mud solids into the res-

[a)]''Selected research articles'' are ones chosen occasionally by the Editor-in-Chief that are judged (a) to have a subject of wide acoustical interest, and (b) to be written for understanding by broad acoustical readership.

[b)]Now at Shell U.K. Exploration & Production, Shell-Mex House, Strand, London WC2R 0DX, United Kingdom.

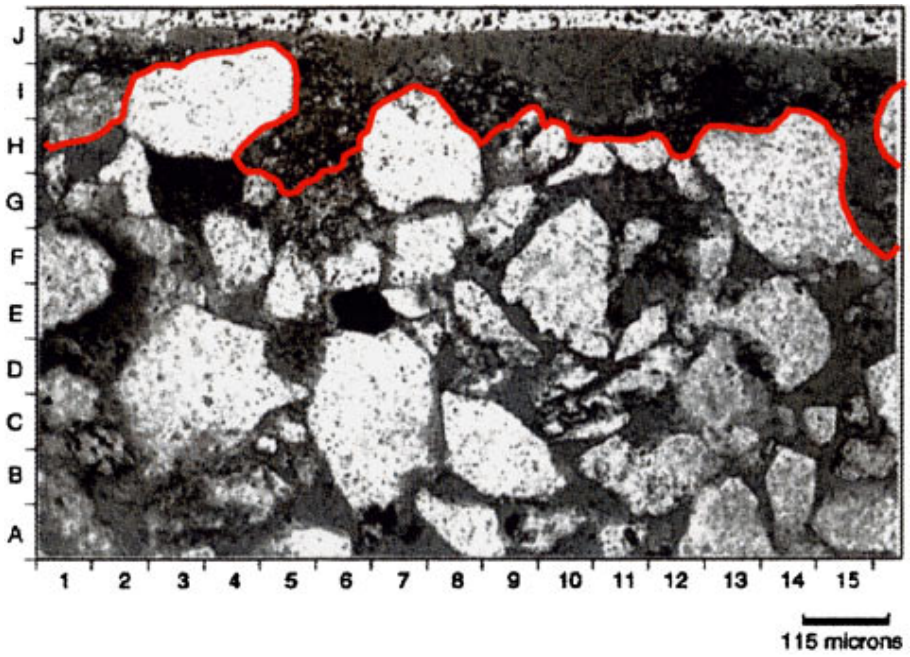

FIG. 1. Thin section in plane polarized light of a typical sample after drawdown with crude oil, showing that the impairment layer on the surface of the wellbore face (zone above red line) is not thicker than about 1 pore depth (e.g., H-I 5-6). The reservoir rock is a fine to medium grained sandstone. From Francis *et al.* (1995).

ervoir. Laboratory experiments by Francis *et al.* (1995) indicate that mud particles can invade the porous formation, creating a thin permeability barrier by plugging the pore throats exposed to the wellbore face. This thin impairment layer, with a thickness less than 0.5 mm, acts as a flow impedance and its presence reduces the flow of hydrocarbons into the well. The impairment layer is considered to be the dominant form of permanent permeability damage (Francis, 1997). The layer is not removed by drawdown of crude oil during production and can only be removed through extensive and time consuming cleaning measures. The laboratory core-flood experiments carried out under reservoir conditions by Francis *et al.* (1995) show that the impairment layer permeability is a factor of 100 to 20 000 less than the formation permeability. The thin impairment layer reduces the average core permeability with a factor of 2 to 150. Figure 1 shows a typical photomicrograph of a sandstone sample from the core-flood experiments after simulating mud invasion and subsequent back production of crude oil through the sample. The shallow invasion of mud solids is shown in this figure. Detailed examination of the cores shows no evidence of mud solids invasion deeper into the cores, fines migration, scale precipitates or emulsions.

There is currently no technology available to detect the impairment layer as a function of position along the wellbore. As a first step toward such a technology, this paper investigates the behavior of borehole Stoneley waves in a model consisting of a borehole penetrating a porous formation, where a thin layer of low permeability separates the well from the reservoir. Since the Stoneley wave is a surface wave that propagates along the borehole, its propagation characteristics are sensitive to properties of the region near the borehole wall. Winkler *et al.* (1989) have investigated the behavior of borehole Stoneley waves in permeable formations from an experimental and theoretical point of view and have demonstrated the significance of poro-elastic wave propagation theory in the borehole geometry. In the following section we describe the impairment model as well as the theory behind the model. The two subsequent sections show numerical results and address the validity of the model.

I. THE IMPAIRMENT MODEL

Figure 2 shows the impairment model in which we investigate the properties of borehole Stoneley wave propagation. The model consists of a fluid-filled borehole (blue) in a porous formation with porosity φ, the reservoir (yellow). The borehole is separated from the formation by a thin layer of low permeability, the impairment layer (red). The borehole fluid is treated as an acoustic medium and the reservoir as a poro-elastic medium (Biot, 1956a,b; Rosenbaum, 1974). In the following, the index 0 is used to indicate the acoustic medium, and the index 1 to indicate the poro-elastic medium. As waves travel along the borehole wall, the perturbed pressure of the borehole fluid, P_0, and that of the pore fluid, P_1, are related to each other via Darcy flow through the impairment layer. For the poro-elastic medium, two displacement fields must be distinguished, U_{r1} for the pore fluid and u_{r1}

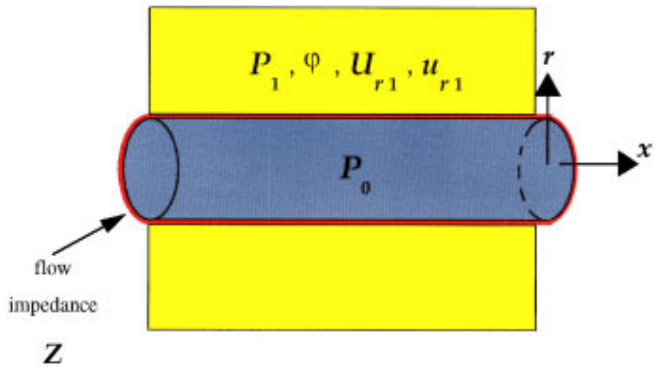

FIG. 2. Impairment model. The impaired layer (red) is described with a single parameter, Z, which is the flow impedance. See also main text. The coordinates r and x are the radial and axial coordinate, respectively.

for the solid frame, where the index r indicates the radial component. The flux, $\varphi(\dot{U}_{r1}-\dot{u}_{r1})$, through the impairment layer is related to the differential pressure, P_0-P_1, in the following way

$$\varphi(\dot{U}_{r1}-\dot{u}_{r1})=\frac{P_0-P_1}{Z}. \tag{1}$$

According to Darcy's law, the flow impedance, Z, can be written as

$$Z=\frac{d}{\kappa_{\rm imp}/\eta}, \tag{2}$$

which is the ratio of impairment layer thickness, d, and impairment mobility, $\kappa_{\rm imp}/\eta$, where $\kappa_{\rm imp}$ is the impairment layer permeability and η the pore fluid viscosity. Note that the impedance is a function of the pore fluid viscosity. Equations (1) and (2) combine into a continuity condition [Eq. (7)] at the boundary between the borehole fluid and the formation. Rosenbaum (1974) also uses this boundary condition. In the literature of well engineering and reservoir simulation (e.g., Woods, 1990) it is common to describe an impaired zone by its skin factor, s. The impairment impedance Z is simply related to s by

$$Z=\frac{R}{\kappa_0/\eta}\,s, \tag{3}$$

where R is the borehole radius and κ_0 the formation permeability. In principle s (and therefore Z) could be negative when, for example, there are deeply penetrating perforations in a cased hole. In this article we consider positive values for Z only.

There is a total of four boundary conditions:

$$U_{r0}=(1-\varphi)\,u_{r1}+\varphi\,U_{r1}, \tag{4}$$

$$-P_0=\tau_{rr1}-\varphi\,P_1, \tag{5}$$

$$0=\tau_{rz1}, \tag{6}$$

$$P_0-P_1=-i\,\omega\,Z\,\varphi\,(U_{r1}-u_{r1}). \tag{7}$$

Equation (4) reflects the continuity of average radial displacement, required by the balance of fluid volume and Eq. (5) the continuity of average normal stress. Since fluids have no shear strength, Eq. (6) prescribes a vanishing shear stress at the borehole wall.

A total of 13 model parameters (Table I) is needed to define the impairment model. Johnson *et al.* (1994a,b) describe how all of the parameters entering into Biot theory can be independently measured. Because the mobility of the reservoir pore fluid is controlled by viscous forces at low frequencies and by inertial forces at high frequencies, a dynamic permeability, $\tilde{\kappa}(\omega)$, is used, where ω is angular frequency. More precisely, a complex tortuosity, $\tilde{\alpha}(\omega)$, is calculated to determine the Biot general elastic coefficients and the three velocities for the Biot waves: the fast compressional wave, the slow compressional wave and the shear wave. See Johnson *et al.* (1987) for more details. The complex tortuosity is related to dynamic mobility, $\tilde{\kappa}(\omega)/\eta$, as follows:

TABLE I. Parameters of the impairment model and their values for the numerical simulations. The formation parameter values are typical for a fluid-filled sandstone reservoir.

Fluid-filled borehole	Fluid specific attenuation	$Q_{\rm MUD}^{-1}$	0.0037
	Fluid density	ρ_0	1.00 g/cm^3
	Fluid slowness	SF	666 μs/m
	Hole radius	R	14.5 cm
Impairment layer	Impairment mobility @ $d=0.5$ mm	$\kappa_{\rm imp}/\eta$	0.1–100 mD/cp
Porous formation	Formation mobility	κ_0/η	25–2500 mD/cp
	Bulk density	ρ_b	2.37 g/cm^3
	Compressional wave slowness	SP	279 μs/m
	Grain bulk modulus	K_s	35.0 GPa
	Pore fluid density	ρ_f	1.00 g/cm^3
	Pore fluid bulk modulus	K_f	2.24 GPa
	Porosity	φ	0.20
	Shear wave showness	SS	472 μs/m

$$\frac{\tilde{\kappa}(\omega)}{\eta}=\frac{i\varphi}{\tilde{\alpha}(\omega)\omega\,\rho_f}. \tag{8}$$

The complex tortuosity can be calculated from the formation mobility, κ_0/η:

$$\tilde{\alpha}(\omega)=\alpha_\infty+\frac{i\varphi}{\omega\,\rho_f}\left[\frac{\kappa_0}{\eta}\right]^{-1}\left[1-\frac{i\omega}{\omega_c}\right]^{1/2} \tag{9}$$

with the critical angular frequency, ω_c, defined as

$$\omega_c=\frac{2\,\varphi}{\rho_f\,\alpha_\infty}\left[\frac{\kappa_0}{\eta}\right]^{-1}. \tag{10}$$

The critical frequency is that frequency for which viscous and inertial forces are of the same order of magnitude (Johnson *et al.*, 1987). The tortuosity at infinite frequency, α_∞, is related to the electrical conductivity of the fluid-filled pores (Brown, 1980) through $\alpha_\infty=F\varphi$, where F is a geometrical factor referred to as the formation resistivity factor. Details are given in Johnson and Sen (1981). Using Archie's law, $F=\varphi^{-m}$, where the cementation exponent, m, is typically 2 for sandstones, yields

$$\alpha_\infty=\frac{1}{\varphi}. \tag{11}$$

After the Biot general elastic coefficients and the velocities for the three Biot waves are calculated (e.g., Liu and Johnson, 1997), the boundary conditions are evaluated at the borehole wall and the wave equation is solved to determine Stoneley wave slowness and attenuation, which are quantities that can be measured with full-waveform sonic logging tools. The details of the method are further discussed in the Appendix.

TABLE II. Biot velocities v_{c1}, v_{c2}, and v_{sh} and critical frequency f_c for frequencies of 1.0 and 5.0 kHz.

κ_0/η [mD/cp]	2500		250		25	
f [kHz]	1.0	5.0	1.0	5.0	1.0	5.0
v_{c1} [m/s]	3587 $-2i$	3591 $-3i$	3586 $-0i$	3586 $-1i$	3586 $-0i$	3586 $-0i$
v_{c2} [m/s]	293 $-183i$	491 $-107i$	84 $-80i$	200 $-157i$	26 $-26i$	58 $-57i$
v_{sh} [m/s]	2119 $-6i$	2129 $-6i$	2117 $-1i$	2118 $-3i$	2117 $-0i$	2117 $-0i$
f_c [kHz]	5	5	51	51	510	510

II. NUMERICAL SIMULATIONS

To investigate the behavior of Stoneley wave propagation, we calculate Stoneley wave slowness and attenuation for various values of impairment impedance and formation mobility. We choose to specify the impairment layer in terms of the impairment mobility, κ_{imp}/η [mD/cp] for a reference thickness $d=0.5$ mm, which is the same reference thickness used in the experimental work of Francis *et al.* (1995) to measure impairment in the laboratory. Note that Eq. (2) shows how to compute the impairment impedance from κ_{imp}/η and d.

Whereas the model consists of 13 parameters (Table I) we focus on the role of impairment mobility and reservoir mobility and use realistic fixed values for the other 11 parameters. We have computed Stoneley wave dispersion curves for reservoir mobilities of 2500, 250, and 25 mD/cp in the frequency range of 500 to 5000 Hz. This frequency range is typical for sonic logging tools when acquiring Stoneley waveforms. Table II gives values for the velocities v_{c1}, v_{c2}, and v_{sh}, which are the formation's fast and slow compressional wave velocities and shear wave velocity, respectively, as derived from the formation parameters in Table I. Furthermore, Table II gives values for the critical frequency, $f_c=\omega_c/2\pi$ [see Eq. (10)]. For frequencies less than f_c viscous forces dominate Stoneley wave fluid flow in the formation, while for frequencies higher than f_c inertial forces dominate the flow. Rather than going into details, we summarize the following general characteristics of the fluid pressure $|P_0|$, $|P_1|$, and the differential radial displacement, $U_{r1}-u_{r1}$ observed for the impairment model. For an open hole with no impairment, i.e., $\kappa_{\text{imp}}/\eta\to\infty$, fluid pressure is continuous across the borehole wall and maximum differential radial displacement, i.e., maximum fluid flow, occurs at the borehole wall. For a closed or fully impaired hole, i.e., $\kappa_{\text{imp}}/\eta=0$ mD/cp, fluid pressure drops discontinuously across the borehole wall and there is no fluid flow at the borehole wall. For impaired wells, i.e., for values of impairment mobility $\kappa_{\text{imp}}/\eta\in\langle 0,\infty\rangle$, fluid pressure and flow at the borehole wall are bound by the open hole and closed hole cases. Furthermore, for a given value of reservoir mobility and impairment mobility, an increase in frequency causes fluid pressure and fluid flow to decay more rapidly radially into the formation. Another observation is that, for a given frequency and impairment mobility, the decay is more rapid for lower values of reservoir mobility. This is due to the fact that the wavelength of the slow P-wave decreases with decreasing reservoir mobility.

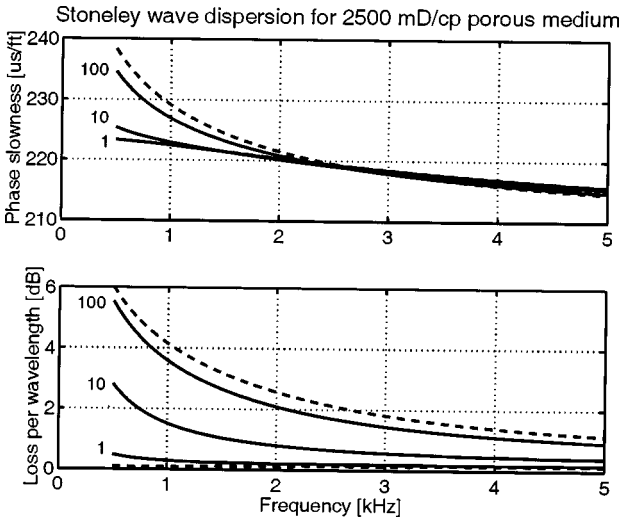

FIG. 3. Dispersion curves for a sandstone reservoir rock with a formation mobility $\kappa_0/\eta=2500$ mD/cp for various values of impairment mobility κ_{imp}/η. Each curve is labeled with the corresponding value of impairment mobility κ_{imp}/η in mD/cp. Dispersion curves for the open hole with no impairment and closed, fully impaired hole are shown as dashed lines. If dashed line is not visible it overlays with a solid curve. Amplitude loss per wavelength equals $27.287\,53^*Q^{-1}$ [Eq. (A35)].

To discuss the observed Stoneley wave dispersion characteristics we present the complex wave number, k_x^{St} [Eq. (A35)], in terms of phase slowness, S [μs/ft], and amplitude loss per wavelength [dB] which is proportional to Q^{-1}. Figures 3 and 4 show the results for a reservoir mobility of 2500 and 250 mD/cp, respectively. The figures show that Stoneley wave dispersion in an impaired well becomes nearly identical to that in a closed, fully impaired well if impairment mobilities are less than about 1 mD/cp. Furthermore, Stone-

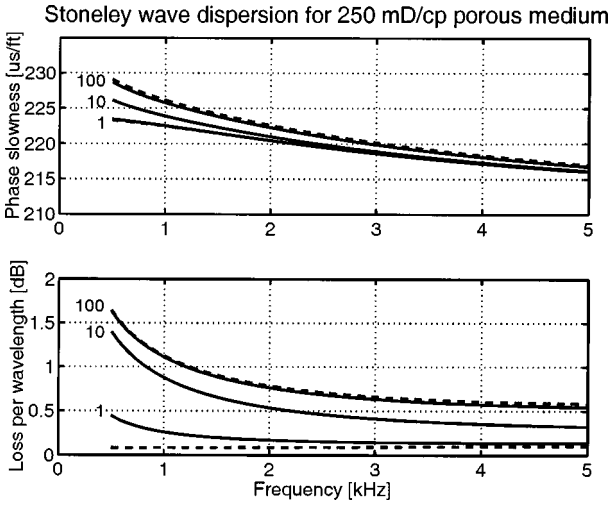

FIG. 4. As Fig. 3 but for a sandstone with a formation mobility of 250 mD/cp.

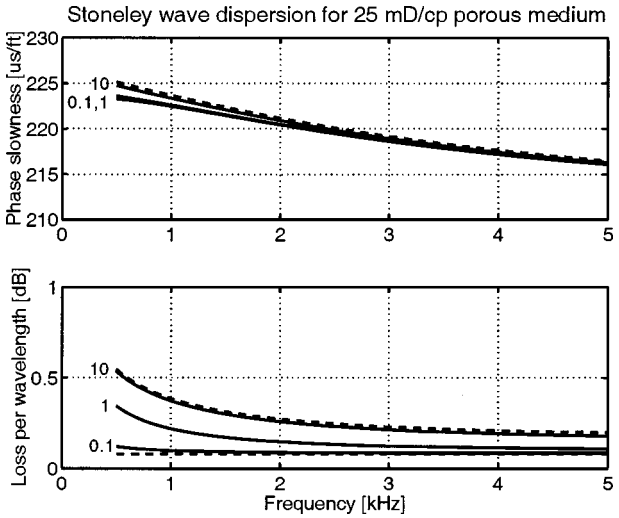

FIG. 5. As Fig. 3 but for a sandstone with a formation mobility of 25 mD/cp.

ley wave dispersion becomes nearly identical to that in a fully open hole with no impairment when impairment mobilities are larger than about 100 mD/cp. In between these two extremes, i.e., for impairment mobilities between about 1 to 100 mD/cp, the presence of the thin impairment layer gradually changes the curves from closed hole dispersion to open hole dispersion (see Figs. 3 and 4). The maximum variability in Stoneley wave slowness and attenuation at 500 Hz is about 15 μs/ft and 6 dB per wavelength for a reservoir mobility of 2500 mD/cp and 6 μs/ft and 1.5 dB per wavelength for a reservoir mobility of 250 mD/cp. This is the variability between the open hole without an impairment layer and the closed, fully impaired borehole.

Figure 5 shows the dispersion curves for a reservoir mobility of 25 mD/cp. For such a small value of reservoir mobility (i.e., ''tight reservoirs'') the range of impairment mobility for which the dispersion curves are different from closed and open hole dispersion is about 0.1 to 10 mD. However, the differences between the dispersion curves in Fig. 5 are quite small in terms of slowness (<2 μs/ft) as well as loss per wavelength (<0.5 dB). Table III gives values for the skin factor s in Eq. (3) for the various impairment scenarios in Figs. 3, 4 and 5.

TABLE III. Skin factor s for the scenarios of Figs. 3–5, where $\kappa_{\rm imp}/\eta$ [mD/cp] is the impairment layer mobility and κ_0/η [mD/cp] the formation mobility. The values of the dimensionless skin factor s range between 0.01 and 9.

$\kappa_{\rm imp}/\eta$ [mD/cp]	κ_0/η [mD/cp]		
	2500	250	25
100	0.1	0.01	⋯
10	1	0.1	0.01
1	9	1	0.1
0.1	⋯	⋯	1

III. DISCUSSION

The impairment model discussed in the previous sections is a relatively simple model, as the impaired zone is characterized by one single parameter, the impairment impedance. Schmitt (1988) has presented a more complicated and more computing intensive model that may be interpreted as an impairment model. The model of Schmitt consists of a circular borehole in a porous formation, where a thin porous layer is placed between the borehole and formation. The thin layer is a Biot medium characterized by 11 parameters, which are listed in Table IV. The boundary conditions are no-slip conditions similar to Eqs. (4) through (7). To compare the two models we first use Eq. (2) to calculate impairment impedance for Schmitt's model, then convert the impedance into impairment mobility to find that $\kappa_{\rm imp}/\eta = 15$ mD/cp. Formation mobility and borehole radius in Schmitt's model are 1500 mD/cp and 12 cm. Figure 6 shows the comparison of Stoneley wave velocity and attenuation. The similarity in Stoneley wave dispersion for the two models reflects the fact that the thickness of Schmitt's porous layer is less than the wavelength of the slow P-wave, which is 4.72 cm at 1 kHz and 2.11 cm at 5 kHz. As a consequence, the gradient of fluid pressure in Schmitt's thin porous layer (the impairment layer) is constant.

TABLE IV. Parameters for the porous thin layer in the model of Schmitt (1988). See Eq. (2) and Table I for parameter definition.

$\kappa_{\rm imp}$	300 mD	K_s	37.9 GPa
η	1 cp	ρ_f	1.00 g/cm
d	1 cm	K_f	2.25GPa
ρ_b	2.337 g/cm^3	φ	0.19
SF	666.7 μs/m	SS	480.8 μs/m
SP	267.7 μs/m		

Tang (1994) and Liu and Johnson (1997) have modeled Stoneley waves in a system where the well is separated from the porous formation by an elastic membrane. This membrane is meant to mimic the mudcake that builds up inward at the borehole wall. The boundary conditions used for the membrane model allow for slip between the membrane and formation. To shed light on the connection between the membrane model and the impairment model, let us assume that the thickness of the membrane reduces to zero. In this case, the boundary conditions in Eqs. (4), (5), and (6) are identical for both models. The boundary condition that specifies pressure communication between borehole and formation for the membrane model, however, is

$$P_0 - P_1 = W_{MC}\,\varphi\,(U_{r1} - u_{r1}), \tag{12}$$

which is physically different from the impairment model [see Eq. (7)]: the membrane stiffness, $W_{MC}+0i$, is constant and real-valued for the membrane model, whereas the impairment model has a constant flow impedance, Z, such that the impairment layer stiffness $W_i(\omega) = -i\omega Z$ is purely imaginary and depends on frequency. For the membrane model the differential pressure $P_0 - P_1$ is proportional to the differential fluid displacement while for the impairment model it is proportional to differential fluid velocity (flow velocity).

Liu and Johnson (1997) present a low-frequency approximation for the membrane model [Eq. (58) in Liu and Johnson] which gives the complex Stoneley wave number, $k_x^{St}(\omega)$, as a function of frequency [e.g., Eq. (A35) in the Appendix]. Because of the mathematical correspondence be-

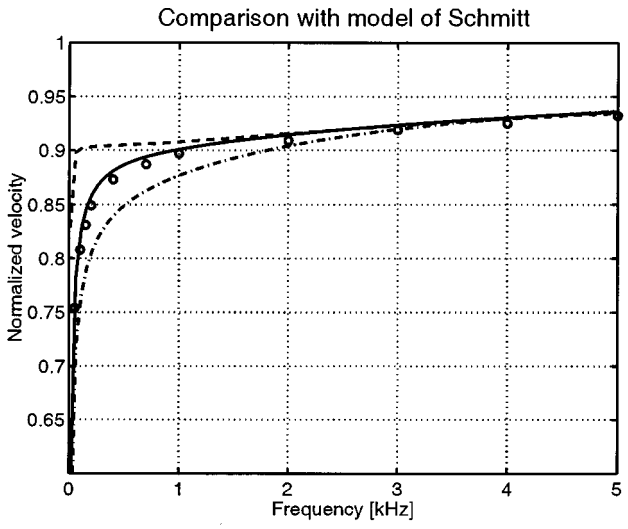

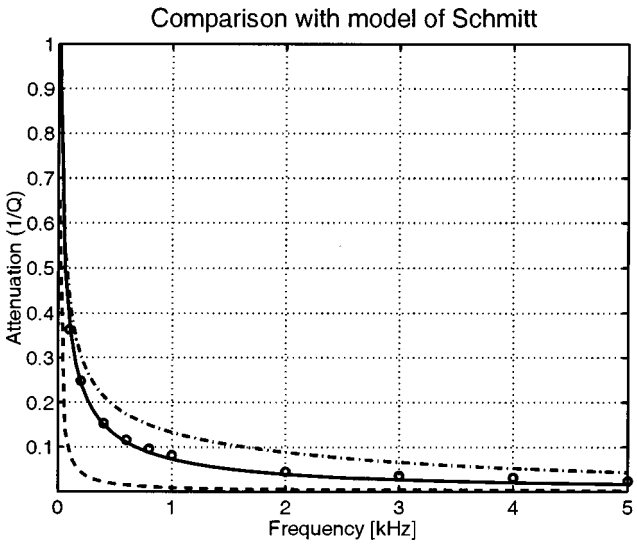

FIG. 6. Comparison between our impairment model and the radially layered model of Schmitt (1988). (Top) Solid curve is the phase velocity, $S^{-1}(\omega)$ [Eq. (A35)], normalized with the pore fluid velocity, calculated for the impairment model with $\kappa_{\text{imp}}/\eta = 15$ mD/cp. Open dots are data points picked by hand from Fig. 2 of Schmitt's paper. Dash-dotted curve is calculated for an open hole with no impairment. Dashed curve is calculated for the impairment model with $\kappa_{\text{imp}}/\eta = 1$ mD/cp. (Bottom) Same comparison, but now for attenuation Q^{-1}.

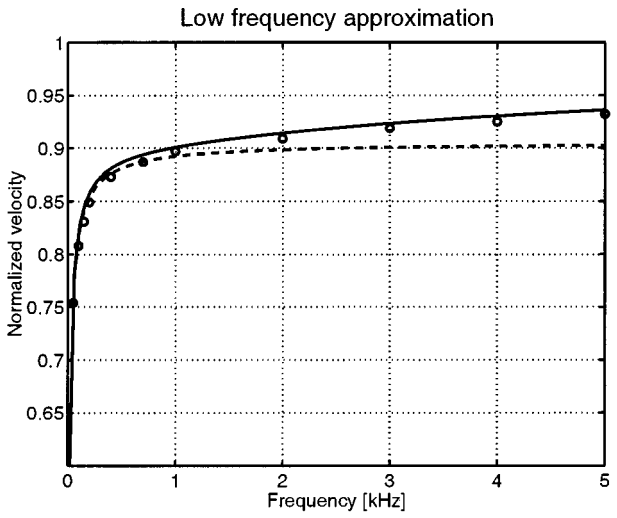

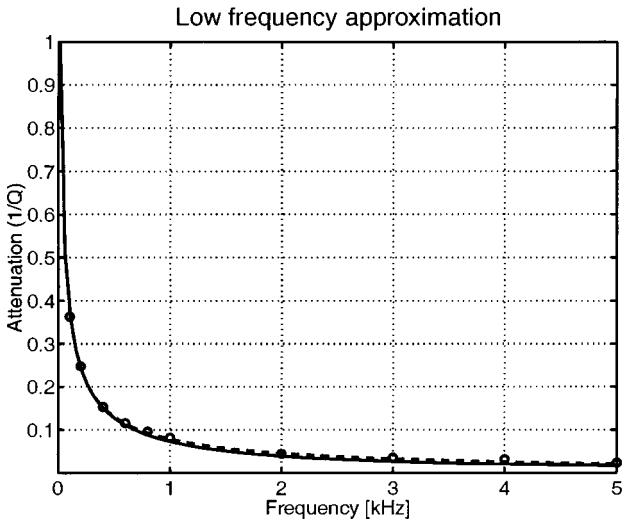

FIG. 7. Comparison between the exact representation of the impairment model (solid) and the low-frequency approximation (dashed) in Eq. (13). The top figure shows normalized velocity, $S^{-1}(\omega)$, and bottom figure attenuation, Q^{-1}. The data points picked by hand from Fig. 2 of Schmitt (1988) have also been added.

tween the membrane model and the impairment model, their Eq. (58) is valid for the impairment model and can be rewritten as follows, substituting an impairment layer thickness of zero:

$$[k_x^{St}(\omega)]^2 = \omega^2 \left[SF^2 + \frac{\rho_0}{\rho_b} SS^2 + \frac{2}{[W_i(\omega) + W_p(\omega)] SS^2 R} \frac{\rho_b}{} \right]. \tag{13}$$

The low-frequency approximation illustrates that the Stoneley wave number consists of three contributions. The right hand side of Eq. (13) shows a borehole fluid contribution of SF^2, where SF is borehole fluid slowness, a frequency independent formation contribution $SS^2(\rho_0/\rho_b)$, where SS is formation shear wave slowness, and a frequency dependent contribution related to permeability effects,

$$\frac{1}{SS^2} \frac{2\rho_b}{[W_i(\omega) + W_p(\omega)] R}, \tag{14}$$

where $W_p(\omega)$ is a stiffness due to the permeability of the formation in the open hole without impairment (Liu and Johnson, 1997). The impairment layer acts as an additional flow impedance, $Z = -W_i(\omega)/i\omega$, in series with that due to open hole fluid flow. The accuracy of the low-frequency approximation is illustrated in Fig. 7. The parameter values are the same as in Fig. 6. For frequencies below 1 kHz the approximation is within 2% of the exact theory for velocity and it is much better for attenuation.

IV. CONCLUSIONS

We have presented a model for borehole Stoneley wave propagation in a porous rock in the presence of skin effects. The parametrization of the model is based on laboratory core flood experiments that suggest the presence of a thin layer of

low permeability at the borehole wall. This permeability barrier, also referred to as impairment layer, may reduce the inflow of crude oil from the porous reservoir throughout the lifetime of a well; it is not a mudcake. The impairment layer is parameterized by a single parameter, the impairment impedance, or alternatively the impairment mobility at a specified thickness of the impairment layer. This parameter is related to the skin factor commonly used in well technology and reservoir simulation.

For Stoneley wave logging frequencies between 500 to 5000 Hz, the main effect of the impairment layer is to change the dispersion of Stoneley waves. Using parameters that are typical for a sandstone formation and using a porosity of 0.20 we find that for sandstones with a low reservoir mobility of 25 mD/cp the impairment layer changes Stoneley wave slowness and attenuation by at most 2 μs/ft and 0.5 dB per wavelength. For sandstones with an intermediate reservoir mobility of 250 mD/cp, the maximum change in slowness and attenuation at 500 Hz caused by the presence of the impairment layer is 6 μs/ft and 1.5 dB per wavelength. For sandstones with relatively high reservoir mobility of 2500 mD/cp this maximum change increases to 15 μs/ft and 6 dB per wavelength. Whereas we have not addressed the inverse problem of estimating the impairment impedance from measurements of Stoneley wave dispersion, it appears that such inverse problem will yield the best-resolved results for oil reservoirs of high permeability and low viscosity.

ACKNOWLEDGMENTS

The authors thank Chris Kimball, Paul Francis, Bikash Sinha, Bart van der Linden and Kees van der Kolk for helpful discussions while preparing this manuscript. B.T. thanks Kees de Groot, William Prins and John Ullo for their effort and support.

APPENDIX: DISPERSION RELATION

To derive the dispersion relation for borehole Stoneley waves in the presence of a permeability barrier, displacement potentials are defined in a fashion similar to, e.g., Winkler *et al.* (1989). We use a circular cylinder coordinate system where r and x are the radial and axial co-ordinates, respectively, and the x-axis is chosen parallel to the borehole axis (see Fig. 2 in main text). Since the Stoneley waves travel parallel to the borehole axis they vary as $\exp i(k_x x-\omega t)$, where k_x is the axial wave number, ω is frequency and t is time.

In the axial wave number–frequency domain, the displacement potential for acoustic waves in the borehole fluid (medium 0) is defined as

$$\Phi_0(k_x,\omega,r)=H_0^{(1)}(k_{r0}\,r)+A_0(k_x,\omega)\,J_0(k_{r0}\,r). \quad \text{(A1)}$$

In the permeable medium (medium 1) penetrated by the borehole, poro-elasticity prescribes the existence of three wave types; three potentials must be defined:

$$\Phi_{1c1}(k_x,\omega,r)=B_{1c1}(k_x,\omega)\,H_0^{(1)}(k_{r1c1}\,r), \quad \text{(A2)}$$

$$\Phi_{1c2}(k_x,\omega,r)=B_{1c2}(k_x,\omega)\,H_0^{(1)}(k_{r1c2}\,r), \quad \text{(A3)}$$

$$\Psi_{1sh}(k_x,\omega,r)=D_{1sh}(k_x,\omega)\,H_1^{(1)}(k_{r1sh}\,r), \quad \text{(A4)}$$

where Φ_{1c1} and Φ_{1c2} represent the fast and slow compressional wave, respectively, and Ψ_{1sh} represents the shear wave. $H_0^{(1)}$ and $H_1^{(1)}$ are Hankel functions of the first kind and J_0 is a Bessel function. The radial wave numbers k_{r0}, k_{r1c1}, k_{r1c2} and k_{r1sh} are equal to $(\omega^2/v^2-k_x^2)^{1/2}$, where v is the velocity of acoustic waves in the borehole fluid, the fast compressional wave, the slow compressional wave and the shear wave, respectively. Chang *et al.* (1988) give expressions for these velocities. We will now determine phase slowness and specific attenuation by solving the boundary conditions [Eqs. (4) through (7) in main text].

In the borehole the radial displacement, U_{r0}, and fluid pressure, P_0, are

$$U_{r0}=\frac{\partial\Phi_0}{\partial r}, \quad \text{(A5)}$$

$$P_0=\rho_0\omega^2\Phi_0, \quad \text{(A6)}$$

where ρ_0 is the borehole fluid density. In the poro-elastic medium the radial and axial displacements in the solid are

$$u_{r1}=\frac{\partial\Phi_{1c1}}{\partial r}+\frac{\partial\Phi_{1c2}}{\partial r}-ik_x\Psi_{1sh}, \quad \text{(A7)}$$

$$u_{x1}=ik_x(\Phi_{1c1}+\Phi_{1c2})+\frac{\partial\Psi_{1sh}}{\partial r}+\frac{\Psi_{1sh}}{r}, \quad \text{(A8)}$$

the radial and axial displacements in the pore fluid are

$$U_{r1}=G_+\frac{\partial\Phi_{1c1}}{\partial r}+G_-\frac{\partial\Phi_{1c2}}{\partial r}-ik_xG_{sh}\Psi_{1sh}, \quad \text{(A9)}$$

$$U_{x1}=ik_x(G_+\Phi_{1c1}+G_-\Phi_{1c2})+G_{sh}\left[\frac{\partial\Psi_{1sh}}{\partial r}+\frac{\Psi_{1sh}}{r}\right], \quad \text{(A10)}$$

where G_+, G_-, and G_{sh} are the potential factors described in Liu and Johnson (1997). Pore fluid pressure, P_1, and the normal stress, τ_{rr1}, and tangential stress, τ_{rz1}, on the solid are

$$P_1=-\frac{1}{\varphi}(Rd_{1f}+Qd_{1s}), \quad \text{(A11)}$$

$$\tau_{rr1}=(P-2N)d_{1s}+Qd_{1f}+2N\frac{\partial u_{r1}}{\partial r}, \quad \text{(A12)}$$

$$\tau_{rz1}=N\left(ik_xu_{r1}+\frac{\partial u_{z1}}{\partial r}\right), \quad \text{(A13)}$$

where P, Q, R and N are the Biot constants referred to as general elastic coefficients (Biot and Willis, 1957) and

$$d_{1s}=-\omega^2\left(\frac{\Phi_{1c1}}{v_{c1}^2}+\frac{\Phi_{1c2}}{v_{c2}^2}\right), \quad \text{(A14)}$$

$$d_{1f}=-\omega^2\left(G_+\frac{\Phi_{1c1}}{v_{c1}^2}+G_-\frac{\Phi_{1c2}}{v_{c2}^2}\right). \quad \text{(A15)}$$

Note that N is the shear modulus of the porous medium. Biot and Willis (1957) use a slightly different notation where

$P-2N=A$. The velocities v_{c1} and v_{c2} are the fast and slow compressional wave velocities, respectively.

We now substitute Eqs. (A5)–(A13) and (A1)–(A4) into the four boundary conditions specified in the main text and evaluate the resulting expressions at the borehole wall, $r=R$, which gives a system of four equations with four unknowns. In matrix form we can write

$$\begin{pmatrix} m_{11} & m_{12} & m_{13} & m_{14} \\ m_{21} & m_{22} & m_{23} & m_{24} \\ 0 & m_{32} & m_{33} & m_{34} \\ \varphi m_{21} & m_{42} & m_{43} & m_{44} \end{pmatrix} \cdot \begin{pmatrix} A_0 \\ B_{1c1} \\ B_{1c2} \\ D_{1sh} \end{pmatrix} = \begin{pmatrix} s_1 \\ s_2 \\ 0 \\ \varphi s_2 \end{pmatrix} \tag{A16}$$

or, in short notation,

$$\mathbf{M}(k_x,\omega)\cdot \begin{pmatrix} A_0 \\ B_{1c1} \\ B_{1c2} \\ D_{1sh} \end{pmatrix} = \mathbf{s}(k_x,\omega). \tag{A17}$$

The matrix elements are

$$m_{11}=-k_{r0}J_1(k_{r0}R), \tag{A18}$$

$$m_{12}=k_{r1c1}H_1^{(1)}(k_{r1c1}R)*(1-\varphi+G_+\varphi), \tag{A19}$$

$$m_{13}=k_{r1c2}H_1^{(1)}(k_{r1c2}R)*(1-\varphi+G_-\varphi), \tag{A20}$$

$$m_{14}=ik_xH_1^{(1)}(k_{r1sh}R)*(1-\varphi+G_{sh}\varphi), \tag{A21}$$

$$m_{21}=-\rho_0\omega^2J_0(k_{r0}R), \tag{A22}$$

$$m_{22}=C_+\frac{\omega^2}{v_{c1}^2}H_0^{(1)}(k_{r1c1}R)+2N\,k_{r1c1}^2 \times\left[H_0^{(1)}(k_{r1c1}R)-\frac{H_1^{(1)}(k_{r1c1}R)}{k_{r1c1}R}\right], \tag{A23}$$

$$m_{23}=C_-\frac{\omega^2}{v_{c2}^2}H_0^{(1)}(k_{r1c2}R)+2N\,k_{r1c2}^2 \times\left[H_0^{(1)}(k_{r1c2}R)-\frac{H_1^{(1)}(k_{r1c2}R)}{k_{r1c2}R}\right], \tag{A24}$$

$$m_{24}=2ik_xk_{r1sh}N\left[H_0^{(1)}(k_{r1sh}R)-\frac{H_1^{(1)}(k_{r1sh}R)}{k_{r1sh}R}\right], \tag{A25}$$

$$m_{32}=-2ik_xk_{r1c1}N\,H_1^{(1)}(k_{r1c1}R), \tag{A26}$$

$$m_{33}=-2ik_xk_{r1c2}N\,H_1^{(1)}(k_{r1c2}R), \tag{A27}$$

$$m_{34}=\left(2k_x^2-\frac{\omega^2}{v_{sh}^2}\right)N\,H_1^{(1)}(k_{r1sh}R), \tag{A28}$$

$$m_{42}=-i\omega Z\,k_{r1c1}\varphi^2(1-G_+)H_1^{(1)}(k_{r1c1}R)+\frac{\omega^2}{v_{c1}^2} \times(Q+G_+R)H_0^{(1)}(k_{r1c1}R), \tag{A29}$$

$$m_{43}=-i\omega Z\,k_{r1c2}\varphi^2(1-G_-)H_1^{(1)}(k_{r1c2}R)+\frac{\omega^2}{v_{c2}^2} \times(Q+G_-R)H_0^{(1)}(k_{r1c2}R), \tag{A30}$$

$$m_{44}=\omega Z\,k_x\varphi^2(1-G_{sh})H_1^{(1)}(k_{r1sh}R), \tag{A31}$$

where J_1 is a Bessel function, v_{sh} the velocity of the Biot shear wave and C_+ and C_- are defined as

$$\begin{aligned} C_+&=P-2N+G_+Q+Q+G_+R, \\ C_-&=P-2N+G_-Q+Q+G_-R. \end{aligned} \tag{32}$$

The source terms in **s** are

$$\begin{aligned} s_1&=k_{r0}H_1^{(1)}(k_{r0}R), \\ s_2&=\rho_0\omega^2H_0^{(1)}(k_{r0}R). \end{aligned} \tag{A33}$$

Borehole modes, including the Stoneley wave, are found by solving the dispersion relation

$$\text{Det}\ \mathbf{M}(k_x,\omega)=0. \tag{A34}$$

For each individual mode, Eq. (A34) is numerically solved with a root-finding algorithm. The borehole Stoneley wave is that mode traveling at the highest phase slowness for any single frequency. The Stoneley wave number, $k_x^{St}(\omega)$, is related to phase slowness, $S(\omega)$, and specific attenuation, Q^{-1}, as follows:

$$k_x^{St}(\omega)=\omega\,S(\omega)\left[1+\frac{i}{2Q}\right]. \tag{A35}$$

This equation is the dispersion relation used to compute Stoneley wave propagation in the presence of skin effects.

Biot, M. A. (**1956a**). ''Theory of propagation of elastic waves in a fluid-saturated porous solid, I. Low frequency range;'' J. Acoust. Soc. Am. **28**, 168–178.

Biot, M. A. (**1956b**). ''Theory of propagation of elastic waves in a fluid-saturated porous solid, II. High frequency range;'' J. Acoust. Soc. Am. **28**, 179–191.

Biot, M. A., and Willis, D. G. (**1957**). ''The elastic coefficients of the theory of consolidation,'' J. Appl. Mech. **24**, 595–601.

Brown, R. J. S. (**1980**). ''Connection between formation factor for electrical resistivity and fluid-solid coupling factor in Biot's equations for acoustic waves in fluid-filled porous media,'' Geophysics **45**, 1269–1275.

Chang, S. K., Liu, H., and Johnson, D. L. (**1988**). ''Low-frequency tube waves in permeable rocks,'' Geophysics **53**, 519–527.

Cheng, C. H., and Toksöz, M. N. (**1981**). ''Elastic wave propagation in a fluid-filled borehole and synthetic acoustic logs,'' Geophysics **46**, 1042–1053.

Cheng, C. H., Jinzhong, Z., and Burns, D. R. (**1987**). ''Effects of in-situ permeability on the propagation of Stoneley (tube) waves in a borehole,'' Geophysics **52**, 1279–1289.

Esmersoy, C., Koster, K., Williams, M., Boyd, A., and Kane, M. (**1994**). ''Dipole shear anisotropy logging,'' presented at the 64th Ann. Int. Mtg., Soc. Explor. Geophys., Expanded abstracts, 1139–1142.

Esmersoy, C., Chang, C., Kane, M., Coates, R. T., Tichelaar, B. W., and Quint, E. (**1998**). ''Acoustic imaging of reservoir structure from a horizontal well,'' The Leading Edge **17**, 940–946.

Francis, P. (**1997**). ''Dominating effects controlling the extent of drilling-induced formation damage,'' presented at the SPE European Formation Damage Conference, The Hague, SPE 38182, Soc. Petrol. Engin., Expanded abstracts, 365–373.

Francis, P. A., Eigner, M. R. P., Patey, I. T. M., and Spark, I. S. C. (**1995**). ''Visualization of drilling-induced formation damage mechanisms using

reservoir condition core flood testing,'' presented at the SPE European Formation Damage Conference, The Hague, SPE 30088, Soc. Petrol. Engin., Expanded abstracts, 101–115.
Harrison, A. R., Randall, C. J., Aron, J. B., Morris, C. F., Wignall, A. H., and Dworak, R. A. (**1990**). ''Acquisition and analysis of sonic waveforms from a borehole monopole and dipole source for the determination of compressional and shear speeds and their relation to rock mechanical properties and surface seismic data,'' presented at the SPE Annual Technical Conference and Exhibition, New Orleans, SPE 20557, Soc. Petrol. Engin., Expanded abstracts.
Hatchell, P. J., and Cowles, C. S. (**1992**). ''Flexural borehole modes and measurement of shear-wave azimuthal anisotropy,'' 62nd Ann. Internat. Mtg., Soc. Explor. Geophys., Expanded abstracts, 201–204.
Johnson, D. L., and Sen, P. N. (**1981**). ''Multiple scattering of acoustic waves with application to the index of refraction of fourth sound,'' Phys. Rev. B **24**, 2486–2496.
Johnson, D. L., Hemmick, D. L., and Kojima, H. (**1994a**). ''Probing porous media with first and second sound. I. Dynamic permeability,'' J. Appl. Phys. **76**, 104–114.
Johnson, D. L., Koplik, J., and Dashen, S. (**1987**). ''Theory of dynamic permeability and tortuosity in fluid-saturated porous media,'' J. Fluid Mech. **176**, 379–400.
Johnson, D. L., Plona, T. J., and Kojima, H. (**1994b**). ''Probing porous media with first and second sound. II. Acoustic properties of water-saturated porous media,'' J. Appl. Phys. **76**, 115–125.
Kimball, C. V., and Marzetta, T. L. (**1984**). ''Semblance processing of borehole acoustic array data,'' Geophysics **49**, 274–281.
Kurkjian, A. L., and Chang, S. (**1986**). ''Acoustic multipole sources in fluid-filled boreholes,'' Geophysics **51**, 148–163.
Liu, H., and Johnson, D. L. (**1997**). ''Effects of an elastic membrane on tube waves in permeable formations,'' J. Acoust. Soc. Am. **101**, 3322–3329.
Mueller, M. C. (**1991**). ''Acquisition of shear velocity information with the dipole array sonic tool (in the Gulf Coast Tertiary of Texas),'' presented at the 61st Ann. Internat. Mtg., Soc. Explor. Geophys., Expanded Abstracts, 127–132.
Rosenbaum, J. H. (**1974**). ''Synthetic microseismograms: Logging in porous formations,'' Geophysics **39**, 14–32.
Schmitt, D. P. (**1988**). ''Effects of radial layering when logging in saturated porous formations,'' J. Acoust. Soc. Am. **84**, 2200–2214.
Schmitt, D. P., Bouchon, M., and Bonnet, G. (**1988**). ''Full-wave synthetic acoustic logs in radially semiinfinite porous media,'' Geophysics **53**, 808–823.
Sinha, B. K., Liu, Q., and Kostek, S. (**1996**). ''Acoustic waves in pressurized boreholes: a finite difference formulation,'' J. Geophys. Res. **101**, 173–25,180.
Sinha, B. K., Norris, A. N., and Chang, S. K. (**1994**). ''Borehole flexural modes in anisotropic formations,'' Geophysics **59**, 1037–1052.
Tang, X. M. (**1994**). ''Effects of mudcake on the measurement of fluid flow properties using borehole waves,'' presented at the 64th Ann. Internat. Mtg., Soc. Explor. Geophys., Expanded Abstracts, 78–81.
Tang, X. M., Cheng, C. H., and Toksöz, M. N. (**1991**). ''Dynamic permeability and borehole Stoneley waves: A simplified Biot-Rosenbaum model,'' J. Acoust. Soc. Am. **90**, 1632–1646.
Tichelaar, B. W., and Hatchell, P. J. (**1997**). ''Inversion of 4-C borehole flexural waves to determine anisotropy in a fractured carbonate reservoir,'' Geophysics **62**, 1432–1441.
Tsang, L., and Rader, D. (**1979**). ''Numerical evaluation of the transient acoustic waveform due to a point source in a fluid-filled borehole,'' Geophysics **44**, 1706–1720.
Williams, D. M., Zemanek, J., Angona, F. A., Dennis, C. L., and Caldwell, R. L. (**1984**). ''The long space acoustic logging tool, presented at 25th Ann. Logging Symposium, Soc. Prof. Well-log Anal.
Winbow, G. A. (**1988**). ''A theoretical study of acoustic S-wave and P-wave velocity logging with conventional and dipole sources in soft formations,'' Geophysics **53**, 1334–1342.
Winkler, K. W., Liu, H., and Johnson, D. L. (**1989**). ''Permeability and borehole Stoneley waves: Comparison between experiment and theory,'' Geophysics **54**, 66–75.
Woods, E. G. (**1990**). ''Well management: Designing and controlling production parameters,'' in *Reservoir Management*, SPE Monograph Vol. 13, edited by C. C. Mattax and R. L. Dalton (Soc. Petrol. Engin., Richardson, TX).

One-channel time-reversal in chaotic cavities: Theoretical limits

Carsten Draeger[a] and Mathias Fink

Laboratoire Ondes et Acoustique, URA CNRS 1503, Université Paris VII Denis Diderot – Ecole Supérieure de Physique et de Chimie Industrielles de la Ville de Paris, 10 Rue Vauquelin, 75005 Paris, France

(Received 15 December 1997; accepted for publication 5 October 1998)

One-channel time-reversal experiments in closed chaotic cavities produce excellent, but not perfect, time-reversed focusing. This paper investigates such experiments by a simple eigenmode analysis of the system. It shows that the process is, even for long reversed signals, subject to an information loss during recording and re-emission which prevents perfect time-reversal. This fact can be expressed by a simple equation, called the cavity equation, which states that the signal of a one-channel time-reversal is equal to the signal of a perfect time-reversal after convolution with the backscattering impulse response of the reversal point (i.e., from this point to this point). The latter convolution describes the introduction of the loss of information. Furthermore, arguments are presented suggesting that one third of the total energy of the time-reversed wave field is actually contained in the refocusing wavefront. The predictions are verified by numerical finite-difference time-domain simulations. [S0001-4966(99)04201-0]

PACS numbers: 43.20.−f, 43.20.Fn, 43.20.Ks, 43.25.Rq [DEC]

INTRODUCTION

Unlike experiments using acoustic time-reversal mirrors, one-channel time-reversal can be easily obtained as it requires only one transmit and one receive channel, and a closed propagation medium with negligible absorption. Like every time-reversal experiment, it is a two-step process: In the first step, a short signal is injected at one point, *A*, and produces a reverberating wave field inside the cavity. At a second point, the reversal point *B*, amplitude and phase of the field is recorded over a long time. Then, in the second step, the cavity is cleared, the signal is time-reversed and reinjected at *B*. In this way, we obtain a sharp, focused peak at the initial source point *A*. Experiments[1] have shown that the focusing quality increases with the size of the time-reversal window, i.e., the duration of the reversed signal. This increase has been quantified by a simple statistical model, inspired by ray trajectories inside the cavity. However, for long windows, a saturation regime is entered where the focusing quality can no more be improved. Then, the amplitude of the refocused signal observed in *A* increases linearly with the reversed time but the shape of the peak and of the (temporal) sidelobes is not affected. The phenomenon of these residual sidelobes is not explained in a satisfactory way by the statistical model. Also, the choice of a cavity in the shape of a chaotic billiard has so far only been explained by the need of ergodic ray dynamics. However, a ray description of the wave field can hardly be justified, even if its conclusions fit to experimental data.

In this paper, we describe the time-reversal process using an approximate eigenmode decomposition of the wave field. Besides reconfirming the refocusing ability, this description is able to explain the saturation regime and provides additional explanations for the advantages due to the chaotic shape of the cavity. It is shown that an information loss occurs at the reversal point *B* and that this inhibits a perfect time-reversal, i.e., the creation of a wave field that behaves exactly as if time was counting backwards. The main idea is the following: By injection of a short pulse during the first step in *A*, the system acquires a certain eigenmode distribution. A long signal is recorded at *B* that can be interpreted as a superposition of all eigenfrequencies of the system. If the signal is sufficiently long and degeneracy is negligible (condition presumably enhanced by the level repulsion of a chaotic wave billiard), these eigenfrequencies are well resolved. During the injection of the reversed signal, every frequency excites then exclusively the corresponding eigenmode. To produce a perfectly reversed wave field, every reinjected eigenmode should have the same weight as during the first step of the experiment. However, *B* measures and injects each eigenmode with a factor proportional to the value of its eigenfunction at this point. In particular, the eigenmodes having a node in *B* cannot be measured at all. This confusion of the eigenmode weights is the origin of the information loss mentioned above, in the sense that the information about the wave field's eigenmode distribution can only be measured or reproduced in a distorted way by *B*.

We have to emphasize that a perfect time-reversal cannot be expected *a priori* in this case. Unlike ''usual'' time-reversal experiments, one-channel time-reversal as presented here is not a scattering experiment. In this case, time-reversal symmetry does not guarantee the possibility of a perfect reversal in the same way as it does in the case of the model of the ''closed time-reversal cavity,''[2] which reverses all outgoing wavefronts, since outgoing wavefronts cannot be defined here.

Section I presents some consequences of this information loss on the temporal shape of the refocused signal at a given point, expressed in a simple equation called here the cavity equation. Section II evaluates the importance of the noise introduced into the system by the information loss in terms of energy. The analysis suggests that, in general, the

[a]Current affiliation: Department of Electrical Engineering, University of Rochester, Rochester, NY 14627, Electronic mail: draeger@ee.rochester.edu

reversed wave field contains (energetically) two-thirds of noise and one-third of desired wave.

I. THE CAVITY EQUATION

Let $h_{XY}(t)$ be the impulse response from point X to point Y, i.e., the signal measured in Y after a Dirac excitation in X. After injection of the signal $f(t)$ in A, we observe hence in B the convolution $f(t)*h_{AB}(t)$. In a one-channel time-reversal process, this signal is time-reversed and reinjected in B, thus giving in A the signal $f(-t)*h_{AB}(-t)*h_{BA}(t)$. [This signal immediately implies refocusing: Reciprocity demands that $h_{AB}=h_{BA}$, and thus, $h_{AB}(-t)*h_{BA}(t)=\int d\tau\, h_{AB}(t+\tau)h_{AB}(\tau)$ is the autocorrelation function of h_{AB}, which has its maximum at $t=0$.] We are now going to compare this signal to the perfectly reversed situation. If we observe the wave field at the source point A during the first step of the experiment, we obtain the signal $f(t)*h_{AA}(t)$, i.e., a signal with a strong first peak due to the initial emission, followed by a long series of reflections from the boundary. We call h_{AA} the backscattering impulse response of A. A perfect time-reversal should reproduce in A exactly the reversed signal, i.e., $f(-t)*h_{AA}(-t)$. We show in the following that the information loss can be taken into account by a simple convolution of this signal by the backscattering impulse response $h_{BB}(t)$ of B. This fact is expressed in the cavity equation:

$$h_{AB}(-t)*h_{BA}(t)=h_{AA}(-t)*h_{BB}(t). \tag{1}$$

This equation is, of course, only valid in the context of an excitation function $f(t)$.

A. Derivation of the cavity equation

For simplicity, we suppose a scalar wave field φ inside the cavity, and a homogeneous wave speed c so that the wave equation is given by

$$\left(\frac{1}{c^2}\frac{\partial^2}{\partial t^2}-\nabla^2\right)\varphi(\mathbf{x},t)=F(\mathbf{x},t),$$

where F is the excitation function. Let $\psi_n(\mathbf{x})$ be the eigenmodes of the cavity with $\nabla^2\psi_n=-k_n^2\psi_n$ and eigenfrequency $\omega_n=c\cdot k_n$. The ψ_n form an orthonormal basis of the system and the wave field can be expressed as a superposition of the eigenmodes:

$$\varphi(\mathbf{x},t)=\sum_n \varphi_n(t)\psi_n(\mathbf{x}).$$

As we are interested in impulse responses, we suppose $F(\mathbf{x},t)=F\delta(\mathbf{x}-A)\delta(t)$. The φ_n are then given by

$$\varphi_n(t)=\begin{cases}\dfrac{Fc^2}{\omega_n}\psi_n(A)\sin(\omega_n t), & t>0\\ 0, & t\leqslant 0,\end{cases}$$

and the impulse response h_{AB} becomes (with $Fc^2=1$):

$$h_{AB}(t)=\sum_n \psi_n(A)\psi_n(B)\frac{\sin(\omega_n t)}{\omega_n}\quad (t>0).$$

(Besides, reciprocity $h_{AB}=h_{BA}$ can be directly seen here.)

From this signal recorded in B, a part $\Delta T=[t_1;t_2]$ is reversed. For the second step of the experiment, we introduce the new time variable t_R, so that refocusing occurs at $t_R=0$. Hence, we reinject at B the signal

$$h_{AB}^{\Delta T}(-t_R)=\begin{cases}h(-t_R), & t_R\in[-t_2,-t_1]\\ 0, & \text{elsewhere}\end{cases}.$$

So, one obtains the refocused signal in A:

$$\begin{aligned}S_{\Delta T}(t_R)&=h_{AB}^{\Delta T}(-t_R)*h_{AB}(t_R)\\ &=\int_{t_1}^{t_2}d\tau\, h_{AB}(t_R+\tau)h_{AB}(\tau)\\ &=\sum_n 1/\omega_n\psi_n(A)\psi_n(B)\sum_m 1/\omega_m\psi_m(A)\psi_m(B)\cdot I_{mn}\end{aligned} \tag{2}$$

where

$$I_{mn}=\int_{t_1}^{t_2}d\tau\,\sin(\omega_n(t_R+\tau))\sin(\omega_m\tau).$$

The integral I_{mn} can be written as

$$\begin{aligned}I_{mn}&=\int_{t_1}^{t_2}d\tau[\sin(\omega_n t_R)\cos(\omega_n\tau)\\ &\quad+\cos(\omega_n t_R)\sin(\omega_n\tau)]\sin(\omega_m\tau)\\ &=\frac{1}{2}\sin(\omega_n t_R)\int_{t_1}^{t_2}d\tau[\sin((\omega_m-\omega_n)\tau)\\ &\quad+\sin((\omega_m+\omega_n)\tau)]\\ &\quad+\frac{1}{2}\cos(\omega_n t_R)\int_{t_1}^{t_2}d\tau[\cos((\omega_m-\omega_n)\tau)\\ &\quad-\cos((\omega_m+\omega_n)\tau)].\end{aligned}$$

The second term of each integral gives a contribution of order $1/(\omega_m+\omega_n)\ll\Delta T$, which can be neglected. Thus, we obtain

$$I_{mn}\cong\begin{cases}\dfrac{1}{2}\dfrac{\sin(\omega_n t_R)}{\omega_m-\omega_n}[-\cos((\omega_m-\omega_n)t_2)+\cos((\omega_m-\omega_n)t_1)]\\ \quad+\dfrac{1}{2}\dfrac{\cos(\omega_n t_R)}{\omega_m-\omega_n}[\sin((\omega_m-\omega_n)t_2)-\sin((\omega_m-\omega_n)t_1)], & \text{if } \omega_m\neq\omega_n\\ \frac{1}{2}\Delta T\cos(\omega_n t_R), & \text{if } \omega_m=\omega_n.\end{cases} \tag{3}$$

We are mostly interested in the second term of I_{mn}. Supposing that the eigenmodes are not degenerate, then $\omega_n=\omega_m \Leftrightarrow n=m$, and this term represents the diagonal elements in the sum over n and m. The first term of (3) is only important if the difference $\omega_m-\omega_n$ is small, i.e., for neighboring eigenfrequencies. In the case of a chaotic cavity, next neighbors tend to repulse each other; if the characteristic distance $\Delta\omega$ is sufficiently large so that $\Delta T \gg 1/\Delta\omega$, the nondiagonal terms of I_{mn} are negligible compared to the diagonal contributions, and one obtains

$$I_{mn}=\tfrac{1}{2}\delta_{mn}\Delta T\,\cos(\omega_n t_R)+O(1/\Delta\omega). \tag{4}$$

In the limit $\Delta T\to\infty$, the signal obtained in A by a reversal in B is finally given by

$$S_{\Delta T}(t_R)=\frac{1}{2}\,\Delta T\sum_n\ \frac{1}{\omega_n^2}\,\psi_n^2(A)\,\psi_n^2(B)\cos(\omega_n t_R).$$

This expression explains some properties that have been observed experimentally. The time dependence, given by $\cos(\omega_n t_R)$, implies the experiment's focusing property: If the frequency distribution can be considered as random, the only constructive interference of the sum we can expect is around $t_R=0$. This also agrees with the symmetry observed with respect to this point in time. Furthermore, the equation shows the obvious proportionality of the amplitude with ΔT.

The convolution of h_{AA} and h_{BB} is evaluated in the same way. As the two signals are of infinite length, the convolution integral diverges. So we define a convolution $\underset{(\Delta T)}{*}$, restricted to the interval ΔT, and we compare the result to $S_{\Delta T}$ in the limit $\Delta T\to\infty$:

$$\begin{aligned}C_{\Delta T}(t)&=h_{AA}(-t)\underset{(\Delta T)}{*}h_{BB}(t)\\&=\int_{t_1}^{t_2}d\tau\,h_{BB}(t+\tau)h_{AA}(\tau)\\&=\sum_n\,1/\omega_n\psi_n^2(B)\sum_m\,1/\omega_m\psi_m^2(A)I_{mn}.\end{aligned} \tag{5}$$

Here, I_{mn} is the same integral as in (3) and (4); its term δ_{mn} reduces the double sum to its diagonal elements. So we obtain immediately

$$S_{\Delta T}(t)=C_{\Delta T}(t)\quad(\Delta T\to\infty),$$

and

$$h_{AB}^{\Delta T}(-t)*h_{BA}(t)=h_{AA}(-t)\underset{(\Delta T)}{*}h_{BB}(t)\quad(\Delta T\to\infty).$$

This is our cavity equation (1). For simplicity, we omit the range ΔT. Of course, the equation is only valid in the context of an excitation function $f(t)$ which convolves the impulse responses.

B. Discussion

The convolution of the perfect signal $h_{AA}(-t)$ by h_{BB} introduces a reduction of the reversal quality. In fact, h_{BB} is a signal with a high peak at $t=0$ due to the initial emission and a long series of reflections afterwards. The more h_{BB} is similar to a single Dirac peak, the lesser the effect of the convolution and the better the reversal quality. So the relative amplitude of the series of multiple reflections in h_{BB} should be reduced in order to improve the refocused signal. This could be done, for example, by choosing a larger cavity: The amplitude level of the multiple reflections is related to the mean energy density, which is lower for larger systems (if the injected energy is the same). However, as the density of eigenfrequencies increases also, the characteristic level spacing $\Delta\omega$ is smaller and one has to reverse a longer signal.

The cavity equation is valid for long reversed intervals. When reversing small time-reversal windows, noise is introduced into the refocused signal by the nondiagonal terms of I_{mn} in (2) and (5). We do not give a quantitative description of this noise herein, as it is already described in Ref. 1. The equation may also be valid in some regular cavities with negligible level degeneracy. However, as there is no level repulsion, the convergence of the equation with increasing ΔT will be slower, i.e., one has to reverse longer signals to obtain good focusing.

C. Generalization

If we observe the signal of the reversed wave field at a point C other than the source point A, the cavity equation can simply be generalized:

$$S_\infty^C=h_{AB}(-t)*h_{BC}(t)=h_{AC}(-t)*h_{BB}(t).$$

Again, the result of the one-channel time-reversal is equal to a convolution of the perfectly reversed signal $h_{AC}(-t)$ and the backscattering impulse response h_{BB} of B.

As our system is linear, the introduction of several reversal points $B,C,D,\ldots$ can be taken into account by summing up the refocused signals for each transducer:

$$S_\infty^A=h_{AA}(-t)*[h_{BB}(t)+h_{CC}(t)+h_{DD}(t)+\cdots].$$

In this case, h_{BB} is replaced by the sum $H(t)=[h_{BB}(t)+h_{CC}(t)+h_{DD}(t)+\cdots]$ in the cavity equation. One can then draw the same conclusion for H as for h_{BB}: The smaller the series of multiple reflections, the better the focusing. The initial peaks of h_{BB}, h_{CC}, etc. superpose in a constructive way, thus the amplitude of the peak of H increases linearly with the number N of reversal points. If these points are far from each other, one may suppose an uncorrelated superposition of the multiple reflections. In this case, their rms level increases proportionally with $\sqrt{N}$. Hence, the peak-to-sidelobes ratio grows with the number of points, i.e., the information loss is reduced by using several reversal points. However, of course, the ratio cannot be better than that of a perfect time-reversal that also produces temporal sidelobes (multiple reflections in the h_{AA} signal).

D. Verification by numerical simulations

We have carried out a finite difference simulation in the time domain to verify the validity of the cavity equation (1). We simulate a chaotic scalar cavity in the shape of a disk with one segment cut off (Fig. 1).[3] It is described by a grid of 384×384 points with a step of $\Delta x=0.053$ mm, giving a diameter of 20.5 mm. The boundary of the cavity is defined by Dirichlet conditions, i.e., the field is set to zero. We use a

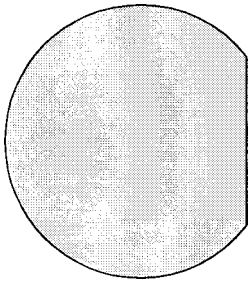

FIG. 1. Chaotic billiard in shape of a disk with one segment cut off.

temporal step of $\Delta t = 0.0094\ \mu$s and a uniform sound-speed parameter of 4000 m/s=4 mm/μs. As we are interested in long propagation times, the dispersion introduced by the numerical scheme cannot be simply neglected. However, dispersion has been shown to be harmless in time-reversal experiments as it is compensated by the process. [Besides, it is easy to see that the derivation of the cavity equation (1) is not altered by a frequency-dependent sound speed.] Thus, we do not need to take this fact into account.

The points A and B are located inside the cavity, and, in this case, far from the boundary and from each other. The impulse responses are measured by emitting a numerical Dirac at one of these points, and measuring at both of them. The impulse responses are then convolved over an interval ΔT. A final convolution is applied with an excitation function with a 1-MHz central frequency and a bandwidth of 100%. Figure 2(a) and (b) show the left- and the right-hand side of the cavity equation for an interval length of $\Delta T = 420\ \mu$s, respectively. The agreement of both signals confirms the equation.

Also of interest is the validity of the equation in the transition from small to great values of ΔT. The characteristic period of time to separate the eigenfrequencies is given by $\Delta T \gg T_H = 1/\Delta\omega$. The number of eigenmodes below a given frequency ω is approximately equal to $N(\omega) = (S/4\pi c^2)\omega^2$ (Refs. 4–6), where S is the surface of the cavity. Hence, we find $T_H = 1/\Delta\omega = \partial N/\partial\omega = S/2\pi c^2\omega$, which is, in our case (surface 300 mm^2, frequency 1 MHz), equal to 19 μs. The time interval $\Delta T = 420\ \mu$s is much greater than this value. Taking a shorter interval, $\Delta T = 210\ \mu$s, we find that $h_{AB}(-t)*h_{BA}(t)$ is clearly different from $h_{AA}(-t)*h_{BB}(t)$ (Fig. 3). If we compare Figs. 2(a) and 3(a), which represent the result of a one-channel time-reversal with windows of size 420 and 210 μs, respectively,

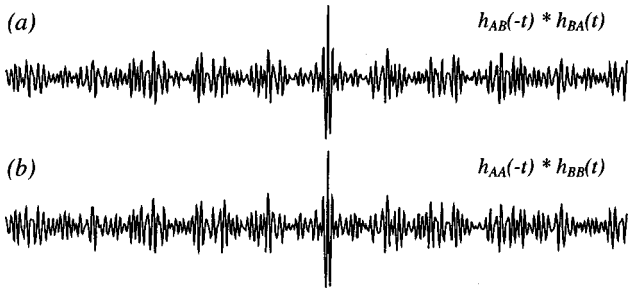

FIG. 2. Verification of the cavity equation by numerical simulations. The excitation signal is here of central frequency 1 MHz (bandwidth 100%); the convolution has been carried out over an interval of $\Delta T = 420\ \mu$s.

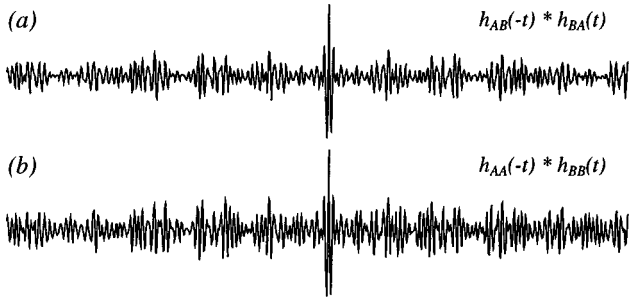

FIG. 3. Same as Fig. 2, but using an interval of $\Delta T = 210\ \mu$s. The cavity equation loses its validity.

we find only a small difference between them. The signal seems already to be in the saturation regime. Thus, $h_{AB}(-t)*h_{BA}(t)$ tends towards the limiting signal more quickly with ΔT than $h_{AA}(-t)*h_{BB}(t)$. This can be seen in the derivation of the cavity equation: The noise introduced into the system for short time-reversal windows is represented by the nondiagonal terms of I_{mn}, and the expected value of $\psi_n(A)\psi_n(B)\psi_m(A)\psi_m(B)$ in (2) is less than the expected value of $\psi_n^2(A)\psi_m^2(B)$ in (5) for $n \neq m$.

II. THE ENERGY OF THE REFOCUSED PEAK

The cavity equation (1) provides information about the temporal shape of the refocused signal at a given point, but does not compare the noise to the refocusing wave in terms of energy. To obtain this comparison, the energy of a perfectly reversed wave and the energy of the refocused peak obtained by a time-reversal in B must be considered. In the first case, the total energy of the system is in the refocused peak; in the second case, only a part of the energy is actually focused, while the rest is distributed as noise in the cavity that cannot be reduced by reversing longer intervals.

A. Theory

Leaving a proportionality factor aside, the field reversed by B is given by

$$\varphi_{TR(B)}(\mathbf{x},t_R) = \sum_n \frac{1}{\omega_n^2}\,\psi_n(A)\psi_n(\mathbf{x})\psi_n^2(B)\cos(\omega_n t_R).$$

The expression for the field initially emitted at A is

$$\varphi_A(\mathbf{x},t) = \sum_n \frac{1}{\omega_n}\,\psi_n(A)\psi_n(\mathbf{x})\sin(\omega_n t) \quad \text{for } t>0,$$

so the reversal of this formula gives the perfectly reversed field. Its time dependence is a sine, while for the one-channel it is a cosine. In view of this, it is more useful to compare the one-channel time-reversal to the temporal primitive of the perfect wave, i.e., to

$$\varphi_{\text{perfect}TR}(\mathbf{x},t_R) = \sum_n \frac{1}{\omega_n^2}\,\psi_n(A)\psi_n(\mathbf{x})\cos(\omega_n t_R).$$

Thus, the only difference between $\varphi_{TR(B)}$ and $\varphi_{\text{perfect}TR}$ is the factor $\psi_n^2(B)$ inside the sum. The energy of the wave field is the sum of kinetic and potential energy. This energy is given (again leaving a proportionality factor aside) by

$$E[\varphi]=\int dV\left(\left(\frac{\partial\varphi}{\partial t}\right)^2+c^2(\boldsymbol{\nabla}\varphi)^2\right).$$

The second term of this integral can be transformed by Green's formula:

$$\int dV(\boldsymbol{\nabla}\varphi)^2=\int_{\text{contour}} dn\ \varphi\ \frac{\partial\varphi}{\partial n}-\int dV\ \varphi\nabla^2\varphi.$$

The integral on the contour of the cavity vanishes with Dirichlet or Neumann boundary conditions. In the case of perfect time-reversal, the energy can then be calculated as

$$\begin{aligned}E[\varphi_{\text{perfect}TR}]&=\int dV\left(\left(\frac{\partial\varphi_{\text{perfect}TR}}{\partial t_R}\right)^2\right.\\&\quad\left.-c^2\varphi_{\text{perfect}TR}\nabla^2\varphi_{\text{perfect}TR}\right)\\&=\int dV\left(\sum_n\ \frac{-1}{\omega_n}\ \psi_n(A)\psi_n(\mathbf{x})\sin(\omega_n t_R)\right)^2\\&\quad-c^2\int dV\left(\sum_n\ \frac{1}{\omega_n^2}\ \psi_n(A)\psi_n(\mathbf{x})\cos(\omega_n t_R)\right)\\&\quad\times\left(\sum_n\ \frac{-k_n^2}{\omega_n^2}\ \psi_n(A)\psi_n(\mathbf{x})\cos(\omega_n t_R)\right).\end{aligned}$$

The double sum is reduced to a single sum due to the orthonormality relation $\int dV\ \psi_n\psi_m=\delta_{mn}$. With $\omega_n=c\cdot k_n$ and $\sin^2(\omega_n t_R)+\cos^2(\omega_n t_R)=1$, one obtains, finally,

$$E[\varphi_{\text{perfect}TR}]=\sum_n\ \frac{1}{\omega_n^2}\ \psi_n^2(A).$$

In the same way, the energy of the at B reversed wave field is found to be

$$E[\varphi_{TR(B)}]=\sum_n\ \frac{1}{\omega_n^2}\ \psi_n^2(A)\psi_n^4(B).$$

For this field, we estimate the energy of the peak by comparing the squared amplitude of the peak at A at $t_R=0$ to the perfect field:

$$E_{\text{peak}}[\varphi_{TR(B)}]=\left(\frac{\varphi_{TR(B)}(A,t_R=0)}{\varphi_{\text{perfect}TR}(A,t_R=0)}\right)^2 E[\varphi_{\text{perfect}TR}].$$

Then, we find the peak energy to total energy ratio as

$$\begin{aligned}&\frac{E_{\text{peak}}[\varphi_{TR(B)}]}{E[\varphi_{TR(B)}]}\\&=\left(\frac{\Sigma_n(1/\omega_n^2)\psi_n^2(A)\psi_n^2(B)}{\Sigma_n(1/\omega_n^2)\psi_n^2(A)}\right)^2\ \frac{\Sigma_n(1/\omega_n^2)\psi_n^2(A)}{\Sigma_n(1/\omega_n^2)\psi_n^2(A)\psi_n^4(B)}\\&=\frac{(\Sigma_n(1/\omega_n^2)\psi_n^2(A)\psi_n^2(B))^2}{\Sigma_n(1/\omega_n^2)\psi_n^2(A)\psi_n^4(B)\Sigma_n(1/\omega_n^2)\psi_n^2(A)}.\end{aligned}\tag{6}$$

As we do not know the eigenmode distribution, we cannot evaluate this expression directly. However, in chaotic cavities, one may use a statistical approach. It is widely conjectured[5,7] that an eigenmode of a chaotic system with ballistic trajectories inside can be considered as a superposition of a large number of plane waves with random amplitude and phase. This implies that the amplitude of an eigenmode at an interior point has a Gaussian distribution and is correlated over a short distance of the order of one wavelength. Thus, we approximate the energy ratio by replacing the sums in (6) by their expectation values $\langle ...\rangle$:

$$\frac{E_{\text{peak}}[\varphi_{TR(B)}]}{E[\varphi_{TR(B)}]}\cong\frac{(\Sigma_n(1/\omega_n^2)\langle\psi_n^2(A)\psi_n^2(B)\rangle)^2}{\Sigma_n(1/\omega_n^2)\langle\psi_n^2(A)\psi_n^4(B)\rangle\Sigma_n(1/\omega_n^2)\langle\psi_n^2(A)\rangle}.$$

For a Gaussian distribution of width σ, $\langle\psi^2\rangle=\sigma^2$. The higher moments can be calculated using the formula $\langle\psi^{2k}\rangle=1\cdot3\cdots(2k-1)\sigma^{2k}$.

If A and B are interior points sufficiently far apart for not to be correlated, then

$$\langle\psi_n^2(A)\psi_n^4(B)\rangle=\langle\psi_n^2(A)\rangle\langle\psi_n^4(B)\rangle=3\sigma^6$$

and

$$\langle\psi_n^2(A)\psi_n^2(B)\rangle=\sigma^4,$$

thus

$$\frac{E_{\text{peak}}[\varphi_{TR(B)}]}{E[\varphi_{TR(B)}]}\cong\frac{1}{3}.$$

Hence, we obtain from our approximate analysis that one-third of the energy is contained in the part of the wave forming the refocused peak and the other two-thirds appear as background noise in the cavity.

One particular case is given by the situation $A=B$; the location of the initial emission coincides with the reversal point. Then

$$\langle\psi_n^4(A)\rangle=3\sigma^4\ \text{ and }\ \langle\psi_n^6(A)\rangle=15\sigma^6,$$

thus,

$$\frac{E_{\text{peak}}[\varphi_{TR(B=A)}]}{E[\varphi_{TR(B=A)}]}\cong\frac{3}{5}.$$

For $A=B$, we expect to have 60% of the energy in the peak, hence a better result. Intuitively, this improvement can be understood for example by the fact that A, unlike B, cannot be on a node of one of the excited eigenmodes.

B. Verification by numerical simulations

To verify these results by simulations, we cannot simply determine the part of the energy in the peak. However, one may interpret these energy ratios not only as being the part of the peak during focusing, but it may be seen in general as the part of the energy forming the refocusing wave field. Thus, we should observe similar energy inhomogeneities in the case of a perfect and a one-channel time-reversal.

A new simulation was carried out on a grid of 512×512 points, using a step of $\Delta x=0.04$ mm, giving a cavity diameter of 20.5 mm. The excitation signal had a central frequency of 5 MHz and a bandwidth of 100%, and the temporal step was $\Delta t=0.0071\ \mu$s for a uniform sound-speed parameter of 4 mm/μs.

We have separated our numerical cavity into an upper and a lower half (Fig. 4), along its symmetry axis. The

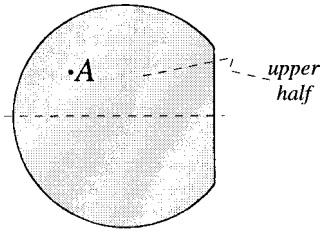

FIG. 4. In our example, the source point A is located in the upper half of the cavity.

source (and focal) point A is located in the upper half. We are now going to calculate the energy fraction $R_{\mathrm{up}}(t) = E_{\mathrm{up}}(t)/E_{\mathrm{tot}}(t)$ contained in this part of the cavity. First, we record R_{up} during the initial emission. The temporal evolution is given in Fig. 5. At the beginning, $R_{\mathrm{up}}=1$ because the energy is still near the source. Then, the wavefronts are reflected and propagate into the lower half, where they are reflected again. The energy goes back and forth several times until it acquires an almost uniform distribution ($R_{\mathrm{up}}=0.5$) inside the system, which continues. A perfect time-reversal should reproduce the scene backwards: Beginning with a (long-lasting) uniform distribution, R_{up} should start oscillating stronger and stronger until culminating at the value 1 at $t_R=0$. Then, the wave diverges again and restarts the same ''damped'' oscillations as before.

In a time-reversal at $B(\neq A)$, we obtain only one-third of the energy in the refocusing wave. Supposing the other two-thirds are uniformly distributed throughout the cavity, we obtain for the energy fraction in the upper half

$$R_{\mathrm{up}}^{TR(B)}(t_R) = \tfrac{1}{3} + \tfrac{1}{3} R_{\mathrm{up}}^{\mathrm{perfect}TR}(t_R).$$

Figure 6 shows a good agreement of this prediction and the value of $R_{\mathrm{up}}^{TR(B)}(t_R)$ actually observed in the simulation. In the case of $B=A$, the relation becomes

$$R_{\mathrm{up}}^{TR(A)}(t_R) = \tfrac{1}{5} + \tfrac{3}{5} R_{\mathrm{up}}^{\mathrm{perfect}TR}(t_R),$$

and the comparison of this prediction and the simulation is presented in Fig. 7. A good match is evident, even though

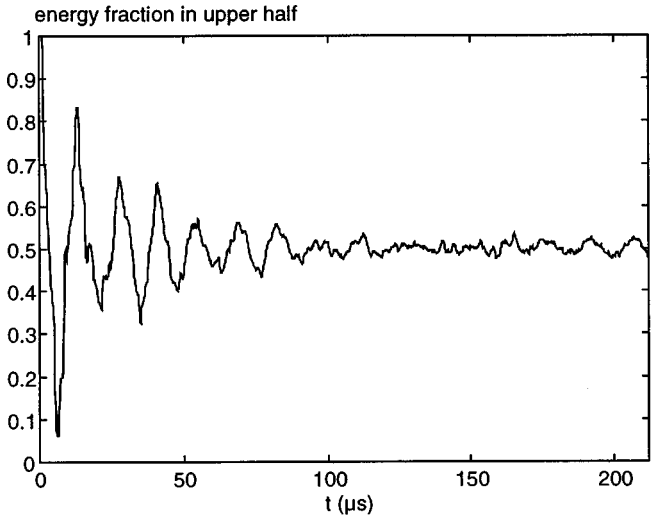

FIG. 5. The fraction of the total energy that is located in the upper half of the cavity during the initial emission.

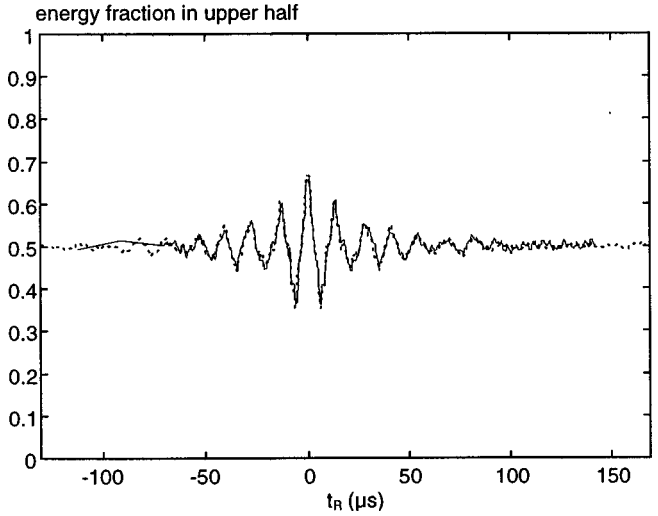

FIG. 6. Fraction of the total energy located in the upper half during refocusing for $A\neq B$: Comparison between theoretical prediction (dashed line) and simulation.

the maximum value of the simulation is lower than the expected one (53% of the energy in the peak versus a prediction of 60%).

III. CONCLUSION

In this paper, we have given a theoretical description of the one-channel time-reversal process in closed chaotic cavities using an approximate eigenmode analysis of the wave field. It mainly describes the process in the saturation regime, i.e., for long time-reversal windows. As the eigenfrequencies of chaotic cavities repulse each other, the signal recorded by the reversal point B after an initial excitation in A is a superposition of well-resolved frequencies, each one corresponding to exactly one eigenmode. Hence, during the reversal step, every frequency of the reversed signal excites mainly its own eigenmode and transmits the right phase to obtain focusing, but, in general, not the right amplitude. The phenomenon of residual (temporal) sidelobes, observed in experiments, is thus explained by this loss of (amplitude) in-

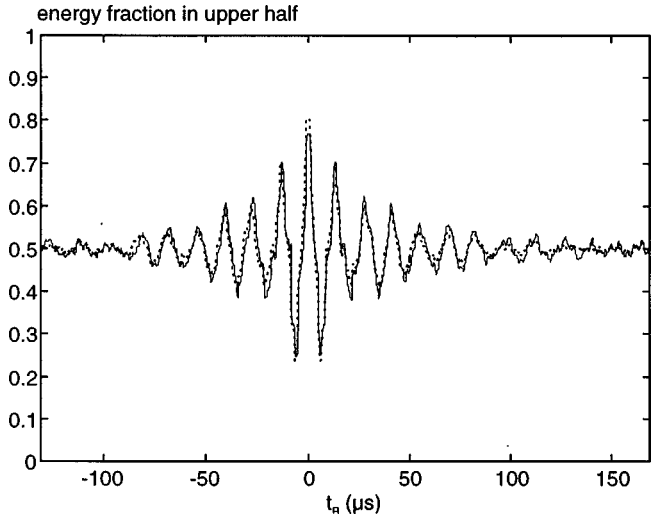

FIG. 7. Same as Fig. 6, for $B=A$.

formation occurring at the reversal point. In fact, B is unable to reproduce the exact weight of each eigenmode because it ''hears'' each eigenfrequency more or less, depending on the amplitude of the eigenmode at this point. One might say that the subjective point of view at B inhibits the creation of a perfectly reversed wave field.

The temporal shape of the refocused signal at a given point of the cavity can be easily compared to the perfectly reversed signal, as the shape results from a temporal convolution of the latter with the backscattering impulse response of B. This relation is expressed in the cavity equation: $h_{AB}(-t)*h_{BA}(t)=h_{AA}(-t)*h_{BB}(t)$. It shows again that the information loss occurs entirely at B. The information loss yields a residual noise in the reversed wave field, in which energy has been shown to be, in general, two-thirds of the total energy in the cavity, while the refocused part of the wave has been shown to carry one-third.

Hence, one may also interpret this result in the sense that this value represents the amount of energy of a wave field in a chaotic cavity that can be controlled using a single, randomly chosen emitting point. A chaotic shape of a given medium might then be useful for the wave field control. Knowing certain characteristics of the reversal point (for example, the amplitude of each eigenmode), one might even compensate for the subjectivity of B and obtain an almost perfect control of the wave field (except the eigenmodes having a node at B). We are now trying to obtain a perfectly reversed wave field by taking this compensation into account in the reversed signal.

ACKNOWLEDGMENTS

We would like to thank A. Derode, O. Legrand, F. Mortessagne, B. van Tiggelen, and R. Weaver for useful discussions.

[1] C. Draeger, J. C. Aime, and M. Fink, ''One-channel time-reversal in chaotic cavities: Experimental results,'' J. Acoust. Soc. Am. **105**, 618–625 (1999).
[2] D. Cassereau and M. Fink, ''Time-reversal of ultrasonic fields—Part III: Theory of the closed time-reversal cavity,'' IEEE Trans. Ultrason. Ferroelectr. Freq. Control **39**, 579–592 (1992).
[3] L. A. Bunimovitch, ''On the ergodic properties of nowhere dispersing billards,'' Commun. Math. Phys. **65**, 295–312 (1979).
[4] M. V. Berry, in *Les Houches 1981—Chaotic Behaviour of Deterministic Systems* (North-Holland, Amsterdam, 1983), pp. 171–271.
[5] S. W. McDonald and A. N. Kaufman, ''Wave chaos in the stadium: Statistical properties of short-wave solutions of the Helmholtz equation,'' Phys. Rev. A **37**(8), 3067–3086 (1988).
[6] R. Balian and C. Bloch, ''Distribution of Eigenfrequencies for the Wave Equation in a Finite Domain,'' Ann. of Phys. **60**, 401–447 (1970).
[7] R. L. Weaver and J. Burkhardt, ''Weak Anderson localization and enhanced backscatter in reverberation rooms and quantum dots,'' J. Acoust. Soc. Am. **96**, 3186–3190 (1994), and references therein.

One-channel time-reversal in chaotic cavities: Experimental results

Carsten Draeger,[a] Jean-Christian Aime, and Mathias Fink
Laboratoire Ondes et Acoustique, URA CNRS 1503, Université Paris VII Denis Diderot – Ecole Supérieure de Physique et de Chimie Industrielles de la Ville de Paris, 10 Rue Vauquelin, 75005 Paris, France

(Received 15 December 1997; accepted for publication 5 October 1998)

Experiments are presented that show the feasibility of reconstructing a point source using acoustic time-reversal with a single transmitter/receiver. The propagation medium is a closed 2-D silicon cavity with chaotic ray dynamics and negligible absorption. Injection of a short pulse at one point yields a long signal at a second one; by reversing a part of this signal, we obtain a focus at the initial injection point. The characterization of the focus was observed by scanning with an optical interferometer and by measuring the signal at the focal spot. With circular converging wavefronts, the reconstructed focus was excellent (corresponding to an aperture of 360°), but not perfect. The increase in quality of the focus with growing length of the reversed signal is described by a statistical ray model. Despite the irreversibility in classical chaos (due to strong sensitivity to initial conditions), the underlying chaotic ray dynamics is useful in this case. © *1999 Acoustical Society of America.* [S0001-4966(99)04301-5]

PACS numbers: 43.20.−f, 43.20.Dk, 43.20.Fn, 43.25.Rq [DEC]

INTRODUCTION

Acoustic time-reversal mirrors are devices able to generate the time-reversed counterpart of a given wave, usually emitted by a point-like source.[1–5] This is done by measuring the incident acoustic field over a large surface, using an array of piezoelectric transducers. The signal of each channel is recorded, time-reversed, and finally re-emitted by the same element. This process creates a wave with the same shape as the incident one, but propagating in the opposite direction, thus focusing on the location of the initial source. One of the main problems of acoustic time-reversal experiments is the need of independent transmit/receive channels for every transducer element. A reduction of the number of elements generally implies a smaller aperture, and thus larger focal spots. In several experiments, it has been observed that multiple reflections and scattering tend to enhance focusing quality in resolution and amplitude. Roux *et al.*[6] carried out time-reversal experiments in waveguides: The reflections on the boundary artificially enlarge the aperture of the time-reversal mirror and thus reduce the focal spot size. Derode *et al.*[7] performed time-reversal experiments through multiply scattering media. Besides the surprising temporal recompression of the reversed signals, the focal spot size corresponds more closely to an aperture associated with the size of the multiple scattering medium rather than to the physical aperture of the mirror itself. In both cases, the information contained in the wider angles, which is lost for small apertures, is redirected or scattered onto the active surface of the mirror, which thus may be reduced. The price to pay for this gain of information is a longer recording time for the signal.

In this study, we examine the reduction of the receivers down to one. In this case, the propagation medium has to be a closed cavity to avoid information loss at infinity, with very weak absorption to allow recording over a long period of time. We have chosen a 2-D silicon wafer as the propagation medium; waves are injected and measured by transversal transducers, fixed to aluminum cones. It will be shown that our measurements are consistent with the hypothesis that the shape of the cavity is of crucial importance. In fact, we use a cavity with chaotic ray dynamics: The information contained in each ray emitted by the source can only be recorded if the ray, after several reflections, passes sufficiently near the time-reversal transducer. This behavior is ensured by ergodicity, which can be easily obtained by choosing a cavity in the shape of a *chaotic billiard*. Such a cavity also ensures mixing of the ray angles.

However, we have to point out one fundamental difference of this setup as compared with the experiments cited above. This is no longer a scattering experiment where we measure the outgoing waves after scattering from the medium. In the closed cavity, we measure instead the wave field at some given point inside the medium. Thus, unlike in scattering experiments, the wavefronts here continue to propagate in the medium after being measured and may even be measured again after several reflections at the boundary. This possibility of a multiple measurement is a disadvantage; it will be shown that it ultimately leads to a reduction of the quality of the time-reversed wave field.

In Sec. I, we present the general characteristics of our experimental setup. Section II shows how one-channel time-reversal experiments are carried out, and presents the spatial and temporal focusing properties. It turns out that the focusing quality increases with the length of the reversed signal. Section III describes this growth by a statistical approach of the ray dynamics of the cavity. Section IV gives two examples of cavities, where the assumption of ergodicity is not fulfilled, and the time-reversal process fails to work properly.

[a]Current affiliation: Department of Electrical Engineering, University of Rochester, Rochester, NY 14627. Electronic mail: draeger@ee.rochester.edu

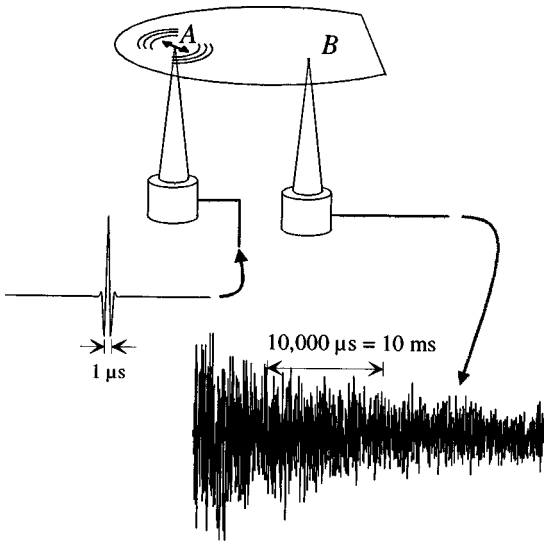

FIG. 1. Elastic waves are injected by means of transversal transducers fixed to Al-cones. A short signal, injected at one of the transducers, *A*, creates a long-lasting, reverberating wave field: The signal obtained at a second point, *B*, is slowly decaying.

I. EXPERIMENTAL SETUP AND SYSTEM PROPERTIES

The propagation media we use are circular wafers of 100- or 125-mm diameter, with a segment of variable size cut off (between 4% and 75% of the diameter). A billiard of the same shape has been shown to have chaotic trajectories.[8] The wafers are 525 μm thick and cut parallel to the plane (100) of the crystal lattice. If we neglect anisotropy, only three modes of propagation exist in the frequency range we used (around 1 MHz): *SH* waves with a nondispersive velocity around 5000 m/s, the Lamb mode S_0 with approximately 8300 m/s, and the highly dispersive A_0 mode with respective phase and group velocity of 2600 ± 100 m/s and 4400 ± 200 m/s. During the typical scale of time (1 ms) of an experiment, the waves are reflected between 40 and 80 times at the boundary. The *SH* and S_0 waves are coupled by reflections at the border of the cavity; the A_0 mode propagates independently. Besides, the A_0 propagation is isotropic in the plane. While, by definition, the *SH* mode has no normal surface displacement, this displacement of the S_0 mode is only very weak, as this mode is quasilongitudinal in the frequency range we use. The A_0 mode, being quasitransversal, is the only mode having sufficient normal surface displacements to be detected by an optical interferometer. This mode also has stronger coupling to the surrounding air, which results in a higher decay rate.

Sound injection and measurement is done by transversal transducers fixed to Al cones whose tips touch the wafer (Fig. 1). This technology has initially been developed by J.-P. Nikolovsky in our school for sound injection in glass plates.[9] It permits a point-like coupling to the system with negligible perturbation of the wave field. The tip of the cone acts as a dipole source and/or measuring point. The A_0 and S_0 waves are mainly emitted in directions around the polarization axis *x*, and the *SH* waves travel in the perpendicular directions (Fig. 2). It turns out that the use of a dipole source is not the best choice as it permits *a priori* only dipole focusing in time-reversal experiments. However, using a trick, we show in Sec. II how it is possible to obtain monopole focusing. Also, in Sec. IV, we point out how the use of a dipole source reveals interesting aspects of the chaotic behavior of the medium.

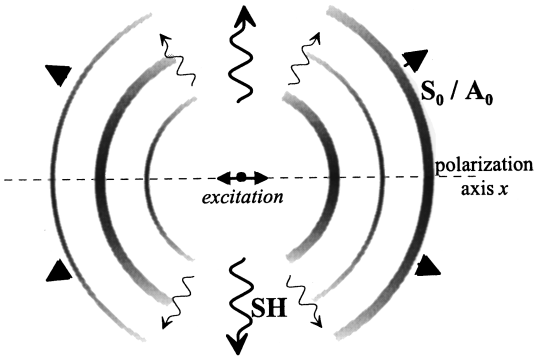

FIG. 2. The modes S_0 and A_0 are mostly emitted in directions around the polarization axis *x* of the dipole source point, the *SH* waves mainly in the perpendicular directions.

Injection of a short pulse in one of the transducers, *A*, creates inside the cavity a reverberating acoustic field with weak attenuation. In fact, the signal observed (after preamplification) by a second transducer, *B*, is slowly decaying (Fig. 1) with a decay period thousands of times longer than the injected signal (1 μs). Figure 3 shows the intensity decay on a logarithmic scale. One observes indeed two different regimes: During the first few milliseconds, the mode A_0 dominates, but decreases relatively quickly with a period of approximately 3 ms, thus revealing the slow decay of the coupled S_0/SH waves (10 to 20 ms, depending on the wafer's size). The length of the signals to be time-reversed (the time-reversal windows) is, with a maximum of 2 ms, always small compared to the latter decay period, and the intensity level inside the window will be considered as constant in the regime S_0/SH. For experiments involving the A_0 mode, we give only qualitative results.

The electronics of the time-reversal mirror provide for the initial emission a short sinusoidal burst of 1 MHz central frequency and a Gaussian envelope of width 0.4 μs, with an

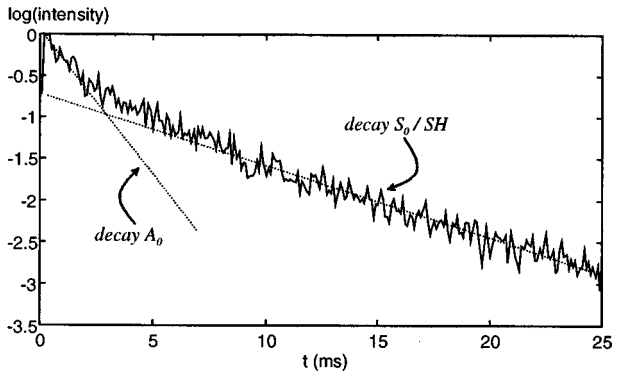

FIG. 3. Decay of the average intensity received at point *B* after injection of a short signal in *A*. For relatively short propagation times, the Lamb mode A_0 dominates. But as this mode is better coupled to the surrounding air, it decreases more quickly than the S_0 and *SH* modes that are permanently converted into each other at the boundary.

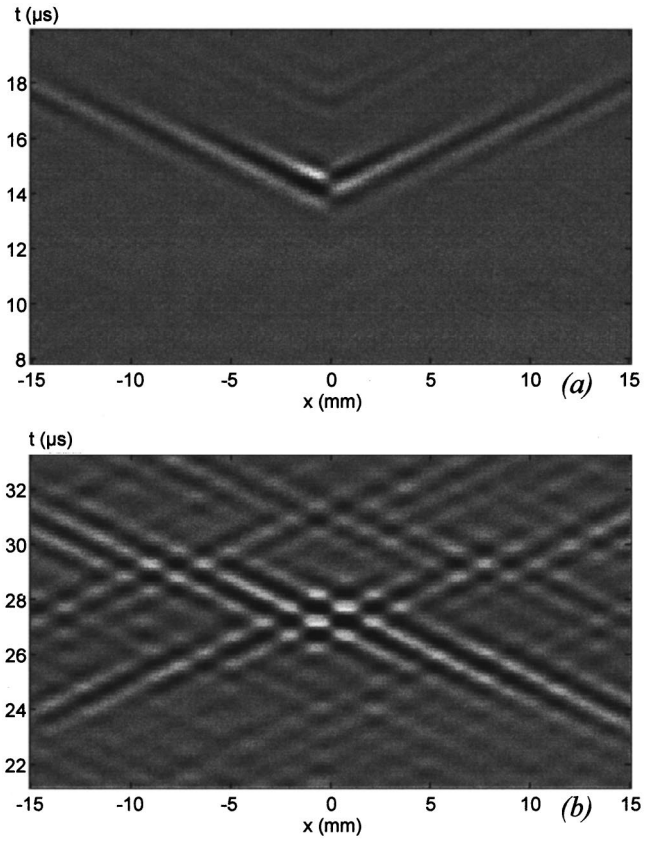

FIG. 4. *B*-scans of the normal surface displacement as measured with an optical interferometer along the polarization axis *x* of the dipole source *A* (at $x=0$), (a) during the initial emission, (b) during refocusing. The *B*-scans have been obtained using a spatial step of 0.1 mm and a sampling frequency of 15 MHz.

amplitude between 10 and 80 V into a 50-Ω impedance. The received signals are digitized using 8 bits with a sampling frequency of either 7.5, 10, or 15 MHz.

II. THE TIME-REVERSAL EXPERIMENT

In the first step of the experiment, the transducer at *A* emits a short pulse at $t=0$. At point *B*, the signal is recorded and, after time-reversal and amplification, a part $\Delta T=[t_1,t_2]$ (the time-reversal window) is reinjected at this same point during the second step. Using a new (simply shifted) variable of the time scale t_R, we start re-emission at $t_R=-t_2$. This leads to a focusing in *A* at $t_R=0$.

A. Spatial recompression

We used a heterodyne Mach–Zehnder type of interferometer that was developed in our laboratory by D. Royer[10] to scan the acoustic field of the A_0 wave around the point *A*. The wafer is, in this case, mounted on a set of two motors able to translate the system in two dimensions, parallel to its surface. The emission is then repeated for every point where the time variation of the field is to be recorded. Figure 4(b) shows a *B*-scan of the normal surface displacement on the polarization axis *x* of *A* after a time-reversal of 1.5 ms in *B*. It has to be compared to the direct emission of the short pulse in *A*, shown in Fig. 4(a). In both figures, one observes

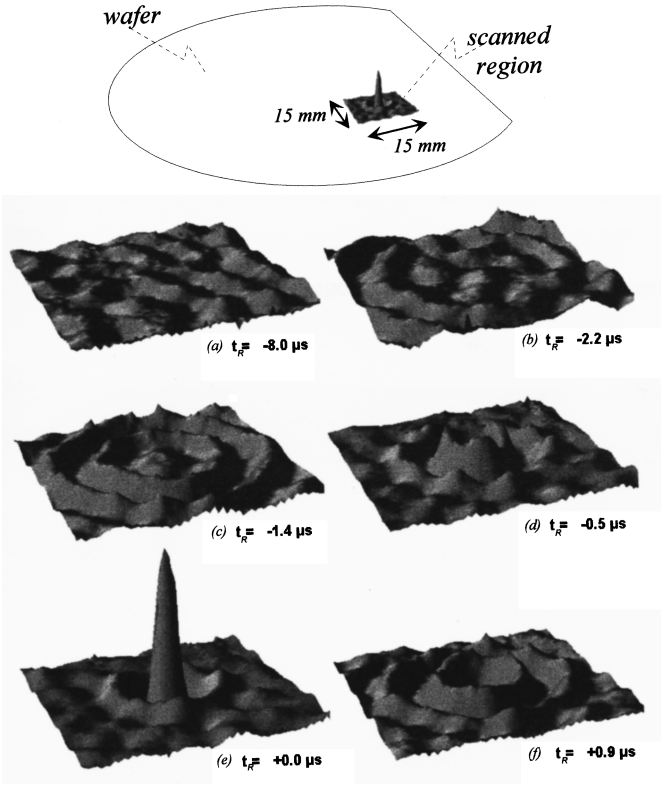

FIG. 5. Linear representation of the monopole refocusing A_0 wave, measured by the interferometer. Note the circular shape of the wavefronts and the background noise level, best seen in (a): One-channel time-reversal produces excellent, but not perfect, results.

the dipole character. However, if the *B*-scan of (b) was the real time-reversal of (a), there should be no outgoing wave after focusing. This is a common property of all time-reversal experiments: The energy in the system is not sucked out at the moment of focusing (which would be the time-reversal of the initial energy injection), so that the wave diverges again afterwards. Also, one can see some noise level elsewhere than the converging and diverging wavefronts. In summary, Fig. 4(a) and (b) show that it is possible to obtain a good, but not perfect, time-reversal with a one-channel time-reversal in *B*. But for a quantitative evaluation, a monopole focusing is preferable.

We have used a trick to obtain a monopole focal spot using transversal transducers. In the first step, the short pulse is now injected by the transducer at *B* instead of *A*. Instead of the second transducer, we use the interferometer to record the signal at point *A*. Being sensitive to normal surface displacements, the interferometer acts as a monopole receiver. The reciprocity principle tells us that the signal obtained is exactly the same as the one that would be recorded with a monopole emitter in *A* and a dipole receiver in *B*. Thus, this signal can be used to simulate a time-reversal experiment with a monopole source at *A* and a dipole reversal point at *B*. In the second step, we reinject a part of the signal at *B*. This leads to a monopole focusing at *A*. A linear representation of the A_0 wave field around the focal spot is given in Fig. 5. It has been measured on a square of 15×15 mm with a step of 0.25 mm for a time-reversal window of size 2 ms. One observes circular incoming wavefronts which focus at $t_R=0$ in

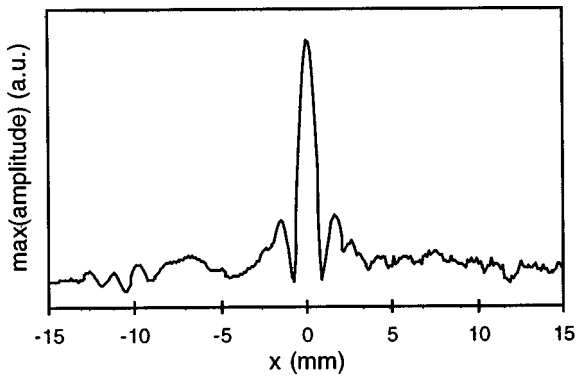

FIG. 6. Cut through the focal spot.

A. This means that in a closed reflecting medium, using a single emission point (the reversal point *B*), it is possible to obtain a focusing quality which corresponds to an angular aperture of 360°. But there is a certain noise level inside the system. This shows that the spatial recompression of the time-reversal process is less than perfect far from the focus. However, the cut through the focal spot, shown in Fig. 6, has a width of 1.1 mm for a central wavelength of 2.6 mm. This indicates that the A_0 wave is almost perfectly focused near the peak.

B. Temporal recompression

Again using transducers for both *A* and *B*, we now observe the refocused signal at *A* after time-reversal at *B*. One obtains a sharp peak at $t_R=0$, standing out from more or less temporal sidelobes (Fig. 7). If we change the position of the time-reversal window, the peak does not change in shape or amplitude, unlike the sidelobes (Figs. 8). As the medium is linear, the signal obtained by a reversal of a long window (which can be cut into several small windows) is the same as the superposition of the contributions of all the small windows. This implies that the amplitude of the peak increases linearly with ΔT (which stands, depending on the context, for the interval $[t_1,t_2]$ of the time-reversal window or, as here, for its length). It means also that higher amplitudes at the focus can be obtained not only by emission of a stronger, but also with a longer, signal. Excluding the possibility of a destructive superposition of the (temporal) sidelobes, their rms value increases linearly with $\sqrt{\Delta T}$ if the contributions of different windows are perfectly uncorrelated, or faster if they are not.

In Fig. 9, we present refocused signals for different window sizes, and, in Fig. 10, the peak/sidelobe intensity ratio. From a certain value of ΔT on (about 1 ms), the shape of the sidelobes does not seem to change any more. The intensity ratio, which increases linearly for small ΔT, saturates for

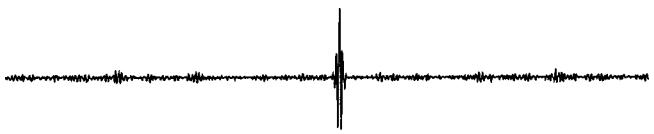

FIG. 7. Refocused signal obtained at *A* after a time-reversal of 1600 μs at *B*. The presented signal is about 210 μs long.

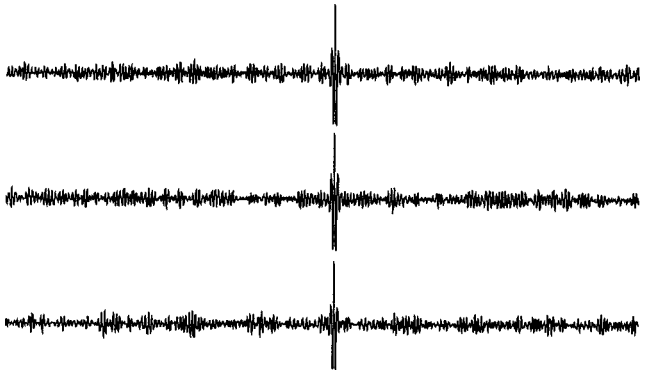

FIG. 8. Refocused signals for different time-reversal windows of same size (120 μs). The sidelobes change, but the peak is not altered.

high values. The refocused signal $s_{\Delta T}(t_R)$ approaches then an asymptotic shape, $S_\infty(t_R)$, and increases linearly with ΔT: $s_{\Delta T}(t_R)=\Delta T\cdot S_\infty(t_R)$, for $\Delta T\to\infty$. In particular, for large time-reversal windows, the refocused signal does not depend on their position, but only on their length. We consider the refocused signal $s_{\Delta T}(t_R)$ as a superposition of two contributions: A first part, $\Delta T\cdot S_\infty(t_R)$, which does not change in shape and which contains the peak as well as certain unavoidable sidelobes, called *residual sidelobes*. The

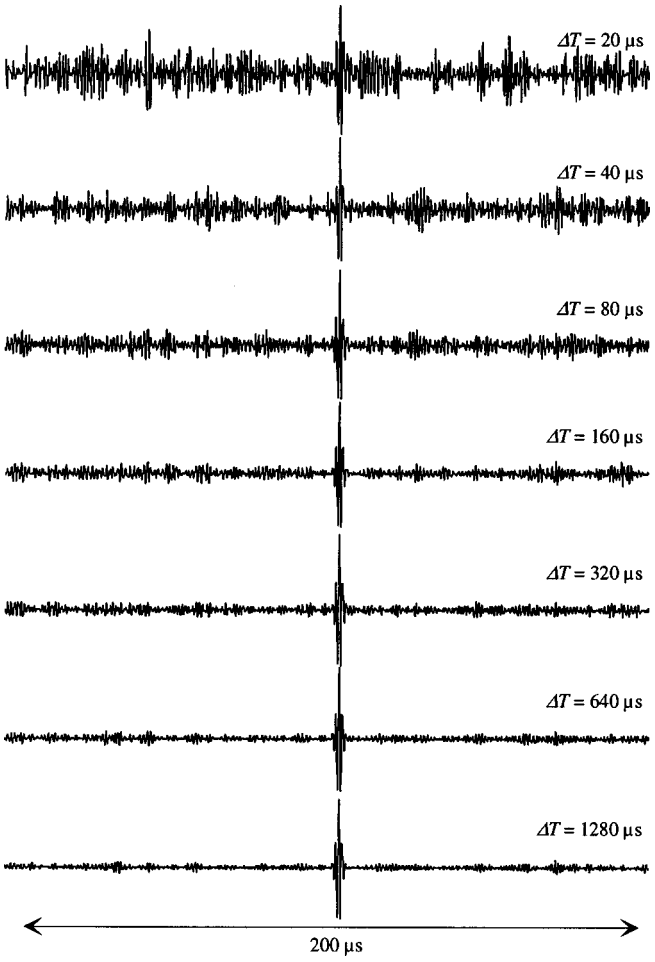

FIG. 9. Refocused signals for different time-reversal window sizes. The quality of the focus increases with the size. (Each amplitude has been normalized by a division by ΔT.)

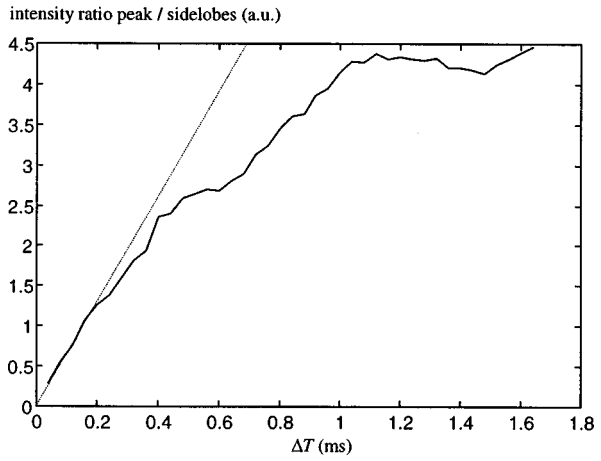

FIG. 10. For small time-reversal window sizes, the peak/sidelobe intensity ratio increases linearly, but enters a saturation regime for longer reversed signals.

second part changes with position and size of the window and can hence be reduced by reversing a longer signal. We designate it *noise*: $s_{\Delta T}(t_R)=\Delta T\cdot S_\infty(t_R)+\text{noise}$. This noise is not a measurement noise that can be reduced by averaging over several acquisitions. On the contrary, this noise is reproducible from one acquisition to the other; its origin is only in the limited size of the time-reversal window.

III. THE RAY MODEL

A. Introduction

In this section, we propose a simple statistical approach to explain the noise appearance. It is inspired by ray trajectories inside the cavity. The description of the wave field by a ray approximation is mostly intuitive and even difficult to justify as the radius of curvature of the cavity is relatively small and the paths are long. However, as we shall see, it fits exactly the experimental observations of the signal-to-noise ratio. The main idea is the following: In the first step of the experiment, imagine that A emits acoustic rays in all directions. (For simplicity, let A and B be monopole sources/receivers and the short pulse be a δ-function.) As the cavity is ergodic, every ray passes after more or less reflections sufficiently near B to be measured. The signal obtained is then a series of pulses, each one corresponding to a particular path between A and B. In the second step, a part of this signal is time-reversed and reinjected at B. Unlike a time-reversal mirror that creates the reversed wavefront in front of its active surface, B does not send back each peak only in the direction where the corresponding ray came from, but in all directions. Rays taking the ''good'' direction trace exactly their path back and arrive at $t_R=0$ at A. At this point, they superpose in a constructive way, giving the refocusing peak. All the rays taking ''bad'' directions may also superpose, thus giving rise to noise. But their superposition may be considered as random, thus increasing more slowly with the length of the time-reversal window than the refocusing peak: The signal-to-noise ratio is higher for longer reversed signals.

B. Calculation of the signal-to-noise ratio

Let $h(t)=h_{AB}(t)=h_{BA}(t)$ be the impulse response from A to B. Imagine that $h(t)$ is a superposition of Dirac pulses with arrival time t_i and amplitude A_i:

$$h(t)=\sum_i A_i\delta(t-t_i).$$

[This assumption is not strictly true as, in 2D, the impulse response is *not* giving δ-peaks, but peaks of type $\mathrm{H}(t-r/c)\cdot(t^2-r^2/c^2)^{-1/2}$, where H is the Heaviside step function, r the distance and c the wave speed. However, for long distances and short pulses, the only effect of the different impulse response is a change in shape of the received signal, which can be formally included in the excitation function $f(t)$ emitted by A that convolves finally the impulse response.]

We define $\rho(t)=\langle\Sigma_i\delta(t-t_i)\rangle$ as the average density of ray arrival times. The brackets $\langle.\rangle$ are defined as an ensemble average over all possible pairs of points (A,B). Of course, the impulse response is different for every pair of points, but because of the ergodic character of the cavity, we expect the same statistical properties. Let $\overline{A}(t)=\langle A(t)\rangle$ denote the average amplitude as a function of time, and $\overline{A^2}(t)=\langle A^2(t)\rangle$ denote the average of its square. As excitation signal $f(t)$, we take a short pulse centered around $t=0$ and with $\int dt\ f(t)=0$, i.e., of average zero. The signal measured at B is then

$$S_{AB}(t)=h(t)*f(t)=\sum_i A_i f(t-t_i)$$

and its expectation value is

$$\langle S_{AB}(t)\rangle=\int dt_i\ \rho(t_i)\overline{A}(t_i)f(t-t_i).$$

We assume that $\rho\overline{A}$ varies slowly enough during the duration of f so that the integral vanishes: $\langle S_{AB}(t)\rangle=0$.

We reinject a part of the signal $\Delta T=[t_1,t_2]$ in B. The part of the reversed impulse response is

$$h^{\Delta T}(-t_R)=\begin{cases}h(-t_R), & t_R\in[-t_2,-t_1]\\ 0, & \text{elsewhere}\end{cases}.$$

Due to reciprocity, the impulse response from B to A is the same as the one from A to B, and we obtain for the signal at A after reversal in B (for $\Delta T\gg$ width of f)

$$S_R(t_R)=f(t_R)*(h^{\Delta T}(-t_R)*h(t))$$

$$=f(t_R)*\int_{\Delta T}d\tau\ h(\tau)h(t_R+\tau).$$

As h is a Dirac function for every arrival time, $h(\tau)h(t_R+\tau)$ is nonzero if and only if τ and $t_R+\tau$ correspond to two arrival times. Let $t_i=\tau$ and $t_j=t_R+\tau=t_R+t_i$, then the signal can be written

$$S_R(t_R)=\sum_{t_i\in\Delta T}\ \sum_{t_j}A_iA_jf(t_R-(t_j-t_i)).$$

Hence, the refocused signal is a superposition of many elementary signals $f(t)$. We are going to split this sum into

three parts. The first one, responsible for the refocusing peak at $t_R=0$, is given by $t_i=t_j$, i.e., the diagonal elements of the double sum:

$$S_{\text{peak}}(t_R)=f(t_R)\sum_{t_i\in\Delta T}A_i^2.$$

The second part can be evaluated by assuming a random superposition of the elementary signals, given by all pairs (t_i,t_j) whose difference behaves as a random variable. We call them *uncorrelated pairs* (t_i,t_j) and the corresponding part of the signal *incoherent noise*.

$$S_{\text{noise}}(t_R)=\sum_{\substack{t_i\in\Delta T\\ t_i\neq t_j\text{uncorr.}}}A_iA_jf(t_R-(t_j-t_i)).$$

This sum contains almost all pairs of arrival times. But there are also pairs $t_i\neq t_j$ that are correlated. This fact can be ascribed to rays that, with origin at *A*, pass over this same point before arriving at *B* and to rays passing over *B* several times during propagation. These pairs give rise to the residual sidelobes, the third part of the sum:

$$S_{\substack{\text{residual}\\ \text{sidelobes}}}(t_R)=\sum_{\substack{t_i\in\Delta T\\ t_i\neq t_j\text{corr.}}}A_iA_jf(t_R-(t_j-t_i)).$$

The latter sum cannot be evaluated *as is*; the residual sidelobes are not described in a satisfactory way by our ray model. However, a model using a decomposition of the wave field in eigenmodes of the cavity gives a complete description of this phenomenon. It is published in a second paper.[11]

Now we want to evaluate the signal-to-noise ratio, i.e., the peak-to-noise ratio.

The expectation value of the peak is

$$\langle S_{\text{peak}}(t_R)\rangle=f(t_R)\int_{\Delta T}dt_i\ \rho(t_i)\overline{A^2}(t_i).$$

The expression $\rho\overline{A^2}=I_0$ represents the average intensity measured in *B* during the first step. Assuming an ergodic lossless cavity, its value must be constant in time, thus

$$\langle S_{\text{peak}}(t_R)\rangle=f(t_R)I_0\Delta T.$$

The amplitude of the peak is proportional to the excitation function and the window size ΔT. It does not depend on the density of arrival times or the corresponding amplitudes. The incoherent noise is, of course, of average zero. Its variance is given by

$$\begin{aligned}\langle S_{\text{noise}}^2(t_R)\rangle&=\left\langle\sum_{\substack{t_i\in\Delta T\\ t_i\neq t_j\text{uncorr.}}}A_iA_jf(t_R-(t_j-t_i))\sum_{\substack{t_i'\in\Delta T\\ t_i'\neq t_j'\text{uncorr.}}}A_{i'}A_{j'}f(t_R-(t_j'-t_i'))\right\rangle\\&=\left\langle\sum_{\substack{t_i\in\Delta T\\ t_i\neq t_j\text{uncorr.}}}A_i^2A_j^2f^2(t_R-(t_j-t_i))\right\rangle+\left\langle\sum_{\substack{t_i\in\Delta T\\ t_i\neq t_j\text{uncorr.}}}A_iA_jf(t_R-(t_j-t_i))\sum_{\substack{t_i'\in\Delta T\\ t_i'\neq t_i,t_j'\neq t_j\\ t_i'\neq t_j'\text{uncorr.}}}A_{i'}A_{j'}f(t_R-(t_j'-t_i'))\right\rangle.\end{aligned}$$

In these sums, several terms are excluded corresponding to correlated or same-arrival times. As these terms are small in number compared to the other ones, we commit only a small error by reintroducing them, but supposing them uncorrelated. The average of the double-sum terms can then be changed to a product of two averages, in which each factor is equal to the noise average $\langle S_{\text{noise}}(t_R)\rangle$ that is zero. The only contribution is given by the diagonal terms. Thus,

$$\langle S_{\text{noise}}^2(t_R)\rangle=\int_{\Delta T}dt_i\int dt_j\ \rho(t_i)\overline{A^2}(t_i)\rho(t_j)\overline{A^2}(t_j)\times f^2(t_R-(t_j-t_i)).$$

We replace $\rho\overline{A^2}$ by I_0. The integral over t_j simplifies to $E_f=\int dt\ f^2(t)$, the ''energy'' of the excitation function. One obtains finally

$$\langle S_{\text{noise}}^2\rangle=E_fI_0^2\Delta T,$$

independent from t_R.

The peak-to-noise ratio is found to be

$$R_{\text{p/n}}=\max\langle S_{\text{peak}}(t_R)\rangle/\sqrt{\langle S_{\text{noise}}^2\rangle}=(\max(f(t))/\sqrt{E_f})\sqrt{\Delta T},$$

which is proportional to the square root of ΔT. Thus, a short signal of high amplitude is better suited for high signal-to-noise ratios than a longer signal with a lower peak value, but containing the same energy.

C. Comparison with experiments

The signal-to-noise ratio calculated above is not convenient for the description of experimental data. First, we prefer a value which does not depend on the shape of the signal. We consider, therefore, the energy of the peak instead of its maximum:

$$E_{\text{peak}}^{\text{exp}}=\int dt_R\ S_{\text{peak}}^2(t_R);$$

$$E_{\text{peak}}^{\text{theory}}=\int dt_R\langle S_{\text{peak}}^2(t_R)\rangle=E_fI_0^2\Delta T^2.$$

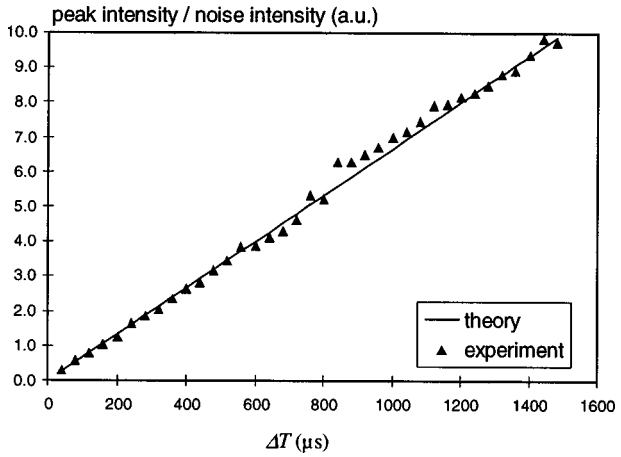

FIG. 11. Evolution of the peak/noise intensity ratio (after subtraction of the residual sidelobes) for increasing time-reversal windows.

Second, as we cannot directly measure the variance of the noise, we estimate its value by taking the average over a window Δt_R in the refocused signal. (Given the ergodic character of the system, this should be a good estimator.) The energy of the noise inside this interval is given by

$$E_{\text{noise}}^{\text{exp}} = \int_{\Delta t_R} dt_R \; S_{\text{noise}}^2(t_R);$$

$$E_{\text{noise}}^{\text{theory}} = \int_{\Delta t_R} dt_R \langle S_{\text{noise}}^2 \rangle = E_f I_0^2 \Delta T \Delta t_R .$$

The theoretical ratio is linear in ΔT:

$$E_{\text{peak}}^{\text{theory}} / E_{\text{noise}}^{\text{theory}} = \Delta T / \Delta t_R .$$

Third, we do not have direct access to the incoherent noise as it is superposed to the residual sidelobes. However, the difference of two refocused signals, $S_{\Delta T_1} - S_{\Delta T_2}$, for two nonoverlapping time-reversal windows ΔT_1 and ΔT_2 of the same size, erases the peak and the residual sidelobes. The noise behaves like a refocused signal obtained by a window of size $\Delta T = \Delta T_1 + \Delta T_2$. These facts have been taken into account to obtain the experimental data in Fig. 11. The agreement is excellent. Note that the straight line is the theoretical ratio, drawn without fit to the experimental data. This justifies thus, *a posteriori*, the model.

IV. TIME-REVERSAL IN REGULAR CAVITIES

In order to show the importance of the ergodic and mixing character of the cavity, we present here two examples of cavities, where this assumption is not, or not completely, fulfilled.

A. Rectangular cavities

Rectangles are a favorite example of regular billiards. The angle of the trajectory is a constant of motion and so the path of a ray can be predicted in the long term. By symmetry considerations, it is easy to see that a one-channel time-reversal in a rectangular cavity produces several focal spots other than the source point *A*, with different amplitudes. (In fact, there are up to nine.) In the experimental setup shown in Fig. 12, some of these image points superpose at A'. Figure 13 presents a *C*-scan, taken at the focusing instant, showing the monopole at *A* and its image at A', symmetrical to the reversal point *B*. The fact that *B* is a dipole source gives another interesting aspect to this experiment: *B* is only able to emit or receive in directions around its polarization axis. As the angle of each ray is conserved, the monopole focal spots at *A* and A' no longer have circular symmetry, but are biased by the directivity pattern of the reversal point.

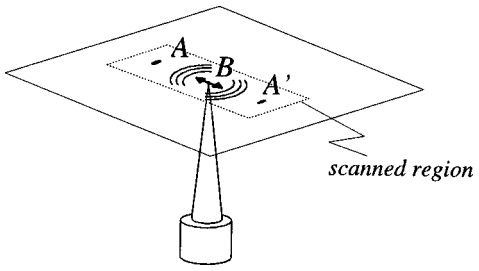

FIG. 12. One-channel time-reversal in rectangular cavities produces several focal spots. In this particular configuration (*A* located on the polarization axis of *B*, which is parallel to one side of the rectangle), some of them are superposed in A'.

B. Temporal dependence of mixing

Chaotic cavities whose shape is only slightly different from the regular case do not reveal their ergodic properties over short time-scales. For the *C*-scans presented in Fig. 14, we have used an almost circular wafer, with a segment of only 4% of the diameter cut off. In circular billiards, the constant of motion is the angular momentum. If *A* and *B* are at the same distance from the center, this would lead, just as in the case of rectangular billiards, to monopole focal spots with the directivity pattern of the dipole reversal point. In the case of our almost regular cavity, the time-reversal of the first 2 ms ($\Delta T = [0;2\text{ ms}]$) shows exactly this behavior [Fig. 14(a)]. If one reverses instead the following two milliseconds ($\Delta T = [2\text{ ms};4\text{ ms}]$), the focal spot is of circular symmetry [Fig. 14(b)]. Obviously, the angular momentum of a ray is conserved over medium periods of time. To be mixed, the ray has to be reflected at least once at the small part of the boundary where the segment is cut off. And only a mixing of the angular momenta allows rays to approach the focal spot from other sides than the directivity pattern of the reversal point.

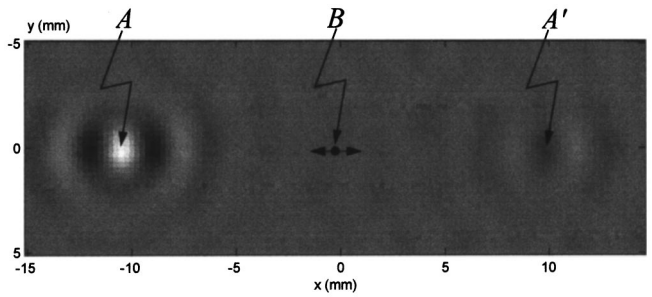

FIG. 13. *C*-scan of two (monopole) focal spots in a rectangular cavity as measured by an optical interferometer. The converging wavefronts are no more circular, but biased by the directivity pattern at the reversal point *B*.

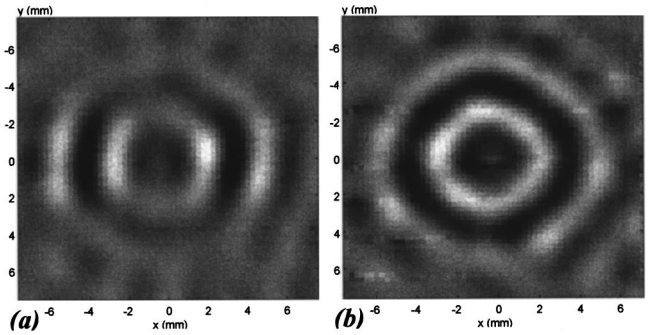

FIG. 14. *C*-scans of the refocused waves in a weakly chaotic billiard. (a) Time-reversal of a window directly after emission ($\Delta T=[0,2000\ \mu s]$) still shows the directivity pattern of the reversal point. (b) Ray angles mix after longer trajectories ($\Delta T=[2000\ \mu s,4000\ \mu s]$) and arrive from all directions at the focal spot.

V. CONCLUSION

Acoustic time-reversal experiments usually need large arrays of transducers. In this paper, we present experiments proving the possibility of reducing the number of elements down to one by using multiple reflections inside the propagation medium. The experiments are carried out with a 2-D silicon wafer, wherein the injection of a short ultrasonic pulse at one point reverberates over a very long time. The signal is recorded at a second point, time-reversed and reemitted. We obtain an excellent focusing at the initial source location.

The focusing peak has been observed using two methods: First, we scanned the field of one propagation mode (A_0) around the focal spot using an optical interferometer. One is able to obtain circular converging wavefronts that collapse at the initial source point and diverge afterwards. However, a certain noise level cannot be avoided. Second, we observe the refocused signal using the transducer located at the initial source. We obtain a short peak standing out from more-or-less temporal sidelobes. The refocused signal depends crucially on the size of the time-reversal window, i.e., the length of the reversed signal. The amplitude of the peak increases linearly with the reversed time; the peak to sidelobes level improves. For long time-reversal windows, a saturation regime is entered where the sidelobes can no more be reduced. The increase of the focusing quality with the reversed time can be successfully described by a simple statistical model, inspired by ray trajectories inside the cavity. However, the residual sidelobes are not taken into account by this model. A more rigorous analysis, based on an eigenmode decomposition of the wave field, explains this phenomenon and is presented in a second paper dealing with the theoretical limits of the time-reversal process.[11]

The use of a chaotic cavity is of crucial interest. First, its ergodic ray dynamics ensures that every ray emitted by the source point can be recorded by the reversal point. Second, we give examples of regular cavities wherein the one-channel time-reversal does not work properly. Third, a theoretical analysis, given in another paper, also takes advantage by assuming some properties of chaotic wave billiards such as, for example, spectral rigidity. While classical chaos inhibits time-reversal experiments due to strong sensitivity to initial conditions, the wave chaos of this case is actually useful.

One-channel time-reversal experiments can be easily reproduced. Unlike usual time-reversal experiments which need, in general, up to 100 transducers and the corresponding independent transmit/receive electronics, one-channel experiments have an extremely simple and low-cost experimental setup. Only two transducers are needed, and one transmit and one receive channel. We used a 2-D cavity in our experiments, but a 3-D cavity should work as well.

Our lab is currently working towards a better characterization of the time-reversal experiments in the transition from regular to chaotic cavities. We also want to try waveguides with a cross section in the shape of a chaotic billiard to obtain time-reversed focusing using a time-reversal mirror with fewer transducer elements.

ACKNOWLEDGMENTS

The authors would like to thank J. P. Nikolovsky for the production of the Al-cones, D. Royer and J. L. Thomas for experimental help, and A. Derode for useful discussions.

[1] M. Fink, ''Time-Reversal Acoustics,'' Phys. Today **50**(3), 34–40 (1997).
[2] M. Fink, ''Time-reversal of ultrasonic fields-Part I: Basic Principles,'' IEEE Trans. Ultrason. Ferroelectr. Freq. Control **39**, 555–566 (1992).
[3] F. Wu, J. L. Thomas, and M. Fink, ''Time-reversal of ultrasonic fields-Part II: Experimental Results,'' IEEE Trans. Ultrason. Ferroelectr. Freq. Control **39**, 567–578 (1992).
[4] D. Cassereau and M. Fink, ''Time-reversal of ultrasonic fields-Part III: Theory of the closed time-reversal cavity,'' IEEE Trans. Ultrason. Ferroelectr. Freq. Control **39**, 579–592 (1992).
[5] D. Cassereau and M. Fink, ''Focusing with plane time-reversal mirrors: An efficient alternative to closed cavities,'' J. Acoust. Soc. Am. **94**, 2373–2386 (1993).
[6] P. Roux, B. Roman, and M. Fink, ''Time-reversal in an ultrasonic waveguide,'' Appl. Phys. Lett. **70**(14), 1811–1813 (1997).
[7] A. Derode, P. Roux, and M. Fink, ''Robust Acoustic Time Reversal with High-Order Multiple Scattering,'' Phys. Rev. Lett. **75**(23), 4206–4209 (1995).
[8] L. A. Bunimovitch, ''On the ergodic properties of nowhere dispersing billards,'' Commun. Math. Phys. **65**, 295–312 (1979).
[9] J. P. Nikolovsky and D. Royer, ''Local and selective detection of acoustic waves at the surface of a material,'' IEEE Ultrason. Symp. Proc. (1997).
[10] D. Royer and E. Dieulesaint, ''Optical detection of sub-angström mechanical displacements,'' IEEE Ultrason. Symp. Proc. , 527–530 (1986).
[11] C. Draeger and M. Fink, ''One-channel time-reversal in chaotic cavities: Theoretical limits,'' J. Acoust. Soc. Am. **105**, 611–617 (1999).

On energy definition in electromagnetism: An analogy with viscoelasticity

J. M. Carcione[a)]
Osservatorio Geofisico Sperimentale, P.O. Box 2011 Opicina, 34016 Trieste, Italy

(Received 15 March 1998; accepted for publication 7 October 1998)

Electromagnetic media as, for instance, imperfect dielectrics, semiconductors, and materials with magnetic losses, have time- (and frequency-) dependent permittivity, magnetic permeability, and electric conductivity, and, therefore, energy dissipation and pulse distortion occurs. The electromagnetic Umov–Poynting's theorem is reinterpreted in light of the theory of viscoelasticity in order to define the stored and dissipated energy densities in the time domain. A simple dielectric relaxation model equivalent to a viscoelastic mechanical model illustrates the analogy that identifies electric field with stress, electric induction with strain, dielectric permittivity with reciprocal bulk modulus, and resistance with viscosity. © *1999 Acoustical Society of America.*
[S0001-4966(99)04801-8]

PACS numbers: 43.20.Bi, 43.20.Wd [DEC]

INTRODUCTION

Energy-balance equations are important for characterizing the energy stored and the transport properties in a field. However, the definition of stored (free) energy and energy dissipation rate is controversial, both in electromagnetism[1] and viscoelasticity.[2] The problem is particularly intriguing in the time domain, since different definitions may give the same time-average value for harmonic fields. This ambiguity is not present when the constitutive relation can be described in terms of springs and dashpots (e.g., Refs. 3 and 4). That is, when the system can be defined in terms of internal variables and the relaxation function has an exponential form.[5] Christensen[6] and Golden and Graham[7] give a general expression of the viscoelastic energy densities which is consistent with the mechanical model description.

Formal analogies, in the mathematical sense, exist between electromagnetism and other fields like mechanics[8] and viscoelasticity. In this case, Carcione and Cavallini,[9] for instance, show an analogy for vector wavefields and material properties that allows the acoustic and electromagnetic problems to be solved with the same analytical methodology. In this work, the stored electric and magnetic energies are defined in terms of the viscoelastic expression by using the analogy. The theory is applied to a simple dielectric relaxation process that is mathematically equivalent to the Zener model or standard linear solid viscoelastic rheology.[10]

It is important to point out that the theory cannot be applied to the whole range of electromagnetic (e.m.) problems, since a mathematical analogy may not necessarily imply a physical analogy. In viscoelasticity, the real part of the complex moduli (describing pure deformation modes) is positive, and the presence of intrinsic dissipation implies velocity dispersion and vice versa (Kramers–Krönig relations[11,12]). These properties preclude the use of the theory for an ionized gas whose complex permittivity may, in some cases, be negative (e.g., Ref. 13), or for a lossless dispersive dielectric that does not satisfy the Kramers–Krönig relations.

The definition of energy is important in a large number of applications where it is necessary to know how the energy transferred by the e.m. field is related to the strength of the field. This context involves the whole electrical, radio, and optical engineering, where the medium can be assumed dielectrically and magnetically linear. In particular, the Debye model has been applied to bioelectromagnetics[14,15] in the analysis of the response of biological tissues, and to geophysics, in the simulation of ground-penetrating radar wave propagation through wet soils.[16,17,18]

I. MAXWELL'S EQUATIONS AND CONSTITUTIVE RELATIONS

Maxwell's equations for isotropic dispersive media, in the absence of external electric and magnetic currents, are

$$\nabla\times\mathscr{E}=-\frac{\partial\mathscr{B}}{\partial t}, \tag{1}$$

$$\nabla\times\mathscr{H}=\frac{\partial\mathscr{D}}{\partial t}+\mathscr{J}, \tag{2}$$

where $\mathscr{E}$ is the electric field, $\mathscr{H}$ is the magnetic field, $\mathscr{D}$ is the electric induction, $\mathscr{B}$ is the magnetic induction, and $\mathscr{J}$ is the conduction current. The symbol $\times$ denotes the vector product.

For time-harmonic fields with time dependence $\exp(i\omega t)$, where ω is the angular frequency, Eqs. (1) and (2) read

$$\nabla\times\mathbf{E}=-i\omega\mathbf{B}, \tag{3}$$

$$\nabla\times\mathbf{H}=i\omega\mathbf{D}+\mathbf{J}, \tag{4}$$

respectively, where **E**, **D**, **H**, and **B** are the corresponding time-harmonic fields.

We consider constitutive relations $\mathscr{D}(\mathscr{E})$ and $\mathscr{B}(\mathscr{H})$ of the form

$$\mathscr{D}=\epsilon*\frac{\partial\mathscr{E}}{\partial t} \tag{5}$$

a)Electronic mail: carcione@gems755.ogs.trieste.it

and

$$\mathscr{B}=\mu * \frac{\partial \mathscr{H}}{\partial t} \tag{6}$$

(i.e., nonmoving media), where ϵ and μ are the dielectric permittivity and magnetic permeability functions, and * denotes time convolution. Similarly, generalized Ohm's law can be written as

$$\mathscr{J}=\sigma * \frac{\partial \mathscr{E}}{\partial t}, \tag{7}$$

where σ is the conductivity function.

For harmonic fields, the constitutive relations read

$$\mathbf{D}=\mathscr{F}\left(\frac{\partial \epsilon}{\partial t}\right)\mathbf{E}, \quad \mathbf{B}=\mathscr{F}\left(\frac{\partial \mu}{\partial t}\right)\mathbf{H}, \tag{8}$$

and

$$\mathbf{J}=\mathscr{F}\left(\frac{\partial \sigma}{\partial t}\right)\mathbf{E}, \tag{9}$$

where $\mathscr{F}(\cdot)$ is the Fourier transform operator. For convenience, the medium properties are denoted by the same symbols, in both the time and the frequency domains, i.e.,

$$\mathscr{F}\left(\frac{\partial \epsilon}{\partial t}\right) \rightarrow \epsilon, \ldots, \text{etc}\ldots$$

II. UMOV–POYNTING'S THEOREM FOR HARMONIC FIELDS

The scalar product of the complex conjugate of Eq. (4) with $\mathbf{E}$, use of $\nabla\cdot(\mathbf{E}\times\mathbf{H}^*)=(\nabla\times\mathbf{E})\cdot\mathbf{H}^*-\mathbf{E}\cdot(\nabla\times\mathbf{H}^*)$, and substitution of Eq. (3) gives Umov–Poynting's theorem for harmonic fields,

$$-\nabla\cdot\mathbf{P}=\tfrac{1}{2}\,\mathbf{J}^*\cdot\mathbf{E}-2i\omega(u_e-u_m), \tag{10}$$

where

$$\mathbf{P}=\tfrac{1}{2}\mathbf{E}\times\mathbf{H}^* \tag{11}$$

is the complex Umov–Poynting vector, and

$$u_e=\tfrac{1}{4}\mathbf{E}\cdot\mathbf{D}^*, \quad u_m=\tfrac{1}{4}\mathbf{B}\cdot\mathbf{H}^*, \tag{12}$$

are the harmonic (complex) (di)electric and magnetic energy densities. The symbol * denotes complex conjugate.

Substitution of the constitutive relations (8) and (9) into Eq. (10) yields

$$2i\nabla\cdot\mathbf{P}=-\omega(\epsilon_T^*|\mathbf{E}|^2-\mu|\mathbf{H}|^2), \tag{13}$$

where

$$\epsilon_T=\epsilon-\frac{i}{\omega}\,\sigma. \tag{14}$$

Taking real and imaginary parts of (13) gives

$$\begin{aligned} 2\,\mathrm{Im}(\nabla\cdot\mathbf{P}) &= \omega[\mathrm{Re}(\epsilon_T)|\mathbf{E}|^2-\mathrm{Re}(\mu)|\mathbf{H}|^2] \\ &= \text{power energy density}, \end{aligned} \tag{15}$$

$$\begin{aligned} 2\,\mathrm{Re}(\nabla\cdot\mathbf{P}) &= \omega[\mathrm{Im}(\epsilon_T)|\mathbf{E}|^2+\mathrm{Im}(\mu)|\mathbf{H}|^2] \\ &= \text{rate of dissipated energy}, \end{aligned} \tag{16}$$

respectively. The time-average energy densities are such that

$$\begin{aligned} &\tfrac{1}{4}\,\mathrm{Re}(\epsilon)|\mathbf{E}|^2=\mathrm{Re}(u_e) \quad \text{stored (di)electric} \\ &-\tfrac{1}{2}\,\omega^{-1}\,\mathrm{Im}(\sigma)|\mathbf{E}|^2=\mathrm{Im}(u_\sigma) \quad \text{stored electric} \\ &\tfrac{1}{4}\,\mathrm{Re}(\mu)|\mathbf{H}|^2=\mathrm{Re}(u_m) \quad \text{stored magnetic} \\ &\tfrac{1}{4}\,\mathrm{Im}(\epsilon)|\mathbf{E}|^2=\mathrm{Im}(u_e) \quad \text{dissipated (di)electric} \\ &\tfrac{1}{2}\,\omega^{-1}\,\mathrm{Re}(\sigma)|\mathbf{E}|^2=\mathrm{Re}(u_\sigma) \quad \text{dissipated electric} \\ &\tfrac{1}{4}\,\mathrm{Im}(\mu)|\mathbf{H}|^2=\mathrm{Im}(u_m) \quad \text{dissipated magnetic}, \end{aligned} \tag{17}$$

where

$$u_\sigma=\tfrac{1}{2}\omega^{-1}\mathbf{J}^*\cdot\mathbf{E}=\tfrac{1}{2}\omega^{-1}\sigma^*|\mathbf{E}|^2 \tag{18}$$

is the (complex) electric energy density.

III. ENERGY DEFINITION IN ELECTROMAGNETISM

Time-average energies for harmonic fields are precisely defined. Let us consider, for instance, the formulation of the energy balance equation given in Oughstun and Sherman.[1] Upon taking the scalar product of Eq. (1) with $\mathscr{H}$ and Eq. (2) with $\mathscr{E}$ and taking the difference, Oughstun and Sherman (Ref. 1, Eq. 2.2.5) obtain

$$-\nabla\cdot\mathscr{P}=\mathscr{J}\cdot\mathscr{E}+\frac{\partial U}{\partial t}, \tag{19}$$

where $\mathscr{P}=\mathscr{E}\times\mathscr{H}$ is the Umov–Poynting vector and U is the total energy per unit volume given by

$$U=U_e+U_m, \tag{20}$$

with

$$\frac{\partial U_e}{\partial t}=\mathscr{E}\cdot\frac{\partial \mathscr{D}}{\partial t}, \tag{21}$$

the time rate of (di) electric energy density, and

$$\frac{\partial U_m}{\partial t}=\mathscr{H}\cdot\frac{\partial \mathscr{B}}{\partial t}, \tag{22}$$

the time rate of magnetic energy density.

The time average of the scalar product of two harmonic vector fields, with the same oscillation frequency, is given by

$$\langle \mathscr{A}\cdot\mathscr{B}\rangle=\tfrac{1}{2}\,\mathrm{Re}(\mathbf{A}\cdot\mathbf{B}^*). \tag{23}$$

Note that taking the time average of Eqs. (19) yields

$$-\langle\nabla\cdot\mathscr{P}\rangle=\tfrac{1}{2}\,\mathrm{Re}(\mathbf{J}^*\cdot\mathbf{E})+2\omega[\mathrm{Im}(u_e)-\mathrm{Im}(u_m)], \tag{24}$$

which can be obtained from Eq. (10) by taking its real part. Equation (24) gives the balance of the rate of dissipated energy density and is equivalent to Eq. (16).

We now review some of the statements discussed by Oughstun and Sherman.[1]

(1) Poynting's theorem *provides a mathematically consistent formulation of energy flow* (p. 24). This does not preclude the existence of an alternative formulation. For instance, Jeffreys[19] gives an alternative energy balance,

implying a new interpretation of the Poynting vector (see also the interesting discussion in Robinson[20] and Jeffreys[21]).

(2) *... it cannot be definitely concluded that the time rate of energy flow at a point is uniquely given by the value of the Poynting vector at that point, for one may add to the Poynting vector any solenoidal vector field without affecting the statement of conservation of energy...* (p. 26). In fact, as the authors state, there is no strictly valid justification for the accepted interpretation of the Poynting vector.

(3) *... one cannot, in general, express the electric energy density and the dissipation separately in terms of the dielectric permittivity and electrical conductivity of a dispersive medium* (p. 31). In the general case [i.e., the time-domain equation (19)], it is not possible to separate the stored energies from the dissipated energies. Relating u_e and U_e gives [see Eq. (2.2.38)],

$$\mathrm{Im}(u_e)=\frac{1}{2\omega}\left\langle\frac{\partial U_e}{\partial t}\right\rangle, \tag{25}$$

and no relationship of this type for the real part of u_e. The same reasoning applies to the magnetic energy. We present in the next section an alternative definition where energy can be, in principle, separated between stored and dissipated.

(4) For time-harmonic fields, the separation is shown in Eq. (17). However, there is no relation between the time-average energies defined in Eq. (17) and the time averages of U_e, U_m (p. 36). In the next section, a link between harmonic energy densities and transient energy densities is obtained.

Note that Oughstun and Sherman [Ref. 1, Eq. (2.1.19)] use an $\exp(-i\omega t)$ time dependence.

IV. UMOV–POYNTING'S THEOREM FOR TRANSIENT FIELDS

Poynting's theorem (19), omitting Oughstun and Sherman's interpretation of the energies, is

$$-\boldsymbol{\nabla}\cdot\mathscr{P}=\mathscr{J}\cdot\mathscr{E}+\mathscr{E}\cdot\frac{\partial\mathscr{D}}{\partial t}+\mathscr{H}\cdot\frac{\partial\mathscr{B}}{\partial t}. \tag{26}$$

Let us consider a stored (di)electric (free) energy density of the form

$$W_e(t)=\frac{1}{2}\int_{-\infty}^{t}\int_{-\infty}^{t}K(t-\tau_1,t-\tau_2)\times\mathscr{D}'(\tau_1)\cdot\mathscr{D}'(\tau_2)d\tau_1\,d\tau_2, \tag{27}$$

where the prime denotes the first-order derivative with respect to the argument. Hunter (Ref. 3, p. 545) and Golden and Graham (Ref. 7, p. 12) define a similar form for the linear viscoelastic case. The underlying assumptions are that the dielectric properties of the medium do not vary with time (nonaging material), and, as in the lossless case, the energy density is quadratic in the electric field. Moreover, the expression includes a dependence on the history of the electric field. However, it is important to note that the above assumption as to the structure of the formula for the free energy density is by no means the only possible one (see Rabotnov,[22] p. 72). Moreover, as we shall see below, the general expression of the free energy is not uniquely determined by the relaxation function.

Differentiating W_e yields

$$\frac{\partial W_e}{\partial t}=\frac{\partial\mathscr{D}}{\partial t}\cdot\int_{-\infty}^{t}K(t-\tau_2,0)\mathscr{D}'(\tau_2)d\tau_2+\frac{1}{2}\int_{-\infty}^{t}\int_{-\infty}^{t}\frac{\partial}{\partial t}K(t-\tau_1,t-\tau_2)\mathscr{D}'(\tau_1)\cdot\mathscr{D}'(g t_2)d\tau_1\,d\tau_2. \tag{28}$$

The constitutive relation (5) can be rewritten as

$$\mathscr{E}=\beta*\frac{\partial\mathscr{D}}{\partial t}, \tag{29}$$

where $\beta(t)$ is the dielectric impermeability function, satisfying

$$\frac{\partial\epsilon}{\partial t}*\frac{\partial\beta}{\partial t}=\delta(t),\quad \epsilon_\infty\beta_\infty=\epsilon_0\beta_0=1,\quad \epsilon(\omega)\beta(\omega)=1, \tag{30}$$

with the subindices ∞ and 0 corresponding to the limits $t\to 0$ and $t\to\infty$, respectively. If

$$\beta(t)=K(t,0)H(t), \tag{31}$$

where $H(t)$ is the Heaviside function, then,

$$\int_{-\infty}^{t}K(t-\tau_2,0)\mathscr{D}'(\tau_2)d\tau_2=\mathscr{E}(t), \tag{32}$$

and (28) becomes

$$\mathscr{E}\cdot\frac{\partial\mathscr{D}}{\partial t}=\frac{\partial W_e}{\partial t}+D_e, \tag{33}$$

where

$$D_e(t)=-\frac{1}{2}\int_{-\infty}^{t}\int_{-\infty}^{t}\frac{\partial}{\partial t}K(t-\tau_1,t-\tau_2)\times\mathscr{D}'(\tau_1)\cdot\mathscr{D}'(\tau_2)d\tau_1\,d\tau_2 \tag{34}$$

is the rate of dissipation of (di) electric energy density. Note that the relation (31) does not determine the stored energy, i.e., this can not be obtained from the constitutive relation. However, if we assume that

$$K(t,\tau_1)=G(t+\tau_1), \tag{35}$$

such that

$$\beta(t)=G(t)H(t), \tag{36}$$

this choice will suffice to determine K, and

$$W_e(t)=\frac{1}{2}\int_{-\infty}^{t}\int_{-\infty}^{t}G(2t-\tau_1-\tau_2)\mathscr{D}'(\tau_1)\cdot\mathscr{D}'(\tau_2)d\tau_1\,d\tau_2, \tag{37}$$

$$D_e(t) = -\int_{-\infty}^{t}\int_{-\infty}^{t} G'(2t-\tau_1-\tau_2)\mathscr{D}'(\tau_1) \cdot \mathscr{D}'(\tau_2)\,d\tau_1\,d\tau_2. \tag{38}$$

Equation (35) is consistent with the corresponding theory implied by mechanical models.[6] Breuer and Onat[23] discuss some realistic requirements from which $K(t,\tau_1)$ must have the reduced from $G(t+\tau_1)$.

Let us calculate the time average of the stored energy density for monochromatic fields. Although $\mathscr{D}(-\infty)$ does not vanish, the transient contained in (37) vanishes for sufficiently large times, and this equation can be used to compute the average of time-harmonic fields. The change of variables $\tau_1 \to t-\tau_1$ and $\tau_2 \to t-\tau_2$ yields

$$W_e(t) = \frac{1}{2}\int_0^{\infty}\int_0^{\infty} G(\tau_1+\tau_2)\mathscr{D}'(t-\tau_1) \cdot \mathscr{D}'(t-\tau_2)\,d\tau_1\,d\tau_2. \tag{39}$$

Using (23), the time average of Eq. (39) is

$$\langle W_e\rangle = \tfrac{1}{4}\,\omega^2|\mathbf{D}|^2 \times \int_0^{\infty}\int_0^{\infty} G(\tau_1+\tau_2)\cos[\omega(\tau_1-\tau_2)]\,d\tau_1\,d\tau_2. \tag{40}$$

A new change of variables $u=\tau_1+\tau_2$ and $v=\tau_1-\tau_2$ gives

$$\langle W_e\rangle = \frac{1}{8}\,\omega^2|\mathbf{D}|^2\int_0^{\infty}\int_{-u}^{u} G(u)\cos(\omega v)\,du\,dv = \frac{1}{4}\,\omega|\mathbf{D}|^2\int_0^{\infty} G(u)\sin(\omega u)\,du. \tag{41}$$

From Eq. (36), and using integration by parts, we have that

$$\mathrm{Re}\left[\mathscr{F}\left(\frac{\partial\beta}{\partial t}\right)\right] = \mathrm{Re}[\beta(\omega)] = G(\infty)+\omega\int_0^{\infty}[G(t)-G(\infty)]\sin(\omega t)\,dt. \tag{42}$$

Using the property

$$\omega\int_0^{\infty}\sin(\omega t)\,dt = 1, \tag{43}$$

we obtain

$$\mathrm{Re}[\beta(\omega)] = \omega\int_0^{\infty} G(t)\sin(\omega t)\,dt. \tag{44}$$

Substituting Eq. (44) into Eq. (41), and since $\mathbf{E}=\beta(\omega)\mathbf{D}$, we finally get

$$\langle W_e\rangle = \tfrac{1}{4}|\mathbf{D}|^2\ \mathrm{Re}[\beta(\omega)] = \mathrm{Re}(u_e). \tag{45}$$

A similar calculation shows that $\langle D_e\rangle = 2\omega\ \mathrm{Im}(u_e)$.

Similarly, the magnetic term on the right-hand side r.h.s. of Eq. (26) can be recasted as

$$\mathscr{H}\cdot\frac{\partial\mathscr{B}}{\partial t} = \frac{\partial W_m}{\partial t} + D_m, \tag{46}$$

where

$$W_m(t) = \frac{1}{2}\int_{-\infty}^{t}\int_{-\infty}^{t} F(2t-\tau_1-\tau_2).\mathscr{B}'(\tau_1) \cdot\mathscr{B}'(\tau_2)\,d\tau_1\,d\tau_2, \tag{47}$$

$$D_m(t) = -\int_{-\infty}^{t}\int_{-\infty}^{t} F'(2t-\tau_1-\tau_2).\mathscr{B}'(\tau_1) \cdot\mathscr{B}'(\tau_2)\,d\tau_1\,d\tau_2, \tag{48}$$

are the stored magnetic energy density and rate of dissipation of magnetic energy density, respectively, such that

$$\mathscr{H} = \gamma * \frac{\partial.\mathscr{B}}{\partial t}, \quad \gamma(t) = F(t)H(t), \tag{49}$$

with γ the magnetic impermeability function.

The rate of dissipated electric energy density can be defined as

$$D_\sigma(t) = -\int_{-\infty}^{t}\int_{-\infty}^{t}\Sigma(2t-\tau_1-\tau_2)\mathscr{E}'(\tau_1) \cdot\mathscr{E}'(\tau_2)\,d\tau_1\,d\tau_2, \tag{50}$$

where

$$\mathscr{J} = \sigma * \frac{\partial\mathscr{E}}{\partial t}, \quad \sigma(t) = \Sigma(t)H(t). \tag{51}$$

Formally, the stored energy density due to the electric currents out of phase with the electric field, satisfies

$$\frac{\partial W_\sigma}{\partial t} = \mathscr{J}\cdot\mathscr{E} - D_\sigma. \tag{52}$$

In terms of the energy densities, Eq. (26) becomes

$$-\boldsymbol{\nabla}\cdot\mathscr{P} = \frac{\partial}{\partial t}(W_\sigma+W_e+W_m)+D_\sigma+D_e+D_m, \tag{53}$$

and the correspondences with the averaged time-harmonic values are

$$\begin{aligned}&\langle W_e\rangle = \mathrm{Re}(u_e), \quad \langle W_m\rangle = \mathrm{Re}(u_m),\\ &\langle D_e\rangle = 2\omega\ \mathrm{Im}(u_e),\\ &\langle D_\sigma\rangle = 2\omega\ \mathrm{Re}(u_\sigma),\\ &\langle D_m\rangle = -2\omega\ \mathrm{Im}(u_m).\end{aligned} \tag{54}$$

Note that $\langle\mathscr{J}\cdot\mathscr{E}\rangle$ is equal to the rate of dissipated energy density $\langle D_\sigma\rangle$, and that

$$\left\langle\frac{\partial W_e}{\partial t}\right\rangle = 0, \tag{55}$$

in contrast with Oughstun and Sherman's result (25). The same property holds for the stored electric and magnetic energy densities.

There are other alternative time-domain expressions for the energy densities whose time-average values coincide

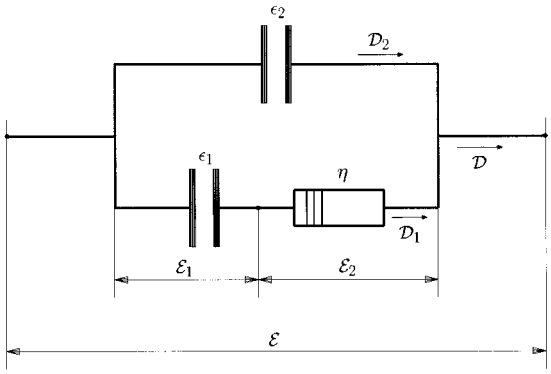

FIG. 1. This electric circuit is equivalent to a purely dielectric relaxation process, where ϵ_1 and ϵ_2 are the capacitances, η is a resistance, $\mathscr{E}$ is the electric field, and $\mathscr{D}$ is the electric induction.

with those given in Eqs. (54), but fail to match the energy in the time domain. For instance, the following definition,

$$W_e' = \tfrac{1}{2}\mathscr{E}\cdot\mathscr{D}, \tag{56}$$

as the stored (di) electric energy density, and

$$D_e' = \frac{1}{2}\left(\mathscr{E}\cdot\frac{\partial\mathscr{D}}{\partial t} - \mathscr{D}\cdot\frac{\partial\mathscr{E}}{\partial t}\right), \tag{57}$$

as the rate of dissipation, satisfy Eq. (53) and $\langle W_e'\rangle = \langle W_e\rangle$ and $\langle D_e'\rangle = \langle D_e\rangle$. However, W_e' is not equal to the energy stored in the capacitors for the Debye model given in the next section [see Eqs. (69) and (71)].

V. EXAMPLE

It is well known that the Debye model used to describe the behavior of dielectric materials[24] is mathematically equivalent to the Zener or standard linear solid model used in viscoelasticity. The following example uses this model to illustrate the concepts presented in the previous section.

A. Debye-type dielectric model

Let us consider a capacitor C_2 in parallel with a series connection between a capacitor C_1 and a resistance R. This circuit obeys the following differential equation:

$$U + \tau_U\frac{\partial U}{\partial t} = \frac{1}{C}\left(I + \tau_I\frac{\partial I}{\partial t}\right), \tag{58}$$

where $U = \partial V/\partial t$, I is the current, V is the voltage, and

$$C = C_1 + C_2, \quad \tau_U = R\left(\frac{1}{C_1} + \frac{1}{C_2}\right)^{-1}, \quad \tau_I = C_1 R. \tag{59}$$

From the point of view of a pure dielectric process, we identify U with $\mathscr{E}$ and I with $\mathscr{D}$ (see Fig. 1). Hence, the dielectric relaxation model is

$$\mathscr{E} + \tau_{\mathscr{E}}\frac{\partial\mathscr{E}}{\partial t} = \frac{1}{\epsilon_0}\left(\mathscr{D} + \tau_{\mathscr{D}}\frac{\partial\mathscr{D}}{\partial t}\right), \tag{60}$$

where

$$\epsilon_0 = \epsilon_1 + \epsilon_2, \quad \tau_{\mathscr{E}} = \frac{1}{\eta}\left(\frac{1}{\epsilon_1} + \frac{1}{\epsilon_2}\right)^{-1}, \quad \tau_{\mathscr{D}} = \epsilon_1/\eta, \tag{61}$$

with η a parameter that introduces the dissipation. Note that ϵ_0 is the static (low-frequency) permittivity and $\epsilon_\infty = \epsilon_0\tau_{\mathscr{E}}/\tau_{\mathscr{D}} = \epsilon_2 < \epsilon_0$ is the optical (high-frequency) permittivity.

We have that

$$\epsilon(t) = \epsilon_0\left[1 - \left(1 - \frac{\tau_{\mathscr{E}}}{\tau_{\mathscr{D}}}\right)\exp(-t/\tau_{\mathscr{D}})\right]H(t), \tag{62}$$

$$\beta(t) = G(t)H(t) = \frac{1}{\epsilon_0}\left[1 - \left(1 - \frac{\tau_{\mathscr{D}}}{\tau_{\mathscr{E}}}\right)\exp(-t/\tau_{\mathscr{E}})\right]H(t) \tag{63}$$

and

$$\epsilon(\omega) = \beta^{-1}(\omega) = \epsilon_0\left(\frac{1 + i\omega\tau_{\mathscr{E}}}{1 + i\omega\tau_{\mathscr{D}}}\right). \tag{64}$$

Equation (64) can be rewritten as

$$\epsilon(\omega) = \epsilon_\infty + \frac{\epsilon_0 - \epsilon_\infty}{1 + i\omega\tau_{\mathscr{D}}}. \tag{65}$$

For instance, the permittivity (65) describes the response of polar molecules, such as water, to the e.m. field.[16,25]

Substituting Eq. (63) into Eq. (29) and defining the internal variable

$$\xi(t) = \phi\,\exp(-t/\tau_{\mathscr{E}})H(t) * \mathscr{D}, \quad \phi = \frac{1}{\epsilon_0\tau_{\mathscr{E}}}\left(1 - \frac{\tau_{\mathscr{D}}}{\tau_{\mathscr{E}}}\right), \tag{66}$$

yields

$$\mathscr{E} = \frac{1}{\epsilon_\infty}\mathscr{D} + \xi, \tag{67}$$

where ξ satisfies

$$\frac{\partial\xi}{\partial t} = \phi D - \frac{\xi}{\tau_{\mathscr{E}}}. \tag{68}$$

The (di)electric energy density is that stored in the capacitors,

$$W_e = \frac{1}{2\epsilon_1}\mathscr{D}_1\cdot\mathscr{D}_1 + \frac{1}{2\epsilon_2}\mathscr{D}_2\cdot\mathscr{D}_2, \tag{69}$$

where $\mathscr{D}_1$ and $\mathscr{D}_2$ are the respective electric inductions. Since $\mathscr{D}_2 = \epsilon_2\mathscr{E}$, $\mathscr{D} = \mathscr{D}_1 + \mathscr{D}_2$, and $\epsilon_\infty = \epsilon_2$, we obtain

$$\mathscr{D}_1 = -\epsilon_\infty\xi, \tag{70}$$

where Eq. (67) has been used. Note that the internal variable is closely related to the electric field acting on the capacitor in series with the dissipation element. Substitution of the electric fields into Eq. (69), and after some calculations, yields

$$W_e = \frac{\epsilon_\infty}{2}\left[\left(\frac{\epsilon_\infty}{\epsilon_0 - \epsilon_\infty}\right)\xi\cdot\xi + \mathscr{E}\cdot\mathscr{E}\right]. \tag{71}$$

Let us verify that Eq. (37) is in agreement with Eq. (71). From Eqs. (63) and (66) we have

$$G(t) = \epsilon_0^{-1} - \phi\tau_{\mathscr{E}}\exp(-t/\tau_{\mathscr{E}}). \tag{72}$$

Replacing Eq. (72) into Eq. (37), and after some algebra, yields

$$W_e=\frac{1}{2\epsilon_0}\,\mathscr{D}\cdot\mathscr{D}-\frac{1}{2}\,\phi\tau_{\mathscr{E}}\left[\exp\left(-\frac{t}{\tau_{\mathscr{E}}}\right)H(t)*\frac{\partial}{\partial t}\,\mathscr{D}(t)\right]^2, \tag{73}$$

where the exponent 2 means the scalar product. Using Eqs. (66) and (68) gives

$$W_e=\frac{1}{2\epsilon_0}\,\mathscr{D}\cdot\mathscr{D}-\frac{1}{2\phi\tau_{\mathscr{E}}}\,(\phi\tau_{\mathscr{E}}\mathscr{D}-\xi)\cdot(\phi\tau_{\mathscr{E}}\mathscr{D}-\xi). \tag{74}$$

Using $\epsilon_\infty\tau_{\mathscr{D}}=\epsilon_0\tau_{\mathscr{E}}$, and a few calculations, shows that the expression in (74) is equal to the stored energy density (71). This equivalence can also be obtained by avoiding the use of internal variables. However, the introduction of these variables is a requirement to obtaining a complete differential formulation of the e.m. equations. This formulation is the basis of most simulation algorithms.[17,18]

The rate of dissipated energy density is

$$D_e=\frac{1}{\eta}\,\frac{\partial\mathscr{D}_1}{\partial t}\cdot\frac{\partial\mathscr{D}_1}{\partial t}, \tag{75}$$

which from Eqs. (70) and (68) becomes

$$D_e=\frac{1}{\eta}\left(\frac{\epsilon_\infty}{\tau_{\mathscr{E}}}\right)^2(\phi\tau_{\mathscr{E}}\mathscr{D}-\xi)\cdot(\phi\tau_{\mathscr{E}}\mathscr{D}-\xi). \tag{76}$$

Taking into account the previous calculations, it is easy to show that substitution of Eq. (72) into Eq. (38) gives Eq. (76).

B. Zener viscoelastic model

Fabrizio and Morro (Ref. 5, p. 42) define a viscoelastic solid with internal variables, for which the free (stored) energy density can be uniquely determined. For simplicity, we only consider dilatational deformations, since this choice does not affect the analysis of the problem. If T is the hydrostatic stress, E is the dilatation (trace of the strain tensor) and ξ is the internal variable, the constitutive relation and growth equation are

$$T=\beta_0E+\xi \tag{77}$$

and

$$\frac{\partial\xi}{\partial t}=-\alpha\xi-\beta E, \tag{78}$$

respectively, where α, β_0, and β are real and positive constants. Integration of (78) yields

$$\xi(t)=-\beta\,\exp(-\alpha t)H(t)*E(t). \tag{79}$$

It can be easily shown that Eqs. (77) and (78) correspond to a Zener mechanical model consisting of a spring of constant $k_1=\beta_0(-1+\alpha\beta_0/\beta)$ in parallel with a dashpot of viscosity $\nu=\beta_0^2/\beta$, together in series connection with a spring of constant $k_2=\beta_0$ (Fig. 2).

The relaxed and unrelaxed moduli are

$$G_\infty=\beta_0-\beta/\alpha,\quad G_0=\beta_0, \tag{80}$$

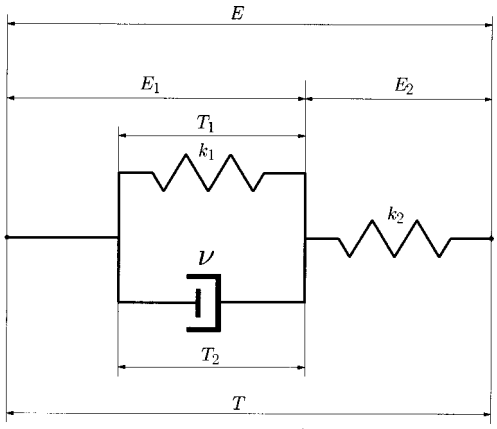

FIG. 2. The Zener viscoelastic model is mathematically equivalent to the electric circuit represented in Fig. 1. k_1 and k_2 are the springs constants, ν is the viscosity of the dashpot, E is the strain, and T is the stress.

respectively, and the relaxation times are

$$\tau_E=\beta_0(\alpha\beta_0-\beta)^{-1},\quad \tau_T=1/\alpha\quad(\tau_E>\tau_T). \tag{81}$$

The relaxation function is

$$G(t)=\alpha^{-1}[\alpha\beta_0-\beta+\beta\,\exp(-\alpha t)]. \tag{82}$$

Assuming that the potential energy is stored in the springs, we have that

$$W_e=\tfrac{1}{2}(k_1E_1^2+k_2E_2^2), \tag{83}$$

where E_1 and E_2 are the dilatations of the springs. Since $T=k_2E_2$ and $E=E_1+E_2$, and using (77), we obtain

$$E_1=-\xi/\beta_0,\quad E_2=E+\xi/\beta_0. \tag{84}$$

Note that the internal variable is closely related to the dilatation on the spring that is in parallel with the dashpot. Substitution of the dilatations into Eq. (83) yields

$$W_e=\frac{1}{2}\left[\left(\frac{\alpha}{\beta}-\frac{1}{\beta_0}\right)\xi^2+\frac{1}{\beta_0}\,(\beta_0E+\xi)^2\right]. \tag{85}$$

For isothermal processes, the free energy coincides with the stored energy. In general, the free energy is not unique (Ref. 5, p. 57). However, for exponential relaxation functions having one internal variable, like the Zener model, the free energy is unique.[26]

Day's free energy for Zener systems (Ref. 5, p. 61) is

$$\psi_D=\frac{1}{2}\,G_\infty E^2+\frac{1}{2}\left\{(G_0-G_\infty)^{-1/2}\times\int_0^\infty G'(s)[E(t)-E(t-s)]ds\right\}^2, \tag{86}$$

where G' is the first-order derivative of the relaxation function. Since

$$\int_0^\infty G'(s)ds=-\beta/\alpha,\quad \int_0^\infty G'(s)E(t-s)ds=\xi,$$

and using Eq. (80), Eq. (86) becomes

$$\psi_D=\frac{1}{2}\left(\beta_0-\frac{\beta}{\alpha}\right)E^2+\frac{\beta}{2\alpha}\left(E+\frac{\alpha}{\beta}\,\xi\right)^2=W_e. \tag{87}$$

This equation differs from the particular form obtained by Fabrizio and Morro (Ref. 5, p. 61) when only dilatational deformations are considered. The cause is a notation error in the book's equation.[27]

The rate of energy density dissipated in the dashpot is

$$D_e=\nu\left(\frac{\partial E_1}{\partial t}\right)^2, \tag{88}$$

which from Eqs. (84) and (78) becomes

$$D_e=\frac{1}{\beta}\,(\alpha\xi+\beta E)^2. \tag{89}$$

C. Mathematical analogy

The mathematics of the viscoelastic problem is the same as for the dielectric relaxation model previously introduced, since the mathematical equivalence identifies $\mathscr{E}$ with stress T and $\mathscr{D}$ with strain E. Then, from the analogy between stress and electric field, strain and electric induction, internal variables, and bulk modulus and dielectric impermeability, Day's free energy (86) in the electromagnetic case reads

$$\psi_D=\frac{1}{2\epsilon_\infty}\,\mathscr{D}\cdot\mathscr{D}+\frac{1}{2}\left\{\left(\frac{1}{\epsilon_0}-\frac{1}{\epsilon_\infty}\right)^{-1/2}\times\int_0^\infty G'(s)[\mathscr{D}(t)-\mathscr{D}(t-s)]ds\right\}^2, \tag{90}$$

where the exponent 2 means the scalar product.

Comparing Eqs. (72) and (82) we obtain the equivalences

$$\frac{\beta}{\alpha}=\frac{1}{\epsilon_\infty}-\frac{1}{\epsilon_0},\quad \beta_0=\frac{1}{\epsilon_\infty},\quad \alpha=\frac{1}{\tau_{\mathscr{E}}}. \tag{91}$$

Substituting these equivalences into Eq. (85), the electromagnetic stored energy density (71) is obtained.

On the other hand, applying the analogy and substituting the equivalences (91) into Eq. (89), yields the electromagnetic rate of dissipated energy density (76).

The complete correspondence between the dielectric and the viscoelastic models is

fields			properties		
$\mathscr{E}$	$\leftrightarrow$	T	ϵ_∞	$\leftrightarrow$	β_0^{-1}
$\mathscr{D}$	$\leftrightarrow$	E	$\tau_{\mathscr{D}}$	$\leftrightarrow$	τ_E
$\mathscr{E}_1$	$\leftrightarrow$	T_1	$\tau_{\mathscr{E}}$	$\leftrightarrow$	τ_T ,
$\mathscr{E}_2$	$\leftrightarrow$	T_2	η	$\leftrightarrow$	ν^{-1}
$\mathscr{D}_1$	$\leftrightarrow$	E_1	ϵ_1	$\leftrightarrow$	k_1^{-1}
$\mathscr{D}_2$	$\leftrightarrow$	E_2	ϵ_2	$\leftrightarrow$	k_2^{-1}
ξ	$\leftrightarrow$	ξ			

(92)

where the symbols can be identified in Figs. 1 and 2.

VI. REMARKS

It is important to keep in mind that Eq. (37) holds when $\mathscr{D}(t\to\infty)=0$, an assumption that is violated by time-harmonic fields. However, after the transient regime (large times after application of the field), the time average of W_e gives $\langle u_e\rangle$, and, for Debye-type dielectric processes (exponential relaxation functions), W_e is the energy stored in the capacitors.

Day's free energy [Eq. (90)] is unique for exponential dielectric functions with one internal variable. Actually, Day's free energy is a particular form of Eq. (37). Both energies coincide for Debye-type dielectric processes.

[1] K. E. Oughstun and G. C. Sherman, *Electromagnetic Pulse Propagation in Causal Dielectrics* (Springer-Verlag, New York, 1994).
[2] G. Caviglia and A. Morro, *Inhomogeneous Waves in Solids and Fluids* (World Scientific, Singapore, 1992).
[3] S. C. Hunter, *Mechanics of Continuous Media* (Wiley, New York, 1983).
[4] F. Cavallini and J. M. Carcione, ''Energy balance and inhomogeneous plane-wave analysis of a class of anisotropic viscoelastic constitutive laws,'' in *Waves and Stability in Continuous Media*, edited by S. Rionero and T. Ruggeri (World Scientific, Singapore, 1994), pp. 47–53.
[5] M. Fabrizio and A. Morro, *Mathematical Problems in Linear Viscoelasticity*, Studies in Applied Mathematics Vol. 12 (SIAM, Philadelphia, 1992).
[6] R. M. Christensen, *Theory of Viscoelasticity. An Introduction* (Academic, New York, 1971).
[7] J. M. Golden and G. A. C. Graham, *Boundary Value Problems in Linear Viscoelasticity* (Springer-Verlag, New York, 1988).
[8] P. Hammond, *Energy Methods in Electromagnetism* (Clarendon, Oxford, 1981).
[9] J. M. Carcione and F. Cavallini, ''On the acoustic-electromagnetic analogy,'' Wave Motion **21**, 149–162 (1995).
[10] C. Zener, *Elasticity and Anelasticity of Metals* (University of Chicago, Chicago, 1948).
[11] H. A. Kramers, ''La diffusion de la lumiere par les atomes,'' Atti Congr. Intern. Fisica, Como **2**, 545–557 (1927).
[12] R. Krönig, ''On the theory of the dispersion of x-rays,'' J. Opt. Soc. Am. **12**, 547–557 (1926).
[13] L. P. Felsen and N. Marcuvitz, *Radiation and Scattering of Waves* (Prentice-Hall, Englewood Cliffs, NJ, 1973).
[14] T. M. Roberts and P. G. Petropoulus, ''Asymptotics and energy estimates for electromagnetic pulses in dispersive media,'' J. Opt. Soc. Am. A **13**, 1204–1217 (1996).
[15] P. G. Petropoulos, ''The wave hierarchy for propagation in relaxing dielectrics,'' Wave Motion **21**, 253–262 (1995).
[16] G. Turner and A. F. Siggins, ''Constant *Q* attenuation of subsurface radar pulses,'' Geophysics **59**, 1192–1200 (1994).
[17] J. M. Carcione, ''Ground-penetrating radar: Wave theory and numerical simulations in lossy anisotropic media,'' Geophysics **61**, 1664–1677 (1996).
[18] T. Xu and G. A. McMechan, ''GPR attenuation and its numerical simulation in 2.5 dimensions,'' Geophysics **62**, 403–414 (1997).
[19] C. Jeffreys, ''A new conservation law for classical electrodynamics,'' SIAM (Soc. Ind. Appl. Math.) Rev. **34**, 386–405 (1993).
[20] F. N. H. Robinson, ''Poynting's vector: Comments on a recent paper by Clark Jeffreys,'' SIAM (Soc. Ind. Appl. Math.) Rev. **36**, 633–637 (1994).
[21] C. Jeffreys, ''Response to a Commentary by F. N. H. Robinson,'' SIAM (Soc. Ind. Appl. Math.) Rev. **36**, 638–641 (1994).
[22] Y. N. Rabotnov, *Elements of Hereditary Solid Mechanics* (Mir, Moscow, 1980).
[23] S. Breuer and E. T. Onat, ''On the determination of free energy in linear viscoelastic solids,'' Z. Angew. Math. Phys. **15**, 184–190 (1964).
[24] A. R. Von Hippel, *Dielectrics and Waves* (Wiley, New York, 1962).
[25] P. Debye, *Polar Molecules* (Dover, New York, 1929).
[26] D. Graffi, and M. Fabrizio, ''Non unicità dell'energia libera per materiali viscoelastici,'' Atti Accad. Naz. Lincei, Cl. Sci. Fis. Mat. Nat. Rend. **LXXXIII**, 209–214 (1989).
[27] A. Morro, personal communication.

Transducer field modeling in anisotropic media by superposition of Gaussian base functions

Martin Spies
Fraunhofer-Institut Zerstörungsfreie Prüfverfahren (IZFP), Universität, Geb. 37, 66123 Saarbrücken, Germany

(Received 12 January 1998; accepted for publication 13 October 1998)

Anisotropic structural materials like fiber composites, but also columnar-grained stainless steels, raise considerable problems for ultrasonic inspection due to the well-known wave propagation phenomena of skewing, splitting and distortion. In this respect, simulation and optimization in ultrasonic nondestructive testing have gained a considerable importance. Among a variety of methods for transducer field calculation, beam superposition has proven to be highly efficient. In this article, a Gaussian beam approach for anisotropic media is presented. The Gaussian base functions are obtained from relationships previously derived for Gaussian wave packets. Each function is furnished with coefficients fixing the beam waists and their position. To test the approach, the case of a piston radiator is addressed for general transversely isotropic media. Using Gaussian beam superposition instead of—as a reference—applying a point source superposition technique leads to an enormous reduction in computer run time. © *1999 Acoustical Society of America.* [S0001-4966(99)05101-2]

PACS numbers: 43.20.Bi, 43.20.Fn [DEC]

INTRODUCTION

Difficulties in the inspection of anisotropic materials arise from those inherent effects like beam splitting, beam distortion and deviation between wave propagation and energy flow. Therefore, high interest has been dedicated to anisotropic wave propagation in the last few years. Respective studies consider plane wave theory as well as propagation of pulses in these media. Extending the scope to inhomogeneous materials, the theory gets unavoidably more complex. However, most of these models suffer from limited capability as they are approximative in character—assuming plane waves or certain beam functions—and/or require high computation time. More decisively, these approaches do not account for transducer-radiated wave fields, thus they are also unable to consider ultrasonic pulse radio frequency (RF) signals. To overcome these drawbacks, Rose *et al.*[1] have presented a numerical integration model using scalar Green's functions as point sources, derived for transversely isotropic media exhibiting mild anisotropy. In recent studies,[2–5] the modeling of ultrasonic transducer-radiation in transversely isotropic and orthotropic media with arbitrary orientation has been addressed by using a point source superposition technique. This generalized point source synthesis method (GPSS) is based on Rayleigh's surface integral and includes the influence of the material's stress-free surface onto the directivity patterns of normal and transverse point sources. Apart from using superposition of point sources, modeling of transducer-generated wave fields is also possible applying beam-superposition techniques. Newberry and Thompson[6] have introduced a model for anisotropic media employing Gauss-Hermite beams, while pure Gaussian beam techniques are known for isotropic media.[7,8]

In this article, a Gaussian beam approach for anisotropic media is presented which corresponds to the isotropic Gaussian beam superposition method by Wen and Breazeale (W&B[9]). The Gaussian base functions are obtained from the relationships previously derived for Gaussian wave packets which have been applied to general transversely isotropic media previously.[10] The procedure used in obtaining the transducer field solutions is analogous to that used to get a series solution to a boundary value problem. Starting with the respective wave equation, a solution that is used as a base function is established, then the relevant boundary conditions are expressed in terms of a set of base functions. Eventually, as described in Ref. 9, the coefficients of the base functions have to be determined so that the superposition of the single field solutions satisfies the boundary conditions.

In Sec. I, the derivation of the Gaussian base functions for anisotropic media is described. Also, a short comparison with isotropic Gaussian beam theory is given. Numerical results are shown and discussed in Sec. II, where—although the results presented here are valid for arbitrary anisotropy—the evaluations are performed for the case of transversely isotropic (TI) media. For comparison, the GPSS method is employed. In the calculations, beam parameters given by W&B[9] for a piston radiator are used.

I. THEORY

The equation of motion for the displacement vector $\underline{\mathbf{u}}$ in a homogeneous anisotropic solid reads

$$(\underline{\nabla}\cdot\underline{\underline{\underline{\mathbf{C}}}}\cdot\underline{\nabla})\cdot\underline{\mathbf{u}}(\underline{\mathbf{R}},t)-\varrho\,\frac{\partial^2}{\partial t^2}\underline{\mathbf{u}}(\underline{\mathbf{R}},t)=-\underline{\mathbf{f}}(\underline{\mathbf{R}},t), \tag{1}$$

and is explicitly dependent on space $\underline{\mathbf{R}}$ and time t. Here $\underline{\nabla}$ is the gradient vector, ϱ is the material density, and $\underline{\mathbf{f}}$ accounts for the volume force density. The elastic stiffness tensor $\underline{\underline{\underline{\mathbf{C}}}}$ depends on the elastic constants, which—for transversely isotropic media—are C_{11}, C_{33}, C_{44}, C_{66}, and C_{13}.

The consideration of plane wave solutions of Eq. (1) for these media shows that there exists one pure shear wave mode. This wave is usually called the *SH* wave, while the coupled waves are called the quasilongitudinal (qP) and quasitransverse (qSV) wave since their polarization is in general not purely longitudinal and transverse, respectively. The relationships characterizing these waves have been given in Ref. 10 for transversely isotropic media with arbitrary spatial orientation (TIA-media) and are summarized in Appendix A.

A. Gaussian wave packets

A solution to the homogeneous ($\underline{\mathbf{f}}=\underline{\mathbf{0}}$) equation of motion (1), which is in the form of a localized pulse, has been obtained by Norris.[11] This solution is governed by a Gaussian envelope and therefore called Gaussian wave packet (GWP). Starting with displacement vector $\underline{\mathbf{u}}$ in the general form

$$\underline{\mathbf{u}}(\underline{\mathbf{R}},t)=\underline{\mathbf{U}}(\underline{\mathbf{R}},t)e^{j\omega\phi(\underline{\mathbf{R}},t)}, \tag{2}$$

$$\underline{\mathbf{U}}(\underline{\mathbf{R}},t)=\sum_{n=0}^{\infty}(j\omega)^{-n}\underline{\mathbf{U}}^{(n)}(\underline{\mathbf{R}},t), \tag{3}$$

and introducing a high frequency and a second-order Taylor-series approximation with respect to space and time for phase $\phi(\underline{\mathbf{R}},t)$, the GWP solution follows in the notation adopted in this article as

$$\begin{aligned}\underline{\mathbf{u}}_\alpha(\underline{\mathbf{R}},t)=U\,\hat{\underline{\mathbf{u}}}_\alpha\,&\exp[j\underline{\mathbf{K}}_\alpha\cdot(\underline{\mathbf{R}}-\overline{\underline{\mathbf{R}}(t)})]\\&\cdot\left[\frac{\det\underline{\underline{\mathbf{M}}}_\alpha(t)}{\det\underline{\underline{\mathbf{M}}}(0)}\right]^{1/2}\exp\left[j\omega\,\frac{1}{2}(\underline{\mathbf{R}}-\overline{\underline{\mathbf{R}}(t)})\right.\\&\left.\cdot\underline{\underline{\mathbf{M}}}_\alpha(t)\cdot(\underline{\mathbf{R}}-\overline{\underline{\mathbf{R}}(t)})\right],\end{aligned} \tag{4}$$

where α designates the wave type. Thus, the GWP is initially in the form of a plane wave which is modulated by a Gaussian envelope in all directions about the pulse center $\overline{\underline{\mathbf{R}}(0)}$ and which travels along a particular ray. Let t be the ray parameter along that ray, then at time $t\geqslant 0$, the pulse center has propagated to

$$\overline{\underline{\mathbf{R}}(t)}=\overline{\underline{\mathbf{R}}(0)}+t\underline{\mathbf{c}}_\alpha, \tag{5}$$

where $\underline{\mathbf{c}}_\alpha$ is the group velocity; furthermore, $\hat{\underline{\mathbf{u}}}_\alpha$ and $\underline{\mathbf{K}}_\alpha$ are the (plane wave) polarization and wave vectors. The Gaussian shape is determined by the complex envelope matrix $\underline{\underline{\mathbf{M}}}$, its time dependence is given by

$$\underline{\underline{\mathbf{M}}}_\alpha(t)=\underline{\underline{\mathbf{M}}}(0)\cdot(\underline{\underline{\mathbf{I}}}+t\underline{\underline{\mathbf{N}}}_\alpha\cdot\underline{\underline{\mathbf{M}}}(0))^{-1}. \tag{6}$$

The evolution of the initial matrix $\underline{\underline{\mathbf{M}}}(0)$ with time t is governed by the real-valued matrix $\underline{\underline{\mathbf{N}}}_\alpha$, which is defined as

$$\underline{\underline{\mathbf{N}}}_\alpha=\partial\underline{\mathbf{c}}_\alpha/\partial\underline{\mathbf{K}}, \tag{7}$$

and which is related to the curvature of the slowness surface. Since it governs the spreading of the packets as these move through the medium, $\underline{\underline{\mathbf{N}}}$ is called the spreading matrix.

An axisymmetric pulse as generated, for example, by a piston transducer insonifying in the x-z plane, is described by

$$\underline{\underline{\mathbf{M}}}(0)=M_1^0\underline{\underline{\mathbf{I}}}+(M_3^0-M_1^0)\hat{\underline{\mathbf{K}}}\,\hat{\underline{\mathbf{K}}}, \tag{8}$$

where $\hat{\underline{\mathbf{K}}}$ designates the direction of insonification and where the quantities M_1^0 and M_3^0 are related to the initial width and length of the GWP. The corresponding envelope matrices $\underline{\underline{\mathbf{M}}}_\alpha(t)$ can be obtained according to their evolution equation (6). The explicit expressions for $\underline{\mathbf{c}}_\alpha$, $\hat{\underline{\mathbf{u}}}_\alpha$, $\underline{\mathbf{K}}_\alpha$, $\underline{\underline{\mathbf{N}}}_\alpha$, and $\underline{\underline{\mathbf{M}}}_\alpha$ have for TIA media been given in Ref. 10 and are summarized in Appendix B.

B. Gaussian base functions

The initial ansatz used for the derivation of the GWP solutions is similar to that of time-harmonic Gaussian beams (GB). The GB solutions are of infinite extent in the direction of propagation, whereas the GWP theory includes an extra degree of freedom in that the pulse is of finite length. In the limit as this length becomes infinite, it reduces to time-harmonic GB theory.

Mathematically, the special case of a GWP of infinite length is obtained by setting the parameter which refers to the pulse length in ray direction equal to zero, i.e.,[12]

$$M_3^0=0. \tag{9}$$

Setting $\overline{\underline{\mathbf{R}}(t)}=\underline{\mathbf{0}}+t\underline{\mathbf{c}}_\alpha$ and obeying that $\underline{\mathbf{K}}_\alpha\cdot\underline{\mathbf{c}}_\alpha=\omega$ allows us to write Eq. (4) as

$$\begin{aligned}\underline{\mathbf{u}}_\alpha(\underline{\mathbf{R}},t)=&\frac{U\,\hat{\underline{\mathbf{u}}}_\alpha\exp(-j\omega t)}{[(1+t\,M_1^0S_1^\alpha)(1+t\,M_1^0S_2^\alpha)]^{1/2}}\\&\cdot\exp[j\,\underline{\mathbf{K}}_\alpha\cdot\underline{\mathbf{R}}+j\omega\,\tfrac{1}{2}(\underline{\mathbf{R}}-t\underline{\mathbf{c}}_\alpha)\\&\cdot\underline{\underline{\mathbf{M}}}_\alpha(t)\cdot(\underline{\mathbf{R}}-t\underline{\mathbf{c}}_\alpha)],\end{aligned} \tag{10}$$

where $\det\underline{\underline{\mathbf{M}}}_\alpha(t)=\det\underline{\underline{\mathbf{M}}}(0)/(1+t\,M_1^0S_1^\alpha)(1+t\,M_1^0S_2^\alpha)$ has been used, S_1^α and S_2^α being the eigenvalues of $\underline{\underline{\mathbf{N}}}_\alpha$.[10,11] To obtain the GB functions in a form similar to the solutions given by W&B[9] for the isotropic case, ray parameter t [Eq. (5)] is replaced according to

$$t=(\underline{\mathbf{R}}\cdot\hat{\underline{\mathbf{K}}})/(\underline{\mathbf{c}}_\alpha\cdot\hat{\underline{\mathbf{K}}}). \tag{11}$$

Thus, suppressing the time-harmonic factor $e^{-j\omega t}$ and replacing M_1^0 by M, the Gaussian base functions follow from Eq. (10). The field solution is then written as a superposition of a series of base functions with different parameters U_n and M_n according to

$$\underline{\mathbf{u}}_\alpha(\underline{\mathbf{R}}) = \sum_{n=1}^{N} U_n \underline{\hat{\mathbf{u}}}_\alpha \exp[j \underline{\mathbf{K}}_\alpha \cdot \underline{\mathbf{R}}] \times \frac{(\underline{\mathbf{c}}_\alpha \cdot \underline{\hat{\mathbf{K}}})}{\sqrt{(\underline{\mathbf{c}}_\alpha + M_n S_1^\alpha \underline{\mathbf{R}}) \cdot \underline{\hat{\mathbf{K}}}} \sqrt{(\underline{\mathbf{c}}_\alpha + M_n S_2^\alpha \underline{\mathbf{R}}) \cdot \underline{\hat{\mathbf{K}}}}} \cdot \exp\left[\frac{j\omega}{2(\underline{\mathbf{c}}_\alpha \cdot \underline{\hat{\mathbf{K}}})} \underline{C}_\alpha \cdot \underline{\underline{\mathbf{M}}}_{\alpha,n}^{\mathrm{GB}} \cdot \underline{C}_\alpha \right], \tag{12}$$

where

$$\underline{C}_\alpha = (\underline{\mathbf{c}}_\alpha \cdot \underline{\hat{\mathbf{K}}}) \underline{\mathbf{R}} - (\underline{\mathbf{R}} \cdot \underline{\hat{\mathbf{K}}}) \underline{\mathbf{c}}_\alpha . \tag{13}$$

In analogy to GWP theory, $\underline{\underline{\mathbf{M}}}_{\alpha,n}^{\mathrm{GB}}$ will be called the beam shape matrix. For TIA media, it results as

$$\underline{\underline{\mathbf{M}}}_{\alpha,n}^{\mathrm{GB}} = M_{1\alpha}^{\mathrm{GB}} \underline{\underline{\mathbf{I}}} + M_{2\alpha}^{\mathrm{GB}} \underline{\hat{\mathbf{K}}}\,\underline{\hat{\mathbf{K}}} + M_{3\alpha}^{\mathrm{GB}} [\underline{\mathbf{a}}\,\underline{\mathbf{a}} - (\underline{\mathbf{a}} \cdot \underline{\hat{\mathbf{K}}})(\underline{\hat{\mathbf{K}}}\,\underline{\mathbf{a}} + \underline{\mathbf{a}}\,\underline{\hat{\mathbf{K}}})], \tag{14}$$

$$M_{1\alpha}^{\mathrm{GB}} = \frac{M_n}{(\underline{\mathbf{c}}_\alpha + M_n S_1^\alpha \underline{\mathbf{R}}) \cdot \underline{\hat{\mathbf{K}}}}, \tag{15}$$

$$M_{2\alpha}^{\mathrm{GB}} = M_{3\alpha}^{\mathrm{GB}} - \frac{M_n}{(\underline{\mathbf{c}}_\alpha + M_n S_2^\alpha \underline{\mathbf{R}}) \cdot \underline{\hat{\mathbf{K}}}}, \tag{16}$$

$$M_{3\alpha}^{GB} = \frac{M_n^2 (\mathcal{G}_\alpha - S_2^\alpha)(\underline{\mathbf{R}} \cdot \underline{\hat{\mathbf{K}}})}{\underline{\hat{\mathbf{K}}} \cdot (\underline{\mathbf{c}}_\alpha + M_n S_1^\alpha \underline{\mathbf{R}})(\underline{\mathbf{c}}_\alpha + M_n S_2^\alpha \underline{\mathbf{R}}) \cdot \underline{\hat{\mathbf{K}}}}, \tag{17}$$

where $\mathcal{G}_\alpha$, S_1^α, and S_2^α are given in Appendix B. The free parameters in Eq. (12) are the (complex) amplitudes U_n and the quantities M_n, which are the complex beam waist parameters of the GB functions, and N is the number of GB functions needed. The next step is to make Eq. (12) satisfy the boundary conditions by properly determining the coefficients of base functions, i.e., the beam waist parameters M_n and the amplitudes U_n, as is commonly done in finding a series solution to a boundary value problem. This has been described by W&B, so the reader is referred to their paper. In the next subsection, it is shown how the expressions presented above are related to isotropic Gaussian beam theory.

C. Comparison with isotropic GB theory

Introducing isotropic conditions leads to

$$\underline{\mathbf{c}}_\alpha = v_\alpha \underline{\hat{\mathbf{K}}}, \quad (\underline{\mathbf{c}}_\alpha \cdot \underline{\hat{\mathbf{K}}}) = v_\alpha , \quad S_1^\alpha = S_2^\alpha = v_\alpha^2, \tag{18}$$

where v_α designates the modulus of phase velocity. Setting $\underline{\hat{\mathbf{K}}} = \underline{\mathbf{e}}_z$, Eq. (14) transforms into

$$\underline{\underline{\mathbf{M}}}_{\alpha,n}^{\mathrm{GB,iso}} = \frac{M_n}{v_\alpha (1 + M_n v_\alpha z)} (\underline{\underline{\mathbf{I}}} - \underline{\mathbf{e}}_z \underline{\mathbf{e}}_z), \tag{19}$$

where $\underline{\mathbf{R}} = (x,y,z)$ has been used. Then, with $r^2 = x^2 + y^2$, Eq. (12) is put into the form

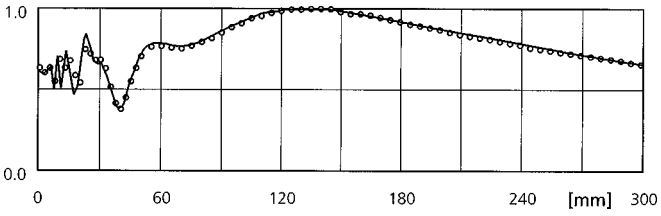

FIG. 1. On-axis field profile behaviour of longitudinal normal transducer in 0°-weld specimen (GPSS: solid curve, GB: dotted curve).

$$\underline{\mathbf{u}}_\alpha^{\mathrm{iso}}(\underline{\mathbf{R}}) = \sum_{n=1}^{N} \underline{\hat{\mathbf{u}}}_\alpha \frac{U_n}{1 + M_n v_\alpha z} \exp\left[j\omega \left(\frac{z}{v_\alpha} + \frac{M_n r^2}{2(1 + M_n v_\alpha z)} \right) \right]. \tag{20}$$

Comparison with the formulation by W&B [Eq. (C2) of Appendix C] relates their beam parameters A_n and B_n directly to U_n and M_n according to

$$U_n = A_n \tag{21}$$

$$M_n = 2j/(\omega B_n). \tag{22}$$

In the following section, numerical examples are presented, where beam parameters given in Ref. 9 have been used.

II. EXAMPLES AND DISCUSSION

The superposition of Gaussian base functions acccording to Eq. (12) is illustrated by simulating normal transducers insonifying into austenitic weld metal specimens exhibiting transversely isotropic symmetry. A ten-term GB solution is applied; the corresponding coefficients used are those determined by W&B for a piston radiator for values of wave number $\times$ radiator radius $ka = 107.8$. For comparison, computationally efficient versions of the GPSS method[3,4] are applied. The piston transducer is modeled by superposition of Huygens' point sources under neglect of the effect of the stress-free material's surface on the point source directivities. In order to account for a realistic transducer, these directivities are usually included in the GPSS calculation,[2] while for the GB method the coefficients for the individual beams would have to be determined correspondingly.

Figures 1 and 2 show the field profiles obtained for a longitudinal (qP) normal probe of 10-MHz frequency and 20-mm diameter, insonifying into an austenitic weld material with grains parallel to the surface. Both the on-axis behavior and the distribution at increasing distances z from the transducer agree well with the GPSS results. It can be seen that discrepancies exist only in the extreme near-field and in the outer side lobe structure.

Insonification into a nonsymmetry direction leads to beam skewing, as shown in Figs. 3 and 4 for a 2.25-MHz, 20-mm-diam probe generating *SH* waves. In this example, the grain orientation is at 30° to the surface. Again, good agreement between the GB and the GPSS results is found.

The most striking feature of the anisotropic GB method is the enormous savings in computer run time. The GPSS calculation performed for the longitudinal normal probe requires the superposition of about 7850 point sources,

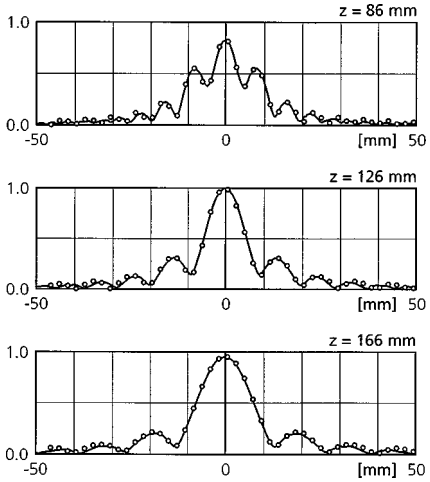

FIG. 2. Field profile distribution of longitudinal normal probe at increasing distances z from the transducer in weld specimen with grains at 0° to the surface (GPSS: solid curve, GB: dotted curve).

whereas the GB results have been obtained with only 10 beams superposed. Accordingly, run time is reduced to less than a thousandth of GPSS run time. This reduction is particularly significant at high frequencies, where GPSS requires higher discretization to fulfill the sampling theorem. Crucial to the GB method are the individual beam parameters U_n and M_n, which have to be evaluated according to the displacement distribution close to the radiator surface. Several approaches for their determination are available.[8,9] Although these parameters depend on the material's (anisotropic) propagation properties, application of the W&B values in the above examples leads to no significant differences in the displacement distribution calculated for the radiator surface as compared to the isotropic case. Principally, the beam parameters characterizing the transducer to be modeled would have to be determined separately for each anisotropic material considered. However, since specimen preparation—required to perform the calibration measurements—is usually tedious in the case of anisotropic complex-structured materials, the necessary supply data for the optimization procedure could be obtained from synthetic GPSS data.

Finally, it has to be mentioned that the presented relationships are valid for convex and concave parts of the slowness surface.[11] For inflection points—which in the above example occur for qSV-waves—cubic phase terms and higher-order transport terms would have to be considered.[13] For this case, an exact transducer field formulation presented previously could be used as a reference.[14]

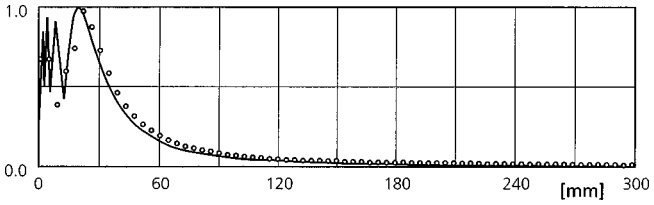

FIG. 3. On-axis field profile behavior of shear normal transducer in 30°-weld specimen (GPSS: solid curve, GB: dotted curve).

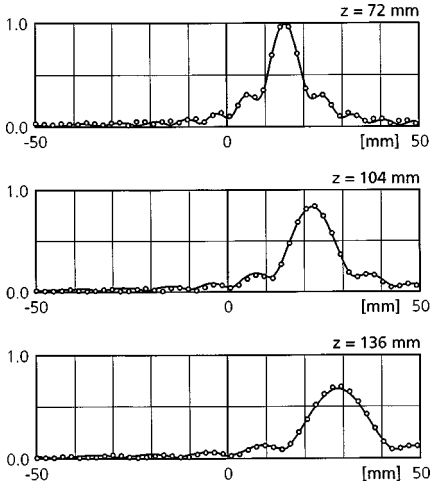

FIG. 4. Field profile distribution of shear normal probe at increasing distances z from the transducer in weld specimen with grains at 30° to the surface (GPSS: solid curve, GB: dotted curve).

ACKNOWLEDGMENTS

The author would like to express his thanks to Professor W. Arnold and Professor M. Kröning, IZFP, Saarbrücken, Germany, for their interest in and support of the subject.

APPENDIX A: PLANE WAVE RELATIONSHIPS

The plane harmonic wave solutions of (1), i.e., the solutions to the homogeneous ($\underline{\mathbf{f}}=\underline{\mathbf{0}}$) equation of motion, are in the form

$$\underline{\mathbf{u}}_\alpha = U\,\underline{\hat{\mathbf{u}}}_\alpha \exp[jK_\alpha \underline{\hat{\mathbf{K}}}\cdot\underline{\mathbf{R}}], \tag{A1}$$

where $\underline{\hat{\mathbf{K}}}$ is the propagation direction. The wave numbers K_α are given by the dispersion relations as[10]

$$K_{SH}^2 = \varrho\,\omega^2/[C_{44}+(C_{66}-C_{44})(\underline{\mathbf{a}}\cdot\underline{\hat{\mathbf{K}}})^2], \tag{A2}$$

$$K_{qSV,qP}^2 = \varrho\,\omega^2(B\pm(B^2-4A)^{1/2})/(2A), \tag{A3}$$

where

$$\begin{aligned} A = {} & C_{33}C_{66}+(\underline{\mathbf{a}}\cdot\underline{\hat{\mathbf{K}}})^2 \\ & \times[C_{33}(C_{11}-2C_{66})-C_{13}(C_{13}+2C_{66})] \\ & +(\underline{\mathbf{a}}\cdot\underline{\hat{\mathbf{K}}})^4[(C_{11}-C_{66})(C_{66}-C_{33})+(C_{13}+C_{66})^2], \end{aligned} \tag{A4}$$

$$B = C_{33}+C_{66}+(\underline{\mathbf{a}}\cdot\underline{\hat{\mathbf{K}}})^2(C_{11}-C_{33}). \tag{A5}$$

The discrimination into the pure transverse wave (SH: shear horizontal) and the two quasiwaves (qSV: quasishear vertical, qP: quasipressure) becomes apparent when the respective polarizations $\underline{\hat{\mathbf{u}}}_\alpha$ are considered, which are given by

$$\underline{\hat{\mathbf{u}}}_{SH} = \mathcal{N}_{SH}(\underline{\mathbf{a}}\times\underline{\hat{\mathbf{K}}}), \tag{A6}$$

$$\underline{\hat{\mathbf{u}}}_{qSV,qP} = \mathcal{N}_{qSV,qP}(F_1^{qSV,qP}\,\underline{\hat{\mathbf{K}}}+F_2^{qSV,qP}\,\underline{\mathbf{a}}). \tag{A7}$$

The abbreviated quantities can be found in Ref. 10. The group velocities are given by

$$\underline{\mathbf{c}}_\alpha = v_\alpha\underline{\hat{\mathbf{K}}}+\mathcal{F}_\alpha v_\alpha(\underline{\mathbf{a}}\cdot\underline{\hat{\mathbf{K}}})(\underline{\underline{\mathbf{I}}}-\underline{\hat{\mathbf{K}}}\,\underline{\hat{\mathbf{K}}})\cdot\underline{\mathbf{a}}, \tag{A8}$$

where

$$\mathcal{F}_{SH}=\frac{C_{66}-C_{44}}{C_{44}+(C_{66}-C_{44})(\underline{\mathbf{a}}\cdot\underline{\hat{\mathbf{K}}})^2}, \tag{A9}$$

$$\mathcal{F}_{qSV,qP}=\frac{1}{2A}\left(y_A+2(\underline{\mathbf{a}}\cdot\underline{\hat{\mathbf{K}}})^2 z_A\pm\frac{F_1-(\underline{\mathbf{a}}\cdot\underline{\hat{\mathbf{K}}})^2 F_2}{\sqrt{B^2-4A}}\right), \tag{A10}$$

$$y_A=C_{33}(C_{11}-2C_{66})-C_{13}(C_{13}+2C_{66}), \tag{A11}$$

$$z_A=(C_{11}-C_{66})(C_{66}-C_{33})+(C_{13}+C_{66})^2, \tag{A12}$$

$$F_1=[C_{66}^2-C_{11}C_{33}][C_{66}-C_{33}] -(C_{13}+C_{66})^2(C_{33}+C_{66}), \tag{A13}$$

$$F_2=F_1+[C_{66}^2-C_{11}C_{33}][C_{66}-C_{11}] -(C_{13}+C_{66})^2(C_{11}+C_{66}). \tag{A14}$$

APPENDIX B: GWP RELATIONSHIPS

Using Eqs. (7) and (A8) yields the spreading matrix for wave type α according to[10]

$$\underline{\underline{\mathbf{N}}}_\alpha=S_1^\alpha\underline{\underline{\mathbf{I}}}-\mathcal{G}_\alpha\underline{\hat{\mathbf{K}}}\,\underline{\hat{\mathbf{K}}}+(S_2^\alpha-\mathcal{G}_\alpha)[\underline{\mathbf{a}}\,\underline{\mathbf{a}}-(\underline{\mathbf{a}}\cdot\underline{\hat{\mathbf{K}}})(\underline{\hat{\mathbf{K}}}\,\underline{\mathbf{a}}+\underline{\mathbf{a}}\,\underline{\hat{\mathbf{K}}})]. \tag{B1}$$

In this representation, use is made of its eigenvalues S_1^α and S_2^α, which are obtained as

$$S_1^{SH}=\frac{C_{44}}{\varrho}, \tag{B2}$$

$$S_2^{SH}=\frac{C_{44}}{\varrho}\,\frac{C_{66}}{C_{44}+(C_{66}-C_{44})(\underline{\mathbf{a}}\cdot\underline{\hat{\mathbf{K}}})^2}, \tag{B3}$$

$$S_1^{qSV,qP}=v_{qSV,qP}^2(1-\mathcal{F}_{qSV,qP}(\underline{\mathbf{a}}\cdot\underline{\hat{\mathbf{K}}})^2), \tag{B4}$$

$$S_2^{qSV,qP}=v_{qSV,qP}^2[1+\mathcal{F}_{qSV,qP}(1-2(\underline{\mathbf{a}}\cdot\underline{\hat{\mathbf{K}}})^2) +(\mathcal{F}_{qSV,qP}^2+\mathcal{E}_{qSV,qP})(\underline{\mathbf{a}}\cdot\underline{\hat{\mathbf{K}}})^2(1-(\underline{\mathbf{a}}\cdot\underline{\hat{\mathbf{K}}})^2)], \tag{B5}$$

where $\mathcal{F}_{qSV,qP}$ is given above and $\mathcal{E}_{qSV,qP}$ is

$$\mathcal{E}_{qSV,qP}=\frac{2}{A}\left\{z_A-(y_A+2(\underline{\mathbf{a}}\cdot\underline{\hat{\mathbf{K}}})^2 z_A)\mathcal{F}_{qSV,qP}\mp\frac{B(C_{13}+C_{66})^2[(C_{66}-C_{11})(C_{66}-C_{33})-(C_{13}+C_{66})^2]}{(B^2-4A)^{3/2}}\right\}. \tag{B6}$$

In Eq. (B1), the quantities $\mathcal{G}_\alpha$ are defined as

$$\mathcal{G}_{SH}=\frac{C_{44}}{C_{66}}S_2^{SH}, \tag{B7}$$

$$\mathcal{G}_{qSV,qP}=v_{qSV,qP}^2[1-2\mathcal{F}_{qSV,qP}(\underline{\mathbf{a}}\cdot\underline{\hat{\mathbf{K}}})^2 -(\mathcal{F}_{qSV,qP}^2+\mathcal{E}_{qSV,qP})(\underline{\mathbf{a}}\cdot\underline{\hat{\mathbf{K}}})^4]. \tag{B8}$$

APPENDIX C: ISOTROPIC GB FUNCTIONS ACCORDING TO W&B

For an axially symmetric sound (or light) beam, with its axis in the z-direction, the (scalar) velocity potential is in cylindrical coordinates written in the form[9]

$$\phi=u(r,z)\exp(jkz), \tag{C1}$$

where k designates the wave number. The GB solution given by W&B is in the form

$$u(r,z)=\frac{A}{B+(2j/k)z}\exp\left[-\frac{r^2}{B+(2j/k)z}\right], \tag{C2}$$

where A and B are arbitrary constants. The only restriction to its validity is $(ka)^2\gg 1$, where a is half the beam diameter at the waist. Thus, the field solution follows as a series of base functions as

$$\phi(r,z)=\frac{j}{k}\sum_{n=1}^{N}\frac{A_n}{B_n+(2j/k)z}\exp\left[jkz-\frac{r^2}{B_n+(2j/k)z}\right]. \tag{C3}$$

[1] J. L. Rose, K. Balasubramaniam, and A. Tverdokhlebov, ''A Numerical Integration Green's Function Model for Ultrasonic Field Profiles in Mildly Anisotropic Media,'' J. Nondestruct. Eval. **8**, 165–179 (1989).

[2] M. Spies, ''Transducer-Modeling in General Transversely Isotropic Media Via Point-Source-Synthesis. Theory,'' J. Nondestruct. Eval. **13**, 85–99 (1994).

[3] M. Spies and M. Kröning, ''A Computationally Efficient Modeling Code for SH-Wave Propagation in Austenitic Welds Using an Explicit Space-Time Green's Function,'' in *Review of Progress in QNDE*, edited by D. O. Thompson and D. E. Chimenti (Plenum, New York, 1996), Vol. 15, pp. 145–152.

[4] M. Spies and M. Kröning, ''Accelerated Space-Time Modeling of Quasi-Longitudinal Waves in Austenitic Weld Structures,'' in *Review of Progress in QNDE*, edited by D. O. Thompson and D. E. Chimenti (Plenum, New York, 1997), Vol. 16, pp. 1175–1182.

[5] M. Spies and M. Kröning, ''Elastic Wavefield Modeling for Arbitrarily Oriented Orthotropic Media,'' in *Review of Progress in QNDE*, edited by D. O. Thompson and D. E. Chimenti (Plenum, New York, 1998), Vol. 17, pp. 1163–1170.

[6] B. P. Newberry and R. B. Thompson, ''A Paraxial Theory for the Propagation of Ultrasonic Beams in Anisotropic Solids,'' J. Acoust. Soc. Am. **85**, 2290–2300 (1989).

[7] J. M. Klosner, L. B. Felsen, I. T. Lu, and Z. Grossfeld, ''Three-Dimensional Source Field Modeling by Self-Consistent Gaussian Beam Superposition,'' J. Acoust. Soc. Am. **91**, 1809–1822 (1992).

[8] C. P. Hsieh, S. Kostek, and F. Stanke, ''Gaussian Beam Modeling of Ultrasonic Transducers Using Nearfield Experimental Data,'' in *Review of Progress in QNDE*, edited by D. O. Thompson and D. E. Chimenti (Plenum, New York, 1993), Vol. 12, pp. 919–924.

[9] J. J. Wen and M. A. Breazeale, ''A Diffraction Beam Field Expressed as the Superposition of Gaussian Beams,'' J. Acoust. Soc. Am. **83**, 1752–1756 (1988).
[10] M. Spies, ''Elastic Waves in Homogeneous and Layered Transversely Isotropic Media: Plane Waves and Gaussian Wave Packets. A General Approach,'' J. Acoust. Soc. Am. **95**, 1748–1760 (1994).
[11] A. N. Norris, ''A Theory of Pulse Propagation in Elastic Anisotropic Solids,'' Wave Motion **9**, 509–532 (1987).
[12] If M_1^0 is also set equal to zero, Eq. (4) describes the plane wave solutions.
[13] V. T. Buchwald, ''Elastic Waves in Anisotropic Media,'' Proc. R. Soc. London, Ser. A **253**, 563–580 (1959).
[14] M. Spies, ''Elastic Wave Propagation in Transversely Isotropic Media. II: The Generalized Rayleigh-Function and an Integral Representation for the Transducer Field. Theory,'' J. Acoust. Soc. Am. **97**, 1–13 (1995).

Nonlinear surface acoustic waves in crystals

Mark F. Hamilton, Yurii A. Il'inskii, and Evgenia A. Zabolotskaya
Department of Mechanical Engineering, The University of Texas at Austin, Austin, Texas 78712-1063

(Received 22 July 1998; revised 30 October 1998; accepted 2 November 1998)

A theory for nonlinear surface acoustic waves in isotropic solids [E. A. Zabolotskaya, J. Acoust. Soc. Am. **91**, 2569–2575 (1992)] is generalized to include the anisotropy of crystals. There is no restriction to material symmetry, orientation of the free surface with respect to crystal axes, or propagation direction in the plane of the free surface. Numerical simulations of waveform distortion, shock formation, and harmonic propagation curves are presented for two different cuts of potassium chloride. © *1999 Acoustical Society of America.* [S0001-4966(99)02802-7]

PACS numbers: 43.25.Fe, 43.35.Pt [HEB]

INTRODUCTION

Advances in theories for nonlinear elastic surface waves have been motivated to a large extent by the development of surface acoustic wave (SAW) devices that perform nonlinear signal processing operations.[1] Much of the theoretical work is restricted to isotropic solids, a review of which is provided in an earlier article.[2] SAW devices employ piezoelectric crystals, and material anisotropy substantially complicates the analysis of nonlinear effects on surface waves. The present article extends a theory developed previously for isotropic solids[3] to describe the evolution of nonlinear surface waves in crystals without any restriction to material symmetry, orientation of the free surface with respect to crystal axes, or propagation direction in the plane of the free surface. Inclusion of piezoelectric effects[4] will be described in a separate article.

Rigorous analyses of nonlinear surface waves in isotropic solids date back to the work of Kalyanasundaram and coworkers.[5–8] Their multiple scale approach was extended by Planat[9] and Lardner[10] to include effects of anisotropy. Planat presented numerical calculations of harmonic propagation curves for various cuts of quartz. Results for the first five harmonics were shown, although only eight harmonics were retained in the computations. Previous work[11] indicates that truncation of the spectrum at such low order has produced anomalous oscillations in harmonic propagation curves reported in investigations of surface waves in isotropic solids. Only very weak nonlinearity, and therefore no shock formation, can be modeled with so few harmonics. Moreover, it is unclear from Planat's article how his nonlinearity matrix depends on frequency.

The theory developed by Lardner[10] for nonlinear surface waves in materials with arbitrary anisotropy was used by Lardner and Tupholme[12] to perform calculations for cubic crystals. Only one geometry was considered, in which the free surface is a plane of symmetry, and the propagation direction is along one of the crystal axes. For this case surface waves exhibit simple exponential attenuation with depth as in isotropic solids (i.e., the wave numbers normal to the surface are imaginary), rather than the oscillatory depth dependence that is more typical in crystals (in which case the vertical wave numbers have nonzero real parts). Lardner calculated propagation curves for the first three harmonics for a surface wave in magnesium oxide.

By introducing a coordinate system that travels with the wave, Parker[13] avoided the multiple scale approach employed by Planat[9] and Lardner.[10] Although Parker's theory was developed for general anisotropic media, numerical simulations were presented only for isotropic solids. We demonstrate here that the present theory reduces to the result obtained earlier by one of the authors[3] for isotropic solids, which in turn has been shown[2] to be equivalent to Parker's theory in the same limit, even though the two theories were derived by entirely different methods. Parker's theory was extended by Kalyanasundaram *et al.*[14] to include effects of diffraction in directional surface wave beams, but no simulations were reported. Diffraction effects have also been included in the isotropic limit of the present theory,[2] for which both analytical and numerical solutions were given.[15]

The theoretical investigation presented here employs the Hamiltonian formalism used previously to describe nonlinear surface waves in isotropic solids.[3] The nonlinearity matrix obtained for isotropic solids has proven to be especially convenient for both interpretation of spectral interactions and development of evolution equations in the time domain.[16–18] The formalism entails calculation of the Hamiltonian to cubic order in the particle displacement for surface waves in anisotropic solids, selection of generalized coordinates, and derivation of coupled spectral equations for the particle velocity in a coordinate system that travels with the surface wave. Numerical simulations of waveform distortion, shock formation, and harmonic propagation curves are presented for two different cuts of a potassium chloride crystal.

The final form of the spectral evolution equation was reported in an earlier publication[19] without derivation or definition of terms in the nonlinearity matrix, and the theory was verified recently via comparison with measurements of shock formation in laser-generated surface waves in crystalline silicon.[20]

I. LINEAR THEORY

We begin with a review of linear theory for surface wave propagation in a crystal because it forms the basis for the nonlinear theory developed in Sec. II. The evolution equations obtained for nonlinear surface waves are assumed

to resemble the linear solution insofar as the depth dependence of each frequency component is taken to be the same as in linear theory.[2] Furthermore, results from linear theory are required to construct the nonlinearity matrix. We shall follow mainly the notation employed in the thorough review of surface waves by Farnell.[21]

A. Basic relations

In the absence of piezoelectric effects, the equation of motion for the particle displacement vector u_i as a function of the stress tensor σ_{ij} in a homogeneous elastic solid with density ρ is

$$\rho \frac{\partial^2 u_i}{\partial t^2} = \frac{\partial \sigma_{ij}}{\partial x_j}. \tag{1}$$

The general linear relation between the stress and strain for an arbitrary anisotropic solid is

$$\sigma_{ij} = c_{ijkl} e_{kl}, \tag{2}$$

where

$$e_{ij} = \frac{1}{2}\left(\frac{\partial u_i}{\partial x_j} + \frac{\partial u_j}{\partial x_i} \right) \tag{3}$$

is the linearized strain tensor. The elastic stiffness tensor c_{ijkl} is symmetric with respect to permutation of indices in each pair ij and kl, as well as with respect to permutation of the pairs themselves, i.e., $i \leftrightarrow j$, $k \leftrightarrow l$, $ij \leftrightarrow kl$. This symmetry permits Eq. (2) to be written

$$\sigma_{ij} = c_{ijkl} \frac{\partial u_k}{\partial x_l}, \tag{4}$$

the substitution of which into Eq. (1) yields the linear wave equation

$$\rho \frac{\partial^2 u_i}{\partial t^2} = c_{ijkl} \frac{\partial^2 u_k}{\partial x_j \partial x_l}. \tag{5}$$

Because of the symmetries involved, it is common to report values of the stiffness constants using the following abbreviated index notation:[22]

$$c_{ijkl} \rightarrow c_{IJ}. \tag{6}$$

The standard mapping is $(11) \rightarrow 1$; $(22) \rightarrow 2$; $(33) \rightarrow 3$; $(23,32) \rightarrow 4$; $(13,31) \rightarrow 5$; $(12,21) \rightarrow 6$. One may therefore regard the stress and strain tensors as six-component vectors and the elastic stiffness tensor as a six-by-six matrix. In Sec. III, numerical calculations of nonlinear surface waves are presented for a cubic crystal. In a coordinate system associated with the crystal axes, the stiffness matrix c_{IJ} for a cubic crystal has 12 nonzero elements, but only 3 are independent:

$$\begin{aligned} &c_{11} = c_{22} = c_{33}, \\ &c_{12} = c_{21} = c_{13} = c_{31} = c_{23} = c_{32}, \\ &c_{44} = c_{55} = c_{66}. \end{aligned} \tag{7}$$

The matrix c_{IJ} for an isotropic solid possesses the same nonzero elements, but only two are independent:

$$c_{11} = \lambda + 2\mu, \quad c_{12} = \lambda, \quad c_{44} = \mu, \tag{8}$$

where λ and μ are the Lamé constants.

If we seek a plane wave solution of the form

$$u_i = \alpha_i e^{i(\mathbf{k}\cdot\mathbf{x} - \omega t)} \tag{9}$$

where $\mathbf{k} = (k_1, k_2, k_3)$ and $\mathbf{x} = (x_1, x_2, x_3)$, substitution into Eq. (5) yields a homogeneous set of linear algebraic equations for α_i (the Christoffel equation):[23]

$$\rho \omega^2 \alpha_i = c_{ijkl} k_j k_l \alpha_k. \tag{10}$$

Equation (10) determines solutions of the wave equation in the form of homogeneous plane waves. When all k_i are real, the solutions correspond to bulk waves. Introducing the wave number k, phase velocity c, and unit vector $\mathbf{n} = (n_1, n_2, n_3)$ along $\mathbf{k}$, i.e.,

$$k = |\mathbf{k}|, \quad c = \omega/k, \quad n_i = k_i/k, \tag{11}$$

we may rewrite Eq. (10) in the form

$$\rho c^2 \alpha_i = c_{ijkl} n_j n_l \alpha_k. \tag{12}$$

The phase speed c of bulk waves is determined by requiring the existence of a nontrivial solution of Eq. (12):

$$\det(\Gamma_{ik} - \rho c^2 \delta_{ik}) = 0, \tag{13}$$

where δ_{ik} is the Kronecker delta and

$$\Gamma_{ik} = c_{ijkl} n_j n_l \tag{14}$$

is the Christoffel matrix.

Equation (13) is cubic in c^2. The three roots are the squares of the velocities of the three types of bulk waves that can propagate along a given direction $\mathbf{n}$. The velocity c depends on the propagation direction $\mathbf{n}$, but it does not depend on frequency. For an isotropic solid, the wave that propagates with the highest velocity is a compressional wave, and the other two are shear waves with different polarizations but with the same propagation speed.

B. Surface waves

Equation (5) also admits solutions that correspond to inhomogeneous plane waves. In this case $\mathbf{k}$ is complex. The inhomogeneous waves are constituent parts of the surface wave—a linear combination of inhomogeneous waves is constructed in such a way as to satisfy the boundary condition on the free surface of the crystal.

We now make a distinction between crystal axes, in reference to which the stiffness constants c_{ijkl} are normally provided, and a coordinate system that is aligned with the free surface of a crystal and provides a more convenient reference frame for describing surface wave propagation. We thus specify a coordinate system in which the (x_1, x_2) plane coincides with the stress-free surface of the crystal, and x_3 is the outward normal to that plane such that the crystal occupies the half-space $x_3 \leqslant 0$. In terms of this coordinate system the inhomogeneous plane waves are expressed as

$$u_i = \alpha_i e^{ik(\mathbf{l}\cdot\mathbf{x} - ct)}. \tag{15}$$

The components of $\mathbf{l} = (l_1, l_2, l_3)$ in the (x_1, x_2) plane, l_1 and l_2, are real, whereas l_3 may be complex, and $\mathbf{l}$ is normalized such that the magnitude of its projection in the (x_1, x_2) plane is unity, i.e., $l_1^2 + l_2^2 = 1$. At angular frequency ω the phase

speed along the free surface is thus $c=\omega/k$, and k is identified as the wave number corresponding to propagation along that surface.

For a plane wave that propagates along the x_1 axis we have $l_1=1$ and $l_2=0$, and we denote the complex quantity l_3 by ζ:

$$\mathbf{l}=(1,0,\zeta). \tag{16}$$

Equation (15) becomes

$$u_i=\alpha_i e^{i\zeta k x_3} e^{i(kx_1-\omega t)}, \tag{17}$$

and instead of Eq. (12) we have

$$\rho c^2 \alpha_i = c_{ijkl} l_j l_l \alpha_k . \tag{18}$$

Here, the stiffness constants c_{ijkl} are defined in terms of the coordinate system associated with the free surface and propagation direction. Values of the stiffness constants are normally provided in the coordinate system associated with the crystal axes, and therefore a transformation of the stiffness matrix is usually required, as discussed in detail by Auld.[22] Equation (18) has a nontrivial solution for

$$\det[\Gamma_{ik}(\zeta)-\rho c^2 \delta_{ik}]=0, \tag{19}$$

where

$$\Gamma_{ik}=c_{ijkl} l_j l_l . \tag{20}$$

Substitution of Eq. (16) into (20) yields

$$\begin{aligned}
\Gamma_{11}&=c_{11}+2c_{15}\zeta+c_{55}\zeta^2,\\
\Gamma_{22}&=c_{66}+2c_{46}\zeta+c_{44}\zeta^2,\\
\Gamma_{33}&=c_{55}+2c_{35}\zeta+c_{33}\zeta^2,\\
\Gamma_{12}&=c_{16}+(c_{14}+c_{56})\zeta+c_{45}\zeta^2,\\
\Gamma_{13}&=c_{15}+(c_{13}+c_{55})\zeta+c_{35}\zeta^2,\\
\Gamma_{23}&=c_{56}+(c_{36}+c_{45})\zeta+c_{34}\zeta^2,
\end{aligned} \tag{21}$$

where $\Gamma_{ik}=\Gamma_{ki}$.

With c regarded as a parameter, Eq. (19) is a sixth-order algebraic equation in terms of ζ. Since all coefficients in this equation are real, the roots ζ must be either real or complex conjugate pairs. Real roots correspond to the bulk waves described in Sec. I A. All roots are imaginary for surface (Rayleigh) waves in isotropic solids.

In the anisotropic half-space under consideration, all displacement components of any surface wave must vanish as $x_3\to-\infty$. To satisfy this condition, only roots for which $\mathrm{Im}\,\zeta<0$ are allowed [see Eq. (17)], and there are three such roots for any given value of c. The vector components α_i correspond to each of these roots according to Eq. (18), and a linear combination is constructed with the three corresponding terms given by Eq. (15). Each of these three terms has the same phase velocity c but a different value of ζ for each of the three roots. The assumed solution thus becomes

$$u_i=\sum_{s=1}^{3} C_s \alpha_i^{(s)} e^{ik(\mathbf{l}_s\cdot\mathbf{x}-ct)}=\sum_{s=1}^{3} C_s \alpha_i^{(s)} e^{i\zeta_s k x_3} e^{i(kx_1-\omega t)}, \tag{22}$$

where $\mathbf{l}_s=(1,0,\zeta_s)$. The coefficients C_s are chosen to satisfy the stress-free boundary condition

$$\sigma_{i3}=0 \quad \text{at } x_3=0. \tag{23}$$

From Eq. (4) we have $c_{i3kl}(\partial u_k/\partial x_l)=0$ at $x_3=0$, and Eq. (22) yields

$$c_{i3kl}\sum_{s=1}^{3} C_s \alpha_k^{(s)} l_l^{(s)}=0, \tag{24}$$

where $l_i^{(s)}$ are the components of $\mathbf{l}_s$.

It remains to solve Eqs. (18) and (24) for the wave speed c, eigenvalues ζ_s, eigenvectors $\alpha_i^{(s)}$, and coefficients C_s. For Rayleigh waves in isotropic solids, simple analytic expressions may be derived for ζ_s, $\alpha_i^{(s)}$, and C_s in terms of c, the value of which is determined by the root of a cubic polynomial. For surface waves in anisotropic solids, each of these quantities must be obtained numerically. The algorithm employed in the present investigation is described in Appendix A. See Ref. 21 for further discussion.

II. NONLINEAR THEORY

The theory for nonlinear surface waves in crystals is developed using the method introduced previously to model nonlinear Rayleigh waves in isotropic solids.[3] The method involves calculating the Hamiltonian at cubic order in the wave variables, choosing appropriate generalized coordinates, and deriving evolution equations in terms of slowly varying harmonic amplitudes. The model has no restriction with regard to crystal symmetry, orientation of the free surface with respect to the crystal axes, or propagation direction in the plane of the free surface.

A. Hamiltonian formalism

The Hamiltonian is written in the form

$$H=T+V+W, \tag{25}$$

where T is the kinetic energy, V is the potential energy at quadratic order in the particle displacement, and W is the potential energy at cubic order associated with nonlinear wave interaction. The energies are expressed initially in terms of the harmonic amplitudes $a_n(t)$ appearing in the following generalized form of Eq. (22):

$$u_i(x,z,t)=\sum_n a_n(t) u_{ni}(z) e^{ink x}, \tag{26}$$

where

$$u_{ni}(z)=\sum_{s=1}^{3} C_s \alpha_i^{(s)} e^{ink\zeta_s z} \tag{27}$$

and $u_{ni}=u^*_{(-n)i}$. Here, $x\equiv x_1$ is the coordinate along the direction of propagation, and $z\equiv x_3$ is normal to and directed outward from the free surface of the crystal. The vector $\mathbf{l}$ is thus defined by Eq. (16).

The functions a_n are chosen to be the generalized coordinates, in which case the corresponding momenta are defined by

$$p_n=\frac{\partial T}{\partial \dot{a}_n}, \tag{28}$$

and Hamilton's canonical equations become

$$\dot{a}_n = \frac{\partial H}{\partial p_n}, \quad \dot{p}_n = -\frac{\partial H}{\partial a_n}, \tag{29}$$

where the dots signify time derivatives. This general framework is identical to that used for nonlinear Rayleigh waves in isotropic solids.[3]

B. Energy relations

Before proceeding to the calculation of T, V, and W in Eq. (25), we present defining relations for the elastic (strain) energy in a crystal. The general expression we use for the elastic energy (per unit volume) is

$$\mathcal{E} = \tfrac{1}{2} c_{ijkl} e_{ij} e_{kl} + \tfrac{1}{6} d_{ijklmn} e_{ij} e_{kl} e_{mn} + \cdots . \tag{30}$$

Here the exact expression for the (Lagrangian) strain tensor is employed:

$$e_{ij} = \frac{1}{2}\left(\frac{\partial u_i}{\partial x_j} + \frac{\partial u_j}{\partial x_i} + \frac{\partial u_k}{\partial x_i}\frac{\partial u_k}{\partial x_j} \right), \tag{31}$$

where $e_{ij} = e_{ji}$. The nonlinear stiffness tensor d_{ijklmn} is symmetric with respect to permutation of the indices within each of the pairs *ij*, *kl*, and *mn*, and it is also symmetric with respect to permutation of the pairs themselves. As in linear theory, the symmetries permit the abbreviated index notation associated with Eq. (6) to be used:

$$d_{ijklmn} \rightarrow d_{IJK}. \tag{32}$$

In a coordinate system aligned with the crystal axes there are 20 nonzero elements of d_{IJK} for a cubic crystal, but only the following 6 are independent:[12]

$$\begin{aligned} &d_{111} = d_{222} = d_{333}, \\ &d_{112} = d_{113} = d_{122} = d_{133} = d_{223} = d_{233}, \\ &d_{123}, \quad d_{144} = d_{255} = d_{366}, \\ &d_{155} = d_{166} = d_{244} = d_{266} = d_{344} = d_{355}, \quad d_{456}. \end{aligned} \tag{33}$$

For isotropic solids only three of these elements are independent, and d_{IJK} may be expressed, for example, in terms of Landau's third-order elastic constants A, B, and C:[24]

$$\begin{aligned} &d_{111} = 2(A + 3B + C), \quad d_{112} = 2(B + C), \\ &d_{123} = 2C, \quad d_{144} = B, \\ &d_{155} = \tfrac{1}{2}A + B, \quad d_{456} = \tfrac{1}{4}A. \end{aligned} \tag{34}$$

Substitution of Eq. (31) into (30) yields, to cubic order in the displacement,

$$\mathcal{E} = \mathcal{E}_2 + \mathcal{E}_3, \tag{35}$$

where

$$\mathcal{E}_2 = \frac{1}{2} c_{ijkl} \frac{\partial u_i}{\partial x_j} \frac{\partial u_k}{\partial x_l}, \tag{36}$$

$$\mathcal{E}_3 = \frac{1}{2} c_{ijkl} \frac{\partial u_i}{\partial x_j} \frac{\partial u_p}{\partial x_k} \frac{\partial u_p}{\partial x_l} + \frac{1}{6} d_{ijklmn} \frac{\partial u_i}{\partial x_j} \frac{\partial u_k}{\partial x_l} \frac{\partial u_m}{\partial x_n}. \tag{37}$$

The expression for $\mathcal{E}_3$ may be simplified by rewriting the first term as

$$\frac{1}{2} c_{ijkl} \frac{\partial u_i}{\partial x_j} \frac{\partial u_p}{\partial x_k} \frac{\partial u_p}{\partial x_l} = \frac{1}{2} c_{ijln} \delta_{km} \frac{\partial u_i}{\partial x_j} \frac{\partial u_k}{\partial x_l} \frac{\partial u_m}{\partial x_n}. \tag{38}$$

The tensor $c_{ijln}\delta_{km}$ is not symmetric with respect to permutation of the pairs *ij*, *kl*, and *mn*, but only its symmetric part is required in Eq. (38) and the following substitution may be made:

$$c_{ijln}\delta_{km} \rightarrow \tfrac{1}{3}(c_{ijln}\delta_{km} + c_{jnkl}\delta_{im} + c_{jlmn}\delta_{ik}). \tag{39}$$

Equation (37) may thus be rewritten

$$\mathcal{E}_3 = \frac{1}{6} d'_{ijklmn} \frac{\partial u_i}{\partial x_j} \frac{\partial u_k}{\partial x_l} \frac{\partial u_m}{\partial x_n}, \tag{40}$$

where

$$d'_{ijklmn} = d_{ijklmn} + c_{ijln}\delta_{km} + c_{jnkl}\delta_{im} + c_{jlmn}\delta_{ik}. \tag{41}$$

Although d'_{ijklmn} is symmetric with respect to permutation of the pairs *ij*, *kl*, and *mn*, unlike d_{ijklmn} it is not symmetric with respect to permutation of indices within these pairs.[24] An abbreviated notation given by $d'_{ijklmn} \rightarrow d'_{IJK}$ must therefore have nine values for each of the new indices: (11)→1; (22)→2; (33)→3; (23)→4; (13)→5; (12)→6; (32)→7; (31)→8; (21)→9. Using this notation, Lardner and Tupholme[12] list the 45 nonzero elements of d'_{IJK} for cubic crystals, and they identify the 10 of these elements that are independent.

1. Kinetic energy

The kinetic energy (per unit area) is given by

$$T = \frac{\rho}{2\lambda} \int_x^{x+\lambda} \int_{-\infty}^{0} \dot{u}_i^2 \, dx \, dz, \tag{42}$$

where $\lambda = 2\pi/k$ here is the wavelength at the fundamental frequency in the Fourier expansion of u_i, and the summation convention applies to $\dot{u}_i^2 \equiv \dot{u}_i \dot{u}_i$. Substitution of Eq. (26) yields

$$T = \frac{\rho}{2} \sum_n \dot{a}_n \dot{a}_{-n} \int_{-\infty}^{0} |u_{ni}|^2 \, dz. \tag{43}$$

We introduce the notation

$$\beta_i^{(s)} = C_s \alpha_i^{(s)} \tag{44}$$

in Eq. (27) and let $z' = |n| k z$ to obtain

$$\int_{-\infty}^{0} |u_{ni}|^2 \, dz = \frac{1}{|n|k} \int_{-\infty}^{0} \left| \sum_{s=1}^{3} \beta_i^{(s)} e^{i\zeta_s z'} \right|^2 dz'. \tag{45}$$

The vectors $\beta_i^{(s)}$ may be normalized such that

$$\int_{-\infty}^{0} \left| \sum_{s=1}^{3} \beta_i^{(s)} e^{i\zeta_s z'} \right|^2 dz' = 1, \tag{46}$$

in which case Eq. (43) reduces to

$$T = \frac{\rho}{2k} \sum_n \frac{\dot{a}_n \dot{a}_{-n}}{|n|}. \tag{47}$$

2. Potential energy

The quadratic part of the potential energy (per unit area) is given by

$$V=\frac{1}{\lambda}\int_{x}^{x+\lambda}\int_{-\infty}^{0}\mathcal{E}_2\,dx\,dz. \tag{48}$$

The explicit relation for $\mathcal{E}_2$ given by Eq. (36) is not needed to evaluate the integral. Instead, Eq. (48) may be rewritten[3]

$$V=-\frac{1}{2\lambda}\int_{x}^{x+\lambda}\int_{-\infty}^{0}u_i\frac{\partial\sigma_{ij}}{\partial x_j}dx\,dz. \tag{49}$$

Elimination of the stress tensor using the momentum equation $\partial\sigma_{ij}/\partial x_j=\rho\ddot{u}_i$ and substitution of Eq. (26) yields

$$V=\frac{1}{2}\rho c^2 k\sum_{n}|n|a_n a_{-n}. \tag{50}$$

3. Interaction energy

The wave interaction energy (per unit area) is given by

$$W=\frac{1}{\lambda}\int_{x}^{x+\lambda}\int_{-\infty}^{0}\mathcal{E}_3\,dx\,dz, \tag{51}$$

or, following substitution of Eq. (40),

$$W=\frac{d'_{ijklmn}}{6\lambda}\int_{x}^{x+\lambda}\int_{-\infty}^{0}\frac{\partial u_i}{\partial x_j}\frac{\partial u_k}{\partial x_l}\frac{\partial u_m}{\partial x_n}dx\,dz. \tag{52}$$

It is evident that substitution of Eq. (26) into (52) yields an expression of the form

$$W=\sum_{n_1+n_2+n_3=0}w_{n_1n_2n_3}a_{n_1}a_{n_2}a_{n_3}, \tag{53}$$

where n_1, n_2, and n_3 are harmonic numbers associated with sum and difference frequency generation (not to be confused with the unit vector components n_i used only in Sec. I A), and $w_{n_1n_2n_3}$ is the matrix that characterizes the strength of the corresponding wave interactions.

To develop an expression for the matrix $w_{n_1n_2n_3}$ we begin by considering the contribution to W from the summation over positive n_1 and n_2, and denote this by

$$\overline{W}=\sum_{\substack{n_1>0,\,n_2>0,\\ n_3=-(n_1+n_2)}}\overline{w}_{n_1n_2n_3}a_{n_1}a_{n_2}a_{n_3}. \tag{54}$$

The symmetry of d'_{ijklmn} with respect to permutation of the index pairs *ij*, *kl*, and *mn* leads to symmetry of $w_{n_1n_2n_3}$ with respect to permutation of n_1, n_2, and n_3, and permits W to be expressed as

$$W=3(\overline{W}+\overline{W}^*). \tag{55}$$

Therefore only $\overline{W}$, or $\overline{w}_{n_1n_2n_3}$, needs to be calculated:

$$\overline{w}_{n_1n_2n_3}=w_{n_1n_2n_3}\quad\text{for } n_1,n_2>0. \tag{56}$$

After substituting Eq. (26) into (52) and integrating we obtain

$$\overline{w}_{n_1n_2n_3}=-\frac{k^2}{3}\sum_{s_1,s_2,s_3=1}^{3}\frac{n_1n_2n_3F_{s_1s_2s_3}}{n_1\zeta_{s_1}+n_2\zeta_{s_2}+n_3\zeta^*_{s_3}}, \tag{57}$$

where

$$F_{s_1s_2s_3}=\tfrac{1}{2}d'_{ijklmn}\beta_i^{(s_1)}\beta_k^{(s_2)}[\beta_m^{(s_3)}]^*l_j^{(s_1)}l_l^{(s_2)}[l_n^{(s_3)}]^*. \tag{58}$$

As shown in Appendix B, the matrix $F_{s_1s_2s_3}$ is a generalization of the parameters α, β, γ, etc., that were used in earlier articles on nonlinear Rayleigh waves in isotropic solids.[3,25]

The same expression $F_{s_1s_2s_3}$ appears in Eq. (70) below for the nonlinearity matrix in the evolution equation for the velocity components. Evaluation of $F_{s_1s_2s_3}$ requires (1) transformation of the stiffness tensors c_{ijkl} and d_{ijklmn} into the coordinate system associated with the free surface of the crystal and the direction of propagation in that plane, and (2) solution of the linear eigenvalue problem to determine the quantities $\beta_i^{(s)}$ (the normalized values of $\alpha_i^{(s)}$) and $l_i^{(s)}$. See Sec. I B and Appendix A.

C. Dynamical equations

We now express the energy relations in terms of a new set of canonical variables that permits simplified dynamical equations to be derived for the nonlinear evolution of progressive plane waves. Specifically, the new set of harmonic amplitudes $b_n(t)$ is defined according to[2,3]

$$a_n=b_ne^{-i|n|\omega t}+b^*_{-n}e^{i|n|\omega t}, \tag{59}$$

$$\dot{a}_n=-i|n|\omega(b_ne^{-i|n|\omega t}-b^*_{-n}e^{i|n|\omega t}), \tag{60}$$

with the momentum related to Eq. (60) via Eqs. (28) and (47):

$$p_n=\frac{\rho}{k}\frac{\dot{a}_{-n}}{|n|}. \tag{61}$$

Substituting Eq. (60) in (47), Eq. (59) in (50), and combining the results in Eq. (25) yields

$$H=2\rho c^2k\sum_{n}|n|b_nb^*_n+W. \tag{62}$$

At this point we may follow precisely the algebra used for nonlinear Rayleigh waves and proceed immediately to the result[3]

$$\dot{b}_n=-\frac{i}{2\rho c}\frac{\partial W}{\partial b^*_n}. \tag{63}$$

It remains to express Eq. (63) explicitly in terms of b_n.

The formal procedure is to substitute Eq. (59) in (54), which produces a summation of terms containing exponentials of the form $\exp[i(l+m+n)\omega t]$. As examined in detail for nonlinear Rayleigh waves,[2] averaging the result in time over a fundamental period $2\pi/\omega$ yields at dominant order only those terms for which $l+m+n=0$. These terms are associated with spectral interactions in progressive plane waves. The terms for which $l+m+n\neq0$ account for the negligible effect due to interaction between spectral components that propagate in opposite directions. For the purpose of expressing W in terms of b_n it is therefore expedient to consider *a*

priori only progressive wave propagation, say in the $+x$ direction. In this case Eq. (59) is replaced by

$$a_n = b_n e^{-in\omega t}, \quad n>0,$$
$$= b^*_{-n} e^{i|n|\omega t}, \quad n<0, \tag{64}$$

the substitution of which in Eq. (54) yields

$$\overline{W} = \sum_{n_1,n_2>0} \overline{w}_{n_1 n_2 n_3} b_{n_1} b_{n_2} b^*_{n_1+n_2}. \tag{65}$$

Equation (65) is the same result that is obtained by using Eq. (59) and averaging. Substitution of Eq. (65) into (55) and then evaluation of the derivative in Eq. (63) gives, for $n_1, n_2>0$,

$$\dot{b}_n = -\frac{3i}{2\rho c}\left(\sum_{n_1+n_2=n} \overline{w}_{n_1,n_2,-n} b_{n_1} b_{n_2} + \sum_{n_1} \overline{w}^*_{n_1,n,-(n+n_1)} b^*_{n_1} b_{n+n_1} + \sum_{n_2} \overline{w}^*_{n,n_2,-(n+n_2)} b^*_{n_2} b_{n+n_2} \right). \tag{66}$$

The second and third summations are equivalent and may be combined, and the result may be written, for $n>0$,

$$\dot{b}_n = -\frac{3i}{2\rho c}\left(\sum_{m=1}^{n-1} \overline{w}_{m,n-m,-n} b_m b_{n-m} + 2\sum_{m=n+1}^{\infty} \overline{w}^*_{m-n,n,-m} b_m b^*_{m-n} \right). \tag{67}$$

Equation (67), with $\overline{w}_{n_1 n_2 n_3}$ defined in Eq. (57), describes the nonlinear evolution in time of a plane progressive surface wave in a crystal. The first summation accounts for sum frequency generation, the second for difference frequency generation.

D. Evolution equations

The desired form of the evolution equation is in terms of particle velocity rather than displacement, and as a function of propagation distance rather than time. Thus define the velocity amplitudes $v_n(t)$ by

$$v_n = -in\omega b_n, \tag{68}$$

in terms of which Eq. (67) becomes, for $n>0$,

$$\dot{v}_n = \frac{n^2\omega}{2\rho c^3}\left(\sum_{m=1}^{n-1} S_{m,n-m} v_m v_{n-m} - 2\sum_{m=n+1}^{\infty} S^*_{n,m-n} v_m v^*_{m-n} \right), \tag{69}$$

where the nonlinearity matrix is given by

$$S_{n_1 n_2} = \sum_{s_1,s_2,s_3=1}^{3} \frac{F_{s_1 s_2 s_3}}{n_1\zeta_{s_1} + n_2\zeta_{s_2} - (n_1+n_2)\zeta^*_{s_3}}, \tag{70}$$

and $F_{s_1 s_2 s_3}$ is defined in Eq. (58). In general, there may be up to $3^3=27$ terms in the summation for $S_{n_1 n_2}$.

For isotropic solids there are only seven terms in the summation, all of them real, and $S_{n_1 n_2}$ reduces to the nonlinearity matrix $R_{n_1 n_2}$ used in previous work[2,11,15–18,26] for Rayleigh waves according to

$$R_{n_1 n_2} = -(\Lambda^3/\mu) S_{n_1 n_2}, \tag{71}$$

where

$$2\Lambda^2 = \xi_t + \frac{1}{\xi_t} + \eta^2\left(\xi_l + \frac{1}{\xi_l} \right) + 4\eta, \tag{72}$$

$\xi_t = (1-c^2/c_t^2)^{1/2}$, $\xi_l = (1-c^2/c_l^2)^{1/2}$, $\eta = -2\xi_t/(1+\xi_t^2)$, c_t is the propagation speed of bulk shear waves in the solid, and c_l is the speed of bulk compressional waves (see also Appendix B). The shear modulus μ renders $R_{n_1 n_2}$ dimensionless ($F_{s_1 s_2 s_3}$, and therefore $S_{n_1 n_2}$, have the same dimensions as the stiffness constants), and the expression for Λ follows from the normalization in Eq. (46).

Equation (69) is suitable for initial value problems, in which a spatial waveform is known at an instant in time and a description of the field is desired at later times. However, one is usually concerned with boundary value problems, in which a known waveform is radiated from a source at a given location, and the evolution of the wave as a function of propagation distance is of interest. A rigorous derivation of the transformation of Eq. (69) from an evolution equation in time to one in space has been provided for the case of isotropic solids.[2] Although the same formal procedure may be followed here for crystals, the result is the same. The space derivative $c(dv_n/dx)$ appears in place of the time derivative $\dot{v}_n$, and Eq. (69) becomes, for $n>0$,

$$\frac{dv_n}{dx} = \frac{n^2\omega}{2\rho c^4}\left(\sum_{m=1}^{n-1} S_{m,n-m} v_m v_{n-m} - 2\sum_{m=n+1}^{\infty} S^*_{n,m-n} v_m v^*_{m-n} \right), \tag{73}$$

where here $v_n = v_n(x)$, and the particle velocity vector is reconstructed as in Eq. (26):

$$v_i(x,z,t) = \sum_{n=1}^{\infty} v_n(x) u_{ni}(z) e^{in(kx-\omega t)} + \text{c.c.}, \tag{74}$$

where

$$u_{ni}(z) = \sum_{s=1}^{3} \beta_i^{(s)} e^{ink\zeta_s z}. \tag{75}$$

The spectral components for $n<0$ are given by $v_n = v^*_{-n}$.

Equation (73) is an appropriate form of the evolution equation for numerical integration. We now present an alternative form that reveals the symmetry properties of the nonlinearity matrix. Equation (73) may be rewritten as follows, with the summation on the right side performed over all indices, negative as well as positive:

$$\frac{dv_n}{dx} = \frac{n^2\omega}{2\rho c^4} \sum_{l+m=n} \frac{lm}{|lm|} S_{lm(-n)} v_l v_m. \tag{76}$$

The nonlinearity matrix in Eq. (70), expressed here as a function of three indices, is symmetric over permutation of these indices:

$$S_{n_1n_2n_3}=S_{n_2n_1n_3}=S_{n_3n_2n_1}=S_{n_1n_3n_2}. \tag{77}$$

When one of the indices is negative and two are positive, Eq. (70) becomes, with $n_1+n_2+n_3=0$,

$$S_{n_1n_2n_3}=\sum_{s_1,s_2,s_3=1}^{3}\frac{F_{s_1s_2s_3}}{n_j\kappa_{s_j}+i|n_j|\xi_{s_j}}, \tag{78}$$

where $\zeta_s=\kappa_s-i\xi_s$ has been separated into its real and imaginary parts, and the standard summation convention is employed:

$$n_j\kappa_{s_j}+i|n_j|\xi_{s_j}\equiv\sum_{j=1}^{3}(n_j\kappa_{s_j}+i|n_j|\xi_{s_j}). \tag{79}$$

When two of the indices are negative and one is positive, the value of the matrix is obtained from Eq. (78) by using the relation

$$S_{n_1n_2n_3}=S^*_{(-n_1)(-n_2)(-n_3)}. \tag{80}$$

It was shown previously[26] that the permutation symmetries in Eq. (77) guarantee conservation of energy for nonlinear surface waves in isotropic solids. The same analysis applies to nonlinear surface waves in crystals, and the same spectral form of the conservation law is obtained:

$$\sum_{n=1}^{\infty}\frac{|v_n|^2}{n}=\text{const.} \tag{81}$$

III. NUMERICAL RESULTS

It is convenient for numerical solution of Eq. (73) to employ the following dimensionless form:

$$\frac{dV_n}{dX}+A_nV_n=\frac{n^2}{8|S_{11}|}\left(\sum_{m=1}^{n-1}S_{m,n-m}V_mV_{n-m}-2\sum_{m=n+1}^{N}S^*_{n,m-n}V_mV^*_{m-n}\right), \tag{82}$$

where

$$V_n=v_n/v_0,\quad X=x/x_0, \tag{83}$$

v_0 is a characteristic velocity amplitude, and

$$x_0=\frac{\rho c^4}{4|S_{11}|\omega v_0} \tag{84}$$

is a length scale that characterizes the shock formation distance for a surface wave radiated at angular frequency ω and with amplitude v_0. The nonlinearity matrix element S_{11} appearing in Eqs. (82) and (84) corresponds to second harmonic generation, and for isotropic solids its magnitude is closely related to the overall nonlinearity of the material.[18] After $S_{n_1n_2}$ is calculated according to Eq. (70) [see the paragraph following Eq. (58)], Eq. (82) is solved using a standard Runge–Kutta algorithm. The *ad hoc* absorption term A_nV_n is required for numerical stability when shocks are formed, and the upper limit N in the second summation restricts the set of harmonics to $1\leqslant n\leqslant N$. The energy relation associated with Eq. (82) is[26]

$$\frac{d}{dX}\sum_{n=1}^{N}\frac{|V_n|^2}{n}=-2\sum_{n=1}^{N}A_n\frac{|V_n|^2}{n}, \tag{85}$$

which for $A_n=0$ becomes

$$\sum_{n=1}^{N}\frac{|V_n|^2}{n}=\text{const.} \tag{86}$$

Equation (81) is recovered for $A_n=0$ and $N=\infty$.

Calculations are presented for propagation in steel (a representative isotropic solid) and in potassium chloride (KCl, a cubic crystal). Steel is considered here in order to verify that calculations obtained from the present algorithm for arbitrary crystals reproduce results obtained in earlier investigations of surface waves in isotropic solids.[3,11] In addition, results for an isotropic solid provide a useful basis of comparison for the new results obtained here for crystals. The boundary condition for each case corresponds to a monofrequency source at $X=0$:

$$V_1=1,\quad V_{n>1}=0. \tag{87}$$

We let $A_n=n^2A_1$ to model thermoviscous losses exhibiting quadratic frequency dependence, with $A_1=0.025$. The absorption is sufficiently weak that the propagation appears lossless up to the point of shock formation, and the shocks exhibit well defined jumps. All calculations were performed with $N=200$ harmonics.

The linear and nonlinear stiffness constants used to calculate the elements of the nonlinearity matrix for steel are the same as in earlier work.[3,11] In Fig. 1(a) and (b) are shown the calculated horizontal ($V_x=v_x/v_0$) and vertical ($V_z=v_z/v_0$) components of the particle velocity waveform at two distances from the source ($X=0$ corresponds to the source waveform). It is seen that x_0 (the distance at which $X=1$) is an appropriate measure of the shock formation distance in this case. Shown in Fig. 1(c) are the magnitudes $|V_n|$ of the harmonics as functions of X. The calculated waveform distortion and harmonic propagation curves are in complete agreement with earlier work, where extensive discussion of these results is provided.[3,11]

The values of c_{IJ} and d_{IJK} for KCl were obtained from the table provided by Lardner and Tupholme,[12] in which the values of d_{IJK} are repeated from the list compiled by Hearmon.[27] Two different cuts of KCl are chosen to illustrate propagation of surface waves in a crystal. In the first case the free surface is the (111) plane, and in the second it is the (001) plane. Figure 2 shows normalized propagation speeds $C=c/(c_{44}/\rho)^{1/2}$ for surface waves in these two planes, where ϕ is the angle with respect to the projection of any crystal axis in the plane of the cut, and c_{44} is the stiffness constant in the crystal coordinate system. For an isotropic solid c_{44} equals the shear modulus μ, in which case $C=1$ would correspond to a value of c equal to the propagation speed of a bulk shear wave. There is a 60-degree periodicity for the propagation speed in the (111) plane of KCl, and a 90-degree periodicity in the (001) plane.

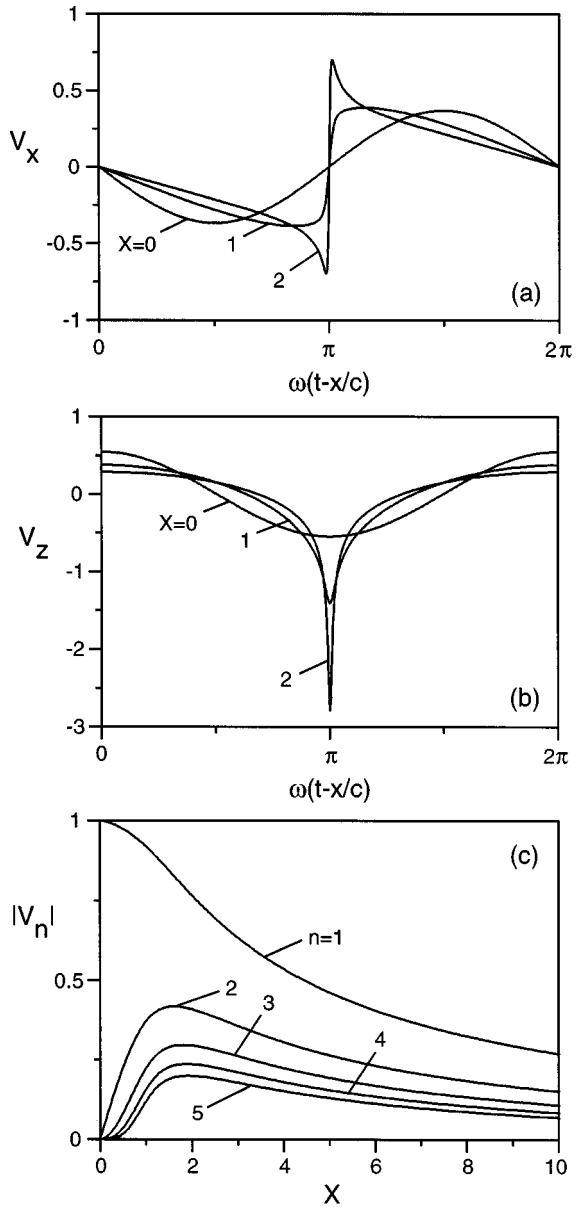

FIG. 1. Nonlinear surface waves in steel: (a) horizontal and (b) vertical velocity waveforms and (c) harmonic propagation curves.

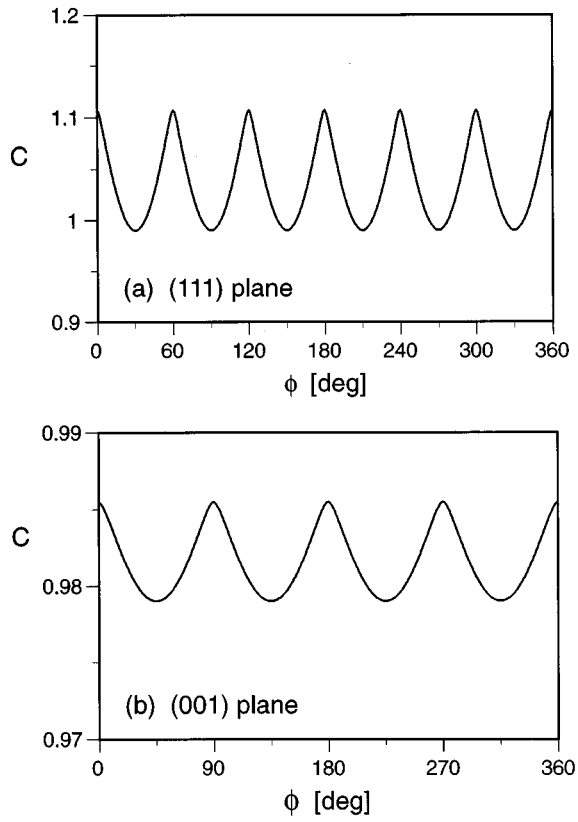

FIG. 2. Dependence of the normalized surface wave speed $C=c/(c_{44}/\rho)^{1/2}$ in KCl for propagation in the (a) (111) and (b) (001) planes. The angle ϕ is with respect to the projection of any crystal axis in the specified plane, e.g., the $[11\bar{2}]$ direction in (a) and the [100] direction in (b).

We first consider nonlinear propagation of a surface wave in the (111) plane of KCl. The direction of propagation is taken to be along the projection of one of the crystal axes, e.g., $\phi=0$ in Fig. 2(a), or say the $[11\bar{2}]$ direction. Because of the symmetry of this geometry there are only two velocity components in the surface wave, the (horizontal) component along the direction of propagation, V_x, and the (vertical) component along the normal to the surface, V_z. In this case $V_y=0$, where $y\equiv x_2$. The quantity x_0 is again a reasonable estimate of the shock formation distance. Note that waveform distortion occurs in a direction opposite that in steel, namely, positive portions of the horizontal velocity waveform recede in time (i.e., arrive later than the zero crossings), and negative portions advance. Accordingly, in the portion of the waveform where the horizontal component forms a shock, the vertical component forms a positive spike, whereas the spike is negative in steel. In contrast with isotropic solids, waveform distortion in KCl is not symmetric (the asymmetry is more noticeable in the vertical component). The reason for the asymmetry is that the elements of $S_{n_1n_2}$ are complex for KCl, whereas they are real for steel. Nevertheless, the harmonic propagation curves in Fig. 3(c) are very similar to those for the isotropic case, Fig. 1(c).

We now consider surface wave propagation in the (001) plane, with the direction of propagation taken to be one of the crystal axes, e.g., $\phi=0$ in Fig. 2(b), or say the [100] direction. Because of the symmetry for this cut and propagation direction, one might expect results that are similar to those for an isotropic solid. Moreover, the elements of matrix $S_{n_1n_2}$ are real in this case, as they are for all isotropic solids. Typical waveforms are shown in Fig. 4(a) and (b). Again there are only two velocity components, V_x and V_z, with $V_y=0$. Here, the nonlinearity has the same sign as nonlinearity in steel, with positive portions of the horizontal velocity waveform advancing in time and negative portions receding. Otherwise, the waveform evolution is substantially different from that in steel, and x_0 is no longer an indication of the shock formation distance. Since $S_{11}^{\text{steel}}/S_{11}^{\text{KCl}}=50$ for this case, the rate of second harmonic generation in steel is much greater than in KCl (for the cut and propagation direction under consideration). However, the differences in the waveform distortion depicted in Figs. 1 and 4 are due mainly to the relative rate of third harmonic generation. Specifically, we have $S_{12}^{\text{steel}}/S_{11}^{\text{steel}}=0.71$ as compared with $S_{12}^{\text{KCl}}/S_{11}^{\text{KCl}}=0.037$, showing that in KCl the efficiency of third har-

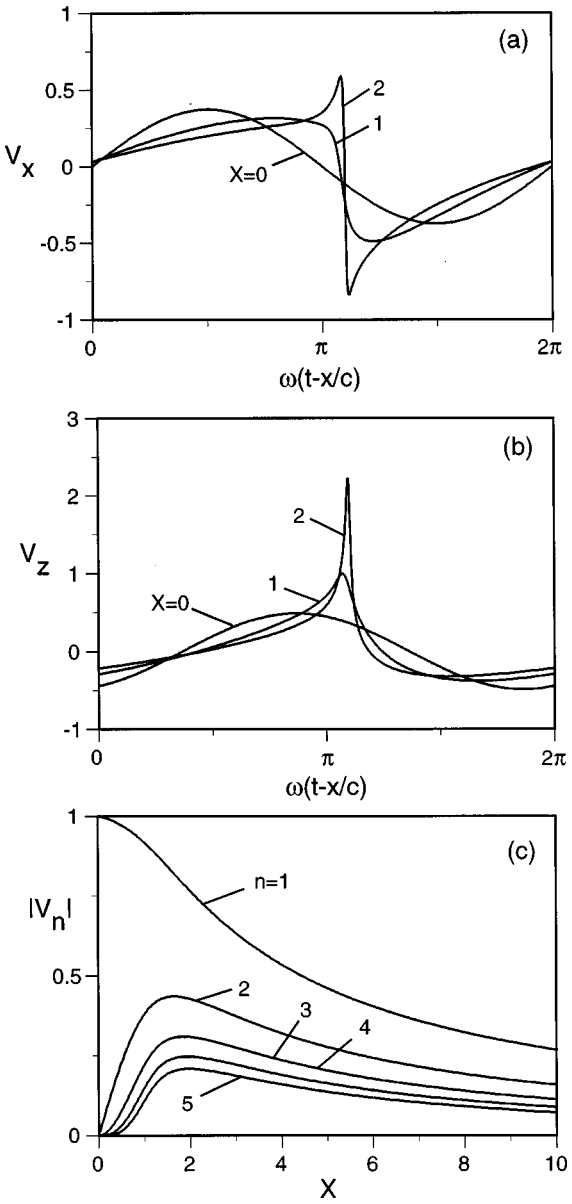

FIG. 3. Nonlinear surface waves in the (111) plane of KCl, for propagation along the projection of one of the cubic axes: (a) horizontal and (b) vertical velocity waveforms and (c) harmonic propagation curves.

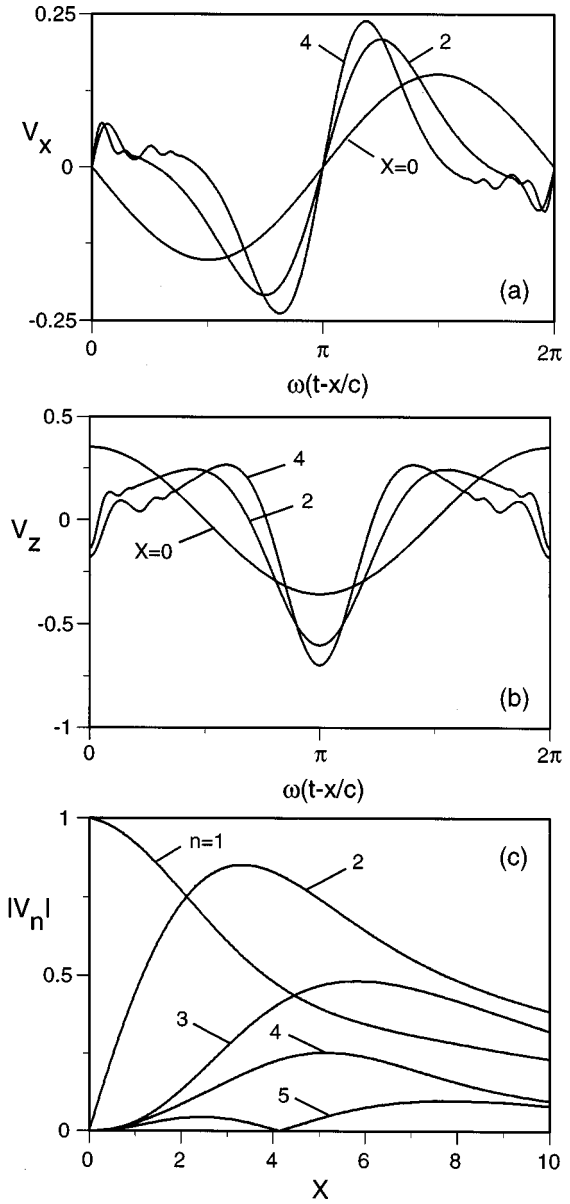

FIG. 4. Nonlinear surface waves in the (001) plane of KCl, for propagation along one of the cubic axes: (a) horizontal and (b) vertical velocity waveforms and (c) harmonic propagation curves.

monic generation is very poor, and therefore shock formation does not occur.

Because the energy in the wave is confined initially to the fundamental and second harmonic components, the second harmonic is seen in Fig. 4(c) to attain an amplitude equal to that of the fundamental at $X \simeq 2$, where the amplitudes of all higher harmonics are still relatively small. This fact permits investigation of second harmonic generation analytically near the source by ignoring third and higher harmonic generation completely. As shown in Appendix C, the analytic solution in this case, for no absorption, is

$$|V_1| = \operatorname{sech}(X/2\sqrt{2}), \tag{88}$$

$$|V_2| = \sqrt{2}\tanh(X/2\sqrt{2}). \tag{89}$$

These equations are compared in Fig. 5 (dashed lines) with the numerical results in Fig. 4(c) for $n=1$ and $n=2$ (solid lines). Agreement for the fundamental component is reasonable up to $X \simeq 5$, and for the second harmonic up to $X \simeq 2$. Equations (88) and (89) are in perfect agreement with numerical solutions of Eq. (82) for $N=2$ and $A_n=0$. Equations (88) and (89) coincide with the solution for two-wave interaction in nonlinear optics,[28] but the physical mechanisms that restrict the number of interacting waves are different in the two cases. In nonlinear optics it is dispersion, and in our case it is the inefficiency of third harmonic generation. The harmonic propagation curves in Fig. 4(c) are most unusual for nonlinear acoustic waves in nondispersive media.

IV. SUMMARY

Spectral evolution equations for nonlinear surface waves in crystals were derived within the theoretical framework developed previously for Rayleigh waves in isotropic solids.[3] There are no restrictions with regard to symmetry of the crystal, orientation of the free surface with respect to the

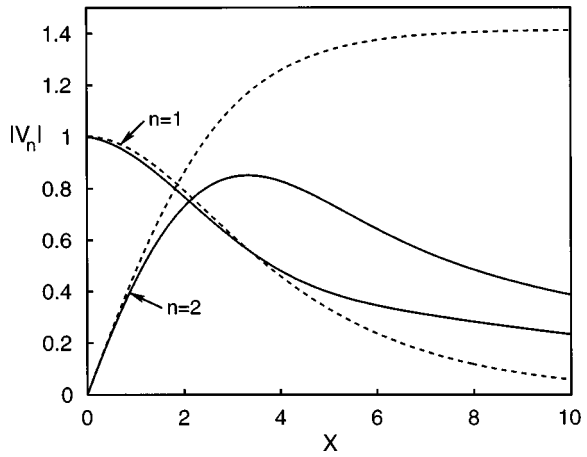

FIG. 5. Comparison of Eqs. (88) and (89) (dashed lines) with the curves for $n=1$ and $n=2$ in Fig. 4(c) (solid lines).

crystal axes, or the direction of propagation in the plane of the free surface. Numerical simulations of waveform distortion, shock formation, and harmonic propagation curves were presented for surface waves in two different cuts of a potassium chloride crystal. In one case the nonlinear distortion leading to shock formation resembles the evolution process in isotropic solids. In the other, the low efficiency of third harmonic generation prevents shock formation and leads to unusually strong second harmonic generation for a nondispersive medium.

ACKNOWLEDGMENTS

Discussions with Ronald Kumon are gratefully acknowledged. This work was supported by the National Science Foundation, the Office of Naval Research, and the Schlumberger Foundation.

APPENDIX A: NUMERICAL SOLUTION OF THE EIGENVALUE PROBLEM

Here we describe the numerical procedure used to solve Eqs. (18) and (24). Begin by introducing the dimensionless notation

$$q=\rho c^2/c_{44}, \quad G_{ik}=\Gamma_{ik}/c_{44}, \tag{A1}$$

such that Eqs. (18) and (19) may be written

$$(G_{ik}-q\,\delta_{ik})\alpha_k=0, \tag{A2}$$

$$\det(G_{ik}-q\,\delta_{ik})=0, \tag{A3}$$

where $G_{ik}=G_{ik}(\zeta)$. The stiffness constant c_{44} was chosen as a normalization factor because for an isotropic solid $c_{44}=\mu$ and thus $q=c^2/c_t^2$, where $c_t=(\mu/\rho)^{1/2}$ is the propagation speed of bulk shear waves. The value of q is thus expected to be of order unity. If we regard q as a known parameter, Eq. (A3) may be solved for ζ, the substitution of which in Eq. (A2) determines α_k. We refer to ζ and α_k as the eigenvalues and eigenvectors, respectively, of the linear system. The solutions for ζ and α_k are used to refine the estimate of q as described below, and the procedure is repeated iteratively until a desired accuracy is achieved.

We thus begin with an assumed value of q and express Eq. (A2) in matrix form:

$$(\mathbf{G}-q\mathbf{I})\boldsymbol{\alpha}=\mathbf{0}, \tag{A4}$$

where $\mathbf{I}$ is the identity matrix and, using Eqs. (21), we may write

$$\mathbf{G}=\mathbf{G}_0+\mathbf{G}_1\zeta+\mathbf{G}_2\zeta^2. \tag{A5}$$

With

$$\mathbf{A}=\mathbf{G}_2, \quad \mathbf{B}=\mathbf{G}_1, \quad \mathbf{C}=\mathbf{G}_0-q\mathbf{I}, \tag{A6}$$

Eq. (A4) takes the form

$$(\mathbf{A}\zeta^2+\mathbf{B}\zeta+\mathbf{C})\boldsymbol{\alpha}=\mathbf{0}, \tag{A7}$$

where

$$\mathbf{A}=\begin{pmatrix} c_{55} & c_{45} & c_{35} \\ c_{45} & c_{44} & c_{34} \\ c_{35} & c_{34} & c_{33} \end{pmatrix}, \tag{A8}$$

$$\mathbf{B}=\begin{pmatrix} 2c_{15} & c_{14}+c_{56} & c_{13}+c_{55} \\ c_{14}+c_{56} & 2c_{46} & c_{36}+c_{45} \\ c_{13}+c_{55} & c_{36}+c_{45} & 2c_{35} \end{pmatrix}, \tag{A9}$$

$$\mathbf{C}=\begin{pmatrix} c_{11}-q & c_{16} & c_{15} \\ c_{16} & c_{66}-q & c_{56} \\ c_{15} & c_{56} & c_{55}-q \end{pmatrix}. \tag{A10}$$

To solve Eq. (A7) for ζ we multiply by $\mathbf{A}^{-1}$ and define

$$\mathbf{B}'=\mathbf{A}^{-1}\mathbf{B}, \quad \mathbf{C}'=\mathbf{A}^{-1}\mathbf{C} \tag{A11}$$

to obtain

$$(\mathbf{I}\zeta^2+\mathbf{B}'\zeta+\mathbf{C}')\boldsymbol{\alpha}=\mathbf{0}. \tag{A12}$$

It is convenient for numerical purposes to rewrite Eq. (A12) as

$$\begin{pmatrix} \mathbf{0} & \mathbf{I} \\ -\mathbf{C}' & -\mathbf{B}' \end{pmatrix}\begin{pmatrix} \boldsymbol{\alpha} \\ \boldsymbol{\beta} \end{pmatrix}=\zeta\begin{pmatrix} \boldsymbol{\alpha} \\ \boldsymbol{\beta} \end{pmatrix}. \tag{A13}$$

The equivalence of Eqs. (A12) and (A13) is confirmed by eliminating $\boldsymbol{\beta}$ in the latter. Equation (A13) may now be solved using standard methods for finding eigenvalues of the matrix

$$\mathbf{Z}=\begin{pmatrix} \mathbf{0} & \mathbf{I} \\ -\mathbf{C}' & -\mathbf{B}' \end{pmatrix}. \tag{A14}$$

There are six eigenvalues of $\mathbf{Z}$. The desired eigenvalues are the three for which $\mathrm{Im}\,\zeta_s<0$. With the three values of ζ_s in hand, the corresponding eigenvector components $\alpha_k^{(s)}$ are determined (to within a constant C_s) by Eq. (A2).

The three constants C_s are determined by Eq. (24),

$$c_{i3kl}\sum_{s=1}^{3} C_s\alpha_k^{(s)}l_l^{(s)}=0, \tag{A15}$$

which may be rewritten, with the summation convention applied to the index s, as

$$D_{is}C_s=0, \tag{A16}$$

where [recall Eq. (16)]

$$D_{is}(q)=c_{i3k1}\alpha_k^{(s)}(q)+c_{i3k3}\alpha_k^{(s)}(q)\zeta_s(q). \tag{A17}$$

Nontrivial solutions for the constants C_s require that the determinant of the matrix D_{is} vanish. The eigenvalues and eigenvectors calculated above are substituted in Eq. (A17), and the result is used evaluate the function

$$f(q)=|\det D_{is}(q)|^2. \tag{A18}$$

A new value of q is chosen, the corresponding eigenvalues ζ_s and eigenvectors $\alpha_k^{(s)}$ are calculated, and the procedure is repeated until $f(q)$ is sufficiently close to zero. The final values of the matrix elements D_{is} are then inserted in Eq. (A16) to solve for the constants C_s.

APPENDIX B: ISOTROPIC SOLIDS

It is important to verify that the present theory for nonlinear surface waves in arbitrary anisotropic solids indeed reduces to the earlier theory[2,3] for nonlinear Rayleigh waves in isotropic solids. We shall perform this comparison in terms of the interaction energy W, because, as seen from Eq. (63) and the evolution equations that follow, this energy function determines completely the nonlinear properties of surface waves within the framework of the theory.

Begin by substituting Eq. (57) in (54) to obtain (recall that overbars signify $n_1, n_2>0$)

$$\overline{W}=\frac{k^2}{3}\sum_{n_1+n_2+n_3=0} a_{n_1}a_{n_2}a_{n_3} \times\sum_{s_1,s_2,s_3=1}^{3}\frac{n_1n_2|n_3|F_{s_1s_2s_3}}{n_1\zeta_{s_1}+n_2\zeta_{s_2}+n_3\zeta_{s_3}^*}. \tag{B1}$$

For an isotropic solid ζ_s is imaginary,

$$\zeta_s=-i\xi_s, \tag{B2}$$

and s assumes only two values because there are only two bulk wave modes, shear (transverse) and compressional (longitudinal), in an isotropic solid:

$$s=t,l. \tag{B3}$$

Specifically, we have[2,3]

$$\xi_t=\sqrt{1-c^2/c_t^2},\quad \xi_l=\sqrt{1-c^2/c_l^2}, \tag{B4}$$

where c_t is the propagation speed of a bulk shear wave in an isotropic solid, and c_l is the speed of a bulk compressional wave. Given that ζ is imaginary, and taking into account the form of the eigenvectors used in previous work,[2,3] it can be shown that $F_{s_1s_2s_3}$ in Eq. (58) must also be imaginary, i.e.,

$$\mathrm{Re}\,F_{s_1s_2s_3}=0. \tag{B5}$$

We therefore let

$$\hat{F}_{s_1s_2s_3}=(\Lambda^3/\mu)\,\mathrm{Im}\,F_{s_1s_2s_3}, \tag{B6}$$

where the dimensionless factor Λ defined in Eq. (72) accounts for the normalization in Eq. (46), and the shear modulus μ, which renders $R_{n_1n_2}$ dimensionless, was used as a normalization factor in the theory for isotropic solids.[3] Equation (B1) thus becomes

$$\overline{W}=-\frac{\mu k^2}{3\Lambda^3}\sum_{n_1+n_2=|n_3|} a_{n_1}a_{n_2}a_{|n_3|}^* \times\sum_{s_1,s_2,s_3=t,l}\frac{n_1n_2|n_3|\hat{F}_{s_1s_2s_3}}{n_1\xi_{s_1}+n_2\xi_{s_2}+|n_3|\xi_{s_3}}. \tag{B7}$$

The expression derived previously for the Rayleigh wave interaction energy in an isotropic solid is [Eq. (2) of Ref. 25]

$$W_{\mathrm{R}}=-\mu k^2\sum_{n_1+n_2+n_3=0} a_{n_1}a_{n_2}a_{n_3}|n_1n_2n_3| \times\left(\frac{\alpha}{|n_1|\xi_t+|n_2|\xi_t+|n_3|\xi_l}+\frac{\beta}{|n_1|\xi_t+|n_2|\xi_l+|n_3|\xi_l} +\frac{\gamma}{|n_1|\xi_l+|n_2|\xi_l+|n_3|\xi_l}-\frac{\delta n_1n_2/|n_1n_2|}{|n_1|\xi_t+|n_2|\xi_t+|n_3|\xi_l} -\frac{\varepsilon n_1n_2/|n_1n_2|}{|n_1|\xi_l+|n_2|\xi_l+|n_3|\xi_l}-\frac{\nu n_1n_2/|n_1n_2|}{|n_1|\xi_l+|n_2|\xi_l+|n_3|\xi_l}\right). \tag{B8}$$

We now compare Eqs. (B7) and (B8). Whereas Eq. (B7) is symmetric with respect to permutation of the indices n_1, n_2, and n_3, Eq. (B8) is not. To write the latter in symmetric form it is necessary to average Eq. (B8) with respect to permutation of (n_1,n_2,n_3), after which the summation may be written as follows for $n_1,n_2>0$:

$$\overline{W}_{\mathrm{R}}=-\frac{\mu k^2}{3}\sum_{n_1+n_2=|n_3|} a_{n_1}a_{n_2}a_{|n_3|}^*|n_1n_2n_3|\Bigg[\alpha\left(\frac{1}{|n_1|\xi_t+|n_2|\xi_t+|n_3|\xi_l}+\frac{1}{|n_1|\xi_t+|n_2|\xi_l+|n_3|\xi_t}+\frac{1}{|n_1|\xi_l+|n_2|\xi_t+|n_3|\xi_t}\right) -\delta\left(\frac{1}{|n_1|\xi_t+|n_2|\xi_t+|n_3|\xi_l}-\frac{1}{|n_1|\xi_t+|n_2|\xi_l+|n_3|\xi_t}-\frac{1}{|n_1|\xi_l+|n_2|\xi_t+|n_3|\xi_t}\right) +\beta\left(\frac{1}{|n_1|\xi_t+|n_2|\xi_l+|n_3|\xi_l}+\frac{1}{|n_1|\xi_l+|n_2|\xi_l+|n_3|\xi_t}+\frac{1}{|n_1|\xi_l+|n_2|\xi_t+|n_3|\xi_l}\right)+\frac{\varepsilon}{|n_1|\xi_l+|n_2|\xi_l+|n_3|\xi_t} +\frac{3\gamma}{|n_1|\xi_l+|n_2|\xi_l+|n_3|\xi_l}+\frac{\nu}{|n_1|\xi_l+|n_2|\xi_l+|n_3|\xi_l}\Bigg]. \tag{B9}$$

Equations (B7) and (B9) are consistent and can be compared term-by-term to show that

$$\hat{F}_{111}=0, \quad \hat{F}_{112}=\alpha-\delta,$$
$$\hat{F}_{211}=\hat{F}_{121}=\alpha+\delta, \quad \hat{F}_{122}=\hat{F}_{212}=\beta, \tag{B10}$$
$$\hat{F}_{221}=\beta+\varepsilon, \quad \hat{F}_{222}=3\gamma+\nu.$$

In Ref. 3, the new parameters α', β', and γ' were introduced to express Eq. (B8) more concisely as

$$W_{\mathrm{R}}=-\mu k^2 \sum_{n_1+n_2+n_3=0} a_{n_1}a_{n_2}a_{n_3}|n_1n_2n_3| \times\left(\frac{\alpha'}{|n_1|\xi_t+|n_2|\xi_t+|n_3|\xi_l}+\frac{\beta'}{|n_1|\xi_t+|n_2|\xi_l+|n_3|\xi_l} +\frac{\gamma'}{|n_1|\xi_l+|n_2|\xi_l+|n_3|\xi_l}\right), \tag{B11}$$

the symmetric form of which is, for $n_1, n_2>0$,

$$\overline{W}_{\mathrm{R}}=-\frac{\mu k^2}{3} \sum_{n_1+n_2=|n_3|} a_{n_1}a_{n_2}a^*_{|n_3|}|n_1n_2n_3| \times\left[\alpha'\left(\frac{1}{|n_1|\xi_t+|n_2|\xi_t+|n_3|\xi_l}+\frac{1}{|n_1|\xi_t+|n_2|\xi_l+|n_3|\xi_t} +\frac{1}{|n_1|\xi_l+|n_2|\xi_t+|n_3|\xi_t}\right)+\beta'\left(\frac{1}{|n_1|\xi_t+|n_2|\xi_l+|n_3|\xi_l} +\frac{1}{|n_1|\xi_l+|n_2|\xi_l+|n_3|\xi_t}+\frac{1}{|n_1|\xi_l+|n_2|\xi_t+|n_3|\xi_l}\right) +\frac{3\gamma'}{|n_1|\xi_l+|n_2|\xi_l+|n_3|\xi_l}\right]. \tag{B12}$$

Comparison of Eqs. (B7) and (B12) yields

$$\hat{F}_{111}=0,$$
$$\hat{F}_{211}=\hat{F}_{121}=\alpha', \tag{B13}$$
$$\hat{F}_{122}=\hat{F}_{212}=\beta',$$

as well as

$$\frac{\hat{F}_{112}+\hat{F}_{221}}{\xi_t+\xi_l}+\frac{\hat{F}_{222}}{2\xi_l}=\frac{\alpha'+\beta'}{\xi_t+\xi_l}+\frac{3\gamma'}{2\xi_l}. \tag{B14}$$

Using Eqs. (B13) to eliminate α' and β' in Eq. (B14) and solving for γ' yields

$$\gamma'=\frac{2\xi_l(\hat{F}_{112}+\hat{F}_{221}-\hat{F}_{211}-\hat{F}_{122})}{3(\xi_t+\xi_l)}+\frac{\hat{F}_{222}}{3}. \tag{B15}$$

Equations (B10) are substituted in Eq. (B15) to eliminate $\hat{F}_{s_1s_2s_3}$ from the expression for γ', and they are substituted in Eqs. (B13) to express α' and β' in terms of unprimed quantities. The results are

$$\alpha'=\alpha+\delta, \quad \beta'=\beta,$$
$$\gamma'=\gamma+\frac{1}{3}\left(\nu+\frac{2\xi_l(\varepsilon-2\delta)}{\xi_t+\xi_l}\right), \tag{B16}$$

which reproduce exactly the relations obtained previously for isotropic solids.[3]

APPENDIX C: ANALYTIC SOLUTION FOR TWO-WAVE INTERACTION

Here we derive an analytic solution of Eq. (82) for the case in which nonlinear interaction is restricted to the fundamental and second harmonic in the absence of absorption. Equation (82) reduces for $N=2$ and $A_n=0$ to the two coupled equations

$$\frac{dV_1}{dX}=-\frac{S^*_{11}}{4|S_{11}|}V_1^*V_2, \tag{C1}$$

$$\frac{dV_2}{dX}=\frac{S_{11}}{2|S_{11}|}V_1^2. \tag{C2}$$

Letting

$$V_n=\hat{V}_n e^{i\theta} \tag{C3}$$

yields

$$\frac{d\hat{V}_1}{dX}=-\frac{(S_{11}e^{i\theta})^*}{4|S_{11}|}\hat{V}_1^*\hat{V}_2, \tag{C4}$$

$$\frac{d\hat{V}_2}{dX}=\frac{S_{11}e^{i\theta}}{2|S_{11}|}\hat{V}_1^2. \tag{C5}$$

Now choose θ such that $S_{11}e^{i\theta}=|S_{11}|$ to obtain

$$\frac{d\hat{V}_1}{dX}=-\frac{1}{4}\hat{V}_1^*\hat{V}_2, \tag{C6}$$

$$\frac{d\hat{V}_2}{dX}=\frac{1}{2}\hat{V}_1^2. \tag{C7}$$

Monofrequency source radiation is assumed, for which the boundary condition at $X=0$ is expressed

$$\hat{V}_1=V_0, \quad \hat{V}_2=0. \tag{C8}$$

With V_0 taken to be real (and positive), and since Eqs. (C6) and (C7) have only real coefficients, we may seek real solutions for $\hat{V}_1$ and $\hat{V}_2$, in which case $\hat{V}_1^*=\hat{V}_1$. Now multiply Eq. (C6) by $\hat{V}_1$, Eq. (C7) by $\frac{1}{2}\hat{V}_2$, and add the results to obtain

$$\frac{d\hat{V}_1^2}{dX}+\frac{1}{2}\frac{d\hat{V}_2^2}{dX}=0. \tag{C9}$$

Integration of Eq. (C9) yields

$$\hat{V}_1^2+\tfrac{1}{2}\hat{V}_2^2=V_0^2, \tag{C10}$$

where the integration constant was determined by the boundary condition, Eqs. (C8). Equation (C10) agrees with Eq. (86). Using Eq. (C10) to eliminate $\hat{V}_1^2$ from Eq. (C7) gives, following separation of variables,

$$dX=\frac{4d\hat{V}_2}{2V_0^2-\hat{V}_2^2}. \tag{C11}$$

Integration yields

$$X = \frac{\sqrt{2}}{V_0} \ln\left(\frac{\sqrt{2}V_0 + \hat{V}_2}{\sqrt{2}V_0 - \hat{V}_2} \right), \tag{C12}$$

where the integration constant was again determined by Eqs. (C8).

Solving Eq. (C12) for $\hat{V}_2$ yields

$$\hat{V}_2 = \sqrt{2}V_0 \tanh(V_0 X/2\sqrt{2}) \tag{C13}$$

for the second harmonic, the substitution of which in Eq. (C10) gives

$$\hat{V}_1 = V_0 \operatorname{sech}(V_0 X/2\sqrt{2}) \tag{C14}$$

for the fundamental. From Eq. (C3) we have $|V_n| = |\hat{V}_n|$, and therefore setting $V_0 = 1$ in correspondence with Eq. (87) yields Eqs. (88) and (89).

[1] *Recent Developments in Surface Acoustic Waves*, edited by D. F. Parker and G. A. Maugin, Springer Series on Wave Phenomena, Vol. 7 (Springer-Verlag, Berlin, 1988); see the papers in the section entitled ''Nonlinear Surface Acoustic Waves and Applications,'' pp. 1–78.

[2] E. Yu. Knight, M. F. Hamilton, Yu. A. Il'inskii, and E. A. Zabolotskaya, ''General theory for the spectral evolution of nonlinear Rayleigh waves,'' J. Acoust. Soc. Am. **102**, 1402–1417 (1997).

[3] E. A. Zabolotskaya, ''Nonlinear propagation of plane and circular Rayleigh waves in isotropic solids,'' J. Acoust. Soc. Am. **91**, 2569–2575 (1992).

[4] M. F. Hamilton, Yu. A. Il'inskii, and E. A. Zabolotskaya, ''Nonlinear surface wave propagation in a piezoelectric material,'' J. Acoust. Soc. Am. **100**, 2567(A) (1996).

[5] N. Kalyanasundaram, ''Nonlinear surface acoustic waves on an isotropic solid,'' Int. J. Eng. Sci. **19**, 279–286 (1981).

[6] N. Kalyanasundaram, R. Ravindran, and P. Prasad, ''Coupled amplitude theory of nonlinear surface acoustic waves,'' J. Acoust. Soc. Am. **72**, 488–493 (1982).

[7] N. Kalyanasundaram and G. V. Anand, ''Periodic Rayleigh waves of finite amplitude on an isotropic solid,'' J. Acoust. Soc. Am. **72**, 1518–1523 (1982).

[8] N. Kalyanasundaram, ''Nonlinear mixing of surface acoustic waves propagating in opposite directions,'' J. Acoust. Soc. Am. **73**, 1956–1965 (1983).

[9] M. Planat, ''Multiple scale analysis of the nonlinear surface acoustic wave propagation in anisotropic crystals,'' J. Appl. Phys. **57**, 4911–4915 (1985).

[10] R. W. Lardner, ''Nonlinear surface acoustic waves on an elastic solid of general anisotropy,'' J. Elast. **16**, 63–73 (1986).

[11] D. J. Shull, M. F. Hamilton, Yu. A. Il'insky, and E. A. Zabolotskaya, ''Harmonic generation in plane and cylindrical nonlinear Rayleigh waves,'' J. Acoust. Soc. Am. **94**, 418–427 (1993).

[12] R. W. Lardner and G. E. Tupholme, ''Nonlinear surface waves on cubic materials,'' J. Elast. **16**, 251–265 (1986).

[13] D. F. Parker, ''Waveform evolution for nonlinear surface acoustic waves,'' Int. J. Eng. Sci. **26**, 59–75 (1988).

[14] N. Kalyanasundaram, D. F. Parker, and E. A. David, ''The spreading of nonlinear elastic surface waves,'' J. Elast. **24**, 79–103 (1990).

[15] D. J. Shull, E. E. Kim, M. F. Hamilton, and E. A. Zabolotskaya, ''Diffraction effects in nonlinear Rayleigh wave beams,'' J. Acoust. Soc. Am. **97**, 2126–2137 (1995).

[16] M. F. Hamilton, Yu. A. Il'insky, and E. A. Zabolotskaya, ''Local and nonlocal nonlinearity in Rayleigh waves,'' J. Acoust. Soc. Am. **97**, 882–890 (1995).

[17] M. F. Hamilton, Yu. A. Il'insky, and E. A. Zabolotskaya, ''Evolution equations for nonlinear Rayleigh waves,'' J. Acoust. Soc. Am. **97**, 891–897 (1995).

[18] E. Yu. Knight, M. F. Hamilton, Yu. A. Il'inskii, and E. A. Zabolotskaya, ''On Rayleigh wave nonlinearity, and analytical approximation of the shock formation distance,'' J. Acoust. Soc. Am. **102**, 2529–2535 (1997).

[19] M. F. Hamilton, Yu. A. Il'inskii, and E. A. Zabolotskaya, ''Nonlinear surface wave propagation in crystals,'' in *Nonlinear Acoustics in Perspective: Proceedings of the 14th International Symposium on Nonlinear Acoustics*, edited by R. J. Wei (Nanjing U.P., Nanjing, 1996), pp. 64–69.

[20] R. E. Kumon, M. F. Hamilton, Yu. A. Il'inskii, E. A. Zabolotskaya, P. Hess, A. Lomonosov, and V. G. Mikhalevich, ''Pulsed nonlinear surface acoustic waves in crystals,'' in *Proceedings of the 16th International Congress on Acoustics*, edited by P. K. Kuhl and L. A. Crum (Acoustical Society of America, New York, 1998), Vol. III, pp. 1557–1558.

[21] G. W. Farnell, ''Properties of elastic surface waves,'' in *Physical Acoustics*, edited by W. P. Mason (Academic, New York, 1970), Vol. 6, pp. 109–166.

[22] B. A. Auld, *Acoustic Fields and Waves in Solids*, 2nd ed. (Krieger, Malabar, FL, 1990), Vol. I.

[23] L. D. Landau and E. M. Lifshitz, *Theory of Elasticity* (Pergamon, New York, 1986), 3rd ed.

[24] A. N. Norris, ''Finite-amplitude waves in solids,'' in *Nonlinear Acoustics*, edited by M. F. Hamilton and D. T. Blackstock (Academic, Boston, 1998), Chap. 9.

[25] E. A. Zabolotskaya, ''Nonlinear propagation of Rayleigh waves,'' Opt. Acoust. Rev. **1**, 133–140 (1990–91).

[26] M. F. Hamilton, Yu. A. Il'insky, and E. A. Zabolotskaya, ''On the existence of stationary nonlinear Rayleigh waves,'' J. Acoust. Soc. Am. **93**, 3089–3095 (1993).

[27] R. F. S. Hearmon, ''The elastic constants of crystals and other anisotropic materials; The third- and higher-order elastic constants,'' in *Landolt-Börnstein: Numerical Data and Functional Relationships in Science and Technology*, edited by K.-H. Hellwege and A. M. Hellwege (Springer-Verlag, New York, 1979), Group III, Vol. 11, pp. 245–286.

[28] J. A. Armstrong, N. Bloembergen, J. Ducuing, and P. S. Pershan, ''Interactions between light waves in a nonlinear dielectric,'' Phys. Rev. **127**, 1918–1939 (1962).

A coherent line source in a turbulent atmosphere

Erik M. Salomons[a)]
TNO Institute of Applied Physics, P.O. Box 155, 2600 AD Delft, The Netherlands

(Received 3 February 1998; revised 1 October 1998; accepted 30 October 1998)

The sound field of a coherent line source in a nonrefracting, turbulent atmosphere is studied. An expression for the sound pressure level in the frequency domain is developed, based on a discretization of the line source into a set of point sources. Atmospheric turbulence is taken into account by the mutual coherence function. Numerical computations for various turbulent atmospheres show that the geometrical attenuation is 3 dB per distance doubling (3 dB/dd) at a small distance (cylindrical spreading), 6 dB/dd at a large distance (spherical spreading), and 7.5 dB/dd in a transition region. The anomalous value of 7.5 dB/dd is confirmed by an analytic approximation. Next, a computational method in the time domain is developed, for arbitrary wave forms emitted by the source. Atmospheric turbulence is taken into account in this method by including random fluctuations of the acoustic travel times, based on the spectral density of the travel time correlation function. For a harmonic coherent line source, the method yields results that agree with results computed in the frequency domain. © *1999 Acoustical Society of America.*
[S0001-4966(99)02502-3]

PACS numbers: 43.28.Fp, 43.28.Hr, 43.28.Mw [LCS]

INTRODUCTION

A finite line source generates a field with cylindrical spreading at small distance and spherical spreading at large distance. As a consequence, the sound pressure level decreases with 3 dB per distance doubling at small distance, and 6 dB per distance doubling at a large distance. The transition from cylindrical to spherical spreading occurs at a distance that depends on the length of the line source.[1] Moreover, the transition distance is smaller for an incoherent line source (i.e., a set of incoherent point sources along a line) than for a coherent line source (e.g., a pulsating cylinder). Atmospheric turbulence causes a reduction of the coherence of the field of a coherent line source. Therefore, atmospheric turbulence is expected to reduce the transition distance from cylindrical to spherical spreading. This effect is investigated in this paper.

The propagation of sound waves from a line source to a receiver at a large distance is affected by various effects: geometrical attenuation (cylindrical or spherical spreading), atmospheric attenuation, atmospheric refraction, and ground reflections. In principle, these effects are not independent of each other. In many practical situations, however, the effects may be considered as independent, approximately. In this paper, only the effect of geometrical attenuation is studied, and the influence of atmospheric turbulence on it. It should be noted that the influence of turbulence on the geometrical attenuation is probably not independent of atmospheric refraction in situations where the receiver is in a refractive shadow.

The most obvious example of a physical realization of a coherent line source is a vibrating cylinder (tube). Another example is a one-dimensional array of coherent sound sources (e.g., loudspeakers). Finally, we mention two examples of nonlinear coherent line sources, a supersonic projectile,[2,3] and a spark source;[4] it should be noted that the analysis presented here cannot be applied directly to these sources, since nonlinear effects are ignored.

I. HARMONIC COHERENT LINE SOURCE

A. Discretization

We consider the system shown in Fig. 1, with a set of coherent, harmonic monopole sources along a finite line segment of length $2\Delta y$. This system represents a discretized approximation of a continuous line source. We will study the variation of the field in the direction perpendicular to the line source, in a nonrefracting, turbulent atmosphere. A rectangular xy coordinate system is used. The monopole sources are located on the y axis at positions (x_j, y_j), with $x_j = 0$ and $y_j = (j-1)\,\delta y - \Delta y$, where $j = 1,2,...,N$. The receiver is located on the x axis, at position (x,y), with $y = 0$. The complex sound pressure field at the receiver is

$$p = \sum_{j=1}^{N} p_j, \tag{1a}$$

with

$$p_j = p_0 \frac{\exp(i[kr_j + S_j - \omega t])}{r_j / r_0}, \tag{1b}$$

the contribution of source j, where p_0 is a constant pressure, ω the angular frequency, $k = \omega/c_0$ the wave number (with c_0 the average sound speed in the atmosphere), $r_0 = 1$ m, $r_j = \sqrt{x^2 + y_j^2}$, and S_j a fluctuating phase, with zero time average: $\langle S_j \rangle = 0$. The phase fluctuations S_j originate from sound speed fluctuations and wind speed fluctuations, i.e., atmospheric turbulence. It should be noted that amplitude fluctuations are neglected here, as these are assumed to saturate and are always considerably smaller than phase fluctuations.[5]

a)Electronic mail: salomons@tpd.tno.ni

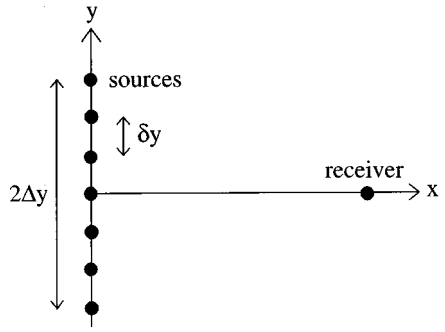

FIG. 1. A system with monopole sources on the y axis and a receiver on the x axis.

In the limit of vanishing distance δy between neighboring sources, the field (1) is identical with the field of a harmonically pulsating cylinder (for large kx). To demonstrate this, we set $S_j=0$ and $\Delta y\to\infty$. Omitting the factor $\exp(-i\omega t)$ in Eq. (1), we find for the pressure amplitude

$$p=\frac{p_0}{\delta_y}\int_{-\infty}^{\infty}\frac{\exp(ik\sqrt{x^2+y^2})}{\sqrt{x^2+y^2}/r_0}\,dy. \tag{2}$$

Evaluating the integral (for large k) by the method of stationary phase,[6] we find

$$p=\frac{p_0 r_0}{\delta y}\sqrt{\frac{2\pi}{kx}}\exp\left(ikx+i\frac{1}{4}\pi\right). \tag{3}$$

The amplitude of the field of a pulsating cylinder of radius b and infinite length is[7] $p=p_c H_0^{(1)}(kx)$, with $p_c=-w_c i\times\rho c_0/H_0^{(1)\prime}(kb)$, where w_c is the vibration velocity of the cylinder, ρ the density of the atmosphere, and $H_0^{(1)\prime}$ is the derivative of the Hankel function $H_0^{(1)}$. For large kx, we find[8]

$$p=p_c\sqrt{\frac{2}{\pi kx}}\exp\left(ikx-i\frac{1}{4}\pi\right). \tag{4}$$

This agrees with Eq. (3) if we set $p_0=-ip_c\delta y/(\pi r_0)$.

B. Mean squared sound pressure

It is assumed that the phase fluctuations S_j are slow compared with the harmonic variations of the field (frozen medium approximation[9]). Then the time-averaged squared sound pressure is obtained from Eq. (1) as (omitting the constant $r_0=1$ m):

$$\begin{aligned}\langle p^2\rangle&=\left\langle\frac{1}{2}\left(\sum_{j=1}^{N}p_j\right)\left(\sum_{m=1}^{N}p_m\right)^*\right\rangle\\&=\frac{1}{2}p_0^2\sum_{j=1}^{N}\sum_{m=1}^{N}\frac{\langle\cos(kr_j-kr_m+S_j-S_m)\rangle}{r_j r_m}\\&=\frac{1}{2}p_0^2\sum_{j=1}^{N}\sum_{m=1}^{N}\frac{\cos(kr_j-kr_m)}{r_j r_m}\Gamma_{jm},\end{aligned} \tag{5}$$

with Γ_{jm} the mutual coherence function (MCF), defined as[10,11]

$$\Gamma_{jm}=\langle\exp(i(S_j-S_m))\rangle=\langle\cos(S_j-S_m)\rangle. \tag{6}$$

To derive an integral expression for a continuous line source, we consider the limit of vanishing distance δy between neighboring sources. Then we can replace the double sum in Eq. (5) by a double integral (denoting y_j and y_m as y and y', respectively):

$$\langle p^2\rangle=\frac{p_0^2}{2(\delta y)^2}\int_{-\Delta y}^{\Delta y}\int_{-\Delta y}^{\Delta y}\frac{\cos(kr-kr')}{rr'}\Gamma(y-y')dy\,dy'. \tag{7}$$

This integral expression for the mean squared sound pressure is a new result, and will be used in the following sections.

C. The mutual coherence function (MCF)

For the MCF we use the expression[5,12]

$$\Gamma(\rho)=\exp\left(-\frac{1}{2}\sqrt{\pi}\mu_0^2k^2xL\left\{1-\frac{\Phi(\rho/L)}{(\rho/L)}\right\}\right), \tag{8}$$

which is valid for a Gaussian correlation function of the fluctuating acoustical index of refraction μ (defined as $\mu=c_0/c-1$, with c the fluctuating sound speed and c_0 the average sound speed):

$$\langle\mu(y)\mu(y')\rangle=\mu_0^2\exp(-\rho^2/L^2). \tag{9}$$

Here $\rho=y-y'$ (or $\rho=y_j-y_m$ in discrete form), μ_0 is the rms value of μ, L is the correlation length, and $\Phi(z)=\int_0^z\exp(-u^2)du=\frac{1}{2}\sqrt{\pi}\,\mathrm{erf}(z)$, where $\mathrm{erf}(z)$ is the error function.

D. The incoherent limit

In the limit $\mu_0^2\to\infty$, all sources are incoherent. In this case, $\Gamma_{jm}=0$ for $j\neq m$ and $\Gamma_{jj}=1$, and we obtain from Eq. (5),

$$\langle p^2\rangle=\frac{1}{2}p_0^2\sum_{j=1}^{N}\frac{1}{r_j^2}. \tag{10}$$

The corresponding integral expression for a continuous line source is

$$\langle p^2\rangle=\frac{p_0^2}{2\delta y}\int_{-\Delta y}^{\Delta y}\frac{1}{x^2+y^2}\,dy. \tag{11}$$

This gives

$$\langle p^2\rangle=\frac{p_0^2}{\delta y}\frac{1}{x}\arctan\frac{\Delta y}{x}. \tag{12}$$

A comparison of Eqs. (7) and (11) yields the following formal expression for the incoherent limit ($\mu_0^2\to\infty$) of the MCF:

$$\Gamma(y-y')=\delta y\,\delta(y-y'), \tag{13}$$

where $\delta(y-y')$ is the Dirac delta function.

E. Numerical examples

Figure 2 shows numerical examples of the sound pressure level as a function of distance x, for the two frequencies $f=400$ and 1000 Hz, and the three source lengths $2\Delta y=10$, 100, and 1000 m. A number of sources

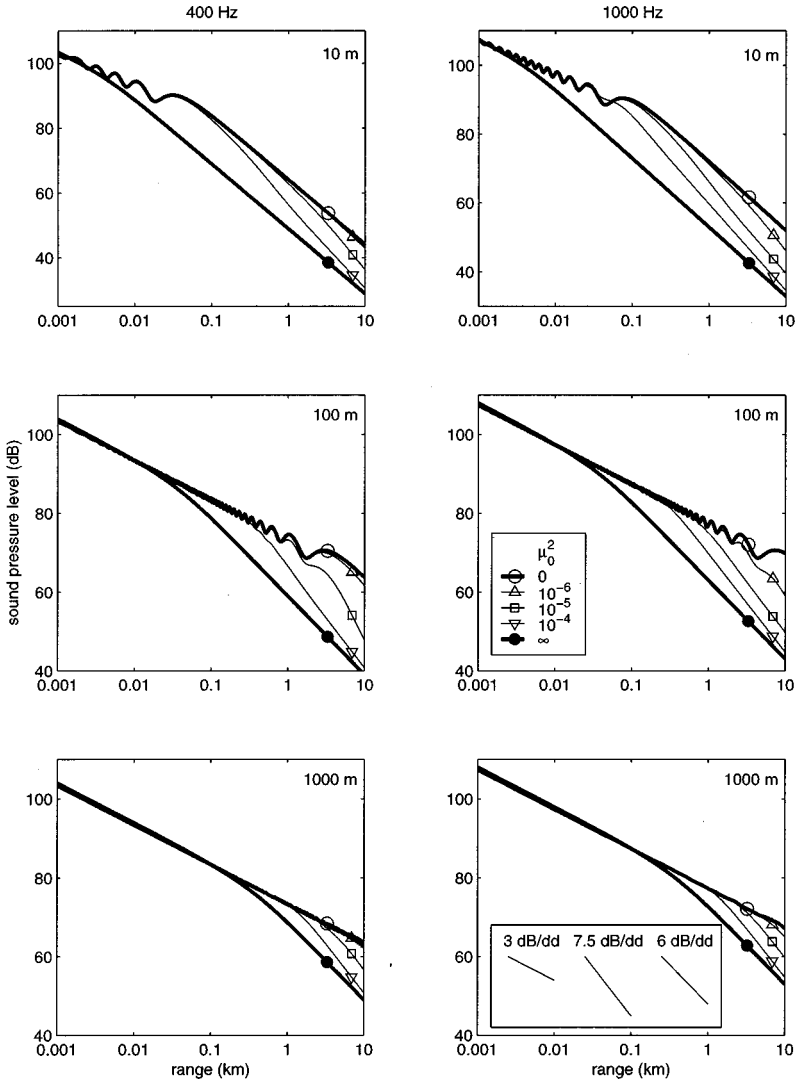

FIG. 2. The sound pressure level as a function of distance, for five values of μ_0^2 (see the legend), source lengths $2\Delta y = 10$, 100, and 1000 m (from top to bottom), and frequencies 400 Hz (left column) and 1000 Hz (right column). Slopes of 3, 7.5, and 6 dB per distance doubling (dd) are indicated.

$N = 2\Delta y f/125$ was used (Δy in m, f in Hz), so that $\delta y \approx \frac{1}{3}\lambda$. We used $p_0 = \sqrt{2}$ Pa, so that the sound pressure level $L_p = 10\log(\langle p^2\rangle/p_{\text{ref}}^2)$ of a single monopole source is 94 dB at a distance of 1 m ($p_{\text{ref}} = 20\,\mu$Pa).

The oscillating thick curves for $\mu_0^2 = 0$ are computed with Eq. (5) with $\Gamma_{jm} = 1$ (the oscillations will be explained in Sec. I F 2). The thick curves for $\mu_0^2 = \infty$ are computed with Eq. (12), but the use of Eq. (10) gives essentially the same result. The number of sources N indicated above was chosen so that the levels for $\mu_0^2 = 0$ and $\mu_0^2 = \infty$ are approximately equal for small values of the range x. For larger N, the curves are shifted but retain their shapes. The thin curves for $\mu_0^2 = 10^{-6}$, 10^{-5}, 10^{-4} are computed with Eq. (5), using Eq. (8) for the MCF. Following Daigle *et al.*,[5] we use $L = 1.1$ m. These authors also report that μ_0^2 varied roughly between 10^{-6} and 10^{-5} for their measurements. The value $\mu_0^2 = 10^{-4}$ represents extremely strong turbulence.

Figure 2 shows that the transition from cylindrical spreading ($dL_p/d\log x = -10$ dB, 3 dB per distance doubling) to spherical spreading ($dL_p/d\log x = -20$ dB, 6 dB per distance doubling) occurs at a smaller distance for an incoherent line source than for a coherent line source. The curves for the incoherent limit $\mu_0^2 = \infty$ show the transition at $x \approx \Delta y$, independent of the frequency. This will be explained in Sec. I F 1. The curves for the coherent limit $\mu_0^2 = 0$ show the transition at $x = \Delta y^2/\lambda$, where λ is the wavelength. This will be explained in Sec. I F 2. The curves for $\mu_0^2 = 10^{-6}$, 10^{-5}, 10^{-4} show a gradual transition from the coherent limit to the incoherent limit. The slope in the transition region is $dL_p/d\log x = -25$ dB (7.5 dB per distance doubling). This will be explained in Sec. I F 3.

F. Transition from cylindrical to spherical spreading

1. The incoherent limit $\mu_0^2 = \infty$

For $x/\Delta y \to \infty$, Eq. (12) for the incoherent limit reduces to

$$\langle p^2\rangle = N\frac{p_0^2}{2x^2}, \tag{14}$$

with $N = 1 + 2\Delta y/\delta y \approx 2\Delta y/\delta y$ the number of sources. This corresponds to spherical spreading. For $x/\Delta y \to 0$, $\arctan \Delta y/x \to \pi/2$, so that Eq. (12) reduces to

$$\langle p^2\rangle = \frac{\pi p_0^2}{2x\,\delta y}, \tag{15}$$

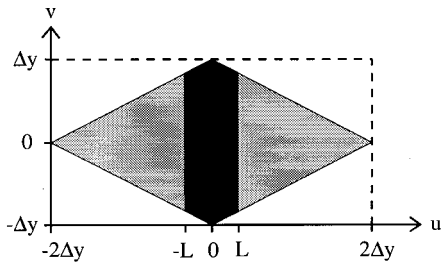

FIG. 3. The grey area is the integration area in the uv plane. The narrow black band around $u=0$ is the region where the MCF is significantly different from zero.

representing cylindrical spreading. Inspection of the arctan function yields that the transition occurs at $x \approx 2\Delta y/\pi \approx \Delta y$, in agreement with the work of Rathe.[1]

2. The coherent limit $\mu_0^2=0$

The oscillations in the curves for $\mu_0^2=0$ in Fig. 2 can be explained in terms of Fresnel zones.[2] The difference in the source–receiver distance between the point source at $y=0$ and the point source at $y=\Delta y$ is

$$\Delta r=\sqrt{x^2+\Delta y^2}-x\approx\frac{\Delta y^2}{2x}, \tag{16}$$

for $x \gg \Delta y$. Equating this difference to $(n-\frac{1}{2})\lambda$ with $n=1,2,3,...$, gives

$$x_n=\frac{\Delta y^2}{(2n-1)\lambda}. \tag{17}$$

The maxima in the oscillating curves occur at $x=x_n$. At $x=x_1$, the first Fresnel zone just fits on the line source. With increasing distance $x>x_1$, the phase differences between the point sources on the line source become small, and the line source behaves as a compact source with spherical spreading.

3. The case $0<\mu_0^2<\infty$

For $x \gg \Delta y$, Eq. (7) can be simplified. We set $r \approx r' \approx x$ in the denominator, and $kr-kr' \approx (k/2x)(y^2-y'^2)$ in the numerator:

$$\langle p^2\rangle=\frac{p_0^2}{2x^2(\delta y)^2}\int_{-\Delta y}^{\Delta y}\int_{-\Delta y}^{\Delta y}\cos\left(\frac{k}{2x}(y-y')(y+y')\right)\times\Gamma_x(y-y')dy\,dy', \tag{18}$$

where the x dependence of the MCF has been indicated by a subscript. We perform a coordinate transformation $(y,y') \rightarrow (u,v)$:

$$u=y-y', \quad v=\tfrac{1}{2}(y+y'), \tag{19}$$

with a Jacobian equal to unity. The integration area in the uv plane is shown in Fig. 3. The MCF is given by Eq. (8), which we write as

$$\Gamma_x(u)=\exp\left(-ax\left(1-\frac{\Phi(u/L)}{u/L}\right)\right), \tag{20}$$

with

$$a=\tfrac{1}{2}\sqrt{\pi}\mu_0^2k^2L. \tag{21}$$

Now we assume $ax>1$, so that $\Gamma(u)\approx 0$ if $|u|$ is larger than a value of the order of the correlation length L (see Fig. 3). Therefore, the integration area can be replaced by an infinite rectangle with vertical sides at $u=\pm\infty$, and horizontal sides at $v=\pm\Delta y$ (cf. Ishimaru[13]). We obtain

$$\langle p^2\rangle=\frac{p_0^2}{2x^2(\delta y)^2}\int_{-\infty}^{\infty}\int_{-\Delta y}^{\Delta y}\cos\left(\frac{k}{x}uv\right)\Gamma_x(u)dv\,du \tag{22}$$

or

$$\langle p^2\rangle=\frac{2p_0^2\Delta y}{x^2(\delta y)^2}\int_0^{\infty}H_x(u)\Gamma_x(u)du, \tag{23}$$

with

$$H_x(u)=\sin\left(\frac{k\Delta y}{x}u\right)\Big/\left(\frac{k\Delta y}{x}u\right). \tag{24}$$

To evaluate the MCF given by Eq. (20), we use the series expansion[8]

$$\Phi(z)=z-\tfrac{1}{3}z^3+O(z^5). \tag{25}$$

Neglecting terms of order z^5 and higher, we get

$$\Gamma_x(u)=\exp(-\tfrac{1}{3}axu^2/L^2). \tag{26}$$

We will consider two limiting cases, x small and x large.

a. x small. For small x, $\Gamma_x(u)\approx 1$, and

$$\langle p^2\rangle=\frac{2p_0^2}{kx(\delta y)^2}\int_0^{\infty}\frac{\sin u'}{u'}du'=\frac{p_0^2\pi}{kx(\delta y)^2}, \tag{27}$$

representing cylindrical spreading. This solution is valid only in a limited region (dependent on frequency), since in the foregoing we assumed that x is large $(x \gg \Delta y)$.

b. x large. For large x, $H_x(u)\approx 1$, and we use Eq. (26) to obtain

$$\langle p^2\rangle=\frac{2p_0^2\Delta y}{x^2(\delta y)^2}\int_0^{\infty}\exp\left(-\frac{1}{3}ax\frac{u^2}{L^2}\right)du, \tag{28}$$

or

$$\langle p^2\rangle=\frac{\pi^{1/4}\sqrt{6L}p_0^2\Delta y}{(\delta y)^2\mu_0kx^{5/2}}. \tag{29}$$

If ax is very large, we should use Eq. (13) instead of Eq. (26), and obtain

$$\langle p^2\rangle=\frac{p_0^2\Delta y}{x^2\delta y}, \tag{30}$$

which coincides with Eq. (14), the incoherent limit.

Equation (29) yields sound pressure levels that are in good agreement with the exact levels, represented in Fig. 2 by the thin curves (although Fresnel oscillations cause some deviations, for 400 Hz and $2\Delta y=100$ m). The slope $dL_p/d\log x=-25$ dB is confirmed by Eq. (29).

II. COMPUTATIONAL METHOD IN THE TIME DOMAIN

In this section we briefly describe a computational method in the time domain, for a coherent line source in a turbulent atmosphere. For some applications, this method may be more practical than the computational method in the frequency domain, described in Sec. I.

The line source is discretized in the same way as in Sec. I, with point sources at $y=y_j$. The field at the receiver is written as

$$p(t)=\sum_{j=1}^{N} \frac{w_j(t-r_j/c_0+\delta t_j)}{r_j}, \tag{31}$$

where the function $w_j(t)$ determines the emitted wave form of point source j, $t-r_j/c_0$ is the retarded time, and δt_j is a fluctuation of the acoustic travel time from source j to the receiver (this fluctuation is caused by atmospheric turbulence). The harmonic line source studied in Sec. I corresponds to the case that all $w_j(t)$ are equal to the same harmonic function.

For the construction of random realizations of the travel time fluctuations δt_j we start from the correlation function of the travel time:[5,12]

$$B_t(\rho)=\frac{1}{2}\sqrt{\pi}\mu_0^2 xL\frac{\Phi(\rho/L)}{(\rho/L)}. \tag{32}$$

We perform a spectral decomposition:[14,15]

$$B_t(\rho)=\int_{-\infty}^{\infty}\cos(\kappa\rho)V(\kappa)d\kappa\approx\Delta\kappa\sum_n \cos(\kappa_n\rho)V(\kappa_n), \tag{33}$$

with $V(\kappa)$ the spectral density, which we compute by the inverse Fourier transform:[14,15]

$$V(\kappa)=\frac{1}{\pi}\int_0^{\infty}\cos(\kappa\rho)B_t(\rho)d\rho$$

$$\approx\frac{\Delta\rho}{\pi}\sum_m \cos(\kappa\rho_m)B_t(\rho_m). \tag{34}$$

Random realizations of the travel times t_j are computed with the expression

$$t_j\equiv t(y_j)=\sqrt{2\Delta\kappa}\sum_n \cos(\kappa_n y_j+\phi_n)\sqrt{V(\kappa_n)}, \tag{35}$$

with random phase angles ϕ_n. It is easily verified that this expression yields the correlation function $B_t(\rho)=\langle t(y+\rho)t(y)\rangle$ given by Eq. (33). The fluctuations are given by $\delta t_j=t_j-\langle t_j\rangle$.

Our numerical implementation is as follows (cf. Chevret *et al.*[16]). First a set $\rho_m=m\Delta\rho$ $(m=0,1,...,N_\rho)$ is chosen, with $\Delta\rho=0.02$ m and $N_\rho\Delta\rho=300$ m. The corresponding set $\kappa_n=n\Delta\kappa$ $(n=0,1,...,N_\kappa)$ is generated, with $\Delta\kappa=2\pi/(N_\rho\Delta\rho)$ and $N_\rho\Delta\kappa=6\ \mathrm{m}^{-1}$ (the cutoff at $\kappa=6\ \mathrm{m}^{-1}$ can be considered as a low-pass filter). The spectral density $V(\kappa_n)$ is computed with Eq. (34). Next, random realizations of the set t_j are computed with Eq. (35), and the fluctuations $\delta t_j=t_j-\langle t_j\rangle$ are obtained.

The above method was tested for the harmonic line sources studied in Sec. I, by reproducing the results computed with Eq. (5), shown in Fig. 2. It was found that averaging the squared sound pressure over 100 random realizations yields sufficiently accurate results.

III. CONCLUSIONS

The field of a coherent line source in a turbulent atmosphere has been studied. An expression has been developed for the sound pressure level in the frequency domain, based on a discretization of the line source into a set of point sources. Atmospheric turbulence is taken into account by the mutual coherence function. Numerical computations have shown that the geometrical attenuation is 3 dB per distance doubling (3 dB/dd) at a small distance (cylindrical spreading), 6 dB/dd at a large distance (spherical spreading), and 7.5 dB/dd in a transition region. The anomalous value of 7.5 dB/dd has been confirmed by an analytic approximation.

Further, a computational method in the time domain has been developed. Atmospheric turbulence is taken into account in this method by including random fluctuations of the acoustic travel times, based on the spectral density of the travel time correlation function. For a harmonic coherent line source, the method yields results that agree with results computed in the frequency domain.

In this study we have focused on the variation of the geometrical attenuation with propagation distance in a turbulent atmosphere. Other propagation effects have been ignored, such as atmospheric refraction, atmospheric absorption, ground reflections, and nonlinear effects. In many practical situations, one may assume that the geometrical attenuation is approximately independent of these effects.

[1] E. J. Rathe, ''Note on two common problems of sound propagation,'' J. Sound Vib. **10**, 472–479 (1969).

[2] A. D. Pierce, *Acoustics. An Introduction to its Physical Principles and Applications* (American Institute of Physics, Woodbury, 1991), pp. 242–243, 606–615.

[3] A. P. Dowling and J. E. Ffowcs Williams, *Sound and Sources of Sound* (Ellis Horwood Limited, Chichester, 1983), Sec. 9.1.

[4] W. M. Wright and N. W. Medendorp, ''Acoustic radiation from a finite line source with N-wave excitation,'' J. Acoust. Soc. Am. **43**, 966–971 (1968).

[5] G. A. Daigle, J. E. Piercy, and T. F. W. Embleton, ''Line-of-sight propagation through atmospheric turbulence near the ground,'' J. Acoust. Soc. Am. **74**, 1505–1513 (1983).

[6] E. Skudrzyk, *The Foundations of Acoustics* (Springer-Verlag, Wien, 1971), pp. 58–65.

[7] M. C. Junger, ''The physical interpretation of the expression for an outgoing wave in cylindrical coordinates,'' J. Acoust. Soc. Am. **25**, 40–47 (1953).

[8] *Handbook of Mathematical Functions*, edited by M. Abramowitz and I. A. Stegun (Dover, New York, 1970), Eqs. 7.1.5, 9.1.3, 9.2.3.

[9] R. B. Stull, *An Introduction to Boundary Layer Meteorology* (Kluwer, Dordrecht, 1988), pp. 5–6.

[10] M. M. Fitelson, ''Coherence function for cylindrically spreading waves in a random medium,'' J. Acoust. Soc. Am. **56**, 53–57 (1974).

[11] V. I. Tatarskii, ''Review of scintillation phenomena,'' in *Wave Propagation in Random Media (Scintillation)* (The Society of Photo-Optical Instrumentation Engineers, Bellingham, Washington, and The Institute of Physics Publishing, Bristol and Philadelphia, 1993), pp. 2–15.

[12] V. E. Ostashev, V. Mellert, R. Wandelt, and F. Gerdes, ''Propagation of sound in a turbulent medium. I. Planes waves,'' J. Acoust. Soc. Am. **102**, 2561–2570 (1997); V. E. Ostashev, F. Gerdes, V. Mellert, and R. Wan-

delt, ''Propagation of sound in a turbulent medium. II. Spherical waves,'' *ibid.* **102**, 2571–2578 (1997).
[13] A. Ishimaru, *Wave Propagation and Scattering in Random Media* (Academic, New York, 1978), p. 356.
[14] V. I. Tatarski, *Wave Propagation in a Turbulent Medium* (McGraw-Hill, New York, 1961), pp. 3–26, 122–156, 173–188.
[15] V. I. Tatarskii, *The Effects of the Turbulent Atmosphere on Wave Propagation* (Israel Program for Scientific Translations, Jerusalem, 1971), pp. 1–33, 218–258.
[16] P. Chevret, Ph. Blanc-Benon, and D. Juvé, ''A numerical model for sound propagation through a turbulent atmosphere near the ground,'' J. Acoust. Soc. Am. **100**, 3587–3599 (1996).

Calculated coherence and extinction of sound waves propagating through anisotropic, shear-induced turbulent velocity fluctuations

D. Keith Wilson
U.S. Army Research Laboratory, ATTN: AMSRL-IS-EE, 2800 Powder Mill Road, Adelphi, Maryland 20783-1197

(Received 14 February 1998; revised 18 October 1998; accepted 30 October 1998)

Previous calculations of the coherence and extinction of sound waves propagating through turbulence have almost always used isotropic models for the turbulence. However, low-frequency sound waves are strongly affected by energy-subrange turbulence structure, which is anisotropic by nature. In this paper, coherence and extinction are calculated using several anisotropic models for turbulent velocity fluctuations in the neutral atmospheric shear layer. New anisotropic versions of the Gaussian and von Kármán models are developed. The Kristensen *et al.* spectral model [Boundary-Layer Meteorol. **47**, 149–193 (1989)] and Mann's rapid-distortion, constant shear model [J. Fluid Mech. **273**, 141–168 (1994)] are also considered. The turbulence models all predict that the crosswind extinction distance is longer than the along-wind value, although they disagree as to the extent of the lengthening: depending on the model, the ratio of crosswind to along-wind extinction varies from 2.1 to 13. These results point to the need for good experiments. Similarly, coherence of the propagating wavefronts is predicted to persist over longer distances in the crosswind direction. [S0001-4966(99)02702-2]

PACS numbers: 43.28.Fp, 43.20.Fn, 43.28.Py [LCS]

INTRODUCTION

Much previous research in the area of wave propagation through turbulence has focused on scattering from the small-scale motions of the inertial subrange.[1] But several studies,[2–9] some now decades old, provide convincing evidence that the larger-scale energy-subrange motions are also important for acoustic propagation through the atmosphere. An obvious situation in which energy-subrange scattering should be important occurs when the wavelength of the sound falls within the energy subrange (i.e., the wavelength is comparable to or larger than the turbulence outer scale). This situation occurs often in practical applications. Consider, for example, near-ground propagation through the atmospheric surface layer when shear (as opposed to buoyancy) production of turbulence dominates. The outer scale for propagation in a surface shear layer is roughly equal to the height of the propagation path. Hence if the wavelength is comparable to or larger than the height, energy-subrange scattering is significant.

But there are also less obvious circumstances, dependent upon the propagation geometry and the wave statistic being considered, in which the energy subrange becomes important. For example, phase fluctuations in line-of-sound propagation are driven by the most energetic turbulent motions along the propagation path. Since the largest scale motions are generally the most energetic, the energy subrange generally contributes most strongly to the phase fluctuations. Therefore energy subrange scattering can be important even for wavelengths very small compared to the outer scale. This fact is evident from several acoustical studies (Refs. 7–9), and has even been discussed in the context of optical propagation by Lawrence and Strohbehn[10] among others.

Unfortunately, calculation of the effects of energy-subrange turbulence on wave scattering is an inherently difficult subject. Unlike the inertial subrange, there are no universal statistical treatments available for the energy subrange. Turbulent motions in the energy subrange depend on the energetics of a particular flow, and are statistically anisotropic (dependent on orientation) and inhomogeneous (dependent on position) as a result. An example of anisotropy is that the variance for turbulent velocity fluctuations in the direction of the mean wind is several times larger than the variance for vertical velocity fluctuations. An example of inhomogeneity is the dependence of the variances on the height above the ground. Similar manifestations of anisotropy and inhomogeneity are evident in the turbulence length scales.

The subject of this paper is the effect of turbulence anisotropy on acoustic propagation. Statistical inhomogeneity is also introduced by assuming that the length scales of the turbulence are proportional to height. The specific case considered is that of a shear-driven, neutral atmospheric surface layer. *Neutral*, in the terminology of geophysical fluid dynamics, means an absence of buoyancy effects. Hence radiative heating and cooling of the ground (and the resulting vertical density contrasts in the overlying air) are neglected. This leaves wind shear as the dominant mechanism for generating the turbulence. Atmospheric conditions are usually nearly neutral when skies are cloudy and the wind is strong. By neglecting buoyantly generated turbulence, I do not intend to imply that this sort of turbulence is unimportant for acoustic wave propagation. The restriction to shear instabilities here is only for simplicity, and hopefully later studies can incorporate buoyancy instabilities.

The derivation of the turbulence models considered in

this paper is more rigorous than for the model developed in an earlier study by Wilson and Thomson.[8] Specifically, the models used here are consistent with the incompressibility property of the turbulent velocity field. All model parameters are chosen on the basis of atmospheric measurements, as opposed to the approximate scaling arguments that were used to infer some parameters in the Wilson and Thomson model. Furthermore, most of the models in this paper have a realistic inertial subrange. One drawback of the models considered here is that they are much more complex than Wilson and Thomson's.

Much of the turbulence modeling effort in this paper derives from the previous work of Kristensen *et al.*[11] They developed an anisotropic spectral model for turbulence and applied it to turbulence originating from various instability mechanisms, including the surface-layer shear. In this paper, I apply the Kristensen *et al.* model to acoustic propagation. Two simplified versions of the Kristensen *et al.* model are also developed: an anisotropic von Kármán model, and an anisotropic Gaussian model. These three models based on the work of Kristensen *et al.* are the subject of Sec. II.

A fourth model considered in this paper, due to Mann,[12] uses an entirely different approach than the one taken by Kristensen *et al.* It is based on rapid distortion theory, which hypothesizes that the shear distortions to an eddy can be calculated from linearized Navier–Stokes equations. The Mann model is summarized in Sec. III.

Before discussing the turbulence models, however, I will consider in Sec. I the equations needed for the acoustical calculations. The equations are based on those developed by Dashen[13] for propagation through random, anisotropic, and inhomogeneous media. Dashen's equations were derived using a path integral approach that assumes the validity of the parabolic approximation to the wave equation, as well as the Markov approximation. They are equivalent to equations given by Rytov *et al.*[14] and Ostashev[15] when specialized to the case of propagation through statistically isotropic and homogeneous turbulence.

I. EXTINCTION AND COHERENCE FOR PROPAGATION THROUGH ANISOTROPIC, RANDOM MEDIA

In this paper, only the first and second moments of the forward-scattered sound field will be considered. Propagation is assumed to be ''line-of-sound;'' that is, ground reflections and refraction are neglected. Validity of the Markov approximation is assumed, which most importantly requires that the outer scale of the turbulence and the coherence radius of the sound field are much larger than the wavelength.[14,15]

Let us designate the acoustic pressure field generated by a point source at the origin as $p(x',\mathbf{r}'_\perp)$. Here the x' axis is the nominal direction of propagation, $\mathbf{r}'$ is the receiver location, and $\mathbf{r}'_\perp=\mathbf{r}'-x'\,\mathbf{e}'_1$ is the separation transverse to the propagation path, with $\mathbf{e}'_1$ being the unit vector along the x' axis. (Primes are used in this paper for the coordinate system aligned with the direction of propagation; unprimed coordinates will be used later for the system having the x axis aligned with the mean wind.) Assuming the validity of the parabolic approximation to the wave equation, as well as the Markov approximation, the mean coherent pressure field decreases exponentially and is given by[13,15]

$$\langle p(x',\mathbf{r}'_\perp)\rangle = p_0(x',\mathbf{r}'_\perp)\exp\left(-\frac{\Phi^2}{2}\right), \tag{1}$$

where $p_0(x',\mathbf{r}'_\perp)=\exp(ik_0r')/(4\pi r')$ is the pressure in the absence of turbulence, k_0 is the acoustic wave number, and Φ is the rms phase fluctuation determined using first-order geometric optics. It can be shown that[13]

$$\Phi^2 \simeq k_0^2 x' \int_{-\infty}^{\infty} R(s\mathbf{e}'_1)\,ds, \tag{2}$$

where $R(\mathbf{r})$ is the three-dimensional (3-D) correlation function of $\mu=1-n$, n being the index of refraction. If we define the integral length scale in the direction of propagation as

$$\mathcal{L}=\frac{1}{\sigma^2}\int_0^{\infty} R(s\mathbf{e}'_1)\,ds, \tag{3}$$

where σ^2 is the variance of μ, the rms phase fluctuation becomes

$$\Phi^2 \simeq 2\sigma^2 k_0^2 x' \mathcal{L}. \tag{4}$$

The distance at which the mean pressure decays to $1/e$ times its value in the absence of turbulence is therefore

$$\xi=(\sigma^2 k_0^2 \mathcal{L})^{-1}. \tag{5}$$

In this paper ξ is called the *extinction distance*. An alternative expression for the extinction distance, which will be useful later on, involves the *two-dimensional (2-D) correlation function*

$$b(\mathbf{r}'_\perp)=\frac{1}{2\pi}\int_{-\infty}^{\infty} R(\mathbf{r}'_\perp+x'\mathbf{e}'_1)dx'. \tag{6}$$

Since $b(\mathbf{0})=(\sigma^2/\pi)\mathcal{L}$, the extinction distance is equal to $\xi=[\pi k_0^2 b(\mathbf{0})]^{-1}$.

The mutual coherence function (MCF), which represents the cross correlation between harmonic signals received by a pair of sensors whose separation is transverse to the direction of propagation, is given by[13,15]

$$\Gamma(x',\boldsymbol{\rho}'_\perp)=\frac{\langle p(x',\mathbf{r}'_\perp)p^*(x',\mathbf{r}'_\perp+\boldsymbol{\rho}'_\perp)\rangle}{p_0(x',\mathbf{r}'_\perp)p_0^*(x',\mathbf{r}'_\perp+\boldsymbol{\rho}'_\perp)}=\exp\left[-\frac{1}{2}D_\phi(\boldsymbol{\rho}'_\perp)\right], \tag{7}$$

where $D_\phi(\boldsymbol{\rho}'_\perp)$ is the phase structure function of first-order geometric optics, and $\boldsymbol{\rho}_\perp$ is the separation between the sensors. It is assumed that the separation is perpendicular to the direction of propagation. The phase structure function is equal to

$$D_\phi(\mathbf{r}'_\perp)=4\pi k_0^2 x'[b(\mathbf{0})-b(\mathbf{r}'_\perp)]. \tag{8}$$

It is convenient to define a *2-D structure function* as

$$d(\mathbf{r}'_\perp)=2[b(\mathbf{0})-b(\mathbf{r}'_\perp)], \tag{9}$$

so that

$$D_\phi(\mathbf{r}'_\perp)=2\pi k_0^2 x' d(\mathbf{r}'_\perp). \tag{10}$$

Note that the 2-D structure function can be written as

$$d(\mathbf{r}'_\perp) = \frac{1}{2\pi} \int_{-\infty}^{\infty} D(\mathbf{r}'_\perp + s\mathbf{e}'_1)\, ds, \tag{11}$$

where $D(\mathbf{r})$ is the usual 3-D structure function encountered in the turbulence literature, given by

$$D(\mathbf{r}) = \langle [n(\mathbf{r}) - n(\mathbf{0})]^2 \rangle = 2[R(\mathbf{0}) - R(\mathbf{r})]. \tag{12}$$

The coherence radius $\mathbf{r}_c$ is defined as the value of $\boldsymbol{\rho}'_\perp$ for which $\Gamma = 1/e$. It is the root of the equation

$$d(\mathbf{r}_c) = (\pi k_0^2 x')^{-1}. \tag{13}$$

In this paper, it is assumed that the main contribution to the index-of-refraction fluctuations comes from turbulent velocity fluctuations. This approximation is usually a very reasonable one for the atmosphere, particularly for neutral conditions.[16] As a result, $\mu \simeq v_i/c_0$, where v_i is the turbulent velocity fluctuation in the direction of propagation.[15] Hence we can replace the correlation function for μ with $R_{ii}(\mathbf{r})/c_0^2$ (no summation of repeated indices implied), where $R_{ij}(\mathbf{r}) = \langle v_i(\mathbf{0}) v_j(\mathbf{r}) \rangle$ is the cross-correlation function between v_i and v_j. Our final equations for the mean pressure and coherence are

$$\langle p(x', \mathbf{r}'_\perp) \rangle = p_0(x', \mathbf{r}'_\perp) \exp\left[-\frac{\pi}{c_0^2} k_0^2 x' b_{ii}(\mathbf{0}) \right], \tag{14}$$

and

$$\Gamma(x', \mathbf{r}'_\perp) = \exp\left[-\frac{\pi}{c_0^2} k_0^2 x' d_{ii}(\mathbf{r}'_\perp) \right], \tag{15}$$

where $b_{ii}(\mathbf{r})$ is the 2-D correlation function of the velocity fluctuation in the direction of propagation and $d_{ii}(\mathbf{r})$ is the corresponding 2-D structure function.

According to the two previous equations, we must calculate the 2-D correlation (and structure) functions of the turbulence to determine the acoustic extinction and coherence. However, it is not always convenient to compute the 2-D correlations directly from their definitions in terms of the 3-D correlation function, because the turbulence models are usually developed in the wave number spectral domain rather than in the spatial domain. Hence it is worthwhile to develop some relationships that give the 2-D correlation directly in terms of the spectra. Such relationships can be derived on the basis that the 3-D correlations R_{ij} and spectral densities Φ_{ij} constitute a Fourier transform pair:

$$R_{ij}(\mathbf{r}) = \int \Phi_{ij}(\mathbf{k}) \exp(i\mathbf{k}\cdot\mathbf{r})\, d^3k, \tag{16}$$

$$\Phi_{ij}(\mathbf{k}) = \frac{1}{(2\pi)^3} \int R_{ij}(\mathbf{r}) \exp(-i\mathbf{k}\cdot\mathbf{r})\, d^3r. \tag{17}$$

By Fourier transforming Eq. (16) with respect to r_1 and then setting $k_1 = 0$, we find

$$b_{ij}(\mathbf{r}_\perp) = \int \Phi_{ij}(\mathbf{k}_\perp) \exp(i\mathbf{k}_\perp \cdot \mathbf{r}_\perp)\, d^2k_\perp. \tag{18}$$

In the general case of anisotropic turbulence, the 2-D correlations depend on the direction of the propagation as well as the direction of the sensor displacement $\mathbf{r}'_\perp$. But let us consider for a moment the case of isotropic turbulence, for which the 3-D spectra can be determined from the energy spectrum $E(k)$ using the following equation:[17]

$$\Phi_{ij}(\mathbf{k}) = \frac{E(k)}{4\pi k^2} \left(\delta_{ij} - \frac{k_i k_j}{k^2} \right). \tag{19}$$

By substituting Eq. (18) into (16), setting $i = j$, and rewriting the integration in cylindrical coordinates, we find

$$b_{ii}(r_\perp) = \frac{1}{2} \int_0^\infty \frac{E(k_\perp)}{k_\perp} J_0(k_\perp r_\perp)\, dk_\perp, \tag{20}$$

where J_0 is the cylindrical Bessel function. Note that in isotropic turbulence, the 2-D structure function depends only on the magnitude of $\mathbf{r}_\perp$.

In the next section of this paper, several anisotropic turbulence models will be considered that are based on a suggestion due to Kristensen *et al.*[11] According to this suggestion, the 3-D spectral tensor in anisotropic turbulence can be modeled approximately with the equation

$$\Phi_{ij}(\mathbf{k}) = \sum_{m=1}^{3} A_m(k) \left(\delta_{mi} - \frac{k_m k_i}{k^2} \right) \left(\delta_{mj} - \frac{k_m k_j}{k^2} \right). \tag{21}$$

The A_m's are three independent scalar energy functions. When $A_1(k) = A_2(k) = A_3(k) \equiv A(k)$, the equation for the 3-D spectra reduces to the one for isotropic turbulence, with $E(k) = 4\pi k^2 A(k)$. In general, $E(k) = \frac{4}{3}\pi k^2 [A_1(k) + A_2(k) + A_3(k)]$. If one assumes validity of the Kristensen *et al.* spectral tensor, the 2-D correlation becomes

$$b_{ii}(r_\perp) = 2\pi \int_0^\infty A_i(k_\perp) J_0(k_\perp r_\perp) k_\perp\, dk_\perp. \tag{22}$$

This result implies $b_{ii}(r_\perp)/2\pi$ and $A_i(k_\perp)$ are a Hankel-transform pair. Also note that the Kristensen *et al.* equation for the 3-D spectral tensor causes the 2-D correlation to be independent of the direction of sensor separation $\mathbf{r}'_\perp$, as in isotropic turbulence. However, the 2-D correlation *does* depend on the orientation of the propagation path when the Kristensen *et al.* tensor is used, unlike the case of isotropic turbulence. It needs to be stressed that the Kristensen *et al.* tensor for the 3-D spectra does not constitute a fully general description of anisotropic turbulence. As mentioned above, the 2-D correlation in anisotropic turbulence will depend, in general, on the direction of $\mathbf{r}'_\perp$.

II. MODELS BASED ON THE KRISTENSEN *ET AL.* ANISOTROPIC TENSOR

The turbulence models derived in this section are all based on previous suggestions made by Kristensen *et al.*[11] In my view, their paper weaves together three particularly significant ideas, which can be considered separately for the purposes of this paper. The first of these ideas hypothesizes a particular equation for the 3-D spectral density tensor, given above as Eq. (21). Although the Kristensen *et al.* spectral density tensor does represent a reasonable first step toward

incorporating anisotropy, it also has some shortcomings. For example, it predicts zero covariance between the along-wind and vertical velocity fluctuations, although this covariance is intrinsically nonzero in a shear layer.

The second main idea in the Kristensen *et al.* paper is a mathematical procedure for determining the three scalar energy functions from 1-D spectral densities, such as can be observed by spatially fixed wind sensors (anemometers). This procedure will be discussed in more detail shortly. The third idea is a versatile three-parameter equation used to model the observed 1-D spectral densities.

A total of three different statistical models for anisotropic turbulence will be considered in this section. All are developed using the Kristensen *et al.* 3-D spectral density tensor, along with their procedure for determining the three scalar energy functions from the 1-D spectra. However, for the first and second models (the anisotropic von Kármán and Gaussian models), the equations used for the 1-D spectra are simpler than the Kristensen *et al.* equation, containing two parameters instead of three. My reason for considering anisotropic versions of the von Kármán and Gaussian models is that the isotropic forms of these models have been employed extensively in atmospheric acoustics; therefore, it is interesting to see how they can be generalized. The third model considered uses the Kristensen *et al.* 1-D spectral equation verbatim and hence is exactly the same as their model for neutral surface-layer turbulence. It is simply repeated here (in condensed form) for convenience. No isotropic version of the full Kristensen *et al.* model has been employed previously in wave propagation studies.

A. Anisotropic von Kármán model

Derivation of an anisotropic model, which reduces to the popular von Kármán model in the isotropic limit, is outlined in this section. The reader may wish to refer to Wilson[18] or Kristensen *et al.*[11] to fill in some of the details. We start by considering the family of 1-D turbulence velocity spectra having the wave number axis parallel to the direction of the mean wind. These spectra can be measured by recording time series with an anemometer fixed to a tower and then converting the time series to an approximate spatial series by invoking Taylor's ''frozen turbulence'' hypothesis.[19] The Fourier transform of the approximate spatial series can then be used to determine the spatial spectra. The spectrum of the velocity component aligned with the direction of the mean wind, called the ''longitudinal'' spectrum, is modeled by the equation[20]

$$F_L(k)=\frac{1}{B(\frac{1}{2},\frac{1}{3})}\frac{\sigma_1^2\ell_1}{(1+k^2\ell_1^2)^{5/6}}, \tag{23}$$

where k is the turbulence wave number, $B(x,y)=\Gamma(x)\Gamma(y)/\Gamma(x+y)$ is the beta function, σ_1^2 is the variance of the longitudinal velocity, and ℓ_1 is a length scale parameter. The coordinate system has the x_1 axis aligned with the mean wind, and the x_3 axis vertical. In isotropic turbulence, the ''transverse'' or ''crosswind'' (horizontal and perpendicular to the mean wind) spectrum $F_T(k)$ and the ''vertical'' spectrum $F_V(k)$ are equal to[19]

TABLE I. Values for the turbulent velocity variances σ_i^2 used in the isotropic von Kármán model and the anisotropic models based on Kristensen *et al.*'s spectral tensor. The variances are normalized by u_*^2, the square of the friction velocity.

Direction	Isotropic von Kármán model	Anisotropic models
	σ_i^2/u_*^2	σ_i^2/u_*^2
Along wind ($i=1$)	2.97	4.77
Crosswind ($i=2$)	2.97	2.68
Vertical ($i=3$)	2.97	1.46

$$F_T(k)=F_V(k)=\frac{1}{2}\left[F_L(k)-k\frac{dF_L(k)}{dk}\right]. \tag{24}$$

Since

$$F_L(k)-k\frac{dF_L(k)}{dk}=\frac{1}{B(\frac{1}{2},\frac{1}{3})}\frac{\sigma_1^2\ell_1}{(1+k^2\ell_1^2)^{5/6}}\times\left(1+\frac{5}{3}\frac{k^2\ell_1^2}{1+k^2\ell_1^2}\right),$$

natural choices for $F_T(k)$ and $F_V(k)$ are

$$F_T(k)=\frac{1}{2B(\frac{1}{2},\frac{1}{3})}\frac{\sigma_2^2\ell_2}{(1+k^2\ell_2^2)^{5/6}}\left(1+\frac{5}{3}\frac{k^2\ell_2^2}{1+k^2\ell_2^2}\right) \tag{25}$$

and

$$F_V(k)=\frac{1}{2B(\frac{1}{2},\frac{1}{3})}\frac{\sigma_3^2\ell_3}{(1+k^2\ell_3^2)^{5/6}}\left(1+\frac{5}{3}\frac{k^2\ell_3^2}{1+k^2\ell_3^2}\right). \tag{26}$$

When the variances σ_i^2 are all equal, and the length scales ℓ_i all equal, Eqs. (23), (25), and (26) reduce to the 1-D spectra of the isotropic von Kármán model. By defining

$$F_0(\sigma,\ell,h,\nu;k)=\frac{\sigma^2\ell}{B(\frac{1}{2},\nu)}\frac{1}{(1+k^2\ell^2)^{\nu+1/2}}\left(1+\frac{hk^2\ell^2}{1+k^2\ell^2}\right), \tag{27}$$

we can conveniently abbreviate Eqs. (23), (25), and (26) as $F_L(k)=F_0(\sigma_1,\ell_1,0,\frac{1}{3};k)$, $F_T(k)=(\frac{1}{2})F_0(\sigma_2,\ell_2,\frac{5}{3},\frac{1}{3};k)$, and $F_V(k)=(\frac{1}{2})F_0(\sigma_3,\ell_3,\frac{5}{3},\frac{1}{3};k)$.

The parameters in the anisotropic von Kármán model can be selected by matching the variances and inertial-subrange asymptotes in the Kaimal *et al.*[21] empirical equations for neutral surface-layer turbulence. The procedure for doing so is straightforward and described in the Appendix, with the results given in Tables I and II. It should be pointed out that the requirement of isotropy in the inertial subrange ($k\ell_i\gg 1$) implies that only four of the six parameters in the anisotropic von Kármán model are independent. Specifically, we must have $\sigma_1^2\ell_1^{-2/3}=\sigma_2^2\ell_2^{-2/3}=\sigma_3^2\ell_3^{-2/3}$. The values in Tables I and II for the isotropic von Kármán model were chosen by setting $\sigma_{\text{avg}}^2=(\sigma_1^2+\sigma_2^2+\sigma_3^2)/3$, and ℓ from the requirement $\sigma_{\text{avg}}^2\ell^{-2/3}=\sigma_1^2\ell_1^{-2/3}$, etc. Note that the variances are all proportional to u_*^2, the friction velocity (defined in the Appendix), and the length scales are all proportional to z, the height. The 1-D spectra for the anisotropic

TABLE II. Values for the length scales and other parameters used in the various turbulence models. The length scales are normalized by z, the height from the ground.

Direction	von Kármán (isotropic)	von Kármán (anisotropic)	Gaussian (anisotropic)	Kristensen *et al.* (anisotropic)	
	ℓ_i/z	ℓ_i/z	L_i/z	l_i/z	μ_i
Along wind ($i=1$)	1.79	3.64	6.21	5.24	0.52
Crosswind ($i=2$)	1.79	1.53	3.59	2.52	0.49
Vertical ($i=3$)	1.79	0.617	0.774	0.59	0.68

von Kármán model are plotted in Fig. 1. In this figure, the curves labelled ''Kristensen *et al.*'' are nearly identical to the Kaimal *et al.* empirical equations. The von Kármán spectra therefore have sharper spectral peaks than the empirical results.

Determination of the extinction distance for propagation in the along-wind direction is a simple matter when the 1-D spectrum $F_L(k)$ is known. Using the Fourier transform relations, one can show that $b_{11}(\mathbf{0})=F_L(0)$, so $F_L(0)$ can be used in place of $b_{11}(\mathbf{0})$ in Eq. (14). But it is not true that $b_{22}(\mathbf{0})=F_T(0)$ or $b_{33}(\mathbf{0})=F_V(0)$. Therefore in the crosswind direction, we are forced to use Eq. (22), with $r_\perp=0$:

$$b_{22}(0)=2\pi\int_0^\infty A_2(k_\perp)k_\perp\,dk_\perp\,, \tag{28}$$

and similarly in the vertical direction. Now it is evident that we must calculate the scalar energy functions $A_2(k)$ and $A_3(k)$ to determine the extinction distances in the crosswind and vertical directions. It is necessary to find all of the $A_i(k)$ to calculate the 2-D structure functions needed for the MCF.

Fortunately Kristensen *et al.*[11] have devised a method for determining the $A_i(k)$ from $F_L(k)$, $F_T(k)$, and $F_V(k)$. Their method is based on the following equations, which they derive:

$$A_1(k)=\frac{k}{4\pi}\frac{d}{dk}\frac{1}{k}\frac{dF_L(k)}{dk}+\frac{1}{2\pi}[-\beta(k^{-2})-\zeta(k^{-2})], \tag{29}$$

$$A_2(k)=\frac{k}{4\pi}\frac{d}{dk}\frac{1}{k}\frac{dF_L(k)}{dk}+\frac{1}{2\pi}[\alpha(k^{-2})-3\beta(k^{-2})-\zeta(k^{-2})], \tag{30}$$

and

$$A_3(k)=\frac{k}{4\pi}\frac{d}{dk}\frac{1}{k}\frac{dF_L(k)}{dk}+\frac{1}{2\pi}[-\alpha(k^{-2})-3\beta(k^{-2})-\zeta(k^{-2})]. \tag{31}$$

(These equations are actually in a slightly different, but equivalent, form than the one given by Kristensen *et al.*[11] The function ζ was not defined in their paper.) The first term in Eqs. (29)–(31) represents the isotropic contribution. By differentiation of Eq. (23), this term is found to be

$$\frac{k}{4\pi}\frac{d}{dk}\frac{1}{k}\frac{dF_L(k)}{dk}=\frac{55\sigma_1^2}{36\pi B(\frac{1}{2},\frac{1}{3})}\frac{k^2\ell_1^5}{(1+k^2\ell_1^2)^{17/6}}. \tag{32}$$

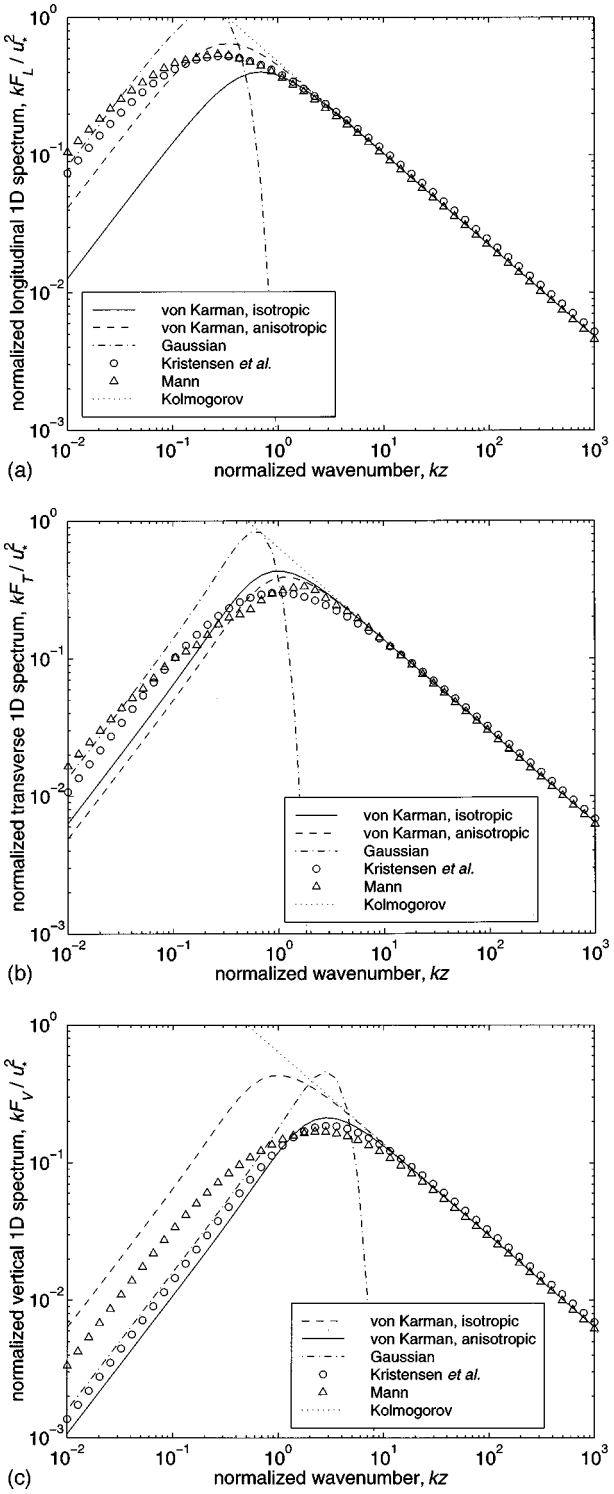

FIG. 1. (a) Modeled one-dimensional spectra for fluctuations of the along-wind velocity component, $F_L(k)$, for the various turbulence models. (b) Modeled one-dimensional spectra for fluctuations of the crosswind velocity component, $F_T(k)$. (c) Modeled one-dimensional spectra for fluctuations of the vertical velocity component, $F_V(k)$. In each plot the spectrum has been multiplied by k/u_*^2, where k is the wave number in the along-wind direction and u_* is the friction velocity.

Derivation of the terms in Eqs. (29)–(31) involving the functions $\alpha(s)$, $\beta(s)$, and $\zeta(s)$ begins by defining the ''residual'' functions

$$f(s)=[F_T(k)-F_V(k)]s^2 \tag{33}$$

and

$$g(s)=\{F_L(k)-kF_L'(k)-[F_T(k)+F_V(k)]\}s^2, \tag{34}$$

where $s\equiv k^{-2}$. From Eqs. (23)–(27), we find

$$f(s)=\frac{s^2}{2}[F_0(\sigma_2,\ell_2,\tfrac{5}{3},\tfrac{1}{3};s^{-1/2})-F_0(\sigma_3,\ell_3,\tfrac{5}{3},\tfrac{1}{3};s^{-1/2})] \tag{35}$$

and

$$g(s)=\frac{s^2}{2}[2F_0(\sigma_1,\ell_1,\tfrac{5}{3},\tfrac{1}{3};s^{-1/2})-F_0(\sigma_2,\ell_2,\tfrac{5}{3},\tfrac{1}{3};s^{-1/2}) -F_0(\sigma_3,\ell_3,\tfrac{5}{3},\tfrac{1}{3};s^{-1/2})]. \tag{36}$$

The functions $\alpha(s)$, $\beta(s)$, and $\zeta(s)$ in Eqs. (29)–(31) can be determined from the integrals[11]

$$\alpha(s)=\frac{s^{+1/\sqrt{2}}}{\sqrt{2}}\int_0^s t^{1-1/\sqrt{2}}f'''(t)\,dt - \frac{s^{-1/\sqrt{2}}}{\sqrt{2}}\int_0^s t^{1+1/\sqrt{2}}f'''(t)\,dt, \tag{37}$$

$$\beta(s)=\frac{s^{1/3}}{3}\int_0^s t^{2/3}g'''(t)\,dt, \tag{38}$$

and

$$\zeta(s)=-s^{-1}\int_0^s t^2 g'''(t)\,dt. \tag{39}$$

Hence we need to solve integrals of the form

$$I(\sigma,\ell,q;s)=\frac{qs^q}{2}\int_0^s t^{1-q}\frac{d^3}{dt^3}[t^2F_0(\sigma,\ell,\tfrac{5}{3},\tfrac{1}{3};t^{-1/2})]\,dt. \tag{40}$$

With this definition, we have

$$\alpha(s)=I\left(\sigma_2,\ell_2,\frac{1}{\sqrt{2}};s\right)-I\left(\sigma_3,\ell_3,\frac{1}{\sqrt{2}};s\right) +I\left(\sigma_2,\ell_2,-\frac{1}{\sqrt{2}};s\right)-I\left(\sigma_3,\ell_3,-\frac{1}{\sqrt{2}};s\right), \tag{41}$$

$$\beta(s)=2I(\sigma_1,\ell_1,\tfrac{1}{3};s)-I(\sigma_2,\ell_2,\tfrac{1}{3};s) -I(\sigma_3,\ell_3,\tfrac{1}{3};s), \tag{42}$$

and

$$\zeta(s)=2I(\sigma_1,\ell_1,-1;s)-I(\sigma_2,\ell_2,-1;s) -I(\sigma_3,\ell_3,-1;s). \tag{43}$$

It can be shown that

$$\frac{d}{dt}F_0(\sigma,\ell,h,\nu;t^{-1/2})=\frac{\nu(\nu-h+\frac{1}{2})}{\nu+\frac{1}{2}}\frac{\ell^2}{s^2} \times F_0\left(\sigma,\ell,\frac{h(\nu+\frac{3}{2})}{\nu-h+\frac{1}{2}},\nu+1;t^{-1/2}\right),$$

from which follows recursively the triple derivative needed in Eq. (40),

$$\frac{d^3}{dt^3}[t^2F_0(\sigma,\ell,\tfrac{5}{3},\tfrac{1}{3};t^{-1/2})] =-\frac{140}{27}\frac{\ell^6}{s^4}F_0\left(\sigma,\ell,-\frac{23}{15},\frac{10}{3};t^{-1/2}\right).$$

Using the definition of the incomplete beta function $B_z(a,b)$ [e.g., Eq. (6.6.1) in Abramowitz and Stegun[24]], we can now write the function I as

$$I(\sigma,\ell,q;k^{-2})=\frac{4675}{432}\frac{q\sigma^2\ell^3}{B(\frac{1}{2},\frac{1}{3})}(k\ell)^{-2q} \times[\tfrac{23}{15}B_{1/(1+k^2\ell^2)}(\tfrac{11}{6}-q,3+q) -B_{1/(1+k^2\ell^2)}(\tfrac{11}{6}-q,2+q)]. \tag{44}$$

Substitution of this result into Eqs. (41)–(43) yields the functions $\alpha(s)$, $\beta(s)$, and $\zeta(s)$, and hence the three scalar energy functions.

The 2-D correlation functions now follow by substituting the scalar energy functions into Eq. (22). The isotropic contribution to the 2-D correlation is found by integrating Eq. (32). This integration presents no great difficulties and we find

$$b_{iso}(\sigma_1,\ell_1;r)=\int_0^\infty\left[\frac{k^2}{2}\frac{d}{dk}\frac{1}{k}\frac{dF_L(k)}{dk}\right]J_0(kr)\,dk =\frac{2\sigma_1^2\ell_1}{\sqrt{\pi}\Gamma(\frac{1}{3})}\left(\frac{r}{2\ell_1}\right)^{5/6} \times\left[K_{5/6}\left(\frac{r}{\ell_1}\right)-\frac{r}{2\ell_1}K_{1/6}\left(\frac{r}{\ell_1}\right)\right]. \tag{45}$$

To find the anisotropic contributions, we need to calculate integrals of the form

$$\overline{I}(\sigma,\ell,q;r)=\int_0^\infty I(\sigma,\ell,q;k^{-2})J_0(kr)k\,dk, \tag{46}$$

in which $I(\sigma,\ell,q;s)$ contains incomplete beta functions. Not surprisingly, the integral has no solution in terms of common higher functions such as Bessel functions. One possible approach to solving the integral is to rewrite the incomplete beta functions as Meijer's G-functions. (Discussions of G-functions can be found in Erdélyi *et al.*[22] and Gradshteyn and Ryzhik.[23]) This can be done by first converting the incomplete beta function to a hypergeometric function having argument $-(k\ell)^{-2}$, using Eqs. (6.6.8) and (15.3.4) in Abramowitz and Stegun.[24] Next the hypergeometric function is recast as a G-function using Eq. (74), Sec. 5.6, and Eq. (9), Sec. 5.3, from Erdélyi *et al.*,[22] with result

$$B_{1/(1+k^2\ell^2)}(a,b)=\frac{(k^2\ell^2)^{-a-1}}{\Gamma(a+b)} \times G_{22}^{21}\left(k^2\ell^2\left|\begin{matrix}2,a+2\\ a+1,a+b+1\end{matrix}\right.\right). \tag{47}$$

It is now possible to calculate $\overline{I}(\sigma,\ell,q;r)$ using Eq. (7.822.1) in Gradshteyn and Ryzhik.[23] We find

$$\overline{I}(\sigma,\ell,q;r)=\frac{q\sigma^2\ell}{2\sqrt{\pi}\Gamma(\frac{1}{3})}\left(\frac{r}{2\ell}\right)^{11/3}\times\left[G_{42}^{22}\left(\frac{4\ell^2}{r^2}\middle|\begin{matrix}\frac{17}{6},2,\frac{23}{6}-q,\frac{17}{6}\\ \frac{17}{6}-q,\frac{35}{6}\end{matrix}\right)-\frac{5}{2}G_{42}^{22}\left(\frac{4\ell^2}{r^2}\middle|\begin{matrix}\frac{17}{6},2,\frac{23}{6}-q,\frac{17}{6}\\ \frac{17}{6}-q,\frac{29}{6}\end{matrix}\right)\right]. \tag{48}$$

The G-functions can be converted to a lower order using a recursion relation [Eq. (12), Sec. 5.3 in Ref. 22], and a reduction formula [Eq. (7), Sec. 5.3 in Ref. 22]. The result is

$$\overline{I}(\sigma,\ell,q;r)=\frac{q\sigma^2\ell}{2\sqrt{\pi}\Gamma(\frac{1}{3})}\left(\frac{r}{2\ell}\right)^{11/3}\times\left[G_{13}^{21}\left(\frac{r^2}{4\ell^2}\middle|\begin{matrix}q-\frac{11}{6}\\ -\frac{11}{6},-1,q-\frac{17}{6}\end{matrix}\right)-8G_{13}^{21}\left(\frac{r^2}{4\ell^2}\middle|\begin{matrix}q-\frac{11}{6}\\ -\frac{5}{6},-1,q-\frac{17}{6}\end{matrix}\right)+\frac{13}{2}G_{13}^{21}\left(\frac{r^2}{4\ell^2}\middle|\begin{matrix}q-\frac{11}{6}\\ \frac{1}{6},-1,q-\frac{17}{6}\end{matrix}\right)-G_{13}^{21}\left(\frac{r^2}{4\ell^2}\middle|\begin{matrix}q-\frac{11}{6}\\ \frac{7}{6},-1,q-\frac{17}{6}\end{matrix}\right)\right]. \tag{49}$$

[Equation (9), Sec. 5.3 in Ref. 22, was also used to derive this result.] For the 2-D correlation function in the along-wind direction, we now have from Eq. (29)

$$b_{11}(r)=b_{iso}(\sigma_1,\ell_1;r)-\overline{\beta}(r)-\overline{\zeta}(r), \tag{50}$$

where, from Eq. (42),

$$\overline{\beta}(r)=2\overline{I}(\sigma_1,\ell_1,\tfrac{1}{3};r)-\overline{I}(\sigma_2,\ell_2,\tfrac{1}{3};r)-\overline{I}(\sigma_3,\ell_3,\tfrac{1}{3};r). \tag{51}$$

Equations for $b_{22}(r)$, $b_{33}(r)$, $\overline{\alpha}(r)$, and $\overline{\zeta}(r)$ follow with obvious replacements.

Since routines for computing Meijer's G-functions are not widely available, it is often impractical to calculate the 2-D correlations by using Eq. (49).[25] Rather, they must be calculated by performing the integration in Eq. (46) numerically.

B. Anisotropic Gaussian model

Although it is rather unrealistic, the isotropic Gaussian model has proven quite popular. The main advantage of the isotropic Gaussian model is that the equations for the correlation and spectral functions are easily obtainable. The disadvantage is that it does not accurately describe the inertial subrange. In this section we explore how the isotropic Gaussian model can be generalized to the anisotropic case. The basic assumption is that the longitudinal correlation function has the form

$$R_L(r)=\sigma_1^2\exp\left(-\frac{r^2}{L_1^2}\right). \tag{52}$$

By Fourier transforming the correlation function, we find

$$F_L(k)=\frac{\sigma_1^2L_1}{2\sqrt{\pi}}\exp\left(-\frac{k^2L_1^2}{4}\right). \tag{53}$$

As mentioned previously, $F_T(k)=F_V(k)=(\frac{1}{2})[F_L(k)-kF_L'(k)]$ in isotropic turbulence. Hence a natural choice for $F_T(k)$ is

$$F_T(k)=\frac{\sigma_2^2L_2}{4\sqrt{\pi}}\left(1+\frac{k^2L_2^2}{2}\right)\exp\left(-\frac{k^2L_2^2}{4}\right), \tag{54}$$

and similarly for $F_V(k)$.

Since Gaussian models do not, by nature, have a realistic inertial subrange, it is reasonable to select the model parameters to obtain the best possible fit to spectral characteristics of the energy subrange, such as variances and integral length scales. A reasonable approach (described in the Appendix) is to select the parameters to reproduce the variances and integral length scales of the Kaimal *et al.*[21] empirical equations. The results are shown in Tables I and II, and the 1-D spectra are plotted and compared to other models in Fig. 1. As one would expect, the Gaussian spectra are satisfactory in the energy subrange ($kz\ll 1$), but very poor in the inertial subrange ($kz\gg 1$).

As for the von Kármán model, we determine the scalar energy functions A_i using Eqs. (29)–(31). For the Gaussian model, the isotropic term in those equations is

$$\frac{k}{4\pi}\frac{d}{dk}\frac{1}{k}\frac{dF_L(k)}{dk}=\frac{\sigma_1^2k^2L_1^5}{32\pi^{3/2}}\exp\left(-\frac{k^2L_1^2}{4}\right). \tag{55}$$

Using the same method as before to calculate $\alpha(s)$, $\beta(s)$, and $\zeta(s)$, we arrive at the residual functions

$$f(s)=\frac{s^2}{2}[G_0(\sigma_2,L_2;s^{-1/2})-G_0(\sigma_3,L_3;s^{-1/2})],$$

and

$$g(s)=\frac{s^2}{2}[2G_0(\sigma_1,L_1;s^{-1/2})-G_0(\sigma_2,L_2;s^{-1/2})-G_0(\sigma_3,L_3;s^{-1/2})],$$

where the function G_0, defined by

$$G_0(\sigma,L;k)=\frac{\sigma^2L}{2\sqrt{\pi}}\left(1+\frac{k^2L^2}{2}\right)\exp\left(-\frac{k^2L^2}{4}\right), \tag{56}$$

appears in place of F_0 in the von Kármán model. We again need to find integrals of the form given by Eq. (40), although with the function G_0 replacing F_0. It can be shown that

$$\frac{d^3}{dt^3}[t^2 G_0(\sigma,L;t^{-1/2})] = \frac{\sigma^2 L}{2\sqrt{\pi}}\left[\left(-\frac{5L^6}{64t^4}+\frac{L^8}{128t^5}\right)\times\exp\left(-\frac{L^2}{4t}\right)\right].$$

The integrals can be written as incomplete gamma functions [e.g., Eq. (6.5.1) in Ref. 24], with result

$$I(\sigma,L,q;s) = \frac{q\sigma^2 L^3}{8\sqrt{\pi}}\left(\frac{4s}{L^2}\right)^q\left[\Gamma\left(3+q,\frac{L^2}{4s}\right) - \frac{5}{2}\Gamma\left(2+q,\frac{L^2}{4s}\right)\right]. \quad (57)$$

The functions $\alpha(s)$, $\beta(s)$, and $\zeta(s)$ can now be determined using Eqs. (41)–(43).

The isotropic contribution to the 2-D correlation function is

$$b_{iso}(\sigma_1,L_1;r) = \frac{\sigma_1^2 L_1}{2\sqrt{\pi}}\left(1-\frac{r^2}{L_1^2}\right)\exp\left(-\frac{r^2}{L_1^2}\right). \quad (58)$$

[If only this isotropic contribution is used to calculate the 2-D correlation function, the results for the extinction and coherence can be shown to be equivalent to Eqs. (22) and (24) in Ostashev *et al.*[26]] Calculation of the anisotropic contributions to the 2-D structure function requires us to integrate the product of an incomplete gamma function and a Bessel function. This integration can be done by rewriting the incomplete gamma functions as confluent hypergeometric functions, using Eqs. (13.1.33) and (13.6.28) in Abramowitz and Stegun.[24] The relationship is $\Gamma(a,x) = e^{-x/2}x^{a/2-1/2}W_{a/2-1/2,-a/2}(x)$, where $W_{\kappa,\mu}(\bullet)$ is Whittaker's function. The integration can now be performed using Gradshteyn and Ryzhik's[23] Eq. (7.672.2), with result

$$\overline{I}(\sigma,L,q;r) = \frac{3q\sigma^2 L}{2\sqrt{\pi}(1-q)}\left[{}_2F_2\left(4,1-q;1,2-q;-\frac{r^2}{L^2}\right) - \frac{5}{4}\,{}_2F_2\left(3,1-q;1,2-q;-\frac{r^2}{L^2}\right)\right], \quad (59)$$

where ${}_2F_2(\bullet)$ is a generalized hypergeometric function. As was the case with the anisotropic von Kármán model, the Gaussian result for the 2-D correlation function again involves a higher function for which computational routines are not commonly available. Hence it is usually most practical to calculate the 2-D correlation function by numerically integrating Eq. (46). Even the simple Gaussian model, when generalized to the anisotropic case, eludes convenient solution for the 2-D correlation function.

C. Kristensen *et al.* model

Krasnenko *et al.*[27] have previously suggested using the Kristensen *et al.* model[11] to calculate statistics of acoustic field fluctuations. The Kristensen *et al.* model uses equations very similar to the von Kármán model, except that in place of F_0 [defined in Eq. (27)] we instead use the new function H_0, defined by

$$H_0(\sigma,l,\mu,h;k) = \frac{l\sigma^2}{\pi}\frac{1}{\{1+[kl/a(\mu)]^{2\mu}\}^{5/6\mu}}\times\left\{1+\frac{h[kl/a(\mu)]^{2\mu}}{1+[kl/a(\mu)]^{2\mu}}\right\}, \quad (60)$$

where $a(\mu)=\pi\mu/B(1/2\mu,1/3\mu)$. The 1-D spectra are

$$F_L(k) = H_0(\sigma_1,l_1,\mu_1,0;k), \quad (61)$$

$$F_T(k) = \tfrac{1}{2}H_0(\sigma_2,l_2,\mu_2,\tfrac{5}{3};k), \quad (62)$$

and

$$F_V(k) = \tfrac{1}{2}H_0(\sigma_3,l_3,\mu_3,\tfrac{5}{3};k). \quad (63)$$

The parameters l_i are integral length scales. The parameters μ_i control the sharpness of the spectral peak; larger values give a sharper peak. Setting the $l_i = a(\mu_i)\ell_i$ and $\mu_i = 1$ reproduces the anisotropic von Kármán model. Kristensen *et al.* chose the parameters in their model to approximate the empirical spectra of Kaimal *et al.*,[21] and the resulting values are shown in Tables I and II. Note that the μ_i's are significantly less than 1, indicating that the actual spectra have broader peaks than in the von Kármán model. The 1-D spectra from the Kristensen *et al.* model (Fig. 1) virtually match the empirical spectra determined by Kaimal *et al.*

Derivation of the scalar energy functions $A_i(k)$ proceeds much as it did in Sec. II A, except that the equations become somewhat more complicated due to the more complicated form for the 1-D spectra. The first term in Eqs. (29)–(31), representing the isotropic spectra, is found by differentiation of Eq. (61) to be

$$\frac{k}{4\pi}\frac{d}{dk}\frac{1}{k}\frac{dF_L(k)}{dk} = \frac{5\sigma_1^2}{12\pi^2 a^{2\mu_1}(\mu_1)}\times\frac{k^{2\mu_1-2}l_1^{2\mu_2+1}}{\{1+[kl_1/a(\mu_1)]^{2\mu_1}\}^{5/6\mu_1+2}}\times\{2-2\mu_1+\tfrac{11}{3}[kl_1/a(\mu_1)]^{2\mu_1}\}. \quad (64)$$

The remaining terms in Eqs. (29)–(31), involving the functions $\alpha(s)$, $\beta(s)$, and $\zeta(s)$, represent the anisotropic contributions. Since the reader can refer to Kristensen *et al.*[11] for the solution for these functions, only the final results will be repeated here:

$$\alpha(s) = \gamma_0\left(\frac{1}{\sqrt{2}},\sigma_{22},l_2,\mu_2;s\right) - \gamma_0\left(\frac{1}{\sqrt{2}},\sigma_{33},l_3,\mu_3;s\right) + \gamma_0\left(-\frac{1}{\sqrt{2}},\sigma_2,l_2,\mu_2;s\right) - \gamma_0\left(-\frac{1}{\sqrt{2}},\sigma_3,l_3,\mu_3;s\right), \quad (65)$$

$$\beta(s) = 2\gamma_0(\tfrac{1}{3},\sigma_1,l_1,\mu_1;s) - \gamma_0(\tfrac{1}{3},\sigma_2,l_2,\mu_2;s) - \gamma_0(\tfrac{1}{3},\sigma_3,l_3,\mu_3;s), \quad (66)$$

and

$$\zeta(s)=2\gamma_0(-1,\sigma_1,l_1,\mu_1;s)-\gamma_0(-1,\sigma_2,l_2,\mu_2;s)-\gamma_0(-1,\sigma_3,l_3,\mu_3;s). \tag{67}$$

The function γ_0 is given by

$$\gamma_0(q,\sigma,\ell,\mu;s)=\frac{1}{96\pi}\frac{q\sigma^2\ell^3}{\mu a^2(\mu)}\eta^q\sum_{n=1}^{4}C_n(\mu)B_{\eta^{\mu}/(1+\eta^{\mu})}\times\left(\frac{11}{6\mu}-\frac{q}{\mu},n+\frac{q-1}{\mu}\right), \tag{68}$$

where

$$\eta\equiv\frac{a^2(\mu)}{\ell^2}s, \tag{69}$$

and

$$\begin{aligned}C_1(\mu)&=40(1-\mu)(1-2\mu)(2-\mu),\\ C_2(\mu)&=\frac{140}{3}(1-\mu)(1-2\mu)(5+6\mu),\\ C_3(\mu)&=\frac{10}{9}(5+6\mu)(5+12\mu)(7-12\mu),\\ C_4(\mu)&=\frac{10}{27}(5+6\mu)(5+12\mu)(5+18\mu).\end{aligned} \tag{70}$$

To find the 2-D structure function, we need to solve the integral Eq. (22), with the scalar energy functions given by Eqs. (29)–(31). Integrals of the form

$$\overline{\gamma}_0(q,\sigma,L,\mu;r)=\int_0^{\infty}\gamma_0(q,\sigma,L,\mu;k^{-2})J_0(kr)k\,dk$$

must be calculated, where $\gamma_0(\bullet)$ incorporates incomplete beta functions with the wave number raised to fractional powers. I have been unable to find a method for calculating these integrals, even in terms of Meijer's *G*-functions, as was possible for the von Kármán model. Fortunately, it is not difficult to find the 2-D structure function by numerical integration.

III. MANN'S RAPID-DISTORTION MODEL

The Mann model[12] is based on *rapid distortion theory*, which models shear-induced distortions to eddies by using a linearized solution to the Navier–Stokes equations. A constant (height-independent) mean shear is assumed in the solution. A full discussion of rapid distortion theory and Mann's model is beyond the scope of this paper. However, the relevant equations will be summarized and applied to acoustic propagation. Mann's equations for the 3-D autospectra are

$$\Phi_{11}(\mathbf{k})=\frac{E(k_0)}{4\pi k_0^4}[k_0^2-k_1^2-2k_1k_{30}\zeta_1+(k_1^2+k_2^2)\zeta_1^2], \tag{71}$$

$$\Phi_{22}(\mathbf{k})=\frac{E(k_0)}{4\pi k_0^4}[k_0^2-k_2^2-2k_2k_{30}\zeta_2+(k_1^2+k_2^2)\zeta_2^2], \tag{72}$$

and

$$\Phi_{33}(\mathbf{k})=\frac{E(k_0)}{4\pi k^4}(k_1^2+k_2^2). \tag{73}$$

In these equations, $E(k)$ is the initial (before the onset of shear distortion) energy spectrum. The von Kármán spectrum is used for $E(k)$, which can be written in the form[20]

$$E(k)=\frac{55}{9B(\frac{1}{2},\frac{1}{3})}\frac{\sigma_M^2k^4\ell_M^5}{(1+k^2\ell_M^2)^{17/6}}, \tag{74}$$

where σ_M^2 and ℓ_M are the variance and length scale parameters, respectively. The initial wave number is

$$\mathbf{k}_0=(k_1,k_2,k_{30}), \tag{75}$$

where $k_{30}=k_3-\beta k_1$. The parameter β is called the nondimensional *eddy lifetime*. Mann's equation for β [Eq. (3.3) in Ref. 12] involves a hypergeometric function. However, β can also be expressed in terms of the incomplete beta function, which is sometimes more convenient since the incomplete beta function can be computed by using widely available routines:[18]

$$\beta=\frac{\sqrt{3}\Gamma}{k\ell_M}\left[B_{1/(1+k^2\ell_M^2)}\left(\frac{1}{3},\frac{5}{2}\right)\right]^{-1/2}. \tag{76}$$

The ζ_i are wave-number-dependent functions, given by the equations

$$\zeta_1=C_1-\frac{k_2}{k_1}C_2,\quad \zeta_2=\frac{k_2}{k_1}C_1+C_2, \tag{77}$$

where

$$C_1=\frac{\beta k_1^2(k_0^2-2k_{30}^2+\beta k_1k_{30})}{k^2(k_1^2+k_2^2)} \tag{78}$$

and

$$C_2=\frac{k_2k_0^2}{(k_1^2+k_2^2)^{3/2}}\arctan\left[\frac{\beta k_1(k_1^2+k_2^2)^{1/2}}{k_0^2-\beta k_{30}k_1}\right]. \tag{79}$$

In his initial paper, Mann[12] determined the free parameter Γ (not to be confused with the MCF) by a least-squares fit to two atmospheric data sets. The resulting values for Γ were 2.6 and 3.2. More recently, Mann[28] determined Γ by fitting his model to various empirical spectral models, and found Γ in the range 3.0 to 4.5. A somewhat simpler alternative method for determining Γ is used in this paper. Specifically, Γ is chosen such that the ratio σ_1^2/σ_3^2 matches the anisotropic models discussed earlier. From Table I, this ratio should be 4.77/1.46=3.27. The desired value of Γ, found using numerical integration, is 3.58.[18] To force σ_1^2 equal to $4.77u_*^2$ when $\Gamma=3.58$, we need to set[18]

$$\sigma_M^2=1.52u_*^2 \tag{80}$$

in the initial von Kármán spectrum. The length scale ℓ_M is obtained by setting the dissipation rate of turbulent kinetic energy to $u_*^3/\kappa z$, where $\kappa\simeq0.40$ is von Kármán's constant.[29] The result is[18]

$$\ell_M=0.587z. \tag{81}$$

TABLE III. Normalized values $\overline{\xi}$ of the extinction distance for several turbulence models. The normalized value must be multiplied by $c_0^2/(k_0^2 u_*^2 z)$ to obtain the actual distance ξ.

Model	$\overline{\xi}$, along wind	$\overline{\xi}$, crosswind	Cross/along-wind ratio
Kristensen *et al.*	0.0400	0.104	2.59
von Kármán, isotropic	0.252	0.252	1.00
von Kármán, anisotropic	0.0770	0.234	3.04
Gaussian, anisotropic	0.0381	0.0815	2.14
Mann	0.141	1.84	13.0
Wilson and Thomson	0.0332	0.245	7.40

The 1-D spectra for the Mann model must be determined numerically, by integrating over k_2 and k_3. For example,

$$F_L(k_1) = \int_{-\infty}^{\infty}\int_{-\infty}^{\infty} \Phi_{11}(\mathbf{k})\, dk_2\, dk_3 . \tag{82}$$

The 1-D spectra are plotted and compared to the other turbulence models in Fig. 1. On the whole, the Mann model agrees well with the Kristensen *et al.* model, the main distinction being that the energy-subrange levels for $F_V(k_1)$ are somewhat higher. This overall agreement is quite satisfactory considering that the Mann model has only three parameters, compared to nine in Kristensen *et al.*

The 2-D correlation functions can be found using Eq. (18). Since $\Phi_{ii}(\mathbf{k}_\perp)$ depends on the orientation of $\mathbf{k}_\perp$, the double integral cannot be reduced to a single one involving a Bessel function as in Eq. (22). However, if we restrict ourselves to sensor separations along just one of the orthogonal coordinate axes, Eq. (18) can be simplified somewhat. For example, if propagation is in the along-wind direction and the sensors are separated in the crosswind direction, the 2-D correlation function of interest is $b(r_2,0) = b_{11}(r_2,0)/c_0^2$, where

$$b_{11}(r_2,0) = \int_{-\infty}^{\infty}\left[\int_{-\infty}^{\infty} \Phi_{11}(0,k_2,k_3)\, dk_3\right] \exp(ik_2 r_2)\, dk_2 . \tag{83}$$

The advantage of this equation is that the full Fourier transform needs to be performed along just one axis. A simple numerical integration can be performed along the other axis.

Note that the 2-D structure functions in the Mann model depend on the direction of the displacement. This behavior distinguishes the Mann model from the ones in Sec. II based on the Kristensen *et al.* spectral tensor.

IV. RESULTS AND DISCUSSION

A. Extinction distance

Extinction distances calculated for the various turbulence models discussed in Secs. II and III are shown in Table III. Also shown are calculations for the isotropic von Kármán model, and the Wilson and Thomson model (retaining the second and third terms only).[8] ''Along wind'' is the x_1 direction, and ''crosswind'' is the x_2 direction. The values in the table are the actual extinction distance normalized by $c_0^2/(k_0^2 u_*^2 z)$. This normalization factor arises from Eq. (14), and the fact that the 2-D structure function $d_{ii}(\mathbf{r}_\perp)$ is proportional to $u_*^2 z$ for all of the shear-layer models considered in this paper. [The velocity variances are proportional to u_*^2 and the length scales to z. The function $d_{ii}(\mathbf{r}_\perp)$ therefore has dimensions of velocity variance times length.]

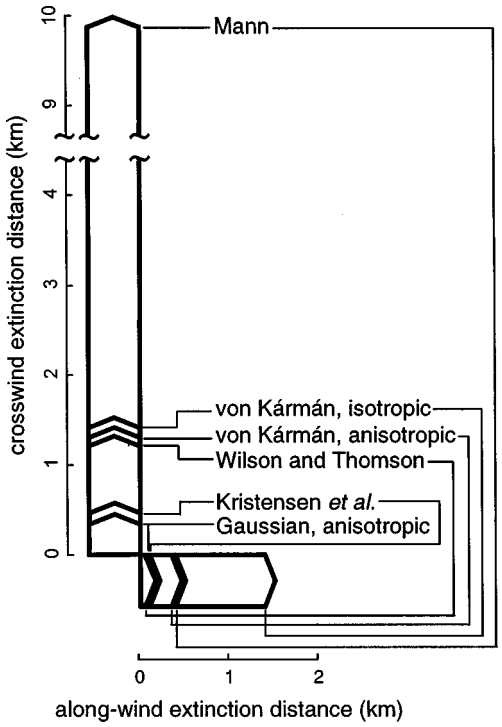

FIG. 2. Extinction distances for the various turbulence models. The calculations are for a frequency $f = 500$ Hz, height $z = 1$ m, friction velocity $u_* = 0.5$ m/s, and sound speed $c_0 = 340$ m/s. (Lengths of the arrows indicate the extinction distance.)

A graphical comparison of the model predictions is shown in Fig. 2, which is for the particular case $f = 500$ Hz, $z = 1$ m, $u_* = 0.5$ m/s, and $c_0 = 340$ m/s. The value for u_* is representative of moderately strong winds. Note that the relative *proportions* between the various distances plotted in Fig. 2 are *independent* of the particular values used for f, z, u_*, and c_0.

All of the anisotropic models predict an extinction distance in the along-wind direction that is much shorter than the isotropic von Kármán model. In the crosswind direction, the Mann model predicts an extinction distance much longer than the isotropic von Kármán model. Predicted distances from the anisotropic von Kármán, and Wilson and Thomson, models are just slightly shorter than the isotropic von Kármán model prediction in the crosswind direction. Predicted distances from the remaining models are all considerably shorter.

For all of the anisotropic models, the predicted extinction distance in the crosswind direction is longer than in the along-wind direction. The ratio of crosswind to along-wind extinction varies from 2.14 for the Gaussian model to 13.0 for the Mann model. In fact, all of the models based on the Kristensen *et al.* spectral tensor have ratios much less than the Mann model. This behavior could indicate that some of the assumptions regarding symmetry of the turbulence, which are inherent to the Kristensen *et al.* spectral tensor

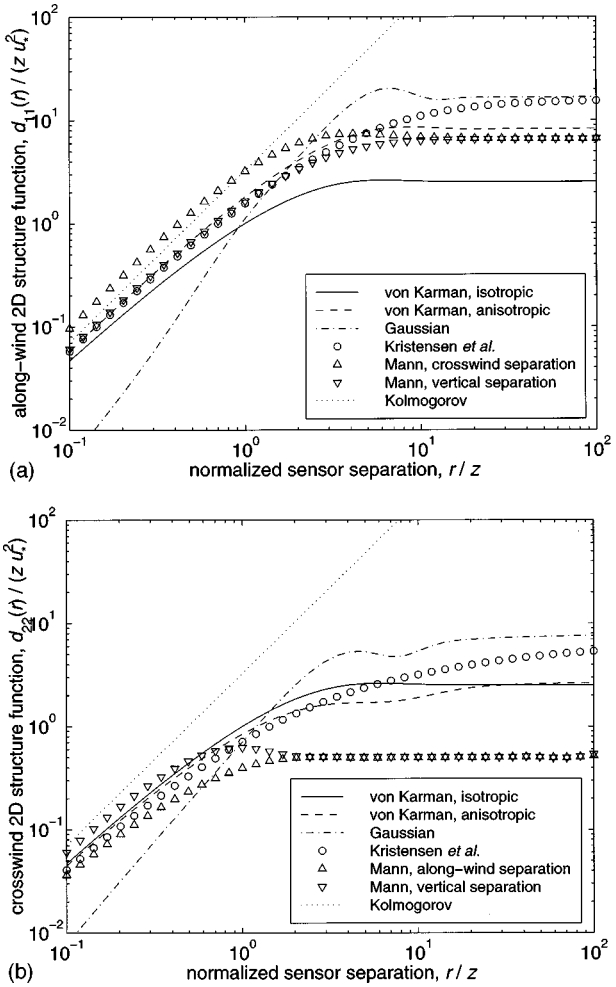

FIG. 3. Two-dimensional structure function as a function of sensor separation for the various turbulence models. (a) Along-wind propagation. (b) Crosswind propagation.

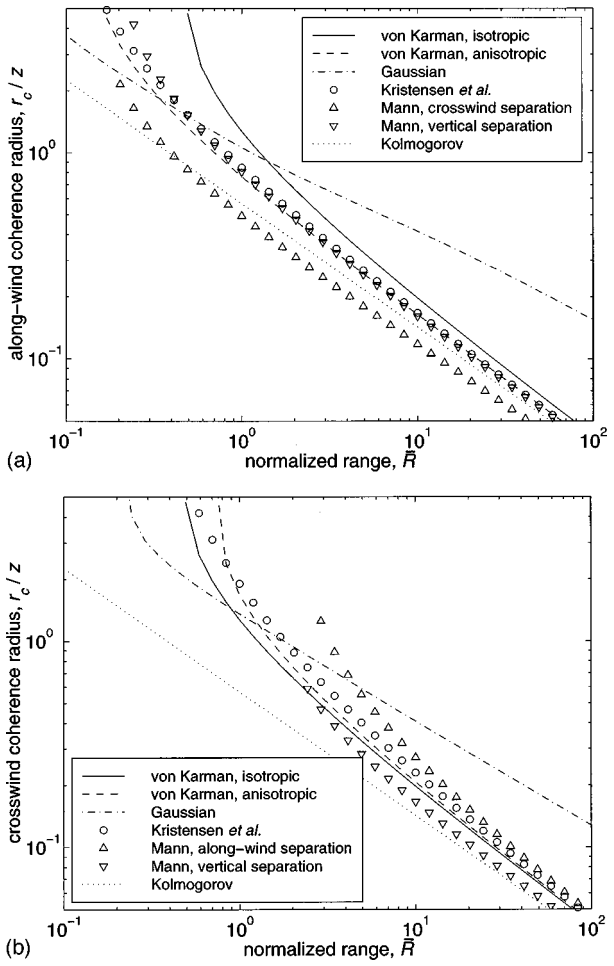

FIG. 4. Coherence radius as a function of normalized range for the various turbulence models. (a) Along-wind propagation. (b) Crosswind propagation.

(but not to the Mann model), do not work well in this application.

B. Two-dimensional structure function

Predictions of the 2-D structure function for the various models are shown in Fig. 3. Also shown in the figures are predictions from the Kolmogorov (inertial subrange) model.[30] As discussed in Sec. I, the 2-D structure function of the turbulence determines coherence of the acoustic wave. The plots clearly show that the Kolmogorov model only works well when the ratio of the sensor separation to the height, r/z, is much less than 1. Convergence to the Kolmogorov prediction as r/z decreases is very slow. Conversely, the Gaussian model is reasonable only in the energy subrange, where r/z is much greater than 1. A peculiar (and probably unphysical) characteristic of the Gaussian model is the appearance of local peaks in the 2-D structure function, at $r/z \approx 6$ in the along-wind direction [Fig. 3(a)] and $r/z \approx 3$ in the crosswind direction [Fig. 3(b)].

In the along-wind direction [Fig. 3(a)], the energy-subrange 2-D structure function is larger for all of the anisotropic models than for the isotropic von Kármán model. The main reason for this behavior is that the anisotropic models all use a longer length scale for the along-wind direction. In the crosswind direction [Fig. 3(b)], the results are mixed. The 2-D structure function is larger for the Kristensen *et al.* and Gaussian models than for the isotropic von Kármán model; for the Mann model, the function is considerably smaller, equal to about 1/10 the Kristensen *et al.* model predictions for large r/z. The essential cause of this behavior is that the Mann model predicts a very small length scale for the crosswind velocity fluctuations in the crosswind direction. Symmetries inherent to the other anisotropic models, including the Kristensen *et al.* model, lead to larger values for this length scale.

For the Mann model, note that the structure functions for both horizontal and vertical separations are nearly the same for very small r/z (the inertial subrange), diverge for moderate separations, and then become equal again for large separations. The reason for the similarity in the inertial subrange is isotropy in that part of the spectrum. They become equal for large separations because $b_{ii}(r,0)$ and $b_{ii}(0,r)$ both approach zero for large r/z, so that the 2-D structure function in the two cases is $d_{ii}(r,0) \simeq d_{ii}(0,r) \simeq 2b_{ii}(0,0)$.

C. Coherence radius

In terms of the 2-D structure function for the turbulent velocities, the coherence radius [Eq. (13)] is the root of the equation

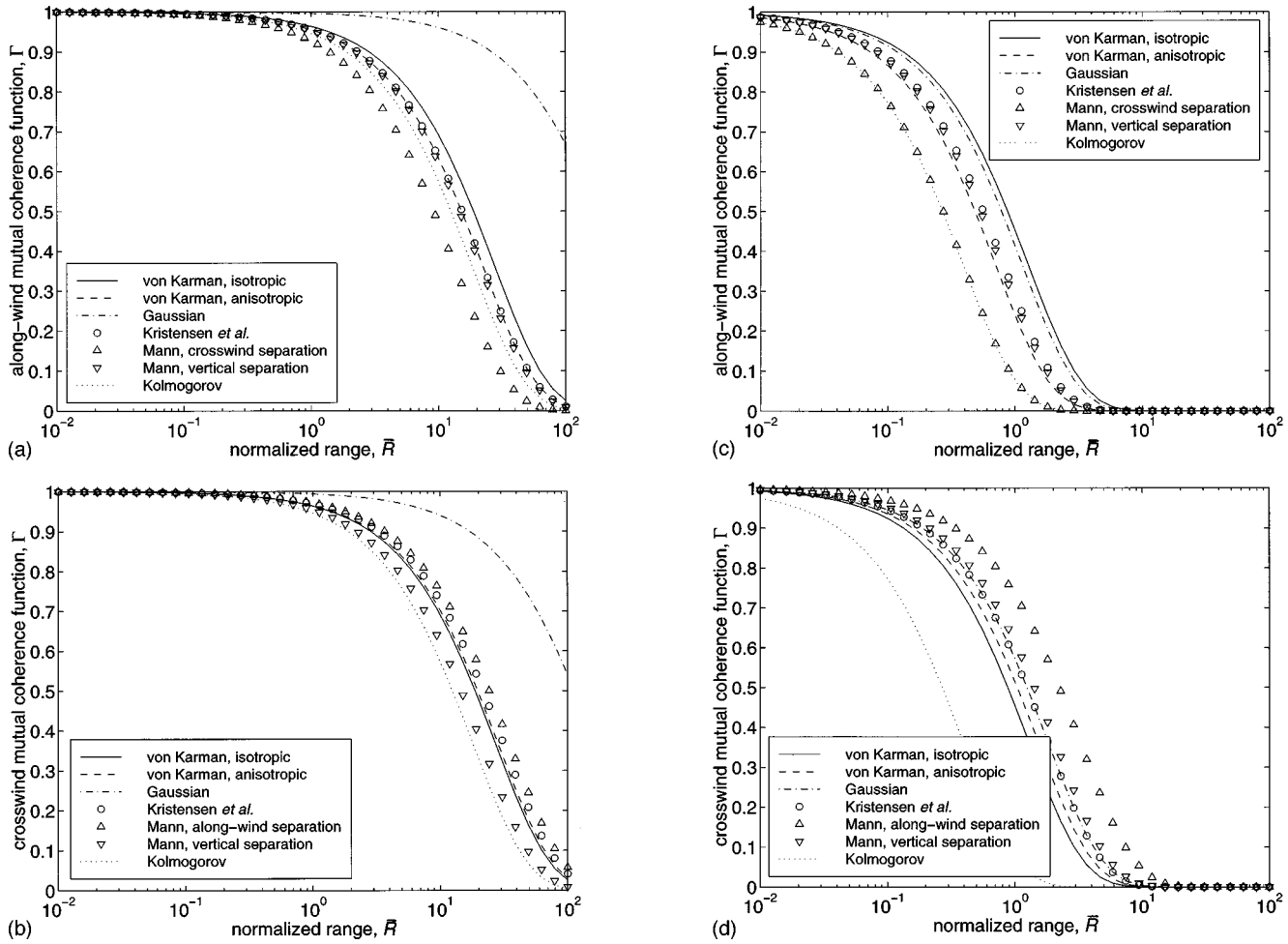

FIG. 5. Mutual coherence function (MCF) as a function of normalized range for the various turbulence models. (a) Along-wind propagation, ratio of sensor separation to height $r/z=0.1$. (b) Crosswind propagation, ratio of sensor separation to height $r/z=0.1$. (c) Along-wind propagation, ratio of sensor separation to height $r/z=1$. (d) Crosswind propagation, ratio of sensor separation to height $r/z=1$.

$$d_{ii}(\mathbf{r}_c)=c_0^2/(\pi k_0^2 x'). \tag{84}$$

Let us define a normalized 2-D structure function for the velocities as $\overline{d}_{ii}(\mathbf{r}_c)=d_{ii}(\mathbf{r}_c)/(zu_*^2)$. Then, if we also define a normalized propagation distance

$$\overline{R}=\frac{4x'k_0^2zu_*^2}{c_0^2}, \tag{85}$$

the equation to be solved becomes

$$\overline{d}_{ii}(\mathbf{r}_c)=4/(\pi\overline{R}). \tag{86}$$

The roots of this equation, as a function of $\overline{R}$, are plotted in Fig. 4(a) and (b), which shows the along-wind and crosswind directions, respectively.

When $\overline{R}$ exceeds 10, the Kolmogorov model works reasonably well in both directions. However, the Gaussian model is poor at these long ranges, because it does not have a realistic inertial subrange. For shorter ranges ($\overline{R}<1$) in the along-wind direction, the anisotropic models predict shorter coherence radii than the isotropic von Kármán model. In the crosswind direction, however, most of anisotropic models predict longer coherence radii than the isotropic von Kármán model. An exception is the Mann model for vertical separations, which predicts a coherence radius slightly less than the isotropic von Kármán model.

D. Mutual coherence function

Predictions of the mutual coherence function [MCF, Eq. (15)] for the various turbulence models, as a function of the normalized range $\overline{R}$, are shown in Fig. 5. Plots (a) and (b) are MCFs for the along-wind and crosswind directions with the sensor separation equal to 0.1 times the height; plots (c) and (d) are for the along-wind and crosswind directions with the separation equal to the height.

When $r/z=0.1$ [the case considered in Fig. 5(a) and (b)], all models except the Gaussian give fairly similar predictions. This is because inertial-subrange turbulence is most important for this small sensor separation, and all of the models except the Gaussian have a realistic inertial subrange. The Gaussian model predicts too little turbulent energy in the inertial subrange and therefore leads to a coherence that is unrealistically high. For the anisotropic von Kármán, Kristensen *et al.*, and Mann models, the predicted coherence in the along-wind direction is less than for the isotropic von Kármán model. The main reason for this behavior is that the

anisotropic models have a higher velocity variance in this direction. In the crosswind direction, the curve for the isotropic von Kármán model falls about midway between the various anisotropic models.

Differences between the models become more pronounced when $r/z=1$ [the case considered in Fig. 5(c) and (d)]. For this separation the energy-subrange characteristics become very important. The Kolmogorov model predicts much lower coherence than the others because it incorporates no ''roll-off'' in the energy spectrum for small wave numbers. Again, in the along-wind direction, the coherence predictions for the anisotropic models are less than for the isotropic von Kármán model. In the crosswind direction, all of the anisotropic models now predict higher coherence than the isotropic von Kármán model. The Mann model predicts the highest coherence in the crosswind direction, particularly for along-wind sensor separations.

V. CONCLUDING REMARKS

The effects of turbulence anisotropy on acoustic propagation were explored in this paper, using several rigorously derived models for the turbulence spectrum in a shear layer. Anisotropy effects were found to be very significant, sometimes resulting in order-of-magnitude corrections to predictions from an isotropic von Kármán model. Dramatic differences between along-wind and crosswind predictions were found in the anisotropic models: predictions of the extinction distance in the crosswind direction were about 2 to 13 times longer than in the along-wind direction, and coherence of the propagating wave persists over much longer distances in the crosswind direction than along-wind.

The various anisotropic turbulence models considered in this paper were found to yield very different propagation predictions, even though the parameters for the models were all chosen based on the same set of empirical spectra measured by Kaimal *et al.*[21] The three models derived from Kristensen *et al.*'s 3-D spectral density tensor (the anisotropic Gaussian, anisotropic von Kármán, and Kristensen *et al.* models) yielded less dramatic differences between the along-wind and crosswind characteristics than Mann's rapid distortion model. Furthermore, predictions from the three models based on Kristensen *et al.*'s spectral tensor differed significantly from each other, despite their underlying mathematical similarities. These results indicate that the predictions are very sensitive to the exact form of the energy-subrange model, so that it will probably be difficult to develop accurate quantitative predictions for energy-subrange effects on scattering.

The Mann model is likely the most realistic one available for an atmospheric shear layer, since it does not incorporate *ad hoc* assumptions about statistical symmetries of the turbulence field. Mann's model is also not much more difficult to apply than the ones based on Kristensen *et al.*'s spectral tensor.

Although the comparisons in this paper are a useful first step toward understanding the effects of anisotropic turbulence on acoustic propagation, field experiments are of course needed to establish and quantify its true importance. Application of the models in this paper is unfortunately hampered by ground reflections and atmospheric refraction. For example, the predictions cannot be expected to hold in a shadow region, since the ''line-of-sound'' scattering theory is invalid there. Hence it would be very worthwhile to include reflection and refraction in subsequent work on propagation through anisotropic turbulence. Other important topics for future research are incorporation of large-scale (buoyancy-driven) turbulence, and development of simpler turbulence models that retain the acoustically most significant features of the anisotropic turbulence.

ACKNOWLEDGMENTS

The author thanks Jakob Mann of the Risø National Laboratory (Denmark) for his helpful comments.

APPENDIX: PARAMETER SELECTION FOR THE ANISOTROPIC VON KÁRMÁN AND GAUSSIAN MODELS

Velocity statistics in a neutral shear layer are typically scaled by the friction velocity u_*, which equals $\sqrt{\tau/\rho}$, τ being the Reynolds stress and ρ the fluid density.[19] The appropriate length scale is z, the height from the ground.[19]

Kaimal *et al.*[21] made extensive measurements of the 1-D spectra of atmospheric turbulence, and devised a set of empirical equations that fit their measurements for neutral conditions. Their equations are parametrized on the basis of u_* and z. I have chosen the parameters for the anisotropic von Kármán and Gaussian models to reproduce certain features of the Kaimal *et al.* empirical spectra. The spectral variances measured by Kaimal *et al.* are given in Table I, and these values were used for the variances in both the anisotropic von Kármán and Gaussian models.

The length scales in the von Kármán model were chosen to reproduce the inertial-subrange asymptote determined by Kaimal *et al.* Specifically, in the inertial subrange the following equation must hold:[21]

$$F_L(k)=\frac{\alpha}{2}\epsilon^{2/3}k^{-5/3}, \tag{A1}$$

where $\epsilon=u_*^3/\kappa z$ is the dissipation rate of turbulent kinetic energy, and α and κ are constants whose values are approximately 0.52 and 0.40, respectively.[29] Taking the limit of Eq. (23) for large $k\ell_1$, and solving for ℓ_1, we find

$$\ell_1=\left[\frac{2\sigma_1^2}{\alpha B(\frac{1}{2},\frac{1}{3})}\right]^{3/2}\frac{\kappa z}{u_*^3}\simeq 0.350\frac{\sigma_1^3 z}{u_*^3}\simeq 3.64z. \tag{A2}$$

The length scales ℓ_2 and ℓ_3 follow similarly by using the inertial-subrange relationship[19]

$$F_T(k)=F_V(k)=\tfrac{4}{3}F_L(k), \tag{A3}$$

with results given in Table II.

Because the Gaussian model does not possess an inertial subrange, some other method is needed for determining its length scale parameters. A reasonable method is to equate the integral length scales in the Gaussian model to those implied by the Kaimal *et al.*[21] measurements. Taking the

zero-wave-number limits of the Kaimal *et al.* empirical equations, we find $l_1 = 5.50z$, $l_2 = 1.59z$, and $l_3 = 0.343z$. Likewise taking the zero-wave-number limits of Eqs. (53) and (54), we have the relationships

$$l_1 = \frac{\sqrt{\pi}}{2} L_1, \quad l_2 = \frac{\sqrt{\pi}}{4} L_2, \quad l_3 = \frac{\sqrt{\pi}}{4} L_3.$$

The values given in Table II now follow.

[1] For a discussion of the various subranges of turbulence and their roles in acoustic wave propagation, the reader may find helpful D. K. Wilson, J. G. Brasseur, and K. E. Gilbert, ''Acoustic scattering and the spectrum of atmospheric turbulence,'' J. Acoust. Soc. Am. (in press).

[2] U. Ingard, ''A review of the influence of meterological conditions on sound propagation,'' J. Acoust. Soc. Am. **25**, 405–411 (1953).

[3] F. M. Weiner and D. N. Keast, ''Experimental study of the propagation of sound over ground,'' J. Acoust. Soc. Am. **31**, 724–733 (1959).

[4] C. I. Chessel, ''Observations of the effects of atmospheric turbulence on low-frequency sound propagation,'' J. Acoust. Soc. Am. **60**, 29–33 (1976).

[5] S. D. Roth, ''Acoustic propagation in the surface layer under convectively unstable conditions,'' Ph.D. thesis, Graduate Program in Acoustics, Pennsylvania State University, 1983.

[6] W. Wilken, ''Korrelation lokaler Schallpegelschwankungen bei der Schallausbreitung in der bodennahen Grenzschicht,'' Acustica **66**, 104–108 (1988) (Correlation of local sound pressure fluctuations for propagation in the near-ground boundary layer).

[7] J. M. Noble, H. E. Bass, and R. Raspet, ''The effect of large-scale atmospheric inhomogeneities on acoustic propagation,'' J. Acoust. Soc. Am. **92**, 1040–1046 (1992).

[8] D. K. Wilson and D. W. Thomson, ''Acoustic propagation through anisotropic, surface-layer turbulence,'' J. Acoust. Soc. Am. **96**, 1080–1095 (1994).

[9] D. E. Norris, ''Atmospheric acoustic propagation: characterization of magnitude and phase variability,'' Ph.D. thesis, Graduate Program in Acoustics, Pennsylvania State University, 1998.

[10] R. S. Lawrence and J. W. Strohbehn, ''A survey of clear-air propagation effects relevant to optical communications,'' Proc. IEEE **58**, 1523–1545 (1970).

[11] L. Kristensen, D. H. Lenschow, P. Kirkegaard, and M. Courtney, ''The spectral velocity tensor for homogeneous boundary-layer turbulence,'' Boundary-Layer Meteorol. **47**, 149–193 (1989).

[12] J. Mann, ''The spatial structure of neutral atmospheric surface layer turbulence,'' J. Fluid Mech. **273**, 141–168 (1994).

[13] R. Dashen, ''Path integrals for waves in random media,'' J. Math. Phys. **20**, 894–920 (1979).

[14] S. M. Rytov, Y. A. Kravtzov, and V. I. Tatarskii, *Principles of Statistical Radio Physics, Part 4: Wave Propagation through Random Media* (Springer-Verlag, Berlin, 1989).

[15] V. E. Ostashev, *Acoustics in Moving Inhomogeneous Media* (E&FN Spon, London, 1997).

[16] D. K. Wilson, ''A brief tutorial on atmospheric boundary-layer turbulence for acousticians,'' in *Seventh International Symposium on Long Range Sound Propagation* (Ecole Centrale de Lyon, Lyon, France, 1996), pp. 111–121.

[17] G. K. Batchelor, *The Theory of Homogeneous Turbulence* (Cambridge U. P., Cambridge, 1953).

[18] D. K. Wilson, ''Anisotropic turbulence models for acoustic propagation through the neutral atmospheric surface layer,'' Technical Report No. ARL-TR-1519, U.S. Army Research Laboratory, 2800 Powder Mill Road, Adelphi, MD 20783 (1998).

[19] H. A. Panofsky and J. A. Dutton, *Atmospheric Turbulence: Models and Methods for Engineering Applications* (Wiley, New York, 1984).

[20] D. K. Wilson, ''Turbulence models and the synthesis of random fields for acoustic wave propagation calculations,'' Technical Report No. ARL-TR-1677, U.S. Army Research Laboratory, 2800 Powder Mill Road, Adelphi, MD 20783 (1998).

[21] J. C. Kaimal, J. C. Wyngaard, Y. Izumi, and O. R. Coté, ''Spectral characteristics of surface layer turbulence,'' Q. J. R. Meteorol. Soc. **98**, 563–589 (1972).

[22] A. Erdélyi, W. Magnus, F. Oberhettinger, and F. G. Tricomi, *Higher Transcendental Functions* (McGraw-Hill, New York, 1953), Vol. 1.

[23] I. S. Gradshteyn and I. M. Ryzhik, *Table of Integrals, Series, and Products* (Academic, San Diego, 1994).

[24] M. Abramowitz and I. A. Stegun, *Handbook of Mathematical Functions* (Dover, San Francisco, 1965), pp. 675–679.

[25] H. J. Auvermann has drawn to my attention the availability of routines for computing Meijer's *G*-functions in the commercial software package Mathematica. I am not aware at present of similar routines available from other sources.

[26] V. E. Ostashev, V. Mellert, R. Wandelt, and F. Gerdes, ''Propagation of sound in a turbulent medium. I. Plane waves,'' J. Acoust. Soc. Am. **102**, 2561–2570 (1997).

[27] N. P. Krasnenko, A. L. Afanas'ev, and A. P. Rostov, private communication.

[28] J. Mann, ''Wind field simulation,'' Probabilistic Engineering Mechanics **13**, 269–282 (1998).

[29] U. Högström, ''Review of some basic characteristics of the atmospheric surface layer,'' Boundary-Layer Meteorol. **78**, 215–246 (1996).

[30] D. K. Wilson, ''Performance bounds for acoustic angle-of-arrival arrays operating in atmospheric turbulence,'' J. Acoust. Soc. Am. **103**, 1306–1319 (1998).

Reverberation in waveguides with rough surfaces

David H. Berman
Department of Physics and Astronomy, University of Iowa, Iowa City, Iowa 52242

(Received 23 January 1998; accepted for publication 13 October 1998)

An impedance formalism for treating scattering at multiple rough boundaries in waveguides with depth-varying sound speeds is developed. The formalism is used to give a compact result for the time history of multiply scattered reverberant sound. In general, the multiple scattering contribution to reverbation decays more slowly than the single scattering contribution. When attenuation mechanisms other than surface scattering are small, the reverberant field has a diffusive character, and this leads to algebraic ($\sim 1/t$) decay of the reverberation of originally pulsed signals. As a by-product of the formalism, conventional reverberation models are derived from ''first principles.'' The derivation provides the precise form of the scattering strength used in such models. In addition, it shows that the mean field should be used for propagation to and from the scattering surface. Finally, the computations present the possibility of treating the scattering by two rough boundaries simultaneously. © *1999 Acoustical Society of America.* [S0001-4966(99)01602-1]

PACS numbers: 43.30.Gv, 43.30.Hw, 43.20.Mv [DLB]

INTRODUCTION

Recent work by Maradudin and co-workers[1–3] has shown that multiple scattering from a surface that supports bound surface waves gives rise to the phenomenon of enhanced backscattering. Enhanced backscattering occurs not only from a surface which separates two half-spaces, but also from a surface which is one boundary of a bounded layer which supports guided waves. Enhanced backscattering is concerned with plane waves incident on these surfaces: what is enhanced is the plane wave scattering amplitude in the exact backscatter direction. The aim of present work is to examine what happens to waves from a point source which are incident on rough surfaces from within a waveguide.

Although it is not entirely explicit, the key to developing a multiple scattering formalism in Ref. 4 is the use of nonlocal impedance boundary conditions. Within a waveguide nonlocal impedance conditions can be satisfied on two surfaces simultaneously by using the analogs of plane waves: waves of a given horizontal wave vector, but with vertical dependence appropriate to the sound speed profile. Then the boundary conditions can be satisfied formally by superpositions of such waves. Using impedance boundary conditions circumvents the need to decompose waves in the waveguide into up- and downgoing components in order to use plane wave scattering amplitudes. (See, for example, Refs. 5–7.) The coefficients of the superposition depend on the source location and can be written formally in terms of an operator $g=1/(g_0^{-1}-Z)$, where Z is a random operator related to the impedances of the bounding surfaces and g_0 is a nonrandom operator involving known solutions of the wave equation in the waveguide, evaluated at the surfaces. The surface Green's function, g involves only quantities evaluated at the bounding surfaces. The treatment of random operators like g has been worked out in detail and is summarized in the appendix of Ref. 4. The field within the waveguide can be written in terms of g, or rather the related scattering operator $t=v/(1-g_0v)$ (where $v=Z-M$, and M is an effective impedance) and derivatives of the mean Green's function of the field in the waveguide evaluated at the surfaces. The result given below in Eq. (29) simply states that the fluctuation of the field within the waveguide is obtained by propagating to the interfaces from the source using the mean Green's function, scattering at the interfaces using t, and then propagating from the surfaces to the receiver again using the mean Green's function.

Multiple scattering enters the picture first in the computation of the mean Green's function which obeys boundary conditions involving an effective impedance. It was shown in Ref. 8 that when the correlation length of surface roughness is short compared to the skip distance between surface encounters, the effective impedance is well approximated by the effective impedance of the surface when it separates two homogeneous half-spaces.

However, the multiple scattering with which we are concerned here arises in computing the second moment of the Green's function. As pointed out by Kirkpatrick,[9] the infinite sum of certain scattering diagrams gives rise to diffusive behavior in the second moment, at least in the case of sound scattered by random volume inhomogeneities. In addition, there is another class of scattering diagrams, the maximally crossed diagrams, which can be summed and give rise to enhanced backscattering on the one hand, and on the other hand, to a sort of ''fossil'' sound which does not appear even to diffuse away from the source, at least in one and two dimensions. These same kinds of sums occur for surface scattering once it has been cast into a similar formalism. Furthermore, the layered waveguide we have in mind here is primarily two-dimensional. These effects require that the only attenuation mechanism is the scattering of the coherent field into the incoherent field. It seems unlikely that this is ever realistic for sound in the ocean, and the maximally crossed diagrams will not be treated here. However, even with other attentuation mechanisms present, the diffusive behavior leads to reverberation which decays more slowly in time than conventional treatments of reverberation[7] would predict.

In Sec. I we describe the impedance formalism. In Sec. II we discuss the Bethe–Salpeter equation and the computation of the second moment of fields scattered at boundaries of a waveguide. Note that the formalism allows the scattering from two bounding rough surfaces to be treated simultaneously. In Sec. III we present details of the computation of reverberation time histories of pulsed signals. The conventional, single scatter, result is contained in Eq. (84) while a multiple scattering contribution to reverberation is given in Eq. (90). The results apply to a fully three-dimensional environment with isotropic roughness. Other authors[10–12] have used ideas similar to those used here for treating multiple surface scattering, but I believe the final results here are both more explicit for reverberation and more concise.

I. IMPEDANCE FORMALISM

Consider a layer bounded by a rough interface just above $z=z_0$ and another interface just below $z=z_1<z_0$. Between z_0 and z_1 the medium has a sound speed profile $c=c(z)$ which depends only on the depth z. The effects of roughness can be described by nonlocal impedance boundary conditions on the flat imaginary surfaces at z_0 and z_1. By this we mean that if $G(\mathbf{R},z;\mathbf{R}_s,z_s)$ is the Green's function for sound in the layer (where $\mathbf{R}$ is a horizontal position and the subscript s refers to the source location), then on the flat surface $z=z_0$ all fields, including $G(\mathbf{R},z;\mathbf{R}_s,z_s)$, must satisfy

$$G(\mathbf{R},z_0;\mathbf{R}_s,z_s)=\int d\mathbf{R}'\, Z_0(\mathbf{R},\mathbf{R}')\partial_z G(\mathbf{R}',z_0;\mathbf{R}_s,z_s). \tag{1}$$

A similar condition must hold on the flat surface at z_1, but with the impedance Z_0 replaced by another impedance, $Z_1(\mathbf{R},\mathbf{R}')$, appropriate to the lower interface. It is more convenient to work with horizontal Fourier transforms of these functions since the sound speed is presumed independent of horizontal position. Then, in terms of horizontal wave vectors we write the boundary conditions as

$$G(\mathbf{Q},z_0;\mathbf{K},z_s)=\int d\mathbf{P}\, Z_0(\mathbf{Q},\mathbf{P})\partial_z G(\mathbf{P},z_0,\mathbf{K},z_s) \tag{2}$$

and

$$G(\mathbf{Q},z_1;\mathbf{K},z_s)=-\int d\mathbf{P}\, Z_1(\mathbf{Q},\mathbf{P})\partial_z G(\mathbf{P},z_1,\mathbf{K},z_s). \tag{3}$$

The minus in the last equation is for later convenience and the convention regarding factors of 2π is

$$G(\mathbf{Q},z_0;\mathbf{K},z_s)=\frac{1}{(2\pi)^2}\int \exp(-i\mathbf{Q}\cdot\mathbf{R}+i\mathbf{K}\cdot\mathbf{R}_s) \times G(\mathbf{R},z_0,\mathbf{R}_s,z_s)\, d\mathbf{R}\, d\mathbf{R}_s. \tag{4}$$

An argument for boundary conditions of this form is given in Appendix A, where it is also shown how the impedance is related to the scattering amplitude. In first-order perturbation theory, for example, if the surface at z_0 were Dirichlet, then $Z_0(\mathbf{Q},\mathbf{P})$ would be given by $-h(\mathbf{Q}-\mathbf{P})$ where $h(\mathbf{Q})$ is the Fourier transform of the surface profile, $z=h(\mathbf{R})=\int h(\mathbf{K})\exp(i\mathbf{K}\cdot\mathbf{R})\, d\mathbf{K}$.

The Green's function $G(\mathbf{Q},z;\mathbf{K},z_s)$ must satisfy the depth separated wave equation

$$\left[\partial_z^2+\left(\frac{\omega^2}{c(z)^2}-\mathbf{Q}^2\right)\right]G(\mathbf{Q},z;\mathbf{K},z_s) =-\delta(z-z_s)\,\delta(\mathbf{Q}-\mathbf{K}) \tag{5}$$

in addition to the boundary conditions. This Green's function can be conveniently constructed from canonical regular solutions, $e^{\pm}(\mathbf{Q},z)$, of the homogeneous depth separated wave equation and the Neumann Green's function $\Phi(\mathbf{Q},z;\mathbf{K},z_s)$ which satisfies Eq. (5) and the simple boundary conditions

$$\partial_z\Phi(\mathbf{Q},z_0;\mathbf{K},z_s)=\partial_z\Phi(\mathbf{Q},z_1;\mathbf{K},z_s)=0. \tag{6}$$

The canonical regular solutions of the homogeneous depth separated wave equation play the role of plane waves in the half-space problem. We will require $e^{\pm}$ to satisfy

$$e^+(\mathbf{Q},z_0)=1,\quad \partial_z e^+(\mathbf{Q},z_0)=0, \tag{7}$$

$$e^-(\mathbf{Q},z_1)=1,\quad \partial_z e^-(\mathbf{Q},z_1)=0. \tag{8}$$

The Neumann Green's function, in turn, can be constructed from these functions as follows:

$$\Phi(\mathbf{Q},z;\mathbf{K},z_s) =\begin{cases} \dfrac{-1}{W(\mathbf{Q})}e^+(\mathbf{Q},z)e^-(\mathbf{Q},z_s)\,\delta(\mathbf{Q}-\mathbf{K}), & z\geqslant z_s, \\ \dfrac{-1}{W(\mathbf{Q})}e^-(\mathbf{Q},z)e^+(\mathbf{Q},z_s)\,\delta(\mathbf{Q}-\mathbf{K}), & z<z_s. \end{cases} \tag{9}$$

Here $W(\mathbf{Q})$ is the Wronskian

$$W(\mathbf{Q})=\partial_z e^+(\mathbf{Q},z)e^-(\mathbf{Q},z)-e^+(\mathbf{Q},z)\partial_z e^-(\mathbf{Q},z) =\partial_z e^+(\mathbf{Q},z_1)=-\partial e^-(\mathbf{Q},z_0). \tag{10}$$

Now write the Green's function $G(\mathbf{Q},z;\mathbf{K},z_s)$ as a superpostion of $e^{\pm}$ and Φ

$$G(\mathbf{Q},z;\mathbf{K},z_s)=e^+(\mathbf{Q},z)\chi^+(\mathbf{Q},\mathbf{K};z_s) +e^-(\mathbf{Q},z)\chi^-(\mathbf{Q},\mathbf{K};z_s)+\Phi(\mathbf{Q},z;\mathbf{K},z_s). \tag{11}$$

The Neumann Green's function Φ accounts for the δ-function source. The coefficients $\chi^{\pm}$ are independent of receiver depth z but dependent on the source depth z_s and are to be chosen to account for the impedance boundary conditions. The boundary conditions provide two linear equations for the two unknown coefficients $\chi^{\pm}$ and these are most conveniently written as a matrix operator equation

$$[E(\mathbf{Q},\mathbf{P})-Z(\mathbf{Q},\mathbf{P}')\partial E(\mathbf{P}',\mathbf{P})]\chi(\mathbf{P},\mathbf{K};z_s) =-\phi(\mathbf{Q},\mathbf{K};z_s). \tag{12}$$

Integration over repeated wave vectors is implied as well as two-by-two matrix multiplication. The matrix operators here are given by

$$E(\mathbf{Q},\mathbf{P})=\delta(\mathbf{Q}-\mathbf{P})\begin{pmatrix} e^+(\mathbf{Q},z_0) & e^-(\mathbf{Q},z_0)\\ e^+(\mathbf{Q},z_1) & e^-(\mathbf{Q},z_1)\end{pmatrix}$$

$$=\delta(\mathbf{Q}-\mathbf{P})\begin{pmatrix} 1 & e^-(\mathbf{Q},z_0)\\ e^+(\mathbf{Q},z_1) & 1\end{pmatrix}, \tag{13}$$

$$\partial E(\mathbf{Q},\mathbf{P})=\delta(\mathbf{Q}-\mathbf{P})\begin{pmatrix} \partial_z e^+(\mathbf{Q},z_0) & \partial_z e^-(\mathbf{Q},z_0)\\ -\partial_z e^+(\mathbf{Q},z_1) & -\partial_z e^-(\mathbf{Q},z_1)\end{pmatrix}$$

$$=-\delta(\mathbf{Q}-\mathbf{P})W(\mathbf{Q})\begin{pmatrix} 0 & 1\\ 1 & 0\end{pmatrix}, \tag{14}$$

and

$$Z(\mathbf{Q},\mathbf{P})=\begin{pmatrix} Z_0(\mathbf{Q},\mathbf{P}) & 0\\ 0 & Z_1(\mathbf{Q},\mathbf{P})\end{pmatrix}. \tag{15}$$

In writing E and ∂E in this way the relation between derivatives obtained from the Wronskian in Eq. (10) has been used.

The remaining undefined quantities in Eq. (12) are

$$\phi(\mathbf{Q},\mathbf{K})=\begin{pmatrix}\Phi(\mathbf{Q},z_0;\mathbf{K},z_s)\\ \Phi(\mathbf{Q},z_1;\mathbf{K},z_s)\end{pmatrix}, \tag{16}$$

and

$$\chi(\mathbf{Q},\mathbf{K};z_s)=\begin{pmatrix}\chi^+(\mathbf{Q};\mathbf{K},z_s)\\ \chi^-(\mathbf{Q};\mathbf{K},z_s)\end{pmatrix}. \tag{17}$$

A formal solution to Eq. (12) is

$$\chi=\frac{1}{\partial E}\frac{1}{E/\partial E-Z}(-\phi)=\frac{1}{\partial E}\frac{1}{g_0^{-1}-Z}(-\phi), \tag{18}$$

where now E and ∂E; etc. denote the operators whose kernels are given above. In the case of flat surfaces for which Z is diagonal in wave vector, one can show that the modal poles associated with the original Neumann Green's function ϕ (the zeros of W) are replaced by poles arising from zeros of the determinant of $g_0^{-1}-Z$. These coincide with the solutions of the conventional dispersion relation,[13]

$$1-R_0R_1=0, \tag{19}$$

once the reflection amplitudes R are written in terms of impedances.

Equation (18) suggests defining a *surface* Green's function

$$g=\frac{1}{g_0^{-1}-Z} \tag{20}$$

in which all terms are evaluated on the bounding surfaces. Note, however, that the sound speed structure within the waveguide is built in to g via the function $e^-(\mathbf{Q},z)$. The surface Green's function can now be formally manipulated exactly as in Ref. 4. The average of g over an ensemble of rough bounding surfaces defines an effective impedance operator, M, which for a statistically stationary ensemble is diagonal in wave number, by

$$\langle g\rangle=\frac{1}{g_0^{-1}-M}. \tag{21}$$

The surface Green's function, g, before averaging, can be written using the averaged Green's function and a scattering operator t as

$$g=\langle g\rangle+\langle g\rangle t\langle g\rangle, \tag{22}$$

where t is given by

$$t=\frac{1}{1-v\langle g\rangle}v=v\frac{1}{1-\langle g\rangle v} \tag{23}$$

and

$$v=Z-M. \tag{24}$$

The effective impedance can be found iteratively by noting that the average of t must vanish.

The statistics of the field in the waveguide are the statistics the scattering operator t. To make this assertion we need to show explicitly how fluctuations of the field within the waveguide are related to t. From Eq. (11) the field within the waveguide is given by

$$G(\mathbf{Q},z;\mathbf{K},z_s)=[e^+(\mathbf{Q},z),e^-(\mathbf{Q},z)]\begin{pmatrix}\chi^+(\mathbf{Q},\mathbf{K},z_s)\\ \chi^-(\mathbf{Q},\mathbf{K},z_s)\end{pmatrix}+\Phi(\mathbf{Q},z;\mathbf{K},z_s)$$

$$=[e(z)]^T\frac{1}{\partial E}[\langle g\rangle+\langle g\rangle t\langle g\rangle](-\phi)+\Phi. \tag{25}$$

First take the mean of G, then take z derivatives and let z first approach z_0 and then z_1. Because Φ is constructed so that its derivatives vanish on z_0 and z_1 we find

$$\begin{pmatrix}\partial_z\langle G(\mathbf{Q},z_0;z_s)\rangle\\ \partial_z\langle G(\mathbf{Q},z_1;z_s)\rangle\end{pmatrix}=\sigma_3\langle g\rangle(-\phi). \tag{26}$$

The two-by-two constant matrix σ_3 is just

$$\sigma_3=\begin{pmatrix}1 & 0\\ 0 & -1\end{pmatrix}. \tag{27}$$

It arises here because there is a $-\partial_z e^+(\mathbf{Q},z_1)$ in the definition of ∂E. Derivatives of $\langle G\rangle$ give rise to derivatives of $e^{\pm}$ producing a matrix ∂E which is cancelled by its inverse which appears in Eqs. (18) and (26).

We can also average G and take vertical derivatives from the right, that is on z_s, and then let z_s approach z_0 and z_1. The details are given in Appendix B with the result

$$[\langle G(\mathbf{Q},z;\mathbf{K},z_0)\rangle\overleftarrow{\partial}_{z_0},\langle G(\mathbf{Q},z;\mathbf{K},z_1)\rangle\overleftarrow{\partial}_{z_1}]$$

$$=-[e^+(\mathbf{Q},z),e^-(\mathbf{Q},z)]\frac{1}{\partial E}\langle g\rangle\sigma_3. \tag{28}$$

Also in Appendix B it is shown that the effective impedance, M, relates the mean field to its derivatives, just as Z relates a realization of the field to its derivatives. Equations (28) and (26) used in Eq. (25) show that the fluctuation of the field within the waveguide is given by

$$\Delta G=[\langle G\rangle\partial]^T\sigma_3 t\sigma_3\partial\langle G\rangle. \tag{29}$$

The scattered field is obtained by propagating to the interfaces with the mean field, scattering with t, and then propa-

gating from the interfaces to the receiver, again using the mean field. This result is reminiscent of the Helmholtz–Kirchhoff integral; the appearance of σ_3 is likely a reflection of the need to use both outward or both inward derivatives at the bounding surfaces.

One word of caution is necessary. The utility of this formalism for forming moments of the fluctuating field might depend on having the impedance, Z, be a Gaussian random field. This is because the algebra of resummation seems to require that all moments of Z factorize into second moments. If so, then the results here are limited to a first-order (in surface roughness) approximation for the impedance, and to roughness described by Gaussian statistics. If non-first-order approximations for Z are used, there is no guarantee that higher-order cumulants will not be significant.

II. SECOND MOMENT OF THE FLUCTUATING FIELD

The principal result of the last section, Eq. (29), means that if we want to find the incoherent contribution to the second moment of the fluctuating field

$$\langle|\Delta G(R,z,t;R_s=0,z_s,t_s=0)|^2\rangle$$
$$=\int d\omega_1\, d\omega_2 \int d\mathbf{Q}_1\, d\mathbf{Q}_2 \int d\mathbf{K}_1\, d\mathbf{K}_2 e^{i(\omega_1-\omega_2)t}$$
$$\times e^{i(\mathbf{Q}_1-\mathbf{Q}_2)\cdot\mathbf{R}}\langle\Delta G(\mathbf{Q}_1,\mathbf{K}_1,\omega_1)\Delta G(\mathbf{Q}_2,\mathbf{K}_2,\omega_2)\rangle,$$

in general, we must consider correlations of tt^* where t and t^* differ in frequency, outgoing horizontal wave vector, and incoming wave vector. Because we will always assume that surface roughness is statistically homogeneous, it is convenient to use sum and difference variables defined by

$$\Omega=(\omega_1+\omega_2)/2,\quad \omega=\omega_1-\omega_2,$$
$$\mathbf{Q}=(\mathbf{Q}_1+\mathbf{Q}_2)/2,\quad \mathbf{p}=\mathbf{Q}_1-\mathbf{Q}_2, \tag{30}$$
$$\mathbf{K}=(\mathbf{K}_1+\mathbf{K}_2)/2,\quad \mathbf{k}=\mathbf{K}_1-\mathbf{K}_2.$$

In this way we are naturally led to consider

$$\langle t(\mathbf{Q}+\mathbf{q}/2,\mathbf{K}+\mathbf{k}/2,\Omega+\omega/2)t^*(\mathbf{Q}-\mathbf{q}/2,\mathbf{K}-\mathbf{k}/2,\Omega-\omega/2)\rangle$$
$$=\tau_{\mathbf{Q},\mathbf{K}}(\mathbf{q}|\Omega,\omega)\,\delta(\mathbf{q}-\mathbf{k}), \tag{31}$$

where τ is defined by this equation and the δ-function follows from the assumed statistical homegeneity.

Fortunately, machinery for computing moments of this type has been described in a number of places.[4,9,14] What makes the present context somewhat distinctive is that there is multimodal propagation in a waveguide. In fact, we will make a pole approximation for both the mean surface Green's function, $\langle g\rangle$, and the mean Green's function $\langle G\rangle$ within the waveguide. The location of the poles is the same. We will therefore write

$$\langle G(\mathbf{P},z;\mathbf{Q},z_s)\rangle=G(\mathbf{P};z,z_s)\,\delta(\mathbf{P}-\mathbf{Q}) \tag{32}$$

with $G(\mathbf{P};z,z_s)$ given by

$$G(\mathbf{P};z,z_s)=\sum_m \frac{-u_m(z)u_m(z_s)}{P^2-(k_m+i\Delta_m)^2}. \tag{33}$$

The $u_m(z)$ are the normal modes of the mean field in the waveguide which satisfy the separated Helmholtz equation with sound speed profile $c(z)$ and ''effective'' impedance boundary conditions at z_0 and z_1. [Effective impedance boundary conditions are given by Eq. (B5) in Appendix B. What is a bit strange here is that, in general, M will have off-diagonal elements. This means that the value of u_m on z_0 is a linear combination, determined by the elements of the matrix M, of its derivatives on z_0 *and* on z_1, and, likewise, the value of u_m on z_1 is a different linear combination of its derivatives on z_0 *and* on z_1.] This expression for G used in Eq. (31) and then in Eq. (4) gives the following expression for the mean Green's function in spatial variables:

$$\langle G\rangle(\mathbf{R},z,\mathbf{R}_0,z_0,\Omega)$$
$$=(-i/4)\sum_m u_m(z)u_m(z_0)H_0^1[(k_m+i\Delta_m)|\mathbf{R}-\mathbf{R}_0|]. \tag{34}$$

The factor $(-i/4)$ is consistent with the right-hand side of Eq. (5). We will assume that the right-hand side depends on frequency, Ω, primarily through the frequency dependence of the modal wave numbers, $k_m=k_m(\Omega)$. The imaginary part of the modal wave number, Δ_m, gives the attenuation of the mth mode of the *mean* field.

Returning to Eq. (31), recall that t is a 2×2 matrix operator and that tt^* is the outer product of such operators. Were we to insert indices, $\tau_{\mathbf{Q},\mathbf{K}}$ would carry four discrete indices. [See Eq. (70) below.] Following Brown *et al.*,[4] τ is the reducible vertex function. It is related to the irreducible vertex function, U, by

$$\tau=U+U\mathcal{G}U. \tag{35}$$

Here $\mathcal{G}$ is the two-point surface Green's function defined by

$$\langle g_{i_1,j_1}(\mathbf{P}+\mathbf{p}/2,\mathbf{K}+\mathbf{k}/2,\Omega+\omega/2)g_{i_2,j_2}$$
$$\times(\mathbf{P}-\mathbf{p}/2,\mathbf{K}-\mathbf{k}/2,\Omega-\omega/2)^*\rangle$$
$$=\mathcal{G}^{i_1,i_2;j_1,j_2}_{\mathbf{P},\mathbf{K}}(\mathbf{p}|\Omega,\omega)\,\delta(\mathbf{p}-\mathbf{k}). \tag{36}$$

Indices in Eq. (31) are inserted similarly. The simplest contribution to the irreducible vertex function is the single-rung ladder diagram, which is a regular function of wave number and frequency.

Roughly speaking, the irreducible vertex function, U, describes multiple scattering which is statistically correlated, while the two-point Green's function $\mathcal{G}$ describes the whole sequence of correlated scattering followed by uncorrelated propagation, followed by correlated scattering, etc., as described in the Bethe–Salpeter equation[4,9]

$$[\langle g^*\rangle^{-1}-\langle g\rangle^{-1}]\mathcal{G}=[\langle g^*\rangle-\langle g\rangle](1+U\mathcal{G}). \tag{37}$$

Our strategy for computing τ is to approximate U, find $\mathcal{G}$ from Eq. (37), and then use the result in Eq. (35). Note that, in contrast to Brown *et al.*, $\langle g^*\rangle$ denotes the complex conjugate at frequency $\Omega-\omega/2$, while $\langle g\rangle$ refers to the surface Green's function at frequency $\Omega+\omega/2$, and these are both 2×2 matrix operators.

It is convenient to work in a basis in which $\langle g\rangle^{-1}$ is diagonal. Because of the assumed statistical homogeneity,

eigenstates are labeled by horizontal wave vectors, **P**. For each **P** there are two eigenstates and we will write

$$\langle g\rangle^{-1}\psi_s(\mathbf{P})=\lambda_s(\mathbf{P})\psi_s(\mathbf{P}), \tag{38}$$

for $s=1,2$. The subscript s distinguishes the two eigenstates, ψ_s, and corresponding eigenvalues, λ_s, both of which are frequency dependent. In this basis, the Bethe–Salpeter equation, Eq. (37), becomes

$$\begin{aligned}[\lambda_{s_1}(\mathbf{P}+\mathbf{q}/2)-\lambda^*_{s_2}(\mathbf{P}-\mathbf{q}/2)]&\mathcal{G}^{s_1,s_2;v_1,v_2}_{\mathbf{P},\mathbf{Q}}(\mathbf{q})\\ &=\left[\frac{1}{\lambda^*_{s_2}(\mathbf{P}-\mathbf{q}/2)}-\frac{1}{\lambda_{s_1}(\mathbf{P}+\mathbf{q}/2)}\right](\delta_{s_1,v_1}\delta_{s_2,v_2}\delta(\mathbf{P}-\mathbf{Q})\\ &\quad+U^{s_1,s_2;u_1,u_2}_{\mathbf{P},\mathbf{K}}(\mathbf{q})\mathcal{G}^{u_1,u_2;v_1,v_2}_{\mathbf{K},\mathbf{Q}}(\mathbf{q})).\end{aligned} \tag{39}$$

It is understood here that there is a sum over the indices u_i and integration over the intermediate wave vector, **K**. There is no sum on the indices s_i nor on v_i. Both $\mathcal{G}$ and the irreducible vertex function U depend on both Ω and ω.

As will be seen in the next section, at large times, reverberation is determined by the singularities of $\mathcal{G}$ as $\omega\to 0$. In turn, the singularities of $\mathcal{G}$ arise because for some values of the horizontal wave vector one of the eigenvalues vanishes. The wave vectors at which one of the eigenvalues vanishes, $|\mathbf{P}|=k_m+i\Delta_m$, $m=1,...,N$, are the modal horizontal wave numbers. In the vicinity of $k_m+i\Delta_m$ let λ_1 be the eigenvalue which vanishes at $k_m+i\Delta_m$. In finding $\mathcal{G}$, restrict attention to only the elements $\mathcal{G}^{1,1;1,1}$ and $U^{1,1;1,1}$; these presumably give the most singular part of $\mathcal{G}$ and determine long time reverberation. For the moment we can now drop the discrete indices with the understanding that we will always be concerned with indices only equal to one, corresponding to the vanishing eigenvalue.

Following the literature[1] we make a pole approximation for $1/\lambda(+)-1/\lambda(-)$ writing

$$\begin{aligned}&\frac{1}{\lambda(\mathbf{P}+\mathbf{q}/2,\Omega+\omega/2)}-\frac{1}{\lambda^*(\mathbf{P}-\mathbf{q}/2,\Omega-\omega/2)}\\ &\quad\approx\sum_{m=1}^{N}\frac{g_m}{(\mathbf{P}+\mathbf{q}/2)^2-(k_m(\Omega+\omega/2)+i\Delta_m)^2}\\ &\qquad-\frac{g_m}{(\mathbf{P}-\mathbf{q}/2)^2-(k_m(\Omega-\omega/2)-i\Delta_m)^2}\\ &\quad\approx\sum_{m=1}^{N}\frac{g_m}{(\mathbf{P})^2-(k_m(\Omega)+i\Delta_m)^2}-\frac{g_m}{(\mathbf{P})^2-(k_m(\Omega)-i\Delta_m)^2}\\ &\quad\approx\sum_{m=1}^{N}2\pi i g_m\delta(P^2-k_m^2).\end{aligned} \tag{40}$$

This sequence of approximations assumes first that $1/\lambda$ can be written as a sum of simple poles, that the residues, g_m, are real, that we are interested in small frequency differences ω and small wave vectors **p**, and that the damping of the coherent field is sufficiently small that $\mathcal{T}[1/(x-i\Delta)]\to\pi i\delta(x)$.

The δ-functions in Eq. (40) will drive the solution of the Bethe–Salpeter equation and they suggest the *ansatz*

$$\mathcal{G}_{\mathbf{K},\mathbf{Q}}(\mathbf{q})=\sum_{m,n}\delta(P^2-k_m^2)\phi_{k_m\hat{\mathbf{K}};k_n\hat{\mathbf{Q}}}(\mathbf{q})\delta(Q^2-k_n^2). \tag{41}$$

The term in square brackets on the left side of Eq. (39) can be expanded to first order in the difference frequency, ω, and in the difference wave vector, **q**, since we are interested in long times. Long times will force $|\mathbf{q}|$ to be small; after a long time sound will have diffused so that slowly varying spatial wave vectors dominate the distribution of sound. Substituting our *ansatz* for $\mathcal{G}$ and integrating $|\mathbf{P}|$ over a small neighborhood of k_m, and $|\mathbf{Q}|$ over a neighborhood of k_n gives the following set of coupled integral equations

$$\begin{aligned}[2i\,\mathrm{Im}\,\lambda(\hat{\mathbf{P}}k_m|\Omega)+\mathbf{q}\cdot\partial_{\mathbf{P}}\lambda(k_m\hat{\mathbf{P}}|\Omega)&\\ +\omega\partial_\Omega\lambda(k_m\hat{\mathbf{P}}|\Omega)]\phi_{k_m\hat{\mathbf{P}};k_n\hat{\mathbf{Q}}}(\mathbf{q})&\\ =-4\pi i g_m\delta_{m,n}\delta(\hat{\mathbf{P}}-\hat{\mathbf{Q}})-\pi i g_m&\\ \times\int\sum_{m'}d\theta_K\,U_{k_m\theta_P;k_{m'}\theta_K}(\mathbf{q})\phi_{k_{m'}\theta_K;k_n\theta_Q}(\mathbf{q}).&\end{aligned} \tag{42}$$

The angle θ_P is the angle $\hat{\mathbf{P}}$ makes with some axis, etc. The factor of 4 comes from $\delta(P^2-k_m^2)=\delta(P-k_m)/(2k_m)$ for positive P, and the analogous result for the δ-function in Q.

The imaginary part of λ arises both from intrinsic dissipative processes and from scattering of the mean field into the incoherent field. The Ward identity[1,4,14] implies

$$\begin{aligned}\mathrm{Im}\,\lambda(k_n)&=\frac{-2k_n(\alpha_n+\epsilon_n)}{g_n}\\ &=\frac{-2k_n\alpha_n}{g_n}-\pi^2\sum_m g_m U^{l=0}_{k_m,k_n}(\mathbf{0}|\Omega,0)).\end{aligned} \tag{43}$$

See Appendix C. The contribution to modal decay caused by scattering at the boundaries is ϵ_m; that caused by other dissipative mechanisms is α_m. The complex modal wave number is $k_m+i\Delta_m=k_m+i(\epsilon_m+\alpha_m)$.

Also shown in Appendix C are results for the derivatives of λ:

$$\partial_{\mathbf{P}}\lambda(k_m)=\frac{2k_m\hat{\mathbf{P}}}{g_m} \tag{44}$$

and

$$\partial_\Omega\lambda(k_m)=\frac{-2k_m}{g_m v_{gm}}, \tag{45}$$

where v_{gm} is the modal group velocity. In order to make the scattering in the Bethe–Salpeter equation self-adjoint, it is useful to absorb factors of g_m into ϕ by writing

$$\psi_{k_m\hat{\mathbf{P}};k_n\hat{\mathbf{Q}}}(\mathbf{q})=\frac{1}{g_m}\phi_{k_m\hat{\mathbf{P}};k_n\hat{\mathbf{Q}}}(\mathbf{q})\frac{1}{g_n}. \tag{46}$$

Then the Bethe–Salpeter equation for ψ can be written

$$\left[2k_m\alpha_m+i\mathbf{q}\cdot\hat{\mathbf{P}}k_m-i\omega\frac{k_m}{v_{gm}}\right]\psi_{k_m\theta_P;k_n\theta_Q}(\mathbf{q}|\Omega,\omega)$$
$$=2\pi\delta_{m,n}\delta(\theta_P-\theta_Q)+\int d\theta_K\sum_{m'}\Lambda_{m,\theta_P;m'\theta_K}$$
$$\times(\mathbf{q}|\Omega,\omega)\psi_{k_{m'}\theta_K;k_n\theta_Q}(\mathbf{q}|\Omega,\omega). \tag{47}$$

The left side of this equation can be recognized as a free-streaming operator: Fourier transformation with respect to **q**, calling the Fourier conjugate variable **R**, and with respect to ω, calling its conjugate variable time, t, gives

$$\left[2k_m\alpha_m-k_m\hat{\mathbf{P}}\cdot\nabla+\frac{k_m}{v_{gm}}\frac{\partial}{\partial_t}\right]\psi$$

for left-hand side of Eq. (47). If the right-hand side were zero, this equation would govern the free motion of a swarm of particles with velocities whose direction is random but whose magnitude is v_{gm}, the group velocity of the mth mode. (The term $2k_m\alpha_m$ represents a loss of particles of this type, independent of direction, i.e., absorption.) The right-hand side of Eq. (47) is analogous to the collision term in the Boltzmann equation. It describes the collisions of the particles initially having velocity $v_{gm'}\hat{\mathbf{K}}$ which after collision have velocities $v_{gn}\hat{\mathbf{P}}$.

The scattering operator, Λ, is given by

$$\Lambda_{m,\theta_P;m'\theta_K}(\mathbf{q}|\Omega,\omega)=\frac{\pi}{2}\left[g_mU_{k_m,\theta_P;k_{m'}\theta_K}(\mathbf{q}|\Omega,\omega)g_{m'}-\frac{4}{\pi}\delta_{m,m'}\epsilon_mk_m\right]. \tag{48}$$

Because of the Ward indentity (energy conservation), the scattering operator satisfies

$$\sum_{m'}\int d\theta_K\,\Lambda_{m,\theta_P;m'\theta_K}(0|\Omega,0)$$
$$=0=\sum_m\int d\theta_P\,\Lambda_{m,\theta_P;m'\theta_K}(0|\Omega,0). \tag{49}$$

When the α_m are small, the behavior of ψ as $\omega\to0$ and $\mathbf{q}\to0$ is dominated by the projection of ψ onto its isotropic and modal average. Using standard projection operator techniques[15] on Eq. (47) gives for the modal and angular average of ψ

$$\left[2\langle k\alpha\rangle-i\omega\left\langle\frac{k}{v}\right\rangle+q^2\frac{1}{2N}\sum_{m,n}k_m\left[\frac{1}{\Lambda^{(1)}}\right]_{m,n}k_n\right]\overline{\psi}(\mathbf{q}|\Omega,\omega)=1 \tag{50}$$

as ω and **q** tend to zero. To be precise, $\overline{\psi}$ is given by

$$\overline{\psi}(\mathbf{q}|\Omega,\omega)=\frac{1}{2\pi N}\int d\theta_P\,d\theta_Q\sum_{m,n=0}^{N}\psi_{k_m\theta_P;k_n\theta_Q}(\mathbf{q}|\Omega,\omega). \tag{51}$$

The matrix $\Lambda^{(1)}$ is given by

$$\Lambda^{(1)}_{m,n}=\int\frac{d\theta_P}{\sqrt{2\pi}}\frac{d\theta_Q}{\sqrt{2\pi}}e^{-i\theta_P}\Lambda_{k_m\theta_P;k_n\theta_Q}(\mathbf{q}|\Omega,\omega)e^{i\theta_Q}, \tag{52}$$

and

$$\left[\frac{1}{\Lambda^{(1)}}\right]_{m,n}$$

denotes the m,n element of the matrix inverse of $\Lambda^{(1)}$. The average of the ratio of wave number to group velocity is

$$\left\langle\frac{k}{v}\right\rangle=\frac{1}{N}\sum_{m=0}^{N}\frac{k_m}{v_{gm}}, \tag{53}$$

and

$$\langle k\alpha\rangle=\frac{1}{N}\sum_{m=0}^{N}k_m\alpha_m. \tag{54}$$

Comparing with Eq. 4.4 in Ref. 9 shows that the diffusion coefficient here should be identified as

$$D(\Omega)=\left(\frac{1}{\langle k/v\rangle}\right)\frac{1}{2N}\sum_{m,n}k_m\left[\frac{1}{\Lambda^{(1)}}\right]_{m,n}k_n. \tag{55}$$

The contribution of $\mathcal{G}$ to τ is given by the second term in Eq. (35). Using $\overline{\psi}$ and the δ-function ansatz for $\mathcal{G}$ gives

$$\mathcal{G}^{u_1,u_2;v_1;v_2}_{\mathbf{P},\mathbf{K}}(\mathbf{p})\approx\frac{1}{8\pi N}\sum_{m,n}\delta(P-k_m)\frac{g_m}{k_m}\overline{\psi}\frac{g_n}{k_n}$$
$$\times\delta(K-k_n)\delta_{u_1,1}\delta_{u_2,1}\delta_{v_1,1}\delta_{v_2,1}. \tag{56}$$

Filling in the details of the operator multiplication in $U\mathcal{G}U$ gives

$$(U\mathcal{G}U)^{\alpha,\beta;\gamma,\delta}_{\mathbf{Q},\mathbf{Q}'}(\mathbf{q}|\Omega,\omega)$$
$$=\frac{1}{8\pi N}\sum_{m,n}\int d\theta_P\,d\theta_K\,U^{\alpha,\beta;1,1}_{\mathbf{Q};k_m\hat{\mathbf{P}}}(\mathbf{q}|\Omega,\omega)g_m$$
$$\times\overline{\psi}g_nU^{1,1;\gamma,\delta}_{k_n\hat{\mathbf{P}};\mathbf{Q}'}(\mathbf{q}|\Omega,\omega). \tag{57}$$

The Ward identity (see Appendix C) can be written as

$$i\pi\sum_n\int d\theta_K\,g_nU^{1,1;\gamma,\delta}_{k_n\hat{\mathbf{K}};\mathbf{Q}'}(\mathbf{0}|\Omega,0)$$
$$=M_{\delta,\gamma}(\mathbf{Q}')-M^*_{\gamma,\delta}(\mathbf{Q}')\equiv2i\Sigma_{\delta,\gamma}(\mathbf{Q}'), \tag{58}$$

with a similar result for the transpose resulting from reciprocity. Using this and our result for $\overline{\psi}$ in Eq. (57) gives

$$(U\mathcal{G}U)^{\alpha,\beta;\gamma,\delta}_{\mathbf{Q},\mathbf{Q}'}(\mathbf{q}|\Omega,\omega)$$
$$=\frac{1}{\pi^2 2\pi N}\Sigma_{\beta,\alpha}(\mathbf{Q})\frac{i}{\langle k/v\rangle[\omega+i\xi+iq^2D(\Omega)]}\Sigma_{\delta,\gamma}(\mathbf{Q}'), \tag{59}$$

where $\xi=2\langle k\alpha\rangle/\langle k/v\rangle$, and where we let $\mathbf{q}\to0$ in $U(\mathbf{q}|\Omega,0)$. This is the expression for multiple scattering that will be used in the next section to compute long-time reverberation. Reference 16 shows how to relax the $\mathbf{q}\to0$, $\omega\to0$ limit in the case of resonant volume scattering.

It should be pointed out that the denominator in Eq. (59), when $\xi\to0$, is just the Fourier transform of the Green's function for the diffusion equation

$$\frac{\partial P}{\partial t}+D\nabla^2 P=-\delta(\mathbf{R})\,\delta(t).$$

Hence Eq. (59) is telling us that over long times sound diffuses between scattering events. In this approximation, the second moment has lost much of its wave character.

III. REVERBERATION

In this section the formalism described above will be applied to computing the second moment of pressure fluctuations arising from a point source in a layered medium with one rough interface. In the process, Ellis's model for reverberation will be rederived, but with some small differences. The advantage of the present derivation is that it can be seen from ''first principles'' what the scattering function must be. In addition, we will show that the multiple scattering contribution to reverberation has an algebraic decay with time, if intrinsic attenuations can be ignored. Even if intrinsic attenuations cannot be ignored, the multiple scattering contribution to reverberation decays more slowly in time than the single scattering contribution, and for long enough time will dominate the single scattering contribution.

A. Conventional reverberation

The starting point for the computation is Eq. (29), and the main mathematical issue is how to deal with the multidimensional integrations that are needed. The pressure at $(\mathbf{r},t)$ caused by a narrow-band pressure source at $\mathbf{r}_0=(\mathbf{R}_0,z_s)$ is

$$p(\mathbf{r},t)=\int\frac{d\omega}{2\pi}e^{-i\omega t}G(\mathbf{R},z;\mathbf{R}_0,z_s;\omega)\hat{a}(\omega), \tag{60}$$

where $\mathbf{r}=(\mathbf{R},z)$. The source function, $\hat{a}(\omega)$, is the Fourier transform of

$$a(t)=\mathrm{Re}\,e^{-i\omega_c t}b(t), \tag{61}$$

where $b(t)$, the complex envelope of the source signal,[17] is slowly varying with respect to the carrier wave, $e^{-i\omega_c t}$. Then

$$a(\omega)=[\hat{b}(\omega-\omega_c)+\hat{b}^*(-\omega-\omega_c)]/2. \tag{62}$$

The received pressure can also be written in terms of its complex envelope, $\tilde{p}(\mathbf{r},t)$, by

$$p(\mathbf{r},t)=\mathrm{Re}\,e^{-i\omega_c t}\tilde{p}(\mathbf{r},t), \tag{63}$$

with $\tilde{p}(\mathbf{r},t)$ given by

$$\tilde{p}(\mathbf{r},t)=\int\frac{d\omega}{2\pi}e^{-i\omega t}G(\mathbf{r},\mathbf{r}_0,\omega+\omega_c)\hat{b}(\omega). \tag{64}$$

The magnitude of $\tilde{p}$ is the quantity usually measured, and here we will be concerned with its fluctuations, in particular with

$$C(\mathbf{r},t)\equiv\langle\Delta\tilde{p}(\mathbf{r},t)\Delta\tilde{p}^*(\mathbf{r},t)\rangle. \tag{65}$$

The complex envelope of the emitted signal is related to the total acoustic energy generated by the source, E_0, by

$$E_0=\frac{1}{16\pi^2\rho_0 c_0}\int|\hat{b}(\omega)|^2\,d\omega. \tag{66}$$

Here ρ_0 and c_0 are the density and sound speed at the source, respectively.

To compute the mean square envelope fluctuation $C(\mathbf{r},t)$ we need to ''unpack'' Eq. (29) for ΔG to obtain

$$\begin{aligned}\Delta\tilde{p}(\mathbf{r},t)=\int\frac{d\omega}{2\pi}e^{-i\omega t}\frac{d\mathbf{P}}{2\pi}\frac{d\mathbf{K}}{2\pi}e^{i\mathbf{P}\cdot\mathbf{R}}e^{-i\mathbf{K}\cdot\mathbf{R}_0}(-1)^i\partial_{z_i}\\ \times\langle G(\mathbf{P},z,z_i,\omega+\omega_c)\rangle t^{i,j}(\mathbf{P},\mathbf{K};\omega+\omega_c)(-1)^j\partial_{z_j}\\ \times\langle G(\mathbf{K},z_j,z_s,\omega+\omega_c)\rangle\hat{b}(\omega).\end{aligned} \tag{67}$$

Here, z_i, $i=0,1$, refers to the level of the imaginary plane adjacent to either the upper or lower bounding rough surface while z_s is the source depth. There is an implicit sum over i and j and the factors $(-1)^i$ are just a simple way to incorporate the matrix σ_3. To understand this expression it is useful to replace the wave vector dependence of the mean fields by the corresponding spatial dependence using

$$\langle G(\mathbf{P},z,z_i,\omega+\omega_c)\rangle=\int d\mathbf{R}'\,e^{-i\mathbf{P}\cdot\mathbf{R}'}\langle G(\mathbf{R}',z,z_i,\omega+\omega_c)\rangle. \tag{68}$$

After translating the dummy variables of integration the fluctuation of the pressure becomes

$$\begin{aligned}\Delta\tilde{p}(\mathbf{r},t)=\int\frac{d\omega}{2\pi}e^{-i\omega t}\frac{d\mathbf{P}}{2\pi}\frac{d\mathbf{K}}{2\pi}d\mathbf{s}\,d\mathbf{s}'\\ \times(-1)^i\partial_{z_i}\langle G(\mathbf{R}-\mathbf{s},z,z_i,\omega+\omega_c)\rangle\\ \times e^{i\mathbf{P}\cdot\mathbf{s}}t^{i,j}(\mathbf{P},\mathbf{K};\omega+\omega_c)e^{-i\mathbf{K}\cdot\mathbf{s}'}(-1)^j\partial_{z_j}\\ \times\langle G(\mathbf{s}'-\mathbf{R}_0,z_j,z_s,\omega+\omega_c)\rangle\hat{b}(\omega).\end{aligned} \tag{69}$$

Results of this type were used by Ellis and Yang[7,18] and others to compute reverberant and scattered fields. The result here is distinctive in that (*a*) derivatives of the mean field are used to propagate to and from the scattering at the boundary, (*b*) there is a precise prescription for the scattering amplitude, t, in terms of the impedance even if t cannot be computed exactly, and (*c*) there are two rough bounding surfaces. This equation, Eq. (69), is still formally exact. However, the ninefold integral in Eq. (69) is daunting. The dimensionality will be reduced by expanding the phase difference of the Green's functions to first order in spatial separations and to first order in the deviation of the frequency from the carrier frequency.

Computing $C(\mathbf{r},t)$ doubles the number of integrations. The dummy variables of integration for $\Delta\tilde{p}$ will be denoted with subscripts ''1'' and the variables of integration giving $\Delta\tilde{p}^*$ with subscripts ''2.'' It will then be convenient to introduce sum and difference variables because the statistical homogeneity of t,

$$\begin{aligned}\langle t^{i_1,j_1}(\mathbf{P}_1,\mathbf{K}_1,\Omega+\omega/2+\omega_c)t^{i_2,j_2}(\mathbf{P}_2,\mathbf{K}_2,\Omega-\omega/2+\omega_c)^*\rangle\\ =\tau^{i_1,i_2;j_1,j_2}_{(\mathbf{P}_1+\mathbf{P}_2)/2_1(\mathbf{K}_1+\mathbf{K}_2)/2}(\mathbf{P}_1-\mathbf{P}_2|\Omega+\omega_c,\omega)\\ \times\delta(\mathbf{P}_1-\mathbf{P}_2-(\mathbf{K}_1-\mathbf{K}_2))\end{aligned} \tag{70}$$

is best expressed in these variables, and because, in expanding phases to first order in the difference variables, the error

is only of third order. Therefore, make the following changes of variable:

$$\Omega=(\omega_1+\omega_2)/2,\quad \omega=\omega_1-\omega_2,$$
$$\mathbf{P}=(\mathbf{P}_1+\mathbf{P}_2)/2,\quad \mathbf{p}=\mathbf{P}_1-\mathbf{P}_2,$$
$$\mathbf{K}=(\mathbf{K}_1+\mathbf{K}_2)/2,\quad \mathbf{k}=\mathbf{K}_1-\mathbf{K}_2, \tag{71}$$
$$\mathbf{R}_1=(\mathbf{s}_1+\mathbf{s}_2)/2,\quad \boldsymbol{\rho}_1=\mathbf{s}_1-\mathbf{s}_2,$$
$$\mathbf{R}_2=(\mathbf{s}_1'+\mathbf{s}_2')/2,\quad \boldsymbol{\rho}_2=\mathbf{s}_1'-\mathbf{s}_2'.$$

Using Eq. (70) eliminates one integral leaving

$$C(\mathbf{r},t)=\frac{1}{(2\pi)^6}\int d\Omega\, d\omega \int d\mathbf{P}\, d\mathbf{K}\, d\mathbf{p}\int d\mathbf{R}_1\, d\mathbf{R}_2\, d\boldsymbol{\rho}_1\, d\boldsymbol{\rho}_2 e^{-i\omega t}\partial_{z_{i_1}}\langle G(\mathbf{R}-\mathbf{R}_1-\boldsymbol{\rho}_1/2,z,z_{i_1},\Omega+\omega_c+\omega/2)\rangle$$
$$\times\partial_{z_{i_2}}\langle G^*(\mathbf{R}-\mathbf{R}_1+\boldsymbol{\rho}_1/2,z,z_{i_2},\Omega+\omega_c-\omega/2)\rangle e^{i\mathbf{P}\cdot\boldsymbol{\rho}_1}e^{i\mathbf{p}\cdot(\mathbf{R}_1-\mathbf{R}_2)}e^{-i\mathbf{K}\cdot\boldsymbol{\rho}_2}\tau^{i_1,i_2;j_1,j_2}_{\mathbf{P},\mathbf{K}}(\mathbf{p}|\Omega+\omega_c,\omega)(-1)^{i_1+i_2+j_1+j_2}$$
$$\times\partial_{z_{j_1}}\langle G(\mathbf{R}_2-\mathbf{R}_0+\boldsymbol{\rho}_2/2),z_{j_1},z_s,\Omega+\omega_c+\omega/2)\rangle\partial_{z_{j2}}\langle G^*(\mathbf{R}_2-\mathbf{R}_0-\boldsymbol{\rho}_2/2),z_{j_2},z_s,\Omega+\omega_c-\omega/2)\rangle$$
$$\times b(\Omega+\omega/2)b^*(\Omega-\omega/2). \tag{72}$$

This equation is still exact.

Assume that the source produces a pulse of finite duration. Then for long times after the pulse is emitted one can reasonably expect that only distant portions of the surface contribute to the integral. This means that the Green's functions, which are of the form shown in Eq. (34), can be evaluated asymptotically using

$$H_0^{(1)}(kR)\sim\sqrt{\frac{2}{\pi kR}}e^{-i\pi/4}e^{ikR}. \tag{73}$$

In the special case of a rough Dirichlet surface, to lowest order in the surface roughness, τ is simply the spectrum of surface heights,

$$\tau_{\mathbf{P},\mathbf{K}}(\mathbf{p}|\Omega,\omega)=S(\mathbf{P}-\mathbf{K}). \tag{74}$$

(Because to lowest order τ is the correlation of impedances, τ in this case does not involve vertical components of the wave vectors. This is one of the simplifying features of the impedance formalism.) Thus, in this case, τ is independent of $\mathbf{p}$, $\mathbf{P}+\mathbf{K}$, Ω, and ω. Integration over $\mathbf{p}$ will give a δ-function in $\mathbf{R}_1-\mathbf{R}_2$. Integration over $(\mathbf{P}+\mathbf{K})/2$ gives $\delta(\boldsymbol{\rho}_1-\boldsymbol{\rho}_2)$. Integration over $\mathbf{P}-\mathbf{K}$ will give the correlation function of surface heights, $C_h(\boldsymbol{\rho}_1+\boldsymbol{\rho}_2)=C_h(2\boldsymbol{\rho}_1)$. This means that the region of integration over $\boldsymbol{\rho}_1$ will be limited to a few correlation lengths of the surface roughness. Thus, for large time t we can expect

$$|\mathbf{R}-\mathbf{R}_1|\gg|\boldsymbol{\rho}_1|/2\approx L_c. \tag{75}$$

In fact, a reasonable estimate of $|\mathbf{R}-\mathbf{R}_1|$ is $|\mathbf{R}-\mathbf{R}_1|\approx v_g t$ where v_g is a typical modal group velocity. The upshot of this argument is that if $t\gg L_c/v_g$, then the phases of the Green's functions can be expanded as

$$e^{ik_m|\mathbf{R}-\mathbf{R}_1\pm\boldsymbol{\rho}_1/2|}\approx e^{ik_m|\mathbf{R}-\mathbf{R}_1|\pm ik_m(\widehat{\mathbf{R}-\mathbf{R}_1})\cdot\boldsymbol{\rho}_1/2}, \tag{76}$$

etc. It will simply be assumed that this same argument can be used in the case of more complicated expressions for τ. Be aware, however, that in the case of a fluid–fluid boundary, τ will contain vertical wave numbers and corresponding branch points. These may be problematic for modes near cut off. In any event, it is assumed that for long times the scattering takes place far from the source and receiver, and then at the scattering location, the incident field has a locally plane wave character. This is what it means to expand to first order in ρ_1 or ρ_2. In the phases, modal wave numbers will be expanded to first order in ω using

$$k_m(\Omega+\omega_c+\omega/2)\approx k_m(\Omega+\omega_c)+\omega/(2v_{gm}), \tag{77}$$

where v_{gm} is the group velocity of the mth mode at the center frequency $\Omega+\omega_c$. The narrow-band assumption limits ω and Ω to values much less than the center frequency. Outside of the phases only zeroth-order terms in these expansions will be used. Making all these approximations gives

$$C(\mathbf{r},t)=\frac{1}{(2\pi)^6 16(2\pi)^2}\sum_{m,n}\int d\Omega\, d\omega\int d\mathbf{P}\, d\mathbf{K}\, d\mathbf{p}\int d\mathbf{R}_1\, d\mathbf{R}_2\, d\boldsymbol{\rho}_1\, d\boldsymbol{\rho}_2\, e^{-i\omega t}\frac{u_m^2(z)u_m'(z_{i_1})u_m'(z_{i_2})u_n'(z_{j_1})u_n'(z_{j_2})u_n(z_s)^2}{k_m k_n|\mathbf{R}-\mathbf{R}_1||\mathbf{R}_2-\mathbf{R}_0|}$$
$$\times(-1)^{i_1+i_2+j_1+j_2}\exp[-2\Delta_m|\mathbf{R}-\mathbf{R}_1|-2\Delta_n|\mathbf{R}_2-\mathbf{R}_0|-ik_m(\widehat{\mathbf{R}-\mathbf{R}_1})\cdot\boldsymbol{\rho}_1+ik_n(\widehat{\mathbf{R}_2-\mathbf{R}_0})\cdot\boldsymbol{\rho}_2]$$
$$\times\exp[i\mathbf{P}\cdot\boldsymbol{\rho}_1-i\mathbf{K}\cdot\boldsymbol{\rho}_2+i\mathbf{p}\cdot(\mathbf{R}_1-\mathbf{R}_2)]\tau^{i_1,i_2;j_1,j_2}_{\mathbf{P},\mathbf{K}}(\mathbf{p}|\Omega+\omega_c,\omega)$$
$$\times\exp[i\omega|\mathbf{R}-\mathbf{R}_1|/v_{gm}+i\omega|\mathbf{R}_2-\mathbf{R}_0|/v_{gn}]\hat{b}(\Omega+\omega/2)\hat{b}^*(\Omega-\omega/2). \tag{78}$$

There should really be a fourfold sum over mode numbers. However, terms such as $\exp[i(k_m-k_{m'})|\mathbf{R}+\mathbf{R}_1|$ have been dropped under the assumption that these will oscillate rapidly except when $m=m'$. The integral over $\boldsymbol{\rho}_1$ gives $(2\pi)^2\delta(\mathbf{P}-k_m\times(\widehat{\mathbf{R}-\mathbf{R}_1}))$ and over $\boldsymbol{\rho}_2$ gives $(2\pi)^2\delta(\mathbf{K}-k_n(\widehat{\mathbf{R}_2-\mathbf{R}_0}))$ giving

$$C(\mathbf{r},t)=\frac{(2\pi)^4}{(2\pi)^6 16(2\pi)^2}\sum_{m,n}\int d\Omega\, d\omega\int d\mathbf{p}\int d\mathbf{R}_1\, d\mathbf{R}_2(-1)^{i_1+i_2+j_1+j_2}\frac{u_m^2(z)u_m'(z_{i_1})u_m'(z_{i_2})u_n'(z_{j_1})u_u'(z_{j_2})u_n(z_s)^2}{k_m k_n|\mathbf{R}-\mathbf{R}_1||\mathbf{R}_2-\mathbf{R}_0|}$$

$$\times\tau^{i_1,i_2;j_1j_2}_{k_m(\widehat{\mathbf{R}-\mathbf{R}_1}),k_n(\widehat{\mathbf{R}_2-\mathbf{R}_0})}(\mathbf{p}|\Omega+\omega_c,\omega)\exp[-2\Delta_m|\mathbf{R}-\mathbf{R}_1|-2\Delta_n|\mathbf{R}_2-\mathbf{R}_0|]\exp[+ip\cdot(\mathbf{R}_1-\mathbf{R}_2)]$$

$$\times\exp\{-i\omega[t-|\mathbf{R}-\mathbf{R}_1|/v_{gm}-|\mathbf{R}_2-\mathbf{R}_0|/v_{gn}]\}\hat{b}(\Omega+\omega/2)\hat{b}^*(\Omega-\omega/2). \tag{79}$$

We will assume that the bandwidth of the pulse is sufficiently small that Ω can be neglected relative to ω_c within τ and that the modal wave numbers k_m, modes $u_m(z)$, and group velocities v_{gm} are to be evaluated at ω_c.

To get conventional reverberation results such as in Ref. 7 consider only the contribution to τ from the irreducible vertex function and set $\mathbf{p}=0$ and $\omega=\Omega=0$ in $U_{\mathbf{P},\mathbf{K}}(\mathbf{p}|\Omega+\omega_c,\omega)$, assuming that U is well behaved in this limit. Then the integration over $\mathbf{p}$ gives $(2\pi)^2\delta(\mathbf{R}_1-\mathbf{R}_2)$. Furthermore, assume that the source and receiver are separated only vertically so that we can let $\mathbf{R}=\mathbf{R}_0=0$. Assume also that $U_{-k_m\widehat{\mathbf{R}}_1,k_n\widehat{\mathbf{R}}_1}$ is independent of the direction of $\widehat{\mathbf{R}}_1$. Then the mean square fluctuation of the pressure envelope is

$$C(\mathbf{r},t)=\frac{1}{(32\pi)}\sum_{m,n}\int_0^\infty RdR(-1)^{i_1+i_2+j_1+j_2}\frac{u_m^2(z)u_m'(z_{i_1})u_m'(z_{i_2})u_n'(z_{j_1})u_n'(z_{j_2})u_n'(z_s)^2}{k_m k_n R^2}$$

$$\times U^{i_1,i_2;j_1,j_2}_{-k_m\hat{\mathbf{R}},k_n\hat{\mathbf{R}}}(\mathbf{0}|\omega_c,0)e^{-2(\Delta_m+\Delta_n)R}\int e^{-i\omega[t-R(1/v_{gm}+1/v_{gn})]}\hat{b}(\Omega+\omega/2)\hat{b}^*(\Omega-\omega/2)\,d\omega\,d\Omega, \tag{80}$$

where, again, k_m, ϵ_m, u_m, etc. are evaluated at the carrier frequency, ω_c.

Finally, suppose for the sake of concreteness, that $\hat{b}$ is Gaussian,

$$\hat{b}(\omega)=A\exp[-\omega^2/(2B^2)],$$

in order to see how things work out. The double frequency integral in Eq. (80) is

$$\int e^{-i\omega[t-R(1/v_{gm}+1/v_{gn})]}\hat{b}\left(\Omega+\frac{\omega}{2}\right)\hat{b}^*\left(\Omega-\frac{\omega}{2}\right)d\Omega\,d\omega$$

$$=A^2 2\pi B^2\exp\left[-\left(t-R\left(\frac{1}{v_{gm}}+\frac{1}{v_{gn}}\right)\right)^2B^2\right], \tag{81}$$

and the normalization of $\hat{b}$ in terms of the total energy gives

$$|A|^2\sqrt{\pi B^2}=16\pi^2\rho_0 c_0 E_0. \tag{82}$$

Hence $C(\mathbf{r},t)$ becomes

$$C(\mathbf{r},t)=\frac{16\pi^2\rho_0 c_0 E_0}{32\pi}\sum_{m,n}\int_0^\infty dR\,(-1)^{i_1+i_2+j_1+j_2}$$

$$\times\frac{u_m^2(z)u_m'(z_{i_1})u_m'(z_{i_2})u_n'(z_{j_1})u_n'(z_{j_2})u_n(z_s)^2}{k_m k_n R}$$

$$\times U^{i_1,i_2;j_1,j_2}_{-k_m\hat{\mathbf{R}}+k_n\hat{\mathbf{R}}}(\mathbf{0}|\omega_c,0)$$

$$\times\exp[-2(\Delta_m+\Delta_n)R]\sqrt{4\pi B^2}$$

$$\times e^{-[t-R(1/v_{gm}+1/v_{gn})]^2B^2}. \tag{83}$$

This leaves just the range integral in Eq. (83). However, if $t\gg 1/B$, i.e., the observations take place at a time long compared to the duration of the pulse, and if the decay rate is small enough that

$$2(\epsilon_m+\epsilon_n)\frac{v_{gm}v_{gn}}{v_{gm}+v_{gn}}\frac{1}{B}\ll 1,$$

then the Gaussian behaves like a δ-function

$$\sqrt{4\pi B^2}e^{-(t-R(1/v_{gm}+1/v_{gn})B)^2}$$

$$\approx\frac{2\pi(v_{gm}+v_{gn})}{v_{gm}v_{gn}}\delta\left(R-t\frac{v_{gm}v_{gn}}{(v_{gm}+v_{gn})}\right).$$

Now the range integral can be done giving

$$C(\mathbf{r},t)=\pi^2\rho_0 c_0 E_0\sum_{m,n}(-1)^{i_1+i_2+j_1+j_2}$$
$$\times\frac{u_m^2(z)u_m'(z_{i_1})u_m'(z_{i_2})u_n'(z_{j_1})u_n'(z_{j_2})u_n(z_s)^2}{k_m k_n t}$$
$$\times U^{i_1,i_2;j_1,j_2}_{k_m\mathbf{R},-k_n\hat{\mathbf{R}}}(\mathbf{0}|\omega_c,0)$$
$$\times\exp\left[-2(\Delta_m+\Delta_n)t\frac{v_{gm}v_{gn}}{(v_{gm}+v_{gn})}\right]. \tag{84}$$

This is basically Ellis' result. It differs only in some details. First, group velocities have replaced phase velocities. Second, instead of a somewhat ill-defined scattering strength, we use here the irreducible vertex function which in turn is expressed in terms of impedance fluctuations and in terms of horizontal wave vectors. It is this last fact that probably accounts for differences in numerical factors. The normal modes here are normalized so that for Dirichlet surfaces, $\int u_n(z)^2\,dz=1$ and the dimension of the normal modes here is $1/\sqrt{\text{Length}}$.

B. Reverberation with multiple scattering

We now compute the contribution to reverberation that comes from including the second term in $\tau=U+U\mathcal{G}U$. Starting again from Eq. (79), the pole structure of $\mathcal{G}$ means that it is not possible to ignore the $\mathbf{p}$ and ω dependence of the $U\mathcal{G}U$ contribution to τ. Using Eq. (59) gives, taking $\mathbf{R}=\mathbf{R}_0=0$,

$$C^{\text{mult.}}(\mathbf{r},t)=\frac{i(2\pi)^4}{((2\pi)^6 16(2\pi)^2)\pi^2\langle k/v\rangle 2\pi N}\sum_{m,n}\int d\Omega\,d\omega\,d\mathbf{p}\,d\mathbf{R}_1\,d\mathbf{R}_2(-1)^{i_1+i_2+j_1+j_2}$$
$$\times\frac{\Sigma_{i_1,i_2}(k_m)u_m^2(z)u_m'(z_{i_1})u_m'(z_{i_2})u_n'(z_{j_1})u_n'(z_{j_2})u_n(z_s)^2\Sigma_{j_1,j_2}(k_n)}{k_m k_n R_1 R_2[\omega+i\xi+ip^2D(\omega_c)]}e^{-2\Delta_m R_1-2\Delta_n R_2}$$
$$\times\exp[-i\mathbf{p}\cdot(\mathbf{R}_1-\mathbf{R}_2)]e^{-i\omega(t-R_1/v_{gm}-R_2/v_{gn})}\hat{b}(\Omega+\omega/2)\hat{b}^*(\Omega-\omega/2). \tag{85}$$

Write the frequency denominator as

$$\frac{1}{[\omega+i\xi+ip^2D(\omega_c)]}=i\int_0^\infty dy\,e^{i[\omega+i\xi+ip^2D(\omega_c)]y}. \tag{86}$$

Then the $\mathbf{p}$ integral (two-dimensional) is Gaussian:

$$\int d\mathbf{p}e^{i\mathbf{p}\cdot(\mathbf{R}_2-\mathbf{R}_1)-p^2Dy}=\frac{\pi}{Dy}e^{-(\mathbf{R}_2-\mathbf{R}_1)^2/(4Dy)}. \tag{87}$$

The pressure fluctuation now becomes

$$C^{\text{mult.}}(\mathbf{r},t)=\frac{i(2\pi)^4}{((2\pi)^6 16(2\pi)^2)\pi^2\langle k/v\rangle 2\pi N}\sum_{m,n}\int d\Omega\,d\omega\int_0^\infty dy\,d\mathbf{R}_1\,d\mathbf{R}_2(-1)^{i_1+i_2+j_1+j_2}$$
$$\times\frac{\pi\Sigma_{i_1,i_2}(k_m)u_m^2(z)u_m'(z_{i_1})u_m'(z_{i_2})u_n'(z_{j_1})u_n'(z_{j_2})u_n(z_s)^2\Sigma_{j_1,j_2}(k_n)}{k_m k_n R_1 R_2 Dy}e^{-2\Delta_m R_1-2\Delta_n R_2}$$
$$\times\exp[-(\mathbf{R}_2-\mathbf{R}_1)^2/(4Dy)]e^{i[\omega+i\xi]y}e^{-i\omega(t-R_1/v_{gm}-R_2/v_{gn})}\hat{b}(\Omega+\omega/2)\hat{b}^*(\Omega-\omega/2). \tag{88}$$

For large times t, we expect that only small values of ω will contribute to the integral. Hence, replace ω by 0 in b and b^*. The remaining ω integration gives $2\pi\delta(y-(t-|\mathbf{R}_1|/v_{gm}-|\mathbf{R}_2|/v_{gn}))$. This allows the y integral to be performed:

$$C^{\text{mult.}}(\mathbf{r},t)=\frac{i(2\pi)^4}{((2\pi)^6 16(2\pi)^2)\pi^2\langle k/v\rangle 2\pi N}\sum_{m,n}\int d\Omega\,d\mathbf{R}_1\,d\mathbf{R}_2(-1)^{i_1+i_2+j_1+j_2}$$
$$\times\frac{\pi(2\pi)\Sigma_{i_1,i_2}(k_m)u_m^2(z)u_m'(z_{i_1})u_m'(z_{i_2})u_n'(z_{j_1})u_n'(z_{j_2})u_n(z_s)^2\Sigma_{j_1,j_2}(k_n)}{k_m k_n R_1 R_2 D(t-R_1/v_{gm}-R_2/v_{gn})}$$
$$\times e^{-2\Delta_m R_1-2\Delta_n R_2}\exp[-(\mathbf{R}_2-\mathbf{R}_1)^2/(4D(t-R_1/v_{gm}-R_2/v_{gn}))]e^{-\xi(t-R_1/v_{gm}-R_2/v_{gn})}\hat{b}(\Omega)\hat{b}^*(\Omega), \tag{89}$$

provided $(t-R_1/v_{gm}-R_2/v_{gn})\geqslant 0$. Because of the damping in $e^{-2\Delta_m R_1-2\Delta_n R_2}$, both R_1 and R_2 are restricted to values less than a few times $1/\Delta_m$. For t much larger than $(1/(v_{gm}\Delta_m)+1/(v_{gn}\Delta_n))$ we can replace $\exp[-(\mathbf{R}_2-\mathbf{R}_1)^2/(4D(t-R_1/v_{gm}-R_2/v_{gn}))]$ by unity and $1/(D(t-R_1/v_{gm}-R_2/v_{gn}))$ by $1/Dt$. Then the integrations over $\mathbf{R}_i$ can be done with the result

$$C^{\text{Mult.}}(\mathbf{r},t)=\frac{\rho_0 c_0 E_0}{2\pi N\langle k/v\rangle}\sum_{m,n}(-1)^{i_1+i_2+j_1+j_2}\frac{\Sigma_{i_1,i_2}(k_m)u_m^2(z)u_m'(z_{i_1})u_m'(z_{i_2})u_n'(z_{j_1})u_n'(z_{j_2})u_m(z_s)^2\Sigma_{j_1,j_2}(k_n)}{k_m k_n 4\Delta_m\Delta_n 2D(\omega_c)t}e^{-\xi t}. \tag{90}$$

In the limit of vanishing intrinsic attenuation, $\xi=0$, $C^{\text{Mult.}}\sim 1/t$; there is only algebraic, not exponential, decay of the reverberation. Also in this limit, Δ_m and $\Sigma(k_m)$ will be proportional for small roughness. $C^{\text{Mult.}}$ then vanishes as the scattering vanishes only because the diffusion constant, D, becomes infinite. For another instance of diffusive reverberation, see Ref. 19. It is claimed there that reverberation in the ocean was observed to follow a power law of the form

$$p^2\sim At^{-4}$$

for surface scattering according to Ref. 20. I am not sure that these observations have survived the test of time, and it is not clear why the decay is faster than that proposed here.

Even when $\xi\neq 0$, it can happen that α is smaller than any of the Δ_m, in which case, the decay of $C^{\text{Mult.}}$ will be slower than the single scatter (from U) contribution to $C^{\text{Mult.}}$. For example, suppose there is only a single propagating mode. Then Eq. (84) takes the form

$$C(\mathbf{r},t)\sim B\frac{e^{-2(\epsilon_1+\alpha_1)v_{g1}t}}{t},$$

while the multiple scattering contribution, Eq. (90), takes the form

$$C^{\text{Mult.}}(\mathbf{r},t)=A\frac{e^{-2\alpha_1 v_{g1}t}}{Dt}.$$

Recall that ϵ_m accounts for the modal attenuation caused by surface roughness, while α accounts for the modal attenuation caused by other mechanisms. Clearly the multiple and single scattering contributions to reverberation are qualitatively similar. However, it is also clear that the multiple scattering contribution decays more slowly than the single scatter contribution. At some time, depending on the various constants A, B, D, α, etc., multiple scattering will dominate single scattering. However, at such times, or at times sufficiently long so that these results for single and multiple scattering are valid, the reverberation signals might be too small to be actually detectable. Since these results concerning the relative size of the single and multiply scattered fields are evidently new, I suspect that no experiment has been designed to distinguish the two. More computation is required to determine the feasibility of such an experiment. In a realistic ocean setting, I would speculate that intrinsic attenuation, α, is so large that algebraic decay will never be observed. However, it seems important to know how to compute the decay rate for reverberation. Should one use α or $\epsilon+\alpha$? This can only be settled by experiment and by an actual computation of the magnitudes of the single and multiple scattering contributions.

IV. SUMMARY AND DISCUSSION

A first-principles computation of reverberation has been presented. Approximations needed to obtain conventional reverberation models have been delineated, resulting in some small corrections and in a better understanding of what function should be used to describe the scattering *per se*. The impedance formalism for describing scattering in a complicated environment has been shown to be a convenient starting point. The contribution of multiple scattering to reverberation has been shown to result in algebraic decay rather than exponential decay of the signal when there is little intrinsic attenuation. However, in general, both the single- and multiple-scattering contributions to reverbation involve a product of exponential and $1/t$ decay. The multiple-scattering contribution appears to decay more slowly than the single-scatter contribution.

The computations presented here are completely analogous to those presented in Refs. 9 and 16 for the scattering of scalar waves by volume inhomogeneities. They are distinct in (1) the treatment of multi-modal propagation and (2) in that the scattering occurs at boundaries. Similar ideas have been numerically implemented by Schmidt and Kuperman.[21] The results here provide an analytic baseline for those computations.

The principal approximations and assumptions for this computation are the following:

(1) Scattering can be described by a nonlocal impedance function for any one realization of an ensemble of rough surfaces. As indicated in Appendix A, this use of the impedance is reasonably well founded. It underlies not only this work, but is implicit in the work of Maradudin, as well.
(2) The computation cannot proceed without assuming statistical homogeneity. Is the ocean really statistically homogeneous? Probably only over limited scales.
(3) Equation (34) for τ and Eq. (37), the Bethe–Salpeter equation, are exact. However, when the irreducible vertex function, U, is approximated as a simple ladder diagram, these cease to be exact. It is difficult to assess the error incurred by using the ladder approximation. For a discussion in the context of electron localization see Ref. 14. The analysis there seems to indicate that when there is no intrinsic attenuation, in addition to ladder diagrams, the maximally crossed diagrams will be important.
(4) Liberal use was made of pole approximations both for the mean Green's function and for the two-point Green's function. For the mean field, this means that branch-cut contributions are ignored. This is normally a reasonable approximation for far-field computations. I assume that if I confine my interest to long times, I need only consider the far field.
(5) In the treatment of the Bethe–Salpeter equation it was assumed further that (a) only the most singular part of $\mathcal{G}$ is needed for long time results, and (b) that this most singular behavior is dominated by the vanishing eigenvalues of the free-streaming operator, i.e., the left side of

Eq. (37), and by the vanishing eigenvalues of the scattering operator, Λ. This is consistent with conventional treatments of transport phenomena derived from the Boltzman equation.[15]

(6) What is not clear is how large the elapsed time t needs to be for these assumptions and approximations to be valid. Computation of the next term in a systematic asymptotic expansion is required to address this issue. Perhaps it is possible to make mean-free-path arguments to assess the validity of these approximation, but that would be another paper.

(7) In computing the multiple integral in Eq. (72) the far-field assumption, Eq. (73), was used, and it was assumed that at the scattering events, the wave field is locally like a plane wave, at least horizontally. Furthermore, the bandwidth of pulses needs to be sufficiently narrow that only a low-order expansion of modal wave numbers in frequency is needed. In obtaining Ellis's result, the expression for U is unevaluated. One can use the ladder approximation, or try to infer U from measurement if the multiple scattering contribution can be neglected.

The multiple scattering result is necessarily more problematic than the single scattering result. However, once one accepts the idea of sound *intensity* diffusing between scattering events, Eqs. (89) and (90) become more understandable, if not more believable. First, the various modes and derivatives appear because the field propagates via the mean field from the source to the various surfaces in a wavelike fashion, and the field propagates from the surface to the receiver also in a wavelike fashion via the mean field. There is a pair of Green's functions for the former and a pair for the latter propagation. Each Green's function contains a sum of products of two modal functions. Hence there are eight modal functions.

The factor $\exp[-(\mathbf{R}_2-\mathbf{R}_1)^2/(4D(t-R_1/v_{gm}-R_2/\times v_{gn}))]/(D(t-R_1/v_{gm}-R_2/v_{gn}))$ in Eq. (89) describes the diffusion of the second moment between scattering events at $\mathbf{R}_1$ and $\mathbf{R}_2$. If the total round trip time is t, and the time to propagate from the source to $\mathbf{R}_2$ is determined by the group velocity v_{gn} and from $\mathbf{R}_1$ to the receiver by the group velocity v_{gm}, this leaves the time $(t-R_1/v_{gm}-R_2/v_{gn})$ to diffuse from $\mathbf{R}_2$ to $\mathbf{R}_1$. The factors $\exp(-2\Delta_m R_1-2\Delta_n R_2)$ describe the decay of the mean field first from the source to $\mathbf{R}_2$ and second from $\mathbf{R}_1$ to the receiver (here co-located with the source). The scattering allows all modes to contribute. The precise form of the diffusion constant, D, requires the detailed analysis leading to Eq. (54). The appearance of the decay constants Σ in Eq. (89) follows from Eq. (57) and the Ward identity–in effect from conservation of energy. All of which is to say that Eq. (89) is understandable, even if the approximations leading to it appear somewhat opaque.

Finally, we note again that the exponential decay rate for multiple scattering is controlled by mechanisms other than surface scattering; the decay arising from surface scattering is contained in ϵ_m and these disappeared from the Bethe–Salpeter equation when the scattering operator Λ was constructed in Eq. (48) and the Ward identity was applied in Eq. (49). The exponential decay rate for single scattering is controlled by a sum of surface scattering and other decay mechanisms.

I have not attempted to include the contribution of maximally crossed diagrams to the scattering. In the limit of no intrinsic scattering these will give rise to a signal that does not decay in time at all because, in this case the diffusion coefficient, D, is proportional to ω. This, means that the sound does not leave the region from which it was generated.[9] It is hard to believe that this can be a significant effect in underwater acoustics, so I have chosen not to investigate the maximally crossed diagrams here.

ACKNOWLEDGMENTS

The work was supported in part by the Office of Naval Reseach. It owes much (more than is indicated by the footnotes) to the clear presentations by A. A. Maradudin in the papers cited below.

APPENDIX A: NONLOCAL IMPEDANCE

This appendix discusses nonlocal impedance boundary conditions. Reference 22 shows that Green's functions, and hence arbitrary fields, in the presence of a single rough boundary can be represented as superpositions of scattering states of the form

$$\psi(\mathbf{R},z)=\int d\mathbf{K}\,d\mathbf{Q}e^{i\mathbf{Q}\cdot\mathbf{R}}[e^{-iq_z z}\delta(\mathbf{Q}-\mathbf{K}) + e^{iq_z z}T(\mathbf{Q}|\mathbf{K})]A(\mathbf{K}). \tag{A1}$$

Here $T(\mathbf{Q}|\mathbf{K})$ is the scattering amplitude for a downgoing plane wave of horizontal wave vector $\mathbf{K}$ to scatter into an upgoing plane wave of horizontal wave vector $\mathbf{Q}$. Impedance boundary conditions relate this field and its z derivative along a horizontal plane. If differentiation and integration can be interchanged, then the z derivative of the field ψ at z is given by

$$\frac{\partial\psi(\mathbf{R},z)}{\partial z}=\int d\mathbf{K}\,d\mathbf{Q}e^{i\mathbf{Q}\cdot\mathbf{R}}(-iq_z)[e^{-iq_z z}\delta(\mathbf{Q}-\mathbf{K}) - e^{iq_z z}T(\mathbf{Q}|\mathbf{K})]A(\mathbf{K}). \tag{A2}$$

Since the amplitudes $A(\mathbf{K})$ appear both in the field and its derivative, there is surely some direct relation between the two. To get at this relation, form the horizontal Fourier transform of the derivative of the field:

$$\frac{\partial\hat{\psi}(\mathbf{Q},z)}{\partial z}\equiv\frac{1}{(2\pi)^2}\int e^{-i\mathbf{Q}\cdot\mathbf{R}}\frac{\partial\psi(\mathbf{R},z)}{\partial z}d\mathbf{R} = \int d\mathbf{K}-iq_z[e^{-iq_z z}\delta(\mathbf{Q}-\mathbf{K}) - e^{iq_z z}T(\mathbf{Q}|\mathbf{K})]A(\mathbf{K}). \tag{A3}$$

For flat surfaces $T(\mathbf{Q}|\mathbf{K})$ is proportional to a δ function and it is a simple matter to solve for A in terms of the vertical derivative. For rough surfaces, in which T is not diagonal in horizontal wave vector, I *assume* that it is still possible to invert (A3) for A in terms of the z derivative of the field. The relationship is linear and must take the form

$$A(\mathbf{K})=\int f(\mathbf{K},\mathbf{Q})[e^{iq_z z}/(-iq_z)]\frac{\partial\hat{\psi}(\mathbf{Q},z)}{\partial z}d\mathbf{Q}. \quad \text{(A4)}$$

The function $f(\mathbf{K},\mathbf{Q})$ is the kernel of the inverse of the operator whose kernel is

$$\delta(\mathbf{Q}-\mathbf{K})-e^{2iq_z z}T(\mathbf{Q}|\mathbf{K}).$$

Formally we can write

$$A=\frac{1}{1-e^{2i\beta z}T}\left(\frac{e^{i\beta z}}{-i\beta}\right)\frac{\partial\hat{\psi}}{\partial z}. \quad \text{(A5)}$$

Substituting Eq. (A4) for A into Eq. (A1) and rearranging the order of integrations and using the inverse Fourier transform gives

$$\psi(\mathbf{R},z)=\int d\mathbf{K}\,d\mathbf{Q}\,d\mathbf{P}\Bigg\{e^{i\mathbf{Q}\cdot\mathbf{R}}[e^{-iq_z z}\delta(\mathbf{Q}-\mathbf{K}) + e^{iq_z z}T(\mathbf{Q}|\mathbf{K})]f(\mathbf{K},\mathbf{P})\frac{e^{ip_z z}}{-ip_z}e^{-i\mathbf{P}\cdot\mathbf{R}'}\Bigg\} \times\frac{\partial\psi(\mathbf{R}',z)}{\partial z}d\mathbf{R}'. \quad \text{(A6)}$$

In this way, the nonlocal impedance of Eq. (1) of the text can be identified as the integral over **K**, **Q**, and **P** of the expression in braces in the equation above. A more formal expression for the impedance is

$$Zi\beta=\frac{1+e^{i\beta z}Te^{i\beta z}}{1-e^{i\beta z}Te^{i\beta z}}. \quad \text{(A7)}$$

Here β is diagonal in horizontal wave vector and gives the vertical component of the wave vector, i.e., $\beta(\mathbf{Q})=\sqrt{\omega^2/c^2-\mathbf{Q}^2}$.

APPENDIX B: THE MEAN FIELD

In this appendix, Eq. (28) of the text is derived. Writing out some of the details of Eq. (25) gives

$$\begin{aligned}&\langle G(\mathbf{Q},z,z_s)\rangle\\ &=[e^+(\mathbf{Q},z),e^-(\mathbf{Q},z)]\frac{1}{\partial E}\langle g\rangle(-\phi)+\Phi(Q,z,z_s)\\ &=[e^+(\mathbf{Q},z),e^-(\mathbf{Q},z)]\frac{1}{\partial E}\langle g\rangle\frac{1}{W(\mathbf{Q})}\begin{pmatrix}e^-(\mathbf{Q},z_s)\\ e^+(\mathbf{Q},z_s)\end{pmatrix}\\ &\quad+\Phi(Q,z,z_s). \quad \text{(B1)}\end{aligned}$$

Here Eqs. (7) and (8) have been used to simplify ϕ. Taking the depth derivative with respect to z_s and first letting $z_s\to z_0$ and then $z_s\to z_1$ gives

$$\begin{aligned}&[\partial_{z_s}\langle G(\mathbf{Q},z,z_s)\rangle|_{z_s=z_0},\partial_{z_s}\langle G(\mathbf{Q},z,z_s)\rangle|_{z_s=z_1}]\\ &=[e^+(\mathbf{Q},z),e^-(\mathbf{Q},z)]\frac{1}{\partial E}\langle g\rangle\frac{1}{W(\mathbf{Q})}\\ &\quad\times\begin{pmatrix}\partial_{z_0}e^-(\mathbf{Q},z_0) & 0\\ 0 & \partial_{z_1}e^+(\mathbf{Q},z_1)\end{pmatrix}. \quad \text{(B2)}\end{aligned}$$

The derivatives of Φ vanish at $z_s=z_0$ and at $z_s=z_0$ because by construction Φ satisfies Neumann boundary conditions. Now Eq. (10) for the Wronskian, $W(\mathbf{Q})$, yields Eq. (28).

Now the role of the effective impedance can also be demonstrated. Equation (B1) can be evaluated first for $z=z_0$ and then for $z=z_0$ to give

$$\begin{pmatrix}\langle G(z_0;z_s)\rangle\\ \langle G(z_1;z_s)\rangle\end{pmatrix}=\left(-E\frac{1}{\partial E}\langle g\rangle+1\right)\phi, \quad \text{(B3)}$$

which we abbreviate as

$$\langle G\rangle=[1-g_0^{-1}\langle g\rangle]\phi. \quad \text{(B4)}$$

Equation (26) of the text allows us to write ϕ in terms of $\partial\langle G\rangle$ which, when combined with the last equation for $\langle G\rangle$, gives

$$\begin{aligned}\langle G\rangle&=-[1-g_0^{-1}\langle g\rangle]\langle g\rangle^{-1}\sigma_3\partial\langle G\rangle\\ &=[g_0^{-1}-\langle g\rangle^{-1}]\sigma_3\partial\langle G\rangle=M\sigma_3\partial\langle G\rangle. \quad \text{(B5)}\end{aligned}$$

Hence M is indeed the impedance operator for the mean field.

APPENDIX C: DERIVATION OF EQS. (43)–(45)

Derivations of Eqs. (43)–(45) of the text are presented here.

In the notation of this paper, the Ward identity given in Ref. 4 is

$$\sum_{\alpha,\beta}[\langle g\rangle_{\alpha,\beta}-\langle g\rangle^*_{\alpha,\beta}]U^{\alpha,\beta;\mu,\nu}=M_{\nu,\mu}-M^*_{\mu,\nu}. \quad \text{(C1)}$$

The Greek indices denote pairs consisting of a horizontal wave vector and a discrete index denoting the upper or lower scattering surface. Using such pairs in Eq. (C1) gives

$$\begin{aligned}&\int d\mathbf{P}\sum_{i_1,i_2}[\langle g\rangle_{i_1,i_2}(\mathbf{P}|\Omega)-\langle g\rangle^*_{i_2,i_1}(\mathbf{P}|\Omega)]\\ &\quad\times U^{i_1,i_2;j_1,j_2}_{\mathbf{P},\mathbf{Q}}(\mathbf{p}=\mathbf{0}|\Omega,0)\\ &\quad=M_{j_2,j_1}(\mathbf{Q}|\Omega)-M_{j_1,j_2}(\mathbf{Q}|\Omega)^*. \quad \text{(C2)}\end{aligned}$$

The difference wave vector **p** is forced to vanish because the mean surface Green's function, $\langle g\rangle$, is diagonal in wave vector. The irreducible vertex function, U, also has a δ function but this is the same as that attached to the full expression for the self-energy, M. The Ward identity requires that the impedance be Hermitian. For penetrable surfaces, for example, fluid–fluid interfaces, the impedance, in general, will not be Hermitian. Its non-Hermiticity reflects the possibility of energy loss to the exterior of the wave guide. If, however, we restrict attention to normal modes and large horizontal wave numbers, the corresponding part of the impedance will be Hermitian. It may be possible to account for the non-Hermitian part of the impedance in what is called intrinsic attenuation, α_m, below, but this is just speculation.

As in the text, it is useful to have the indices i_1 and i_2 refer to eigenvectors of $\langle g\rangle(\mathbf{P})$ rather than surfaces. This is accomplished by inserting an orthogonal transformation and redefining U. Again we argue that it is now the 1,1 elements

of $\langle g\rangle$ that dominate the sum on the left of Eq. (C2), i.e., $1/\lambda(\mathbf{P})$. If the pole approximation, Eq. (39), is used in Eq. (C2), then

$$i\pi\int d\theta_P \sum_m g_m U^{1,1;j_1,j_2}_{k_m,\theta_P;\mathbf{Q}}(\mathbf{0}|\Omega,0)=2i\Sigma_{j_2,j_1}, \tag{C3}$$

where

$$\Sigma_{j_2,j_1}(\mathbf{Q}|\Omega)=\frac{M_{j_2,j_1}(\mathbf{Q}|\Omega)-M_{j_1,j_2}(\mathbf{Q}|\Omega)^*}{2i}. \tag{C4}$$

It is also convenient to define

$$H_{j_2,j_1}(\mathbf{Q}|\Omega)=\frac{M_{j_2,j_1}(\mathbf{Q}|\Omega)+M_{j_1,j_2}(\mathbf{Q}|\Omega)^*}{2}. \tag{C5}$$

Both H and Σ are Hermitian matrices. Furthermore, from its definition, $g_0^{-1}=E(\partial E)^{-1}$, it can be seen that g_0^{-1} is Hermitian in the absence of intrinsic attenuation mechanisms.

We can relate Σ to the imaginary part of the modal wave numbers. Suppose that ψ_0 is an eigenvector of $g_0^{-1}-H$ with eigenvector λ_0. If ψ is the corresponding eigenvector of $\langle g\rangle=g_0^{-1}-M=g_0^{-1}-H-i\Sigma$ with eigenvalue λ, then if Σ is small,

$$\lambda\approx\lambda_0-i\langle\psi_0|\Sigma|\psi_0\rangle\approx\lambda_0-i\Sigma_{1,1}. \tag{C6}$$

Since $\Sigma_{1,1}$ is real, the correction to λ_0 is pure imaginary.

We are interested not so much in the eigenvalue λ as in the zeros of λ, because these are the modal wave numbers. Suppose that $k_m+i\alpha_m$ is a zero of λ_0,

$$\lambda_0(k_m+i\alpha_m)=0. \tag{C7}$$

We can expect a small imaginary part α if there is some small amount of intrinsic damping showing up in a non-Hermitian part of g_0^{-1}. For the zeros of the perturbed eigenvalue write

$$\lambda(k_m+i\alpha_m+i\epsilon_m)=0. \tag{C8}$$

Expanding to first order in ϵ_m gives

$$\lambda(k_m+i\alpha_m)+\frac{\partial\lambda(k_m+i\alpha_m)}{\partial k_m}i\epsilon_m$$

$$=0=-i\Sigma_{1,1}(k_m+i\alpha_m)+\frac{\partial\lambda(k_m+i\alpha)}{\partial k_m}i\epsilon_m, \tag{C9}$$

or

$$\epsilon_m=\frac{1}{\partial\lambda(k_m+i\alpha_m)/\partial k_m}\Sigma_{1,1}(k_m+i\alpha_m). \tag{C10}$$

Here ϵ_m represents the damping of the mth normal mode resulting from scattering of the coherent field at the boundaries of the waveguide. The derivative in Eq. (C10) can be related to other quantities by recalling that near a zero of λ we have written

$$\frac{1}{\lambda(Q)}=\frac{g_m}{Q^2-(k_m+i\Delta_m)^2}\approx\frac{g_m}{2k_m(Q-(k_m+i\Delta_m)}, \tag{C11}$$

where $\Delta_m=\alpha_m+\epsilon_m$. This means that

$$\frac{\partial\lambda(k_m+i\alpha_m)}{\partial k_m}=\frac{2k_m}{g_m}, \tag{C12}$$

and that the damping resulting from scattering is

$$\epsilon_m=\frac{g_m}{2k_m}\Sigma_{1,1}(k_m). \tag{C13}$$

Equation (C11) also gives

$$\mathrm{Im}\,\lambda(k_m)=-\frac{2k_m}{g_m}\Delta_m, \tag{C14}$$

as in the left side of Eq. (43).

Finally, Eq. (45) results from considering the full frequency dependence of the eigenvalue, $\lambda=\lambda(k_m(\Omega)|\Omega)$ absorbing the imaginary contributions into k_m. The condition that k_m be a modal wave number is

$$\lambda(k_m(\Omega)|\Omega)=0. \tag{C15}$$

If the frequency Ω varies, the eigenvector changes both through its explicit dependence on Ω and through the dependence of the wave number on Ω:

$$\frac{\partial\lambda}{\partial k_m}\frac{\partial k_m}{\partial\Omega}+\frac{\partial\lambda}{\partial\Omega}=0, \tag{C16}$$

which implies

$$\frac{\partial\lambda}{\partial\Omega}=\frac{-2k_m}{g_m v_{gm}}. \tag{C17}$$

In writing this last result the definition of the modal group velocity

$$v_{gm}=1/\frac{\partial k_m}{\partial\Omega} \tag{C18}$$

has been used.

[1] R. M. Fitzgerald, A. A. Maradudin, and F. Pincemin, ''Scattering of a scalar wave from a two-dimensional randomly rough Neumann surface,'' Waves Random Media **5**, 381–411 (1995).

[2] A. R. McGurn and A. A. Maradudin, ''Localization effects in the elastic scattering of light from a randomly rough surface,'' J. Opt. Soc. Am. B **4**, 910–926 (1987).

[3] J. A. Sánchez-Gil, A. A. Maradudin, J. Q. Lu, V. D. Freilikher, M. Pustilnik, and I. Yurkevich, ''Scattering of electromagnetic waves from a bounded medium with a random surface,'' Phys. Rev. B **50**, 15353–15368 (1994).

[4] G. Brown, V. Celli, M. Haller, A. A. Maradudin, and A. Marvin, ''Resonant light scattering from a randomly rough surface,'' Phys. Rev. B **31**, 4993–5005 (1985).

[5] H. P. Bucker and H. E. Morris, ''Normal-mode reverberation in channels or ducts,'' J. Acoust. Soc. Am. **44**, 827–828 (1968).

[6] F. Ingenito, ''Scattering from an object in a stratified medium,'' J. Acoust. Soc. Am. **82**, 2051–2059 (1987).

[7] D. D. Ellis, ''A Shallow-water normal mode reverberation model,'' J. Acoust. Soc. Am. **97**, 2804–2814 (1995).

[8] D. H. Berman, ''Computing effective reflection coefficients in layered media,'' J. Acoust. Soc. Am. **101**, 741–748 (1997).

[9] T. R. Kirkpatrick, ''Localization of acoustic waves,'' Phys. Rev. B **31**, 5746–5755 (1985).

[10] A. G. Voronovich, *Wave Scattering from Rough Surfaces* (Springer-Verlag, Berlin, 1994), p. 29 ff.

[11] N. P. Zhuk, O. A. Tret'yakov, and A. G. Yarovoi, ''Relationship of the equivalent impedance of a rough surface to the scattering characteristics,'' Sov. Phys. Acoust. **32**, 247–249 (1986).

[12] N. P. Zhuk, O. A. Tret'yakov, and A. G. Yarovoi, ''Characteristics of the

fluctuation component of a sound field in a layered medium with a rough boundary,'' Sov. Phys. Acoust. **33**, 283–285 (1987).
[13] L. M. Brekhovskikh, *Waves in Layered Media*, translated by R. T. Beyer (Academic, San Diego, 1980). pp. 410–414.
[14] D. Vollhardt and P. Wölfle, ''Diagrammatic, self-consistent treatment of the Anderson localization problem in $d \leqslant 2$ dimensions,'' Phys. Rev. B **22**, 4666–4679 (1980).
[15] J. J. Duderstat and W. R. Martin, *Transport Theory* (Wiley, New York, 1979), p. 238 ff.
[16] D. Livdan and A. A. Lisyansky, ''Diffusion of classical waves in random media with microstructure resonances,'' J. Opt. Soc. Am. A **13**, 844–850 (1996).
[17] A. D. Whalen, *Detection of Signals in Noise* (Academic, Orlando, 1971), pp. 59–60.
[18] T. C. Yang, ''Scattering from boundary protuberances and reverberation imaging,'' J. Acoust. Soc. Am. **93**, 231–242 (1993).
[19] D. G. Crighton, A. P. Dowling, J. E. Ffowcs Williams, M. Heckl, and F. G. Leppington, *Modern Methods in Analytical Acoustics* (Springer-Verlag, Berlin, 1992), pp. 628–630.
[20] R. P. Chapman, ''Sound Scattering in the Ocean,'' in *Underwater Acoustics*, edited by V. M. Albers (Plenum, New York, 1967), Vol. 2, Chap. 9.
[21] H. Schmidt and W. A. Kuperman, ''Spectral representations of rough interface revereberation in stratified ocean waveguides,'' J. Acoust. Soc. Am. **97**, 2199–2209 (1995).
[22] D. H. Berman, ''Completeness of Scattering States for Rough Interfaces,'' Ann. Phys. (N.Y.) **222**, 212–228 (1992).

A complete energy conservation correction for the elastic parabolic equation

Michael D. Collins[a)]
Naval Research Laboratory, Washington, DC 20375

William L. Siegmann
Rensselaer Polytechnic Institute, Troy, New York 12180

(Received 17 January 1997; revised 8 October 1998; accepted 28 October 1998)

A complete energy conservation correction is derived to improve the accuracy of the elastic parabolic equation for range-dependent problems. The correction is complete in the sense that it is valid for problems involving a broad spectrum of horizontal wave numbers. It is a linear condition that associates the incident and transmitted fields on a vertical interface with arrays of point sources having the appropriate energy flux densities. It is a generalization of a complete energy conservation correction for the acoustic parabolic equation [J. Acoust. Soc. Am. **94**, 975–982 (1993)]. © *1999 Acoustical Society of America.* [S0001-4966(99)02002-0]

PACS numbers: 43.30.Ma [SAC-B]

INTRODUCTION

The parabolic equation method is an efficient approach for solving range-dependent propagation problems.[1] Recent topics of interest in parabolic equation modeling include techniques for handling elastic layers[2–5] and conserving energy in range-dependent problems.[6–8] One of the key remaining goals is to develop an approach for accurately handling range-dependent problems involving fluid and elastic layers. In this paper, we resolve part of this problem by deriving a complete energy conservation correction for the elastic parabolic equation.

The parabolic equation method is based on factoring an operator to obtain an outgoing wave equation that can be solved efficiently as an initial value problem in range. The factorization is exact when the medium is range independent. Many range-dependent problems can be solved by approximating the medium as a sequence of range-independent regions, using the parabolic equation method to propagate the field through each region, and neglecting energy that is backscattered at the vertical interfaces between regions. Transmitted fields can be obtained using energy conservation[6–8] and single scattering[9,10] corrections. Energy conservation corrections have proven to be more effective for the acoustic case. The elastic case has not been fully resolved.

Since outgoing wave equations contain only one range derivative, their solutions cannot be forced to satisfy all of the conditions at a vertical interface. Accurate solutions can be obtained by conserving energy flux. An implementation based on the standard expression for this quantity would involve a nonlinear interface condition. Partial energy conservation corrections are linear conditions based on the assumption of a narrow horizontal wave number spectrum. They provide accurate solutions to many acoustics problems.[6,7] It is possible to obtain linear conditions without resorting to the narrow spectrum approximation. The complete energy conservation correction for acoustic media is a linear condition that handles a broad spectrum of horizontal wave numbers.[8]

A partial energy conservation correction has been derived for elastic media.[8] Since this approximation lacks robustness, we have derived a complete energy conservation correction for the elastic case. Although the derivation is based on approximations, the complete correction should be accurate for many range-dependent problems. For the acoustic case, the complete correction associates the incident and transmitted fields with arrays of point sources having the appropriate energy flux densities.[8] A similar interpretation applies to the complete correction for the elastic case. Before deriving the correction, we discuss the elastic parabolic equation, self-starter[11,12] (which is used to interpret the correction), and normal mode solution (which is used to derive the correction).

I. THE ELASTIC PARABOLIC EQUATION

We consider a two-dimensional problem and work in Cartesian coordinates, where z is the depth and the range x is the horizontal distance from a source. A range-dependent elastic waveguide is divided into a sequence of range-independent regions. The equations of motion are solved in each region with the elastic parabolic equation, which is derived in this section. A method for approximating transmitted fields at the vertical interfaces between regions is derived in Sec. IV. The wave speeds c_p and c_s are related to the density ρ and the Lamé parameters λ and μ by $\rho c_p^2 = \lambda + 2\mu$ and $\rho c_s^2 = \mu$. We work in the frequency domain and remove the factor $\exp(-i\omega t)$ from the dependent variables, where ω is the circular frequency and t is time.

The equations of motion,[5]

$$(\lambda+2\mu)\frac{\partial^2\Delta}{\partial x^2}+(\lambda+2\mu)\frac{\partial^2\Delta}{\partial z^2}+\rho\omega^2\Delta+2\frac{\partial\mu}{\partial z}\frac{\partial^2 w}{\partial x^2}+\omega^2\frac{\partial\rho}{\partial z}w+\left(\frac{\partial\lambda}{\partial z}+2\frac{\partial\mu}{\partial z}\right)\frac{\partial\Delta}{\partial z}+\frac{\partial}{\partial z}\left(\frac{\partial\lambda}{\partial z}\Delta\right)+2\frac{\partial}{\partial z}\left(\frac{\partial\mu}{\partial z}\frac{\partial w}{\partial z}\right)=0, \tag{1}$$

a)Electronic mail: collins@ram.nrl.navy.mil

$$\mu \frac{\partial^2 w}{\partial x^2} + \mu \frac{\partial^2 w}{\partial z^2} + \rho\omega^2 w + (\lambda + \mu) \frac{\partial \Delta}{\partial z} + \frac{\partial \lambda}{\partial z} \Delta + 2 \frac{\partial \mu}{\partial z} \frac{\partial w}{\partial z} = 0, \tag{2}$$

are valid in each range independent region, where Δ is the dilatation and w is the vertical displacement. The horizontal displacement u and stresses σ_{xx}, σ_{zz}, and σ_{xz} are related to Δ and w by the equations

$$\frac{\partial u}{\partial x} = \Delta - \frac{\partial w}{\partial z}, \tag{3}$$

$$\sigma_{xx} = (\lambda + 2\mu)\Delta - 2\mu \frac{\partial w}{\partial z}, \tag{4}$$

$$\sigma_{zz} = \lambda \Delta + 2\mu \frac{\partial w}{\partial z}, \tag{5}$$

$$-\frac{\partial \sigma_{xz}}{\partial x} = \frac{\partial \sigma_{zz}}{\partial z} + \rho\omega^2 w = \frac{\partial}{\partial z}(\lambda\Delta) + 2\frac{\partial}{\partial z}\left(\mu \frac{\partial w}{\partial z}\right) + \rho\omega^2 w. \tag{6}$$

The normal stress σ_{zz} and tangential stress σ_{xz} vanish at the boundaries $z=0$ and $z=H$. Placing the depth operators appearing in Eqs. (1) and (2) into the matrices L and M, we obtain

$$L \frac{\partial^2 \mathbf{U}}{\partial x^2} + M\mathbf{U} = \mathbf{0}, \tag{7}$$

$$\mathbf{U} = \begin{pmatrix} \Delta \\ w \end{pmatrix}. \tag{8}$$

The absence of a $\partial/\partial x$ term in Eq. (7) is an advantage for parabolic equation applications, which are based on factoring an operator. Since L and M commute with $\partial/\partial x$ in each range-independent region, we can factor the operator in Eq. (7) to obtain

$$\left(\frac{\partial}{\partial x} + iK\right)\left(\frac{\partial}{\partial x} - iK\right)\mathbf{U} = \mathbf{0}, \tag{9}$$

where $K = (L^{-1}M)^{1/2}$. The outgoing solution of Eq. (9) satisfies the parabolic equation,

$$\frac{\partial \mathbf{U}}{\partial x} = iK\mathbf{U}. \tag{10}$$

The implementation of Eq. (10) is based on the formula

$$\mathbf{U}(x + \Delta x) = \exp(iK\,\Delta x)\mathbf{U}(x), \tag{11}$$

a rational approximation of the operator $\exp(iK\,\Delta x)$, and numerical techniques.[13,14]

II. THE SELF-STARTER

The self-starter[11,12] is an efficient approach for obtaining an initial condition for Eq. (10). In this section, we generalize the self-starter to the case of an arbitrary source. The form of the self-starter provides a physical interpretation of the energy conservation correction. We first consider the case of a medium that consists of homogeneous layers. In each layer, we define the compressional potential ϕ and shear potential ψ so that

$$u = \frac{\partial \phi}{\partial x} - \frac{\partial \psi}{\partial z}, \tag{12}$$

$$w = \frac{\partial \phi}{\partial z} + \frac{\partial \psi}{\partial x}. \tag{13}$$

We place an arbitrary combination of compressional and shear sources at $x=0$. In each layer, the potentials satisfy

$$\frac{\partial^2}{\partial x^2}\begin{pmatrix} \phi \\ \psi \end{pmatrix} + \frac{\partial^2}{\partial z^2}\begin{pmatrix} \phi \\ \psi \end{pmatrix} + \begin{pmatrix} k_p^2 & 0 \\ 0 & k_s^2 \end{pmatrix}\begin{pmatrix} \phi \\ \psi \end{pmatrix} = 2\rho^{-1/2}\omega^{-2}\delta(x)\begin{pmatrix} -iA_p \\ A_s \end{pmatrix}, \tag{14}$$

where $k_p = \omega/c_p$, $k_s = \omega/c_s$, $A_p(z) = 0$ for a shear source, and $A_s(z) = 0$ for a compressional source.

Integrating Eq. (14) over an arbitrarily small range interval about $x=0$ and rearranging, we obtain

$$\lim_{x \to 0^+} \rho\omega^2 \frac{\partial}{\partial x}\begin{pmatrix} \phi \\ \psi \end{pmatrix} = \rho^{1/2}\begin{pmatrix} -iA_p \\ A_s \end{pmatrix}. \tag{15}$$

From Eqs. (2), (3), (12), (13), and (14), we obtain

$$\rho\omega^2 \frac{\partial \phi}{\partial x} = -(\lambda + 2\mu)\frac{\partial}{\partial x}\nabla^2 \phi = -(\lambda + 2\mu)\frac{\partial}{\partial x}\left(\frac{\partial u}{\partial x} + \frac{\partial w}{\partial z}\right) = -(\lambda + 2\mu)\frac{\partial \Delta}{\partial x}, \tag{16}$$

$$\rho\omega^2 \frac{\partial \psi}{\partial x} = -\mu \frac{\partial}{\partial x}\nabla^2 \psi = \mu \frac{\partial}{\partial x}\left(\frac{\partial u}{\partial z} - \frac{\partial w}{\partial x}\right) = (\lambda + 2\mu)\frac{\partial \Delta}{\partial z} + \frac{\partial \lambda}{\partial z}\Delta + \rho\omega^2 w + 2\frac{\partial \mu}{\partial z}\frac{\partial w}{\partial z}. \tag{17}$$

The terms in Eq. (17) that involve derivatives of λ and μ apply to the general case involving inhomogeneous layers. Since there is a range derivative on the right side of Eq. (16) but not Eq. (17), we handle the compressional and shear components separately. Substituting Eqs. (16) and (17) into Eq. (15) and using Eq. (10) to replace the x derivative for the compressional case, we obtain

$$\rho^{-1/2} QK\mathbf{U}_p = \begin{pmatrix} A_p \\ 0 \end{pmatrix}, \tag{18}$$

$$\rho^{-1/2} Q\mathbf{U}_s = \begin{pmatrix} 0 \\ A_s \end{pmatrix}, \tag{19}$$

where $\mathbf{U} = \mathbf{U}_p + \mathbf{U}_s$ and

$$Q = \begin{pmatrix} \lambda + 2\mu & 0 \\ (\lambda + 2\mu)\dfrac{\partial}{\partial z} + \dfrac{\partial \lambda}{\partial z} & \rho\omega^2 + 2\dfrac{\partial \mu}{\partial z}\dfrac{\partial}{\partial z} \end{pmatrix}. \tag{20}$$

For the general case involving inhomogeneous layers, we rearrange Eq. (7) and place compressional and shear source terms on the right side to obtain

$$\frac{\partial^2 \mathbf{U}}{\partial x^2} + K^2 \mathbf{U} = 2i\delta(x) Q^{-1} \begin{pmatrix} \rho^{1/2} A_p \\ 0 \end{pmatrix} + 2i\delta(x) K Q^{-1} \begin{pmatrix} 0 \\ \rho^{1/2} A_s \end{pmatrix}. \tag{21}$$

Integrating Eq. (21) over an arbitrarily small range interval about $x=0$, we obtain

$$\lim_{x \to 0^+} \frac{\partial \mathbf{U}}{\partial x} = iQ^{-1} \begin{pmatrix} \rho^{1/2} A_p \\ 0 \end{pmatrix} + iKQ^{-1} \begin{pmatrix} 0 \\ \rho^{1/2} A_s \end{pmatrix}. \tag{22}$$

We obtain Eqs. (18) and (19) from Eq. (22) by using Eq. (10) to replace $\partial/\partial x$ on the left side and handling the terms on the right side separately. Rearranging Eqs. (18) and (19) and applying Eq. (11), we obtain

$$\mathbf{U}_p(x) = K^{-1} \exp(iKx) Q^{-1} \begin{pmatrix} \rho^{1/2} A_p \\ 0 \end{pmatrix}, \tag{23}$$

$$\mathbf{U}_s(x) = \exp(iKx) Q^{-1} \begin{pmatrix} 0 \\ \rho^{1/2} A_s \end{pmatrix}. \tag{24}$$

To avoid singularities at the source location, the self-starter can be implemented using Eqs. (23) and (24) at $x = x_0$, where x_0 is comparable to a wavelength. In cylindrical geometry, it is necessary to account for cylindrical spreading and apply the correction factor $K^{1/2}$ to the self-starter.[11,12] For this case, Eqs. (18) and (19) become

$$\rho^{-1/2} Q K^{1/2} \mathbf{U}_p = \begin{pmatrix} A_p \\ 0 \end{pmatrix}, \tag{25}$$

$$\rho^{-1/2} Q K^{-1/2} \mathbf{U}_s = \begin{pmatrix} 0 \\ A_s \end{pmatrix}. \tag{26}$$

III. THE NORMAL MODE SOLUTION

In this section, we describe the normal mode solution of Eq. (21). The properties of this solution and the projection operator associated with the normal modes are used to derive the energy conservation correction in the following section. The depth separated eigenvalue problem for Eq. (21) is

$$K^2 \mathbf{U}_j = k_j^2 \mathbf{U}_j, \tag{27}$$

$$\mathbf{U}_j = \begin{pmatrix} \Delta_j \\ w_j \end{pmatrix}, \tag{28}$$

where $\mathbf{U}_j$ and k_j^2 are the jth mode and eigenvalue.

The projection operator associated with the normal modes is defined in terms of the displacements and stresses.[15–17] From Eqs. (3), (4), and (6), we obtain

$$\begin{pmatrix} \sigma_{xx} \\ w \end{pmatrix} = R\mathbf{U}, \tag{29}$$

$$\frac{\partial}{\partial x} \begin{pmatrix} u \\ -\sigma_{xz} \end{pmatrix} = S\mathbf{U}, \tag{30}$$

$$R = \begin{pmatrix} \lambda + 2\mu & -2\mu \dfrac{\partial}{\partial z} \\ 0 & 1 \end{pmatrix}, \tag{31}$$

$$S = \begin{pmatrix} 1 & -\dfrac{\partial}{\partial z} \\ \dfrac{\partial}{\partial z}\lambda & 2\dfrac{\partial}{\partial z}\mu\dfrac{\partial}{\partial z} + \rho\omega^2 \end{pmatrix}. \tag{32}$$

The projection operator is defined by

$$(\mathbf{U}, \tilde{\mathbf{U}}) = \int_0^H (R\mathbf{U})^t S \tilde{\mathbf{U}}\, dz, \tag{33}$$

where $\mathbf{U}$ and $\tilde{\mathbf{U}}$ are arbitrary and the superscript t denotes the transpose. In the Appendix, we show that the projection operator is symmetric and that the modes can be normalized so that

$$(\mathbf{U}_i, \mathbf{U}_j) = \delta_{ij}, \tag{34}$$

for distinct eigenvalues.

Assuming continuous depth dependence and applying integration by parts to Eq. (33), we obtain

$$(\mathbf{U}, \tilde{\mathbf{U}}) = -2\mu w \left(\tilde{\Delta} - \frac{\partial \tilde{w}}{\partial z} \right) \Big|_0^H + \int_0^H \mathbf{U}^t T \tilde{\mathbf{U}}\, dz, \tag{35}$$

$$T = \begin{pmatrix} \lambda + 2\mu & -(\lambda + 2\mu)\dfrac{\partial}{\partial z} \\ \dfrac{\partial}{\partial z}(\lambda + 2\mu) & \rho\omega^2 \end{pmatrix}. \tag{36}$$

An arbitrary field can be expressed in terms of the normal modes as

$$\mathbf{U} = \sum_j a_j \mathbf{U}_j, \tag{37}$$

$$a_j = (\mathbf{U}, \mathbf{U}_j). \tag{38}$$

For the compressional line source $A_p(z) = \delta(z - z_0)$ in a homogeneous layer, it follows from Eqs. (23), (35), and (38) that

$$a_j = \omega^{-2} k_j \rho^{-1/2} (\lambda + 2\mu) \Delta_j \exp(ik_j x)\big|_{z=z_0}. \tag{39}$$

For the shear line source $A_s(z) = \delta(z - z_0)$, in a homogeneous layer it follows from Eqs. (24), (35), and (38) that

$$a_j = \omega^{-2} \rho^{-1/2} \left((\lambda + 2\mu) \frac{\partial \Delta_j}{\partial z} + \rho\omega^2 w_j \right) \exp(ik_j x) \Big|_{z=z_0}. \tag{40}$$

The quantities appearing on the right sides of Eqs. (39) and (40) are proportional to the entries of $Q\mathbf{U}_j$, which are the compressional and shear parts of the mode.

IV. ENERGY CONSERVATION

In this section, we derive a method for approximating transmitted fields across vertical interfaces. To simplify the derivation, we assume that the elastic parameters are sufficiently smooth so that integration by parts can be performed without introducing interface terms, range dependence occurs away from $z=0$ and $z=H$ so that only a small error is introduced by ignoring boundary terms that arise from integration by parts (i.e., the boundary terms are nearly equal on

each side of a vertical interface), and the imaginary parts of the Lamé parameters (which account for attenuation) are small perturbations.

The energy flux through a vertical interface[18] is proportional to

$$E = \mathrm{Im} \int_0^H (u^* \sigma_{xx} + w^* \sigma_{xz}) dz. \tag{41}$$

Rearranging Eq. (41), we obtain

$$E = -\mathrm{Im} \int_0^H (u \sigma_{xx}^* - w^* \sigma_{xz}) dz. \tag{42}$$

From Eqs. (10) and (30), we obtain

$$\begin{pmatrix} u \\ -\sigma_{xz} \end{pmatrix} = -iSK^{-1}\mathbf{U}. \tag{43}$$

From Eqs. (29), (42), and (43), we obtain

$$E = \mathrm{Re} \int_0^H (R\mathbf{U})^* SK^{-1}\mathbf{U}\, dz. \tag{44}$$

To further simplify the derivation, we assume that $\mathbf{U}$ is dominated by propagating modes. Since the attenuation is assumed to be small, the imaginary parts of these modes and the corresponding eigenvalues are perturbations that can be neglected. From the modal representation, the properties of the modes, and Eq. (44), we obtain

$$E = \int_0^H (RK^{-1/2}\mathbf{U})^* SK^{-1/2}\mathbf{U}\, dz. \tag{45}$$

Applying integration by parts to Eq. (45) and neglecting boundary terms, we obtain

$$E = \int_0^H (K^{-1/2}\mathbf{U})^* T(K^{-1/2}\mathbf{U}) dz. \tag{46}$$

To simplify the integrand in Eq. (46), we apply the factorization $T = \tilde{G}\, DG$, where

$$\tilde{G} = \begin{pmatrix} 1 & -(\lambda+2\mu)\dfrac{\partial}{\partial z}\dfrac{1}{\rho\omega^2} \\ 0 & 1 \end{pmatrix}, \tag{47}$$

$$D = \begin{pmatrix} (\lambda+2\mu)\left(1 + \dfrac{\partial}{\partial z}\dfrac{1}{\rho\omega^2}\dfrac{\partial}{\partial z}(\lambda+2\mu)\right) & 0 \\ 0 & \rho\omega^2 \end{pmatrix}, \tag{48}$$

$$G = \begin{pmatrix} 1 & 0 \\ \dfrac{1}{\rho\omega^2}\dfrac{\partial}{\partial z}(\lambda+2\mu) & 1 \end{pmatrix}. \tag{49}$$

Substituting the factorization into Eq. (46), performing integration by parts, and neglecting boundary terms, we obtain

$$E = \int_0^H (GK^{-1/2}\mathbf{U})^* D(GK^{-1/2}\mathbf{U}) dz. \tag{50}$$

To further simplify the derivation, we consider the limit of gradual depth dependence and neglect terms involving depth derivatives of the material properties to obtain

$$\Delta + \frac{\lambda+2\mu}{\rho\omega^2}\frac{\partial^2\Delta}{\partial z^2} = -\frac{\lambda+2\mu}{\rho\omega^2}\frac{\partial^2\Delta}{\partial x^2} = \frac{\lambda+2\mu}{\rho\omega^2}K^2\Delta, \tag{51}$$

where $K^\gamma\Delta$ and $K^\gamma w$ denote the entries of $K^\gamma\mathbf{U}$ and γ is arbitrary. From Eqs. (48), (49), (50), and (51), we obtain

$$E = \omega^{-2}\int_0^H (|A_p|^2 + |A_s|^2) dz, \tag{52}$$

$$A_p = \rho^{-1/2}(\lambda+2\mu)K^{1/2}\Delta, \tag{53}$$

$$A_s = \rho^{-1/2}\left((\lambda+2\mu)\frac{\partial}{\partial z}(K^{-1/2}\Delta) + \rho\omega^2 K^{-1/2} w\right). \tag{54}$$

Energy can be conserved across a vertical interface by conserving A_p and A_s across the interface. These quantities are closely related to the potentials. The quantity A_p reduces to the quantity conserved in the complete correction for the acoustic case.[8]

The implementation of the correction involves the solution of two boundary value problems. The incident field $\mathbf{U}_a$ propagates in region a. The transmitted field $\mathbf{U}_b$ propagates on the other side of the vertical interface in region b. We compute A_p and A_s using the equations

$$\begin{pmatrix} A_p \\ B_s \end{pmatrix} = \rho_a^{-1/2} Q_a K_a^{1/2}\mathbf{U}_a, \tag{55}$$

$$\begin{pmatrix} B_p \\ A_s \end{pmatrix} = \rho_a^{-1/2} Q_a K_a^{-1/2}\mathbf{U}_a. \tag{56}$$

We discard the quantities B_p and B_s, which are defined by Eqs. (55) and (56), and compute $\mathbf{U}_b = \mathbf{U}_p + \mathbf{U}_s$ using the equations

$$\rho_b^{-1/2} Q_b K_b^{1/2}\mathbf{U}_p = \begin{pmatrix} A_p \\ 0 \end{pmatrix}, \tag{57}$$

$$\rho_b^{-1/2} Q_b K_b^{-1/2}\mathbf{U}_s = \begin{pmatrix} 0 \\ A_s \end{pmatrix}. \tag{58}$$

As in the acoustic case,[8] the complete correction is related to the self-starter. Comparing Eqs. (57) and (58) with Eqs. (25) and (26), we observe that the field is associated with arrays of compressional and shear point sources that have the appropriate energy flux densities. This physical interpretation suggests that the complete correction should provide accurate solutions for many problems despite the assumptions that were made in the derivation. The solutions of Eqs. (57) and (58) can be obtained using the approach for implementing the self-starter.

Generalizations of partial corrections for the acoustic case can be obtained by making approximations in Eqs. (53) and (54). By applying the approximation $K \cong k_0$, which was used in Ref. 6 for the acoustic case, the conserved quantity is reduced to $\rho^{-1/2} Q\mathbf{U}$. A natural generalization of the approximation $K \cong k_p$, which was used in Ref. 7 for the acoustic case, is to conserve the quantities

$$\tilde{A}_p = \rho^{-1/2} c_p^{-1/2}(\lambda+2\mu)\Delta, \tag{59}$$

$$\tilde{A}_s = \rho^{-1/2} c_s^{1/2}\left((\lambda+2\mu)\frac{\partial\Delta}{\partial z} + \rho\omega^2 w\right). \tag{60}$$

The quantity $\tilde{A}_p$ is conserved in the partial correction of Ref. 8, which provides improved accuracy. The partial corrections do not require the approximation of the fourth root of an operator or the separate treatment of the compressional and shear components. The partial correction involving c_p and c_s should provide greater accuracy, as it does in the acoustic case.

V. CONCLUSION

We have derived a complete energy conservation correction for the elastic parabolic equation. With this improvement, the elastic parabolic equation should be accurate for many range-dependent problems. The correction is valid for problems involving a broad spectrum of horizontal wave numbers. As in the acoustic case, the incident and transmitted fields are associated with arrays of point sources having the appropriate energy flux densities. The correction is based on the assumption of gradual range dependence and predicts that energy does not couple between shear and compressional waves across a vertical interface in this limit. The next logical step in the development of the elastic parabolic equation is to implement the corrections derived in Sec. IV. This might require special rational approximations to avoid instabilities and a formulation in a different set of dependent variables[8] to facilitate the treatment of sloping interfaces.

ACKNOWLEDGMENT

This work was supported by the Office of Naval Research.

APPENDIX: ORTHOGONALITY OF THE MODES

We show that the modes are orthogonal with respect to the projection operator for an arbitrary stratified elastic medium. We first show that the projection operator is symmetric for problems involving continuous depth dependence. From Eqs. (31), (32), and (33), we obtain

$$(\mathbf{U},\tilde{\mathbf{U}}) = \int_0^H \left\{ \left[(\lambda+2\mu)\Delta - 2\mu \frac{\partial w}{\partial z} \right] \left(\tilde{\Delta} - \frac{\partial \tilde{w}}{\partial z} \right) + w \left[\frac{\partial}{\partial z}(\lambda \tilde{\Delta}) + 2 \frac{\partial}{\partial z} \left(\mu \frac{\partial \tilde{w}}{\partial z} \right) + \rho \omega^2 \tilde{w} \right] \right\} dz. \tag{A1}$$

Expanding the terms in Eq. (A1) and rearranging, we obtain

$$(\mathbf{U},\tilde{\mathbf{U}}) = \int_0^H \left[(\lambda+2\mu)\Delta\tilde{\Delta} + \rho\omega^2 w\tilde{w} - 2\mu \left(\Delta \frac{\partial \tilde{w}}{\partial z} + \tilde{\Delta} \frac{\partial w}{\partial z} \right) + 2\mu \frac{\partial w}{\partial z} \frac{\partial \tilde{w}}{\partial z} - \lambda \Delta \frac{\partial \tilde{w}}{\partial z} + w \frac{\partial}{\partial z}(\lambda \tilde{\Delta}) + 2w \frac{\partial}{\partial z} \left(\mu \frac{\partial \tilde{w}}{\partial z} \right) \right] dz. \tag{A2}$$

Applying integration by parts to Eq. (A2), we obtain

$$(\mathbf{U},\tilde{\mathbf{U}}) = w \left(\lambda \tilde{\Delta} + 2\mu \frac{\partial \tilde{w}}{\partial z} \right) \Bigg|_0^H + \int_0^H \left[(\lambda+2\mu)\Delta\tilde{\Delta} + \rho\omega^2 w\tilde{w} - (\lambda+2\mu) \left(\Delta \frac{\partial \tilde{w}}{\partial z} + \tilde{\Delta} \frac{\partial w}{\partial z} \right) \right] dz. \tag{A3}$$

Since $\sigma_{zz}=0$ at $z=0$ and $z=H$, the boundary terms vanish in Eq. (A3). From the symmetry of the integrand in Eq. (A3), we conclude that $(\mathbf{U},\tilde{\mathbf{U}})=(\tilde{\mathbf{U}},\mathbf{U})$. Since the boundary terms in Eq. (A3) involve w and σ_{zz}, which are continuous across horizontal interfaces, we conclude that symmetry holds for problems involving piecewise continuous depth dependence.

To simplify the remaining analysis, we approximate (to arbitrary accuracy) a waveguide involving piecewise continuous depth variations in the elastic properties with a waveguide involving N homogeneous layers. In each layer, the ith normal mode satisfies

$$k_i^2 \Delta_i = \frac{d^2\Delta_i}{dz^2} + \frac{\rho\omega^2}{\lambda+2\mu}\Delta_i, \tag{A4}$$

$$k_i^2 w_i = \frac{\lambda+\mu}{\mu}\frac{d\Delta_i}{dz} + \frac{d^2 w_i}{dz^2} + \frac{\rho\omega^2}{\mu} w_i. \tag{A5}$$

Substituting two arbitrary modes into Eq. (35) and using Eqs. (A4) and (A5), we obtain

$$k_i^2(\mathbf{U}_i,\mathbf{U}_j) = -2\sum_{m=1}^{N-1} \left((\lambda+\mu)\frac{d\Delta_i}{dz} + \mu\frac{d^2 w_i}{dz^2} + \rho\omega^2 w_i \right) \left(\Delta_j - \frac{dw_j}{dz} \right) \Bigg|_{z_m}^{z_{m+1}} + \sum_{m=1}^{N-1} \int_{z_m}^{z_{m+1}} \left[\left((\lambda+2\mu)\frac{d^2\Delta_i}{dz^2} + \rho\omega^2\Delta_i \right) \times \left(\Delta_j - \frac{dw_j}{dz} \right) + \left(\frac{\lambda+\mu}{\mu}\frac{d\Delta_i}{dz} + \frac{d^2 w_i}{dz^2} + \frac{\rho\omega^2}{\mu} w_i \right) \left((\lambda+2\mu)\frac{d\Delta_j}{dz} + \rho\omega^2 w_j \right) \right] dz, \tag{A6}$$

where the mth layer lies within $z_m < z < z_{m+1}$.

Expanding the terms in Eq. (A6) and applying integration by parts, we obtain

$$k_i^2(\mathbf{U}_i,\mathbf{U}_j) = -\sum_{m=1}^{N-1}\left[\rho\omega^2 w_j\left(\Delta_i - \frac{dw_i}{dz}\right) + \left(\lambda\frac{d\Delta_i}{dz} + 2\mu\frac{d^2w_i}{dz^2} + 2\rho\omega^2 w_i\right)\left(\Delta_j - \frac{dw_j}{dz}\right)\right]\Bigg|_{z_m}^{z_{m+1}}$$

$$+\sum_{m=1}^{N-1}\int_{z_m}^{z_{m+1}}\left[\rho\omega^2\left(\Delta_i\Delta_j - \frac{dw_i}{dz}\frac{dw_j}{dz} + \frac{\rho\omega^2}{\mu}w_i w_j\right)\right.$$

$$\left.+(\lambda+2\mu)\left(\frac{d\Delta_i}{dz}\frac{d^2w_j}{dz^2} + \frac{d\Delta_j}{dz}\frac{d^2w_i}{dz^2} + \frac{\lambda}{\mu}\frac{d\Delta_i}{dz}\frac{d\Delta_j}{dz}\right) + \frac{(\lambda+2\mu)\rho\omega^2}{\mu}\left(w_i\frac{d\Delta_j}{dz} + w_j\frac{d\Delta_i}{dz}\right)\right]dz. \tag{A7}$$

We use the symmetry of the integrand in Eq. (A7) and a similar expression for $k_j^2(\mathbf{U}_j,\mathbf{U}_i)$ to obtain

$$k_i^2(\mathbf{U}_i,\mathbf{U}_j) - k_j^2(\mathbf{U}_j,\mathbf{U}_i) = \sum_{m=1}^{N-1}\left[\left(\lambda\frac{d\Delta_j}{dz} + 2\mu\frac{d^2w_j}{dz^2} + \rho\omega^2 w_j\right)\left(\Delta_i - \frac{dw_i}{dz}\right)\right.$$

$$\left.-\left(\lambda\frac{d\Delta_i}{dz} + 2\mu\frac{d^2w_i}{dz^2} + \rho\omega^2 w_i\right)\left(\Delta_j - \frac{dw_j}{dz}\right)\right]\Bigg|_{z_m}^{z_{m+1}}. \tag{A8}$$

The interface and boundary terms in Eq. (A8) involve the x derivatives of σ_{xz} and u. The interface terms cancel because σ_{xz} and u are continuous across interfaces. The boundary terms vanish because $\sigma_{xz}=0$ at $z=0$ and $z=H$. We therefore obtain

$$0 = k_i^2(\mathbf{U}_i,\mathbf{U}_j) - k_j^2(\mathbf{U}_j,\mathbf{U}_i)$$

$$= (k_i^2 - k_j^2)(\mathbf{U}_i,\mathbf{U}_j) \Rightarrow (\mathbf{U}_i,\mathbf{U}_j) = \delta_{ij}. \tag{A9}$$

The second equality in Eq. (A9) follows from the symmetry of the projection operator, which we demonstrated using the assumption that σ_{zz} and w are continuous across interfaces and that $\sigma_{zz}=0$ at $z=0$ and $z=H$. All of the interface and boundary conditions were therefore used to arrive at Eq. (A9).

[1] F. B. Jensen, W. A. Kuperman, M. B. Porter, and H. Schmidt, *Computational Ocean Acoustics* (American Institute of Physics, New York, 1994), pp. 343–412.

[2] R. R. Greene, ''A high-angle one-way wave equation for seismic wave propagation along rough and sloping interfaces,'' J. Acoust. Soc. Am. **77**, 1991–1998 (1985).

[3] M. D. Collins, ''A higher-order parabolic equation for wave propagation in an ocean overlying an elastic bottom,'' J. Acoust. Soc. Am. **86**, 1459–1464 (1989).

[4] B. T. R. Wetton and G. H. Brooke, ''One-way wave equations for seismoacoustic propagation in elastic waveguides,'' J. Acoust. Soc. Am. **87**, 624–632 (1990).

[5] M. D. Collins, ''Higher-order parabolic approximations for accurate and stable elastic parabolic equations with application to interface wave propagation,'' J. Acoust. Soc. Am. **89**, 1050–1057 (1991).

[6] M. B. Porter, F. B. Jensen, and C. M. Ferla, ''The problem of energy conservation in one-way models,'' J. Acoust. Soc. Am. **89**, 1058–1067 (1991).

[7] M. D. Collins and E. K. Westwood, ''A higher-order energy-conserving parabolic equation for range-dependent ocean depth, sound speed, and density,'' J. Acoust. Soc. Am. **89**, 1068–1075 (1991).

[8] M. D. Collins, ''An energy-conserving parabolic equation for elastic media,'' J. Acoust. Soc. Am. **94**, 975–982 (1993).

[9] M. D. Collins and R. B. Evans, ''A two-way parabolic equation for acoustic backscattering in the ocean,'' J. Acoust. Soc. Am. **91**, 1357–1368 (1992).

[10] J. T. Goh and H. Schmidt, ''A hybrid coupled wave-number integration approach to range-dependent seismoacoustic modeling,'' J. Acoust. Soc. Am. **100**, 1409–1420 (1996).

[11] M. D. Collins, ''A self-starter for the parabolic equation method,'' J. Acoust. Soc. Am. **92**, 2069–2074 (1992).

[12] R. J. Cederberg and M. D. Collins, ''Application of an improved self-starter to geoacoustic inversion,'' IEEE J. Ocean Eng. **22**, 102–109 (1997).

[13] M. D. Collins, ''A split-step Padé solution for parabolic equation method,'' J. Acoust. Soc. Am. **93**, 1736–1742 (1993).

[14] M. D. Collins, ''Generalization of the split-step Padé solution,'' J. Acoust. Soc. Am. **96**, 382–385 (1994).

[15] I. Herrera, ''Contribution to the linearised theory of surface wave transmission,'' J. Geophys. Res. **69**, 4791–4800 (1964).

[16] A. McGarr and L. E. Alsop, ''Transmission and reflection of Rayleigh waves at vertical boundaries,'' J. Geophys. Res. **72**, 2169–2180 (1967).

[17] B. L. N. Kennett, ''Guided wave propagation in laterally varying media—I. Theoretical development,'' Geophys. J. R. Astron. Soc. **79**, 235–255 (1984).

[18] A. Ben-Menahem and S. J. Singh, *Seismic Waves and Sources* (Springer-Verlag, New York, 1981), p. 31.

Normal mode oscillation of a sphere with solid–gas–solid structure

H. Oda[a] and I. Suzuki
Department of Earth Sciences, Okayama University, Okayama 700, Japan

(Received 2 March 1998; revised 19 October 1998; accepted 20 October 1998)

A free oscillation study was made for a heterogeneous sphere with three-layered spherical shell structure composed of an inner spherical sample, middle gas, and outer solid layers in order to apply resonant sphere technique (RST) to elasticity measurements at high pressures. The spheroidal modes of the sphere are classified into ''sample,'' ''gas,'' and ''container'' modes, whose strain energy distributions are localized in the sample, gas, and outer layers, respectively. The sample modes, whose frequencies provide information about the elastic constants of the spherical sample, are more strongly excited than the gas and container modes when putting a vibrational source on the surface of spherical sample in the three-layered sphere and measuring the resonance spectrum on the sample sphere. The localization of strain energy is due to a large difference in acoustic impedance between gas and solid layers. All the resonant frequencies increase with increasing pressure in the gas layer, but the pressure derivatives of resonant frequencies of gas modes are larger than those of sample and container modes. Thus the pressure curves of gas modes frequently intersect those of sample and container modes. At pressures where the sample or container modes intersect the gas modes, modal interchange takes place only between spheroidal modes of ${}_nS_l$ and ${}_{n'}S_{l'}$ satisfying the conditions of $l=l'$ and $n-n'=\pm 1$. To avoid such an interchange, the gas layer should be kept thin. © *1999 Acoustical Society of America.* [S0001-4966(99)01202-3]

PACS numbers: 43.35.Cg [HEB]

INTRODUCTION

The elastic constants of the Earth's materials provide us with important information regarding the structure and composition of the Earth's interior. It is especially important to investigate effects of pressure and temperature on the elastic constants in material science and earth science. Consequently, a number of methods have been developed and applied for measuring the elastic constants of solids. The resonance method is a technique to determine the elastic constants from the measured resonance spectrum of a vibrating solid. The method is classified into several kinds, depending on a specimen's shape used for the spectral measurements. In particular, the method using a spherical specimen, which is called ''resonant sphere technique'' (RST), has been successfully applied to elasticity measurements of anisotropic materials at room temperature and ambient pressure (e.g., Suzuki *et al.*, 1992; Oda *et al.*, 1994). The RST has merit in that it is amenable to quite small specimens, i.e., specimens with dimensions less than 1 mm. Furthermore, the ''buffer method'' was devised for applying the resonance method to the elasticity measurements at high temperatures (Goto and Anderson, 1988). This method has been employed to trace the temperature variations of elastic constants of solids by rectangular parallelepiped resonance (RPR) method (e.g., Isaak *et al.*, 1992). The first application of the buffer method to RST was made to measure the elastic constants of calcium oxide specimen up to 1200 K (Oda *et al.*, 1992). A more complete compendium of the available high-temperature elasticity data from the resonance technique is found in Anderson and Isaak (1995).

The cavity resonance method (CRM) was proposed by Ohno *et al.* (1991) for elasticity measurements of solids by RST at high pressures. In the CRM, a spherical specimen is placed in the center of a spherical container which is filled by pressurized gas to compress the specimen. The resonance spectrum of the spherical specimen is then measured under hydrostatic pressure. Recently Isaak *et al.* (1998) presented a method to evaluate the pressure effects on the rigidity modulus that take into account the finite viscosity of the pressurizing gas. Their study addressed only the pure toroidal modes. We assumed zero gas viscosity, but extend the theory to spheroidal modes where gas viscosity is less important. Thus our study provides the means by which pressure effects on compressional moduli may ultimately be obtained from RST.

In order to determine the elastic constants from resonant frequencies of a spherical sample vibrating in pressurized gas, it is necessary to account for frequency shifts due to small deformations of the spherical sample by hydrostatic pressure and due to exchange of vibrational energy from the spherical sample to the gas layer. The first effect on the frequencies can be easily evaluated, but the latter effect is more problematic. We treat the sample oscillation in a pressurizing gas as the free oscillation of a three-layered sphere in which an inner spherical solid specimen is surrounded by a high-pressure gas layer and an outer solid layer. Because it is possible to calculate the free oscillation frequencies for a radially heterogeneous sphere with solid–gas–solid configuration, the elastic constants are determined in the usual way by minimizing, in a least squares sense, the differences be-

[a]Electronic mail: lfee0688@cc.okayama-u.ac.jp

tween measured and computed frequencies of the sample mode oscillations of the three-layered sphere. However, the sample mode oscillations have not been studied in detail for a sphere with solid–gas–solid configuration. Since the configuration is similar to that of the deep Earth, inner core (solid)–outer core (fluid)–mantle (solid), our study is of broader interest than the immediate problem of using RST to determine the pressure effects of elasticity.

We investigate how the sample mode oscillations are affected by increasing pressure in the gas layer of the three-layered sphere, and discuss problems in identifying sample oscillation modes under pressure. Furthermore, we point out the optimal conditions for correctly measuring the resonance spectrum of the inner spherical specimen by CRM.

I. THEORETICAL BACKGROUND

Free oscillations of a radially heterogeneous sphere with isotropic elasticity are classified into toroidal and spheroidal modes, and their solutions are numerically obtained for each mode. Here we briefly review the theory to calculate the free oscillation frequencies of the elastically isotropic sphere with solid–gas–solid structure, assuming that the viscosity in gas layer is zero. According to Takeuchi and Saito (1972), the equation of motion of an elastic body in spherical coordinate (r,θ,ϕ) is given by

$$\boldsymbol{\rho}\frac{\partial^2\mathbf{u}}{\partial t^2}=(\operatorname{div}\mathbf{T}_r,\operatorname{div}\mathbf{T}_\theta,\operatorname{div}\mathbf{T}_\phi)+\frac{1}{r}(-T_{\theta\theta}-T_{\phi\phi},\ T_{r\theta}-T_{\phi\phi}\cot\theta,T_{\phi r}+T_{\theta\phi}\cot\theta), \tag{1}$$

where ρ is density, $\mathbf{u}$ is the displacement vector, and $\mathbf{T}_r$, $\mathbf{T}_\theta$, and $\mathbf{T}_\phi$ denote stress vectors acting across the planes normal to the r, θ, ϕ axes. When the origin of the spherical coordinates is at the center of a sphere, the displacement vector $\mathbf{u}$ and stress vector $\mathbf{T}_r$ of the freely oscillating sphere can be expressed by

$$\begin{aligned}\mathbf{u}&=ry_1(r)\boldsymbol{\nabla}\times[\mathbf{r}Y_l^m(\theta,\phi)],\\ \mathbf{T}_r&=ry_2(r)\boldsymbol{\nabla}\times[\mathbf{r}Y_l^m(\theta,\phi)]\end{aligned} \tag{2}$$

for toroidal modes and

$$\begin{aligned}\mathbf{u}&=y_1(r)[\mathbf{r}Y_l^m(\theta,\phi)]+ry_3(r)\boldsymbol{\nabla}[Y_l^m(\theta,\phi)],\\ \mathbf{T}_c&=y_2(r)[\mathbf{r}Y_l^m(\theta,\phi)]+ry_4(r)\boldsymbol{\nabla}[Y_l^m(\theta,\phi)]\end{aligned} \tag{3}$$

for spheroidal modes, where $Y_l^m(\theta,\phi)$ is the spherical harmonic function specified by angular order, l, and azimuthal order, m, and $\mathbf{r}$ is the unit vector in the radial direction. The symbol ''$\times$'' denotes cross product of two vectors and $\boldsymbol{\nabla}$ is defined by

$$\boldsymbol{\nabla}=\left(\frac{\partial}{\partial r},\frac{1}{r}\frac{\partial}{\partial\theta},\frac{1}{r\sin\theta}\frac{\partial}{\partial\phi}\right). \tag{4}$$

Therefore the problem is to find radial eigenfunctions $y_1(r)$, $y_2(r)$, $y_3(r)$, and $y_4(r)$ satisfying the equation of motion.

Equation (1) gives the motion for the radially heterogeneous sphere and can be expressed in a simple form by using $y_1(r)$, $y_2(r)$, $y_3(r)$, and $y_4(r)$:

$$\frac{d\mathbf{y}}{dr}=\mathbf{A}(r)\mathbf{y}(r). \tag{5}$$

The motion-stress vectors $\mathbf{y}(r)$ are given by

$$\begin{aligned}\mathbf{y}(r)&=[y_1(r),y_2(r)]^t,\\ \mathbf{y}(r)&=[y_1(r),y_2(r),y_3(r),y_4(r)]^t\end{aligned} \tag{6}$$

for toroidal and spheroidal modes, respectively, and ''t'' means the transpose of the matrix. The coefficient matrix $\mathbf{A}(r)$ is written as

$$\mathbf{A}(r)=\begin{bmatrix}\dfrac{1}{r} & \dfrac{1}{\mu}\\ \dfrac{\mu(l-1)(l+2)}{r^2}-\omega^2\rho & -\dfrac{3}{r}\end{bmatrix} \tag{7}$$

for toroidal modes, and

$$\mathbf{A}(r)=\begin{bmatrix}-\dfrac{2\lambda}{(\lambda+2\mu)r} & \dfrac{1}{\lambda+2\mu} & \dfrac{\lambda l(l+1)}{(\lambda+2\mu)r} & 0\\ -\omega^2\rho+\dfrac{4\mu(3\lambda+2\mu)}{(\lambda+2\mu)r^2} & \dfrac{-4\mu}{(\lambda+2\mu)r} & -\dfrac{2\mu(3\lambda+2\mu)l(l+1)}{(\lambda+2\mu)r^2} & \dfrac{l(l+1)}{r}\\ -\dfrac{1}{r} & 0 & \dfrac{1}{r} & \dfrac{1}{\mu}\\ -\dfrac{2\mu(3\lambda+2\mu)}{(\lambda+2\mu)r^2} & -\dfrac{\lambda}{(\lambda+2\mu)r} & -\omega^2\rho+\dfrac{4\mu(\lambda+\mu)l(l+1)}{(\lambda+2\mu)r^2}-\dfrac{2\mu}{r^2} & -\dfrac{3}{r}\end{bmatrix} \tag{8}$$

for spheroidal modes, where ω is angular frequency, and λ and μ are Lame's constants depending on the r coordinate.

The motion-stress vectors $\mathbf{y}(r)$ can be obtained for a given value of ω by solving Eq. (5) by means of the conventional Runge–Kutta–Gill's method. When the spherical surface $(r=a)$ is stress-free, we must find the free oscillation frequency ω for which the solutions of $\mathbf{y}(r)$ satisfy the boundary condition $y_2(a)=0$ in the case of toroidal mode oscillation or $[y_2(a),y_4(a)]=0$ in the case of spheroidal mode oscillation. This is a typical boundary value problem

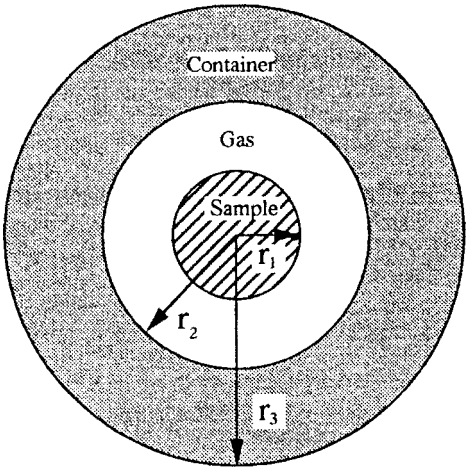

FIG. 1. Model of spherical shell structure which is composed of sample (Fe), gas (He), and container (WC) layers. Radii of sample, gas, and container layers are denoted by r_1, r_2, and r_3, respectively. The elastic constants, density and other parameters of each layer are given in Table I.

and the practical procedures to find their solutions are presented in detail by Saito (1988).

II. FREE VIBRATION OF A THREE-LAYERED SPHERE

Figure 1 shows a three-layered sphere composed of an inner spherical sample of iron (Fe), middle layer of helium gas (He) and outer layer of tungsten carbide (WC). The elastic constants, density, and other parameters of each layer are given in Table I. The helium gas is used as a pressure medium to compress the spherical sample. Such a model is called ''cavity model.''

The numerical solution of free oscillation of the three-layered sphere was obtained by solving Eq. (5) using the computer program ''Disper80'' (Saito, 1988). In order to examine characteristics of the normal mode of the three-layered sphere, we investigated the distribution of strain energy in the sphere. The strain energy can be expressed as

$$W=\int \varepsilon_{ij}T_{ij}\,dv, \tag{9}$$

where ε_{ij} and T_{ij} are strain and stress tensors, respectively, and the summation convention is assumed for repeated indices. Integration of Eq. (9) is performed over the entire volume of the sphere. Calculating the stress and strain tensors from the displacement solutions of Eqs. (2) and (3) and substituting them into (9), we have

$$W=\int_0^a E(r)dr, \tag{10}$$

where the strain energy density function $E(r)$ is defined by

$$E(r)=\frac{(ry_2)^2}{\mu}+(l-1)(l+2)\mu(y_1)^2 \tag{11}$$

for toroidal modes and

$$\begin{aligned}E(r)&=E_\mu(r)+E_K(r)\\&=\frac{1}{\lambda+2\mu}(ry_2)^2+l(l^2-1)\\&\quad\times(l+2)\mu(y_3)^2+\frac{l(l+1)}{\mu}(ry_4)^2\\&\quad+\frac{\mu(3\lambda+2\mu)}{\lambda+2\mu}\{2y_1-l(l+1)y_3\}^2\end{aligned} \tag{12}$$

for spheroidal modes. The $E_\mu(r)$ and $E_K(r)$ are strain energy densities to which the rigidity and bulk moduli contribute, respectively.

When a vibration source is put on the surface of the inner sample, the strain energy of toroidal modes is confined only to the inner sphere because the toroidal displacements are not excited in the gas layer in the case of zero gas viscosity. Isaak *et al.* (1998) consider the effect of finite gas viscosity on the toroidal vibrations, and they show that when the pressurizing gas is helium the effects are small. Thus, to a close approximation, the toroidal oscillations of the inner spherical sample may be regarded as ''sample modes.'' In contrast to the toroidal oscillation, spheroidal mode displacements are excited over the entire space of the three-layered sphere. Nevertheless, strain energy localization is seen in the spheroidal modes. Figure 2 shows the distribution of strain energy density of three spheroidal modes. We find three characteristic modes called ''sample,'' ''gas,'' and ''container'' modes, whose strain energy distributions are localized in sample, gas, and container layers, respectively. Such a localization of strain energy is due to a large difference in acoustic impedance between gas and solid layers.

III. PRESSURE DEPENDENCE OF FREE OSCILLATION FREQUENCIES

Free oscillation frequencies of the three-layered sphere were calculated with changing pressure in the gas layer. Pressure changes in density and elastic constants of the three layers and a slight decrease in sample volume due to confining pressure were accounted for when calculating the free oscillation frequency spectrum. The pressure derivatives of the elastic constants in each layer are listed in Table I. The elasticity and density data of the helium gas at high pressures are from Nishitake and Hanayama (1975). Another spectrum was calculated for a single iron sphere under the same hydrostatic pressure condition by assuming no transfer of vibrational energy from the iron sphere and that the density, radius, and elastic constants of the iron sphere and their pressure changes are the same as those of the inner specimen of the three-layer configuration.

Frequency spectra of the three-layered sphere and the single iron sphere at 0.1 MPa pressure are shown in Fig. 3 by classifying the vibration modes into sample, gas, and container modes. In a given frequency range there are many more gas and container modes than sample modes. At low pressure, the spectrum of the sample does not vary so much when going from the single sphere to the sample mode of the three-layer configuration. Figure 4 depicts the pressure dependencies of a sample mode and its equivalent mode for the

TABLE I. Parameter values of cavity model.

	Density (g/cm^3)	Radius (mm)	Elastic constants (GPa) K	μ
Sample Fe	7.789	2.384	165.0	79.5
Gas He	$2.5E-04$	5.0	$2.4E-04$	⋯
Container WC	15.1	8.5	391.0	219.0
			$\partial K/\partial P$	$\partial\mu/\partial P$
Sample Fe			5.0	1.9
Gas He			[a]	
Container WC			6.0	2.5

[a]Pressure variation of sound velocity α (km/s) in gas layer is expressed by $\alpha=0.99239+5.4467P-24.270P^2+80.028P^3$.

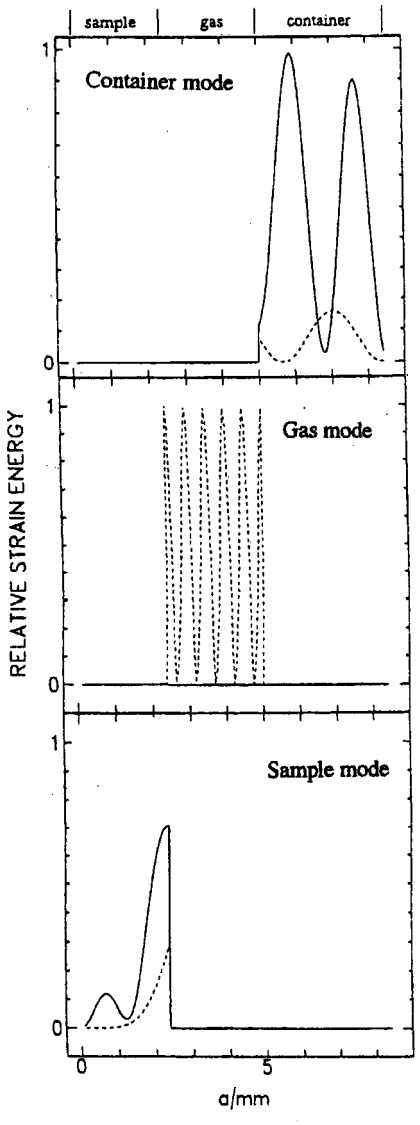

FIG. 2. Distribution of strain energy density of spheroidal modes of the three-layered sphere. The horizontal axis indicates distance measured from the center of the sphere. The strain energy density normalized by the maximum value of $E(r)$ is shown by dividing into two parts, $E_\mu(r)$ (solid line) and $E_k(r)$ (dashed line), to which the rigidity and bulk moduli contribute [see Eq. (12)].

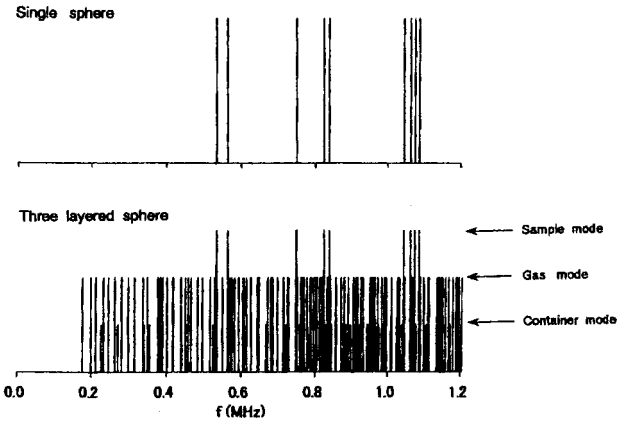

FIG. 3. Comparison between resonance spectra of the three-layered sphere and the single iron sphere at pressure of 0.1 MPa. Sample, gas, and container modes are indicated by long, intermediate, and short bars, respectively.

single sphere. In both cases the frequencies become larger with increasing pressure. The increase in frequencies is attributed to changes in elastic constants, density, and volume for the single sphere and to those in each layer for the three-layered sphere. The sample mode frequency is nearly equal to the resonant frequency of the single sphere at low pressure, but diverges from the single sphere frequency as pressure increases. The difference in acoustic impedance between gas and solid layers decreases as pressure increases, thus allowing vibrational energy to more readily transfer from the solid sphere to the gas layer. Consequently, the sample mode frequency deviates from the resonant frequency of the single sphere and the pressure derivatives of frequencies for the two cases are not equal. If the frequency difference is evaluated and accounted for, we obtain the resonant frequencies of a single sphere from spectral measurements on the three-layered sphere. We emphasize, however, that determining the frequency shifts due to vibrational energy transfer implies that the elastic constants of the sample are already known at elevating pressure. In order to avoid such complications, we recommend evaluating the sample's elastic constants from a least squares fit of the measured and calculated spectra for the full three-layered system. In this

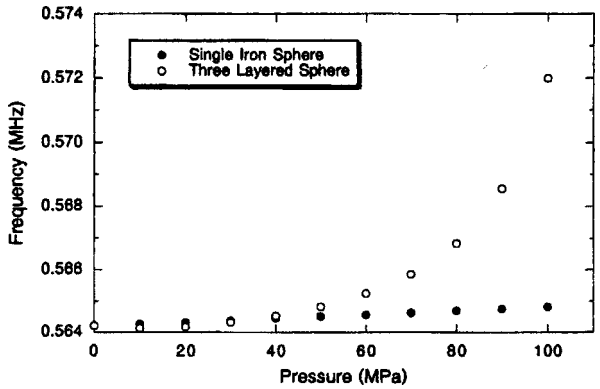

FIG. 4. Pressure dependence of resonant frequencies of the single sphere (solid circles) and sample mode (open circles) of the three-layer configuration. The oscillation mode is ${}_0S_2$ for the single sphere and ${}_5S_2$ for the sample mode, and both modes are equivalent.

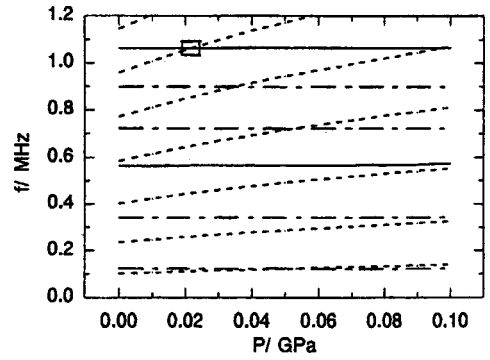

FIG. 5. Pressure dependence of resonant frequencies of sample (solid line), gas (dashed line), and container (dotted and dashed line) modes, which are equivalent to the ${}_nS_2$ modes. A small rectangular region is magnified in Fig. 6.

case care is required in order to identify what modes of spheroidal oscillations are equivalent to measured sample modes. Therefore we investigate the behavior of the sample modes in response to elevating pressure in a gas layer.

Figure 5 shows the pressure dependence of frequencies of spheroidal modes, ${}_nS_2$, where ''n'' and ''2'' are radial and angular order numbers, respectively. Each of these modes belongs to one of sample, gas, and container modes. All the free oscillation frequencies increase with increasing pressure. The gas modes show the largest increase in frequencies against a pressure increase because of the larger compressibility of gas. Thus their pressure curves frequently intersect those of sample and container modes (Fig. 5). In order to observe details of the intersection between the pressure curves of resonant frequencies, a small rectangular region containing an intersection between sample and gas modes is magnified in Fig. 6 (see Fig. 5). The frequencies of ${}_{10}S_2$ and ${}_{11}S_2$ modes gradually approach as the confining pressure increases up to the intersection pressure and separate above the pressure. Thus the sample mode is equivalent to the ${}_{11}S_2$ mode below the intersection pressure, but to the ${}_{10}S_2$ mode above the pressure. This result means that an interchange from ${}_{11}S_2$ mode to ${}_{10}S_2$ mode takes place in the vicinity of the intersection on the pressure curve of the sample mode. Reverse interchange also occurs on the pressure curve of gas mode. Therefore the intersection between the pressure curves of sample and gas modes is interpreted as interchange from ${}_{11}S_2$ to ${}_{10}S_2$ on the sample mode and from ${}_{10}S_2$ to ${}_{11}S_2$ on the gas mode. Such an interchange occurs only between the spheroidal modes, ${}_nS_l$ and ${}_{n'}S_{l'}$, satisfying the conditions of $l=l'$ and $n-n'=\pm 1$, and the modal interchanges do not take place in the case of single sphere oscillation. This result means that one should be aware of change

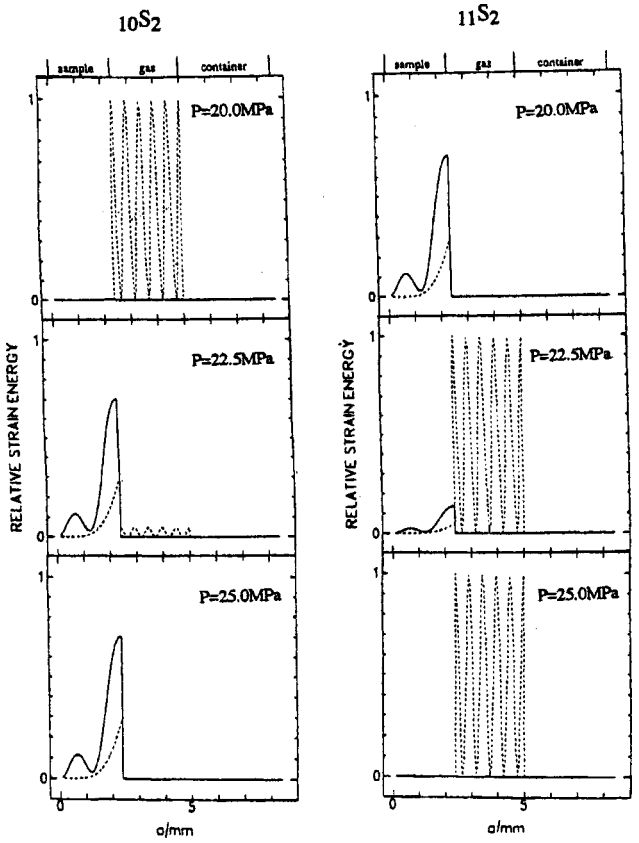

FIG. 7. Strain energy distribution of ${}_{10}S_2$ and ${}_{11}S_2$ modes at three confining pressures, 20, 22.5, and 25 MPa. See the caption of Fig. 2 for the solid and dashed lines.

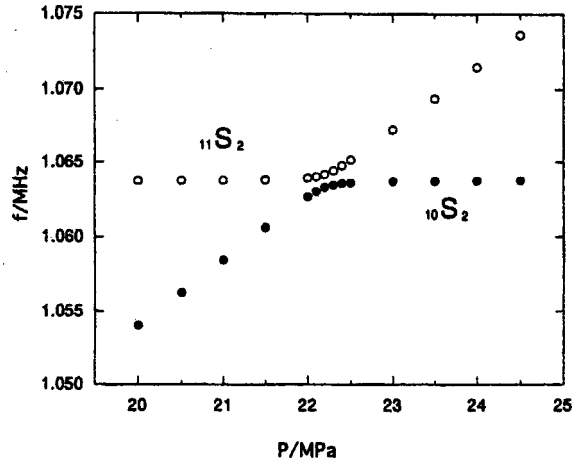

FIG. 6. Detailed pressure dependence of the frequencies of ${}_{10}S_2$ (solid circles) and ${}_{11}S_2$ (open circles) modes in the pressure interval between 20 and 25 MPa.

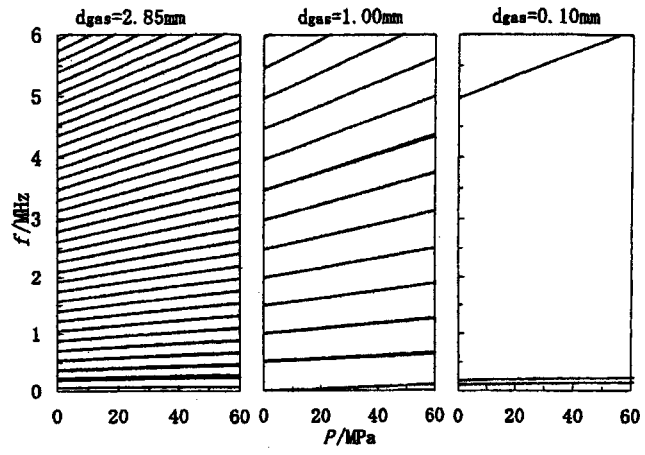

FIG. 8. Pressure dependence of the resonant frequencies of gas modes for different thickness of gas layer, d_{gas}. The left, middle, and right panels correspond to the cases of $d_{\mathrm{gas}}=2.85$, 1.0, and 0.1 mm, respectively.

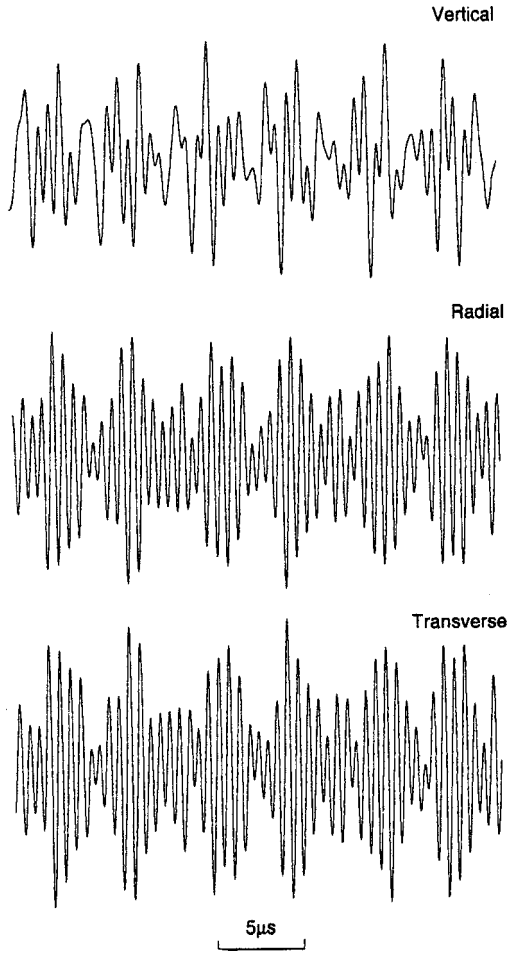

FIG. 9. Theoretical waveforms generated by a double couple point sources located on a pole of the sample. The observation point is on the opposite pole. The top, middle, and bottom traces show vertical, radial, and transverse components, respectively.

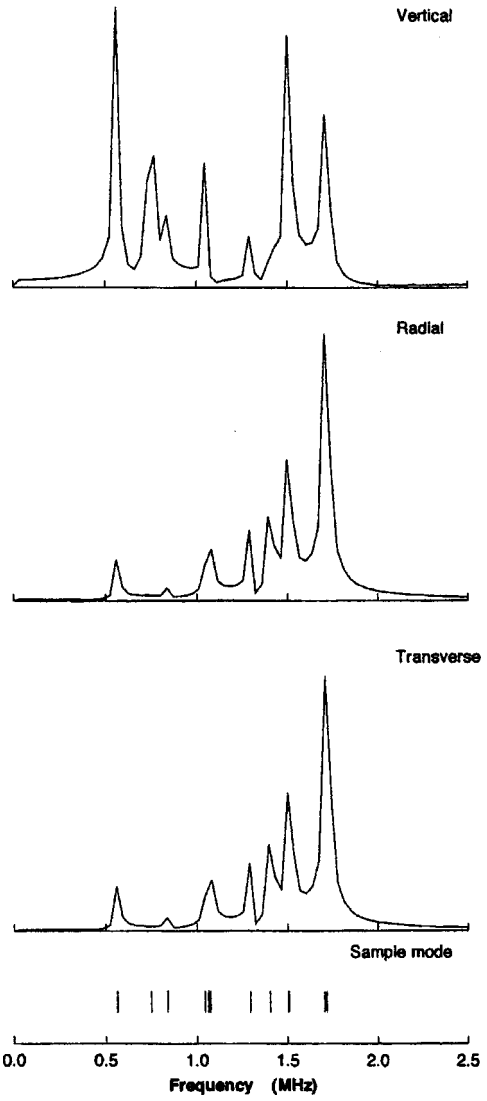

FIG. 10. Amplitude spectra of the theoretical waves of vertical, radial, and transverse components. The bottom figure indicates the frequency spectrum of sample modes.

in radial order numbers of spheroidal modes when tracing sample mode frequencies against pressure.

Figure 7 shows the strain energy distribution of the ${}_{10}S_2$ and ${}_{11}S_2$ modes under different confining pressures. As the pressure increases, the distribution shows that the ${}_{10}S_2$ mode changes from gas mode to sample mode and the ${}_{11}S_2$ mode changes reversely. The resonance modes in the vicinity of the intersection are intermediate between sample and gas modes. In general, a spheriodal mode of a three-layered sphere with solid–gas–solid structure shows the feature of the sample, gas, or container mode at a confining pressure, but the mode changes into other modes as the confining pressure increases.

IV. DISCUSSION AND CONCLUSION

As seen in Figs. 5 and 6, intersection between the pressure curves of resonant frequencies may make it difficult to identify spheroidal oscillation modes measured in the vicinity of the intersection. The misidentification of resonance modes is a source of errors in the elastic constants determined from the resonant frequencies. In order to avoid problems in mode identification, it is necessary to either not use frequencies measured at the intersection of pressure curves in the elasticity inversion analysis or use a configuration for which the number of gas modes is minimized. The pressure dependencies of resonant frequencies of gas modes were calculated for different thicknesses of gas layer in order to find optimal conditions for identifying sample mode frequencies. As seen in Fig. 8, the frequency interval between adjacent gas modes increases as the thickness of gas layer is reduced. Thus, the possibility of misidentification of sample modes in the resonance spectrum is lessened in the case of a three-layered sphere with a thinner gas layer.

Because there are a number of resonance modes in the free oscillation of a three-layered sphere with solid–gas–solid structure, knowing the relative amplitudes of the resonance modes is useful for extracting the sample modes from the resonance spectrum. Assuming the same situation as the cavity resonance experiment where a pair of source and receiver is set at opposite poles on the surface of the spherical sample, we synthesized waveforms of elastic waves generated by the point source and then calculated amplitude spectra of the synthesized waveforms. The synthesis of the elastic

waves was carried out at ambient pressure by means of normal mode superposition method (Gilbert and Dziewonski, 1975), where the eigenfunctions of 550 modes including 12 sample modes were used. Figures 9 and 10 depict the synthesized waveforms and their amplitude spectra, respectively. The amplitude spectra show several clear peaks that correspond to the sample modes, but no spectral peaks of gas and container are found. This result indicates that the excitation of gas and container modes are sufficiently weak on the surface of the sample in comparison with that of sample mode. Thus even if the resonance spectrum of the three-layered sphere is complicated because a large number of gas and container modes are excited, sample modes can be easily identified in the resonance spectrum measured on the spherical sample.

In summary we have addressed problems related to the use of RST for elasticity measurements under high pressure. We investigated normal mode oscillation of a sphere with spherical shell structure composed of three layers: solid spherical sample, gas, and solid container shell. The results obtained are summarized as follows.

(1) The resonance modes of a sphere with solid–gas–solid structure are classified into sample, gas, and container modes, whose strain energy distributions are localized into sample, gas, and container layers, respectively.
(2) All resonant frequencies increase with increasing gas pressure and the increase in frequency of gas mode is largest. When tracing the pressure change of resonant frequencies, a spheroidal mode shows feature of sample, gas, or container mode at one hydrostatic pressure, but changes into other modes as pressure increases.
(3) At a pressure where a pressure curve of sample or container mode intersects that of gas mode, modal interchange takes place only between spheroidal modes of ${}_nS_l$ and ${}_{n'}S_{l'}$ satisfying the conditions of $l=l'$ and $n-n'=\pm 1$. Thus it is very important to identify what modes of spheroidal oscillation correspond to measured sample modes. The interchange may be an origin for misidentification of resonance mode measured in the vicinity of the intersection pressure. To avoid occurrence of the modal interchange, the gas layer should be thinned.
(4) Sample modes are much more strongly excited than those of gas and container modes when the resonance spectrum is measured on the surface of the inner sample and a vibrational source is put on the sample surface.

ACKNOWLEDGMENTS

The authors thank H. Kikuchi and S. Onishi for their help in calculating resonant frequencies and synthesizing elastic wave forms. They are also grateful to D. G. Isaak and an anonymous reviewer for giving critical comments to revise the first version of this manuscript.

Anderson, O. L., and Isaak, D. G. (**1995**). ''Elastic constants of mantle minerals at high temperature,'' in Mineral Physics and Crystallography, edited by T. J. Ahrens (American Geophysical Union, Washington DC), pp. 64–97.

Gilbert, F., and Dziewonski, A. M. (**1975**). ''An application of normal mode theory to the retrieval of structural parameters and source mechanisms from seismic spectra,'' Philos. Trans. R. Soc. London, Ser. A **278**, 187–269.

Goto, T., and Anderson, O. L. (**1988**). ''Apparatus for measuring elastic constants of single crystals by a resonance technique up to 1825 K,'' Rev. Sci. Instrum. **59**, 1405–1408.

Isaak, D. G., Anderson, O. L., and Oda, H. (**1992**). ''High-temperature thermal expansion and elasticity of calcium-rich garnets,'' Phys. Chem. Miner. **19**, 106–120.

Isaak, D. G., Carnes, J. D., Anderson, O. L., and Oda, H. (**1998**). ''Elasticity of fused silica spheres under pressure using resonant ultrasound spectroscopy,'' J. Acoust. Soc. Am. **104**, 2200–2206.

Nishitake, T., and Hanayama, Y. (**1975**). ''Velocity of ultrasound wave in helium, argon and nitrogen gases at high pressure,'' J. Phys. Soc. Jpn. **39**, 1065–1067.

Oda, H., Anderson, O. L., Isaak, D. G., and Suzuki, I. (**1992**). ''Measurements of elastic properties of single-crystal CaO up to 1200 K,'' Phys. Chem. Miner. **19**, 96–105.

Oda, H., Isoda, S., Inouye, Y., and Suzuki, I. (**1994**). ''Elastic constants and anelastic properties of an anisotropic periclase sphere as determined by the resonant sphere technique,'' J. Geophys. Res. **99**, 15517–15527.

Ohno, I., Nishitake, T., Hanayama, Y., Kimura, M., and Kumazawa, M. (**1991**). ''The resonance method to determine the pressure and temperature variations of elastic constants,'' Engineering Science Preprints-28, 28th Annual Meeting in the Society of Engineering Science.

Saito, M. (**1988**). ''Disper80, A subroutine package for calculation of seismic normal-mode solutions,'' in *Seismological Algorithms*, edited by D. J. Doornbos (Academic, New York), pp. 293–319.

Suzuki, I, Oda, H., Isoda, S., Saito, T., and Seya, K. (**1992**). ''Free oscillation of an elastically anisotropic sphere and its application to determining the elastic constants of rutile,'' J. Phys. Earth **40**, 601–616.

Takeuchi, H., and Saito, M. (**1972**). ''Seismic surface waves, in *Method in Computational Physics, Vol. 11*, edited by B. A. Bolt (Academic, New York), pp. 217–295.

Backscattering enhancements due to retroreflection of ultrasonic leaky Rayleigh waves at corners of solid elastic cubes in water

Karen Gipson[a] and Philip L. Marston[b]
Department of Physics, Washington State University, Pullman, Washington 99164-2814

(Received 11 August 1998; revised 2 November 1998; accepted 2 November 1998)

Backscattering enhancements can be important for interpreting acoustical images of scatterers. Experiments were performed on a solid stainless steel cube in water in order to investigate a significant mechanism for producing a large backscattered signal. Enhanced high-frequency backscattering is observed when the block is rotated such that the incident acoustic wave strikes one of its flat surfaces in the vicinity of the coupling angle for launching a leaky Rayleigh wave at the steel–water interface. This enhancement can be explained as a retroreflection of the leaky wave at a corner of the block, which results in a reversal of the incident wave vector and thus produces a large backscattered signal. The magnitude of the peak backscattered pressure is approximated using a convolution formulation [P. L. Marston, J. Acoust. Soc. Am. **97**, 34–41 (1995)]. Observed backscattering enhancements support the validity of the convolution formulation to approximate the general magnitude of the peak pressure, as well as being consistent with the dephasing predicted by that theory as the block is rotated away from the coupling angle. Tilting the block while maintaining the coupling angle reduces the backscattered amplitude because of changes in the reflection coefficients at the corner as well as increased attenuation.
[S0001-4966(99)03002-7]

PACS numbers: 43.35.Pt [HEB]

INTRODUCTION

The scattering characteristics of certain canonical shapes, such as spheres and infinite cylinders, have been studied using analytical solutions expressed as a partial-wave series.[1,2] However, many scatterers are not amenable to analytical solutions; even an object as simple as an elastic rectangular parallelepiped precludes a partial-wave solution, since the wave equation is not separable for such a geometry. Hence, other methods must be employed to predict or explain the scattering properties of such shapes. Chinnery *et al.*[3] and Thorne *et al.*[4] have recently analyzed the scattering by cubes at low frequencies; however, different scattering mechanisms are expected to dominate at high frequencies. Ray methods have proven useful for describing high-frequency scattering for a variety of cases,[5,6] and such methods are heuristically appealing because they provide visualization of specific physical processes that may contribute to scattering. In the present work we investigate a specific high-frequency backscattering enhancement observed for a solid stainless steel cubical block that is submerged in water. It is noteworthy that related manifestations of the retroreflection process discussed herein may be relevant to a variety of elastic objects with corner truncations and that such enhancements may be important for interpreting the sonar images of objects with corners.

A leaky Rayleigh wave is launched on a fluid-loaded flat elastic surface when an acoustic wave is incident on the flat surface such that the incident acoustic wave vector's component along the interface matches the wave vector of the Rayleigh wave on the interface.[7] The incident angle for which such wave coupling occurs is called the Rayleigh angle and is commonly expressed by the trace velocity matching condition $\theta_R = \sin^{-1}(c/c_R)$, where c is the speed of sound in the water and c_R is the phase velocity of the leaky Rayleigh wave. Since c_R is supersonic with respect to c, the Rayleigh wave will leak radiation into the water; by reciprocity we see that radiation leaks into the water at the Rayleigh angle. If the cubical block of this investigation is rotated such that the acoustic wave in water is incident on one of the flat faces of the block in the vicinity of the Rayleigh angle, a leaky Rayleigh wave is launched on the face. When this wave reaches the edge of the face, part of it is reflected and propagates to the adjacent edge forming the corner, where part of it is reflected again. A ray diagram of the process of interest is shown in Fig. 1. This process is termed retroreflection: for a 90° corner, the final result is that the wave vector of the leaky Rayleigh wave is reversed. Since the outgoing wavefront associated with this leaky radiation is locally flat[5] and directed back toward the source, the retroreflection process can result in a large contribution to the farfield backscattered pressure.

For an elastic object with flat surfaces and corners, significant backscattering can occur from the process described above or from specular reflection off one of the flat faces. However, specular reflection requires that two of the Euler angles of the surface normal be narrowly constrained.[8] In contrast, the requirements for the retroreflection process to contribute to backscattering are (a) that a leaky Rayleigh wave be launched on the surface, and (b) that this wave

[a]Present address: Department of Physics, University of Puget Sound, 1500 North Warner, Tacoma, WA 98416.
[b]Electronic mail: marston@wsu.edu

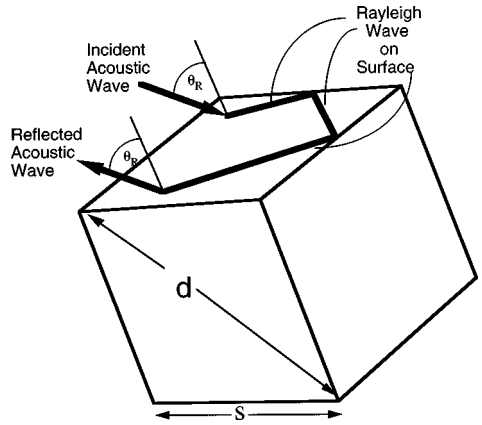

FIG. 1. The retroreflection process. If the acoustic wave is incident in the vicinity of the Rayleigh angle, a leaky Rayleigh wave will be launched on the flat surface of the block. When the associated ray reaches the corner, it will be partially reflected at each edge, with the result that the wave vector is reversed as shown. The Rayleigh wave will thus retroreflect acoustic radiation in the backscattering direction with a flat wavefront. Other rays parallel to the one shown contribute to the flat wavefront. The radiation due to subsequent reflections of the leaky waves is neglected due to the damping rate at the high frequencies under consideration.

survive the successive reflections at the edges of the solid. The former requirement narrowly constrains one of the Euler angles: the acoustic wave must be incident near the Rayleigh angle. In Sec. I we present the experimental methods and observations that confirm the existence of the retroreflected backscattered signal for incidence near the Rayleigh angle when conditions are favorable for satisfying the second requirement, and the angular width associated with rotation is found to be relatively broad. In addition, it is observed that the second requirement places only weak restrictions on a second angle, which can be connected to the tilt angle of the block. This suggests that the mechanism under investigation is more likely to be observed than specular reflection from one of the flat faces of the block; we will see in Sec. III that the experiments and theory of this investigation substantiate that idea.

The theoretical analysis of the retroreflected wave in Sec. II is based on a convolution formulation discussed by Marston,[9–11] specialized to the present case of leaky Rayleigh waves. The dependence of the result of Sec. II on the rotation and tilt angles of the block are derived in Appendices A and B, respectively. In Appendix C we explain the modifications required to account for the finite launch region, while a correction to plane wave incidence due to the finite nature of the separation distance of the transducer and the target is given in Appendix D. (Other corrections to and justifications of some of the approximations in the theory are presented in Ref. 12.) In Appendix E we discuss the normalization of the data, and comparisons between the theoretical predictions and the experimental observations appear in Sec. III.

I. OBSERVATION OF THE RETROREFLECTED SIGNAL

The experiments were performed in a redwood tank of 12-ft diam and 8-ft depth, which held approximately 6500

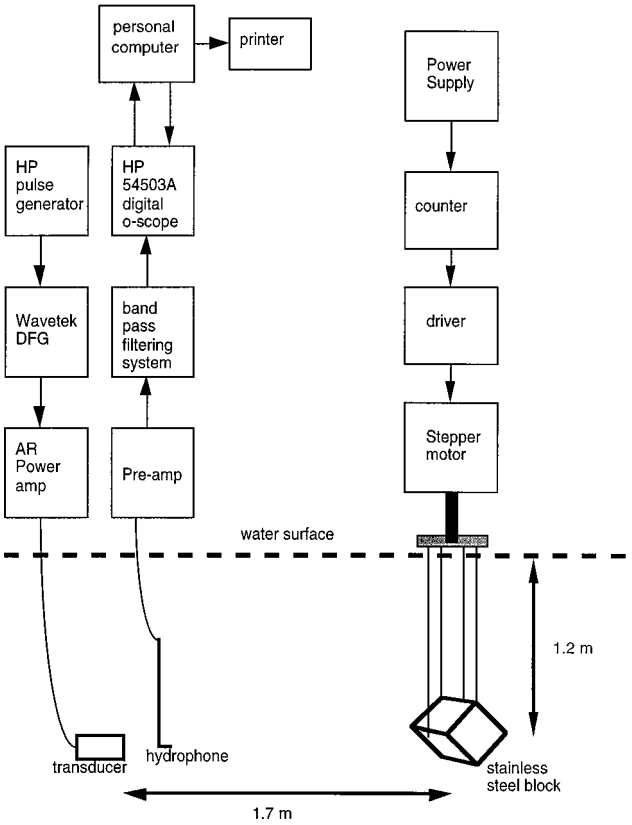

FIG. 2. The experimental setup for measuring the dependence of backscatter on rotation and tilt.

gallons of water. The experimental setup and associated electronics are shown in Fig. 2. The experiment was centered in the tank, with the source and target separated by a distance of approximately 1.7 m in order to ensure uniform ensonification across the target while isolating the signals backscattered by the target from those reflected from the tank walls. The source was a 0.95-cm diam piston transducer (Panametrics model V309), which was driven with 1.5-MHz five-cycle sine wave bursts generated by the Wavetek digital function generator and gated by a Hewlett-Packard pulse generator. A small bent-tip hydrophone was positioned a distance of 50 cm in front of the source (between the source and the target) to detect the backscattered signal, which was amplified and filtered before being sent to the Hewlett-Packard digital oscilloscope. The data were averaged over many identical events by the HP scope and manually time windowed to isolate the peak signal at each angular step before being recorded by a computer.

The target was a solid stainless steel 303 cubic block 6.00 cm on a side. The material parameters of the target were measured from a sample of the material from which the target was constructed; the relevant material parameters and those of the surrounding water are shown in Table I and are needed to calculate the Rayleigh velocity and attenuation.[7,11] The size of the target was chosen so that its dimensions would be somewhat larger than the Rayleigh wave attenuation length of 2.88 cm for the frequency used in the experiments but not so large as to significantly compromise plane wave illumination within the constraints of the scattering

TABLE I. Material parameters for the experiment. The parameters for the block and surrounding water are used to determine the Rayleigh angle, and the parameters for the calibration sphere are used to determine the magnitude of the specular contribution to its form function in the backscattering direction.

	Density, ρ (in g/cm^3)	$c_{\text{Longitudinal}}$ (in mm/μs)	c_{shear} (in mm/μs)
Block (SS 303)	7.81	5.762	3.140
Sphere (SS 440c)	7.455	6.110	3.254
Water	0.998	1.479	

facility. The block was suspended from the rotary stage by four thin stainless steel wires in order to inhibit it from swinging after being rotated; care was taken to preserve the reflecting surface of the block when attaching the suspension wires. (See Appendix E.) The tilt angle was varied by adjusting the lengths of two of the suspension wires and was determined to the nearest 0.1° by measuring the deflection of a laser beam reflected from a mirror mounted on the top surface of the block. The rotary stage was driven by a stepper motor, which enabled the rotation angle to be incremented by 0.05°. The high inertia of the target motivated manual collection of the data to ensure that the block was motionless during the signal averaging process.

In the first set of experiments, the block was suspended such that its diagonal was level, so that a surface wave on the block would strike each of the edges forming the retroreflecting corner at a 45° angle. For this orientation the horizontal incident wave vector, the normal to the illuminated face, and a diagonal of that face all lie in a horizontal plane. (This is termed the untilted block for reasons to be explained subsequently.) The block was then rotated about a vertical axis through its center using the rotary stage, which varied the angle at which the incoming rays were incident on the front face of the block. In this manner, the dependence of the backscattered signal on the rotation angle θ was investigated. Examples of the farfield signals are shown in Fig. 3; the large signal near 35 μs in Fig. 3(a) corresponds to the predicted time for the first return from the mechanism under consideration. Due to the relatively high rate of radiation damping at high frequencies, subsequent returns from multiple reflections are not expected to contribute significantly to backscattering in the high-frequency regime. Therefore the pressure magnitude at a given angle was determined from an average over several cycles of the first return. The pressure magnitudes were normalized as discussed in Appendix E to produce the backscattering form function as a function of θ plotted in Fig. 4. (The dotted and dashed curves in Fig. 4 are theoretical dephasing relationships derived in Appendix A by the convolution method to be discussed subsequently.) The data in Fig. 4 confirm that the backscattered signal has a maximum for incidence near the Rayleigh angle and decreases as the angle of incidence differs from the region of the Rayleigh angle, supporting the hypothesis that a leaky Rayleigh wave is launched on the surface of the block and retroreflected around the corner to yield a large backscattering contribution.

In the second set of experiments, the block was held at

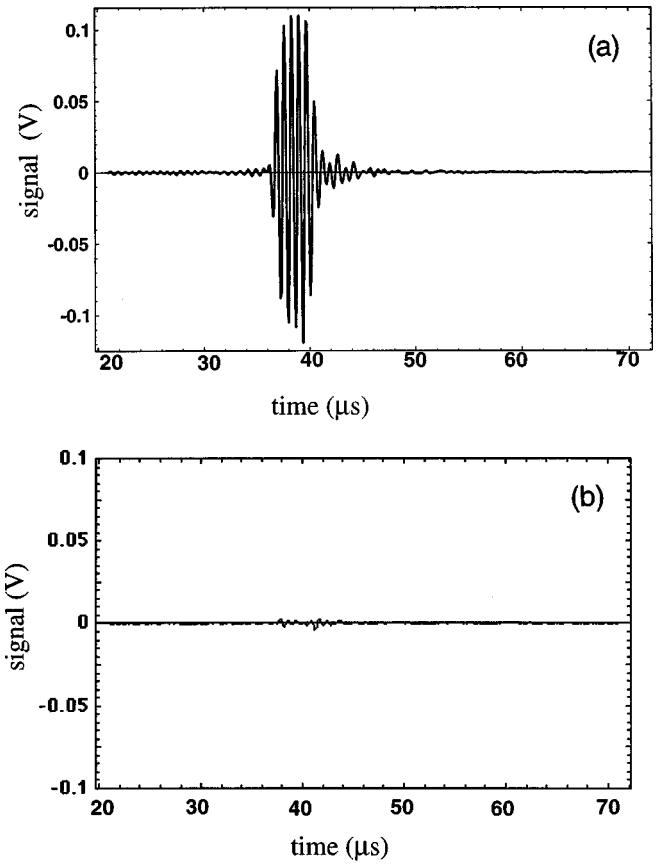

FIG. 3. Examples of backscattered signals, with time $t=0$ set to correspond to the specular reflection from the face of the block. (a) The backscattered signal from the block for $\theta=29.9$ degrees, and (b) the corresponding signal for $\theta=32.0$ degrees. The signal is significantly greater in (a) than in (b) due to the excitation of the ray shown in Fig. 1.

the Rayleigh angle (the experimentally determined maximum in the absence of tilt) while the tilt angle was varied such that the diagonal of the block's ensonified surface was no longer horizontal. As shown in Fig. 5, tilting the block by an angle γ causes the Rayleigh wave to strike the edges forming the corner at complementary angles $\gamma \pm 45°$. Since

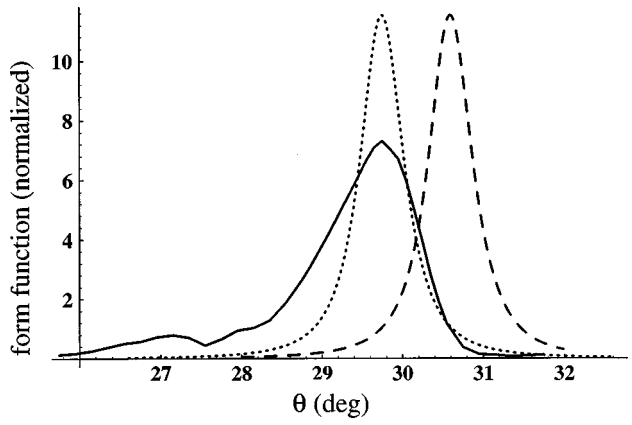

FIG. 4. The backscattering form function magnitude as a function of the rotation angle. The solid curve shows the data, the dashed curve is the theoretical dephasing relationship derived in Appendix A, and the dotted curve is the theoretical dephasing curve taking the rotation angle as an adjustable parameter. The form function is normalized as discussed in Appendix D.

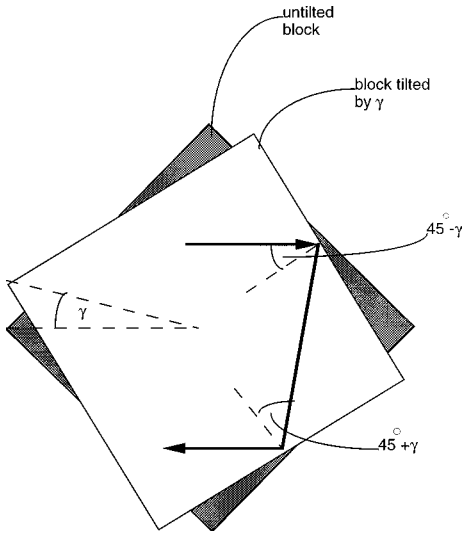

FIG. 5. The effects of block tilt on Rayleigh wave propagation on the block's face. Tilting the block causes the Rayleigh wave to strike each of the edges forming the corner at different angles as well as resulting in a longer pathlength across the corner.

edge reflection coefficients depend on the angle of incidence, the angles $\gamma \pm 45°$ are expected to have different reflection coefficients than the 45° angles of the untilted case. In addition, tilting the block results in increased attenuation due to a longer pathlength as the surface wave travels across the corner. In Appendix B we demonstrate that the product of the two reflection coefficients with the attenuation factor will be largest when the Rayleigh wave strikes each of the edges at a 45° angle. This elucidates why having the diagonal level is considered the untilted block: the backscattered pressure should decrease as the block is tilted away from that orientation. Figure 6 displays the backscattered pressure as a function of tilt angle γ. The dots representing the data are normalized with respect to the value at $\gamma = 0$ and clearly confirm the expectation that the backscattered pressure decrease as the block is tilted away from $\gamma = 0$. (The solid curve in Fig. 6 is the theoretical tilt degradation curve derived in Appendix B by quantifying the above considerations, and will be discussed in more detail in Sec. III.)

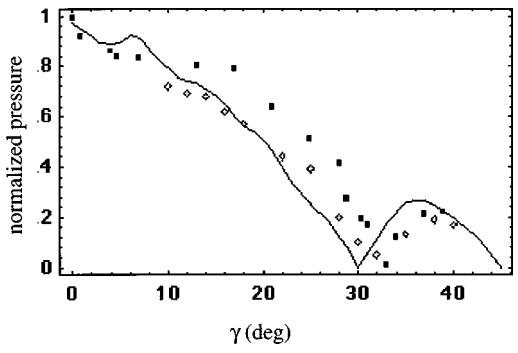

FIG. 6. Backscattered pressure as a function of tilt angle. The dots and boxes represent two sets of data, while the solid curve is the theoretical tilt degradation relationship derived in Appendix B. Both the data and the theory have been normalized with respect to backscattered pressure for the untilted block.

II. DEVELOPMENT OF AN APPROXIMATE MODEL

Following the development of Marston *et al.*,[10] an approximation for the backscattered pressure can be obtained by expressing the outgoing leaky wave field near the scatterer as a spatial convolution of the incident pressure and a function describing the response of the scattering surface to a spatially localized pressure, employing the concept of an image block to account for the reflection at the corner, and then using the Rayleigh–Sommerfeld propagation integral[5] to construct the farfield amplitude. Time harmonic waves are assumed; an $\exp(-i\omega t)$ time dependence is suppressed throughout the development. The initial calculation is performed for the maximum backscattering case: the acoustic wave is incident on the untilted block at the Rayleigh angle. In addition, the block is initially approximated as a semi-infinite corner. After obtaining an expression for the magnitude of the backscattered pressure for this idealized case, a correction accounting for the finite size of the block is introduced. (The details of that correction are presented in Appendix C.) The resulting expression gives an approximate prediction of the peak farfield backscattered pressure due to the retroreflection process under investigation, Eq. (8). As mentioned in the Introduction, the dependence of the backscattered pressure on rotation and tilt angles is analyzed in Appendices A and B, respectively. These results are discussed in Sec. III.

Due to the two edge reflections of the Rayleigh wave associated with the retroreflection process (see Fig. 1), the prediction of the pressure amplitudes relies on an approximation of the magnitude of the two amplitude reflection coefficients. We use the Rayleigh wave reflection coefficients calculated by Gautesen using a numerical transform method for Rayleigh wave reflections on an elastic quarter-space bounded by a vacuum.[13] The value of Poisson's ratio used in Gautesen's calculation ($\frac{1}{3}$) is sufficiently close to the calculated value for the stainless steel block (0.289) that the discrepancy can be neglected for the present purpose of testing the ability of the analysis to explain the general magnitude of the observed signal. However, we note that using Gautesen's coefficients neglects any effects of radiation on the reflection coefficient product B introduced in Eq. (4); the presence of fluid loading will decrease the actual reflection coefficients somewhat since some energy can leak into the fluid.

For the case of the untilted block, the leaky Rayleigh wave strikes each of the edges forming the corner at a 45° angle, which corresponds to the angular region of the largest product of the edge reflection coefficients. We begin the convolution formulation by approximating the scatterer as an elastic half-space, which is a reasonable approximation for the present case of high-frequency acoustic waves incident on a flat face of the block. In addition, the response of the surface is assumed to be uniform in a direction transverse to the propagation of the leaky wave. This allows the surface response to be approximated as a convolution with a spatial *line* response given by a one-dimensional integral.[9] Although such an approximation does not fully represent the reflecting corner, the error it introduces to the final result is ameliorated by attenuation effects, as shown in Ref. 12 by applying the more complicated approximation method of Ref. 11 in a spe-

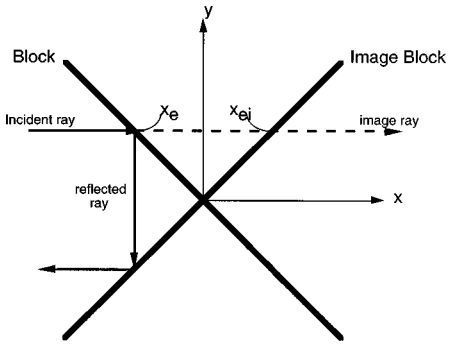

FIG. 7. Image plane depiction of the retroreflection process. The reflection around the corner may be viewed as propagation onto the image block as shown, with an appropriate factor accounting for energy losses at each reflecting edge. For the case of the untilted block shown, the Rayleigh wave strikes each edge at a 45 degree angle, so that $x_e=-y$ and $x_{ei}=y$.

cial case. Defining x to be the initial (horizontal) propagation direction of the leaky Rayleigh wave on the surface of the block, the leaky wave contribution to pressure field at a point x' relative to a line source at a surface coordinate $x=0$ can be expressed as a convolution of the spatial line response with the incident pressure:

$$p_{\mathrm{R}}(x')=\int_{-\infty}^{x'} p_i(x)h(x'-x)dx, \tag{1}$$

where the subscript R denotes that this is the pressure contribution due to leaky Rayleigh waves, and the one-sided spatial line response $h(x)$ can be written as[9]

$$h(x\geqslant 0)\approx -2\alpha\exp(-\alpha x)\exp(ik_R x+i\varphi_b), \tag{2}$$

where k_R and α are the real and imaginary components of the complex leaky wave number, associated with Rayleigh wave propagation and attenuation, respectively, and φ_b is a background phase constant. In the experiments, plane wave incidence is assumed; thus, we write the incident pressure as $p_i(x)=p_0\exp(ik_x x)$, where p_0 is taken to be real.

Next, we consider propagation of the Rayleigh wave around the corner as propagation onto an image block, as shown in Fig. 7. We assume for the time being that the acoustic wave is incident at the Rayleigh angle, so that $k_x=k_{\mathrm{R}}$, resulting in a phase matching of the incident pressure and response function terms in the convolution integral of Eq. (1). This allows the magnitude of the leaky pressure field in the $x'=0$ plane to be expressed as

$$|p_{\mathrm{R}}(0)|=p_0\int_{-\infty}^{x_e}|h(-x)|dx, \tag{3}$$

where x_e is the x coordinate of the position at which the propagating Rayleigh wave strikes the edge of the infinite corner. The integration is truncated at x_e because the illumination ends there. Since we are currently considering the case of a 90° corner with 45° incidence of the Rayleigh wave, we see from Fig. 7 that $x_e=-y$, and Eq. (3) simplifies to $2p_0\exp(-\alpha y)$. The retroreflected leaky Rayleigh wave will experience attenuation as it propagates in the x direction, as well as losing energy in the reflection processes at each of the edges forming the corner. The magnitude of the outgoing pressure field at an arbitrary point on the surface in the image quadrant is thus

$$|p_{\mathrm{R}}(x,y)|=2p_0B\exp(-\alpha x)\exp(-\alpha|y|), \tag{4}$$

where B is the product of the edge reflection coefficients, which depend on the angles at which the leaky Rayleigh wave impinges on the reflecting edges. For the purpose of approximating the modulus of the backscattered amplitude, it is not necessary to show the cumbersome expressions for the phase in Eq. (4). This is because the outgoing wavefront is locally flat within the relevant radiating portion of the block's surface, so that there is no ambiguity as to any variation of phase along coordinates transverse to a given backscattered ray that is radiated from the block's surface.

The ray analysis is only used near the block; the far-field backscattered pressure is subsequently determined by substituting Eq. (4) for the leaky pressure field at the surface of the block into the Rayleigh propagation integral,[5]

$$p_{lsca}(x_s,y_s,z_s)=-\frac{1}{2\pi}\int\int_{-\infty}^{\infty}dx'\,dy'\,p_{\mathrm{R}}(x',y',0)\times\frac{\partial}{\partial z_s}\left(\frac{\exp(ikr')}{r'}\right), \tag{5}$$

where (x_s,y_s,z_s) is the far-field observation point and $r'=[(x_s-x')^2+(y_s-y')^2+z_s^2]^{1/2}$. The plane over which the integration is performed, called[5] the ''exit plane,'' is defined so as to approximate p_{R} as constant in phase, and therefore corresponds to a plane of the leaky wavefront leaving the surface. Since the Rayleigh wave is attenuated by radiation damping as it travels along the block's surface, the maximum contribution to the backscattered pressure will come from a point just after reflection at the corner of the block; we therefore define the origin of the exit plane to correspond to the point of that maximum contribution. The wave field is propagated geometrically from the block to the adjacent exit plane which touches the corner of the block. We choose the coordinates of the exit plane such that its y axis coincides with the y axis previously defined for the image block's surface, while its x axis is rotated about the y axis by θ_{R}. Thus, a point (x_i,y_i) on the image block is projected to the point (x',y') on the exit plane according to

$$x'=x_i\cos\theta_{\mathrm{R}}; \tag{6a}$$

$$y'=y_i. \tag{6b}$$

The exit plane is considered to be semi-infinite; its lower boundaries are determined by the edges forming the corner of the block. Since the radiation leaks only from the surface of the block, the outgoing wavefront is bounded by the projection of the ray that leaves the edge of the block. Letting x_{ei} denote the image of x_e, this projection is given by $x'_e=x_{ei}\cos\theta_{\mathrm{R}}$. From Fig. 7 we see that $x_{ei}=y_i$ for the present case of a 90° corner with 45° incidence, and using Eq. (6b) we obtain $x'_e=y'\cos\theta_{\mathrm{R}}$. Since $\cos\theta_{\mathrm{R}}\leqslant 1$, we see that the projection of the corner of the block onto the image plane is thus larger than the physical corner.

The propagation integral of Eq. (5) is simplified by restricting attention to far-field observation points using the Fraunhofer approximation of the phase,[5] which is applicable because the effective dimensions of the radiating region are limited by the length L discussed below. Since the phase of p_R is constant in the exit plane, the phase of the integrand is constant for the backscattering case of $x_s = y_s = 0$. From symmetry, we see that the integration has equal contributions from two regions; showing only one of these and introducing a factor of 2 to account for the other integration region, Eq. (5) thus becomes

$$|p_{\text{scat}}| = \frac{4p_0 B}{\lambda r} \int_0^\infty dy' \int_{x_e'}^\infty dx' \exp(-\alpha y') \times \exp(-\alpha x' (\cos\theta_R)^{-1}), \tag{7}$$

where $x_e' = y' \cos\theta_R$, as previously discussed, and $\lambda = 2\pi/k$ is the wavelength of the acoustic wave in water. We define the Rayleigh wave attenuation length as $L = \alpha^{-1}$. (With this definition the Rayleigh wave experiences $1/e$ attenuation for $x = L$.) The integration of Eq. (7) thus yields

$$|p_{\text{scat}}| = \frac{2BL^2}{\lambda r} p_0 g \cos\theta_R, \tag{8}$$

where the integration result has $g = 1$. The integration result is supplemented by introducing a geometrical correction factor $g \leqslant 1$ in order to account for the finite size of the block. The derivation of g is presented in Appendix C.

Using the normalization convention discussed in Appendix E allows Eq. (8) to be rewritten as a form function, which elucidates its dependence on frequency. Applying Eq. (E4) to Eq. (8) eliminates the dependence on r and p_0 while introducing a factor of $1/s\sqrt{3/(2\pi)}$, where s is shown in Fig. 1. The frequency dependence of the resulting form function is thus seen to be embedded in the terms L, λ, and g. (The frequency dependence of the geometrical correction factor g arises from its dependence on L.) In order to explicitly determine the form function's dependence on k, we can use $\lambda = 2\pi/k$ and $L = 1/\alpha$, and rewrite the latter expression in terms of k by noting that α can be written as $\alpha = (\alpha/k_R) \times (k_R/k)k$, where the parenthetical factors are constants. The term k_R/k is simply equal to $\sin\theta_R$, and we can define a new variable $\beta = \alpha/k_R$ to represent the first term. (For the parameters in Table I, $\beta = 0.011$.) The resulting form function is

$$|f_{\text{cube}}| = \left(\frac{2B\cos\theta_R}{\sqrt{6\pi}(\beta \sin\theta_R)^2} \right) \frac{g}{ka_{\text{cube}}}, \tag{9}$$

where the bracketed terms do not depend on frequency, and $a_{\text{cube}} = s/2$ is the half-width of the cube, defined so that ka_{cube} is a dimensionless frequency. Figure 8 shows a plot of $|f_{\text{cube}}|$ as a function of ka_{cube}. The decrease of $|f_{\text{cube}}|$ for low frequencies arises from the decrease in g, while the decrease for high frequencies arises from the $1/k$ dependence evident in Eq. (9). Note that the increase of L at very low frequencies may result in resonances, but Eq. (9) predicts only the contribution for the first retroreflected return. The frequency used in this experiment corresponds to $ka_{\text{cube}} = 190$, which is approximately the optimum frequency predicted by Eq. (9). The attenuation length L is sufficiently small that any contributions to the backscattering due to the Rayleigh waves transmitted across the faces of the cube beyond the reflecting edges have been neglected in our analysis.

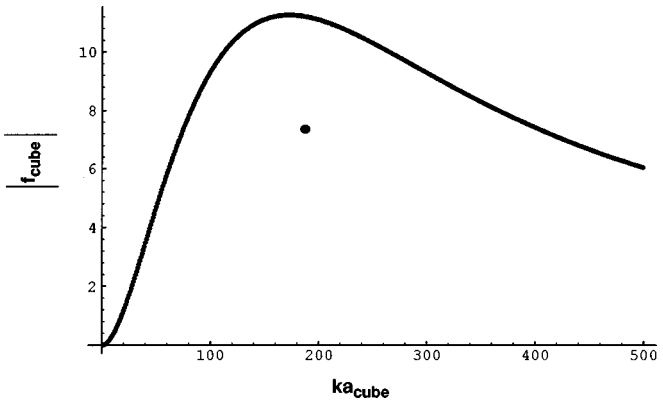

FIG. 8. Frequency dependence of the form function. The curve above is plotted from Eq. (9) to elucidate the frequency dependence of the backscattered return. The experimental parameters correspond to $ka_{\text{cube}} = 190$, and the dot indicates the observed form function at that frequency. At low ka_{cube}, the assumption that subsequent Rayleigh wave reflections are negligible breaks down and the form function is expected to exhibit structure due to resonances.

III. DISCUSSION

The Rayleigh angle and attenuation length are calculated from elasticity theory using the shear and longitudinal speeds of the block, its density, and the density and sound speed of the surrounding water.[14] The parameters in Table I predict a Rayleigh speed of 2.908 mm/μs, with an attenuation length L of 2.88 cm. Using the trace velocity matching condition, the theoretical prediction for the Rayleigh angle is thus 30.6°. The geometric factor g for the experimental parameters is determined to be 0.688 (see Appendix C), and the wavelength λ is determined from the water temperature to be 0.986 mm for the frequency used. The specular contribution[5] to the form function for the calibration sphere is determined from the parameters in Table I to have a magnitude of 0.938. Thus, we find that for the untilted block the peak backscattering form function magnitude is predicted from Eqs. (E2) and (E5) to be 11.5. Experimentally, the peak retroreflected form function for the data shown in Fig. 4 was approximately 7.3. These results are in relatively good agreement; the elevated theoretical prediction is consistent with the elevated values of the reflection coefficients (due to neglecting the effects of fluid loading) and the effects of assuming a transversely uniform wave on the surface. In addition, the size of the scattering facility prevented a sufficient separation distance to ensure that the farfield conditions assumed in the theory were rigorously satisfied.

Figure 4 is a plot of the normalized backscattering form function versus the incident angle. The solid data curve clearly shows that the backscattered pressure has a local maximum; the experiments place this maximum at an average angle of 30.0°. The dashed curve in Fig. 4 was determined by evaluating the theoretical dephasing relationship of Eq. (A6) at 0.01° steps over an 8° interval and normalizing to

the peak form function predicted by Eqs. (E2) and (E5). The dotted curve is a shifted version of the dashed curve, offset by the 0.6° discrepancy between the measured and predicted Rayleigh angles in order to facilitate comparison between the experimental results and the theoretical predictions. The justification of this angular shift is based on the finite distance between the source and the target, as discussed in Appendix D. It is seen in Fig. 4 that the theory describes the general features of the data. The observed peak magnitude is of the same order of magnitude as that predicted by the theory, and the width of the data curve is also in general agreement with the theoretical width based on the dephasing of the incident acoustic wave with respect to the Rayleigh surface wave. Ray tracing with diffraction predicts a backscattering angular width of order λ/L, corresponding to approximately 2° for the experimental parameters of this study; the data and theory curves in Fig. 4 substantiate that prediction. The structure visible in the 26°–28° range of the data curve in Fig. 4 is visible in every dataset, but is unaccounted for by the present (approximate) theory.

Figure 6 is a plot of the normalized backscattered pressure as a function of tilt angle when the acoustic wave is incident at the Rayleigh angle. The theory curve was determined from the degradation factor of Eq. (B4), using the appropriate reflection coefficients to determine B for each value of g, and was normalized to the experimental value for $\gamma=0$. Again, we note general agreement between the theory and observations, and it is noteworthy that the signal degrades relatively slowly with block tilt. The observed dip in the data appears to be associated with a zero of the Rayleigh wave reflection coefficient predicted by Gautesen's calculations[13] to occur at $\gamma=30°$ for a Poisson's ratio of $\frac{1}{3}$. The slight discrepancy in the observed angle of the dip may be due to the slight dissimilarity of the Poisson's ratio of the block (0.289) from the assumed value of $\frac{1}{3}$.

Although the necessity for incidence at the Rayleigh angle narrowly constrains one of the Euler angles, Fig. 6 demonstrates that the effect is observable for almost any tilt of the block, placing very weak restrictions on a second angle. The symmetry inherent in tilting the block downward instead of upward allows Fig. 6 to be reflected about $\gamma=0°$, and the symmetry of the four corners of the face allows the resulting 90° curve to be periodically extended to create a 360° curve. Since the 360° curve has so few nulls, we can approximate the solid angle associated with retroreflection as $(\lambda/L)\sin\theta_R$. In contrast, the solid angle for high-frequency backscattering due to specular reflection is of order $(\lambda/d)^2$, where d is shown in Fig. 1. For metal objects in water, the Rayleigh angle is typically 28°–30°.[15] Thus, we see that for high-frequency underwater scattering, elastic objects with corner truncations that satisfy the simple requirement $d>L$ will be more likely to produce detectable backscattered signals through the retroreflection process described in this paper than through specular reflection.

As mentioned in the Introduction, the convolution formulation presented in Sec. II also has an application to other shapes of scatterers. For example, this method has been applied to backscattering due to the retroreflection of Lamb waves by corner truncations on plates.[10,16] Geometrical ray tracing predicts that any corner truncation of angle $180°/n$, where n is an even integer, will exhibit the retroreflection process.[10] Although the present work focused on 90° corners, Dodd observed retroreflective contributions to backscattering for plates having both 45° and 90° corner truncations, and the observed peak backscattered pressure ratio was in good agreement with a theoretical prediction from a one-dimensional analysis analogous to that presented in Sec. II.[16] Though we are not aware of the publication of sonar images demonstrating enhanced target visibility from this mechanism, images have been published for other situations where the visibility of the edge of a target is enhanced due to reflection of a leaky wave.[17]

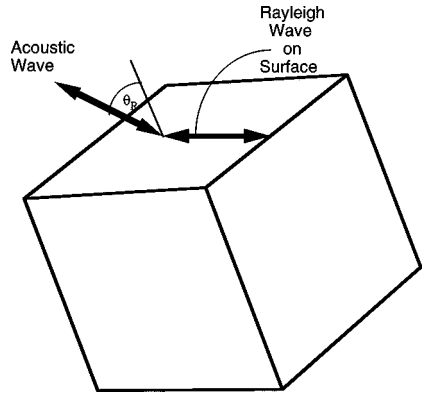

FIG. 9. Single-bounce edge reflection. Backscattering can also occur when the block is tilted such that its edges are level ($\gamma=45$ degrees) so that only one edge is involved in the reflection process. The signal from this type of reflection has a larger amplitude but a smaller angular width than the corner retroreflection which is the main topic under investigation.

It is also noteworthy that the tilt degradation experiments of the present investigation revealed a very large signal for $\gamma=45°$, which was omitted from the data displayed in Fig. 6 because it corresponds to a slightly different mechanism. That mechanism is depicted in Fig. 9 and may be termed a single-bounce edge reflection. Since the mechanism shown in Fig. 9 requires that γ lie close to 45°, it is relatively unlikely to be observed for a randomly oriented cube; its analysis is outside the scope of the present paper.

ACKNOWLEDGMENTS

This research was supported by the Office of Naval Research. Portions of related research on the scattering by the corners of plates (Refs. 10 and 16) were carried out while one of the authors (P.L.M.) was a Visiting Scientist at the Applied Research Laboratories of University of Texas and was supported by the ARL:UT Independent Research and Development Program.

APPENDIX A: DEPHASING OF BACKSCATTERED PRESSURE WITH INCIDENT ANGLE

Equation (8) represents the backscattered pressure when the acoustic wave is incident at the Rayleigh angle. For incidence at other angles, the phase terms in the convolution integral do not cancel but instead lead to a transverse phase

dependence on the block's surface and a modified prefactor. If the incident pressure has $k_x \neq k_R$, then the pressure for $x=0$ and $y \geqslant 0$ is found from Eq. (1) to be

$$p_R(0,y) = -2p_0 \frac{\alpha}{\alpha + i\,\Delta k} \exp(-i\,\Delta k\, y + i\varphi_b) \times \exp(-\alpha y), \tag{A1}$$

where $\Delta k = k_x - k_R$. To account for propagation and attenuation of the Rayleigh wave on the image plane and its reflection at the edges, Eq. (A1) is multiplied by $B\exp(ik_R x)\exp(-\alpha x)$. The constant phase surfaces on the image block are thus no longer oriented in the y direction, but instead are found to be given by lines of slope $k_R/\Delta k$. The phase dependence can be viewed as a skewing of the rays at the edge of the block, before propagation onto the image block. The rays that correspond to the direction of propagation of the wavefronts are described by lines of slope $-\Delta k/k_R$; these make an angle φ with the x axis, where φ is given by

$$\tan\varphi = \frac{-\Delta k}{k_R} = \frac{k_R - k_x}{k_R}, \tag{A2}$$

where the fact that $\tan\varphi$ is an odd function means that Eq. (A2) retains the information of whether k_x is greater or less than k_R, so that both cases may be analyzed simultaneously.

A simple method of approximating the skewing uses a parameter $\beta = -\tan\varphi$, with φ defined as in Eq. (A2). Taking the exit plane along the block's surface, the leaky wave pressure for $y \geqslant 0$ on the surface is obtained from Eq. (A1) by allowing for paraxial propagation along x and by using $\Delta k = \beta k_R$ in the y term:

$$p_R(x,y) = -2p_0 \frac{\alpha B}{\alpha + i\,\Delta k} \exp(-i\beta k_R y - \alpha y + i\varphi_b) \times \exp(i(k_R + i\alpha)x). \tag{A3}$$

The leaky wave contribution to the far-field pressure is then found using the far-field form of the Rayleigh–Sommerfeld propagation integral [see our Eq. (5) and Eq. (6) of Ref. 5]:

$$p_{ff} = \frac{-ik}{2\pi r}\cos\theta \exp(ikr) \int_{-\infty}^{\infty}\int_{x_b}^{\infty} p_R(x,y) \times \exp(-ikx\sin\theta)\,dx\,dy, \tag{A4}$$

where r is the distance from the point (0,0) on the block's surface to the far-field evaluation point, and the lower integration limit of x, $x_b = x_b(y)$, depends on the edge of the block. Substituting Eq. (A3) into Eq. (A4) and evaluating the integral gives the magnitude of the far-field pressure as

$$|p_{ff}| = \frac{4p_0 B}{\lambda r}\cos\theta \left|\frac{\alpha}{\alpha + i\,\Delta k}\right| \frac{1}{|\alpha + i\,\Delta k|} \frac{1}{|2\alpha + i\beta k_R + i\,\Delta k|}, \tag{A5}$$

using summetry for $y<0$. Note that for $\theta = \theta_R$, Eq. (A5) reduces to Eq. (8), as expected. Furthermore, Eq. (A5) gives the ratio of the result for $\theta \neq \theta_R$ to the result for $\theta = \theta_R$ as

$$\left|\frac{p_{scat}(\theta \neq \theta_R)}{p_{scat}(\theta = \theta_R)}\right| = \frac{\cos\theta}{\cos\theta_R} F_1 F_2; \tag{A6a}$$

$$F_1 = \frac{1}{1 + (kL)^2(\sin\theta - \sin\theta_R)^2}; \tag{A6b}$$

$$F_2 = \frac{1}{\sqrt{1 + (jkL)^2(\sin\theta - \sin\theta_R)^2}}, \tag{A6c}$$

where j is a parameter accounting for the wavefront skew on the block's surface: taking $j = \frac{1}{2}$ ($\beta = 0$) neglects the effects of wavefront skew while $j = 1$ ($\beta = \Delta k/k_R$) includes the effects. (As seen in Ref. 12, the results are very similar for the two cases.) The main consequence of dephasing is through the terms Δk in (A5). The theoretical dephasing curve plotted in Fig. 4 was generated by evaluating Eq. (A6) with $j = \frac{1}{2}$ for 0.01° steps over an 8° interval, normalizing the results to the peak pressure magnitude predicted by Eq. (E2), and using Eq. (E5) to express the results in terms of a dimensionless form function.

APPENDIX B: SIGNAL DEGRADATION WITH BLOCK TILT

The calculations in Sec. II are for an untilted block; backscattering will decrease when the block is tilted for two reasons: (a) the Rayleigh wave will strike the reflecting edges at different angles, which have different reflection coefficients; and (b) the Rayleigh wave will travel a greater distance as it cuts across the corner of the block, resulting in increased attenuation. If the block is tilted by an angle γ, the Rayleigh wave will be incident on one reflecting edge at $45° + \gamma$ and the other at $45° - \gamma$ (see Fig. 5), so that both the reflection coefficients contributing to the product B in Eq. (8) are altered. Approximating the Rayleigh wave reflection coefficients for the case under investigation as the corresponding values on an elastic quarter-space bounded by a vacuum, as determined by Gautesen,[13] it is found that the *product* of the two reflection coefficients is greatest in the angular region near $\gamma = 0°$. Any tilt away from that angle will therefore tend to decrease the amplitude of the wave after retroreflection and subsequently decrease the backscattered pressure.

The increased attenuation will also tend to decrease the backscattered pressure; this effect can be quantified by geo-

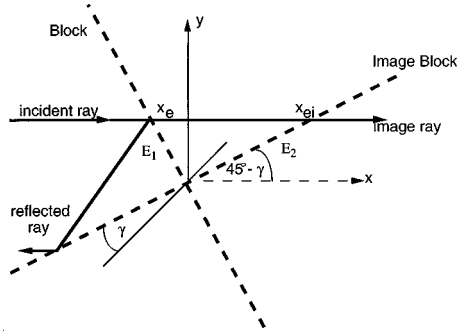

FIG. B1. Image plane for the tilted block. The distance across the corner is the same as the distance $X_c = x_{ei} - x_e$, which can be determined from the triangle with sides X_c, E_1, and E_2, as discussed in the text. X_c is longer than the corresponding distance for the untilted block, resulting in a decrease in amplitude due to extra attenuation.

metrical analysis of the change in pathlength resulting from tilting the block. From Fig. 7 we can see that for the untilted block the pathlength across the corner is $2y$. Figure B1 shows the corresponding figure when the block is tilted by an angle γ. From the figure we can see that the path across the corner, $X_c = x_e - x_{ei}$, is the hypotenuse of a triangle having the edges of the corner labeled by E_1 and E_2 as its other two sides, where E_1 and E_2 are given by

$$E_1 = \frac{y}{\cos(45° - \gamma)}; \tag{B1}$$

$$E_2 = \frac{y}{\sin(45° - \gamma)}. \tag{B2}$$

Substituting Eqs. (B1) and (B2) into the Pythagorean theorem and making trigonometric simplifications shows the pathlength across the corner to be a function of y and γ:

$$X_c(y, \gamma) = 2y \frac{1 + (\tan \gamma)^2}{1 - (\tan \gamma)^2}. \tag{B3}$$

Repeating the steps leading to Eq. (8) with the geometry shown in Fig. B1 shows that after the integration over x', the integrand $\exp(-2\alpha y')$ is replaced by $\exp(-\alpha X_c(y', \gamma))$. The subsequent integration over y' gives increased attenuation from the increased pathlength, which results in an amplitude factor of

$$K(\gamma) = \frac{1 - (\tan \gamma)^2}{1 + (\tan \gamma)^2}. \tag{B4}$$

The above analysis may be repeated for a block tilted by $-\gamma$, in which case the arguments of Eqs. (B1) and (B2) are replaced by $45° + \gamma$. Such substitutions result in Eq. (B3) for the pathlength so that Eq. (B4) is the correct tilt degradation factor, regardless of the direction of tilt.

The dephasing curve shown in Fig. 6 was generated by discretizing Gautesen's graphical presentation of Rayleigh wave reflection coefficients, multiplying the tilt degradation factor $K(\gamma)$ by the product of the coefficients at $45° + \gamma$ and $45° - \gamma$ for each value of γ in 1° steps over the interval plotted, and normalizing with respect to the measured amplitude at $\gamma = 0$. The curve may be reflected about $\gamma = 45°$ and $\gamma = 0°$ as desired to generate a tilt degradation curve valid for the complete 360° tilt range of the block. It is noteworthy that the retroreflected signal is detectable for almost any tilt of the block. The weak local maximum predicted near γ of 7° in Fig. 6 is the result of features of the reflection coefficient calculated by Gautesen.

APPENDIX C: CORRECTION TO THE APPROXIMATION OF A SEMI-INFINITE BLOCK

To represent the finite nature of the block, the lower limit of integration in Eq. (3) and both the upper and lower integration limits in Eq. (5) are modified. Letting d represent the block diagonal, Fig. C1 shows that for the untilted case we can write the lower limit of the x integration on the block in Eq. (3) as $x_0 = -(d - x_e) = -d + y$, while the upper limits on the image block become $x_{oi} = d - x_{ei} = d - y$ for the x integration and $d/2$ for the y' integration. The modifications to Eq. (3) give the pressure on the image block as

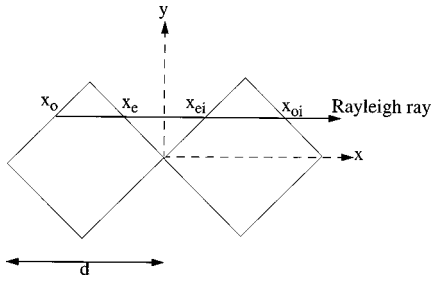

FIG. C1. Integration limits for the finite block. As seen from the sketch, the x integration limits on the block are x_0 to x_e, and on the image block they are x_{ei} to x_{oi}. The y integration extends from $-d/2$ to $d/2$. Evaluating Eqs. (5) and (7) with these corrected limits gives Eq. (C3).

$$|p_R(x,y)| = 2Bp_0 \exp(-\alpha x)\exp(-\alpha y) \times [1 - \exp(-\alpha d)\exp(2\alpha y)], \tag{C1}$$

where the bracketed factor modifies the result of Eq. (4) for the infinite corner. Substituting this result into Eq. (5) with the appropriate modifications to the integration limits discussed above and defining the dimensionless parameter $\zeta = d/L$, gives the far-field pressure as

$$|p_{scat}| = \frac{2BL^2 p_0 \cos \theta_R}{\lambda r}[1 - 2\zeta \exp(-\zeta) - \exp(-2\zeta)]. \tag{C2}$$

Comparing Eq. (C2) to Eq. (9) yields the geometrical correction factor g:

$$g(\zeta) = 1 - 2\zeta \exp(-\zeta) - \exp(-2\zeta). \tag{C3}$$

For these experiments, $d = 8.48$ cm and $L = 2.88$ cm so that $g = 0.688$.

APPENDIX D: ESTIMATION OF ANGULAR UNCERTAINTY DUE TO FINITE SEPARATION DISTANCE

In this Appendix we analyze the effect that the finite distance between the source and target has on the angle at which the incident wave strikes the corner of the block. Because of radiation damping, the largest contribution to backscattering will come from leaky rays with a detachment point very near the launch point, i.e., those launched just prior to the retroreflection around the corner. Therefore, the peak backscattered pressure will occur at the angle associated with incidence on the block's corner rather than at its center. The situation is illustrated in Fig. D1, where it can be seen that the angle of incidence on the corner is larger than the angle of incidence at the block's center by δ. Since the experimental angle θ is measured at the center of the block, the peak backscattered signal is expected to occur at the angle $\theta - \delta$. The present analysis approximates the transducer as a point source, so that the results give only an upper bound on δ rather than an exact value.

Letting C represent the distance from the transducer to the center of the block and d represent the diagonal of the block, it is found that $\tan \delta = a/c = A/C$, with a and A defined as in Fig. D1. Reference to the figure shows that c

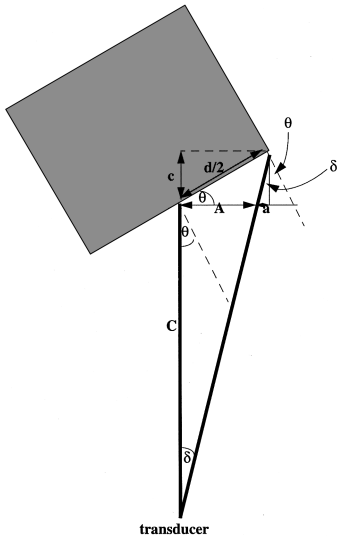

FIG. D1. Geometrical analysis of the effect of the finite separation distance on the incident angle. From the sketch it can be seen that if θ is the angle of incident at the center of the block, then the angle of incidence on the corner is $\theta+\delta$.

$=(d/2)\sin\theta$ and $A+a=(d/2)\cos\theta$. Solving this system of equations yields $\delta=\arctan[(\tan\theta(1+(2C)/(d\sin\theta)))^{-1}]$. Substituting in the measured values of $d=8.48\,\text{cm}$, $C=170\,\text{cm}$, and $\theta=29.9°$ from the experiment gives a predicted shift of $-1.21°$. The measured angular discrepancy of $-0.7°$ is well within this upper bound. Therefore, the angular shift of the theoretical dephasing curves in Fig. 4 is justified on the basis of the finite distance between the source and the target.

APPENDIX E: NORMALIZATION OF DATA

In this Appendix we explain how the measured pressure amplitudes are converted to form function magnitudes (such as plotted in Fig. 4). The target was a solid stainless steel 303 cubic block 6.00 cm on a side and was suspended from the rotary stage by four thin stainless steel wires, as shown in Fig. E1. The measured pressure amplitudes were initially

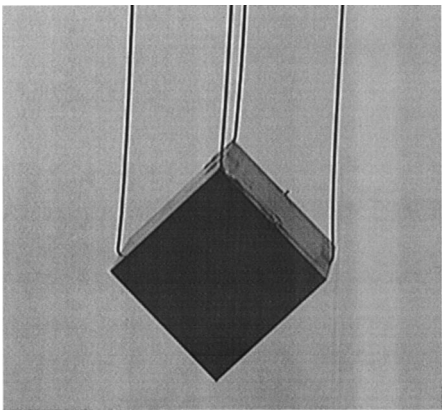

FIG. E1. Photograph of the cubical target. The target was a solid stainless cube 6.00 cm on a side and was suspended by four thin stainless steel wires. The wires were welded to the top face of the cube so as not to affect the reflecting surface, which was the front face of the block. The wires attached to the apex were fixed, and the tilt of the block was adjusted by changing the lengths of the two side wires.

calibrated to the measured specular return from a calibration sphere for each experiment.[5] The calibration sphere used in these experiments was a solid sphere of radius 3.49 cm composed of stainless steel 440c. After each dataset, the block was removed from the water and replaced by the sphere, with time traces ensuring that the front surface of the sphere was at the same location as the block's reflecting surface. Using p_0 to represent the magnitude of the incident pressure, the magnitude of the pressure backscattered to a far-field observation point a distance r from a sphere of radius a is known to be expressible as[5]

$$|p_{\text{sph}}|=p_0\frac{a|f_{\text{spec}}|}{2r}, \tag{E1}$$

where f_{spec} is the specular form function of the sphere. In the high-frequency limit the magnitude of f_{spec} can be approximated as $|\rho_E c_L-\rho c|/|\rho_E c_L+\rho c|$, where ρ_E and c_L are the density and longitudinal wave speed of the elastic solid and ρ and c are the density and speed of sound in the surrounding water. Using parameters in Table I, we find that $|f_{\text{spec}}|\cong 0.938$ for the experiments of this chapter. From Eq. (8) we can see that calibrating the data in this way eliminates the dependence of the backscattering amplitude on incident pressure and observation point; specifically, Eq. (8) yields

$$\frac{|p_{\text{scat}}|}{|p_{\text{sph}}|}=\frac{4BL^2g\cos\theta_{\text{R}}}{\lambda a|f_{\text{spec}}|}. \tag{E2}$$

A form function for the cube was subsequently defined by normalization with respect to a reference sphere of the same projected area, as introduced by Chinnery *et al.* for scattering by cubes in the low-frequency regime.[3] We have chosen to follow Chinnery's form function convention, despite the fact that the scattering pattern in the low-frequency regime includes resonances that are not relevant to our high-frequency tone burst measurements. A generic form function is defined from power considerations to be[3]

$$|f|=\sqrt{\frac{4\pi r^2}{A}}\frac{|p_{\text{scat}}|}{|p_0|}, \tag{E3}$$

where A is the projected cross-sectional area of the scatterer. Note that for a sphere, $A=\pi a^2$, so that Eq. (E3) gives the same result as Eq. (E1). However, for a cube, the projected cross-sectional area will depend on the orientation of the cube; therefore the average projected cross-sectional area $\langle A\rangle=3s^2/2$ is used. This gives the form function of the cube as

$$|f_{\text{cube}}|=\frac{2r}{s\sqrt{3/(2\pi)}}\frac{|p_{\text{scat}}|}{|p_0|}. \tag{E4}$$

Since Eq. (E4) has the structure of a form function of a sphere of radius $a_{\text{ref}}=s\sqrt{3/(2\pi)}$, the form function can be interpreted as referenced to a sphere having the same projected area as the cube. Equation (E1) can be used to eliminate the dependence on r and p_0, yielding an expression for the form function of the cube in terms of the ratio of the pressure magnitude backscattered by the cube to the pressure magnitude of the specular return from the calibration sphere. The result is

$$|f_{\text{cube}}| = \frac{a|f_{\text{spec}}|}{s\sqrt{3/(2\pi)}} \frac{|p_{\text{scat}}|}{|p_{\text{sph}}|}. \tag{E5}$$

This normalization is applied to both the measured pressure ratios and the theoretical pressure ratio given by Eq. (E2). In the experiments of this chapter, $a = 1.75\,\text{cm}$, $s = 6.00\,\text{cm}$, and $|f_{\text{spec}}| = 0.938$, so that the prefactor is found to be 0.790.

[1] R. R. Goodman and R. Stern, ''Reflection and transmission of sound by elastic spherical shells,'' J. Acoust. Soc. Am. **34**, 338–344 (1962).

[2] L. Flax, G. C. Gaunaurd, and H. Uberall, ''Theory of resonance scattering,'' in *Physical Acoustics*, edited by R. N. Thurston (Academic, New York, 1981), Vol. 15, pp. 191–293.

[3] P. A. Chinnery, V. F. Humphrey, and J. Zhang, ''Low-frequency acoustic scattering by a cube: Experimental measurements and theoretical predictions,'' J. Acoust. Soc. Am. **101**, 2571–2582 (1997); P. A. Chinnery, J. Zhang, and V. F. Humphrey, ''Acoustic scattering by nonmetallic and metallic cubes in the elastic resonance regime: Experimental measurements and combined finite element/boundary element modeling,'' *ibid.* **102**, 60–66 (1997).

[4] P. D. Thorne, S. Sun, J. Zhang, I. Bjorno, and T. Mazoyer, ''Measurements and analysis of acoustic backscattering by elastic cubes and irregular polyhedra,'' J. Acoust. Soc. Am. **102**, 2705–2713 (1997).

[5] P. L. Marston, ''Geometrical and catastrophe optics methods in scattering,'' in *Physical Acoustics*, edited by R. N. Thurston and A. D. Pierce (Academic, Boston, 1992), Vol. 21, pp. 1–234.

[6] P. L. Marston, ''GTD for backscattering from elastic spheres and cylinders and the coupling of surface elastic waves with the acoustic field,'' J. Acoust. Soc. Am. **83**, 25–37 (1988).

[7] H. L. Bertoni and T. Tamir, ''Unified theory of Rayleigh-angle phenomena for acoustic beams at liquid–solid interfaces,'' Appl. Phys. **2**, 157–172 (1973).

[8] W. G. Neubauer and L. R. Dragonette, ''Monostatic reflection from a rigid rectangular plane,'' J. Acoust. Soc. Am. **41**, 656–661 (1967).

[9] P. L. Marston, ''Leaky waves on weakly curved scatterers. II. Convolution formulation for two-dimensional high-frequency scattering,'' J. Acoust. Soc. Am. **97**, 34–41 (1995).

[10] P. L. Marston, S. S. Dodd, and C. M. Loeffler, ''Retroreflective backscattering of sound in water due to leaky waves on facets, plates, and corner truncations: approximate theory,'' J. Acoust. Soc. Am. **94**, 1861(A) (1993).

[11] P. L. Marston, ''Spatial approximation of leaky wave surface amplitudes for three-dimensional high-frequency scattering: Fresnel patches and application to edge-excited and regular helical waves on cylinders,'' J. Acoust. Soc. Am. **102**, 1628–1638 (1997).

[12] K. Gipson, ''Leaky Rayleigh wave ultrasonic backscattering enhancements: Experimental tests of theory for tilted solid cylinders and cubes,'' Ph.D. thesis, Washington State University, 1998.

[13] A. K. Gautesen, ''Scattering of an obliquely incident Rayleigh wave in an elastic quarter-space,'' Wave Motion **8**, 27–41 (1986).

[14] L. M. Brekhovskikh, *Waves in Layered Media* (Academic, New York, 1980).

[15] W. G. Neubauer, ''Ultrasonic reflection of a bounded beam at Rayleigh and critical angles for a plane liquid–solid interface,'' J. Appl. Phys. **44**, 48–55 (1973).

[16] S. S. Dodd, C. M. Loeffler, and P. L. Marston, ''Retroreflective backscattering of sound in water due to Lamb waves on plates with corners,'' J. Acoust. Soc. Am. **94**, 1765(A) (1993).

[17] G. Kaduchak, C. M. Wassmuth, and C. M. Loeffler, ''Elastic wave contributions in high-resolution acoustic images of fluid-filled, finite cylindrical shells in water,'' J. Acoust. Soc. Am. **100**, 64–71 (1996).

Acoustic recovery of lost power in pulse tube refrigerators

G. W. Swift, D. L. Gardner, and S. Backhaus
Condensed Matter and Thermal Physics Group, Los Alamos National Laboratory, Los Alamos, New Mexico 87545

(Received 18 May 1998; accepted for publication 21 October 1998)

In an efficient Stirling-cycle cryocooler, the cold piston or displacer recovers power from the gas. This power is dissipated into heat in the orifice of an orifice pulse tube refrigerator, decreasing system efficiency. Recovery of some of this power in a pulse tube refrigerator, without sacrificing the simplicity and reliability inherent in a system with no cold moving parts, is described in this paper. In one method of such power recovery, the hot ends of both the regenerator and the pulse tube are connected to the front of the piston driving the refrigerator. Experimental data is presented demonstrating this method using a thermoacoustic driver instead of a piston driver. Control of time-averaged mass flux through the refrigerator is crucial to this power recovery, lest the refrigerator's cooling power be overwhelmed by a room-temperature mass flux. Two methods are demonstrated for control of mass flux: a barrier method, and a hydrodynamic method based on turbulent irreversible flow. At $-55\,^{\circ}\mathrm{C}$, the refrigerator provided cooling with 9% of the Carnot coefficient of performance. With straightforward improvements, similar refrigerators should achieve efficiencies greater than those of prior pulse tube refrigerators and prior standing-wave thermoacoustic refrigerators, while maintaining the advantages of no moving parts. © *1999 Acoustical Society of America.* [S0001-4966(99)00802-4]

PACS numbers: 43.35.Ud [HEB]

INTRODUCTION

As illustrated in Fig. 1(a) and (b), the orifice pulse tube refrigerator[1] (PTR) may be regarded as a Stirling refrigerator in which the cold moving parts have been replaced by stationary components. A reduction in efficiency may accompany this simplification in hardware, for a number of reasons. The most obvious cause of reduced efficiency is that work is absorbed and dissipated into waste heat in the orifice of the orifice PTR, whereas it is recovered at the cold piston of the Stirling machine and delivered back to the hot end of the system, either directly (via a displacer) or indirectly (via a crankshaft). Kittel[2] has shown that this orifice dissipation, regarded as a loss inherent to the orifice PTR, causes the coefficient of performance COP (i.e., the efficiency) of orifice PTRs to be bounded by T_C/T_H, significantly less than the Carnot COP $T_C/(T_H-T_C)$ which bounds Stirling refrigerators. (T is temperature and the subscripts C and H refer to cold and hot, respectively.) This inherent loss is most severe for $T_C \sim T_H$, thus far preventing practical use of orifice PTRs in noncryogenic applications such as food refrigeration and air conditioning. Orifice dissipation loss is also important in cryogenic systems: In one large orifice PTR with which we are familiar,[3,4] having 2 kW of cooling power at 125 K, orifice dissipation comprises 30% of the entropy generation and lost available work[5] in the refrigeration system (excluding losses in its thermoacoustic driver).

Acoustic transmission lines and inertances can pass acoustic power with little dissipation, while shifting the magnitude and phase of oscillatory pressure dramatically. This suggested to us that they could perform the work-recovery function of the Stirling's cold piston, while preserving the PTR's no-moving-parts advantage. This can be accomplished by at least two methods, illustrated schematically in Fig. 1(c) and (d) for a piston-driven pulse tube refrigerator. In the first method, an acoustic transmission line replaces the orifice, inertance, and compliance, connecting between the hot heat exchanger of the pulse tube and the back side of the drive piston. Most of the power that would previously have been dissipated in the orifice travels along the transmission line to the back side of the piston, helping move the piston and hence reducing the power required of the motor. In the second method, an inertance (or short transmission line) and a compliance between the piston and the aftercooler produce substantial amplitude and phase shifts between them, with the hot heat exchanger of the pulse tube connected at the *front* of the piston. In this method, the power previously dissipated in the orifice is delivered directly to the *front* of the piston and thereby added to the power supplied by the piston, reducing the power required of the motor. Thus, for both methods, system efficiency can be greater than for conventional orifice PTRs.

The fundamental idea behind these methods (and others) was fully anticipated over ten years ago by Ceperley,[6] whose early publications on ''traveling wave heat engines'' (including refrigerators) inspired the beginnings of thermoacoustics research here at Los Alamos. Ceperley realized that the essence of Stirling equipment is a regenerator in which the pressure and volumetric velocity oscillations are substantially in phase, and that an acoustic network with essentially toroidal topology [e.g., in our Fig. 1(c) or (d)] containing the Stirling heat-exchange components can provide such phasing. He showed that efficiencies near 80% of the Carnot efficiency are, in principle, possible with such configurations.

However, Ceperley did not discuss two features that we find are vital for practical operation of such refrigerators and

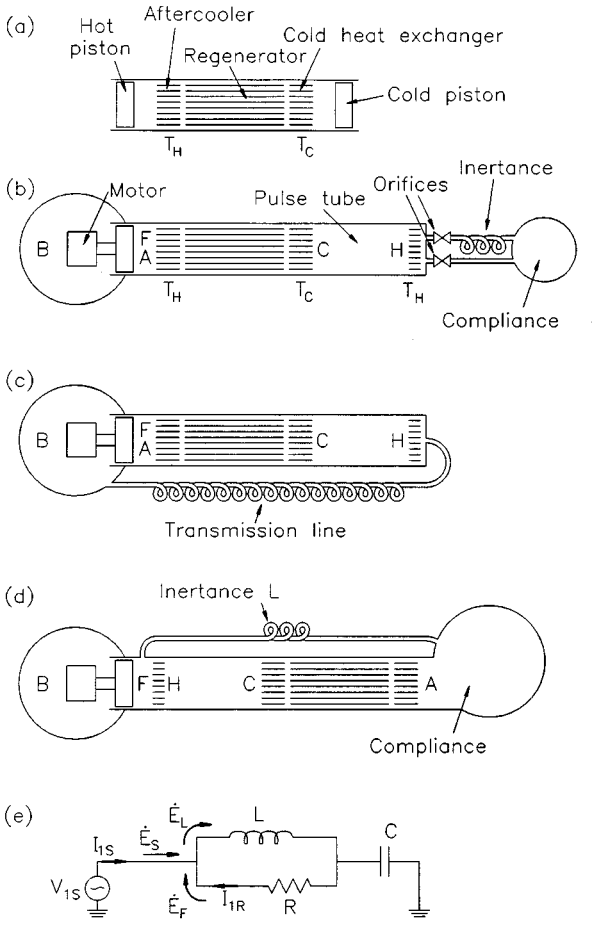

FIG. 1. Schematics of (a) Stirling cycle refrigerator (omitting details such as motor, crankshaft, etc.), (b) orifice pulse tube refrigerator, in which the cold piston of the Stirling cycle refrigerator is replaced by passive components, (c) pulse tube refrigerator with transmission-line feedback, and (d) pulse tube refrigerator with lumped boost configuration. To avoid confusion with the pulse tube's hot heat exchanger, the heat exchanger at the hot end of the regenerator is called the aftercooler. Capital letters in (b) through (d) label locations in the refrigerators: B—back of piston; F—front of piston; A—aftercooler; C—cold heat exchanger; H—hot heat exchanger; and L—inertance. The pistons move sinusoidally in time; the gas velocity in the regenerator is generally from aftercooler to cold heat exchanger while the pressure is high and generally in the opposite direction while the pressure is low. (e) Electric circuit crudely analogous to the acoustic network of (d).

engines. First, a thermal insulation column, namely the pulse tube itself in PTR practice, must insulate the ''remote'' heat exchanger (cold for refrigerators, hot for engines) from ambient temperature. The heat leak along a pulse tube can be as small as 5% of the cooling power of a PTR[7] using a tapered[8] pulse tube, although 15%–40% is typical.[9] Second, something must be done to prevent significant time-averaged mass flow from circulating around the torus. Gedeon[10] has discussed causes of such mass flow and the large heat flux it can carry.

To discuss these concepts quantitatively and in more detail, we take the essential physics to be spatially one-dimensional, with x specifying the coordinate along the direction of oscillatory gas motion. We use the conventional counter-clockwise phasor notation, so that time-dependent variables are expressed as

$$\xi(x,t)=\xi_m(x)+\mathrm{Re}[\xi_1(x)e^{i\omega t}], \tag{1}$$

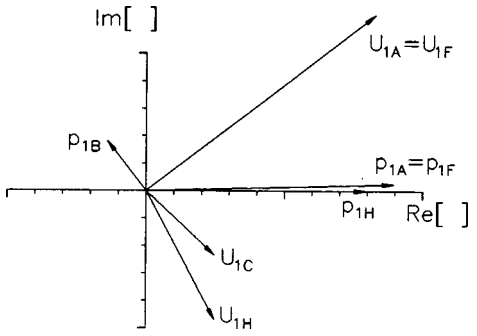

FIG. 2. Typical phasor diagram. Cryogenic pulse tube refrigerators with sufficient power to employ inertances have phasors similar to these, with p_1 in the pulse tube slightly smaller in magnitude than at the aftercooler, and usually lagging in phase; and with U_1 leading pressure at the aftercooler and lagging at both ends of the pulse tube. Pressure phasors are plotted as p_1/p_m, with each mark on the axes representing 0.01. Velocity phasors are plotted as U_1/Sa, where S is pulse tube area and a is sound speed, with each mark on the axes representing 0.001.

with the mean value ξ_m real, and with $\xi_1(x)$ complex to account for both the magnitude and phase of the oscillation. We adopt an acoustical point of view,[11] using the vocabulary of acoustic resistance, inertance, compliance, and transmission line to discuss the lumped and distributed impedances associated with the components of the PTR. This approach has been successful previously, even within regenerators.[12–15] In a minor departure from most prior PTR literature, which has focused on pressure p_1 and mass flux $\dot{M}_1$ as the oscillatory quantities of most interest, we will generally use the conventional acoustic variables p_1 and volumetric velocity U_1; the latter is related to mass flux simply via $\dot{M}_1=\rho_m U_1$, where ρ is the mass density. We take x and U_1 positive in the direction of positive acoustic power flow, for example to the right through the regenerators and pulse tubes in Fig. 1(a)–(c), and to the left through the transmission line in Fig. 1(c).

Some very general, almost unavoidable features of phasor diagrams for efficient cryogenic orifice PTRs are shown in Fig. 2, where the extra, capitalized subscripts on p_1 and U_1 correspond to the location labels in Fig. 1(b). We adopt the arbitrary convention that the phase of the pulse tube pressure is zero, so p_{1H} falls on the real axis. Typically the pressure drop along the pulse tube itself is immeasurably small, and that across the heat exchangers is negligible compared to that across the regenerator, which is in turn small compared to $|p_1|$, so $p_{1C}\cong p_{1H}$ and p_{1A} must lie close to p_{1H}, as shown in Fig. 2. Typically the time-averaged energy flux through the regenerator is small.[16] Applying energy conservation to the cold heat exchanger then shows that the cooling power $\dot{Q}_C$ is approximately equal to the total power flowing away from the cold heat exchanger in the pulse tube. The open nature of the pulse tube suggests that this total power flowing along it is the acoustic power $\frac{1}{2}\mathrm{Re}[p_1\tilde{U}_1]$, where the tilde signifies complex conjugation; in fact, heat can flow from hot to cold in the pulse tube, so the acoustic power is an upper bound of the cooling power:

$$\dot{Q}_{C,\mathrm{gross}}\leqslant \tfrac{1}{2}\mathrm{Re}[p_{1C}\tilde{U}_{1C}]. \tag{2}$$

Hence, in Fig. 1(a)–(d) acoustic power must flow in the di-

rection we have defined as positive x, so U_{1A}, U_{1C}, and U_{1H} must lie in the right half-plane in Fig. 2. An idealized refrigerator might be imagined with negligible entrained gas volume, so that U_1 would be independent of x in the pulse tube, $\rho_m U_1$ would be independent of x in the regenerator, and in particular the phase of U_1 would be constant throughout the refrigerator. As is well known,[1] nonzero gas volume causes x dependence in U_1, proportional to the compliance of the components and to $i\omega p_1$. This leads to a spread in phase of U_1 through the system, with U_1 at small x (i.e., toward the aftercooler) leading. The most efficient regenerator operation is achieved for the phase of p_1 falling somewhere between the phases of U_1 at the two ends of the regenerator. In orifice PTRs, this can be achieved using inertance[17,18] or a double inlet.[19] Viscous pressure drop occurs throughout the regenerator, so $p_{1A}-p_{1C}\cong p_{1A}-p_{1H}$ must be in phase with (parallel to) some weighted average of U_1 in the regenerator. Both $|U_1|$ and viscosity are highest at the regenerator's hot end, so the weighted average is dominated by U_{1A}, generally ensuring that p_{1H} lags p_{1A}. Finally, to the extent that the volume V_B on the back side of the piston is simply a compliance,

$$p_{1B}=j\frac{\gamma p_m}{\omega V_B}U_{1F}, \tag{3}$$

so p_{1B} must lead $U_{1F}=U_{1A}$ by 90°. Often the gas volume on the back side is large enough that $|p_{1B}|$ is much smaller than $|p_{1F}|$. These features are also illustrated in Fig. 2.

As discussed in the first paragraph, in an orifice PTR, the acoustic power

$$\dot{W}_H=\frac{\omega}{2\pi}\int_0^{2\pi/\omega}p(t)U(t)dt=\frac{1}{2}\mathrm{Re}[p_{1H}\tilde{U}_{1H}] \tag{4}$$

exiting the hot end of the pulse tube is lost, dissipated into heat in the orifice. This is typically nearly equal to the gross cooling power given in Eq. (2). To recover this acoustic power, thereby bringing the inherent efficiency limit of PTRs up to the Carnot limit, we can incorporate either of two low-loss acoustic connections shown in Fig. 1(c) and (d). The first method is described briefly in the next section: As shown in Fig. 1(c), a transmission line feeds the power recovered from the hot end of the pulse tube to the back side of the drive piston at p_{1B}. In Sec. II, we describe the second, more interesting method, shown in Fig. 1(d), in which the pulse tube delivers the recovered power directly to the front of the driver at p_{1F}, while the inertance delivers the drive power to the aftercooler. To convey the generality of the two methods, we describe them qualitatively for a piston driver in Secs. I and II, but we present experiments based on the second method using a thermoacoustic driver in Secs. III, IV, and V. In common with the double-inlet PTR,[19] both of these methods unfortunately permit second-order mass streaming through the refrigerator; in Sec. V we discuss our progress toward simple control of this important effect. Finally, in Sec. VI we present some conclusions and challenges for future development.

The idea that acoustic power will naturally circulate clockwise through the networks of Fig. 1(c) and (d) seems surprising, until we consider the LRC circuit of Fig. 1(e), a textbook electrical circuit crudely analogous to the acoustic network of Fig. 1(d). Many of us have derived expressions for the ac currents in each component of this circuit, but seldom do we consider the time-averaged electric power flows $\dot{E}$. By energy conservation, the time-averaged power $\dot{E}_S=\frac{1}{2}\mathrm{Re}[V_{1S}\widetilde{I_{1S}}]$ flowing from the voltage source into the circuit must equal the time-averaged power $\dot{E}_L-\dot{E}_F$ dissipated in the resistor. (In this idealized circuit, no time-averaged power can be absorbed in the dissipationless inductor L nor flow into the dissipationless capacitor C.) Ordinary ac circuit analysis easily yields the fed-back power

$$\dot{E}_F=\frac{1}{2}\mathrm{Re}[V_{1S}\widetilde{I_{1R}}]=\frac{|V_{1S}|^2}{2R}\frac{\omega^2LC(1-\omega^2LC)}{(1-\omega^2LC)^2+(\omega L/R)^2}, \tag{5}$$

with the sign convention as shown in the figure. Hence, whenever $\omega^2LC<1$, the directions of time-averaged power flow are as shown in the figure; positive electric power $\dot{E}_F$ flows *out* of the end of the resistor closest to the voltage source!

I. ACOUSTIC POWER RECOVERY

A. Transmission line configuration

Figure 1(c) illustrates an acoustic transmission line connecting the hot end of the pulse tube with the back side of the drive piston. A transmission line[20] obeys the equations

$$p_1(x)=p_{1i}\cos kx-i\frac{\rho_m a}{S}U_{1i}\sin kx, \tag{6}$$

$$U_1(x)=U_{1i}\cos kx-i\frac{S}{\rho_m a}p_{1i}\sin kx, \tag{7}$$

which show how p_1 and U_1 evolve with x along the transmission line, given their initial values p_{1i} and U_{1i} at $x=0$. The cross-sectional area of the transmission line is S, and a is the sound speed. [We omit the subscript m on variables such as a which, in principle, should be expressed as in Eq. (1) but whose oscillatory parts are of no interest in this work.] If the wave vector k is real, these equations describe a lossless transmission line, with $\frac{1}{2}\mathrm{Re}[p_1\tilde{U}_1]$ independent of x; losses in the transmission line (due to viscosity and thermal conductivity) can be included by using complex k.

From Eq. (6), a transmission line can connect the hot end of the pulse tube with the back side of the piston if its length l and area S are chosen such that

$$p'_{1B}=p_{1H}\cos kl-i\frac{\rho_m a}{S}U_{1H}\sin kl, \tag{8}$$

with the new value of p'_{1B} determined by a modified version of Eq. (3), accounting for the volumetric velocity flowing into V_B from the end of the transmission line:

$$p'_{1B}=j\frac{\gamma p_m}{\omega V_B}\left(U_{1F}-U_{1H}\cos kl+i\frac{S}{\rho_m a}p_{1H}\sin kl\right). \tag{9}$$

Because Eqs. (8) and (9) are complex, they represent four real equations in the four unknowns l, S, $\mathrm{Re}[p'_{1B}]$, and $\mathrm{Im}[p'_{1B}]$, so they will generally have a solution. The curves

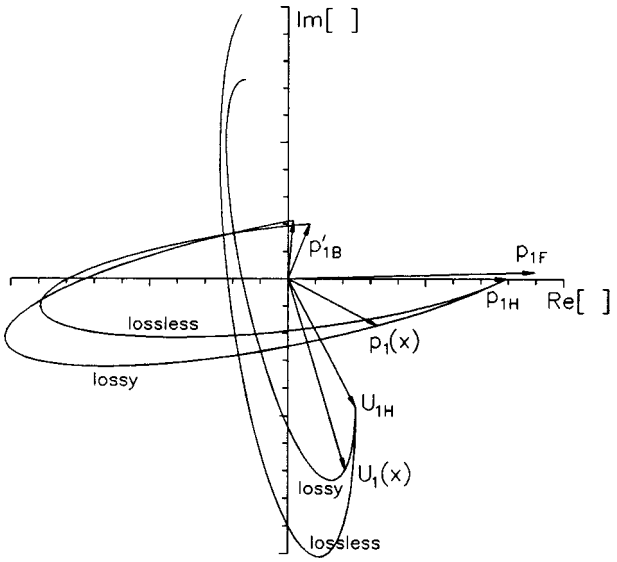

FIG. 3. Typical phasor diagrams for lossless (inner curves) and lossy (outer curves) transmission lines connected between pulse tube and back of piston. The transmission line's initial phasors p_{1H} and U_{1H} are the same as in Fig. 2.

in Fig. 3 illustrate Eqs. (6) and (7) when l and S are chosen correctly for the PTR whose phasors were shown in Fig. 2. The phasors are functions of x, following ellipses for the idealized, lossless (real k) transmission line; p_{1H}, U_{1H}, and S determine the eccentricity and orientation. The realistic, lossy transmission line yields similar curves, almost ellipses if the losses are sufficiently small, as shown in Fig. 3. Even for the lossy line, a substantial fraction of the acoustic power exiting the hot end of the pulse tube is delivered to the back of the drive piston, as shown by the reduction of the pressure difference across the piston from $p_{1F}-p_{1B}$ in Fig. 2 to $p_{1F}-p'_{1B}$ in Fig. 3. These figures are based on preliminary design calculations for a 100 K, helium-filled PTR having a gross cooling power of a few kW, which is typical of the cooling power we have been considering for liquefaction of natural gas.[3]

Although we decided to discuss this configuration here because it is easy to understand, we did not pursue it experimentally, because the more compact layout of the ''boost'' configuration discussed below was so appealing.

B. Lumped boost configuration

A second method to feed acoustic power from the hot end of the pulse tube back to the driver is illustrated in Fig. 1(d). The hot end of the pulse tube is connected directly to the front of the piston, while the aftercooler is connected through an acoustic network comprising an inertance and a compliance. We call this the ''lumped boost'' configuration because lumped acoustic impedances are used to boost $|p_{1A}|$ slightly above $|p_{1F}|$. (A ''distributed boost'' configuration, in which a short transmission line replaces the inertance and compliance, is also feasible.) In the lumped boost configuration, we will no longer neglect the flow resistance of the pulse tube's hot heat exchanger; its resistance R_H must be such that

$$p_{1H}-p_{1F}=R_H U_{1H}. \tag{10}$$

The compliance ensures that the volumetric velocity U_{1L} through the inertance differs from that at the aftercooler:

$$U_{1L}=U_{1A}+j\frac{\omega V_A}{\gamma p_m}p_{1A}, \tag{11}$$

where V_A is the volume of the compliance, so that the pressure difference across the inertance is

$$p_{1F}-p_{1A}=j\omega\frac{\rho_m l}{S}\left(U_{1A}+j\frac{\omega V_A}{\gamma p_m}p_{1A}\right), \tag{12}$$

where l and S are the length and area of the inertance. Taking the phasors at H and A to be given and combining Eqs. (10) and (12) to eliminate p_{1F}, we obtain a single complex equation in the unknowns R_H, V_A, l, and S, often with many possible solutions. Phasors for one such solution are shown in Fig. 4, where the refrigerator's end-point phasors are again the same as in Fig. 2.

The drive power is of course $\frac{1}{2}\,\mathrm{Re}[(p_{1F}-p_{1B})\widetilde{U_{1F}}]$ in both Fig. 1(b) and (d). If the compliance on the back side of the piston can be considered lossless, $\mathrm{Re}[p_{1B}\widetilde{U_{1F}}]=0$, so the drive power is simply $\frac{1}{2}\,\mathrm{Re}[p_{1F}\widetilde{U_{1F}}]$. In the lumped-boost case, $|U_{1F}|=|U_{1L}-U_{1H}|$ is rather large—much larger in Fig. 4 than in Fig. 2—so the amplitude of the piston motion in Fig. 1(d) must be much greater than in Fig. 1(b) or (c). Nevertheless, the power required of the piston is much less in Fig. 1(d) than in Fig. 1(b), because the phase angle between p_{1F} and U_{1F} is so large. Furthermore, the large magnitude of $|U_{1F}|$ presents no problem whatsoever if a pistonless thermoacoustic engine is used to drive the refrigerator.

II. APPARATUS

Encouraged by all these ideas, we proceeded to experiments with the lumped boost configuration. To use an existing driver[21] to power the experimental refrigerator, and to avoid the expense of building large hardware, we chose to test these ideas with a scale-model PTR that was approximately *similar*, in the technically strict sense of the word, to what would be required for a kW helium design. We built a ''half-scale'' PTR, filled with 2.4 MPa argon and operated at 23 Hz. It can be shown[22,23] that this is *similar* to a full-scale, 40-Hz, 3-MPa helium system, as long as the temperatures are high enough that argon can be regarded as an ideal gas. The physical phenomena and dimensionless combinations of variables in the half-scale argon PTR are all the same as at full scale in helium, just as a scale-model airplane in a wind tunnel and a full-sized airplane in flight share the same aerodynamics. The primary advantage of our half-scale argon model is that all powers are reduced by a factor of 16.7. A disadvantage is that we should keep this PTR's cold temperature greater than about 200 K, so that the argon is approximately an ideal gas. (Argon's critical point is 151 K, 4.9 MPa. At 2.4 MPa, it liquefies at 134 K.) Hence, our experiments can be regarded both as an easy exploration of some phenomena involved in acoustic recovery of otherwise

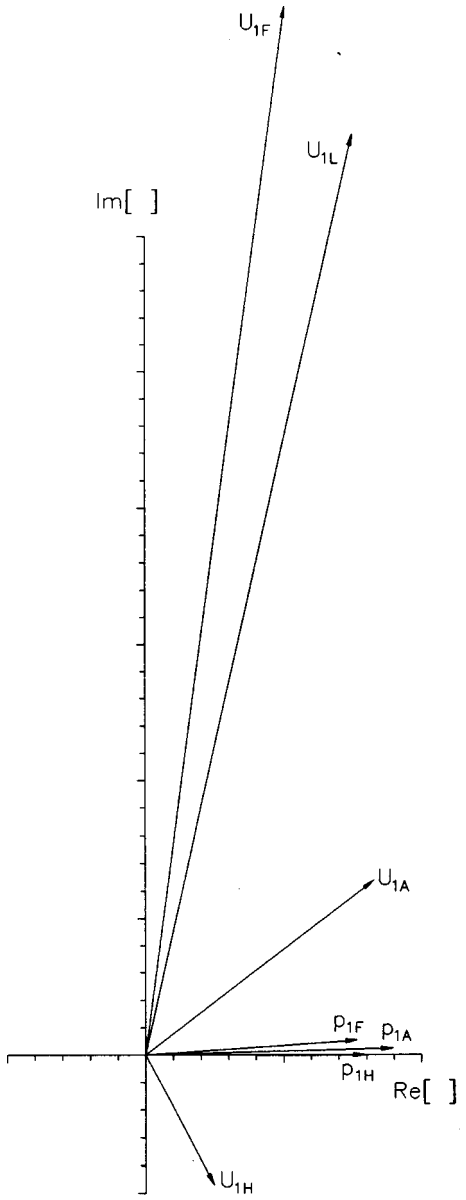

FIG. 4. Typical phasor diagrams for lumped boost configuration. The endpoint phasors p_{1H}, U_{1H}, p_{1A}, and U_{1A} are the same as in Fig. 2. The simple lumped impedances cause $p_{1H}-p_{1F}$ to be in phase with U_{1H}, $U_{1A}-U_{1L}$ to lag p_{1A} by 90°, and $p_{1F}-p_{1L}$ to lead U_{1L} by 90°.

lost power in PTRs, and as testing of an accurate scale model of a particular large refrigerator, with scaling details given in Table I.

In designing this hardware, we often sacrificed expected performance for versatility, ease of construction, and speed of design, because we correctly anticipated having to make many modifications in order to understand the behavior of such a novel apparatus. The system we built, illustrated in Fig. 5, is based on the lumped boost configuration of Fig. 1(d), but driven by a thermoacoustic engine instead of a piston and motor.

The heart of the refrigerator, its regenerator, was made of a 2.1-cm-thick stack of 400-mesh (i.e., 400 wires per inch) twilled-weave stainless-steel screens punched at 6.1-cm diameter. The total weight of the screens in the regenerator was 170 g. We calculated the hydraulic radius[24,25] of this

TABLE I. Scale factors to convert experimental data obtained with argon in this paper to numbers relevant to a larger helium-filled refrigerator. Multiply experimental data in this paper by the number in the table to obtain the expected result for the larger refrigerator. (Heat leaks that depend on the thermal conductivity of air, metal, or plastic do not scale.)

Variable	Multiplier
length	2
temperature	1
frequency	1.58
pressure	1.32
velocity	3.16
volumetric velocity	12.6
power	16.7

regenerator to be approximately 12 μm, based on its geometry and weight; in thermoacoustic calculations presented throughout the rest of this paper, we use 11 μm because this value gave the best agreement with our preliminary experiments in the ''traditional PTR'' configuration discussed below. The hydraulic radius is much smaller than the argon's thermal penetration depth (100 μm at 300 K), as required of a good regenerator. The stainless-steel pressure vessel around the regenerator had a wall thickness of 1.4 mm.

The pulse tube was a simple open cylinder, 3.0-cm id and 10.3 cm long, with 0.8-mm wall thickness. Its diameter is, of course, much greater than the argon's viscous penetration depth (90 μm at 300 K), and its length is greater than the 1-cm gas displacement amplitude in it at a typical operating point near $|p_1|/p_m \sim 0.1$. At each end, a few 35-mesh copper screens served as simple flow straighteners, to help maintain something resembling oscillatory plug flow in the pulse tube. We expected that argon's high density (relative to helium, which is almost universally used in PTRs) enhances the gravitational stability of this plug flow, so that careful flow straightening and tapering[8] would be unnecessary. This need for gravitational stability dictated the orientation of the refrigerator assembly with respect to vertical.

The cold heat exchanger between the regenerator and pulse tube was a 1.8-Ω length of NiCr ribbon wound zigzag on a fiberglass frame. Wires from the heater and a thermometer passed axially along the pulse tube to leak-tight electrical feedthroughs at room temperature. The two water-cooled heat exchangers (aftercooler and hot heat exchanger) were of shell-and-tube construction, with the Reynolds number of order 10^4 at $|p_1|/p_m \sim 0.1$ in the argon inside the 1.7-mm-diam, 18-mm-long tubes. The aftercooler had 365 such tubes, and the hot heat exchanger had 91.

The inertance was a simple metal tube with 2.2-cm id and 21-cm length, with 7-degree cones as shown in Fig. 5 at both ends to reduce turbulent end effects. The inertance and the refrigerator components were sealed to the flat plates above and below by rubber O-rings to enable easy modifications. The flat plates were held at a fixed separation by flange extensions and a cage of stout tubes through which long bolts passed, not shown in the figure. The compliance was half an ellipsoid with 2:2:1 aspect ratio, with a volume of 950 cm^3.

For simplicity, we insulated the cold parts of the apparatus with fiber-foam water-pipe insulation from the local

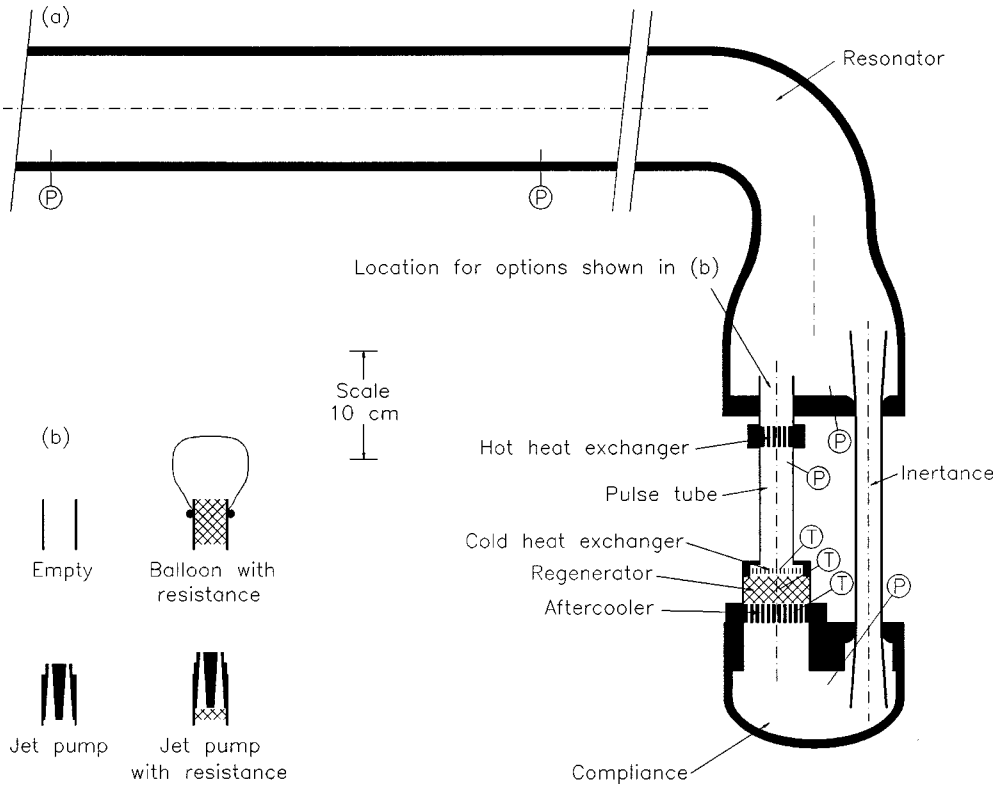

FIG. 5. (a) Drawing of the apparatus, in the inertance-boost configuration of Fig. 1(d). The dash–dot lines show local axes of cylindrical symmetry. Acoustic power circulates clockwise through the inertance and refrigerator part of the apparatus. ''P'' shows the location of a pressure sensor, and ''T'' the location of a temperature sensor. The heavy flanges around the aftercooler and hot heat exchanger contain water jackets. O-rings, most flanges, and bolts are omitted for clarity. The inside boundaries of the pressure vessel are to scale. (b) In the course of the measurements, these four options were used above the hot heat exchanger in (a). In each of the two cross-sectional views of the jet pump, two of the four tapered holes are shown.

hardware store. Type-K thermocouples measured temperatures in and near the regenerator. The 1.6-mm-diam thermocouple probe used to measure T_H was in the aftercooler, in the argon in one of the 365 tubes, touching the tube wall. The 0.8-mm-diam thermocouple probe used to measure T_C was standing freely in the argon between the cold heat exchanger and the flow straightener at the cold end of the pulse tube. Because of the different attachments of the T_C and T_H thermocouples, we believe that T_C represents the average temperature of the cold gas while T_H approximates the metal surface temperature in the aftercooler. The 0.8-mm-diam thermocouple probe whose temperature we will call T_{mid} was inserted into the very center of the regenerator, in a well that was drilled radially through the pressure-vessel wall and the screens. (Additional thermocouples outside the pressure vessel near the cold heat exchanger and the middle of the regenerator were used to confirm the internal temperature measurements.) Three piezoresistive pressure sensors (Endevco) in the compliance, pulse tube, and upper flat plate detected p_{1A}, p_{1H}, and p_{1F}, respectively, and two more sensors in the middle of the resonator were used to measure the acoustic power[26] flowing down the resonator from the thermoacoustic driver to the refrigerator. All pressure signals were detected with a lock-in amplifier.

A. First measurements

Preliminary measurements checked our implementation of the two-microphone acoustic-power measurement method[26] using the two sensors in the middle of the resonator. In these measurements, the PTR at the end of the resonator was replaced by a simple variable acoustic load comprising an adjustable valve R and a compliance C. Pressure sensors on either side of the valve allowed determination of the power dissipated in this RC network.[26] Figure 6 shows measurements of the two-microphone power as a function of dissipation in the RC network, at two pressure amplitudes in the resonator. The slopes in Fig. 6 are unity, demonstrating consistency between the RC and two-microphone methods. The region of large scatter in the measurements plotted in

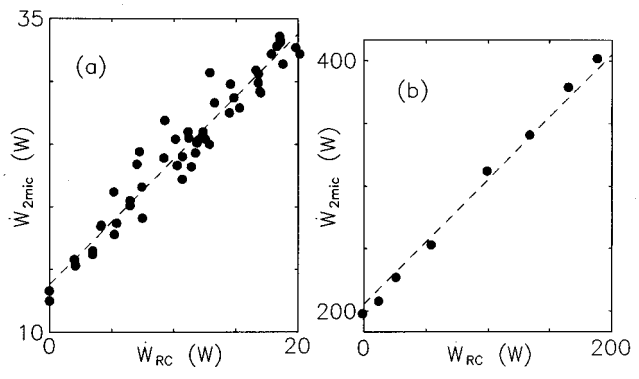

FIG. 6. Points show measured acoustic power $\dot{W}_{2\mathrm{mic}}$ passing the two-microphone location in the resonator, as a function of measured acoustic power $\dot{W}_{\mathrm{RC}}$ dissipated at the end of the resonator. For these preliminary measurements, an RC network replaced the refrigerator, inertance, and compliance of Fig. 5. The lines have slopes unity. (a) $|p_{1F}|/p_m = 0.038$ and (b) $|p_{1F}|/p_m = 0.094$.

Fig. 6(a) is due to thermoacoustic engine instability.[27] Fortunately, this instability was not encountered when the refrigerator was in place.

In Fig. 6(a) and (b), the offsets at zero RC dissipation are measures of the dissipation of acoustic power in that portion of the resonator between the two-microphone location and the RC network. This dissipation is up to four times greater than would be calculated for laminar acoustic dissipation, and is consistent with the turbulent dissipation calculations[28,29] of `DeltaE` Versions 3 and 4, assuming a pipe roughness factor of 1×10^{-3} for the resonator. This roughness factor is used in calculations of dissipation in the resonator and the inertance in the remainder of this paper.

To gain experience with our refrigerator, we made preliminary measurements with our PTR components (the regenerator, pulse tube, and three associated heat exchangers in Fig. 5) in the traditional PTR configuration shown in Fig. 1(b). Although PTR impedance networks at the hot end of the pulse tube are sometimes as simple as a single adjustable orifice and a compliance,[1] or a fixed lossy inertance and a compliance,[18] we used the configuration shown in Fig. 1(b), with two adjustable orifices (valves) and a fixed inertance in series with the compliance. The two valves allow independent control of both the magnitude and phase of the network's acoustic impedance.[21] In this traditional configuration, the refrigerator's performance was roughly as we had expected. At $|p_{1H}|/p_m=0.06$, the refrigerator cooled to $-115\,^{\circ}\mathrm{C}$ and had 20 W of net cooling power at $-50\,^{\circ}\mathrm{C}$; at $|p_{1H}|/p_m=0.08$ this cooling power was 40 W. Measurement of p_1 in the compliance and pulse tube, and knowledge of the gas volume in each component, allowed[21,28] us to infer U_1 throughout the refrigerator. The measured cooling power at $-50\,^{\circ}\mathrm{C}$ was about 10 W less than the inferred gross cooling power $\mathrm{Re}[p_{1H}\widetilde{U_{1C}}]/2$. We estimate that external heat leak contributes approximately half of this difference, with the balance due mostly to heat transport through the regenerator. In these preliminary measurements with the PTR in the traditional configuration, the most efficient operating points approached 5% of Carnot's coefficient of performance, using the net cooling power (i.e., electric resistance heater power, uncorrected for heat leak) and the two-microphone acoustic power in the calculations.

Next, we configured the refrigerator in the lumped boost configuration as shown in Fig. 5(a) [with the ''empty'' option of Fig. 5(b) installed above the pulse tube's hot heat exchanger]. The results were immediately disappointing: The refrigerator did not cool below 19 °C, essentially the temperature of the cooling water supplied to the water-cooled heat exchangers that day. (The aftercooler temperature $T_H=26\,^{\circ}\mathrm{C}$ for these measurements.) However, the pressure phasors seemed to be close to our expectations and the refrigerator's disappointing ''cold'' temperature was very strongly independent of heat load applied to the ''cold'' heat exchanger—e.g., at $|p_{1H}|/p_m=0.07$ an applied load of 70 W raised T_C to only 35 °C, as shown by the half-filled circles in Fig. 7. We concluded that the acoustic phenomena and gross cooling power were substantially as planned. Thus, we suspected that extremely vigorous streaming was effectively keeping the cold heat exchanger thermally anchored to the aftercooler, overwhelming the otherwise satisfactory thermoacoustic cooling power.

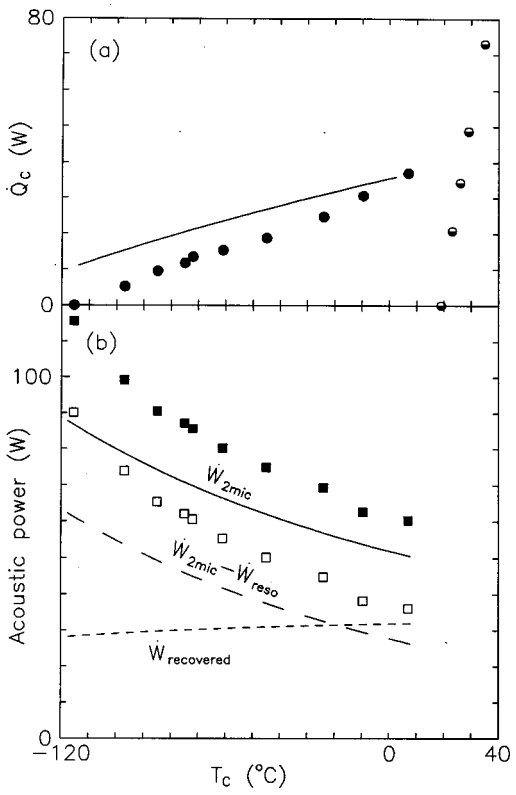

FIG. 7. Powers as a function of cold temperature T_C. The half-filled circles show measured cooling power with no balloon or other attempt to mitigate streaming ($|p_{1H}|/p_m=0.068$). The filled symbols and lines are with the balloon blocking streaming, at $|p_{1H}|/p_m=0.054$. (a) Cooling power. The experimental points show the electric power applied to the cold heat exchanger to maintain a given T_C. The line is the corresponding calculation. (b) Acoustic powers. The experimental points show measurements at the two-microphone location in the resonator; the solid line is the corresponding calculation. The open squares show the inferred acoustic power delivered to the refrigerator network, obtained by subtracting the calculated resonator dissipation from the measured two-microphone power. The long-dash line is the corresponding calculation. The short-dash line shows calculated values of recovered power (i.e., the acoustic power passing through the balloon).

III. SUPPRESSION OF STREAMING

A. Barrier method

It is essential that the time-averaged mass flow $\dot{M}$ through a PTR be near zero, to prevent a large steady energy flux $\dot{M}c_p(T_H-T_C)$ from flowing to the cold heat exchanger (where c_p is the gas' isobaric specific heat per unit mass). Such a steady energy flux would add an unwanted thermal load to the cold heat exchanger. In a traditional PTR configuration such as shown in Fig. 1(b), $\dot{M}$ is exactly zero; otherwise, mass would accumulate (or deplete, depending on sign) steadily in the compliance as a function of time. Gedeon[10] has discussed how nonzero $\dot{M}$ can arise in Stirling and pulse-tube cryocoolers whenever a closed-loop path exists for steady flow. Our lumped boost configuration clearly provides such a path; hence, we must understand and minimize $\dot{M}$.

Henceforth, we extend the complex notation introduced in Eq. (1) to second order by writing time-dependent variables as

$$\xi(x,t)=\xi_m(x)+\mathrm{Re}[\xi_1(x)e^{i\omega t}] + \xi_{2,0}(x)+\mathrm{Re}[\xi_{2,2}(x)e^{i2\omega t}]. \quad (13)$$

The final term, which oscillates at angular frequency 2ω, is of no interest here, but the time-averaged second-order term, with subscript ''2,0,'' is of great interest.

Gedeon argues that the second-order time-average mass flow

$$\dot{M}_2=\tfrac{1}{2}\mathrm{Re}[\rho_1\tilde{U}_1]+\rho_m U_{2,0} \quad (14)$$

is of primary concern. In acoustics, such second-order mass flow is known as streaming.[30] Gedeon shows that $\frac{1}{2}\mathrm{Re}[\rho_1\tilde{U}_1]=\rho_m\dot{W}_2/p_m$ in a regenerator, where $\dot{W}_2=\frac{1}{2}\mathrm{Re}[p_1\tilde{U}_1]$ is the acoustic power passing through the regenerator. Hence, $\frac{1}{2}\mathrm{Re}[\rho_1\tilde{U}_1]$ *must* be nonzero, and efficient regenerator operation requires that

$$U_{2,0}=-\tfrac{1}{2}\mathrm{Re}[\rho_1\tilde{U}_1]/\rho_m=-\dot{W}_2/p_m. \quad (15)$$

The consequences of ignoring this requirement can be severe. If $\dot{M}_2>0$, an undesired, streaming-induced heat load

$$\dot{Q}_{\mathrm{loss}}\sim\dot{M}_2 c_p(T_H-T_C) \quad (16)$$

flows from hot to cold through the regenerator. (If $\dot{M}_2<0$, such heat flows from hot to cold through the pulse tube, with equally harmful effect.) For $U_{2,0}=0$, the ratio of $\dot{Q}_{\mathrm{loss}}$ to the ordinary regenerator loss $\dot{H}_{\mathrm{reg}}$ is of the order of

$$\frac{\dot{Q}_{\mathrm{loss}}}{\dot{H}_{\mathrm{reg}}}\sim\frac{\gamma}{\gamma-1}\frac{(T_H-T_C)}{T_H}\frac{\dot{W}_H}{\dot{H}_{\mathrm{reg}}} \sim\frac{\gamma}{\gamma-1}\frac{(T_H-T_C)}{T_C}\frac{\dot{Q}_{C,\mathrm{gross}}}{\dot{H}_{\mathrm{reg}}}, \quad (17)$$

where $\dot{W}_H$ is the hot-end acoustic power and $\dot{Q}_{C,\mathrm{gross}}$ is the gross cooling power [see Eq. (2)]. In the third expression, each of the three fractions is >1 for cryocoolers; hence their product is $\gg 1$, and the unmitigated streaming-induced heat load would be much greater than the ordinary regenerator loss.

The steep slope $d\dot{Q}_C/dT_C$ shown in the half-filled circles in Fig. 7 provides an estimate of $\dot{M}_2$ in our refrigerator's ''empty'' configuration. Over the narrow temperature range of these data, gross cooling power and all other acoustic phenomena should be approximately constant and regenerator loss should be small, so the slope of the data should reflect Eq. (16): $-d\dot{Q}_{\mathrm{loss}}/dT_C=\dot{M}_2 c_p$. The experimental data yield $\dot{M}_2=9$ g/s. With Eq. (14) and our estimate that $\rho_m\dot{W}_2/p_m\sim 1$ g/s, this suggests that $\rho_m U_{2,0}$ was an order of magnitude larger than $\frac{1}{2}\mathrm{Re}[\rho_1\tilde{U}_1]$ for these measurements.

To quickly confirm our suspicion that the initial poor refrigerator performance shown as half-filled circles in Fig. 7 was due to such streaming, we installed a large rubber balloon (from a party-supplies store) above the pulse tube's hot heat exchanger, with the balloon protruding up into the resonator, as shown in Fig. 5(b). We rolled the balloon's collar completely up its neck and partly onto its body, so that tension in the rubber could not hold the balloon's surface against the sharp upper edge of the 3.1-cm-diam tube over which it was stretched. The balloon's limp volume was about 100 cm^3. We expected that this limp balloon would be acoustically transparent, but would block streaming flow completely.

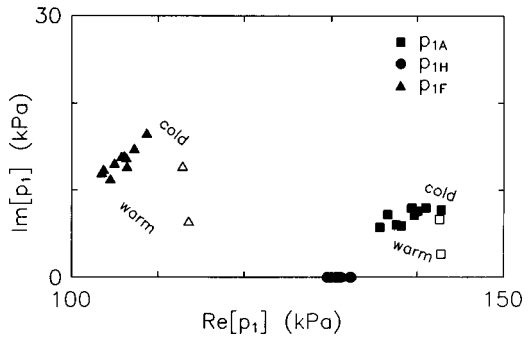

FIG. 8. Pressure phasors for measurements with balloon blocking streaming, at $|p_{1H}|/p_m=0.054$. The zero of phase has been chosen to set the phase of p_{1H} to zero, consistent with the other figures in this paper. The traditional phasor lines from the origin to each phasor have been eliminated to avoid clutter. Note the suppressed zero. The filled symbols are measurements; open symbols are calculations at the extreme values of T_C, with p_{1H} matched to the experimental values. The uppermost or rightmost symbols correspond to T_C near $-115\,^\circ$C; the lowermost or leftmost symbols correspond to T_C above $0\,^\circ$C.

At the same time, we installed extra resistance above the hot heat exchanger as shown in Fig. 5(b), because our earlier ''empty'' measurements had indicated that a larger flow resistance there was needed to make the phase of p_{1A} lead that of p_{1H}. The resistance comprised 130 g of 60 mesh copper screen packed into a volume 3 cm in diameter and 4 cm long. During fabrication, this screen was accidentally flattened and crushed to a higher density than expected, thereby providing more resistance than we wanted. Hence, we are uncertain of its hydraulic radius, which would otherwise have been approximately 100 μm. Fortunately, the system-performance calculations described below are not very sensitive to details in this component. We selected 60 μm as a reasonable estimate of the as-built hydraulic radius of this component, using this value in all calculations.

With the balloon in place, the refrigerator performed well, much like it had in the traditional PTR configuration described above, confirming our suspicion that enforcing $\dot{M}\equiv 0$ is the key to successful operation of this type of thermoacoustic system. The balloon survived without visible damage for 36 h of operation at $|p_{1H}|/p_m$ ranging from 0.04 to 0.10, more than enough time to obtain measurements.

In one set of measurements, we kept $|p_{1H}|/p_m=0.054$, while varying T_C from $-115\,^\circ$C to $7\,^\circ$C by adjusting the electric heater power $\dot{Q}_C$ at the cold heat exchanger. ($T_H=13\,^\circ$C throughout.) Figure 7 shows the resulting experimental cooling power and acoustic power requirements and Fig. 8 shows the experimental pressure phasors, together with some calculations of these and other variables. The calculations use `DeltaE`,[28] with geometry, mean pressure, fre-

TABLE II. The essential sequence of segments used in the DeltaE calculations described in this paper. (Free targets have been omitted for clarity.) The shooting-method guesses include T_m, complex p_1, and complex U_1 at the beginning, the complex branch impedance at the ''tbranch,'' and the heat flows at the aftercooler and cold heat exchanger. The shooting-method targets include T_H (at both aftercooler and hot heat exchanger), T_C, complex p_{1H}, the complex p_1 matching condition at the union, and the complex impedance at the ''hardend.''

	Segment type	Comment
0	BEGIN	at the two-microphone location
1	ISODUCT	long part of resonator
2	ISOCONE	conical adapter in resonator
3	ISODUCT	a little more resonator
4	TBRANCH	into the inertance
5	ISOCONE	cone at top of inertance
6	ISODUCT	the inertance
7	ISOCONE	cone at bottom of inertance
8	COMPLIANCE	the compliance
9	ISODUCT	short passage
10	TXFRST	aftercooler
11	STKSCREEN	regenerator
12	HXMIDL	cold heat exchanger
13	STKDUCT	pulse tube
14	TXLAST	hot heat exchanger
15	SXLAST	extra resistance
16	SOFTEND	terminates ''tbranch'' sequence
17	UNION	attaches 16 to the end of 3
18	HARDEND	ensures no U_1 leaks out

quency, p_{1H}, T_H, and T_C set to experimental conditions. (For those who are interested, Table II shows the sequence of DeltaE segments used in the calculations.)

In Fig. 8, p_{1F} and p_{1A} lead p_{1H}, with $|p_{1F}|<|p_{1H}|<|p_{1A}|$, consistent with the discussion leading up to Fig. 4. The measured and calculated phasors are in reasonably good agreement, showing that we understand the overall acoustic behavior of this network. Indeed, we can regard the complex differences $p_{1A}-p_{1H}$, $p_{1H}-p_{1F}$, and $p_{1F}-p_{1A}$ as indications of the impedances of the intervening components and the volumetric velocities through them [cf. Eqs. (10) and (12)]. From this viewpoint, the agreement between measured and calculated p_{1A} might be taken to indicate, for example, that we understand U_1 through the regenerator to within 10%–30% in magnitude and 10°–40° in phase.

In Fig. 7, the cooling power drops and the two-microphone acoustic power rises as T_C decreases. The calculations, which are in reasonable agreement with the experiments, provide insight to the main causes of these trends. First, the calculated gross cooling power $\dot{W}_C = \frac{1}{2}\mathrm{Re}[p_{1C}\tilde{U}_{1C}]$ is nearly constant at 40 W, independent of T_C, for these measurements. As discussed near Eq. (2), under the most ideal circumstances this would be the cooling power. The decrease in calculated $\dot{Q}_C$ below 40 W as T_C decreases is nearly proportional to T_H-T_C and is almost entirely due to heat flux through the regenerator. The difference between measured and calculated $\dot{Q}_C$ is also proportional to T_H-T_C, rising to 10 W at $T_C=-120\,°\mathrm{C}$. This could easily be due to a combination of ordinary heat leak through our insulation and streaming- or jet-driven convection in the pulse tube. Second, under the most ideal circumstances—with 40 W of cooling power and with Carnot's COP$=T_C/(T_H-T_C)$—the required net acoustic power would be $\dot{W}=(40\ \mathrm{W})(T_H-T_C)/T_C$, which rises from zero at $T_C=T_H$ to 35 W at $T_C=-120\,°\mathrm{C}$. This accounts for most of the 40 W rise in calculated $\dot{W}_{2\mathrm{mic}}$ with falling T_C in the figure. The measurements of $\dot{W}_{2\mathrm{mic}}$ exceed calculations by roughly 20%, for unknown reasons. Some 25 W of $\dot{W}_{2\mathrm{mic}}$ can be attributed to dissipation in the resonator between the two-microphone location and the refrigerator; this has been subtracted to yield the open squares and associated dashed line. Approximately 5 W of acoustic power is dissipated in the flow resistance under the balloon, 15 W is lost due to viscosity in the regenerator and adjacent heat exchangers, and 10 W is dissipated in the inertance.

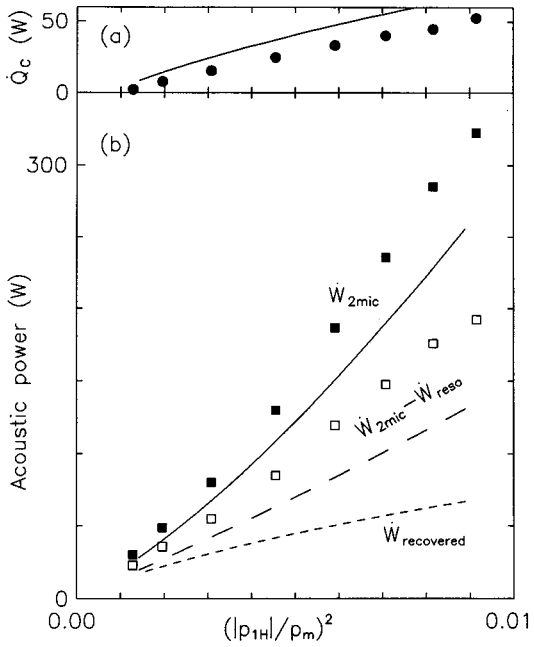

FIG. 9. Powers at $T_C=-60\,°\mathrm{C}$, as a function of pressure amplitude. (a) Cooling power. (b) Acoustic powers. The symbols have the same meaning as in Fig. 8.

If this were a traditional orifice PTR, $\dot{W}_C=40$ W would be dissipated in the orifice. In Fig. 7, the calculated fedback acoustic power $\dot{W}_{\mathrm{recovered}}$, which is of primary interest in this investigation, is near 30 W; hence, approximately 75% of $\dot{W}_C$ is recovered, fed back into the resonator. Note that, at the highest temperatures, $\dot{W}_{\mathrm{recovered}}$ is comparable to $\dot{W}_{2\mathrm{mic}}-\dot{W}_{\mathrm{reso}}$; in other words, at these temperatures feedback reduces the acoustic power delivered from the resonator to the refrigerator by roughly half.

In a second set of measurements with the balloon blocking streaming, we varied $|p_{1H}|$ while holding T_C constant near $-60\,°\mathrm{C}$. Unsurprisingly, the pressure phasors resembled those of Fig. 8 in phases and in degree of agreement between measurement and calculation. Cooling power and acoustic powers are displayed in Fig. 9. Again, calculations are in reasonably good agreement with experiment. Cooling power is proportional to $|p_{1H}|^2$, as expected. The difference between calculated and measured cooling power is roughly 5 W at the lowest amplitudes, consistent with the corresponding difference in Fig. 7; this difference increases at higher

amplitudes, for unknown reasons. The measurements of $\dot{W}_{2\mathrm{mic}}$ exceed calculations by roughly 20%, as they did in Fig. 7. At the highest amplitudes, resonator dissipation is a large fraction of $\dot{W}_{2\mathrm{mic}}$; subtracting resonator dissipation from $\dot{W}_{2\mathrm{mic}}$ leaves both calculated and measured $\dot{W}_{2\mathrm{mic}}$ proportional to $|p_{1H}|^2$, as expected. Again, the calculated $\dot{W}_{\mathrm{recovered}}$ is somewhat larger than the cooling power, is most of $\dot{W}_C$, and is large enough that in its absence the acoustic power $\dot{W}_{2\mathrm{mic}}-\dot{W}_{\mathrm{reso}}$ delivered from the resonator to the refrigerator would have to be significantly larger.

B. Hydrodynamic method

The measurements with the balloon convinced us that the acoustic aspects of the lumped-boost network were functioning as expected. However, we feared that the balloon would not be reliable enough for long-term practical use, so we returned our attention to the more challenging issue of streaming suppression. From among several options (including series bellows, fans, and parallel check valves) we chose to investigate asymmetry in hydrodynamic end effects to suppress streaming.

Gedeon[10] shows that $\dot{M}_2$ will be zero only if a nonzero $\Delta p_{2,0}$ exists across the regenerator, consistent with, and causing, the viscous flow of the correct $U_{2,0}$ in the regenerator. In a simple orifice PTR, this pressure difference appears automatically, because the topology imposes $\dot{M}_2=0$. However, when a regenerator is connected with other components in a ''loop'' topology, such as shown in Fig. 1(c) or (d) or such as in a double-inlet PTR, the topology does not ensure $\dot{M}_2=0$; rather, it ensures that $\oint(dp_{2,0}/dx)dx=0$ around the loop. To obtain the correct $U_{2,0}$ in the regenerator in ''loop'' systems, we must design the other components of the loop so that they impose the correct $\Delta p_{2,0}$ across the regenerator.

The required $\Delta p_{2,0}$ can be estimated using the low-Reynolds-number limit of Fig. 7-9 of Kays and London[25]

$$\frac{dp}{dx}\simeq-\frac{6U\mu}{Sr_h^2} \tag{18}$$

for the pressure gradient in a screen bed of cross-sectional area S and hydraulic radius r_h, where U is the volumetric velocity and μ is the viscosity. (The numerical factor depends weakly on the volumetric porosity of the bed.) With Eq. (15) for U, this yields

$$\Delta p_{2,0}\simeq\frac{6}{Sr_h^2p_m}\int_{\mathrm{reg}}\mu_m(x)\dot{W}_2(x)dx \tag{19}$$

for the pressure difference across the regenerator when $\dot{M}_2\equiv0$. (The viscosity's x dependence is due to the temperature gradient.) For our apparatus at typical operating conditions, $\Delta p_{2,0}$ is of the order of a few hundred Pa.

In the limit of low viscosity or large tube diameters and in the absence of turbulence, $p_{2,0}$ would be described by some acoustic version of the Bernoulli equation. This suggests that an acoustically ideal loop connecting the two ends of the regenerator would impose across the regenerator a pressure difference of the order of $\Delta[\rho_m u_1\tilde{u}_1]$, where u_1 is the complex velocity amplitude. (Such an ideal loop might include a pulse tube, transmission line, and compliance, without heat exchangers or other components with small passages.) This pressure difference is typically much smaller than the $\Delta p_{2,0}$ given in Eq. (19) that is required for $\dot{M}_2=0$. Hence, to produce the required $\Delta p_{2,0}$, we need an additional physical effect or structure in the loop, relying on turbulence, viscosity, or some other physical phenomenon not included in the Bernoulli equation.

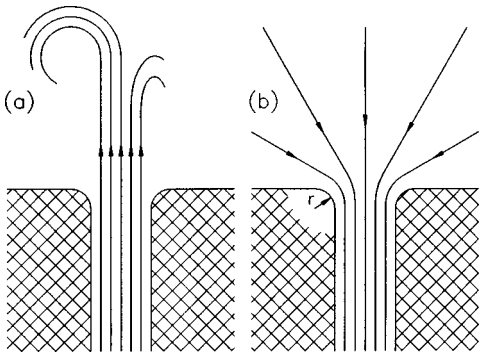

FIG. 10. Illustration of asymmetric flow at high Reynolds number at the transition between a small tube and open space. (a) Outflow. (b) Inflow, for which the radius r of rounding of the lip is important.

Asymmetry in hydrodynamic end effects can produce this required $\Delta p_{2,0}$. In a tapered transition between a small-diameter tube, where $|u_1|$ is large, and a large-diameter tube, where $|u_1|$ is small, turbulence would be avoided and Bernoulli's equation would hold if the taper were sufficiently gentle. At the opposite extreme, for an abrupt transition, we expect large $|u_1|$ to generate significant turbulence, and further we expect the oscillatory pressure drop across the transition to reflect the phenomena known as ''minor losses''[31] in high-Reynolds-number steady flow. If the gas displacement amplitude is much greater than the tube diameter, we also expect that the flow would at any instant have little memory of its past history, so that the acoustic behavior can be deduced from careful time integration of the steady-flow phenomena.

Ideally, the pressure at each instant of time could be described by the ordinary, steady-flow Bernoulli equation. At abrupt transitions, deviations of the pressure from this ideal are called ''head loss'' or ''minor loss'' in steady flow, with the lost pressure Δp_{ml} given by

$$\Delta p_{ml}=K\,\tfrac{1}{2}\rho u^2, \tag{20}$$

where K is the minor-loss coefficient, which is well known[31,32] for many transition geometries, and u is the velocity. For our purposes, the most important fact about K is that it depends strongly on the direction of flow through the transition. In the example shown in Fig. 10, a small tube is connected to an essentially infinite open space. When the gas (at velocity u inside the tube) flows out of the tube, a jet occurs, and kinetic energy is lost to turbulence downstream of the jet; $K_{\mathrm{out}}=1$. In contrast, when gas flows into the tube, the streamlines in the open space are widely and smoothly dispersed; K_{in} varies from 0.5 to 0.04, with smaller values for larger radius r of rounding of the edge of the entrance.

If $u=|u_1|\sin\omega t$, we can calculate the time-averaged pressure drop by integrating Eq. (20) in time:

$$\overline{\Delta p_{ml}}=\frac{\omega}{2\pi}\left(\int_0^{\pi/\omega}K_{\rm out}\frac{1}{2}\rho|u_1|^2\sin^2\omega t dt - \int_{\pi/\omega}^{2\pi/\omega}K_{\rm in}\frac{1}{2}\rho|u_1|^2\sin^2\omega t dt\right)$$
$$=\tfrac{1}{8}\rho|u_1|^2(K_{\rm out}-K_{\rm in}). \quad (21)$$

This is the source of $\Delta p_{2,0}$ that we will use. Such simple control of $\dot{M}_2$ is not without penalty, however; acoustic power is dissipated at a rate

$$\dot{E}=S\frac{\omega}{2\pi}\int_0^{2\pi/\omega}\Delta p_{ml}u dt$$
$$=S\frac{\omega}{2\pi}\left(\int_0^{\pi/\omega}K_{\rm out}\frac{1}{2}\rho|u_1|^3\sin^3\omega t dt - \int_{\pi/\omega}^{2\pi/\omega}K_{\rm in}\frac{1}{2}\rho|u_1|^3\sin^3\omega t dt\right)$$
$$=\frac{1}{3\pi}\rho|u_1|^2|U_1|(K_{\rm out}+K_{\rm in}) \quad (22)$$
$$=\frac{8}{3\pi}\overline{\Delta p_{ml}}|U_1|\frac{K_{\rm out}+K_{\rm in}}{K_{\rm out}-K_{\rm in}}, \quad (23)$$

where S is the area of the small tube. Equation (23) shows that the best way to produce a desired $\overline{\Delta p_{ml}}$ is to insert the device at a location where $|U_1|$ is small, and to shape it so that $K_{\rm out}-K_{\rm in}$ is as large as possible.

In our refrigerator, $|U_1|$ is smallest at the cold heat exchanger, but that is an unsuitable location for adding a dissipative structure. The hot heat exchanger has only slightly larger $|U_1|$, and already requires some extra dissipation to ensure that p_{1A} leads p_{1H} slightly, so we chose the space above the hot heat exchanger, previously occupied by the balloon and extra resistance, as the location for our experiments on asymmetry in end effects for streaming control. We installed what we call the ''jet pump,'' a brass block bored through with four identical tapered holes, each 5.3 cm long, 10 mm diam at the lower end, and 4 mm diam at the upper end, as shown in Fig. 5(b). We expected that end effects at the small ends of the holes would be strongly asymmetric, causing the desired $\overline{\Delta p_{ml}}$, while the velocities at the large ends of the holes would be small enough that minor losses would be negligible and the tapers joining the ends would be gradual enough to prevent minor losses in between.

To investigate the control of $\overline{\Delta p_{ml}}$ through the dependence of $K_{\rm in}$ on the radius r of rounding of the entrance, we made a series of temperature measurements with the jet pump in our refrigerator, at $|p_{1H}|/p_m\simeq 0.06$ with no heat applied at the cold heat exchanger, with each measurement having a different entrance rounding at the small ends of the tapered holes in the jet pump. At this pressure amplitude, the Reynolds number of the oscillatory flow was 2×10^5 and the gas displacement amplitude $|U_1|/\omega S\sim 0.2$ m at the jet. The results of this series of temperature measurements are shown

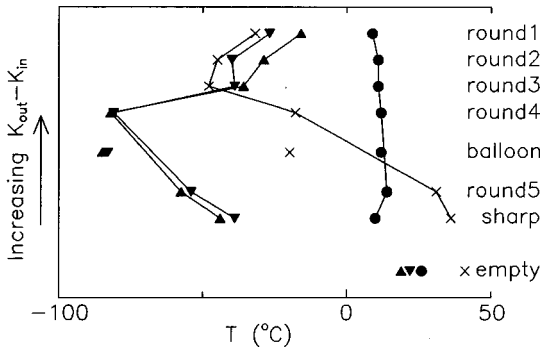

FIG. 11. Temperatures in and near the regenerator as the hardware above the hot heat exchanger was changed. Circles, aftercooler temperature T_H; ×, mid-regenerator internal temperature $T_{\rm mid}$; erect triangles, cold heat exchanger internal temperature T_C; inverted triangles, cold heat exchanger external temperature. Lines link the six jet-pump data sets, which are arranged vertically in order of increasing strength of jet pump. Measurements under comparable conditions with the balloon and with no attempt to mitigate streaming (''empty'') are inserted into the sequence at appropriate vertical locations.

in Fig. 11. We began this tedious process with sharply machined edges (''sharp'' in Fig. 11) at the small ends of the four holes. Next, we rounded and polished the edges of the holes to $r\sim 0.5$ mm (''round1''), and then we proceeded to machine away ~ 0.1 mm at a time from the flat upper end of the jet pump (''round2'' through ''round5''), thus removing ever more of the rounded edges and returning the entrances ever closer to ''sharp.'' Also shown for comparison in the figure are data from the balloon measurements and from our preliminary measurements with no attempt to mitigate streaming [corresponding to the ''empty'' configuration of Fig. 5(b) and the lowest half-filled circle in Fig. 7].

Figure 11 is qualitatively consistent with the discussion of streaming and its control presented above, and in particular with the expected increase of $\overline{\Delta p_{ml}}$ with decreasing $K_{\rm in}$ as determined by the radius of rounding of the entrances. With no attempt to control streaming (''empty''), the cold and hot temperatures T_C and T_H were nearly equal, and the temperature $T_{\rm mid}$ in the middle of the regenerator was 20° warmer than the others. In this circumstance, $\dot{M}$ was large and positive (i.e., flowing through the regenerator from hot to cold). With such large $\dot{M}$, the middle of the regenerator was thermally tied to the average gas temperature on the hot end of the regenerator (which happened to be about 20° warmer than the aftercooler metal surface temperature T_H), and this warm gas flowing up through the regenerator delivered a large heat load to the cold heat exchanger, as implied by Eq. (17), keeping T_C high. With the ''sharp'' and ''round5'' versions of the jet pump, a nonzero $\overline{\Delta p_{ml}}$ reduced $\dot{M}$, thereby lowering the temperatures. With the ''round4'' version of the jet pump, we were fortunate to arrive at the value of $K_{\rm in}$ that generated exactly the $\overline{\Delta p_{ml}}$ needed to force $\dot{M}\simeq 0$, so the temperatures were very nearly equal to those we observed when the balloon enforced $\dot{M}\equiv 0$. More well-rounded versions of the jet pump (''round3'' through ''round1'') reduced $K_{\rm in}$ and hence generated even greater $\overline{\Delta p_{ml}}$, causing $\dot{M}<0$; in these cases, the cold heat exchanger was loaded by warm gas flowing down through the pulse tube, and the mid-

regenerator temperature felt the thermal influence of gas flowing steadily from the cold end of the regenerator.

Furthermore, the phase of p_{1A} increased steadily from ''round1'' through ''round5'' and ''sharp,'' consistent with the increase in the effective resistance to U_1 of the jet pump with increasing K_{in} that we expect based on Eq. (22).

Hoping that we understood all the important features of this apparatus, we made final modifications. We upgraded our computer model of the apparatus to incorporate the minor losses of Eq. (22), both at the small end of the jet pump and at both ends of the inertance. The model results suggested that system performance would be improved if we added some extra resistance above the hot heat exchanger, so we inserted 25% of our copper screen resistance under the jet pump; together with the resistance of the jet pump itself, this provided a total resistance that left p_{1A} nearly in phase with p_{1H} and yielded calculated performance superior to that we had observed with the balloon. We rounded and polished the jet pump hole entrances again, repeating abbreviated measurements of temperatures and iteratively smoothing the entrances until we returned to temperatures comparable to ''round4'' in Fig. 11. We then proceeded with more extensive measurements.

In one set of measurements with this final jet-pump configuration, we kept $|p_{1H}|/p_m = 0.054$ while varying T_C by adjusting the electric heater power $\dot{Q}_C$ at the cold heat exchanger. These conditions are comparable to those for the ''balloon'' and ''empty'' data shown in Fig. 7. The results are shown in Fig. 12. The mid-regenerator temperature was 20 °C for $T_C = -80$ °C, indicating that the jet pump was too weak, with nonzero $\dot{M}$ flowing from hot to cold through the regenerator. Nevertheless, the cooling power is far greater than it was for the ''empty'' data, showing that the jet pump was far better than nothing at suppressing streaming. At high T_C the calculated and measured cooling powers are in good agreement; here, a small nonzero $\dot{M}$ has less effect on the net cooling power. At lower T_C the measured cooling power is significantly lower than the calculated values (and lower than the balloon measurements), as the small nonzero $\dot{M}$ consumes a significant fraction of the cooling power. The acoustic powers are negligibly affected by small $\dot{M}$, so the agreement between measured and calculated $\dot{W}_{2\text{mic}}$ is as good as it was for the balloon measurements. Both calculated cooling power and calculated $\dot{W}_{2\text{mic}}$ are better than for the balloon case, because of the better choice of total flow resistance above the hot heat exchanger discussed in the previous paragraph.

In a second set of measurements, we varied $|p_{1H}|$ while holding T_C constant near -55 °C; these conditions are comparable to the balloon measurements shown in Fig. 9. The results are shown in Fig. 13. In Fig. 13(a), the experimental cooling power exhibits interesting structure, which we believe is due to nonzero $\dot{M}$. A local maximum in $\dot{Q}_C$ occurs at $(|p_{1H}|/p_m)^2 = 0.0025$, for which $T_{\text{mid}} = 10$ °C as shown in Fig. 13(c). This value of T_{mid} is comparable to that we observed with the balloon at this T_C, suggesting that $(|p_{1H}|/p_m)^2 = 0.0025$ happens to obtain $\dot{M} \simeq 0$ with this jet

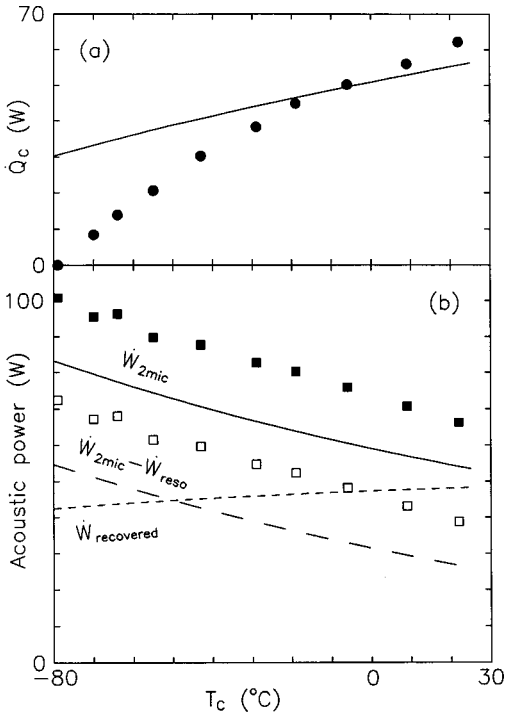

FIG. 12. Powers as a function of cold temperature T_C, with final configuration with jet pump and small extra resistance, at $|p_{1H}|/p_m = 0.054$. $T_H = 12$ °C throughout. (a) Cooling power. The experimental points show the electric power applied to the cold heat exchanger to maintain a given T_C. The line is the corresponding calculation. (b) Acoustic powers. The experimental points show measurements at the two-microphone location in the resonator; the solid line is the corresponding calculation. The open squares show the inferred acoustic power delivered to the refrigerator network, obtained by subtracting the calculated resonator dissipation from the measured two-microphone power. The long-dash line is the corresponding calculation. The short-dash line shows calculated values of the recovered power (i.e., the acoustic power passing through the balloon).

pump r. At lower $|p_{1H}|$, the T_{mid} measurements imply $\dot{M} < 0$; at higher $|p_{1H}|$, they imply $\dot{M} > 0$. In both cases, cooling power is reduced significantly by this streaming. The experimental acoustic power $\dot{W}_{2\text{mic}}$ in Fig. 13(b) is in reasonable agreement with calculations over the whole range of $|p_{1H}|$, with no obvious feature near the $\dot{M} \simeq 0$ amplitude, again confirming our expectation that nonzero $\dot{M}$ has little effect on purely acoustic phenomena.

However, the dependence of $\dot{M}$ on amplitude implied by Fig. 13 suggests that our understanding is incomplete: Eq. (19) for the pressure difference required across the regenerator and Eq. (21) for the pressure difference produced by the jet pump are both quadratic in amplitude, so if they conspire to make $\dot{M} \simeq 0$ at one amplitude, then they should do so at all amplitudes. Furthermore, there is a significant difference between the results of these two equations. Using calculated powers and velocities at $(|p_{1H}|/p_m)^2 = 0.0025$ in Fig. 13, Eq. (19) yields 200 Pa while Eq. (21) yields 2 kPa (assuming $K_{\text{out}} - K_{\text{in}} \sim 0.7$). Rough estimates show that a large number of other components and phenomena in the apparatus may each contribute tens to hundreds of Pa to $\oint (dp_{2,0}/dx)dx$. Representative examples include the gravitational head due to the cold gas in the cold components, minor losses at the inertance ends, boundary-layer streaming in the inertance,

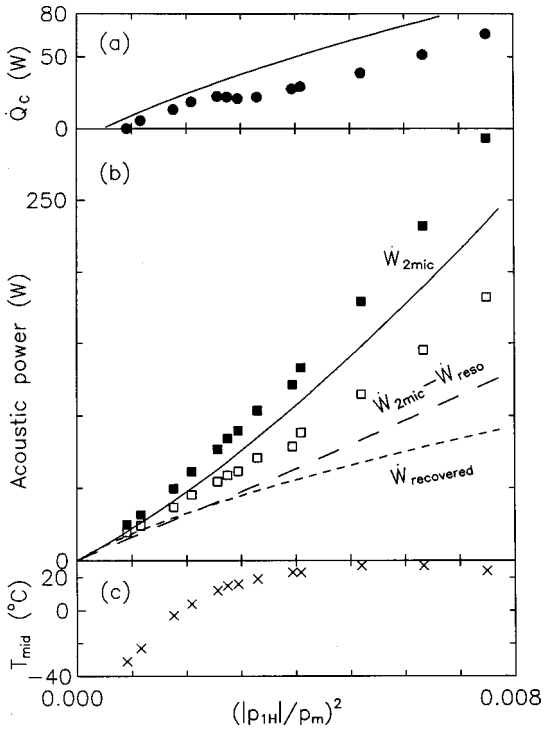

FIG. 13. Powers and mid-regenerator temperature at $T_C = -55\,^{\circ}\mathrm{C}$, as a function of pressure amplitude, with final configuration with jet pump and small extra resistance. $T_H = 13\,^{\circ}\mathrm{C}$ throughout. The symbols have the same meaning as in Fig. 12. (a) Cooling power. (b) Acoustic powers. (c) Mid-regenerator temperature.

and Gedeon's streaming in the extra resistance below the jet pump. Additional evidence that such components are contributing significantly to streaming is provided by the steep slope $d\dot{Q}_C/dT_C$ observed in our original, ''empty'' configuration and discussed below Eq. (17), which suggests that the ''empty'' configuration had a large nonzero $\Delta p_{2,0}$ across the regenerator, with its sign driving $U_{2,0}$ in the same direction as $1/2\,\mathrm{Re}[p_1 \tilde{U}_1]$.

The sensitivity of $\dot{M}$ to small details, illustrated in Figs. 11 and 13(a), suggests that practical use of a jet pump to suppress streaming in this type of refrigerator will require convenient adjustability in the jet pump or in some other $\dot{M}$-controlling part of the acoustic network.

IV. CONCLUSIONS

The $\dot{M} \simeq 0$ operating points in Fig. 13 are the most efficient operating points observed in these measurements. At the points near the relative maximum in cooling power in Fig. 13(a), the experimental coefficient of performance $\mathrm{COP} = \dot{Q}_C/\dot{W}_{2\mathrm{mic}} = 0.29$, so that the second-law efficiency is 9%. [The second-law efficiency is $\mathrm{COP}/\mathrm{COP}_{\mathrm{Carnot}}$, where $\mathrm{COP}_{\mathrm{Carnot}} = T_C/(T_H - T_C)$.] This is not as high as today's best traditional orifice PTRs[17] (10%–20% of Carnot) or standing-wave thermoacoustic refrigerators[33] (20% of Carnot), but it is high enough to show that this type of refrigerator has promise. If we deduct the calculated resonator dissipation from the experimental $\dot{W}_{2\mathrm{mic}}$, we obtain a second-law efficiency of 13%. We are confident that we can design much more efficient systems, based on the lessons we've described in this paper. For example, in our present refrigerator the inertance should have had a larger diameter and more streamlined ends; constraints of our existing hardware prevented such apparently straightforward modifications. Even simple improvements to our thermal insulation and use of a tapered pulse tube[8] could improve performance significantly, by increasing net cooling power with no cost to acoustic power.

We have discovered no reasons to doubt Ceperley's conclusion that efficiencies much greater than half of Carnot's are possible; we believe he was correct to suggest that traveling-wave refrigerators offer the potential for excellent performance with the simplicity of no moving parts. However, in addition to following Ceperley's ideas, it is vital to suppress time-averaged mass flux through such a refrigerator, and to use a thermal buffer column such as the pulse tube of a traditional PTR.

These same principles also apply to engines, which will be the subject of a paper in the near future.

Much more overall exploration remains to be done. Here, we have investigated the transmission-line configuration briefly, and the lumped boost configuration in more detail. It seems likely that other traveling-wave configurations can be discovered; they may offer advantages in efficiency or size. We used a balloon and a jet pump to suppress streaming; again, it seems likely that other, possibly better methods remain to be discovered. Quantitative understanding of all the sources of $\Delta p_{2,0}$ in the network will also be challenging.

In addition to these general research issues, considerable engineering effort will be required to determine how such techniques might impact specific applications such as cryogen liquefaction, cooling of superconducting electronics, or food refrigeration.

ACKNOWLEDGMENTS

This work has been funded by the Offices of Basic Energy Sciences and Fossil Energy in the U. S. Department of Energy. We thank Vince Kotsubo for useful conversations regarding the diagnosis and suppression of streaming.

[1] R. Radebaugh, ''A review of pulse tube refrigeration,'' Adv. Cryog. Eng. **35**, 1191–1205 (1990).
[2] P. Kittel, ''Ideal orifice pulse tube refrigerator performance,'' Cryogenics **32**, 843–844 (1992).
[3] Cryenco, Inc., 3811 Joliet, Denver, CO 80239.
[4] G. W. Swift, ''Thermoacoustic natural gas liquefier,'' in Proceedings of the DOE Natural Gas Conference, Houston, TX, March 1997.
[5] A. Bejan, *Advanced Engineering Thermodynamics* (Wiley, New York, 1997), 2nd ed.
[6] P. H. Ceperley, ''Gain and efficiency of a short traveling wave heat engine,'' J. Acoust. Soc. Am. **77**, 1239–1244 (1985), and references therein.
[7] G. W. Swift, M. S. Allen, and J. J. Wollan, ''Performance of a tapered pulse tube,'' to be published in the Proceedings of the 10th International Cryocooler Conference, Monterey CA, May 1998.
[8] J. R. Olson and G. W. Swift, ''Acoustic streaming in pulse tube refrigerators: Tapered pulse tubes,'' Cryogenics **37**, 769–776 (1997).
[9] R. Radebaugh, personal communication.
[10] D. Gedeon, ''DC gas flows in Stirling and pulse-tube cryocoolers,'' in *Cryocoolers 9*, edited by R. G. Ross (Plenum, New York, 1997), pp. 385–392.
[11] L. E. Kinsler, A. R. Frey, A. B. Coppens, and J. V. Sanders, *Fundamentals of Acoustics* (Wiley, New York, 1982).

[12] B. J. Huang and C. W. Lu, ''Dynamic response of regenerator in cyclic flow system,'' Cryogenics **33**, 1046 (1993).
[13] B. J. Huang and C. W. Lu, ''Linear network analysis of regenerator in a cyclic-flow system,'' Cryogenics **35**, 203 (1995).
[14] G. W. Swift and W. C. Ward, ''Simple harmonic analysis of regenerators,'' J. Thermophys. Heat Transfer **10**, 652–662 (1996).
[15] J. H. Xiao, ''Thermoacoustic theory for cyclic flow regenerators. Part I: Fundamentals,'' Cryogenics **32**, 895 (1992).
[16] For an ideal gas, specific heat c_p is constant and the hydrodynamic contribution to the time-averaged energy flux is $\overline{\rho(t)c_pT(t)U(t)}$, where the overbar denotes time average. If the gas is in perfect thermal contact with the regenerator matrix, $T(t)\equiv T_m$ is constant. If also the time-average mass flux $\overline{\rho(t)U(t)}$ through the regenerator is zero, then $\overline{\rho(t)c_pT(t)U(t)}=0$.
[17] R. Radebaugh, ''Advances in cryocoolers,'' in *Proceedings of the 16th International Cryogenic Engineering Conference/International Cryogenic Materials Conference* (ICE16/ICMC) (Elsevier Science, Oxford, 1997), pp. 33–44.
[18] S. W. Zhu, S. L. Zhou, N. Yoshimura, and Y. Matsubara, ''Phase shift effect of the long neck tube for the pulse tube refrigerator,'' in *Cryocoolers 9*, edited by R. G. Ross (Plenum, New York, 1997), pp. 269–278.
[19] S. Zhu, P. Wu, and Z. Chen, ''Double inlet pulse tube refrigerators: An important improvement,'' Cryogenics **30**, 514 (1990).
[20] P. M. Morse and K. U. Ingard, *Theoretical Acoustics* (McGraw–Hill, New York, 1968) Chap. 6.2.
[21] D. L. Gardner and G. W. Swift, ''Use of inertance in orifice pulse tube refrigerators,'' Cryogenics **37**, 117–121 (1997).
[22] Briefly, similitude requires that reduction of all dimensions of the apparatus by a factor of 2 is accompanied by a reduction of all thermophysical length scales in the gas by a factor of 2. Here, the relevant thermophysical length scales are the acoustic wavelength $\lambda=a/f$ and the viscous penetration depth $\delta_\nu=\sqrt{\mu/\pi f\rho}$. Reducing these lengths by a factor of 2 determines the frequency and pressure necessary to make argon in the half-scale apparatus *similar* to helium in the full-scale apparatus. For a more complete treatment (discussing the temperature dependence of μ and K, similarity of Prandtl number, and other effects), see Ref. 23.
[23] J. R. Olson and G. W. Swift, ''Similitude in thermoacoustics,'' J. Acoust. Soc. Am. **95**, 1405–1412 (1994).
[24] The hydraulic radius is the ratio of gas volume to gas–solid contact surface area.
[25] W. M. Kays and A. L. London, *Compact Heat Exchangers* (McGraw-Hill, New York, 1964).
[26] A. M. Fusco, W. C. Ward, and G. W. Swift, ''Two-sensor power measurments in lossy ducts,'' J. Acoust. Soc. Am. **91**, 2229–2235 (1992).
[27] G. W. Swift, ''Analysis and performance of a large thermoacoustic engine,'' J. Acoust. Soc. Am. **92**, 1551–1563 (1992).
[28] W. C. Ward and G. W. Swift, ''Design environment for low amplitude thermoacoustic engines (DeltaE),'' J. Acoust. Soc. Am. **95**, 3671–3672 (1994). Fully tested software and users guide available from Energy Science and Technology Software Center, U. S. Department of Energy, Oak Ridge, TN. To review DeltaE's capabilities, visit the Los Alamos thermoacoustics web site at http://rott.esa.lanl.gov/. For a beta-test version, contact ww@lanl.gov (Bill Ward) via Internet.
[29] M. Iguchi, M. Ohmi, and K. Maegawa, ''Analysis of free oscillating flow in a U-shaped tube,'' Bull. JSME **25**, 1398 (1982).
[30] W. L. M. Nyborg, ''Acoustic streaming'' in *Physical Acoustics*, edited by W. P. Mason (Academic, New York, 1965), Vol. IIB, p. 265.
[31] R. W. Fox and A. T. McDonald, *Introduction to Fluid Mechanics* (Wiley, New York, 1985).
[32] V. L. Streeter, *Handbook of Fluid Dynamics* (McGraw-Hill, New York, 1961)
[33] S. L. Garrett, J. A. Adeff, and T. J. Hofler, ''Thermoacoustic refrigerator for space applications,'' J. Thermophys. Heat Transfer **7**, 595–599 (1993).

Sensitivity measurements of piezoelectric polymer hydrophones from 0.2–2 MHz using a broadband-pulse technique

Gerald R. Harris and Paul M. Gammell
Food and Drug Administration, Center for Devices and Radiological Health, Rockville, Maryland 20850

(Received 12 August 1998; accepted for publication 23 October 1998)

It is widely recognized that the sensitivity of hydrophones used to measure medical diagnostic ultrasound fields should be uniform over several octaves above the center frequency (i.e., above the mean of the upper and lower −3 dB frequencies in the transmitted acoustic-pressure spectrum). However, a bandwidth extending to at least ten times *below* the diagnostic pulse-center frequency is needed for accurate (error ≈5%) measurement of the peak rarefactional pressure. Since at present it is not common for manufacturers of medical-use hydrophones to provide sensitivity information below 1–2 MHz, a study was undertaken to determine these low-frequency sensitivities. The technique uses broadband, plane-wave pressure pulses generated by electrical short-pulse excitation of a thick piezoelectric ceramic disk. The hydrophone response is calculated from measurements of the source transducer and hydrophone-voltage waveforms. The frequency responses of both needle-type and spot-poled membrane polymer hydrophones were measured using this technique. The spot-poled membrane hydrophones had −3-dB bandwidths extending below 0.2 MHz, the lower limit for the calibration technique. The needle-type hydrophones studied, however, all exhibited a response roll-off of greater than 3 dB in the frequency range studied. Therefore, given the above bandwidth criterion as a function of diagnostic pulse-center frequency, the sensitivity to at least 0.2 MHz should be established for diagnostic-use hydrophones, because a uniform response below 1 MHz cannot be assumed. [S0001-4966(99)01002-4]

PACS numbers: 43.38.Fx, 43.20.Px, 43.30.Yj [SLE]

INTRODUCTION

Recent work has shown that the low-frequency response of medical-use hydrophones may be important for accurate pulse measurements, particularly of the peak rarefactional pressure, an important quantity for assessing the likelihood of cavitation onset.[1] However, frequency-response data below 1–2 MHz typically are not provided for commercial hydrophones designed for measurements in medical ultrasound fields. A technique for generating broadband-pressure pulses was therefore applied as an efficient means to measure the low-frequency response of miniature hydrophones used in biomedical ultrasonics.

Both needle-type and spot-poled membrane piezoelectric polymer hydrophones were studied. These hydrophones are described below, followed by a discussion of the calibration technique. Then the frequency-response measurements are presented and discussed, with special attention given to the results for the needle-type hydrophones, which display a low-frequency roll-off in response that appears to be due primarily to diffraction at the needle tip.

I. DESCRIPTION OF HYDROPHONES

Both the needle-type and spot-poled membrane hydrophones had the piezoelectric polymer polyvinylidene fluoride (PVDF) as the sensitive element. In the basic needle-type hydrophone design, a circular piece of poled, metal-coated PVDF film, usually 25 μm or less in thickness and 1 mm or less in diameter, is attached to the end of a hollow metal tube of similar diameter. In the spot-poled membrane design, a sheet of PVDF film is stretched across a support frame several centimeters or more across. Only a small central region of the film, typically 1 mm or less in extent, is rendered piezoelectrically active by a spot-poling procedure. Electrodes (covering the poled spot) and contiguous electrical leads are vacuum deposited onto the film. A common variation is the bilaminar membrane design, in which two identical film layers are glued together and the outer surfaces are metal coated to provide an electrical shield.

Eleven hydrophones were included in the study. Six were needle-type hydrophones from four commercial sources, and three were spot-poled membrane hydrophones from three commercial sources. Two other spot-poled membrane hydrophones made in the authors' laboratory also were included. The five membrane hydrophones consisted of three single-layer and two bilaminar types, and in two of the single-layer designs, the polymer film had a soft rubber backing.

Table I lists the designations and geometrical diameters of the hydrophones; that is, the diameters defined by the dimensions of the active elements of the hydrophones. All hydrophone signals except for N1 and N6 were fed to an amplifier having a nominal gain of 40 dB, an input impedance of 500 kΩ, and a −3-dB bandwidth of 10 kHz to 20 MHz. Integral preamplifiers were used with hydrophones N1, N3, N6, M1, and M3. Preamplifier −3-dB bandwidths extended from less than 30 kHz to greater than 20 MHz.

TABLE I. Geometrical diameters of hydrophones.

Hydrophone ID N=Needle M=Membrane	Geometrical diameter (mm)
N1	1.0
N2	1.0
N3	0.6
N4	0.4
N5	0.5
N6	0.2
M1	1.0
M2	1.0
M3	0.5
M4	0.6
M5	0.2

II. MEASUREMENT TECHNIQUE

The frequency response was measured using a technique for generating broadband, plane-wave acoustic pulses in water via short-pulse excitation of a thick piezoelectric transducer.[2] Figure 1 contains a diagram of the source transducer, electrical pulse generator, and hydrophone under test. If the applied voltage pulse has a duration that is short compared to the acoustic transit time through the transducer, two distinct planar stress waves are radiated from each face. The amplitudes of these pressure pulses are determined by the magnitudes of the mechanical-load impedances relative to that of the transducer. For the materials shown, the wave radiated into the air backing is negligibly small.

The source used for these measurements was a 6.35-cm-diam, 2.54-cm-thick, lead zirconate titanate transducer (Navy type I). In Ref. 2 it was shown that for this transducer type and thickness, the spectra of the radiated front-face pressure pulse, $P_I(f)$, and the electrical excitation pulse, $V_T(f)$, [related respectively to temporal pressure and voltage pulses $p_I(t)$ and $\nu_T(t)$] are proportional for frequencies above approximately $f=0.2$ MHz. For this restricted frequency range, $F(s)$ in Eq. (1) of Ref. 2 can be dropped, giving

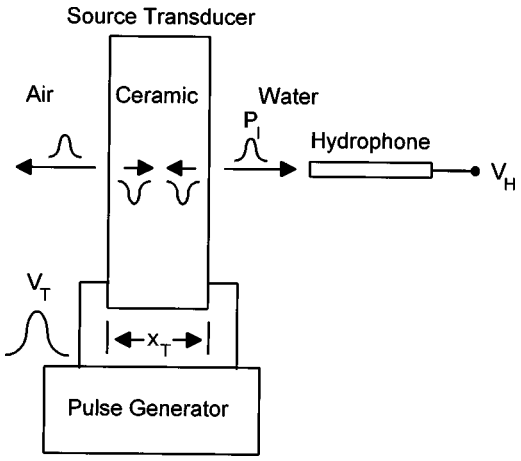

FIG. 1. Diagram of source transducer, electrical pulse generator, and hydrophone.

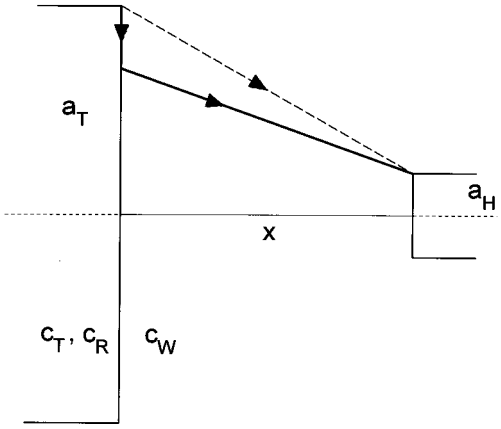

FIG. 2. Diagram of waves traveling from the source transducer boundary to the hydrophone. −−− propagation path of edge wave; ——— propagation path of head wave.

$$P_I(f)=\frac{h_{33}\epsilon_{33}^{s}z_W}{x_T(z_W+z_T)}\cdot V_T(f)=\frac{e_{33}z_W}{x_T(z_W+z_T)}\cdot V_T(f)$$
$$=KV_T(f), \tag{1}$$

where the negative sign in Ref. 2 has been ignored for convenience. Here, h_{33} and e_{33} are piezoelectric constants, ϵ_{33}^{s} is the clamped dielectric permittivity, and z_W and z_T are the water and transducer specific acoustic impedances. (For the relationship $e_{33}=h_{33}\epsilon_{33}^{s}$, see, e.g., Ref. 3.)

For Eq. (1) to be useful in practice, the front-face plane-wave pulse radiated into water, $p_I(t)$, must be isolated in time from the other components of the radiated field, most notably the pulse from the back face of the source transducer, and waves originating at the source boundary. By proper selection of the source dimensions and hydrophone location, such temporal isolation is possible. To see this, first consider only the pulse from the back face (i.e., neglect for the moment source-boundary effects). In this case, Eq. (1) is valid until the pulse radiated from the back face of the source transducer reaches the hydrophone. That is, if the source transducer and hydrophone are separated by axial distance x, and if the source is excited at time $t=0$, then Eq. (1) is valid for times $t<t_{\max}$, where

$$t_{\max}=t_M+x/c_W<x_T/c_T+x/c_W. \tag{2}$$

Here, c_T and c_W are the longitudinal wave velocities in the source transducer and water, respectively, and t_M is the desired temporal-measurement window, which can be no greater than x_T/c_T, the transit time through the source transducer. (Also, t_M is greater than the duration of the source-transducer excitation pulse.)

Now considering source-boundary effects, further temporal restrictions regarding Eq. (1) are related to the arrival at the hydrophone of edge and head waves that originate at the source boundary.[4,5] The hydrophone distance x must be small enough so that these waves arrive at the hydrophone after time $t_{\max}$. To determine the limiting values on x, consider each of these waves separately, as depicted in Fig. 2.

Edge waves: Edge waves arise due to diffraction at the source boundary. The time, t_E, that the edge wave takes to first reach the perimeter of a coaxially aligned hydrophone is

$$t_E = \frac{\sqrt{x^2 + (a_T - a_H)^2}}{c_W}, \tag{3}$$

where a_T and a_H are the source transducer and hydrophone radii, respectively. For t_E to be greater than $t_{\max}$, the limiting value of x, x_{Elim}, is

$$x_{\text{Elim}} < \frac{(a_T - a_H)^2 - (c_W t_M)^2}{2 c_W t_M}. \tag{4}$$

Head waves: As described in Refs. 4 and 5, radial modes excited in the source transducer give rise to lateral waves that originate at the source perimeter. As the lateral waves propagate inward along the transducer–water interface, head waves are radiated into the water. Two lateral waves are launched at the interface, traveling at the longitudinal and shear-wave velocities of the source transducer. For this analysis, only the longitudinal wave need be considered because of its greater velocity. This velocity, c_R, differs from c_T in that c_T is the velocity of the longitudinal wave traveling parallel to the polar axis of the transducer, whereas c_R is measured perpendicular to the polar axis.

Equation (4) in Ref. 4 can be solved for the time of arrival of the nearest head wave at the perimeter of a coaxially aligned hydrophone [cf. Ref. 5, Eq. (16)]

$$t_H = \frac{a_T - a_H + x\sqrt{(c_R^2/c_W^2 - 1)}}{c_H}. \tag{5}$$

It is assumed that $c_R > c_W$. For t_H to be greater than $t_{\max}$, the limiting value of x, x_{Hlim}, is

$$x_{\text{Hlim}} < \frac{c_W(a_T - a_H - c_R t_M)}{c_R - \sqrt{c_R^2 - c_W^2}}. \tag{6}$$

Equation (6) is valid in the conical region whose base is the circular source-transducer surface and whose apex is the axial point $x_{\text{Hmax}} = a_T[(c_H/c_W)^2 - 1]^{0.5}$. In theory, head waves cease to exist on axes beyond this point, although in practice the transition is more gradual.[4,5]

For the source transducer used in this study, $a_T = 3.18$ cm, $x_T = 2.54$ cm, $c_T = 0.46$ cm/μs, and $c_R = 0.39$ cm/μs. Taking $c_W = 0.149$ cm/μs, $t_M = 5.0$ μs, and a maximum a_H of 0.05 cm from Table I gives $x_{\text{Elim}} = 6.2$ cm, $x_{\text{Hlim}} = 5.9$ cm, $x_{\text{Hmax}} = 7.6$ cm, and $x_T/c_T = 5.5$ μs. For the $x < x_{\text{Hmax}}$ region considered, x_{Hlim} is always less than x_{Elim}. Using $x = x_{\text{Hlim}}$ in Eq. (2) gives $t_{\max} = 44$ μs.

In the actual measurements, the hydrophones were located on the source-transducer axis between $x = 1.5$ cm and $x = 6$ cm. As expected, no discernable position-dependent differences were found in the pulses measured with the hydrophones throughout this range over the 5-μs measurement interval.

Because axial points are equidistant from the circular-source perimeter, the edge- and head-wave components arrive in phase. Therefore, positioning the hydrophones on the axis was easily accomplished by spatially maximizing these pulse components. However, it should be noted that positioning is not critical to the measurements because of the plane-wave nature, and therefore position independence, of $p_I(t)$ over a large portion of the paraxial field of the source transducer.[4] (The attenuation of water can be neglected for frequencies below 2 MHz.)

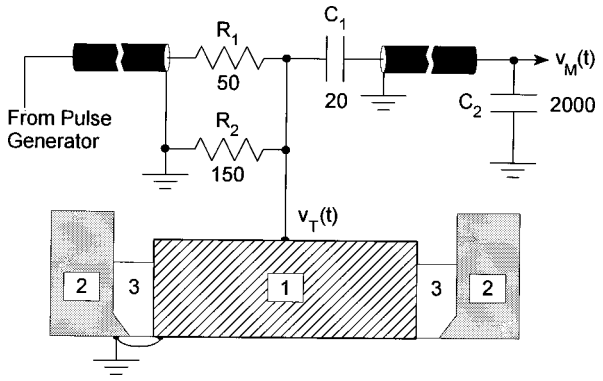

FIG. 3. Source-transducer schematic with partial view of transducer and housing in cross section. (1) 6.35-cm diameter by 2.54-cm thick, piezoelectric ceramic source transducer (Navy type I), (2) metal housing; (3) silicone rubber. Resistance and capacitance values are in ohms and picofarads, respectively. The two coaxial-cable symbols represent the cable connections between R_1 and C_1 (both located inside the transducer housing along with R_2) and the pulse generator and C_2, respectively.

Having established the measurement conditions under which Eq. (1) is valid, the hydrophone sensitivity can be determined. The hydrophone sensitivity at frequency f, $M(f)$, is the ratio of the hydrophone-voltage spectrum, $V_H(f)$, to the incident pressure pulse, $P_I(f)$. Using Eq. (1),

$$M(f) = V_H(f)/KV_T(f), \tag{7}$$

again, for $f > 0.2$ MHz. Thus, with Eq. (7) a broadband hydrophone-sensitivity response can be computed from measurements of $\nu_T(t)$ and the hydrophone's output voltage, $\nu_H(t)$, in response to $p_I(t)$. As mentioned above, since $p_I(t)$ is largely position independent, spatial averaging by the hydrophone is not an issue, and no spatial-averaging correction factors need be calculated and applied to $M(f)$ unless a_H approaches a_T.

A schematic of the source transducer is shown in Fig. 3. The separation between the cylindrical-transducer surface and the housing was approximately 0.8 cm. The unipolar-voltage pulse from the pulse generator (model 605B, Cober Electronics) had a maximum amplitude of 2200 V into 200 Ω, and a variable pulse width down to a minimum of 0.1–0.2 μs (-6 dB). Resistive divider R_1–R_2 helped match the source and load, thus minimizing both pulse ringing and fall time. Noninductive power resistors were used (MS Series, Caddock Electronics.)

Source-transducer voltage $\nu_T(t)$ was monitored using the capacitive divider C_1–C_2. C_1, an rf high-voltage ceramic capacitor (UFP1 Series, Murata Electronics), was mounted inside the transducer housing along with R_1 and R_2. C_2, comprising two 1000-pF silvered mica capacitors in parallel, was located externally to minimize rf pick-up. If the attenuation of the capacitive divider is denoted A, then the monitored voltage, $\nu_M(t)$, is

$$\nu_M(t) = A\nu_T(t) = \frac{C_1}{C_1 + C_2 + C_C + C_{\mathrm{IN}}}\nu_T(t), \tag{8}$$

where C_C is the capacitance of the 1-m coaxial cable connecting the source transducer to C_2, and C_{IN} is the input capacitance of the waveform analyzer used to record $\nu_M(t)$ (Tektronix DSA602 with 11A34 amplifier).

With $V_M(f) = AV_T(f)$, Eq. (7) is

$$M(f) = \frac{AV_H(f)}{KV_M(f)}. \tag{9}$$

From impedance analyzer measurements of capacitance (Hewlett-Packard model 4192A), the ratio A was determined to be 0.0103. Also, from published transducer material values in Ref. 6, $e_{33} = 15.1\,\mathrm{C/m^2}$ and $z_T = 34.5\times10^6\,\mathrm{N\cdot s/m^3}$. With $z_W = 1.49\times10^6\,\mathrm{N\cdot s/m^3}$, $K = 24.6\,N/(\mathrm{V\cdot m^2})$, which gives

$$M(f) = 4.19\times10^{-4}\frac{V_H(f)}{V_M(f)}\,\mathrm{V/Pa}, \tag{10}$$

or,

$$M_{\mathrm{dB}}(f) = 20\log\frac{V_H(f)}{V_M(f)} - 187.6\ \ \mathrm{dB}\ \ re:\ \ 1\ \ \mathrm{V/\mu Pa}. \tag{11}$$

Note that the sensitivity in Eq. (11) is referred to the output of the 40-dB amplifier mentioned in Sec. I. Voltages $\nu_H(t)$ and $\nu_M(t)$ were recorded using the waveform analyzer for the 11 hydrophones, and spectra were calculated from 0.2 to 2 MHz for use in Eq. (11). Measurements were made in water having a temperature of $21.0\pm1.0\,^\circ\mathrm{C}$ and an electrical conductivity of $2.0\pm1.0\ \mu\mathrm{S/cm}$.

Five microseconds of temporal data were recorded; i.e., $t_M = 5\ \mu\mathrm{s}$. Over this 5-μs interval, 512 data points were taken. Before performing the fast Fourier transforms (FFT), the waveforms were windowed to suppress any truncation effects, as discussed in Ref. 2. Then the waveform-data arrays were zero filled to achieve a record length of 4096 points, resulting in an FFT-frequency resolution of 25 kHz.

III. RESULTS

Example plots of the monitored voltage $\nu_M(t)$ and hydrophone voltage $\nu_H(t)$ for hydrophones N2 and M1 are shown in Fig. 4(a) and (b). For comparative purposes the plots are normalized to a peak amplitude of 1. The maximum value of $\nu_M(t)$ in Fig. 4 was 7 V. Taking $p_I(t)$ as $K\nu_T(t) = (K/A)\nu_M(t)$, a monitored voltage of 7 V corresponds to a temporal-peak pressure of about 17 kPa, a pressure amplitude much less than these hydrophones typically measure. Therefore, waveform averaging of the hydrophone signals (up to 512 averages using the waveform analyzer) was performed for noise reduction. The rise time and -6-dB pulse duration of $\nu_M(t)$ in Fig. 4 are 48 and 113 ns, respectively. As stated above, $t_M = 5\ \mu\mathrm{s}$. However, only 3 μs are shown in Fig. 4 for easier viewing and comparison of the pulses.

Figures 5 and 6 contain the magnitude responses for the needle-type and spot-poled membrane hydrophones, respectively. Equation (11) was used, but, except for N1 and N6, the 40-dB gain of the hydrophone amplifier was subtracted, so the sensitivities plotted are referred to the input of this amplifier. Also, 20 dB was subtracted from the sensitivity of N1 in Fig. 5 to decrease the size of the vertical scale.

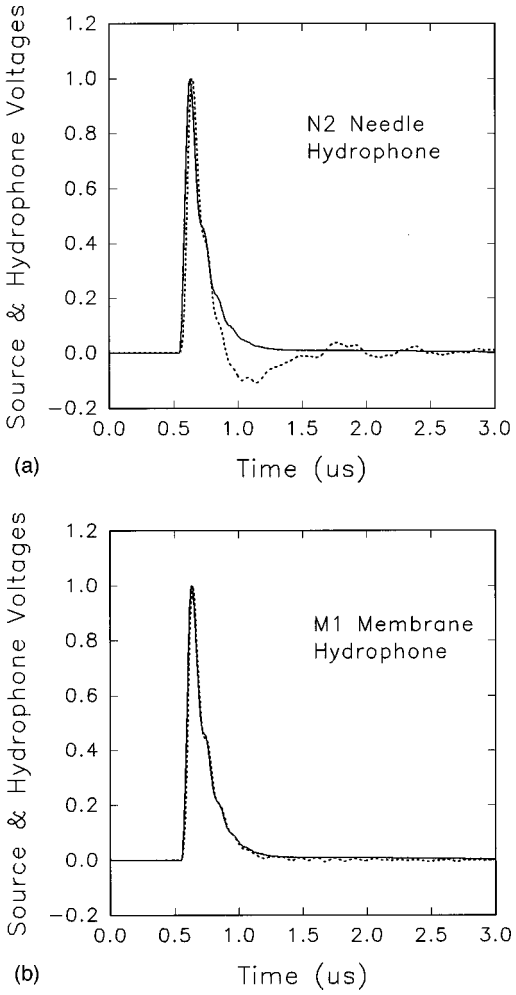

FIG. 4. The monitored source-transducer voltage, $\nu_M(t)$, and the hydrophone voltage, $\nu_H(t)$, for (a) needle-type hydrophone N2 and (b) spot-poled membrane hydrophone M1; ——— $\nu_M(t)$, ····· $\nu_H(t)$. Each plot is normalized to a peak amplitude of 1.

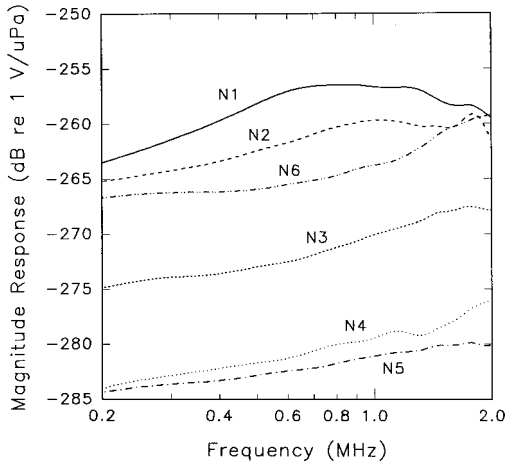

FIG. 5. Sensitivity versus frequency plots for the needle-type hydrophones. 20 dB has been subtracted from the sensitivity of N1.

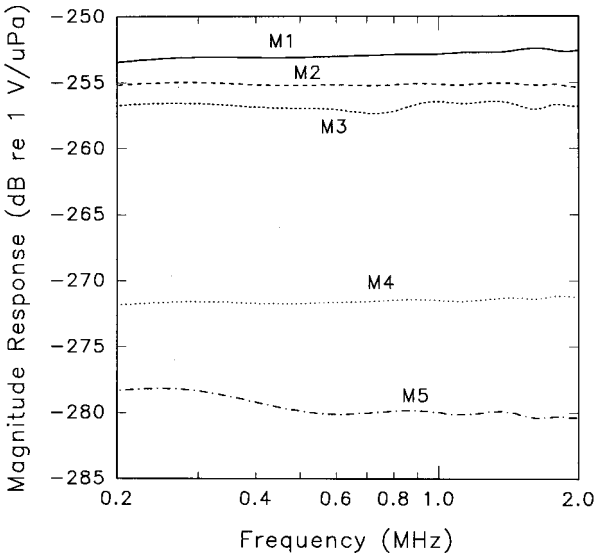

FIG. 6. Sensitivity versus frequency plots for the spot-poled membrane hydrophones.

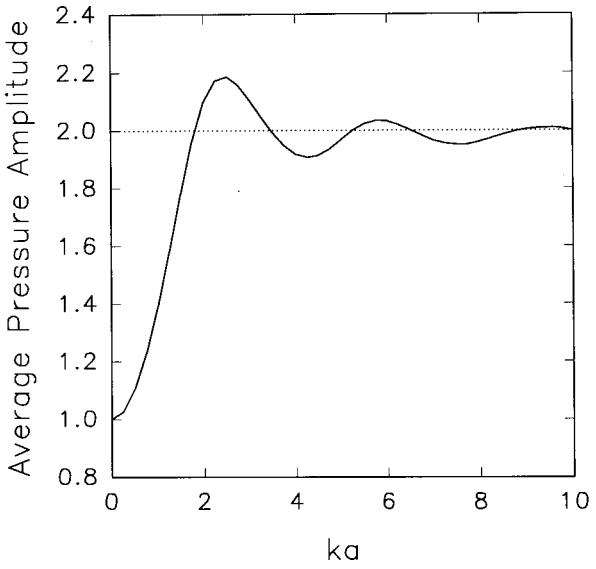

FIG. 7. Acoustic pressure spatially averaged over the end of a rigid, semi-infinite cylindrical rod vs *ka* for sound normally incident on the end of the cylinder. For the plot, it is assumed that the amplitude of the incident wave, p_i, is unity.

IV. DISCUSSION

A. Low-Frequency sensitivity

The low-frequency sensitivity of piezoelectric receivers usually is assumed to be limited by the RC time constant associated with the loading (e.g., amplifier) resistance and total capacitance of the receiver, cable, and amplifier.[7] For typical hydrophones such as those used in medical ultrasound exposimetry, this limit is less than 50 kHz. From the spot-poled membrane hydrophone results in Fig. 6, this simple electrical analysis seems to be adequate, since no significant deviations from a flat, uniform response are seen. For the needle-type hydrophones, however, this model is insufficient to explain the low-frequency roll-offs observed in Fig. 5.

Theoretical models have shown that other factors associated with the needle-type hydrophone's geometry and construction can affect the low-to-mid-range frequency response, including surface waves in the backing material,[8] and, more importantly in the present study, diffraction effects at the needle tip.[9–11] To illustrate this latter effect, consider the plot in Fig. 7. This plot, constructed from calculations in Ref. 11, shows the acoustic pressure spatially averaged over the end of a rigid, semi-infinite cylindrical rod vs ka, where k is the wave number ($2\pi/\lambda$), λ is the acoustic wavelength in the propagation medium (e.g., water), and a is the cylinder radius. The sound is incident normal to the end of the rod. Modeling the needle-type hydrophone as this rod, the acoustic field at the needle tip can be considered to comprise the incident pressure wave with amplitude p_i, and a wave diffracted at the edge of the circular tip. When λ is much smaller than the needle-tip diameter (high-frequency or large-ka case), the diffracted wave averages to zero over the tip, and the pressure at the tip is twice the incident pressure due to total reflection of the incident wave from the end of the rigid surface. As λ becomes large compared to the tip diameter, the diffracted component vanishes and the average pressure at the tip approaches that of the incident pressure. In between these two extremes, when the wavelength and tip diameter are similar, diffraction-induced interference effects produce the oscillatory behavior seen in Fig. 7. Here, the pressure amplitude averaged over the tip rises with frequency from its initial value of p_i, reaching a peak of $2.18p_i$ at $ka=2.4$, and then eventually settling to the final value of $2p_i$. This theoretical response passes through the -3-dB point ($re{:}2p_i$) at $ka=1.03$. Thus, the larger the needle diameter, the lower in frequency the response extends.

To examine the needle-type hydrophone results in light of this model, the sensitivities in Fig. 5 were replotted on a linear scale in Fig. 8, with each plot normalized to unity at $ka=1.81$, the value at which the average pressure in Fig. 7 first reaches 2.0. With a sound speed of 1.49 mm/μs, this ka value corresponds to $fd=0.86$, where f is in MHz and d

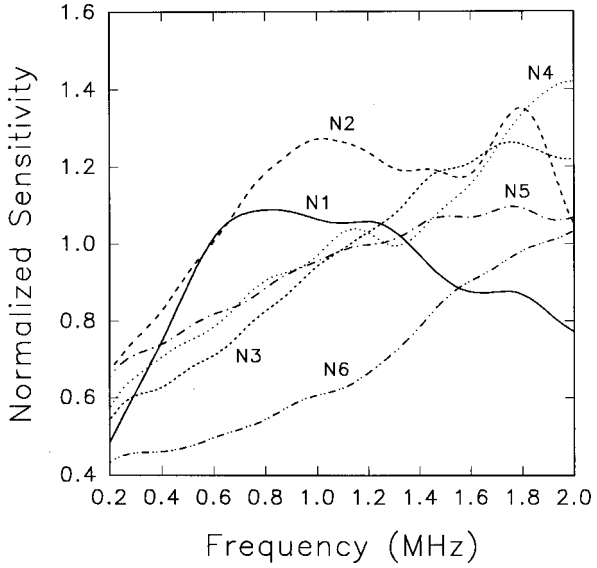

FIG. 8. Normalized sensitivity vs frequency plots for needle-type hydrophones.

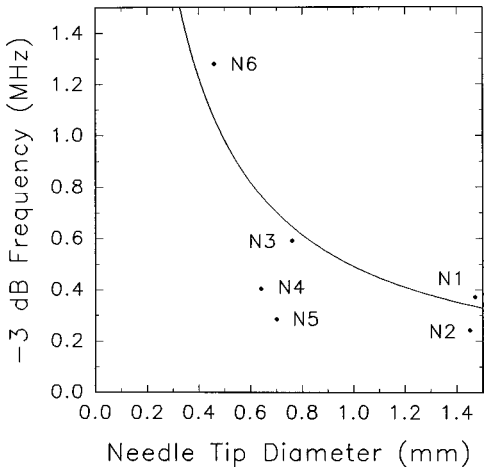

FIG. 9. −3-dB frequencies relative to the response at $f=0.86/d$. The solid curve is the theoretical result for the pressure spatially averaged over the end of a rigid, semi-infinite cylindrical rod (i.e., $f=0.49/d$). The individual points are taken from the experimental results for the six needle-type hydrophones.

$=2a$ is in mm. Figure 9 contains the −3-dB frequencies relative to the value at $f=0.86/d$ for the six needle-type hydrophones, d being the needle-tip diameters (which are, of course, larger than the geometrical diameters given in Table I). At the −3-dB point, $ka=1.03$ corresponds to $fd=0.49$; also plotted in Fig. 9 is the function $f=0.49/d$, the theoretical −3-dB result for the rigid-rod model. Points to the left of this curve would represent hydrophones having a broader low-frequency response than that predicted by the model.

Regarding comparisons with the model, needle-type hydrophones typically are hollow cylinders (rather than rigid rods) containing the center conductor as well as backing materials and coatings of unspecified acoustic impedances. Also, the geometrical and needle-tip diameters differ. Furthermore, the needle diameter of N4 increases to 1 mm about 2 mm from the tip, and for both N3 and N5 the needle body near the tip is tapered. In addition, the tip of N5 is rounded rather than flat, as with the other hydrophones (which also made determining d more difficult). Thus, while direct comparisons are hampered by these deviations from the rigid-rod model, based on the needle-type hydrophones studied it appears that an enhanced low-frequency response may be achieved by altering the size, shape, or composition of the hydrophone near the tip. Increasing the geometrical diameter would, of course, exacerbate errors due to spatial averaging.

B. Calibration accuracy

The main sources of error in the sensitivity results presented in Figs. 5 and 6 come from the systematic uncertainties associated with the factors in Eq. (9), along with the gain accuracy of the 40-dB amplifier used.

Capacitive-divider attenuation, A: The overall error in determining this capacitive ratio is estimated to be ±5%, the main component being the stray capacitance associated with mounting C_1.

Transducer constant, K: The piezoelectric and dielectric transducer properties are subject to batch fluctuations and aging.[6] However, it is implied in Ref. 6 that the reported value of the piezoelectric constant e_{33} should vary by no more than approximately ±10%. Assuming that the combined uncertainties of the specific acoustic impedances and transducer thickness contribute no more than ±5%, an error of ±15% can be assigned to K.

Hydrophone and monitored-voltage spectra, $V_H(f)$ and $V_M(f)$: Here, the error depends not on the accuracy of the waveform analyzer used to record $\nu_H(t)$ and $\nu_M(t)$, but on the precision of the input attenuators, since a voltage ratio is being measured. This error should be less than ±5%.

Amplifier gain: The gain of the rated 40-dB amplifier was measured to be 39.87±0.03 dB from 0.2 to 2.0 MHz, for an error of less than ±0.5%.

Following the calculation procedure in Ref. 12, the estimated systematic uncertainty in the absolute-sensitivity data due to the above factors is ±19% (at the 95%-confidence level). It should be noted that if the data in Figs. 5 and 6 are considered as only relative responses, then a sensitivity measurement at a single frequency by an independent (and possibly more accurate) calibration technique may be used to obtain the broadband absolute response. In this regard, for single-frequency calibrations, laser interferometry has been used above about 400 kHz,[9] and three-transducer reciprocity has been used up to 500 kHz.[13]

With regard to the lower limit of 0.2 MHz, this limit applies only if Eq. (1) is used to compute $P_I(f)$. If a substitution method using the thick-transducer technique is employed, in which the spectral response of the hydrophone under test is compared to that of a reference hydrophone having known frequency response, then the lower-frequency limit, as well as calibration accuracy, will be determined by the response data available for the reference hydrophone. Furthermore, if $p_I(t)$ is measured directly, such as by interferometric means, as reported in Ref. 14, then the theoretical considerations used in Ref. 2 to calculate the lower-frequency limit do not apply.

V. CONCLUSIONS

The objective of this investigation was to use a thick-transducer, short-pulse technique to measure the low-frequency sensitivity of piezoelectric polymer hydrophones currently used in biomedical ultrasound exposimetry. With regard to the measurement technique, a chief advantage was the ability to obtain broadband calibration data in a single measurement, as opposed to the more time-consuming single-frequency techniques based on reciprocity or interferometry. Also, because of the plane-wave nature of the pulses, there was no need for precise source-hydrophone positioning or corrections for hydrophone spatial averaging. However, sensitivity was poor since the source transducer was neither focused nor operated in a resonant mode, so hydrophone-signal amplification and waveform averaging were necessary. Although not of concern for the present study, it may be noted that hydrophone-phase response also is available in addition to the amplitude-response results presented.

For the spot-poled membrane hydrophone sensitivities, no significant deviation from a flat, uniform response was seen. The needle-type hydrophones, on the other hand, all displayed a roll-off in low-frequency response at frequencies

considerably higher than that due to the RC time constant. The roll-off frequency was affected by the size and shape of the needle tip, an outcome in qualitative agreement with a diffraction-based model for the spatially averaged pressure on the end of a rigid, semi-infinite cylindrical rod.

Needle-type hydrophones have advantages over spot-poled membrane hydrophones in several practical instances, such as when measuring close to the source transducer. However, a roll-off in response calls the use of these devices into question when accurate knowledge of the pressure waveform is required, particularly with regard to measuring the peak rarefactional pressure in pulsed waveforms displaying significant finite-amplitude distortion. Therefore, altering the shape or composition of the needle to improve the low-frequency response could be an important design consideration.

[1] G. R. Harris, ''Are current hydrophone low frequency response standards acceptable for measuring mechanical/cavitation indices?,'' Ultrasonics **34**(6), 649–654 (1996).

[2] G. R. Harris, M. R. Myers, and P. M. Gammell, ''The response of transiently-excited thick transducers at low frequencies,'' J. Acoust. Soc. Am. **100**, 3115–3120 (1996).

[3] P. Schnabel, ''Dispersion of thickness vibrations of piezoceramic disk resonators,'' IEEE Trans. Sonics Ultrason. **25**, 16–24 (1978).

[4] G. R. Harris, E. F. Carome, and H. D. Dardy, ''An analysis of pulsed ultrasonic fields as measured by PVDF spot-poled membrane hydrophones,'' IEEE Trans. Sonics Ultrason. **30**, 295–303 (1983).

[5] J. C. Baboux, F. Lakestani, and M. Pedrix, ''Theoretical and experimental study of the contribution of radial modes to the pulsed ultrasonic field radiated by a thick piezoelectric disk,'' J. Acoust. Soc. Am. **75**, 1722–1731 (1984).

[6] H. Jaffe and D. A. Berlincourt, ''Piezoelectric transducer materials,'' Proc. IEEE **53**, 1372–1386 (1965).

[7] W. S. Burdic, *Underwater Acoustic System Analysis* (Prentice-Hall, Englewood Cliffs, NJ, 1984), pp. 77–79.

[8] Y. Nakamura and T. Otani, ''Study of surface elastic wave induced on backing material and diffracted field of a piezoelectric polymer film hydrophone,'' J. Acoust. Soc. Am. **94**, 1191–1199 (1993).

[9] S. P. Robinson, ''A comparison of the frequency response of membrane and needle probe PVDF hydrophones,'' in *Physics in Medical Ultrasound II*, edited by D. Evans and K. Martin (Institute of Physical Sciences in Medicine, York, UK, 1988), pp. 79–86.

[10] B. Fay, G. Ludwig, C. Lankjaer, and P. A. Lewin, ''Frequency response of PVDF needle-type hydrophones,'' Ultrasound Med. Biol. **20**, 361–366 (1994).

[11] D. S. Jones, ''Scattering of a scalar wave by a semi-infinite rod of circular cross section,'' Philos. Trans. R. Soc. London, Ser. A **247**, 499–528 (1955).

[12] R. C. Preston, D. R. Bacon, and R. A. Smith, ''Calibration of medical ultrasonic equipment-procedures and accuracy assessment,'' IEEE Trans. Ultrason. Ferroelectr. Freq. Control **35**, 110–121 (1988).

[13] S. P. Robinson and G. R. Doré, ''Uncertainties in the calibration of hydrophones at NPL by the three-transducer spherical-wave reciprocity method in the frequency range 10 kHz to 500 kHz,'' NPL Report RSA(EXT)0054 (National Physical Laboratory, Teddington, Middlesex, UK, November 1994).

[14] J. C. Baboux, H. Djelouah, and M. Pedrix, ''Interferometric measurements of transient ultrasonic fields: application to hydrophone calibration,'' in *Proceedings of the 1988 IEEE Ultrasonics Symposium* (IEEE, New York, 1988), pp. 857–861.

Bifurcation and chaos in flexural vibration of a baffled plate in mean flow

Sean F. Wu
Department of Mechanical Engineering, Wayne State University, Detroit, Michigan 48202

Jason Zhu
General Motors Truck Group, Mail Code 483-326-151, 3300 General Motors Road, Milford, Michigan 48380-3726

(Received 6 May 1998; accepted for publication 27 October 1998)

This paper presents the results of an analytic and numerical investigation of flexural vibration of a finite plate clamped to an infinite baffle in mean flow. Attention of the present paper is focused on: (1) the physical mechanisms that lead to unstable conditions for a clamped plate in mean flow; (2) the effects of mean flow, plate aspect ratio and length to thickness ratio, and the structural nonlinearities on the instabilities; and (3) the onset of bifurcation and chaos in plate flexural vibration beyond critical mean flow speeds. In carrying out these analyses, the plate flexural displacements are solved by the Galerkin method. The critical mean flow speeds are determined by a general stability theory and the Routh algorithm. Results show that the instabilities of a baffled plate are mainly caused by an added stiffness due to acoustic radiation in mean flow, but controlled by the structural nonlinearities. The added stiffness is shown to be negative and increase quadratically with the mean flow speed. Hence, as the mean flow speed approaches a critical value, the added stiffness may null the overall stiffness of a plate, leading to an unstable condition. Note that without the inclusion of the structural nonlinearities, the plate has only one equilibrium position, namely, its undeformed flat position. Under this condition, the amplitude of plate flexural vibration would grow exponentially in time everywhere, known as absolute instability. With the inclusion of structural nonlinearities, the plate may possess multiple equilibria. When the mean flow speed exceeds the critical values, the plate may be unstable around all equilibria, jumping from one equilibrium position to another. Since this jumping is random, the plate flexural vibration may seem chaotic. This chaotic behavior disappears, however, when viscous damping is introduced. Accordingly, the plate settles down to a ''buckled-down'' position owning to the hydraulic fluid-loading effect. [S0001-4966(99)01902-5]

PACS numbers: 43.40.Dx, 43.40.Rj [CBB]

INTRODUCTION

Analyses of dynamic and acoustic responses of fluid-loaded structures in subsonic and supersonic flows have long been topics of great interest.[1–6] Applications of these studies can be found in the designs of aircraft fuselage and underwater vehicles. Previous studies have shown that the characteristics of the dynamic and acoustic responses of an elastic structure may be quite different when there is mean flow. The most significant change is the onset of instabilities, such as those depicted by Brazier-Smith and Scott[7] for an infinite plate subject to a time-varying external excitation. Using the causality principle, Brazier-Smith and Scott demonstrated numerically that the response of an infinite plate could become unstable in mean flow. When the mean flow speed is below a critical value, the plate response may be convectively unstable if the excitation frequency is below the upper limit of the spatial instability. Here convective instability is defined as an exponential growth in the plate flexural vibration amplitude as the disturbance propagates in the downstream direction. When the mean flow speed exceeds the critical value, the plate response may become absolute unstable. Namely, the amplitude of plate vibration may grow exponentially in time at any point under any excitation frequency.

Brazier-Smith and Scott's numerical analyses were confirmed by Crighton and Oswell's asymptotic analysis.[8] In particular, Crighton and Oswell shed light on the onset of convective instability: an infinite plate may draw energy from mean flow to sustain the growth in the amplitude of plate flexural vibration. Also, they derived an analytic formulation for depicting the critical mean flow speed beyond which absolute instability would occur. This critical mean flow speed is shown to depend on fluid/structure density ratio and compressional wave speeds ratio. According to Crighton and Oswell's formula, absolute instability may occur for an infinite steel plate in water, disregarding its thickness, when the mean flow speed exceeds 14.9 m/s. For the same plate in air, absolute instability may occur when the mean flow speed exceeds merely 0.02 m/s! These predictions are indeed startling. However, Crighton and Oswell's analysis[8] provides no explanations to the onset of absolute instability.

Actually, the phenomenon of absolute instability described above[7,8] may have little practical significance, because, first of all, an infinite plate is nonexistent and second, no one has ever observed it in reality. Nonetheless, this phenomenon has fascinated the first author of the present paper. The lack of physical explanation to such a phenomenon has motivated him to look further into this problem.

In two recent papers,[9,10] it has been found that absolute

instability may be attributable to an added stiffness effect due to acoustic radiation in mean flow. This added stiffness is negative and its value increases quadratically with the mean flow speed. As the mean flow speed approaches a critical value, the added stiffness may null the overall stiffness of a plate, thus leading to an unstable condition.

The objective of the present paper is to give a more detailed and in-depth analysis of the characteristics of plate flexural vibration around critical mean flow speeds. Since an infinite plate does not exist in reality, a finite plate is considered. To simplify the problem, the plate is assumed to be clamped to an infinite baffle, and to be in contact with a fluid on one side but in vacuum on the other side. Also taken into account is the effect of the structural nonlinearities induced by in-plane forces and shearing forces due to stretching of plate bending motion.

It is emphasized that the inclusion of the structural nonlinearities are not meant for analyzing large-amplitude vibrations, but rather for keeping the amplitude of plate flexural vibration from growing unboundedly. The inclusion of the nonlinearities also allows one to gain valuable insight into the characteristics of plate flexural vibration, for example, bifurcation and chaos, which cannot be acquired from the analysis of a linear system.

Attention of this paper is focused on: (1) the physical mechanisms leading to unstable conditions of a baffled plate in mean flow; (2) the effects of mean flow speed, plate aspect and length to thickness ratios, and the structural nonlinearities on the instabilities; and (3) the onset of bifurcation and chaos in plate flexural vibration beyond critical mean flow speeds. Section I presents the basic equations of motion for a fluid-loaded plate in mean flow. Section II gives the approximate solutions to plate flexural vibration by using Galerkin's method. The effect of mean flow on stability of a baffled plate is analyzed in detail in Sec. III. Section IV depicts stability charts of a baffled plate under various aspect ratios, length to thickness ratios, and fluid to structure density ratios. Section V illustrates the numerical results of transition of plate flexural vibration from stable to unstable conditions when the mean flow speed exceeds the critical values. In particular, it shows that this transition may be random and plate flexural vibration may be chaotic.

It is worth pointing out that while absolute instability has never been observed in reality, chaos in flexural vibration of a clamped plate has been observed experimentally.[11] This random vibration has a direct impact on resulting acoustic radiation. The studies of the instability mechanisms of a clamped plate in mean flow may eventually lead to a better understanding of why there is a sudden increase in the overall sound pressure level beyond certain mean flow speed.[12]

I. FUNDAMENTAL EQUATIONS

Consider a finite plate of length L, width b, and thickness h that is clamped to an infinite and rigid baffle (see Fig. 1). In analyzing flexural vibration, it is assumed that: (1) the plate is in contact with fluid of density ρ and sound speed c on one side ($z>0$) and in vacuum on the other side; (2) the fluid moves at a uniform, constant speed U in the x-axis direction; and (3) the amplitude of plate flexural vibration remains small at all times such that it does not alter significantly the steady flow pattern.

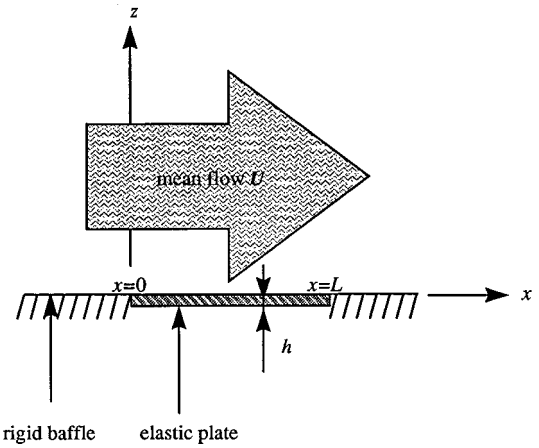

FIG. 1. Schematic of a baffled plate in mean flow.

Under these assumptions, the equation that governs plate flexural vibration can be written as[9,10]

$$\mathcal{L}_1\{w(x,y,t)\}-\mathcal{L}_2\{w(x,y,t)\}-\mathcal{L}_3\{w(x,y,t)\} = P\left(x,y,\frac{h}{2},t\right), \tag{1}$$

where w is the plate flexural displacement in the z-axis direction, P represents any external pressure excitation, and $\mathcal{L}_j$, $j=1$ to 3, are differential and integral operators operating on w.

Physically, the operator $\mathcal{L}_1$ represents the sum of plate stiffness, inertia, and damping forces per unit area, $\mathcal{L}_2$ stands for the effect of in-plane forces and shearing forces per unit area due to stretching of plate bending motion, and $\mathcal{L}_3$ describes the fluid-loading effect that acts back on the plate surface. Mathematically, these operators are defined by

$$\mathcal{L}_1 = D\nabla^4+\rho_p h\frac{\partial^2}{\partial t^2}+d\frac{\partial}{\partial t}, \tag{2a}$$

$$\mathcal{L}_2 = N_x\frac{\partial^2}{\partial x^2}+N_y\frac{\partial^2}{\partial y^2}+2N_{xy}\frac{\partial^2}{\partial x\,\partial y}, \tag{2b}$$

$$\mathcal{L}_3 = \rho\left(\frac{\partial}{\partial t}+U\frac{\partial}{\partial x}\right)\int_0^L\int_0^b\left[\mathrm{G}(\vec{r}|\vec{r}_o)\left(\frac{\partial}{\partial\tau}+U\frac{\partial}{\partial x_o}\right)\right]_\tau dx_o\,dy_o, \tag{2c}$$

where $D=Eh^3/12(1-\nu^2)$, is the plate flexural rigidity, here E and ν are the Young's modulus and the Poisson's ratio, respectively, ρ_p is the plate density, d is the plate viscous damping coefficient per unit area, N_x and N_y are the stress resultants in the x- and y-axis directions, respectively, and N_{xy} is the projection of the shearing forces in the z axis.[13] Because of the inclusion of N_x, N_y, and N_{xy}, Eq. (1) is nonlinear containing cubic nonlinearities.

The symbol $[\,]_\tau$ in Eq. (2c) implies that the quantities inside the square brackets are to be evaluated at the retarded time, $\tau=t-\Delta t$, and G represents the Green's function which for a subsonic mean flow speed can be written as[9,14]

$$G(\vec{r}|\vec{r}_o)=-\frac{1}{2\pi\sqrt{(x-x_o)^2+(1-M^2)[(y-y_o)^2+z^2]}}, \tag{3}$$

where M is the mean flow Mach number and Δt is the time required for the signal to travel from the source to receiver,

$$\Delta t=\frac{M(x-x_o)+\sqrt{(x-x_o)^2+(1-M^2)[(y-y_o)^2+z^2]}}{c\sqrt{1-M^2}}. \tag{4}$$

At the joints with the baffle, the plate satisfies the clamped boundary conditions

$$\begin{aligned} &w(0,y,t)=w(L,y,t)=w(x,0,t)=w(x,b,t)=0,\\ &\left.\frac{\partial w}{\partial x}\right|_{x=0}=\left.\frac{\partial w}{\partial x}\right|_{x=L}=\left.\frac{\partial w}{\partial y}\right|_{y=0}=\left.\frac{\partial w}{\partial y}\right|_{y=b}=0. \end{aligned} \tag{5}$$

II. APPROXIMATE SOLUTIONS VIA THE GALERKIN METHOD

Equation (1) represents a nonlinear, partial differential/integral equation. Because of the complexities involved in this equation, analytic solutions cannot be found. Hence, the Galerkin method is used to derive approximate solutions. Since in this paper we are interested in the effect of mean flow on the characteristics of the plate flexural vibration responses, it is sufficient to examine the homogeneous solutions of Eq. (1). Accordingly, we set the forcing function P on the right side of Eq. (1) to zero.

For convenience sake, let us first nondimensionalize variables in Eq. (1),

$$\begin{aligned} &(\bar{x},\bar{x}_o)=\frac{(x,x_o)}{L},\quad (\bar{y},\bar{y}_o)=\frac{(y,y_o)}{b},\quad \bar{t}=\frac{1}{\phi^2}\left(\frac{c_0 t}{h}\right),\\ &\phi=\frac{L}{h},\quad \eta=\frac{b}{L},\quad \sigma=\frac{\rho}{\rho_p},\\ &\xi=\phi^2\left(\frac{d}{\rho_p c_0}\right),\quad \zeta=\sigma^{1/2}\phi^{3/2}\left(\frac{U}{c_0}\right), \end{aligned} \tag{6}$$

where a bar over a variable implies a dimensionless quantity, ϕ represents the plate length to thickness ratio, η stands for the plate aspect ratio, σ describes the fluid/plate density ratio, ξ indicates the viscous damping ratio, ζ depicts the dimensionless mean flow speed, and $c_0=c_p/\sqrt{12}$ represents a scaled compressional wave speed, where c_p is the plate compressional wave speed.[15]

Next, the plate flexural displacement is expanded in terms of n normal modes in the $\bar{x}$-axis direction (longitudinal modes) and m normal modes in the $\bar{y}$-axis direction (lateral modes),[13]

$$\bar{w}(\bar{x},\bar{y},\bar{t})=\sum_{i=1}^{n}\sum_{j=1}^{m} W_i(\bar{x})W_j(\bar{y})\bar{C}_{ij}(\bar{t}), \tag{7}$$

where $W_i(\bar{x})$ and $W_j(\bar{y})$ satisfy the prescribed boundary conditions (5), and $\bar{C}_{ij}(\bar{t})$ are the dimensionless time-dependent coefficients for coupling of the ith longitudinal mode to the jth lateral mode.

Substitute Eq. (7) into (1), multiply the resultant equation by $W_k(\bar{x})$ ($k=1$ to n) and then integrate it over $\bar{x}$ from 0 to 1. Next, multiply the resultant equation by $W_l(\bar{y})$ ($l=1$ to m) and integrate it over $\bar{y}$ from 0 to 1. This process yields a set of homogeneous, nonlinear, second-order ordinary differential equations, which can be written in an indicial form as[14]

$$\Phi_{klij}\ddot{\bar{C}}_{ij}(\bar{t})+\Psi_{klij}\dot{\bar{C}}_{ij}(\bar{t})+\chi_{klij}\bar{C}_{ij}(\bar{t})+\Xi_{klij}\bar{C}_{ij}(\bar{t})=0, \tag{8}$$

where Φ_{klij}, Ψ_{klij}, and χ_{klij} represent the effects of plate inertia, viscous damping, and stiffness, respectively, and Ξ_{klij} stands for the effect of structural nonlinearities and contains quadratic powers of the unknown coefficients $\bar{C}_{ij}(\bar{t})$.

To facilitate integrations in Eq. (2c), the symmetry property of the Green's function G is utilized to replace $\partial G(\vec{r}|\vec{r}_o)/\partial x$ by $-\partial G(\vec{r}|\vec{r}_o)/\partial x_o$. Next, the chain rule is employed to transfer the derivative of G with respect to x_o to $w(x_o,y_o,\tau)$. Finally, the clamped boundary conditions (5) are used to eliminate w and its first derivative evaluated at the edges. If we further limit ourselves to the case in which the time required for an acoustic signal to traverse the characteristic dimension of the plate is much less than the characteristic period of the signal, then the time delay Δt in Eq. (2c) can be neglected. Such a compactness condition is justifiable for low Mach number flows[16] ($M\ll 1$), which is the case under consideration in the present paper.

Note that the above procedures are valid for clamped boundary conditions only. For other boundary conditions such as simply-supported conditions, the slope of the flexural displacement will be discontinuous at the edges of the plate. Accordingly, the Dirac delta function should be used to account for the contributions from these discontinuities along the edges. Evaluations of the integral in Eq. (2c) can then be facilitated by using this delta-type function and the corresponding boundary conditions at the edges.

Once this is done, the expressions of Φ_{klij}, Ψ_{klij}, χ_{klij}, and Ξ_{klij} for a subsonic flow can be written as

$$\Phi_{klij}=\delta_{ik}\delta_{jl}+\frac{\eta\sigma\phi}{2\pi\sqrt{1-M^2}}\Theta^{(0)}_{klij}, \tag{9a}$$

$$\Psi_{klij}=\xi\delta_{ik}\delta_{jl}+\frac{\eta\zeta\sqrt{\sigma\phi}}{\pi\sqrt{1-M^2}}\Theta^{(1)}_{klij}, \tag{9b}$$

$$\chi_{klij}=\left[\lambda_i^4+\frac{\lambda_j^4}{\eta^4}\right]\delta_{ik}\delta_{jl}+\frac{2}{\eta^2}\theta_{ik}\theta_{jl}+\frac{\eta\zeta^2}{2\pi\sqrt{1-M^2}}\Theta^{(2)}_{klij}, \tag{9c}$$

$$\begin{aligned} \Xi_{klij}=6(1-\nu^2)\bar{C}_{pq}(\bar{t})\bar{C}_{rs}(\bar{t})[&\theta_{pr}\theta_{ik}\beta_{jlqs}\\ &+\theta_{qs}\theta_{jl}\beta_{ikpr}-\gamma_{pr}\gamma_{sq}\gamma_{ik}\gamma_{jl}], \end{aligned} \tag{9d}$$

where δ_{ij} represent the Kronecker delta, λ_i is the eigenvalue of the ith normal mode, and θ_{ik}, γ_{ik}, β_{jlqs}, and $\Theta^{(\nu)}_{klij}$ are defined by

$$\theta_{ik}=\int_0^1 \frac{\partial^2 W_i(\bar{x})}{\partial \bar{x}^2} W_i(\bar{x}) W_k(\bar{x})\, d\bar{x}, \tag{10a}$$

$$\gamma_{ik}=\int_0^1 \frac{\partial W_i(\bar{x})}{\partial \bar{x}} W_k(\bar{x})\, d\bar{x}, \tag{10b}$$

$$\beta_{jlqs}=\int_0^1 W_j(\bar{y}) W_l(\bar{y}) W_q(\bar{y}) W_s(\bar{y})\, d\bar{y}, \tag{10c}$$

$$\Theta_{klij}^{(\upsilon)}=\int_0^1\int_0^1 W_k(\bar{x}) W_l(\bar{y})\, d\bar{x}\, d\bar{y} \times \int_0^1\int_0^1 \frac{W_j(\bar{y}_o)[\partial^{(\upsilon)} W_i(\bar{x}_o)/\partial x_0^{(\upsilon)}]}{\sqrt{(\bar{x}-\bar{x}_o)^2+\eta^2(1-M^2)(\bar{y}-\bar{y}_o)^2}}\, d\bar{x}_o\, d\bar{y}_o, \tag{10d}$$

where the superscript (υ) in Eq. (10d) indicates the order of derivatives with respect to x_o ($\upsilon=0$, 1, and 2).

Physically, the terms on the right side of Eq. (9a) represent the effect of mass for each mode of the plate and that of the added mass due to fluid loading, respectively. The terms on the right side of Eq. (9b) describe the effect of viscous damping associated with each mode and that of the added damping induced by acoustic radiation in the presence of mean flow, respectively. The square-bracketed term on the right side of Eq. (9c) indicates the sum of stiffness of the ith longitudinal mode and that of the jth lateral mode; the second term implies the stiffness due to coupling between the longitudinal and lateral modes; and the last term depicts the added stiffness due to acoustic radiation in mean flow. The terms on the right side of Eq. (9d) stand for the effect of added stiffness due to structural nonlinearities.

Thus, by using the Galerkin method the nonlinear, partial differential/integral equation (1) is reduced a set of coupled, nonlinear, second-order ordinary differential equations. If only the first longitudinal and lateral modes are considered, then Eq. (8) becomes a standard Duffing-type equation. The approximate solution to such an equation using multiple scales or averaging method has been documented extensively.[17–20] For an arbitrary number of longitudinal and lateral modes, however, analytic solutions cannot be obtained even for the first-order approximation. Under this circumstance, numerical solutions can be obtained by using the Gear method.[21]

III. MEAN FLOW EFFECTS ON PLATE FLEXURAL VIBRATION

To examine how mean flow changes the plate flexural vibration responses, we need first to determine the equilibrium positions around which a plate vibrates. One such equilibrium coincides with the plate's original undeformed position. The inclusion of structural nonlinearities, however, generates new equilibria. These additional equilibrium positions are derived explicitly in this section, which enables us to determine the critical mean flow speeds and to understand the mechanisms that govern the plate stabilities.

In the preceding section, we have derived the characteristic equation (8) for a baffled plate in mean flow. As an example of analyzing the plate stability, let us consider one lateral mode ($m=1$) and two longitudinal modes ($n=2$). Accordingly, Eq. (8) can be rewritten as a set of two homogeneous, nonlinear, second-order ordinary differential equations. To facilitate the analysis, we introduce an auxiliary set of variables Y_i to replace these two equations by four first-order, ordinary differential equations

$$Y_1=\bar{C}_{11}(\bar{t}), \tag{11a}$$

$$Y_2=\dot{\bar{C}}_{11}(\bar{t}), \tag{11b}$$

$$Y_3=\bar{C}_{21}(\bar{t}), \tag{11c}$$

$$Y_4=\dot{\bar{C}}_{21}(\bar{t}). \tag{11d}$$

This transformation results in a phase space[22] defined by Y_i and $\dot{Y}_i$,

$$\dot{Y}_1=Y_2, \tag{12a}$$

$$\dot{Y}_2=-\frac{\alpha_1}{\alpha_{01}}Y_1-\frac{\xi}{\alpha_{01}}Y_2-\frac{\alpha_3}{\alpha_{01}}Y_4-\frac{\alpha_4}{\alpha_{01}}Y_1^3-\frac{\alpha_5}{\alpha_{01}}Y_1Y_3^2, \tag{12b}$$

$$\dot{Y}_3=Y_4, \tag{12c}$$

$$\dot{Y}_4=-\frac{\alpha_2}{\alpha_{02}}Y_3-\frac{\xi}{\alpha_{02}}Y_4+\frac{\alpha_3}{\alpha_{02}}Y_2-\frac{\alpha_5}{\alpha_{02}}Y_1^2Y_3-\frac{\alpha_6}{\alpha_{02}}Y_3^3, \tag{12d}$$

where the coefficients α_{ij} are given by

$$\alpha_{01}=1+\frac{\eta\sigma\phi}{2\pi}\Theta_{1111}^{(0)}, \tag{13a}$$

$$\alpha_{02}=1+\frac{\eta\sigma\phi}{2\pi}\Theta_{2121}^{(0)}, \tag{13b}$$

$$\alpha_1=\lambda_1^4+\frac{2\theta_{11}^2}{\eta^2}+\frac{\lambda_1^4}{\eta^4}+\frac{\eta\zeta^2}{2\pi}\Theta_{1111}^{(2)}, \tag{13c}$$

$$\alpha_2=\lambda_2^4+\frac{2\theta_{11}\theta_{22}}{\eta^2}+\frac{\lambda_1^4}{\eta^4}+\frac{\eta\zeta^2}{2\pi}\Theta_{2121}^{(2)}, \tag{13d}$$

$$\alpha_3=\frac{\eta\zeta\sqrt{\sigma\phi}}{\pi}\Theta_{1121}^{(1)}, \tag{13e}$$

$$\alpha_4=6(1-\nu^2)\left(1+\frac{1}{\eta^4}\right)\beta_{1111}\theta_{11}^2, \tag{13f}$$

$$\alpha_5=6(1-\nu^2)\left(\beta_{1111}\theta_{11}\theta_{22}+\frac{3}{\eta^4}\beta_{1122}\theta_{11}^2\right), \tag{13g}$$

$$\alpha_6=6(1-\nu^2)\left(\beta_{1111}\theta_{22}^2+\frac{1}{\eta^4}\beta_{2222}\theta_{11}^2\right). \tag{13h}$$

Equation (12) allows us to use a general stability theory[23] to examine the stabilities at the fixed points or equilibrium positions determined by setting the right side of Eq. (12) to zero, namely,

$$Y_2=0, \tag{14a}$$

$$(\alpha_1+\alpha_4 Y_1^2+\alpha_5 Y_3^2)Y_1=0, \tag{14b}$$

$$Y_4=0, \tag{14c}$$

$$(\alpha_2+\alpha_5 Y_1^2+\alpha_6 Y_3^2)Y_3=0. \tag{14d}$$

Solutions to Eq. (14) are given by

$$\tilde{Y}_1=\tilde{Y}_2=\tilde{Y}_3=\tilde{Y}_4=0, \tag{15a}$$

$$\tilde{Y}_2=\tilde{Y}_3=\tilde{Y}_4=0, \quad \tilde{Y}_1=\pm\sqrt{-\frac{\alpha_1}{\alpha_4}}, \tag{15b}$$

$$\tilde{Y}_1=\tilde{Y}_2=\tilde{Y}_4=0, \quad \tilde{Y}_3=\pm\sqrt{-\frac{\alpha_2}{\alpha_6}}, \tag{15c}$$

$$\begin{aligned}&\tilde{Y}_2=\tilde{Y}_4=0, \quad \tilde{Y}_1=\pm\sqrt{\frac{\alpha_2\alpha_5-\alpha_1\alpha_6}{\alpha_4\alpha_6-\alpha_5^2}},\\ &\tilde{Y}_3=\pm\sqrt{\frac{\alpha_1\alpha_5-\alpha_2\alpha_4}{\alpha_4\alpha_6-\alpha_5^2}},\end{aligned} \tag{15d}$$

where the symbol $\tilde{Y}$ implies a fixed point or an equilibrium position. Note that solutions given by Eqs. (15) must be real in order for these equilibria to be meaningful.

Clearly, the equilibrium position given by Eq. (15a) corresponds to the plate's original undeformed position, and the rest are induced by structural nonlinearities. The stabilities around each of these equilibria can now be examined.

Taking the derivative of Eqs. (14) with respect to time, we obtain

$$\mathcal{J}(Y)\{\dot{Y}\}=0, \tag{16}$$

where $\mathcal{J}(Y)$ is a Jacobian matrix. Assume a form of solution to Eq. (16) as

$$\{Y\}=\{|Y|\}e^{\Lambda\bar{t}}, \tag{17}$$

where Λ represents the eigenvalues of the system and $\{|Y|\}$ stands for the amplitude of $\{Y\}$. Substituting Eq. (17) into (16) leads to the following characteristic equation,

$$\sum_{n=0}^{4}\Omega_n\Lambda^n=0, \tag{18}$$

where Ω_n are given by

$$\Omega_0=\Gamma_1\Gamma_2-4\alpha_5^2\tilde{Y}_1^2\tilde{Y}_3^2, \tag{19a}$$

$$\Omega_1=\xi(\Gamma_1+\Gamma_2), \tag{19b}$$

$$\Omega_2=\xi^2+\alpha_3^2+\alpha_{01}\Gamma_2+\alpha_{02}\Gamma_1, \tag{19c}$$

$$\Omega_3=\xi(\alpha_{01}+\alpha_{02}), \tag{19d}$$

$$\Omega_4=\alpha_{01}\alpha_{02}, \tag{19e}$$

where $\Gamma_{1,2}$ are given by

$$\Gamma_1=\alpha_1+3\alpha_4\tilde{Y}_1^2+\alpha_5\tilde{Y}_3^2, \tag{20a}$$

$$\Gamma_2=\alpha_2+\alpha_5\tilde{Y}_1^2+3\alpha_6\tilde{Y}_3^2. \tag{20b}$$

The stability theorem for linear systems[24] states that a system is stable if and only if the roots of the characteristic equation all lie in the left-half Λ plane, excluding the imaginary axis. This theorem is also applicable to the system under consideration. One way of determining whether the roots of the polynomial equation (18) all lie in the left-half Λ plane without actually solving Eq. (18) is via use of the Routh algorithm,[24] which yields the following inequalities:

$$\Omega_0>0, \quad \Omega_1>0, \quad \Omega_2>0, \quad \Omega_3>0, \quad \Omega_4>0, \tag{21a}$$

$$\Omega_2\Omega_3-\Omega_1\Omega_4>0, \tag{21b}$$

$$\Omega_1(\Omega_2-\Omega_1\Omega_4)-\Omega_0\Omega_3^2>0. \tag{21c}$$

Substituting Eq. (19) into Eq. (21) then leads to the following conditions,

$$\xi>0, \quad \alpha_{01}>0, \quad \alpha_{02}>0, \quad \Gamma_1>0, \quad \Gamma_2>0, \tag{22}$$

which must all be satisfied in order for the system defined by Eq. (12) to be stable.

Equation (22) may shed light on the mechanisms that govern the instabilities of a finite plate in the presence of mean flow. The first inequality in Eq. (22) requires that the damping ratio ξ be positive. This condition is automatically satisfied because the damping coefficient d is positive. In the special case of an undamped system, $\xi=0$, the roots of the polynomial equation all lie on the imaginary axis and the system is marginally stable, if other conditions in Eq. (22) are satisfied. The second and third inequalities in Eq. (22) require that α_{01} and α_{02} be positive. From Eqs. (13a) and (13b), we see that these quantities consist of the plate aspect ratio, the fluid/structure density ratio, and the added mass due to fluid loading, which are all positive. Therefore these two conditions are satisfied automatically.

The last two inequalities in Eq. (22) require both Γ_1 and Γ_2 be positive. Substituting the plate's undeformed equilibrium position given by Eq. (15a) into (20), we obtain $\Gamma_1=\alpha_1$ and $\Gamma_2=\alpha_2$. The quantities $\alpha_{1,2}$ represent the effect of the stiffness and that of the added stiffness due to acoustic radiation in mean flow [see Eqs. (13c) and (13d)], respectively. The former is positive, while the latter is negative because $\Theta^{(2)}_{1111}$ and $\Theta^{(2)}_{2121}$ are negative [see Eq. (10)]. This is obvious because for a plate with clamped boundary conditions, we have $\partial^2 W_i(\bar{x})/\partial\bar{x}^2=-\lambda_i^2 W_i(\bar{x})$.[9,10] Hence the values of $\Theta^{(2)}_{klij}$, which involve integrations of the product of $\partial^2 W_i(\bar{x})/\partial\bar{x}^2$ and $W_i(\bar{x})$, are always negative.

Without mean flow, the added stiffness is identically zero. Hence α_1 and α_2 are always positive, which means $\Gamma_1>0$ and $\Gamma_2>0$ and the plate is stable around its undeformed equilibrium position. When there is mean flow and when the mean flow speed is low, the effect of the added stiffness is small. Therefore α_1 and α_2 are positive, $\Gamma_1>0$ and $\Gamma_2>0$, and the plate is still stable. However, the values of α_1 and α_2 decrease quadratically with the increase of the mean flow speed. When the mean flow speed exceeds the critical values such that the added stiffness overpowers the plate's own stiffness, then α_1 and/or α_2 may be negative and the plate may become unstable.

The plate aspect and length to thickness ratios have a direct impact on the overall stiffness. The larger the plate

aspect and length to thickness ratios are, the smaller the plate overall stiffness is and the more unstable the plate tends to be.

The critical mean flow speeds can be determined by setting Γ_1 and Γ_2 to zero, which is equivalent to setting α_1 and α_2 to zero. From Eqs. (13c) and (13d), we obtain

$$u_{\mathrm{cr},1}=c_0\sqrt{-\frac{2\pi}{\eta\sigma\phi^3\Theta^{(2)}_{2121}}\left(\lambda_2^4+\frac{2\theta_{11}\theta_{22}}{\eta^2}+\frac{\lambda_1^4}{\eta^4}\right)}, \quad (23a)$$

$$u_{\mathrm{cr},2}=c_0\sqrt{-\frac{2\pi}{\eta\sigma\phi^3\Theta^{(2)}_{1111}}\left(\lambda_1^4+\frac{2\theta_{11}^2}{\eta^2}+\frac{\lambda_1^4}{\eta^4}\right)}. \quad (23b)$$

Note that the number of critical mean flow speeds is determined by that of normal modes selected in the characteristic equation (8) or, equivalently, the order of matrix in Eq. (8). In this particular case, the order of matrix in Eq. (8) is two, thus leading to two critical speeds.

Suppose that $u_{\mathrm{cr},1}<u_{\mathrm{cr},2}$. Then at the first critical mean flow speed $U=u_{\mathrm{cr},1}$, we have $\alpha_1>0$ and $\alpha_2=0$. The plate's original equilibrium position remains unchanged. At this equilibrium position [see Eq. (15a)], $\Gamma_1=\alpha_1>0$ and $\Gamma_2=\alpha_2=0$. The last inequality in Eq. (22) is marginally satisfied and the plate is stable.

When $u_{\mathrm{cr},1}<U<u_{\mathrm{cr},2}$, we have $\alpha_1>0$ and $\alpha_2<0$. In this case, a new equilibrium position given by Eq. (15c) emerges in addition to the original equilibrium position given by Eq. (15a). However, the plate is unstable at the original equilibrium position because $\Gamma_1=\alpha_1>0$ and $\Gamma_2=\alpha<0$ there, while stable at the new equilibrium position because $\Gamma_1=\alpha_1-\alpha_2\alpha_5/\alpha_6>0$ and $\Gamma_2=-2\alpha_2>0$. [Note that in order for the equilibrium position given by Eq. (15c) to exist, α_6 must be positive. In fact, Eqs. (10) and (13) show that α_4, α_5, and α_6 are all positive.] When $U=u_{\mathrm{cr},2}$, we have $\alpha_1=0$ and $\alpha_2<0$. In this case, the equilibrium position given by Eq. (15c) co-exists with the original equilibrium position. Once again, the plate is unstable at the original equilibrium position because $\Gamma_1=\alpha_1=0$ and $\Gamma_2=\alpha_2<0$ there, but stable at the new equilibrium position because $\Gamma_1=-\alpha_2\alpha_5/\alpha_6>0$ and $\Gamma_2=-2\alpha_2>0$.

When the mean flow speed exceeds both critical values, $U>u_{\mathrm{cr},1}$ and $U>u_{\mathrm{cr},2}$, then both α_1 and α_2 are negative. Under this condition, there are three equilibria given by Eqs. (15a), (15b), and (15c), respectively. The equilibrium position given by Eq. (15d) cannot be realized. This is because Eq. (15d) requires either of the following sets of inequalities to hold,

$$\begin{cases}\alpha_2\alpha_5>\alpha_1\alpha_6,\\ \alpha_4\alpha_6>\alpha_5^2,\end{cases} \text{ and } \begin{cases}\alpha_1\alpha_5>\alpha_2\alpha_4,\\ \alpha_4\alpha_6>\alpha_5^2,\end{cases} \quad (24a)$$

or

$$\begin{cases}\alpha_2\alpha_5<\alpha_1\alpha_6,\\ \alpha_4\alpha_6<\alpha_5^2,\end{cases} \text{ and } \begin{cases}\alpha_1\alpha_5<\alpha_2\alpha_4,\\ \alpha_4\alpha_6<\alpha_5^2.\end{cases} \quad (24b)$$

Since $\alpha_1<0$ and $\alpha_2<0$, the conditions of Eq. (24a) lead to

$$\alpha_5^2<\alpha_4\alpha_6, \quad (25a)$$

while those of Eq. (24b) result in

$$\alpha_5^2>\alpha_4\alpha_6, \quad (25b)$$

which are contradictory to each other.

Under this mean flow speed the plate is unstable around its original equilibrium position given by Eq. (15a) because $\Gamma_1=\alpha_1<0$ and $\Gamma_2=\alpha_2<0$. At the equilibrium position given by Eq. (15b), we have $\Gamma_1=-2\alpha_1>0$ and $\Gamma_2=\alpha_2-\alpha_1\alpha_5/\alpha_4$. In order for the plate to be stable, Γ_2 must be positive, namely, $\alpha_2>\alpha_1\alpha_5/\alpha_4$. On the other hand, at the equilibrium position given by Eq. (15c), we have $\Gamma_1=\alpha_1-\alpha_2\alpha_5/\alpha_6$ and $\Gamma_2=-2\alpha_2>0$. The stable condition (22) requires $\Gamma_1>0$, which yields $\alpha_1>\alpha_2\alpha_5/\alpha_6$. These two inequalities may be satisfied depending upon the values of α_1, α_2, α_4, α_5, and α_6, which represent the effects of the plate stiffness and the added stiffness due to acoustic radiation in mean flow. In most situations, however, the plate cannot be stabilized permanently at either one of these two equilibrium positions. Instead, it vibrates at one equilibrium position for a while and then jumps to another. Consequently, plate flexural vibration may seem unstable, yet its amplitude is always bounded.

It must be pointed out that these instabilities are caused by structural nonlinearities. Without the inclusion of structural nonlinearities, there is only one equilibrium position, i.e., the undeformed flat position. Under this condition, the amplitude of plate vibration would grow exponentially in time when the mean flow speed exceeds the critical value. With the inclusion of structural nonlinearities, the overall amplitude of vibration is bounded, but the plate may vibrate at the equilibrium positions other than its original one. In particular, when the mean flow speed exceeds certain critical values, plate vibration may become so unstable that it jumps from one equilibrium position to another. Further, this jumping may be random and plate vibration may seem to be chaotic.

IV. STABILITY CHARTS FOR FINITE PLATES IN MEAN FLOW

In the preceding section, we have derived explicit formulations for predicting critical mean flow speeds $u_{\mathrm{cr},i}$ for a baffled plate. These critical speeds are shown to be correlated to the plate stiffness and the added stiffness due to acoustic radiation in mean flow. Specifically, the values of $u_{\mathrm{cr},i}$ depend on the plate aspect ratio, length to thickness ratio, and fluid/structure density ratio. To acquire a better understanding of these correlations, we present in this section the stability charts for different types of elastic plates under different flow conditions.

As before, let us consider a finite plate with clamped boundary conditions. Under this condition, the plate normal modes are given by[13]

$$W_k(x)=\sigma_k\left[\sin\left(\frac{\lambda_k x}{L}\right)-\sinh\left(\frac{\lambda_k x}{L}\right)\right]+\left[\cos\left(\frac{\lambda_k x}{L}\right)-\cosh\left(\frac{\lambda_k x}{L}\right)\right], \quad (26a)$$

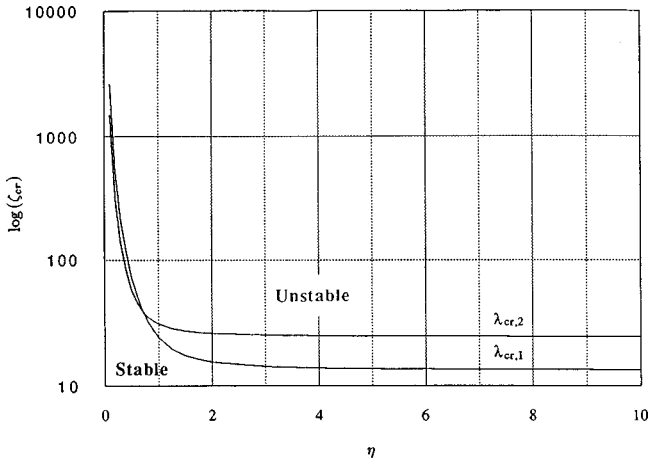

FIG. 2. Dimensionless mean flow speeds versus the plate aspect ratio.

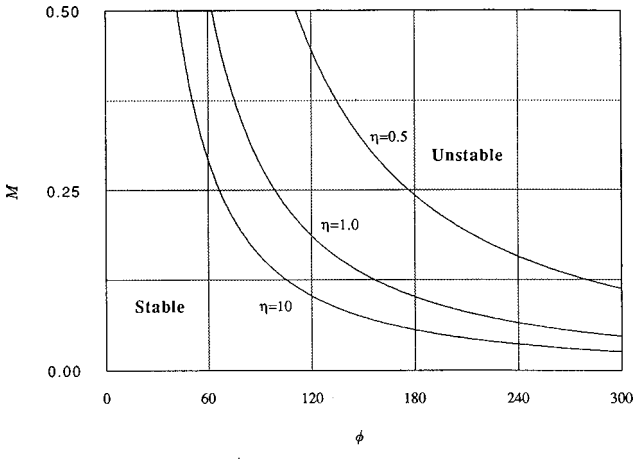

FIG. 3. Stability chart of a steel plate in contact with water on one side and vacuum on the other side at fixed plate aspect ratios.

$$W_i(y)=\sigma_i\left[\sin\left(\frac{\lambda_i y}{b}\right)-\sinh\left(\frac{\lambda_i y}{b}\right)\right]+\left[\cos\left(\frac{\lambda_i y}{b}\right)-\cosh\left(\frac{\lambda_i y}{b}\right)\right], \tag{26b}$$

where σ_i represents the ith modal ratio

$$\sigma_i=\frac{\sin\lambda_i+\sinh\lambda_i}{\cos\lambda_i-\cosh\lambda_i}, \tag{27}$$

where λ_i is the ith eigenvalue determined by $\cos\lambda_i\cosh\lambda_i=1$. The first three eigenvalues are given by $\lambda_1=4.73\,004$, $\lambda_2=7.8532$, and $\lambda_3=10.9956$. Accordingly, the first three modal ratios are -0.9825, -1.0008, and $-0.99\,997$. For a large value of i, $\lambda_k\to(2k+1)\pi/2$ and $\sigma_i\to-1$.

Note that the normal modes $\{W(x)\}$ and $\{W(y)\}$ are orthogonal to each other

$$\int_0^L W_k(x)W_l(x)\,dx=\begin{cases}L & \text{for } k=l,\\ 0 & \text{for } k\neq l;\end{cases}$$
$$\int_0^b W_i(y)W_j(y)dy=\begin{cases}b, & \text{for } i=j,\\ 0, & \text{for } i\neq j.\end{cases} \tag{28}$$

However, the products of $\{W(x)\}$ or $\{W(y)\}$ and their derivatives are not necessarily orthogonal.

The dimensionless mean flow speed ζ is defined in Eq. (6). Using the critical mean flow speeds given by Eq. (23), we can write

$$\zeta_{\mathrm{cr},1}=\sqrt{-\frac{2\pi}{\eta\Theta^{(2)}_{2121}}\left(\lambda_2^4+\frac{2\theta_{11}\theta_{22}}{\eta^2}+\frac{\lambda_1^4}{\eta^4}\right)}, \tag{29a}$$

$$\zeta_{\mathrm{cr},2}=\sqrt{-\frac{2\pi}{\eta\Theta^{(2)}_{1111}}\left(\lambda_1^4+\frac{2\theta_{11}^2}{\eta^2}+\frac{\lambda_1^4}{\eta^4}\right)}. \tag{29b}$$

The values of $\Theta^{(2)}_{1111}$ and $\Theta^{(2)}_{2121}$ can be evaluated numerically using the standard Gaussian quadrature techniques by substituting the normal modes given by Eq. (26) into Eq. (10).

Figure 2 depicts the curves of critical dimensionless mean flow speeds [expressed as $\log(\zeta_{\mathrm{cr},i})$] versus the plate aspect ratio η, which defines the stability boundaries of a finite plate in mean flow. The area below both curves represents the stable region where the plate vibrates around its undeformed equilibrium position. The area between the curves indicates the region where the plate vibrates around the equilibrium positions other than its original undeformed one. The area above both curves implies the region where the plate is unstable.

Figure 2 demonstrates that the larger the plate aspect ratio is, the more unstable the plate tends to be, while the smaller the plate aspect ratio is, the more stable the plate becomes in the presence of mean flow. This is because a large aspect ratio ($\eta\geqslant 1$) tends to reduce the stiffness of the lateral modes and those of coupling between the longitudinal and lateral modes [see Eq. (9c)]. Meanwhile, it increases the added stiffness induced by acoustic radiation in mean flow, which always works against the plate's own stiffness. As a result, the overall stiffness is reduced and the plate becomes less stable. On the other hand, a small aspect ratio ($\eta\leqslant 1$) tends to increase the stiffness of the lateral modes and those of coupling between the longitudinal and lateral modes, while it decreases the added stiffness due to acoustic radiation in mean flow. Consequently, the overall stiffness is enhanced and the plate becomes more stable in mean flow.

Also, Fig. 2 shows that the critical mean flow speeds approach constant values at large aspect ratios. Numerical results demonstrate that $\zeta_{\mathrm{cr},1}=13.4$ at $\eta=10$, and $\zeta_{\mathrm{cr},1}\to 13.33$ as $\eta\to\infty$. This implies that for a finite length but infinitely wide plate, the vibration responses may be unstable when the dimensionless mean flow speed exceeds $\zeta_{\mathrm{cr},1}=13.33$. Note that the square of $\zeta_{\mathrm{cr},1}$ is

$$\zeta^2_{\mathrm{cr},1}=13.33^2=177.68, \tag{30}$$

which is in excellent agreement with the analytic solution[6] of the critical value, $\zeta^2_{\mathrm{cr}}=177$, obtained by using the Galerkin method with a single mode approximation for a two-dimensional panel in mean flow.

The formulations derived in this paper also enable us to examine the correlations between mean flow speeds and fluid/structure density ratio, plate length to thickness ratio, and plate aspect ratio. Figures 3 and 4 illustrate the stability charts for a steel plate in water with a fluid/structure density ratio $\sigma=0.1282$ and that for an aluminum plate in water with

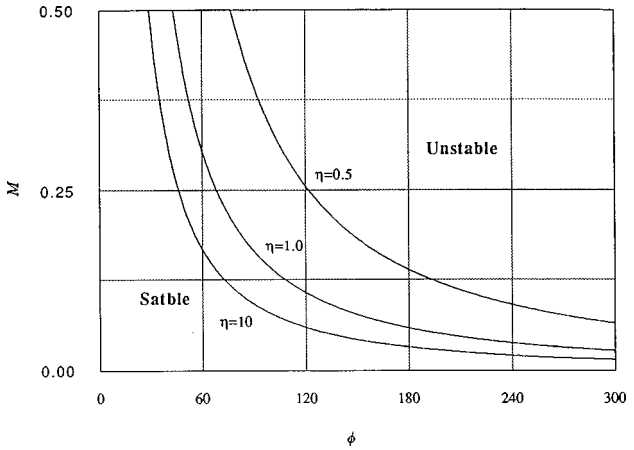

FIG. 4. Stability chart of an aluminum plate in contact with water on one side and vacuum on the other side at fixed plate aspect ratios.

$\sigma=0.3704$, respectively. Results show that for a fixed aspect ratio η and fluid/structure density ratio σ, the thinner the plate (i.e., the larger the value of $\phi=L/h$), the lower the critical mean flow Mach number, and the more unstable the plate. On the other hand, for a fixed length to thickness ratio ϕ and fluid/structure density ratio σ, the larger the aspect ratio η, the lower the critical mean flow Mach number, and the more unstable the plate. Finally, for a fixed length to thickness ratio ϕ and aspect ratio η, the larger the value of fluid/structure density ratio σ, the more unstable the plate.

V. BIFURCATION AND CHAOS IN PLATE VIBRATION IN MEAN FLOW

In this section, we demonstrate numerical results of the flexural displacements of a baffled plate in mean flow. In particular, we display transition of plate vibration from a stable condition to an unstable one as the mean flow speed exceeds its critical values.

First, we consider a steel plate in water with a mass density $\rho_p=7800(\mathrm{kg/m^3})$, a length $L=2.5$ (m), a width $b=1.25$ (m), and a thickness $h=0.003$ (m). Accordingly, the plate aspect ratio $\eta=0.5$, the length to thickness ratio $\phi=833.3$, and the fluid/structure density ratio $\sigma=0.1282$,

Substituting these values into Eq. (6) yields a dimensionless mean flow speed $\zeta=8288.36M$, where M is typically below 0.01 for most engineering applications. Accordingly, Eq. (29) gives the dimensionless critical mean flow speeds $\zeta_{\mathrm{cr},1}=57.97$ and $\zeta_{\mathrm{cr},2}=74.23$. In what follows, we calculate the amplitudes of plate flexural vibration at a fixed point with $M=0.005$, 0.008, and 0.01, or equivalently, $\zeta=41.44$, 66.31, and 82.99, which corresponds to the dimensionless mean flow speed regimes, $\zeta<\zeta_{\mathrm{cr},1}<\zeta_{\mathrm{cr},2}$, $\zeta_{\mathrm{cr},1}<\zeta<\zeta_{\mathrm{cr},2}$, and $\zeta_{\mathrm{cr},1}<\zeta_{\mathrm{cr},2}<\zeta$, respectively.

As in all nonlinear systems, the responses are sensitive to the initial conditions. In this paper, we choose to give the plate an initial displacement with a zero initial velocity, namely, $Y_1(0)=Y_3(0)=0.05$, and $Y_2(0)=Y_4(0)=0$. The plate flexural vibration responses subject to these initial conditions are obtained by solving (12) using the Gear method.[21]

Figure 5 displays the time history of the dimensionless plate flexural displacement and the corresponding phase

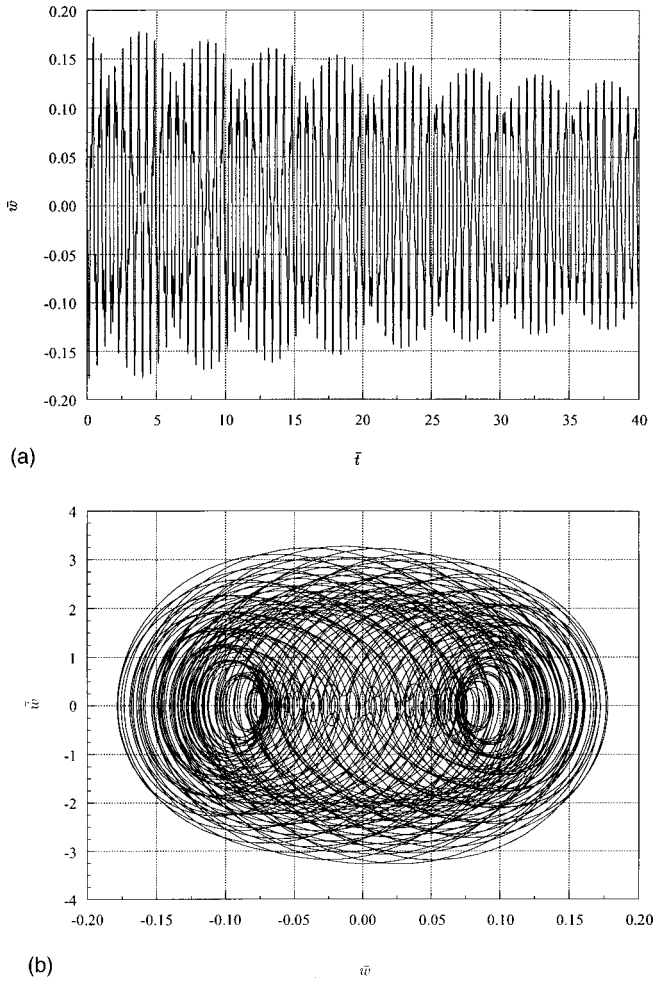

FIG. 5. Responses of flexural vibration for a steel plate with $\eta=0.5$, $\xi=0.5$, and $M=0.005$, i.e., $\zeta<\zeta_{\mathrm{cr},1}<\zeta_{\mathrm{cr},2}$. (a) Time history. (b) Phase plane.

plane evaluated at $\bar{x}=0.75$ and $\bar{y}=0.5$ with a damping ratio $\xi=0.5$ and a mean flow Mach number $M=0.005$, or $\zeta=41.44$. Since the mean flow speed is below the critical values ($\zeta<\zeta_{\mathrm{cr},1}<\zeta_{\mathrm{cr},2}$), the plate is stable around its undeformed equilibrium position, and vibrational motion is pseudo-periodic.

Here the effect of structural nonlinearities on plate flexural vibration is clearly visible. Without the inclusion of structural nonlinearities, the response would consist of contributions from the selected lateral and longitudinal modes only, which are coupled through the stiffness matrix and fluid loading. With the inclusion of structural nonlinearities, the responses include contributions not only from the selected modes, but also from their harmonics. Also, the amplitude of plate vibration is damped out by the viscous damping.

Next, we increase the Mach number to $M=0.008$, or $\zeta=66.31$. Since $\zeta_{\mathrm{cr},1}<\zeta<\zeta_{\mathrm{cr},2}$, the plate is unstable at its undeformed equilibrium position, but stable at a new equilibrium position. The time history of plate flexural vibration and the corresponding phase plane at $\bar{x}=0.75$ and $\bar{y}=0.5$ with a viscous damping ratio $\xi=0.5$ are illustrated in Fig. 6.

In this case, the main characteristics of plate flexural vibration remain essentially unchanged, namely, motion is

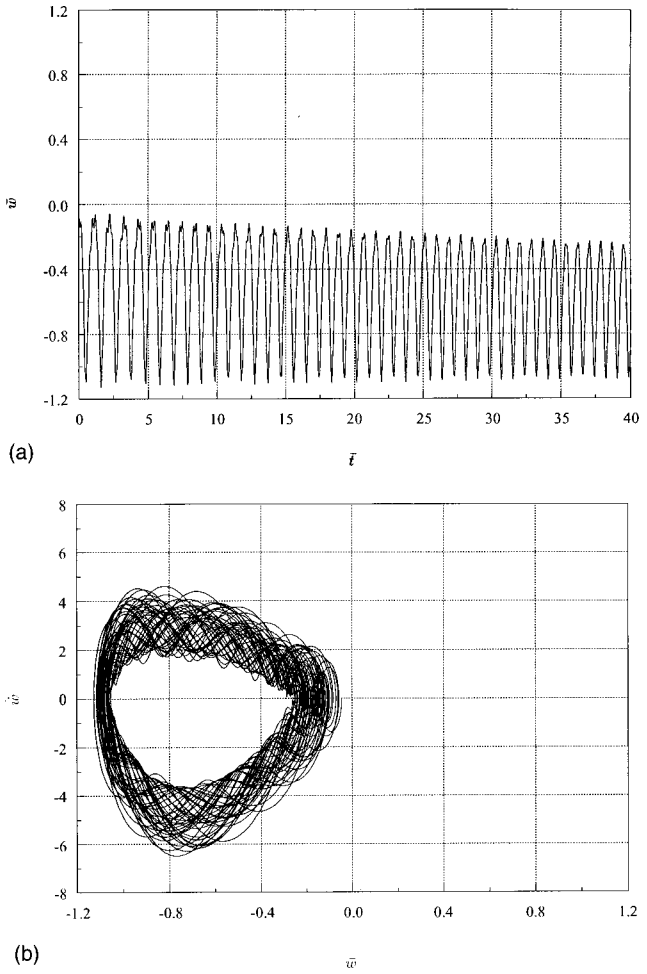

FIG. 6. Responses of flexural vibration for a steel plate with $\eta=0.5$, $\xi=0.5$, and $M=0.008$, i.e., $\zeta_{cr,1}<\zeta<\zeta_{cr,2}$. (a) Time history. (b) Phase plane.

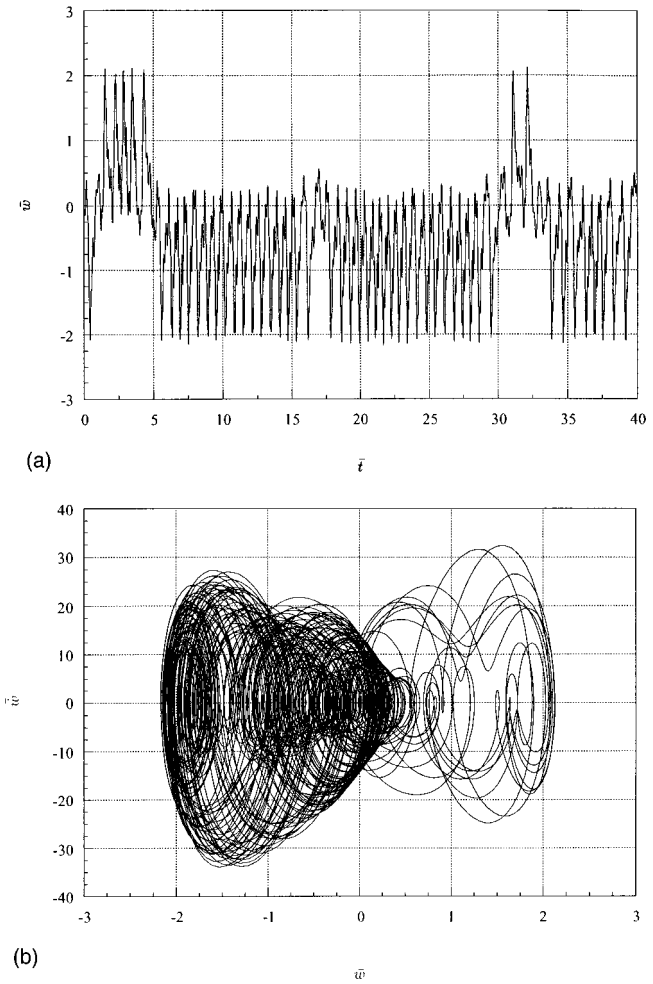

FIG. 7. Responses of flexural vibration for an undamped steel plate with $\eta=0.5$, $\xi=0.0$, and $M=0.01$, i.e., $\zeta_{cr,1}<\zeta_{cr,2}<\zeta$. (a) Time history. (b) Phase plane.

pseudo-periodic and consists of contributions from both the selected modes and their harmonics. The most striking differences are the change of the equilibrium position and the increase in the vibration amplitudes. Note that even without viscous damping, the plate can still be stabilized at a buckled-down equilibrium position owing to the fluid-loading effect.

When the Mach number is raised to $M=0.01$, or $\zeta=82.88$, the dimensionless mean flow speed exceeds both critical values, $\zeta>\zeta_{cr,2}>\zeta_{cr,1}$. Under this condition, the plate has three equilibrium positions given by Eqs. (15a), (15b), and (15c), respectively. However, the plate cannot be stabilized at any equilibria in an undamped situation. Figure 7(a) demonstrates that when $\xi=0$, plate flexural vibration becomes unstable, jumping from one equilibrium position to another. Moreover, these jumps are purely random and therefore flexural vibration is chaotic. This chaotic behavior is confirmed in the corresponding phase plate [see Fig. 7(b)]. Under this circumstance, the viscous damping may become a stabilizing factor. Figure 8 shows that when viscous damping is introduced, say, $\xi=0.5$, the jumping among the equilibria disappears and the plate settles down to a buckled-down position.

To better understand the chaotic behavior of a baffled plate in mean flow, we now calculate the dimensionless vertical displacements of the equilibria as the mean flow Mach number increases. As an example, we consider an undamped steel plate ($\xi=0$) with $\eta=0.5$, $\phi=833.3$, and $\sigma=0.1282$.

Figure 9 indicates that at very low Mach numbers ($\zeta<\zeta_{cr,1}<\zeta_{cr,2}$), the dimensionless vertical displacement of the

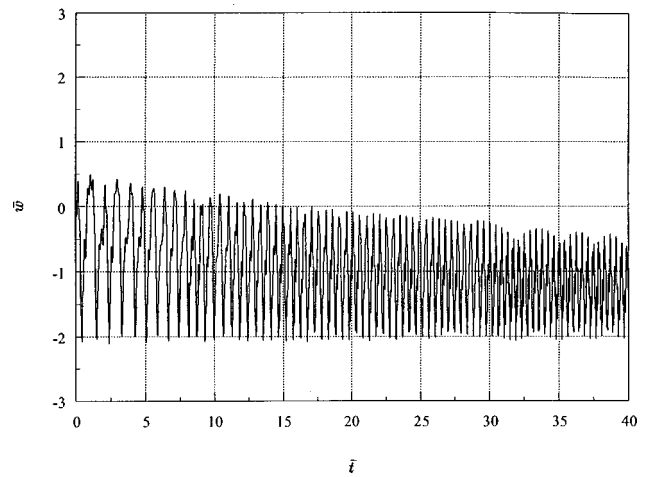

FIG. 8. Time history of plate flexural vibration for a damped steel plate with $\eta=0.5$, $\xi=0.5$, and $M=0.01$, i.e., $\zeta_{cr,1}<\zeta_{cr,2}<\zeta$.

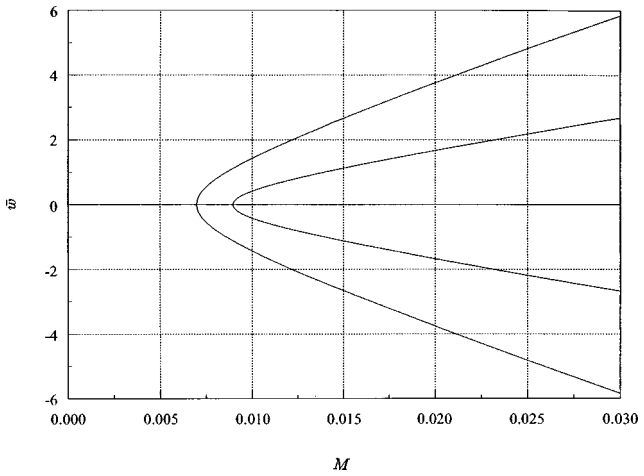

FIG. 9. Bifurcations in equilibria for a steel plate with $\sigma=0.1282$, $\phi=833.3$, and $\eta=0.5$.

equilibrium position is identically zero. This represents the stable situation in which the plate vibrates around its undeformed equilibrium position. When the mean flow Mach number exceeds a critical value, $\zeta_{cr,1}<\zeta<\zeta_{cr,2}$, the vertical displacements of the equilibria bifurcate to a symmetric pair. Mathematically, this corresponds to the situation in which the plate can vibrate around either a buckled-up or buckled-down position. However, the former is unstable because of the fluid loading effect which exerts a downward pressure on the plate surface. Hence the plate ends up with a buckled-down position. The buckling displacement increases monotonically with the Mach number M. When M exceeds a second critical values, $\zeta_{cr,1}<\zeta_{cr,2}<\zeta$, another bifurcation emerges and the plate has two pairs of equilibria. However, the plate cannot be stabilized permanently at any of the equilibria. Instead, it jumps from one equilibrium position to another in a random manner and flexural vibration may seem chaotic.

Figures 10 and 11 demonstrate similar bifurcation phenomena for a baffled plate with the same length to thickness ratio ϕ and fluid/structure density ratio σ, but larger aspect ratios at $\eta=1$ and $\eta=10$, respectively. As pointed out earlier, the larger the plate aspect ratio, the more unstable the plate. This trend is reflected in Figs. 10 and 11 in that bifurcations occur at lower Mach numbers as η increases.

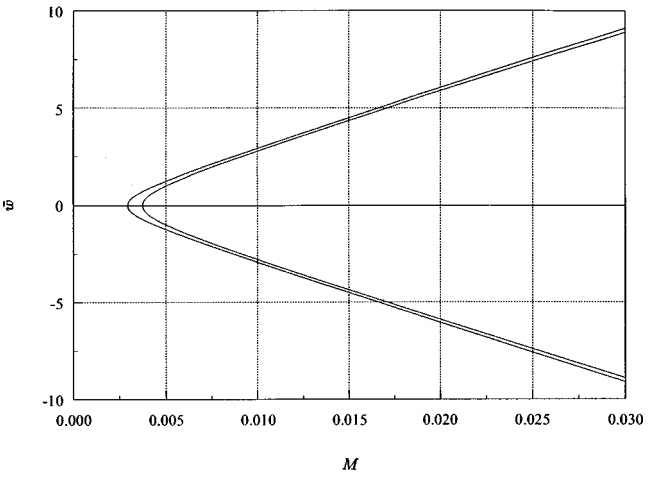

FIG. 10. Bifurcations in equilibria for a steel plate with $\sigma=0.1282$, $\phi=833.3$, and $\eta=1$.

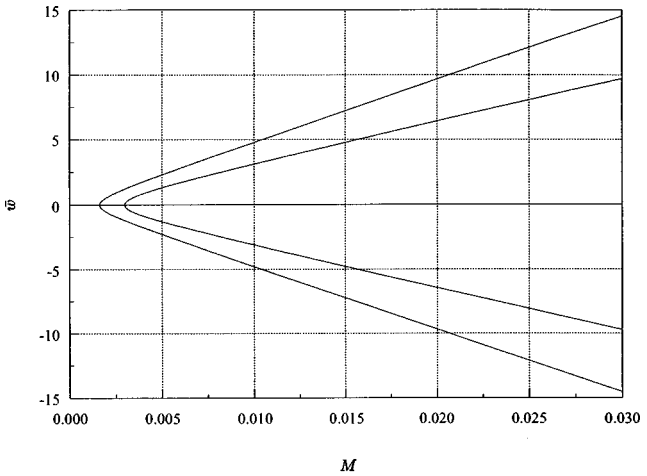

FIG. 11. Bifurcations in equilibria for a steel plate with $\sigma=0.1282$, $\phi=833.3$, and $\eta=10$.

For a plate with a fixed aspect ratio η and fluid/structure density ratio σ, the stability increases with the decrease of the length to thickness ratio ϕ. Figure 12 displays the bifurcation curves when ϕ is reduced by half to 416.7 or, equivalently, the thickness is doubled. Comparing the results of Fig. 12 to those of Fig. 10, we see clearly a delay in bifurcations as the mean flow speed increases. On the other hand, when the plate thickness is halved or the length to thickness ratio ϕ is doubled to 1666.7, bifurcations occur at a much lower Mach number (see Fig. 13). Accordingly, the plate becomes less stable in the presence of mean flow.

VI. CONCLUSIONS

The free responses of a baffled, clamped rectangular plate wetted on one side by a fluid moving at a constant, uniform velocity (and in vacuum on the other side) is investigated. The equations of motion for the plate flexural displacement are solved, taking into account the fluid-loading effect on the wetted side, as well as nonlinear inplane forces

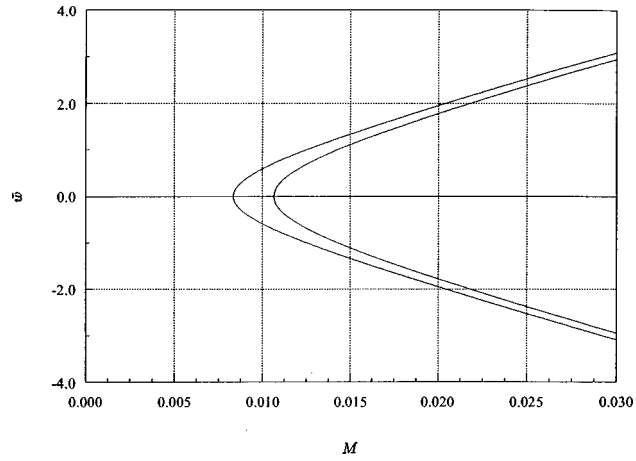

FIG. 12. Bifurcations in equilibria for a steel plate with $\sigma=0.1282$, $\phi=416.6$, and $\eta=1$.

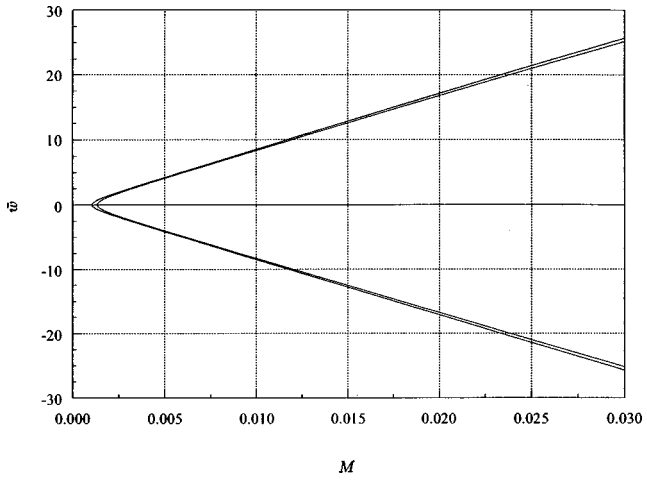

FIG. 13. Bifurcations in equilibria for a steel plate with $\sigma=0.1282$, $\phi=1666.7$, and $\eta=1$.

and share stresses. It is shown that ideal plates with these boundary conditions have more than one equilibrium positions, and the plate flexural vibration may become unstable under certain mean flow speeds. When the mean flow speed exceeds a critical value, the plate may be unstable around its original undeformed position, but stable around a buckled-down position with a larger amplitude. When the mean flow speed exceeds all the critical values, the plate may become unstable around all equilibria. Under this condition, the plate may jump randomly from one equilibrium position to another. This chaotic behavior disappears, however, when viscous damping is introduced. Note that without the inclusion of the structural nonlinearities, the plate has only one equilibrium position. Under this circumstance, the amplitude of plate flexural vibration would grow exponentially in time everywhere as the mean flow speed exceeds a critical value, known as absolute instability. With the inclusion of the nonlinearities, the plate may possess multiple equilibria, but may not be stable at all equilibrium positions beyond certain mean flow speeds. Under this condition, plate flexural vibration may become chaotic. Nonetheless, the overall amplitude is always bounded.

ACKNOWLEDGMENT

This work was supported by Office of Naval Research Grant No. N00014-89-J-3138.

[1] E. H. Dowell, ''Flutter of infinitely long plates and shells—Part I: Plate,'' AIAA J. **4**, 1370–1377 (1966).
[2] E. H. Dowell, ''Nonlinear oscillations of a fluttering plate. II,'' AIAA J. **5**, 1856–1862 (1967).
[3] E. H. Dowell, ''Flutter of a buckled plate as an example of chaotic motion of a deterministic autonomous system,'' in *Aeroelasticity of Plates and Shells* (Noordhoff International, Leyden, The Netherlands, 1974).
[4] C. H. Ellen, ''Stability of clamped rectangular plates in uniform subsonic flow,'' AIAA J. **10**, 1716–1717 (1972).
[5] C. H. Ellen, ''The stability of simply supported rectangular surfaces in uniform subsonic flow,'' J. Appl. Mech. **40**, 68–72 (1973).
[6] A. Kornecki, E. H. Dowell, and J. O'Brien, ''On the aeroelastic instability of two-dimensional panels in uniform incompressible flow,'' J. Sound Vib. **47**, 163–178 (1976).
[7] P. R. Brazier-Smith and J. F . Scott, ''Stability of fluid flow in the presence of a complaint surface,'' Wave Motion **6**, 547–560 (1984).
[8] D. C. Crighton and J. E. Oswell, ''Fluid loading with mean flow. I. Response of an elastic plate to localized excitation,'' Philos. Trans. R. Soc. London **335**, 557–592 (1991).
[9] S. F. Wu and L. Maestrello, ''Responses of finite baffled plate to turbulent flow excitation,'' AIAA J. **33**, 13–19 (1995).
[10] S. F. Wu and J. Zhu, ''Stability analysis of a nonlinear plate in mean flow,'' J. Comput. Acoust. **5**, 137–155 (1997).
[11] L. Maestrello, ''Nonlinear response and acoustic radiation from a curved panel structure,'' J. Comput. Acoust. **104**(3), Pt. 2, 1801 (1998).
[12] D. G. Crighton, ''Aeroacoustics of jet flows at low Mach number,'' in *Theoretical and Computational Acoustics '97*, edited by D. Lee *et al.* (Scientific Publishing, Singapore, 1998).
[13] A. W. Leissa, *Vibration of Plates* (NASA, Scientific Information Division, Washington, DC, 1969), Chap. 10, pp. 267–284.
[14] J. Zhu, ''Acoustic and dynamic responses of fluid-loaded plates in mean flow,'' Ph.D. dissertation, Wayne State University, Detroit, Michigan, 1995.
[15] M. G. Junger and D. Feit, *Sound, Structures and Their Interaction* (MIT, Cambridge, MA, 1972), Chap. 2, pp. 37–40.
[16] M. J. Lighthill, ''On sound generated aerodynamically I. General theory,'' Proc. R. Soc. London, Ser. A **211**, 564–587 (1952).
[17] W. S. Loud, ''On periodic solutions of Duffing's equation with damping,'' J. Math. and Phys. (Cambridge, MA) **34**, 173–178 (1955).
[18] D. E. Newland, ''On the methods of Galerkin, Ritz, and Krylov-Bogoluibov in the theory of nonlinear vibrations,'' Int. J. Mech. Sci. **7**, 159–172 (1965).
[19] L. L. Chao and D. L. Sikarskie, ''A new type of nonlinear approximation with application to the Duffing equation,'' International Journal of Nonlinear Mechanics **9**, 179–191 (1974).
[20] A. H. Nayfeh and D. T. Mook, *Nonlinear Oscillations* (Wiley-Interscience, New York, 1979), Chap. 2, pp. 56–59.
[21] C. W. Gear, *Numerical Initial-Value Problems in Ordinary Differential Equations* (Prentice–Hall, Englewood Cliffs, NJ, 1971).
[22] L. Meirovitch, *Methods of Analytical Dynamics* (McGraw–Hill, New York, 1979), Chap. 2, pp. 91–97.
[23] J. Guckenheimer and P. Homes, *Nonlinear Oscillations, Dynamical Systems, and Bifurcations of Vector Fields* (Springer-Verlag, New York, 1983).
[24] K. Ogata, *Modern Control Engineering* (Prentice–Hall, Englewood Cliffs, NJ, 1970).

Aeroelastic structural acoustic control

Robert L. Clark and Kenneth D. Frampton
Department of Mechanical Engineering and Materials Science, Duke University, Durham, North Carolina 27708-0300

(Received 4 March 1998; accepted for publication 27 October 1998)

Static, constant-gain, output-feedback control compensators were designed to increase the transmission loss across a panel subjected to mean flow on one surface and a stationary, acoustic half-space on the opposite surface. The multi-input, multi-output control system was based upon the use of an array of colocated transducer pairs. The performance of the static-gain, output-feedback controller was compared to that of the full state-feedback controller using the same control actuator arrays, and was found to yield comparable levels of performance for practical limitations on control effort. Additionally, the resulting static compensators proved to be dissipative in nature, and thus the design varied little as a function of the aeroelastic coupling induced by the fluid–structure interaction under subsonic flow conditions. Several parametric studies were performed, comparing the effects of control-effort penalty as well as the number of transducer pairs used in the control system. [S0001-4966(99)01302-8]

PACS numbers: 43.40.Vn [PJR]

LIST OF SYMBOLS

$\mathbf{A},\mathbf{B},\mathbf{C},\mathbf{D}$	state space matrices
a	panel length (chord)
a_a	external speed of sound
b	panel width (span)
D	$EI/(1-\nu^2)$, stiffness
D_{mn}	aerodynamic influence coefficient
$H_{mn}(t)$	aerodynamic influence function
$I_{mn}(t)$	aerodynamic influence function
M	Mach number
M_n	mass matrix
N	number of plate expansion modes
$p^a(x,y,z,t)$	aerodynamic pressure
$p^{\text{tbl}}(x,y,z,t)$	TBL pressure
$q_n(t)$	plate generalized coordinate
$Q_n^a(t)$	aerodynamic generalized force
$Q_n^c(t)$	cavity generalized force
$Q_n^{\text{tbl}}(t)$	TBL generalized force
s	tU_a/a
S	plate surface
S_{mn}	aerodynamic influence coefficient
t	time
U_a	free-stream velocity
$w(x,y,t)$	panel displacement
x,y,z	Cartesian coordinates
ξ_s	structural-damping ratio
Λ_m	cavity modal volume
$\Psi_n(x,y)$	plate modal expansion functions
$\phi^a(x,y,z,t)$	aerodynamic velocity potential
ρ_a	external fluid density
ρ_s	plate density

INTRODUCTION

The active control of low-frequency sound transmission to the interior of modern aircraft is of particular interest for stochastic noise sources such as that presented by the turbulent boundary layer (TBL). In a recent study, Clark and Frampton (1996) demonstrated the importance of including aeroelastic coupling for predicting the resulting sound radiation in the presence of mean flow. Thomas and Nelson (1995) investigated linear quadratic regulator (LQR) theory and linear quadratic Gaussian (LQG) theory for the control of panels subjected to stochastic noise sources shaped in frequency to capture the dynamics of TBL noise. However, the aeroelastic coupling was not considered in this earlier study. The current study combines the analysis of a panel including aeroelastic coupling and the use of static compensation for the active control of sound transmission across a panel subjected to a stochastic noise source.

The purpose and contribution of this work is to detail the performance which can be achieved in active structural acoustic control of aeroelastic systems through the use of static (constant-gain, output-feedback) compensation on square (equal inputs and outputs) systems with colocated transducers. The dual Levine–Athans method (Toivonen, 1985; Makila and Toivonen, 1987) was implemented to design a static compensator which was optimal with respect to a frequency-weighted cost function and chosen control-effort penalty. The system model was based upon a panel with pinned-boundary conditions, residing within an infinite baffle, and subjected to mean flow on one surface and a stationary acoustic half-space on the opposite. Radiation filters were designed to predict the rms sound power radiated into the half-space as outlined by Baumann *et al.* (1991), and linearized potential-flow theory was used in the aerodynamic model. The aeroelastic coupling was created as detailed by Frampton and Clark (1996), which provided a means for constucting a state-variable model of the aeroelastic, structural acoustic system.

The work presented herein provides a comparison be-

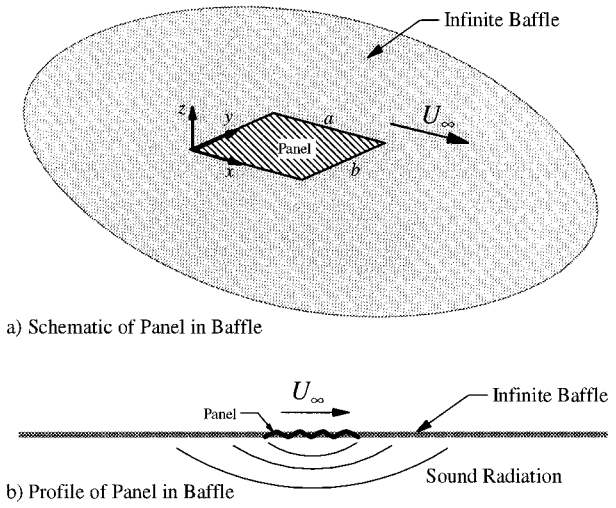

FIG. 1. Schematic diagram of aeroelastic, structural acoustic system.

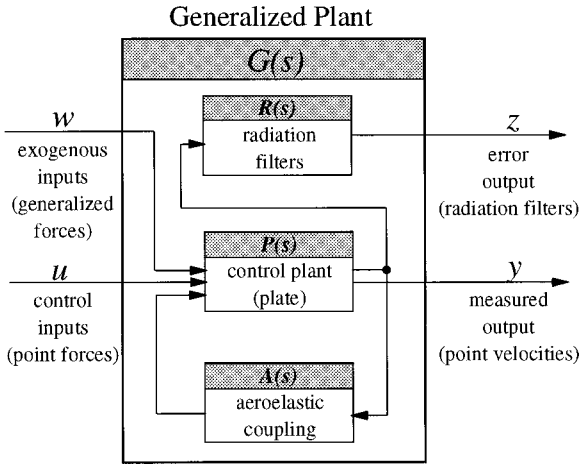

FIG. 2. Block diagram of generalized plant.

tween direct output-feedback control with static compensation (constant-gain feedback) and full state-feedback control (LQR). The LQR design for state feedback was computed to provide an upper bound on the performance which can be expected given the locations of the control actuators chosen. In all cases, for reasonable levels of control-effort penalty, active control systems incorporating static compensation yield performance which is comparable to that achieved with full state feedback. A parametric study is performed in this work, comparing the control system performance as a function of dynamic pressure under subsonic flow conditions. Additionally, the effect of control-effort penalty, the number of colocated control actuators used, and implementation of controllers designed for alternative flow conditions were studied. Results from this study indicate that a single, static, dissipative compensator can be designed to operate over all dynamic pressures corresponding to subsonic flow, increasing the transmission loss across the panel. Advantages of static compensation are less complexity in the control system implementation and the ease of generating a dissipative controller which is robust to model uncertainty.

I. MODEL DEVELOPMENT

A schematic diagram of the system is illustrated in Fig. 1. As depicted in Fig. 1(a), the panel is positioned within an infinite baffle, and air with mean velocity U_∞ flows over the surface of the panel in the x-direction. The panel has dimensions a and b in the x- and y-direction, respectively, with out-of-plane displacement occurring in the z-direction. As illustrated in Fig. 1(b), the opposite side of the panel is subject to a zero mean velocity (no-flow) condition, and the sound power radiated to this half-space is computed through the implementation of radiation filters derived from the Rayleigh integral.

A block diagram of the coupled system is illustrated in Fig. 2. Central to the block diagram are the panel dynamics, $P(s)$, which in this study were obtained from an assumed modes approach (Meirovitch, 1967). As illustrated, the output of the panel dynamics, $P(s)$, is coupled through the aerodynamic system, $A(s)$, which constitutes the aerodynamic response to the panel. This feedback through the fluid couples the panel modes and can potentially lead to divergence at Mach numbers less than 1 or flutter at Mach numbers greater than 1 in extreme cases. The dynamic coupling of the panel to the fluid influences the sound power radiated to the interior, as was demonstrated previously by Clark and Frampton (1996). The velocity of the panel in generalized coordinates is also coupled to the radiation filters, $R(s)$, which can be used to predict the sound power radiated as illustrated in Fig. 2. The generalized plant, $G(s)$, is the combination of all dynamics required for the design and synthesis of the control system.

The description of the aeroelastic, structural acoustic system can be divided into three sections: (1) panel model, $P(s)$; (2) aerodynamic model, $A(s)$; and (3) radiation-filter model, $R(s)$. Each of these models will be discussed in the following subsections.

A. Panel model

The partial differential equation of motion describing a thin, uniform panel including external-fluid loading and TBL loading can be expressed as follows:

$$\rho_s \frac{\partial^2 w(x,y,t)}{\partial t^2} + D\left[\frac{\partial^4 w(x,y,t)}{\partial x^4} + \frac{\partial^4 w(x,y,t)}{\partial x^2\,\partial y^2} + \frac{\partial^4 w(x,y,t)}{\partial y^4}\right] + p^a(x,y,z=0,t) + p^{\mathrm{tbl}}(x,y,z=0,t) = 0. \quad (1)$$

The coordinate system for the panel and associated flow was illustrated in Fig. 1. Note that the dynamic effect of the stationary, acoustic half-space is not considered in the model of the structural dynamic response of the panel.

A separable expansion solution is assumed using the *in vacuo* orthogonal panel eigenfunctions and generalized coordinates of the form

$$w(x,y,t) = \sum_{n=1}^{N} \Psi_n(x,y) q_n(t). \quad (2)$$

Substituting Eq. (2) into Eq. (1), multiplying by an arbitrary expansion function, $\Psi_m(x,y)$, and integrating over the domain yields a set of ordinary differential equations of the form

$$M_n[\ddot{q}_n(t)+\omega_n^2 q_n(t)]+\rho_a U_a^2 Q_n^a(t)+Q_n^{\mathrm{tbl}}(t)=0, \tag{3}$$

where the aerodynamic generalized forces are

$$Q_n^a(t)=\int_0^b\int_0^a \frac{p^a(x,y,z=0,t)}{\rho_a U_a^2}\Psi_n(x,y)dx\,dy, \tag{4}$$

and the turbulent boundary layer generalized forces are

$$Q_n^{\mathrm{tbl}}(t)=\int_0^b\int_0^a p^{\mathrm{tbl}}(x,y,z=0,t)\Psi_n(x,y)dx\,dy. \tag{5}$$

For the purpose of this study, $Q_n^{\mathrm{tbl}}(t)$ was chosen to be spectrally white and was used to excite each structural mode of the panel uniformly with stochastic independence. The desire was to place greater emphasis on characterizing the maximum transmission loss which could be achieved with the active control system, as opposed to detailing the operation with a frequency-shaped disturbance.

B. Aerodynamic model

Recent efforts by Frampton *et al.* (1996) and Frampton and Clark (1996) have been devoted to the development of reduced-order models of aerodynamics associated with full potential-flow theory cast in state-variable form. Clark and Frampton (1996) also detailed the implications of aeroelastic coupling on structural acoustic radiation. A brief overview of the aeroelastic model is presented herein and greater detail can be found in the references provided.

1. Transform solution to the linearized potential-flow generalized forces

Consider the case of a simply supported panel with the following eigenfunctions:

$$\Psi_n(x,y)=\sin\left(\frac{n\pi}{a}x\right)\sin\left(\frac{m\pi}{b}y\right). \tag{6}$$

The aerodynamic generalized forces, $Q_n^a(t)$, are found by solving the partial differential equation describing the velocity potential in an inviscid, irrotational fluid moving parallel to the *x*-axis

$$\nabla^2\phi^a-\frac{1}{a_\infty^2}\left[\frac{\partial^2\phi^a}{\partial t^2}+2U_a\frac{\partial^2\phi^a}{\partial x\,\partial t}+U_a^2\frac{\partial^2\phi^a}{\partial x^2}\right]=0. \tag{7}$$

subject to the boundary conditions for a panel embedded in an infinite baffle

$$\left.\frac{\partial\phi^a}{\partial z}\right|_{z=0}=\begin{cases}\dfrac{\partial w}{\partial t}+U_a\dfrac{\partial w}{\partial x}, & \text{on the plate,}\\ 0, & \text{off the plate,}\end{cases} \tag{8}$$

and a finiteness or radiation condition as *z* approaches infinity.

The solution can be obtained by taking a Laplace transform with respect to time and a double-Fourier transform with respect to the *x* and *y* spatial coordinates. The transformation is applied to Eqs. (7), (8), and Bernoulli's equation

$$p^a=-\rho_a\left[\frac{\partial\phi^a}{\partial t}+U_a\frac{\partial\phi^a}{\partial x}\right], \tag{9}$$

while incorporating Eq. (2). Details of the solution are discussed by Dowell (1967, 1975).

The solution yields the generalized aerodynamic forces on the panel which are given here as

$$Q_n^a(t)=\sum_{m=1}^{N} Q_{mn}^a(t), \tag{10}$$

where $Q_{mn}^a(t)$ is the force on the *n*th panel mode due to motion of the *m*th panel mode such that

$$Q_{mn}^a(t)=q_m(t)S_{mn}+\dot{q}_m(t)D_{mn}+\int_0^t q_m(\tau)H_{mn}(t-\tau)d\tau+\int_0^t \dot{q}_m(\tau)I_{mn}(t-\tau)d\tau, \tag{11}$$

where

$$S_{mn}=\frac{1}{M}\int_0^a\int_0^b\frac{\partial\Psi_m}{\partial x}\Psi_n\,dy\,dx, \tag{12}$$

$$D_{mn}=\frac{1}{MU_a}\int_0^a\int_0^b\Psi_m\Psi_n\,dy\,dx, \tag{13}$$

$$H_{mn}(t)=-\frac{U_a}{4\pi^2M^2}\int_{-\infty}^{\infty}\int_{-\infty}^{\infty}G_{mn}i\alpha\sqrt{\alpha^2+\gamma^2}\times e^{-i\alpha U_a t}J_1[a_\infty t\sqrt{\alpha^2+\gamma^2}]d\alpha\,d\gamma, \tag{14}$$

$$I_{mn}(t)=-\frac{1}{4\pi^2M^2}\int_{-\infty}^{\infty}\int_{-\infty}^{\infty}G_{mn}\sqrt{\alpha^2+\gamma^2}\times e^{-i\alpha U_a t}J_1[a_\infty t\sqrt{\alpha^2+\gamma^2}]d\alpha\,d\gamma, \tag{15}$$

and

$$G_{mn}=\int_0^a\int_0^b\Psi_m(x,y)e^{-i(\alpha x+\gamma y)}dy\,dx\int_0^a\int_0^b\Psi_n(x,y)\times e^{i(\alpha x+\gamma y)}dy\,dx. \tag{16}$$

More information on this modeling technique may be found in the reference by Frampton *et al.* (1996). A method of approximating the generalized forces and constructing the reduced-order model for the aeroelastic coupling can be found in the references by Clark and Frampton (1996) and Frampton and Clark (1996).

A plot of the aeroelastic response of the panel as a function of Mach number is presented in Fig. 3. The results presented were computed from the H_2 norm of the system, consisting of inputs corresponding to forces in generalized structural coordinates and outputs corresponding to velocities in generalized structural coordinates. The frequency response depicted in Fig. 3 represents the rms power associated with the system outputs when driven by independent, stochastic noise sources. (Greater detail of system norms can be found in the reference by Boyd and Barratt, 1991.) As illustrated, the dynamics of the aeroelastic system vary significantly as a function of Mach number, and significant energy dissipation due to the fluid-structure coupling is noted near Mach 0.9.

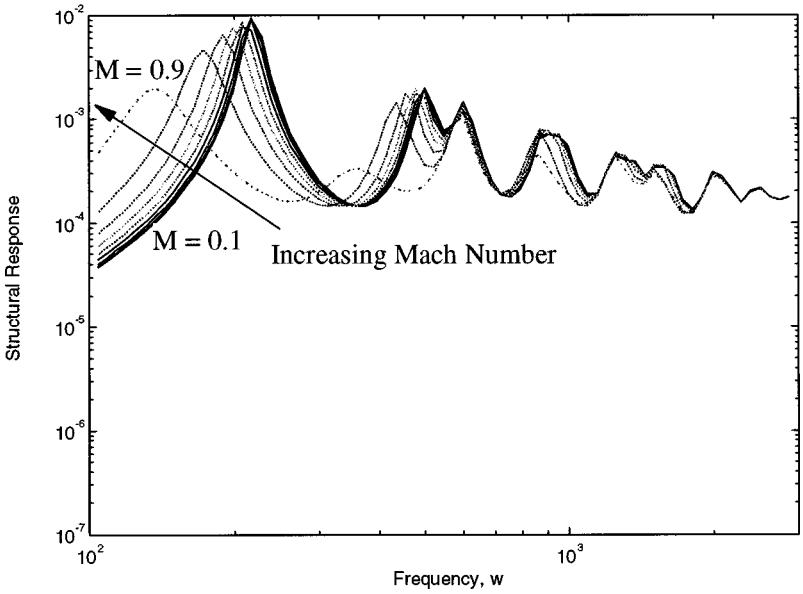

FIG. 3. rms structural response of an aeroelastic system.

C. Radiation filter model

Radiation filters were originally introduced by Baumann *et al.* (1991) for active structural acoustic control such that the dynamic response of the system could be augmented to incorporate additional states (radiation modes) which provide a measure of sound power radiated. The objective of the work was to produce a cost functional in the LQR/LQG formulation which, when minimized, would guarantee optimal performance with respect to structural acoustic control as opposed to structural control. The augmentation of system dynamics in the formulation of a ''frequency-shaped'' cost was originally proposed and detailed by Gupta (1980) and was extended to other exemplary applications. Thomas and Nelson (1995) also utilized the radiation filters for their feedback control-system realization, and the basic formulation for the filters can be found in their paper and that of Baumann *et al.* (1991).

For the infinite baffle, a frequency-dependent expression for the power radiated can be rendered by integrating an expression for the acoustic intensity over the hemisphere. Since the pressure can be obtained from Rayleigh's integral, the far-field acoustic intensity in the half-space is easily obtained. The form of the radiated power is

$$\Pi = \frac{1}{\pi}\int_0^\infty \mathbf{V}^H(j\omega)\mathbf{M}(j\omega)\mathbf{V}(j\omega)d\omega, \tag{17}$$

where Π is the total radiated power, $\mathbf{V}(j\omega)$ is matrix of the Fourier transform of modal velocities, and $\mathbf{M}(j\omega)$ represents the frequency-dependent interaction between structural modes required to compute the radiated power. The self- and mutual-radiation efficiencies of the structural modes can be readily obtained from this matrix as outlined by Lomas and Hayek (1977), and more recently by Cunnefare (1991).

If the Laplace domain equivalent of the matrix $\mathbf{M}(j\omega)$ is expressed as $\mathbf{M}(s)$, then one can express the matrix in terms of a filter and its parahermitian conjugate

$$\mathbf{M}(s) = \mathbf{R}^T(-s)\mathbf{R}(s), \tag{18}$$

where $\mathbf{R}(s)$ is the radiation filter as detailed by Baumann *et al.* (1991). This filter can be obtained through spectral factorization, as outlined by Francis (1986), and a state-variable model for the filter can be used to augment the system dynamics. The time-averaged sound power radiated from the structure when driven by a white-noise excitation can thus be computed from the output of these augmented states. For greater detail of the design of radiation filters, the reader is referred to the work of Baumann *et al.* (1991).

The radiation filters used in the work presented herein were compared against the self- and mutual-radiation efficiencies for several exemplary structural modes in the prior work by Clark and Frampton (1996). In Fig. 4, the rms sound power is plotted as a function of frequency. As in the previous section, the inputs correspond to independent, stochastic forces in generalized coordinates. However, for this case, the output of the generalized plant, $G(s)$, corresponding to the rms sound power is presented. Again, the effect of energy dissipation due to aeroelastic coupling is evident, and less sound power is radiated with increasing Mach number for the same level of forcing input. It should be noted that the response results presented here are normalized by the forcing input or TBL pressure-fluctuation levels. In reality, these pressure fluctuations are proportional to dynamic pressure or (for a fixed altitude) Mach number squared (Dowell, 1975). Hence, the dimensional or actual responses will increase with Mach number relative to those normalized responses shown here. For example, as one goes from $M=0.1$ to $M=0.9$, the increase will be by a factor of $(0.9/0.1)^2=81$. This may be important in practice, if the control authority of the actuators is limited (see Sec. II). Details of the plate and fluid properties used to generate the results presented are documented in Sec. III.

II. CONTROLLER SYNTHESIS

For the purpose of comparison, two different types of control laws, state feedback and output, constant-gain feedback, were investigated. Both sought to minimize a linear

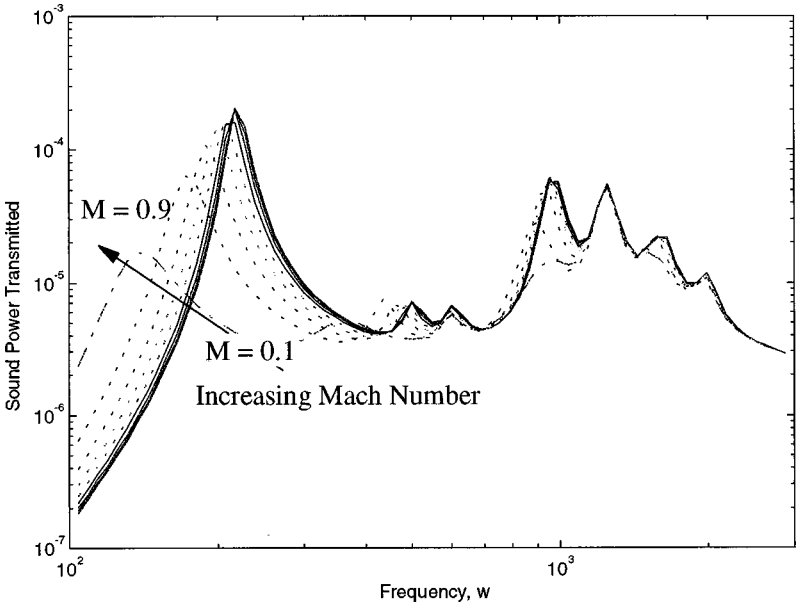

FIG. 4. rms structural acoustic response of an aeroelastic system.

quadratic cost function which balanced performance with control effort. State-feedback methods are well suited for this problem and optimal LQR gains provide an upper bound to obtainable performance. However, the same problem can be posed with constraints such that the control action consists of a matrix of constant gains applied to the sensor signals. Although this type of control is far more restrictive than state feedback, the ease of implementation makes its consideration important.

A. State-feedback control

The optimal control problem for the system,

$$\dot{\mathbf{x}} = \mathbf{A}\mathbf{x} + \mathbf{B}_c\mathbf{u}_c, \tag{19}$$

$$\mathbf{y}_p = \mathbf{C}_p\mathbf{x}, \tag{20}$$

is to find the input signal, $\mathbf{u}_c$, which minimizes the cost function

$$J = \int_0^\infty \mathbf{y}_p^T\mathbf{Q}\mathbf{y}_p + \mathbf{u}_c^T R\mathbf{u}_c\, dt, \tag{21}$$

where $\mathbf{Q}$ is a semipositive definite performance weighting, R is the positive definite control-effort penalty, $\mathbf{y}_p$ is the performance output, and $\mathbf{u}_c$ is the actuator-control signal. The performance output is a weighted measure of the acoustic radiation and can be written as a linear function of the augmented states, i.e., $\mathbf{y}_p = \mathbf{C}_p\mathbf{x}$. Therefore, Eq. (21) can be written

$$J = \int_0^\infty \mathbf{x}^T\tilde{\mathbf{Q}}\mathbf{x} + \mathbf{u}^T R\mathbf{u}\, dt, \tag{22}$$

where $\tilde{\mathbf{Q}} = \mathbf{C}_p^T\mathbf{Q}\mathbf{C}_p$. For state feedback, the input is of the form $\mathbf{u} = -\mathbf{K}\mathbf{x}$, and the minimization of Eq. (21) yields the well-known linear quadratic regulator [Kalman *et al.* (1963); Anderson *et al.* (1990)]. This approach is often used for generating an optimal linear-control law, and its application to structural acoustic problems has been detailed elsewhere [Baumann *et al.* (1991); Thomas and Nelson (1995)].

Implementation of a state feedback-control law requires full knowledge of the state, which typically must be estimated from a limited set of measurements. When employing radiation filters, especially those derived from curve fitting, the augmented plant can become very high order. This makes practical implementation of a state estimator difficult. Nevertheless, the state-feedback gains provide an upper bound for the performance of the simpler constant-gain controllers. They are computed here for comparison and closed-loop results are derived assuming perfect state information is available.

B. The dual Levine–Athans algorithm

The minimization of Eq. (21) can also be carried out under the assumption that $\mathbf{u} = \mathbf{G}\mathbf{y}_s = \mathbf{G}\mathbf{C}_s x$, where $\mathbf{y}_s$ is the output signal from available measurements. This implies that the control signal is generated as a constant-gain matrix times the sensor signals. This choice of control input forms a parametric LQ problem, and several techniques of obtaining the optimal controller have been investigated (Makila and Toivonen, 1987). However, unlike the state-feedback case, there is still no guaranteed unique solution. The approach taken here is a variation on the method proposed by Levine and Athans (1970), and its development follows Toivonen (1985). It has the advantage of being globally convergent to a solution from a stabilizing initial guess, and the solution satisfies the necessary conditions for optimality.

Consider the cost function in Eq. (21); by letting $\mathbf{u} = \mathbf{G}\mathbf{C}_s\mathbf{x}$ we can write

$$J = \int_0^\infty \mathbf{x}^T(\tilde{\mathbf{Q}} + \mathbf{C}_s^T\mathbf{G}^T R\mathbf{G}\mathbf{C}_s)\mathbf{x}\, dt. \tag{23}$$

This cost function depends on initial conditions of the state. Given random initial conditions with $E[\mathbf{x}(0)^T\mathbf{x}(0)] = \mathbf{P}$, the cost can then be expressed using the trace operator as

$$J = \mathrm{tr}[(\tilde{\mathbf{Q}} + \mathbf{C}_s^T\mathbf{G}^T R\mathbf{G}\mathbf{C}_s)\mathbf{L}] = \mathrm{tr}(\mathbf{K})\mathbf{P}, \tag{24}$$

where $\mathbf{K}$ and $\mathbf{L}$ satisfy the equations

$$0 = \mathbf{K}\mathbf{A}_c + \mathbf{A}_c^T\mathbf{K} + \mathbf{C}_s^T\mathbf{G}^T R\mathbf{G}\mathbf{C}_s + \tilde{\mathbf{Q}}, \tag{25}$$

$$0 = \mathbf{L}\mathbf{A}_c + \mathbf{A}_c^T\mathbf{L} + \mathbf{P}, \tag{26}$$

with $\mathbf{A}_c = \mathbf{A} - \mathbf{B}\mathbf{G}\mathbf{C}_s$. The gain

$$\mathbf{G}_{\text{opt}} = R^{-1}B^T\mathbf{K}\mathbf{L}\mathbf{C}_s^T(\mathbf{C}_s\mathbf{L}\mathbf{C}_s^T)^{-1}, \tag{27}$$

is a stationary point on the loss function, i.e., $dJ/d\mathbf{G} = 0$. Therefore, $\mathbf{G}_{\text{opt}}$ satisfies the necessary conditions for optimality.

The procedure for calculating $\mathbf{G}_{\text{opt}}$ involves first determining an initial gain matrix, $\mathbf{G}_0$, which stabilizes the system. Equation (27) is then solved for $\mathbf{L}$, and the nonlinear equations

$$0 = \mathbf{K}\mathbf{A}_c + \mathbf{A}_c^T\mathbf{K} + \mathbf{C}_s^T\mathbf{G}^T R\mathbf{G}\mathbf{C}_s + \tilde{\mathbf{Q}}, \tag{28}$$

$$\mathbf{G} = \mathbf{G}_0 + \theta(R^{-1}\mathbf{B}^T\mathbf{K}\mathbf{L}\mathbf{C}_s^T(\mathbf{C}_s\mathbf{L}\mathbf{C}_s^T)^{-1} - \mathbf{G}_0), \tag{29}$$

must be solved for $\mathbf{G}$ and $\mathbf{K}$. The scalar parameter θ is constrained to $0 < \theta < 1$, and can be adjusted downward to ensure that $J(\mathbf{G}) < J(\mathbf{G}_0)$. The numerical algorithm proceeds by iterating on Eqs. (26), (28), and (29), and updating $\mathbf{G}$ until $|\mathbf{G}_{i+1} - \mathbf{G}_i| < \epsilon$. In practice, $\mathbf{G}_0 = 0$ was used as the initial stabilizing gain matrix and $\mathbf{P}$ was chosen to be $\mathbf{B}_d^T\mathbf{B}_d$, where $\mathbf{B}_d$ described a disturbance input influence matrix. Convergence of the algorithm on the 281-state model typically occurred within 25 iterations.

III. DESCRIPTION OF MODEL

The following parameters were used to construct the model used in this study: $a = 0.60$ m, $b = 0.51$ m, $h_s = 0.0022$ m, $E_s = 7.1 \times 10^{10}$ Pa, $\rho_s = 2700$ kg/m^3, $\xi_s = 0.05$, $\rho_a = 0.42$ kg/m^3, and $a_a = 300$ m/s. The plate modes included in the structural model correspond to the first 30 modes of the structure (ordered by natural frequency). However, only the first ten modes and the structural acoustic interaction of these modes were included in the model of the radiation filters. As detailed by Clark and Cox (1996), more modes are required in the structural model to compute the optimal static compensator and predict realistic closed-loop performance. However, fewer modes are required to accurately predict the sound power radiated over the desired bandwidth of emphasis for structural acoustic control. Additionally, the aerodynamic coupling between the structure and the fluid was limited to the first ten modes, as the influence is most significant over the desired bandwidth for these modes.

The material properties of the panel correspond to that of aluminum and the aerodynamic properties correspond to an altitude of 10 km. It should be noted that a realistic estimate of the damping ratio $\xi = 0.05$ was incorporated in the model to provide reasonable predictions of performance for actual aircraft panels.

The number of disturbance inputs equaled the number of structural modes included: 30. The disturbance path corresponded to independent excitation of all structural modes concurrently in generalized coordinates with a spectrally white input, which effectively assumes a uniform spatial distribution of the TBL pressures over the panel. While it can be argued that this method of excitation ignores the frequency-shaped weighting which would result from realistic TBL noise sources, it does serve to isolate the aeroelastic, structural acoustic coupling of the panel and provide a means for evaluating the active insertion loss (AIL) as detailed by Smith and Clark (1996).

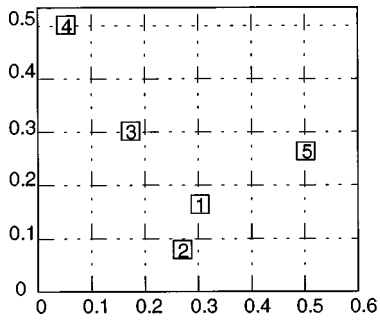

#	x(%)	y(%)
1	0.50	0.32
2	0.45	0.15
3	0.28	0.57
4	0.08	0.97
5	0.83	0.50

FIG. 5. Schematic diagram of structure with corresponding transducer-pair locations.

The number of colocated transducer pairs used in the closed-loop system was varied between one and five. Point force and colocated point-velocity sensors were selected for this preliminary study due to the positive real behavior of such colocated transducer pairs. The locations of the control forces were selected randomly so as not to emphasize the control of any particular structural mode. The positions are displayed in the schematic diagram presented in Fig. 5. In addition to the displayed locations of the actuators in physical coordinates, the locations are tabulated in percent of the structure length in the *x*- and *y*-dimensions, respectively. The transducer pairs are numbered, and when one pair is used for control, the transducer pair labeled 1 is used, when three pairs are used for controls, transducer pairs labeled 1, 2, and 3 are used.

IV. RESULTS

Results presented in this section detail the performance of static compensation and compare this with state-feedback control for a single-input, single-output (SISO), three-input, three-output (3I3O), and five-input, five-output (5I5O) control system with colocated transducers. For the cases considered here, the augmented model has 281 states: 60 structural states, 55 aerodynamic states, and 166 states for the radiation filters. Clearly, state estimation for this *reduced-order* model of the system is not reasonable. However, closed-loop performance using static compensation is compared to full state feedback to provide a means of evaluating the performance of a practical implementation of the active structural acoustic control system. The dimension of the colocated array, the control effort penalty, and the effect of variation in Mach number (dynamic pressure) are studied parametrically to provide insight into the physics and practical implementation issues such as robustness to variation in plant dynamics. For each test case presented, the rms sound power radiated by the structure and the rms structural response to a random excitation are plotted as a function of frequency. These values represent the sum of the square of the singular values at each frequency for the MIMO transfer function from disturbance to acoustic power and modal velocity, respectively. Addi-

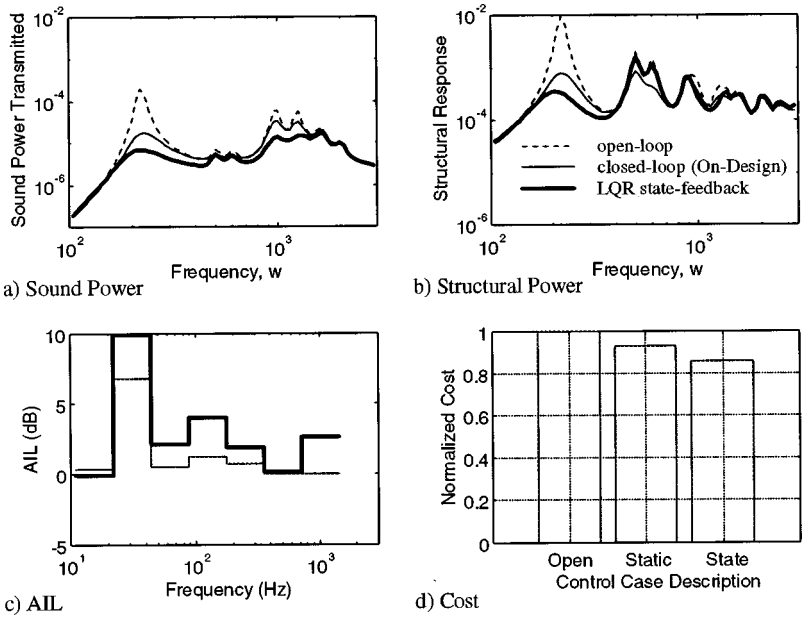

FIG. 6. Comparison of open- and closed-loop response for static and state-feedback control utilizing three colocated transducer pairs and a control-effort penalty of $R=10^{-5}$ for a flow condition of Mach 0.1.

tionally, the normalized cost function (ratio of closed loop to open loop) are plotted as is the active insertion loss (AIL) (Smith and Clark, 1996) for each active control system implementation.

A. Typical result

All of the results presented in this section will follow the general format outlined in this typical result. As illustrated in Fig. 6, results summarizing the (a) sound power transmitted, (b) the structural response, (c) the AIL, and (d) the normalized cost for a Mach number of 0.1 are presented. In Fig. 6(a), the static compensator is compared to full state feedback with the same performance and control-effort penalty ($R=10^{-5}$). Three colocated point-force actuators and point-velocity sensors as illustrated in Fig. 5 and described in Sec. III were used for the case presented. As illustrated in Fig. 6(a), significant levels of attenuation are achieved near the fundamental mode of the panel. Additionally, the results presented in Fig. 6(b) indicate that the static compensator is dissipative, as the response of the out-of-bandwidth structural modes are not increased. The AIL is presented in Fig. 6(c), and as indicated, as much as 9 dB of attenuation is achieved in the octave band containing the fundamental panel mode. The AIL decreases with increasing frequency as is expected for an active structural acoustic control (ASAC) system. The normalized cost illustrated in Fig. 6(d) demonstrates that the state-feedback controller results in better overall performance, but for the given control-effort penalty, results achieved with static compensation are acceptable.

Test cases at higher subsonic Mach numbers were selected and are presented in the following subsections. However, rather than discuss each case independently, the results of various parametric cases are compared.

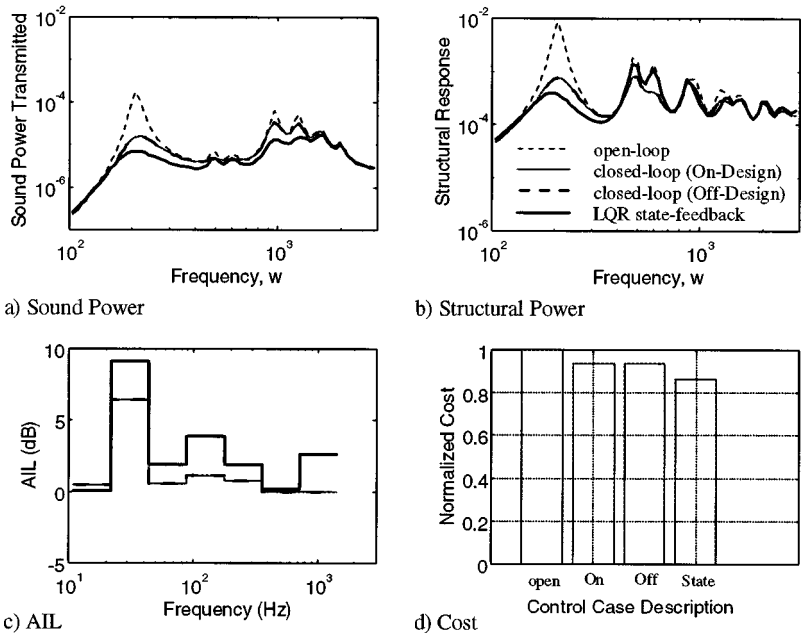

FIG. 7. Comparison of open- and closed-loop response for static and state-feedback control utilizing three colocated transducer pairs and a control-effort penalty of $R=10^{-5}$ for a flow condition of Mach 0.5, including an off-nominal design.

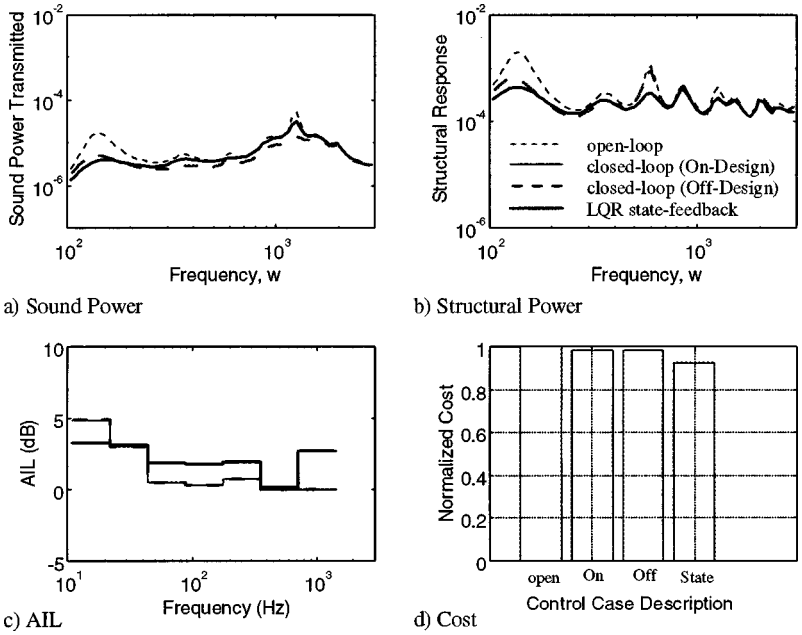

FIG. 8. Comparison of open- and closed-loop response for static and state-feedback control utilizing three colocated transducer pairs and a control-effort penalty of $R=10^{-5}$ for a flow condition of Mach 0.9, including an off-nominal design.

B. Variation in the Mach number and off-nominal design

In the following test cases, the control-effort penalty was maintained at $R=10^{-5}$; however, in addition to presenting the results for the optimal state-feedback controller and the optimal static compensator for each Mach number, the static compensator designed for operation at $M=0.1$ was also implemented for comparison of an *off-nominal design* and to provide a measure of robustness. As in the previous test case presented, three colocated transducer pairs were used to control the system. While the test cases presented are limited to Mach numbers of 0.5 and 0.9, additional test cases at Mach numbers ranging from 0.1 to 0.9 in increments of 0.1 were studied with similar results. For the results presented in Fig. 7, the Mach number was increased to 0.5. As illustrated in Fig. 7(a), the sound power transmitted in proximity to the resonant frequency corresponding to the fundamental mode was attenuated significantly. Due to the dissipative nature of the controller, spillover into higher-order structural modes was not a problem, and as much as 8 dB of AIL was achieved in the octave band containing the fundamental resonance. Additionally, one observes that the closed-loop response corresponding to the *off-nominal* design case yielded performance virtually identical to that achieved with the optimal static compensator. Thus, while the increase in Mach number altered the resonant behavior of the system, the static compensator design was relatively insensitive to this change in dynamics.

The Mach number was increased to 0.9, nearing the speed of sound, and as was illustrated in Figs. 3 and 4, the dynamics of the resonant behavior and inherent damping of the system were radically modified. An optimal static compensator was designed for this flow condition, and the closed-loop performance is compared to that of the off-

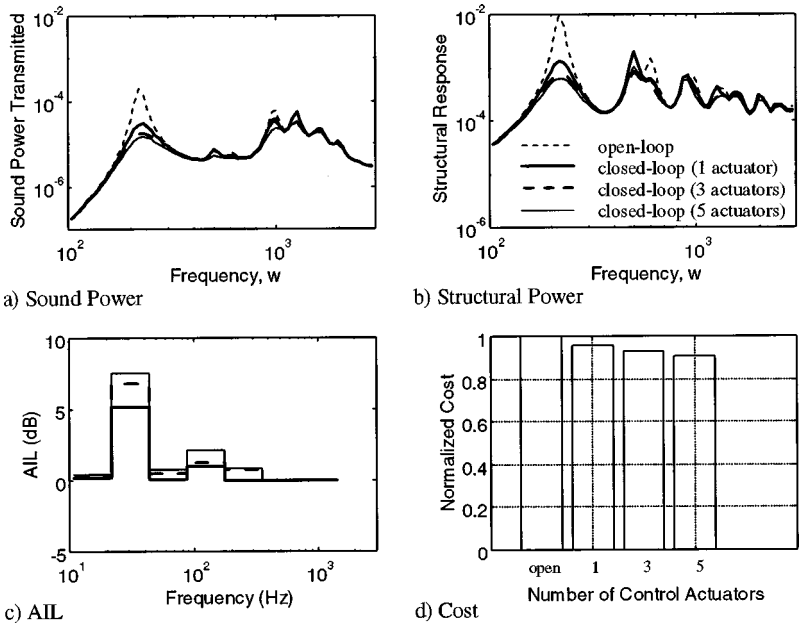

FIG. 9. Comparison of open- and closed-loop response for static compensation and variation in the number of transducer pairs implemented with a control-effort penalty of $R=10^{-5}$ and a flow condition of Mach 0.1.

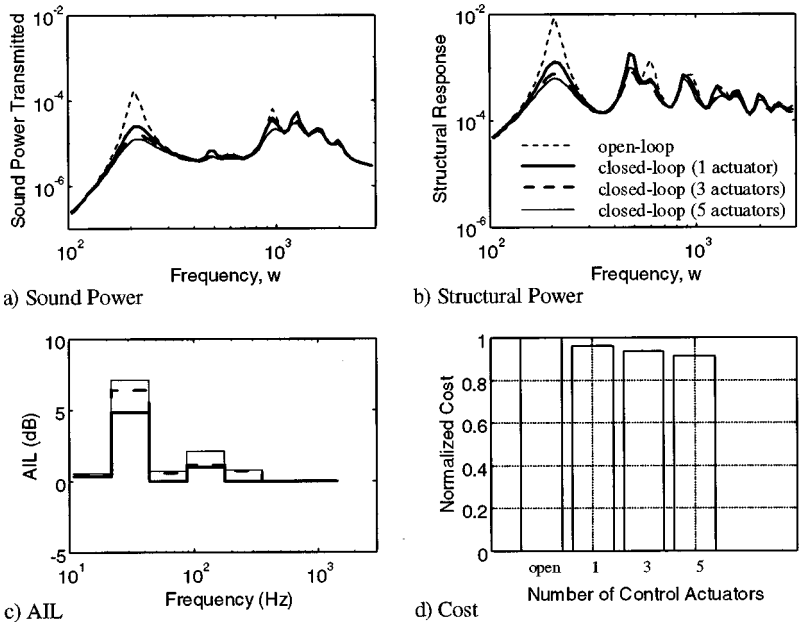

FIG. 10. Comparison of open- and closed-loop response for static compensation and variation in the number of transducer pairs implemented with a control-effort penalty of $R=10^{-5}$ and a flow condition of Mach 0.5.

nominal design and the optimal state-feedback controller in Fig. 8. As illustrated in Fig. 8(c), the AIL reaches a maximum of 5 dB in the octave band containing the fundamental mode. It is of interest to note that the static compensator performs better in this octave band than the state-feedback controller. This result is most likely due to the fact that the static compensator cannot modify the dynamics as a function of frequency, and thus couples most efficiently to the volumetric mode of the panel. Alternatively, the added-input impedance due to the aerodynamics decreases the performance penalty associated with the response in the octave band of the fundamental mode, hence, the state-feedback controller expends less effort at low frequency and more effort at high frequency. As in the results presented for the previous test case, the static compensator designed for operation at $M=0.1$ resulted in nearly identical performance to that of the static compensator designed for $M=0.9$. Due to the dissipative nature of the static compensators designed, spillover into higher-order structural modes was not a problem for the nominal or off-nominal control-system designs.

While the coefficients of the static compensators differed by 2% or 3%, the overall performance of the closed-loop system varied little as a function of Mach number or dynamic pressure for subsonic flow, including the test cases not presented in this article.

C. Variation in number of colocated transducer pairs

For the results presented in this section, the radiation filters were used to generate the performance penalty and the control-effort penalty was set to $R=10^{-5}$. This level of control-effort penalty was chosen since it provided reasonable control gains and associated control forces. The number

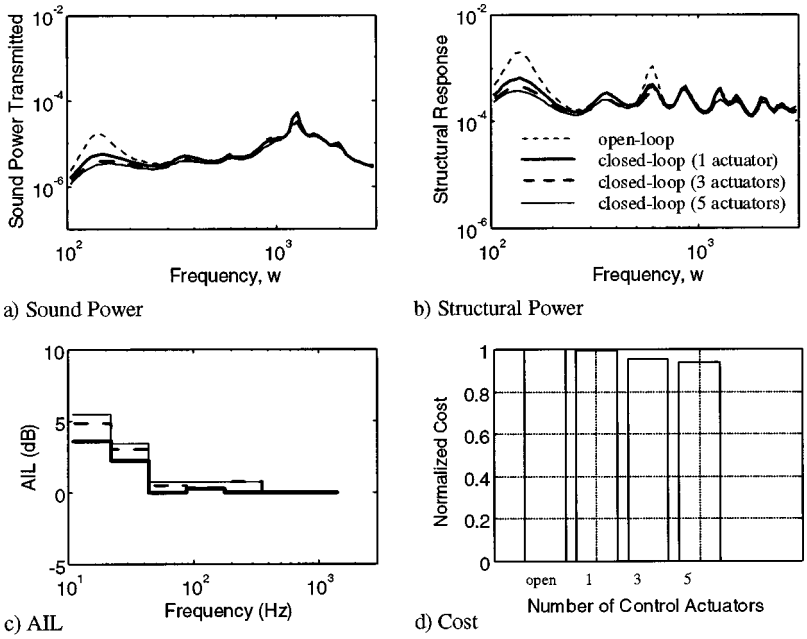

FIG. 11. Comparison of open- and closed-loop response for static compensation and variation in the number of transducer pairs implemented with a control-effort penalty of $R=10^{-5}$ and a flow condition of Mach 0.9.

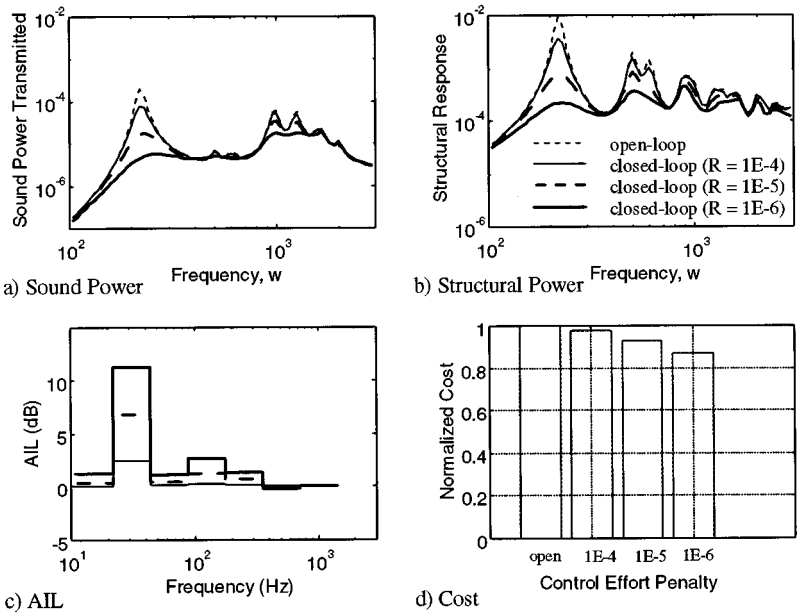

FIG. 12. Comparison of open- and closed-loop response for static compensation and variation in the control-effort penalty for a structure configured with three colocated transducer pairs and a flow condition of Mach 0.1.

of colocated transducer pairs was varied to demonstrate the effect of increasing transducer-pair order on performance.

In Figs. 9, 10, and 11, the closed-loop performance of static compensators for Mach numbers of 0.1, 0.5, and 0.9, respectively, are presented. Results from test cases corresponding to compensators incorporating 1, 3, and 5 colocated transducer pairs positioned on the panel as described in the previous section and illustrated in Fig. 5 are compared. Rather than discuss each test case and figure independently, general trends observed in all three figures are discussed concurrently. As indicated in (a) and (c) of Figs. 9, 10, and 11, the performance of the closed-loop system for decreasing the sound power transmitted increases with increasing order of colocated transducer pairs used in the control system for each Mach number. However, one should also recognize that the frequency-dependent characteristic of the controller does not change significantly with increasing transducer order. For example, the AIL of the control system improves in each octave band; however, the general trend in each octave band is the same. Additionally, as indicated in (b) of Figs. 9, 10, and 11, spillover into higher-order structural modes was not a problem. This result is again due to the dissipative nature of the controller.

D. Variation in the control-effort penalty

In the final set of comparisons, the variation in control-effort penalty is compared. For each of the test cases presented, the number of colocated transducer pairs was fixed at 3, and the Mach numbers used were 0.1, 0.5, and 0.9. The trends of the results presented in Figs. 12, 13, and 14, are discussed concurrently.

As was the case with increasing the number of transducer pairs used to control the aeroelastic, structural acoustic system, decreasing the control-effort penalty also results in improved performance. Although not shown graphically, the

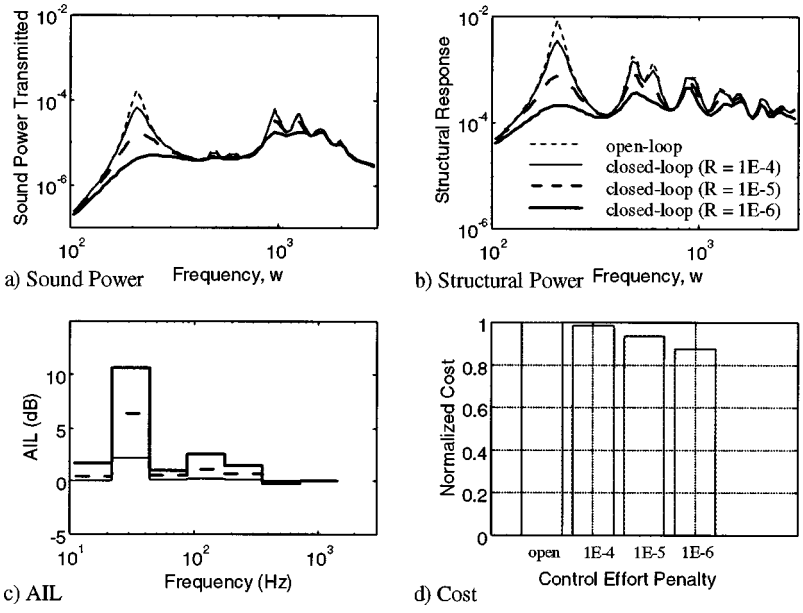

FIG. 13. Comparison of open- and closed-loop response for static compensation and variation in the control-effort penalty for a structure configured with three colocated transducer pairs and a flow condition of Mach 0.5.

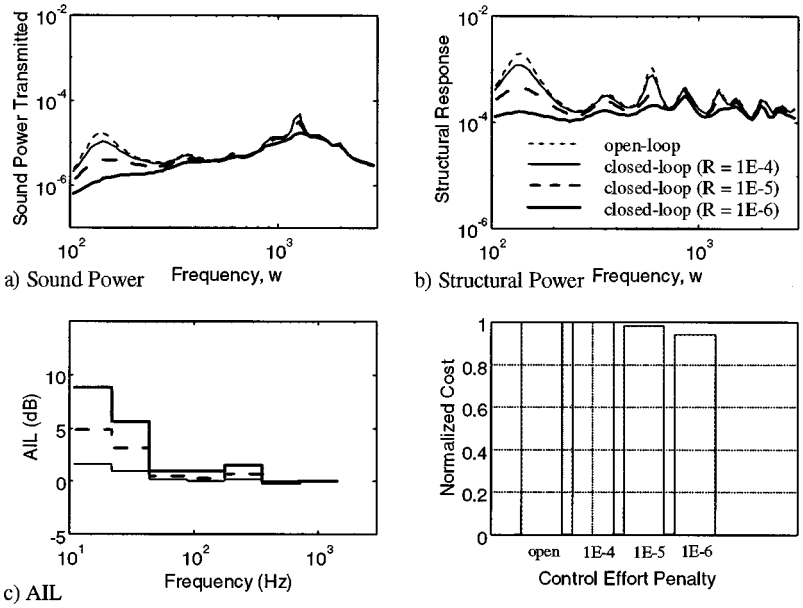

FIG. 14. Comparison of open- and closed-loop response for static compensation and variation in the control-effort penalty for a structure configured with three colocated transducer pairs and a flow condition of Mach 0.9.

ratio of control energy to disturbance energy was computed as a function of frequency. For a control-effort penalty of $R=10^{-4}$, the ratio of the control energy to disturbance energy is much less than 1, by more than an order of magnitude at any given frequency. For $R=10^{-5}$, the ratio is one order of magnitude less, which upon considering the performance achieved is an acceptable level of control effort. However, for $R=10^{-6}$, the ratio of control energy to disturbance energy is of the same order of magnitude over portions of the bandwidth. In general, a ratio less than 1 is desired for practical implementation. Using feedback control generally results in an increase in the input impedance of the system and a corresponding decrease in the control effort required. For practical reasons, one would not choose to implement a controller which requires as much energy as the disturbance imposes. However, for sake of comparison, the performance of a system implementing such a controller is presented (corresponding to $R=10^{-6}$). As illustrated in Figs. 12(c), 13(c), and 14(c), the AIL increases as the control-effort penalty is decreased. The legend for the lines is illustrated in (a) of each figure. All of the resulting static compensators were dissipative and the performance improved as the control-effort penalty was decreased. For reasons previously outlined, the static compensator resulting from a control effort penalty of $R=10^{-5}$ would be selected for practical implementation due to the relative performance achieved and the fact that the ratio of control energy to input energy is less than unity for this case.

V. CONCLUSIONS

A method of designing static-gain compensators for direct, output-feedback control of aeroelastic, structural acoustic systems was presented. Results from this work demonstrate that the sound transmission across a panel subjected to mean flow on one surface and a stationary half-space on the other can be decreased significantly through the use of colocated transducer pairs and simple static-gain, output-feedback control.

Further, results from this study demonstrate that the static-gain compensator design is relatively insensitive to variations in dynamic pressure (Mach number for fixed fluid properties), and thus a controller designed to operate at low subsonic speeds (Mach 0.1) is equally effective at higher subsonic speeds (Mach 0.9). The resulting controller is thus robust to variations in plant dynamics associated with aeroelastic coupling when multi-input, multi-output, colocated rate-feedback control is employed. While state-feedback control was shown to be more effective over the bandwidth, considering the order of the dynamic system, state estimation does not provide a practical alternative. For control systems designed with reasonable levels of control energy, the closed-loop performance of the static-gain compensator compared well with the full state-feedback control system design.

Future work will be devoted to the practical realization of the proposed control system. Additionally, the use of distributed piezoelectric transducers will also be considered.

ACKNOWLEDGMENTS

The authors would like to gratefully acknowledge the support of the National Science Foundation under the CAREER Program Award: CMS-95-01470. Additionally, the authors would like to thank David E. Cox of the Guidance and Controls Branch of the NASA-Langley Research Center for his helpful comments.

Anderson, B., and Moore, J. (**1990**). *Optimal Control: Linear Quadratic Methods* (Prentice-Hall, Englewood Cliffs, NJ).

Baumann, W. T., Saunders, W. R., and Robertshaw, H. H. (**1991**). ''Active Suppression of Acoustic Radiation from Impulsively Excited Structures,'' J. Acoust. Soc. Am. **90**, 3202–3208.

Boyd, S., and Barratt, C. (**1991**). *Linear Controller Design: Limits of Performance* (Prentice-Hall, Englewood Cliffs, NJ).

Clark, R. L., and Frampton, K. D. (**1997**). ''Aeroelastic Structural Acoustic Coupling: Implications on the Control of Turbulent Boundary Layer Noise Transmission,'' J. Acoust. Soc. Am. **102**, 1639.

Clark, R. L., and Cox, D. E. (**1997**). ''Multi-Variable Structural Acoustic

Control with Static Compensation,'' J. Acoust. Soc. Am. **102**, 2748–2756.
Cunefare, K. A. (**1991**). ''The Minimum Multimodal Radiation Efficiency of Baffled Finite Beams,'' J. Acoust. Soc. Am. **90**, 2521–2529.
Dowell, E. H. (**1967**). ''Generalized Aerodynamic Forces on a Flexible Plate Undergoing Transient Motion,'' Q. Appl. Math. **26(3)**, 2267–2270.
Dowell, E. H. (**1975**). *Aeroelasticity of Plates and Shells* (Noordhoff International, Groningen, The Netherlands).
Frampton, K. D., Clark, R. L., and Dowell, E. H. (**1996**). ''State-Space Modeling for Aeroelastic Panels Subject to Linearized Potential Flow Aerodynamic Loading,'' AIAA J. Aircraft **33**(4), 816–822.
Frampton, K. D., and Clark, R. L. (**1997**). ''State Space Modeling of Aerodynamic Forces on a Plate Using Singular Value Decomposition,'' AIAA J. **34**(12), 2627–2631.
Francis, B. (**1986**). *A Course in H_∞ Control Theory* (Springer-Verlag, New York).
Gupta, N. K. (**1980**). ''Frequency Shaped Cost Functionals: Extension of Linear-Quadratic-Gaussian Design Methods,'' J. Guid. Control. Dyn. **3**(6), 529–535.
Kalman, R. E., Ho, Y., and Narendra, K. S. (**1963**). ''Controllability of Linear Dynamical Systems,'' in *Contributions to Differential Equations*, Vol. 1 (Wiley, New York).
Levine, W. S., and Athans, M. (**1970**). ''On the Determination of the Optimal Constant Output Fedback Gains for Linear Multivariable Systems,'' IEEE Trans. Autom. Control. **AC-15**(1), 44–48.
Lomas, N. S., and Hayek, S. I. (**1977**). ''Vibration and Acoustic Radiation of Elastically Supported Rectangular Plates,'' J. Sound Vib. **52**(1), 1–25.
Makila, P. M., and Toivonen, H. T. (**1987**). ''Computational Methods for Parametric LQ Problems—A Survey,'' IEEE Trans. Autom. Control. **AC-32**(8), 658–671.
Meirovitch, L. (**1967**). *Analylical Methods in Vibrations* (Macmillan, New York).
Smith, G. C., and Clark, R. L. (**1998**). ''The Influence of Frequency-shaped Cost Functionals on the Structural Acoustic Control Performance of Static, Output Feedback Controllers,'' J. Acoust. Soc. Am. **104**, 2236–2245.
Thomas, D. R., and Nelson, P. A. (**1995**). ''Feedback Control of Sound Radiation from a Plate Excited by a Turbulent Boundary Layer,'' J. Acoust. Soc. Am. **98**, 2651–2662.
Toivonen, H. T. (**1985**). ''A Globally Convergent Algorithm for the Optimal Constant Output Feedback Problem,'' Int. J. Control **41**, 1589–1599.

The measurement of frame motion in flexible porous materials

K. Khirnykh
School of Engineering Systems and Design, South Bank University, London SE1 0AA, United Kingdom

A. Cummings
School of Engineering, University of Hull, Hull HU6 7RX, United Kingdom

(Received 8 April 1998; revised 21 September 1998; accepted 28 September 1998)

This paper describes a method for measuring the vibrational velocity of the solid skeleton of a flexible porous sound-absorbing material. The method is based on a simple electromagnetic principle, involving a thin conductor that is structurally connected to the frame of the absorbent and placed in a magnetic field. The sample test results that are presented here demonstrate that links may be established between acoustic data and frame velocity measurements. In the presence of a high-amplitude sound field, measurements showed that the velocity of the frame exhibits very nonlinear properties, which cannot be explained by nonlinearities in the airborne sound wave. © *1999 Acoustical Society of America.* [S0001-4966(99)04001-1]

PACS numbers: 43.50.Gf, 43.20.Jr, 43.50.Yw [MRS]

INTRODUCTION

Porous media have many applications in acoustics, mainly as sound absorbents. One such use is in dissipative mufflers, where structural motion of the solid frame of the absorbent can—at certain frequencies—have a significant effect on the sound-absorbing properties of the material. There has recently been interest in frame motion effects in porous media[1–3] and this work continues.

As a part of a theoretical, numerical, and experimental study[4,5] of the interaction between high-intensity sound and lightweight flexible porous media, we carried out measurements of the structural motion of the frame of the material as well as of sound pressure and acoustic particle velocity, up to frequencies of several hundred Hertz. Clearly, even small accelerometers cannot be used to measure frame motion in lightweight media such as glass fiber or plastic foams because of the mass-loading effect, and some alternative method must be employed. Laser methods might seem attractive, but they could only be used to measure the vibrational motion of the surface of the material and would also require the use of transparent walls in a duct containing the porous material. An alternative method was devised in the present investigation, involving the use of a thin metallic wire passing through the porous material and placed normal to a magnetic field. The electromotive force between the ends of the wire then gave a measure of the average vibrational velocity of the material along the length of the wire, normal to the axis of the wire and to the direction of the magnetic field. This method is the antithesis of remote sensing methods such as laser techniques, in that the sensing element is actually built into the test structure. The present method can, in principle, also be applied at levels of acoustic excitation lower than those employed in the present study.

In this paper, the above experimental technique for the measurement of frame vibration is outlined, the experimental apparatus is described and some experimental results are presented and discussed.

I. A NEW METHOD OF MEASUREMENT OF THE FRAME VELOCITY

A. Principles of the method and sources of error in the measurements

For the sake of simplicity it will be assumed that a one dimensional sound wave passes through a flexible porous medium and that the structural motion is also one dimensional, in the x direction, as illustrated in Fig. 1.

The motion of the frame of the porous medium will be driven by the oscillatory fluid motion via the fluid/structural coupling mechanism involving both viscous and (at high acoustic levels) inertial forces. A magnetic field is applied to the porous medium and is assumed to be uniform and directed normally to the x axis. A thin, flexible, metallic wire having a thin surface layer of adhesive is threaded through the pores of the material (which is assumed to be of a sufficiently open structure so as to permit this without any significant distortion of its structure), and runs normal to the x axis and to the direction of the magnetic field.

In general, the electromotive force (emf) over a length L of the wire will be given by

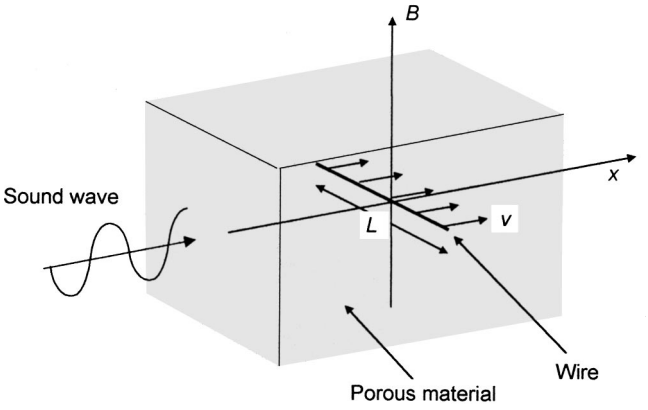

FIG. 1. Orientation of sound propagation, wire, and magnetic field.

$$E = \int_L (\mathbf{v} \times \mathbf{B}) \cdot d\mathbf{L}, \tag{1}$$

where **v** is the velocity vector of the wire at any point, **B** is the magnetic field vector at the same point, and $d\mathbf{L}$ is the relative position vector between the ends of an element of wire having length dL. In the present case, if **v**, **B**, and $d\mathbf{L}$ are assumed always to be normal to one another and $|\mathbf{B}|$ is assumed constant, we may write Eq. (1) simply as

$$E = \int_L v B \, dL = \langle v \rangle B L, \tag{2}$$

where $\langle v \rangle$ is the average of v along the length of the wire. Provided B—the magnitude of the magnetic field strength—is known, the emf E, developed along the length of the wire embedded in the porous medium, gives a measure of the average vibrational velocity of the wire along its length.

For Eq. (2) to give a measure of the vibrational velocity of the solid frame of the porous medium in the *absence* of the wire, it must be assumed that the wire has the same vibrational velocity as the frame and furthermore that the presence of the wire does not affect the frame motion. A detailed analysis of this problem is beyond the scope of the present investigation and would involve the solution of the equations of motion of the frame and wire in two dimensions, including both compressional and shear wave effects in the frame. Instead, we rely here on experimental data indicating that there is no significant dependence of the measured frame velocity on the diameter of the wire, for a given wire material. The experimental arrangement is described in Sec. II, but it is only the experimental data, taken for two differing thicknesses of wire, that are of interest at this point. The test material was ''Bulpren'' foam of 72 pores per inch (ppi) (see Sec. II for further details), and the wires used were of tinned copper, 40 and 140 μm diameter. These wires were threaded through the absorbent by using a fine needle. Two notionally identical, but different, samples of foam were employed in the tests and the wires were inserted at the same position in both samples. Two separate samples were used because it was assumed that the damage incurred to the sample by insertion of the wire would render the sample useless for further tests once the wire had been removed. The test frequency was 120 Hz, and—for identical incident sound fields in the two cases—the rms velocity amplitude of frame vibration was found to differ by 5% between the two tests. This small difference could have been attributable to variations in mechanical properties between the two samples of foam as much as to the effect of the mass of the wire, and in any case was taken to signify that, for the range of wire thickness and for materials similar to those used in the tests, there was no significant mass-loading effect of the wire on the absorbent. Time constraints precluded the repetition of these tests at higher frequencies, but it is thought that the wire and frame velocities would be closely similar up to at least 1 kHz, particularly in the case of the 40-μm wire. Any inertial effects caused by the wire—likely to be significant only at high frequencies—could be minimized by the use of a smaller diameter wire.

It is almost inevitable that there would be ''end effects'' in this method of measurement of the frame velocity, caused by small lengths of wire moving in the magnetic field but not embedded in the porous medium, since the ends of the wire would need to bend at some point in order to accommodate the motion of the wire. These can be minimized by careful design and should, in any case, be small. Some idea of their magnitude is given in the following subsection on calibration.

A further possible source of error, that could, in principle, be of concern at higher frequencies, relates to any structural resonance effects that might occur in the unsupported lengths of wire within the absorbent, between the points at which it is in contact with the solid frame of the porous medium. Again, a detailed treatment of this effect is hardly possible unless comprehensive information is available concerning the effective boundary conditions at the contact points and the distribution of unsupported lengths of wire. We can, however, make order-of-magnitude estimates of the resonance frequencies. The 140-μm-diam wire was used in the great majority of the experimental tests in view of its relative robustness and ease of handling, so we base our estimates on this. The coarser of the two foam sound-absorbing materials used in the experiments had 42 ppi, so that a typical pore dimension was about 0.6 mm. Supposing the wire was effectively simply supported every five pore dimensions, we may now estimate[6] the fundamental resonance of an unsupported length of wire—in isolation from the rest of the wire—as $f_1 = (\pi/2l^2)\sqrt{EI/\rho A}$, where l is the

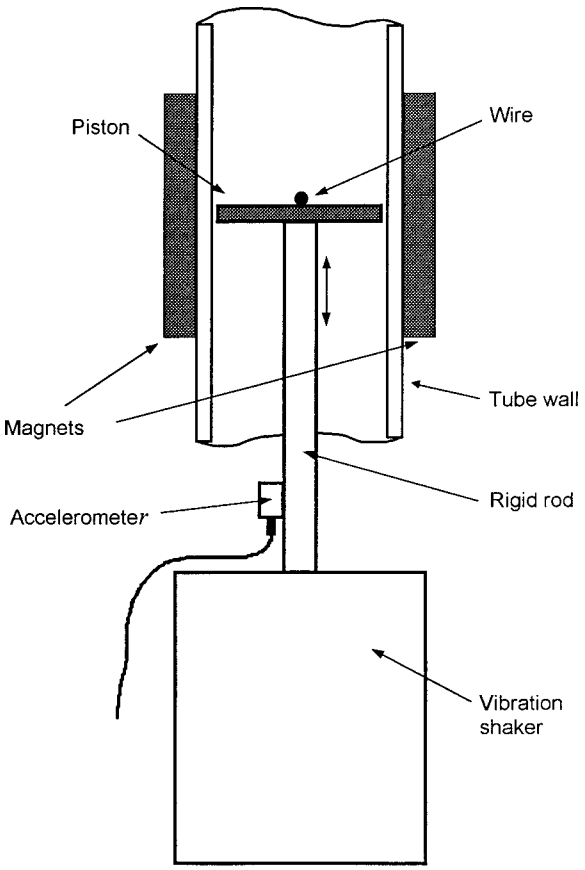

FIG. 2. Calibration arrangement.

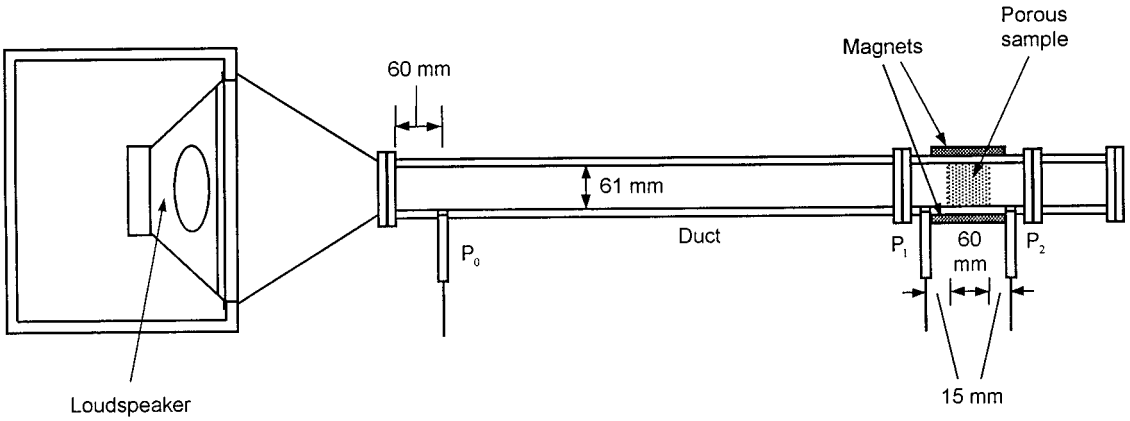

FIG. 3. Experimental apparatus.

length of the wire between supports, E is the Young's modulus of the wire material, ρ its density, I its second moment of area about the neutral plane, and A its cross-sectional area. For a copper wire as above with $l=3$ mm, we find $f_1 \approx 22$ kHz, which is well above the frequency range of interest. It is likely that l has been overestimated here, but even if the wire were supported only every ten pore dimensions, we should have $f_1 \approx 4.5$ kHz, which is still safely clear of the upper frequency of interest. It therefore seems unlikely that resonance effects in the wire should be of any concern.

B. Calibration of the system

The magnetic field in the experimental apparatus was provided by two identical ferrite permanent magnets, measuring $100\times151\times25$ mm. These were clamped firmly to opposite sides of a perspex tube with 19-mm walls and an internal cross section of 61×61 mm (see Sec. II for details). The distance between the opposite faces of the magnets was therefore 99 mm. The magnetic field strength at the position of the wire was measured by means of a Gauss meter with a Hall probe, and was found to vary between 0.05856 and 0.0602 Tesla along the length of the wire, the average value being 0.0596 Tesla. This figure is accurate to about 1%.

Although the emf measured at the ends of the wire should be proportional to the frame velocity via a coefficient which can be directly calculated from a knowledge of the magnetic field strength and length of the wire (see Sec. I A), a separate test was carried out in order to assess the magnitude of any extraneous effects that might cause departures from the theoretical estimates of frame velocity.

A rod of nonferromagnetic plastic material was attached to a Brüel & Kjær (B&K) vibration exciter type 4809 and placed in the section of the rectangular tube in which the porous samples were tested. A conducting wire, 140 μm in diameter, was glued to a square piston of side 55 mm, which was attached to the upper end of the rod as shown in Fig. 2. The length of the (aluminum) rod was such that no axial vibrational resonance effects occurred within the frequency range of the calibration experiments.

Because the voltage to be detected was very low it was necessary to amplify the signal, and accordingly an amplifier with a gain of 1300 was built. The amplifier was battery powered and had a very high input impedance in order to reduce noise caused by possible ground loops and extraneous induction effects. The voltage signal from the wire was fed to the amplifier through conducting wires that were glued to the tube walls in order to eliminate spurious signals caused

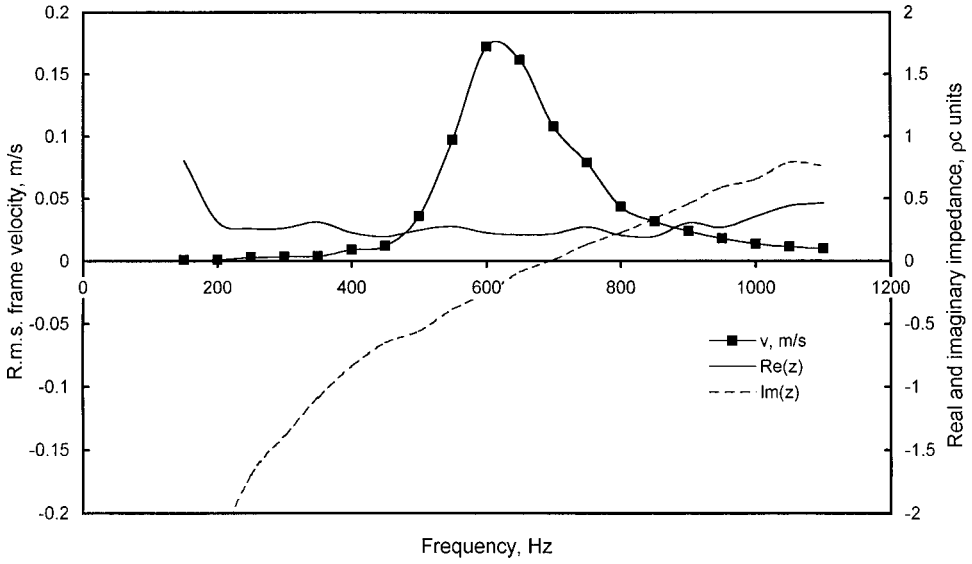

FIG. 4. Filtren, 40-mm cavity, 140 dB: impedance and frame velocity.

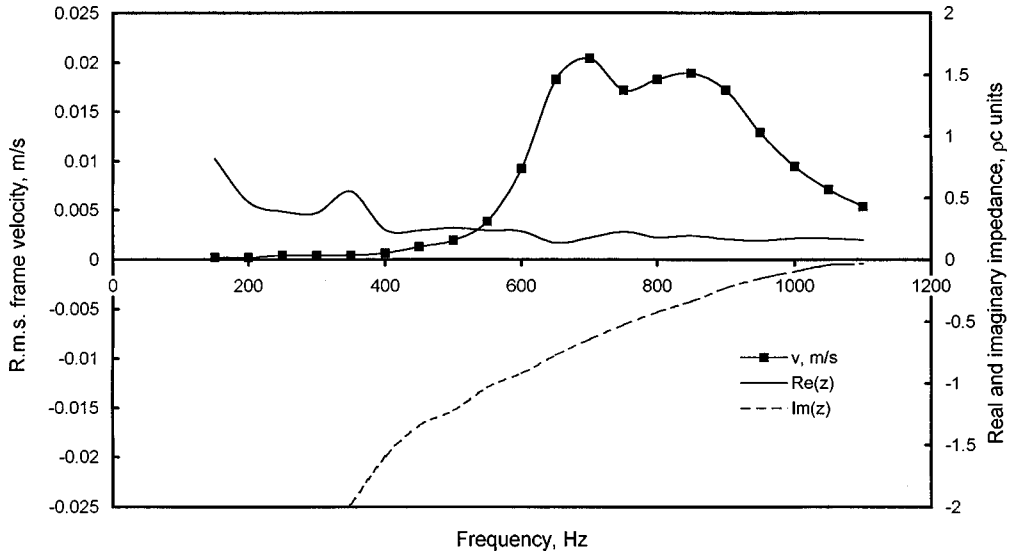

FIG. 5. Filtren, hard wall, 140 dB: impedance and frame velocity.

by vibration. A twisted pair of conducting wires was used away from the vicinity of the magnets in order to minimize the picking up of electromagnetic noise. The sensing wire passed through very small holes in opposite walls of the tube, from the sample to the exterior, and was soldered to the conducting wires.

The voltage signal from the wire was compared to the integrated signal from the accelerometer (B&K type 4332, with B&K charge amplifier type 2635) over a range of frequencies from 120 to 300 Hz, appropriate factors being applied to yield the inferred rms velocity signals. These velocity signals were in good agreement, the maximum discrepancies being about 2.5%, which could be accounted for by the small inaccuracy in measuring the amplifier gain, end effects leading to a small uncertainty in the length of the wire (see Sec. I A) and errors in measurement of the magnetic field strength. Tests were not carried out at lower or higher frequencies, but there was no reason to suppose that the resulting data would have shown any different trends.

II. THE EXPERIMENTAL APPARATUS

Figure 3 shows a test apparatus consisting of a JBL 2206H 300-mm-diam cone loudspeaker, mounted in an enclosure and coupled by means of a square-section conical horn to a perspex tube of 61×61 mm internal cross section and 19-mm wall thickness, as mentioned in Sec. I B. The two identical ferrite magnets of dimensions 100×151×25 mm were secured by an aluminum G-clamp to the outer surfaces of opposite walls of the perspex tube. To reduce possible distortion of the magnetic field, only nonmagnetic nylon bolts were used in the tube structure, in the neighborhood of the test section. Three microphones were used to detect the sound field at certain points in the tube; all were B&K

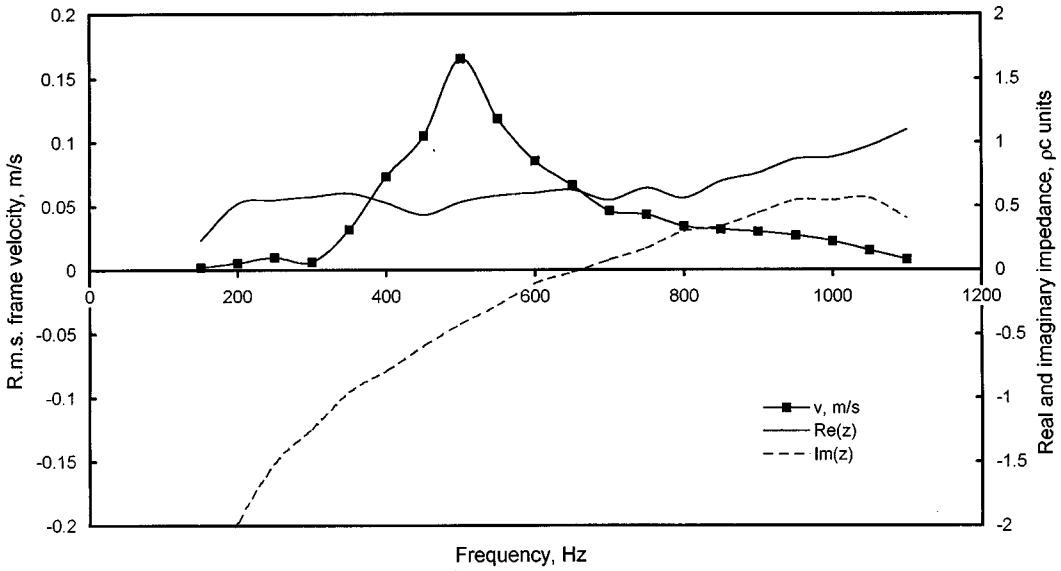

FIG. 6. Bulpren, 40-mm cavity, 140 dB: impedance and frame velocity.

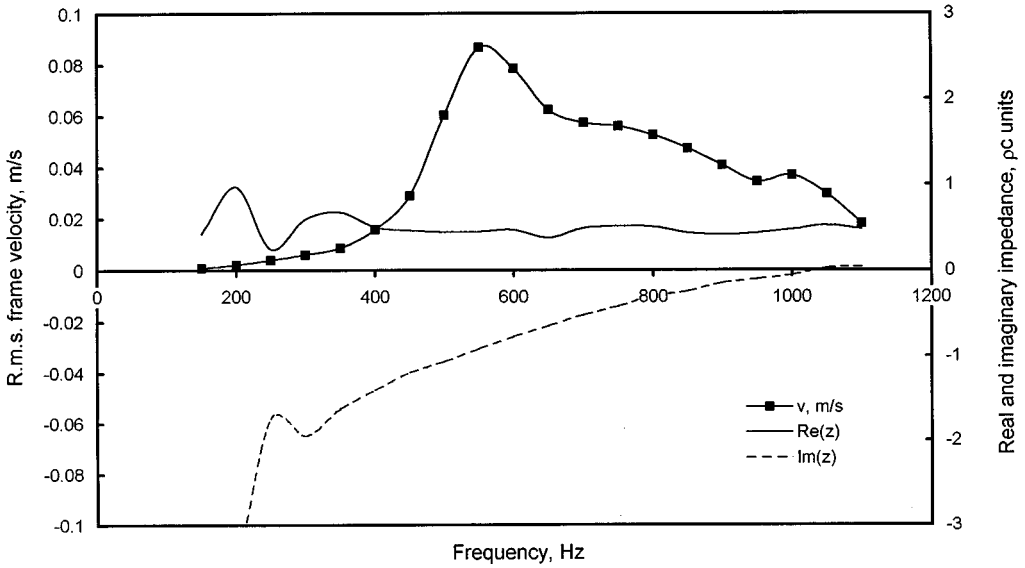

FIG. 7. Bulpren, hard wall, 140 dB: impedance and frame velocity.

1/4-in. condenser microphones, type 4136. Microphones P_1 and P_2, positioned in the side walls approximately 15 mm on either side of the sample, were used to measure sound-pressure level (SPL) in front of and behind the sample. Microphones P_0 and P_1 were used to measure the impedance of the sample and cavity or termination behind the sample by using a two-microphone technique.[7] All tests were conducted with discrete frequency excitation.

The possibility of flanking transmission across the test sample, via bending waves in the walls, needs to be considered here. Cummings[8] has studied internal/external sound transmission through the walls of flexible rectangular section ducts and has shown that wall vibration is only important near and above the lowest transverse structural resonance frequency of the duct walls. Below about half this frequency, the walls are effectively rigid and flanking can be neglected. This lowest resonance, in the case of plane waves in a square duct, may be approximated by that of a Euler beam made from a strip of the wall material, clamped at both ends and with a length equal to the transverse internal wall width. Thomson's[6] table of frequency formulas for Euler beams with various boundary conditions was again used here to estimate the lowest structural resonance frequency of the duct walls. Published data on the mechanical properties of perspex, together with the wall thickness and width for the experimental tube, yield a fundamental wall frequency of 9460 Hz, which is 8.6 times higher than the upper limit of the measured data in the present investigation (1100 Hz). Therefore, the tube walls may be assumed rigid and flanking transmission can be neglected.

The experiments were carried out with two types of porous materials: ''Bulpren'' S75 5734 foam with 72 ppi and ''Filtren'' 2145 foam with 42 ppi. The foam samples had dimensions of $60\times61\times61$ mm. Both these materials were fully reticulated polyurethane foams. The samples were cut to fit snugly within the tube.

A series of tests was carried out with the two types of sample: (i) with a cavity and (ii) with a rigid termination. The arrangement shown in Fig. 3 shows a cavity behind the sample. When the tests involved a rigid termination, microphone P_2 was removed. To test the consistency of the results, three wires were embedded in each sample: one centrally positioned and two displaced 10 mm to the right and left, respectively, in the x direction. The frame velocity data presented later in this paper were taken from the centrally placed wire; the two adjacent wires typically gave almost the same signal, indicating that the frame velocity in the central part of the sample was not very sensitive to x.

III. SOME EXPERIMENTAL RESULTS

The principal aim of the experiments was to test the experimental technique and to study the behavior of frame motion at different frequencies and sound-pressure levels. During the experiments the following quantities were measured: (i) velocity of the frame at the position of the wire, (ii) sound-pressure signal in front of and behind the porous sample (the latter in cases where there was a cavity behind the sample), (iii) impedance at the surface of the sample facing the sound source.

The rms value of the frame velocity was measured for sound-pressure levels in front of the sample (at microphone P_1) equal to 130 and 140 dB and in the frequency range from

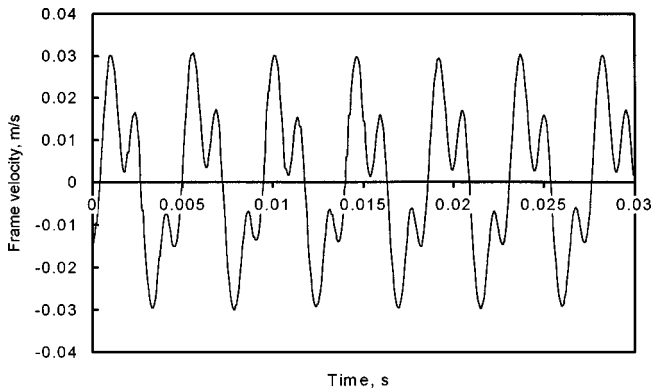

FIG. 8. Filtren, 80-mm cavity, 155 dB, 220 Hz: frame velocity versus time.

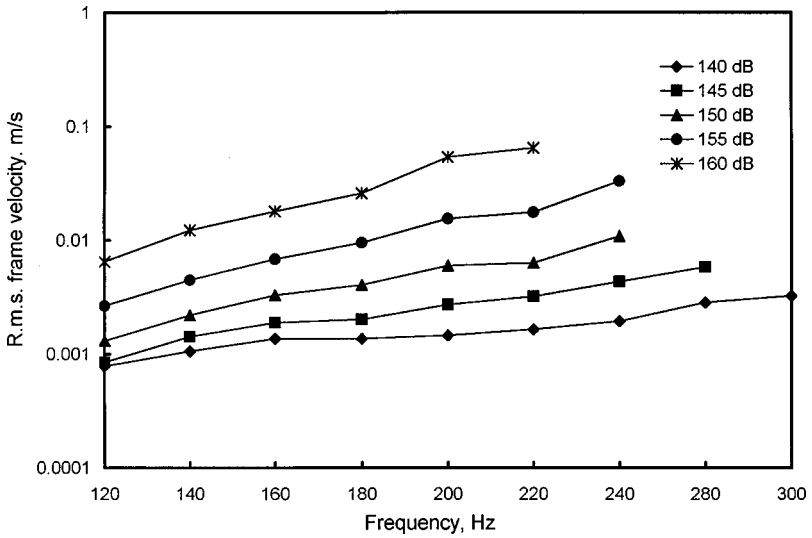

FIG. 9. Filtren, 80-mm cavity, 220 Hz: rms frame velocity at different sound-pressure levels.

150 to 1100 Hz. Additional data included values of impedance at the surface of the sample, measured by the use of the two-microphone method. Plots of rms frame velocity, together with the real and imaginary parts of the impedance at the surface of the sample facing the sound source, are shown in Figs. 4–7, for Filtren and Bulpren with both a 40-mm backing cavity and a rigid termination, at a sound-pressure level (at microphone P_1) of 140 dB. The Filtren sample with the cavity (Fig. 4) shows a maximum in the frame velocity at a slightly lower frequency than the first resonance frequency of the sample/cavity system. This might represent a structural resonance of the sample, weakly coupled to the resonance of the fluid phase of the system, or simply a peak in the structural response caused by the enhanced particle velocity in the sample near the fluid resonance frequency. Since there are no distinct features in the impedance curves near the structural velocity peak, it can be assumed that structural/fluid coupling is weak.

The Filtren plots (Fig. 5) with a rigid backing show a higher fluid resonance frequency (as expected) and a broader and lower structural velocity peak, at a rather higher frequency than that in Fig. 4. These data might suggest the forcing of a structural mode by the fluid motion, again with no evidence of strong structural/acoustic coupling. The Bulpren plots (Figs. 6 and 7), with and without a backing cavity, show similar features, overall, to those exhibited in Figs. 4 and 5, though both structural and fluid resonance frequencies are a little lower than those observed in the case of Filtren.

At higher incident sound levels, significant third harmonic distortion was evident in the frame motion. Figure 8 shows an example of a frame velocity/time history, with a Filtren sample and an 80-mm cavity, at 220 Hz and a sound-pressure level at microphone P_1 of 155 dB. Although—at these high sound-pressure levels—some harmonic distortion of the acoustic signal was present, it was clear from the experimental data that the frame itself exhibited significantly nonlinear dynamic structural behavior. The rms frame velocity versus frequency is shown in Fig. 9 for a range of incident sound levels (again at microphone P_1), and some evidence of a ''softening spring'' behavior is evident, since the spacing of the curves on the logarithmic velocity scale increases with equal increments in sound level. Studies of the static behavior of fully reticulated plastic foams (see, for example, the book by Gibson and Ashby[9]) show an initially linear elastic behavior of the frame in tension—with eventual stiffening at higher strains—and an initially linear behavior

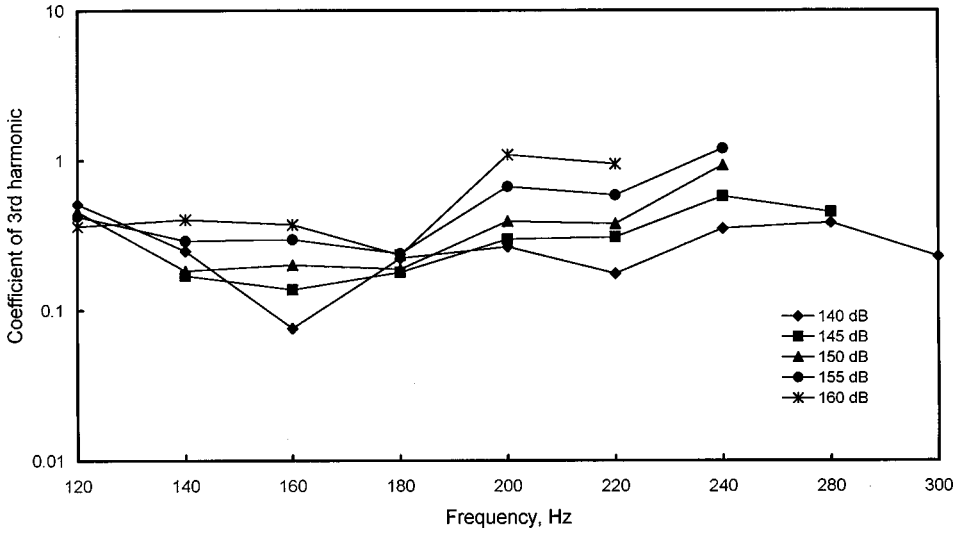

FIG. 10. Filtren, 80-mm cavity, 220 Hz: coefficient of third harmonic of frame velocity at different sound-pressure levels.

in compression, soon followed by a softening characteristic caused by frame buckling, and eventual stiffening. It is thought that dynamic frame buckling may be responsible for the softening spring characteristics apparent in Fig. 9.

In Fig. 10, the third harmonic amplitude coefficient for Filtren with an 80-mm cavity, at 220 Hz, is shown as a function of frequency at various incident sound levels. It can be seen that there is a general increase in third harmonic coefficient as the sound level increases, and that it can exceed unity at certain frequencies, when the sound level is 155–160 dB.

The experimental data presented in Figs. 4–10 are all, of course, dependent on the structural boundary conditions imposed by the walls of the tube on the sides of the test sample. These boundary conditions would depend on whether the sample was loose or tight fitting in the tube or whether it was glued in place. In the present case, where the purpose of the experiments was mainly to demonstrate the experimental technique, the precise nature of the boundary conditions was not very important. In cases where *in situ* data (for example, the vibration levels of the absorbent in dissipative mufflers) were required, representative structural boundary conditions for the porous material would have to be preserved.

IV. CONCLUSIONS

The main point of this paper has been to describe a simple method of measuring the vibrational velocity of the solid frame of a flexible porous material. This method is quite robust, with an accuracy that is fairly easy to establish; in the present case, this is estimated to be approximately $\pm 3\%$. The method has several desirable features: (i) it does not involve the use of any device (such as an accelerometer) that would mass load the material, (ii) the velocity can be measured in regions of the material away from the surface, (iii) the method does not require penetration of laser light into the inner regions of the porous medium, and (iv) it yields a space average of the vibrational velocity along the length of a wire that is embedded in the material (thereby avoiding any spurious local variations in velocity amplitude). Its main disadvantages would seem to be that magnets have to be placed on either side of the wire and that the measurement of a three dimensional vibrational velocity field could involve a cumbersome arrangement of wires and magnets. While these drawbacks could create difficulty in some circumstances, skillful design of the apparatus could enable the ready measurement of two-dimensional velocity fields in many situations.

The experimental data presented were taken at fairly high sound-pressure levels, and significant structural nonlinearity of the test samples was noted.

ACKNOWLEDGMENTS

This research was supported by the Science and Engineering Research Council, under Research Grant GR/J47873. The authors also wish to acknowledge the assistance of Dr. A. G. I. Jenner, of the Department of Physics at the University of Hull, in the measurement of magnetic field strength.

[1] J.-F. Allard, *Propagation of Sound in Porous Media* (Elsevier Science, Barking, 1993), Chap. 6.
[2] J. S. Bolton, N.-M. Shiau, and Y. Kang, J. Sound Vib. **191**, 317 (1996).
[3] R. Panneton and N. Atalla, J. Acoust. Soc. Am. **100**, 346 (1996).
[4] K. Khirnykh, A. Cummings, and B. M. Shield, *Proceedings of Euronoise '95*, Lyon, France, Vol. 3, p. 841 (CETIM, Senlis, 1995).
[5] K. Khirnykh, A. Cummings, and B. M. Shield, *Proceedings of Inter-Noise 95*, Newport Beach, CA, Vol. 1, p. 449 (Noise Control Foundation, Poughkeepsie, NY, 1995).
[6] W. T. Thomson, *Theory of Vibration with Applications* (Prentice-Hall, Engelwoods, Cliffs, NJ, 1981), 2nd ed., p. 220.
[7] I. V. Lebedeva and S. P. Dragan, Meas. Tech. **8**, 52 (1988).
[8] A. Cummings, J. Sound Vib. **61**, 327 (1978).
[9] L. J. Gibson and M. F. Ashby, *Cellular Solids* (Cambridge U.P., Cambridge, 1997), 2nd ed., Chap. 5.

A boundary integral formulation for the prediction of acoustic scattering from periodic structures

Y. W. Lam
University of Salford, Salford M5 4WT, United Kingdom

(Received 3 March 1998; revised 16 September 1998; accepted 5 October 1998)

The scattering of sound by reflecting surfaces is an important feature in room acoustics. The boundary element method has been shown in the past to be an accurate method to calculate the scattering pattern of complex surfaces. However, this numerical method is expensive to use on large surfaces where a large number of elements is required. This paper proposes a method of reducing the number of boundary elements required to model large, but periodic, structures. The method is based on a consideration of the relationship between the field variables at two points exactly one period apart. The problem is reduced to the modeling of just one period of the structure. In cases of plane-wave incidence, the prediction using this method agrees very well with the prediction obtained by modeling the complete structure. With the point source in the near field of the surface, the incidence field is no longer periodic and the assumption of a constant periodic factor does not hold. In this case, it is shown that the method can still be used with a simple modification to the periodic formulation, and produces good agreements with the full structure predictions and with measurements. © *1999 Acoustical Society of America.* [S0001-4966(99)05301-1]

PACS numbers: 43.55.Br, 43.55.Ka, 43.20.Fn [JDQ]

INTRODUCTION

Scattering surfaces play an important role in room acoustics and are often used to promote the diffusion of sound. The ability to characterize the scattering property of these surfaces is highly desirable in the design of room acoustics. The prediction of the scattering pattern or polar response of the surface can provide the acoustic designers with information to judge the sound field distribution. One may also use the scattering pattern to derive a single figure coefficient, much like the well-established absorption coefficient, to rank the diffusion performance of surfaces. Although a universally accepted formulation of such a single figure coefficient is still not available, efforts are being made to achieve this goal.[1,2]

The boundary element method has been shown by previous research to be an accurate and effective method for the prediction of scattering from complex surfaces.[3] The method is flexible enough to handle virtually any arbitrarily shaped, regular and locally reacting surface. It is also highly adaptable and can be modified to take advantage of specific features of a problem, such as the two-dimensional, thin panel, and axisymmetric formulations.[4,5] However, one limitation of the boundary element method is the large number of elements required to model large surfaces. In room acoustics, the scattering surfaces are usually quite large. The two-dimensional and thin panel formulations can be used to reduce the size of the problems on a large variety of surfaces, but it is still not practical to model very large surfaces that are formed by periodic structures. Examples are the quadratic diffusers used in concert halls, which often consist of a combination of several periods of a prime quadratic sequence, and profiled metal cladding walls, which are commonly used in industrial and leisure buildings.

The modeling of periodic structures using the boundary element method has been carried out by M. Heckel[6] to calculate the radiation from a vibrating profiled cladding. Her formulation uses a superposition of plane waves at discrete angles with the cladding acting as an acoustic diffraction grating. There was, however, no evidence to suggest how successful the formulation was. We also note that, in practical scattering problems, the number of periods in a periodic structure is finite, and it seems more intuitive and efficient to formulate the problems in terms of geometrical periods rather than superimposed plane waves. This paper outlines such a formulation. To limit the scope of the investigation, the formulation is carried out for two-dimensional problems. The extension to three dimensions should be a straightforward procedure. Predictions using this periodic formulation will be compared with predictions using the usual formulation to model the full structure, and with measurements performed on both small and large periodic structures.

I. PERIODIC FORMULATION

The boundary integral equations can be written as follows:[4]

$$\int_S \left[p(\mathbf{r}_q) \frac{\partial G(\mathbf{r}_p|\mathbf{r}_q)}{\partial \mathbf{n}_q} - \frac{\partial p(\mathbf{r}_q)}{\partial \mathbf{n}_q} G(\mathbf{r}_p|\mathbf{r}_q) \right] dS = \begin{cases} p(\mathbf{r}_p) - p_{\text{inc}}(\mathbf{r}_p), & \mathbf{r}_p \in V_{\text{ext}}, \\ \frac{1}{2} p(\mathbf{r}_p) - p_{\text{inc}}(\mathbf{r}_p), & \mathbf{r}_p \in S, \\ -p_{\text{inc}}(\mathbf{r}_p), & \mathbf{r}_p \in V_{\text{int}}, \end{cases} \tag{1}$$

where $p(\mathbf{r}_q)$ is the pressure on the surface at point $\mathbf{r}_q$, $\mathbf{n}_q$ is the outward normal, $p_{\text{inc}}(\mathbf{r}_p)$ is the incident pressure at receiver position $\mathbf{r}_p$, V_{int} is the interior volume enclosed by the surface S, and V_{ext} is the volume external to S. The Green's function for the two-dimensional problem is

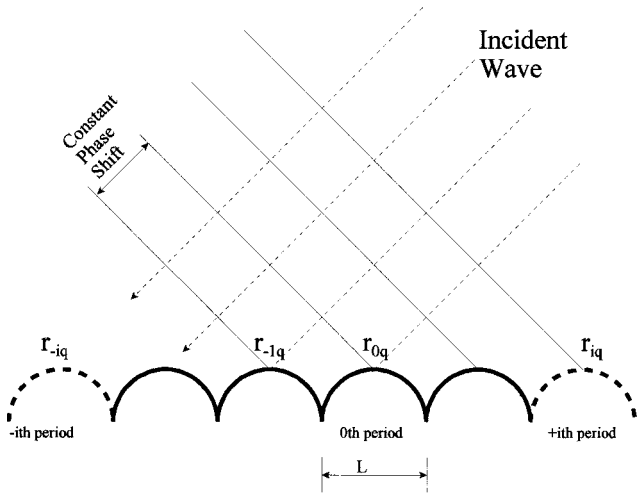

FIG. 1. Plane-wave incidence on a periodic structure.

$$G(\mathbf{r}_p|\mathbf{r}_q)=\frac{j}{4}H_0^{(2)}(k|\mathbf{r}_p-\mathbf{r}_p|),$$

where $H_0^{(2)}$ is the Hankel function of order zero. The integral equation can be solved if the surface impedance is known. Here the scattering surface is assumed to be hard, i.e., $\partial p(\mathbf{r}_q)/\partial \mathbf{n}_q=0$ inside the integral.

For the periodic structure shown in Fig. 1, the integral equation with the receiver position $\mathbf{r}_{0p}$ on the 0th period of the surface can be written as

$$\sum_{i=-\infty}^{\infty}\int_{S_i}\left[p(\mathbf{r}_{iq})\frac{\partial G(\mathbf{r}_{0p}|\mathbf{r}_{iq})}{\partial \mathbf{n}_{iq}}\right]dS=\frac{1}{2}p(\mathbf{r}_{0p})-p_{\mathrm{inc}}(\mathbf{r}_{0p}). \quad (2)$$

For free waves in a periodic structure, Bloch's theorem[7] states that all field quantities at two points exactly one period apart are related by the same factor. For excited waves, the variation in the field quantities will be modulated by the excitation. In the case of plane-wave incidence, the incident wave between two points exactly one period apart (periodic points) differs by a constant phase factor, but the relationship between the *total* pressure at periodic points will be modified by the scattered wave. The scattered wave can be considered in two parts. The first is the image reflection of the incident wave as if the surface were flat, rigid, and of infinite extent. This part has the same periodic phase shift as the incident wave on the surface. The second part is the additional wave field created by the surface variations that deviate from the flat, rigid, and infinite conditions. If this second part of the scattered wave is weak, the relationship between the total pressure at periodic points will still be dominated by the corresponding variation of the incident field. An example is the scattering from finite-size rigid plane surfaces for which Kirchhoff's approximation, that the total surface pressure is given by the doubling of the incident pressure, often produces good predictions. The validity of this assumption in this context will be thoroughly tested in later sections.

Assuming that the surface pressure on the periodic structure at two periodic points, i.e., points that are exactly one period apart, is related by a constant factor $e^{\gamma L}$, where γ is generally complex, then

$$p(\mathbf{r}_{0q})=e^{\gamma L}p(\mathbf{r}_{1q})=e^{2\gamma L}p(\mathbf{r}_{2q})=\cdots=e^{i\gamma L}p(\mathbf{r}_{iq}), \quad (3)$$

where i indexed the ith period. Here the constant factor is determined by the ratio of the incident pressure between any two periodic points,

$$e^{\gamma L}=\frac{p_{\mathrm{inc}}(\mathbf{r}_{iq})}{p_{\mathrm{inc}}(\mathbf{r}_{(i-1)q})}. \quad (4)$$

The integral equation (2) with the $\mathbf{r}_{0p}$ on the surface can now be written as

$$\int_{S_0}\left[p(\mathbf{r}_{0q})\sum_{i=-\infty}^{\infty}e^{i\gamma L}\frac{\partial G(\mathbf{r}_{0p}|\mathbf{r}_{iq})}{\partial \mathbf{n}_{0q}}\right]dS$$
$$=\tfrac{1}{2}p(\mathbf{r}_{0p})-p_{\mathrm{inc}}(\mathbf{r}_{0p}), \quad (5)$$

which can be discretized and solved in the usual way. Note that since the structure is periodic, the normal vectors are the same at corresponding periodic points. Hence the vector $\mathbf{n}_{iq}$ can be replaced by $\mathbf{n}_{0q}$ in the integral.

Since the asymptotic form of the two-dimensional Green's function (given by the Hankel function) at a large distance is inversely proportional to the square root of the distance, it may be expected that the summation inside the integral should converge quickly. In practice, since all structure must be finite and have a finite number of periods, one may conveniently choose the physical number of periods to be the limit of the summation. The effect on the accuracy of having only a finite number of periods will be tested later on a surface that has only a small number of periods.

A further reduction of the problem can be achieved if we assume that the thickness of the scattering object is small. This is often true, since most reflectors in room acoustics are constructed from thin panels. Also, when the surface is large, the effect of its rear side is small and modeling it as a rigid, thin object should not introduce significant errors. With the thin panel assumption, Eq. (5) can be further reduced to[4]

$$\int_{S_{01}}\left[(p(\mathbf{r}_{0q1})-p(\mathbf{r}_{0q2}))\sum_{i=-\infty}^{\infty}e^{i\gamma L}\frac{\partial^2 G(\mathbf{r}_{0p}|\mathbf{r}_{iq})}{\partial \mathbf{n}_{0q}\partial \mathbf{n}_{0p}}\right]dS$$
$$=-\frac{\partial p_{\mathrm{inc}}(\mathbf{r}_{op})}{\partial \mathbf{n}_{0p}}, \quad (6)$$

where the additional subscripts 1 and 2 index the front and back faces of the thin object, and the integral is now over just the front face S_{01} of one period of the structure. The exterior pressure, with $\mathbf{r}_p$ in the exterior region V_{ext}, is calculated by

$$p(\mathbf{r}_p)=\int_{S_{01}}\left[(p(\mathbf{r}_{0q1})-p(\mathbf{r}_{0q2}))\sum_{i=-\infty}^{\infty}e^{i\gamma L}\frac{\partial G(\mathbf{r}|\mathbf{r}_{iq})}{\partial \mathbf{n}_{0q}}\right]dS$$
$$+p_{\mathrm{inc}}(\mathbf{r}_p). \quad (7)$$

II. PLANE-WAVE INCIDENCE

The above formulation, represented by Eqs. (6) and (7), is applied to a periodic structure consisting of 21 half-cylinders, as shown in Fig. 1. Each cylinder has a diameter of 0.115 m, which is about 1.7 wavelengths at the highest test frequency of 5000 Hz used in this study. The half-

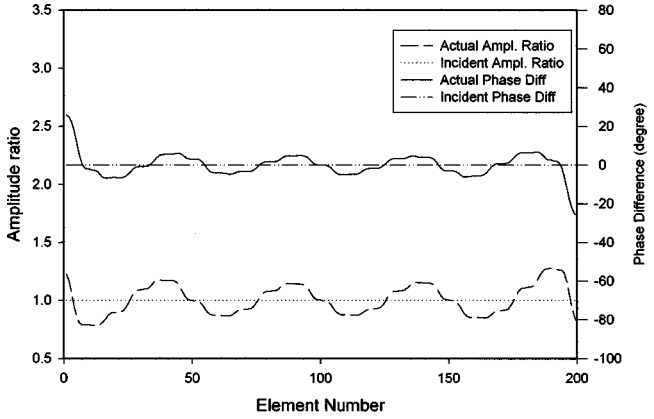

FIG. 2. Relationship between points one period apart. Normal incidence plane wave at 630 Hz. The amplitude ratios and phase differences are calculated according to Eq. (8).

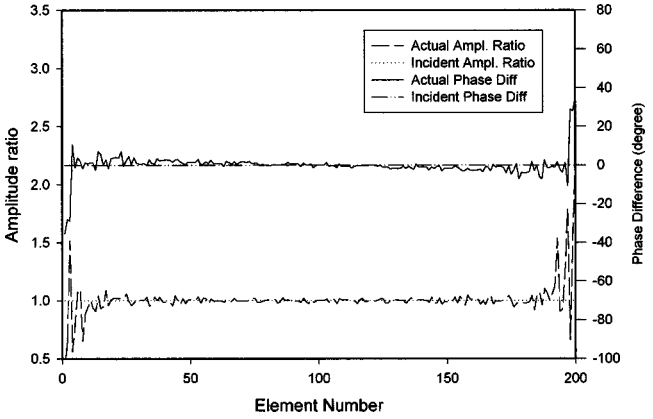

FIG. 3. Relationship between points one period apart. Normal incidence plane wave at 5000 Hz. The amplitude ratios and phase differences are calculated according to Eq. (8).

cylinders are placed side by side without gaps. The configuration corresponds to an experimental setup which will be discussed in the next section.

The source is located sufficiently in the far field so that plane-wave incidence can be assumed on the surface. The pressure difference across the front and back faces, $p(\mathbf{r}_{oq1}) - p(\mathbf{r}_{oq2})$, was calculated by the periodic formulation, Eq. (6), and by applying the full boundary integral formulation, Eq. (2), to the full structure of all 21 cylinders. The equations were solved by dividing the surface of integration into discrete boundary elements in the usual way. In this study, ten elements were used for each half-cylinder, giving a element size of about 1/4 wavelength at the highest test frequency of 5000 Hz. This is considered to be the maximum size that can be tolerated before the constant pressure assumption that is used to discretize the boundary integral into elements is seriously violated. With this mesh resolution, 210 elements were required in the full model but only 10 were required in the periodic model. The solution time for the surface pressure at a single frequency was 23 s for the full model and about 1 s for the periodic model on a Pentium II 300-MHz desktop computer.

The amplitude ratio and phase difference between points one period apart in successive periods are calculated from the full structure formulation as follows:

$$\text{Amplitude Ratio} = \left| \frac{p(\mathbf{r}_{(-1)q1}) - p(\mathbf{r}_{(i-1)q2})}{p(\mathbf{r}_{iq1}) - p(\mathbf{r}_{iq2})} \right|, \tag{8}$$

$$\text{Phase Difference} = \text{Phase Angle of} \left(\frac{p(\mathbf{r}_{(i-1)q1}) - p(\mathbf{r}_{(i-1)q2})}{p(\mathbf{r}_{iq1}) - p(\mathbf{r}_{iq2})} \right).$$

The result for normal incidence is shown in Figs. 2 and 3 for the 630- and 5000-Hz case. The ''element number'' used to label the x-axis corresponds to the numbering index of the boundary elements used in the model. The elements are numbered sequentially from one end of the structure to the other. Element 1 is at the source end of the structure when the source is offset from the center line (oblique incidence). Since ten elements were used for each period, each set of consecutive ten elements corresponds to a period of the structure.

For a plane incident wave, the amplitude ratio is 1 and at normal incidence the phase difference is 0. The constant factor $e^{\gamma L}$, determined from the incident wave by Eq. (4), is therefore equal to 1 in this case. These figures therefore show the deviation in the actual structure from this assumption. At high frequencies, such as in Fig. 3, the deviation is generally small except at the edges of the structure. At low frequencies, such as in Fig. 2, the deviation is higher throughout the entire panel because the size of the panel in relation to the wavelength is smaller and edge effects become more important. In these cases, the deviation can be as high as 10° in the middle of the panel. The effect of the deviations in the phase of the surface pressure on the prediction of the exterior far-field sound field is, however, small, as can be seen in the far-field polar responses in Figs. 4 and 5 for a receiver at far field (100 m). The dB values of the scattered pressure shown in these and subsequent figures are normalized to the incident pressure at 0°. The periodic and full structure predictions agree well. This is not surprising since, at normal incidence, the excitation is identical over each period. Therefore both the structure and the excitation are periodic with the same period. The surface pressure over each period should therefore be the same except for the variation created by the

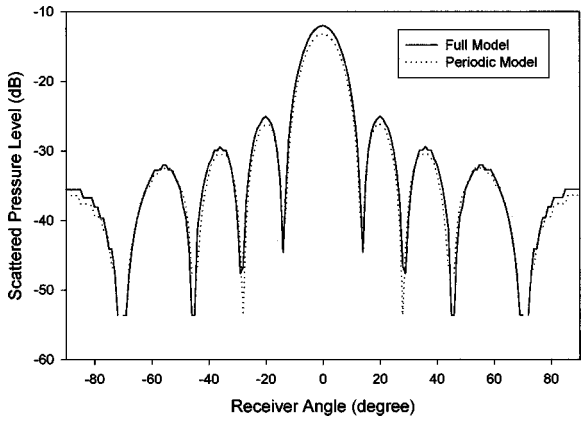

FIG. 4. Predicted far-field polar responses. Normal incidence plane wave at 630 Hz.

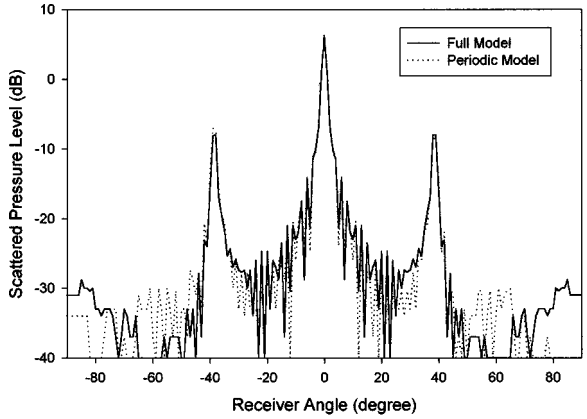

FIG. 5. Predicted far-field polar responses. Normal incidence plane wave at 5000 Hz.

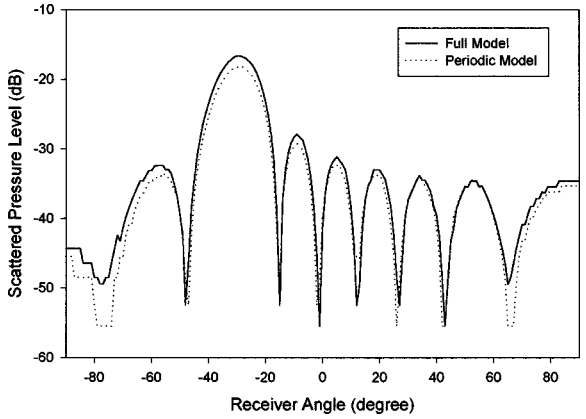

FIG. 7. Predicted far-field polar responses. 30° incidence plane wave at 630 Hz.

finite-size edge diffraction effect. The assumption of the periodic formulation is mostly satisfied with $e^{\gamma L}=1$. The periodic prediction should therefore agree with the full structure prediction, as is indeed the case.

The next set of results shows the surface pressure relationship between periods for a plane-wave incidence at 30° to the normal. At oblique incidence, the excitation created by the incident wave no longer has the same period as that of the structure. There is a constant phase shift in the incident wave at points that are exactly one structural period apart. The assumption that the surface pressures at periodic points are related by the same constant factor as that of the incident wave can be further tested in this result.

Figure 6 shows the total surface pressure and incident pressure relationships between periodic points. They are very similar to the normal incidence case except that the phase difference is now shifted from zero. Again the deviation from the incident pressure relationship is generally small. The agreement between the polar response predicted by the periodic formulation and that by the full structure model is also very good, as can be seen in Fig. 7. This result strongly suggests that the relationship of the incident wave over successive periods can be used successfully to represent the relationship between the surface pressure, at least in the case of plane-wave incidence.

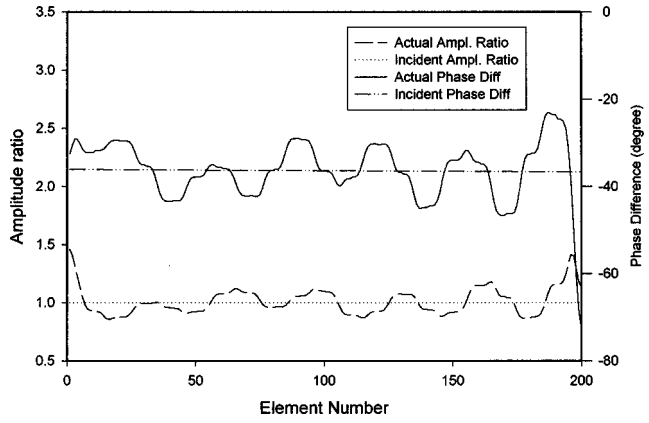

FIG. 6. Relationship between points one period apart. 30° incidence plane wave at 630 Hz. The amplitude ratios and phase differences are calculated according to Eq. (8).

The periodic formulation is also successful in the prediction of near-field polar responses. Figure 8 shows the case with a receiver at 1-m radius. The periodic prediction agrees very well with that predicted by the full integral formulation. An under-prediction of 1–2 dB in the sound-pressure level is seen in this case. Generally both over- and under-predictions occur in other cases and the error margins are similar to that observed here.

III. NEAR-FIELD SOURCE AND EXPERIMENTAL RESULTS

When the source is located in the near field of the surface, the incident wave is no longer a plane wave. In the two-dimensional case, the wave will be cylindrical and an additional phase and amplitude variation will be introduced by the cylindrical curvature, as can be seen in Fig. 9, which shows the general source, receiver, and object geometries of a near-field configuration used in this study. In this case, the incident pressure is no longer related by a constant factor at periodic points on the surface. Under such circumstances, the simple assumption of a constant relating factor for the surface pressure cannot hold; see Fig. 10, which shows the amplitude and phase relationship between successive periodic points on the 21 half-cylinder structure with the source at 2 m, normal incidence. The periodic formulation using this assumption produces significant errors in the calculation of

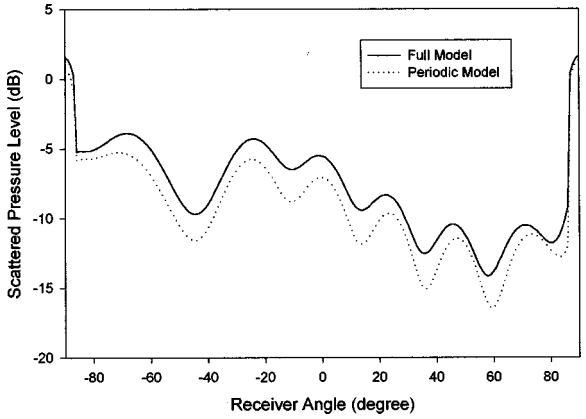

FIG. 8. Predicted near-field polar responses. 30° incidence plane wave at 630 Hz.

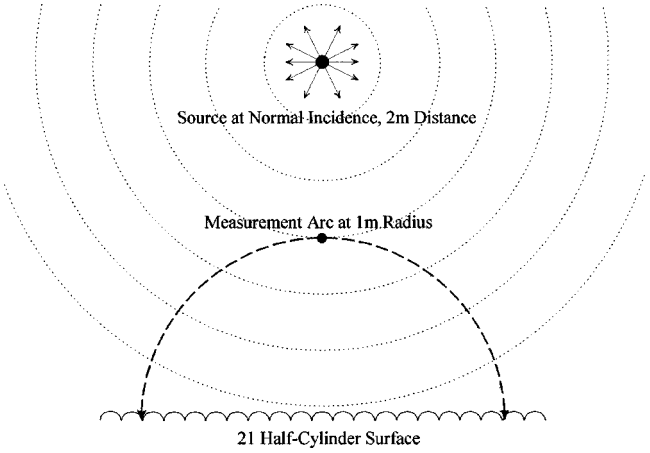

FIG. 9. Source, receiver, and scattering surface geometries for the near-field study.

the external pressure, as shown clearly in Figs. 11 and 12 for 0 and 30° incidence, respectively. The data predicted by this constant factor periodic formulation are labeled ''Constant Periodic'' in the figures. As can be seen, its predictions of the shapes of the polar responses, especially in the 30° case, are not in agreement with those predicted by the full structure model. Given the large deviation of the surface pressure phase factor from a constant factor, as shown in Fig. 10, this is hardly surprising.

The near-field source configuration is nevertheless an important case to consider since most laboratory measurements of large surfaces, due to limitation in space, will have the source not too far from the surface. The experimental setup, which produced the measured results shown in Figs. 11 and 12, and later figures, has the source at a radius of 2 m from the surface and a receiver radius of 1 m. Even at the lowest measuring frequency of 630 Hz, the 2-m source radius is less than the minimum far-field distance of 2.7 m, estimated from the usual formula of $W^2/4\lambda$,[8] where W is the total width of the surface, which is equal to 21×0.115 m in this case. To deal with this problem, we observe from Fig. 10 that, although the phase factor is not a constant, it follows almost exactly the phase shift of the incident pressure. This agrees with our assumption of weak nonimage scattering,

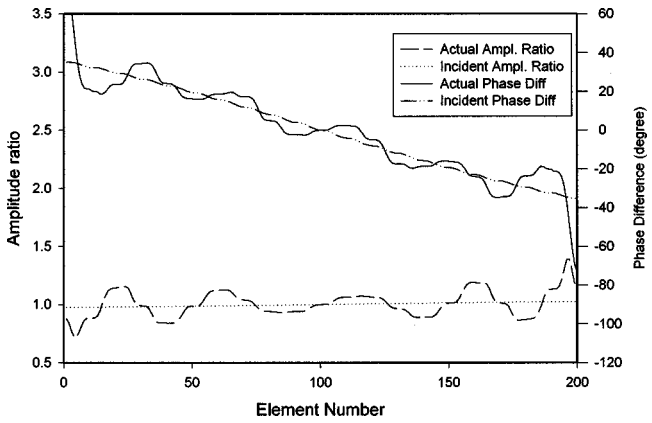

FIG. 10. Relationship between points one period apart. Near-field normal incidence at 630 Hz. The amplitude ratios and phase differences are calculated according to Eq. (8).

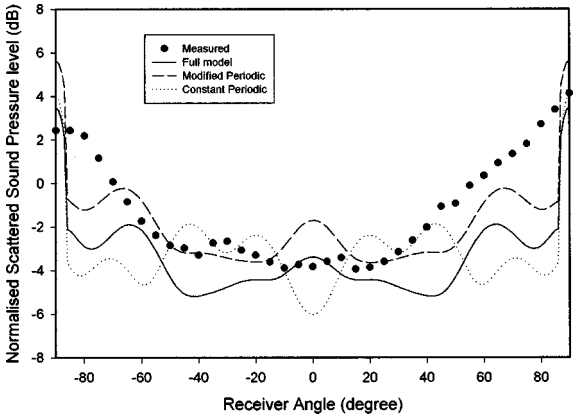

FIG. 11. 1/3-octave near-field polar responses at 1 m at 630 Hz. Near-field source at 2 m, normal incidence.

that the surface pressure relationship between successive periodic points is imposed predominantly by the incident field. It seems therefore appropriate to modify the constant factor periodic formulation by introducing a variable factor that is determined by the incident field at the points of interest. The surface integral equation (6) is modified accordingly, to give

$$\int_{S_{01}}\left[(p(\mathbf{r}_{0q1})-p(\mathbf{r}_{0q2}))\sum_{i=-\infty}^{\infty}\Lambda_{0i}\,\frac{\partial^2 G(\mathbf{r}_{0p}|\mathbf{r}_{iq})}{\partial\mathbf{n}_{0q}\partial\mathbf{n}_{0p}}\right]dS$$

$$=-\frac{\partial p_{\mathrm{inc}}(\mathbf{r}_{0p})}{\partial\mathbf{n}_{0p}}, \tag{9}$$

where

$$\Lambda_{0i}=\frac{p_{\mathrm{inc}}(\mathbf{r}_{iq})}{p_{\mathrm{inc}}(\mathbf{r}_{0q})}$$

and the integral equation (7) for the exterior pressure is similarly modified by replacing the factor $e^{i\gamma L}$ by the factor Λ_{oi}.

The result of applying this modification can be seen in Figs. 11 and 12. The data labeled ''Modified Periodic'' are predicted by this modified periodic formulation. The improvement in the prediction is obvious. The shapes of the polar scattered patterns predicted by the modified formulation are almost identical to those predicted by the full model, although there is a shift in the absolute amplitude of about 2 dB in the normal incidence case.

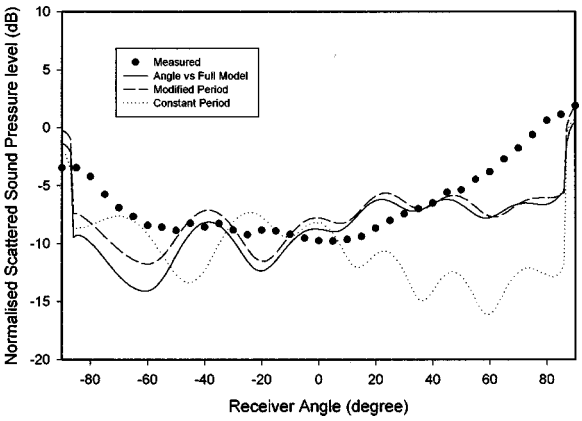

FIG. 12. 1/3-octave near-field polar responses at 1 m at 630 Hz. Near-field source at 2 m, 30° incidence.

The measured data shown in the figures were obtained by RRG Diffusor Systems, Inc., using an array of microphones located at a 1-m radius and separated at 5° intervals. The scattering surface was laid on a hard baffle and measurements were performed in 1/3-octave frequency bands. The polar scattering with the scattering sample in place and with no scattering sample (the background measurement) were measured. The background data were then subtracted from the scattering data to remove the direct sound and the room effect. The fast Fourier transform (FFT) of this response was divided by the 1/distance scaled loudspeaker response, which is measured 37 times with the loudspeaker in the scattering sample position on axis to each microphone. The deconvolved scattered data were then windowed to isolate them from any remaining interference. The subtraction and deconvolution procedure, however, introduces residue noise into the data. Measured data are therefore less reliable when the scattered energy is low (at receiver angles far away from the geometrical reflection angles), and also when the microphone is close to the surface or baffle (at large receiver angles). In most cases this affects the measured data at (absolute) receiver angles greater than 60°.

To allow comparisons in 1/3-octave bands, predictions were made at five single frequencies in each 1/3-octave band at logarithmically equal intervals. The scattered pressures were then energy averaged to give the 1/3-octave results. The use of five frequency points for the averaging was enough to smooth out most of the single-frequency specific interferences.

Unfortunately, precise information on the normalization used to generate the measured data was not clear and we cannot compare directly the absolute amplitudes of the predicted and measured scattering patterns. Nevertheless, the shapes of the patterns can be compared. This is not a serious problem in our work, since ultimately the shape of the scattering pattern is what characterizes the distribution of the scattered energy and hence the diffusion performance of the surface. In Figs. 11 and 12, and subsequent figures that show the measured data, the absolute amplitudes of the predicted scattering patterns are, as before, normalized to the incident pressure at 0°. The measured polar patterns are referenced to give dB values similar to the predicted patterns at 0°. However, since this normalization of the measured data is not precisely the same as the predictions, the measured data should not be used to judge the relative accuracy in the *amplitudes* of the predictions. For example, both the modified and the constant periodic predictions may seem to have better agreement with the measured data in terms of amplitude than the full model within the angular ranges of -50 to $-10°$ and 10 to 40° in Fig. 11, but this is purely because the measured data were normalized to give a similar amplitude at exactly 0° to that predicted by the full model. If the normalization were changed to shift the measured data down by 2 dB, then the full model data would have far better agreement with the measured data. The result in Fig. 12 is more clear-cut. The modified periodic and the full model predictions clearly agree well with each other and have much better agreement with the measured data than the constant periodic model.

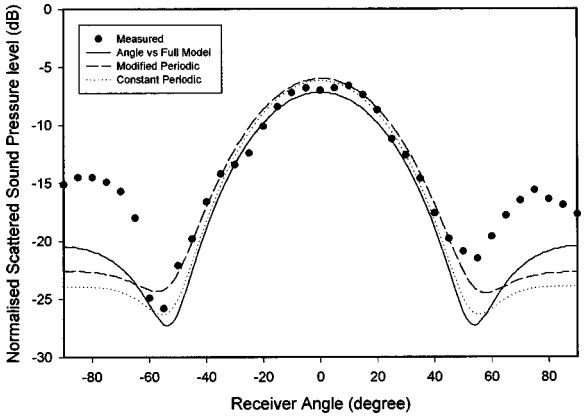

FIG. 13. 1/3-octave polar response of a surface with six half-cylinders at 630 Hz, normal incidence.

Overall, the predicted scattering patterns agree fairly well with the measured results except at near grazing angles when the receiver is close to the surface.

A second, smaller scattering surface with six periodic half-cylinders was also measured. The experimental setup is again the same as that for the 21-cylinder surface: the source is at 2-m normal incidence and the receivers are at 1-m radius. With this smaller surface, the estimated minimum far-field distance is 1.7 m at 5000 Hz, and the source is therefore in the far field even at 5000 Hz. The receiver distance, however, changes from near to far field depending on the frequency and angle. The purpose of this test is to determine if the periodic formulation can adequately model structures that have only a small number of periods and therefore have stronger influence from the edges.

Figures 13 and 14 show the predicted and measured scattering patterns at 630 and 5000 Hz, respectively. The agreement between both predictions and measurement is very good at the lower frequency when the source is well in the far field. At the higher frequency, the agreement is good near the main scattering beam from about -30 to 30°. Significant deviations develop at higher scattering angles where the scattering energy is low. Surprisingly, the modified periodic formulation agrees slightly better with the measurement at these angles than the full structure model. This is, however, more likely to be caused by the background or residue

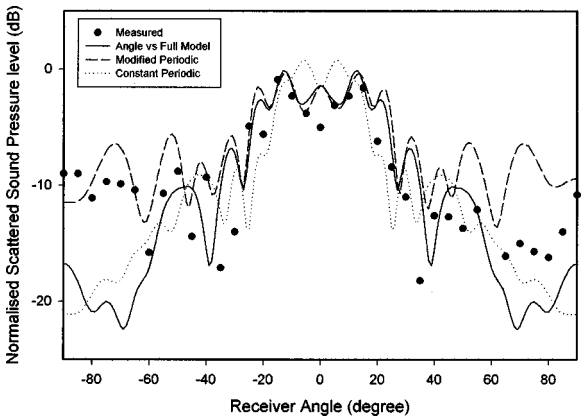

FIG. 14. 1/3-octave polar response of a surface with six half-cylinders at 5000 Hz, normal incidence.

TABLE I. Diffusion coefficients calculated from predicted polar responses of the surface with 21 half-cylinders. Plane wave incidence.

	Normal incidence receivers 100 m		30° incidence receivers 100 m		30° incidence receivers 1 m	
Frequency (Hz)	Full	Periodic	Full	Periodic	Full	Periodic
630	0.23	0.23	0.26	0.28	0.71	0.65
1250	0.16	0.19	0.18	0.22	0.79	0.76
2500	0.29	0.16	0.19	0.21	0.73	0.75
5000	0.13	0.13	0.16	0.19	0.71	0.70

noise in the measurement that was discussed earlier.

Interestingly, in Fig. 14, both the full model and the less accurate constant periodic model predicted large interference dips in the scattering pattern while the modified periodic model did not. It should, however, be noted that the surface under investigation here has only six periods. With such a small number of periods, edge diffractions will have a significant effect on the accuracy of both periodic formulations. Within the main scattering beam, from about -30 to 30°, the modified periodic model still has much better accuracy than the constant periodic model and agrees very well with the full model. At larger angles both periodic models are significantly affected by the edge effect and are both in error. Results from all the frequencies tested on this surface indicated that the modified model has a slight tendency to predict less sharp interference dips than the full model, but the difference is generally not as large as that shown in Fig. 14. Figure 13 is a more typical result.

IV. DIFFUSION COEFFICIENTS

As mentioned earlier in the Introduction, it is desirable to be able to calculate from the polar pattern a single figure coefficient, which one may call the diffusion coefficient, to describe the diffusion performance of a surface. A number of procedures for such a coefficient have been proposed in the past but all have certain difficulties which need to be resolved.[9,10] There are yet no universally accepted definitions for the diffusion coefficient, although efforts are being made to develop one.[1,2] Here we choose a simple procedure to calculate a diffusion coefficient from the polar response as a means of investigating the accuracy of the prediction methods in determining a single figure coefficient. The physical meaning of the chosen coefficient is based on the angular energy distribution and is considered sufficient to give an adequate representation of the diffusion performance.

The calculation is again based on the two-dimensional approach. Let the energy at each polar receiver angle be E_i, and the total energy summing over all the receiver angles be E_T, then an indication of how the scattering pattern deviates from an ideal uniform scattering can be calculated as

$$d=1-\frac{\Sigma_i^N|(E_i-E_T/N)|}{E_T}, \tag{10}$$

where N is the total number of receivers positioned at a constant angular interval $\Delta\theta$. This will give a value of 1 for a uniform scattering field. However, when the field is totally specular, i.e., the energy is concentrated within a specular angle range $\theta_s=n_s\cdot\Delta\theta$ such that $E_i=E_s$ within θ_s, but otherwise is equal to 0, then the total energy $E_T=E_s\cdot n_s$ and the equation gives

$$d=1-\frac{n_s(E_s-n_sE_s/N)+(1-n_s)(n_sE_s/N)}{n_sE_s}$$

$$=1-2\left(1-\frac{n_s}{N}\right), \tag{11}$$

which is negative when the specular angle is smaller than $N/2$. To obtain a coefficient that gives a value of 0 for totally specular reflection, one can normalize the summation term of the equation by the factor indicated by the totally specular case,

$$d=1-\frac{\Sigma_i^N|(E_i-E_T/N)|}{E_T2(1-n_s/N)}. \tag{12}$$

This definition works well in the far field when the specular angle range is small. In the near field it will work if the specular energy is uniformly distributed over the specular angle range. Unfortunately, in practice this is seldom the case and the normalization gives rise to negative values when n_s is large. To avoid this complication, we choose to remove the $(1-n_s/N)$ term from the normalization, so that

$$d=1-\frac{\Sigma_i^N|(E_i-E_T/N)|}{2E_T}. \tag{13}$$

The result will be similar to that using the full normalization in the far field when the specular angle range is small. In the near field the specular angle range is large and the scattering pattern is ''flatter'' than in the far field. Without the $(1-n_s/N)$ term in the normalization, the value of d will always be larger in the near field. The coefficient is bound between 0 and 1.

Using the above definition, the diffusion coefficients of the 6- and 21-cylinder surfaces were calculated from the polar responses. The result is summarized in Tables I and II. The modified periodic formulation was used to calculate the coefficients in the columns labeled ''Periodic.''

The results are consistent with the findings on the polar responses. With plane-wave incidence, the periodic formulation and the full structure model results are very similar. The changes in the values of the diffusion coefficient with the source and receiver configurations agree particularly well.

Measured data were only available in the near field (Table II). Even here the two predictions generally agree well with each other, and their diffusion coefficient values

TABLE II. Diffusion coefficients calculated from predicted and measured near-field polar responses. Source at 2 m and receivers at 1 m.

	6 Half-cylinders Normal incidence				21 Half-cylinders Normal incidence				21 Half-cylinders 30° incidence			
Frequency (Hz)	Measured	Full	Periodic	Constant	Measured	Full	Periodic	Constant	Measured	Full	Periodic	Constant
630	0.55	0.46	0.45	0.43	0.73	0.86	0.71	0.84	0.63	0.78	0.77	0.68
1250	0.46	0.42	0.44	0.36	0.78	0.90	0.84	0.89	0.80	0.75	0.80	0.77
2500	0.39	0.56	0.62	0.54	0.76	0.67	0.67	0.88	0.59	0.68	0.67	0.75
5000	0.54	0.42	0.60	0.36	0.78	0.74	0.68	0.82	0.80	0.64	0.62	0.72

are also close to those calculated from the measured responses. The trend of variations in the coefficient is again well predicted. As expected, the value of the coefficient increases as the receiver moves into the near field of the surfaces. The differences between the predicted and measured values are generally within 0.15 and in most cases less than 0.1. Even in cases where the deviation is high (e.g., in the six-cylinder results), the corresponding polar responses do not seem to be significantly different (Figs. 13 and 14) except at large scattering angles where the scattered energy is low. Overall the coefficients calculated from the modified periodic formulation are as accurate as those calculated from the full model prediction in both the near and far fields and for both the small and large periodic surfaces.

Also shown under the columns labeled ''Constant'' in Table II are the coefficients calculated by the constant periodic model. Generally the constant periodic model shows slightly larger deviations from the full model and measurements than the modified model. Its prediction of the frequency dependence of the coefficient in the 21-cylinder case is also poor.

V. CONCLUSIONS

A boundary element method formulation that uses the periodic property of a structure has been developed. The formulation is based on the assumption that the surface pressure at two points exactly one period apart on a periodic structure is related by a factor that can be determined from the incident sound field. For plane-wave incidence, the factor is constant and is given by the phase shift between the incident pressure at the two periodic points. When the source is in the near field, the factor is not constant but can still be calculated from the individual ratio of the incident pressure at each pair of periodic points. This formulation has been shown to have an accuracy similar to that obtained by modeling the full structure in the prediction of the near- and far-field scattering patterns of both large and small periodic structures, except at scattering angles where the scattered energy is low. The prediction also compares well with measurements.

The predicted and measured scattering patterns were used to calculate a coefficient that can be used to describe the scattering performance of a surface. Again the agreement between the coefficients calculated from predictions and measurements is good. The trend of variations is particularly well predicted. The deviations in the absolute values are mostly within 0.1. However, further work is required to judge the significance of such a difference in values.

The multiple half-cylinder surfaces used in this study are smooth except at the joints between cylinders. In other scattering surfaces such as the quadratic residue diffusers (QRDs), there can be more sharp edges on the surface. Diffractions from these sharp edges may affect the weak non-image scattering assumption that is essential to the periodic formulation. An indication of the validity of applying the assumption to QRDs can be obtained from the work of Cox and Lam.[3] It was shown in their work that the scattering surface of a QRD can be represented satisfactorily by a flat surface with variable admittance in a boundary element model. The admittance of a well can be derived simply from the phase change of plane waves propagating up and down the well. This suggests that diffractions from the well edges can be ignored. One should therefore be able to apply the periodic formulation to a series of QRDs with each QRD modeled as a flat surface with variable admittance. Further work is required to confirm this suggestion.

ACKNOWLEDGMENTS

The author wishes to thank Dr. P. Antonio of RRG Diffusor Systems Inc. for providing the measurement data on the two periodic surfaces. This work is funded by the UK's Engineering and Physical Science Research Council under Grant No. L13124.

[1] P. D'Antonio, ''The disc project: Directional scattering coefficient determination and auralization of virtual environments,'' *Proceedings of NoiseCon 93* (1993), pp. 259–264.
[2] T. J. Hargreaves, T. J. Cox, Y. W. Lam, and P. D'Antonio, ''Diffusion parameters for auditorium surfaces,'' Proceedings of Institute of Acoustics (UK) **19**, 19–27 (1997).
[3] T. J. Cox and Y. W. Lam, ''Prediction and evaluation of the scattering from quadratic residue diffusers,'' J. Acoust. Soc. Am. **95**, 297–305 (1994).
[4] T. Terai, ''On calculation of sound fields around three dimensional objects by integral equation methods,'' J. Sound Vib. **69**, 71–100 (1980).
[5] A. F. Seybert, B. Soenarko, F. J. Rizzo, and D. J. Shippy, ''A special integral equation formulation for acoustic radiation and scattering for axisymmetric bodies and boundary conditions,'' J. Acoust. Soc. Am. **80**, 1241–1247 (1986).
[6] M. A. Heckl, ''Acoustic optimisation of profiled cladding of buildings,'' Proceedings of Institute of Acoustics (UK) **15**, 267–274 (1993).
[7] F. Bloch, ''Uber die Quantenmechanik der Elektronen in Kristallgittern,'' Z. Phys. **52**, 555–600 (1928).
[8] L. E. Kinsler, A. R. Frey, A. B. Coppens, and J. V. Sanders, *Fundamentals of Acoustics* (Wiley, New York, 1982), 3rd ed. Eq. (8.58), p. 188.
[9] J. Angus, A. C. Marvin, J. Clegg, and J. F. Dawson, ''A practical metric for evaluating sound diffusers,'' *Proceedings of 98th Audio Engineering Society Convention*, preprint 3955 (D5) (1995).
[10] T. J. Cox, ''Diffusion parameters for baffled diffusers,'' *Proceedings of 99th Audio Engineering Society Convention* (1995).

Insights into linear and nonlinear cochlear transduction: Application of a new system-identification procedure on transient-evoked otoacoustic emissions data[a)]

Geetha Krishnan[b)]
Department of Computer Science, Carnegie Mellon University, Pittsburgh, Pennsylvania 15213

Mark E. Chertoff
Department of Hearing and Speech, University of Kansas Medical Center, School of Allied Health, Kansas City, Kansas

(Received 7 July 1997; revised 23 September 1998; accepted 25 September 1998)

Transient-evoked otoacoustic emissions (TEOAE) were used to characterize linear and nonlinear cochlear transduction using a new system-identification procedure. In this technique, a computational model of the system is first developed. From the measured stimulus and response records, spectral-density functions and multiple coherence functions are calculated. The coherence functions allow the characterization of linear/nonlinear processes as a function of frequency. Summations of linear and nonlinear coherences provide a goodness-of-fit of the chosen model. Finite impulse response pulses with a bandwidth of 1–8 kHz were used to evoke otoacoustic emissions. Eleven adults with normal hearing served as subjects. Third- and fifth-order polynomial models were used to model the data, and the results indicate that the fifth-order model is a better fit to the TEOAE data. The results of this study suggest that this system-identification procedure can be successfully applied to model cochlear transduction using a broadband stimulus. Most importantly, coherence functions provide useful insights into linear and nonlinear cochlear processes and have the potential to be developed as a clinical measure for monitoring changes in cochlear status. [S0001-4966(99)03101-X]

PACS numbers: 43.64.Bt, 43.64.Jb, 43.64.Ri [RDF]

INTRODUCTION

The auditory system, like most biological systems, is nonlinear. The nature of auditory nonlinearities has been examined at various levels of the auditory system using a variety of approaches. One approach has been to examine distortion products or combination tones generated in the cochlea when stimulated with a two-tone complex signal. The most easily detected and well-studied combination tones are distortion products of the form $2f1-f2$, and $f2-f1$, where $f1$ and $f2$ are frequencies of the primary tones of a two-tone complex, with $f1<f2$. Distortion products have been examined in cochlear microphonics (Dallos, 1973), in the nerve discharges of the auditory-nerve fibers (Goldstein and Kiang, 1968), from basilar-membrane vibrations (Robles *et al.*, 1991), and more recently, using evoked otoacoustic emissions recorded from the outer ear canal (Kemp, 1979; Probst *et al.*, 1991).

Evoked otoacoustic emissions are acoustic energy generated in the cochlea in response to acoustic stimulation and are measured from the ear canal of humans and animals. Acoustic distortion products evoked using a two-tone complex stimulus, also known as distortion-product otoacoustic emissions (DPOAE), have provided strong evidence for the existence of nonlinear active mechanical processes in the cochlea (Kemp, 1979; Kim *et al.*, 1980). Emissions evoked with a transient, such as a click, also exhibit nonlinear behavior (Kemp, 1978), which is evident from the nonlinear growth of the input/output (I/O), function. Numerous studies have since linked the outer-hair cells (OHC) of the cochlea as the source of the active nonlinear processes that generate otoacoustic emissions (Mountain, 1980; Zurek *et al.*, 1982; Brownell, 1983; Lonsbury-Martin *et al.*, 1987; Brown *et al.*, 1989; Veuillet *et al.*, 1991; Moulin *et al.*, 1993).

In recent years, DPOAE amplitude and I/O growth functions have been used to examine nonlinear processes of the cochlea. Although DPOAE I/O functions can provide information about cochlear transduction, they are difficult to interpret because they vary as a function of such factors as $f2/f1$ ratio, primary level of the stimuli, and primary frequency, even in normal-hearing subjects (Nelson and Kimberley, 1992; Lasky *et al.*, 1994). Therefore, to completely characterize cochlear transduction for all frequencies at once, or to monitor changes in its nonlinear processes, it would be necessary to obtain I/O functions for DPOAEs over a multitude of stimulus parameters. A technique that could characterize the properties of the transduction process for all frequencies of interest would provide new insights into the linear and nonlinear processes of signal transduction in the cochlea.

A recent development in the field of random data analysis is a linear/nonlinear system-identification technique (Bendat, 1990) that is well suited for characterizing nonlinear systems, such as cochlear transduction, using a broadband

[a)]Presented in part at the Third Joint Meeting of the Acoustical Society of America and Acoustical Society of Japan, Honolulu, Hawaii, Dec. 1996 [J. Acoust Soc. Am. **100**, 2628(A) (1996)].
[b)]Electronic mail: geetha@cs.cmu.edu

input. In this system-identification technique, a computational model of the system consisting of nonlinear elements in series with unknown linear filters is first developed. From the measured input and output data, spectral-density functions and multiple coherence functions are calculated. The cumulative coherence functions provide a goodness-of-fit of the model to the data. The coherence functions may be further examined to characterize linear/nonlinear processing as a function of frequency. Filters that optimally characterize the nonlinear system are calculated using statistical techniques related to regression analysis. The identification of the system can be accomplished using either Gaussian or transient signals, and is performed in the frequency domain.

There are several advantages to applying this system-identification technique to nonlinear systems. First, as the analysis is done in the frequency domain, the results are presented as single-dimensional functions of frequencies that are easier to interpret than the multidimensional results of the time-domain, kernel-based approaches (Wickesberg *et al.*, 1984; Wickesberg and Geisler, 1984; Shi and Hecox, 1991; Dijk *et al.*, 1993). The potential for developing this technique into a clinical diagnostic procedure lies in the advantage that the outputs from this procedure are functions of frequency that are easy to interpret.

Second, with this technique, nonlinear systems may be modeled as arbitrary linear systems in parallel with arbitrary nonlinear systems. Any number of nonlinear paths may be in parallel with the linear system. This flexibility in the use of numerous nonlinear paths allows us to approximate system nonlinearities using polynomial equations of any order. This is important because accurate modeling of the nonlinear properties of cochlear transduction will require polynomials greater than third order (Weiss and Leong, 1985). Furthermore, this procedure yields *uncorrelated* outputs from the different paths in the model. From these uncorrelated outputs, coherence measures can be computed which reveal the relative contributions of energy from the various nonlinear paths to the overall response, e.g., otoacoustic emissions. In contrast, kernel-based approaches are computationally complex for orders higher than two, and kernels of consecutive orders are not mutually independent (Shi and Hecox, 1991). Finally and most importantly, a broadband signal, such as a transient signal, can be used as input to the cochlea. This allows stimulation of the entire length of the cochlea simultaneously, providing us with a complete characterization of the cochlea. It has been shown that emissions evoked with a transient, such as a click, have nonlinear I/O growth function (Kemp, 1978). However, the nonlinearities in transient-evoked emissions have not been characterized, mainly due to the lack of analytical techniques that are computationally manageable. The coherence functions obtained from this procedure may be used to characterize the nonlinear components of TEOAE. Besides, we need to have a better understanding of the responses of the cochlea to other types of signals, such as noise and clicks. As de Boer (1993) has rightly stated, ''There is no reason why the field of nonlinear studies cannot be extended to encompass other phenomena or other cases such as noise or click responses.''

The chief goal of this study is to determine the feasibility of using this system-identification technique to describe the relationship between the input: a transient signal, and the output: evoked otoacoustic emissions. Bendat's system-identification technique has been used to characterize the auditory system of Mongolian gerbils using cochlear microphonic data (Chertoff *et al.*, 1994; Chertoff *et al.*, 1996).

The goals of this study were to demonstrate the applicability of this system-identification technique to study cochlear processing to broadband input. Specifically, the linear and nonlinear components of TEOAEs will be studied using coherence measures.

I. SYSTEM-IDENTIFICATION PROCEDURE

A. Goals and procedure

The primary goal in system identification is to decipher the properties of an unknown system given the input and output measured from the system. The first step is to model the unknown system based on reasonable assumptions about the system and its nonlinear components. One such model is illustrated in Fig. 1(a). This is a single input/single output system with a linear system in parallel with finite-memory nonlinear systems. a_1, a_2, and $a_3 \ldots a_n$ are linear filters and $g_2[x(t)]$ and $g_3[x(t)] \cdots g_n[x(t)] \cdots$ are zero-memory nonlinear systems. The cascade of a zero-memory nonlinearity and a linear filter results in a more general class of nonlinearities, called a finite-memory nonlinearity.

For our purpose we defined a third-order polynomial model where the $g_2(x)$ and $g_3(x)$ were defined to be a squarer and a cuber followed by filters, a_2 and a_3, respectively. In the frequency-domain representation, $X_1(f)$, $X_2(f)$, and $X_3(f)$ are the Fourier transforms of $x(t)$, $x^2(t)$, and $x^3(t)$, respectively. This frequency-domain representation can be extended to any arbitrary number of $g_n[x(t)]$ as $X_n(f)$ followed by the corresponding $A_n(f)$. The fifth-order polynomial model is an extension of the third-order model, with a fourth-order and fifth-order zero-memory nonlinear systems which are in series with corresponding filters. The nonlinear model shown in Fig. 1(a) can be replaced by multi-input/single-output model and represented in the frequency domain as shown in Fig. 1(b). The derivation of frequency-domain formulas and the demonstration of the equivalence of single-input/single-output models to multiple-input/single-output models are presented in detail in Bendat (1990) and will not be dealt with here. Figure 1(b) shows the representation of the *n*-th order polynomial model as multi-input/single-output model in the frequency domain. Capitalized variables, $X_1(f), X_2(f), X_2(f), \ldots, X_n(f)$; $A_1(f), A_2(f), A_3(f), \ldots, A_n(f)$; $Y_1(f)$, $Y_2(f)$; $Y_3(f), \ldots, Y_n(f)$; $Y(f)$ and $N(f)$ are Fourier transforms of their associated time-domain waveforms, $x(t), x^2(t), x^3(t), \ldots, x^n(t)$; $y_1(t), y_2(t), y_3(t), \ldots, y_n(t)$; $y(t)$ and $n(t)$, respectively. The inputs from the different paths are correlated. The purpose of the analysis is to estimate the unknown systems, $A_1(f), A_2(f), A_3(f), \ldots, A_n(f)$. The system properties are estimated from simultaneous measurements of the input, $X(f)$ and output, $Y(f)$, so that the noise term, $N(f)$ is minimized. The term $N(f)$ accounts for the joint effects of measurement noise and modeling error. The estimation of the A filters requires the calcu-

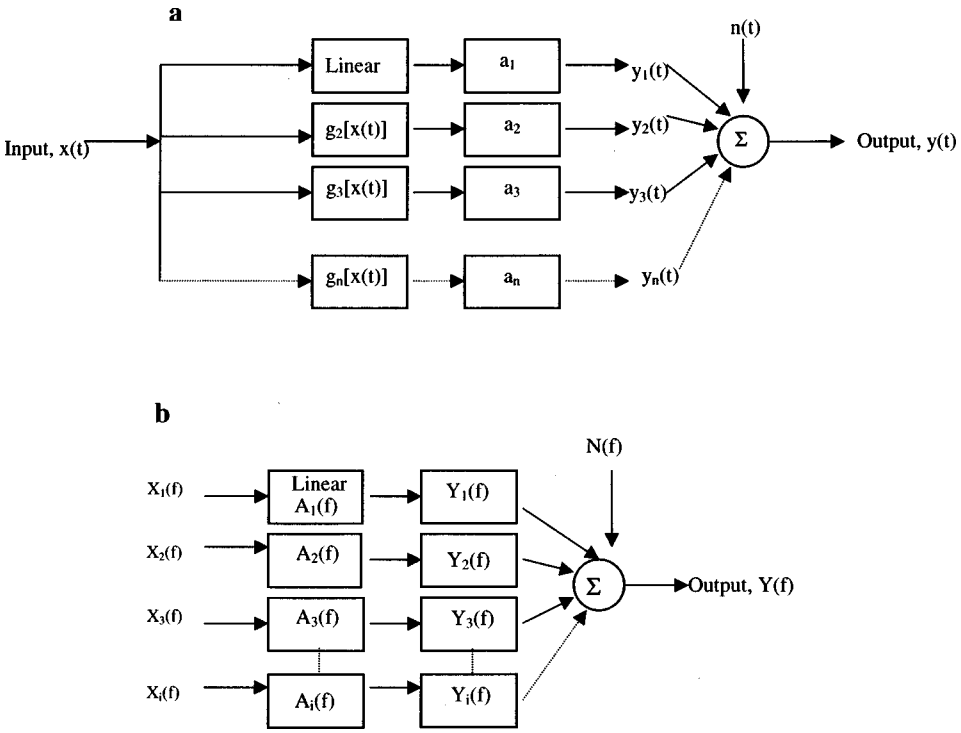

FIG. 1. (a) A time-domain model of a single-input/single-output system with a linear system in parallel with a finite memory nonlinear system. The linear filters are represented by $a_1, a_2, a_3, \ldots, a_n$. The zero-memory nonlinear systems are represented by $g_2[x(t)]$ and $g_3[x(t)]\cdots g_i[x(t)]$. $y_1(t), y_2(t), y_3(t), \ldots, y_n(t)$ are outputs from the different paths. $Y(t)$ is the summated output and $n(t)$ represents the noise term. (b) A frequency-domain model of a multi-input/single-output model which is equivalent to the single-input/single-output model shown in Fig. 1(a). The terms, $X_1(f), X_2(f), X_3(f), \ldots, X_n(f)$ are the spectrum of respective time-domain signals for the different paths. $A_1(f), A_2(f), A_3(f), \ldots, A_n(f)$ are the corresponding filters in the frequency domain. $Y_1(f), Y_2(f), Y_3(f), \ldots, Y_n(f)$ are the output spectra from the different paths. $Y(f)$ is the summated output spectrum of the system. $N(f)$ is the noise spectrum.

lation of autospectral (S_{xx}, S_{yy}) and cross-spectral (S_{xy}) density functions between inputs and outputs of the various paths. The next step is to uncorrelate the multiple inputs by using an ordered set of ''conditioned,'' or what are known statistically as ''residual,'' input records. Coherence measures, $\gamma^2_{u_i y}(f)$, are then computed from the uncorrelated input and the output spectral-density functions. It is important to understand that the coherence measures have been computed after uncorrelating the multiple inputs. This means, for example, that the third-order coherence is an indicator of how much of the output can be explained by the third-order path after subtracting the effects of the first- and second-order path. Thus, the third-order coherence function reflects only third-order distortions ($2f1-f2$, $2f2-f1$, $3f1$,... etc.) and not lower-order distortion products. To summarize, an *n*th-order polynomial does indeed generate distortion products lower than *n*th order, but an *n*th-order coherence function reflects only *n*th-order distortion products (since the effects of the lower-order distortion products have been subtracted out during the uncorrelation process). This, in fact, is the strength of this procedure as it allows us to use coherence functions as a measure of distortion from the different nonlinear paths. Coherence values lie between 0 and 1, and their magnitude is related to the degree of association between the input of a path and the total output. The coherence functions are summed algebraically to yield a cumulative coherence function that provides a measure of the model's overall goodness-of-fit. The closer the cumulative coherence is to 1, the better the fit. The goodness-of-fit with which the system under consideration can be identified depends largely on the zero-memory nonlinearity one chooses for the model and the amount of noise in the measurements (Bendat, 1990; Bendat and Piersol, 1993). Formulas for calculating spectral-density functions, estimation of *A* filters and coherence functions are not provided here, as they are available in Bendat (1990) and Bendat and Piersol (1993).

B. Selection of models

It is generally agreed that the outer-hair-cell transduction process plays a central role in the generation of cochlear nonlinearities that are observed in evoked otoacoustic emissions (Anderson and Kemp, 1979; Kim, 1980; Kemp, 1982; Zwicker, 1983; Brown, McDowell, and Forge, 1989; Patuzzi *et al.*, 1989). Although the exact nonlinearity is still unknown, researchers are in agreement that the OHC transduction function is a general compressive nonlinearity. Cody and Russell (1987) have shown that the I/O function for OHCs exhibits saturation. The saturation effects may be modeled by the function, x^α with values of α between 0 and 1 (Smoorenburg, 1972). Zwicker (1986), for his ''preprocessing'' model, assumed a power function with an exponent of 0.4 (up to levels of 40 dB SPL).

Simulation experiments were done to test whether or not the polynomial models would adequately model a compressive nonlinearity of the type x^α, where α was set to 0.4. A system composed of the compressive nonlinearity x^α followed by a Butterworth filter with a low-pass cutoff of 4 kHz and a rolloff of 18 dB/octave was simulated. The input, $x(t)$, was an ensemble of 30 records. The input $x(t)$ was passed through the nonlinear system and the corresponding output $y(t)$ was obtained. Both third-order and fifth-order polynomial models were used to analyze the simulated $x(t)$ and $y(t)$. Bendat's procedure was used to identify the filters in the linear and the nonlinear paths. These calculated filters were used to derive the original Butterworth filter that was cascaded with the x^α nonlinearity. The derived Butterworth filters were then compared with the original Butterworth filter to see how well the third- and fifth-order polynomials-

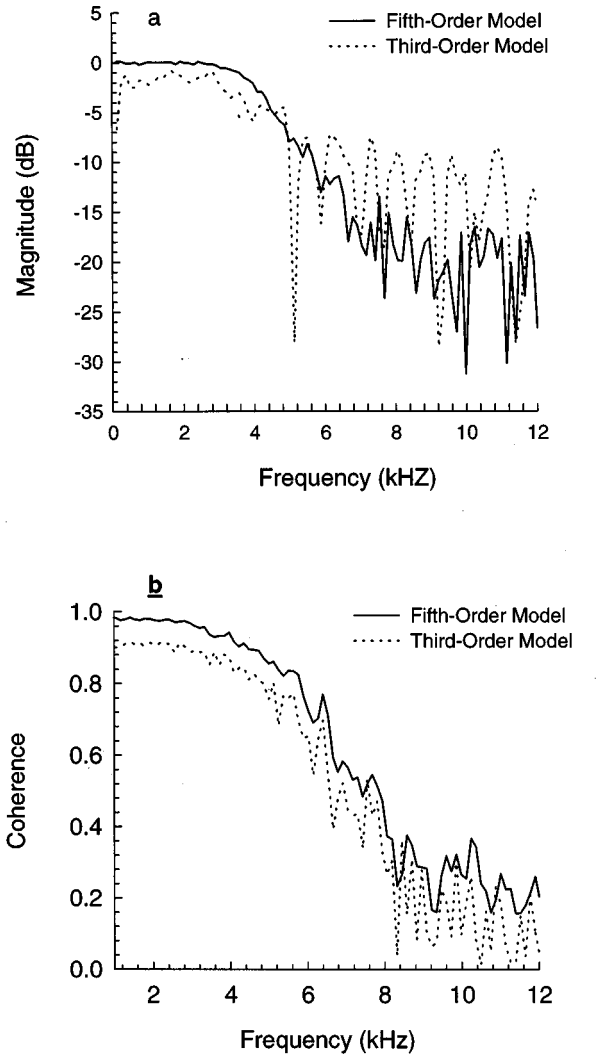

FIG. 2. (a) Estimated filters using the fifth- and third-order polynomial model for the simulation experiment where the x^{α} nonlinearity was low-pass filtered using a Butterworth filter with a 4-kHz cutoff and a rolloff of 18 dB/octave. The dotted line represents the estimated filter from the third-order model and the solid line represents the filter from the fifth-order model. (b) Cumulative coherence function from the third- and fifth-order models for the simulation experiment. The dotted line represents third-order cumulative coherence and the solid line represents fifth-order cumulative coherence.

could model the compressive nonlinearity x^{α}. The filter cutoff and rolloff from the fifth-order model [Fig. 2(a)] corresponded with the actual Butterworth filter, whereas the third-order model estimate did not yield the appropriate cutoff frequency and rolloff of the filter. Furthermore, the cumulative coherence was used to measure the goodness-of-fit of the two models. The cumulative coherence functions from the third-order and the fifth-order polynomial models are shown in Fig. 2(b). There was an increase in mean cumulative coherence, from 89% for the third-order to 96% for the fifth-order model. The increase in coherence, although seemingly small, was accompanied by better approximation of the original filter with the fifth-order polynomial. These results suggest that a compressive nonlinearity of the type x^{α} can be adequately modeled with a polynomial of sufficiently high order.

In a previously reported study, using Bendat's procedure, we modeled TEOAE data using a third-order polynomial function (Krishnan and Chertoff, 1995). In this paper, both third-order and fifth-order polynomial functions are fit to TEOAE data and the results from the two polynomial models are compared. Bendat's technique is not limited to using polynomial models. Any nonlinear function can be used for the $g(x)$ term. However, in this study, polynomials were chosen to model the compressive nonlinearity for two reasons: First, any general nonlinearity such as the power function with an exponent between 0 and 1 can be expanded into a Taylor or Laurent infinite series which converges over a limited range. Therefore, by using a sufficiently high-order polynomial model, we can model any arbitrary nonlinearity over a limited range of input amplitudes. In this study, the range is for input amplitudes up to 92 dB SPL (p–p) which is the peak-to-peak value of the finite impulse response (FIR) pulse used to evoke the emissions. Second, recent studies have found differences in the suppressive effects on odd-order and even-order distortion products in response to ipsilateral and contralateral stimulation to tones and broadband noise. These differences have been attributed to different sources of nonlinearities within the cochlear partition (Kirk and Johnstone, 1993; Chang and Norton, 1997), and more specifically, to the properties of the receptor potentials of the OHCs (Chang and Norton, 1997). The power spectrum of TEOAE of guinea pigs also show changes corresponding to the frequency of the signal used for overstimulation (Ueda *et al.*, 1997). The proposed procedure in this study will allow a detailed examination of the effects of such overstimulation on the linear and nonlinear components of TEOAEs. Our long-term goal is to use coherence measures to examine the effects of drug and noise exposure in animal models and humans. The choice of a polynomial model has some clear advantages in that the changes in the nonlinear coherence functions can be examined for the different orders. This could be potentially used as a clinical and research tool for monitoring the cochlea when normal functioning is disrupted. The coherence functions that are obtained from a polynomial model from the different nonlinear paths provide a measure of proportion of energy from the different nonlinear paths relative to total output. That is, we will be able to examine the contributions of the odd-order and even-order distortions to the output. On the other hand, if a general nonlinear function is used for the $g(x)$ term, we could only obtain the coherence function for the linear path and the nonlinear path. Furthermore, the use of a compressive function requires that we specify values for a number of parameters. For example, if the nonlinearity is modeled with x^{α}, then the model needs to be tested for a range of values of α. If a hyperbolic tangent function is used to model the nonlinearity, then various rectification factors need to be tested. With the use of a polynomial model, the system parameters are derived from the procedure. One disadvantage is that we may need to increase the order of the polynomial model to improve the fit. It should be emphasized that although the approach under investigation is strictly functional, having no structural implications, it will allow us to describe the system transfer characteristics that transform a broadband stimulus into a response.

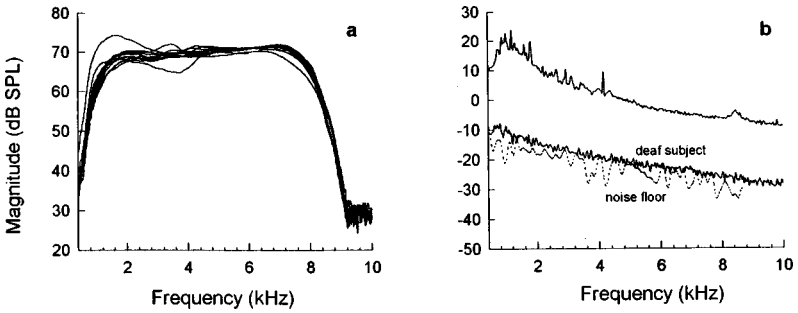

FIG. 3. (a) Input spectral-density function (S_{xx}) for 11 subjects. (b) Mean output spectral-density functions (S_{yy}) averaged across subjects. The bottom-most plot shows the output spectrum for the control subject who is deaf (solid line). The dotted line in the same panel marks the noise floor.

II. GENERAL METHODS

A. Subjects

Eleven normal-hearing adults between the ages of 18 and 40 years served as subjects. Subjects were included in the study if their pure-tone thresholds were 15 dB HL or better for octave frequencies between 250 and 8000 Hz. Tympanograms showed normal middle-ear function. All subjects had a negative history of extreme exposure to noise or use of ototoxic drugs and familial hearing loss. One subject with profound deafness served as a control.

B. Stimulus generation

The transient stimulus for evoking otoacoustic emissions consisted of a band-limited signal (1000 to 8000 Hz) that was generated by a finite impulse response (FIR) filter. The stimulus (2404 points) was generated in MATLAB (The Mathworks, 1993) and uploaded to an array processor (AP2, Tucker-Davis Technologies). The D/A output sampled at 65.536 kHz was sent to an attenuator (PA4, Tucker-Davis technologies) and delivered to a transducer (Knowles BP 1712). The stimulus was measured in each individual ear canal with a microphone (Knowles EK 3133). The signal had a flat frequency spectrum with an overall sound-pressure level of 70 dB across frequencies.

C. Data acquisition

Otoacoustic emissions were recorded with a custom-built probe that housed the transducer and microphone. The output of the microphone was high-passed at 400 Hz (Krohn-Hite) and low-passed at 10 kHz (Stanford, SR560), and amplified with a gain of 10 000 (Stanford, SR560). The amplifier was off for the first 3 ms after stimulus onset to prevent saturation of the amplifier. The signal was routed to an A/D converter (Tucker-Davis) for time-domain averaging, and an artifact reject routine rejected signals that saturated the A/D converter.

D. Experimental protocol

The first session for every subject included an audiological evaluation, which consisted of obtaining pure-tone thresholds, a tympanogram, and an otoscopic examination. The choice of a test ear was random, unless one ear was better than the other on audiological measures, in which case the better ear was chosen. Each subject was seated in a comfortable recliner in a sound-treated booth and allowed to relax during recording. Subjects were given breaks as needed. Test sessions lasted for 30–40 min.

A spectral-equalization procedure preceded recording of emissions. Details of this procedure are presented in Chertoff and Chen (1996). Briefly, this involved obtaining the ear canal's transfer function using an initial probe signal. The inverse of the transfer function was convolved with the desired signal, and the ''conditioned signal'' was obtained. The conditioned signal, when delivered into the ear canal of the individual, resulted in a flat frequency response. This flat-spectrum signal was then used to evoke otoacoustic emissions. The beginning of emissions was set at 4.5 ms from time zero. The actual energy in the FIR pulse begins 0.75 ms after time zero. So, emission responses measured from 4.5 ms from time zero are actually 3.75 ms from stimulus onset. Each recording was done for 30 ms.

A total of 30 stimulus/response records was obtained for each subject. Each emission record was obtained with 500 averages. A break occurred during recording if the stimulus changed drastically, due to displacement of the probe or if the subject needed a break. Following such breaks, the spectral-equalization procedure was repeated prior to additional data collection.

E. Models for system identification

System identification was performed using two models. The first was a third-order polynomial model. The second was an extension of the third-order model, with the addition of fourth- and fifth-order nonlinear paths [Fig. 1(a) and (b)]. The analyses were performed on 30 stimulus and 30 emission records for each of the 11 subjects and one control subject, who was profoundly deaf. Spectral-density functions were computed from fast Fourier transforms of 2048 points. From the input and output spectral-density functions, the frequency response and the phase response were obtained. Coherence measures were obtained for each path, and the cumulative coherence was calculated to test the models' goodness-of-fit. The coherence measures obtained for the two models were compared.

III. RESULTS

A. Spectral-density functions

Otoacoustic emissions were present for all 11 normal subjects in response to FIR pulse. In Fig. 3(a), the autospectral-density function for the stimulus (S_{xx}) is shown

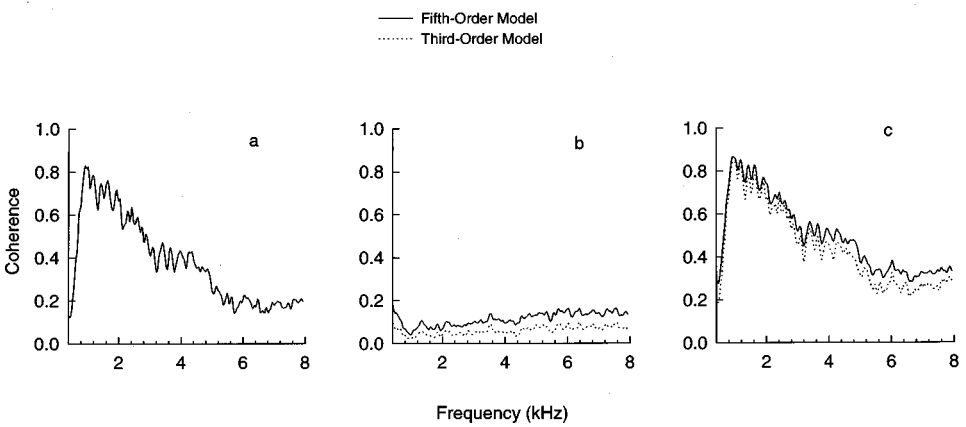

FIG. 4. Dotted lines represent coherence estimates from the third-order model. Solid lines represent coherence estimates from the fifth-order model. (a) Mean linear coherence. (b) Mean nonlinear coherence. (c) Mean cumulative coherence.

for each of these subjects. The spectral equalization resulted in a flat spectrum for most subjects for frequencies between 1 and 8 kHz. Figure 3(b) shows the mean autospectral-density function (S_{yy}) of the response averaged across subjects. The bottom curve shows the autospectral-density function of the response for the control subject with profound deafness, which coincided with the noise floor. This comparison shows that the responses from the 11 subjects were biological and above the noise floor.

B. Comparison of third- and fifth-order models

Figure 4(a)–(c) show the two models' mean coherence functions averaged across all normal subjects. The linear coherence function [Fig. 4(a)] is identical for both models. Figure 4(b) shows that the total nonlinear coherence from the fifth-order model is higher than that from the third-order model. Figure 4(c) shows that the cumulative coherence function from the fifth-order model is higher than that from the third-order model. There was an increase in the mean cumulative coherence of approximately 10% from the third- to the fifth-order model. This suggests that the fifth-order model provides a better fit to the otoacoustic emissions data. This increase of 10% is important, as the results of the simulation experiment suggests that small increases (7% in simulation experiment) are accompanied by a more accurate estimation of the properties of the original filter.

C. Coherence functions

The linear coherence functions for all subjects are presented in Fig. 5. These plots were obtained from the fifth-order model analysis. The nonlinear coherences are grouped according to even order (Fig. 6) and odd order (Fig. 7). From each of the coherence functions, the proportion of energy was averaged across frequency bands (1–2, 2–4, 4–6, and 6–8 kHz). The mean coherence as a function of frequency bands is shown in Fig. 8(a)–(e). The proportion of energy in these bands was examined and compared with the results reported in the acoustic distortion-product literature.

1. Linear coherence

For most subjects, linear coherences of at least 0.75 are seen for frequencies up to 1–2 kHz, as seen in Fig. 5. This trend is clearly seen in Fig. 8(a). Individuals show varying rates of decline in coherence values. For example, some subjects show a gradual decline in coherence from 2 to 4 kHz (e.g., S1), while for others, the decline is more abrupt (e.g., S4), and the bandwidth for which relatively high coherence values are present differs among individuals. The last panel of Fig. 5 (S12) shows the linear coherence function for the subject with profound deafness. It is near zero, indicating no degree of linear relation between input and output.

2. Even-order coherence

The second- and fourth-order coherence functions are shown for all subjects in Fig. 6. Second-order coherence functions reveal relatively high coherence values for a narrow frequency region below 1 kHz for most subjects. This may reflect second-order distortion-product terms of the form $f2-f1$, generated in the second-order path.

3. Odd-order coherence

The third- and fifth-order coherence functions are shown in Fig. 7 for all subjects. One consistent pattern among subjects is that the third-order coherence increases steadily for all subjects for frequencies between 1 and 8 kHz [Fig. 8(c)] This is perhaps due to the distortion-product terms of the form $3f1$, $2f1+f2$, or $2f2+f1$ generated in the third-order path. The fifth-order coherences are generally lower than the third-order coherences. However, there are exceptions. For example, S2 has a large peak in the fifth-order coherence function below 2 kHz, and the corresponding third-order coherence measures for that frequency region are lower. Similar to the third-order coherence, the fifth-order coherence also shows an increase from 1–2 and 6–8 kHz [Fig. 8(e)].

IV. DISCUSSION

A. Cochlear processing of broadband input

This analysis provides strong evidence that nonlinearities higher than third order are generated in the cochlea and that they can be detected in TEOAEs. In addition to second- and third-, fourth- and fifth-order nonlinearities were found for all 11 subjects.

Although the most commonly and easily detected distortion-product emissions to two-tone stimulation are third order, there is now evidence that the nonlinear cochlear

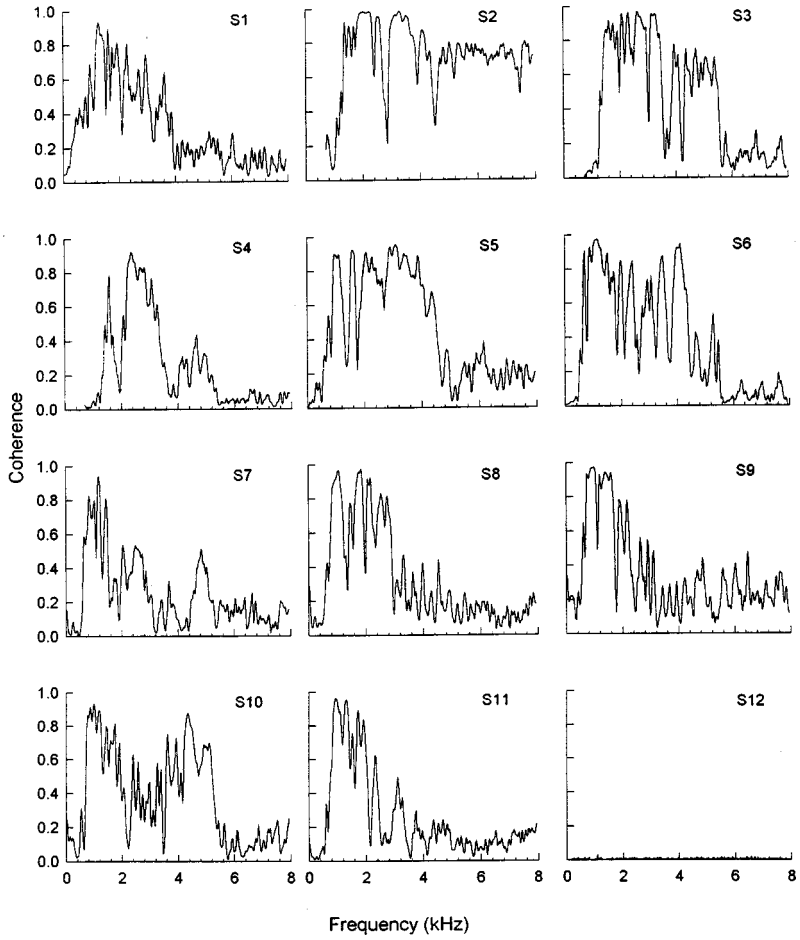

FIG. 5. Linear coherence functions shown for all subjects. The last panel (S12) shows linear coherence function that is close to zero for the control subject, who is profoundly deaf. This coincides with the noise floor.

transduction requires a model that is higher than third order. Weiss and Leong (1985), for example, have used a hyperbolic tangent function to model the channel conductance of the OHCs as a function of angular displacement of the stereociliary tuft. Patuzzi *et al.* (1989) have used a ninth-order polynomial to model the mechanical-to-electrical OHC transduction. More recently, Evans *et al.* (1991) fitted the voltage-length change function of the OHCs using a second-order Boltzmann equation. For the same data, they also reported that a fifth-order polynomial function did not adequately describe the saturation at extreme voltages. The data presented here also is in support of this, as the cumulative coherence does not equal 1, even for the fifth-order model. These nonlinear relations of the different but related cochlear processes indicate that a complete characterization of the nonlinear transduction has to include nonlinearities of orders higher than fifth. Although the fifth-order polynomial is a better fit than the third-order model to the TEOAE data presented here, future work in the use of this procedure should focus on higher-order polynomial models or other nonlinear functions to completely characterize cochlear transduction, and thereby improve the cumulative coherence.

Fifth- and higher-order DPOAEs have been reported in two-tone experiments in rabbits (Lonsbury-Martin *et al.*, 1987), gerbils, guinea pigs, and humans (Brown and Williams, 1993; Brown and Gaskill, 1990). However, the most commonly detected DPOAE in two-tone stimulation experiments under a variety of stimulus conditions in humans is the $2f1-f2$ frequency (Probst *et al.*, 1991). One possible explanation for the differences in detecting distortion products of higher orders using broadband stimuli, as seen in this study and in two-tone experiments, is that the cochlea responds differently to the different types of signals. With broadband stimulation there is a greater opportunity for interactions among frequencies, whereas, with two-tone stimuli the interactions are much less. This is an important difference between the distortion products evoked with two-tone stimuli and broadband stimuli. Interactions can also occur between numerous primary frequencies, between distortion products and primaries resulting in the generation of higher-order distortion products. Interactions between the various spectral components can actually result in the enhancement or attenuation of certain frequencies depending on individual system properties and phase relations between the forward- and backward-traveling waveforms. It has been noted that $2f1-f2$ and $3f1-2f2$ DPOAEs were larger in amplitude, and hence easily measured, when the stimuli were close in frequency (Gaskill and Brown, 1990). The closeness of frequencies in broadband input can result in detectable higher-order nonlinearities. With the use of broadband input, the level of fifth-order nonlinearities may be higher than two-tone DPOAEs due to enhancement of certain spectral components, consequently resulting in better signal/noise ratio.

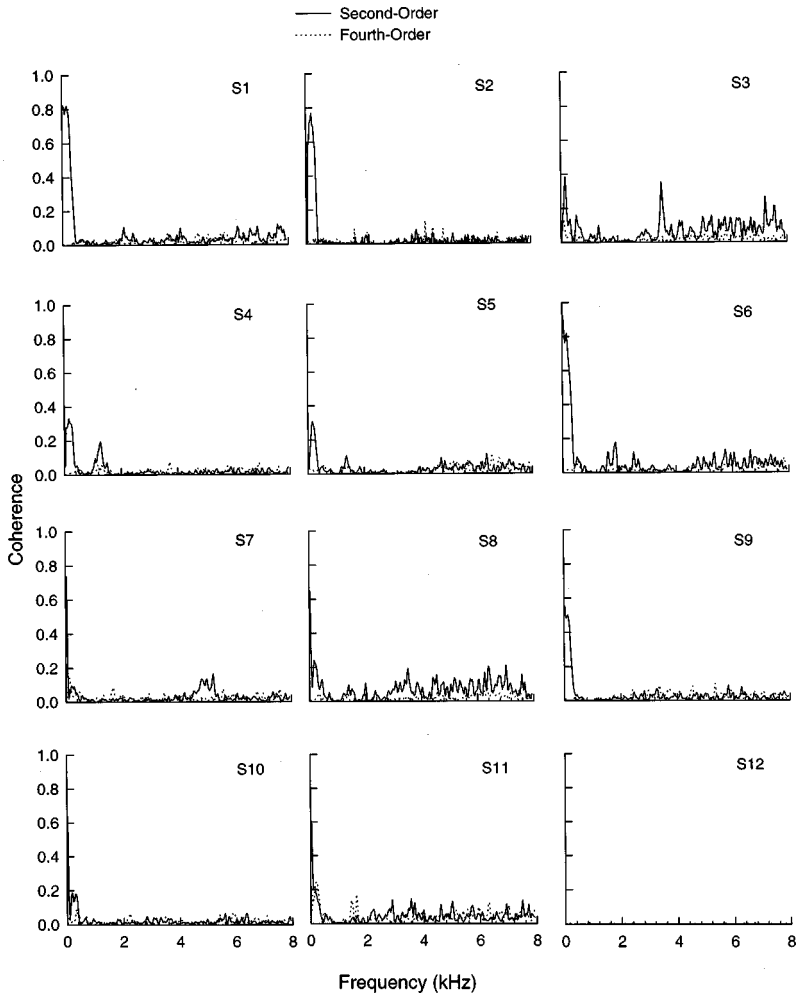

FIG. 6. Even-order coherence functions shown for all subjects. The second-order coherence functions are shown as solid lines and the fourth-order functions are shown as dotted lines.

B. Coherence functions: Further insights into linear and nonlinear processes

The coherence values reflect the proportion of energy from each path relative to the total energy of the response. Comparisons of linear and nonlinear coherence between frequency bands reveal interesting trends. For most subjects, the linear coherence was relatively high below 4 kHz, and decreased above 4 kHz. This is evident from the linear coherence functions.

The study's observations of an increase in third-order nonlinear coherence between 4 and 6 kHz are consistent with the two-tone $2f1-f2$ DPOAEs. In a recent study, Lonsbury-Martin *et al.* (1990) reported a substantial increase in the level of $2f1-f2$ DPOAEs in the frequency region between 4 and 6 kHz. They examined the level of DPOAEs as a function of the geometric mean frequencies of the primaries. An increase in $2f1-f2$ amplitude of approximately 10 dB between 1 and 6 kHz for stimulus levels of 75 and 85 dB SPL was reported. Similar increases were reported by Gaskill and Brown (1990) for $2f1-f2$ levels as a function of the primary frequency, $f1$. As noted by Lonsbury-Martin *et al.* (1990), this increase in the distortion-product levels for high frequencies, despite the possible attenuation by the middle ear, implies that at high frequencies the levels of distortion products are likely to be very large within the cochlea. These observations are supported by our results on the increase in the nonlinear coherences between 1 and 6 kHz and the corresponding decline in the mean linear coherences. The notable increase in total nonlinear coherence for the higher frequencies, 4–6, and 6–8 kHz, compared to 1–2 kHz observed in the present study, suggests that cochlear processing is more nonlinear for this frequency range compared to 1–2 kHz. Based on these findings, it is reasonable to conclude that a considerable amount of high-frequency energy in evoked emissions is due to distortions from nonlinear processes.

There are anatomical and physiological characteristics that distinguish the high-frequency (basal) and the low-frequency (apical) regions of the cochlea. *In vivo* studies suggest differences in tuning curves of the nerve fibers innervating the basal and apical ends of the cochlea. Fibers with high characteristic frequencies are more sharply tuned than those with low characteristic frequencies (Kiang *et al.*, 1965). Much of the differences between the high- and the low-frequency tuning appear to be related to differences in OHCs at the base and apex of the cochlea. One significant difference is that basal OHCs receive greater efferent input than the apical cells (Spoendlin, 1969, 1979). It is well known that contralateral stimulation, which presumably excites the efferent system, reduces the level of acoustic distortion products (Puel and Rebillard, 1990; Veuillet *et al.*, 1991). Furthermore, while the loss of basal cells has an im-

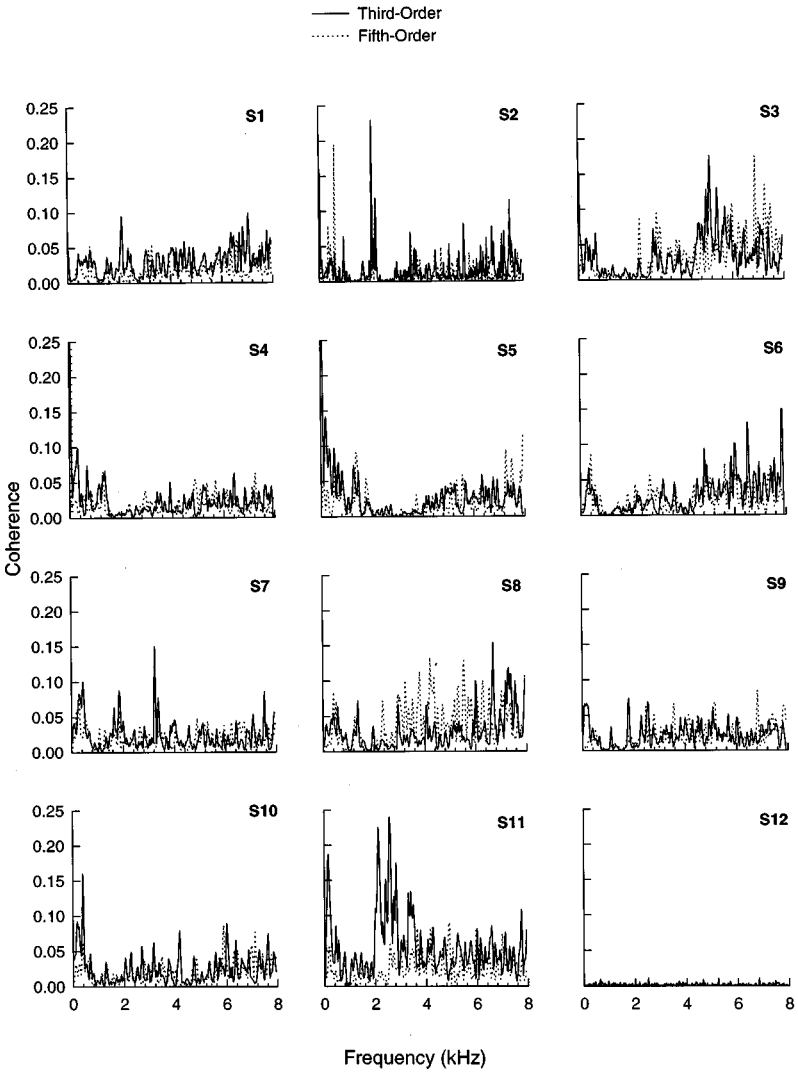

FIG. 7. Odd-order coherence functions for all subjects. The cubic coherence functions are shown as solid lines and the fifth-order functions are shown as dotted lines.

mediate effect on frequency sensitivity, the loss of apical cells is not necessarily reflected in threshold shifts (Altschuler *et al.*, 1992). Thus, the inherent sharper tuning and higher sensitivity of the basal cells may result in the generation of distortions of higher levels for high frequencies, compared to the low frequencies. Two other explanations are possible. First, the higher density of OHCs in the basal region compared to the apical region may also render the basal region relatively more sensitive, and consequently generate distortions of higher levels. Second, the stimulus used in this study had a flat spectrum that could result in relatively greater energy in the high-frequency region, resulting in greater stimulation and more distortion in the basal region of the cochlea. Comparisons of linear and nonlinear coherence functions have provided some insights into linear and nonlinear cochlear processing of broadband input.

It is difficult, however, to compare absolute distortion-product levels with nonlinear coherence measures because they measure different quantities. For example, levels of $2f1-f2$ cannot be directly compared with third-order coherence values. Third-order coherence reflects the percentage of all third-order distortions that are not statistically correlated to the first and second orders. The point that needs to be emphasized is that coherence functions provide a new and different measure of nonlinear processes. They are a measure of distortion that indicates the amount of uncorrelated energy added from the nonlinear paths to the output. The relative changes in the odd- and even-order coherences in response to changes in the cochlear status can, however, be compared with relative changes in the even- and odd-order DPOAEs. Future investigations along this line will likely provide a better understanding of the source of generation of the two types of emissions.

V. CONCLUSIONS

The primary goal of this study was to use a system-identification technique to understand linear and nonlinear processing in the cochlea for broadband input. The most important outcome of this study is the demonstration that Bendat's system-identification technique can be usefully applied to the study of linear and nonlinear properties of cochlear transduction. Furthermore, the coherence measures that are obtained through this procedure offer insights into linear and nonlinear cochlear processing of broadband signals. The coherence functions are functions of frequency, from which we can obtain frequency-specific information, and this information can be related to the localized status of the cochlea.

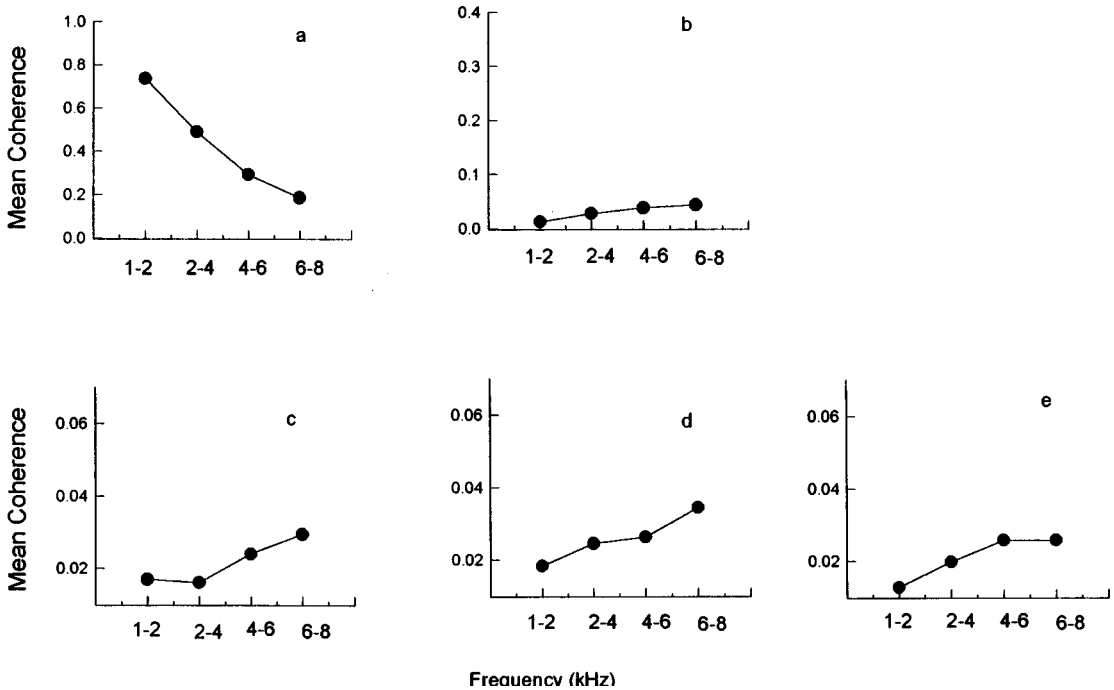

FIG. 8. (a) Mean linear coherence averaged across subjects shown as a function of frequency bands. (b) Mean second-order coherence averaged across subjects shown as a function of frequency bands. (c) Mean third-order coherence averaged across subjects shown as a function of frequency bands. (d) Mean fourth-order coherence averaged across subjects shown as a function of frequency bands. (e) Mean fifth-order coherence averaged across subjects shown as a function of frequency bands.

Additionally, these functions provide a measure of goodness-of-fit of the chosen model. In this study, third-order and fifth-order polynomial models were used to find the least-squares fit to the I/O relations, and the cumulative coherence showed that the fifth-order model is a better fit than the third-order model to the otoacoustic emissions data, evoked using a broadband FIR pulse. At this time, the characterization of the properties of the cochlear transduction is by no means complete. The total coherence for the fifth-order model is still less than 1 and this suggests that further improvement in the model is in order. One such improvement would be to use other nonlinear functions such as the hyperbolic tangent function, Boltzmann equation, or a polynomial model of a higher order for the zero-memory nonlinearity. Additionally, improvement in the cumulative coherence may also occur with reduction in the noise term. This may be possible if the number of input/output records used in the computation was increased.

Most importantly, coherence measures which are functions of frequency are useful indices of linear and nonlinear processes: It is conceivable that changes in the cochlear status due to different causes will show differences in coherence functions from the different nonlinear paths. Changes in trends as well as relative changes in coherence from the different paths may prove to be relevant factors in the clinical monitoring of cochlear status. The application of Bendat's system-identification procedure is by no means limited to otoacoustic emissions data. Physiological responses obtained using other techniques can be subjected to a similar analysis and the linear and nonlinear properties of responses can be characterized. For example, cochlear microphonic responses may also be obtained using broadband input and the linear/nonlinear processes involved in evoking these responses may be characterized and compared with those obtained using otoacoustic emissions.

Bendat's system-identification procedure offers an opportunity to compare TEOAE analysis with DPOAEs evoked with two-tone signals. For example, one study that is underway examines the effects of aspirin on DPOAEs and the relative changes in coherences of different orders. Currently, there is a lack of consensus on whether or not TEOAEs and DPOAEs are generated by a common source. A comparative analysis of relative changes in DPOAEs and the nonlinear components of TEOAEs, in a given model, such as guinea pigs or humans, will undoubtedly shed more light on this issue.

The focus of this paper has been on the coherence function, because of its potential as a clinical tool. Other outputs of this procedure are the spectral-density functions, and the A filters. The spectral-density functions are calculated for the set of stimulus and response records (please see Sec. I: System identification technique). The phase plot of the spectral-density function obtained from the response records can be potentially useful in the development of a measure of latency of emissions. The A filters can be used to predict system responses to other stimuli or stimulus conditions. These are just some of the avenues that are open for future work using this technique.

Last, this procedure is computationally feasible and provides us with a coherence measure, which is a potential clinical tool. A full understanding of the cochlear processes can be more successfully attained through the blending of several approaches and cross-validating empirical findings through different analytical techniques.

ACKNOWLEDGMENTS

This research was done at the University of Kansas, School of Allied Health, Department of Hearing and Speech, Kansas City, Kansas, and is based on part of the doctoral thesis by Geetha Krishnan. We wish to thank John Belmont, John Ferraro, of the University of Kansas Medical Center, and Christopher Schweitzer of Audiologic, Boulder, Colorado, for their helpful discussions and comments. We also thank several participants at the third joint meeting of the ASA and ASJ (Dec. 1996 in Honolulu, Hawaii) who demonstrated interest in this paper and provided very helpful comments. We would also like to thank the reviewers for their comments and suggestions.

Altschuler, R. A., Raphael, Y., Prosen, C. A., Dolan, D. F., and Moody, D. B. (**1992**). ''Acoustic stimulation and overstimulation in the cochlea: A comparison between basal and apical turns of the cochlea,'' in *Noise-Induced Hearing Loss*, edited by A. Dancer, D. Henderson, R. Salvi, and R. Hamernik (Mosby Year Book, St. Louis, MO).

Anderson, S. D., and Kemp, D. T. (**1979**). ''The evoked cochlear mechanical response in laboratory primates,'' Arch. Otorhinolaryngol. **224**, 47–54.

Bendat, J. S. (**1990**). *Nonlinear System Analysis and Identification from Random Data* (Wiley, New York).

Bendat, J. S., and Piersol, A. G. (**1993**). *Engineering Applications of Correlation and Spectral Analysis* (Wiley, New York).

Boer, E. de (**1993**) ''Some like it active,'' in *Proceedings of the International Symposium on Biophysics of Hair Cells and Sensory Systems*, edited by H. Duifhuis, J. W. Horst, P. van Dijk, and S. M. Netten (World Scientific, Singapore), pp. 3–22.

Brown, A. M., McDowell, B., and Forge, A. (**1989**). ''Acoustic distortion products can be used to monitor the effects of chronic gentamyacin treatment,'' Hearing Res. **42**, 43–156.

Brownell, W. E. (**1983**). ''Observations of a motile response in isolated outer hair cells,'' in *Mechanisms of Hearing*, edited by W. R. Webster and L. M. Aitken (Monash University, Clayton, Victoria), pp. 5–10.

Brown, A. M., and Gaskill, S. A. (**1990**). ''Can basilar membrane tuning be inferred from distortion measurement?,'' in *The Mechanics and Biophysics of Hearing*, edited by P. Dallos, C. D. Geisler, J. W. Mathews, M. A. Ruggero, and C. R. Steele (Springer-Verlag, Berlin), pp. 164–169.

Brown, A. M., and Williams, D. M. (**1993**). ''A second filter in the cochlea,'' in *Biophysics of Hair Cell Sensory Systems*, edited by H. Duifhuis, J. W. Horst, P. van Dijk, and S. M. Netten (World Scientific, Singapore), pp. 72–77.

Chang, K. W., and Norton, S. J. (**1997**). ''Efferently mediated changes in the quadratic distortion product $(f2-f1)$,'' J. Acoust. Soc. Am. **102**, 1719–1733.

Chertoff, M. E., and Chen, J. (**1996**). ''An *in-situ* calibration routine for click stimuli,'' J. Am. Acad. Audiol. **7**, 130–136.

Chertoff, M. E., Krishnan, G., Ator, G. A., and Hixon, D. A. (**1994**). ''Auditory evoked potential measures of auditory nonlinearities in gerbil,'' Abst. Assoc. Res. Otolaryngol. **98**, 25.

Chertoff, M. E., Steele, T., Ator, G. A., and Bian, L. (**1996**). ''Characterizing cochlear mechano-electric transduction using a nonlinear systems identification procedure,'' J. Acoust. Soc. Am. **100**, 3741–3753.

Cody, A. R., and Russell, I. J. (**1987**). ''The responses of hair cells in the basal turn of the guinea pig cochlea to tones,'' J. Physiol. **383**, 551–569.

Dallos, P. (**1973**). ''Nonlinear Distortion,'' in *The Auditory Periphery: Biophysics and Physiology* (Academic, New York), pp. 395–421.

Dijk, P. van, Wit, H. P., and Segenhout, J. M. (**1993**). ''Wiener kernel analysis of auditory nerve fiber response in the frog,'' in *Proceedings of the International Symposium on Biophysics of Hair Cells and Sensory Systems*, edited by H. Duifhuis, J. W. Horst, P. van Dijk, and S. M. Netten (World Scientific, Singapore).

Evans, B. N., Hallworth, R., and Dallos, P. (**1991**). ''Outer hair cell electromotility: The sensitivity and vulnerability of the DC component,'' Hearing Res. **1**, 1–17.

Gaskill, S. A., and Brown, A. M. (**1990**). ''The behavior of the acoustic distortion product, $2f1-f2$, from the human ear and its relation to auditory sensitivity,'' J. Acoust. Soc. Am. **88**, 821–839.

Goldstein, J. L., and Kiang, N. Y. S. (**1968**). ''Neural correlates of the aural combination tone $2f1-f2$,'' IEEE Trans. **56**, 981–992.

Kemp, D. T. (**1978**). ''Stimulated acoustic emissions from within the human auditory system,'' J. Acoust. Soc. Am. **64**, 1386–1391.

Kemp, D. T. (**1979**). ''Evidence of mechanical nonlinearity and frequency selective wave amplification in the cochlea,'' Arch. Otolaryngol. **224**, 37–45.

Kemp, D. T. (**1982**). ''Cochlear echoes: Implications for noise-induced hearing loss,'' in *New Perspectives on Noise-Induced Hearing Loss*, edited by R. P. Hamernik, D. Henderson, and R. Salvi (Raven, New York).

Kiang, N. Y. S., Watanabe, T., Thomas, E. C., and Clark, L. F. (**1965**). *Discharge Patterns of Single Fibers in the Cat's Auditory Nerve* (MIT, Cambridge, MA).

Kim, D. O., Molnar, C. E., and Mathews, J. W. (**1980**). ''Cochlear mechanics: nonlinear behavior in two-tone responses as reflected in cochlear nerve fiber responses and in ear-canal sound pressure,'' J. Acoust. Soc. Am. **67**, 1704–1721.

Kirk, D. L., and Johnstone, B. M. (**1993**). ''Modulation of $f2-f1$: evidence for a GABA-ergic efferent system in apical cochlea of the guinea pig,'' Hearing Res. **67**, 20–34.

Krishnan, G., and Chertoff, M. E. (**1995**). ''Quantifying cochlear linear and nonlinear processes using nonlinear system-identification technique and otoacoustic emissions,'' presented at the 18th meeting of the Association for Research in Otolaryngology, St. Petersburg Beach, Florida.

Lasky, R. E., Snodgrass, E., and Hecox, K. (**1994**). ''Distortion-product otoacoustic emission input/output functions as a function of frequency in human adults,'' J. Am. Acad. Audiol. **5**, 183–194.

Lonsbury-Martin, B. L., Martin, G. K., Probst, R., and Coats, A. C. (**1987**). ''Acoustic distortion products in rabbit ear canal. I. Basic features and physiological vulnerability,'' Hearing Res. **28**, 173–189.

Lonsbury-Martin, B. L., Harris, F. P., Stagner, B. B., Hawkins, M. D., and Martin, G. K. (**1990**). ''Distortion product emissions in humans: I. Basic properties in normally hearing subjects,'' Ann. Otol. Rhinol. Laryngol. **147**, 3–14.

MATLAB (**1993**). ''High Performance numeric computation and visualization software,'' The Mathworks, Inc.

Moulin, A., Collet, L., and Duclaux, R. (**1993**). ''Contralateral auditory stimulation alters acoustic distortion products in humans,'' Hearing Res. **65**, 193–210.

Mountain, D. C. (**1980**). ''Changes in endolymphatic potential and crossed bundle stimulation alters cochlear mechanics,'' Science **210**, 71–72.

Nelson, D. A., and Kimberley, B. P. (**1992**). ''Distortion-product emissions and auditory sensitivity in human ears with normal hearing and cochlear hearing loss,'' J. Speech Hear. Res. **35**, 1142–1159.

Patuzzi, R. B., Yates, G. K., and Johnstone, B. M. (**1989**). ''Outer hair cell receptor current and sensorineural hearing loss,'' Hearing Res. **42**, 47–72.

Probst, R., Lonsbury-Martin, B., and Martin, G. K. (**1991**). ''A review of otoacoustic emissions,'' J. Acoust. Soc. Am. **89**, 2027–2067.

Puel, J. L., and Rebillard, G. (**1990**). ''Effect of contralateral sound stimulation on the distortion product $2f1-f2$: Evidence that the medial efferent system is involved,'' J. Acoust. Soc. Am. **87**, 1630–1635.

Robles, R., Ruggero, M. A., and Rich, N. C. (**1991**). ''Two-tone distortion in the basilar membrane of the cochlea,'' Nature (London) **349**, 413–414.

Shi, Y., and Hecox, K. E. (**1991**). ''Nonlinear system identification by m-pulse sequences: Application to Brainstem auditory evoked responses,'' IEEE Trans. Biomed. Eng. **38**, 834–845.

Smoorenburg, G. F. (**1972**). ''Combination tones and their origin,'' J. Acoust. Soc. Am. **52**, 615–632.

Spoendlin, H. (**1969**). ''Innervation patterns in the organ of corti of the cat,'' Acta Oto-Laryngol. **67**, 239–259.

Spoendlin, H. (**1979**). ''Neural connections of the outer hair cell system,'' Acta Oto-Laryngol. **87**, 381–387.

Ueda, H., Tsuge, H., Hattori, T. (**1997**). ''Changes in evoked otoacoustic emissions in the guinea pig after pure-tone acoustic overstimulation,'' J. Acoust. Soc. Am. **101**, 3577–3582.

Veuillet, E., Collet, L., and Duclaux, R. (**1991**). ''Effect of contralateral auditory stimulation on active cochlear micromechanical properties in human subjects: dependence on stimulus variables,'' J. Neurophysiol. **65**, 724–735.

Weiss, T. F., and Leong, R. (**1985**). ''A model for signal transmission in ear having hair cells with free-standing stereocilia IV. Mechanoelectrical transduction stage,'' Hearing Res. **20**, 175–195.

Wickesberg, R. E., and Geisler, D. C. (**1984**). ''Artifacts in Wiener kernels

using Gaussian white noise,'' IEEE Trans. Biomed. Eng. **BME-31**(6), 454–461.
Wickesberg, R. E., Dickson, J. W. Gibson, M. M., and Geisler, D. C. (**1984**). ''Wiener kernel analysis of anteroventral cochlear nucleus neurons,'' Hearing Res. **14**, 155–174.
Zurek, P. M., Clark, W. W., and Kim, D. O. (**1982**). ''The behavior of acoustic distortion products in the ear anals of chinchillas with normal or damaged ears,'' J. Acoust. Soc. Am. **72**, 774–780.
Zwicker, E. (**1986**). ''A hardware cochlear nonlinear preprocessing model with active feedback,'' J. Acoust. Soc. Am. **80**, 146–153.

Evoked otoacoustic emissions arise by two fundamentally different mechanisms: A taxonomy for mammalian OAEs

Christopher A. Shera[a] and John J. Guinan, Jr.
Eaton-Peabody Laboratory of Auditory Physiology, Massachusetts Eye and Ear Infirmary, 243 Charles Street, Boston, Massachusetts 02114 and Department of Otology and Laryngology, Harvard Medical School, Boston, Massachusetts 02115

(Received 2 June 1998; accepted for publication 27 October 1998)

Otoacoustic emissions (OAEs) of all types are widely assumed to arise by a common mechanism: nonlinear electromechanical distortion within the cochlea. In this view, both stimulus-frequency (SFOAEs) and distortion-product emissions (DPOAEs) arise because nonlinearities in the mechanics act as ''sources'' of backward-traveling waves. This unified picture is tested by analyzing measurements of emission phase using a simple phenomenological description of the nonlinear re-emission process. The analysis framework is independent of the detailed form of the emission sources and the nonlinearities that produce them. The analysis demonstrates that the common assumption that SFOAEs originate by nonlinear distortion requires that SFOAE phase be essentially independent of frequency, in striking contradiction with experiment. This contradiction implies that evoked otoacoustic emissions arise by two fundamentally different mechanisms within the cochlea. These two mechanisms (linear reflection versus nonlinear distortion) are described and two broad classes of emissions—reflection-source and distortion-source emissions—are distinguished based on the mechanisms of their generation. The implications of this OAE taxonomy for the measurement, interpretation, and clinical use of otoacoustic emissions as noninvasive probes of cochlear function are discussed. [S0001-4966(99)02202-X]

PACS numbers: 43.64.Jb, 43.64.Kc, 43.64.Bt [BLM]

INTRODUCTION

During the 20 years since Kemp's (1978) discovery, otoacoustic emissions (OAEs) have become widely used, both as research tools and as clinical diagnostic and screening aids (e.g., Kemp *et al.*, 1986; Norton and Stover, 1994; Whitehead *et al.*, 1996a; Robinette and Glattke, 1997). Interpretation of measured otoacoustic responses is grounded on an underlying picture of the origin of evoked OAEs. All categories of evoked OAEs are commonly regarded as originating in nonlinear distortion, presumably through the electromotile responses of outer hair cells (Brownell, 1990). These nonlinearities in cochlear mechanics are thought to act as ''sources'' of backward-traveling waves (Kemp, 1978; de Boer, 1983; Allen and Neely, 1992). Kemp (1997) describes the physical mechanism—often simply abstracted as ''nonlinear stimulus re-emission'' by cellular ''emission generators''—in a recent review:

> ''The model of the phenomenon adopted at that time [circa 1978] is still relevant. It is that ... a nonlinearity at the peak of the traveling wave turns around or scatters back some of the traveling wave energy, and returns both stimulus frequency and intermodulation signals back to the middle ear.''

We epitomize in Table I the major elements of this ''common view''—and the nonlinear-distortion model that underlies it—as culled from the literature (e.g., Kemp, 1980, 1998; Probst *et al.*, 1991; Allen and Neely, 1992; Allen and Lonsbury-Martin, 1993; Patuzzi, 1996; Hartmann, 1997).[1]

In this paper, *we argue that the common view cannot be correct*. For although the nonlinear-distortion model accounts for distortion products, it cannot explain stimulus-frequency or transiently evoked emissions, in particular their phase, which rotates rapidly with frequency at low sound levels. Although considerably elaborated, our central argument is similar in spirit to that first used by Kemp and Brown (1983a) and later formalized by others (Strube, 1989; Shera and Zweig, 1993b; Zweig and Shera, 1995) to distinguish ''wave-'' and ''place-fixed'' emission mechanisms. By combining our argument with data on emission phase, we conclude that at low sound levels stimulus-frequency and transiently evoked emissions must arise by mechanisms fundamentally different from pure distortion products.[2] We therefore distinguish two classes of emissions—reflection- and distortion-source emissions—based on the mechanisms of their generation. Our mechanism-based taxonomy has important implications for the measurement, interpretation, and use of otoacoustic emissions as noninvasive probes of cochlear function.[3]

I. DEFINITIONS AND BACKGROUND

Otoacoustic emissions are typically classified according to the stimulus waveform and related details of the measurement paradigm (e.g., Zurek, 1985). Initially, we follow suit by distinguishing two classes of evoked emissions based on the relationship between the emissions and the stimuli used to elicit them:[4]

[a]Electronic mail: shera@epl.meei.harvard.edu

TABLE I. Synopsis of the ''common view'' of evoked emissions presented in the literature.

Common view of evoked emissions
• Evoked otoacoustic emissions arise through nonlinear stimulus ''re-emission'' by cellular ''emission generators'' (e.g., outer hair cells). • Stimulus re-emission occurs because electromechanical nonlinearities—principally those near the peak of the traveling-wave envelope—act as ''sources'' of backward-traveling waves. • SFOAEs and DPOAEs both arise through nonlinear distortion (e.g., SFOAEs can be thought of as ''zeroth-order'' DPOAEs arising from distortion at the first harmonic).

(i) Echo emissions comprise stimulus-frequency and transiently evoked emissions (SFOAEs and TEOAEs), grouped together because they occur at the frequency (or frequencies) of stimulation, whether the stimulus is a pure tone or an acoustic transient.

(ii) Distortion-product emissions (DPOAEs) occur at frequencies not present in the evoking stimulus (e.g., at the frequency $2f_1-f_2$ in response to stimulus tones at frequencies f_1 and f_2).

Our use of the distortion-product nomenclature is standard, and we introduce the term ''echo emissions'' simply as a convenient shorthand. In the common view these two classes of evoked emission both arise from nonlinear electromechanical distortion within the cochlea. Preparatory to further analysis, we review basic properties of echo emissions at low sound levels.

A. Characterizing echo emissions at low levels

As one sweeps the frequency of an acoustic stimulus tone, the pressure in the human ear canal, P_{ec}, varies as shown in Fig. 1. As the stimulus level is lowered, a regular oscillatory component appears superposed on a more smoothly varying ''background'' response. Whereas the shape of the background depends on the acoustics of the ear canal and middle ear, the oscillatory component represents an acoustic interference pattern created by the superposition of the stimulus tone and a second tone at the same frequency originating from within the cochlea (Kemp, 1978, 1979a,b). The relative amplitude of the oscillatory component grows as the stimulus level is reduced, until, at the sound levels near threshold shown in Fig. 2 ($\lesssim$5 dB SL), the interference pattern becomes approximately independent of sound level, indicating that stimulus and response are linearly related (Zwicker and Schloth, 1984; Shera and Zweig, 1993a). Similar quasi-periodic oscillations appear in the frequency spectra of the responses to low-level acoustic transients (e.g., Zwicker and Schloth, 1984).[5] At frequencies near 1500 Hz, the frequency spacing Δf_{OAE} between adjacent spectral maxima is approximately 100 Hz in human ears.

1. Interpretation using the cochlear traveling-wave reflectance, R

We interpret evoked emissions as indicating the presence of backward-traveling waves within the cochlea. To characterize their properties, we define the *cochlear traveling-wave reflectance*, *R*, as the complex ratio of the out-going (or emitted) pressure wave to the in-going (or stimulus) wave at the basal end of the cochlea near the stapes (Shera and Zweig, 1993a):[6]

$$R(f;A)\equiv\left.\frac{P_{\text{out-going}}}{P_{\text{in-going}}}\right|_{\text{stapes}}, \tag{1}$$

where *R* depends on both the frequency, *f*, and amplitude, *A*, of the stimulus. The cochlear reflectance provides a phenomenological characterization of the emission process as seen from the base of the cochlea.[7]

By regarding the intervening middle ear as a linear, two-port network, one can relate the cochlear reflectance, *R*, to measurements of ear-canal pressure, P_{ec} (Shera and Zweig, 1993a). When the emission amplitude is small relative to the stimulus ($|R|\ll 1$), the relation reduces to the simple formula[8]

$$\frac{P_{ec}(f;A)}{P_{ec}(f;A_{ref})}\approx\frac{A}{A_{ref}}[1+m(f)R(f;A)], \tag{2}$$

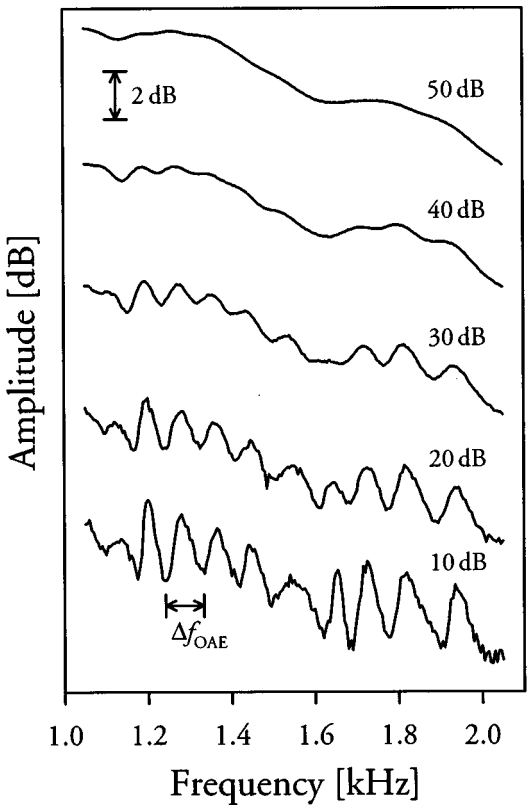

FIG. 1. Frequency dependence of ear-canal pressure and its variation with sound level in a normal human ear. The curves, offset vertically from one another for clarity, represent the normalized amplitude of the ear-canal pressure, P_{ec}, measured with a constant voltage applied to the earphone driver (Shera and Zweig, 1993a). The approximate sensation level of the stimulus tone at 1300 Hz is indicated on the right. At the highest level the pressure amplitude varies relatively smoothly with frequency. As the stimulus level is lowered, sound generated within the cochlea combines with the stimulus tone to create an oscillatory acoustic interference pattern that appears superposed on the smoothly varying background seen at high levels. Near 1500 Hz, the frequency spacing Δf_{OAE} between adjacent spectral maxima is approximately 100 Hz. Data from Shera and Zweig (1993a).

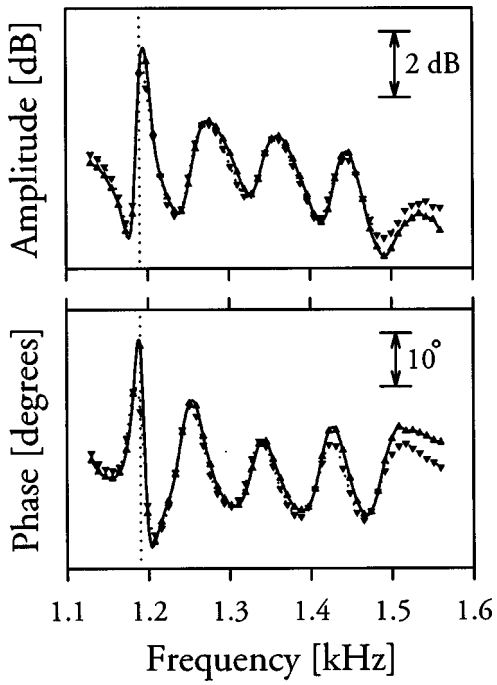

FIG. 2. Linearity at low levels manifest by measurements of the ear-canal pressure, P_{ec}, normalized by the amplitude of the earphone-driver voltage, at sound levels of 5 dB SL (▲) and 0 dB SL (▼) relative to threshold at 1300 Hz. The vertical dotted line marks the frequency of a known spontaneous emission. Aside from a small drift in the background—probably the result of slow changes in middle-ear cavity pressure and/or variations in the temperature of the recording microphone—the two functions nearly superpose, indicating that the response appears linear at these near-threshold levels. Adapted from Fig. 6 of Shera and Zweig (1993a).

where A is the stimulus amplitude and A_{ref} is a high-level reference amplitude at which the relative amplitude of the emissions is negligible (e.g., in humans $A_{ref} \approx 60$ dB SPL). The complex function $m(f)$ characterizes round-trip middle-ear transmission and varies relatively slowly with frequency (Shera and Zweig, 1993a).

At sound levels near threshold, R becomes independent of level, indicating that the emitted wave varies linearly with the stimulus. Solving Eq. (2) for mR using measurements of P_{ec} yields a function of slowly varying amplitude and rapidly rotating phase (Shera and Zweig, 1993a). Typical results, obtained from the measurements of Fig. 2 in the low-level linear regime, are shown in Fig. 3. Although the function $m(f)$ characterizing middle-ear transmission is not known in detail, middle-ear transfer functions vary relatively slowly with frequency compared to the oscillations in the ear-canal pressure spectrum (e.g., Puria *et al.*, 1997; Puria and Rosowski, 1997). The frequency dependence of the product mR is therefore primarily that of the reflectance R. Reference to Fig. 3 shows that[9]

$$\text{Emission measurements} \Rightarrow \begin{cases} |R| \approx \text{slowly varying} \\ \angle R \approx \text{locally linear with } f. \end{cases} \tag{3}$$

Over frequency intervals corresponding to a few oscillations in the pressure spectrum (i.e., over intervals a few times the size of Δf_{OAE}), the reflectance R has the approximate form[10]

$$R(f) \approx |R| e^{-2\pi i f \tau}, \tag{4}$$

where the amplitude $|R| \approx$ constant and $\tau \approx 10$ ms near 1500 Hz. Whereas the amplitude of the reflectance varies slowly, its phase rotates rapidly, circling one full period over the frequency interval $\Delta f_{OAE} \approx 1/\tau$. Since the largest contributions to the emission are believed to originate near the peak of the forward-traveling wave, the approximate constancy of $|R|$ suggests—via the cochlear mapping between frequency and position—that all points along the cochlear partition are about equally effective at reflecting the traveling wave. The linear variation of $\angle R$ with frequency suggests the presence of a delay (in this case, of about 10 ms).

Although deduced from measurements of stimulus-frequency emissions, Eq. (4) can be reinterpreted in the time domain to provide a description of transiently evoked emissions valid in the low-level linear regime: The echo evoked by a narrow-band tone burst is a scaled (by a factor $|R|$) and delayed (by τ seconds) version of the stimulus waveform (e.g., Wilson, 1980; Norton and Neely, 1987).[11] Having characterized the properties of echo emissions at low levels, we next consider whether they can originate through nonlinear distortion.

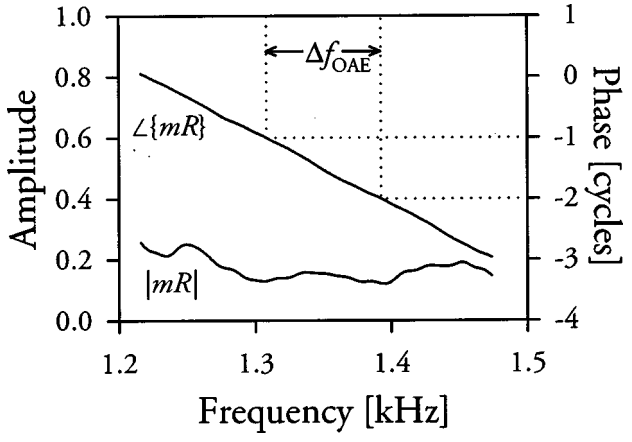

FIG. 3. Amplitude and phase of mR versus frequency computed from a subset of the data in Fig. 2 that avoids the spontaneous emission (Shera and Zweig, 1993a). The curves indicate that R has a slowly varying amplitude and a locally linear phase (assuming m is slowly varying). The frequency interval Δf_{OAE} between spectral maxima in ear-canal pressure corresponds to a full rotation of the phase of R. Data from Shera and Zweig (1993a).

II. DO ECHO EMISSIONS ARISE BY NONLINEAR DISTORTION?

A. The nonlinear-distortion model

The nonlinear-distortion model that underlies the common view of evoked emissions is illustrated schematically in Fig. 4. When the cochlear response is nonlinear, traveling waves can induce spatial distortions in the mechanics that act as ''sources'' of backward-traveling waves. In addition to accounting for distortion-product emissions, the model also appears to provide a natural explanation for echo emissions. For example, the observation that $|R| \approx$slowly varying—that is, that all points ''reflect'' about equally—might be naturally explained by supposing that the sources that generate the backward-traveling wave are induced by the wave itself through nonlinearities in the mechanics (Kemp, 1978, 1979a;

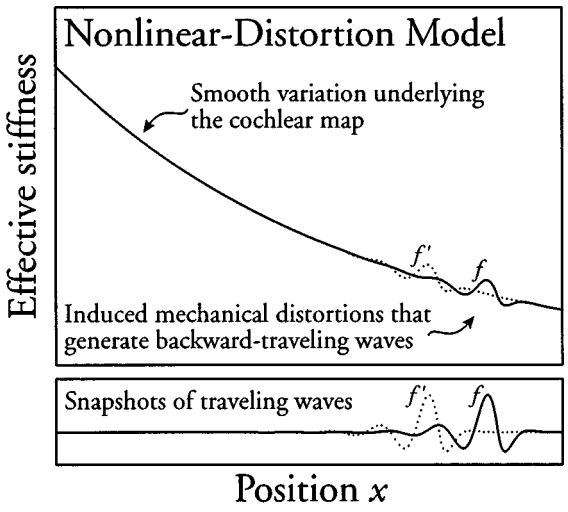

FIG. 4. Mechanical distortions induced by pure-tone stimulation. When the cochlear response is nonlinear, the traveling wave (bottom panel) is presumed to induce distortions in the mechanics (top panel) that act as sources of backward-traveling waves. In the example shown here, the traveling wave induces distortions in the effective stiffness of the cochlear partition (e.g., via nonlinearities in the mechanisms of force generation by outer hair cells). The dotted line shows how the region of induced mechanical distortion moves with the wave envelope as the stimulus frequency is increased from f to f'.

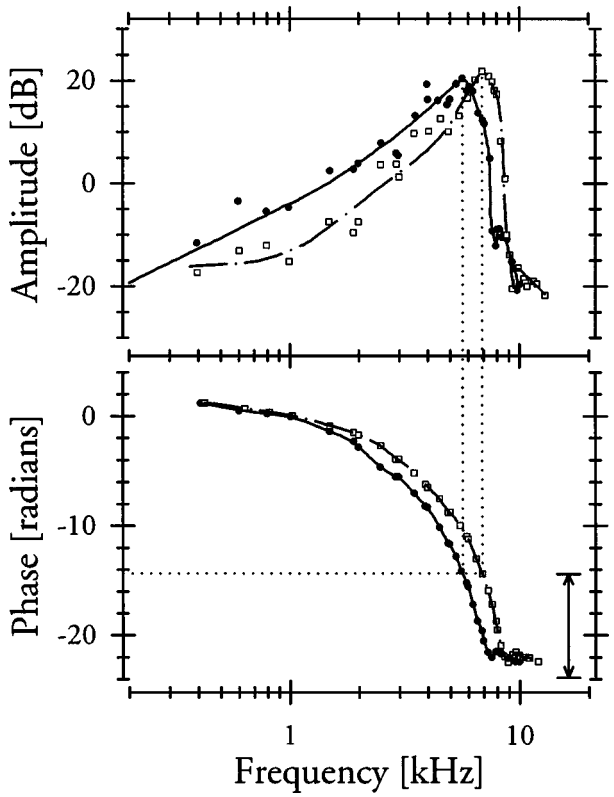

FIG. 5. Constancy of phase accumulation at the peak of the wave envelope. The figure shows Rhode's (1971, Fig. 8) measurements of basilar-membrane transfer functions (i.e., basilar membrane to malleus displacement ratios) at two nearby positons along the basilar membrane ($\Delta x \approx 1.5$ mm). As indicated by the dotted lines, the total phase accumulation at the peak of the transfer function (horizontal line) is not a strong function of frequency (vertical lines). The scale bar (double-headed arrow) in the lower right-hand corner provides an estimate of the relative phase accumulation necessary to account for the rapid rotation of $\angle R$ (see footnote 12). Relative to the scale bar, the observed difference in phase accumulation is negligible.

de Boer, 1983; Allen and Neely, 1992). And, since the phase of R has the form of a delay, it is natural to associate that delay with wave travel to and from the site of generation of the re-emitted wave.

An attractive feature of the nonlinear-distortion model is its implicit unification of echo and distortion-product emissions through a common origin in cochlear nonlinearity. Intuitively, the model seems to account naturally for both striking features of the frequency dependence of R (i.e., $|R| \approx$slowly varying, since the induced sources depend on the form and strength of cochlear nonlinearities, which presumably vary relatively slowly with position; and $\angle R \approx$locally linear with frequency, due to the round-trip traveling-wave delay between the stapes and the site of re-emission).

In what follows, we analyze the model more carefully and show that *the nonlinear-distortion model*—despite its apparent virtues—*actually predicts a constant reflectance phase, in striking contradiction with experiment*.

B. Can the nonlinear-distortion model account for $\angle R$?

To simplify the analysis of the model without sacrificing any essential feature, we assume that the forward-traveling wave is re-emitted by a nonlinear source induced at the *peak* of the traveling wave. Recall that $\angle R$ represents the accumulated phase shift between the out- and in-going waves at the stapes. In our simplified nonlinear-distortion model, this phase shift can be written as the sum of three components:

$$\angle R = \Delta\theta_{\text{forward-travel}} + \Delta\theta_{\text{re-emission}} + \Delta\theta_{\text{reverse-travel}}, \qquad (5)$$

representing phase shifts due to forward and reverse wave propagation (i.e., between the stapes and the site of re-emission at the peak of the wave envelope) and any phase shift due to the re-emission process itself. Consistency with the data of Fig. 3 requires that the sum of these phase shifts rotate rapidly with frequency. Does the model agree with experiment?

1. Phase shifts due to wave travel cannot account for $\angle R$

First, we consider phase shifts due to wave travel. Does $\Delta\theta_{\text{forward}}$ rotate rapidly with frequency? Figure 5 answers this question using measurements of basilar-membrane motion. The figure shows the phase accumulated by the forward-traveling wave as it propagates from the stapes to the peak of its envelope at its characteristic place. Perhaps surprisingly, the phase accumulation at the peak of the wave envelope is almost independent of frequency:

$$\underset{\text{measurements}}{\text{Basilar-membrane}} \Rightarrow \Delta\theta_{\text{forward-travel}} \approx \text{constant}. \qquad (6)$$

For comparison, the scale bar in Fig. 5 illustrates the phase shift necessary to account for the estimated change in $\angle R$ over the same frequency range.[12] Relative to the scale bar, the observed difference in the phase accumulation is negligible.

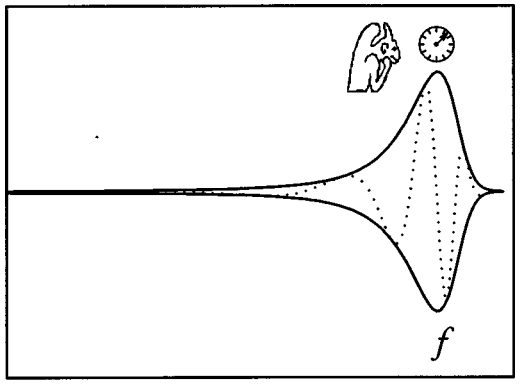

FIG. 6. The demon emitter. Charged with generating emissions by pushing and pulling on the basilar membrane, the demon needs to determine the stimulus frequency in order to create a backward-traveling wave with the correct relative phase. To determine the stimulus frequency the demon must compare the period of basilar-membrane vibration with the ticking of a ''clock.'' The only clock available, however, is the local resonator that determines the characteristic frequency.

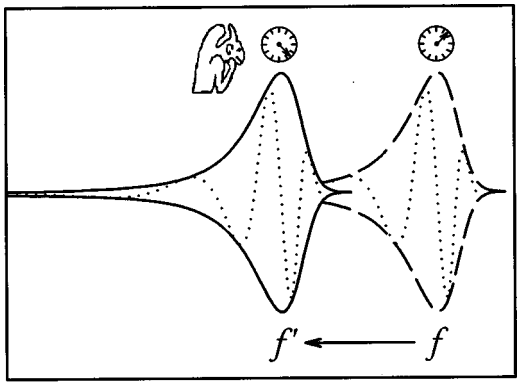

FIG. 7. When the stimulus frequency is changed (e.g., from $f \rightarrow f'$), the envelope of the traveling wave shifts along the basilar membrane. Because the demon moves with the wave, changing the stimulus frequency changes the demon's local time reference correspondingly. As a result, the demon cannot detect changes in stimulus frequency and thus cannot generate backward-traveling waves whose phase depends on that frequency.

The constancy of $\Delta\theta_{\text{forward}}$ is an immediate consequence of the approximate local scaling symmetry (Zweig, 1976; Siebert, 1968; Sondhi, 1978) manifest by basilar- and tectorial-membrane transfer functions (Rhode, 1971; Gummer *et al.*, 1987; Rhode and Cooper, 1996) and neural tuning curves (e.g., Kiang and Moxon, 1980; Liberman, 1978). Local scaling symmetry implies that rather than depending on position and frequency independently, basilar-membrane transfer functions depend on the two variables x and f only in the single combination $f/f_{\text{cf}}(x)$, where $f_{\text{cf}}(x)$ is the cochlear position-frequency map. When the cochlear map is exponential, the symmetry implies that traveling-wave envelopes are locally ''shift-similar,'' with the number of wavelengths in the traveling wave nearly independent of frequency. Compared to the higher frequency wave, the lower frequency wave travels further along the cochlea and requires a longer time to reach its peak. But *both waves travel the same number of wavelengths*, and the total phase accumulation is therefore the same.

Although we have no direct measurements of the phase shift $\Delta\theta_{\text{reverse}}$,[13] standard cochlear models[14] predict that

$$\Delta\theta_{\text{reverse-travel}} \approx \Delta\theta_{\text{forward-travel}}. \tag{7}$$

Consequently,[15]

$$\begin{matrix}\text{Measurements} \\ \text{and models}\end{matrix} \Rightarrow \Delta\theta_{\text{round-trip}} \approx \text{constant}. \tag{8}$$

For the nonlinear-distortion model of echo emissions to agree with experiment, the phase rotation of $\angle R$ must originate in $\Delta\theta_{\text{re-emission}}$. To test whether this is possible, we consider the thought-experiment of the demon emitter.

2. Phase shifts due to re-emission cannot account for $\angle R$

Rather than bog ourselves down in the model-dependent—and, for our purposes, irrelevant—details of a particular nonlinear re-emission mechanism, we argue more generally by imagining that emissions are generated within the cochlea by a tiny demon who ''surfs'' the peak of the envelope of the traveling wave, where the effects of nonlinear distortion are presumably greatest (see Fig. 6).[16] The demon, agent for nonlinear distortion, is charged with launching backward-traveling waves by pushing and pulling on the basilar membrane. In the process, the demon introduces the phase shift $\Delta\theta_{\text{re-emission}}$. Can the demon supply the frequency dependence necessary to produce the observed form of $\angle R$?

At first sight, the answer appears to be ''Yes.'' For example, when the ear is stimulated with a pure tone the demon simply determines the stimulus frequency and consults a formula he keeps in his pocket that tells him how to compute, as a function of frequency,[17] the phase with which he must push and pull (relative to the local motion of the basilar membrane) in order to produce the appropriate value of $\Delta\theta_{\text{re-emission}}$.[18]

How does the demon determine the stimulus frequency?[19] From his position atop the traveling-wave envelope the demon counts the number of times the basilar membrane rises and falls and compares that number with the ticking of a ''clock.'' But what clock does he have available? The demon's time reference is the local ''resonator'' that determines the characteristic frequency, f_{cf}, at his location.[20] The demon's clock therefore ticks at intervals proportional to $1/f_{\text{cf}}$,[21] counting out time in units appropriate to his position along the cochlear partition.

Suppose that we fix the stimulus frequency at some value, f. Because the demon sits at the peak of the traveling wave (i.e., at the characteristic place corresponding to frequency f), he sees the basilar membrane undergo one oscillation for every tick of his clock (since $f/f_{\text{cf}}=1$). The demon concludes that the stimulus has unit frequency (in units of cycles/clock-tick) and, after evaluating his formula, pushes and pulls on the basilar membrane appropriately. For example, at unit frequency the demon might push downwards on the basilar membrane during every upwards zero-crossing of its local motion.

Now suppose that we increase the stimulus frequency to the value f' as illustrated in Fig. 7. By increasing the fre-

quency, we shift the envelope of the traveling wave basalwards towards the stapes. And the demon, because he surfs the envelope, is carried along with the wave (just as the sources induced by nonlinear distortion move with the wave; cf. Fig. 4). Again the demon determines the stimulus frequency by counting the number of basilar-membrane oscillations per clock tick. But note that *because he moved with the wave, the demon now uses a different clock*. He now uses the local resonator corresponding to his new location, and that resonator ticks at time intervals of $1/f'_{\rm cf}$. Thus, once again, the demon measures a frequency of 1 cycle/clock-tick (since $f'/f'_{\rm cf}=1$) and, after consulting his formula, pushes and pulls with the same relative phase that he did for frequency f.

Although the stimulus frequency changes ($f\rightarrow f'$), the demon's clock changes correspondingly ($f_{\rm cf}\rightarrow f'_{\rm cf}$). As a result, the demon cannot detect the change and so pushes and pulls with the same relative phase at all stimulus frequencies. The demon—a proxy for nonlinear distortion, or, indeed, any emission mechanism that moves with the wave envelope—cannot generate backward-traveling waves with a phase shift that depends on frequency:[22]

$$\underset{\text{experiment}}{\text{Thought}} \Rightarrow \Delta\theta_{\text{re-emission}} \approx \text{constant}. \tag{9}$$

As suggested by the appearance in the thought-experiment of the relative frequency $f/f_{\rm cf}(x)$, this conclusion can be understood, equivalently, as a consequence of local scaling symmetry (Shera and Zweig, 1993b; Zweig and Shera, 1995).

By combining the predicted phase shifts due to wave travel and reflection we conclude that *the nonlinear-distortion model predicts a constant reflectance phase, in striking contradiction with experiment*:

$$\underset{\text{distortion model}}{\text{Nonlinear}} \Rightarrow \angle R \approx \text{constant}. \tag{10}$$

Although the measured $\angle R$ varies rapidly with frequency, the nonlinear-distortion model predicts a constant value for each of the three component phase shifts in Eq. (5). *This contradiction effectively rules out nonlinear distortion as the origin of echo emissions at low levels.*

Note that our analysis of the nonlinear-distortion model is independent of the detailed form of the emission sources and the nonlinearities that produce them. Made above for simplicity, the assumption that emissions originate from a single point (e.g., from the peak of the wave envelope) is not critical to the conclusion. The argument is easily generalized—by considering many demons surfing many different parts of the wave—to include emissions created over a broad region of the cochlea.

C. Testing the predictions of the thought-experiment using DPOAEs

Our analysis of the nonlinear-distortion model can be tested experimentally by measuring the frequency dependence of emission phase under circumstances where the generation mechanism is *known* to be scaling-symmetric nonlinear distortion. Central to the argument is the notion that changing the stimulus frequency simply shifts the resulting wave pattern (and thus any nonlinear emission sources) along the basilar membrane. As a consequence of local scaling symmetry, this shift corresponds to a simple frequency rescaling that results in approximate constancy of both $\Delta\theta_{\text{round-trip}}$ and $\Delta\theta_{\text{re-emission}}$. Note, however, that similar arguments should apply to *any* measurement paradigm for which an approximate frequency scaling of the stimulus is maintained.

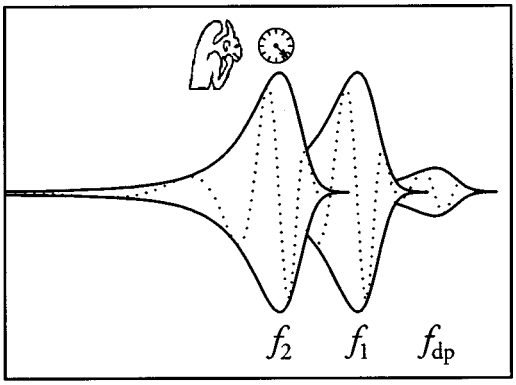

FIG. 8. The demon, responsible here for generating DPOAEs, generates the $2f_1-f_2$ distortion product from his position near the peak of the f_2 traveling wave. When the primary frequency ratio f_2/f_1 is held constant during the frequency sweep, the stimulus and distortion-product wave patterns are simply translated along the cochlear partition. As before, the demon is unable to detect changes in the stimulus frequencies and, consequently, generates a DPOAE with constant phase.

Specifically, the analysis should apply to the generation of distortion-product otoacoustic emissions when the primary-frequency ratio, f_2/f_1, is held fixed (see Fig. 8).[23] When the cochlear position-frequency map is exponential, a constant frequency ratio corresponds to a constant distance along the basilar membrane; the constant ratio f_2/f_1 thus fixes the spatial separations and relative phase relationships (referenced to stapes motion) of the primary traveling waves.[24] So imagine, for example, that the demon—responsible now for generating distortion-products—surfs the peak of the envelope of the f_2 traveling wave. Since the local resonator ticks at a rate proportional to f_2, the demon measures the primary frequencies as f_1/f_2 and 1, values that do not change as the two-tone complex is swept along the cochlea (since the frequency ratio f_2/f_1 is held constant).[25] The analysis thus predicts that for fixed f_2/f_1, the demon emitter should be unable to detect changes in the primary frequencies. Consequently, the resulting emission phase should be roughly constant.

Figure 9 provides a test of this prediction in the human ear. The figure shows the phase of the cubic distortion product $2f_1-f_2$ measured[26] at fixed $f_2/f_1=1.2$. As predicted, the emission phase is essentially independent of frequency,[27] varying by less than half a cycle over most of the nearly three octave range of the figure.[28] In contrast, SFOAE phase measured in the same subject varies by more than 30 cycles over the same frequency range.[29] Measurements in other subjects (total $n=3$) are consistent with these results, and Kemp and Brown have reported similar findings (Kemp and

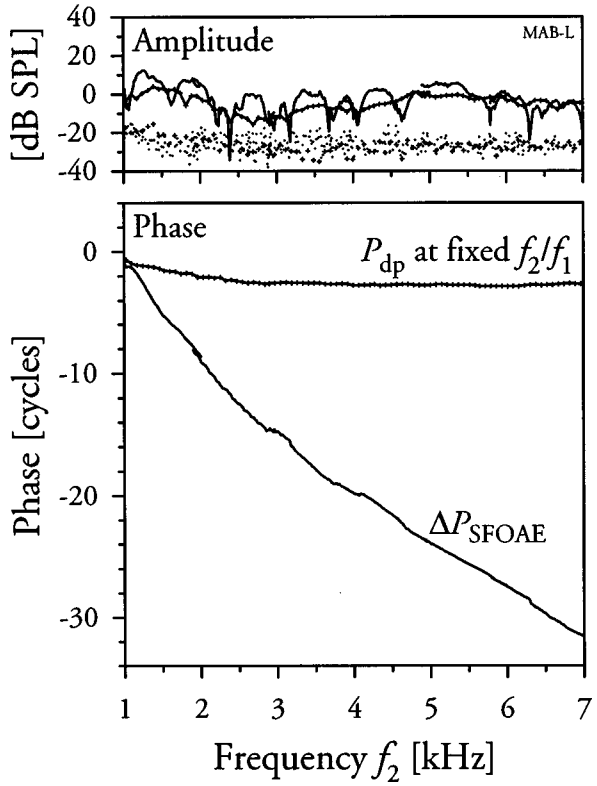

FIG. 9. Constancy of ''frequency-scaled'' DPOAE phase. The solid curves with small crosshairs (+) show the amplitude and phase of P_{dp}, the human $2f_1-f_2$ cubic distortion product measured while holding the ratio of the primary frequencies fixed (at $f_2/f_1=1.2$ with primary levels $\{L_2,L_1\}=\{40,50\}$ dB SPL). With the ratio f_2/f_1 fixed, the primary traveling waves maintain an approximately constant separation along the basilar membrane. To reduce the confounding effects of reflection-source emissions (see Sec. IV C below), the DPOAE was measured in the presence of a 55-dB SPL suppressor tone near $2f_1-f_2$ (e.g., Kemp and Brown, 1983b; Heitmann *et al.*, 1998). (Although the suppressor tone substantially reduced the DPOAE fine structure, it had little effect on the secular variation of the phase important here.) Shown for comparison are measurements in the same subject of ΔP_{SFOAE}, the stimulus-frequency emission obtained using a variant of the suppression method (e.g., Guinan, 1990; Kemp *et al.*, 1990) with probe and suppressor levels of {40,55} dB SPL, respectively. The dotted lines in the upper panel show the approximate measurement noise floor. Note that the data shown here were obtained over several measurement sessions; as a consequence of variations in system calibration, small discontinuities are sometimes visible near session boundaries. Detailed methods for both measurements are presented in the Appendix.

Brown, 1983b; Kemp, 1986). Our abstract thought-experiment thus correctly predicts the striking frequency independence of the phase of emissions generated by frequency-scaled (or ''scaling-symmetric'') nonlinear distortion.[30]

This result supports the argument of Sec. II B—and its contrast with the frequency dependence of echo-emission phase rules out nonlinear distortion as the origin of echo emissions at low levels. If echo emissions and distortion products shared a common origin in cochlear nonlinearity, echo-emission phase, like the phase of $2f_1-f_2$ measured at fixed f_2/f_1, would be essentially independent of frequency. But instead, echo-emission phase rotates rapidly. Contrary to the common view, echo emissions apparently arise by mechanisms fundamentally different from distortion products. When measured with comparable paradigms (i.e., stimuli that preserve the approximate frequency scaling of the stimulus wave pattern characterizing the measurement of stimulus-frequency emissions), echo and distortion-product emissions manifest profound differences in the frequency dependence of their phase that contradict the notion, succinctly expressed by Brass and Kemp (1993), that ''SFOAEs can be thought of as zero-order DPs, and thus as part of the DP series.''

III. ECHO EMISSIONS ARISE BY COHERENT REFLECTION

If echo emissions do not arise by nonlinear distortion, how do they originate? The (mistaken) prediction of the nonlinear-distortion model that $\angle R \approx$ constant hinges on the essential feature that the emission sources move with the wave. The resulting contradiction with experiment suggests that rather than ''surfing'' the wave envelope like the demon, the perturbations that reflect the wave may instead be fixed in space. Thus, rather than being ''re-emitted'' by ''emission generators'' induced through nonlinear distortion, the traveling wave simply scatters off pre-existing irregularities in the mechanics.

The recent theory of coherent reflection filtering (Shera, 1992; Shera and Zweig, 1993b; Zweig and Shera, 1995) characterizes this scattering and indicates that at low stimulus levels echo emissions arise via coherent reflection from the ''random'' impedance perturbations characteristic of cochlear anatomy (Engström *et al.*, 1996; Bredberg, 1968; Wright, 1984; Lonsbury-Martin *et al.*, 1988). Although the impedance perturbations may be densely and randomly distributed along the cochlear partition, the tall, broad peak of the traveling wave localizes the effective scattering to a region spanning the peak of the wave envelope. Most scattered wavelets combine out of phase and cancel one another out. But a simple analog of Bragg's law[31] from x-ray crystallography (Brillouin, 1946) enables a subset of scattered wavelets to combine coherently and form a large reflected wave having the characteristics of echo emissions observed experimentally. In this model, wavelets scattered over an extended region of the cochlea interfere with one another to create a region of coherent reflection that sweeps along the cochlear partition as the frequency is varied. This interference between multiple scattered wavelets precludes the representation of $\angle R$ as a simple sum of phase shifts due to wave propagation and reflection [e.g., along the lines of Eq. (5)]. Nevertheless, the theory predicts that the delay parameter τ—which characterizes the local average phase slope of R in Eq. (4)—equals twice the peak group delay of the basilar-membrane transfer function. Details of the theory, including its many predictions and applications, are presented elsewhere (e.g., Zweig and Shera, 1995; Talmadge *et al.*, 1998a).

IV. DISCUSSION

The arguments we present here demonstrate that the ''common view''—which attributes all otoacoustic emissions, both echo emissions and distortion products, to nonlinear distortion—cannot be correct. Although many argue that otoacoustic emissions share a common origin in co-

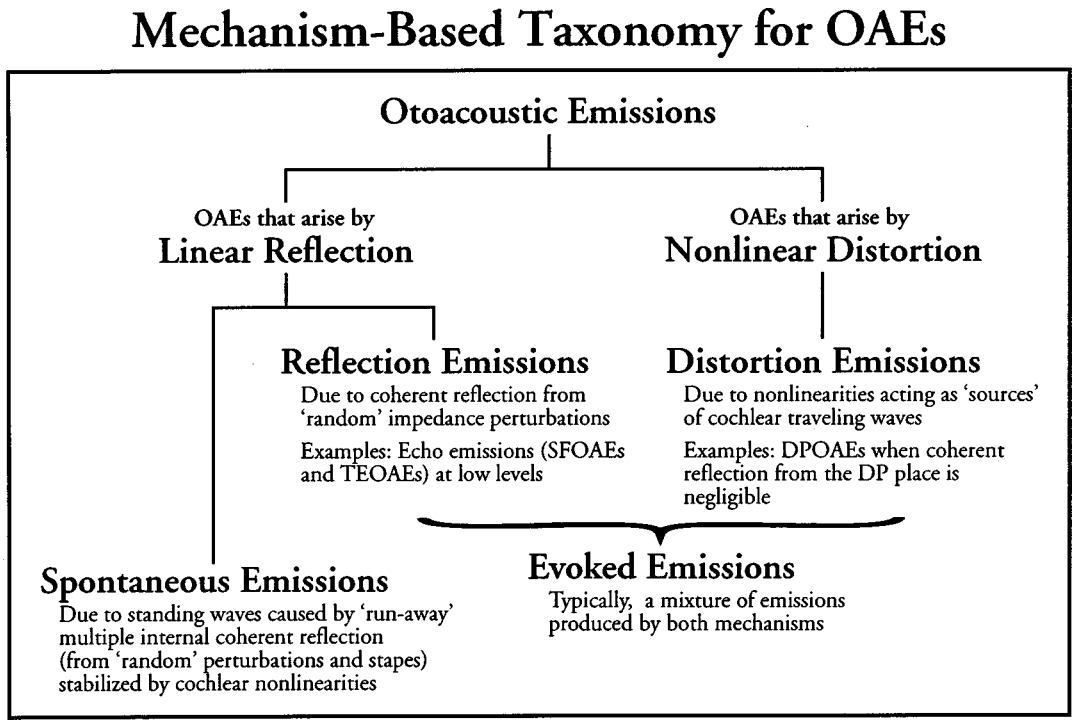

FIG. 10. Proposed mechanism-based taxonomy for mammalian otoacoustic emissions. For conciseness, the names ''reflection-source'' and ''distortion-source'' emissions are here shortened to ''reflection'' and ''distortion'' emissions, respectively.

chlear nonlinearity—that, as Kemp (1997) puts it, ''nonlinearity is at the heart of OAE generation''—we argue that OAEs arise by two fundamentally different mechanisms (i.e., linear coherent reflection[32] versus nonlinear distortion).

A. A mechanism-based taxonomy for otoacoustic emissions

To codify this fundamental distinction we propose a taxonomy for mammalian otoacoustic emissions based on the mechanisms of their generation. This OAE taxonomy, the simplest consistent with current data, is presented in Fig. 10.

Our mechanism-based taxonomy divides evoked otoacoustic emissions into two broad classes:

(i) *Reflection-source emissions*, in which backward-traveling waves arise through the linear (coherent) reflection of forward-traveling waves by pre-existing perturbations in the mechanics (e.g., echo emissions such as SFOAEs and TEOAEs measured at low sound levels); and

(ii) *Distortion-source emissions*, in which backward-traveling waves arise through sources induced by nonlinear distortion (e.g., pure DPOAEs[2]).

Whereas distortion-source emissions would not occur in the absence of cochlear nonlinearities, the coherent reflection responsible for reflection-source emissions is a linear process. The taxonomy is thus consistent with the observations (cf. Fig. 2) that at sound levels near threshold echo-emission amplitude grows linearly with the amplitude of the stimulus (e.g., Kemp and Chum, 1980; Wit and Ritsma, 1979; Wilson, 1980; Zwicker and Schloth, 1984; Shera and Zweig, 1993a) and the principle of superposition holds (Zwicker, 1983). These observations would be more difficult to explain if echo emissions arose through nonlinear distortion.[33]

The conclusion that reflection-source emissions arise through linear coherent reflection may appear to conflict with the well-known level dependence of stimulus-frequency and transiently evoked emissions, which exhibit a nonlinear growth in amplitude at all but the lowest sound levels (cf. Figs. 1 and 2). We emphasize, however, that nonlinear growth with level does not imply that reflection-source emissions arise by a nonlinear process. Rather, the theory of coherent reflection filtering suggests that the nonlinear growth should be understood as a consequence of the level-dependent amplification of forward and reverse traveling waves (Zweig and Shera, 1995), as schematized in Fig. 11. Since the outer hair cells are limited in the forces they can

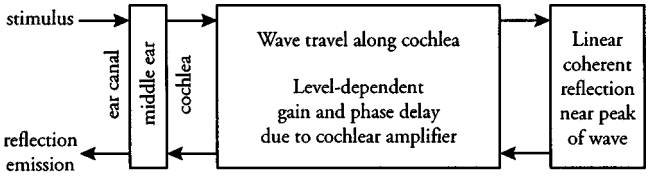

FIG. 11. Simplified conceptual model for the generation of reflection-source emissions. Reflection-source emissions arise from a region of linear coherent reflection near the peak of the traveling-wave envelope. Incident and reflected waves undergo level-dependent gains and phase delays while traveling to, from, and within the scattering reigon. At medium and high stimulus levels, reflection-source emissions therefore exhibit a nonlinear growth with sound level. Note that although they appear separated here for clarity, the regions of coherent reflection and maximal gain overlap within the cochlea. Figure 12 fleshes out this conceptual model (by including phase shifts due to wave propagation) and extends the model to illustrate the mixing of reflection- and distortion-source emissions that occurs during the generation of DPOAEs.

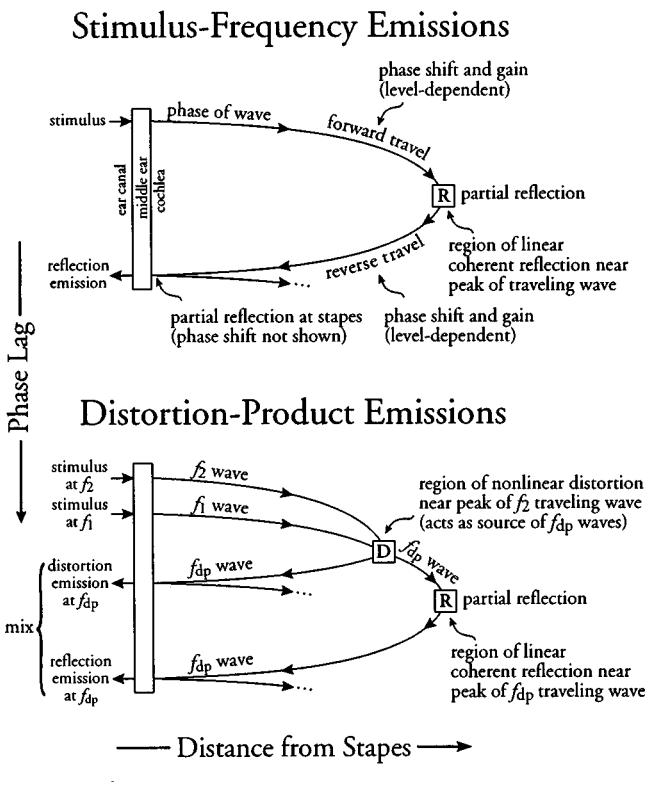

FIG. 12. Schematic diagrams illustrating the generation of stimulus-frequency (top) and distortion-product emissions (bottom) at low sound levels. Both diagrams show phase lags relative to stimulus phase (lag increasing downward) of forward- and backward-traveling waves versus distance from the stapes. At low levels, SFOAEs arise from a region of coherent reflection (**R**) near the peak of the traveling-wave envelope. Stimulus and reflected waves undergo level-dependent gains and phase delays while traveling to and from the scattering region. The generation of low-level DPOAEs is more complicated and involves the mixing of reflection and distortion emissions in the ear canal. A region of nonlinear distortion (**D**) near the peak of the f_2 wave generates waves at frequency f_{dp} that propagate in both directions: The backward-traveling wave propagates to the ear canal as a distortion-source emission; the forward-traveling wave undergoes partial coherent reflection (**R**) near the peak of its wave envelope, generating a second backward-traveling wave that propagates to the ear canal as a reflection-source emission. The DPOAE measured in the ear canal is thus a mixture of emissions arising not just from two spatially distinct regions, but from two fundamentally different mechanisms. Backward-traveling waves arriving at the stapes are partially reflected, creating new forward-traveling waves (arrows with three dots) that subsequently undergo partial coherent reflection themselves. The resulting (infinite) series of multiple internal reflections is truncated for clarity. Note that possible phase shifts due to reflection are not shown.

produce, traveling-wave amplitudes are compressive functions of sound level, with the greatest compression occurring near the peak of the wave envelope, where scattering is maximal. Although the propagation of traveling-wave energy is a nonlinear function of sound level, the physical mechanisms responsible for reversing the direction of that propagation (i.e., coherent reflection from perturbations in the mechanics) are essentially linear.

In our taxonomy, spontaneous emissions are grouped with reflection-source emissions. As originally suggested by Kemp (1980), spontaneous emissions may result from a process of ''run-away'' multiple internal reflection stabilized by cochlear nonlinearities. In the view espoused in the taxonomy, multiple cycles of propagation, amplification, and coherent reflection[34] create narrow-band cochlear standing waves measurable in the ear canal (Zweig and Shera, 1995; Talmadge and Tubis, 1993; Talmadge *et al.*, 1997).

When we argue that reflection- and distortion-source emissions arise by different mechanisms, we mean that the processes responsible for creating backward-traveling waves differ for the two emission types. For example, although the backward-traveling waves created by nonlinear distortion may arise, at least in part, through the action of nonlinear cellular demons (OHCs) pushing and pulling on the basilar membrane, reflection-source emissions do not result directly from OHC forces. Rather, we argue that reflection-source waves arise by the linear, ''passive'' scattering of the forward-traveling wave off more or less random perturbations in the mechanics. Although the waves created by this scattering may then be amplified through the collective action of the ''cochlear amplifier,'' the backward-traveling waves themselves are not fundamentally the product of nonlinear force generation by outer hair cells.

Once generated, however, backward-traveling waves produced by either mechanism propagate basally to the stapes (from which they may be partially reflected), through the middle ear, and out into the ear canal. While propagating, emissions of both types undergo delays, phase shifts, and gains (e.g., due to the cochlear amplifier or reverse middle-ear transmission), as illustrated in Fig. 12. Thus, although their mechanisms of generation are fundamentally different, both emission types traverse a similar pathway on their way to the ear canal, and both are potentially vulnerable to modifications or disruptions of this pathway (e.g., to changes in outer-hair-cell function, middle-ear transfer characteristics, etc.). Although a common dependence on propagation pathways from cochlea to ear canal presumably introduces correlations in reflection- and distortion-source emission amplitude, the taxonomy emphasizes that their respective mechanisms of generation—and hence their dependence on underlying parameters of cochlear mechanics—remain fundamentally distinct.

Although identifying what we suggest are the two principal branches of the OAE family tree, our taxonomy makes no attempt to adumbrate the sub-branches. For example, in some species (e.g., rodents and rabbits), considerable evidence suggests that distortion-source emissions can be usefully divided into subtypes, conventionally designated the ''active or low-level component'' and the ''passive or high-level component'' (e.g., Norton and Rubel, 1990; Mills and Rubel, 1994; Whitehead *et al.*, 1992a,b, 1995; Whitehead, 1998).[35] The differential vulnerability of these two distortion components to physiological insult suggests that they arise from different mechanisms within the cochlea.[36] And although coherent reflection from ''random'' mechanical perturbations appears to be the dominant reflection mechanism in the normal primate ear, reflection by other mechanisms may contribute in some circumstances. For example, incoherent reflection from large punctate perturbations may dominate in certain pathologies or in specialized cochleae, such as in the ''auditory fovea'' of the CF-FM bat (e.g., Kössl and Vater, 1995), in which the mechanical properties of the cochlear partition change rapidly with position. When

coupled with knowledge of the underlying mechanisms, a more complete identification of the different emission subtypes could presumably prove of considerable value in the application of OAEs to noninvasive diagnostics.

B. Relation to the conventional classification of OAEs

As the taxonomy implies, we argue that backward-traveling waves originating by coherent reflection and nonlinear distortion constitute the elemental OAE ''building blocks'' that combine to form evoked emissions measured in the ear canal (i.e., echo emissions and DPOAEs). In any given measurement, the two types mix in varying degrees dependent on the species, the stimulus parameters, and the state of the cochlea. For example, although presumably arising largely by coherent reflection, echo emissions measured at medium and high stimulus levels may contain significant energy from distortion-source waves created by nonlinear distortion (e.g., Yates and Withnell, 1998; Withnell and Yates, 1998).

The OAE taxonomy thus provides a mechanism-based alternative to the conventional classification scheme, which classifies emissions based principally on the stimuli used to elicit them (e.g., TEOAEs, SFOAEs, and DPOAEs). *The mixing of reflection- and distortion-source emissions in the ear canal precludes any fixed correspondence between the two schema*. At low levels, however, echo emissions (i.e., TEOAEs and SFOAEs) arise predominantly through linear coherent reflection. And under circumstances when coherent reflection from the f_{dp} place can be neglected, DPOAEs arise predominantly from distortion-source waves due to nonlinear distortion. Thus, in these special cases, the division of evoked emission into ''echo emissions'' and ''distortion products''—a division made at the beginning of this paper based on the relative spectral content of the stimulus and the emission—corresponds to a fundamental difference in generation mechanism as well.[37] As commonly measured, however, evoked OAEs typically represent mixtures of the different emission types. We therefore find the conventional, stimulus-based emission nomenclature more confusing than helpful for understanding the origin and properties of OAEs.

C. An example of reflection- and distortion-source mixing

Our taxonomy and its identification of the fundamental OAE ''building blocks'' provides a framework that simplifies the often bewildering complexity of OAE phenomenology. The phenomenon of DPOAE fine structure, for example, can be understood in terms of the mixing of the two OAE ''building blocks.'' As originally suggested by Kim (1980), much of DPOAE fine structure apparently arises through the interference of two distinct sources located near the f_2 and f_{dp} places (e.g., Kim, 1980; Kemp and Brown, 1983b; Shera and Zweig, 1992). Although the ''two-source'' model for DPOAEs now appears well established (e.g., Gaskill and Brown, 1990; Brown *et al.*, 1996; Engdahl and Kemp, 1996; Brown and Beveridge, 1997; Talmadge *et al.*, 1997, 1998b; Heitmann *et al.*, 1997, 1998; Fahey and Allen, 1997; Siegel *et al.*, 1998), our taxonomy goes further and identifies these two sources as arising not simply from two distinct locations, but from *two different mechanisms*: a distortion source near the f_2 place and a coherent reflection from the f_{dp} place. (The combined process is illustrated in the bottom panel of Fig. 12, where the distortion- and reflection-source regions are denoted **D** and **R**, respectively.) Indeed, as our argument demonstrates for the frequency-scaled, fixed-f_2/f_1 paradigm, it is fundamentally this difference in emission-source *mechanism*—and *not*, as is often implied (e.g., Brown *et al.*, 1996), the difference in source *location*—that is ultimately responsible for the different frequency dependencies of the phase of the emissions arising from the two interfering sources. Thus, as commonly measured, *DPOAEs actually comprise a mixture of backward-traveling waves that arise by two fundamentally different mechanisms within the cochlea*. By matching measurements of DPOAE fine structure with predictions obtained using the model of coherent reflection filtering, Talmadge *et al.* (1999) provide elegant experimental corroboration of these ideas.

The relative mix of the two OAE ''building blocks'' measured in the ear canal presumably depends on stimulus parameters such as frequency and level. For example, Fig. 12 predicts that variations in the DPOAE mix should occur as a consequence of any change in the relative amplitudes of the net forward- and backward-traveling distortion-source waves emanating from **D**. Mechanisms that may produce such changes include suppression by the primaries (e.g., Kanis and de Boer, 1997; Shera and Guinan, 1997), nonlinearities in the effective forward and reverse ''load impedances'' (Shera and Zweig, 1991, 1992; Fahey and Allen, 1997), and phase-dependent interference between distortion-source wavelets within the DP source region (e.g., van Hengel, 1996; Neely and Stover, 1997; Kemp and Knight, 1999). Variations in the relative mix would also be expected as a result of any mechanism (e.g., suppression) that affects the cochlear amplifier in the region between **D** and **R** and thereby modifies the strength of the reflection-source emissions that scatter back from **R** (e.g., Kemp and Brown, 1983b; Kummer *et al.*, 1995; Heitmann *et al.*, 1998).

Several studies can be interpreted in this light as providing evidence for stimulus-dependent mixing. For example, the data of Fahey and Allen (1997) in cat suggest that the relative amplitude of the distortion- and reflection-source components varies with the primary level ratio, L_2/L_1. Similarly, Kemp's (1986) measurements in human ears suggest a dependence on the ratio f_2/f_1. At values of f_2/f_1 relatively close to one ($f_2/f_1 \lesssim 1.1$), the frequency dependence of the $2f_1-f_2$ DPOAE shows regular variations (nulls) in amplitude and a more rapidly rotating phase distinctly different from the nearly constant amplitude and phase obtained at larger values of f_2/f_1 (cf. Fig. 9). These features appear consistent with the view that the measured DPOAE arises from a variable f_2/f_1-dependent mix of waves from two distinct sources, and, furthermore, that these two sources—in accordance with their respective identities as sources of nonlinear distortion and coherent reflection—produce emissions with very different frequency dependence in their phase. Applying the reasoning of Sec. II B to emissions evoked by any frequency-scaled stimulus (e.g., fixed

f_2/f_1), we hypothesize that (1) a nearly frequency-independent phase implies that the OAE arises mainly by nonlinear distortion, whereas (2) a rapidly rotating phase implies that the OAE arises mainly by coherent reflection.

D. The taxonomy resolves OAE ''paradoxes''

The taxonomy provides a conceptual framework that helps resolve issues that appear paradoxical if all emissions are regarded as sharing a common origin in nonlinear distortion. For example, consider the observations that

(i) whereas primates tend to have large SFOAEs and TEOAEs, many SOAEs, and small DPOAEs, rabbits and guinea pigs have the relative amplitudes and/or prevalence of these emissions reversed (e.g., Zurek, 1985; Whitehead *et al.*, 1996a); and

(ii) whereas SFOAEs and SOAEs are abolished by aspirin administration, DPOAEs can remain almost unchanged (e.g., Martin *et al.*, 1988; Wier *et al.*, 1988).

In the common view these observations are largely unintelligible and, indeed, are often presented as paradoxes. For if all emissions shared a common origin in cochlear nonlinearity, their relative amplitudes would be expected to vary together, both between species and in response to aspirin or other ototoxic drugs.[38] Our taxonomy resolves these ''paradoxes'' by recognizing fundamental differences in the mechanisms of OAE generation. As shown below, when differences in their mechanisms of generation are taken into account, the observation that the different emission types can be ''decoupled,'' both between species and by certain experimental manipulations and/or pathologies, is no longer surprising (indeed, it is predicted).

First, consider species differences in OAE amplitude and prevalence. Whereas distortion-source emissions depend on the form and magnitude of cochlear nonlinearities (e.g., on the effective ''operating point'' along hair-cell displacement-voltage transduction functions), reflection-source emissions depend strongly on the size and spatial arrangement of micromechanical impedance perturbations (e.g., on variations in hair-cell number and geometry). In the light of these different dependencies, species differences between the two emission types no longer appear mysterious: They simply reflect differences across species in the respective factors underlying emission generation. Indeed, the theory of coherent reflection filtering provides an interesting hypothesis to explain the striking species differences in reflection-emission amplitudes (Zweig and Shera, 1995): The model predicts that disorderly patterns of impedance perturbations produce large reflections whereas orderly patterns produce only small reflections.[39] Correspondingly, in contrast to the cellular disorder characteristic of the primate organ of Corti, anatomical regularity constitutes an ''impressive feature'' of the rodent cochlea (e.g., Wright, 1984). Thus, the theory of coherent reflection filtering accounts naturally for the relative amplitudes of reflection emissions in humans (large) and guinea pig (small).[40]

Next, consider the effects of aspirin on OAEs. Once reflection- and distortion-source emissions are understood as separate emission types, a number of possible explanations for their differential responses arise. For example, the experiments of Martin *et al.* (1988) suggest that aspirin may somehow reduce the gain of the cochlear amplifier while preserving the nonlinearities responsible for generating distortion emissions. Although a reduction in the gain of the cochlear amplifier would be expected to have a dramatic effect on reflection emissions—which arise from scattering near the peak of the traveling wave, where the gain is presumably largest—the effect on distortion-source emissions could be significantly less. To see this, note that suppression studies indicate that distortion-source waves appear to be generated predominantly in the region of maximum overlap between the primaries near the peak of the f_2 traveling wave (e.g., Brown and Kemp, 1984; Kummer *et al.*, 1995). The region of nonlinear distortion (**D** in Fig. 12) is therefore often significantly basal to the f_{dp} place (near **R**). For example, the generation of cubic distortion products at the frequency $f_{dp}=2f_1-f_2$ at a primary-frequency ratio of $f_2/f_1\approx 1.25$ occurs at the frequency ratio $f_{dp}/f_2\approx 0.6$, corresponding to roughly three-quarters of an octave. At the low and medium sound-pressure levels for which the amplifier gain is significant, this frequency ratio corresponds to a distance from the f_{dp} place larger than the width of the traveling-wave envelope.[41] Thus, the distortion source lies basal to the region of maximal gain for the f_{dp} traveling wave (see Fig. 12), and, consequently, the backward-traveling distortion-source wave experiences relatively little amplification as it travels to the stapes. The resulting DPOAE would thus appear relatively insensitive to the gain of the cochlear amplifier at the distortion-product frequency.[42]

Note, however, that the analysis is complicated by possible mixing of the emission types, specifically by contributions to the measured DPOAE from reflection-source emissions scattered back from the f_{dp} place. Although aspirin may have little effect on the distortion source (**D**), the argument outlined above predicts a decrease in the magnitude of any concomitant reflection-source emissions (due to reductions in the f_{dp} amplifier gain near **R**) and thus significant changes in the resulting distortion-product microstructure. Unfortunately, the measurements reported by Martin *et al.* do not permit an evaluation of this prediction.[43] Nevertheless, the general idea that reflection-source emissions may be more sensitive to changes in the f_{dp} amplifier gain is consistent with the observation that the emission component from the f_{dp} place (i.e., the coherent reflection) is differentially diminished by presumed reductions in the amplifier gain due to efferent feedback evoked by contralateral noise (Brown and Beveridge, 1997).

E. Implications of the taxonomy for the use of OAEs

As a consequence of their different origins, reflection- and distortion-source emissions presumably manifest different dependencies on cochlear pathologies. However, the mixing of the two emission types confounds an understanding of their individual characteristics and clouds the assessment of their different utilities as clinical diagnostic and screening aids. As a result, it is of considerable theoretical and practical interest to isolate and characterize the properties of each emission type (and related subtypes) separately,

to understand the factors that control their mixing, and to determine their individual correlations with cochlear pathology.

Although some degree of mixing among the OAE ''building blocks'' may prove unavoidable, several existing measurement techniques hold promise for at least partially separating the two types of emissions. For example, reflection-source emissions can be studied at low sound levels using methods that do not cancel the low-level linear components of the response (e.g., Kemp and Chum, 1980; Shera and Zweig, 1993a). And in DPOAE measurements, the confounding contributions of reflection-source emissions can be substantially reduced by using a third primary tone with frequency near f_{dp} to suppress amplification of the reflection-source emissions that scatter back from this location (e.g., Kemp and Brown, 1983b; Heitmann *et al.*, 1998). Alternatively, the reflection- and distortion-source components of DPOAEs may be separable based on onset latency, either in the time (e.g., Whitehead *et al.*, 1996b; Talmadge *et al.*, 1998b) or the frequency domain (e.g., Brown *et al.*, 1996). Note that extracting or suppressing individual components of an evoked emission may be more difficult—and problems of interpretation correspondingly greater—when the respective regions of wave generation [e.g., the regions of nonlinear distortion (**D**) and coherent reflection (**R**) in Fig. 12] overlap extensively within the cochlea. For DPOAEs, significant overlap can be expected when using primary-frequency ratios close to one.

Our taxonomy predicts that reflection- and distortion-source emissions—when properly separated and studied—will manifest considerable differences in their correlations with particular cochlear pathologies. Clinical measurement of both types of evoked emissions will presumably be needed to maximize the power and specificity of OAEs as noninvasive probes of cochlear function.

ACKNOWLEDGMENTS

We gratefully acknowledge many stimulating discussions with Jont B. Allen, Paul F. Fahey, David T. Kemp, Nelson Y. S. Kiang, Stephen T. Neely, Sunil Puria, Carrick L. Talmadge, and George Zweig and thank John R. Iversen, M. Charles Liberman, William T. Peake, John J. Rosowski, and three anonymous reviewers for their helpful critical readings of and comments on the manuscript. The work was supported by NIDCD/NIH Grant Nos. DC00108, DC03494, DC00119, and DC00235.

APPENDIX: MEASUREMENT METHODS

This appendix outlines the methods used to obtain the distortion-product and stimulus-frequency emission data shown in Fig. 9. All measurements were performed with subjects comfortably reclined in a sound-proofed, vibration-isolated chamber (Ver *et al.*, 1975), well shielded from sources of electrical interference (Golka, 1994). Stimulus waveforms were generated and responses acquired and averaged digitally using a Spectrum Signal Processing PC/C31 DSP board with two Burr-Brown analog daughter modules providing eight channels of synchronized analog I/O. The hardware was computer controlled using a custom data-acquisition system implemented in LabVIEW and supplemented with hand-coded time-domain artifact-rejection and synchronous-averaging routines. Acoustic signals were transduced at sampling rates of 59.94 kHz using a calibrated Etymotic Research ER-10c DPOAE probe system supplemented with an ER-3A earphone whose sound-delivery tube was threaded through the ER-10c foam ear-tip. Measurement frequency resolution was always sufficient to resolve ambiguities due to phase unwrapping. Control experiments in a small cavity indicated that the measurement-system distortion was at or below the noise floor (typically less than -25 dB SPL). Treatment of human subjects was in accordance with protocols approved by the Human-Studies Committee at the Massachusetts Eye and Ear Infirmary.

Measurement of DPOAEs: To reduce reflection-source contributions to the measured emission (see Sec. IV C), DPOAEs were measured in the presence of a suppressor tone with frequency near $2f_1-f_2$ (e.g., Kemp and Brown, 1983b; Heitmann *et al.*, 1998). Although the suppressor tone substantially reduced the DPOAE fine structure, it had little effect on the more secular variation of the phase of primary interest in the context of this paper.

At each measurement frequency the acoustic stimulus had the form

$$\text{stimulus}=\underbrace{\langle XX\ldots X\rangle}_{\#\geqslant M}, \tag{A1}$$

where X represents a periodic 4096-sample ($\approx$68.33 ms) segment containing an integral number of periods of the stimulus waveform. The waveform consisted of three frequency components: a component at each of the two primary frequencies, f_1 and f_2, and a third component at the suppressor frequency, f_s, near $2f_1-f_2$. The phase of each component was adjusted to produce an upwards zero-crossing (sine-phase) at the beginning of each X segment. The respective stimulus levels $\{L_1,L_2,L_s\}$ were {50,40,55} dB SPL. To minimize artifactual distortion, the three component waveforms were delivered synchronously through separate earphones.

Measurements were made versus frequency by sweeping f_2 from high frequencies to low while varying f_1 to keep the primary-frequency ratio at the fixed value $f_2/f_1=1.2$. The suppressor frequency was also swept, with $f_s=2f_1-f_2+\Delta f_s$ and $\Delta f_s=43.9$ Hz.[44] The periodic segments X were presented repeatedly until a total of $M=32$ corresponding artifact-free responses[45] were collected; at each frequency the total stimulus duration was therefore $\geqslant 32\times 68.33$ ms $\approx$2.2 s. To reduce unwanted transients the waveform was ramped on and off by pre- and postpending two additional segments (indicated by the angled brackets $\langle$ and $\rangle$) with envelopes of half Blackman windows with 2.5-ms rise and fall times. After digitizing the resulting ear-canal pressure, responses to the segments X were averaged and the amplitude and phase of the $2f_1-f_2$ distortion component extracted using Fourier analysis.

Measurement of SFOAEs: Stimulus-frequency emissions were measured using a variant of the suppression method

(e.g., Guinan, 1990; Kemp *et al.*, 1990; Brass and Kemp, 1991, 1993; Souter, 1995). In this method, the emission is obtained as the complex (or vector) difference between the ear-canal pressure at the probe frequency measured first with the probe tone alone and then in the presence of a stronger suppressor tone at a nearby frequency.

At each measurement frequency the acoustic stimulus had the form

$$\text{stimulus}=\underbrace{\langle XX\ldots X\rangle}_{\#\geqslant M}, \tag{A2}$$

where X represents a periodic (5×4096)-sample ($\approx$341.66 ms) segment consisting of two components:

$$X=\begin{cases}\pi_1\Pi_2\Pi_3\pi_4\pi_5\Pi_6\Pi_7\pi_8 & \text{(probe earphone)},\\ o_1O_2O_3\langle_4\sigma_5\Sigma_6\Sigma_7\rangle_8 & \text{(suppressor earphone)}.\end{cases} \tag{A3}$$

Each component consisted of four long (uppercase) and four short (lowercase and angled brackets) intervals. The long intervals were each 4096 samples ($\approx$68.33 ms) in duration and contained an integral number of periods of the probe (Π_i), suppressor (Σ_i), and zero (O_i) waveforms, respectively. The short intervals were one-fourth the duration of the long intervals (i.e., 1024-samples or $\approx$17.08 ms) and did not, in general, contain an integral number of periods of the corresponding waveform. The short intervals π_i, σ_i, and o_1 allowed for response settling time and contained segments of the probe, suppressor, and zero waveforms, respectively. The short intervals $\{\langle_4,\rangle_8\}$ were used to ramp the suppressor tone {on,off} using the {first,second} half of the Blackman window. The two components of X were synchronized and presented simultaneously through separate earphones. Note that whereas the probe tone played continuously during the measurement, the suppressor tone cycled on and off repeatedly due to alternation of the zero and suppressor waveforms. The probe and suppressor levels $\{L_p,L_s\}$ were {40,55} dB SPL.

Measurements were made versus probe frequency by sweeping both probe and suppressor from high frequencies to low, with $f_s=f_p+\Delta f_s$ and $\Delta f_s=43.9$ Hz. The periodic segments X were played repeatedly until a total of $M=64$ corresponding artifact-free responses were collected; at each frequency the total stimulus duration was therefore $\geqslant64\times341.66$ ms$\approx$22 s. To reduce unwanted transients the probe waveform was ramped on and off by pre- and postpending two additional segments [indicated by the angled brackets $\langle$ and $\rangle$ in Eq. (A2)] with envelopes of half Blackman windows with 2.5-ms rise and fall times. After digitizing the resulting ear-canal pressure, responses to all probe-alone segments (i.e., all segments Π_2 and Π_3) were averaged to form Y_p; similarly, the responses to all probe+suppressor segments (i.e., all segments Π_6 and Π_7) were averaged to form Y_{p+s}. From these averaged response waveforms, the complex amplitudes of the f_p components of the ear-canal pressure, denoted $P_p(f_p)$ and $P_{p+s}(f_p)$, were extracted using Fourier analysis. The complex quantity $\Delta P_{SFOAE}(f_p)$ was then defined as

$$\Delta P_{SFOAE}(f_p)\equiv P_p(f_p)-P_{p+s}(f_p)e^{-2\pi i\Delta N\Delta T f_p}, \tag{A4}$$

where the complex exponential compensates for the phase shift in the probe due to the time interval, $\Delta N\Delta T$, between the probe-alone and probe+suppressor segments. Here, ΔT is the sampling interval (reciprocal of the sampling rate), and ΔN represents the total number of these intervals that separate the two segments:

$$\Delta N=\#\text{ samples }(\Pi_2\Pi_3\pi_4\pi_5)=2\tfrac{1}{2}\times4096=10\,240. \tag{A5}$$

Note that when the two segments are separated by an integral number of periods of the probe waveform, the phase shift modulo 2π is zero.

Due to the long averaging time and high-frequency resolution (the probe frequency was typically decremented in steps of approximately 15 Hz), Fig. 9 shows data obtained over several measurement sessions. Unwrapped phase curves from the different sessions were patched together by shifting them vertically by integer multiples of 2π to obtain a (nearly) continuous curve. As a consequence of variations in system calibration, small discontinuities are sometimes visible in both amplitude and phase at the ''seams'' near session boundaries.

[1]In the common view, stimulus-frequency emissions (SFOAEs) are regarded as ''zeroth-order'' distortion-products (DPOAEs) produced by the degenerate primary stimulus pair $f_1=f_2$ (e.g., Brass and Kemp, 1993; Kemp, 1998). Patuzzi (1996), for example, argues this point from an operational perspective:

> ''The nonlinear growth of ear canal sound pressure with stimulus level is easily explained by a nonlinear input admittance to the ear canal, due to the nonlinear input admittance of the cochlea. Because the sound level in the ear canal does *not* scale proportionately with the stimulus level, the sound level predicted at low stimulus levels on the basis of linear extrapolation from high stimulus levels does not agree with that actually measured. The difference between the expected and measured acoustic waveforms is often attributed to the presence of a 'stimulus frequency OAE,' when it is just as easily explained by a nonlinear cochlear input admittance and an error of extrapolation. The measurement of SFOAEs can be viewed as an analysis of the first harmonic of the nonlinear input admittance. [...] Just as the SFOAEs represent the nonlinear growth of the first harmonic of the cochlear input admittance, the DPOAEs can be viewed as two-tone interactions due to the nonlinearity of the cochlear input admittance.''

[2]We use the qualifier ''pure'' here because distortion products measured in the ear canal are often *mixtures* of emissions generated by both distortion- and reflection-source mechanisms. We elaborate on this point in Sec. IV below.

[3]A preliminary account of this work has been presented elsewhere (Shera and Guinan, 1998).

[4]In this paper, we focus on acoustically evoked otoacoustic emissions; emissions evoked by direct electrical stimulation of the organ of Corti are not considered.

[5]In a normal ear, the threshold hearing curve often manifests corresponding peaks and valleys (e.g., Elliot, 1958; Thomas, 1975; Long, 1984); at levels near threshold, a swept tone of constant driver level moves alternately into and out of perception (e.g., Kemp, 1979b; Cohen, 1982).

[6]The symbol ''$\equiv$'' denotes equivalence—it means that the quantity on the left (in this case, the cochlear reflectance) is defined by the quantity on the right (here, the complex ratio of forward- and backward-traveling pressure waves at the stapes).

[7]Although we later conclude that the terminology is physically appropriate, the term ''reflectance'' should not be understood to imply any tacit assumption of a particular emission mechanism.

[8]Equation (2) neglects terms proportional to $R^2,R^3,\ldots$ that arise due to multiple internal reflection within the cochlea (see Shera and Zweig, 1993a; Zweig and Shera, 1995). See also Fig. 12 of this paper.

[9]A wider range of emission data from humans (Shera and Zweig, 1993a) shows that there exist extended frequency regions well characterized by statements (3) punctuated by short ''anomalous regions'' in which the re-

flectance varies more rapidly (see also Fig. 9 and footnote 29).

[10]Over a wider frequency range, R varies roughly as

$$R \approx R_0 e^{-2\pi i N \ln(f/f_{\max})},$$

where $f_{\max}$ is the maximum frequency of hearing. Except near ''anomalous regions'' (see footnote 9), both the complex amplitude R_0 and the dimensionless parameter N generally vary slowly with frequency (Shera and Zweig, 1993a). By expanding $\angle R$ in a power series about an arbitrary reference frequency one can show that the effective ''delay,'' τ, appearing in Eq. (4) varies inversely with frequency as $\tau(f) = N/f$. The parameter N thus represents the delay measured in units of the stimulus period.

[11]For simplicity, we have ignored dispersive effects due to sound transmission through the middle ear. The echo described here is that which would be measured at the basal end of the cochlea near the stapes (i.e., at the point where the reflectance R is defined).

[12]We wish to compare the observed change in $\Delta\theta_{\text{forward}}$ with the value predicted using the assumption that $\angle R \approx 2\Delta\theta_{\text{forward}}$. [The factor of 2 arises from round-trip travel; see Eq. (7).] The change, $\Delta\{\angle R\}$, in the phase of R over the frequency interval Δf_{cf} between the characteristic frequencies of the two measurement points can be estimated as follows. Since $\angle R$ rotates through 2π radians over the interval Δf_{OAE} between spectral maxima, the interval Δf_{cf} between the characteristic frequencies of the two measurement points corresponds to a phase shift of roughly

$$\Delta\{\angle R\} \approx 2\pi \Delta f_{\text{cf}} / \Delta f_{\text{OAE}}.$$

Unfortunately, the frequency spacing Δf_{OAE} between emission spectral maxima has not been measured in the squirrel monkey. However, measurements of SFOAEs at frequencies of 1–2 kHz in the rhesus monkey (Lonsbury-Martin *et al.*, 1988) indicate that $\Delta f_{\text{OAE}}/f \approx \frac{1}{13}$—compared with roughly $\frac{1}{15}$ at similar frequencies in humans (Shera and Zweig, 1993a)—suggesting that species differences may be small among primates. Using the human value yields

$$\Delta\{\angle R\} \approx 2\pi 15 \Delta f_{\text{cf}}/f_{\text{cf}} \approx 6\pi,$$

where the ratio $\Delta f_{\text{cf}}/f_{\text{cf}} \approx |f_{\text{cf}}(x_1) - f_{\text{cf}}(x_2)| / \sqrt{f_{\text{cf}}(x_1) f_{\text{cf}}(x_2)} \approx \frac{1}{5}$ has been estimated from the data in Fig. 5. Under the assumption that $\angle R \approx 2\Delta\theta_{\text{forward}}$, the predicted change in $\Delta\theta_{\text{forward}}$ is $\frac{1}{2}\Delta\{\angle R\}$ (i.e., approximately 3π, as shown by the scale bar in Fig. 5). Note that human emission measurements suggest that the ratio $\Delta f_{\text{OAE}}/f$ decreases at higher frequencies (Zweig and Shera, 1995); our calculation based on the value of $\Delta f_{\text{OAE}}/f$ near 1 kHz may therefore underestimate the value of $\Delta\{\angle R\}$ at 6 kHz.

Alternatively, the value of $\Delta\{\angle R\}$ can be estimated directly from the data in Fig. 5 using the theory of coherent reflection filtering (see Sec. III), which predicts the relation $\Delta f_{\text{OAE}}/f \approx 1/2f\tau_{\text{group}}$, where τ_{group} is the transfer-function group delay measured at the characteristic frequency (Zweig and Shera, 1995). Calculating the slope of the transfer-function phase from the data in Fig. 5 yields the value $\Delta f_{\text{OAE}}/f \approx \frac{1}{8}$, an estimate that implies a value of $\Delta\{\angle R\}$ roughly half that obtained above. Because the transfer-function phase varies more rapidly when the amplitude response is sharper, the estimates of τ_{group} and $\Delta\{\angle R\}$ obtained here from Fig. 5 presumably underestimate the values characteristic of healthy preparations at low sound levels (cf. Zweig and Shera, 1995).

The obvious uncertainty in these various estimates notwithstanding, the value of $\Delta\{\angle R\}$ consistently appears many times greater than the observed change in $\Delta\theta_{\text{forward}}$.

[13]Direct determination of phase shifts due to reverse propagation may now be possible using careful measurements of OAEs evoked by focal electrical stimulation of the cochlear partition (e.g., Nakajima *et al.*, 1994, 1999).

[14]For nice reviews, see the series by de Boer (1980, 1984, 1991).

[15]Even if $\Delta\theta_{\text{forward}}$ and $\Delta\theta_{\text{reverse}}$ are not numerically equal, the constancy of $\Delta\theta_{\text{round-trip}}$ follows so long as $\Delta\theta_{\text{reverse}} \approx$ constant, as expected in an approximately scaling-symmetric cochlea.

[16]Our thought experiment alludes, of course, to ''Maxwell's demon'' (e.g., Maxwell, 1871; Leff and Rex, 1990), a ''very observant and neat-fingered being'' invented by Maxwell to illustrate the statistical character of the second law of thermodynamics. Compared to Maxwell's demon, our demon is rather myopic, but is capable of doing work.

[17]The demon's phase formula may depend not only on the frequency of basilar-membrane vibration, but also on its local amplitude. We focus here, however, on changes in stimulus frequency and assume, for simplicity, that the stimulus amplitude is held constant during the measurement (e.g., as it was during the frequency sweeps shown in Fig. 1).

[18]Of course, the demon must also determine, from his measurements of basilar-membrane displacement, how *hard* he must push in order to generate an emission with the correct relative amplitude, $|R|$.

[19]Despite an aptitude for pushing and pulling, the demon is no omniscient or omnipotent being. Rather, the demon is but a stand-in for unspecified biophysical mechanisms and, consequently, must make do with the tools he finds at hand.

[20]Every transverse section of the cochlear partition may exhibit, in addition to the macromechanical oscillator tuned to f_{cf}, various micromechanical oscillators, modes of vibration, or other processes with different resonant frequencies and/or characteristic time scales (e.g., tectorial-membrane resonances, membrane time constants, efferent feedback signals, etc.). At each location, the cochlear partition may therefore contain not one but multiple ''clocks;'' and these multiple clocks could, in principle, be arranged to enable the demon to detect changes in the stimulus frequency. However, so long as the emission process does not depend sensitively on the relative values of these additional resonant frequencies [e.g., because the micromechanical oscillators have nearly the same spatial dependence as $f_{\text{cf}}(x)$ (e.g., Allen and Fahey, 1993) and/or because the relevant time scales are either much larger or much smaller than $1/f_{\text{cf}}$], then each location along the cochlear partition can effectively be regarded as having a single independent clock. At low and moderate sound levels, this assumption is supported both by the existence of scaling symmetry and, most compellingly, by the measurements of emission phase presented in Sec. II C. These measurements suggest that even if additional clocks exist, the demon (i.e., the source of nonlinear distortion) does not consult them while generating distortion-product emissions.

[21]With no loss of generality we can take the proportionality constant to be unity.

[22]More precisely, the demon cannot generate backward-traveling waves with a phase shift that depends *reproducibly* on frequency. The demon could, however, generate a stochastic frequency dependence by pushing and pulling on the basilar membrane at random. Such a strategy would, of course, be at odds with the repeatability of the emission measurements.

[23]In the nonlinear-distortion model, stimulus-frequency emissions simply correspond to the limiting case $f_2/f_1 = 1$.

[24]A constant ratio f_2/f_1 fixes not only the spatial separation between the envelopes of the primary traveling waves, but also the distances between all resulting distortion-product waves whose frequencies fall in the exponential portion of the cochlear map. *Proof*: If $\alpha \equiv f_2/f_1 =$ constant, then

$$f_{\text{dp}}/f_2 = (nf_1 - mf_2)/f_2 = n/\alpha - m = \text{constant},$$

for all values of n and m.

[25]For simplicity, we have assumed here that the demon is able to separate the complex temporal waveform of basilar-membrane vibration into its component frequencies. To the demon sitting at the f_2 place, the two-tone complex might look like a sinusoid of frequency $\frac{1}{2}(1 + f_1/f_2)$, amplitude modulated at the frequency $\frac{1}{2}(1 - f_1/f_2)$, where frequencies are measured in the demon's local units (i.e., in units of f_2).

[26]Measurement methods are detailed in the Appendix.

[27]The near constancy of ''frequency-scaled'' DPOAE phase differs from the more rapid phase rotation obtained when DPOAEs are measured using a stimulus paradigm (e.g., fixed f_1, fixed f_2, or fixed $2f_1 - f_2$) for which the cochlear wave pattern is not simply translated along the cochlear partition (e.g., Kimberley *et al.*, 1993; O Mahoney and Kemp, 1995). The strong dependence of the observed phase gradient on the measurement paradigm argues against any naive equivalence between DPOAE phase gradients and ''wave travel times'' within the cochlea.

[28]The slow variation in DPOAE phase apparent in the data at frequencies less than roughly 3 kHz may reflect a gradual breaking of scaling symmetry in the apical turns of the cochlea. Deviations from scaling at similar frequencies are apparent in the shapes of cat auditory-nerve tuning curves (e.g., Kiang and Moxon, 1980; Liberman, 1978).

[29]Although we focus here on SFOAE phase, a few remarks about SFOAE amplitude may be helpful. In particular, we emphasize that the irregular variations in SFOAE amplitude, $|\Delta P_{\text{SFOAE}}|$, apparent in the top panel of Fig. 9 should not be confused with the quasi-periodic oscillations in ear-canal pressure amplitude, $|P_{\text{ec}}|$, seen in Figs. 1 and 2. Whereas oscillations in $|P_{\text{ec}}|$ arise due to acoustic interference between stimulus and emission caused by the quasi-periodic cycling of SFOAE phase (or, equivalently, the locally linear variation of $\angle R$) with frequency, the variations in

$|\Delta P_{\mathrm{SFOAE}}|$ result from changes in SFOAE amplitude (or, equivalently, changes in $|R|$). Frequency intervals where $|R|$ changes rapidly are known as ''anomalous regions'' (Shera and Zweig, 1993a; see also footnote 9). The theory of coherent reflection filtering accounts for the origin and properties of these irregular variations in $|R|$ with frequency (Zweig and Shera, 1995).

[30]The analysis here can be ''inverted'' by asking ''What constraint does the striking frequency independence of fixed-f_2/f_1 DPOAE phase place on cochlear mechanics?'' That constraint might reasonably be expected to take the form of a symmetry principle enforcing the empirical relation $\angle P_{\mathrm{dp}} \approx$ constant. The arguments presented here identify the underlying symmetry principle as local scaling symmetry.

[31]Bragg's law—formulated by English physicists W. H. Bragg and his son, W. L. Bragg—states that when monochromatic x rays are incident upon a crystal, diffracted beams of maximal intensity occur when the x rays that scatter back from different atomic layers within the crystal combine in phase with one another.

[32]It may be worth remarking that the principal and eponymous conclusion of this paper—namely, that mammalian OAEs arise by two fundamentally different mechanisms—while certainly consistent with the theory of coherent reflection filtering, is by no means logically dependent upon it. So far as the logic of the present paper is concerned, the existence of a plausible candidate theory for the origin of reflection-source emissions is no more than a happy coincidence.

[33]These observations are not conclusive of linearity both because the measurements have only limited precision and because *ad hoc* nonlinear systems can always be constructed that will mimic the response of a linear system to a finite collection of test signals.

[34]Just as with stimulus-frequency emissions, the forward-traveling wave scatters off perturbations in the mechanics of the cochlear partition located near the peak of the wave envelope. The backward-traveling wave reflects from the impedance mismatch at the stapes (Shera and Zweig, 1991, 1992).

[35]The extent to which these two components reflect actual distortion-source subtypes—as opposed to uncontrolled-for, level-dependent mixing of reflection- and distortion-source emissions (see Sec. IV C and Fig. 12 below)—remains an important open question.

[36]Two distortion components with differential sensitivity to acoustic trauma have also been identified in the alligator lizard (Rosowski *et al.*, 1984).

[37]To clarify the distinction we maintain between ''echo'' and ''reflection-source'' emissions: As defined in Sec. I, the term ''echo emissions'' is simply a convenient shorthand for stimulus-frequency and transiently evoked emissions; as defined by the taxonomy in Sec. IV A, the term ''reflection-source emissions'' refers to OAEs that arise by linear reflection. At low levels, echo emissions are examples of reflection-source emissions.

[38]Indeed, based on their observations Martin *et al.* (1988) suggested that SFOAEs and DPOAEs may arise by different mechanisms, a suggestion fleshed out by the taxonomy presented here.

[39]Orderly patterns of impedance perturbations typically do not contain significant components at the spatial frequencies for which scattering is coherent (Zweig and Shera, 1995).

[40]Concomitant with the small amplitudes of rabbit and rodent reflection-source emissions is the absence of pronounced DPOAE fine-structure (e.g., Whitehead *et al.*, 1992a; Whitehead, 1998). Both observations can be understood—with reference to Fig. 12—as a consequence of the relatively small amplitude of the reflection-source emission (**R**) scattered back from the f_{dp} place.

[41]At low sound-pressure levels, the width of the traveling-wave envelope can be approximated by using local scaling symmetry to convert the bandwidth of the basilar-membrane transfer function (or neural tuning curve) to a spatial distance using the cochlear map (e.g., Liberman, 1982; Greenwood, 1990). For comparison with the ratio $f_{\mathrm{dp}}/f_2 \approx 0.6$ calculated in the text, the upper-frequency $Q_{10\mathrm{dB}}$-point on the f_{dp} transfer function occurs at the frequency

$$f_{Q_{10}} \approx f_{\mathrm{dp}}(1+1/2Q_{10}).$$

For a realistic Q_{10} of order 10, this yields a frequency ratio of $f_{\mathrm{dp}}/f_{Q_{10}} \approx 0.95$, corresponding to a distance along the cochlear partition spanning less than a semitone in characteristic frequency.

[42]Of course, distortion amplitudes also depend on amplifier gains at the primary frequencies f_1 and f_2. However, because the amplifier gain saturates at high sound levels, these effects are likely to be small at the sound levels used by Martin *et al.* (i.e., 80 dB SPL).

[43]In addition, the high primary sound levels they employed may well have suppressed the gain of the f_{dp} amplifier, reducing the reflection component even in the absence of aspirin ototoxicity.

[44]To preserve the frequency scaling of the stimulus waveform, the suppressor frequency f_s should, ideally, be swept while maintaining a fixed frequency ratio f_s/f_{dp} rather than the constant frequency difference $\Delta f_s = f_s - f_{\mathrm{dp}}$ used here. However, the frequency-quantization constraints imposed by our use of digital stimulus generation and time-domain averaging precluded our use of a constant-f_s/f_{dp} paradigm. Nonetheless, control experiments suggest that the phase $\angle \Delta P_{\mathrm{dp}}$ is not especially sensitive to the precise value of f_s. Similar remarks apply to the measurement of SFOAEs discussed below.

[45]The time-domain responses Y_n and Y_{n+1} to stimulus segments X_n and X_{n+1} were judged to contain an artifact if

$$\max_i |Y_{n+1}[i] - Y_n[i]| > Y_{\mathrm{rejection}},$$

where $Y[i]$ represents the ith sample of Y, and $Y_{\mathrm{rejection}}$ is the rejection threshold (set on a per subject and per session basis). When an artifact was detected, both responses were discarded and neither Y_n nor Y_{n+1} added to the final average. We adopted this artifact-rejection scheme primarily because of the ease with which it could be implemented in real time (cf. Keefe and Ling, 1998).

Allen, J. B., and Fahey, P. F. (**1993**). ''A second cochlear-frequency map that correlates distortion product and neural tuning measurements,'' J. Acoust. Soc. Am. **94**, 809–816.

Allen, J. B., and Lonsbury-Martin, B. L. (**1993**). ''Otoacoustic emissions,'' J. Acoust. Soc. Am. **93**, 568–569.

Allen, J. B., and Neely, S. T. (**1992**). ''Micromechanical models of the cochlea,'' Phys. Today **45**, 40–47.

Brass, D., and Kemp, D. T. (**1991**). ''Time-domain observation of otoacoustic emissions during constant tone stimulation,'' J. Acoust. Soc. Am. **90**, 2415–2427.

Brass, D., and Kemp, D. T. (**1993**). ''Suppression of stimulus frequency otoacoustic emissions,'' J. Acoust. Soc. Am. **93**, 920–939.

Bredberg, G. (**1968**). ''Cellular patterns and nerve supply of the human organ of Corti,'' Acta Oto-Laryngol. Suppl. **236**, 1–135.

Brillouin, L. (**1946**). *Wave Propagation in Periodic Structures* (McGraw–Hill, New York).

Brown, A. M., and Beveridge, H. A. (**1997**). ''Two components of acoustic distortion: Differential effects of contralateral sound and aspirin,'' in *Diversity in Auditory Mechanics*, edited by E. R. Lewis, G. R. Long, R. F. Lyon, P. M. Narins, C. R. Steele, and E. L. Hecht-Poinar (World Scientific, Singapore), pp. 219–225.

Brown, A. M., and Kemp, D. T. (**1984**). ''Suppressibility of the $2f_1 - f_2$ stimulated acoustic emission in gerbil and man,'' Hearing Res. **13**, 29–37.

Brown, A. M., Harris, F. P., and Beveridge, H. A. (**1996**). ''Two sources of acoustic distortion products from the human cochlea,'' J. Acoust. Soc. Am. **100**, 3260–3267.

Brownell, W. E. (**1990**). ''Outer hair cell electromotility and otoacoustic emissions,'' Ear Hearing **11**, 82–92.

Cohen, M. F. (**1982**). ''Detection threshold microstructure and its effect on temporal integration data,'' J. Acoust. Soc. Am. **71**, 405–409.

de Boer, E. (**1980**). ''Auditory physics. Physical principles in hearing theory. I,'' Phys. Rep. **62**, 88–174.

de Boer, E. (**1983**). ''Wave reflection in passive and active cochlea models,'' in *Mechanics of Hearing*, edited by E. de Boer and M. A. Viergever (Martinus Nijhoff, The Hague), pp. 135–142.

de Boer, E. (**1984**). ''Auditory physics. Physical principles in hearing theory. II,'' Phys. Rep. **105**, 142–226.

de Boer, E. (**1991**). ''Auditory physics. Physical principles in hearing theory. III,'' Phys. Rep. **203**, 125–231.

Elliot, E. (**1958**). ''A ripple effect in the audiogram,'' Nature (London) **181**, 1076.

Engdahl, B., and Kemp, D. T. (**1996**). ''The effect of noise exposure on the details of distortion product otoacoustic emissions in humans,'' J. Acoust. Soc. Am. **99**, 1573–1587.

Engström, H., Ades, H. W., and Andersson, A. (**1966**). *Structural Pattern of the Organ of Corti* (Williams and Wilkins, Baltimore).

Fahey, P. F., and Allen, J. B. (**1997**). ''Measurement of distortion product phase in the ear canal of the cat,'' J. Acoust. Soc. Am. **102**, 2880–2891.
Gaskill, S. A., and Brown, A. M. (**1990**). ''The behavior of the acoustic distortion product, $2f_1-f_2$, from the human ear and its relation to auditory sensitivity,'' J. Acoust. Soc. Am. **88**, 821–839.
Golka, R. K. (**1994**). ''Laboratory-produced ball lightning,'' J. Geophys. Res. **99**, 10679–10681.
Greenwood, D. D. (**1990**). ''A cochlear frequency-position function for several species—29 years later,'' J. Acoust. Soc. Am. **87**, 2592–2605.
Guinan, J. J. (**1990**). ''Changes in stimulus frequency otoacoustic emissions produced by two-tone suppression and efferent stimulation in cats,'' in *Mechanics and Biophysics of Hearing*, edited by P. Dallos, C. D. Geisler, J. W. Matthews, M. A. Ruggero, and C. R. Steele (Springer-Verlag, New York), pp. 170–177.
Gummer, A. W., Smolders, J. W. T., and Klinke, R. (**1987**). ''Basilar membrane motion in the pigeon measured with the Mössbauer technique,'' Hearing Res. **29**, 63–92.
Hartmann, W. M. (**1997**). *Signal, Sound, and Sensation* (AIP, Woodbury, NY).
Heitmann, J., Waldman, B., Schnitzler, H. U., Plinkert, P. K., and Zenner, H.-P. (**1997**). ''Suppression growth functions of DPOAE with a suppressor near $2f_1-f_2$ depends on DP fine structure: Evidence for two generation sites for DPOAE,'' Assoc. Res. Otolaryngol. Abs. **20**, 83.
Heitmann, J., Waldman, B., Schnitzler, H. U., Plinkert, P. K., and Zenner, H.-P. (**1998**). ''Suppression of distortion product otoacoustic emissions (DPOAE) near $2f_1-f_2$ removes DP-gram fine structure—Evidence for a secondary generator,'' J. Acoust. Soc. Am. **103**, 1527–1531.
Kanis, L. J., and de Boer, E. (**1997**). ''Frequency dependence of acoustic distortion products in a locally active model of the cochlea,'' J. Acoust. Soc. Am. **101**, 1527–1531.
Keefe, D. H., and Ling, R. (**1998**). ''Double-evoked otoacoustic emissions. II. Intermittent noise rejection, calibration and ear-canal measurements,'' J. Acoust. Soc. Am. **103**, 3499–3508.
Kemp, D. T. (**1978**). ''Stimulated acoustic emissions from within the human auditory system,'' J. Acoust. Soc. Am. **64**, 1386–1391.
Kemp, D. T. (**1979a**). ''Evidence of mechanical nonlinearity and frequency selective wave amplification in the cochlea,'' Arch. Otorhinolaryngol. **224**, 37–45.
Kemp, D. T. (**1979b**). ''The evoked cochlear mechanical response and the auditory microstructure—Evidence for a new element in cochlear mechanics,'' Scand. Audiol. Suppl. **9**, 35–47.
Kemp, D. T. (**1980**). ''Towards a model for the origin of cochlear echoes,'' Hearing Res. **2**, 533–548.
Kemp, D. T. (**1986**). ''Otoacoustic emissions, travelling waves and cochlear mechanisms,'' Hearing Res. **22**, 95–104.
Kemp, D. T. (**1997**). ''Otoacoustic emissions in perspective,'' in *Otoacoustic Emissions: Clinical Applications*, edited by M. S. Robinette and T. J. Glattke (Thieme, New York), pp. 1–21.
Kemp, D. T. (**1998**). ''Otoacoustic emissions: Distorted echoes of the cochlea's travelling wave,'' in *Otoacoustic Emissions: Basic Science and Clinical Applications*, edited by C. I. Berlin (Singular, San Diego), pp. 1–59.
Kemp, D. T., and Brown, A. M. (**1983a**). ''A comparison of mechanical nonlinearities in the cochleae of man and gerbil from ear canal measurements,'' in *Hearing—Physiological Bases and Psychophysics*, edited by R. Klinke and R. Hartmann (Springer-Verlag, Berlin), pp. 75–82.
Kemp, D. T., and Brown, A. M. (**1983b**). ''An integrated view of cochlear mechanical nonlinearities observable from the ear canal,'' in *Mechanics of Hearing*, edited by E. de Boer and M. A. Viergever (Martinus Nijhoff, The Hague), pp. 75–82.
Kemp, D. T., and Chum, R. A. (**1980**). ''Observations on the generator mechanism of stimulus frequency acoustic emissions—Two tone suppression,'' in *Psychophysical Physiological and Behavioural Studies in Hearing*, edited by G. V. D. Brink and F. A. Bilsen (Delft U.P., Delft), pp. 34–42.
Kemp, D. T., and Knight, R. (**1999**). ''Virtual DP reflector explains DPOAE 'wave' and 'place' fixed dichotomy,'' Assoc. Res. Otolaryngol. Abs. **22**, 396.
Kemp, D. T., Bray, P., Alexander, L., and Brown, A. M. (**1986**). ''Acoustic emission cochleography—Practical aspects,'' Scand. Audiol. Suppl. **25**, 71–95.
Kemp, D. T., Brass, D., and Souter, M. (**1990**). ''Observations on simultaneous SFOAE and DPOAE generation and suppression,'' in *Mechanics and Biophysics of Hearing*, edited by P. Dallos, C. D. Geisler, J. W. Matthews, M. A. Ruggero, and C. R. Steele (Springer-Verlag, New York), pp. 202–209.
Kiang, N. Y. S., and Moxon, E. C. (**1980**). ''Tails of tuning curves of auditory-nerve fibers,'' J. Acoust. Soc. Am. **68**, 1115–1122.
Kim, D. O. (**1980**). ''Cochlear mechanics: Implications of electrophysiological and acoustical observations,'' Hearing Res. **2**, 297–317.
Kimberley, B. P., Brown, D. K., and Eggermont, J. J. (**1993**). ''Measuring human cochlear traveling wave delay using distortion product emission phase responses,'' J. Acoust. Soc. Am. **94**, 1343–1350.
Kössl, M., and Vater, M. (**1995**). ''Cochlear structure and function in bats,'' in *Hearing by Bats*, edited by A. N. Popper and R. R. Fay (Springer-Verlag, New York), pp. 191–234.
Kummer, P., Janssen, T., and Arnold, W. (**1995**). ''Suppression tuning characteristics of the $2f_1-f_2$ distortion-product otoacoustic emission in humans,'' J. Acoust. Soc. Am. **98**, 197–210.
Leff, H. S., and Rex, A. F., editors (**1990**). *Maxwell's Demon: Entropy, Information, Computing* (Princeton U.P., Princeton).
Liberman, M. C. (**1978**). ''Auditory-nerve response from cats raised in a low-noise chamber,'' J. Acoust. Soc. Am. **63**, 442–455.
Liberman, M. C. (**1982**). ''The cochlear frequency map for the cat: Labeling auditory-nerve fibers of known characteristic frequency,'' J. Acoust. Soc. Am. **72**, 1441–1449.
Long, G. R. (**1984**). ''The microstructure of quiet and masked thresholds,'' Hearing Res. **15**, 73–87.
Lonsbury-Martin, B. L., Martin, G. K., Probst, R., and Coats, A. C. (**1988**). ''Spontaneous otoacoustic emissions in the nonhuman primate. II. Cochlear anatomy,'' Hearing Res. **33**, 69–94.
Martin, G. K., Lonsbury-Martin, B. L., Probst, R., and Coats, A. C. (**1988**). ''Spontaneous otoacoustic emissions in the nonhuman primate. I. Basic features and relations to other emissions,'' Hearing Res. **33**, 49–68.
Maxwell, J. C. (**1871**). *Theory of Heat* (Longmans, Green, London).
Mills, D. M., and Rubel, E. W. (**1994**). ''Variation of distortion product otoacoustic emissions with furosemide injection,'' Hearing Res. **77**, 183–199.
Nakajima, H. H., Olson, E. S., Mountain, D. C., and Hubbard, A. E. (**1994**). ''Electrically evoked otoacoustic emissions from the apical turns of the gerbil cochlea,'' J. Acoust. Soc. Am. **96**, 786–794.
Nakajima, H. H., Naidu, R. C., Hubbard, A. E., and Mountain, D. C. (**1999**). ''Forward and reverse traveling waves in the cochlea,'' Assoc. Res. Otolaryngol. Abs. **22**, 333.
Neely, S. T., and Stover, L. J. (**1997**). ''A generation of distortion products in a model of cochlear mechanics,'' in *Diversity in Auditory Mechanics*, edited by E. R. Lewis, G. R. Long, R. F. Lyon, P. M. Narins, C. R. Steele, and E. L. Hecht-Poinar (World Scientific, Singapore), pp. 434–440.
Norton, S. J., and Neely, S. T. (**1987**). ''Tone-burst-evoked otoacoustic emissions from normal-hearing subjects,'' J. Acoust. Soc. Am. **81**, 1860–1872.
Norton, S. J., and Rubel, E. W. (**1990**). ''Active and passive ADP components in mammalian and avian ears,'' in *Mechanics and Biophysics of Hearing*, edited by P. Dallos, C. D. Geisler, J. W. Matthews, M. A. Ruggero, and C. R. Steele (Springer-Verlag, Berlin), pp. 219–226.
Norton, S. J., and Stover, L. J. (**1994**). ''Otoacoustic emissions: An emerging clinical tool,'' in *Handbook of Clinical Audiology*, edited by J. Katz (Williams and Wilkins, Baltimore), pp. 448–462.
O'Mahoney, C. F., and Kemp, D. T. (**1995**). ''Distortion product otoacoustic emission delay measurement in human ears,'' J. Acoust. Soc. Am. **97**, 3721–3735.
Patuzzi, R. (**1996**). ''Cochlear micromechanics and macromechanics,'' in *The Cochlea*, edited by P. Dallos, A. N. Popper, and R. R. Fay (Springer-Verlag, New York), pp. 186–257.
Probst, R., Lonsbury-Martin, B. L., and Martin, G. K. (**1991**). ''A review of otoacoustic emissions,'' J. Acoust. Soc. Am. **89**, 2027–2067.
Puria, S., and Rosowski, J. J. (**1997**). ''Measurement of reverse transmission in the human middle ear: Preliminary results,'' in *Diversity in Auditory Mechanics*, edited by E. R. Lewis, G. R. Long, R. F. Lyon, P. M. Narins, C. R. Steele, and E. L. Hecht-Poinar (World Scientific, Singapore), pp. 151–157.
Puria, S., Peake, W. T., and Rosowski, J. J. (**1997**). ''Sound-pressure measurements in the cochlear vestibule of human-cadaver ears,'' J. Acoust. Soc. Am. **101**, 2754–2770.
Rhode, W. S. (**1971**). ''Observations of the vibration of the basilar membrane in squirrel monkeys using the Mössbauer technique,'' J. Acoust. Soc. Am. **49**, 1218–1231.
Rhode, W. S., and Cooper, N. P. (**1996**). ''Nonlinear mechanics in the apical

turn of the chinchilla cochlea *in vivo*,'' Aud. Neurosci. **3**, 101–121.
Robinette, M. S., and Glattke, T. J., editors (**1997**). *Otoacoustic Emissions: Clinical Applications* (Thieme, New York).
Rosowski, J. J., Peake, W. T., and White, J. R. (**1984**). ''Cochlear nonlinearities inferred from two-tone distortion products in the ear canal of the alligator lizard,'' Hearing Res. **13**, 141–158.
Shera, C. A. (**1992**). ''Listening to the Ear,'' Ph.D. thesis, California Institute of Technology.
Shera, C. A., and Guinan, J. J. (**1997**). ''Measuring cochlear amplification and nonlinearity using distortion-product otoacoustic emissions as a calibrated intracochlear sound source,'' Assoc. Res. Otolaryngol. Abs. **20**, 51.
Shera, C. A., and Guinan, J. J. (**1998**). ''Reflection emissions and distortion products arise by fundamentally different mechanisms,'' Assoc. Res. Otolaryngol. Abs. **21**, 344.
Shera, C. A., and Zweig, G. (**1991**). ''Reflection of retrograde waves within the cochlea and at the stapes,'' J. Acoust. Soc. Am. **89**, 1290–1305.
Shera, C. A., and Zweig, G. (**1992**). ''Analyzing reverse middle-ear transmission: Noninvasive Gedankenexperiments,'' J. Acoust. Soc. Am. **92**, 1371–1381.
Shera, C. A., and Zweig, G. (**1993a**). ''Noninvasive measurement of the cochlear traveling-wave ratio,'' J. Acoust. Soc. Am. **93**, 3333–3352.
Shera, C. A., and Zweig, G. (**1993b**). ''Order from chaos: Resolving the paradox of periodicity in evoked otoacoustic emission,'' in *Biophysics of Hair Cell Sensory Systems*, edited by H. Duifhuis, J. W. Horst, P. van Dijk, and S. M. van Netten (World Scientific, Singapore), pp. 54–63.
Siebert, W. M. (**1968**). ''Stimulus transformations in the peripheral auditory system,'' in *Recognizing Patterns*, edited by P. A. Kolers and M. Eden (MIT, Cambridge), pp. 104–133.
Siegel, J. H., Dreisbach, L. E., Neely, S. T., and Spear, W. H. (**1998**). ''Vector decomposition of distortion-product otoacoustic emission sources in humans,'' Assoc. Res. Otolaryngol. Abs. **21**, 347.
Sondhi, M. M. (**1978**). ''Method for computing motion in a two-dimensional cochlear model,'' J. Acoust. Soc. Am. **63**, 1468–1477.
Souter, M. (**1995**). ''Stimulus frequency otoacoustic emissions from guinea pig and human subjects,'' Hearing Res. **90**, 1–11.
Strube, H. W. (**1989**). ''Evoked otoacoustic emissions as cochlear Bragg reflections,'' Hearing Res. **38**, 35–45.
Talmadge, C. L., and Tubis, A. (**1993**). ''On modeling the connection between spontaneous and evoked otoacoustic emissions,'' in *Biophysics of Hair Cell Sensory Systems*, edited by H. Duifhuis, J. W. Horst, P. van Dijk, and S. M. van Netten (World Scientific, Singapore), pp. 25–32.
Talmadge, C. L., Tubis, A., Piskorski, P., and Long, G. (**1997**). ''Modeling otoacoustic emission fine structure,'' in *Diversity in Auditory Mechanics*, edited by E. R. Lewis, G. R. Long, R. F. Lyon, P. M. Narins, C. R. Steele, and E. L. Hecht-Poinar (World Scientific, Singapore), pp. 462–471.
Talmadge, C. L., Tubis, A., Long, G. R., and Piskorski, P. (**1998a**). ''Modeling otoacoustic emission and hearing threshold fine structures,'' J. Acoust. Soc. Am. **104**, 1517–1543.
Talmadge, C. L., Long, G. R., Tubis, A., and Dhar, S. (**1998b**). ''Study of cochlear reflectance using distortion product otoacoustic emissions,'' Assoc. Res. Otolaryngol. Abs. **21**, 345.
Talmadge, C. L., Long, G. R., Tubis, A., and Dhar, S. (**1999**). ''Experimental confirmation of the two-source interference model for the fine structure of distortion product otoacoustic emissions,'' J. Acoust. Soc. Am. **105**, 275–292.
Thomas, I. B. (**1975**). ''Microstructure of the pure-tone threshold,'' J. Acoust. Soc. Am. Suppl. 1 **57**, S26–S27.
van Hengel, P. W. J. (**1996**). ''Emissions from cochlear modelling,'' Ph.D. thesis, Rijksuniversiteit Groningen.
Ver, I. L., Brown, R. M., and Kiang, N. Y. S. (**1975**). ''Low-noise chambers for auditory research,'' J. Acoust. Soc. Am. **58**, 392–398.
Whitehead, M. L. (**1998**). ''Species differences of distortion-product otoacoustic emissions: Comment on ''Interpretation of distortion product otoacoustic emission measurements. I. Two stimulus tones'' [J. Acoust. Soc. Am. **102**, 413–429 (1997)],'' J. Acoust. Soc. Am. **103**, 2740–2742.
Whitehead, M. L., Lonsbury-Martin, B. L., and Martin, G. K. (**1992a**). ''Evidence for two discrete sources of $2f_1-f_2$ distortion-product otoacoustic emission in rabbit: I. Differential dependence on stimulus parameters,'' J. Acoust. Soc. Am. **91**, 1587–1607.
Whitehead, M. L., Lonsbury-Martin, B. L., and Martin, G. K. (**1992b**). ''Evidence for two discrete sources of $2f_1-f_2$ distortion-product otoacoustic emission in rabbit: II. Differential physiological vulnerability,'' J. Acoust. Soc. Am. **92**, 2662–2682.
Whitehead, M. L., Lonsbury-Martin, B. L., Martin, G. K., and McCoy, M. J. (**1996a**). ''Otoacoustic emissions: Animal models and clincal observations,'' in *Clinical Aspects of Hearing*, edited by T. R. V. D. Water, A. N. Popper, and R. R. Fay (Springer-Verlag, New York), pp. 199–257.
Whitehead, M. L., Stagner, B. B., Martin, G. K., and Lonsbury-Martin, B. L. (**1996b**). ''Visualization of the onset of distortion-product otoacoustic emissions and measurement of their latency,'' J. Acoust. Soc. Am. **100**, 1663–1679.
Whitehead, M. L., Stagner, B. B., McCoy, M. J., Lonsbury-Martin, B. L., and Martin, G. K. (**1995**). ''Dependence of distortion-product otoacoustic emissions on primary levels in normal and impaired ears. II. Asymmetry in L_1, L_2 space,'' J. Acoust. Soc. Am. **97**, 2359–2377.
Wier, C. C., Pasanen, E. G., and McFadden, D. (**1988**). ''Partial dissociation of spontaneous otoacoustic emissions and distortion products during aspirin use in humans,'' J. Acoust. Soc. Am. **84**, 230–237.
Wilson, J. P. (**1980**). ''Evidence for a cochlear origin for acoustic re-emissions, threshold fine-structure and tonal tinnitus,'' Hearing Res. **2**, 233–252.
Wit, H. P., and Ritsma, R. J. (**1979**). ''Stimulated acoustic emissions from the human ear,'' J. Acoust. Soc. Am. **66**, 911–913.
Withnell, R. H., and Yates, G. K. (**1998**). ''Enhancement of the transient-evoked otoacoustic emission produced by the addition of a pure tone in the guinea pig,'' J. Acoust. Soc. Am. **104**, 344–349.
Wright, A. A. (**1984**). ''Dimensions of the cochlear stereocilia in man and in guinea pig,'' Hearing Res. **13**, 89–98.
Yates, G. K., and Withnell, R. H. (**1998**). ''Intermodulation distortion in click-evoked otoacoustic emissions,'' Assoc. Res. Otolaryngol. Abs. **21**, 17.
Zurek, P. M. (**1985**). ''Acoustic emissions from the ear: A summary of results from humans and animals,'' J. Acoust. Soc. Am. **78**, 340–344.
Zweig, G. (**1976**). ''Basilar membrane motion,'' in *Cold Spring Harbor Symposia on Quantitative Biology, Volume XL, 1975* (Cold Spring Harbor Laboratory, Cold Spring Harbor, NY), pp. 619–633.
Zweig, G., and Shera, C. A. (**1995**). ''The origin of periodicity in the spectrum of evoked otoacoustic emissions,'' J. Acoust. Soc. Am. **98**, 2018–2047.
Zwicker, E. (**1983**). ''Delayed evoked oto-acoustic emissions and their suppression by gaussian-shaped pressure impulses,'' Hearing Res. **11**, 359–371.
Zwicker, E., and Schloth, E. (**1984**). ''Interrelation of different oto-acoustic emissions,'' J. Acoust. Soc. Am. **75**, 1148–1154.

Response phase: A view from the inner hair cell

M. A. Cheatham[a] and P. Dallos
Communication Sciences and Disorders, Audiology and Hearing Sciences, Hugh Knowles Center, Frances Searle Building, Northwestern University, Evanston, Illinois 60208-3550

(Received 2 June 1998; revised 9 October 1998; accepted 23 October 1998)

Inner hair cell (IHC) responses are recorded from the apical three turns of the guinea pig cochlea in order to define the relationship between hair cell depolarization and position of the basilar membrane. At low frequencies, inner hair cell depolarization is generally observed near basilar membrane velocity to scala vestibuli, reflecting the putative freestanding nature of the IHC's stereocilia. While this is consistent with previous IHC results, independent of location, and with neural responses for fibers with low best frequencies, it is inconsistent with single-unit results from the base of the cochlea, where response phase is associated with basilar membrane velocity to scala tympani. Results suggest that the temporal disparity between IHC and neural data from the base of the cochlea may relate to several factors that influence transmembrane voltage in IHCs. First, extracellular voltages (Ingvarsson, 1981; Sellick *et al.*, 1982; Russell and Sellick, 1983) can potentially affect low- and high-frequency regions differently because electrical interactions are more likely in the base of the cochlea than in the apex (Dallos, 1983, 1985). Second, waveform distortion and kinetic properties associated with voltage-dependent ion channels in the IHC's basolateral membrane can both influence response phase by adding harmonic components and lagging the receptor potential by as much as 90 deg. Third, the velocity dependence of IHCs in the apex appears to extend to higher frequencies than the velocity dependence demonstrated for IHCs in the base of the cochlea. These features, which influence the timing of discharges in the auditory nerve, are compared and evaluated.
[S0001-4966(99)01702-6]

PACS numbers: 43.64.Ld, 43.64.Nf, 43.64.Tk [RDF]

INTRODUCTION

Auditory-nerve fibers with low best frequencies (BF) tend to generate spikes for low-level, low-frequency inputs during the time when the basilar membrane is moving to scala vestibuli (SV); i.e., when basilar membrane velocity is maximum in the direction of SV. Conversely, auditory-nerve fibers innervating the base of the cochlea tend to respond near scala tympani (ST) velocity. A transition separates these regions where preferred phase is easily designated. These general trends, defined by Ruggero *et al.* (1996), have been studied and/or replicated to varying degrees by several investigators in the chinchilla (Ingvarsson, 1981; Ruggero and Rich, 1983, 1987), guinea pig (Konishi and Nielsen, 1978; Maceri *et al.*, 1982; Oshima and Strelioff, 1983), gerbil (Sokolich *et al.*, 1976; Oshima and Strelioff, 1983), and cat (Cai and Geisler, 1996a). The state of the art on this subject, however, is reflected in the extensive recordings obtained by Ruggero and his colleagues (Ruggero *et al.*, 1996).

Although hair cell measurements are difficult and, therefore, much less extensive than those from auditory-nerve fibers, data from the apex of the cochlea demonstrate that IHCs depolarize at low frequencies near SV velocity (Dallos and Santos-Sacchi, 1983; Dallos, 1985; Cheatham, 1993). This is in harmony with neural records obtained in the chinchilla for fibers with low BFs. Interestingly, IHCs from the base of the cochlea also respond to SV velocity at low stimulus frequencies (Sellick and Russell, 1980; Nuttall *et al.*, 1981; Russell and Sellick, 1983; Patuzzi and Yates, 1987), which is difficult to reconcile with single-unit responses from the high-frequency region of the cochlea. In order to clarify the relationship between IHC and neural responses, this report provides additional data from IHCs in the apical three turns of the guinea pig cochlea. Results from third and fourth turns correspond to neural data obtained for fibers with low BFs. Data from the second turn, however, may provide insights into the temporal disparities between IHC and neural responses at more basal regions of the cochlea.

Ideally, it would be important to provide IHC data from the basal turn to compare with the results presented here. In other words, apply the lateral approach to hair cell recording (Dallos *et al.*, 1982) in all four cochlear turns. Unfortunately, this approach has not been successful in the high-frequency region of the cochlea. This may relate to position of the access window over scala media. In the basal turn, outer hair cells are short and a flatter electrode track is required to avoid disruption of the tectorial membrane. Consequently, the lower position of the window may interfere with attachment of the basilar membrane to the spiral ligament. Because of these difficulties, the results in this report from the apical three turns are compared with measurements from first-turn IHCs collected by other investigators using the scala tympani approach, which requires penetration of the basilar membrane (Sellick and Russell, 1980; Nuttall *et al.*, 1981; Russell and Sellick, 1983; Patuzzi and Yates, 1987; Cody and Mountain, 1989). Taken together, the experimental results may

[a]Electronic mail: m-cheatham@nwu.edu

further our understanding of how signals are processed prior to spike initiation in the auditory nerve.

I. METHODS

The cochlea is exposed in anesthetized guinea pigs using the traditional ventrolateral approach (Dallos *et al.*, 1982). Because it is practical to record from only one turn in any given preparation, a single window is made over scala media in turns 2, 3, or 4, where BFs are approximately 4000, 1000, and 250 Hz, respectively. After traversing the spiral ligament and the endolymphatic space, the recording electrode encounters Hensen cells at the edge of the organ of Corti (OC). Ideally, the electrode track is roughly parallel to but below the reticular lamina, thereby optimizing chances for hair-cell recordings. Additional details can be obtained from previous publications (Dallos, 1985; Cheatham and Dallos, 1992). All animal care procedures were approved by the National Institutes of Health and by Northwestern University's Institutional Review Committee.

In these experiments, receptor potentials are recorded from individual IHCs. These potentials are produced by the receptor current flowing through resistances associated with the cell's basolateral membrane. Stimulus-related responses are also measured in the organ of Corti fluid space. These measures reflect outer hair cell (OHC) receptor currents which are proportional to local basilar membrane displacement (Dallos, 1973; Nedzelnitsky, 1974; Dancer and Franke, 1980). Consequently, the voltages recorded from the OC fluid space are used to determine the position of the basilar membrane. In other words, the motion pattern of the basilar membrane is estimated locally in the same general area as the hair cell recordings and no corrections are required to compensate for traveling wave and/or synaptic delays. The OC measure is preferable to that at the round window for at least two reasons. First, there is usually a disparity between the round window location at which basilar membrane motion is estimated and the place along the cochlear partition where a nerve fiber innervates its hair cell target. Thus, traveling-wave delays must be estimated and compensated. Second, the electroanatomy in the hook region is complex (Weiss *et al.*, 1969; Dallos *et al.*, 1971), with the result that the CM suffers from phase cancellation (Whitfield and Ross, 1965) as local and remote hair cell generators interact. This electrical complication makes estimation of basilar membrane position from round window recordings less accurate when compared to measures from the OC fluid space. The organ of Corti potentials, made in the same general area as the hair cell recordings, are also preferable to those from perilymphatic scalae because the length constant within the organ may be shorter (Geisler *et al.*, 1990).

Stimuli are produced by a single earphone (Beyer DT-48) and the input sound pressure levels are measured in the ear canal utilizing a miniature microphone (Knowles BT-1751). Because the latter is nonlinear at high levels, distortion in the sound is determined in a coupler using a 1/2-in. Brüel & Kjaer condenser microphone (type 4134). Measurements are not made in the ear canal because of contamination by distortion products generated in the cochlea and fed back through the middle ear as otoacoustic emissions. At the highest levels used in these experiments, i.e., 75 dB, the second harmonic is at least 65 dB down from the fundamental at 40 Hz. Using this result, one can estimate harmonic response magnitudes due to distortion in the sound (Dallos *et al.*, 1969). When compared to these calculations, the physiological responses reported here for the 40 Hz fundamental are at least an order of magnitude greater than the predicted magnitude of the artifact. Even though distortion levels may be higher when measured in the ear canal (Ruggero *et al.*, 1996, Table 1), they are still estimated to be lower than the levels required to produce the results reported here.

Electrical measurements are made from individual IHCs and from the organ of Corti fluid space. Responses are amplified, low-pass filtered to control aliasing, and gain-controlled to avoid saturating the analog-to-digital converter. The averaged-response waveforms are plotted versus time relative to the beginning of the time window used in the averaging process. In order to emphasize detailed aspects of the responses, waveform segments are plotted for two stimulus periods. This procedure is clarified by using two abscissas: one in time, the other in periods.

In order to assay the magnitudes of individual components from distorted responses, averaged-response waveforms are digitally filtered off-line. These manipulations are performed using IGOR PRO (WaveMetrics, Lake Oswego, OR 97035) equipped with the Igor Filter Design Laboratory. In this program, filtered outputs appear in phase with the input because phase changes associated with the filter are removed. This in-phase or noncausal filtering allows small phase variations to be quantified. Design macros implement either low- or high-pass filters by using the McClellan–Parks–Rabiner technique. Attenuations in the reject band are at least 40 dB down from the passband, where rippling is less than ± 0.02 dB. In the low-pass case, the passband is 0–50 Hz, while in the high-pass case, the reject band is 0–50 Hz. IGOR PRO is also used to subtract OC from IHC waveforms, allowing the IHC's basolateral membrane potential to be determined (Russell and Sellick, 1983; Cody and Mountain, 1989). This is useful because the release of neurotransmitter is proportional to the potential difference across the presynaptic membrane (Katz and Miledi, 1967).

II. RESULTS

In this report, the term ''response phase'' refers to the time during a single period of a low-frequency sinusoid when the hair cell depolarizes, thereby inducing transmitter release and, presumably, increasing discharge rate (Flock, 1971). Consequently, IHC data are evaluated to determine when the voltage gradient across the cell's basolateral membrane becomes more positive relative to that in quiet, and to relate this to the instantaneous position of the basilar membrane. An IHC recording from the fourth turn is used to introduce these ideas and results.

A. Fourth turn

Figure 1 displays IHC and OC waveforms for a 100 Hz stimulus presented at 40 dB. Two cycles are displayed to demonstrate temporal aspects of the responses. Because the BF of this IHC is 270 Hz, the 100 Hz input produces a large

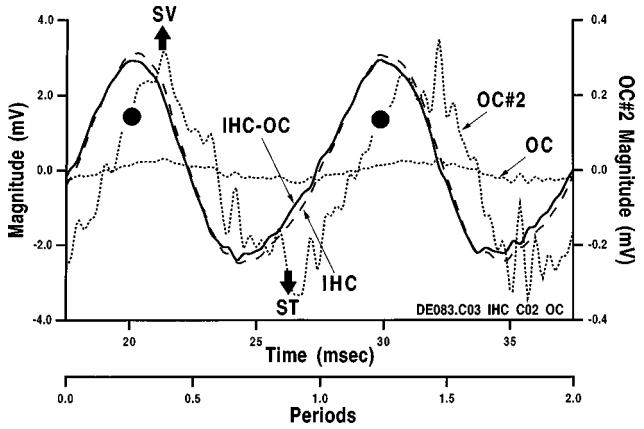

FIG. 1. Data in this figure were collected from fourth turn at 100 Hz (40 dB). Organ of Corti responses are plotted with dotted lines, the IHC response with dashed lines, and the subtracted IHC–OC response with solid lines. In this and subsequent figures, response magnitudes are plotted versus time relative to the beginning of the time window used in the averaging process. Although the second abscissa indicates only two periods of the stimulating sinusoid, the tone burst was 40 ms long. Symbols are placed on the OC waveform guided by eye to indicate when the IHC–OC potential is maximally positive relative to the position of the basilar membrane. The OC#2 response is plotted using the right ordinate so that temporal comparisons can be made between intracellular and extracellular measures. In this and all figures, sound pressure level is measured in dB *re*: 20 μPa.

ac receptor potential which exceeds that produced in the OC fluid space. Although the left ordinate applies to both IHC and OC responses, the OC waveform is replotted as OC#2 using the ordinate on the right, where an expanded scale facilitates temporal comparisons. The phase lead demonstrated here between IHC and OC potentials is thought to reflect the freestanding nature of the IHC stereocilia (Lim, 1972) and the consequent velocity dependence of the IHC input (Dallos *et al.*, 1972). The fourth waveform, plotted with solid lines, is obtained by subtracting the OC from the IHC response. Because of the large disparity in magnitude between intracellular and extracellular responses at this apical location, the IHC–OC curve is virtually identical to that for the IHC. In other words, intracellular ac responses recorded in the apex of the cochlea are much larger in magnitude than those measured nearby in the OC fluid space, with the result that the IHC transducer largely determines the transmembrane voltage.

In order to determine the timing of hair cell depolarizations relative to the position of the basilar membrane, the OC response is interpreted in the following way. The positive phase of this cochlear microphonic (CM) response is associated with basilar membrane displacement to SV; the negative phase with displacement to ST. This relationship is based on evidence suggesting that the CM reflects outer hair cell (OHC) receptor currents (Dallos and Cheatham, 1976), and that OHCs respond to basilar-membrane displacement (Békésy, 1960; Dallos *et al.*, 1972). Hence, the local CM also reflects basilar membrane displacement. Based on this association, one concludes that the IHC plotted in Fig. 1 depolarizes between basilar membrane velocity to SV and basilar membrane displacement to SV. This is indicated by the filled circles placed on the OC waveform at the time when the IHC–OC potential, which drives transmitter release, is maximally positive.

B. Third turn

An IHC response from third turn, where BF is 1000 Hz, is shown in Fig. 2. At the top, both IHC and OC response waveforms are displayed for a 200 Hz stimulus presented at 50 dB. The IHC–OC function is not included because it is virtually identical to the IHC response. As in Fig. 1, the input is below BF and the IHC response leads the potential recorded in the OC fluid space by ~45 deg. These temporal features are shown by comparing the OC response with that from the IHC. Waveforms are also included for higher frequency inputs, again presented at 50 dB. For 600 Hz (center), the IHC and OC responses are nearly in phase and the IHC depolarizes for basilar membrane displacements to SV similar to observations in first-turn IHCs (Sellick and Russell, 1980; Nuttall *et al.*, 1981; Russell and Sellick, 1983; Patuzzi and Yates, 1987; Cody and Mountain, 1989). This is because the velocity sensitivity of the IHC transducer is expressed only at low frequencies.

At the bottom of Fig. 2, the IHC waveform at 1200 Hz lags behind the OC response. This shift is thought to reflect low-pass filtering associated with the hair cell's basolateral membrane (Sellick and Russell, 1980; Dallos and Santos-Sacchi, 1983). Based on information collected from third-turn IHCs, the cutoff frequency of this filter is estimated to be ~470 Hz (Dallos, 1984). Therefore, IHC responses at high frequencies should decrease in magnitude by 6 dB/octave and the IHC phase should lag behind the OC response by 90 deg. The CM does not show a similar phase lag because this extracellular ac potential reflects OHC receptor currents and not OHC receptor potentials (Russell and Sellick, 1983; Dallos and Evans, 1995). Therefore, the OHC basolateral membrane does not act as a low-pass filter on the OC response.

C. Second turn

Because low-frequency response phase depends on the BF of single auditory-nerve fibers (Ruggero *et al.*, 1996) and presumably on their place of innervation along the cochlear spiral, it is helpful to examine this feature in hair cells with higher BFs. Information was, therefore, collected from second-turn IHCs where BFs are ~4000 Hz. In the top panel of Fig. 3, the IHC ac receptor potential at 150 Hz exceeds in magnitude and leads in phase the extracellular CM response. At 1200 Hz, however, the IHC and the IHC–OC responses both lag behind the OC measurement, consistent with filtering by the IHC's basolateral membrane (Sellick and Russell, 1980; Dallos and Santos-Sacchi, 1983). In other words, these patterns are qualitatively similar to those seen in Fig. 2. Because of the relatively larger OC response at 1200 Hz, the subtracted waveform differs from the IHC receptor potential. In fact, the temporal disparity is exaggerated when the IHC's basolateral membrane potential (IHC–OC) is compared with the OC response.

Although these measures from the second turn are consistent with those obtained elsewhere along the cochlear par-

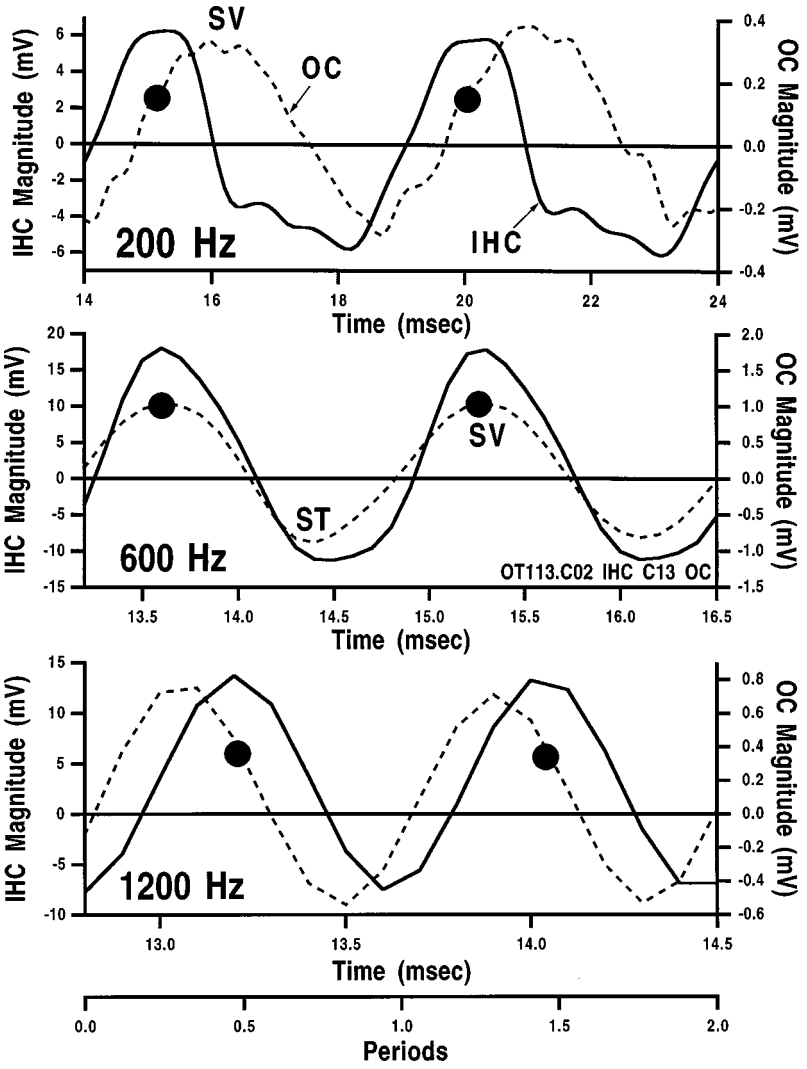

FIG. 2. Data are provided for IHC (solid lines) and OC (dotted lines) responses recorded in third turn at three different frequencies. All inputs were presented at 50 dB. A zero line is included for reference. Although only two stimulus periods are displayed, the tone burst duration was 40 ms.

tition, it is instructive to look for indications where this characterization might not apply. This is because single units with high BFs exhibit a response phase that differs from that for units with low BFs. Based on previous suggestions that extracellular voltages can influence transmitter release at very low frequencies (Ingvarsson, 1981; Sellick *et al.*, 1982; Russell and Sellick, 1983), a 40 Hz input was chosen to increase separation between the stimulus frequency and the cell's BF. These second-turn results, displayed in Fig. 4 for OC, IHC, and IHC–OC records, are not typical of the responses usually encountered at this location and plotted in Fig. 3. In fact, the IHC response (thin solid lines) at 40 Hz and 65 dB is slightly lagging behind that recorded in the OC fluid space (dotted lines). The response phase estimated from the difference potential, IHC–OC (bold solid lines), lies in the region between basilar membrane displacement to SV and basilar membrane velocity to ST. This is indicated by the symbol placed on the OC waveform. Although this is an unusual IHC response pattern, it is similar to responses recorded in single units with comparable BFs. For example, fibers in the chinchilla auditory nerve with BFs in the transition region express a response phase just leading ST velocity at low frequencies (Ingvarsson, 1981; Ruggero and Rich, 1989; Ruggero *et al.*, 1996).

Data collected from the same IHC at 40 Hz and 75 dB are plotted in Fig. 5. The IHC waveform (thin solid lines) indicates that depolarization occurs between SV displacement and ST velocity. However, when the OC response is subtracted from the intracellular response (bold solid lines), two positive peaks emerge. These data at 40 Hz indicate that only after subtracting the extracellular response are two occurrences of hair-cell depolarization expressed within the cycle. This is probably because the second peak of depolarization coincides with the ST phase of the cochlear microphonic. Because an extracellular negativity tends to depolarize IHCs, this is the excitatory phase of the CM response. Consequently, the timing of hair cell depolarizations is affected by the relative magnitudes of extracellular and intracellular voltages.

Because these responses are distorted at 75 dB, the waveforms were digitally filtered off-line and plotted in the center panel of Fig. 5 to reveal changes in response phase for the fundamental versus the higher-order harmonics. These filtered responses represent difference potentials (IHC–OC) obtained after both high- and low-pass filtering. This is done to indicate the ways in which extracellular and intracellular responses are integrated and filtered by the hair cell's basolateral membrane. The low-pass filtered OC waveform is ap-

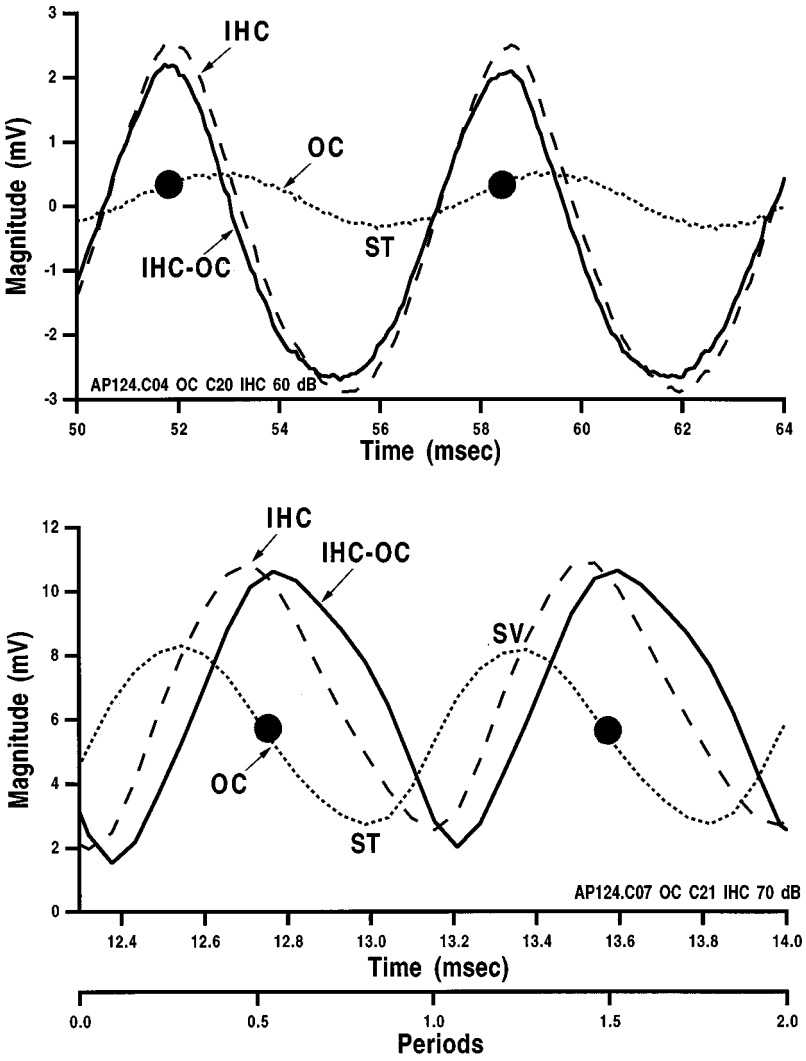

FIG. 3. This figure provides results from a second-turn IHC (dashed lines) and from the OC fluid space (dotted lines). The IHC–OC difference potential (solid lines) is also included to approximate the IHC's basolateral membrane voltage. Results at the top are for 150 Hz at 60 dB; those at the bottom for 1200 Hz at 70 dB. The OC response at 1200 Hz has been shifted vertically to facilitate comparisons with the IHC results (actually, the dc response in the extracellular space is small). The tone burst at 150 Hz (1200 Hz) was 50 (40) ms long. Although the first cycle at 1200 Hz is somewhat larger than the second, this is most likely due to noise, because only 40 presentations were averaged. In other words, this cell is not different from all other IHCs that do not exhibit adaptation.

pended to indicate position of the basilar membrane. Comparisons between the OCLP response and the subtracted low-pass waveform [(IHC–OC)LP] reflect phase differences between the IHC's basolateral membrane potential and the extracellularly recorded response at the fundamental (OCLP). The subtracted high-pass response [(IHC–OC)HP] reflects the harmonic content of the voltage gradient across the cell's basolateral membrane. The source of this nonlinearity is suggested in the lower panel, where low- and high-pass filtered IHC and OC waveforms are compared. In spite of the fact that the OC response at the fundamental is larger than the IHC response, the harmonic content of the intracel-

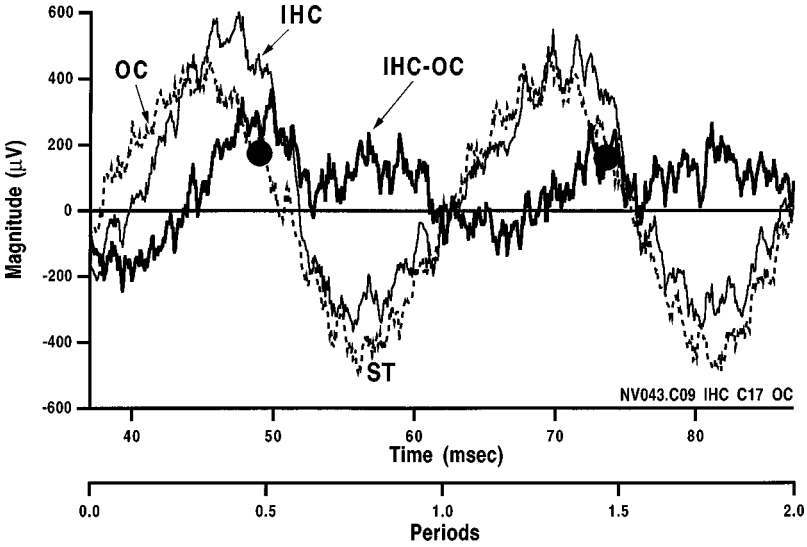

FIG. 4. Results from an unusual second-turn IHC are shown here for 40 Hz at 65 dB. Again waveforms are included for the IHC (thin lines), OC (dotted lines), and the IHC–OC (bold lines) responses. The OC response is used to designate position of the basilar membrane with the negative phase of the response indicating displacement to ST. The duration of the 40-Hz tone burst was 105 ms.

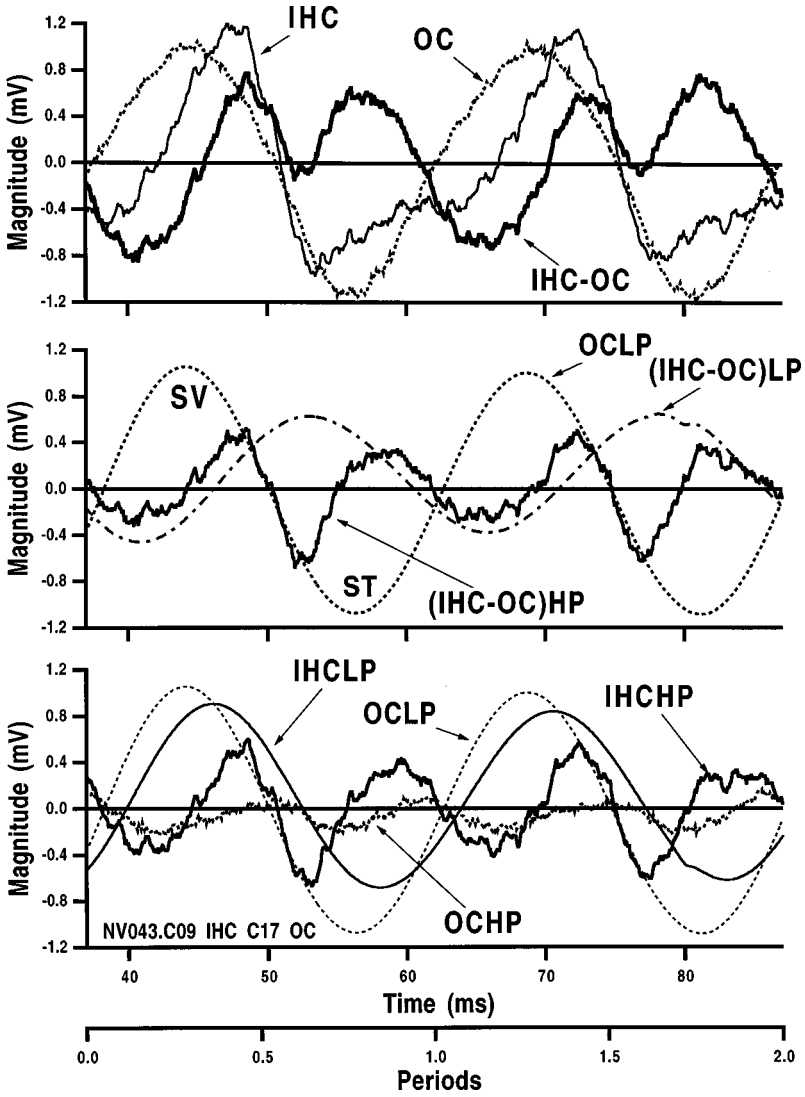

FIG. 5. These results are from the same IHC and the same level series as in Fig. 4. The data here, however, were collected at 75 dB. Line styles in the top panel are the same as those in Fig. 4. In the center panel, difference potentials are computed by subtracting IHC and OC responses and then high- and low-pass filtering the subtracted waveforms. The low-pass filtered OC waveform, plotted with dotted lines, is appended to indicate position of the basilar membrane. The bottom panel shows high- and low-pass filtered waveforms for both OC and IHC responses. The high- (low-) pass condition is plotted with thick (thin) lines.

lular response (IHCHP) exceeds that measured just outside the cell. In other words, the IHC response is more nonlinear than the one measured in the OC fluid space. Consequently, the more distorted intracellular response appears to reflect nonlinearities associated with voltage-dependent channels in the cell's basolateral membrane, as well as nonlinearities associated with the hair cell transducer. These harmonic components tend to produce an apparent phase lag of the depolarizing phase of the hair cell's basolateral-membrane potential (i.e., IHC–OC).

III. DISCUSSION

A. The frequency and level dependence of response phase

The single-unit literature indicates that response phase at low frequencies depends on BF. A preference for SV velocity is demonstrated, but only for neurons innervating the apex of the cochlea. Fibers targeting the base respond during basilar membrane velocity to ST (Ruggero *et al.*, 1996). This contrasts with results from IHCs, where depolarizations have generally been recorded near basilar membrane velocity to SV, independent of location (Sellick and Russell, 1980; Dallos and Santos-Sacchi, 1983; Patuzzi and Yates, 1987; Cody and Mountain, 1989). In order to deal with this discrepancy, it has been suggested that transmitter release could be driven by dominant, extracellular voltages with the result that single units would be expected to respond during ST displacement (Ingvarsson, 1981; Sellick *et al.*, 1982; Russell and Sellick, 1983). In this case, the voltage gradient across the IHC's basolateral membrane becomes relatively more positive during the negative phase of the CM response, which coincides with basilar membrane displacement to ST.

Data collected here in the apex of the cochlea indicate that IHC responses are larger and more nonlinear than those recorded outside the cell in the OC fluid space. This implies that extracellular voltages would not drive transmitter release (Dallos, 1983, 1985). However, in the base of the cochlea, gross extracellular responses at low frequencies are distorted (Ruggero *et al.*, 1986) and sometimes larger than IHC responses (Russell and Sellick, 1983). These differences may relate to the signal-to-BF ratio. Because this can be several octaves for single units with high BFs, thresholds on the tails of tuning curves are relatively high. Consequently, neural-response phase could lead ST displacement by as much as 90 deg, reflecting changes in wave shape as the CM response becomes more distorted. In other words, as the CM wave-

form becomes more square in shape, stimulation due to it occurs earlier in time. Because single units fire when their threshold is crossed, this may explain why neural phases lead ST displacement.

At somewhat higher levels, the IHC's receptor potential begins to dominate the transmembrane potential, with the result that a preference for SV velocity should be expressed. This transition has been demonstrated in the high-frequency region of the cochlea (Sellick *et al.*, 1982; Cody and Mountain, 1989), where IHCs respond near ST displacement at threshold levels, and near SV velocity at somewhat higher levels. These variations in response phase probably depend on differences between inner and outer hair cell excitation; specifically, the velocity dependence of the IHC input that serves to increase its threshold at low frequencies, thereby allowing extracellular voltages from OHCs to influence transmitter release.

Unfortunately, empirical determination of the degree to which extracellular voltages influence transmembrane potential is difficult to obtain. This is because penetration of the cell changes its electrical characteristics (Kros and Crawford, 1990; Kros, 1996; Zeddies and Seigel, 1995, 1996), making quantitative comparisons between IHC and OC responses difficult. Not only is the receptor potential decreased because the membrane resistance is reduced, but the basolateral membrane itself is linearized compared to its normal *in vivo* behavior. This makes it difficult to quantify the effect of phase shifts and nonlinearities produced by voltage-dependent ion channels in the IHC's basolateral membrane. Because of these complications, IHC and OC responses could appear similar in magnitude because of the leak associated with electrode penetration which is largely unavoidable in all sharp microelectrode recordings.

B. Simulation of response phase

A simple summation of sinusoids (i.e., not the solution of an elaborate hair cell model) is used to demonstrate that the addition of appropriate signals can produce a series of response patterns that is useful in deciphering the various phase shifts measured in the peripheral auditory system. In this effort, contributions are added as if they were produced by nonlinear cochlear elements, including the IHC transducer and voltage-dependent ion channels located in the cell's basolateral membrane. Extracellular voltages are also incorporated. The resulting changes in transmembrane voltage produced by pertinent combinations are provided in Fig. 6. In part (A), the IHC response (dashed lines) exceeds in magnitude and leads in phase the response measured in the OC fluid space (dotted lines) at low frequencies. This configuration reflects dominance by the IHC transducer, with the result that the voltage gradient across the cell's basolateral membrane, plotted with solid lines, is positive for SV velocity. This pattern, though idealized, is reasonably similar to those shown in Figs. 1, 2, and 3 and corresponds to that for nerve fibers with low BFs where discharge rate also increases near basilar membrane velocity to SV.

Part (B) of Fig. 6 depicts the case where the OC response exceeds that in the IHC with the result that the transmembrane potential depolarizes near displacement to ST. This simulation may apply to very low-frequency responses in the base of the cochlea, where the velocity dependence of the IHC transducer acts as a high-pass filter and reduces input to the cell (Sellick *et al.*, 1982; Russell and Sellick, 1983; Cody and Mountain, 1989). In this case, it is possible that single units with high BFs respond closer to ST velocity, reflecting a squaring of the OC waveform at moderate and high levels. Although this simulation depicts a much larger extracellular response, Russell and Sellick (1983) demonstrate that even when the IHC potential exceeds or is commensurate with the OC response, the extracellular voltage can influence the waveform of the transmembrane potential, as shown in Figs. 3 and 5. Thus, the voltage that drives transmitter release reflects a complex interaction between extracellular and intracellular responses. Although IHCs in the apex are also velocity dependent, electrical interactions are not likely here (Dallos 1983, 1985) because the CM is very small compared to the intracellular response. This is because low-frequency inputs are much closer to BF in the apex than in the base of the cochlea, with the result that cells respond in the ''tip region'' of the traveling wave.

Inner hair cell harmonic components also influence the timing of hair cell depolarizations and, ultimately, the timing of transmitter release. This is represented in Fig. 6(C), where interactions between the fundamental and the second harmonic result in two peaks of depolarization similar to the results plotted in Fig. 5. Depending on the relative phase between fundamental and harmonic components, and the degree to which they cancel and/or reinforce one another, one or multiple depolarizations can develop per cycle. In other words, the presence of harmonic components can influence the degree to which there is more than one preferred time for spikes to occur during a single period of a low-frequency input (Johnson, 1980; Ruggero and Rich, 1983; Horst *et al.*, 1990; Cai and Geisler, 1996a). Because the CM response is usually more linear than that recorded inside the cell (Fig. 5 and Cody and Mountain, 1989), the degree to which multiple peaks occur postsynaptically also depends on the relative magnitudes of intracellular and extracellular voltages. This was indicated in Fig. 5, where two peaks of depolarization emerge after the OC response is subtracted from that recorded inside the IHC. This possibility, that extracellular voltages influence postsynaptic responses, assumes that OC voltages will be significant, relative to IHC receptor potentials, even if the cell is not invaded by the microelectrode.

Although results from first-turn IHCs are not included here, it has been reported that the IHC ac receptor potential leads the CM by 90 deg at 40 Hz, after which it falls rapidly to zero degrees between 200 and 300 Hz (Sellick and Russell, 1980; Russell and Sellick, 1983). This suggests that the phase lead between IHC and OC responses is expressed in the base of the cochlea, but only at very low frequencies. In fact, another first-turn IHC (Russell and Sellick, 1983) did not exhibit a velocity dependence even at 30 Hz, where the ac receptor potential was in phase with the CM recorded in the OC. This indicates that the cell depolarized when the basilar membrane was displaced to SV. At 250 Hz, the ac receptor potential produced by this same cell was lagging behind the CM by ~45 deg. This phase lag is consistent with

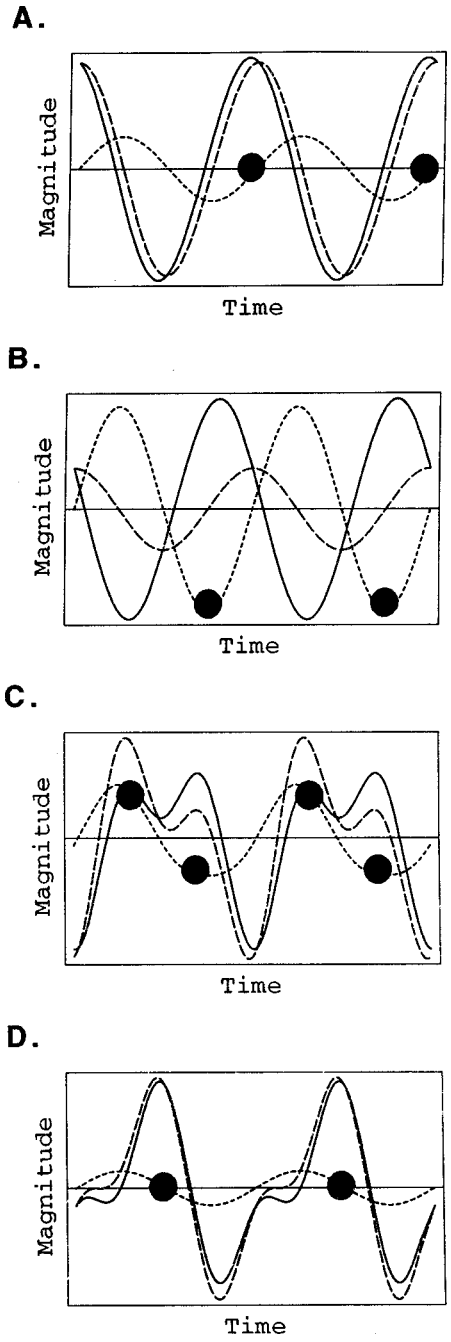

FIG. 6. Computer simulations demonstrate conditions where transmitter release is dominated by the IHC transducer [part (A)], the extracellular CM response [part (B)], and by IHC harmonic components [part (C)]. In all panels, two cycles are shown and the line styles are as follows: IHC, dashed; OC, dotted; transmembrane potential, solid. In part (A), the IHC transducer controls the voltage gradient across the cell's basolateral membrane with the result that the cell depolarizes for SV velocity, as indicated by the symbols. A similar response phase also characterizes single units with low BFs. In part (B), the extracellular CM, measured in the OC fluid space, controls transmitter release. The transmembrane potential is positive during basilar-membrane displacement to ST. For both panels (A) and (B), a phase lead of 90 deg for the fundamental component is incorporated. Contributions by IHC harmonic components, as in part (C), result in two depolarizations per cycle. This was achieved by adding 70% second harmonic, i.e., the second harmonic was 3 dB down from the fundamental. Finally, the simulation in panel (D) shows the fundamental component of the IHC response lagging behind the OC potential. This represents basal-turn responses at ~500 Hz where the IHC transducer responds to SV displacement and ion channels in the cell's basolateral membrane contribute a phase lag. Significant second-harmonic distortion (50%) is also assumed.

estimates (Zeddies and Siegel, 1995) of the kinetics of voltage-dependent ion channels. Based on these data obtained in the base of the cochlea, the simulation in panel (D) of Fig. 6 represents an input at ~500 Hz, where there is no velocity dependence. The simulation includes energy at the second harmonic and assumes a phase lag due to channel activity. In this case, maximum depolarization occurs near basilar membrane velocity to ST. This is evident in the records even when the OC response is not subtracted. This response phase is similar to that observed for single units in the base of the cochlea (Ruggero *et al.*, 1996; Cai and Geisler, 1996a).

The distortion and phase shift produced by voltage- and time-dependent channel activity should be considered when evaluating response phase. It is difficult, however, to quantify these contributions because all *in vivo* hair cell recordings invariably compromise channel kinetics. In fact, the receptor potential usually reflects the transducer impedance because of the leak that shunts the basolateral membrane when the electrode penetrates the cell. If this leak is relatively minor, then low-pass filtering by the membrane will shape the receptor potential and contribute a phase lag between intracellular and extracellular responses. Because IHC responses rarely reflect balanced contributions from both transducer and basolateral membrane impedances, the magnitude and phase changes, as well as the distortions contributed by channel activity, are not fully reflected in hair cell recordings.

C. Implications for postsynaptic responses

The schematic in Fig. 7 represents response phase plotted as a function of stimulus frequency and expressed relative to the motion pattern of the basilar membrane. Responses for the apex of the cochlea are presented in the top panel. Functions for the CM (dot–dashed lines), measured in the OC fluid space, indicate that the positive (negative) phase of this cochlear potential is associated with SV (ST) displacement throughout the frequency range depicted here. This is because the CM reflects OHC receptor currents (Dallos and Cheatham, 1976), and OHCs probably respond to basilar-membrane displacement at all frequencies (Dallos *et al.*, 1972). Thus, the phase changes on the right ordinate are plotted relative to basilar membrane displacement to SV. The function representing input to the IHC transducer (dashed lines) exhibits a velocity dependence for low frequencies with the result that IHC responses are measured near SV velocity. This preference reflects high-pass filtering associated with ciliary mechanics (Dallos and Cheatham, 1990). As stimulus frequency increases, IHC response phase changes to SV displacement, reflecting entrainment of the hair bundle (Freeman and Weiss, 1990) or possibly a loose contact between the IHC stereocilia and the overlying tectorial membrane. In other words, at higher frequencies, the IHCs can respond to basilar membrane displacement even when there is no firm attachment between the IHC stereocilia and the overlying tectorial membrane. The function plotted with solid lines combines high-pass filtering associated with the IHC transducer and low-pass filtering associated with the hair cell's basolateral membrane. As response phase moves

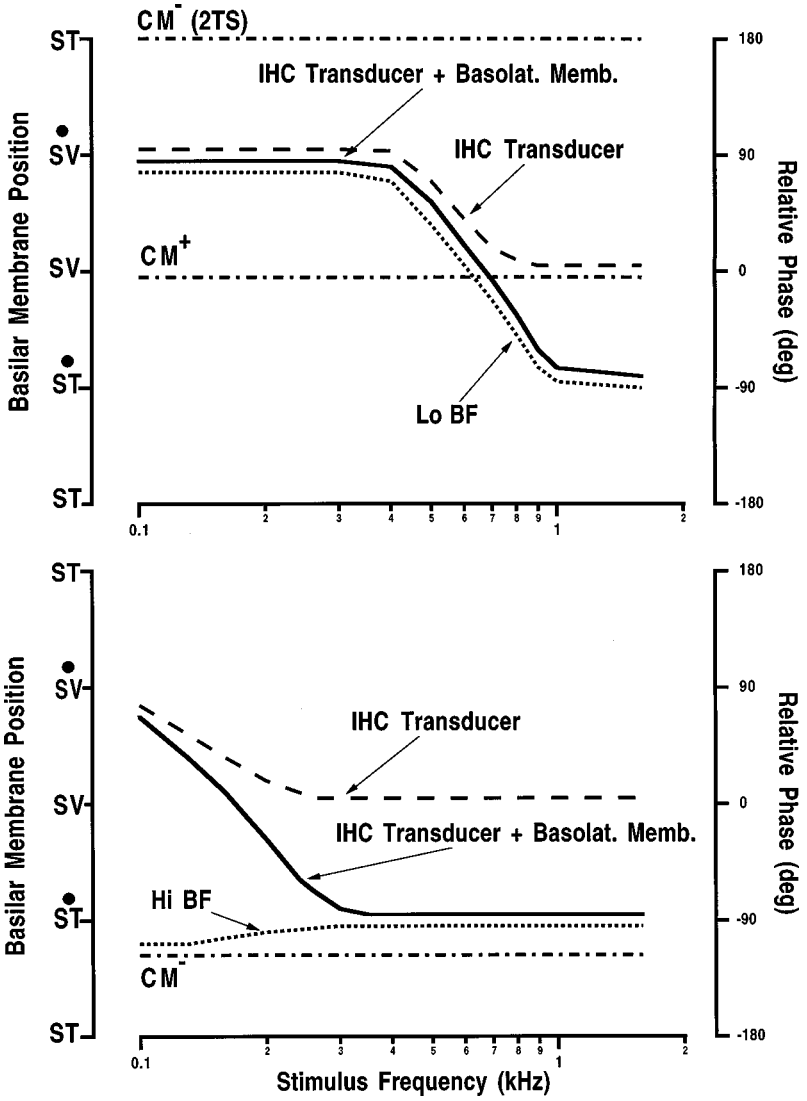

FIG. 7. These schematics are designed to summarize response phase for hair-cells and single-units in the apex (top panel) and base (bottom panel) of the cochlea. Because single-unit results in the chinchilla (Ruggero *et al.*, 1996) are the most extensive, they form the basis for these representations. The left ordinate represents basilar membrane position; the right, response phase plotted relative to SV displacement, with positive numbers indicating phase leads. The top panel indicates that the IHC transducer (dashed lines) responds to SV velocity at low frequencies. In other words, a 90 deg lead is expressed relative to the positive phase of the CM response (dot–dashed lines), which is associated with basilar membrane displacement to SV. As stimulus frequency increases, however, IHC excitation coincides with basilar membrane displacement to SV. In this case, the time of excitation is ~180 deg out of phase with the negative CM response. The phase of excitation for single units with low BFs (solid lines) indicates that they also respond to SV velocity at low frequencies. The IHC data reported here suggest that these neural responses should pass through SV displacement and finally settle at ST velocity as stimulus frequency increases. Above ~1000 Hz, the 1/4-cycle disparity between the single unit and the IHC transducer reflects the 90 deg phase lag associated with low-pass filtering by the IHC's basolateral membrane. For single units with high BFs, depicted at the bottom, a preference for ST velocity is demonstrated throughout the frequency range depicted here. The negative phase of the CM response is plotted near ST velocity to reflect nonlinearities associated with the high levels required to reach threshold for inputs well below BF.

from SV velocity to ST velocity (see also Figs. 2 and 3), the function displays a 90 deg lead at low frequencies and a 90 deg lag above ~1000 Hz, when measured relative to the positive phase of the CM response. This smooth transition is suggested by modeling efforts (Dallos, 1984) that show the corner frequencies of the low- and high-pass filters to be well matched. Finally, the function plotted with dotted lines represents the expected excitation phase for single units with low BFs, based on the IHC results. This function parallels that for the IHC transducer plus the basolateral membrane. These results imply that single units should respond to basilar membrane velocity but responses should be ~180 deg out of phase at 200 versus 1200 Hz. Predictions are not made for higher-frequency inputs because of the several stages of low-pass filtering associated with synaptic processes (Weiss and Rose, 1988a, b; Kidd and Weiss, 1990).

The bottom panel in Fig. 7 represents the basal, high-frequency region of the cochlea. Thus, these hair-cell and single-unit responses are obtained well below BF. The representation demonstrates that IHCs are velocity sensitive, but only at very low frequencies below ~200 Hz. This is why the IHC transducer function plateaus at SV displacement near 300 Hz, a lower frequency than in the apex. The combined function, for the IHC transducer plus the basolateral membrane, plateaus at ST velocity but, again, at lower frequencies than in the apex. The negative phase of the CM is also included because this phase of the extracellular response can induce transmitter release at very low frequencies. This function, however, is positioned closer to ST velocity, rather than ST displacement, to reflect a squaring of the CM waveform. This is done because the CM is distorted at the high levels required to reach threshold for inputs well below BF (Ruggero *et al.*, 1986). The function for single units with high BFs (dotted lines) is drawn to reflect control of transmitter release by the IHC transducer and basolateral membrane above ~300 Hz and control by the extracellular CM below ~200 Hz. In other words, the excitation phase at ST velocity probably reflects both intracellular and extracellular influences. The CM is not thought to control transmitter release at higher frequencies because it does not exceed the IHC receptor potential in magnitude (Russell and Sellick, 1983). Although single units in the apex also respond to

basilar membrane velocity, their responses at 200 and 1200 Hz are expected be ~180 deg out of phase. Consequently, the phases of excitation for high- and low-BF units should be in phase at 1200 Hz, but out of phase at 200 Hz.

It is emphasized that a preference for SV velocity is not exhibited in single units with high BFs. This may relate to observations where the phase lead associated with ciliary mechanics is only expressed at very low frequencies in IHCs with high BFs. For example, data obtained from first-turn IHCs (Sellick and Russell, 1980; Russell and Sellick, 1983) indicate that hair cell depolarizations occur for basilar membrane displacements to SV above ~200 Hz. Anatomical evidence is consistent with this possibility because the tallest stereocilia at the base of the cochlea are found on inner, rather than outer, hair cells (Lim, 1980; Wright, 1984). This observation is worth pointing out because it is the height of the stereocilia, in combination with the configuration of the subtectorial space, that determines input to the IHC. In spite of this caveat, the transition region where OHC stereocilia become shorter than IHC stereocilia occurs at a place along the cochlear partition (Eldredge *et al.*, 1981) that is similar to the place where response phase changes in the single-unit recordings (Ruggero *et al.*, 1996). It is, therefore, possible that the difference in response phase, for low- versus high-BF nerve fibers, relates to the wider frequency range over which the velocity dependence of the IHC transducer contributes to apical IHC responses. In fact, Dallos and Santos-Sacchi (1983) state that the median frequency producing an IHC phase lead of 45 deg, relative to the OC response, is 340 Hz. This is well above that for basal-turn IHC responses that are, on average, in phase with the OC response above ~200 Hz (Sellick and Russell, 1980; Russell and Sellick, 1983).

In addition to a spatial variation in the degree of coupling between the IHC stereocilia and the tectorial membrane (Ruggero and Rich, 1987), it is conceivable that ion-channel density for IHCs varies longitudinally along the cochlear spiral, as demonstrated for OHCs (Housley and Ashmore, 1992). This could influence the frequency at which a criterion phase lag is expressed, with the result that voltage-dependent ion channels could contribute a larger phase lag in the base versus the apex of the cochlea for a given low-frequency input. In other words, a 90 deg phase lag might occur at lower frequencies in the base of the cochlea. This implies that single units with high BFs would respond to ST velocity at lower frequencies than in the apex, as shown in Fig. 7.

It is also proposed that IHCs in the basal half of the cochlea may be more nonlinear than their apical counterparts. Even though a criterion ac receptor potential is produced at the same sound-pressure level in first- and third-turn IHCs, a 20 dB higher level is required to produce the same criterion dc response at the apical recording location (Russell and Sellick, 1978; Cheatham and Dallos, 1999). In other words, the IHCs are equally sensitive, but they differ in the degree of asymmetry exhibited in their transducer functions. Consequently, harmonic components may influence response phase to a greater degree in the high-frequency region of the cochlea.

D. The phase of excitation versus the phase of suppression

The frequency dependence of response phase depicted in Fig. 7 should be considered when evaluating the temporal relationships between single-tone excitation and two-tone suppression for low-frequency suppressors below BF. In contrast to reports demonstrating variations in the timing of excitation for single-tone inputs, the phase of two-tone suppression is relatively constant. Data indicate that the time of suppression, within a single cycle of a low-frequency suppressor, occurs near basilar membrane displacement to ST when the suppressor is introduced at its lowest effective level. This preference has been demonstrated in IHC ac receptor potentials (Patuzzi and Sellick, 1984; Cheatham and Dallos, 1997), in single-unit discharge rates (Ingvarsson, 1981; Patuzzi *et al.*, 1984a; Temchin *et al.*, 1997), and in cochlear mechanics (Patuzzi *et al.*, 1984b; Rhode and Cooper, 1993; Cooper, 1996). The association of suppression with basilar membrane displacement to ST, and with the negative phase of the CM response, is shown at the top of Fig. 7. It is thought to reflect asymmetries in the outer hair cell transducer, such that basilar membrane displacements to ST effectively bias the transducer in the off position (Geisler *et al.*, 1990; Cheatham and Dallos, 1997), thereby reducing the gain of the cochlear amplifier.

Confusion develops when the phase of suppression is compared with the phase of excitation for the low-frequency suppressor alone. In fact, the various temporal relationships observed between excitation and suppression could relate to the frequency and level dependence of response phase indicated here and well documented at the single-unit level (Ruggero *et al.*, 1996). Although not very common (Cai and Geisler, 1996b), there are instances where the phases of both excitation and suppression coincide with basilar membrane displacement to ST (Sachs and Hubbard, 1981; Sellick *et al.*, 1982). In this case, the most parsimonious explanation is that excitation for the low-frequency suppressor alone is related to the extracellular CM, as in Fig. 6(B). More often, however, the phases of suppression and excitation differ, suggesting that variations in response phase for single tones may underlie these differences. Representations in Fig. 7 indicate that, depending on BF, various temporal relationships can exist between the time of excitation for the low-frequency suppressor alone and the time of suppression in the two-tone case.

IV. SUMMARY

Simply characterizing the IHC transducer can sometimes reveal very little about how signals are conveyed to the auditory nerve. In fact, in order to understand this transfer of information, one must take into account contributions from ion channels located in the cell's basolateral membrane, which serves to integrate intracellular and possibly extracellular voltages. Data indicate that apical IHCs depolarize near SV velocity, reflecting the velocity dependence of the IHC transducer at low frequencies. However, as stimulus frequency increases, the time of depolarization shifts to SV displacement, reflecting the possibility of a visco–elastic cou-

pling between the hair bundle and the tectorial membrane. Although a similar pattern has been documented for first-turn IHCs, the transition between SV velocity and SV displacement appears to occur at lower frequencies than the transition demonstrated for apical IHCs. This suggests that the velocity dependence of the IHC transducer would be expressed in basal-turn responses, but only for very low-frequency inputs. Consequently, above ~200 Hz, IHCs with high BFs probably respond to SV displacement. This, coupled with waveform distortion and the kinetics of ion-channel gating in the cell's basolateral membrane, places the time of maximum transmitter release near ST velocity. Because IHCs in the base appear to be more asymmetrical than their apical counterparts, harmonic components influence the timing of hair-cell depolarizations to a greater degree in the high-frequency region of the cochlea. For frequencies below ~200 Hz, the difference in response phase between apex and base may well result from extracellular voltages that potentially influence transmitter release in the high-frequency region of the cochlea.

ACKNOWLEDGMENTS

Work supported (in part) by grant number 5 R01 DC00089, Studies in Cochlear Hair Cell Transduction, from the National Institute on Deafness and Other Communication Disorders, National Institutes of Health. Comments by Jonathan Siegel and Mario Ruggero are appreciated.

Békésy, G. von (**1960**). *Experiments in Hearing* (McGraw-Hill, New York).
Cai, Y., and Geisler, C. D. (**1996a**). ''Temporal patterns of the responses of auditory-nerve fibers to low-frequency tones,'' Hearing Res. **96**, 83–93.
Cai, Y., and Geisler, C. D. (**1996b**). ''Suppression in auditory-nerve fibers of cats using low-side suppressors: I. Temporal aspects,'' Hearing Res. **96**, 94–112.
Cheatham, M. A. (**1993**). ''Cochlear function reflected in mammalian hair cell responses,'' Prog. Brain Res. **97**, 13–19.
Cheatham, M. A., and Dallos, P. (**1992**). ''Physiological correlates of off-frequency listening,'' Hearing Res. **59**, 39–45.
Cheatham, M. A., and Dallos, P. (**1997**). ''Low-frequency modulation of inner hair cell and organ of Corti responses in the guinea pig cochlea,'' Hearing Res. **108**, 191–212.
Cheatham, M. A., and Dallos, P. (**1999**). ''Contributions by inner and outer hair cells to the summating potential,'' Abs. Assoc. Res. Otolaryngol., #723.
Cody, A. R., and Mountain, D. C. (**1989**). ''Low-frequency responses of inner hair cells: evidence for a mechanical origin of peak splitting,'' Hearing Res. **41**, 89–99.
Cooper, N. P. (**1996**). ''Two-tone suppression in cochlear mechanics,'' J. Acoust. Soc. Am. **99**, 3087–3098.
Dallos, P. (**1973**). *The Auditory Periphery* (Academic, New York).
Dallos, P. (**1983**). ''Some electrical circuit properties of the organ of Corti. I. Analysis without reactive elements,'' Hearing Res. **12**, 89–119.
Dallos, P. (**1984**). ''Some electrical circuit properties of the organ of Corti. II. Analysis including reactive elements,'' Hearing Res. **14**, 281–291.
Dallos, P. (**1985**). ''Response characteristics of mammalian cochlear hair cells,'' J. Neurosci. **5**, 1591–1608.
Dallos, P., and Cheatham, M. A. (**1976**). ''Production of cochlear potentials by inner and outer hair cells,'' J. Acoust. Soc. Am. **60**, 510–512.
Dallos, P., and Santos-Sacchi, J. (**1983**). ''AC receptor potentials from hair cells in the low-frequency region of the guinea pig cochlea,'' in *Mechanisms of Hearing*, edited by W. R. Webster and L. M. Aitkin (Monash U.P., Clayton, Australia), pp. 11–16.
Dallos, P., and Cheatham, M. A. (**1990**). ''Effects of electrical polarization on inner hair cell receptor potentials,'' J. Acoust. Soc. Am. **87**, 1636–1647.
Dallos, P., and Evans, B. N. (**1995**). ''High-frequency motility of outer hair cells and the cochlear amplifier,'' Science **267**, 2006–2009.
Dallos, P., Schoeny, Z. G., Worthington, D. W., and Cheatham, M. A. (**1969**). ''Some problems in the measurement of cochlear distortion,'' J. Acoust. Soc. Am. **46**, 356–361.
Dallos, P., Schoeny, Z. G., and Cheatham, M. A. (**1971**). ''On the limitations of cochlear-microphonic measurements,'' J. Acoust. Soc. Am. **49**, 1144–1154.
Dallos, P., Billone, M. C., Durrant, J. D., Wang, C.-y., and Raynor, S. (**1972**). ''Cochlear inner and outer hair cells: Functional differences,'' Science **177**, 356–358.
Dallos, P., Santos-Sacchi, J., and Flock, Å (**1982**). ''Intracellular recordings from cochlear outer hair cells,'' Science **218**, 582–584.
Dancer, A., and Franke, R. (**1980**). ''Intracochlear sound pressure measurements in guinea pigs,'' Hearing Res. **2**, 191–205.
Eldredge, D. H., Miller, J. D., and Bohne, B. A. (**1981**). ''A frequency-position map for the chinchilla cochlea,'' J. Acoust. Soc. Am. **69**, 1091–1095.
Flock, Å. (**1971**). ''Sensory transduction in hair cells,'' in *Handbook of Sensory Physiology*, Volume I, edited by W. R. Loewenstein (Springer-Verlag, New York), pp. 396–441.
Freeman, D. M., and Weiss, T. F. (**1990**). ''Hydrodynamic forces on hair bundles at high frequencies,'' Hearing Res. **48**, 31–36.
Geisler, C. D., Yates, G. K., Patuzzi, R. B., and Johnstone, B. M. (**1990**). ''Saturation of outer hair cell receptor currents causes two-tone suppression,'' Hearing Res. **44**, 241–256.
Horst, J. W., Javel, E., and Farley, G. R. (**1990**). ''Coding of spectral fine structure in the auditory nerve. II: Level dependent nonlinear responses,'' J. Acoust. Soc. Am. **88**, 2656–2681.
Housley, G. D., and Ashmore, J. F. (**1992**). ''Ionic currents of outer hair cells isolated from the guinea-pig cochlea,'' J. Physiol. (London) **448**, 73–98.
Ingvarsson, K. (**1981**). ''Dynamics of cochlear hair cells as inferred from cochlear potentials and responses from auditory nerve fibers,'' Ph.D. Dissertation, Northwestern University, Evanston, IL 60208.
Johnson, D. H. (**1980**). ''The relationship between spike rate and synchrony in responses of auditory-nerve fibers to single tones,'' J. Acoust. Soc. Am. **68**, 1115–1122.
Katz, B., and Miledi, R. (**1967**). ''A study of synaptic transmission in the absence of nerve impulses,'' J. Physiol. (London) **192**, 407–436.
Kidd, R. C., and Weiss, T. F. (**1990**). ''Mechanisms that degrade timing information in the cochlea,'' Hearing Res. **49**, 181–207.
Konishi, T., and Nielsen, D. W. (**1978**). ''The temporal relationship between basilar membrane motion and nerve impulse initiation in auditory nerve fibers of guinea pigs,'' Jpn. J. Phys. **28**, 291–307.
Kros, C. J. (**1996**). ''Physiology of mammalian cochlear hair cells,'' in *The Cochlea*, edited by P. Dallos, A. N. Popper, and R. R. Fay (Springer-Verlag, New York), pp. 318–385.
Kros, C. J., and Crawford, A. C. (**1990**). ''Potassium currents in inner hair cells isolated from the guinea-pig cochlea,'' J. Physiol. (London) **421**, 263–291.
Lim, D. J. (**1972**). ''Fine morphology of the tectorial membrane: Its relationship to the organ of Corti,'' Arch. Otolaryngol. **96**, 199–215.
Lim, D. J. (**1980**). ''Cochlear anatomy related to cochlear mechanics. A review,'' J. Acoust. Soc. Am. **67**, 1686–1695.
Maceri, D. R., Sokolich, W. G., and Strelioff, D. (**1982**). ''A reinvestigation of the response phase of auditory nerve fibers in guinea pigs,'' Abs. Assoc. Res. Otolaryngol. p. 10.
Nedzelnitsky, V. (**1974**). ''Measurement of sound pressure in the cochlea of anesthetized cats,'' in *Facts and Models of Hearing*, edited by E. Zwicker and E. Terhardt (Springer-Verlag, Berlin), pp. 45–53.
Nuttall, A. L., Brown, M. C., Masta, R. I., and Lawrence, M. (**1981**). ''Inner hair cell responses to velocity of basilar membrane motion in the guinea pig,'' Brain Res. **211**, 171–174.
Oshima, W., and Strelioff, D. (**1983**). ''Responses of gerbil and guinea pig auditory nerve fibers to low-frequency sinusoids,'' Hearing Res. **12**, 167–184.
Patuzzi, R. B., and Sellick, P. M. (**1984**). ''The modulation of the sensitivity of the mammalian cochlea by low frequency tones. II. Inner hair cell receptor potentials,'' Hearing Res. **13**, 9–18.
Patuzzi, R. B., and Yates, G. K. (**1987**). ''The low-frequency response of inner hair cells in the guinea pig cochlea: implications for fluid coupling and resonance of the stereocilia,'' Hearing Res. **30**, 83–98.
Patuzzi, R. B., Sellick, P. M., and Johnstone, B. M. (**1984a**). ''The modu-

lation of the sensitivity of the mammalian cochlea by low frequency tones. I. Primary afferent activity,'' Hearing Res. **132**, 1–13.
Patuzzi, R. B., Sellick, P. M., and Johnstone, B. M. (**1984b**). ''The modulation of the sensitivity of the mammalian cochlea by low frequency tones. III. Basilar membrane motion,'' Hearing Res. **13**, 19–27.
Rhode, W. S., and Cooper, N. P. (**1993**). ''Two-tone suppression and distortion production on the basilar membrane in the hook region of cat and guinea-pig cochlea,'' Hearing Res. **66**, 31–45.
Ruggero, M. A., and Rich, N. C. (**1983**). ''Chinchilla auditory-nerve responses to low frequency tones,'' J. Acoust. Soc. Am. **73**, 2096–2108.
Ruggero, M. A., and Rich, N. C. (**1987**). ''Timing of spike initiation in cochlear afferents: Dependence on site of innervation,'' J. Neurophysiol. **58**, 379–403.
Ruggero, M. A., and Rich, N. C. (**1989**). '' 'Peak-splitting': intensity effects in cochlear afferent responses to low frequency tones,'' in *Cochlear Mechanisms—Structure, Function and Models*, edited by J. P. Wilson and D. T. Kemp (Plenum, London), pp. 259–266.
Ruggero, M. A., Robles, L., and Rich, N. C. (**1986**). ''Cochlear microphonics and the initiation of spikes in the auditory nerve: Correlations of single-unit data with neural and receptor potentials recorded from the round window,'' J. Acoust. Soc. Am. **79**, 1491–1498.
Ruggero, M. A., Rich, N. C., Shivapuja, B. G., and Temchin, A. N. (**1996**). ''Auditory-nerve responses to low-frequency tones: Intensity dependence,'' Aud. Neurosci. **2**, 159–185.
Russell, I. J., and Sellick, P. M. (**1978**). ''Intracellular studies of hair cells in the guinea pig cochlea,'' J. Physiol. (London) **284**, 261–290.
Russell, I. J., and Sellick, P. M. (**1983**). ''Low-frequency characteristics of intracellularly recorded receptor-potentials in guinea-pig cochlear hair cells,'' J. Physiol. (London) **338**, 179–206.
Sachs, M. B., and Hubbard, A. E. (**1981**). ''Responses of auditory-nerve fibers to characteristic-frequency tones and low-frequency suppressors,'' Hearing Res. **4**, 309–324.
Sellick, P. M., and Russell, I. J. (**1980**). ''Responses of inner hair cells to basilar membrane velocity during low frequency auditory stimulation in the guinea pig cochlea,'' Hearing Res. **2**, 439–446.
Sellick, P. M., Patuzzi, R., and Johnstone, B. M. (**1982**). ''Modulation of responses of spiral ganglion cells in the guinea pig cochlea by low frequency sound,'' Hearing Res. **7**, 199–221.
Sokolich, W. G., Hamernik, R. P., Zwislocki, J. J., and Schmiedt, R. A. (**1976**). ''Inferred response polarities of cochlear hair cells,'' J. Acoust. Soc. Am. **59**, 963–974.
Temchin, A. N., Rich, N. C., and Ruggero, M. A. (**1997**). ''Low-frequency suppression of auditory-nerve responses to characteristic-frequency tones,'' Hearing Res. **113**, 29–56.
Weiss, T. F., and Rose, C. (**1988a**). ''Stages of degradation of timing information in the cochlea: A comparison of hair-cell and nerve-fiber responses in the alligator lizard,'' Hearing Res. **33**, 167–174.
Weiss, T. F., and Rose, C. (**1988b**). ''Comparisons of synchronization filters in different auditory receptor organs,'' Hearing Res. **33**, 175–179.
Weiss, T. F., Peake, W. T., and Sohmer, H. S. (**1969**). ''Intra-cochlear responses to tones,'' MIT Quart. Progr. Rep. **94**, 305–316.
Whitfield, I. C., and Ross, H. F. (**1965**). ''Cochlear microphonic and summating potentials and the outputs of individual hair cell generators,'' J. Acoust. Soc. Am. **38**, 126–131.
Wright, A. (**1984**). ''Dimensions of the cochlear stereocilia in man and the guinea pig,'' Hearing Res. **13**, 89–98.
Zeddies, D. G., and Siegel, J. H. (**1995**). ''Physiologically based model of the inner hair cell,'' Abs. Assoc. Res. Otolaryngol., p. 53.
Zeddies, D. G., and Siegel, J. H. (**1996**). ''Influence of the basolateral membrane on receptor potentials in a simulated inner hair cell,'' Abs. Assoc. Res. Otolaryngol., p. 184.

Analog very large-scale integrated (VLSI) implementation of a model of amplitude-modulation sensitivity in the auditory brainstem

André van Schaik[a)]
MANTRA Centre for Neuromimetic Systems, Swiss Federal Institute of Technology, CH-1015 Lausanne, Switzerland

Ray Meddis
Centre for the Neural Basis of Hearing, Department of Psychology, Essex University, Colchester, Essex CO4 3SQ, United Kingdom

(Received 4 February 1998; revised 31 August 1998; accepted 29 October 1998)

An analog very large-scale integrated (VLSI) implementation of a model of signal processing in the auditory brainstem is presented and evaluated. The implementation is based on a model of amplitude-modulation sensitivity in the central nucleus of the inferior colliculus (CNIC) previously described by Hewitt and Meddis [J. Acoust. Soc. Am. **95**, 2145–2159 (1994)]. A single chip is used to implement the three processing stages of the model; the inner-hair cell (IHC), cochlear nucleus sustained-chopper, and CNIC coincidence-detection stages. The chip incorporates two new circuits: an IHC circuit and a neuron circuit. The input to the chip is taken from a ''silicon cochlea'' consisting of a cascade of filters that simulate basilar membrane mechanical frequency selectivity. The chip which contains 142 neurons was evaluated using amplitude-modulated pure tones. Individual cells in the CNIC stage demonstrate bandpass rate-modulation responses using these stimuli. The frequency of modulation is represented spatially in an array of these cells as the location of the cell generating the highest rate of action potentials. The chip processes acoustic signals in real time and demonstrates the feasibility of using analog VLSI to build and test auditory models that use large numbers of component neurons. [S0001-4966(99)03102-1]

PACS numbers: 43.64.Qh, 43.64.Bt [RDF]

INTRODUCTION

The complexity of auditory signal processing in the auditory periphery and brainstem requires sophisticated modeling techniques. Computational modeling of individual stages has already been shown to be a successful approach to characterizing the processes involved. However, when it is necessary to characterize the response of the system as a whole, even high-speed computers may require very long run times. There are approximately 10 000 inner-hair cells (IHCs), 30 000 afferent auditory-nerve (AN) fibers and tens of thousands of neurons in the cochlear nucleus alone. Very large-scale integrated (VLSI) circuitry offers the possibility of evaluating such complex models in real time. Below, we present an initial attempt to exploit analog VLSI technology to simulate a complex system involving inner-hair cells, ventral cochlear nucleus (VCN) sustained-chopping stellate cells, and coincidence-detecting neurons in the central nucleus of the inferior colliculus (CNIC). Although none of the individual cells is modeled in great detail by the electronic circuits, the VLSI system is nevertheless capable of implementing the signal-processing principles exploited by the biological system.

The highly parallel architecture of the auditory periphery and auditory brainstem is well suited to analog VLSI technology because of the case of replicating individual circuits once the design details of a single unit have been decided. For example, all IHCs appear to operate according to the same principles; it is only the input that differs between cells. If a suitable circuit can be designed to simulate their operation, they can be readily replicated in large numbers. The IHC and neurons to be described below occupy approximately the same area on the chip with a density of approximately 4000 neurons (or IHCs) per square centimeter. When IHCs and neurons are combined on a single chip, the response of large assemblies of neurons to complex stimuli is more easily evaluated in real time.

A number of seminal studies using analog VLSI technology have already attempted to simulate individual stages of mammalian auditory-signal processing. Lyon and Mead (1988) produced an early simulation of cochlear mechanical filtering, this has been followed by a number of other studies (Fragnière *et al.*, 1997; Lazzaro and Mead, 1989a; Lyon, 1991; Liu *et al.*, 1991; Sarpeshkar *et al.*, 1996; Watts *et al.*, 1992; Watts, 1993). Lazzaro (1992) has attempted to simulate mechanical-to-electrical transduction analogous to that occurring at the level of the IHC. Others (for example, Mahowald and Douglas, 1991; Mead, 1989; Rasche *et al.*, 1997; Sarpeshkar *et al.*, 1992) have developed models of neurons but only Lazzaro (Lazzaro and Mead, 1989b, 1989c; Lazzaro, 1991) appears to have used VLSI neurons to simulate aspects of auditory processing. In the study described below,

[a)]Present address: Auditory Neuroscience Lab., Dept. of Physiology, University of Sydney, NSW 2006, Australia.

we build upon these pioneering efforts to show how three different stages of auditory processing can be combined on a single chip to simulate the response of arrays of CNIC units to acoustic stimulation.

The circuit is based on a previous computer model of amplitude-modulation sensitivity of single neurons in the inferior colliculus (Hewitt and Meddis, 1994). The original model was able to simulate the rate response of a single CNIC unit as a function of the rate of amplitude modulation of sinusoidal signals. As such, it represented a testable model of the anatomical and physiological basis of the behavior of these cells as observed in animal preparations (Rees and Palmer, 1989; Langner and Schreiner, 1988). If, however, the model could be extended to represent the simultaneous activity of arrays of such cells, each with a different best-modulation frequency (BMF), its behavior might have relevance to psychoacoustic theories concerning the perception of pitch. Langner *et al.* (1998) have presented evidence that an orderly orthogonal arrangement of cells in the CNIC can be observed with respect to their best frequency (BF) for pure tones and their BMF for modulated tones. While such arrays of cells could be simulated using conventional digital computers, the required processing time can be prohibitive. This was seen as a suitable opportunity to explore the power of analog VLSI circuitry.

Section I summarizes the model as given by Hewitt and Meddis (1994). Section II contains the details of the hardware implementation of the model components. Section III evaluates the model in terms of its ability to represent the behavior of a single CNIC unit. Section IV shows how amplitude modulation may be represented across an array of hardware CNIC cells.

I. MODEL

As far as possible, the hardware was designed to simulate exactly the processing in the four-stage model described by Hewitt and Meddis (1994). This is represented in Fig. 1. Some compromises were necessary when designing the VLSI chip. These will be detailed when describing the hardware implementation in Sec. II. The description immediately below refers to the original software model that inspired the project.

Stage 1 is the mechanical filtering of the cochlea.

Stage 2 is a model of the functioning of an inner-hair cell in response to the mechanical stimulation of the basilar membrane. The model is based directly on that published earlier by Meddis (1986, 1988). The output of the cell is characterized as the probability of occurrence of an action potential in an auditory-nerve fiber synapsing with the cell. An important characteristic of the hair-cell model is that the response adapts over time to a constant stimulus. The output from the cell is half-wave rectified and has a low-pass frequency characteristic with a corner frequency in the region of 1 kHz.

Stage 3 simulates the activity of stellate cells in the VCN that show a sustained-chopping response to pure tones and are thought to have excitatory projections to the CNIC. Each cell receives inputs from a large number of hair cells with similar receptive fields. In the original version of the

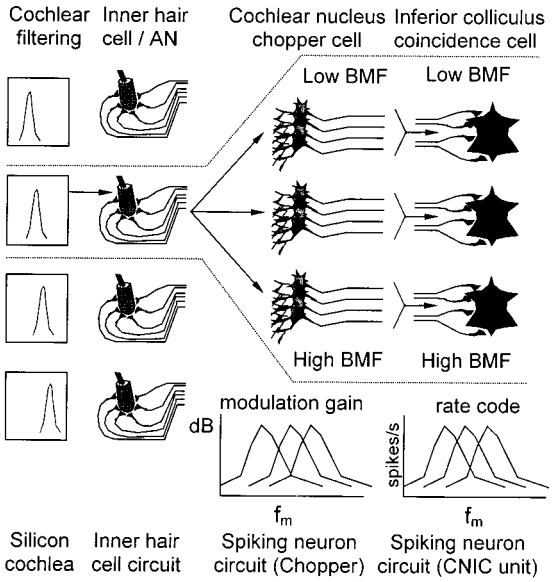

FIG. 1. Proposed neural circuit for amplitude-modulation sensitivity in the inferior colliculus. Abbreviations: BMF-best-modulation frequency. Adapted from Hewitt and Meddis (1994).

model, 60 inputs were used, but later studies (Meddis and O'Mard, 1997) have suggested that 30 might be a more appropriate number. The inputs to a VCN cell are in the form of spikes delivered by auditory-nerve (AN) fibers. They are thought to contact the receiving cell on its dendrites, where substantial low-pass filtering occurs. As a consequence, a continuous, high-frequency tone stimulus results in a steady input current that maintains a steady pressure on the membrane potential and causes it to rise regularly above threshold. The cell responds with a stream of action potentials at a rate determined mainly by its own membrane characteristics (Arle and Kim, 1990; Banks and Sachs, 1991; Hewitt *et al.*, 1992). This rate is its ''intrinsic frequency'' and varies from cell to cell. Detailed studies of models of this process show that these processes can be used to explain the tendency of these cells to synchronize their action potentials to the peaks of amplitude-modulated sinusoids when, and only when, the rate of modulation is close to the intrinsic frequency of the cell (Hewitt *et al.*, 1992).

Stage 4 simulates the observation that some cells in the CNIC respond with a firing-rate increase when the rate of amplitude modulation of a stimulus is close to a narrow range of frequencies characteristic of the particular cell. The model makes the assumption that certain cells in the CNIC receive input from a number of sustained-chopping cells in the VCN and respond only when a number of these inputs are simultaneously active. The inputs are assumed to come from VCN cells with similar intrinsic frequencies. Normally, the spike activity in these inputs will be random with respect to one another, and the CNIC cell will notice few coincidences. However, when the acoustic stimulus is amplitude modulated at a rate sympathetic to the VCN sustained-chopping cells, their activity will be synchronized as each cell spikes at the crest of the amplitude-modulation wave. As a result, the CNIC cell will receive many coincidental inputs and will respond with an increased rate of firing. This model has been shown to simulate rate-modulation functions ob-

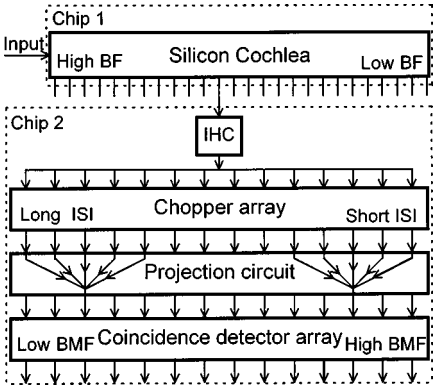

FIG. 2. Implementation of the amplitude-modulation sensitivity model.

served in cells in the inferior colliculus (Rees and Palmer, 1989) It is important to note that the rate–BMF of the CNIC cell depends upon the intrinsic frequencies of the VCN cells that are providing its input. It depends only weakly upon the membrane characteristics of the CNIC cell itself.

II. HARDWARE IMPLEMENTATION

The software implementation is based on carefully modeled individual cells. This would be very hard to achieve with the hardware implementation, since hardware implementations do not have the flexibility or the precision of software implementations. A detailed hardware model of an individual neuron can only be implemented with large and complex circuits (see, for instance, Rasche *et al.*, 1997), which would prohibit the implementation of a large number of these neurons on a single chip. The main advantage of a hardware implementation, however, is that it can simulate a model in real time, even when the number of elements and stages in the model becomes large. We have therefore kept the individual elements small and simple, under the hypothesis that the signal processing in the brain that we try to model depends more on the availability of a large number of neurons than on the exact details of operation of each individual neuron.

The hardware model (Fig. 2) aims to implement the signal processing performed at the different stages of the software model presented in the previous section, not the details of each element. In fact, we only use naming such as IHC, cochlear nucleus (CN) chopper and CNIC to allow the reader to compare the stages in the hardware with those in the original model. They do not imply that the hardware elements are detailed models of their biological counterparts.

The VLSI implementation uses two chips (Fig. 2). The first chip is an electronic simulation of the mechanical filtering of the cochlea and consists of series of bandpass filters corresponding to stage 1 in the model description above. This silicon cochlea has already been described in detail by van Schaik *et al.* (1995). This chip has a number of outputs, each simulating the response of the basilar membrane at a different point along its length. Only one output is fed to the second chip. As a consequence, each chip represents a single frequency-selective ''channel'' and additional chips will be required to represent the full range of channels. For all of the evaluations described below, the center frequency (CF) of the cochlear filter is set to 5 kHz.

The second chip contains the hardware implementation of stages 2–4 of the model: one inner-hair cell (IHC) circuit that models the average output of several IHCs from a small section along the basilar membrane and two arrays of the same spiking neuron circuit, simulating the signal processing of neurons in the VCN and the CNIC, respectively. The same spiking neuron circuit is used to simulate a sustained chopper (VCN) or a coincidence detector neuron (CNIC). Technical details concerning component values are given in the Appendix (see also van Schaik, 1997).

A. Inner-hair cell circuit

The IHC stage is implemented using three main circuit components (Fig. 3). The first component simulates the asymmetrical, saturating response of the IHC receptor potential to mechanical deflection of the stereocilia. It consists of two stages: a compressive function and a circuit to add a bias to the membrane potential. The bias also guarantees spontaneous activity in the absence of any input. The second component implements the low-pass filtering of the membrane potential. The third component introduces adaptation to constant stimulation. The output of the circuit is a continuous current, which can be interpreted as the instantaneous spike probability on a biological auditory nerve. Alternatively, we can interpret this output as the equivalent of the excitatory postsynaptic current generated in a chopper cell by a number of AN fibers from a small section along the basilar membrane that contact this chopper cell. The hardware implementation does not attempt to replicate the detailed mechanisms of the IHC model used in the original paper, but does simu-

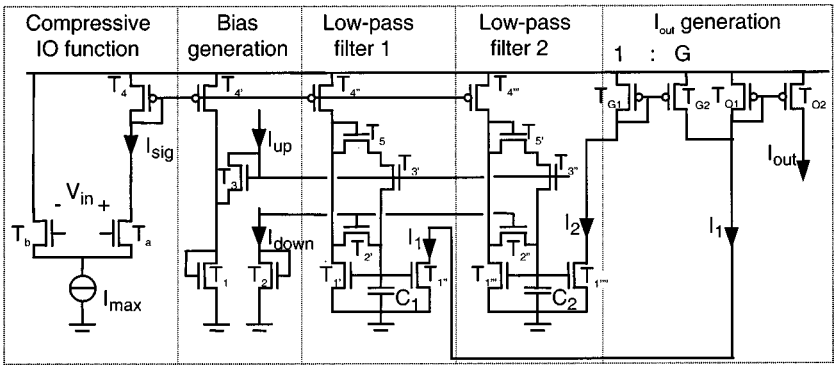

FIG. 3. Circuit diagram for the IHC stage.

late those features of the IHC response to acoustic stimulation that are important for the operation of the AM sensitivity model.

1. Static inner-hair cell voltage response

Hudspeth and Corey (1977) have shown that the relation between bundle deflection and the percentage of open-ion channels has a sigmoidal form with a certain offset, so that 20% of the channels are open at equilibrium. This can be easily modeled using two transistors T_a and T_b) as a differential pair (see Fig. 3) for which the current I_{sig} through transistor T_a is a sigmoidal function between 0 and $I_{\max}$ of the input voltage V_{in}, as we shall see in the measurement of Fig. 4(a). By using a differential pair with one transistor (T_b) four times as large as the other (T_a), only 20% of the bias current will flow through the smaller transistor (T_a) when V_{in} equals zero.

2. Dynamic IHC voltage response

The phase locking of the inner-hair cell can be modeled using a low-pass filter with a cutoff frequency of about 1 kHz (Rose *et al.*, 1967; Palmer and Russell, 1986). This implies a time constant equal to $\tau = 1/2\pi f = 0.16$ ms to model this effect. Obtaining such large time constants is one of the main problems in modeling comparatively slow brain elements with analog VLSI circuits. If the precision of the value of the time constant is not an important issue, then large time constants can be realized using the current mirror shown in the low-pass filter blocks in Fig. 3. This current mirror creates a nonlinear low-pass filter for which I_{up} controls the maximum rise speed and I_{down} sets the maximum fall speed of the voltage on the capacitor C_1. Using this circuit, the time constant will vary as a function of signal level for both the low-pass filter and the adaptation circuits. The time constant can be increased by as much as a factor of 3 for a 20-dB increase in signal level. This is a problem, and to avoid any difficulties in evaluating the later stages, all tests were made at the same signal levels.

3. IHC adaptation

A form of adaptation similar to the adaptation seen on the auditory nerve can be obtained in the IHC circuit by taking a weighted difference between I_1 and a second low-pass-filtered version of I_{sig}. When we use a larger capacitor in the second filter, its output I_2 will react more slowly to an onset of I_{sig} than I_1 does. In the circuit, the value $C_2 = 3C_1$ is used. The actual output current of the IHC circuit is given by $I_{\text{out}} = I_1 - GI_2 + I_{\text{spont}}$ and is created with two additional current mirrors, as shown in Fig. 3. The value G is the gain of this additional current mirror and controls the ratio between the peak response and the sustained response of the circuit. G should be smaller than 1 in order to keep a sustained response to the input signal. I_{spont} can be used to adapt the ''spontaneous rate of firing'' of the inner-hair-cell model independently of the signal levels of I_1 and I_2.

4. Test results

Figure 4(a) shows the measurements of the current I_1, which is the equivalent of the receptor potential in the real inner-hair cell, as a function of the input voltage. Comparison with the intracellular-voltage response to hair displacement as measured by Hudspeth and Corey (1977) shows good agreement. Although the differential pair has been designed to have an output current equal to 20% of the maximum current at zero input voltage, the measurement shows an output current equal to 30% of the maximum current in this case. This is probably due to the mismatch of the differential pair transistors.

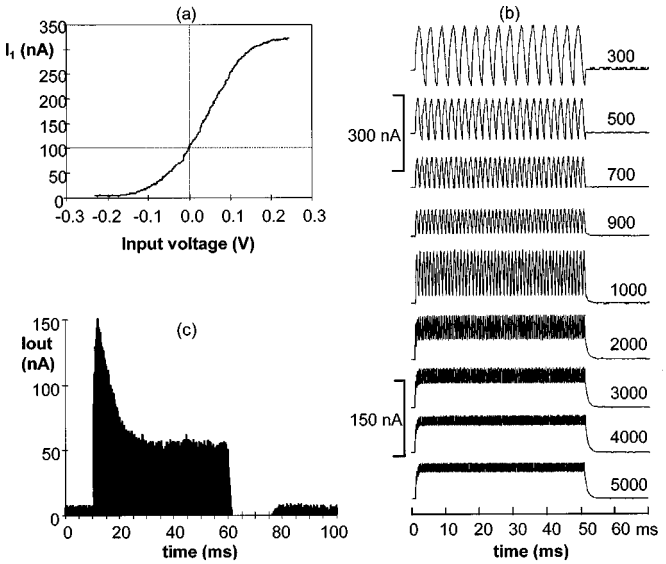

FIG. 4. IHC circuit output. (a) Static relation between I_1 and V_{in}, (b) variation of I_1 for pure-tone inputs at different frequencies, (c) Output current of the IHC circuit after weighted subtraction of I_2 from I_1.

Figure 4(b) shows the response of the current I_1 to pure-tone stimulation at frequencies between 300 Hz and 5 kHz. These results are comparable to those of Palmer and Russell (1986).

The final output current of the circuit in is given by $I_{\text{out}} = I_1 - GI_2 + I_{\text{spont}}$. Using I_{spont}, G, V_{up}, and V_{down} creates an output signal [Fig. 4(c)] similar to the post stimulus time histogram (PSTH) of a single auditory nerve when stimulated with a 5-kHz pure tone. The time constant of adaptation is around 10 ms.

5. Other IHC circuits

The only other analog VLSI implementation of an inner-hair cell known to the authors was implemented by Lazzaro (1992). The circuit is of a size and complexity comparable to the circuit presented here, but does not model the low-pass-filtering behavior of the IHC that causes a reduction in phase locking at frequencies above 1 kHz. This reduction of phase locking is essential for the operation of the AM sensitivity model.

B. Basic neuron circuit

The neuron implementation [Fig. 5(a)] has been kept as simple as possible in order to maximize the number of neurons that could be included on a single chip of size 5 mm^2. The circuit models the main features of a neuron needed to obtain chopping or coincidence-detecting behavior. It con-

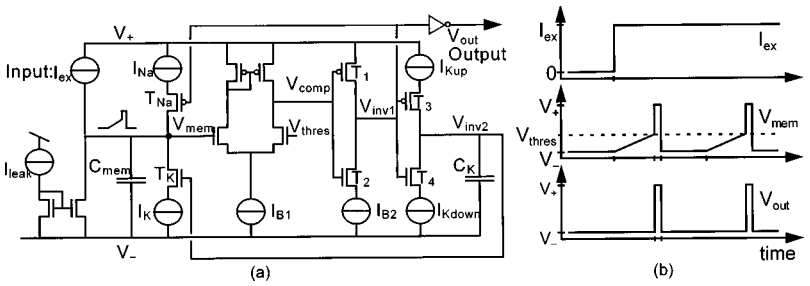

FIG. 5. (a) Circuit details of the VLSI neuron. (b) Example of the response of the membrane potential (V_{mem}) and the output signal (V_{out}) to a dc input current (I_{cx}).

sists of three main components corresponding to auditory-nerve input, membrane potential, and spike generation, respectively.

1. Neuron membrane potential

The membrane of a biological neuron is modeled by a membrane capacitance, C_{mem}; the membrane-leakage current is controlled by the current source, I_{leak}. In the absence of any input ($I_{\mathrm{ex}}=0$), the membrane voltage will be drawn to its resting potential (controlled by V_-) by this leakage current. Excitatory inputs simply add charge to the membrane capacitance. If an excitatory current larger than the leakage current is injected, the membrane potential will increase from its resting potential. This membrane potential, V_{mem}, is compared with a controllable threshold voltage, V_{thres}, using a basic transconductance amplifier driving a high-impedance load. If V_{mem} exceeds V_{thres}, an action potential will be generated [Fig. 5(b)].

2. Neuron-spike generation

The generation of the action potential in the neuron circuit is patterned after the biological neuron, in which an increased sodium conductance creates the upswing of the spike and in which the delayed blocking of the sodium channels plus delayed increase of the potassium conductance creates the downswing. The circuit model is as follows: If V_{mem} rises above V_{thres}, the output voltage of the comparator V_{comp} will rise to the positive power supply. The output of the following inverter V_{inv1} will thus go low, thereby making the *p*-channel metal oxide (PMOS) transistor $\mathrm{T_{Na}}$ conduct and thus allowing the current I_{Na} to pull up the membrane potential. At the same time, however, a second inverter will allow the capacitance C_K to be charged at a rate controlled by the current I_{Kup}. As soon as the voltage V_{inv2} on C_K is high enough to allow conduction of the *n*-channel metal oxide (NMOS) transistor T_K whose gate it controls, the current I_K will be able to discharge the membrane capacitance.

Two different time constants govern the spike-generation process. The current I_{Kup} which charges C_K controls the spike width, since the delay between the onset of conduction of $\mathrm{T_{Na}}$ and the onset of conduction of T_K is inversely proportional to I_{Kup}. If V_{mem} now drops below V_{thres} the output of the first inverter V_{inv1} will become high, blocking conduction of $\mathrm{T_{Na}}$ cutting off the current I_{Na}.

Furthermore, the second inverter will then allow C_K to be discharged by the current I_{Kdown}. If I_{Kdown} is small, the voltage on C_K will decrease only slowly, and as long as this voltage stays high enough to keep T_K conductive and allow I_K to discharge the membrane, it will be impossible to stimulate the neuron if I_{ex} is smaller than I_K. Therefore I_{Kdown} can be said to control the ''refractory period'' of the neuron.

Finally, I_{B1} and I_{B2} are two bias currents needed to limit the power consumption of the circuit; they do not influence the spiking behavior of the neuron in any major way.

3. Other neuron circuits

Several analog VLSI neurons have been published (for example, Mahowald and Douglas, 1991; Lazzaro and Mead, 1989a; Mead, 1989; Rasche *et al.*, 1997; Sarpeshkar *et al.*, 1992), and they can be divided into two categories. The first category, which contains the neuron circuit presented here, was started by Mead (1989). It uses a small circuit as a neuron model that tries to capture just the essentials needed for a given processing task. The goal in this case it to put a large number of these neurons on a chip to study their behavior as a group. Most of the neurons published in this group, however, are too simple for the AM sensitivity model, because they do not implement a refractory period, which is needed to control the intrinsic chopping rate of the choppers, nor do they include membrane leakage, which is needed to set the temporal selectivity of the coincidence-detector neuron. One neuron circuit, published by Sarpeshkar *et al.* (1992), is very similar to the neuron circuit presented here and could have been used for the AM sensitivity model. The circuit presented here is just slightly larger, but allows parameters such as the spiking threshold, spike width, and refractory-period duration to be controlled independently, which is not the case in Sarpeshkar's neuron. The second category of neuron circuits, started by Mahowald and Douglas (1991), tries to model a single neuron in great detail by implementing the hardware equivalent of Hodgkin–Huxley models. These neuron circuits, however, are not useful for the implementation of the AM sensitivity model because they are simply too big. For example, a recent publication of such a neuron by Rasche *et al.* (1997) describes a chip of the same size as our complete AM sensitivity model (4 mm^2), but the chip contains only a single neuron that emulates a cortical pyramidal cell.

C. VCN sustained-chopper model

The input to the neuron comes directly from the IHC and is a current representing the probability of an action potential in the afferent auditory-nerve fibers that contact a real VCN chopper neuron. Ideally, this should be in the form of discrete, stochastic spike events. Unfortunately, the generation of random events proved difficult using this technol-

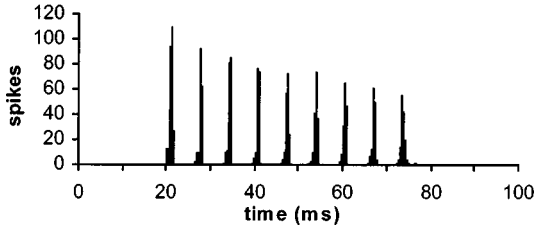

FIG. 6. Measured sustained-chopping response of a neuron on the chip.

ogy. The use of probabilities is not problematic for this particular application because the input to real cells comes from a large number of fibers and is strongly low-pass filtered at the cell dendrite. The net effect is roughly the same, but the electronic neuron remains more regular, i.e., sustains chopping longer, than its biological counterpart. The difficulty in generating random spikes will need to be overcome in the future, however, for other applications such as bushy cells. The neuron circuit described above (in conjunction with the IHC circuit) produces a sustained-chopping response when stimulated with a 5-kHz pure tone (Fig. 6). The rate at which the cell chops is controlled by the current I_{Kdown}, which is varied systematically across the array. The minimum- and maximum-chopping rates used for this project were 90 and 180 spikes per s, respectively.

D. VCN–CNIC projections

Each CNIC unit receives input from a range of VCN neurons at the previous level. The width of this range can be varied under operator control. The strongest input comes from the corresponding neuron in the VCN array. Inputs to the left and right are attenuated by a factor depending upon the distance from the CNIC unit to the VCN unit. The circuit that creates this connectivity, shown in Fig. 7, uses only two transistors, one input wire, and one output wire per CNIC neuron.

The operation of this circuit may be understood as follows: When a spike arrives at synapse 3, for instance, the current I_{syn3} will flow through the switch for the duration of the spike. Part of this current will flow directly through the transistor T_{G3}; the output current I_{ex3} will be equal to this

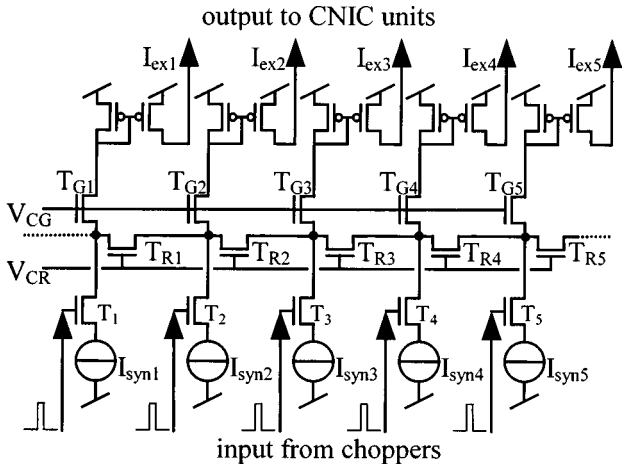

FIG. 7. The lateral-diffusion network circuit.

current. The rest of the current flows into the network to either side of the node which connects the different synapses laterally. If we assume that the network extends infinitely to the left and to the right, equal amounts of current will flow left and right. At the neighboring nodes these currents will split again, partially continuing to flow through the lateral transistors and the rest creating the output currents I_{ex2} and I_{ex1}. In this way, a current injected at a certain node in the network creates a symmetrical distribution of output currents; the largest output current occurs at the same node as the injection, and the amplitudes of the output currents decrease as the node gets farther away. It can be shown that when the transistors are operated in the weak inversion region, the distribution of currents is an exponential function given by:

$$\frac{I_{\mathrm{exj}}}{I_{\mathrm{syni}}} = \alpha e^{-d_{ij}/L}, \quad \alpha = \frac{1-e^{-1/L}}{1+e^{-1/L}}, \quad L = e^{(V_{CG}-V_{CR})/2nU_T}, \tag{1}$$

where d_{ij} is the distance in number of lateral transistors between output j and input i, n is the slope factor of the transistors (about 1.5), and U_T is the thermal voltage, which is 25 mV at room temperature. V_{CG} and V_{CR} are the bias voltages that are used to set L. In the experiments of this paper, a diffusion length L of about 3 has been used. Furthermore, since the circuit is completely linear in the current domain, we can apply the superposition principle, so that the current at a given output node is simply the sum of the individual effects of the input currents at the input nodes.

E. IC coincidence-detecting neuron model

The neuron circuit of Fig. 5 can also be used to create a coincidence-detecting neuron. In this case, the membrane time constant should be short, so that the neuron does not integrate its input over an extended period of time. If the input to the neuron consists of excitatory current spikes with an amplitude that ensures that no single spike can make the membrane potential reach the threshold voltage, multiple spikes will have to arrive simultaneously, or in very quick succession, in order to create output spikes. A way to reduce the membrane time constant is to reduce the membrane capacitance C_{mem}, which also saves considerable silicon area, since the capacitors are the largest structures on the chip. The second capacitor C_K can also be reduced in size to save space since the refractory period of the coincidence-detector cell does not play as important a role as it does for the chopper neuron.

III. SINGLE-UNIT SIMULATION

The output of the three types of units in the VLSI model has been characterized (Fig. 8) as a function of input-signal intensity, using a 5-kHz pure tone filtered by the silicon cochlea and taken at the output of the cochlear filter with a 5-kHz best frequency. The input intensity that just evokes spikes from the CN unit has been chosen as the 0-dB point. The IHC circuit does not actually generate spikes, but its current output is representative of a spike probability; in order to present it in the same graph, the current has been

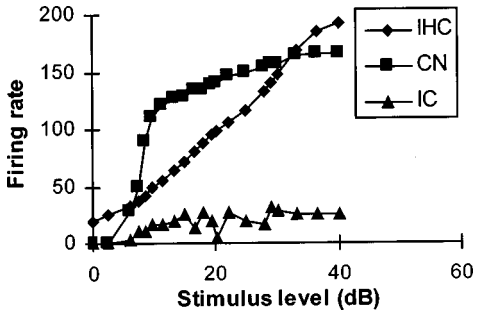

FIG. 8. Rate-intensity functions of the three types of units in the VLSI model for a 5-kHz pure-tone input. Stimulus intensity is given in dB relative to the spiking threshold of the CN unit.

converted into a spike rate, using an arbitrary scaling factor. Saturation of the IHC output, which is shown in Fig. 3(a), cannot be measured in the complete system, because the silicon cochlea cannot deal physically with sounds of such large amplitude. We do see in Fig. 8, however, that both the CN unit and the inferior colliculus (IC) unit saturate before the IHC unit does.

The spike activity of a chopper circuit will synchronize to the envelope of an amplitude-modulated, high-frequency tone. This will only occur, however, when the rate of AM is similar to the intrinsic rate of firing of the cell as controlled by the current I_{Kdown}. While synchronization is best at a particular frequency, it will still occur to a narrow range of frequencies above and below its best-modulation frequency. For any given rate of AM, some choppers will produce a stream of spikes synchronized with the amplitude modulation. As a result, the spikes produced by this group will be synchronized with each other and capable of driving a coincidence detector.

Synchronization of similar choppers by amplitude modulation at the appropriate modulation frequency can be seen in the oscilloscope traces of Fig. 9. When the input signal is either above or below BMF, the choppers do not synchronize to the input signal, and they therefore do not synchronize to each other either.

Activity in a coincidence-detector (CD) cell is generated by synchronized inputs from the chopper neurons. Pure-tone stimuli do not produce correlated activity across neighboring chopping cells, and they do not produce a rate rise in these CD units. Neighboring choppers with similar BMFs are connected to a single CD coincidence detector through the lateral-diffusion network. This network ensures that the CD unit is most strongly stimulated by a single chopper and that the neighbors of this chopper on either side stimulate the CD unit with a strength that falls off with distance. When this network is used with a diffusion length of about 3, then only three choppers on either side of the central chopper will have a noticeable effect on the CD unit. The CD input current will thus be maximal when these seven choppers spike simultaneously. The threshold of the CD unit can be set to require seven simultaneous input spikes using the I_{syni} current source (Fig. 7). When this is the case, the CD unit will only generate a spike if the inputs are perfectly correlated, i.e., when an appropriate modulation frequency is present. However, this setting would allow very little variation in the intrinsic chopping rate of the chopper units on the chip. In order to relax the constraints a little, the threshold has been adapted so that three neighboring chopper units spiking simultaneously are sufficient for reaching the threshold of firing of the CD cell. Furthermore, the oscilloscope trace in Fig. 9 shows very little noise on the IHC output. With such a deterministic IHC output, the synchronization will be far stronger than in biology at the BMF, and also disappear more quickly for frequencies above or below BMF. We have also observed very strong synchronization of the choppers to every second or third cycle of AM for modulation frequencies close to two or three times the BMF of the unit when this stimulus is used. In order to obtain a more biological behavior of both the chopper units and the CD units, we have explicitly added noise to the IHC output current. We have increased the noise level and measured the synchronization of the choppers to the signal [Fig. 10(a)], until the degree of synchrony to the stimulus envelope of the evoked activity of a chopper unit at different modulation frequencies roughly matches that of a biological chopper and of the computer model as presented by Meddis and O'Mard (1997). The sensitivity of the CD unit using these settings to amplitude modulation is shown in Fig. 10(b) for a single unit on the chip. Unfortunately, no data was available for a real IC neuron with a best-modulation frequency in the 130-Hz range. We have therefore plotted the data for a 52-Hz BMF unit from the Hewitt and Meddis' (1994) paper in the same figure (original data from Rees and Palmer, 1989). It can be seen that the VLSI CD unit has a more selective modulation-transfer function (MTF) than the IC neuron, but is of the same order of magnitude and shape.

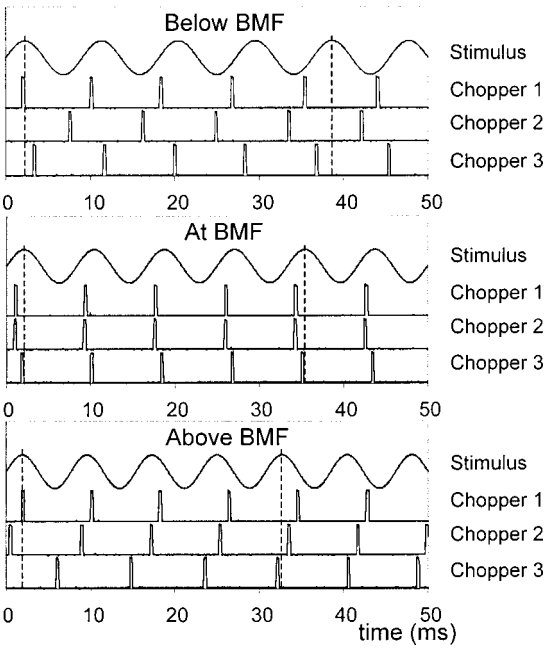

FIG. 9. Oscilloscope traces of the input signal to the IHC circuit and the output traces of three similar choppers on the chip; (a) below BMF, (b) at BMF, and (c) above BMF.

The degree of synchrony for the choppers has been measured from their period histograms using the vector-strength metric (Goldberg and Brown, 1969). Vector strength (r) is calculated as:

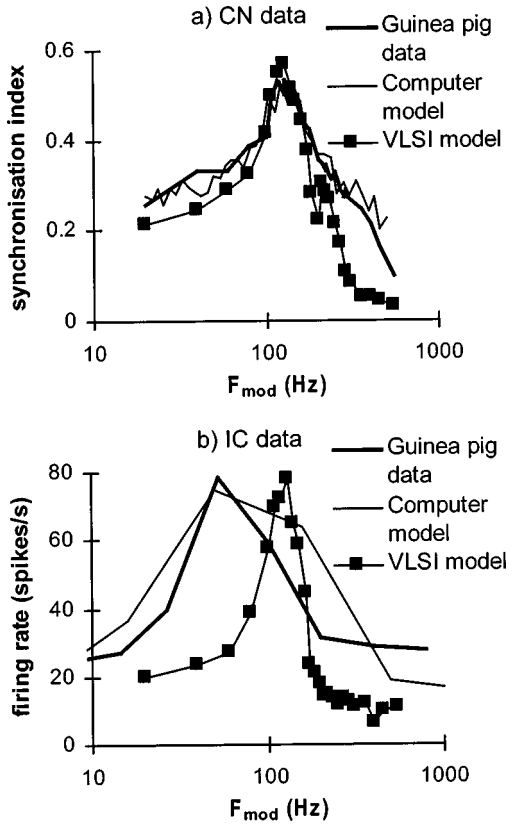

FIG. 10. (a) Vector strengths for the CN unit measured on guinea pig and Meddis' original computer model (Meddis and O'Mard, 1997) and the VLSI implementation. (b) AM sensitivity of an IC coincidence-detecting unit.

$$r = \frac{\sqrt{[\Sigma_0^{K-1} R_k \cos 2\pi(k/K)]^2 + [\Sigma_0^{K-1} R_k \sin 2\pi(k/K)]^2}}{\Sigma_0^{K-1} R_K}, \tag{2}$$

where K is the number of bins in the period histogram, and R_k is the magnitude of the kth bin.

IV. MULTIUNIT REPRESENTATION OF AM SENSITIVITY

While physiological studies are typically restricted to the measurement of the response of a single cell, the modeler can simulate the simultaneous response of large numbers of units. An overview of the operation of the chip as a whole is shown in Fig. 11, which illustrates measurements of the choppers and the coincidence detectors, respectively. In order to show the principle of operation clearly, a non-noisy output of the IHC circuit has been used for these measurements. Figure 11(a) shows the chopping rate of all choppers in the array when stimulated with a 5-kHz pure tone. The chopping rate increases along the array for a given stimulus intensity, due to the decreasing refractory period of the choppers in the array. Because of unavoidable component mismatch, the chopping rate, or intrinsic frequency of the cell, is a noisy function of the position in the array.

Figure 11(b) shows the spiking rate of the choppers when stimulated with a 5-kHz signal which is amplitude modulated at 120 Hz at 50% modulation depth. Most choppers are unaffected by the introduction of modulation, but those units whose intrinsic frequencies are close to 120 Hz

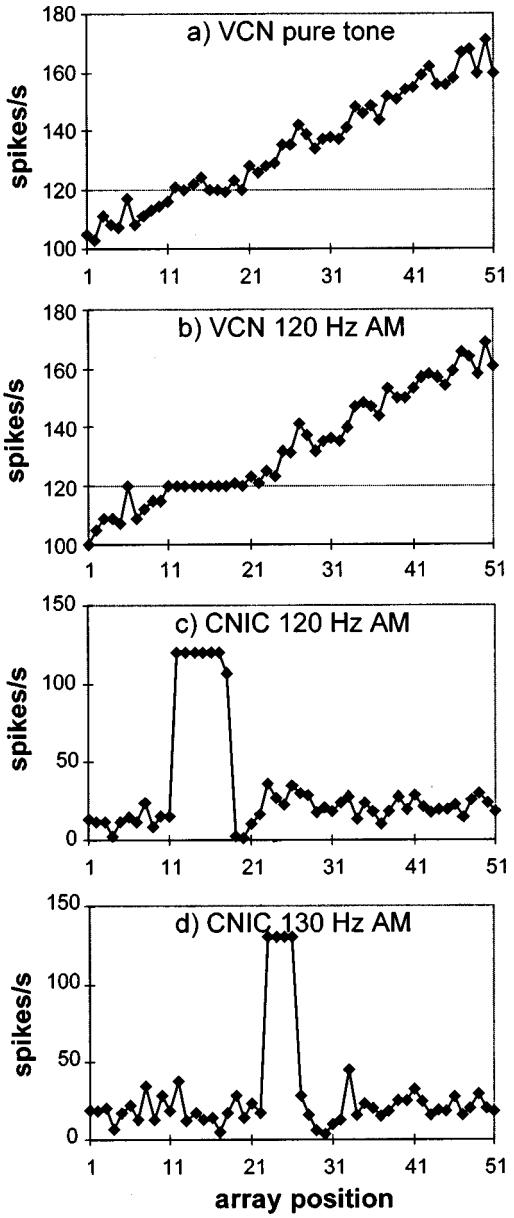

FIG. 11. (a) Average spiking rate of the choppers in the array in response to a pure-tone stimulus. (b) Average chopping rate in response to the pure-tone amplitude modulated at 120 Hz and 50% depth. (c) AM sensitivity of the coincidence-detecting neurons in response to the 120-Hz AM stimulus. (d) Response of the coincidence detectors to a 130-Hz AM stimulus. Note that only the central 51 of the 71 neurons in each array are shown.

are recruited to fire at the same rate as the modulation. It is also the case that these choppers fire at the same phase each modulation period, and are therefore phase locked to the modulation signal. The response of the CD neurons to the input from the choppers is summarized in Fig. 11(c). A small range of CD cells shows a high rate of firing. These are the cells that receive input from the choppers that are synchronized to the 120-Hz amplitude-modulated input signal. Figure 11(d) shows the response for a signal modulated at 130 Hz. The position of the responding CD unit moves to the right of the array. There are fewer CD neurons responding to the 130-Hz modulation than to the 120-Hz modulation, i.e., the peak in Fig. 11(d) is narrower than the peak in Fig. 11(c). This is caused by the random variations of component values

accidentally giving rise to more choppers with an intrinsic chopping rate closer to 120 than to 130 Hz. This fact may be checked in Fig. 11(a).

V. DISCUSSION

The primary goal of this project was to explore the feasibility of using VLSI technology to overcome the speed restrictions inherent in conventional computational modeling of signal processing in the auditory periphery and brainstem. The success of the project suggests that future modeling efforts should definitely consider using this approach. The pressure to use real-time, highly parallel architectures will increase as modelers reach beyond the IC to the thalamus and, eventually, the cortex. VLSI technology appears to have the capacity to meet the additional signal-processing needs. This is especially true for analog VLSI, continuous-time implementations, which operate per definition in real time.

The demonstration has many shortcomings. The project used only a very small chip incorporating one hair cell and 142 neurons. The difficulty experienced in obtaining physiologically accurate cochlear bandpass filters on the input chip restricted the stimuli to pure tones and AM tones that were not affected by this limitation. The IHC circuit has time constants that were dependent (unrealistically) on signal level. We have not been able to solve the problem of how to generate stochastic streams of spikes in the hardware implementation of inputs to the VCN chopper units. The hardware neurons were relatively primitive and only captured the simplest properties necessary to characterize the relevant characteristics of sustained chopping units. These problems will need to be solved before the technology can be used as a general-purpose modeling tool. Nevertheless, the present circuit has demonstrated the feasibility of an alternative approach to modeling complex signal processing in the brainstem.

In fact, the restraints imposed by the new technology did result in some unexpected new perspectives. First, the model works well without a stochastic input to the chopper cells, even though this was assumed to be essential to the success of the original computational model. The low-pass filtering of the dendritic inputs to real VCN choppers is likely, in any case, to attenuate much of the random fine-structure of the AN input. In the hardware model, the natural variation in intrinsic frequency of neighboring choppers is responsible for the decorrelation of spike activity that distinguishes steady-tone stimuli from amplitude-modulated tones. This may also be the case in the auditory nervous system. Second, in the original model, the chopper cells feeding the CNIC coincidence detectors were established as exclusive groups of choppers with identical intrinsic frequencies within a group. This was shown to be unnecessary by the VLSI model, which tolerated limited variation in intrinsic frequency and was able to use the output from one VCN chopper to feed a number of CD cells. This was a useful economy on our small VLSI chip and is a potential economy for the nervous system itself.

In the model, the best rate-modulation frequency of a CD unit is determined by the membrane characteristics of the chopping units that supply its input. The intrinsic chopping rate of the CD cell is not relevant. It is interesting, in this regard, that Rees *et al.* (1997) have recently found that CNIC cells with a highly regular (chopping) response to pure tones are not the cells that have the best response to amplitude modulation. The model described here would predict that a pronounced intrinsic regularity would impair the ability of the CNIC to respond to the intrinsic rhythms of the VCN chopping units, and is therefore consistent with the physiology.

The chip described above contained only 142 neurons. A 1-cm^2 chip could hold 4000 neurons. It is not known how many sustained-chopper cells there are in the VCN, but estimates of the number of multipolar cells (of which only some are sustained choppers) suggest something in the region of 28 000 in the cat (Liberman, 1990). If half of these are sustained choppers and half of the units on the chip are reserved for CNIC units, about eight identical chips would be required to represent a complete model of this AM sensitivity model using 1-cm^2 chips. If, say, 30 chips were used to represent a useful number of channels, each covering a small range of frequencies, there would be space to include other aspects of VCN functioning such as the response of bushy and octopus cells, known to be present in the human cochlear nucleus (Adams, 1996). Each chip would be identical except for the input, which would derive from a different filter tap in the silicon cochlea.

VI. CONCLUSIONS

An analog VLSI device has successfully implemented a model of the complex interaction of a large assembly of neurons in the auditory brainstem thought to be responsible for processing amplitude-modulated acoustic stimuli. The device prepares the way for large-scale implementations representing a similar number of neurons to those found in the mammalian brainstem.

ACKNOWLEDGMENTS

This work was supported by the Swiss National Science Foundation. We are grateful to Eric Fragnière and Eric Vittoz for continuous practical support throughout this project.

APPENDIX

A. Implementation: Technical details

The chip described in this paper has been integrated in ES2's 1.0-μm CMOS technology ECPD 10.

The channel width-over-length ratios (W/L) of the transistors in the IHC circuit and the neuron circuit are given in Table AI and Table AII, respectively. For all measurements a 5-V power supply has been used.

The bias currents of the IHC circuit were determined as follows. $I_{\max}$ directly sets the maximum value of I_1 and has been set to 330 nA, as may be seen in Fig. 4(a). The adaptation gain G was about 2/3, so that the sustained output of the IHC circuit was about 1/3 of the maximum output at the onset of the stimulus, as may be seen in Fig. 4(c). Finally, I_{up}

TABLE AI. IHC circuit-device geometry.

Transistor	W/L (μm)
T_a	5/5
T_b	20/5
T_1, $T_{1'}$, $T_{1''}$, $T_{1'''}$, $T_{1''''}$	5/10
T_2, $T_{2'}$, $T_{2''}$	5/5
T_3, $T_{3'}$, $T_{3''}$	5/5
T_4, $T_{4'}$, $T_{4''}$, $T_{4'''}$	5/10
T_5, $T_{5'}$	2
Capacitor	C (pF)
C_1	5
C_2	15

and I_{down} have been adapted to obtain the output of I_1 for different input frequencies shown in Fig. 4(b) and are both on the order of 0.5 nA.

The design of the neuron has been kept very simple: all transistors that function as switches are 5 by 2 microns and all others are 5 by 5 microns (Table AII). The capacitors C_{mem} and C_K are 10 pF for the chopper implementation and 1 pF for the CD neuron implementation, respectively.

Different bias currents and voltages influence the behavior of the neuron. Some of the variables, however, have little influence, or influence only factors that can be easily fixed, such as the spike width. In order to generate a fixed-width, fixed-height spike, I_{Na} should be much larger than the leakage current I_{leak} or than the input current I_{ex}. In order to be able to bring the membrane potential back down at the end of the spike, I_K should in turn be larger than I_{Na}. The exact values of I_{Na} and I_K, however, are not critical. Both I_K and I_{Na} are currents in the 1-μA range, with I_K about twice as large as I_{Na}. The width of the spike depends almost exclusively on I_{Kup}, which has been adapted to yield a spike 0.3-ms wide. This yields a value for I_{Kup} of about 0.1 μA. The function of the bias currents I_{B1} and I_{B2} is only to limit the current flow through the threshold comparator, and through the first inverter. Their exact value is not important either, and has been set equal to I_K. The threshold voltage V_T influences the time the neuron needs to integrate a constant input from the end of the refractory period to the onset of the output spike. When both the input amplitude and the threshold voltage are doubled, the effective integration time will stay constant. In other words, doubling the threshold voltage is equivalent to reducing the input current by half. In the experiments in this paper, a threshold voltage of 3 V has been used.

The two remaining biases, I_{Kdown} and I_{leak}, have quite a large influence on the spiking behavior of the neuron. I_{Kdown} controls the duration of the refractory period of the neuron, and thereby sets the intrinsic chopping rate or limits the maximum spiking rate of the neuron. I_{Kdown} is made to vary along the chopper array, so that the intrinsic chopping rate of the neurons is 100 spikes per s at one end and 200 spikes per s at the other end. This means that, in either case, the refractory period is at least several ms. In order to create such long refractory periods, I_{Kdown} has to be small, on the order of 1 nA. For the coincidence-detecting neuron, I_{Kdown} is used to limit its maximum rate, which has been adjusted to about 200 spikes per s. The same I_{Kdown} as for the fastest chopper can thus be used for all coincidence-detector neurons.

TABLE AII. Neuron circuit-device geometry.

Transistor	W/L (μm)
T_{Na}, T_K, T_1, T_2, T_3, T_4	5/2
others	5/5
Capacitor	C (pF)
C_{mem}	10, 1
C_K	10, 1

I_{leak} plays an important role in creating the coincidence-detector behavior. The input to the coincidence-detector neuron is in the form of fixed-width, fixed-height current spikes which are passed through the lateral-diffusion network. The amplitude of the output-current spikes of the chopper and the lateral-diffusion length L are set, using I_{syni} and V_{CR} plus V_{CG}, respectively (Fig. 7), so that the input-spike current for the coincidence detector is larger than I_{leak} when the input comes from one of the seven most proximal chopper neurons only. I_{leak}, thus, limits the number of choppers that influence the coincidence detectors for a given setting of I_{syni}, V_{CR}, and V_{CG}. I_{leak} should, however, be used to set the temporal window of the coincidence detection, since it does this independently of other bias values. A relatively high I_{leak} ensures that the membrane potential returns quickly to the resting potential after a single-input spike. When a single-input spike is not strong enough to charge the membrane capacitance up to the threshold voltage, several spikes have to arrive in quick succession to elicit spikes from the coincidence-detector cell. The temporal window within which the spikes have to arrive is controlled by I_{leak}. An I_{leak} on the order of 10 nA has been used, which results in a temporal window on the order of 1 ms. Next, I_{syni}, V_{CR}, and V_{CG} should be adapted to get the desired number of choppers that influence the coincidence detector. Finally, the threshold voltage V_T of the coincidence detector should then be adapted, so that the coincidence detector spikes when a few of the input spikes from the choppers are simultaneous. In order to obtain a diffusion length L on the order of 3, V_{CR} and V_{CG} have been set to 2.66 and 2.74 V, respectively. I_{syni} is about 80 nA and V_T is 3 V.

A difference in the role of I_{leak} for the chopper neurons stems from the fact that the input to the chopper neurons is a directly injected, continuous analog current and not in the form of current spikes. When the membrane potential is at rest, only an input current larger than I_{leak} will be able to drive the membrane potential towards the threshold voltage. When the input current is larger than I_{leak}, the current that effectively charges the membrane capacitor is given by $I_C = I_{\text{ex}} - I_{\text{leak}}$. For the chopper neurons, I_{leak} thus functions as a stimulation threshold and acts to subtract a constant value from the input current. In the tests in this paper, however, I_{leak} has been minimized to a value well below 1 nA and its effect on the chopper neurons is therefore negligible.

Adams, J. C. (**1996**). ''Neural circuits in the human auditory brainstem,'' in *Auditory Basis of Speech Perception*, edited by W. Ainsworth and S. Greenberg (Dept. Neuroscience, Keele University, Keele, UK).

Arle, J. E., and Kim, D. O. (**1991**). ''Neural modeling of intrinsic and spike-discharge properties of cochlear nucleus neurons,'' Biol. Cybern. **64**, 273–283.

Banks, M. I., and Sachs, M. B. (**1991**). ''Regularity analysis in a compartmental model of chopper units in the anteroventral cochlear nucleus,'' J. Neurophysiol. **65**, 606–629.

Fragnière, E., van Schaik, A., and Vittoz, E. A. (**1997**). ''An analogue VLSI model of active cochlea,'' Analog Integr. Circuits Signal Process. **13**, 19–36.

Goldberg, J. M., and Brown, P. B. (**1969**). ''Responses of binaural neurons to dichotic stimulation,'' J. Neurophysiol. **32**, 940–958.

Hewitt, M. J., and Meddis, R. (**1994**). ''A computer model of amplitude-modulation sensivity of single units in the inferior colliculus,'' J. Acoust. Soc. Am. **95**, 2145–2159.

Hewitt, M. J., Meddis, R., and Shackleton, T. M. (**1992**). ''A computer model of a cochlear-nucleus stellate cell: Responses to amplitude-modulated and pure-tone stimuli,'' J. Acoust. Soc. Am. **91**, 2096–2109.

Hudspeth, A. J., and Corey, D. P. (**1977**). ''Sensitivity, polarity and conductance change in the response of vertebrate hair cells to controlled mechanical stimuli,'' Proc. Natl. Acad. Sci. USA **74**, 2407–2411.

Langner, G., and Schreiner, C. E. (**1988**). ''Periodicity coding in the inferior colliculus of the cat: I. Neuronal mechanisms,'' J. Neurophysiol. **60**, 1799–1822.

Langner, G., Schreiner, C. E., and Biebel, U. W. (**1998**). ''Functional implications of frequency and periodicity coding in the auditory midbrain,'' in *Psychophysical and Physiological Advances in Hearing*, edited by A. R. Palmer, A. Rees, A. Q. Summerfield, and R. Meddis (Whurr, London), pp. 243–249.

Lazzaro, J., and Mead, C. (**1989a**). ''Circuit models of sensory transduction in the cochlea,'' in *Analog VLSI Implementations of Neural Networks*, edited by C. Mead and M. Ismail (Kluwer Norwell), pp. 85–101.

Lazzaro, J., and Mead, C. (**1989b**). ''Silicon modeling of pitch perception,'' Proc. Natl. Acad. Sci. USA **86**, 9597–9601.

Lazzaro, J., and Mead, C. (**1989c**). ''A silicon model of auditory localization,'' Neural Comput. **1**, 41–70.

Lazzaro, J. P. (**1991**). ''A silicon model of an auditory neural reprcsentation of spectral shape,'' IEEE J. Solid-State Circuits **26**, 772–777.

Lazzaro, J. P. (**1992**). ''Temporal adaptation in a silicon auditory nerve,'' in *Advances in Neural Information Processing Systems Vol. 4*, edited by J. Moody, S. Hanson, and R. Lippmann (Morgan Kaufmann, San Mateo, CA), pp. 813–820.

Liberman, C. M. (**1991**). ''Central projections of auditory nerve fibres of differing spontaneous rate. I. Anteroventral cochlear nucleus,'' J. Comp. Neurol. **313**, 240–258.

Liu, W., Andreou, A., and Goldstein, M. (**1991**). ''Analog VLSI implementation of an auditory periphery model,'' in *Advanced Research in VLSI* (MIT, Cambridge, MA), pp. 153–163.

Lyon, R. F. (**1991**). ''Analog implementations of auditory models,'' in *Proceedings of the DARPA Workshop-Speech and Natural Language* (Morgan Kaufmann, San Mateo, CA).

Lyon, R. F., and Mead, C. A. (**1988**). ''An analog electronic cochlea,'' IEEE Trans. Acoust., Speech, Signal Process. **36**, 1119–1134.

Mahowald, M., and Douglas, R. (**1991**). ''A silicon neuron,'' Nature (London) **354**, 515–518.

Mead, C. A. (**1989**) *Analog VLSI and Neural Systems* (Addison-Wesley, Reading, MA).

Meddis, R. (**1986**). ''Simulation of mechanical to neural transduction in the auditory receptor,'' J. Acoust. Soc. Am. **79**, 702–711.

Meddis, R. (**1988**). ''Simulation of mechanical to neural transduction: Further studies,'' J. Acoust. Soc. Am. **83**, 1056–1063.

Meddis, R., and O'Mard, L. P. (**1997**). ''Modeled chop-S and pauser/build-up responses in the cochlear nucleus: further studies,'' ARO Midwinter research meeting, abstract 454.

Palmer, A. R., and Russell, I. J. (**1986**). ''Phase-locking in the cochlear nerve of the guinea pig and its relation to the receptor potential of inner hair-cells,'' Hearing Res. **24**, 1–15.

Rasche, C., Douglas, R. J., and Mahowald, M. (**1997**). ''Characterization of a Pyramidal Silicon Neuron,'' in *Neuromorphic Systems: Engineering Silicon from Neurobiology*, edited by L. S. Smith and A. Hamilton (World Scientific, London), pp. 15–21.

Rees, A., and Palmer, A. R. (**1989**). ''Neuronal responses to amplitude-modulated and pure-tone stimuli in the guinea pig inferior colliculus, and their modification by broadband noise,'' J. Acoust. Soc. Am. **85**, 1978–1994.

Rees, A., Sarbaz, A., Malmierca, M. S., and LeBeau, F. E. N. (**1997**). ''Regularity of firing of neurons in the inferior collliculus,'' J. Neurophysiol. **77**, 2945–2965.

Rose, J. E., Brugge, J. F., Anderson, D. J., and Hind, J. E. (**1967**). ''Phase-locked response to low-frequency tones in single auditory nerve fibers of the squirrel monkey,'' J. Neurophysiol. **30**, 767–793.

Sarpeshkar, R., Lyon, R. F., and Mead, C. A. (**1996**). ''An analog VLSI cochlea with new transconductance amplifiers and nonlinear gain control,'' in *Proceedings of the IEEE International Conference on Circuits and Systems, Atlanta, GA* (IEEE, New York), Vol. 3, pp. 292–295.

Sarpeshkar, R., Watts, L., and Mead, C. (**1992**). ''Refractory Neuron Circuits,'' *CNS Technical Report*, CNS-TR-92-08, California Institute of Technology, Pasadena, CA.

van Schaik, A., Fragniere, E., Vittoz, E. (**1996**). ''Improved silicon cochlea using compatible lateral bipolar transistors,'' in *Advances in Neural Information Processing Systems, Vol. 8*, edited by D. Touretzki, M. C. Mozer, and M. E. Hasselmo (MIT Press, Boston, MA), pp. 671–677.

van Schaik, F. A. (**1997**). ''Analogue VLSI Building Blocks for an Electronic Auditory pathway,'' Ph.D. thesis 1764, Swiss Federal Institute of Technology (Presses Polytechniques Romandes, Lausanne).

Watts, L. (**1993**). ''Cochlear Mechanics: Analysis and Analog VLSI,'' Ph.D. thesis, California Institute of Technology, Pasadena, CA.

Watts, L., Kerns, D. A., Lyon, R. F., and Mead, C. A. (**1992**). ''Improved implementation of the silicon cochlea,'' IEEE J. Solid-State Circuits **SC-27**, 692–700.

Masker laterality and cueing in forward-masked intensity discrimination[a)]

Robert S. Schlauch,[b)] Bart R. Clement, Dennis T. Ries, and Jeffrey J. DiGiovanni
Department of Communication Disorders, University of Minnesota, Minneapolis, Minnesota 55455

(Received 17 March 1997; revised 2 November 1998; accepted 3 November 1998)

Forward-masked intensity discrimination was measured as a function of level in experiments designed to reveal insights into the mechanism(s) underlying the midlevel elevation of the Weber fraction. The standard and maskers were 1.0-kHz tones that were separated by 100 ms. Performance was measured for listeners with normal hearing using an adaptive procedure. In experiment 1, intensity discrimination was measured in the presence of an ipsilateral masker (80 dB SPL), a contralateral masker (93 dB SPL), and a binaural (dichotic) masker produced by combining the ipsilateral and contralateral maskers. Listeners perceived only the contralateral masker in the binaural-masker condition. The contralateral masker produced a small midlevel elevation of the Weber fraction. The ipsilateral masker and the binaural masker produced a large, midlevel elevation of the Weber fraction. Experiment 2 found that a two-tone masker resulted in a reduction (improvement) in the Weber fraction for some conditions, but the midlevel elevation remained for all subjects in this cue-tone condition. Experiment 3 demonstrated that cross talk could not account for all of the masking observed with contralateral maskers. Taken together, the results suggest that a single complex mechanism or multiple mechanisms may be responsible for the masking seen in these experiments. On the basis of the cueing results, it is concluded that a portion of the masking is due to cognitive factors; however, a sensory mechanism cannot be ruled out for the remaining portion, based on the results of these experiments. Finally, a small but significant amount of masking due to contralateral maskers places the mechanism for this outcome central to the cochlear nucleus. [S0001-4966(99)03402-5]

PACS numbers: 43.66.Ba, 43.66.Dc, 43.66.Fe [WJ]

INTRODUCTION

When pure-tone intensity discrimination is measured in the presence of a high-level forward masker that is turned off 100 ms prior to the onset of the standard, the Weber fraction is elevated relative to the Weber fraction measured in the absence of a masker. Surprisingly, the largest elevation of the Weber fraction is observed for midlevel standards (Zeng *et al.*, 1991). Several studies have attempted to identify the site of the mechanism or mechanisms causing this midlevel elevation of the Weber fraction.

Zeng and Shannon (1995) examined forward-masked intensity discrimination in several conditions in electrical and acoustical hearing. In electrical hearing, they observed elevated Weber fractions for midlevel standards in listeners with cochlear implants, but not in listeners with cochlear-nucleus implants. In acoustical hearing, a large elevation of the Weber fraction occurred for midlevel standards when the masker and standard were presented to the same ear; the masking effect was much smaller when the masker and standard were presented to different ears. The small amount of masking observed for contralateral maskers in acoustical hearing was argued to be consistent with cross hearing. In other words, the high-level masker (typically 90 dB SPL) in these conditions could have exceeded interaural attenuation by an amount sufficient to result in ipsilateral masking in the ear with the standard tone. Taken together, Zeng and Shannon's (1995) results suggest that the site of the mechanism responsible for the midlevel elevation of the Weber fraction in forward-masked intensity discrimination is either the auditory nerve or the cochlear nucleus.

Zeng *et al.* (1991) argue that a possible physiological correlate to the midlevel elevation of the Weber fraction may be the differential recovery from adaptation of auditory-nerve fibers. The spontaneous-firing rates of auditory-nerve fibers are bimodally distributed, as are fiber thresholds (Liberman, 1978). Fibers with low spontaneous rates (SR) tend to have, on average, higher thresholds for a criterion increase in rate than fibers with high SR (Liberman, 1978). Relkin and Doucet (1991) reported that low-SR fibers also have a slower recovery time from prior stimulation than do high-SR fibers. If intensity changes are coded by the firing rate of low-SR and high-SR auditory fibers, the midlevel elevation of the Weber fraction may be related to this slow recovery from prior stimulation of the low-SR fibers. For midlevel standards in the presence of a forward masker, high-SR fibers are saturated by the standard and presumably unable to code intensity changes, whereas low-SR fibers, whose rate-intensity functions normally code midlevel stimuli, would be adapted still by the masker. By contrast, low- and high-level standards would not show an elevation of the Weber fraction. For low-level standards, intensity changes would be coded by high-SR fibers with their rapid recovery from prior stimulation. At high levels, changes

[a)]Portions of this paper were presented at the 129th meeting of the Acoustical Society of America in Washington, DC [Clement and Schlauch, J. Acoust. Soc. Am. **97**, 3276(A) (1995)].

[b)]Electronic mail: Schla001@maroon.tc.umn.edu

would be coded by low-SR fibers because they would be operating in a more optimal region of their response curve.

The findings of Zeng and Shannon (1995) suggest a peripheral origin for the elevation of the Weber fraction seen for forward-masked intensity discrimination, but other studies imply a central influence on the midlevel elevation of the Weber fraction. For instance, the finding that backward-masked intensity discrimination produces a midlevel elevation of the Weber fraction (Plack and Viemeister, 1992) seems inconsistent with the idea that the mechanism responsible for the masking is related to the slow recovery from adaptation of low-SR fibers in the auditory nerve. Although separate mechanisms may cause the elevation observed in forward and backward masking, assuming dual mechanisms is not parsimonious, given the similarity of the data under both conditions. Further, a recent study by Schlauch *et al.* (1997) shows that the elevation of the Weber fraction is greatest when the masker and standard are perceptually similar. In their study, a short-duration masker resulted in more masking than a long-duration masker, a finding inconsistent with studies of adaptation of auditory-nerve fibers (Harris and Dallos, 1979) and a study of the effect of masker duration in forward-masked detection (Kidd and Feth, 1982). It should be noted that Harris and Dallos (1979), in their study of neural adaptation, did not use stimuli identical to those of Schlauch *et al.* (1997), but all of the neural studies of adaptation, to date, report an increase in the amount of adaptation as masker duration is increased (Young and Sachs, 1973; Smith, 1977; Harris and Dallos, 1979).

Given the conflicting hypotheses to account for the midlevel elevation of the Weber fraction (midlevel bump) in forward-masked intensity discrimination, a series of experiments was completed to examine possible mechanisms responsible for this phenomenon.

I. EXPERIMENT 1. DO SUBJECTS SHOW A MIDLEVEL BUMP IF THEY ARE UNAWARE THAT AN IPSILATERAL MASKER IS PRESENT?

As noted earlier, maskers and standards presented to the same ear result in a large elevation of midlevel Weber fractions for forward-masked intensity discrimination, whereas when the masker and standard are presented to different ears, the Weber fraction is elevated, but to a much smaller extent (Zeng and Shannon, 1995). If the amount of masking seen in forward-masked intensity discrimination requires conscious awareness and the listener were somehow made unaware that an ipsilateral masker was present, the midlevel elevation of the Weber fraction should be reduced or eliminated. On the other hand, if the masking effect remained large when the listener was unaware of the presence of the ipsilateral masker, the outcome would be consistent with a sensory or cognitive process that occurs without conscious awareness.

The ''Stenger principle'' provides a means for making a listener unaware that an ipsilateral masker is present. The Stenger principle states that when tones that are identical except for level are presented simultaneously to each ear of a person with normal hearing, the listener perceives the tone only in the ear with the greatest intensity (Martin, 1997). Stenger (1907) developed a test based on this idea to identify persons who are feigning a unilateral hearing loss (described in Rintelmann and Schwan, 1991). The original test was administered with matched tuning forks struck with different amounts of force, but the modern version of this test is administered typically by presenting one tone 10 dB below the person's admitted threshold in the ear with the feigned loss, and the other tone 10 dB above threshold in their other (better) ear. No response is observed to this dichotic stimulus in most persons feigning a substantial unilateral loss, even though the 10-dB sensation-level (SL) tone in the better ear results in an unequivocal response every time it is presented monotically. The Stenger test is very effective (84%) at identifying persons feigning a unilateral loss when the presentation level to the poorer ear exceeds that of the better ear by more than 10 dB (Kinstler *et al.*, 1972). In other words, the more intense tone must be 11 dB or greater in level than the level of the less-intense tone to make the less-intense tone imperceptible.

Our experiment made use of the Stenger principle to render subjects unaware that a masker was present in the same ear as the standard tone in a forward-masked intensity discrimination experiment.

A. Method

Three listeners, aged 42, 24, and 30 years, served as subjects. All had hearing within normal limits (10 dB HL or better) for octave intervals between 0.25 and 8.0 kHz. Further, hearing thresholds were symmetrical, within 10 dB, between ears at each frequency that threshold was assessed. Two subjects (1 and 3) had considerable experience in psychoacoustic experiments. The other subject (2) had never participated in a psychoacoustic experiment previously. All listeners were given several hours of practice at the tasks in this study prior to data collection.

B. Stimuli

Maskers and standards were 1.0-kHz pure tones that were digitally generated at a sampling rate of 20.0 kHz by a custom-designed 16-bit digital-to-analog (D/A) converter. The output of the D/A converter was low-pass filtered with a cutoff frequency of 8.0 kHz. Three channels were employed. The standard and increment were generated using separate channels that were mixed before being presented to the headphones. The increment was added in phase with the standard. A third channel produced the masker tone. Maskers and standards were 100 ms. All stimuli had 5-ms cosine-squared onset and offset ramps.

Before data collection began, potential subjects were screened to determine if the Stenger principle held true for a 13-dB difference in level between ears.[1] Subjects were presented with a 50-trial block. Half of the trials contained a moderate-to-high level, 1.0-kHz tone for 300 ms. The remaining trials contained the same high-level, 300-ms tone, along with a tone that was 13 dB lower, presented simultaneously to the other ear. The level for the higher-level tone was randomly assigned a value for a given trial of between 50 and 90 dB SPL. The level was randomized to eliminate a potential loudness cue. Subjects were asked to judge for each trial whether the tone was presented to one ear or to both ears

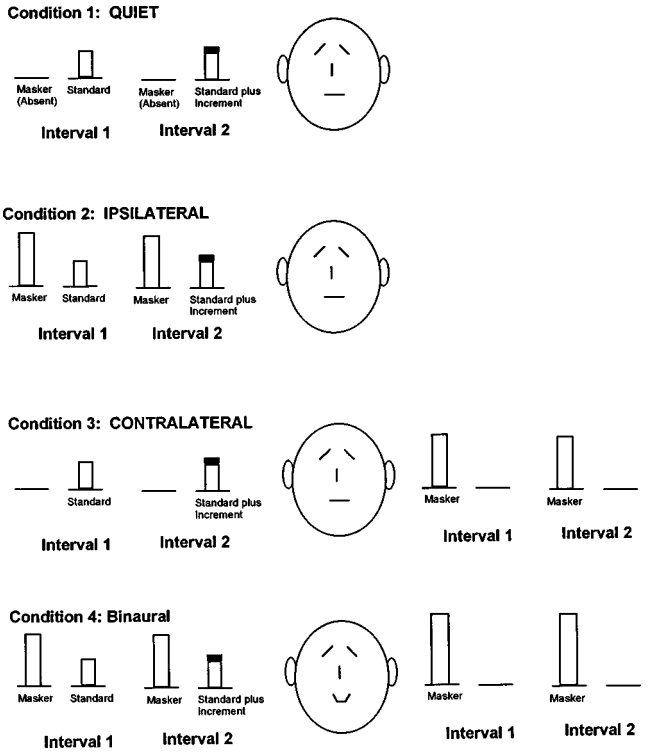

FIG. 1. A schematic drawing representing the four conditions of experiment 1. The increment appears in interval 2 for each of these examples, but it had an equal probability of occurring in either interval in the actual experiment.

simultaneously. No feedback was given regarding performance and trials were separated by 3 s. Lights marked the listening interval. Seven subjects had to be screened before three were found who performed at or near chance for this task (performance$<$0.6; chance$=$0.5). Binaural diplacusis may be responsible for four subjects being able to discriminate the binaural condition from the monaural (Newby, 1979). Burns (1982) reports pitch-intensity functions are significantly different in each ear of some, but not all, listeners. These differences in pitch across ears may have provided a cue to identify the presence of the dichotic stimulus in our four listeners who failed the screening by scoring significantly above chance.

C. Procedure

Intensity discrimination was measured as a function of level for the three subjects for whom the Stenger principle held. For each of four conditions, intensity discrimination was assessed for standard levels ranging from 20 to 80 dB in 10-dB steps. Performance was measured with a two-interval, forced-choice (2IFC) adaptive procedure using a decision rule that targeted 79.4%-correct performance (Levitt, 1971). For every incorrect response, the level of the tone added in phase with the standard was increased by 3 dB, whereas three consecutive correct responses resulted in a reduction in the level of the increment by the same amount. Subjects were given visual feedback regarding the accuracy of their responses following each trial. The Weber fraction for a single block was calculated based on the mean of reversals in stimulus-level direction within a given block. Weber fractions were based on a minimum of three 50-trial blocks that were collected during separate testing sessions (on three different days). If the standard deviation of those three blocks exceeded 3.5 dB, additional blocks, up to as many as eight, were completed. The order of conditions was selected randomly; once a condition was selected, one block for each of the seven standard levels was collected. The four conditions are described below and are also shown schematically in Fig. 1. Subjects listened to stimuli through headphones (Telephonics, TDH-39).

D. Conditions

Condition 1 (quiet): Intensity discrimination was measured in the absence of a masker. The standard was a 1.0-kHz tone. The inter-interval delay was 500 ms. This condition served as a baseline condition, so that the degree of masking in subsequent conditions could be quantified relative to intensity discrimination in the absence of a masker. The right ear was arbitrarily chosen for this condition for each of the subjects.

Condition 2 (ipsilateral masker): Intensity discrimination was measured in the presence of an ipsilateral forward masker that preceded each interval of the 2IFC task. The delay between the masker offset and the onset of the standard (zero voltage) was 100 ms. Both the masker and the standard were 1.0-kHz tones. The masker was fixed in level at 80 dB SPL.

Condition 3 (contralateral masker): In this condition, intensity discrimination was measured in the presence of a contralateral masker that was fixed in level at 93 dB SPL. The task, temporal sequence, and frequency of stimuli were all the same as those of condition 2.

Condition 4 (binaural masker): This condition was employed to induce the Stenger effect. The task, temporal sequence, and frequency of stimuli were the same as those of the previous conditions. Forward maskers were presented simultaneously to each ear of a listener. The masker level was fixed at 80 dB SPL in the ear ipsilateral to the standard tone, and 93 dB SPL in the ear contralateral to the standard tone.

E. Results

Figure 2 illustrates Weber fractions as a function of level for the four conditions in experiment 1. In quiet (condition 1), subjects 1 and 2 show a gradual reduction in the Weber fraction as level increases, a result known as the near miss to Weber's law (McGill and Goldberg, 1968). Subject 3 shows a midlevel elevation of the Weber fraction in quiet. Florentine *et al.* (1987) found individual differences of this sort for Weber fractions in quiet in their study of intensity discrimination.

An ipsilateral masker (condition 2) resulted in a large elevation of the Weber fraction for low and moderate levels of the standard; only a small elevation was found for the highest level of the standard (80 dB SPL). Prior published investigations of forward-masked intensity discrimination with a 100-ms delay between the masker and standard generally find the largest elevation for midlevel standards (Zeng and Turner, 1992). A reason for this difference may be that we used identical durations for the masker and standard (100

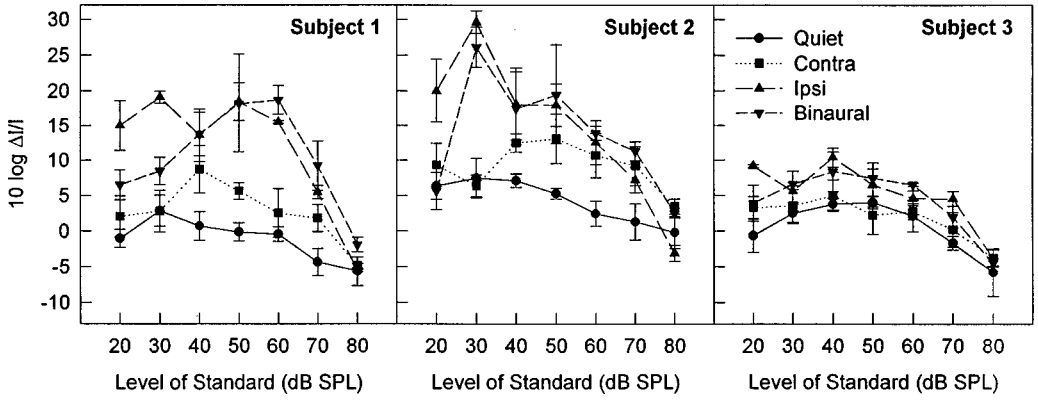

FIG. 2. The Weber fraction (dB) as a function of level for the four conditions of experiment 1 for each subject. Circles represent the quiet condition. Ipsilateral, contralateral, and binaural maskers are represented by triangles, squares, and triangles, respectively. Error bars represent plus- and minus-one standard deviation.

ms), whereas most prior studies employed a masker that was much longer in duration than the standard [e.g., 100 ms for the masker and 25 ms for the standard in Zeng and Turner (1992)]. Schlauch *et al.* (1997) argue that identical duration maskers and standards result in masking due to perceptual similarity, which has its greatest effects for low-level standards.

A contralateral masker (condition 3) resulted in a midlevel elevation of the Weber fraction for subjects 1 and 2. By contrast, subject 3 showed little or no masking for a contralateral masker. This small amount of masking observed for contralateral maskers is consistent with the results of earlier studies (Plack *et al.*, 1995; Zeng and Shannon, 1995).

The binaural masker (condition 4) elevated Weber fractions in a manner very similar to that for the ipsilateral masker, even though the subjects only perceived the higher-level contralateral masker. All of the subjects showed less masking for the binaural masker than for the ipsilateral masker for the lowest-standard levels (20 dB SPL for all subjects and 30 dB SPL for subjects 1 and 2). This improvement in performance seen when the second masker was added may be due to a lateralization cue. That is, in the binaural condition the masker was lateralized to the ear contralateral to the standard, which may have made it easier for the listener to dissociate the masker and standard than when they were both perceived to have originated in the same ear. In any event, a lateralization cue does not appear to be effective for reducing masking for the higher-level standards in this study. A similar outcome is seen in the data of Plack *et al.* (1995), who used equal-level binaural maskers in a forward-masked intensity discrimination experiment.

II. EXPERIMENT 2. DOES A TONAL CUE PRESENTED SIMULTANEOUSLY WITH THE MASKER REDUCE THE MASKING SEEN IN FORWARD-MASKED INTENSITY DISCRIMINATION?

It has been suggested that temporal uncertainty resulting from employing maskers and standards with similar frequencies and bandwidths increases the amount of forward masking in a detection task (Moore and Glasberg, 1982) and an intensity discrimination task (Schlauch *et al.*, 1997). That is, perceptually similar maskers and standards result, for some conditions, in more masking than ones that are perceptually dissimilar. In our experiment 1, where maskers and standards were employed that were identical in every respect except for level, some portion or all of the masking effect may have been due to the perceptual similarity of the masker and standard. In this second experiment, the masker was modified to help subjects distinguish the masker from the standard. To accomplish this, we used a two-tone complex for our masker and a single tone for the standard. The frequencies of the masker complex were 1.0 kHz and 4.133 kHz, whereas the standard frequency was 1.0 kHz. The 4.133-kHz tone is not harmonically related to the frequency of the standard and these two tones are separated sufficiently to avoid masking. Pilot data for subjects 1 and 2 (a few standard levels were sampled) confirmed that the 4.133-kHz tone alone resulted in no elevation of the Weber fraction.

A. Subjects

Subjects 1 and 2, who showed the greatest amount of masking in experiment 1, participated along with two additional subjects (subjects 3 and 4) who were recruited for this experiment. The two new recruits were young adults who met the same criteria for participation as noted in the methods for experiment 1. Subjects 3 and 4 were not administered the Stenger screening test.

B. Stimuli and procedure

Stimulus generation and procedure were identical to those of experiment 1. The only difference was that the masker was a two-tone complex comprised of 1.0-kHz and 4.133-kHz tones, rather than a single, 1.0-kHz tone. The level of each masker was 80 dB SPL.

Pilot data showed that subjects 3 and 4 produced only a small amount of masking with 100-ms maskers and standards. To increase the amount of masking, these subjects were run using 10-ms standards and maskers. Subjects 1 and 2 were run using 100-ms maskers and standards.

C. Results

Adding the remote-frequency cue to the ipsilateral condition resulted in reduced Weber fractions at several standard levels for three of the four subjects. Figure 3 summarizes the results. The greatest reduction occurred for the lowest-level standards for subject 2. Schlauch *et al.* (1997) reported a similar finding for one of their subjects in a condition that employed 10-ms maskers and 10-ms standards in a forward-masked intensity discrimination task. The increase in masking shown by subject 3 in the cue-tone condition is a result of masking by the 4.133-kHz tone. Masking data collected with the 4.133-kHz tone alone showed elevated jnd's even when the masker level was reduced to 60 dB SPL.

III. EXPERIMENT 3. CAN CROSS HEARING ACCOUNT FOR THE BUMP SEEN IN CONDITIONS WITH CONTRALATERAL MASKERS?

This experiment was designed to examine whether the elevation of the Weber fraction for midlevel standards in the contralateral-masker condition is due to the masker tone crossing over to the same ear as the standard tone. If the masker were crossing over to the ear with the standard tone, the skull would attenuate it. The amount of this attenuation, known as interaural attenuation, ranges from 40 to 75 dB for persons wearing TDH earphones mounted in supra-aural cushions (Snyder, 1973). The mean value of interaural attenuation at 1.0 kHz, measured in a group of 228 persons with complete unilateral hearing loss, is 60 dB (Snyder, 1973). Using 40 dB as the most conservative estimate of interaural attenuation, an ipsilateral forward-masking condition was set up in which we presented the maximum amount of ipsilateral masking that could have occurred during the contralateral condition. If contralateral masking is the result of the masker crossing over to the ear with the standard tone, the results for this low-level ipsilateral-masker condition should produce the same amount of masking that was seen with the high-level contralateral masker, or more.

A. Subjects, stimuli, and procedure

The subjects from experiment 2 participated in this experiment. The stimuli and procedures were identical to those of the ipsilateral-masker condition in experiment 2, with the exception that the masker level was set to 53 dB SPL and the masker was a single, 1000-Hz tone. This level represents the greatest amount of crossover that may have occurred in the contralateral condition employing the 93-dB SPL contralateral masker. For subjects 1 and 2, Weber fractions were measured only for the two midlevel standards that yielded the most masking (masked–quiet) in the presence of the contralateral masker (40 and 50 dB SPL for subject 1 and 50 and 60 dB SPL for subject 2). For subjects 3 and 4, Weber fractions were measured for standard levels of 40, 50, and 60 dB SPL.

B. Results

The results of these measurements are shown in Fig. 4. All of the measurements obtained with the 53-dB SPL masker yielded Weber fractions that are smaller than those

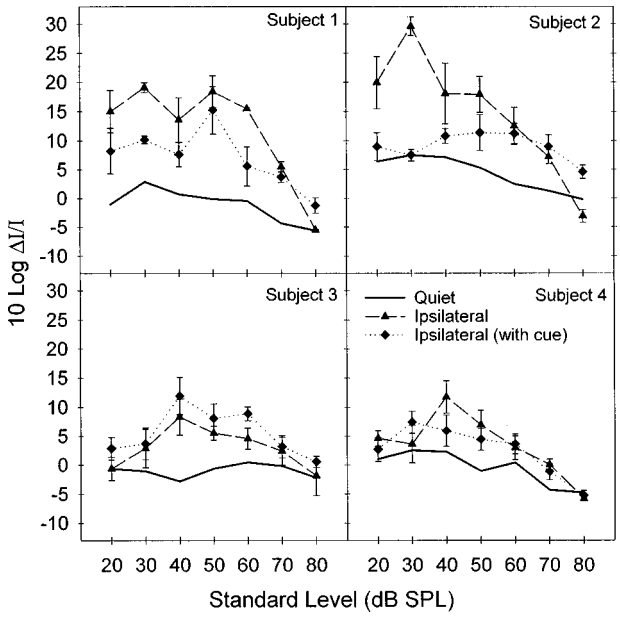

FIG. 3. The Weber fraction (dB) for the condition with an ipsilateral two-tone masker (triangles). For comparison, data are shown for a quiet condition and for an ipsilateral masker condition (data for Subjects 1 and 2 are from experiment 1). Quiet data are shown by a solid line, whereas data for the ipsilateral single-tone masker are shown as diamonds.

obtained with the contralateral masker. Further, this low-level masker yielded Weber fractions that are only slightly elevated and nearly identical in size to those obtained in the quiet condition of experiment 1. Thus, cross hearing cannot account for the full effect of contralateral masking observed in experiment 1. The finding that a 53-dB SPL masker results in only a small increase in the Weber fraction is consistent with the results of Zeng and Turner (1992) and Plack *et al.* (1995).

IV. GENERAL DISCUSSION

The finding that a contralateral masker produced substantially less masking than a binaural masker, even though the two masker conditions were indistinguishable, supports the idea that the midlevel elevation of jnd's in forward-masked intensity discrimination is the result of a mechanism that does not require conscious awareness. Contrary to early descriptions of this phenomenon where the putative mechanism was believed to be associated with adaptation in the auditory nerve (Zeng and Turner, 1992), the present results and those of some other recent studies suggest that it is at least partly due to more central mechanisms. For instance, the result in the current study that the midlevel elevation of jnd's seen with a contralateral masker cannot be accounted for by cross hearing suggests that the mechanism is located within the superior olive, the first station of binaural interaction, or even higher in the auditory system. Other evidence inconsistent with an explanation based on adaptation is the finding that the masker acts to increase rather than to decrease the subjective magnitude of the standard or standard plus signal (Carlyon and Bevridge, 1993; Zeng, 1994), and the finding that short-duration maskers can produce more masking than long-duration maskers (Schlauch *et al.*, 1997).

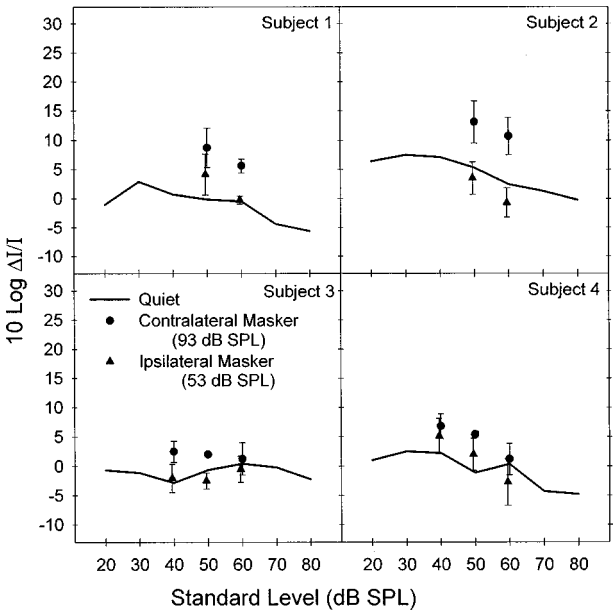

FIG. 4. The Weber fraction (dB) for a low-level masker (53 dB SPL) is shown as an upward-pointing arrow. For comparison, data for a quiet condition and for a contralateral masker are shown for the four participants in experiment 2 as solid lines and circles, respectively. Data for subjects 1 and 2 are from experiment 1. Note that the low-level masker produces less masking than the contralateral masker for all comparisons.

Our results suggest that a portion of the masking observed in our study could be accounted for by cognitive factors. When a two-tone complex was used to help listeners distinguish the masker from the standard, an improvement in performance was observed for some listeners, but the midlevel elevation of the Weber fraction remained. Plack and his colleagues (Plack *et al.*, 1995; Plack, 1996b) have suggested that the memory trace may be corrupted or that the variance of the memory trace may be increased by the presence of the masker in forward-masked intensity discrimination. There is evidence that a forward masker enhances the loudness of midlevel standards and introduces substantial variance in a listener's estimate of that loudness (Zeng, 1994). Plack and his colleagues demonstrated that a stimulus placed in close temporal proximity to the standard, either before or after the standard, results in an improvement in performance compared to a condition where the proximal stimulus was not present. These results demonstrate that listeners are able to make use of the proximal stimulus, but this outcome is not inconsistent with the idea that a sensory mechanism is responsible for the midlevel elevation of jnd's in forward-masked intensity discrimination. Plack (1996b) suggests that the role of the reference signal may be to modulate the sensory trace in a manner that provides the listener with a temporal profile. Changes in the temporal profile would enable listeners to identify the interval with the increment based on a within-interval comparison rather than a comparison of absolute levels across intervals. Plack (1996b) described a temporal model which predicted that the nature of a temporal cue would differ depending on whether the proximal stimulus was presented before or after the standard. Consistent with the model, two groups of subjects trained on tasks with different cues performed poorly when they switched tasks. Although this result is interesting, it does not address the mechanism underlying the midlevel elevation of jnd's.

The midlevel elevation of jnd's in backward masking is another result that is difficult to account for by a peripheral sensory mechanism (Plack and Viemeister, 1992). One possibility, which seems unlikely, is that different mechanisms are responsible for the elevation of jnd's in forward and backward masking; studies have shown that the effects of forward and backward masking on intensity discrimination and loudness are similar under a variety of conditions (Plack and Viemeister, 1992; Plack, 1996a). Another possibility is that masking in forward-masked intensity discrimination reflects a process of central origin known as an ''automatic process.''

An automatic process describes behavior in focused-attention tasks where subjects are unable to ignore an irrelevant stimulus (Schneider *et al.*, 1984). In one example, subjects asked to visually identify a letter in isolation take less time to respond than when they are asked to identify the same target letter in the context of a flanking letter. The longer response time is cited as evidence that subjects automatically processed the flanking letter along with the target letter, even though they knew in advance the location of the flanking letter and that it was irrelevant to the task. Schneider *et al.* (1984, p. 21) state that one defining feature of an automatic process is that it ''demands resources in response to an external stimulus, regardless of the subjects' attempts to ignore the distraction.'' They also state that a possible function of an automatic process is to bias or prime memory for subsequent inputs. In the case of forward- (or backward-) masked intensity discrimination, a high-level stimulus results in an assimilation of subjective magnitudes of moderate-level stimuli that are similar in frequency and presented in close temporal proximity to the high-level stimulus. Plack (1996a) argues that such a process may reflect long-term integration of intensity. Long-term integration of intensity of stimuli with similar spectra may promote perceptual streaming (attending to an auditory source over time). Plack (1996a) notes that such a process would not likely be deleterious to speech perception, given that fine spectral distinctions are not obscured by this type of masking and that intensity processing used for recognizing auditory objects is relative rather than absolute.

V. CONCLUSIONS

The midlevel elevation of the intensity jnd is determined almost entirely by the masker input to the ipsilateral ear rather than by the perceived location of the masker. However, a small elevation of the intensity jnd does occur with a contralateral masker, a finding that is not due to acoustic cross talk. Also, a cue tone reduces the amount of forward masking in some listeners. The reduction in the Weber fraction due to cueing and the finding that contralateral masking is not due to cross talk support the notion that a portion of the masking seen in these conditions is not the result of a peripheral sensory mechanism. On the other hand, conscious awareness of the ipsilateral masker is not necessary for masking to occur. This implies that the mechanism respon-

sible for the midlevel elevation of the Weber fraction is the result of a cognitive process that occurs without conscious awareness, or that a portion of the masking is likely the result of a sensory mechanism.

ACKNOWLEDGMENTS

We are grateful to Dr. Chris Plack for his helpful comments during the review process. Discussions with Dr. Plack about the definitions of concepts such as ''cognitive'' and ''conscious awareness'' were particularly illuminating. This work was supported by NIH-NIDCD R29 DC01542.

[1]Hafter and Kimball (1980) have found that well-trained listeners given feedback are able to identify correctly ($d'=1$) the presence of a low-level tone that is as much as 45 to 50 dB below the level of a tone presented simultaneously to the other ear. The three listeners they tested differed considerably in their ability to do this task, even with training. Subtle differences in the perception of dichotically and monotically presented tones make identification of differences easier when the stimuli are presented in a same/different task such as in Hafter and Kimball's (1980) experiment, rather than our experiment, where short-term memory traces of both examples were not as readily accessible and feedback was not provided.

Burns, E. M. (**1982**). ''Pure-tone pitch anomalies. I. Pitch-intensity effects and diplacusis in normal ears,'' J. Acoust. Soc. Am. **72**, 1394–1402.
Carlyon, R. P., and Bevridge, H. A. (**1993**). ''Effects of forward masking on intensity discrimination, frequency discrimination, and the detection of tones in noise,'' J. Acoust. Soc. Am. **93**, 2886–2895.
Florentine, M., Buus, S., and Mason, C. R. (**1987**). ''Level discrimination as a function of level for tones from 0.25 to 16 kHz,'' J. Acoust. Soc. Am. **81**, 1528–1541.
Hafter, E. R., and Kimball, P. (**1980**). ''The threshold for binaural interaction,'' J. Acoust. Soc. Am. **67**, 1823–1825.
Harris, D. M., and Dallos, P. (**1979**). ''Forward masking of auditory nerve fiber responses,'' J. Neurophysiol. **42**, 1083–1107.
Kidd, G., and Feth, L. L. (**1982**). ''Effects of masker duration in pure-tone forward masking,'' J. Acoust. Soc. Am. **72**, 1384–1386.
Kinstler, D. B., Phelan, J. G., and Lavender, R. W. (**1972**). ''The Stenger and speech Stenger tests in functional hearing loss,'' Audiology **11**, 187–193.
Levitt, H. (**1971**). ''Transformed up–down methods in psychoacoustics,'' J. Acoust. Soc. Am. **49**, 467–477.
Liberman, M. C. (**1978**). ''Auditory nerve response from cats raised in a low-noise chamber,'' J. Acoust. Soc. Am. **63**, 442–455.
Martin, F. N. (**1997**). *Introduction to Audiology* (Allyn and Bacon, Boston).
McGill, W. J., and Goldberg, J. P. (**1968**). ''A study of the near miss to Weber's law and pure-tone intensity discrimination,'' Percept. Psychophys. **4**, 105–109.
Moore, B. C. J., and Glasberg, B. R. (**1982**). ''Contralateral and ipsilateral cueing in forward masking,'' J. Acoust. Soc. Am. **71**, 942–945.
Newby, H. A. (**1979**). *Audiology* (Prentice-Hall, Englewood Cliffs, NJ).
Plack, C. J. (**1996a**). ''Loudness enhancement and intensity discrimination under forward and backward masking,'' J. Acoust. Soc. Am. **100**, 1024–1030.
Plack, C. J. (**1996b**). ''Temporal factors in referential intensity coding,'' J. Acoust. Soc. Am. **100**, 1031–1042.
Plack, C. J., Carlyon, R. P., and Viemeister, N. F. (**1995**). ''Intensity discrimination under forward and backward masking: Role of referential coding,'' J. Acoust. Soc. Am. **97**, 1141–1149.
Plack, C. J., and Viemeister, N. F. (**1992**). ''Intensity discrimination under backward masking,'' J. Acoust. Soc. Am. **92**, 3087–3101.
Relkin, E. M., and Doucet, J. R. (**1991**). ''Recovery from forward masking in the auditory nerve depends on spontaneous firing rate,'' Hearing Res. **55**, 215–222.
Rintelmann, W. F., and Schwan, S. A. (**1991**). ''Pseudohypacusis,'' in *Hearing Assessment*, edited by W. F. Rintelmann (Pro Ed, Austin, TX).
Schlauch, R. S., Lanthier, N., and Neve, J. (**1997**). ''Forward masked intensity discrimination: Duration effects and spectral effects,'' J. Acoust. Soc. Am. **102**, 461–467.
Schneider, W., Dumais, S. T., and Shiffrin, R. M. (**1984**). ''Automatic and control processing and attention,'' in *Varieties of Attention*, edited by R. Parasuraman and D. R. Davies (Academic, New York).
Smith, R. L. (**1977**). ''Short-term adaptation in single auditory nerve fibers: Some postimulatory effects,'' J. Neurophysiol. **40**, 1098–1112.
Stenger, P. (**1907**). ''Simulation and dissimulation of ear diseases and their identification,'' Deutsche Medizinsche Wochenschrift **33**, 970–973.
Snyder, J. M. (**1973**). ''Interaural attenuation characteristics in audiometry,'' Laryngoscope **83**, 1847–1855.
Young, E., and Sachs, M. B. (**1973**). ''Recovery from sound exposure in auditory nerve fibers,'' J. Acoust. Soc. Am. **54**, 1535–1543.
Zeng, F.-G. (**1994**). ''Loudness growth in forward masking: Relation to intensity discrimination,'' J. Acoust. Soc. Am. **96**, 2127–2132.
Zeng, F.-G., and Shannon, R. V. (**1995**). ''Possible origins of the nonmonotonic intensity discrimination function in forward masking,'' Hearing Res. **82**, 216–224.
Zeng, F.-G., and Turner, C. W. (**1992**). ''Intensity discrimination in forward masking,'' J. Acoust. Soc. Am. **92**, 782–787.
Zeng, F.-G., Turner, C. W., and Relkin, E. M. (**1991**). ''Recovery from prior stimulation. II. effects upon intensity discrimination,'' Hearing Res. **55**, 223–230.

Amplitude-modulation detection at low- and high-audio frequencies[a)]

David A. Eddins
Psychoacoustics Laboratory, Department of Speech and Hearing Sciences, Indiana University, Bloomington, Indiana 47405

(Received 9 February 1998; accepted for publication 16 October 1998)

Estimates of temporal acuity under comparable conditions at low- and high-audio frequencies are rare. The present study used the amplitude-modulation detection paradigm to estimate temporal acuity over a range of audio frequencies from 800 to 12 800 Hz. Amplitude-modulation detection was measured as a function of modulation frequency for bandlimited noise carriers, and the resulting temporal modulation-transfer functions were used to characterize temporal acuity. The most important result from the two experiments reported is that systematic manipulations of carrier upper-cutoff frequency produced estimates of temporal acuity that did not vary from 800 to 12 800 Hz. When the modulated noise bands were filtered after modulation to control for potential spectral cues, the low-pass cutoff of the modulation-transfer function varied with the carrier bandwidth. However, when the standard stimulus was a quasifrequency-modulated (QFM) noise and the signal was an unfiltered, amplitude-modulated noise, the low-pass cutoff of the modulation-transfer function was independent of carrier bandwidth. These results are consistent with a growing body of evidence demonstrating that auditory temporal acuity is constant throughout most of the audible frequency range. [S0001-4966(99)00402-6]

PACS numbers: 43.66.Mk [JWH]

INTRODUCTION

A number of authors have suggested that the ability of the auditory system to process amplitude fluctuations is limited more by the central auditory system than by the resonant properties of the peripheral auditory system. This position is supported, at one level, by recent data which show that the detection of amplitude modulation depends little on the spectral location of the carrier stimulus (e.g., Eddins, 1993), and on another level by models of amplitude-modulation detection that have required extremely broad predetection filters to account for the behavioral data (e.g., Viemeister, 1979; Forrest and Green, 1987; Strickland and Viemeister, 1997). While such models may be helpful in predicting the type of temporal information that is available to the auditory system, they are often physiologically unrealistic, lacking analogs to important physiological properties such as basilar-membrane filtering. Dau and colleagues (Dau, 1996; Dau *et al.*, 1996; Dau *et al.*, 1997a,b) and Holube and Kollmeier (1996) recently introduced a model of auditory perception that includes a number of physiologically relevant elements, including a filter bank representing basilar-membrane filtering. The model predicts with extraordinary accuracy the perception of amplitude modulation and other auditory phenomena. The portion of the stimulus passing through a given basilar-membrane filter channel undergoes half-wave rectification, low-pass filtering (1000 Hz), and nonlinear adaptation before being delivered to a second bank of filters tuned to a range of envelope frequencies. This modulation-filter bank is the most notable feature of the model, as it provides the basis for the fine temporal resolution required in tasks such as amplitude-modulation detection. It is important, however, to recognize that the decision stage of the model integrates the output from all of the peripheral channels within the spectral range of the input signal.

With the modulation-filter-bank model, Dau *et al.* (1997b) simulated amplitude-modulation detection using the same stimulus conditions as reported by Eddins (1993) and obtained modulation-transfer functions that were very close to the original behavioral results. The stimulus conditions allowed a comparison of modulation thresholds obtained for equivalent absolute-noise bandwidths at different carrier frequencies. In this case, the first stage of the model included very different basilar-membrane filter properties for low- and high-frequency carriers. Because filter bandwidths increased with increasing carrier frequency, the number of filter channels decreased with increasing carrier frequency. Despite variation in the number of active filters and their bandwidths with changes in carrier frequency, the predicted results, like the behavioral results of Eddins, indicated no difference in detection across carrier frequency. Thus, it appears that this spectral integration includes a trade between the number of filter channels and their bandwidths. The empirical results of Eddins and subsequent reports by Strickland and Viemeister (1997) and Dau (1997b) have demonstrated such spectral integration over a carrier frequency range of 500 to 5000 Hz. Other psychophysical paradigms demonstrating similar spectral integration include temporal gap detection (e.g., Eddins *et al.*, 1992) and modified masking-period patterns (e.g., Eddins, 1998). Combining these results with studies of gap detection with sinusoids (e.g., Moore *et al.*, 1993; Shailer and Moore, 1987) and Huffman sequences (Green, 1973), there is strong evidence that temporal acuity does not depend upon

[a)]A portion of this research was presented at the 135th meeting of the Acoustical Society of America [D. A. Eddins, J. Acoust. Soc. Am. **103**, 2842 (A) (1998)].

the stimulus frequency, at least over the range of 500 to 5000 Hz.

The modulation-filter-bank model predicts similar spectral integration at much higher carrier frequencies. Indeed, unless one assumes markedly different auditory processing at high- and low-audio frequencies, estimates of temporal acuity should be comparable throughout most of the audible frequency range. A number of investigators have explored temporal resolution at high-audio frequencies (e.g., >5000 Hz) with disparate results. For example, measurements of amplitude-modulation detection in bandlimited noise by Rodenberg (1977) and Viemeister (1979) resulted in modulation-transfer functions with −3-dB bandwidths that increased with increasing center frequency over the range 200 to 10 000 Hz. In these studies, however, stimulus bandwidth and frequency region covaried, making it difficult to interpret the influence of frequency region on the pattern of results. Measures of temporal gap detection using bandlimited noise with center frequencies as high as 14 000 Hz (Fitzgibbons, 1984; Buus and Florentine, 1985) have revealed shorter gap-detection thresholds with increasing frequency. In these studies, however, the bandwidth and frequency region also covaried. More recently, Snell *et al.* (1994) systematically varied stimulus bandwidth and frequency region and reported gap-detection thresholds that were shorter at midfrequencies than at lower and higher frequencies. These results are not consistent with previous gap-detection results and may have been influenced by audible clicks in the standard interval of the gap-detection task. One goal of the present study was to evaluate auditory temporal acuity over a broad range of audio frequencies (800 to 12 800 Hz) using the amplitude-modulation detection paradigm.

A second motivation for the present experiments was to explore the apparent discrepancies in the literature concerning the influence that stimulus bandwidth may have upon estimates of auditory temporal acuity. Strong bandwidth effects have been reported in experiments on amplitude-modulation detection (e.g., Eddins, 1993) and temporal gap detection (e.g., Eddins *et al.*, 1992), for which explanations have included limits imposed by intensity discrimination and variations in the acoustic properties of the stimuli themselves. In terms of amplitude-modulation detection, Strickland and Viemeister (1997) suggested that changes in the *low-pass cutoff* of the modulation-transfer function with changes in stimulus bandwidth, reported by Eddins (1993) and others, were largely a result of the stimulus generation technique used in those experiments.

Differences in methods of stimulus generation arise from different approaches to minimizing the spectral cues that result from the amplitude modulation of bandlimited noise. Sinusoidal amplitude modulation of a bandlimited noise produces side components above and below the spectral edges of the carrier band. The presence of these components provides a spectral cue in the detection task. In many investigations of modulation detection, the side components have been removed by filtering after amplitude modulation. This equates the spectrum of the modulated signal to that of the unmodulated standard. Such filtering, however, reduces the effective modulation depth. This reduction is greatest for high-modulation frequencies and for narrow-noise bandwidths. An alternative approach is to match the magnitude spectrum of the unmodulated standard to that of the AM signal. This may be accomplished by adding side components to the unmodulated standard at $f_c \pm f_m$, where f_c is the frequency of a given carrier component and f_m is the modulation frequency. The side components have magnitudes identical to the those of the AM signal and phases that are either chosen randomly from a uniform distribution ($0–2\pi$) or phases that are shifted $\pi/2$ radians relative to the respective carrier component. In the latter case, the phase shift of the side components results in a carrier and side components that approximate the central-most components of an FM stimulus. Such a stimulus is termed quasifrequency modulation, or QFM (e.g., Mathes and Miller, 1947). Thus, the magnitude spectra of the standard and signal are statistically identical, but their phase spectra, and therefore their waveforms, are quite different. The distributions of instantaneous amplitude values for noise bands with random or QFM sidebands and random noise without sidebands are nearly identical and are quite different from the distribution of instantaneous amplitudes for a sinusoidally amplitude-modulated noise. Using such a QFM standard, Strickland and Viemeister (1997) reported little effect of stimulus bandwidth on the shape of the modulation-transfer function.

The main goal of the present study was to characterize the temporal acuity of the auditory system over a broad range of audio frequencies using the amplitude-modulation detection paradigm. This was accomplished in two experiments using the two different stimulus generation techniques outlined above. Experiment 1 extended the measurements reported by Eddins (1993), using the filter-after-modulation technique, to frequencies as high as 12 800 Hz. Experiment 2 was essentially a replication of experiment 1, but rather than filtering the amplitude-modulated signal after modulation, a QFM standard stimulus was used to control for spectral cues.[1] Thus, a direct comparison of the results from experiments 1 and 2 can allow determination of whether the bandwidth effect reported by Eddins (1993) was a result of filtering-after-amplitude modulation rather than some property associated with bandlimited noise or auditory perception. Experiment 2 also extends the measurement of modulation detection using a QFM standard to upper-cutoff frequencies as high as 12 800 Hz.

I. METHODS

A. Procedures

An adaptive, two-interval, two-alternative forced-choice method with a three-down, one-up tracking algorithm was used to estimate the modulation depth, 20 log *m*, corresponding to 79.4%-correct detection (Levitt, 1971). The adaptive procedure varied modulation depth using a 5-dB step size for the first three reversals in the adaptive track and a step size of 2 dB thereafter. Modulation-detection thresholds were estimated by averaging the modulation depth at each of the last even number of reversals, excluding the first three reversals. The final threshold for a condition was taken as the average

threshold across three 60-trial blocks. A fourth block was included if the standard deviation across the first three exceeded 2.5 dB. Each trial consisted of two 400-ms observation intervals marked by LEDs and separated by a 400-ms silent interval. Subject responses were followed by visual feedback. Stimuli were presented via ER-2 (Etymotic) insert earphones and testing was conducted in a sound-attenuating chamber.

B. Stimulus generation

All stimuli were generated using a digital-array processor (TDT AP2) and a 16-bit D/A converter with a sampling period of 25.0 μs (40 000-Hz sampling rate). In experiment 1, a broadband noise was generated in the time domain. When required, the broadband noise was amplitude modulated at the desired modulation frequency and depth. A subsequent Fourier transform yielded a complex buffer pair (magnitudes and phases) which was digitally bandpass filtered by setting the Fourier components outside the desired passband to a value of zero. An inverse fast Fourier transform (FFT) on the complex buffer pair then yielded a waveform having the desired spectral and temporal characteristics.

In experiment 2, a different four-step technique was used for stimulus generation. First, a bandlimited-noise carrier with the desired bandwidth and upper-cutoff frequency (UCF) was produced by filling portions of two 16 384-point buffers with the appropriate component magnitudes (Rayleigh distributed) or phases (uniformly distributed from 0 to 2π radians). Upper $(f+fm)$ and lower $(f\text{-}fm)$ side components were then created for each carrier component, such that when added to the carrier, either amplitude-modulated noise (AM) or quasifrequency-modulated (QFM) noise was produced (see Mathes and Miller, 1947). The phase relation of the side components to the corresponding carrier component determined whether AM or QFM was produced. For AM, the side components had the same starting phase as the corresponding carrier component. For QFM, the starting phase of the side components was shifted $\pi/2$ radians relative to the corresponding carrier component. The magnitude of a side component relative to the magnitude of the corresponding carrier component determined the depth of modulation. After adding the ensemble of side components to the carrier components, an inverse FFT yielded a noise waveform having the desired spectral and temporal characteristics.

In both experiments, independent noise stimuli were presented on each observation interval. The stimulus duration was 409.6 ms, including 10-ms $\cos^2$ onset and offset ramps. The magnitude spectra were scaled so that each noise sample had the same overall energy, corresponding to a pressure-spectrum level of 45 dB SPL.

C. Data analysis

One means of data analysis involved obtaining the best-fitting low-pass-filter function to each modulation-transfer function to better characterize the shape and sensitivity of each function. Specifically, for each subject and each bandwidth–UCF combination, the threshold data were fit with the transfer function of a simple low-pass filter of the form: $10\log_{10}[k/(1+(\omega\tau)^2)]$, where $\omega=2\pi f_m$ and $\tau=1/(2\pi f_c)$. Here, f_m is the modulation frequency, f_c is the -3 dB bandwidth, and k is the height or gain of the function at the y intercept $(f_m=0)$. Note that the fitting procedure merely provides a convenient way to summarize the data across the various spectral conditions. Best-fitting low-pass functions should not be interpreted as representing the low-pass-filter stage present in traditional envelope detector models (e.g., Viemeister, 1979).

TABLE I. Stimulus conditions in experiment 1 parsed by bandwidth (rows) and upper-cutoff frequency (columns). The first column shows the four stimulus bandwidths with the modulation frequencies reported at that bandwidth in parentheses. Cell entries in columns two through six indicate the total number of subjects per condition. Individual subject numbers are in parentheses.

	Upper-cutoff frequency (Hz)				
Bandwidth (Hz)	1600	3200	6400	9600	12 800
400 (4–64)	4 (1–4)	5 (1–5)	4 (1–4)	4 (1–4)	5 (1–5)
800 (4–128)	5 (1–5)	5 (1–5)	5 (1–5)	5 (1–5)	5 (1–5)
1600 (4–256)	⋯	5 (1–5)	5 (1–5)	5 (1–5)	5 (1–5)
3200 (4–256)	⋯	⋯	4 (2–5)	4 (2–5)	4 (2–5)

II. EXPERIMENT 1

A. Listeners

Five listeners ranging in age from 22 to 24 years participated in experiment 1. All had normal middle-ear function based on a screening tympanogram (*Y*, 226 Hz) and pure-tone thresholds $\leqslant$15 dB HL at octave frequencies from 250 to 8000 Hz as measured using an ER-3A earphone (ANSI, 1989). Pure-tone thresholds from 9000 to 13 000 Hz were $\leqslant$27 dB SPL as measured using an ER-2 earphone. Sound-pressure levels for the ER-2 earphones correspond to levels measured in a Zwislocki 2-cc coupler with an ER 1-08 adaptor. None of the listeners had previous experience in psychoacoustic listening tasks. Listeners were paid an hourly wage and received a 10% bonus upon completion of the study.

B. Conditions

Amplitude-modulation thresholds were estimated by determining the minimum modulation depth necessary to discriminate noise that was sinusoidally amplitude modulated from unmodulated noise. Specific noise bandwidths and upper-cutoff frequencies are listed in Table I, along with the listeners who participated in each condition.

Upper-cutoff frequencies above 12 800 Hz were not included in these experiments because of the rather dramatic loss of hearing sensitivity above this frequency experienced by typical, young, college-aged listeners (e.g., 20–25 years; see Green *et al.*, 1987). The original set of measurement conditions included modulation frequencies from 4 to 512 Hz in octave intervals with the stipulation that the modulation frequency not exceed one-half of the stimulus bandwidth. During data collection, a threshold run was discarded if the modulation depth requested by the tracking procedure was less than 0 dB $[20\log(1/m)]$, which would have resulted in

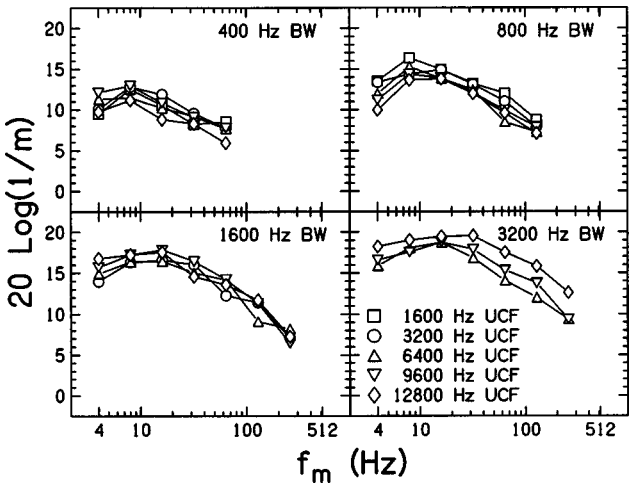

FIG. 1. Mean thresholds for amplitude-modulation detection as a function of modulation frequency with sensitivity to modulation at threshold expressed in terms of $20 \log(1/m)$. Each panel represents a different noise bandwidth and the symbols denote the different noise-band upper-cutoff frequencies.

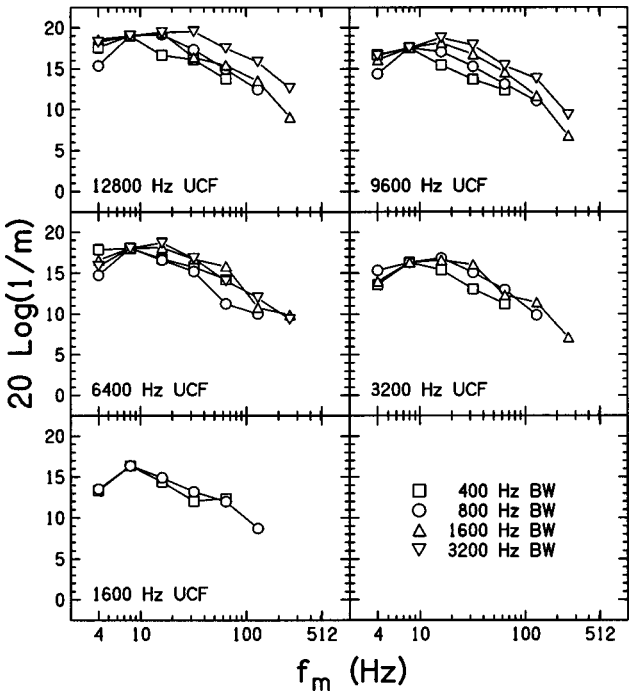

FIG. 2. Threshold data from Fig. 1 replotted with noise bandwidth as the parameter and each panel representing a different noise-band upper-cutoff frequency. Threshold functions in each panel are normalized to the highest threshold at the 8-Hz modulation frequency.

overmodulation. As a result of this protocol, threshold estimates could not be obtained at the highest modulation frequency for a given noise bandwidth in over 80% of the cases. Therefore, thresholds will only be reported for modulation frequencies of 4 to 64 Hz at the 400-Hz bandwidth, 4 to 128 Hz at the 800-Hz bandwidth, and 4 to 256 Hz at the 1600- and 3200-Hz bandwidths. Of the 484 conditions outlined in Table I, the protocol prevented the estimate of threshold ten additional times, spanning nine different conditions. Due to time constraints, listeners 1 and 5 completed only 14 of the 17 bandwidth–upper-cutoff combinations, as shown in Table I.

C. Results and discussion

Modulation thresholds were consistent across the individual listeners and thus only the mean data will be shown. Each panel in Fig. 1 represents a different noise bandwidth and displays the sensitivity to modulation at threshold on the ordinate and modulation frequency on the abscissa. The different symbols indicate upper-cutoff frequency. For each bandwidth–upper-cutoff-frequency combination, the resulting modulation-transfer function shows the characteristic low-pass form. There is considerable overlap among the plotted functions and little systematic difference in the height or the shape of the modulation-transfer functions across the different upper-cutoff frequencies. Comparing the data across the four panels, it is clear that the peak or maximum sensitivity to modulation increases with increasing bandwidth. Using the threshold at a modulation frequency of 8 Hz to compare sensitivity to modulation across frequency, and averaging across upper-cutoff frequencies, sensitivity increases from 12.4 to 18.2 dB as the bandwidth increases from 400 to 3200 Hz. It is rather difficult to compare the shapes across bandwidths, so the data have been replotted in Fig. 2, with all of the bandwidth conditions at a given upper-cutoff frequency shown in the same panel. Bandwidths are distinguished by the different symbols. To further facilitate the comparison of function shape, the transfer function for each UCF has been normalized to the maximum threshold obtained for the 8-Hz modulation frequency. The data for the 9600-Hz upper cutoff (top right) show the largest influence of noise bandwidth on the shape of the transfer function. Here, there is a systematic increase in the low-pass cutoff with increasing noise bandwidth. A similar, though less dramatic, result was obtained at the 12 800-Hz and 3200-Hz upper-cutoff frequencies. This bandwidth effect is less clear at the upper cutoffs of 6400 and 1600 Hz.

Following the fitting procedure outlined above, estimates of the time constant, τ, and the sensitivity parameter, k, were obtained. These values are shown in Fig. 3 as a function of noise bandwidth with τ values in the upper panel and $10 \log_{10}(k)$ values in the lower panel. The symbols indicate the five upper-cutoff frequencies and represent average values across listeners. Beginning with the upper panel, it is clear that τ varies little with upper-cutoff frequency over the range of 1600 to 12 800 Hz, as indicated by the overlapping symbols. In addition, there is a systematic decrease in τ with increasing noise bandwidth. For comparison, the solid line shows the time-constant estimates reported by Eddins (1993). Since his data varied little with upper-cutoff frequency, the solid line represents an average across upper cutoffs of 600, 2200, and 4400 Hz. The results from the two studies show remarkable agreement, and the present measurements extend the previous results to substantially higher upper-cutoff frequencies, demonstrating that the detection of amplitude modulation does not depend on the frequency of the carrier over the range of 1600 to 12 800 Hz. When combined with the results of Eddins (1993), that range extends from 600 to 12 800 Hz.

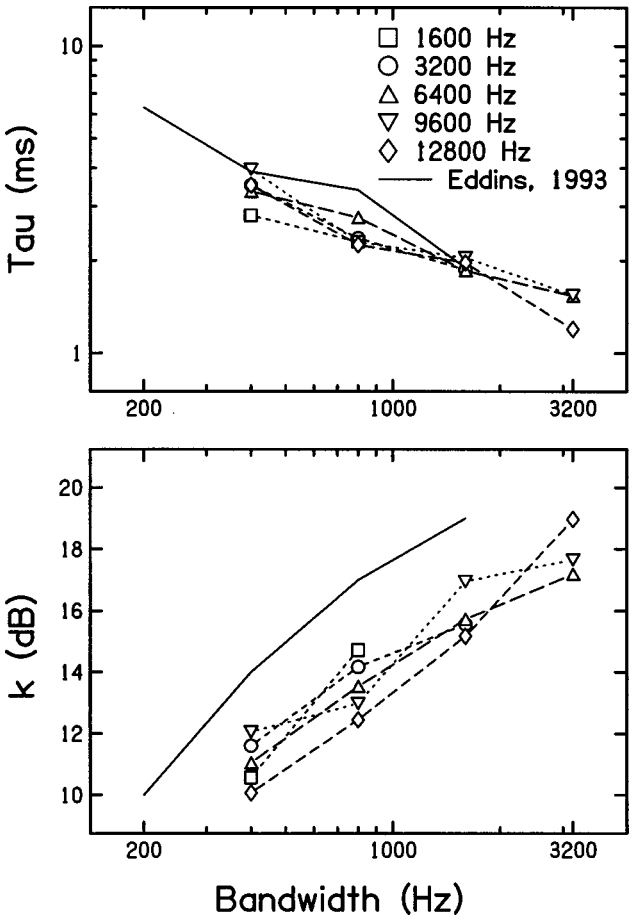

FIG. 3. Constants estimated by the fitting procedure and averaged across listeners (see the description in text). The upper panel shows the time constant, τ, as a function of noise bandwidth. The symbols represent different upper-cutoff frequencies. The lower panel shows the sensitivity to modulation, k, as a function of bandwidth at the same upper-cutoff frequencies. The solid lines in the two panels represents estimates taken from Eddins (1993), averaged across the upper-cutoff frequencies of 600, 2200, and 4400 Hz.

The lower panel of Fig. 3 shows a systematic increase in sensitivity to modulation with increasing noise bandwidth. Again, the pattern of results at low upper-cutoff frequencies is similar to those reported by Eddins (1993), as shown by the solid line. Listeners in the present experiment, however, had consistently lower sensitivity to modulation at each noise bandwidth. This likely reflects individual differences in listeners' ability to detect amplitude modulation. For a given bandwidth, there is considerable overlap among the different upper-cutoff frequencies, demonstrating little change in sensitivity to modulation with upper-cutoff frequency.

In addition to changes in the sensitivity to modulation with increasing bandwidth, the estimated -3-dB bandwidths increased and associated time constants decreased with increasing bandwidth (Fig. 3, upper panel). To determine whether this bandwidth effect resulted from restrictions in the effective modulation depth imposed by filtering after modulation, experiment 2 included the same spectral conditions as in experiment 1 but used a QFM standard to match the magnitude spectrum of the AM signal, rather than filtering after modulation to match the spectrum of the unmodulated standard.

III. EXPERIMENT 2

A. Listeners

Four new listeners ranging in age from 19 to 25 years participated in experiment 2. All had pure-tone thresholds of 15 dB HL or better at octave frequencies from 250 to 8000 Hz and normal middle-ear function based on a screening tympanogram (Y, 226 Hz). Pure-tone thresholds for listeners 1 and 2 were less than 20 dB SPL from 9000 to 13 000 Hz. For listener 4, thresholds gradually increased from 10 dB at 9000 Hz to 32 dB SPL at 13 000 Hz. Thresholds for listener 3 increased from 14 to 52 dB over the same range. None of the listeners had previous experience in psychoacoustic listening tasks. Listeners were paid an hourly wage and received a 10% bonus upon completion of the study.

B. Conditions

Noise bandwidths were 400, 800, and 1600 Hz at upper-cutoff frequencies of 3200, 6400, 9600, or 12 800 Hz. A 3200-Hz bandwidth was included at each of the three-higher upper cutoffs. Modulation frequencies ranged from 4 to 128 Hz for the 400-Hz bandwidth, 4 to 256 Hz at the 800- and 1600-Hz bandwidths, and 4 to 512 Hz at the 3200-Hz bandwidth. Again, threshold runs were discarded if the modulation depth requested by the tracking procedure would have resulted in overmodulation (i.e., 20 log $(1/m)<0$ dB). As a result, 12 out of 448 (112 conditions $\times 4$ subjects) threshold estimates could not be obtained. In cases where a threshold estimate could not be obtained for a particular subject, the mean thresholds reported below represent the mean of the remaining subjects.

A spectral analysis of the analog signals revealed low-level distortion at the frequency of modulation, approximately 55 dB below the spectral level of the bandlimited-noise stimuli. After extensive listening experience, several of the listeners reported hearing a low pitch associated with this distortion when the modulation frequency was 512 Hz, but not for lower modulation frequencies. For those listeners, sensitivity to modulation was better at 512 Hz than at the 256 Hz modulation frequency, suggesting that the distortion was indeed a cue for detection at 512 Hz. Listeners who did not report such a pitch sensation had poorer sensitivity to modulation at 512 than at 256 Hz.[2] To mask distortion components at the frequency of modulation, a low-pass noise (0 to 600 Hz, No=35 dB SPL) was included in all conditions. The low-pass noise was generated in the same manner as the carrier band and both were played simultaneously (409.6 ms) via separate D/A converters. The two noises were mixed using a dual-channel adder (TDT SM1).

C. Results and Discussion

Modulation thresholds were consistent across the four listeners and the mean modulation-detection thresholds are shown in Fig. 4. Each panel represents a different noise bandwidth, with the symbols denoting the various upper-cutoff frequencies. The pattern of thresholds with modulation frequency is similar to those in experiment 1, showing the characteristic low-pass form with considerable overlap in

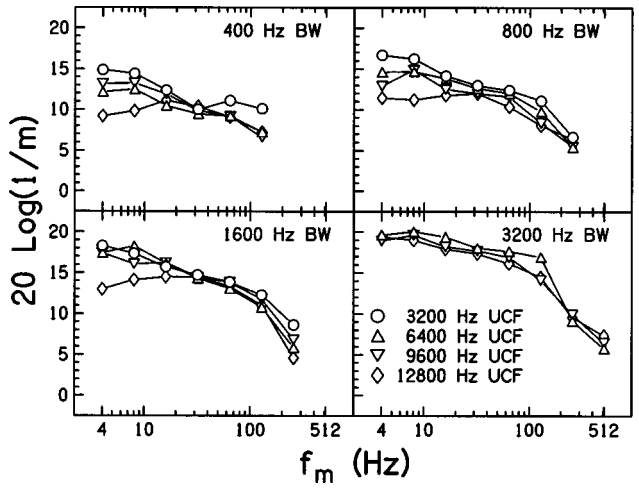

FIG. 4. Amplitude modulation-detection thresholds as a function of modulation frequency from experiment 2. As in Fig. 1, each panel represents a different noise bandwidth and the symbols denote the different noise-band upper-cutoff frequencies.

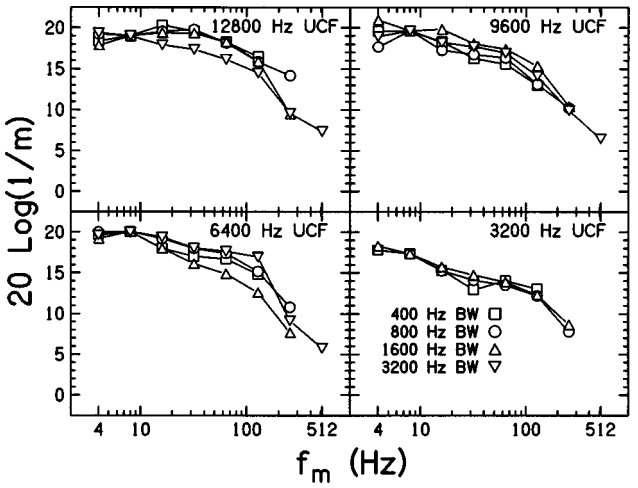

FIG. 5. Data replotted from Fig. 4 with thresholds from the different upper-cutoff frequencies shown in separate panels. The data in each panel are normalized to the highest threshold at the 8-Hz modulation frequency.

thresholds from the different upper-cutoff frequencies. A close comparison of the data in Figs. 1 and 4 reveal two differences in the results from experiments 1 and 2. First, the modulation-transfer functions from experiment 2 are flatter, especially for the narrower bandwidths, reflecting a higher low-pass cutoff frequency. Second, while there was little effect of signal frequency in experiment 1, experiment 2 reveals a reduced sensitivity to modulation at the 12 800-Hz upper-cutoff frequency for modulation frequencies of 4 and 8 Hz, at least for the narrower bandwidths. For modulation frequencies greater than 8 Hz, there was no systematic variation across the four upper-cutoff frequencies. The effect of stimulus bandwidth on the sensitivity to modulation is apparent when comparing across the different panels of Fig. 4. As in experiment 1, the modulation-transfer functions shift upward with increasing noise bandwidth, with sensitivity increasing from about 12 dB at the 400-Hz bandwidth to about 20 dB at the 3200-Hz bandwidth.

To better compare the shape of the transfer functions across noise bandwidth, the thresholds in Fig. 4 have been replotted in Fig. 5 with upper-cutoff frequency represented in the different panels and bandwidth shown by the symbols. As in Fig. 2, each transfer function has been normalized to the maximum threshold obtained at the 8-Hz modulation frequency for a given upper-cutoff frequency. Unlike the data in Fig. 2, there is no systematic influence of stimulus bandwidth on the shape of the function. The results of the curve-fitting procedure described above are shown in Fig. 6, with τ and k values in the same format as in Fig. 3. The solid lines in each panel represent values taken from experiment 1, averaged across upper-cutoff frequency. The τ values in the upper panel show little systematic variation with noise bandwidth, unlike those of experiment 1. Sensitivity to modulation, $10 \log_{10}(k)$, on the other hand, increased with increasing bandwidth, much the same as in experiment 1.

As noted above, sensitivity to modulation was reduced at modulation frequencies of 4 and 8 Hz in the 12 800-Hz upper-cutoff condition relative to the other three upper-cutoff frequencies. It is possible that this result reflects reduced audibility at the highest upper-cutoff frequency. For two listeners, however, pure-tone thresholds were <20 dB SPL from 8000 to 13000 Hz, yet they also demonstrated reduced sensitivity to modulation at 4 and 8 Hz. To further evaluate the possibility that stimulus audibility contributed to this reduced sensitivity, the two listeners who demonstrated the greatest difference in modulation detection at 3200 and

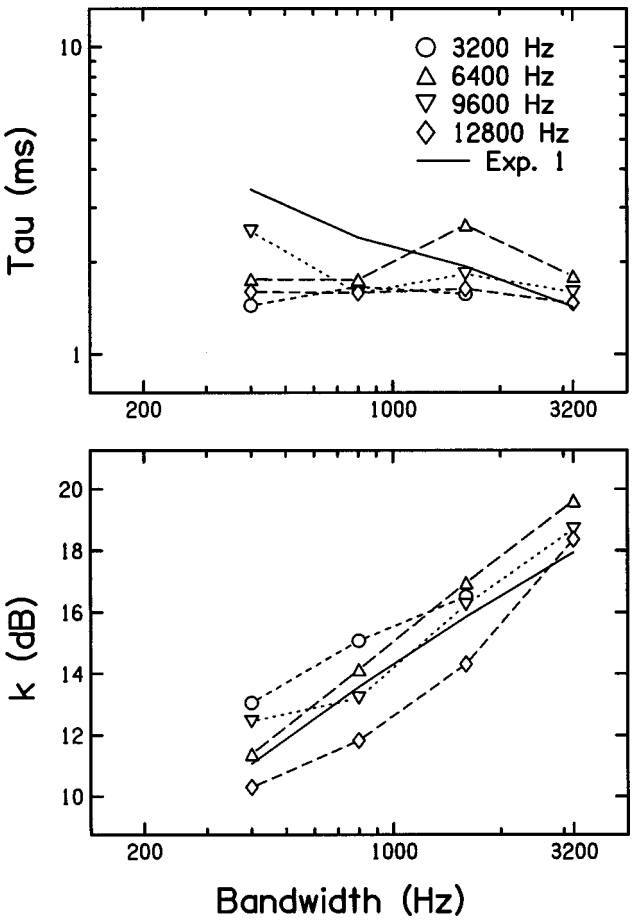

FIG. 6. Constants estimated by the fitting procedure, averaged across the listeners of experiment 2. The solid lines represent estimates taken from experiment 1, averaged across the different upper-cutoff frequencies.

12 800 Hz ($f_m = 8$ Hz) were retested on a subset of conditions in which the spectrum level was increased from 45 to 60 dB SPL. These conditions included a 400-Hz bandwidth, modulation frequencies of 8 and 16 Hz, and upper cutoffs of 3200 and 12 800 Hz. For both listeners, thresholds were nearly identical at the two spectral levels, further indicating that audibility cannot account for the reduced sensitivity to modulation.

A second possibility is that, under typical conditions, modulation detection is enhanced by a spread of excitation to more basal regions of the cochlea, as suggested by Zwicker (1956). Furthermore, the masking-period patterns reported by Zwicker (1976) indicated that this enhancement of modulation depth was greatest for low-modulation frequencies (<64 Hz). Though three of the four subjects of experiment 2 had rather good hearing sensitivity up to 13 000 Hz, it is very likely that this sensitivity declined rapidly at slightly higher frequencies, although thresholds were not measured above 13 000 Hz. If that were the case, then there would be little benefit from an upward spread of excitation for the highest-frequency condition. Others have argued, however, that if inherent fluctuations of the noise carriers limit modulation detection, then the upward spread of excitation would provide little benefit, as both the fluctuations of the noise and the applied modulation would be enhanced (e.g., Maiwald, 1967; Dau *et al.*, 1997a). These authors further argue that, since the nonlinear effects of upward spread of excitation are highly level dependent, modulation detection in narrow-band noise should also be level dependent. There is no empirical evidence to indicate such a level dependence. At this time, there is no clear explanation for the reduced sensitivity to modulation at 4 and 8 Hz, with a UCF of 12 800 Hz.

Although no model simulations are reported here, the present data are entirely consistent with predictions based upon the modulation-filter-bank model of auditory processing mentioned in the introduction (Dau *et al.*, 1997a,b). That model has been used to demonstrate spectral integration of temporal information in various tasks including modulation detection. Using stimuli that were filtered after modulation (cf. experiment 1), the model predicted essentially no effect of stimulus frequency region for audio frequencies from 600 to 4400 Hz, and predicted an inverse relation between carrier bandwidth and the low-pass cutoff of the modulation-transfer function. Of course, the model was subject to the same stimulus limitations imposed by filtering after modulation seen in experiment 1, namely a modulation frequency-dependent reduction in modulation depth. If model simulations were based upon AM vs. QFM stimuli, as in experiment 2, such a reduction in modulation depth would not be present and there would be no basis for a bandwidth effect. To consider model predictions for increases in the carrier frequency to 12 800 Hz, note that the modulation-filter-bank stage is independent of audio frequency, whereas basilar-membrane filtering is simulated by a bank of gammatone filters in the audio-frequency domain with bandwidths proportional to their center frequency. An extension of these basic elements to audio frequencies as high as 13 000 Hz would continue to predict a trading relation between the number of active basilar-membrane filters and the width of those filters when presented with stimuli of fixed absolute bandwidth. Processing in the modulation frequency domain would remain the same, resulting in model predictions in agreement with the present data.

IV. SUMMARY AND CONCLUSIONS

Thresholds for the detection of amplitude modulation were measured as a function of the modulation frequency using bandlimited-noise carriers. The resulting modulation-transfer functions may be used to characterize auditory temporal acuity. Two important issues addressed by these experiments concerned whether estimates of auditory temporal acuity vary across carrier frequency and whether previously reported changes in the shape of the modulation-transfer function with stimulus bandwidth are directly related to the technique of filtering after modulation. The following conclusions can be drawn on the basis of the two experiments reported.

(1) When the stimuli were bandpass filtered after amplitude modulation (experiment 1), the resulting modulation-transfer functions varied systematically with carrier bandwidth, resulting in wider -3-dB bandwidths, shorter time constants, and increased sensitivity to modulation with increasing carrier bandwidth.
(2) When the standard stimulus was a quasifrequency-modulated (QFM) noise and the signal was an unfiltered, amplitude-modulated noise (experiment 2), the shape of the resulting modulation-transfer functions varied little with carrier bandwidth, but the sensitivity to modulation improved with increasing bandwidth.
(3) Combined, one may conclude from the two experiments that the common technique of filtering after modulation reduces the effective modulation depth substantially, having the greatest effect for high-modulation frequencies and narrow-noise bandwidths.
(4) Temporal acuity, as estimated by amplitude-modulation detection, does not vary over a range of audio frequencies from 600 to 12 800 Hz.

ACKNOWLEDGMENTS

The author would like to thank Leah Talley and Rachel Manegold for assistance in data collection and analysis. Ann Clock Eddins and Brian C. J. Moore, and an anonymous reviewer provided helpful comments on previous versions of this paper.

APPENDIX: MODULATION DETECTION WITH AND WITHOUT A LOW-PASS NOISE MASKER

During the course of experiment 1 it became apparent that at least one of the listeners was able to use low-level distortion at the frequency of modulation to improve modulation detection when the modulation frequency was 512 Hz. The distortion at the frequency of modulation had a spectral level of -10 dB SPL, or approximately 55 dB below the spectrum level of the nominal signal. This led to the use of a 600-Hz low-pass noise masker in experiment 2. To evaluate how a low-pass masker might influence modulation detection

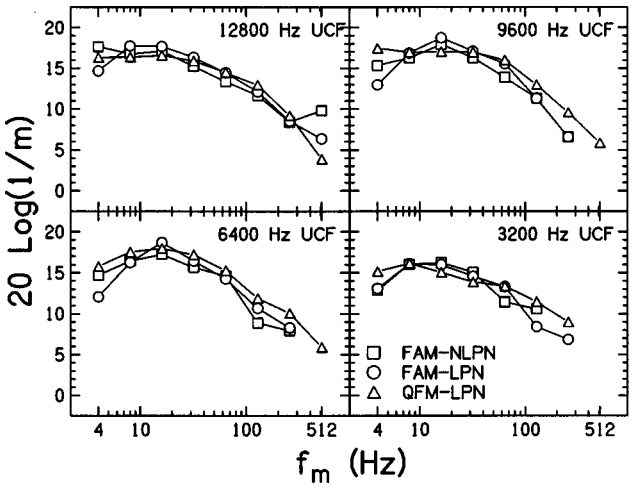

FIG. A1. Amplitude modulation-detection thresholds as a function of modulation frequency for three stimulus manipulations: filtering after modulation with no low-pass noise masker (FAM–NLPN, squares), filtering after modulation with low-pass noise (FAM–LPN, circles), and the QFM technique with low-pass noise (QFM–LPN; triangles). The noise-carrier bandwidth was 1600 Hz, presented at a spectral level of 45 dB SPL. The 600-Hz low-pass noise, when presented, had a spectral level of 35 dB SPL and was gated with the carrier stimulus.

at other modulation frequencies, the following measurements were conducted. Modulation-transfer functions were obtained using the filtering-after-modulation technique with and without a 600-Hz low-pass noise masker. The stimulus conditions included a 1600-Hz bandwidth at upper-cutoff frequencies of 3200, 6400, 9600, and 12 800 Hz and modulation frequencies in octave steps from 4 to 512 Hz. Three of the listeners from experiment 1 participated. These listeners also participated in a pilot experiment using the QFM technique of experiment 2. Since that pilot experiment employed the spectral conditions outlined above, those data are included here for comparison.

Figure A1 shows modulation-detection thresholds for the three stimulus manipulations: filtering after modulation with no low-pass noise (FAM–NLPN), filtering after modulation with low-pass noise (FAM–LPN), and the QFM technique with low-pass noise (QFM–LPN). All data points represent the mean across three listeners with the exception of the 512-Hz modulation frequency at the 12 800-Hz upper cutoff, in which case reliable thresholds could be measured for only two of the three listeners. Several data points are missing at modulation frequencies of 256 and 512 Hz, where at least two listeners failed to achieve reliable threshold estimates. In general, the modulation-transfer functions in each panel are quite similar, indicating no strong effects of the presence of low-pass noise. One notable exception occurs at the 12 800-Hz UCF, $f_m = 512$ Hz, where detection was clearly best in the FAM–NLPN condition, presumably reflecting the use of distortion at the modulation frequency to detect the signal. When masking was added, the threshold dropped markedly. A second exception occurs at the 4-Hz modulation frequency, where the presence of low-pass noise resulted in reduced sensitivity to modulation by about 1.9 dB. The low-pass noise did not reduce sensitivity at other modulation frequencies. Using the low-pass filter-fitting technique described in the Sec. I, mean τ values were 1.6 and 1.7 ms with and without the low-pass noise, and were 1.2 ms for the QFM conditions. These results are consistent with the data from the main experiments. What is clear from these data is that low-pass filtering had a negligible effect on the general form of the modulation-transfer function for these stimulus conditions. One may conclude, therefore, that it is reasonable to compare the data of experiments 1 and 2 despite differences in the presence of a low-pass masker.

[1]Pilot experiments have shown that modulation detection does not depend upon the choice of QFM or random-phase side components for the noise standard. QFM noise bands were chosen as the standard in experiment 2 to be consistent with several experiments in progress in which the discrimination of AM and QFM tones is being measured.

[2]Low-level distortion at the frequency of modulation also was present in the stimuli of experiment 1. Indeed, one of the five listeners (listener 1) in experiment 1 did have reliable threshold estimates at the 512-Hz modulation frequency, and those thresholds were better than her thresholds at the 256-Hz modulation frequency. When specifically asked, that subject reported hearing a low pitch associated with the modulation frequency. The other four listeners may not have benefitted from this potential cue, consistent with the fact that those listeners could not detect modulation at a rate of 512 Hz.

In addition to masking distortion at the modulation frequency, it is also possible that the presence of the low-pass noise in experiment 2 influenced the form of the modulation-transfer function. If so, then it would be difficult to compare the results of experiment 1, which did not include a low-pass masker, to those of experiment 2. As shown in the Appendix, modulation detection with and without the low-pass noise was nearly identical for three of the five listeners in experiment 1. Thus, it is unlikely that differences between experiments 1 and 2 reflect the presence of the low-pass masker in experiment 2.

Strickland and Viemeister (1997) reported a similar phenomenon at a modulation frequency of 512 Hz and attributed the improved detection at high-modulation frequencies to aural-distortion products. An informal series of measurements in our lab, however, failed to reveal detectable changes in the level of otoacoustic emissions in the region of the modulation frequency when comparing unmodulated and amplitude-modulated noise using stimuli identical to those of experiment 1.

ANSI (**1989**). ANSI S3.6-1989 ''American National Standard Specifications for Audiometers'' (American National Standards Institute, New York).

Buus, S., and Florentine, M. (**1985**). ''Gap detection in normal and impaired listeners: The effect of level and frequency,'' in *Time Resolution in Auditory Systems*, edited by A. Michelsen (Springer-Verlag, New York), pp. 159–170.

Dau, T (**1996**). ''Modeling auditory processing of amplitude modulation,'' Doctoral Thesis, University of Oldenburg.

Dau, T., Kollmeier, D., and Kohlrausch, A. (**1996**). ''A quantitative model of the effective signal processing in the auditory system. I. Model structure,'' J. Acoust. Soc. Am. **99**, 3615–3622.

Dau, T., Kollmeier, D., and Kohlrausch, A. (**1997a**). ''Modeling auditory processing of amplitude modulation. I. Detection and masking with narrowband carriers,'' J. Acoust. Soc. Am. **102**, 2892–2905.

Dau, T., Kollmeier, D., and Kohlrausch, A. (**1997b**). ''Modeling auditory processing of amplitude modulation. II. Spectral and temporal integration,'' J. Acoust. Soc. Am. **102**, 2906–2919.

Eddins, D. A. (**1993**). ''Amplitude modulation detection in narrowband noise as a function of carrier frequency and bandwidth,'' J. Acoust. Soc. Am. **93**, 470–479.

Eddins, D. A. (**1998**). ''Estimates of auditory temporal processing using modified masking period patterns,'' J. Acoust. Soc. Am. (submitted for publication).

Eddins, D. A., Hall, J. W., and Grose, J. H. (**1992**). ''The detection of temporal gaps as a function of absolute bandwidth and frequency region,'' J. Acoust. Soc. Am. **91**, 1069–1077.

Fitzgibbons, P. J. (**1984**). ''Temporal gap resolution in narrow-band noises with center frequencies from 6000 to 14 000 Hz,'' J. Acoust. Soc. Am. **75**, 566–569.

Forrest, T. G., and Green, D. M. (**1987**). ''Detection of partially filled gaps in noise and the temporal modulation transfer function,'' J. Acoust. Soc. Am. **82**, 1933–1943.

Green, D. M. (**1973**). ''Temporal acuity as a function of frequency,'' J. Acoust. Soc. Am. **54**, 373–379.
Green, D. M., Kidd, G., and Stevens, K. N. (**1987**). ''High-frequency audiometric assessment of a young adult population,'' J. Acoust. Soc. Am. **81**, 485–494.
Holube, I., and Kollmeier, D. (**1996**). ''Speech intelligibility prediction in hearing-impaired listeners based on a psychoacoustically motivated perception model,'' J. Acoust. Soc. Am. **100**, 1703–1716.
Levitt, H. (**1971**). ''Transformed up–down methods in psychoacoustics,'' J. Acoust. Soc. Am. **49**, 467–477.
Maiwald, D. (**1967**). ''Die Berechnung von Modulationsschwellen mit Hilfe eines Funktionsschemas,'' Acustica **18**, 193–207.
Mathes, R. C., and Miller, R. L. (**1947**). ''Phase effects in monaural perception,'' J. Acoust. Soc. Am. , 780–797.
Moore, B. C. J., Peters, R. W., and Glasberg, B. R. (**1993**). ''Detection of temporal gaps in sinusoids: Effects of frequency and level,'' J. Acoust. Soc. Am. **93**, 1563–1570.
Rodenberg, M. (**1977**). ''Investigation of temporal effects with amplitude modulated signal,'' in *Psychophysics and Physiology of Hearing*, edited by E. F. Evans and J. P. Wilson (Academic, London), pp. 429–437.
Shailer, M., and Moore, B. C. J. (**1987**). ''Gap detection and the auditory filter: Phase effects using sinusoidal stimuli,'' J. Acoust. Soc. Am. **81**, 1110–1117.
Snell, K. B., Ison, J. R., and Frisina, D. R. (**1994**). ''The effects of signal frequency and absolute bandwidth on gap detection in noise,'' J. Acoust. Soc. Am. **96**, 1458–1464.
Strickland, E. A., and Viemeister, N. F. (**1997**). ''The effects of frequency region and bandwidth on the temporal modulation transfer function,'' J. Acoust. Soc. Am. **102**, 1799–1810.
Viemeister, N. F. (**1979**). ''Temporal modulation transfer functions based upon modulation thresholds,'' J. Acoust. Soc. Am. **66**, 1364–1380.
Zwicker, E. (**1956**). ''Die elementaren Grundlagen zur Bestimmung der Informationskapzität des Gehörs,'' Acustica **6**, 356–381.
Zwicker, E. (**1976**). ''Masking period patterns of amplitude modulated pure tones,'' Acustica **36**, 113–120.

Some aspects of the lateralization of echoed sound in man. II. The role of the stimulus spectrum[a)]

Daniel J. Tollin[b)]
The Sensory Research Unit, Department of Experimental Psychology, The University of Oxford, Oxford OX1 3UD, United Kingdom

G. Bruce Henning[c)]
Center for Vision and Image Sciences, Department of Psychology, The University of Texas, Austin, Texas 78712

(Received 29 December 1997; revised 1 July 1998; accepted 8 October 1998)

The lateralization of clicks and their ''echoes'' was investigated with a view to determining the role of spectral characteristics in lateralization. Lateralization-discrimination performance was measured in a number of two-interval, two-alternative forced-choice experiments using three pairs of binaural clicks designed to elucidate how spectral cues are used in lateralization. The stimulus in one observation interval comprised a diotic click followed, after the interclick interval (ICI), by a dichotic click with either (1) an interaural time delay or (2) an interaural amplitude difference. The dichotic click was in turn followed, after an ICI of the same size, by another diotic click. In the second observation interval, the signals to the two ears were interchanged. The stimulus has the property that the signals delivered to the two ears had either (1) identical energy-density spectra but nonzero interaural-phase differences (IPDs) or (2) zero IPDs but nonidentical energy-density spectra. Under certain circumstances, observers perceived these stimuli as arising from the side of the head opposite that which would be predicted from the direction of the interaural cue in the temporal waveform. Joint consideration of the psychophysical data and the spectral characteristics of the stimuli strongly suggest a spectral ''dominance region'' for lateralization near 750 Hz, observers' lateralization performance was determined predominantly by the IPD cues from this region. In general, the results demonstrate that echoes of transients that arrive within about 2–3 ms of an initial transient are not suppressed, but have a substantial effect on lateralization through their contribution to the resultant spectral characteristics. The results contradict models that represent the precedence effect as the temporary suppression or inhibition of directional information in echoes over 2–3 ms after an initial transient.
[S0001-4966(99)02302-4]

PACS numbers: 43.66.Pn, 43.66.Mk, 43.66.Ba [DWG]

INTRODUCTION

Acoustic reflections abound in virtually every environment. Nonetheless, our ability to localize a sound to its source is accurate and appears to depend on directional information in the sound that arrives at the ears first. It has been proposed that the auditory system avoids the problem of reflections by selectively suppressing directional information in reflections that arrive within a few milliseconds of the sound that reaches the ears first via the most direct path (Wallach, Newman, and Rosenzweig, 1949; Zurek, 1980, 1987). The phenomenon is called the *precedence effect* (Wallach *et al.*, 1949).

Two pairs of clicks or brief, broadband noise bursts presented over headphones are often used to simplify the study of the precedence effect and an important parameter is the delay between the first arriving sound and its first ''echo''—the interclick interval (ICI) (Zurek, 1987; Blauert, 1997). Two commonly used stimulus configurations are shown in Fig. 1: The type I configuration (top panel), in which a dichotic click precedes a diotic click by the ICI, and the type II configuration (bottom panel), in which a dichotic click follows a diotic click. These configurations are used in forced-choice lateralization-discrimination paradigms to measure interaural time delay (ITD) thresholds in the dichotic click as a function of ICI (Zurek, 1976, 1980; Gaskell, 1978, 1983; Saberi and Perrott, 1990; Tollin, 1998a; Tollin and Henning, 1998a). The ICI affects the relative precision of lateralization based on information in either the first arriving sound or the echo. For ICIs between about 1 and 10 ms there are two classical features of the precedence effect: (1) ITD thresholds from type I configurations are constant and approximate the thresholds for a dichotic stimulus with no echo, and (2) type II ITD thresholds are 2–8 times larger (Zurek, 1976, 1980; Gaskell, 1978, 1983).

However, a different result appears with ICIs less than about 0.4 ms where the lateralization of both type I and type II stimuli depends on the interaural information in the sum of

[a)]Portions of this work were reported at the 3rd joint meetings of the Acoustical Society of America and the Acoustical Society of Japan, 2–6 December 1996, Honolulu, Hawaii [J. Acoust. Soc. Am. **100**, 2593 (A) (1996)].

[b)]Present address: Department of Physiology, University of Wisconsin-Madison, 290 Medical Sciences Building, 1300 University Ave., Madison, WI 53706.

[c)]On leave from the Sensory Research Unit, Department of Experimental Psychology, The University of Oxford, U.K.

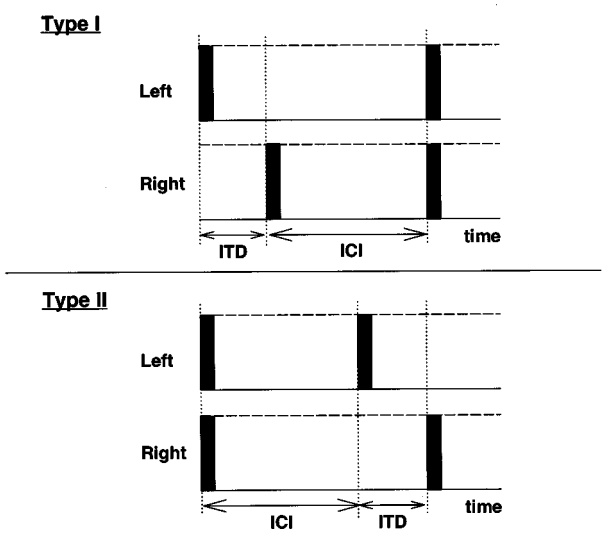

FIG. 1. Two stimulus configurations commonly used in discrimination studies of the precedence effect. The top panel shows the type I stimulus and the bottom panel, the type II.

the direct and echo clicks (Gaskell, 1978, 1983; Tollin and Henning, 1998a). Gaskell (1983) and Tollin (1998a) have suggested that the spectral characteristics of the stimuli determine how the type I and type II stimuli with small ICIs are lateralized. Their analyses concern what Warnke (1941) called *summing localization*—for short ICIs the perceived location of a direct sound and one of its echoes appears at some location determined jointly by the localization cues of both (e.g., Blauert, 1997, p. 204).

The temporal upper bound of summing localization with clicks is often assumed to be around 1.0 ms (Blauert, 1997), so the results and analyses of Gaskell (1983) and Tollin and Henning (1998a) for small ICIs can be assumed to relate solely to the phenomenon of summing localization. Results from other studies, however, indicate ''summing localization'' for ICIs larger than 1.0 ms. For example, both Wallach *et al.* (1949) and Yost and Soderquist (1984), using ICIs of 2 and 1 ms, respectively, found that the function relating the ITD of a first click required to center the intracranial image when the echo click had a fixed ITD was nonmonotonic. A monotonic function might be expected if the sensitivity to directional information in the ''echo'' click was reduced by the mechanism that produces the precedence effect. Moreover, when the first click had zero ITD and the echo click had a $+800$-μs ITD, Wallach *et al.*'s observers consistently reported that the stimulus was on the side of the head *opposite* the side expected from the ITD in the echo. Blauert and Cobben (1978) also observed consistent and regular anomalies in the localization of pairs of narrow-band transients for ICIs up to 3.0 ms (the largest ICI they used), and concluded that the delayed signal (i.e., the echo) obviously codetermined the perceived location of the click pair. Finally, Tollin and Henning (1998a) measured type II ITD thresholds that oscillated between moderate and high values as a function of ICI for ICIs up to 3.2 ms. All these results are difficult to reconcile with the traditional explanation of the precedence effect; that is to say, the results are not indicative of a mechanism which completely inhibits or reduces the effectiveness of the directional information contained in echoes arriving within a few milliseconds of the first click (for reviews, see Zurek, 1987; Blauert, 1997).

Subjective reports from studies of the precedence effect (e.g., Blauert, 1997 p. 216; Yost and Soderquist, 1984; Saberi and Perrott, 1995) share some striking similarities with reports from time-intensity trading experiments (e.g., Hafter and Jeffress, 1968)—diffuse, spacious, and ambiguous images are commonly reported. Observers in time-intensity trading experiments can sometimes discern two separate images, one associated with the interaural delay and one associated with the interaural-level difference (Hafter and Jeffress, 1968). This suggests independent roles for interaural time and level cues in time-intensity trading and may be similar in the lateralization of echoed sounds.

The interaural cues that are important to observers in the lateralization (or localization) of echoed sounds, however, are not readily apparent from their temporal waveforms. To gain further insight, spectral cues must be examined.

A. The problem

A direct sound and one identical (or highly correlated) echo (Fig. 1) produce an energy-density spectrum with periodic ripples (i.e., a comb filter). The periodicity of the cosinusoidal ripple is inversely proportional to the ICI. For each signal configuration shown in Fig. 1, there are two different time lags, one for each ear. Because the time lags differ, the rate of ripple in their resultant energy-density spectra differs; with the type II stimulus in Fig. 1, the rate of ripple in the right-ear signal will be slightly higher than in the left-ear signal. Thus, there will be interaural differences in energy density whose sign and size depends on both frequency and the delays between the clicks in each ear. The ratio of the left- and right-ear energy densities, the relative-energy-density spectrum (RED), displays the differences in energy density at the two ears and the associated interaural-level differences (ILDs) that affect lateralization. The interaural phase-difference (IPD) spectrum is also important, but as Gaskell has pointed out, provided the ITDs as well as the ICIs are identical, the IPD spectrum for the type I and type II stimuli will be identical (Gaskell, 1978, 1983; Tollin, 1998a).

Gaskell concluded that for ICIs greater than about 600 μs, the resultant spectral characteristics alone do not account in any simple way for the differences in lateralization in the two configurations. Although the IPD spectra of the type I and type II configurations are identical when their ICIs and ITDs are the same, the RED spectra for the two conditions are different; it is not immediately clear how these differences can explain the observed discrepancy in performance for ICIs greater than 600 μs (Zurek, 1980; Gaskell, 1983; Yost and Soderquist, 1984). However, this does not establish that the observers were not using the spectral characteristics for greater ICIs.

We investigated the role of spectral cues in the lateralization of clicks particularly to determine the roles of the RED- and IPD-based cues, using stimuli designed specifically to avoid the problems two-click stimuli raise. The re-

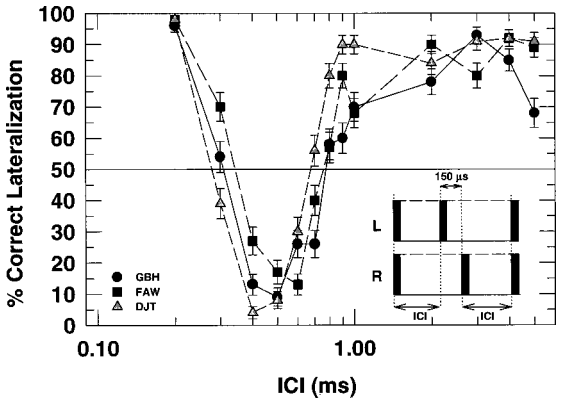

FIG. 2. The percentage of correct lateralization as a function of the ICI in ms (logarithmic axis) for three observers when the stimulus was the three-click stimulus shown in the inset. Each data point is based on 100 observations.

sults indicate the temporal limits over which lateralization cues are influenced by the spectra of the entire stimulus.

I. THREE-CLICK STIMULI: ITD IN THE SECOND PAIR

We can take advantage of the property of the Fourier transform that relates the energy-density spectrum of a given signal to the energy-density spectrum of its time-reversed pair: (1) The energy-density spectrum for a signal with a pure-time delay is identical to the energy-density spectrum of the undelayed signal, and (2) reversing time (i.e., playing the signal backward) does not affect the energy density either (Papoulis, 1962). Time-reversed stimulus pairs, then, have two important properties relevant to our study: (1) since their energy-density spectra are identical, the RED (in dB) will be zero for all frequencies so that (2) the signals differ only in their phase spectra and produce nonzero IPDs.

The three-binaural-click stimulus shown in the inset of Fig. 2 satisfies the conditions above; it is comprised of three equal-amplitude binaural clicks with an ITD of 150 μs in the second pair; the first and last clicks are diotic. Two ICIs are defined as those intervals between the onsets of the elements of the stimulus indicated in the inset of Fig. 2 and were identical in size to ensure that one signal was simply a time-reversed version of the other. In a companion publication, Tollin (1998b) derives the general equations used here to compute the spectral characteristics, including the RED and IPD.[1] When all the clicks are of equal amplitude, the energy-density spectra for the left- and right-ear signals of the three-click stimulus shown in Fig. 2 are identical, so the RED will be zero for all frequencies. However, the IPD will be nonzero at most frequencies and thus provides the *only* spectral cue to noncentral lateralization.

A. Experiment 1

1. Methods

The observers' ability to lateralize the stimuli of Fig. 2 was investigated. The experimental system was based on the Tucker–Davis Technologies (TDT) System II. The signals for the left and right ears were constructed digitally on a TDT AP2, downloaded to the dynamic memory of a TDT DA3-4 analog-to-digital converter (DAC), and converted to full-scale analog voltages (16 bit) by separate DACs at a rate of 200 kHz. The left and right signals were independently attenuated (TDT PA4), low-pass filtered at 10 kHz (Kemo VBF/3, 24 dB/octave), and delivered in parallel via three TDT HB6 high-impedance dual-channel headphone buffers to three matched pairs of TDH-39 earphones driven in phase and mounted in Grason–Stadler 001 muffs.

The stimuli were constructed from sums of scaled and delayed 20-μs clicks. The response to a single 20-μs click over the TDH-39 earphones had a total duration of approximately 500 μs [measured using a 6-cc coupler and a condenser microphone to observe the signal on an oscilloscope (Gaskell, 1978)]. The level of a single click corresponded to approximately 30 dB SL.

A two-interval, two-alternative forced-choice discrimination paradigm was employed in which the observers were required to indicate which of two observation intervals contained the left-most-appearing stimulus. The stimulus in the inset of Fig. 2 represents the stimulus configuration for only one observation interval and, on the basis of the ITD shown, was designated the ''correct'' stimulus. In the second interval, the signals to the ears were reversed. The ITD in the second pair of clicks was fixed at 150 μs because, in the absence of a second echo, observers achieve at least 70% correct over the 0.8–to 6.4-ms range of ICIs which elicit the precedence effect (Tollin and Henning, 1998a; Tollin, 1998a). Three experienced observers with normal hearing (including the two authors, DJT and GBH) from the study of Tollin and Henning (1998a) participated in these experiments. They received no additional practice sessions. Preliminary experiments revealed some ICIs for which performance was consistent but anomalous in that lateralization performance was near 10% correct (Tollin and Henning, 1996); the stimuli were lateralized consistently but in the direction *opposite* that which would have been expected from the ITD. Consequently, in order not to confuse the observers, we gave no feedback.

One of 13 ICIs between 0.1 and 5 ms was psuedorandomly chosen (without replacement) and held constant for 50 presentations. On each trial, the probability that the ITD in the middle click led in the left ear in the first observation interval was 0.5. The beginning of a trial was marked by briefly illuminating an LED on each observers response box. LEDs were also used to indicate the onsets of the two observation intervals, which were separated by a 600-ms pause. After the observation intervals, the observers had a 1-s response interval before the next trial began. Once all the 13 ICIs were used, the process was repeated to yield 100 observations from each observer at each ICI.

2. Results

Figure 2 shows the percent-correct lateralization as a function of ICI. (The error bars in this and all subsequent plots indicate the range of performance corresponding to ± 1.0 standard deviation, assuming that the numbers of correct responses were binomially distributed.) As ICI increases from 0.2 to 0.5 ms, the observers' performance decreases from near 100% correct to 8%–17% ''correct.'' Thus, from

good lateralization at a short ICI in the sense consistent with the ITD in the middle click, the observers go to consistent but *anomalous* lateralization at an ICI of 0.5 ms. As the ICI increases from 0.5 to 1.0 ms, the observers' performance rises from 8%–17% to 68%–90% correct. By an ICI of 2.0 ms, the observers generally achieve performance levels greater than 75% correct.

Anomalous lateralization occurs for ICIs from 0.3 to approximately 0.8 ms. Here, the observers perceived the stimulus configuration in the inset of Fig. 2 as coming from the right, even though the 150-μs ITD in the second pair of clicks favors the left ear. The total stimulus duration is twice the ICI plus the ITD, so that anomalous lateralization occurred for stimuli with total durations from 0.75 to about 1.75 ms.

3. Discussion

It has been suggested that the precedence effect with clicks operates optimally at ICIs between 1 and 2 ms (Wallach *et al.*, 1949; Zurek, 1987; Litovsky *et al.*, 1997). Consistent with this view, Tollin and Henning (1998a) found that for a type II configuration, the same three observers require an ITD of about five times that needed to lateralize a single dichotic click for ICIs in the range of *total* durations for which they show anomalous lateralization here. Gaskell (1983) and Saberi and Perrott (1990) report similar observations with their type II stimuli. In all three of these studies, the largest increases in the ITD threshold occurred with type II stimuli with ICIs between about 1 to 2 ms. It is not surprising, then, that it has been suggested that the precedence effect with clicks operates optimally at these ICIs.

It is tempting to attribute the decreased lateralizability in the two-click experiments to the effects of an echo-suppression mechanism which suppresses directional information in clicks that arrive a few milliseconds after the leading click (e.g., Zurek, 1980, 1987). But our results with three-click stimuli suggest that this is not the case. A mechanism that suppressed directional information in an echo presented 0.6 ms after the direct click would surely suppress the directional information in another echo added only 0.75 ms later (i.e., 1.35 ms after the direct click). But the data of Fig. 2 clearly show that the presence of the third click substantially influenced the perception of these stimuli, even when it was presented up to 2 ms after the direct click. Anomalous lateralization with the three-click stimuli should never occur if the directional information in the first and second echoes were simply suppressed; suppression would lead to performances near 50% correct; no suppression at all would lead to performance near 100% correct. The observers, however, perform consistently near 10%.

B. Supplementary experiment 1

There is considerable similarity between three-click stimuli and the type II configuration: The only lateralization cue in each configuration is an ITD which, after the ICI follows a diotic click that, on its own, provides no useful cue for lateralization in a discrimination task. The three-click stimulus is simply a type II stimulus followed, after an ICI of the same size, by an additional diotic echo. In this experiment, we investigate the effect of adding a second diotic echo 1.45 ms after the onset of the first click on the lateralization of the preceding type II stimulus by manipulating the amplitude of the second echo.

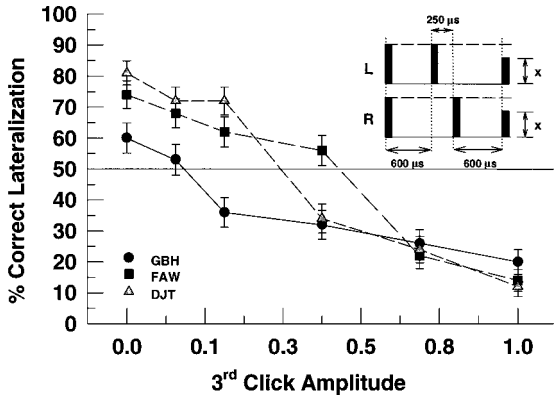

FIG. 3. The percentage of correct lateralization as a function of the amplitude, *x*, of the third binaural pair of clicks relative to the amplitude of the preceeding clicks in the stimulus shown in the inset. The stimulus was a three-click stimulus with an ICI of 600 μs and an ITD of 250 μs. Each data point is based on 100 observations.

1. Methods

The stimulus comprised three binaural clicks with an ICI of 600 μs and an ITD of 250 μs in the first echo; the amplitude of the diotic second echo was manipulated. The inset of Fig. 3 shows the stimulus configuration presented in one observation interval. The experiment was identical to the first experiment except that here, one of six relative amplitudes, *x*, of the third pair of clicks was selected and held constant for 50 trials. Each amplitude was used twice to yield 100 observations per amplitude for each of the same three observers.

2. Results

Figure 3 shows the percentage of correct lateralization judgments as a function of the normalized amplitude of the third pair of clicks (a value of 1.0 corresponds to the 30-dB SL level of our standard click). As the amplitude increased from 0.0 to 1.0, the performance of all observers *decreased* from 60%–80% to 10%–20% correct.

The 250-μs ITD required for consistent and correct performances with zero amplitude (i.e., a type II stimulus) would, on the lines of previous ''explanations'' of the precedence effect, be attributed to suppression of the directional information in the echo click. However, if the directional information in the second pair of clicks were indeed suppressed, one might reasonably expect that the directional information in the third click added a short time later should also be suppressed. Consequently, the third click should have either (1) not affected performance or, (2) because it had zero ITD, simply reinforced a central location. In the former case, performance should not have changed for any amplitude and in the latter case, performance should have approached 50% correct. Neither of these results occurred. The addition of a third pair of clicks, the second echo, contrib-

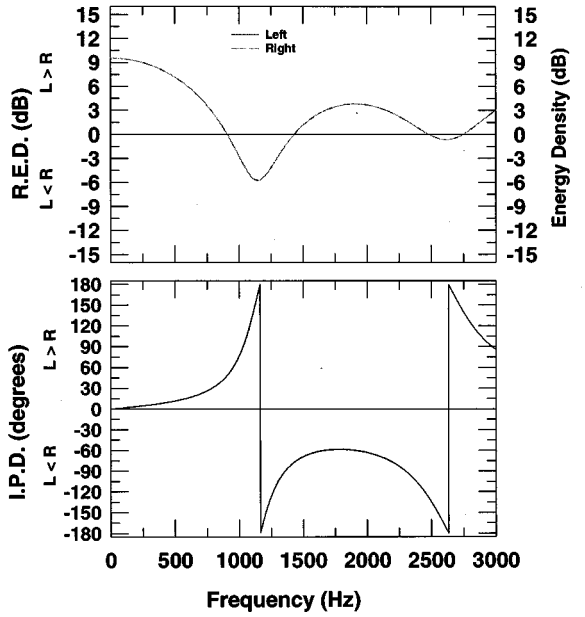

FIG. 4. The right-hand ordinate of the top panel shows the energy-density spectra for the stimuli delivered to the left (solid line) and right (dashed line) ears for the three-click stimulus with an ICI of 200 μs and an ITD of 150 μs in the middle click. The left-hand ordinate of the top panel shows the relative-energy density, RED, over the same frequency range. The bottom panel shows the interaural-phase delay (IPD) in degrees for both stimuli.

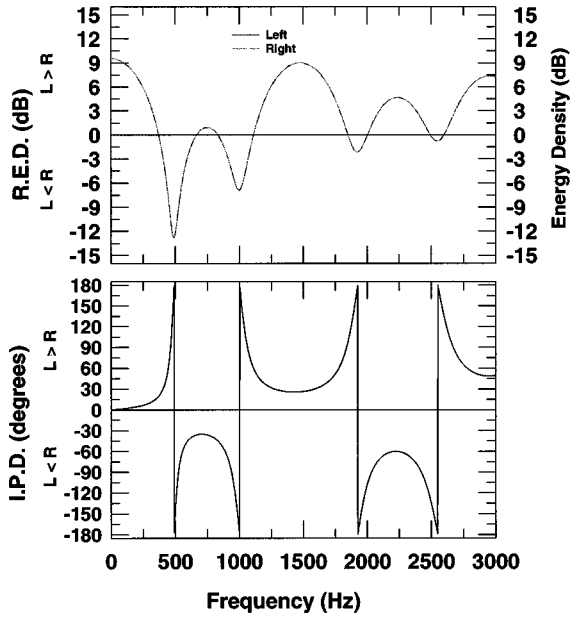

FIG. 5. The spectral characteristics for the three-click stimulus with an ICI of 600 μs and an ITD of 150 μs in the middle click.

uted substantially to the overall perception of the complex, even when its amplitude was 18 dB below the amplitude of the preceding clicks. Thus, neither the information in the second nor the third pair of clicks was suppressed, and echo suppression does not explain the data in Fig. 2 or 3. We require an alternative explanation.

C. Spectral characteristics

Consider the spectral characteristics of the three-click stimuli of experiment 1 for three different ICIs chosen because observers lateralized them differently. The spectral characteristics were computed by specializing the general equations derived in Tollin (1998b) for the three-click stimulus shown in the inset of Fig. 2. The top panel of Fig. 4 shows the energy densities (dB, right-hand ordinate) for the left- and right-ear stimuli which were easily and correctly lateralized—the stimulus had an ICI of 200 μs and an ITD of 150 μs. The energy-density spectra for the left- and right-ear signals are identical so that only one spectrum can be seen and, consequently, the relative-energy density (RED dB, left-hand ordinate) is zero.

The bottom panel of Fig. 4 shows the IPD (in degrees) over the same frequency range. The IPD spectrum provides the *only* cue to noncentral lateralization. The IPD leads in the left ear for frequencies up to nearly 1250 Hz. Further, the energy-density spectra in the top panel reveal that there is energy in this low-frequency region. Since the binaural system is known to be most sensitive to interaural-phase differences for frequencies below 1500 Hz (Rayleigh, 1907; Zwislocki and Feldman, 1956; Henning, 1983), and given that there is energy in the low-frequency region, the highly consistent lateralization achieved by all the observers might reflect their use of the IPD cue around 750 Hz. At 750 Hz, the IPD is on the order of $+30°$ (a left-ear lead of approximately 110 μs).

When the ICI was 600 μs, the observers showed highly consistent but anomalous lateralization near 10% correct. Figure 5 shows the spectral characteristics where, in the frequency ranges 0–500 and 1000–2000 Hz, the IPD shows the left ear leading. If the observers used the IPD cues in either of these frequency regions, they would achieve consistent performances at least better than 50% correct. But given the low energy in the band of frequencies around 500 Hz it is unlikely that the IPD cues from this region could be used. Had the observers used the band of frequencies just below 1500 Hz—where the energy density is high—lateralization above 50% correct would have been expected. But lateralization of this stimulus is consistent and anomalous.

The spectra in Fig. 5 show that in the frequency region between 500–1000 Hz, the IPD favors the right side. At 750 Hz, there is an IPD of $-35°$, which corresponds to an ITD of about 130 μs favoring the right ear. The energy-density spectrum reveals that the intensity of the band of frequencies around 750 Hz was only 8 dB below the levels in the bands centered on 1500 Hz and the lower-frequency regions. If the observers used the IPD information from this region, they would be expected to achieve consistent but anomalous levels of performance and they do; the observers get about 10% correct. The IPDs in the spectral region centered on 2500 Hz are also consistent with the anomalous lateralization. [Note that Henning (1983) has shown that for high-frequency transients, observers are not sensitive to the IPD *per se*, but rather the group delay—the local rate of change of the IPD spectrum. The rapid rates of change of the IPD spectrum of our stimulus occur where the energy density is not zero, so that very large group delays are present and this frequency region remains a possible source of information.]

Finally, when the ICI was 1000 μs, all three observers

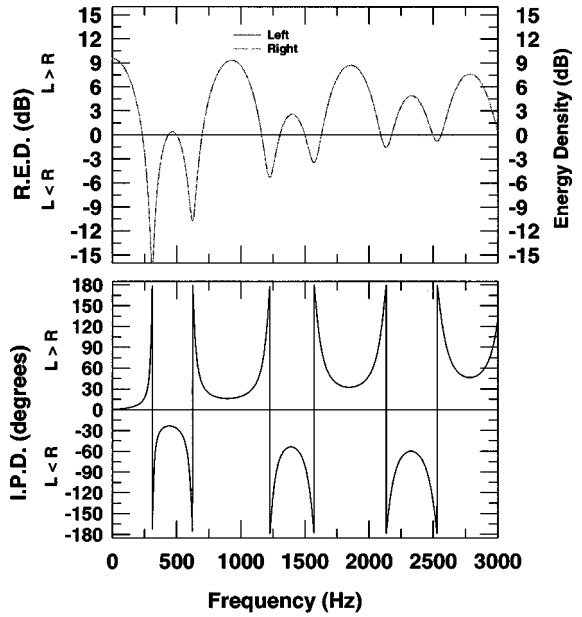

FIG. 6. The spectral characteristics for the three-click stimulus with an ICI of 1000 μs and an ITD of 150 μs in the middle click.

achieved performances of 70% correct or better. Figure 6 shows the relevant spectra. The IPDs favoring the left ear now occupy a region from just above 600 to 1200 Hz and the energy density shows a local maximum near 900 Hz. The observers' performance might be due to their using the interaural-phase information in that frequency region, since the IPD at 900 Hz is $+15°$—a left-ear lead of 45 μs and consistent with performance. The observers did not seem to be distracted by the large negative IPDs near 500 Hz, even though at 500 Hz there is also a local energy maximum. At 500 Hz there is an IPD of $-27°$, 150 μs favoring the right ear. If the observers used the lateralization information in this region, consistent but anomalous lateralization might be expected. This was not the case, showing that the observers did not rely on the IPD information from this region.

D. Discussion

Anomalous lateralization similar to that observed here is not new; it has been observed elsewhere with clicks (Gaskell, 1983; Wallach *et al.*, 1949) and with brief noise bursts (Zurek, 1980). Anomalous localization has also been reported with broad- and narrow-band clicks (David and Hanson, 1962; Blauert and Cobben, 1978). Anomalous performance has usually been observed with two-click stimuli in response to changes in the interaural *amplitude* of a zero-ITD echo which follow a simultaneous equal-amplitude diotic pair. The anomalous lateralization observed here was produced by an interaural *delay* in the second pair of three equal-amplitude clicks.

Further consideration of the spectral characteristics of the three-click stimuli at the remaining ICIs suggested that the observers used the interaural-phase differences from the frequency band around 750 Hz when they could. This seemed to be the case even when the level in the band was 8 dB below neighboring bands. Provided the ICI was 1 ms or less, lateralization performance could be accounted for by

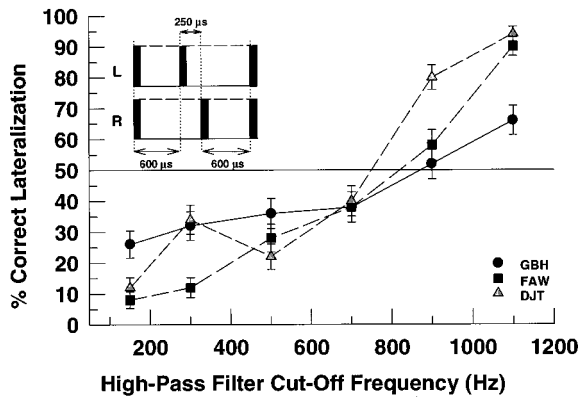

FIG. 7. The percentage of correct lateralization as a function of the high-pass-filter cutoff frequency for three observers for the three-click stimulus with an ITD in the dichotic second pair of clicks of 250 μs and an ICI of 600 μs. Each point represents 100 observations.

assuming that the observers used (or gave more weight to) the IPD cues in the band around 750 Hz. The hypothesis that the spectral characteristics near 750 Hz were responsible for anomalous lateralization was tested in two supplementary experiments. We reasoned that if removing the interaural spectral characteristics consistent with the anomalous lateralization by filtering or making them inaudible by masking removed anomalous lateralization, then those interaural spectral characteristics were likely to be responsible for the anomalous lateralization.

E. Supplementary experiment 2 a: Effects of high-pass filtering

The three-click stimulus, shown in the inset of Fig. 7, had an ICI of 600 μs and an ITD of 250 μs. The solid lines

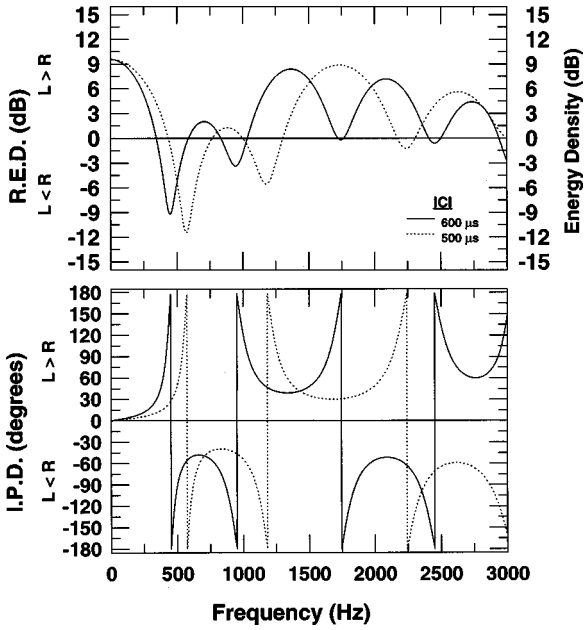

FIG. 8. The spectral characteristics of the two three-click stimuli used in supplementary experiments 2 a and 2 b. The solid lines in each panel show the spectral characteristics for the three-binaural-click stimulus with an ICI of 600 μs and ITD of 250 μs and the dotted lines show the characteristics for the stimulus with an ICI of 500 μs an ITD of 150 μs.

in the top and bottom panels of Fig. 8 show spectra of this stimulus. Our hypothesis predicts anomalous lateralization consistent with the IPD around 750 Hz. By selectively filtering out the components near 750 Hz, it should be possible to see whether the IPDs there were indeed responsible for lateralization.

1. Methods

The same observers participated and the signal generation, experimental apparatus, and the lateralization task were as described in Sec. II A 1, except that the filters were operated in high-pass mode using six high-pass cutoff frequencies between 125 and 1100 Hz. One cutoff frequency was chosen and held constant for 50 trials. Once all six cutoff frequencies had been exhausted, the process was repeated resulting in 100 observations for each cutoff frequency per observer.

2. Results

Figure 7 shows percentage-correct lateralization as a function of the high-pass cutoff frequency. When the cutoff was 200 Hz, observers' lateralization was consistent but anomalous (8%–26% correct). As the cutoff frequency rose to 750 Hz, lateralization approached chance performance (50%). When the cutoff frequency was raised to 1100 Hz, correct performance was achieved for two observers (90%–94%), 66% for the other. Anomalous lateralization disappeared when the 750-Hz band was removed.

One reasonable strategy for observers in these and other precedence-effect experiments (and presumably in actual acoustical environments) where the resultant spectral characteristics of the signals at the two ears may be quite complex, might be to use the interaural cues from only the frequency regions with the most energy. Inspection of the energy density of our stimulus (Fig. 8, solid lines) shows that the unfiltered stimulus has its maximum near 1300 Hz. The sign of the IPD in this region agrees with the ITD in the temporal waveform, so observers using information from this region would achieve performance *at least* greater than chance. But the data show that the observers do not behave in this manner. Rather, they appear to use the IPD cues near the local energy-density peak near 750 Hz.

There are, however, two frequency regions over which the IPD is consistent with anomalous lateralization: one near 750 Hz and the other near 2225 Hz. The data from the current experiment show that when frequencies below about 900 Hz are attenuated, anomalous lateralization disappears. When the high-pass cutoff frequency was 1100 Hz, all observers lateralized the stimuli significantly above chance, with their consistent, correct lateralization in agreement with the positive IPD near 1250 Hz. The results of this experiment, then, support our hypothesis that the anomalous lateralization of this stimulus arises from information the observers take from the region near 750 Hz.

F. Supplementary experiment 2 b: Effects of masking

A continuous pure tone was used to mask the 750-Hz frequency band in a three-click stimulus (not shown) with an ICI of 500 μs and an ITD of 150 μs in the second click; the dotted lines in the panels of Fig. 8 show its spectral characteristics. The IPD in the local energy-density peak near 850 Hz opposes the direction indicated by the ITD in the temporal waveform. Thus, we predict anomalous lateralization for this stimulus.

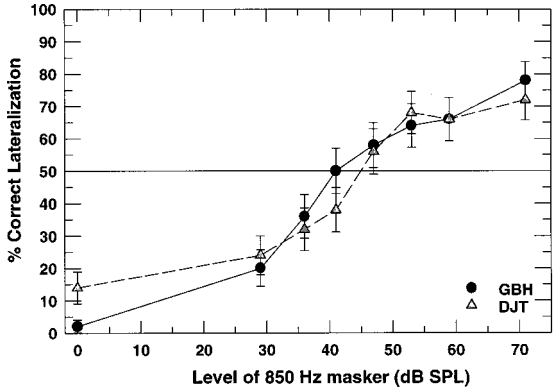

FIG. 9. The percentage of correct lateralization as a function of the level (in dB SPI) of a continuous 850-Hz tone for two observers when the stimulus was a three-click stimulus with an ICI of 500 μs and an ITD of 150 μs. Each point is based on 50 observations.

1. Methods

A continuous pure tone of 850 Hz, generated by a TDT WG2 waveform generator, was added with zero interaural-phase difference to the three-click stimuli through a TDT SM3 weighted-signal mixer. The level of the tone (dB SPL) was controlled via a TDT PA4 digital attenuator. Masker level was held constant for 50 trials and lower masker levels were used before higher. Aside from these additions, the experimental apparatus and psychophysical task were as described in Sec. I A 1. Two observers participated in this experiment.

2. Results

Figure 9 shows percentage-correct lateralization as a function of the level (dB SPL) of the 850-Hz masking tone. When the tone was not present, the observers lateralized anomalously (2% and 14% correct) as predicted. As the masker level increased, performance also increased. At a level of about 45 dB SPL, both observers were at chance performance. With further increases, performance increased above chance, so that at 71 dB SPL, both observers achieved near 75% correct.

Components in the band near 850 Hz were progressively masked by the tone as its level increased. Fletcher (1953) reports that an 800-Hz tone at 40 dB SPL provides 20 dB of masking over a band of frequencies between about 650 and 1000 Hz, corresponding to the bandwidth of the local energy-density peak near 850 Hz. With the tone at 45 dB SPL, both observers were near 50% correct. Thus, one way of interpreting the results is that the masking of the components near 850 Hz reduces the effectiveness of the interaural-phase-difference cues from that band, so for the observers to achieve the correct lateralization they exhibit, they must use cues from a different spectral location. But which? One pos-

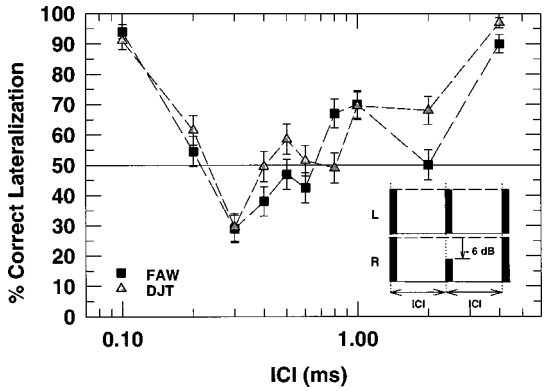

FIG. 10. The percentage of correct lateralization as a function of the ICI in ms (logarithmic axis) for two observers when the stimulus was the three-click stimulus shown in the inset. Each data point is based on 100 observations.

sible insight comes from the observers' reports that the clicks sounded higher pitched when the masker level was 53 dB SPL or greater than when the masker was either not present or at low levels. Examination of the IPD spectrum reveals that in the frequency regions between 1200 and 2250 Hz, the IPD is positive—consistent both with the observers' performance levels near 75% correct and their subjective impressions. Presumably, then, the observers were forced to use the interaural-spectral cues in this region when the masker level exceeded about 45 dB SPL and prevented their using information from their preferred spectral region near 750 Hz.

II. THREE-CLICK STIMULI—AMPLITUDE DIFFERENCE IN SECOND PAIR

We have explored observers' abilities to use interaural phase cues. However, IPDs are only one of the cues to lateralization. Stimuli can also be lateralized with interaural amplitude or energy differences (Tollin, 1998a). In this section, we use a stimulus (shown in the inset of Fig. 10) which has the unique property that the IPD spectrum is zero at all frequencies but the RED is nonzero. The stimulus comprises three clicks with equal ICIs and no interaural-time differences. Rather there is an interaural-*amplitude* ratio of 6 dB in the second click. Observers lateralize a single click with an interaural-amplitude ratio of 6 dB on the side receiving the more-intense click with 100% accuracy (Tollin, 1998a). For this stimulus, the RED represents the *only* interaural cue for noncentral lateralization, as the IPD is zero for all frequencies.

A. Experiment 3

The experiment investigated the ability to lateralize the three-click stimulus as a function of ICI. The stimulus, shown in the inset of Fig. 10, would be expected to be lateralized to the left on the basis of the interaural-amplitude difference favoring the left ear. The experimental apparatus and psychophysical procedure were as described in section Sec. I A 1. Ten values of ICI ranging from 0.1 to 5 ms were used. One of the values of ICI was chosen and held constant

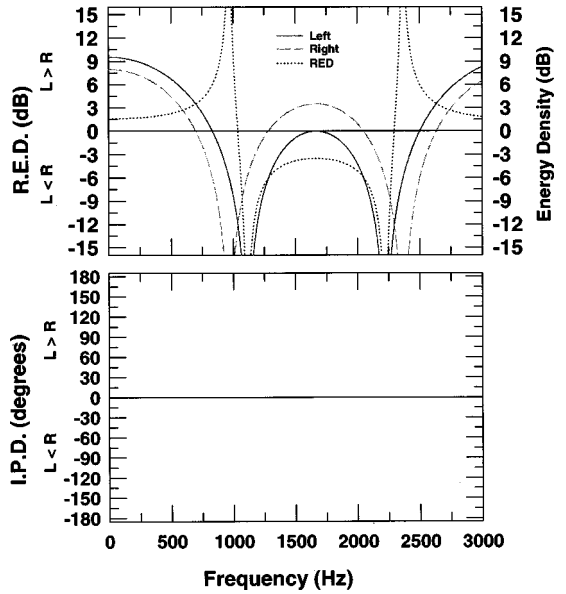

FIG. 11. The spectral characteristics of the three-click stimuli with an ICI of 300 μs and a 6-dB interaural-amplitude difference in the second pair of clicks.

for 50 trials. The process was repeated once all values were used to produce 100 observations for each of the two observers for each ICI. Two observers participated.

B. Results

Figure 10 shows the percentage-correct lateralization as a function of ICI. As the ICI increases from 0.1 to 0.3 ms, performance drops from greater than 90% correct to 30% correct. With an ICI of 0.3 ms, the observers hear the stimulus on the opposite side of the head from that expected from the interaural-amplitude difference in the second click. For ICIs from 0.3 to 0.6 ms, one observer lateralizes the stimuli somewhat anomalously (performance around or below 50% correct), while the other observer performs near chance. For ICIs greater than 1.0 ms, performance by and large improves so that by 4.0 ms, performance is 90% correct or better.

C. Spectral characteristics

The spectral characteristics of this stimulus were considered for each ICI we used but, in the interest of brevity, the spectral characteristics for only the 0.3-ms ICI condition are shown in Fig. 11. The IPD is zero for all frequencies. There are two regions in the frequency range shown where the RED favors the left ear, and one favoring the right. Only the RED in the region centered near 1500 Hz is consistent with the anomalous lateralization exhibited by the observers. But consideration of the RED around 1500 Hz for the stimulus with an ICI of 0.6 ms, where the observers performed at chance or slightly anomalously, reveals a positive RED over a large band; consequently, higher levels of performance would have been expected had the observers used the RED cues from this region.

When the interaural level of the second click pair was manipulated, no fixed spectral region could be found that yielded interaural-spectral characteristics consistently in

agreement with the observers' behavior. One possible explanation for this finding is that there may be no ''dominant region'' for interaural-level cues as there is for interaural time or phase cues (Bilsen and Raatgever, 1973). This is consistent with observers' roughly equal sensitivity to interaural-level cues across frequency (Mills, 1960; Grantham, 1984; Yost and Dye, 1988).

III. DISCUSSION

We have reviewed several instances where neither lateralization nor localization was consistent with the notion of simple postonset suppression of directional information in echoes. Consideration of the spectral characteristics of our various three-click stimuli revealed that spectral cues near 750 Hz were consistent with many of the observed results, particularly where the observers exhibited highly consistent, but anomalous lateralization. Consideration of the time-domain representation of the anomalously lateralized stimuli does not reveal why a particular stimulus configuration should be anomalously lateralized. Examination of the interaural phase-difference (IPD) and relative energy-density (RED) spectra, however, revealed cues which, if used by the observers, would clearly lead to anomalous lateralization.

A. Comparisons with other studies

Gaskell (1983) considered the spectral characteristics of the stimuli for which her observers exhibited anomalous lateralization—20-μs clicks in a type II configuration with no interaural delays, rather an interaural-amplitude ratio of 6 dB in the echo pair and ICIs between 100 and 600 μs. For ICIs less than 600 μs. Gaskell demonstrated a large band of low frequencies over which the IPD spectrum favored the ear *opposite* that in which the higher-amplitude click occurred, consistent with the anomalous lateralization.

Based on our findings with three-click stimuli, we considered the spectral characteristics near 750 Hz for Gaskell's stimuli with ICIs greater than 600 μs. For ICIs between 0.8 and 1.2 ms, the sign of the IPD near 750 Hz is consistent with the sign of the ILD and we would predict nonanomalous performance, as was observed. However, for ICIs between approximately 1.4 and 2.0 ms, the IPD around 750 Hz opposess the ILD. Thus, anomalous lateralization would be expected if IPD were the only cue, but for this stimulus, there are also substantial differences in the left- and right-ear energy densities consistent with the ILD in the echo. Consistent with the use of IPD around 750 Hz, however, one observer's performance decreases substantially and one observer's performance actually drops below 50% correct as the ICI is raised from 1.4 to about 1.6 ms. As the ICI is raised from 2.0 to 2.4 ms, all Gaskell's observers exhibit a dramatic increase in their performance levels. This increase in performance coincides with a transition in the 750-Hz region of the sign of the IPD opposing the ILD to the sign of the IPD consistent with the ILD. Finally, at an ICI of 2.8 ms, the sign of the IPD is again in opposition to the ILD and, if the observers were sensitive to the IPD, would result in decreased performance relative to that at 2.4 ms. Performance for two (of three) observers does, in fact, show the decrease. These are important observations; even though Gaskell manipulated ILDs (and not ITDs), the resultant spectra contained nonzero IPDs whose signs are consistent with or oppose the sign of the ILD, depending on the ICI. (Future experiments on the precedence effect measuring the precision of ILD discrimination in transients should take this into account.)

Zurek (1980) also observed anomalous lateralization in his study of the amplitude-based precedence effect using pairs of 1-ms rectangularly gated Gaussian noise bursts. Zurek (1987) suggested that his results might arise from multiple temporal interactions between the leading and the lagging bursts, provided that the ICI is short enough and that the interaural-amplitude ratio of the second binaural pair of bursts is large, so that there are, in effect, only three clicks; viz., the diotic first click followed, in effect, by a single lagging click presented to one ear only. According to Zurek, the observer may actually perceive *two* interaural delays, one equal to zero due to the coincident initial pair, and another longer ITD due to the interaction between the leading click in one ear and the lagging click in the other. With this stimulus, the direction of the longer ITD is opposite the interaural-amplitude difference and, as Zurek pointed out, anomalous lateralization could result.

At first glance, Zurek's model is wholly consistent with our anomalous results. Consider the putative multiple temporal interactions occurring with a three-click stimulus which can be conveniently summarized by those elements of the broadband cross-correlation function that fall within approximately ± 650 μs of zero—the physiologically meaningful range of interaural delays normally encountered by adult human observers (Kuhn, 1987). The cross-correlation function for a three-click stimulus with an ICI of 600 μs and an ITD of 150 μs contains equal-amplitude peaks at delays of 0 and -600 μs, and a peak of half that amplitude at a delay of 150 μs. [A large peak also occurs at a delay of 750 μs (ICI $+$ITD) that falls outside the range of physiologically reasonable delays.] The large peak at -600 μs is consistent with the anomalous lateralization of this particular stimulus (see Fig. 2), as Zurek might predict.

The cross-correlation model also has some success in conditions that do not lead to anomalous lateralization. Consideration of the cross correlation of a three-click stimulus with an ICI of 1000 μs and ITD of 150 μs yields a peak within the physiological range at 0-μs delay, and a peak of half that amplitude at $+150$ μs, all the other peaks occur at delays well outside the physiologically reasonable range. The observers lateralized this particular stimulus correctly, achieving performance levels of 70% correct or better, consistent with the 150-μs delay. Thus, it seems the cross-correlation model might also be applicable to conditions leading to nonanomalous lateralization.

The cross-correlation model is appealing because it is simple and seems to be compatible with the data for several different stimulus configurations. But a natural question is whether its predictions are compatible with the performance differences between the two-click type I and type II stimuli. Unfortunately, here the theory breaks down because, for identical ICIs and identical ITDs, the cross correlation for the

type I stimulus is identical to that for the type II (Zurek, 1976; Gaskell, 1978, 1983; Tollin, 1998a). Even for small ICIs, where the model seems to be most applicable, it cannot, on its own, explain the robust differences in performance observed with the type I and type II stimuli as Gaskell (1978, 1983) pointed out.

The cross-correlation model also cannot explain why observes' lateralization in supplementary experiment 2 b could be driven from highly anomalous to correct by simply increasing the level of a diotic pure-tone masker. The model might predict that lateralization performance would tend toward 50% with increasing masker level, but performance greater than 50% should not occur. But, the addition of a masking tone to the three-click stimulus produced performance near 90% correct. Clearly, then, the model cannot explain many important aspects of the precedence effect.

One way to preserve the model is to evoke echo suppression—suppression that somehow inhibits the directional information from echoes arriving later than about 1 ms from the onset of the first wavefront is often assumed (Zurek, 1980, 1987; Lindemann, 1986). Such postonset inhibitory theories are attractive because their predictions agree qualitatively with experimental results from a wide range of studies and appear to help account for the failure of the cross-correlation model.

However, our results with three clicks demonstrate that the directional information in clicks presented up to 2–3 ms after the first click is not suppressed. Rather, echoes that arrive as late as 2–3 ms after the initial click affect the spectral characteristics of the sum of the first arriving signal and its echoes in ways that have a substantial effect on lateralization.

B. Temporal integration and sound localization

One interpretation of our results, then, is that the auditory system analyzes sums of delayed transients on the basis of their short-term spectral characteristics with a time constant on the order of at least 2–3 ms, and that these short-term spectral characteristics are important in sound localization. A time constant of about 2–3 ms arises for several reasons. First, the IPD spectrum near 750 Hz for a three-click stimulus with an ICI of 2 ms and an ITD of 150 μs suggests that this stimulus should have been lateralized anomalously, but all observers achieved performances of 80% correct or better (Fig. 2). So, spectral considerations failed to predict observers' performances when the total duration of the three-click stimuli was greater than 4 ms.

Second, monaural temporal-order discrimination of transients with identical energy-density spectra fails for signals shorter than 2–3 ms (Ronken, 1970; Patterson and Green, 1970; Green, 1971; Resnick and Feth, 1974; Henning and Gaskell, 1981). Third, Hall and Lumis (1973) demonstrated that the monaural detection of click pairs in the presence of a notched-noise masker depends on ICI and the spectral location of the notch for ICIs up to just above 2 ms. They showed that detection thresholds oscillated between higher and lower values as a function of ICI in a manner predictable from the energy-density spectrum of the click pairs at the spectral location of the notch.

Further, it has not escaped our notice that the impulse response of the ear canal, pinna, head, shoulders, and torso—whose Fourier transform yields head-related transfer functions—can have total durations near 2 ms (Wightman and Kistler, 1997). Because ''reflections'' from these structures influence localization through their effects on the resultant spectral characteristics of the sounds reaching the ears, a time constant of at least 2 ms again seems appropriate.

C. A ''dominance region'' in the precedence effect

It is well known that observers are most sensitive to interaural time and phase differences for frequencies around 700 Hz (Zwislocki and Feldman, 1956). Bilsen and Raatgever (1973) found a ''dominant-region'' effect whereby the frequency components around 700 Hz were much more effective in the lateralization of broadband noise than were neighboring components. Likewise, Henning (1983), using an 800-Hz-wide transient with an interaural-group delay of 200 μs centered on different frequencies, showed that such stimuli were predominantly lateralized according to the IPDs in the spectral region near 700 Hz. Wightman and Kistler (1992) also established that low-frequency ITD cues are of primary importance in localizing sounds on the horizontal plane in virtual space (and presumably also in ''real'' environments). They found that the low-frequency ITDs completely dominated their observers' judgments of the horizontal positions of virtual-sound sources even when the high-frequency localization cues—interaural-level differences and monaural spectral cues—signaled positions different from that indicated by the low-frequency ITD.

The results of our experiments with the three-click stimuli with an ITD in the second pair are also consistent with this interpretation; the observers appear to lateralize primarily on the basis of the IPD in the region around 750 Hz provided the total duration is less than 2–3 ms. In other words, these results demonstrate that the dominant-region effect also holds for stimulus conditions under which the precedence effect is assumed to operate. We found no such region for interaural-level differences (i.e., REDs).

Others have also investigated the role of spectral dominance in the precedence effect (Blauert and Divenyi, 1988; Divenyi, 1992; Shinn-Cunningham *et al.*, 1995; Saberi, 1996; Yang and Grantham, 1997; Tollin and Henning, 1998b). But aside from Tollin and Henning (1998b), the role of spectral dominance was investigated by independently changing the spectral composition of the direct and echo stimuli. These studies showed that a lead stimulus containing primarily low frequencies will make more difficult the use of the directional information in an echo containing primarily high frequencies, but not vice versa. The present experimental paradigm transcends those techniques and shows more directly that, even for stimuli in which both direct and echoed sounds are broadband and identical, the IPD in the spectral region around 750 Hz is of particular importance.

Two important issues remain. First, in light of the findings that the dominant-region effect holds in our three-click

experiments, a re-examination of why the ITD sensitivity for type II stimuli is much worse than the for type I stimuli with the same ICI is in order. For ICIs less than about 3 ms, can performance be predicted from the type I and type II spectral characteristics around 750 Hz? The second issue of importance concerns the situation where the direct and ''echo'' sounds are uncorrelated. As the direct and echoed sound become uncorrelated, their resultant spectral characteristics diverge considerably from those produced for correlated sounds. Zurek (1980) considered this possibility and measured ITD thresholds for type I and type II stimuli under two different conditions; the direct- and echo-noise burst were either (1) identical, or (2) uncorrelated. His data showed that for ICIs between about 1 and 10 ms, ITD jnd's were roughly the same under both conditions; substantially elevated for the type II stimulus but not for the type I. The implication of Zurek's findings is that the resultant spectral characteristics alone are not necessary to produce a precedence effect with broadband transients. But as we showed in this paper, Zurek's data do not preclude the important role for the resultant spectral characteristic of delayed and added transients or highly correlated sounds in lateralization and localization. These important issues warrant discussion and will be considered in detail in a forthcoming paper.

IV. CONCLUSIONS

To simplify the investigation of the role of the spectral characteristics in lateralization, three-click stimuli were designed to have either (1) nonzero interaural-phase differences (IPDs), or (2) nonzero relative-energy densities (REDs). When the IPD was the only spectral cue, observers' performance was consistent with their using IPDs in a band of frequencies around 750 Hz, provided the total stimulus duration was less than about 2–3 ms. Additional masking and filtering experiments confirmed that the observers used IPD information from this region. The results support the notion of a dominant region for the lateralization in the spectral region around 750 Hz. Joint consideration of the behavioral data and the spectral characteristics for the stimulus with zero IPDs and nonzero REDs revealed no equivalent region for interaural-level differences. Our results demonstrate that echoes that arrive within 2–3 ms of an initial click are not suppressed, but play a substantial role in lateralization through their contribution to the spectral characteristics of 2–3 ms epochs that contain the direct sound and its echoes. The findings challenge the hypothesis that the precedence effect is most effective, in the sense that the directional information in echoes is suppressed, with click stimuli for ICIs between approximately 1–2 ms (Wallach *et al.*, 1949; Gaskell, 1983; Yost and Soderquist, 1984; Saberi and Perrott, 1990; Litovsky *et al.*, 1997).

ACKNOWLEDGMENTS

This work was carried out in The Sensory Research Unit, Department of Experimental Psychology, The University of Oxford, U.K. as a part of the first author's doctoral dissertation. Financial support was provided to the first author through an O.R.S. Award, a St. Catherine's College (Oxford) Graduate Fellowship, and a University of Oxford Overseas Bursary. The first author was supported by NIH NIDCD grants No. DC00045 and No. DC00116 during the preparation of the manuscript. Both authors would also like to thank Drs. E.R. Hafter, D. McFadden, and W. Grantham (the Associate Editor) and two anonymous reviewers for their comments on the manuscript.

[1]See AIP Document No. E-PAPS: E-JASMAN-105-023902 for the derivation of the general equations used to compute the spectral characteristics for the various three-binaural-click stimulus configurations used in the paper. E-PAPS document files can be retrieved free of charge from our FTP server (http://www.aip.org/epaps/epaps.html) or from ftp.aip.org in the directory/epaps/. For further information, E-mail: paps@aip.org or Fax: 516-576-2223.

Bilsen, F. A., and Raatgever, J. (**1973**). ''Spectral dominance in binaural lateralization,'' Acustica **28**, 131–132.
Blauert, J. (**1997**). *Spatial Hearing* (MIT, Cambridge, MA).
Blauert, J., and Cobben, W. (**1978**). ''Some considerations of binaural cross correlation analysis,'' Acustica **39**, 96–104.
Blauert, J., and Divenyi, P. L. (**1988**). ''Spectral selectivity in binaural contralateral inhibition,'' Acustica **66**, 267–274.
David, E. E., and Hanson, R. L. (**1962**). ''Binaural hearing and free field effects,'' Proceedings of the Fourth International Congress on Acoustics, Copenhagen, 1962, Paper H24 (unpublished).
Divenyi, P. L. (**1992**). ''Binaural suppression of non-echoes,'' J. Acoust. Soc. Am. **91**, 1078–1084.
Fletcher, H. (**1953**). *Speech and Hearing in Communication* (Van Nostrand, Princeton, NJ), p. 155.
Gaskell, H. (**1978**). ''Some aspects of the localization of transient sounds in man.'' Doctoral dissertation, The University of Oxford, U.K.
Gaskell, H. (**1983**). ''The precedence effect,'' Hearing Res. **11**, 277–303.
Grantham, D. W. (**1984**). ''Interaural intensity discrimination: Insensitivity at 1000 Hz,'' J. Acoust. Soc. Am. **75**, 1191–1194.
Green, D. M. (**1971**). ''Temporal auditory acuity,'' Psychol. Rev. **78**, 540–551.
Hafter, E. R., and Jeffress, L. A. (**1968**). ''Two image lateralization of tones and clicks,'' J. Acoust. Soc. Am. **44**, 563–569.
Hall, J. L., and Lummis, R. C. (**1973**). ''Thresholds for click pairs masked by band-stop noise,'' J. Acoust. Soc. Am. **54**, 593–599.
Henning, G. B. (**1983**). ''Lateralization of low-frequency transients,'' Hearing Res. **9**, 153–172.
Henning, G. B., and Gaskell, H. (**1981**). ''Monaural phase sensitivity with Ronken's paradigm,'' J. Acoust. Soc. Am. **70**, 1669–1673.
Kuhn, G. F. (**1987**). ''Physical acoustics and measurements pertaining to directional hearing,'' in *Directional Hearing*, edited by W. A. Yost and G. Gourevitch (Springer-Verlag, New York), pp. 3–25.
Lindemann, W. (**1986**). ''Extension of a binaural cross-correlation model by contralateral inhibition: II. The law of the first wavefront,'' J. Acoust. Soc. Am. **80**, 1623–1630.
Litovsky, R. Y., Rakerd, B., Yin, T. C. T., and Hartmann, W. M. (**1997**). ''Psychophysical and physiological evidence for a precedence effect in the median sagittal plane,'' J. Neurophysiol. **77**, 2223–2226.
Lord Rayleigh (**1907**). ''On our perception of sound direction,'' Philos. Mag. **3**, 456–464.
Mills, A. W. (**1960**). ''Lateralization of high-frequency tones,'' J. Acoust. Soc. Am. **32**, 132–134.
Papoulis, A. (**1962**). *The Fourier Integral and Its Applications* (McGraw-Hill, New York).
Patterson, J. H., and Green, D. M. (**1970**). ''Discrimination of transient signals having identical energy spectra,'' J. Acoust. Soc. Am. **48**, 894–905.
Resnick, S. B., and Feth, L. L. (**1975**). ''Discriminability of time-reversed click pairs: intensity effects,'' J. Acoust. Soc. Am. **57**, 1493–1499.
Ronken, D. (**1970**). ''Monaural detection of a phase difference between clicks,'' J. Acoust. Soc. Am. **47**, 1091–1099.
Saberi, K. (**1996**). ''Observer weighting of interaural delays in filtered impulses,'' Percept. Psychophys. **58**, 1037–1046.
Saberi, K., and Perrott, D. R. (**1990**). ''Lateralization thresholds obtained

under conditions in which the precedence effect is assumed to operate,'' J. Acoust. Soc. Am. **87**, 1732–1737.
Saberi, K., and Perrott, D. R. (**1995**). ''Lateralization of click-trains with opposing onset and ongoing interaural delays,'' Acustica **81**, 272–275.
Shinn-Cunningham, B. G., Zurek, P. M., Durlach, N. I., and Clifton, R. K. (**1995**). ''Cross-frequency interactions in the precedence effect,'' J. Acoust. Soc. Am. **98** 164–171.
Tollin, D. J. (**1998a**). ''Some aspects of the lateralization of echoed sound in man,'' Doctoral dissertation, The University of Oxford, U.K.
Tollin, D. J. (**1998b**). ''Some aspects of the lateralization of echoed sound in man. IIb: Derivations of the spectral characteristics for arbitrary binaural-click stimuli'' (submitted to AIP E-PAPS, see footnote 1).
Tollin, D. J., and Henning, G. B. (**1998a**). ''Some aspects of the lateralization of echoed sound in man. I. The classical interaural delay-based precedence effect,'' J. Acoust. Soc. Am. **104**, 3030–3038.
Tollin, D. J., and Henning, G. B. (**1998b**). ''Across-frequency integration in the precedence effect,'' in *Psychophysical and Physiological Advances in Hearing*, edited by A. R. Palmer, A. Rees, A. Q. Summerfield, and R. Meddis (Whurr, London), pp. 329–335.
Tollin, D. J., and Henning, G. B. (**1996**). ''Anomalous lateralization in the precedence effect with novel two echo stimuli,'' J. Acoust. Soc. Am. **100**, 2593A.
Wallach, H., Newman, E. B., and Rosenzweig, M. R. (**1949**). ''The precedence effect in sound localization,'' Am. J. Psychol. **62**, 315–337.
Warnke, H. (**1941**). ''The fundamentals of room-related stereophonic reproduction in sound films,'' Akust. Zh. **6**, 174–188.
Wightman, F. L., and Kistler, D. J. (**1992**). ''The dominant role of low-frequency interaural time differences in sound localization,'' J. Acoust. Soc. Am. **91**, 1648–1661.
Wightman, F. L., and Kistler, D. J. (**1997**). ''Factors affecting the relative salience of sound localization cues,'' in *Binaural and Spatial Hearing in Real and Virtual Environments*, edited by R. H. Gilkey and T. A. Anderson (Erlbaurn, Hillsdale, NJ), pp. 1–23.
Yang, X., and Grantham, D. W. (**1997**). ''Cross-spectral and temporal factors in the precedence effect: Discrimination suppression of the lag sound in free-field,'' J. Acoust. Soc. Am. **102**, 2973–2983.
Yost, W. A., and Dye, R. (**1988**). ''Discrimination of interaural differences of level as a function of frequency,'' J. Acoust. Soc. Am. **83**, 1846–1851.
Yost, W. A., and Hafter, E. R. (**1987**). ''Lateralization,'' in *Directional Hearing*, edited by W. A. Yost and G. Gourevitch (Springer-Verlag, New York), pp. 49–84.
Yost, W. A., and Soderquist, D. R. (**1984**). ''The precedence effect revisited,'' J. Acoust. Soc. Am. **76**, 1377–1383.
Zurek, P. M. (**1976**). ''An investigation of the binaural perception of echoed sound.'' Doctoral dissertation, Arizona State University.
Zurek, P. M. (**1980**). ''The precedence effect and its possible role in the avoidance of interaural ambiguities,'' J. Acoust. Soc. Am. **67**, 952–964.
Zurek, P. M. (**1987**). ''The precedence effect,'' in *Directional Hearing*, edited by W. A. Yost and G. Gourevitch (Springer-Verlag, New York), pp. 85–106.
Zwislocki, J., and Feldman, R. S. (**1956**). ''Just noticeable differences in dichotic phase,'' J. Acoust. Soc. Am. **28**, 860–864.

Effects of stimulation mode on threshold and loudness growth in multielectrode cochlear implants

Monita Chatterjee[a)]
Department of Auditory Implants and Perception, House Ear Institute, 2100 West Third Street, Los Angeles, California 90057

(Received 29 June 1998; accepted for publication 21 October 1998)

The effect of increasing the separation between the two members of a stimulating electrode pair was studied in four users of the Nucleus-22 cochlear implant. Two experiments were performed. In experiment 1, detection threshold for a 200-ms, 500-pulses/s biphasic pulse train was measured as the spatial separation between the active and return electrodes was increased. In experiment 2, loudness-growth functions were measured as the electrode separation was increased. The results of experiment 1 indicate that (a) threshold decreases monotonically toward an asymptote (monopolar threshold) as the electrode separation is increased and (b) the threshold versus electrode separation function is similar across subjects and electrode location. The results of experiment 2 indicate that loudness L is related to the current amplitude I by a simple exponential function: $L = e^{\beta I}$, where β, the exponent of the loudness function, is, to a first approximation, linearly related to the separation between the electrodes of the stimulating pair. Thus, dynamic range and the shape of loudness growth can be directly linked to the spatial separation between active and return electrodes. [S0001-4966(99)00602-5]

PACS numbers: 43.66.Ts, 43.66.Cb, 43.66.Ba, 43.64.Me [DWG]

INTRODUCTION

Current cochlear-implant technology is sophisticated enough to allow the clinician freedom to select certain important parameters of stimulation. Depending upon the device, some of these parameters may be the frequency limits of the analysis filters (frequency allocation table), the dynamic range, the compression ratio, and the mode of stimulation (spatial distance separating the active and return electrodes along the cochlea). From an applied perspective, this last parameter is of considerable interest because of its impact on thresholds and, consequently, on battery life and the potential to miniaturize external hardware. From a theoretical point of view, the effect of changing the spatial extent of the stimulating field along the cochlea has implications for signal processing in the electrically stimulated auditory system. In this paper, we describe a detailed study of the quantitative relation between stimulation mode, threshold, and loudness growth in four users of the Nucleus-22 device.

For pulsatile electrical stimuli, the spread of excitation with increasing electrode separation depends upon many factors, including the geometry and impedance of the structures within the electric field, the distance of the neurons from the electrodes, as well as the degree of myelination and other structural features of the neurons (for a review, see Rattay, 1990). Generally speaking, it seems reasonable to assume that the number of neurons responding to the stimulus increases with increasing separation between the two electrodes of a stimulating pair. If threshold is determined by some form of integration of neural activity in the cochlea, increasing the electrode separation should result in a reduction in threshold. Indeed, it is a common observation that broad excitation across the tonotopic axis of the cochlea (as in monopolar stimulation, where the return electrode is a distant electrode placed elsewhere in the body) results in lower thresholds than focused excitation (as in bipolar stimulation, where the active and return electrodes are adjacent to each other), in addition to narrower dynamic ranges (Shannon, 1983; Abbas and Brown, 1991; Shephard *et al.*, 1993; Pfingst *et al.*, 1995).

One source of the large variability in cochlear implant patients' performance is often thought to lie in the variability of nerve-survival patterns across patients. Although there does appear to be a relationship between the total spiral ganglion-cell *count* and etiology of deafness (Nadol, 1997), the relationship between patterns of neural degeneration and factors such as etiology, duration of deafness, age, etc, are not well understood. Anatomical studies of spiral ganglion-cell counts in different regions of the human cochlea (Zimmerman *et al.*, 1995) show considerable variation along the length of the cochlea both within and across patients. Overall, survival appears to be better in the apical half than in the basal half of the cochlea.

We speculate that the rate at which threshold declines with increasing electrode separation should be determined at least partially by the pattern of surviving neurons. Thus, in a patient with a uniform pattern of surviving neurons from base to apex, thresholds should decline continuously with increasing electrode separation, whereas in a patient with large irregularities in nerve-survival patterns, the function may have plateaus or discontinuities. In addition, in patients with irregular nerve-survival patterns, the shape of the threshold vs electrode-separation function should depend strongly upon electrode location in the cochlea. In experiment 1 of the present study, we address these questions by directly measuring threshold as a function of stimulation

a)Electronic mail: monita@hei.org

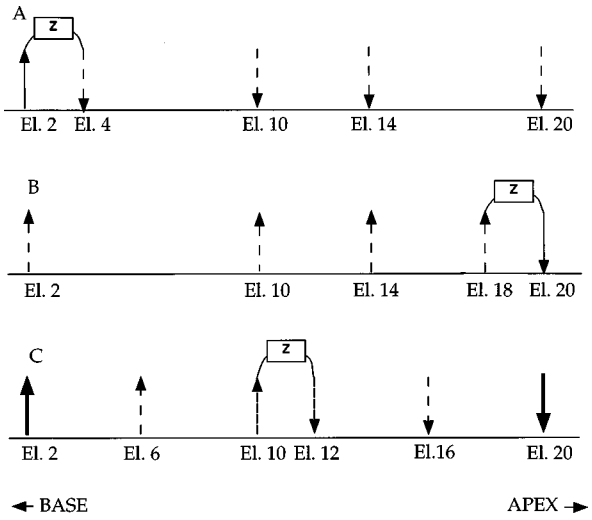

FIG. 1. Schematic illustrations of the different kinds of electrode pair configurations used in the experiments. (A) The active electrode of the pair is fixed at Electrode 2, and electrode separation is changed by changing the return electrode. (B) The return electrode is fixed at Electrode 20, and the electrode separation is changed by changing the active electrode. (C) The electrode separation is changed by changing both active and return electrodes, but their respective distances from Electrode 11 are equal. In (A) and (B), the solid and dashed lines indicate the fixed and variable electrodes, respectively. In (C), the different lines indicate different electrode pairs and current paths. Thus, Electrode 10 is the active electrode, and Electrode 12 is the return electrode in the pair forming the narrowest stimulation mode. The arrows indicate the direction of current flow (upward arrow indicates the active electrode, downward arrow indicates the return electrode). The box labeled ''*Z*'' represents the impedance in the current path.

mode while parametrically varying electrode location.

If the system is nonlinear, the relationship between electrode separation and the resulting neural excitation may be quite different for stimuli presented at threshold compared with stimuli presented above threshold. Such a difference would be reflected in loudness-growth functions obtained at various electrode separations. While it has been observed that dynamic range (in microamperes) is narrower for wider electrode separations, the exact quantitative relationship between the growth of loudness within the dynamic range and electrode separation has not been systematically explored. The aim of experiment 2 of this study was to discover the shape of the function relating the slope of loudness growth to electrode separation, and to relate the findings to the results of experiment 1.

A. Terminology

Figure 1 shows different arrangements of electrode pairs for the same stimulation mode (or electrode separation). In the Nucleus-22 system, electrodes are numbered 1–22 from the base to the apex. Note that in the experiments described here, the apical member of the electrode pair is always the return electrode. In Fig. 1(A), the basal member of the pair is fixed, and the electrode separation is changed by changing the apical member. In Fig. 1(B), the apical member of the pair is fixed, and the separation is changed by changing the basal member of the pair. In Fig. 1(C), the apical and basal members of the pair both change, keeping their respective distances from El. 11 equal. We will refer to these different ways of changing the electrode separation as ''electrode configuration.'' The absolute location of the fixed electrode of the pair will be referred to as ''electrode location.'' The number of electrodes separating the active and return electrodes is referred to as ''stimulation mode'' by some manufacturers. In this paper, we refer to it interchangeably as ''electrode separation'' or ''stimulation mode,'' represented by the variable M, where $M=1$ for the bipolar stimulation mode (active and return electrodes adjacent to each other), and $M=21$ for the widest possible separation, where the active and return electrodes are El. 1 and El. 22, or vice versa. For instance, in one configuration, the basal electrode was fixed, and the apical electrode was varied. Thus, electrode pairs were (2,4), (2,6), (2,8), etc., or (10,12), (10,14), (10,16), etc. We refer to these series as $(2,2+M)$ or $(10,10+M)$. In a second type of configuration, the apical electrode was fixed, while the basal electrode was changed to change the electrode separation [e.g., electrode pairs were (18,20), (16,20), (14,20), etc., referred to as (20-M,20)]. In a third type of manipulation, electrode pairs were chosen to be symmetrically spaced around electrode 11 (for example, electrode pairs were (10,12), (9,13), (8,14), etc., referred to as $(11-M+1,11+M-1)$. Note that the spatial distance separating adjacent electrodes along the array is 0.75 mm. Thus, for the broadest possible separation in the Nucleus-22 system ($M=21$), the spatial distance between electrodes is 15.75 mm.

It is important to recognize that the stimulating pulse is biphasic—thus, the ''active'' electrode receives the positive phase first, while the ''return'' electrode receives the negative phase first. The phases are reversed in the second half-cycle. Depending upon the stimulus configuration, the distance from the electrode, etc., neurons may respond to both phases of the pulse (see Rattay, 1990).

I. METHODS

Subjects were four postlingually deafened adult male users of the Nucleus-22 cochlear-implant system with varying levels of speech recognition in quiet. Table I lists scores they

TABLE I. Subjects, etiology of deafness, and scores obtained on two sound-only tests. The two right-most columns show values of ''*c*'' and ''*k*'' obtained from Fig. 8 for each subject.

Subject	Etiology of deafness	NU6 word list	CUNY sentences, sound only	Value of ''*c*'' from Fig. 8	Value of ''*k*'' from Fig. 8
N3	Unknown	24%	79.4%	0.0038	0.0009
N4	Trauma	70%	99.02%	0.0047	0.0012
N7	Unknown	48%	99.02%	0.0035	0.0010
N14	Unknown	18%	47%	0.0066	0.0014

recently obtained on one run each of the NU6 word list test (percent of words correctly identified out of a recorded list of 50 words uttered by a male speaker presented at 70 dB SPL; Tillman and Carhart, 1966) and on the CUNY sentence test (Boothroyd *et al.*, 1985; percent of words correct out of a recorded list of 12 sentences, female speaker, 70 dB SPL) without the aid of lipreading. Apart from routinely scoring higher on all speech tests administered in the laboratory, subjects N4 and N7 are able to use their implant to communicate over the telephone with little difficulty, while subjects N3 and N14 are unable to do so. All the subjects have acquired considerable experience in psychophysical tasks as a result of having participated in many experiments in our laboratory.

Stimuli were delivered through a custom research interface (Shannon *et al.*, 1990). All stimuli were 200-ms-long trains of 200-μs/phase, biphasic pulses, presented at 500 pulses/s. Accurate estimates of current delivered were obtained from the manufacturer's amplitude-calibration tables for each subject's device.

Thresholds were measured using a 3-down, 1-up, two-interval, forced-choice paradigm, converging at the 79.4%-correct point (Levitt, 1971). The amplitude of the pulse train was adaptively adjusted until a minimum of eight reversals or a maximum of 12 reversals were completed in 60 trials or less. The initial (first three reversals) and final step sizes were 2 and 0.5 dB, respectively. The mean of the last eight reversal points was calculated for each threshold measure, and the mean and standard deviation of at least two measures were calculated for each threshold estimate.

Loudness-growth functions were measured according to the following procedures:

The subject was presented with a soft stimulus (one presentation of the 200-ms, 500-pulses/s pulse train) close to threshold. By pressing the left- and right mouse buttons, the subject could increase or decrease the level of the stimulus in small incremental steps. The subject was asked to increase the level until the loudness reached a maximum acceptable level. Along the way, the subject indicated to the experimenter the relative loudness at each stage. This gave us an idea of the approximate dynamic range for each mode of stimulation. For this procedure, the subject received a single presentation of the stimulus each time he pressed a mouse button.

Subjects tended to be conservative in estimating the maximum acceptable level during the first session. In pilot runs, a subject would sometimes estimate a stimulus to be only moderately loud, even though its amplitude had been set to the maximum level previously obtained. We would then increase the amplitude in very small steps, until the subject estimated it to be at the maximum acceptable loudness. Based upon pilot runs, a minimum of eight amplitude levels was selected to cover the dynamic range. At each amplitude selected, the subject was presented with a sequence of six presentations of the same stimulus (stimulus set). The first presentation was intended as a cue to alert the subject. Next, the remaining five repetitions were presented to the subject (interstimulus interval was 300 ms). An LED flashing in synchrony with each presentation served as a visual cue. The subject was asked to select a number from a scale of 0 (don't hear it) to 100 (too loud) to match the subjective magnitude of the perceived overall loudness of the stimulus set. This procedure was used because during pilot runs, some subjects occasionally reported changes in the loudness of the stimulus between the first and third presentations of the stimulus.

Before beginning the data collection procedure, the subject was presented with an ascending sequence (0.2-dB steps) of the 200-ms pulse train from threshold to the maximum acceptable level, in order to give them some orientation as to the range of stimuli that might be used as well as to ensure that the loudest stimuli were not too loud. A minimum of three to a maximum of eight repetitions were performed for each loudness function. Thus, each loudness function corresponds to at least 24 loudness estimates (a minimum of eight amplitude steps and three repetitions at each step). Whenever possible, the data were obtained on two separate days, three to four repetitions on each day. For a particular electrode pair, all the repetitions for a given day were performed in one session lasting approximately one half h. The mean and standard deviation of all loudness estimates made for a particular electrode pair were computed at each amplitude.

At current levels close to threshold, subjects did not always hear all six presentations, but were asked to judge the loudness of the ones that were audible. As the softest sound was always presented at a higher level than threshold, subjects never used ''0'' to judge the loudness, but fractions were allowed and often used.

The experimenter ensured a rough randomization of the presentation sequence of the stimuli. For each repetition, stimuli were presented in a different order (decided previously by the experimenter). The softest and loudest sounds were most easily recognized by subjects, while sounds in between the two ends of the range were more difficult to judge.

Loudness functions were obtained for the (20-M,20) configuration in all four subjects (results shown in Fig. 6). The remaining electrode locations and configurations were chosen arbitrarily for each subject.

II. RESULTS AND ANALYSIS

A. Amplitude units

It may be useful at this point to address the issue of amplitude units used in electrical vs acoustic stimulation. To accommodate the wide dynamic range of normal sensory systems, the stimulus is often described in logarithmic units. In electrical stimulation of the cochlear-deafened auditory system, the peripheral compressive nonlinearity is absent. As a result, the dynamic range of the system is limited, and the input to the auditory nerve can be directly expressed in microamperes of current or nanocoulombs of charge. In listeners with auditory brainstem implants as well as sizable residual hearing in one ear, Zeng and Shannon (1992) have shown that, in order to achieve loudness balance between the electrical and acoustic stimuli in the two sides, current amplitude (in microamperes) in the implanted side must be pro-

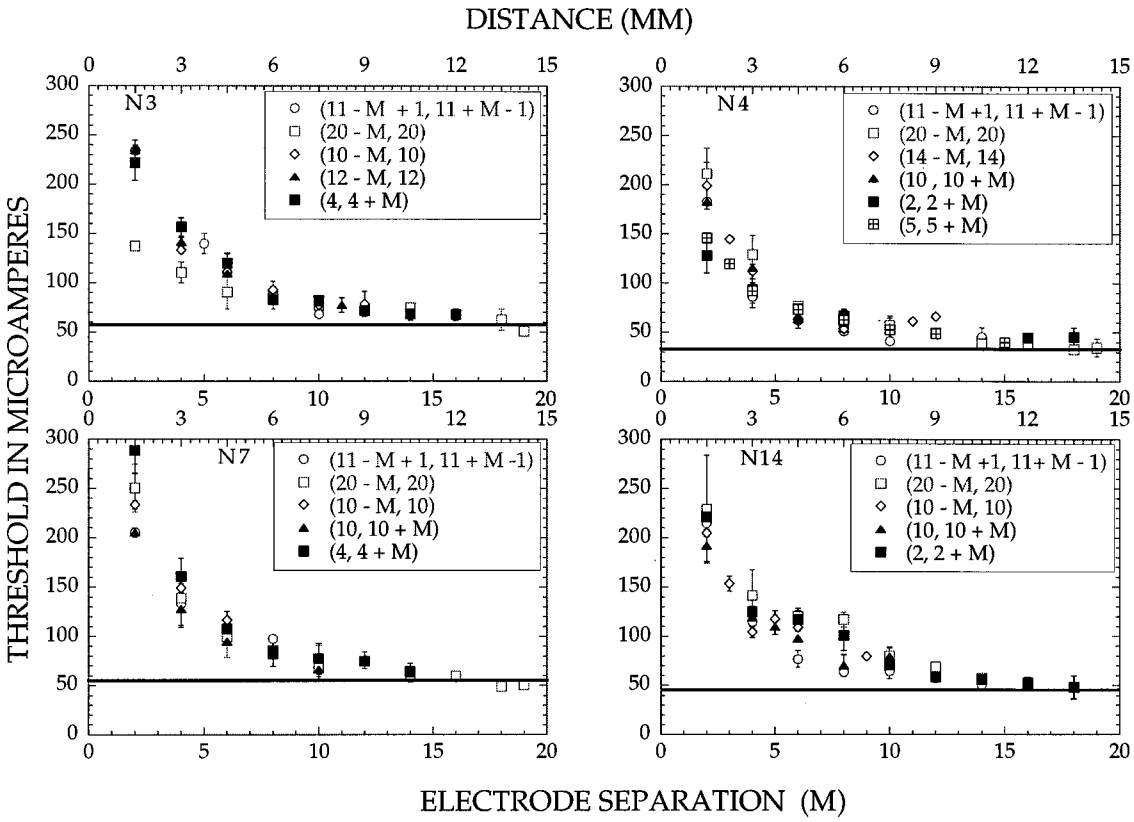

FIG. 2. Thresholds in microamperes as a function of electrode separation *M*, for the four subjects and different electrode configurations (shown in the insets). For each electrode separation *M*, the upper abcissa shows the distance separating the active and return electrodes of the pair in mm. Error bars represent ±1 standard deviation. The horizontal line across each plot represents the mean pseudomonopolar threshold [El. (1,22), $M=21$] for each subject.

portional to dB SPL in the other side. It appears, therefore, that linear units are appropriate in the context of electrical stimulation. The data presented here are plotted using linear microamperes.

B. Experiment 1: The shape of the threshold vs electrode-separation function

Figure 2 plots the threshold in microamperes as a function of electrode separation. Each panel corresponds to data obtained in one subject. Within each panel, each symbol represents data corresponding to a different electrode configuration and/or location. In general, and as expected, thresholds decrease with wider electrode separation. It is apparent that the functions are very similar across subjects, as well as within subjects, across the various configurations and locations. For each subject, for the most focused stimulation, thresholds are most diverse across electrode location (i.e., the data points show greatest scatter for $M=2$), presumably reflecting local variations along the cochlea. Beyond $M=6$ (a separation of 4.5 mm), the functions converge toward a minimum threshold. Presumably, this minimum threshold corresponds to that obtained with monopolar stimulation (Pfingst *et al.*, 1995).

We obtained the threshold for the widest electrode separation [i.e., electrode pair (1,22), corresponding to $M=21$] in each subject. We refer to this as a pseudomonopolar stimulation mode. For each subject, this threshold is shown by the horizontal line across each plot in Fig. 2. To facilitate comparison across subjects and conditions, we normalized the ordinate to the threshold difference between $M=2$ and $M=21$. The result is shown in Fig. 3 for each subject. Symbols show results from different electrode configurations. It is apparent from inspection of Figs. 2 and 3 that the normalized threshold vs electrode-separation function is relatively independent of subjects and electrode configurations. This suggests that the change of threshold with electrode separation can be adequately described by a single function.

If we assume that the threshold decays exponentially from the bipolar threshold T_{BP} (corresponding to $M=1$) until it asymptotes to the monopolar threshold T_{MP}, we can use the following equation to describe the decay:

$$T-T_{MP}=(T_{BP}-T_{MP})e^{-\alpha x}, \tag{1}$$

where T is the measured threshold in microamperes for a particular electrode configuration, x corresponds to the distance separating the electrodes in the array [$x=(M)*0.75$ mm], and α^{-1} represents the space constant. In all cases, T_{BP} can be measured. Although true monopolar stimulation is not possible in the Nucleus-22 system, an approximate value is obtained by measuring the threshold for the pseudomonopolar condition [threshold for electrode pair (1,22), shown by the horizontal lines in Fig. 2]. Thus, α is the only parameter to be adjusted to fit the data. Figure 4 shows examples of the equation applied to the data obtained in two subjects, for the electrode configuration (20-M,20). The values of α and the correlation coefficient R are indicated in the figure. The high values of R (>0.95) suggest that, based on only two measurements—the bipolar threshold

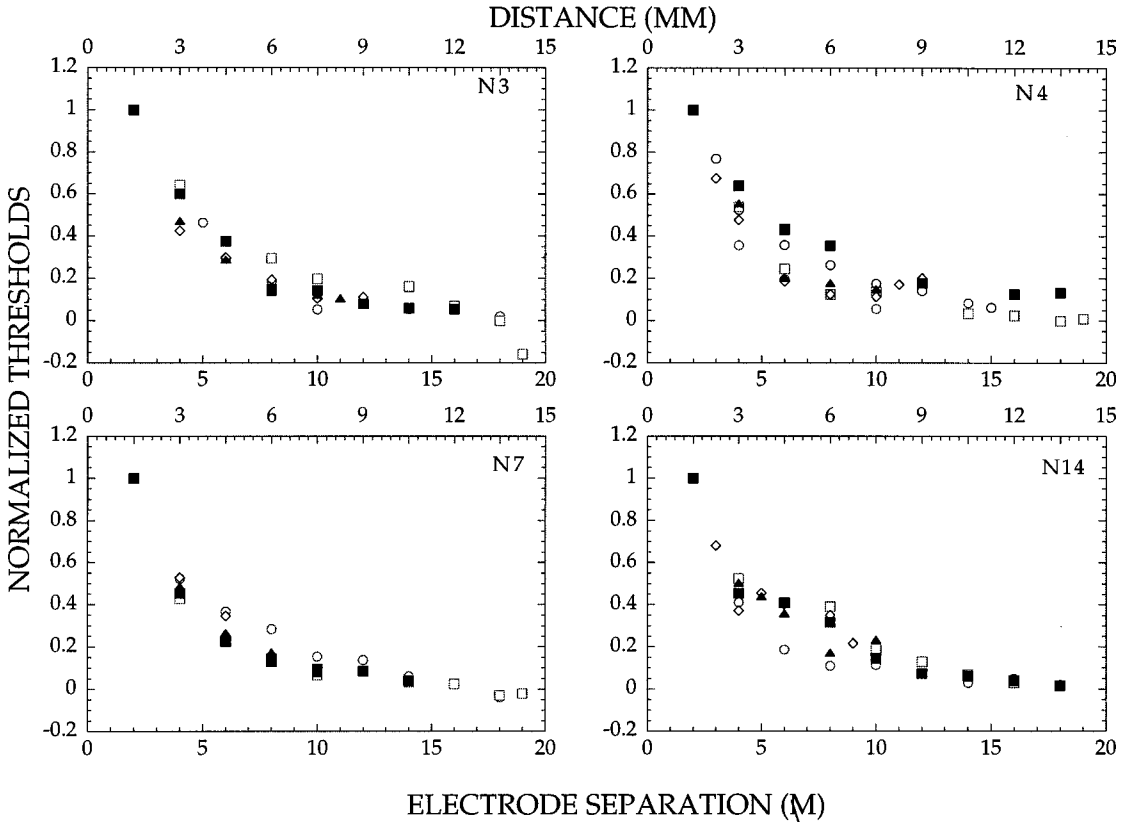

FIG. 3. The data from Fig. 2, normalized by subtracting the pseudomonopolar ($M=21$) threshold from each data point and then dividing by the threshold difference between $M=2$ and $M=21$. The symbols are the same as in Fig. 2.

and the monopolar or pseudomonopolar threshold—we can predict the threshold for all other electrode separations.

The present results are in qualitative agreement with similar data in cochlear-implant subjects reported by Pfingst *et al.* (1995) using a lower pulse rate of stimulation, and with electrically evoked auditory brainstem response (EABR) threshold vs electrode-separation functions measured by Abbas and Brown (1991). Overall, the threshold changes smoothly with electrode separation. The functions are independent of electrode configuration, electrode location, and subject, leading us to conclude that, at least in the present set of subjects, irregularities in nerve-survival patterns do not play a large role in determining the threshold function.

This experiment can also be considered an electrical analog of Fletcher's famous band-widening experiments which led to the concept of critical bandwidth (Fletcher, 1940). From this viewpoint, the threshold vs electrode-separation function is a measure of the spatial width of a channel. The data suggest that beyond a spatial separation of 3–4.5 mm (4–6 electrodes), recruitment of distant neurons does not contribute significantly to the threshold. This estimate is in agreement with many other measures of channel separability (e.g., Shannon, 1983; Tong and Clark, 1986; Lim *et al.*, 1989; McKay *et al.*, 1995; Chatterjee and Shannon, 1998) in multichannel electrical stimulation of the cochlea.

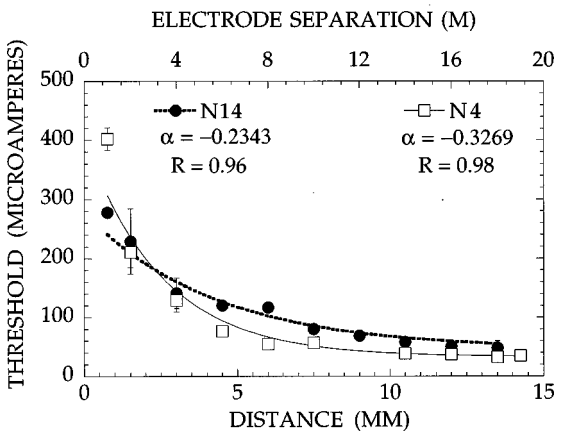

FIG. 4. Threshold versus electrode-separation data (filled circles and open squares) and curve fits (intermittent and solid lines) for two subjects using the electrode configuration (20-M,20). The inverse of the space constant, α, and the correlation coefficient R are indicated for each fit.

C. Experiment 2: Growth of loudness as a function of electrode separation

As loudness estimates made by subjects showed substantial variability, the observations for a particular function were made on two separate days whenever it was possible to do so. Figure 5 shows examples of loudness estimates made by subjects N3 and N7 on two different days. Although the standard deviations on each day were large, the mean functions did not differ greatly from day to day. For purposes of analysis, a grand mean and standard deviation was computed from all recorded estimates corresponding to each amplitude and electrode pair for each subject (across the different days).

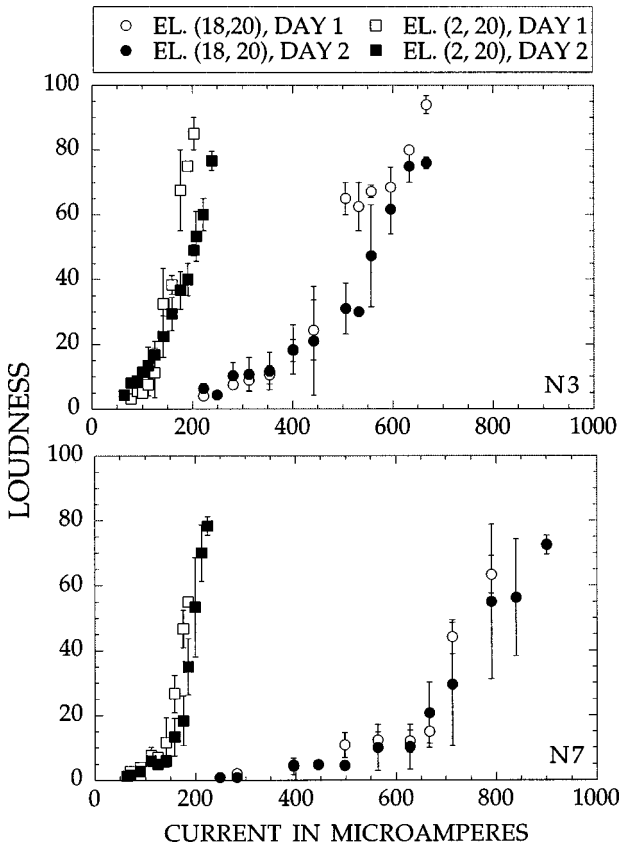

FIG. 5. Two sets of loudness estimates made by subjects N3 and N7 on two different days. The electrode pairs are indicated. Error bars represent ±1 standard deviation.

Figure 6 shows loudness-growth functions in all subjects measured using three different stimulation modes ($M=2$, $M=10$, and $M=18$), with the electrode configuration (20-M,20). In agreement with a large body of previous work (e.g., Shannon, 1981, 1985; Zeng and Shannon, 1992, 1994) the functions suggest that an expansive nonlinearity relates the amplitude of the current pulses to estimated loudness. The intermittent lines in Fig. 6 are curve fits with the equation

$$L = e^{\beta I}, \tag{2}$$

where β is a constant, and I represents the amplitude of the current pulses in microamperes. In all cases, the equation fit the data with a correlation coefficient greater than 0.9. (Power functions also fit the data well, but required an additional parameter.)

Inspection of the data reveals a consistent pattern. In agreement with observations of previous investigators, the dynamic range is widest for the narrowest electrode separation, and narrowest for the widest electrode separation. Consistent with this qualitative observation, the exponent β is smallest for the narrowest electrode separation and largest for the widest electrode separation.

Further examples of loudness estimates made by subjects using different sets of electrode pairs are shown in Fig. 7. Again, the intermittent lines show the curve fits obtained using Eq. (2).

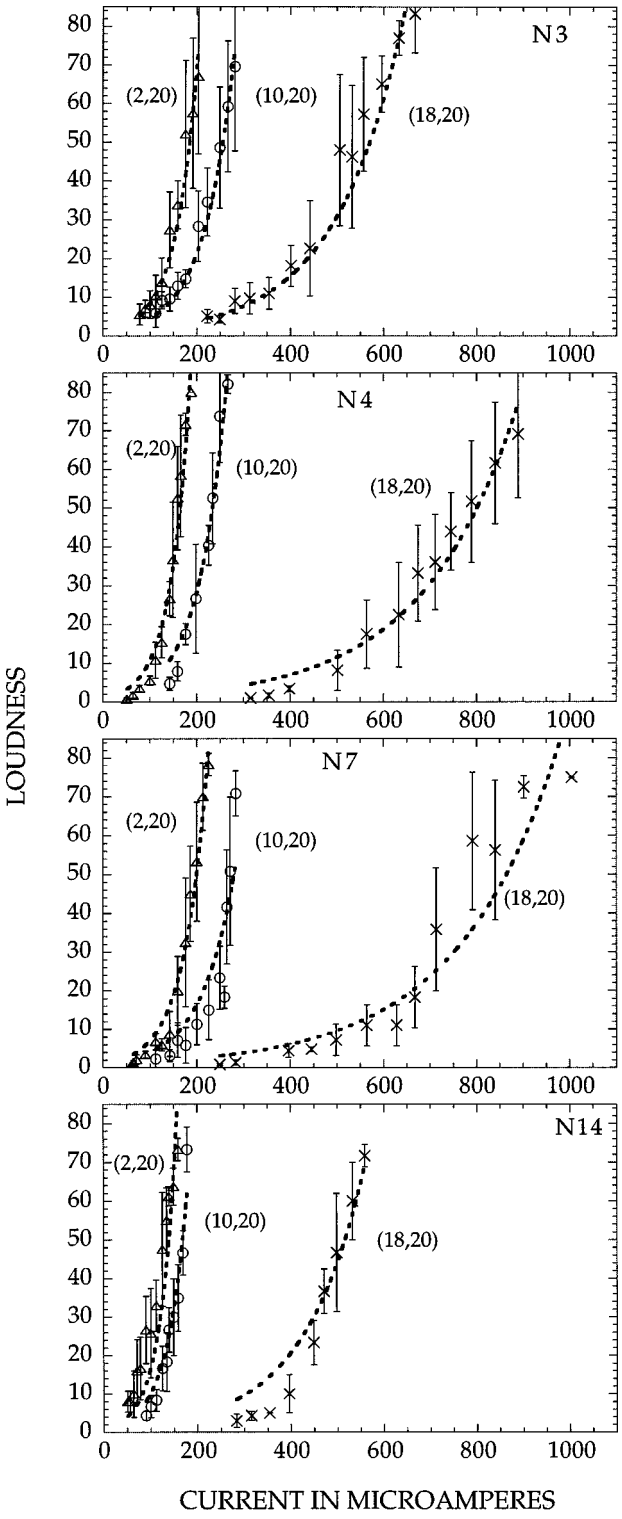

FIG. 6. Loudness functions obtained in four subjects using electrodes (18,20), (10,20), and (2,20). The intermittent lines represent curve fits using Eq. (2) (see the text). Error bars represent ±1 standard deviation.

We measured a number of loudness functions in each subject. Curve fits using Eq. (2) were used to obtain the exponent in each case. To quantify the relationship between the rate of growth of loudness and the spatial separation between electrodes, we plotted the values of β obtained from all the loudness functions obtained in each subject, against the electrode separation M (Fig. 8). Regardless of electrode

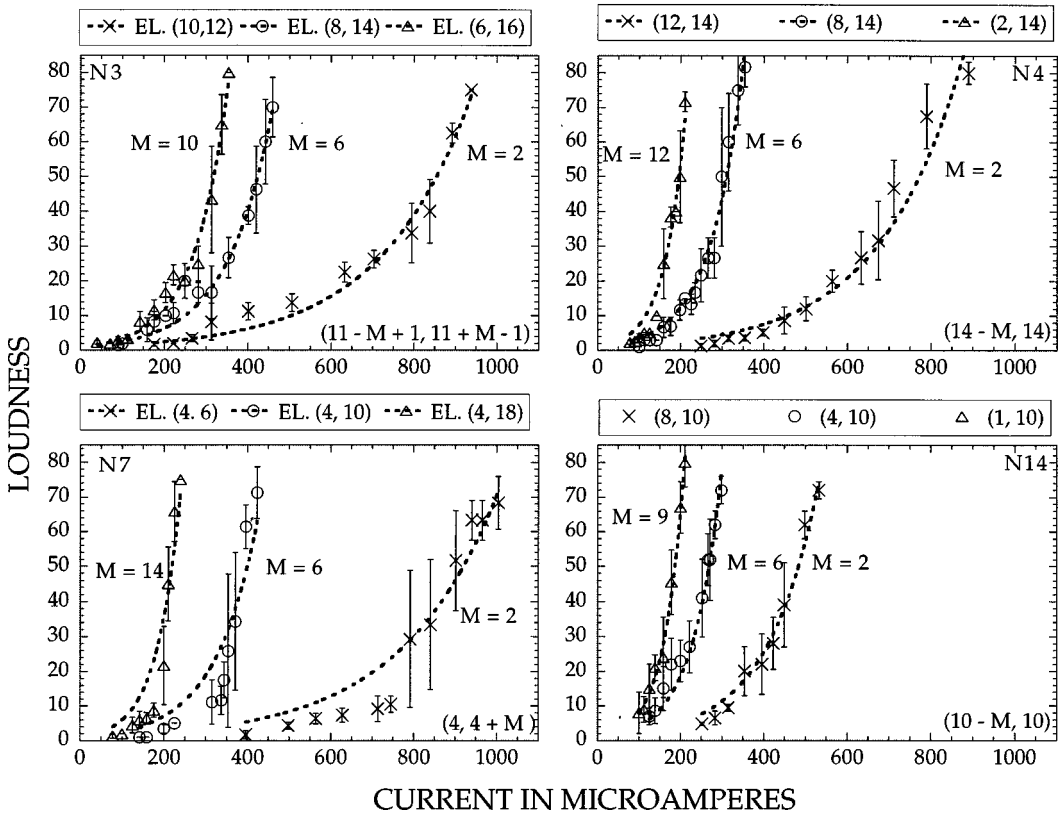

FIG. 7. Further examples of loudness estimates made by the four subjects. The electrode pairs stimulated are indicated above each plot. The intermittent lines represent curve fits using Eq. (2). Error bars represent ±1 standard deviation.

configuration, the derived exponents fall along a single, monotonically increasing function of electrode separation. By inspection, a linear relationship between β and M seems a reasonable first approximation.[1] The lower panel in Fig. 8 shows a scatter plot of the exponents derived from each subject's data, together with linear approximations (the equations are shown adjacent to the plot). We can therefore replace β in Eq. (2) with $(c+kM)$, where c and k are constants. We would thus have

$$L = e^{(c+kM)I}. \tag{3}$$

Or, if x represents the electrode separation in mm, $0.75^*(M) = x$, and

$$L = e^{[c+k(x/0.75)]I}. \tag{4}$$

From Fig. 8, c ranges from 0.0035 to 0.0066 and k ranges from 0.0009 to 0.0014.

We have thus obtained a simple and direct relationship between the spatial separation between electrode pairs in mm and loudness. At least for the stimuli used in this experiment, the exponent of the loudness function depends only on the electrode separation. The relationship between the distance x and the exponent β can be approximated by a simple linear function, the slope k and intercept c of which show some small subject dependence.

For a fixed current amplitude I and different electrode separations $M1$ and $M2$, the corresponding loudnesses $L1$ and $L2$ are related by

$$\frac{L1}{L2} = e^{k(M1-M2)I}, \tag{5}$$

or, in terms of x:

$$\frac{L1}{L2} = e^{k[(x1-x2)/0.75]I}. \tag{6}$$

Thus, for fixed I, increasing the electrode separation by m electrodes increases the loudness by a factor of e^{kmI}. At low-current levels, the change in loudness with m is small, but as I increases, the change is amplified by the expansive nature of the nonlinearity.

Conversely, for a fixed separation M and different levels of stimulation $I1$ and $I2$, the corresponding loudnesses $L1$ and $L2$ are related by

$$\frac{L1}{L2} = e^{(c+kM)(I1-I2)}. \tag{7}$$

Thus, for a particular electrode separation M, the change in loudness for a given change in current is controlled by the value of M. For small M, the change in loudness with I is small, but as M increases, the exponential function amplifies the change.

For a fixed loudness $L = e^n$, the current amplitude I and the separation M are related by $(c+kM)I = n$. Thus, electrode separation and current amplitude have a reciprocal relation at equal loudness.

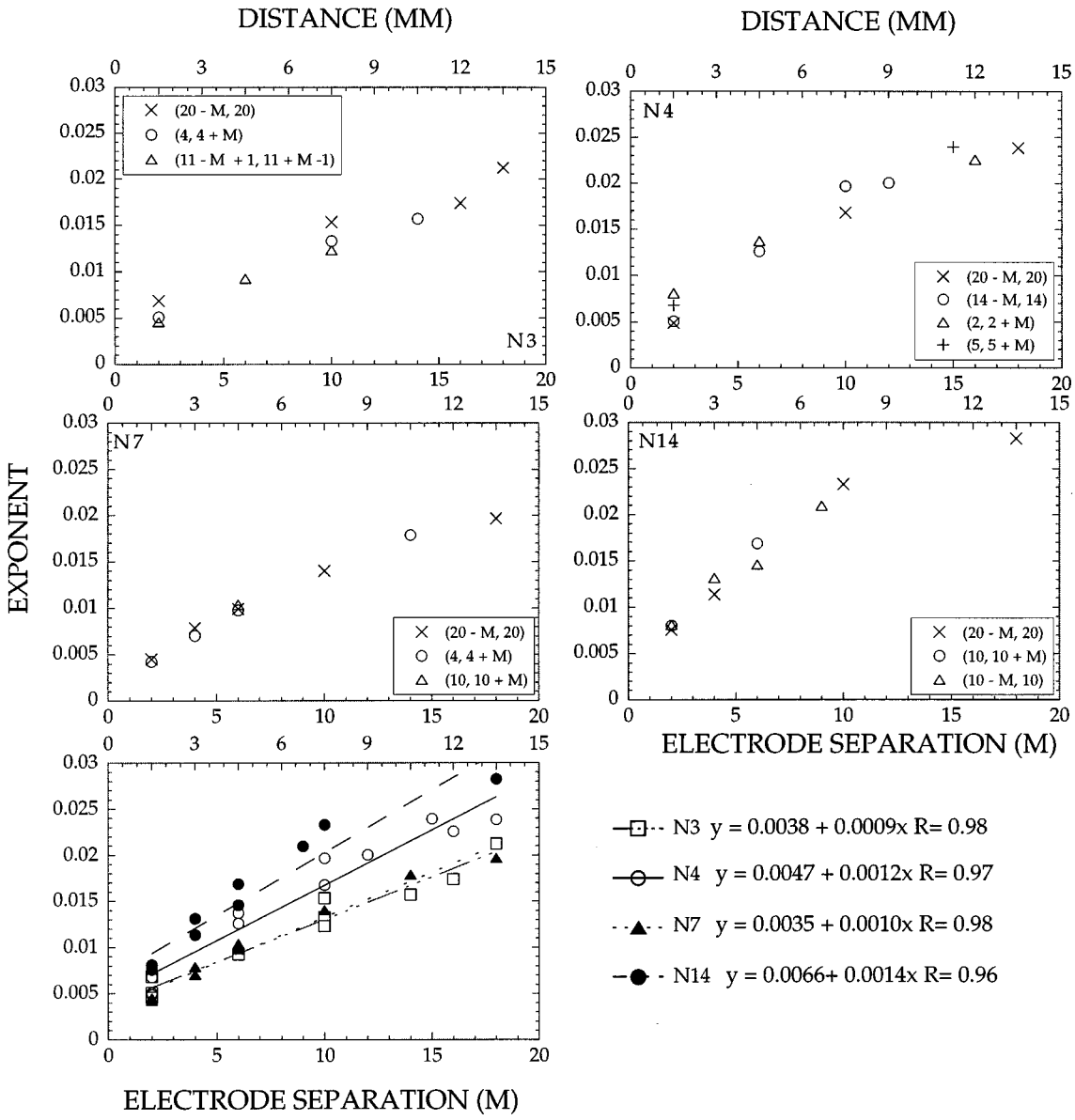

FIG. 8. Upper four panels: Exponents obtained by curve-fitting a large number of loudness functions such as those in Figs. 5 and 6, as a function of the electrode separation. Each symbol represents a different electrode configuration (indicated in the insets). Lower panel: Exponents for each subject pooled and plotted together as a function of electrode separation. Each symbol represents exponents from one subject. The lines represent the linear curve fits (equations shown adjacent to the plot).

It is evident from the above analysis that the two terms, current amplitude I and the electrode separation-related term $(c+kM)$, affect loudness in comparable ways. An increase in one variable changes the subject's sensitivity to the other. Table I shows the values of c and k obtained from Fig. 8, alongside the other potentially relevant information about each subject. Although the values of c and k are largest for subject N14, who is the poorest performer, inspection of the data revealed no orderly relationship between these values for the other subjects and their speech-recognition scores.

III. DISCUSSION

The results of the experiments described here show a clear and consistent dependence of both the exponent of the loudness function and threshold on the separation between active and return electrodes. These relationships hold regardless of the electrode configuration, electrode location, and the differences among subjects in the benefit gained from their implant. Notwithstanding the small number of subjects in this study, this consistency of the results, together with the qualitative agreement with other studies in this area, suggests that these findings may be a fundamental and potentially important aspect of loudness perception in electrical stimulation.

At different electrode locations, thresholds obtained using the more focused stimulation modes showed considerable scatter, suggesting that irregularities do exist in the nerve-survival pattern. However, such local irregularities in nerve survival do not result in large differences in the functions relating threshold and loudness growth to the electrode separation. This may possibly be due to the integration of activity across neurons, resulting in a spatial low-pass filter-

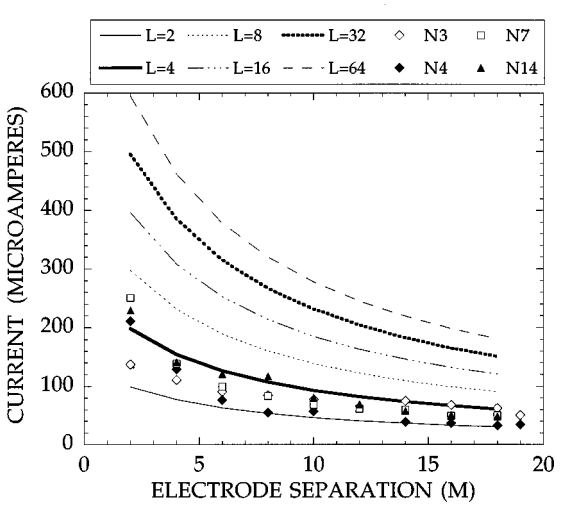

FIG. 9. Equal-loudness functions predicted from Eq. (8), assuming $c=0.0050$ and $k=0.0010$. Each line corresponds to a different fixed loudness ($L=2,4,...,64$). The data points, replotted from Fig. 2, represent the threshold versus electrode-separation data corresponding to the electrode configuration (20-M,20), for the four subjects indicated. Each symbol represents data from one subject.

ing, or smoothing effect, when the spatial extent of the stimulus is increased.

A. Relationship between threshold and suprathreshold measures

Because of the expansive nature of the nonlinearity relating loudness to electrode separation and current amplitude, the effect of the electrode separation on loudness is much larger at high-current levels than at threshold. By setting the loudness L in Eq. (3) to a fixed value $L0$, we can predict the current I required at a given electrode separation M, as follows:

$$I=\frac{\ln(L0)}{c+kM}. \tag{8}$$

From Fig. 8, for the subjects included in the present study, c ranges from 0.0035 to 0.0066, and k ranges from 0.0009 to 0.0014. For the purposes of this discussion, we choose $c=0.0050$ and $k=0.0010$, both intermediate values in their respective ranges. Given these values, we can describe I as a function of M for a particular loudness. Equal loudness plots were constructed from Eq. (8), for different values of L ranging from 2 to 64. Each line in Fig. 9 represents a doubling of loudness. It is evident from the figure that for small M, a large change in I is required to produce a doubling in perceived loudness, whereas for large M, a small change in I will produce a doubling in perceived loudness. The data points shown at the bottom of the figure correspond to the thresholds measured in the four subjects for the electrode configuration (20-M,20).

Most of the threshold data fall in between the lines corresponding to $L=2$ and $L=4$. While the methodological differences between experiments 1 and 2 do not allow for precise quantitative comparisons between the (presumably more objective) threshold data and the predicted equal-loudness functions, the fact that the form of the predicted equal-loudness function at low-current levels is a good approximation to the threshold vs electrode separation data suggests that similar mechanisms may be operating both at and above threshold.

B. Underlying mechanisms and implications for auditory models

The threshold data obtained in this study are in qualitative agreement with results from experiments using the (physiological)-evoked auditory brainstem response in subjects using the Nucleus-22 device (Abbas and Brown, 1991) and with psychophysical data obtained by Pfingst *et al.* (1995). In the Abbas and Brown (1991) study, correlations were also observed between the psychophysical threshold and the physiological EABR thresholds. The same study measured the growth of the EABR peak as a function of stimulus amplitude. Consistent with the results presented here, they found that the EABR exhibits the widest dynamic range for the most focused stimulation. Although they did not measure loudness functions, the authors found that the psychophysical dynamic range was correlated with the slope of the EABR growth function. Shephard *et al.* (1993) also found that the EABR growth function steepened with increasing electrode separation in the cat cochlea. These qualitative similarities are reassuring, and suggest that the psychophysical relationships described here have a basis in peripheral processing. The evoked EABR data are well approximated by the output of Frijns' detailed model of auditory-nerve responses to electrical stimulation (Frijns, 1995), which assumes that the EABR magnitude is determined by a simple sum of activity across the neural population without incorporating any nonlinearities in the input/output function of the auditory neurons.

The precise transformations leading to the psychophysical functions, of course, cannot be determined precisely at our current state of knowledge. For instance, the EABR grows linearly with current amplitude, but the loudness function grows exponentially with current amplitude. If we think of the EABR as broadly representative of the output of a peripheral processing stage, and the loudness function as broadly representative of a central processing stage, the difference between the growth functions may imply the presence of an expansive nonlinearity in between the two stages of processing. An exponential nonlinearity of this nature has been proposed by Zeng and Shannon (1992,1994). Their model of loudness assumes a compressive cochlear nonlinearity, followed by an expansive central nonlinearity. They suggest that for cochlear-implant patients, loudness grows as an exponential function of current amplitude because the cochlear nonlinearity is absent.

For such a model to work, information processing by auditory neurons would have to be similar in electric and acoustic stimulation. Although relatively little is known about the physiological responses of auditory centers to electrical stimuli, the known differences between auditory and electrical stimulation need to be considered before direct comparisons are performed. It is known that auditory neurons in deafened cochleae demonstrate little or no spontaneous firing, and respond with almost perfect synchronization

to electrical stimuli. In contrast, with a normal cochlea, auditory neurons are spontaneously noisy and show poorer synchronization to (acoustically presented) periodic stimuli (Hartmann and Klinke, 1990; Dynes and Delgutte, 1992). Because of their strong synchronization, the firing rates of electrically stimulated auditory neurons show saturation at the rate corresponding to the stimulus period. Thus, regardless of current amplitude, the same neuron will saturate at 200 spikes/s when stimulated at 200 pulses/s, and at 800 spikes/s when stimulated at 800 pulses/s (Javel, 1990). In normal acoustic hearing, the stochastic firing of the neurons results in a dynamic range that is relatively independent of the periodicity of the stimulus. In addition, their dynamic ranges are related to their thresholds and spontaneous activity, which appear to be controlled by the output of the inner hair cell–auditory-nerve synapse. These factors are presumably absent in electrical stimulation of neurons in deafened cochleae. It is apparent from this discussion that, however tempting, comparisons between electric and acoustic stimulation will only be relevant when all the known variables involved in the two modes of stimulation are taken into account.

The present results suggest that current amplitude and the electrode separation along the cochlea play comparable roles in the function determining loudness growth. This fundamental finding is difficult to explain in terms of current models of auditory processing of electric and acoustic stimuli. In normal hearing, it is known that the total loudness of a wideband signal is equal to the sum of the loudness it evokes within each auditory filter (Zwicker *et al.*, 1957; Zwicker and Scharf, 1965). Thus, a wideband signal sounds louder than a narrow-band signal of the same total energy. In electrical stimulation, one may speculate that as the separation between the two electrodes of a stimulating pair is increased, their respective fields interact less and less, and they may function more and more like a pair of true monopoles. If so, the neural populations responding to a widely separated electrode pair may be more independent than neural populations responding to a narrowly separated electrode pair. If similar mechanisms are at play in both acoustic and electric stimulation, the summation of loudness across independent channels may indeed result in lower thresholds and steeper loudness functions for the more widely separated electrode pair.

IV. CONCLUDING REMARKS

The decay of threshold with electrode separation can be quantified using an exponential function, with an asymptote at monopolar threshold. The present work also suggests a simple, robust relation between the stimulation mode and the rate of loudness growth. Although the small size of the subject pool is a disadvantage of this study, the findings are strengthened by the fact that the relationships show consistency regardless of the large intersubject variability in speech recognition with the implant.

The present experiments have been restricted to stimulation with a single electrode pair. The growth of loudness may be quite different when stimulation with multiple pairs of electrodes is considered. Further experimentation is clearly necessary in order to define the parameter space of loudness perception in electrical stimulation.

ACKNOWLEDGMENTS

The author thanks Qian-Jie Fu for the software used to run the experiments. Fan-Gang Zeng, Robert Shannon, Steven Otto, Mark Robert, and the reviewers of the Journal are thanked for helpful comments. Lendra Friesen is thanked for the subjects' scores listed in Table I. We are grateful to our subjects for their enthusiastic participation in the experiments. We thank Dawna Mills and Darlene Fragale of the House Ear Clinic for their help in identifying subjects. Jim Heller, Vena Margo, and Cochlear Corporation are thanked for providing us with the calibration tables for each subject. Work supported by NIDCD RO1 DC01526-05.

[1]Similar relationships were observed when the loudness estimates were plotted against dB microamperes (*re*: 1 microampere), and exponential functions were fit to the data. While the resulting exponents varied linearly with the electrode separation *M*, the slopes and the intercepts were different. These relationships can be derived algebraically.

Abbas, P. J., and Brown, C. J. (**1991**). ''Electrically evoked auditory brainstem response: growth of response with current level,'' Hearing Res. **51**(1), 123–137.

Boothroyd, A., Hanin, L., and Hnath, T. (**1985**). *CUNY Laser Videodisk of Everyday Sentences* (Speech and Hearing Sciences Research Center, City University of New York).

Chatterjee, M., and Shannon, R. V. (**1998**). ''Forward masked excitation patterns in multielectrode electrical stimulation,'' J. Acoust. Soc. Am. **103**, 2565–2572.

Dynes, S. B. C., and Delgutte, B. (**1992**). ''Phase-locking of auditory-nerve discharges to sinusoidal electric stimulation of the cochlea,'' Hearing Res. **58**, 79–90.

Fletcher, H. (**1940**). ''Auditory patterns,'' Rev. Mod. Phys. **12**, 47–65.

Frijns, J. H. M. (**1995**). ''Cochlear Implants. A Modelling Approach,'' Ph.D. dissertation, Leiden University.

Hartmann, R., and Klinke, R. (**1990**). ''Response characteristics of nerve fibers to patterned electrical stimulation,'' in *Models of the Electrically Stimulated Cochlea*, edited by J. M. Miller and F. A. Spelman (Springer-Verlag, New York).

Javel, E. (**1990**). ''Acoustic and electrical encoding of temporal information,'' in *Models of the Electrically Stimulated Cochlea*, edited by J. M. Miller and F. A. Spelman (Springer-Verlag, New York).

Levitt, H. (**1971**). ''Transformed up–down methods in psychoacoustics,'' J. Acoust. Soc. Am. **49**(2, Pt. 2), 467–477.

Lim, H. H., Tong, Y. C., and Clark, G. M. (**1989**). ''Forward masking patterns produced by intracochlear electrical stimulation of one and two electrode pairs in the human cochlea,'' J. Acoust. Soc. Am. **86**, 971–980.

McKay, C. M., McDermott, H. J., and Clark, G. M. (**1995**). ''Loudness summation for two channels of stimulation in cochlear implants: effects of spatial and temporal separation,'' Ann. Otol. Rhinol. Laryngol. **166**, 230–233.

Nadol, Jr., J. B. (**1997**). ''Patterns of neural degeneration in the human cochlea and auditory nerve: Implications for cochlear implantation,'' Otolaryngol.-Head Neck Surg. **117**, 220–228.

Pfingst, B. E., Miller, A. L., Morris, D. J., Zwolan, T. A., Spelman, F. A., and Clopton, B. M. (**1995**). ''Effects of electrical current configuration on stimulus detection,'' Ann. Otol. Rhinol. Laryngol. **104**(9, Pt. 2), Suppl. 166, 127–131.

Rattay, F. (**1990**). *Electrical Nerve Stimulation. Theory, Experiments and Applications* (Springer-Verlag, New York).

Shannon, R. V. (**1981**). ''Growth of loudness for sinusoidal and pulsatile electrical stimulation,'' Ann. Otol. Rhinol. Laryngol. **90** Suppl. 82, 13–14.

Shannon, R. V. (**1983**). ''Multichannel electrical stimulation of the auditory nerve in man. II. Channel interaction,'' Hearing Res. **12**, 1–6.

Shannon, R. V. (**1985**). ''Threshold and loudness functions for pulsatile stimulation of cochlear implants,'' Hearing Res. **18**, 135–143.

Shannon, R. V., Adams, D. D., Ferrel, R. L., Palumbo, R. L., and Grandgenett, M. (**1990**). ''A computer interface for psychophysical and speech research with the Nucleus cochlear implant,'' J. Acoust. Soc. Am. **87**, 905–907.

Shephard, R. K., Hatsushika, S., and Clark, G. M. (**1993**). ''Electrical stimulation of the auditory nerve: The effect of electrode position on neural excitation,'' Hearing Res. **66**, 108–120.

Tillman, T. W., and Carhart, R. (**1966**). ''An expanded test for speech discrimination utilizing CNC monosyllabic words,'' Northwestern University Auditory Test No. 6, *Technical Report No. SAM-TR-66-55* (USAF School of Aerospace Medicine, Brooks Air Force Base, Texas).

Tong, Y. C., and Clark, G. M. (**1986**). ''Loudness summation, masking, and temporal interaction for sensations produced by electric stimulation of two sites in the human cochlea,'' J. Acoust. Soc. Am. **79**, 1958–1966.

Zeng, F.-G., and Shannon, R. V. (**1992**). ''Loudness balance between electric and acoustic stimulation,'' Hearing Res. **60**, 231–235.

Zeng, F.-G., and Shannon, R. V. (**1994**). ''Loudness-coding mechanisms inferred from electric stimulation of the human auditory system,'' Science **264**, 564–566.

Zimmermann, C. E., Burgess, B. J., and Nadol, Jr., J. B. (**1995**). ''Patterns of degeneration in the human cochlear nerve,'' Hearing Res. **90**, 192–201.

Zwicker, E., and Scharf, B. (**1965**). ''A model of loudness summation,'' Psychol. Rev. **72**, 3–26.

Zwicker, E., Flottorp, G., and Stevens, S. S. (**1957**). ''Critical bandwidth in loudness summation,'' J. Acoust. Soc. Am. **29**, 548–557.

Investigation of the effects of temporal and spatial interactions on speech-recognition skills in cochlear-implant subjects

Chandra S. Throckmorton[a] and Leslie M. Collins[b]
Department of Electrical Engineering, Duke University, Durham, North Carolina 27708-0291

(Received 30 March 1998; accepted for publication 5 November 1998)

Forward masking was investigated as a measure of spectral and temporal interactions. Such interactions may adversely affect speech recognition in cochlear-implant subjects. Seven subjects, implanted with the Nucleus 22 device, performed a forward-masking task. They also performed an electrode-discrimination task in order to measure spectral interactions without temporal interactions. Correlation analysis indicated a significant relationship between data obtained in the two tasks ($p<0.1$). The two tasks were also correlated with the subjects' scores from five measures of speech recognition. Forward masking and electrode discrimination were strongly correlated with measures requiring consonant and phoneme recognition, respectively. These results indicate that the relationship between forward masking and speech recognition may be due, in part, to a lack of spectral resolution. The data also indicate that consonants may be more readily masked than vowels. Forward-masking data measured for all clinically programmed electrodes in three of the seven subjects were used with a model of the spectral maxima sound processor (SMSP) to estimate the number of electrodes stimulated during a consonant that might be masked by prior presentation of a vowel. These results suggest that temporal interactions across electrodes may be a factor in speech-recognition abilities of some cochlear-implant subjects. [S0001-4966(99)03902-8]

PACS numbers: 43.66.Ts, 43.66.Dc, 43.71.Ky, 43.64.Me [JWH]

INTRODUCTION

The design of speech processors for cochlear implants relies on several assumptions regarding subjects' perceptual response to electrical stimulation. These assumptions are that each electrode is distinct both spatially and temporally, or equivalently that electrode interactions do not occur. More fundamentally, it is often assumed that each electrode stimulates a unique population of neurons, and that stimulation of one electrode does not affect the perceptual response to stimulation that is applied to other electrodes. When these assumptions are invalid, the information to be transmitted through the electrode array may be distorted, or in the most extreme case, imperceptible. Thus, the evaluation of such assumptions, as well as evaluation of potential remediation strategies that could be implemented when the assumptions are not met, is of significant interest to researchers in implant psychophysics.

Several methods for evaluating such interactions and their effects on speech-processing algorithms have been proposed and evaluated in the literature. These methods can be broadly categorized as methods that are used to evaluate spectral or spatial interactions, and methods that are used to evaluate temporal interactions. In practice, some methods overlap these two categories. Techniques used to evaluate abnormalities in the spectral structure elicited by electrical stimulation include pitch ranking and pitch scaling (Shannon, 1983; Townshend *et al.*, 1987; Busby *et al.*, 1994; Busby and Clark, 1997; Collins *et al.*, 1997), multidimensional scaling (McKay *et al.*, 1996), and electrode discrimination (Busby *et al.*, 1993; Busby and Clark, 1996; Zwolan *et al.*, 1997). Techniques that have been used to investigate temporal interactions include gap detection (Shannon, 1983), as well as forward masking (Shannon, 1983; Tong and Clark, 1986; Lim *et al.*, 1989; Shannon, 1990; Blamey *et al.*, 1993; Chatterjee and Shannon, 1998). However, gap detection and forward masking may also be used to assess spatial interactions since each measure is affected by neural population overlap (Shannon, 1983, 1990; Chatterjee and Shannon, 1998).

The study of electrode interactions allows researchers and clinicians to both quantify the amount of interaction and assess the effectiveness of current methods of speech processing. Factors that can be evaluated regarding the speech-processing algorithms include the set of electrodes that are stimulated, the order in which electrodes are stimulated, and the rate at which they are stimulated. Most of the studies listed above have indicated that electrode interactions do in fact occur, sometimes with deleterious effects. Townshend *et al.* (1987), Zwolan *et al.* (1997), Busby *et al.* (1997), and Collins *et al.* (1997) have discussed possible methods for reducing information distortion and/or loss due to indiscriminable electrodes and unusual ordering of the pitch percept. These methods include removing indiscriminable electrodes from those available for stimulation and reordering the electrodes into tonotopic order. In addition, Merzenich and White (1977), among others, have recommended sequential stimulation rather than simultaneous stimulation of electrodes in order to reduce the summation of electrical fields. This approach also reduces masking effects; however, as Shannon (1983, 1990), Tong and Clark (1986), Lim *et al.*

[a]Electronic mail: cst@ee.duke.edu
[b]Electronic mail: lcollins@ee.duke.edu

(1989), and Chatterjee and Shannon (1998) have shown, forward-masking effects have not been eradicated by sequential stimulation.

Forward-masking studies in both normal-hearing and implanted individuals have suggested that the elevated thresholds observed in forward-masking tasks in which the masker and probe are in close proximity are a result of the refractoriness of the underlying neural population. The amount of the threshold shift observed in masking tasks can thereby be assumed to be proportional to the amount of neural population overlap. Under these assumptions, forward-masking data can potentially be used to estimate the excitation patterns that occur in the cochlea. As such, in a ''textbook'' case, the amount of masking measured for a probe stimulus should decrease monotonically as distance between the probe and masker excitation increases. Deviations from this expected pattern may, in some cases, be indicative of a ''nonideal'' cochlea, and may suggest variability in current paths or nerve survival in implanted subjects.

Since forward masking also occurs in normal-hearing subjects (Jesteadt *et al.*, 1982 and others), the issue becomes not whether forward masking occurs, but whether it negatively affects the implanted individual's speech-recognition skills. One hypothesis is that forward-masking effects correspond to reduced spectral resolution, which can negatively affect speech recognition. This reduced spectral resolution can also be quantified through electrode-discrimination paradigms. A second hypothesis is that forward masking may be considered a measure of temporal interactions, which in turn may adversely affect speech recognition. It is well known that consonant recognition is consistently poorer in cochlear-implant subjects than vowel recognition (Dowell *et al.*, 1982; Blamey *et al.*, 1987; Tye-Murray and Tyler, 1989; Dorman *et al.*, 1991; Tyler and Moore, 1992; Pelizzone *et al.*, 1993; Doyle *et al.*, 1995). One possible explanation for this difference is that, through the phenomenon of forward masking, the energy in a vowel renders the information in a following consonant imperceptible. Both of these hypotheses are explored in this paper.

Because of the large number of masker/probe pairs, data collected in previous forward-masking studies have been limited to a few of the available combinations. Thus, the effects of the delay time between masker and probe, masker level (Chatterjee and Shannon, 1998; Shannon, 1990), masker position (Shannon, 1983), and distance between masker and probe (Lim *et al.*, 1989; Chatterjee and Shannon, 1998) have been studied for only a few combinations of masker and probe electrodes. By varying masker level, masker–probe delay, and probe location for a basal-, apical-, and centrally located masker, Chatterjee and Shannon (1998) noted a possible connection between poorer speech recognition and greater susceptibility to changes in forward-masking parameters. In the present study, data on seven subjects representing a wide range of speech-recognition skills were gathered; thus, it was possible to examine the correlation between speech recognition and forward masking, a topic which has not previously been explored in a rigorous fashion.

In this study, forward-masking patterns were measured for all active electrodes in three subjects implanted with the Nucleus 22 device. In addition, forward-masking patterns were measured for a masker located near the center of the array in four subjects, also implanted with the Nucleus 22 device. Electrode discrimination was measured for all seven subjects. With this data, the relationship between forward-masking effects, electrode discrimination, and speech-recognition ability was investigated. Correlation coefficients between average-masking levels and speech-recognition scores were calculated, and two hypotheses based on these results were investigated. Based on the potential temporal effects of forward masking on speech recognition, the first hypothesis that was investigated was that forward masking causes consonant information to be lost as a result of a previous stimulation occurring in response to a vowel. The possible ramifications of the first hypothesis were estimated through a model of the SMSP speech-processing algorithm (McDermott *et al.*, 1992). The second hypothesis considered forward masking to be a measure of spectral resolution, and its relationship with electrode discrimination, another measure of spectral resolution, was investigated.

I. METHODS

A. Subjects and equipment

One male and two female subjects implanted with the Nucleus 22 device completed the forward-masking task for all of their functioning electrodes, producing masking patterns for each electrode in the form suggested by Lim *et al.* (1989). Additional subjects, one female and three male, completed the forward-masking task for one centrally located electrode. These seven subjects also completed an electrode-discrimination task to determine which electrode pairs in their array were indiscriminable. All subjects had at least 6-months experience with their device. The demographic information for these subjects is presented in Table I. All of the subjects who participated in this study used either bipolar+1 (BP+1) or BP+2 modes of stimulation. In the remainder of this paper, when a specific electrode is referenced, it is the more basal of the bipolar pair (e.g., for the BP+1 mode of stimulation, electrode 1 refers to the bipolar pair [1,3]). The 22 electrodes in the array are ordered sequentially from base (1) to apex (22).

Stimuli were delivered to subjects through an implanted receiver/stimulator driven by a Cochlear Corp. Spectra 22 processor connected to a Cochlear Corp. Dual Processor Interface (DPI). Stimuli were presented in the psychophysical procedures via custom-designed software which interfaced to the device through the DPI and Cochlear Corp. IF4 board. These procedures were run on an IBM personal computer that also controlled the DPI. A color monitor was used to cue the subjects and display feedback information when applicable. Subjects indicated the chosen interval on each trial by depressing the appropriate key on the computer keyboard. The use of human subjects as described in this manuscript was approved by the Duke University Institutional Review Board and the National Institute on Deafness and other Communication Disorders.

TABLE I. Demographic information for the implanted subjects.

Subject	Sex	Age (years)	Age at onset of profound deafness (years)	Age at implantation (years)	Mean/standard deviation of dynamic range across all active electrodes (in μA)	Mode of stimulation
S1	M	71	25	62	122/20.2	BP+1
S2	M	72	16	62	643/176	BP+1
S3	M	65	20	57	517/309	BP+2
S4	F	74	57	66	254/62.5	BP+1
S5	F	48	41	45	535/60.6	BP+1
S6	F	40	23	33	483/104	BP+1
S7	M	60	56	57	184/50.0	BP+2

B. Stimuli

In all of the experimental tasks, the stimuli presented consisted of biphasic rectangular pulses with a constant phase duration of 200 μs/phase, and were presented at a stimulation rate of 500 pps. The loudness of the stimuli was adjusted by changing the amplitude of the stimuli. For the tasks designed to measure threshold level, comfort level, loudness balance level, and electrode discrimination, the stimulus duration was 300 ms and the interstimulus interval was 500 ms.

For the forward-masking task, the duration of the masker was 300 ms, and the duration of the probe was 20 ms. The delay between masker and probe was 2 ms, while the delays between intervals and trials were each 500 ms. Since the elevation of the threshold of the probe is the quantity of interest to evaluate masking effects, unmasked thresholds for all electrodes were also measured using a stimulus duration of 20 ms.

C. Tasks

1. Loudness balancing

In order to perform the loudness-balancing task, it was first necessary to measure the threshold and maximum-comfort level for each of the functioning electrodes. Both were measured using a method of adjustment in which the subject controlled the amplitude of the stimulus using the stimulus-control knob associated with the DPI. For each electrode, the subject adjusted the amplitude until threshold and maximum-comfort level were achieved. The stimulating software controlled the current in ''current level'' units, which vary in size but average approximately 0.16-dB of current. Subsequently, these amplitude values, which range from 1 to 239, are referred to as ''cochlear-device amplitude steps.'' Once the thresholds and maximum-comfort levels of all the functioning electrodes were measured, the task was repeated. The largest values of threshold and maximum-comfort levels for each electrode were assumed to be the correct values.

To loudness balance the stimuli on each electrode, subjects were asked to adjust the loudness of a stimulus presented to one of their electrodes to the loudness of a stimulus presented to a central reference electrode. The amplitude of the stimulus that was presented on the reference electrode was adjusted by the subject to achieve a comfortable loudness level prior to beginning the loudness-balance task. Stimulation alternated continuously between the reference electrode and the test electrode until the subject indicated that a balance had been achieved. At this point, the balanced value was recorded.

This task was performed six times for each electrode comparison. On three of these runs, the initial amplitude of the test electrode was set at its threshold, and the subject increased its amplitude to match the reference electrode's loudness level. In the remaining three runs, the test electrode's initial amplitude was set to a level slightly below the maximum-comfort level, and the subject decreased its amplitude to match its loudness to that of the reference electrode. The six measured values were then averaged for each test electrode, and this average value was considered the loudness-balanced value and was used in the forward-masking task as the masker stimulus level. This procedure was used to avoid subject bias, and to bracket the ''equally loud'' range of stimuli. At the completion of all comparisons, all electrodes were stimulated in sequential order at the loudness-balance level to verify the results of the loudness-balance procedure.

Presenting the maskers at loudness-balance level implies that the actual current levels at which the maskers are presented will differ across subjects and electrodes. Since increasing the current level at which a masker is presented also increases the forward-masking effects produced by that masker, some of the masking effects recorded in this study are probably due to presenting maskers at different current levels. However, one of the goals of this study was to investigate the relationship between speech recognition and forward masking. Speech processors attempt to present speech at a comfortable loudness level for each individual subject; thus, a particular acoustic stimulus may be presented to different subjects at different current levels. Therefore, forward-masking effects for a particular acoustic stimulus will be influenced both by the physiological differences between subjects as well as by the differences in current levels. With this in mind, the maskers were presented at a comfortable loudness level rather than at absolute-current level.

2. Probe threshold baseline measurement

In order to assess forward-masking effects as accurately as possible, each electrode's 20-ms threshold was measured using an adaptive 2 down/1 up two-interval forced choice (2IFC) procedure. After each incorrect response, the signal amplitude was increased by one step, and it was decreased after two correct responses. To estimate the threshold, the

TABLE II. Masker/probe pairs that were measured at least twice to verify the masking level. The asterisk indicates that the second measurement was greater than the first measurement.

Subject	(Masker, probe) pairs	Differences between first and second measurements (dB *re*:1 μA)/dynamic range of probe (dB *re*: 1 μA)
S1	(13,13)	14.31/24.28
S4	(10,8)	6.99/26.26
	(12,14)	*10.00/30.05
S5	(17,19)	14.77/29.51
	(18,5)	13.80/29.03
	(4,19)	18.06/28.64
S6	(6,19)	22.70/28.64
	(12,10)	11.46/27.21
	(17,18)	15.91/28.31
	(2,4)	18.63/26.11
S7	(2,15)	16.34/25.75
	(19,3)	0.00/27.03

final eight of the 14 reversals obtained were averaged. This converges on the signal amplitude, which produces 70.7%-correct responses (Levitt, 1971). The step size used in the adjustment was one cochlear-device amplitude step. One interval contained the electrode stimulation, while the other interval contained an equal duration of silence. Feedback was provided. The subject's task was to choose the interval in which the electrode was stimulated.

3. Forward-masking procedure

A 2 down/1 up adaptive 2IFC procedure was used to measure the change in the threshold of a particular electrode (probe) due to a preceding stimulation either on the same electrode or a different electrode (masker). The step size used in the adjustment was one cochlear-device amplitude step, and feedback was provided to the subjects. An exhaustive procedure was performed in which each functioning electrode served as a masker. All available odd-numbered electrodes were used as probes. In addition, the two electrodes on either side of the masker as well as the masker electrode also served as probe electrodes. In one interval, only the masker was stimulated while in the other, stimulation of the masker was followed by 2 ms of silence and then stimulation of the probe. The intervals were randomized so that the probe was equally likely to occur in either interval. The total duration of each interval was identical.

The masker amplitude was fixed at the loudness-balanced level, and the initial amplitude of the probe was set so that it was easily detectable. The subject's task was to choose which of the two intervals contained the probe stimulus. The last eight of 14 reversals were averaged to obtain one data point for each masker/probe combination, except when results which were strongly inconsistent with the expected pattern of results were observed during measurement. When this occurred, the combination was tested at least twice to verify that the measurement was not due to laxity on the part of the subject. Table II lists these combinations for each subject, as well as the changes in the measured values. In all cases except one, the second measurement of the masked threshold was lower than the first measurement, and the lower values were considered the masked thresholds.

Although testing each masker/probe pair once is certainly suboptimal, one of the goals of this study was to investigate forward-masking effects across all possible combinations of electrodes for three subjects. Using an adaptive procedure, all three subjects required approximately 1 year of psychophysical testing to complete this protocol (at an average of one test session per week). Future studies will investigate the extent of the variability associated with single versus multiple measurements. The variability by the lack of averaging data affects all of the analyses in this study. However, assuming that the masked thresholds consisted of some overestimation as well as underestimation, the effects of the variation due to single-point measurements in the correlation analysis were probably decreased by using average masking levels rather than the single-point measurements. Furthermore, in the estimation of the number of masked electrodes per consonant, the estimates probably contain some overestimation and underestimation due to single-point measurements, and thus, only the average over all the consonants was considered for comparison between subjects.

4. Electrode discrimination

For the four subjects who completed the forward-masking task for only a central electrode, electrode-discrimination data reported in Collins *et al.* (1997) were utilized. Discriminability between electrodes for the three subjects completing the forward-masking task for all of their functioning electrodes was determined using a 2IFC fixed-level procedure. The amplitudes of stimulation for the electrodes were fixed at loudness-balance levels. Discrimination was measured in 60 trial blocks for each electrode pair, and a d' value was calculated. For each trial, either the same electrode was stimulated in both intervals or each interval corresponded to a stimulus presented on different electrodes. Thus, the subject's task was to decide whether the intervals contained stimulations which were the ''same'' or ''different.'' The presentation of same and different stimuli were equally likely, and feedback was provided after each response.

5. Speech-recognition measurement

The speech-recognition skills of the seven subjects were measured using four speech-recognition tests. The nine-choice closed-set Iowa medial vowel test was administered. In this test, each of the nine stimuli (heed, had, heard, hud, who'd, hawed, hid, head, and hood) were presented five times in random order (Tyler *et al.*, 1986). The Cochlear Corp. version of the 14-choice closed-set Iowa medial consonant-recognition task was administered, in which each of the fourteen stimuli (apa, aba, ama, ana, ata, ada, ava, afa, aga, aka, asa, aza, asha, and aja) were presented five times in random order (Tyler *et al.*, 1986). The NU6 Monosyllabic Words test (Tillman *et al.*, 1966), which was scored for the 50 possible words and 150 possible phonemes, was admin-

istered, along with the CID Everyday Sentences test (Davis *et al.*, 1978), which was comprised of 20 sentences with a total of 100 key words. Taped stimuli were presented to the subjects in a double-walled, acoustically insulated booth (LAC, Bronx, NY). All tests were administered during the last test session of the experiment. The stimuli were presented once, and the subjects recorded their own responses. The subjects used their clinically programmed speech processors during speech-recognition testing. Results are reported as percent correct.

D. Speech processor model

This model was used to investigate possible masking effects on consonants which may occur as a result of the stimulation pattern of a vowel in subjects implanted with the Nucleus 22 device. A model of the spectral maxima sound processor (SMSP) strategy, as described in McDermott *et al.* (1992), was implemented. With this model, it was possible to predict which electrodes would be stimulated in response to various speech tokens along with their corresponding levels of stimulation. The input to this model consisted of the Iowa Medial Consonant test words (Tyler *et al.*, 1986).

McDermott *et al.* (1992) estimate that six pulses can be presented to the electrode array every 4 ms. Based on this estimate, N nonoverlapping 4-ms windows of the test word were processed by the model, where $4N$ was the duration of the stimulus. Each window of speech data produced 16 spectral peaks corresponding to the output of 16 filters (McDermott *et al.*, 1992). Of these 16 peaks, the six largest, along with their corresponding filter numbers, were stored. Thus, each test word produced a filter matrix and a spectral-amplitude matrix which were of dimensions N by 6. The two matrices derived were independent of a particular subject.

The filter numbers were mapped to the set of 16 most apical, available electrodes. The filter with the highest passband was mapped to the most basal electrode of the set, while the filter with the lowest passband was mapped to the most apical of the set. Thus, the filter matrix was mapped to a matrix of electrodes.

The spectral amplitudes were converted to current based on the method described by Skinner *et al.* (1991). It was necessary to assume a maximum-stimulation level in order to carry out this procedure. Normally, the maximum-stimulation level would be set by the subject on their device using the sensitivity control to adjust the automatic gain control. In order to simulate a ''best case'' scenario, the largest amplitude contained within the spectral-amplitude matrix was mapped to the maximum-comfort level, and the other values were mapped accordingly. In this way, the spectral-amplitude matrix was converted into a current-level matrix.

The final stage of this process involved calculating whether the electrodes that are stimulated in response to a vowel would mask the stimuli that occur in response to a consonant following the vowel. For each test word, the electrode matrix and the current-level matrix were separated into phonemes so that these effects could be investigated. Since forward-masking data was gathered under the two conditions that the masker was of 300-ms duration and at loudness-balance level, it was necessary to analyze the data under these conditions. In this analysis, the first condition was matched by looking at the effects of vowels on subsequent consonants, since the vowels typically consist of repeated stimulation of six electrodes for a ''long'' duration.

The second condition was addressed by scaling the current levels of the maskers to loudness-balance level. For each masker, the ratio of the loudness-balance level to the actual-current level was calculated. The largest ratio was used to scale the consonant-current levels, and all the maskers were assumed to be at loudness-balance level so that the measured data could be used. However, all but one of the masker levels calculated using the model were greater than the loudness-balance level as a result of using the largest ratio. Since masking effects increase with masker level (Jesteadt *et al.*, 1982; Lim *et al.*, 1989; Chatterjee and Shannon, 1998), actual masking would be greater than the masking calculated with this model.

To calculate the masking effects vowels have on consonants, a representative window of the vowel phoneme was selected to represent the stimulation pattern that occurs in response to a vowel. Each electrode contained within the vowel window was considered a masker. Calculating the masking effect of the vowel electrodes on the consonant electrodes required use of the forward-masking data gathered across the whole array. If a masker/probe combination was not measured, a value was interpolated from the preceding and subsequent probe measurements. Based on this analysis, the number of electrodes stimulated in response to a consonant that were masked by the vowel stimulus could be calculated.

TABLE III. Speech-recognition scores of all seven subjects using five different measures. Scores are reported as percent correct.

Subject	NU6 (W) (%)	NU6 (P) (%)	CID (%)	Consonants (%)	Vowels (%)
S1	12	27	25	28	62
S2	0	0	0	10	24
S3	8	26	9	27	44
S4	18	49	79	41	84
S5	20	39	56	33	67
S6	12	45	43	46	71
S7	34	55	81	53	59

II. RESULTS

A. Speech recognition

Table III lists the percent correct scores achieved on the NU6 words, NU6 phonemes, Iowa medial vowels, Iowa medial consonants, and the CID sentences tests. Clearly, speech-recognition abilities varied widely across subjects. No ceiling effects were noted on any of the test materials.

B. Masking

The relationship between the masked-probe threshold and its unmasked threshold was examined. Masking patterns, examples of which are shown in Figs. 1–4, were generated for all subjects for each electrode that was used as a masker. These figures plot the measured masking level as a function

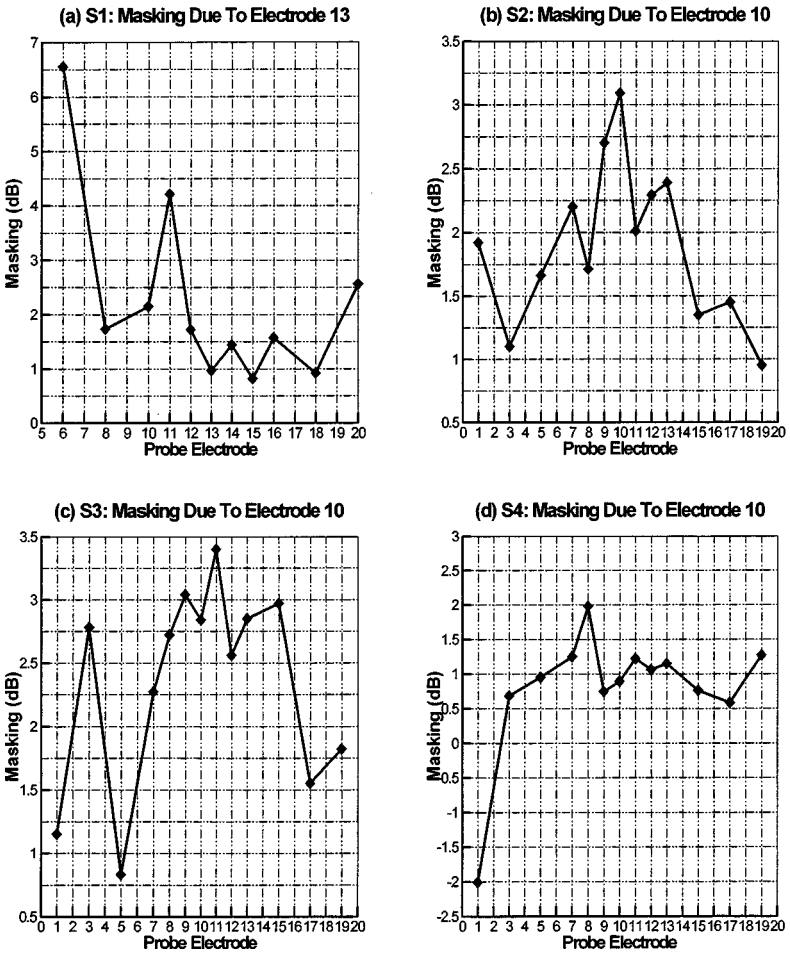

FIG. 1. Masking patterns for those subjects who only completed the forward-masking task for a centrally located electrode. The symbols indicate masker/probe pairs that were measured. The electrodes used as maskers were (a) electrode 13 for S1, (b) electrode 10 for S2, (c) electrode 10 for S3, and (d) electrode 10 for S4.

of the probe electrode number. Each panel in Figs. 1–4 represents the masking pattern measured for a particular masker. Each data point plotted in a panel, shown with a diamond symbol, represents the average of the final eight reversals measured in the adaptive procedure for the probe identified on the abscissa. In order to compare masked levels across probe electrodes, the difference of the masked and unmasked thresholds was normalized, as suggested by Lim *et al.* (1989). The normalization was performed using a ratio of loudness-balanced levels to threshold levels. Thus, the masking level for probe electrode j due to masker i, m_{ij}, was calculated via

$$m_{ij} = (T_j^{\mathrm{msk}} - T_j^{20}) \frac{\mathrm{LB}_i - T_i}{\mathrm{LB}_j - T_j}.$$

T_j and T_i are the 300-ms unmasked thresholds of the probe and masker in dB, LB_j and LB_i are the loudness-balanced levels of the probe and masker in dB, T_j^{msk} is the masked threshold of the probe in dB, and T_j^{20} is the 20-ms unmasked threshold of the probe in dB. A masking level of 0 dB indicates that no masking occurred.

Figure 1 displays the masking patterns resulting from this method of analysis for the four subjects who completed the forward-masking task for one centrally located electrode (S1–S4). Figures 2–4 contain four representative masking patterns for the three subjects who completed the full study (S5–S7). These patterns were selected to illustrate the patterns that were obtained at various locations across the array (apical, mid, and basal), as well as to illustrate the variety of patterns which was obtained.

Theoretically, the most masking should occur when the masker and probe are located at the same electrode, and masking should decrease monotonically as the distance between masker and probe electrodes increases. In addition, the amount of masking should never be less than zero. Although the maximum masking occurred under these conditions for some maskers and subjects, as shown in Fig. 1(b), this was not always the case. An example of a pattern in which the peak in the masking pattern is not located at the masker is shown in Fig. 2(a). In general, however, higher levels of masking did occur for probe electrodes located close to the masker electrode.

In addition, masking patterns did not necessarily decrease monotonically as the distance between the masker and probe electrodes increased. These results are similar to those observed by Chatterjee and Shannon (1998), Lim *et al.* (1989), and Shannon (1983). Chatterjee and Shannon (1998) observed nonmonotonic masking patterns in the majority of their subjects. They also observed that peaks in the masking patterns were not coincident with the masker location for one of the masker/probe combinations obtained from two of their four subjects. Lim *et al.* (1989) and Shannon (1983) both reported nonmonotonic masking functions from their subjects.

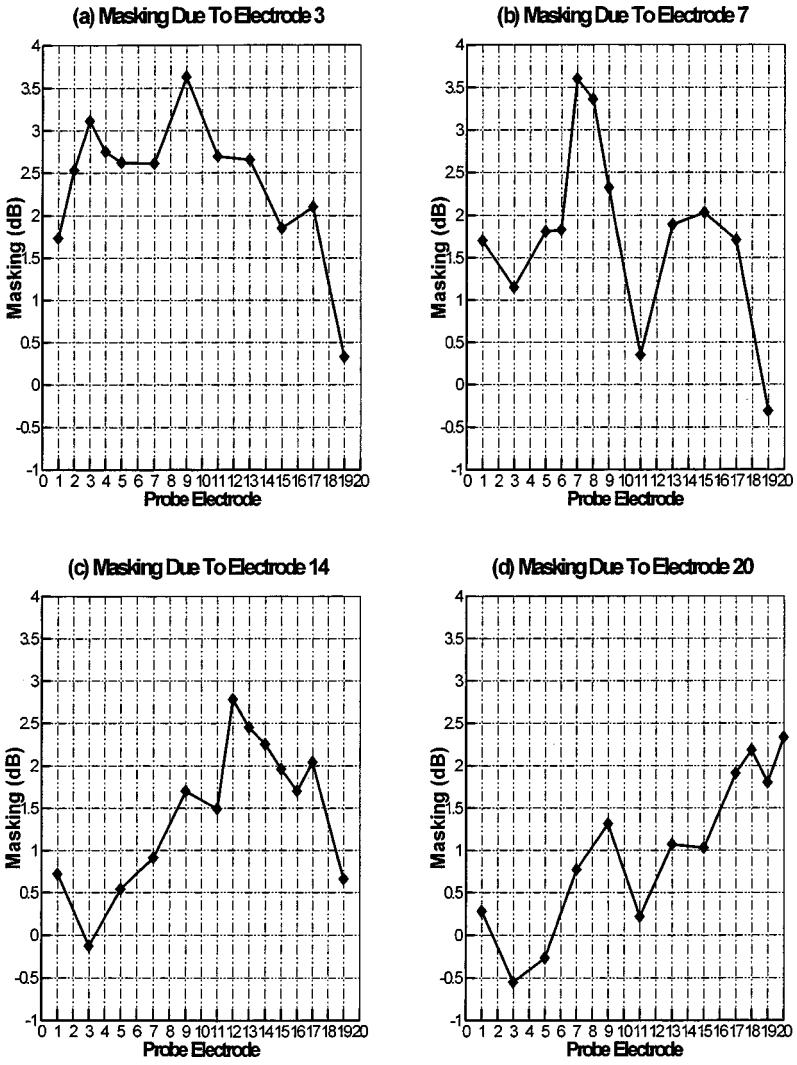

FIG. 2. Four of S5's 20 masking patterns chosen as representative. The symbols mark masker/probe pairs for which forward masking was measured.

To quantify these effects, Table IV lists the number of times the peak in the masking pattern occurred at the masker location for each of the three subjects who completed the complete masking study. In addition, Table IV lists the number of times the masker location was either adjacent to the peak in the pattern, or was the second-highest peak in the masking pattern. The final row of Table IV lists the number of maskers for which masking patterns were measured. Clearly, the degree to which the various subjects' data conforms to the expected pattern in which a peak occurs at or nears the masker is subject dependent. Subject S7, whose data follows the expected pattern more closely than the other subjects, has higher speech-recognition scores than subjects S5 and S6. It is interesting to note that the majority of the subjects who participated in previous masking studies all had relatively high speech-recognition scores. This fact, in addition to the fact that only a few masker–probe combinations were measured, may help explain why there were relatively few instances in which the peak in the masking pattern was not located at the location of the masker in these previous studies.

The data from this study indicates that not only does the maximum masking occur for probes at locations other than the masking electrode in some cases, but some combinations of probe and masker result in masking data less than 0 dB. Negative masking levels occur when the masked threshold is less than the unmasked threshold. Similar results can also be seen in data from other studies (Shannon, 1990; Chatterjee and Shannon, 1998). The adaptive procedure was not restricted to presenting probe stimulus levels that were strictly greater than the 20-ms unmasked thresholds; thus, it is possible that negative masking levels are a result of experimental variability in estimates of both masked and unmasked thresholds.

The data also indicates that maskers affect large portions, if not all, of the electrode array rather than only raising the thresholds of neighboring electrodes. These results are similar to those described in previous studies (Shannon, 1983; Lim *et al.*, 1989; Chatterjee and Shannon, 1998). The extent to which a masker affects the threshold of a probe electrode can be deduced by noting the distance between the probe and the masker at which the masking pattern falls to zero. For example, subjects S1, S2, S3, and S4 showed patterns of results in which the masking patterns either never reached zero (S1, S2, and S3), or reached zero for only one of the most distant electrodes (subject S4, electrode 1) for a masker located in the center of the array. Most subjects showed such electrode interactions, out to a spacing of 10–15 electrodes in some cases. The exception to this pat-

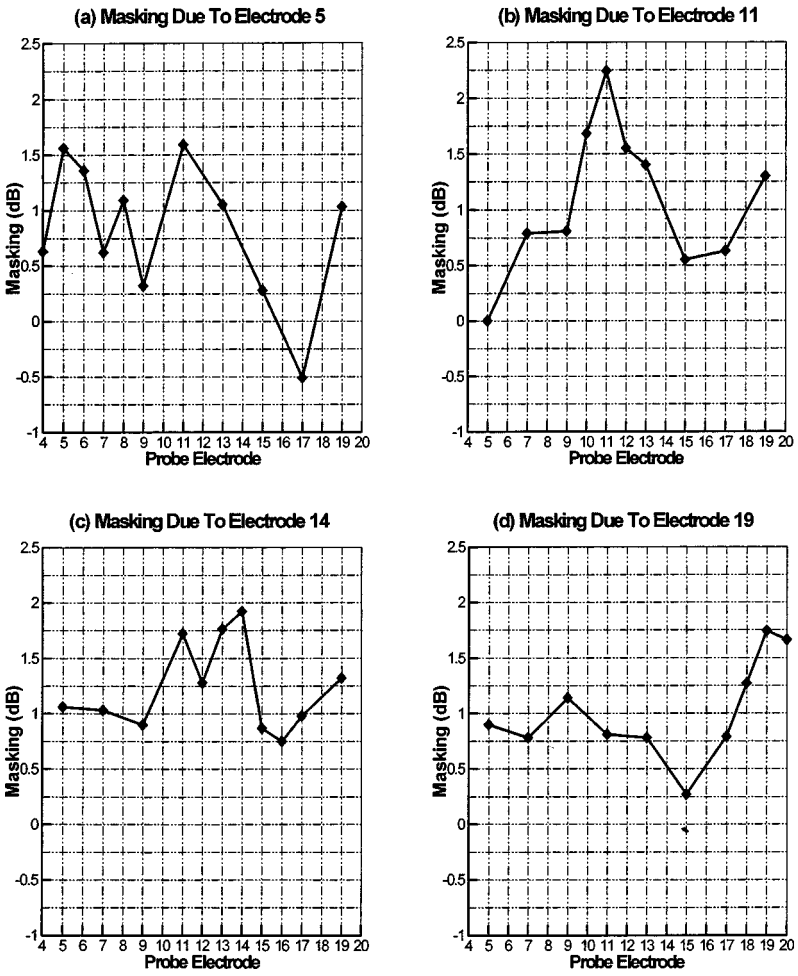

FIG. 3. Four of S6's 17 masking patterns chosen as representative. The symbols mark masker/probe pairs for which forward masking was measured.

tern is subject S7, whose masking patterns tended to fall to zero within approximately four electrodes.

In order to summarize all of the masking patterns collected, Fig. 5 contains the average of all of the masking patterns for subjects S5, S6, and S7. For each subject, the masking patterns obtained for each masker were aligned at the masker and then averaged. The resulting average of the masking patterns is plotted versus probe distance from the masker electrode. The results shown in Fig. 5 indicate that S5 experiences greater masking effects in terms of both amplitude and width of the masking pattern, while S6 differs from S5 mostly in the width of the average masking pattern. In addition, unlike S5 and S7, S6's average pattern increases in masking level, on the apical side, as the distance between masker and probe increases. The amplitude of the masking pattern can be considered to represent the degree of temporal interactions experienced by the subject, while the breadth of the masking pattern can be considered the extent of spatial interactions (i.e., the deficiency in spectral resolution). It should be noted that as the distance between masker and probe increases, the points along the average masking pattern are calculated using fewer measurements. For a subject with 20 functioning electrodes, the point representing a distance of 18 electrodes between masker and probe is the result of only one masking level (that measured for masker electrode 1 and probe electrode 19), while the point representing a distance of 0 electrodes is the average of 20 masking levels (each functioning electrode as masker and probe). Thus, the variance in the estimates of the average masking patterns increases with increasing electrode separation.

To obtain another measure of the variation in spectral resolution across subjects, the average electrode spacing required to reduce the interaction to zero for subjects S5–S7 was calculated. These electrode spacings are listed in Table V. The averages were calculated only for those patterns that decreased to within 0.5 dB of 0 dB. The average spacing required for subject S5 is 8.7 mm, for subject S6 it is 4.6 mm, and for subject S7 it is 2.6 mm. The spatial constant for electrical stimulation reported by Black and Clark (1980) was 2–3 mm which is similar to the average spacing required for subject S7, but substantially lower than that observed for subject S5 and, to some degree, S6. Subject S7, who has the highest speech-recognition scores of these three subjects, exhibits the smallest average spacing required to achieve minimal channel interactions. The differences between the average spacing for each of the three subjects are significantly different ($p<0.005$).

To obtain a relative measure of the amount of electrical interaction generated by a particular masker, an average masking level was calculated across all probe electrodes for each masker as

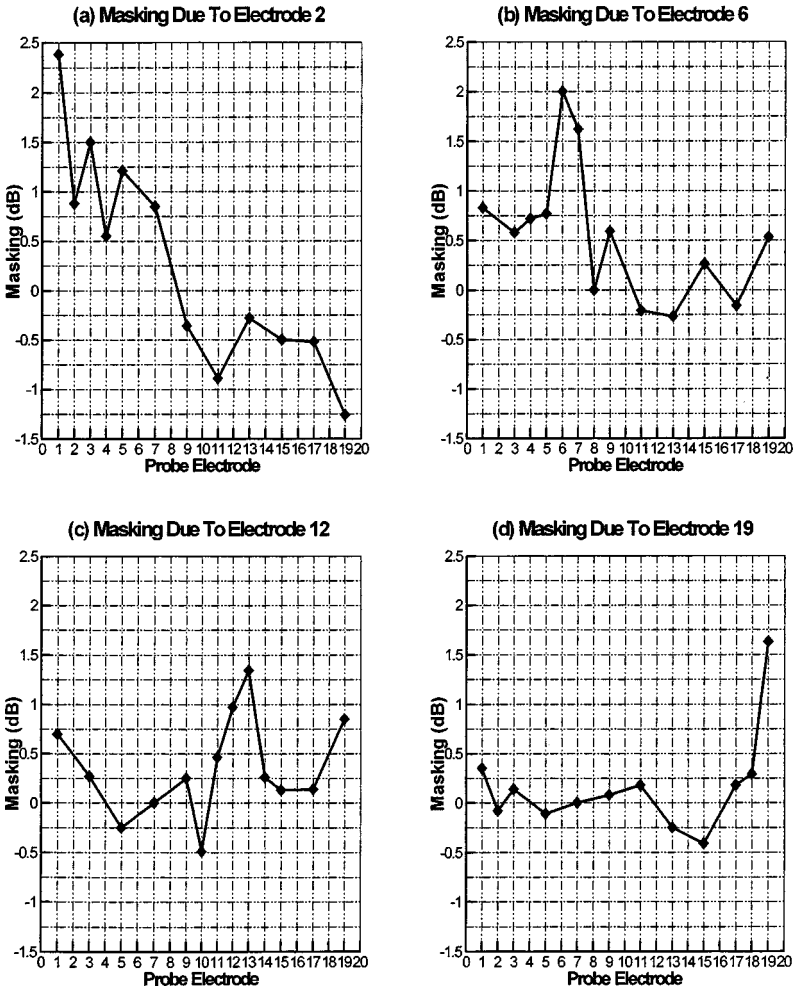

FIG. 4. Four of S7's 19 masking patterns chosen as representative. The symbols mark masker/probe pairs for which forward masking was measured.

$$m_i^{\mathrm{av}} = \frac{1}{P} \sum_{j=1}^{P} m_{ij},$$

where m_i^{av} is the average masking level for masker i, P is the number of probe electrodes measured for masker i, and m_{ij} is the normalized masking level measured at probe j as a result of masker i. Figure 6 shows the average masking levels calculated for each subject. A single point is plotted for those subjects for whom only a central electrode was tested. The average masking level includes effects from both temporal and spatial interactions (i.e., amplitude and breadth of a masking pattern) measured for a particular masker. Noticeable differences in average masking levels exist across subjects. Subjects S1, S2, S3, and S5 experience more masking on the average than subject S6, who in turn experiences more average masking than subject S4 and S7.

For each subject, Table VI lists average speech-

TABLE IV. Analysis of similarity between theoretical masking results and results obtained in this study.

Subject	S5	S6	S7
Number of times peak in masking pattern occurred when the probe was at the masker location	7	3	11
Number of times peak in masking pattern occurred for the probe adjacent to the masker location, or the peak at the probe at the masker location was the second-highest peak	10	7	7
Total number of maskers tested	20	17	19

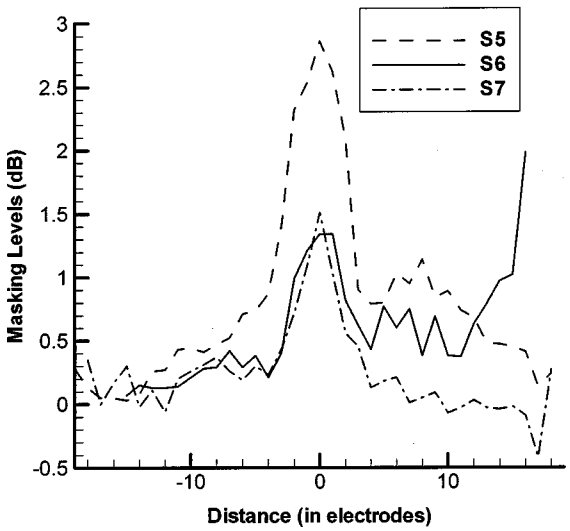

FIG. 5. Average of all masking patterns for S5, S6, and S7. The patterns are plotted with respect to the probe's distance from the masker.

TABLE V. Analysis of the spatial extent of masking for three subjects. Average distance from the masker electrode to the probe electrode at which interactions are minimized are reported in both electrode-to-electrode distance and mm. The differences between the average distance measures for all three subjects are statistically different ($p<0.005$).

Subject	Average distance from masker electrode to probe whose threshold is within 0.5 dB of unmasked threshold
S5	11.6 electrodes/8.7 mm
S6	6.2 electrodes/4.65 mm
S7	3.5 electrodes/2.63 mm

recognition scores along with the average masking level at a centrally located electrode. In general, the order of the subjects in terms of average masking effects (least to greatest) is similar to the order of their speech recognition capabilities (greatest to least).

C. Electrode discrimination

The spectral resolution of the seven subjects was examined by determining the number of electrode pairs which were indiscriminable. The number of indiscriminable electrodes for subjects S1–S4 was determined from data obtained in an earlier study reported by Collins *et al.* (1997). The number of indiscriminable electrodes for subjects S5–S7 was determined using a same/different task (2IFC) from which a d' value was determined. When $d'<1$, the electrode pair was considered to be indiscriminable. The number of indiscriminable electrodes for each subject is listed in Table VI, in the order of least to greatest average masking level. In general, the lower number of indiscriminable pairs corresponds to the higher average speech scores. Since the number of indiscriminable pairs may be used as a measure of spectral resolution, a correlation analysis between the number of indiscriminable pairs and speech-recognition scores was performed. Furthermore, the correlation between the

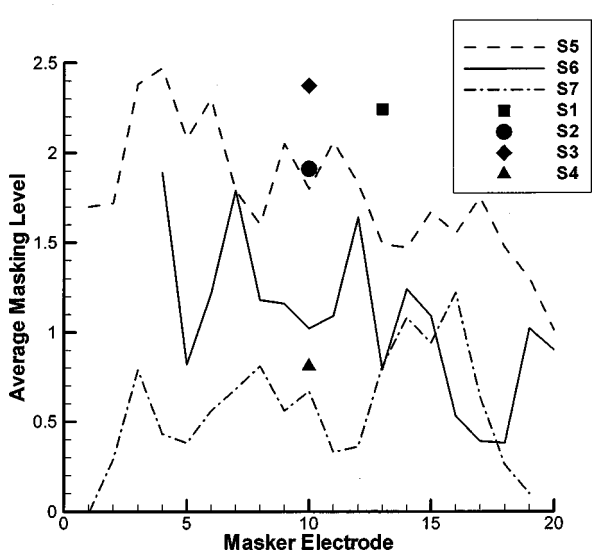

FIG. 6. Plot of the average masking levels due to each masker. Since subjects S1–S4 had only the masking effects of one electrode measured, their average masking amounts are represented by a single point. Subjects S5–S7 have average masking amounts for each functioning electrode in their array.

TABLE VI. Average speech-recognition and masking data for each of the seven subjects. Subjects are ordered in increasing level of average masking. This corresponds closely to an orderly decrease in average speech-recognition score. The number of indiscriminable electrode pairs for each subject is included.

Subject	Average masking at center electrode (dB)	Average speech-recognition score (% correct)	Number of indiscriminable electrodes
S7	0.67	55.2	4
S4	0.81	54.2	1
S6	1.64	43.4	1
S5	1.80	43.0	4
S2	1.91	6.8	11
S1	2.24	30.8	5
S3	2.37	22.8	6

number of indiscriminable pairs and average masking levels was calculated to investigate the possible extent to which forward masking may be related to spatial interactions.

D. Correlation analysis

In order to determine whether a statistical relationship exists between the forward-masking data and speech-recognition scores, the average masking level for each of the seven subjects' central electrodes as well as their speech-recognition scores were used to calculate the nonparametric Spearman rank-order correlation coefficients. These correlation coefficients are listed in Table VII. A strong correlation exists between the average masking levels and three of the five speech-recognition measures. This result suggests two hypotheses for the statistically significant relationship between the types of interactions that can be measured using forward masking and speech-recognition abilities of cochlear-implant subjects. The hypotheses are that a correlation between speech-recognition ability and forward-masking effects exists due to the temporal interactions measured by forward masking, or it exists due to the spectral interactions which both forward masking and speech recognition measure. An interesting observation is that the strongest correlations occur with NU6 phonemes (0.89), Iowa medial consonants (0.86), and CID sentences (0.86), which are significant at $p<0.05$, while the relationship between vowel perception and average masking level is not significant. These results lend some support for the first hypothesis that, due to temporal interactions, consonants which follow vowels may be masked by vowels, thereby reducing speech-recognition scores that include evaluation of consonant perception.

Another possible explanation for the strong correlation between forward masking and speech-recognition skills is that both are affected by spectral resolution. This hypothesis was investigated through electrode discrimination, which provides a measure of spectral resolution which may be affected less by temporal interactions. The number of indiscriminable electrode pairs for each subject was correlated with average masking levels to investigate the extent to which average masking levels may be related to spectral resolution. The number of indiscriminable electrodes was also correlated with each speech-recognition measure to es-

TABLE VII. The Spearman-correlation coefficients calculated using the average masking levels of each subject's centrally located electrode and the subjects' speech-recognition scores, using the number of indiscriminable electrodes and the subjects' speech-recognition scores, and the average masking levels of the centrally located electrodes and the number of indiscriminable electrodes. The bold entries are significant at $p<0.05$, and the entries with the asterisks are significant at $p<0.10$.

	NU-6 (word)	NU-6 (phoneme)	CID sentences	Iowa med. vowels	Iowa med. consonants	Avg. masking level
Avg. masking level	0.74*	**0.89**	**0.86**	0.50	**0.86**	···
Number of indiscriminable electrodes	0.64	**0.84**	0.77*	**0.93**	**0.84**	0.73*

timate the influence of spectral resolution on speech recognition. The results of this analysis are also presented in Table VII. Spectral resolution, measured by electrode discrimination, was strongly correlated with vowel recognition as expected (0.93), as well as consonant recognition (0.84), and phoneme recognition (0.84). It was less strongly correlated with average masking level, which is a measure of both temporal and spatial interaction. The strong correlation of the number of indiscriminable pairs with the measures of phoneme recognition suggest that the relationship between average masking levels and the Iowa medial consonants and NU6 phonemes may be due to lack of spectral resolution rather than temporal interactions alone; however, temporal interactions may have stronger influences on word recognition represented in CID sentences and NU6 words.

E. Model-based analysis of temporal interactions

The ramifications of possible temporal interactions were considered through a model of the SMSP. Each consonant test word entered in the model of the SMSP produced a percentage of consonant electrodes masked by the vowel ''a.'' The percentages from the test words were averaged, and Table VIII lists the averages for the three subjects who completed the full forward-masking study. In general, the model predicted that subjects with more masking effects would experience a reduction in the salience of consonant cues as a result of vowel-like stimulation. Due to the high variance seen for both S5 and S6, the difference in their averages is not statistically significant; however, the difference between S7's average and those of S5 and S6 is statistically significant at $p<0.05$.

TABLE VIII. The estimated average percentage of consonant electrodes masked by the preceding-vowel phoneme window for those subjects who completed the forward-masking study for all of their functioning electrodes. The difference between S7's average percentage and those of S5 and S6 is statistically significant at $p<0.05$.

Subjects	Average percentage
S5	13.02
S6	18.69
S7	5.33

III. DISCUSSION

In this study, masking patterns were obtained with a centrally located electrode serving as masker for seven subjects. In a more exhaustive study, masking patterns for all possible maskers were obtained for three of these subjects. Substantial variability was observed in the individual masking patterns obtained from each subject. This variability is probably due, in part, to the single measurements used to obtain the masking patterns. However, the masking patterns for S5, S6, and S7 based on the average of the single measurements (Fig. 5) showed distinct features predicted by a hypothetical masking pattern. A peak occurred when the masker and probe were the same electrode, and the patterns showed a monotonic decrease from the peak. As the distance between the probe and the masker increases, the number of single measurements in the average decreases, which may explain the decrease in monotonicity in the tails of the average masking patterns. However, if the extreme points in the tails are excluded, S6 still appears to experience a noticeable increase in masking in the right-hand tail. This may be due to physical features within the cochlea of S6. In addition, small negative masking levels as seen for S7 may be explained by experimental variability in measuring thresholds using a single measurement. The adaptive procedure was used to measure the 20-ms thresholds in an attempt to eliminate/minimize such events by providing an accurate measure of unmasked threshold.

Despite the anomalies in the masking patterns, two important insights into the interactions between electrodes stimulated within a narrow time frame are provided by the patterns. First, electrodes in close proximity to one another tend to cause the greatest masking effects. This is a result that has also been observed in other studies of forward masking, including Lim *et al.* (1989), Shannon (1983), and Chatterjee and Shannon (1998). Maskers also tend to elevate probe thresholds across the entire electrode array, rather than merely at neighboring electrodes. This suggests the possibility that subjects may suffer much greater information loss than is commonly assumed. If only neighboring electrodes were affected, then information loss would be bounded by instances in which neighboring electrodes were stimulated sequentially. If, however, the whole array can be affected, any electrode stimulation might be masked by any previous stimulation. Speech-processing strategies that utilize spa-

tially staggered pulses, such as continuous interleaved sampling (CIS), may reduce these effects.

The evidence that some subjects do suffer greater masking effects than others (e.g., the greater amplitude and width of S5's average masking pattern) led to the consideration of how these masking effects might be related to the subject's ability to recognize and understand speech. The statistically significant correlation between the speech-recognition scores and the average masking levels of the central electrodes of the seven subjects suggested a relationship between information loss and forward masking. Two hypotheses for this relationship were considered. The first was that the loss was due to the temporal effect of vowel stimulation masking consonant stimulation. The second was that forward masking also provided a measure of spectral resolution, in addition to temporal resolution, and degradations in spectral resolution led to poorer speech recognition. The strong correlation of the average masking levels with speech-recognition measures that were not strongly correlated with electrode discrimination offers some support for the temporal-interaction hypothesis. However, the statistically significant correlation between average masking levels and electrode discrimination suggests that at least part of the correlation between average masking levels and speech recognition is due to spectral resolution. Thus, the correlation between average masking levels and speech recognition may be the result of both spectral and temporal interactions. If forward masking causes changes in temporal characteristics of speech, the effects on speech recognition may be significant since several studies (Shannon *et al.*, 1995; Boothroyd *et al.*, 1996) which removed spectral information from speech data have shown that temporal cues provide much of the information necessary for phoneme identification.

The 80–100-ms gap between the first vowel and the subsequent consonant in the Iowa medial consonant test words (Tyler *et al.*, 1986) suggests that the masking effects that the preceding vowel might have on the consonant probably affects only those electrodes which are weak in amplitude (e.g., transition periods, antiresonances), since masking effects decrease as the gap between masker and probe increases. The possibility that the vowel has some masking effect on the consonant for a gap of this duration does exist since Shannon (1990) and Chatterjee and Shannon (1998) have shown that masking effects still occur for a gap of this duration for speakers with good speech-recognition skills.

Studies of medial stop consonants in normal-hearing subjects have shown that the consonant–vowel (CV) transition, when the closure duration is short, is the main cue for identifying the consonants for normal-hearing subjects (Dorman and Raphael, 1980; Tartter *et al.*, 1983). Thus, if the vowel stimulation masks, to some extent, the CV transition, it may affect consonant recognition. However, it is more likely that the vowel may mask the vowel–consonant (VC) transition period. The role of the VC transition in consonant and word recognition for normal-hearing subjects is the subject of several studies (Tartter *et al.*, 1983; Streeter and Nigro, 1979; Dorman and Raphael, 1980). For short closure durations, both Dorman *et al.* (1980) and Tartter *et al.* (1983) agreed that the VC transition had some effect on consonant recognition, but that the CV transition was the main cue. Streeter and Nigro (1979) showed that an absent VC transition had no significant effect on distinguishing words from nonwords, but if the VC transition conflicted with the CV transition in place or manner, then word perception decreased. Thus, if forward masking by a vowel on a consonant does not completely eradicate the VC transition, but rather warps the transition in terms of manner or place identification, it is possible that this would affect word recognition. It is interesting to note that average masking level was correlated with NU-6 word ($p<0.10$) and CID sentences ($p<0.05$), while electrode discrimination was not correlated significantly with NU-6 words at all and was less correlated with CID sentences ($p<0.10$). Future studies including more subjects and more repetitions of the measurements will be necessary to further investigate the hypotheses presented in this paper. Furthermore, data collected with more repetitions will allow estimation of which electrodes in individual consonants may be masked. This would provide a method for investigating whether the VC transition periods may be masked by vowel stimulation, thus reducing word comprehension.

ACKNOWLEDGMENTS

We express our thanks and appreciation to the subjects who gave us their time and effort. Also, we thank Dr. Terry Zwolan, Dr. Paul Kileny, and Ms. Pat Roush for their help in contacting and recruiting subjects, and Dr. David W. Smith, Dr. Roger Miller, and Dr. Rich Tyler and one anonymous reviewer for their valuable input. We are indebted to Cochlear Corp. for providing equipment necessary to carry out this study. This research was supported by NIH Grant No. 5R03-DC-03136-02.

Black, R. C., and Clark, G. M. (**1980**). ''Differential electrical excitation of the auditory nerve,'' J. Acoust. Soc. Am. **67**, 868–874.

Blamey, P. J., and Dooley, G. J. (**1993**). ''Pattern recognition and masking in cochlear implant patients,'' Prog. Brain Res. **97**, 271–8.

Blamey, P. J., Dowell, R. C., Brown, A. M., Clark, G. M., and Seligman, P. M. (**1987**). ''Vowel and consonant recognition of cochlear implant patients using formant-estimating speech processors,'' J. Acoust. Soc. Am. **82**, 48–57.

Boothroyd, A., Mulhearn, B., Gong, J., and Ostroff, J. (**1996**). ''Effects of spectral smearing on phoneme and word recognition,'' J. Acoust. Soc. Am. **100**, 1807–1818.

Busby, P. A., and Clark, G. M. (**1996**). ''Electrode discrimination by early-deafened cochlear implant patients,'' Audiology **35(1)**, 8–22.

Busby, P. A., and Clark, G. M. (**1997**). ''Pitch and loudness estimation for single and multiple pulse per period electric pulse rates by cochlear implant patients,'' J. Acoust. Soc. Am. **101**, 1687–95.

Busby, P. A., Tong, Y. C., and Clark, G. M. (**1993**). ''Electrode position, repetition rate, and speech perception by early- and late-deafened cochlear implant patients,'' J. Acoust. Soc. Am. **93**, 1058–67.

Busby, P. A., Whitford, L. A., Blamey, P. J., Richardson, L. M., and Clark, G. M. (**1994**). ''Pitch perception for different modes of stimulation using the cochlear multiple-electrode prosthesis,'' J. Acoust. Soc. Am. **95**, 2658–69.

Chatterjee, M., and Shannon, R. V. (**1998**). ''Forward masked excitation patterns in multielectrode electrical stimulation,'' J. Acoust. Soc. Am. **103**, 2565–72.

Collins, L. M., Zwolan, T. A., and Wakefield, G. H. (**1997**). ''Comparison of electrode discrimination, pitch ranking, and pitch scaling data in postlingually deafened adult cochlear implant subjects,'' J. Acoust. Soc. Am. **101**, 440–55.

Davis, H., and Silverman, S. R. (**1978**). *Hearing and Deafness* (Holt, Rinehart, and Winston, New York).
Dorman, M. F., and Raphael, L. J. (**1980**). ''Distribution of acoustic cues for stop consonant place of articulation in VCV syllables,'' J. Acoust. Soc. Am. **67**, 1333–1335.
Dorman, M. F., Dankowski, K., McCandless, G., Parkin, J. L., and Smith, L. (**1991**). ''Vowel and consonant recognition with the aid of a multichannel cochlear implant,'' Q. J. Exp. Psychol. A **43**(3), 585–601.
Dowell, R. C., Martin, L. F., Tong, Y. C., Clark, G. M., Seligman, P. M., and Patrick, J. F. (**1982**). ''A 12-consonant confusion study on a multiple-channel cochlear implant patient,'' J. Speech Hear. Res. **25**(4), 509–16.
Doyle, K. J., Mills, D., Larky, J., Kessler, D., Luxford, W. M., and Schindler, R. A. (**1995**). ''Consonant perception by users of Nucleus and Clarion multichannel cochlear implants,'' American Journal of Otology **16**(5), 676–81.
Jesteadt, W., Bacon, S. P., and Lehman, J. R. (**1982**). ''Forward masking as a function of frequency, masker level, and signal delay,'' J. Acoust. Soc. Am. **71**, 950–62.
Levitt, H. (**1971**). ''Transformed up–down methods in psychoacoustics,'' J. Acoust. Soc. Am. **49**, 467.
Lim, H. H., Tong, Y. C., and Clark, G. M. (**1989**). ''Forward masking patterns produced by intracochlear electrical stimulation of one and two electrode pairs in the human cochlea,'' J. Acoust. Soc. Am. **86**, 971–80.
McDermott, H. J., McKay, C. M., and Vandali, A. E. (**1992**). ''A new portable sound processor for the University of Melbourne/Nucleus Limited multielectrode cochlear implant,'' J. Acoust. Soc. Am. **91**, 3367–71.
McKay, C. M., McDermott, H. J., and Clark, G. M. (**1996**). ''The perceptual dimensions of single-electrode and nonsimultaneous dual-electrode stimuli in cochlear implantees,'' J. Acoust. Soc. Am. **99**, 1079–1090.
Merzenich, M. M., and White, M. W. (**1977**). ''Cochlear implants: The interface problem,'' in *Functional Electrical Stimulation: Applications in Neural Prostheses*, edited by F. T. Hambrecht and J. B. Reswick (Marcel Dekker, New York), Vol. 3, pp. 321–340.
Pelizzone, M., Boex, C., and Montandon, P. (**1993**). ''Vowel and consonant identification tests can be used to compare performances in a multilingual group of cochlear implant patients,'' ORL. J. Otorhinol. Relat. Spec. **55**(6), 341–6.
Shannon, R. V. (**1983**). ''Multichannel electrical stimulation of the auditory nerve in man. I. Basic psychophysics,'' Hearing Res. **11**(2), 157–89.
Shannon, R. V. (**1983**). ''Multichannel electrical stimulation of the auditory nerve in man. II. Channel interaction,'' Hearing Res. **12**(1), 1–16.
Shannon, R. V. (**1990**). ''Forward masking in patients with cochlear implants,'' J. Acoust. Soc. Am. **88**, 741–4.
Shannon, R. V., Zeng, F. G., Kamath, V., Wygonski, J., and Ekelid, M. (**1995**). ''Speech recognition with primarily temporal cues,'' Science **270**, 303–4.
Skinner, M. W., Holden, L. K., Holden, T. A., Dowell, R. C., Seligman, P. M., Brimacombe, J. A., and Beiter, A. L. (**1991**). ''Performance of postlinguistically deaf adults with the Wearable Speech Processor (WSP III) and Mini Speech Processor (MSP) of the Nucleus multi-electrode cochlear implant,'' Ear Hear. **12**(1), 3–22.
Streeter, L. A., and Nigro, G. N. (**1979**). ''The role of medial consonant transitions in word perception,'' J. Acoust. Soc. Am. **65**, 1533–1541.
Tartter, V. C., Kat, D., Samuel, A. G., and Repp, B. H. (**1983**). ''Perception of intervocalic stop consonants: The contributions of closure duration and formant transitions,'' J. Acoust. Soc. Am. **74**, 715–725.
Tillman, T. W., and Carhart, T. (**1966**). ''An expanded test for speech discrimination utilizing CNC monosyllabic words'': Northwestern University Auditory Test No. 6. Technical Report No. SAM-TR-66-55, USAF School of Aerospace Medicine, Brooks Air Force Base, Texas.
Tong, Y. C., and Clark, G. M. (**1986**). ''Loudness summation, masking, and temporal interaction for sensations produced by electric stimulation of two sites in the human cochlea,'' J. Acoust. Soc. Am. **79**, 1958–66.
Townshend, B., Cotter, N., Van Compernolle, D., and White, R. L. (**1987**). ''Pitch perception by cochlear implant subjects,'' J. Acoust. Soc. Am. **82**, 106–15.
Tye-Murray, N., and Tyler, R. S. (**1989**). ''Auditory consonant and word recognition skills of cochlear implant users,'' Ear Hear. **10(5)**, 292–8.
Tyler, R. S., and Moore, B. C. (**1992**). ''Consonant recognition by some of the better cochlear-implant patients,'' J. Acoust. Soc. Am. **92**, 3068–77.
Tyler, R. S., Preece, J. P., and Tye-Murray, N. (**1986**). The Iowa Phoneme and Sentence Tests (a laser video disc with consonant, vowel, and sentence tests), Department of Otolaryngology—Head and Neck Surgery, The University of Iowa, Iowa City, IA.
Zwolan, T. A., Collins, L. M., and Wakefield, G. H. (**1997**). ''Electrode discrimination and speech perception in postlingually deafened adult cochlear implant subjects,'' J. Acoust. Soc. Am. **102**, 3673–3685.

Blowing pressure, power, and spectrum in trumpet playing

N. H. Fletcher[a] and A. Tarnopolsky
School of Aerospace and Mechanical Engineering, Australian Defence Force Academy, Canberra 2600, Australia

(Received 15 April 1998; revised 6 October 1998; accepted 28 October 1998)

Measurements of sound output as a function of blowing pressure are reported for a group of experienced trumpet players. The study identifies several common features, namely (1) a threshold blowing pressure approximately proportional to the frequency of the note being played, (2) an extended region in which the sound output rises by about 15 dB for each doubling of blowing pressure, and (3) a saturation region in which sound output rises by only about 3 dB for a doubling of blowing pressure. Some players are able to blow with maximum pressures as high as 25 kPa, which is significantly greater than normal systolic blood pressure. A simple theory is presented that provides a physical explanation for the acoustical behavior, but a detailed treatment requires solution of the nonlinear coupled equations both for the lip-valve mechanism and for nonlinear wave propagation in the instrument tube. Frequency analysis of the sound shows a basic spectral envelope determined by the resonance properties of the mouthpiece cup and the radiation behavior of the bell, supplemented by an extension to increasingly high frequencies as the blowing pressure is increased. This high-frequency behavior can be attributed to nonlinear wavefront steepening during sound propagation along the cylindrical bore of the instrument. [S0001-4966(99)02102-5]

PACS numbers: 43.75.Fg, 43.75.St [WJS]

INTRODUCTION

Blowing technique is a vital part of the playing of any wind instrument, and it is therefore rather surprising that the study of physical parameters such as blowing pressure has attracted so little attention. The foundations of such a study for many wind instruments were laid as long ago as 1965 by Bouhuys,[1] but the only subsequent detailed measurements of which we are aware are those on the flute by Fletcher[2] and on woodwind reed instruments by Fuks and Sundberg.[3] The only papers on trumpet performance technique of which we are aware are those of Luce and Clark,[4] who examined spectral properties of the sound, and of Bertsch,[5] who studied the sounds produced by different trumpet players but did not correlate these with blowing pressure. There have, of course, been many papers on various more mechanical aspects of sound production in brass instruments that will be referred to later.

Bouhuys' results for the trumpet are summarized as follows. The blowing pressure measured in the mouth ranged from about 30 to 100 mm Hg (4 to 13 kPa) for high notes played *pp* and *ff*, respectively. Corresponding figures for low notes are omitted from the graph. The acoustic power output ranged from about 20 μW to 1 mW for low notes and from 200 μW to 30 mW for high notes. The overall acoustic efficiency was 0.01% to 0.03% for low notes and 0.03% to 1% for high notes, the higher efficiencies applying to fortissimo playing. In each case only one note and two dynamic levels were measured, and the radiated sound power was estimated from on-axis measurements in a normal room.

It is the purpose of the present paper to report more extensive measurements of blowing technique for a group of trumpet players, with detailed studies on one professional player, and to interpret these findings acoustically.

I. MEASUREMENTS

Measurements were made on three players: a professional orchestral trumpeter (GC), and two experienced amateur players (NH and KB). In the measurements to be reported, they all played standard B♭ trumpets, but some measurements were also made of GC playing a B♭ cornet, and a piccolo trumpet in A. A catheter tube, about 2 mm in external diameter, was inserted in one corner of the player's mouth and the blowing pressure was measured on one of two bourdon gauges that had been calibrated against a water manometer. Acoustic measurements were made at a distance of 1–1.5 m from the horn mouth on the axis of the instrument and later corrected to the equivalent level at 1 m distance. The A-weighted sound pressure level was noted and the sound itself recorded for later analysis. In the case of player GC, the measurements were made in an anechoic chamber, while for the other two players a normally furnished living room was used. Because the frequency response of the microphones used fell off above 16 kHz, the reported measurements extend only to this frequency.

The playing tests consisted of a series of steady notes of given pitch played with increasing loudness from pianissimo up to the fortissimo limit for the particular player. The note pitches covered the whole compass of each instrument in an appropriately transposed CFCF . . . sequence, or something close to that.

Figure 1 summarizes the measured results for professional GC playing a standard B♭ trumpet. Several points are

[a]Permanent address: Research School of Physical Sciences and Engineering, Australian National University, Canberra 0200, Australia. Electronic mail: neville.fletcher@anu.edu.au

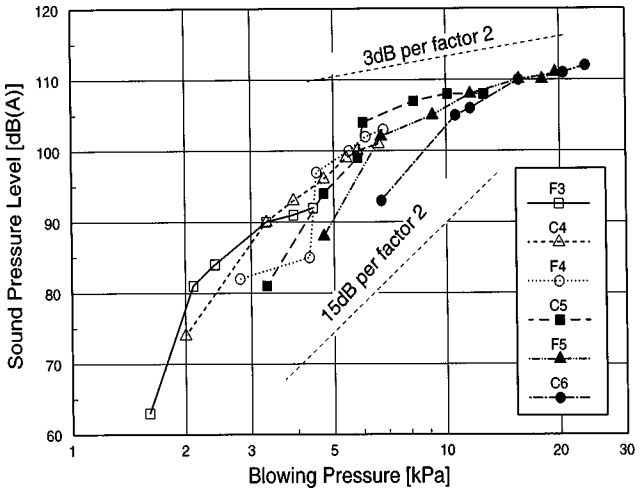

FIG. 1. Equivalent SPL at 1 m produced by player GC on a standard B♭ trumpet in an anechoic chamber, as a function of blowing pressure.

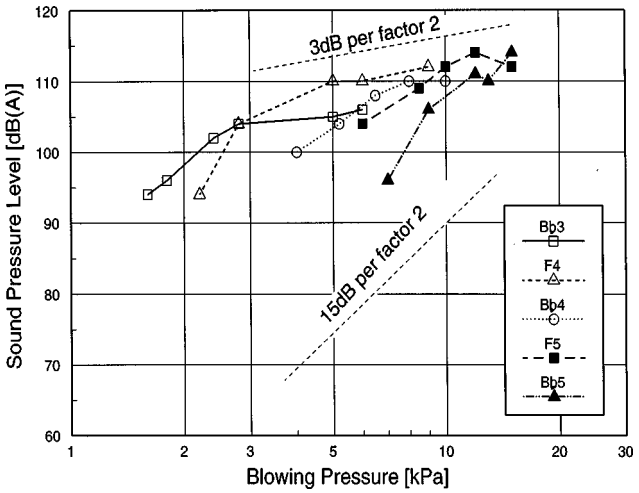

FIG. 2. Equivalent SPL at 1 m produced by player NH on a standard B♭ trumpet, as a function of blowing pressure.

worthy of immediate note. The first is that, in agreement with Bouhuys and the common knowledge of players, there is a threshold pressure required for the sounding of any note, and this threshold increases steadily with the pitch of the note. Second, there is an upper limit to the pressure that can be used for any note, and again this limit increases as we ascend the scale. It is noteworthy that the highest blowing pressure used by this particular player, who is of solid physique, is about 25 kPa. This pressure is much higher than the normal systolic (maximum) blood pressure, which is typically only about 18 kPa, so that it is small wonder that the player reported physiological difficulties when required to play at this level! To appreciate the magnitude of this pressure excess, the graph should be replotted with blowing pressure on a linear scale. Physiological measurements by Fiz *et al.*[6] on the maximum expiratory pressure that can be achieved by trumpet players—not while playing the trumpet, or indeed while actually expelling air—yielded a value of 23 ± 5 Pa, in confirmation of the general level of this result, while they found that similarly fit young men who did not play any brass instrument were able to achieve expiratory pressures of only 19 ± 1 Pa. Presumably muscle training accounts for this difference.

Figures 2 and 3 show similar measurements for players NH and KB. If the two figures are superimposed, then they roughly replicate the measurements in Fig. 1, but player NH, who had a stocky physique similar to that of GC, used only the louder part of the range, while KB, who was much slighter of build and had been criticized by his teacher for not playing vigorously enough, used only the quieter part. The maximum blowing pressure used by KB was only about 7 kPa while NH used pressures up to about 15 kPa.

The professional player GC thus had a much greater range of dynamics and employed a much greater blowing-pressure range than either of the other players, a conclusion that is perhaps not surprising. The measured sound pressure levels should not be compared between players more closely than ±3 dB, because the acoustic environments were somewhat different, but the maximum A-weighted level of about 110 dB for high notes is in good agreement with the maximum measured by Bertsch,[5] as also is the dynamic range.

Figure 4 shows the threshold pressure required by each of the three players to produce notes of various pitches. In all cases, the threshold pressure is very nearly proportional to the frequency of the note being played, but there is a range of about a factor of 2 in the slope of this characteristic, with the professional player GC having threshold pressures within the range spanned by the other two players.

During the course of the study, similar measurements were made of the playing technique of GC on a B♭ cornet and a piccolo trumpet in A. In each case the blowing pressures and sound pressure levels were very similar to those measured for the same notes on the trumpet, with the threshold pressures for the highest notes on the A trumpet appropriately extrapolated upwards.

II. SPECTRAL ANALYSIS

To supplement the measurement of sound pressure level, a recording was made, at a distance of about 1.5 m on the instrument axis, of the sound produced by professional player GC for each note. It is well known that the upper

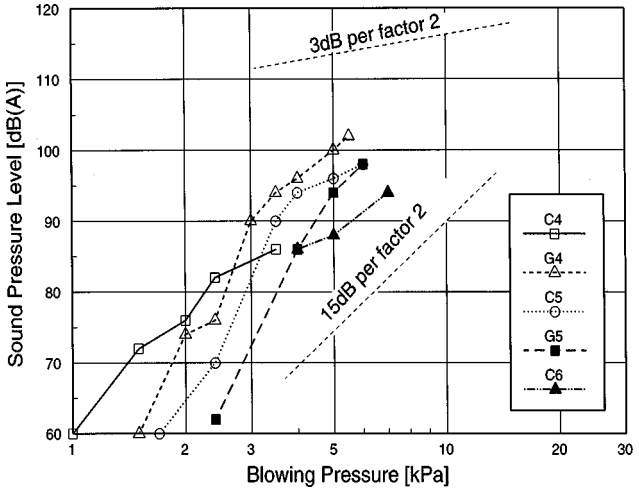

FIG. 3. Equivalent SPL at 1 m produced by player KB on a standard B♭ trumpet, as a function of blowing pressure.

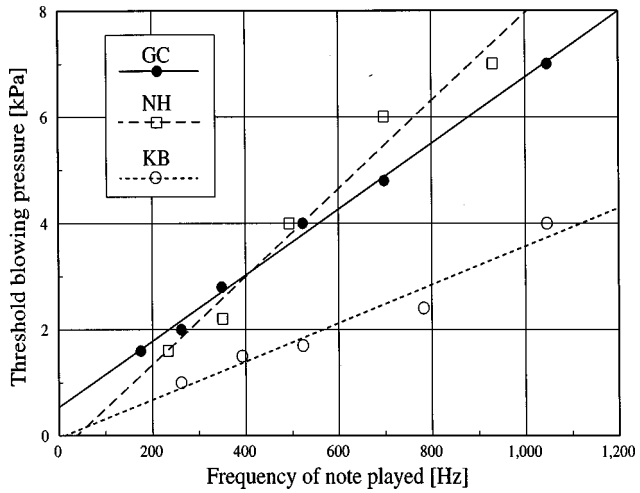

FIG. 4. Threshold blowing pressure used by players GC, NH, and KB to produce notes of various pitches. The sequence of notes played by each player is not exactly the same.

partials of the trumpet sound increase in level relative to the fundamental at high loudness levels, giving incisive brilliance to trumpets in the orchestra. The object here was to investigate this change in timbre over the whole range of playing levels.

Investigations of the envelope of the trumpet spectrum by Luce and Clark[4] characterized it as consisting of two frequency regions. Below the radiation cutoff of the bell, typically about 1000 Hz, the radiated power rose slowly with frequency, typically at 2 to 4 dB/octave, while above cutoff the envelope fell at 15 to 25 dB/octave. They found that the slope below cutoff increased and the slope above cutoff decreased as the intensity level was increased. These measurements apply, not to individual notes, but rather to the average spectrum over the entire instrument.

The present measurements broadly confirm these results, but introduce new detail because they relate to individual notes rather than to the overall spectral envelope. Figure 5

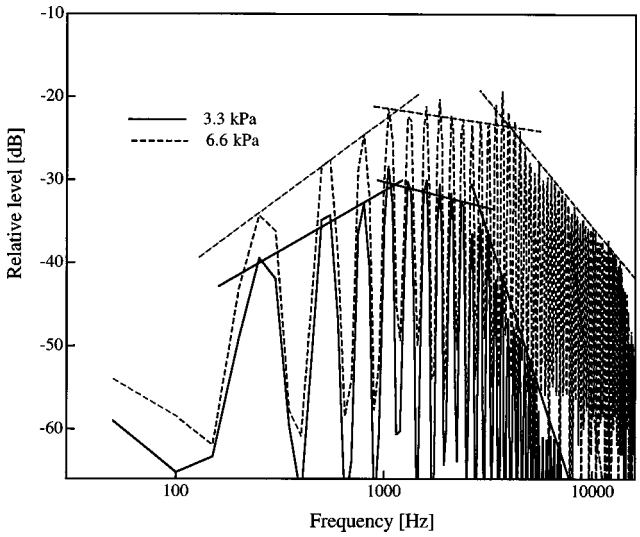

FIG. 5. Spectrum of the note C4 played softly and loudly on a B♭ trumpet. The three slope regions and their transitions are clearly evident, as is the shift with playing level.

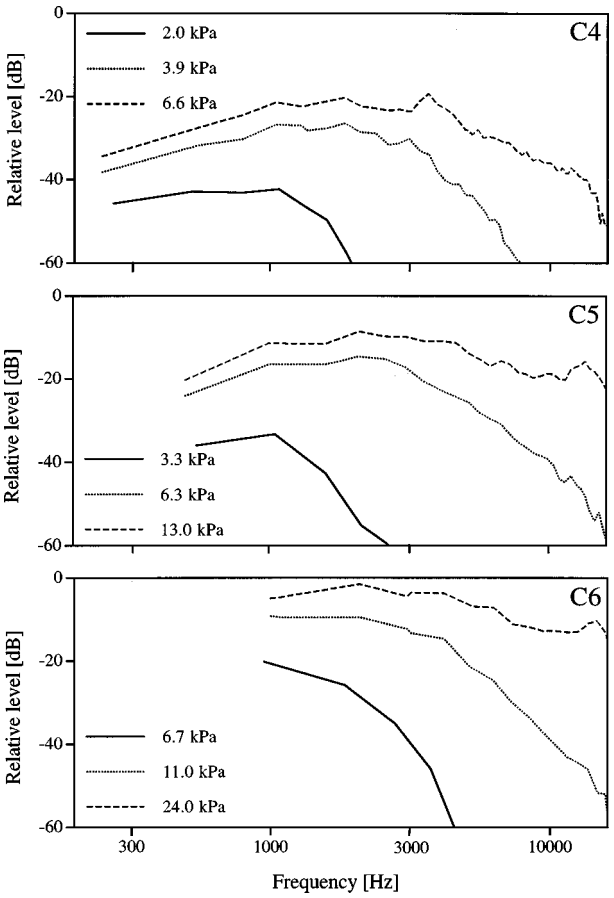

FIG. 6. Spectral development of the noted C_4, C_5, and C_6 as functions of blowing pressure, as played on a B♭ trumpet by GC.

shows typical acoustic spectra for the low note C_4 played softly and loudly on a B♭ trumpet. It is clearly tempting to characterize these spectra in terms of three slopes: a rise of about 6 dB/octave below about 1000 Hz, a nearly constant slope from 1000 Hz to an upper transition at 2–3 kHz which increases with dynamic level, and an upper section with slope about −30 dB/octave at low levels and only about −10 dB/octave at the higher level shown. It is more realistic, however, to examine the spectral envelopes for a wide range of notes and dynamic levels, as shown in Fig. 6. This makes it clear that it is difficult to assign these slopes in an unambiguous manner. What does seem clear, however, is that there is a basic low-level spectral envelope with a characteristic that rises towards a maximum near 1000 Hz and then declines at higher frequencies, as shown by the full curves. On top of this is some other mechanism that extends the envelope to increasingly higher frequencies as the dynamic level is increased. We see below that there is a simple theoretical justification for this interpretation.

III. DESCRIPTIVE THEORY

The sound generation mechanism in brass instruments depends upon the motion of the player's lips, which constitute a pressure-controlled valve. The actual behavior of the lips is certainly complex, for they consist of soft tissue that can support various types of wavelike oscillatory behavior,[7] rather as can the human vocal folds. For our present pur-

poses, however, such detail is not required, and we can use a simple mass-and-spring model. The operation of such simplified valves has been discussed in detail in several publications—for a detailed exposition and list of references the reader is referred to the book by Fletcher and Rossing.[8] The particular case of brass-players' lips has been investigated by Martin,[9] by Elliott and Bowsher,[10] by Yoshikawa,[11] by Adachi and Sato,[12] and by Copley and Strong.[13]

The essence of this mechanism is that the player's lips are driven open and closed by the oscillating sound pressure in the instrument mouthpiece. Details depend upon whether the valve is of the ''outward-swinging door'' $(+,-)$ or ''sliding door'' $(+,+)$ type, or something in between.[11–15] Unlike the ''inward-swinging door'' $(-,+)$ reed valves in woodwind instruments, a brass-player's lips can act as an acoustic generator only within a narrow frequency band quite close to their natural mechanical resonance frequency.[14] This resonance frequency is determined by their vibrating mass and their muscle tension. There is a threshold blowing pressure necessary to initiate the lip vibration that is determined by the lip tension (and is thus related to the lip vibration frequency) and by the acoustic impedance of the instrument and of the player's mouth cavity.[14]

We can put together a simple theory to describe the operation of this lip-valve generator. Suppose that $p_0(f)$ is the threshold gauge pressure in the mouth for excitation of the lip valve when producing a note of frequency f. If it is assumed that the lips are initially held closed, then to a first approximation this pressure will be that which is needed to force the lips open against the lip tension force T, and so will be proportional to T. If the vibrating mass m of the lips were independent of their tension, then their resonant frequency f would be proportional to $(T/m)^{1/2}$, so that we should expect $p_0(f)$ to be proportional to f^2. The structure of the soft tissue in the lips, however, is such that their vibrating mass m decreases markedly with increasing muscular tension. The measurements of Elliott and Bowsher[10] suggest that $m \propto 1/T$, so that it is a better approximation to write

$$p_0(f) = Kf, \tag{1}$$

where K is a constant. This expression agrees well with the experimental data in Fig. 4, which gives a value of about 7 Pa/Hz for K in the case of player GC, 8 Pa/Hz for NH, and 4 Pa/Hz for KB.

Once the lips are forced open by a blowing pressure p greater than p_0, they oscillate in resonance with the instrument horn, because the skilled player has chosen the tension to match the note he wishes to play. The lip vibration is approximately sinusoidal, because the frequency is near resonance, and the vibration amplitude is about equal to the equilibrium lip opening, so that the lips just close once in each cycle.[9] It is thus a reasonable assumption to write the linear opening x of the lips as

$$x = A(p - p_0)(1 + \cos 2\pi f t), \tag{2}$$

where p is the blowing pressure in the mouth and A is another constant, the magnitude of which is inversely proportional to lip tension, and thus to the frequency of the note being played. A is typically about 10^{-7} m Pa^{-1} for a high note, so that the lip opening would reach 1 mm for a blowing pressure 10 kPa above p_0 if it behaved linearly. It should be recognized, however, that the relation (2) cannot hold for very high pressures. Instead, the lip opening x will saturate, because of tissue nonlinearity and also the constraining effect of the mouthpiece, at a value not much more than 1 mm. This can be added as an upper limit to the relation (2).

Equation (2) actually conceals a great deal, for it does not show how the oscillating mouthpiece pressure actually leads to regeneration and thus to vibration of the lips. For this detail, the reader is referred to one of the more complete treatments of brass instruments.[8,10] In brief, however, the oscillating mouthpiece pressure is the main driver of lip motion, and the sounding frequency may be either a little above or below both the lip resonance and the horn resonance, depending upon the geometry of lip motion. For our present purposes, consideration of these details is unnecessary.

The lip opening is typically elliptical, but the axial ratio decreases as the lip opening increases. It is not feasible to model this exactly, but an interpolation is adequate. If the axial ratio of the ellipse remained constant, then the opening area S would vary as x^2, while if the width of the opening remained constant, then S would be simply proportional to x. It is therefore a reasonable approximation to take the area of the opening to be

$$S \approx Cx^{3/2}, \tag{3}$$

where C is a constant, the magnitude of which can be estimated to be about 0.05 $\mathrm{m}^{1/2}$ for typical lip-opening shapes.

At any instant, the quasi-static Bernoulli flow through the lips is then

$$U = (2/\rho)^{1/2}(p - p_1)^{1/2} S = B(p - p_1)^{1/2} x^{3/2}, \tag{4}$$

where p_1 is the back-pressure in the instrument mouthpiece, and B is another constant, of magnitude about 0.06 $\mathrm{m}^2\ \mathrm{kg}^{-1}$, as can be seen from (2) and (3). This back-pressure can be evaluated from the fact that the instrument operates at a resonance, so that its input impedance is nearly purely resistive and has a magnitude R that is typically of order 10^8 Pa m^{-3} s, allowing a bore diameter of about 8 mm and an effective Q-value of around 10 for the resonances. We consider later a refinement in which the magnitude of R varies with frequency. In any case, the back-pressure is $p_1 = RU$. Substituting this in (4), and squaring, leads to the quadratic equation

$$U^2 + B^2 R x^3 U - B^2 p x^3 = 0, \tag{5}$$

which has the solution

$$U = \frac{B^2 R x^3}{2}\left[\left(1 + \frac{4p}{B^2 R^2 x^3}\right)^{1/2} - 1\right]. \tag{6}$$

A. Power and efficiency

Equation (6) can be solved to find the component $\tilde{U}(nf)$ of the flow at the frequency nf of the nth harmonic by substituting (2) for x, performing a Fourier transform numeri-

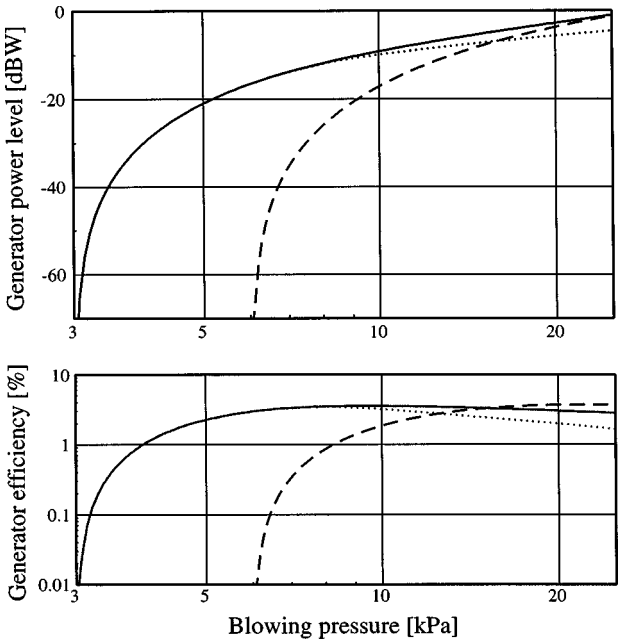

FIG. 7. Calculated acoustic power (in decibels relative to 1 W) produced by the lip generator, and the overall pneumatic efficiency of this generator, both as functions of blowing pressure. Two cases are plotted, corresponding to two notes an octave apart. In the case of the lower note, the dotted curve shows the behavior if the lip opening is limited to 1 mm.

cally, and retaining just the term at this frequency. The acoustic power supplied by the generator to the instrument is then

$$\Pi = \frac{1}{2} R \sum_n \tilde{U}(nf)^2. \tag{7}$$

Figure 7 shows the result of two such calculations for notes an octave apart, 250 and 500 Hz, using the parameter values given in the text and assuming $K = 7$ Pa/Hz in (1), as for player GC. Quantitative details of this calculation should not be given much attention, because the parameters involved were only roughly estimated and only terms up to $n = 3$ were included in the summation, but the overall behavior is significant. The acoustic power supplied by the lip generator rises sharply from zero as the blowing pressure exceeds the threshold value p_0, and settles down to a slope of about 5 to 15 dB per doubling of blowing pressure. If the lip aperture is limited by nonlinearity, however, then the characteristic turns over to a smaller slope at high blowing pressures as shown by the dotted portion of the curve for the lower note. For the higher note, the lip displacement reaches this limit only at about 20 kPa. These curves are individually very similar to the measured curves for individual notes in Fig. 1, though the quantitative agreement is not particularly good. The maximum calculated generator power is about 1 W at a blowing pressure of 25 kPa for no lip motion limitation, and about 0.3 W if the opening is limited to 1 mm. No upper limit to the blowing pressure appears in the case of the lower of the two notes.

Actually the consideration of terms up to only $n = 3$ in (7) is an adequate approximation, because we are dealing with the acoustic power supplied by the lip generator to the mouthpiece, not with the radiated sound. As discussed in the next section, the relative levels of upper harmonics in the mouthpiece flow, and thus in the mouthpiece pressure, are small compared to their relative levels in the radiated sound.

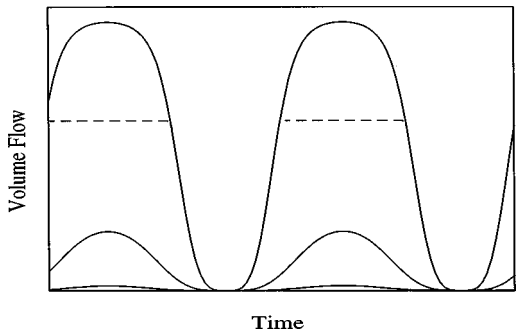

FIG. 8. Calculated lip flow waveforms for a trumpet at low, medium, and high playing levels. The broken curve shows the behavior if the lip opening is limited to 1 mm. The waveforms of the mouthpiece pressure are identical under the assumptions of the calculation.

The quantity plotted in Fig. 7 is not, as we have noted, the radiated acoustic power, but rather the acoustic power produced by the lip generator. Much of this power is dissipated in viscous and thermal losses to the walls of the instrument, and typically less than 10% is radiated as sound. The radiation efficiency itself behaves like the radiation resistance at the open bell of the instrument, and so rises at 6 dB/octave up to the radiation cutoff frequency, which is typically about 1000 Hz for a trumpet, above which it remains constant. We discuss the development of the radiated spectrum in the next section, but for the present we accept that the calculated maximum generator power of 1 W for high notes is therefore expected to result in only about 100 mW of acoustic output power. The measurements in Fig. 1 show a maximum sound pressure level of 110 dB at 1 m, which would correspond to about 1 W of radiated power from an isotropic radiator, since the A-weighting has little effect on total power measured over the frequency range of the trumpet. The trumpet radiation pattern is, however, far from uniform, so that the total radiated power is probably not much more than 100 mW. For lower notes, the transfer efficiency to radiation will be even smaller and, in particular, the lower-frequency full curve of Fig. 8 should be depressed by 6 dB relative to the higher-frequency curve because of the frequency dependence of the radiation resistance. The calculations are thus in better agreement with experiment than might have been expected from their approximate nature.

We might note the implications of this analysis for total acoustic efficiency, as measured by Bouhuys.[1] The total input pneumatic power is approximately $\Pi_0 = pU_0$, where U_0 is the zero-frequency flow component in the Fourier transform calculation above and we have neglected oscillations in mouth pressure. The generator efficiency is then simply Π/Π_0. This efficiency is also plotted in Fig. 7, and ranges from about 0.1% for very soft playing up to about 3% for loud playing, though this efficiency decreases slightly if the lip aperture is limited. Reducing these figures by a factor of about 10 for high notes and as much as 100 for low notes to convert them to radiated acoustic power gives overall efficiencies in remarkably good agreement with those measured by Bouhuys.[1]

B. Spectrum

Solution of Eq. (6) for the flow through the lip valve shows that it has the form in Fig. 8. Since we have assumed a constant value for the input resistance R at the harmonic resonance peaks, the mouthpiece pressure has the same form. For very soft playing the waveform is reasonably sinusoidal, but at higher levels it has a markedly distorted shape, with a plateau for large lip opening, when the flow is limited by the resonant horn resistance and the consequent mouthpiece back-pressure, and a rather sharp decrease to zero as the lips close. This calculation is in good qualitative agreement with the mouthpiece pressure measurements of Elliott and Bowsher.[10]

A flow with this shape has a spectrum that is nearly constant up to a frequency about n times that of the fundamental, where n is the mark/space ratio of the waveform when it is approximated by a rectangular wave. This conclusion, however, derives from the unduly simplified assumption that the resistive part R of the input impedance is the same at all the low resonances of the instrument. For a real trumpet this is not so, for the Helmholtz-type resonance of the volume of the mouthpiece cup, vented through the constricted back-bore and loaded by the characteristic impedance of the instrument bore, produces a resonant envelope to the input impedance, as investigated by Benade.[16] This leads to an envelope for R that rises to a broad peak with a Q value around 5, typically at 500–1000 Hz, and then decreases, and we should expect to find evidence of this in the spectrum. It is not difficult in principle to substitute such a frequency variation for R back into Eqs. (5)–(7), but we shall not bother to do this in detail. It suffices to note that such a procedure would certainly modify the spectrum of the power supplied by the lip-valve generator to reflect a similar mouthpiece resonance. This then explains the common envelope feature seen in all the low-level curves of Fig. 6.

We must now seek to explain the origin of the increased level and apparent actual power gain in the high-frequency components observed in loud playing. That there is indeed a discrepancy between the spectrum measured in the mouthpiece cup and that of the radiated sound is well known, and part of the explanation lies with the radiation behavior of the instrument horn. This is not entirely simple, as discussed by Benade and Jansson,[17] but the general conclusion is that there is a cut-off frequency, around 1 kHz, below which the radiated sound level rises at 6 dB/octave relative to the internal sound pressure, and above which the relation is flat. These considerations, together with the mouthpiece resonance, have been built into a generalized linear model for the transfer function between mouthpiece pressure and radiated sound by Elliott *et al.*[18] They conclude that, above the radiation cutoff, there is little if any power loss, at least for small signal levels where the linear approximation is valid. While this consideration is clearly important in determining the balance between low-frequency and high-frequency components of the radiated sound, it fails to explain the apparent power gain at high frequencies observed in loud playing.

This high-frequency discrepancy in the spectrum has been investigated by Beauchamp.[19] He reported that there is indeed a marked excess in the level of high-frequency components in the radiated sound, particularly above the radiation cutoff frequency, and that this level varies greatly with playing conditions, often appearing as an actual power gain. The explanation of this behavior has been given by Hirschberg *et al.*[20] who showed that it arises from nonlinear acoustic propagation behavior, particularly in the long cylindrical part of the instrument bore. Such nonlinear propagation behavior has been discussed in detail by Beyer,[21] but a brief semiquantitative discussion will be adequate here.

As we have already seen, the mouthpiece pressure p_0 rises each cycle to nearly the blowing pressure in the player's mouth, and thus perhaps as high as 25 kPa or about 180 dB relative to the normal reference level. While the pressure in the main bore is probably lower than this by a factor of at least 3, the level is sufficiently high that the propagation behavior is significantly nonlinear. This can be seen from an examination of a wave of even 2 kPa amplitude, in which the peak acoustic particle velocity is about 5 $\mathrm{m\,s^{-1}}$. Since the cylindrical part of the bore is around 1 m long, this leads to a convective transit-time gain of perhaps 0.05 ms for the high-frequency components in the compressive part of the propagating wave. The result is a steepening of the leading edge of this wave that increases as the pressure amplitude increases. In extreme cases a shock wave may even develop. Adiabatic temperature rise in the wave enhances the effect.

The result of this nonlinear propagation behavior is a transfer of energy from the low-frequency components of the mouthpiece waveform to higher harmonics, the extent of this transfer increasing as the blowing pressure is increased. Because of the initial rise of radiation resistance below cutoff, this transfer increases the radiated sound energy as well as providing an apparent power gain at high frequencies. This leads to an even greater increase in the subjectively perceived loudness, because the wider sound spectrum has less auditory masking, as discussed by Plomp.[22]

While we shall not attempt to investigate these phenomena in any detail in the present paper, it is possible to draw some semiquantitative conclusions from the experimental data. Referring to Fig. 6, we see that, while fitting straight lines as in Fig. 5 is not generally convincing, it is possible to describe the high-frequency extent of each curve by giving the frequency above which the harmonics are more than 20 dB below the spectral peak. This information is plotted in Fig. 9. The highest frequency measurements are limited by the frequency response of the microphone, and points shown as 16 kHz may well be higher. These results show that the high-frequency extension of the spectrum, and by implication wavefront steepening, increases about linearly with blowing pressure, which is what we should expect from the discussion in the previous paragraphs. For a given blowing pressure, the effects of wavefront steepening are less pronounced for higher notes.

It is not difficult to see the general reasons for this behavior, if we make the assumptions that extension of the spectrum above the frequency determined by the mouthpiece resonance and the radiation cutoff, namely about 1000 Hz, is caused almost entirely by nonlinear propagation effects, and that the magnitude of these nonlinear effects is proportional to the pressure amplitude in the propagating wave. Both

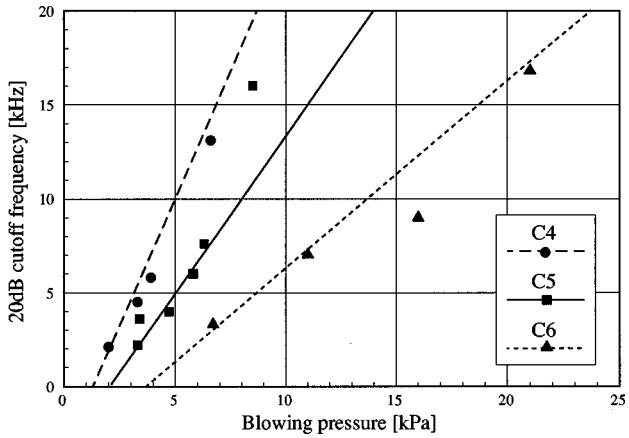

FIG. 9. Frequency at which the spectral envelope falls 20 dB below its peak value, as a function of blowing pressure, for three notes played on a B♭ trumpet. The lines have been drawn according to the prescription discussed in the text.

these assumptions are reasonable in terms of the discussion above, but require detailed justification.

Since the pressure in the instrument bore is proportional to the pressure $p_1 = RU$ in the mouthpiece, it is necessary first to examine the flow U through the lips, as given by (6), with the lip opening x given by (2). It is not possible to derive simply an expression for the extension of the spectrum as a function of blowing pressure for a given note pitch, but we seek rather to see how this extension, whatever it is, scales with pitch and blowing pressure. Suppose therefore that the flow $U(f,p)$ refers to a note of fundamental frequency f played with blowing pressure p. We seek to know the flow $U(\alpha f, \beta p)$ for a note of fundamental frequency αf played with blowing pressure βp. To increase the lip vibration frequency by a factor α requires an increase in lip tension and a decrease in lip moving mass by the same factor α, as discussed in relation to Eq. (1). This increases the threshold pressure p_0 by a factor α and changes the constant A in (2), and thus the value of x at a given pressure, by a factor α^{-1}. Similarly, to a reasonable approximation, increase in the blowing pressure by a factor β increases x by a factor β if the threshold is ignored.

Returning to (6), we find that the expression $4p/B^2R^2x^3$ is typically of order unity for $x \approx 1$ mm, which makes approximation difficult. If x is a good deal larger than this, then $U \approx p/R$, while if x is smaller, then $U \approx Bp^{1/2}x^{3/2}$. Adopting the latter expression and using the argument in the previous paragraph leads to the result

$$U(\alpha f, \beta p) \approx \beta^2 \alpha^{-3/2} U(f,p). \tag{8}$$

This means that, if the note frequency is raised by a factor α and the blowing pressure by a factor $\beta = \alpha^{3/4}$, then the flow, and hence the pressure and the spectral result, are all unchanged. This argument ignores the niceties of threshold pressure, and so holds only well above threshold. The upshot of this simplified argument is to suggest that, whatever the harmonic development curve for a note of sounding frequency f played with pressure p, this can be transformed to the corresponding curve for sounding frequency αf by increasing all the plotted blowing pressures by a factor $\alpha^{3/4}$. The exact value of the exponent in this prescription depends upon the behavior of lip opening shape embodied in Eq. (3). This may vary a little from player to player, but the extreme values are 0.5 and 1.

Referring to Fig. 9, we have a reference curve for the lowest frequency f that is a straight line not passing through the origin. The approximate relation given above then suggests that the curve for frequency $2f$ can be derived by simply multiplying all the pressures in the reference curve by $2^{3/4} \approx 1.7$, and the curve for frequency $4f$ by multiplying all the pressures in the reference curve by $4^{3/4} \approx 2.8$. The lines in the figure have been drawn to this prescription, and fit the experimental data quite well, which gives some measure of confirmation to the assumptions. For much larger blowing pressures and lip openings, we must turn to the result $U \approx p/R$, which suggests that all curves tend to the same asymptote in the limit of high pressures. It does not appear that this asymptote has been reached in the experimental data.

It must be emphasized that this argument is lacking in rigor and serves simply to provide a possible basis for explanation for the observed behavior. A proper analysis clearly requires explicit consideration of the pressure waveform and frequency and quantitative treatment of the nonlinear propagation.

IV. CONCLUSIONS

This experimental study has established, in a general way, the blowing technique used by typical trumpet players. In particular, we recognize the following features:

(1) a threshold blowing pressure for sounding of each note, this pressure rising linearly with the frequency of the note to be played;
(2) a rapid rise of radiated sound output for blowing pressures above threshold, settling down to a regime in which sound output power rises about 15 dB for each doubling of blowing pressure, the sound power for a given blowing pressure being nearly independent of the pitch of the note being played;
(3) a saturation regime, in which the sound output power rises only slowly with increasing blowing pressure, a doubling of blowing pressure increasing the sound level by only about 3 dB.

While this represents the general pattern of performance technique, there is a good deal of variation between individual performers in relation to the pressure range used, and thus the tone quality produced. At a more detailed level, these differences may also depend upon lip shape and musculature and upon learned playing technique. Some variation is also to be expected between trumpets with different mouthpiece sizes and bore diameters, though the range of variation among standard instruments is not large.

A first-order theoretical consideration suggests the underlying physics responsible for these results, in terms of the flow behavior of the vibrating lip-valve generator and nonlinear wave propagation in the main bore of the instrument. These considerations give expressions for the acoustic input power at the instrument mouthpiece, the spectrum of which is then modified by nonlinear propagation behavior in the

instrument bore, which steepens the wavefronts and transfers acoustic energy from low to high harmonics. These high harmonics are more efficiently radiated, produce a narrower radiation pattern, and enhance both the subjective loudness of the tone and its ability to rise above the general orchestral background.

Although manifestly incomplete in many details, the theoretical treatment outlined does appear to capture the essence of the performance technique used by trumpet players and to provide a skeleton upon which a more detailed understanding could be built.

ACKNOWLEDGMENTS

We are grateful to the trumpet players who participated in this study, and to Dr. A. Hirschberg, who provided perceptive comments on the first version of the paper. This work is part of a program supported by a grant from the Australian Research Council.

[1] A. Bouhuys, ''Sound-power production in wind instruments,'' J. Acoust. Soc. Am. **37**, 453–456 (1965).
[2] N. H. Fletcher, ''Acoustical correlates of flute performance technique,'' J. Acoust. Soc. Am. **57**, 233–237 (1975).
[3] L. Fuks and J. Sundberg, ''Blowing pressures in reed woodwind instruments,'' in *Quart. Prog. Status Rep., Speech Music and Hearing*, Royal Inst. Tech., Stockholm, No. 3/1996, pp. 41–56.
[4] D. Luce and M. Clark, ''Physical correlates of brass instrument tones,'' J. Acoust. Soc. Am. **42**, 1232–1343 (1967).
[5] M. Bertsch, ''Variabilities in trumpet sounds,'' Proc. Inst. Acoust. **19**(5), 401–406 (1997).
[6] J. A. Fiz, J. Aguilar, A. Carreras, A. Teixido, M. Haro, D. O. Rodenstein, and J. Morera, ''Maximum respiratory pressures in B♭ trumpet players,'' Chest **104**, 1203–1204 (1993).
[7] R. D. Ayers, ''New perspectives on the brass instruments,'' in *Proceedings of the International Symposium on Musical Acoustics*, Leavenworth, WA, 1998 (Acoustical Society of America, Woodbury, NY, 1998), pp. 129–134.
[8] N. H. Fletcher and T. D. Rossing, *The Physics of Musical Instruments* (Springer-Verlag, New York, 1992), Chaps. 13 and 14.
[9] D. W. Martin, ''Lip vibrations in a cornet mouthpiece,'' J. Acoust. Soc. Am. **13**, 305–308 (1942).
[10] S. J. Elliott and J. M. Bowsher, ''Regeneration in brass wind instruments,'' J. Sound Vib. **83**, 181–217 (1982).
[11] S. Yoshikawa, ''Acoustical behavior of brass player's lips,'' J. Acoust. Soc. Am. **97**, 1929–1939 (1995).
[12] S. Adachi and M. Sato, ''On the transition of lip vibration states in the brass instrument,'' in *Proceedings of the International Symposium on Musical Acoustics*, Dourdan, France, 1995 (IRCAM, Paris, 1995), pp. 17–22.
[13] D. C. Copley and W. J. Strong, ''A stroboscopic study of lip vibrations in the trombone,'' J. Acoust. Soc. Am. **99**, 1219–1226 (1996).
[14] N. H. Fletcher, ''Excitation mechanisms in woodwind and brass instruments,'' Acustica **43**, 63–72 (1979).
[15] N. H. Fletcher, ''Autonomous vibration of simple pressure-controlled valves in gas flows,'' J. Acoust. Soc. Am. **93**, 2172–2180 (1993).
[16] A. H. Benade, *Fundamentals of Musical Acoustics* (Oxford U. P., New York, 1976), pp. 400–405.
[17] A. H. Benade and E. V. Jansson, ''On plane and spherical waves in horns with nonuniform flare,'' Acustica **31**, 80–98 (1974).
[18] S. J. Elliott, J. Bowsher, and P. Watkinson, ''Input and transfer response of brass wind instruments,'' J. Acoust. Soc. Am. **72**, 1747–1760 (1982).
[19] J. W. Beauchamp, ''Analysis of simultaneous mouthpiece and output waveforms of wind instruments,'' in Audio Eng. Soc. Preprint No. 1626 (1980); also ''Inference of nonlinear effects from spectral measurements of wind instrument sounds,'' J. Acoust. Soc. Am. **99**, 2455A (1996).
[20] A. Hirschberg, J. Gilbert, R. Msallam, and A. P. J. Wijnands, ''Shock waves in trombones,'' J. Acoust. Soc. Am. **99**, 1754–1758 (1996).
[21] R. T. Beyer, *Nonlinear Acoustics* (US Naval Sea Systems Command, 1974).
[22] R. Plomp, *Aspects of Tone Sensation* (Academic, New York, 1976), Chap. 5.

Discrimination of musical instrument sounds resynthesized with simplified spectrotemporal parameters[a)]

Stephen McAdams[b)]
Laboratoire de Psychologie Expérimentale (CNRS), Université René Descartes, EPHE, 28 rue Serpente, F-75006 Paris, France and Institut de Recherche et de Coordination Acoustique/Musique (IRCAM/CNRS), I place Igor-Stravinsky, F-75004 Paris, France

James W. Beauchamp[b)]
School of Music and Department of Electrical and Computer Engineering, University of Illinois at Urbana-Champaign, 2136 Music Building, 1114 West Nevada Street, Urbana, Illinois 61801

Suzanna Meneguzzi
Laboratoire de Psychologie Expérimentale (CNRS), Université René Descartes, EPHE, 28 rue Serpente, F-75006 Paris, France and IRCAM, I place Igor-Stravinsky, F-75004 Paris, France

(Received 17 November 1997; revised 21 September 1998; accepted 23 September 1998)

The perceptual salience of several outstanding features of quasiharmonic, time-variant spectra was investigated in musical instrument sounds. Spectral analyses of sounds from seven musical instruments (clarinet, flute, oboe, trumpet, violin, harpsichord, and marimba) produced time-varying harmonic amplitude and frequency data. Six basic data simplifications and five combinations of them were applied to the reference tones: amplitude-variation smoothing, coherent variation of amplitudes over time, spectral-envelope smoothing, forced harmonic-frequency variation, frequency-variation smoothing, and harmonic-frequency flattening. Listeners were asked to discriminate sounds resynthesized with simplified data from reference sounds resynthesized with the full data. Averaged over the seven instruments, the discrimination was very good for spectral envelope smoothing and amplitude envelope coherence, but was moderate to poor in decreasing order for forced harmonic frequency variation, frequency variation smoothing, frequency flattening, and amplitude variation smoothing. Discrimination of combinations of simplifications was equivalent to that of the most potent constituent simplification. Objective measurements were made on the spectral data for harmonic amplitude, harmonic frequency, and spectral centroid changes resulting from simplifications. These measures were found to correlate well with discrimination results, indicating that listeners have access to a relatively fine-grained sensory representation of musical instrument sounds. [S0001-4966(99)00202-7]

PACS numbers: 43.66.Jh, 43.75.Wx [WJS]

INTRODUCTION

It has been traditional to view musical sounds in terms of a spectral model that describes them as a series of sinusoidal components, each having an amplitude and a frequency. Often, as is the case in this article, these sounds have frequencies which are harmonically related to a fundamental frequency, or at least approximately so. While many experiments on timbre have used fixed frequencies and fixed relative amplitudes (Miller and Carterette, 1975; Plomp, 1970; Preis, 1984; von Bismarck, 1974), analyses of musical instrument sounds reveal that these parameters have a great deal of variation, leading to the conjecture that these variations are responsible, in large part, for the uniqueness of the individual sounds.

For example, we can think of the amplitudes (A) and frequencies (f) varying over time (t) and having two parts, a smoothly or slowly moving part (1) and a more rapidly changing microvariation part (2):

$$A_k(t) = A1_k(t) + A2_k(t), \tag{1}$$

$$f_k(t) = f1_k(t) + f2_k(t), \tag{2}$$

where k refers to the harmonic number. Alternatively, since we consider only quasiharmonic sounds here, we can also break the frequency into two other parts:

$$f_k(t) = k\overline{f_0}(t) + \Delta fi_k(t), \tag{3}$$

where $\overline{f_0}$ is the fundamental frequency averaged over several harmonics and Δfi_k is an inharmonic frequency deviation, both varying over time.

Figure 1 gives a block diagram of a spectral representation model using the parameters of Eqs. (1) and (2), which is also an additive, sine-wave-synthesis model. The question to be explored in this article is: to what degree can these parameters be simplified, without making them discriminable, with respect to sounds containing the full amount of information? A given sound can be reconstituted with high quality from the full representation using time-varying additive synthesis. However, such a representation is quite data inten-

[a)]Portions of these results were presented at the 133rd meeting of the Acoustical Society of America (Beauchamp *et al.*, 1997).

[b)]Address correspondence to either S. McAdams at IRCAM (Electronic mail: smc@ircam.fr) or to J. Beauchamp at UIUC (Electronic mail: j-beauch@uiuc.edu).

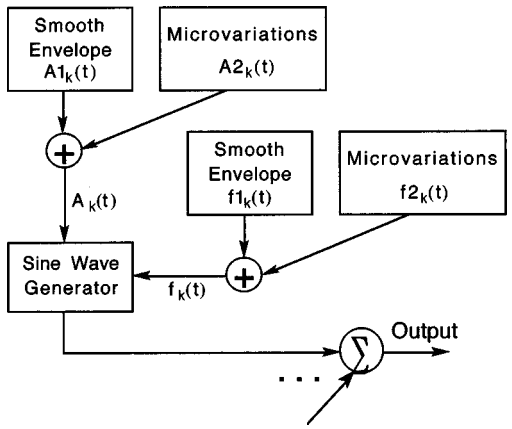

FIG. 1. Spectral-representation model using smooth and microvariation envelopes for amplitude and frequency. Each harmonic *k* is summed with the others to form the total output by additive synthesis.

sive. Any possibility of reducing the data would alleviate storage problems and accelerate the process of synthesis, which is particularly important for real-time sound synthesis. Also, one might hope that such simplifications would lead to the possibility of streamlined synthesis control using a few well-chosen, perceptually relevant parameters. Most important for us, however, is that knowledge about the sensitivity of human listeners to certain kinds of sound simplifications may provide clues for understanding the sensory representation of musical sounds. Specifically, this study is aimed at determining the relative perceptual importance of various spectrotemporal features which we have suspected are important for making timbral distinctions and for judging sound quality.

A few researchers have already addressed the problem of perceptually relevant data reduction using discrimination paradigms. Grey and Moorer (1977) used a rectangular-window, heterodyne-filter analysis algorithm and time-varying additive synthesis to prepare their stimuli based on 16 sounds from various bowed-string, woodwind, and brass instruments of duration 0.28 to 0.40 s. They asked their subjects (musical listeners) to discriminate between five versions of the sounds: (1) the digitized original analog tape recording, (2) a complete synthesis using all time-varying amplitude and frequency data resulting from the analysis stage, (3) a synthesis using a small number of line-segment approximations to the amplitude and frequency envelopes, (4) the same modification as version (3) with removal of low-amplitude initial portions of attack transients, and (5) the same modification as (3) with frequencies fixed in harmonic relation to the fundamental frequency (frequency-envelope flattening). Listeners heard four tones in two pairs and had to determine which pair contained a different tone. They were allowed to respond ''no difference heard.'' Discrimination scores were computed as the probability that the correct interval was chosen plus half the probability that a no difference response was given (ostensibly to simulate random guessing on those trials).

An important result was the low discrimination scores for comparisons of versions (2) and (3), which ranged from 0.48 to 0.80 (depending on the instrument), with an average of only 0.63. This indicated that microvariations in amplitude and frequency are usually of little importance, implying the possibility for significant data reduction. However, the authors gave no algorithm for fitting the straight lines to the data or criteria for error, but stated only that the number of segments varied between four and eight per parameter over each tone's duration. Also, since the tones were short and some segments were needed to fit attack transients, it is not clear how these results can be extrapolated for longer sounds. Discrimination rates between versions (3) and (4) and between (3) and (5) were similarly low, averaging 0.65 (range: 0.55 to 0.74) and 0.68 (range: 0.56 to 0.92), respectively. The results indicated that there were significant differences among the 16 instruments.

In general, discrimination rates for single simplifications were low, and relatively high rates (above 0.85) only occurred for multiple simplifications. For example, the average discrimination rate between versions (1) and (5), where three simplifications were combined, was 0.86. From our experience, these figures seem low. We can only conjecture that this was due to the short tones used, to noise on the analog tape used for stimulus presentation which may have masked some parameter variation details, and perhaps even to the experimental instructions which specifically oriented listeners toward differences in quality of articulation and playing style rather than toward any audible difference.

Charbonneau (1981) extended Grey and Moorer's study [based on their version (3) representation] by constructing instrumental sounds that maintained their global structure, while simplifying the microstructure of the amplitude and frequency envelopes of each harmonic partial. The first simplification was applied to the components' amplitude envelopes, each component having the same amplitude envelope (calculated as the average harmonic-amplitude envelope) scaled to preserve its original peak value and start- and end times. (This is similar to our amplitude-envelope coherence simplification; see Sec. I below.) The second simplification was similarly applied to the frequency envelopes, each having the same relative frequency variation as the fundamental, meaning that the sound remained perfectly harmonic throughout its duration (similar to our frequency-envelope coherence simplification; see Sec. I below). The third simplification resulted from fitting the start- and end-time data to fourth-order polynomials. Listeners were asked to evaluate the timbral differences between original [version (3)] and simplified sounds on a scale from 0 (no difference) to 5 (large difference). Results indicated that the amplitude-envelope simplification had the greatest effect. However, as for the Grey and Moorer study, the strength of the effect depended on the instrument.

Sandell and Martens (1995) used a different approach to data reduction. The harmonic time-frequency representation derived from a phase-vocoder analysis was treated as a data matrix that could be decomposed into a number of linearly recombinable principal components from either a temporal or a spectral perspective. The recombination of the appropriately weighted principal components can be used to regenerate the signal of a given instrument sound. These authors estimated the number of principal components necessary to

achieve a simplified sound that was not reliably discriminated from a sound reconstructed from the full (though down-sampled) analysis data. From these results, they could then compute the proportion of data reduction possible without compromising perceived sound quality. They achieved considerable data reduction for the three instruments tested, but the amount varied a great deal across instruments. One interpretation problem that often plagues perceptually oriented principal components analyses on acoustic data (see also, Repp, 1987) is that the perceptual nature and relevance of the individual components is most often difficult to conceive. For example, it is not clear that they could represent perceptual dimensions with clearly defined acoustic characteristics along which stimuli could be varied intuitively in sound synthesis.

This reservation notwithstanding, the results of these three studies demonstrate that timbre changes result from simplification of the signal representation. In fact, it is clear from the two earlier studies that the simplifications performed on temporal parameters, and specifically on time-varying functions of amplitude and frequency, influence to a greater or lesser degree the discrimination of musical sounds.

In the present study, we sought to determine precisely the extent to which simplified spectral parameters affect the perception of synthesized instrumental sounds, using tones of 2-s duration and without the use of straight-line approximations. We measured the discrimination of several kinds of simplifications for sounds produced by instruments of various families of resonators (air column, string, bar) and types of excitation (bowed, blown, struck). Two of the simplifications we chose (amplitude-envelope coherence and spectral-envelope smoothness) were derived from previous studies on timbre perception and corresponded to acoustic parameters that are highly correlated with perceptual dimensions revealed by multidimensional scaling techniques (Grey and Gordon, 1978; Iverson and Krumhansl, 1993; Krimphoff *et al.*, 1994; McAdams *et al.*, 1995). The other four simplifications related to the perceptibility of microvariations of amplitude and frequency over time, with much having been written about the latter (Brown, 1996; Dubnov and Rodet, 1997; McAdams, 1984; Sandell and Martens, 1995; Schumacher, 1992).

In addition, various combinations of these simplifications were applied to the sounds in groups of two, three, or four. We hypothesized that accumulated simplification along several perceptual dimensions would increase discrimination. Below, we present the technique used for analyzing and synthesizing the stimuli, followed by a description of the discrimination experiment. The results are then discussed in terms of musical synthesis and the perceptual representation of musical signals.

I. ANALYSIS/SYNTHESIS METHOD

Seven prototype musical instrument sounds were selected for analysis using a computer-based phase-vocoder method (Beauchamp, 1993). This phase vocoder is different than most in that it allows tuning of the fixed analysis frequency (f_a) to coincide with the estimated fundamental frequency of the input signal. The analysis method yields the frequency deviations between harmonics of this analysis frequency and the corresponding frequency components of the input signal, which are assumed to be at least approximately harmonic relative to its fundamental.

A. Signal representation

For each sound, an analysis frequency was chosen that minimized the average of the harmonic frequency deviations. Thus, a time-varying representation was achieved for each sound according to the formula

$$s(t)=\sum_{k=1}^{K} A_k(t)\cos\left(2\pi\int_0^t (kf_a+\Delta f_k(t)dt)+\theta_k(0)\right), \tag{4}$$

where

$s(t)=$ sound signal,
$t=$ time in s,
$k=$ harmonic number,
$K=$ number of harmonics,
$A_k(t)$ is the amplitude of the kth harmonic at time t,
$f_a=$ analysis frequency,
$\Delta f_k(t)$ is the kth harmonic's frequency deviation, such that $kf_a+\Delta f_k(t)$ is the exact frequency of the kth harmonic, and
$\theta_k(0)$ is the initial phase of the kth harmonic.

The parameters used for synthesis that were simplified in this study are $A_k(t)$ and $\Delta f_k(t)$. No attempt was made to simplify $\theta_k(0)$. Although $A_k(t)$ and $\Delta f_k(t)$ were only stored as samples occurring every $1/(2f_a)$ s, the signal was approximated with reasonable accuracy at a much higher resolution (sample frequency 22 050 or 44 100 Hz) by using linear interpolation between these values. Synthesis was accomplished by additive (or Fourier) synthesis of the harmonic sine waves.

B. Prototype sounds

Sounds of the instruments clarinet, flute, harpsichord, marimba, oboe, trumpet, and violin were selected in order to have one representative from each of several families of instruments whose tones are at least approximately harmonic. Five of the sounds were taken from the McGill University Master Samples recordings, one from Prosonus (oboe), and one (trumpet) had been recorded at the UIUC School of Music. An attempt was made to select sounds that were of high quality, that represented the instruments well, and that had fundamental frequencies close to 311.1 Hz (E-flat 4), a note within the normal playing range of these instruments.[1] Since synthesis was accomplished by an additive method based on Eq. (1), it was easy to alter the stimuli's fundamental frequencies (f_a) to be exactly 311.1 Hz. Table I gives some basic characteristics of the prototype sound signals.

C. Analysis method

The phase vocoder method used for analysis consists of the following steps:

TABLE I. Data for the seven instrument sounds used in the study. For McGill source recordings, the numbers indicate volume:track-index. For Prosonus recordings, they indicate woodwinds volume:band-index. Attack (t_1) is the time in the original sound at which the attack was estimated to end. Decay (t_2) is the time in the original sound at which the decay was estimated to begin. The marimba and harpsichord, being impulsively excited instruments, have no sustain portions. The marimba, being shorter than the target 2-s duration, was stretched rather than shortened, and so the attack and decay values were not used.

	Source of original recording	Original fundamental frequency (Hz)	Original duration of sound, t_L (s)	Number of harmonics used in analysis, K	Attack, t_1 (s)	Decay, t_2 (s)
Clarinet (Cl)	McGill (2:10-14)	311.4	3.81	70	0.05	3.50
Flute (Fl)	McGill (9:86-04)	311.0	2.31	70	0.25	2.10
Harpsichord (Hc)	McGill (11:95-06)	311.1	2.97	70	0.04	2.97
Marimba (Mb)	McGill (3:04-23)	312.2	1.83	70	...	...
Oboe (Ob)	Prosonus (W1:04-04)	311.8	2.98	30	0.15	2.20
Trumpet (Tp)	UIUC	350.0	2.43	31	0.32	1.30
Violin (Vn)	McGill (9:63-03)	311.1	4.94	66	0.22	4.10

(1) Band-limited interpolation of the input signal to produce a power-of-two number of samples per analysis period ($1/f_a$), which is the lowest possible to exceed the number of original samples in this time interval.
(2) Segmentation of the input signal into contiguous frames whose lengths are equal to twice the analysis period ($2/f_a$) and which overlap by half an analysis period ($f_a/2$).
(3) Multiplication of each signal frame by a Hamming window function whose length is two analysis periods ($2/f_a$).
(4) Fast Fourier transform (FFT) of the resulting product to produce real and imaginary components at frequencies 0, $f_a/2$, f_a, $3f_a/2$,..., $f_s/2-f_a$, where f_s is the sampling frequency. Components which are not positive integer multiples of f_a are discarded.
(5) Right-triangle solution of each retained real and imaginary part to give the amplitude and phase of each harmonic.
(6) Computation of the frequency deviation for each harmonic by a trigonometric identity which essentially gives the difference in phase between frames for each harmonic.
(7) Storage of the harmonic-and frequency-deviation data in an ''analysis file.'' The number of harmonics stored is less than $f_s/(2f_a)$. The analysis file for each sound is the basis for further sound processing.

Further details of this procedure are discussed by Beauchamp (1993).

The analysis system may be viewed as a set of contiguous bandpass filters which have identical bandwidths (f_a) and are centered at the harmonics of the analysis frequency (f_a). The basic assumption is that the signal consists of harmonic sine waves which line up with the filters such that each filter outputs one of the sine waves. The analysis gives the amplitude and frequency of each sine wave. When the sine waves are summed, the signal is almost perfectly reconstructed. In fact, the sine-wave sum can be viewed as that created by processing the input signal by the sum of the bandpass-filter characteristics. It can be shown that this sum is flat within ± 1 dB over the range $[f_a/2, f_s/2]$. Figure 2 shows a block diagram of the basic analysis/ synthesis system and Fig. 3 shows a typical set of amplitude and frequency data.

D. Types of simplification

Spectral simplifications were performed on the analysis data, after which the sounds were synthesized by the additive method. In order that sound duration would not be a factor in the study, most of the sounds were shortened to a 2-s duration by resampling the analysis data. Rather than resampling at a uniform rate, the sounds were resampled to preserve their attack and decay portions and shorten their interior portions while retaining their microstructural variations in amplitude and frequency. This was done by first observing the sound's rms amplitude given by

$$A_{\mathrm{rms}}(t) = \sqrt{\sum_{k=1}^{K} A_k^2(t)}, \tag{5}$$

and then identifying by eye the time intervals corresponding to the attack and decay as $(0,t_1)$ and (t_2,t_L) (see Table I for chosen values of t_1 and t_2), where t_L is the original sound duration. The marimba was an exception to this procedure, since its original duration was 1.83 s. The data for this instrument were simply stretched to obtain a duration of 2 s,

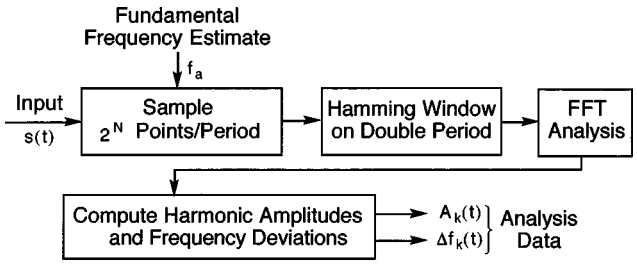

FIG. 2. Method for time-varying spectral analysis that yields the amplitude and frequency deviations for each harmonic k. The exact frequency for harmonic k is given by $f_k = k\, f_a + \Delta f_k(t)$, where f_a is the analysis fundamental frequency.

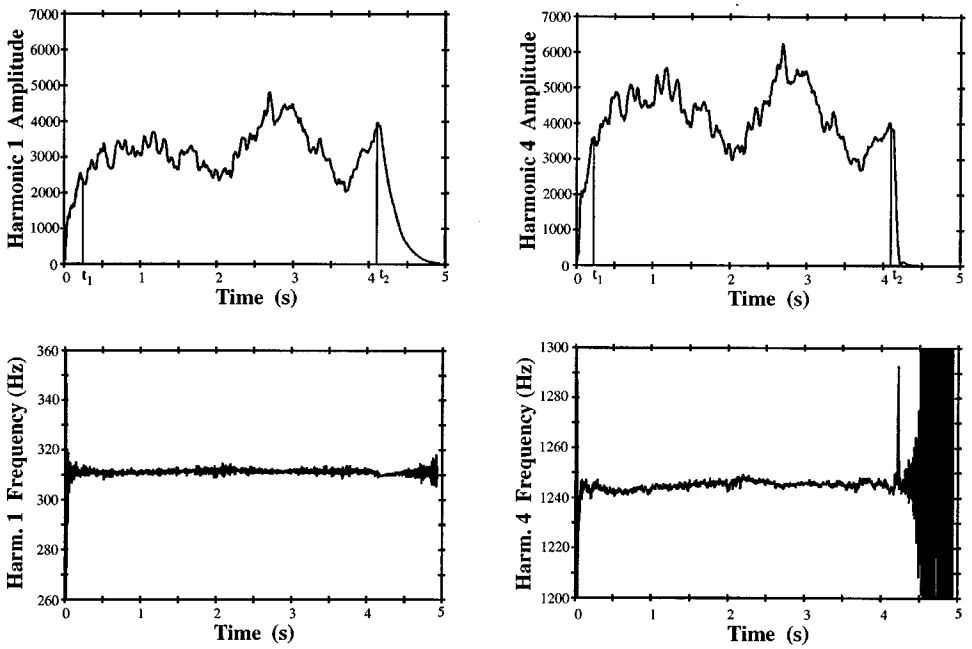

FIG. 3. Example spectral-analysis data for original violin tone (left column: first harmonic; right column: fourth harmonic; upper row: amplitude envelopes; lower row: frequency envelopes). Note the difficulty in reliably estimating the frequency of harmonic 4 when its amplitude approaches zero. Attack (t_1) and decay (t_2) boundaries are indicated.

and no notable degradation of the musical quality of the original was noted by the authors.

Second, for each harmonic amplitude and frequency deviation, the time intervals (t_1, t_1+2) and (t_2-2, t_2) were cross-faded using a cubic function to minimize any discontinuities. Thus, between the times t_1 and t_2, the sound was transformed from what it sounded like in the region of time t_1 to what it sounded like in the region of time t_2 over a period of $2-(t_1+t_L-t_2)$ s. This gave each sound a total duration of 2 s. In order for this method to work properly, we assumed that each sound had a microstructure which was statistically uniform over the interval (t_1, t_2). Since the sounds selected had no vibrato, this assumption seemed to be valid, and the resulting synthesized sounds were judged by the authors to be free of artifacts. Details on the duration-shortening algorithm are given in Appendix A. Figure 4 shows a set of data corresponding to Fig. 3 after application of the duration-shortening algorithm. Note that t_1 and t_2 are indicated in Fig. 3.

Finally, the seven duration-equalized prototype sounds were compared, and amplitude multipliers were determined such that the sounds were judged by the authors to have equal loudness. When the sounds were synthesized with the shortened duration, the amplitude multipliers, and a synthesis fundamental frequency of 311.1 Hz, they were judged to be equal in loudness, pitch, and duration. (It should be mentioned, however, that this equalization was not central for the present study, since each discrimination pair was always derived from a single prototype sound.) The equalized sounds then served as the reference sounds for this study, and their corresponding data sets are henceforth referred to as the analysis data.

Six primary simplifications of the analysis data were performed prior to synthesis. Each of these simplifications constitutes a major reduction in the amount of data used for synthesis.

1. Amplitude-envelope smoothness (AS)

The objective of this operation was to remove microvariations or noise in the harmonic amplitude over time, as these had been shown to be perceptually salient in previous work by Charbonneau (1981). These envelopes $A_k(t)$ were processed by a second-order recursive digital filter having a Butterworth response and a smoothing cutoff frequency of 10 Hz. This essentially removed all microdetail in the amplitude envelopes. However, we did not smooth the attack portions of the envelopes $(0 \leqslant t \leqslant t_1)$ since we only wished to determine the importance of microdetail in the amplitude envelopes thereafter. Smoothing the attack portions would have slowed the attacks, unintentionally affecting discrimination of the simplified sounds from their corresponding reference sounds. In order to avoid discontinuity, the attack portion of each amplitude envelope was cross-faded into the subsequent smoothed portion over a few frame points corresponding to the delay of the filter. In this way, the attack portions were essentially unaltered by the smoothing operation (see Table I for t_1 values).

2. Amplitude-envelope coherence (AC) (spectral envelope fixing)

The objective was to test the effect of eliminating *spectral flux* (defined as the change in shape of a spectral envelope over time) without changing the rms amplitude envelope or the average spectrum. Spectral flux has been found to be an important perceptual dimension of timbre (Grey, 1977; Krumhansl, 1989; Krimphoff *et al.*, 1994). To eliminate spectral flux, the amplitude envelope $A_k(t)$ for each har-

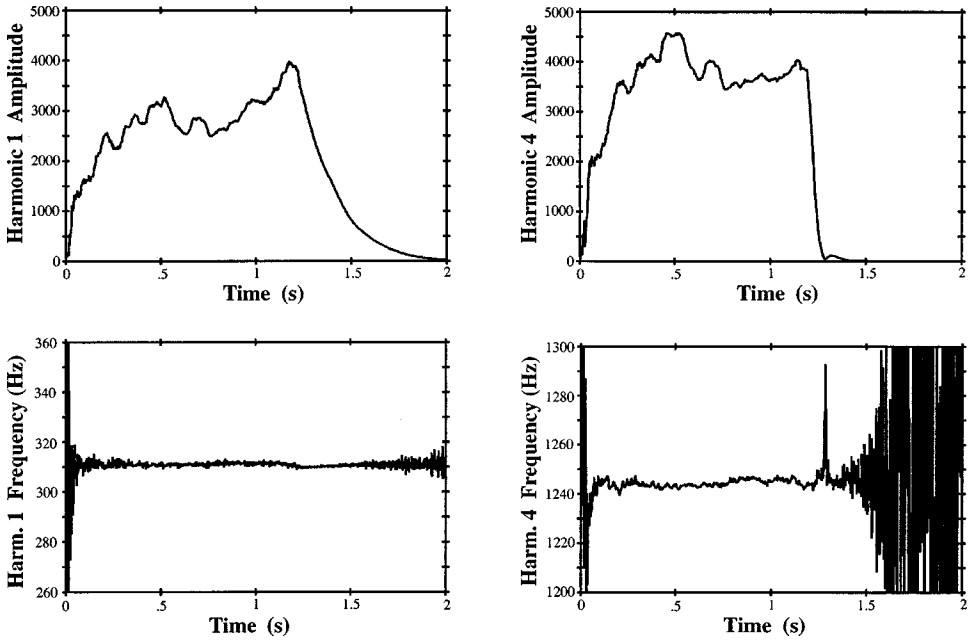

FIG. 4. Example spectral-analysis data for violin tone with duration reduced to 2 s (left column: first harmonic; right column: fourth harmonic; upper row: amplitude envelopes; lower row: frequency envelopes).

monic k was replaced by a function which was proportional to the rms envelope and the average amplitude of the harmonic. Thus, the harmonic-amplitude ratios $[A_2(t)/A_1(t)$, etc.] were fixed during the course of the sound. In addition, the amplitudes were scaled in order to preserve the rms envelope under this transformation. The formula for this transformation is:

$$A_k(t) \leftarrow \frac{\overline{A_k} A_{\mathrm{rms}}(t)}{\sqrt{\Sigma_{k=1}^{K} \overline{A_k}^2}}, \tag{6}$$

where $\overline{A_k}$ signifies the time average of the kth harmonic amplitude over the sound's duration and $\leftarrow$ signifies the replacement operation. Note that with this transformation, all amplitude envelopes of all harmonics have the same shape, albeit with different scale factors.

3. Spectral envelope smoothness (SS)

The question to be answered here is whether jaggedness or irregularity in the shape of a spectrum is perceptually important. For example, the clarinet has a characteristically ''jagged'' up-and-down spectral envelope due to weak energy in the low-order, even harmonics. A smoothing of this spectral envelope would give it more of a low-pass form. Spectral-envelope smoothness was found by Krimphoff *et al.* (1994) to correspond to the third dimension of Krumhansl's (1989) 3D space. To test this, the time-varying spectra were smoothed with respect to frequency. To accomplish this, at each time frame each harmonic amplitude was replaced by the average of itself and its two neighbors (except for endpoint harmonics number 1 and K, where averages of themselves and their neighbors were used)

$$A_1(t) \leftarrow \frac{A_1(t)+A_2(t)}{2}, \tag{7a}$$

$$A_k(t) \leftarrow \frac{A_{k-1}(t)+A_k(t)+A_{k+1}(t)}{3}, \quad k \notin \{1,K\}, \tag{7b}$$

$$A_K(t) \leftarrow \frac{A_{K-1}(t)+A_K(t)}{2}. \tag{7c}$$

This smoothing algorithm is not unique and may not be optimal, but it is perhaps the simplest one can imagine. According to this algorithm, the smoothest possible spectrum is one that follows a straight-line curve (i.e., $A_k = a + b \cdot k$), since such a spectral envelope would not be altered by this transformation.

Figure 5 compares the time-varying amplitude spectrum of a reference sound with those obtained after increasing amplitude-envelope smoothness, amplitude-envelope coherence, and spectral-envelope smoothness algorithms have been applied. The effect of these operations on the reference time-varying spectrum is readily apparent.

4. Frequency envelope smoothness (FS)

We wished to test the auditory importance of frequency microvariations in a parallel fashion to that of amplitude microvariations. Therefore, the envelopes $\Delta f_k(t)$ were processed similarly to the $A_k(t)$ envelopes in amplitude-envelope smoothing described above, except that smoothing was done over the entire sound's duration, including the attack phase. This operation did not grossly affect the frequency variation during the attack, as amplitude-envelope smoothing would have affected amplitude variation during that period had it included the attack.

5. Frequency envelope coherence (FC) (harmonic frequency tracking)

Here, we wanted to test the discriminability of inharmonicity among a sound's partials, even if it sometimes occurs

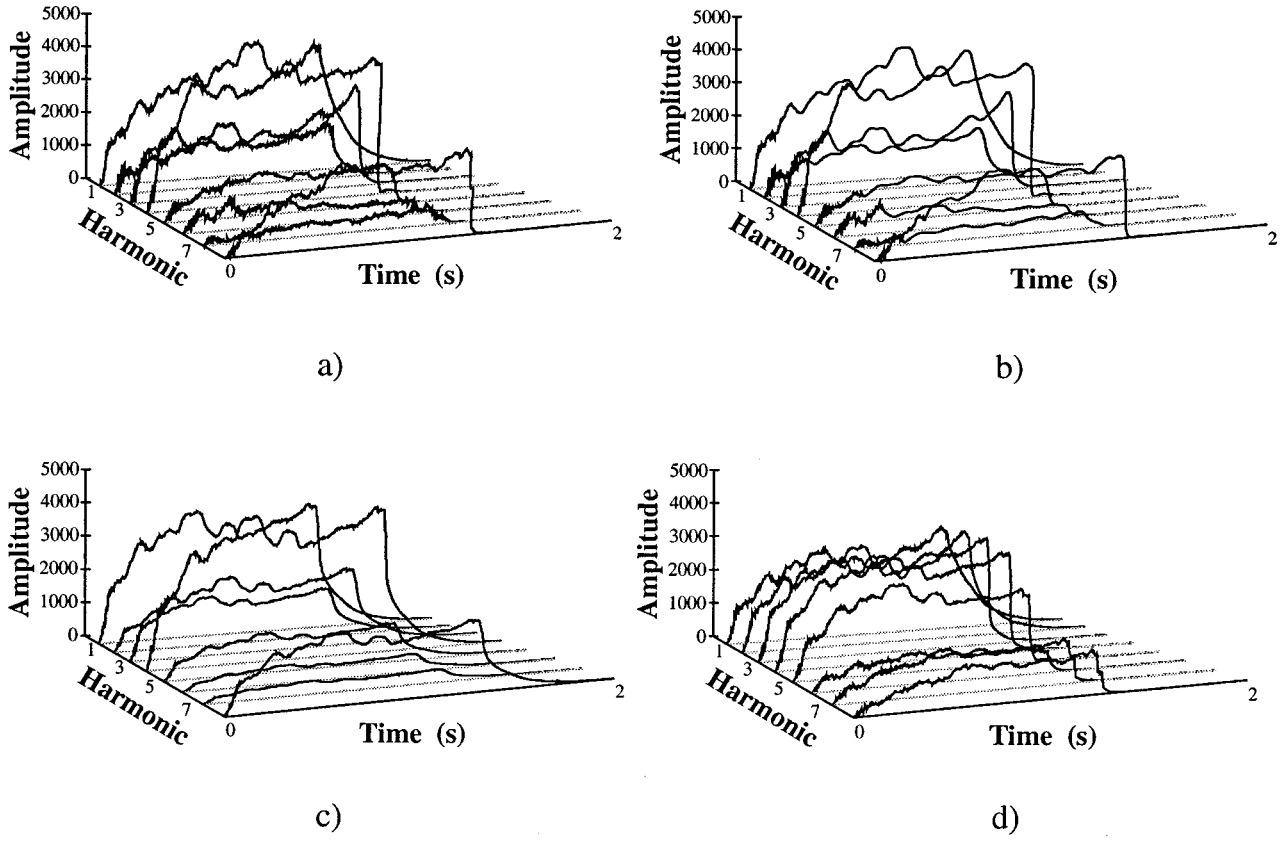

FIG. 5. Simplifications of amplitude envelopes for harmonics 1 to 8: (a) full violin-tone analysis data (reference sound) (b) after amplitude-envelope smoothing, (c) after rms envelope substitution (amplitude-envelope coherence), (d) after spectral-envelope smoothing.

only momentarily. Analogously to the amplitude-envelope coherence case, all frequency envelopes over time are tied together in a perfect harmonic relation. First, an average temporal-frequency contour was computed on the envelope for the first five harmonics, and then the individual harmonic contours were set equal to this contour multiplied by their respective harmonic numbers.

$$f_K(t) \leftarrow k\overline{f_0(t)}, \tag{8}$$

where $\overline{f_0(t)}$ is defined by

$$\overline{f_0(t)} = \frac{\Sigma_{k=1}^{5} A_k(t)\,(1/k)\,f_k(t)}{\Sigma_{k=1}^{5} A_k(t)}. \tag{9}$$

With this method, the strongest harmonics among the first five receive the ''highest votes'' for determining the average fundamental frequency of the sound. The measured frequency of the first harmonic could have been used instead of $\overline{f_0}$. However, it is possible that the first harmonic may be weak in amplitude, which with phase-vocoder analysis would result in a poorly defined frequency envelope (Moorer, 1978). This method obviates that problem.

6. Frequency envelope flatness (FF)

This simplification tested listeners' abilities to discriminate the combination of no frequency variations and no inharmonicity, as after this operation is performed, neither are present in the synthesized sounds. Indeed, there is no frequency envelope, as each harmonic's frequency is set equal to the product of its harmonic number (k) and the fixed analysis frequency (f_a). This operation had previously been found to have an effect on discrimination by Grey and Moorer (1977) and Charbonneau (1981).

Figure 6 shows a reference set of harmonic-frequency envelopes in comparison to those which have been simplified by frequency-envelope smoothing, frequency-envelope coherence, and frequency-envelope flattening.

Each simplification is accompanied by a certain amount of data reduction. Formulas for data reduction are given in Appendix B.

II. EXPERIMENTAL METHOD

A. Subjects

The 20 subjects were aged 19 to 35 years and reported no hearing problems. They included ten musicians (six males, four females) and ten nonmusicians (four males, six females). Musicians were defined as being professionals, semiprofessionals, or having at least 6 years of practice on an instrument and playing it daily. Nonmusicians were defined as having practiced an instrument for not more than 2 to 3 years in their childhood or adolescence, and no longer playing. The subjects were paid for their participation with the exception of three who were members of the auditory-perception team at IRCAM.

B. Stimuli

The seven instruments chosen belong to the air column (air reed, single reed, lip reed, double reed), string (bowed,

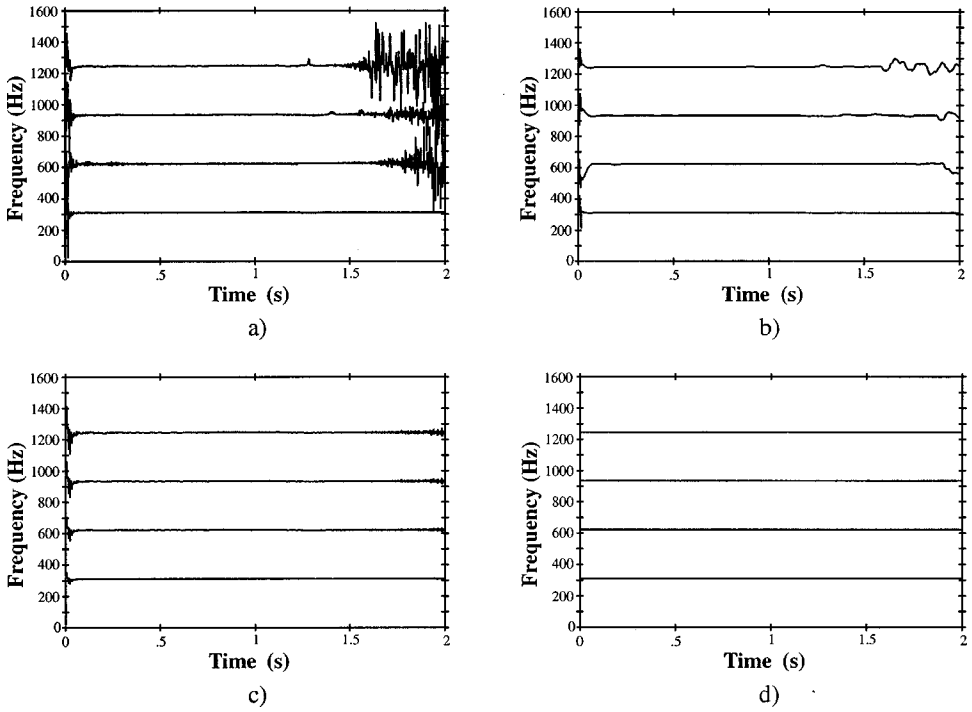

FIG. 6. Simplifications of frequency envelopes for harmonics 1 to 4: (a) full violin-tone analysis data (reference sound), (b) after frequency-envelope smoothing, (c) after average frequency-envelope substitution (frequency-envelope coherence), (d) after replacement by fixed harmonics (frequency-envelope flattening).

plucked), and bar (struck) families: clarinet, flute, harpsichord, marimba, oboe, trumpet, and violin. Each was analyzed and synthesized with the reference sound-analysis data (before modification). In no case could the original recorded sound be discriminated from the full synthesis when presented in an AA–AB discrimination paradigm at better than 64%.[2] The sounds were stored in 16-bit integer format on hard disk. All ''reference'' sounds (full synthesis) were equalized for fundamental frequency (311.1 Hz or E-flat 4) and for duration (2 s) (see Sec. I D for a description of the technique for equalizing duration in synthesis). They were also equalized for loudness in an adjustment procedure by the authors. The different kinds of simplifications and their combinations that were applied to the stimuli are illustrated graphically in Fig. 7. Six simplifications concerned a single parameter, three concerned two parameters, and one each concerned three and four parameters.[3] The 11 simplified sounds for each instrument were synthesized with the method described above on a NeXT computer. They were equalized for loudness within each instrument in an adjustment procedure by the authors.

C. Procedure

A two-alternative forced-choice (2AFC) discrimination paradigm was used. The listener heard two pairs of sounds (AA–AB) and had to decide if the first or second pair contained two different sounds. The dependent variable was the d' measure of sensitivity to the physical difference derived from signal-detection theory using a 2AFC model (Green and Swets, 1974; Macmillan and Creelman, 1991). The trial structure could be one of AA–AB, AB–AA, BB–BA, or BA–BB, where A represents the reference sound and B one of the 11 simplifications. This paradigm has the advantage of presenting to the listener both a ''same'' pair and a ''different'' pair between which the different one must be detected. All four combinations were presented for each simplification and for each instrument. The two 2-s sounds of each pair were separated by a 500-ms silence, and the two pairs were separated by a 1-s silence. On each trial, a button labeled (in French) ''The first pair was different: key 1'' appeared on the left of the computer screen and a button labeled ''The second pair was different: key 2'' appeared on the right. The computer would not accept a response until all four sounds in a trial had been played. This was indicated by a dimming of the labels on the buttons during sound presentation.

For each instrument, a block of 44 trials was presented to the subjects (four trial structures$\times$11 simplifications). Each block was presented twice in succession, and performance for each simplification was computed on eight trials for each subject. Seven pairs of blocks were presented corresponding to the seven instruments. The total duration of the experiment was about two h and 20 min. For 13 subjects, the experiment was divided into two sessions performed on different days, with four instruments on one day and three instruments on the other. For seven other subjects, it was performed in one day with several pauses between instruments.

The experiment was controlled by the PSIEXP interactive program (Smith, 1995) running on a NeXT computer. Subjects were seated in a Soluna S1 double-walled sound-isolation booth facing a window through which the computer screen was visible. Sounds were converted through NeXT digital-to-analog converters, amplified through a Canford power amplifier, and then presented through AKG K1000

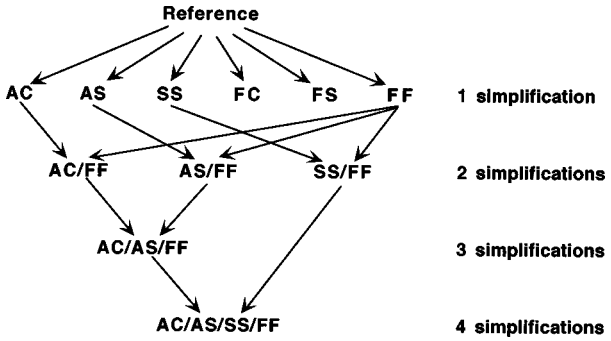

FIG. 7. Schema illustrating the accumulation of stimulus simplifications. For key, see Table II.

open-air headphones at a level of approximately 70 dB SPL as measured with a Bruel & Kajer 2209 sound-level meter fitted with a flat-plate coupler.

At the beginning of the experiment, the subject read instructions and asked any necessary questions of the experimenter. Five or six practice trials (chosen at random from the instrument being tested) were presented in the presence of the experimenter before the first block for each instrument. Then the two experimental blocks for that instrument were presented. The order of presentation of the 44 trials was random within each block, and the order of presentation of the instruments was randomized for each subject.

III. RESULTS

Discrimination rates were computed for each simplification of each instrument's reference sound across the four trial structures and two repetitions for each subject. The means across both groups of subjects for the 11 simplifications on seven instrument sounds are given in Table II and plotted in Fig. 8. Accumulated simplifications involving amplitude-envelope coherence (AC), amplitude-envelope smoothness (AS), and spectral-envelope smoothness (SS) are joined by lines to visualize the effect of accumulation. In general, spectral-envelope smoothness and amplitude-envelope coherence simplifications were the most easily discriminated, followed by coherence (FC) and flatness (FF) of frequency envelopes, and finally amplitude-(AS) and frequency-(FS) envelope smoothness. With one exception, the accumulation of simplifications improved discrimination, attaining nearly perfect discrimination for all instruments. The pattern of discrimination differences across simplification types is very different for each instrument, suggesting that the acoustic structure of each sound is affected differentially by these simplifications.

To evaluate the different factors included in this experiment, several statistical analyses were performed. The dependent variable in these analyses was the d' index of sensitivity (derived from proportion-correct discrimination rates in Table A.5.2 from Macmillan and Creelman, 1991). A global mixed analysis of variance (ANOVA) was performed on between-subjects factor musical training (2) and within-subjects factors instrument (7) and simplification (11). Mixed ANOVAs on musical training and simplification were also performed for the data of each instrument individually.

TABLE II. Results of discriminating six basic simplifications and five combinations of simplifications compared to the reference sounds (complete resynthesis of the originals after frequency, duration, and loudness matching). Key: AC=amplitude-envelope coherence, AS=amplitude-envelope smoothness, SS=spectral-envelope smoothness, FC=frequency-envelope coherence, FS=frequency-envelope smoothness, FF=frequency-envelope flatness, Cl=clarinet, Fl=flute, Hc=harpsichord, Mb=marimba, Ob=oboe, Tp=trumpet, Vn=violin.

	Instrument							
Simplification	Cl	Fl	Hc	Mb	Ob	Tp	Vn	Mean
AC	0.81	0.96	0.97	0.97	0.75	0.98	0.95	0.91
AS	0.56	0.80	0.79	0.59	0.54	0.73	0.59	0.66
SS	0.98	0.97	0.96	0.99	0.99	0.82	0.99	0.96
FC	0.69	0.72	0.93	0.50	0.53	0.77	0.70	0.69
FS	0.56	0.59	0.84	0.67	0.72	0.81	0.69	0.70
FF	0.70	0.72	0.91	0.62	0.48	0.82	0.73	0.71
AC/FF	0.86	0.98	0.97	0.96	0.94	0.99	0.99	0.95
AS/FF	0.69	0.94	0.92	0.65	0.81	0.86	0.71	0.80
SS/FF	1.00	0.99	0.97	0.98	0.98	0.89	0.98	0.97
AC/AS/FF	0.87	0.98	0.98	0.97	0.86	1.00	0.98	0.95
AC/AS/SS/FF	0.99	0.98	0.98	0.98	0.99	0.97	1.00	0.99

For the data within each instrument, Tukey–Kramer HSDs (''honestly significant differences'') were computed to determine the critical difference between condition means at a significance level of 0.05. This technique allows a robust comparison among all means of a data set by the simultaneous construction of confidence intervals for all pairs (Ott, 1993). Finally, in order to determine which simplifications were reliably different from chance performance, single-sample *t*-tests were performed against a hypothetical mean of 0.50 with probabilities being corrected for multiple tests with the Bonferroni adjustment.

A. Effects of musical training

Musicians discriminated simplifications from reference sounds slightly better overall than nonmusicians (86.8% vs 82.2%) by 3.0% to 7.1% across instruments [$F(1,18) = 8.05$, $p < 0.05$].[4] There was no interaction of this factor with other factors in the global analysis. In the individual ANOVAs, there were significant main effects of musical training for four of the seven instruments [flute: $F(1,18) = 5.01$, $p < 0.05$; marimba: $F(1,18) = 9.76$, $p < 0.01$; oboe: $F(1,18) = 6.99$, $p < 0.05$; violin: $F(1,18) = 5.70$, $p < 0.05$], and there were significant musical training by simplification interactions for two instruments [clarinet: $F(10,180) = 2.93$, $p < 0.05$; violin: $F(10,180) = 2.55$, $p < 0.05$]. So overall, there was a small effect of musical training that was globally reliable and present in the majority of instruments but which varied differently across simplification conditions in only two of the instruments. Given the small size of the effect, we will not consider it any further.

B. Effects of instrument

In the global ANOVA, there were highly significant effects of instrument [$F(6,108) = 28.80$, $p < 0.0001$], simplification [$F(10,180) = 237.97$, $p < 0.0001$], and their interaction [$F(60,1080) = 9.87$, $p < 0.0001$]. This strong interaction revealed very large differences in the effects of a given sim-

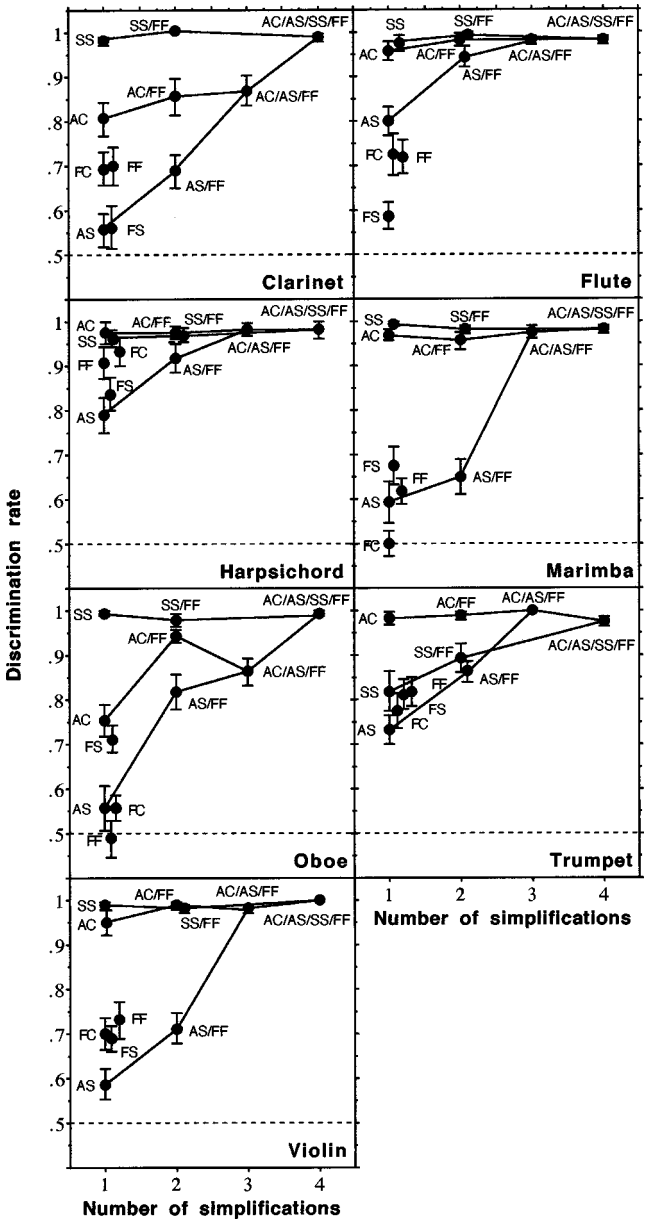

FIG. 8. Discrimination rates as a function of the number of simplifications performed on sounds from seven instruments. The letter codes refer to the simplification types (see Table II caption). Simplifications involving AS, AC, and SS are connected to visualize the effect of their accumulation. The vertical bars represent ±1 standard error of the mean. Chance performance is at 0.5. Some points have been displaced laterally for visibility.

plification across instruments. We will therefore only consider differences among simplifications within the individual ANOVAs for each instrument.

C. Effects of the simplifications and their accumulation

The main effect of simplification was highly significant ($p<0.0001$) for all seven instruments [clarinet: $F(10,180)=40.14$; flute: $F(10,180)=41.14$; harpsichord: $F(10,180)=11.54$; marimba: $F(10,180)=71.82$; oboe: $F(10,180)=43.40$; trumpet: $F(10,180)=22.05$; violin: $F(10,180)=81.65$], indicating a large variation in discriminability of the different types of simplification. Single-sample *t*-tests adjusted for multiple tests indicated that only nine of the 42 single simplifications were *not* discriminated above chance. These include AS and FS for the clarinet, FS for the flute, AS and AC for the marimba, AS, FC, and FF for the oboe, and AS for the violin. Note that no single simplification is ''successful'' (i.e., indistinguishable from the reference sound) for all seven instruments. However, amplitude-envelope smoothness was only reliably discriminated from the reference in flute, harpsichord, and trumpet. In order to evaluate the significance of the differences among simplifications, a clustering organization is projected onto the mean data in Fig. 9 in which means that are smaller than the critical Tukey–Kramer HSD for that instrument are enclosed in a bounded region. The critical differences are listed in Table III. In general, simplifications involving amplitude-envelope coherence (AC) and spectral-envelope smoothness (SS) are found in the highest cluster, showing near-perfect discrimination for most instruments, although AC is less well discriminated in the clarinet and oboe, and SS is less well discriminated in the trumpet.

As a general rule, the discrimination of a multiple simplification was roughly equal to the discrimination of the constituent simplification which had the highest discrimination rate. For example, take the clarinet sound. Discrimination was near chance for AS, around 70% for FF, about 80% for AC, and nearly perfect for SS. Accumulating AS and FF gave a rate no different from that for FF. Similarly, AC/FF and AC/AS/FF had rates no different from that of AC, while SS/FF and AC/AS/SS/FF were not different from SS alone. This rule held for 32 of the 35 multiple-simplification conditions. Thus, there were only three cases where the accumulation of two simplifications was better discriminated than either of the constituent simplifications: AS/FF was better than AS and FF for the flute, and AC/FF and AS/FF were better than their constituents for the oboe. There was only one case where an accumulated simplification resulted in a *decrease* in discrimination performance: AC/AS/FF was discriminated worse than AC/FF for the oboe, suggesting that the addition of the amplitude-envelope smoothness reduced the effect of amplitude-envelope coherence and/or frequency-envelope flatness. Taken together, these results suggest that it is generally sufficient to examine the individual effects of a single, ''most-potent'' simplification for each instrument to explain the behavior of their combinations. In order to compare across instruments, the discrimination rates for the six single simplifications are shown for each instrument in Fig. 10.

IV. MEASUREMENTS OF SPECTRAL DIFFERENCES BETWEEN REFERENCE AND SIMPLIFIED SOUNDS

A. Amplitude and frequency errors

The effect of the simplifications on sounds was directly measured from the analysis file data by computing normalized rms differences between reference and simplified sounds. Accordingly, for the amplitude simplifications, we measured the relative difference between reference (*Ar*) and

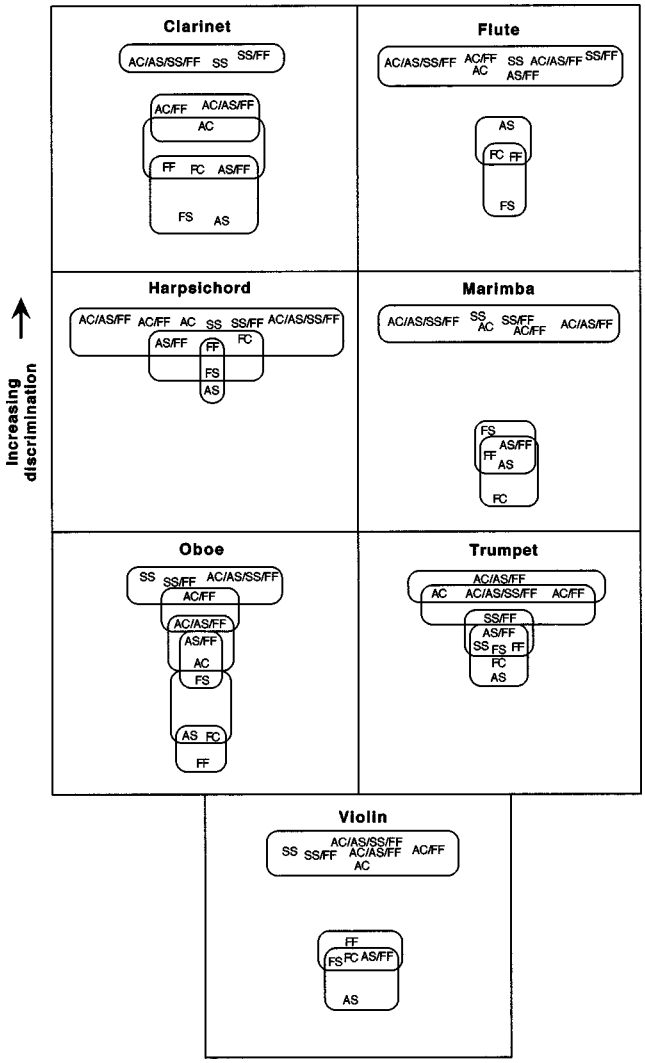

FIG. 9. Schematic representation of significant differences between means as revealed by Tukey–Kramer HSD tests. Discrimination performance is organized along the vertical dimension within each panel, as in Fig. 8. Simplifications with means whose differences are not bigger than the critical difference (see Table III) are enclosed within a bounded region. In the oboe data, for example, FF is not significantly different from AS and FC but is different from FS. However, AS and FC are not significantly different from FS.

simplified (*As*) time-varying amplitude spectra (which are assumed to represent sounds having the same mean frequencies and same duration) using

$$\mathrm{ERR}_{\mathrm{amp}}=\frac{1}{I}\sum_{i=1}^{I}\left(\frac{\Sigma_{k=1}^{K}(As_k(i)-Ar_k(i))^2}{\Sigma_{k=1}^{K}As_k(i)\cdot Ar_k(i)}\right)^{1/2}, \tag{10}$$

TABLE III. Critical Tukey–Kramer differences for the mean discriminations of simplifications computed across both groups of subjects.

Instrument	Critical difference
Clarinet	0.217
Flute	0.196
Harpsichord	0.226
Marimba	0.187
Oboe	0.207
Trumpet	0.215
Violin	0.170

where i is the number of the analysis time frame and I is the total number of frames. $\mathrm{ERR}_{\mathrm{amp}}$ can vary between 0 and 1. In our set of sounds, it varied between about 0.01 and 0.58. With this formula, the error at any instant relative to the amplitude at that instant is computed. Due to the amplitude product in the denominator, Eq. (10) accentuates low-amplitude portions, giving them the same weight as high-amplitude portions. It is assumed here that proportional-amplitude errors are more relevant than absolute-amplitude errors. The normalized squared errors are accumulated over harmonics and are then averaged over time. One could argue that this might be improved by first accumulating amplitudes by critical bands before averaging, but this would complicate the calculation considerably and would not guarantee any improved result.

In a similar manner, for the frequency simplifications, we measured the difference between reference (*fr*) and simplified (*fs*) series of time-varying frequency data using

$$\mathrm{ERR}_{\mathrm{freq}}=\frac{1}{If_a}\sum_{i=1}^{I}\left(\frac{\sum_{k=1}^{K}\left(\frac{(Ar_k(i)(fs_k(i)-fr_k(i))}{k}\right)^2}{\Sigma_{k=1}^{K}Ar_k^2(i)}\right)^{1/2}. \tag{11}$$

Frequency differences are divided by the harmonic number k, because we assume that they are intrinsically amplified linearly with k. The frequency difference for each harmonic k is weighted by its amplitude, giving greater votes to higher-amplitude harmonics. This is beneficial because lower-amplitude harmonics tend to have more oscillation in their frequency data, which is an artifact of the analysis process and not representative of the sound itself (Moorer, 1978). Besides averaging over time, we normalize by the average fundamental frequency (f_a), so that the results are presented as a proportion of the fundamental. The values of $\mathrm{ERR}_{\mathrm{freq}}$ in our set of sounds were very low (between 0.0009 and 0.0134).

The amplitude and frequency-error results for the six basic simplifications for the seven instruments are shown in Tables IV and V, respectively. The mean d' scores are plotted in Fig. 11 as a function of the logarithm of the error values for the amplitude (a) and frequency (b) simplifications. Although there is some dispersion in the plot, the overall relations between listener-obtained discrimination scores and the objective measurements are clear. For most cases, larger errors predict higher sensitivity. If discrimination scores are expressed in terms of d', $\log(\mathrm{ERR}_{\mathrm{amp}})$ explains 77% of the variance in discrimination performance for single-amplitude simplifications. The amount of variance explained increases to 88% if the outlying point due to the AC condition for the marimba is removed. Note that the various amplitude simplifications are quite different overall in their discriminability (AS<AC<SS).

The picture is quite different for the frequency simplifications. First, the data are much more scattered, indicating that $\mathrm{ERR}_{\mathrm{freq}}$ explains much less variance than did $\mathrm{ERR}_{\mathrm{amp}}$ for corresponding conditions; explained variance in d' by $\log(\mathrm{ERR}_{\mathrm{freq}})$ is only 34% but increases dramatically to 57% when the outlying point due to the FF condition for the oboe

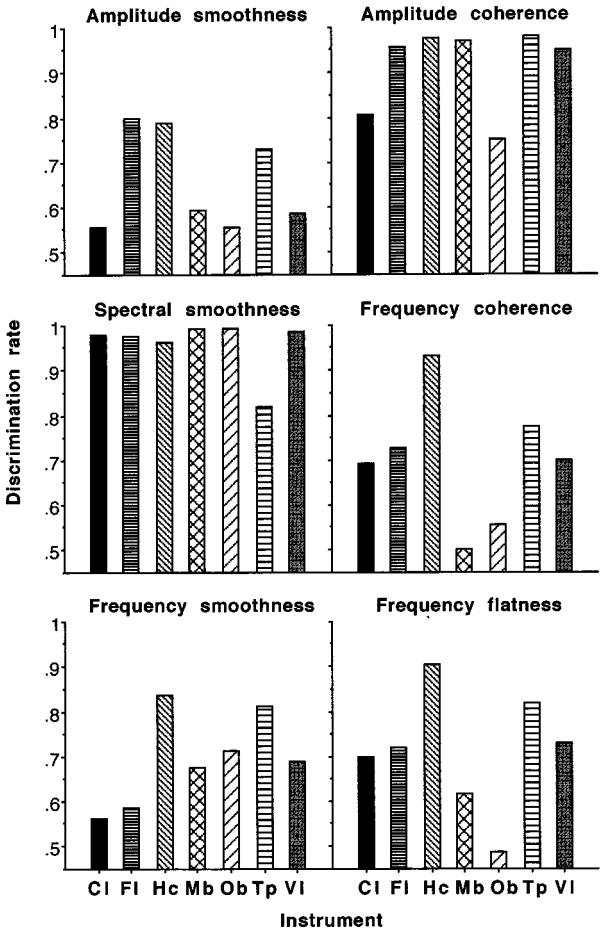

FIG. 10. Discrimination rates for the seven different instrument sounds having been simplified in six ways (see the text for a complete description). For instrument key, see Table II.

is removed. Second, there is a much greater overlap between the conditions indicating that there is a less systematic effect of the simplification condition and that each simplification type affects the various instruments to very different degrees.

B. Effect of spectral-amplitude changes on centroid

Since the centroid of the spectrum has been shown to be strongly correlated with one of the most prominent dimensions of multidimensional-scaling representations of timbral differences (Grey and Gordon, 1978; Iverson and Krumhansl, 1993; Kendall and Carterette, 1996; Krimphoff *et al.*, 1994; Krumhansl, 1989; Wessel, 1979), one might conjecture that a listener's ability to detect spectral-amplitude modifications is due to detection of attendant centroid changes rather than to the modifications themselves. Although in synthesized tones spectral centroid can be controlled independently of other spectral-amplitude modifications, they are not necessarily separable in musical instrument tones. Nonetheless, we have found them to be statistically independent to a substantial degree in a number of our stimuli.

We define time-varying normalized spectral centroid (SC) to be

TABLE IV. Relative spectral differences between reference and simplified spectra for basic and accumulated amplitude simplifications. The values represent ERR_{amp} [Eq. (10)]. Note that the values for basic simplifications and those simplifications accumulated with the FF simplification would be identical, since the FF operation has no effect on the amplitudes. For key, see Table II caption.

	Instrument						
Simplification	Cl	Fl	Hc	Mb	Ob	Tp	Vn
AC	0.100	0.164	0.204	0.033	0.122	0.280	0.350
AS	0.017	0.024	0.035	0.016	0.020	0.024	0.015
SS	0.565	0.324	0.258	0.505	0.377	0.143	0.401
AC/AS/FF	0.101	0.165	0.207	0.035	0.124	0.280	0.350
AC/AS/SS/FF	0.578	0.342	0.282	0.508	0.418	0.299	0.511

$$\mathrm{SC}(i)=\frac{\Sigma_{k=1}^{K} kA_k(i)}{\Sigma_{k=1}^{K} A_k(i)}. \tag{12}$$

To test the degree to which an amplitude simplification affects the centroid, we calculate the rms-amplitude-weighted mean centroid change based on the centroids of the simplified (SCs) and reference (SCr) spectra:

$$\overline{\Delta \mathrm{SC}}=\frac{\sum_{i=1}^{I}\left|\frac{\mathrm{SC}s(i)}{\mathrm{SC}r(i)}-1\right|\cdot A_{\mathrm{rms}}(i)}{\Sigma_{i=1}^{I} A_{\mathrm{rms}}(i)}. \tag{13}$$

This quantity is zero if there is no difference in centroid and it is unbounded, although for our simplifications $\overline{\Delta \mathrm{SC}}$ attained a maximum value of 0.3.

Of course, the amplitude-envelope coherence (AC) simplification may result in a large centroid change for tones with a great deal of spectral flux, since it was designed to eliminate any centroid change during the course of a sound. However, centroid effects, some quite sizable, also occur for AS and SS operations, although the changes induced by AS are generally much less than those due to the other two amplitude simplifications. Table VI gives a list of the average relative centroid changes for the three amplitude simplifications. Mean discrimination data (d') are plotted as a function of $\overline{\Delta \mathrm{SC}}$ in Fig. 11(c). Note that these averages are based on magnitudes of the SC changes. Further inspection of Table VI reveals that for the instruments tested, centroid increases in stimuli with spectral-envelope smoothness are always positive, whereas for the other two simplifications, the change in centroid can go in either direction—even during the sounds. The logarithm of the mean centroid change ex-

TABLE V. Relative spectral differences between reference and simplified spectra for basic frequency simplifications. The values represent ERR_{freq} [Eq. (11)]. Note the values for FF would override all accumulations of this operation with other simplifications. For key, see Table II caption.

	Instrument						
Simplication	Cl	Fl	Hc	Mb	Ob	Tp	Vn
FC	0.001	0.002	0.010	0.001	0.003	0.003	0.003
FS	0.001	0.004	0.013	0.003	0.008	0.004	0.003
FF	0.002	0.005	0.013	0.003	0.010	0.007	0.004

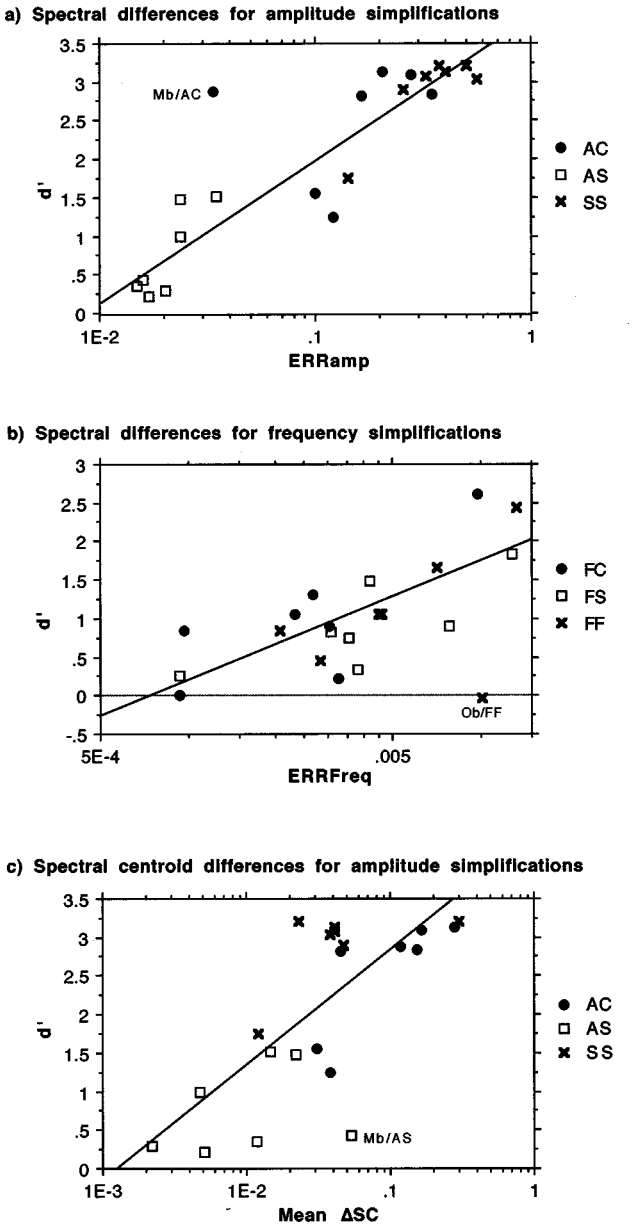

FIG. 11. Discrimination scores (d') plotted as functions of the logarithms of three objective measures [ERR_{amp} (a), ERR_{freq} (b), and $\overline{\Delta SC}$ (c)] for the single amplitude and frequency-envelope simplifications indicated for each panel. The linear regression lines were computed without one outlying point indicated in each panel: Mb/AC in (a), Ob/FF in (b), and Mb/AS in (c), since the removal of these single points resulted in dramatic increases in the correlation coefficients in each case (see the text for complete descriptions of the objective measures).

plains 54% of the variance in d', but this value increases to 65% when the outlying point due to the marimba in the AS condition is removed.

V. DISCUSSION

The discrimination data show that the sensitivity of listeners to simplifications of musical instrument spectra depends on the parameter modified and the instrument sound processed, while being relatively unaffected by the musical training of the listeners. The interaction between type of simplification and instrument is most likely due to a combination of the perceptual salience of the parameter simplified and the strength of that parameter in the particular sound. From Fig. 10 it is quite obvious that spectral-envelope smoothness and amplitude-envelope coherence are the most discriminable simplifications. However, spectral-envelope smoothness causes a smaller perceptual change for the trumpet than the other instruments, which is not unexpected since its spectrum is quite smooth to begin with. For this latter instrument, amplitude-envelope coherence is the most discriminable simplification, due to the strong degree of spectral flux present in brass tones (Grey, 1977). Further, the amplitude-envelope coherence simplification is much less discriminable for the clarinet and oboe because their spectra do not undergo as much spectral flux as most other instruments (Grey, 1977).

The other simplifications result in lesser discrimination scores, either because these involve parameters of lesser perceptual salience or because the parameters have insufficient strength to result in higher scores. Again, scores depend on the instrument tested. Amplitude-envelope smoothness seems to be most important for the flute, trumpet, and harpsichord, the former two because of their relatively large temporal variations and the latter because of its effect on the decay curves.

Objective measures of average spectral ($\overline{\Delta SC}$) and spectrotemporal change (ERR_{amp},ERR_{freq}) were developed in an attempt to quantify the acoustic cues that give rise to the discrimination performance. Figure 11 clearly shows that the three amplitude simplifications (AC, AS, and SS) have different effects on changes in amplitude-envelope structure and consequently that they are discriminated to differing degrees as well. Spectral-envelope smoothness is almost always the most easily detected, followed by amplitude-envelope coherence, and finally by amplitude-envelope

TABLE VI. Average relative-magnitude change of centroid [$\overline{\Delta SC}$, Eq. (13)] for the three basic amplitude simplifications and two accumulations of those simplifications. Note that centroids would not be appreciably affected by the FF simplification since the frequency variations were less than 1% during the significant amplitude portions of the sounds. A minus sign indicates that, on average, the centroid for the simplified sound decreased compared to the reference sound. For key, see Table II caption.

	Instrument						
Simplification	Cl	Fl	Hc	Mb	Ob	Tp	Vn
AC	0.031	0.045	0.279(−)	0.118(−)	0.038	0.166	0.155
AS	0.005(−)	0.023	0.015(−)	0.054(−)	0.002(−)	0.005	0.012(−)
SS	0.039	0.041	0.047	0.299	0.023	0.012	0.042
AC/AS/FF	0.031	0.046	0.282(−)	0.117(−)	0.038	0.166	0.156
AC/AS/SS/FF	0.058	0.061	0.284(−)	0.359	0.038	0.168	0.156

smoothness, which gives performance not far from chance for four of the seven instrument sounds.

Similarly, note that for most sounds the effect of amplitude-envelope smoothness on spectral centroid change (mean=0.016) is much less than that of amplitude-envelope coherence (0.119), with the flute being the only exception (0.023 vs 0.045, respectively). Indeed, the flute has a comparatively high discrimination score for amplitude-envelope smoothness (0.80), whereas the marimba with amplitude smoothness has a moderately high spectral-centroid change (0.054) and a relatively low discrimination rate (0.59). Also, surprisingly, the flute has a high discrimination score for the amplitude-coherence simplification (0.96), even though its change of centroid (0.041) is slightly less than the amplitude-based simplifications (overall mean for the three, 0.045). On the other hand, we see that in comparison to the amplitude-envelope coherence, spectral-envelope smoothness causes moderate to high centroid changes (0.02–0.30), with the trumpet (0.01) being the obvious exception as mentioned above. The marimba exhibits a large relative centroid change (0.30), but this is true because the marimba's sound is dominated by its fundamental. In this case, spectral-envelope smoothness makes a profound change by introducing a second harmonic which was originally nonexistent. Note, however, that spectral-envelope smoothness will have an effect on any jagged spectrum, regardless of whether the spectrum is changing or not, whereas amplitude-envelope coherence only affects sounds with time-varying spectra. Since spectral-envelope smoothness inherently affects the centroid, we cannot tell whether discrimination is due to this effect or directly to the change of spectral-envelope fine structure, but it is probably due to a combination of these effects.

All of the amplitude simplifications produce changes in both $\mathrm{ERR}_{\mathrm{amp}}$ and $\overline{\Delta \mathrm{SC}}$ measures. Further, these two objective measures partially explain the variance in discrimination performance and yet are not strongly correlated between them ($r=0.61$). This suggests that they may both contribute to the discrimination of amplitude-related changes in the spectrotemporal morphology of the simplified instrument sounds. To test this idea, the logarithms of both parameters were selected as independent variables in a stepwise regression across single-amplitude simplifications with d' as the dependent variable. This technique tests the independent contribution of each parameter, which only enters the regression if its contribution is statistically significant (F-to-enter=4, in our case). Both parameters successfully enter into the regression. The final result is given by the following linear regression equation, by which 83% of the variance in the data is explained:

$$d' = 4.34 + 1.35 \cdot \log(\mathrm{ERR}_{\mathrm{amp}}) + 0.64 \cdot \log(\overline{\Delta \mathrm{SC}}). \qquad (14)$$

It becomes clear from this analysis that there are at least two perceptual cues contributing to discrimination performance in these sound simplifications.

The striking thing about the frequency-related simplifications is their relative weakness in creating discriminable differences in the stimuli. This result may be due primarily to the fact that, in normal instrument sounds without vibrato, the amount of frequency variation is relatively small. Indeed, as can be gleaned from Table V, the largest change in frequency variation created by flattening or smoothing the frequency envelopes is for the harpsichord and is on the order of 1.3%; the next largest is on the order of 1% produced by frequency flattening of the oboe. It is perhaps surprising, therefore, that so much has been written in the literature about the importance of frequency microvariations in the creation of naturalness in synthetic sounds (Dubnov and Rodet, 1997; McAdams, 1984; Sandell and Martens, 1995; Schumacher, 1992). Nonetheless, there are certainly classes of musical sounds where pitch contour plays an important role in musical expressiveness, such as vibrato and portamento, particularly in vocal and bowed-string sounds.

The effect of combining amplitude-related and frequency-related cues for the accumulated simplifications is less clear in the data, however. In a stepwise regression of the entire set of d' scores on all three objective measures, only $\mathrm{ERR}_{\mathrm{amp}}$ entered significantly into the regression and then explained only 63% of the total variance. So, while individual cues seem to explain a large portion of the variance for the basic simplifications, their combined use in judging accumulated simplifications remains uncertain. This may be due in part to the judgment strategy discussed above, namely that listeners respond to the most salient parameter in an accumulation of parameters. In the discrimination data, there are only four out of 35 cases where an accumulation gives higher discrimination scores than the best of its component simplifications: AC/FF is better than either component for the oboe, and AS/FF is better than either component for clarinet, flute, and oboe. If our objective measures are truly indicative of the perceptual cues being used by listeners to perform the task, they should have a similar pattern to the discrimination data with accumulations having the same or slightly higher values than their constituent simplifications. Globally this is the case (see Tables IV, V, and VI): AC/AS/FF is approximately equal to AC for all seven instruments in terms of both $\mathrm{ERR}_{\mathrm{amp}}$ and $\overline{\Delta \mathrm{SC}}$, and AC/AS/SS/FF is approximately equal to or slightly higher than SS or AC in all seven instruments in terms of $\mathrm{ERR}_{\mathrm{amp}}$, although it is quite a bit higher for clarinet, flute, and marimba in terms of $\overline{\Delta \mathrm{SC}}$. The combination of the psychophysical data and the objective measurements would thus seem to globally support the most-potent cue judgment strategy.

VI. CONCLUSIONS

The results of this study point very strongly to (1) spectral-envelope shape (jagged vs smooth) and (2) spectral flux (time variation of the normalized spectrum) as being the most salient physical parameters that we have studied related to timbre discrimination, followed in order by (3) the presence of frequency variation, (4) frequency incoherence (inharmonicity), (5) frequency microvariation, and (6) amplitude microvariation. Simplifications (reductions or eliminations) of these parameters give rise to changes in the spectrotemporal morphology of an instrument sound's sensory representation, to which both musician and nonmusician

listeners are very sensitive. This sensitivity is only slightly greater in musicians than in nonmusicians. The level of discrimination resulting from the modifications was globally greater for the amplitude simplifications than for the frequency simplifications, with the exception of amplitude smoothing. Thus, musical-sound synthesis should pay particular attention to spectral-envelope fine-structure and spectral flux if a high degree of audio quality is to be ensured.

Objective measures were defined that predict a great deal of the discrimination performance. These measures are related to changes in the amplitude envelopes and the spectral centroid for amplitude simplifications, and to changes in the frequency envelopes for frequency simplifications. Since discrimination can be predicted by physical measurement of differences in the time-varying spectra, it appears that the importance of these parameters is in direct proportion to the extent to which they actually vary in musical sounds, as we have shown with the strong interaction between simplification type and musical instrument. Further work is needed to examine the relative perceptual sensitivity of listeners to these different physical factors. We have also shown that if several parameters are varied simultaneously, listeners appear to use the most salient one, and their discrimination performance can, for the most part, be predicted on the basis of it alone. While it is likely that this acute sensitivity to the fine-grained spectral and temporal structure of the musical sounds exists across the entire range of pitch, dynamics, and articulation possible on each instrument, further research will be needed to determine the relative importance of the different objective parameters in different regions of an instrument's musical ''space.''

ACKNOWLEDGMENTS

We would like to thank Sophie Savel for running subjects in the control experiment, Bennett Smith for the wonders of PSIEXP, as well as John Hajda and two anonymous reviewers for helpful comments.

APPENDIX A

We can write the reduced-duration harmonic amplitude envelope as

$$A_k(t) \leftarrow \begin{cases} A_k(t), & 0 \leqslant t < t_1, \\ (1-\alpha(x)) \cdot A_k(t) + \alpha(x) \cdot A_k(t+t_2-t_3), & \\ \quad t_1 \leqslant t < t_3, & \\ A_k(t+t_L-2), & t_3 \leqslant t \leqslant 2, \end{cases} \tag{A1}$$

where

$$t_3 = 2-(t_L-t_2), \quad \alpha(x) = 3x^2 - 2x^3, \quad x = \frac{(t-t_1)}{(t_3-t_1)},$$

and t_L is the duration of the original sound.

Note that $\alpha(x)$ is a cubic spline with the following properties:

(1) The derivative of $\alpha(x)$ with respect to x is zero at $x=0$ and $x=1$,
(2) $\alpha(0)=0$,
(3) $\alpha(1)=1$.

The same method obviously applies to the harmonic-frequency envelopes.

APPENDIX B

Since the data rate for each harmonic amplitude or frequency envelope is originally $2f_a$, the overall data rate for K harmonic amplitude and frequency envelopes is $4K \cdot f_a$.

Amplitude-envelope smoothing (AS) and frequency-envelope smoothing (FS) essentially reduce the data rate for each harmonic envelope from $2f_a$ to $2f_c$, where f_c is the filter cutoff frequency. If only amplitude-envelope smoothing were applied, the data rate for K harmonics would be reduced to $2K \cdot f_c + 2K \cdot f_a = 2K \cdot (f_c + f_a)$. In our case, since $f_a = 311$ Hz and $f_c = 10$ Hz, the data reduction factor would be $4.311/[2 \cdot (10+311)] = 1.94$. The same result would apply if only frequency-envelope smoothing were applied. On the other hand, if both were applied the new total data rate would be $4K \cdot f_c$, and the data reduction factor would be f_a/f_c. In our case, this is $311/10 = 31.1$, i.e., there is only a substantial overall data reduction if both amplitude- and frequency-envelope smoothing are applied.

Spectral-envelope smoothing does not reduce the data rate very much, at least not with the current definition of smoothing. Since the order of the smoothing function is 2, the reduction is approximately a factor of 2.

Amplitude- (AC) and frequency coherence (FC) simplifications essentially replace multiple envelopes by single envelopes. If one of these simplifications were applied, the data rate falls from $4K \cdot f_a$ to $2K \cdot f_a + 2f_a = 2(K+1) \cdot f_a$. So, the data reduction factor would be approximately 2. If both were applied, the data reduction factor would be exactly K, the number of harmonics. In our case, this varies from 30 to 70, depending on the instrument.

The data rate for flattened frequency envelopes is zero. So, if frequency flattening (FF) is applied, the data rate goes from $4K \cdot f_a$ to $2K \cdot f_a$, a factor of 2 reduction.

Data rates after combinations of data simplifications can be calculated from the individuals. For example, if AC and FF are combined, the data rate becomes $2f_a$. For AS and FF, it would be $2K \cdot f_c$. For SS and FF, it is $K \cdot f_a$. For AC, AS, and FF, it is $2f_c$. For AC, AS, SS, and FF, it is just f_c. The corresponding data-reduction factors are for AC/FF, $2K$; for AS/FF, $2f_a/f_c$; for SS/FF, 4; for AC/AS/FF, $2K \cdot f_a/f_c$; for AC/AS/SS/FF; $4K \cdot f_a/f_c$.

[1]We were unable to find a trumpet tone of suitable quality recorded at E-flat 4, so we used a tone recorded by author J.B. which was within a whole tone of that pitch, *F*4. When resynthesized at E-flat 4, it sounded perfectly natural to all of the authors.

[2]A control experiment designed to test discrimination of the digitized recordings and the fully analyzed–resynthesized sounds was conducted with six listeners. Each subject performed 40 trials for each instrument using the paradigm described in Sec. II C. The discrimination rates for oboe, clarinet, flute, harpsichord, marimba, trumpet, and violin were 0.62, 0.54, 0.59, 0.64, 0.53, 0.57, and 0.53, respectively. Chance performance would be at 0.50 in this two-alternative forced-choice paradigm. Discrimination rates above

0.55 are significantly different from chance ($p<0.05$) by an exact binomial test for 240 trials (6 listeners×40 trials). Therefore, the full reconstructions were discriminated from the original recordings in four of the seven cases (oboe, harpsichord, marimba, and trumpet), although their discrimination rates are still quite low. That the discrimination scores are as high as 64% is actually quite surprising, given that the authors could not discriminate them informally. The subjects must have been operating from extremely subtle cues which only became obvious upon repeated listening. Two possible cues are phase differences and low-frequency noise differences between the original and synthetic cases. Improvements in the analysis/synthesis algorithms should be able to close this gap in the future. However, for this study we are confident that the vast majority of the spectrotemporal features survived the analysis/synthesis process intact. Moreover, the duration-shortened resynthesized sounds were created to be the reference sounds, so our conclusions, which relate to these sounds, are not affected by this finding.

[3]Audible artifacts were sometimes noticeable with the AC and SS simplifications. Amplitude-envelope coherence created two types of artifacts: a ''shh'' noise at the end of the sound (clarinet) or a kind of general muting of the sound (harpsichord, marimba, and trumpet). In fact, in rendering the amplitude envelopes coherent, one increases the amplitude of weak harmonics that start later and end earlier in parts of the signal that are near the noise floor. The frequency estimation is not very precise for these temporal regions of such harmonics (Moorer, 1978), and by increasing their amplitude, the existing imprecise fluctuations in frequency become clearly audible. The spectral-envelope smoothing creates a kind of gargling sound in the flute, marimba, and trumpet. This simplification also increases the level of weak harmonics whose representations have been corrupted by stronger neighbors due to channel leakage, thus amplifying fluctuations due to imprecise estimation of their frequency. These two kinds of artifacts disappear or are notably reduced when combined with frequency coherence or frequency flatness, since the frequency fluctuations producing the artifacts are then reduced or eliminated.

[4]Probabilities are corrected where necessary by the Geisser–Greenhouse epsilon (Geisser and Greenhouse, 1958), which is a conservative adjustment to account for inherent correlations among repeated measures.

Beauchamp, J. W. (**1993**). ''Unix workstation software for analysis, graphics, modifications, and synthesis of musical sounds,'' *94th Convention of the Audio Engineering Society*, Berlin (Audio Engineering Society, New York), Preprint 3479 (L-I-7).

Beauchamp, J. W., McAdams, S., and Meneguzzi, S. (**1997**). ''Perceptual effects of simplifying musical instrument sound time-frequency representations,'' J. Acoust. Soc. Am. **101**, 3167.

Brown, J. C. (**1996**). ''Frequency ratios of spectral components of musical sounds,'' J. Acoust. Soc. Am. **99**, 1210–1218.

Charbonneau, G. R. (**1981**). ''Timbre and the perceptual effects of three types of data reduction,'' Comput. Music J. **5(2)**, 10–19.

Dubnov, S., and Rodet, X. (**1997**). ''Statistical modeling of sound aperiodicities,'' in *Proceedings of the International Computer Music Conference*, 1997, Thessaloniki (International Computer Music Association, San Francisco), pp. 43–50.

Geisser, S., and Greenhouse, S. W. (**1958**). ''An extension of Box's results on the use of the *F* distribution in multivariate analysis,'' Ann. Math. Stat. **29**, 885–891.

Green, D. M., and Swets, J. A. (**1974**). *Signal Detection Theory and Psychophysics* (Krieger, Huntington, NY).

Grey, J. M. (**1977**). ''Multidimensional perceptual scaling of musical timbres,'' J. Acoust. Soc. Am. **61**, 1270–1277.

Grey, J. M., and Gordon, J. W. (**1978**). ''Perceptual effects of spectral modifications on musical timbres,'' J. Acoust. Soc. Am. **63**, 1493–1500.

Grey, J. M., and Moorer, J. A. (**1977**). ''Perceptual evaluations of synthesized musical instrument tones,'' J. Acoust. Soc. Am. **62**, 454–462.

Iverson, P., and Krumhansl, C. L. (**1993**). ''Isolating the dynamic attributes of musical timbre,'' J. Acoust. Soc. Am. **94**, 2595–2603.

Kendall, R. A., and Carterette, E. C. (**1996**). ''Difference thresholds for timbre related to spectral centroid,'' in *Proceedings of the 4th International Conference on Music Perception and Cognition, Montreal*, pp. 91–95 (Faculty of Music, McGill University).

Krimphoff, J., McAdams, S., and Winsberg, S. (**1994**). ''Caractérisation du timbre des sons complexes. II. Analyses acoustiques et quantification psychophysique,'' Journal de Physique **4**(C5), 625–628.

Krumhansl, C. L. (**1989**). ''Why is musical timbre so hard to understand?,'' in *Structure and Perception of Electroacoustic Sound and Music*, edited by S. Nielzén and O. Olsson (Excerpta Medica, Amsterdam), pp. 43–53.

Macmillan, N. A., and Creelman, C. D. (**1991**). *Detection Theory: A User's Guide* (Cambridge U.P., Cambridge).

McAdams, S. (**1984**). ''Spectral Fusion, Spectral Parsing, and the Formation of Auditory Images,'' unpublished Ph.D. dissertation, Stanford University, Stanford, CA, App. B.

McAdams, S., Winsberg, S., Donnadieu, S., De Soete, G., and Krimphoff, J. (**1995**). ''Perceptual scaling of synthesized musical timbres: Common dimensions, specificities, and latent subject classes,'' Psychol. Res. **58**, 177–192.

Miller, J. R., and Carterette, E. C. (**1975**). ''Perceptual space for musical structures,'' J. Acoust. Soc. Am. **58**, 711–720.

Moorer, J. A. (**1978**). ''The use of phase vocoder in computer music applications,'' J. Audio Eng. Soc. **24**, 717–727.

Ott, R. L. (**1993**). *An Introduction to Statistical Methods and Data Analysis* (Duxbury, Belmont, CA).

Plomp, R. (**1970**). ''Timbre as a multidimensional attribute of complex tones,'' in *Frequency Analysis and Periodicity Detection in Hearing*, edited by R. Plomp and G. F. Smoorenburg (Sijthoff, Leiden), pp. 397–414.

Preis, A. (**1984**). ''An attempt to describe the parameter determining the timbre of steady-state harmonic complex tones,'' Acustica **55**, 1–13.

Repp, B. H. (**1987**). ''The sound of two hands clapping: An exploratory study,'' J. Acoust. Soc. Am. **81**, 1100–1109.

Sandell, G. J., and Martens, W. L. (**1995**). ''Perceptual evaluation of principal-component-based synthesis of musical timbres,'' J. Audio Eng. Soc. **43**, 1013–1028.

Schumacher, R. T. (**1992**). ''Analysis of aperiodicities in nearly periodic waveforms,'' J. Acoust. Soc. Am. **91**, 438–451.

Smith, B. K. (**1995**). ''PSIEXP. An environment for psychoacoustic experimentation using the IRCAM Musical Workstation'', in *Program of the SMPC95: Society for Music Perception and Cognition, Berkeley, CA*, edited by D. L. Wessel (University of California, Berkeley).

von Bismarck, G. (**1974**). ''Sharpness as an attribute of the timbre of steady sounds,'' Acustica **30**, 159–172.

Wessel, D. L. (**1979**). ''Timbre space as a musical control structure,'' Comput. Music J. **3(2)**, 45–52.

Perception of complex tones and its analogy to echo spectral analysis in the bat, *Megaderma lyra*

Katrin Krumbholz[a] and Sabine Schmidt
Zoologisches Institut der Ludwig-Maximilians-Universität München, Luisenstrasse 14, 80333 München, Germany

(Received 27 March 1998; accepted for publication 2 October 1998)

The gleaning bat *Megaderma lyra* emits broadband echolocation sounds consisting of multiple frequency components. The present study investigates into which perceptual qualities the spectral characteristics of echoes may be translated in the auditory system of *M. lyra*. Three bats were trained in a 2-AFC behavioral experiment to classify nine complex tones, which spectrally resembled *M. lyra*'s sonar calls, into two perceptual categories. Then the bats' spontaneous responses to unknown complex tones were recorded. The results show that the animals based their classifications of the complex tones on a sound quality which was mediated by their broadband frequency spectra. The bats used the training stimuli as *spectral templates* and classified the test stimuli according to their *broadband spectral similarity* with the learned patterns. Assuming that passive hearing and echo processing are governed by similar perceptual qualities and subject to similar limitations, the perceptual mode which was used by the bats to compare the multicomponent spectral patterns in the reported experiments could serve as a powerful tool for the spectral analysis of *M. lyra*'s multicomponent echoes. The analogy between the perception of complex tones and echo spectral analysis in *M. lyra* is theoretically elaborated in the ''formant-mode'' model. [S0001-4966(99)04501-4]

PACS numbers: 43.80.Ka, 43.80.Lb, 43.66.Gf, 43.66.Hg [FD]

INTRODUCTION

Audition is the most important sense by which echolocating bats acquire information about their environment. They perceive their environment acoustically by emitting calls and analyzing the returning echoes. Moreover, audition plays an important role in the context of intraspecific communication. Finally, passive listening is essential for prey detection in gleaning bats like *Megaderma lyra*.

The echolocation calls with which bats scan their environment are species specific (Neuweiler, 1990). However, they are also situation dependent, i.e., different bat species use echolocation calls of similar time-frequency structure in similar behavioral contexts (Schnitzler and Henson, 1980). When bats are taxing the distance of objects or analyzing their structure, they emit broadband signals which most commonly have a downward frequency-modulated structure. From a theoretical viewpoint, downward frequency-modulated signals with a broad bandwidth allow an optimal performance of an echolocation system that processes the noisy echoes with an adaptive filter that is tuned to the corresponding call (Glaser, 1974; Hänsler, 1996). Further, the dimensions of objects encountered by an echolocating bat are often comparable to the wavelengths of the echolocation signals. Thus, echoes are hardly ever reflected geometrically. Instead, bats perceive the surrounding objects as if they were two- or three-dimensional irregular gratings which reflect a multitude of echoes that form a complex interference pattern. In order to identify the reflecting target, the bat has to analyze the frequency transfer function of the reflection. This can only be accomplished with a broadband echolocation sound (Beuter, 1980).

M. lyra exclusively relies on short and broadband echolocation sounds (Möhres and Neuweiler, 1966; Schmidt, 1992). The average echolocation call of *M. lyra* covers a frequency range from about 20 to 120 kHz. It consists of up to six harmonically related frequency components, each of which is linearly downward frequency-modulated. The frequency of the first harmonic may sweep from about 23 to 18 kHz. The individual frequency components appear as distinct peaks in the composite frequency spectrum of *M. lyra*'s echolocation calls. (Schmidt, 1992; Hanke *et al.*, 1997). Broadband signals of either noiselike or harmonic frequency structure are also important elements of the communication repertoire of *M. lyra* (Leippert, 1994). Finally, the rustling noises that *M. lyra* uses to detect a prey moving on the substrate are broadband and extend into the ultrasonic range (Neuweiler, 1989).

A behavioral study (Schmidt, 1988, 1992) indicates that, in the echolocation context, *M. lyra* evaluates the characteristic changes in the spectral content of the perceived echoes in order to identify certain geometric features of the reflecting target. Schmidt (1988, 1992) presented phantom echoes to the bats which consisted of two delayed replicas of their echolocation calls. The delays of the two echoes differed by a few microseconds. The animals classified the two-wavefront phantom echoes on the basis of their spectral interference profile. It is the aim of the present study to investigate into which perceptual qualities the spectral characteristics of the echoes are translated by the auditory

[a]To whom correspondence should be directed: Centre for the Neural Basis of Hearing, Department of Physiology, University of Cambridge, Cambridge CB2 3EG, United Kingdom, Electronic mail: katrin.krumbholz@mrc-cbu.cam.ac.uk

system of the bats. In the perception of human listeners, the partials in harmonic complex tones within a certain range of fundamental frequencies tend to fuse to elicit a single collective pitch sensation approximately corresponding to the fundamental frequency of the tone complex. This pitch sensation, often referred to as the virtual or residue pitch, is not attributable to a single partial in the tone complex. Actually it is still perceived even if the fundamental component is not physically present in the spectrum (see, e.g., de Boer, 1985). On the other hand, the spectral pitch of a single resolved partial can be heard out in a complex tone. This analytic mode of pitch perception often requires a considerable amount of training in human subjects (Lichte, 1941). Other nonpitch sensory qualities of complex tones depend on the broadband level profile of the component frequencies. The quality of vowels depends on the number and frequency positions of the widely spaced maxima in the harmonic level profile, the formant peaks (Peterson and Barney, 1952; Chistovich and Lublinskaya, 1979). In studies of profile analysis, subjects are distinguishing a complex tone with a flat level profile from a similar complex tone in which the level of one frequency component is incremented (Green, 1988). Thereby, subjects are comparing the level of the incremented component with the levels of the unaltered partials. Preisler and Schmidt (1995, 1998) showed that *M. lyra* can classify quasi-static harmonic complex tones both according to their collective pitch and on the basis of their actual frequency spectrum. They studied the behavioral responses of *M. lyra* to harmonic complex tones that comprised a frequency range similar to the bat's own echolocation calls. The bats were trained to classify complete complex tones as higher or lower pitched than a fixed reference frequency. The spectra of the training signals were confined to the frequency regions either above or below the reference frequency. After training, the bats' spontaneous responses to incomplete harmonic complexes were tested. One or more of the lowest harmonics were missing in their spectra. The test stimuli provided the animals with conflicting information: their fundamental frequencies were lower than the reference frequency whereas their frequency spectra contained only harmonics above the reference. Individual animals classified the ambiguous test stimuli consistently either as lower or higher pitched than the reference—showing that they referred either to the collective pitch of the harmonic tones or to the frequencies of the physically present components.

Schmidt (1995) proposed that *M. lyra* might separate the variable and the invariable information in the perceived echoes into two independent perceptual dimensions. In human speech perception, the different aspects of spectral information are separated into percepts of timbre and pitch (Peterson and Barney, 1952). The harmonic frequency structure would provide the bats with an invariable information and could, analogous to the situation in human speech perception, be translated into a percept of collective pitch. The perception of collective pitch is essentially independent of the relative levels of single partials (Patterson, 1973; Preisler, 1993). The pitch information may be used by the bat to recognize its own calls and to associate a perceived echo correctly with the corresponding emission in a call sequence. On the other hand, the actual level profile of the frequency components in the echo, comparable to the formant structure of speech vowels, depends on the geometry of the reflecting target as well as its spatial position and would thus constitute the variable part of echo information. The bats may use the latter for target identification.

In the present study we examined whether bats that spontaneously classify harmonic complex tones according to their physical frequency spectra could be trained to alter their decision criterion and base their classifications on the collective pitch of the complex tones. Further, we investigated the principles that govern the spectral mode of perception in *M. lyra*. Did the ''spectral listeners'' in the study of Preisler and Schmidt (1995) resolve and compare the spectral pitches of single partials in the complex tones? Or did the bats evaluate the frequencies of the partials in the complex tones on a broad bandscale similar to human subjects that evaluate the frequency positions of the formant peaks in vowel spectra? It is conceivable that the bats analyze not only the relative levels but also the average frequencies of the modulated harmonic components in the spectra of perceived echoes. We present a theoretical scheme for this assumption which is based on the pitch models for modulated sounds (Feth, 1974; Feth and O'Malley, 1977; Feth *et al.*, 1982).

I. MATERIALS AND METHODS

A. Experimental setup

Signals were generated digitally with a DSP board (AP2, TDT) and digital-to-analog converted with a sampling rate of 250 kHz (DA3-2, TDT). They were fed into a low-pass filter (Krohn-Hite 3323) with a cutoff frequency of 100 kHz, attenuated (Elementa), amplified (Harman/Kardon HK6100), and finally presented via a magnetostatic loudspeaker (Technics EAS 10 TH800C). The frequency transfer function of the loudspeaker was linearly decreasing by about 10 dB between 3 and 100 kHz within a $\pm$3-dB range. The experiments were carried out in a sound-attenuated room ($2.5\times3\times2.2$ m^3). The bat's starting position was in the hind upper part of the room. The loudspeaker was mounted at a distance of about 2 m away and 1.5 m below the starting place and was directed to the position of the bat's head. Two feeding dishes were mounted symmetrically on either side of the loudspeaker. The experimenter was seated behind the loudspeaker.

B. Procedure

The experiments were carried out using a two-alternative, forced-choice behavioral (2-AFC) paradigm. In each trial, the experimenter triggered the signal presentation via a computer keyboard. The bat had to respond to the signals by flying to either the right or the left feeding dish. Signal presentation was stopped after the bat had made its choice and the response was stored in the computer memory. During the training periods, the bats had to acquire the correct right–left classifications for a fixed set of training stimuli. Responses to training stimuli were rewarded with a mealworm only if the bat chose the correct side. When the bats correctly classified the training stimuli in more than

90% of the cases, test trials were interspersed among the training trials with a probability of 25%. In the test trials, any choice of a feeding dish was rewarded in order not to influence the spontaneous classifications of the bats. Both training and test stimuli were chosen in a random order. About 30 responses of each bat were collected for each test stimulus to establish the percentage value of choices to the right side for that stimulus. According to a one-dimensional χ^2-test applied to a sample of $N=30$ responses, a fraction of 75% choices to one side differs from the chance value of 50% at a highly significant level of $p<0.01$ (Zöfel, 1988). A four-field χ^2-test was applied to examine whether differences between the responses to two test stimuli were significant (Zöfel, 1988).

C. General properties of signals

Stimuli were pure or complex tones with an overall duration of 400 ms. They had linear on and off ramps with a duration of 2 ms. After a trial had been started, stimuli were presented with an interstimulus interval of 1.2 s until the bat responded. During the initial training, each stimulus was preceded by a reference tone of 23 kHz. The silent gap between reference and experimental stimulus was 400 ms and the interpair interval was 1.2 s. After the bats had memorized the frequency of this reference, the reference tone was omitted in the stimulus presentations, as *M. lyra* is known to have an excellent absolute pitch (Schmidt *et al.*, 1995). All data of the experiments described below were collected without presentation of the 23-kHz reference. The stimuli were presented at an overall level of 47 ± 3 dB.

D. Experimental animals

The experiments were performed with three individuals of the bat species *M. lyra* (one male and two females). All three bats had participated in earlier psychoacoustic experiments. During the experimental sessions the bats were fed on mealworms. In addition, a small house mouse was supplied every two weeks. The bats' weight was monitored daily. The bats were kept in a dimly illuminated flight room at 28 °C where they had free access to water.

The experiments in this study are noninvasive and therefore do not require an animal experimentation approval. Permission to keep and breed *M. lyra* in fulfillment of § 11, Abs. 1, S. 1, No. 1 Tiersch *G* has been given to the Zoologisches Institut der Universität München by the Städtisches Veterinäramt der Landeshauptstadt München, dated 6 November 1992.

II. EXPERIMENT 1: SPONTANEOUS CLASSIFICATION OF HARMONIC SPECTRA

By using the experimental paradigm employed by Preisler and Schmidt (1995, 1998), we first tested whether the bats that were to take part in the subsequent experiments would base their spontaneous pitch judgments of harmonic tones on the collective pitch of the tone complexes or on the content of their physical frequency spectra. Three bats were trained to classify pure tones as higher or lower pitched than

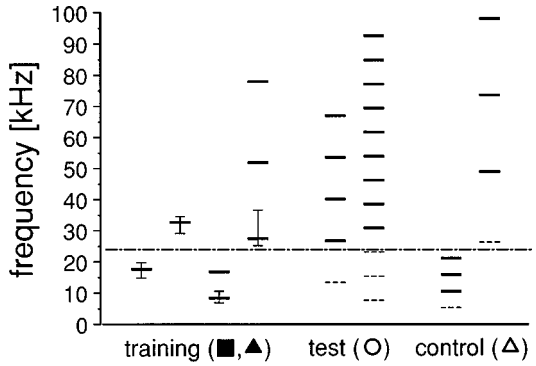

FIG. 1. Spectral composition of training, test, and control stimuli that were used in experiment 1. The long, dash–dotted line indicates the pure tone reference of 23 kHz; the solid lines show the presented harmonics, the dashed lines show the omitted harmonics of the experimental stimuli, respectively. The vertical bars denote the range of pure tone and fundamental frequencies that were used in the training stimuli. Only two examples of a total of six test and four control stimuli are shown. The symbols for the different stimulus types correspond to those used in Fig. 2.

a fixed pure tone reference of 23 kHz (see Fig. 1, training). The six low pitched training tones had frequencies between 14.8 and 19.8 kHz and were rewarded at the left feeding dish. The frequencies of the four high pitched training tones ranged between 29.2 and 34.7 kHz. They were rewarded at the right feeding dish. In a second step, complete harmonic complex tones consisting of two or three harmonics were presented as training stimuli. Six of the harmonic tones had fundamentals between 6.9 and 10.6 kHz and their frequency spectra were confined to the region below 23 kHz. The other four harmonic tones had fundamental frequencies between 25.3 and 36.8 kHz and thus their spectra contained only frequencies higher than 23 kHz (Fig. 1, training). The bats transferred the pitch classification from the pure tones to the complex tones without further training. Test stimuli were six incomplete harmonic tones with fundamental frequencies between 7.0 and 16.9 kHz. All harmonic components with frequencies below the reference of 23 kHz were missing in the test stimuli, i.e., their frequency spectra were confined to the region above 23 kHz, whereas their collective pitches were below the 23 kHz reference (Fig. 1, test). Control trials were interspersed among the test trails. The four control stimuli had fundamental frequencies of 5.3, 7.3, 26.3, and 30.9 kHz (Fig. 1, control). They were missing-fundamental-stimuli consisting of two or three harmonics. The frequency spectra of the control stimuli with fundamental frequencies below or above the reference of 23 kHz were confined to the frequency region below or above the reference, respectively. The individual results of the three animals are shown in Fig. 2. Responses to the test and control stimuli are denoted by open symbols. All three bats classified the test stimuli as ''higher than the reference'' although their fundamental frequencies and, accordingly, their collective pitches were below 23 kHz. The control stimuli were classified as higher or lower than the reference according to their spectral content. The animals thus judged the test stimuli according to their actual frequency spectra.

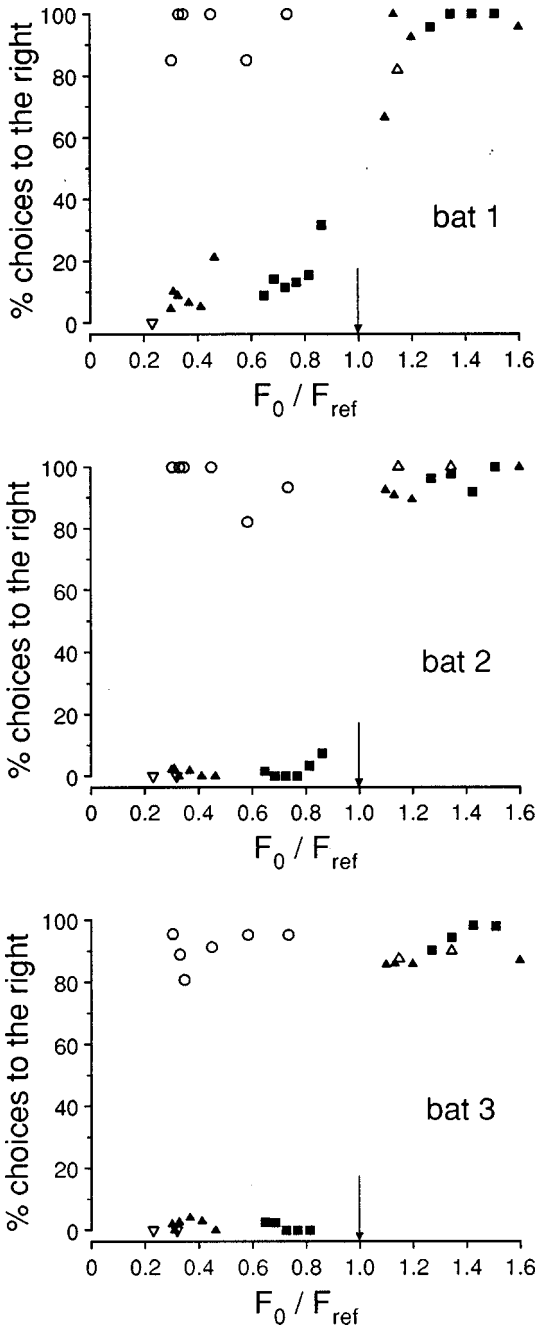

FIG. 2. Individual responses of three bats in experiment 1 expressed as the percentage of choices to the right side. The abscissa shows the pure tone and the fundamental frequencies of the respective training, test, and control stimuli normalized by the reference frequency of 23 kHz (arrow). The different symbols denote the responses to the pure tone (solid squares) and the complex tone (solid triangles) training stimuli as well as to the test (open circles) and control (open triangles) stimuli. Note that all test stimuli are classified to the right side by all three bats, indicating that there is no spontaneous classification of collective pitch in these individuals.

III. EXPERIMENT 2: CAN BATS BE *TRAINED* TO CLASSIFY HARMONIC TONES ACCORDING TO COLLECTIVE PITCH?

The aim of this experiment was to investigate whether the bats could be *trained* to classify harmonic complex tones according to their fundamental frequencies.

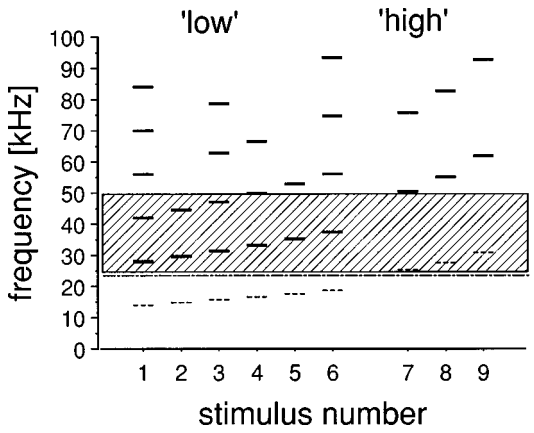

FIG. 3. Frequency content (solid lines) of ''low'' and ''high'' training stimuli of experiment 1 with fundamental frequencies below and above 23 kHz (long, dash–dotted line) respectively. The abscissa shows the stimulus numbers as used in Table I. The fundamentals were omitted in the frequency spectra (dashed lines). Please note that the ''high'' training stimuli contain no spectral energy in the hatched frequency region below 50 kHz.

A. Training stimuli

Training stimuli were a set of nine harmonic complex tones consisting of two to five adjacent harmonics (see Fig. 3). Six of the training stimuli had fundamental frequencies between 14 and 18.7 kHz which were, apart from one exception, identical with the frequencies of the low pitched pure tone training stimuli used in experiment 1. The animals were rewarded for selecting the left feeding dish in response to these stimuli. They will in the following be referred to as the ''low'' training stimuli. The fundamental frequencies of the three ''high'' training stimuli were ranging between 25.3 and 30.9 kHz. They were identical with the frequencies of three of the high pitched pure tone training stimuli of experiment 1. In the presence of these stimuli, the bats were rewarded at the right feeding dish. The fundamental was omitted in the frequency spectra of all training stimuli so that they contained only harmonics above 23 kHz. The spectral content of all training stimuli is listed in Table I. The training stimuli are labeled with numbers 1 to 9.

B. Rationale of test stimuli and decision models

After training, the bats classified the ''low'' and the ''high'' training stimuli correctly on the left and the right

TABLE I. Spectral content of ''low'' and ''high'' training stimuli. The fundamental frequency is indicated by F_0. The physically present harmonics are given in column 3, the rewarded side is given in column 4.

Stimulus No.	F_0 (kHz)	Harmonics	Rewarded side
1	14.0	2–6	left
2	14.8	2–3	left
3	15.7	2–5	left
4	16.6	2–4	left
5	17.6	2–3	left
6	18.7	2–5	left
7	25.3	2–3	right
8	27.5	2–3	right
9	30.9	2–3	right

side, respectively. Still, this does not mean that they actually classified the nine training stimuli according to their collective pitch. Rather, the bats could have acquired three different decision criteria during the training period, each of which would have enabled them to classify the set of training stimuli correctly. Apart from the collective pitch, the frequency of the lowest partial of the training stimuli would have provided a usable cue in the classification task. The second harmonic is the lowest frequency component in all training stimuli (see Fig. 3). Therefore, the frequency of the lowest partial in the ''high'' training stimuli is higher than 50 kHz whereas the ''low'' stimuli contain at least one partial whose frequency is substantially lower than 50 kHz (see the hatched frequency region below 50 kHz in Fig. 3). In humans, the spectral pitches of the lowest and the highest partials tend to be heard out most easily from a tone complex (Moore *et al.*, 1984; Moore and Ohgushi, 1993). Finally, the bats could have memorized the sound of each training stimulus together with the required right–left classification. In this case, the bats possibly attended to a sound quality that was mediated by the broadband spectral composition of the training stimuli. The three optional decision criteria will in the following be referred to as collective pitch A, spectral pitch of lowest partial B, and broadband spectral composition C, respectively.

After the training period, unknown harmonic and inharmonic complex tones, whose spectral composition differed from that of the training stimuli, were presented to the bats (they will be described in the next paragraph). To establish a quantitative relation between the bats' actual decision behavior and the three possible decision criteria A, B, and C, the decision criteria were expressed by scalar numerical measures. The collective pitch criterion A is expressed by the fundamental frequency F_0 of the tone complexes normalized by the reference frequency F_{ref} of 23 kHz. The criterion of lowest partial B is expressed by the frequency of the lowest harmonic in the presented tone complexes (F_{low}) divided by 50 kHz. If the bats attended to a sound quality mediated by the broadband spectral composition of the training stimuli (criterion C), they must have judged the unknown test stimuli according to their perceptual similarity to the learned training stimuli. In order to obtain a measure for decision criterion C, we assumed that the perceptual similarity of the complex tones is determined by the similarity of their broadband frequency spectra. Therefore, we first determined the spectral similarity of each test stimulus with each of the ''low'' and ''high'' training stimuli. The spectral similarity of two tone complexes was expressed in terms of a spectral correlation coefficient. As the frequency spectrum of a quasistatic complex tone is composed of the arbitrarily narrow peaks of the partial tones, the correlation between two complex tones which have no partials in common would equal zero. The complex tones were therefore converted into a spectrally smeared 'internal representation.' Thereby each delta peaked partial tone at frequency f was convoluted with a normal density function to yield the smeared representation $E_f(u)$. Here E_f is a function of frequency u given by

$$E_f(u)=\frac{1}{\sigma(f)\sqrt{2\pi}}\exp\left\{\frac{-(u-f)^2}{2\sigma(f)^2}\right\}. \tag{1}$$

The standard deviation $\sigma(f)$ of the density function was set equal to *M. lyra*'s critical bandwidth at the frequency f of the respective partial tone. It is given by $\sigma(f)=4.9(f/50)^{1.71}$ (Schmidt *et al.*, 1995). The functions $E_f(u)$ may be regarded as approximations of the distribution of excitation for one partial with frequency f (Moore and Glasberg, 1983) or as the probability density of the random variable describing the measurement of f by the auditory system (Goldstein, 1973). The correlation coefficients between the internal representations of two tone complexes with N and M components were calculated according to

$$\mathrm{crr}(C_1^N,C_2^M)=\frac{\int E_{C_1^N}(u)E_{C_2^M}(u)\,du}{\sqrt{\int E_{C_1^N}(u)^2\,du\int E_{C_2^M}(u)^2\,du}}, \tag{2}$$

where C_1^N and C_2^M are the N- and M-dimensional vectors containing the partial frequencies of the two tone complexes. $E_{C_1^N}$ and $E_{C_2^M}$ are the respective internal representations. The integral in the numerator of Eq. (2) was calculated with the boundary condition that each partial in either tone complex was matched with only one partial in the other tone complex. In the next step, the maxima of the spectral similarities of a test stimulus S with the sets of ''low'' and ''high'' training stimuli were calculated. The maximum spectral similarity of S to the ''low'' stimuli was subtracted from the maximum similarity to the set of ''high'' stimuli

$$\begin{aligned}C(S)&=\max\{\mathrm{crr}(S,H);H\in H\}-\max\{\mathrm{crr}(S,L);L\in L\}\\&=\max_{\text{'high'}}-\max_{\text{'low'}},\end{aligned} \tag{3}$$

and this value was taken as a measure for the broadband spectral criterion C. In Eq. (3), L and H denote the sets of ''low'' and ''high'' training stimuli, respectively.

Schmidt (1988, 1992) used a comparable model of spectral correlation to explain the discrimination performance of *M. lyra* for phantom target echoes of the bats' own echolocation sounds. The correlation between two complex spectra in Eq. (2) defines an angular measure of spectral similarity. Other possible measures could be defined by the Euclidean distance or equivalent metrics between the smeared internal representations of two wideband spectra (cf. Schmidt, 1992).

C. Composition of test stimuli

A set of test stimuli was designed to investigate which of the three decision criteria A, B, or C was used by the bats to classify the training stimuli. The test stimuli can be grouped into three classes. Two examples of each class are shown in Fig. 4. The spectral content of all test stimuli are listed in Table II.

Class 1 contained seven test stimuli that differed from the training stimuli only in fundamental frequency and the total number of higher harmonics (Fig. 4, class 1). The class 1 stimuli are labeled with numbers 10 to 16 in Table II. They consisted of two to five adjacent harmonics and like in the training stimuli the fundamental component was omitted in their spectra. The fundamental frequencies of the class 1

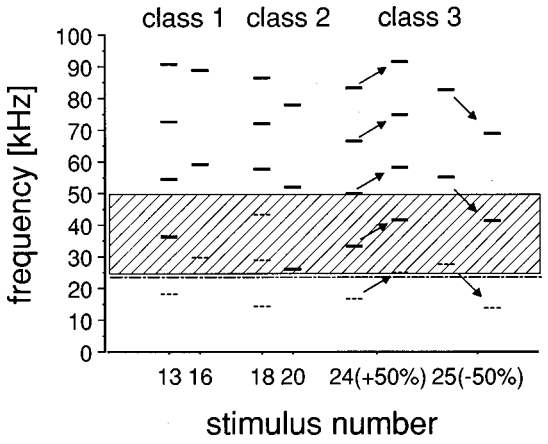

FIG. 4. Spectral composition (solid lines) of the test stimuli used in experiment 2. Two examples of each of the three classes of test stimuli are shown together with their respective stimulus numbers. The inharmonic tone complexes (class 3) are shown with the respective unshifted harmonic complexes (for further explanations see Fig. 3).

stimuli were either higher or lower than 23 kHz and differed from those of the ''low'' and ''high'' training stimuli.

Class 2 of the test stimuli contained five harmonic complex tones (Fig. 4, class 2). Three of the class 2 stimuli (numbers 17 to 19) had fundamental frequencies below 23 kHz, similar to the ''low'' training stimuli. However, unlike in the ''low'' training stimuli, not only the fundamental component but up to three of the lower harmonics were missing in their frequency spectra. Stimuli 18 and 19 consisted only of harmonics above 50 kHz (see Fig. 4, class 2). In this respect, they resembled the ''high'' training stimuli. The two other class 2 stimuli (numbers 20 and 21) had fundamental frequencies of 26 and 31.8 kHz and consisted of the first three harmonics. In contrast to the ''high'' training stimuli, these two test stimuli therefore contained spectral energy well below 50 kHz (see Fig. 4, class 2).

The four tone complexes of class 3 test stimuli (numbers 22 to 25) were shifted out of the harmonic frequency relation by 50% of the fundamental frequency (Fig. 4, class 3; two examples are shown together with the respective unshifted, harmonic tone complexes). In human listeners, such highly inharmonic tones do not elicit any unambiguous percept of the collective pitch (de Boer, 1985). For the inharmonic tones of class 3, the collective pitch criterion A was set to one, as chance performance must be expected for these stimuli without a well-defined collective pitch. Spectrally, class 3 stimuli resembled the ''low'' training examples: they all contained spectral energy below 50 kHz and in all but one case the frequency spacing between the partials was smaller than 23 kHz.

TABLE II. Spectral content of test stimuli of experiment 2. The fourth column highlights the most important attributes of the stimuli (e.g., class, region of F_0 and F_{low} and inharmonic shift in percentage of the F_0 of the respective unshifted complex tone). For further explanations see Table I.

Stimulus No.	F_0 (kHz)	Harmonics	Attributes
10	13.0	2–5	class 1, $F_0<23$ kHz
11	15.3	2–6	class 1, $F_0<23$ kHz
12	16.3	2–3	class 1, $F_0<23$ kHz
13	18.2	2–5	class 1, $F_0<23$ kHz
14	26.8	2–3	class 1, $F_0>23$ kHz
15	28.4	2–3	class 1, $F_0>23$ kHz
16	29.6	2–3	class 1, $F_0>23$ kHz
17	12.1	3–7	class 2, $F_{low}<50$ kHz
18	14.4	4–6	class 2, $F_{low}>50$ kHz
19	17.1	3–4	class 2, $F_{low}>50$ kHz
20	26.0	1–3	class 2, $F_{low}<50$ kHz
21	31.8	1–3	class 2, $F_{low}<50$ kHz
22	12.8	2–6	class 3, +50% shift
23	18.7	2–5	class 3, −50% shift
24	16.6	2–5	class 3, +50% shift
25	27.5	2–3	class 3, −50% shift

D. Results of experiment 2

The bats responded to the seven test stimuli of class 1 with a highly significant preference for either one or the other side. Seemingly, the animals judged these test stimuli according to their fundamental frequency: harmonic complexes with a fundamental frequency lower or higher than 23 kHz were classified similar to the ''low'' or ''high'' training stimuli, respectively. However, the test stimuli of class 1 are also spectrally most similar to the corresponding ''low'' and ''high'' training stimuli. It will be shown below that the criteria of lowest partial B and broadband spectral composition C are also both compatible with the bats' behavior for class 1 stimuli.

Assuming that the bats used the collective pitch criterion A, their responses to class 2 test stimuli are not in accordance with the fundamental frequencies of these test stimuli. Stimuli 18 and 19 which had fundamentals below 23 kHz but spectrally more resembled the ''high'' training examples were classified as the ''high'' training stimuli with a clear preference for the right side. The two complete harmonic tones 20 and 21 whose fundamentals were higher than 23 kHz but which comprised partials well below 50 kHz were classified as the ''low'' training stimuli with a clear preference to the left side by two of the bats whereas one bat chose both sides about equally often in response to these two stimuli.

Finally, test stimuli of class 3, which are expected to elicit no unambiguous percept of collective pitch and spectrally resembled the ''low'' training stimuli in that they contained partials with frequencies lower than 50 kHz, were readily categorized as similar to the ''low'' training stimuli by all three bats.

The individual results of the three animals are plotted in Figs. 5, 6, and 7 as a function of the numerical measures of the three decision criteria A, B, and C. As expected, all three decision criteria divide the training and class 1 stimuli (filled squares and open circles) into two well-separated categories, yielding a monotonic relation between the respective decision variables and the animals' responses to these stimuli. However, the relation between the decision behavior and the fundamental frequency criterion A becomes nonmonotonic for the critical test stimuli of classes 2 and 3 (see arrows in Figs. 5, 6, and 7, A). Therefore, it can clearly be excluded that the bats used the collective pitch as their decision criterion in this experiment. In the case of bat 1 (Fig. 5), the lowest partial criterion B can also be excluded as the deci-

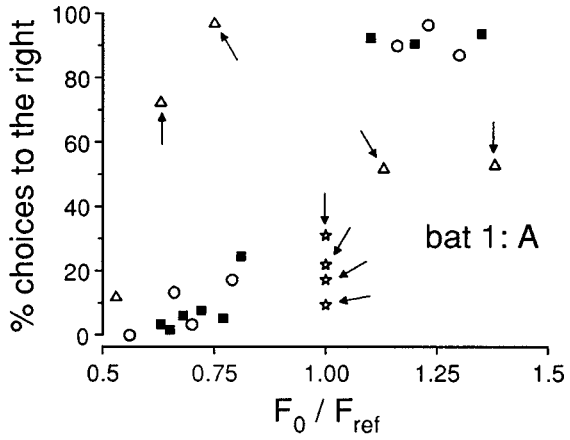

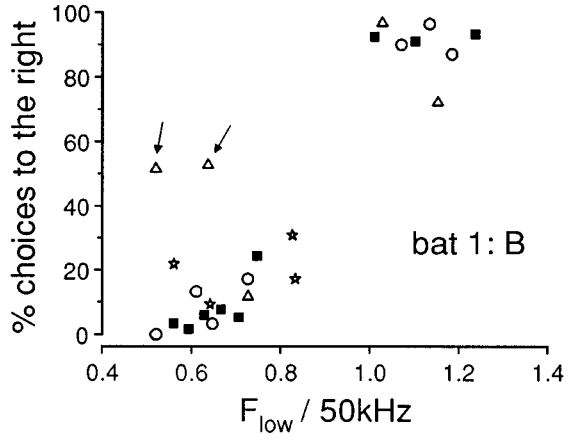

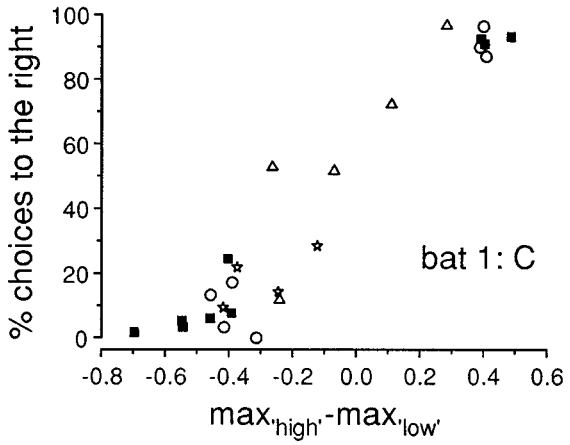

FIG. 5. Individual responses of bat 1 expressed as the percentage of choices to the right side plotted as a function of the decision criteria collective pitch *A*, pitch of resolved partial *B* and broadband spectral composition *C* (see text for explanation). Responses to training stimuli (filled squares), class 1 (open circles), class 2 (open triangles) and class 3 (open stars) test stimuli are characterized by different symbols. Systematic deviations from a monotonic decision function are indicated by arrows.

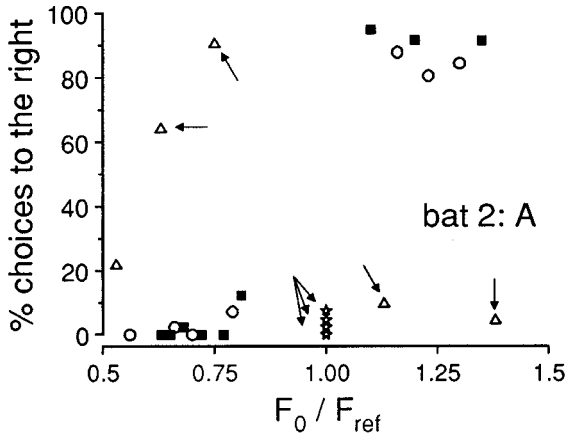

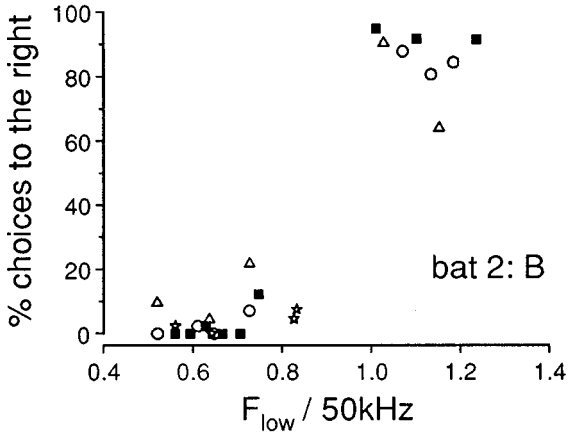

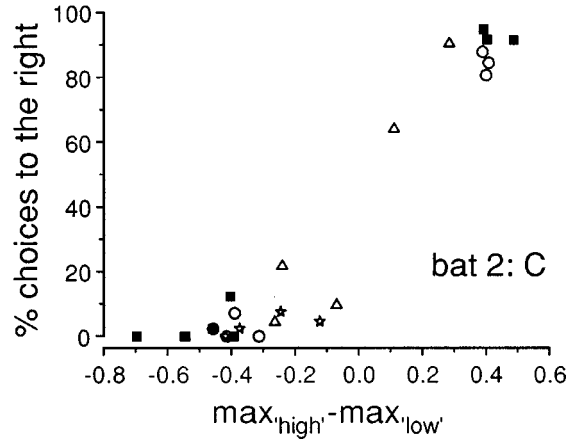

FIG. 6. Individual responses of bat 2 (for further explanations see Fig. 5).

sion variable. Bat 1 showed chance performance in response to the two complete harmonic tones 20 and 21. Had bat 1 based its decisions on the spectral pitch of the lowest partial, it should have classified these stimuli as the ''low'' training stimuli with a clear preference to the left side (see arrows in Fig. 5, B). As the ''low'' training stimuli, both test stimuli 20 and 21 contain a partial well below 50 kHz. For bats 2 and 3, however, the numerical representations of both decision criteria B and C are monotonically related to the actual decision behavior (Figs. 6 and 7, B, C). Further testing was needed in the case of these two bats to distinguish between decision criteria B and C.

IV. EXPERIMENT 3: BROADBAND SPECTRAL ANALYSIS VERSUS RESOLUTION OF A SINGLE PARTIAL

A. Stimuli and conditions

Only bats 2 and 3 participated in this experiment. In experiment 2, these two bats had classified the complete harmonic tones 20 and 21 which consisted of the first three

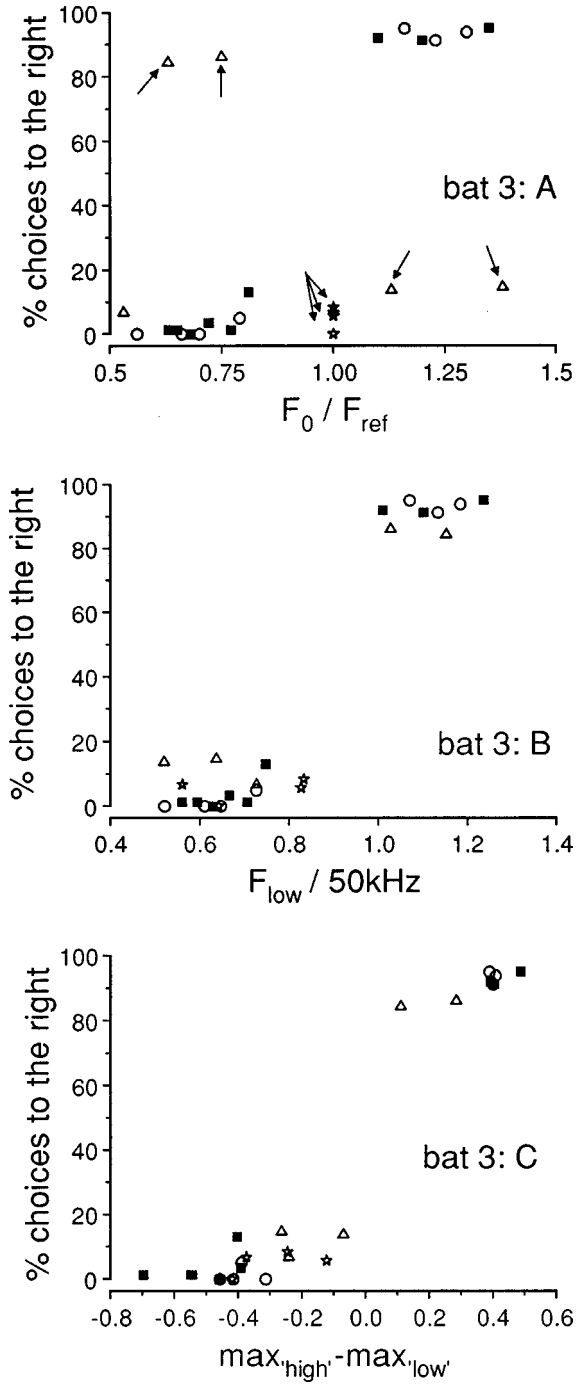

FIG. 7. Individual responses of bat 3 (for further explanations see Fig. 5).

harmonics of a fundamental frequency of 26 and 31.8 kHz, respectively, as the ''low'' training stimuli with a significant preference to the left side. The two stimuli 20 and 21 were now added to the set of 'high' training stimuli (numbers 7 to 9, see Table I). Contrary to the bats' spontaneous classifications, responses to the two complete harmonic tones were then only rewarded at the right feeding dish. Assuming that bats 2 and 3 based their decisions on the spectral pitch of the lowest frequency component in the complex tones (criterion B), this new training should have forced them to change their decision criterion from the lowest partial criterion B to the broadband spectral composition criterion C. The lowest frequency component of the two new ''high'' training stimuli

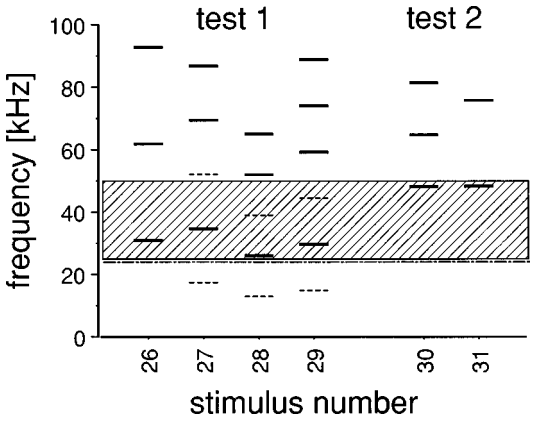

FIG. 8. Spectral content of the two sets of test stimuli used in experiment 3 together with their stimulus numbers. The hatched bar denotes the frequency region below 50 kHz.

was lower than 50 kHz. If the bats decided according to the spectral pitch of the lowest component they would have chosen the right side only in response to stimuli with a lowest frequency component higher than 50 kHz (like the old ''high'' training stimuli 7 to 9). Therefore the new training would have made criterion B useless and it would have forced the bats to attend to spectral similarities in the frequency region above 50 kHz.

If a bat managed to reverse its classifications of stimuli 20 and 21 in no more than one week, its spontaneous responses to a set of four new test stimuli were recorded. The spectra of the four test stimuli are shown in Fig. 8, test 1. Their spectral content is given in Table III (numbers 26 to 29). One test stimulus (number 26) was another complete harmonic tone with a fundamental frequency of 30.9 kHz. The other three (numbers 27 to 29) were harmonic tones with fundamental frequencies between 13 and 17.4 kHz which consisted of adjacent harmonics in the frequency region above 50 kHz and contained only even number harmonics in the region below 50 kHz. Test stimuli 27 to 29 thus spectrally resembled the ''low'' training stimuli in the frequency region above 50 kHz and they were similar to the newly learned ''high'' training stimuli 20 and 21 in the region below 50 kHz. If a bat kept choosing the left side in response to the complete harmonic tones 20 and 21 in more than 75% of the trials after the given time of one week, training was stopped and two other test stimuli, labeled with numbers 30 and 31, were presented (see Fig. 8, test 2 and Table III). Both of them were inharmonic complex tones with a lowest frequency component of 48 kHz. Stimulus 30

TABLE III. Spectral content of test stimuli of experiment 3. For further explanations see Table II.

Stimulus No.	F_0 (kHz)	Harmonics	Attributes
26	30.9	1–3	test 1
27	17.4	2, 4, and 5	test 1
28	13.0	2, 4, and 5	test 1
29	14.8	2, 4–6	test 1
30	16.6	2–3	test 2, +89% shift
31	27.5	2–3	test 2, −25% shift

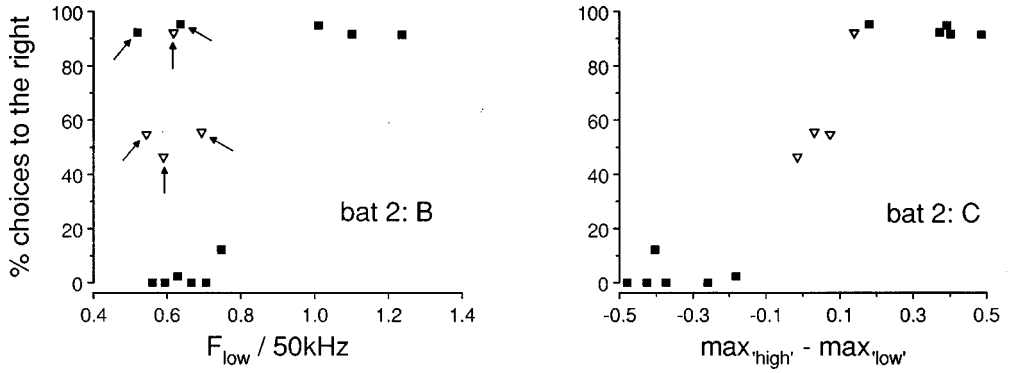

FIG. 9. Individual responses of bat 2 to the new training stimuli illustrated in Fig. 8, test 1, plotted as a function of the two spectral variables B and C. The responses to training stimuli are characterized by solid squares, responses to test stimuli are given as open triangles. Systematic deviations from a monotonic decision function are indicated by arrows.

consisted of three partials with a frequency spacing of 16.6 kHz whereas the two component frequencies of stimulus 31 were separated by 27.5 kHz.

B. Results of experiment 3

1. Bat 2

When responses to the complete harmonic tones 20 and 21 were rewarded on the right side only, bat 2 learned to fully reverse its classifications of these two stimuli in only about five days. Note that the training for experiment 2 had required a much longer time of about two months. This shows that, like bat 1, bat 2 also must have had a concept of the broadband spectral patterns of the ''low'' and ''high'' training stimuli. A complete revision of the decision criterion would certainly have required a longer training time. Bat 2 spontaneously transferred the new classification of the complete harmonic tones to a different fundamental frequency of 30.9 kHz (test stimulus 26). The animal responded to the three new test stimuli 27 to 29 about equally often on both sides (mean % choices to the right=52.5% for all three stimuli for a total of $N=139$ decisions). Obviously, the animal noticed the spectral congruence of these test stimuli with the ''low'' training stimuli in the frequency region above 50 kHz and was at the same time puzzled by their similarity with the newly learned ''high'' training stimuli 20 and 21 in the region below 50 kHz. Bat 2's results for the four new test stimuli are plotted in Fig. 9 as a function of the two spectral decision criteria B and C. The spectral correlations of criterion C were in this case calculated using the enlarged set of ''high'' training stimuli (numbers 7 to 9, 20, and 21). The relation between decision data and the resolved partials criterion B is nonmonotonic not only for the test stimuli (open triangles) but also for the new training stimuli (filled squares; see arrows in Fig. 9, B) whereas the broadband spectral criterion C yields a good match to the observed behavior (Fig. 9, C).

Bat 2 had classified the complete harmonic tones 20 and 21 differently from bat 1 in experiment 2. The present results indicate that this was not because bat 2 used a different decision criterion. Rather, it seems that during the training of experiment 2, bat 2 had learned to focus its spectral comparison on the frequency region below 50 kHz. The ''low'' and ''high'' training stimuli of experiment 2 differ most obviously in this frequency region (see the hatched bar in Fig. 3). The second training forced bat 2 to more strongly consider the high-frequency spectral properties of the experimental stimuli.

2. Bat 3

Bat 3 had also spontaneously classified the complete harmonic tones 20 and 21 as the ''low'' training stimuli in experiment 2. However, unlike bat 2, this animal did not learn to reverse its classifications of these two stimuli. After one week of training it kept choosing the left side in response to stimuli 20 and 21 in more than 75% of the cases even though it was not rewarded for these responses. We therefore stopped the new training and tested bat 3's spontaneous responses to the inharmonic complex tones 30 and 31 (see Fig. 8, test 2). The two parts of Fig. 10 show this bat's responses to the new test stimuli 30 and 31 (open triangles) as a function of the two spectral criteria B and C. Criterion B cannot separate these test stimuli, because their lowest partials have the same frequency. The observed difference between the responses to the test stimuli 30 and 31 is correctly mapped by criterion C. Bat 3 classified test stimulus 31 with a significantly greater preference to the right side (% choices to the right=69.7, $N=33$) than stimulus 30 (% choices to the right=43.3, $N=30$; $\chi^2=4.47$, $p=0.035$). Stimulus 31 spectrally more resembles the ''high'' training stimuli due to the wider spacing of its frequency components (see Fig. 8, test 2). This shows that the animal based its decisions on spectral similarity in the frequency region above 50 kHz if the region below 50 kHz did not provide any usable information. Bat 3 probably most strongly considered spectral similarities in the frequency region below 50 kHz and can thus be said to have made use of both criteria B and C, depending on the spectrum of a given test stimulus.

V. DISCUSSION

The three bats that participated in the present experiments were ''spectral listeners'' as they based their spontaneous pitch judgments of harmonic complex tones on the spectral pitches of the component partial tones. The bats' responses to the test stimuli of experiment 2 proved that the animals did not adopt the collective pitch of harmonic tones as their decision criterion during the training of experiment

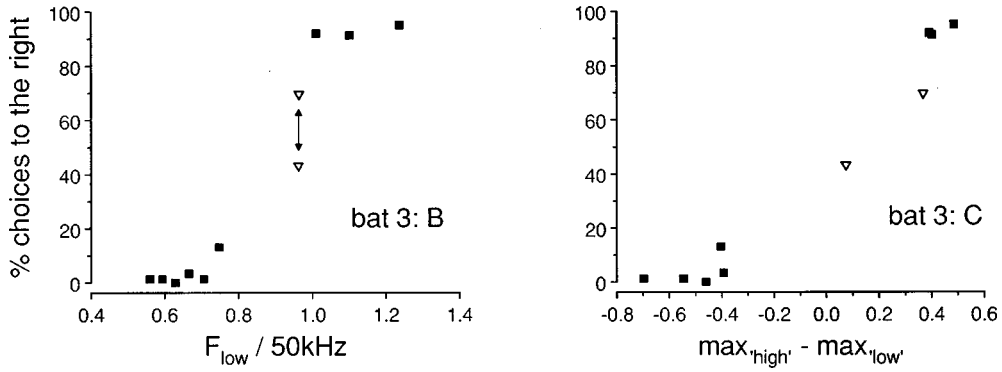

FIG. 10. Individual responses of bat 3 to the two new test stimuli shown in Fig. 8, test 2, as a function of the spectral decision criteria B and C (for further explanations see Fig. 9).

2. In earlier studies (Preisler and Schmidt, 1995, 1998; Schmidt *et al.*, 1995), on the other hand, some bats managed to spontaneously classify harmonic tones according to collective pitch. These individual differences in behavior may be attributable to differences in the distinctiveness of collective pitch perception. Differences in the individual predisposition to the perception of collective pitch have been reported for human subjects (Preisler, 1993). Alternatively, the use of collective pitch by *M. lyra* may be context dependent and may have been impeded by the specific experimental situation. After all, the experimental situation differed from the echolocation context as the animals were passively listening to the stimuli. Therefore, there was no need to attribute the stimuli to any preceding sonar call.

The ''high'' training stimuli do not contain spectral energy in the frequency region below 50 kHz (see hatched frequency region in Fig. 3). The ''low'' training stimuli all contain at least one partial whose frequency is substantially lower than 50 kHz. Experiment 3 revealed that some animals were using this general distinguishing property to a limited extent. However, the animals did not base their decisions exclusively on the pitch of a single partial, although the lowest partial in the training stimuli would have provided a usable criterion. Rather, it seems that all animals had acquired a concept of the broadband spectral compositions of the ''low'' and ''high'' training stimuli. They used the training stimuli as spectral templates for the classification task and classified the unknown test stimuli according to their broadband spectral similarity to individual training stimuli. For their decisions, two animals put a strong weight on spectral similarities in the frequency region below 50 kHz. However, they too had the information in the high-frequency region at their disposal and could switch to it if the low-frequency region did not provide any unambiguous cues. This shows that *M. lyra* can differentially judge the spectral similarity of complex tones in different frequency regions. The bats are able to recognize that certain frequency regions contain more relevant information than others.

Thus, none of the animals had performed a genuine pitch comparison in the present experiments. The bats rather classified the experimental stimuli on the basis of a sensory quality that is mediated by their broadband frequency spectra. The bats' decisions show that the spectral correlation between two complex tones can be taken as a scalar numerical measure for the perceptual similarity between them (see Figs. 5–7, C). As all test and training stimuli have flat amplitude spectra, the correlations between their spectra are determined by the number and frequencies of their partial tones. Correspondingly, the sensory quality that we consider also depends on the number and frequencies of the partials in the complex tones in analogy to the timbre of vowels that is determined by the number and the frequency positions of their widely spaced formant peaks (Chistovich and Lublinskaya, 1979). The sound quality of vowels seems to depend on the relative levels L_1 and L_2 of two formant peaks only if the frequency separation between the two formants is not larger than some critical value. In that case, the two formants can be replaced by a single formant with a frequency that depends on L_2-L_1 in a ''center of gravity'' like manner. The relative levels of widely spaced formants have a minor effect on the vowel quality as long as they are detected. In profile analysis, on the other hand, discriminations are made on the basis of a sound quality that is exclusively determined by the relative levels of the partial tones at least if broadband spectra with widely spaced partials are concerned (Richards *et al.*, 1989). In this respect, the present experimental paradigm has to be distinguished from the profile analysis approach as only complex tones with flat amplitude spectra were used. It can rather be compared to studies of vowel perception if the partial tones in the ultrasonic multicomponent spectra used in the present study are regarded as analogues to the widely spaced formant peaks in a vowel spectrum. Remez *et al.* (1981) investigated a similar analogy between speech sounds and stimuli consisting of discrete partials with frequencies corresponding to the formant peaks.

A. Potential relevance for echolocation: The ''formant-mode'' model of echo perception

The results of the present experiments show that the broadband spectral analysis is a dominant and flexible sensory tool in the bat *M. lyra*. It provides the bat with a measure by which it can estimate the similarity between complex spectral patterns on a broad bandscale and which enables the bat to distinguish between information bearing and irrelevant frequency regions. The bats' remarkable performance in the classification tasks of the present experiments suggest that *M. lyra*'s auditory system is specialized on the analysis of broadband sounds consisting of multiple distinct frequency

components. Under the assumption that passive listening and echolocation in *M. lyra* at least partly involve similar modes of auditory processing, it can be conjectured that the broadband spectral analysis observed for complex tones also plays an important role for the echolocation of *M. lyra*, as this bat's sonar calls exhibit a harmonic multicomponent frequency structure similar to that of harmonic complex tones. In the following we will develop a theoretical framework which relates the perception of quasi-static complex tones investigated in the present experiments to the analysis of the spectral characteristics of echoes in *M. lyra*.

The downward frequency-modulated echolocation calls of *M. lyra* have very short durations. In the laboratory, echolocation calls are shorter than 2 ms (Hanke *et al.*, 1997). If the bat tracks a prey, calls become as brief as 0.4 ms. The modulation rates are correspondingly high. For a typical 1-ms call the modulation rate of the first harmonic component ranges between 4000 and 5000 Hz/ms. For human subjects, there is experimental evidence that the limit of temporal resolution that is commonly measured for spectrally static sounds is also approximately valid for frequency-modulated signals (Madden, 1994). This means that the instantaneous frequency of a dynamic signal is not perceived with an arbitrarily sharp resolution on the temporal scale. The auditory system averages frequency over a certain span of time. Experimental results indicate that for humans this averaging time is in the range of a few milliseconds which is comparable to what is observed in measurements of gap or increment detection (Plomp, 1964; Shailer and Moore, 1983; Moore *et al.*, 1996). Feth and co-workers have proposed the IWAIF (intensity-weighted average of instantaneous frequency) model for the short-time frequency averaging process (see, e.g., Feth *et al.*, 1982, 1995). The model assumes that the auditory system computes a weighted average of the instantaneous frequency, the IWAIF value, with a temporal weighting function equal to the instantaneous intensity of the signal. In the frequency domain, the IWAIF value of a signal corresponds to the ''center of gravity'' of the signal's power spectrum (Anantharaman and Krishnamurthy, 1993).

Gap detection experiments with the echolocating bat *Tadarida brasiliensis* indicate that this species' temporal acuity in passive listening does not vastly excel the human performance (Nitsche, 1993). Nitsche (1992) showed that *T. brasiliensis* is unable to distinguish between an upward and a downward frequency-modulated signal if the duration of the sweeps is shorter than about 4 ms. The synthetic sweeps had a similar frequency content as the echolocation calls of *T. brasiliensis*. The observed temporal threshold exceeds the average duration of *Tadarida*'s approach phase echolocation calls. Thus, in view of the brevity of *M. lyra*'s echolocation calls, it is hardly conceivable that the bat perceptually resolves the time structure of its echolocation calls. More likely, *M. lyra* evaluates the average qualities of the frequency components in the calls, like their overall levels and their average frequencies or IWAIF values.

Assume that the nth frequency component in an echolocation call of *M. lyra* sweeps down from the starting frequency $f_s(n)$ to the end frequency $f_e(n)$. The overall level

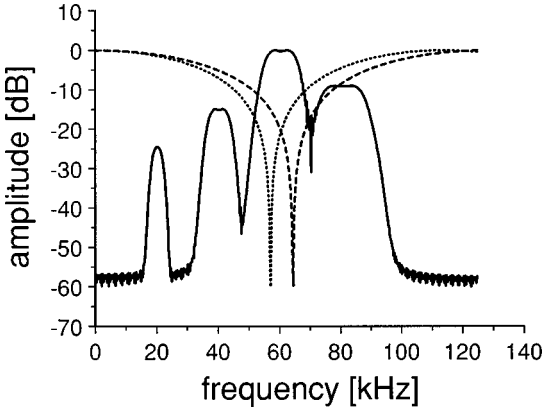

FIG. 11. Two just discriminable reflector transfer functions corresponding to ideal two surface targets with surface distances of 1.3 (dashed line) and 1.5 mm (dotted line). The solid line shows an idealized magnitude spectrum of a typical approach phase echolocation call of *M. lyra*. The two reflectors would yield IWAIF values of the third frequency component differing by 6.9 kHz.

of the nth frequency component is determined by the integral

$$A_n = \int_{f_e(n)}^{f_s(n)} |S(f)|^2 \, df. \tag{4}$$

Here, $|S(f)|$ denotes the magnitude spectrum of the echolocation call. Similarly, the IWAIF value of the nth component is defined by its ''center of gravity''

$$f_n = \frac{\int_{f_e(n)}^{f_s(n)} f|S(f)|^2 \, df}{\int_{f_e(n)}^{f_s(n)} |S(f)|^2 \, df} \tag{5}$$

(compare Anantharaman and Krishnamurthy, 1993). If an echolocation call is reflected by a structured target, the frequency transfer function $|R(f)|$ of the reflection will be imprinted onto the magnitude spectrum of the call. This will change the relative overall level of the nth frequency component according to

$$B_n = \int_{f_e(n)}^{f_s(n)} |R(f)|^2 |S(f)|^2 \, df. \tag{6}$$

As was pointed out in the Introduction, *M. lyra* might evaluate these changes in the relative overall levels of the frequency components to identify the transfer function of the reflection. The bat would thus derive the target structure from a profile analysis of the emission and its echo. However, the average frequencies of the components are also changed by the reflection. The IWAIF value of the nth frequency component in the echo can be written as

$$v_n = \frac{\int_{f_e(n)}^{f_s(n)} f|R(f)|^2 |S(f)|^2 \, df}{\int_{f_e(n)}^{f_s(n)} |R(f)|^2 |S(f)|^2 \, df}. \tag{7}$$

A reflection can shift the IWAIF values of the frequency components by considerable amounts. The dashed lines in Fig. 11 show two reflection transfer functions that are just discriminable by *M. lyra* (from Schmidt, 1992). They correspond to reflections at ideal two-front targets with a distance of 1.3 and 1.5 mm between the two surfaces, respectively. The solid line in Fig. 11 shows an idealized magnitude spec-

trum of a typical approach phase echolocation call of *M. lyra* (Hanke *et al.*, 1997; Schmidt, 1992). The IWAIF value of the third partial calculated with Eq. (4) differs for the two transfer functions by as much as 6.9 kHz. Hence, the average pitches of the partials are, in fact, highly variable characteristics of the echo spectrum that might carry a great deal of information about the reflecting target. Therefore, *M. lyra* probably not only evaluates the relative overall levels of the components in the echoes but also their average frequency positions. This notion is supported by the results of the present experiments: they show that *M. lyra* can simultaneously memorize a multitude of spectral patterns each consisting of several frequency components. The bat is able to classify unknown patterns by comparing the frequency positions of their spectral components with those in the learned patterns. This remarkable performance matches with the predictions of the IWAIF model showing that the frequencies of the spectral components in the echoes mediate information about the reflecting object. Hence, *M. lyra* possibly derives target structure from a broadband spectral analysis which may be seen as a combination of a profile analysislike mode of perception and a vowellike mode of perception. In the auditory system of *M. lyra*, object structures are probably represented as spectral patterns determined by the relative levels and the average frequencies of the up to six components in the bat's sonar echoes. Unknown objects may thus indeed be classified on the basis of a spectral comparison of the perceived echoes with these learned patterns as has been proposed in Schmidt (1992).

Although the relations between the average frequencies v_n of the components in echoes depend on the reflection transfer function and can significantly deviate from the harmonic relation, collective pitch perception may still play an important role for the association of a perceived echo with the corresponding emission in the call sequence as was conjectured by Schmidt (1995). Moore and Glasberg (1986) have shown that a mistuned component in an otherwise harmonic complex tone still significantly contributes to the collective pitch of the complex even if the mistuning is sufficiently large so that the component is heard out as a separate tone.

B. The role of the perception of roughness for the analysis of echo spectra

In the ''formant-mode'' model it is assumed that the time structure of the echolocation calls is not perceptually resolved due to the high frequency-modulation rates. An interesting alternative hypothesis concerning the perceptual dimensions involved in spectral echo processing by *E. fuscus* has been proposed by Miller (1997) (see also Nitsche and Miller, 1996). He suggested that the spectral changes in the echoes might be translated into a perception of roughness. A ripple on the wideband spectrum of a downward-modulated frequency component appears as an envelope modulation of its temporal waveform. The perception of these temporal envelope fluctuations may become important if the ripple on the echo spectrum is too fine to be spectrally resolved by the bandpass filters of the inner ear. However, due to the high-frequency modulation rates of *E. fuscus*' echolocation calls, the behaviorally relevant envelope fluctuations are rather fast in the range of several kilohertz. In a behavioral experiment, Miller (1997) presented bats of the species *E. fuscus* with envelope-modulated phantom echoes of their own echolocation calls and measured the just-detectable modulation depth as a function of the modulation frequency. Moderate and very high modulation frequencies between 1 and 9 kHz were tested. Miller's (1997) results indicate that *E. fuscus* detects an envelope modulation with a depth between 20% and 50% even at the high modulation frequencies. It cannot be excluded, however, that the bats used the spectral sidebands that are an inevitable consequence of envelope modulation (see, e.g., Ambardar, 1995). The envelope fluctuations that are brought about by the interference of multiple echo wavefronts, on the other hand, are not associated with spectral sidebands. More experimentation is therefore needed to further investigate whether roughness perception plays a role in the context of target fine structure analysis.

C. Constraints of the frequency structure of echolocation calls

In the ''formant-mode'' model it is assumed that *M. lyra* perceives the spectral changes between calls and echoes as changes in the average frequency positions and the relative overall levels of the modulated frequency components in its multicomponent echolocation calls. The model therefore suggests that target fine structure is represented in the form of *discrete* spectral patterns in the auditory system of *M. lyra*. The echolocation calls of other bat species do not exhibit such a pronounced multicomponent structure as *M. lyra*'s calls. The broadband portions of *E. fuscus*' echolocation calls, for example, have relatively flat power spectra in the perceptually relevant frequency region (e.g., Modgans *et al.*, 1993; Moss and Schnitzler, 1989; Surlykke, 1992). Assuming that *E. fuscus* infers target fine structure from the spectral characteristics of the echoes (Modgans and Schnitzler, 1990; Simmons *et al.*, 1990), the bat has to analyze the differences between the *continuous* power spectra of call and echo. The concept of a discrete representation of echo spectra would thus not be applicable in a spectral model of echolocation in *E. fuscus*. Concepts for the representation of continuous spectral profiles, like the ripple analysis model (e.g., Shamma *et al.*, 1995), have to be employed.

If a sonar call with a more or less flat power spectrum is reflected from an extended target, the frequency positions of the peaks and notches in the echo spectrum stand in a direct reciprocal relationship to the fine delay differences of the interfering partial echoes. Saillant *et al.* (1993) have exploited this fact in a computational model for echolocation in *E. fuscus* which is referred to as the SCAT model. In the SCAT model, the frequency spectrum of the echo is directly translated into the temporal domain of fine range differences.

D. Spectral versus temporal perspective in modeling approaches

The spectral models of echolocation, like the ''formant-mode'' model presented above, are based on the assumption that bats identify target fine structure by analyzing the power

spectra of calls and echoes. They do not, however, necessarily imply that the geometric structure of the target is reconstructed in the identification process. The spectral models are thus compatible with the assumption that the high-frequency phase information which is present in the multi-wavefront reflection of an echolocation call is lost in the auditory system of the bats. Hence, a spectral model predicts that targets with identical frequency transfer profiles but different phase functions cannot be distinguished by bats. Range-reversed targets, for example, would lead to ambiguities (compare Menne, 1988).

The SCAT model represents a compromise between a purely spectral model and a fully phase-sensitive cross-correlator (compare also Simmons *et al.*, 1979, 1996). The model is a spectral model in the sense that in its initial stages, the perceived echo is translated into a succession of dechirped short-time power spectra. The short-time spectra are represented by the smoothed output of a set of bandpass filters. They correspond to the distribution of excitation along the frequency-place dimension of the auditory system and are therefore comparable to the smeared internal representation of sounds that was used in the present study to compute the spectral correlation coefficients. In the spectral transformation block of the SCAT model, the short-time power spectra of the echoes are converted into a distribution along the temporal domain, referred to as the range distribution. The transformation from the frequency to the time domain can be coarsely regarded as an inverse Fourier cosine transform of the short-time power spectra with a set of modified cosine functions. Not all phase information in the echo is lost by the formation of the short-time power spectra. Therefore, the range distribution contains more information than a mere autocorrelation of the echo with itself. The autocorrelation function of a signal corresponds via the Fourier cosine transform in a one-to-one manner to its power spectrum (Wiener, 1930) and would thus lead to the same ambiguities for range reversed targets. However, the range distribution of the SCAT model contains less information than a cross-correlation between the echo and the corresponding call because part of the high frequency fine structure is smoothed by a low-pass filter. Although the SCAT model still requires a considerable temporal resolution, it is physiologically more plausible than a cross correlator.

Both the purely spectral models, like the ''formant-mode'' model, as well as the SCAT model (Saillant *et al.*, 1993) are concerned with the question of which perceptual dimensions the frequency transfer function of a spatially extended target are translated into. The SCAT model translates the frequency content of the echo into a distribution along a one-dimensional range axis. The geometrical fine structure of a target can be described by a one-dimensional range axis only if it is assumed that the propagation vectors of the interfering wavefronts in a multi-wavefront echo are approximately parallel. This assumption is justified if the distance between the bat and the target is very large and when small targets, e.g., single insects in the open air, are tracked from a distance that is large in comparison to the dimension of the target. However, it certainly does not apply when echoes from slightly different incident angles, which cannot be spatially resolved, interfere, as is the case in the presence of a structured object and densely cluttered background. Here, the representation of target geometry on a small scale, as any representation of space, requires three range dimensions. Further on, the reflection transfer function of each target itself depends on the actual angle of incidence of the echolocation call. The recognition of a certain target must therefore be a complex cognitive process which probably involves the analysis of multiple call-echo pairs and the comparison of the actual estimates with a set of learned patterns. The results of the present study suggest that *M. lyra* performs this comparison along the spectral dimension. Thereby, *M. lyra* probably simultaneously processes different features of the echo spectrum. The relative levels and absolute frequency positions of the echo components may be compared to learned spectral patterns corresponding to certain target structures in a similar way as the test stimuli of experiments 2 and 3 were compared to the training stimuli. Additionally, the frequency relations between the echo components may be perceived as a collective pitch which provides target-independent information. The analysis of the different spectral features of the echoes thus allows the acoustical characterization of targets and object recognition without an explicit translation of the echo spectrum to an ambiguous spatial dimension.

ACKNOWLEDGMENTS

This study was supported by the Deutsche Forschungsgemeinschaft, SFB 204 ''Gehör,'' München. The authors would like to thank Professor G. Neuweiler and Dr. A. Preisler for their support.

Ambardar, A. (**1995**). *Analog and Digital Signal Processing*, Foundations in Engineering Series (PWS Publishing).

Anantharaman, J. N., and Krishnamurthy, A. K. (**1993**). ''Intensity-weighted average of instantaneous frequency as a model for frequency discrimination,'' J. Acoust. Soc. Am. **94**, 723–729.

Beuter, K. J. (**1980**). ''A new concept of echo evaluation in the auditory system of bats,'' in *Animal Sonar Systems*, edited by R.-G. Busnel and J. F. Fish (Plenum, New York), pp. 747–761.

Chistovich, L. A., and Lublinskaya, V. V. (**1979**). ''The 'center of gravity' effect in vowel spectra and critical distance between the formants: psychoacoustical study of the perception of vowel-like stimuli,'' Hearing Res. **1**, 185–195.

de Boer, E. (**1985**). ''Auditory Time Constants: A Paradox?,'' in *Time Resolution in Auditory Systems*, edited by A. Michelsen (Springer-Verlag, Berlin), pp. 141–158.

Feth, L. L. (**1974**). ''Frequency discrimination of complex periodic tones,'' Percept. Psychophys. **15**, 375–379.

Feth, L. L., and O'Malley, H. (**1977**). ''Two-tone auditory spectral resolution,'' J. Acoust. Soc. Am. **62**, 940–947.

Feth, L. L., Krishnamurthy, A. K., and Zhang, T. (**1995**). ''Detection of combinations of frequency modulation: An application of the IWAIF model,'' in *Advances in Hearing Research, Proceedings of the 10th International Symposium on Hearing*, edited by G. A. Manley, G. Klump, C. Köppl, H. Fastl, and H. Oeckinghaus (World Scientific, Singapore), pp. 338–343.

Feth, L. L., O'Malley, H., and Ramsey, J. (**1982**). ''Pitch of unresolved two-component complex tones,'' J. Acoust. Soc. Am. **72**, 1403–1412.

Glaser, W. (**1974**). ''Zur Hypothese des Optimalempfangs bei der Fledermausortung,'' J. Comp. Physiol. **94**, 227–248.

Goldstein, J. L. (**1973**). ''An optimum processor theory for the central formation of the pitch of complex tones,'' J. Acoust. Soc. Am. **54**, 1496–1516.
Green, D. M. (**1988**). *Profile Analysis—Auditory Intensity Discrimination*, Oxford Psychology Series No. 13 (Oxford U.P., New York).
Hanke, S., Pillat, J., and Schmidt, S. (**1997**). ''Echolocation in the gleaning bat, *Megaderma lyra*, when hunting terrestrial prey,'' in *Göttingen Neurobiology Report 1997*, Vol. II, edited by N. Elsner and H. Wässle (Georg Thieme Verlag, Stuttgart), p. 367.
Hänsler, G. (**1996**). *Statistische Signale, Grundlagen und Anwendungen* (Springer-Verlag, Berlin).
Leippert, D. (**1994**). ''Social Behavior on the Wing in the False Vampire, *Megaderma lyra*,'' Ethology **98**, 111–127.
Lichte, W. H. (**1941**). ''Attributes of complex tones,'' J. Exp. Psychol. **28**, 455–480.
Madden, J. P. (**1994**). ''The role of frequency resolution and temporal resolution in the detection of frequency modulation,'' J. Acoust. Soc. Am. **95**, 454–462.
Menne, D. (**1988**). ''Designing critical experiments on the detection and estimation in echolocating bats,'' in *Animal Sonar—Processes and Performance*, edited by P. E. Nachtigall and P. W. B. Moore (Plenum, New York), pp. 387–411.
Miller, L. A. (**1997**). ''The detection of amplitude modulated echoes by the Big Brown Bat, Eptesicus,'' in *Abstracts of the 20th Annual Midwinter Research Meeting of the ARO*, edited by G. R. Popelka, p. 91.
Modgans, J., and Schnitzler, H.-U. (**1990**). ''Range resolution and the possible use of spectral information in the echolocating bat, *Eptesicus fuscus*,'' J. Acoust. Soc. Am. **88**, 754–757.
Modgans, J., Schnitzler, H.-U., and Ostwald, J. (**1993**). ''Discrimination of two-wavefront echoes by the big brown bat, *Eptesicus fuscus*: behavioral experiments and receiver simulations,'' J. Comp. Physiol. A **172**, 309–323.
Möhres, F. P., and Neuweiler, G. (**1966**). ''Die Ultraschallorientierung der Großblatt-Fledermäuse (Chiroptera-Megadermatidae),'' Zeitschrift für vergleichende Physiologie **53**, 195–227.
Moore, B. C. J., and Glasberg, B. R. (**1983**). ''Suggested formulae for calculating auditory-filter bandwidths and excitation patterns,'' J. Acoust. Soc. Am. **74**, 750–753.
Moore, B. C. J., and Glasberg, B. S. R. (**1986**). ''Thresholds for hearing mistuned partials as separate tones in harmonic complexes,'' J. Acoust. Soc. Am. **80**, 479–483.
Moore, B. C. J., and Ohgushi, K. (**1993**). ''Audibility of partials in inharmonic tones,'' J. Acoust. Soc. Am. **93**, 452–461.
Moore, B. C. J., Glasberg, B. R., and Shailer, M. J. (**1984**). ''Frequency and intensity difference limens for harmonics within complex tones,'' J. Acoust. Soc. Am. **75**, 550–561.
Moore, B. C. J., Peters, R. W., and Glasberg, B. R. (**1996**). ''Detection of decrements and increments in sinusoids at high overall levels,'' J. Acoust. Soc. Am. **99**, 3669–3677.
Moss, C. F., and Schnitzler, H.-U. (**1989**). ''Accuracy of target ranging in echolocating bats: acoustic information processing,'' J. Comp. Physiol. A **165**, 383–393.
Neuweiler, G. (**1989**). ''Foraging Ecology and Audition in Echolocating Bats,'' Trends in Ecology & Evolution **4**, 160–166.
Neuweiler, G. (**1990**). ''Auditory adaptations for prey capture in echolocating bats,'' Physiol. Rev. **70**, 615–641.
Nitsche, V. (**1992**). ''Thresholds for auditory temporal order in the bat *Tadarida brasiliensis*,'' in *Rythmogenesis in Neurons and Networks*, Proc. 20th Göttingen Neurobiol. Conf., edited by N. Elsner and W. Richter (Georg Thieme Verlag, Stuttgart), p. 230.
Nitsche, V. (**1993**). ''Gap detection in the bat *Tadarida brasiliensis*,'' in *Gene Brain Behavior*, Proc. 21th Göttingen Neurobiol. Conf., edited by N. Elsner and M. Heisenberg (Georg Thieme Verlag, Stuttgart), p. 261.
Nitsche, V., and Miller, L. A. (**1996**). ''Detection of amplitude modulation in the sonar echoes by the Big Brown Bat, *Eptesicus fuscus*,'' in *Göttingen Neurobiology Report 1996*, Vol. II, edited by N. Elsner and H.-U. Schnitzler (Georg Thieme Verlag, Stuttgart), p. 240.
Patterson, R. D. (**1973**). ''The effects of relative phase and number of components on residue pitch,'' J. Acoust. Soc. Am. **53**, 1565–1572.
Peterson, G. E., and Barney, H. L. (**1952**). ''Control methods used in a study of the vowels,'' J. Acoust. Soc. Am. **24**, 175–184.
Plomp, R. (**1964**). ''Rate of decay of auditory sensation,'' J. Acoust. Soc. Am. **36**, 277–282.
Preisler, A. (**1993**). ''The influence of the spectral composition of complex tones and of musical experience on the perceptibility of virtual pitch,'' Percept. Psychophys. **54**, 589–603.
Preisler, A., and Schmidt, S. (**1995**). ''Virtual Pitch Formation in the Ultrasonic Range,'' Naturwissenschaften **82**, 45–47.
Preisler, A., and Schmidt, S. (**1998**). ''Spontaneous classifications of complex tones at high and ultrasonic frequencies in the bat, *Megaderma lyra*,'' J. Acoust. Soc. Am. **103**, 2595–2607.
Remez, R. E., Rubin, P. E., Pisoni, D. B., and Carell, T. D. (**1981**). ''Speech perception without traditional speech cues,'' Science **212**, 947–950.
Richards, V. M., Onsan, Z. A., and Green, D. M. (**1989**). ''Auditory profile analysis: Potential pitch cues,'' Hearing Res. **39**, 27–36.
Saillant, P. A., Simmons, J. A., and Dear, S. P. (**1993**). ''A computational model of echo processing and acoustic imaging in frequency-modulated echolocating bats: The spectrogram correlation and transformation receiver,'' J. Acoust. Soc. Am. **94**, 2691–2712.
Shailer, M. J., and Moore, B. C. J. (**1983**). ''Gap detection as a function of frequency, bandwidth and level,'' J. Acoust. Soc. Am. **74**, 467–473.
Schmidt, S. (**1988**). ''Evidence for a spectral basis of texture perception in bat sonar,'' Nature (London) **331**, 617–619.
Schmidt, S. (**1992**). ''Perception of structured phantom targets in the echolocating bat, *Megaderma lyra*,'' J. Acoust. Soc. Am. **91**, 2203–2223.
Schmidt, S. (**1995**). ''The psychophysics of hearing by bats,'' in *Fechner Day '95, Proceedings of the 11th Annual Meeting, International Society of Psychophysics*, Cassis, France, edited by C. A. Possamai, pp. 91–96.
Schmidt, S., Preisler, A., and Sedlmeier, H. (**1995**). ''Aspects of pitch perception in the ultrasonic range,'' in *Advances in Hearing Research, Proceedings of the 10th International Symposium on Hearing*, edited by G. A. Manley, G. Klump, C. Köppl, H. Fastl, and H. Oeckinghaus (World Scientific, Singapore), pp. 374–382.
Schnitzler, H.-U., and Henson, O. W. (**1980**). ''Performance of airborne animal sonar systems I. Microchiroptera,'' in *Animal Sonar Systems*, edited by R.-G. Busnel and J. F. Fish (Plenum, New York), pp. 109–181.
Shamma, S. A., Vranic-Sowers, S., and Versnel, H. (**1995**). ''Representation of spectral profiles in the auditory system: Theory, physiology and psychoacoustics,'' in *Advances in Hearing Research*, edited by G. A. Manley, G. M. Klump, C. Köppl, H. Fastl, and H. Oeckinghaus (World Scientific, Singapore), pp. 432–441.
Simmons, J. A., Fenton, M. B., and O'Farell, M. (**1979**). ''Echolocation and pursuit of prey by bats,'' Science **203**, 16–21.
Simmons, J. A., Moss, C. F., and Ferragamo, M. (**1990**). ''Convergence of temporal and spectral information into acoustic images of complex sonar targets perceived by the echolocating bat, *Eptesicus fuscus*,'' J. Comp. Physiol. A **166**, 449–470.
Simmons, J. A., Saillant, P. A., Ferragamo, M. J., Haresign, T., Dear, S. P., Fritz, J., and McMullen, T. A. (**1996**). ''Auditory Computations for Biosonar Target Imaging in Bats,'' in *Auditory Computations*, edited by H. L. Hawkins, T. A. McMullen, A. N. Popper, and R. R. Fay (Springer-Verlag, Berlin), pp. 401–468.
Surlykke, A. (**1992**). ''Target ranging and the role of time-frequency structure of synthetic echoes in the big brown bat, *Eptesicus fuscus*,'' J. Comp. Physiol. A **170**, 83–92.
Wiener, N. (**1930**). ''Generalized harmonic analysis,'' Acta Math. **55**, 117–258.
Zöfel, P. (**1988**). *Statistik in der Praxis* (Gustav Fischer Verlag, Stuttgart).

LETTERS TO THE EDITOR

This Letters section is for publishing (a) brief acoustical research or applied acoustical reports, (b) comments on articles or letters previously published in this Journal, and (c) a reply by the article author to criticism by the Letter author in (b). Extensive reports should be submitted as articles, not in a letter series. Letters are peer-reviewed on the same basis as articles, but usually require less review time before acceptance. Letters cannot exceed four printed pages (approximately 3000–4000 words) including figures, tables, references, and a required abstract of about 100 words.

Experimental determination of the effective structure-function parameter for atmospheric turbulence

D. K. Wilson[a)]
U.S. Army Research Laboratory, 2800 Powder Mill Road, Adelphi, Maryland 20783

D. I. Havelock and M. Heyd
Institute for Microstructural Science, National Research Council, Ottawa, Ontario K1A 0R6, Canada

M. J. Smith, J. M. Noble, and H. J. Auvermann
U.S. Army Research Laboratory, 2800 Powder Mill Road, Adelphi, Maryland 20783

(Received 13 November 1997; revised 7 November 1998; accepted 9 November 1998)

The effective structure-function parameter for scattering by atmospheric turbulent velocity fluctuations has normally been assumed to be $C_{\text{eff}}^2=4C_V^2/c_0^2$, where C_V^2 is the velocity structure-function parameter and c_0 the sound speed. However, a new derivation by Ostashev [Waves Random Media **4**, 403–428 (1994)], which takes into account the vectorial nature of the wind velocity field, suggests that $C_{\text{eff}}^2=22C_V^2/3c_0^2$. An experiment was designed to determine the correct value of the coefficient. Sound-pressure amplitude variances were monitored for several discrete frequencies between 380 and 3800 Hz, at distances up to 250 m. Cup and hot-wire anemometers were used to determine C_V^2. A theory for scattering by inertial-subrange turbulence was then used to calculate the C_{eff}^2 coefficient from the amplitude variance and C_V^2. Datasets recorded under different atmospheric conditions yielded different relationships between the coefficients and failed to verify either the 4 or 22/3 value. Some possible explanations for this behavior are discussed, including the need for more realistic meteorological modeling. [S0001-4966(99)04302-7]

PACS numbers: 43.28.Fp [LCS]

An acoustic wave propagating through the atmosphere is affected by turbulent fluctuations in wind velocity and temperature. Following the ideas of Kolmogorov,[1] the statistics of the turbulent fluctuations for each of these fields can be characterized by a structure-function parameter (SFP), C_v^2 and C_T^2, respectively. It is useful to define an ''effective'' SFP for the acoustic wave that combines the effects of the velocity and temperature fluctuations into a single parameter C_{eff}^2. Normally this effective SFP has been assumed to have the form

$$C_{\text{eff}}^2=\frac{C_T^2}{T_0^2}+a_v\frac{C_v^2}{c_0^2}, \tag{1}$$

where T_0 is the average temperature, c_0 the average sound speed, and a_v a constant coefficient. Tatarskii[2] suggested that $a_v=4$, and this value has been used in much subsequent work. However, a more recent derivation by Ostashev,[3] which rigorously accounted for the vectorial nature of the wind velocity field, resulted in $a_v=22/3$. The objective of the experiment described in this Letter was to determine the correct value for the coefficient a_v.

The experiment was performed at a small airport located east of the city of Ottawa, Ontario. Acoustic measurements of a series of pre-recorded tones were conducted with an array of electret microphones, located on the ground surface at intervals of 25 m, out to a distance of 650 m. The signals from this array were amplified and then transmitted to an equipment trailer, where they were filtered, digitized, and recorded. The test tones, at frequencies ranging from 380 to 3800 Hz, were produced with a standard horn-type loudspeaker, which was located on the top of a 1-m tower. Wind velocity and temperature were simultaneously recorded with a cup-type anemometer at 2-m height, a hot-wire anemometer at 2 m, and several temperature sensors on a 10-m tower. The cup anemometer and thermometers had a sampling rate of 0.5 Hz, whereas the hot-wire anemometer signals were filtered with a 250-Hz lowpass filter and sampled

[a)]Electronic mail: dkwilson@arl.mil

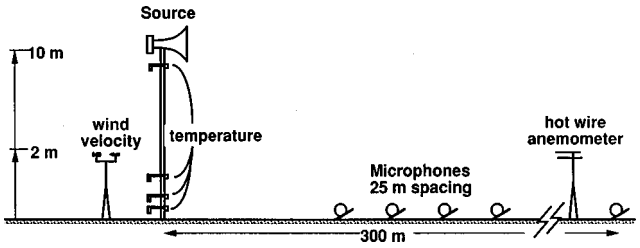

FIG. 1. Sideview showing location of the experimental equipment.

at 1000 Hz. The layout of the experiment is shown in Fig. 1. Further details on the test site, microphone array, and signal processing can be found in Havelock *et al.*[4]

Our method for determining the velocity coefficient in the C_{eff}^2 equation was to compare the variance in the log-amplitude fluctuations of the sound pressure to the SFPs that were estimated from the meteorological measurements. The equation for the log-amplitude pressure variance of a spherically propagating wave is[2]

$$\langle \chi^2 \rangle = 0.031 C_{\text{eff}}^2 k^{7/6} X^{11/6}, \tag{2}$$

where $k = 2\pi f/c_0$, f is the frequency, and X is the source–receiver separation (range). In our trials, the contribution of temperature fluctuations to C_{eff}^2 was small, so that $C_{\text{eff}}^2 \simeq a_v C_v^2/c_0^2$. Hence, by determining $\langle \chi^2 \rangle$ as a function of frequency and range from the microphone signals, and determining C_v^2 from the cup and/or hot-wire anemometer measurements, we should be able to evaluate a_v.

Our method for determining C_v^2 is based on the definition

$$\langle [v(\boldsymbol{r}+\Delta\boldsymbol{r}) - v(\boldsymbol{r})]^2 \rangle = C_v^2 (\Delta \boldsymbol{r})^{2/3}, \tag{3}$$

where $\boldsymbol{r}+\Delta\boldsymbol{r}$ and $\boldsymbol{r}$ are the locations of two sensors, and v is the component of the velocity field aligned with $\Delta\boldsymbol{r}$. For this equation to be valid, Δr must be within the inertial subrange.[1] Assuming the validity of Taylor's hypothesis, which states that the turbulence is ''frozen'' as the wind moves it past a stationary sensor, we have for the velocity SFP,

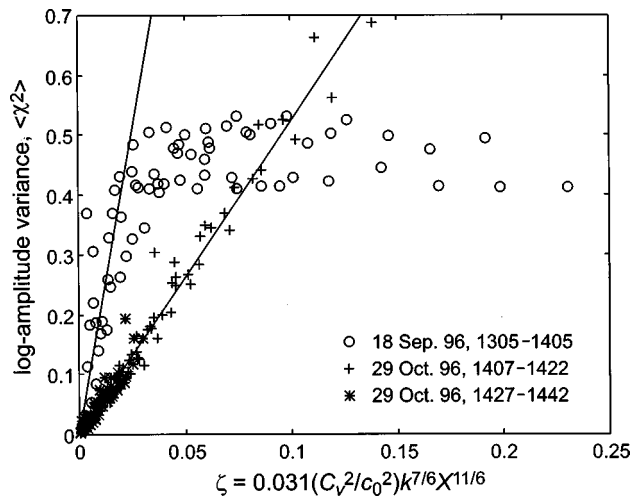

FIG. 2. Log-amplitude variance for the two datasets, as a function of the parameter $\zeta = 0.031(C_v^2/c_0^2)k^{7/6}X^{11/6}$. The lines are least-squares fits to the initial, linear sections of the data.

TABLE I. Summary of the results of the experiment. The coefficient for the effective structure-function parameter is a_v.

Date	C_v^2 ($m^{4/3}/s^2$)	a_v
18 September 1996	0.14	20
29 October 1996	0.088	5.2

$$C_v^2 = \frac{\langle [u(t+\Delta t) - u(t)]^2 \rangle}{(U\Delta t)^{2/3}}, \tag{4}$$

in which t is time, U is the mean wind speed, and u is the wind fluctuation in the direction of the mean. Our calculations for C_v^2 were made using the hot-wire anomemometer data, and are for separations $\Delta r = U\,\Delta t = 1$ m. The reason for selecting 1 m is that this value is less than the height of the anemometer (2 m), yet large enough to avoid the high-frequency roll-off in the sensor response.

The first dataset we consider, lasting 15 min, was recorded between 1350 and 1405 on 18 September 1996. The skies were mostly clear, winds were rather light ($U = 2.5$ m/s) but highly variable, and propagation was roughly cross-wind. A temperature lapse condition resulted in upward refraction. There were six test tones, at 1225, 1550, 2125, 2575, 3250, and 3800 Hz. The value for C_v^2 determined from the hot-wire anemometer was 0.14 $m^{4/3}/s^2$. The circles in Fig. 2 are $\langle \chi^2 \rangle$ for this dataset, plotted vs $\zeta = 0.031(C_v^2/c_0^2)k^{7/6}X^{11/6}$. Only ranges $X < 250$ m are included on the plot, since a shadow zone was evident at longer ranges. Based on Eqs. (1) and (2), the slope of the data points should be a_v. Although the data do collapse fairly well onto a line for small ζ, saturation is evident for $\zeta \gtrsim 0.03$. [Saturation effects were observed some time ago for optical propagation in the atmosphere (e.g., Ref. 5), and more recently for acoustic propagation by Daigle *et al.*[6] For this particular dataset the onset of saturation is complicated by the upward refraction.] The line shown in Fig. 2 is a least-squares fit to those data for which $\zeta < 0.03$. The slope of the line is 20. This is substantially greater than the values 4 or 22/3 suggested by theory.

The second dataset we consider is actually a combination of two 15 min sessions, one from 1407 to 1422 on 29 October 1996, and the other from 1427 to 1442 on the same day. Skies were clear on this afternoon, winds were moderate ($U = 3.4$ m/s), and propagation was downwind. The first session used tones at 1000, 1350, 1700, 2300, 2900, and 3500 Hz, whereas the second used tones at 380, 500, 600, 700, 820, and 940 Hz. The reason why we have combined the two sessions for this analysis is that they collapse nearly onto a single line, suggesting that C_v^2 was stationary through the time period covering the two sessions. The value of C_v^2 determined for the period 1407 to 1442 was 0.088 $m^{4/3}/s^2$. The corresponding plot of $\langle \chi^2 \rangle$ vs ζ is shown in Fig. 2. The line fitted to the combined dataset has a slope of 5.2, which falls between the theoretical values of 4 and 22/3.

Clearly, our experiment has been inconclusive in verifying either $a_v = 4$ or $a_v = 22/3$. The two datasets (summarized in Table I) yielded inconsistent results. It is unclear whether the difference in the slopes between the two datasets is due

to the orientation between the wind and propagation direction or some other factor. In future work, it would be desirable to collect a greater number of datasets.

Although the exact reason why the measured values of a_v differed from the theoretical ones is unclear, there are several possibilities. First, the data could be moderately affected by a large-scale (energy-subrange) turbulence structure, which is anisotropic and dependent on atmospheric conditions. Second, the covariance between temperature and velocity has been assumed negligible in both the theory and data analysis. Although this assumption has a well established precedence in the literature, the covariance term may actually be more significant than the temperature term,[7] and therefore may not be negligible. Finally, C_v^2 was assumed to be independent of height, which is probably a poor assumption. For example, in a surface layer where shear generation of turbulence dominates, $C_v^2 \propto z^{-2/3}$ (e.g., Ref. 8). If the sound in our experiment travels a straight path, simple calculations show that the average value of C_v^2 over the propagation path is 1.03 times the value measured by the hot-wire anemometer at 2 m—a small correction. If there is refraction, however, the correction can be significantly different.

Although the results of this experiment are inconclusive in verifying either $a_v = 4$ or $a_v = 22/3$, they do indicate the need for more realistic meteorological modeling in order to obtain accurate predictions of sound field statistics.

[1] A. N. Kolmogorov, ''The local structure of turbulence in incompressible viscous fluid for very large Reynolds numbers,'' C. R. Acad. Sci. URSS **30**, 301–305 (1941).

[2] V. I. Tatarskii, *The Effects of the Turbulent Atmosphere on Wave Propagation* (Keter, Jerusalem, 1971).

[3] V. E. Ostashev, ''Sound propagation and scattering in media with random inhomogeneities of sound speed, density and medium velocity,'' Waves Random Media **4**, 403–428 (1994).

[4] D. I. Havelock, X. Di, G. A. Daigle, and M. R. Stinson, ''Spatial coherence of a sound field in a refractive shadow: Comparison of simulation and experiment,'' J. Acoust. Soc. Am. **98**, 2289–2302 (1995).

[5] M. E. Gracheva, ''Research into the statistical properties of the strong fluctuations of light when propagated in the lower layer of the atmosphere,'' Izv. Vuz. Radiofiz. **10**, 775–787 (1967).

[6] G. A. Daigle, J. E. Piercy, and T. F. W. Embleton, ''Line-of-sight propagation through atmospheric turbulence near the ground,'' J. Acoust. Soc. Am. **74**, 1505–1513 (1983).

[7] D. K. Wilson, ''A brief tutorial on atmospheric boundary-layer turbulence for acousticians,'' in *7th International Symposium on Long Range Sound Propagation* (Ecole Centrale de Lyon, Lyon, France, 1996), pp. 111–121.

[8] R. B. Stull, *An Introduction to Boundary Layer Meteorology* (Kluwer, Dordrecht, Germany, 1988).

Incorporation of thermal overlap effects into multiple scattering theory

D. Julian McClements,[a] Yacine Hemar,[b] and Norbert Herrmann
Biopolymers and Colloids Research Laboratory, Department of Food Science, University of Massachusetts, Amherst, Massachusetts 01003

(Received 17 October 1997; revised 6 August 1998; accepted 2 November 1998)

Existing multiple scattering theories do not give accurate predictions of the ultrasonic properties of concentrated emulsions because overlap of thermal waves generated by the droplets in the presence of an ultrasonic field is not taken into account [McClements, J. Acoust. Soc. Am. **91**, 849–853 (1992)]. Recently, a core-shell model was developed which accounts for the effects of thermal overlap, but ignores multiple scattering, intrinsic absorption and visco-inertial effects [Hemar *et al.*, J. Phys. II **7**, 637–647 (1997)]. A multiple scattering theory is combined with the core-shell model to obtain a new theory that overcomes the limitations of each of the individual theories. The new theory gives excellent agreement with experimental measurements of the attenuation spectra of concentrated monodisperse emulsions. © *1999 Acoustical Society of America.* [S0001-4966(99)02902-1]

PACS numbers: 43.35.Bf [HEB]

INTRODUCTION

Ultrasonic spectrometry is finding increasing use as an analytical tool for characterizing the properties of concentrated emulsions.[1,2] Commercial instruments have recently become available which can rapidly and nondestructively measure both the disperse phase volume fraction and droplet size distribution of emulsions.[3–5] These instruments measure the attenuation coefficient of an emulsion over a wide range of frequencies (typically from 1 to 150 MHz), and then use ultrasonic scattering theory to find the droplet size distribution and concentration that gives the best fit between the theoretical predictions and the measured attenuation spectra.[1,6,7] The theory used to interpret the attenuation spectra is normally based on a single scattering theory, developed orginally by Epstein and Carhart[8] and then extended by Allegra and Hawley,[9] although corrections for multiple scattering are often included.[1,10] This approach gives excellent agreement with experimental measurements in fairly dilute emulsions ($\phi<0.15$), but may lead to significant deviations between the theory and experiment at higher droplet concentrations.[10]

In the long wavelength regime, the principal form of attenuation in emulsions with low density contrast is the heat flow which occurs between a droplet and its surroundings when the droplet is in the presence of an ultrasonic wave.[11,12] The extent of these thermal losses depends on the magnitude of the temperature gradient between the droplet and its surroundings. The Epstein–Carhart–Allegra–Hawley (ECAH) theory assumes there are no interactions between neighboring droplets, so that the heat generated by one droplet flows directly into the continuous phase.[8,9] In practice, the heat generated by a droplet may propagate into a neighboring droplet, and therefore the temperature gradient between a droplet and its surroundings is reduced, which leads to a decrease in the attenuation. This phenomenon was used to account for the fact that measurements of the attenuation coefficient of emulsions were lower than those predicted by multiple scattering theories at high droplets concentrations.[10,13] Recently, Hemar *et al.*[14] developed a core-shell model to account for the influence of the overlap of the thermal waves generated by the droplets on the ultrasonic properties of concentrated emulsions. Nevertheless, this model is limited because it does not take into account multiple scattering, intrinsic absorption or visco-inertial effects. In this article, we combine a multiple scattering theory with the core-shell model to develop a new theory that overcomes the limitations of each individual theory.

I. MULTIPLE SCATTERING THEORY

A variety of multiple scattering theories are available to relate the ultrasonic properties of emulsions to their microstructure, composition, and thermophysical properties.[15–17] These theories are based on a mathematical analysis of the propagation of ultrasonic waves through an ensemble of particles. One of the most widely used is the Waterman and Truell theory, which is given by the following expression in the long wavelength limit:[15]

$$\left(\frac{K}{k_1}\right)^2=\left(1-\frac{3i\phi A_0}{(k_1r)^3}\right)\left(1-\frac{9i\phi A_1}{(k_1r)^3}\right). \tag{1}$$

Here K is the complex propagation constant of the emulsion ($=\omega/c+i\alpha$), k_1 is the complex propagation constant of the continuous phase ($=\omega/c_1+i\alpha_1$), c is the ultrasonic velocity, α is the attenuation coefficient, ω is the angular frequency, i is $\sqrt{-1}$, ϕ is the dispersed phase volume fraction, r is the droplet radius, and A_0 and A_1 are the monopole and dipole scattering coefficients of the individual droplets.

Epstein and Carhart[8] developed a theory that could be used to calculate the scattering coefficients of individual

[a]Corresponding author. Electronic mail: mcclements@foodsci.umass.edu
[b]Current address: Hannah Research Institute, Ayr KA6 5HL, Scotland.

droplets surrounded by an infinite liquid, which was later extended by Allegra and Hawley.[9] In the long wavelength regime, the following explicit expressions for the monopole and dipole scattering coefficients were derived:[9]

$$A_0 = -\frac{ik_1 r}{3}\left((k_1 r)^2 - (k_2 r)^2 \frac{\rho_1}{\rho_2}\right) - \frac{i(k_1 r)^3(\gamma_1 - 1)}{b_1^2}\left(1 - \frac{\beta_2 C_{P1}\rho_1}{\beta_1 C_{P2}\rho_2}\right) H, \tag{2}$$

$$A_1 = \frac{i(k_1 r)^3(\rho_2 - \rho_1)(1 + T + is)}{\rho_2 + \rho_1 T + i\rho_1 s}, \tag{3}$$

where

$$H = \left[\frac{1}{(1 - ib_1)} - \frac{\tau_1}{\tau_2}\frac{\tan(b_2)}{\tan(b_2) - b_2}\right]^{-1},$$

$$b_1 = \frac{(1+i)r}{\delta_{T,1}}, \quad b_2 = \frac{(1+i)r}{\delta_{T,2}},$$

$$\delta_{T,i} = \sqrt{\frac{2\tau_i}{\rho_i C_{Pi}\omega}}, \quad \delta_S = \sqrt{\frac{2\eta_1}{\rho_1 \omega}}, \tag{4}$$

$$T = \frac{1}{2} + \frac{9\delta_S}{4r}, \quad s = \frac{9\delta_S}{4r}\left(1 + \frac{\delta_S}{r}\right).$$

Here, the density is ρ, the specific heat capacity is C_P, the coefficient of volume expansion is β, the thermal conductivity is τ, the viscosity is η, and the ratio of specific heats is γ. The subscripts 1 and 2 refer to the continuous and dispersed phases, respectively. The parameters δ_T and δ_S are referred to as the thermal and viscous skin depths, respectively, and are related to the distance that the thermal and shear waves generated by a droplet penetrate into the surrounding liquid.[13] The above equations give excellent agreement with experimental measurements for most dilute emulsions ($\phi < 0.15$), and for more concentrated emulsions under certain experimental conditions, i.e., relatively large droplet sizes and high frequencies.[10,11]

Recently, it has been shown that significant deviations occur between the above theory and experimental measurements when the thermal waves generated by neighboring droplets overlap with one another, i.e., at low frequencies and/or in highly concentrated emulsions.[10,14,18] This effect has been accounted for theoretically using a ''core-shell'' model.[14] In this theory, it is assumed that each emulsion droplet is surrounded by a shell of the continuous phase, which is itself surrounded by an effective medium, whose properties are determined by the composition of the whole emulsion (Fig. 1). The thickness of the shell is approximately equal to the average distance between the droplets in an emulsion.

The core-shell model does not take into account multiple scattering, intrinsic absorption or visco-inertial losses.[14] In this article, we show that a more comprehensive theory of ultrasonic propagation in emulsions can be developed by combining multiple scattering theory with the core-shell model to overcome each of their individual limitations.

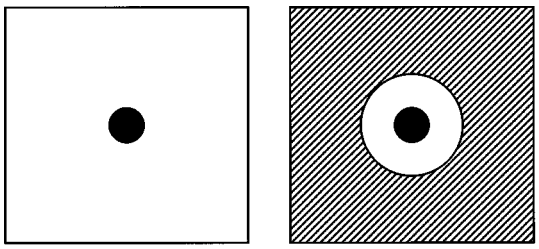

FIG. 1. Schematic diagram of the core-shell model used to take into account thermal overlap effects in the multiple scattering theory.

The approach we adopt in this paper is to compare the analytical expression for the complex propagation constant of an emulsion derived using the core-shell model with that derived using ultrasonic scattering theory under the same approximations, i.e., no intrinsic absorption, no multiple scattering and no visco-inertial losses. By comparing these expressions we show that they are identical except for a single ''thermal term,'' which includes the thermal overlap effects in the core-shell model. The multiple scattering theory is therefore extended by replacing the original thermal term with the one from the core-shell model.

To compare the two approaches under the same assumptions we have to derive an expression for the traditional ultrasonic scattering theory [Eq. (1)] which ignores intrinsic absorption, multiple scattering and visco-inertial effects. Allegra and Hawley[9] showed that the intrinsic losses are contained in the first term on the right-hand side of Eq. (2), so that these losses can be ignored by dropping this term. The visco-inertial effects originate because of the density difference between the droplets and surrounding liquid, and so these losses can be ignored by setting $\rho_1 = \rho_2$, so that A_1 equals zero. The multiple scattering effects are due to ϕ^2 terms in Eq. (1), and therefore these losses can be ignored by dropping these terms. Finally, the following expression for the complex propagation constant of an emulsion is obtained from Eqs. (1)–(3):

$$\left(\frac{K}{k_1}\right)^2 = \left(1 - \frac{3\phi(\gamma_1 - 1)}{b_1^2}\left(1 - \frac{\beta_2 C_{P1}\rho_1}{\beta_1 C_{P2}\rho_2}\right) H\right), \tag{5}$$

where $\gamma_1 (= 1 + T_a \beta_1^2 c_1^2 / C_{P1})$ is the ratio of specific heats in the continuous phase and T_a is the absolute temperature. This equation can be rearranged to give:

$$\left(\frac{K}{k_1}\right)^2 = \left(1 + i\frac{3\phi}{\omega r^2}\frac{T_a}{\kappa_1}\left(\frac{\beta_1}{C_{P1}\rho_1} - \frac{\beta_2}{C_{P2}\rho_2}\right) H \tau_1\right), \tag{6}$$

where the adiabatic compressibility is κ. This equation is analogous to Equation 15 in Ref. 14, but with $H = A\kappa_1 / \kappa_0 \tau_1$, where A is the term in the core-shell model which takes into account the thermal overlap effects (see Equation 24 in Ref. 14) and κ_0 is the volume averaged compressibility of the emulsion [$\kappa_0 = \phi\kappa_2 + (1 - \phi)\kappa_1$].

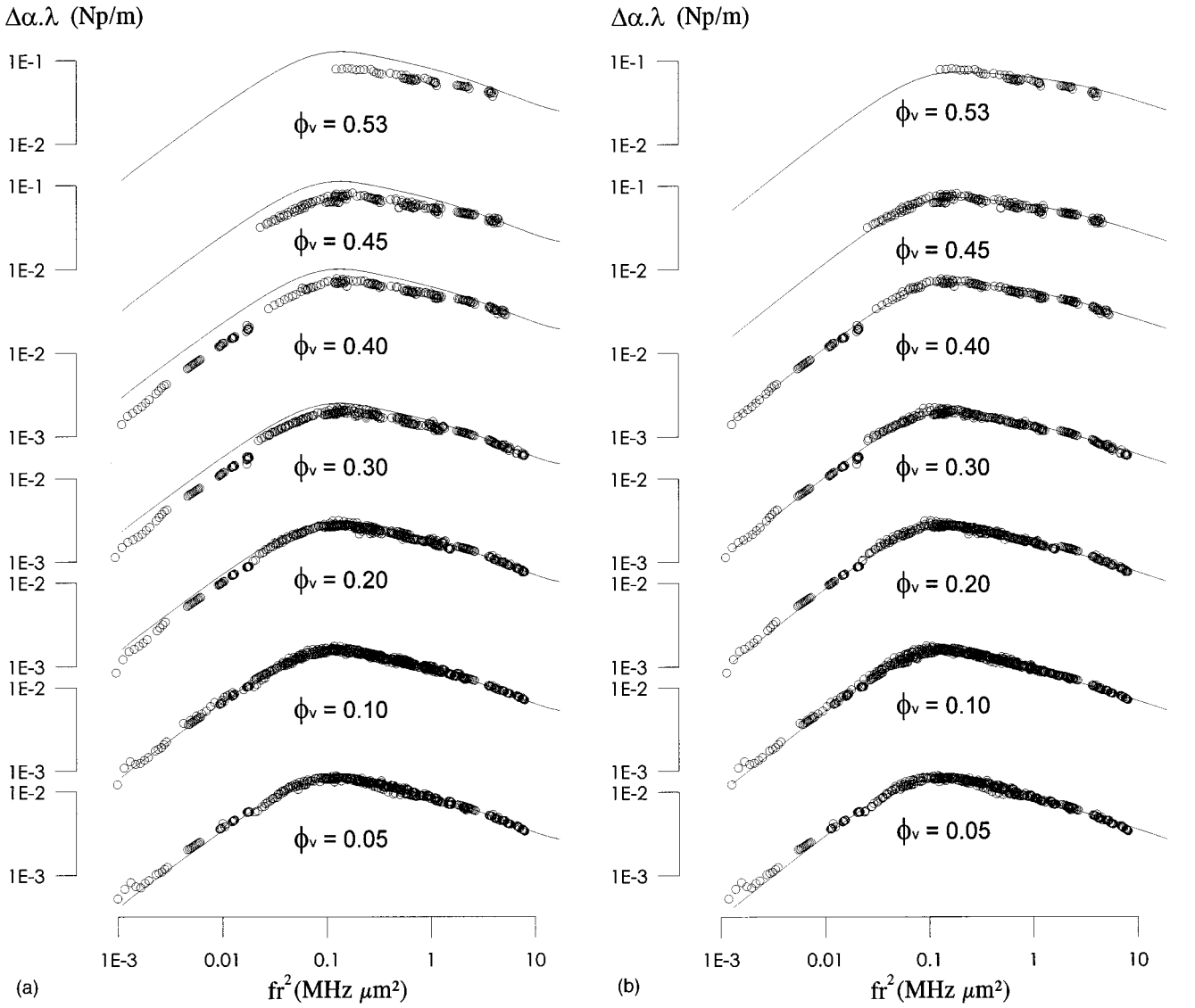

FIG. 2. Comparision of predicted and measured ultrasonic attenuation spectra of *n*-hexadecane oil-in-water emulsions. The open circles are experimental measurements, the full lines are computed using the theory. (a) The data for the traditional ultrasonic scattering theory and (b) the data for the new theory.

We can therefore extend the multiple scattering theory to include thermal overlap effects by replacing the H term given above [Eq. (4)] with the expression derived by Hemar *et al.*:[14]

$$H=\frac{\tau_2\kappa_1}{\kappa_0}\frac{n_2r-\tanh(n_2r)}{EC+FD}\times\left[2\kappa_3\left(\frac{g_1-g_3}{g_2-g_1}\right)n_1x(n_3x+1)+C(1+n_1r)+D(1-n_1r)\right], \tag{7}$$

where

$$g_i=\frac{\beta_i}{\rho_iC_{Pi}},$$

$$C=e^{n_1(x-r)}[\tau_1(n_1x-1)+\tau_3(n_3x+1)],$$

$$D=e^{-n_1(x-r)}[\tau_1(n_1x+1)-\tau_3(n_3x+1)],$$

$$E=\tau_2n_2r+[\tau_1(n_1r+1)-\tau_2]\tanh(n_2r),$$

$$F=\tau_2n_2r-[\tau_1(n_1r-1)+\tau_2]\tanh(n_2r),$$

where $n_i=(1-i)/\delta_{Ti}$ and x is the radius of the shell of continuous phase which surrounds the droplets:[14]

$$x=\frac{r}{\sqrt{3\phi}}. \tag{8}$$

The thermophysical properties of the effective medium which surrounds the shell are given by the following expressions:[14]

$$\rho_3=(1-\phi)\rho_1+\phi\rho_2, \tag{9}$$

$$\kappa_3=(1-\phi)\kappa_1+\phi\kappa_2, \tag{10}$$

$$\rho_3C_{P3}=(1-\phi)\rho_1C_{P1}+\phi\rho_2C_{P2}, \tag{11}$$

$$\tau_3=\tau_1\frac{1+2\phi\chi-2(1-\phi)\zeta\chi^2}{1-\phi\chi-2(1-\phi)\zeta\chi^2}, \tag{12}$$

where

$$\chi = \frac{\tau_2 - \tau_1}{\tau_2 + 2\tau_1}, \quad \zeta = 0.21068\phi - 0.04693\phi^2.$$

It should be noted that the H term given by Eq. (7) tends to that given by Eq. (4) when the spacing between the droplets is much greater than the length of the thermal skin depth, i.e., $x \gg \delta_{T,1}$. This condition is met when emulsions are sufficiently dilute, the frequency is sufficiently high or the particles are sufficiently large:

$$f \gg \left(\frac{\tau_1}{\rho_1 C_{P,1} \pi}\right)\left(\frac{\sqrt[3]{\phi}}{r}\right)^2. \tag{13}$$

It should also be noted that the value of A_0 [Eq. (2)], corrected for thermal overlap effects, can be used in the Lloyd and Berry[16] or Ma *et al.*[17] multiple scattering theories, as well as in the Waterman and Truell[15] theory.

In this study we have been principally concerned with the properties of emulsions in which the density contrast between the droplets and the surrounding liquids is low, so that the dominant form of attenuation is the thermal losses. In systems where there is a relatively high density contrast it would also be necessary to take into account the effect of the overlap of the shear waves generated by the droplets.[19]

II. COMPARISION WITH EXPERIMENTAL MEASUREMENTS

The original and extended multiple scattering theories are compared with experimental measurements of the ultrasonic attenuation spectra of concentrated monodisperse hexadecane oil-in-water emulsions in Fig. 2. These measurements were made using an interferometric technique that has been described in detail elsewhere.[18] The particle size of the emulsions was determined by finding the value which gave the best fit between the measured attenuation spectra and that predicted by either the original theory [Fig. 2(a)] or the extended theory [Fig. 2(b)] for the 10% oil-in-water emulsions. These particle sizes were then used in all of the subsequent calculations. The extended multiple scattering theory gives excellent agreement with the experimental measurements across the whole range of frequencies and droplet concentrations [Fig. 2(b)], whereas the original multiple scattering theory overpredicts the attenuation coefficient at the lower frequencies, particularly in concentrated emulsions ($\phi > 0.15$) [Fig. 2(a)]. These results clearly show that our theory is more useful than the existing theory for interpreting ultrasonic spectra in concentrated emulsions.

III. CONCLUSIONS

The multiple scattering theory has been extended to take into account the overlap of the thermal waves generated by the droplets on the ultrasonic attenuation spectra of emulsions. This theory has been shown to give better predictions of the ultrasonic properties of concentrated emulsions than the traditional multiple scattering theory in concentrated emulsions. The development of this theory should enable manufacturers of instruments that utilize ultrasonic spectrometry to characterize emulsions to extend them to higher droplet concentrations.

ACKNOWLEDGMENTS

This material is based upon work supported by the Cooperative State Research, Education and Extension Service, U.S. Department of Agriculture, under Agreement No. 97-35503-4371.

[1] D. J. McClements, ''Principles of Ultrasonic Droplet Size Determination,'' Langmuir **12**, 3454–3461 (1996).
[2] M. J. W. Povey, *Ultrasonic Techniques for Fluid Characterization* (Academic, San Diego, CA, 1997).
[3] F. Alba, ''Ultrasound spectroscopy: A sound approach to sizing of concentrated particulates,'' in *Handbook on Ultrasonic and Dielectric Characterization Techniques for Suspended Particulates*, edited by V. A. Hackely and J. Texter (American Chemical Society, Westerville, OH, 1998).
[4] A. Dukhin, ''Acoustic and Electroacoustic Spectroscopy,'' in *Handbook on Ultrasonic and Dielectric Characterization Techniques for Suspended Particulates*, edited by V. A. Hackely and J. Texter (American Chemical Society, Westerville, OH, 1998).
[5] U. Riebel, ''Ultrasonic extinction and velocity in dense suspensions,'' in *Handbook on Ultrasonic and Dielectric Characterization Techniques for Suspended Particulates*, edited by V. A. Hackely and J. Texter (American Chemical Society, Westerville, OH, 1998).
[6] U. Riebel and F. Loffler, ''The fundamentals of particle size analysis by means of ultrasonic spectrometry.'' Part. Part. Syst. Charact. **6**, 135–143 (1989).
[7] A. S. Dukhin and P. J. Goetz, ''Acoustic and electroacoustic spectroscopy,'' Langmuir **12**, 4336–4344 (1996).
[8] P. S. Epstein and R. R. Carhart, ''The absorption of sound in suspensions and emulsions'' J. Acoust. Soc. Am. **25**, 553–565 (1953).
[9] J. R. Allegra and S. A. Hawley, ''Attenuation of sound in suspensions and emulsions: Theory and experiments.'' J. Acoust. Soc. Am. **51**, 1545–1564 (1972).
[10] D. J. McClements, ''Comparision of multiple scattering theories with experimental measurements in emulsions,'' J. Acoust. Soc. Am. **91**, 849–853 (1992).
[11] D. J. McClements and M. J. W. Povey, ''Scattering of ultrasound by emulsions,'' J. Phys. D **22**, 38–47 (1989).
[12] A. S. Dukhin, P. J. Goetz and C. W. Hamlet, ''Acoustic spectroscopy for concentrated polydisperse colloids with low density contrast,'' Langmuir **12**, 4998–5003 (1996).
[13] D. J. McClements, ''Ultrasonic determination of depletion flocculation in oil-in-water emulsions containing a non-ionic surfactant,'' Colloids Surf., A **90**, 25–35 (1994).
[14] Y. Hemar, N. Herrmann, P. Lemarechal, R. Hocquart, and F. Lequeux, ''Effect medium model for ultrasonic attenuation due to the thermo-elastic effect in concentrated emulsions,'' J. Phys. II **7**, 637–647 (1997).
[15] P. C. Waterman and R. Truell, ''Multiple scattering of waves,'' J. Math. Phys. **2**, 512–537 (1962).
[16] P. Lloyd and M. W. Berry, ''Wave propagation through an assembly of spheres,'' Proc. Phys. Soc. London **91**, 678–688 (1967).
[17] Y. Ma, V. K. Varadan, and V. V. Varadan, ''Comments on ultrasonic propagation in suspensions,'' J. Acoust. Soc. Am. **87**, 2779–2782 (1990).
[18] N. Herrmann, ''Application de Techniques ultrasoneres a l'etude de dispersions,'' Ph.D. thesis, Universite Louis Pasteur, Strassbourg, France, 1996.
[19] A. S. Dukhin and P. J. Goetz, ''Acoustic spectroscopy for concentrated polydisperse colloids with high density contrast,'' Langmuir **12**, 4987–4997 (1996).

Comment on "Enhancement of the transient-evoked otoacoustic emission produced by the addition of a pure tone in the guinea pig" [J. Acoust. Soc. Am. 104, 344–349 (1998)]

Tianying Ren[a)]
Oregon Hearing Research Center, Department of Otolaryngology and Head & Neck Surgery, Oregon Health Sciences University, 3181 SW Sam Jackson Park Road, Portland, Oregon 97201-3098

Alfred L. Nuttall
Oregon Hearing Research Center, Department of Otolaryngology and Head & Neck Surgery, Oregon Health Sciences University, 3181 SW Sam Jackson Park Road, Portland, Oregon 97201-3098 and Kresge Hearing Research Institute, Department of Otolaryngology, Head & Neck Surgery, The University of Michigan, 1301 East Ann Street, Ann Arbor, Michigan 48109

(Received 23 September 1998; accepted for publication 11 November 1998)

Recently, Withnell and Yates [J. Acoust. Soc. Am. **104**, 344–349 (1998)] reported a pure tone acoustic enhancement of the transient-evoked otoacoustic emission (TEOAE). They state that their data conflict with the existing theory that the TEOAE represents a one-to-one frequency response to stimulus component frequencies. Therefore, they interpreted the observed enhancement as a result of a complex interaction on the basilar membrane of hypothetical intermodulation distortion products. This Letter reviews recent data and proposes an alternative interpretation that the enhancement results from an impedance discontinuity at the pure tone characteristic frequency (CF) location. TEOAEs at frequencies below this tone are reflected from its CF location rather than from their own CF locations. © *1999 Acoustical Society of America.* [S0001-4966(99)04002-3]

PACS numbers: 43.64.Jb, 43.64.Kc, 43.64.Bt [BLM]

To explore the origin of the transient-evoked otoacoustic emission (TEOAE), Withnell and Yates (1998) extended the work of Sutton (1985) to study the effect of a pure-tone suppressor on the TEOAE with a variety of stimulus spectra and pure-tone suppressors in guinea pig. They hypothesized that a pure tone suppressed a region on the basilar membrane (BM) that roughly matches the suppressor excitation pattern on the BM, with maximum suppression occurring in the region of the pure-tone frequency. If TEOAE generators act independently, then, with the addition of a 70 dB SPL tone, a reduction in the amplitude of the TEOAE power spectrum over a range of frequencies is expected, with the predominant effect being a maximal reduction of the emission near the tone frequency. Enhancement of the emissions is not expected at any frequency. However, they found enhancement in the amplitude of the response spectrum at frequencies corresponding to BM regions apical to the tone. The authors state their finding indicates that the TEOAE does not result solely from independent generators along the BM and interpreted the pure-tone-induced enhancement as a contribution of intermodulation distortion to the TEOAE.

In order to study the interaction between mechanical–electrical and electrical–mechanical transductions of outer hair cells *in vivo*, Ren and Nuttall (1998a) observed the acoustically induced changes in the electrically evoked otoacoustic emission (EEOAE). It was found that a pure tone enhanced the EEOAE fine structure at frequencies below the acoustic frequency and suppressed the overall level of the EEOAE at frequencies above the acoustic frequency. In addition, the EEOAE at frequencies approximately one-half octave lower than the acoustic frequencies were relatively more enhanced or showed relatively less suppression than at other frequencies. As a possible mechanism of acoustic enhancement, Ren and Nuttall suggested that the acoustic stimulus creates an impedance discontinuity at its characteristic frequency (CF) location, leading to a change in the reflected electrically evoked traveling wave, which may enhance or suppress the EEOAE by the vector summation of two waves.

In our laboratory, a novel signal processing method has subsequently been developed to detect the multiple components of the EEOAE. We found that the EEOAE generated by extracochlear electrical stimulation consists of a short delay component (SDC), with a short time delay, and a long delay component (LDC), having a long time delay (Ren and Nuttall, 1998b). The SDC is proposed as the reverse propagated wave from the electrode location; the LDC is proposed as the reflected forward-propagated wave, which originates at the electrode location, travels apically, and is reflected near the CF location. Intravenous furosemide (50 mg/kg) completely suppressed the LDC but not the SDC. A simultaneously presented pure tone altered the power distribution of the LDC: the power level of the LDC below the frequency of the acoustic pure tone increased and that above the tone frequency decreased (Ren and Nuttall, 1998b). These data demonstrate that the intracochlear reflection pattern of the electrically evoked energy was altered by the pure tone, strongly supporting the interpretation that the acoustic modulation of the EEOAE results from change in intracochlear reflection patterns.

Although the above two studies (Withnell and Yates,

a)Electronic mail: rent@ohsu.edu

1998; Ren and Nuttall, 1998a) may appear different, there exist relevant similarities. First, in the study by Withnell and Yates, clicks are wide bandwidth stimuli, as shown by stimulus spectra in their Figs. 1–4. In the study by Ren and Nuttall, a constant current with swept frequency across a wide frequency range was used to evoke the mechanical energy from the electromotility of outer hair cells (Ashmore, 1987; Brownell *et al.*, 1985; Dallos *et al.*, 1991; Santos-Sacchi, 1989). This electrically evoked vibration retropropagates to the external ear canal to form the EEOAE. But conventional forward waves propagate along the BM (Nuttall and Ren, 1995). Note that the wide frequency response of the EEOAE (Ren and Nuttall, 1995) indicates the wide bandpass feature of the forward-propagated wave because of the isotropic property of the BM (Allen and Fahey, 1992). Thus, in both studies, the effective stimulus is wideband. The only difference is that the click evokes simultaneous traveling waves while the swept frequency current causes traveling waves at different times. Thus, the TEOAE is similar to what we described as the LDC of the EEOAE (Ren and Nuttall, 1998b).

It has been suggested that the origin of the TEOAE involves reflections from impedance discontinuities (Kemp, 1986; Kemp and Chum, 1980; Prieve *et al.*, 1996; Probst *et al.*, 1986). Similarly, the LDC of the EEOAE is proposed to be reflected energy from the CF sites when acoustical energy is originally generated by the electrically stimulated cochlear partition near the electrode.

Although the ear canal-measured EEOAE is the vector summation of the reverse wave from the cochlear partition near the electrode and the reflected wave from the CF place, the EEOAE transfer functions (Fig. 2 B, Ren and Nuttall, 1998a) show a similar complex pattern of acoustic enhancement as that revealed by the TEOAE (Figs. 1–4, Withnell and Yates). A simultaneous pure tone increased the amplitude of the emissions at frequencies below the tone frequency and decreased the amplitude in frequencies at and above the tone frequency for both EEOAE and TEOAE. The fine structure, i.e., the amplitude variation, of the emissions was enhanced in the frequency range below tone frequency and suppressed in the frequency range at and above the pure-tone frequency. In addition, we demonstrated that the nonlinear phase/frequency function of the EEOAE became linear when a pure tone (10 kHz, 80 dB SPL) was simultaneously presented (Fig. 4 B, Ren and Nuttall, 1998a).

Withnell and Yates state that if the TEOAE represents a one-to-one frequency response to component frequencies of the stimulus, then simultaneous presentation of a pure tone should suppress those TEOAE components, which are close to the pure-tone frequency. It is true that the simultaneous presentation of a pure tone suppresses the BM vibration induced by a click near the pure-tone frequency in the same way as does two-tone suppression (Geisler and Nuttall, 1997). However, it is not necessary that the amplitude of the TEOAE follow the changes in BM vibration, because the TEOAE is presumably composed of the reflected acoustic energy from the CF location on the BM, and the amplitude of the TEOAE is determined by the amplitude of the incident wave, the BM reflection coefficient, and transmission efficiency of the reflected wave. The simultaneously presented pure tone causes a traveling wave with maximum vibration at its CF place, resulting in an impedance discontinuity. Traveling waves at frequencies below the pure-tone frequency encounter the impedance discontinuity and are reflected from the CF location of the pure tone rather than from their own CF locations. The reflection coefficient for traveling waves from the pure tone CF site may be higher than that from the CF places of frequencies below the tone frequency because of the high magnitude of the vibration and the nonlinear mechanical properties of the BM. Although this may be a passive reflected wave without magnification by hypothetical cochlear amplifier, the transmission efficiency of the reflected energy from the pure tone CF location could be higher than that from the CF locations below the pure-tone frequency due to the change in reflection location from the apical region to base. This proposed model can account for the data presented in Withnell and Yates' Figs. 1–4, where the amplitude of the TEOAE at frequencies below the tone frequency was enhanced.

Important experimental evidence against the interpretation that TEOAE enhancement induced by simultaneous presentation of a pure tone results from intermodulation distortion product (DP) is that acoustic enhancement of the EEOAE does not require intermodulation products. In the experiment by Ren and Nuttall (1998a), a constant current with swept frequency and a pure tone were delivered to the cochlea, and the EEOAE was measured at the frequencies of the electrical current. Neither a DP produced by different EEOAE frequency components nor a DP caused by interaction between electrically evoked traveling waves and pure-tone-induced waves contributed to the data since the EEOAE was measured at the stimulus frequency rather than at any DP frequency.

Whereas a TEOAE present outside the stimulus passband (above 10 kHz) (Fig. 4; Withnell and Yates) is consistent with intermodulation distortion energy contributing to the TEOAE, such energy of the TEOAE evoked by 0–5 kHz is not evident in the bandwidth stimulus (Figs. 2 and 3, Withnell and Yates). Since the single-tone burst evoked TEOAE also shows bandpass features rather than a single frequency peak on the spectrum (Yoshikawa *et al.*, 1998), TEOAE energy outside the single-tone bandwidth is not evidence that TEOAE is generated by the mechanism of the DP production. It can be concluded that TEOAE energy outside the stimulus passband may not be an indicator of DP production in the cochlea.

It is essential to have two normal traveling waves at $f1$ and $f2$ frequency locations to generate DPs. It is also well documented that the presentation of a pure tone near $f1$ or $f2$ frequency can suppress the DPs (Brown and Kemp, 1984; Martin *et al.*, 1987). Even if DPs could be generated by some frequency components of an acoustical click, these DPs likely are suppressed by other frequency components of the same click stimulus. In addition, the simultaneously presented pure tone can also suppress the click-evoked DPs in the same way as the suppression of the two acoustical primaries-evoked DPs.

Withnell and Yates (1998) stated ''The net result would depend on the precise way in which the remaining inter-

modulation products sum, but any outcome presumably is possible from suppression to enhancement.'' However, neither experimental result nor a theoretical model supporting this interpretation was presented in their paper. In our paper (Ren and Nuttall, 1998a) and in this letter, the proposed model for the acoustically evoked changes in the intracochlear reflection pattern predicts frequency dependent enhancement.

In summary, based on recent findings in acoustic enhancement of the EEOAE, it is proposed in this letter that acoustically induced change in intracochlear reflection can interpret the enhancement of the TEOAE. This alternative theory not only satisfactorily interprets the TEOAE enhancement data presented by Withnell and Yates but also is consistent with other studies that the TEOAE represents a one-to-one frequency response to component frequencies of the stimulus (Kemp and Chum, 1980; Kemp, 1986; Probst *et al.*, 1986; Prieve *et al.*, 1996).

ACKNOWLEDGMENTS

The authors gratefully acknowledge an anonymous reviewer's thoughtful suggestions, and Nadine Brown for editorial help. Supported in part by research Grant Nos. 2 P01 00078 and R01 DC 00141 from the National Institute of Deafness and Other Communication Disorders, National Institutes of Health; Research Funds of the American Otological Society, Inc.; the Medical Research Foundation of Oregon; and Department of Veterans Affairs-Rehabilitation Research and Development Service.

Allen, J. B., and Fahey, P. F. (**1992**). ''Using acoustic distortion products to measure the cochlear amplifier gain on the basilar membrane,'' J. Acoust. Soc. Am. **92**, 178–188.

Ashmore, J. F. (**1987**). ''A fast motile response in guinea-pig outer hair cells: the cellular basis of the cochlear amplifier,'' J. Physiol. (London) **388**, 323–347.

Brown, A. M., and Kemp, D. T. (**1984**). ''Suppressibility of the 2 $f1$-$f2$ stimulated acoustic emissions in gerbil and man,'' Hearing Res. **13**, 29–37.

Brownell, W. E., Bader, C. R., Bertrand, D., and de Ribaupierre, Y. (**1985**). ''Evoked mechanical responses of isolated cochlear outer hair cells,'' Science **227**, 194–196.

Dallos, P., Evans, B. N., and Hallworth, R. (**1991**). ''Nature of the motor element in electrokinetic shape changes of cochlear outer hair cells,'' Nature (London) **350**, 155–157.

Geisler, C. D., and Nuttall, A. L. (**1997**). ''Two-tone suppression of basilar membrane vibrations in the base of the guinea pig cochlea using 'low-side' suppressors,'' J. Acoust. Soc. Am. **102**, 430–440.

Kemp, D. T. (**1986**). ''Otoacoustic emissions, travelling waves and cochlear mechanisms,'' Hearing Res. **22**, 95–104.

Kemp, D. T., and Chum, R. (**1980**). ''Properties of the generator of stimulated acoustic emissions,'' Hearing Res. **2**, 213–232.

Martin, G. K., Lonsbury-Martin, B. L., Probst, R., Scheinin, S. A., and Coats, A. C. (**1987**). ''Acoustic distortion products in rabbit ear canal. II. Sites of origin revealed by suppression contours and pure-tone exposures,'' Hearing Res. **28**, 191–208.

Nuttall, A. L., and Ren, T. (**1995**). ''Electromotile hearing: evidence from basilar membrane motion and otoacoustic emissions,'' Hearing Res. **92**, 170–177.

Prieve, B. A., Gorga, M. P., and Neely, S. T. (**1996**). ''Click- and tone-burst-evoked otoacoustic emissions in normal-hearing and hearing-impaired ears,'' J. Acoust. Soc. Am. **99**, 3077–3086.

Probst, R., Coats, A. C., Martin, G. K., and Lonsbury-Martin, B. L. (**1986**). ''Spontaneous, click-, and tone burst-evoked otoacoustic emissions from normal ears,'' Hearing Res. **21**, 261–275.

Ren, T., and Nuttall, A. L. (**1995**). ''Extracochlear electrically evoked otoacoustic emissions: a model for in vivo assessment of outer hair cell electromotility,'' Hearing Res. **92**, 178–183.

Ren, T., and Nuttall, A. L. (**1998a**). ''Acoustical modulation of electrically evoked otoacoustic emission in intact gerbil cochlea,'' Hearing Res. **120**, 7–16.

Ren, T., and Nuttall, A. L. (**1998b**). ''Multiple origins of the electrically evoked otoacoustic emission,'' in *Abstracts of the Twenty-First Annual Midwinter Research Meeting of the Association for Research in Otolaryngology*, edited by G. R. Popelka (Association for Research in Otolaryngology, Mt. Royal, NJ), p. 179.

Santos-Sacchi, J. (**1989**). ''Asymmetry in voltage-dependent movements of isolated outer hair cells from the organ of Corti,'' J. Neurosci. **9**, 2954–2962.

Sutton, G. J. (**1985**). ''Suppression effects in the spectrum of evoked otoacoustic emissions,'' Acustica **58**, 57–63.

Withnell, R. H., and Yates, G. K. (**1998**). ''Enhancement of the transient-evoked otoacoustic emission produced by the addition of a pure tone in the guinea pig,'' J. Acoust. Soc. Am. **104**, 344–349.

Yoshikawa, H., Smurzynski, J., and Probst, R. (**1998**). ''Otoacoustic emissions evoked by single-tone burst and two-tone burst complexes,'' in *Abstracts of the Twenty-First Annual Midwinter Research Meeting of the Association for Research in Otolaryngology*, edited by G. R. Popelka (Association for Research in Otolaryngology, Mt. Royal, NJ), p. 88.

Reply to "Comment on 'Enhancement of the transient-evoked otoacoustic emission produced by the addition of a pure tone in the guinea pig'" [J. Acoust. Soc. Am. 105, 919–921 (1999)]

Graeme K. Yates[a] and Robert H. Withnell[b]
The Auditory Laboratory, Department of Physiology, The University of Western Australia, Nedlands, 6907, Western Australia, Australia

(Received 5 November 1998; accepted for publication 11 November 1998)

In a recent paper Withnell and Yates [J. Acoust. Soc. Am. **104**, 344–399 (1998)] suggested that the TEOAE might be comprised of significant quantities of intermodulation distortion energy, based on a series of suppression experiments involving the measurement of the TEOAE with the addition of a pure tone. Ren and Nuttall [J. Acoust. Soc. Am. **105**, 919–921 (1999)] have suggested an alternative explanation for our experiments, wherein a pure tone produces a local impedance change in the nonlinear mechanical properties of the basilar membrane: emission energy at frequencies below the frequency of the pure tone is suggested to arise from reflections at this impedance discontinuity. In this Letter, a response to their hypothesis is given, arguing that it is not consistent with experimental findings, and that, in fact, the TEOAE is comprised predominantly of intermodulation distortion energy [Yates and Withnell, Assoc. Res. Otolaryngol. Abstr. **21**, 5 (1998)]. [S0001-4966(99)04102-8]

PACS numbers: 43.64.Jb, 43.64.Kc, 43.64.Bt [BLM]

We thank Dr. Ren and Dr. Nuttall for their letter offering an alternative interpretation for the findings of Withnell and Yates (1998), although we do observe at the outset that we had already considered and rejected a similar explanation in that paper.

The most important finding of Withnell and Yates (1998) was the absence of strong, frequency-specific suppression of the transient-evoked otoacoustic emission (TEOAE) by a simultaneously presented pure tone, as Sutton (1985) had found previously but Kemp and Chum (1980) had not. The mixture of enhancement and suppression of the TEOAE at frequencies quite unrelated to the tone was an unexpected and entirely secondary finding. To explain our results, we proposed that the TEOAE might be composed of significant quantities of intermodulation distortion energy, generated by interactions between the spectral components of the stimulus click at a continuum of places along the cochlea. In such a proposal, the addition of a pure tone would reduce the click-evoked basilar membrane vibration at, and basal of, the characteristic place of the tone, thereby reducing the amount of intermodulation energy produced at that place. Significant quantities of intermodulation distortion energy would still be generated by activity at other, more apical sites on the basilar membrane, and the result at any given response frequency would depend upon the precise phase relationship between the suppressed and unsuppressed energy. Such a proposal, it was noted, provided a satisfactory explanation for the results of Avan *et al.* (1993, 1995, 1997), findings which were discordant with an independent generator hypothesis (Kemp, 1986; Probst *et al.*, 1986; Prieve *et al.*, 1996). Indeed, it was Prieve *et al.* (1996) who recognized that an independent generator hypothesis for the TEOAE was inconsistent with the level-dependent nonlinear nature of the cochlea.

Ren and Nuttall (1999) have offered an alternative explanation for our findings: namely that the addition of a pure tone produces a local impedance change in the nonlinear mechanical properties of the basilar membrane. Traveling waves at frequencies below the pure-tone frequency encounter the impedance discontinuity and are reflected from the CF location of the pure tone rather than their own CF locations (Ren and Nuttall, 1999). This purportedly provides a mechanism for the observed enhancement of the TEOAE at frequencies below the tone frequency. There is no evidence in the literature, however, of reflections of traveling waves of low frequency caused by simultaneous presentation of higher frequency tones, and such an alternative explanation does not explain the fact that no suppression of the TEOAE was routinely observed at the frequency of the pure tone. Ren and Nuttall argue that suppression of the TEOAE might not be a necessary concomitant of basilar membrane suppression because under their model the component of the wave reflected from the tone CF place may be greater than that from the emission CF place, leading to either enhancement or suppression. However, in the case of suppression of the TEOAE that we were looking for, the characteristic place of the suppressor and of the response frequencies we expected to suppress were one and the same place. It is therefore immaterial which reflection dominates: if the amplitude of the click-induced basilar membrane vibration were reduced, then the TEOAE must necessarily also be reduced.

A readily examinable consequence of the Ren and Nuttall model is that if energy at frequencies below that of the pure tone is reflected from the impedance discontinuity created by the tone (so dominating the total reflected energy at those frequencies), then the group delay of such energy will

[a]Electronic mail: gyates@cyllene.uwa.edu.au
[b]Electronic mail: rwithnel@cygnus.uwa.edu.au

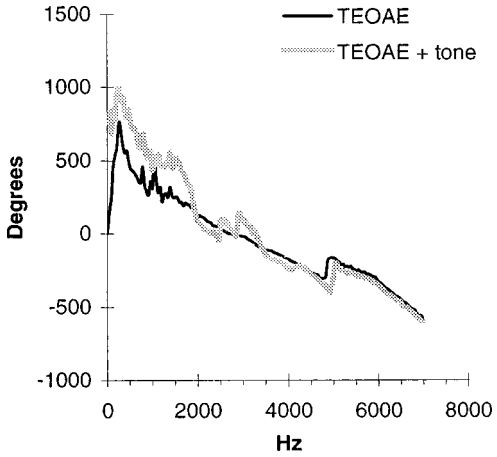

FIG. 1. Phase response data for a TEOAE recorded in response to a 0- to 7-kHz click stimulus with and without the addition of a 5 kHz tone. Phase data below ~1500 Hz is noise.

be less than for the same energy without the pure tone present (which must propagate to its own characteristic place and then back again to the stapes). The difference in group delay will be most manifest at frequencies lower than the pure-tone frequency. Thus, while we hesitate to introduce new data in a communication of this kind, we feel obliged to provide an example of previously unpublished phase data from the suppression experiments of Withnell and Yates (1998). Phase data typically showed the group delay to remain unchanged at frequencies lower than that of the frequency of the added pure tone: Fig. 1 provides an example for the TEOAE in response to a 0- to 7-kHz click, with and without the addition of a 5-kHz pure tone [corresponds to Fig. 1 of Withnell and Yates (1998)]. In fact, Fig. 1 shows no change in the group delay of the TEOAE across the frequency range of the stimulus following the addition of the 5-kHz pure tone.

Ren and Nuttall concede that TEOAE energy outside of the stimulus passband (above 10 kHz) in Fig. 4 of Withnell and Yates (1998) is consistent with intermodulation distortion energy contributing to the TEOAE (Ren and Nuttall, 1999), but also observe that no energy is evident outside of the stimulus passband for Figs. 2 and 3. Closer inspection of Fig. 3 in fact reveals that, with the addition of a 6-, 9-, or 12-kHz tone, there is energy in the TEOAE outside the stimulus passband (0–5 kHz). However, Ren and Nuttall (1999) argue that since the single-tone burst evoked TEOAE also shows bandpass features rather than a single frequency peak on the spectrum (Yoshikawa *et al.*, 1998), TEOAE energy outside the single-tone bandwidth is not evidence that the TEOAE is generated by the mechanism of the DP production, and so they suggest it can be concluded that TEOAE energy outside the stimulus passband may not be an indicator of DP production in the cochlea. However, the experiments of Yoshikawa *et al.* (1998), which they cite, were not carried out with pure tones but rather with cosine-modulated tones of 5-ms duration. Such stimuli have a −20-dB bandwidth of about 600 Hz, very close to, but slightly narrower than, the bandwidth of the responses reported. At center frequencies in the range 1–3 kHz, as used by Yoshikawa *et al.*, there is ample opportunity for intermodulation to occur in a ~300-Hz band. Thus, the experiments of Yoshikawa *et al.* cannot be taken as evidence for production of other frequencies by a single frequency stimulus.

Ren and Nuttall's alternative explanation for the findings of our paper (Withnell and Yates, 1998) is based on their recently reported experiments (Ren and Nuttall, 1998). In this paper, they describe their findings for the electrically evoked otoacoustic emission (EEOAE), stimulated from an extra-cochlear electrode, with the addition of an acoustical pure tone. The present letter (Ren and Nuttall, 1999) claims that the EEOAE in Ren and Nuttall (1998) was enhanced below the pure-tone frequency and suppressed above, but inspection of their figures (Ren and Nuttall, 1998) shows that the response was predominantly one of suppression at all frequencies, apart from a band of enhancement about one-half octave wide and just below the tone frequency. As we commented in our original paper, our TEOAEs were enhanced and suppressed in a far less predictable manner by a pure tone. Ren and Nuttall (1999) draw their parallel between these EEOAE findings and our TEOAE findings based on a claimed similarity between clicks being wideband stimuli and the EEOAE being obtained in response to a constant current with swept frequency across a wide frequency range. However, in a nonlinear system, the sweeping of frequency, which is essentially the presentation of a single frequency at any one time, is not equivalent to a click which presents all frequencies simultaneously.

Ren and Nuttall's (1998) basic observations are in conflict with many reports of interactions between EEOAEs and tonal acoustical stimuli (e.g., Mountain and Hubbard, 1989; Xue *et al.*, 1993; Nakajima *et al.*, 1996, 1998; Kirk and Yates, 1996), all of which report only enhancement of EEOAE responses, except for the case of electrical frequencies close to or just above the local CF of the electrode site, regardless of the frequency of the tone. Ren and Nuttall's (1998) technique would appear to approximate an injection of electrical current into the basal region of the cochlea (the delay times of the EEOAEs would support this). They show some evidence of propagation of a traveling wave from the effective site of electrical stimulation, but not such direct evidence as has been described previously (Kirk and Yates, 1994), where it was demonstrated that acoustical tonebursts could forward-mask compound action potentials generated by the electrically evoked traveling waves, and that electrically evoked traveling waves could forward-mask acoustically generated compound action potentials.

There is no doubt that acoustical tones may modulate the amplitude of EEOAEs, but little direct evidence to indicate that they change intracochlear reflection patterns of traveling waves. Recently, Kirk and Yates (1998) showed that acoustically induced vibration of the basilar membrane directly modulates the EEOAE in direct proportion to the mean open probability of mechanical-to-electrical transduction channels of outer hair cells, and have also suggested that a small shift in outer hair cell operating point could explain acoustic enhancement. Alternatively, Mountain and Hubbard have, for some time, claimed that enhancement of the EEOAE is due to release of the basilar membrane vibrations from a negative feedback loop at low frequencies. No reso-

lution of these competing explanations is yet available, but there is considerably more direct evidence for both of these suggestions than for the reflection hypothesis of Ren and Nuttall (1999).

Finally, we reported in February of this year at the Midwinter Meeting of the Association for Research in Otolaryngology (Yates and Withnell, 1998) that intermodulation distortion energy does indeed contribute to the TEOAE. Our experiments using high-pass filtered clicks demonstrated the presence of physiological vulnerable energy, not present in the original stimulus, both above and below the stimulus passband. This provides unequivocal evidence that the TEOAE is comprised of intermodulation distortion energy; indeed, we were able to demonstrate in this report that the TEOAE is predominantly comprised of intermodulation distortion energy.

ACKNOWLEDGMENTS

We wish to thank Dr. Des Kirk and Dr. Robert Patuzzi for their assistance with the preparation of this response. Supported by the National Health and Medical Research Council of Australia and the Department of Physiology, The University of Western Australia. R.H.W. is the recipient of a postgraduate scholarship from the Department of Physiology.

Avan, P., Bonfils, P., Loth, D., and Wit, H. (**1993**). ''Temporal patterns of transient-evoked otoacoustic emissions in normal and impaired cochleae,'' Hearing Res. **70**, 109–120.

Avan, P., Bonfils, P., Loth, D., Elbez, M., and Erminy, M. (**1995**). ''Transient-evoked otoacoustic emissions and high-frequency acoustic trauma in the guinea pig,'' J. Acoust. Soc. Am. **97**, 1–9.

Avan, P., Elbez, M., and Bonfils, P. (**1997**). ''Click-evoked otoacoustic emissions and the influence of high-frequency hearing losses in humans,'' J. Acoust. Soc. Am. **101**, 2771–2777.

Kemp, D. (**1986**). ''Otoacoustic emissions, travelling waves and cochlear mechanisms,'' Hearing Res. **22**, 95–104.

Kemp, D. T., and Chum, R. (**1980**). ''Properties of the generator of stimulated acoustic emissions,'' Hearing Res. **2**, 213–232.

Kirk, D. L., and Yates, G. K. (**1994**). ''Evidence for electrically evoked travelling waves in the guinea pig cochlea,'' Hearing Res. **74**, 38–50.

Kirk, D. L., and Yates, G. K. (**1996**). ''Frequency tuning and acoustic enhancement of electrically evoked otoacoustic emissions in the guinea pig cochlea,'' J. Acoust. Soc. Am. **100**, 3714–3725.

Kirk, D. L., and Yates, G. K. (**1998**). ''Enhancement of electrically evoked oto-acoustic emissions associated with low-frequency stimulus bias of the basilar membrane towards *scala vestibuli*,'' J. Acoust. Soc. Am. **104**, 1544–1554.

Mountain, D. C., and Hubbard, A. E. (**1989**). ''Rapid force production in the cochlea,'' Hearing Res. **42**, 195–202.

Nakajima, H. H., Olson, E. S., Mountain, D. C., and Hubbard, A. E. (**1996**). ''Acoustic overstimulation enhances low-frequency electrically evoked otoacoustic emissions and reduces high-frequency emissions,'' Aud. Neurosci. **3**, 79–99.

Nakajima, H. H., Mountain, D. C., and Hubbard, A. E. (**1998**). ''Nonlinear characteristics of electrically evoked otoacoustic emissions,'' Hearing Res. **122**, 109–118.

Prieve, B. A., Gorga, M. P., and Neely, S. T. (**1996**). ''Click- and toneburst-evoked otoacoustic emissions in normal-hearing and hearing-impaired ears,'' J. Acoust. Soc. Am. **99**, 3077–3086.

Probst, R., Coats, A. C., Martin, G. K., and Lonsbury-Martin, B. L. (**1986**). ''Spontaneous, click- and toneburst-evoked otoacoustic emissions from normal ears,'' Hearing Res. **21**, 261–275.

Ren, T., and Nuttall, A. L. (**1999**). ''Comment on 'Enhancement of the transient-evoked otoacoustic emission produced by the addition of a pure tone in a guinea pig [J. Acoust. Soc. Am. 104, 344–349 (1998)],' '' J. Acoust. Soc. Am. **105**, 919–921.

Ren, T., and Nuttall, A. L. (**1998**). ''Acoustical modulation of electrically evoked otoacoustic emission in intact gerbil cochlea,'' Hearing Res. **120**, 7–16.

Sutton, G. J. (**1985**). ''Suppression effects in the spectrum of evoked otoacoustic emissions,'' Acustica **58**, 57–63.

Withnell, R. H., and Yates, G. K. (**1998**). ''Enhancement of the transient-evoked otoacoustic emission produced by the addition of a pure tone in the guinea pig,'' J. Acoust. Soc. Am. **104**, 344–349.

Xue, S., Mountain, D. C., and Hubbard, A. E. (**1993**). ''Acoustic enhancement of electrically-evoked otoacoustic emissions reflects basilar membrane tuning: Experimental results,'' Hearing Res. **70**, 121–126.

Yates, G. K., and Withnell, R. H. (**1998**). ''Intermodulation distortion in click-evoked otoacoustic emissions,'' Abstracts of the Twenty-First Annual Midwinter Research Meeting A.R.O., Association for Research in Otolaryngology, p. 5.

Yoshikawa, H., Smurzynski, J., and Probst, R. (**1998**). ''Otoacoustic emissions evoked by single-tone burst and two-tone burst complexes,'' Assoc. Res. Otolaryngol. Abstr. **21**, 88.

PROGRAM OF

Joint Meeting

The 137th regular Meeting of the Acoustical Society of America

2nd Convention of the European Acoustics Association: Forum Acusticum

integrating the 25th German Acoustics DAGA meeting

Berlin, Germany • 15–19 March 1999

NOTE: All Journal articles and Letters to the Editor are peer reviewed before publication. Program abstracts, however, are not reviewed before publication, since we are prohibited by time and schedule.

MONDAY AFTERNOON, 15 MARCH 1999 POSTER GALLERY, 12:00 TO 6:20 P.M.

Posters from various technical sessions remain on display in the Poster Gallery

Also, the following poster sessions are scheduled:
Poster Session 1pPAe
Poster Session 1pPPb
Poster Session 1pSCb

MONDAY AFTERNOON, 15 MARCH 1999 ROOM H3010, 1:55 TO 6:20 P.M.

Session 1pAA

Architectural Acoustics: Concert and Opera Halls: Case Studies of New Halls; Opera Houses

Leo L. Beranek, Cochair
975 Memorial Drive, Suite 804, Cambridge, Massachusetts 02138-5755, USA

Jürgen Meyer, Cochair
Physikalisch-Technische Bundesanstalt, Bundesalle 100, 38116 Braunschweig, Germany

Chair's Introduction—1:55

Invited Papers

2:00

1pAA1. Acoustic design of the Tsuyama Music Cultural Hall based on the preference theory. Y. Ando, Y. Suzumura (Grad. School of Sci. and Technol., Kobe Univ., Rokkodai, Nada, Kobe, 657-8501 Japan, andoy@kobe-u.ac.jp), and I. Yamamoto (Arch. & Env. Res. Ltd., Kobe, Japan)

The city of Tsuyama is located about 100 kilometers west of Kobe. The fundamental shape of the plan and cross sections of the hall were designed by applying the theory of subjective preference [Ando, *Architectural Acoustics* (AIP Press/Springer-Verlag, New York, 1998)]. Special attempts made in the acoustic design of this hall are: (1) a number of columns distributed in front of the walls at the audience level and on the stage: This may keep a small value of the IACC and a certain initial time delay gap between the direct sound and the first reflection, making an increase of the subjective preference for both listeners and musicians; (2) a stage enclosure with the canopy of several triangular reflectors at adjustable height for musicians, to control the preferred delay time of the reflections in performing a certain type of music; and (3) the shape of the rear wall of the stage, to control the IACC for listeners.

2:20

1pAA2. The new Konzertsaal of the KKL Center, Lucerne, Switzerland. I. Acoustics design. Russell Johnson and Eckhard Kahle (Artec Consultants, Inc., 114 W. 26th St., 9th Fl., New York, NY 10001-6812, ek@artec-usa.com)

The 1840 seat concert hall is the first of three halls that will eventually make up the Culture and Convention Center in Lucerne. It was inaugurated on 19 August 1998 to widespread critical acclaim. The hall is the home of the Lucerne International Music Festival, one of the most prestigious international festivals dedicated to symphonic music. The room will first be presented and illustrated, and an outline will be given of the basic acoustics design features such as room shape, seat count, and balcony design. Then, focus will shift to more specific acoustic design features, such as the reverberance chamber surrounding the main audience chamber, the two-part moving canopy with both horizontal and vertical reflecting surfaces, and the acoustically diffusing surface finish on most of the side wall area of the hall.

2:40

1pAA3. The new Konzertsaal of the KKL Center, Lucerne, Switzerland. II. Preliminary acoustical measurements. Eckhard Kahle, Russell Johnson, and Brian Katz (Artec Consultants, Inc., 114 W. 26th St., 9th Fl., New York, NY 10001-6812, ek@artec-usa.com)

The newly opened Concert Hall in Lucerne is the home of the International Music Festival with its extremely varied programs. Furthermore, the remainder of the year requires this hall to provide an appropriate acoustic environment for an even wider range of performances, ranging from conferences and other speech events to symphony orchestra, amplified popular music, ethnic music, and organ recitals. In a town with a population of 60 000, it will also be necessary to accommodate a varying number of audience members. For all these reasons, several elements of acoustic variability have been included in the design of the hall. During the first months of the inaugural season, the settings of the variable acoustics features of the hall were documented for each individual performance in the form of a logbook. This paper will discuss the use of the acoustical elements for selected performances taken from the ongoing log. The results of preliminary acoustical measurements and subjective listening impressions for the selected performances will be given. Furthermore, objective measurements were recorded in the hall at various stages of construction.

3:00

1pAA4. The acoustics evolution of Chicago's Orchestra Hall: A case study. R. Lawrence Kirkegaard (Kirkegaard and Assoc., Inc., 4910 Main St., Downers Grove, IL 60515)

Originally opened in 1904, Chicago's Orchestra Hall was immediately recognized as acoustically flawed due to low reverberation times, poor bass response, a crowded stage, and poor on-stage hearing conditions. In 1991, the Orchestral Association of Chicago decided to renovate and expand Orchestra Hall into a comprehensive Symphony Center for music in Chicago. The core of the project was a commitment to improve the acoustics to the extent feasible within the constraints of the site and the historic beauty of the hall. The Association contracted directly with Kirkegaard and Associates as acoustical consultants to work in parallel with the architects, Skidmore Owings and Merrill. The renovated hall reopened in the fall of 1997, with completion of acoustics work delayed until summer of 1998. The renovated hall is beautiful architecturally, and its acoustics has been gratifyingly improved. This paper describes the history and results of the remodeling. Test data as well as subjective assessments will be discussed and important acoustics lessons shared.

3:20

1pAA5. Yokohama Minato Mirai Hall. Hideki Tachibana (Inst. of Industrial Sci., Tokyo Univ., Roppongi 7-22-1, Minato-ku, Tokyo, 106-8558 Japan, tachibana@iis.u-tokyo.ac.jp) and Hiroyuki Kimura (Nikken Sekkei Ltd., Kouraku 2-1-2, Bunkyou-ku, Tokyo, 112-0004 Japan)

The Yokohama Minato Mirai Hall was planned as a complex cultural facility on the waterfront of Yokohama City and was opened in June 1998. In this building, a large concert hall with 2020 seats (mainly for symphony concerts) and a small concert hall with 400 seats mainly for chamber music are included. For the design and construction of this building, an acoustic design and research group consisting of architects, acousticians, and building engineers was set up and such various acoustic problems as room acoustics, sound insulation between rooms and facades, prevention of structure-borne sound from subway by floating floor construction, and noise reduction of the air-conditioning system were investigated by cooperative work in the group. For the acoustic design of the two halls, computer simulation based on geometrical acoustics and a 1/10 scale model experiment were performed for checking room shape and auralization studies. During and after the construction, acoustic measurements were carried out under various conditions. Before the opening, test concerts were performed with an audience, and acoustic data under occupied conditions were obtained. In this paper, the outline of the design process and the acoustic characteristics of the two halls are introduced.

3:40–4:00 Break

4:00

1pAA6. Acoustical design of the Marienkirche concert hall, Neubrandenburg. Henrik E. Möller and Tapio Lahti (Akukon Oy Consulting Engineers, Kornetintie 4 A, FIN-00380 Helsinki, Finland, henrik.moller@akukon.fi)

St. Mary's medieval gothic cathedral in Neubrandenburg, Germany, was ruined at the end of World War II. Two decades ago a decision was made to turn it into a concert hall. The design started in 1996 with the architectural competition, won by Architects Pekka Salminen. The hall will be a combination of old brick walls and mullioned windows, joined with modern glass and concrete. The back wall and the ceiling are made of glass. An audience of 1200 maximum is divided into three blocks: stalls, a balcony, and a tier behind the stage. The initial properties were promising: rectangular, 21 m wide, 18 m high, and with inherent diffusion. The

acoustical design was challenged by the restriction of not to touch the old restored side walls. A full-audience reverberation time of 2.0 s was set as a goal. Other objectives were moderate reverberation rise in bass, strong spaciousness and lateral energy. The acoustics were designed with a computer using the Odeon hall design program. Main new elements of acoustical control are a cloud array above the stage, triangular sails near the side wall cornices, and glass reflectors beside the stage. The hall is expected to be inaugurated in autumn 1999.

4:20

1pAA7. Festspielhaus Bayreuth—The unique acoustic situation. Karlheinz Müller (Müller-BBM, Robert-Koch-Str. 11, 82152 Planegg b. Munich, Germany)

The Festspielhaus in Bayreuth is the only opera house of the world which was founded and mostly designed by a composer. Richard Wagner himself founded the festival society and was one of the main designers of the opera house, the stage situation, and the pit. It is a very modern opera house, far away from the typical aristocratic or common theater of the times of 1876. The open house has a special acoustic situation. What are the reasons for this acoustic situation? Especially the sunken-pit design is subject to endless controversial discussions. All the maintenance work of the last years had the priority not to destroy the typical mysterious sound of the original Festspielhaus. Although all part of the whole house are now redecorated, the typical Wagnerian sound has been perfectly conserved.

4:40

1pAA8. Acoustics of opera houses: A cultural heritage. Patrizio Fausti, Roberto Pompoli, and Nicola Prodi (Dip. di Ingegneria, Univ. di Ferrara, via Saragat 1, 44100 Ferrara, Italy, pompoli@ing.unife.it)

An important part of contemporary Italian musical culture has developed inside historical opera houses. An outstanding opera repertory was especially conceived to match these places, both from the architectural and the acoustical points of view. But, while extensive attention is devoted to architectural and historical aspects, the acoustical characteristics of an opera house, that is, the set of listening attributes which make such a place unique among all spaces for music, are still nowadays hardly recognized as being paramount. In fact they can be rightly considered a relevant cultural heritage in Italy and can thus be called acoustical heritage. This new kind of heritage calls for accurate study and attention, both from the scientific and social points of view. To preserve the heritage for future generations, it is necessary to know it precisely and to elaborate means of accurate description. A project with the participation of international specialists has been established to agree on a standardized procedure for acoustic measurements specific to Italian historical opera houses in order to investigate the pecularity of these places. The aim of the project is to give a state-of-the-art acoustic documentation fo some theaters with the possibility of later applying up-to-date acoustical analysis.

5:00

1pAA9. New subjective and objective data on 20 opera houses of the world. Leo L. Beranek (975 Memorial Dr., Ste. 804, Cambridge, MA 02138-5755) and Takayuki Hidaka (Takenaka Res. and Development Inst., Chiba, 270-1395, Japan)

Acoustical measurements have been made in opera houses of Europe, Japan, the United States, and Argentina using the same equipment: dodecahedron loudspeaker, stretched impulses, and monaural and binaural sensing devices. The measuring positions were 3 on-stage and 2 in-pit for sources, and 8 to 17 in audience areas for sensors. Quantities measured as a function of frequency were reverberation time RT, early decay time EDT, clarity C80, deutlichkeit D, time gravity Tg, early to reverberant energy ratio as a function of cutoff time $C(t)$, strength G, interaural cross correlation IACC, IACCE, and IACCL, stage support ST1 and ST2, initial-time-delay gap ITDG, and reflectograms. International opera conductors were contacted by mail to rate 20 opera houses, with satisfactory responses. An attempt is made to correlate the objective data with the subjective ratings. Early results indicate that IACCE3 and ITDG are definite indicators. Others seem important in a certain type of opera house.

5:20

1pAA10. Acoustic considerations in the redevelopment of the Royal Opera House, London. Rob Harris (Arup Acoustics, Parkin House, 8 St. Thomas St., Winchester, Hampshire SO23 9HE, UK)

The Royal Opera House, Covent Garden is currently closed for a major redevelopment. It is scheduled to re-open in December 1999 with a refurbished and extended main auditorium, a studio theater seating 400, major new ballet studios and facilities for the Royal Ballet, new and refurbished opera and chorus rehearsal rooms, and a completely new backstage, with full wagon facilities and a double height flytower. This paper discusses the acoustic philosophy behind the design and reports the design solutions and the progress on site to date. Matters of particular interest include the approach to the preservation/enhancement of the acoustic of the main house, the dynamics of the ballet studios, the exceptionally large and complex acoustic scenery doors and the acoustic variability incorporated into the studio theater, which is a box-in-box construction.

5:40

1pAA11. Acoustic quality in the Theatre ''Palafenice,'' Venice. Lamberto Tronchin (DIENCA-CIARM, Viale Risorgimento 2, 40136 Bologna, Italy)

The burning of the Teatro La Fenice, in Venice, has also been a tragedy for the acoustical community. The Municipality of Venice decided to build a tense-structure (called PalaFenice) on the isle of Tronchetto, as a temporary auditorium for operas and concerts. The use of such a structure provokes many different acoustic problems, quite different from those already known to musicians at La Fenice. In this paper the acoustic quality of the theatre has been analyzed, and compared to the acoustic measurement already

performed in the former La Fenice theatre. Binaural measurements have been performed in the hall using the impulse response technique (including absorption of the ceiling), and a dummy head located at different listening positions. According to ISO 3382, many acoustic parameters have been evaluated, like listening level, ITDG, reverberation time, IACC, and others, and their values have been mapped. Also, Ando's quality maps of preferences, with reference to two different kinds of musical signals, was accomplished from experimental measurements. The measurements pointed out an unsuitable behavior of the structure at low frequency and low reverberation time and intelligibility in the hall. Finally, an hypothesis of the acoustic chamber has been formulated.

6:00

1pAA12. Orchestra shells: Acoustical and practical design considerations. Daniel E. Commins (commins acoustics workshop, 15, rue Laurence Savart, F-75020 Paris, France and 350 Fifth Ave., New York, NY 10118, comminsacoustics@compuserve.com)

A hall or an outdoor facility is rarely used for a single type of artistic program. Often, it is necessary to design an orchestra shell that transforms theoretically a theatre or an opera house into a concert hall. The acoustical criteria for opera or concerts are quite different; the design of an orchestra shell that would create proper acoustical conditions on stage for the musicians and in the hall for the audience can be quite complex. The larger the hall and the proscenium opening, the harder it is to come up with an adequate solution. The major problems are the following: architecture and aesthetics, acoustical efficiency, ensemble conditions, acoustic response, diffusion, size, weight, transformation time, and storage. Some progress has been made over the last few years, but the problem remains complex. This paper will attempt to explain the design and construction process and will provide recent examples of small and large shells: Ravinia, Lille concert hall, Gradignan, Porto Teatro S. João, Opera Garnier in Paris, Staatsoper in Munich, and Serralves auditorium in Porto.

Contributed Posters

The following posters will be on display in the Poster Gallery from Monday to Wednesday, 15–17 March. Contributors will be at their posters from 10:00 a.m. to 12:00 noon on Wednesday, 17 March.

1pAA13. Acoustical modifications of the interior design of a 50-ft chapel. Catherine Sémidor and Emmanuel Merida (ERIAC Ecole d'architecture et de paysage de Bordeaux Domaine de Raba, 33405 Talence Cedex, France, catherine.semidor@bordeaux.archi.fr)

In order to organize congresses, the University of Sciences in Bordeaux has bought a building with a chapel which will be modified to become both a lecture room and a place for music entertainment with a small orchestra. This paper deals with an interdisciplinary study from the acoustical inventory to the proposition of the new interior design, realized simultaneously by the acoustician team, the architect, and the university. The place, a church, is notable for its high reverberation time. Given this characteristic, a modified MLS software permitting measurements in such halls was tested. The numerical simulation was ajusted from the room-acoustics measured criteria. This reliable model became the base of the study to validate the architectural choices leading to the ''right acoustics'' for the ''right place.'' Among several acoustical solutions, the one presenting the more practical application was chosen. The design concept developed for this hall actually permits a variable acoustics to achieve the right level of reverberance for music and good speech clarity for lectures. The results of measurements carried out in the newly opened chapel will be compared with the computed criteria of the last model.

1pAA14. The acoustical properties of large studios. Bojan Ivancevic, Hrvoje Domitrovic, and Sinisa Fajt (Faculty of E. E. and Computing, Dept. of Electroacoustics, Unska 3, HR-10000 Zagreb, Croatia, bojan.ivancevic@fer.hr)

New studios for Croatian Radio-Television were planned with the starting user conditions. The background noise level must fulfill $N15$ or $N20$ criteria. Demanded reverberation time for a 400 m^2 radio studio is $Tr=0.6$ s, for TV studios of the same area, $Tr=0.7$ s, and for the 1000 m^2 TV studio, reverberation time is 1 s. Since all three studios with built-in control rooms were built in an urban area with excessive noise, it was necessary to obtain very good protection against noise, and at the same time, using the same elements, achieve the desired reverberation time. Special attention was given to flutter echoes and achievement of diffuse sound fields. The inner shell construction was built up using special acoustical building blocks. Besides using double walls, the broad analysis was done in order to avoid any possible problem in sound insulation. The achieved coincident frequency for walls and floors is 7.6 Hz, and this is quite satisfactory. The computer simulation was used during the design of internal sound-absorbing and reflecting surfaces. Described solutions take care of all user demands, as well as the usage particularities of such spaces. The measurements of relevant acoustical parameters were done after the building was finished.

1pAA15. The sound quality of the Teatro Comunale in Treviso, Italy. Lamberto Tronchin (DIENCA-CIARM, Viale Risorgimento, 2 40136 Bologna, Italy)

The Teatro Comunale of Treviso was designed at the same time as the Teatro La Fenice of Venice, in the middle of the 19th century. Treviso being so close to Venice, the reputation of the Venetian Theatre, just rebuilt after the burning of 1836, influenced the municipality of this little town, which decided to design the Theatre with the same shape as la Fenice. After the burning of 1996, and following the disappointment of losing such unique architecture and sound quality, acoustical measurements were performed in many Italian theatres, especially in historic theatres where acoustical measurements were never before undertaken. In this paper, the results of the acoustic measurements are presented. According to ISO 3382, binaural measurements, with a dummy head, have been performed in 25 positions in the hall, with different positions of the sound source in the proscenium. Acoustical parameters, such as EDT, G, LE were calculated from the impulse responses and mapped. Also, Ando's quality maps of preferences, with reference to two different kinds of musical signals, were accomplished from experimental measurements. From the measurements, a good behavior of the theatre has been pointed out, even if some limitations in some positions have been discovered.

Session 1pAB

Animal Bioacoustics: Animal Electrophysiological Acoustics

Philip H.-S. Jen, Cochair
Division of Biological Sciences, University of Missouri, Columbia, Missouri 65211, USA

Alexander Ya. Supin, Cochair
Institute of Ecology and Evolution, Russian Academy of Science, 33 Leninsky Prospect, 117071, Moscow, Russia

Invited Papers

2:00

1pAB1. ''Internal spectra'' in the dolphin's auditory system obtained by a minimal-masking technique. Alexander Ya. Supin and Vladimir V. Popov (Inst. of Ecology and Evolution, Russian Acad. of Sci., 33 Leninsky Prosp., 117071 Moscow, Russia)

To understand signal processing in the auditory system, it is of importance to know the ''internal spectrum'' representations of test stimuli, i.e., profiles of excitation along the frequency-representation axis. Such profiles may be obtained using a ''minimal-masking'' technique: An excitation profile is reflected by a masking curve (masker level dependence on frequency) when a masking criterion is not the threshold response to the probe stimulus but the threshold masking effect—a very small standard decrease of the probe response. The dolphin's auditory system provides good opportunities for such measurements because of the large amplitude and high consistency of the auditory brain-stem-evoked potentials (ABR). Minimal-masking curves were obtained in bottlenosed dolphins for various probe stimuli: narrow-band, rectangular, and rippled spectrum stimuli. At low stimulus levels, the profiles reproduced the stimulus spectrum well, except for a little wider bandwidth; this widening corresponded to the bandwidth of peripheral auditory filters. Stimuli with rectangular spectra evoked excitation profiles with enhanced edges, thus indicating enhancement of spectral contrast by lateral effects. Stimuli with rippled spectra evoked profiles reproducing ripples; however, edge ripples were also markedly enhanced. At high stimulus levels, all stimulus types evoked excitation profiles markedly expanded to high frequencies, far beyond the stimulus bandwidth.

2:20

1pAB2. Effect of removing physiologically relevant sound-localization parameters on tuning properties of barn owl tectal neurons. Hermann Wagner, Iris Poganiatz (Inst. Biologie II, RWTH Aachen, Kopernikusstrasse 16, D-52074 Aachen, Germany), Israel Nelken, and Gilad Jacobson (Hebrew Univ., Ein Karem, Jerusalem 91120, Israel)

Barn owls use the interaural time difference (ITD) for locating sounds in azimuth and the interaural level difference (ILD) for locating sounds in elevation. Neurons in the optic tectum have spatially restricted receptive fields. Recently, Keller *et al.* [Hearing Res. **118**, 13–34 (1998)] have demonstrated that the spatial patterns of responses were almost indistinguishable in response to virtual [stimuli filtered with head-related transfer functions (HRTFs)] and to free-field stimulation in neurons of the inferior colliculus. The inferior colliculus provides input to the optic tectum. The spatial restriction of tectal neurons is mainly due to their sensitivity to ITD and ILD. This paper deals with the effect of removing ITD and/or ILD from the virtual stimuli on the tuning of tectal neurons. HRTFs of two barn owls were recorded, and noise stimuli with ITDs, ILDs, filtered with HRTFs, filtered with HRTFs but containing no ITDs, and filtered with HRTFs but without ILDs were used in the experiments. Preliminary results suggest that removal of ITDs or ILDs caused a substantial loss of spatial tuning in tectal neurons. These results support earlier findings that suggested an essential role of the tectal neurons in sound-localization behavior. [Work supported by GIF.]

2:40

1pAB3. Temperature effects on the auditory system: An amphibian case history. Peter M. Narins (Dept. of Physiological Sci., Univ. of California, Los Angeles, 405 Hilgard Ave., Los Angeles, CA 90095)

The inner ear of anurans is unique in that it contains three organs specialized for sound reception. The amphibian papilla (AP), the basilar papilla (BP), and the saccule (S) are anatomically distinct, spatially separate organs each with its own complement of sensory hair cells and overlying tectorial structure. The BP and portions of the AP respond exclusively to airborne sounds, whereas other portions of the AP and the S exhibit sensitivity both to airborne sounds and to substrate-borne vibrations. Measurements from the auditory periphery of *Rana pipiens pipiens* suggest that in contrast to BP fibers, AP fiber tuning is highly temperature-dependent. Moreover, hair cells from the rostral AP and S exhibit a clear temperature dependence in their intracellular current step response, unlike caudally located AP and BP cells. Finally, spontaneous otoacoustic emissions, which presumably reflect hair cell motility, are highly temperature-dependent despite the fact that the upper portion of the emission frequency range (600–1600 Hz) corresponds to the domain of the BP. A model is presented that attempts to reconcile these disparate results. [Work supported by NIDCD Grant No. DC-00222.]

3:00

1pAB4. Lateral inhibition in frequency tuning of central auditory neurons. Philip H.-S. Jen (Div. of Biological Sci., Univ. of Missouri, Columbia, MO 65211, pjen@biosci.mbp.missouri.edu)

Previous studies have shown that frequency tuning curves (FTCs) of auditory neurons in the inferior colliculus (IC) are composed of an excitatory area that is either neighbored by an inhibitory area on one flank or is sandwiched by two inhibitory areas. Neurons that are responsible for excitatory and inhibitory areas are likely neighboring neurons. Whereas this neural lateral inhibition sharpens frequency tuning and provides a means to reduce ambiguity in encoding frequency at high stimulus intensities, neurons with two-flank lateral inhibitory areas have larger Q_n values and smaller excitatory areas than neurons with one-flank inhibitory areas. The closer the inhibitory area is to the excitatory area, the sharper the frequency tuning becomes. The Q_n values of IC neurons tend to increase with the ratio of inhibitory area to excitatory area. Application of bicuculline and/or strychnine broadens FTCs of many IC neurons and completely or partially abolishes the inhibitory areas. Corticofugal pathways sharpen the FTC by narrowing the excitotory area and broadening the lateral inhibitory areas. [Work supported by NSF.]

Contributed Papers

3:20

1pAB5. Paradoxical lateral suppression in the dolphin's auditory system. Vladimir V. Popov and Alexander Ya. Supin (Inst. of Ecology and Evolution, Russian Acad. of Sci., 33 Leninsky Prosp., 117071 Moscow, Russia)

A paradoxical phenomenon was found in the auditory system of dolphins: weak sounds suppressed the brain-evoked potential responses to much stronger sounds. This occurred when the brain-evoked potentials were elicited by rhythmically amplitude-modulated sounds at modulation rates from a few hundred to more than a thousand Hz. The rhythmic-evoked response (the so-called envelope-following response) was markedly suppressed by addition of another sound of higher frequency and down to 40 dB lower intensity than the amplitude-modulated stimulus. This phenomenon was called the paradoxical lateral suppression. Only the sustained rhythmic response was a subject of this suppression, while the transient on-response to the stimulus onset was not suppressed, thus indicating that the suppression influenced the ability of evoked potentials to follow rapid amplitude modulations. At certain conditions the paradoxical lateral suppression prevents weak sounds from being masked by stronger ones. When a complex sound consists of two carriers—a higher-level, lower-frequency and a lower-level, higher-frequency, the paradoxical lateral suppression results in that evoked responses follow modulation of the weaker carrier, not the stronger one. It may help a dolphin to perceive weaker echo signals in the background of stronger emitted pulses.

3:40

1pAB6. Analysis of the role of inhibition in shaping responses to sinusoidally amplitude-modulated signals in the auditory system. George D. Pollak (Dept. of Zoology, Univ. of Texas, Austin, TX 78712)

Neurons in the inferior colliculus (IC) typically respond with phase-locked discharges to low rates of sinusoidal amplitude modulated (SAM) signals and fail to phase-lock to higher SAM rates. The hypothesis that these properties are shaped by the integration of phase-locked excitation and inhibition, as they are in lower nuclei, was tested. Responses were recorded from IC neurons evoked by SAM signals before and during the iontophoretic application of bicuculline, a competitive antagonist for $GABA_A$ receptors, strychnine, a competitive antagonist for glycine receptors, and the $GABA_B$ receptor blocker, phaclofen. The hypothesis that inhibition shapes responses to SAM signals in the IC was not confirmed. In more than 90% of the IC*c* neurons tested, the range of SAM rates to which they phase-locked was unchanged after blocking inhibition with bicuculline, strychnine, or phaclofen, applied either individually or in combination. These results illustrate that the same response property, phase-locking restricted to low SAM rates, is formed in more than one way in the auditory brainstem. In lower nuclei, the mechanism is coincidence of phase-locked excitation and inhibition, whereas in IC the same response feature is formed by a different but unknown mechanism. [Work supported by NICD.]

4:00

1pAB7. Measurement of impulse noise-induced temporary threshold shift in endangered and protected animals—Two case studies. Ann E. Bowles, Larry Wolski, Erik Berg, and Pamela K. Yochem (Hubbs-Sea World Res. Inst., 2595 Ingraham St., San Diego, CA 92109, annb1@san.rr.com)

Sonic booms at levels typical for supersonic airlines (<3 psf) are considered harmless to hearing based on laboratory studies. However, data on laboratory animals are difficult to generalize to other species. Wildlife present a particular problem because experimental efforts to induce permanent threshold shift (PTS) cannot be conducted for ethical or management reasons. Instead, ''significant'' temporary threshold shift (TTS) has been proposed as a conservative damage risk criterion (DRC). With this in mind, two series of experiments were conducted using simulated *N* waves at levels up to 6 psf, rise time down to 0.4 ms, and 100- or 300-ms duration—one on seals and sea lions and a second on the desert tortoise. Level of the least-detectable auditory brainstem response (ABR) was used to estimate best sensitivity before and after exposure. Small immediate threshold shifts ($\sim$5 dB) were detected in pinnipeds and larger ($\sim$20 dB) shifts in desert tortoises. The greater impact on desert tortoises may be explained by their greater best sensitivity at low frequencies. No PTS was detected. Thresholds for TTS were therefore detected in both species and may be useful in establishing DRCs for animals. [Work supported by NASA, Contract No. NAS1-20101 and USAF, Contract No. F33615-89-D-4003.]

Session 1pEA

Engineering Acoustics: 3D Loudspeaker Reproduction Methods

Neil A. Shaw, Cochair
Menlo Scientific Acoustics, Inc., P.O. Box 1610, Topanga, California 90290-1610, USA

Diemer de Vries, Cochair
Laboratory of Acoustic Imaging and Sound Control, Delft University of Technology, P.O. Box 5046, 2600 GA Delft, The Netherlands

Chair's Introduction—1:55

Invited Papers

2:00

1pEA1. Factors in the performance of systems for the production of virtual acoustic environments. P. A. Nelson, O. Kirkeby, Y. Kahana (Univ. of Southampton, Southampton SO17 1BJ, England), and H. Hamada (Tokyo Denki Univ., Tokyo, Japan)

This paper will describe recent progress in the development of systems designed to present, at the ears of a listener, the signals necessary to produce the illusion in the listener of the existence of a ''virtual'' source of sound. Attention will be restricted to systems which use a relatively small number of loudspeakers whose input signals are determined by optimal processing of the signal to be associated with the virtual source. It will be demonstrated that the form of the sound field produced is crucial to the success of such systems. Emphasis will be given to a system that uses two very closely spaced loudspeakers to transmit a particular form of sound field which most easily produces the iteraural time delay associated with a given virtual source position. Results will be presented of subjective experiments and of numerical simulations of the sound field. Factors determining the system performance will be discussed, particularly with regard to front–back confusions and individual differences in head related transfer functions. It will also be shown that systems using four louspeakers can significantly reduce the degree of front–back confusion even when assuming a relatively simple model of the listener's HRTF.

2:20

1pEA2. Creating virtual surround using dipole and monopole pressure fields. John W. Norris (Harman Multimedia, Harman Intl., 8500 Balboa Blvd., Northridge, CA 91329)

The objective of virtual 3-D sound technology is to convey to the listener an accurate impression of an acoustic environment. This is accomplished by conveying a realistic directional impression of sounds. Most of the successful techniques for doing this are based on the head-related transfer function (HRTF). In this paper a new method that creates the desired pressure field using dipole and monopole pressure fields will be presented. The object is to recreate locally the pressure field an actual sound source would produce, in a neighborhood of the listener's ears. One of the drawbacks of using HRTF's is that they have the pinna characteristics of the ears used to make the measurement, and so introduce the associated notches and peaks into the transfer function. The listener then has to ''in effect'' listen through these ears. And as pinna characteristics vary widely between individuals, the introduced notches and peaks associated with the measured pinnas may not correlate with the listener's. Thus by approximating the pressure field in the neighborhood of the ears, it is no longer necessary to create artifical peaks and notches in the transfer functions.

2:40

1pEA3. Spatial sound reproduction with wave field synthesis. Marinus M. Boone and Diemer de Vries (TU Delft, Lab. of Acoust. Imaging and Sound Control, P.O. Box 5046, 2600 GA Delft, The Netherlands, rinus@akst.tn.tudelft.nl)

Wave field synthesis is a reproduction technique developed at TU Delft, that enables the generation of high-quality three-dimensional spatial sound fields. The benefit of the method is that spatial impressions are highly independent of the position of the listeners within a large listening area. In short, the method uses a limited number of audio channels that are reproduced by generating plane and spherical wave fields with arrays of loudspeakers that surround the listening place. Applications include spatial sound reproduction in the home and in cinemas, sound reinforcement in theaters, teleconferencing with large video screens, and variable acoustics.

3:00

1pEA4. Comparison of virtual sound source positioning with amplitude panning and Ambisonic reproduction. Holger Strauss and Jörg Buchholz (Inst. of Commun. Acoust., Ruhr-Univ. Bochum, D-44780 Bochum, Germany, strauss@ika.ruhr-uni-bochum.de)

Different kinds of panning algorithms can be applied to render virtual sound sources in pantophonic or periphonic loudspeaker setups. One popular method is constant energy amplitude panning, where only the loudspeakers nearest to the virtual sound source are used for sound reproduction. Another well established reproduction method is Ambisonics, which uses the spherical harmonics theory in combination with knowledge from psychoacoustics to render virtual sound sources by simultaneously using all loudspeakers in a setup. Technical details and background information on both algorithms are given, and technical implementation issues (e.g., required computational effort) are discussed. A series of psychoacoustic listening tests was performed to evaluate virtual sound source localization with both reproduction methods for a six-loudspeaker pantophonic and an eight-loudspeaker periphonic setup. Localization accuracy and the subjects' reaction time were measured. The results show that the localization blur does not depend on the virtual sound source position for Ambisonics, while amplitude panning causes a high localization blue for virtual sources between the loudspeakers and a low localization blur for images close to the loudspeakers. Similar results were found in tests carried out to ascertain how dependent the reaction time is on the virtual sound source position.

3:20

1pEA5. Modification of electrodynamic loudspeakers for 3-D spatialization. E. Grigori Evreinov and V. Alexander Agranovski (Lab. for DIIS, Specvuzavtomatika Design Bureau, 44/5-13 Lenin St., 344038 Rostov-on-Don, Russia, asni@ns.rnd.runnet.ru)

The modification of electrodynamic loudspeakers was developed on a separation base of management cues by spatial and acoustic sound attributes. A loudspeaker has a single diaphragm and segmented surround, because a diaphragm embodiment in a kind of several adjacent parts evokes the losses and distortions at a sound reproduction of low frequencies. Surround's segments have an electrical control by their mechanical properties (a density). It allows the regulation of a velocity of the diaphragm fluctuations in appropriate zones. Thus a redistribution of a sound pressure (or of an acoustic energy) in the near-field or in the immediate neighborhood of pinna occurs according to the changes of spatial coordinates of sound objects. Offered construction provides a spatial localization of sound objects in the near field, even with using a single loudspeaker.

3:40

1pEA6. Sound focusing in reverberating rooms: The time-reversal approach. Sylvain Yon, Christian Dorme, and Mathias Fink (Lab. Ondes et Acoust., Univ. Paris VII/E.S.P.C.I., U.M.R. C.N.R.S. 7587, 10 rue Vauquelin, 75231 Paris Cedex 05, France)

Time reversal is already known as an efficient ultrasonic method to focus through inhomogeneous or multidiffusive media. The presence of pointlike reflectors in these media allows applications of this technique in fields like nondestructive testing, medical imaging, or underwater acoustics. An extension of this technique in audible range acoustics is presented. An array of 70 microphone/loudspeaker couples is used to refocus sound inside of a reverberating room. At a desired focal point, directivity patterns are measured and compared with those obtained by focusing with a cylindrical beamforming technique through the same antenna. Time reversal is shown to strongly improve the focal spot pattern (beamwidth and sidelobes level). These results are related to the ability of time reversal to compensate for reverberation and scattering induced in the studied room. The process acts as a spatio-temporally matched filter to the propagation transfer function of the desired focal point through the room. It makes this technique an auto-adaptive focusing system to a random 3-D cavity. Theory, experimental results, and future applications will be described.

4:00–4:20 Break

4:20

1pEA7. Algorithm for the design of broadband, constant-beamwidth, point-element linear arrays with constant sidelobe level. Joseph B. Gaalaas and Elmer L. Hixson (Dept. of Elec. and Comput. Eng., Univ. of Texas, Austin, TX 78712)

An algorithm has been designed that allows one to calculate the individual element weights, as a function of frequency, required to achieve specified values of sidelobe level and half-power beamwidth. The arrays considered had linear geometry and an odd number of evenly spaced, point elements. The input parameters are the sidelobe level, half-power beamwidth, and the number of elements. For different values of the input parameters, the bandwidth that produced realizable solutions was determined numerically. Upon choosing values for the input parameters that yield realizable solutions, the weighting functions for each element are determined by an explicit calculation. An array may be combined with a scaled version of itself to increase the bandwidth. The element weights for an octave bandwidth broadside array were calculated using this algorithm and this array was combined with a scaled version of itself to extend the bandwidth to two octaves. Microphone and loudspeaker arrays based on these calculated weights were implemented with a digital signal processor. Measurements of the directivity patterns in an anechoic room were compared to the desired directivity patterns to assess the design procedure. [Work supported by NSF Graduate Research Fellowship and Uniden Endowed Thrust 2000 Fellowship.]

4:40

1pEA8. A sound transducer with a flat, flexible diaphragm working with bending waves. Daniela L. Manger (Manger Products, Industriestr. 17, D-97638 Mellrichstadt, Germany)

From the time of the idea to the finally working sound transducer, a period of over 20 years was necessary. The time has been needed for development and research in manufacturing and materials. It took a long time until new synthetic and magnetic materials were available with their best fitting mechanical behaviors. Nowadays it is possible to present a wideband sound transducer working from 100 Hz up to 35 kHz. It follows time precise without any mechanical energy storage the incoming signal. The special structure of the flat and flexible diaphragm works concentrically only with bending waves. A simple mechanical model, theoretical equations and measurements will be presented in comparison to the omnipresent Rice–Kellogg piston loudspeaker. The advantages in perception and hearing will be shown with regard to physiological behaviors of the hearing sense.

5:00

1pEA9. FEM simulations of horn loudspeakers and their experimental verification. Armin Jost and Reiner Kressmann (Inst. for Electroacoustics, Merckstr. 25, D-64293 Darmstadt, Germany, kre@uet.tu-darmstadt.de)

Horn loudspeakers are in common use for sound reinforcement of large rooms because of their high efficiency. In the design of horn loudspeakers, special care has to be taken on the horn's geometry and its interaction with the properties of the driver. In the present work, the finite-element analysis of these coupled acoustical–mechanical systems is compared with classical analytical and finite-difference methods. All simula-

tions are compared with experimental data, obtained from two different horn loudspeakers: First, a folded bass cabinet transducer and, second, a midrange horn loudspeaker. The bass cabinet is 50×54×104 cm in size; the midrange horn measures 40×44×44 cm. Both cabinets are made from wood; therefore, the horn's geometry can only be approximated to the ideal exponential characteristics. In general, the effect of finite horn length, resulting in reflections at the mouth due to mismatch in acoustical impedance, has to be considered. The bass horn, especially, has to be simulated very precisely, since this loudspeaker shows higher impedance mismatch. The finite-element simulations carried out with ANSYS show excellent agreement with the measurements. The sound-pressure level generated was investigated as a function of frequency and angle of radiation.

5:20

1pEA10. New numerical simulation tool for the design of electromagnetic transducers. Michael Schinnerl, Hermann Landes, Manfred Kaltenbacher, Reinhard Lerch (Dept. of Elec. Measurement Technol., Univ. of Linz, Altenbergerstr. 69, A-4040 Linz, Austria, michael.schinnerl@jk.uni-linz.ac.at), and Joachim Schöberl (Univ. of Linz, A-4040 Linz, Austria)

Due to the high geometric complexity and the interaction of different physical field types, like mechanical displacement, acoustic pressure, and magnetic induction, the design of electromagnetic transducers is a challenge for the developers. Since the fabrication of prototypes and experimental-based design is a lengthy and costly process, needs for appropriate numerical simulation tools arise. In this paper, a simulation program is presented which is especially adapted to multifield problems like the one described above. First, the description of the underlying physical fields (acoustic, mechanical, and magnetic) with partial differential equations (PDE) and their coupling is reported. The solution of these PDEs is based on either finite-element methods (FEM), boundary-element methods (BEM), or coupled FE-BE methods, depending on the considered problem type. However, these numerical techniques yield to long computer time, especially in the 3-D case. Therefore, a multigrid solver has been developed which enables considerably faster solutions of the presented numerical tasks. Finally, two application examples, the calculation of an EMAT (electromechanical acoustic transducer) in transmitting and receiving mode and the prediction of the sound field of a vibrating machine part, show the reliability of the simulations.

5:40

1pEA11. Determination of structure of the NARMAX model for dynamic loudspeaker using the orthogonal algorithm. Piotr Pruchnicki and Andrzej Dobrucki (Wroclaw Univ. of Technol., Inst. of Telecommunications and Acoust., Wyb. S. Wyspianskiego 27, 50-370 Wroclaw, Poland)

NARMAX is a general method for modeling of nonlinear systems. In the paper, an application of this method for modeling of nonlinearities in dynamic loudspeakers is presented. In most cases, a polynomial representation of the NARMAX model causes an ill-conditioned equation system which indicates that the use of orthogonalization is necessary to solve the system. The high number of coefficients is the main disadvantage of the NARMAX method, and it results in an erroneous model, and an algorithm for identification of coefficients that is noneffective. A modification of the orthogonal algorithm (classical Gram–Schmidt) is presented. It is based on the premise that the coefficient providing the highest error reduction ratio is chosen in every step of the algorithm. The creation of the model stops when the given accuracy is achieved. This way leads to the choice of only the most significant coefficients. The work and effectiveness of this modified algorithm for systems with given nonlinearities at different levels of accuracy of the model are presented in the paper.

6:00

1pEA12. A proposal to adopt Maxwell distribution as a measure of acoustic field diffuseness in a reverberation room. Matias Han, W. Budhiantho (Dept. of Elec. and Computer Eng., Satya Wacana Christian Univ., Jl. Diponegoro 52-60, Salatiga 50711, Indonesia), and Elmer L. Hixson (Univ. of Texas, Austin, TX 78712)

The existence of an acoustic velocity vector resultant field which follows Maxwell distribution in a reverberation room indicates 3-D diffuseness of the field. Therefore, Maxwell distribution is a better measure for the sound-field diffuseness than Gaussian distribution given by the acoustic pressure in the same room that does not have a directional information. A Gaussian distributed pressure field does not always give a satisfactory diffuseness. The acoustic velocity vector resultant was measured using total energy density sensor. Theoretical and experimental investigations are given to support this proposal.

Session 1pED

Education in Acoustics: Acoustics Education 2000

Daniel R. Raichel, Cochair
Department of Mechanical Engineering, City College of New York, 140 Street and Convent Avenue, New York, New York 10031, USA

Roberto Pompoli, Cochair
Engineering Department, University of Ferrara, Via G. Saragat 1, 44100 Ferrara, Italy

Chair's Introduction—1:55

Invited Papers

2:00

1pED1. Acoustics education in France: Past, present and future. B. Hamonic (bernard.hamonic@eurobretagne.fr)

Acoustics is the science of sound. The interdisciplinary nature of acoustics implies the broad scope of acoustics education and the necessity to teach it at various levels of the student education, from high school to Ph.D. In the 1960s acoustics was not an important part of the French education system. Progressively teaching acoustics at a higher education level became natural and, in the 1990s, France was the only country to give a diploma between six and eight years after the secondary studies leaving certificate (Bac in french). The quality of this diploma was directly related to the emergence in France of research teams specialized in acoustics. Teaching acoustics at a secondary level came into effect only in 1994 for senior high school students. This presentation will first summarize the current acoustics education system in France with its characteristic in secondary education (senior high school) and higher education, univerities (first, second, and third cycle), engineering schools (French typcial system), etc. The future of acoustic education seems directly related to computer-based courses, the emergence of videotapes and videodiscs demonstration experiments, internet communication, etc. Reflection toward teaching acoustics in France in the future will then be addressed.

2:20

1pED2. Survey of the university institutions teaching acoustics in Poland. Edward Hojan (Inst. of Acoust., Adam Mickiewicz Univ., PL-60-769 Poznań, Matejki 48/49, Poland)

Higher education in Poland is either state owned or private. The total number of students in the institutions of higher education at the university level amounts to 630 000, which makes 15 students per 1000 citizens. As a rule, the education provided by state-owned schools is free. Among the state-owned educational institutions, presently in Poland, there are 13 universities, 18 technical universities, 8 musical academies, and 12 medical academies in which acoustics (or only psychoacoustics) is learned at selected branches of the studies The subject of acoustics is not provided in private schools. In this survey a directory of schools will be given with the details of studies where acoustics is available, including the numbers of students, hours, and the topics taught in the lectures and tutorials.

2:40

1pED3. Acoustics education in the Low Countries. Adrianus J. M. Houtsma (IPO, P.O. Box 513, 5600 MB Eindhoven, The Netherlands)

This presentation is an overview of acoustics education programs found at universities and professional colleges in the Netherlands and Flanders. As has happened in many other academic areas, the traditional organization of educational programs along disciplinary lines has to a large extent made a place for an organization based on application areas. In university programs on acoustics, one finds clusters of specialized subjects that seem to be typical for schools or departments, such as audiology, audiometry, and speech therapy in medical schools, phonetics, music, and speech in humanities departments, and architectural acoustics, noise control, imaging, and fundamentals in applied sciences or engineering departments. Several professional colleges offer courses that are focused on measurement techniques, insulation properties of materials, and noise control in buildings and structures. A fundamental and broad treatment of acoustics, followed by a treatment of specialized applications in the areas of noise control engineering, architectural acoustics, or electroacoustics as elective options, is found in the Advanced Acoustics Course, organized by the Dutch and the Belgian acoustical societies and taught annually in Antwerp.

3:00

1pED4. State and trends of acoustics education in Germany. Peter Költzsch (TU Dresden, Dept. of Elec. Eng., Inst. of Tech. Acoust., Mommsenstraße 13, D-01062 Dresden, Germany, peter.koeltzsch@iname.com)

An overall view of the state of the education in the field of acoustics in Germany, Austria, and Switzerland is given in ''Guide to Acoustics Studies'' (2nd ed., July 1998, edited by DEGA). In Germany, acoustics is taught at 63 institutes (23 universities, 16 universities of technology, and 3 universities for music, art film, or television). In connection with education, the following problem

is of great interest: How is the discipline of acoustics integrated into the traditional faculties of German universities? The present state is: integration of acoustics in mechanical, electrical, environmental engineering *et al*. On the other hand, a characteristic problem also is the existence of a ''strong'' acoustics institute at a university with a considerable research and education potential and, on the other hand, smaller special acoustics research and education capacities in all those scientific disciplines in which acoustics plays an important role. Here the question emerges whether it is more expedient for the development of acoustics to ''keep'' so-called ''acoustics pets'' in several faculties or to found a central acoustics institute to satisfy all requirements at the institutes and at the university in all. However, into which faculty should this ''acoustics institute'' be integrated then?

3:20

1pED5. Acoustics education in Ukraine. Stanislav M. Mayevskyy and Leonid M. Gelman (Dept. of Nondestructive Testing, Natl. Tech. Univ. of Ukraine, 37, Peremogy pr., Kiev, 252056, Ukraine)

Acoustics education in Ukraine is considered. In more than 40 universities, students learn acoustics: in the acoustics department of the National Technical University in Ukraine (only one department in Ukraine) and many related departments such as Nondestructive Testing, Physics, Electrical Engineering, etc. Acoustical specializations of departments are presented. The most promising and developing acoustical specialization is biomedical acoustics.

3:40–4:00 Break

4:00

1pED6. Education in acoustics: The Italian experience. Roberto Pompoli (Eng. Dept., Univ. of Ferrara, via G. Saragat 1, 44100 Ferrara, Italy, rpompoli@ing.unife.it)

Education in acoustics is a topic which has been discussed for many years in different international conferences: ICA, Inter-Noise, Forum Acusticum, etc. Tor Kihlman, analyzing in two papers [Proc. ICA'95, 311–314; Proc. Inter-Noise'96, 87–90] the education programs for students in technical faculties, arrives at the conclusion that two kinds of curricula are needed: one for students who are not specializing in acoustics and another one for students who are specializing in this field. He proposes some strategies to be followed in order to obtain better results when teaching acoustics in the technical faculties. Starting from these considerations, and taking into account on one hand the experience of education in acoustics in Italy, and on the other the analysis of the data collected by the author (in charge of education for the EAA), some possible solutions are proposed for a better coordination of the programs betweens the institutions and for the establishment of a European network of experts and teachers who are willing to move to different universities for short periods. The project could be coordinated by the EAA and funded by the European Commission.

4:20

1pED7. Education on acoustics in Spain and Latin America. Manuel Recuero (Departamento de Ingeniería Mecánica y Fabricación, Universidad Politécnica de Madrid, Ctra. Valencia Km. 7, 28031 Madrid, Spain, mrecuero@diac.upm.es), Constantino Gil, and Antonio Minguez (Universidad Politécnica de Madrid, 28031 Madrid, Spain)

Education in acoustics was incorporated as a part in engineering education in 1969, and from then to today it has had several transformations. In this paper, the results obtained from this education during the last years and how it is today are presented. Also presented are the conclusions reached from the theoretical and experimental knowledge points of view in the last three decades. The present situation of this type of education in the Spanish countries in South America are also expounded: development, implementation, years of teaching, etc. The paper is a summary of the education in acoustics in the Spanish universities with their curricula, laboratories, facilities, and so on, and the premises for the future.

4:40

1pED8. UK education in acoustics. C. G. Rice (Inst. of Sound and Vib. Res., The University, Southampton SO17 1BJ, UK, cgr@soton.ac.uk)

To definitively report on the status of acoustics education in the UK must be regarded as a challenging task. The areas of interest are even wider than the normally accepted classification of acoustic subjects (e.g., PACS), and the variety of situations to which such knowledge can be applied in practice is daunting. However, whatever the level of expertise required of practitioners in acoustics, everyone ought to be educated within a framework of life-long learning and continuing professional development. In the UK such formal educational and training requirements needed to practice the profession of acoustics have been specified, and it is in this context that UK education in acoustics will be reviewed. Formal educational requirements leading to chartered engineer status for individuals (e.g., CEng and FEANI EurIng) have been laid down by the UK Engineering Council in their ''Standards and Routes to Registration (SARTOR)'' document. These procedures were compiled by members from the professional engineering institutions and include guidelines for the accreditation of university degree courses. The Institute of Acoustics plays an important role in the implementation of such procedures. Information relating to the wider role of the importance of acoustics education in nonengineering disciplines will also be presented.

5:00

1pED9. Education in acoustics: Fundamentals and peculiarities. Nikolai A. Dubrovsky (Andreyev Acoust. Inst., #4 Shvernika Ul., Moscow 117036, Russia), Albert A. Dogadov, and Alexandr S. Sigov (Moscow State Inst. of Radiotechnology, Electron. and Automation, Moscow 117454, Russia)

An historical background of university and technical high school education in acoustics in Russia is considered. Basic features of Soviet concepts of training in acoustics are discussed. Main advantages are deep and broad training in basic and applied disciplines, a system of the ''base'' research centers for early research activity of students under leadership of active scientists, and reporting by students of their results in science and technology at conferences and seminars. These advantages had been very positive for the Soviet planned economy. The main drawbacks are redundancy and rigidity of this education system. Transition to free market society forced the modification of basic concepts of education in acoustics: to introduce flexible education similar to European and American ones, to train students in new areas of acoustics intended to enhance the quality of life (ecology, medicine), to provide optional training in acoustics (common or individual), to meet requirements of private enterprises to education of selected students. A new approach to training of foreign students is developed: transition from special high schools for foreigners to joint education of foreigners with Russian citizens in many state educational centers. The role of the Russian Acoustical Society in exchange of education methodology between training centers in Russia is presented.

5:20

1pED10. Acoustics: A route to science literacy in the 21st Century. Thomas D. Rossing (Phys. Dept., Northern Illinois Univ., DeKalb, IL 60115)

Two trends have been apparent during the second half of the 20th Century: the disappearance of acoustics from physics curricula and the decline in the percentage of students who take physics, both in schools and universities. The relationship, if any, between these trends is well worth discussing. More intriguing, however, is the likelihood that acoustics, with its rather wide appeal to students and to the public, can serve as a vehicle to promote science literacy.

MONDAY AFTERNOON, 15 MARCH 1999 ROOM MA004, 2:00 TO 6:20 P.M.

Session 1pMU

Musical Acoustics: Sound Production of Wind Instruments

William J. Strong, Cochair
Department of Physics, Brigham Young University, Provo, Utah 84602, USA

D. Murray Campbell, Cochair
Department of Physics and Astronomy, University of Edinburgh, Edinburgh EH9 3JZ, UK

Invited Papers

2:00

1pMU1. A comparison of wind instrument time-variant spectra. James W. Beauchamp (School of Music and Dept. of Elec. and Comput. Eng., Univ. of Illinois at Urbana–Champaign, 2136 Music Bldg., 1114 W. Nevada, Urbana, IL 61801, j-beauch@uiuc.edu)

Musical instruments can be compared in terms of the sound spectra that they produce. First, they may be compared in terms of spectral envelope, which allows an observation of change of amplitude with respect to frequency. Moreover, the spectra change with respect to time, usually with a burst of low-amplitude, broadband spectrum initiating the attack phase, followed by a gradual increase of spectral centroid. The so-called ''steady state'' may actually include some interesting changes, depending on performance expressivity. The final decay phase is perhaps the least manipulable by the performer, and is generally characterized by a gradual lowering of the centroid as the amplitude decreases. A centroid-indexed family of spectral envelopes based on data for several tones with different fundamental frequencies gives a good average picture of the spectra for a particular instrument. However, this representation fails to take into account special details such as pitch-dependent and harmonic-dependent spectral features. While such special details are least important for the brass, they are very important for the woodwinds, and several features of the clarinet, oboe, saxophone, and flute will be illustrated and compared.

2:20

1pMU2. Sound production of flue organ pipes. Andras Miklos and Judit Angster (Fraunhofer-Institut Bauphysik, Nobelstr. 12, D-70569 Stuttgart, Germany, angster@ibp.fhg.de)

For understanding the sound production of flue organ pipes, the acoustic properties of the two main components, the acoustic resonator and the air jet generator at the labium (flue + upper lip), have been investigated separately. It was found that the formant structure of the stationary sound spectrum is mostly determined by the geometry of the pipe, including the location, size, and shape of the openings (mouth and open end), while the attack is strongly influenced by the air jet generator. An influence of the wall

vibrations on the stationary sound has been also found, but this effect could be neglected until the wall is not too thin. The spectra of the stationary sound radiated by the openings are markedly different. The analysis of their formant structures implies that the source of the radiation is the acoustic flow at the openings. Experiments performed on labium models and pipes with damped acoustic resonators show that an edge tone with characteristic spectrum appears first during the attack. Its sound field may excite the acoustic resonator purely acoustically, preceding the development of the coupling between jet and acoustic oscillations. This assumption has been supported by the experiments discussed in the paper.

2:40

1pMU3. Sound production in flue instruments: A review. Benoit Fabre, Marc-Pierre Verge (Laboratoire d'Acoustique Musicale, Univ. Paris VI, 11 rue de Lourmel, 75015 Paris, France, fabreb@ccr.jussieu.fr), and Avraham Hirschberg (TUE, 5600 MB Eindhoven, The Netherlands, A.Hirschberg@phys.tue.nl)

The introduction of computer implementation of numerical methods, 40 years ago, has opened the way towards quantitative modeling of the sound production in flue instruments. This has induced a first wave of new research initiated in the late 1960s by the precursor work of Bechert, Cremer, Ising and Coltman. The breakthrough of real-time sound synthesis in the last decade has allowed the judgment of models on the basis of the sound which they produce. With this breakthrough ''verbal'' modeling such as the controversy between Helmholtz and Rayleigh about the nature of the sound source at the labium (volume source or dipole) is now a historical curiosity. However, it has became clear that lumped models as used in sound synthesis will remain semi-empirical caricatures. It has appeared that direct numerical simulation of the details of the flow including the effect of turbulence is still impossible. One observes, therefore, a shift back towards experimental studies such as that of jet response to acoustical excitation, the effect of nicks, the effect of chamfers, the influence of materials, Coanda effect induced by turbulence, etc. A review of these recent studies will be presented.

3:00

1pMU4. A Rayleigh wave model for the lip reed: Qualitative aspects. R. Dean Ayers (Dept. of Phys. and Astron., California State Univ., Long Beach, 1250 Bellflower Blvd., Long Beach, CA 90840, rdayers@csulb.edu), Richard P. Birkemeier, and Lowell J. Eliason (California State Univ., Long Beach, CA 90840)

The stroboscopic technique of Daniel W. Martin [J. Acoust. Soc. Am. **13**, 305–308 (1942)] has been updated by using a video camera. Improved magnification and resolution show that the upper lip's motion is complicated: a Rayleigh wave propagates downstream in a thin, passive layer of flesh. Muscles of the embouchure are used to adjust the tension and dimensions of that layer. The lips of accomplished performers show a wide range of detailed behaviors, due in some cases to asymmetry in the lip structure. The fact that players must find their own particular techniques for efficient control of the Rayleigh wave is significant for brass pedagogy. Seeing their lips in motion may help beginning players to advance more rapidly. Results of a preliminary survey among accomplished performers and beginners will be presented. [Work supported in part by the Scholarly and Creative Activities Committee and the College of Natural Sciences and Mathematics at CSULB.]

3:20

1pMU5. Self-excitation in woodwinds: From a particular model to a generic model. Ana Barjau, Vincent Gibiat (Dept. of Mech. Eng., Polytech. Univ. of Catalunya, Diagonal 647, 08028 Barcelona, Spain), and Vincent Gibiat (ESPCI, 75231 Paris Cedex 05, France)

The process of sound production in a double-reed woodwind is based upon two mechanisms: the Bernoulli mechanism, which is associated only with the reed and air dynamics, and the coupling mechanism, which represents the interaction between the bore and the reed. A realistic model, close to the physical reality of the system, leads to satisfactory simulated results compared to experimental measures. However, the great number of parameters and variables appearing in the mathematical formulation makes it difficult to predict the final behavior of the system. In this paper, the realistic model is presented, and progressive simplifications are done to reduce the formulation to a single equation containing a few control parameters and a single variable. The progressive models are discussed and applied to simulate the internal pressure at the input section of the instrument. Different behaviors are then evident: from more traditional ones (periodic states) to quasiperiodic and chaotic signals.

3:40

1pMU6. Some comments on the artificial blowing of the reed woodwind instrument. Tohru Idogawa (1-14-39 Gakuen-cho, Higashi-kurume, Tokyo 2030021, Japan, RXE07320@nifty.ne.jp)

Important results were obtained by artificial blowings of the reed woodwind instruments: Many states of air column vibrations can be excited under a fixed fingering and a fixed embouchure; these states have their respective regions of blowing pressure in which frequency and waveform of the air column vibration change slightly and continuously as the blowing pressure is varied; a sudden transition from one state to another takes place irreversibly at a blowing pressure, the upper (or lower) boundary of the state, when

blowing pressure is increased (or decreased) gradually. It will be presented that the above-described results are not necessarily valid for a conical brass pipe (0.63 m long), which has the same apex angle as that of the bassoon, blown by the mouthpiece of the soprano saxophone. One of the vibratory states excited has changed to another state without transition. When a cylindrical brass pipe, which has about the same length as that of the clarinet, has been artificially blown with the clarinet mouthpiece, the reed has been easily broken, which has rarely been observed for the clarinet.

4:00–4:20 Break

4:20

1pMU7. Differences between cylindrical and conical reed instruments. Jean-Pierre Dalmont (Lab. d'Acoust. de l'Univ. du Maine, UMR CNRS 6613, 72085 Le Mans, France)

Most investigations on reed instruments have been carried out on clarinet probably because this is the most common reed instrument. However, the extrapolation of the results to conical instruments is risky. The fact that internal clarinet spectrum does not contain even harmonics is not the only difference. For example the transfer function between input and output pressure is very different: this makes a saxophone, for lower notes, much louder than a clarinet. On the other hand, application of linear analysis near the threshold of oscillation to conical reed instruments is limited: because of the inverse bifurcation, small oscillations do not exist for conical reed instruments. This is confirmed by the observation that it is clearly much easier to play pianissimo with a clarinet than with a saxophone or an oboe. The saturation mechanism seems also to be different for conical and cylindrical instruments. On a saxophone the saturation occurs at a lower mouth pressure because of the existence of more than one regime at the fundamental frequency. All these aspects will be discussed with reference to simplified physical models and illustrated by experiments using artificial blowing. [This work has been done in collaboration with C. J. Nederveen, J. Gilbert, and J. Kergomard.]

Contributed Papers

4:40

1pMU8. A complete period-doubling cascade on a cromorn. Vincent Gibiat (LOA/ESPCI CNRS UMR 7587, 10 rue Vauquelin, 75231 Paris Cedex 05, France, Vincent.Gibiat@espci.fr) and Michele Castellengo (Univ. Paris, Paris, Cedex 05, France)

The cromorn is a very simple double reed instrument of the Renaissance which shares with the recorder the valuable property that there is no contact between the musician's lips and the double reed, allowing one to study it without any human intervention and so to control the parameters of the sound production. This has been studied by varying the blowing pressure from small values to the pressure needed to obtain the normal sound of the instrument and then by decreasing it. The sound has been recorded and analyzed in time frequency domain. A complete cascade of period-doubling bifurcations has been obtained following the increase of the pressure. Two chaotic regions have been found, one just after the third period doubling and another after a period tripling. For the lowest pressure in the decreasing process the coupling of the reed and the bore becomes too weak and the reed squeaks. The instrument is simple enough to follow the schematic given by Maganza *et al.* for cylindrical instruments and it will be shown that the decrease of the pressure is equivalent to the sharpening of the nonlinear function which relates pressure and flow that gives the possibility of period doublings.

5:00

1pMU9. The motion of air-driven free reeds. James P. Cottingham, C. Joseph Lilly, and Christopher H. Reed (Phys. Dept., Coe College, Cedar Rapids, IA 52402, jcotting@coe.edu)

An earlier study on free reeds from reed organs [P. D. Koopman and J. P. Cottingham, Reed Organ Soc. Bull. **15**, No. 3–4, 17–23 (1997)] yielded information about the variation in amplitude of reed vibration with pressure, but few further details on the reed motion. A more thorough set of measurements of the motion of these reeds has been done, including the use of a variable impedance transducer to measure reed displacement and a laser vibrometer system to measure reed velocity. For reeds from reed organs, at low to moderate blowing pressures, the reed motion at each point is nearly sinusoidal and the reed profile at maximum amplitude closely approximates that calculated for a cantilevered beam vibrating in the first mode. At blowing pressures considerably higher than normal playing pressure, strong indications of the presence of the second beam mode are observed. The nearly sinusoidal reed motion at normal pressure contrasts with the sound pressure waveform near the reed which, as a result of the valve action of the reed, roughly resembles a pulse wave. Similar measurements on accordion reeds yield somewhat contrasting results.

5:20

1pMU10. A new algorithm to simulate nonlinear propagation in a tube of any shape. Application to a real-time physical model of trumpetlike instruments. Christophe Vergez and Xavier Rodet (IRCAM, Paris, 1 pl. Igor Stravinsky, 75014 Paris, France)

When air pressure is low enough, wave propagation in a pipe can be considered linear to a reasonable degree. When the pressure level increases, this simplification becomes more and more inaccurate since high pressure values travel faster than low pressure values. The speed of propagation is thus a function of the pressure level. A new time-domain approach is proposed to simulate nonlinear propagation of a sound wave in a tube of any shape. This constraint-based algorithm does not prevent the derivative of the signal from breaking, as it happens when a shock wave occurs. Moreover, the algorithm allows the carrying out of nonlinear propagation even once a shock has occured. Thus, as expected the distorsion of a sinusoidal wave into a N-wave of progressively decreasing amplitude was observed. Moreover, without any additional computational cost, this technique provides fractional delay variation as needed for continuous tube's variations in length. The nonlinear propagation algorithm is included in the real-time high-quality physical model of trumpetlike instruments. Simulation shows a great improvement in the sound quality since this algorithm allows subtle nuances in the timbre as well as hard brassy effects.

5:40

1pMU11. Blowing and breathing in the woodwinds: Generation and control of input parameters. Leonardo Fuks (UFRJ–Rio de Janeiro Federal Univ., School of Music, Rua do Passeio 98, Rio de Janeiro, 20021-290, Brazil, leonardo@speech.kth.se)

Wind instruments, being more than an extension to the performer's body, are strongly connected to the respiratory system. Such a relationship permits a multiple and fine control of input parameters, enabling wide ranges of tone variation and expressiveness, but also imposes constraints concerning muscular demands for aerodynamic energy supply, breathhold times, and lung capacity, among others. The present investigation combined physiological and acoustical approaches, focusing on reed woodwinds under naturalistic playing conditions. Airflow and blowing pressure used by professional players were shown to be systematic in rehearsed tasks and to depend on pitch and dynamic level, instrument type, and reed characteristics, suggesting that musical training involves the incorporation and adjustment of the mechanical properties of the system to the musician's technique. Blowing pressure sensation was assessed by a psychophysical method, showing a quasi-linear behavior. Respiratory movements, decomposed into rib cage and abdominal contributions, have been recorded and analyzed during performance by an inductive plethysmographic method, providing insights to the musicians' use of the respiratory system. The ever-changing pulmonary air composition was shown to affect fundamental frequency to some extent. [The research work presented in this paper was carried out at KTH, Stockholm, and was sponsored by a Brazilian CAPES scholarship.]

6:00

1pMU12. Swiss horns and their harmonicity. Rolphe F. Fehlmann (Swiss Software Eng. College, Dept. of CAD/CAM Eng., Morgartenstr. 2, CH-3012 Berne, Switzerland)

Earlier it has been shown that there exists an optimal curved waveguide for musical purposes exhibiting a sequence of harmonic resonance modes [R. F. Fehlmann, in Intl. Congress on Acoustics, III (1995), pp. 417–421]. The radiation of some ekmelic overtones even consists of elliptical waves [R. F. Fehlmann, J. Acoust. Soc. Am. **103**, 2774 (A) (1998)]. According to the hypothesis of Risset/Mathews [J.-C. Risset and M. V. Mathews, Phys. Today **22**(2), 23–30 (1969)], the ''warmth'' of a sound source is due to the inharmonicity of the musical tones. However, in this paper, it is shown that this is not the case for the well-known ''warm and melancholic'' sound of the Swiss horns and thus questions the reasoning of Risset/Mathews.

MONDAY AFTERNOON, 15 MARCH 1999 ROOM H107, 1:55 TO 6:00 P.M.

Session 1pNSa

Noise: Urban Noise and Soundscapes

Joseph Pope, Cochair
Pope Engineering Company, P.O. Box 236, Newton Centre, Massachusetts 02459, USA

Brigitte Schulte-Fortkamp, Cochair
Acoustics/Physics, University of Oldenburg, D-26111 Oldenburg, Germany

Chair's Introduction—1:55

Contributed Papers

2:00

1pNSa1. Trading level for number of aircraft immissions: A full-factorial laboratory design. Joachim Vogt (Univ. of Dortmund, Dept. 14, Organisational Psych., D-44221 Dortmund, Germany, VOGT@WAP-MAIL.FB14.UNI-DORTMUND.DE) and Karl Theodor Kalveram (Univ. of Duesseldorf, D-40221 Duesseldorf, Germany)

To what extent can the number of overflights be increased without enhancing annoyance, if airplanes become softer? An original B737 take-off sound (A-weighted sound-pressure level: $L_{max}=76$ dB) was either reduced or amplified by 4.8 dB. In a 3×3 factorial design, nine groups of ten subjects were exposed for 27 min to 3, 9, or 27 copies of one of these three sounds. Regarding energy equivalence defined by $L_{eqA}=$const, a 4.8-dB sound-pressure reduction compensated for three times the number of the higher level, achieving constant Leq levels in the diagonals of the design. After noise exposure, cardiovascular responses and the subject ratings of loudness, annoyance, and quality of an imagined living area with comparable noise load were analyzed statistically. Comparison of the equal-energy conditions revealed no difference regarding heart rate and blood pressure, but subjective loudness increased with both level and number, and 27 soft aircraft were rated extremely loud. However, annoyance decreased, when 3 loud overflights were converted to 9 medium events, but increased again under 27 soft events. Imagined living quality always decreased with increasing numbers of events, and could not be compensated for by energy-preserving reduction of single-event levels. Conclusion: Beyond 10 events per 30 min the number probably has an increasing over-energetic impact on subjective noise effects.

2:20

1pNSa2. Calculation of noise contours for Belgian airports. Elisabeth M. J. Peeters, Jan Thoen (Laboratorium voor Akoestiek en Thermische Fysica, K. U. Leuven, Celestijnenlaan 200D, 3001 Leuven, Belgium), and Ghislain Geusens (Regie der Luchtwegen, 1030 Brussels, Belgium)

Noise contours are an objective way to represent the long-term noise load from departing and arriving aircraft. Many major European airports have a long history of noise contour calculations and related land use planning. For Belgian airports, several noise contour calculations have been made since the 1970s, but have always been based on limited information. Recently, noise contours for the airports of Brussels, Antwerp, and Ostend have been calculated based on detailed flight information. Long-term noise measurements around Brussels airport validated the accuracy of the Brussels airport noise contours. Up to today, neither for the development of noise contours, nor for the land use planning based on airport noise contours, official guidelines or practices exist, and new houses can still be built around the airports. On the other hand, with international harmonization efforts in mind, Belgian airports are not, as some other European airports restrained by legislation, based on dated technology noise contours, but have taken the opportunity to choose noise descriptors and calculation methods based on current evolutions in the international ways of calculating noise contours, as well as on international guidelines.

2:40

1pNSa3. Normalized noise spectra of aircraft take-off and landing operations. J. Salvador Santiago and Jose Pons (Instituto de Acustica, C.S.I.C.-c/Serrano 144, 28006 Madrid, Spain, ssantiago@fresno.csic.es)

At Madrid-Barajas Airport, a new runway will enter into service in the year 1999, located to the NW of the two existing ones. This fact implies a new configuration of flight paths, both for take-off and landing operations, and a new definition of the areas adjacent to the airport as regards the noise impact on the population. An ad-hoc regulation states that the dwellings within the area covered by the isophones of $L_{\text{eq day}}=65$ dB and $L_{\text{eq night}}=55$ dB, for the future situation in the year 2010, have to be supplemented by the airport operator with an acoustic insulation to achieve an internal noise level of $L_{\text{eq day}}=35$ dB and $L_{\text{eq night}}=30$ dB. The noise spectra that will be used for measuring the actual insulation of the buildings have been determined along the isophones $L_{\text{eq}}=80$ dB to $L_{\text{eq}}=55$ dB, in steps of 5 dB, for take-off and landing operations, by means of *in situ* tape recordings of 938 aircraft operations, recorded simultaneously in six measuring stations. Out of 5245 valid recordings, 2749 with enough signal-to-noise ratio were analyzed in 1/3 octave bands, and the results presented as spectra normalized to 0 dB.

3:00

1pNSa4. Noise problems, savage approaches. From ''just forget it,'' to physical violence. Fernando J. Elizondo-Garza (Laboratorio de Acustica, UANL-FIME, P.O. Box 20 ''F,'' Cd. Universitaria, San Nicolas, 66450, N. L., Mexico, fjelizon@ccr.dsi.uanl.mx)

Different approaches and/or philosophies that can be used to face a noise problem are described and commented on. Both the classical noise control procedures and the savage approaches that go from simply ''forget it,'' to physical violence, are considered.

3:20

1pNSa5. Can population density be used to determine ambient noise levels? Catherine M. Stewart (Oak Ridge Inst. of Sci. and Education (ORISE), Postgrad. Internship Prog., U.S. Army Ctr. for Health Promotion and Preventive Medicine, Environ. Noise Prog., 5158 Blackhawk Rd., Aberdeen Proving Ground, MD 21010-5422), William A. Russell, Jr., and George A. Luz (U.S. Army Ctr. for Health Promotion and Preventive Medicine, Environ. Noise Prog., Aberdeen Proving Ground, MD 21010-5422)

In 1974, the U.S. Environmental Protection Agency (USEPA) published a report endorsing the day–night average sound level (DNL) for nationwide use. Included in this report was an equation predicting DNL from the number of people per square mile. The equation was based on monitoring from 100 sites throughout the U.S. To determine whether the 1974 equation still provided a realistic estimate 25 years later, monitoring was conducted at 50 sites in Baltimore County, Maryland. Population density ranged from 600 to 13 000 people per square mile. To explore seasonal differences and test–retest reliability, the monitoring was conducted for 24 h in the summer and 24 h in the winter. The results are compared to those of the USEPA.

3:40

1pNSa6. Development of a curve to predict community annoyance due to transportation noise exposure. Lawrence S. Finegold (U.S. Air Force Res. Lab., Wright–Patterson AFB, OH 45433, LFinegold@falcon.al.wpafb.af.mil)

This paper presents a brief review of the history of the development of a curve to predict community annoyance in response to transportation noise sources beginning with the original ''Schultz curve'' [J. Acoust. Soc. Am. **64**, 377 (1978)]. This seminal article provided the results of a large-scale database meta-analysis (i.e., a secondary analysis of previously published data) using data from the 11 published transportation-elated community annoyance social surveys. The Schultz curve, which relates general transportation noise exposure (in terms of day–night average sound level, DNL) and the percent of a community ''highly annoyed'' (%HA) has been used for decades in environmental impact analyses in much of the world. The community annoyance database used by Schultz has been updated with additional social survey data, nearly tripling its original size in the initial Fidell *et al.* [J. Acoust. Soc. Am. **89**, 221–233 (1991)] analysis. A more recent version of this meta-analysis by Finegold *et al.* [Noise Control Eng. **42**(1), 25–30 (1994)] differs from the Fidell *et al.* analysis on several technical issues and includes 400 data points from 22 international social surveys. The results of the Finegold *et al.* analysis have recently been adopted as part of a U.S. standard on environmental noise (ANSI S12.9-1996/Part 4). This paper reviews the details of this meta-analysis.

4:00–4:20 Break

4:20

1pNSa7. A field study about the effects of low-frequency noise on man. Ana M. Verzini, Carlos A. Frassoni, and Aldo H. Ortiz (Centro de Investigaciones Acusticas y Luminotecnicas UNC, Cordoba, Argentina)

During the last few years, several shopping centers have been placed in residential neighborhoods of Cordoba City, and inhabitants' complaints about noise have been reported. The present paper is a field study about the effects produced by very low-frequency noise on people's health and quality of life. It was carried out in different zones of Cordoba City, where considerable levels of noise in the frequencies below 163 Hz and also in infrasounds had been detected. The generating sources were air conditioning systems, industrial plants, and traffic noise. One hundred people between 21 and 65 years old were surveyed, and the measurements of noise were done in front of each interviewed person's home, with a B&K analyzer, type 2144 and microphone B&K type 4193. Noise levels in dBLin, dBA, dBLin below 163 Hz and dBLin below 20 Hz were found, and due to the multivaried characteristics of the research and the categorical variables used, data from the questionnaire and noise levels were analyzed by means of the multiple correspondence factorial analysis. Several relationships were found among type of noise, sociodemographics, and moderator variables, and effects of noises. [This study was supported by a grant of CONICET.]

4:40

1pNSa8. How information about the source influences noise annoyance. Karl T. Kalveram, Juergen Dassow (Univ. of Duesseldorf, Inst. of General Psych., Universitaetsstr. 1, 40225 Duesseldorf, Germany), and Joachim Vogt (Univ. of Dortmund, Dortmund, Germany)

Annoyance following noise exposure can be considered to convey a ''possible loss of fitness signal'' (PLOF-signal), indicating that the individual's Darwinian fitness decreases if she or he continues to stay in that situation. Especially, nonfamiliar conspecifics appearing in the habitat diminish fitness of the inhabitants because they are going to use the same but restricted resources. Therefore, sounds carrying the information that they are manmade are likely to evoke more annoyance than other sounds of equal level and spectral density. In an experiment, subjects were exposed to recorded sounds of ocean surf and party murmur. Both sounds were carefully equalized regarding spectral energy and overall level [$L_{\text{eq(A)}}=52$ dB]. In the ''manmade'' sound condition, subjects felt significantly more annoyed and were significantly more impaired in a free recall memory test. However, physiological stress indices (potassium/sodium measured in saliva) did not discriminate significantly between the conditions. The results support the hypothesis that considered biologically, the main function of noise annoyance is to warn a person that fitness may diminish, but not to induce actual stress. This explains the frequently reported finding that noise, although annoying, causes only little or even no physiological stress reactions.

5:00

1pNSa9. Use of immersive sound in a museum exhibition. Peter Coulter (Powerhouse Museum, P.O. Box K346, Haymarket, Sydney, Australia 2000, peterc@phm.gov.au)

Studies have shown [Schaffer, World Sound Project (1997)] that in our environment, which includes our community, traffic and motorized sounds are growing at a faster rate than nonmotorized human sounds, suggesting that because motorized sound is low-information, high-intensity, it tends to desensitize the populace and results in less social interaction. One role of museums is to preserve a balance of sounds, as a sanctuary from our environment, and explore the consequence of our motorized culture. At the Powerhouse Museum, an exhibition has opened, December 1998, entitled ''Cars and Culture'' which examines the consequence of cars. In the exhibition there is an immersive sound space that has been created using an ambisonic sound system. This soundscape is discussed. An experiment was devised where the degree of sound immersiveness was varied for a number of visitors and their reactions were measured.

5:20

1pNSa10. Loudness evaluation of urban soundscapes by a cross-modal matching method. Patrick Susini (Inst. de Recherche et de Coordination Acoust./Musique (IRCAM), 1 place Igor-Stravinsky, F-75004 Paris, France, susini@ircam.fr) and Valerie Maffiolo (Lab. d'Acoust. Musicale, Paris Cedex 05, France)

In a previous study, loudness of a time-varying pure tone was evaluated using a cross-modal matching method. In this procedure, the loudness was matched to an equivalent muscular force. Subjects had to judge the instantaneous and global loudness using a proprioceptive input device with force feedback. Using this technique, subjects could respond easily, rapidly, continuously, and with feedback concerning their evaluation. The present study examines the relation between instantaneous and global loudness of 16 urban soundscapes lasting about 20 s using the same method. First, the procedure is individually calibrated with 1-s soundscapes presented at different sound-pressure levels. The data obtained for each subject fit well with a linear relation on a log–log scale between the sound-pressure level in dB and the associated force in log Newtons. Then, the global judgments are performed under two experimental conditions: one with instantaneous loudness evaluation during stimulus presentation and one without. Good correlation was found between these two judgments. The global judgment and the average over the instantaneous matching contour are nearly identical. In addition, a fluction factor (FI) calculated on the loudness judgment contour reflects the degree of movement produced by the subject as well as the presence of discriminable sources.

5:40

1pNSa11. Is pleasantness for soundscapes dimensional or categorical? Valerie Maffiolo, Michele Castellengo (Lab. d'Acoust. Musicale, Univ. Paris 6, case 161, 4 place Jussieu, F-75252 Paris Cedex 05, France, maffiolo@ccr.jussieu.fr), and Daniele Dubois (CNRS, UPR 9017, INALF, ENS, Montrouge, France)

This paper focuses on methodological issues regarding the dimensional or categorical properties of pleasantness for soundscapes. Sixteen sequences of urban soundscapes were recorded and reproduced with their real sound intensity, using techniques previously validated to produce the illusion of a real environment. The sequences were processed using two methods: free categorization and pair comparisons. The categorization method consisted of asking subjects to sort out the sequences according to pleasantness and to verbally qualify their categories. In the pair comparison task, subjects had first to choose, for each pair, which sequence was the most pleasant, and then to rate the pleasantness dissimilarity between the two sequences on a nine-point scale. Categories and ratings were processed through a cluster analysis and interpreted in connection with a psycholinguistic analysis of the verbal comments. Binary choices were transformed onto a dimensional representation of pleasantness. The main results lead to the discussion of the influence of procedures and data representations of the interpretation of pleasantness for soundscapes, and suggest that the dimensional aspect of pleasantness is more an artifact of representation than an intrinsic property of soundscapes. Unpleasant soundscapes seem to be more adequately represented as a specific category of sounds rather than values ranging on a scale.

Contributed Poster

This poster will be on display in the Poster Gallery from Monday to Wednesday, 15–17 March. The author will be at the poster from 2:00 p.m. to 4:00 p.m. on Tuesday, 16 March.

1pNSa12. Assessment of low-frequency noise in dwellings. New Polish recommendations. Marianna Mirowska (Bldg. Res. Inst., Acoust. Dept., Ksawerow 21 02-656 Warsaw, Poland)

The paper presents the new Polish recommendations for evaluation of low-frequency noise penetrating into dwellings from appliances installed inside or outside of building. Based on measurement data of annoyance noise, epidemiological investigations of the influence of noise on the health of exposed inhabitants, laboratory tests of thresholds of narrow- and broadband noise perception, review of the present literature, the new assessment criteria was proposed. In order to assess the noise spectra measured in dwellings, the A10 characteristics as the rating curve have been accepted. Its L levels for one-third-octave bands are determined by relation: $L_{A10} = 10$ kA. The low-frequency noise occurs as annoying when the sound pressure levels of noise exceeds the levels of A10 curve and exceeds the background noise by more than: 10 dB for tone noise and 6 dB for broadband noise.

Session 1pNSb

Noise: Noise from Air-Conditioning, Ventilating and Industrial Fans

Jean Tourret, Cochair
CETIM, Industrial Acoustics Department, B.P. 80067, F-60304, Senlis, France

Robert Schlinker, Cochair
United Technologies Research Center, 411 Silver Lane, East Hartford, Connecticut 06108, USA

Invited Papers

2:00

1pNSb1. Fan noise—In-duct sound power—What are we measuring and why? W. T. W. Cory (Woods of Colchester Ltd., Tufnell Way, CO4 AR Colchester, Essex, UK, Bill.Cory@woods-fans.com)

The paper will review the history of the measurement of fan noise. Early standards will be described and related to the state of knowledge existing at the time. The need for reliable methods of measuring the noise in-duct was foreseen at an early stage. This required the development of microphone shields able to ensure accurate readings of noise in a moving airstream. The relationship of in-duct levels to those measured around the fan in reverberent or free-field conditions will be discussed. Finally, the forthcoming ISO standards will be introduced and the recognized need for a number of different levels to be recorded.

2:20

1pNSb2. In-duct fan sound power measurement. Part I. Review of general problem. Wolfgang Neise and Frank Arnold (DLR-Institut fuer Antriebstechnik, Abteilung Turbulenzforschung Berlin, Mueller-Breslau-Strasse 8, 10623 Berlin, Germany, Wolfgang.Neise@dlr.de)

Many technical fan installations involve a duct on the inlet side and/or outlet side of a fan. Therefore the need arises for a measurement method for determination of the sound power radiated by fans or other fluid handling sources into a duct. In the paper the problems associated with such a method are discussed: Axial standing waves due to sound reflection from the duct end, acoustic loading of the source, turbulent flow pressures superimposed on the sound field, flow noise generated by flow/microphone probe interaction (self noise), discrimination between sound pressures and turbulent flow pressures, measurement position in the duct in view of higher-order mode sound propagation and directional characteristic of the microphone probe used, and modal distribution of sound power. Early and recent work on the above topics is reviewed. A brief description of the standarized in-duct method ISO 5136 (1990) is given.

2:40

1pNSb3. In-duct fan sound power measurement. Part II. Revision of ISO 5136. Wolfgang Neise and Frank Arnold (DLR-Institut fuer Antriebstechnik, Abteilung Turbulenzforschung Berlin, Mueller-Breslau-Strasse 8, 10623 Berlin, Germany, Wolfgang.Neise@dlr.de)

In recent investigations problems with the present version of the in-duct method ISO 5136 (1990) became apparent which indicate that a revision of the standard is necessary. The two major problem areas are: (1) Swirl flow existing in the test duct may interfere with the microphone probe to give too high sound power levels. Farzami and Guedel [1992 Proc. Fan Noise, CETIM Senlis, France, pp. 375–380] showed that this problem can be solved by placing a flow straightener between the fan outlet and measurement plane. (2) By comparison with other methods of sound power determination [Holste and Neise, JSV **152**, 1–26 (1992)], the sound power levels obtained by using the in-duct method are too low by several decibels in the frequency region of higher-order mode sound propagation. It is shown that the discrepancy between the results of the in-duct method and other methods is caused by the so-called modal correction C4 which is to account for the directivity characteristic of the microphone fitted with a turbulence screen in view of the propagation angle of the higher-order duct modes. Experimental and theoretical results are presented for a new combined frequency correction C34 which includes the effects of the superimposed mean flow on the sensitivity and directivity of the microphone probe as well as on the modal sound propagation and characteristics in the duct.

3:00

1pNSb4. Numerical method and software package for prediction of pressure pulsation in centrifugal ventilators. S. Timouchev (InteRe Ltd., DG, 19 Apt. 11, Engels St. 141400 Khimki, Moscow Reg., Russia, irico@glas.apc.org)

A numerical method and software package was developed for designers and researchers in the field of vibration and noise problems in centrifugal ventilators. The numerical procedure is based on a representation of unsteady compressible liquid flow as a form of vortex (pseudo-sound) and acoustic mode superposition. It gives a possibility to determine absolute amplitudes of pressure pulsation in the ventilator casing induced by unsteady interaction between nonuniform flow outgoing from a centrifugal impeller volute tongue or diffuser vanes, so-called blade passing tones. Inupt data includes 2-D ventilator geometry and operation mode. Acoustic impedance boundary conditions can be defined with a circuit specification or by direct inlet and outlet specific complex

impedance definition. It is possible to take into account local wall-specific complex impedance to study a coating effect on reduction of pressure pulsation. Output data represents: unsteady pressure map in the ventilator casing; amplitude distribution map for any selected harmonic; pressure versus time curves with accompanied spectrum information at any point selected by user; total vibration load vectors acting on the ventilator volute casing; and static pressure, velocity, and vorticity distribution in the centrifugal impeller. Validation of the software was completed on the centrifugal pump air model with more than 400 measuring points for two different radial gaps. The mismatch with experimental data is mostly 1.5–2.0 dB of unsteady pressure amplitude. Effects of radial clearance, number and form of impeller blades, exit and wall impedance are considered as well. The successful validation of the numerical method shows a good prospect in optimizing centrifugal ventilator geometry with improving vibration and noise characteristics at the draft stage and reducing refinement costs.

3:20

1pNSb5. Modeling centrifugal fan blade trailing edge noise. Robert H. Schlinker, Bruce L. Morin, C. D. Coffen, and Roger L. Davis (United Technologies Res. Ctr., 411 Silver Ln., East Hartford, CT 06108, schlinrh@utrc.utc.com)

Centrifugal fan noise contains numerous aeroacoustic mechanisms, one of them being trailing edge noise due to turbulent boundary layer flows convecting over the blade trailing edge. A fundamental research program was conducted to develop a trailing edge noise database and assess the ability of existing aeroacoustic models to predict this mechanism. The database included unsteady surface pressure spectra, trailing edge wake characteristics, and acoustic sound power. To focus on trailing edge noise, a mixed flow radial fan was simulated with a circumferential array of nonrotating vanes located in a radial diffuser. Both loaded and unloaded vane geometries were tested to simulate varying pressure gradients in an actual fan blade passage. It was demonstrated that the trailing edge noise mechanism can be accurately predicted if the trailing edge wall pressure spectrum is known *a priori*. However, for radial fans the strong adverse pressure gradients appear to rule out the existence of a ''universal'' wall spectrum shape typically observed in flat plate zero pressure gradient boundary layer flows. Hence, futher trailing edge noise modeling needs to focus on predicting surface pressure spectrum shape, in addition to, amplitude and frequency content.

3:40–4:00 Break

Contributed Papers

4:00

1pNSb6. Aeroacoustic response of a six-bladed axial fan to installation effects. Jean-Guillaume Lalanne, Hans Boden, and Mats Abom (Dept. of Vehicle Eng./MWL S-10044 Stockholm, Sweden, jgl@fkt.kth.se)

First, the effects of the duct on the aeroacoustic response of an axial fan have been studied experimentally and theoretically. The loading effect was modeled by a 1D model in the plane-wave frequency domain. This model was validated experimentally by changing duct lengths and fan positions. Second, an experimental characterization of the inflow turbulence has been done. Single degree-of-freedom statistical parameters have been measured as autocorrelation and temporal autospectrum for the axial turbulence components in order to estimate the integral scale and turbulence intensity. In parallel (the fan being located between an anechoic room and a reverberant room), sound pressure and sound-power measurements have been carried out. Different grids and supercritical screens have been designed to change the inflow conditions. The next task is to determine the spectral pattern in both the temporal frequency and tangential wave number domains and correlate it to acoustic response. Only the tonal part of the spectrum is considered. [Work supported by EEC.]

4:20

1pNSb7. Experimental determination of the fluctuating pressure on a rotating fan blade as a source of acoustic noise. Michael Stremel and Thomas Carolus (Institut fuer Fluid und Thermodynamik, Fachgebiet: Stroemungsmaschinen, Universitaet-Gesamthochschule Siegen, 57068 Siegen, Germany)

The fluctuating pressure on the rotating blades is a significant quantity responsible for the noise emitted from axial fans. In order to compute the noise from flow field data, a model is required which describes the fluctuations as a function of flow parameters. The paper presents the fluctuating pressure, measured on the rotating blade of a fan under different operating conditions. The turbulence intensity and the spectral density of the turbulent inflow velocity fluctuations are varied and measured. From CFD calculations quantities, such as boundary layer thickness, shape parameter, etc., of the flow around the blades are deduced and used as parameters. Simultaneously, the noise emitted from the fan is measured and compared to the fluctuating blade pressure.

4:40

1pNSb8. Aeroacoustics of axial propeller: Applying to an acoustic wind tunnel and optimization of an axial propeller for cooling system. Y. Dupont (Sciences Industries Conseils, 14, avenue de Sceaux, 78000 Versailles, France)

A simplified model is more convenient to predict design parameter effects on operating characteristics and radiated noise of a propeller. Thus, the aeroacoustic design software, DECIVENT, is used for subsonic axial flow fan, mounted as well in reduced systems like cooling systems as in greater structures like test wind tunnel. For a given flow rate and with the blades specified in cylindrical sections, the total pressure and torque are provided by the following computations: (i) outlet velocity triangle by solving radial balance, (ii) lift coefficient by a conformal transformation, and (iii) lift and drag forces, evaluated with considerations of laminar or turbulent boundary layer stall. The outlet relative velocity and force fields allow one to compute the radiated noise whose components are (i) loading noise, computed by Lighthill's model, and (ii) broadband noise computed by Fukano's model. Correlations with tests show the validity of this methodology. This software, weak customer in computational duration, may be

connected with an optimization software which, after some hundred iterations, allows one to exhibit the best compromise. Two propellers design by these means will be presented: one for a preliminary plan of an acoustic wind tunnel, and one for a cooling system.

5:00

1pNSb9. Experimental investigation of noise sources in cross-flow fans. Michael Herrmann,[a] Wolfgang Neise (DLR-Institut für Antriebstechnik, Abteilung Turbulenzforschung Berlin, Mueller-Breslau-Strasse-8, 10623 Berlin, Germany, Wolfgang.Neise@dlr.de), and Robert H. Schlinker (United Technologies Research Ctr., East Hartford, CT 06108)

Cross-flow fans are unusual types of blowers which operate in a fundamentally different way from axial or centrifugal fans. The flow enters and leaves the impeller in a direction vertical to its axis and passes the blade row twice, first radially inward and then radially outward. Hence, cross-flow fans are basically two-stage fans. Aerodynamic and acoustic modeling of cross-flow fans is extremely difficult because of the complexity of the flow field in the rotating impeller channels with a reversal of the flow direction during each revolution and large regions of severe flow separations. To obtain experimental input data for modeling efforts, experiments were performed with a scaled up model fan. The fan was installed in an open-inlet/ducted outlet test rig. Measurements were made of the unsteady pressures on the impeller blades and on the fan casing, in particular the vortex wall. The flow fields inside the impeller and at its outer periphery were studied by using hot wire anemometry and a three-hole probe. The effect of different casing geometries was examined. A simple model for broadband noise radiation involving surface dipole sources as suggested in an early paper by Sharland [JSV **1**, 302–322 (1964)] predicts the spectrum measured in an anechoically terminated outlet duct reasonably well for a medium frequency range. [a] Now with Behr GmbH & Co., Mauserstrasse 3, 70469 Stuttgart, Germany

5:20

1pNSb10. Practical approach to ANC of fan noise with feedback compensation. Petr Koníček and Ondřej Jiříček (CTU in Prague, FEE, Dept. of Phys., Technicka 2, 166 27 Prague, Czech Republic, jiricek@fel.cvut.cz)

Attenuation of low-frequency noise is a difficult task using passive methods. This paper presents the results of a fan noise reduction in a duct with circular cross section and a small diameter using active noise control. The control algorithm is designed for the optimum least square control in the time domain and contains acoustic feedback compensation. This algorithm was used for the attenuation of noise generated by a small axial fan. The discrete components of noise were totally canceled and the broadband component was reduced. The results of our project will be used for betterment of the working environment.

5:40

1pNSb11. Noise from airborne air conditioning system. Oleksander I. Zaporozhets and Vadim I. Tokarev (Acoust. Lab., Kyiv Intl. Univ. of Civil Aviation, 1, Ave. Cosmonaut Komarov, Kyiv, 252058 Ukraine, zap@elan-ua.net)

A prediction model for noise produced by an air conditioning system in an aircraft pressurized compartment is described. It is based on analysis of the sound flow energy in air conditioning system channels, including both the generation attenuation effects of the acoustic oscillations within the system. Differences in calculations from those usually used in stationary air conditioning systems for industrial, public, and residential buildings are discussed. The mechanism of noise generation by compressors, cooling turbine, separated flows in regulator, and jet flows from the pipe nozzle are investigated. The calculation results are obtained and carried out for different operational airplane conditions. Optimum tasks for operation conditions of an air conditioning system for noise impact criterion are formulated and solved.

Contributed Posters

These posters will be on display in the Poster Gallery from Monday to Wednesday, 15–17 March. Authors will be at their posters from 10:00 a.m. to 12:00 noon on Tuesday, 16 March.

1pNSb12. Rotational noise generation in peripheral fans. Volkmar Weise (TU Bergakademie Freiberg Institut f. Fluidmechanik und Fluidenergiemaschinen Lampadiusstr. 2, D-09596 Freiberg, Germany)

Peripheral fans are used in technical applications where radial and axial fans cannot supply the required pressure ratio at a low mass flux rate. Characteristic for peripheral fans is their high noise emission in the range above 1000 Hz. In comparison to the theory of noise generation in axial fans the sound sources in peripheral fans are not only the rotational blade forces. From an aeroacoustic viewpoint the main difference between axial fans and peripheral fans is the stripper which is necessary to separate inlet and outlet. The sound generation at the outlet is related to the circulating flow between rotor and side channel. This circulation is the main reason for the momentum and energy transfer from the rotor to the gas. The stripper divides the flow in the side channel from the flow between the blades. The result is the modulation of the circulating flow with monopole sources of aerodynamic noise. At the inlet the relief of the blade chambers filled with higher pressure proved to be the main aeroacoustic source by time-dependent periodical mass flux. According to the theory of aerodynamic sound generation this expansion flow represents a monopole source of noise. [Work supported by DFG.]

1pNSb13. Experiences with attenuation of low-frequency noise in duct. Ondřej Jiříček and Petr Koníček (CTU in Prague, FEE, Dept. of Phys., 166 27 Prague, Czech Republic, jiricek@fel.cvut.cz)

Fan noise still represents a serious component of noise pollution in the working place. Fan noise contains both random and discrete frequency components. This paper presents results of experiments with the ANC system useful for low noise design of air-conditioning systems. Computer simulation and measurements were used to examine the performance of the tested feedforward system. The control algorithm is designed for the optimum least square control in the time domain. Experimental results of an investigation of active control of sound are presented.

Session 1pNSc

Noise: Railway Noise I

Paul J. Remington, Cochair
BBN Systems and Technologies, 10 Moulton Street, Cambridge, Massachusetts 02138, USA

Markus Hecht, Cochair
Institut für Strassen- und Schienenverkehr, Fachgebiet Schienenfahrzeuge, Sekr. SG-14, Salzufer 17-19, D-10587 Berlin, Germany

Chair's Introduction—2:15

Invited Papers

2:20

1pNSc1. The effects of rail support stiffness on railway rolling noise. David J. Thompson, Chris J. C. Jones, and Guillaume de France (Inst. of Sound and Vib. Res., Univ. of Southampton, Highfield, Southampton SO17 1BJ, UK, djt@isvr.soton.ac.uk)

Rolling noise from trains is radiated by both wheel and track vibrations, the track being dominant in many cases. The stiffness of the rail fastener system, especially the elastomeric rail pad usually inserted between the rails and the sleepers, has a significant influence on the noise emitted by the track. Railways are increasingly using softer pads to reduce potential damage to sleepers and ballast. Softer pads decouple the rail from the sleeper. This reduces the noise from the sleeper but also reduces the decay of vibration with distance along the rail and hence leads to an increase of the noise radiated by the rail. The paper describes experimental and theoretical work to investigate the influence of pad stiffness on the dynamic and acoustic behavior of track. The vibrational behavior has been measured on a dedicated 36-m section of railway track, with different types of rail pad installed. The results are compared with predictions using theoretical models of the track behavior. This allows the effective pad stiffness and damping to be determined, laboratory measurements also being available for comparison. The attenuation of vertical and lateral vibration along the track is measured in order to estimate the effect on radiated noise.

2:40

1pNSc2. Time domain simulation of railway noise. Anders Nordborg (ABB Corporate Research, Appl. Mech., SE-72178 Vasteras, Sweden)

The most difficult problem concerned with railway noise generation is the process occurring in the contact region during rolling. The following computation efficient time domain model determines the vertical rail deflection by use of Green's function of a periodically supported beam. Nonlinear Hertzian contact mechanics are used, less realistic, however, than a discretized contact region allowing for rough surfaces. The wheel is as yet a rigid mass. More advanced contact and wheel models can readily be included later. Calculation results include the following observations. The contact force peaks sharply precisely above the support points, followed by a short loss of rail–wheel contact, also for smooth rails. Vibrations of the rail pinned–pinned mode are impossible to eliminate by removing surface roughnesses, because the excitation is above all caused by forward wheel velocity together with discrete supports. The response amplitude increases with forward velocity. Optimum pad stiffness depends on corrugation amplitude. These new findings should be considered when trying to noise optimize track constructions.

3:00

1pNSc3. Short pitch corrugation on straight tracks—Theory and numerical simulation. Steffen Müller and Klaus Knothe (ABB Res. Ctr., Speyerer Str. 4, 69115 Heidelberg, Germany and Tech. Univ. of Berlin, Marchstr. 12, 10587 Berlin, Germany, steffen.mueller@decrc.abb.de)

Simulation models (Frederick, Sinclair, Valdivia, Hempelmann) which have been developed during the last 20 years showed the formation of short pitch corrugation to be a frequency constant mechanism, where a track mode about 1000 Hz dominates the corrugation process. Based on this, however, it is difficult to explain the relatively small variation in wavelength with vehicle speed which is observed in practice. In this presentation a sophisticated linear wheel-rail model is introduced which could help in resolving this contradiction. The transient dynamics is described by a feedback loop: Fluctuations in the contact geometry and the creepages cause varying contact forces. This produces fluctuating relative displacements between wheel and rail which in turn change the contact geometry and the creepages again. The simulation of the long-term behavior shows how the rail surface is damaged after a high number of wheel passages. Based on numerical results it is demonstrated that, due to contact mechanical effects, short pitch corrugation is growing within a fixed wavelength band, which could explain why the wavelength varies only a little with vehicle speed. The presented model is therefore a good basis for future research on how short pitch corrugation can be suppressed.

3:20

1pNSc4. On the determination of dynamic properties of elastic rail fastenings. Rolf J. Diehl and Paul Hofmann (Müller–BBM, Robert-Koch-Strasse 11, D-82152 Planegg, Germany)

The dynamic properties of the resilient layers of rail-fastening systems play an important role for sound and vibration emission from railway lines. In order to achieve low sound radiation from the rails, a rather stiff fastening for the rail is advisable, whereas for vibration minimization rather soft fixtures would be preferred. The dynamic properties of fastening systems are determined from measurements. In order to have comparable results, a CEN standard is currently being written which is consistent with the method described in ISO 10846 for laboratory measurements of the dynamic stiffness. The method and examples for results will be discussed. For the optimization of the setup for a given situation [track, vehicles, speed(s), operating conditions, surroundings], theoretical models are useful tools. In addition, such models can be used to predict the future impact. Apart from the prediction model itself, the quality of a prediction depends on the reliability of the input data. Results of calculations with the rail/wheel impedance model RIM will be shown to demonstrate the effect of different vertical stiffnesses of the rail fastening and its frequency dependence on the emitted sound and vibration levels.

3:40

1pNSc5. Reduction of ground-borne noise from rail systems. George P. Wilson (Wilson, Ihrig & Assoc., Inc., 5776 Broadway, Oakland, CA 94618)

Over the last 35–40 years there has been an ever increasing awareness of ground-borne noise from rail system train operations and an increasing need for mitigation. In response there have been extensive and continuing efforts to develop rail fixation and support systems which will reduce or control the ground-borne noise which originates at the wheel/rail interface. The rail fixation systems have varied from simple resilient boots on sleepers or resilient pads under rail fixation plates to elaborate concrete floating slab trackforms. Intermediate mitigation designs have included ballast mats, booted duo-block sleepers, and many configurations of resilient rail fixation baseplate assemblies. A review of the various types of ground-borne noise mitigation trackform designs is presented along with indication of the effectiveness for each type or class of design. Further, characteristics or design parameters of the various classes of design which result in poor performance are discussed, particularly for floating slab trackform.

4:00–4:20 Break

Contributed Papers

4:20

1pNSc6. STV: Silencing goods traffic. Part 2: Demonstrating practical low noise solutions. J. Lub (NS Technisch Onderzoek, P.O. Box 8125, NL-3503, RC Utrecht, The Netherlands)

The Dutch national project, Quiet Rail Traffic (Stiller Treinverkeer STV), aims at an overall A-weighted noise reduction of at least 10 dB for day-to-day goods traffic, with a maximum achievable reduction of 16 dB. The project has as goals the development of validated design and analysis methods, and the demonstration thereof by means of the construction and testing of two prototype quiet goods wagons and a prototype quiet track construction. Validation tests will be performed in November 1998. Static and pass-by noise and vibration tests are conducted with two prototype container carrying wagons, loaded with containers and a reference vehicle. The goods wagons are equipped with laser-cladded wheels, composite brake blocks, drum brakes, magnetic brakes, and wheel skirts. They are operated on a continuously laid slab track construction with embedded rail. The rail type is of a newly designed type, optimized for noise reduction and application in track designs with continuous rail support. Mini-barriers and sound absorption material are applied to the track. A telemetry system is used for measuring wheel noise. The improvements achieved by the total prototype wagon/track combination and components are compared to the predicted noise reduction and data collected in the reference phase of the project.

4:40

1pNSc7. The real sound emission of ''Rasengleis.'' P. Fuerst (cdf Schallschutz Dresden, Wilhelm-Liebknecht-Straße, 6, D-01257 Dresden, Germany, cdf-Schallschutz-DD@t-online.de)

The ''Rasengleis'' (railway lines which are covered by meadow and bedded on conventional ballasted tracks) has indeed a lower noise emission level. Various investigations focusing on the acoustical behavior of the ''Rasengleis'' were carried out in the last years. The results were rather different. The first sequence of measurements took place **before** changing the construction of the second part of the railway line. That was to counterbalance errors due to locality, time (the last measurement was carried out almost 2 years later than the first one), and other ambient conditions. The levels could be easily compared among each other using the results of the reference point. Additionally, the measurements were repeated after at least a year to take aging processes of the meadow into account. Two different types of trams were used. They differ among other things in the kind of absorption used for the wheels. One wheel type contains rubber parts stressed of shearing (Tatra T4D), the other wheel rubber parts are stressed of pressure (Bochum). ''Rasengleis'' reduces noise emission depending on the kind of wheel up to 3 dB (minimum 2 dB). There will be measured levels of drive past, standardized values, and sonograms.

5:00

1pNSc8. Structure-borne noise reduction in a railway tunnel in Cologne by means of a ballastless mass–spring-system-type Züblin with discrete Sylodyn® bearings and dynamically soft Sylodyn® ballast mats. Rüdiger G. Wettschureck (Getzner Werkstoffe GmbH, P.O. Box 162, D-82025 Grünwald/Munich, Germany, Wet@getzner-werkstoffe.de), Franz Breuer (Peutz Consult GmbH, D-40599 Düsseldorf, Germany), Markus Tecklenburg (Getzner Werkstoffe GmbH, Bürs/Bludenz, Germany), and Horst Widmann (Ed. Züblin AG, D-70567 Stuttgart, Germany)

In the vicinity of Chorweiler (a suburb of Cologne) there is a tunnel in the double track of German Railways between Cologne and Düsseldorf which was built for airborne noise protection reasons. On both sides of this tunnel there are very close housing areas built during the last years. The structure-borne noise of the rail traffic caused a considerable interference with the residents. In 1997 measures to reduce the railway vibrations were installed in both tracks of a 970-m-long tunnel section. In one part of the tunnel, 230 m long, a mass–spring system with a natural frequency of 11 Hz, using discrete bearings, was installed. The rest of the tunnel was equipped with ballast mats tuned to extremely low dynamic stiffening and

to main line axle loads (push–pull trains of commuter traffic Rhein/Ruhr) with a specific static stiffness of 0.03 N/mm^3 [according to DB-TL 918071, Edition June (1988)]. The efficiency of these reduction measures, that means their insertion loss, was estimated by means of lumped-parameter models, and measurements of the structure-borne noise during train passages were carried out on identical measuring points before and after the structural alterations in the tunnel and in adjacent buildings. The measurement results show a good correspondence with the calculations and completely confirm the high expectations set in the measures.

5:20

1pNSc9. Short pitch corrugation on straight tracks—Practical experiences. Thomas Klimpel and Klaus Knothe (Tech. Univ. of Berlin, Inst. of Aviation, Dept. of Design, Marchstr. 12, 10587 Berlin, Germany)

One possibility to reduce rolling noise is to reduce roughness excitation. The basis of the paper is measurements of profile irregularities on a test section of the track between Baarn and Amersfoort in the networks of Nederlandse Spoorwegen (NS). In one of two segments, periodic wear pattern (short pitch corrugation) appears with wavelength from 3.5 to 4 cm, whereas the second one is uncorrugated. The line is used only in one direction and mainly by passenger cars with medium speed. Starting from the measured track data, systematic calculations with the program of Müller, which is presented in a separate paper, have been undertaken. The aim is to estimate the roughness growth and to find hints about how the growth can be stopped or at least reduced. In Müller's paper it is explained in detail that roughness growth is restricted to a wavelength range between 2 and 10 cm. Numerical results will be presented in order to clarify how different track components influence the RGG process. The model only takes into account wear as a long-term mechanism. It shall be discussed how the long-term behavior is influenced by plastic deformation, hardness variations, or different values of micro-roughness.

5:40

1pNSc10. A reciprocal method to evaluate low, close to track noise barriers. P. F. van Tol (NS Technisch Onderzoek, Postbus 8125, 3503 RC, Utrecht, The Netherlands) and H. A. Holties (M+P Raadgevende Ingenieurs, 1430 AH, Aalsmeer, The Netherlands)

In the framework of the Dutch program Quiet Train Traffic (Stiller Trein Verkeer) low, close to track barriers and absorptive layers on a slab track have been investigated. Following numerical calculations on low, close to track barriers and absorptive layers an experimental study has been made in order to evaluate the different solutions. A special test site has been constructed, which acoustically resembles a slab track. It enables a quick mounting and dismounting of different low, close to track barriers and absorptive layers on the slab. Using a reciprocal measurement method the acoustical performance (insertion loss) of different solutions has been determined. One of the advantages of a reciprocal method is that the noise reduction for different noise sources on a freight train, such as wheels, rails, and wagon superstructure, due to absorptive layers and low, close to track barriers is easily identified. Note that this stationary method is very efficient since no train passby is necessary. It is explained that a real train passby may be simulated by combining the measurements over multiple angles. Finally, a comparison will be made between the experimental and the numerical results.

MONDAY AFTERNOON, 15 MARCH 1999 ROOM H2032, 1:55 TO 4:00 P.M.

Session 1pNSd

Noise: Airframe Noise

Ulf Michel, Cochair
DLR, Institut für Antriebstechnik Abt. Turbulenzforschung, Müller-Breslau-Strasse 8, 10623 Berlin, Germany

Michele G. Macaraeg, Cochair
Aerodynamic and Acoustic Methods Branch, NASA Langley Research Center, MS 128, Hampton, Virginia 23186, USA

Chair's Introduction—1:55

Invited Papers

2:00

1pNSd1. The ''Owl'' as a challenge in airframe noise research. Geoffrey M. Lilley (ICASE, NASA Langley Res. Ctr., Hampton, VA 23681 and Dept. of Aeronautics and Astronautics, Univ. of Southampton, Southampton SO17 1BJ, UK)

The ''silent'' flight of the ''owl'' has captured the attention of the aeronautical community for over 50 years. The silent flight, resulting from changes in the flight feathers of the ''owl'' from all other birds, notably the leading edge comb, the trailing edge fringe, and the upper wing covering of the velvety down feathers, has been known and carefully documented by biologists, ornithologists, and aeronautical engineers. Many of the noise characteristics of an ''owl'' have similarities with airframe noise. By training owls to fly with the leading edge comb removed Kroeger *et al.* (1971) established that the leading edge comb was essential for stable flight at its high lift and low speed. However Kroeger's measurements showed that the ''owl'' had a broadband radiated noise spectrum indicating that the flow in the adverse pressure gradient on the rear upper surface was turbulent at the wing trailing edge. The present paper describes the effect of the trailing edge fringe and the down feathers on the noise spectrum generated by the owl and why the owl remains silent to its prey in spite of their excellent hearing above 2 kHz.

2:30

1pNSd2. Airbus airframe noise reduction—A European harmonized research effort. Werner Dobrzynski (DLR, Institut für Entwurfsaerodynamik, Abt. Technische Akustik, Lilienthalplatz 7, 38108 Braunschweig, Germany)

Very large aircraft—such as the planned Airbus A3XX—require correspondingly high lift forces and extended landing gear structures, thus causing potentially very high airframe noise levels during the landing approach. This problem was realized by the Airbus Consortium, and the first relevant research initiatives date back to the early 1990s. Soon after, initial research at DLR began under contract to Airbus Industrie, dedicated to landing gear airframe noise. Recognizing the general challenge of research for aircraft noise reduction at that time, a European Noise Reduction Initiative (ENRI) was proposed, dealing with both engine and airframe noise. Subsequent technical discussions, however, led to separate programs for engine and airframe noise research, the latter being initiated under the acronym RAIN (reduction of airframe and installation noise). RAIN encompasses analytical and experimental work to describe, predict, and reduce the noise both from landing gears and high lift devices. In parallel, national research programs began: In France wind tunnel and flyover experiments relate to the whole aircraft airframe noise characteristics, while corresponding research in Germany focuses on high lift devices noise. In Great Britain, noise modeling is performed for landing gear noise prediction. These national efforts are coordinated by the Airbus partner companies (3E-program).

3:00

1pNSd3. Directivity of flap side-edge noise as observed with a phased microphone array on landing aircraft. Ulf Michel and Weiyang Qiao[a] (DLR, Müller-Breslau-Str. 8, 10623 Berlin, Germany)

The sound emissions of a large number of aircraft landing at the airport of Frankfurt/Main, Germany, were studied with an 8- by 8-m phased microphone array consisting of 111 irregularly distributed microphones. The data reduction procedure takes account of the motion of the sound sources. The measurement procedure is described and results for the directivity of flap side-edge noise of various aircraft types are reported. Flap side-edge noise is an important airframe noise source on many aircraft and can be clearly identified with the phased array. The variation of this noise source between different aircraft types is considerable, which indicates a substantial noise reduction potential. [a] Permanent address: NW Polytechnical Univ., Xian, PROC.

3:30

1pNSd4. Simulation of acoustic scattering from a trailing edge. Bart A. Singer, Kenneth S. Brentner, David P. Lockard (NASA Langley Res. Ctr., Hampton, VA 23681-2199, b.a.singer@larc.nasa.gov), and Geoffrey M. Lilley (ICASE, Hampton, VA 23681-2199)

Unsteady two-dimensional flow calculations were performed about a thin NACA airfoil with a bluff-body vortex generator positioned at 98% chord. The bluff body produced unsteady vortex shedding, which simulated large coherent eddies in a boundary layer. The shed vortices interacted and occasionally paired as they convected past the sharp trailing edge of the airfoil. The CFD calculations clearly showed acoustic waves emanating from the airfoil trailing edge. The Ffowcs Williams and Hawkings equation [J. E. Ffowcs Williams and D. L. Hawkings, Philos. Trans. R. Soc. A **264**, 321–342 (1969)] was used to compute the acoustic field generated by the unsteady aerodynamic field. Directivity maps and Mach-number scalings have been obtained and compared with the theoretical predictions for trailing-edge noise. The noise below the airfoil displays characteristics typical of a sound field scattered from a sharp edge. The noise above the airfoil is more complicated; it contains significant contributions from both the scattered acoustic field and the bluff-body vortex generator. The effects of spanwise correlation length and the choice of integration surface will also be discussed.

Session 1pNSe

Noise: Jet Acoustics

Michael Fisher, Cochair
Institute of Sound and Vibration Research, The University, Southampton SO17 1BJ, UK

Philip J. Morris, Cochair
Department of Aerospace Engineering, Pennsylvania State University, 233P Hammond Building, University Park, Pennsylvania 16802, USA

Invited Papers

4:30

1pNSe1. The noise spectrum of isotropic turbulence. Geoffrey M. Lilley (ICASE, NASA Langley Res. Ctr., Hampton, VA 23681 and Dept. of Aeronautics and Astronautics, Univ. of Southampton SO17 1BJ, UK)

Proudman's solution for the noise radiated from isotropic turbulence at low Mach numbers and high Reynolds numbers was reviewed by Lilley (1994) following the simulation of Sarkar and Hussaini (1993). It was suggested (Lilley, 1996) that the Lighthill–Proudman theory could be used for the prediction of the radiated acoustic power from turbulent free shear flows in the absence of shock waves. In this approximation the Lighthill ''filter function'' was used with distributions of the turbulent kinetic energy, the temperature fluctuations, and the turbulent length scale. The results were compared with experimental measurements. But the method (Lilley, 1996) was only concerned with the total acoustic power. Modifications to this theory are required for the estimation of the spectrum and directivity of the radiated sound. The frequency resolution in time-dependent RANS calculation (TRANS) is limited by the grid used. In most, the large scale structure of the turbulence is resolved and consequently the energy containing scales captured. But the high-frequency part of the spectrum is poorly defined. Present work discusses two models for the high-frequency spectral decay and some of the properties of the high-frequency spectrum in turbulent shear layers.

5:00

1pNSe2. Jet noise of subsonic aircraft: An aeroengine manufacturer's perspective. A. J. Kempton (Installations Eng., Rolls-Royce plc, Derby, UK)

These papers trace the history of jet noise reduction from early pure jets to modern engines with high bypass ratios. Choice of engine cycle is important in reducing jet noise, but there is also the need to balance the requirements of cost, weight, and specific fuel consumption, in addition to minimizing other engine noise sources. Some techniques for reducing jet noise are illustrated. Forced mixers on long-cowl engines are effective in reducing low-frequency jet noise, but can cause an increase in high frequencies (especially in flight). For larger aircraft with more powerful engines, where the noise problem is most severe, installation issues dictate somewhat against long-cowl configurations. The current challenge is therefore to achieve similar noise reductions to forced mixers but on short-cowl engines. In the future, the requirement for further noise reductions might result in much more novel aeroplane and engine configurations. Jet noise experiments can easily give misleading results unless the facilities and rigs are designed to avoid contamination by excess noise and to provide correct simulation of boundary layers and other aerodynamic parameters (including flight simulation). Fortunately, testing at reduced scale is acceptable for noise. Advanced measurement techniques (like source location) can be very beneficial in aiding understanding.

5:30

1pNSe3. Industry perspective on jet noise—Prediction and reduction requirements. David H. Reed, T. R. S. Bhat, and W. T. Conley (Boeing Commercial Airplane Group, Seattle, WA)

Spectacular growth of airline passenger traffic, nearly tenfold since 1970, has been fueled by a steady trend toward lower cost airfares made possible by technological achievements in airframe and aircraft engine design. Of all the advancements in aircraft design, none has been more important than that of the high bypass ratio (HBPR) turbofan engine, first introduced in 1969 on the Boeing 747. Since then, HBPR turbomachinery noise technology has kept pace with other engine refinements, allowing newer aircraft to meet increasingly stringent community noise requirements. Even more advanced turbomachinery and nacelle noise technology is now at hand as a result of government/industry efforts in both Europe and the United States. Engines with substantially lower fan noise will be introduced. Jet noise will remain the major obstacle to further noise reduction. Since the majority of new commercial aircraft over the next 20 years will be powered by HBPR engines, research in jet noise must be a major priority. This paper examines

the needs for jet noise reduction across the range of commercial aircraft types, and suggests technology development efforts including CFD tools for jet characterization, active flow control, installation effects, and novel suppression devices. This paper also discusses challenges in jet noise technology for supersonic airliners.

Contributed Paper

6:00

1pNSe4. Intensive narrow-band noise of oscillating circular gas jet. Andrew G. Semenov and V. Andrew Rimsky-Korsakov (N. N. Andreev Acoust. Inst., Russian Acad. of Sci., 4 Shvernik St., 117036 Moscow, Russia, bvp@acoins.msk.ru)

Self-sustained oscillations of a jet issuing from a circular nozzle in an impedance plane into unbounded space or interacting with various obstacles, such as a parallel plane or a coaxial rigid circle, are analyzed. In the problem statement region of the circular jet inner boundary, alternative deflection during self-interaction or interaction with obstacles is considered as an axisymmetric monopole (volume) source of axial sound waves inside the jet cylinder directed to the jet root. By means of the corresponding 1-D boundary value problem solution, Nyquist stability criteria are derived for oscillations inside the cylindrical volume bounded by jet boundaries. Conditions favorable for jet boundary axially symmetric self-sustained oscillations excitation are found and their relations to the problem basic parameters are predicted, both for subsonic and supersonic jet cases. The proposed method could be used in various practical jet-obstacle interaction noise-generation problem analyses.

MONDAY AFTERNOON, 15 MARCH 1999 ROOM MA043, 2:20 TO 5:40 P.M.

Session 1pPAa

Physical Acoustics: Scattering

Richard Stern, Cochair
Applied Research Laboratory, Pennsylvania State University, P.O. Box 30, State College, Pennsylvania 16801

Adriano Alippi, Cochair
Department of Energetics, University of Rome, ''La Sapienza,'' via Scarpa 14, 00161 Rome, Italy

Contributed Papers

2:20

1pPAa1. Studies of scattering from differently shaped objects using the TLM technique. Ulf Kristiansen (Acoust., Dept. of Telecommunication, Norwegian Univ. of Sci. and Technol., O. S. Bragstads plass 2B N-7034 Norway) and Nicolas Brachet (ESM2, Technopole de Chateau-Gombert, 13451 Marseille, France)

The transfer line method (TLM) can be regarded as a discretized version of Huygen's principle. Wave energy propagates along a system of lines connecting regularly spaced node points. An energy packet reaching a node along a certain line will at the next time step be split up and reradiated into all the lines connected to that node. Wave propagation is therefore regarded as a discretized process in space and time with local updating rules. Special rules are applied for reflecting, absorbing, and partially absorbing surfaces. The method has been used for some time in electromagnetic wave propagation, but not so much in acoustic studies. The present study is a 2-D investigation of the scattering of sound pulses from objects having different shapes: circular, triangular, and rectangular. Performing this in the time domain allows the following of the scattering process in detail.

2:40

1pPAa2. Space-wave number representation of transient waves. Experimental determination of the space location origin of Lamb waves on cylindrical shells. Loic Martinez, Jean Duclos, and Alain Tinel (LAUE UPRESA CNRS 6068, BP 4006, Pl. R. Schuman, 76610 Le Havre, France, loic.martinez@lemel.fr)

A new space-frequency-wave number representation is introduced. This representation is obtained by space-sliding window FFT of the space-frequency representation. This new method is used to experimentally define the space origin of the pulse-generated Lamb wave on an air-filled cylindrical shell immersed in water (relative thickness is equal to 0.03). The space-wave number slices also allow the measurement of the Lamb-wave complex wave numbers and their propagation direction (reduced frequencies range from 20 to 1000). The reflected field is experimentally separated from multiple propagating Lamb waves. This efficient method is complementary to the surface wave analysis method (S.W.A.M.) [Martinez *et al.*, 16th ICA and 135th ASA Congress, II, 1359–1360 (1998)]. In particular, the space-wave number representations are not limited by space windowing. The experimental results confirm the theoretical computations performed on waves propagating on a plane plate.

3:00

1pPAa3. Scattering by cylindrical shells: The Scholte–Stoneley wave nature. Naum Veksler, Jean-Louis Izbicki, and Jean-Marc Conoir (LAUE, CNRS UPRESA 6068, Pl. R. Schuman, 76610 Le Havre, France)

A systematic study of the A wave revolving around circular cylindrical elastic shells immersed in water is performed. The resonance frequencies and halfwidths have been computed for a wide range of the b/a ratio (b is the inner radius and a the outer one). The A-wave evolution is studied from the case of the quasisolid cylinder to the case of the very thin shell (b/a equal to 0.99). The resonances are computed from the complex frequency plane; it is then possible to get the dispersion curves of the A wave. The phase velocities dispersion curves, plotted against the adimensional variable ktd (kt is the shear wave number and d the thickness of the shell), practically coincide in the low-frequency range. The resonance halfwidths are small in this frequency range. The A wave is a bending type wave. At higher frequencies, the A wave becomes analogous to a diffracted Franz wave.

3:20

1pPAa4. Sound scattering by Gauss beam from cylindrical objects. I. L. Oboznenko, E. I. Oboznenko (Dept. of Electron., NTUU Kiev Polytech. Inst., Kiev 252056, Ukraine), and Vladimir I. Genis (Drexel Univ., Philadelphia, PA 19104)

Practically, when diagnosing vessels by focusing array, the vessel is radiated not by the plane wave, but a time-limited beam. Here one can see the results of theoretical and experimental research of Gauss beam sound scattering from cylindrical objects with wave resistance different from the medium. Well-known results of sound scattering on cylinders with limited sizes are wrong in reality, because of limiting the vertical size of the cylinder. In fact, all the objects, including the cylinder, are radiated by a nonconcentrated beam, like a Gauss beam. Theoretical and experimental results of Gauss beam scattering in the band of parameter $\alpha = a/w$ (where a-cylinder radius; w-Gauss beam width on e^{-1} range) from 10^{-6} (quasi-plane wave) to 100 (super-narrow beam) show, that a scattered wave spectrum changes very substantially. This point needs caution, and immediately changes classic results for the plane wave. Also, the sound beam echo-signal spectrum in the reverse direction gives one the ability to classify and to differ objects as ''more soft'' or ''more hard'' with respect to medium (for wave resistance it differs up to 5%–10% from medium). This permits the classification of cylindrical foreign inclusions or defects of little vessels like post-, precapillaries.

3:40–4:00 Break

4:00

1pPAa5. Scattering from cylindrical structures with various end-cap shapes. Angie Sarkissian and Louis R. Dragonette (Naval Res. Lab., Code 7132, Washington, DC 20375-5350, angie@aqua.nrl.navy.mil)

The scattered field from a cylindrical structure near the forward direction is computed using the Kirchhoff approximation of scattering from a screen. The effects of varying the shape of the end-caps are examined by carrying out target strength computations for various shapes. The cylindrical region is modeled to be impenetrable while the effects of varying the reflectivity of the end-cap regions are examined. [Work supported by ONR.]

4:20

1pPAa6. Complex poles of Lamb waves propagating along anisotropic and absorbing fluid-loaded plates. Marc Deschamps and Olivier Poncelet (Laboratoire Mecanique Physique, Univ. Bordeaux 1, 351 Cours de la Liberation, 33405 Talence Cedex, France)

This work presents theoretical and experimental investigations on Lamb wave generation along anisotropic immersed plates. The structure of these guided waves is strongly dependent on the nature of the source (transient source, bounded beam . . .). An incident plane wave for which the signal is time-limited is considered, and leads to transient Lamb waves mathematically defined by complex frequencies. These frequencies are the poles of the reflection/transmission coefficients of the fluid-loaded plates. This point of view, recently developed for isotropic plates, is completely different from the classic approach in terms of leaky Lamb waves, which are harmonic waves. New interesting results are then obtained for the NDT of thin anisotropic plates: the dispersion curves calculated for complex frequencies are very different from those calculated for real frequencies (harmonic waves). Moreover, some modes have a negative imaginary part of the frequency that implies transient phenomena increasing with time. The waveforms of the reflected signals are obtained and explained by the calculation of a contour integral in the complex frequency plane. The roles of anisotropy and absorbing effects are discussed.

4:40

1pPAa7. Experimental determination of the angular width of plate modes. Guy Durinck, Willy Thys (IRC, Katholieke Univ. Leuven, Campus Kortrijk, B-8500 Kortrijk, Belgium), Pascal Rembert, and Jean-Louis Izbicki (Univ. du Havre, 76610 Le Havre, France)

The reflection and transmission coefficient of a plate can be expressed as a function of frequency at fixed angle of incidence or as a function of angle of incidence at fixed frequency. In the first situation, the transmission coefficient can be considered as a superposition of frequency resonances, while in the latter case it can be considered as a superposition of angular resonances [R. Fiorito, W. Madigosky, and H. Uberall, J. Acoust. Soc. Am. **66**, 1857–1866 (1979)]. Using this approximation the properties of frequency resonances of a plate can be determined experimentally [Derible *et al.*, Ultrasonics International 93 Conf. Proc. 483–486 (1993)]. In this work, this approximation is used to determine the properties of the angular resonances. The transmission coefficient as a function of frequency is determined for a large set of angles of incidence by insonifying the plate with an ultrasonic pulse. Then, at fixed frequency, the data are plotted as a function of angle of incidence. The properties of the angular resonances are extracted using the Argand representation of the transmission coefficient. A comparison with theoretical values is made.

5:00

1pPAa8. Wedge diffraction analyzed by localized response function of the boundary value problem. Mitsuhiro Ueda (Tokyo Inst. of Technol., Dept. of IDE, O-okayama, Meguro-ku, Tokyo, 152-8552 Japan, ueda@ide.titech.ac.jp)

A new diffraction principle called virtual discontinuity principle of diffraction, abbreviated by VDPD, which is formulated by considering the wave propagation in a space seen by an observer virtually, has been proposed by this group. The boundary value problem is formulated using VDPD and the Green's theorem. Then it becomes clear that the response function, which shows mutual dependence of the potential on the surface of the object, is composed of two components. One of them is localized near the edges of the object that can be seen by the observer. The other is not localized, just like the response function used in the BEM formulation of the boundary value problem. The observer in the free space can always see the edge of a wedge. Thus the boundary value problem for the wedge diffraction can be formulated using the localized response function only. As a result of the localization near the edge, sampling points of the potential can be limited near the edge. Thus in spite of the infinite size of the wedge, the numerical procedure to solve the problem is simplified remarkably.

5:20

1pPAa9. Modal scattering from orifices. Jane L. Horner, Björn A. T. Petersson (Dept. of Aeronautical and Automotive Eng., Loughborough Univ., Loughborough LE11 3TU, UK, j.l.horner@lboro.ac.uk.), and Richard Lyons (Loughborough Univ., Loughborough LE11 3TU, UK)

When considering a sound wave traveling through a circular orifice in a rigid baffle, both the reflected and scattered field have to be established on the incident side of the orifice. Previous investigations have used Hankel transforms to establish the amplitudes of these two waves. This study concentrates on the coupling of the modes in the scattered and reflected fields, with the object of the investigation being to determine if a modal approach may be taken to describe the reflected sound fields from such an orifice. Results are shown in the form of the modal contributions to the integrand which must be used to obtain the scattered field.

Session 1pPAb

Physical Acoustics: Ultrasonic Non-Destructive Evaluation and Time Reversal Techniques

R. Glynn Holt, Cochair
Department of Aerospace and Mechanical Engineering, Boston University, Boston, Massachusetts 02215, USA

Walter Arnold, Cochair
Fraunhofer Institute for Nondestructive Testing, University, Building 37, D-66123, Saarbrücken, Germany

Contributed Papers

2:00

1pPAb1. Reflection coefficient of a Stonely–Scholte wave: An experimental investigation. Edouard Mouton and Manell E. Zakharia (CPE Lyon, LASSSO (LISA, EP92 CNRS), 43 Bd. du 11 Novembre 1918, BP 2077, Bat. 308, F 69616, Villeurbanne Cedex, France)

The Stoneley–Scholte waves are becoming more and more popular in both sediment characterization and nondestructive testing (computation of material and sediment properties, flaw or obstacle detection). When dealing with a 3-D obstacle, the coupling of these evanescent waves with the elastic waves in the target and the continuity conditions may have several definitions. In theoretical papers, some authors choose to impose the continuity of each component of the wave, some others the continuity of the sum vector. A specific tank experiment has been designed and conducted. Its specific goal is to define the continuity conditions that have to be used in future works. A special-purpose mock-up has been built up that contains two different blocks molded in an epoxy resin. One block is ''mechanically hard'' (duraluminum) and the other one is more ''soft'' (PVC). The geometry of both blocks has been especially optimized in order to enhance the reflection and refraction phenomena. For each material, two interfaces were considered: a perpendicular one and sloping one (wih respect to the direction of propagation of surface waves). Frequency range is centered around 100 kHz with an investigation thickness of a few centimeters.

2:20

1pPAb2. Characterization of bonding quality of composites with the nonlinear modulation method. Dimitri Donskoy, Alexander Ekimov, and Alexander Sutin (Stevens Inst. of Technol., 711 Hudson St., Hoboken, NJ 07030)

The nonlinear ultrasonic nondestructive testing technique is emerging as a valuable tool for material characterization and diagnostics. The most widely used nonlinear method is based on measurements of harmonic distortion of the probing ultrasonic wave. Another approach, developed by the authors, utilizes effect of modulation of ultrasound by low-frequency vibration. This method is more sensitive to various material and structural flaws, such as cracks, debonding, delamination, etc. It is also much easier to implement in practice. The present work focuses on characterization of bonding quality of composite plates used in the aerospace industry. The test was performed on 14 samples with various (known) degrees of bonding. The ultrasonic frequencies in the range of 50 kHz to 1.5 MHz were examined to determine the most sensitive frequencies. The modulating vibrations were in much lower frequency range up to 1 kHz. It was found that the average (across the frequency range) normalized modulation level is proportional to the bonding quality and can be used for its quantitative assessment.

2:40

1pPAb3. Sound scattering and transmission through cylindrical layer with concentrated defects. Vladimir I. Genis (School of Biomed., Eng., Sci. and Health Systems, Drexel Univ., Philadelphia, PA 19104) and Elena I. Oboznenko (NTUU Kiev Polytech. Inst., Kiev 252056, Ukraine)

An experimental method of defect detection in a cylindrical shell is proposed. Defects are the cylindrical hollows (the projections) on the outside or the inside of the shell, filled up, and encircled by water. The defect diameter makes up 1–2 mm (0–0,95) h long, where h—is a shell thickness. The inverse sound scattering field and pass wave field on the shell axis were measured in the sound acoustic beam. Experimental investigations were compared with theoretical investigations by changing the shell wave dimension in the 2–20 range (the 3-D resilience theory). The presence of the shell resonance clears surges and its inside liquid pillar as lengthening of the defect gradually results in their being illegible. The long defects reduce discrimination of the resonance system shell water. The through defect and the Helmholtz resonator are similar. The measurement results of the shells with defects and without were compared, when the shell was radiated by narrow sound beam (the beam width 10–15 times as much as the defect diameter). The theoretical calculation and experimental measurements of the nondefective shell are practically identical. The proposed method serves for defect presence (or absence) definition in pipelines, blood vessels, and others.

3:00

1pPAb4. Modeling of ultrasonic wave interaction with alumine and silica inclusions in steel. Noelle Mercier (LG2mS Acoustique, Univ. de Compiegne, BP 20529, Compiegne, France, Noelle.Mercier@utc.fr) and Nazir Chebbo (Univ. Libanaise, IUT de Saida, BP 813, Saida, Liban)

To progress in the characterization or discrimination of flaws in ultrasonic nondestructive testing, it is essential to have a good knowledge of the interaction of incident ultrasonic waves with these flaws and to model the echographic signals. The flaws considered here are of volumetric type. They have been simulated, in 2-D geometry, by circular cylinder forms. The developed model calculates the stemming time signal of the longitudinal or transverse wave diffused by a cylinder made of a fluid medium, an empty cavity, an elastic, or a rigid solid. The used method is based on the usual modal theory. The time signal is obtained by the Fourier transform of the multiplied monochromatic components, for each frequency, by the spectral response of the transducer. The presented results concern the case of two elastic media which simulate inclusions in steel. The convergence of the modal series, for a quite small flaw, is relatively rapid even for high frequencies. A comparison is presented between experimental and numerical results obtained in retrodiffusion, using a transducer of 10-MHz nominal frequency, for alumine and silica inclusions of about 300 μm. Whereas the beam aspect is not taken into account, the wave curves are similar.

3:20

1pPAb5. Depth profiling of residual stress in steel by laser ultrasonics. Weimin Gao, Silvio Elton, X. Kruger,[a] Christ Glorieux, Kris Van de Rostyne, Walter Lauriks, Jan Thoen, and Jacques Charlier[a] (Laboratorium voor Akoestiek en Thermische Fysica, Katholieke Universiteit Leuven, Belgium)

Depth profiling of residual stress in steel is of great interest in many practical applications. Conventional techniques are either destructive (x-ray diffraction and hole drilling) or with obvious restriction (Barkhausen noise). This paper presents a noncontact and nondestructive laser ultrasonics method for determining the depth profile of the residual stress layer in steel samples. It is known that surface acoustic waves penetrate into solids to a depth proportional to the wavelength. They are expected to be dispersive in the presence of gradients in physical properties such as residual stress. Based on the dispersion theory, the depth dependence of an effective velocity $v(z)$, which is related to the stress profile $S(z)$, can be fitted from the frequency dependence of the phase velocity $v(w)$. Due to the advantage of wide bandwidth, laser-generated and -detected surface acoustic waves (SAW) offer a promising nondestructive stress depth profiling method. The profiles obtained by SAW are compared with the stress data obtained by other techniques. [a] Also at Service de Métallurgie Physique, Université Libre de Bruxelles, Belgique.

3:40–4:00 Break

4:00

1pPAb6. Measurements of pulsed velocity field generated by circular and rectangular piezoelectric transducers directly coupled to a block of aluminum. N. Ouarradi and B. Piwakowski (Ecole Centrale de Lille, P.B. 48, Villeneuve d'Ascq 59650, France)

A new computational tool Discrete Representation Acoustic Modelling/Solid (DREAM/S), has been developed for computing the displacement field generated by a pulse-excited transducer, directly coupled to an elastic half-space. It allows the separate determination of different components (shear, compressional, radial, axial) of displacement. This method is based on the spatial pulse response approach and gives directly the transient time-domain field. DREAM/S has already been validated mathematically in regard to analytic and exact methods. The main objective of this paper is to show the experiments performed in order to validate this software. First, a brief presentation of DREAM/S and elementary examples of computing are given. Afterward, the experimental results obtained in the case of circular and rectangular transducers directly coupled to a block of aluminum are presented and compared with the ones obtained by DREAM/S. This comparison displays a good agreement and confirms the high precision of this approach. In order to facilitate the interpretation of multichannel records, including the direct and edge waves and the reverberations from the borders of the model, both computed and recorded signals are displayed in specific format, usually applied in the geophysical imaging.

4:20

1pPAb7. Quality assessment of adherent and fusion-welded joints in silicon wafers by nonlinear ultrasound. A. Wegner, A. Koka, S. Hirsekorn, and W. Arnold (Fraunhofer-IZFP, Univ., Bldg. 37, D-66123 Saarbruecken, Germany, wegner@izfp.fhg.de)

The interest in fusion-welded silicon wafers has increased recently because of their excellent electrical and mechanical properties. Typical applications are in acceleration and pressure sensors. The interface of room temperature bonded wafers contains a physically adsorbed water layer. Bond temperatures higher than 373 K cause a reduction of the adsorbed water by diffusion and thus an increase in bond strength. If electronical components are protected by surrounding silicon wafers, the joining temperature must not be higher than 673 K. The bond strength of the interface essentially defines the reliability of the components. Therefore, a nondestructive method to evaluate the bond quality is required. Binding forces are nonlinear and cause a nonlinear modulation of transmitted or reflected ultrasonic waves. Inhomogeneities in bond strength of an interface can be imaged by the local ultrasonic amplitudes of the insonified frequency and of its higher harmonics measured interferometrically in transmission. A quantitative evaluation of the image data yields information about the variations in bond strength and the size of delaminations and of weakly bonded areas. This paper presents experimental and theoretical investigations of the interface of bonded silicon wafers exploiting the nonlinear transmission of ultrasound. The data are compared to destructive tests.

4:40

1pPAb8. Ultrasonic weld testing using the laser vibrometer detection of a time-reversed A wave. Bruno Morvan, Alain Tinel, and Jean Duclos (L.A.U.E, Univ. du Havre, Pl. R. Schuman, BP 4006, 76610 Le Havre, France, morvan@iut.univ-lehavre.fr)

This study presents a method of weld inspection by a surface wave called A wave. The A wave propagates without attenuation in an immersed plane plate, so it is suitable for a long-range inspection of large structures. The studied structure consists of a brass plate perpendicularly soldered on to another one. For convenience, the welding is discontinuous and a nonsoldered zone is chosen as reference. The A wave is very dispersive, so a time-reversed method is used to temporally focus it on the weld: this improves the signal-to-noise ratio. An immersed transducer transmits a reversed A-wave signal. A laser vibrometer collects, at several locations along a line parallel to the weld, the incident A-wave signal and its reflection on the weld. At each position, owing to the A-wave time-reversal excitation, the two detected signals have the same duration. The correlation of the two signals allows one to determine the time delay between the incident and the reflected signal. Once the group velocity is known, the topography of the weld can be built and the defects localized.

5:00

1pPAb9. One-bit time reversal through high-order multiple scattering media. Arnaud Derode, Arnaud Tourin, and Mathias Fink (Laboratoire Ondes et Acoustique ESPCI—Universite Denis Diderot Paris VII 10, rue Vauquelin 75231 Paris Cedex 05, France, arnaud.derode@espci.fr)

A time-reversal mirror (TRM) is an adaptative device that can focus an ultrasonic wave through an inhomogeneous medium. In a typical experiment, a pointlike source transmits a pulse that propagates through the medium. The distorted wavefronts are recorded by a 128-tranducer array. The 128 signals are digitized over 8 bits, stored in a memory, time reversed, and retransmitted by the array through the medium: the resulting wave converges onto the source, despite the inhomogeneities. In the presence of high-order multiple scattering, the TRM still works and takes advantage of it to refocus a pulse with a finer spatial resolution than in a homogeneous medium. Moreover, it is shown that the TRM is still able to focus a wave even if the recorded scattered wave is encoded over 1 bit, only its sign being used. Reducing the number from 8 bits to 1 does not appear to change the lateral resolution; the signal-to-noise ratio is a little higher. Thus the 1-bit TRM appears to be a very robust and low-cost focusing device. Experiments were carried out in a water tank through a random collection of 2400 parallel steel rods.

5:20

1pPAb10. Characterization of time-reversed elastic waves in ergodic billiards. Julien de Rosny, Carsten Draeger, and Mathias Fink (Lab. Ondes et Acoust., Univ. Paris 7, URA CNRS 1503, ESPCI, 10 rue Vauquelin, 75231 Paris Cedex 05, France, julien.derosny@espci.fr)

One year ago, this laboratory showed experimentally and numerically that an elastic wave can be time reversed in a highly reflecting cavity with a single pointlike source [Draeger and Fink, J. Acoust. Soc. Am. **101**, 3090(A) (1997)]. This is possible because the cavity is low dissipative and its shape is ergodic. Now the properties of this experiment are better understood. Clearly, two parameters are involved. The first one (T) is the beginning of the time reversal window; the second one is its duration ΔT. The lowest value of T which gives an isotropic focusing is the ''angular mixing time;'' it may be related to the ergodicity time. There is another characteristic time: beyond a certain limit, increasing ΔT does not im-

prove the quality of focusing any longer. This ''saturation time'' is very dependent on the initial pulse length; it is analogous to the Heisenberg time. Also, the difference beteween the perfect theoretical time reversal and the experimental one is explained.

5:40

1pPAb11. Backscattering time-reversal of acoustic waves in random media. Arnaud Tourin, Arnaud Derode, and Mathias Fink (Lab. Ondes et Acoust. Univ. Paris VII-ESPCI 10 rue Vauquelin, 75005 Paris, France)

Three years ago, the first experiments showing the reversibility of acoustic waves propagating through high-order multiple scattering media were reported [A. Derode, P. Roux, and M. Fink, Phys. Rev. Lett. **75**, 4206 (1995)]. These experiments were performed in a transmission mode by means of a time reversal mirror (TRM). Here, new time-dependent experimental results obtained in a backscattering mode are reported. The experiment can be described as follows: the TRM used is a linear array of 128 transducers. One of the elements transmits a pulsed wave into the sample which is a random set of 2400 steel rods. In the 128 recorded backscattered signals, short windows are selected which are time-reversed and retransmitted. Surprisingly, it is found that the synthesized time-reversed waves revive their past and converge onto the initial emitting element, despite disorder. Thus the image of the source is recreated, what is referred to as the mirror effect. The spatial refocusing is found to be improved when selecting windows farther and farther in the backscattered signals. The refocused spot time-evolution is well explained by a simple model including both single and multiple scattering contributions.

Contributed Poster

This poster will be on display in the Poster Gallery from Monday to Wednesday, 15–17 March. Author will be at the poster from 10:00 a.m. to 12:00 noon on Tuesday, 16 March.

1pPAb12. A correlation-measuring system for ultrasonic NDT using maximum length sequences. Torsten Niederdraenk (SIEMENS Audiologische Technik GmbH, D-91050 Erlangen, Germany) and Rainer Thaden (Institut fuer Technische Akustik, RWTH Aachen, D-52056 Aachen, Germany)

In the field of nondestructive material testing (NDT), the advantages of a correlation-measuring technique can be used. In particular, the better dynamic range and gain in the signal-to-noise ratio provide a good possibility of investigating strongly scattering or absorbing materials. The application of maximum length sequences as excitation signals permits the performing of the correlation procedure by using the Fast Hadamard transform (FHT), a very fast correlation algorithm. In nondestructive material testing, a number of special requirements has to be fulfilled. Apart from the driving conditions of the piezoelectric transducers, measurements in NDT often require high measuring frequencies. Based on former developments, a measuring system has been developed that provides a high testing rate; even when using MLS signals of order $n=16$, a rate of 20 Hz is obtained. A partially parallel calculation structure of the FHT gives a vivid looking presentation of the measuring results.

MONDAY AFTERNOON, 15 MARCH 1999 ROOM MA041, 2:00 TO 6:00 P.M.

Session 1pPAc

Physical Acoustics: Nonlinear Acoustics

Lawrence A. Crum, Chair
Applied Physics Laboratory, University of Washington, 1013 N.E. 40th Street, Seattle, Washington 98105, USA

Contributed Papers

2:00

1pPAc1. Higher order effects in finite-amplitude sound fields. Sigve Tjøtta (Dept. of Math., Univ. of Bergen, Johs. Brunsgt. 12, 5007 Bergen, Norway and Dept. of Phys. Univ. of Oslo, P.O. Box 1048 Blindern, NO316 Oslo, Norway)

Nonlinear effects associated with intense sound fields in fluids are considered theoretically. Special attention is directed to the study of higher-order effects that cannot be described within the standard propagation models of nonlinear acoustics (the KZK and Burgers equations). The analysis is based on the fundamental equations of motion for a homogeneous, thermoviscous fluid, for which thermal equations of state exist. Model equations are derived and used to analyze nonlinear sources for generation of flow and heat, and other changes in the ambient state of the fluid. Fluctuations in the coefficients of viscosity and thermal conductivity caused by the sound field are accounted for. Also considered are nonlinear effects induced in the fluid by surface waves in the transducer. The intensity and absorption of finite-amplitude sound waves are calculated, and related to the sources for generation of higher-order effects.

2:20

1pPAc2. Modeling and simulating finite-amplitude propagation through time-varying inhomogeneous absorbing media. Ibrahim M. Hallaj (Appl. Phys. Lab, Univ. of Washington, 1013 NE 40th St., Seattle, WA 98105, ibrahim@apl.washington.edu), Robin O. Cleveland (Boston Univ., Boston, MA 02215), and Steven G. Kargl (Univ. of Washington, Seattle, WA 98105)

A model equation is derived for three-dimensional wave propagation through an inhomogeneous, time-varying medium. The model equation accounts for arbitrary inhomogeneities, finite-amplitude distortion, and absorption. The effect of time dependence of the background medium parameters is included in the equation. An ordering scheme based on the characteristic time of the evolution of each parameter allows one to evaluate their relative importance. A two-dimensional version of the wave equation is solved in the time-domain using finite-difference methods. Explicit, implicit, and operator splitting techniques were used in the solution to overcome numerical instabilities. Results from the code are compared to known solutions for some simple geometries in homogeneous and

step indexed media. Various modeling and numerical schemes for treating the absorption on the computational domain interior and at the boundaries of the domain will be presented. [Work supported by ONR and DARPA.]

2:40

1pPAc3. Second-harmonic component in the focused beam transmitted through a weakly dispersive liquid layer. Shigemi Saito (Faculty of Marine Sci. and Technol., Tokai Univ., 3-20-1 Orido, Shimizu, Shizuoka, 424-8610 Japan, ssaito@scc.u-tokai.ac.jp)

The characteristic of the nonlinearly generated second-harmonic component in the focused beam which transmits through a layer consisting of weakly dispersive liquid is theoretically and experimentally investigated. In a focused beam, a destructive interference takes place, within the post focal region, between two portions of second-harmonic components which are generated in the pre- and post-focal regions. This is due to the phase delay of the second-harmonic component passing through the focal region relative to the fundamental component. When a weakly dispersive layer is inserted into the focal region, a phase advance occurs for the second-harmonic component passing through the layer due to slightly higher sound-speed for second-harmonic frequency, together with the phase delay due to diffraction. Then the effect of the destructive interference is degraded to result in amplitude increase of the second-harmonic component within the post-focal region. The experiment for a layer of water–oil mixture employed as a dispersive liquid is compared with the nondispersive case and demonstrates the validity of theoretical prediction.

3:00

1pPAc4. Investigation of nonlinear wave distortion in a focal and post-focal region in water. Grazyna Grelowska, Eugeniusz Kozaczka (Naval Acad., ul. Smidowicza 71, 81-919 Gdynia, Poland), and Grazyna Lypacewicz (Polish Acad. of Sci., 00-049 Warsaw, Poland)

The subject of interest is sources of finite amplitude. Focusing sources belonging to both of the two main differentiated groups of such sources have been examined. The first one consists of sources with additional lens, and the second one of the single-element PZT sources. Previous investigations concerned mainly phenomena occurring close to the source—in a prefocal and a focal region. The phenomena appearing at the longer distances in the post-focal region, where the nonlinear wave distortion is obviously considerably greater than in a pre-focal region, is the main topic of this paper. Experiments are conducted in measurements of spatial pressure distribution in a beam radiated by: (1) a single PZT element focused source with a fundamental frequency of 1.5 MHz, (2) a PZT plane circular source coupled with the plano-concave lens with a frequency of 1.0 MHz. A PVdF hydrophone with diameter of 1 mm was used as a pressure probe. The results of the experiments are compared to the theoretically predicted ones. The sound field was modeled by the KZK equation with the equivalent boundary condition adequate to the actual boundary condition.

3:20

1pPAc5. The decay of pulses with complex structure according to Burgers' equation. Sergey N. Gurbatov, Galina Pasmanik (Dept. of Radiophys., Nizhny Novgorod State Univ., Nizhny Novgorod 603600, Russia), and Bengt O. Enflo (KTH, S-10044 Stockholm, Sweden)

Nonlinear plane acoustic waves propagating through a fluid are studied using Burgers' equation in the two cases: small viscosity and viscosity tending to zero. The evolution of initial pulses with monochromatic and noise carrier is considered. The initial pulses are characterized by two length scales. The length scale for substantial changes of the modulation function is much greater than the corresponding scale of the carrier. Some simple pulses with only one length scale are also studied, since their properties are important for the studies of pulses with two scales. With increasing time, the initial pulses are deformed and shocks appear. The shocks then merge, and finally a finite pulse ends up with an N wave and a periodic signal with a sawtooth wave. The decrease of the energy of the wave with time is investigated for pulses with both monochromatic and noise carrier and for vanishing and finite but small viscosity. How the characteristics of the final waves depend on the characteristics of the initial waves is also investigated. Both numerical and analytical methods are used.

3:40

1pPAc6. Investigation of the process of self-demodulation of acoustic waves in the river sand. Veniamin E. Nazarov, Vladimir Yu. Zaitsev (Inst. of Appl. Phys., Russian Acad. of Sci., 46 Uljanov St., 603600 Nizhny Novgorod, Russia), and Andrey B. Kolpakov (Inst. of Civil Architecture, 603600 Nizhny Novgorod, Russia)

Experimental investigation and theoretical description of nonlinear self-demodulation of a pulsed high-frequency acoustic wave and propagation of the secondary low-frequency acoustic pulses in dry and water-saturated sand are carried out. The dependence of the propagation time of the video pulses upon the initial static pressure and the relation of the duration and the form of the secondary pulses with the form of the envelope of the initial high-frequency wave were studied. In order to describe the observed dependences, nonlinear equations of state for the considered grain media were suggested. Using the equations, analytical expressions for the demodulated pulse forms were derived. On the basis of matching the theoretical predictions and experimental data, linear and nonlinear acoustic parameters of the sand are determined. The obtained results may be applied to analysis of seismic signals and used for development of seismoacoustic sensing methods, primarily for diagnostic applications of nonlinear effects.

4:00–4:20 Break

4:20

1pPAc7. Effects of micro bubbles vibration for increase of acoustic streaming. Shinichi Sakamoto and Yoshiaki Watanabe (Dept. of Electron., Doshisha Univ., Kyotanabe, Kyoto 610-0321, Japan, tr0141@mail4.doshisha.ac.jp)

The effects of the existence of micro bubbles in water for the increasing of acoustic streaming velocity are experimentally discussed. Velocity of acoustic streaming is observed on the sound axis by LDV (laser Doppler velocimeter). Acoustic streaming is generated by continuous ultrasonic sound transmitted by some PZT transducers whose diameter is 15 mm and resonant frequencies are 2.98 or 3.46 MHz. Sound pressures of ultrasonic sound are set to 80, 160, and 240 kPa at the last peak position on the sound axis. Micro bubbles are generated by extracting water with a syringe mechanism, decreasing the pressure of water down to 6.4% below static pressure. Average radius of micro bubbles is approximately 220 μm. The experimental results clearly show the velocity of acoustic streaming increases; the velocity increases from 9 to 13.5 mm/s when the micro bubbles exist. The harmonics are observed when the micro bubbles are generated. The mechanism for the increase of acoustic streaming is discussed from the point of view of the nonlinear effect of the bubble vibration.

4:40

1pPAc8. Anomalously high elastic nonlinearity and frequency-independent Q-factor as complementary properties of microinhomogeneous solids. Vladimir Zaitsev[a)] (Katholieke Univ., Leuven, Belgium)

During the last few decades, a wide class of media demonstrating anomalously high elastic nonlinearity was experimentally revealed (e.g., rocks, grainy materials, concretes). Their nonlinear parameters often exceeded those of homogeneous liquids and solids by several orders of magnitude, whereas linear elastic properties remained ''normal.'' Just the same, materials often possess an almost frequency-independent Q-factor, which also is quite different from homogeneous liquids. These acoustical peculiarities may be evidently attributed to the influence of structural microinhomogeneities (e.g., cracks, grains, etc.) typical of the mentioned media. Recently, a few physical models describing nonlinearity of grainy

and crack-containing materials were proposed, while the description of the dissipation (almost frequency-independent Q-factor) still is restricted to phenomenological models. The report presents a rather demonstrative model of microinhomogeneous solids, which allows for explanation of the mentioned facts. It follows naturally that the microinhomogeneities may not cause significant change of linear elasticity, whereas a sharp increase of elastic nonlinearity and occurrence of the frequency-independent Q-factor appear to be complementary manifestations of the same microstructure. The model readily allows one to relate medium structural features with its elastic and dissipative properties. [Work supported partially by RFBR and Academic Board of KUL.] [a] Permanent address: Inst. of Appl. Phys. RAS, 46 Uljanova St., Nizhny Novgorod, 603600, Russia.

5:00

1pPAc9. Dissipation in solids: Thermal oscillations of atoms. Adnan Akay and Cem Celik (Carnegie Mellon Univ., Pittsburgh, PA 15213)

Dissipation in a solid is related to the increase in the average kinetic energy of its atoms as a result of external excitation. This paper investigates the relationship between vibration field of a nonlinear lattice of atoms and its energy absorption properties. Numerical results show that a nonlinear lattice accepts energy when excited within its resonance bands. The width of the resonance bands increases with increased nonlinearity, eventually leading to their overlap.

5:20

1pPAc10. ''Acoustical modeling'' according to the theory of the common networks—Taking into account nonlinear effects. Joern Huebelt and Ennes Sarradj (TU Dresden, Inst. fuer Technische Akustik, Mommsenstr. 13, 01062 Dresden, Germany)

One method to model the electroacoustical transducer consists of describing its basic system components using lumped elements according to the theory of the common networks. In the past this technique has been widely used. However, the validity of the underlying simplifications has to be proofed in particular cases. The modeling of the acoustic behavior of a signal horn shall demonstrate the efficiency of this method. In a first step, a linear model in the frequency domain was established. It turned out that for a more exact simulation, the consideration of nonlinear effects is necessary. Due to the extension to nonlinear components, the analysis of the system has to be carried out in the time domain. The model provides the possibility to include the results of the FEM analysis or the BEM analysis, for those system parts which cannot be reduced to lumped elements. Moreover, it enables a relatively fast and inexpensive examination of the system characteristics compared to the FEM or the BEM analysis and can be easily adapted to similar horn types.

5:40

1pPAc11. On ambiguity in the description of sources and the choice of the acoustic variable. Ricardo E. Musafir (PEM/COPPE and DHS/EE, Universidade Federal do Rio de Janeiro, C.P. 68503, RJ, 21945-970 Brazil, rem@serv.com.ufrj.br)

In a homogeneous medium at rest, a classical problem of source ambiguity is expressed by the fact that one cannot differentiate between the fields of a volume displacement point monopole and of a volume acceleration isotropic point quadrupole. In more complex situations, a similar identity concerning the fields of more elaborate combination of point sources can be shown to exist. This reflects the fact that, since two types of energy are involved in the propagation, one cannot tell, from the wave field alone, of which type was the action responsible for originating the wave, there existing, ideally, always a way of representing a ''mass'' source by a combination of ''momentum'' sources and vice versa. It is shown, however, that, depending on the choice of the acoustic variable—and thus on the operations needed in order to combine the continuity and momentum equations into a single equation, this elegant picture may not be clearly displayed in the wave equation. The particular case of the use of the stagnation enthalpy as dependent variable is examined as an example, the analysis being used to discuss its adequacy as a variable for aerodynamic noise problems.

Contributed Poster

This poster will be on display in the Poster Gallery from Monday to Wednesday, 15–17 March. Author will be at the poster from 10:00 a.m. to 12:00 noon on Tuesday, 16 March.

1pPAc12. Nonlinear effect of the inertia of the fluid on acoustic streaming in cylindrical guides. Ludovic Menguy and Jöoel Gilbert (Lab. d'Acoust. de l'Univ. du Maine UMR CNRS 6613, Ave. Olivier Messiaen, 72085 Le Mans Cedex 9, France)

Acoustic streaming is the mean flow created by a high sound level wave. Classical treatment [J. W. S. Rayleigh, Philos. Trans. R. Soc. London **175**, 1–21 (1884)] considers that in cylindrical guides a standing acoustic wave creates a symmetrical toroidal vortex (slow streaming) due to the action of Reynolds stress forcing resisted by viscosity. A perturbation method followed by a time averaging applied to the conservation equations leads to the equations describing the behavior of the mean flow velocity in a cylindrical air-filled guide. According to a dimensional analysis, the effect of the fluid inertia cannot be neglected if the streaming becomes perceptible. This effect, previously studied for free or semi-infinite space, is controlled in the case of a waveguide by the dimensionless parameter $\mathrm{Re}_{nl}=\mathrm{M}^2/\mathrm{Sh}^2$ (M and Sh are the acoustic Mach number and the Shear number). Numerical resolution of this nonlinear system of equations (Newton–Raphson method) is performed using nonslip conditions on the tube wall and mass flux conservation accross the section of the tube. Results indicate that inertia distorts perceptibly the streamlines, and renders vortex pattern unsymmetrical. A comparison of slow and nonlinear acoustic streaming is finally achieved.

Session 1pPAd

Physical Acoustics: Cavitation Physics and Sonoluminescence I

Werner Lauterborn, Cochair
Drittes Physikalisches Institut, Universität Göttingen, Burgerstrasse 42-44, D-37073 Göttingen, Germany

Ronald A. Roy, Cochair
Department of Aerospace and Mechanical Engineering, Boston University, Boston, Massachusetts 02215, USA

Invited Papers

2:00

1pPAd1. Sonoluminescence: Current status and future perspectives. Lawrence A. Crum and Thomas J. Matula (Appl. Phys. Lab., Univ. of Washington, 1013 NE 40th St., Seattle, WA 98105)

Considerable recent attention has been directed at the phenomenon of sonoluminescence, especially since the discovery of single-bubble sonoluminescence (SBSL), in which a single, stable, acoustically levitated gas bubble can be made to pulsate with a sufficiently large amplitude to emit light each acoustic cycle. It appears that exciting physics may be associated with this phenomenon. When a sufficiently strong acoustic field is propagated through a liquid containing microscopic cavitation nuclei, similar optical emissions can be observed, although the spectrum of this multiple bubble sonoluminescence (MBSL) often possesses characteristics of the host liquid and its constituents, unlike the spectra of SBSL, which has no discernible bands or lines. Nevertheless, MBSL spectra should be able to shed considerable light on the discipline of sonochemistry. Relevant aspects of the current status of SBSL and MBSL research will be reviewed, some speculations on future directions will be offered. [Work supported in part by the NSF.]

2:20

1pPAd2. The cavitation collapse on a sub-ns time scale. B. Gompf, R. Pecha, and W. Eisenmenger (1. Physikalisches Inst., Univ. Stuttgart, Pfaffenwaldring 57, D-70550 Stuttgart, Germany)

A single sonoluminescing air bubble trapped in the pressure maximum of a resonant sound field in water is an ideal model system to investigate the end phase of the cavitation collapse. The dynamics of these single bubbles can be characterized with Mie-scattering. In earlier experiments, the scattered light was detected with photomultiplier tubes (PMT) where the time resolution is limited by the response of the PMT and no spatial resolution is possible. Using a streak camera, the scattered light can be recorded with high spatial and temporal resolution. The streak images show that at the minimum radius the scattered light intensity is not only a function of $R(t)$ anymore, and the changes in the refractive indices inside the bubble and in the highly compressed water surrounding the bubble have to be considered. Together with the width and intensity of the emitted light pulses, the results represent a complete data set for the end phase of the bubble collapse.

2:40

1pPAd3. Measuring cavitation conditions by multibubble sonoluminescence. Kenneth S. Suslick, William B. McNamaraIII, and Yuri T. Didenko (Univ. of Illinois, 600 S. Mathews Ave., Urbana, IL 61801, ksuslick@uiuc.edu)

Multibubble sonoluminescence (MBSL) arising from ultrasonic irradiation of solutions containing volatile transition metal carbonyls have been collected and analyzed. The principal emission is the atomic line spectrum from excited states of the metal atoms. This metal atom MBSL has been used to determine the effective emission temperature of cavitation as a function of the dissolved gas, and the effects of changes in the ratio of the heat capacities and of the thermal conductivity of the dissolved gas have been examined. The results strongly support a simple near-adiabatic compression model of cavitation. The results also indicate that the continua in MBSL spectra are due to emission from small molecules, and not due to plasma emission. [Work supported by the NSF and in part by the DOE.]

3:00

1pPAd4. Simulation of bubble motion in acoustic cavitation. Robert Mettin, Stefan Luther, Claus-Dieter Ohl, and Werner Lauterborn (Drittes Physikal. Inst., Univ. Göttingen, Bürgerstrasse 42-44, D-37073 Göttingen, Germany, R.Mettin@physik3.gwdg.de)

The motion of cavitation bubbles in an acoustic field is investigated both experimentally and numerically. To simulate the experimental results, a particle approach is employed which calculates the trajectories of many individual bubbles. For this purpose, added mass, drag, and Bjerknes forces are considered, and nucleation and coalescence of bubbles are modeled. Though the particle model is based on simplifying assumptions, it can reproduce different cavitation structure types observed in experiments. [Work partially supported by ''Graduiertenkolleg Strömungsinstabilität und Turbulenz.'']

3:20

1pPAd5. Bubble dynamics and SBSL in a variable acceleration environment. R. Glynn Holt, Ronald A. Roy, and Sean C. Wyatt (Dept. of Aerosp. and Mech. Eng., Boston Univ., 110 Cummington St., Boston, MA 02215, rgholt@bu.edu)

In order to prepare for pending experiments in variable g environments, some of the multiple effects caused by the time-varying acceleration of acoustic resonators used in bubble levitation experiments were considered. The coupled effects of the induced changes in ambient pressure (due to a changing hydrostatic head) and bubble position (due to a change in the buoyant body force) were modeled. Changing the ambient pressure, while holding the acoustic pressure amplitude constant, causes changes in the radial bubble response and diffusive equilibrium requirements. Changing the bubble levitation position causes both the local acoustic pressure amplitude and gradient to change, which will again impact bubble response. If the bubble is required to remain in a stable diffusive equilibrium, both of these effects will force the bubble equilibrium radius to change. Finally, by using an empirical relation for emitted SL intensity versus bubble response, the variation of emitted light intensity as a function of the changing ambient acceleration is obtained. Where possible, these results are compared to experimental data. [Work supported by NASA.]

3:40–4:00 Break

Contributed Papers

4:00

1pPAd6. Single-bubble large-scale cavitation. Vadim A. Simonenko, Vladimir N. Nogin, Nikolay G. Karlykhanov, Gennadiy V. Kovalenko (Russian Federal Nuclear Ctr., ITP, P.O. Box 245, 456770 Snezhinsk, Chelyabinsk region, Russia, sva@sva.ch70.chel.su), and William C. Moss (Lawrence Livermore Natl. Lab., Livermore, CA 94550)

Recent successes in experimental and theoretical studies of single-bubble sonoluminescence (SBSL) suggest the possibility of achieving high energy densities in the collapsed bubble. Scaling analyses and efficient ways for cavitation enhancement are discussed, with particular attention to the geometrical size of the system components and ambient pressure level. The goal is to increase the energy density in the collapsed bubble and increase the size and mass of the heated region. Theoretical estimations and results of direct hydrodynamic numerical simulations are presented for a prospective system with a 0.01- to 0.1-mm-radius gas-filled cavity that is surrounded by a 0.3-m-radius liquid-filled shell. The liquid-filled shell is surrounded by two concentric gas-filled spherical shells. The inner shell contains pressurized hydrogen, whereas, the outer shell contains oxygen. The initial rarefaction phase, which caused bubble expansion, is caused by a sudden release of the hydrogen gas into the outer oxygen-filled shell. The subsequent compression phase results from the combustion of the hydrogen and oxygen gases. [Work was partly supported by CRDF].

4:20

1pPAd7. Single-bubble sonoluminescence: Investigation of the emitted pressure wave with a streak camera and a fiber-optic probe hydrophone. R. Pecha, Z. Q. Wang, B. Gompf, and W. Eisenmenger (1. Physikalisches Inst., Univ. Stuttgart, Pfaffenwaldring 57, D-70550 Stuttgart, Germany)

In the collapse end phase of single-bubble sonoluminescence (SBSL), in addition to a short light pulse, a spherical pressure wave is emitted by the bubble into the surrounding liquid. This pressure wave was investigated with two different methods: (1) If the bubble is illuminated by a laser beam, laser light is Mie-scattered by the bubble itself, but also by the outgoing pressure pulse. The scattered light of both was recorded with a streak camera with a spatial resolution of 8 μm and a temporal resolution of 500 ps. From the time-dependent radial distance of the pressure pulse $r(t)$ from the bubble, the velocity $v(t)$ can be determined. The speed of sound in the vicinity of the bubble is increased in comparison to normal conditions. This change in the sound velocity was used to estimate the amplitude of the pressure pulse. (2) At a distance of 2.5 mm from the bubble, a fiber-optic probe hydrophone with a spatial resolution of 100 μm and a rise time of 5 ns was used to measure the pressure wave. Measurements depending on the amplitude of the driving sound field, the gas concentration, and the temperature of the water will be presented.

4:40

1pPAd8. Experimental observations of the effect of ambient pressure on single-bubble sonoluminescence. M. Dan, J. D. N. Cheeke (Phys. Dept., Concordia Univ., 1455 de Maisonneuve Blvd. W., Montreal, QC H3G 1M8, Canada, manas@alcor.concordia.ca), and L. Kondic (Duke Univ., Durham, NC 27708)

The experimental observations of the influence of ambient pressure on single-bubble sonoluminescence will be presented. In the SBSL regime as the ambient pressure was decreased only about 10%, the SL intensity increased significantly as predicted [L. Kondic, C. Yuan, and C. K. Chan, Phys. Rev. E **57**(1), R32–R35 (1998)]. There was an increase of about five times in SL intensity as the ambient pressure was decreased by about 10%–12%, at constant driving acoustic pressure. This increment continued until a certain value of the ambient pressure, below which the bubble became unstable and vanished. The equilibrium radius and the maximum radius of the SBSL bubble both incerased with decrease of ambient pressure. This observation provides valuable insight into the mass flow mechanism between the bubble and the liquid, and gives the first direct confirmation of ''argon bubble hypothesis.'' [Work supported by NSERC and Concordia Seagram Fund for Innovative Research.]

5:00

1pPAd9. Parameter space of single-bubble sonoluminescence for various liquid temperatures. D. Felipe Gaitan (NCPA, Univ. of Mississippi, University, MS 38677) and R. Glynn Holt (Boston Univ., Boston, MA 02215)

In a previous paper by the authors [Phys. Rev. Lett. **77**, 3791 (1996)], the region of parameter space (acoustic pressure, ambient bubble radius) in which stable single-bubble sonoluminescence (SBSL) occurs in an air–water system driven at 20.6 kHz was described as a function of the dissolved gas concentration. In this paper, new data (ambient radius, maximum radius, expansion ratio, as well as the emission and extinction thresholds) will be presented for the SBSL parameter space at various liquid temperatures for different gases and liquids. [Work supported by the Office of Naval Research.]

5:20

1pPAd10. Molecular dynamics approach for a sonoluminescing bubble. Burkhard Metten, Thomas Kurz, and Werner Lauterborn (Drittes Physikalisches Institut, Univ. Goettingen, Burgerstr. 42-44, D-37073 Goettingen, Germany, metten@dpi.physik.uni-goettingen.de)

Up to now the numerical calculations for the converging shock or compression wave model of sonoluminescence have been based primarily on continuum methods. Here an alternative approach by molecular dynamics simulation is shown to be feasible with today's computer memory and speed. Both approaches are compared. Results of the simulations are presented for the scaling behavior with the number of particles, for different boundary conditions (spherical and ellipsoidal bubbles) and for one and

more species in the bubble. The dependence of the light intensity and pulse duration on the sphericity of the bubble is discussed. [Work supported by the Graduiertenkolleg Stroemungsinstabilitäten und Turbulenz.]

5:40

1pPAd11. Single-bubble sonoluminescence in water during transitions from hypergravity to low gravity on NASA's KC-135 aircraft and laser-beam extinction methods for studying bubble dynamics. David B. Thiessen, Jeremy E. Young, Mark J. Marr-Lyon, Ben R. Dzikowicz, and Philip L. Marston (Dept. of Phys., Washington State Univ., Pullman, WA 99164-2814)

The sound field which drives SBSL also provides the radiation force which counteracts the average buoyancy of the bubble. One consequence is that the location of the bubble should be altered by the effective acceleration of gravity g_e. Variations in g_e may alter the physical processes giving rise to luminescence. This group's previous experiments have confirmed that SBSL is not automatically quenched in the reduced and enhanced g_e conditions in an aircraft undergoing parabolic flight trajectories [D. B. Thiessen *et al.,* in *Proc. of the 4th Microgravity Fluid Phys. Conf.* (NASA, 1998), pp. 379–383]. The new experiments were carried out with the SBSL chamber in contact with a constant-pressure gas-filled chamber. During intervals of negligible drift in the SBSL intensity, there can be a rapid intensity rise (with a relaxation time of about 5 s) of about 4% as g_e is decreased from 1.8 to near 0 g, but the increase is not seen in all data sets. In related work, diagnostics based on monitoring laser-beam extinction with a photocell [J. S. Stroud and P. L. Marston, J. Acoust. Soc. Am. **94**, 2788–2792 (1993)] is applied to SBSL bubbles in the laboratory. [Work supported by NASA.]

MONDAY AFTERNOON, 15 MARCH 1999 POSTER GALLERY, 2:00 TO 4:00 P.M.

Session 1pPAe

Physical Acoustics: Acoustic Evaluation of Materials (Poster Session)

Torsten Niederdraenk, Cochair
Siemens Audiologiesche Technik GmbH, D-91050 Erlangen, Germany

Jean Francois Allard, Cochair
Institut d'Acoustique et de Mecanique de l'Universite du Maine, UMR CNRS 6613, av. Olivier Messiaen, F-72085 Le Mans, Cedex 9, France

Contributed Papers

All posters will be on display in the Poster Gallery from Monday to Wednesday, 15–17 March. Authors will be at their posters from 2:00 p.m. to 4:00 p.m. on Monday, 15 March.

1pPAe1. Acoustic emission signals from the sol–gel transition of tetraethoxysilan (TEOS) and sodium silicate solutions. Jadwiga Rzeszotarska, Feliks Rejmund (Inst. of Fundamental Technolog. Res., Polish Acad. of Sci., Swietokrzyska 21, 00-049 Warsaw, Poland, freymund@ippt.gov.pl), and Jerzy Ranachowski (Polish Acoust. Society, 00-049 Warsaw, Poland)

Sol–gel processes have been used extensively to prepare oxide materials (glasses and ceramics). The acoustic emission (AE) method with broadband piezoelectric transducer (up to 500 kHz) was used to control the evolution of slow gel formation from organic TEOS and fast formations from sodium silicate as the precursors of silica. The obtained dependencies of the AE count rate and rms values versus time characterize the dynamic of the cross-linking and desolvation processes under ambient conditions. The frequency distribution analysis of individual power spectra provides an activity estimation of integral parts of processes. In sodium silicate solutions the spectra of low frequency (17–70 kHz) were mainly observed. On the other hand, the most representative spectra from the gelation of TEOS display at three basic ranges; 16–20 kHz, 200–230 kHz, and 400–470 kHz. The relative intensities of spectra in these ranges were changed considerably during the gel formation. [Work partly supported by KBN Grant No. T 07B 047 15.]

1pPAe2. Ultrasonic velocity and absorption in the binary mixtures of 1-butanol with isomeric butanediols at 298.15 K. Edward Zorebski and Michal Zorebski (Inst. of Chemistry, Silesian Univ., Szkolna 9, 40-006 Katowice, Poland, emz@tc3.ich.us.edu.pl)

From the early days of ultrasonic technology, ultrasonic velocity and ultrasonic absorption have been a rich source of information on the structure and condition of the materials trough in which the ultrasonic waves are propagated. Here an investigation into binary mixtures (in the whole concentration range) of 1-butanol with 1,2-butanediol and 2,3-butanediol at 298.15 K is reported. For the ultrasonic velocity measurements at 2.15 MHz, the pulse-echo-overlap method was used and the ultrasonic absorption in the frequency range 10–200 MHz was determined by the standard pulse technique, where the amplitude of the first transmitted pulse was registered as a function of distance. The results were compared with the previous data for 1-butanol with 1,3-butanediol and 1,4-butanediol and discussed in terms of molecular interactions in highly associated liquids.

1pPAe3. Ultrasonic study of ionic association in aqueous solutions of lanthanide salts. Birutė Voleišienė, Gintara Miglinienė, and Algirdas Voleišis (Ultrasound Res. Ctr., Kaunas Univ. of Technol., Studentų str. 50, LT-3031 Kaunas, Lithuania, ulab@tef.ktu.lt)

The association reactions between trivalent ions of lanthanum, cerium, neodymium, gadolinium, erbium, ytterbium, and nitrate or sulphate ligands has been investigated from ultrasound velocity dispersion measurement data. It is assumed that ultrasound velocity dispersion in aqueous solutions of lanthanide nitrates and sulphates is caused by an association process. The ultrasound velocity was measured by the ultrasonic laser interferometer within the frequency range of 3–200 MHz. The rates of formation of inner sphere complexes $[LnNO_3]^{2+}_{aq}$ and $[LnSO_4]^{+}_{aq}$ were calculated and the interaction between individual ions Ln(III) and water molecules is discussed across the series. A comparison of relaxation parameters for the nitrate solutions with corresponding sulphates was made. It has been shown that a magnitude of an ultrasound dispersion may be the quantity of complexation. Ultrasound velocity dispersion for nitrate solutions is much smaller than that of more diluted lanthanide sulphate solutions. The lanthanide nitrates form predominantly outer sphere complexes with some inner sphere substitution. In order to produce an appreciable amount of inner complexes in nitrate solutions for a similar dispersion and relaxation, a tenfold higher concentration of the nitrates must be used.

1pPAe4. Effect of wall adsorption on the photoacoustic detection of ammonia with a 1.53-μm DFB diode laser. Andreas Hebach, Andras Miklos, and Peter Hess (Inst. of Physical Chemistry, Univ. of Heidelberg, Im Neuenheimer Feld 253, D-69120 Heidelberg, Germany, andreas.miklos@urz.uni-heidelberg.de)

The adsorption of ammonia molecules (and other polar molecules such as nitrogendioxide, water, etc.), on the walls of the photoacoustic (PA) detector influences the accuracy of the concentration measurement. This effect becomes larger for small concentrations and depends on the direction of the concentration change. This means that a hysteresis of the PA signal is observed between measurements carried out by decreasing and by increasing the concentration. The adsorption problem was reduced considerably by performing the measurements in a continuous flow. For measurements with high flow rate a new photoacoustic detector was developed. The differential design provides good flow and electronic noise suppression. The PA signal has been generated by tuning a 40-mW, 1.53-μm GEC-Marconi DFB laser to the absorption peak of ammonia at 1527 nm. The dependence of the PA signal on the flow rate of ammonia–nitrogen mixtures with different concentrations was investigated. In another experiment the hysteresis of the PA signal was investigated by increasing and decreasing the concentration in several steps, but maintaining the same total flow rate. It was found that a higher flow rate results in a smaller error of the concentration measurement and a shorter response time of the PA detector.

1pPAe5. The effects of ultrasonic waves on dye penetration with cellulose fabrics dyed by vinylsulphonic dyes. Vesna Ignjatovič, Mile Novakovič (Faculty of Technol., Leskovac Bulevar, oslobo/enja 124, 16000 Leskovac, vesnateh@tehfin.tehfak.ni.ac.yu), and Milena Miljkovič (Leskovac Bulevar, 16000 Leskovac)

Research has shown that ultrasound traveling in the form of waves through liquids causes the effect of cavitation. Cavitation is manifested in a continuous creation and disappearance of vacuums within the liquid. Therefore, interruptions are created in the liquid, that is, strong forcing waves are made. The cavitation strikes are used in solid matter destruction, emulsion creation, greasy surface cleansing, and the like. The ultrasonic energy has been applied in textile industry, for the most part in soaking processes, and textile washing and cleaning. There is research indicating that ultrasonic energy can be used in dyeing of cotton with direct and reactive dyes, of polyamid and wool with acid dyes, and of polyester and acetate fibers with disperse dyes. Based on previous research, this paper is an account of an experiment whose aim was to implement the latest achievements in vibration and ultrasonic theory in textile dyeing technologies. Thus cotton knitwear has been dyed with vinylsulphonic reactive dye, with and without the use of ultrasonic energy, and with the introduction of an air bubble in the dye tub with the application of ultrasonic energy. Previous experiments have shown that ultrasound contributes to greater dye absorption from the tub, so that equal distribution dyeing with the use of ultrasound requires less dye, shorter period of dyeing, less power consumption, and at the same time the pollution of waste waters is reduced. All these characteristics make this procedure economically and ecologically affordable. So as to intensify the process, this research has been directed towards the introduction of an air bubble in the dyeing tub which is under the effect of ultrasound. Dye absorption from the tub and dye penetration in the fabric have been monitored by means of spectrophotometry (absorption and reflection spectrophotometry). Previous research projects have not been able to explain completely the fundamental interaction of ultrasound and fibers, that is, reactive dyes in water, and with that, in the process of dyeing itself. Therefore, future work will deal with this problem. [This paper is a part of research done for the requirements of the project titled ''Modern Approaches in New Dyeing Procedure Development for Optimal Pollution of the Environment,'' and financed by Science and Technology Ministry of Serbia.]

1pPAe6. The effects of ultrasonic energy on reactive dye absorption in the presence of reduced quantities of salt. Mile Novakovič, Vesna Ignjatovič (Faculty of Technol., Leskovac Bulevar oslobo/enja 124, 16000 Leskovac, vesnateh@tehfin.tehfak.ni.ac.yu), and Milena Miljkovič (Leskovac Bulevar, 16000 Leskovac)

Ultrasonic energy has shown a wide range of application possibilities in many fields of human craftsmanship, and its application in textile industry has been a matter of research for a number of years. For the time being, the best results have been achieved in other research still being done in laboratories. This paper presents a part of the overall research done within the project ''Modern Approaches in New Dyeing Procedure Development for Optimal Pollution of the Environment,'' financed by Science and Technology Ministry of Serbia. One of the predetermined objectives of the project is to examine the possibility of ultrasonic energy application in technological processes of dyeing cellulose fabrics by vinylsulphonic dyes. Having that in mind, it is necessary to systematically investigate all of the aspects of ultrasonic energy effects on textile substrata, the dye, and the relation of dye solution and fiber. In the experiments, cellulose microfiber knitwear has been dyed with vinylsulphonic dyes according to the on-line procedure, at a stable temperature, with the addition of varying quantities of salt. Concerning the fact that salt has the ability of enhancing dye absorption from the tub, and that ultrasonic energy helps the process of absorption, the quantity of salt required may be reduced, and thus reduce the cost of dyeing and the pollution of waste waters. Dye absorption from the tub has been monitored by means of absorption spectrophotometry. With the method of reflection spectrophotometry, spectral remission curves have been measured, K/S values calculated, and respectively the relative intensity of dyeing on the fabric determined.

1pPAe7. Acoustic emission (AE) generated by thermomechanical stress in ceramics. Przemyslaw Ranachowski (Inst. of Fundamental Technolog. Res., Polish Acad. of Sci., Swietokrzyska 21, 00-049 Warsaw, Poland)

The thermomechanical long-term toughness of electrotechnical porcelain of long-rod insulators was investigated. The objects were stressed in thermostat to 63% of nominal strength. The cyclic temperature changes from −25 deg to 40 deg were applied. This treatment corresponds to real environmental conditions on insulators of high-voltage lines. The AE

method was used for monitoring the gradual destruction process during the test. The initiation and propagation of microcracks correlate with AE count rate. It was stated that the magnitudes of consecutive maxims of count rate during the cooling part of the cycle depend on the advancement of material destruction. The increase of these maxims means reduction of ceramics toughness related with multiplication of microcracks number and larger probability of critical cracks appearance. When the ceramics retains its strength, the maxims have approximately the same value in consecutive test cycles. The AE method was successfully applied in product certification procedure and control of electric power system. The degree and parameters of porosity of ceramics have been defined on the basis of velocity and attenuation of ultrasound. The good agreement of theoretical and experimental data was obtained. [Work supported by KBN Grant No. T 07B 03413.]

MONDAY AFTERNOON, 15 MARCH 1999 ROOM H1012, 1:55 TO 6:20 P.M.

Session 1pPPa

Psychological and Physiological Acoustics: Recent Advances in Models of Auditory Processing

William A. Yost, Cochair
Parmly Hearing Institute, Loyola University, 6525 North Sheridan Road, Chicago, Illinois 60626, USA

Torsten Dau, Cochair
AG Medizinische Physik, University of Oldenburg, D-26111 Oldenburg, Germany

Chair's Introduction—1:55

Invited Papers

2:00

1pPPa1. Modeling within- and across-channel processing of amplitude modulation. Torsten Dau (AG Medizinische Physik, Univ. of Oldenburg, Oldenburg, Germany)

Recently, a model was presented in which a modulation filterbank was introduced to analyze the envelope fluctuations at the output of each excited peripheral auditory filter [Dau *et al.*, J. Acoust. Soc. Am. **102**, 2892–2905 (1997)]. As a decision stage, an optimal detector was applied which combines all modulation-filter outputs linearly, assuming independent observations. The model accounts for temporal modulation transfer functions (TMTF) with narrow band and broadband carriers as well as for modulation masking data. The model does not cover conditions which require across-channel processing, such as modulation detection interference (MDI). In this case, the auditory system seems to combine information across frequency channels whose responses are temporally modulated. A new modeling approach is presented that integrates the modulation-filter outputs across frequency channels prior to the decision stage, while preserving the original model's ability to describe TMTFs and modulation masking. To further ensure the possibility of predicting spectral masking, a low-frequency part of the modulation spectrum, including the dc component, is processed separately within each peripheral channel. The model can account for the main features of MDI, but it does not account for comodulation masking release.

2:20

1pPPa2. Computer models of the auditory periphery. Ray Meddis (Ctr. for the Neural Basis of Hearing at Essex, Essex Univ., Colchester CO4 3SQ, UK, rmeddis@essex.ac.uk)

Enough is now known about the auditory periphery to allow the development of useful computational models. These accept an arbitrary acoustic stimulus and predict the response of auditory nerve fibers. Current models are largely based on linear filters representing the mechanical frequency selectivity of the cochlear. Nonlinear models would be more appropriate if they could be developed in a form that replicated physiological measurements. This paper describes one approach that combines a nonlinear model of frequency selectivity with a revised inner hair cell model. The nonlinear filters are evaluated using published data collected at three sites on the basilar membrane. They behave nonlinearly at frequencies close to best frequency and linearly at remote frequencies. They show appropriate impulse responses and patterns of two-tone suppression. The hair cell model incorporates a simple account of the receptor potential and retains a previously developed reservoir model of synaptic flow. An innovation includes a model of the discrete release of transmitter quanta that explicitly assumes a presynaptic origin for the stochastic nature of the auditory nerve response. The combined model gives a useful account of the differences between low-, medium-, and high-spontaneous rate fibers that is consistent with earlier physiological speculation.

2:40

1pPPa3. Modeling the effects of peripheral compression on temporal processing. Andrew J. Oxenham (Dept. of Speech-Lang. Pathol. & Audiol., Northeastern Univ., Boston, MA 02115)

Most psychoacoustic models to date have assumed that the peripheral auditory system can be treated as a bank of quasilinear bandpass filters. Physiological studies have shown that this approximation holds only for damaged cochleae: the response of the basilar membrane in a healthy cochlea to sounds around the characteristic frequency is highly nonlinear and compressive over a wide range of sound-pressure levels. Many aspects of psychoacoustic performance can be explained by taking these nonlinear characteristics into account. Short-term temporal integration in simultaneous and forward masking (where signal detectability improves with increasing signal duration), the critical masking interval (where the detectability of a brief signal temporally centered in a masker decreases with increasing masker duration), and the nonlinear growth of forward masking can be modeled with relatively simple assumptions if a physiologically reasonable nonlinearity is included. Similarly, some aspects of temporal processing in listeners with cochlear hearing impairment can be well described by making the reasonable assumption that cochlear compression is reduced or absent. Thus the altered temporal processing shown in some tasks by hearing-impaired listeners may in many cases be due to reduced cochlear compression and not to more central processing deficits. [Work supported by the NIH/NIDCD.]

3:00

1pPPa4. Recent advances in models of binaural detection and localization. H. Steven Colburn (Hearing Res. Ctr. and Biomed. Eng., Boston Univ., 44 Cummington St., Boston, MA 02215, colburn@enga.bu.edu)

There has been a significant increase in the mathematical modeling of binaural phenomena in the past couple of years by a number of research groups. Available review chapters [e.g., Colburn, in *Auditory Computation* (Springer-Verlag, New York, 1996); Stern and Trahiotis, in *Handbook of Perception* (Academic, New York, 1996)] do not include this new material. Recent advances were stimulated in part by the availability of more powerful computational tools and in part by recent data that include more complex stimulus situations such as noise waveforms with interaural time differences but no interaural intensity differences and vice versa [van de Par and Kohlrausch, J. Acoust. Soc. Am. (1998)]. This presentation reviews recent developments in binaural modeling with particular attention given to models of binaural detection and sound localization. Both pink-box models, which incorporate available information from auditory physiology, and black-box models are considered. [Work supported by NIDCD Grant No. R01 DC00100.]

3:20

1pPPa5. Temporal models of pitch processing. William A. Yost (Parmly Hearing Inst., Loyola Univ. Chicago, 6525 N. Sheridan Rd., Chicago, IL 60626)

Most models of pitch perception assume three basic stages of processing: cochlear filtering, haircell/neural transduction, and pitch extraction. In temporal models of pitch processing the pitch extraction stage is often based on autocorrelationlike processes. This talk will review our work using regular interval stimuli to study temporal models of pitch perception. Work with regular interval stimuli suggests that temporal models of pitch processing can account for the pitch and pitch strength of complex sounds with both resolved and unresolved harmonics. The pitch and pitch strength of regular interval stimuli appears to be based on the temporal properties of the waveform fine structure. Human and animal psychophysical results, physiological recordings from the cochlear nucleus, and model results will be presented. [Work supported by NIDCD and AFOSR.]

3:40–4:00 Break

Contributed Papers

4:00

1pPPa6. Cochlear wavelength representation of acoustic frequency content. Timothy A. Wilson (Dept. of Elec. Eng., Univ. of Memphis, Memphis, TN 38152-6574)

Peak-to-peak wavelengths of the sinusoidal steady-state response of a simple cochlear model (i.e., incompressible, inviscid, linear fluid in a rigid box-shaped chamber with a linear stiffness-damping-mass cochlear-partition model having exponential parameter variation with place) were examined. For a wide range of mechanical parameter values and for a wide range of cochlear places (at least those basalward of the best place, though sometimes extending through the best place toward the cutoff regime), the wavelengths were found to be (1) a decreasing, approximately linear function of the logarithm of the stimulus frequency, and (2) a decreasing, approximately linear function of cochlear place. A simple algorithm for estimating the instantaneous frequency of sinusoidal signal components of complex signals (both constant frequency and chirps), as well as that of the center frequency of pulse- and noise-excited resonances, was developed. Estimator performance for the cases of signals plus noise and of noisy wavelength measurements will be presented.

4:20

1pPPa7. Evaluation of a physiological ear model for the simulation of nonlinear masking effects. Frank Baumgarte (Inst. fuer Theoret. Nachrichtentechnik und Informationsverarbeitung, Univ. of Hannover, Appelstr. 9A, D-30167 Hannover, Germany)

A physiological model of the human auditory system with the aim at generating masked thresholds for arbitrary sound signals was presented at the previous DEGA meeting. The main parts of the ear model are an active nonlinear cochlear model and a threshold detector which evaluates changes in specific loudness. It was shown that the ear model is able to rebuild the level dependency of spectral and temporal masking patterns,

the asymmetry of masking between noise and tone, and the different detection thresholds for amplitude and frequency modulation. This study presents new simulation results for nonlinear masking effects. These results indicate that the nonlinear ear model allows demonstration of other nonlinear psychoacoustical effects such as the additivity of masking, suppression, and distortion product detection. Since the physiological ear model represents a unified approach covering the most important masking effects of arbitrary sounds, it is suitable for applications such as perceptual audio coding. An improved coding efficiency is expected due to the more accurate masked thresholds generated by the ear model in comparison to results from psychoacoustical models commonly used in audio coding which neglect many of the nonlinear effects of auditory perception. [Work supported by DFG.]

4:40

1pPPa8. Physiological measurements and mathematical models for interaural pathways. Hans-Peter Rangol (Zoologisches Institut, Johann Wolfgang Goethe Univ., Frankfurt am Main, Germany, hprangol@gmx.de)

The middle-ear cavities of birds, reptiles, and anurans are often connected through a tube, which can act as an interaural pathway between both eardrums. Such an arrangement of acoustically effective structures is described as a pressure-difference receiver. It is generally assumed that pressure-difference receivers enhance the skills for directional hearing in animals. Sound pressures and phases were measured with probe-microfones in the interaural pathway from Zebra Finches during azimuthal rotation. The results show pressure differences between right and left middle ear, which are dependent on the azimuth and the frequency of the applied sound. A mathematical model was constructed, which gives the resulting pressure and phase of two overlaying waves that travel different distances. Assuming one wave traveling through the pathway and a second around a sphere, the resulting wave from dependency on azimuth and frequency was calculated. The pattern shows the same characteristic pressure differences as the physiological measurements. The same procedures were performed with a sphere as a hardware model for a head with an interaural pathway. The results show again the expected characteristics. The combination of physiological measurements, mathematical modeling, and testing this model with hardware models gives a meaningful explanation for the acoustical properties of middle ears as a basis for psychological acoustics.

5:00

1pPPa9. A network model for the functional architecture of the mammalian medial superior olivary nucleus. Claus Weiland (Dept. of Zoology, J. W. Goethe Univ., Frankfurt/Main, Germany)

The mammalian MSO is part of the superior olivary complex, the lowest level in the auditory pathway, which receives binaural input. The microarchitecture of the anatomical convergence of both paths is considered as fundamental for the nucleus' function in time-domain processing. This architecture is mostly, according to a proposal of Jefress [L. Jefress, J. Comp. Physiol. Psychol., 35–39 (1948)], interpreted as a network of coincidence detectors. However, the topographic organization of the afferent innervation of the MSO shows much more complexity as is assumed in this model. The connection scheme of the afferent fibers indicates even aspects of terminal divergence, which should result in broadly tuned neurons instead of sharply tuned coincidence detectors. This study proposes a network model for the processing of interaural time delays (ITD) in the MSO based on connection patterns and response properties of the MSO fusiform cells. Instead of local coincidence detection, coding of ITD's is distributed over a cluster of fusiform cells, where each individual cell's degree of stimulus resolution is considered as low. While in the Jefress model each delay line is processed as a single channel, cluster formation based on MSO's multipolar cells could be a mechanism for sampling over these different channels.

5:20

1pPPa10. Modeling the precedence effect: Mechanisms of onset enhancement in binaural lateralization models. Roberto M. Dizon and H. Steven Colburn (Hearing Res. Ctr. and Biomed. Eng. Dept., Boston Univ., 44 Cummington St., Boston, MA 02215, dizon@bu.edu)

The general behaviors of several cross-correlation-based lateralization models in response to dynamic impulsive stimuli, specifically those that elicit the precedence effect, are presented as a means of gaining insight into the contribution of individual stages of the models to precedencelike performance. In general, an enhancement of activity at onset relative to later activity in the model outputs (or equivalently, a temporary post-onset suppression in activity) is associated with the relative perceptual emphasis of early portions of stimuli as described by the precedence effect. Onset enhancement in cross-correlation models has thus far only been exhibited using dynamic mechanisms such as that used in a model by Lindemann [J. Acoust. Soc. Am. (1986)]. This work evaluates the dynamic properties of several cross-correlation models that include mechanisms of onset enhancement. These mechanisms include that of Lindemann's model, peripheral mechanisms such as adaptation, and a physiologically based inhibition mechanism adapted from the IC model of Cai, Carney, and Colburn [J. Acoust. Soc. Am. (1998)]. In this work, binaural models are created from various permutations of the mechanisms described above, and the final and intermediate model outputs in response to a few sample stimuli are shown and compared. [Work supported by ONR and NIH (NIDCD R01 DC00100).]

5:40

1pPPa11. A model of primary sensations, pitch, loudness, and timbre, of sound signals. Y. Ando (Grad. School of Sci. and Technol., Kobe Univ., Rokkodai, Nada, Kobe, 657-8501 Japan, andoy@kobe-u.ac.jp)

Primary sensations, pitch, loudness, and timbre, of a given source signal and sound field are described based on the model of the auditory–brain system [Ando, *Architectural Acoustics* (AIP/Springer-Verlag, New York, 1998)]. The model consists of the autocorrelation and interaural cross-correlation mechanisms. (Note that the power density spectrum is identical with the ACF.) In order to describe timbre, the human cerebral hemisphere specialization for the temporal and spatial factors of sound fields is taken into consideration in a similar manner as the subjective preference. Here, timbre is defined by a remaining primitive sensation that cannot be expressed by only pitch and loudness. [Work was partially supported by the Ministry of Education, Grant-in-Aid for Scientific Research (C), 9838022, 1998.]

6:00

1pPPa12. The mechanisms underlying temporal pitch perception studied with sequences of filtered clicks. Christian Bering and Christian Kaernbach (Inst. für Allgemeine Psych., Univ. Leipzig, Seeburgstr. 14-20, 04 103 Leipzig, Germany)

In order to probe the mechanisms underlying temporal pitch perception it is necessary to eliminate all spectral cues from the stimulus, i.e., to use stimuli that cannot be resolved by the cochlea. High-pass filtered clicks combined with the corresponding low-pass filtered noise prove to be especially suitable for the construction of stimuli with specific temporal properties. These stimuli allow for the testing of specific hypotheses concerning temporal processing in the auditory system. The present study compares psychophysical results, obtained with periodic and aperiodic click sequences with single-cell simulations of chopper cells in the ventral cochlear nucleus. The latter are thought to explain the observed sensitivity to temporal regularity.

Session 1pPPb

Psychological and Physiological Acoustics: Cross-Spectral Processing (Poster Session)

Torben Poulsen, Chair
Department of Acoustic Technology, Technical University of Denmark, Building 352, DK-2800 Lyngby, Denmark

Contributed Papers

All posters will be on display in the Poster Gallery from Monday to Wednesday, 15–17 March. Authors will be at their posters from 2:00 p.m. to 4:00 p.m. on Monday, 15 March.

1pPPb1. Effect of target versus distracter-tone frequency region and variance on sample discrimination of frequency differences. Donna L. Neff, Rebecca L. Wrage, and Walt Jesteadt (Boys Town Natl. Res. Hospital, 555 N. 30th St., Omaha, NE 68131, neff@boystown.org)

This experiment examined how performance in a complex frequency-discrimination task was influenced by the frequency region and relative frequency variability of target versus distracter tones. In a 2IFC sample-discrimination task, normal-hearing listeners were asked to select the interval containing target tones drawn from the higher of two overlapping Gaussian frequency distributions. The target distributions were placed in one of three frequency regions: ''low'' (500 Hz), ''middle'' (1414 Hz), or ''high'' (4000 Hz). For a particular target region (e.g., low), two distracter tones were then drawn at random and added, one from each of the Gaussian distributions at the two remaining frequency regions (e.g., middle and high). All distributions were equivariant on a logarithmic frequency scale. Based on the CoRE model [R. A. Lutfi and K. A. Doherty, J. Acoust. Soc. Am. **96**, 3443–3450 (1994)], it was predicted that tones with greater variance would have a greater influence on performance independent of frequency region. The results indicate that the influence of variance depends on the frequency region of targets versus distractors, with notable individual differences and training effects. [Work supported by NIDCD.]

1pPPb2. Detection of tones of unexpected frequency in amplitude-modulated noise. Matthew B. Fitzgerald and Beverly A. Wright (Audiol. and Hearing Sci. Prog., 2299 N. Campus Dr., Northwestern Univ., Evanston, IL 60208-3550)

The percentage of correct detections of tonal signals presented in wideband sinusoidally amplitude modulated (SAM) noise, or noise with SAM and unmodulated regions, was measured for an expected signal of 1000 Hz and unexpected signals of 200, 600, 1400, and 1800 Hz. The level of each signal was set so the signal could be detected on 85% of trials when presented by itself. When the noise was 100% SAM at 10 Hz, six of nine listeners detected at least one unexpected signal on over 70% of trials. When a 400-Hz wide region centered at 1000 Hz was unmodulated and the remaining wideband noise was SAM, or vice versa, all three listeners still detected at least one unexpected signal on over 70% of trials. With unmodulated noise, all unexpected signals were detected at chance. These results suggest most listeners monitor multiple auditory filters when detecting tonal signals in noise that is entirely or partially SAM. This listening strategy may be related to, but not responsible for, the better detectability of signals in wideband SAM than unmodulated noise, because here signal levels in SAM noise were similarly low for listeners who did or did not detect unexpected signals. [Work supported by NIH/NIDCD.]

1pPPb3. A behavioral reverse correlation technique to decipher early auditory feature coding. Christian Kaernbach (Inst. für Allgemeine Psych., Univ. Leipzig, Seeburgstr. 14-20, 04 103 Leipzig, Germany)

Certainly people do not perceive auditory stimuli as a bunch of time-varying spectral components, but what else could provide a format for early auditory feature coding? This question has been dealt with extensively in vision, revealing sensitivity to waveletlike stimuli and to simple object feature elements. Up to now there has been no attempt to decipher the alphabet of hearing at a coding level higher than that of sinusoidal phonons on the auditory nerve. The present study demonstrates a behavioral reverse correlation technique revealing which kind of features will be detected in random stimuli (noise). When a noise segment is repeatedly presented, it will elicit simple percepts, equivalent to the detection of lines, circles, or faces in random dot images. When these percepts are masked by another noise segment, in about 60% of the cases there is a clear-cut difference of masking level depending on the sign of the masker. By adding up sign-sensitive maskers in the correct polarity, one gets the ''noison'' that elicits this specific percept. The noisons presented in the talk represent only a random selection of possible auditory features, but they give an indication of the potential scope of feature specifications.

1pPPb4. Internal representation of spectral information in dependence of signal type and auditory filter bandwidth. Bernhard Laback and Werner A. Deutsch (Acoust. Res. Lab., Austrian Acad. of Sci., Liebigg. 5, 1010 Vienna, Austria)

Previous studies have shown that enhancement of the spectral background (lower level spectral components) improves intelligibility as well as listening comfort of music signals in subjects with broader than normal auditory filters. This is in contrast to reported results on speech perception in noise, yielding reduced intelligibility as a result of spectral contrast reduction. A proposed model for the internal object representation by separation of ''spectral layers'' accounts for these opposing effects. ''Spectral layers,'' corresponding to different sound sources [in music: dominant/accompanying musical voices; in speech-in-quiet: formant peaks/modulation sidebands of the peaks (transitions); in speech-in-noise: speech foreground/speech background/noise components] are represented in coherent spectral amplitudes. The audibility of ''spectral layers'' is derived from individual masking properties. Pilot experiments with speech tokens and short music fragments agree relatively well with the model predictions: The effect of either increasing or reducing the spectral contrast on discrimination highly depends on the distribution of the perceptually relevant acoustical information in the ''spectral layers'' relative to their audibility. Performance varies for different signal types (simultaneous musical voices, vowel, consonant). [Work supported by the Austrian Academy of Sciences.]

1pPPb5. Amplitude modulation discrimination interference (MDI) and speech intelligibility for normal-hearing and hearing-impaired subjects. Jan Koopman, Rene van der Horst, and Wouter A. Dreschler (Dept. of Exp. Audiol., Academic Medical Ctr., P.O. Box 22660, NL-1100 DD, Amsterdam, The Netherlands, j.koopman@amc.uva.nl)

Modulation detection interference is the decrease of sensitivity for amplitude modulation when the target is presented in the presence of modulating maskers [W. A. Yost and S. J. Sheft, J. Acoust. Soc. Am. **85**(2), 848–857 (1989)]. A typical MDI experiment was carried out in which the maskers were located at 500 and 4000 Hz and the target at 1400 Hz (covering the range of speech frequencies). The modulation depths of the maskers were held steady at 0, 0.18, or 0.30. The modulation rates were 4, 8, or 16 Hz. Also, speech intelligibility was measured by a sentence test in continuous noise. Both experiments were carried out for six normal-hearing and six hearing-impaired subjects. All signals were presented at MCL level. Both groups of subjects were most sensitive for amplitude modulations when they were presented in the presence of the nonmodulating maskers or without any masker at all; the sensitivity decreased by 8 dB for normal-hearing subjects and 6 dB for hearing-impaired subjects for the modulated masker condition. The modulation threshold also increased for increasing reference modulation depths. The amplitude modulation discrimination sensitivity showed a significant correlation with the critical signal-to-noise ratios for speech intelligibility.

1pPPb6. Comodulation masking release in bit-rate reduction systems. Martin D. Vestergaard,[a] Karsten B. Rasmussen, and Torben Poulsen (Dept. of Acoust. Technol., Bldg. 352, Tech. Univ. of Denmark, DK-2800 Lyngby, Denmark, kbr@dat.dtu.dk)

It has been suggested that the level dependence of the upper masking slope be utilized in perceptual models in bit-rate reduction systems. However, comodulation masking release (CMR) phenomena lead to a reduction of the masking effect when a masker and a probe signal are amplitude modulated with the same frequency. In bit-rate reduction systems the masker would be the audio signal and the probe signal would represent the quantization noise. Masking curves have been determined for sinusoids and 1-Bark-wide noise maskers in order to investigate the risk of CMR, when quantizing depths are fixed in accordance with psycho-acoustical principles. Masker frequencies of 500 Hz, 1 kHz, and 2 kHz have been investigated, and the masking of pure tone probes has been determined in the first four 1/3 octaves above the masker. Modulation frequencies between 6 and 20 Hz were used with a modulation depth of 0.75. A CMR of up to 10 dB was obtained at a distance of 6 Bark above the masker. The amount of CMR was found to depend on the presentation level of the masker; a higher masker level leads to a higher CMR effect. Hence, the risk of CMR affecting the subjective performance of bit-rate reduction systems cannot be ruled out. [a] Currently at Oticon Research Centre Eriksholm, 243 Kongevejen, DK-3070 Snekkersten, Denmark, mve@oticon.dk

1pPPb7. Comodulation masking release (CMR) for multiple temporal envelope maskers. Lee Mendoza (Dept. of Commun. Sci. and Disord., Louisiana State Univ., 163 M&DA, Baton Rouge, LA 70803, lmendoz@lsu.edu)

Thresholds for a pure-tone signal were measured in masking noise composed of multiple noise bands. In some conditions, one group of flanking bands (consisting of half of the flanking bands) was comodulated, and independent of the other group of comodulated flanking bands in terms of temporal envelope. The center frequencies of the flanking bands were arranged such that noise bands from the two groups were spectrally interleaved. In these conditions, the band of noise centered on the signal was a combination of two noise bands, which were each comodulated with one group of flanking bands. CMR was obtained but was not of the magnitude observed when all noise bands shared a common temporal envelope. Potential cues in the multiple envelope maskers included the information in the summed representation of the flanking bands, and the degree of temporal envelope correlation between the on-signal band and the flankers. Additional stimulus conditions examined the viability of these cues. The results of these experiments support an envelope correlation explanation for the CMR observed with the multiple temporal envelope maskers. [Work supported by the Louisiana Board of Regents.]

1pPPb8. An exploration of coherence masking protection in a spectral profile discrimination task. Peter J. Bailey (Dept. of Psych., Univ. of York, York YO10 5DD, UK, pjb1@york.ac.uk)

Gordon [P. C. Gordon, Percept. Psychophys. **59**, 232–242 (1997)] has reported a form of masking protection, in which identification thresholds for noise-masked target signals are lower when a nondistinctive cosignal is present. Gordon suggested that target signals are protected from masking as a result of their perceptual coherence with the cosignal. The experiment reported here sought to show whether cosignals enhance performance in a task involving discrimination of spectral profiles. The target signals were increments in the level of components in a complex tone (harmonics $1-7$, $F0=125$ Hz), with the third harmonic incremented in one trial interval and the fifth harmonic in the other. Discrimination threshold increments were measured for four well-practiced listeners in three conditions. In one condition, the complex tone was presented alone, without a cosignal. In the two cosignal conditions, harmonics 8–40 were added, with either a vowellike or a flat spectral profile. Average threshold increments were similar in the three conditions, and no listener showed reliably smaller threshold increments when a cosignal was present. Cosignals may confer protection from the effects of noise masking, but they do not necessarily enhance performance in other auditory tasks. [Work supported by UK MRC.]

1pPPb9. Auditory profile analysis: Effects of asynchrony and ear of presentation. Nicholas I. Hill and Peter J. Bailey (Dept. of Psych., Univ. of York, York YO10 5DD, UK, nih1@york.ac.uk)

The ability of listeners to detect an increment in the level of a 1-kHz tone relative to four flanking tones (having frequencies of 0.16, 0.40, 2.50, and 6.25 kHz) was examined under four conditions of presentation. In two conditions all five tones were presented monaurally to the listener's right ear, while in the other two conditions the 1-kHz tone was presented to the left ear with the flanking tones presented to the right. For each of the two spatial configurations, the tones were either gated on and off at the same time or else the 1-kHz tone was gated on 100 ms before, and off 100 ms after the flanking tones. The flanking tones were always gated on and off simultaneously and had a duration of 200 ms. The overall level of the stimuli was randomized on each presentation. Average thresholds in the two asynchronous conditions were approximately 10-dB higher (signal re: pedestal amplitude) than those in the synchronous, monotic condition. Ear differences alone resulted in an average elevation in threshold of 3 dB. These results suggest that asynchrony is more effective than spatial cues in preventing intensity information from being combined across frequency. [Work supported by UK MRC.]

Session 1pSAa

Structural Acoustics and Vibration: Inverse Problems in Structural Acoustics I

Sean F. Wu, Cochair
Department of Mechanical Engineering, Wayne State University, Detroit, Michigan 48202, USA

Björn A. Petersson, Cochair
Department of Aeronautical and Automotive Engineering, Loughborough University of Technology, Loughborough, Leicestershire LE11 3TU, UK

Chair's Introduction—1:55

Invited Papers

2:00

1pSAa1. An overview of the inverse problem for sound reconstruction in interior spaces. Earl G. Williams (Naval Res. Lab., Washington, DC 20375)

Calculation of the sound field between noise sources and a closed two-dimensional measurement surface is an inverse propagation problem. A powerful and popular method for the reconstruction of sound fields in this space is based on boundary element methods applied to the Helmholtz integral equation. Unfortunately, due to the numerical nature of these solutions, the physics associated with backtracking (backpropagating) the field from the measurement surface to the source surfaces is hidden. Analytic models are used to view this backpropagation as a deconvolution operation on the measured field. The nature of this deconvolving function (called the inverse propagator) is examined; it is a singular function, it is spatially local, and it *unsoothes* the measured pressure field. An understanding of the nature of the inverse propagator is critical to successful solution of the inverse problem by BEM methods (especially the regularization process), as well as the sucessful development of three-dimensional sound projection methods for sound synthesis. Furthermore, this understanding leads to new insights into the solution of the inverse problem. [Work supported by ONR and NASA.]

2:20

1pSAa2. Problem of reconstructing the full vibration field from limited data. Yuri I. Bobrovnitskii (Lab. of Structural Acoust., Mech. Eng. Res. Inst., M. Kharitonievsky 4, Moscow 101830, Russia, bobrovni@orc.ru)

The problem of expanding the vibration field from the measured points to unmeasured (inaccessible) points is posed and solved. This field reconstruction problem is one of the inversion problems of structural dynamics and acoustics. The procedure of handling it is the following: the full vibration field under study is described by a mathematical model containing a certain number of parameters (e.g., a modal model with the mode amplitudes as the model parameters); the values of these parameters are identified from the limited data; the field of the structure is then computed using this model. The main result of the present submission is that there exists the best mathematical model (containing a finite number of parameters) which gives the minimal error of describing the field in unmeasured points. Another result presented is that there also exists the optimal volume of the measurement data. The paper contains a general theory, equations relating the error to the measurement accuracy and the data volume, and some computer simulation results. Discussion of how to choose the best field mode using only the measurement data is also presented.

2:40

1pSAa3. An overview of reconstructing acoustic pressure fields using the HELS method. Sean F. Wu (Dept. of Mech. Eng., Wayne State Univ., 5050 Anthony Wayne Dr., Detroit, MI 48202)

The acoustic pressures radiated from complex vibrating structures are reconstructed by using the Helmholtz equation least-squares (HELS) method [Wang and Wu, J. Acoust. Soc. Am. **102**, 2020–2032 (1997); Wu and Yu, *ibid.* **104**, 2054–2060 (1998)]. Specific examples include an engine block and the interior space of a passenger vehicle. These structures are of arbitrary shapes and geometry, containing sharp edges and corners, and abrupt changes in surface contour. To test the robustness of the HELS method, measurements of field acoustic pressures are taken over a planar surface at a certain distance away from the structure. The reconstructed acoustic pressures, however, extend over the entire (nonplanar) surface of the structure. Note that the input data in these cases are not error free due either to measurement uncertainties or to the loss of the near-field effect. On the other hand, reconstructed acoustic pressures consist of predominantly the near-field effect. Hence the problem becomes mathematically ill-posed. To overcome this ill-posedness difficulty, an optimization scheme is developed which enables one to obtain satisfactory reconstruction results with a relatively few number of measurements in the field. The HELS method is shown to be effective in the low- to mid-frequency range, and can become a robust noise diagnostic tool for analyzing structure-borne sounds. [Work supported by NSF.]

3:00

1pSAa4. Some inverse problems in structural acoustics. D. N. Ghosh Roy (SFA, Inc., 1401 McCormick Dr., Landover, MD 20785), J. A. Warner, and L. S. Couchman (Naval Res. Lab., Washington, DC 20375-5350)

Fundamental problems of direct and inverse solutions of the multidimensional Helmholtz equation in structural acoustics are discussed. Inversion of an obstacle from the far-field pattern is compared to that of a medium and/or an inhomogeneity. An overview of various methods of solving these problems is presented. The linear techniques for a medium and/or inhomogeneity problem and some intrinsically nonlinear methods of inversion for an obstacle are described. Four nonlinear methods are compared, namely, the ansatz of potential over an internal curve, the dual space method using the Herglotz wave functions, methods based on the Rayleigh hypothesis, and the most recent method of shape differentiation combined with the Padé approximation. The efficacy and advantages of the last technique are illustrated by numerically reconstructing both penetrable and impenetrable obstacles of various shapes and orientations. The robustness of the method in regard to the initial conditions and regularization are demonstrated and its extension to elasticity and an acoustical shell structure are presented. Finally, some open questions and future directions are discussed.

3:20

1pSAa5. Identification of forces by the RIFF method. C. Pezerat and J. L. Guyader (Lab. Vibs. Acoust. de l'INSA de Lyon, 20 avenue A. Einstein, 69621 Villeurbanne Cedex, France)

The goal of this presentation is to show the application of a test bed which should permit the identification of forces created by an engine when it is not possible to measure them directly. The interest of this experimentation is to have an idea of the forces in the real situation. The mechanism consists of fixing the engine on a known plate which has characteristics related to those of the real situation. To identify forces exciting the plate, the method used, the RIFF method, is based on the computation of the force distribution, i.e., the second member of the equation of motion of the plate, from the knowledge of the flexural displacements. The main difficulty of this inverse problem comes from uncertainties in data that produce a high noise level in the result. To overcome this instability, two regularization techniques are presented. The first approach is based on singular value decomposition (SVD), consisting of eliminating the singular values of the operator applied on displacements. The second approach is based on high wave number filtering. Formulations of techniques are presented and experimental results are shown in order to validate both approaches.

3:40

1pSAa6. Source localization on a ''fuzzy structure'' beam using matched-field processing. David Feit and Matthew Craun (Carderock Div. Naval Surface Warfare Ctr., 9500 MacArthur Blvd., West Bethesda, MD 20817-5700)

Matched-field processing (MFP), a technique originally developed by the underwater acoustic community [Baggeroer, Kuperman, and Mikhalevsky, IEEE J. Ocean Eng. **18**, 401–424 (1993)] for source localization, is used to localize the source of excitation on a flexurally vibrating beam to which is attached a ''fuzzy structure (FS).'' The FS, for this study, consists of a set of flexurally vibrating strips, of randomly varying lengths, attached at uniformly spaced points along the length of the beam. MFP differs from classical inverse methods in that it does not require an inversion of the system model. Instead it correlates or ''matches'' observed signals with solutions of the equations of motion for a range of excitation points using a variety of linear and nonlinear methods. In this paper several different MFP algorithms are used and compared where the observed or simulated data is measured both globally, along the entire length of the beam, or locally over a limited region of the structure. Successful localization is found to be dependent on frequency. For lightly damped structures, the MFP localization results become ambiguous at the resonance frequencies of the structure. [Work supported by ILIR Program CDNSWC.]

4:00

1pSAa7. Inverse scattering of acoustic waves by two elastic shells in water. G. C. Gaunaurd (Naval Surface Warfare Ctr., Carderock Div., Code 684, West Bethesda, MD 20817-5700) and H. Huang (Consultant, Bowie, MD 20715)

The key problem of inverse scattering consists of the identification of an unknown target from its scattering pattern (form-function). For a single, simple-shaped target in an infinite medium, the problem has been solved elsewhere. There is present interest in the case of two elastic shells, with centers a distance d apart, insonified by a (distant) sonar, operating at frequency f, in a boundless sea. The determination of the scattering pattern of such a double-shell target was analyzed by this group earlier [viz., J. Acoust. Soc. Am. **98**, 2149–2156 (1995)]. That direct solution is now built upon to solve the associated inverse problem. From the form-function of the two shells—assumed equal—which is also assumed given in two arbitrary directions, it is determined: (a) that there are actually two interacting shells (i.e., spatial resolution), (b) their separation d, (c) the pair orientation angle α, (d) the shape and size of the shells, (e) their thickness, h, and (f) their material composition. This information is all extracted from features in the form-functions, using the detailed procedure explained here, which accounts for all orders of multiple scattering, since the shells could be close to each other, and thus be strongly interacting. A way to obtain/measure the two needed form-functions is using ultra-wideband (UWB) interrogating waveforms or UWB processing. [Work partially supported by the ILIR Program of NSWC-CD.]

4:20–4:40 Break

4:40

1pSAa8. An inversion approach based on multiple-aspect resonance analysis of finite cylindrical shells in water. Alessandra Tesei, Warren L. J. Fox, and Alain Maguer (SACLANT Undersea Res. Ctr., La Spezia, Italy)

Inverse scattering of fluid-loaded, elastic, thin-walled cylindrical shells is addressed by multiple-aspect resonance analysis. A set of aspect-dependent acoustic phenomena is selected from membrane wave and resonance scattering theories, which are expected to be backscattered by fluid-filled or empty thin-walled shells and to give rise to resonance phenomena in the *ka* range (1,50). The features selected are from spatial axial modes, and Lamb-type, Scholte–Stoneley, and shear helical waves. The last three wave families are significant only over a small range of target aspects near broadside, with the width of this range depending on shell properties. Approximate equations are formulated relating resonance behavior in the aspect-frequency domain, to target parameters such as shell outer radius, thickness, length, and material. The inverse methodology is validated on experimental data from a steel cylindrical shell with flat end-caps, filled with air or water and suspended in the water column. The target was continuously rotated on the plane of its longitudinal axis while insonified by broadband pulses. Good agreement between theory and experiment encourages the extension of the approach to more complex scatterers for classification purposes. [Work partially supported by EC (MAST DEO project).]

5:00

1pSAa9. High spatially sampled interior acoustic measurements of a turboprop aircraft for near-field acoustic holography (NAH) algorithm development. Peter C. Herdic,[a] Brian H. Houston (Naval Res. Lab., Code 7136, Washington, DC 20375), and Earl G. Williams (Naval Res. Lab., Washington, DC 20375)

Experimental results are reported of in-flight acoustic responses acquired by scanning a dense array of microphones within an aircraft interior. High data quality was obtained in several measurement sets. This database will ultimately be used for inverse and forward projections of the measured, enclosed acoustic surface to determine the velocity of the fuselage skin and the entire interior acoustic field. A discussion of the experimental design methodology will include approaches to measure the in-flight pressure field coherently during the execution of a scan, spatial sampling requirements based on measured vibration over an arc of the fuselage wall, and the effect of ambient noise on the measurement. The in-flight acoustic response shows spatial variation throughout the interior with dominant blade passage harmonics. Two ground-based (engine off) measurement scans were performed where excitation by an internal acoustic source and a point force applied to a frame assist in identification of interior acoustic modes and structural resonances. [Work supported by NASA, Langley.] [a] Also SFA, Inc.

5:20

1pSAa10. Force spectra identification by FRF matrix inversion: A sensor placement criterion. Matthias Blau (TU Dresden, Inst. fuer Technische Akustik, D-01062 Dresden, Germany)

Excitation force spectra are a key quantity in structure-borne sound characterization. In this paper, the identification of multiple broadband force spectra by FRF matrix inversion is considered. Because of the notorious sensitivity of inverse methods to small errors in measured data, such measurements must be carried out with extreme care. One major decision that could heavily affect the accuracy of the final results concerns the placement of the vibration response sensors. To date, this is often accomplished by just putting them as close as possible to the force input points, or by subjective judgment, or by considering the condition number of the FRF matrix as a criterion. In this paper, an alternative criterion is proposed which takes into account that, especially in the frequency region up to a few hundred Hz, the resulting errors are often dominated by measurement noise-induced bias on response spectra estimates.

5:40

1pSAa11. Experimental reconstruction of the vibration field in a cylindrical shell. Alexander A. Kochkin (Lab. of Structural Acoust., Mech. Eng. Res. Inst., M. Kharitonievsky 4, Moscow 101830, Russia, kochkin@hotmail.com)

The problem of reconstruction of a vibration field in an unmeasured region of a thin cylindrical shell is considered. The forced vibrating shell of finite dimension is divided into two parts: the first part (the measurement region) is accessible for measuring any vibration characteristics while the second part (the reconstruction region) is considered as ''inaccessible.'' The problem is solved using the general approach–see the presentation by Yu. I. Bobrovnitskii at this Special Session. The vibration field of the shell was modeled by a finite sum of normal waves, amplitudes of which were determined by equating the modeling values to the data. The SVD technique was used in the inverse procedure for parameter identification. Most attention was paid to finding an appropriate method for choosing the best model of the shell which minimized the reconstruction error. For the measurement error 0.08 of the experiment conducted, the reconstruction error varied from 0.2 to 0.7 as the measurement region diminished from 0.7 to 0.3.

Session 1pSAb
International Workshop on Active Noise and Vibration Control

Structural Acoustics and Vibration: Signal Processing and Controllers for Active Control

Richard J. Silcox, Cochair
Structural Acoustics Branch, NASA Langley Research Center, Hampton, Virginia 23681-2199, USA

Boaz Rafaely, Cochair
Signal Processing and Control Group, Institute of Sound and Vibration Research, University of Southampton, Southampton, SO17 1BJ, UK

Invited Papers

2:00

1pSAb1. Iterative feedback control design for active vibration control. Sandor M. Veres (School of Electron. and Elec. Eng., Univ. of Birmingham, Edgbaston B15 2TT, UK, s.m.veres@bham.ac.uk)

Model-based robust feedback control design is widespread: a parametric model is identified with some measure of the unmodeled dynamics present in the most advanced approaches. In off-line design, often open-loop experiments are used which can fail to provide satisfactory models because the identification criterion does not serve the aims of feedback robustness. Another frequent problem is possible large bias of the parametric part because of wrong model orders. In the best case large bias comes with large bounds of the unmodeled dynamics in the H-infinity or the L-1 norms. The conclusion is that the use of a plant model is the source of considerable problems while it has so far seemed a natural approach to controller design. In this paper a new ''model-free'' approach will be outlined for designing feedback vibration controllers. This will be based on a direct search using a sequence of iterative experiments. The experiments will alternate between two types: with and without the vibration source being active. The iterations of the controller parameters allowed by the sequence of experiments will lead to a sequence of improvements of control performance. This will be verified experimentally with reduction of sound-induced low-frequency vibration of a glass plate.

2:20

1pSAb2. Predictive feedback and feedforward control for systems with unknown disturbances. Jer-Nan Juang (Structural Dynam. Branch, NASA Langley Res. Ctr., Hampton, VA 23681) and Kenneth Eure (NASA Langley Res. Ctr., Hampton, VA 23681)

This paper presents the theory and implementation of a hybrid controller for general linear systems by incorporating a feedforward path in the feedback control. The generalized predictive control is extended to include a feedfoward path in the multi-input multi-output cases. There are cases in acoustic-induced vibration where the disturbance signal is not available to be used by the hybrid controller, but a disturbance model is available. In this case the disturbance model may be used in the feedback controller to enhance performance. In practice, however, neither the disturbance signal nor the disturbance model is available. This paper presents the theory of identifying and incorporating the noise model into the feedback controller. Implementations are performed on a test plant and regulation improvements over the case where no noise model is used are demonstrated.

2:40

1pSAb3. Constrained beamformer optimization for antenna arrays. Marcus Bronzel (Dept. of Elec. Eng., TU Dresden, Helmholtzstr. 18, 01062 Dresden, Germany, bronzel@ifn.et.tu-dresden.de) and Holger Boche (Heinrich Hertz Inst. fuer Nachrichtentechnik, 10587 Berlin, Germany)

A common problem for hands-free voice terminals and for smart antennas in future mobile communication systems is to optimize the directional response of an array of microphones or antennas in order to enhance the signal-to-noise-and-interference ratio (SINR). Digital beamforming (DBF) algorithms are commonly used for spatial filtering, which effectively results in more benign channel characteristics with reduced interference and delay spread. A new constrained beamforming (CBF) algorithm is presented which allows optimum beam steering and interference cancellation for arbitrarily spaced directions for signals-of-interest (SOI) as well as for interfering waveforms. The proposed CBF combines the properties of the Bartlett and the Capon beamformer [L. C. Godara, ''Application of antenna arrays to mobile communications, Part II: Beam-forming and direction of arrival considerations, Proc. of the IEEE **85**, 1193–1245 (1997)] while maintaining minimum power requirements. It is shown that the result can be interpreted as the beam vector representation using special interpolating fundamental functions. [Work supported by BMBF.]

3:00

1pSAb4. Real-time identification of multiple modes using IIR filters. Tae W. Lim (Dept. of Aerosp. Eng., The Univ. of Kansas, 2004 Learned Hall, Lawrence, KS 66045, tlim@aerospace.ae.ukans.edu)

Infinite impulse response (IIR) filter design is investigated in this work for the real-time identification of modal parameters such as natural frequencies, damping ratios, and mode shapes of vibrating structures or acoustic medium. This investigation is mainly aimed at identifying multiple modes simultaneously using a new structure of IIR filters. The previous algorithm [Lim, Cabell, and Silcox, J. Vib. Acoust. **118**, 649–656 (1996)] was limited to the identification of one or two modes due to its complexity of converting identified IIR filter coefficients to modal parameters. The new IIR filter structures are designed to allow direct conversion of filter coefficients to modal parameters and to facilitate the identification of multiple modes. The new approach provides promise for a realistic application of the algorithm for narrow-band signals, which typically contain multiple frequencies. The new IIR filter structure is described in detail in this paper. Results of the multiple mode identification are presented using the new approach. [This research was supported by Structural Acoustics Branch, NASA Langley Research Center.]

3:20

1pSAb5. Predictive control for suppression of vibration induced by flow noise. Minh Q. Phan (Dept. of Mech. and Aerosp. Eng., Princeton Univ., Princeton, NJ 08544, mqphan@princeton.edu), Kenneth Eure, and Jer-Nan Juang (NASA Langley Res. Ctr., Hampton, VA 23681)

Predictive control is based on an intuitively appealing concept where the current control action is based on a prediction of the system controlled output at some time step in the future. Originated from chemical process engineering, several predictive control methods have emerged, including model algorithmic control (MAC), dynamic matrix control (DMC), extended prediction self-adaptive control (EPSAC), extended horizon adaptive control, multistep multivariable adaptive regulator (MUSMAR), and generalized predictive control (GPC). Sharing a similar philosophy, the details of these controllers are different from each other due to different choices of cost functions, constraints, and dynamic models. Almost all of them are model-based methods. A data-based treatment of predictive control will be presented, and it will be shown how it is an effective tool to suppress flow-induced vibrations. In this approach, the predictive controller gains are synthesized directly from input–output data instead of working through an intermediate identification model. Experimental results will be used to illustrate the benefit of this data-based treatment of predictive control over conventional model-based approach. A technique will be developed to avoid drifting of the controller gains identified with closed-loop data, and comparison with other conventional methods such as conditional updating, dither, and leakage will be made.

3:40–4:00 Break

Contributed Papers

4:00

1pSAb6. Multichannel signal decorrelation using a new generalization of the prediction error filter. Jonathan G. Cook and Steve J. Elliott (Inst. of Sound and Vib. Control, Signal Processing and Control Group, Highfield, Southampton SO17 1BJ, UK, jgc@isvr.soton.ac.uk)

In many multichannel adaptive active control systems the convergence speed is limited by the correlations between the reference signal channels. This paper describes a causal digital filter capable of reducing multiple channel correlated colored input data to an underlying set of uncorrelated unit variance white signals. This filter is the inverse of the spectral factorization matrix for this data set. The problem is approached in two steps. In the first step it is shown analytically that a single-point delay prediction error filter (PEF) will produce white output error data from multiple non-white inputs. The flaw in this process is that there is an inherent matrix of gains which scales and correlates the output channels. In the second step, a technique is presented to derive this matrix of gains from the spectral density matrix of the filter output and thus calculate the appropriate inverse filter. The output from this two-step process is uncorrelated, unit variance and white. The complete signal reduction algorithm is then demonstrated for multiple-channel simulated signals and is finally calculated and tested on correlated road noise data.

4:20

1pSAb7. Nonlinear adaptive controller for electrodynamic transducers without additional sensor. Stefan Irrgang and Wolfgang Klippel (Klippel GmbH, Aussiger Str. 3, 01277 Dresden, Germany, klippel-gmbh@t-online.de)

Nonlinearities inherent in common transducers (woofers, shakers) produce new spectral components (distortion) in the reproduced sound which affect the perceived sound quality and impair active noise and vibration control. Recent research has shown that these nonlinear mechanisms are predictable and a nonlinear control can compensate for these distortions by inverse preprocessing of the electric input signal. Adaptive schemes have been developed to adjust the control parameters to the particular transducer and to cope with parameter uncertainties due to heating and aging. The adaptive controller requires an acoustic or mechanic output signal derived from the transducer. Using an additional sensor increases the costs and is impractical under harsh environment. However, a motional signal can also be derived from the back-induced EMF by monitoring the input current of the transducer only. Following this approach a nonlinear adaptive observer is implemented in a digital control system providing a robust and cost-effective solution for audio applications and active noise control.

4:40

1pSAb8. Fast convergence algorithms for active noise control in vehicles. Luis Vicente and Enrique Masgrau (Dept. of Electron. Eng. and Commun., Univ. of Zaragoza, Zaragoza E50015, Spain, lvicente@posta.unizar.es)

When the reference signal for the FXLMS algorithm is taken from an acoustic sensor, convergence can be very slow due to great eigenvalue spread. Using a nonacoustic sensor, such as a tachometer, cancellation of narrow-band noise in the sensed fundamental frequency and harmonically related ones can be achieved very fast, although other periodic noises and the underlying broadband noise will remain. Backward prediction errors resulting at the various stages of an adaptive lattice predictor (ALP) represent a time-domain orthogonalization of the input signal. An ALP structure, with the acoustic reference as input signal, before a FXLMS, makes up the FXGAL algorithm. Due to orthogonalization, FXGAL is significantly faster compared to FXLMS with reference from a microphone. When compared to FXLMS with a tachometer signal, it is not faster but it can cancel every periodic noise, independently of the harmonical relation between them, as well as the underlying broadband noise. Depending on the relative weights of the different components (periodic harmonically

related, periodic nonharmonically related, and broadband noise) in the reference signal, the FXGAL algorithm can be an excellent alternative to FXLMS. Comparative results between FXLMS (with acoustic and nonacoustic reference) and FXGAL will be presented. [Work supported by CONSI+D-DGA.]

5:00

1pSAb9. Application of nonlinear adaptive signal processing techniques to blind source separation and interference suppression. H. Leon Sibul, J. Micheal Roan, and A. Gregory Babich (Appl. Res. Lab., Penn State Univ., P.O. Box 30, State College, PA 16804-0030)

In active noise and vibration control it is important to identify independent noise generation mechanism and sources. In all large physical systems only a mixture of noise sources can be observed. The mixture model can be either linear or nonlinear. Recently there has been an explosion of significant research literature on blind deconvolution. In blind deconvolution, the actual mixture model and source signals are not known; however, in the theoretical development it is assumed that sources are statistically independent. In practice, good results have been obtained even if sources are not independent. If the mixture model is linear, statistically independent noise sources can be separated by blind deconvolution techniques that are based on the theory of the independent component analysis (ICA). We implement ICA by a cascade of the linear adaptive algorithm that is based on singular value decomposition (SVD) and a nonlinear algorithm that is based on a radial-basis function (RBF) neural network. A RBF neural network can also approximate the inverse of the nonlinear mixture model. We use a fast RBF updating algorithm for adaptation of the nonlinear network. Theoretical results are illustrated by computer simulations. Results are compared with linear adaptive signal processing algorithms. [This research has been supported by ONR, Dr. Kam Ng, Program Officer.]

5:20

1pSAb10. Digital filters used in the feedback loop of an ANR earplug. Veronique Zimpfer, Karl Buck (French German Res. Inst., BP 34, F-68301, Saint Louis Cedex, France), and Nicole Gache (CPE Lyon, LASSSO, Villeurbanne Cedex, France)

Commercially available active hearing protectors are usually implemented as ear muffs with an analog driven feedback loop. The active attenuation bandwidth of these devices is limited to about 800 Hz. Moreover, it is not possible to adapt the analog system for specific noise events or to the user's morphology. Active earplugs allow one to extend the bandwidth of the active protection to frequencies higher than 2 kHz. A digital feedback system has been implemented for active earplugs, in order to allow an adaptation to different noises and users. As the acoustic delays are too short to obtain a causal system when using FIR filters, the filters have been implemented as IIR type filters. The paper presents numerical simulations of different possible algorithms, used for the cascaded IIR filter of the ANR system. It shows how numerical errors are propagated in cascaded Bi-Quad implementations, and how an optimum signal-to-noise ratio may be obtained. The numerical predictions and experimental results will be presented and compared. As these filters will be used in a closed-loop feedback system, a numerical simulation of the behavior of the closed-loop system, including the electroacoustic transfer function of the ear plug, will be presented.

5:40

1pSAb11. A control friendly software to convert a low-cost DSP board into a powerful active noise controller. Antonio Minguez (Instituto de Investigación del Automovil INSIA, Universidad Politécnica de Madrid, Ctra. Valencia Km. 7, 28031 Madrid, Spain, aminguez@diac.upm.es) and Manuel Recuero (Universidad Politécnica de Madrid, 28031 Madrid, Spain)

A windows environment software has been developed in order to convert the low cost EZ-KIT Lite DSP board of Analog Devices into a powerful monochannel active noise controller. The software, developed with LabVIEW, downloads the code to the EZ-KIT Lite and permits one to modify in real time any working parameter until obtaining the optimal control performance. Among the parameters to control are the gain inputs, outputs, low-pass filters, and dc removing. There are three types of adaptive algorithms that can be used: filtered-X/U LMS, multiple adaptive notch, and a genetic algorithm. All these algorithms are implemented in such a way that it is not necessary to do any previous cancellation path estimation. Also implemented is internal generator that produces up to four simultaneous tones added with a white noise. As it is said before, any parameter of the algorithms and of the generator can also be easily changed in real time, when the cancellation is in progress. This permits one to obtain the best parameters before implementing an active noise controller in any application.

6:00

1pSAb12. Adaptive compensation of noise in a sonar system. Kai Wicker and Egidius Arens (STN Atlas Elektronik GmbH, Sebaldsbrücker Heerstr. 235, D-28305 Bremen, Germany)

The performance of a sonar system on a ship is strongly influenced or even limited by its own and other ship's noise. Its own noise can have different sound sources. The engine causes disturbing line spectra, the auxiliary equipment can radiate both harmonic signals and white or colored noise signals. Due to the viscous flow during ship movement, disturbing noise can also arise. Interaction between the hydrodynamic flow and the whole ship structure can excite the ship's own modes, which results in strong natural oscillations (flow noise-induced resonances). Additionally, other loud ships can disturb the sonar processing, too. An adaptive noise reduction method is presented. It is suited to reduce a ship's own machinery noise, and, with slight variations, also jamming targets. The output of the adaptive method can be calculated in the time domain as well as in the frequency domain. Working in the time-domain, techniques are available which reduce the numerical expense, but some reasons suggest the calculation in the frequency domain. Calculations based on both simulated data and real data recorded at sea are presented.

Session 1pSCa

Speech Communication: Speech Quality in Telecommunications

Hans-Wilhelm Gierlich, Cochair
HEAD Acoustics GmbH, Ebertstrasse 30a, 52134 Herzogenrath-Kohlscheidt, Germany

Mark E. Perkins, Cochair
AT&T, 101 Crawfords Corner Road, Holmdel, New Jersey 07733, USA

Chair's Introduction—1:55

Invited Papers

2:00

1pSCa1. Methods for subjective assessment of service quality: Milestones to customer-centered quality engineering. Harald Klaus (Quality and Acceptability of Tele-Services, Deutsche Telekom Berkom GmbH, Goslarer Ufer 35, 10589 Berlin, Germany)

In a liberalized market, the opinion of the customer about the quality of an entire service is a key issue for success. In the telecommunication market, technology evolves very rapidly to intelligent and integrated applications. Therefore, new views and methods for the assessment of quality aspects have to be developed in time. The first part of the presentation gives an overview of subjective assessment methods for speech as well as for audio and video applications. Furthermore, practical aspects of quality testing are discussed. In the second part, issues and trends for customer-centered quality engineering are outlined.

2:20

1pSCa2. Speech quality and the E-model. Ute Jekosch and Sebastian Möller (Inst. of Commun. Acoust., Ruhr-Universität Bochum, D-44780 Bochum, Germany, jekosch@ika-ruhr-uni-bochum.de)

The E-model is a quality prediction model for network planning purposes. Its use is going to be recommended by the ITU-T. In comparison with both listening-only and conversation tests the model often shows high predictive power. Accordingly, network planners have high confidence in its applicability. However, until now it is not yet discretely understood which aspects of quality are actually covered by E-model predictions. To name only two, uncertainties do exist, e.g., for the mode of communication (listening only or conversation) and user-related factors. In the talk, a schematic is presented which covers, besides speech-communication-related elements (one-way voice transmission quality, communication effectiveness, ease of communication) also human-factor-related and service-related elements (comfort, costs). It is shown that matters are simplified by exclusively using the MOS as the basis for a thorough verification of the model. In the course of verification, measures of user acceptance, expectation, etc., are needed in order to understand how human- and service-related features influence the users' perception of the quality of service. An approach is presented to obtain subjective judgments other than MOS on a scale which is closely related to the scale of the model, namely the transmission rating factor R.

Contributed Papers

2:40

1pSCa3. Hands-free car kits—A performance discussion of ''state-of-the-art'' solutions. Frank Kettler, Hans Wilhelm Gierlich, and Winfried Krebber (HEAD acoustics GmbH, Ebertstrae 30a, 52134 Herzogenrath, Germany)

The increasing demand for hands-free solutions in vehicles partly results from safety reasons. In several countries, the use of handsets is already prohibited for drivers. From the technical point of view, not only the ''hands-free problem''—acoustical stability and echo—has to be solved. The environmental conditions, i.e., noise level and position of microphone and loudspeaker, are extremly critical. Technical implementations include various signal processing methods such as echo cancellers, noise reduction algorithms, and level switching devices. Typically they work in conjunction with codecs (GSM or others). Consequently, speech transmission quality is influenced in various ways. Comparative measurements carried out with eight different hands-free car kits are discussed in this presentation. The test setup guarantees reproducible conditions using the auditory part of a driving simulator, artificial head technology, and a codec simulator. The determination of important objective parameters was carried out with adapted test signals, while real speech samples were used for subjective evaluation. Measurement setup and relevant parameters concerning speech transmission quality are briefly discussed. A number of listening examples demonstrate differences between various implementations.

3:00

1pSCa4. Scenarios for economic conversation tests in telephone speech quality assessment. Stephan Wiegelmann, Sebastian Möller, and Ute Jekosch (Inst. of Commun. Acoust., Ruhr Univ. Bochum, D-44780 Bochum, Germany, moeller@ika.ruhr-uni-bochum.de)

In telephony, there is a permanent need for auditory testing of the effect of different types of impairment on speech communication quality. Though quality perception is different in listening-only and conversation situations, for economic (time and money) reasons, in most cases only listening-only tests are carried out to assess telephone speech quality. For some parameters, however, conversation tests are mandatory, as the parameter under investigation affects only the conversation situation (e.g., echo, delay). In order to overcome the limitations of conversation tests, new scenarios have been developed which allow the testing of around three times as many circuit conditions within one test session compared to conventional conversation test scenarios. The scenarios cover everyday situations of information exchange, and meet most of the basic require-

ments of quality assessment scenarios (naturalness, balance, comparability, clarity). The scenarios are available in three languages and have been successfully used by different telecommunication test laboratories. Comparison with listening-only test results shows that differences exist between the two types of quality judgments, which underlines the necessity for conversation tests in order to get more valid quality judgments. Modifications of the scenarios for mobile and Internet telephony situations are presented.

3:20

1pSCa5. Expectation in quality assessment of Internet telephony. Sebastian Möller and Joachim Riedel (Inst. of Commun. Acoust., Ruhr Univ. Bochum, D-44780 Bochum, Germany, moeller@ika.ruhr-uni-bochum.de)

Telephony from Internet terminals is getting more and more popular. Thus it is interesting to know which level of quality one user expects from a connection established from a computer terminal in relation to a normal wirebound telephone. For mobile situations, it has been shown that the lower expectation results in more favorable quality judgments in comparison with wirebound systems when assessing physically equal connections. The user's expectation includes call motivation, attitude, experience, emotions, etc., and it will have an important influence on his/her perception of and judgment on quality. A conversation test has been carried out in order to investigate the quality impact due to Internet-typical impairments (absolute delay, low-bitrate codecs), both for users of a conventional wirebound telephone and an Internet terminal. In contrast to what can be observed for mobile phones, it turns out that the expectation level of potential users may result in a disadvantage effect, i.e., quality expectation is so high that Internet terminal connections are rated worse than conventional ones for physically equal connections. The situation is different for subjects who never operated a computer terminal before. Results are discussed regarding user groups and the consequences for the assessment of Internet terminal telephony.

3:40

1pSCa6. Speech quality evaluation: Auditory and instrumental procedures. Frank Kettler, Hans Wilhelm Gierlich, and Ekkehard Diedrich (HEAD acoustics GmbH, Ebertstrae 30a, 52134 Herzogenrath, Germany and Deutsche Telekom Berkom GmbH, 10589 Berlin, Germany)

The complexity of signal processing in modern communications requires advanced test procedures. This goes both for telecommunication networks and for terminal equipment. Hands-free telephones (HFT) are a typical example of telecommunication equipment showing a nonlinear, time-variant, and speech-controlled transmission characteristic. In addition, the performance depends heavily on the environmental conditions like test rooms or ambient noise. New test procedures, both auditory and instrumental, have been developed during the last few years to determine quality aspects of HFT's. The principles of auditory tests as conversational tests, specific double-talk tests, and a new realization of listening-only tests are discussed. These procedures are used for both parameter identification and value selection. The parameters found to be auditory relevant have been identified, and advanced tests for quality parameters—determining the auditory quality—were developed.

4:00–4:20 Break

4:20

1pSCa7. Psychoacoustically motivated objective speech quality evaluation procedures, PSQM, and improvements. John G. Bereends and Andries P. Hekstra (KPN Res., P.O. Box 421, NL- 2260 AK Leidschendam, The Netherlands)

PSQM (Perceptual Speech Quality Measure), measuring speech quality objectively, has been standardized by ITU-T as recommendation P.861. PSQM characterizes the perception of the (degraded) output speech signal of the system in comparison to the (ideal) input speech. A perceptual model is used that maps input and output signals onto psychophysical representations using psychophysical equivalents of frequency (Bark) and intensity (compressed Sone). The quality of the device under test is determined with a simple cognitive mapping from the differences in the psychophysical representation to the perceived speech quality in terms of Mean Opinion Scores (MOS). Within an ITU benchmark testing a limited set of unknown codec distortions the PSQM showed high correlations (around 0.97) between subjectively perceived and objectively measured speech quality. When applying PSQM to a wide variety of real world distortions two major limitations show up: First, dynamic time warping effects, as they will be found, e.g., in Internet telephony, cause a degradation in correlation. Second, the perceptual model that is used within the PSQM method is too simple to account for a wide variety of distortions. This presentation discusses extensions to the PSQM method that allows application to real world distortions.

4:40

1pSCa8. Noise reduction in acoustic signals using the perceptual coding and intelligent decision systems. Rafal Krolikowski and Andrzej Czyzewski (Tech. Univ. of Gdansk, WETI, Sound Eng. Dept., 80-952 Gdansk, Poland)

A new algorithm of broadband, nonstationary noise reduction was engineered employing the perceptual approach to the removal of noise from acoustic signals. It enables analysis and processing of sound according to characteristics of hearing sense, and employs a decision system to automatically adjust thresholds of masking. The presented algorithm provides an extension of perceptual coding applications, because it makes possible the reduction of noise included in source signals. Although noisy components of a signal may occur randomly, it is possible to estimate the noise distribution on the basis of signal analysis in silence passages of the transmission. Subsequently, the decision should be made as to the masking curves' parameter settings which will make the noise inaudible. That is the reason why an intelligent approach is used in modeling some interrelations between available noise patterns and the noise affecting consecutive portions of useful signals. The decision system was implemented in various ways using fuzzy reasoning, rough set approach, and modified feedforward neural networks with functional links. The proposed methods of noise reduction and obtained results of noisy speech processing are presented in the paper. [Work supported by the Committee for Scientific Research, Poland, Grant No. 8 T11D 021 12.]

5:00

1pSCa9. Application of auditory contours to speech quality measurements. Peter Daniel, Manfred Zollner (Neutrik Cortex Instruments, Erzb.-Buchberger-Allee 14, D-93051 Regensburg, Germany, daniel@neutrik-cortex.de), and Wolfgang Ellermeier (Univ. Regensburg, 93040 Regensburg, Germany)

For the development of instrumental speech quality measures it is important to model human auditory signal processing. The ITU-T standard P.861 for telephone transmission quality, however, neither takes into account the time-frequency resolution of the human ear nor its masking properties. Moreover the abstraction or contorization processes occurring in speech perception are disregarded. Terhardt proposed to use spectral pitch as the primary auditory contour. In our approach it is derived from the part-tone time-pattern (PTTP) originally conceptualized by Heinbach [Acustica **67**, 242–256 (1988)]. The PTTP is extracted from an aurally adequate spectral analysis. A new instrumental method based on differences of auditory contours will be presented. The results will be compared with other instrumental methods and with data from subjective listening tests.

5:20

1pSCa10. Application of automatic speech recognition to evaluation of speech transmission quality in analog communication systems. Wojciech Majewski and Wojciech Myslecki (Inst. of Telecommunications and Acoust., Wroclaw Univ. of Technol., Wybrzeze Wyspianskiego 27, 50-370 Wroclaw, Poland, majewski@aipsa.ita.pwr.wroc.pl)

The preliminary results of application of automatic recognition of isolated words to objective evaluation of speech transmission quality in analog telephone channels are presented. A memoryless, finite state recognition system with LPC, FFT, and BF-FFT (where the speech signal was filtered in Bark bands) parametrization was applied. In classification stage a dynamic time warping and nearest-neighbor algorithm were utilized. Nonsense word lists consisting of 100 logotoms were recorded in a studio by a professional male speaker and utilized next as a test material. Speech transmission quality was examined in laboratory models of telephone channels with frequency bands of 300–3400, 400–2500, and 100–6000 Hz for speech-to-white-noise ratios in the range of +15 to −15 dB. The results of objective measurements expressed in percent of logotoms correctly recognized by the recognition system were compared under the same transmission conditions with subjectively measured logotom intelligibility. The best agreement between subjective and objective evaluation of speech transmission quality was obtained for automatic speech recognition utilizing BF–FFT parametrization. The results of objective evaluation of speech transmission quality by means of the presented method are encouraging and the experiments will be continued for other communication channels (e.g., digital) and different distortions and disturbances.

5:40–6:00 Discussion

MONDAY AFTERNOON, 15 MARCH 1999 POSTER GALLERY, 2:00 TO 6:00 P.M.

Session 1pSCb

Speech Communication: Data Based Speech Synthesis and Analysis I (Poster Session)

Andy Harsin, Chair
Lucent Technologies/Bell Labs Advanced Technologies, 101 Crawfords Corner Road, Holmdel, New Jersey 07733, USA

Contributed Papers

All posters will be on display in the Poster Gallery from Monday to Wednesday, 15–17 March. Authors will be present at their posters on Monday, 15 March. To allow contributors an opportunity to see other posters, authors of odd-numbered papers will be at their posters from 2:00 p.m. to 4:00 p.m. and authors of even-numbered papers will be at their posters from 4:00 p.m. to 6:00 p.m.

1pSCb1. Automatic syllabic boundary extraction from connected speech. Andy Harsin (Lucent Technologies/Bell Labs Adv. Technologies, 101 Crawfords Corner Rd., 1L-513, Holmdel, NJ 07733)

A computational algorithm is presented which locates syllabic boundaries in connected speech. Filtered, digitized speech is processed in two stages. The first stage is an auditory front end which filters the digitized speech into critical bandwidths. The critical bands are amplitude-scaled according to a standard frequency/amplitude function, then low-frequency amplitude modulations in the 2–30-Hz range are emphasized according to a perceptual modulation sensitivity function. Next, the critical bands are low-pass filtered at 100 Hz and decimated at a rate of 25:1. Then they are low-pass filtered at 100 Hz, again creating acoustic envelopes of the processed speech, one for each critical band. During the second stage of processing, an autocorrelation-based algorithm is run on the envelopes. The local minima of this algorithm are pooled across the critical-band envelopes, yielding syllabic boundaries. The utterances used to develop and test this algorithm were taken from the Harvard Phonetically Balanced Sentences. Currently, the algorithm places boundaries within a few tens of milliseconds of where a phonemic syllabification would place them. Work continues on fine-tuning the algorithm. Another goal is to compare the algorithm's performance against human listeners'. [The author wishes to acknowledge the support of Lucent Technologies in conducting this project.]

1pSCb2. Issues in the design of an advanced unit selection method for natural sounding concatenative synthesis. Andrew Breen and Peter Jackson (BT Labs., Martlesham Heath, Ipswich IP5 3RE, UK)

This paper describes a method for selecting units from a database of recorded speech, for use in a concatenative speech synthesizer. The simplest approach is to store one example of every possible unit. A more powerful method is to have multiple examples of each unit. The challenge for such a method is to provide an efficient means of selecting units from a practical inventory, to give the best approximation to the desired sequence in some clearly specified way. The approach used in BT's Laureate system uses mixed *N*-phone units. In theory, such units could be of arbitrary size, but in practice they are constrained to a maximum of three phones. This method dynamically generates the unit sequence based on a global cost. Units are selected using purely phonologically motivated criteria, without reference to acoustic features, either desired or available within the inventory. A sophisticated method of unit selection does not, however, guarantee natural sounding synthesis. The process of signal generation plays an equally important part. The style of speech generated by such an approach is highly influenced by the underlying nature of the original recorded speech data. The paper will discuss this and other limitations of purely concatenative synthesis.

1pSCb3. System for wideband speech coding based on recursive filterbanks. Ralf Th. Pietsch and Arild Lacroix (Institut für Angewandte Physik, Johann Wolfgang Goethe Univ., D-60054 Frankfurt am Main, Germany)

Wideband speech coding becomes increasingly important because of the enhanced quality due to the extended frequency range. Possible applications are in various fields partly with fixed and partly with variable data rates: synchronous and asynchronous transmission over digital networks, mobile telephony, and multimedia systems. In this context a system is presented which is well suited for dialog communication. The signal analysis and synthesis is done by filterbanks based on recursive filters. The use of recursive filters implies short system delays in the filterbank. However, phase distortions are present and have to be considered carefully. Different methods were implemented to reduce phase distortions and to compensate group delay peaks. Coding is based on redundance and irrelevance reduction. The irrelevance reduction is implemented by the exploitation of psychoacoustical masking effects. Encoder and decoder are running on a single DSP32C signal processor in real time. The achieved data rate for good speech quality is 32 kbit/s and below.

1pSCb4. Selection of cross-fade regions for concatenation of demisyllable units. Nicholas J. Kibre (Panasonic Technologies, Inc., Speech Technol. Lab.)

This paper describes how overlap regions are identified in demisyllabic filter trajectory concatenation units used in a residually excited formant synthesis system, currently being developed at PTI/STL [Pearson, Kibre, and Niedzielski, ICSLP 1998]. This approach has been shown to produce clear and human-like synthetic speech, but as in other concatenative methods smooth transitions in cross-fade regions are essential to sound quality. This can best be obtained if a nucleus region is identified for each segment type which has consistent filter trajectories in all tokens. Database size precludes manual tuning and labeling, and this paper considers and compares two approaches to automating this task. The first of these is a rule-based approach, in which observation and phonological theory are used to formulate an ideal cross-fade region for each segment. Each token is searched for its best match to this definition, as determined according to penalty weights for different kinds of deviation from it. The second is a statistical approach utilizing HMMs to model the cross-fadable nuclear region of each segment type, as well as the adjacent transition regions. Rather than manually marking these regions in the training data, embedded training can be used to discover optimal definitions for the three phases.

1pSCb5. Blind separation of speech signals in the frequency domain. Jörn Anemüller (AG Medizinische Physik, Carl von Ossietzky Universität Oldenburg, 26111 Oldenburg, Germany)

Blind source separation algorithms try to reconstruct original signals, e.g., multiple speakers, from knowledge of their superpositions, using solely the mutual statistical independence of the source signals as criterion for separation. However, application of existing algorithms to acoustic superpositions is limited by the complex nature of room transfer functions and by the use of nonlinear computations. Expanding on our previous work, we linearize the acoustic source separation problem by moving to the frequency domain [Anemüller and Gramss, DAGA (1998)] and eliminate the need for computation of nonlinear functions by using a multiple decorrelation approach. Thus, our algorithm exploits the highly redundant structure of, e.g., speech signals in order to reduce the computational cost. Results of separation experiments are presented.

1pSCb6. A combined wideband speech and audio coder using human articulatory and auditory models. Guangyu Wang (Univ. of Kiel, Inst. of Network and System Theory, D-24143 Kiel, Germany)

The modern high-quality speech and audio coding algorithms are mostly based on human articulatory models. On the other hand, high-quality audio coders are mostly based on models of human auditory system. However, neither of these two methods can provide acceptable performance for both music and speech. In this paper a coder is proposed which operates for both wideband speech and audio signal. The structure of the coder is based on both human articulatory and auditory models. In the first part the LPC parameters are drawn using the conventional autocorrelation method in order to simulate the human articulatory system. With LPC parameters the redundancy of input signal in time domain is removed. In the second part of the coder, the LPC residual signal is further transformed into frequency domain through MLT (modulated lapped transform). The MLT coefficients are then quantized in frequency domain using the human auditory properties such as masking property. The informal listening test has shown that the proposed coder provides very good quality for wideband speech and for most music signals.

1pSCb7. Evaluation of monaural and binaural speech enhancement for robust auditory-based automatic speech recognition. Michael Kleinschmidt, Thomas Wittkop, and Birger Kollmeier (AG Medizinische Physik, Universität Oldenburg, D-26111 Oldenburg, Germany)

A major deficiency in state-of-the-art automatic speech recognition systems is the lack of robustness in additive and convolutive noise. The model of auditory perception, as developed by Dau *et al.* [J. Acoust. Soc. Am. **99**, 3615–3622 (1996)] for psychoacoustical purposes, partly overcomes these difficulties when used as a front-end for speech recognition. Especially in combination with locally-recurrent neural networks (LRNN) the model output, called ''internal representation'' had been shown to provide highly robust feature vectors [Tchorz and Kollmeier, J. Acoust. Soc. Am. (submitted)]. To further improve the performance of this auditory-based LRNN recognition system in background noise, different speech enhancement methods were examined. The minimum mean-square error (MMSE) short-term spectral amplitude estimator (STSA), as proposed by Ephraim and Malah [IEEE Trans. Acoust., Speech, Signal Process. **32**, 1109–1121 (1984)], was compared to a binaural Wiener filter [Wittkop *et al.*, this meeting], based on directional and coherence cues. Both noise reduction algorithms yield highly improved recognition rates in nonreverberant noisy conditions, while the performance in clean speech is not significantly affected. The algorithms were also evaluated in real-world reverberant conditions with speech-simulating noise and jammer speech.

1pSCb8. A text-to-speech oriented comparison of English and Polish intonation. G. Demenko (A. Mickiewicz Univ., Inst. of Linguist., Miedzychodzka 5,60-371 Poznan, Poland) and W. Jassem (Inst. of Fundamental Technol. Res., Warszawa, Poland)

Current analyses of Polish intonation in terms of $F0$ tracings indicate that it is possible to represent the melodies in the two languages within one descriptive framework, much as in the ''British'' tradition. The basic structure of an intonation phrase can be represented as ([([wPT])+[sPT]) +[NT (+NT)], where NT is the nuclear tune, sPT is the strong (accented) prenuclear tune, and wPT is the weak (unaccented) prenuclear tune. A monosyllabic sPT and a monosyllabic NT are accented, as is the first syllable of a sPT or NT of more than one syllable. The chief structural difference between E and P is that P allows mononuclear intonation phrases only, while E has a special case of a binuclear IP. If rise-fall-rise in NT position can be shown to be an independent NT in E, then this NT does not exist in P. Most of the tunes have quite similar realizations at the phonetic level. The widest differences between E and P with respect to intonation are obtained in their semantic/pragmatic meanings and in the occurrence frequencies. $F0$ traces have confirmed the linguistic structure of an intonation phrase. The importance of dynamic parameters, i.e. those

which describe the relations in the adjacent vowels/syllables describing the set of intonation structures under investigation, was tested by means of neural networks.

1pSCb9. Blind dereverberation using short-time cepstrum frame subtraction. Jean van Eeghem, M. Tohyama (Kogakuin Univ., Inst. of Comput. Acoust. and Hearing, Tokyo, Japan), and T. Koike (NTT Adv. Technol., Tokyo, Japan)

A blind dereverberation method that can be used to separate reverberant speech into an impulse response and a dry speech contribution is presented by the authors. This method is based on the assumption that the contribution of an impulse response to reverberant speech varies slowly compared to that of the dry speech. Processing the reverberant signal for short-time frames and using the special properties of the cepstrum domain, allows a recursive scheme to remove the equal impulse response contributions. Although short-time frames are processed, the effects of an amply longer impulse response can be separated from the dry speech. The assumption of a constant impulse response in only two frames and the iterative processing make the method inherently robust to changes in the impulse response. An ambiguous linear phase addition when calculating the inverse cepstrum constitutes one of the problems to limit the dereverberation performance.

1pSCb10. A robust unit selection system for speech synthesis. Alistair Conkie (AT&T Labs. Res., 180 Park Ave., Florham Park, NJ 07932)

There has been interest for many years in diphone-based speech synthesis and, recently, a rapidly increasing interest in unit selection-based synthesis (as illustrated by interest in the CHATR system). The limits of both systems are well known. While intelligibility is generally very high for diphone-based systems, the resulting signals do not sound completely natural. This happens for several reasons, amongst them the limited number of phone variants present in a typical system, and the cost of concatenating at diphone boundaries. For unit selection synthesis, typically phone-based, it is possible to produce sentences that sound surprisingly natural and intelligible from a large database. However, quality is often not consistent, and the main difficulties appear to be related to selecting acoustically appropriate units from a large database with the correct prosodic characteristics. Typically no prosody modification is done. In an effort to capture the best features of both systems a unit-selection and synthesis algorithm has been devised that allows finer control than the CHATR system (version 0.8), both by applying selective prosody modification and by exercising finer control over the units that get chosen for synthesis. Results of experiments based on this version of unit selection synthesis will be presented.

1pSCb11. Vocal-tract parameter estimation from formant patterns. Heiko Freienstein, Knut Müller, and Hans Werner Strube (Drittes Physikalisches Institut, Univ. of Göttingen, D-37073 Göttingen, Germany)

A method is proposed to estimate individual vocal-tract parameters from formant frequency patterns. Vocal-tract parameters, such as scaling factors of vocal-tract length and area were determined in reference to the given area function of an articulatory synthesizer. These individual parameters of various speakers are expected to be suitable to normalize speakers in automatic speech recognition. It has been shown by Schroeder (1967) that there is a linear relationship between relative formant frequency deviation $\delta\omega/\omega$ and a relative area perturbation $\delta A/A$ of the area function. Further, a similar relationship can be derived for length perturbation of an area function. The presented method is based on the inverse relationship: deviations of the formant frequency pattern of a speaker relative to the reference speaker are attributed to length and area perturbations of the area function of the reference speaker. A pilot study using synthetic speech showed promising results: estimated vocal-tract area functions were in good agreement with natural area functions. In the present study the method is extended to real speech. Investigations are carried out on speech samples of a German data base (PhonDat) to find speaker-specific parameters. [Work supported by Deutsche Forschungsgemeinschaft (Str 255/7-2).]

1pSCb12. Blueprint of a biomechanical model of vocal tract structures. F. Reiner Wilhelms-Tricarico (Res. Lab. of Electron., 50 Vassar St., Cambridge, MA 02139)

A new biomechanical model of the vocal tract is under construction. Structures of the tract will be represented in a three-dimensional finite-element model. In contrast to a previous pilot project [see Wilhelms–Tricarico, J. Acoust. Soc. Am. **97**, 3085–3098 (1995)], this model will make use of tri-quadratic finite elements and uses implicit time stepping methods. The new model comprises the entire oral floor and the tongue as a system consisting of a small number of finite elements. It will incorporate modeling of collision and sliding between the tongue and the teeth and the hard palate, as well as a moving mandible and hyoid bone. Algorithmic and implementation details will be presented.

1pSCb13. Phonetic recognition of Arabic figures based on formant analysis via artificial neural network. A. I. El Mallawany (Housing & Bldg. Res. Ctr. Dokki, P.O. Box 1770, Cairo, Egypt), M. I. Abdallah (Zagazig Univ., Zagazig, Egypt), M. Abd El Gawad, and H. S. Sedik (Housing & Bldg. Res. Ctr. Dokki, Cairo, Egypt)

This paper describes a speaker recognition for dependent and independent speaker systems based on the formant analysis technique. Also, this system is used for Arabic figure recognition. Linear predictive code (LPC) is applied for extracting the formants of the Arabic digits from 0–9. After training and selecting the proper network structure, the recognition accuracy is found to be 98.8% for the dependent system while it is 78.8% for the independent case. Recognition accuracy for independent speaker is improved to 95.5% when grouping the Arabic digits into three groups.

1pSCb14. On processing speech and non-speech signals in acoustics. Rostislav Pazukhin (Inst. of Modern Philology IFO, Pedagogical College WSP, 13/15 Armii Krajowej Ave., Czenstokhova, PL 42-201, Poland)

In a nonspeech communication, the pitch, duration, formants arrangement, and other acoustic features are *bearers of coded information*. Certain meanings are assigned to them by convention. The processing of nonspeech signals, consists in distinguishing and, subsequently, interpreting them. Speech oral messages are not, by contrast, amenable to such one-average ''technology.'' Each oral utterance betrays a two-layer organization. Here, true information carriers are coded *articulary changes* within the speech channel. Such gestures may be successfully ''read'' directly in TADOMA communication (by the hand placed against the face of the speaker), or in the ''inner speech'' (through bioimpulses announcing rudimentary movements of our speech organs). Mostly, however, the invisible articulations need applying certain ''echo-effects'' to become perceivable. Usually, the ''echoes'' of the voice, noise, whistle, and light (cf. ''lip-reading'') are used. Accordingly, the acoustician's mission in speech processing ought to be reduced to restoring—from the sound characteristics of utterances—the invisible changes within the throat of the speaker (through an improved ''inverse mapping, the directional hearing methodology, etc.''?). Starting from these data, physiologists and linguists could decipher messages using ''lexicon of speech gestures.''

Session 1pSP

Signal Processing in Acoustics and Psychological and Physiological Acoustics: Auditory Displays

Elizabeth M. Wenzel, Cochair
NASA Ames Research Center, MS 262-2, Moffett Field, California 94035-1000, USA

Jens Blauert, Cochair
Communication Acoustics, Ruhr-Universität Bochum, D-44780 Bochum, Germany

Chair's Introduction—1:55

Invited Papers

2:00

1pSP1. Virtual concerts in virtual spaces—in real time. Tapio Lokki, Lauri Savioja, Jarmo Hiipakka, Rami Hanninen (Telecommunications Software and Multimedia Lab., Helsinki Univ. of Technol., P.O. Box 5400, FIN-02015 HUT, Finland, Tapio.Lokki@hut.fi), Ville Pulkki, Riitta Vaananen (Helsinki Univ. of Technol., FIN-02015 HUT, Finland), Jyri Huopaniemi (Speech and Audio Systems Lab., 00045 Nokia Group, Finland), Tommi Ilmonen, and Tapio Takala (Helsinki Univ. of Technol., FIN-02015 HUT, Finland)

The DIVA system is an experimental interactive real-time virtual environment with synchronized sound and animation components. The system provides real-time automatic character animation and visualization, dynamic behavior control of virtual actors, interaction through motion analysis, sound generation with physical models of musical instruments, and three-dimensional sound auralization. The combined effect of 3-D visual and acoustic elements creates stronger immersion than would be possible with either alone. As a demonstration, a virtual band with four artificial musicians has been implemented. The user interacts with the virtual musicians by showing the tempo with a baton, like real conductors do. The animated band follows the gestures of the conductor and another user controls the viewpoint of the audience. Due to the real-time acoustic modeling and sound rendering, both users hear the auralized music in a real concert hall.

2:20

1pSP2. Perceptual criteria for eliminating reflectors and occluders for efficient rendering of environmental sound. William L. Martens and Jens Herder (Univ. of Aizu, Tsuruga, Ikki-machi, Aizu-Wakamatsu City, Fukushima, 965-8580 Japan)

Given limited computational resources available for rendering spatial sound imagery, it is important to determine effective means for choosing what components of the rendering will provide the most audible differences in the results. Rather than begin with an analytic approach that attempts to predict audible differences on the basis of objective parameters, subjective tests were executed to determine the audible difference made by two types of sound obstruction: reflectors and occluders. Single-channel recordings of 90 short speech sounds were made in an anechoic chamber in the presence and absence of these two types of obstructions, and as the angle of those obstructions varied over a 90-deg range. These recordings were reproduced over a single loudspeaker in that anechoic chamber, and listeners were asked to rate how confident they were that the recording of each of these 90 stimuli included an obstruction. The results revealed the conditions under which these obstructions have a significant impact on the perceived spatial image. These confidence ratings were incorporated into an evaluation function used in determining which reflectors and occluders are most important for rendering.

2:40

1pSP3. Auditory displays using loudspeaker reproduction in a car cabin. Winfried Krebber and Hans W. Gierlich (HEAD acoustics GmbH, Ebertstr. 30 a, D-52134 Herzogenrath, Germany, winfried.krebber@head-acoustics.de)

Playback of binaural sounds generated by an auditory display is normally made by headphones. For automotive applications such as driving simulation or sound design, however, loudspeaker reproduction is often required. A setup using a cabin-specific four-channel loudspeaker arrangement is presented and discussed. In order to get a sufficient 3-D sound, the loudspeakers have to be equalized carefully. Best results could be achieved using individualized HRTF sets. The quality of loudspeaker reproduction in comparison to headphone reproduction was evaluated by several psychoacoustic experiments. Localization and distance perception experiments show that loudspeaker reproduction does not achieve the same quality as individualized headphone reproduction. However, for simulator applications the achieved quality is quite sufficient.

3:00

1pSP4. Spatial auditory displays for speech communications: A comparison of free-field and virtual acoustic environments. Todd Nelson (AFRL/HECP, 2255 H St., Wright–Patterson AFB, OH 45433-7022, tnelson@al.wp.afb.mil), Mark Ericson (AFRL/HECB, Wright–Patterson AFB, OH 45433-7901), Robert Bolia (Veridian, Dayton, OH 45440), and Richard McKinley (AFRL/HECB, Wright–Patterson AFB, OH 45433-7901)

The ability of listeners to monitor the simultaneous presentation of multiple speech signals was evaluated in free-field and virtual acoustic environments. Two acoustic environment conditions (free-field and virtual) were combined factorially with two spatial conditions (spatially separated and nonspatially separated), eight simultaneous talker conditions (1, 2, 3, 4, 5, 6, 7, and 8), and two sex of critical speech signal (male and female) to provide 64 experimental conditions. A within-subjects design was used. Participants, four males and four females, were required to detect and identify the presentation of critical speech signals among a background of nonsignal speech events. Speech stimuli consisted of a call sign and a color–number combination contained within a carrier phrase (e.g., ''Ready TIGER go to WHITE ONE now.''). The USAF Air Force Research Laboratory's (AFRL) Auditory Localization Facility—a 277-speaker geodesic sphere housed within an anechoic chamber—was used for free-field presentation, and AFRL's 3-D auditory display generators were employed for virtual presentation. Results indicated that spatial separation of the speech stimuli enhanced performance efficiency of the free field and the virtual conditions. Implications for the design of spatial auditory displays to enhance communication effectiveness and situation awareness are discussed.

3:20

1pSP5. Sonification of range information for 3-D space perception. Evangelos E. Milios, Bill Kapralos, and Sotirios Stergiopoulos (Dept. of Comput. Sci., York Univ., North York M3J 1P3, Canada, eem@cs.yorku.ca)

A device is presented that allows 3-D space perception by sonification of range information obtained via a point laser range sensor. The laser range sensor is worn by the user, who scans space by pointing the laser beam in different directions. The resulting stream of range measurements is then converted to an auditory signal whose frequency or amplitude varies with the range. This device differs from existing navigation aids for the visually impaired. Such devices use sonar ranging whose primary purpose is to detect obstacles for navigation, a task to which sonar is well suited due to its wide beam width. In contrast, the purpose of this device is to allow users to perceive the details of 3-D space that surrounds them, a task to which sonar is ill suited, due to artifacts generated by multiple reflections and to limited range. Preliminary trials demonstrate that the user is able to detect corners and depth discontinuities accurately with ease and to perceive the size of the surrounding space.

3:40

1pSP6. Auditory perception of rolling balls. Mark Houben, Luuk Franssen, Dik Hermes (IPO, Ctr. for Res. on User-System Interaction, P.O. Box 513, NL 5600 MB Eindhoven, The Netherlands, houben@ipo.tue.nl), Armin Kohlrausch, and Berry Eggen (IPO and Philips Res. Labs., Eindhoven, The Netherlands)

Two experiments investigating the perception of recorded sounds of rolling wooden balls are reported. In the first experiment, whether subjects can identify differences in the size of rolling wooden balls, is studied. In the second experiment, the velocity of rolling balls is varied. Real recordings of wooden balls rolling over a wooden plate were presented pairwise, with a 700-ms pause in between. The stimuli had a duration of 800 ms and were presented at equal SPL. Subjects had to decide which of the two sound examples was created by the larger (first experiment) or faster ball (second experiment) (2I2AFC procedure). The results of the first experiment show that subjects are able to identify differences in the size of rolling balls, except for the stimulus pair with the smallest relative difference in diameter of 14%. The second experiment reveals that most subjects can clearly discriminate between rolling balls with different velocities, if the relative difference exceeds about 30%. However, some subjects had difficulties in labeling the sounds correctly, resulting in percentage correct responses close to 0%. It is to be expected that labeling errors will disappear when subjects receive feedback about the correctness of their responses.

4:00–4:20 Break

Contributed Papers

4:20

1pSP7. A filtering model for efficient rendering of the spatial image of an occluded virtual sound source. William L. Martens, Jens Herder, and Yoshiki Shiba (Univ. of Aizu, Tsuruga, Ikki-Machi, Aizu-Wakamatsu City, Fukushima, 965-8580 Japan)

Rendering realistic spatial sound imagery for complex virtual environments must take into account the effects of obstructions such as reflectors and occluders. It is relatively well understood how to calculate the acoustical consequence that would be observed at a given observation point when an acoustically opaque object occludes a sound source. But the interference patterns generated by occluders of various geometries and orientations relative to the virtual source and receiver are computationally intense if accurate results are required. In many applications, however, it is sufficient to create a spatial image that is recognizable by the human listener as the sound of an occluded source. In the interest of improving audio rendering efficiency, a simplified filtering model was developed and its audio output submitted to psychophysical evaluation. Two perceptually salient components of occluder acoustics were identified that could be directly related to the geometry and orientation of a simple occluder. Actual occluder impulse responses measured in an anechoic chamber resembled the responses of a model incorporating only a variable duration delay line and a low-pass filter with variable cutoff frequency.

4:40

1pSP8. Communication and 3-D sound: Speech intelligibility and speaker recognition. Rob Drullman and Adelbert W. Bronkhorst (TNO Human Factors Res. Inst., Kampweg 5, 3769 DE Soesterberg, The Netherlands)

In a 3-D auditory display, sounds are presented over headphones in a way that they seem to originate from virtual sources in a space around the listener. The possible merits of such a display were investigated with respect to speech intelligibility and speaker recognition against a background of competing speech. Various conditions were investigated: speech material (words or sentences), presentation mode (monaural, binaural, or

3D), number of competing speakers (1–4), and virtual position of the speakers (in 45° steps around the frontal horizontal plane). Average results for 12 listeners show an increase of speech intelligibility for a 3-D presentation, with more than two competing speakers compared to conventional monaural or binaural presentation. The acuity to recognize a speaker is slightly better and the time required for recognition is significantly shorter for a 3-D presentation in the presence of two or three competing speakers. Although absolute localizability of a speaker is rather poor, spatial separation appears to have a significant effect on communication. For either speech intelligibility, speaker recognition, or localizability, no difference is found between the use of an individualized 3-D auditory display and a general display. [Work supported by the Royal Netherlands Navy.]

5:00

1pSP9. Simplified auralization of reflections in a virtual auditory environment. Bernd Dürrer (Inst. of Commun. Acoust., Ruhr Univ. Bochum, Geb. IC 1/132, 44780 Bochum, Germany, duerrer@ika.ruhr-uni-bochum.de)

Based on the mirror-image method, a system for generating virtual auditory environments can simulate reflections using virtual sound sources. During the auralization process, the signal of each virtual sound source has to be convolved with the appropriate pair of HRTFs. In this investigation, a simplified model based only on interaural time and intensity differences was used for the auralization of higher-order reflections: This approach greatly reduces the necessary computational effort. Stimuli using the simplified model were compared in listening tests with stimuli using convolution with HRTFs. The tests were performed with artificial-head HRTFs (17 subjects) and individual HRTFs (9 subjects). In addition to the reduction of computational costs, significant perceptual effects on the extent of the auditory event were noted which are believed to be beneficial for certain applications (e.g., telecommunications). The usability of this model was evaluated in a speech intelligibility test in a concurrent speakers scenario. [Work supported by the EU project AUDIS (Esprit No. 22352).]

5:20

1pSP10. Design criteria for auditory virtual environments. Jörg Sahrhage (Inst. of Commun. Acoust., Ruhr Universität Bochum, 44780 Bochum, Germany, sahrha@ika.ruhr-uni-bochum.de)

During the last decade a large variety of different systems and technologies for generating auditory virtual environments emerged, ranging from low-cost displays for computer games to high-end interactive and immersive systems comprising real-time head tracking and more or less authentic room simulation. Auditory virtual environment generators employing different technological approaches have been developed for various application areas like navigation aids, teleconferencing systems, virtual control rooms, integrated multi-modal VE generators, or even as tools for psychophysical research. Depending on the particular application, perceptually relevant parameters (e.g., responsiveness, smoothness, and authenticity) will be identified on the basis of psychophysical knowledge. Further, an attempt will be made to derive and quantify adequate physical design criteria. An overview of the available auditory VE generators will be followed by a careful analysis and comparison of the system's alleged capabilities and technological constraints. These will be checked against the proposed application-dependent design criteria.

5:40

1pSP11. A sound judgment depending on the urban visual setting? Stephanie Viollon and Catherine Lavandier (Univ. de Cergy, IUT Dept. Genie Civil, Rue d'Eragny, Neuville sur Oise, 95031 Cergy Pontoise Cedex, France, viollon@u-cergy.fr)

In a number of experiments carried out in the experimental psychology field, audition and vision proved to provide information which interacted each other. What about the audio–visual interactions in the city? The first aim of this research was to develop an experimental procedure involving methodological parameters best suitable to test the influence of the visual setting on the sound judgment in the complex sound environment. The second one was to apply it to various urban situations. In a series of simulation tests, participants rated some urban sound stimuli and this, under different visual conditions varying according to the degree of urbanization. An artificial audio–visual environment was specifically created. The experimental methods were based on three types, involving different structures of presentation of the audio–visual combinations. For each of them (except for the completely random one), two types of orders of presentation of both the visual and sound sequences were defined. The results for all the experiments were commented on and compared. The best suitable experimental method was validated. The present results point out that the visual influence was many sided. Some clusters of sound stimuli and sound variables were defined according to the visual influence exerted.

6:00–6:20

Discussion and demonstration sign-up

Attendees may ask questions of session authors and may sign up to attend a demonstration of DIVA (1pSP1), or to present their own sound samples, in a high quality studio environment. Nearly all sound formats up to 12 channels can be reproduced for listener groups of up to 20 persons. The studio is located nearby.

Session 1pUW

Underwater Acoustics: Wave Propagation: Session in Honor of Leonid M. Brekhovskikh I

Peter N. Mikhalevsky, Cochair
SAIC, 1710 Goodridge Drive, McLean, Virginia 22102, USA

Nikolai Dubrovsky, Cochair
N.N. Andreyev Acoustics Institute, 4 Shvernika Street, 117036 Moscow, Russia

Invited Papers

2:00

1pUW1. Acoustic thermometry of ocean climate (ATOC). Walter Munk (Scripps Inst. of Oceanogr., Univ. of California, San Diego, 9500 Gilman Dr., La Jolla, CA 92093) and ATOC consortium

The purpose of ATOC is to monitor ocean variability over scales exceeding 1 year and 5000 km, using the method of ocean acoustic tomography. ATOC takes advantage of the favorable condition in the sound channel for low-frequency propagation. By forming long-range averages, the very intense mesoscale variance is reduced by two orders of magnitude to permit the detection of the relatively weak climate signals. Results of 15 months of transmissions from a source off Monterey, California will be shown. The exploration of the oceans by acoustics dates back to the use of acoustic depth meters and the navigation of drifting buoys. With the modern development led by Brekhovskikh, the move is toward matched-field methods which attempt to interpret the entire recorded sound field in terms of the pertinent ocean parameters.

2:40

1pUW2. Leonid Brekhovskikh: The man and the scientist. Nikolai A. Dubrovsky (Andreyev Acoust. Inst., #4 Shvernika Ul., Moscow 117036, Russia, dubrov@akin.ru)

L. Brekhovskikh was one of the main founders and a first Director of the Acoustics Institute (AI) of the USSR Academy of Sciences (1954). He contributed a lot in the selection of young gifted scientists and engineers as AI staff, formation of the main branches of research in AI, construction of new buildings and experimental setups, and promoted a new approach to design and construction of the research vessels *Sergei Vavilov* and *Petr Lebedev*. The active creative work of L. Brekhovskikh in AI (1963–1980) became even more intensive after he left the director's position. It relates to new theoretical achievements, fruitful and numerous experiments in the ocean, organizing the famous Zvenigorod conferences on ocean acoustics, and publishing the fundamental treatise ''Acoustics of the Ocean.'' Brekhovskikh possesses the personal features that facilitate his achievements in science. He is a very gifted, amicable, benevolent, reserved, purposeful, concentrated, and rational person. Sport exercises and yoga practice have considerably supported his creative efforts for decades.

3:20

1pUW3. Theory of sound propagation in the ocean: A tribute to L. M. Brekhovskikh. Finn B. Jensen (SACLANTCEN, Viale S. Bartolomeo 400, 19138 La Spezia, Italy, jensen@saclantc.nato.int)

This presentation will be an account (from a personal perspective) of the impact L. M. Brekhovskikh's first (and now classic) book on *Waves in Layered Media* from 1960 has had on the development of modern-day numerical models for solving ocean acoustic problems. A whole generation of acoustic modelers, starting in the early 1970s, devoted a career to developing computer codes that would predict sound propagation through a realistic ocean environment, including refraction, scattering, and diffraction of sound within the water column itself, as well as reflection and scattering at ocean boundaries (sea surface and seabed). Not everybody realized that much of the underlying theory had been developed years before and presented in the monograph by Brekhovskikh in 1960 (English edition). In fact, much of the numerical work undertaken in the 1970s and 1980s was merely an automation—through the use of a computer—of solution procedures already outlined by Brekhovskikh. Few, if any, have contributed more to establishing a sound theoretical foundation for ocean acoustics, and L. M. Brekhovskikh's influence on the field can hardly be overestimated.

3:40

1pUW4. Development of underwater acoustics in China and L. M. Brekhovskikh's early activities in China. Dinghua Guan (Inst. of Acoust., Chinese Acad. of Sci., Beijing 100 080, PROC, zrh@canna.ioa.ac.cn)

In this paper the early activities and influence of L. M. Brekhovskikh in the development of underwater acoustics in China are reviewed. The activity of Brekhovskikh as an invited underwater acoustics expert in the formulation of the 12-year plan of S&T development of China in 1956 is described. This paper reviews the early development of underwater acoustics in China, including the visit of Chinese experts to the Institute of Acoustics in Russia, the first joint Sino–Russian experiment in the South China Sea, and the training of young Chinese scientists. The monograph ''Waves in Layered Media'' has had a large influence on Chinese underwater acoustics. This paper also reviews part of the research on underwater acoustics in China. The ray-mode theory was developed, improved, and used in propagation, reverberation, and noise field modeling in shallow water. The relationship between rays and normal modes was analyzed and proved. The influence of sea bottom in shallow water was expressed in terms of angular dependence of bottom reflection loss. Wave theory for long-range reverberation was developed. MFP, MMP, and other methods of positioning and inversion was developed. Internal waves and their influence on sound propagation were studied.

4:00–4:20 Break

4:20

1pUW5. The tangent plane approximation and related approaches in rough surface scattering theory. Alexander G. Voronovich (NOAA/ Environ. Technol. Lab., 325 Broadway, Boulder, CO 80303, agv@etl.noaa.gov)

The tangent plane approximation (TPA) was introduced into the theory of wave scattering from rough surfaces by L. M. Brekhovskikh in 1952. This method corresponds to the semi-classical (WKB) approximation and is the second ''classical'' method (after the small perturbation method introduced into this realm by Rayleigh in 1907) that is widely used for the solution of wave propagation problems. Development of this approach significantly increased the capabilities to solve practical tasks and produced a long-lasting effect on other theoretical developments. For example, the operator expansion method or the small-slope approximation developed recently could be considered as a generalization of the TPA. The first part of the talk will be devoted to a demonstration of the relationship between TPA and different ''nonclassical'' approaches developed later. In many but not all instances, TPA could be obtained as a zeroth-order iteration of an appropriate integral equation for surface sources (for this reason TPA is also called the Kirchhoff approximation). However, some other approaches to the approximate solution of this integral equation based on smoothness of the rough surface are also possible. Corresponding enhancements of the TPA will be considered also for the case of impedance surface.

4:40

1pUW6. Leonid M. Brekhovskikh and his scientific school. Yury P. Lysanov (Andreyev Acoust. Inst., 4 Shvernik Str., Moscow, 117036 Russia, bvp@asu.acoins.msk.su)

The following items will be discussed: The first meeting with L. M. Brekhovskikh (1951), the Acoustics Laboratory at the Lebedev Physics Institute, L. M. Brekhovskikh and the organization of the Acoustics Institute, a collection of young scientists and post-graduates from many Russian cities for the new Institute, a post-graduate studentship, new problems in ocean acoustics, wave scattering by rough surfaces, Brekhovskikh's approximation (the tangent plane method), the growth of international relations, the Second and Fourth International Congresses on Acoustics (USA, 1956; FRG, 1959), all-union Acoustical Conference in Moscow (1958), the great role of L. M. Brekhovskikh in educating young scientists in ocean acoustics and oceanology (lectures at the Moscow State University and the Moscow Institute of Physics and Technology), scientific seminars under the supervision of L. M. Brekhovskikh (Sukhumi, Zvenigorid, Moscow), and Brekhovskikh's books and papers and their fundamental contribution to ocean acoustics and oceanology.

5:00

1pUW7. Applications of the waveguide invariant approach. William A. Kuperman, Gerald L. D'Spain, Hee Chun Song, and Aaron M. Thode (Marine Physical Lab., Scripps Inst. of Oceanogr., La Jolla, CA 92093-0704)

The waveguide invariant approach [S. D. Chuprov, *Acoustics of the Ocean: Current Status*, edited by Brekhovskikh and Andreevoi (Nauka, Moscow, 1982), pp. 71–91; L. M. Brekhovskikh and Y. P. Lysanov, *Fundamentals of Ocean Acoustics*, 2nd ed. (Springer-Verlag, Berlin, 1991), pp. 139–145] summarizes the dependence of robust interference phenomenon on the ocean environment by a parameter denoted ''β.'' This elegant approach is based on the dependence of group speed on phase speed for general classes of environments. It has been used to describe interference patterns in the range-frequency plane for range-independent and two-dimensional, mildly range-dependent environments. The approach is extended to include the third dimension, azimuth dependence. Furthermore, an analogous derivation for describing the ambiguity structure of a broadband linear matched-field processor reveals that the trajectories of sidelobes of such a processor in the range-frequency plane are also subject to the same invariant description. A connected result is that the focus of a phase-conjugate array can be shifted away from or toward the original probe source by a process directly related to the waveguide invariant formalism. These new applications have all been experimentally verified.

5:20

1pUW8. Wave diffraction at reflection and propagation in layered media. Oleg A. Godin (School of Earth and Ocean Sci., Univ. of Victoria, P.O. Box 3055, Victoria, BC V8W 3P6, Canada, ogodin@uvic.ca)

In his theory of waves in layered media, L. M. Brekhovskikh has systematically employed integral representations of the field in terms of plane or quasi-plane waves, with all the other useful representations of the field derived from this exact solution. It is this approach that enabled him to efficiently study, and for the first time gain a deep insight into and a quantitative description of the fundamental diffraction phenomena accompanying total reflection, guided propagation, and formation of caustics in inhomogeneous media. In this presentation, L. M. Brekhovskikh's work on wave diffraction in layered media, including his concept of diffracted rays, study of ray and beam displacement at reflection, investigation of ray theory and the WKBJ approximation domains of validity, and an exact solution for a range-dependent benchmark problem, are reviewed. Recent developments in the theory of acoustic propagation in inhomogeneous media are traced back to the ideas first introduced and explored by L. M. Brekhovskikh.

5:40

1pUW9. My life, my teachers, pupils, and friends. Leonid M. Brekhovskikh (Acoust. Wave Propagation Lab., P. P. Shirshov Oceanology Inst. of the Russian Acad. of Sci., 36 Nakhimovsky Av., Moscow, 117851 Russia, leon@rav.sio.rssi.ru)

The presentation will cover the following topics: Childhood dreams: Have they become a reality? Why and how did I become an acoustician? Sixty years of creativity in the golden times of Russian science, including oceanography and ocean acoustics. Contact with which outstanding persons did influence my world outlook? What could I pass on to my pupils? What does the ''iron mode of life'' mean? What is the short- and long-term future of Russian science from my point of view?

Posters from various technical sessions remain on display in the Poster Gallery.

Posters from sessions which contain both lecture and poster presentations will be attended by the authors as listed below.

10:00—12:00

1pNSb12	Weise, Volkmar	Rotational noise generation in peripheral fans
1pNSb13	Jiricek, Ondrej	Experiences with attenuation of low frequency noise in duct
1pPAb12	Niederdraenk, Torsten	A correlation-measuring-system for ultrasonic NDT using maximum length sequences
1pPAc12	Menguy, Ludovic	Non-linear effect of The inertia of The fluid on acoustic streaming in cylindrical guides
2pNSa12	Peters, Juergen	Prediction of railway induced vibration by means of transfer functions

Also, the following poster sessions are scheduled:
Poster Session 2aMU (in MA141)
Poster Session 2aPPb

Session 2aAAa

Architectural Acoustics: Modeling of Halls; Halls with Special Features

Jürgen Meyer, Cochair
Physkalisch-Technische Bundesanstalt, Bundesalle 100, 38116 Braunschweig, Germany

Leo L. Beranek, Cochair
975 Memorial Drive, Suite 804, Cambridge, Massachusetts 02138-5755, USA

Chair's Introduction—7:55

Invited Papers

8:00

2aAAa1. Room acoustic simulation in the planning of concert halls and opera houses. Eckard Mommertz (Müller-BBM, Robert-Koch-Straße 11, D-82152 Planegg, Germany)

In room acoustic planning and design of concert halls and opera houses, computerized prediction of sound transmission gains an increasing significance. The room acoustic simulation may give a more reliable prediction of the room acoustic conditions to be expected. Furthermore, the visualized and auralized results have a positive effect on the communication between acoustician and architect. In this paper, the requirements as well as present possibilities and limitations of room acoustic prediction in practice are described by means of exemplary current building projects. Some important aspects such as coupled volumes, diffuse wall reflections, curved surfaces, or grazing sound transmission above the audience are discussed.

8:20

2aAAa2. Scale model experiences in concert and opera hall design. Takayuki Hidaka (Takenaka R&D Inst., 1-5-1, Otsuka, Inzai, Chiba, 270-1395 Japan, hidaka.takayuki@takenaka.co.jp)

Scale model experiments were executed for two concert halls and two opera houses which recently opened in Tokyo. Based on the geometrical acoustic analysis by using CAD model, effective room shapes were studied so as to minimize the extra labor at the scale model test. Then, 1:10 scale models made of wood and proper acoustical materials were constructed. Up-to-date digital signal processing technique was applied in order to improve the accuracy of the experiment. Also, several new ideas concerning the sound source, receivers, scale modeled seatings, and how to calibrate the air absorption were introduced, intended for the precise prediction of the room acoustical parameters. Thus, monaural parameters RT, EDT, C80, D, G, and ST, and binaural parameter IACC were measured in the scale models, and they were compared with those measured in real halls. The accuracy and problems of this method were discussed with the acoustical data found here.

8:40

2aAAa3. Recent multi-purpose hall designs in Denmark with physically variable acoustics. Anders Chr. Gade (Dept. of Acoust. Technol., Tech. Univ. of Denmark, Bldg. 352, DK 2800 Lyngby, Denmark, gade@dat.dtu.dk) and Niels Vilhelm Jordan (Jordan Akustik, Gevninge, Denmark)

This paper describes two recent Danish multi-purpose hall designs, in which acoustic variability has been accomplished in different ways: through variable absorption and variable volume, respectively. The different approaches were chosen in order to insure that not only reverberation time (T) and so clarity (C), but also the strength parameter (G) could be varied in a favorable direction in view of the prescribed uses of the halls. The hall with variable absorption is the assembly hall in the new extension to the Royal Library in Copenhagen to open in fall 1999. This hall will seat 600 people and be used for chamber music concerts, symphony orchestra rehearsals, and amplified speech. For the latter two functions, a reduction in G along with reduction in T was considered favorable. The hall with variable volume is the recently opened Esbjerg Musikhus seating 1100 and equipped with a full stage house. This hall is used for symphonic concerts and musicals as well as drama and conferences. In this hall, maintaining or even increasing G along with a reduction in T is advantageous, especially in the drama theatre mode. The paper will describe the design of these two halls along with acoustic measurement results.

9:00

2aAAa4. Variable-volume/coupled-volume response at Sala Julio Prestes. Christopher N. Blair (Jaffe Holden Scarbrough Acoustics, 114A Washington St., Norwalk, CT 06854) and José Augusto Nepomuceno (Acústica & Sônica, 05416-011 São Paulo-SP, Brazil)

Sala Julio Prestes (opening in early 1999) is an adaptive conversion of a railway station in São Paulo, Brazil into a traditional ''shoe-box'' concert hall. A unique feature of this 1600-seat room is the ceiling, formed in 15 large, tightly spaced, coffered panels. The nine central panels can be raised or lowered independently, while the six edge panels move in symmetric pairs. When the ceiling pieces move together, the room volume can be incrementally adjusted, from a minimum of approximately 12 000 m^3 to a maximum of about 28 000 m^3. When the pieces are placed at different levels, various coupled-volume conditions between the lower audience chamber and the volume above the ceiling are also possible. The coupled response is further tunable by provision of absorptive banners which can be deployed in the space above the ceiling panels. Acoustic measurements and binaural recordings of orchestral excerpts in this room with an audience are planned for late 1998 and early 1999. This paper presents preliminary results of these efforts, including recorded musical examples played with various ceiling configurations.

9:20

2aAAa5. Links between concert hall geometry, objective parameters, and sound quality. Robert Essert (Arup Acoustics, Boston House, 36-38 Fitzroy Square, London W1P 5LL, UK)

For decades, the design of concert halls was driven by considerations of time history alone (T60, C80, ITDG), and as a result, little importance was attached to room geometry. The subjective importance of binaural dissimilarity has been a strong, though often simplistic, influence on recent designs. While listening experience has shown which fundamental room forms sound better than others, computer modeling and statistical analysis have enabled systematic investigation of the degree to which the geometry affects the sound. Using simple parametric models, this study will investigate effects of surface parallelism, concavity, and convexity on spatial and monaural objective acoustical parameters and on essential subjective attributes.

9:40

2aAAa6. Consistency in acoustic design when building symphonic performance halls. Christopher Jafe, Mark Holden, and Robert Lilkendey (Jaffe Holden Scarbrough Acoustics, Inc., 114A Washington St., Norwalk, CT, cjaffe@jhsacoustics.com)

The acoustic success of all concert hall designs depends on meeting the subjective response of the audience and the performers. Since it is now possible to correlate subjective preferences of listeners and players with quantitative physical acoustic criteria, it is axiomatic that the acoustician should be consistent in setting acoustic environmental criteria for all spaces programmed for symphony performances. This paper describes the application of key physical acoustic criteria related to hall liveness, warmth, and intimacy in the design of rectangular and surround concert halls, multiuse proscenium style performances spaces, and symphonic music pavilions. In addition, the authors will illustrate how the consistent application of these same acoustic criteria can enable the practitioner to develop successful symphony halls and virtual concert facilities utilizing electronic reflected energy systems (ERES). All of the facilities described in this paper incorporated the reflections corelated to listener and performer preferences and were extremely well received by audiences, performers, and the press.

10:00

2aAAa7. Hammerson Hall, The Living Arts Centre in Mississauga, Ontario. Robert Wolff and Damian Doria (Artec Consultants, Inc., 114 W. 26th St., 9th Fl., New York, NY 10001-6812, dd@artec-usa.com)

This paper describes how adjustable acoustics features, effective micro and macro shaping, low background noise levels, and appropriate seat count contribute to a high-quality flexible performance environment. Diagrams, graphs, and images explain the techniques. Hammerson Hall is a concert theater designed to provide suitable acoustic environments for such varied performance media as symphony orchestra, chamber orchestra, recital ensembles, opera, musical theatre, ballet, dance, popular music, speech plays, comedy, lectures, and meetings. The room accommodates 1233 patrons for events when an orchestra is in the pit or on a concert

platform, but it can quickly accommodate 1315 patrons for events where seats are located on seating wagons on the orchestra pit lift. Hammerson Hall is basically rectangular in shape; however, architectural elements make it appear to be curvilinear. The room also has flexible acoustic absorption and volume. Horizontal balconies and shelves act as reflectors, lateralizing sound energy for acoustic music events.

10:20–10:40 Break

Contributed Papers

10:40

2aAAa8. Assessing and optimizing the acoustical parameters of concert halls for Korean traditional music. Kyoungsoo Park, Koeng-Mo Sung (School of Elec. Eng., Seoul Natl. Univ., Seoul, Korea, med@acoustics.snu.ac.kr), and Yeongha Choi (Dept. of Audio Production, Dong-Ah Broadcasting College)

The western music has been studied for many decades in acoustical viewpoint. Many objective parameters are developed for the purpose of assessing the concert halls and optimal values of them were studied. Oriental music, however, and musics of the other cultures have not been studied well yet and neither is Korean traditional music. Although Korean traditional music is somewhat different from western music in sense of the structure of instruments, the style, and the concert halls, something making common people feel the music to be beautiful may have many factors in common. In this paper, a few acoustical parameters of Korean concert halls have been studied by that assumption. Many parameters of traditional concert halls and modern concert halls for Korean traditional music have been measured. The halls were modeled for computer simulation and then varied to find optimal conditions of the halls for Korean traditional music by listening to artificially generated live music in the simulated virtual halls. The method of assessing and finding the optimal condition proposed in this paper may be applied to the other cultural music, too.

11:00

2aAAa9. Acoustical design of the Walt Disney Concert Hall in Los Angeles. Yasuhisa Toyota (Nagata Acoust., Inc., Hoshino-Bldg. 8F, 5-23-13 Sendagaya, Shibuya-ku, Tokyo 151-0051, Japan, toyota@nagata.co.jp)

A completely new concert hall is scheduled to be opened in the downtown of Los Angeles. The hall was named the Walt Disney Concert Hall, after the late Walt Disney, since the project was started based on the donation of 50 million dollars by Mrs. Disney. The hall was designed as a monopurpose concert hall mainly for orchestral music and is scheduled to be a home hall of the Los Angeles Philharmonic Orchestra and Esa-Pekka Slonen, the Music Director of the orchestra. The hall has approximately 2400 seats and widely spread seating arrangements around the stage like the Berlin Philharmonic hall and the Suntory Hall in Tokyo. Computer simulation studies were carried out to determine the room shape, and acoustic tests with 1/10 scale model were introduced in the final process of the design stage. Construction work is scheduled to start in March 1999, and be completed in 2002. Acoustical design of the hall, especially on its room acoustics and the results of the 1/10 scale model tests, will be reported.

11:20

2aAAa10. The acoustics evolution of Chicago's orchestra hall: Construction details. Dawn R. Schuette and Scott D. Pfeiffer (Kirkegaard and Assoc., 4910 Main St., Downers Grove, IL 60515)

Chicago's Orchestra Hall is a space that has undergone numerous modifications in its 94-year history. Recent efforts have been the most substantial, producing significant changes. This paper will supplement an invited paper by presenting details of design and construction methods that resulted in the acoustic improvements. Particular issues to be discussed will include construction methods of adding volume to an existing and operating building, details of massive construction used to increase bass response, and techniques of sealing fireproofing, plaster, and concrete within the acoustic volume.

11:40

2aAAa11. Sopukka, the new experimental stage of the Turku City Theatre. Anssi Ruusuvuori (Akukon Oy Consulting Engineers, Kornetintie 4 A, FIN-00380 Helsinki, Finland, anssi.ruusuvuori@akukon.fi)

Sopukka, the new experimental stage of the City Theatre of Turku, Finland, was built inside the frame of the old small stage. The new stage was designed as a ''black box,'' with movable seating areas for 80 to 150 spectators. The main design goal was flexibility, which would allow as many different staging arrangements as possible. Because of the lack of traditional stage area, the main acoustical design goal was to have an even distribution of sound from any part of the room to any possible seating area. As the ceiling was too high for useful reflections, it had to be absorbed, and the reflecting surfaces were designed as separate elements. The first idea was to hang movable reflecting panels from the ceiling, but the idea was dropped because their moving and adjustment for different settings would have been too cumbersome. Instead, the walls were equipped with fixed diffusers, formed by curved surfaces inside rectangular boxes. These diffusers reflect sound evenly across the room and also back to the performers. The building was completed in March 1997. It has been used for musicals, childrens' plays, and experimental theatre. The acoustics has been considered very favorable.

12:00

2aAAa12. Excellent acoustics *and* a low RT? A case study of the recent renovation of the Kennedy Center Concert Hall, Washington, DC. Christopher Jaffe, Paul Scarbrough, Russell Cooper, and Pamela Clements (Jaffe Holden Scarbrough Acoustics, Inc., 114A Washington St., Norwalk, CT 06854)

In October 1997, the renovated Concert Hall at the Kennedy Center reopened to critical acclaim. The hall is designed on the shoebox model, but with an audience of 2759 and a volume of 250 cubic feet per person, its occupied midfrequency reverberation time was below the 2.0 s that is now considered fundamental to acoustical excellence. The musicians were also having difficulties hearing on stage. The acoustic redesign involved rebuilding the stage with reshaped walls, an acoustical canopy, resonant floor, orchestra risers, seating at stage sides and rear, and refurbished organ. Parterrre walls were added at orchestra level to increase side reflections. Since the ceiling could not be raised, reverberation was enhanced by building small reverberation chambers beside the stage and reducing seat count. Removing parts of the upper side balconies created an area near the stage where the sound field could develop without audience absorption. Changes also included echo control, new seats, and new stage HVAC system. The paper presents data from acoustical measurements and computer models made before and after the renovation, and discusses the combination of acoustical parameters that enables the hall to achieve such high acclaim despite its relatively low reverberation time.

Contributed Poster

This poster will be on display in the Poster Gallery from Monday to Wednesday, 15–17 March. Author will be at poster from 10:00 a.m. to 12:00 noon on Wednesday, 17 March.

2aAAa13. CAAD—Computer aided architectural and acoustical design. Marius Smigelschi, Alexandru Badescu, and Radu Pana (Inst. of Architecture, Bucharest, Romania)

The computer program ''AUDIO'' is intended to encourage architects to include (integrate) the room acoustics study in the architectural design from its very beginning, by using in both ways, interactively, the same computer descriptions (AUTOCAD environment) of the room. The main stages of the design are: first: – first architectural variants: – 2-D acoustical comparison, improvement of the room shape in plan, longitudinal, and transversal sections; second: – architectural 3-D model: – 3-D detailed shape analysis, proposed absorbtion characteristics of room boundaries; third: – architectural details and specifications: – proposals for finishings and materials, taken from the database of the program. In both 2- and 3D stages the program is based on a very performant ray-tracing method. *Entry*: – room boundaries taken from the architectural model and internally processed (boundary area, volume), audience area, sources (characteristics and location), *acoustical processing*: – in almost real time, the complete history of impingements (collisions), that is almost statistical, – *output*: graphic representation of first 2–4 reflections, equal contours on the audience surface of up to ten chosen parameters, (reverberation time, sound level, clarity, spatial impression, lateral efficiency, time gravity point . . .), detailed impulse response, reverberation time, and the same ten parameters for any reception point.

TUESDAY MORNING, 16 MARCH 1999 ROOM H2032, 7:55 A.M. TO 12:00 NOON

Session 2aAAb

Architectural Acoustics and Noise: Modeling of Noise in Work Rooms

Murray Hodgson, Cochair
Occupational Hygiene Program, University of British Columbia, 2206 East Mall, Vancouver, British Columbia V6T 1Z3, Canada

Wolfgang Probst, Cochair
ACCON GmbH, Graefelfingerstrasse 133A, D-81375 Munich, Germany

Chair's Introduction—7:55

Invited Papers

8:00

2aAAb1. Prediction of noise in workrooms including extended sources, directivity of radiation, and screening. W. Probst (ACCON GmbH, Graefelfinger Str. 133 A, 81375 Munich, Germany, Wolfgang.Probst@accon.de)

For many years the mirror image method has been used to calculate noise levels in workrooms. Fittings are taken into account by a fitting density defined by Kuttruff and extended to this application by Jovicic. In a research program financed by BAUA Dortmund it was examined how directivity of radiation and screening can be integrated. A removable screen was installed in different halls and it measured the sound distribution in the shadow region, which was produced by a uniformly radiating loudspeaker radiating white noise. Calculation of the same situation by taking into account screening showed that only low orders of reflection are influenced by the screen. This gives the necessary information for a modification of software programs to include screening. Similar to this procedure, a loudspeaker with high directivity was used as source with known emission to measure sound decay curves in workrooms. The same situation was calculated by mirroring the complete directivity of the source. Measured and calculated levels are in good agreement. With these techniques the German standard VDI 3760 for noise calculation in rooms can be improved in the next years.

8:20

2aAAb2. Experiences with the application of a software for noise prediction in workrooms. Jürgen H. Maue (Berufsgenossenschaftliches Institut für Arbeitssicherheit—BIA, Alte Heerstraße 111, D-53757 Sankt Augustin, Germany, J.Maue@hvbg.de)

For a couple of years, the BIA has been using a computer program for the calculation of room acoustic parameters and the prediction of sound pressure levels at the workplace. Experiences gathered with the program in connection with industrial consulting activities are presented and illustrated by examples. The software is based on a calculation method referred to in the German VDI guideline 3760 (image sound source method) requiring a mean degree of complexity in the description of the room. The software comprises a large library, indicating sound absorption coefficients for all tested materials. The program is mainly used for planning room acoustic improvements and new workrooms. Noise prediction in connection with production changes (replacement of machinery, new productions) is also possible. In some cases of hearing damage, the program was used for a retrospective determination of

noise exposure at former workplace. A comparison of the calculated spatial sound decay curves and the thus-derived room acoustic parameters with the measurement readings showed good correspondence. The development of noise maps and the consequent presentation of the achievable noise reduction by means of concrete measures has become an important instrument for motivating and convincing companies.

8:40

2aAAb3. Is it worth applying sound particle scattering methods to sound propagation in factory halls?—Results and comparisons of some simulations. Uwe M. Stephenson (Fachhochschule Hamburg, Fb Bauingenieurwesen, Hebebrandstr. 1, D-22297 Hamburg, Germany, U.M.Stephenson@t-online.de)

Sound particle simulation, a version of ray tracing, is meanwhile a well-established method in room acoustics. In usual closed rooms, sound propagation is dominated by multiple reflections. In factory halls, the problem arises that a lot of inner sound scattering obstacles (machines, etc.) may practically not be registered in detail. A principal deficiency of ray tracing is the impossibility of taking diffraction into account. Often only a mean level decay per distance is of interest. Therefore, it is a well-founded and -tested semi-analytical approach of using only a mean scattering surface area per volume $q = S/(4V)$ and combining that with a simple mirror image source method for rectangular rooms (German guideline VDI 3760). With the sound particle method, this multiple scattering is directly simulated in a Monte Carlo manner. This has several advantages: rooms of arbitrary form, diffuse reflecting surfaces, and inhomogeneous distributions of scattering bodies may be simulated. Meanwhile, on modern PCs, computation times lie in the range of only a few minutes. A disadvantage is the much higher effort of defining the (often uncertain!) input data. Some recent results of simulations of typical setups in factory halls (not computable by common methods) are presented and compared.

9:00

2aAAb4. Modeling of noise in factory workrooms—A practical perspective. David N. Lewis (Unilever Research, Port Sunlight, Wirral L48 6EU, UK, David.N.Lewis@Unilever.com)

It has been known for a considerable time that classical diffuse field theory cannot be applied to workrooms where either of the floor dimensions are greater than approximately five times the ceiling height [H. J. Sabine, Proc. Third Annual Noise Abatement Symposium, Vol. 3, 10 October (1952)]. In such large workrooms there are often many sources of noise and the benefits of alternative noise control stategies are often not obvious. Computerized methods of noise prediction in factory workrooms were first developed in Unilever around 1979. The first major application and validation of the technique was on a project to reduce noise in a manufacturing facility in 1980. The main tool for noise prediction is an in-house package which calculates the combined effect of multiple sources at all points 1 m apart within the building. Source sound power, directivity, and the propagation curves for the building are input, the latter having been derived from ray tracing predictions, empirical models, or measurement. The technique has been used successfully on numerous projects in the last 20 years and is a valued tool for illustrating the likely benefits of acoustic treatment or defining noise control specifications. An overview of the technique and its application is presented.

9:20

2aAAb5. Modeling of sound fields in enclosed spaces with absorbent room surfaces. Stephen M. Dance and Bridget M. Shield (South Bank Univ., SESD, Borough Rd., London SE1 0AA, UK, dances@sbu.ac.uk)

Commercial computer models are now generally available for the prediction of sound levels in industrial workshops. Four models have been used in this investigation; including RAYNOISE v3.0, RAMSETE v1.3, RAYSCAD+v3.3, and FAME v1.0. These models were validated in rooms with highly absorbent room surfaces using standard and Millington-based absorption coefficients. The rooms included hypothetical, performance, experimental, and industrial spaces. Measurement data were available for the six central octave bands. The results are presented for sound levels and reverberation time, in addition to which the execution time for each model is detailed. It was found that Millington-based absorption coefficients provided consistently more accurate predictions for each type of space than standard absorption coefficients.

9:40

2aAAb6. PlantNoise system for the prediction, visualization, and auralization of industrial noise during computer walk-through. Murray Hodgson, Nelson Heerema, and Kurtis Halingten (Occupational Hygiene Prog. and Dept. of Mech. Eng., U. B. C., 3rd Fl., 2206 East Mall, Vancouver, BC V6T 1Z3, Canada, hodgson@mech.ubc.ca)

PlantNoise, a novel hardware and software system for predicting, visualizing, and auralizing noise in typical industrial workrooms, is described and demonstrated. It is simple, rapid, accurate, and user-friendly, responding to the needs of industrial practitioners. Input data describing a workroom and its noise sources are input. The workroom floor-plan is visualized, along with the noise sources, a 1-m receiver grid, and a receiver icon. Octave-band and total noise levels, and octave-band reverberation times, are predicted at the receiver location, using new empirical models, and are displayed. The noise is also auralized, using a sound card. The receiver can be ''walked-through'' the workroom arbitrarily under user control. Visualized and auralized data are updated in real time. Noise contours can be plotted. At any time, the workroom can be modified—for example, to introduce noise-control measures—and the modified noise visualized and auralized.

10:00

2aAAb7. An adaptive beam tracing method for room acoustics prediction. Yiu W. Lam and Ian Drumm (Dept. of Acoust. and Audio Eng., Univ. of Salford, Salford M5 4WT, UK)

A new adaptive beam-tracing algorithm was developed and implemented into a computer model to predict the propagation of sound in enclosed spaces. Unlike previous beam-tracing methods, the model predicts a near perfect geometrical representation of a propagating sound field by adaptively tailoring it to the shape of the reflecting surfaces. Using this adaptive approach, problems such as gaps and overlaps between beams, and the ambiguity of reflection direction when a beam hits more than one surface can be eliminated. In addition, the beam tracing can start with only a small number of beams. Child beams are generated automatically upon each reflection to adapt to the complexity of the room. This method runs faster than traditional beam and ray-tracing methods in the early part and faster than the image method in the later part of the reverberation process. Diffuse reflections are handled by a radiant exchange process and combined with the specular reflections to calculate the impulse response of a room. This model is applied to several spaces with representative workspace shapes and fittings and the result is compared with traditional prediction methods. The suitability of using diffuse reflections to model the effect of factory fittings is investigated.

10:20–10:40 Break

Contributed Papers

10:40

2aAAb8. Call center as an acoustical challenge. Ernst Joachim Voelker and Sabine Fischer (Inst. for Acoust. and Bldg. Phys., Kiesweg 22, 61440 Oberursel, Germany)

Call centers differ from the standard open plan offices in that telephone calls using headsets lead to special types of activities at the working places. Phone calls with clients produce almost simultaneously an A-weighted speech-noise level of around 52–58 dB when, for instance, 12 or 18 neighboring working places are occupied. On the other hand, the background noise produced by all persons working is much lower at around 43–45 dB in well-known open plan offices when quiet work (such as paperwork) is being performed, or when employees are absent. In both cases, there are certain levels of privacy expected. Call centers belong to grade three privacy with a permitted signal-to-noise ratio of around 9 dB. Many room acoustical properties must be considered, such as the falling off of sound levels with increasing distances, avoidance of disturbing sound reflections, short reverberation times, and well-designed sound barriers which must have a soundproofing quality and a high sound absorption. Measurements in existing call centers can be related to the grades of privacy within a certain field of confidence. The same applies to other open plan offices. Artificial background noise such as sound conditioning must be introduced in order to reach the privacy accommodations.

11:00

2aAAb9. Acoustic quality at workplaces. Lia Kortchmar, Michael Vorländer (Inst. of Tech. Acoust., RWTH Aachen, Templergraben 55, D-52056 Aachen, Germany, lia@akustik.rwth-aachen.de), and Jules G. Slama (PEM-COPPE-UFRJ, Rio de Janeiro, Brazil)

The pursuit of a methodology to elucidate the workplaces issue is a challenge within the area of acoustic quality. The matter involves the search for subjective attributes to be employed on rating acoustic quality judgements. In this search for evaluation strategies, it is appropriate to associate a physical property of the enclosure to a subjective feature. Objective measures offer an intermediate description between design and the subjective effect. The emphasis here is on the objective attributes significant for sound perception. This work looks at some practical experience gained from the connection between experimentally measured values and subjective sensations related to sound quality at workplaces. Information is crossed among the different techniques used for its evaluation. The qualitative features of extremely nondiffuse sound fields are examined by the analyses of the physical properties, objective measures, and subjective quality of various types of rooms. [This work has been carried out at the Institute of Technical Acoustics at the RWTH Aachen University in collaboration with the Federal University of Rio de Janeiro (COPPE/UFRJ).]

11:20

2aAAb10. Modeling huge sound sources in a room acoustical calculation program. Claus L. Christensen (Dept. of Acoust. Technol., DTU, Bldg. 352, DK-2800 Lyngby, Denmark, clc@dat.dtu.dk)

A room acoustical model capable of modeling point sources, line sources, and surface sources is presented. Line and surface sources are modeled using a special ray-tracing algorithm detecting the radiation pattern of the surfaces of the room. Point sources are modeled using a hybrid calculation method combining this ray-tracing method with image source modeling. With these three source types it is possible to model huge and complex sound sources in industrial environments. Compared to a calculation with only point sources, the use of extended sound sources is shown to improve the agreement with measured data.

11:40–12:00 Discussion

Session 2aAB

Animal Bioacoustics: Physics of Animal Bioacoustics I

James H. Miller, Cochair
Department of Ocean Engineering, University of Rhode Island, Narragansett, Rhode Island 02882, USA

Christine Erbe, Cochair
Institute of Ocean Sciences, 9860 West Saanich Road, Sidney, British Columbia V8L 4B2, Canada

Invited Papers

8:00

2aAB1. Insect sounds in agriculture. Robert Hickling (Natl. Ctr. for Phys. Acoust., Univ. of Mississippi, University, MS 38677)

Insects make sounds, either in the course of normal activity (for example, eating or moving about), or to communicate. To investigate activity sounds, it is generally necessary to have a quiet environment, which occurs naturally in grain or soil, and can be created artificially in a soundproof box or anechoic chamber. These sounds can be used to detect pests in agricultural commodities, such as rice weevils in grain, grubs in soil, fruit-fly larvae in fruit, and bollworm in cottom bolls. Examples can be heard on the internet [www.olemiss.edu/~lee/]. A brief discussion is presented of sound transmission in grain and soil. Sound does not appear to be used for communication by larvae. However some grubs in soil may use sound to warn off other grubs from their feeding areas. Acoustic communication appears to be important to ants. Results are presented of sounds made by the black imported fire ant *Solenopsis richteri*. Examples can be heard on the internet [www.olemiss.edu/~hickling/]. It is shown how ants can make use of the near-field properties of a simple sound source in air. [Work supported by the USDA.]

8:20

2aAB2. Directional hearing in small animals: Tympanal mechanics and evolutionary innovations. Daniel Robert (Inst. for Zoology, Zurich Univ., Winterthurerstr. 190, CH-8057 Zurich, Switzerland)

Tympanal hearing is an evolutionary innovation that occurred at least twice independently in flies (Diptera). Both in Tachinidae and Sarcophagidae fly families, hearing organs evolved that are located on the anterior thorax and that present two thin tympanal membranes rigidly connecting to a pair of mechano-receptive sensory organs. Remarkably, the small interaural distance (1 mm) constitutes a serious challenge for directional hearing at 3–6 kHz. The mechanical response of these ears to incident random noise was investigated by microscanning laser Doppler vibrometry. Mechanical transfer functions of tympanal displacements show that the ipsi- and contralateral tympana vibrate with an unexpectedly large amplitude difference and interaural delay [R. N. Miles *et al.*, J. Acoust. Soc. Am. **98**, 3059–3070 (1995)]. The deflection shape analysis shows that in both cases the tympanal membranes are mechanically coupled across the animals midline. However, morphological and biomechanical evidence indicates that the process of mechanical coupling differs between both families, indicating the presence of two alternative and distinct mechanisms for directional sensitivity. This biomechanical and morphological study exemplifies how evolutionary innovation can generate original and specific solutions to the general problem of directional auditory processing. [Work supported by NIH, NSF, and the Swiss Science Foundation.]

8:40

2aAB3. Directional hearing in grasshoppers: Biophysical mechanisms and animal performance. Marc Holderied, Johannes Schul, Dagmar v. Helversen, and Otto v. Helversen (Inst. of Zoology II, Univ. of Erlangen, Staudtstr. 5, 91054 Erlangen, Germany, mholderi@biologie.uni-erlangen.de)

Grasshopper hearing organs are pressure difference receivers: two tympana are connected by air-filled tracheal sacs. Sound reaches a tympanum's outer surface directly and its inner surface through these sacs. Recently, Michelsen and Rohrseitz determined the transfer function of these sacs and developed a biophysical model to predict directional hearing. Tympanal nerve recordings made in Erlangen revealed that this model can predict hearing even for complex stimulus situations with two sound sources emitting pure tones of varying phase and amplitude. Behavioral tests using broadband grasshopper songs showed that a 1-dB intensity difference between two lateral sound sources is sufficient for correct lateralization. It is, however, difficult to predict actual interaural intensity differences for broadband noise by model calculation. A direct method to determine the actual interaural intensity difference necessary for correct lateralization is to decouple the two tympana. For this purpose, light magnetomechanical earphones for free-moving grasshoppers were developed. Lateralization performance using earphones was similar to acoustic stimulation. The possible influence of coherence in broadband signals to the model is discussed.

9:00

2aAB4. Middle ear adaptations in an old world amphibian. Peter M. Narins, Alejandro P. Purgue (Dept. of Physiological Sci., Univ. of California, Los Angeles, 405 Hilgard Ave., Los Angeles, CA 90095), and Edwin R. Lewis (Univ. of California, Berkeley, CA 94720)

Each tympanic membrane (TM) of males of the Old World frog *Petropedetes parkeri* is decorated with a single, prominent, fleshy papilla during the breeding season. The papilla is composed of a nonossified, spongiform tissue that contain fluid-filled canals that terminate at or near the papillar surface. Roughly three-quarters of the papillar mass is located on the outer surface of the TM, while one-quarter is found on the inner TM surface. Injecting sound into the vocal cavity and measuring the vibration response of a point of the tympanic membrane using laser Doppler vibrometry revealed that the papilla vibrates little in response to sound, but clear modes are observed on the remaining portion of the TM. Moreover, the Fourier transform of the impulse response of the male's intact TM exhibits a peak at ~750 Hz, close to the dominant frequency of the male's advertisement call (780 Hz). This tuning is interpreted as an adaptation for broadcasting of the call from the eardrums of the male. Surgically removing the papilla resulted in a surprising change in the TM response properties. [Work supported by NIDCD Grant Nos. DC-00222 to PMN and DC-00112 to ERL.]

9:20

2aAB5. The traveling-wave amplifier model of the cochlea adapted to dolphins. Lars N. Andersen (Dept. of Math. Modeling, Bldg. 321, Tech. Univ. of Denmark, 2800 Lyngby, Denmark, nonboe@eivind.imm.dtu.dk) and Whitlow W. L. Au (Hawaii Inst. of Marine Biol., Kailua, HI 96734)

The traveling-wave amplifier (TWA) model of the cochlea [A. Hubbard, Science **259**, 68–71 (1993)] has been shown to produce outputs that compare quite well with experimental data. A TWA model with parameters adjusted to fit the physiological properties of the dolphin cochlea was used as part of a sonar signal discrimination system. The system was tested on a cylinder wall thickness discrimination problem. Broadband echoes from cylinders with different wall thicknesses were aligned using a matched filter and envelope detection. The aligned signals were used as inputs to the TWA model and energy from different locations along the cochlea model were computed in time increments. Data were reduced by principal component analysis and finally classified by a neural network. Results from the experiment demonstrate the potential of the framework.

Contributed Papers

9:40

2aAB6. An excitation of surface acoustic waves in the ear canal. E. Grigori Evreinov (Lab. for DIIS, Specvuzavtomatika Design Bureau, 44/5-13 Lenin St., Rostov-on-Don, Russia, 344038, evreinovg@usa.net)

Usually electrodynamic loudspeakers have a small flexibility of the diaphragm. Therefore, at sound reproduction of low frequencies, a coupling space between the diaphragm and the ear must be hermetic. In a range of high frequencies, distortions are stipulated by the presence of reflected sound waves, and depend on the ear canal's position in the closed sound space. There is a coupled acoustic resonant system which consists of the pinna, the eardrum, and the ear canal. Sound oscillations excited in a cartilaginous part of the outer ear are partly reflected, but an absorbed component is spread through subcutaneous conjunctive tissue toward an attachment place of the tympanic membrane via surface acoustic waves (SAW). The hearing thresholds' data received by use of a special sound conductor which is generating SAW, in a range of frequencies 125–8000 Hz, did not show statistic distinctions regarding measurings carried out via conventional tonal audiometry. It is supposed that mechanical energy necessary for excitation of auditory sensation with the help of oscillations spreading through the conjunctive tissue of the ear canal is required even less than at the creation of equivalent levels of air pressure because an amplitude of acoustic oscillations is directly attached to the eardrum edge.

10:00–10:20 Break

10:20

2aAB7. Sound production in wasps and ants (*Hymenoptera*). Gunther Tschuch (Inst. f. Zoologie d. Univ., Entwicklungsbiologie, Domplatz 4, D-06099 Halle, Germany, tschuch@zoologie.uni-halle.de) and Denis J. Brothers (Univ. of Natal, Scottsville, Pietermaritzburg 3209, South Africa)

Some species of ants (*Formicidae*) and stinging wasps (some *Sphecidae, Bradynobaenidae, Rhopalosomatidae,* and all species of *Mutillidae*) possess stridulatory organs without resonance structures. The stridulatory organs occur in both sexes between the 3rd and 4th, 4th and 5th, or 5th and 6th abdominal tergites. The sphecid wasp *Pseudoplisus phaleratus* makes use of all three positions. The main part of the stridulatory organ is an area of 60 to 200 very regular ripples with species-specific ripple distances of 1.2 to 5 μm. To prevent mechanical destruction of the ripples during sound production, the force is spread over a width of more than 100 μm. The signals are optimized to serve as warning signals. Frequently wasps and ants present the acoustical signals together with optical (aposematic coloration) and chemical signals (allomones). The potential predators (e.g., lizards, mammals) are phylogenetically very diverse. Therefore the acoustical signals must have a broad frequency spectrum. The mechanisms used for the production of such spectra were investigated by laser vibrometry. The signals were analyzed by cepstrum and by an adaptive optimal-kernel time-frequency representation [D. L. Jones and R. G. Baraniuk, IEEE Trans. Signal Process. **43**, 2361–2371 (1995)]. [Work supported by DFG.]

10:40

2aAB8. The target strength of the northern right whale (*Eubalaena glacialis*). James H. Miller (Dept. of Ocean Eng., Univ. of Rhode Island, Narragansett, RI 02882), David C. Potter (Woods Hole Oceanogr. Inst., Woods Hole, MA 02543), Thomas Weber, and James Felix (Univ. of Rhode Island, Narragansett, RI 02882)

The greatest cause of anthropogenic mortality in great whales is ship strikes. Avoiding collisions, which are almost exclusively with baleen whales, may be critical to the survival of the northern right whale (*Eubalaena glacialis*). A potential solution to this problem is the use of an active forward-looking obstacle avoidance sonar. This sonar could alert the ship's crew of the presence of the whales or other obstacles at useful maneuvering ranges. The prediction of these detection ranges depends on the reflectivity of the whales. The focus of this study is the determination of target strength of the right whale. In May and September of 1998, a prototype phased-array sonar was mounted on the bow of a 25-m research vessel to collect these measurements. The sonar used a CW ping with a frequency of 87 kHz, a duration of 2 ms, a source level of 175 dB *re*: 1 μPa at 1 m. The receive array consisted of an 8×8 element array with BD wavelength spacing. The frequency was chosen to be inaudible to the baleen whales. Target strengths were also collected for humpback whales (*Megaptera novaeangliae*), and compare well with previously published data. [Work supported by NMFS and NSF.]

11:00

2aAB9. Modeling animal FM tones using a cubic spline interpolation. Etienne Douaze (Dolphin Study Group, Tropical Marine Sci. Inst., 14 Kent Ridge Rd., Singapore 119 223), Eric Delory, John Potter (Tropical Marine Sci. Inst., Singapore 119 223), and Elizabeth Taylor (Tropical Marine Sci. Inst., Singapore 119 223)

The use of FM tones for communication is widespread among birds and mammals. Analysis of these signals by biologists is currently limited to a qualitative visual inspection of spectrograms and manual logging of discrete signal features from a spectrogram window. Human-related measurement errors are usually not considered and a robust numerical model of animal FM tones is lacking. A model should take at least three signal parameters into account: frequency and amplitude modulation, and the harmonic content. In this work a numerical model for animal FM tone fundamentals is presented. A piecewise polynomial interpolation is used to fit bottlenose dolphin (*Tursiops truncatus*) FM tones, commonly called whistles, from manually logged spectrogram fundamentals. Cubic splines are used to achieve the best visual fit to the signal fundamental by controlling locally the slope and the curvature of the curve fit. A smoothing factor, calculated from an independent experiment on six human subjects, is applied to the interpolation to adjust for human measurement errors. Dolphin tone fundamentals are modeled with a set of 80 coefficients, a number conveniently independent of signal duration because longer dolphin whistles are observed to be associated with a lesser degree of frequency modulation.

11:20

2aAB10. Physical constraints on blue whale sound production mechanisms derived from matched-field processing. Aaron M. Thode, Gerald L. D'Spain, and William A. Kuperman (Marine Physical Lab., Scripps Inst. of Oceanogr., Univ. of California, La Jolla, CA 92093-0205)

Matched-field processing (MFP) is a technique for estimating the range and depth of an acoustic source using data collected from a multiple hydrophone array. Physical constraints on the sound production mechanism used by blue whales can be established using this method, including a vocalizing animal's depth, depth and range changes during vocalization, source level estimates, and removal of propagation effects from the animal's source signature. Data are presented from a 1996 experiment off the California Channel Islands that contain a 30-min. sequence wherein a single individual produces 10 pulses and 22 FM sweeps from distances up to 5 km away. The animal appears to vocalize at depths between 15 and 25 m during both types of vocalizations, and swims with horizontal speeds between 2 to 5 m/s. The source levels generated by a type A call vary from 176–192 dB re:1 μPa @ 1 m over a 10- to 100-Hz band, consistent with previous estimates [W. C. Cummings, J. Acoust. Soc. Am. **50**, Pt. 2, p. 1193]. The type B source levels will also be analyzed and discussed. [Work supported by ONR.]

11:40

2aAB11. Using broadband humpback whale vocalizations to locate nonvocal whales in shallow water. Nicholas C. Makris, Yi-San Lai (MIT, 77 Massachusetts Ave., Cambridge, MA 02139), and Douglas H. Cato (Defence Sci. and Technol. Organization, Pyrmont, NSW 2009, Australia)

In a previous paper [Makris and Cato, J. Acoust. Soc. Am. **96**, 3270 (1994)], it was shown that a vocal member of a humpback whale herd can be used as a source of opportunity to locate nonvocal members with a passive towed array. That analysis employed full-field but narrow-band propagation and scattering models to emphasize the high spatial array gains available. In the present paper, full-field simulations are performed to determine the structure of actual broadband humpback whale vocalizations after scattering from whales in a shallow-water waveguide. The simulations show that the time signature of a whale vocalization is significantly altered during each of the three stages of (1) propagating from vocal to nonvocal whale, (2) scattering from the nonvocal whale, and (3) propagating from the nonvocal whale to a receiver. The large time-bandwidth gains available in humpback vocalizations then cannot be optimally exploited without first modeling broadband propagation and scattering of the whale vocalization for the given waveguide and bistatic geometry. This raises serious questions about whether the humpbacks themselves, who have limited spatial gains over the noise, can actively detect nonvocal herd members with their vocalizations, as was discussed in the above reference.

12:00

2aAB12. Anthropogenic ocean noise: Negligible or negligent impact? Darlene Ketten (Woods Hole Oceanogr. Inst., Woods Hole, MA and Harvard Med. School, Boston, MA 02114, dketten@whoi.edu) and John R. Potter (Acoust. Res. Lab., NUS, Singapore 117596)

The increasing use of the oceans is accompanied by rising acoustic pollution. From explosive transients to the nearly continuous drone of ships, anthropogenic noise accompanies virtually every human activity in the sea. Anthropogenic noise has the potential for significant impact on marine species, especially marine mammals, yet existing data are insufficient to predict accurately any but the grossest consequences. There are almost no controlled data on how the acoustic environment is changing as a result of human activity. There is also little information on how marine mammals respond physically and behaviorally, either to intense transients or to a long-term background increase in ambient noise. Ignorance and resulting caution in testing potentially harmful acoustic devices may be seriously hampering our learning progress and the development of effective acoustic deterrents that could decrease marine mammal by-catch. This work discusses the current understanding of acoustic trauma and ambient noise characteristics in the context of what is known about marine mammal hearing and its variations. The work focuses on how species vary in their potential for impact and on determining whether acoustically vulnerable species coincide with acoustic ''hot spots'' in the ocean where Man's activities may damage hearing and disrupt key behaviors.

Session 2aAO

Acoustical Oceanography: Innovations in Fish and Plankton Acoustics I

Kenneth G. Foote, Cochair
Institute of Marine Research, P.O. Box 1870, Nordnes, N-5024 Bergen, Norway

David A. Demer, Cochair
Southwest Fisheries Science Center, P.O. Box 271, La Jolla, California 92038, USA

Invited Papers

8:00

2aAO1. A seven-octave-bandwidth echo sounding system for application to fish and zooplankton. Kenneth G. Foote, Tor Knutsen (Inst. of Marine Res., P.O. Box 1870 Nordnes, N-5024 Bergen, Norway, tor@imr.no), Philip R. Atkins, Claire Bongiovanni, David T. I. Francis (Univ. of Birmingham, Birmingham B15 2TT, UK), Peter K. Eriksen, and Tom Mortensen (RESON A/S, DK-3550 Slangerup, Denmark)

A new echo sounder has been designed and built for measuring broadband acoustic scattering signatures of fish and zooplankton (BASS), which is also the name of the underwriting EU MAST-III project. Development of the system is described in terms of four elements: (1) acoustics, consisting of seven nominally octave-bandwidth transducers spanning the frequency range 25 kHz to 3.2 MHz, depth rated to 300 m, (2) electronics, for control of the transmission and echo reception processes, (3) man–machine interface, allowing remote operation of the transducers and electronics by a menu-driven personal computer, and (4) housing, including mounting of transducers on a bracket and packaging of electronics in a proximate pressure vessel. The system is presently configured for use as a vertical sonde, with ship-derived power. Early *in situ* applications to euphausiids and Norwegian spring-spawning herring observed on cruises in October and December 1998 are described. The issue of calibration is addressed. Supporting work on modeling the backscattering cross section of marine organisms based on measurement of their morphology and physical properties, and on measuring the same cross section *ex situ* in a so-called mesocosm of approximate volume 100 cubic meters, is mentioned. [Work supported by the EU through RTD Contract No. MAS3-CT95-0031.]

8:20

2aAO2. A multiple-frequency method for potentially improving the accuracy and precision of *in situ* target strength measurements. David A. Demer (Southwest Fisheries Sci. Ctr., P.O. Box 271, La Jolla, CA 92038, ddemer@ucsd.edu), Michael A. Soule (Sea Fisheries Res. Inst., Cape Town, South Africa), and Roger P. Hewitt (Southwest Fisheries Sci. Ctr., La Jolla, CA 92038)

The effectiveness of a split-beam echosounder system to reject echoes from unresolvable scatterers, thereby improving the measurements of *in situ* target strengths (TS) of individuals, is dramatically enhanced by combining synchronized signals from two or more adjacent split-beam transducers of different frequencies. The accuracy and precision of the method was determined through simulations and controlled test tank experiments using multiple standard spheres and 38- and 120-kHz split-beam echosounders. By utilizing the angular positional information from one of the split-beam transducers, additional corresponding TS measurements were shown to be obtainable from a juxtaposed single-beam transducer. Both methods were utilized to extract *in situ* TS measurements of Antarctic scatterers simultaneously at 38, 120, and 200 kHz. The ultimate efficiency of the multiple-frequency technique is shown to be limited by phase measurement precision, which in turn is limited by the scattering complexity of targets and the receiver bandwidth. Imprecise phase measurements also result in significant beam-compensation uncertainty in split-beam measurements. Differences in multi-frequency TS measurements provided information about the identity of constituents in a mixed species assemblage. The taxa delineation method has potential, but is limited by compounding measurement uncertainties at the individual frequencies and sparse spectral sampling.

8:40

2aAO3. The investigation of physiologically controlled resonance scattering data from fish using a new acoustic approach. C. Feuillade (Naval Res. Lab., Stennis Space Center, MS 39529-5004, cf@nrlssc.navy.mil)

Low-frequency acoustic scattering from fish is typically dominated by the swimbladder resonance response. Swimbladders are physically similar to bubbles, and it has been traditionally assumed that, as with bubbles, resonance frequency measurements may be directly used to calculate the swimbladdeer volume. Typically, swimbladder models used to interpret fisheries scattering data, and thus determine fish size and abundance, have adopted this premise. Questions are raised, however, by one set of measurements on depth-adapted Atlantic cod by Sand and Hawkins [J. Exp. Biol. **58**, 797–820 (1973)], which indicates resonance frequencies much higher, and with more rapid depth variations, than can be realistically explained using such simple assumptions. They argued that the anomalous resonances they observed were actively controlled by the fish, and not just a passive property of the swimbladders. To investigate this phenomenon, a new model was recently developed which incorporates both viscous and elastic properties of fish flesh as variables influencing swimbladder scattering [J. Acoust. Soc. Am. **103**, 3245–3255 (1998)]. This presentation will demonstrate how this model provides a basis for understanding the physiological behavior of the fish, and a starting point for determining which species of fish may be reliably surveyed using the traditional approach.

9:00

2aAO4. Fisheries and plankton acoustics: State of the art and beyond. David N. MacLennan (Marine Lab., P.O. Box 101, Victoria Rd., Aberdeen AB11 8DB, Scotland, MacLennan@marlab.ac.uk)

Acoustical methods are well established as a means of remotely observing aquatic organisms. The range of applications reported in the literature is wide, from studies of isolated animals to populations extending over large areas. The geometric scale of target organisms is similarly huge, from microscopic plankton to the largest of marine mammals. The information required from acoustical investigations may be simple quantities like abundance estimates, or more descriptive output like species identification. In each case, there are different problems to be considered. The multi-disciplinary nature of acoustical techniques is important. Success depends on a combined appreciation of scattering physics, animal physiology, statistics, and sonar technology to mention just some of the contributing fields. The historical context is explained, leading to a critical review of recent developments. To a large extent, the driving force has been new technology, especially the rapid growth of computing power. It is important to ensure that appropriate scientific research is done to achieve the benefits of new technology, in acoustics as in other fields, for a better understanding of the living resources in the sea and fresh waters.

Contributed Papers

9:20

2aAO5. Acoustic observations of the annual cycle of fish and plankton populations in the Beaufort Sea. Robert Pinkel (Scripps Inst. of Oceanogr., 9500 Gilman Dr., La Jolla, CA 92093-0213)

During the period November 1997 through September 1998, a 160-kHz Doppler sonar was operated at the SHEBA ice camp. During this period, the camp drifted clockwise around the Beaufort Sea. The sonar, constructed at the Marine Physical Laboratory of the Scripps Institution of Oceanography, transmitted coded pulses with an 8-kHz bandwidth and recorded echo intensity, spectral bandwidth, and mean Doppler shift. The fall 1997 data featured very weak return echoes. Distinct hard targets were observed over ~5% of the profile. These have been tentatively identified as Arctic Cod. With changing season and camp location, both plankton and fish populations have evolved significantly. Algorithms have been implemented to track the discrete hard targets and the underlying continuum planktonic population through the course of the year.

9:40

2aAO6. Acoustic abundance estimation of midwater animals. Kenneth G. Foote and Ingolf Roettingen (Inst. of Marine Res., P.O. Box 1870 Nordnes, N-5024 Bergen, Norway, ingolf.rottingen@imr.no)

The echo integration method of estimating the abundance of midwater animals, specifically pelagic fish and zooplankton, is reviewed. The roles of the modern scientific echo sounder and complementary postprocessing system are emphasized, but requirements imposed by availability of the target animals to surveying by vertical transducer beam, environment including weather and possible presence of other significant scatterers, and the animal itself, are mentioned. The process of converting acoustic measurements of animal density to abundance over the survey region is illustrated in detail for the case of Norwegian spring-spawning herring (Clupea harengus) when wintering in a fjord system. A simple explanation is given for continued interest in the scattering properties of midwater animals, specifically their backscattering and extinction cross sections. The constant need for positive scatterer identification, as through physical capture or optical registration, or, failing these, acoustic classification, is described. The usefulness of geostatistics in estimating abundance and the variance of the abundance estimate, as well as in quantifying the observed spatial distributional properties of the animal, is mentioned. [Partial support of the EU through RTD Contract Nos. AIR2-CT94-1007 and MAS3-CT95-0031 is acknowledged.]

10:00–10:20 Break

10:20

2aAO7. Use of acoustics in large tuna trophic-habitat characterization in French Polynesia. Arnaud Bertrand (ORSTOM, BP 70, 29280 Plouzane, France, arnaud.bertrand@orstom.fr)

Tuna have a high metabolic rate, yet they often live in regions characterized by low primary productivity rates. Improving knowledge on tuna-habitat trophic relationship is of main importance for understanding tuna distribution and catchability. Distribution of large tuna food webs, i.e., micronekton, was described in French Polynesia at depths up to 500 m using acoustics and pelagic trawls. At large scale, acoustics profile response, morphological characterization of acoustic structures, and quantitative descriptors of sound scattering variability were used. Due to water masses advection and oxygen limitation main micronektonic production was localized 8 degrees south of the equatorial upwelling. At a smaller scale, micronekton was classified into seven scattering type: gas-filled swimbladder fish, absent swimbladder fish, gas-bearing invertebrates, cephalopods, fluidlike crustacean, fluidlike jelly-fish, and elastic-shelled invertebrates. Qualitative and quantitative aspects of the scattering structures were also described. Then scattering structure composition and the tuna trophic interest of aggregations was determined.

10:40

2aAO8. Multi-frequency measures and models of Lake whitefish (*Coregonus clupeaformis*) backscatter from Lake Michigan. J. Michael Jech, John K. Horne (CILER, Univ. of Michigan, 2205 Commonwealth Blvd., Ann Arbor, MI 48105, jech@glerl.noaa.gov), Lee A. Powell, and James H. Grandt (Univ. of Wisconsin, Madison, WI 53706)

To improve chances for discriminating and identifying fish and zooplankton species, more acoustic information is better. Multifrequency, digital echosounders increase information bandwidth by increasing the number discrete frequencies transmitted and received through multiple transducers. Multifrequency data provide a range of aural perspectives just as colored spotlights accent different components of a painting. Lake whitefish (*Coregonus clupeaformis*) represent an increasing biomass in Lake Michigan and have a disproportionately large, single-chambered swimbladder relative to the body volume. Frequency-dependent, echo amplitude predictions from a Kirchhoff-ray mode model were compared to *in situ* backscatter measurements of constrained and free ranging lake whitefish at five discrete frequencies (38, 50, 120, 200, and 420 kHz). In addition to geometric scattering, backscattering characteristics of whitefish in the resonance region were also modeled. This combination of theoretical model prediction and multifrequency measures allows the quantification of the importance of intraspecies backscatter variability due to fish sizes and behavior. [Work supported by ONR.]

11:00

2aAO9. Status and distribution of the dolphins in the Black Sea—By the acoustically improved line transect sampling technique. Ali C. Gucu (Inst. of Marine Sci., Middle East Tech. Univ., P.O. Box 28, Erdemli, 33731, Icel, Turkey, gucu@ims.metu.edu.tr)

Although dolphins are an endangered species, until 1983 they had been harvested in the Black Sea. Due to severe ecological changes taking place in this sea, the fish stocks experienced a decline within the last decade. The dolphins preying upon fish stocks were adversely affected and their population size was shrunk due to food shortage. But there is an ever growing lobbying on the government for legalizing dolphin fishery, because fishermen believe that the dolphin population has increased since the ban of dolphin fishery, resulting in an increased predation over the fishes

by dolphins, causing fishery to collapse in 1989. The aim of this study is to assess dolphin population size within the Turkish EEZ. One of the best techniques to assess the population size of dolphins is the line transect sampling. Being a direct visual census method, the major disadvantage of this technique is the probability of detection, which is not a uniform unity; as far as the eye can see is the basis of the line transect sampling. This disadvantage was eliminated acoustically by using fisheries' acoustic devices, and the sounds of the dolphin recorded by a scientific echosounder were used to detect the existence of the animals on the transect.

11:20

2aAO10. Schools and clusters: Interannual variability in the aggregative behavior of North Sea herring from acoustic surveys. Richard Aukland and David Reid (Marine Lab. Aberdeen, Victoria Rd., P.O. Box 101, Aberdeen AB11 9DB, Scotland, UK, reiddg@marlab.ac.uk)

Commercially exploited pelagic fish species have a strong tendency to aggregate together. Individual fish aggregate into schools of varying sizes and schools will also tend to aggregate into clusters of many schools. If the stock abundance changes, it is expected that the pattern of these aggregations will change. The numbers, sizes, densities of the schools, and clusters may be expected to change with changing stock level. Such changes will in turn influence the conduct of both fishing and survey activities. A knowledge of fish aggregation patterns and the processes involved should improve the reliability of stock monitoring techniques and provide an understanding of the impact of exploitation on dynamically changing populations. Using image processing techniques a database of schools has been developed from data recorded during acoustic surveys for herring in the NW North Sea between 1993–1998. Positional, morphometric, environmental, and energetic descriptors have been computed for each school. The paper will present the results of the analysis of this database, giving particular attention to variation in schooling and clustering patterns, and the spatial distribution of these aggregations, in relation to the changing herring stock size in the period 1993–1998.

11:40

2aAO11. Assessing the relationships between oceanographic parameters and fish distribution: Methodological access and potential problems. Patrick Schneider (Inst. de Ciencias del Mar, Paseo Juan de Borbon, s/n, 08039 Barcelona, Spain, patrick@icm.csic.es)

The management of living resources, such as fish, is depending on the information available on the interrelationships between these resources and other factors—biotic or nonbiotic—prevailing in the system of interest. As far as the impact of oceanographic parameters on the distribution of pelagic fish is concerned, little is known. A profound understanding of distributional patterns of fish, of shifts in distribution, and the interactions between environmental factors and distribution requires at first the simultaneous acquisition of both acoustic and oceanographic data. Haul data and hydroacoustic data, gathered on five small scale surveys in two Mediterranean areas simultaneously with data for temperature, salinity, sigma-*t*, and currents, was compared visually and statistically to reveal possible interrelations. As new methods needed to assess the interrelations between environmental and acoustic data are still being developed or adapted from other applications within the scientific community, methodological problems related with this approach are discussed and preliminary results and implications for further investigations and survey designs are presented. Further, new techniques for visualizing survey data are presented and discussed with the objective to open new insights in well-known data. [This work has been financed by the European Commission under Contract No. FAIRGT950139.]

12:00

2aAO12. Observation and extraction of three-dimensional information on fish schools. John Simmonds (Marine Lab., Aberdeen AB11 9DB, Scotland), Francois Gerlotto (ORSTOM, Montpellier, France), Paul Fernandes, and David MacLennan (Marine Lab., Aberdeen AB11 9DB, Scotland)

The paper describes the performance calibration and use of a 90-deg sector scanning sonar for the collection and extraction of information on the 3D structure of fish schools. The equipment, which consists of a 455-kHz 60-beam sector scanning sonar linked to a PC is described briefly. The specific calibration problems of a high-frequency instrument with multiple beams is discussed and calibration data from on-axis and beam shape measurements are presented. The deployment of the instrument for data collection at sea and the data collection methods are described. Examples of the data collected are given. A three-dimensional data processing algorithm is presented along with results of reconstruction from selected schools. The statistical properties of within school data are discussed along with indications of the precision of internal structures that can be evaluated using the sonar. The development of this system is supported by the European research program, AIR.

Session 2aEA

Engineering Acoustics: Silicon Sensors

Ilene J. Busch-Vishniac, Cochair
Whiting School of Engineering, Johns Hopkins University, 3400 North Charles Street, Baltimore, Maryland 21218-2694, USA

Gerhard M. Sessler, Cochair
Institute for Telecommunications and Electroacoustics, Darmstadt University of Technology, Merckstrasse 25, D-64283 Darmstadt, Germany

Chair's Introduction—7:55

Invited Papers

8:00

2aEA1. Silicon microphones: An overview. Marc Fischer and Gerhard M. Sessler (Inst. for Telecommun. and Electroacoust., Darmstadt Univ. of Technol., Merckstrasse 25, 64283 Darmstadt, Germany)

Over the past few years, silicon micromachining has become a well-established technology. This development was promoted by the expectation that new types of sensors and actuators can be fabricated at low cost. Very early, attempts were made to realize acoustic sensors by the use of micromachining. Only now, the first commercial silicon microphones are available. This paper presents an overview of the technology and discusses different principles to build silicon microphones. There are acoustic sensors, e.g., the capacitive silicon microphone, which are designed by downscaling classical transducers. As opposed to this, there are new types of sensors, making use of novel transduction principles, or of the possibility to integrate active elements on the silicon substrate. The focus of this paper is on the following principles: the capacitive microphone in either single-chip or two-chip design, the piezoelectric microphone with organic or ceramic piezolayer, the piezoresistive microphone utilizing monocrystalline or polycrystalline silicon, the optical microphone based on modulating light propagation in a micromechanical waveguide, and the FET microphone, consisting of an acoustically modulated field-effect transistor. Each transducer will be discussed briefly, including the typical technological process necessary for its design.

8:20

2aEA2. Silicon micromachined microphone chip at Siemens. Alfons Dehé, Thomas Bever, Stephan Schmitt, Sven Michaelis, Hans-Jörg Timme, Ewald Pettenpaul (Siemens AG, Semiconductor Group, HL HF T SNS, Balanstr. 73, D-81617 Munich, Germany), Klaus Oppermann, and Robert Aigner (Siemens AG, D-81739 Munich, Germany)

Applications ranging from hearing aids over communication to noise cancellation open up a high volume market for low-cost, batch producible and reliable microphones. To obey these conditions, a single-chip capacitive microphone has been developed at Siemens, utilizing a modified standard CMOS process with adjacent bulk micromachining. In a first step, the microphone is integrated with a source follower, enabling low output impedance of the signal. The technology allows for the future integration of advanced circuitry. The microphone consists of an acoustically sensitive polycrystalline silicon membrane and a highly perforated back-plate as the counter electrode. To achieve highly sensitive devices, special emphasis was given to the stress of the polycrystalline silicon membrane, which should be slightly tensile. Another key issue during the fabrication and in operation is to prevent stiction of the sensitive membrane. Since the overall chip size is below 3-mm side length, surface mounting in low-cost SMD packages is possible.

8:40

2aEA3. A low-voltage silicon condenser microphone for hearing instrument applications. Pirmin Rombach, Matthias Müllenborn, Udo Klein (Microtronic A/S, Byleddet 12-14, DK-4000 Roskilde, Denmark), Lis Nielsen, and Roger Frehoff (Mikroelektronik Ctr., DTU, DK-2800 Lyngby, Denmark)

Silicon microphones have been the subject of investigations since the early 1980s. Due to their poor performance, no silicon microphone for hearing instrument applications has been commercially available until today. Usually the sensitivity of the electromechanical transducer is too low. Thus the input-related noise of the following preamplifier stage becomes dominant and results in a high equivalent input-related noise. Here a silicon condenser microphone with the potential for hearing instrument applications will be presented. To get the best properties for the different mechanical parts, e.g., membrane and back plate, a dedicated process sequence has been developed. Therefore, circuitry and mechanical parts have to be produced separately and mounted later in a stacking process. The microphone has a 2×2 mm^2, 0.4 μm-thick membrane and an air gap of 1.0 μm. Wafers with different membrane stress have been produced. The microphones have been acoustically, mechanically, and electrically characterized, partly on wafer-scale, and compared with an acoustical/electrical lumped element model. The sensitivity for the low-stress microphones using a 1.5 V power supply is about 7.0 mV/Pa and the input related A-weighted noise is 23 dB SPL, including the preamplifier. Due to a conservative layout, the parasitic capacitance is about 50%. An increase of 2–3 mV/Pa sensitivity and hence 3 dB SPL less noise can therefore be achieved by design optimization.

9:00

2aEA4. Silicon capacitive microphones with corrugated diaphragms. Quanbo Zou and Rongming Lin (School of MPE, Nanyang Technol. Univ., Singapore 639798)

Several miniature silicon capacitive microphones that are newly developed, including a single-chip fabricated condenser microphone and a floating-electrode-electret microphone, and a double-chip fabricated condenser microphone, will be presented. All these microphones take advantage of the corrugated diaphragm technique, which has been proven to be an excellent technique for highly sensitive structures. This technique has greatly improved the performance of the silicon capacitive microphones, especially the sensitivities and noise levels. High reproducibility of the microphone performance has also been achieved as the result of the reduction of the thin-film initial stress effects on the mechanical membranes. Moreover, the corrugation technique makes it possible to integrate easily the electric circuits on the single chip that contains the microphone. Overall design considerations for various microphones will be presented, followed by the finite-element analyses for the mechanical properties of the diaphragms and backplates. Fabrication processes for these microphones are briefly described. Finally, the experimental results are compared with the calculations. The study shows that the single-chip fabricated condenser and electret microphones with integrated preamplifiers have higher sensitivities or greater potentials compared with other capacitive microphones of the same diaphragm sizes, and many promising applications can be expected.

9:20

2aEA5. A novel microelectromechanical system (MEMS) design for an underwater acoustic field sensor. Thomas G. Bifano, Robin O. Cleveland, Debora A. Compton, and Allan D. Pierce (Dept. of Aerosp. and Mech. Eng., Boston Univ., 110 Cummington St., Boston, MA 02115, adp@enga.bu.edu)

A concept for underwater acoustic imaging exploits current technology for constructing MEMS devices from silicon wafers. Anisotropic etching creates frustum-shaped (pyramids with tops cut off) holes in a wafer chip; the bonding of two such chips creates double frustum-shaped holes, each analogous to an hour glass. The front side of each hole is a tapered duct with a baffled open end. The acoustic disturbance generated by an incident plane wave magnifies as the flow converges toward the waist. The back half of the double frustum is covered by a third silicon layer and acts as a Helmholtz resonator, the waist being the neck. The manufacturing process places a thin membrane across the waist which oscillates sychronously with the acoustically induced fluid motion. An appropriate design can achieve fluid velocities at the neck much larger than what would be associated with the incident acoustic wave in free space, and exploratory experiments confirm this. The oscillating membrane is sensed by an optical system, and theoretical extrapolation of the measured displacement amplitude yields a measurement of the amplitude of the incident acoustic wave. [Work supported by Indian Head Divison, Naval Surface Warfare Center, as part of the DARPA Sonoelectronics Program.]

9:40–10:00 Break

Contributed Papers

10:00

2aEA6. Slot silicon microphone: Analytical and experimental study. Zdenek Skvor (CTU Prague, Technicka 2, 166 27, Prague 6, Czech Republic) and Axel Stoffel (FH Furtwangen, Furtwangen im Schwarzwald, Germany)

The diaphragm, as an acoustically active part of the electrostatic silicon transducer, is usually located in the front of the transducer, and the size of the substrate plate determines the entire size of the assembly. It is possible to place on the substrate plate a higher number of sensors and thus obtain a higher sensitivity of the whole system. The increasing number of diaphragms provokes the enlargement of the frontal area of the assembly and the device loses its miniature size. In this contribution a new arrangement is presented of electrostatic or similar pressure sensors with an indirect pressure excitation of their diaphragms and with a small frontal area of the assembly [A. Stoffel and Z. Skvor, Slot microphone, Applic. for U.S. Patent 9,010,032]. Together with an adjacent plate, the substrate plate with diaphragms forms a thin rectangular air-gap with constant or variable cross section and with frontal or frontal and lateral opening. The analytical description is based on the solution of the two-dimensional Helmholtz equation and the transfer function was derived with respect to visco-thermal losses and was experimentally verified.

10:20

2aEA7. Model measurement of the microphone array. Libor Cerny (Dept. of Radioelectronics, CTU Prague, Technicka 2, 166 27, Prague 6, Czech Republic, CERNYL@FELD.CVUT.CZ)

The use of silicon has allowed the fabrication of microphones with integrated electronic circuitry and the development of the FET microphone. The introduction of lithographic technique has resulted in microphones with very small (1 mm^2) diaphragms with specially shaped backplates. The application of corrugated diaphragms ensures promising future development of silicon microphones. On the basis of this work the arrangement can be prepared for an encapsulation of a miniature microphone chip. Frequency response of the microphone arrays of various types was measured on models in an enlarged scale. It was proven by the numerical results and by the measurements on the model that this manner of encapsulation is possible and advantageous. It was concluded that there is a satisfactory agreement between the analytical description and experimental results of model measurements. The measurement can be transposed to frequency ranges in the ratio of wavelength and dimensions and the damping of modes can be calculated. This problem solution is cheaper than measurement of the miniature microphone chip [Z. Kvor, ''Study of the Air-gap and the Influence of the Microphone Position on the Substrate Plate,'' Report Copernicus CP 940515 (1997), P. R. Scheeper, Sensors and Actuators **A44**, 1–11 (1994)].

10:40

2aEA8. Theoretical and experimental study of the electrostatic transducer with a nonplanar back plate. Jan Skvor (Dept. of Radioelectronics, CTU-Prague, Technicka 2, 166 27, Prague 6, Czech Republic, skvorjan@feld.cvut.cz)

Usually the electrostatic transducer as a microphone or pressure sensor is formed by a circular or rectangular membrane and a planar back electrode with holes. The number, the diameter, and the position of the holes in the back electrode determine the acoustic impedance of the air-gap and especially the damping of the transducer. The aim of this contribution is to show the possibility of the realization of a transducer with a thin diaphragm and a back electrode of convex shape and without holes. The convex shape of the back electrode, because of the nonuniform displacement distribution over the membrane, has a small influence on the transducer sensitivity, but a very high influence on the membrane damping. In

the contribution is shown the application of the theory of this type of transducer with a circular membrane vibrating in the fundamental mode with approximate parabolic distribution of membrane displacement and a paraboloidal back electrode without the holes. This transducer modification is applicable for classical and silicon micro-mechanical technologies [Z. Skvor and J. Skvor, Proc. 4th Congress on Acoust., SFA, Marseille (1997), Vol. 1, pp. 63–66].

11:00

2aEA9. A comparison of surface transverse wave propagation on quartz and gallium orthophosphate. Emmanuel Bigler and Jean-Bernard Briot (Laboratoire de Physique et Métrologie des Oscillateurs Associé à l'Université de Franche-Comté, Besançon, France and 25044 Besancon Cedex, France, bigler@lpmo.univ-fcomte.fr)

Gallium orthophosphate ($GaPO_4$) is a piezoelectric material (32-class) with the same symmetry as quartz, but with a higher electromechanical coupling factor and richer possibilities of temperature-compensated acoustic modes in a wide range of temperatures, mainly at high temperatures above 300 °C. Surface transverse waves (STWs) can be generated on both quartz and $GaPO_4$ crystals on Y-rotated plates, so it is interesting to compare both materials on this respect. It is shown that a temperature-compensated orientation exists on $GaPO_4$ for STWs, but with a lower velocity (2500 m/s) than for quartz (5100 m/s). Propagation of STWs on $GaPO_4$ under an array of metal strips or grooves is studied and dispersion curves for grooves, aluminum, and gold strips are presented. It is shown that energy trapping near the surface will occur in all cases, allowing STW resonators to be built on $GaPO_4$. The sensitivity of STW devices on $GaPO_4$ to metal thickness and geometrical parameters of electrodes will be investigated. Possible applications to high-temperature devices will be discussed. [This work is supported by CEC, Thomson Microsonics (France) and CNRS (France).]

11:20

2aEA10. An integrated-optical silicon microphone with a Fabry–Pérot cavity as modulator. Martin Klaiber (Inst. for Telecommunications and Electroacoustics, Darmstadt Univ. of Technology, Merckstr. 25, 64283 Darmstadt, Germany)

A new construction principle for an integrated-optical microphone is presented. It uses a Fabry–Pérot cavity as modulator. This combines the very sensitive interferometric multiple reflection scheme with a direct intensity modulation. The microphone consists of two chips, the carrier chip and the membrane chip. Both are fabricated in silicon using standard semiconductor technology. The membrane chip is mounted on top of the carrier chip, so that both chips together form the Fabry–Pérot cavity. Unmodulated primary light is generated by a laser diode and partially transmitted to the microphone via a 3-dB coupler. A single fiber, which is attached to the bottom side of the carrier chip, connects the coupler and the microphone. The incoming light is modulated in the Fabry–Pérot cavity by the membrane deflection and is reflected back into the fiber. It passes the coupler in reverse direction and is thereby partially transmitted to a receiver device, e.g., a photo diode. The main advantage of this kind of microphone is that a very low inherent noise level (<30 dB/A) can be achieved with a relatively simple design.

11:40

2aEA11. Development of compact fiber-optic microphones. Young C. Cho, Charles K. Gary, Meric Ozcan (NASA Ames Res. Ctr., MS 269-3, Moffett Field, CA 94035-1000, ycho@mail.arc.nasa.gov), and Thomas George (Jet Propulsion Lab., Pasadena, CA 91109)

Advanced pressure sensors have been developed at NASA Ames Research Center, using fiber-optic technology. The development includes: compact size microphone for aeroacoustic measurements in wind tunnels with minimized flow–sensor interaction, and compact size pressure sensors for real-time measurements of flow transition over an airfoil. A prototype pressure sensor was designed and fabricated with a silicon nitride diaphragm mounted on a miniaturized ferrule. The sensor has a 3-mm diameter. Preliminary tests demonstrated excellent performance. The frequency response is steady and uniform within the design frequency limit, 100 to 5000 Hz. Its sensitivity, measured in terms of signal-to-noise ratio, is almost 10 dB better than the best condenser microphone available in a similar size (0.125-in diameter), and is better than any existing fiber-optic pressure sensor by at least three orders of magnitude. The overall performance of this sensor exceeds the initial expectation. The compact size and light weight of these sensors provide several advantages. The small size could allow tens of hundreds of sensors to be used together for applications such as microphone arrays. The flow–sensor interaction is smaller, providing more accurate measurements of pressure fluctuation of air flows over flight surfaces.

Session 2aMU

Musical Acoustics: Modeling Versus Measurements of Wind Instruments

Avraham Hirschberg, Cochair
Eindhoven University of Technology, N-LAAG, P.O. Box 513, 5600 MB Eindhoven, The Netherlands

Shigeru Yoshikawa, Cochair
Department of Acoustical Design, Kyushu Institute of Design, 4-9-1 Shiobara, Minami-Ku, Fukuoka 815-8540, Japan

Chair's Introduction—7:55

Invited Papers

8:00

2aMU1. Mouth tones of flue organ pipes: A control of sound aesthetics. Michele Castellengo (Laboratoire d'Acoustique Musicale, Universite Paris 6, 11 Rue Lourmel 75015 Paris, France)

The quality of the steady sound of organ pipes is determined by pipe geometry and blowing pressure. In contrast to this, the attack transient is controlled by both the voicer and to some extent by the player. The initial part of the transient is related to the so-called ''mouth tones,'' which will be discussed in some detail. On the basis of analyses of the sound production of many organs, the importance of mouth tones during the attack transients of some characteristic stops is shown: Diapason family with initial broadband noises; stopped and chimney pipes with inharmonic ''pings;'' Viola stop of the Italian organ with long and intense mouth tones persisting during the stationary sound. As frequency content of mouth tones is directly dependent on the air velocity at the flue, any variation of the pallet opening time in the mechanical action or small uncontrolled fluctuations existing in the wind channel produce many variations in the attack transients. Such variations due to the mouth tones give life to the perceived sound quality of the organ, an instrument where sound production is hardly influenced by the musician.

8:30

2aMU2. Numerical calculations of woodwind impedances without adequate experimental data: Personal experiences. William J. Strong (Dept. of Phys. and Astron., Brigham Young Univ., Provo, UT 84602)

Some numerical calculations of impedances of an oboe showed relatively good qualitative agreement with experimental data [G. R. Plitnik and W. J. Strong, J. Acoust. Soc. Am. **65**, 816–825 (1979)]. With the apparent success of the numerical method, input impedances were calculated for a number of ''woodwind-like'' structures. On the basis of these calculations a paper was prepared and submitted for publication. Some six months after its submission it was returned with numerous comments regarding errors in its content. A recurring comment from the reviewer was ''the digital computer where used alone has contributed directly to most of the difficulties of this paper.'' Previous to receiving the reviewer's comments the author was using the same numerical method to calculate resonance frequencies of a flute. Difficulty was being experienced in getting reasonable agreement with experimental results. However, after incorporating empirical data into the representation of toneholes rather good results were obtained with the numerical method [W. J. Strong, N. H. Fletcher, and R. K. Silk]. A brief history of these experiences will be presented along with pertinent details from the papers and the reviewer's comments.

9:00

2aMU3. Flow and upstream impedance in wind instruments. P. L. Hoekje (Dept. of Phys. and Astron., Baldwin-Wallace College, 275 Eastland Rd., Berea, OH 44017)

The salient features of the behavior of a wind instrument can be explained by the now-common model of an air column resonator coupled with a flow controller; this paper presents clarifications in that model. The reed flow controller is driven by a pressure difference p and generates a flow u; its nonlinearity spreads energy across the spectrum, converting energy from the dc energy source of the player's breath. The instrument air column is characterized by its input impedance $Z_d = p_d / u_d$, where the subscript d denotes the downstream side of the reed. Upstream is the player's airway, characterized by $Z_u = p_u / u_u$ and controlled by the player. The sum $(Z_d + Z_u)$ provides feedback to the reed, and when Z_u is comparable to Z_d, the playing qualities of the instrument appear to change. The flow waveform can be estimated from $u_d = p_d / Z_d$, which can then be compared to predictions from dynamical models of the reed motion. To the extent that the reed is incompressible, then $u_d = -u_u$, and Z_u can be estimated from the measurements $(Z_d p_u / p_d)$. Evidence will also be presented of the nonlinearity of the air column response at loud playing levels.

2aMU4. Why are historical brass instruments hard to play in tune? D. Murray Campbell (Dept. of Phys. and Astron., Univ. of Edinburgh, Edinburgh EH9 3JZ, UK)

Historical cup-mouthpiece instruments, especially those from the Renaissance and Baroque periods, have the reputation of being harder to play in tune than modern brass instruments. This paper considers what is meant by ''playing in tune'' from both acoustical and musical standpoints, and surveys acoustical features of some early cup-mouthpiece instruments which may have contributed to their reputation for uncertain intonation. Three different classes of instruments are distinguished. The first includes instruments of fixed acoustical length, such as the natural trumpet; the second includes instruments in which the acoustical length may be lengthened by moving a slide or depressing valves, as on the trombone and the valved trumpet; the third includes cup-mouthpiece instruments in which the acoustical length can be decreased by opening fingerholes, such as the cornetto and the serpent. Different considerations affect intonation in each class of instrument. Experimentally derived input impedance curves, frequency spectra of played notes, and threshold pressure measurements using artificial lips are presented and discussed in the context of intonation sensitivity.

9:40–10:00 Break

Contributed Posters

Posters will be on display in Room MA141 on Tuesday, 16 March, from 10:00 a.m. to 12:20 noon to allow contributors an opportunity to see other posters, contributors of odd-numbered papers will be at their posters from 10:00 a.m. to 11:00 a.m. and contributors of even-numbered papers will be at their posters from 11:00 a.m. to 12:00 noon.

2aMU5. Modeling of air-jet-driven instruments: An unstable jet driven by pressure gradient. Seiji Adachi (Dept. of Information Sci. and Technol., Aichi Prefectural Univ., Nagakute, Aichi, 480-1198 Japan)

A new model of the jet deflection is developed to understand the sound production of an organ flue pipe, which is representative of air-jet-driven instruments. This model provides a dynamical equation governing the displacement of a jet, which has the aerodynamical instability and is driven by the acoustic pressure gradient in the direction perpendicular to jet travel. Due to the instability, the growth factor of the deflection becomes exponential, as found in measurements of the jet movement such as hot-wire anemometry and flow visualization. The oscillation condition of an experimental E4 organ pipe is examined by considering the phase difference between the jet displacement at the labium and the acoustic pressure at the mouth. The sound is simulated by means of the physical modeling technique. The simulated pipe behavior is compared with that found in an actual pipe. Similarities and differences found in the transition between oscillation regimes are discussed.

2aMU6. Variation of frequency with blowing pressure for an air-driven free reed. James P. Cottingham, Christopher H. Reed, and Michael Busha (Phys. Dept., Coe College, Cedar Rapids, IA 52402, jcotting@coe.edu)

In free reed instruments, an approximately linear decrease of playing frequency with increasing blowing pressure is normally observed. Laboratory measurements on harmonium-type reeds from an American reed organ have shown additionally that at very low pressure there is a small region of increasing frequency with increasing blowing pressure, and at extremely high blowing pressures, the frequency of reed vibration increases rapidly with increasing pressure. Measurements of growth and damping rates confirm the previously reported result [A. O. St. Hilaire, T. A. Wilson, and G. S. Beavers, J. Fluid Mech. **49**, 805–815 (1971)] that at low air-flow rates aerodynamic forces add to the mechanical damping of the vibrating reed, but at higher flow rates, the aerodynamic forces contribute negative damping, resulting in self-sustained oscillations. Measurements of reed damping or growth rates have been made over a wide pressure range. Incorporation of these values along with other appropriate parameters in Fletcher's model of reed vibration [N. H. Fletcher, Acustica **43**, 63–72 (1979)] permit theoretical calculation of the variation in frequency with pressure for the air-driven free reed. The results of these calculations agree well with experimental data.

2aMU7. Jet and vortex behaviors visualized during the starting transient in organ pipes. Shigeru Yoshikawa (Dept. of Acoust. Design, Kyushu Inst. of Design, Fukuoka, 815-8540 Japan, shig@kyushu-id.ac.jp)

Three types of transient jet behaviors are demonstrated using slow-motion pictures (2 to 30 pictures per second) taken by a high-speed digital video camera (1297 or 1440 pps). (1) The jet issuing from the flue almost always deviates toward the pipe outside and results in a large vortexlike trajectory. When the lower surface of this outwardly curved jet just touches the edge tip, a tiny vortex is likely to be formed beneath the edge. This vortex introduces the first stimulus from the jet to the pipe inside, and in turn significant disturbances are created along the jet. As communicated to the pipe, these disturbances gradually become periodic and well-organized to build a jet wave. This tiny vortex beneath the edge yields a smooth and fast build-up. (2) A much faster build-up is realized when the jet impinges the edge straightforwardly and divides into the two from the jet center. However, this case is rare. (3) A much slower build-up is caused when the blowing pressure is relatively low and a small vortex tends to stand between the flue and the edge. This stagnant vortex may yield a ''two-crest'' jet wave prior to the formation of an ordinal ''one-crest'' jet wave.

2aMU8. Foot resonance in an organ pipe. Claire Segoufin, Benoit Fabre (LAM, UPMC case 161, 4 place Jussieu, 75252 Paris cedex 05, France, segoufin@ccr.jussieu.fr), Vincent Rioux, Munetaka Yokota, Malte Kob, and Mendel Kleiner (Chalmers Univ. of Technol., Gothenburg, S-41279, Sweden)

Pressure measurements in the foot of an organ pipe under playing conditions show acoustical pressure fluctuations induced by the acoustic field in the pipe. Fluctuations of the pressure difference between the foot and the mouth of the instrument results in jet velocity fluctuations that can absorb or produce acoustic energy depending on relative phase with the acoustic pressure in the mouth of the pipe. In most flue organ stops, pipe dimensions indicate that the first pipe resonance and the Helmholtz foot resonance should lie close to each other at least for one pipe in the stop. The present work was triggered by the question of knowing why this does not seem to bother organ builders. Measurements of Helmholtz foot resonances as a function of the driving pressure carried on a pipe with adjustable foot volume are presented. Measurements indicate a damping of the resonance due to the flow through the mouth that can be accounted for by

an elementary model of the flow through the mouth. Analysis indicates that, unlike recorder playing, the jet velocity guarantees an efficient damping.

2aMU9. Analysis of time-frequency structure of woodwinds' sounds, with usage of discrete wavelet transform. Magdalena Klapper (Dept. of Computer Sci., Univ. of Mining and Metallurgy, Cracow, Poland)

The purpose of this paper is a presentation of analysis results of sounds of woodwinds. The aim of the research was to observe the characteristic properties of the time-frequency structure of particular instruments' sounds, considering the sound register and dynamics. Special attention was paid to the range of tone color registers and possible loudness of sound within them. A trial was undertaken to define the reasons for the division of the instruments' scale in several tone color registers. The mathematical methods used to perform the time-frequency analysis of the instruments' sounds were: mainly multilevel discrete wavelet transform, and also traditional methods: fast Fourier transform and short-time Fourier transform. Discrete wavelet transforms seems to be an especially useful tool for observation of changes of sound parameters. The methods mentioned above vary in distribution of time-frequency analysis. Each of them delivers fragmentary information of the time-frequency structure of the sound; however, they are complementary to one another. Within the framework of the paper a comparison of the analysis results of instrument sounds of quite different properties of time-scale structure are presented.

2aMU10. Attack transients of free reed organ pipes. Jonas Braasch (Inst. of Commun. Acoust., Ruhr Univ., D-44780 Bochum, Germany, braasch@ika.ruhr-uni-bochum.de) and Christian Ahrens (Ruhr Univ., D-44780 Bochum, Germany)

Free reed pipes in organs have fallen out of favor, because they were reputated to have a sluggish attack transient. To test this theory, the starting transients of the *''Klarinette 8 ft''* pipes were measured on the new Klais organ in the Auditorium Maximum, Bochum. Further measurements to determine the role of the wind pressure were done on the wind chest of the Klais workshop in Bonn. The transients of the free reed pipes were compared to those of bound reed pipes and diapason pipes (measured on the same organ). As the results show, the attack transient of the free reed pipes was indeed slower than that of bound reed pipes, but on the same order of that of diapason pipes. However, in contrast to the free reed pipes, diapason pipes have a noticeable broadband noise preceding the sound. In addition, there is a delay between the onset of the first-order harmonic and the onset of the higher-order harmonic in the starting transient of the free reed pipe. This effect is not usually found in the transient of diapason pipes.

2aMU11. Noise quality of transient sounds: Perception of ''hiss'' and ''cough'' in a flue organ pipe. Vincent Rioux, Daniel Västfjäll, Munetaka Yokota, and Mendel Kleiner (Dept. of Appl. Acoust., Chalmers Univ. of Technol., S-41279 Göteborg, Sweden)

According to an expert organ builder, the onomatopoeia ''hiss'' and ''cough'' must be distinguished from the well-known general term ''chiff'' in order to describe the characteristic bursts of noise occuring during the transient of many flue organ pipes. These particular sounds can be adjusted and aligned to a certain aesthetic, but this matter has not yet been much discussed by organ experts. This exploratory study mainly relies on a computer-based listening test which has been carried out on two groups of people (musicians and acousticians). The experiment focused on the participants perception of ''hiss'' and ''cough'' and also on their ability to extract the ''noisy'' part from the harmonic components. Even though the sounds were quite similar, the noise/harmonic separation task was successful for a large number of subjects. This supports the hypothesis of a natural perceptual difference between the noise bursts and the concomitant harmonic setup and also the validity of this decomposition. To differentiate and identify ''cough'' and ''hiss'' sounds, however, is a much more elaborate task which requires much experience.

2aMU12. Experimental investigations of wall influences on woodwind instrument sound. Cornelis J. Nederveen (Acacialaan 20, 2641 AC Pijnacker, The Netherlands) and Jean-Pierre Dalmont (Université du Maine, 72085 Le Mans Cedex 9, France)

Influences of wall vibrations and thermal/viscous dissipation at the walls on loudness and sound quality of some woodwind instruments (clarinets, recorders, organ flue pipes) were investigated experimentally. Instruments with various wall thicknesses and wall porosities were studied. Wall vibrations were not found to influence the air oscillations except for a very thin-walled cylindrical organ flue pipe. For this pipe, level increases of 3 dB and perceptible sound quality changes were observed when the upper part of the pipe was clamped. From input impedance measurements of instruments geometrically identical, but varying in wall porosity, it was found that the quality factor of the resonances could vary by a factor of 2. The sound level produced by blowing these instruments appeared (at a certain blowing pressure) to be proportional to the real part of the input impedance. The pressure level at which a recorder overblows appeared to increase with the input impedance. Besides wall damping, variations in the bore, which determine the exact positioning of eigenfrequencies, were also found to affect loudness and sound spectrum.

2aMU13. Mechanical response of artificial buzzing lips. John S. Cullen (Dept. of Phys. and Astron., Univ. of Edinburgh, Edinburgh EH9 3JZ, UK), Jöel Gilbert (l'Université du Maine, 72085 Le Mans Cedex 9, France), and D. Murray Campbell (Univ. of Edinburgh, Edinburgh, UK)

Brass instruments sound when the coupling between the acoustical resonator (the instrument) and the mechanical oscillator (the lips) results in a self sustained oscillation. It is the aim of this investigation to characterize experimentally the mechanical response of the lips and to examine its influence on the lip motion observed under near-threshold playing conditions. In this investigation artificial latex rubber lips replace the lips of a human player. Particular emphasis is placed on studying the development of the mechanical response as the embouchure is tightened or as airflow through the lips is introduced. The effect of the acoustical coupling provided by the mouthpiece is investigated. Also presented are playing test measurements, carried out at a level just above the threshold of oscillation. The artificial lips are used to excite resonators of various acoustical lengths; for each resonator the relation of the playing frequency to the nearest lip and resonator resonance frequencies is examined and the measured phase difference between lip opening area and mouthpiece pressure is compared with the phase angles of lip mechanical response and resonator input impedance at the playing frequency. The observed oscillation threshold behavior is compared with that predicted by theoretical physical models.

2aMU14. Reed instruments, from small to large periodic oscillations. Jöel Gilbert, Jean-Pierre Dalmont, and Jean Kergomard (Lab. d'Acoust. de l'Univ. du Maine, UMR CNRS 6613, Ave. Olivier Messiaen, 72085 Le Mans Cedex 9, France)

Reed instruments are physical systems which can be considered as self-sustained oscillators. The ''normal operation'' of the instrument corresponds to the establishment of a permanent periodic regime. On the one hand, the behavior of the small periodic oscillations in the fixed point (threshold) vicinity is well known: the bifurcation's nature and the oscillation's characteristics depend on both the excitator and the resonator. On the other hand, a theory has been developed for lossless resonators coupled with the excitator: compared to experimental results, this theory is relevant for large amplitude oscillations. The matching between the analytical solutions of the two theories is not instantaneous. The matching is

studied using the harmonic balance technique with the continuation method coming from known analytical results near the threshold. The bifurcation graphs are constructed for different resonators. The particular resonator with two harmonic resonances is discussed in detail. The role of the octave regime is unexpected: the octave is matched to some of the fundamental regimes. Some resonators (cylinder, lattice of cylinders, cone) are arranged on an artificial mouth designed for single-reed woodwinds. Measurements of periodic regimes are compared to the theoretical results. A movie will be shown.

2aMU15. A virtual reconstruction of the trumpet. Lamberto Tronchin and Alessandro Cocchi (DIENCA—CIARM Viale Risorgimento, 2 40136 Bologna, Italy, tronchin@ciarm.ing.unibo.it)

Virtual reconstructions of musical/instruments have already been analyzed in past years on violins. The ''virtual'' instruments can be used in subjective listening tests for the evaluation of the sound quality of different instruments, as well as in the restoration of ancient instruments, and for preliminary listening tests on new designed instruments. In this paper, the trumpet is treated as a linear system, characterized by its impulse response. From the IRs measured in different positions in the trumpet, an inverse numeric filter of three trumpets has been obtained, through a new developed technique. From the recording of some original pieces of music, sampled directly inside one of the trumpets, an ''anechoic'' signal has been obtained by convolution with the inverse filter calculated in the same position. The ''anechoic'' signal, convolved with the IRs just measured in the other trumpets, produced a signal containing all the acoustic characteristics of the instruments, avoiding all nonacoustic phenomena, and allowed the realization of ''virtual'' reconstruction of the trumpet. The first results of the listening tests confirm the similarity between the direct acoustic recording and the convolution technique also for the trumpet, as well as already found for the violins.

2aMU16. The wave digital filter brass mouthpiece model. Maarten van Walstijn (Faculty of Music, Univ. of Edinburgh, 12 Nicholson Square, Edinburgh EH8 9DF, Scotland) and Murray Campbell (Univ. of Edinburgh, Edinburgh, Scotland)

Wave digital filter (WDF) techniques are applied to develop an efficient discrete-time two-port mouthpiece model that can be used in traveling-wave based modeling of brass instruments. WDF's were principally developed for simulation of analog networks, and are used here to discretize the classical first-order lumped element mouthpiece model [J. Backus, J. Acoust. Soc. Am. **60**, 470–480 (1976)]. The model is segmented into two-port units that are individually mapped to the digital domain using the two-port WDF approach [S. Lawson and A. Mirzai, *Wave Digital Filters* (Ellis Horwood, London, 1990)]. The realizability of the filter structure is ensured by choosing the port resistances in between the units such that delay-free loops are avoided. The two-port mouthpiece can be directly coupled to models of the lips and leadpipe, although special care must be taken concerning the local characteristic impedance. The WDF mouthpiece model is easy to plug in, its parameters are very intuitive, and it has low computational costs, which makes it particularly suitable for physical modeling with musical sound synthesis purposes. The functioning of the WDF brass mouthpiece model will be further illustrated in a digital wave guide modeling application of a trumpet, wherein all model parameters are derived from measured data.

2aMU17. A computer program for optimization of brass instruments. Part I. Concept, implementation. Wilfried Kausel, Paul Anglmayer, and Gregor Widholm (Inst. f. Wiener Klangstil, Univ. f. Music and Performing Arts in Vienna, Vienna, Austria)

Computer optimization is used to improve characteristics of real world systems. Different strategies are known and have successfully been applied in areas like filter design, circuit synthesis, layout, etc. Common to all optimization methods is the need for mathematical models and target functions evaluating to a single number, reflecting the sum on all deficiencies depending on variables to be varied. In a brass instrument optimizer these variables are representing physical dimensions which later on can be changed by the instrument maker (e.g., by inserting sleeves or modifying the bore). In the target function, differences between actual and desired characteristics like intonation or responsiveness are calculated, weighted, and added. Because these characteristics can only be derived from the instrument's calculated input impedance, physical modeling is required. Systematically and algorithmically, the optimizer approaches the best possible instrument step by step, varying optimization variables. It is directed by the result and tendency of the target function which is evaluated after each step. The brass instrument optimization program introduced here makes computer optimization available for musical instrument manufacturers. Much expert knowledge like defining target functions, specifying optimization variables, and modeling instruments are hidden from the user, making the tool easy enough to work with.

2aMU18. A computer program for optimization of brass instruments. Part II. Applications, practical examples. Paul Anglmayer, Wilfried Kausel, and Gregor Widholm (Inst. f. Wiener Klangstil, Univ. f. Music and Performing Arts in Vienna, Vienna, Austria)

The brass instrument optimization program presented in Part I has been used in a variety of practical cases, demonstrating its power for the improvement of existing brass instruments. In the first and possibly most difficult step, bore lists describing the instrument's geometry have to be obtained. Sometimes data can be imported directly from a CAD system, otherwise mechanical measurements must be done. Next, the dimensions which are to be varied by the program have to be specified. Constraints can be defined. Specific parametric modification rules representing typical working steps of instrument makers (inserting sleeves, narrowing and widening of certain areas) can be applied. Finally, optimization targets have to be defined. Any combination of intonation, impedance magnitude matching, shape, or envelope goals in user-defined frequency intervals is possible. The optimizer will search for the best possible compromise. During the optimization run, all activities can be observed on screen, and target parameters can be adjusted dynamically. In practical examples, real instruments have been optimized and the proposed modifications have been performed by an instrument maker. Measurements and evaluation results made before and after the modifications have been compared. It was shown that the actual performance improvement matches the predicted one well.

2aMU19. Directivity measurement of a singer. Malte Kob and Harald Jers (Inst. of Tech. Acoust., Tech. Univ. Aachen, Templergraben 55, D-52056 Aachen, Germany)

The convenient method of using broadband excitation for fast and accurate evaluation of narrow-band directivity cannot be applied to the human vocal tract. If the voice itself is used as the excitation, the variable properties of the vocal tract change with each differently pronounced phoneme, and therefore a vowel does not yield the same directivity as a consonant. Additionally, the nonstationary character of the voice does not allow for simple measurements with one scanning microphone. In the method described here, the singer stands on a turntable and sings a glissandolike vowel through at least one octave. The sound-pressure level is recorded with two microphones, one as a reference attached to the singer's nose and the other at a 2-m distance. The spectra of both signals are calculated with a sufficiently long FFT, and the levels are subtracted. For each position of the turntable and every angle of elevation, the spectra are stored on disk and postprocessed within a MATLAB environment. Measured directivity plots of several human singers are compared with those of an artificial singer that has been built to reproduce the singing voice accurately.

Session 2aNSa

Noise: Community Noise Annoyance

Brigitte Schulte-Fortkamp, Cochair
Acoustics/Physics, University of Oldenburg, D-26111 Oldenburg, Germany

Sanford Fidell, Cochair
BBN Technologies, 21128 Vanowen Street, Canoga Park, California 91303, USA

Chair's Introduction—7:55

Panel:

B. Berglund, Sweden
D. Botteldooren, Belgium
S. Fidell, USA
T. Gjestland, Norway
R. Guski, Germany
T. Kaku, Japan
P. Lercher, Austria
H. Miedema, The Netherlands
B. Schulte-Fortkamp, Germany
M. Vallet, France

Invited Papers

8:00

2aNSa1. Limits of utility of dosage-response analysis for predicting the Prevalence of annoyance. Rainer Guski (Dept. of Psych., Ruhr Universitaet Bochum, D-44780 Bochum, Germany, Rainer.Guski@Ruhr-Uni-Bochum.De)

Dose-response analyses from field studies are essential parts of the information necessary for establishing limits for tolerable noise immissions within the sites (e.g., residential areas with certain immissions) and persons actually studied. But they have their limits when (1) dose-response data are compared between independent studies, (2) annoyance data are extrapolated to other sites, other immission types, levels resp. numbers of noise events, other people, or future times, and (3) the effect of noise abatement programs is predicted. These limitations are presented, using empirical data for illustration purposes. The discussion concentrates (a) on methodological aspects of measuring annoyance, (b) methodological aspects of converting continuous annoyance scales to the percentage of highly annoyed people, and (c) on the contribution of nonacoustic factors to annoyance and to empirical dose-response relationships. It is concluded that dose-response analyses must not be discarded, but their limited utility should be kept in mind.

8:20 Panel Discussion chaired by M. Vallet

8:40

2aNSa2. Joint noise annoyance: A field evaluation of models concerning road and railway exposure. Peter Lercher (Inst. of Social Medicine, Univ. of Innsbruck, A-6020 Innsbruck, Austria, Peter.Lercher@uibk.ac.at) and Ulrich Widmann (Mller BBM, D-82152 Planegg bei Munchen, Germany)

There is still controversy about how to deal appropriately with a noise exposure situation where two noise sources are of equal importance to an exposed population. Reanalyzing an older German study [Planungsbro Obermeyer (1983)] Ronnebaum *et al.* (1996) have shown that in a situation where no source is dominant and both sources produce more than 53 dB, Leq, overall annoyance is less than annoyance of the most annoying source. In an ongoing large-noise survey ($N = 2000$) in the Austrian part of the Alps (TYROL) legal requirements force noise ingenieurs to use simple energy summation models in the absence of state of the art alternatives. Selected models [Flindell (1983), DELTA Acoustic & Vibration (1995)] are evaluated in a complex topographical situation (narrow valley with residential areas on the slopes) where noise annoyance due to railway noise has increased over the last decade in spite of a constant number of train passages. The results of this evaluation will be reported and discussed in terms of its usefulness for environmental risk assessments.

9:00 Panel Discussion chaired by T. Gjestland

9:20

2aNSa3. Social survey of the annoyance of low-frequency aircraft ground noise. S. Fidell, L. Silvati, S. Lind, and K. Pearsons (BBN Technologies, 21128 Vanowen St., Canoga Park, CA 91303)

Concerns about the appropriateness of representing low-frequency aircraft ground and near-ground noise in A-weighted units, and about the adequacy of standard interpretive criteria for assessing community response to low-frequency noises, are becoming more common at large civil airports. Residents of a neighborhood adjacent to a busy runway were interviewed to determine the annoyance of runway sideline noise at frequencies below 100 Hz, and of its audible manifestations inside homes. Extensive measurements were made to estimate low-frequency noise contours in the interviewing area, and street addresses of respondents were geo-coded to permit

assignment of low-frequency noise levels to each household. Residents who were highly annoyed by low-frequency sideline noise were concentrated in areas with maximum sound levels summed in one-third octave bands between 25 and 80 Hz (inclusive) that were in excess of 75–80 dB. These levels are consistent with Hubbard's (1980) estimates of low-frequency airborne sound levels capable of inducing secondary emissions in light architectural elements of residences.

9:40 Panel Discussion chaired by R. Guski

10:00–10:20 Break

10:20

2aNSa4. Measurements of noise annoyance: Decisions on appropriate evaluation procedures in field and laboratory settings. Brigitte Schulte-Fortkamp (Acoust./Phys., Univ. of Oldenburg, D-26111 Oldenburg, Germany)

The complicated context of noises that are annoying has to be taken into account to measure annoyance adequately. The measurement has to provide insight information improving the understanding of the complex processes causing the annoyance judgments built up in ranking results, e.g., based on categorical judgments. Another problem will be defined by asking which procedure is more or less sufficient to solve the problems of annoyance measurements or should those measurements be carried out in studies combining both field and laboratory. There is the necessity of a consensus that studies on annoyance have to include the context of activities or interference of activities. Two laboratory studies based on a field study evaluating noise from different sources are carried out in different countries. The results point out the context sensitivity of any judgment as well as the measurement procedure guarantee a detailed characterizing of the noises. The subjective judgments correlate with those parameters relevant for the living situation of each subject. For the laboratory experiments the context is defined by associations evoked by the noises presented. Results of both of the studies strongly demonstrate the need for measurements including the context evaluation and an integrative procedure of field and laboratory studies.

10:40 Panel Discussion chaired by P. Lercher

11:00

2aNSa5. Predicting the joint annoyance of multiple noise sources. Birgitta Berglund and Mats E. Nilsson (Inst. of Environ. Medicine, Karolinska Inst. and Dept. of Psych., Stockholm Univ., S-106 91 Stockholm, Sweden)

Noise annoyance is always linked to a complex of environmental noises (noise emission) even if source-specific annoyance is possible to report. Therefore, there is a lack of agreement between total or joint annoyance predicted from source emissions and the actual annoyance reported under field conditions. Models developed from laboratory experiments are commonly pure mathematical constructs based on simple energy summation of totally overlapping sound, whereas the field conditions require yet undeveloped mathematical models that account for perceptual-cognitive integration processes. To be successful in predicting joint annoyance of multiple noise sources, it is necessary that the integration of information derived from noise emission(s) is modeled, rather than simply to sum mathematically noise-source emissions. Important factors for perceptual-cognitive integration processes are kinds of noise sources, their levels, time pattern of joint emissions, discernibility of sounds, and the role these play in the soundscape. Existing models can to varying degree accommodate these factors, but it seems necessary that new models particularly take into account the time pattern of joint emissions as well as the role of sounds in (perceived) soundscapes.

11:20 Panel Discussion chaired by H. Miedema

11:40

2aNSa6. Predicting overall reaction to multiple noise sources. Jiro Kaku (Kobayasi Inst. Phys. Res., 3-20-41 Higashimotomati, Kokubunji, Tokyo, 185-0022, Japan), Tohru Kato (Otemon Gakuin Univ., Ibaraki, Osaka, 567-8502, Japan), Sonoko Kuwano (Osaka Univ., Osaka, 565-0871, Japan), and Seiichiro Namba (Takarazuka Univ., Hyogo, 665-0803, Japan)

The validity of models predicting overall human response to complex sound environments, which are constituted of road traffic and railway noises, is discussed using results of psychological experiments carried out both in a laboratory and outdoors, as well as by using results of social surveys. Existing predictive models (energy summation model, independent effects model, response summation model, and so on) were applied to the data. The result shows that the simple energy summation model gives the poorest predicting ability in every case. It suggests that differences of response among different noise sources must be considered. The effective level D of road traffic noise relative to railway noise was calculated using Ollerhead's response summation model as approximately 10 dB in the laboratory experiment. The D values decreased as compared to the above value in cases of field experiments and social surveys, but it was still clear that the contribution of road traffic noise to the overall judgment was greater than that of railway noise. Judging from the coefficient of determination and standard errors shown in the results, the independent effects model seems to be the most suitable to predict the overall human response to complex sound environments.

12:00 Panel Discussion chaired by D. Botteldooren

Session 2aNSb

Noise: Computational Aeroacoustics I: Numerical Simulation of Jet and Shear Flow Noise

Christopher K. W. Tam, Cochair
Department of Mathematics, Florida State University, Tallahassee, Florida 32306-4510, USA

Philippe Lafon, Cochair
Department of Acoustics and Vibration Mechanics, Electricité de France, 1, Avenue de Général de Gaulle, 92141 Clamart, Cedex, France

Invited Papers

8:00

2aNSb1. Jet noise simulations using the nonlinear disturbance equations. Philip J. Morris (Dept. of Aerosp. Eng., Penn State Univ., 233P Hammond Bldg., University Park, PA 16802)

Large eddy simulations (LES) of turbulent high Reynolds number flows require significant computational resources if scales in the inertial subrange are to be resolved. However, solutions of the Reynolds-averaged Navier–Stokes (RANS), with an appropriate turbulence model, can provide an efficient and accurate solution for the time-averaged flow. The present formulation recasts the Navier–Stokes equations into equations for the nonlinear perturbations about the RANS approximation to the mean flow. The instantaneous fluctuations are decomposed into a time-averaged component, a resolved large-scale perturbation about this mean, and an unresolved small-scale perturbation. A subgrid scale (SGS) model is used to describe the unresolved scales. The resulting equations are solved on parallel computers using a domain decompositon strategy. Calculations are performed for both circular and rectangular jets. The grid used for the numerical simulations is described. The turbulent fluctuations in the jet, including the time average of the nonlinear perturbations, are presented. Direct simulations of the near and far fields of the jets are given. The jet far field is computed by both direct simulations and with a Ffowcs Williams and Hawkings method. Comparisons are made with available experimental data. [Work supported by NASA Langley Research Center.]

8:30

2aNSb2. Numerical simulation of jet noise: Fundamental issues, progress and outlook. Sanjiva K. Lele (Dept. of Aeronautics and Astronautics and Dept. of Mech. Eng., Stanford Univ., Durand Bldg., Stanford, CA 94305-4035)

High-speed jets remain noisy and loud today. Can high-fidelity numerical simulations provide a new and unique vantage point in future studies of jet-noise and its suppression? What physical and numerical challenges must be overcome in such computational approaches? What features of jet turbulence must be explicitly computed? What is the impact of ''sub-grid'' scale models, and what precautions must be exercised to avoid ''spurious'' sources? These fundamental issues will be discussed in the first part of the talk. Recent progress in simulations of high-speed jets, including large eddy simulation (LES), will be presented. The need to examine carefully the interplay between the effects of numerical approximation and physical models being used, will be stressed. The role of reduced-complexity model problems related to jet noise will be discussed and results on sound generation from shock-vortex interaction in a jet mixing layer will be highlighted. Open issues in jet simulations and jet noise modeling will be stressed throughout. This talk includes collaborative work with colleagues Jon Freund, Bendiks-Jan Boersma, Ted Manning, Tim Colonius, and Parviz Moin. [Financial support was (in part) provided by AFOSR under Grant No. F49620-98-1-0355 and NASA under Grant No. NAG 2-1213.]

9:00

2aNSb3. Numerical simulation of jet screech tones. Christopher K. W. Tam (Dept. of Mathematics, Florida State Univ., Tallahassee, FL 32306-4510)

Screech tones are discrete frequency sounds radiated from imperfectly expanded supersonic jets. The tones are generated by a feedback loop driven by the large-scale instability waves of the jet flow. In the plume of an imperfectly expanded jet is a quasiperiodic shock cell structure. Screech tones are produced by the interaction of the instability waves and the shock cells as the former passes through the latter. Although the screech phenomenon has been studied over many years, many of its features are still not understood. Presently, there are accurate tone frequency prediction formulas. However, there is no known way to predict tone intensity. In this study, the screech phenomenon is investigated through numerical simulation using CAA methods. The simulation reproduces all the characteristic features of jet screech, including the staging phenomenon. The computed screech frequencies and intensities are found to compare well with experimental measurements. Numerical results on the effects of jet temperature also compare well with experiments. The favorable agreements indicate that numerical simulation is a valuable tool for investigating the jet screech phenomenon. [Work supported by NASA Lewis Research Center Grant NAG 3–2102.]

9:30

2aNSb4. Inviscid and viscous computations of supersonic jets. San-Yih Lin (Inst. of Aeronautics and Astronautics, Natl. Cheng Kung Univ., 70101, Tainan, Taiwan, ROC)

Numerical investigations of unsteady flow fields and associated sound radiations due to supersonic jets are performed numerically. The axisymmetric Euler and Navier–Stokes equations are solved by two numerical methods, modified Osher–Chakravarthy and WENO. The Reynolds numbers based on the jet diameter and the axial velocity are from 700 to 70 000. For higher Reynolds number flows, the large-eddy equations are used to accurately capture the large-scale vortical structures. The Smagorinsky model is chosen and the Smagorinsky constant is carefully chosen to avoid excessive damping of large-scale fluctuations. The boundary condition treatments are also studied. Two numerical methods are compared with each other to see the effect of dissipation of each method. Kirchhoff's integration method is applied to calculate the far-field noise, with the sound source obtained from the calculated time-dependent near field. Details of the flow structures, such as mean flow distributions, shear layer, and the corresponding sound pressure level, are investigated. It is noted that the sound-pressure level obtained by the Euler solver is very high even in the downstream of the jet. Three-dimensional computations are also performed roughly to understand more complicated structures of jet flows.

10:00–10:20 Break

10:20

2aNSb5. Direct numerical simulation of sound generation in turbulent shear flows. Tim Colonius (California Inst. of Technol., Mail Code 104-44, Pasadena, CA 91125)

Direct numerical simulations of turbulent shear flows and their radiated acoustic fields have provided new insights into the mechanisms of sound generation, as well as the efficacy and limitations of the acoustic analogy approach. At present, these computations are expensive, and limited to relatively low Reynolds number and canonical flows. The computational approach consists of using high-order accurate numerical methods, together with accurate and robust nonreflecting and buffer-zone boundary conditions. This talk will focus on the results of computations of sound generated in mixing layers, jets, and open cavity flows. The relationship between linear stability waves in the flow and the radiated acoustic field is examined, in the context of a forced subsonic mixing layer and a fully turbulent supersonic round jet. For the subsonic flow, the acoustic sources can be modeled as wave packets, which radiate a superdirective acoustic field. For the supersonic jet, the directly computed (i.e., nonlinear source) acoustic field is compared to predictions based on radiating stability waves. Finally, the flow/acoustic instabilities in the subsonic flow over an open cavity are examined, and control strategies for reducing the internal acoustic load are explored. [Work supported by NSF (CTS-9501349) and AFOSR (F49620-98-1-0095).]

10:50

2aNSb6. Vortex dynamics, transition to turbulence, and aeroacoustics in rectangular free jets. Fernando F. Grinstein (Lab. for Computational Phys. and Fluid Dynam., Naval Res. Lab., Washington, DC 20375-5344)

An overview of recent studies of compressible, rectangular, free jets is presented, with special focus on understanding the dynamics and topology of coherent vortical structures controlling the jet development, and identifying major near-jet noise generation mechanisms. Relevant issues of subgrid and supergrid modeling in free-jet numerical simulations are addressed in this context. The vortex dynamics underlying axis-switching and vortex bifurcation phenomena are examined, including: the roles of self-induced vortex-ring deformation, reconnection, braid vortices, aspect ratio (AR), and the transition to turbulence from laminar initial jet conditions. Qualitatively different vorticity geometries characterizing the near field of low-AR, $M<2$, ideally expanded, rectangular jets are demonstrated, involving: (i) self-deforming and (ii) bifurcating vortex rings; interacting ring and rib (braid) vortices—including, (iii) single ribs aligned with corner regions ($AR>1$), and (iv) rib pairs aligned with the corners ($AR=1$); (v) smaller-scale, elongated, ''worm'' vortices in the turbulent jet regime. The near-field entrainment of low-AR rectangular jets is shown to be largely determined by the characteristic geometry of the ring–rib interactions; progress in the study of noise-generation mechanisms in low-AR jets is discussed. [Work sponsored by AFOSR, ONR, and the DoD HPC-MP.]

11:20

2aNSb7. Use of linearized Euler equations for subsonic flow noise prediction. Philippe Lafon (Electricité de France, Dept. of Acoust. and Vib. Mech., avenue du Général de Gaulle, 92141 Clamart Cedex, France)

The introduction of efficient numerical techniques like Tam's DRP scheme allows one to develop aeroacoustic modeling based on Euler equation solvers and applied on realistic configurations. It is already clear that the system of Euler equations is the most complete one in order to compute acoustic propagation in fluids, but the way to calculate noise generation with the same equations needs to be established. So, it is necessary to introduce in the propagation calculation some information coming from a previous or a simultaneous flow calculation. One approach is to try to define source terms for the Euler equations as it was set up for Lighthill's or Lilley's equation. Others approaches can rely on the coupling of the two equation systems by domain decomposition or by introducing disturbances linked to flow calculation. The SNGR model belongs to the first category. A source term is defined by analogy with Lilley's equation. A stochastic space time turbulent field is used in order to avoid expensive LES or DNS flow computations. This approach is mainly applied to the calculation of noise radiated by internal flows where the methods based on the classical acoustic analogy do not work easily.

11:50

2aNSb8. Analysis of sound generated by free shear flows using direct numerical simulations. Eldad J. Avital, Kai H. Luo, and Neil D. Sandham (Dept. of Eng., Queen Mary & Westfield College, Mile End Rd., London E1 4NS, UK)

The sound produced by large-scale structures in free shear flows is investigated using direct numerical simulations (DNS). Both temporal and spatial DNS approaches are investigated, with special attention given to the former due to its lower computational cost. It is shown that the temporal approach can be used to investigate Mach-wave generation but not the general sound emitted by large-scale subsonic sources. Consequently, temporal DNS data of supersonic mixing layers undergoing transition to turbulence are analyzed. Two dominant Mach waves are found, each of which is identified with vortical features in the flow. The spatial DNS approach is then investigated to study the effect of the computational box size on the sound calculation. A large-scale model is used to show that the low-subsonic case is more restrictive in that sense than the supersonic one. The first case is further investigated by calculating the basic radiation emitted by axisymmetric jets, using the compact Lighthill and Mohring–Kambe formulations. Boundary corrections are developed and tested to reduce the box size effect and to improve the agreement between the two formulations. Finally, the effect of the retarded-time variation along the jet is discussed.

TUESDAY MORNING, 16 MARCH 1999 ROOM H2013, 8:35 TO 11:40 A.M.

Session 2aNSc

Noise: Hearing Conservation Program Effectiveness

Larry H. Royster, Cochair
MAE Department, North Carolina State University, Raleigh, North Carolina 27695-7910, USA

Laszlo Matéfi, Cochair
Department of Occupational Medicine, Swisss Accident National Insurance Fund, Suva, Fluhmattstrasse 1, CH-6002 Lucerne, Switzerland

Chair's Introduction—8:35

Invited Papers

8:40

2aNSc1. Hearing conservation for workers in British Columbia and Canada. Christine Harrison (Workers' Compensation Board of British Columbia, Hearing Conservation Section, 6951 Westminster Hwy., Richmond, BC V6B 5L5, Canada, charrison@wcb.ca)

Comprehensive hearing conservation programs for noise-exposed workers in British Columbia have existed since 1978. From 1978 to 1996, a program consisted of engineered noise controls, hearing protection use, and annual hearing tests. In 1996 more statutory components were added: exposure monitoring of workers, posting of noisy work areas, education and training, and annual review of the program. Several administrative aspects of the province-wide program are unique; for example, all hearing tests are recorded on a single, standardized computer form and submitted to the central data base of the Workers' Compensation Board. Industries which have submitted hearing tests include forestry, construction, and manufacturing. The construction program itself is unique in a number of aspects. As of 1998, well over one million audiometric records (each of which includes information regarding occupation, years of noise exposure, threshold values, hearing protection use, nonoccupational noise exposure, age, gender, and more) are in the data base. Analysis of this data has only begun, but interesting trends have been identified. These trends will be presented, with a discussion of methods of program evaluation, as well as an overview of hearing conservation practices across Canada.

9:00

2aNSc2. Distortion product otoacoustic emissions—Valuable method for hearing conservation programs? Laszlo Matéfi (Dept. of Occupational Medicine, Swiss Accident National Insurance Fund, Suva, Fluhmattstrasse 1, CH-6002 Lucerne, Switzerland)

Pure tone audiometry as a screening method for hearing conservation programs has been well established for years. However, it takes a certain time, requires a good cooperation of the patient, and indicates only the damage already caused. Otoacoustic emissions and especially the distortion products have recently been discussed as an alternate method for screening examinations. In the context of this prevention program, some hundred subjects have been examined as usually pure tone audiometry and in addition by measuring the distortion product otoacoustic emissions. The evaluation has been done in the context with the hearing loss measured by pure tone audiometry, with the history of noise exposure, and with the reliability of the distortion product otoacoustic emissions. The present

results show that there is no reliable association between neither distortion products and hearing loss measured by pure tone audiometry nor between the distortion products and the noise exposure history. The only association found was between important hearing loss measured by pure tone audiometry and absence of distortion products. So, it can be said that distortion product otoacoustic emissions are not a reliable method to be used as screening measurement in hearing conservation programs.

9:20

2aNSc3. Hearing thresholds of pupils and apprentices between the ages of 15–19 years. Karl Körpert (AUVA-HUB, A. Stifterstraße 65, A-1200 Wien, Austria)

Since the early 1990s, several authors have reported on the decreasing hearing ability of young people. The audiograms of the 15–19-year-old men and women show a pronounced dip at 4 and 6 kHz, which was not observable a decade before. This fact was observed also in the hearing conservation programs applied to nonoccupationally noise-exposed apprentices in Austria. A commonly suggested reason for that is increased noise exposure in leisure time. To find out if there are differences between apprentices and pupils of the same age, respectively, if information campaigns run during the last years led to an improvement in the hearing status, audiometric investigations were performed in factories and schools in 1992 and 1997. The results of these measurements and relation to leisure time behavior, investigated by questioners, will be reported.

9:40–10:00 Break

10:00

2aNSc4. Assessment of hearing conservation program implemented in chosen plants in Poland. Krystyna Pawlas (Inst. of Occupational Medicine and Environ. Health, 13 Koscielna str., 41-200 Sosnowiec, Poland, kape@imp.sosnowiec.pl)

In Poland, as in other industrialized countries, noise is a serious problem of occupational medicine. On the basis of the Polish state law, managers of noisy plants are obliged to implement the hearing conservation program. The program consists of noise measurement, noise reduction by technical means, periodical hearing examination of workers exposed to noise, use of hearing protectors, and training of workers. Nevertheless, 30% of all new cases of occupational diseases recognized every year in Poland are the noise-induced hearing loss (NIHL). Most cases of NIHL are recognized in the mining and metallurgical industries. One of the projects previously carried out analyzed the efficiency of medical prophylaxis [J. Grzesik and K. Pawlas, Ochrona Zdrowia Publicznego **96**, 516–523 (1985), in Polish]. Hearing conservation programs performed in chosen plants (mines and foundries) were evaluated. Each point of the hearing conservation program was investigated on the basis of the data collected in the plants. Hearing protector devices used by workers were examined, too. The researchers discovered weak points in the activities of health services and occupational hygiene departments as well as of managers and workers.

10:20

2aNSc5. ANSI S12.13: Using audiometric data variability to assess hearing conservation success or failure. Julia D. Royster (Environ. Noise Consultants, Inc., P.O. Box 30698, Raleigh, NC 27622-0698, EFFECTIVE_HCPS@compuserve.com) and Larry H. Royster (North Carolina State Univ., Raleigh, NC 27695-7910)

In 1991, draft standard ANSI S12.13 was published, offering methods for using the variability in audiometric data as an indicator of the effectiveness of hearing conservation programs (HCPs) in protecting noise-exposed personnel from occupational hearing loss. In contrast to methods which require many years of data before hearing thresholds of noise-exposed groups may be compared to control groups, ANSI S12.13 methods may be applied to as few as two successive audiograms. If high variability is found between successive audiograms, it may be due either to unreliable testing (a problem in itself) or to inadequate protection from noise, allowing a temporary and eventually permanent threshold shift to occur. In either case, the evaluator is alerted that the HCP is ineffective. Identifying poor audiometry prevents erroneous decisions from being made based on bad data, both for individuals and for groups. This information enables the evaluator to make needed improvements to the HCP. Examples of analyses will be shown to illustrate patterns of results indicating both procedural problems and insufficient protection. Experience with ANSI S12.13 confirms the value of two simple procedures.

10:40

2aNSc6. An overview of hearing conservation practices in the U.S.A. Larry H. Royster (North Carolina State Univ., P.O. Box 7910, Raleigh, NC 27695-7910) and Julia D. Royster (Environ. Noise Consultants, Inc., P.O. Box 30698, Raleigh, NC 27622-0698, EFFECTIVE_HCPS@compuserve.com)

Federal governmental regulations dealing with the prevention of occupational noise-induced hearing loss began in 1969 with the publication of the Walsh–Healey Act and was extended to general occupations when the U.S. Department of Labor published the OSHA (U.S. Occupational Safety and Health Administration) regulations in 1971. Finally, required procedures for developing an acceptable hearing conservation program were promulgated in 1983. This presentation will briefly review the history and implementation of the OSHA regulations in U.S. industry. In addition, the present activities by U.S. industry in implementing the OSHA regulations and by OSHA in enforcing them will be reviewed to answer the question: ''Is the present implementation of the OSHA noise regulations effective in preventing noise-induced hearing loss in U.S. occupational environments?''

Contributed Papers

11:00

2aNSc7. Research strategies for evaluating effectiveness of industrial hearing loss prevention programs (HLLP). Mary M. Prince, John R. Franks, Carol Merry, and Michael Colligan (Natl. Inst. for Occupational Safety and Health (NIOSH), 4676 Columbia Pkwy., Cincinnati, OH 45226)

NIOSH recommends that hearing loss prevention programs (HLPPs) be implemented for all workers whose unprotected 8-h TWA exposures equal or exceed 85 dB and that the programs include at least the following components: (1) initial and annual audits of procedures, (2) noise exposure assessment, (3) engineering and administrative control of noise exposures, (4) audiometric surveillance and evaluation, (5) use of hearing protectors (for exposures $>$85 dB, regardless of duration), (6) education and motivation, (7) recordkeeping, and (8) program evaluation. All components except program evaluation and routine in-hour audits are generally discussed in the Occupational Safety and Health Administration (OSHA) Hearing Conservation Amendment (HCA). This paper presents research approaches for systematically evaluating OSHA-mandated hearing conservation programs. The intent of such research is to (a) develop methods for evaluating hearing conservation programs that can be used across several industrial sectors and (b) identify ways in which ''hearing conservation'' can effectively become ''hearing prevention'' programs. General approaches are presented for each program element and data collection issues are discussed with specific examples of how various methods can been used for program evaluation. The goal of such research strategies is to identify the best predictors of program effectiveness.

11:20

2aNSc8. Assessment of methods for determining field-equivalent sound levels from real-ear and manikin measurements. Dorte Hammershoei and Henrik Moller (Acoust. Lab., Aalborg Univ., Fredrik Bajers Vej 7 B4, DK-9220 Aalborg O, Denmark)

The usual method of measuring noise with a sound-level meter at the position of the exposed person, but with the person absent, is not applicable for sound sources placed close to the ears. For measurement of the noise emission from such sources, the coupling between the sound source and the ear must be similar to that of the real life situation. This can be achieved by using the microphone in real ear technique (the MIRE technique) or the manikin technique as described in the upcoming ISO 11904, parts 1 and 2, respectively. For evaluation and comparison with traditional criteria, the measured ear or manikin sound-pressure levels are subsequently converted into either free-field or diffuse-field equivalent sound-pressure levels. The uncertainty of the final result depends on the method used. For the MIRE technique, the uncertainty is mainly related to the statistical uncertainty as determined by the variation between humans and the number of subjects used. For the manikin technique, the uncertainty is mainly related to the deviation of the manikin's acoustical characteristics from those of humans. The paper presents an overview of the methods and examples of practical results.

Contributed Poster

This poster will be on display in the Poster Gallery from Monday to Wednesday, 15–17 March. The author will be at the poster from 10:00 a.m. to 12:00 noon on Wednesday, 17 March.

2aNSc9. The confounding influence of collapsing the ear canal on audiological assessment of noise-exposed workers. Michel Picard, Chantale Tremblay, and Veronique Dumont (Ecole d'orthophonie et d'audiologie, Univ. de Montreal, Montreal, QC H3C 3J7, Canada, Picardmi@magellan.umontreal.ca)

Collapsing of the ear canal resulting from using supra-aural earphones has been studied in a group of 52 noise-exposed workers. Prevalence and audiometric manifestations of collapsing the ear canal were determined based on comparison of pure-tone air-conduction thresholds obtained when insert earphones are substituted for supra-aural ones in the same individuals. Results indicate that as many as 17% of candidates showed in one ear or the other, threshold elevations of 6.6 dB on average at 3 kHz, of 8.1 dB on average at 4 kHz, and of 9 dB on average at 6 kHz as a result of shifting from insert to supra-aural earphones. This finding is of special concern when considering the particular attention paid for the correct positioning of the two types of devices, and the systematic tearing of the tragus in the anterior direction to force the ear canal opening in the positioning of supra-aural earphones. It suggests supra-aural earphones may partially collapse the entrance of the ear canal as a result of the excess pressure applied to the pinna. A model that may help predict the effects of this insidious yet pervasive condition of collapsing ear canals on hearing thresholds of noise-exposed workers will be discussed.

Session 2aPAa

Physical Acoustics: Thermoacoustics I

Cila Herman, Cochair
Department of Mechanical Engineering, Johns Hopkins University, 3400 North Charles Street, Baltimore, Maryland 21218, USA

Martin Wetzel, Cochair
BMW AG, Hufelandstrasse, 80788 Muenchen, Germany

Chair's Introduction—7:55

Invited Papers

8:00

2aPAa1. Thermoacoustic natural gas liquefier. Gregory W. Swift (Condensed Matter and Thermal Phys. Group, Los Alamos Natl. Lab., Los Alamos, NM 87545) and John J. Wollan (Cryenco, Inc., Denver, CO 80239)

An experimental thermoacoustic natural-gas liquefier has been built and tested. It comprises a standing-wave thermoacoustic engine and a traveling-wave refrigerator (a pulse-tube refrigerator). The engine and refrigerator share a common resonator, filled with 3 MPa helium gas and operating at 40 Hz. The engine is heated by external combustion of natural gas, while the refrigerator cools and liquefies a methane stream, so the complete system functions as a natural-gas-fired natural-gas liquefier having no moving parts. Both the engine and refrigerator have operated above 20% of their respective Carnot efficiencies. Compared to other thermoacoustics research hardware, this experimental system is very powerful, with up to 20 kW of acoustic power delivered from the engine to the resonator and up to 2 kW of refrigeration power at 130 K provided by the refrigerator. Nevertheless, much larger systems will be required for commercial success. [Work supported by the Office of Fossil Energy in the U.S. DOE and by Cryenco, Inc.]

8:20

2aPAa2. A pistonless Stirling engine—A new direction in thermoacoustics. Scott N. Backhaus and Gregory W. Swift (Condensed Matter and Thermal Phys. Group, Los Alamos Natl. Lab., Los Alamos, NM 87545)

Due to its thermodynamic reversibility, the Stirling cycle has an inherent advantage in thermal efficiency over the standard, irreversible standing-wave thermoacoustic cycle. The main disadvantage of the Stirling cycle has been the need for high-pressure, sliding piston seals. Building significantly on the ideas of Ceperley [J. Acoust. Soc. Am. **66**, 1508 (1979)], a thermoacoustic version of a 1-kW Stirling engine has been constructed and tested. This engine enjoys both the efficiency advantage of the Stirling cycle and the no-moving-parts advantage of thermoacoustics. In this first attempt, experimental data show that the engine has an efficiency above 35% of the Carnot efficiency, much higher than that of any prior thermoacoustic engine. [Work supported by the Office of Basic Energy Sciences in the U.S. DOE.]

8:40

2aPAa3. The thermoacoustic oscillator as a musical instrument. Werner Lauterborn and Georg Müller (Drittes Phys. Inst., Univ. Göttingen, Bürgerstr. 42-44, D-37073 Göttingen, Germany)

The air in a tube with a short stack of thin parallel plates inside starts to oscillate when a steep heat gradient is applied. The known device can be considered as an oscillator, more specifically a thermoacoustic oscillator (TAO). It radiates sound when the tube is open to the ambient air. The pitch is determined by the tube length. Thus different pitches can be generated by altering the tube length, allowing the possibility to build musical instruments based on TAOs. As in other instruments with tubes, there are several possibilities to alter the tube length. It may be adjusted by holes that are opened and closed as in a recorder, or by a sliding piston with a hole in it to transmit the sound to the exterior. With the sliding piston, trombonelike sliding sounds can be generated. Examples of musical sounds out of a TAO will be given. A thermoacoustic organ is easily conceivable consisting of TAOs of different lengths played by keys opening and closing the respective TAOs.

9:00

2aPAa4. Measurements of the performance of a thermoacoustic refrigerator prototype. B. L. Minner, J. E. Braun, and L. Mongeau (School of Mech. Eng., Purdue Univ., West Lafayette, IN 47907)

The performance of a thermoacoustic prototype designed for a cooling capacity of 140 W and operating stack end temperatures of 282 and 306 K was measured. The device was operated using a 55%–45% helium–argon mixture at a mean pressure lower than or equal to 20 bars. The electrodynamic moving coil driver coupled to the half-wavelength resonator was tuned such that the system resonance frequency (i.e., the operating frequency) was around 180 Hz. The stack was made of a coiled polyester film and nylon filament spacers. The secondary system included finned-tube heat exchangers with water as the operating fluid. The power delivered to the driver coil was measured using a power meter. The cooling power was estimated from the water-side temperature drop across the heat exchangers measured using thermopiles, and from the water flow rate. Acoustic pressure, piston acceleration, and temperature measurements were also made at various locations inside the resonator. The measured values were compared with predictions obtained using DeltaE.

9:20

2aPAa5. Measurements of thermoacoustic functions for unusual stacks. Gabriela Petculescu and Larry A. Wilen (Dept. of Phys. and Astron., Ohio Univ., Athens, OH 45701, wilen@helios.phy.ohiou.edu)

Following earlier work [G. Petculescu and L. A. Wilen, J. Acoust. Soc. Am. **103**, 2841(A) (1998)], a volume-modulation technique is employed to measure directly the complex compressibility of gas in a stack. When a temperature gradient is imposed on the stack, the complex compressibility is sensitive to thermoacoustic effects which can be measured to high precision. These effects depend on both thermal and viscous properties of the gas. Direct measurements of the thermoviscous functions analogous to $F(\lambda)$ and $F(\lambda_T)$ will be presented for unusual geometry stacks, such as conical shapes or stacks constructed from reticulated vitreous carbon (RVC). The behavior of a stack with a sharp temperature gradient approximating a temperature discontinuity will also be described. Time permitting, nonlinear effects may also be discussed. [Work supported by the Office of Naval Research and Ohio University Research and Sponsored Programs.]

9:40

2aPAa6. Conventional heat exchanger design methods and their applicability to thermoacoustics. Cila Herman (Dept. of Mech. Eng., Johns Hopkins Univ., 3400 N. Charles St., Baltimore, MD 21218, herman@titan.me.jhu.edu)

Heat exchangers (HEX) play an important role in many engineering applications, and well established methods for their modeling and optimization are available. Conventional heat exchangers take advantage of forced convection or phase change to transport thermal energy from the hot to the cold fluid, as opposed to thermoacoustic applications where the mean velocity of the oscillatory flow is zero. Conventional HEX are typically classified according to flow arrangement and type of construction. The most commonly implemented methods for HEX analysis are the logarithmic mean temperature difference (LMTD) method and the number of transport units (NTU) approach. Both methods require a set of input parameters and the analysis yields, for example, the appropriate heat exchanger size, i.e., the heat transfer surface area, and type that achieve the desired fluid outlet temperature. The applicability of conventional heat exchanger design methods to thermoacoustic HEX is explored. HEX design solutions developed for thermoacoustics are analyzed in light of the LMTD and NTU approaches. Key differences and issues requiring further research are addressed in the study. [Work supported by the Office of Naval Research.]

10:00–10:20 Break

10:20

2aPAa7. Computational analysis of a thermoacoustic refrigerator. Thomas Schneider, Rupert Klein (FB Mathematik & Informatik, Freie Universität, D-14195 Berlin, Germany), Etienne Besnoin, and Omar M. Knio (Johns Hopkins Univ., Baltimore, MD 21218)

The velocity and temperature fields in an idealized, parallel-plate, thermoacoustic refrigerator are analyzed using a low-Mach-number computational approach. Two-dimensional unsteady calculations of the flow field in the neighborhood of the stack and heat exchangers are performed using: (a) a semi-implicit, finite-volume, Godunov-type, compressible flow solver, and (b) a vorticity-based scheme for stratified flows. The first model is used to address the limiting case of plates with vanishingly small thickness, while the second model is used to analyze finite blockage effects. The predictions of both models are compared to each other and are used to study the effect of heat exchanger properties on the thermal performance of the device. [The work of T.S. and R.K. is supported by DFG. The work of E.B. and O.M.K. is supported by the Office of Naval Research.]

10:40

2aPAa8. Effects of gas mixture on a thermoacoustic refrigerator driven at high amplitudes. Matthew E. Poese and Steven L. Garrett (Grad. Prog. in Acoust., P.O. Box 30, State College, PA 16804, matt@sabine.acs.psu.edu)

Measurements of a thermoacoustic refrigerator driven at pressure ratios up to 6%, with a He/Ar gas mixture have been reported [M. E. Poese and S. L. Garrett, ''Performance measurements of a thermoacoustic refrigerator driven at high amplitudes,'' Proc. 16th Intl. Congress Acoust. and 135th meeting Acoust. Soc. Am. **2**, 809–810 (1998)] and show a 15% lower heat pumping power at 6% pressure ratio compared to the fourfold increase in heat pumping power expected by doubling the pressure ratio from 3%. To further characterize the high-amplitude performance, measurements with other gas mixtures (He/SF_6 and He/Xe) were made. These experiments show that while the He/Xe mixture enables the machine to operate with a larger COPR than with a He/Ar mixture, the nonlinear cooling power degradation is more severe: 10% at a 3% pressure ratio and 20% at 6%. Experiments with a He/SF_6 mixture show no significant increase in COPR compared to a He/Ar mixture, only a positive shift of the COPR curve with cooling power of about 1.5 in 15 W. [Work supported by Office of Naval Research, NASA, through the Pennsylvania Space Grant Consortium and the Applied Research Lab through the Enrichment and Foundation Program. The authors thank Scott Diehl for generous help with making these measurements.]

11:00

2aPAa9. Experimental verification of Rayleigh's interpretation for thermoacoustic Sondhauss-type oscillations. Guadalupe Huelsz and Eduardo Ramos (Centro de Investigación en Energía, UNAM, AP 34 CP 62580, Temixco, Mor. Mexico)

A century ago, Rayleigh [J. W. S. Rayleigh, *The Theory of Sound* (Dover, New York, 1945), Vol. 2, Sec. 322] gave a qualitative explanation of the acoustic power production in terms of the relative phase of the pressure wave and the heat transferred to the fluid. In quantitative terms his interpretation is equivalent to saying that a wave is promoted if the absolute value of this relative phase is less than $\pi/2$, otherwise the wave is attenuated. The authors have demonstrated [G. Huelsz and E. Ramos, Int. Comm. Heat Mass Transfer **22**, 71–80 (1995)] that in standing waves Rayleigh's criterion for acoustic power production can be translated to the relative phase of the pressure and the temperature oscillations in the limit when the distance to the solid boundary goes to zero; if the absolute value of this quantity is larger than $\pi/2$ there is local acoustic power production. In the experimental work reported here, this criterion was used to provide

experimental verification for Rayleigh's interpretation of the acoustic power production in a standing wave parallel to a wall with an axial temperature gradient. [Partial support for this work has been provided by DGAPA-UNAM IN103197 and CONACYT G0044E projects.]

11:20

2aPAa10. Thermoacoustic resonator and its sound source: Model of the coupling and experiments. Pierrick Lotton, Helene Bailliet, Michel Bruneau (Laboratoire d'Acoustique, IAM UMR 6613, Univ. du Maine, 72085 Le Mans Cedex 9, France, lotton@laum.univ-lemans.fr), and Vitali Gusev (Univ. du Maine, 72 085 Le Mans Cedex 9, France)

Current thermoacoustic devices typically consist of a sound source loaded by both a ''rear'' cavity and the ''front'' thermoacoustic resonator. The main element placed in the resonator is a stack supporting a temperature gradient, sandwiched between heat exchangers. In thermoacoustic refrigerators, heat transfer along the stack depends on the acoustic power flux available. In the framework of a previous model [Bailliet *et al.*, ''Coupling between loudspeakers and thermoacoustic cavities,'' submitted to Acta Acustica], this acoustic power can be determined knowing the electrical voltage applied to the source, an electrodynamic loudspeaker, the goal being to optimize the coupling between the loudspeaker and the thermoacoustic resonator. However, in this model, the temperature gradient along the stack is set to zero. The main purpose of this paper is to include in this model the temperature gradient along the stack. The expression of the input acoustic impedance of the thermoacoustic resonator is modified using an approximated analytical solution of the linear equation for the acoustic pressure inside the stack. The efficiency of the coupled system is expressed, yielding the highest acoustic power flux available in the stack (controlled in this study by LDA measurements) for a given electrical voltage applied to the loudspeaker.

TUESDAY MORNING, 16 MARCH 1999 ROOM MA042, 7:55 A.M. TO 12:20 P.M.

Session 2aPAb

Physical Acoustics: Ultrasonic Imaging: Diagnostic Methods in Material Testing and Medicine

Walter Arnold, Cochair
Fraunhofer Institute for Nondestructive Testing, University, Building 37, D-66123 Saarbrücken, Germany

Bernhard R. Tittmann, Cochair
Department of Engineering Science and Mechanics, Pennsylvania State University, University Park, Pennsylvania 16802, USA

Chair's Introduction—7:55

Invited Papers

8:00

2aPAb1. Acoustic wave field imaging and measurement by scanning probe methods. Eduard Chilla (Paul-Drude Inst. for Solid State Electron., Nanoacoustics Group, Hausvogteiplatz 5-7, D-10117 Berlin, Germany, e.chilla@pdi-berlin.de)

Acoustic waves are widely utilized for the investigation of elastic properties of solids and layered systems. However, since the spatial resolution is limited due to Abbe's criteria, small structures can not be investigated by elastic waves using conventional techniques. These limitations can be overcome by applying scanning probe methods. A scanning acoustic force microscope (SAFM) and a scanning acoustic tunneling microscope (SATM) for the measurement of high-frequency surface acoustic waves were developed. The methods are based on the mixing at the nonlinearities of the tip-to-sample interactions. The amplitude and phase of the surface oscillation can be imaged with a lateral resolution in the nanometer range. The phase velocities of surface acoustic wave for propagation distances as small as 20 nm were measured. By using the SATM the surface oscillation was measured on the atomic scale. The SAFM was applied for the investigation of high-frequency interdigital transducers up to some GHz. Scattering and dispersion of elastic waves were studied. Recently, it has been shown that in-plane polarized surface acoustic waves can be detected by using a scanning acoustic probe technique. The phase velocity of Love waves in quartz-layered systems was determined.

8:20

2aPAb2. Acoustic images at the nanometer scale—Why and how? Andrew Kulik, Emmanuel Dupas, Frederic Oulevey, Delphine Gourdon, Nancy Burnham, and Gerard Gremaud (Ecole Polytechnique Federale de Lausanne, Phys. Dept., CH-1015 Lausanne, Switzerland, root@igahpse.epfl.ch)

For years, researchers have attempted super-resolution acoustical images. Using a subwavelength detector one can map acoustical fields with a spatial resolution determined by the size of the detector. A breakthrough approach is to use an atomic force microscope (AFM) in order to detect ultrasound. The lateral resolutions that have been achieved by various groups are better than 50 nm. Different methods are in use to generate and detect the signal. Three main setups have been developed: (i) Contact-mode medium-frequency (typically 500 kHz) low-amplitude methods (SLAM), (ii) ''mechanical diode'' high-frequency (typically 5 MHz) high-amplitude pulsed setups (UFM), and (iii) contact-mode high-frequency (typically 5–400 MHz) methods using mixing of two ultrasonic waves through the nonlinearity of the tip–sample interaction. All three systems map different properties of the sample and have advantages and disadvantages. An overview of these methods will be illustrated by images and measurements.

8:40

2aPAb3. Atomic force acoustic microscopy: Acoustical imaging on the nm scale. Ute Rabe and Sigrun Hirsekorn (Fraunhofer Inst. for Nondestructive Testing, Bldg. 37, Univ., D-66123 Saarbruecken, Germany, rabe@izfp.fhg.de)

High-resolution imaging techniques are important tools in materials evaluation and nondestructive testing. Conventional acoustical imaging techniques allow the determination of elastic properties and defect detection with a spatial resolution dependent on the wavelength of the imaging ultrasound. Research work over the last years has shown that this limit can be overcome by combining atomic force microscopy (AFM) with acoustic microscopy. Inducing ultrasonic vibrations in the contact formed by the sample surface with the sensor tip of an AFM opens its high lateral resolution to ultrasonic imaging. Different measurement techniques in which linear and nonlinear effects play a role are possible and have been demonstrated experimentally. An overview of the imaging techniques will be given. Theoretical models which allow the explanation of the image contrast and the derivation of quantitative surface qualities will be discussed.

9:00

2aPAb4. Material characterization using micro-machined air transducers. Butrus T. Khuri-Yakub, F. Levent Degertekin, Sean T. Hansen, and Neville R. Irani (Stanford Univ., E. L. Ginzton Lab., Stanford, CA 94305, khuri-ya@ee.stanford.edu)

This paper presents the application of micro-machined ultrasonic air transducers (MUT) to material characterization. The transducers are made of thin membrane capacitors with very thin vacuum gaps. A system analysis that details the design of the transducers and the transmitter and receiver electronics to deliver over a 100-dB dynamic range while operating in the 1–5-MHz range is presented. The transducers and electronics system are used both in pulse–echo and pitch–catch modes to evaluate materials. In transmission and reflection, the system is used to image defects in carbon epoxy composites. Transducers are designed, using Lamb wave theoretical calculations, to excite selected Lamb wave modes in composite and other materials. The transducers are then used to characterize the composites with respect to defect detection (via Lamb wave velocity changes) and material characterization (via slowness curve inversion).

9:20

2aPAb5. Imaging with a 16 000-element 2-D array. Ken Erikson and Tim White (Lockheed Martin, 2 Forbes Rd., Lexington, MA 02421)

Imaging with acoustical lenses in the low MHz frequency range using fully populated 2-D arrays offers the potential for high-resolution, real-time, 3D volume imaging, together with low power and low cost. A 2-D composite-piezoelectric receiver array bonded directly to a large custom-integrated circuit is the enabling technology for a new implementation of the original acoustical imaging paradigm. This 128×128 (16 384 total) element transducer hybrid array (THA) uses massively parallel, on-chip signal processing and is intended for medical and underwater imaging applications. The system under development, which is the acoustical analog of a video camera, will be discussed in this paper.

9:40–10:00 Break

Contributed Papers

10:00

2aPAb6. Time-domain ultrasound diffraction tomography. T. Douglas Mast (Appl. Res. Lab., Penn State Univ., University Park, PA 16802, mast@sabine.acs.psu.edu)

A quantitative ultrasonic imaging method employing time-domain scattering data is presented. This method provides tomographic images of inhomogeneous media using scattering measurements made on a surface surrounding the medium of interest, e.g., on a circle for two-dimensional problems or on a sphere for three-dimensional problems. These scattering data are used to construct a time-domain analog of the far-field scattering operator. Images of compressibility variations are then reconstructed using a coherent combination of the far-field scattered waveforms, delayed and summed in a manner that numerically focuses on the unknown medium. This approach is closely related to synthetic aperture imaging; however, unlike conventional synthetic-aperture methods, the present method provides quantitative reconstructions of compressibility variations, analogous to frequency-compunded filtered backpropagation images weighted by the spectrum of the incident wave. Example reconstructions, obtained using synthetic data for two-dimensional scattering of wideband pulses, show that the time-domain reconstruction method can provide image quality superior to single-frequency reconstructions for objects of size and contrast relevant to medical imaging problems such as ultrasonic mammography. Reconstructions also illustrate the dependence of image quality on the number of incident-wave insonifications and on the range of scattering angles available for measurements.

10:20

2aPAb7. Transient elastography in biological tissues. Laurent Sandrin, Stefan Catheline, and Mathias Fink (ESPCI—LOA, 10 rue Vauquelin, 75005 Paris, France, laurent.sandrin@espci.fr)

Elastography is used in different ways to characterize soft tissues. Ophir uses static elastography to estimate strains in the tissue after a quasi-static compression. Strains can also be measured by sonoelasticity using mechanically forced low-frequency vibrations and the ultrasonic pulsed Doppler method (Parker and Sato). These techniques are subjected to bias due to unknown boundary conditions. In this article a technique called transient elastography is presented which is not sensible to boundary conditions. It uses a low-frequency pulsed vibration ($\sim$100 Hz) and a cross-correlation technique to measure displacements on the order of 1 μm. This technique was first developed for one-dimensional measurements on the axis of the ultrasonic transducer. It is now used with an array of 64 transducers to get time-dependent two-dimensional displacements at a rate of 2000 frames per second. Movies of the shear wave propagation

through homogeneous and inhomogeneous phantoms and biological tissues have been obtained. It will be discussed how to inverse near-field data in order to recover the medium shear viscosity and elasticity fields.

10:40

2aPAb8. Comparison between first and second harmonic imaging in ultrasound tomography. D. Kourtiche, A. Chitnalah, and M. Nadi (Lien, Université H. Poincaré, Nancy 1, BP 239, 54506, Vandoeuvre, France, kourtich@lien.u-nancy.fr)

In biomedical ultrasound imaging, quality of images can be enhanced using the second harmonic generated by nonlinear distorsion in the biological medium. Recent works have showed that the use of harmonics improves lateral resolution. The goal of this paper is to show the advantage of ultrasound tomography imaging using the second harmonic. The method of image reconstruction is based on diffraction Fourier theorem which relates the Fourier transform of the measured scattered field with the Fourier transform of the object function. This experimental setup is based on a 3-MHz circular transducer 2 cm in diameter. The transmitted field is measured by a wide bandwidth hydrophone 1 mm in diameter. A cylindrical object is centered at 10 cm from the emitting transducer. A mechanical system permits the translation of the hydrophone step by step $(\lambda/2)$. For each position, the signal is detected by a numerical oscilloscope and digitized. Data are transferred to the PC for posttreatment. The first and the second harmonics are then obtained from measurement by FFT. Tomographic imaging is obtained from the first and second harmonic measurements. These images are compared and the performance of the second harmonic imaging in terms of resolution is discussed.

11:00

2aPAb9. Amplitude dependence of down-converted acoustic waves due to a nonlinear force interaction. E. Dupas (Dept. of Phys., EPFL, CH-1015 Lausanne, Switzerland), G. Behme (Paul Drude Inst., Berlin, Germany), A. Kulik, N. A. Burnham (EPFL, CH-1015 Lausanne, Switzerland), E. Chilla, and H.-J. Froehlich (Paul Drude Inst., Berlin, Germany)

The interpretation of atomic force microscopy (AFM) data suffers from the lack of a detailed knowledge of the nonlinearity of the tip-sample force interaction. The AFM output signal as a function of the amplitude of two independent acoustic oscillations has been experimentally investigated in order to determine the interaction's power law. Two complementary experiments were performed: (1) Two separate 500-kHz acoustic waves were propagated within the cantilever and through a cleaved mica sample; (2) 200-MHz surface acoustic waves (SAW) excited surface oscillations on a quartz sample in contact with the cantilever. In both experiments, the signals were amplitude modulated at a low frequency in order to record the dc mixing term. The cantilever vibration amplitudes at the modulation frequency, as well as at the difference frequency, were recorded using a lock-in amplifier. The experimental results have been compared with a physical model assuming a nonlinearity of the form $F(1/d)^n$, with F being the force, d the penetration depth, and n lying between 0 and 5. This model predicts an output signal depending approximately quadratically on each of the oscillation amplitudes. This approach to force interaction analysis will be evaluated.

11:20

2aPAb10. Double focus technique for quantitative measurements in time-resolved acoustic microscopy. Volker Haenel and Bernhard Kleffner (Fraunhofer Inst. of Biomed. Eng., Ultrasound Dept., Ensheimer Str. 48, D-66386 St. Ingbert, Germany)

Simultaneous measurement of sound velocity and thickness of thin specimens is a well-known technique in time-resolved acoustic microscopy. However, the applicability is restricted, because a substrate in contact with the back of the sample is required. Furthermore, the substrate must have an area without coating, because a reference signal from the substrate's surface is needed. In order to overcome these performance limitations, a double focus technique has been developed. By focusing the lens on the front, and afterwards on the back of the sample, only signals from the sample itself are required. Based on a simple geometrical model, the relevant acoustical equations for sound velocity and thickness were deduced analytically. Afterwards the method was applied to PVDF film in order to experimentally examine the feasibility of the approach. The measured results were compared with reference values and showed reasonable agreement. Based on these experiments, the influence of factors limiting the precision of the model, for example the spherical aberration, will be discussed, yielding an approach for an improved model. Eventually, the significance of the results for applying the method to manufacturing processes of thin films or foils, especially for online process control, will be described.

11:40

2aPAb11. A new method for nonlinear nondestructive testing of developing defects inside inhomogeneous solids. Vadim A. Robsman (Dept. of Information Technol., Transport Construction's Res. Inst., 1 Kolskay St., 129329 Moscow, Russia) and Oleg V. Rudenko (Moscow State Univ., 119899, Moscow, Russia)

Nonlinear acoustic interactions in defect solids subjected to the growing force load are studied both experimentally and theoretically. Three types of nonlinear processes are considered, which can be named as ''wave–defect'' interaction, ''defect–defect'' interaction (through the acoustic radiation), and the ''defect–secondary radiation'' one. Acoustic signals passed through the different building materials and constructions being under a load were recorded, as well as pulses radiated by growing defects at the increase in load. The nonlinear parameter of defect solid containing cracks was evaluated from the measured data. A new mathematical model describing the kinetics of statistical ensemble of cracks and based on nonlinear integrodifferential equation was developed. At an increase in force applied to the solid (including extremely high load up to a destructive one) new phenomena were observed, namely, jumps from one statistical distribution to another, radically different stages of nonlinear transformations in frequency spectra, and transitions from dynamic to stochastic behavior. Such processes can serve as new highly sensitive indicators of the defect solid structure and as a forerunner of catastrophic destruction.

12:00

2aPAb12. Investigations in ultrasonic tomography. Jean-Pierre Lefebvre, Philippe Lasaygues, Armand Wirgin, Sebastien Delamare (CNRS—Laboratoire de Mecanique et d'Acoustique, 31 chemin Joseph Aiguier, 13402 Marseille Cedex 20, France, lefebvre@lma.cnrs-mrs.fr), and Serge Mensah (Ecole Superieure de Mecanique de Marseille, IMT, 13451 Marseille Cedex 20, France)

Ultrasonic tomography (UT) is a technique to reconstruct the spatial distribution of some physical parameter of an object from measurements of the scattered field. The measurements are made for more or less dense sets of emitter and receiver positions and of frequencies of the interrogating wave. This inverse scattering problem was solved by using a Born approximation that leads to a particularly simple and attractive linear relation between the object function (OF) and the scattered field, particularly in the far-field (2-D or 3-D Fourier transform), making it possible, in principle, to reconstruct the OF in near real time for a sufficiently large set of scattering data. Ultrasonic tomography was investigated numerically and experimentally. Numerical simulations, using ideal measures with ideal objects, allow the examination in detail of the influence of various parameters such as the object's dimension and contrast, transducers bandwidth, etc. It allows one to analyze what happens when the Born approximation is no longer valid (high frequencies, high contrasts), to find limits of quantitative and qualitative imagery, and to imagine various improvement procedures (e.g., superresolution procedures leading to high resolution with low frequencies). Experimentations (with a mechanical and an antenna-based system) show the applicability of the method for medical and materials applications.

Posters will be on display in the Poster Gallery from Monday to Wednesday, 15–17 March. Authors will be at their posters from 2:00 p.m. to 4:00 p.m. on Tuesday, 16 March.

2aPAb13. Nonlinear acoustic testing of defects for the evaluation of risk for insurance of thermal electric power stations. Vadim A. Robsman and Yury V. Novak (Dept. of Information Technol., Transport Construction's Res. Inst., 1 Kolskay St., 129329 Moscow, Russia)

The testing of defects in buidings, smoke tubes, groundworks of turbine generators, and other principal constructions of an electric power station without their removal from service was performed. Both externally exited acoustic pulses with narrow-band spectrum and acoustic emission pulses caused by vibration of power equipment were used as sources of structural information. Harmonics generation was observed at a small concentration of defects. Increase in concentration causes the growth of higher harmonic intensity and the broadening of their spectral lines. In highly damaged constructions, the spectral lines merge together into a continuous wideband spectrum. Acoustic emission can complicate the spectral distribution by introducing the random frequency components. It was discovered that the analysis of different stages of nonlinear evolution of spectra makes it possible to distinguish the different kinds of internal defects and, consequently, to predict the risk of emergency. This approach was put into use recently for insurance of thermal energy plants in Russia.*l*

2aPAb14. Experience in nonlinear wave testing of constructions inside the earthquake area. Vadim A. Robsman and V. E. Stepanyan (Dept. of Information Technol., Transport Construction's Res. Inst., 1 Kolskay St., 129329 Moscow, Russia)

In large-scale experiments on damaged engineering constructions disposed inside an earthquake area, the new nonlinear acoustic phenomena were observed which offer the possibility to evaluate the degree of damage and the strength of constructions. Specifically, the different parts of buildings (ground works, walls, etc.) were tested, as well as bridges damaged by catastrophic earthquake in Speatak, Armenia (1988). Such nonlinear technology was verified in the laboratory using a test seismic installation. Nonlinear testing was used later at the deep tunnel construction in rocks to predict the possible injury. Nonlinear effects were recorded in both transient internal radiation and in signals (regular and noise waves) generated by an external source. The direct relation was discovered between the rate of development of nonlinear distortion of spectra and the degree of damage of constructions subjected to earthquake shock.

2aPAb15. Experiments in solids using air-coupled ultrasound. D. A. Hutchins, D. R. Billson, and C. S. McIntyre (Univ. of Warwick, Coventry CV4 7AL, UK)

Electrostatic (capacitance) transducers have been designed and constructed for the imaging of solids in air, at frequencies of up to 1 MHz. The devices use a micromachined silicon backplate and a flexible membrane. The sensitivity and bandwidth of the resultant devices is such that signals can be propagated through solid samples in air. Examples will be given of imaging experiments in a wide range of materials, including fiber-reinforced polymer composites, paper, and metals. Measurements of material property can also be made, and examples will be given of how such measurements can be made at various temperatures. Particular reference will be made to measurements where it is possible to study changes in structure, by measurement of the elastic properties of the material.

TUESDAY MORNING, 16 MARCH 1999 ROOM MA041, 7:55 TO 11:20 A.M.

Session 2aPAc

Physical Acoustics: Interaction of Acoustic Fields with Suspended Particles I

Robert E. Apfel, Cochair
Faculty of Engineering, Yale University, 9 Hillhouse Avenue, New Haven, Connecticut 06520-8286, USA

Ewald Benes, Cochair
Institut für Allgemeine Physik, Vienna University of Technology, A-1040 Vienna, Austria

Chair's Introduction—7:55

Invited Paper

8:00

2aPAc1. Separation of aerosol fine particles by high-power ultrasound. Juan A. Gallego-Juarez, Iziar Gonzalez-Gomez, and Enrique Riera F. de Sarabia (Instituto de Acustica, CSIC, Serrano, 144, 28006 Madrid, Spain, jgallego@fresno.csic.es)

The application of high-intensity acoustic fields to an aerosol can produce the agglomeration of the suspended particles, shifting their size distribution to a large range. Acoustic agglomeration is a process in which acoustic forces cause particles to interact and eventually to collide. The complex mechanism of this process involves orthokinetic and hydrodynamic effects. The orthokinetic effect

refers to direct collisions produced among particles of different size and/or density which are differently entrained by the acoustic field. The hydrodynamic effects refer to particle interactions generated through the surrounding fluid by hydrodynamic forces induced by the acoustic field. One important hydrodynamic effect is the acoustic wake effect which is related to the asymmetry of the flow field around the moving particles. Acoustic agglomeration has a potential use in the separation of fine particles (smaller than 2.5 μm) which are emitted from industrial and residential combustion and from vehicle exhaust. In this paper recent theoretical and experimental advances in the knowledge of the basic mechanisms of acoustic agglomeration are presented, together with some results about the improvement of fine particle separation efficiency of conventional filters when the aerosol is previously treated with high-power ultrasound. [The authors acknowledge the support of CICYT-AMB96-A211-C02.]

Contributed Papers

8:20

2aPAc2. Studying drop cluster and array behavior using an acousto-electric levitator. Yibing Zheng and Robert E. Apfel (Dept. of Mech. Eng., Yale Univ., New Haven, CT 06520-8286, yibing.zheng@yale.edu)

An acousto-electric levitator is developed for studying the formation and behavior of drop clusters and arrays. The device enables us to form suspended 2-D drop clusters and arrays by using electric and acoustic fields to levitate and manipulate drops. The spacing and the size of drops can be easily controlled by varying electric and/or acoustic field intensities. Experiments have been done on single- and multi-component drops, such as octane and dodecane, which are primary materials in natural fuels. Studies are focused on the evaporation rate of each drop due to the interaction in the array. The acoustic frequency has been increased from 28 kHz to more than 150 kHz so that generation and control of smaller drops, associated with spray combustion, are possible. The formation process of clusters and arrays, and the force balance among drops are analyzed. A theoretical calculation based on the diffusion-controlled model is compared with these experimental results. This high-frequency acoustic levitator is also used to study solid particle clusters whose size is around 10 μm by using a mixture of solid particles and liquid, and then letting the liquid evaporate. [Work supported by NASA through JPL Grant No. 958722 and NASA Grant No. NAG3-2147.]

8:40

2aPAc3. Generation of a standing wave field using crossing sound beams for acoustic micromanipulation. Teruyuki Kozuka, Toru Tuziuti, Hideto Mitome (Natl. Industrial Res. Inst. of Nagoya, AIST, 1-1 Hirate-cho, Kita-ku, Nagoya 462-8510, Japan, kozuka@nirin.go.jp), Toshio Fukuda, and Fumihito Arai (Nagoya Univ., Furo-cho, Chikusa-ku, Nagoya 464-8603, Japan)

A novel sound-field generation method for noncontact manipulation of particles has been studied experimentally. Although it was possible to trap particles in water at nodes of a standing wave field generated between a transducer and a reflector and to transport them using a frequency-shifting operation, there were several problems, such as unstable force due to resonance of the sound field and different movement of trapped particles. The present paper describes a method to generate a standing wave field using plural sound sources without a reflector. When two transducers were settled with their sound-beam axes crossing to each other, a standing wave field was generated in the crossing region. Changing the mutual phase of transmitting signals between the transducers, the sound field was shifted laterally, keeping the same form. When polystyrene particles were poured with a pipette into the sound field, they were trapped at the nodes of the sound-pressure distribution and were transported stably. Using three transducers whose sound-beam axes were crossed at an angle of 120° to each other in a plane, a standing wave field was generated with a hexagonal node pattern, and two-dimensional manipulation of a particle was accomplished.

Invited Papers

9:00

2aPAc4. Ultrasonic micromanipulation of particles and effects of acoustic streaming. Hideto Mitome, Teruyuki Kozuka, and Toru Tuziuti (Natl. Industrial Res. Inst. of Nagoya, AIST, 1 Hirate-cho, Kita-ku, Nagoya 462-8510, Japan, mitome@nirin.go.jp)

Noncontact manipulation of particles suspended in water has been studied using action of acoustic radiation pressure. A standing wave field in an unconfined vessel was used but the sound field was not necessarily resonant. When alumina suspension was poured into the sound field, particles were trapped and formed agglomeration. Changing the frequency continuously, the agglomerated particles were transported along the sound beam axis corresponding to the changes of wavelength. Selecting an appropriate frequency increment, they were transported in the opposite direction at different positions. Using a line-focused transducer with a back electrode divided into strips, it was possible to transport the particles perpendicular to the sound beam axis. A combination of these techniques realized two-dimensional manipulation without contact. Generation of acoustic streaming from the transducer to the reflector was observed even in the standing wave field due to nonuniformity of the sound field. To suppress this phenomenon for the stable manipulation, use of a tone-burst wave was proposed, noting the differences in the characteristic time between the streaming and trapping; the former is much longer than the latter and it is possible to keep the effective trapping force unchanged while suppressing the generation of streaming.

9:20

2aPAc5. Studies of particle separation using acoustophoresis. Todd L. Brooks and Robert E. Apfel (Dept. of Mech. Eng., Yale Univ., New Haven, CT 06520-8286, todd.brooks@yale.edu)

Particles in a liquid medium can be manipulated using the acoustic radiation force generated by a high-intensity ultrasonic standing wave. The resulting motion of the particles depends on the relative contrasts in particle density and compressibility with the surrounding host liquid. This allows the possibility of a separation technique that can distinguish particles based on these elastic properties, which is not possible with other separation methods. A flow-through resonator has been designed in which an acoustic standing wave is oriented perpendicular to the direction of fluid flow. This allows incoming particles to be moved perpendicular to the flow so that they can be separated into separate streams at the output end. Results will be shown for several different types of particles in a range of sizes (5−100 μm). There is also a secondary force which can cause an attraction between particles. This force is usually considered negligible except when particles are very close together. Some preliminary calculations will be shown predicting the effects of the secondary particle force and these will be compared to observations. [Work supported by NASA through Grant No. NAG8-1351.]

9:40–10:00 Break

10:00

2aPAc6. Analysis of composite resonators for ultrasonic micromanipulation and separation. Martin Gröschl, Felix Trampler, Ewald Benes (Institut für Allgemeine Physik, Vienna Univ. of Technol., Wiedner Hauptstraße 8/134, A-1040 Wien, Austria, groeschl@iap.tuwien.ac.at), and Helmut Nowotny (Vienna Univ. of Technol., A-1040 Wien, Austria)

Piezoelectric composite resonators for the separation or manipulation of particles dispersed in a liquid by means of acoustic forces are investigated theoretically and experimentally. Such devices typically comprise at least four material layers: a piezoelectric transducer, a carrier (e.g., glass), the liquid (suspension), and an acoustic reflector. A mathematical matrix model for multilayer structures [M. Gröschl, Acust. Acta Acust. **84**, 432–447 (1998)] is used to calculate the electric admittance spectrum of the resonator and results are compared to measurements obtained with a specialized computer-controlled measuring system. Additionally, the model allows the calculation of the spatial course of electric and acoustic field quantities (e.g., displacement amplitude, energy flow, energy density) along the multilayer structure. To characterize resonators for particle separation, the *resonator performance number* is introduced, which is a measure for the stored acoustic energy in the liquid (suspension) with respect to the total electric energy supplied by the driving source. It is shown that, for a given setup, the performance number depends strongly on frequency. The frequency range of maximum performance numbers defines the optimal operating range of the particle separator. [Work supported in part by the European Commission, Project # FMRX-CT97-0156.]

10:20

2aPAc7. Scattering enhancements and resonator frequency shifts resulting from the interaction between ultrasonic fields and suspended particles and bubbles. Philip L. Marston (Dept. of Phys., Washington State Univ., Pullman, WA 99164-2814), Christopher S. Kwiatkowski (Washington State Univ., Pullman, WA 99164-2814), and Harry J. Simpson (Naval Res. Lab., Washington, DC 20375-5350)

The radiation pressure of ultrasonic standing waves in water is known to cause suspended particles to migrate to energetically preferred locations. The spatial periodicity of the resulting bands of enhanced particle concentration makes possible significant acoustic signatures of this migration even if the volume fraction for the initially uniform spatial distribution is quite small. Our initial approach used acoustic Bragg scattering of a tilted high-frequency probe beam from the induced layers [H. J. Simpson and P. L. Marston, J. Acoust. Soc. Am. **98**, 1731–1741 (1995); in *Nonlinear Acoustics*, edited by M. F. Hamilton and D. T. Blackstock (Academic, San Diego, 1998), Chap. 14]. The scattering is enhanced because the particles in the induced layers scatter sound with what amounts to the same phase. This effect was also observed with a probe wave collinear with the pump standing wave [C. S. Kwiatkowski, Ph.D. thesis, Washington State University, 1997]. The particle migration can also shift the frequency of the standing wave resonance [C. S. Kwiatkowski and P. L. Marston, J. Acoust. Soc. Am. **103**, 3290–3300 (1998)] and a related frequency shift with dilute bubble clouds has also been observed. [Work supported by the Office of Naval Research.]

10:40

2aPAc8. Agglomeration and collection of suspended particles using resonant acoustic fields within porous media. Donald L. Feke and Alan E. Penrod (Dept. of Chemical Eng., Case Western Reserve Univ., Cleveland, OH 44106-7217)

The collection of micron- to millimeter-size solids from flowing suspensions is of fundamental importance in many chemical and materials processing technologies. Recently, a technique has been developed that enables the collection of such solids within porous meshes and other filtration media having pore size up to 200 times larger than the particles being retained. This is accomplished by energizing the filtration medium with a low power, one-dimensional resonant acoustic field. In laboratory tests, collection efficiencies up to 90% have been achieved. The retention of the solids by the porous medium is reversible, and the solids can be easily flushed from the filter as soon as the acoustic field is terminated. In this presentation, data that illustrate the agglomeration and collection effects will be provided. The three possible mechanisms that can cause the observed phenomena will be discussed. In order to model the particle collection phenomena, a particle trajectory analysis has been completed. In this model, the path of individual particles toward elements of the porous mesh are calculated as a function of the fluid flow conditions and the acoustic force acting between the particle and collector. Design strategies for optimization of the particle collection phenomena will also be presented.

11:00

2aPAc9. Ultrasonic cell micro-manipulation and separation. W. T. Coakley (School of Biosciences, Cardiff Univ., Cardiff CF1 3TL, UK)

The manipulation of small (<5-μm-diam) eukaryotic cells and of bacteria (ca. 1.5-μm diameter) has been examined here in a number of batch and flow systems containing ultrasonic standing waves. The The different systems, involving plane and tubular ultrasonic transducers and a range of acoustic pathlengths, have been designed to treat suspension volumes of analytical scale, i.e., 5 ml to 50 μl for both single-sample and ''on-line'' situations. The frequencies employed range from 1–12 MHz. Removal efficiencies of 99.5% have been achieved for yeast and for the bacterium *Escherichia coli*. The influence of secondary cell–cell interaction forces in determining the cell concentration dependence of harvesting efficiency in batch sedimentation systems is considered. The contributions of pulsing and of field modulation techniques to achieving high harvesting efficiencies are illustrated. Applications of standing wave radiation forces to (i) levitate cells in suspension for microscopic examination of cell interactions; (ii) to enhance particle agglutination immunoassay detection of cells or cellular products, and (iii) accelerate the aqueous biphasic separation of cells are presented. [Work supported by BBSRC and EU.]

Session 2aPAd

Physical Acoustics: Cavitation Physics and Sonoluminescence II

Ronald A. Roy, Cochair
Department of Aerospace and Mechanical Engineering, Boston University, Boston, Massachusetts 02215, USA

Werner Lauterborn, Cochair
Drittes Physikalisches Institut, Universität Göttingen, Bürgerstrasse 42-44, 37073 Göttingen, Germany

Invited Papers

8:00

2aPAd1. Stimulating sonoluminescence. Joachim Holzfuss and Matthias Rüggeberg (Inst. für Angew. Physik, TU Darmstadt, Schlossgartenstr. 7, 64289 Darmstadt, Germany)

Single-bubble sonoluminescence is characterized by the light emission of an acoustically driven bubble in a liquid. It is due to an enormous compression of the bubble volume, where a change in volume by six orders of magnitude is followed by a violent collapse. The question has been asked if the violence of the collapse can still be increased. In the theory of nonlinear dynamical systems, methods have been developed to control systems toward higher energetic response. As a complex system that is excited within a resonant cell is being dealt with, harmonic series expansions of the driving signal have been used. It is shown that already two-mode signals with optimized amplitudes and phases are able to boost sonoluminescence. The difficulties concerning multimode signals are analyzed experimentally and numerically. The effects of nonsinusoidal excitation concerning spatial and temporal bubble dynamics are presented. [Work supported by the DFG (SFB 185).]

8:20

2aPAd2. Sonoluminescence light emission. Sascha Hilgenfeldt (DEAS, Harvard Univ., 29 Oxford St., Cambridge, MA 02138, sascha@stokes.harvard.edu), Detlef Lohse (Univ. of Twente, The Netherlands), and Siegfried Grossmann (Univ. of Marburg, Marburg, Germany)

Extending the hydrodynamical/chemical approach to single-bubble sonoluminescence (SBSL) to include light emission, it is shown that a few well-known, simple physical concepts are sufficient to account for the observed characteristics of emitted light pulses: Rayleigh–Plesset bubble dynamics, polytropic gas heating, dissociation of molecular gases, and thermal radiation of optically thin bodies. With these ingredients, a model can be developed which yields correct widths, shapes, intensities, and spectra for the pulses of emitted SBSL light. These quantities all depend in a characteristic way on each other, as well as on experimental parameters like driving pressure, water temperature, or dissolved gas concentration. A direct comparison of the theoretical results to experimental findings shows good agreement. The theory furthermore predicts that strongly forced xenon bubbles should show a dependence of the pulse width on light wavelength, in contrast to argon bubbles. Moreover, if upscaled SBSL bubbles of larger size at larger driving pressures can be created (e.g., using smaller driving frequencies), the resulting light emission intensities should be greatly increased.

8:40

2aPAd3. Computed optical emissions from a star in a jar. William Moss (Lawrence Livermore Natl. Lab., L-200, 7000 East Ave., Livermore, CA 94550, wmoss@llnl.gov)

A sonoluminescing bubble has been modeled as a thermally conducting, partially ionized plasma. The model accounts for most of the observed experimental trends, including (i) the asymmetric pulse shape; (ii) the temperature and driving pressure dependence of the pulse width and intensity; and (iii) spectral shapes, in particular, the 300-nm peak in the spectrum of xenon sonoluminescence. The agreement between the calculations and the data, as well as the models predictions of almost every experimental trend, leave little doubt that the spectral and temporal properties of the emissions of a single sonoluminescing bubble are due to adiabatic- or shock-initiated thermal emission from a cool dense plasma. [Work was performed under the auspices of the U. S. Department of Energy by Lawrence Livermore National Laboratory under Contract No. W-7405-Eng-48.]

9:00

2aPAd4. Water vapor and sonoluminescence. Andrew J. Szeri and Brian D. Storey (Univ. of California, Dept. of Mech. Eng., Berkeley, CA 94720-1740, aszeri@me.berkeley.edu)

In recent work, it has been shown that segregation of gas mixtures within sonoluminescence bubbles is driven by strong thermal and pressure gradients inside the bubble [B. D. Storey and A. J. Szeri, ''Mixture segregation within sonoluminescence bubbles,'' in review]. Although these rather exotic types of diffusive transport are often neglected, they are of crucial importance in a number of applications. These effects conspire to increase the fraction of the lighter gas in a mixture of noble gases near the center, and to increase the fraction of the heavier gas near the bubble wall at the moment of extreme collapse. This results in a greater energy concentration at the bubble center. While the temperature and pressure peaks have a duration (FWHM) of only a few hundred

picoseconds at most, it has been found that appreciable mixture segregation persists for several orders of magnitude longer. Armed with this new understanding of how gas mixtures behave, it is possible to investigate more deeply the question of water vapor within the bubble. Several investigators have shown that the presence of water vapor has important consequences for compression versus shock heating, for hydrodynamics of the bubble collapse, and for chemistry.

Contributed Papers

9:20

2aPAd5. Optimal resonant stimulation of sonoluminescence. Matthias Rüggeberg and Joachim Holzfuss (Inst. fuer Angew. Physik, TU Darmstadt, Schlossgartenstr. 7, 64289 Darmstadt, Germany)

In single-bubble sonoluminescence, a bubble is levitated and forced to oscillate by a standing sound wave. Once per cycle, at the maximum compression of the bubble volume, the emission of a pulse of visible light is observed; due to the strong bubble collapse, a shock wave is emitted in the liquid also. It was found that these shock waves can be visualized by the means of a schlieren method. Using a stroboscopic illumination of the bubble, its dynamical behavior and the shocks can be recorded in slow motion by a video camera. Experimentally measured velocities of the shock waves were compared with numerical calculations. Further, the recorded shock waves contain information about the bubble position and collapse time. In the regime of instable sonoluminescence, sudden changes in bubble position depending on bubble size were observed. The phenomenon in the context of interactions of the bubble with the complex sound field is discussed. [Work supported by the DFG (SFB 185).]

9:40–10:00 Break

10:00

2aPAd6. Sonoluminescing bubbles rectify argon: Comparing predictions with latest experiments. Sascha Hilgenfeldt (Div. of Eng. and Appl. Sci., Harvard Univ., 29 Oxford St., Cambridge, MA 02138) and Detlef Lohse (Univ. of Twente, 7500 AE Enschede, The Netherlands, lohse@tn.utwente.nl)

For the ASA meeting in Hawaii in 1996, the Session Chair, Robert Apfel, posed a challenge to the theoreticians working on single-bubble sonoluminescence (SBSL): experiments should be suggested and predictions made. The crucial predictions following from the hydrodynamical/chemical approach to SBSL were phase diagrams for SBSL bubbles, the rectification of argon in SBSL air bubbles, the existence of stable nitrogen bubbles, and the ejection of chemical reaction products from the SBSL bubble [S. Hilgenfeldt, D. Lohse, and M. Brenner, Phys. Fluids **8**, 2808 (1996); D. Lohse *et al.*, Phys. Rev. Lett. **78**, 1359 (1997); D. Lohse and S. Hilgenfeldt, J. Chem. Phys. **107**, 6986 (1997)]. Meanwhile, many beautiful experiments have been done by Crum and Matula, by Apfel and Ketterling, by Gaitan and Holt, by Suslick *et al.*, by Barber, Putterman *et al.*, and by many others. In this talk a comparison between these experiments and above predictions is presented.

10:20

2aPAd7. Sonoluminescence and acoustics within nonlinearly driven cavities. Ralf Guenther (Naturwissenschaftliches und Medizinisches Institut (NMI), D-72770 Reutlingen, Germany, guenther@nmi.de)

The field distributions inside a nonlinearly driven cavitation bubble are obtained as a function of the dynamics of the bubble radius. They represent a straightforward generalization of standing wave solutions within a one-dimensional cavity to nonlinearly driven cavities. By coupling the solution to the Rayleigh–Plesset equation, a bubble equation is obtained which includes heat transfer from the bubble to the liquid and the spatial variation of the pressure field. The range of validity of the perturbational solution is dependent on the nature of the bubble content, and is largest for monoatomic gases. The inclusion of the internal field distributions into the simulation of the bubble dynamics is possible with very small computational effort. Applications to sonoluminescence are discussed. [Work supported by the German Ministry of Education and Research.]

10:40

2aPAd8. The search for electrical discharges from single- and multi-bubble sonoluminescence. Vassilious J. Bezzerides, Thomas J. Matula, and Lawrence A. Crum (Appl. Phys. Lab., Univ. of Washington, 1013 NE 40th St., Seattle, WA 98105, matula@apl.washington.edu)

Previous research supported the notion that electrical discharges resulted from the collapse of bubbles in cavitation fields [G. Giminez and F. Goby, in *Cavitation and Inhomogeneities in Underwater Acoustics*, edited by W. Lauterborn (Springer-Verlag, New York, 1980), pp. 101–107]. Further research was performed in a cavitation field, as well as with a single cavitating bubble. The cavitation field was generated in a standing wavefield using gassy water, resulting in a small confined region of cavitation. Single-bubble cavitation was also performed in this system, but with degassed water. Two methods were used to detect electrical pulses. In one case a small probe consisting of two fine wires coupled to a low-current differential amplifier was placed near the cavitation bubble(s). Signals were only observed when the probe was in contact with the cavitation field (no signals were observed in the single-bubble system). The second method utilized a coiled loop of wire surrounding the levitation cell, connected to a high-bandwidth lock-in amplifier. In this case, the reference frequency was scanned from about 25 kHz to more than 20 MHz. Signals were observed at harmonics of the drive frequency. [This research supported by DOE-EM.]

11:00

2aPAd9. Multibubble sonoluminescence at 2 MHz: Optical spectral data and attempt at interpretation. T. Lepoint, E. Hankenne, F. Lepoint-Mullie, and N. Vogelet (Lab. de Sonochimie et d'Etude de la Cavitation, Institut Meurice, Av. Emile Gryzon 1, B-1070 Brussels, Belgium)

In order to obtain information on the physical conditions created by transient cavitation bubbles imploding at acoustic frequencies (fac) of therapeutic interest, the UV–visible spectral distribution of multibubble sonoluminescence at 1.7 MHz is focused on. Original optical spectra (wavelength range: 220–950; resolution: 0.24 nm) will be reported for aqueous solutions containing various alkali-metals chlorides and dissolved noble gases. Special emphasis will be put on the profile of $D1$ and $D2$ lines associated with the reduced metals [i.e., (i) their blending toward the red zone (much less than for fac 20 kHz); (ii) the absence of measurable shift and broadening; (iii) the absence of fusion of the D lines]. Several scenarios for (i) the reduction of the cation and (ii) the surrounding of the emitting metal atoms will be discussed. [The present authors—particularly T.L. and F. L-M.—are very grateful to Dr. J-L. Domanchain and G. Nivez (Jobin-Yvon I.S.A.).]

11:20

2aPAd10. The stability of microbubbles and sonoluminescence. U. H. Augsdörfer,[a] A. K. Evans, and D. P. Oxley (The Sci. and Eng. Res. Ctr., De Montfort Univ., Leicester LE1 7BH, England)

Sonoluminescence (SL), the light emission of a micron-sized bubble of gas trapped in water by an acoustic field, is associated with the collapse of a bubble nonlinearly oscillating under the sound field. Recent advances have made it possible to trap a single bubble at the pressure antinode of a standing wave, where it collapses and reexpands with the periodicity of the applied sound and emits light with every cycle. A critical feature of SL is the spherical symmetry of the bubble. If the collapse is violent, irregularities in the spherical shape of the bubble may develop towards the end of the collapse. As a result, the bubble may get destroyed shortly after the collapse. Due to the microscopic size of the bubble, molecular fluctuations constitute an additional force to which the gas–liquid interface is exposed. This additional force causes irregularities in the spherical shape of the bubble. The stability of a bubble is discussed by analyzing results obtained from hydrodynamic calculations of the bubble dynamics and the fluid dynamical processes outside the bubble taking molecular fluctuations into consideration. Results of these calculations reveal a surprising stability behavior and are in good agreement with observed behavior in single-bubble SL experiments. [a] ua@dmu.ac.uk

11:40

2aPAd11. Numerical simulations of stationary single-bubble sonoluminescence. Vladimir N. Nogin, Nikolay G. Karlykhanov, Gennadiy V. Kovalenko, and Vadim A. Simonenko (Russian Federal Nuclear Ctr., ITP, P.O. Box 245, 456770 Snezhinsk, Chelyabinsk region, Russia, sva@sva.ch70.chel.su)

In one-dimensional approximation, the approach was developed to simulate the regime of stationary behavior (groves, collapse, and rebouncing) for a gas-filled single bubble located in the center of a spherical water-filled vessel under an external resonant periodic sound field. The simulations were performed for realistic equations of state for water and gas (air or argon), with identification of the shock wave in the bubble, with account of surface tension on the water–gas interface, and heat conduction for the matter in the bubble (molecular and radiative). The bubble radius dependence versus time was obtained for varying external conditions: amplitude and frequency of acoustic field, temperature of water, and magnitude of surface tension. Calculated parameters for a stationary bubble (pressure in bubble vicinity, minimal and stationary radii of bubble) were demonstrated to show a good agreement with experimental data. [Work supported by CRDF.]

TUESDAY MORNING, 16 MARCH 1999 ROOM H1012, 7:55 A.M. TO 12:20 P.M.

Session 2aPPa

Psychological and Physiological Acoustics: The Role of Peripheral Compression in Hearing

Mary Florentine, Cochair
Department of Speech, Language Pathology and Audiology, Northeastern University, 1000 Forsythe Street, Boston, Massachusetts 02115, USA

Brian C. J. Moore, Cochair
Department of Experimental Psychology, University of Cambridge, Downing Street, Cambridge CB2 3EB, UK

Chair's Introduction—7:55

Invited Papers

8:00

2aPPa1. Amplification and compression in the cochlea. Ian Russell (School of Biological Sci., Univ. of Sussex, Falmer, Brighton BN1 9QG, UK, I.J.Russell@sussex.ac.uk)

The large dynamic range of the auditory system is due to processes within the cochlea which amplify low-level and compress high-level signals. Both the amplification and compression are associated with outer hair cell function and are reflected in their voltage responses to tones. Outer hair cells control the mechanical properties of the cochlear partition for frequencies close to the peak of the traveling wave which propagates along it. Thus they also control the mechanical input to the inner hair cells and excitation of the auditory nerve fibres. The amplification of basilar membrane responses can exceed 60 dB for high-frequency, low-level tones close to the characteristic frequency of the measurement place. For responses to levels above about 40 dB SPL, hair cell and basilar membrane responses are compressive and increase at a rate close to 0.2 dB per dB SPL. The cochlear efferent system has been implicated in controlling compression, but indications of the underlying mechanism of compression can be gained from measurements of the spatial distribution of basilar membrane responses both along its length and width, and from temporal changes in these responses to tones.

8:40

2aPPa2. Measurements of peripheral compression using forward masking and pulsation threshold. Christopher J. Plack (Dept. of Psych., Univ. of Essex, Wivenhoe Park, Colchester CO4 3SQ, UK) and Andrew J. Oxenham (Dept. of Speech-Lang. Pathol. and Audiol., Northeastern Univ., Boston, MA 02115)

Development of a reliable psychophysical measure of the basilar-membrane (BM) response function is of great importance, not least as a diagnostic tool for sensorineural hearing loss. Described here are attempts to estimate the response function using forward masking and pulsation threshold. Both techniques measure, in effect, the masker level needed to mask a higher frequency signal as a

function of signal level. In the forward-masking design, the signal is a 4-ms tone burst presented 2 ms afer a 100-ms masker. In the pulsation-threshold design, 200-ms signal bursts are alternated with 200-ms masker bursts and the listener determines the masker level at which the signal just begins to sound ''continuous'' as opposed to ''pulsed.'' This is assumed to occur when the masker and signal excitation levels are equal at the BM place tuned to the signal. The experiemnts are based on the finding that the BM response function is roughly linear for stimuli with frequencies well below characteristic frequency (CF). A plot of masker level at threshold against signal level provides, therefore, an estimate of the BM response to the (CF) signal. Results from normal and impaired listeners will be presented and the relative merits of the techniques discussed.

9:00

2aPPa3. Nonlinear cochlear processing of harmonic complexes. Marjorie R. Leek (Army Audiol. and Speech Ctr., Walter Reed Army Med. Ctr., Washington, DC 20307, leek@wrair-emh1.army.mil)

Some harmonic complexes with component phases that change monotonically with harmonic frequency are characterized by temporal waveforms with relatively flat envelopes. With an appropriate choice of component phases, the fine structure within periods represents an upward or downward sweep of instantaneous frequency. One such class of phase selections creates ''Schroeder-phase waveforms,'' named after the developer of the phase algorithm. These stimuli have been used recently in a number of psychoacoustic studies because of some intriguing characteristics of the waveforms, along with some compelling hypotheses regarding the interactions of the waveforms with cochlear processing mechanisms. Properties of Schroeder waveforms will be discussed in relation to hypotheses regarding internal alteration of waveform shapes by normal and impaired cochlear processing. Studies will be reviewed that involve the effects of phase selection on discrimination of temporal waveforms, as well as masking by Schroeder-phase stimuli in normal and impaired auditory systems. Results from these studies appear to reflect properties of the traveling wave within the cochlea, as well as evidence of active nonlinear gain in normal cochleas. [Work supported by NIH DC00626.]

9:20

2aPPa4. Loudness and ABR findings with short signals: More compression than expected? Birger Kollmeier, Jesko Verhey, Oliver Wegner, and Torsten Dau (AG Medizinische Physik, Universität Oldenburg, Germany)

Previous work on loudness perception was primarily focused on stationary stimuli. However, knowledge about the processing and perception of temporally varying sounds is of special interest for various applications, such as, e.g., speech perception and hearing aids. We therefore studied the loudness of brief sounds both with psychophysical and electrophysiological methods (i.e., auditory evoked potentials) as a function of the stimulus bandwidth. The loudness summation effect appeared to be larger for brief stimuli than for long stimuli. Also, the magnitude of wave V in ABR recordings for brief stimuli with equal subjective loudness was found to depend on the stimulus bandwidth. Both results indicate that the effective compression for short signals is larger than for long signals. This finding is in conflict with predictions derived with current loudness models or with a model of the effective processing in the auditory system. The consequences of these findings for the nonlinear compression stage in auditory models will be discussed.

9:40

2aPPa5. On the relation between peripheral compression and the growth of loudness. Søren Buus (Commun. and Digital Signal Processing Ctr., ECE Dept. (409 DA), Northeastern Univ., 110 Forsyth St., Boston, MA 02115), Mary Florentine (Northeastern Univ., Boston, MA 02115), Torben Poulsen (Tech. Univ. Denmark, DK 2800 Lyngby, Denmark), and Hannes Müsch (Northeastern Univ., Boston, MA 02115)

This presentation reviews similarities and differences between normal listeners' pure-tone loudness functions and the compressive basilar-membrane, BM, input-output function. Loudness matches between pure tones and multitone complexes with widely separated components reveal that the loudness function can be modeled by a modified power function with local exponents around unity near threshold and 0.2 at moderate levels [S. Buus *et al.*, J. Acoust. Soc. Am. **104**, 399–410 (1998)]. Loudness matches between short and long tones show that the SPL difference at equal loudness is a nonmonotonic function of SPL and is largest at moderate levels [S. Buus *et al.*, J. Acoust. Soc. Am. **101**, 669–680 (1997)]. These data can be explained by a loudness function that is flattest at moderate levels, where its local exponent also is around 0.2. This value is close to that obtained for BM input-output functions. The steepening of the loudness function at low levels is qualitatively similar to BM measurements. The steepening at high levels is absent in BM data when the state of the animals' cochleae is carefully controlled. One possible explanation is that the cochleae of normal adult listeners are in worse condition than those of carefully treated animals. [Work supported by NIH/NIDCD.]

10:00

2aPPa6. Relationship between loudness perception and peripheral compression in subjects with unilateral cochlear hearing loss. Brian C. J. Moore, Deborah A. Vickers (Dept. of Exp. Psych., Univ. of Cambridge, Cambridge CB2 3EB, England), Christopher J. Plack (Univ. of Sussex, Brighton BN1 9QG, England), and Andrew J. Oxenham (Northeastern Univ., Boston, MA 02115)

Loss of compression on the basilar membrane (BM) associated with outer hair cell damage (OHC) is thought to be the main factor underlying loudness recruitment in people with cochlear heating loss. To assess this idea, subjects with unilateral cochlear hearing loss were tested. Recruitment was measured by obtaining loudness matches between tones presented alternately to the two ears. Compression was estimated from the slopes of growth-of-masking functions in forward masking. The ratio of slopes for a masker centered well below the signal frequency and a masker centered at the signal frequency gives a measure of BM compression at the place corresponding to the signal frequency [A. J. Oxenham and C. J. Plack, J. Acoust. Soc. Am. **101**, 3666–3675 (1997)]. The measures of loudness recruitment were used to derive a parameter HL_{OHC}, the amount of the hearing loss attributable to OHC damage [B. C. J. Moore and B. R. Glasberg, Auditory Neurosci. **3**, 289–311 (1997)]. The value of HL_{OHC} is directly related to the amount of recruitment. The estimated compression decreased systematically as HL_{OHC} increased from 0 to 55 dB. These results are consistent with the idea that loudness recruitment is directly related to loss of compression on the BM. [Work supported by the MRC, UK.]

Contributed Papers

10:40

2aPPa7. Nonlinear amplification in the cochlea—Implications of a computer model. Martin Steurer (Dept. of Otorhinolaryngology, Univ. of Vienna, Waehringer Guertel 18-20, A-1090 Vienna, Austria)

In the cochlear amplifier the output is fed back to the input. Namely, the contraction of the outer hair cells (OHCs) is believed to be controlled by the deflection of the ciliary bundle caused by the movements of the tectorial membrane. The contraction of the OHCs leads to an intensified movement of the basilar and tectorial membrane, and by this closing the loop. Such a model implies minimal response time of up to 300 ms to reach the steady state of amplification and even more time to return from maximum amplification to zero movement (except thermal movement). These time limits can be reduced when accepting intensity-dependent optimal frequencies of the cochlea amplifiers. The optimum frequency defined by best phase shift at a certain place of the basilar membrane starts nearby the characteristic frequency of the basilar membrane and increases with increasing intensity. Therefore, the peak amplification for a fixed frequency moves in the apical direction with increasing intensity. The results of this model simulated on a computer show improved time responses and explain how to control phase shifts for the optimum frequency in the cochlear amplifier.

11:00

2aPPa8. Monaural, cross-frequency coincidence detection as a mechanism for decoding perceptual cues provided by the cochlear amplifier. Michael G. Heinz (Speech and Hearing Sci. Prog., MIT, Cambridge, MA 02139 and Hearing Res. Ctr., Boston Univ., Boston, MA 02215, mgheinz@mit.edu), Laurel H. Carney, and H. Steven Colburn (Boston Univ., Boston, MA 02215)

Basilar membrane (BM) response properties associated with the cochlear amplifier are consistent with broadened BM tuning as level increases from approximately 20 to 90 dB SPL or higher. Associated with broadened tuning are compressive BM magnitude responses and level-dependent phase changes. To evaluate the perceptual significance of the cochlear amplifier, the associated nonlinear response properties of the auditory nerve (AN) and physiologically realistic mechanisms for decoding the perceptual cues they provide were studied. Most AN fibers' rate and synchrony responses to tones are saturated above 40 dB SPL; however, nonlinear phase changes with level are encoded in AN responses up to 90 dB SPL or higher. Broadened tuning produces an increase in the correlation between adjacent AN fibers. Monaural coincidence detection is a physiologically realistic mechanism that can extract nonlinear phase cues across AN fibers with similar characteristic frequencies over a wide dynamic range. Methods from statistical decision theory [Colburn, J. Acoust. Soc. Am. **54**, 1458–1470 (1973)] were combined with an analytical AN model to provide a quantitative framework for evaluating the potential of a coincidence detector to explain human performance in pure-tone intensity and frequency discrimination. [Work supported by NIH Grant No. T32DC00038 and NSF Grant No. 9601215.]

11:20

2aPPa9. Benefits of nonlinear active gain for detection of brief probes in Schroeder-phase complex maskers. Van Summers and Philip Seitz (Army Audiol. and Speech Ctr., Walter Reed Army Med. Ctr., Washington, DC 20307-5001, vsummers@erols.com)

Masking period patterns for positive and negative Schroeder-phase complexes were determined for tonal probes at 1 and 4 kHz. Maskers included components from 200–5000 Hz of a 100-Hz fundamental. The 5-ms probes had onsets occurring 153, 155.5, 158, 160.5, or 163 ms following masker onset. For listeners with normal hearing, thresholds in the positive Schroeder-phase masker varied by as much as 25 dB depending on the position of the probe within the masker period. Thresholds in the negative Schroeder-phase maskers were nearly constant as probe onset varied. The maskers were more nearly equal in effectiveness for listeners with sensorineural hearing loss and in testing at high presentation levels. The findings support an interpretation involving differences in the shape of the basilar-membrane waveform generated by each masker, and influences of nonlinear active gain on these internal responses. The positive Schroeder-phase masker appears to produce a highly modulated basilar membrane response. Nonlinear active gain enhances the signal-to-masker ratio for signals presented during low-amplitude ''troughs'' of these modulated internal waveforms. Consistent with this account of the present findings, active gain is reduced or eliminated at high presentation levels and with cochlear damage.

11:40

2aPPa10. Loudness fluctuation and temporal masking in normal and hearing-impaired listeners. Josef Chalupper (Inst. of Man-Machine-Commun., Tech. Univ. München, Arcisstr. 21, D-80333 München, Germany, cha@mmk.e-technik.tu-muenchen.de)

The model of fluctuation strength as proposed by Fastl is based on the level difference ΔL between the maximum and minimum of the temporal masking pattern of dynamically varying sounds. Compared to normal-hearing subjects this level difference can be strongly reduced in hearing-impaired listeners. Recent findings, however, suggest that perceived fluctuations in hearing-impaired listeners are magnified by recruitment. Based on fitted loudness fluctuations—measured by a categorical scaling procedure—for each subject a ''uniform loud noise'' was generated, having equal loudness across all critical bands. These noises were amplitude modulated with different rates and depths. In experiment 1, subjects had to judge ''how strong (not how fast) fluctuates the loudness'' by marking one of seven verbal categories. In experiment 2, the ΔL's of the various noises were measured by determining the thresholds in the envelope's maximum and minimum. Although measured level differences were markedly reduced in the hearing impaired, the perceived loudness fluctuations are nearly the same for normal and hearing-impaired listeners. These results support the idea that the model of fluctuation strength can be applied to hearing-impaired listeners by transforming the difference in level into the corresponding individual difference in loudness. [Work supported by Geers.]

12:00

2aPPa11. Relation of long-term adaptation to the loudness-function slope. William Hellman (Dept. of Phys. and Hearing Res. Ctr., Boston Univ., 590 Commonwealth Ave., Boston, MA 02215, hellman@buphyc.bu.edu) and Rhona Hellman (Northeastern Univ., Boston, MA 02115)

The decline in loudness over time, defined as simple loudness adaptation, is modeled by introducing temporal factors into the nonadapted loudness function. This modification generates effective time-dependent intensity and threshold shifts. Model predictions for several frequencies are in accord with recent psychophysical measures [Hellman *et al.*, J. Acoust. Soc. Am. **101**, 2176–2185 (1997)]. In contrast to the time constant description of adaptation, the present method produces a direct connection to properties of the loudness function. A consequence of this connection is the demonstration that the increase in loudness adaptation with decreases in SL is linearly related to the loudness-function slope in log–log coordinates. Moreover, the good agreement between the measured and predicted loudness-adaptation data implies a consistency and stability in the use of numbers for loudness judgments.

Session 2aPPb

Psychological and Physiological Acoustics: Spatial Factors in Binaural Hearing (Poster Session)

D. Wesley Grantham, Chair
Bill Wilkerson Center for Otolaryngology and Communication Science, Department of Speech and Hearing Science, Vanderbilt University Medical Center, Nashville, Tennessee 37212, USA

Contributed Papers

Posters will be on display in the Poster Gallery from Monday to Wednesday, 15–17 March. Authors will be at their posters from 10:00 a.m. to 12:00 noon on Tuesday, 16 March.

2aPPb1. Near-field localization in echoic rooms. Scott Santarelli, Norbert Kopco, Barbara G. Shinn-Cunningham (Dept. of Cognit. and Neural Systems, Boston Univ., 677 Beacon St., Boston, MA 02215, shinn@cns.bu.edu), and Douglas Brungart (Armstrong Lab., Wright–Patterson AFB, OH 45433-7901)

The current study examines the ability of subjects to indicate the distance and direction of sources within 1 m of the head in a medium-sized, echoic classroom. Two conditions were tested in the same group of subjects. In the first, subjects were seated in the center of the room, relatively far from any hard reflective surfaces. In the second condition, subjects were located at the same position in the room, but a 12×4 enamel-covered wallboard was positioned next to the listener to create an additional artificial wall approximately 6 in. from the left ear of the listeners. The initial hypothesis was that previous localization results from tests in anechoic space would be nearly indistinguishable from the results in the first condition, since for sources near the head, the direct-to-reverberant energy ratio in this first condition would be very large. However, it was believed that the addition of a single, short-latency echo might bias some localization judgments, particularly judgments of distance and elevation. Instead the results indicate that localization accuracy and variability are comparable for the two echoic conditions, but that both measures of localization ability are worse in echoic conditions than in anechoic conditions.

2aPPb2. The effect of sentence onset asynchrony on call sign detection and message intelligibility in a simulated ''cocktail party.'' Brian D. Simpson (Dept. of Psych., Wright State Univ., 3640 Colonel Glenn Hwy., Dayton, OH 45435, bsimpson@sdl.psych.wright.edu), Robert S. Bolia (Veridian, Dayton, OH 45431), Mark A. Ericson, and Richard L. McKinley (Air Force Res. Lab., Wright–Patterson Air Force Base, OH 45433-7901)

Previous research has demonstrated that the spatial separation of multiple simultaneous talkers improves detection and intelligibility of a critical speech signal among non-signal speech events [Nelson *et al.*, J. Acoust. Soc. Am. **103**, 2341–2342(A) (1998); M. L. Hawley *et al.*, J. Acoust. Soc. Am. **99**, 2596(A) (1996)]. However, few findings on the effects of varying phrase onsets have been reported [J. C. Webster and P. O. Thompson, J. Acoust. Soc. Am. **26**, 396–402 (1954)]. The purpose of the present study was to investigate the effect of varying the interval between sentence onsets on call sign detection and message intelligibility. The relative onset times of two to eight temporally overlapping phrases were varied systematically in both spatially separated and nonspatially separated conditions on the horizontal plane. The phrases were presented virtually to five normal-hearing listeners. All possible temporal positions of the target phrase were examined. Results will be discussed in the context of listening to speech in real-world situations. [Work supported by AFOSR.]

2aPPb3. Speech intelligibility in real and virtual adverse auditory environments. Nancy L. Vause (U.S. Army Res. Lab., Human Res. and Eng. Directorate, Aberdeen Proving Ground, MD 21005) and D. Wesley Grantham (Vanderbilt Univ. Med. Ctr., Nashville, TN 37212)

The purpose of this investigation was to examine the effects of real and virtual adverse conditions on speech intelligibility. The experiment was designed to examine the effect of presentation method on speech intelligibility in conditions of noise and reverberation as signal-to-noise ratio was systematically varied. Additionally, this investigation evaluated the influence of talker gender on speech intelligibility in anechoic and reverberant environments as a function of signal-to-noise ratio and presentation method. Speech intelligibility scores were obtained from 21 normal hearing subjects using a nonsense syllable test. The syllables were recorded in three environments (diotic anechoic, virtual anechoic, and virtual reverberant) with three signal-to-noise ratios (0, 5, 9 dB) using two simultaneous masking sources. The findings indicate that (a) traditional diotic presentation of these stimuli degrades speech intelligibility compared to virtual presentation and may not accurately represent real-world performance; (b) the signal-to-noise ratios did not influence performance trends between presentation modes, as intelligibility improved with increasing SNR; (c) reverberation decreased intelligibility although the effects were not as dramatic as expected; and (d) using these stimuli, the female talker tokens were more easily identified than male talkers in a virtual presentation, but not generally for diotic presentation. [Work supported by NICDC and U.S. Army.]

2aPPb4. Monaural and binaural minimum audible angles for virtual sound sources. Robert S. Bolia (Veridian, 5200 Springfield St., Dayton, OH 45431, rbolia@falcon.al.wpafb.af.mil), Alan D. Musicant, and Daniel A. Gajewski (Middle Tennessee State Univ., Murfreesboro, TN 37132)

A number of researchers have employed the minimum audible angle (MAA) paradigm to investigate the precision with which listeners can discriminate differences of sound-source location in the free field [A. W. Mills, J. Acoust. Soc. Am. **30**, 237–246 (1958); W. M. Hartmann and B. Rakerd, *ibid.* **85**, 2031–2041 (1989)]. Surprisingly, this has been done only for binaural listening conditions, although Man's capacity for monaural localization is well documented [J. R. Angell and W. Fite, Psych. Rev. **8**, 225–246 (1901); R. A. Butler, R. A. Humanski, and A. D. Musicant, Perception **19**, 241–256 (1990)]. In the present study, monaural and binaural MAAs were determined using a broadband stimulus for seven virtual sound-source positions in the horizontal plane. Listeners indicated via a three-alternative, forced-choice paradigm whether the stimulus presented in the second interval appeared to move clockwise, counterclockwise, or not at all, with respect to that presented in the first interval.

Results will be discussed in terms of data obtained in previous studies of binaural MAA, and compared with data on monaural and binaural localization acuity.

2aPPb5. The cocktail party effect with conversational speech. James W. Kondash, Robert H. Gilkey, Scott K. Isabelle, and Brian D. Simpson (Dept. of Psych., Wright State Univ., Dayton, OH 45435)

Most often the cocktail party effect has been evaluated for relatively simple stimuli (e.g., isolated words or simple sentences masked by noise) in anechoic environments. Here, a stimulus situation is used which is similar to that employed by Plomp [Acustica **34**, 200–211 (1976)] (i.e., continuous discourse for both target and masker) in a reverberant room. However, instead of asking subjects to make a subjective judgment of intelligibility, the ''tracking procedure'' of DeFillipo and Scott is used [J. Acoust. Soc. Am. **63**, 1186–1192 (1978)] to simulate a conversation. This procedure measures the number of words per minute (WPM) successfully transmitted between the target talker and the subject. Preliminary results show increases in WPM of about 20% when the masker is separated from the target by 90 deg in the horizontal plane relative to the case when both the target and masker are at the same location in front of the subject. (The change in S/N necessary to maintain constant WPM between these conditions indicates that the magnitude of the effect is similar to that observed by Plomp.) Separating the target and masker(s) in elevation has little effect on WPM. [Work supported by AFOSR and the Ohio Board of Regents.]

2aPPb6. Monaural azimuth sound localization with linguistic and nonlinguistic stimuli. Barbara S. Muller and Pierre Bovet (Dept. of Psych., Univ. of Geneva, 9 rte de Drize, 1227 Geneva, Switzerland, Barbara.Muller@pse.unige.ch)

Many studies have been conducted to measure monaural azimuth sound localization performances with different sounds varying in frequency and complexity, but few are using language. This experimental design included phonologically and semantically different sentences, that is, they either contained fricative consonants or not, and all sentences were presented right way out or reversed. Analysis of response correctness of 30 subjects showed that localization performance is better with the left ear than with the right ear, but that neither the phonological nor the semantic aspect of the stimuli have any influence on localization accuracy. Analysis of response times of the subjects revealed an effect of the stimuli's nature. Reversed sentences as well as those containing fricative consonants need more time to be localized than other stimuli. These results suggest that monaural sound localization is independent of phonological or semantic attributes of the signal, but that linguistic stimuli are processed more quickly than nonlinguistic ones.

2aPPb7. Aided and unaided performance on a clinical test of sound localization. Joan Besing, Janet Koehnke (U.S. Army Res. Lab, Human Res. and Eng. Directorate, AMSRL-HR-SD, Bldg. 520, Aberdeen Proving Ground, MD 21005, jkoehnke@arl.mil), Patrick M. Zurek, Kosuke Kawakyu (Sensimetrics Corp.), and Jennifer Lister (Univ. of South Alabama)

A test of sound field localization using two small loudspeakers has been developed to evaluate performance on this task in typical clinical settings. The intensity-difference stereophony technique, incorporating interspeaker intensity differences, is used to create phantom sound images in the horizontal plane at locations between the actual loudspeakers. When the intensity of the stimulus from the speakers is the same, the source is perceived straight ahead; as the interspeaker intensity difference increases, the perceived source location moves toward the speaker with the more intense stimulus. Using speakers located at ± 40 degrees, localization of short phrases has been measured for subjects with normal hearing and subjects with hearing loss. The subjects with hearing loss were tested with and without their hearing aids. Results indicate that subjects with normal hearing have good localization with errors averaging 8.0 degrees. Unaided, subjects with hearing loss generally have larger localization errors than subjects with normal hearing, although there is a wide range of performance. With their hearing aids, the majority of subjects with hearing loss have poorer localization than without their hearing aids. Repeated administration of this test over a period of days or weeks indicates good test–retest reliability. [Work supported by NIH, NIDCD/SBIR No. DC02435.]

2aPPb8. Auditory spatial attention influences discrimination of interaural time differences: Evidence from a probe-signal paradigm. Andrew J. Sach, Nicholas I. Hill, and Peter J. Bailey (Dept. of Psych., Univ. of York, York YO10 5DD, UK, a.sach@psych.york.ac.uk)

Performance on a same–different ITD discrimination task was used as a metric for auditory spatial attention. In several variants of a probe-signal procedure, attention was directed as detailed below. In all experiments, performance was better for signals lateralized on the expected side of the head. In experiment 1, a lateralized auditory cue preceded the signal. Lest this functioned not simply as an attentional cue but also as a spatial landmark, experiment 2 used no cue but manipulated expectation by presenting trials more frequently on a particular side. To establish whether the effects in experiment 2 generalized to all sounds within the spatial focus or were attributable simply to greater familiarity with the expected stimulus, a rove was incorporated in the pitch (experiment 3) or the timbre (experiment 4) of the signals on each trial. Experiment 5 introduced trial-by-trial visual cueing which, necessarily endogenous, provided evidence for top–down attentional control. Further work established whether analogous effects are seen on a frequency discrimination task, and when sounds are lateralized by IID. [Work supported by UK BBSRC.]

2aPPb9. Effects of low-frequency thresholds on sound-source identification in the frontal horizontal plane using interaural time difference cues. Stuart Gatehouse, Catherine Lever, Christian Lorenzi, and Patrick Howell (MRC Inst. of Hearing Res., Royal Infirmary, Glasgow G31 2ER, Scotland)

Eight listeners with symmetric sensorineural hearing loss were investigated using a sound-source identification paradigm, to study localization abilities in noise for sources in the frontal horizontal plane. Stimulae were low-pass filtered click trains making available the primary cue of interaural time differences. Compared to performance of a normally hearing reference group, the listeners with sensorineural hearing loss exhibited systematic deficits in localization ability which were strongly related to hearing level. However, parallel detection experiments also showed deficits and the localization data might be a function of simple audibility. The listeners were further tested using a number of binaural hearing aid fittings for which detectability was returned to levels displayed by the normal-hearing listeners. Aided localization ability did improve but still showed residual deficits compared to the normal-hearing references and, furthermore, still had a systematic relationship with hearing level. The gradient of this relationship was approximately half that in the unaided data. The results suggest that sensorineural hearing loss compromises the use of interaural time difference cues to achieve sound-source identification and that the deficit is in part independent of audibility considerations.

2aPPb10. Acoustic weapons? Sources and propagation of strong sound. Jürgen Altmann (Experimentelle Physik III, Universität Dortmund/Institut für Experimentalphysik III, Ruhr-Universität Bochum, 44780 Bochum, Germany, Altmann@EP3.Ruhr-Uni-Bochum.DE)

Acoustic weapons are under research and development in a few countries. Reliable information is scarce; allegations, mainly in the military press, have stressed the infrasound region. By means of a literature review and own analysis potential strong sources from infra- to ultrasound were identified. Speakers with horns, sirens, and whistles can produce acoustic powers of kilowatts to tens of kilowatts. Explosive blasts have no upper limit. Repetitive explosions, e.g., of a fuel–air mixture, might produce powers on the order of megawatts. Most sources would be too large to be

handheld. Propagation of strong sound to some distance meets several problems, however. Diffraction impedes or prevents directed propagation, in particular at low frequencies. Sound of high intensity propagates nonlinearly, deforming into shocked waves with strong attenuation. The level at a given distance depends in a complicated way on details, such as source level, source size, frequency, wavefront form, and humidity. Keeping certain sound-level limits, e.g., at the ears of targeted people, would require very complex processing and automatic control. Acoustic weapons may turn out cumbersome and may not add important new options for the military; this could facilitate preventive limits up to a ban.

TUESDAY MORNING, 16 MARCH 1999 ROOM H2036, 7:55 TO 10:00 A.M.

Session 2aSAa

Structural Acoustics and Vibration: Inverse Problems in Structural Acoustics II

Bjorn A. Petersson, Cochair
Department of Aeronautical and Automotive Engineering, Loughborough University of Technology, Loughborough, Leicestershire LE11 3TU, UK

Sean F. Wu, Cochair
Department of Mechanical Engineering, Wayne State University, Detroit, Michigan 48202, USA

Chair's Introduction—7:55

Contributed Papers

8:00

2aSAa1. Parameter estimation of layered structures with one accessible surface. G. Dixon, J. L. Horner, and B. A. Petersson (Dept. of A.A.E.T.S., Loughborough Univ., Ashby Rd., Loughborough, Leicestershire LE11 3TU, UK, g.dixon@lboro.ac.uk)

It is frequently desirable, for inspection purposes, to test a layered structure nonintrusively. In practice, it is not always possible, or convenient, to access both surfaces. The aim of this paper is to determine the accuracy with which the parameters of a layered structure can be found, measurements being taken from only one surface. Using a matrix propagator model, a layer over a half-space is examined. Modeling point excitation, the sensitivity of the response to changes in the parameters of the layers are presented. The information gained will support an extended study, focusing upon systems with many layers, some of which may be composed of inhomogeneous materials.

8:20

2aSAa2. Order tracking using the Vold–Kalman tracking filter. Svend Gade, Henrik Herlufsen, and Hans Konstantin-Hansen (Brüel & Kjær, Skodsborgvej 307, DK-2850 Nærum, Denmark, sgade@bk.dk)

The Vold–Kalman filter allows for the high-performance simultaneous tracking of orders in systems with multiple independent axles. The interactions associated with close and crossing orders give rise to beating and complex psychoacoustic phenomena. With this new filter and using multiple tachometer references, waveforms as well as amplitude and phase may be extracted without the beating interactions. The Vold–Kalman filter provides several filter shapes for optimum resolution and stopband suppression. Orders extracted as waveforms have no phase bias, and may hence be used in synthesis and tailoring. The input to Vold–Kalman filtering is time history data. The class of algorithms based on Kalman filters shows no data between preselected orders, but has fine resolution, and is independent of slew rates. The calculation speed may be an issue if a large number of orders is to be extracted. This paper shows an example of the various steps of order tracking using the Vold–Kalman method applied on a simple single-shaft motor. Filter shapes are discussed and an example of decoupling of orders from a multishaft system is demonstrated. The Vold–Kalman filter is implemented in PULSE, the Brüel & Kjær Multianalysis System.

8:40

2aSAa3. Characterization of complex systems from inverse radiative transfer measurements. John Burkhardt (Dept. of Mech. Eng., U.S. Naval Acad., Annapolis, MD 21402)

A technique is proposed for the characterization of complex systems using measurements of time-dependent backscattered acoustic intensity. Utilizing a statistical model of system disorder, radiative transfer theory is used to model backscattered acoustic intensity. An algorithm for the estimation of system characteristics from observed backscatter is developed and presented. The technique is tested by numerically simulating the backscattered acoustic intensity from a disordered acoustic half-space with prescribed characteristics. Inversely estimated system characteristics are then compared with known system parameters.

9:00

2aSAa4. Indirect determination of input forces generated by the pump of a watercraft under operating conditions: Some guidelines. J-M. Janin, Y. Champoux, and N. Attala (G.A.U.S., Dept. of Mech. Eng., Univ. of Sherbrooke, Sherbrooke, QC J1K 2R1, Canada, Jean-Marc.Janin@gaus.gme.usherb.ca)

Engineers are currently able to calculate the dynamic characteristics of a complex structure using numerical tools. However, from an optimization point of view, it would be more valuable to predict correctly the actual response of the structure under working conditions. That requires that the engineers have the ability to determine precisely the input forces that are injected to the structure while operating. The direct measurement of the input forces is often impossible. That is due to the difficulties in mounting

transducers and to the additional modifications it implies on the structure. Indirect measurement of forces has already been applied to a few industrial structures with some success, but no guidelines on the method have been given yet. In this paper, the work that has been done on the determination of the forces generated by the pump of a watercraft under real operating conditions, i.e., in the water, where direct measurements are made with difficulty, is presented. A comparison of the different inversion techniques (pseudoinversion, TLS) has been made. Attention here has been focused on clearly defining limitations and guidelines concerning the use of indirect force measurement methods in order to obtain results with a good confidence level.

9:20

2aSAa5. Sensor proximity error in the conformal near-field acoustic holography and its solution by using the nonsingular boundary integral equation. Jeong-Guon Ih and Sung-Chon Kang (Ctr. for Noise and Vib. Control, Dept. of Mech. Eng., Korea Adv. Inst. of Sci. & Technol., Taejon 305-701, Korea, ihih@sorak.kaist.ac.kr)

In the conformal near-field acoustic holography (NAH) using the boundary element method (BEM), the transfer matrix relating the vibro-acoustic properties of source and field depends solely on the geometrical condition of the problem. This kind of NAH is known to be very powerful in dealing with the sources having irregular boundaries. When the vibro-acoustic source field is reconstructed by using this conformal NAH, one tends to position the sensors as close as possible to the source surface in order to get rich information on the nonpropagating wave components. The conventional acoustic BEM based on the Kirchhoff–Helmholtz integral equation has the singularity problem in the very-near field of the source surface: computation error increases very rapidly as approaching from the far field. This problem originated from the singular kernel of the fundamental solution of the BIE and can influence the reconstruction accuracy. In this paper, the holographic BIE is reformulated to remove the singularity by introducing an additional propagating plane wave. Reconstructed results by the conventional and the nonsingular BIE are compared for a simple radiator model. It is observed that the nonsingular formulation can yield accurate vibro-acoustic transfer matrix and thus improve the resolution of the reconstructed source field.

9:40

2aSAa6. A vibroacoustic inverse problem regularized by SVD technique coupled with Miller's method. C. Marquis-Favre (LASH/DGCB URA CNRS 1652, ENTPE, rue M. Audin, 69518 Vaulx-en-Velin, France, Cathy.Marquis@entpe.fr), N. Hamzaoui, and C. Boisson (LVA, INSA, 69621 Villeurbanne, France)

This communication presents the resolution of a vibroacoustic inverse problem. This latter is a typical ill-posed problem introduced by a Fredholm integral equation of the first kind. This formulation is used in the mathematical model established for an approach dealing with numerical construction of the vibroacoustic transfer function for sound radiation prediction from an industrial structure operating in its real environment [Marquis *et al.*, ICA (1995)]. The construction of the vibroacoustic transfer function is based on the use of acoustic pressures and vibratory velocity measurements defining the structure *in situ*. The acoustic pressures are data for computation of a density function allocated to points sources distributed on the structure. This calculation lies in solving a vibroacoustic inverse problem. This is carried out with the SVD technique. The regularization process is based on the Miller's method using *a priori* information on the solution and on the measurement errors contaminating the data. Some numerical simulations for an academic vibroacoustic system illustrate the sensitivity of different parameters and their influence on the application conditions of the approach. Some practical indications concerning SVD and the regularization are given and some results show the regularization effects and the consequences in the presence of measurements errors.

TUESDAY MORNING, 16 MARCH 1999 ROOM EB301, 10:00 A.M. TO 12:20 P.M.

Session 2aSAb
International Workshop on Active Noise and Vibration Control

Structural Acoustics and Vibration: Active Control of Structural Vibration

M. Osman Tokhi, Cochair
Department of Automatic Control and Systems Engineering, University of Sheffield, Sheffield S1 3JD, UK

Andy Von Flotow, Cochair
Hood Technology Corporation, 1750 Country Club Road, Hood River, Oregon 97031, USA

Invited Papers

10:00

2aSAb1. Nonlinear modeling of the forward path in a mechanical active control system. Linus Pettersson, Lars Hakansson, Ingvar Claesson, and Thomas Lago (Dept. of Appl. Signal Processing, ITS/HK-R, 372 25 Ronneby, Sweden, LINUSPETTERSSON@ITS.HK-r.se)

In most active control applications the estimate of the forward path is closely related to the performance of the controlled system. Nonlinearities in the forward path are most likely to degrade the performance. In the active control of machine tool vibration in a lathe, the plant under control principally consists of two physical parts: amplifier and a tool holder construction with integrated actuators. One applicable actuator type was used and it was based on highly magnetostrictive material. However, these types of actuators generally have nonlinear behavior. To obtain deeper understanding on the dynamic properties of the plant under control and thereby obtain a solid base for the feedback control of the machine tool vibration, nonlinear modeling of the forward path was proposed. Two methods were used: The approach of neural networks and the reverse multiple-input single-output by Bandat have been used in order to describe the forward path as accurately as possible. In the active control system of machine tool vibration in a lathe the forward path is the transfer from the actuator amplifier to the output from the accelerometer mounted on the toolholder shank in the toolholder construction.

10:20

2aSAb2. Control of vibration of flexible manipulators. M. O. Tokhi (Dept. of Automatic Control and Systems Eng., The Univ. of Sheffield, Mappin St., Sheffield S1 3JD, UK, o.tokhi@sheffield.ac.uk)

Flexible manipulator systems are receiving increasing attention due to their advantages over conventional rigid manipulators. The advantages of flexible manipulators are faster response, lower energy consumption, relatively smaller actuators, higher payload to weight ratio and, in general, less overall cost. However, due to their flexible nature, induced vibrations appear in the system during and after a positioning motion. This implies that in developing a control strategy for such systems, both the rigid body as well as flexible motion (vibration) have to be taken into account. A considerable amount of research work has already been carried out on the vibration control of flexible manipulators. These range from open-loop control to closed-loop control strategies of fixed and adaptive nature. This paper presents an investigation into the development of several approaches for vibration control of flexible manipulators. A single-link flexible manipulator is considered. Open-loop control techniques, including Gaussian-shaped and filtered command methods, and closed-loop control approaches of fixed and adaptive nature, including joint-based collocated control and hybrid collocated and non-collocated control, are developed. These are verified within simulation and practical rig-based environments. Finally, a comparative assessment of the performance of these strategies in vibration suppression of flexible manipulators is provided.

Contributed Papers

10:40

2aSAb3. Real-time control of a vibrating plate excited by a turbulent boundary layer. Emmanuel Friot, Marc Georgelin (CNRS-LMA, 31 Chemin Joseph Aiguier, 13402 Marseille Cedex 09, France, friot@lma.cnrs-mrs.fr), Christophe Durand, and Gilles Robert (LMFA, 69131 Ecully, France)

Optimal feedback control was designed and successfully implemented to reduce the vibrations of a steel plate excited by a turbulent boundary layer. One side of the plate was equipped with piezoelectric sensors and actuators. The other side was imbedded in the wall of the CNRS-LMFA anechoic wind tunnel. Measurements of the wall pressure at flow speed ranging from 70 to 130 m/s showed that the plate was excited by a standard boundary layer; the parameters of a Corcos model for the wall pressure were identified from flow data. For control a state-space model for the plate was first identified from the actuator-to-sensor transfer functions; nine plate modes in the 0–1000-Hz range were taken into account. Covariance matrices for the boundary layer excitation were also identified from vibration data. An optimal linear quadratic Gaussian (LQG) controller was then designed from the plate and noise model. The LQG algorithm was implemented on the CNRS-LMA multichannel control system and tested at three flow velocities. A 10-dB reduction of the vibration level was achieved for the three modes mostly excited by the boundary layer.

11:00

2aSAb4. Semiactive damping of vibration in mixing or propelling systems. George Vachtsevanos and Peng Wang (School of Elec. and Computer Eng., Georgia Inst. of Technol., Atlanta, GA 30332-0250, gjv@ee.gatech.edu)

Vibration damping for mixing or propelling systems is investigated in this research, through the use of semiactive control techniques. The mixing or propelling systems considered consist of a motor mounted on some support, a long shaft driven by the motor, and a propeller. Such sytems can be found in many engineering areas like chemical and materials engineering. Because the shaft is long and the propeller is working in liquids, occurrence of vibrations in such a system is inevitable. Damping of the vibration is critical to prolong the life of the motor and thus of the whole system. However, it is difficult to establish an accurate mathematical model for the operation of the mixing or propelling systems since they involve a great deal of material characteristics and structure dynamics. This paper proposes a dynamic wavelet neural network to model the relationship between vibration observations and operating parameters. This model is them employed to design a semiactive controller regulating the operating variables so that vibrations can be damped. Experimental and simulation results are presented. The experimental setup consists of an AC motor, a triaxial transducer, a data acquisition module, in addition to LABVIEW software from a Dual-400-MHz Pentium-II workstation.

11:20

2aSAb5. A distributed active vibration absorber for sound radiation and vibration control. C. R. Fuller and P. E. Cambou (Vib. and Acoust. Labs., Mech. Eng. Dept., Virginia Tech, Blacksburg, VA 24061)

This paper discusses the analytical and experimental development of a distributed active vibration absorber (DAVA) designed to reduce sound radiation and vibration over extended areas of elastic structures. The distributed vibration absorber, in contrast to the classical vibration absorber, consists of a continuous active elastic layer covered with a continuous mass distribution. The distribution of the mass layer can be optimally designed to reduce either sound radiation or vibration over selected areas or frequency bands for particular structures. The paper first discusses an analytical model of the DAVA based upon variational techniques and used in conjunction with a genetic algorithm to design the mass distribution optimally. Simulated results on vibration and sound radiation control for a vibrating beam are presented and are compared to experimental realizations of the DAVA. The analytical and experimental tests confirm that the DAVA can passively attenuate vibration and sound radiation through an extended area and over an extended frequency range. The DAVA is shown to outperform the classical point vibration absorber significantly. The introduction of an active signal to the DAVA is seen to provide significant additional sound and vibration reduction. The DAVA is demonstrated to provide effective passive and active vibration and sound control in a conformal, compact, skin treatment. [Work funded by the ONR, Dr. Kam Ng, Technical Monitor.]

11:40

2aSAb6. Multichannel feedback control for the isolation of equipment from base vibration. Marc J. Serrand and Stephen J. Elliott (ISVR, Univ. of Southampton, Highfield, Southampton SO17 1BJ, UK, msc97ms@isvr.soton.ac.uk)

Passive systems for the isolation of equipment from base vibration involve an inherent compromise between good high-frequency isolation, which requires low values of isolator damping, and limited excitation of the rigid body modes, which requires high values of isolator damping. It is known that a single-channel active control system using ''skyhook damping,'' in which a secondary force acts in proportion to the absolute velocity of the equipment, can give good damping in a lumped mass-spring-damper system without compromising the high-frequency isolation. In this experimental study a multichannel skyhook damper was used to study the isolation of a rigid mass from the vibrations of a flexible base plate. With the actuators and sensors wired together and the system excited symmetrically, a single-channel controller was initially implemented which not only showed reductions in the equipment vibration of up to 40 dB at the heave resonance at 15 Hz, but also showed substantial reductions at modes of the flexible base plate below about 200 Hz. The multichannel controller was also able to control the pitching mode of the equipment which is apparent when the system is not excited symmetrically.

12:00

2aSAb7. Smart/intelligent vibration and shock control by active or semi-active means. George J. Stein (Inst. of Mater. and Machine Mech., Slovak Acad. of Sci., Račianska 75, P.O. Box 95, SK-830 08 Bratislava 38, Slovak Republic, ummsste@savba.savba.sk)

In this contribution, some results of investigation of an electro-pneumatic active vibration control system for use in driver's seats will be given first. The system uses a common air spring as the force generator and either a flow control or pressure control proportional valve to generate the active force. The structures of the linear controller, employing both the feed-back ''sky-hook''-type additional damping and the feed-forward vibration control for both types of electro-pneumatic transducers, will be illustrated. Both systems, of different control structure, are capable of mitigation of the vibration exposure of the driver by 8 to 10 dB, measured by a standardized method. The theoretical possibility of use of active or semi-active vibration control systems for smart/intelligent vibration and shock control will be briefly discussed. The idea is to use already available active or semi-active means to rapidly modify the damping properties of a linear oscillatory system according to commands based on fast evaluation of input vibration and so intelligently adapt the structure to the character of vibration excitation.

Session 2aSCa

Speech Communication: Data Based Speech Synthesis II

Nick Campbell, Cochair
Advanced Telecommunication Research Laboratory, Hikari-dai 2-2, Seika-cho, Kyoto 619-02, Japan

Juergen Schroeter, Cochair
AT&T Laboratories–Research, 180 Park Avenue, Florham Park, New Jersey 07932-0971, USA

Chair's Introduction—7:55

Invited Papers

8:00

2aSCa1. Rules, measures, and corpora for speech synthesis. Yoshinori Sagiksaka (ATR-ITL, Kyoto, Japan)

A speech synthesis system is characterized by three factors: control rules, evaluation measures for rule development, and speech corpora to quantify and test these rules. In traditional speech synthesis by rule, the latter two factors have not been clearly acknowledged as system building constituents. Unclear acknowledgment of these two factors has often made it difficult for researchers to develop and evaluate a system consistently with objective measures. At ATR, corpus-based speech synthesis was proposed more than a decade ago to cope with this deficiency. In this talk, research efforts in corpus-based synthesis are overviewed to show how these three factors have been studied. Through this introduction, it is stressed that both clear formulation of engineering problems and basic scientific investigation of human mechanism are quite important to build a system efficiently and to understand human characteristics properly in a scientific fashion. To figure out the future problems, research efforts combining subjective evaluation and objective measures will also be introduced on the control of temporal characteristics for speech synthesis.

8:20

2aSCa2. An overview of Microsoft's Whistler text-to-speech system. X. D. Huang (Microsoft Research, Redmond, WA 98052)

The data-driven approach can significantly facilitate the process of creating text-to-speech (TTS) systems for a new language, a new voice, or a new style. As such, Whistler TTS engine was designed to benefit from automatically constructed model parameters. Efforts to improve Whistler with the use of additional training data and better learning algorithms that make full use of these data will be reviewed. Training data have been augmented for a number of speakers. To better use these data, the hidden Markov model speech recognition system has been used to segment the training corpora and select more representative acoustic units. The classification and regression tree was used for both grapheme to phoneme conversation and unseen triphone generalization. Speech signal reconstruction was based on the mixed excitation source-filter model that leads to better compression of the acoustic inventory. A number of ways to smooth the spectral parameters were also studied to minimize the concatenation distortion. To improve automatically extracted prosodic templates, the learning process was refined with an analysis-by-synthesis approach. However, the coverage remains a challenge for the data-driven approach to make Whistler produce synthetic speech that resembles the original speaker. This is especially true for the prosody model.

8:40

2aSCa3. Data-driven speech synthesis. Nick Campbell (ATR-ITL, Kyoto, 619-02 Japan)

Described in this paper are the theoretical background and implementation of a speech synthesis engine that uses an index of features describing a natural speech source to provide pointers to waveform segments that can then be re-sequenced to form novel utterances. By efficiently labelling the features in speech that are minimally sufficient to describe the perceptually relevant variation

in acoustic and prosodic characterisitcs, reduce the task of synthesis to ''retrieval'' rather than ''replication,'' and is reduced reuse of original waveform segments is possible without the need for (perceptually damaging) signal processing. The drawback of this system is that it requires a large corpus of natural speech from one speaker, but current improvements in data-storage devices and cpu technology have overcome this problem. The style of the corpus speech determines the style of the synthesis, but experiments with corpora of emotional speech confirm that by switching source corpora one can easily control the speaking style. By shifting ''knowledge'' out of the synthesizer into the source data an engine is produced that can work on any adequately labelled speech corpus. The interesting work for the future lies in determining which features are relevant to capture the variation in speech, and how they can be best described.

9:00–9:20 Discussion

9:20

2aSCa4. The AT&T Next-Gen TTS System. Mark C. Beutnagel, Alistair D. Conkie, Juergen Schroeter, Yannis Stylianou, and Ann K. Syrdal (AT&T Labs—Res., 180 Park Ave., Florham Park, NJ 07932-0791, jsh@research.att.com)

The new AT&T TTS system for general U.S. English text is based on best-choice components picked from the AT&T Flextalk TTS, the Festival System from the University of Edinburgh, and ATR's CHATR system. From Flextalk, it employs text normalization, letter-to-sound, and (optionally) baseline prosody generation. Festival provides general software-engineering infrastructure (modularity) for easy experimentation and competitive evaluation of different algorithms or modules. Finally, CHATR's unit selection was modified to guarantee the intelligibility of a good n-phone ($n=2$ would be diphone) synthesizer while improving significantly on perceived naturalness relative to Flextalk. Each decision made during the research and development phase of this system was based on formal subjective evaluations. For example, the best voice found in a test that compared TTS systems built from several speakers gave a 0.3-point head start (on a 5-point rating scale) in quality over the mean of all speakers. Similarly, using our Harmonic-plus-Noise speech representation gave us a 0.25-point advantage over standard TD-PSOLA. Finally, not performing prosodic modifications (other than some smoothing across concatenation points) on the units but using the system-generated prosody as a target in unit selection, 0.4 points were gained on overall quality. In conclusion, the new system combines the best of rule-based and data-driven worlds in TTS technology to deliver on the long-standing promise of truly natural-sounding synthesis.

9:40

2aSCa5. Domain-specific prominence-based concatenation. Thomas Portele (IKP, Univ. of Bonn, Bonn, Germany)

Some recent approaches to unlimited text-to-speech conversion do not use ''designed'' inventories of concatenative units like diphones. Instead, an annotated corpus of read speech is searched for the realization of a speech segment whose features best match the corresponding ones demanded by the synthesis input. Crucial for this approach are the size and the variety of the corpus, the number and kind of annotations, and the definition of ''best match'' based on these annotations. In this implementation, the parameter ''perceived prominence'' is relied on as the most important parameter for the selection of a prosodically appropriate realization. A previous investigation with a German corpus indicated, however, that a corpus has to be very large in order to allow prosodic variations (e.g., different focus placements) of one utterance while retaining an acceptable intelligibility, if no post-selection signal modification is applied. The application of the same procedure to an American English corpus with domain-specific utterances (travel planning) indicates that the restriction to specific domains yields better results, but that signal manipulation is inevitable in order to obtain intelligible speech.

10:00–10:20 Break

10:20

2aSCa6. Phonetic transcriptions—Aligning canonical and pronunciation forms. Diane Hirschfeld (Tech. Acoust. Lab., Dresden Univ. of Technol., 01062 Dresden, Germany)

In database preparation for concatenative speech synthesis, the alignment of canonical and pronunciation form phone sequences plays a key role for further processing. Syllabification and word boundary detection are based on canonical transcriptions, but accent detection and phrasing is coupled to the speech signal and therefore to the pronunciation form. In text-to-speech processing, canonical transcriptions are available. Unit selection is done on the speech signal and has to take into account the realized phone sequence. If a good alignment of canonical and pronunciation form of the database is available, pronunciation variants are generated implicitly in unit selection. Finally, correct alignment of phone sequences is interesting for other disciplines, too (i.e., generation of pronunciation lexica for recognition). On the bases of manual alignment for our database of a male speaker of German, the most frequent deviations from the canonical form are categorized and assigned to syllable constituents and phone combinations. For automatic alignment, a system of articulatory/acoustic features of phone combinations is developed. Similarity measures are derived from this feature system for a given phone sequence. The presented algorithm is evaluated in relation to manual alignment results.

10:40–11:00 Discussion

11:00

2aSCa7. HMM-based database segmentation and unit selection for concatenative speech synthesis. Holzapfel Martin (SIEMENS AG ZT IK 5, 81739 Munich, Germany, Martin.Holzapfel@mchp.siemens.de)

In the proposed paper methods for improved HMM-based segmentation and unit selection for concatenative speech synthesis from a large corpus will be presented. The proposed algorithm is based on triphone HMMs. For training only the database to be segmented and its canonical phonetic transcription are used. Experiments on the optimization of these HMMs for segmenation are reported. Results in changes of the HMM topology, overadaption to the database, and variations on the acoustical features will be highlighted. Special attention is given to the tree-based clustering of the models according to their phonetic context. Contrary to other approaches, the clustering is performed on phone-model level. The clustering-tree is the basis of the phonetically motivated selection of the phone-sized speech units. Using the binary membership of those clusters as selection criterion results in a target conflict on the size of those clusters. (Tight phonetic description versus prosodic and contextual variety in one cluster.) Using the distance of the resulting nodes of the tree offers a still discrete but much finer scaled phonetic selection criterion overcoming the above-mentioned shortcomings. These techniques decreased the distances of the segmentation from manual labeling and significantly improved the overall quality of the Siemens TTS System PAPAGENO.

11:20

2aSCa8. Waveform models for data-driven speech synthesis. Michael W. Macon (Oregon Grad. Inst., 20000 NW Walker Rd., Beaverton, OR 97006)

Many ''data-driven'' models for synthesizing speech rely on concatenating waveforms extracted from a database. However, the number of perceptually important degrees of freedom in speech make it unlikely that enough data could be collected to cover all combinations of phonetic variables. By utilizing models that can transform the waveform in perceptually relevant ways, the space of acoustic features covered by the data can be expanded. The minimal requirement for such a model is parametric control of the fundamental frequency and duration. In addition to this, dimensions such as voice quality characteristics (breathiness, creak, etc.), phonetic reduction, and voice identity can be altered to expand the range of effects realizable from a given database. A few classes of models have been proposed to allow varying degrees of control over these dimensions. Trade-offs between flexibility, fidelity, and computational cost exist with each. This paper will describe common threads running through the best-known approaches, including handling of nonperiodic components and sensitivity to measurement errors. Although each of these approaches has its own merits, none has been proven to satisfy all the desired properties for synthesis simultaneously. The limits of some of the simplifying assumptions underlying these methods will be demonstrated, and areas needing improvement will be outlined.

11:40

2aSCa9. Concatenative synthesis with subwords for restricted-prosody applications. Marian Macchi and Dan Kahn (E-Speech Corp., Princeton, NJ)

For applications of text-to-speech in which the message prosody is restricted, very-high-quality speech can be achieved by concatenation of prerecorded words without physical modifications to the recorded words, if the words were spoken with the appropriate prosody. However, if the vocabulary is unlimited or changeable, it is necessary to have strategies for producing out-of-vocabulary words. Experiments were done with concatenating subword units from a prerecorded inventory to produce names (First name + last name pairs) spoken in isolation, a message set that is rich in phonemic and word-level prosody but extremely restricted in phrasal prosody. In the present approach, the use of rules predicting duration, pitch, and coarticulatory smooth was minimized. Those phonetic events that minimize distortion when functioning as splice points were identified, and then units were defined as the interval between these phonetic events. The units are labeled in terms of constituent phonemes, stress, word structure, intonation, and adjacent phonemes. Some of the labels were then collapsed into equivalence categories. Physical manipulations of the units were limited to time-domain smoothing of pitch at the concatenation boundary. Work is under way to optimize the set of splice points and maximize the size of the equivalence classes.

12:00–12:20 Discussion

Session 2aSCb

Speech Communication: Cross Language and L2 Phonetics I

James E. Flege, Cochair
Department of Rehabilitation Sciences, University of Alabama, Birmingham, Alabama 35294-0019, USA

Ocke-Schwen Bohn, Cochair
English Department, Aarhus University, DK-8000 Aarhus C, Denmark

Chair's Introduction—7:55

Invited Papers

8:00

2aSCb1. Spoken word recognition by non-native listeners. Ann R. Bradlow (Dept. of Linguist., Northwestern Univ., 2016 Sheridan Rd., Evanston, IL 60208, abradlow@nwu.edu)

While the ability to perceive novel phoneme contrasts is necessary for accurate spoken word recognition by non-native listeners, it is likely that novel phoneme perception functions in a linguistically meaningful manner only once the contrast in question signals a known lexical contrast. In other words, knowledge of the sound-based structure of the target language lexicon is just as important for non-native speech perception as experience with the structure of the target language phoneme inventory. In order to understand non-native speech perception fully, there is a need to investigate recognition of word-sized units by non-native listeners using stimulus materials that are well controlled in terms of the sound-based structure of the target language lexicon. Accordingly, how non-native listeners recognize English words under conditions known to affect spoken word recognition by native English listeners was investigated. Results showed that the ability to take advantage of consistent surface phonetic information, such as a consistent talker across items, is a perceptual skill that transfers easily from first to second language perception. However, non-native listeners had particular difficulty with words that are easily confused with other similar sounding words, suggesting that non-native word recognition may be compromised when fine phonetic discrimation at the segmental level is required.

8:20

2aSCb2. The role of speaking rate in the perception of L2 speech. Murray J. Munro (Dept. of Linguist., Simon Fraser Univ., Burnaby, BC V5A 1S6, Canada, mjmunro@sfu.ca)

Previous work has shown that late second language (L2) learners typically speak more slowly than native speakers, and that speaking rate tends to correlate with overall L2 proficiency. However, the role of rate in native listeners' judgments of the global accentedness of L2 speech has not yet been established. Because rate tends to covary with proficiency, it is not known, for instance, whether the poorer global accent judgments typically assigned to slow L2 speech are due to rate differences or to other properties (such as segmental accuracy). This paper is a synthesis of the results of a series of experiments addressing this relationship. The effect of rate differences on evaluations of global accentedness of sentence-length utterances was assessed by compressing and expanding L2 speech and presenting it to listeners for accentedness ratings. Rate differences accounted for a small but significant portion of the variance in listeners' judgments. Overall, slightly accelerated L2 speech tended to be rated more highly than slower speech. These results are discussed in the context of rate measurements from a variety of types of L2 speech samples. The discrepancy between typical L2 production rates and native listeners' rate preferences is examined. [Work supported by SSHRC.]

8:40

2aSCb3. Toward further understanding of second language speech learning: An approach utilizing speech technology. Reiko Akahane-Yamada (ATR Human Information Processing Res. Labs., Kyoto, 619-0288 Japan, yamada@hip.atr.co.jp)

Recent training studies have clarified several aspects of second language (L2) learning. However, many questions still remain unanswered, and further training studies are necessary. In this paper, today's speech technology was applied to speech perception and production training. First, new speech resynthesis algorithm (STRAIGHT) was used to enhance training stimuli. Japanese speakers were trained to identify English /r/ and /l/ using several versions of synthetic stimuli with different manipulations. All the versions showed equivalent training effect as the original stimuli, suggesting that this resynthesis technique has a potential to enhance training materials. Second, two attempts were made to build an automated speech production training system, focusing on the issue of how to provide useful feedback for learners. Spectrogram and HMM-based speech recognition scores were attempted as feedback, and Japanese speakers were trained to produce /r/ and /l/. Subjects with either feedback improved significantly from pretest to posttest in their production ability as evaluated by human judges. A correlation was also found between evaluation scores obtained from HMM and human judges, further supporting the applicability of a HMM-based speech recognition system. Various approaches to optimize L2 speech training methods will be discussed in the context of the theories of speech perception/production development.

9:00

2aSCb4. Non-natives' production of vowels in conversational speech. Thorsten Piske, James E. Flege (Dept. of Rehabilitation Sci., Univ. of Alabama, 503 Voker Hall, Birmingham, AL 35294-0019), Ian R. A. MacKay (Univ. of Ottawa, Ottawa, ON K1N 6N5, Canada), and Diane Meador (Speech and Lang. Sci. Res. Lab., Juneau, AK 99802)

The aim of this study was to determine if native speakers of Italian can ever learn to produce accurately English vowels not found in Italian. A recent study [J. E. Flege, I. R. A. MacKay, and D. Meador, J. Acoust. Soc. Am., under review], in which native Italian subjects were asked to repeat real words presented via a loudspeaker, showed that early but not late bilinguals produced English /ɪ ʊ ɚ/ accurately. None of the subjects, however, did so when asked to repeat nonwords. But what about the most crucial evidence—conversational speech? Here a new technique with satisfactory experimental control ws developed to assess vowels produced in conversational speech. Speech samples were obtained from the same 90 subjects who participated in the earlier study. The subjects' production of /ɪ ʊ ɚ/ (not found in Italian) and /i æ o/ was evaluated auditorily by native English-speaking listeners. Preliminary results indicate that early bilinguals can learn to produce /ɪ ʊ ɚ/ accurately in conversational speech, but that only a declining proportion of subjects do so as the age of learning English increases. High scores for /o/, which is much like an Italian vowel, were obtained. This suggested that listeners are not unduly influenced by overall degree of foreign accent in the samples examined.

9:20

2aSCb5. Age of learning affects the learning of L2 pronunciation but not morphosyntax. James E. Flege (Dept. of Rehabilitation Sci., VH503, Univ. of Alabama, Birmingham, AL 35294, jeflege@uab.edu), Grace Yeni-Komshian (Univ. of Maryland, College Park, MD 20742), and Serena Liu (Univ. of Alabama, Birmingham, AL 35294)

Many studies have shown that performance in a second language (L2) decreases as the age of L2 learning increases, but such findings are difficult to interpret because many factors are confounded with age. Here we assessed the overall degree of foreign accent in English sentences, and scores obtained on a 144-item grammaticality judgment test (GJT). The subjects were 240 Koreans who differed according to their age of arrival (AOA) in the United States (2 to 23 years). As AOA increased, foreign accents grew stronger and the GJT scores decreased steadily. However, when variables confounded with AOA were controlled using a subgroup matching technique, AOA was found to exert a significant effect on the foreign accent ratings but not on the GJT scores. Total years of education in the United States, but not language use or AOA, significantly affected scores for a subset of GJT items that tested rule-based, generalizable aspects of English morphosyntax. Conversely, language use, but not education or AOA, affected the scores for GJT sentences testing lexically based aspects of morphosyntax. Age effects on L2 pronunciation thus appear to be real. However, differences in morphosyntactic knowledge may instead be due to age-related variation in education or English-language use.

9:40–10:00 Break

10:00

2aSCb6. On what it takes to predict perceptual difficulty in cross-language vowel perception. Ocke-Schwen Bohn (English Dept., Aarhus Univ., DK-8000 Aarhus C, Denmark), Winifred Strange (CUNY Grad. Ctr., New York, NY), and Sonja A. Trent (Univ. of South Florida, Tampa, FL)

According to current models of cross-language speech perception and second language (L2) speech learning, perceptual difficulty depends upon how listeners map the phonetic segments of the foreign language onto their native language (L1) categories. A number of indirect methods have been suggested for predicting perceptual difficulty, e.g., contrastive phonemic analyses and acoustic comparisons of L1 and L2 sounds. This presentation summarizes recent studies which directly assessed perceptual assimilation patterns for North German vowels (as perceived by American English listeners) and for British English vowels (as perceived by Danish listeners). Vowels were produced in CVC syllables in various consonantal contexts in both citation form and sentence frames. As expected, contrastive phonemic analyses were not good predictors of assimilation patterns. Somewhat surprisingly, acoustic comparisons didn't always predict assimilation patterns either. In particular, measures of acoustic similarity from ''canonical'' forms didn't predict acoustic similarity for coarticulated vowels, nor did these measures predict perceptual similarity. Our results strongly suggest that perceptual difficulty in cross-language speech perception cannot be predicted using indirect methods, nor can difficulty be predicted by perceptual studies of citation form utterances. Instead, successful predictions of perceptual difficulty must be based on direct assessments of assimilation patterns. [Work supported by NIDCD.]

10:20

2aSCb7. Phonemic repertoire effects in lexical activation. Anne Cutler (MPI for Psycholinguist., P.O. Box 310, 6500 AH Nijmegen, The Netherlands)

Languages differ in the size and makeup of their phonemic repertoire. Phoneme-detection experiments have shown that speakers of languages with large, confusable vowel repertoires (English, Dutch) differ in their expectations of phonetic variability from speakers of languages with small distinct vowel repertoires (Spanish, Japanese). The present study asks whether these different expectations also constrain the activation of spoken words, via two word reconstruction experiments, in which listeners reconstruct from nonwords (e.g., *eltimate*) a real word by changing just one phoneme (*ultimate, estimate*). Dutch listeners responded significantly faster and made fewer errors when required to change vowels as opposed to consonants; when allowed to change any phoneme, they altered vowels significantly more often than consonants, and vowel responses were made more rapidly than consonant responses. This suggests that for these listeners, vowel information constrains lexical activation less tightly (allows more potential alternative candidates) than consonant information. In a language with few, distinct vowels, however, this weaker constraint of vowel information on lexical activation is not found: Spanish subjects, in the same task, responded equally rapidly and accurately whether required to alter vowels or consonants; when allowed to change any phoneme, they marginally preferred to alter consonants rather than vowels.

10:40

2aSCb8. Native-language phonetic and phonological constraints on perception of non-native speech contrasts. Catherine Best (Dept. of Psychol., Wesleyan Univ., Middletown, CT 06459 and Haskins Labs, 270 Crown St., New Haven, CT 06511, best@haskins.yale.edu)

Adults discriminate many non-native speech contrasts poorly, especially from an unfamiliar language that is not (yet) an L2. The Perceptual Assimilation Model (PAM) [Best *et al.*, JEP: HPP **14**, 34 560 (1988)] posits that this difficulty stems from knowledge of both the phonological functions and the phonetic details of native speech segments. Thus, discrimination of an unfamiliar contrast depends not only on whether it resembles a native phonological contrast, but also on perceived goodness of fit between the non-native segments and native phonetic category(s). Cross-language comparisons support PAMs prediction that perceptual assimilation of contrasting non-native segments to a single native category yields poorer discrimination than assimilation to two categories (TC contrasts). Discrimination is worst if both phones are equally similar to a single category (SC), substantially better if they differ in category goodness (CG), near ceiling for TC assimilations, and good to excellent for consonants that fail to be assimilated as speech, instead being perceived as nonspeech events (non-assimilable: NA). Recent findings indicate that, as predicted, SC, CG, and TC assimilations are associated with preferential activation of left hemisphere language regions, whereas NA stimuli yields bilateral brain activation. Other findings with fluent bilinguals indicate a persisting L1 effect on non-native consonant discrimination even if their L2 is acquired prior to 5 years. [Work supported by NICHHD and NIDCD.]

11:00

2aSCb9. Cortical representation of language in monolinguals and bilinguals. Jacques Mehler (CNRS VA1198, 54 B. D. Raspail, Paris 75006, France)

A presentation will be made of experiments trying to evaluate language representation in monolingual and bilingual subjects. The impact of distance of the languages on the cortical representations of L1 and L2 will be thus evaluated. Furthermore, also considered will be the age at which L2 has been acquired and the degree of proficiency that the bilinguals have attained in L2. Data will be presented from PET, fMRI, MEG, and high-density evoked potentials. Results tend to show that level of proficiency is more important than age of acquisition to explain the cortical representation of L2. Comparing and contrasting standard psycholinguistic evaluations with imaging studies, the respective advantages and shortcomings will be discussed. In the second part of the presentation the hypothesis that languages can be arranged into a limited number of classes will be explored. A review of work showing that infants discriminate a change of language only if the test and habituation languages have different rhythmical properties will be presented. The notion that languages can be sorted into rhythmical classes can be evaluated experimentally and results will be presented.

11:20

2aSCb10. Research in cross-language and second-language speech perception and production: Issues, trends, and future directions. Winifred Strange (Speech and Hearing Sci., CUNY Grad. School, 33 W. 42nd St., New York, NY 10036-8099)

Theoretical and methodological advances presented in the preceding papers of this special session will be summarized and critiqued. Suggestions for future research will be offered. The comments offered in this talk are intended to generate discussion by the participants and audience of the special session.

11:40–12:20 Discussion

Session 2aSP

Signal Processing in Acoustics: Acoustic Image Synthesis for Arbitrary Listeners

Anthony J. Brammer, Cochair
IMS/ASP, National Research Council, M-36 Montreal Road, Ottawa, Ontario K1A OR6, Canada

Adelbert W. Bronkhorst, Cochair
Perception Department, TNO Human Factors Research Institute, P.O. Box 23, 3769 ZG Soesterberg, The Netherlands

Chair's Introduction—7:55

Invited Papers

8:00

2aSP1. Are individualized head-related transfer functions required for auditory information displays? Elizabeth M. Wenzel (NASA Ames Res. Ctr., M.S. 262-2, Moffett Field, CA 94035-1000, bwenzel@mail.arc.nasa.gov) and Durand R. Begault (San Jose State Univ., Moffett Field, CA 94035-1000)

In aerospace applications, spatial cues in auditory displays can allow an astronaut, ground-controller, or other human operator to take advantage of their natural ability to localize sounds in three-dimensional space. Synthetic localization of acoustic images can be used to enhance situational awareness, improve segregation of multiple audio signals through selective attention, and provide a means of detecting a desired signal against noise for enhanced speech intelligibility. A number of studies in the literature have suggested that individualized head-related transfer functions (HRTFs) produce the best localization performance for a given listener in a spatial auditory display. However, it is often impractical to measure the HRTFs for each potential user of an aerospace display. Further, whether or not individualized cues are required may depend upon the nature of the task that is being aided. For example, a communications display may not require individualized cues to enhance speech intelligibility, while a display that represents the direction of incoming aircraft to an air traffic controller may benefit from individualized HRTFs. This paper describes some of the spatial auditory displays that have been investigated at NASA Ames and discusses the efficacy of using nonindividualized cues in the context of various aerospace tasks.

8:20

2aSP2. Localization in real life and with individual, nonindividual, and artificial head binaural recordings. Henrik Moller (Acoust. Lab., Aalborg Univ., Fredrik Bajers Vej 7 B4, DK-9220 Aalborg O, Denmark)

Human sound localization was studied in real life (1), and with binaural recordings made in the ears of the listener him/herself (2), in the ears of other humans (3), and with artificial heads (4). The localization with individual binaural recordings turned out to be identical to that of real life. An increased number of errors was seen for nonindividual binaural recordings, especially in terms of confusions between median plane sources. It proved possible to select human ''recording heads'' that offered recordings which gave more favorable results than others. The highest number of errors was seen with artificial head recordings. This is surprising, since the artificial heads aim at replicating the acoustics of the ''average'' human. Measurements of head-related transfer functions confirmed differences between data obtained with artificial heads and those obtained from humans. The paper gives an overview of experiments and measurements carried out at Aalborg University over a number of years.

8:40

2aSP3. Relearning sound localization with new ears. P. M. Hofman, A. J. Van Opstal, and J. G. A. Van Riswick (Dept. of Medical Phys. and Biophys., Univ. of Nijmegen, Geert Grooteplein 21, NL-6525 EZ Nijmegen, The Netherlands)

Because the inner ear is not organized spatially but tonotopically, sound localization relies on the neural processing of implicit acoustic cues. To determine a sound's position, the brain must learn and calibrate these individual cues, using accurate spatial feedback from other sensorimotor systems. Experimental evidence for such a system has been demonstrated in barn owls, but not in humans. In this study, the existence of ongoing spatial calibration in the adult human auditory system is demonstrated. The spectral elevation cues of human subjects were disrupted by modifying their outer ears (pinnae) with molds. Although localization of sound elevation was dramatically degraded immediately after the modification, accurate performance was steadily reacquired. Interestingly, learning the new spectral cues did not interfere with the neural representation of the original cues, as subjects could localize sounds with both normal and modified pinnae.

9:00

2aSP4. Explaining individual differences in head-related transfer functions. Frederic L. Wightman and Doris J. Kistler (Waisman Ctr., Univ. of Wisconsin, 1500 Highland Ave., Madison, WI 53705, Wightman@waisman.wisc.edu)

The fidelity of virtual auditory images is degraded by differences between the listener's head-related transfer functions (HRTFs) and the HRTFs used to synthesize the virtual images. Middlebrooks (this meeting) argues that simple frequency scaling accounts for many of these individual differences. In an attempt to understand more fully both the capabilities and limitations of frequency scaling, the HRTFs from 100 individuals were analyzed. The difference between each pair of HRTFs was expressed as a single number, the average of the squared dB differences at 40 log-spaced frequencies from 0.12 to 12 kHz. A multidimensional scaling analysis (ALSCAL) was performed on the resulting difference matrix. A two-dimensional solution accounted for over 80% of the total variance. The frequency scaling factor needed for the optimal fit of each individual's HRTF set to the HRTF set at the center of the 2-D solution was then determined. The correlation between the optimal frequency scalar and the coordinate of each HRTF set on one dimension of the scaling solution was over 0.95. Attempts to reveal a physical basis for the second dimension have been less successful. [Work supported by NIH, NASA, and ONR.]

9:20

2aSP5. Adapting head-related transfer functions to individual listeners. Adelbert W. Bronkhorst (TNO Human Factors Res. Inst., P.O. Box 23, 3769 ZG Soesterberg, The Netherlands, bronkhorst@tm.tno.nl)

A highly efficient data reduction scheme will be described that captures the interindividual variability, present in head-related transfer functions (HRTFs), in only a limited number of parameters. The techniques used are principal component analysis and least-squares fitting of orthogonal spherical functions. The distortions introduced by the data reduction were evaluated using a distance measure based on the dB differences between HRTFs within 1/6 octaves. The distance measure correlates strongly with results of listening tests in which original HRTFs were compared with HRTFs reconstructed from the compressed data. Adaptation of HRTFs to an individual can be performed by reconstructing a set of HRTFs using estimated parameter values. Two methods for estimating these values will be discussed: prediction based on anthropometrical data and optimization using a simple listening test.

9:40–10:00 Break

Contributed Papers

10:00

2aSP6. The contribution of spectral cues to human sound localization. Erno H. Langendijk and Adelbert W. Bronkhorst (TNO Human Factors Res. Inst., Kampweg 5, 3796 DE Soesterberg, The Netherlands, erno@tm.tno.nl)

The contribution of spectral cues to human sound localization was investigated by removing cues in 1/2-, 1-, or 2-octave bands in the frequency range above 4 kHz. Localization responses were given by placing an acoustic pointer at the same apparent position as a virtual target. The pointer was generated by filtering a 100-ms harmonic complex with equalized head-related transfer functions (HRTFs). Listeners controlled the pointer by a hand-held stick that rotated about a fixed point. In the baseline condition the target, a 200-ms noise burst, was filtered with the same HRTFs as the pointer. In other conditions the spectral information within a certain frequency band was removed by replacing the directional transfer function within this band with the average transfer of this band. Analysis of the data showed that the effect of bandwidth is larger than that of center frequency. There appears to be an interaction between center frequency and target position. Effects related to center frequency varied substantially among listeners. This indicates that listeners use different cues when localizing sounds from a certain direction.

10:20

2aSP7. Sound localization using other people's ears. John C. Middlebrooks (Kresge Hearing Res. Inst., Univ. of Michigan, 1301 E. Ann St., Ann Arbor, MI 48109-0506, jmidd@umich.edu)

When subjects attempt to localize virtual targets that have been synthesized with directional transfer functions (DTFs) recorded from other subjects' ear canals, they typically show a considerable increase in localization error relative to the condition in which DTFs are recorded from their own ear canals. This study explored intersubject differences in DTFs and developed a procedure to reduce such differences, thereby improving virtual localization. DTFs varied systematically among subjects in regard to the center frequencies of spectral features such as peaks and notches. Generally, spectral features appeared at lower frequencies in the DTFs of larger subjects and at higher frequencies in DTFs of smaller subjects. Characteristic errors in virtual localization could be related to frequency differences between spectral features in the listener's own DTFs and those with which virtual targets were synthesized. Scaling transfer functions in frequency by an optimal scalar could reduce intersubject variance in DTFs, sometimes by more than 50%. Frequency scaling of DTFs resulted in corresponding improvements in virtual localization. In the majority of cases, optimal frequency scaling reduced by more than half the increase in error that resulted from listening through another subject's ears. [Work supported by ONR Grant No. N00014-94-0481 and NIH Grant No. DC00420.]

10:40

2aSP8. Holophony versus ambisonic: Deriving a hybrid method for 3-D sound reproduction in videoconferencing. Rozenn Nicol and Marc Emerit (France Telecom CNET, 2 Ave. Pierre Marzin, 22307 Lannion Cedex, France, rozenn.nicol@cnet.francetelecom.fr)

Current research in videoconferencing intends to introduce 3-D reproduction methods both for image and sound. This paper will deal only with the problem of 3-D sound reproduction. First, one specific requirement must be borne in mind: in a videoconference, the listening area has to be wide, since it is addressed to several listeners. Two approaches have been considered: Holophony—acoustical equivalent to holography—and ambisonic. In a previous paper, it has been shown that these two methods are based on the same principle, i.e., physical reconstruction of the acoustical 3-D field, which appears as the most relevant solution to obtain an extensive listening area. However, holophony and ambisonic achieve opposite compromises between system complexity (number of signals recorded, number of microphones and loudspeakers) and reconstruction performance (accuracy, size of listening area, implementation opportunities). The two approaches are compared in order to point out a hybrid method, which optimizes the result. First studies focus on sound pick-up and show that ambisonic is more efficient concerning the coding of spatial information. In this paper, this analysis will be completed, first by examining the sound reproduction step, and second by studying the method robustness toward the actual behavior of transducers.

Session 2aUWa

Underwater Acoustics, Acoustical Oceanography, and Physical Acoustics: Acoustics and the Comprehensive Test Ban Treaty I

Arthur B. Baggeroer, Cochair
Department of Ocean Engineering, Massachusetts Institute of Technology, 77 Massachusetts Avenue, Cambridge, Massachusetts 02139, USA

Martin W. Lawrence, Cochair
Provisional Technical Secretariat, Comprehensive Nuclear-Test-Ban Treaty Organization, Vienna International Centre, P.O. Box 1200, A-1400 Vienna, Austria

Invited Papers

8:20

2aUWa1. Overview of the hydroacoustic monitoring system for the Comprehensive Nuclear-Test-Ban Treaty. Martin W. Lawrence (Provisional Tech. Secretariat, Comprehensive Nuclear-Test-Ban Treaty Organization, Vienna Intl. Ctr., A-1400 Vienna, Austria, mlawrence@ctbto.org)

A global hydroacoustic monitoring system is being implemented for use in verification of the Comprehensive Nuclear-Test-Ban Treaty (CTBT). This system will provide hydroacoustic monitoring of all the world's oceans for 24 h a day, every day of the year, into the indefinite future. This unique resource will utilize two types of station. One type will be based on a hydrophone at the SOFAR axis depth, cabled back to shore. The other will be based on a seismometer on a small island using detection of the T-phase signal. This latter station relies on a signal which has propagated predominantly through the ocean, but has been converted to seismic energy at the margin of the island. This new application of hydroacoustics highlights a number of scientific questions which have not been adequately addressed. Progress in implementation of this network will be described.

8:40

2aUWa2. Acoustic source calculations for nuclear bursts. Douglas B. Clarke, Philip E. Harben, and David B. Harris (Lawrence Livermore Natl. Lab., Livermore, CA)

Research has been conducted on the source term for long-range underwater propagation of signals from nuclear explosions in and above the ocean, in support of CTB monitoring objectives. A suite of source-region simulations is reviewed to study the variation of wave properties and source-region energy partition as a function of height or depth of burst. The multistep calculation combines LLNL's CALE hydrodynamics code in the strong shock region with NRL's weak shock code, NPE, at intermediate ranges. The source term calculations are intended as a starter field for long-range linear propagation models to obtain signature estimates at normal observational ranges. Calculations are presented to examine the effect of sea ice below an air burst on acoustic coupling into the water column. The ice was modeled as a continuous elastic layer 5-m thick at the water surface, and the source as a 1-Kt explosion 50 m above the ice. Calculations with and without the ice layer predict a moderate, but noticeable reduction in coupled acoustic energy in signals observed at the 10 000-m range. [Work performed under the auspices of the U. S. Department of Energy by the Lawrence Livermore National Laboratory under Contract No. W-7405-ENG-48.]

9:00

2aUWa3. Hydroacoustic monitoring of the oceans. Y. Caristan (CEA/DASE, BP. 12, 91680 Bruyers Le Chatel, France, caristan@dase.bruyeres.cea.fr)

In order to verify compliance with this Treaty, an international Monitoring System based on four technologies, seismology, infrasounds, hydroacoustic, and radionuclides, shall be implemented. Therefore, a network of hydrophones and seismic T-wave stations has been designed and evaluated in terms of detectability and location capability. Hydroacoustic waves generated by an undersea explosion or by oceanic earthquakes are propagating over several thousands of kilometers within an oceanic waveguide called So.F.A.R., channel (sound fixing and ranging) as shown by Ewing and Tolstoy (1950). When they are reaching any continental slope or island they are converted in seismic T-waves which are recorded by seismographs. By using both numerical simulations and experimental analysis, a methodology has developed which allows to better understand and quantify the effects of the source parameters and of the propagation characteristics (specifically on the So.F.A.R. channel and of the continental slope) on the recorded waveforms. The results obtained should be useful to improve the evaluation of detectability and location capability of the future hydroacoustic network and should provide some effective guidance to the site survey process. For that purpose and also to have a better understanding of the source parameters and of the acoustic wave propagation, a methodology has developed using both a numerical simulation and an experimental analysis.

9:20

2aUWa4. Hydroacoustics in monitoring the comprehensive test ban treaty. John A. Orcutt (Inst. of Geophys. and Planetary Phys. (0225), Scripps Inst. of Oceanogr., La Jolla, CA 92093, jorcutt@igpp.ucsd.edu)

The Comprehensive Test Ban Treaty was signed by the U. S. in 1996 and many other nations have since joined in supporting the treaty. On a planet which is more than 70% covered by oceans, only 11 sites will monitor acoustic propagation in the oceans. The capabilities of the system are further limited through the avoidance of any directionality capability at the sites and five of the sites are simply seismometers located on islands. Several research projects become very important in developing understanding to the level needed to remove some of the more substantial problems introduced by this limited capability. In particular, the coupling of acoustic to seismic wave propagation in the vicinity of islands is an important issue. Research has demonstrated that the efficiency of coupling, for example, is highly dependent on azimuth and, hence, the offshore morphology. Additional work is required to develop a predictive capability for coupling. Typically hydrophones in the ocean detect far more events than seismometers on land. This, coupled with the slow speed of propagation, makes location of events difficult. Research involving the joint location of events using hydrophones and seismometers will be reviewed.

9:40

2aUWa5. Automated detection of underwater explosions by the IMS hydroacoustic network. Hyrum Laney, Paul Dysart, Herbert Freese (Science Applications Intl. Corp., 1710 Goodridge Dr., McLean, VA 22102, dysart@osg.saic.com), Douglas Brumbaugh, Ronan Le Bras, and Jeffrey Hanson (Science Applications Intl. Corp., San Diego, CA 92121)

An important component of the CTBT monitoring system is the 11-station hydroacoustic network designed to monitor the oceans for unannounced underwater explosions. Explosions that do not breach the sea surface consist of a series of pulses due to gas bubble oscillations. The period of oscillation is a well-known function of the yield and detonation depth for explosives up to several thousand kilograms of TNT equivalent. The presence of a bubble pulse is a strong indicator of an explosive source and, therefore, is useful in event characterization. Examples of underwater explosions, which can be used to calibrate signal processing algorithms and propagation models, are rare. A set of explosive and other impulsive events recorded on hydrophones at Wake Island and Point Sur, CA is presented. These include the French nuclear tests, volcanic events, and chemical explosions. The set also includes pressure time-series simulated using a normal-mode propagation model. The automatic signal processor has been developed to search the real cepstrum for peaks using a noise-spectral equalization algorithm similar to those used in passive sonar. Examples illustrate complications due to range, depth, ambient noise, and waveguide distortion.

10:00–10:20 Break

10:20

2aUWa6. Characterization of reflected hydroacoustic signals for ctbt localization. Jeffrey Angell, Ted Farrell, and Jay Pulli (GTE/BBN Technologies, Arlington, VA 22209)

The sparse nature of the proposed IMS hydroacoustic network implies that maximizing the information from each sensor is critical to overall network performance for nuclear event localization. Performance may be enhanced using information contained in late-time reflected arrivals from continental shelves, islands, and seamounts. The primary focus here is to characterize reflected signals and determine the conditions under which reflections are likely to occur. Several data sets, including a 1970 ship-scuttling explosion conducted in the North Atlantic (CHASE 21 event) are analyzed. Travel-time ellipses and bearing estimates generated from measured arrival times of waveform envelopes are used to determine possible geographic locations of acoustic reflections. Environmental characteristics at these locations are examined in order to understand the conditions under which reflections are likely to occur. Time- and frequency-domain characteristics of both the direct arrivals and reflections are measured and discussed. [Work sponsored by Defense Special Weapons Agency Contract Number DSWA01-97-C-0164.]

Contributed Papers

10:40

2aUWa7. Modeling hydroacoustic waveform envelopes for comprehensive test-ban treaty monitoring. Yevgeniy Y. Dorfman (BBN Technologies, 70 Fawcett St., Cambridge, MA 02138) and Jay J. Pulli (BBN Technologies, Rosslyn, VA 22209)

Robust and accurate localization of explosion events in the oceans requires modeling signal arrival times for a number of receivers. Additional information contained in the waveform envelope may also be used to recover other source properties and reduce the probability of false alarms in nuclear explosion monitoring. The feasibility of efficient envelope modeling was investigated by comparing adiabatic normal-mode model predictions with explosion data. The KRAKEN computer code, combined with appropriate dispersion curve interpolation, was used to compute modal shapes and wave numbers in each range segment. To facilitate CTBT knowledge base development, the model has been used to illustrate the various factors that contribute to the shape of the received hydroacoustic waveform envelope, and provide design feedback for sensor placement and data analysis algorithms. The model was compared with data for two source–receiver paths: (a) the Chase21 ship scuttling explosion on 25 June 1970 off the New Jersey coast and recorded at the Ascension Island hydroacoustic array; and (b) nuclear explosions on Mururoa Atoll and received at the hydrophone at Point Sur, California. Adiabatic normal-mode approach was found inadequate for source and receiver located far from the SOFAR axis. [Work supported by U.S. DOE, Office of Nonproliferation and National Security.]

11:00

2aUWa8. Propagation modeling of *T*-phase time series via RDOASES. Brian Sperry (MIT/WHOI Joint Prog. in Oceanogr. and Ocean Eng., Woods Hole Oceanogr. Inst., Woods Hole, MA 02543), Henrik Schmidt, and Arthur Baggeroer (MIT, Cambridge, MA 02139)

Properly situated earthquakes and explosive sources often radiate acoustic energy into the oceanic waveguide and are thereby detectable at long ranges. Details of how this energy actually couples into the ocean remain elusive. Recent development of a range-dependent version of OASES has made it possible to model acoustic propagation in range-

varying, elastic environments. It has been very successful in investigating the effect of epicenter depth for *T*-phase excitation on a sloping bottom. The present study extends earlier work to consider time-domain characteristics of the arrival and their dependence upon properties of the source and its surrounding region. The general environment considered here is a Munk sound-speed profile and sloping bottom out to a range of 30 km, after which the bottom depth is constant. The seismoacoustic field is computed using RDOASES, and then projected onto the local mode shapes. The complex mode coefficients are propagated to a distant receiving array, where the time-domain signal is synthesized. Understanding the source excitation in terms of mode and frequency content is critical to interpreting the arrival structure. At teleseismic ranges, the dependence of group delays on mode number and frequency leads to significant time spreading of the various signal components.

11:20

2aUWa9. Normal-mode composition of earthquake T phases recorded in the deep ocean. Gerald L. D'Spain, Lewis P. Berger, William A. Kuperman (Scripps Inst. of Oceanogr., La Jolla, CA 92093-0704), Jeff L. Stevens, and G. Eli Baker (Maxwell Technologies, San Diego, CA 92123-1506)

For upslope propagation in an ocean environment, the place(s) where underwater acoustic field energy couples into the land seismic field is determined by the local water depth and the normal-mode composition of the acoustic energy, to first approximation. Therefore, the use of earthquake-generated T phases as natural probes of water-to-land coupling characteristics is aided by knowledge of their modal makeup. During the 1989 VAST experiment, conducted in 5000-m-deep water in the midlatitude Northeast Pacific Ocean (34.0 deg N, 140.0 deg W), the Marine Physical Lab deployed a 200-element, 3000-m-aperture vertical hydrophone array from R/P FLIP. Several earthquakes generated detectable T phases during the 11-day recording period and the modal composition of five such events, including one on land, have been determined. Because of the extended nature of the T-phase source region, the individual modes are uncorrelated, permitting an eigenanalysis of the data cross spectral matrix at a given frequency to provide approximate mode amplitude and eigenfunction information. Results indicate that for the predominant T-phase energy around 5 Hz, the first four or five modes are important, with the mode having largest amplitude often not being the lowest one. [Work supported by ONR and DSWA.]

11:40

2aUWa10. Progress in the implementation of the T-phase subnetwork for monitoring the oceans. Marta Galindo Arranz (Provisional Tech. Secretariat, Comprehensive Nuclear-Test-Ban Treaty Organization, Vienna Intl. Ctr., A-1400 Vienna, Austria, mgalindo@ctbto.org)

For the first time seismic technology is being used for monitoring the oceans, detecting and evaluating acoustic signals. Five seismic stations, called T-phase stations, are being established to complement six hydrophone stations, thus constituting the hydroacoustic international monitoring network. This T-phase subnetwork is mostly localized in the northern hemisphere and has been designed to work in synergy with the seismic network. Many technical difficulties arise at the time of installing new T-phase stations, due to lack of some relevant scientific knowledge. The T-phase stations are located on small islands with abrupt bathymetric properties and an open view of the ocean. Within this environment it is necessary to find the optimum distance from the coastline in order to achieve a compromise between sea-induced noise and good T-phase detection capability. Other open questions include the details of how acoustic energy is coupled into seismic energy, as well as how factors such as location and seasonal variations of the SOFAR channel affect the acoustic-to-seismic coupling. These questions are investigated at each site survey, upgrading, or new installation within the subnetwork. Results of these investigations will be presented as well as possible implications for technical specifications of the T-phase stations.

12:00

2aUWa11. Perturbative eigenvalue techniques for global-scale hydroacoustic pulse propagation. Gregory J. Orris, John S. Perkins, and Laurie T. Fialkowski (Naval Res. Lab., Washington, DC 20375)

Because of the computational difficulties associated with three-dimensional acoustic propagation on global scales in the ocean, current models require a hybrid approach. In the Global-Scale Ocean Acoustic Raytrace Model, horizontal refraction of eigenrays is accomplished by first separating the vertical dependence of the field from the horizontal dependence and solving for the vertical eigenvalues and eigenmodes. This approximation is valid as long as the ocean medium is adiabatic in the horizontal direction. The eigenvalues and eigenmodes directly affect the local phase speed and group velocity, and consequently, refraction and travel time of a given ray. If Fourier synthesis is used in conjunction with another full-field method to obtain time-domain results along a horizontally refracted ray, then the computing requirements of determining the local eigenvalue spectrum as a function of frequency can become overly burdensome. An approach based on perturbation methods is introduced that can be used to compute the eigenvalue spectrum quickly at frequencies close to those at which the spectrum has already been determined, yet far enough away in frequency to be useful for the Fourier synthesis of pulse propagation. [Work supported by the U.S. Department of Energy, Office of Non-proliferation and National Security, Office of Research and Development, Contract No. DE-A101-95IS20011.]

Session 2aUWb

Underwater Acoustics: Rapid Ocean Environmental Assessment

Ronald A. Wagstaff, Cochair
Code 7183, Naval Research Laboratory, Stennis Space Center, Mississippi 39529-5004, USA

Jürgen Sellschopp, Cochair
SACLANT Undersea Research Center, Viale San Bartolomeo 400, 19138 La Spezia, Italy

Invited Papers

8:00

2aUWb1. Rapid response, a demonstration of ocean assessment capabilities. Jürgen Sellschopp and Tuncay Akal (SACLANT Undersea Res. Ctr., Viale San Bartolomeo 400, 19138 La Spezia, Italy)

The suitability of sound waves as a carrier of information in the ocean is known to be highly variable. In the past, the assessment of the controlling environmental parameters has typically been subject to post-cruise analysis and often took years. SACLANT Undersea Research Centre and NATO's organization for military oceanography agreed upon a three-year series of surveys in the Mediterranean Sea aimed at the development of a methodology for rapid environmental assessment (REA). A large number of research ships and patrol aircraft were provided by various nations. Researchers of numerous institutes were engaged in the REA trials. Time-invariant parameters such as bottom properties were measured directly or determined by inversion. The results were transferred for optional replacement in a standard database. Time-dependent parameters such as the sound velocity structure were predicted by means of real-time ocean models initialized and updated with survey data. The infrastructure for timely delivery of REA products and forecasts was developed, the main requirements being appropriate data channels and data fusion capacity. Rapid response was the first demonstration by the research community that the critical characteristics of the acoustic environment can be provided by the end of a mission.

8:20

2aUWb2. Rapid assessment of undersea ambient noise. Ronald A. Wagstaff (Naval Res. Lab., Stennis Space Center, MS 39529-5004) and Reginald D. Hollett (SACLANT Undersea Res. Ctr., La Spezia, Italy)

Undersea ambient noise is a critical parameter in determining the performance of passive sonar systems, and sometimes active systems. There are many properties of the ambient noise that must be considered in a rapid ambient noise field assessment, including mean and percentile levels as a function of frequency, temporal and spatial variation, vertical and horizontal directionality, and depth dependence. In addition, rapid interpretation and extrapolation of the measured and analyzed ambient noise results require a credible onboard ambient noise prediction model and collateral noise model input measurements of oceanographic, acoustic, meteorological, and noise source parameters, e.g., sea and swell height, wind speed, and the positions, speeds, courses, and lengths of near and distant ships. Finally, turnkey data processing programs and time proven analysis procedures must be utilized with onboard graphics and word processing capabilities to generate the assessment document onboard in final form. The methods and techniques used by the SACLANT Undersea Research Centre (SACLANTCEN) and the Naval Research Laboratory (NRL) for rapid onboard assessment of the ambient noise are presented and discussed. [Work supported by Project 01 of SACLANTCEN and the Office of Naval Research through the management of the WISPR Filter Development and Evaluation Project by NRL.]

8:40

2aUWb3. Summary of bottom reverberation findings and model/data comparisons during three rapid environmental assessment trials. John R. Preston (ARL, Penn State Univ., P.O. Box 30, State College, PA 16804) and Dale D. Ellis (Defence Res. Establishment Atlantic, Dartmouth, NS B2Y 3Z7, Canada)

From August 1996 through February 1998 the authors participated with SACLANTCEN in three rapid environmental assessment (REA) trials, including experiments for bottom reverberation. Eight sites were visited: three sites south of Sicily, three sites in the Ionian Sea, and two sites in the Atlantic near the Straits of Gibraltar. SUS charges were used as sources. The receivers were a nested horizontal array with 128 elements spaced at 0.5, 1, and 2 m and a second horizontal array with 32 elements spaced at 0.18 m. Sets of nearly monostatic recordings were analyzed in frequency bands from 80 to 4000 Hz. Polar plots of the beam time series were superimposed on bathymetric charts, revealing a number of scattering features not on the charts. The results illustrate the use of directional reverberation measurements as a useful remote-sensing tool. Another objective of the reverberation experiments was to quickly invert for estimates of scattering and geo-acoustic parameters that can be used in a wider variety of conditions. The horizontal array data were compared with the generic sonar model (GSM) predictions for selected cases. A summary of the model parameters found at the eight sites is presented. [Work partially supported by ONR.]

9:00

2aUWb4. Shallow-water REA using autonomous ocean sampling networks. Henrik Schmidt, James G. Bellingham (MIT, Cambridge, MA 02139), and Allan Robinson (Harvard Univ., Cambridge, MA 02138)

Environmental management and naval operations in coastal waters are severely limited by a lack of oceanographic predictive capability associated with the strong spatial gradients and temporal variability inherent to such environments. A key to improving the predictive capability is a measurement system which can provide data in close to real time for assimilation into oceanographic circulation models. In that regard, the Autonomous Ocean Sampling Network (AOSN) combines small, autonomous underwater vehicles (AUV) with an underwater communication and navigation network to provide an ocean measurement system with real-time data access and adaptive sampling capabilities. The acoustic communication capability of the AOSN allows for feedback to the sensor platforms of uncertainties of the field estimates, information which can then be used to redistribute the AOSN resources optimally. The development of a new observation and prediction capability combining the AOSN with efficient coastal circulation models is the objective of an ongoing multidisciplinary research effort, but the feasibility has already been demonstrated through a series of field deployments. The results of these experiments are reviewed, and the potential for this new rapid environmental assessment capability for littoral environments is discussed.

9:20

2aUWb5. Rapid assessment of bottom backscattering. Tuncay Akal and Anthony P. Lyons (SACLANT Undersea Res. Ctr., Viale San Bartolomeo 400, 19138 La Spezia, Italy)

There is a strong need to obtain information about the expected acoustic reverberation environment that will be encountered in various shallow-water sites to aid in planning and evaluating the effectiveness of operational systems. A new technique is being developed at the SACLANT Undersea Research Centre to quickly sense the mean reverberation levels of a shallow-water area. A prototype device and analysis algorithms have been developed and used as part of rapid response operations. The system transmits and receives acoustic signals from an 80-kHz transducer and simultaneously calculates the quantitative acoustic response of the seafloor. The reverberation measurements made so far have concentrated on mapping the mean seafloor scattering level (backscattering strength) and amplitude statistics over an area for various grazing angle regimes. Differences in scattering strength between high and low reverberation zones within an operational area were significant, with differences in mean level reaching 10–12 dB. Additionally, the reverberation measurements were compared with other techniques to verify relevant bottom-type classification. The experimental technique and data obtained from different areas are presented.

9:40

2aUWb6. *In-situ* update of geoparameter databases. Charles Holland, John Osler, Edward McDonald, and Carlo Ferla (SACLANT Undersea Res. Ctr., 19138 La Spezia, Italy, holland@saclantc.nato.int)

Low- and mid-frequency system performance is often controlled and degraded by bottom interaction, especially in littoral regions. However, performance prediction models generally give unreliable estimates of bottom interaction. The poor estimates are most often due to the databases that drive the models rather than the model physics. In this study a new approach is taken in rapid environmental assessment for overcoming this problem. The concept is to use *in-situ* propagation data to extract geoacoustic information about the bottom which is then used to update the bottom database. An analogous approach has long been employed for the water column, where *in-situ* bathythermograph (BT) data are used to update historical databases. While techniques for screening/merging BT data are now under development, there are no comparable techniques for treating bottom geoacoustic data. In this paper, a high-level methodology for updating bottom databases with *in-situ* measurements is outlined. The methodology includes a series of critical questions sequenced to lead to decisions about the robustness of the historical databases in a given region and the potential for database update. Results of the methodology, i.e., the *in-situ* measurements, modeling, and resulting bottom geoparameter database updates, from several littoral areas, will be shown.

10:00–10:20 Break

Contributed Papers

10:20

2aUWb7. Preliminary results from at-sea tests of the Autonomous Buoyed Environmental Sensor System (ABES). J. Mark Stevenson (Acoust. Branch, Space and Naval Warfare Systems Ctr., San Diego, CA) and John L. Newton (Ocean Sensors, Inc., San Diego, CA)

ABES is an autonomous oceanographic measurement system which provides relatively dense spatial and temporal sampling of the highly variable shallow-water ocean environment. Compared to more traditional sampling methods, ABES is low cost; albeit providing slightly lower measurement accuracy and resolution. ABES is not intended to replace existing high-resolution oceanographic instrumentation, but fill the niche for a low-cost, lower-resolution system that would provide higher spatial sampling. The instrument is a sensor string connected to a cylindrical electronics canister. The prototype sensor string contains one electromagnetic current meter, three tilt sensors, three magnetoresistive compasses, and ten conductivity, temperature, and depth sensors. These sensors are distributed along a 40-m cable. A system controller, GPS receiver, and spread-spectrum radio are housed in the 1-m-long electronics canister. Together, these components weigh 10 kg in air and occupy a volume of 5 l. Data collected during three at-sea tests in 1998 and compared to traditional CTD measurements suggest that ABES can effectively define the temporal and spatial characteristics of the shallow-water environment. [Work supported by ONR 321-SS and 322-PO.]

10:40

2aUWb8. Estimation of modal eigenvalues from an arbitrary distribution of receivers in a planar array. Subramaniam D. Rajan (Sci. Solutions, Inc., 18 Clinton Dr., Hollis, NH 03049)

Acoustic propagation in shallow-water areas is strongly influenced by the acoustic properties of the sediment layers. Many approaches have been proposed for obtaining the acoustic properties of the sediment layers. A simple and powerful approach has been the inversion algorithms based on modal eigenvalues [Rajan *et al.*, J. Acoust. Soc. Am. **82**, 998–1017 (1987)]. The performance of this approach has been demonstrated in field

experiments. In these field experiments, the data were obtained on a linear synthetic aperture horizontal array. In recent years there has been an effort to extend the procedure to cover wider areas so that the range-dependent properties of the sediment can be determined. A means of achieving this objective is to collect the acoustic data on a planar array of receivers from which the range-dependent properties of the sediment can be obtained. Schemes for extracting modal eigenvalues of the propagating modes from data acquired on a curvilinear track with nonuniform grid spacing will be presented and the performance of the schemes evaluated using synthetic and field data.

11:00

2aUWb9. Bottom reflection phase inversion using modal dispersion curves. B. T. Cox and P. Joseph (Inst. of Sound and Vib. Res., Univ. of Southampton, Southampton SO17 1BJ, UK)

A technique to obtain an estimate of the seabed reflection coefficient phase from modal dispersion curves is presented. The technique is demonstrated on experimental data with a frequency range of 4 to 100 kHz in a 10-cm-deep water waveguide. Thirteen modal dispersion curves, defined as the pressure amplitude as a function of frequency and horizontal wave number, were obtained by measuring the acoustic pressure as a function of range and performing a Hankel transform. Initial attempts have produced estimates of the phase that are in close agreement with an independent estimate obtained by measuring the seabed wave speeds and density. [Work sponsored by EPSRC and DERA (Winfrith).]

11:20

2aUWb10. Extracting sea-bottom information from reverberation data. Dale D. Ellis (Defence Res. Establishment Atlantic, P.O. Box 1012, Dartmouth, NS B2Y 3Z7, Canada, ellis@drea.dnd.ca) and John R. Preston (The Pennsylvania State Univ., State College, PA 16804)

Reverberation measurements contain information about both the scattering and propagation effects. This paper will discuss our efforts to extract bottom loss and bottom scattering from reverberation data, including at-sea results obtained during three recent Rapid Environmental Assessment (REA) trials with the SACLANT Undersea Research Centre. There is often a strong interrelationship between the bottom loss and scattering, and attempts to deal with the uniqueness of the extracted parameters are discussed. Earlier attempts using another simplified, but automated, inverse scheme indicated very good agreement with independently measured bottom loss. In the recent REA trials the initial bottom loss was obtained using some *a priori* geologic information for the experiment area. Then the bottom parameters were manually adjusted to obtain a good fit to the data from several nearby locations and array headings. The best fits were obtained by first adjusting the bottom loss to fit the rate of decay, and then adjusting the strength of the Lambert coefficient to fit the level.

11:40

2aUWb11. Estimation of the channel scattering function. Steven Kay (Dept. of Elec. Eng., Univ. of Rhode Island, Kingston, RI 02881, kay@ele.uri.edu) and S. Bradford Doyle (Naval Undersea Warfare Ctr. Div., Newport, RI 02841)

The estimation of the range-Doppler scattering function for an arbitrarily spread (underspread or overspread) channel is addressed. Conventional methods typically require collection of reverberation data from many pings over time to characterize the channel accurately. A new method is proposed based on a minimum mean-square error (MMSE) estimator of a single realization of the channel's time-varying frequency response. Next, a two-dimensional autoregressive spectral estimation technique is used as a scattering function estimator. This approach does not suffer from the usual convolutional smoothing with the signal ambiguity function encountered with Fourier-based methods. The method is compared to traditional methods through simulation. Insight into signal design based on this new method is also provided. [Work supported by NUWC Division, Newport.]

Posters from various technical sessions remain on display in the Poster Gallery.

Posters from sessions which contain both lecture and poster presentations will be attended by the authors as listed below.

.

2:00–4:00

1pNSa12	Mirowska, Marianna	Assessment of low frequency noise in dwellings. New Polish recommendations
2aPAb13	Robsman, Vadim A.	Nonlinear acoustics testing of defect for evaluation of risk of insurance of the therman electric power stations
2aPAb14	Robsman, Vadim A.	Experience in nonlinear wave testing of constructions inside the earthquake area
2aPAb15	Hutchins, D. A.	Experiments in solids using air-coupled ultrasound
3aNSb12	Murphy, William J.	Four protectors in search of a rating system
3aNSb13	Zannin, Paulo H. T.	Effects of cup, cushion, headband force, and foam lining on the attenuation of earmuffs

Also, the following poster sessions are scheduled:
Poster Session 2pSCb
Poster Session 2pSPb

Session 2pAAa

Architectural Acoustics: Worship and Theatre Spaces

Emmanuel G. Tzekakis, Cochair
Department of Architecture, Aristotle University of Thessaloniki, 540 06, Thessaloniki, Greece

Daniel E. Commins, Cochair
Commins Acoustics Workshop, 15 rue Laurence Savart, F-75020 Paris, France

Chair's Introduction—1:55

Contributed Papers

2:00

2pAAa1. The acoustical design of a new open air theater in Thessaloniki, Greece. Emmanuel G. Tzekakis (Dept. of Architecture, Aristotle Univ. of Thessaloniki, 540 06, Thessaloniki, Greece) and Gottfried Schubert (Consultant in Acoust., Athens, Greece, emil49@compulink.gr)

The international experience in the design of open air theaters is limited. Most new theaters are used exclusively with electroacoustic installations, because they are very large or in very noisy surroundings. As a result, no new architectural or acoustical breakthroughs are available. The new theater reported in this paper is a 5000 seat open air theater, with a shape derived from the ancient Greek prototypes, optimized for best listening conditions without electroacoustic installations. The background noise level reduction and the geometry of the theater were the main concerns of the acoustical design. Modeling tools were used to predict the final acoustical conditions. Measurements made in the almost ready theater indicate that using known and reliable prototypes in a careful way results in high quality acoustical conditions.

2:20

2pAAa2. The ancient Greek theater and its acoustical quality for contemporary performances. Gottfried Schubert (Consultant in Acoust., 22 Apolonos Str., 153 44, Kantza Pallini, Athens, Greece, emil49@compulink.gr) and Emmanuel G. Tzekakis (Aristotle Univ. of Thessaloniki, 540 06, Thessaloniki, Greece)

The acoustical quality of the ancient Greek theater is often described as a phenomenon with mythical dimensions. According to recent experiences with contemporary theater performances at famous historical ancient Greek theaters, the acoustical situation is much more simple and even more problematic than described. To understand the real situation, it is helpful to review the evolution of the ancient theater in terms of construction as well as the theater play as a religious and cultural event. The Dionysus Theater of Athens is one of the most important examples to base this review on. Modern theater festivals also take place in the ancient theater of Epidaurus, which compared to many others, is in a remarkably good condition especially after its restoration. Nevertheless, the scene building is missing and this leads to several acoustical problems. The Epidaurus Theatre is used as an example for the description of the experiences with contemporary performances in ancient Greek theaters.

Posters from various technical sessions remain on display in the Poster Gallery.

Posters from sessions which contain both lecture and poster presentations will be attended by the authors as listed below.

.

2:00–4:00

1pNSa12	Mirowska, Marianna	Assessment of low frequency noise in dwellings. New Polish recommendations
2aPAb13	Robsman, Vadim A.	Nonlinear acoustics testing of defect for evaluation of risk of insurance of the therman electric power stations
2aPAb14	Robsman, Vadim A.	Experience in nonlinear wave testing of constructions inside the earthquake area
2aPAb15	Hutchins, D. A.	Experiments in solids using air-coupled ultrasound
3aNSb12	Murphy, William J.	Four protectors in search of a rating system
3aNSb13	Zannin, Paulo H. T.	Effects of cup, cushion, headband force, and foam lining on the attenuation of earmuffs

Also, the following poster sessions are scheduled:
Poster Session 2pSCb
Poster Session 2pSPb

Session 2pAAa

Architectural Acoustics: Worship and Theatre Spaces

Emmanuel G. Tzekakis, Cochair
Department of Architecture, Aristotle University of Thessaloniki, 540 06, Thessaloniki, Greece

Daniel E. Commins, Cochair
Commins Acoustics Workshop, 15 rue Laurence Savart, F-75020 Paris, France

Chair's Introduction—1:55

Contributed Papers

2:00

2pAAa1. The acoustical design of a new open air theater in Thessaloniki, Greece. Emmanuel G. Tzekakis (Dept. of Architecture, Aristotle Univ. of Thessaloniki, 540 06, Thessaloniki, Greece) and Gottfried Schubert (Consultant in Acoust., Athens, Greece, emil49@compulink.gr)

The international experience in the design of open air theaters is limited. Most new theaters are used exclusively with electroacoustic installations, because they are very large or in very noisy surroundings. As a result, no new architectural or acoustical breakthroughs are available. The new theater reported in this paper is a 5000 seat open air theater, with a shape derived from the ancient Greek prototypes, optimized for best listening conditions without electroacoustic installations. The background noise level reduction and the geometry of the theater were the main concerns of the acoustical design. Modeling tools were used to predict the final acoustical conditions. Measurements made in the almost ready theater indicate that using known and reliable prototypes in a careful way results in high quality acoustical conditions.

2:20

2pAAa2. The ancient Greek theater and its acoustical quality for contemporary performances. Gottfried Schubert (Consultant in Acoust., 22 Apolonos Str., 153 44, Kantza Pallini, Athens, Greece, emil49@compulink.gr) and Emmanuel G. Tzekakis (Aristotle Univ. of Thessaloniki, 540 06, Thessaloniki, Greece)

The acoustical quality of the ancient Greek theater is often described as a phenomenon with mythical dimensions. According to recent experiences with contemporary theater performances at famous historical ancient Greek theaters, the acoustical situation is much more simple and even more problematic than described. To understand the real situation, it is helpful to review the evolution of the ancient theater in terms of construction as well as the theater play as a religious and cultural event. The Dionysus Theater of Athens is one of the most important examples to base this review on. Modern theater festivals also take place in the ancient theater of Epidaurus, which compared to many others, is in a remarkably good condition especially after its restoration. Nevertheless, the scene building is missing and this leads to several acoustical problems. The Epidaurus Theatre is used as an example for the description of the experiences with contemporary performances in ancient Greek theaters.

2:40

2pAAa3. Acoustic measurement of Shakespeare's Globe Theatre, London. Russell Richardson and Bridget M. Shield (South Bank Univ., 103 Borough Rd., London SE1 0AA, UK, richarjr@sbu.ac.uk)

In the late 1960's, Sam Wanamaker initiated the reconstruction in London of the theatre built for William Shakespeare's company of players in the late 16th century. The theatre was built in the traditional manner to be as faithful to the original as surviving documentation allows, and has a circular auditorium with an open roof. The theatre was opened for performances in the summer of 1997. An acoustic survey of the theatre has been carried out. Measurements have been made of reverberation time (RT), early decay time (EDT), clarity index (C50), definition (D50), and rapid speech transmission index (RASTI) within the theatre's auditorium. Various source positions were chosen on the stage after consultation with voice coaches and actors at the theatre, and receiver positions were chosen to provide uniform coverage of all the major audience areas. The results of these measurements indicate that, despite the theatre's open-air construction, the amount of early energy provided to most audience areas results in reasonable levels of speech intelligibility, although achieving an adequate speech sound level is more of a problem. This is clearly exacerbated by the theatre's open-air design, and its position in central London under the main flight path to London's Heathrow Airport. The reverberant characteristics of the auditorium are generally within acceptable limits for modern theatres.

3:00

2pAAa4. Acoustical evaluation of auditoria in Taiwan built before 1975. Weihwa Chiang and Zenjang Juang (Taiwan Univ. of Sci. and Tech., 43, Section 4, Keelung Rd., Taipei City 106, Taiwan, WHCH@mail.ntust.edu.tw)

Investigations were conducted regarding the acoustical characteristics of existing auditoria built before 1975. Discussions of the historical evolution since Japanese occupation were followed by architectural and acoustical analysis of 21 cases. Although many auditoria built during Japanese occupation were not designed for musical performances, they are more reverberant but smaller than the ones built after World War II. However, 62% of the selected cases were constructed with windows with 4 mm or thinner glazing on sidewalls or around the upper perimeter. Analysis of two auditoria were made regarding the performances of room acoustics, background noise control, and sound system. The room acoustics in both auditoria are suitable for chamber music but are too dry and too loud for orchestra music. Average background noises reach NC40 with AC off and NC50 with AC on. Both sound systems could not give correct directions of sound images, although they provide acceptable output level (96 dB SPL) and speech intangibility (STI 0.57) in the 2000-Hz band. With growing concerns about energy preservation in Taiwan, the current study could provide useful information for renovating or remodeling an existing auditorium. [Work supported by the National Science Foundation of Taiwan.]

3:20

2pAAa5. Restoration by means of sound reinforcement of a church of the Renaissance. Jose Romero-Faus, Alicia Gimenez-Perez, Albert Marin-Sanchis, and Antonio Sanchis-Sabater (Appl. Phys. Dept., High Tech. School of Industrial Eng., Polithechnic Univ. of Valencia, P.O. Box 22012, 46080 Valencia, Spain, agimenez@fis.upv.es)

This work summarizes the project of the acoustic restoration of a Church of the Renaissance, XV Century, after the architectural restoration carried out in it throughout the last 10 years, with volume, 9000 m^3; total surface, 3000 m^2; room constant, $R=1110$ m^2; reverberation time to 500 Hz, 1.8 s; inteligibility from the altar to the last banks, 0.34; loss of sound level, 7 dB. Since the acoustic response for the music and the song was good, the one which should improve above all was the intelligibility. Specifically, this project was undertaken to provide a uniform sound coverage to all the hearing zone, an adequate sound level, the nonexistence of perceptible late reflections, and the adequate intelligibility characteristic of the room. Bearing in mind, furthermore, that the acoustics of the enclosure could not be improved by means of acoustic materials, the adopted solution was to use an electroacoustic system, putting a centralized cluster of loudspeakers over the altar, to 8 m of height, that assured the sufficient sound reinforcement. This solution improved the intelligibility, which became 0.53, as well as the coverage field. These results have been validated by means of a ray tracing program.

3:40

2pAAa6. Acoustical problems in mosques: A case study on the three mosques in Istanbul. Zerhan Karabiber (Yildiz Tech. Univ., Faculty of Architecture, Dept. of Bldg. Phys., Besiktas, 80750, Istanbul, Turkey, karabi@yildiz.edu.tr)

Although worshiping places of different great religions, such as churches, synagogues, and mosques, have in general similar acoustical requirements, they still have authentic needs. In acoustical literature, there are many works on church acoustics whereas almost none on mosque acoustics. This fact is one of the main reasons for the neglect of acoustics in the newly built mosques. In mosque designs, where it is very difficult to avoid classical forms, traditional mosque types are repeated rather frequently. However, in this repetition, acoustics is often neglected and the result is acoustically poor mosques. The aim of this work is the acoustical assessment of ancient mosques for the development of ''acoustical criteria in mosque design.'' In this paper, three mosques, built in the Ottoman Empire period, in Istanbul, are evaluated from an acoustical point of view. Effects of the changes on the noise climate are shown and room acoustics is examined. Attempts were made to constitute basic principles of acoustical comfort conditions in mosques.

Contributed Posters

These posters will be on display in the Poster Gallery from Monday to Wednesday, 15–17 March. Authors will be at their posters from 10:00 a.m. to 12:00 noon on Wednesday, 17 March.

2pAAa7. Room acoustical measurements and architectural documentation of auditoriums in Berlin considering the speech intelligibility in dependence of spatial distribution of sound fields. Peter S. Krämer (GEBRA Gesellschaft für Bau- und Raumakustik mbH, Agricolastr. 26, D-10555 Berlin, Germany)

Measurements of spatial room acoustical impulse responses were performed to provide a database for the examination of speech intelligibility (SI) in real rooms. As is well known, the spatial distribution of reflections can influence the SI, especially in reverberant rooms. Nevertheless, the qualitative and quantitative dependences are mostly unknown. Room acoustical measurements thus were realized using a dodecahedron loudspeaker for measuring reverberation time, an interference-free loudspeaker with omnidirectional characteristic for recording impulse responses, and an artificial speaker and a dummy head microphone for measurements of SI criteria and recording of logatom syllables. A specially constructed spaced four-capsule microphone in tetrahedron arrangement was used for measuring also. The four-microphone analysis technique can recognize intensity and direction of the early reflections [Odjija and Krämer (1999)]. Results of the measurements will be documented and published on a CD-ROM, together with the architectural data of the auditoriums. First results of the room acoustical measurements are presented. Prior studies have shown that reproducing the measured binaural cues with headphones does

not influence the SI significntly. Subjective measurements of SI and analysis of spatial dependences will be performed in a second stage of the project.

2pAAa8. Simulated acoustic field in mudejar-gothic churches. Miguel Galindo, Teofilo Zamarreno, Sara Giron (Dept. Fisica Aplicada, Universidad de Sevilla, Spain, teofilo@cica.es), Juan J. Sendra, and Jaime Navarro (Dept. Construcciones Arquitectonicas, Universidad de Sevilla, Spain)

The most significant acoustic parameters in a set of mudejar-gothic churches were measured (all the churches were located in the city of Seville). From the analysis of these data important conclusions were otained about the behavior of the reverberant field versus source–receiver distance [J. Sendra *et al.*, *Computational Acoustics and its Environmental Applications—II* (Computation on Mechanics Publications, Southampton, 1997), pp. 139–148] from Barron's revised theory [Barron *et al.*, J. Acoust. Soc. Am. **84**, 618–628 (1988)] and the relations between several acoustics quality descriptors: C80, D50, and RASTI [Zamarreno *et al.*, Proceedings Acustica-98, Lisbon (1998)]. The three most representative churches were chosen to carry out a computer simulation with the RAYNOISE software. Absorption coefficient values used in the model have been adjusted using measured reverberation time data, and thus the results were obtained for the other acoustic parameters in the different octave bands. It was proven that, in general, simulated values are coherent with the experimental results. Moreover, according to other authors [L. Marshall, J. Acoust. Soc. Am. **94**, 2251–2261 (1994)], it has also been proven that C80 and D50 indices need no spectral analysis and their broadband values and their averages in significant bands (500–2000 Hz) are indifferent.

TUESDAY AFTERNOON, 16 MARCH 1999 ROOM H105, 4:15 TO 6:20 P.M.

Session 2pAAb

2p TUE. PM

Architectural Acoustics: Perceptual Aspects in Rooms

Hideki Tachibana, Cochair
Institute of Industrial Science, Tokyo University, Roppongi 7-22-1, Minato-ku, Tokyo 106-8558, Japan

Roberto Pompoli, Cochair
Engineering Department, University of Ferrara, Via G. Saragat 1, 44100 Ferrara, Italy

Chair's Introduction—4:15

Invited Paper

4:20

2pAAb1. An evaluation of scattered reflections in sound fields. Y. Suzumura, Y. Ando (Grad. School of Sci. and Technol., Kobe Univ. Rokkodai, Nada, Kobe 657-8501 Japan, 966d852n@kobe-u.ac.jp), M. Oowaki (Kumagai-Gumi Tech. Res. Labs., Tsukuba, Japan), Toshiki Iizuka, and I. Yamamoto (Arch. & Env. Res. Ltd., Kobe, Japan)

Although a large number of studies have been made on a theory of scattering, no studies have been attempted to evaluate the scattered sound fields in a concert hall. This paper will show an evaluation method of sound fields that involve scattered reflection by a circular-columns array installed in front of both side walls. Measurements were performed by use of a 1/10 scale model of the concert hall. Here, scattered sound fields are evaluated by four acoustic factors (SPL, DT1, Tsub; IACC, and in addition WIACC and tauIACC). It is found that the IACC and Dt1 of the sound fields of the concert hall are improved with use of the circular columns array.

Contributed Papers

4:40

2pAAb2. Listener perception of spatial impression and auditory source width and their influence on overall impression in real rooms and headphone studies. Martin A. Gold (Dept. of Architecture, Univ. of Florida, Gainesville, FL 32611-5702)

Comparisons of listener evaluations of music in real room situations and in headphone listening studies were used to assess the contribution of reverberance, loudness, auditory source width (ASW), and spatial impression on the overall impression of music listening and to evaluate their role as independent acoustic variables. Room studies were conducted using large numbers of average listeners at designated locations with a live sound source. Headphone listening studies were conducted using anechoic recordings with simulated acoustic environments (early reflections and reverberation) having different configurations of early and late sound energy. Directional components of the early and late energy were independently modeled as part of the experiment (Gold, 1994). Regression models were conducted to assess the interrelationship of independent variables on listener overall impression. In many cases, independent elements could be identified as contributing to overall impression; however, these elements were not the same in each case. For example, in cases where reverberance is not present, loudness and ASW become greater contributors. In addition, an attempt was made to find out if there is a listener distinction between ASW (a widening of the source sound) and spatial impression (the quality of being immersed in the sound).

5:00

2pAAb3. Controls of a modulated delay time of reflection enhancing subjective preference. Junko Atagi, Yoichi Ando (Grad. School of Sci. and Technol., Kobe Univ., Rokkodai, Nada, Kobe, 657-8501 Japan, 968d803n@kobe-u.ac.jp), and Yasutaka Ueda (Hazama Corp., Karima, Tsukuba, 305-0822 Japan)

Previously, the most preferred delay time of reflection for time-invariant sound fields corresponds to the effective duration of the autocorrelation function (τ_e) of source signals [Ando, *Concert Hall Acoustics* (Springer-Verlag, New York, 1985)]. However, the SPL fluctuation in a real room is fluctuated and the model of such a time-variant system is proposed by the direct sound and the varying delay time of reflection [Ueda and Ando, J. Acoust. Soc. Am. **102**, 2771–2775 (1997)]. To realize more excellent sound fields than time-invariant sound fields, a method of controlling a modulation of the delay time of reflection is discussed. Experiments are performed on the modulation methods to enhance subjective preference in a sound field. The following methods are examined to control the delay time of reflection in the experiment: (1) sinusoidally modulated delay time, (2) random modulated delay time, (3) delay time corresponding to the change of the running τ_e of the source signal, and (4) fixed delay time of reflection at the minimum value of the running τ_es.

5:20

2pAAb4. Effect of closely spaced high-frequency reflections on perception of music. Paul T. Calamia and Scott D. Pfeiffer (Kirkegaard & Assoc., 4910 Main St., Downers Grove, IL 60515)

Experience in three concert halls with complaints about harsh high-frequency response led to the investigation of acoustic effects in these halls. The use of wall treatments intended to be acoustically diffusive or transparent, or intended to make a fan-plan more similar to a shoe-box hall, resulted in repetitive, closely spaced, high-frequency reflections. Effects have been measured in place and in laboratory simulations. Examples of the wall treatments and corresponding measurements will be discussed, as will recommendations for achieving a more desirable frequency response.

5:40

2pAAb5. Influence of sensory interactions between vision and audition on the perceptual characterization of room acoustics. Chrysanthy Nathanail (Laboratoire d'Acoustique Musicale, Université Paris VI, Tour 66, Case 161, 4, place Jussieu, 75252, Paris Cedex 05, France), Catherine Lavandier (Université Cergy-Pontoise), Jean-Dominique Polack (Université Paris VI, France), and Olivier Warusfel (Ircam, Paris 75004, France)

Broad evidence on sensory interactions between vision and audition suggests that visual information available to listeners-spectators in concert halls is likely to interfere in the evaluation process of the acoustical quality. The influence of the stage visual distance on the auditory apparent distance was studied in four magnitude estimation paradigms. Sound stimuli providing successive impressions of auditory distance were generated by a virtual room acoustics processor (''Spatialisateur'') in binaural format and presented separately or coupled with 3-D concert hall pictures. Subjects were asked to judge the auditory distance. Pilot experiments I and II obtain a first qualitative observation of the effects and study a progressive change observed at the responses. Main experiments III and IV adopt two different procedures of stimuli presentation and improved sound reproduction and attempt a first objective evaluation of the results. The analysis of variance performed on the responses reveals a small offset-type influence of the visual stimuli on the auditory distance: i.e., the same auditory stimuli appear more distant when presented with distant stage views. In addition, differences between *unimodal* (auditory stimuli alone) and *bimodal* tests suggest that vision enhances the ''depth'' of the auditory field and provides a spatial frame of reference for auditory judgments.

6:00

2pAAb6. Perception of sweep sounds caused by reflective pulse train in a rectangular reverberation room. Kenji Kiyohara, Ken'ichi Furuya, Masashi Tanaka, and Yutaka Kaneda (NTT Human Interface Labs., 3-9-11, Midori-cho, Musashino-shi, Tokyo, 180-8585 Japan)

Elevated frequency sweep sounds were perceived when a pulsive sound (a handclap) was generated in a rectangular reverberation room. The mechanism of this phenomenon was investigated. First, reflection of the pulsive sound (a pulse train) was simulated using the image method. The sweep sounds were also perceived in the simulated pulse train. It was assumed that the pulse train, whose intervals decreased inversely in proportion to time, caused the sweep sound sensation. The existence of such a pulse train was confirmed in the simulated pulse train. Then, this phenomenon was investigated theoretically based on algebraic number theory. A pulse train whose intervals decrease inversely proportional to time becomes a pulse train of equal intervals when it is represented on the power of time (t^2) axis. On the other hand, considering a cubic room for simplicity, reflective pulse sounds arrive at $(l^2+m^2+n^2)L^2/c^2$ on the t^2 axis (l, m, n: positive integer, L: room dimension, c: sound velocity). The number theory proves that $(l^2+m^2+n^2)$ covers almost all integers. In other words, reflective pulsive sounds arrive with equal time intervals of L^2/c^2 on the t^2 axis. This algebraic regularity causes a listener to experience the sweep sound sensation.

Contributed Posters

These posters will be on display in the Poster Gallery from Monday through Wednesday, 15–17 March. Authors will be at their posters from 10:00 a.m. to 12:00 noon on Wednesday, 17 March.

2pAAb7. Appropriate bandwidth and integration time for measurements of the degree of interaural cross correlation as a measure of apparent source width in concert halls. Masayuki Morimoto (Environ. Acoust. Lab., Faculty of Eng., Kobe Univ., Nada, Kobe, 657-8501 Japan, mrmt@kobe-u.ac.jp) and Kazuhiro Iida (Matsushita Comm. Ind. Co., Ltd., Saedo, Tsuzuki, Yokohama, 224-8539 Japan)

ISO 3382 Annex suggests using the degree of interaural cross correlation (ICC) as a measure of apparent source width (ASW), while mentioning that the choice of bandwidth for test signals and the integration time are uncertain. Needless to say, what is important for a physical measure is that it is well correlated with the subjective effect, in this case ASW. This paper describes psychological experiments to investigate the appropriate bandwidth for test signals and the integration time for measuring ICC to evaluate ASW. The experimental results indicate that (1) measurements of ICC with 1/3-oct bands are preferred for evaluating ASW, whereas the use of wide band and 1/1-oct band signals as described in the ISO standard are not, and (2) measurement of ICC for all reflections including both the early reflections and later reverberant sound is most suitable for evaluating ASW, rather than the early reflections alone.

2pAAb8. The interrelation between the music sound clarity index C_{80} and the subjective evaluation of the hall acoustics. Vytautas J. Stauskis (Vilnius Gediminas Tech. Univ., Sauletekio al. 11, LT 2040, Vilnius, Lithuania)

It has been established by acoustic investigations in actual halls that the clarity index C_{80} may have optimum recommended values, while subjectively the sounding of music in those halls may be evaluated as poor. Three halls were selected for investigations: (1) a church with the volume of 27 000 m^3, (2) Vilnius Opera Theatre with the volume of 8700 m^3, and (c) a concert hall with the volume of 4900 m^3. In hall (1), the values of C_{80} are from -1.4 to -3.9 dB. The reverberation time is 6.6 s. According to subjective evaluations, the acoustics of this hall is suitable neither for classical nor romantic music. In hall (2), the values of C_{80} vary from -1.1 to 2.4 dB in all rows in the stalls. The reverberation time is very short and varies between 1.2 s. The sound of an orchestra in the hall is evaluated as very poor. In hall (3), the values of C_{80} are within the range of -1.0 to 2.8 dB and the reverberation time is 1.55 s. The sound of chamber music is evaluated as good, while that of symphony music is evaluated as satisfactory. This shows that this subjective indicator may not provide full characterization of the hall acoustics.

TUESDAY AFTERNOON, 16 MARCH 1999 ROOM MA001, 2:00 TO 5:40 P.M.

Session 2pAB

Animal Bioacoustics: Physics of Animal Bioacoustics II

Whitlow W. L. Au, Cochair
Hawaii Institute of Marine Biology, P.O. Box 1106, Kailua, Hawaii 96734, USA

Roland Aubauer, Cochair
Institute of Zoology II, University of Erlangen, Staudtstrasse 5, D-91058 Erlangen, Germany

Invited Paper

2:00

2pAB1. Biophysics of peripheral auditory systems in three teleost fish. Mardi C. Hastings (Dept. of Mech. Eng., Ohio State Univ., 206 W. 18th Ave., Columbus, OH 43210)

Many types of auditory systems are found in the more than 20 000 different species of teleost fish. These unique sensors may detect extremely small acoustic particle velocities as well as acoustic pressure. Auditory bandwidths may range from very low frequencies to ultrasonic regimes depending on the species. Several experimental studies conducted over the last 15 years have yielded data which indicate that auditory sensitivity, bandwidth, and source localization are primarily controlled by the biomechanics of the periphery. In these studies *in vivo* displacements of peripheral auditory organs were measured noninvasively in response to tones emitted from an underwater speaker. The measurements were then correlated with mathematical models formulated from the basic physics of each system. Results are presented for three different species, goldfish (*Carassius auratus*), oscars (*Astronotus ocellatus*), and shad (*Alosa sapidissima*), and compared with auditory capabilities determined in behavioral and physiological studies reported in the literature.

Contributed Papers

2:20

2pAB2. Development of a software package calculating zones of influence on marine mammals around industrial noise sources. Christine Erbe and David M. Farmer (IOS—Ocean Acoust., 9860 W. Saanich Rd., Sidney, BC V8L 4B2, Canada, erbec@dfo-mpo.gc.ca)

A software package is presented which estimates zones of interference around underwater noise sources affecting marine mammals. An ocean sound propagation model based on ray theory computes the spreading of complex underwater sound such as broadband animal vocalizations and man-made noise. On a grid of receiver locations (representing the affected marine mammal), the received signal and noise sound spectra are compared. Given a species-specific audiogram, the software package plots zones of audibility around the noise source. Given species-specific vocalizations, zones of masking are plotted based on results obtained during an earlier study which measured masked hearing thresholds of a beluga vocalization in icebreaker noise with a trained beluga whale. Tools developed during this study (such as an artificial neural network and critical band methods) are incorporated in the software package and can be used to predict zones of masking for industrial noise other than the types directly measured with the beluga. Zones of discomfort, injury, and hearing loss could be plotted if thresholds were known or using current estimates. The software package is applicable to a variety of ocean environments requiring location-specific physical oceanography input data.

2:40

2pAB3. Whistle signals of sturgeons and cetaceans. Larissa K. Tolstoganova (17, V. Krasnoselskaya, Moscow 107140, Russia, tesler@vniro.ecosrv.fipc.ru)

There are a lot of recordings of acoustic signals emitted by cetaceans and a few studies on sturgeon sounds. The signal analysis showed that all heard species of sturgeons and likewise cetaceans produce whistles and impulse signals consisting of broadband pulses. Sturgeon whistles may be separated into tone whistle with line spectrum, narrow-band whistle with narrow-band spectrum, FM whistle with narrow-band or broadband summary spectrum, and line or narrow-band instantaneous spectra. Acipenser stellatus, for example, emit tone and narrow-band signals consisting of one to seven components. The first component frequency is 2 to 3.5 kHz. The highest one is up to 16 kHz. Acipenser baeri and Acipenser guldenstadti emit all signal types. The frequency spectrum is up to 18 kHz. More often Acipenser Baeri produce FM whistles having one to five components

which frequency varies directly as the square or cube of time. The minimal frequency of the first component is 1.0–3.5 kHz. The frequency range of the component is up to 2.5 kHz. Acipenser guldenstadti more often produce FM whistles having one to three components, which frequency varies inversely as the square root of time. The frequency range of the component is up to 7 kHz.

3:00

2pAB4. Validation of a system for synthesizing distant signatures of underwater explosions for sea mammal hearing studies. Joseph A. Clark (CDNSWC, Code 734, Bethesda, MD 20084 and COMB, Ste. 236, Columbus Ctr., 701 E. Pratt St., Baltimore, MD 21202), Jane A. Young (CDNSWC, Bethesda, MD 20084 and COMB, Baltimore, MD 21202), and Joel B. Gaspin (IHNSWC, Indian Head, MD 20640)

A system for synthesizing distant signatures of underwater explosions was described in an earlier talk [J. A. Clark and Jane A. Young, J. Acoust. Soc. Am. **102**, 3177(A) (1997)]. The system is now being used to study expected temporary threshold shifts (TTS) of sea mammals near underwater explosive test ranges in the Baltic sea. The results of these studies will be used to define safe range criteria for mammal hearing which will then be incorporated into the methodology for assessing potential damage to marine mammal hearing. Typical underwater explosion signals (time histories) were selected from an extensive set of blast signals computed for a variety of charge weights, explosion depths, ranges from the blast, and water conditions specified by sound-speed profiles and water depths. The selected signals were synthesized and measured at the location of the test mammals (bottlenose dolphins). The fidelity of the synthesized signals to the computed waveforms was determined by comparing such characteristics as peak pressures, positions of major spikes in the time histories, and one-third octave band energy spectra. Examples of typical signals used for the TTS studies and their measured characteristics will be presented.

3:20

2pAB5. Information entropy of humpback whale song. Ryuji Suzuki, John R. Buck (Dept. of Elec. and Computer Eng. and Ctr. for Marine Sci. and Tech., Univ. of Massachusetts, North Dartmouth, MA 02747), and Peter L. Tyack (Woods Hole Oceanogr. Inst., Woods Hole, MA 02543)

Many theories of nonhuman animal communication posit a first-order Markov model in which the next signal depends only on the current one. Such a model precludes a hierarchical structure to the communication signal. Information theory and signal processing provide quantitative techniques to estimate the underlying complexity of an arbitrary signal or symbol sequence. These techniques are applied to humpback whale songs and demonstrate that any first-order Markov model fails to attain the underlying bound of complexity in these songs. Humpback songs are symbolized into alphabet sequences using spectrograms and self-organizing neural nets [Walker, unpublished]. The entropy of the song sequence is measured with a first-order parametric Markov model, and with a nonparametric sliding window method [Kontoyiannis *et al.*, IEEE Trans. Info. Theory **44**, 1319–1327 (1998)]. Preliminary analyses suggest that the entropy of the first-order Markov model is significantly higher than that of the nonparametric model, meaning that any first-order Markov source cannot reasonably model humpback songs. Furthermore, it is found that the symbolized song statistics are locally but not globally stationary, implying that these songs possess a hierarchical structure. [Work supported by NSF Ocean Sciences.]

3:40

2pAB6. Ultrasound-mediated transformation of prokaryotic cells. Jane A. Young (CDNSWC, Code 725, Bethesda, MD 20084 and COMB, Ste. 236, Columbus Ctr., 701 E. Pratt St., Baltimore, MD 21202), Joseph A. Clark (CDNSWC, Bethesda, MD 20084 and COMB, Baltimore, MD 21202), and William R. Jones (Univ. of Maryland, Baltimore, MD 21202)

Ultrasound-mediated transfection of mammalian cells has been reported in the literature [Kim *et al.*, ''Ultrasound-mediated transfection of mammalian cells,'' Human Gene Therapy **7**, 1339–1346 (July 10, 1996)]. Optimum results were obtained using continuous wave insonification at a carrier frequency of MHz, peak pressures of 319–411 kPa, exposure times of 20–60 s, and ambient temperatures 23–37 °C. Cavitation was shown to be a key mechanism for the insertion of plasmid DNA into cells. Prokaryotic cells appear to present a greater challenge to ultrasound approaches because of their smaller size and stronger membranes. This talk will report results of a series of ultrasound-mediated transformation experiments on prokaryotic cells, specifically bacteria. Conditions required to obtain a lethal dose for 50% of the cells (LD50) and transformation of cells will be presented. Effects of peak pressure levels, pulse duration, quiescent time between pulses, static pressure, and number of exposures will be discussed. This work could have broad applications, from disinfection of aquacultural and agricultural systems to genetic engineering.

4:00–4:20 Break

4:20

2pAB7. On interfacing physics with electrophysiology in echolocation in bats. Daniel R. Raichel (Dept. of Mech. and Aerosp. Eng., CUNY Grad. School, City College of CUNY, New York, NY 10031, raichel@juno.com) and Mathew J. Palakal (Indiana Univ.–Purdue Univ. at Indianapolis, Indianapolis, IN 46202)

In animal echolocation, reflected signals carry far more information than is generally realized. The real, nonlinear nature of sound propagation and the sensitivity of reflected sound to the effects of the target and its environs provide a matrix M representative of both probe and reflected signals that lends itself to real-time spectral processing and formation of acoustical images. This process necessitates a sensitivity to signals at least two or more octaves beyond the fundamentals of the probe signals, combined with a high degree of resolution in the frequency, signal strength, and phase domains. The information feeds into the neurological system at the rate of dM/dt, enabling neurological processing of the high-frequency downward pulses ranging from 20 to 100 kHz used by echolocation bats as well as pure FM pulses and CF-FM combination pulses used by certain species of bats. The multi-dimensional matrix also accommodates the duration and repetition rates of these pulses which are continuously altered according to the perceptual demand during echolocation. Electrophysiological data suggests that the specialized delay-sensitive neurons that are present in various regions of the auditory pathway allow the animal to obtain fine delay acuity and target discrimination ability in cluttered environments, with nanosecond resolution.

4:40

2pAB8. Biosonar in a textured world. Rolf Müller and Roman Kuc (Intelligent Sensors Lab., Elec. Eng. Dept., Yale Univ., New Haven, CT 06520-8284, rolf@isl.eng.yale.edu)

Capabilities of bats to analyze spectral profiles have been demonstrated by several researchers. However, suggestions as to the informational content of the biologically accessible features in terms of the echo-generating process are not yet entirely convincing. Invoking a general analogy to visual color perception does not provide an operational definition of the hypothetical perceptual mechanism. The proposed mechanisms are mostly restricted to a scenario, where the spacing of two reflectors may be determined via the resulting comb-filter transfer function. The generality of this concept is curtailed by most natural surfaces constituting aggregates of multiple reflecting facets with a pronounced random component to their arrangement. Classification of natural textures is conceived to be a pivotal capability which may underly performance in several tasks probably performed by the animals, e.g., landmark identification and control of scanning movement. In order to understand how the demands of texture classification relate to the key features of biological sonar systems, the following steps are taken: Starting from a database of textures typical of bat's habitats (i.e., foliage), the implications of two paramount attributes of biological sonar systems are studied: sensor mobility and a joint time-frequency representation encoded in spike patterns.

5:00

2pAB9. Modeling the role of nonhuman vocal membranes in phonation. Hanspeter Herzel (Inst. Theor. Biol., Humboldt Univ., Invalidenstr. 43, D-10115 Berlin, Germany, h.herzel@biologie.hu-berlin.de), Patrick Mergell (Univ. Erlangen--Nuremberg, Bohlenplatz 21, D-91054 Erlangen, Germany), and Tecumseh Fitch (Harvard/MIT Speech and Hearing Sci., Cambridge, MA 02138)

Although the mammalian larynx exhibits little structural variation compared to sound-producing organs in other taxa (birds or insects), there are some morphological features which could lead to significant differences in acoustic functioning, such as air sacs and vocal membranes. The vocal membrane (or ''vocal lip'') is a thin upward extension of the vocal fold that is present in many bat and primate species. The vocal membrane was modeled as an additional geometrical element in a two-mass model of the larynx. It was found that vocal membranes of an optimal angle and length can substantially lower the subglottal pressure at which phonation is supported, thus increasing vocal efficiency, and that this effect is most pronounced at high frequencies. The implications of this finding are discussed for animals such as bats and primates which are able to produce loud, high-pitched calls. Modeling efforts such as this provide guidance for future empirical investigations of vocal membrane structure and function, can provide insight into the mechanisms of animal communication, and could potentially lead to better understanding of human clinical disorders such as sulcus vocalis.

5:20

2pAB10. Middle ear frequency characteristics of Norwegian cattle. Magne Kringlebotn (Dept. of Phys., Norwegian Univ. of Science and Technol., N-7034 Trondheim, Norway)

Preliminary results indicate that for a constant sound pressure to the tympanic membrane, the mean low-frequency asymptote value for the volume displacement in the inner ear windows of Norwegian cattle as compared to human ears is less by about 8 dB, while above about 2 kHz the volume displacement becomes increasingly larger than in the human ear. If mean amplitude responses are roughly approximated by straight lines above 1 kHz, the slope for cattle ears is about -4 dB/oct as compared to an earlier measured value of -16 dB/oct for the human ear. Mean resonance frequencies are nearly equal, both about 0.8 kHz. The phase of the windows volume displacement relative to the sound pressure at the tympanic membrane is close to zero below 0.2 kHz, and falls to about -4π at 20 kHz. Earlier phase measurements in human ears indicating a phase change of less than 2π are believed to be in error.

TUESDAY AFTERNOON, 16 MARCH 1999 ROOM H1058, 2:00 TO 6:00 P.M.

Session 2pAO

Acoustical Oceanography: Innovations in Fish and Plankton Acoustics II

Chris Feuillade, Cochair
Naval Research Laboratory, Stennis Space Center, Mississippi 39529-5004, USA

David N. MacLennan, Cochair
Marine Laboratory, P.O. Box 101, Victoria Road, Aberdeen AB11 8DB, UK

Contributed Papers

2:00

2pAO1. High-resolution target strength measurements in deep water. Egil Ona and Ingvald Svellingen (Inst. of Marine Res., P.O. Box 1870, 5024 Bergen, Norway, egil.ona@imr.no)

High-resolution target strength data can only be claimed valid in situations where it can be safely shown to be much less than one target per pulse volume. Many fish species occur in densities and at depths where this demand hardly can be met with standard, hull-mounted, survey transducers. This paper describes a new and simple method for obtaining such data with some examples of target strength and target tracking data obtained in deep water at three different cruises. The system used is the Simrad EK-500 split beam echo sounder, connected to an oil-filled ES38D, pressure-resistant transducer, on cable lengths from 400-800 m. The transducer was lowered as a probe the desired depth, often inside or close to the fish layer, with the vessel stationary, or slowly drifting. For maximizing the number of detections per fish, the echo sounder was operated at maximum pulse repetition frequency. Recordings shown are from three different species, small myctophid fishes at 200–400 m, hake at 200–400 m, and herring at 50–400 m. High-quality target strength distributions were frequently obtained in less than 1 h at a typical target strength station.

2:20

2pAO2. A summary of target strength observations on fishes from the shelf off West Africa. Ingvald Svellingen and Egil Ona (Inst. of Marine Res., P.O. Box 1870, 5024 Bergen, Norway, egil.ona@imr.no)

In many areas, and in tropical waters in particular, it may be difficult to fulfill the resolution criteria for high-quality target strength measurements both with respect to density and species mixing. Since 1985 target strength data have been collected periodically during cruises with R/V DR. FRIDTJOF NANSEN in West African waters. As a first attempt to establish a reasonably correct target strength for important species in the area, swimbladder morphology was studied and compared with species from the North Atlantic. After 1986, *in situ* target strength data was collected off Morocco and in Namibian waters using split-beam echo sounders. Data from the following species have been analyzed and discussed: Pilchard (*Sardina Pilchardus*), horse mackerel (*Trachurus Capensis*), hake (*Merluccius Capensis*), and myctophids. Only data which were considered to be of high quality have been analyzed. The calculated average target strength for pilchard are several decibels higher than the currently applied target strength of North Sea herring, but not very different from other reported target strength of sardine in other areas. Also, the target strength of horse mackerel is high compared to the presently applied target strength. For hake, the measured target strength are comparable to reported data for gadoids.

2:40

2pAO3. Resonance frequencies of absorption lines due to pelagic fish. Orest Diachok (Naval Res. Lab., Washington, DC 20375)

Resonance frequencies, f_0, of absorption lines due to pelagic fish with swim bladders change at twilight in accord with systematic changes in their depths and separations. Measurements of f_0 at night, and calculations of f_0, based on measurements of the effective radius, r_0, and eccentricity, ε, of sardine swim bladders, and the average depth of dispersed sardines at night, are in good agreement. This result implies that swim bladder compression by internal organs did not have a large effect on r_0 and ε during this experiment. Close agreement between laboratory measurements and calculated values of f_0 of individual physotomes suggests that this inference is generally valid. Possible exceptions to this ''rule'' will be considered in the context of Ona's (1990) laboratory observations of the effects of internal organs on swim bladder compression, and measurements of the state of internal organs of fish in the ocean. The resonance frequencies of absorption lines attributed to sardines in schools, $f_0' \approx 0.6 f_0$. This result is consistent with a modified form of d'Agostino and Brennan's (1988) equation for the fundamental mode of a bubble cloud. Their equation accounts for realistic numbers of fish per school (10^4–10^5). Modifications, which account for realistic separations between fish in schools and school eccentricity, will be presented. [Work supported by ONR.]

3:00

2pAO4. Modeling the target strength of Calanus finmarchicus. David T. I. Francis (School of Electron. and Elec. Eng., Univ. of Birmingham, Edgbaston, Birmingham B15 2TT, UK, francist@ee-admn.bham.ac.uk), Kenneth G. Foote, Tor Knutsen (Inst. of Marine Res., N-5024 Bergen, Norway), and Lucio Calise (Centro Marino Internazionale, I-09072 Torregrande (OR), Italy)

The boundary element method is applied to the copepod Calanus finmarchicus, treated as a composite body, with fluidlike oil sac embedded in a fluidlike, mostly transparent prosome. The generally complex shapes of the two bodies are modeled on the basis of the actual dorsal- and lateral-aspect cross sections, as observed by videomicroscopy with the living, unanaesthetized animal encased in a droplet of sea water. Physical properties of the two bodies, namely mass density and longitudinal-wave sound speed, are derived through a combination of measurement and inference. Computations of backscattering cross section as a function of orientation and frequency are presented over the range 25 kHz to 3.2 MHz for a number of specimens. A sensitivity analysis is performed to quantify some uncertainty in the assumed values of the physical properties. [Support by the following is acknowledged: EU through RTD Contract No. MAS3-CT95-0031, Norwegian Research Council through Grant No. 113809/122, and Bergen Large-Scale Facility (LSF) for Marine Pelagic Food Chain Research.]

3:20

2pAO5. Comparing predictions from backscatter models to *in situ* measurements of a dual-chambered, swimbladdered fish. John K. Horne, J. Michael Jech (CILER, Univ. of Michigan, 2205 Commonwealth Blvd., Ann Arbor, MI 48105, horne@glerl.noaa.gov), and Paul D. Walline (Israel Oceanograph. and Limnological Res., Tiberias, Israel 14102)

Most acoustic backscatter models predict echo amplitudes of single or aggregations of fish with single-chambered swimbladders. Lavnun (*Acanthobrama terraesanctae*), a planktivorous fish in Lake Kinneret, Israel, possesses a dual-chambered swimbladder. Target strength, length, frequency, or aspect relationships do not exist for this commercially important species. What is the most appropriate way to model backscatter amplitudes from single and aggregations of fish with multi-chambered swimbladders? Carrier frequency, organism length, organism aspect, and swimbladder shape all influence amplitudes of returned echoes. Predicted backscatter amplitudes and intra-species variance predictions from an anatomically-based Kirchhoff-ray mode model were compared to *in situ* measures of lavnun backscatter at 120 and 420 kHz. The lavnun swimbladder was modeled as a single chamber (with equivalent volume of both chambers), as two independent chambers, and as two acoustically interacting chambers. Wider application and comparison of theoretical models to field measurements increases understanding of factors influencing backscatter amplitude and variability for all fish species, and should improve methods for identifying organisms. [Work supported by ONR and US–Israel BSF.]

3:40

2pAO6. Comparison of Ayu target strength estimates determined from tank measurement and calculations. Kouichi Sawada (Natl. Res. Inst. of Fisheries Eng., Ebidai, Hasaki, Kashima, Ibaraki, 314-0421 Japan, ksawada@nrife.affrc.go.jp), Masahiko Yoshida (Mie Univ., Mie, 514-8507 Japan), Yoichi Miyanohana (Natl. Res. Inst. of Fisheries Eng., Ibaraki, 314-0421 Japan), and Kunio Shirakihara (Mie Univ., Mie, 514-8507 Japan)

Ayu, *Plecoglossus altivelis*, is one of the most popular freshwater fish which can be seen in many rivers in Japan. Especially in the North Basin of Lake Biwa, Ayu is the highest predator. It is important to know the spatial and temporal variations of Ayu biomass to understand the predator's effect to the food chain in the lake. Acoustic survey has been conducted since 1995. There is little information about the target strength (TS) of Ayu. Since Ayu has an open swimbladder, it is necessary to measure TS before the swimbladder was deflated by the suspension method in a tank. Target strength of live Ayu was measured in a tank and a three-dimensional image of swimbladder was obtained by an x-ray computer tomography (CT) system. In addition, a side and a dorsal image of the swimbladder were obtained by a soft x-ray system. All measurements were done in live condition. Kirchhoff approximation was used for the calculation on the basis of the three-dimensional image of swimbladder. A deformed cylinder model and a prolate spheroid model were also used for the calculation on the basis of side and dorsal image of the swimbladder. Calculation and measurement are compared and discussed in this paper.

4:00–4:20 Break

4:20

2pAO7. Analyzing ship-borne acoustic Doppler current profiler measurements to estimate the vertical and spatial distribution of southern Black Sea zooplankton. Funda Erkan and Ali C. Gucu (Inst. of Marine Sci., Middle East Tech. Univ., P.O. Box 28, Erdemli, 33731, Icel, Turkey, funda@ims.metu.edu.tr)

The acoustic Doppler current profiler was used in Summer–Autumn 1996 and 1997 cruises of R/V BILIM of Middle East Technical University to study the distribution of zooplankton in the southern Black sea. The backscattered signal intensity is compared with macro and mesozooplankton samples collected with Nansen closing net and 30-L Niskin water samplers. Analyzing the taxonomic groups and the length distribution of the individuals in the samples, size classification has been done. Total cross-sectional areas of the zooplankton in the length classes were compared with the resultant MVBS values. Highly significant correlations were observed. The relations between acoustic units and the size classes of zooplankton were presented by an empirical model which described a high percent of the total variance. The data sets from basin-wide surveys were used to obtain spatial distribution of zooplankton in the southern Black Sea. The spatial distribution of zooplankton was to a great extent determined by hydrography of the Black Sea. Daily migration patterns of zooplankton were studied, and the descending and ascending rates of different zooplankton groups were also calculated.

4:40

2pAO8. Analysis of the neuro-fuzzy classifiers for fish species identification from acoustic echoes. Andrzej Stepnowski, Dung Tran Van, and Joanna Maciolowska (Tech. Univ. of Gdansk, Acoust. Dept., 80-952 Gdansk, Poland, astep@pg.gda.pl)

Some of the variety of classification methods have been recently implemented also for fish species identification from their acoustic echoes. The classification systems employing artificial neural networks and fuzzy logic separately are not satisfactory, so the combined neuro-fuzzy approach were carried out. A couple of neuro-fuzzy classifiers were built and tested using the NEFCLASS program, which discovered the rules and found the shape of membership functions for determining correct class categories for a given input data set. The systems were tested on fish echoes acquired by DT4000 digital echo sounder. The results are promising with reference to the classifiers performance and their generalization abilities.

5:00

2pAO9. Improving echograms' resolution by wideband pulse compression and dynamic focusing. Manell E. Zakharia (CPE Lyon, LASSSO (LISA, EP92 CNRS), 43 Bd. du 11 Novembre 1918, BP 2077, Bat. 308, F 69616, Villeurbanne Cedex, France)

Improving the resolution of fisheries' sounder echograms (i.e., reducing the confusion volume) can be achieved by improving either the axial or the angular resolution. On one hand, the range (i.e., time) resolution can be improved without any degradation of the signal-to-noise ratio by using frequency-modulated signals associated with pulse compression. Axial resolution can be considerably enhanced by using wideband signals. On the other hand, due to the angular spreading of the sonar beam, the lateral resolution is proportional to the range. Improving the angular resolution can only be achieved by using a larger array (only possible on the receiving side). Nevertheless, such a solution has a severe limitation as it reduces the volumes sampled at short range, leading to an angular undersampling of the biomass. Dynamic focusing can be used to overcome this problem. Its principle is simple: the shorter the range, the smaller the array (i.e., the larger the angular aperture). The use of such a technique needs a compromise between the acceptable beam divergence and the system complexity. Both techniques will be applied to real data and echograms will be displayed and compared to the ones obtained with a standard system.

5:20

2pAO10. Bergen acoustic buoy (BAB)—A tool for remote monitoring of marine resources. Olav Rune Godo and Atle Totland (Inst. of Marine Res., P.O. Box 1870, 5024 Bergen, Norway)

Marine resource abundance monitoring is often accomplished by means of research vessel acoustic surveys. Vessel time is limited and expensive, and optimal and cost-efficient utilization is required. Such vessels have clear limitations in observing the true acoustic distribution, density, and acoustic properties of marine organisms due to noise and light emitted during surveying and sampling. A potential solution to some of the emerging problems is a remote operated acoustic device, which can be used to monitor distribution, density, movements, and properties of marine organisms under natural and survey vessel affected conditions. In this paper a new concept for a remote operated acoustic data logger is presented which can give an online presentation of the acoustic information. The system is built on the new Simrad General Purpose Transceiver (GPT) operated through a standard windows NT interface. The technical specification and operational features will be presented and exemplified with experience from the first sea trials. The system is designed to meet demands from other applications, e.g., a drop sonde and towed underwater function, and future development of the concept is discussed.

5:40

2pAO11. Design of a transducer-driving system scanning around an aquatic target in an indoor tank. Ken Ishii, Tsuyoshi Okumura, Kouichi Sawada, and Yoichi Miyanohana (Natl. Res. Inst. of Fisheries Eng., Ebidai Hasaki, Kashima, Ibaraki, 314-0421 Japan)

A squid has been specified as a kind of fish that has to been managed scientifically. Estimation of its resources via acoustic surveys is required. But the basic data of the target strength (TS) of a squid are limited. So far, in the measurements of the TS pattern of fish, echo levels are observed while changing the aspect of a fish. On the other hand, since a squid is more fragile than a fish, and unstable in shape, the rotating unit of fish is not available for a squid. So the positioning system that makes a transducer scan precisely around an aquatic target suspended in the water has been designed. This system is loaded in the electric flatcar, the probe of which can move three dimensionally, on the top of a tank which is 10 m in width, 15 m in length, and 10 m in depth. It is hoped that precise TS pattern measurements are possible so that the target is suspended without damage owing to this transducer-driving system. The detail of control software and an example of measurements and subjects are described in this paper.

Session 2pEA

Engineering Acoustics: Microphones, Measurements, Etc.

George S. K. Wong, Cochair
Institute for National Measurement Standards, National Research Council, Montreal Road, Ottawa, Ontario K1A OR6, Canada

Gunnar Rasmussen, Cochair
G.R.A.S. Sound & Vibration aps, Skelstedet 10B, 2950 Vedbaek, Denmark

Chair's Introduction—1:55

Contributed Papers

2:00

2pEA1. A microphone without a membrane. Joerg Sennheiser (Sennheiser Electron. GmbH & Co. Kg, Am Labor 1, 30900 Wedemark, Germany)

In all microphones used today, the component which affects the quality most is the membrane. The frequency response and the signal-to-noise ratio of a microphone depend on the best possible coupling of this mechanical component to the acoustic sound field and on its oscillatory behavior. In the mass production of membranes within narrow tolerances, properties such as geometry, mass, stiffness, native modes, etc. have a great effect on the quality and are often problematic. There is therefore great interest in finding a working principle for microphones which does not require a membrane. A possible way out is to utilize the well-known thermal anemometer principle: An electrically heated wire is cooled down in an air flow. The resistance change in the wire is a measure of the air speed and thus of the velocity. If the heat capacity of the heated sensor is reduced by micromechanical techniques, this principle can also be used to measure the acoustical volume velocity at higher frequencies. The expected limits and first readings are shown via the models realized.

2:20

2pEA2. A simple optical microphone. Wolfgang Niehoff (Sennheiser Electron. GmbH & Co. Kg, Am Labor 1, 30900 Wedemark, Germany)

In the past, a number of different working principles have been suggested for optical microphones, but many of these require a high degree of technical sophistication. Thus some suggestions are based on the interferometric principle, whilst others would utilize frequency modulation of laser light via a variable mirror (membrane) situated in the laser resonator. Light intensity modulation is a much more simple approach: A light beam emitted from an optical fiber is aimed at a reflecting membrane. The beam reflected from the membrane is captured by a second optical fiber and fed into a photodiode. Depending on the movement of the membrane, more or less light is launched into a second optical fiber. The photoelectric current of the photodiode thus expresses the movement of the membrane, and with it the sound field, as an electrical signal. As optical fibers transmit light with very few losses, the actual optoacoustic transducer can be positioned at a long distance from the light source and the photodiode. This allows problem-free use of the optoacoustic transducer in the presence of very strong electromagnetic fields (e.g., MRI). It is possible to improve upon this principle via simple modifications. The electroacoustic characteristics achieved are discussed and a model is presented.

2:40

2pEA3. Microphone calibration techniques. Gunnar Rasmussen (G.R.A.S. Sound & Vib. aps, Skelstedet 10B, Vedbaek, Denmark)

Primary calibration of microphones is well described and standardized by IEC 1094-2 using the reciprocity technique. When the standard microphone is calibrated, a reference source is needed for transfer of the calibration value to the acoustical measuring devices or systems employing the working measurement microphone. A reliable transfer device is the pistonphone. Another method may be the use of a comparison against a working standard microphone. Sound reference sources called ''calibrators'' are standarized by IEC in 60942:1997. Sound calibrators may often be inferior in accuracy and stability to the systems they are being applied to. They should therefore be labelled check devices. Other techniques have been employed for many years. The use of a reference voltage coupled to the system input is widely used. This may be extended to incorporate the preamplifier and incorporate features like modulating the polarization voltage whether internal or external or incorporating the cartridge capacity into a capacitive voltage divider. These techniques do not allow a calibration but only supply a means of injecting a signal in the electrical system to check the ability to transfer a signal. Calibration is not obtained.

3:00

2pEA4. Optical measuring and calibration techniques for microphones. Gottfried K. Behler and Michael Vorländer (Inst. of Tech. Acoust., Univ. of Aachen, Templergraben 55, 52056 Aachen, Germany)

Microphone measurement techniques are normally based on acoustical excitation and electrical derivation of either the voltage or the current output of the transducer. With condenser microphones, electrical excitation can be used as well. Calibration of microphones based on acoustical excitation therefore is quite time consuming, and sensitive for several errors originating in inaccurate sound-field properties and environment conditions. Measurements of the microphone membrane velocity with optical means like the laser Doppler vibrometer technique offer an accurate, touchless method to derive the local movement at almost each point of the membrane. Excitation of the membrane can be accomplished by direct feeding of the transducer (due to its reversible construction), which provides highest accuracy for the derivation of either current or voltage at the terminals of the transducer. From the knowledge of the vibration characteristics and the excitation properties, the ''differential transducer sensitivity'' defined at each surface point can be derived. With numerical methods, like the discrete solution of the Helmholtz equation or BEM, the radiated sound can be calculated, and finally the overall microphone radiation pattern and sensitivity can be calculated. The described techniques were applied to different types of microphones. The measurement and calculation results will be shown.

3:20

2pEA5. New design concepts for the construction of an omnidirectional sound source. Christos A. Goussios, George V. Papanikolaou (Dept. of Elec. and Computer Eng., Aristotle Univ. of Thessaloniki, Univ. Campus 540 06, Thessaloniki, Greece), and George M. Kalliris (Aristotle Univ. of Thessaloniki, Thessaloniki, Greece)

This paper presents a study for the optimum design and construction of an omnidirectional point source. The point source model of theoretical acoustics is used as an elementary unit for electroacoustic measurements in the area of room and free-field acoustics. The spherical radiation requirement for the entire acoustic spectrum and the finite dimensions of the point source model contradict the construction in practice. This is because of high-frequency beaming and the existing dimensions of radiators. A new design approach of using horn loaded cone loudspeakers and properly placed high-frequency diffusers was used to minimize these problems. Twelve radiators loaded on pentagon-shaped horns were placed in a dodecahedron topology to build a practical point source with a useful frequency response of 80–16 000 Hz and an omnidirectional radiation pattern up to 12 000 Hz. The results display improvement in the radiation pattern compared to those of the already existing point sources, due to the use of horns and diffusers. Increase in the sound pressure level is also displayed because of the obvious increase of the directivity index of each individual radiating element.

3:40

2pEA6. Simulation of ultrasonic fields in composite media with planar boundaries. Liudas Mažeika and Rymantas J. Kažys (Ultrasound Res. Ctr., Kaunas Univ. of Technol., Studentų str. 50, LT-3031, Kaunas, Lithuania, liudas.mazeika@tef.ktu.lt)

In this paper the method and fast algorithm for simulation of ultrasonic fields exited by the direct or angular transducers in media with a few thick layers are presented. The method exploits regularities of the disk-shaped transducer field in a homogeneous medium, adapting it to a multilayered medium, the boundaries of which are not necessarily parallel. It was assumed that at any point the pulse response of the transducer must be of the similar shape, consisting of the fragments corresponding to the plane and the edge waves. The additional parameters of the pulse response are evaluated solving a system of nonlinear equations. These parameters are used to find some equivalent point in pulse response for a homogeneous medium with adequate values of parameters. The method proposed allows the evaluation of ultrasonic field structure in the solids when the immersion technique is used or inside tanks when ultrasonic waves pass through a wall. The simulation and experimental results presented show a good correspondence with the field structure calculated using other methods.

4:00

2pEA7. Wideband ultrasonic piezoelectric microphones. Vygantas Augutis and Darius Gailius (Varpo 10-12, Kaunas 3028, Lithuania, dagail@tef.ktu.lt)

Microphones with an air coupling multiple matching layer and fiber damper were developed. The method for calculation of the characteristics of the transducers is presented. The signal-to-noise ratio (SNR) of these microphones is about 10 dB lower than the SNR ratio of capacitive microphones, but they are more suitable for use in dusty and wet conditions. The frequency range of these microphones is 10–100 kHz. The system for the measurement of the characteristic of microphones was developed. Short acoustic pulses, generated by the electical spark, were used as a wideband probing acoustic signal. Serious attention was paid to the estimation of instability of the spark-generated acoustic pulses. Several modifications of developed microphones, their characteristics, and fields of application are presented.

4:20–4:40 Break

4:40

2pEA8. A simple method to estimate the absorption coefficient of porous absorbers. Ulrich Ackermann (Dept. of Mech. Eng., Märkische Fachhochschule Iserlohn, Postfach 2061, D-58590 Iserlohn, Germany)

To estimate the attenuation D of silencers under practical conditions, the formula of Piening is used: $D=1.5\alpha CL/A$ (C is the circumference, L the length, and A the cross-sectional area of the absorbing duct). For most of the porous absorbers the absorption coefficient α can be estimated by the very simple relation $\alpha=0.9\log(fd)-X$ $(0\leqslant\alpha\leqslant1)$, where f is the frequency in Hz and d the thickness of the absorber in cm. For different porous absorbers the constant X can be derived from measurements in small test rigs, where only a few materials are needed. For mineral wool with a density between 20 and 40 kg/m^3, $X=2{,}4$, and for snow with a density of 270 kg/m^3, $X=2{,}65$, e.g., the Piening formula together with the relation for α gives a simple method to calculate the space for splitter- or tube-silencers in ducts, e.g., without knowing the acoustical performance of the porous absorber exactly.

5:00

2pEA9. A simple device for flow resistance measurements. Dag Holmberg and Erling Nilsson (Dept. of Eng. Acoust., LTH, Lund Univ., P.O. Box 118, SE221 00 Lund, Sweden, Dag.Holmberg@kstr.lth.se)

A simple device for static measurements of flow resistance on thin porous materials is developed and evaluated. The device consists of a duct with a piston which is driven at a steady low speed. This generates a flow of air with constant volume velocity. The duct ends with a cavity with an interface to the outside where the sample is mounted. The differential pressure between the cavity and the outside is measured. In order to prevent nonlinear effects, the speed of the piston is kept so low that the constant velocity of the air is of the same order of magnitude at the sample as the rms velocity of sound waves at approximately 100 dB SPL. The device is so constructed that it is possible to measure samples of standard dimensions, e.g., cloth mounted at different perforated frames, if the speed of the moving piston is accordingly adjusted to match the open area. The performance of the device is tested and discussed.

5:20

2pEA10. Experimental investigation of bending waves in ultrasonic reactors. Torsten Niederdraenk (Siemens Audiologische Technik GmbH, D-91050 Erlangen, Germany) and Rainer Thaden (Institut fuer Technische Akustik, RWTH Aachen, D-52056 Aachen, Germany)

A number of practical applications like ultrasonic cleaning, sonochemistry, and others use the effects of high, intense ultrasound. In general, the high-pressure sound fields can be obtained by different arrangements of piezoelectric compound transducers, which have to be optimized according to each application. A commonly used setup is a planar array transducer, consisting of one or more transducer elements. A tool to design and develop the transducer arrangements is given by simulations of the electromechanical equivalent circuit, although the results are often based on several assumptions. This paper reports on vibroacoustic investigations of compound transducer arrangements. Laser-optical measurements give evidence for arising bending waves on the radiating surface of the transducers that may affect the generated sound field and which have some effect on the total power distribution. The influence of bending waves has been included in the equivalent circuit; some simulations are presented.

5:40

2pEA11. Underwater acoustic tank evaluation of acoustic properties of samples using spectrally dense signals. Carlos Ranz-Guerra and Pedro Cobo-Parra (Inst. de Acstica, C/Serrano 144, 28006, Madrid, Spain, iacrg32@fresno.csic.es)

This paper deals with exploring the availability and reliability of subtraction techniques, based on spectrally dense signals such as maximum length sequences, in evaluating the echo reduction losses and transmitting properties of samples of interest in underwater acoustics. These techniques, first employed in air acoustics, were adapted to the underwater environment. Experimental results show how a measurement can be accomplished and the limitations produced by the actual available combination of soft, hardware and tank and samples dimensions. [The authors wish to acknowledge the help given by the CICYT, Project AMB97-1175-C03-01, for allowing them to use the software, hardware, and related facilities in carrying out the work described by this paper.]

6:00

2pEA12. Mechanical impedance of wheeled tractor steering mechanism. Stanislovas Merkevičius and Ričardas Vagusevičius (Lithuanian Univ. of Agriculture, Agriculture Eng. Faculty, Occupational Prevention and Eng. Management Dept., Kaunas–Acad. 4324, Lithuania)

There are fairly many wheeled tractors of 6 kN class made in CIS (Community of Independent States). The characteristics of noise and vibration are inadequate for valid standards. Vibrations of especially high levels having the effect on hands are generated through the steering wheel to the person's (operator's) hands. If fitting in vibroisolating or vibrodepherisating elements to the driving mechanism details junctions (joints), it is partly possible to lessen the vibration level having the effect on the person. It would be more effective and more rational to discuss the possibilities of absorbing spreading vibration and vibroisolation when there is enough information about the vibration of the steering wheel mechanism. Applying the methods of mechanical impedance, the mathematical model of steering mechanism, consisting of the steering wheel mechanism and the steering wheel has been made, giving an opportunity to analyze the interaction of the steering wheel, the person (operator), and the spreading vibration.

TUESDAY AFTERNOON, 16 MARCH 1999 ROOM MA004, 1:55 TO 6:20 P.M.

Session 2pMU

Musical Acoustics: Musical Acoustics and the Musician

Thomas D. Rossing, Cochair
Physics Department, Northern Illinois University, DeKalb, Illinois 60115, USA

Anders Askenfelt, Cochair
Department of Speech, Music, and Hearing, Royal Institute of Technology, P.O. Box 70014, 10044 Stockholm, Sweden

Chair's Introduction—1:55

Invited Papers

2:00

2pMU1. The perception of music by the human brain: An introductory course. Juan G. Roederer (Geophysical Inst., Univ. of Alaska—Fairbanks, Fairbanks, AK 99775-7320)

The study of the perception of music is a fascinating interdisciplinary endeavor in which musicians, neuroscientists, psychologists, physicists, and physiologists work together. Recent advances in the understanding of how musical sounds are detected in the ear, converted into neural signals, processed, and interpreted in the brain make the subject very attractive for an elective introductory university course. It is possible to present many subject matters in a generally understandable way, without the requirement of previous knowledge beyond that of secondary level [J. G. Roederer, *Physics and Psychophysics of Music*, 3rd ed. (Springer-Verlag, New York, 1995); German edition: *Physikalische und Psychoakustische Grundlagen der Musik* (Springer-Verlag, Heidelberg)]. In such a course, many puzzling questions can be addressed (and answered!): Why do people perceive only *one* pitch when they listen to a musical tone made up on many harmonics? Why are there musical scales? Why is pitch resolved so well, despite the ''bad'' frequency analysis in the inner ear? What happens in the brain when sounds are imagined? What is the relationship between music and language? Why do listeners react emotionally to musical sounds? The pedagogical challenges of organizing such an interdisciplinary course will be discussed.

2:20

2pMU2. Musical acoustics, the music student, and the music teacher. Knut Guettler (Norwegian State Acad. of Music, P. B. 5190 Majorstua, 0302 Oslo, Norway, knut.guettler@samson.nmh.no)

Dialogs between musicians and acousticians are not always successful. A lack of common language combined with mutual suspicion of the other person trespassing on ones own professional authority, often restricts what ought to have been a fruitful exchange of knowledge. For the music student, there is, however, a third matter that seriously impedes the possibility of gaining acoustical insight. As for all arts, yearning and intuition are the driving forces in the development of musical and instrumental skills.

Focus on purely technical matters, or even worse, the feeling of being overruled by such, is hardly combinable with a desirable musical progress of the young student. Based on the author's experience as a principal professional player and teacher of music for more than 30 years, this paper gives some suggestions on which and how topics in musical acoustics may be introduced.

2:40

2pMU3. Acoustical training for stringed instrument makers. Bernard E. Richardson (Dept. of Phys. and Astron., Univ. of Wales, Cardiff, P.O. Box 913, Cardiff CF2 3YB, UK, RichardsonBE@Cardiff.ac.uk)

The vast majority of popular stringed instruments found in western culture have been the product of generations of empirical experimentation on the part of craftsmen trying to provide a suitable vehicle for musical expression. In previous centuries, skills and knowledge were passed down from master to pupil during long apprenticeships, but whenever the continuity has been broken, there has been a feeling that various ''secrets'' have been lost. In more recent years, increased leisure time and better education has encouraged many individuals to take up instrument making, either as amateurs or as professionals. Most of these makers work in isolation, so there is now an even greater impetus to ''rediscover'' and communicate past arts. Some of these makers have turned to science to provide rational explanations of the many questions which are inevitably raised during the pursuit of making ''fine'' instruments. Based on the author's experience of his interactions with pupils of violin and guitar making, this paper seeks to explore how scientific investigations can best be communicated to makers and examines to what extent ''scientists'' and ''makers'' can learn from each other.

3:00

2pMU4. Intensive training on acoustics of pipe organs for organ builders and organists. Judit Angster and Andras Miklos (Fraunhofer-Institut Bauphysik, Nobelstr. 12, D-70569 Stuttgart, Germany, angster@ibp.fhg.de)

A special course on acoustics is organized regularly in the Fraunhofer-Institute fr Bauphysik (IBP) for training pipe organ builders, official organ experts, and organists. The title of the 4-day intensive course is ''Pipe Organ and Church Acoustics'' and it is scheduled at the end of January every year, when most of the organ builders are less occupied than in other periods. The number of participants is limited to 20, but the course is repeated in February, if necessary. The working language of the course is German, but English and French are also possible. The curriculum of the course is based on the ongoing research on pipe organs in the IBP and it is divided to three parts: fundamentals of acoustics; recent results of research on organ and church acoustics; and laboratory demonstrations and practical applications. During the demonstrations there is a limited possibility to perform measurements suggested by the participants. The content of the lectures and demonstrations is upgraded every year with the newest results of the research. In this paper the experiences of the eight courses held up to now will be discussed. A short video clip showing some of the laboratory demonstrations will also be presented.

3:20

2pMU5. Acoustic loading exercises in singing training. Ingo R. Titze (Dept. of Speech Pathol. and Audiol. and Natl. Ctr. for Voice and Speech, Univ. of Iowa, Iowa City, IA 52242, ingo-titze@uiowa.edu)

Singing teachers have devised vocal exercises that present variable acoustic loads to the sound source. These exercises consist of lip and tongue trills, nasal consonants, and vowels with small mouth openings (like /u/). Some pedagogues and clinicians have advocated phonating into long and narrow tubes. Since none of these exercises produce either a strong or aesthetically pleasing acoustic output in and of themselves, their merit must lie in facilitating the respiratory and phonatory systems. Recent Hopf bifurcation analysis has shown that inertive acoustic loads, resulting from deliberate constricting and lengthening of some portion of the vocal tract, can lower the oscillation threshold pressure, thereby facilitating the ease of vocal onset. Resistive acoustic loads, either upstream or downstream of the vocal folds, have a less beneficial effect on oscillation threshold pressure. [Work supported by Grant No. P60 DC00976 from the National Institute on Deafness and Other Communication Disorders.]

3:40

2pMU6. Illustrating music performance principles by synthesis. Anders Friberg and Johan Sundberg (Royal Inst. of Technol., Dept. of Speech, Music and Hearing, Drottning Kristinas vg 31, SE-100 44 Stockholm, Sweden, andersf@speech.kth.se)

Music is generally not performed exactly as written. Instead, many small systematic variations of tone duration, pitch, articulation, etc. are found in a performance. These variations may serve the purpose of communicating different emotions or to outline the musical structure. An overview of commonly used principles is presented concerning the performance of different rhythmic patterns, the marking of important notes or chords, musical punctuation, and the hierarchical phrase structure. These principles are encoded in the form of rules implemented in a computer program, where they can be applied on any musical example. The possibility to isolate and change the quantity of the effects generated by each rule makes the system a unique tool for illustrating music performance to music students.

4:00–4:20 Break

4:20

2pMU7. Music acoustics and contemporary musical composition. Gerald Bennett (Swiss Ctr. for Comput. Music, Florhofgasse 6, 8001 Zurich, Switzerland, gbennett@cerfnet.com)

Although it may seem that in the past musical composition got by well without specific knowledge of music acoustics, in fact the acoustical knowledge of each epoch has always determined the representational framework within which the composer formulates his ideas. For the last 50 years, however, composition in the field of electroacoustic music has required far more explicit and detailed

acoustical knowledge than was the case for instrumental music. The relationship between music acoustics and composition today is one of reciprocal influence: frequently research in music acoustics is put to good (if sometimes surprising) use by composers. Sometimes, however, composers' needs have led to important research in music acoustics. The present paper illustrates this reciprocity with examples from the areas of sound synthesis, physical modeling, and the simulation of reverberant spaces, and speaks of the importance of research for contemporary composition. In addition, the author presents a wish list for future work in music acoustics.

4:40

2pMU8. Teaching musical acoustics. R. Dean Ayers (Dept. of Phys. and Astron., California State Univ., Long Beach, CA 90840) and Thomas D. Rossing (Northern Illinois Univ., DeKalb, IL 60115)

Although designed particularly for music students, musical acoustics courses at American universities generally draw a ''mixed bag'' of students with a rather wide variety of backgrounds. This presents some real challenges but also some real rewards. Some of the problems in teaching musical acoustics to heterogenous classes and some of the ways these problems can be dealt with are discussed. Readable textbooks, demonstration experiments, and videotapes help to challenge and motivate the students, but the best way of all to learn the subject is by doing hands-on experiments.

Contributed Papers

5:00

2pMU9. Measurement of performance response differences when striking different areas of a marimba bar. Barry J. Larkin (Dept. of Music, Iowa State Univ., Ames, IA 50011, blarkin@iastate.edu) and Ronald A. Roberts (Iowa State Univ., Ames, IA 50011)

Over the past 40 years, general percussion education manuals have stated that the best place to activate a marimba or xylophone bar is to strike it in the exact center. Over the years, this has become known as the ''best spot,'' and percussion students have been blindly advised to strive always to perform in this manner. Recent re-publications of mallet methods from the early part of the 20th century show that it was a common practice to perform on the end of the accidental bars for speed and superior sound. Also, leading classical marimba performer, Leigh Howard Stevens, has stated his preference for this type of execution. This paper will present spectral analysis results from measurements made at nine different locations on a Great F sharp marimba bar. The results will show the diverse types of responses generated by location changes of as little as an inch.

5:20

2pMU10. Control index of the upright and grand piano actions. Xavier Boutillon (Laboratoire d'Acoustique Musicale, CNRS, Case 161, 4 place Jussieu, 75252 Paris Cedex 05, France) and Robert Grijalva (Univ. of Michigan, Ann Arbor, MI 48109-2085)

The motion of the piano hammer between its resting position and the contact with the strings follows two phases. At first, the motion is imposed by the pianist's finger on the key. When it escapes from the main action, within 2 mm from the string, the hammer possesses the velocity v_e. During the second and brief phase before impact, the hammer is only subject to gravity, friction of its pivoting axis, and to the action of an additional spring in the case of the upright piano. Finally, the hammer hits the strings with velocity v_i. The difference between v_e and v_i, and the threshold on v_e below which the hammer does not even touch the strings, are a nuisance for the musician. Although inevitable, this second phase also affects the aptitude to control nuances, so important in music. To quantify this notion, the control index $i_c = dv_e/dv_i$ is introduced, which can be easily calculated. Its limit is 1 for *fortissimo* but it approaches 0 for *pianissimo*. For the pianist, this corresponds to a steeply increasing difficulty to phrase music at low rather than at high dynamic levels. Differences between the grand and the upright piano will be discussed.

5:40

2pMU11. An artificial neural network model for analysis and synthesis of pianists' performance styles. Roberto Bresin (Royal Inst. of Technol., Dept. of Speech, Music and Hearing, Drottning Kristinas v. 31, 10044 Stockholm, Sweden, roberto@speech.kth.se)

A model for synthesis and analysis of professional pianists' performance styles by means of artificial neural networks (ANNs) is presented. The style of pianists was synthesized using Bruno Repp's measurements [J. Acoust. Soc. Am. **92**, 2546–2568 (1992)] of Schumann's Trumerei as performed by 24 famous pianists. It will be shown that, by using significant score parameters, ANN can learn and reproduce the style of a pianist at a local level. The behavior of the trained ANN and the performance characteristics of the pianists were analyzed by running the trained ANN in a special way. All ANN input neurones were locked to fixed values, except one or two neurones whose input values were allowed to change in time. For example, if one of these neurones is related to the duration of the current note, the output of the ANN gives a curve showing expressive deviations produced by the ANN, when the duration of the note is varying. In this way it is possible to extract behavior rules of performing action of the ANN, and compare them with the performance style of pianists as well as of rule-based performance systems. The model is developed in the Java language and is available on the Internet.

6:00

2pMU12. Experience of students of composition and instrument construction at the National School of Music of UNAM in the auditory normalization of timbre with age and with exposure to different instruments. Eduardo Castro-Sierra (Natl. School of Music (ENM) of the Natl. Autonomous Univ. of Mexico (UNAM), Xicoténcatl No. 126, 04100 México, D.F., Mexico), Martha Gómez-Gama, Miguel Zenker (ENM, UNAM), and Santiago J. Pérez-Ruiz (Section of Acoust. of the Ctr. of Instruments of the Natl. Autonomous Univ. of Mexico)

A study of tonal memory using as stimuli synthesized harmonic sounds with a quasi-square-wave spectrum has been carried out at ENM. The subjects were young boys and girls (age span=8:1–15:6), starting their musical education at the Cycle for Musical Initiation, and young adults of either sex (age span=13:11−42), with experience of from 1 to 10 years in singing, piano, violin, clarinet, flute, trumpet, saxophone, guitar, percussion, or composition at the regular courses of ENM. While the children were adept in retaining in memory tonal changes of a major or a minor second using the synthesized stimuli, the older students showed much greater difficulty with this test, particularly those whose instrument had a timbre closer to that of the square wave (clarinet or saxophone), or who were undertaking studies of composition. Students of composition or instrument construction at the Instrument Construction Workshop of ENM have embarked on a further analysis of auditory normalization of timbres of diverse synthesized or natural sounds of instruments. It is expected that such an experience will allow the students to better conceptualize different timbre combinations as well as the timbre of individual musical instruments.

Session 2pNSa

Noise: Railway Noise II

Markus Hecht, Cochair
Institut für Strassen- und Schienenverkehr, Fachgebiet Schienenfahrzeuge, Sekr. SG14, Salzufer 17-19, D-10587 Berlin, Germany

Paul J. Remington, Cochair
BBN Systems and Technologies, 70 Fawcett, Cambridge, Massachusetts 02138, USA

Chair's Introduction—1:55

Invited Papers

2:00

2pNSa1. Today's railfreight noise situation. Markus Hecht (Institut für Straßen- und Schienenverkehr, Fachgebiet Schienenfahrzeuge, Sekr. SG 14, Salzufer 17-19, D-10587 Berlin, Germany)

In recent years railway freight wagons have tended toward a gradual increase in noise radiation. The reasons have been the transition from slide to roller-axle bearings, more welded joints instead of bolted or riveted ones, the increased number of four-axled wagons instead of two-axled ones, and higher medium speeds. Meanwhile, the competitors on the road and in the air have made substantial progress in noise reduction. The first major step toward quieter trains in railway freight was the decision of the German and the Swiss freight operators DB-Cargo and SBB-Cargo to replace cast iron brake blocks by composite brake blocks. This was done in the US decades ago, but the stopping distances in Europe are much shorter, about one-quarter of those in the US. Therefore, the braking forces are much higher, which results in higher thermal thrust on the running surfaces. A special wheel shape had to be developed to withstand this impact and to reduce the risk of broken wheels. Noise emission from European modern standard freight cars must be reduced by 25 dB. Only then can the existing perception limits at densely used freight lines be reached at night. Measures to achieve this goal will be presented.

2:20

2pNSa2. Cause research and assessment of the acoustic behavior of rail vehicles using SFE AKUSRAIL. Hans Zimmer (SFE GmbH, Ackerstr. 71-76, D-13355 Berlin, Germany)

Many efforts have been made in the past to further develop knowledge of both the interior acoustics and sound emission of rail vehicles using numerical methods. One major advantage of numerical methods is the possibility of forecasting the acoustic behavior (without prototyping) and hence influencing the design of the vehicles, also in terms of acoustic criteria. Another advantage of this ''virtual prototyping'' is that it is possible to determine the contribution of individual components to the sound level within the frequency range analyzed, i.e., to analyze the causes of acoustic behavior. However, strict criteria must be met to satisfy the claim of a useable forecast of acoustic behavior. It must be possible to simulate important acoustic phenomena—such as structure/air coupling, absorption, reflection, emission, etc. The numerical model must be sensitive enough to permit the forecasting of trends. The interaction of rail and vehicle must be taken into consideration as a crucial precondition for identifying and analyzing acoustically critical frequencies. Another decisive criterion, however, is that it must be possible to assess not only the ''actual'' acoustic state, but also the underlying causes. This includes, for instance, knowledge of structure-borne sound paths and the structure and coupling situation.

2:40

2pNSa3. Roughness growth on tread-braked railway wheels: EUROSABOT theoretical studies. Anders Nilsson and Urmas Ross (MWL, Dept. of Vehicle Eng., KTH, S-100 44, Stockholm, Sweden, andersni@fkt.kth.se)

Rail and wheel surface irregularities are the main source of rolling noise. One of the main causes for wheel surface roughness is tread braking. Wheels braked by the most common tread brakes—cast iron blocks—have high roughness levels and, as usual, corrugation with wavelength of 30–100 mm. The Brite Euram research project EUROSABOT deals with new solutions for tread brakes, which would lower the roughness level, prevent the buildup of periodic roughness, and consequently reduce the rolling noise, and at the same time would follow the safety requirements of railway operation. Field measurements, discussed in detail by Stefan Buehler in a companion presentation, in parallel with laboratory studies has distinguished that the interaction of thermo-elastic and vibrational instabilities is the main reason for corrugation generation. Computer simulations describing simultaneously thermodynamical, structural, and acoustic processes of the braking operation have proved to be unpractical for parametric studies and, instead, several simplified models are used. These models have shown that the main parameters affecting roughness growth are Young's modulus and coefficient of thermal expansion of the block material and damping of the system.

3:00

2pNSa4. Eurosabot field measurements—Methods and results. Stefan Bühler (ABB Daimler-Benz Transportation Ltd., Zürcherstrasse 41, P.O. Box CH-8401, Winterthur, Switzerland)

Eurosabot is a European research project focused on rolling noise reduction of block braked railway vehicles. While braking, the interaction between block and wheel generates roughness patterns on the wheel which become the major excitation for rolling noise. The objective was to find a brake block (material and design) which combines the advantages of common cast-iron blocks with lower roughness generation without common drawbacks of other block families. Measurements of most relevant parameters were already available before Eurosabot, but boundary conditions and other parameters were different, inconsistent, or even unknown, which made it difficult to gain a reliable understanding of how roughness is generated. Therefore, Eurosabot's measuring campaigns were focused on strictly simultaneous monitoring of all relevant parameters under known and real boundary conditions. The following parameters were monitored over a long-term period in normal service: wheel and block wear, wheel roughness, braking distance, residual stress (wheel rim). During a concentrated campaign, rail roughness, rail impedance, rail accelerations, sound pressure, and sound power distribution were measured wayside, as well as sound pressure (on board), wheel and block accelerations, wheel and block temperature distribution, and friction coefficient on the vehicle. Results show that this method enables a complete judgment of the behavior of a block.

3:20

2pNSa5. Noise annoyance by freight trains. Anja H. M. Steenbekkers and Ronald G. de Jong (TNO Prevention and Health, P.O. Box 2215, 2301CE Leiden, The Netherlands, rg.dejong@pg.tno.nl)

In The Netherlands a new freight-only railway route, the ''Betuweroute,'' is being planned to carry freight traffic from Rotterdam harbor east into Germany. Inhabitants of areas near the future route are concerned about noise and vibration, and question the relevance of current legislation for a ''freight-only'' line. Results of analyses on existing data show no consistent differences in exposure–response relations between routes with a small or high proportion of freight trains, once the effects of different noise levels are removed. Thus these results do not support the need for special legislative provisions for freight-only lines. However, hardly any freight-only train route was included in the analyses, and concern remains. The most western part of the future Betuweroute is an existing freight-only line, the ''Harbour line.'' Some 109 inhabitants living near this line were interviewed in order to pretest the questionnaire for a social survey in areas along the future Betuweroute. For most homes accurate noise data are available. This offers another opportunity to test the hypothesis that, once the effects of different noise levels are removed, freight trains do not cause more annoyance than passenger trains. The results of this test will be presented.

3:40–4:00 Break

Contributed Papers

4:00

2pNSa6. Experiments and computations of noise reduction by barriers. Erik M. Salomons and A. A. F. M. Beeks (TNO Inst. of Appl. Phys., P.O. Box 155, 2600 AD Delft, The Netherlands)

Experimental and theoretical investigations are presented of the performance of noise barriers in the open air. The experimental work includes full-scale measurements on barriers and scale-model measurements on a barrier in a wind tunnel. The wind tunnel experiments indicate that meteorology has large effects on barrier attenuation. The results of the wind tunnel experiments are compared with results of numerical computations with the parabolic equation method. Good agreement with the experimental data is obtained only if wind speed profiles as measured in the wind tunnel are used in the computations. It is concluded that wind speed gradients induced by the barrier itself reduce the barrier attenuation considerably: reductions as large as 10 dB are found. The use of aerodynamically optimized barriers is proposed in order to minimize this reduction of barrier attenuation.

4:20

2pNSa7. Scale model experiments on new types of noise barriers. Djamel Ouis (Eng. Acoust., Lund Inst. of Technol., P.O. Box 118, S-22100, Lund, Sweden)

This paper is concerned with the results of experiments conducted on some new types of noise barriers. The experiments were conducted in the anechoic chamber at a scale model level and the barriers have different profiles with focus on the so-called forklike topped barrier. The quantity of interest is the sound-pressure level in the zone shadowed by the barrier. The arms of the barrier top were combined in several different ways and angles as well as also being mounted by either hard or soft cylinders to predict the effect of these latter on the edge diffraction phenomenon. The ground is taken either as hard on both sides of the barrier or a combination of hard and soft ground on, respectively, the source and receiver sides. [This work was supported by a grant from TeknikBrostiftelsen in Lund, which is gratefully acknowledged.]

4:40

2pNSa8. Acoustical contribution analysis of railway wheels and tracks. C. Katzenschwanz (IABG GmbH, Einsteinstr. 20, 85521 Ottobrunn, Germany, katzenschwanz@iabg.de), G. Hölzl, L. Willenbrink, and T. Lölgen (Deutsch Bahn AG, D-80939 München, Germany)

In a numerical analysis the contribution of different railway wheels and the track on the sound power and the sound pressure was determined. Two different wheels under different loads and positions were compared. In a first step a unit mechanical excitation in the connection point between the wheel and the rail was used to analyze the structural displacements of each configuration with finite elements. The structural energy on the surface of the wheel and the rail was used to select critical frequencies using boundary elements. In a second step the sound pressure was displayed on visualization planes and the contributions of the wheel and the rail to the sound power and the pressure at different points were discussed for the critical frequencies. It could be shown that the main sound pressure was dominated by the wheel. The bending modes of the wheel contribute a lot to the sound pressure. For optimized wheels the bending stiffness should be therefore increased. The position of the wheel—over the sleeper or in between—did not influence the contribution very much as well as the loading of the wheel.

5:00

2pNSa9. Empirical formulas for noise of high speed trains. Rik van Haaren (NS Tech. Res., P.O. Box 8125, 3503 RC Utrecht, The Netherlands, e.van_haaren@geluid.nsto.ns.nl) and Karel Looijmans (TNO/TPD, 2600 AD Delft, The Netherlands)

Aeroacoustic sources at high-speed trains are dominant noise sources for trains running at high speeds. The pantograph is an important source located at a high position. Therefore, this source cannot be handled by applying noise barriers. Noise measurements are carried out in the DNW windtunnel for a ADtrans pantograph, using a 2-D microphone array. Measurement results show the noise sources at the pantograph to be located in three areas. The top area is the most important source. Extensive tests with several pantograph configurations indicate that the noise is not dominantly emitted by some specific parts, but more by a large number of parts as a whole. By using empirical formulas, models are formulated to estimate the broadband noise emission of the pantograph, as well in amplitude as in spectral distribution. Analysis of the experimental results indicate that the turbulence in the wake is the dominant noise generating mechanism. The noise levels scale with a power of six to the flow velocity. On the basis of the models it is expected that noise reductions in broadband noise up to 10 dB are possible. Inflow turbulence is an important noise-generating mechanism at the foot region; however, this can easily be handled by adapting the flow around the foot region with a spoiler. The numerical models can be used to design low-noise train parts. The detailed noise measurement results supply important information that can be used for the design of acoustically optimal constructions.

5:20

2pNSa10. Calculation of the three-dimensional sound radiation of rails using the multipole approach. Berndt W. Zeitler and Michael Moeser (Institut fuer Technische Akustik, Einsteinufer 25, 10587 Berlin, Germany, zeitler@mach.ut.tu-berlin.de)

Railway noise is of concern where an important factor is the sound radiated from the rail. This has been studied by using a multipole approach. The three-dimensional sound radiation of a vibrating rail can be calculated by approximating the normal velocity on the surface of the rail with the velocity produced by multipole sources within the rail. Their amplitudes are gained by minimizing the surface error by a method of least squares. The sound radiation is then the superposition of the pressure generated by all such multipole sources. It has been calculated considering one or two rails, coherent or not, each moving arbitrarily in the x and y directions (perpendicular to the length of the rail), with or without frequency-dependent ground absorption. The results of the approach are demonstrated.

5:40

2pNSa11. Vibration assessment in buildings from the underground trains. Illya E. Tsukernikov, Samuel A. Rybak, Stanislav A. Kostarev, and Igor A. Nekrasov (Lab. of Acoust. and Vib., Tunnel Assoc., 21 Sadovaya-Spasskaya St., Moscow, 107217, Russia)

The method approved by the Moscow government in 1997, which has been implemented by the regulation ''Guideline for assessment of vibration from underground train operation in dwellings and administrative buildings'' [1998, Moscow, TIMR], is considered. The method is based on the control of nonsteady vibration by two normative parameters: maximum and equivalent values of rms acceleration, and assessment is made as for frequency-weighted quantities, and so in octave frequency bands at the range 22, 5–90 Hz. The method makes it possible to determine the values of maximum effective rms acceleration during the rating time stated. The procedure of equivalent rms acceleration calculation is analogous to one of DIN 4150, part 2, and the train operation schedules during the rating times are used. Results of testing the method at one of the Moscow Metro lines are discussed. Recommendation on the enlargement of the frequency range controlled and on the correction of the criterion of the frequency-weighted rms acceleration assessments are proposed.

Contributed Poster

This poster will be on display in the Poster Gallery from Monday to Wednesday, 15–17 March. The author will be at the poster from 10:00 a.m. to 12:00 noon on Tuesday, 16 March.

2pNSa12. Prediction of railway-induced vibration by means of transfer functions. Juergen Peters and Gerhard Prestele (Moehler + Partner, Schwanthaler Str. 79, D-80336 Muenchen, Germany)

The prediction of train-induced vibrations in urban areas has to meet many, partly contradictory aspects. Accuracy of predicted vibration with respect to disturbance of residents and measures of reduction of ground-borne vibration, unknown conditions of transmission, large number of buildings to investigate, economical and time aspects also have to be taken into account. The extension of an existing above-ground railway into two tracks in dense developement was taken to test a prediction method based on measured transfer functions characterizing the new track. These investigations were done at an intermediate stage of construction without gravel and sleepers. The transfer functions are used to calculate emission spectra based on a known set of train spectra and corresponding transfer functions investigated elsewhere. The train spectra have to match the super/substructure of the new track and characteristics of the train to be predicted (e.g., velocity). Recent results are discussed.

Session 2pNSb

Noise: Noise at the Workplace I

Alice H. Suter, Cochair
Alice Suter & Associates, 575 Dogwood Way, Ashland, Oregon 97520, USA

Gustav A. Sehrndt, Cochair
Consultant, Kapuzinerstrasse 8, D-50737 Cologne, Germany

Chair's Introduction—1:55

Invited Papers

2:00

2pNSb1. The last 100 years of magazine articles on noise. Robert D. Bruce (Collaboration in Science and Technology, Inc., 15835 Park Ten Pl., Ste. 105, Houston, TX 77084)

Articles on ''noise'' that were referenced in the Reader's Guide to Literature (and similar guides) from 1890 to 1990 were reviewed recently. These articles present an interesting history of the spread of knowledge about noise-induced hearing loss. By determining the readership of each magazine and assuming that the information in that magazine was representative of the knowledge of that readership, it is possible to attribute certain levels of knowledge chronologically about noise-induced hearing loss to different segments of society. For example, the first group to learn about noise-induced hearing loss consisted of doctors who directly diagnosed hearing losses. Next to learn were the doctors who read journal articles written by the first doctors. Soon after the medical articles were published, the information propagated to the scientific/engineering and financial communities, and they added their own particular insights on the subject. Considerably later, magazines read by workers and their families published information on noise-induced hearing loss, but seldom with sufficient information to enable workers to protect their own hearing.

2:20

2pNSb2. Combined effects of noise and whole body vibration in the working environment. Marianne Schust and Helmut Seidel (Federal Inst. for Occupational Safety and Health, Office Berlin, Nöldnerstr. 40-42, 10317 Berlin, Germany, arbeitsmedizin@basam.b.shuttle.de)

The simultaneous exposure to noise and whole-body vibration (WBV) is the most frequent combination of physical factors at workplaces. Both factors probably act not-independently of each other. The results of the studies regarding the aural effects indicate that additional exposure to WBV amplifies the temporary threshold shift as well as of the permanent threshold shift. Various parameters, i.e., postural sway, vision, and cardiovascular changes, were investigated in experimental studies to clarify the extraaural physiological effects. The results demonstrate a dependence on the intensity and the frequency spectrum of the noise as well as of the WBV. Mutually amplifying interactions of noise and WBV were observed. The events of experimental research regarding the subjective assessment of exposure conditions suggest the following conclusions: an increase of noise intensity causes stronger sensations of the WBV intensity except for WBV with main frequencies around 2.5 Hz. Changes of WBV intensity have no effect on the subjectively experienced loudness and noise-related annoyance. Compound judgments of the entire situation are influenced by an interaction of noise and WBV. The results are discussed to derive proposals for guidelines considering combined effects.

2:40

2pNSb3. Hearing disorders from combined exposures to noise and solvents: A review. Thais C. Morata (Natl. Inst. for Occupational Safety and Health, 4676 Columbia Pkwy./C 27, Cincinnati, OH 45226, thaiscm@aol.com)

Not until recently was solvent exposure found to have a significantly adverse effect on hearing. In some cases the risk can be comparable to the most potent and best-known occupational factor, excessive noise. In animals, combined exposure to solvents and noise can result in an increased loss of auditory function beyond the simple addition of the effects of each agent. An increased prevalence of hearing loss has been reported in humans as well. The balance function can also be affected by certain industrial chemicals. The importance of these observations becomes clear when the magnitude of exposed populations and the number of potentially hazardous chemicals found in work environments are taken into account. The need for research in this area is further heightened by the fact that there are no guidelines or standards for combined exposures to chemical and physical agents. The present paper reviews the effects of combined exposures to solvents and noise on hearing function and examines study designs, hearing assessment alternatives, and strategies for the analysis of these effects.

3:00

2pNSb4. Communication and warning signal perception. Judy Edworthy (Dept. of Psych., Univ. of Plymouth, Drake Circus, Plymouth, Devon PL4 8AA, UK, jedworthy@plymouth.ac.uk)

Warning signals are used throughout industry and commerce, and often provide vital sources of information. Due to developments in digital technology, it is now possible to deign any sort of auditory signal, some of which may be effective, some of which may not. In this paper a methodology is outlined which takes a step-by-step, user-centered approach to the design and implementation of warning signals in noisy environments with the aim of creating warning signals which are both easy to understand and to act upon. It begins with the selection of referents (the events to be signaled), through an iterative design process which involves tests of appropriateness, learning and confusion, urgency, and recognition, to operational testing which includes adaptation to the noise environment, consideration of the complete warning set, and so on. The methodology is based on a standardized procedure for designing and implementing public information systems [ISO 7001, ''Specification for public information systems'' (1979)]. The paper describes the methodology in detail.

3:20

2pNSb5. Noise exposure, hearing loss, and hearing conservation in the construction industry. Alice H. Suter (Alice Suter & Assoc., 575 Dogwood Way, Ashland, OR 97520)

Workers in certain sectors of the construction industry incur more noise-induced hearing loss than in most other trades. This paper reviews data on noise exposure and hearing loss in the construction industry, gathered mainly in Washington State, British Columbia, Canada, and Sweden. The problem of worker mobility, where temporary employment is typical even for unionized workers, has hampered the implementation of effective hearing conservation programs in the construction industry. Solutions to this problem include a central repository for audiometric test results and information on training and noise control programs. Multiemployer benefit programs concerning health insurance and pensions provide models in the United States. A hearing conservation program specific to construction noise has been successfully implemented in British Columbia, with a resulting decrease in the incidence of noise-induced hearing loss.

3:40

2pNSb6. Assessment and remediation of perceived handicap in subjects with acquired hearing impairment. Lillemor R-M. Hallberg (Nordic School of Public Health, Box 121 33, 420 42 Göteborg, Sweden, Lillemor.Hallberg@nhv.se)

In a treatment-comparison group design, a group-rehabilitation program developed for hearing-impaired individuals and their close relatives was evaluated. The majority of subjects had hearing loss from noise exposure. The aim of the program was to give adequate information, psychosocial support, and training for effective coping strategies. Sixty-six consecutive patients at the hearing clinic were included in a pilot study. Standardized questionnaires, intended to measure ''perceived handicap,'' ''social support,'' ''perceived negative attitudes,'' ''acceptance of hearing loss,'' and ''communication strategies'' (maladaptive behavior, verbal strategies, and nonverbal strategies), were used at the end of the last group session (short-term evaluation) and with postal questionnaires four months later (long-term evaluation). The evaluation showed that the use of maladaptive behavior (e.g., guessing, pretending to hear, and avoiding interactions) was significantly decreased in the treatment group in a short-term as well as in a long-term perspective ($p=0.000$ and $p=0.032$, respectively). The use of verbal strategies was significantly increased in the treatment group after the rehabilitation ($p=0.020$), but this increase did not reach a significant level four months later. Self-reported handicap was decreased in some conditions. Presently, data from ongoing rehabilitation groups are assessed and statistical data analysis will follow.

4:00–4:20 Break

4:20

2pNSb7. Noise control case studies. Keith A. Broughton (Health and Safety Executive, Magdalen House, Bootle, Merseyside L20 3QZ, UK)

Giving advice to owners and employers on how they can introduce methods of controling noise in industrial situations is often difficult. Many years ago the noise specialist inspectors built up a database of successful control methods they witnessed in their normal duties in visiting factories. These were collated into a case study book and sold. Recently this exercise was repeated and the second book, *Sound Solutions*, was issued. Aimed specifically at employers, it gives examples from a wide range of industries of noise problems which have been successfully overcome. It outlines the original problem, gives the solution, and indicates an approximate cost, and gives advice on where such control can be obtained. In the introduction advice is given so that the employer can ask a consultant or engineer questions on the method to be employed to solve a problem, so that they have a better understanding of the control process involved. The guidance is published by the HSE, a department of government.

4:40

2pNSb8. Noise declaration for hand-held machinery. Ilkka Kyttälä (Ministry of Social Affairs and Health, Dept. for Occupational Safety and Health, Box 536, FIN-33101 Tampere, Finland) and Erkko P. Airo (Inst. of Occupational Health, FIN-00370 Helsinki, Finland)

A study on noise declarations and safety of hand-held machinery was executed in Finland in 1995–1996. Acceptable declarations were available for 77% of pneumatic and 94% of combustion-type machinery but only for 50% of electric machinery. This problem of machinery not having noise declaration can be corrected by national or international market control operations. For example, such a project on pneumatic hand-held machinery is going on in Finland by the occupational safety and health administration. The results will be presented at the beginning of 1999. Another problem is that the available noise declarations were usually correct but not

necessarily valid. Laboratory measurements showed that declared values were correct, but the sound-pressure levels at the operator's position were higher in practical use. For example, angle grinders' declared idling SPLs were 80–86 dB, in a workshop they were 90–95 dB, and during metal processing the SPL was 110 dB. The reason for this is obvious: the quiet simulated, standardized operating conditions produce less noise than the typical use. The purpose of the system, the possibility to choose a low-noise machine, is partially lost. Too low declared values may also lead to false conclusions about the need of hearing protection.

Contributed Papers

5:00

2pNSb9. Common problems in noise control projects. Sergio Beristain (Mexican Inst. of Acoust. Lab., Faculty of Elec. and Mech. Eng., Natl. Polytechnic Inst., P.O. Box 75805, 07300 Mexico City, Mexico)

In actual industrial noise control, it is common to face obstacles before being able to analyze the noise, in addition to others arising in the process of analysis and designing the proper solution: usually it is not a new installation, which produces big savings in the future, but noise due to bad installations or irregular growth of industrial plants. This paper discusses the most common problems found in practice, and presents some ideas for facing some of them. Among them are economics, legislation, lack of knowledge or interest, lack of trained personnel for making the installation, etc., and the noise control project itself, which indeed is very important. This means that the noise control specialist should be ready to face conditions fully outside his or her expertise, but completely related to the problem to be solved. There are some additional aspects not related with technique, standards, or economics, which are opposed to the implementation of the designed solution, like culture, education or ''the expectation that nobody will get deaf in the future if they did not get deaf today.'' Knowledge of all of the above limitations is essential to avoid failure in noise control in new or rebuilt installations or in hearing conservation programs.

5:20

2pNSb10. Polish system of workers' protection against noise. Krystyna Pawlas (Inst. of Occupational Medicine and Environ. Health, 13 Koscielna str., 41-200 Sosnowie, Poland, kape@imp.sosnowie.pl)

In Poland, like in other industrial countries, the protection of workers' health against hazards of occupational environment is a subject of many regulations. The basic act is the Code of Labor. Executive regulations connected with the Code are edited by the Ministry of Health and Social Welfare and the Ministry of Labor and Social Affairs. The Ministry of Health controls the organization of occupational health services, e.g., requirements for persons performing health examinations, principles of hearing examination, assessment of hearing disability, and the principle of certification of the hearing damage as occupational disease as well as monitoring of noise at workplaces. The Ministry of Labor establishes maximum allowable levels, organizes safety and hygiene services, and sets the principles of education in the field of occupational hygiene. The Ministry of Labor recommends standards for measuring and assessing noise at workplaces. These regulations are the basis for the hearing conservation programs. Polish legislation has been adjusted recently to harmonize with the currently standing legislation in the European Community. The main principles at present are the same as those accepted by the EC, but there are some differences concerning details of legislation and the organization of medical as well as occupational hygiene services.

5:40

2pNSb11. A DRC-based analysis of the auditory hazard from exposure to impact noises generated by carpentry tools and tasks. Robert M. Lilkendey (Jaffe Holden Scarbrough Acoustics, Inc., 114A Washington St., Norwalk, CT 06854, rlilkendey@jhsacoustics.com)

To assess the risk of hearing from impulsive sounds several countries have developed damage risk criteria (DRC) which establish limits for an exposure to impulse noise based on key parameters of the impulse and a threshold for acceptable hearing loss. The German, French, Dutch, and an adjusted CHABA DRC were used to assess the potential for carpentry-based impact noises to present an auditory hazard to construction workers under normal working conditions. Measurements of impact noise events from compressed air nailguns and common hammering tasks were made in the field and simulated in a laboratory. The peak sound-pressure level, duration, and A-weighted energy of each impact were determined by digitizing the event and then processing the waveform using two impulse noise analysis programs. The maximum number of allowable exposures was calculated for each event based on the levels set by the DRCs and compared to published and observed productivity rates. The results showed that among the four DRCs, the German was the least protective, finding only 5 of the 12 exposures to be hazardous, and the French (7), Dutch (11), and adjusted CHABA (12) incrementally more protective.

6:00

2pNSb12. Auditory damage due to impulses or continuous noise. Gerald Fleischer (Div. of Auditory Res., Univ. of Giessen School of Medicine, D-35392 Giessen, Germany)

In order to determine the detrimental effect of continuous noise versus impulsive noise, a number of groups were examined: school children, university students, soldiers, workers, pilots, and amateur and professional musicians. Auditory performance was determined by means of pure tone audiometry up to 16 kHz. Auditory load throughout life was estimated, using a detailed questionnaire that included the aspects of profession, hobbies, sports, and consumption of music. Occurrence and severity of tinnitus were also determined. It can be shown that impulsive noise is more damaging to the ear than continuous noise of the same L_{eq}. Analyzing the situation at the workplace, it can be concluded that the damaging effects of acoustic impulses are not properly measured by the L_{eq}.

Session 2pNSc

Noise and Physical Acoustics: Experience with Noise Prediction I

Keith Attenborough, Cochair
Faculty of Technology, The Open University, Milton Keynes MK7 6AA, UK

Karl-Wilhelm Hirsch, Cochair
Institut für Lärmschutz, Arnheimer Strasse 107, 40489 Düsseldorf, Germany

Invited Papers

2:00

2pNSc1. Remarks on acoustical descriptors for explosions in air. Karl-Wilhelm Hirsch (Inst. fuer Laermschutz, Duesseldorf, Germany)

Currently, ISO/TC43/SC1/WG51 is collecting ''experiences'' with measuring and predicting shooting noise. One goal of this working group is to write a guideline for the measurement of source data of shooting noise, taking into account the special characteristics of these high energy, impulsive blasts. There are three special aspects with shooting noise: First, there are nonlinear effects close to the source. Second, the strong directivity of blast sources plays a very important role. Third, in contrast to most of the continuous noise sources, blasts are single events which involve coherence effects during source and receiver measurements. Therefore, a dedicated set of emission data has to be introduced to describe a blast source with respect to sound propagation models. The presentation will discuss the definition of a set of appropriate source descriptors for muzzle blasts. The source will be treated as a linear spherical source with directivity. Its intensity will be defined in the far field and its directivity pattern will describe the acoustical strength. The radius of this artificial source depends on the blast energy and is an important parameter when determining the appropriate measurement distance for source measurements.

2:20

2pNSc2. Measurements of acoustical emissions from large-calibre weapons. Christa Korff (Lärm-Meßstelle 1 Bw, WTD 91, D-49716 Meppen, Postfach 1764, Germany)

Extreme pressure waves and a wide frequency band characterize the environment of a firing large-calibre weapon. Here the usual way to gain acoustical source data therefore fails. For this reason an international working group has developed a standard procedure to obtain the sound emission from such weapons. This will be described. The German Ministry of Defense adopted the method to collect the basic source data for a computer model to calculate the emissions of noise caused by the shooting artillery and explosions in the vicinity of military training areas. It supported the experiments that have been carried out in the last years at the Meppen proving ground in northern Germany. There the environmental conditions defined by the working group are met rather well. First experiences with the application of the standard procedure and some results of the model calculations are reported.

2:40

2pNSc3. Source data for small arms noise. Larry L. Pater (U.S. Army Construction Eng. Res. Labs., Champaign, IL)

Small arms source data are required for calculation of far-field noise levels. Advantages and disadvantages of various methods of obtaining source data for small arms noise are discussed, and specific examples are presented. Important issues include nonlinear effects, directivity of muzzle blast and projectile shock noise fields, isobar shapes, wavefront shapes, and blast wave temporal characteristics, particularly shape and duration. A methodology is presented for obtaining source data that is free of inaccuracies due to ground reflections and ground impedance effects. Source data have been measured for a number of small weapons, both rifles and pistols. Example data are presented as waveforms, peak levels, overall sound exposure levels, and spectral distribution of 1/3-octave-band sound exposure levels. Data are presented separately for muzzle blast and projectile shock, and special attention is paid to the effect of interactions of the blast noise sound wave with the ground. [Work supported by U.S. Army.]

3:00

2pNSc4. Results from Norwegian sound propagation experiments. Lars R. Hole (Norwegian Defence Construction Service (NDCS), Oslo mil/Akershus, 0015 Oslo, Norway, larsr@gfi.uib.no)

This paper describes four sound propagation experiments that were undertaken in Norway from 1994 to 1996. Trials were carried out at Finnskogen; a long-range site, and at Haslemoen; a short-range site. Summer and winter conditions were investigated at both sites. Two similar experiments were carried out at each site with and without snow cover. At Finnskogen, an experimental array of 24 by 24 km was set up in a terrain with smooth hills, primarily covered by forest. At Haslemoen, propagation was investigated out to 1.5 km above a uniform forest and a uniform, flat open field of pasture land. One, 8, and 64 kg cylindrical charges of C-4 explosives

were used as sound sources. Measurements of acoustics, seismic ground response, complex ground impedance, and meteorology were carried out simultaneously. This paper gives an overview of the experiments and presents examples of data. An overview of theoretical research based on the collected dataset is also given. Literature for further details is referred. An easily accessible database with all data is available. Detailed information is also given at www.bpof.inter.net.

3:20

2pNSc5. Measured and computed effect of meteorological condition and ground surface on propagation of impulsive sound to 20 km. Michael J. White (Appl. Res. Assoc., 5941 S. Middlefield Rd., Littleton, CO 80123)

The cumulative propagation effects of weather and ground surface on sound exposure levels at long distances from an impulsive sound source are not well established. Measurements of sound exposure and peak pressure at distances up to about 20 km from explosions were made by the U.S. Army for three types of ground conditions. These data, along with measured weather profiles and ground impedance parameters, were used as inputs to the FFP model, for comparison of measurement to prediction. The 1/3-octave band attenuations were calculated for band center frequencies from 1 Hz to 1 kHz, for the measurement microphone locations in the study. A great deal of the variation in signal level from event to event was predicted by the FFP model, without resort to nonlinear propagation effects or to turbulent scattering. Groups of cases with similar signal attenuation with distance and similar weather profiles may provide a reasonable basis for classifying long-distance propagation conditions. Such a classification would have merit as an efficient way to assess long-term noise averages or to estimate the error in short-term predictions of noise levels. [Work supported by USACERL and AMSAA.]

3:40

2pNSc6. Blast noise propagation above a snow cover at Haslemoen, Norway. Donald G. Albert (USACRREL, 72 Lyme Rd., Hanover, NH 03755) and Lars R. Hole (Norwegian Defence Construction Service, Environ. Section, Oslo mil/Akerhus, 0015 Oslo, Norway)

During the short-range winter measurements at Haslemoen, Norway, a series of blast wave forms produced by 1-kg charges of C4 explosive fired 2 m above a dry snow cover 11 to 20 cm thick were recorded after propagating horizontally 100 to 1400 m. In attempting to model these experiments, it was found that the usual viscoelastic treatment of the ground was unable to match the recorded wave forms. A rigid-porous model of the snow cover was required to obtain good agreement. The measured wave forms, with a peak frequency around 50 Hz, show pulse broadening effects similar to those previously seen in pistol shot experiments using higher frequency waves over shorter propagation distances. The modeling predicts an average snow cover depth of 15 cm and effective flow resistivities of $30-41$ kPa s m^{-2}, in agreement with snow pit observations and with previous acoustic measurements over snow. For propagation in the upwind direction, the pulse broadening caused by the snow cover interaction is lessened, but the overall amplitude decay is greater because of refraction of the blast waves.

4:00–4:20 Break

4:20

2pNSc7. Air–ground interaction effects in the propagation of low-frequency impulse noise. Christian Madshus, Amir M. Kaynia (Norwegian Geotechnical Inst., Anal. Div., P.O. Box 3930, Ullevaal Hageby, N-0806 Oslo, Norway, cm@ngi.no), and Lars R. Hole (Norwegian Defence Construction Service, N-0015 Oslo, Norway)

Four large-scale sound propagation experiments performed in Norway from 1994 to 1996 under both summer and winter conditions clearly demonstrate that air–ground interaction has a significant effect on the propagation of low-frequency impulse noise. During the experiments, specific measurements were made for detailed investigation of this interaction. The paper will present the instrumentation used, and some typical measured data. Various numerical simulations of the experiments are made, covering both poro-elastic and visco-elastic description of the ground. Based on the measured data, theoretical considerations, and the numerical simulations, the paper will discuss mechanisms for acoustic energy loss from the air into the ground. Special emphasis will be put on the effect of the interaction of the propagating air pressure with the slow p-waves and with the dispersive Rayleigh waves in the ground. The relative importance of these two interaction mechanisms on the energy loss and thus on the sound attenuation will be examined for various ground conditions.

4:40

2pNSc8. A comparison of engineering methods for predicting ground effect. Keith Attenborough (Faculty of Technol., The Open Univ., Milton Keynes MK7 6AA, England)

Methods for calculating ground effect for broadband noise are reviewed and predictions of these methods are compared with recent data for propagation from a fixed jet engine and measurements over farmland in various states of cultivation. The review includes empirical, standard, and approximate analytical methods. The comparison leads to a discussion and evaluation of their relative merits. [Work supported by EPSRC and BBSRC (UK).]

5:00

2pNSc9. On the applicability of models for outdoor sound. Karsten B. Rasmussen (Dept. of Acoust. Technol., Bldg. 352, Tech. Univ. of Denmark, DK-2800 Lyngby, Denmark, kbr@dat.dtu.dk)

The suitable prediction model for outdoor sound fields depends on the situation and the application. Computationally intensive methods such as parabolic equation methods, FFP methods, and boundary element methods all have advantages in certain situations. These approaches are accurate and predict not only sound pressure levels but also phase information. Such methods are, however, not

always able to predict the sound field for more complicated scenarios involving terrain features, atmospheric wind and temperature gradients, and turbulence. Another class of methods is based upon approximate theory—such methods are inherently less accurate but generally faster in computation and may also provide results for complicated scenarios. The accuracy of different approaches in realistic situations is discussed based upon measured and simulated data.

5:20

2pNSc10. Standardization efforts in Germany on the quality of software products for the prediction of environmental sound emission. Ulrich J. Kurze (Müller-BBM GmbH, Robert-Koch-Str. 11, D-81252 Planegg, Germany)

Based on ISO/IEC 12119 for quality requirements and testing of software packages, a special standard has been drafted for software products designed for noise mapping and related tasks of environmental noise control. The most important aspects are related to the definition and testing of software precision and to an interface suitable for data exchange between various programs. In a first step, the potential consistency of the software calculation procedures with standarized procedures is checked by test cases. Since switches can be set in most programs to accelerate calculation procedures for complex and extended situations, a second step is required to control the precision obtainable by the user for his special application. This is done on a statistical basis. Most of the effort is generally spent with the collection, adjustment, and input of geometrical data. In order to simplify repeated runs for modified situations and to allow for maximum flexibility of users, a common interface has been defined for all acoustically relevant data determined for a first run. This helps avoid errors and allows for data exchange suitable for comparison of different programs and situations.

5:40

2pNSc11. Aircraft noise model corrected by operational and propagation effects. Oleksander I. Zaporozhets, Vadim I. Tokarev (Acoust. Lab., Kyiv Intl. Univ. of Civil Aviation, 1, Ave. Cosmonaut Komarov, Kyiv, 252058 Ukraine, zap@elan-ua.net), Keith Attenborough, and Kai M. Li (The Open Univ., Milton Keynes MK7 6AA, UK)

Although there are mathematical models for predicting aircraft noise, the requirements on their accuracy have recently increased. Possibilities for model improvements are reviewed with respect to both noise source generation characteristics and noise propagation effects. The review indicates that the required corrections are not standard since they depend on the physical model of the noise source. The results of aircraft noise assessment for different types of aircraft and for different models of noise propagation are discussed. Recommendations for their use in computational schemes are made. The most rational method generates the required corrections for each type of aircraft according to the operational and noise propagation conditions in a given situation.

6:00

2pNSc12. FLULA2: Aircraft noise prediction and measurements. Georg Thomann and Rudolf Buetikofer (EMPA, CH-8600 Duebendorf, Switzerland)

Aircraft noise predictions of the program FLULA2 are compared with airport noise monitor measurements and with single flight events. Further, the versatility of using a point source model for simulation is discussed and the implications of accurate noise predictions on land use planning are outlined. The aircraft noise simulation program FLULA2, developed at EMPA, uses a point source with a directivity characteristic in contrast to many other models which use line segments and correction terms. With the powerful model of a moving point source, the level-time history of a single flight can be reconstructed. Thus all acoustic effects (topography, spectral air absorption, ground effects, . . .) may be included and any noise metrics can be calculated. The program is validated by comparing single events (the level-time history of measurements and of calculations) and by comparing the yearly average of measurements at monitoring stations around airports with the L_{eq} predictions. There are variations, but there is no systematic under- or overestimation of the noise calculations compared with the monitors.

Session 2pNSd

Noise: Computational Aeroacoustics II: Methodology and Applications

Sanjiva K. Lele, Cochair
Department of Aeronautics and Astronautics, Stanford University, Stanford, California 94305-4035, USA

Christophe Bailly, Cochair
Laboratoire de Mécanique des Fluides et d'Acoustique, Ecole Centrale de Lyon & UMR CNRS 5509, BP 163, 69131 Ecully, Cedex, France

Invited Papers

2:00

2pNSd1. Aeroacoustic simulations and stochastic approach using linearized Euler's equations. Christophe Bailly and Daniel Juvé (Lab. de Mécanique des Fluides et d'Acoust., Ecole Centrale de Lyon, France and UMR CNRS 5509 BP 163, 69131 Ecully Cedex, France)

Sound generation and propagation in a turbulent flow is a very difficult numerical problem. Indeed, acoustic fluctuations are very small by comparison to the mean and turbulent fields. Linearized Euler's equations provide accurate numerical solutions only in working on perturbations. In the stochastic noise generation and radiation model, the mean flow is calculated by solving the Reynolds-averaged Navier–Stokes equations. Then, Euler's equations are linearized around this mean flow field. A turbulent source term is introduced in the equations, and the turbulent velocity field is modeled by a sum of random Fourier modes. The numerical solution is obtained by using a dispersion-relation-preserving scheme in space, combined with a fourth-order Runge–Kutta algorithm in time. In order to validate the numerical method, radiation of multipolar sources in a uniform and sheared mean flow has been investigated in a two-dimensional case. The calculated solutions favorably compare with analytical solutions or with ray tracing. Then, the SNGR model is applied to a subsonic jet noise in a 3-D geometry. Numerical results and future developments will be discussed.

2:30

2pNSd2. CAA activities at ONERA using LES. Eric Manoha, Bruno Troff, Christelle Seror, Gilles Rahier, and Pierre Sagaut (Office Natl. d'Etudes et de Recherches Aerostatiales (ONERA), Dept. of Computational Fluid Dynam. and Aeroacoustics, BP 72, 92322 Chatillon Cedex, France)

Most CAA applications rely on hybrid methods providing the radiated sound (using the Lighthill analogy, Kirchhoff integral or linearized Euler equations) from unsteady CFD. In that context, LES is widely considered as a compromise between full DNS and unsteady RANS. For two years, ONERA has undertaken studies aiming at understanding and applying LES in CAA. Former works focused on coupling LES to the Lighthill analogy. One typical application was the prediction of the noise generated by vortex shedding at the trailing edge of a thick flat plate. The incompressible LES was performed on a Cartesian mesh using the ONERA ''PEGASE'' code. The far-field noise was computed using the Curle formulation and favorably compared to airfoil noise experiments. More recently, a theoretical study analyzed the contribution of the LES subgrid scale model, or cutoff wave number, to the noise production computed from the Lighthill tensor, concluding that modeling this contribution may be important to correctly estimating the acoustic field. Other CAA applications of LES are now under progress: flap side-edge noise from high-lift devices of landing aircraft, and jet noise, with comparison of the Kirchhoff integral and Lighthill analogy. Coupling LES with linearized Euler equations is also a topic of interest.

3:00

2pNSd3. Low dispersion schemes. Mathematical model and demonstrative cases. Oktay Baysal (Aerosp. Eng. Dept., Old Dominion Univ., Norfolk, VA 23529-0247)

Considering the computational efficiency along with the high-fidelity to the underlying physical principles, significant advances have been achieved in aeroacoustics simulations. This, however, appears to have remained somewhat limited to the modeled periodic noise generation and propagation by assuming linear waves in uniform flow. Toward this goal, some useful applications have been computed with low-dispersion schemes, by solving the linearized Euler and Navier–Stokes equations. In addition to the benchmark cases reported in the CAA Workshops, these included a supersonic jet noise simulation. On the other hand, there are numerous aeroacoustics applications, such as subsonic jet noise and cavity noise, where the linear wave and uniform flow assumptions would be too compromising. Consequently, the linear dispersion-relation-preserving scheme and its boundary conditions have been extended to the nonlinear equations. It has been tested for a number of simple initial-value and periodic-source problems. Presently, a cavity noise problem and its suppression are being computed with this computational model. [Work partially supported by NASA Langley Research Center.]

3:30

2pNSd4. Direct computation of sound generation and radiation from a ''Singing Wire'' (or direct computation of Aeolian tone). Duck Joo Lee and Jae Wook Kim (Aerosp. Eng. Dept., Korea Adv. Inst. of Sci. and Technol. (KAIST), 373-1 Kusong-dong, Yusong-gu, Taejon, Korea 305-701)

Sound from a singing wire, known as ''Aeolian Tone,'' is simulated by directly solving unsteady compressible Navier–Stokes equations. The surface pressure on the surface of the wire in the presence of wind fluctuates periodically and the pressure near the surface radiates as a ''dipole sound.'' The mechanisms of the surface pressure fluctuation are closely related to vortex shedding from the wire. An OHOC (optimized high-order compact) scheme is used to have high resolutions of the flow and the sound. A new formalism of characteristic boundary conditions in the body-fitted generalized coordinates is presented. Extended kinds of numerical boundary conditions for simulating subsonic inflow, nonreflecting outflow, and solid wall are formulated on the basis of characteristics and applied to computational aeroacoustics (CAA). The boundary conditions are applied to actual computation of 2-D wire having a cylindrical cross section on nonuniform and nonrectangular grid meshes. Far-field acoustic pressures due to Karman vortex streets are measured and the Strouhal number is evaluated correctly. The feasibility of using the generalized characteristic boundary conditions is investigated for sound generation owing to an unsteady flow around a body.

4:00–4:20 Break

4:20

2pNSd5. Acoustic radiation due to gust–airfoil and blade–vortex interactions. Ramesh K. Agarwal (Wichita State Univ., Natl. Inst. for Aviation Res., Wichita, KS 67260-0093)

The problem of acoustic radiation due to gust–airfoil and blade–vortex interaction in compressible mean flow is considered numerically. The acoustic perturbation field is calculated by solving the acoustic equations derived from the unsteady Euler equations by linearizing about a steady mean flow and assuming a single frequency disturbance. A computational code is developed which is validated by computing the unsteady loads on a flat plate due to a gust in incompressible flow (Sears problem), and unsteady loads and acoustic radiation due to a compact and noncompact gust in compressible flow. For these three cases the numerical results are compared with the exact analytical solutions and asymptotic solutions. Excellent agreement is obtained. The validated code is then employed to perform parametric studies by varying the Mach number of the mean flow, the angle of attack, and the geometry (thickness and camber) of the airfoil. Conclusions are drawn about the magnitude and phase of acoustic radiation due to gust–airfoil interaction for various Mach numbers, angles of attack, and airfoil geometries. The validated code is also employed to compute the acoustic radiation due to blade–vortex interaction. Calculations are compared with those of other investigations for both the mean flow and the acoustic variables.

4:50

2pNSd6. On the coupling of the inverse problem with computational aeroacoustics. Xiadong Li (Dept. of Jet Propulsion, No. 407, Beijing Univ. of Aeronautics and Astronautics, Beijing 100083, PROC)

This presentation is to survey the recent developments and advances of inverse problems arising from various aeroacoustic applications, with the emphasis on the inverse problem of the Ffowcs Williams and Hawkings (FW–H) equation. Generally an inversion physical model should be first established to relate the sound source with its radiated acoustic field. The main difficultly is that most inverse problems are mathematically ill posed. The singular value decomposition (SVD) technique combined with the Tikhonov regularization method has shown to be a very powerful tool. Also, the generalized cross-validation (GCV) and L-curve criterions are rather suitable for choosing an optimal regularization parameter. Several studies have shown that the aeroacoustic source strength distributions can be reconstructed using the radiated acoustic field data, such as a propeller [X. D. Li and S. Zhou, AIAA J. **34**, 1097–1102 (1996)] or a streamlined body [S. P. Grace, H. M. Atassi, and W. K. Blake, AIAA J. **34**, 2233–2240 (1996)]. The inversion techniques can also be applicable for the spatial transformation of sound field and active noise control. Finally, the possibility of the coupling of the inverse problem with computational aeroacoustics is to be discussed. [Work supported by NSF and ASF of China.]

Session 2pNSe

Noise: Computational Aeroacoustics III: Further Topics

Tim Colonius, Cochair
Mail Code 101-44, California Institute of Technology, Pasadena, California 91125, USA

Eric Manoha, Cochair
Department of Computational Fluid Dynamics and Aeroacosutics, Office National d'Etudes et de Recherches Aerospatiales (ONERA), BP72, 92322 Chatillon, Cedex, France

Contributed Papers

5:20

2pNSe1. Noise computation of a mixing layer using LES simulations. Christophe Bogey, Christophe Bailly, and Daniel Juvé (Lab. de Mécanique des Fluides et d'Acoust., Ecole Centrale de Lyon, France and UMR CNRS 5509 BP 163, 69131 Ecully Cedex, France)

A study of noise computation of a two-dimensional subsonic mixing layer is performed. The first concern is to develop a large eddy simulation (LES) code solving the filtered Navier–Stokes equations to obtain the nonlinear generation of sound. The compact DRP scheme of Tam and Webb is used in space, and the time integration is carried out by a four-step Runge–Kutta algorithm. The boundary conditions of Dong and Tam are implemented. Then, a two-dimensional mixing layer is simulated. The spatial growth, turbulence rates, and spectra are in good agreement with other available studies. The goal is now to use the LES data to calculate the acoustic field generated by the mixing layer. Various methodologies have been investigated. First, the direct exploitation of the LES pressure field reveals tremendous difficulties due to the different orders of magnitude between aerodynamic and acoustic fluctuations. The other approaches consist of using source terms calculated from the LES velocity fluctuations. Two formulations are tested: Lighthill's analogy based on a volume integral over the region encompassing sound sources, and linearized Euler's equations where a source term is added. Numerical results and future developments will be discussed.

5:40

2pNSe2. An error analysis for the lattice gas time domain (LGTD) method in CAA. Victor W. Sparrow (Penn State Univ., Grad. Prog. in Acoust., 157 Hammond Bldg., University Park, PA 16802, sparrow@helmholtz.acs.psu.edu)

One of the most important requirements in computational aeroacoustics (CAA) is that a numerical method have excellent dispersion characteristics. The new lattice gas time domain (LGTD) method has better dispersion characteristics than any other scheme encountered by the author. This talk will first review LGTD in comparison with the better known finite difference time domain (FDTD) method. Then quantitative error estimates will be provided for a benchmark problem from ICASE/LaRC Workshop on Benchmark Problems in CAA [NASA Conf. Pub. 3300, 143–147 (1995)], showing the spectacular performance of the LGTD method. The present work answers some questions raised and extends the findings presented in CEAS/AIAA-95-115 [in Proc. 1st Joint CEAS/AIAA Aeroacoustics Conference, 12–15 June 1995, Munich, Germany, pp. 813–817] and in J. Comp. Acoust. **1**, 423–454 (1994).

6:00

2pNSe3. Reduction of boundary effects in acoustic analogy application to CFD databases. Andreas Wilde and Marco Rose (Technische Univ. Dresden/Mommsenstr., 13/01062 Dresden, Germany, andreas@eakaw2.et.tu-dresden.de)

The calculation of noise generation and radiation using an acoustic analogy is very sensitive to the degree to which the sound-generating flow or rather the flow-simulation model meets the very strict assumptions made when deriving the aeroacoustic analogy. In many cases of technical interest, the popular assumption that there are no nonacoustic flow fluctuations on the boundary of the considered volume (control volume) is not satisfied. In these cases, the analogy has to be extended or an additional volume has to be attached, in which these nonacoustic fluid motions are damped. In this work, two examples of extension of the analogy formulation and of damping zones are studied. While all schemes yield reduction of noise prediction errors, the damping zone schemes are most effective in cancelling spurious noise sources. On the other hand, the extension of the acoustic analogies provides cost-effective ways to reduce noise prediction errors even at low frequencies.

Session 2pNSf

Noise: Harmonization of Noise Ratings

Paul D. Schomer, Cochair
USA CERL, P.O. Box 9005, Champaign, Illinois 61826-9005, USA

Truls Gjestland, Cochair
SINTEF Telecom and Infomatics, O.S. Bragstads plass, Trondheim N-7034, Norway

Joos Vos, Cochair
TNO Human Factors Research Institute, P.O. Box 23, 3769ZG Soesterberg, The Netherlands

Chair's Introduction—2:15

Invited Papers

2:20

2pNSf1. How many ways is it worth slicing the social survey data cake? Sanford Fidell (BBN Technologies, 21128 Vanowen St., Canoga Park, CA 91303)

As when serving portions of cake, social survey findings on the prevalence of noise-induced annoyance may be sliced in many ways to create dosage–response relationships. Schultz (1978) divided ''clustering'' from ''nonclustering'' surveys; FICON (1992) sliced off a few inconvenient data points; several researchers and agencies have found reasons to develop separate relationships for certain noise sources; while yet others question the rationale for developing dosage–response relationships in the first place. Are the various dosage–response relationships usefully different from one another, and artfully enough sliced to support regulatory policy-making or theory development? Might differences among dosage-response relationships inferred by different means reflect statistical artifacts, or the influences of nonacoustic factors? This paper discusses applied and other uses for different slices of the same cake, and how many (more) slices might be useful.

2:40

2pNSf2. Uncertainty in dosage-annoyance relations. Dick B. Botteldooren (Dept. of Information Technol., Univ. of Gent, St. Pietersnieuwstraat 41, 9000 Gent, Belgium) and Truls Gjestland (SINTEF Telecom and Informatics, N-7034 Trondheim, Norway)

Dosage-annoyance relations have traditionally been derived by fitting analytical curves through data gathered from large numbers of field studies. Information on the uncertainty of the relation thus derived is not often given. In this paper the same data set will be examined in several different ways and how this can influence conclusions will be demonstrated. The data set used is taken from Fidell and Barber [J. Acoust. Soc. Am. **89**, 221–233 (1991)]. Transformations of annoyance scales and sound-level measures are assumed to be suitable and are not redone in this work. It is assumed that the average annoyance response of Man is searched and that the dosage-response curves will be used to integrate exposure levels to a single figure that can be used to compare noise impact to a community. This goal is totally different, with respect to uncertainty, from predicting noise annoyance in a particular exposure situation. In this work, individual data are combined, taking into account the different number of data points at different exposure levels and the uncertainty in results from individual studies. Each study is treated as an observation made by an independent expert. Differences to dosage-annoyance relations derived in a more traditional way are discussed. The obvious conclusion is that dosage response relations must be used with caution and that this can well be expressed by taking into account calculation uncertainty accurately.

3:00

2pNSf3. On using ''loudness-weighted'' SEL, LEQ, and DNL to assess noise environments. Paul Schomer (Schomer & Assoc., 2117 Robert Dr., Champaign, IL 61821)

LEQ and DNL are commonly used to assess the long-term noise environments around airports, roads, etc. The fundamental building block to these assessments is the A-weighted sound level or SEL. These are used to compute LEQ or DNL. But many problems have surfaced over the simple use of A-weighting. The A-weighting has been shown to be deficient in assessing sound with strong low-frequency content, and other characteristics, like impulsiveness, are not properly accounted for by the A-weighting. However, no other simple filter has been shown to be superior to the A-weighting filter. One can consider building a more complicated filter that dynamically changes with level and frequency to better reflect human response than does the A-weighting. The equal loudness contours expressed in phons offers a set of curves that can be used to design such a filter. Like A-weighted sound level or A-weighted SEL, signals processed with such a new ''filter'' would be termed ''loudness-weighted'' sound level or ''loudness-weighted'' SEL. This author has analyzed many sounds to illustrate, test, and evaluate the concept of loudness-weighted SEL. This paper discusses the concept of using ''loudness-weighting'' in place of A-weighting and the results indicated by the analysis of many common sounds.

3:20

2pNSf4. Soundscape in cities, limits to the noise limits? Tor Kihlman and Jean Berillon (Dept. of Appl. Acoust., Chalmers Univ. of Technol., SE-41296 Gothenburg, Sweden, tk@ta.chalmers.se)

Today traffic noise due to cars, trains, and airplanes is the main noise source in urban areas. In accordance to the European Commission's Green paper on Future Noise Policy, more than about 250 million people are exposed to A-weighted outdoor levels higher than 55 dB. To improve the situation is a tremendous challenge and the question arises if we are really able to provide a good environment (i.e., levels below 55 dB) for all people in today's cities. In a previous paper [Kihlman and Kropp, Proceedings International Congress on Acoustics, Seattle (1998)], different cities with different structures and automobile dependencies are compared in a general study based on statistical data. A flat regular town structure was assumed without shielding due to, for instance, buildings. In this paper the studies are extended to more common situations including detailed information about traffic flow and the screening of traffic noise due to the building structure. Results are compared with sound maps for different cities.

3:40

2pNSf5. Time-of-day penalty for aircraft noise. H. M. E. Miedema, R. G. de Jong, and H. Vos (TNO-PG, P.O. Box 2215, 2301 CE Leiden, The Netherlands, HME.Miedema@PG.TNO.NL)

Noise metrics differ in the penalty they apply to noise in the evening and the night, and in the definition of these periods. In L_{Aeq} (24 h) no penalties are applied. DNL uses a penalty of 10 dB for the night (22–7 h), and DENL uses a penalty of 5 dB for the evening (19–23 h) and 10 dB for the night (23–7 h). An earlier meta-analysis [J. M. Fields, ''The relative effect of noise at different times of the day—an analysis of existing survey data,'' Hampton, VA, NASA, Report CR-3965 (1986)] did not reveal consistent evidence on the basis of which penalties could be chosen. Data from the 1997 Amsterdan airport study [De Jong *et al.*, ''Hinder, Gezondheid- en Belevingsaspecten in de regio Schiphol,'' TNO-PG, Leiden, Netherlands, report 98.039 (1998); $N=11{,}812$] are used to estimate the time-of-day penalties that give an optimal relation with noise annoyance and self-reported sleep disturbance, respectively. L_{Aeq}'s are available for the following periods: 7–19, 19–22, 22–23, 23–6, and 6–7 h. Penalties are estimated for the whole sample, and for subgroups (e.g., age classes, different levels of noise sensitivity) separately.

4:00–4:20 Break

4:20

2pNSf6. Validation of a new procedure for rating shooting sounds with the help of field survey data. Joos Vos (TNO Human Factors Res. Inst., P.O. Box 23, 3769 ZG Soesterberg, The Netherlands, vos@tm.tno.nl)

In previous laboratory studies it was shown that an almost perfect prediction of the annoyance caused by shooting sounds was obtained on the basis of the outdoor A-weighted and C-weighted sound exposure levels (ASEL and CSEL; L_{AE} and L_{CE}). For single events, the rating sound level, L_r, is given by $L_r=L_{\mathrm{AE}}+\beta(L_{\mathrm{CE}}-L_{\mathrm{AE}})(L_{\mathrm{AE}}-\alpha)+12$ dB. The second term $\beta(L_{\mathrm{CE}}-L_{\mathrm{AE}})(L_{\mathrm{AE}}-\alpha)$ implies (1) that the annoyance is dependent also on the ''heaviness'' of the sound (characterized by $L_{\mathrm{CE}}-L_{\mathrm{AE}}$), and (2) that the additional annoyance ($\beta>0$) increases with ASEL for $L_{\mathrm{AE}}>\alpha$ dB, and decreases with ASEL for $L_{\mathrm{AE}}<\alpha$ dB. In the present study, the procedure for rating shooting sounds, as described above, was validated with the help of data from a German field survey on the annoyance caused by artillery and road-traffic sounds: α and β were determined for which L_r for shooting sound would, overall, numerically correspond to the A-weighted day–night level of equally annoying road-traffic sound. For all relevant impulsive sources, the required ASELs and CSELs received in the various residential areas were determined by TNO Institute of Applied Physics. The results showed that a proper rating sound level was obtained with $\alpha=40$ dB and $\beta=0.025$.

4:40

2pNSf7. A new test of the validity of a maximum single-event-level model in the prediction of the community response to artillery sounds. Edmund Buchta (Inst. für Lärmschutz, Arnheimerstraße 107, D-40489 Düsseldorf, Germany)

It is common, for many environmental sounds, to predict the community response from acoustic measures (such as L_{eq} or L_{dn}) that take the yearly energy-average sound level into account. According to Rylander and colleagues, however, the annoyance is determined mainly by the level of the noisiest events [e.g., see J. Sound Vib. **127**(3), 555–563 (1988); **192**(1), 199–206 (1996)]. The number of those events is less important: the annoyance increases with the number of events up to a saturation point (e.g., for large firearms 1000 shots/year with $L_{\mathrm{CE}}>90$ dB) above which a further increase in number does not affect the annoyance. In the present paper, the usefulness of Rylander's model was tested with the help of data from a German field survey on the subjective effects of artillery sounds [J. Acoust. Soc. Am. (in press)]. The analyses showed that (1) application of a threshold to CSEL results in the loss of important information from residential areas without events above threshold, and (2) saturation, if any, might be observed only from about 70 000 shots/year. It is concluded that for several reasons Rylander's model is inferior to models in which total exchangeability of single-event levels and number of events is assumed.

5:00–5:40
Panel Discussion

Panelists: D. Botteldooren, Belgium
E. Buchta, Germany
S. Fidell, USA
T. Gjestland, Norway
T. Kihlman, Sweden
H. M. E. Miedema, The Netherlands
P. D. Schomer, USA
J. Vos, The Netherlands

TUESDAY AFTERNOON, 16 MARCH 1999 ROOM MA043, 2:00 TO 5:20 P.M.

Session 2pPAa

Physical Acoustics: Thermoacoustics II

Martin Wetzel, Cochair
BMW AG, Hufelandstrasse, 80788 Muenchen, Germany

Cila Herman, Cochair
Department of Mechanical Engineering, Johns Hopkins University, 3400 North Charles Street, Baltimore, Maryland 21218, USA

Invited Papers

2:00

2pPAa1. Advances in pulse tube refrigeration. Ray Radebaugh (Physical and Chemical Properties Div., National Inst. of Sci. and Technol., 325 Broadway, Boulder, CO 80303)

The pulse tube refrigerator is now being developed for a wide variety of cryogenic cooling applications, and it is beginning to replace other types of cryocoolers in many of these applications. This widespread interest occurs because there are no moving parts in the cold end. Most of this development in pulse tube refrigerators began in the mid-1980s with the introduction of the orifice to provide the proper phase relationship between the gas velocity and the pressure. The pulse tube refrigerator has now become the most efficient cryocooler for temperatures of 60 to 120 K. The current state-of-the-art in pulse tube refrigerators is discussed in this paper. Temperatures as low as 2.2 K with two stages and efficiencies as high as 19% of Camot at 80 K in one stage have been achieved. The operating fundamentals are explained very well through the use of thermoacoustic modeling techniques. Recent R&D areas to be discussed are the use of additional orifices, inertance tubes, tapered pulse tubes, dc flow, and thermoacoustic drivers. The fluid dynamics within the pulse tube is still not well understood, and further research in this area is needed to improve performance even further.

2:20

2pPAa2. Thermoacoustic instabilities of highly premixed flames in combustors and boilers. Thomas Sattelmayer and Christian Pankiewitz (Technische Univ. Muechen, Lehrstuhl A fuer Thermodynamik, Boltzmannstrasse 15, D-85748 Garching, Germany)

The attempt to reduce the formation of pollutants from combustion processes has led in recent years to the development of novel low-temperature combustion processes. Confined flames of this type exhibit a number of instability mechanisms, which can lead to unacceptable combustion noise or even to severe damage. The instability mechanisms, which appear in cases of technical interest, are reviewed and explained. It is shown that a realistic model for the description of the instability requires a proper representation of the contribution of the flame as the driving element. To date, nonlinear transfer functions have to be deduced from combustion experiments, but attempts to derive transfer functions numerically have already been published. In the past, modeling efforts were strongly focused on longitudinal modes. Although circumferential modes are of technical importance, they have not yet been fully understood. In this case, a complex interaction of the nonlinear flame with the linear acoustic system has to be taken into account and the transition between modes becomes more important. Since a satisfactory description of the interaction is not yet available, active instability control techniques have been proposed. Their limit in cases of technical interest will be discussed.

2:40

2pPAa3. Thermoacoustic research at ETH Zürich in the 1990s. J. Bösel (Linde Kryotechnik AG, Dättlikonerstrasse 5, CH-8422 Pfungen, Switzerland) and Ch. Trepp (Swiss Federal Inst. of Technol. (ETH) Zürich, CH-8092 Zürich, Switzerland)[a)]

The linear thermoacoustic theory was developed by N. Rott, formerly Professor at the Institute of Aerodynamics at ETH Zürich, in the late 1960s. Since then a couple of research projects in that field have been carried out under the supervision of Prof. Rott, and more recently at the Institute of Process Engineering. The talk will give a short historical summary of the research activities at ETH Zürich and the latest work undertaken at the Institute of Process Engineering will be presented. This research was aimed at increasing the power density of thermoacoustic engines. Instead of the ''stack,'' usually consisting of ''long'' parallel plates, short parallel-plate segments were used, which were randomly oriented to each other. This alternative stack arrangement was expected to benefit from improved heat transfer characteristics and an anisotropic thermal conductivity. The results of a simple numerical model and experiments carried out with a thermoacoustic heat pump confirmed these expectations and will be presented in the talk. [a)] Former affiliation.

Contributed Papers

3:00

2pPAa4. High-efficiency 2-kW thermoacoustic driver. Robert W. M. Smith, Robert M. Keolian, Steven Garrett (Grad. Prog. in Acoust. and Appl. Res. Lab., Penn State Univ., P.O. Box 30, State College, PA 16804), and John Corey (CFIC, Inc./Resonant Power Group, Troy, NY 12180)

A moving-magnet electrodynamic driver will be described which is intended to maintain an acoustic resonance within a thermoacoustic air conditioner containing an inert gas mixture of helium and argon at 30 bar. It is energized by a linear motor with a Bl-product of 41 N/A and a coil resistance of 0.24 Ω. An auxiliary spring system augments the magnetic stiffness (154 kN/m) to provide a driver mechanical resonance frequency near 60 Hz. An Inconel bellows forms a flexure seal which provides an effective piston area that maximizes electroacoustic conversion efficiency by making the Joule heating losses in the coil equal to the mechanical dissipation in the magnetic suspension. The driver's electroacoustic conversion efficiency is predicted to be in excess of 83%. [Work supported by the Office of Naval Research.]

3:20

2pPAa5. Performance of a two-stack annular prime mover. Brent A. Carter and Anthony A. Atchley (Grad. Prog. in Acoust., Penn State Univ., P.O. Box 30, State College, PA 16804, aatchley@psu.edu)

In a previous study, numerical investigations of a two-stack annular thermoacoustic prime mover were made [H. T. Lin *et al.*, J. Acoust. Soc. Am. **102**, 3071(A) (1997)]. The conditions for onset were predicted. The subject of this paper is an experimental investigation of a two-stack annular prime mover. The prime mover, modeled using DeltaE and a MATLAB program, is constructed using an annular aluminum resonator, copper fin heat exchangers, and two parallel plate, glass stacks. The relative position of the two stacks is adjustable within the resonator. Fluid-cooled ambient heat exchangers, and cartridge-heater powered hot heat exchangers are used to apply independent temperature differences across the two stacks. The sound field and temperature within the resonator are measured with a series of microphones and thermocouples distributed along the resonator. The performance of the prime mover is investigated as a function of relative stack position, temperature differences applied to the stacks, and heater power levels. [Work supported by the Office of Naval Research and The Pennsylvania State University Applied Research Laboratory.]

3:40–4:00 Break

4:00

2pPAa6. On validity of mean-field approximation in thermoacoustics. V. Gusev (Laboratorie de Physique de l'Etat Condensé, UPRESA—CNRS 6087, Université du Maine, 72085 Le Mans, Cedex 9, France, vitali@laum.univ-lemans.fr), H. Bailliet, P. Lotton, and M. Brauneau (Université du Maine, 72085 Le Mans, Cedex 9, France)

Thermoacoustic heat flux is convective in its physical nature. In the present communication it is demonstrated that the problem of analytical description of thermoacoustic heat flux is identical to the problem of closing moment hierarchy in the theory of fluid turbulence. In the case of harmonic acoustic oscillations, spatially inhomogeneous time-averaged temperature distribution is related to temperature oscillations at fundamental frequency. However, the first (fundamental) harmonic depends on the second harmonic of temperature field, which in turn is related to the third harmonic, and so on. In analytical models of thermoacoustic devices the harmonics of temperature oscillations are usually neglected. This so-called ''mean-field'' approximation results in the description of thermoacoustic heat transport as a diffusion process (with an effective thermal diffusivity depending on acoustic wave power). In the present communication it is demonstrated that mean-field approximation is not just inappropriate for the description of thermoacoustic heat exchange between gas-separated solid plates, but it is also not valid in all the cases where the characteristic spatial scale of mean temperature variation does not significantly exceed the amplitude of gas displacement in standing acoustic wave (for example, near the terminations of the stacks and heat exchangers). [Work is supported by DGA.]

4:20

2pPAa7. Second-order thermoacoustics. Roger Waxler (Grad. Prog. in Acoust., Penn State Univ., University Park, PA 16804, waxler@math.psu.edu)

A theoretical study is made of nonlinear effects in thermoacoustic stacks. The equations of fluid dynamics and heat transfer are expanded about a mean state with constant pressure and zero velocity but with a nonzero temperature gradient along the stack. The expansion is carried out to second order in Mach number. Using Rott's approach to control the linear terms, the time-independent parts of the second-order terms are studied. A set of coupled equations for the radiation pressure, velocity streaming, and time-averaged temperature are obtained and solved. The transverse heat flux into the stack is obtained. The solutions depend on the pressure and temperature at the ends of the stack, and thus on the details of the nonlinear effects in the resonator. However, it is found that the effects of the resonator on the velocity streaming and radiation pressure can be reduced to two parameters.

4:40

2pPAa8. Nonlinear saturation of thermoacoustic instability. Sergey Karpov and Andrea Prosperetti (Dept. of Mech. Eng., Johns Hopkins Univ., Baltimore, MD 21218)

In earlier work [Watanabe *et al.*, J. Acoust. Soc. Am. **102**, 3484–3496 (1997)] a quasi-one-dimensional nonlinear model for thermoacoustic devices was developed. The model reduces exactly to the well-known Rott theory upon linearization, but numerical work has shown that it is also able to predict nonlinear features in agreement with experiment. In this work, a weakly nonlinear analysis of the model is carried out for conditions close to the linear stability threshold. The level at which the amplitude of the linearly unstable perturbation is predicted to saturate compares favorably with numerical calculations and experiment. On the basis of the result, the effect of several design variables such as nonuniformity of the resonator cross section, stack plate spacing, and others is explored. [Work supported by the Office of Naval Research.]

5:00

2pPAa9. Acoustic boundary layer phenomena near a corrugated surface. James B. Mehl (Dept. of Phys., Univ. of Delaware, Newark, DE 19716-2570, jmehl@udel.edu) and Michael R. Moldover (Physical and Chemical Properties Group, Natl. Inst. of Standards and Technol., Gaithersburg, MD 20899)

Acoustic resonator techniques for measuring thermophysical properties require a quantitative understanding of the viscous and thermal boundary layers. Near smooth solid boundaries, well-known analytic models of boundary layers have been confirmed by careful measurements. Little is known either experimentally or theoretically about the effects of surface roughness on the boundary layers. Roughness effects have been investigated through numerical calculations of the coupled acoustic, thermal, and shear fields near a corrugated interface, i.e., a surface with a profile $y = A \cos qx$. The calculations were carried out in the limit where the acoustic wavelength is much larger than the scale of surface roughness $(A, 2\pi/q)$ or the penetration lengths δ_t and δ_v. Boundary layer phenomena cause phase shifts and energy absorption in the reflection of a plane acoustic wave by a smooth surface. These effects are further modified at a corrugated reflecting surface. The calculated reflection coefficients have been applied to the model relating the speed of sound to the frequencies of spherical and cylindrical acoustic cavity resonances, and to the theoretical model of the Greenspan acoustic viscometer. [Research supported in part by the Office of Naval Research.]

Contributed Posters

These posters will be on display in the Poster Gallery from Monday to Wednesday, 15–17 March. Authors will be at their posters from 10:00 a.m. to 12:00 noon on Wednesday, 17 March.

2pPAa10. How much pressure drop is necessary for heat transfer? I. Rülich and H. Quack (TU Dresden, Institut f. Energiemaschinen und Maschinenlabor, Lehrstuhl f. Kälte- und Kryotechnik, D-01062 Dresden, Germany, ingo@memkul.mw.tu-dresden.de)

In many technical applications, heat has to be transferred from a fluid to a wall. To do this efficiently in a short time and confined volume, the fluid has to be moved by applying a pressure difference. In refrigeration and power processes working with ideal gases, the pressure drop in the heat exchangers plays an important role in the overall efficiency of the cycle. The present work investigated whether the necessary pressure drop to obtain a certain amount of heat transfer can be derived from basic principles at least for Reynolds numbers below 2000. It was found that there exists a lower limit on the order of magnitude of 2 pressure heads per transfer unit. This figure is slightly dependent on the Prandtl number of the fluid. Real heat exchanger geometries have values higher than this minimum value, the magnitude depending on simple shape factors, which were derived from numerical fluid flow calculations and with published experimental data. This work identified how the ideal inner geometry of a regenerator for regenerative power and refrigeration processes should look like. [Work is supported by BMBF Grant No. 13N6619/0.]

2pPAa11. Threshold condition for traveling wave excitation in an annular prime-mover. T. Le Polles, S. Job, H. Bailliet, P. Lotton, M. Bruneau (Laboratoire d'Acoustique, IAM UMR 6613, Université du Maine, 72085 Le Mans, Cedex 9, France), and V. Gusev (Université du Maine, 72085 Le Mans, Cedex 9, France)

The threshold condition for thermoacoustic instability in an annular prime-mover is derived. The region of spatially inhomogeneous temperature distribution (due to the presence of a stack and hot and cold heat exchangers) is assumed to be acoustically thin. The interaction of acoustic waves with the stack is assumed to be quasiadiabatic. Theoretical approach (based on the transformation of differential wave equation into Volterra integral equation, which is solved by iterative procedure) is valid for arbitrary spatial temperature distribution. Nevertheless, it was found that the threshold for the excitation of a traveling acoustic wave does not depend on the details of temperature spatial distribution but just on the ratio of the temperatures of hot and cold heat exchangers. Moreover, the critical temperature ratio does not depend on the thickness of the stack if the acoustic losses inside the heated region are negligible in comparison with acoustic losses in the rest part of the annular system. In this important limiting case critical temperature ratio diminishes when the dimensions of the system are scaled up. [Work supported by DGA.]

Session 2pPAb

Physical Acoustics: Nonlinear Motion of Bubbles and Drops I

R. Glynn Holt, Cochair
Department of Aerospace and Mechanical Engineering, Boston University, Boston, Massachusetts 02215, USA

Joachim Holzfuss, Cochair
Institut für Angewandte Physik, TU Darmstadt, Schlossgartenstrasse 7, D-64289 Darmstadt, Germany

Chair's Introduction—4:15

Invited Papers

4:20

2pPAb1. Acoustic levitation, a theoretical and experimental round up. E. G. Lierke (Battelle Ingenieurtechnik GmbH, Düsseldorfer Straße, 65760 Eschborn, Germany)

A resumé of terrestrial levitation of solid samples and drops in one-axial acoustic standing wave levitators is presented. It concentrates on a normalized theoretical description of drop displacement and deformation in the full dynamic range of the levitation safety factor, the ratio of axial levitation force and sample weight. The range of the initial sample radius a_0 follows from the wave number product $10^{-2}<ka_0<1.5$. Sample properties density ρ and surface tension σ are represented by the Bond number $\mathrm{Bo}=\rho/\sigma \cdot a_0^2 \cdot g_0<2$ (g_0 is gravity constant). The critical Weber number $\mathrm{We}_{\mathrm{crit}}=10$ (ratio of Bernoulli stress and capillary pressure) defines the upper limit of levitation at acoustic Mach numbers $\mathrm{Ma}_{\mathrm{crit}}=\sqrt{5/P_0\kappa_0 \cdot \sigma/a_0}$ (P_0 is static pressure, κ_0 is heat capacity ratio). Resulting temperature variations and acoustic convections, represented by Nusselt and Sherwood numbers, are briefly discussed. A new family of modular, one-axial, acoustic levitators (20, 60, and 100 kHz) with sensor-controlled, calibrated resonance tuning is introduced. The levitators can easily be changed from a ''Bessel mode'' tube version, with minimized gas volume, into an ''open'' version with free radial access to the sample, both optional with superimposed axial gas flow. Some experimental techniques with compatible commercial components, like temperature and humidity sensors, optical accessories (observation and spectroscopy), and microdrop injectors are briefly discussed.

4:40

2pPAb2. Physics of drop formation. Jens Eggers (Univ. of Essen, Dept. of Phys., 45117 Essen, Germany)

A wide variety of technologically relevant processes, like ink-jet printing, spray painting, or internal combustion, depends on a detailed understanding of the underlying mechanism of drop formation. The motion is driven by surface tension, which tries to minimize surface area, thus reducing the minimum radius of a fluid jet to zero in finite time. This singular motion is self-similar as a function of time, and independent of fluid parameters or of initial conditions. The theory is confirmed by experiment without adjustable parameters.

5:00

2pPAb3. Bubble dynamics and nucleation of ice in supercooled water. E. H. Trinh and K. Ohsaka (Jet Propulsion Lab., California Inst. of Technol., Pasadena, CA 91109)

The effects of mechanically induced impulses such as vibration and flow have been used to induce the solid–liquid phase transformation in liquids held below their equilibrium freezing point. Although processes used for grain refining in metallurgy rely on this artificially enhanced nucleation process, there is no clearly identified underlying physical mechanism. Experiments have been conducted with single bubbles immersed in a small volume of supercooled water and trapped in a 22-kHz resonant cell to study the action of both large amplitude radial and shape oscillations. The experimental observations reveal that large-amplitude radial oscillations of micron-size air bubbles induce the nucleation of ice when a minimum supercooling of 5 °C is reached. Shape oscillations and radially nonresonant bubbles do not induce nucleation of ice within the same ''incubation'' time. The appearance of the ice crystal at the location of the trapped bubble strongly suggests a cause and effect correlation between the bubble radial oscillations and the freezing onset, and both sonoluminescing and nonluminescing bubbles appear to induce nucleation. This mechanism also has the additional benefit of allowing the direct measurement of free dendritic growth velocity within a supercooled liquid bulk in the absence of any artificially introduced seed. [Work sponsored by NASA.]

5:20

2pPAb4. Acoustic diagnosis of singing cavitation vortices. Branko Bajic (Brodarski Inst., Holjevca 20, 10020 Zagreb, Croatia, bajic@t-online.de)

The acoustic field generated by hydrodynamic cavitation is usually random and broadband. There is, however, a case in which it is tonal. Indeed, as reported by Higuchi, Arndt, and Rogers [J. Fluids Eng. (Dec. 1989)], and Maines and Arndt [ASME Symp. Cavitation and Multiphase Flow (1995)], cavitating vortices which shed off from a body immersed in a flow may generate a harmonic acoustic signal even if involving no vibrations of the cavitating body. This paper presents the results of the parametric analysis of sound generated by the singing vortices produced in a test on a finite-span hydrodynamic profile immersed in a uniform water flow. A continuous development of the vortex through filling by air was investigated. The acoustic diagnosis of the process of oscillations of the cavitating vortex generating the singing is presented. The issues relevant to the theoretical modeling of the lock-in mechanism are investigated: necessary conditions for the onset and stability of the process, possible influence of water velocity other than through the cavitation number, influence of vortex energy, etc. The relevant peculiarities of the vortex dynamics are revealed. The question if there is a back-influence of the singing on the basic vortex dynamics is considered.

5:40

2pPAb5. Radiation pressure of sound on moving vortices. Andrew G. Semenov, Vadim N. Alexeyev, and Samuel A. Rybak (N. N. Andreev Acoust. Inst., Russian Acad. of Sci., 4 Shvernik St., 117036 Moscow, Russia, bvp@acoins.msk.ru)

This report is devoted to the nonlinear acoustic pressure of sound waves propagating in the vicinity of a rather general class of localized flows induced by the motion of spherically symmetric structures of the type of vortices in the liquid, say, ocean environment. As a result, the mean force exerted on a vortex is considered. The conventional general expression for transport cross section derived in a nonlinear theory of interaction of sound with rigid particles is proven to be incorrect for the vortex–sound interaction case. For the specific case of Hill's vortex mean force, it is shown to be absent both in the traveling and standing sound wave fields. However, the force could be observable if the distribution of mean sound energy in the incident sound field in the limit of vortex dimensions could be characterized by nonzero spatial gradient. A generalized expression for mean force exerted on a localized vortex structure is derived.

6:00

2pPAb6. Bubble size distribution near a pressure antinode. Robert Mettin, Stefan Luther, Claus-Dieter Ohl, and Werner Lauterborn (Drittes Physikal. Inst., Univ. Göttingen, Bürgerstrasse 42-44, 37073 Göttingen, Germany, R.Mettin@physik3.gwdg)

When strong ultrasonic standing wave fields are generated in liquid-filled resonators, cavitation bubbles emerge and build dynamic structures, typically near the pressure antinodes. For technical applications like sonochemical reactions taking place in the resonator, the size distribution of the clustering bubbles is an important parameter. New photographic measurements of bubble sizes are presented, along with numerical size estimates. These are based on Bjerknes force and shape stability calculations for spherical bubbles. [Work partially supported by ''Graduiertenkolleg Strömungsinstabilität und Turbulenz.'']

TUESDAY AFTERNOON, 16 MARCH 1999 ROOM MA041, 2:00 TO 5:20 P.M.

Session 2pPAc

Physical Acoustics: Interaction of Acoustic Fields with Suspended Particles II

Ewald Benes, Cochair
Institut für Allgemeine Physik, Vienna University of Technology, A-1040 Vienna, Austria

Robert E. Apfel, Cochair
Faculty of Engineering, Yale University, 9 Hillhouse Avenue, New Haven, Connecticut 06520-8286, USA

Contributed Papers

2:00

2pPAc1. The acoustic generation of internal flow and rotation of levitated fluid particles. Eugene H. Trinh and Sang K. Chung (JPL/Caltech, 4800 Oak Grove Dr., Pasadena, CA 91109)

The detailed motions of levitated fluid particles in response to acoustic fields have become a topic of renewed interest because of the potential application of containerless processing techniques to a number of fundamental studies in heat or mass transfer and crystal growth. In these situations, acoustic fields are generally used to generate internal circulation to boost the transport rates, or to control the rotational motion of a levitated solution droplet. Two instances where such effects have been discovered and are being exploited will be discussed. The first case involves millimeter-size gas or vapor bubbles ultrasonically trapped in a resonant liquid cell and displaying vigorous internal circulation due to the excitation of high-frequency capillary waves at their interface. The second example deals with the drive of rotational motion of levitated droplets in ambient air and the effects of viscosity on this coupling. The results indicate that acoustic streaming flows are responsible for the generation of this controlled torque. [Work sponsored by NASA.]

2:20

2pPAc2. Whole blood clarification in an ultrasonic standing wave. Caroline M. Cousins, Susan E. Higgins, Medha S. Limaye, Jeremy J. Hawkes, W. Terence Coakley (School of Biosciences, Cardiff Univ., Cardiff CF1 3TL, UK), Peter Holownia, and Christopher P. Price (St. Bartholomew's and Royal London School of Medicine and Dentistry, London E1 2AD, UK)

There has been interest for a number of years in the possibility of separating, for transfusion proposes, blood cells from the suspending plasma in ultrasonic standing waves. On a much smaller scale, there has also been interest in separating cells and plasma so that the latter can be analyzed in single or multiple sample systems. Cells in whole blood occupy about 45% of the suspension volume. It has been shown with a number of different cell types, e.g., yeast and bacteria, that concentrations of this order are not as efficiently harvested by ultrasound as lower concentrations. Removal of cells from 2–5 ml whole blood volumes has been examined here in standing wave fields from plane or tubular transducers. The tubular transducers were driven at frequencies from 0.66 to 3.4 MHz. A range of frequencies, sonication pulsing regimes, and power levels have been established that result in cell separation efficiencies in excess of 99.5% in 5 min under conditions where cavitation has been avoided. The technique is now being applied to the blood of increasing numbers of volunteer donors to establish confidence in the ability to clarify plasma without cell damage. [Work supported by BBSRC and EU.]

2:40

2pPAc3. Viability of plant cells in ultrasonic fields. Hannes Böhm, Kenneth C. Lowe, L. Gregory Briarty, J. B. Power, Michael R. Davey (Life Sci. Dept., Univ. of Nottingham, University Park, Nottingham NG7 2RD, UK), and Ewald Benes (Vienna Univ. of Technol., A-1040 Vienna, AT Austria)

The influence of ultrasonic waves on suspension plant cell cultures (e.g., petunia and carrot) has been investigated. The dependency of viability, cell density, miototic division, and regeneration, on the controlled acoustic parameters' frequency of sound, energy density, treatment time, and wave type, is presented. Special focus is on the investigation of the influence of propagating plane waves, because these allow a spatially almost invariable acoustic pressure amplitude and, as a consequence, the same acoustic parameter values for all cells in the treated suspension volume. [Work supported in part by the European Commission, Contract No. ERBFMRXCT970156.]

3:00

2pPAc4. Viability of yeast cells in propagating ultrasonic waves. Stefan Radel, Aiden J. McLoughlin (Dept. of Industrial Microbiology, Univ. College Dublin, Dublin 4, IE Ireland, radel@iap.tuwien.ac.at), and Ewald Benes (Vienna Univ. of Technol., A-1040 Vienna, AT Austria)

In some recent papers the upper limits for the acoustic pressure amplitudes, in standing wave fields, that exert no measurable influence on viability of various biological cells have been reported. However, the pressure amplitude in a standing wave is periodically varying in space in the direction of sound propagation and, because of radiation pressure, the cells are not homogeneously distributed within the sample volume, resulting in effects arising from the dynamic environments created. Thus standing waves are obviously not appropriate to study the direct influence of sound pressure amplitude on viability data. Therefore, both metabolic activity/viability of yeast cells and their ability to replicate as a function of acoustic frequency and sound pressure amplitude have been investigated in propagating waves. The observed effects are compared to those in crossed beam fields and in standing plane wave fields. The results allow a better forecast and interpretation of viability threshold data relevant in predicting the effects of acoustic parameters in standing wave fields. [Work supported in part by the European Commission, Contract No. ERBFMRXCT970156.]

3:20

2pPAc5. Ultrasonic standing waves to enhance optical particle sizing equipment. Ian L. Holwill and Andy T. Martin (DERA Porton Down, Salisbury, Wiltshire SP4 0JQ, UK, iljholwill@clara.net)

Experiments have been performed using dynamic light scattering (DLS) apparatus to investigate the potential of the use of ultrasonic forces for *in situ* removal of unwanted particles from the measurement volume. Megahertz frequencies were used to move micron-sized particles from the laser beam focus and leave the submicron particles for measurement. Removal of polystyrene latex (PSL) particles down to a diameter of 2 μm was demonstrated while leaving particles with a diameter below 100 nm unaffected to be accurately measured by the DLS technique. Further experiments have been performed on airborne particles in custom-built single-particle light scattering apparatus. The aim of this study was to direct particles toward a laser focus for sizing by forward light scatter measurements. Sub-100 kHz standing waves were used to direct micron-sized particles to a laser beam focus for analysis. Large particles (of the order of 20 μm) were very successfully moved toward the laser focus, and adjustment of the power to the transducers allowed continuous, real-time control of the concentration of particles delivered to the measurement volume. A concentration range of approximately 100:1 was achieved. For smaller particles below 10 μm, the concentration range was limited to 2:1.

3:40–4:00 Break

4:00

2pPAc6. Ultrasonically enhanced sedimentation—Results of an empirical scale-up approach. Johannes Spengler and Martin Jekel (Dept. of Water Quality Control, Sekr. KF 4, Tech. Univ. of Berlin, Strasse des 17, Juni 135, D-10623 Berlin, Germany, wrh@itu201.ut.TU-Berlin.de)

Ultrasonic standing waves are suitable for both coagulation of dilute suspensions and thickening of already settled sludge. For each purpose the right choice of process parameters and reactor design is important. The used ultrasonic effects are acoustic radiation and acoustic as well as hydrodynamic particle interaction forces. Acoustic and convective streaming cause shear stress on particle clusters and can therefore disperse aggregates. To achieve good efficiency at high flow rates, these undesirable streaming effects must be controlled, especially for the realization of larger reactors. One suitable measure is to divide the sonicated volume into several smaller parts separated by thin polyethylene films. Basic investigations in various batch and continuous flow lab systems led to an empirically derived scale-up concept. A prototype 3-MHz transducer array consisting of 16 single piezos used for coagulation has been developed and manufactured in cooperation with ELAC Nautik (Kiel). Preliminary results of two new pilot plants (sonicated volume 10 L for coagulation, respectively, 70 L for thickening) show good performance of the reactors. Comparison with previous lab scale data prove the applicability of the scale-up method as it will be presented at the meeting.

4:20

2pPAc7. Ultrasonic splitting of oil-in-water emulsions. Ralf König, Ewald Benes, Martin Gröschl (Vienna Univ. of Technol., Inst. für Allgemeine Physik, Wiedner Hauptstr. 8-10/134, A-1040 Vienna, AT Austria), and Jens Hald (Tech. Univ. of Denmark, DK-2800 Lyngby, DK Denmark)

Standing resonant ultrasonic wave fields can be utilized for liquid–liquid separation of the dispersed particles and the fluid caused by the acoustic radiation pressure and the induced particle agglomeration or coagulation/coalescence process. For the splitting of oil-in-water emulsions, the available piezoelectric composite transducer technology was improved and a dedicated resonator with crossed plane wave sonication geometry has been developed. The resonator chamber is entirely made of aluminium or tempax glass and the PZT piezoceramic transducer delivers an acoustic energy flow density of up to 24 W/cm^2 into the sonication volume. The chosen resonance frequency is kept stable by automatic frequency control utilizing the maximum true power criterion. Physically and

chemically well-defined low and high density pure laboratory and also industrially used cooling-lubricating oil-in-water emulsion samples have been investigated. The quality of the ultrasonic-induced particle separation/coagulation process is characterized by physical–chemical analysis of the separated oil- and water phase and by determining the change of the particle size distribution of the initial emulsion due to the ultrasonic treatment. [Work supported by the European Commission, Contract Nos. ERBFMBICT960916 and ERBFMRXCT970156.]

4:40

2pPAc8. Acoustic deinking of paper: Pulse effectiveness in particle detachment. Sameer I. Madanshetty and Jogesh B. Chandran (Mech. and Nuclear Eng., 322 Durland Hall, Kansas State Univ., Manhattan, KS 66506-5106)

Deinking remains an important step in environmentally conscious manufacturing of paper. Removing xerographic ink from a print sample using acoustic microcavitation provides an easy method to observe context for studying cavitation-induced erosion at surfaces. Experiments indicate that microcavitation evolves microimplosions which are effective in causing deinking preferentially at ink sites. Acoustic microcavitation is brought about by low megahertz acoustic fields giving rise to micron-size bubbles that live a few microseconds. In exposing a surface to continuous waves for a defined duration, one could obtain cavitation effects in an average, overall sense; the details of nucleation, evolution of inertial events, and the precise interplay of field parameters in effecting cavitation, however, get glossed over. Studying pulsed cavitation using tone bursts at low duty cycles, instead of CW insonification, reveals interesting details of the initiation and evolution of acoustic microcavitation. Specifically, it is found that short-pulse deinking is more effective than long-pulse deinking. This fact seems to raise an anomalous question of how the sample knows it is being visited by a short pulse or a long pulse. Recent experiments operationally demonstrate why short-pulse deinking is more effective. [Work supported by NSF.]

5:00

2pPAc9. Particle filtration by a combination of ultrasound standing waves and laminar flow. Jeremy J. Hawkes, Caroline Cousins, W. Terence Coakley (School of Biosciences, Cardiff Univ., Cardiff CF1 3TL, UK), and Peter J. Keay (Univ. of Luton, Luton, UK)

Radiation forces in ultrasonic standing waves move suspended particles to half-wavelength separations, thus creating concentrated bands of particles separated by cleared medium. Continuous flow filters of one-half wavelength acoustic pathlength (0.25 mm, 3-MHz frequency) are described here in which particles concentrate on the central axis of the flow chamber. This concentration is maintained downstream in a novel laminar flow expansion section where the concentrated particles and clarified suspending phase are removed at separate outlets. The expanded downstream laminar section facilitates the engineering and positioning of efficient removal ports. Filter construction provides observation windows for monitoring of band integrity either parallel or at 90 degrees to the transducer face. The short acoustic pathlength in the present systems allows particle separations at frequencies significantly higher than previously employed in single half-wavelength systems, thus permitting exploitation of higher acoustic pressures without generating order-disrupting cavitation. Results for clarification of polystyrene latex particles, under flow conditions where particles typically spend <1 s in the field, are in excess of 98% and 70% for 9- and 1-μm-diam particles, respectively. [Work supported by BBSRC and EU.]

TUESDAY AFTERNOON, 16 MARCH 1999 ROOM MA005, 2:00 TO 4:20 P.M.

Session 2pPAd

Physical Acoustics: Cavitation Physics and Sonoluminescence III

Werner Lauterborn, Cochair
Drittes Physikalisches Institut, Universität Göttingen, Bürgerstrasse 42-44, 37073 Göttingen, Germany

Ronald A. Roy, Cochair
Department of Aerospace and Mechanical Engineering, Boston University, Boston, Masschusetts 02215, USA

Contributed Papers

2:00

2pPAd1. Experimental investigation of dynamics of sonoluminescing bubbles. Yuichiro Kato, Shigeo Hayashi (Dept. of Appl. Phys. and Chem., Univ. of Electro-Commun., Chofu, Tokyo 182-8585, Japan), Kenji Tanaka, and Hiroshi Kobayashi (Waseda Univ., Shinjuku, Tokyo 169-8555, Japan)

Light scattering was carried out for a cavitation bubble trapped in a spherical flask. A He–Ne laser of 7 mW was used as the light source and the scattering angle was 90 deg. A function generator was used as the trigger source and a digital phospher oscilloscope for averaging the data. Changing the drive voltage resulted in differences in the signal waveform above and below the sonoluminescence threshold; a sonoluminescing bubble had the maximum radius greater than a dark bubble did, but showed smaller rebounds. This suggests that energy concentration is made possible by tight and symmetric collapse of the bubble. Sonoluminescence signals were also retrieved for a few hours with no laser light, and a discontinous drift was noted in the appearance time on the oscilloscope, suggesting that a bubble may have drifted in space discontinuously. [Work supported by Grant-in-Aid for Scientific Research, Ministry of Education, Science, and Culture, Japan.]

2:20

2pPAd2. On the light emission from a collapsing laser-induced cavitation bubble. Claus-Dieter Ohl and Werner Lauterborn (Drittes Physikalisches Inst., Univ. Göttingen, Bürgerstrasse 42–44, Göttingen, Germany)

The collapse of laser-induced cavitation bubbles is accompanied by the emission of light. A detailed experimental study of the properties of the luminescence is presented. The dependence of the luminescence duration on the size of the bubble and on its sphericity prior to collapse is investigated. In aqueous sodium solutions line emission is found. The shape of these lines varies with the sphericity of the collapse. Also, differences in the emission spectrum in the case of spherical and aspherical collapse have been found.

2:40

2pPAd3. Temperature dependency of luminescence from laser-produced cavitation bubbles. Olgert Lindau and Werner Lauterborn (Drittes Physikalisches Inst., Univ. Göttingen, Bürgerstrasse 42-44, D-37073 Göttingen, Germany)

Single laser-produced bubbles emit short light pulses in the collapse phase. This phenomenon is called single-cavitation bubble luminescence (SCBL) in analogy to single-bubble sonoluminescence (SBSL) where the bubbles levitate in an acoustic field. Laser bubbles are produced using a *Q*-switched Nd:YAG laser. The laser beam is focused with an aberration-minimized lens system into a temperature controlled cuvette filled with bidistilled water. A photomultiplier collects the light emitted in the collapse phase of the bubble. Bubble size is monitored with a hydrophone. As laser-produced bubbles are bigger in size than their acoustically driven counterparts, they emit stronger light pulses. The light energy per pulse in dependence on bubble size is reported. SBSL shows a strong dependency on temperature and a similar behavior is expected for SCBL.

3:00

2pPAd4. Single-cavitation bubble luminescence after fs-laser-induced breakdown in water. Cordt Schenke, Thomas Kurz, and Werner Lauterborn (Drittes Physikalisches Inst., Univ. Göttingen, Bürgerstrasse 42-44, D-37073 Göttingen, Germany, cordt@physik3.gwdg.de)

The use of ultrashort, intense laser pulses to induce an optical breakdown has both advantages and disadvantages. One of the most important advantages is the possibility to create cavitation bubbles with a much smaller size than by use of nanosecond pulses. By this, the parameter range of single cavitation bubble luminescence (SCBL) studies can be extended. The dynamics and luminescence of the created bubbles were investigated. Due to self-focusing, the initially formed plasma has a cylindrical shape, which leads to elongated cavitation bubbles. The observed dynamics of the bubbles seems to indicate the formation of two jets penetrating the bubble while collapsing. For the first time, luminescence of bubbles created this way is observed. It seems to arise from the collapse of microbubbles which are created by self-focusing in the prefocal region.

3:20

2pPAd5. Time series analysis of cavitation bubble fields. Stefan Luther, Ulrich Parlitz, and Werner Lauterborn (Drittes Physikalisches Inst., Universität Göttingen, Bürgerstrass e 42-44, D-37073 Göttingen, Germany, luther@physik3.gwdg.de)

Acoustical cavitation bubble fields exhibit spatio–temporal structure formation on multiple scales involved. The temporal scales are the fast, medium, and slow scales given by the period of the driving, the typical relaxation time of the individual bubble motion, and the drift of the filaments, respectively. The spatial scales are the microscopic, mesoscopic, and macroscopic scales given by the bubbles' mean radii, typical bubble distances, and the wavelength of macroscopic disturbances (e.g., sound waves). Prominent examples of the observed structures are, for example, period doubling on a fast temporal scale and a slowly drifting filamentlike bubble distribution on the macroscopic spatial scale. These structures are experimentally investigated using simultaneously measured sequences of images (CCD camera) and acoustic time series (hydrophones). Based on these data the experimentally observed patterns are characterized using image processing techniques (e.g., principal component analysis) and by means of methods of nonlinear time series analysis (e.g., test for stationarity, dimension estimates, surrogate data analysis). The investigations focus on the correlation between spatial and temporal structures on different scales and transitions between them. [Work supported by ''Graduiertenkolleg Strömungsinstabilität und Turbulenz.'']

3:40

2pPAd6. Acoustic bubble traps. Reinhard Geisler, Thomas Kurz, and Werner Lauterborn (Drittes Physikalisches Institut, Universität Göttingen, Bürgerstr. 42-44, D-37073 Göttingen, Germany)

A small, oscillating bubble in a liquid can be trapped in the antinode of an acoustic standing wave field. Bubble stability is required for the study of single-bubble sonoluminescence (SBSL). The properties of the acoustic resonator are essential for the stable trapping of sonoluminescing bubbles. Its acoustic modes were measured by means of holographic interferometry and hydrophones. Flasks of different geometries (spherical, cylindrical, rectangular, ovoid) were investigated as well as different acoustic modes. Higher harmonic modes were used to trap several single, stable sonoluminescencent bubbles within one acoustic resonator (few bubble sonoluminescence, FBSL). This opens up the possibility to study bubble–bubble interactions (secondary Bjerknes forces).

4:00

2pPAd7. Vapor cavitation zone formation in a water layer. Isaac Shreiber (Inst. for Industrial Math., Hanachtom 4/2484311 Beer-Sheva, Israel, isaak@indigo.cs.bgu.ac.il)

This paper deals with a model for the formation of a vapor bubble cavitation zone within a water layer due to a rarefied wave propagating in the water layer. The water in the layer is close to the saturation line (subheated). Models are presented for vapor cavitation zone development, pressure field formation, and the phenomenon of coalescence. The specific feature of the cavitation is a reflected rarefied wave; the growing and floating bubbles generate the swelling of the entire bulk of water; the coalescing and floating bubbles can uplift the water layer and splash it. The gas cavitation phenomenon and a de-aeration technology are also discussed and the Epshtein model for cavitation was developed. The Epshtein model assumes that the essence of water cavitation is the solved gas diffusion into the bubble germs providing for their growth. The peculiarity of the problem is the bubbles get into a periodic acoustic wave and they grow under the rectified diffusion process activity. These large bubbles can escape the cavitating layer.

Session 2pPAe

Physical Acoustics: Surface Roughness

Keith Attenborough, Cochair
Faculty of Technology, The Open University, Milton Keynes MK7 6AA, UK

Ali R. Kolaini, Cochair
ERC-OEL, University of California at Santa Barbara, 6740 Cortona Drive, Goleta, California 93117, USA

Chair's Introduction—1:55

Invited Papers

2:00

2pPAe1. Measurements and models of small-scale surface roughness effects at audio-frequencies in air. Keith Attenborough (Faculty of Technol., The Open Univ., Milton Keynes MK7 6AA, England)

Surface roughness has been found to have an important influence on outdoor ground effect. Indoor and outdoor measurements of roughness effects are reported together with developments of analytical boss theories and numerical predictions using boundary elements. Although the Twersky boss theory including incoherent scatter is found to lead to reasonable agreement with data, it fails to predict measured diffraction grating effects and, overall, the BEM results are in better agreement.

2:20

2pPAe2. Experimental and modeling results for near-grazing propagation over rough surfaces. James P. Chambers and James M. Sabatier (Natl. Ctr. for Physical Acoust., Univ. of Mississippi, University, MS 38677)

Recent experimental work on acoustic propagation over rough surfaces has shown intriguing propagation effects ranging from frequency shifts in the ground interference dip to surface wavelike phenomena. Attempts to model the observed data with an effective impedance formulation have had some success but have met with some problems for certain propagation geometries and surface configurations. Experimental data and modeling results will be presented and discussed for a variety of surfaces ranging in surface properties from impermeable to loosely packed soil and ranging in surface roughness scales from low sloped perturbations to steeply sloped wedges.

2:40

2pPAe3. The influence of millimeter-scale seafloor roughness on measured and predicted high-frequency acoustic backscattering strength. Kevin B. Briggs (Seafloor Sci. Branch, Naval Res. Lab., Stennis Space Center, MS 39529), Darrell R. Jackson (Univ. of Washington, Seattle, WA 98105), and Steve Stanic (Naval Res. Lab., Stennis Space Center, MS 39529)

Seafloor microtopography, as measured by underwater stereo photogrammetry, is systematically characterized concurrently with other sediment properties as model parameters to be used for predicting high-frequency acoustic backscattering from the seafloor as part of field experiments. Typically, seafloor roughness is digitized at 2–5 mm intervals from 35- or 70-mm film transparencies with a stereocomparator capable of 1-mm-scale lateral precision and sub-millimeter-scale vertical accuracy. Relative seafloor height profiles are used to estimate roughness power spectra, which are parameterized as slopes and intercepts of the line fit to the roughness variance regressed on the spatial frequency. According to the composite roughness model developed by APL-UW, the decay of the roughness spectra with increasing spatial frequency (slope) and the spectral strength (intercept) can be used to determine the contribution of the seafloor roughness to the overall backscattering strength. Data from field experiments are presented in order to demonstrate the relationship between seafloor roughness at sub-centimeter scales and high-frequency acoustic scattering. Experimental acoustic data and model predictions are presented from a coarse, shelly sea floor off Jacksonville, Florida, a rippled fine sand in the Quinault Range off Washington, and a very fine sand with subtle seafloor roughness off Tirrenia, Italy. [Work supported by ONR.]

3:00

2pPAe4. Acoustic backscatter from a sandy seafloor with anisotropic roughness. Richard J. Brothers, Gary J. Heald, and Patricia A. G. Thomson (DERA Bincleaves, Weymouth, Dorset, UK)

A high-frequency array was used to gather backscatter data from a sandy seabed with an anisotropic roughness spectrum. The source and receiver were fixed to a pan and tilt head so that the orientation to the seabed could be varied. A significant reduction in the backscatter was observed as the transducer was trained from the across ripple direction to the along ripple direction. The variation in backscatter with respect to the grazing angle is compared with the composite roughness model and modifications have been incorporated to take account of the bedform roughness and local grazing angle. The wideband transducer employed allowed a range of bandwidths (up to 60 kHz) to be used, including short pulse and chirp waveforms. Variation in the number of elements in the beamformed data showed the variation in backscatter due to change in beamwidth. Supporting measurements of the experiment site were made by SACLANTCEN, including stereo photography and grab samples of the sediment.

3:20

2pPAe5. Acoustic remote sensing of seafloor roughness: Resolving ambiguous estimates of roughness spectrum parameters. Christian P. de Moustier and Daniel D. Sternlicht (Marine Physical Lab., Scripps Inst. of Oceanogr., 9500 Gilman Dr., La Jolla, CA 92093-0205)

To predict or model how sound waves interact with the seafloor some parametrization of the roughness of the sediment–water interface is required. Conversely, bottom backscattered echoes contain information about the roughness of the interface, relative to the acoustic wavelength, often mixed with contributions from inhomogeneities in the sediment volume. However, inversions of seafloor roughness parameters from high-frequency (10–100 kHz) acoustic backscatter measurements often produce ambiguous results with numerous plausible parameter combinations fitting a given acoustic backscatter angular dependence curve or an echo envelope shape. Based on the data and on direct or inferred seafloor roughness measurements reported in the literature, and assuming that the relief spectrum of seafloor topography obeys a power law, it is shown that a level of inversion ambiguity can be lifted by setting the roughness spectral exponent to a value appropriate for the sediment type and by iterating on the spectral strength and the allowable amount of sediment volume backscatter. This is illustrated with examples drawn from comparisons between seafloor echo envelope models and measured acoustic backscatter data yielding interface roughness spectral parameters and rms bottom curvatures consistent with the lithology of the areas investigated. [Work supported by ONR N00014-94-1-0121.]

3:40–4:00 Break

4:00

2pPAe6. Stochastic models for scattering by seafloor roughness. Darrell R. Jackson (Appl. Phys. Lab., Univ. of Washington, Seattle, WA 98105)

Models for acoustic scattering by seafloor roughness can be divided into numerical models that treat individual realizations of the random seafloor and stochastic models that provide statistical moments representing the scattered field. Such stochastic models require statistical submodels for seafloor roughness and incorporate acoustic submodels that connect statistics of the scattered field with statistics of the random interface. Thus, one must consider the compatibility of the interface and acoustic submodels. Recent work by various investigators has resulted in a number of improvements over classical perturbation and Kirchhoff results. A variety of seafloor types (e.g., fluid, elastic, layered) can now be treated, and improved acoustic approximations permit application over a wider range of roughness parameters. Questions remain, however, as to the accuracy of the newer models. [Work supported by ONR.]

4:20

2pPAe7. Characterization of small-scale seafloor roughness using close-range digital photogrammetry. Anthony P. Lyons, Warren L. J. Fox, Eric Pouliquen, and Tuncay Akal (SACLANT Undersea Res. Ctr., APO AE 0613-5000, lyons@saclantc.nato.int)

Surface roughness is a fundamental property affecting a variety of physical phenomena including sediment transport and the interaction of acoustic energy with the seafloor. Characterization of bottom roughness and its dynamics is therefore essential for understanding and quantifying the influence of the sediment microtopography. Extensive field measurements of bottom roughness have been taken recently with an end-to-end digital photogrammetry system providing quantitative, two-dimensional surface roughness measurements on spatial scales of approximately a millimeter to a meter. Results of these measurements have shown that sediment surfaces in shallow water are often anisotropic and/or exhibit non-Gaussian height distributions, both of which have the potential to strongly affect seafloor acoustic scatter. For these kinds of surfaces, simple roughness parameters such as rms height or the slope and offset of a power-law representation of the power spectra will not give a sufficiently complete description. Two-dimensional statistical models are needed to capture the anisotropic nature of sediments with oriented features, while for seafloors with peaked forms, it is the phase information in the frequency domain that is required, as this controls the shape characteristics of a surface. Characterization of seafloor roughness based on these ideas will be presented using results from the digital photogrammetry system.

4:40

2pPAe8. Measurement of the effective surface impedance of rough surfaces in laboratory and *in situ*. Christian Nocke (Fraunhofer-Inst. Bauphysik Stuttgart (IBP), Stuttgart Nobelstrasse 12, D-70569 Stuttgart, Germany)

The normal specific acoustic impedance fully characterizes the acoustic behavior of a surface. In this contribution, laboratory and *in situ* results of a novel measurement procedure for this impedance are presented. The acoustic propagation above the surface is most sensitive to the acoustical properties of the surface at small angles of incidence. This effect is utilized to deduce the impedance from measurements of the interference between the direct and reflected sound of a point source above the surface under investigation. For homogeneous and plane surfaces, the absorption coefficient calculated from these impedance values compares well with the results from tube measurements. For rough and/or inhomogeneous surfaces, the measured impedance results must be interpreted as effective values. The reliability of the method has been proved in laboratory measurements for a frequency range between 80 and 4000 Hz. Furthermore, results of the new method from room acoustical applications are presented.

5:00

2pPAe9. The influence of small-scale seafloor surface morphology on acoustic backscattering. Eric Pouliquen, Benoit Zerr, and Anthony P. Lyons (NATO SACLANT Undersea Res. Ctr., Viale S. Bartolomeo, 400 19138 La Spezia, Italy)

Sediment transport induced by current flows and surface gravity waves often causes the formation of nonisotropic features of the seafloor interface. Depending on environmental conditions (e.g., current, sediment type, etc.), these directional ripples may display non-Gaussian or sharply peaked forms. Contrary to RADAR sea surface scattering, these two aspects of the morphology of the seabed

interface have not been deeply considered in the study of scattering of acoustic waves from the seabed. Their influence on backscattering is performed using two-dimensional and three-dimensional models including a finite-difference time-domain model (FDTD), a model based on the integral equation method, and a model based on the Kirchhoff approximation. All these models compute the time response as well as an averaged scattering strength from realistic randomly generated surfaces and profiles. The results of the simulations and acoustic data at high frequency show a sensitivity of the backscattered signals and of the backscattering strengths to both the anisotropy and the sharp nature of the seafloor interface edges.

TUESDAY AFTERNOON, 16 MARCH 1999 ROOM H1012, 1:55 TO 6:20 P.M.

Session 2pPPa

Psychological and Physiological Acoustics and Noise: Application of Psychoacoustics in Rating Environmental Noise

Hugo Fastl, Cochair
Institut of Man-Machine Communication, Technical University of Munich, Arcisstrassse 21, D-80333 Munich, Germany

Manfred T. Kalivoda, Cochair
Wiener Gasse 146/3, A-2380 Perchtoldsdorf, Austria

Sonoko Kuwano, Cochair
Department of Environmental Psychology, Osaka University, 1-2 Yamadaoka, Suita, Osaka, 565-0871 Japan

Chair's Introduction—1:55

Invited Papers

2:00

2pPPa1. A cross-cultural study of the factors of sound quality of environmental noise. Sonoko Kuwano (Dept. of Environ. Psych., Faculty of Human Sci., Osaka Univ., 1-2 Yamadaoka, Suita, Osaka, 565-0871 Japan, kuwano@env.eng.osaka-u.ac.jp), Seiichiro Namba (Takarazuka Univ. of Art and Design, Japan), Mary Florentine (Northeastern Univ., Boston, MA), Zheng Da Rui (Academia Sinica, PROC), Hugo Fastl (Tech. Univ. Munich, Munich, Germany), and August Schick (Oldenburg Univ., Oldenburg, Germany)

The sound quality of various environmental noises was judged using semantic differential in Japan, Germany, the U.S.A., and China. The sounds used were aircraft noise, train noise, road traffic noise, speech, music, and construction noise. As the result of factor analysis, three factors were extracted in Japan and Germany. They were interpreted as ''powerful,'' ''pleasant,'' and ''metallic'' factors. In the U.S., and China, ''powerful'' and ''metallic'' factors were not differentiated. The impression of ''powerful'' factors were found to show high correlation with L_{Aeq} and loudness level based on ISO 532B. There seemed some difference in connotative meanings of the terms ''loud,'' ''noisy,'' and ''annoying'' among the four countries. There was little difference in the impression of high-level aircraft noise, train noise, and road traffic noise among the four countries. They were perceived as negative impression such as ''annoying,'' ''ugly,'' ''unpleasant,'' etc. The validity of other psychophysical measures was examined in relation to these results.

2:20

2pPPa2. Individual noise sensitivity and performance on psychoacoustic tasks. Wolfgang Ellermeier, Monika Eigenstetter, and Karin Zimmer (Inst. fuer Psychologie, Universität Regensburg, 93040 Regensburg, Germany, wolfgang.ellermeier@psychologie.uni-regensburg.de)

In environmental noise surveys, self-reported noise sensitivity turned out to be a major predictor of noise-annoyance reactions. Its relationship to basic measures of auditory functioning, however, has not been systematically explored yet. Therefore, in the present investigation, a sample of 61 unselected listeners was subjected to a battery of psychoacoustic laboratory procedures ranging from threshold determinations to loudness scaling tasks. No significant differences in absolute thresholds, intensity discrimination, simple auditory reaction time, or power-function exponents for loudness emerged, when the sample was split along the median into two groups of ''low'' versus ''high'' noise sensitivity on the basis of scores obtained from a psychometrically evaluated questionnaire [K. Zimmer and W. Ellermeier, Diagnostica **44**, 11–20 (1998)]. Small but systematic differences were found in verbal loudness estimates, and in ratings of the unpleasantness of natural sounds, thus suggesting that self-reported noise sensitivity captures evaluative rather than sensory aspects of auditory processing.

2:40

2pPPa3. Loudness and annoyance of steady-state and temporally varying noise. Rhona Hellman (Dept. of Psych., Northeastern Univ., 360 Huntington Ave., Boston, MA 02115, hellman@neu.edu) and Norman Broner (VIPAC Engineers and Scientists Ltd., Melbourne, Australia 3207)

Loudness and annoyance judgments were obtained by magnitude estimation for low-frequency noises. In one experiment, listeners judged the loudness and annoyance of 10-s noise bursts; in a second experiment, loudness and annoyance judgments of a continuous noise were made at regular temporal intervals over an exposure period of 1 h. All listening was through loudspeakers in an ASHRAE test room. For noise stimuli containing dominant low-frequency tones, the annoyance-to-loudness ratios ranged from 2.0 to nearly 8.0 under steady-state conditions. This large ratio variation was found despite nearly equal A-weighted levels. Moreover, consistent with a recent study [Hellman *et al.*, J. Acoust. Soc. Am. **101**, 2176–2185 (1997)], loudness decreased with time, more at low than at moderate sensation levels (SL). Perceived annoyance exhibited a similar dependence on SL with time, suggesting that loudness and annoyance are related. However, for noise stimuli with spectral peaks at 31.5 and 25 Hz, annoyance declined by a smaller percentage than loudness. This effect produced an increase in the annoyance-to-loudness ratio over the 1-h listening period. [Work supported in part by ASHRAE.]

3:00

2pPPa4. Response to air-cooling machinery noise: A preliminary study. Nancy Franchek, Patricia Davies (1077 Ray W. Herrick Labs., Purdue Univ., West Lafayette, IN 47907-1077), Richard Wood, and Phil Lavrich (United Technologies Carrier, Syracuse, NY 13221)

People living close to commercial properties are often exposed to air-cooling machinery noise. Of primary concern is the awareness of tones in the sounds and how that awareness contributes to the overall annoyance experienced by people exposed to the noise. For noise control, it is most straightforward to control the strength of tonal contributions from components such as fans and compressors. For the class of machinery considered in this study, fan fundamentals are usually around 60 Hz and compressor fundamental frequencies are typically between 500 and 700 Hz. A preliminary study was carried out using 27 sounds that simulated a broad range of possible noises made by this type of air-cooling machinery. The sounds were presented to people who were asked to rate them in terms of tonality and annoyance. Tonality and annoyance ratings only increased when sounds contained at least one compressor tone above a certain threshold level. High correlations were found between objective metrics and the average of the subjects' responses. Recommendations for future research include investigations into the individual effects of changing spectral balance, overall loudness, and tonal contributions for these types of sounds, because changing tonal levels alone affects all of these sound characteristics simultaneously.

3:20

2pPPa5. Binaural assessment of loudness of environmental noise. Anna Preis (I. I. S. Univ. of Tokyo, 7-22-1 Roppongi, Minato-ku, Tokyo, 106 Japan)

Loudness of time-varying environmental noises (two types of car noise and aircraft noise) presented under dichotic and diotic stimulation was investigated via headphones. The stimuli were combinations of signals with increasing and decreasing SPL. The objective was to discover if there is a difference between the noise assessment of these signals presented in diotic and dichotic conditions. The results are compared with previous research, where it was found that for combinations of tone/noise and noise/noise, there was no difference between binaural loudness perceived in diotic and dichotic listening conditions. In the case of stimuli that consist of two tones of different frequency, those presented diotically were perceived to be louder than those presented dichotically.

3:40

2pPPa6. Aspects of global assessment of loudness-equalized interior car sound in stationary driving conditions. Thomas Hempel (Inst. of Commun. Acoust., Ruhr Univ., D-44780 Bochum, Germany)

In listening tests, loudness still turns out to be the most relevant parameter for a subject's assessment regarding interior car sound. In order to investigate further parameters in listening tests, the influence of loudness differences between the sound samples has to be avoided. Minimizing errors, this can be done by equalizing the loudness of presentation of each sample to the median of all samples in the set. It can be found that originally soft cars now yield lower rankings of preference than before. A possible reason might be the loudness of presentation, which is higher than in the real car. A presentation of sound samples, which now are equalized to the loudness originally appearing in those soft cars, could possibly lead to different rankings. Furthermore, global assessments of loudness-equalized interior car sounds were obtained using the method of paired comparisons as well as the method of magnitude estimation.

4:00–4:20 Break

4:20

2pPPa7. Psychoacoustic evaluation of noise emissions. Hugo Fastl (Inst. of Man-Machine-Commun., Tech. Univ. München, Arcisstr. 21, D-80333 München, Germany)

While the psychoacoustic evaluation of noise emissions is already on its way from basic research laboratories in universities to application labs in industry, the psychoacoustic evaluation of noise emissions is not yet widely applied [http://www.mmk.e-technik.tu-muenchen.de/admin/noise.html]. Therefore, psychoacoustic evaluations of noise emissions from road traffic noise, railway noise, aircraft noise, industrial noise, and leisure noise are discussed. As a rule, the overall loudness of a noise emission is larger than the

average of the instantaneous loudnesses of the acoustic events constituting the noise emission. With respect to physical measurements, statistical treatment of loudness values measured according to DIN 45 631 can predict the subjective evaluations of noise emissions for different types of noises. [Work supported by DFG.]

4:40

2pPPa8. Evaluating sequences of environmental noise using the method of absolute judgment in laboratory and outdoor situations. Some methodological considerations. Juergen Hellbrueck and Alfred Zeitler (Catholic Univ. of Eichstaett, Environ. and Health Psych., Ostenstraße 26, D-85072 Eichstaett, Germany, juergen.hellbrueck@ku-eichstaett.de)

It has been shown that the perceived average loudness of a noise sequence can be predicted from the Leq [S. Namba and S. Kuwano, J. Acoust. Soc. Jpn. (E) **1**, 99–106 (1980)] or the percentile loudness N_4 [e.g., H. Fastl, Contributions to Psychological Acoustics. Results of the Fifth Oldenburg Symposium on Psychological Acoustics (1991), pp. 205–216]. While most of the experiments have been conducted in laboratory situations, there is lack of evidence that the results can be transferred to noise situations outside of the laboratory. Context factors and psychological frames of reference play an important role, when environmental noises are rated in real noise situations. Category scaling based on the method of absolute judgment is regarded to be a natural scaling procedure which is inherently associated with psychological theories of frames of reference. Current results of empirical studies on the evaluation of longer periods of traffic noise have proved the applicability of category scales. The method has been used in outdoor settings as well as in laboratory situations, and yielded reliable results in both cases. Therefore, it is proposed to use measurements which are familiar to the subjects, such as absolute judgments, thus having direct access to individuals' perceptions.

5:00

2pPPa9. Application of loudness quantities in a field study. Ulrich Widmann (Müller-BBM, Robert-Kochstr. 11, 82152 Planegg, Germany) and Peter Lercher (Inst. für Social Medicine, Innsbruck, Austria)

The evaluation of noise emissions in field studies is mainly based on the concept of energy-equivalent A-weighted sound level. This averaging method has the advantage of being physically well defined and easy to compute. However, several laboratory studies showed that this method is aurally not adequate and the specific acoustic characteristics of traffic sources cannot sufficiently be discriminated. In a pilot study a good correlation was found between annoyance reactions of residents near a highway after noise abatement measures and perceived loudness. Residents' reactions near the highway could be well predicted using a percentile value of N_5. To predict the reactions for subjects living at larger distances from the source the effect of masking by environmental background noise has to be considered additionally using the psychoacoustic concept of partially masked loudness. The pilot study was restricted to a small number of inhabitants in one village. In a new field study in Austria it was attempted to confirm the preliminary results of the pilot study within a larger population. The ratings of loudness quantities, i.e., different percentile values, and of physical quantities, i.e., energy-equivalent A-weighted level and level percentiles, are investigated.

5:20

2pPPa10. Psychoacoustics and noise abatement in Austria—Some practical experiences. Manfred T. Kalivoda (Wiener Gasse 146/3, A-2380 Perchtoldsdorf, Austria, psia-consutt@eunet.at)

In Austria there are two main fields of application for psychoacoustic methods. For noise from trade and industry the Gewerbeordnung (trade act) does not use any SPL limits. There is a more stringent regulation that says that an industrial plant has to be licensed only if neither a health risk nor intolerable nuisance or annoyance can be expected. The Umweltverträglichkeits-Prüfungs-Gesetz (environmental assessment act) from the year 1994 includes industry and all modes of transport uses the same wording as the Gewerbeordnung. Nevertheless, A-weighted equivalent levels are frequently used for noise assessment in these two fields. There are many situations where it makes no big difference if $L_{A,eq}$ or psychoacoustics is used. However, there is about 10% to 20% of noise problems for which SPL alone is not adequate so wrong conclusions are drawn on the noise impact. psi-A Consult is very experienced in applying psychoacoustics on real noise problems. Some examples, showing the discrepancies between conventional and psychoacoustic noise assessment, are presented here.

5:40

2pPPa11. Factors influencing equal-loudness-level contours. Carsten Reckhardt, Volker Mellert (Physik Akustik Univ. Oldenburg, D-26111, Oldenburg, Germany), and Birger Kollmeier (Univ. Oldenburg, Oldenburg, Germany)

Data on equal-loudness-level contours taken from the literature show considerable differences between the results of different laboratories, even when using the recommended alternative forced-choice (AFC) method. Some of these differences can be attributed to free parameters in the procedures that the experimentator could change. This work investigates the influence of the experimental setup on the resulting curves obtained with an adaptive two-alternative forced-choice procedure for the 30- and 50-phon curves in the range from 200 Hz to 1 kHz. For the adaptive procedure, the amount of change in the resulting equal-loudness-level contours is measured for different free parameters (e.g., initial step size, starting level). It is shown that for a simple adaptive procedure the influence of the starting level is smaller than the range effect when using the method of constant stimuli. The effect of the starting level is reduced when using large initial step size in the adaptive procedure. However, the effect can still amount to 6 dB. This effect diminishes when using an interleaved procedure. The maximum measurement error for the different procedures is estimated. In addition, it is shown that interindividual variance is reduced when the individual threshold is taken into account.

6:00

2pPPa12. Effects of helicopter and aircraft interior noise and vibration on passengers' comfort sensation and subjective well-being. Julia Quehl, August Schick (Dept. of Psych., Inst. for Res. into Man-Environment-Relations, Univ. of Oldenburg, 26111 Oldenburg, Germany, quehl@uni-oldenburg.de), Volker Mellert, Brigitte Schulte-Fortkamp (Univ. of Oldenburg), and Hermann Remmers (Inst. for Tech. and Appl. Phys. (ITAP) GmbH, Oldenburg, Germany)

Apparently passengers' sensation of comfort and subjective well-being are key concepts in the research on user acceptance of helicopter and aircraft systems. The design and development of advanced air transportation technologies require a fundamental, theory-based understanding of these concepts. From the passengers point of view, helicopter and aircraft interior noise and vibration are primary physical factors underlying the perception of comfort and well-being. In various judgmental contexts the influence of exposure to combined interior noise and vibration in helicopters and aircrafts will be analyzed by means of combined psychoacoustical, socioacoustical, and psychological research methods: Field experiments in a flight simulator and during real flight situations as well as laboratory experiments using a sound and vibration reproduction system will be carried out in order to examine the interactive effects of noise and vibration. The aim is to develop a passenger comfort or well-being index for helicopter and aircraft interior environments. The index will be based on the integration of physical predictors for the flight situation and psychological predictors for the passengers' sensation of comfort and well-being.

TUESDAY AFTERNOON, 16 MARCH 1999 ROOM H106, 2:00 TO 6:20 P.M.

Session 2pPPb

Psychological and Physiological Acoustics: Physiological Acoustics

Glennis R. Long, Chair
Department of Audiology and Speech Sciences, Purdue University, West Lafayette, Indiana 47907, USA

Contributed Papers

2:00

2pPPb1. A new HRTF decomposition and the corresponding algorithm for sound spatialization. Eric Dudouet and Jacques Martin (Ctr. Scientifique et Technique du Batiment, 25 rue J. Fourier, 38400 Saint-Martin-d'Heres, France)

Binaural simulations make extensive use of head-related transfer functions (HRTF), so spatializers have to deal with large amounts of data and long computing times to interpolate the HRTF database over the whole space. A better understanding of human auditory localization could lead to a better simulation of localization cues and allow the database and the computing time to be minimized. Principal component analysis on HRTFs, reported by D. J. Kistler and F. L. Wightman [J. Acoust. Soc. Am. **91**, 1637–1647 (1992)], gave only second-order decorrelated base vectors. In order to find simple vectors (bandpass or low-pass), an independent component analysis has been computed for upper-hemisphere preprocessed HRTFs (reported in by M. Emerit *et al.* [Proc. 15th ICA, Trondheim, Norway, (1995) pp. 437–440]). New analyses have been done on a new HRTF data set, on different representations (time, magnitude alone and with phase). These analyses give a small number of base vectors, which can be used to reconstruct any HRTF, with a correlation coefficient near 1, and allow a new spatialization method using 3 IIR filters, derived from independent impulse responses, to be conceived. Source signals are filtered by each of these filters, and linear combination of the results gives the spatialized signal.

2:20

2pPPb2. Vibration characteristics of bone-conducted sound. Stefan Stenfelt, Bo Håkansson (Dept. of Signals and Systems, Chalmers Univ. of Technol., Göteborg, Sweden, stenfelt@s2.chalmers.se), and Anders Tjellström (Sahlgrenska Univ. Hospital, Göteborg, Sweden)

A dry skull, prepared with a layer of damping material in the brain capsule, was used to investigate the vibratory pattern of bone-conducted sound. Three orthogonal vibration responses of the cochleas were measured, by means of accelerometers, in the frequency range 0.1 to 10 kHz. The exciter was attached at different points in the temporal, parietal, and frontal bones. The results revealed a profound low-frequency antiresonance (attenuation) in the ipsilateral transmission path, which was psychoacoustically shown to yield a distinct lateralization effect. It was further shown that the direction of excitation coincides with that of maximum response at the ipsilateral cochlea. No dominating response direction was found for frequencies above the first skull resonance at the contralateral cochlea. An overall higher response level was achieved at the ipsilateral cochlea when the transducer was attached close to the posterior semicircular canal compared with the other excitation points of the skull, for the energy transmission in general and specifically for the direction of excitation. Transcranial attenuation between the cochleas was found to be highly frequency specific, with a maximum of 40 dB in a single direction. Transcranial energy attenuation was less than 10 dB for the investigated frequency range.

2:40

2pPPb3. Estimation of the sound pressure at the eardrum. Herbert Hudde (Inst. of Commun. Acoust., Ruhr Univ., Bochum, Germany) and Andreas Engel (St. Elisabeth Hospital, Bochum, Germany)

In hearing experiments or in audiological investigations, the results usually have to be referred to an appropriate input signal. Typically, the input voltage of a headphone or the sound pressure generated in a free sound field or under a different reference condition are used. In many cases, however, it would be preferable to know the sound pressure at the eardrum, as it is more closely related to the auditory sensation. If headphones are used, the reference to the pressure at drum can be approximately achieved by means of an ear simulator, such as the well-known ear simulator, according to DIN IEC 711. But the ear simulator can only reproduce the acoustical properties of an average ear. The resulting errors depend on various parameters, including those of the headphone used. A considerable portion of the error is caused by the individual ear canals. These errors alone can exceed 10 dB in the audiologically used frequency range up to 8 kHz. Some methods of estimating the pressure at the drum are investigated. Optimum results are obtained if both the sound pressure and the volume velocity at the ear canal entrance are measured. But fairly good results can also be achieved without measuring the volume velocity.

3:00

2pPPb4. Three-dimensional measurements of a physical full-size model of the human middle ear. Henning Taschke (Inst. of Commun. Acoust., Ruhr Univ., Bochum, Germany) and Christian Weistenhofer (Ruhr Univ., Bochum, Germany)

Complete systematical investigations of the vibrational properties of the human middle ear are impossible to carry out by means of temporal bone measurements of a single specimen because of post-mortem changes (time variance), damages to the object to be measured, and the irreversibility of manipulations. Measurements of physical models offer the facility for examining the properties of the human middle ear regardless of the above problems. The quality of the scientific findings obtained from the physical models depends on how good the properties of the real middle ear are reproduced by the elements, forms and materials chosen. A physical full-size model of the human middle ear was developed that allows the use of measurement instrumentation which is applied for real ear measurements. One- and three-dimensional measurements of the physical full-size model will be presented. The quality of the model will be judged by comparisons with real ear measurements and model predictions. The fields of application of the model resulting from this will be discussed.

3:20

2pPPb5. A general model of inner ear pressure responses including ultra-low frequencies. Ernst-J. Haberland (Dept. of ENT and HNS, Univ. of Halle-Wittenberg, Magdeburger Str. 12, D-06097 Halle, Germany) and Hans J. Neumann (City Hospital Martha-Maria, D-06120 Halle, Germany)

Various volume displacement processes act on the inner ear fluids, e.g., via the stapes, via the capillary bed, via the cochlear aqueduct or in the case of ultra-slow processes via pressure homeostasis from tissue. Frequencies below the audible range make a pressure difference in the perilymphatic scales but without any audible traveling wave dispersion. In experiments in guinea pigs, interference patterns were found between audible and low-frequency nonaudible perilymphatic flows in CM recordings. The function of perilymph can be subdivided into the dispersional part and the conventional part. Franke and Dancer [Arch. Otorhinolaryngol. **234**, 213–218 (1982)] described a model of the guinea pig's cochlea in accordance with pressure measurements in the two perilymphatic scales up to low frequencies at the lower boundary of the audible range. In our own experiments, it was measured pressure responses to slow and ultra-slow changes of perilymphatic infusions and aspirations and superimposed incremental volume pulses into the perilymphatic system [Neumann and Haberland, *Biophysikalische Untersuchungen* (Tectum Verlag, Marburg, 1998)]. From these experimental findings was developed an extended model of the passive pressure characteristics of the inner ear system that takes into account nonlinearities and valve characteristics in the convection-relevant slow and ultra-slow movements of perilymph.

3:40–4:00 Break

4:00

2pPPb6. Cochlear fine structure in chinchillas. Glenis R. Long, Lauren Shaffer (Dept. of Audiol. and Speech Sci., Purdue Univ., West Lafayette, IN 47907), William J. Murphy (Natl. Inst. for Occupational Safety and Health, Cincinnati, OH 45226), and Carrick L. Talmadge (Univ. of Mississippi, University, MS 38677)

Spontaneous otoacoustic emissions (SOAEs) and distortion product otoacoustic emissions (DPOAEs) were evaluated in both ears of nine apparently normal-hearing chinchillas selected because preliminary screening indicated that they had SOAEs in at least one ear. All chinchillas show DPOAE fine structure in both ears (even in ears without detectable SOAEs). The spacing of the SOAEs and the characteristics of DPOAE fine structure are compared with OAE measures (obtained using the same procedures) from two species of kangaroo rat (*Dipodomys merriami* and *Dipodomys spectabilis*) that have no SOAEs and no DPOAE fine structure, and human subjects who have fine structure. Similarities and differences between the species are used to evaluate this model of cochlear fine structures further [Talmadge *et al.*, J. Acoust. Soc. Am. **98**, 1517–1543 (1998)].

4:20

2pPPb7. Modulation of distortion product otoacoustic emissions (DPOAE) by low-frequency masker tones in human ears. Torsten Marquardt (Inst. of Sound and Vib. Res., Univ. of Southampton, Southhampton, England), Johannes Hensel, Günther Scholz, and Dieter Mrowinski (Humboldt Univ., Berlin, Germany)

Biasing of the basilar membrane displacement by a loud low-frequency tone causes changes of the DPOAEs depending on the phase of the masker. A corresponding model helps to understand the nonlinear behavior of the cochlea and to improve the diagnosis of inner ear diseases. Up to now, short time Fourier transform has been used to measure the DPOAE suppression pattern. This method has inherent time and frequency resolution limits. Therefore a new approach is presented, where the primaries and all frequencies generated by the process are harmonics of the masker. A rectangular time window with length according to the masker period is used. The part of the spectrum representing the DPOAE signal is regarded as modulated tone, consisting of a DPOAE frequency $(2f1-f2)$ and spectral side frequencies. The time course of the DPOAE suppression pattern is computed by superposition of these complex components. The results are compared with a simulation of the distortions of the outer hair cells' mechano-electrical transfer function. In addition, a cochlear impedance model is verified. Variation of masker frequency results in the expected phase shift of the DPOAE modulation pattern and allows the assessment of the lower cutoff frequency of the human cochlear impedance.

4:40

2pPPb8. Characteristics of amplitude modulation following responses in man. Günter Mauer and Wolfgang H. Doering (Univ. of Technol., RWTH Aachen, ENT-Dept., Audiol., Pauwelsstr. 30, D-52057 Aachen, Germany, mauer@alpha.imib.rwth-aachen.de)

Amplitude modulation following responses (AMFRs) are a subset of envelope following responses (EFRs) and can be recorded from the human scalp. In AMFRs continuous amplitude-modulated (AM) stimuli with carrier frequency f_c and modulation frequency f_m are used. Responses arise at frequency f_m and are largest for modulation frequencies in the range below 100 Hz depending on the subject's age and state of arousal. Multichannel recordings and brain electrical source analysis were carried out to get information about localization of AMFR generators and dependency on modulation frequency of the stimulus. Recording of AMFR seems to yield important information about frequency-specific hearing loss even in the low-frequency range. Responses are assumed to be evoked by neural excitation originating mainly from a basilar membrane region corresponding to the carrier frequency f_c. However, in masking experiments, it could be shown that also regions of the basilar membrane related to frequencies up to several octaves above the carrier frequency contribute to the responses although stimulus bandwidth is very narrow. Models of cochlear mechanics were used to elucidate stimulus-response characteristics and effective stimulation bandwidth. Thresholds of AMFR in normal-hearing and hearing-impaired subjects are in close relation to psychoacoustically determined thresholds for the same stimuli.

5:00

2pPPb9. Excitation and inhibition in the dorsal nucleus of the lateral lemniscus influence binaural response properties of neurons in the rat's inferior colliculus. Jack B. Kelly (Lab. of Sensory Neurosci., 329 Life Sci. Bldg., Carleton Univ., Ottawa K1S 5B6, Canada, jkelly@ccs.carleton.ca)

In vitro brain slice studies have shown that neurons in the rat's dorsal nucleus of the lateral lemniscus (DNLL) are affected by both NMDA and non-NMDA receptor-mediated excitation and glycineric inhibition evoked by electrical stimulation of ascending afferent fibers in the lateral lemnis-

cus and GABAergic inhibition evoked by stimulation of the commissure of Probst [Wu and Kelly, 1996]. The effects of excitatory and inhibitory events in the DNLL on binaural responses in the rat's inferior colliculus are reported here for *in vivo* experiments. Receptor specific antagonists were injected locally into the DNLL before and after recording extracellular single-neuron responses from the contralateral inferior colliculus. Binaural responses were evoked by paired clicks delivered to the two ears. Both NMDA and non-NMDA excitatory amino acid antatonists (NBQX and CPP) produced a release from binaural inhibition and glycinergic and GABAergic antagonists (strychnine and bicuculline) resulted in enhanced binaural inhibition. The results support the idea that the DNLL plays a role in binaural processing through an inhibitory (GABAergic) influence on the contralateral central nucleus of the inferior colliculus. [Research supported by NSERC of Canada.]

5:20

2pPPb10. Sensitivity of auditory units in the frog's midbrain to amplitude decrements. Nikolay G. Bibikov (N. N. Andreyev Acoust. Inst., Shvernik st. 4, Moscow 117036, Russia, BVP@ASU.ACOINS.MSK.SU)

Responses to single and repetitive amplitude decrements in an otherwise steady best-frequency sinusoid were recorded in midbrain auditory units of the curarized grass frog. The modulators were either 1 or 12 full cycles of cosine function (frequencies: 10–100 Hz, maximal modulation depths: 6%–80%). All units were also classified according to their responses to pure tone and AM tone bursts. In some tonic units, which demonstrated enhancement of synchronization in the course of AM tone bursts, enhancement of the rate response to successive amplitude decrements was routinely observed. The response to the first decrement in succession could be omitted, but the probability of highly synchronized firing increased gradually to the end of the series of decrements. The effect could be explained by adaptation of the unit to a new average intensity level. Some onset units, which did not respond to any modulation periods of 100% AM tone bursts, demonstrated a prominent response to a single 10%–20% decrement in a pure tone. The dependence of the response upon duration of decrement (period of a cosine function) usually showed a prominent maximum in the range of 20–50 ms. The response latency increased with the decrement duration, showing that the firing was evoked by an amplitude recovery.

5:40

2pPPb11. Incremental responses in the auditory cortex and the auditory periphery. Robert L. Smith, Dyanne Baptiste (ISR and Dept. of Bioeng. and Neurosci., Syracuse Univ., Syracuse, NY 13244-5290, Bob_Smith@isr.syr.edu), and Bernd Lutkenhoner (Univ. of Munster, Munster, Germany)

When probe tones are added to background sounds, the perception or detectability of the probe is influenced by the time delay from the onset of the background to the onset of the probe. In general, the shorter the time delay, the harder it is to detect or perceive the probe as a separate signal. Possible physiological counterparts of these phenomena were investigated by adding 40-ms-long probe tones to 200-ms-long background tones. The corresponding increment in response was measured in the auditory nerve of anesthetized gerbils, using single-unit and modulation following responses, and in the auditory cortex of awake humans, using a 37-channel Magnetoencephalogram (MEG) and a single equivalent current-dipole model. The auditory nerve responses appear to obey superposition such that the increment in response is independent of the time delay. In contrast, the increment in the MEG response was significantly smaller for small delays than for long delays. The results suggest that the cortical responses behave differently than the peripheral responses, and more closely resemble those obtained psychophysically, although differences in experimental paradigms may also affect comparisons. Hence the difference between peripheral and central effects may reflect a functionally significant change in temporal processing occurring along the auditory pathway.

6:00

2pPPb12. Analyses of continuous brain waves in relation to subjective preference of the sound field. Chiung Yao Chen (Dept. of Architecture, Chaoyang Univ. of Technol., 168 Gifeng E. Rd., Wufeng Taichung, Taiwan, ROC)

Two factors comprising a standard of time are prevailing for designing a music hall: (1) initial time delay gap between the direct sound and the first reflection (Δt_1); (2) subsequent reverberation time (T_{sub}). In brain researches of sound cognition, auditory-evoked potential (AEP) was frequently applied. However, it is undetectable in studying the variation of T_{sub} and Δt_1 by a longer stimulus. In the present study, a method for measuring a human's responses on continuous brain waves (CBW) was arranged with respect to the subjective preference of a music sound field. First, the ''effective duration'' (τ_e) was defined by the effective gap of the initial deduction (0.1 envelope) of the autocorrelation function of CBW. Results show the values of τ_e efficiently prolong ($p_i = 0.05$) on the left hemisphere when the scale values (SVs) of preference increases by changing Δt_1. Second, this relationship was extended to examine changing T_{sub}. The longer ($p_i = 0.01$) τ_e were found as the SVs increased in the range of $T_{\mathrm{sub}} = 0.2$ to 1.2 s. Finally, as the auditory tempo was varied, the differences of values of τ_e show a closer correlation ($r = 0.80$, $p_i = 0.01$) to the differences of SVs on the left hemisphere.

Session 2pSAa

Structural Acoustics and Vibration: Structural Vibration, Radiation and Scattering I

Mauro Pierucci, Cochair
Department of Aerospace and Engineering Mechanics, San Diego State University, San Diego, California 92182-1308, USA

Christiaan Kauffmann, Cochair
Faculty of Technology, Mathematics, and Informatics, Delft University of Technology, P.O. Box 5031, 2600 GA Delft, The Netherlands

Contributed Papers

2:00

2pSAa1. On the acoustic Zeeman effect. Christiaan Kauffmann (Faculty of Tech. Math. and Informatics, Delft Univ. of Technol., P.O. Box 5031, 2600 GA Delft, The Netherlands, kauffman@dv.twi.tudelft.nl)

Thin, square plates subject to uniform boundary conditions vibrating in flexural motion have an enumerable set of resonances, some of them having multiple resonant modes. This holds for plates vibrating *in vacuo*. If the plate motion is subject to fluid loading, the resonant properties modify. Fluid loading induces all resonances to shift downwards (added mass effect), while acoustic radiation contributes to the damping of the modes. These features are well known and understood, although the actual calculation requires considerable computational effort. A perturbation method is presented for dealing with the effect of light fluid loading on the degenerate resonances. Removal of degeneracy is found for repeated modes having different coefficients for added mass and radiation damping. Symmetry is preserved for degenerate resonances that are modified by fluid loading in an identical way. Numerical results are presented that show how resonances split for the modes $u_{mn} \pm u_{nm}$ of simply supported plates, where m and n have the same parity, i.e., $m+n$ is even. Simple physical arguments, like equivalent multipole sources of the mode shapes and their spatial modulation, are used to interpret the results. Mode shapes with the highest degree of symmetry show the largest shift in frequency.

2:20

2pSAa2. HYPERION—A computational tool for the investigation of the sound transmission loss of periodically structured plates. Waldemar Maysenhoelder, Bozica Horvatic, and Klaus Nasshan (Fraunhofer-Inst. f. Bauphysik, Nobelstr. 12, D-70569 Stuttgart, Germany, maysenhoelder@ibp.fhg.de)

HYPERION offers a generalization of Cremer's famous treatment [Akust. Z. **7**, 81–104 (1942)] of the sound transmission of thin homogeneous plates in several respects: (i) periodically inhomogeneous plates, (ii) anisotropic bending stiffness, and (iii) different fluids on both sides of the plate. [A detailed account of the theory including some examples has been given in Acustica/acta acustica **84**, 668–680 (1998).] The spatial periodicity generates propagating and nonpropagating diffracted waves, which may lead to several conspicuous features of the sound transmission loss curve. The most surprising phenomena are total reflection and total transmission below the critical frequency. These and other effects pertaining to refraction, near fields, and diffraction will be illustrated by an 8-min video film. Besides, it is worth mentioning that the computation of the transmission loss for diffuse-field excitation is rather time consuming, since a two-dimensional integration has to be performed over the two angles of incidence. The complexity of the integrand will be demonstrated graphically. [Financial support from the Deutsche Forschungsgemeinschaft is gratefully acknowledged.]

2:40

2pSAa3. A modal synthesis approach to investigate the influence of viscoelastic boundary conditions on the sound radiated from a plate backed cavity. Olivier Chiello, Franck C. Sgard (LASH, DGCB URA CNRS 1652, ENTPE—Rue Maurice Audin, 69518 Vaulx-en-velin Cedex, France, olivier.chiello@entpe.fr), and Noureddine Atalla (Univ. de Sherbrooke, QC J1K 2R1, Canada)

In this paper an efficient formulation is proposed to calculate the sound radiation from a plate with edges viscoelastically restrained against translation and rotation and coupled to a cavity. The viscoelastic constants can be varied arbitrarily along the plate boundary and reproduce simply supported, clamped, free or guided edges as limiting cases. The formulation classically couples a modal expansion for the structure *in vacuo* and the cavity, using a coordinate transformation to calculate the fluid-structure coupled modes. The modal basis associated with the structure *in vacuo* is determined using a free component mode synthesis technique considering the viscoelastic parameters as components with a residual flexibility only. This approach is appropriate to compute the coupled modes efficiently and to perform a parameter study. Numerical examples are presented in the case of a plate excited either mechanically or acoustically. The aim of the study is to determine which boundary parameters have an influence on the acoustic behavior of plates and to develop tools for the pratical design of plate mounting conditions.

3:00

2pSAa4. The structural acoustic optimization of an unstiffened cylinder finite-element model. Sergio De Rosa, Francesco Franco, Mauro Fontana, Romualdo Paino (Dept. of Aeronautical Eng., Univ. of Naples ''Federico II,'' Via Claudio 21, 80125 Naples, Italy, derosa@unina.it), and Antonio Sollo (ALENIA Aerosp.—Aeronautic Div. Viale dell'Aeronautica, Pomigliano D'Arco (NA), Naples, Italy)

The presentation will show some results of an ongoing research, aimed to the tuning of a structural-acoustic optimization procedure. The target is the definition of a design tool in which it will be possible to include, at the same time, the weight and noise limits, together with the stress constraints, for getting reliable aircraft fuselage models. All the new capabilities included in the actual version of the MSC/NASTRAN have been tested. They allow analyzing the structural dynamics, the coupled acoustic response, to evaluate the structural-acoustic sensitivity and the global optimization process. Several similar attempts have been reported in the specific literature but, typically, different solvers have been used for each part of the problem (the structural degrees of freedom, the acoustic ones, and the optimization algorithm). Here, all results concern the application of the same finite-element model for a simplified (unstiffened) cylinder. The thicknesses of the plate elements have been grouped longitudinally and circumferentially, so that it has been possible to evaluate the predictive trends for fixed excitation frequency. Several optimization strategies have also been compared and discussed. They have also verified the optimized structural-acoustic models in output by evaluating the structural-acoustic geometric and dynamic coupling coefficients.

3:20

2pSAa5. Finite element and boundary elements for underground input to SEA calculations. Philippe Jean (Centre Scientifque et Technique du Bâtiment, 24 rue Joseph Fourier, 38400 St. Martin d'Hères, France)

In order to study underground structures with a SEA model, special care must be given to ground loading which affects the behavior of the walls. The use of more precise techniques such as finite elements and boundary element techniques enables a description of complex phenomena and the computation of input to the SEA model. Therefore, several aspects have been analyzed: effect of type and position of source, type of ground, size and shape of the foundation, influence of the superstructure (size and type). Applications to the case of railway type situations are given. The source can be either on the surface or in the ground resulting in the generation of different types of waves.

3:40

2pSAa6. Radiation of sound from a monopole source near a free-flooded cylindrical shell. K. Steven Kim (Signatures Directorate, Carderock Div., Naval Surface Warfare Ctr., 9500 MacArthur Blvd., West Bethesda, MD 20817-5700)

Radiation of sound from an acoustic source changes if there is a structure nearby. Radiated and scattered acoustic pressure fields are obtained when a free-flooded cylindrical shell of finite length is subjected to acoustic waves from a monopole source. By solving integral equations formulated for an elastic thin shell with simply supported boundary conditions at both ends, far-field acoustic pressures are calculated. Cases of various source locations inside and outside a shell are discussed.

4:00–4:20 Break

4:20

2pSAa7. Modeling structure-borne sound transmission via pipe systems to building structures. G. Susanne van der Jagt and Heiko J. Martin (Acoust. Lab., B-FAGO, Eindhoven Univ. of Technol., P.O. Box 513, 5600 MB Eindhoven, The Netherlands, g.s.v.d.jagt@bwk.tue.nl)

In residential buildings many people are annoyed by noise caused by their neighbors, including structure-borne sound caused by drinking water, sanitary, and other installations. In different building regulations, limits are set to the maximum allowable sound level caused by installations in a room. However, predictions of the sound level in the design stage are not possible. In this research, a framework for structure-borne sound transmission models for pipe systems, including source characterization, has been developed. Further, the application possibilities of existing calculation methods in the quantification of the sound transmission have been investigated. For example, the application possibilities of the finite-element method (FEM) and statistical energy analysis (SEA) depend on the element type, including dimensions and material (pipe, mounting, or building structure), the wave type, and the frequency area. By combining both methods, calculations for the whole audible frequency area seem possible. Some models are presented, together with calculated values of characteristic parameters. Measurements can be used to complete and validate the models, for example by using a measurement setup based on the plate method. The interaction between calculations and measurements will form the basis for future research. The future research setup is also presented.

4:40

2pSAa8. Estimating radiation modes for broadband measurement. Scott D. Sommerfeldt and Dong Lin (Dept. of Phys., Brigham Young Univ., Provo, UT 84602-4673, s_sommerfeldt@byu.edu)

Acoustic radiation modes have been investigated as a means of estimating far-field radiated acoustic power, based on structural vibration measurements. One of the difficulties associated with radiation modes is the fact that the mode shapes are frequency dependent. Much of the research in the past associated with radiation modes has focused on the low-frequency range, where the radiation modes are nearly frequency independent. The work reported here is aimed at developing a measurement approach based on radiation modes, which is applicable in the low- and mid-frequency range, where the frequency dependence of the radiation modes cannot be ignored. In general, if a limited number of point vibration sensors are to be used to estimate the radiated acoustic power, the appropriate locations on the structure for those sensors will change for each frequency. However, it will be shown that if one uses distributed sensors, it is possible to use a single sensor configuration to estimate the acoustic radiation over a broad range of frequencies. Numerical results will be shown that indicate the measurement accuracy that can be expected over a range of frequencies up to a normalized frequency of $kL = 15$.

5:00

2pSAa9. Integral formulations for the vibroacoustic characterization of a cello. C. Langrenne and A. Garcia (Laboratoire d'Acoust. du CNAM, 5 rue du Vertbois, 75003 Paris, France)

An isoparametric element formulation is used for implementing the Helmholtz integral formulation associated with arbitrary shaped three-dimensional bodies [M. Bonnet, Eyrolles editions, 1997]. The inverse problem is solved, i.e., the normal velocity distribution is determined on the surface of the instrument. In this way, the direct problem can be solved: the acoustic field can be calculated anywhere (near field, far field). Because of difficulties in solving the inverse problem (ill-posed problem, i.e., of which the solution is very sensitive to the errors of measurements), a regularization method is used to find the nearest solution of the real one [C. Langrenne and A. Garcia, Inter-Noise 97 Proc., Hungary, August 25–27 (1997)]. Experimental vibroacoustic characterization is done from holography measurements, without any contact with the stucture of the instrument, with the help of a robot describing a cylindrical surface.

5:20

2pSAa10. Effect of internal inhomogeneities on acoustic scattering from finite cylindrical shell bounded by hemispherical endcaps. Nicolas Touraine, Dominique Décultot, Gérard Maze (Lab. Acoust. Ultrasonore et Electron. (LAUE), UPRESA CNRS 6068, Université du Havre, Pl. Robert Schuman, 76610 Le Havre, France), Aleksander Klauson, and Jaan Metsaveer (Tallinn Tech. Univ., EE 0026 Tallinn, Estonia)

The acoustic scattering from an air-filled finite cylindrical shell with hemispherical endcaps is considered. In axial incidence, experimental studies have shown formation of compressional wave $S0$ resonances. These resonances are predicted and identified by applying the phase-matching condition over the meridian circumference. However, frequency irregularities observed experimentally on spectra have suggested that the assemblage quality during the manufacturing of the object may be not negligible. Indeed, internal nonuniformities of the shell at the junctions of cylindrical and hemispherical shells are present and modify certain wave propagation phenomena. The aim of this study is to discover these experimental conditions of the studied object through a numerical model with internal annular inhomogeneities localized at the junctions of the substructures and for two different b/a ratios (internal to external radius ratio) equal to 0.97 and 0.99. In the studied frequency range (50–300 kHz), in addition to the $S0$ wave, another peripheral wave A can be generated for the ratio $b/a = 0.97$. The numerical approach is based on the discretization of the shell and determination of its eigenmodes (FEM). Acoustical pressure field is found by the boundary integral equation procedure (BEM). The comparison of numerical and experimental results is presented in frequency and time domains.

5:40

2pSAa11. Designing structures for noise and vibration control with statistical energy analysis. Liangyu Huang and P. K. Raju (Dept. of Mech. Eng., Auburn Univ., Auburn, AL 36849)

Statistical energy analysis (SEA) was initially developed for predicting noise and vibration levels in interior spaces and structures at audio frequencies. The methodology developed in this paper extends traditional statistical energy analysis beyond the prediction of mean-rms vibroacoustic response. An SEA response sensitivity algorithm was formulated to relate variability of design parameters to SEA response variation. The method can be used to sort the design parameters which have the greatest effect on the sound-pressure levels in acoustic spaces. The SEA response variance analysis relates response variance directly to variances in design parameters. This methodology is important for acoustic design of aircraft, ship, and automotive vehicles because it enables the user to qualitatively and quantitatively determine the rank and variations of vehicle interior sound-pressure level with respect to changes in design parameters. When fully developed, this methodology can be a powerful tool for identifying the design changes that would be most effective for controlling noise and vibration from structures.

6:00

2pSAa12. The acoustical power radiated by a planar annular plate for the form of vibrations (0,*n*). W. P. Rdzanek (Inst. of Phys., Pedagogical Univ. of Rzeszów, Rejtana 16a, 35-311 Rzeszów, Poland) and Z. Engel (Mining-Metallurgical Acad., Al. Mickiewicza 30, 30-059 Kraków, Poland)

The acoustic power radiated by a thin annular plate fixed rigidly, with both internal/external edges, into a planar rigid infinite baffle is analyzed. These processes are considered sinusoidal in time. It is assumed that the annular plate vibrates axially symmetric. The radiated acoustic power integral formula is transformed with the introduction of the contour integral at the plane of complex variable. Then the Cauchy theorem about residua is used. An elementary, useful for calculations in case of high frequencies, form of the formula of the radiated acoustic wave is obtained. This formula represents the acoustic power with the assumption that the annular plate vibrates with the *n*th axially symmetric mode.

TUESDAY AFTERNOON, 16 MARCH 1999 ROOM EB301, 2:00 TO 5:00 P.M.

2p TUE. PM

Session 2pSAb

International Workshop on Active Noise and Vibration Control
Structural Acoustics and Vibration: Active Noise Control in Ducts

Scott D. Sommerfeldt, Cochair
Department of Physics and Astronomy, Brigham Young University, Provo, Utah 84602-4673, USA

Gérard Mangiante, Cochair
Laboratoire de Mechanique et d'Acoustique, 31 Chemin Joseph-Aiguier, 13402 Marseille, Cedex 20, France

Invited Papers

2:00

2pSAb1. Development of an active exhaust silencer for combustion engines. Rene Boonen and Paul Sas (KU Leuven, Dept. of Mech. Eng., PMA, Celestijnenlaan 300B, B-3001 Heverlee, Belgium, rene.boonen@mech.kuleuven.ac.be)

A silencer is developed to attenuate engine exhaust noise using active control. The device consists of an electrically driven valve, combined with a buffer volume. Using the mean flow through the valve and the pressure fluctuations in the volume, the valve regulates the flow such that only the mean flow passes the tail pipe outlet. The flow fluctuations are temporally buffered in the volume. A cold engine simulator is developed to experiment with exhaust systems. This device generates realistic exhaust noise and the matching gas flow using compressed air. It allows quick and reliable acoustic and fluid dynamic experiments on exhaust prototypes. The valve is controlled using a nonadaptive feed-forward algorithm. The active silencer reduces the exhaust noise 13 dBA. However, the nonlinear relation between valve stroke and pressure drop limits the performance of the controller. Currently, a feedback controller is being implemented. It improves the performance, but is now limited by the time delay between control valve and the error pressure sensor. Future developments are now focused to compensate the time delay, using a Smith compensator, or repetitive control. Adaptive feed-forward is in consideration also, but this probably will not be ready when the workshop is held. [Work supported by BOSAL International.]

2:20

2pSAb2. Effects of geometric discontinuities and filter lengths on active control in ducts. Denis Duhamel (ENPC-CERAM, 6 et 8 Ave. Blaise Pascal, Cité Descartes, Champs-sur-Marne, 77455 Marne-la-Vallée Cedex 2, France) and Philippe Sergent (STCPVMN, 60321 Compiègne Cedex, France)

The active control is often used to reduce noise propagation in ducts, usually in straight sections. However, industrial ducts often contain discontinuities where the secondary source of an active system can or must be placed. The possibility of active control in such situations is studied and compared to the case of a straight duct. It is shown that a correct position for the secondary source allows one to take advantage of both passive and active attenuations, and can improve the global system. For a right angle or a resonator, simple analytical formulas can be obtained for the active attenuation, and it can be proved that the power output of the secondary source is

null. The influence of other important parameters such as the number of coefficients of the FIR filter in a filtered-X LMS algorithm, and the sampling frequency used for the control or the loss factor in the duct, are also estimated by analytical formulas. This gives, for instance, explanations for the frequency bands over which the control efficiency is low. In each case, comparisons with experimental data are provided and they support the theoretical conclusions quite well.

Contributed Papers

2:40

2pSAb3. An active silencer for harsh environmental conditions. Jan Krüger (Fraunhofer-Inst. Bauphysik Stuttgart (IBP), Stuttgart Nobelstrasse 12, D-70569 Stuttgart, Germany)

Active noise control has proven effective in the reduction of low-frequency noise in ducts, e.g., in air conditioning systems. However, in many applications the capability of proper operation of an active silencer is severely limited by the harsh environment. In fact, higher temperatures, static and dynamic pressure loads, extreme sound power levels, and abrasive flow often prohibit the use of active silencers at all. Appropriate design details for an actively absorbing silencer are presented, leading to a new construction with high performance and durability. Using standard components (microphone, loudspeaker), robust protection measures are developed which can be adapted to particular applications. A computational model derived from the theory of active silencers allows the variation of design parameters and the prediction of the insertion loss. To verify the numerical results, experiments under several acoustical and thermal conditions were conducted.

3:00

2pSAb4. Active noise control of higher-order modes in a rectangular duct using stabilized fast transversal filters. Holger Opfer and Dieter Guicking (Drittes Physikalisches Institut, Universitaet Goettingen, Buergerstr. 42-44, 37073 Goettingen, Germany, holger@physik3.gwdg.de)

For active noise control of sound propagating down a duct in the fundamental mode commercial systems are available. Cancellation of sound also propagating in higher-order modes adds the requirement of higher computational power for the signal processing unit, and stability problems due to source coupling effects. The widely used LMS algorithms need little computational effort, are very stable, but also have a slow tracking behavior to changes in the input signal. Depending on the eigenvalue spread of the input signal's autocorrelation matrix they lead to slow convergence. One method to overcome this problem is to use stabilized fast RLS algorithms which are independent of the statistics of the input signal. A multi-channel stabilized fast transversal filter algorithm has been investigated experimentally in a rectangular duct with respect to its stability, convergence, and performance.

3:20

2pSAb5. A hybrid active–passive system for controlling locomotive exhaust noise. Paul J. Remington (BBN Technol., 70 Fawcett St., Cambridge, MA 02138), Scott Knight, and Douglas Hanna (BBN Technologies, New London, CT 06320-6147)

Diesel electric locomotives represent the primary source of motive power in the U.S. railroad industry, and are a significant source of environmental noise. There is a variety of noise sources on a locomotive; however, two sources will have to be controlled before significant reductions in locomotive noise can be achieved: diesel engine exhaust noise and cooling fan noise. Here a system is described that uses both active and passive components to control broadband exhaust noise below 4 kHz. The active system utilizes eight actuators and eight residual microphones in an adaptive feed-forward configuration to control tonal noise below 200 Hz. The passive system is a compact exhaust silencer designed to control exhaust noise above that frequency while still fitting within the limited space available beneath the locomotive hood. Both active and passive systems will be described in detail, and practical problems encountered in the design of the combined systems will be described. Performance estimates for both the active and passive system will be presented along with the available measurements. [This work was supported under contract to the U.S. Federal Railroad Administration.]

3:40–4:00 Break

4:00

2pSAb6. Active control of pulsating flows in transitory conditions. J. Tartarin and F. Carimantran (Lab. d'Etudes Aerodynamiques, Univ. de Poitiers, bat. H, 40 avenue du Recteur Pineau, 86022 Poitiers, France, Francois.Carrimantran@lea.univ-poitiers.fr)

The active control in a duct in the presence of hot and/or corrosive gasses (e.g., exhaust system) or even heavy fluids (oil, fuel, water, . . .) needs an actuator that is particularly resistant. That's why the LEA designed an original auxiliary source [Hardouin *et al.*, Acta Acustica **1**, 189–198 (1993)]: an oscillating flap which acts in a flow as an aeroacoustic source. Its high efficiency in very low frequencies associated with its little bulk is also another major interest. For active control, because it is a source connected in series with the primary source, an online identification is preferable for better adaptive character. Therefore specific algorithms were developed in frequency domain for command strategies of feedback synchronous type. Other time-frequency domain algorithms were implemented. In view of industrial applications, these different algorithms were experimentally compared, particularly in transitory conditions. Jointly, simulations were led to allow the development and the optimization of exhaust mufflers including the flap and passive devices.

4:20

2pSAb7. Experimental investigations on active suppression of sound propagation in a fluid-filled pipe. Roland Lippold and Joachim Scheuren (Müller-BBM GmbH, Robert-Koch-Straße 11, D-82152 Planegg, Germany, li@mbbm.de)

The control of sound propagating along fluid-filled pipes is complicated because of the strong coupling between the structural and the fluid transmission path. If the propagation along the structural path is supressed (e.g., by passive compensation in the case presented), it is possible to reduce the propagating sound by active means only acting on the fluid. This statement was proved by several experiments. The experimental setup consisted of one pipe made of aluminum (length 4 m, wall thickness 5 mm, inner diameter 90 mm) and two pipes made of steel (3 m / 1.5 m, 2.5 mm, 70 mm) which were connected via 90-deg bends and filled with water. For excitation and compensation of sound in the fluid, shaker driven pistons acting perpendicular to the pipe axes were used. The frequency of the harmonic excitation in the frequency range from 600 up to 800 Hz was known to the compensation algorithm. If the passive compensation of the structural path was sufficient, the reductions of sound pressure in the fluid achieved at and behind the error sensor were between 10 and 20 dB. Otherwise, reductions of the same order were locally restricted to the position of the error sensor.

4:40

2pSAb8. Automobile gas-exchange systems low-frequency noise reduction using active noise control units. Andrei V. Vassiliev (Dept. of Labour and Environ. Protection, Togliatti Polytechnic Inst., Belorusskaya str. 14, Togliatti, 445667 Russia)

The main automobile aerodynamic noise sources radiating into the environment are internal combustion engine gas-exchange systems (intake and exhaust). Practical possibilities of active noise control unit applica-

tions for automobile gas-exchange system low-frequency noise reduction are discussed. Existing technical constructions of active noise control units (including those patented by author) for automobile intake and exhaust noise reduction are concerned. New construction of a unit is proposed. Its peculiarity is joint intake and exhaust noise reduction possibility. The signal of engine rotation frequency pick-up is input into the control system through the low-pass filter and transducer and then transmitted by the loudspeakers through the special waveguides into the zones of compensation near the intake and exhaust pipe open ends. Throttle opening angle is accounted for. Calculative results show the efficiency of such a construction operation.

TUESDAY AFTERNOON, 16 MARCH 1999 ROOM H3010, 2:00 TO 6:20 P.M.

Session 2pSCa

Speech Communication: Data Based Speech Synthesis and Analysis III

Juergen Schroeter, Chair
AT&T Laboratories–Research, 180 Park Avenue, Building 103, Florham Park, New Jersey 07932-0971, USA

Contributed Papers

2:00

2pSCa1. VCV synthesis from muscle commands. Perrier Pascal (ICP-INPG, 46 Av. Felix Viallet, 38031 Grenoble Cedex, France), Yohan Payan (TIMC, IMAG, 38706 La Tronche, France), Joseph Perkell, Majid Zandipour, and Melanie Matthies (MIT, Cambridge, MA 02139)

The biomechanical model of the tongue developed by Payan and Perrier [Speech Commun. **22**, 185–205 (1997)] is used to generate tongue movements in VCV sequences, where V is [i], [a], or [u] and C is the stop consonant [k]. Tissues' elastic properties are accounted for in finite-element modeling, and the mechanisms underlying the production of muscle forces are modeled according to Feldman's Equilibrium Point Hypothesis. Each elementary sound is associated with a target that is described as a static equilibrium position of the tongue, which is likely to vary with the phonemic context. In vowel production, the target is actually supposed to be reached, while the production of stop consonants consists of movements toward virtual targets located beyond the palate, which therefore cannot be reached. The collision of the tongue against the palate is modeled according to a penalty method, based on a nonlinear relationship between contact force and position/velocity of points located on the tongue surface [Marhefka and Orin, IEEE Conf. Robotics and Automation, 1662–1668 (1996)]. The acoustic signal is generated with a one-dimensional low-frequency approximation based on the Kelly–Lochbaum model. Synthetic kinematic and acoustic signals are compared with human speakers' data. [Work supported by CNRS, NSF, and NIH.]

2:20

2pSCa2. Speech synthesis of VCV sequence using a physiological articulatory model. Jianwu Dang (ATR Human Information Res. Labs., 2-2 Hikaridai, Seikacho Soraku-gun, Kyoto, 619-0288 Japan and Univ. of Waterloo, Waterloo, ON N2L 3G1, Canada, jwdang@crg3.uwaterloo.ca) and Kiyoshi Honda (ATR Human Information Res. Labs., 2-2 Hikaridai, Seikacho Soraku-gun, Kyoto, 619-0288 Japan)

A 3-D articulatory model has been constructed based on volumetric MR images for a Japanese male speaker, which is driven by a target-dependent control strategy to produce dynamic articulation for vowel sequences [Dang and Honda, ICSLP98]. This work describes a multi-point control strategy that is developed for generating vowel–consonant–vowel (VCV) sequence. Three control points are located on the mandible, tongue tip, and tongue dorsum, and they are operated in each muscle workspace. Contributions of the tongue and jaw muscles to each control point are evaluated by model simulation, and described as a weighted coefficient. Muscle activation signals are determined according to the articulatory vector from the current position to the target. The total activation pattern of the muscles is the sum of the activation signals calculated for the control points. Dynamic vocal tract shape is obtained by using the activation pattern to excite the model, and compared with MRI movies of VCV sequence for the same speaker [Masaki and Honda, J. Acoust. Soc. Am. **102**, 3166(A) (1997)]. The VCV sequence is synthesized from a set of vocal tact area functions of the model, based on vocal tract widths in the midsagittal and parasagittal planes, and compared with real speech.

2:40

2pSCa3. The FUL speech recognition system. Aditi Lahiri and Henning Reetz (Dept. of Linguist., Univ. of Konstanz, D186, 78462 Konstanz, Germany, aditi.lahiri@uni-konstanz.de)

The featurally underspecified lexicon (FUL) speech recognition system is based on a lexicon where words are represented by radically underspecified phonological features. Features are extracted from the speech stream and are mapped with a ternary logic (match, no-mismatch, mismatch) to the entries in the 100 000-word lexicon without building a segmental representation. The mapping process operates from left to right and allows for certain insertions and deletions of segments of the words in the lexicon. Mismatching features are deactivated from the search. Word candidates remaining after this selection undergo the parallel active prosodic and syntactic parsing of phrase hypothesis. The system is speaker independent and not sensitive to microphone or line conditions and does not need a high signal-to-noise ratio.

3:00

2pSCa4. Parameter estimation from speech signals for tube models. Karl Schnell and Arild Lacroix (Institut für Angewandte Physik, Johann Wolfgang Goethe Univ., D-60054 Frankfurt am Main, Germany)

Discrete time tube models implemented by lattice structures can be used to simulate the propagation of sound waves in the vocal tract. To cover a wide variety of speech sounds, it is necessary to extend the standard all-pole tube model by coupling the nasal tract, and, furthermore, enable the excitation of the tube system at different places in between. The resulting filter structure $H(z)$ now shows poles as well as zeros in the transfer function. The impedance of the lip opening is realized using a model from Laine [U. K. Laine, ''Modeling of lip radiation impedance in the z-domain,'' Proc. ICASSP-82, 1992–1995 (1982)], which includes one pole and one zero in the z-plane. The parameters of the tube model will then be estimated from speech by minimization of an error, which describes the spectral distance between $H(z)$ and the prefiltered speech signal. The prefilter is used for the separation of signal components due to excitation and radiation. A gradient-based optimization is implemented to find the minimum. Following this procedure, the frequency response is able to approximate the spectral envelope of the speech signal. The resulting areas correspond to those obtained by x-ray or NMR investigations.

3:20

2pSCa5. A preliminary study of speech transformation using empirically defined articulatory modes. Brad Story and Ingo Titze (WJ Gould Voice Res. Ctr., Denver Ctr. for the Performing Arts, 1245 Champa St., Denver, CO 80204)

In previous work it has been shown that a speaker-specific set of vocal tract shapes (acquired using MRI) corresponding to vowels can be decomposed into orthogonal components or ''modes,'' and effectively parameterized by the modal coefficients. Furthermore, a nearly one-to-one mapping was found to exist between the modal coefficients of the two most significant modes and the $F1-F2$ formant space. Thus an inverse mapping of time-varying formants extracted from recorded speech back to modal coefficients (and consequently to vocal tract area functions) was made possible; the derived sequence of area functions can be used in a simulation of the original speech utterance. In this study, it is first shown that similar orthogonal modes exist for three additional speakers. It will then be demonstrated that the time-varying modal coefficients determined for a recorded sentence via the inverse mapping of one speaker can also be used to create a sequence of area functions based on one of the other speaker's vocal tracts. A subsequent simulation produces the original sentence but with the vocal tract characteristics of the new speaker. The results also suggest that the time-varying modal coefficients may define common gestures across speakers even though their acoustic characteristics can be different.

3:40

2pSCa6. A neural model for auditory scene analysis. Dekun Yang, Georg F. Meyer, and William A. Ainsworth (Dept. of Commun. and Neurosci., Keele Univ., Keele, Staffs ST5 5BG, UK, dekun@cs.keele.ac.uk)

The fundamental process of auditory scene analysis is the organization of elementary acoustic features in a complex auditory scene into grouped meaningful auditory streams. There are two important issues which need to be addressed for modeling auditory scene analysis. The first issue is concerned with the representation of elementary acoustic features, whilst the second issue is related to the binding mechanism. This paper presents a neural model for auditory scene analysis in which a two-dimensional amplitude modulation (AM) map is used to represent elementary acoustic features and the synchronization of neural oscillators is adopted as the binding mechanism. The AM map captures the modulation frequencies of sound signals filtered by an auditory filterbank. Since the modulation frequencies are the $F0$-related features for voiced speech signals, $F0$-based segregation can be utilized to group the auditory streams. The grouping of $F0$-related features is attained as the formation of the synchronization of nonlinear neural oscillators. Each oscillator is associated with a certain modulation frequency. A set of oscillators are synchronized only when their associated frequencies are harmonically related. The proposed model is tested on synthetic double-vowel identification and the results are in accordance with psychophysical data.

4:00–4:20 Break

4:20

2pSCa7. Noise reduction for speech signals by operations on the modulation frequency spectrum. Hans Werner Strube and Hans Wilmers (Drittes Physikalisches Inst., Univ. Göttingen, D-37073 Göttingen, Germany)

A new method is presented for enhancing the contrast between speech and background noise, which might be useful as a preprocessor for speech recognizers or even for improving the audible speech signal. As in the brain a representation of the acoustic modulation spectrum exists, it is suggested to use similar methods for signal separation. Previous models have shown the possibility of selecting frequency channels based on modulation frequency (MF) analysis, if the signals to be separated have sufficiently different modulations. Instead of selecting or weighting frequency channels, in the present approach the MF spectrum is processed directly. This seems to be less prone to produce ''musical noise.'' The dominant common MF (mostly corresponding to F_0) is enhanced by an adaptive bandpass filter in each frequency channel, and the low-MF components are artificially reconstructed before transforming back. No explicit F_0 measurement is required. Nonstationary sounds (detected by the width of the low-MF part) are specially treated, for instance, by channel-dependent mixing with the original signal. The method is tested with a HMM recognizer (at Univ. Oldenburg) and compared to classic methods such as spectral subtraction. Intelligibility measurements are planned. Examples of processed speech will be presented.

4:40

2pSCa8. Resolution capability of reassigned Fourier spectrum. Dekun Yang, William A. Ainsworth, and Georg F. Meyer (Dept. of Commun. and Neurosci., Keele Univ., Keele, Staffs ST5 5BG, UK, dekun@cs.keele.ac.uk)

High-resolution spectral estimation is important for speech analysis. The conventional Fourier transform technique cannot offer sufficient resolution for speech signals of short durations. The reassignment method has been recently developed to improve the resolution of the Fourier spectrum. The basic idea of the reassignment method is to assign the value of the Fourier spectrum to the gravity center of the region rather than the geometric center of the region. However, the characteristics of the reassigned Fourier spectrum have not been fully understood. This paper is concerned with a detailed investigation of the resolution capability of the reassigned Fourier spectrum. The factors affecting resolution, such as frequency separation and relative amplitude, are studied. The minimal frequency separation which can be resolved in the reassigned Fourier spectrum is determined. As a result, it shows that the reassigned Fourier spectrum has better resolution capability in comparison to the Fourier spectrum. Furthermore, the study shows that the frequency estimator of closely spaced sinusoids has a bias. The bias is due to the interaction of the two sinusoids under the assignment operation. The expression of the bias is derived and shows that the bias can be ignored for most speech signals.

5:00

2pSCa9. Improved spectral resolution via the reassigned Fourier transform. Charles R. Day, William A. Ainsworth, and Georg F. Meyer (Dept. of Commun. & Neurosci., Keele Univ., Keele, Staffordshire ST5 5BG, UK, charles@cs.keele.ac.uk)

A modified form of the Fourier transform, the reassigned Fourier transform (RAFT), uses phase as well as magnitude information. Its properties are shown to be superior for both pure-tone and speech signal analysis. The RAFT technique has the potential to deliver higher resolution spectrograms than the fast Fourier transform (FFT) for a given signal analysis window. The reassignment of energy with respect to both time and frequency, such that the reassignments model the time–frequency fluctuations of the sampled signal, allows the RAFT to deliver higher resolution than the FFT (with the FFT, spectral/temporal analyses place all of the energy at points lying in the center of either a time/frequency sample-window, respectively). In particular, the improved spectral resolution of the RAFT for a given signal analysis window size is compared with that of the FFT for a fundamental speech processing application: pitch tracking. The results indicate that use of the RAFT instead of the FFT allows shorter signal analysis windows to be used. The pitch tracking performance of the RAFT with short analysis windows (e.g., 25 and 12 ms) is better than the FFT. [Work supported by the UK's EPSRC.]

5:20

2pSCa10. Intelligibility enhancement of synthetic speech heard via telephone in a noisy environment. Stefanie Köster and Joachim Mersdorf (Inst. fuer Kommunikationsakustik, Ruhr-Univ. Bochum, Universitätsstr. 150, D-44780 Bochum, Germany)

The intelligibility of synthetic speech, like the intelligibility of natural speech, decreases if it is transmitted via telephone and/or heard in a noisy environment. A natural speaker adapts his speaking style to these hard

speaking conditions in order to restore intelligibility. With new applications for speech synthesis, e.g., navigation systems for cars, the need for adapting synthetic speech to hard speaking conditions arises. Here, the results of intelligibility tests for German databased synthetic speech in comparison to natural speech are presented, and first methods of intelligibility enhancement for synthetic speech are given. It is shown that under the conditions mentioned above unadapted synthetic speech has a lower segmental intelligibility for all phonemes or phoneme clusters than natural speech. For that reason the methods applied affected all speech sounds equally. They are based on prevoius studies of natural speech produced under stress conditions like a noise afflicted environment [Summers *et al.*, J. Acoust. Soc. Am. **84**, 917–928 (1988)]. It is shown that the intelligibility of synthetic speech is improved significantly by these enhancement methods. The results give evidence to an individual adaptation for phonemes or phoneme clusters in future.

5:40

2pSCa11. Query language for access to speech corpora. Andreas Mengel and Ulrich Heid (Inst. of Natural Lang. Processing, Stuttgart Univ., Azenbergstrasse 12, 70174 Stuttgart, Germany, mengel@ims.uni-stuttgart.de)

Typically, speech corpora are designed for the study of speech, its patterns, and their influences. Corpora for synthesis support the extraction and reuse of units in concatenative speech synthesis systems. Recent approaches consider speech segments of variable length, to enhance naturalness. The development of spoken language dialog systems (SLDSs) and similar applications requires dialog corpora with multiple information, such as prosodic labeling, grammatical annotations, dialog acts, etc. For constructing such multilevel corpora and, particularly, for retrieving useful information from there, three aspects are crucial: A theory for the description of the corpora, an effective markup and methods for specifying, and efficiently retrieving relevant portions of the data. MATE (EU Telematics Project LE4-8370) proposes standards for an integrated and consistent multilevel annotation based on the existing TEI standard (Text Encoding Initiative). For the access to massively marked-up speech data, a query language and a query engine have been developed. This allows the retrieval of any combination of data, with linguistic annotations from different levels. The presentation will describe and demonstrate the query language.

6:00

2pSCa12. Prosody templates in word-level synthesis. Frode Holm and Kazue Hata (Speech Technol. Lab., 3888 State St., Santa Barbara, CA 93105)

This paper describes an approach to word-level prosody with the goal of achieving natural-sounding human intonation. This study comprised about 3000 words in sentence initial position, uttered by a female native speaker of American English. From these recordings general $F0$ and duration templates were extracted, initially based on stress-pattern alone. Results with regards to $F0$ templates [F. Holm and K. Hata, ICSLP (1998)] had previously been reported, which showed great promise for a practical synthesis implementation. In this paper duration templates will be focused on. Obtaining temporal prosody patterns is a much harder problem than it is for $F0$ contours. This is largely due to the fact that one cannot separate a high-level prosodic intent from purely articulatory constraints merely by examining individual segmental data. This methodology relies on a concept of stretchability, which gives a clear measure of how much a given cluster of segments can change its duration in natural speech. The higher this measure is, the more of the speaker's intentional temporal adjustment is expected to be found in that cluster. Using this concept, a template-generating procedure has been formulated that achieves a very high prediction rate of a speaker's duration patterns.

TUESDAY AFTERNOON, 16 MARCH 1999 POSTER GALLERY, 2:00 TO 6:00 P.M.

Session 2pSCb

Speech Communication: Cross Language and L2 Processing II (Poster Session)

Winifred Strange, Chair
City University of New York, 33 West 42 Street, New York, New York 10036, USA

Contributed Papers

All posters will be on display in the Poster Gallery from Monday to Wednesday, 15–17 March. Authors will be present at their posters on Tuesday, 16 March. To allow contributors an opportunity to see other posters, contributors of odd-numbered papers will be at their posters from 2:00 p.m. to 4:00 p.m. and contributors of even-numbered papers will be at their posters from 4:00 p.m. to 6:00 p.m.

2pSCb1. The influence of vowel context on the Japanese listener's identification of English voiceless fricatives. William L. Martens and Stephen Lambacher (Univ. of Aizu, Tsuruga, Ikki-machi, Aizu-Wakamatsu City, Fukushima, 965-8580 Japan)

In order to examine the influence of vowel context on the ability of native Japanese speakers to distinguish between English voiceless fricatives, recognition rates from a five-alternative, forced-choice (5AFC) test were analyzed in terms of receiver operating characteristics. This signal-detection-theoretic analysis showed contrasting effects of vowel context on sensitivity versus response bias. Subjects heard each of 75 nonsense syllables spoken by three native speakers of English, and were asked to report whether the syllable they heard contained /f/, /s/, /ʃ/, /θ/, or /h/. Fricative identifiability (measured by the index of sensitivity, d') appeared to be modulated primarily by phonemic and phonetic factors. In contrast, the likelihood of giving one fricative response over another without regard for which fricative is presented (measured by the index of bias, β) appeared to be modulated by more subjective factors such as familiarity with common loan words (words of foreign origin). A cross-linguistic examination of phonemic and phonetic factors revealed possible reasons why the Japanese listener's identification of English fricatives is considerably poorer in particular vowel contexts, and how differences in fricative production can make it more difficult to make certain phonetic distinctions.

2pSCb2. Can English listeners learning Japanese as a second language employ a mora-based segmentation procedure? Takashi Otake (Dept. of English, Dokkyo Univ., 1-1 Gakuen-cho, Soka, Saitama, 340 Japan, otake@dokkyo.ac.jp) and Kiyoko Yoneyama (Ohio State Univ., Columbus, OH 43210)

Previous research has shown that monolingual listeners exploit language-specific segmentation routines, based on linguistic rhythm, not only with native but also with foreign input. Thus monolingual Japanese listeners used a mora-based segmentation procedure with both Japanese and English, while monolingual English listeners, whose linguistic rhythm is different from Japanese, did not use this procedure [Cutler and Otake, JML **33**, 824–844 (1994)]. Bilinguals, however, can inhibit an inappropriate rhythm-based segmentation procedure [Cutler *et al.*, Cogn. Psychol. **24**, 381–410 (1992)]. The present study explored whether English listeners learning Japanese as a second language could employ a mora-based segmentation procedure in Japanese. Three groups of American subjects, whose Japanese proficiency differed, participated in the experiment, using the phoneme monitoring materials of Cutler and Otake (1994). The prediction based on the findings above was that none of these subjects would be sensitive to morae in listening to Japanese. The results, however, showed that all the subject groups were consistently sensitive to morae, which suggests that English listeners can employ a non-native segmentation procedure in a foreign input as long as they have at least begun to acquire the foreign phonology. [Work supported by Fulbright senior research grant and the Telecommunications Advancement Foundation.]

2pSCb3. Intonational foreign accent in the speech of American speakers of German. Matthias Jilka (Inst. of Natural Lang. Processing, Univ. of Stuttgart, Azenbergstr. 12, 70174 Stuttgart, Germany)

The $F0$ patterns typical of German and American English are analyzed within the framework of a category-based description of intonation events as established by the ToBI prosodic transcription system. This description is supplemented by intonation rules for the categories' phonetic implementation. The rules are also the basis for the process of $F0$ generation and resynthesis, which facilitates determining which aspects in non-native speech are responsible for the perception of intonational foreign accent. An analysis of the productions of native speakers of American English who are fluent in German shows a distinct influence of L1 prosodic characteristics on L2. It consists of a transfer of native prosodic settings to L2. Several types of intonational foreign accent are identified. Tonal categories, such as pitch accents or boundary tones, are affected in two ways: either an incorrect category is selected or it is assigned to an inappropriate part of the intonation phrase. Transfer effects are particularly distinct in the American speakers' phonetic realization of corresponding tonal categories. The Americans also maintain other prosodic language-specific features like pitch range. Overall, prosodic behavior in L2 acquisition seems quite similar to segmental behavior and in accordance with current models of segmental L2 acquisition.

2pSCb4. A study of the language dominance effects on bilinguals' voice quality. Marielle Bruyninckx and Bernard Harmegnies (Phonet. Lab Pl. du Parc, 18 B-7000 Mons, France, Marielle.Bruyninckx@umh.ac.be)

This paper examines whether language dominance exerts influences on speaker's voice quality. Ten French–Polish bilingual subjects, split into a French-dominant group and a Polish-dominant group, were selected. They were asked to record five utterances of two balanced texts (one for each language). One FFT-based LTAS was computed for each utterance. The so-obtained 100 spectra were compared by means of a pattern recognition procedure: the SDDD dissimilarity index. Two types of within-speaker comparisons were performed for each subject: within-language comparisons and between-language comparisons. The results show that the average SDDD index values derived from the between-language comparisons score higher than those drawn from within-language matchings. This confirms our earlier results based on different types of bilinguals. The within-language FR/FR SDDD index values tend to score higher in the French-dominant group than the POL/POL ones; the opposite relationship can be observed in Polish-dominant subjects. These results empower one to generalize the idea that language dominance seems to be a significant variable in the characterization of the phonetic behavior of speakers using more than one language.

2pSCb5. Effects of L1 phonotactic constraints on L2 speech perception and production. Satoshi Imaizumi, Yuji Tamekawa (Dept. of Speech and Cognit. Sci., Grad. School of Medicine, Univ. of Tokyo, Bunkyo, Tokyo, 113-0033 Japan), Hidemi Itoh (Tohoku Univ., Sendai, 980-8575 Japan), Toshisada Deguchi (Tokyo Gakugei Univ., Tokyo, 184-8501 Japan), and Koichi Mori (Res. Inst. Natl. Rehabilitation Ctr. for the Disabled, Saitama, 359-8555 Japan)

Effects of L1 phonotactic constraints on L2 speech perception and production were analyzed during the course of audio-visual perceptual training for Japanese adult learners of English by observing articulation of words containing /l/, /r/, and /w/. The speech identification score drastically improved during the training. The improvement in non-native word-initial rl distinction was clearly associated with the changes in the perceptual, articulatory, and neuronal spaces, which represent dissimilarities between the non-native and native phonemes in each domain assessed through perceptual, palatographic, and neuromagnetic measurements. Significant difficulty in identification of consonant-rl clusters, however, remained for some trainees even after one year of training. Analyses of palato-lingual contact patterns during word articulation suggested that more articulatory errors tend to occur in consonant-rl clusters than in other phonotactic contexts in such a way that both /l/ and /r/ are substituted with Japanese /r/ sometimes associated with a vowel inserted. Results suggested that the L2 phonological system can be acquired through a multimodal training, although it is strongly interfered with by L1 phonotactic constraints.

2pSCb6. Patterns of vowel-to-vowel coarticulation in Greek and English. Areti Okalidou (Dept. of Logotherapy, Tech. Educational Inst. of Patras, 263 34 Koukouli, Patra, Greece) and Laura L. Koenig (Haskins Labs., New Haven, CT 06511)

Many previous studies have indicated that coarticulatory behavior differs systematically across languages. One specific hypothesis, made by Manuel and Krakow (1984), is that languages with larger vowel inventories show reduced vowel-to-vowel coarticulation because their crowded vowel spaces impose more stringent requirements for maintaining phonological distinctiveness. The present study is designed (a) to test this prediction in Greek versus English, which have small and large vowel inventories, respectively; and (b) to investigate which parameters of the vowel system are most responsible for shaping language-specific coarticulatory constraints. Adult monolingual speakers of each language were recorded, producing VCV utterances embedded in phonologically similar carrier phrases. Vowels included all five vowels of Greek, /i,e,a,o,u/, and their closest counterparts in American English, and the medial consonant varied between labial and alveolar places of articulation. To provide an independent measure of production variability for each vowel, speakers also produced the vowels in real words of the form /pVt/ or /bVt/, embedded in the same carrier phrases. Preliminary data are presented for two speakers of each language, and discussed in terms of vowel type, distribution within the vowel space, and the size of vowel areas within $F1-F2$ space.

2pSCb7. Production of Japanese durational contrasts by native and nonnative speakers. Yukari Hirata (Univ. of Chicago, Dept. of Linguist., 1010 E. 59th St., Classics 304, Chicago, IL 60637, yh16@midway.uchicago.edu)

Non-native speakers' production of Japanese durational contrasts, and the development of their abilities, are examined in relation to native speakers' production. Two native speakers and two beginning learners produced 2–4 mora words contrasting in either consonant or vowel length. The learners also produced the same set of words after 4 weeks of perceptual training [Y. Hirata, CLS34 Phonetics Panel (forthcoming)]. Acoustic analyses of the native speaker productions indicate durational systematicity not only in the consonant pairs, as in M. Han [Phonetica **49**, 102–127 (1992)], but also in the vowel pairs: the average ratio of short to long vowels was 1:1.8–2.0 regardless of context and speaker. Furthermore, a linear relationship was found between the number of morae and word duration, extending Port *et al.* [J. Acoust. Soc. Am. **81**, 1574–1585 (1987)]. The learners' results before training indicate an inability to produce the durational contrasts, e.g., subject A's average durational ratio for the vowel pairs was 1:1.2. After training, the ratio became closer to that of the native speakers, viz., 1:1.6–1.7, while subject B's did not show a linguistically significant change. Subject A's results contrast even with those of Han's advanced subjects, and illuminate the upper limit for L2 learners with training.

2pSCb8. Acoustic-phonetic analysis of the acquisition of American English tense-lax contrasts by native speakers of Chinese. Catherine L. Rogers (Dept. of Speech and Hearing Sci., Ohio State Univ., 110 Pressey Hall, 1070 Carmack Rd., Columbus, OH 43210, rogers.140@osu.edu)

In a study of the perception of Chinese-accented English by native American English-speaking listeners [C. Rogers and J. Dalby, J. Acoust. Soc. Am. **100**, 2725(A) (1996)], in which performance on seven segmental error category variables was correlated with intelligibility at the sentence level, vowel tenseness was found to be most strongly correlated with connected-speech intelligibility ($r=0.76$, $p<0.001$). Analyses of these results across the eight Chinese speakers showed that the average performance of the four most intelligible speakers (measured in terms of sentence percent-correct performance) on words targeting tense-lax contrasts surpassed that of the four least intelligible speakers by more than 30%. Analyses of both durational and spectral properties of the target lax phonemes /ɪ, ɛ, and ʊ/ produced by the Chinese speakers will (1) explore the acoustic properties responsible for the difference in performance on the target lax phonemes across the two groups of speakers, (2) compare results across the three target phonemes, and (3) investigate the hypothesis that acquisition of the tense-lax contrasts is associated with more nativelike implementation of phenomena realized only at the connected-speech level (e.g., phrase-final lengthening). [Work supported by NIDCD.]

2pSCb9. Perceived vowel quantity in Swedish: Native and British listeners. Dawn M. Behne (Norwegian Univ. of Sci. and Technol., N-7043 Trondheim, Norway), Kirk P. H. Sullivan, and Peter E. Czigler (Ume Univ., SE-901 87 Ume, Sweden)

In many languages, vowels are characterized by their use of contrastive phonological vowel quantity and vowel quality. In Swedish, vowels have traditionally been described as being distinct in quality as well as having a phonological distinction between short and long vowel quantities. In English, however, phonological distinctions among vowels are described as primarily qualitative. This investigation examines the perceptual use of vowel duration and the first two vowel formant frequencies in distinguishing Swedish vowel pairs by three groups of listeners: native Swedish listeners (SS), British English listeners who do not know Swedish (EE), and British listeners who know Swedish well (ES). For each of three pairs of Swedish vowels (IPAKiel[i=DC]IPAKiel-[I], IPAKiel[o=DC]-IPAKiel[O], IPAKiel[A=DC]IPAKiel-[a]), /kVt/ words were resynthesized having ten degrees of vowel duration and ten degrees of $F1$ and $F2$ adjustment. Listeners' responses and reaction times in a rhyming task show that unlike native listeners, L2 (i.e., ES) listeners distinguish Swedish vowel quantity using duration almost exclusively, which is consistent with what they have been taught, whereas TimesEE listeners respond as expected for a comparable English vowel continuum, using both vowel duration and spectra. These results are discussed in terms of the different stategies used by the different listeners.

2pSCb10. Dynamic information in French vowel identification by native and non-native listeners. Terry L. Gottfried and Jonathan S. Neville (Dept. of Psych., Lawrence Univ., Appleton, WI 54912)

French /t/–vowel and /t/–vowel–/t/ syllables were spoken by a native speaker in a constant sentence frame. Target syllables were edited so that native French and non-native listeners heard intact syllables, only the initial and final portion of syllables (silent-center), only initial (initial-only), or only center portions (center-only). Research in American English [e.g., W. Strange, J. Acoust. Soc. Am. **85**, 2135–2153 (1989)] has demonstrated that listeners accurately identify vowels in silent-center consonant-vowel-consonant syllables; identification of initial- or final-only portions is very poor. However, French syllables are more commonly consonant-vowel in structure; for this reason, native listeners might identify initial-only portions nearly as accurately as silent-centers. By contrast, Americans whose second language is French might perform more poorly on silent-center French syllables than on intact syllables, and most poorly on initial-only. Findings suggest that indeed native French listeners identify initial-only syllables as accurately as silent-center and intact syllables, except for confusions of oral-nasal contrasts (e.g., /a/ vs /ɛ/). Native listeners perform significantly better on TV syllables than TVT syllables, especially in silent-center and initial-only conditions. The pattern of errors for non-native listeners is different, particularly with respect to less familiar vowel contrasts (e.g., /u/ vs /y/). [Work supported by Lawrence University Faculty Grant.]

2pSCb11. Training American listeners to perceive Mandarin tones: Transfer to production. Yue Wang, Michelle M. Spence, Allard Jongman, and Joan A. Sereno (Cornell Phonet. Lab., Cornell Univ., Ithaca, NY 14853, yw36@cornell.edu)

Training American listeners to perceive the four Mandarin lexical tones has been shown to be effective [Y. Wang, A. Jongman, and J. A. Sereno, J. Acoust. Soc. Am. **103**, 3090(A) (1998)]. Eight trainees participated in a two-week training program, after which their tone identification accuracy showed an overall 21% increase from the pretest to the posttest, and the improvement was generalized to new stimuli and new talkers. Further studies have now been carried out to investigate whether the tone contrasts gained perceptually can be transferred to the production domain without additional training. Before their perception pretest and after their posttest, the same trainees were recorded, producing a list of 80 Mandarin words bearing the four tones. Their productions were judged by 40 native Mandarin listeners in an identification task. Trainees' posttest tone productions were on average 16% more accurately identified than their pretest productions, indicating significant tone production improvement after perceptual training. Acoustic analyses of the pre- and posttraining productions further reveal the nature of the improvement. Results are discussed in terms of the relationship between non-native tone perception and production as well as learning at the suprasegmental level.

2pSCb12. Point vowels in Japanese mothers' speech to infants and adults. Jean E. Andruski (Audiol. and Speech-Lang. Pathol., Wayne State Univ., 581 Manoogian Hall, 906 W. Warren Ave., Detroit, MI 48202), Patricia K. Kuhl (Univ. of Washington, Seattle, WA 98195), and Akiko Hayashi (Tokyo Gakugei Univ., Koganei, Tokyo 184, Japan)

American, Russian, and Swedish mothers produce acoustically more extreme point vowels (/i/, /u/, and /a/) when speaking to their infants than when speaking to another adult [Kuhl *et al.*, Science **277**, 684–686]. This study examines the three point vowels in Japanese mothers' speech, and

compares the acoustic structure of infant-directed (ID) and adult-directed (AD) tokens. Three target words containing /i/, /u/, and /a/ (bi:zu, batto, bu:tsu = beads, bat, boots) were recorded while mothers conversed with another native-speaking adult, and with their infants, aged either $5\frac{1}{2}$ or $8\frac{1}{2}$ months. $F1$, $F2$, and $F0$ were measured at vowel onset, center, and offset. Acoustic, results will be compared for AD and ID speech, and expansion of the vowel space in Japanese mothers' speech will be examined. [Work supported by NIH HD35465-01S1.]

2pSCb13. Detection of foreign accent by *L*2 English listeners. Kimiko Tsukada (SHLRC, School of ELM, Macquarie Univ., NSW 2109, Australia)

This study investigates the question of whether non-native listeners are capable of differentiating native from non-native English talkers when presented with a specific foreign accent. Seven Japanese listeners (six female, one male), five of whom have lived in English-speaking countries for a minimum of nine years, were asked to identify the native talker in a forced-choice paired comparison task. The stimuli used were monosyllabic English words (in /CVt/ and /CVd/) produced by Australian and Japanese talkers in which vowels were matched on their $F1$, $F2$ at the temporal midpoint and duration. Non-native listeners performed the task more poorly than the native listeners (60% vs 79%). It was observed that some adult non-native listeners have difficulty in recognizing even their own $L2$ speech production [H. Goto, Neuropsychologia **9**, 317–323 (1971)]. Perception errors were spread quite evenly across 11 vowel types. However, vowels such as /ɛ, /æ/, /ʌ/, and /ɔ/ induced more errors. This may be related to the acoustic vowel space of their $L1$ in which, unlike English, the only low vowel /a/ is not cramped by the neighboring vowels. The results revealed large interlistener variability which suggests a complex nature of $L2$ perception.

2pSCb14. Neurophysiologic correlates of cross-language perception of phonetic categories. Anu Sharma and Michael Dorman (Dept. of Speech and Hearing Sci., Arizona State Univ., Tempe, AZ 85257-0102, anu.sharma@asu.edu)

This study examined neurophysiologic correlates of categorical perception of native and non-native phonetic categories. Behavioral and electrophysiologic responses were obtained in Hindi and English listeners, in response to a stimulus continuum of naturally produced, bilabial CV stimuli that differed in VOT from −90 to 0 ms. These speech sounds constitute phonenically relevant categories in Hindi but not in English. As expected, the native Hindi listeners identified the stimuli as belonging to two distinct phonetic categories (/ba/ and /pa/) and their discrimination of a stimulus pair across categories was more accurate than their discrimination of a stimulus pair (of equal VOT change) within the /pa/ category. English listeners discrimination accuracy of within- and across-category pairs was at chance. N100 and MMN cortical-evoked potentials which are considered neural indices of preattentive sensory encoding and discrimination were measured. A double-peaked N100 was elicited in English and Hindi listeners. The first peak was elicited by syllable onset, while the latency of the second peak reflected the VOT lead time. Hindi listeners exhibited robust MMNs for the within- and across-category pairs, while English speakers did not, suggesting that the central sensory representation of certain phonetic categories is at least partially altered by linguistic experience.

2pSCb15. Perceptual training with native Japanese speakers on various L2 sounds. Jesica C. Pruitt (Speech and Hearing Sci., Univ. of Washington, 1417 N. E. 42nd St., Seattle, WA 98105, jcpruitt@u.washington.edu), Reiko Akahane-Yamada (ATR-HIP Res. Labs, Soraku-gun, Kyoto, 619-0288 Japan), Winifred Strange (CUNY Grad. School, New York, NY 10036), Rieko Kubo, and Tomoko Takada (ATR-HIP Res. Labs, Soraku-gun, Kyoto, 619-0288 Japan)

It has been found that adults can more robustly acquire segments in a second language (L2) with identification training which uses highly varied training stimuli, i.e., natural tokens from multiple talkers in multiple phonetic contexts. This approach has been applied systematically in cross-language training studies in which Japanese speakers were trained to acquire AE /r/ and /l/ [Lively et al., J. Acoust. Soc. Am. **96**, 2076–2087 (1994)] as well as AE/ɤ, æ, ʌ/ [Strange and Akahane-Yamada, J. Acoust. Soc. Am. **102**, 3137(A) (1997)]. The current set of experiments expanded this line of research by testing whether the same procedure would be effective in training other consonants (/b/–/v/, /s/–/θ/ and /z/–/ð/) and vowels (11 AE vowels). With both consonants and vowels, the previous results were replicated; subjects showed significant improvement from pretest to posttest and showed generalization to an untrained talker. In the vowel training study, transfer of training across speaking style was further examined. Subjects were trained to distinguish vowels in CVC syllables in a carrier sentence context, and were then tested in both sentence and citation contexts. Interestingly, the improvements were significant for sentence contexts but not for citation. Taken together, these studies further our understanding of the complexities of L2 learning and training.

2pSCb16. Recognition of Portuguese vowels by Galician-speaking and Spanish-speaking listeners. Sergio Feijóo, Santiago Fernández, and Ramón Balsa (Departamento de Física Aplicada, Universidad de Santiago de Compostela, 15706 Santiago, Spain, fasergio@usc.es)

Galician, Portuguese, and Spanish are three romanic languages spoken in the Iberian peninsula. Galician and Portuguese are historically related and keep the same vocalic system of common latin: a, ɛ, e, i, ɔ, o, u. In Spanish the number of vowels was reduced to five: a, e, i, o, u. Nevertheless, Spanish has exerted considerable influence on Galician, contributing to weaken the vocalic contrasts ɛ–e and ɔ–o. The purpose of these experiments was to assess how Galician- and Spanish-speaking listeners perceived the vocalic system of Portuguese. Stimuli were pV syllables pronounced in a carrier phrase, where V was one of the seven vowels. Results show that Galician-speaking listeners have some difficulty in perceiving the contrasts ɛ–e and ɔ–o, probably due to the historical influence of Spanish, and despite the fact that $F1$ and $F2$ of the Portuguese vowels were similar to those reported for Galician vowels. Spanish-speaking listeners identified ɛ–e as a single vowel e, and ɔ–o as a single vowel o, associating the L2 vocalic inventory to their own vocalic system. Discussion is based on the acoustic characteristics of vowels in those languages.

2pSCb17. Aerodynamic constraints on sound change: The case of syllabic sibilants. Alan C. L. Yu (1203 Dwinelle Hall, Dept. of Linguist., Univ. of California, Berkeley, CA 94720-2650, aclyu@socrates.berkeley.edu)

High vowels are known to assimilate in place of articulation and frication to a preceding sibilant. Such an assimilation process is found in an historical sound change from Middle Chinese to Modern Mandarin (e.g., */si/ became [sz] ''poetry''). However, such assibilation is systematically absent when the vowel is followed by a nasal consonant. This paper investigates the co-occurrence restriction between nasalization and frication, demonstrating that pharyngeal pressure is so significantly vented during the opening of the velic valve that the necessary pressure buildup behind the constriction of a fricative is consequently severely diminished, resulting in no audible turbulence. It reports the aerodynamic effects of nasalization on vowels, as spoken by a native speaker of American English (presumed to parallel the phonetic conditions present in Middle Chinese). The results reveal that in comparison to oral vowels the pharyngeal pres-

sure, volume velocity, and particle velocity decrease dramatically when high vowels are nasalized. Based on this study, a physical motivation for the phonological patterns with respect to the interaction between syllabic sibilants and nasal is advanced. [This work is supported by the President's Undergraduate Fellowship 1997–1998.]

2pSCb18. Does interspeaker variation in habitual speaking rate predict the size of the acoustic vowel space? Ying-Chiao Tsao (Dept. of Special Ed./Communicative Disord., Univ. of Nebraska, Kearney, NE 68849, tsaoy@platte.unk.edu) and Gary Weismer (Univ. of Wisconsin, Madison, WI 53706)

In a previous study [Tsao and Weismer, J. Speech Lang. Hear. Res. (1997)], it was demonstrated that interspeaker variation in habitual speaking rate is predictive of interspeaker variation in maximal speaking rate. Thus speakers who are habitually slow speakers do not seem to be able to produce as fast a maximum rate as speakers who are habitually fast. This finding was interpreted to mean that some component of interspeaker variation in habitual speaking rate reflects neurological predispositions, rather than (for example) voluntary ''choices'' of different rates. The present study explores the hypothesis that habitually slow and fast speakers may have differently sized acoustic vowel spaces. The hypothesis is derived from previous observations that within speakers, the size of the acoustic vowel space fluctuates with speaking rate. Results suggest that there is substantial overlap between the vowel spaces of habitually slow and fast speakers, but that the slow speakers do tend to have larger vowel spaces. [Work supported by NIH.]

2pSCb19. Russian vowels in mothers' speech to infants and adults. Jean E. Andruski (Audiol. & Speech-Lang. Pathol., Wayne State Univ., 581 Manoogian Hall, 906 W. Warren Ave., Detroit, MI 48202), Patricia K. Kuhl (Univ. of Washington, Seattle, WA 98195), L. A. Chistovich, E. V. Kozhevnikova, V. L. Ryskina, and E. I. Stolyarova (Early Intervention Inst., St. Petersburg, Russia)

Cross-linguistically, when mothers address their infants they produce acoustically more extreme point vowels (/i/, /u/, and /a/) than they produce when speaking to another adult [Kuhl *et al.*, Science **277**, 684–686 (1997)]. This study examines three nonpoint vowels in Russian (/e/, /o/, /'i/) and compares their acoustics in infant-directed (ID) and adult-directed (AD) speech with the acoustics of Russian point vowels in AD and ID speech. Six target words containing the nonpoint vowels in stressed syllables were recorded while ten mothers conversed with their infant and another adult. $F1$, $F2$, and $F0$ were measured at vowel onset, center, and offset. As with the point vowels, the acoustic structure of all three vowels differs significantly in ID and AD speech. $F2$ tends to move to an acoustically more extreme position in each case. In addition, nonpoint ID vowels show more vowel-inherent formant movement across the course of the vowel. Formant movement may provide an important cue to vowel identity, and its exaggeration in ID speech may increase the likelihood that infants incorporate formant movement into their mental representation of a vowel. Significant differences in formant structure were found for vowels in one-, two-, and three-syllable words, including vowels with short mean durations.

2pSCb20. Identifying novel samples of spoken Korean. Z. S. Bond and Verna Stockmal (Dept. of Linguist., Ohio Univ., Athens OH 45701, zbond1@ohiou.edu)

Listeners can identify familiar foreign languages without understanding them on the basis of their sound or acoustic signature. Listeners need only brief exposure to a novel language to learn to identify it from its sound pattern [Bond *et al.*, Lang. Sci. **20**, 353–367 (1998)]. The current experiments replicated the previous study using a different target language. In the first experiment, listeners distinguished Korean from languages which employ syllable rhythm. In the second experiment, listeners separated Korean from other East Asian languages. In both experiments, listeners made judgments either without exposure (control) or after exposure to 10 min of spoken Korean. Listener responses were converted to A, a nonparametric measure of discriminability. In experiment 1, listeners in the control condition responded at chance, mean $A=0.47$. After exposure, listeners identified Korean above chance levels, mean $A=0.71$. Listeners tended to confuse Korean with Asian languages rather than with African or European languages, suggesting that voice and speech style influenced their judgments. In experiment 2, the control group had extreme difficulty identifying Korean, mean $A=0.28$. Brief exposure enabled listeners to develop a representation of the sound of Korean in that they produced more hits and fewer misses to the target (mean $A=0.71$).

2pSCb21. Acoustic studies comparing Danish vowels, British English vowels, and Danish-accented British English vowels. Anja Steinlen and Ocke-Schwen Bohn (English Dept., Aarhus Univ., DK-8000 Aarhus C, Denmark, engas@hum.aau.dk)

Few studies have examined the production of English vowels by native speakers of languages with vowel inventories as large as, or larger than, English. Danish is such a language, whose vowels are unevenly distributed in the vowel space, with a densely populated upper portion and a sparsely populated lower portion of the vowel space. This paper reports on acoustic comparisons of British English vowels as produced by ten native speakers of British English and of Danish, and of Danish vowels as produced by ten native speakers of Danish. Danish and English vowels were produced in CVC syllables in a variety of consonantal contexts. Acoustic analyses revealed temporal, spectral, and dynamic differences between the vowels produced by the speaker groups. The results of this study suggest that comparisons of vowels across languages, as well as analyses of the productions of non-native speakers, are incomplete and may even be misleading unless the effects of consonantal context are taken into account. The results of this study also provide an interesting test case for Flege's speech learning model, which makes predictions concerning the learnability of foreign language vowels based on their degree of difference from native language categories.

Session 2pSPa

Signal Processing in Acoustics and Engineering Acoustics: Smart Microphones and Audio for Teleconferencing

Gary W. Elko, Cochair
Acoustics and Speech Research, Bell Laboratories, Lucent Technologies, 500 Mountain Avenue, Murray Hill, New Jersey 07974, USA

Jens Blauert, Cochair
Communication Acoustics, Ruhr Universität Bochum, D-44780 Bochum, Germany

Chair's Introduction—1:55

Invited Papers

2:00

2pSPa1. Steerable adaptive first- and second-order differential microphones. Gary W. Elko (Acoust. and Speech Res., Bell Labs, Lucent Technologies, 500 Mountain Ave., Murray Hill, NJ 07974, gwe@research.bell-labs.com)

Directional microphone arrays are spatial filters that can be designed to improve the sound quality of speech in audio telecommunication by removing acoustic signals arriving from undesired directions. Recently, there has been a large interest in adaptive microphone systems (also sometimes referred to as ''smart microphones''), since these systems automatically self-adjust their spatial response to minimize acoustic interference and thereby increase the desired signal-to-noise ratio. The talk will present adaptive first- and second-order differential microphone arrays that have fixed look directions dependent on the array geometry. A generalized version of the adaptive first-order system will then be presented where the look direction can be arbitrarily oriented (independent of the array spatial orientation). The commensurate problem of acoustic echo cancellation with adaptive microphones will also be discussed and some potential solutions given.

2:20

2pSPa2. Integrating acoustic echo cancellation with adaptive beamforming microphone arrays. Walter Kellermann (Lehrstuhl f. Nachrichtentechnik I, Univ. at Erlangen, Nurnberg, Germany, walter.kellermann@e-technik.fh-regensburg.de)

In hands-free and untethered man–machine speed communication, acoustic echo control (AEC) is widely acknowledged as a critical issue determining, e.g., the quality of a full-duplex dialogue, or the speech recognition performance of voice control applications. In comparison to single microphones, microphone arrays (MAs) allow for an improved acoustic front-end by increased spatial selectivity and the flexibility to track moving sources. It is argued that in most cases, however, this will not suffice to eliminate the need for AEC. The most effective solution to AEC is provided by echo cancellation systems, which model the acoustic echo path from the source to the receiver by an adaptive digital filter. While the echo path for a time-invariant MA can be modeled by a single adaptive filter, adaptive beamforming MAs require a time-variant filter capable of tracking the change of the beamforming characteristic instantaneously or, alternatively, one echo canceller for each sensor of the array. Given the considerable computational load for acoustic echo cancelers, a concept is proposed here that limits the beamforming to several fixed beams and foresees one echo canceler for each beam. In addition to computational efficiency, this system provides synergies enhancing the control of the acoustic echo canceler as well as source finding for beamforming.

2:40

2pSPa3. Self-calibrating microphone array. Jens Meyer (Dept. of Electroacoustics, Darmstadt Univ. of Technol., Merckstr. 25, 64283 Darmstadt, Germany, J.Meyer@uet.tu-darmstadt.de)

A popular application for microphone arrays is speech pick up in situations where a close spacing between talker and microphone is not suitable. A beamformer is used to achieve a directivity pattern that maximizes the ratio between the desired signal and noise sources. Here a fixed beamformer is evaluated. A fixed beamformer means that the coefficients are set at one time and then remain constant. Many design methods are known for fixed beamformers. Most of these methods assume ideal microphone array characteristics like precise sensor positions, perfect phase and gain of the sensors, and free-field conditions of the acoustical field. In many practical applications these conditions are not fulfilled. The disregard of the free-field condition in some speech pick-up applications (e.g., array on the top of a monitor, array as a hearing aid) especially can cause severe distortions of the desired beam pattern. This presentation suggests an approach that includes the nonideal effects in the design process of the beamformer. The directivity pattern is therefore measured at some discrete angles. The measured data are then compared with a predetermined directivity pattern and the beamformer coefficients are optimized such that this pattern is approximated as closely as possible.

3:00

2pSPa4. Spatial audio for telepresence. Andrew Rimell (MAES, MLB 3/7, BT Labs., Ipswich, Suffolk IP5 3RE, UK, andrew.rimell@bt.com)

Developments in communications technology, such as audio–visual conferencing and telepresence, have created a new set of demands for audio delivery systems. In the past, a telephone handset, with its limited transducers, was adequate for simple spoken communication; however, future multiuser communication systems and immersive machine interfaces will be greatly enhanced by using high-quality three-dimensional audio. Such three-dimensional sound systems can position individual talkers' voices in space around the user, creating a greater feeling of immersion and improving intelligibility. This presentation discusses the design and implementation of a number of spatial audio system implementations. The applications range from a SmartSpace chair (a single-user environment using a transaural system) through to a VisionDome (a large multiuser environment using a combination of ambisonics and nonlinear panning). Theoretical design and practical implementation issues are discussed, including problems encountered and how they were overcome.

3:20

2pSPa5. Audio teleconferencing systems with sound localization effects. Shigeaki Aoki and Manabu Okamoto (Nippon Telegraph and Telephone Corp., Human Interface Labs. 1-1, Hikarinooka Yokosuka, Kanagawa 239-0847, Japan, aoki@nttspch.hil.ntt.co.jp)

In teleconferencing, conversation should flow naturally between separate sites. The acoustic design should, of course, be able to at least convey the correct volume. However, sound localization is also very important for realizing the kind of virtual reality world that is teleconferencing. Coordinating the visual image (a speaker's face) and the sound image (his or her voice) creates a kind of virtual environment in which the participants at each site feel as if they are having a conversation in the same room. Two prototype teleconferencing systems with sound localization effects have been developed. The more primitive of the two is a small teleconferencing system that can connect two sites with stereo reproduction in a way that utilizes psychological acoustic phenomena. The other is a high-presence system that aims at achieving a high level of ambience among three separate sites. Its features and key technologies are natural images on a large super-high-resolution display, good sound localization from remote locations through the use of a multichannel sound image localization system, and high-definition images as a result of HDTV coding and transmission. The proposed multichannel sound system comprises four subsystems, one each for sound input, reproduction, acoustic feedback control, and transmission.

3:40

2pSPa6. Robust and adaptive spatialized audio for desktop conferencing. Darren B. Ward (School of Elec. Eng., Univ. College, UNSW, Canberra ACT 2600, Australia, d-ward@ee.adfa.oz.au) and Gary W. Elko (Bell Labs, Lucent Technologies, Murray Hill, NJ 07974)

For multi-talker teleconferencing, providing multichannel audio to the listener has been advocated as an alternative to a conventional single audio channel. The use of multichannel audio provides a means of supplying the listener with spatialized audio cues. Specifically, it permits binaural signals to be delivered to the listener, which has distinct advantages for multi-talker teleconferencing. First it allows remote talkers to be virtually placed around the listener, providing the listener with the ability to easily discriminate between talkers based on their virtual location. Second, if a binaural microphone is used to acquire the talker's speech signal, the listener can receive this binaural signal directly. Binaural signals can be delivered to a listener through headphones or using a loudspeaker array (which is more preferable for video conferencing). However, the use of loudspeaker arrays requires the listener's head to be accurately positioned or else the spatialized audio effect will be lost. This paper contains discussion on the means of delivering binaural signals using loudspeaker arrays that allow the listener to move her or his head without losing the spatialized audio effect.

4:00–4:20 Break

4:20

2pSPa7. Chat space models. Michael Cohen (Spatial Media Group, Univ. of Aizu 965-8580, Japan, mcohen@u-aizu.ac.jp)

Shared virtual environments, especially those supporting spatial sound, require generalized control of user-dependent media streams. Nonimmersive perspectives in virtual environments enable fluid paradigms of perception, especially in the context of frames-of-reference for conferencing and musical audition. Traditional mixing idioms for enabling and disabling various sources employ `mute` and `solo` functions, which, along with `cue`, selectively disable or focus on respective channels. Exocentric interfaces which explicitly model not only sources, but also location, orientation, directivity, and multiplicity of sinks, motivate the generalization of `mute`/`solo` & `cue` to `exclude` and `include`, manifested for sinks as `deafen`/`confide` & `harken`, a narrowing of stimuli by explicitly blocking out and/or concentrating on selected entities. Such functions can be applied not only to other users' sinks for privacy, but also to one's own sinks for selective presence. Figurative representations of these functions are introduced, virtual hands to be clapped over avatars' ears and mouths. An audibility protocol is described, comprising `revoke`, `renounce`, `grant`, and `claim` methods, invocable by these narrowcasting commands to control superposition of soundscapes, and a taxonomy of modal narrowcasting functions is proposed. Applications include groupware for collaboration and teaching, teleconferencing and chat spaces, and authoring and manipulation of distributed virtual environments.

4:40

2pSPa8. Spatial voice activity detection using a microphone array noise canceller. Michael W. Hoffman (Univ. of Nebraska, 209N WSEC, Lincoln, NE 68588-0511) and Zhao Li (Motorola, Inc., Austin, TX 78758)

An array of microphones is used for both noise suppression and spatial voice activity detection (SVAD). A generalized sidelobe canceller (GSC) is employed for adaptive interference rejection and the signals in the noise canceller are also exploited to provide desired signal activity detection. The SVAD shows promising results for environments with moderate reverberation and single or multiple interfering sources. For direct-to-reverberant energy ratios of 4 to 11 dB and signal-to-interference power ratios of -10 to 10 dB, speech detection miss rates are generally below 5%, while false alarm rates range from 10% to 40%. Most scenarios generally resulted in the false alarm rates between 10% and 20%. A key advantage of the GSC-based SVAD is its computational simplicity. In addition, the proposed technique is quite suitable for multiple interfering sources as well as nonstationary interference such as competing speakers. The system has been tested with a standard CELP speech coder.

5:00

2pSPa9. Speech reconstruction from a noisy reception signal. Michiko Kazama (Acoust. Consultant, Tokyo, Japan), Mikio Tohyama (Kogakuin Univ., Tokyo, 192-0015 Japan), and Akira Morita (NHK Sci. and Tech. Res. Labs., Tokyo, 157 Japan)

Noise reduction is a fundamental issue of smart microphone systems or a hearing aid. Noise reduction by spectral subtraction has been investigated for speech signals. However, identifying whether frame is a speech or a silence portion is difficult under nonstationary noisy conditions when using this method. Extracting the desired speech based on the sinusoidal wave model [T. Quatieri and R. Mcaulay, IEEE ASSP **34**, 1449–1464 (1986)] was investigated. It was confirmed that intelligible speech sound could be synthesized using only five dominant sinusoidal waves [M. Kazama *et al.*, 5th ICSV 2079–2086 (1997)]. In this article, a new noise reduction method by extracting the dominant sinusoidal waves in each frame (32 ms) according to the energy ratio of the signal to noise was proposed. The signal-to-noise ratio was improved by 10 dB (S/N ratio) when the original S/N ratio was 0 dB. Speech quality could also be improved by reconstructing the higher harmonics from the noisy vowels using the frame-dependent comb filters. This reconstructed speech sound will be demonstrated at the presentation. This method might implement a fundamental technology of the smart microphone systems, including hearing aids. [Work supported by Housou Bunka Fund.]

Contributed Papers

5:20

2pSPa10. Improvements in teleconferencing sound quality and gain before feedback through the use of DML technology. Peter Mapp (Peter Mapp Assoc., Colchester CO3 4JZ, UK) and Henry Azima (New Transducers, Stonehill, Huntingdon, UK)

One of the primary limitations of teleconferencing systems is the premature onset of acoustic feedback. The current trend toward the use of desktop personal computers as the teleconferencing platform, rather than dedicated and acoustically treated video conferencing rooms, further exacerbates the problem. Local, sound reflecting surfaces including the desktop, conference table, or computer screen, etc., can cause undesirable specular reflections from the loudspeakers to occur. These are then picked up by the system microphone(s), causing the formation of strong comb filtering and resultant sound coloration, reduced speech clarity, and reduced gain before feedback. Historically, a number of approaches have been adopted to help overcome such effects, including echo cancelling, phase shifting and ''smart'' microphone techniques. The paper illustrates the effects of such reflections and shows that distributed mode loudspeakers can produce less boundary interactions and comb-filtering effects. Experimental data are presented to show that DML technology can passively offer a 4–7-dB improved gain before feedback advantage over conventional cone devices in typical teleconferencing applications. The fact that significant gains in feedback margin and reductions in potential coloration are achieved without the need for additional DSP or active techniques implies a radically different and advantageous acoustical radiation mechanism.

5:40

2pSPa11. A method for echo cancellation in audio signals using the genetic algorithm. Slawomir K. Zielinski (Tech. Univ. of Gdansk, Sound Eng. Dept., ul. Narutowicza 11/12, 80-952 Gdansk, Poland, slawek@sound.eti.pg.gda.pl)

A new method for echo cancellation is proposed. This method is based on inverse models of systems causing the echo in transmission channels. Parameters of these models are optimized using the genetic algorithm. In general, the inverse models that are used for echo cancellation can be divided into several categories according to their complexity. In the simplest case, the models consist of digital delay lines, scalers, and adders. The more complex models use also a nonlinear filtration, which in the general case may be a nonstationary one. The experiments and informal subjective listening tests showed that the proposed method allows for the perceptually efficient suppression of echo which was caused by multiple reflections providing delayed and scaled copies of the original signal. An additional preprocessing employing a calculation of the correlation function of the input signal can diminish the computational complexity of the proposed algorithm. Some examples of echo cancellation results obtained with the use of the proposed method are presented and illustrated with sound examples.

6:00

2pSPa12. A third octave real time VXI analyzer. Alberto Martin, Manuel Recuero, Juan Manuel Lopez, and Mariano Ruiz (Instituto Universitario de Investigacion del Automovil, Universidad Politecnica de Madrid, Crta. de Valencia Km.7, 28031 Madrid, Spain, amartin@insia.upm.es)

A digital signal processing system with VXI interface has been developed in a C-size board conforming to VXI 1.4 specification, and is made up of two blocks. The first one implements a message VXI interface and the second the digital processing itself, based in a 49-MHz TMS320C31. The system includes a complete software to customize for a specific application. The VXI interface has been gifted with a real time operating system and a software parser for building a SCPI (standard command for programmable instruments) translator. The software developed for the digital signal processing system has been built in several modules written in C language and C30 assembler in order to improve the velocity. The utility of this system is to realize customizable and specific digital signal processing without the necessity of acquiring complex and expensive VXI boards that do not allow modification of the commands, the specific algorithm, or the firmware. In order to show the versatility of the system, a one-third-octave real time analyzer has been developed in agreement with ANSI S1.11.

Session 2pSPb

Signal Processing in Acoustics: Signal Processing (Poster Session)

John Impagliazzo, Chair
Naval Undersea Warfare Center, Code 8212, Building 679, Newport, Rhode Island 02841, USA

Contributed Papers

All posters will be on display in the Poster Gallery from Monday to Wednesday, 15–17 March. Contributors will be at their posters from 2:30 p.m. to 4:30 p.m. on Tuesday, 16 March.

2pSPb1. Improving the performance of ultrasonic range meters. Monica Alonso-Sanudo, Cesar Gracia (ETSI Telecomunicacion, 28040 Madrid, Spain), and Pedro Olmos (CIEMAT, Avda Complutense 22, 28040 Madrid, Spain)

Range meters based on the time of flight of ultrasonic pulses are instruments widely used in a large number of daily operations. However, their performance may be seriously degraded when the environment has plenty of spurious obstacles masking the true target, a situation not rarely encountered in practice. Here some methods to reduce the influence of such echoes on monofrequency, wide-aperture range meters are analyzed. The discussion is focused on the use of that information contained in the pulse that allows one to find most of the target features. Relevant parameters to play with are the ratio between transmitted and received pulse lengths and energies, as well as the time evolution of the echo pattern. These techniques, suited for low-cost and small-size equipment, have been simulated with the help of a simple geometric ray model, showing the significant improvement achieved in the rejection of those spurious echoes that would lead to erroneous range determination if only time counting were implemented. In addition, experimental results obtained with a uP-based prototype employing 40-kHz ultrasound pulses and apertures of 30 deg are presented and discussed.

2pSPb2. Hands-free teleconferencing unit using auxiliary loudspeaker and duo-filter echo canceller DSP. Suehiro Shimauchi, Yoichi Haneda, and Yutaka Kaneda (NTT Human Interface Labs., 3-9-11, Midori-cho, Musashino-shi, Tokyo, 180-8585 Japan, sima@splab.hil.ntt.co.jp)

In many telecommunication systems, hands-free operation is becoming popular. For this to be comfortable and easy, high echo cancellation performance and a simple setup are required. This paper presents a new hands-free teleconferencing unit that consists of a main loudspeaker, an auxiliary loudspeaker, a microphone, and an echo canceller DSP board. The auxiliary loudspeaker is used to reduce the acoustic coupling between the main loudspeaker and the microphone by reproducing the anti-phase sound of the main loudspeaker. Since the auxiliary loudspeaker is set very close to the microphone, its sound level is low enough for users not to hear. Experimental results showed a reduction in acoustic coupling of about 6 dB from 200 Hz to 1 kHz. This unit also incorporates a newly developed acoustic echo canceller (AEC) DSP. The AEC algorithm, which is based on a duo-filter control system [Y. Haneda, S. Makino, J. Kojima, and S. Shimauchi, ''Implementation and Evaluation of an Acoustic Echo Canceller Using Duo-Filter Control System,'' in *Proc. EUSIPCO96* (1996), Vol. 2, pp. 1115–1118], helps to produce good and stable performance even during double-talk.

2pSPb3. Approximation of dummy-head recording technique by a multimicrophone arrangement. Nataliya Tohtuyeva and Volker Mellert (Dept. of Phys. and Acoust., Univ. of Oldenburg, D-26111 Oldenburg, Germany)

Head-related recording and reproduction systems rely on the two-ear microphones of a dummy head. However, the dummy head is sometimes difficult to use, e.g., due to size and weight. Additionally, its geometry, which gives the important diffraction pattern information for sound localization, is fixed. A microphone array, which approximates the head-related transfer functions, has fewer restrictions. Theoretical evaluation of a simple microphone array, which takes psychoacoustic-determined frequency weights for phase and magnitude into account, is presented. Results of practical sound localization test with this array are reported for sound sources in the horizontal plane. [Work supported by the German Science Foundation (DFG).]

2pSPb4. On the subspace methods for direction-of-arrival estimation in underwater acoustics. Miloud Frikel and Victor Barroso (IST/ISR, Av. Rovisco Pais 1, Torre Norte, Piso 7, 1096 Lisbon, Portugal)

The problem of bearing estimation appears in a vast number of applications, e.g., radar, sonar, communication systems,.... In this study, an investigation of the passive angular location of sources in underwater acoustics using an array of sensors is presented. First, eigenstructure/noneigendecomposition methods for direction-of-arrival (DOA) estimation of narrow-band/wide-band signals' wave fronts are studied. The noneigenanalysis-based techniques are emphasized because of their weak computational load. The studied methods are of high resolution such as (music, minimum-norm, their propagator,...). The eigenstructure based techniques on the exploitation of two principal properties: first, the data matrix has $(N-P)$ multiplicity of its smallest eigenvalues, with N and P as the number of sensors and sources, respectively, and the eigenvectors corresponding to the minimal eigenvalues; these methods have better performance than the classical methods. A comparative study of these types of subspace methods is presented. Finally, a robust method to improve the accuracy of the estimation of the direction-of-arrival of the sources is developed. The results of simulations are provided to illustrate the theoretical predictions. [This work was partially funded by FEDER and PRAXIS XXI, under contract PRAXIS/3/3.1/TPR/23/94.]

2pSPb5. Blind source separation. Miloud Frikel, Victor Barroso, and Joao Xavier (IST/ISR, Av. Rovisco Pais 1, Torre Norte, Piso 7, P-1096 Lisboa Codex, Portugal, frikel@isr.ist.utl.pt)

In signal processing the received data can be modeled as a superposition of a finite number of elementary source signals and an additive noise. Generally, in a multi-sensor environment application, such as underwater acoustics, the principal objective is estimating the number and directions

of radiating sources. In the last decade, eigenstructure-based methods yielding resolution have been proposed. However, these methods need the model of sources. In many cases, this model is not available, indeed, there is the appearance of the blind methods. Blind technique refers to lack of knowledge about the mixing system. It assumes very weak assumptions either for signals or mixtures. Blind source separation consists in identifying the sensors/sources transfer matrix and retrieving the source signals without resorting *a priori* information about the above matrix. It exploits only the information carried by the received signals themselves. The potential benefit of such a blind approach is that source separation is essentially unaffected by errors in the propagation model or in array calibration whereas the classical array processing methods assume that the array geometry is known and the sources are in the far field of the array. This contribution deals with blind source separation using second-order statistics. [This work was partially funded by FEDER and PRAXIS XXI, under Contract No. PRAXIS/3/3.1/TPR/23/94.]

2pSPb6. Envelope filtering of signals in the modulation frequency domain and evaluation of fluctuation strength. Cord Walter and Reinhard Weber (Akustik, Physik, Carl-von-Ossietzky Univ. Oldenburg, 26111 Oldenburg, Germany)

Fluctuation strength assessments with predefined envelope variations are commonly performed with synthesized modulated sounds. The intent of the present study is to change gradually the variability of recorded signals' envelopes for subsequent fluctuation strength evaluations. Manipulation of a signal's envelope was achieved by implementing a filter in the modulation frequency domain. Making use of an algorithm developed by R. Koch [B. Kollmeier and R. Koch, J. Acoust. Soc. Am. **95**, 1593–1602 (1994)], time signals are transformed into (waterfall-like) bandpass-time signals (bandwidth 86 Hz) by calculating the spectra of successive frames. From the time-dependent envelopes of the bandpasses, modulation spectra are computed and filtered. Time signals with changed envelopes are resynthesized from the filtered modulation spectra by reversing the former processing stages. The fluctuation strength of the original and modified time signals was computed and compared with the subjective assessments. The results of this comparison are used to validate an algorithm for fluctuation strength calculations of recorded signals.

2pSPb7. Computer-aided systems for prolonged recording and analysis of human bowel sounds. Charalambos A. Dimoulas, George V. Papanikolaou (Dept. of Elec. and Computer Eng., Aristotle Univ. of Thessaloniki, Univ. Campus 540 06, Thessaloniki, Greece), George M. Kalliris, and Costas Pastiadis (Aristotle Univ. of Thessaloniki, Thessaloniki, Greece)

This paper presents the design of noninvasive systems for the investigation of the small bowel motility patterns. The basic idea was to implement dedicated devices for the recording and analysis of human bowel sounds. Properly modified transducers were used for the caption of gastrointestinal sound signals. A data acquisition ambulatory system, consisting of a preamplifier and a recording unit, was initially designed capable for maximum continuous recording of 6 h. After the first experimental results with this system, the necessity for longer recording duration was obvious. For this reason the installation of a computer-based stationary system in a special reformed examination room was the next development step. Triggering of the input data and rejection of the regions with absence of gastrointestinal activity allowed much more recording duration. A computerized signal processing system, which involves equalizing procedures, noise cancellation techniques, and neural network algorithms, was used for the off-line analysis of the recorded data. Novel measures and 2-D and 3-D representation techniques were employed for the exposition of results. The new approach gave flexibility to the system because longer recording times offer more information to the doctor so that the statistical analysis is much more effective and reliable.

TUESDAY AFTERNOON, 16 MARCH 1999 ROOM H104, 2:00 TO 5:40 P.M.

Session 2pUWa

Underwater Acoustics, Acoustical Oceanography, and Physical Acoustics: Acoustics and the Comprehensive Test Ban Treaty II

Arthur B. Baggeroer, Cochair
Department of Ocean Engineering, Massachusetts Institute of Technology, Cambridge, Massachusetts 02139, USA

Martin Lawrence, Cochair
Provisional Technical Secretariat, Comprehensive Nuclear-Test-Ban Treaty Organization, Vienna International Centre, A-1400 Vienna, Austria

Invited Papers

2:00

2pUWa1. Overview of the infrasound monitoring system for the Comprehensive Nuclear-Test-Ban Treaty. Douglas R. Christie (Provisional Tech. Secretariat, Comprehensive Nuclear-Test-Ban Treaty Organization, Vienna Intl. Ctr., A-1400 Vienna, Austria, dchristie@ctbto.org)

A global network of 60 infrasonic array stations is being established as part of a global monitoring system for verification of the Comprehensive Nuclear-Test-Ban Treaty. These ultrasensitive stations, which are distributed as uniformly as possible over the surface of the globe, will be capable of detecting and locating any nuclear explosion in the atmosphere with yields of 1 Kt or more. In addition to nuclear explosions, this network will detect infrasound from a wide range of man-made and naturally occurring sources, including large chemical explosions, meteors, volcanic explosions, aerodynamic infrasound associated with orographic features, and auroral-generated infrasound. The propagation of infrasound in the atmosphere is not, as yet, fully understood. The analysis of data from this network should provide considerable insight into the detailed long-range propagation properties of low-frequency sound in a temporally and spatially inhomogeneous medium.

2:20

2pUWa2. Autonomous hydroacoustic stations in support of CTBT-monitoring technology and event screening. Peter C. Wille (FWG, Klausdorfer Weg 2-24, 24148 Kiel, Germany)

No more than six hydroacoustic receiver stations will be monitoring the three world oceans in the framework of the CTBT. Together with five T-wave stations they will synergetically cooperate with the seismic network which alone can neither provide the required accuracy of localization on the southern hemisphere nor the capability of reliable event discrimination of the oceans. To maintain the function of the sparse hydroacoustic network in case of an irretrievable station breakdown, an autonomous auxiliary unit for temporary replacement of fixed cable connected stations has been developed by FWG. The battery-supplied autonmous station, like the permanent stations, suspends the hydrophone at the depth of the SOFAR channel axis. The lightweight construction permits quick deployment and retrieval. The received acoustic signals are processed for prescreening at the station by algorithms with adjustable criteria to discriminate large explosions from natural events of similar energy turnover such as sea quakes and volcanic eruptions. The characteristics of the signals are transmitted by a surface buoy radio link via low orbit satellites to the data center, together with unprocessed, highly suspicious signals for expert analysis.

2:40

2pUWa3. Adaptation of underwater acoustic propagation models to infrasonic atmospheric propagation. Guy V. Norton, Wayne A. Kinney (Acoust. Simulation, Measurements and Tactics Branch, Code 7180, Naval Res. Lab., Stennis Space Center, MS 39529-5004), Dan J. Ramsdale (Neptune Sciences, Inc., Carriere, MS 39426), and Rodney W. Whitaker (Los Alamos Natl. Lab., Los Alamos, NM 87545)

For decades, the U.S. Navy has been engaged in the development of underwater acoustic propagation models to aid in the design and effective use of sonar systems. Much of the expertise created in this development is applicable (directly or by modification) to challenges associated with the use of infrasonic arrays to monitor CTBT compliance. The results of the modification and adaptation of some existing underwater acoustic propagation models to predict and analyze acoustic-gravity wave signals in both a range-independent and a range-dependent atmosphere will be reported. Examples are given that include the effects of range-dependent winds on received signal amplitude and arrival direction for the case of an airborne explosive source and a ground-based infrasonic receiver. Frequencies of interest are in the band from 0.02 to 10 Hz, and ranges of interest are 1000 km or less. [Work sponsored by the U.S. Department of Energy and the Los Alamos National Laboratory.]

3:00

2pUWa4. Naturally occurring sources of infrasound. Alfred J. Bedard, Jr. (Natl. Oceanic and Atmospheric Administration, Environ. Technol. Lab., Mail Code R/E/ET4, 325 Broadway, Boulder, CO 80303)

There are growing numbers of potential applications for infrasonic observing systems. The evolving International Monitoring System for the nuclear test ban treaty (including 60 infrasonic stations) offers exceptional opportunities to make infrasonic data sets widely available and to explore their uses in geophysical studies. This is especially true because of the ability to perform synergistic studies with seismic and hydroacoustic systems in a processing environment where diverse data sets can be readily melded. Natural infrasound sources such as avalanches, earthquakes, geomagnetic activity, meteors, ocean waves, severe weather, turbulence, and volcanoes offer great resources for international cooperative research programs. Sources of low-frequency sound from civilization processes offer a set of parallel opportunities. This paper will review the broad range of investigations possible using both individual and multiple infrasonic observing systems, as well as infrasonic systems in combination with other remote sensing systems.

Contributed Papers

3:20

2pUWa5. Interpretation of the different infrasounds detected in France during one year in a four-components prototype CTBT station. Elisabeth Blanc, Alexis Le Pichon, and Yves Cansi (CEA-DASE, BP 12, 91680 Bruyeres-Le-Chatel, France, blanc@ldg.bruyeres.cea.fr)

A four-components prototype CTBT station has been installed in France by the Department of Analysis and Monitoring of the Environment of the Atomic Energy Commission, for the development of instrument and methods for infrasound monitoring. The purpose of this paper is to present the characteristics of the main infrasound signals detected during a year. Infrasound from the Concorde supersonic airplane presents different phases corresponding to the different acoustic paths in the different layers of the atmosphere. The number of phases, their apparent velocity, and the signal shape are strongly dependent on the ray trajectory and then on the wind and temperature profiles. Characteristic seasonal variations have been determined. Microbarom signals have been used to follow the evolution of the ocean swell during periods of several days. Severe weather infrasound has been observed, related to lightning activity and convective motions of the atmosphere. Chemical industrial explosions provide interesting well-known sources used for testing the methods and for the development of propagation models. All these events are control events for the permanent evaluation of the detection and location capability of the station. A synthesis of one year's observations is given.

3:40

2pUWa6. Infrasound source location at the prototype international data center. David J. Brown, Charles N. Katz, Ronan Le Bras, Jin Wang, and Anna Gault (SAIC/CMR, Ste. 1450, 1300 N. 17th St., Arlington, VA 22209)

The Prototype International Data Center (PIDC) is developing an operational system to provide temporal and spatial source location information for highly impulsive sources with an equivalent nuclear yield of at least 1 kT in any terrestrial environment. This source information is deduced by a combination of automatic and interactive processing. Detecting the infrasound released by large-scale atmospheric explosions is the most suitable method for the immediate location and characterization of atmospheric sources. The PIDC treats the source location problem uniquely in that a given source can be located using any combination of infrasonic, seismic, or hydroacoustic signals when these signals exist. The highly dynamic aspect of the atmosphere, however, creates problems not traditionally encountered in the seismic or hydroacoustic source location problem. The dynamic nature of these effects will limit the ability to apply detailed propagation models in an automatic operational system, such as is being developed at the PIDC. A seasonal atmospheric model is being used in conjunction with near real-time meteorological data to provide the am-

bient atmospheric conditions required by the physical propagation model. Results obtained from a ground-truth data set will be presented that demonstrate the operation of the PIDC source location procedure.

4:00–4:20 Break

4:20

2pUWa7. Temporal variability in the propagation of infrasonic waves over Hawaii and Alaska. Milton Garces, Kent Lindquist, Roger Hansen (Univ. of Alaska, Fairbanks, AK 99775-7320, milton@hialoha.net), Douglas Drob, and Michael Picone (Naval Res. Lab., Washington, DC 20375)

Temporally varying atmospheric temperature and wind velocity data from ground level up to heights of 250 km are used to compute travel time curves and azimuth deviations for acoustic waves propagating over the CTBT infrasonic array sites of Hawaii and Alaska. An enhanced formulation of the tau-*p* method [Garces *et al.*, Geophys. J. Int. (1998)] permits theoretical estimates of travel times and azimuth deviations for infrasonic waves traveling through a stratified, windy atmosphere. Atmospheric data for the season of Winter is obtained from the Naval Research Laboratory MSISE-90 and HWM-93 models, which include tidal and geomagnetic effects. These data will be supplemented with ground-based and satellite-based atmospheric data. An ensemble of circumstances, encompassing infrasonic wave propagation through anomalous environmental conditions as well as studies on site-specific effects, will be presented. Based on the predicted phases, effective detection and source inversion algorithms will be developed at each array.

4:40

2pUWa8. An optical fiber infrasound sensor. Mark Zumberge and Jonathan Berger (IGPP, Scripps Inst. of Oceanogr., 9500 Gilman Dr., La Jolla, CA 92093-0225, jberger@ucsd.edu)

As part of the International Monitoring System of the CTBT, infrasound signals in the band 0.02 to 4 Hz must be detected in the presence of ambient noise generated chiefly by wind. The effectiveness of acoustic filters employed in standard infrasound sensors is limited by pressure propagation and attenuation characteristics within the filter. To improve the signal-to-noise ratio, an optical fiber instrument for sensing the integrated pressure variations along a line has been designed. The sensor design consists of optical fibers inside a long, fluid-filled tube, deployed along the ground surface. Integrated pressure variations along the fiber's length are sensed by interferometrically monitoring changes in the optical path length of the fiber. The optical fiber sensor can average over kilometer-scale lengths of arbitrary geometry with an averaging bandwidth governed by the speed of light and thus should offer significant practical advantages in reducing the effect of wind noise, increasing the signal-to-noise ratio over a wide bandwidth.

5:00

2pUWa9. One-year analysis of systematic detection and location of infrasounds in a protoype CTBT station. Alexis Le Pichon and Yves Cansi (CEA-DASE, BP 12, 91680, Bruyères-Le-Châtel, France, lepichon@ldg.bruyeres.cea.fr)

Within the framework of the Comprehensive Test Ban Treaty, the Department of Analysis and Monitoring of the Environment (DASE) of the French Atomic Commission has developed an automatic processing software providing detection of coherent infrasound signals. The infrasound's parameters are calculated by using the progressive multichannel correlation method as a real-time detector. Each week, an automatic bulletin summarizes all detections by giving the wave parameters (velocity and azimuth), the amplitude, the frequency range, and the correlation coefficient. The one-year bulletins enable the identification of most of the infrasounds (sonic boom of supersonic aircraft, mining explosions of known quarries, storms, ocean swell). Most of the man-made infrasounds are produced by quarry blasts and the Concorde. Other infrasounds are produced by severe weather (storms, hail). Excluding false detections, an average number of 40 detections is obtained each day. For some infrasounds, statistics show several phases related to the different reflections in the stratosphere and thermosphere with seasonal characteristics. In order to detect coherent signals with poor signal-to-noise ratio (detection in windy period, fine detection of phases with low amplitudes), the thresholds of detections are set at a low level. In the future, this study will help to determine operational thresholds.

5:20

2pUWa10. High-resolution measurements of the angle-of-arrival of infrasonic signals in the range 0.5–5 Hz. Ludwik Liszka (Swedish Inst. of Space Phys., Umea Div. Sorfors 634, S-905 88 Umea, Sweden, ludwik@irf.se)

The method used in the present study is a further development of the threshold filtering technique. Signals are transformed using the Morlet wavelet and a sliding window in the domain of the wavelet coefficient magnitude (spectral density). The procedure results in an ampligram, a graph demonstrating the amplitude and phase of components of the signal corresponding to different spectral densities. The ampligram may be further used to determine the number of independent components of the signal using the principal component analysis. The method offers a possibility to detect the statistical properties of signal components: stochastic and deterministic components may be easily distinguished. The most important applications for infrasound measurements are nonlinear filtering of the signal, extraction of weak deterministic components outside the working range of microphone, extraction of different propagation modes, and high-resolution measurements of the angle-of-arrival. The application described here facilitates measurements of the angle-of-arrival for each propagation mode separately.

Contributed Posters

These posters will be on display from Monday to Wednesday, 15–17 March. Authors will be at their posters from 10:00 a.m. to 12:00 noon on Wednesday, 17 March.

2pUWa11. Surveying infrasonic noise on oceanic islands. Michael A. H. Hedlin, Frank L. VernonIII, Jon Berger, and John A. Orcutt (IGPP, Univ. of California, San Diego, 9500 Gilman Dr., La Jolla, CA 92093-0225, hedlin@ucsd.edu)

An essential step in the establishment of an international monitoring system (IMS) infrasound station is the site survey. The Provisional Technical Secretariat recommends infrasonic noise be recorded with meteorological data at four separate, promising, locations in the vicinity of the nominal station location to identify a secure site which would give the good signal-to-noise while offering easy access to power and telecommunications. A good infrasound station should be sheltered from the prevailing winds by gentle topography, trees, and ground cover and located as far as possible from other natural and cultural noise sources. As the IMS network has been designed to give uniform global coverage, some of the stations will be located on oceanic islands. Noise surveys are being conducted at three locations in the Atlantic: Sao Miguel, Azores; Santiago, Cape Verde; and Ascension Island. These island locations are very important as they provide coverage in a region of great monitoring interest. However, they also offer a range of meteorological, topographical, and habitation conditions which result in few suitable locations to deploy an infrasound array. This paper describes preliminary efforts to characterize infrasonic noise levels on these islands and find locations with the necessary practical requirements.

2pUWa12. On temporal and spatial variations of infrasonic signals at long distances from surface explosions. Sergey N. Kulichkov (Inst. of Atmospheric Phys., Russian Acad. of Sci., Pyzevsky 3, Moscow 109017, Russia)

Temporal and spatial variations of infrasonic signals at the long distances from surface explosions are discussed. The experiments were performed in different seasons during 1989–1991. Surface explosions with yields of 20–70 tons were realized one to two times in a month in runs of four to ten explosions with 10–20-min intervals between them. The receivers were placed both in the zone of acoustic shadow and in the zone of acoustic audibility at the distances about 300 km from the explosions. Signals from more than 60 explosions were recorded. It was observed that the characteristics of infrasonic signals from similar explosions can vary sufficiently both during one hour and during one day. The variations of those during different seasons were observed too.

TUESDAY AFTERNOON, 16 MARCH 1999 ROOM H2053, 2:00 TO 5:00 P.M.

Session 2pUWb

Underwater Acoustics and Signal Processing in Acoustics: Localization, Estimation and Detection in Underwater Acoustics

D. Eric Smith, Chair
Applied Research Laboratories, University of Texas at Austin, Austin, Texas 78713-8029, USA

Contributed Papers

2:00

2pUWb1. Cell noise at the output of a MFP beamformer in shallow water. Newell O. Booth, Phil W. Schey, and Ahmad T. Abawi (Space and Naval Warfare Systems Ctr., Code D881, San Diego, CA 92152-5000)

Measurements of ambient noise in search cells at the output of linear and adaptive beamformers are presented for data from three arrays deployed simultaneously in the SWellEX-96 experiment (200-m water depth off San Diego, CA). Previous papers by the authors have demonstrated the application of matched-field processing (MFP) to the detection and localization of submerged acoustic sources using the SWellEX-96 arrays. In this paper, the arrays (horizontal, vertical, and tilted-vertical lines) were processed to obtain cell noise spectra in noisy and quiet regions of the range, depth, and azimuth search space. Array noise gain measurements quantitatively compare the noise rejection capability of the arrays and processing methods. Frequency, integration time, array orientation, number of elements, and aperture are important parameters. Results are presented for linear and adaptive beamforming methods using plane-wave, focused plane-wave, and MFP steering vectors. [Work sponsored by the Office of Naval Research.]

2:20

2pUWb2. Tracking results from the three-dimensional full field processing (FFP) array and the Santa Barbara Channel experiment. Herbert Freese, Yung Lee, Robert Greene, and Peter Mikhalevsky (SAIC, 1710 Goodridge Dr., McLean, VA)

In March of 1998, SAIC under DARPA sponsorship deployed five 170-m, 30-element, vertical line arrays (VLAs) in 200 m of water in the Santa Barbara Channel. The VLAs were arranged in a pentagon with a 200-m horizontal aperture. Each hydrophone package contained tilt sensors for array localization as well as a thermistor for water temperature measurement. Each VLA also contained four compasses that were used in conjunction with the tilt sensors for passive localization of the array elements. In this presentation the acoustic experiments will be described and a number of results including a comparison of acoustic and nonacoustic localization methods, an environmental characterization, and the results of acoustic measurements using a towed source and surface ships of opportunity will be presented. Specific acoustic results to be presented will include measurements of array signal and noise gain, and the results of tracking the towed source and surface ships using adaptive matched field methods.

2:40

2pUWb3. Comparison of mode-shapes-only source depth estimation with conventional matched field source localization and the impact of array tilt on these processes. Paul Hursky (Lockheed Martin, P.O. Box 180858, Coronado, CA 92178-0858), William S. Hodgkiss, and William A. Kuperman (Scripps Inst. of Oceanogr., San Diego, CA 92093-0701)

Matched field processing (MFP) typically exploits acoustic mode structure using both mode shapes and wave numbers to estimate source location. It is also possible to use mode shapes alone to estimate source depth [E. C. Shang, J. Acoust. Soc. Am. **77**, 1413–1418 (1985); T. C. Yang, *ibid.* **82**, 1736–1745 (1987)]. Measurements of multiple frequency towed source transmissions using a vertical line array spanning the lower duct of a summer sound-speed profile (SwellEx 96) were used to compare conventional MFP processing with several variants of mode-shapes-only depth estimation. Sensitivity of these processes to reduced aperture, array tilt, and signal-to-noise ratio was studied in simulated and measured data. Array tilt mismatch was successfully corrected to improve source localization results significantly.

3:00

2pUWb4. Highly resolved detection in a waveguide with the D.O.R.T. method. Claire Prada, Nicolas Mordant, and Mathias Fink (Lab. Ondes et Acoust., Univ. Paris 7, CNRS, ESPCI, 10 rue Vauquelin, 75005 Paris, France)

The D.O.R.T. method (French acronym for decomposition of the time-reversal operator) is a scattering analysis technique that uses an array of transducers in pulse-echo mode. The method was applied to detection and selective focusing on pointlike scatterers through inhomogeneous media [J. Acoust. Soc. Am. **99**, 2067–2076 (1996)]. Here, laboratory measurements in a water waveguide are presented. Taking advantage of the multiple reflections at the interfaces of the guide, high resolution is achieved with the D.O.R.T. method without using any *a priori* knowledge of the guide. The separation of two scatterers and the selective focusing are obtained with a transverse resolution at least nine times better than the predicted free space limit. The detection of a scatterer placed at less than half a wavelength from the water/air interface is also achieved with good sensitivity. Finally, the impulse response functions of each scatterer to the array is computed as a combination of the eigenvectors of the time-reversal operator obtained at each frequency. Using these impulse Green functions, selective focusing with high temporal and spatial compression is performed.

3:20

2pUWb5. A high-resolution algorithm for wave number inversion using a holographic technique. Philippe Roux, Megan McArthur, Paul Hursky, and William A. Kuperman (Marine Physical Lab., Scripps Inst. of Oceanogr., UCSD, 9500 Gilman Dr., La Jolla, CA 92093-0238, philippe@mpl.ucsd.edu)

The aim of this work is to perform a high-resolution wave number inversion in a noisy shallow water waveguide. A single-frequency source is towed at a constant speed relative to a vertical array. No *a priori* knowledge of the waveguide characteristics is required. The inversion algorithm starts from the holographic representation of the field received from the source on the array. Then, using the recorded field along the source track, a newly modified eigen-matrix pencil was performed to extract the wave numbers. The accuracy of the method is compared to the Cramer–Rao lower bounds. The dependence of the results on the length of the source track, the number of receivers in the array, the signal-to-noise ratio, and the sound velocity profile in the waveguide are discussed. Both experimental and simulated data are reported.

3:40

2pUWb6. Beamforming performance of a V-shaped array of sea-bed geophone sensors. Richard J. Brind and Nick J. Goddard (DERA Winfrith, Winfrith Technol. Ctr., Dorchester, Dorset DT2 8XJ, UK, rjbrind@dera.gov.uk)

Geophone sensors on the sea-bed offer a mechanism for detecting and localizing acoustic sources in the ocean. Recent work is described in which a V-shaped array of sensor units was deployed on the sea-bed in a shallow water location. Each unit consisted of a three-component set of geophones and a hydrophone. Data were obtained on the response of the sensors to noise from ships in the vicinity, and to impacts on the sea-bed remote from the array. The positions of the units were determined by examining the phase of broadband energy at each pair of elements, and applying a least squares fit. The geophone data were then beamformed. Conventional and adaptive beamforming techniques have been applied, and the sensitivity of each to errors in the knowledge of the element positions assessed. The response of the array to noise from nearby ships has been compared to predictions. The beam pattern was found to be superior to that of an equivalent array of acoustic sensors. The ability of the V-shaped configuration in the experiment to resolve the wave number of the incident field has been investigated. The response of the array to energy arriving in the dispersive interface wave propagation path has been examined.

4:00–4:20 Break

4:20

2pUWb7. Transient, tonal, and background noise filtering with wavelet and cosine transforms. Eric Delory and John R. Potter (Acoust. Res. Lab., Tropical Marine Sci. Inst. and Elec. Eng. Dept., Natl. Univ. of Singapore, 27 Engineering Dr., 117596 Singapore, eric@arl.nus.edus.g)

In underwater acoustic signal processing, a major concern has been to extract information from a noisy time series, without over-constraining the estimation. Often, very little is known about the signal or noise and any strict assumption increases the risk of failure in real applications. Here, a new denoising method is presented, tested on three types of real underwater noise sources $(n_1(t), n_2(t), n_3(t))$, each added to an arbitrary signal $s(t)$. Noise class indices respectively refer to snapping shrimp noise, shipping noise, and underwater background noise, which are technically considered as transient, tonal, and broadband pink noise. $s(t)$ is defined as any signal that does not belong to these three classes, thus imposing no strict constraint. The extraction process is performed in three steps, each performing a *noise-specific* orthogonal block transform. First, a one-level Haar wavelet-packet transform is applied to detect transient noise components, using an additive information cost function as a hypothesis test and a simple dot-product to identify and extract them. Second, the denoised signal is reconstructed and decomposed by a one-level cosine-packet transform to identify and extract tonal components in a same manner. After reconstruction, pink noise is removed by thresholding a near-optimal Daubechies wavelet-packet basis.

4:40

2pUWb8. Objective function particularity for shallow water waveguide parameter estimation procedure. Alexey A. Pudovkin (N. N. Andreev Acoust. Institut, North Brunch, Pochtovay St., 3, Severomorsk, Murmansk reg., 184600, Russia, vfo@nordacin.murmansk.su)

The acoustic field observable parameter values and its acoustic field model predictions were compared, when one desired to estimate model parameters. The measurement was completed when its error was known. It is a preferred tool for analysis to describe statistically disalignments of the model predictions and experimental observations; then one tries to avoid it by creating a sophisticated physic model. Stochastic description acceptability is checked by stochastic hypotheses test (SHT). One tests the hypothesis which was used for objective function (OF) conformation, for instance, by maximum likelihood (ML) tenet. The more disalignment, the bigger OF value for acceptable OF. The model parameters are estimated by OF minimization. The ML OF modification is proposed by penalty function (PF) method. The PF takes into account hypothesis test results, which implicate an acceptable physical–stochastic model of the waveguide acoustic field. If SHT does not give cause to reject the acoustic field formation model on acceptable significance level, then it is possible to calculate the estimation error with the use of ML OF and PF. The measurement implementation main difficulty provided for the model finding. This model ought to be rather simple to calculate the error, but at the same time rather complete to describe disalignments correctly.

Contributed Poster

This poster will be on display in the Poster Gallery from Monday to Wednesday, 15–17 March. Author will be at the poster from 10:00 a.m. to 12:00 noon on Wednesday, 17 March.

2pUWb9. Matched-field depth discrimination with active sonar. Granger W. Hickman and Jeffrey L. Krolik (Dept. of Elec. and Computer Eng., Box 90291, Duke Univ., Durham, NC 27708)

This paper concerns the problem of estimating target depth in a shallow ocean using multiple pings from a low-frequency active sonar. Although much work on passive range-depth source localization using full-wave propagation models has been published, little attention has been given to the active sonar problem because of the difficulty in modeling target reflection characteristics. In this paper, active MFP is achieved without knowledge of the target's backscatter coefficients. By assuming the target's aspect and depth are relatively constant during its track, a MFP range-depth estimate is obtained by modeling the changes in the unresolved coherent multipath returns from ping to ping. The MAP range-depth estimate involves a dynamic programming procedure which uses a Markov model of changes in the target backscatter coefficients from ping to ping. Preliminary simulation results suggest that the target depth can be resolved (after approximately ten pings) to within 10 m in a water column 215 m deep. [Work supported by ONR.]

Posters from various technical sessions remain on display in the Poster Gallery.

Posters from sessions which contain both lecture and poster presentations will be attended by the authors as listed below.

10:00–12:00

1pAA13	Semidor, Catherine	Acoustical modifications of the interior design of a 50′ chapel
1pAA14	Ivancevic, Bojan	The acoustical properties of large studios
1pAA15	Tronchin, Lamberto	The sound quality of the Theatre Comunale in Treviso, Italy
2aAAa13	Smigelschi, Marius	CAAD-Computer aided architectural and acoustical design
2aNSc9	Picard, Michel	The confounding influence of collapsing the ear canal on audiological assessment of noise-exposed workers
2pAAa7	Kramer, Peter S.	Room acoustical measurements and architectural documentation of auditoriums in Berlin considering the speech intelligibility in dependence of spatial distribution of sound fields
2pAAa8	Galindo, Miguel	Simulated acoustics field in mudejar-gothic churches
2pAAb7	Morimoto, Masayuki	Appropriate band width and integration time for measurements of the degree of interaural cross-correlation as a measure of apparent source width in concert halls
2pAAb8	Stauskis, Vytautas J.	The interrelation between the music sound clarity index C80 and the subjective evaluation of the hall acoustics
2pPAa10	Ruhlich, I.	How much pressure drop is necessary for heat transfer
2pPAa11	Le Polles, T.	Threshold condition for travelling wave excitation in an annular prime-mover
2pUWa11	Hedlin, Michael A. H.	Surveying infrasonic noise on Oceanic Islands
2pUWa12	Kulichkov, Sergey N.	On temporal and spatial variations of infrasonic signals at long distances from surface explosions
2pUWb9	Hickman, Granger W.	Matched-field depth discrimination with wave sonar
3aNSa5	Schulz, Detlef	Non-occupational noise and hearing capability of children and young adults
3aNSa6	Domitrovic, Hrvoje	Noise levels in dental practice
3aNSa7	Barham, Richard G.	The role of measurement standards in acoustics
3aUWa11	Khelladi, Hassina	Analysis of boundaries' effects in the evaluation of transient ultrasonic fields scattered by a rigid reflector
3aUWa12	Semenov, Andrew G.	Sound scattering by moving inhomogeneity
4aAAb13	Masyukov, Valery A.	Noise transmission through a finite plate: physical approach
4aAAb14	Rebureo, Manuel	Prediction equations of isolating systems: gypsum panels
4pAA13	Jang, Jaehee	System development to reduce floor impact sound in apartment houses
4pAA14	Kustner, Eberhard	Additional improvement of air borne and impact sound insulation of ceilings in prefabricated standard house-buildings
4pAA15	Rodriguez-Manzo, Fausto	Towards a classification of acoustic comfort. A case study of a university classroom
5aAA13	Legrand, Olivier	High frequency asymptotics and random matrix theory in reverberant rooms
5aAA14	Morfey, Christopher L.	Mode counts for rooms and waveguides
5aAA15	Picard Lopez, M. A.	An extension of the transfer function method described in ASTM E 1050-90 for its use in semianechoic conditions
5aAA16	Dutilleux, Guillaume, J. A.	Towards a global *in situ* method for materials acoustic impedance assessment at very low frequencies using evolution strategy
5aAA17	Bosmans, Ivan	Sound absorption properties of suspended ceilings with plastic foils
5pAA8	Becker, Jorg	Four-microphone-array measurements combined with geometrical room acoustic simulation technique
5pAA9	Gomes, Marcio H.	On the accuracy of the assessment of room acoustical parameters using MLS technique and ray-tracing simulation

Also, the following poster sessions are scheduled:

Poster Session 3aAOa

Poster Session 3aPPb

Poster Session 3aUWc

Session 3aABa

Animal Bioacoustics: Evolution in Hearing and Sound Production I

Robert J. Dooling, Cochair
Department of Psychology, University of Maryland, College Park, Maryland 20742, USA

Annemarie Surlykke, Cochair
Center for Sound Communication, Institute of Biology, Odense University, DK-5230 Odense M., Denmark

Invited Papers

8:00

3aABa1. The evolution of tympanate hearing from proprioceptors in ancient grasshoppers. Heiner Roemer (Zoology, Karl-Franzens Univ., A-8010 Graz, Austria) and Moira J. van Staaden (Bowling Green State Univ., Bowling Green, OH 43403)

The ears of modern insects occur on rather different body parts, from head, to thorax, to abdomen, and there is evidence from comparative anatomy and embryology in divergent taxa that they have evolved from proprioreceptors responding to stretch or vibration. Receptor cells of these ears are directly or indirectly coupled to thin cuticular membranes (tympana), which are considered to play important roles in sensitivity and frequency tuning of such ears. This report is on a new set of hearing organs in an ancient grasshopper (*Bullacris membracioides*) without the typical tympanum, but a sensitivity exceeding most tympanate ears. As a result, males are capable of signaling acoustically over up to two km. In addition, within single individuals of this species, six pairs of serially repeated abdominal ears exist which all respond to biologically relevant frequencies and intensities. Altogether, anatomical comparison and results of neurophysiological and behavioral experiments provide strong evidence for the transition in function from proprioreception to airborne sound reception, and for the selective advantage during the evolutionary development of a complex ear structure. [Work supported by Austrian Science Foundation.]

8:30

3aABa2. Evolution of vocal communication in the gray treefrog complex. H. Carl Gerhardt (Univ. of Missouri, Columbia, Columbia, MO 65211, bioscarl@showme.missouri.edu)

The evolution of communication requires changes in both signals and the criteria used by receivers to select signals. The question arises: Do changes occur first in signals, first in receivers, or are tight co-evolutionary changes required in both signals and receivers? In the gray treefrog complex, spectral properties of calls are conserved: in both the diploid ancestral species (Hyla chrysoscelis) and in derived, tetraploid lineages (nominally, H. versicolor) there are two spectral peaks: a dominant band centered at about 2.4 kHz, and a secondary band (-8 to -10 dB) at about 1.2 kHz. Whereas females of the ancestral species have a weak preference for calls consisting only of the secondary band to calls having only the dominant band, females of the derived species strongly prefer calls with just the dominant band. Thus, an evolutionary change in preference has preceded any change in the spectral properties of the call. Temporal differences between the species include pulse rate, pulse duration, and pulse shape. Whereas females of the ancestral species use pulse rate alone for call discrimination, females of the derived species base preferences on all three properties, thus suggesting a co-evolutionary change. [Work supported by NSF and NIMH.]

9:00

3aABa3. Evolution of vocalization behavior in a Madagascar amphibian. Peter M. Narins (Dept. of Physiological Sci., Univ. of California, Los Angeles, 405 Hilgard Ave., Los Angeles, CA 90095) and Edwin R. Lewis (Univ. of California, Berkeley, CA 94720)

Vocalizations of *Boophis madagascariensis (Rhacophoridae)* males were recorded in a mid-elevation rain forest in eastern Madagascar. Call notes made by males of this species were classified into 28 types. This represents the largest known call repertoire of any amphibian. Even considering all iambic notes as variants of one type, there remain eight distinct call notes produced by this species. Morphological analysis of the vocal musculature of *B. madagascariensis* revealed no obvious adaptations for unusual glottal flexibility or function. Playback studies using a subset of the call notes as stimuli were carried out in the animals' natural habitat to determine the functional significance of several of the call notes. One sequence of notes evoked increased call rates from males, other note sequences inhibited males from calling, whereas others appeared to have no effect on male calling rate. Call note pairs occurred inconsistently and unpredictably. The evolutionary significance of an extended vocal repertoire and a random call note production scheme are discussed. [Work supported by NIDCD Grant Nos. DC-00222 to PMN and DC-00112 to ERL.]

9:20

3aABa4. Moths' ears evolved first for bat defense and later for communication. Annemarie Surlykke (Ctr. for Sound Commun., Inst. of Biol., Odense Univ., DK-5230 Odense M., Denmark, ams@dou.dk)

Many moths possess simple ears primarily to alert them to the echolocation calls of hunting bats. Since large targets reflect stronger echoes than small ones, bats should detect moths with large wing and body surface areas at greater distances than small moths. The increased conspicuousness of large moths would reduce their safety margin over bats, unless this is offset by a greater sensitivity of their ears. Results seem to support this: The sensitivity of ears of noctuid moths is significantly dependent on size, with larger moths possessing lower thresholds. If moth ears exist for bat detection, moths that live in bat-free niches should exibit reduced acoustic sensitivity. Studies of moths temporally isolated from bats (flying either in the winter or during the day) have confirmed this expectation. Another effect of the release of predation pressure from bats may be the use of the preexisting ears for sexual acoustic communication. All sonorous noctuoid moths described so far produce sounds in the same frequency range as that emitted by bats, presumably because bat-sensitive ears are the ancestral (plesiomorphic) condition and acoustic communication is a facility aquired later. [Work supported by the Danish National Research Foundation.]

Contributed Paper

9:40

3aABa5. Bats, insects, and the evolution of hearing. Lee A. Miller (Inst. of Biol., Ctr. for Sound Commun., Odense Univ., DK-5230 Odense M., Denmark)

Insectivorous bats appeared in the fossil record about 50 million years ago, or long after certain insects had adopted nocturnal habits. Many of these nocturnal insect species already had complex ears used mainly for intra-specific communication. Due to their physically small size, insects can produce high-frequency sounds most efficiently. Thus many species were ''preadapted'' for hearing bats. Examples would be certain beetles and bush crickets. Some nonhearing insects presumably evolved the capacity to hear the ultrasonic signals of bats. One well-documented case is that of the green lacewing, where the first fossil records of ears appeared after bats evolved. Many species of moths have ears tuned to bat signals, an adaptation that has evolved independently in different families and presumably in direct response to bat predation. All evidence points to a substantial selection pressure applied by bats on nocturnal insects. With the preoccupation of hearing mechanisms to avoid predation, other responses of nocturnal insects to echolocating bats might be overlooked. One example could be the advantage for nocturnal insects to occupy the ''clutter zone'' near or in vegetation, which would mix echoes from the prey with those of clutter. [Work supported by the Danish National Research Foundation.]

WEDNESDAY MORNING, 17 MARCH 1999 ROOM MA001, 10:20 A.M. TO 12:20 P.M.

Session 3aABb

Animal Bioacoustics: Evolution in Hearing and Sound Production II

Darlene R. Ketten, Cochair
Department of Biology, Woods Hole Oceanographic Institution, Woods Hole, Massachusetts 02543

Lee A. Miller, Cochair
Center for Sound Communication, Institute of Biology, Odense University, DK-5230 Odense M., Denmark

Invited Papers

10:20

3aABb1. Temporal resolution in birds and the perception of complex sounds. Robert J. Dooling (Dept. of Psych., Univ. of Maryland, College Park, MD 20742), Marjorie R. Leek (Walter Reed Army Medical Ctr., Washington, DC 20307), and Micheal L. Dent (Univ. of Maryland, College Park, MD 20742)

On many measures of temporal processing, including maximum and minimum temporal integration and duration discrimination, birds show sensitivities similar to those of humans and other mammals. More recent studies on difference limens for short duration tones, discrimination of gaps in sinusoidal markers, and detection of a mistuned harmonic, however, indicate that birds are much more sensitive than humans to certain temporal aspects of complex sounds. Further explorations of auditory temporal analysis by budgerigars (*Melopsittacus undulatus*) are described here, using sets of harmonic complexes with identical long-term spectra but with temporal waveforms differing either in envelope shape or fine structure. Behavioral discrimination and masking data using these temporal complexes show a high degree of temporal resolving power by the avian auditory system. These findings will be discussed in the context of previous studies on temporal modulation transfer functions and temporal windows in the budgerigar. In aggregate, these results strongly support the long-held belief that birds are more sensitive than humans and other mammals to temporal aspects of complex acoustic signals. [Work supported by NIH DC00198.]

10:50

3aABb2. Audiogram, morphological contraints, environmental acoustics, and adaptation. Wolfgang Plassmann and Evelyn Glaser (Dept. of Zoology, J. W. Goethe Univ., Frankfurt/Main, Germany)

Phylogenetic contraints are a severe restriction on the morphological diversity of the peripheral auditory system in mammals. In order to investigate problems of sensory adaptation under selective pressure, one has first of all to show in a model analysis the potential variance of the system and physiological consequences resulting from these variances. On the basis of these theoretical considerations, morphological investigations, and physiological measurements, an attempted explanation of given auditory systems can be offered based on additional field observations. Following this line of argument, the subsequent topics will be adressed: (a) size and allometric relations of middle and inner ear structures will be presented; (b) consequences of morphological size and changes of allometric relation for the audiogram will be discussed by means of theoretical models and experimental studies; (c) sound propagation properties of different environments such as desert, grassy plain, and forest will be demonstrated. Based on these data, possible selective pressure on the peripheral auditory system in various habitats will be discussed in relation to audiograms, vocalization, and abiotic sound.

11:20

3aABb3. Acoustic fatheads: Parallel evolution of underwater sound reception mechanisms in dolphins, turtles, and sea birds. Darlene R. Ketten (Woods Hole Oceanogr. Inst., Woods Hole, MA 02543 and Harvard Med. School, Boston, MA 02114, dketten@whoi.edu), Connie Merigo, Elisabeth Chiddick, Howard Krum (New England Aquarium, Boston, MA 02114), and Edward F. Melvin (Univ. of Washington, Seattle, WA 98105)

Dolphins lack conventional external ear canals, seal ear canals vary widely in size and patency, and sound conduction mechanisms in aquatic birds and turtles are virtually unknown. In this study, computerized tomography (CT) and magnetic resonance imaging (MRI) were used to map densities of tissues associated with the outer, middle, and inner ears of three dolphin, two seal, two turtle, and two sea-bird species. Three-dimensional reconstructions of scan data were used to determine species-specific geometry of tissue groups connected to the middle ear or surrounding the ear canal. The analyses show bundles of coherent fatty tissues emerging from the middle ear in all species examined. Densities of these fats are similar across species and are consistent with sound speeds near that of sea water. In seals and birds, these fats sheathed the external auditory canal. In turtles, the fats formed a discrete column communicating with the surface of the head. In dolphins, the fats formed three distinct bundles: two directed anteriorly along the lower jaw with a third projecting laterally. These findings suggest that all four groups evolved parallel soft tissue mechanisms that act as low impedance channels for underwater sound. [Work supported by Mellon Foundation, Seaver Institute, and Office of Naval Research.]

11:40

3aABb4. The upper frequency range in pigeon hearing: Response properties in auditory nerve and cohlear nucleus—is tuning different in birds? Jean W. Th. Smolders, Marcus Mueller, and Rainer Klinke (Physiologisches Institut III, Theodor-Stern-Kai 7, 60590 Frankfurt am Main, Germany, klinke@em.uni-frankfurt.de)

Information on responses of auditory nerve fibers in birds is generally limited to the low and mid-frequency ranges of hearing, due to anatomical constraints using the standard ganglion cell approach through the opened tympanic recess. Intracranially recorded responses of single units from the auditory nerve and the overlying cochlear nuclei in the pigeon (Columba livia) were compared to those recorded from the ganglion. Characteristic frequencies (CFs) of auditory units ranged from 0.08–5.7 kHz with intracranial compared to 0.06–1.6 kHz with intrascalar recordings. Response properties were qualitatively and quantitatively comparable in the overlapping CF ranges (0.08–1.6 kHz). Mean spontaneous firing rate decreased monotonically with CF. The CF thresholds were lowest (0–5 dB SPL) in the CF range 0.6–1.5 kHz. Mean sharpness of tuning (Q10 dB) varied nonmonotonically with CF, with a maximum near 2 kHz. In addition, Q10 dB of pigeon auditory units up to CFs of 2 kHz was much higher than that of gerbil *(Meriones unguiculatus)* primary fibers in the same CF range, recorded in the same setup. As it is highly improbable that mechanical tuning in birds would by far exceed that in mammals, this finding is further evidence for a difference in avian and mammalian tuning mechanisms. [Work supported by the DFG, SFB 269.]

Contributed Paper

12:00

3aABb5. Adaptations for hearing in background noise. Georg M. Klump, Ulrike Langemann, Ingo Hamann, and Andreas Nieder (Institut fuer Zoologie, Technische Universitaet Muenchen, Lichtenbergstr. 4, D-85748 Garching, Germany, Georg.Klump@bio.tum.de)

Acoustic communication in the natural environment is greatly affected by the ubiquitous background noise. Therefore, vertebrates have evolved mechanisms to efficiently cope with auditory masking. Spectral filtering of the acoustic input is one possibility to improve signal detection. In addition, communication efficiency can be enhanced by exploiting the amplitude fluctuations in background noise. This improvement of signal detection has been termed ''comodulation masking release'' (CMR). CMR has two components: (1) release from masking within the spectral filter (i.e., a critical band) centered on the signal and (2) release from masking by comparison of correlated amplitude fluctuations (i.e., comodulation) across separate spectral filters. An excellent animal model for studying CMR is the European starling, a songbird exhibiting a temporal resolution and frequency selectivity in its auditory system that is similar to the human's processing performance. Psychoacoustic experiments in starlings show a considerable CMR both within and across spectral filters. Furthermore, the range of envelope frequencies is an important determinant of the amount of CMR. Neurophysiological data recorded in the starling's auditory forebrain reveal that the temporal encoding of the stimulus envelope within auditory filters is a major factor determining the amount of CMR. [Work supported by the DFG, FG Hoerobjekte.]

Session 3aAOa

Acoustical Oceanography: Innovations in Fish and Plankton Acoustics III (Poster Session)

Kenneth G. Foote, Chair
Institute of Marine Research, P.O. Box 1870, Nordnes, N-5024, Bergen, Norway

Contributed Papers

All posters will be on display in the Poster Gallery from Monday to Wednesday, 15–17 March. Authors will be at their posters on Wednesday, 17 March. To allow contributors an opportunity to see other posters, contributors of odd-numbered papers will be at their posters from 8:00 a.m. to 10:00 a.m. and contributors of even-numbered papers will be at their posters from 10:00 a.m. to 12:00 noon.

3aAOa1. Comparison of two *in situ* tuna target strength measurement methods. Arnaud Bertrand and Erwan Josse (ORSTOM, BP 70, 29280 Plouzane, France, arnaud.bertrand@orstom.fr)

Two approaches were developed for *in situ* tuna TS measurement in French Polynesia. One consists of coupling split beam TS measurement with sonic tracking of tagged fish. The other one consists of TS measurement on tuna aggregated close to a Fish Aggregating Device. The first method was used on well-identified fish, swimming freely in their environment and allowing observation of the effect of fish behavior on TS up to 500 m of depth. The second method was applied on juvenile fish located close to the surface. In this case, fish were not individually identified and a fish sample was caught by trolling line in order to determine the length and species composition of the aggregation. Both methods are complementary and results are similar according to body length.

3aAOa2. Modeling the target strength of *Meganyctiphanes norvegica*. David T. I. Francis (School of Electron. and Elec. Eng., Univ. of Birmingham, Edgbaston, Birmingham B15 2TT, UK, francist@ee-admn.bham.ac.uk), Tor Knutsen, Kenneth G. Foote (Inst. of Marine Res., N-5024 Bergen, Norway), and Lucio Calise (Centro Marino Internazionale, I-09072 Torregrande (OR), Italy)

The euphausiid *Meganyctiphanes norvegica* is modeled as a fluidlike body having the actual shape of the head and thorax, as reconstructed from dorsal and lateral views recorded with a video camera with macrolens. The mass density has been measured for individual specimens in a density-gradient column, and the longitudinal-wave sound speed in the body, estimated from the measured sound speed through an assemblage of animals in a velocimeter. Theoretical target strength spectra are computed by the boundary element method at a number of discrete frequencies spanning the range 25 kHz to 3.2 MHz. [Support by the following is acknowledged: EU through RTD Contract No. MAS3-CT95-0031, Norwegian Research Council through Grant No. 113809/122, and Bergen Large-Scale Facility (LSF) for Marine Pelagic Food Chain Research.]

3aAOa3. Target strength spectra of swim-bladdered fish. Kenneth G. Foote (Inst. of Marine Res., P.O. Box 1870 Nordnes, N-5024 Bergen, Norway) and David T. I. Francis (Univ. of Birmingham, Edgbaston, Birmingham B15 2TT, UK)

Swim-bladdered fish are modeled by the actual shape of the swimbladder as determined from microtomed sections. Target strength spectra are computed for specimens of pollack (*Pollachius pollachius*) and saithe (*Pollachius virens*). Results obtained with both the Kirchhoff approximation and boundary-element method at each of four ultrasonic frequencies are compared with each other and with measurements of target strength of the same specimens before swim bladder morphometry. [Partial support of the EU through RTD Contract No. MAS3-CT95-0031 is acknowledged.]

3aAOa4. Broad-scale volume backscattering strength measurements in the Black Sea. Erhan Mutlu, Ali C. Gucu, and Ferit Bingel (Inst. of Marine Sci., P.O. Box. 28, 33731, Erdemli, Icel, Turkey)

Enhanced echograms of high-frequency sound (120 and 200 kHz) from entire tracklines surveyed during summer and winter of 1991–1994 were evaluated to observe volume backscattering in the Black Sea. Echo intensities were filtered through two thresholds for distinguishing suspended scatterers from active swimmers (fish). It was postulated that the backscattering by the suspended matters was associated with bathymetry, seasonal stratification and different levels of mixing of water, and daily migration of zooplankton. The scattering was layered in association with the physical structure in the open water. As bottom depth was shoaled, the vertical structure became more homogenous. Biological scatterers were diversified with zooplanktoners and pelagic fish (anchovy and sprat). Copepod and gelatinous organisms (comb-jelly and moon jellyfish) appeared to be responsible for the zooplanktonic scatterers. Changes in seasonal and diurnal migrational patterns of fish were investigated. During the summer, pelagic fish schools were observed in an offshore area, whereas in winter the schools were confined to the coastal area. In regard to the schooling density, higher concentrations were found in winter.

3aAOa5. Wavelet decompositions versus singular value decomposition (SVD) in a fish target strength estimation. Marek Moszynski and Andrzej Stepnowski (Dept. of Acoust., Tech. Univ. of Gdansk, Narutowicza 11/12, 80-952 Gdansk, Poland, marmo@pg.gda.pl)

The fish target strength estimation when using acoustic echoes from a single-beam echosounder is possible after solving ill-conditioned equations where probability density functions (PDFs) of echo level, target strength, and beam pattern are involved. The modified singular value decomposition (SVD) algorithms are typically used in such cases. Unfortunately, this technique often leads to artifactual modes in solution due to Fourier nature of underlying eigenfunctions. The expectation maximization smoothing (EMS) method is used to improve smoothness of solution but by the cost of increasing the time of computation of estimates. D. L. Donoho (1995) proposed the wavelet-vaguelette decomposition (WVD) as

being well suited for solving ill-conditioned equations with inhomogeneous functions. This concept was extended to fish target strength estimation and obtained results were compared to SVD performances.

3aAOa6. Gas cavities in phytoplankton. Dmitry A. Selivanovsky, Igor N. Didenkulov (Inst. of Appl. Phys., 46 Ulyanov St., Nizhny Novgorod, 603600, Russia), and Pavel A. Stunzhas (Shirshov's Inst. of Oceanology, Moscow, 117851, Russia)

Acoustical and related properties of phytoplankton suspensions were investigated in laboratory conditions and *in situ*. A review of studies is present. It was found that cells have gas cavities which allow them to keep a neutral buoyancy. Under sharp compression gas cavities dissolve and recover only under the light exposition. Such properties can explain an anomalous migration of some sound scattering layers. The use of the compression/decompression method allowed us to find gas cavities in blood erythrocites also. The 6.5-MHz acoustic backscattering from phytoplankton suspensions was applied for characterization of reverberation level under the natural condition and compression (up to 5 atm), which allowed us to evaluate a relative volume of gas cavities in cells. Gas cavities increase an acoustical cross section by 2–3 orders. A dispersion of sound velocity in phytoplankton suspensions with the phase and the resonance methods (from 200 Hz to 11 MHz) for six kinds of living cell suspensions was also studied. Both the increase and decrease of sound velocity dispersion with frequency was observed. The effect is different for cells of different kinds. [Work supported in part by RFBR, Russia.]

3aAOa7. Modeling considerations for acoustic scattering by fluidlike elongated zooplankton: Model intercomparisons and recommendations for euphausiids and copepods. Timothy K. Stanton and Dezhang Chu (Dept. of Appl. Ocean Phys. and Eng., Woods Hole Oceanogr. Inst., Woods Hole, MA 02543-1053)

Predictions of acoustic scattering by fluidlike elongated zooplankton are made using the deformed cylinder model and Distorted Wave Born Approximation over a wide range of animal size, shape, material property inhomogeneities, and orientation, as well as acoustic frequency. Each shape represents a digitized form of the shape of a euphausiid or copepod at low-, medium-, and high-resolution sampling of the shape (e.g., at low resolution, a straight smooth finite cylinder is used and at high resolution, a rough tapered bent finite cylinder is used). The results are analyzed in order to determine the conditions under which the various degrees of complexity in modeling the scattering are required. For example, the predictions illustrate that for modeling the scattering for animals near broadside incidence, relatively simple models can be used (smooth homogeneous bodies). However, for animals off broadside, which can be the case for downward-looking echosounders insonifying euphausiids and copepods, roughness and sometimes inhomogeneities must be used to model the scattering accurately (roughness effects dominate scattering well off broadside). Comparisons are made with laboratory data involving euphausiids, shrimp, and copepods. [Work supported by ONR.]

3aAOa8. Inference of material properties of zooplankton from acoustic and conductivity measurements. Dezhang Chu (Dept. of Appl. Ocean Phys. and Eng., Woods Hole Oceanogr. Inst., Woods Hole, MA 02543) and Peter Wiebe (Woods Hole Oceanogr. Inst., Woods Hole, MA 02543)

In order to infer correctly biological information from raw acoustic data, various acoustical models have been developed and much progress has been made both in laboratory experiments and field applications. However, the acoustic properties of biological scatterers, such as sound-speed and density, have a profound influence on the target strength estimate or volume scattering strength. A 1%–2% variation in sound speed and density can lead to an error in target strength prediction by as much as 20 dB or a tenfold bias in biomass estimate, which could be much greater than that due to the choice of different acoustic models. There is a dearth of information about the material properties of the live zooplankton because measurement of them is difficult. An instrumented chamber was used to collect simultaneously acoustic and conductivity data with and without the presence of live zooplankton. The acoustic measurement characterizes both the back- and forward-scattering patterns, while the conductivity measurement provides an estimate of the fraction of volume the animals occupy (volume fraction). The combined information can then be used to infer the material properties of the animal. The experimental results will be presented and discussed. [Work supported by NSF.]

3aAOa9. Digital transducer, novel technology for acoustical oceanography and fisheries research. William Acker, Dan Wiggins (BioSonics, Inc., 4027 Leary Way NW, Seattle, WA 98107, bio@biosonicsinc.com), and Janusz Burczynski (BioSonics Europe, 54036 Marina di Carrara (MS), Italy)

Novel digital transducer architecture designed and produced by BioSonics Inc. offers many advantages over older analog designs. By digitizing the signal at the transducer element, the cable-coupled noise is eliminated. The signal is sampled at a high rate and accuracy (0.13%), and wide instantaneous dynamic ranges (132 dB). This allows simultaneous capture of extremely small and large echoes (single plankton specimen or bottom return) with no loss in detail or signal saturation. The data acquisition system is virtually automatic since most of the decisions are done by software. Row data is stored on PC hard drive. Data acquisition and data analysis software packages are user friendly and operate in Windows™ environment. Many data processing tools are already developed as separate implementaiton of various algorithms. Digital transducers have already been successfully applied in various field projects in both marine and fresh waters: (i) monitoring and estimates of fish and plankton, (ii) fish tracking, and (iii) bottom plants estimate and seabed classification. The digital sonar is available in various packages and it can be installed on different platforms as portable systems for boats and ships, fixed platforms on dams, and in river in systems. The digital transducers are available in a wide range of frequencies (38 kHz to 1 MHz), in a single, dual, or split beam configurations.

3aAOa10. Spheres for calibrating high-frequency broadband echo sounders. Kenneth G. Foote (Inst. of Marine Res., P.O. Box 1870 Nordnes, N-5024 Bergen, Norway), David T. I. Francis (Univ. of Birmingham, Birmingham B15 2TT, UK), Hilde Furset, and Halvor Hobaek (Univ. of Bergen, N-5007 Bergen, Norway)

The notion of standard-sphere broadband calibration [Dragonette *et al.*, J. Acoust. Soc. Am. **69**, 1186 (1981)] is being realized for a new echo sounding system that spans the seven-octave range 25 kHz to 3.2 MHz. Spheres formed of tungsten carbide with 6% cobalt binder, with 10- and 20-mm diameters, have been measured in the laboratory to determine their backscattering spectra over the approximate frequency ranges 0.85–1.3 MHz and 2.9–3.6 MHz. This allows exploration of the wave number radius (ka) product over the nominal ranges 18–28, 36–56, 61–75, and 122–150. Comparison with theoretical expectation, as derived from the standard modal solution using published values for the material properties, is quite good. Confidence in the computations thus enables favorable regions of the backscattering spectra to be sought and exploited in choosing optimal diameters, as has earlier been the case with spheres for calibrating resonant transducers. In the course of checking computations, it was discovered that two independently developed numerical codes yield values

for the backscattering cross section that agree to within 1 part in 10 000 to better than one part in 1 000 000 for ka of the order of 100. [Partial support of the EU through RTD Contract No. MAS3-CT95-0031 is acknowledged.]

3aAOa11. Shark and salmon movement measured by tracking radar-type acoustic transducers. John Hedgepeth, David Fuhriman (BioSonics, Inc., Seattle, WA), Robert Johnson, David Geist (Battelle Memorial Inst., Richland, WA), Norm Bartoo, David Holts (Natl. Marine Fisheries Service, La Jolla, CA), Tim Mulligan, and George Cronkite (Dept. of Fisheries and Oceans, Nanaimo, BC, Canada)

Studies of fish behavior have used a methodology called the tracking transducer. The principle of tracking radar, aligning the antenna beam with a target, was applied with an acoustic split-beam transducer and dual-axis rotators for tracking individual fish over long periods of time. Deviation of the target from the beam axis produces a correction to point the axis toward the target. Initial studies with active acoustics have evolved an acoustic tag tracking method that is proposed for tracking both juvenile salmon and pelagic sharks. The major advance is that active and passive radar-type tracking can be combined in the same instrument. The tracking transducer was first used at Ice Harbor Dam, Snake River, 1995, and in 1996, at The Dalles Dam, Columbia River. Two tracking systems were used to triangulate a small acoustic transmitter in salmonid fish at Lower Granite Dam on the Snake River, Washington. Recently, adult salmon, returning to the Fraser River, were tracked to measure avoidance to surveying vessels. The feasibility for tracking sharks was shown at the Tacoma, Washington Point Defiance Aquarium. A proposed method of simultaneously tracking sharks with echoes and using acoustic tags will allow behavior, abundance, and associated pelagic assemblages to be determined.

3aAOa12. Mechanoreception for food fall detection in deep sea scavengers. Michael Klages (Alfred-Wegener-Inst. for Polar- and Marineresearch Postfach 12 01 61, 27515 Bremerhaven, Germany) and Sergey I. Muyakshin (Inst. of Appl. Phys., Nizhny Novgorod, 603600, Russia)

Although knowledge about functional principles of deep-sea ecosystems is rather scarce, it is assumed that the energy supply for scavengers is restricted to large food falls of dead vertebrates. It is generally accepted that chemoreception is one of the major tools for marine organisms to detect food sources. However, another major source of information may come from hydroacoustical feeding noises produced by scavengers appearing on a cadaver reached the seafloor. The aim of the present study was to investigate whether scavenging crustaceans—pandalid shrimps Pandalus borealis—are able to detect such rare food fall events via mechanoreception or not. These results are based on 228 single experiments indicating that these animals possess the sensitivity to the particle displacement of 0.1–10 mkm in frequency range 30–250 Hz. Therefore, acoustic feeding noises offer a possibility for animals to detect such rare events but only at distances of a few meters. At such small distances chemoreception is presumably more important. However, based on theoretical calculations on the relevance of various types of waves, originating on the water-sediment interface from any object falling on the seafloor, it is proposed that such ''micro seismic events'' may allow resting scavengers even some hundred meters away the detection of this event, most likely followed by chemoreceptive tracking.

3aAOa13. Echogram noise quantification with application to herring observations. Rolf J. Korneliussen (Inst. of Marine Res., P.O. Box 1070, Nordnes, N-5024 Bergen, Norway, rolf@imr.no)

Pushing the limits of scientific echo sounders involves considerations of noise, which is inherently frequency dependent. Suprisingly, perhaps, there is also a dependence on bottom depth. In this work, noise is quantified by measurement for a standard echo sounder, the EK500, at 18, 38, 120, and 200 kHz. Use of empirical relations of noise as a function of range to reduce echogram noise is described in general, and illustrated in particular for data collected on Norwegian spring-spawning herring (Clupea harengus) when wintering in the Vestfjord system. [Work supported by the Norwegian Research Council through Grant No. 113517/120.]

3aAOa14. Preliminary description of swimming activity and estimation of swimming speed of saithe (*Pollachius virens*) at one location in the North Sea. Jens Pedersen (Danish Inst. for Fisheries Res., North Sea Ctr., P.O. Box 101, DK-9850 Hirtshals, Denmark, jp@dfu.min.dk)

Individual saithe were tracked with a split-beam echosounder, while the vessel was drifting, in the area around Eigersundbank in the North Sea and their swimming speed estimated. The average swimming speed was approximately 4 and 1 body lengths per second for small saithe (20–30 cm) and saithe >70 cm, respectively, and a significant inverse relationship between length of the saithe and swimming speed was found. There was clear evidence of diurnal variation in swimming speed of small saithe, as the swimming speed was significantly higher during night (18–06 h) than during day (06–18 h). The number of observations on saithe >70 cm was too small to compare day and night swimming speeds. Although the results indicate higher swimming speeds of saithe in the demersal layer compared to pelagic saithe, significant differences were not found. The duration of acoustic observation time was 36–56 min per 4-h sampling interval during the 24-h cycle. A total of 278 series of saithe were selected, which, according to selection criteria, were accepted as representing tracking of single fish over two pings or more. The species identify of the targets tracked acoustically was verified by trawling in the layers investigated.

Session 3aAOb

Acoustical Oceanography and Underwater Acoustics: Acoustic Tomography and Thermometry I

Uwe Send, Cochair
Institut für Meereskunde, University of Kiel, Düsternbrooker Weg 20, 24105 Kiel, Germany

Robert C. Spindel, Cochair
Applied Physics Laboratory, University of Washington, Seattle, Washington 98105, USA

Invited Papers

8:00

3aAOb1. Meddies and front detection by acoustic tomography. Fabienne Gaillard (Laboratoire de physique des océans—IFREMER, BP 70, 29280, Plouzané, France, fabienne.gaillard@ifremer.fr)

The CAMBIOS experiment was defined within the CANIGO project as an observing array for the Canary basin. A pair of 400-H acoustic tranceivers set up in the middle of the basin provided a 9-month reciprocal series of arrival amplitude versus time sequences, starting in July 1997 and ending in March 1998. In the Canary basin the temperature and current field are perturbed in the upper layers by the meandering and branching of the Azores front, and at mid-depth by the transit of warm and salty coherent structures called meddies. The first analysis of the acoustic measurements will be presented here, with particular attention dedicated to the signature of the front and meddies, both on direct and reciprocal travel times. [Work supported by the MAST III programme under Contract No. MAS3-CT96-0060.]

8:20

3aAOb2. Resonant diurnal internal tides in the North Atlantic. Brian D. Dushaw (Appl. Phys. Lab., College of Ocean and Fisheries Sci., Univ. of Washington, Seattle, WA 98105) and Peter F. Worcester (Univ. of California at San Diego, La Jolla, CA 92093)

Using an acoustic tomography array located midway between Puerto Rico and Bermuda, enhanced diurnal tidal signals associated with the lowest internal-wave mode have been observed. These signals result from a diurnal internal wave with $O(500\text{-km})$ wavelength that is resonantly trapped between the shelf just north of Puerto Rico and the turning latitude, a distance of about 1100 km. The data obtained using the large acoustical array are consistent with the predicted Airy-function variation with latitude of diurnal internal waves near the turning latitude. The existence of this wave is a striking demonstration of the long spatial and temporal coherence of oceanic internal tides.

8:40

3aAOb3. Acoustic monitoring of the transport and temperature variability in the Strait of Gibraltar. Peter F. Worcester (Scripps Inst. of Oceanogr., Univ. of California at San Diego, La Jolla, CA 92093-0225, pworcester@ucsd.edu), Uwe Send (Univ. of Kiel, 24105 Kiel, Germany), Bruce D. Cornuelle, and Christopher O. Tiemann (Univ. of California at San Diego, La Jolla, CA 92093)

Three acoustic transceivers transmitted across the Strait of Gibraltar during April–May 1996 to determine the feasibility of using acoustic methods to measure the transport and average temperature in the Strait. The first arrivals, from ray paths confined to the (lower layer) Mediterranean water, give sum travel times that are remarkably stable, with a slow peak-to-peak variation of only about 3 ms over a two-week period, corresponding to an integrated temperature change of about 70 $\text{m}\,^{\circ}\text{C}$. The difference travel times from a path diagonal to the axis of the Strait show a peak-to-peak tidal variation of about ± 5 ms, corresponding to integrated currents parallel to the acoustic path of about ± 50 cm/s, which is consistent with estimates derived from a moored current meter array. One of the transceivers also had a two-element horizontal receiving array, to determine the feasibility of using arrival angle to measure the current perpendicular to the acoustic path. The measured phase differences are encouragingly similar to phase differences predicted using the current meter data. Later arrivals, from ray paths that sampled the (upper layer) Atlantic water, are much more complicated, in part due to the effects of the internal wave bores present in the Strait.

9:00

3aAOb4. AMOC: Acoustic monitoring of the ocean climate of the Arctic. Ola M. Johannessen and AMOC Group (NERSC, Edv. Griegsvei 3A, 5037 Solheimsviken, Norway and Geophysical Inst., Univ. of Bergen, Bergen, Norway, hanne.sagen@nrsc.no)

The overall objective of AMOC is to develop and design an acoustic system for long-term monitoring of the ocean temperature and ice thickness in the Arctic Ocean, including the Fram Strait, for climate variability studies and global warming detection. The unique combination of the underwater acoustic remote sensing with satellite remote sensing of the ice cover including modeling and data assimilation, in the predicted sensitive climate region of the Arctic Ocean, is perhaps the key solution to monitor global climate changes and early detection of global warming. AMOC has the following specific objectives: (i) Compilation and analysis of existing ocean and ice data from the Arctic Ocean. (ii) Simulation of present and future Arctic Ocean environment to be used as input to acoustic modeling. (iii) Simulation of present and future basin-wide acoustic propagation using natural variability and global warming scenarios to investigate the sensitivity of acoustic methods for global warming detection. (iv) Simulation of present and future acoustic propagation in the Fram Strait to investigate the sensitivity of acoustic methods for monitoring heat and volume fluxes in an area of strong mesoscale eddy activity. (v) Design of an optimal acoustic monitoring system for climate change detection in the Arctic.

9:20

3aAOb5. Sound-signal scintillation approach to acoustic monitoring of the heat and mass transport through the Fram Strait. Konstantin A. Naugolnykh (CIRES, Univ. of Colorado/ETL, NOAA, Boulder, CO 80303), Igor B. Esipov, Oleg B. Ovchinnikov, Yuri I. Tuzhilkin (N. Andreev Acoust. Inst., Moscow, 117036, Russia), and Ola M. Johannessen (Univ. of Bergen, Bergen, Norway)

The computation model of the sound-signal propagation in the Fram Strait environment is considered in application to remote acoustic sensing of the heat and mass transport. A 3-D sound-speed environment has been simulated with respect to the statistical features of the real cross section of the strait obtained from experimental data. The linear four-element transmission array and four-element receiving arrray with equally spaced elements are modeled. Travel time variations of the signals propagating across the strait related to temperature change are calculated and the methods of the temperature retrieval in the complex environment is discussed. Then the travel time perturbations of the sound signals produced by the advection of the small-scale inhomogeneities across the path are considered. The calculation of the time-lagged cross-correlation function of the acoustic field gives the transverse current velocity data. By combining the response from each transmitter–receiver pair in different ways, the transverse current profile is retrieved. Results obtained are used to estimate the potential accuracy of the acoustic sensing of the heat and mass transport through the strait cross section. [Work supported by Environmental and Climate Programme of EC, Project PL970338.]

9:40

3aAOb6. AMOC: Listen to the climate change? Hanne Sagen (NERSC, Edv. Griegsvei 3A, 5037 Solheimsviken, Norway, hanne.sagen@nrsc.no) and Ola M. Johannessen (Univ. of Bergen, Bergen, Norway)

Acoustical methods such as acoustic tomography and thermometry have proved their importance in future long-term monitoring of ocean climate. The scope of this presentation is to show how ambient noise can be used as additional information in a future acoustic monitoring system for the Arctic ocean. To our knowledge, no inversion of ambient noise characteristics to sea ice and ocean parameters has been attempted neither in the MIZ nor the interior of the Arctic Ocean. Key parameters in ocean climate monitoring in the Arctic are averaged ice thickness and averaged ocean temperature profiles. These parameters are very difficult and time demanding to measure by using point measurements, and unavailable using electromagnetic waves. Therefore, special attention has been paid to developing new concepts for measuring ocean stratification and averaged ice thickness. A new concept combining wave models, SAR data, and ambient noise recordings for retrieving the sea ice thickness and elastic parameters of the sea ice in MIZ are presented. Another concept is proposed for use in the MIZ and in the interior Arctic using averaged ambient noise frequency spectra to obtain information about the sea ice and ocean stratification.

10:00–10:20 Break

Invited Paper

10:20

3aAOb7. Acoustic studies of the large-scale ocean circulation. Dimitris Menemenlis (Jet Propulsion Lab., California Inst. of Technol., MS 300-323, 4800 Oak Grove Dr., Pasadena, CA 91109, dimitri@pacific.jpl.nasa.gov)

Detailed knowledge of ocean circulation and its transport properties is prerequisite to an understanding of the earth's climate and of important biological and chemical cycles. Results from two recent experiments, THETIS-2 in the Western Mediterranean and ATOC in the North Pacific, illustrate the use of ocean acoustic tomography for studies of the large-scale circulation. The attraction of acoustic tomography is its ability to sample and average the large-scale oceanic thermal structure, synoptically, along several sections, and at regular intervals. In both studies, the acoustic data are compared to, and then combined with, general circulation models, meteorological analyses, satellite altimetry, and direct measurements from ships. Both studies provide complete regional descriptions of the time-evolving, three-dimensional, large-scale circulation, albeit with large uncertainties. The studies raise serious issues about existing ocean observing capability and provide guidelines for future efforts.

Contributed Papers

10:40

3aAOb8. ATOC or Candide: Toward depth-averaged temperature maps of the North Pacific Ocean. Brian D. Dushaw and the ATOC Group[a] (Appl. Phys. Lab., College of Ocean and Fisheries Sci., Univ. of Washington, Seattle, WA 98105)

The ATOC Project has aquired trans-Pacific acoustic data from two acoustic sources: one located on Pioneer Seamount off the coast of California, the other located north of Kauai, Hawaii. Transmissions from these sources are detected by U.S. Navy SOSUS arrays located throughout the North Pacific. The time series of acoustic travel times from the Pioneer Seamount and Kauai transmissions are about 1 $\frac{1}{2}$ and 1 year long, respectively. Both time series have highly irregular sampling because of marine mammal protocols and temporary cable failures. These acoustic data are used to estimate ocean temperature accurately. At the time of writing this abstract, however, the overlap of the two time series is just beginning. The overlapping time series will for the first time allow estimates of temperature maps of the North Pacific basin using long-range acoustics because the acoustic paths from these sources criss-cross the North Pacific. This

talk will show the initial maps of depth-averaged temperature of the North Pacific Ocean derived using the time series to be collected through Fall 1998. [a] The Acoust. Thermometry of Ocean Climate (ATOC) Group is: A. B. Baggeroer, D. Menememlis [now at JPL], and C. Wunsch (MIT); T. G. Birdsall, K. Metzger (Univ. of Michigan); C. Clark (Cornell Univ.); J. A. Colosi (WHOI); B. D. Cornuelle, M. Dzieciuch [now at ABMF], W. Munk, P. F. Worcester (SIO); D. Costa (Univ. of California, Santa Cruz); B. D. Dushaw, B. M. Howe, J. A. Mercer, R. C. Spindel (APL-UW); A. M. G. Forbes (CSIRO, Hobart).

11:00

3aAOb9. Measurements of multi-megameter travel-time bias and coherence. M. Dzieciuch, P. Worcester (Scripps Inst. of Oceanogr., Univ. of California, San Diego, CA), T. Birdsall, K. Metzger (Univ. of Michigan), B. Howe, J. Mercer, and R. Spindel (Univ. of Washington)

The quality of ocean acoustic travel-time measurements depends on the coherence as well as the bandwidth of the signal. Ocean internal-wave fields are thought to be responsible for the loss of coherence in low-frequency acoustic signals. If the coherence bandwidth is less than the signal bandwidth, it is possible to consider sub-bands of the signal as separate measurements. The separate measurements can then be combined incoherently to improve the quality of the travel-time measurement. Theoretical work and computer simulations also predict that the travel-time of acoustic signals is biased by the ocean internal wave field. The path-integral theory for scattering predicts that the size of the travel-time bias depends on the logarithm of the center frequency of the acoustic signal, thus separate sub-bands would have different travel times and incoherent recombination would not be an optimal procedure. A recent experiment, in which two acoustic signals with different center frequencies were transmitted simultaneously, makes it possible to measure the bias experimentally and to determine the efficiency of sub-band averaging. Preliminary results suggest that the bias is about 50 ms at 3500-km range, which is roughly as large as expected.

11:20

3aAOb10. Reciprocal tomography between ATOC transmitters. James A. Mercer, Brian Dushaw, Bruce M. Howe, Robert C. Spindel (Appl. Phys. Lab., Univ. of Washington, Seattle, WA 98105), Peter F. Worcester (Univ. of California at San Diego, La Jolla, CA 92093), and Kurt Metzger (Univ. of Michigan, Ann Arbor, MI 48109)

The Acoustic Thermometry of Ocean Climate (ATOC) sound sources are located 8 miles north of Kauai, Hawaii and 50 miles west of Half Moon Bay, California. The sources are connected to shore-based electronics by undersea coaxial cables. Recent modifications in the shore-based electronics have permitted the ATOC transducers to serve as hydrophones as well as transmitters. Data collected over this 4-Mm reciprocal path will be presented and discussed in terms of current and internal wave effects. [Work supported by ONR.]

11:40

3aAOb11. Modal structure of low-frequency, broadband receptions at megameter ranges. Kathleen E. Wage, Arthur B. Baggeroer (Res. Lab. of Electron., MIT and Woods Hole Oceanogr. Inst., Woods Hole, MA 02543), and James C. Preisig (Woods Hole Oceanogr. Inst., Woods Hole, MA 02543)

Data from the Acoustic Thermometry of Ocean Climate (ATOC) experiment show that at 3515-km range, each low (axial) mode signal contains a series of arrivals, rather than a single dispersive arrival, which would characterize adiabatic propagation. Short-time Fourier transform (STFT) analysis demonstrates that this multipath structure exhibits frequency-selective fading and significant temporal variability. Despite the complexity of individual receptions, averaging the mode estimates for transmissions at successive four-hour intervals reveals some of the expected dispersion characteristics of a deep water channel. Although this evidence suggests that the modes retain travel-time information at megameter ranges, the complicated nature of the arrivals indicates that a better understanding of mode coupling due to internal waves is required for tomography and matched-field processing applications. This study investigates the temporal and frequency coherence of broadband modes by comparing PE simulations with the ATOC results. Since ambient noise and environmental uncertainty affect the accuracy of mode signal measurements for experimental data, this research also addresses certain practical issues and limitations involved in estimating mode coherence. [Work supported by ONR.]

12:00

3aAOb12. On the existence of nearly stable dynamics in long-range sound propagation through oceanic mesoscale structure. Michael A. Wolfson and Steven Tomsovic (Dept. of Phys., Washington State Univ., Pullman, WA 99164-2814, mwolfson@wsu.edu)

A dynamical system, motivated by ocean acoustic pulse propagation in the horizontal plane along the sound channel axis, is constructed using a potential derived from an idealized mesoscale eddy field. This problem is known to exhibit chaotic behavior in that rays are exponentially sensitive to both their initial condition and the position and strength of the individual eddies. The measure of chaos for the system has been expressed by deriving a Lyapunov exponent which determines the mean growth rate for the envelope of one of the elements of the stability matrix [M. A. Wolfson and F. Tappert, J. Acoust. Soc. Am. (to be published, 1998)]. However, the individual stability matrix elements are seen to fluctuate wildly from one ray to another. It turns out that many rays exhibit absolute traces of the stability matrix with values of $O(1)$ even at basin scale ranges. This implies that much of the dynamics involves only local rotations as the flow evolves in phase space. Estimates are presented for a range-dependent measure of this nearly stable dynamical feature. Its relation to tomographic inversions of some features of mesoscale eddy fields is discussed.

Session 3aBB

Biomedical Ultrasound/Bioresponse to Vibration: HIFU and Thermal Effects

Ronald A. Roy, Cochair
Department of Aerospace and Mechanical Engineering, Boston University, Boston, Massachusetts 02215, USA

Ibrahim Hallaj, Cochair
Applied Physics Laboratory, University of Washington, Seattle, Washington 98105, USA

Contributed Papers

8:00

3aBB1. Numerical simulation of the enhanced heat production in tissue due to the nonlinear character of high-intensity focused ultrasound (HIFU). Siegfried Ginter, Eckard Steiger, and Rainer Riedlinger (Inst. fuer Hoechstfrequenztechnik und Elektronik/Akustik, Univ. Karlsruhe, D-76128 Karlsruhe, Germany)

HIFU is used in thermotherapy to destroy tumors located deep in human tissue by heat. It is well known that HIFU is connected with the generation of higher-frequency components due to nonlinear steepening during propagation. An over-proportional heat generation in tissue occurs with enhanced power input. To obtain fundamental information about an optimal dosage of the applied ultrasound, simulations are necessary. A hot spot in healthy tissue must be avoided and a sufficient heat delivery in the tumor region must be guaranteed. Until now most numerical investigations of thermotherapy with HIFU have been carried out under the assumption of linearity. This means an essential underestimation of heat production. Here an improved model is introduced which enables accurate simulations, including nonlinearities. It consists of a set of nonlinear acoustic equations which ensure an accurate full-wave propagation modeling. A broadband absorption model of typical soft-tissue frequency-power-law character is included to obtain a nonlinear modeled heat source. The thermal behavior is described by a bio-heat-transfers-equation. The complete model is solved by means of a high-order FDTD scheme. Exemplary simulations illustrate the efficiency of this method.

8:20

3aBB2. Hyperthermia therapy using phase conjugation. Philippe Roux, Michael B. Porter, Hee C. Song, and William A. Kuperman (Marine Physical Lab., Scripps Inst. of Oceanogr., UCSD, 9500 Gilman Dr., La Jolla, CA 92093-0238)

One of the advantages of ultrasound phased-array treatments is the noninvasive manner in which ultrasonic energy, and then heat, can be delivered to the treatment volume. However, the heat generated in the medium induces variations in the sound speed, which affects the acoustic focusing and leads to strong effects such as self-focusing or self-defocusing of the sound beam. In this work, a numerical simulation is used to study coupled acoustic-heat propagation in tissue. By simultaneously modeling the propagation of acoustic waves and the diffusion of heat, it was possible to simulate quantitatively acoustic refraction induced by heat in the treatment volume. Finally, using phase conjugation, one procedure to control temperature and maintain the acoustic focusing at the initially desired focal point was developed.

8:40

3aBB3. Diagnostic ultrasound for two-dimensional temperature mapping in hyperthermia and laser-induced tissue coagulation. Hendrik Willig, Annette Pfennig, Volker Haenel, Bernhard Kleffner (Fraunhofer Inst. for Biomed. Eng., Ultrasound Dept., Ensheimer Str. 48, D-66386 St. Ingbert, Germany, willig@ibmt.fhg.de), and Karsten Schwerdtfeger (Universitaet des Saarlandes, Universitaetskliniken, 66421 Homburg, Germany)

Laser-induced tissue heating and coagulation is a common technique in minimally invasive surgery to achieve localized thermal tissue damage. Precision and efficiency of treatment could be improved markedly by noninvasive spatio-temporal temperature monitoring. A method for two-dimensional mapping of tissue temperature as well as tissue structural changes has been investigated *in vitro*. The algorithms are based on the temperature dependence of speed of sound and a combination of additional acoustical parameters in order to consider the expansion of the heated volume, creation of gas bubbles, and carbonization. An approach for motion compensation, as it is necessary for clinical application, will be described in short.

9:00

3aBB4. Noninvasive estimation of tissue temperature via ultrasound frequency shift using a narrow-band transducer. Seong-Wook Song, Koeng-Mo Sung (School of Elec. Eng., Seoul Natl. Univ., Seoul, Korea), Min-Joo Choi (Cheju Natl. Univ.), and Jun-Seok Lim (Sejong Univ.)

When applying the high power focused ultrasound to medical therapy, it is necessary to monitor the temperature change in tissue. Some methods have been proposed to measure this change noninvasively. One of those techniques measures the frequency changes in harmonics which are linear with the temperature changes. The linear coefficient has been defined with the fundamental frequency changes and the temperature changes. This measurement requires at least three harmonics, so that it requires a wideband transducer to estimate the fundamental frequency efficiently. This paper suggests a method to measure the temperature changes noninvasively with only one component of harmonics, under the condition that the proportional constant is defined such as the thermal expansion coefficient. It does not require the wideband transducer. Additionally, it shows the mutual relationship between thermal expansion coefficient, thermal frequency shift coefficient, and thermal speed change coefficient, which are defined in similar form.

9:20

3aBB5. Thermal effect of ultrasound enhancer for transdermal insulin delivery. E. J. Park and S. W. Yoon (Dept. of Phys., Sung Kyun Kwan Univ., 300 Chunchundong, Suwon 440-746, Kyungkido, Republic of Korea, swyoon@yurim.skku.ac.kr)

Ultrasound has been known as a good enhancer for transdermal drug delivery. However, major mechanisms in the ultrasound enhancer to improve the transdermal drug delivery were not well understood. In this

study a simple experiment was designed to simulate the human skin system with rat back skin. An unfocussed 1-MHz ultrasound transducer and a heating wire loop were used as enhancers. Transmitted amounts of insulin with the ultrasound enhancer were increased ten times more than those without any enhancer. The ultrasound enhancer also improved by 25% the enhancement of insulin transportation compared with that due to thermal effect solely by heating wire loop. It was also observed that rapid temperature increase with ultrasound more efficiently enhanced transdermal transport of insulin. The thermal effect of the ultrasound enhancer is suggested as a most likely mechanism for transdermal insulin delivery.

9:40–10:00 Break

10:00

3aBB6. Sound scattering and local heating from pulse-driven microbubbles. Sascha Hilgenfeldt (DEAS, Harvard Univ., 29 Oxford St., Cambridge, MA 02138, sascha@stokes.harvard.edu), Detlef Lohse (Univ. of Twente, 7500 AE Enschede, The Netherlands), and Michael Zomack (Schering AG, Clinical Development, 13342 Berlin, Germany)

Using a bubble dynamical model based on the Rayleigh–Plesset equation, it is shown that the experimentally observed spectra of sound emitted from diagnostic microbubble contrast agents under the action of short, strong ultrasonic pulses can be understood from the interplay of *enhanced sound emission* due to nonlinear bubble oscillations and *enhanced sound damping* due to the occurrence of high frequencies in the emitted spectrum. The latter effect counteracts the pronounced increases in the scattering cross sections in the regime of nonlinear bubble response. Sound absorption furthermore leads to highly localized heating of the liquid (e.g., blood) over a distance of several μm near the collapsing bubble. This temperature rise is, however, too brief and the heated liquid volume too small to be hazardous to the patient's health.

10:20

3aBB7. Numerical modeling of high-intensity focused ultrasound for hemostatic applications. Vera A. Khokhlova (Dept. of Acoust., Phys. Faculty, Moscow State Univ., Moscow 119899, Russia, vera@na.phys.msu.su), Peter J. Kaczkowski, and Lawrence A. Crum (Univ. of Washington, Seattle, WA 98105)

A promising therapeutic application of high-intensity focused ultrasound (HIFU) is hemostasis. In one possible hemostatic application, ultrasound induced heating will be used to stop bleeding during open surgery. To achieve substantial heat deposition on the surface of the bleeding organ, intense acoustic fields will be used, and therefore nonlinear effects on wave propagation in the coupling liquid between the transducer and the treated region must be taken into account. Moreover, nonlinearity can be used to increase the efficiency of heat deposition in shallow tissues by transforming wave energy to higher harmonics. Theoretical characterization of acoustic field is performed using a one-dimensional spherical wave model and the KZK equation. On-axis and off-axis waveforms, spatial distributions of harmonics, acoustic intensity, and heat deposition are calculated numerically in water and in tissue using a frequency-domain scheme. The influence of operating frequency, initial intensity, transducer aperture, amplitude shading, focal depth, and position of the water–tissue interface on acoustic propagation regimes and associated tissue heating is studied. For given absorption properties of the tissue and desirable spatial shape of the thermal lesion, an optimal set of transducer parameters and corresponding nonlinear effects are presented and discussed. [Work supported by DARPA, ONR, CRDF and RFBR.]

10:40

3aBB8. Effect of tone burst ultrasound in combination with PPAA (poly-propyl acrylic acid) on hemolysis of erythrocytes. Tyrone M. Porter, Pierre Mourad, Larry Crum (Appl. Phys. Lab., 1013 NE 40th St., Seattle, WA 98105), Niren Murthy, Alan Hoffman, and Pat Stayton (Univ. of Washington, Seattle, WA 98105)

In this study, high intensity focused ultrasound (HIFU) and PPAA (poly-propyl-acrylic acid) were combined at sublethal doses to achieve hemolysis of human erythrocytes. In a series of experiments, a suspension of erythrocytes (1A passive cavitation detection system) was utilized to monitor the acoustic emissions from the cell suspension during exposure to ultrasound. In the presence of PPAA, there is a significant increase in cavitation and hemolysis during ultrasound exposure at a *p*H of 6.1, but not at a *p*H of 7.4. PPAA is a *p*H-sensitive polymer, changing its conformation and its activity as the solution becomes more acidic, achieving its optimal active state at a *p*H of 6.1. The acoustic data and the activity of PPAA suggest that the polymer, in its active state, provides nucleation sites to the cell suspension and that cell/bubble interaction is the primary mechanism for cell damage.

11:00

3aBB9. The effects of temperature on the characteristics of the focal region in high-intensity focused ultrasound. Francesco P. Curra, Pierre D. Mourad, and Lawrence A. Crum (Appl. Phys. Lab., Univ. of Washington, Seattle, WA 98105)

The application of high-intensity focused ultrasound uses the transformation of ultrasonic energy into thermal energy to raise the temperature of tissue rapidly and induce necrosis of tumor cells. Targeting and control of the heated region and the amount of energy delivered are important issues. These numerical simulations couple sound propagation with the bio-heat equation to investigate tissue heating over time. The temperature rise affects both sound speed and attenuation. These, in turn, influence the spatial boundaries and magnitude of the ultrasonic time average intensity which, in turn, drives the temperature. In this model, the dependence of the sound speed and tissue attenuation on temperature is based on experimental results obtained in pig liver [Bloch *et al.*, Proc. 16th Intl. Cong. Acoust., Seattle, WA, 1065–1066 (1998)]. The results show a spatial shifting of the focal region toward the transducer accompanied by a reduction in the magnitude of the ultrasonic time average intensity depending upon the on-time of the transducer and the initial pressures at which it is driven. The temperature response follows the same behavior, with a spatial shift of the hottest spot and a decrease in its peak value, although thermal conduction tends to counteract the process. [Work supported by DARPA.]

11:20

3aBB10. High-intensity ultrasonic spectra in water and brain tissue. Kristian Jambrosic, Bojan Ivancevic (Faculty of Elec. Eng. and Computing, Unska 3, HR-10000 Zagreb, Croatia, kristian.jambrosic@fer.hr), and Igor Zoric (Faculty of Mining, Geology and Petroleum Eng., HR-10000 Zagreb, Croatia)

A common method of brain tumour surgery is using CUSA (cavitation ultrasonic surgical aspirator). While using CUSA, there is a strong focusing of the ultrasonic field within the cranium. This can cause damage to healthy brain tissue. Therefore, the ultrasonic field intensity at the critical spots must be measured. These measurements cannot be made *in vivo*, thus raising the need for a substitute model. In this paper, frequency spectra of the CUSA probe was measured at its working frequency of 25 kHz in an oval container (simulating the cranium). The measurement was made at few field intensities, using the B&K hydrophone in the container, and the B&K microphone outside it. The medium temperature has been controlled. Calf brain tissue, physiologically similar to human, was used as a substitute model. The same measurement was repeated in water to examine the spectrum difference in high- and low-attenuation media. During the measurement, the occurrence of the cavitation was observed by spectra changes.

Session 3aEA

Engineering Acoustics and Underwater Acoustics: Recent Advances in Underwater Transducers I

Dehua Huang, Cochair
Arichell Technologies, Inc., West Newton, Massachusetts 02165, USA

William J. Marshall, Cochair
BBN Systems and Technologies, Union Station, New London, Connecticut 06320, USA

Lars Kofoed, Cochair
Brüel & Kjær, 2850 Nærum, Denmark

Chair's Introduction—7:55

Invited Papers

8:00

3aEA1. A new deep-submergence broadband multiport underwater sound transducer. John L. Butler and Alexander L. Butler (Image Acoustics, Inc., 97 Elm St., Cohasset, MA 02025)

The back radiation from a transducer is normally isolated from the front radiation in order to avoid cancellation due to the out-of-phase nature of the back radiation. However, this isolation is difficult to achieve if the transducer is broadband and operated under significant ambient pressure encountered in deep submergence applications. The multiport transducer (U.S. Patent 5,184,332) offers a solution to this problem by using free-flooded resonance chambers on both the front and back surfaces of the transducer. It will be shown that with these chambers the acoustic pressure cancellation is avoided and the pressure now adds at frequencies between the two resonance's (which set the bandwidth of the system). A multiport design for a coaxial set of cylinders driven by the two surfaces of a piezoelectric ring transducer will be presented. Results from finite element and circuit analysis models will be presented and shown to agree with measured results on the model fabricated by Massa Products Corporation, Hingham, MA. [Work supported in part by an SBIR through NUWC, Newport, RI.]

8:20

3aEA2. 1-3 piezocomposite underwater transducers. Thomas R. Howarth (Naval Res. Lab., Washington, DC 20375-5350, howarth@nrl.navy.mil)

After over a decade of research (including application in medical ultrasonic products), 1-3 piezocomposite materials are now being utilized in a variety of U. S. Navy underwater transducer applications. This paper will survey a selection of current transducers that feature 1-3 piezocomposites as the active elements. The overview will chronologically present the transducers as they have evolved from the initial design of shaped aperture transceivers for acoustical environmental studies followed by a broadband projector for synthetic aperture sonars. Other transducers include cylindrical- and spherical-shaped constant beamwidth transducers (CBT), a parametric array, subbottom profilers, and acoustic calibration standards. An advanced design featuring an integrated accelerometer, acoustic pressure sensor, and actuation layer will be included. The 1-3 piezocomposite material attributes that are making these transducers useful for underwater applications will be discussed. The direction of future 1-3 piezocomposite-based underwater transducers will conclude the presentation. [This research was supported by the Office of Naval Research Code 333.]

8:40

3aEA3. Biased lead zirconate titanate as a high-power transduction material. James M. Powers (Newport Div., Naval Undersea Warfare Ctr., Newport, RI 02841), Mark B. Moffett (Georgia Tech Res. Inst., Atlanta, GA 30318), Michael D. Jevnager (Naval Undersea Warfare Ctr., Newport, RI 02841), and Stephen S. Gilardi (Interface Eng., Mystic, CT 06355)

High-power, underwater transducers using polarized piezoelectric ceramic material are usually limited in drive amplitude so that depolarization does not occur, but application of a dc bias field in the polarization direction allows the use of higher ac drive fields. To demonstrate the feasibility of a biased operation as a means of achieving higher power, a thin-walled, spherical-shell transducer was constructed of Channel 5800 and tested in NUWC's Acoustic Pressure Tank Facility. The transducer was successfully driven to 33 V/mil (1.3 MV/m) rms with an accompanying bias field of 31 V/mil (1.2 MV/m) and a hydrostatic pressure of 1400 psig (9.65 MPa). The source level was 206 dB//mPa-m at 61 kHz, corresponding to a 10-dB improvement over the usual Navy standard unbiased drive limit of 10 V/mil (0.4 MV/m) rms. [Work supported by ONR.]

9:00

3aEA4. Steered beams using a spatially phased array. W. Jack Hughes (Appl. Res. Lab., Penn State Univ., P.O. Box 30, State College, PA 16804, wjh2@psu.edu)

A spatially phased transducer array has been developed and tested that can form a steered beam without the need for electronically applying phase shifts to an array of elements. In its simplest form, the transducer consists of two channels from spatially shaped cosine and sine apertures, where the sine channel is shifted 90 degrees and then combined with the cosine channel. The transducer produces a beam steered to a desired angle at a specific design frequency in either receive or transmit operation. Several have been fabricated and tested using low-lateral mode transducer materials such as polyvinylidene flouride (PVDF) and 1-3 PZT composite, and electroplated electrodes to form the cosine and sine apertures. The appearance of the electrode has led to calling this a ''doily'' transducer array. Beams were formed that were steered as far as 54 degrees with typical sidelobe levels of −20 dB. The apertures were also geometrically shaped to supress sidelobes along the steering axis. [This work was supported by Kam Ng of ONR.]

9:20

3aEA5. Recent low-frequency sonar transducers and arrays. Didier Boucher (DCN Ingénierie centre Sud, sous-direction lutte sous la mer, BP 30, 83800 Toulon Naval, France)

Research in the field of high-power, low-frequency underwater transducers has been sustained by advances in submarine noise reduction and the promise of long-range detection at low frequencies. The earliest idea came up to use the already available passive towed array sonars as receive arrays in conjunction with additionally towed sound sources. The frequency of the active adjunct idea was of course given by the existing passive arrays. Very promising trials at sea, even in the shallow water environment, soon led to the consideration of full low-frequency active sonar systems (LFASS). Those have now been investigated for nearly two decades. With the emergence of new high-power transduction materials and the rapid evolution of fast computers and powerful modeling techniques, this research field has been fertile ground for transduction innovation. Specifically, high-power transducer developments include performance improvements to conventional piezoelectric ceramic projectors, progress in the exploitation of new active driver materials, and advances in transduction design techniques. While high power, low frequency, wide bandwidth, and high efficiency remain the primary performance objectives behind these developments; low weight, small size as well as medium to deep submergence are desirable physical attributes that require equal attention by the designer. This paper emphasizes the key characteristics of two sea-proven concepts for LFASS: Janus Helmholtz transducers and multihead arrays (international patents). The attention will be particularly focused on measured values of the sound sources. Finally, this paper addresses future trends in terms of sonar array designs for LFASS.

9:40

3aEA6. Recent developments of underwater acoustic transducers in China. Houqing Zhu (Inst. of Acoust., Chinese Acad. of Sci., Beijing 100080, PROC, zhu@tank.ioa.ac.cn)

Some of the recent developments of underwater acoustic transducers in China, such as the Rare-Earth giant magnetostrictive (Terfenol-D underwater acoustic transducers (including 1-kHz free-flooded modified IV flextensional transducer, the 890-Hz free-flooded Terfenol-D hexagonal transducer, and the 2.7-kHz Tonpilz Terfenol-D transducer), the 500-Hz flexible disk piezoelectric high-power transducer, the 450-kHz 2-2 piezoelectric composite underwater acoustic transmitting transducer, the 1-3 piezoelectric composite hydrophone, the 100–10 000-kHz polar glass ceramic hydrophone, the small-size low-frequency narrow beam hydrophone, the acoustic pressure receiver-vibration pick-up compound hydrophone, the large area PVDF hydrophone, etc., are presented in this paper.

10:00–10:20 Break

Contributed Papers

10:20

3aEA7. Development of a compact suspension system for a neutrally buoyant underwater acoustic intensity probe. James A. McConnell (Acoustech Corp., P.O. Box 139, State College, PA 16804)

Practical use of neutrally buoyant underwater acoustic intensity probes requires a suspension system to position them in some preferred orientation with respect to an acoustic field of interest. However, since these probes typically contain a moving coil geophone to facilitate particle velocity measurements, the design of such suspension systems is not trivial. On one hand, theory mandates that the dynamics of the geophone will not be adversely affected by the suspension as long as the mass-spring system created by the probe and the elastic members has a low-resonance frequency and high quality factor relative to that of the geophone. However, by meeting these two design criteria, wave effects (e.g., flexural resonances) in the elastic members can become a limiting factor in the performance of the device, particularly at high frequencies. This paper presents theoretical and experimental results of an effort to design a compact suspension system that embodies the aforementioned design considerations, but has relatively low susceptibilty to flexural resonances. [Work supported by the Acoustics Technology Branch of the Naval Air Warfare Center—Aircraft Division, via the DoD Small Business Innovation Research Program.]

10:40

3aEA8. Comparative study: Flow-induced noise on underwater acoustic pressure, particle velocity, and intensity sensors. James A. McConnell (Penn State Univ., Grad. Prog. in Acoust., P.O. Box 30, State College, PA 16804 and Acoustech Corp., State College, PA 16804, univibe@sabine.acs.psu.edu) and Gerald C. Lauchle (Penn State Univ., State College, PA 16804)

A neutrally buoyant underwater acoustic *p*-*u* intensity probe contains discrete sensors for direct measurement of acoustic pressure and particle velocity [J. A. McConnell and G. C. Lauchle, J. Acoust. Soc. Am. **103**, 2755(A) (1998)]. Intensity is calculated from the cross spectrum between these two quantities. Thus a single probe can be categorized as a compound sensor capable of independently measuring acoustic pressure, particle velocity, and intensity. Using this probe, a comparative study concerning the measurement of all three quantities in the presence of mean flow and an independent sound source was performed. Bias errors, which

result from the flow-induced noise generated by towing the sensor (e.g., a cylindrical body) in cross flow at low speeds through a channel of water, are presented. Other parameters of interest include analysis of experimental pressure–pressure and pressure–velocity correlation functions. The effect of body geometry (e.g., variation in aspect ratio) on the measured bias errors and correlation functions is also presented. [Work supported by the Office of Naval Research, the Naval Submarine League, and the Acoustics Technology Branch of the Naval Air Warfare Center—Aircraft Division, via the DoD Small Business Innovation Research Program.]

11:00

3aEA9. Bias error due to flow-induced noise on a velocity gradient underwater acoustic intensity sensor. Kevin J. Bastyr and Gerald C. Lauchle (Penn State Univ., Grad. Prog. in Acoust., P.O. Box 30, State College, PA 16804, zabour@sabine.acs.psu.edu)

A neutrally buoyant underwater acoustic *u*-*u* intensity probe employs discrete sensors for the direct measurement of acoustic particle velocity at two locations. Active intensity is calculated from the cross spectrum between the two velocity sensors [K. J. Bastyr and G. C. Lauchle, J. Acoust. Soc. Am. **103**, 2755(A) (1998)]. Under quiescent conditions the sensor has no bias error; however, in the presence of mean flow, this is no longer true. A derivation of the bias error that results from performing acoustic intensity measurements in the presence of mean flow is presented. Results show that the bias error due to the turbulent boundary layer generated by fluid flow over the cylindrical body that encapsulates the sensors is proportional to the cross spectrum of the turbulent velocities measured by the sensors. This theoretical derivation is quantified with preliminary experimental data obtained by towing the sensor at low speeds through an open channel of water. [Work supported by Office of Naval Research, Multi-University Research Initiative on Acoustic Transduction, Materials, and Devices.]

11:20

3aEA10. Development and testing of an ultrasonic PMN transducer. Jocelyne Coutte, Christian Granger, Bertrand Dubus, and Jean-Claude Debus (IEMN, Dept. ISEN, UMR CNRS 9929, 41 Bd. Vauban, 59046 Lille Cedex, France, jocelyne.coutte@isen.fr)

Lead magnesium niobate ceramics (PMN) are promising materials for realizing high-power transducers for macrosonics or underwater acoustics because of the large strains at moderate electric field and the low hysteresis. The use of PMN ceramics in transducers presents some difficulties: highly nonlinear properties, temperature and frequency dependence of dielectric permittivity, and dc bias field needed. This paper describes the design, realization, and testing of a 20-kHz transducer. The Langevin-type transducer is made of four PMN-PT rings prestressed by a steel bolt between two-end-masses. The transducer is modeled using electrostrictive finite elements [J. C. Debus *et al.*, J. Acoust. Soc. Am. **103**, 3336–3343 (1998)]. It is optimized in terms of coupling coefficient and radiated acoustic power for in-air or in-water applications. The transducer is tested for several temperatures and various bias voltages and prestresses. Resonance and antiresonance frequencies, coupling coefficients, and vibrational amplitudes are measured and compared to numerical predictions and to experimental results on a reference piezoelectric transducer. [Work supported by a DRET/DCN grant.]

11:40

3aEA11. Thermal analysis of high drive transducer elements. Robert Montgomery and Stephen C. Butler (Naval Undersea Warfare Ctr., Newport, RI 02841, butlersc@code20nl.npt.nuwc.navy.mil)

The increasing demand for high-power, low-cost, compact transducer packages for underwater acoustic applications is leading to concerns of overheating in the active driving piezoelectric ceramic (lead zirconate titanate) elements and the associated passive materials (epoxies and polyurethanes). Pushing a design to its thermal limits can lead to reduced acoustic performance and reliability. There is not much guidance to be found in the literature that provides an analytical approach to cope with thermal issues of piezoelectric ceramics in the design phase. An analytic modeling effort is presented that addresses the thermal issues for compact high drive 31-mode free-flooded ring underwater sonar transducers. In this particular case, the thermal issues proved to be the limiting design concerns over the field and stress-limited cases. However, with modeling (analytical and finite element) and bench testing of components, the proper choice of materials and configuration parameters were determined and the performance goals were subsequently achieved. The approach addresses both the transient thermal response and the steady-state temperature profile that results from high-power, high duty cycle drive. These results may prove useful for other similar designs. [Work supported by ONR.]

12:00

3aEA12. The calibration of extended stationary low-frequency hydroacoustic antennae in the real conditions. Alexander V. Agranovski, Byneev R. Osman, Sergei G. Cygankov, and Alexander V. Rosenberg (SPECVUZAVTOMATIKA Design Bureau, Lab. of Hydroacoustics R & D, 51 Gazetni St., 344007 Rostov-on-Don, Russia, asni@ns.rnd.runnet.ru)

As known, the complex problems of a sea polygon calibration must include solutions of coordinate problems after an antennae systems placement was completed. At calibration, a necessity more frequently arises in a solution of other kinds of coordinate tasks: geometrical form determination for a receiving system; geometrical form determination for a receiving system and coordinates of the main receiving element in the selected immovable coordinate system (absolute fixing); and the self-coordinated determination of a mutual position for emitting points and receiving system elements. The first and second tasks assume that point coordinates are known (e.g., ones were determined by navigation methods), but at a third task they are not known. In the last case, a mutual location of hydrophones and emitting points ought be determined only by means of hydroacoustic measurements. At calibration, other kinds of acoustic signals are used: continuous signal (tonal or narrow-band) and pulsed signal (explosion, pneumatic gun, etc.). In this paper some algorithms for the decision of the above-mentioned tasks at the calibration of extended stationary low-frequency hydroacoustic antennae by using different kinds of emitted signals are described.

Session 3aED

Education in Acoustics: European Demonstrations in Acoustics Education

Lothar Gaul, Cochair
Institut für Mechanik, Universität Stuttgart, Pfaffenwaldring 9, 70550 Stuttgart, Germany

P. K. Raju, Cochair
Department of Mechanical Engineering, Auburn University, Ross 201, Auburn, Alabama 36849, USA

Sally G. Revoile, Cochair
(University of Maryland, Baltimore), Sea Island, Georgia 31561, USA

Chair's Introduction—8:35

Invited Papers

8:40

3aED1. Application of numerical techniques in teaching technical acoustics. Fulop Augusztinovicz (Tech. Univ. of Budapest, Dept. of Telecommunications, Sztoczek u. 2., H-1111 Budapest, Hungary, fulop@hit.bme.hu)

Due to their highly extended visualizing capabilities, numerical methods are very apt at demonstrating acoustic effects and phenomena. Finite-element methods (FEM) are mainly used to describe the sound fields in closed spaces, and boundary element methods (BEM) are well suited to predict radiation from vibrating bodies. Coupled systems can also be analyzed by some hybrid approaches. The paper shows applications of these tools in undergraduate and postgraduate courses of technical acoustics. Starting from the well-known concentrated parameter approach, a more realistic description of basic acoustic elements and systems consisting of acoustic masses, acoustic compliances, Helmholtz resonators, waveguides, etc. can be presented. Based on these examples, the dynamic behavior of acoustic systems such as the existence of standing waves, eigenmodes, and resonance effects can be visualized and understood. Radiation problems can be solved for elementary acoustic sources, demonstrating the basic rules of fluid–structure interaction phenomena. The most advantageous feature of numerical—FEM/BEM—calculation and visualization techniques is its capabilty to handle a large amount of data. Problems can be approached in three dimensions, both in time and frequency domain. Apart from the application areas, the lecture addresses the necessary hardware and software tools to prepare these sorts of demonstration, too.

9:00

3aED2. A library of visualization and auralization examples to support understanding. Jens Blomqvist, Tor Kihlman, and Wolfgang Kropp (Dept. of Appl. Acoust., Chalmers Univ. of Technol., SE-41296 Gothenburg, Sweden, wk@ta.chalmers.se)

In a project financed by the Swedish Council for renewal education a library has been produced containing visualization and auralization examples concerning physical phenomena in acoustics. The main goal of the library is to support the development of a thorough understanding of basic acoustic phenomena. The work was supported by studies in the form of interviews and questionnaires to understand—What are the genuine problems students have in acoustics, mathematics, and physics? How do the students' and teachers' view of acoustics, physics, and mathematics differ? What are suitable measures to achieve a common basis between teacher and student for a successful communication? During the project it became obvious such a library has to be developed together with students from our courses. The library has to be adapted to the students needs and to their mental picture of physics, mathematics, and acoustics. In order to achieve this, a group of students was asked to take part in the project. They directed both content and layout of the library from their own perspective. The results of this work will be presented together with typical examples from the library.

9:20

3aED3. Web-accessible resources for teaching phonetics. Anders Eriksson (Dept. of Phonet., Umeå Univ., S-901 87 Umeå, Sweden, anderse@ling.umu.se)

The paper covers two aspects of the usability of the Internet resources in teaching phonetics. First of all, the Internet may be used to disseminate information and teaching materials. Search facilities provided by normal, search engines are too coarse, however, to be really useful if one wants to find suitable teaching resources (course notes, tutorials etc.). One way to address this problem is to use a structured inventory of hyper-links to relevant materials. A working group within the Socrates/Erasmus thematic network on Speech Communication has set up a searchable inventory of web accessible materials, relevant to teaching phonetics. The principles underlying the structuring of the database will be described and illustrated by examples from the database. A second possible use has to do with Open and Distance Learning (ODL). Phonetics, however, requires both sounds and images to be realistic, and for many areas the possibility to perform experiments is essential. With the advent of internet-based tools like audio and video players and programming languages like Java new possibilities have opened up for realistic, high-quality phonetics resources. The presentation will demonstrate a perception test, which may be run inside a normal web browser and which is accessible over the Internet.

9:40

3aED4. Model of the human speech production based on vocoder techniques. Klaus Fellbaum (Brandenburg Tech. Univ., Cottbus, Germany) and Joerg Richter (Tech. Univ. of Berlin, Berlin, Germany, fellbaum@kt.tu-cottbus.de)

A tutorial is presented with which the student first gets basic knowledge about the human speech production. It is explained that speech is generated by an air flow coming from the lungs which is, in the case of voiced sounds, periodically interrupted by the vocal cords and then modulated with the resonance rooms of the mouth and nasal tract. For voiceless sounds (like ''f,'' ''sch'') the vocal cords are open and the air flow excites the mouth and nasal tract with a noise-like pressure signal. It is therefore adequate to distinguish two components in the speech production: the excitation and the articulation component. In our tutorial, the two components are realized (simulated) by a technical system, known as linear predictive vocoder (LPC vocoder). Its principle is explained by a short text and some graphics and the analogy to the human speech organs is clearly shown. The main emphasis is put on the control parameters of the system—in the main the pitch frequency and the vocal tract parameters (prediction coefficients)—and the effect when.

10:00–10:20 Break

10:20

3aED5. Teaching boundary element methods in acoustics. Lothar Gaul, Marcus Wagner, and Wolfgang Wenzel (Univ. Stuttgart, Inst. A fuer Mechanik, Pfaffenwaldring 9, 70550 Stuttgart, Germany, L.Gaul@mecha.uni-stuttgart.de)

The boundary element method (BEM) provides a powerful tool for the numerical solution of sound fields, because (1) it maps the domain equation on the boundary and thus reduces the problem dimension by one, (2) it provides a nonreflecting boundary on an arbitrary radiating surface, and (3) pressure, velocity, and intensity can be calculated at every field point from the boundary data. The author's concept of teaching BEM in a graduate engineering course is to provide a link with subjects taught in undergraduate engineering mechanics such as rod vibrations, reciprocity principle, influence functions, and finite elements (FE). These subjects are generalized to the field equations of acoustics and elastodynamics. The associated integral equations are derived from the dynamic reciprocity principle. Their kernels are fundamental solutions which turn out to be influence functions of a full space. Boundary formulations of rods and beams recall well-known FE matrices. The fluid–structure interaction of interior and exterior acoustics is formulated by adopting the unsymmetric allocation approach of BEM and a symmetric hybrid BEM which is based on a multifield varational principle. Waves and vibrations in a flexible pipe and the sound radiation from a vibrating tire are treated as examples.

10:40

3aED6. An adaptive, active noise reduction system in closed space. Andrzej Golas and Wojciech Ciesielka (Dept. of Mech. and Vibroacoustics, Univ. of Mining and Metallurgy, Poland, ghgolas@cyf-kr.edu.pl)

In the demonstration an adaptive system of noise reduction is presented. Both the acoustic signals phase compensation and the adaptive digital filtering theory are employed. An incident acoustic wave is identified and a compensation signal is generated using a finite impulse response filter which coefficients are calculated in real time employing an LMS algorithm. The algorithm is implemented on a dSpace card with a signal processor (TMS320C31 Texas Instrument). In the receiving point (artificial head, real listener, receiving transducer) the disturbing signal (white noise filtered in range 50–250 Hz) is reduced by an active adaptive system. The damping coefficient that is obtained in the system varies from 10 to 20 dB. The experiment can be conducted and observed in any interior.

11:00

3aED7. The use of computers in acoustical engineering: A computer-aided electroacoustics course. Juan J. Gomez Alfageme, Manuel Recuero, and Jose L. Sanchez (Dept. of Audiovisual and Commun. Eng., Polytechnic Univ. of Madrid, Ctr. Valencia Km. 7, 28031 Madrid, Spain, alfageme@diac.upm.es)

The teaching of electroacoustics in the audiovisual engineering curriculum has sustained important changes during the last 4 years. The increasing use of computers in the classroom has allowed a new approach to this subject, which needs vast knowledge in physiscs, mathematics, and signal analysis. In the last years our department has developed a computer-aided course in electroacoustics. This course is made in the Windows operating system and programmed in Matlab, for its extended use in engineering departments all over the world. At the moment, the implemented modules are electroacoustic transducer analysis, direct radiation loudspeaker systems, array directivity, sound intensity, electrodynamic loudspeaker distortion, and speech index transmission calculus. All the modules have the same structure using the Matlab object-oriented user interface facilities and use the Matlab resources for graphical representation. Each module makes transducer behavior simulation based on equivalent circuits. The student does not need to have a great deal of knowledge in programming to work with the modules. The structure of different modules will be explained and the results with students in our curriculum will be provided.

11:20

3aED8. Acoustics education at the Stuttgart University. Gerhard Hübner (Universität Stuttgart, ITSM, Pfaffenwaldring 6, D-70550 Stuttgart, Germany, wittstock@itsm.uni-stuttgart.de)

The Stuttgart University is relatively young compared to several other German universities. Nevertheless or fortunately for this reason the developments in Stuttgart's acoustical teaching went off with some remarkable distinctions in its relevant scientific history and present situation. (i) A new teaching focused on noise generation and radiation caused by practical sound sources was started successfully by K. Gösele already in the late 1940s. (ii) Supported and initiated by the requirements of the important industrial area around Stuttgart, an increasing interest of more and more Engineering Departments to include noise and noise control in lectures and

investigations took its origin much earlier than in other places which, in 1993, concluded in the establishment of the ''Work Group of Technical Acoustics and Noise Control at the Stuttgart University'' (ATALUS) where 13 institutes from 6 different faculties organized their exchange of experiences on a broad basis. Furthermore, in 1994 several acoustical lectures are included in the new curriculum ''environmental engineering and protection.'' (iii) Several relevant basic lectures are straightened on the general theory, e.g., focused on numerical methods (BEM, the link of DFEM with the physical phenomenon of sound radiation), propagation and sound power of structure-borne sound in general shaped bars and shells using second-order differential equations, and sound intensity measurement techniques.

11:40

3aED9. Standard and nonstandard Galerkin FEM for numerical acoustics. Frank Ihlenburg (Germanischer Lloyd, Vorsetzen 32, D-20459 Hamburg, Germany, ihl@hamburg.germanlloyd.de)

Over the last decade, several modern nonstandard modifications of the standard Galerkin finite-element method have been developed for, or applied to, the numerical solution of the Helmholtz equation. Most of these concepts, like Galerkin least-squares or bubble methods, have been first developed and demonstrated in one dimension, where also a rigorous analysis of the so-called preasymptotic error behavior of the standard Galerkin FEM is available. In this talk, a short overview of these topics will be given and the extension of the methods/results to higher dimensions will be discussed, where practical problems are formulated.

12:00

3aED10. Courses on acoustics: What is needed? Otto von Estorff (Ocean Eng. II, TU Hamburg-Harburg, D-21071 Hamburg, Germany, estorff@tu-harburg.de)

The constant reduction of allowable noise levels and consumer demand for a better acoustic performance of technical systems put a tremendous pressure on manufacturers. As a consequence, engineers who know about acoustics, and the measures to improve it, are currently looking at numerous job openings. In fact, the industry is seeking intensively in this field. The present paper is related to the contents of courses on acoustics at the university as well as in industry. Its focus is to discuss the question ''What is needed?'' in order to meet the requirements of future acoustic challenges and, of course, the expectations of the student's future employer. Based on the author's experience and a little questionnaire, a possible course content is setup and discussed.

WEDNESDAY MORNING, 17 MARCH 1999 ROOM MA004, 7:55 A.M. TO 12:20 P.M.

Session 3aMU

Musical Acoustics: Musical Instruments and Structural Acoustics I: Experimental Studies, Theoretical Models and Numerical Analysis

Antoine J. Chaigne, Cochair
ENST, Dept. TSI, CNRS URA 820, 46 Rue Barrault, 75634 Paris, Cedex 13, France

Uwe J. Hansen, Cochair
Department of Physics, Indiana State University, Terre Haute, Indiana 47809, USA

Chair's Introduction—7:55

Invited Papers

8:00

3aMU1. Experimental and theoretical studies of the modes of stringed instruments and their relevance for quality control of instrument manufacture. Bernard E. Richardson (Dept. of Phys. and Astron., Univ. of Wales, Cardiff, P.O. Box 913, Cardiff CF2 3YB, UK, RichardsonBE@Cardiff.ac.uk)

This paper reviews various methods for measuring and predicting the modes of vibration of the wooden structures found in instruments of the violin and guitar family. These methods include holographic and speckle interferometry, modal analysis by impact hammer excitation, and the finite element method. Theoretical modeling of stringed instruments has now advanced to the stage where the models can be ''played,'' allowing listening tests to be used to link construction of the instrument with the perceived sound quality in a formal way. Early indications of this work suggest that mode frequencies play a much smaller role in determining the sound quality of an instrument than has previously been assumed, and that greater attention should be paid to the ''ease'' with which modes can be driven by the strings and to the ''source strengths'' of the modes. This paper will put the case for measuring additional modal parameters, such as effective mass and effective stiffness, and discuss their relevance to quality control by the maker during manufacture of an instrument.

8:20

3aMU2. Dynamical behavior evolution of the guitar harmonic plate in the successive construction phases. María J. Elejabarrieta (Dept. Mecánica, Escuela Politécnica Superior de Mondragón Unibertsitatea, Spain), Amaya Ezcurra (Univ. Pública de Navarra, Spain), Carlos Santamaría (Univ. del Pais Vasco, Spain), and José Bretos (Univ. Pública de Navarra, Spain)

The fundamental piece for the quality of the sound of a guitar is its harmonic plate. From the initial phase (gross plate without hole) until the last construction phase (the addition of the structures system), the craftsman has established a series of stages where the acoustical behavior is modified until the definitive guitar is created. This is the reason to establish the effect of each modification in the vibratory response of the harmonic plate. With this purpose an experimental modal analysis and a finite element modeling of all the construction phases in the low-frequency range have been carried out, obtaining information about vibration patterns, eigenfrequencies, quality factors, and spectra. In the three first construction phases, the plate goes from a uniform thickness distribution and no hole to a mouth and variable thicknesses. These changes do not modify the vibration patterns, but they lead to a gradual decrease of the eigenfrequencies and an increase of the vibration amplitude. The vibration patterns are modified when the structures are added. Then, the rigidity of the structure is increased and the resonances present a smaller damping. Likewise, the frequency response function decreases remarkably and the resonances tend to be more uniformly distributed in frequency.

8:40

3aMU3. Numerical simulation of timpani. Patrick Joly, Leïla Rhaouti (INRIA, Domaine de Voluceau-Rocquencourt, BP 105, 78153 Le Chesnay Cedex, France), and Antoine Chaigne (ENST, 75634 Paris Cedex 13, France)

The goal of this work is to achieve sound synthesis via time-domain numerical simulations, with particular interest in the case of timpani. The approach combines the use of a mathematical model, which is supposed to represent accurately the physics of the phenomena, and of modern techniques for the approximation of partial differential equations. The model appears as a system of wavelike equations coupled by fluid–solid interaction conditions. It includes various damping mechanisms as well as a nonlinear model for the mallet–membrane interaction. The numerical approach aims at realizing the best compromise among accuracy, stability, and efficiency. Its main characteristics are the use of finite elements for the space discretization, of a fictitious domain method for a flexible treatment of the geometry of the instrument, and of explicit centered finite differences for the time discretization. Higher-order absorbing boundary conditions are used for simulating the radiation of sound in free space. In the presentation, the main properties of the numerical methods will be emphasized and various numerical results will be compared to experiments.

9:00

3aMU4. Comparison between modal analysis and finite-element modeling of a marimba bar. Antoine Chaigne (ENST, Dept. TSI, CNRS URA 820, 46 Rue Barrault, 75634 Paris Cedex 13, France) and Ingolf Bork (Physikalisch-Technische Bundesanstalt, Braunschweig, Germany)

The sound spectrum of low-tuned marimba bars contains many components that cannot be explained by a simple one-dimensional model of flexural vibrations. A modal analysis has thus been performed on a bass marimba bar C_3 with a fundamental frequency of 130 Hz [outer dimensions: $46\times6\times2.35$ cm (x,y,z), material: rosewood], taking into account two spatial components of vibration. The 20 lowest modes were extracted from this analysis (modal frequencies and mode shapes). A 3-D finite-element analysis of this bar, based on an orthotropic model for the material, has been conducted in parallel. Modal analysis and finite-element modeling yield very similar mode shapes and modal frequencies for the first 12 modes, between 130 and 4000 Hz, which confirms the experimental results and validates the theoretical approach. The discrepancies between measured and calculated frequencies are less than 4% in this frequency range. For higher frequencies, between 4000 and 8000 Hz, the main flexural modes along $0x$, such as the (7,0) and the (8,0) modes, are still correctly predicted. In this range, the three components of the bar motion become significant and the finite-element modeling shows a number of modes which were not detected in the modal analysis.

Contributed Papers

9:20

3aMU5. Investigating the effect of different strutting arrangements on the modes of a guitar soundboard. Mark Lewney and Bernard E. Richardson (Dept. of Phys. and Astron., Univ. of Wales, Cardiff, P.O. Box 913, Cardiff CF2 3YB, Wales, m.lewney@astro.cf.ac.uk)

A spruce soundboard was fitted with a bridge and attached to an experimental rig which provided a fixed edge and uniform backing cavity volume. The rig allowed the same soundboard to be fitted with various standard strutting arrangements. The mode shapes and frequencies were investigated using holographic interferometry. Of particular interest were the *small* changes in mode shapes induced by the different strutting arrangements. Input admittance measurements were made to determine the effective mass of each mode as ''seen'' by the strings. Previous psychoacoustical work [H. A. K. Wright, Proc. Inst. Acoust. **19**(5), 149–154 (1997)] has suggested that effective mass is an important parameter in determining a mode's contribution to the overall sound output, and can be significantly affected by small changes in the mode shape. A new method of determining the effective mass is also presented. [Work supported by EPSRC.]

9:40

3aMU6. Air cavity modes in sound boxes recorded by TV holography. Anna Runnemalm and Nils-Erik Molin (Div. of Exp. Mech., Lule Univ. of Technol., SE-971 87 Lule, Sweden, Anna.Runnemalm@mt.luth.se)

Amplitude and phase distribution of air cavity modes in a rectangular box, in a guitar, and in a violin are measured using TV holography. The box and the top and back plates of the guitar and the violin are made transparent using 5-mm-thick and flat PMMA plates. Standing waves in the enclosed cavities are generated by a loudspeaker. Object laser light is sent through the cavities to a rigid white-painted steel block and reflected back again through the cavities to the optical unit of the TV holography interferometer. Laser light traveling through a sound pressure field will experience a phase delay, since an increased air pressure is accompanied by a higher air density as well as a higher index of refraction which in turn gives a slower speed of the laser light, which generates a phase delay compared to undisturbed air. This often small phase change is made visible by the highly sensitive phase-modulated TV holography technique. The optical system will be described and air cavity modes in a simple rectangular box, in a guitar, and in a violin will illustrate the presentation.

10:00–10:20 Break

Invited Papers

10:20

3aMU7. On the function of the violin bridge. Erik V. Jansson (Dept. of Speech, Music and Hearing, Royal Inst. of Technol. (KTH), SE-100 44 Stockholm, Sweden, erik@speech.kth.se) and Benedykt K. Niewczyk (Violin Workshop, ul Wozna 6, 61-776 Poznan, Poland)

In measured frequency responses of violins of soloist quality a broad maximum is found at about 2.5 kHz which has been called the bridge hill as the violin bridge on rigid support has its major in-plane resonant frequency nearby [E. V. Jansson, Acust./acta acust. **83**, 337–341 (1997)]. Experiments show, however, that the hill rather lies in combined properties of the bridge and of the top plate. It can be influenced both by the properties of the top plate between the f-holes but also by the bridge. The maximum is efficiently excited in the normal main direction of bowing. The force along the bow is transformed into a force couple at the bridge feet which excites the bridge and body. The broad maximum involves resonant motion which is not confined to the bridge alone. [Work supported by KTH, Swedish Natural Science Research Council, Swedish Institute, and Wenner-Gren Center Foundations for Scientific Research.]

10:40

3aMU8. Normal modes of vibration in a violin. Uwe J. Hansen (Dept. of Phys., Indiana State Univ., Terre Haute, IN 47809) and Thomas D. Rossing (Northern Illinois Univ., DeKalb, IL 60115)

The normal modes of vibration of a violin constructed by Carleen Hutchins have been studied using both sinusoidal and impact excitation while the instrument is supported in several different ways. The results from these experiments are compared to those of several previous investigators on the same instrument [see references in Roberts and Rossing, Catgut Acoust. Soc. J. **3**(5), 3–9 (1998)]. The observed operating deflection shapes, from which normal modes are determined, are found to vary with means of support and excitation, but by comparing the various data the normal modes can be determined with reasonable certainty.

11:00

3aMU9. Deconstructing the violin—The road from B to A. George Bissinger (Phys. Dept., East Carolina Univ., Greenville, NC 27858, bissingerg@mail.ecu.edu)

A recently initiated project to measure the elastic and damping material properties, normal mode frequency and shape vibrational properties, and the angular distribution and efficiency of radiation from assembled violins is described. Combining accurate geometries and densities, experimental modal analysis with a scanning laser vibrometer, measurements of bridge-corpus transfer mobilities, and far-field radiation over a sphere, one potential application is to extract the relevant material and vibrational properties for all substructures. Another goal is to generate a finite-element model ''particularized'' to each violin to calculate normal mode radiation from the violin and simulate its sound. Other aspects and applications of the model will also be briefly discussed. [Research supported by the National Science Foundation under Grant No. DMR-9802656.]

11:20

3aMU10. Finite-element analysis of vibrating trombone bell. P. L. Hoekje (Dept. of Phys. and Astron., Baldwin–Wallace College, 275 Eastland Rd., Berea, OH 44017) and Andrew Morrison (Univ. of Northern Iowa, Cedar Falls, IA 50614-0150)

Finite-element analysis (FEA) was used to predict the vibration patterns of an isolated trombone bell. These vibrations are implicated in subtle contributions to the sound field, over and above the primary contribution from the vibrating air column. Holographic interferometry of vibration patterns of an actual bell reveal that most modes exhibit rotational symmetry with vibrating patches of equal size distributed around circumferential rings. Such modes at low frequencies will radiate poorly. However, some patterns observed by holography do not display such symmetry and will have enhanced sound radiation as a result. FEA calculations using a mesh of points with rotational symmetry seem to give only symmetric modes, but lead to elements of unequal sizes and aspect ratios. On the other hand, using the package's AutoMesh feature to redraw the mesh into equal-sized elements for more efficient computation introduces inherent asymmetries into the model, and also breaks the symmetry of the solutions. It is concluded that the observed asymmetries in the holographic data are due to asymmetries in the bell itself, leading to enhanced radiation of sound. [Work supported by the Carver Foundation.]

Contributed Papers

11:40

3aMU11. Simulation and measurement of wall vibrations of a flue organ pipe. Malte Kob (Inst. of Tech. Acoust., Tech. Univ. Aachen, Templergraben 55, D-52056 Aachen, Germany) and Matthias Scholz (Ackerwand 21, D-99423 Weimar, Germany)

The question of whether the vibrations of a metal flue organ pipe contribute to the perceived sound or not is still not completely answered. One result of the research done within the GOArt (Göteborg Organ Art Center) project is that, due to the casting process and the need to save material, the baroque flue organ pipe has considerably thinner walls than a modern pipe. According to an organ builder, the pipe under test is likely to vibrate. To demonstrate the influence of the wall vibrations on the perceived sound, recordings of a blown pipe with and without damping of the wall are carried out. An FE model is created and the radiation for the case of coupled air and structural modes are calculated to enable parametric studies of the influence of the wall properties. The simulations are compared to FRF measurements using MLS excitation of a shaker, laser vibrometer velocity measurements, and subsequent modal analysis. The results indicate that some structural modes significantly change the spectral

components in the *transient* spectra of the blown pipe, whereas in the *stationary* spectrum, the effect is small. [This work was performed at the Department of Applied Acoustics, Chalmers University of Technology, Göteborg, Sweden.]

12:00

3aMU12. An investigation of vibrational and acoustical properties of the violin using MLS and optical holography. Lars H. Morset (Appl. Optics Group, Inst. of Phys., Norwegian Univ. of Sci. and Technol. (NTNU), 7034 Trondheim, Norway, Lars.Morset@phys.ntnu.no)

In this investigation a multi-channel MLS (maximum length sequence) measurement system is used for vibrational and acoustical measurements on the violin. MLS measurements are useful since both phase and magnitude can be measured with great accuracy. In these measurements, both the phase and magnitude influence of the transducers are corrected. Using this tool, the input admittance, the velocity at the feet of the bridge, and the sound pressure at the far field of the violin are measured simultaneously. These parameters give important information about the vibrational and acoustical properties of the violin. A more extensive investigation is also performed. The sound level pressure and phase are measured in several equally spaced positions in the far field of the violin situated in an anechoic chamber. Radiation patterns are found for each mode and the radiated power is calculated. Optical holography is then used to measure the vibrational pattern for the most important modes of the violin body. These acoustical and vibrational measurements are correlated to determine which modes are most important to the radiated sound power.

WEDNESDAY MORNING, 17 MARCH 1999 ROOM H2032, 7:55 TO 9:20 A.M.

Session 3aNSa

Noise: Noise at the Workplace II

Gustav A. Sehrndt, Cochair
Consultant, Kapuzinerstrasse 8, D-50 737, Cologne, Germany

Alice H. Suter, Cochair
Alice Suter & Associates, 575 Dogwood Way, Ashland, Oregon 97520, USA

Chair's Introduction—7:55

Contributed Papers

8:00

3aNSa1. Characteristics of the noise found in day-care centers. Picard Michel and Boudreau Chantal (Ecole d'orthophonie et d'audiologie, Universite de Montreal, Montreal, QC H3C 3J7, Canada, picardmi@magellan.umontreal.ca)

Today's day-care centers are apparently extremely noisy environments. Given the paucity of data on this particular issue, noise measurements were collected for 25 sites with groups of 1.5- to 5-year-old children ($N=4-16$). Noise levels associated with three types of children's activities were studied, namely: unstructured activities of the children; structured ones (e.g., story telling); and lunch time. In addition, measurements were collected for the unoccupied case. A-weighted levels (10–90 percentiles, average levels, L_{Aeq}), and third octave levels will be presented for each measurement condition. Statistical analysis to model the noise in all conditions will also be reported. Of special concern, L_{Aeq} (10 min) indicated frequent readings in excess of 85 dB for all measurement conditions except the unoccupied case. This suggests that children may be at risk of noise-induced hearing loss dependent on the length of stay in the day-care centers. They would only be able to initiate or sustain any meaningful verbal communication activity by using extreme vocal effort to speak loud enough to raise their voice above the din. Obviously, this is quite an alarming situation.

8:20

3aNSa2. Occupational noise in Spanish textile industries. Amando Garcia, Jose V. Garrigues (Dept. de Fisica Aplicada, Univ. of Valencia, Burjassot, Valencia, Spain, 46100, amando.garcia@uv.es), and Ana M. Garcia (Univ. of Valencia, Valencia, Spain, 46022)

This study has been carried out in 20 small-, medium-, and large-sized textile industries located in the provinces of Valencia and Alicante (Spain). A series of noise-level measurements has been carried out in order to evaluate the daily noise exposure levels ($L_{\mathrm{ep,d}}$) for a wide variety of workplaces. About 33% of the workers present during the measurements were exposed to daily mean A-weighted noise levels $L_{\mathrm{ep,d}}$ higher than 85 dB. It has been noticed that personal protection against noise was used only by a minority of these workers. Available data from routine medical examinations have been also analyzed. The observed hearing loss is related to noise exposure level in the corresponding workplaces. In particular, about 48% of the workers exposed to $L_{\mathrm{ep,d}}$ levels higher than 85 dB showed acoustic trauma (hearing losses higher than 40 dB for the 4000-Hz frequency in either ear).

8:40

3aNSa3. What is and should be in the area of noise-protection: Make progress a catalog on noise reduction. Karl Ross (DGUHT, Henlestr. 7, D-97074 Würzburg, Germany)

Noise has a harmful effect on health. Also, More than 10 000 deaths every year in the *ecological domain*, for example, are said to be caused indirectly in this way in Germany. In the area of the *industrial safety*, the following applies: the regulation governing accident prevention under the title ''Noise'' has been in existence since 1975. Annually, more than four million persons are at noisy workplaces and two million hearing screening tests are being carried out. Yet, noise-related illnesses still occur (1996: 11 724 reported illnesses/1252 pension-cases receiving compensation for the first time). The costs of these were over 500 million German Marks altogether. However, company practicians are often not able to plan/carry out noise reduction without intensive support. Therefore, there had been checked more than 200 000 pages for the keynotes ''noise reduction'' or something similar. A new catalog on noise reduction is introduced at this point. It contains more than 400 examples. In it are listed in alphabetical order: the noise-problem with its dB(A) values before and after the decrease, the approximate cost of material, a short description of noise reduction, and a guide to the literature pertaining to special cases. Providing nonbinding advice in the area of industrial safety, the catalog is used at this time as a prototype free of charge. The costs, the protected area, or volume are partly estimated.

9:00

3aNSa4. Ladle crane noise. Jerzy W. Wiciak, Marek Iwaniec, and Ryszard J. Panuszka (Structural Acoust. and Intelligent Mater. Group, Tech. Univ. of Mining and Metallurgy, 30-059 Cracow, al. Mickiewicza 30, Poland, ghpanusz@kinga.cyf-kr.edu.pl)

The present paper considers the vibration analysis of the ladle crane (with hoisting capacity $Q=160$ tons) and noise caused by working units of the crane. The vibroacoustical investigations and theoretical analysis have been applied to the main bridge with box-trapezoid cross section. In the article there is shown comparison of the vibration acceleration and dynamic stress that have been measured in real structure with calculations obtained by means of the finite element method. The noise caused by working units of the crane have been presented for three operating conditions: when the tilting ladle was descending and was hoisting, and pass by load running of the teeming crane. [Work supported by TUMM DS 11.130.557, Cracow, Poland.]

Contributed Posters

These posters will be on display in the Poster Gallery from Monday to Wednesday, 15–17 March. Authors will be at their posters from 10:00 a.m. to 12:00 noon on Wednesday, 17 March.

3aNSa5. Nonoccupational noise and hearing capability of children and young adults. Detlef Schulz, Karin Künzel, and Lars Hentschel (Hochschule für Technik und Wirtschaft Mittweida, Fachbereich MPI, Postfach 1451, D-09644 Mittweida, Germany)

There has been considerable literature over the past decade ascertaining a worsening of the hearing capability of young persons. It is supposed that this may be caused by some peculiarities of the modern way of living, that is, man-made noise (e.g., noisy hobbies). To get insight in some components of the real noise exposure of young people dosimetric measurements were performed in schools as well as in discotheques and as spectators of sports events (football matches and some indoor sports like basketball). For discotheques equivalent sound pressure levels of 95–105 dB(A) are typical; for indoor sports they are in many cases on the same order of magnitude. Persons frequently attending such events may get an exposure which is comparable with occupational noise exposure above the daily average of 85 dB. Furthermore, audiometric testings of children and young adults at the age of 14–25 years were performed. The high-frequency range (8–16 kHz) was taken into special consideration, since it is assumed to be important for the early detection of noise-induced hearing threshold shifts. Hearing thresholds together with the results of questionnaires are presented showing an increasing threshold shift with age already at young people, especially in the frequency region above 10 kHz.

3aNSa6. Noise levels in dental practice. Hrvoje Domitrovic (Faculty of Elec. Eng. and Computing, Dept. of Electroacoustics, Unska 3, HR-10000 Zagreb, Croatia, hrvoje.domitrovic@fer.hr), Ivana Bagic (School of Dental Medicine, Gunduliceva 5, HR-10000 Zagreb, Croatia), and Bojan Ivancevic (Faculty of Elec. Eng. and Computing, HR-10000 Zagreb, Croatia)

Noise can cause unwanted masking of sounds, interference with speech, even pain and injury, and temporary or permanent loss of hearing. Concerning exposure of noise levels at the workplace, industrial plants and huge machines are usually considered. However, there are ''clean'' jobs where people are exposed to significant noise. One example, which will be treated in this paper, is dental practice. In this work it is intended to show the results of SPL measurements that were done at the Dept. of Pedodontics in the School of Dental Medicine Zagreb. One- and two-channel measurements were made using a sound level meter and an artificial head (head-and-torso simulator). Noise levels generated by various dental devices, their spectra, and differences between noise levels in left and right ear (in the dentist's usual working position) were shown. The sound power and subjective sound levels regarding sound source frequency and intensity were determined upon results of these measurements. Special attention was paid to ultrasound and infrasound components, as well as vibrations. Since two Faculty practices with a dozen of dental sets in each were at our disposal, influence of aging and wearing, particularly in mechanical devices, was also considered.

3aNSa7. The role of measurement standards in acoustics. Richard G. Barham (Natl. Physical Lab., Teddington, Middlesex TW11 0LW, UK)

Recent times have seen a marked increase in public awareness of noise as both a cause of nuisance and a hazard to hearing. Consequently, demand for acoustical measurements has grown and is now an important issue across an ever broadening range of industrial sectors. If these measurements are to have any technical validity, it is essential that they be founded on some physical reference quantity or primary standard. In practice, this is achieved by means of a defined measurement infrastructure. In the UK, the National Measurement System serves this purpose and it is the role of the National Physical Laboratory (NPL) to establish the primary measurement standards to underpin the system. While different applications deal with a range of acoustical quantities, they all derive in some way from sound pressure. The primary standard for sound pressure is realized through the calibration of laboratory standard microphones, using the reciprocity method. NPL has for many years been at the forefront of research in this field and most recently has introduced a fully revised reciprocity calibration facility. The paper describes the facility and highlights the latest technical developments. It also discusses the value of third-part accreditation of such facilities.

Session 3aNSb

Noise: Hearing Protector Measurements, Effects, Design and Performance

Elliott H. Berger, Cochair
E·A·R Hearing Protection Products, 7911 Zionsville Road, Indianapolis, Indiana 46268-1657, USA

Guido F. Smoorenburg, Cochair
Hearing Research Laboratories, University Hospital, Utrecht F02504, 3508GA Utrecht, The Netherlands

Chair's Introduction—7:55

Invited Papers

8:00

3aNSb1. The results of a unique Nordic HAKK interlaboratory REAT comparison. Torben Poulsen (Dept. of Acoust. Technol., Tech. Univ. of Denmark, DK-2800 Lyngby, Denmark)

The sound-field requirements in the hearing protector standard ISO 4869-1 are under discussion at present and are likely to be changed in a coming revision of the standard. The Nordic HAKK group comprises representatives from the hearing protector industry, labor protection institutes, audiological clinics, and universities. The test facilities at the laboratories of the members of the Nordic HAKK group cover various ways to fulfill the sound-field requirements of the ISO standard. Therefore, a round robin test was initiated with the aim of determining—and comparing between laboratories—the attenuation of two hearing protectors of the muff type and one of the plug type. The measurements were performed during the meetings of the group and with the group members (min. ten) as test subjects, thus permitting one group of subjects to be used by all laboratories. A statistical analysis of the results is in progress at the time of submission of this abstract. All factors (laboratory, protector-type, test-frequency, test-subject) are significant.

8:20

3aNSb2. Experience with a new ANSI standard for measuring the real-ear attenuation (REAT) of hearing protectors (S12.6-1997). Elliott H. Berger, Ronald W. Kieper, and Donald L. Peyton (E·A·R Hearing Protection Products, 7911 Zionsville Rd., Indianapolis, IN 46268-1657, eberger@compuserve.com)

It has become increasingly apparent during the past 20 years that laboratory-measured values of hearing protector attenuation obtained in conformance with ANSI standards (S3.19-1974, S12.6-1984) bore little correspondence to those obtained by workers in actual occupational settings. The development of a new standard, ANSI S12.6-1997, *Methods for Measuring the Real-Ear Attenuation of Hearing Protectors*, addressed this problem. The new standard includes both experimenter-supervised fit and subject-fit methods. The latter method, designated as method B, requires the use of audiometrically experienced subjects who are naïve in the use of hearing protection. This method is intended to approximate the upper limits to the attenuation that can be expected for groups of occupational users. It yields mean attenuation values, more so for earplugs than earmuffs, that are substantially lower, and standard deviation values that are higher than previously found using ANSI standards. This paper will describe the new S12.6, present method-B test data, compare and contrast the standard to the existing related ISO standard (4869-1:1990), and review the results of ongoing studies designed to evaluate aspects and assumptions of the Method-B protocol. The problems inherent in obtaining and utilizing test panels of inexperienced hearing protection wearers, as well as observations gleaned from working with those subjects for in excess of 30 evaluations, will also be examined.

8:40

3aNSb3. Alternative field methods of measuring hearing protector performance. John R. Franks (Bioacoustics and Occupational Vib. Section, NIOSH, MS C-27, 4676 Columbia Pkwy., Cincinnati, OH 45226-1998)

Real-world tests of hearing protector attenuation are scarce. This study evaluated data from three new field-test methods as compared to the subject-fit data from Method B of ANSI S12.6-1997 for the same protector. The new field-test methods were: fit-check headphone (FCH) method [K. L. Michael, Spectrum **15**, Suppl. 1, 24 (1998)], modified fit-check in sound-field (MFCSF) method, and modified bone conduction loudness balance (MBCLB) method [T. W. Rimmer and M. J. Ellenbecker, Appl. Occup. Environ. Hyg. **12**, 69–75 (1997)], all of which can be administered in small audiometric booths such as are commonly found in industry. Twenty audiometrically competent subjects naive to hearing protector use were tested in the laboratory and for the three field-test methods. The earplug tested was the EAR Express Pod Plug. The results showed that the FCH method and the ANSI A0S12.6 subject-fit method produced similar attenuation levels. The MFCSF method showed decreased attenuation levels at 250 and 500 Hz while the MBCLB attenuations were elevated at 250, 500, and 1000 Hz due to the occlusion effect of the HPD. The results suggest that the FCH method was the most feasible and reliable method for field testing, although it is limited to earplugs. [Portions of work supported by the U.S. EPA IA 75090527.]

9:00

3aNSb4. The attenuation of combinations of ear muffs and ear plugs. Guido F. Smoorenburg (Hearing Res. Labs., Univ. Hospital Utrecht F.02.504, P.O. Box 85500, 3508GA Utrecht, The Netherlands, g.smoorenburg@kmb.azu.nl)

In a number of situations, a single hearing protector (earplug or earmuff) may not provide sufficient hearing protection. This may concern, for example, shooting noise in indoor firing ranges, shooting instructors also outdoors, and jet-engine testing sites. Combinations of earplugs and earmuffs may then be considered. The protection provided by these combinations cannot simply be obtained by adding the attenuation figures provided for the plug and muff individually. A principal limit is set by bone conduction of the sound through the skull to the inner ear. In addition, the total attenuation may be affected by acoustic coupling of the two protectors. It will be demonstrated how to estimate the total attenuation using attenuation measurements of combinations of three earmuffs (Bilsom Comfort, Clark 19A, Peltor H7A) and three earplugs (Bilsom Form, Bilsom Soft, Willson EP100) for 16 subjects and data on bone conduction. The experiment was carefully designed, aiming at a direct comparison of the attenuation for the protectors individually and together, within one subject and with a minimum of replacement of the protectors. The evaluation was based primarily on subjective measurements (REAT method) but the earmuffs have also been measured using miniature microphones in the outer ear canal.

9:20

3aNSb5. Artificial heads versus miniature microphones for measuring active noise-reduction hearing protector performance. Thomas Fedtke and Utz Richter (Physikalisch-Technische Bundesanstalt, Bundesallee 100, D-38116 Braunschweig, Germany)

The results of sound attenuation measurements on hearing protectors with head and torso simulators (HATSs) are quite encouraging if suitable corrections for the bone conduction and the occlusion effect are applied. Yet, the real-ear-at-threshold (REAT) method is still the standardized and most often used procedure to get appropriate measures for the protection provided by passive earmuffs and passive earplugs. With the development of active noise reduction (ANR) hearing protectors, however, the REAT method fails because of the background noise generated by the electronic components of the devices. Furthermore, the limits and the efficiency of such devices cannot be tested with sound-pressure levels near the hearing threshold. Thus there is an urgent need for using either HATSs or probe microphones on humans for the measurement of the ANR performance of a hearing protection device. Attempts to determine the effective attenuation with a combination of REAT and artificial head measurements will be compared with the results of microphone in real ear (MIRE) measurements for several commercially available ANR systems, including noise cancelling headphones. Aspects of validity and uncertainty of the various procedures, as well as practical relevance and ethical considerations, will be discussed.

9:40–10:00 Break

10:00

3aNSb6. Amplitude-sensitive attenuating earplugs. Pascal J. F. Hamery and Armand L. Dancer (French–German Res. Inst. of Saint-Louis, 5 rue du General Cassagnou, BP 34, 68301 Saint-Louis Cedex, France, dancer@newel.net)

The most simple amplitude-sensitive attenuating earplug is made of a plate with one little hole that is inserted in a perforated plug (like Racal Gunfender). That hole presents an acoustic impedance which has essentially a viscous resistance and a nonlinear dependence on the particle velocity in its center [L. J. Sivian, J. Acoust. Soc. Am. **7**, 94–101 (1935); U. Ingard and H. Ising, *ibid.* **42**, 6–17 (1967)]. The dimensions of that hole have been optimized and a new configuration, i.e., an empty cavity with two perforated plates, has been designed. This ''filter'' of small dimensions can easily be fitted into different commercial perforated earplugs. To better understand the experimental results and optimize the acoustic nonlinear ''filter'' dimensions, a theoretical model has been developed. Moreover, an experimental setup is described which allows visualizing the particle velocity inside the cavity with a particle imagery velocity camera which helps to understand the actual behavior of such a nonlinear cavity.

10:20

3aNSb7. Implementation of adaptive digital ANR in hearing protectors. Herman J. M. Steeneken and Jan A. Verhave (TNO Human Factors Res. Inst., P.O. Box 23, 3769ZG Soesterberg, The Netherlands, steeneken@tm.tno.nl)

Present state-of-the-art personal hearing protectors with ANR are mainly based on analog control circuitry. The performance of these systems is fair to good; an additional attenuation for low frequencies of 10–25 dB is obtained. By using a digital control circuitry for feedback gain control and compensatory filtering, a similar performance can be obtained. Digital signal processing allows for real-time control of the system parameters. By using an adaptive algorithm, the system performance can be optimized for individual (acoustic) frequency transfer and for the spectrum of the specific noise to be suppressed. A prototype system has been developed, in which the feedback gain and the frequency response parameters are adaptively controlled. The system uses an (additional) probe to determine the stability of the feedback loop. Other features of digital ANR are: continuous monitoring of the noise dose, transparency at low noise levels in order to improve direct communications and warning signals, and advanced signal processing of speech signals from an intercom. Preliminary results obtained with an add-on system (attached to a standard earmuff) will be presented and compared to the performance of 20 commercially available systems.

10:40

3aNSb8. Use of the Zwicker method to predict signal audibility in noise with hearing protection devices. Martin Liedtke (BIA—Berufsgenossenschaftliches Inst. für Arbeitssicherheit, Alte Heerstrasse 111, D-53754 Sankt Augustin, Germany, M.Liedtke@hvbg.de)

Hearing protection devices (HPDs) can decrease perception of acoustic warning signals. Therefore, specific restrictions are given for the use of HPDs in specific danger areas in Germany. For example, up until 1996, German traffic regulation did not permit use of HPDs while steering a vehicle in road traffic. Within investigations carried out in the 1980s, the audibility of track-layer warning signals was examined during exposure to typical noises and when HPDs were worn. For this purpose, differences in audibility were determined on the basis of the Zwicker method (ISO 532, Method B). As a result, a procedure to predict signal audibility with HPDs was available to select appropriate HPDs for specific situations at work. A special procedure to be carried out if HPDs have to be worn in road traffic was published in 1996 in Germany: A list of hearing protectors realizes a preselection; a final perception test at work under operation conditions carried out by the individual employee and the person responsible for safety indicates the suitability of the HPD. Recent investigations on level-dependent HPDs show that the level of signal audibility seems to depend on the transfer characteristic of the level-dependent HPD.

11:00

3aNSb9. Hearing protection in everyday practice—The gap between expert knowledge and the beliefs of the users. M. L. Barrenas (Dept. of Auiology, Sahlgrens Univ. Hospital, Gothenburg, Sweden)

Many well-informed workers do not use hearing protectors (HPs) as they are taught to. Also, there are differences between what workers know, believe, and do. HPs are used whenever ''necessary'' and taken off when ''the noise levels are low.'' Workers know when the noise is measured at their workplace. However, when there is no feedback from these measurements, the noise levels will be regarded as being ''all right.'' Based upon their own noise rating scale, workers create their own norms for HP usage. By regarding their hearing as normal, even when they know their hearing is impaired, there is no incentive to use HP more often. The great disparity between the knowledge of the experts and the way workers use HP shows that the awareness of damage risk is low. Adaptation to noise and to hearing disability is tremendous! Thus, HP usage is determined by the worker's own noise rating scale, by exchange of opinions between workers, and by their belief of having normal hearing, rather than by the objective noise measurements, information about the need of hearing protection and audiograms. Therefore, the hearing conservation procedures must be renewed according to modern pedagogic principles starting from the perspective of the users, not the experts.

Contributed Papers

11:20

3aNSb10. Acoustic modeling and measurements of hearing protectors for impulsive noise. Samir N. Y. Gerges and Erasmo F. V. Miranda (Federal Univ. of Santa Catarina (UFSC), Mech. Eng. Dept., Lab. Noise and Vib., Cx.P.476, Florianopolis, SC, Brazil, gerges@mbox1.ufcs.br)

REAL is the world-wide common method used for the hearing protector attenuation measurement in accordance with ISO 4869 and ANSI S12.6. This method is not suitable to determine the attenuation of the peak level of impulsive noise, because it measures the attenuation subjectively at low levels of a steady-state sound near the threshold of hearing. Alternative low cost and quick methods are required for assessing hearing protector attenuation for impulsive noise. In this paper a numerical model based on the finite-element method (FEM) for the impulsive noise attenuation prediction of the hearing protector is presented. The insertion loss of the peak level in the time domain is calculated and compared with laboratory measurements.

11:40

3aNSb11. A rating system in search of hearing protectors. William J. Murphy and John R. Franks (Bioacoustics and Occupational Vib. Section, NIOSH, MS C-27, 4676 Columbia Pkwy., Cincinnati, OH 45226-1998)

Previous methods for rating the noise reduction of hearing protection devices (HPDs) have determined the mean attenuation and standard deviations at several octave-band frequencies using real-ear attenuation at threshold (REAT) measurements. Typically, some fraction of the standard deviation is subtracted from the mean attenuation to estimate an assumed protected value for a given percentage of the population. The subtractive correction assumes normally distributed numbers that are linear and not logarithmic. Data from several HPDs were analyzed with a statistical approach which first determined the A-weighted noise reduction for individual measurements. The cumulative distribution of A-weighted noise reduction (CDNRA) was then fit with a combination of two logistic regression curves. The Pearsons correlation coefficients for the model and the data were better than 0.99 for each of four devices analyzed. The CDNRA method yielded reasonable results from data collected from well-fit and poorly fit hearing protectors. In contrast, the NRR method would yield negative NRR values for poorly fit protectors. This paper describes the CDNRA method and looks at the results for an interlaboratory test of four HPDs, as well as additional data collected in the NIOSH Hearing Protector Laboratory. [Portions of work supported by the U.S. EPA IA 75090527.]

Contributed Posters

These posters will be on display in the Poster Gallery from Thursday to Friday, 18–19 March. Authors will be at their posters from 2:00 p.m. to 4:00 p.m. on Thursday, 18 March.

3aNSb12. Four protectors in search of a rating system. William J. Murphy, John R. Franks, Dave A. Harris (Bioacoustics and Occupational Vib. Section, NIOSH, MS C-27, 4676 Columbia Pkwy., Cincinnati, OH 45226-1998), and Jennifer L. Johnson (USA MEDDAC, Hearing Conservation, Ft. Hood, TX 76544)

The EAR Classic, V-51R, Howard Leight Max-1 and EAR Express Pod insert earplug hearing protection devices (HPDs) were tested at the NIOSH Hearing Protector Laboratory using real-ear attenuation at threshold (REAT) according to ANSI S12.6-1997 Method B subject-fit (SF) and ANSI S3.19-1974 experimenter-fit (EF) methods. Several subject panels were created from the NIOSH subject pool which permitted comparisons to the manufacturer's REAT data published on the device's label. For the Classic, NIOSH data agreed with the manufacturer's data. However, for the other devices, the manufacturer's data typically produced higher noise reduction ratings (NRRs) than the NIOSH data. The subject-fit NRR, NRR(SF), results were 17, 1, 12, and 10 dB for the Classic, V-51R, Max and Express, respectively. The REAT variances for the Bilsom V-51R data and the Howard Leight Max were significantly smaller than the NIOSH variances. The NIOSH recommendation that SF data, measured according to ANSI S12.6-1997, be used to rate the performance of a hearing protector, is supported by these results. Application of the NIOSH and OSHA derating schemes to EF NRR either overestimated or underestimated the NRR(SF). [Portions of work supported by the U.S. EPA IA 75090527.]

3aNSb13. Effects of cup, cushion, headband force, and foam lining on the attenuation of earmuffs. Paulo Henrique T. Zannin (Dept. Engenharia Mecanica, Univ. Fed. Parana, Centro Politecnico, Curitiba, PR 81531-990, Brazil)

The essays were undertaken using an artificial head and a diffuse sound field, according to DIN ISO 4869-1. Increasing the cup mass improved the noise attenuation by 17 dB at 100–300 Hz. The coherence function between cup vibration and sound pressure inside the cup has shown that a great amount of sound energy is transmitted to the inside of the cup, at low frequencies. The foam lining of the cup clearly attenuated the sound in the frequency between 2000 and 8000 Hz. Increasing absorbent mass improved attenuation because resonances could be damped. The attenuation measured with a complete earmuff, and the same without the cushion, have shown that sound leakage occurs at frequencies ranging from 100–2000 Hz. The vaseline coating between the skin and the cushion improve the attenuation by less than 5 dB (100–200 Hz). As the headband force increases to a maximal deformation of the cushion, attenuation reaches 20 dB at 200 Hz. The increase in the headband force is, however, a limiting factor in the use of the earmuff, as it becomes too uncomfortable. The same conclusion applied to the increase in the mass of the cup.

WEDNESDAY MORNING, 17 MARCH 1999 ROOM H1028, 8:00 A.M. TO 12:00 NOON

Session 3aNSc

Noise and Physical Acoustics: Experience with Noise Prediction II

Karl-Wilhelm Hirsch, Cochair
Institut für Lärmschutz, Arnheimer Strasse 107, 40489 Düsseldorf, Germany

Keith Attenborough, Cochair
Faculty of Technology, The Open University, Milton Keynes MK7 6AA, UK

Invited Papers

8:00

3aNSc1. Experiences with high-speed algorithms for full-field predictions of long-range sound propagation in the atmosphere. Martin West and Robert A. Sack (Univ. of Salford, Salford M5 4WT, UK)

Algorithms based on a parabolic equation (PE) solution of the Helmholtz equation have in the last few years become popular because of their precision and robustness, as well as their flexibility in dealing with a wide range of ground boundary conditions and meteorological conditions. PE solutions previously had to be performed on powerful workstations, but with recent advances in personal computer (PC) hardware it is possible to obtain limited predictions on more modest computers. The new algorithms being developed by this group have the potential to increase computational speeds of standard PE algorithms by up to two orders.

8:20

3aNSc2. The development of prediction models to control noise levels around UK firing ranges. Geoff Kerry and Martin West (Univ. of Salford, Salford M5 4WT, UK)

Since 1981, many UK firing ranges have used computer-based prediction models to control noise levels in the surrounding countryside. These models take into account local surface conditions and meteorology to provide peak noise level contour maps over distances of up to 30 km. A feature of these models is that peak noise level maps can be produced within a few minutes of the input of meteorological data obtained directly from radiosonde ascents or from mesoscale models. Several new prediction models have been developed at Salford over the years, taking advantage of the ever increasing power of personal computers to improve accuracy and user input and output facilities. This paper will discuss the model developments, including the meteorological preprocessor, illustrate some of the techniques adopted to improve accuracy and speed, and outline future improvements.

8:40

3aNSc3. Measurements and computations of shooting noise. Part 1: Muzzle noise. Erik M. Salomons and Frank H. A. van den Berg (TNO Inst. of Appl. Phys., Stieltjesweg 1, 2600 AD Delft, The Netherlands)

The accuracy of a model for propagation of shooting noise is investigated by comparison with experimental data for muzzle noise and detonation noise of several weapons, over ranges up to 15 km. The caliber of the weapons ranges from 7.62 to 155 mm. The model is based on a database with values of the transmission loss computed with the parabolic equation method for a set of 27 atmospheric sound speed profiles, three ground types, and many different source–receiver configurations. For the comparisons between the model and the measurements, sound-speed profiles are selected from a set of 27 profiles, based on experimental profiles computed from meteorological data collected during the measurements. In general, good agreement is obtained between measured and computed sound levels and spectra. It is found that sound propagation over water yields considerably higher levels than sound propagation over grassland does. Situations with heterogeneous grounds are investigated as well, e.g., consisting of a grass area and a water area. [This work was coordinated and financed by the Dutch Ministry of Defence, Defence Co-ordinator Physical Planning and Environmental Affairs (MODNL-CROMD).]

Contributed Papers

9:00

3aNSc4. Measurements and computations of shooting noise. Part 2: Bullet noise. Frank H. A. van den Berg and Erik M. Salomons (TNO Inst. of Appl. Phys., Stieltjesweg 1, P.O. Box 155, 2600 AD Delft, The Netherlands)

Due to the supersonic speed of the bullet, a shock wave is generated (sonic boom). A method has been developed to compute the generation and propagation of bullet noise on the basis of the geometry of the bullet and its speed. This model also holds for bullet paths of finite length with decreasing bullet speed. The accuracy of this model is investigated by comparison with experimental data for propagation of bullet noise of several weapons, over ranges up to 7 km. The caliber of the weapons ranges from 5.56 to 120 mm. The measurements indicate that nonlinear effects are only important for the first few hundred meters from the bullet path. This is explained by a coherence loss, caused by propagation through the atmosphere. When corrected for this loss, the measurements and calculations of bullet noise compare reasonably well. [This work was coordinated and financed by the Dutch Ministry of Defence, Defence Co-ordinator Physical Planning and Environmental Affairs (MODNL-CROMD).]

9:20

3aNSc5. Calculation of aircraft sound propagation on airports via determination of ground impedance. Reinhard Blumrich (DLR, Institut für Physik der Atmosphäre, D-82234 Weßling, Germany, reinhard.blumrich@dlr.de) and Jürgen Altmann (Ruhr Universität Bochum, 44780 Bochum, Germany)

In the framework of acoustic and seismic monitoring of airports for verifying disarmament or peace-keeping agreements, the propagation of sound emitted by aircraft was investigated. This propagation is strongly affected by the porous ground. A determination of the ground surface impedance allows one to calculate the attenuation and phase shift with distance and height. In the course of aircraft signal measurements at the military airport at Jever, Germany, the surface impedance of the grass-covered ground was determined from c. 60 Hz to 2.2 kHz by measurements of complex transfer functions using (quasi-)white noise and a numerical inversion of the spherical wave reflection factor. A three-parameter impedance model was fitted to the measured impedance. By means of the ground impedance propagation calculations are carried out. In the case of the transfer function measurement signals, the calculated spectra agree very well with the actually measured ones. In the case of the jet aircraft, the simulated spectra fit to those of the measured signals only in general appearances of amplitude, and not in phase. This is probably due to an inaccurate localization of the sound source, its extension and directivity. Wind and temperature gradients were not considered.

9:40–10:00 Break

10:00

3aNSc6. Forecasts of sound propagation by a mesoscale atmospheric model. Svenn O. Haugland (Geophysical Inst., Univ. of Bergen, Allegt. 70, 5018 Bergen, Norway) and Lars R. Hole (Norwegian Defence Construction Service (NDCS), Oslo mil/Akershus, 0015 Oslo, Norway, larsr@gfi.uib.no)

A mesoscale atmospheric model has been used to simulate local wind and temperature profiles in an area with hilly terrain in eastern Norway. Simulated wind and temperature profiles have been used to determine the local sound velocity profiles. The predicted profiles were used as input in an acoustic model. Meterological measurements were carried out in conjunction with measurements of propagation of low frequency (<100 Hz) impulse sound. The predicted atmospheric profiles are compared with profiles measured by meteorological towers and a tethered balloon launched at the site.

10:20

3aNSc7. Meteo-BEM: A new hybrid approach to predict noise barriers' efficiency with meteorological effects, theory, and comparison with experimental results. Eric Premat (ENTPE, DGCB CNRS URA 1652, 2 rue Maurice Audin, 69518 Vaulx-en-Velin Cedex, France) and Yannick Gabillet (CSTB, 38400 Saint-Martin d'Heres, France)

In a complex outdoor environment, meteorological factors have been found to affect the sound field. On one hand, boundary element methods are particularly well adapted to calculate the sound pressure above complex boundaries (various absorbing properties and shapes) in a homogeneous atmosphere. On the other hand, a few models have been recently developed to describe the acoustic propagation in inhomogeneous media

(normal modes, residue series, parabolic equation, fast field program . . .). Meteo-BEM is a new hybrid formulation taking advantage of the power of the boundary element methods, and including meteorological effects using as the appropriate Green's function these recent propagation models in inhomogeneous media. In this paper, the theory of BEM, together with sound propagation in inhomogeneous media, is briefly recalled. The new hybrid model is then presented. The case of a rigid thin-noise barrier on a flat ground under a known sound-speed gradient condition is studied. Results from Meteo-BEM are then compared to measurement data for validation. It is shown that this new model allows one to calculate accurately the sound field in a complex outdoor environment and offers promising further developments.

10:40

3aNSc8. Assessing changes in the noise environment from military training ranges: A case study in forensic acoustics. George A. Luz and Nelson D. Lewis (U.S. Army Ctr. for Health Promotion and Preventive Medicine, 5158 Blackhawk Rd., Abereen Proving Ground, MD 21010-5422)

In response to litigation alleging that an Army installation was making more noise in land adjoining tank and artillery ranges in 1997 than when the owner had purchased the land in 1969, the past weapons noise environment had to be reconstructed from available data. The results, which documented the changes in the training noise environment from 1971 to 1984 to 1997, demonstrated the long-term benefits of the U.S. Army Construction Engineering Research Laboratories' BNOISE computer model. Also discussed is (1) the use of automated noise monitoring data to validate ''busy day'' weapons noise contour maps and (2) the potential for cost savings by combining environmental noise modeling with air, water, and solid waste pollution.

11:00

3aNSc9. Moving point source—A simple model for predicting statistical sound levels in the neighborhood. Edelbert Schaffert and Stefan Becker (BesB GmbH Berlin, Undinestr. 43, 12203 Berlin, Germany)

When predicting the noise produced by moving sound sources (e.g., vehicles, airplanes, etc.) sound-level statistics can be helpful to describe the situation. However, the common sound models only yield the average sound level, and under special circumstances, also the maximum sound level. The calculation model moving sound source also gives sound level and the level-versus-time diagram. For the calculation, first the paths of the sound sources have to be digitalized and divided into parts. Each part will be represented as a point sound source which is active during a certain time slot, which again is based upon the velocities of the moving objects. Sound propagation from all point sources to the point of emission is calculated by using ISO or equivalent standards. This leads to the time versus level diagram and (when the steps from one to another point source are small enough) to the desired statistical levels. The described model, named the moving sound source, has no limitations. It could be easily integrated in commercial sound propagation calculation programs. It was successfully used for the approval of a new racetrack in Germany. Also, the new DIN 45684 (noise of small aircraft) is based on it.

11:20

3aNSc10. Track dispersion in aircraft noise modeling. Rudolf Buetikofer and Stefan Pluess (EMPA, CH-8600 Duebendorf, Switzerland)

Aircraft noise calculations based on clusters of single flight events are compared to results from a set of average flight paths. For the situation of Zurich airport, the aircraft noise was calculated with two different methods for the data input to the noise calculation program. The traditional method consists of defining a main track and several side tracks, each associated with a specific percentage of traffic. Further, an average climb profile was defined for each aircraft type. The definition of these average flight paths is based on the analysis of radar information from the airport. The new method selects for a given aircraft and departure (or landing) procedure from all available radar data sets a representative sample of, e.g., 100 flights, including different seasons, different companies, and different take-off weights. For each individual (real) flight the aircraft noise is calculated and the results are summed up according to the flight statistics. The price is an increase of computation load by a factor of 20, the benefit is a more representative result especially for regions with curved flights where the tracks diverge over a large area.

11:40

3aNSc11. Computational methods for designing a silator—A low-frequency resonator element. Norbert Kalus (Dept. of Math.-Phys.-Chem., TFH Berlin Univ. of Appl. Sci., Luxemburgerstr. 10, D-13353 Berlin, Germany, kalus@tfh-berlin.de)

The silator is a vacuum bubble resonator element which is used as a noise control device and has a low-frequency performance. It consists of an evacuated, lens-shaped, convex cap of sheet metal. The capsule volume can be made as small as desired, since, because of the vacuum inside, there is no air stiffness. The effect of a silator is comparable to that of a Helmholtz resonator, but only a hundredth of the latter's installation volume is needed. Broadband noise control can be achieved by a set of silators tuned to different frequencies. The principles of this silator technology in aeroacoustics were established by Bschorr and Laudien in 1992. The resonant characteristics of such a device are very sensitive to its geometrical properties. The plasticity of the material, the metal forming, and the remaining stresses in the convex cap also influence its effectiveness. The major development problem lies in the extremely small manufacturing tolerances. The tolerances decrease with increasing size and frequency. In this paper, computational methods and results are presented to yield the final design of the silator's shape with a very low resonant frequency. The calculations were performed using the finite-element program MSC/NASTRAN for Windows.

Session 3aNSd

Noise: Aerodynamic Noise of Vehicles

Bernd Barsikow, Cochair
Akustik Data Engineering Office, Kirchblick 9, D-14129 Berlin, Germany

Paul R. Donovan, Cochair
General Motors Proving Grounds, 24-NVL, Milford, Michigan 48380-3726, USA

Chair's Introduction—8:55

Invited Papers

9:00

3aNSd1. Characteristics of the Aeolian tone generated from cylinders in conjunction with pantograph noise control. Hajime Fujita (Dept. of Mech. Eng., Nihon Univ., 1-8 Kanda Surugadai, Chiyoda-ku, Tokyo 101-8308, Japan) and Akio Sagawa (Railway Tech. Res. Inst., Maibara, Shiga 521-0013, Japan)

Aerodynamic sound generated from cylindrical objects, such as in pantographs of trains, is a prime noise source in high-speed vehicles. Characteristics of the aerodynamic sound generated from two-dimensional cylinders are studied experimentally in order to contribute to the prediction and control of high-speed vehicle noise. The effect of the angle of inclination to the mean flow of a circular cylinder, and the effect of the angle of attack of a square cylinder, to the Aeolian tone generation are studied quantitatively, and angle ranges for low noise generation are found in the subcritical Reynolds number range. The relative importance of the cylinder surface pressure fluctuation and its spanwise correlation length to the Aeolian tone generation is revealed. Experiments are extended to the super-critical Reynolds number range for a circular cylinder normal to the mean flow. In the beginning of the surface boundary layer transition, the Strouhal number suddenly jumps up to about twice as much and the Aeolian tone level decreases suddenly about 20 dB. It is found that the decrease of the Aeolian tone level is mainly due to the decrease of the cylinder surface pressure fluctuation. Application to recent pantograph development is discussed.

9:20

3aNSd2. Reducing the sound emission of TRANSRAPID by decreasing the aerodynamic sound sources. Klaus-Peter Schmitz and Hans-Gerd Runde (Industrieanlagen-Betriebsgesellschaft mbH—Magnetbahn–Versuchsanlage—Hermann-Kemper-Straße 23, D-49762 Lathen, Germany, klaus-peter.schmitz@tm.iabg.de)

With the support of the BMBF and in commission of the MVP, the IABG pursues the TRANSRAPID test facility. The TRANSRAPID vehicle TR07 started in 1989 with a very low sound emission. A passby level of 94 dB was measured in a distance of 25 m (free propagation and without soundshields) and a speed of 400 km/h. First investigations with a microphone array pointed out a very calm upper part of the car body and some sound sources in the region of the bow as well as in the region of the levitation and guidance system (LGS). These results showed the low importance of the noise emissions caused by the turbulent boundary layer (TBL) as there was no sound emission found in the upper part of the vehicle. So the sound emission seemed to be caused by aerodynamic sound sources coming from discontinuities of the shape. To reduce the sound emission especially the shape of the bow was modified, the design of the covering plates of the LGS was optimized, and new inner coverings between the vehicle and the guideway were developed. All these changes have decreased the sound emission of the TR07; today a pass-by level of 88.5 dB is realized.

9:40

3aNSd3. Aerodynamic noise from vehicles on the Yamanashi Maglev Test Line. Masaaki Miyamoto, Mikio Yamazaki, Yasuyuki Goto (Linear Express Development Div., Central Japan Railway Co., Chuo-ku, Tokyo, Japan), Makoto Ueno (Railway Tech. Res. Inst., Chuo-ku, Tokyo, Japan), Yasuo Zenda, and Masanobu Iida (Railway Tech. Res. Inst., Kokubunji-City, Tokyo, Japan)

This paper is a report about aerodynamic noise from Maglev vehicles running at an ultra high speed. Maglev running tests have been carried out on the Yamanashi Maglev Test Line and 550 km/h was recorded in December 1997. The noise produced when Maglev vehicles run at high speed consists of almost only aerodynamic noise because of the levitated running of Maglev vehicles. Two types of nose shapes were developed for Yamanashi test cars in order to considerably reduce air drag and aerodynamic noise. The noise measured when Maglev vehicles running on the viaduct at the velocity of 500 km/h will be reported in this paper. Also the rate of increase of noise to velocity and the source of noise of running Maglev vehicles will be reported. In general, it is known that when a high-speed train enters a tunnel, a compression wave is generated ahead of the train and a pulse wave radiates from the exit of the tunnel, and an air pressure booming noise is generated in some cases. This air pressure booming noise is successfully suppressed by setting a hood at the tunnel entrance in this test line.

10:00

3aNSd4. Sound radiation from flow-excited, elastically supported rectangular panels. L. Mongeau, J. Fazio (School of Mech. Eng., Purdue Univ., 1077 Herrick Labs., West Lafayette, IN 47907-1077), and N. Vlahopoulos (Univ. of Michigan, Ann Arbor, MI 48109-2145)

The objective of this study was to evaluate the influence of the viscoelastic properties of glass run weather seals on the interior noise radiated by vehicle window panel vibrations. The vibrational response of a flow-excited rectangular aluminum panel supported on all four edges by a fixture hosting a glass run rubber sealing system was measured in a low-speed wind tunnel. The panel was attached to an acoustically treated enclosure located underneath the wind tunnel test section. The resonance frequencies, damping coefficients, and mode shapes of the panel were measured following established modal analysis procedures. Two different sealing systems were investigated to study the influence of seal compliance and damping factor on the sound transmission loss of the elastically supported panel. The experimental results were compared to predictions obtained using finite-element and boundary element numerical methods. The sensitivity of the radiated sound level to variable seal properties was evaluated. The possible applications of these results to quiet vehicle seal design were considered.

10:20–10:40 Break

10:40

3aNSd5. Wind tunnel noise measurements on full-scale pantograph models. Thomas Lölgen (Dept. of Acoust., Res. and Technol. Ctr., Deutsche Bahn AG, Völckerstr. 5. 80939 München, Germany)

Noise reduction of pantographs is of special importance for the operation of high-speed trains, since the pantograph noise cannot be treated with passive counter measures like sound barriers. Therefore the noise emission of pantographs was investigated in an acoustically treated wind tunnel for air speeds up to 400 km/h. The aims were to determine the noise reduction potential of pantographs, to investigate their aerodynamic behavior, to validate existing theoretical models, and to compare measurement techniques and wind tunnels. The acoustic measurements were carried out using a microphone array system, a parabolic antenna as well as normal microphones. Two pantographs, which are in service today in Germany and Japan, were used as references. Two full-scale models of high-speed pantographs were tested in several configurations. The achieved noise reduction of the models compared to the reference pantographs confirmed the theoretical results.

Contributed Papers

11:00

3aNSd6. Measurements of sound radiated by turbulent wall jets past singularities. Marc C. Jacob (LMFA, UMR CNRS 5509, Ecole Centrale de Lyon BP 163, 69131 Ecully Cedex, France), Alain Louisot (Métraflu, 69130 Ecully, France), and Sylvie Guerrand (Direction de la Recherche et de la Technologie, SNCF, 75379 Paris Cedex 08, France)

Sound radiated by high-speed turbulent wall jets past backward facing steps or shallow cavities is investigated experimentally. Both aerodynamic (laser Doppler and hot wire anemometry) and acoustic measurements (far-field directivity, spectra, and source localizations) are performed. Source localizations show that a backward facing step is a major sound source. Far-field measurements show that it has a strong upstream directivity and radiates in the medium frequency range. Aerodynamical results and an acoustic parametric study suggest that the source is due to the diffraction of the separated shear layer eddies by the sharp edge of the step: this is qualitatively confirmed by existing diffraction models. A shallow cavity (with length exceeding seven times the depth) has a strong downstream and upstream directivity: it can be regarded as a superposition of two acoustically independent sources, a backward facing and an upward facing step. In particular for such cavities and for Reynolds numbers (based on cavity depth) ranging from 40 000 to 470 000 no feedback mechanism and no cavity resonances are observed. [Work supported by the French Ministère des transports.]

11:20

3aNSd7. Boundary-layer noise from high-speed vehicles: Theory and measurement. W. F. KingIII, B. Barsikow, and M. Klemenz (akustik-data Eng. Office, Kirchblick 9, D-14129 Berlin, Germany, akustik_data@compuserve.com)

Wayside noise emitted by the turbulent boundary layer (TBL) on a moving vehicle represents its minimal acoustic radiation. When wayside noise levels for aerodynamically clean vehicles (particularly maglev ones) begin to approach within 3 dB of the TBL noise level, further abatement measures become ineffectual. Knowledge of this lower bound to wayside noise is important to avoid expenditures for useless attempts at further lowering sound levels. The acoustic energy of TBL noise per unit area is low, but its cumulative contribution on a long vehicle could be significant. The present paper comprises two parts. One is a semi-empirical theory of TBL noise. Although Lighthill's acoustic analogy correctly describes TBL noise, this equation cannot be solved without knowledge of the (as yet) unknown source terms. Furthermore, the fluctuating density, the desired solution, appears on both sides of the equation. Hence, a model approach becomes necessary. The present offering is based upon extrapolated parameters describing the burst-sweep cycle within a flat-plate TBL. The second part of the paper summarizes results of array measurements made above the smooth roof of the maglev vehicle Transrapid 07 at speeds up to 400 km/h. Predictions show reasonable agreement with measurements.

11:40

3aNSd8. The relationship between the power level and different parameters of a single vehicle noise. Antonio Reig, Esteban Gaja, Jose Luis Manglano, and Salvador Sancho (ETSII Univ. Politecnica Valencia, Cno Vera s/n, 46022 Valencia, Spain)

This paper is concerned with the description of various factors, such as velocity, gears, and type of vehicle affecting the power level of a vehicle noise; a resume of this dependence will be offered. This work has been done in the Universidad Politecnica de Valencia (Spain) by the Laboratorio de Ingeniera Acoustica within a Thesis Project, with the aim to develop a predictive mathematical model of the urban traffic noise. Measurements were taken with an analyst Bruel mod. 2236, which enables one to obtain power levels in third octave bands by a real-time spectral analysis. The measurements being used are extensively explained in this paper, in particular that special care was taken to avoid noise from other sources that could interfere with the results. The reason why the power level was chosen as the first stage of this study of traffic noise, starting from the single vehicle as the point source, was to comply with the methodology established in the second part of standards ISO 9613, leaving for a second stage the propagation of the urban traffic noise. The final results show the great correlation between speed of the vehicle and power level.

12:00

3aNSd9. Experimental investigations of surface pressure fluctuations related to car interior noise. B. Brähler, I. U. Borchers, L. Schauwecker (Dept. of Vibroacoutics, Daimler Benz Aerosp. Dornier GmbH, Friedrichshafen, Germany, Boris.Braehler@dbag.fdh.daimlerbenz.com), and V. Mellert (Universität Oldenburg, Oldenburg, Germany)

Due to the progress in the reduction of engine noise and tire/road noise for cars, aerodynamically induced noise becomes increasingly important for car interiors and for speeds above 120 km/h. The aerodynamically induced noise is mainly caused by flow separations which may lead to highly intensive surface pressure fluctuations forcing the car housing to vibrate and to radiate. This is the case especially for the windows, which have a relatively small transmission loss. Due to the very strong flow separations behind both the A pillar and the rearview mirror the side windows play a major role as aeroacoustic noise sources in the interior of automobiles. In this study the flow around the side windows of a production car, where there is nearly no vortex separation on the A pillar, is investigated. Therefore, the influences of the A pillar and rearview mirror could be studied independently by generating each source separately. For different configurations measurements of the hydrodynamic pressure fluctuations next to the side window were performed. Dependent on the spatial distribution of the pressure fluctuations significant changes for the car interior noise may be expected. The experimental results suggest a large potential of further reduction of car interior noise due to an aeroacoustic optimization of the flow.

WEDNESDAY MORNING, 17 MARCH 1999 ROOM H110, 8:20 A.M. TO 12:20 P.M.

Session 3aNSe

Noise: IEC61672–The New International Standard for Sound Level Meters

Alan H. Marsh, Cochair
DyTec Engineering, 5092 Tasman Drive, Huntington Beach, California 92649, USA

Hans O. Finke, Cochair
Opferkamp 12, D-38110 Braunschweig, Germany

Invited Papers

8:20

3aNSe1. Introductory remarks. Alan H. Marsh (DyTec Engineering, Inc., 5092 Tasman Dr., Huntington Beach, CA 92649) and Hans-Otto Finke (Opferkamp 12, D-38110 Braunschweig, Germany)

The new International Standard (IEC 61672, sound level meters) is being developed by Working Group 4 for IEC/Technical Committee 29, Electroacoustics. The standard will be published by the International Electrotechnical Commission (IEC). It amalgamates and extends the specifications and test procedures that were given in IEC 60651:1979 for conventional instruments that display sound levels with exponential time weighting and IEC 60804:1985 for integrating-averaging instruments that display time-average sound levels. A sound-level meter conforming to the specifications of IEC 61672 will provide the user with higher-quality measurements than previously available, especially for transient and short-duration sounds. This standard represents the culmination of years of effort by a dedicated team of experts from several countries. This special session will describe the acoustical and electrical characteristics that are required. All presenters of papers in this session are members of Working Group 4.

8:40

3aNSe2. Scope of the new standard. William V. Richings (3 Old Hall Ave., Duffield, Belper, Derbyshire DE56 4GN, UK)

The fundamental requirements for IEC 61672 have not changed. However, practical experience, advances in technology, and current regulations have been taken into account when developing the new standard. The type 0 accuracy category of IEC 651 is almost nonexistent because it is too specialized, while type 3 has been made redundant by the low cost of modern circuitry. Thus the new standard describes only two performance classes corresponding to much improved types 1 and 2 of the previous standard. Important new annexes give detailed procedures for conformance tests and for periodic checks. It is now recognized that the uncertainties of measurement are not negligible and realistic tolerance limits have been specified to include them. Another significant advance for the measurement of impulsive sounds is that a minimum linear operating range of 60 dB is specified for all instruments. Existing and draft European Community Directives call for peak C-weighted measurements and appropriate specifications are given. Requirements for immunity to electrostatic discharges and radio-frequency fields and for radio-frequency emission have been included to cover regulations in Europe and elsewhere. The environmental reference conditions have been changed to 23 °C and 50% relative humidity for consistency with the IEC microphone standards.

9:00

3aNSe3. Free-field response of sound level meters. Gaston Banget-Mossaz and Jean-Noël Durocher (Laboratoire National d'Essais, 75724 Paris, Cedex 15, France, Gaston.Banget@lne.fr)

Within specified ranges, sound level meters should be able to measure a frequency-weighted sound pressure level at a given point, regardless of the direction of sound incidence and the frequency of the sound. Acoustical characteristics of sound level meters are specified in draft IEC 61672 as a function of frequency for plane progressive sound waves of steady sinusoidal signals under free-field conditions. The free-field frequency response of a microphone in a specified reference direction is modified by (a) sound reflected

from the case of the sound level meter, (b) the apparatus that supports the instrument under test, and (c) the frequency response of the system that processes the signals from the microphone. From the simulated influence of sound waves reflected from an instrument equipped with a microphone having a FLAT frequency response, it is shown that linear frequency steps should be preferred to logarithmic frequency steps for evaluation of reflection effects. Test signal frequencies are calculated from the quotient of the speed of sound by the distances from the reflection point on the case to the microphone reference point. Measurement results are shown and comments noted regarding the procedures in the proposed standard for testing acoustical characteristics.

9:20

3aNSe4. Frequency weightings and responses. Peter Hedegaard (Brüel & Kjaer, 2850 Naerum, Denmark)

The first frequency weightings for sound-level meters were described in the 1940s in American and German standards. The well-known A, B, and C frequency weightings were originally designed to match the equal loudness contours described by Fletcher and Munson. These frequency weightings were realizable by simple passive electronic circuits. Even though the frequency weightings in proposed IEC 61672 are unchanged, their use is changed. Frequency weightings are now defined by their poles and zeros, and may be calculated to any degree of precison. Since 1961, other frequency weightings have been standardized for special purposes but are largely obsolete, along with the B weighting. Tolerance limits are discussed for the different performance classes and their changes from 1961 to the present. Wide tolerance limits for the high- and low-frequency ends of the frequency range are necessary to allow for different microphone sizes, manufacturing tolerances, and unattended operation outdoors. The wide limits may cause differences in measurement of sound levels if the sound has strong high- or low-frequency components. Some unsuccessful attempts to solve the problem are discussed. The new Z-weighting, FLAT frequency response, and the use of C-weighting for measurements of peak sound-pressure level, are discussed.

9:40

3aNSe5. Response to steady signals. Theodore J. Kuemmel (Quest Technologies, Inc., 510 S. Worthington St., Oconomowoc, WI 53066)

The level of a steady sinusoidal signal indicated by a sound-level meter should be linearly related to the level of the corresponding signal at the input. Small level-linearity errors over a wide range of input signal levels and signal frequencies are a powerful indicator of the ability of a sound-level meter to square and form the time integral of the sound-pressure signal properly. Errors in level-range controls as well as level linearity are specified in proposed IEC 61672 relative to a fixed reference level difference at the reference frequency for the reference sound-pressure level on the reference level range. At 1 kHz, the extent of the linear operating range is to be at least 60 dB. The Instruction Manual is to state the nominal sound levels at the lower and upper boundaries of the linear operating ranges at specified frequencies. The new standard requires an instrument to have overload and under-range indicators. Level-linearity errors are to be within the tolerance limits up to the first indication of overload. Data will be presented to demonstrate that modern designs for sound-level meters can conform to the specifications for the response to steady sinusoidal electrical signals.

10:00

3aNSe6. Response to nonsteady signals. Ole-Herman Bjor (Norsonic AS, P.O. Box 24, N-3420 Lierskogen, Norway)

A sound-level meter should respond correctly to the frequency-weighted energy of the sound signal, no matter whether the signal comes from a pistol shot or a fan. Most sound signals of interest are transients, some with very short durations and high peak amplitudes. A major part of the proposed IEC 61672 standard describes requirements for the response of a sound-level meter to short duration signals of various levels and durations. Compared with the present standards for sound-level meters, the requirements for measurements of short-duration signals have been improved considerably. After considerable discussion, the Working Group decided to specify and test a sound-level meter with electrical toneburst signals of various durations as extracted from a steady 4-kHz sinusoidal signal. The specifications apply to all kinds of sound-level meters; hence, they are given in terms of maximum F- and S-weighted sound level and in terms of sound exposure level or time-average sound level. The response of the microphone is specified separately. Examples will be shown to demonstrate the ability of modern-design class 1 and class 2 sound-level meters to conform to the specifications of the proposed International Standard.

10:20–10:40 Break

10:40

3aNSe7. Peak C-weighted sound-pressure level. Hiroaki Takinami (Rion Co., Ltd., Kokubunji, Tokyo, Japan)

Peak sound pressure is the greatest absolute value of the instantaneous sound pressure occurring within a stated time interval. Peak sound-pressure levels are measured without exponential time weighting and hence are fundamentally different from maximum sound levels measured with time weighting F or S. Until the development of the new International Standard for sound-level meters in IEC 61672, there was no internationally accepted specification for measurements of the peak level of nonsteady or transient sounds. For short-duration sounds, the value of the peak sound-pressure level depends on the frequency bandwidth of the measuring device; very short-duration signals require a wide bandwidth of uniform frequency response. To permit reproducible measurements of various short-duration sounds, IEC 61672 provides specifications for peak C-weighted sound-pressure levels. Frequency-weighting C has the most uniform response over the widest bandwidth of any internationally standarized frequency weighting. The specification requires that the peak C-weighted levels of a single cycle at 31,5 Hz, 500 Hz, and 8 kHz and positive and negative half cycles of 500-Hz sinusoidal signals be measured within practical tolerance limits. Data will be shown to demonstrate conformance of instruments to the specification.

11:00

3aNSe8. Environmental considerations for sound-level meters. Richard G. Tyler (Cel Instruments Ltd., 35-37 Bury Mead Rd., Hitchin, Herts SG5 1RT, UK)

A sound-level meter should operate as intended over a wide range of environmental conditions. To ensure this objective, IEC 61672 sets limits for the influence of atmospheric conditions and radio-frequency (rf) fields. A limit is also established for the rf emissions from a sound-level meter. Specifications in IEC 61672 for the influence of temperature and humidity on the performance of a sound-level meter are more stringent for class 1 instruments than corresponding specifications in existing standards. The extremes of the temperature–humidity range are reduced for class 2 instruments. Requirements for the effects of atmospheric pressure remain similar. New specifications were added for the effects of static discharges up to 8 kV and for the influence of exposure to a moderate rf field. Limits for the influence on instrument performance of a given rf field, with carrier frequencies from 25 MHz to 1 GHz, should satisfy most existing national and European Union requirements. Tests to demonstrate conformance with these requirements are specified in the proposed International Standard. Test results will be presented, as available, to demonstrate that modern designs for sound-level meters are able to conform to the environmental specifications in IEC 61672.

11:20

3aNSe9. Uncertainties of measurement and IEC 61672. Susan P. Dowson (Ctr. for Mech. and Acoust. Metrology, Natl. Physical Lab., Teddington TW11 0LW, UK)

No measurement is ever exact; there is always an uncertainty associated with it. In the past, international specification standards for the performance of acoustical instruments have not included uncertainties of measurement of the testing laboratory when specifying tolerance limits. However, to demonstrate conclusively whether or not a particular instrument conforms to the specifications of a standard, it is essential that these measurement uncertainties be taken into account. In a recent change of policy, the international committee responsible, IEC TC-29 ''Electroacoustics,'' has decided that all its future standards must include uncertainties of measurement in the tolerance limits specified. This paper will discuss different types of measurement uncertainty and likely contributions to uncertainty budgets. It also explains the difficulties in accumulating the necessary data for inclusion in IEC 61672, and of incorporating the data into the tolerance limits. The reasoning behind the decision to quote a maximum permitted expanded uncertainty of measurement for the testing laboratory separately for each test will also be discussed. Examples will be presented of the determination of expanded uncertainties of measurement for acoustical and electrical signals and their application in assessments of conformance.

Contributed Paper

11:40

3aNSe10. Tolerances of ''A''-weighting at extreme frequencies. Alan D. Wallis and Christopher G. Rice (ISVR Univ. of Southampton, Southampton SO17 1BJ, UK, adwallis@compuserve.com)

Since IEC 123 (sound level meters) there has been an infinite negative tolerance permitted on the frequency weightings at the extremes of frequency. For example, the attenuation of A-weighting at 31.5 Hz was 39.2 dB, with a tolerance of ± 5 dB. At all frequencies below this, the tolerances are $+5$ dB and minus infinity. A similar situation occurs at 8 kHz and above. Thus a sound level meter which did not respond at all to signals below 31.5 Hz or above 8 kHz may well meet the full requirements of the standard. In 1979, IEC 651 kept the same situation for a type 3 instrument, but changed the frequencies at which infinite negative tolerances were permitted to below 20 Hz and above 12.5 kHz for a type 1 instrument. The August 1998 draft of IEC 61672-3CD also has infinite tolerances but now at 16 Hz and 16 kHz for a class 1 and 20 Hz and 8 kHz for a class 2. Many workers suggest that infinite tolerances should no longer be permitted, while others think that they are essential. This paper evaluates both sides of the argument and offers suggested tolerance figures.

Invited Paper

12:00

3aNSe11. Summary. Alan H. Marsh (DyTec Engineering, Inc., 5092 Tasman Dr., Huntington Beach, CA 92649)

The proposed International Standard, IEC 61672, for sound-level meters, differs significantly from the existing standards for such instruments. Existing standards include IEC 60651:1979 for conventional instruments that measure time-weighted and frequency-weighted sound levels and IEC 60804:1985 for integrating-averaging and integrating sound-level meters that measure time-average sound levels and sound exposure levels, respectively. The principal differences and improvements will be highlighted. The anticipated schedule leading to eventual publication by IEC will be indicated.

Session 3aNSf

Noise: Turbomachinery Noise

Johan B. H. M. Schulten, Cochair
National Aerospace Laboratory (NLR), P.O. Box 153, 8300 AD Emmeloord, The Netherlands

Stewart A. L. Glegg, Cochair
Center for Acoustics and Vibration, Department of Ocean Engineering, Florida Atlantic University, Boca Raton, Florida 33431-0991, USA

Chair's Introduction—9:05

Invited Papers

9:10

3aNSf1. On the noise from turbomachinery and ducted fans—A review of prediction methods. Michel Roger (LMFA, UMR CNRS 5509, Ecole Centrale de Lyon, BP 163, 69131 Ecully Cedex, France)

Noise reduction of turbomachines and ducted fans is a major issue in aeronautics, with regard to both environment of airports and passengers. From the theoretical point of view, it is the final result of a whole strategy, involving physical understanding as a starting point and modeling as a tool for searching low-noise solutions. This is true for generating as well as propagating mechanisms. Within that scope, a complete simulation of the whole acoustic process from source to observer is not necessary. A partial model easy to run and able to predict the right trends is enough. The paper is devoted to a state-of-the-art in prediction methods. A presentation is given of both analytical and numerical techniques understood as complementary tools. Limitations of the former and expected future developments of the latter are discussed, together with hybrid techniques coupling computational fluid dynamics for the definition of sources and analytical acoustics. Examples are taken in the literature, not only in connection to turbofan engines, but also to other rotating blade technologies involving rotors and stators. The specificities of each application are used as a guideline for the best-suited approach.

9:40

3aNSf2. Predicting the effects of blade geometry on rotor–stator interaction noise. Nigel Peake (Dept. of Appl. Mathematics and Theoret. Phys., Silver St., Cambridge CB3 9EW, UK, n.peake@damtp.cam.ac.uk)

One of the principal noise generation mechanisms in modern high-bypass turbofan engines corresponds to the interaction between convected vortical disturbances from a rotor and a downstream stator row. In this talk, a method for predicting this noise will be described, which takes full account of the effects of the stator blade geometry. These effects include the distortion of the incident disturbances by the nonuniform flow around the stator, noise generation by flow sources close to the blade leading edges, and refraction as the noise propagates back upstream. The approach adopted involves the use of asymptotic analysis based on the realistic limits of large reduced frequency and small, but nonzero, blade camber and thickness. A new feature of this work concerns the behavior of the noise near modal cutoff. Previous ray-theoretic solutions diverge at these points, but a uniformly valid solution will be presented here which overcomes this difficulty. This makes it possible to use these techniques to predict the response of the stator to a whole turbulence spectrum, and not just to a single gust.

Contributed Papers

10:00

3aNSf3. Numerical analysis and active control of wake/blade-row interaction noise. C. J. Hwang and J. Y. Kuo (Inst. of Aeronautics and Astronautics, Natl. Cheng Kung Univ., Tainan, Taiwan, ROC, hwang@cfhp2.iaa.ncku.edu.tw)

A computational approach for investigating and controlling the wake/blade-row interaction noise through the use of actuators or blowing/suction on the stator blade surfaces is presented in this paper. This approach includes a solution-adaptive finite volume upwind scheme, adaptive/dynamic mesh technique, boundary treatments for aeroacoustic computations, and an active noise control algorithm. A two-dimensional section of a fan stage, which is composed of an upstream rotor and a downstream fan exit guide vane (FEGV), is investigated. By utilizing a rotor wake model, the acoustic fields of the FEGV are presented and analyzed to understand the accuracy and suitability of the present adaptive scheme. Also, the noise generation mechanics are studied. Finally, the active noise control algorithm is introduced. From the computational results, the reduction of noise due to actuators on the blade surfaces is more significant than that of using blowing/suction. The downstream propagating acoustic waves are more difficult to control than the upstream propagating waves. [Work supported by NSC.]

10:20–10:40 Break

10:40

3aNSf4. An analytical model for upstream and downstream sound power from swept blade rows. Stewart A. L. Glegg (Ctr. for Acoust. and Vib., Florida Atlantic Univ., Boca Raton, FL 33431)

This paper will describe an analytical approach which can be used to calculate the upstream or downstream sound power generated by a swept blade row. The blade row is modeled using a linear cascade of flat plates with finite chord. The correct allowance for spanwise loading and gust

convection is included. The value of this approach is that it can be used at very high reduced frequencies which are typically found in broadband fan noise applications. Results will be given which show the problems associated with only considering the noise sources at the leading edges of the blades and ignoring the trailing edges. The effects of blade sweep will also be illustrated by showing the radiated modal sound power as a function of blade sweep. [Work supported by NASA.]

11:00

3aNSf5. A cut-off attenuator with perforated plate in a centrifugal fan and its aeroacoustic experiments. Yadong Lu and Jing Tian (Inst. of Acoust., Chinese Acad. of Sci., P.O. Box 2712, Zhongguancun Rd., No. 17, Beijing 100080, PROC)

A new type of low-noise centrifugal fan with a special cut-off attenuator with a perforated plate has been invented and designed. The principle of noise suppression with this cut-off attenuator and its structure characteristics is introduced in this paper. A series of experimental comparisons of this type of centrifugal fan with a prototype centrifugal fan have been carried out. The experimental results show that the A-weighted noise level of a prototype fan without a cut-off attenuator with a perforated plate is 93 dB. As a result of using this special attenuator, the noise level of a centrifugal fan is decreased to 88.3 dB. Thus, sound attenuation due to this attenuator is 4.7 dB. In addition, decreasing the airflow and keeping the rotating velocity of the fan unchangeable, noise reduction would be 3.5 to 5.0 dB. It can be shown from the spectrum measurements that by using this cut-off attenuator with a perforated plate, not only the discrete frequency noise components of blade passing frequency and its harmonics, which predominate the sound level of a centrigual fan, can be attenuated, but also the broadband noise can be suppressed. Meanwhile, the aerodynamic performance of a centrifugal fan has not been greatly changed. [Work suported by NSFC.]

11:20

3aNSf6. Performance of acoustic liners for jet engine intake ducts. Matthew J. Greaves and Björn A. T. Petersson (Dept. of AAETS, Loughborough Univ., Loughborough LE11 3TU, England, M.J.Greaves@lboro.ac.uk)

In order to meet current and future noise emission regulations, it is necessary to reduce the noise generated by aircraft engines. One method is to line the duct with an attenuating configuration, and acoustic liners employing the Helmholtz resonator concept are now commonplace in jet engine intake ducts. Based on reports of core failure, the question of the mechanisms behind such failures, being the interaction of high sound pressure levels and shock waves with the liners, is addressed. Full-scale experimental pressure data are presented. Moreover, using the experimental data as input to a numerical model for nonrigid cavity walls, the induced stresses are analyzed. Results for typical liner configurations are given, and the nonlinear orifice effects considered. Possible alternative designs are examined and their advantages and disadvantages from an acoustic viewpoint discussed.

11:40

3aNSf7. Acoustical forced oscillation diagnosis method of cracks for turbomachinery. Leonid M. Gelman and Lyudmila V. Kondratyuk (Dept. of Nondestructive Testing, Natl. Tech. Univ. of Ukraine, 37, Peremogy pr., Kiev, 252056, Ukraine)

A new acoustical forced oscillation diagnosis method of fatigue cracks for turbomachinery is proposed. The method uses nonstationary vibration excitation with variable frequency. Turbomachinery rotating details with fatigue cracks were considered as piecewise-linear systems. A new analytical approach and new analytical expressions of spectral density of narrow-band noise of rotating details are proposed. Experimental results of diagnostics of gas-turbine engine compressor blades based on noise emission are presented.

WEDNESDAY MORNING, 17 MARCH 1999 ROOM MA042, 7:55 A.M. TO 12:20 P.M.

Session 3aPAa

Physical Acoustics: Duct Acoustics I

Dirk Ronneberger, Cochair
Drittes Physikalisches Institut, University of Göttingen, Burgerstrasse 42-44, D-37073 Göttingen, Germany

Walter Eversman, Cochair
Mechanical and Aerospace Engineering and Engineering Mechanics, University of Missouri, 202 Mechanical Engineering, Rolla, Missouri 65401, USA

Chair's Introduction—7:55

Invited Papers

8:00

3aPAa1. Energy conservation, time-reversal invariance, and reciprocity. Willi Mohring (MPI fur Stromungsforschung, Box 2853, D-37018 Gottingen, Germany)

The scattering of sound waves at a connection of two different ducts is studied. They may carry a mean flow. The two ducts may differ geometrically or in the wall properties, and the transition from one duct to the other may be smooth or abrupt. The wall is assumed to react linearly, but not necessarily locally. An incident acoustic mode generates transmitted and reflected waves. For potential flow and lossless walls, an energy conservation theorem is valid. There is then also usually an invariance with respect to time reversal, which includes reversal of the mean flow. These properties imply reciprocity with reversed flow. Possible generalizations to vortical mean flow are discussed. These relations can be extended to a certain class of absorbing materials which are important in

engineering and which show significant losses. This class consists of materials which are obtained from lossless materials by complexifying otherwise real material constants. (A resistance can be understood as an imaginary capacitance.) A reciprocity relation can then be obtained by analytic continuation, although there is neither energy conservation nor time-reversal invariance.

8:20

3aPAa2. Acoustic energy estimates in inhomogeneous moving media. F. Farassat (M.S. 461, NASA Langley Res. Ctr., Hampton, VA 23681) and Mark Farris (Midwestern State Univ., Wichita Falls, TX 76308)

In ducted fan engine noise research, there is a need for defining a simple and easy to use acoustic energy conservation law to help in quantification of noise-control techniques. There is a well-known conservation law relating acoustic energy and acoustic energy flux in the case of an isentropic irrotational flow. Several different approaches have been taken to generalize this conservation law. For example, Morfey [J. Sound Vib. (1971)] finds an identity by separating out the irrotational part of the perturbed flow. Myers [J. Fluid Mech. (1986)] is able to find a series of indentities by observing an algebraic relationship between the basic conservation of energy equation for a background flow and the underlying equations of motion. In an approximate sense, this algebraic relationship is preserved under perturbation. A third approach which seems to have not been pursued in the literature is a result known as Noether's theorem. There is a Lagrangian formulation for the Euler equation of fluid mechanics [M. E. Taylor, PDE's, Vol. 3, 1996]. Noether's theorem says that any group action that leaves the Lagrangian action invariant leads to a conserved quantity. This presentation will include a survey of current results regarding acoustic energy and preliminary results on the symmetries of the Lagrangian.

8:40

3aPAa3. A reverse flow theorem and acoustic reciprocity in compressible potential flows. Walter Eversman (Mech. and Aerosp. Eng. and Eng. Mech., Univ. of Missouri–Rolla, Rolla, MO 65401, eversman@umr.edu)

A reverse flow reciprocity theorem for acoustic propagation in compressible potential flows in nonuniform ducts is derived in terms of steady flow and acoustic velocity potentials. A similar result for a quasi-one-dimensional formulation is also presented. The theorem is specialized to investigate the characteristics of the acoustic modal scattering matrices for propagation in transition sections for axially symmetric ducts in the presence of high-speed flow. It is found that reflection coefficients for modes incident at the source plane in direct and reverse flow are related, and in particular, that diagonal elements in the direct and reverse flow reflection coefficient matrices are invariant. The same result is true for modes incident at the termination plane. The transmission coefficient matrix for modes incident at the source plane in direct flow is related to the transmission coefficient matrix for modes incident at the termination plane in reverse flow. Simpler but consistent results are demonstrated in the quasi-one-dimensional case where it is shown that the acoustic power transmission coefficient is invariant to the direction of flow. Numerical results from finite-element solutions are used to support the theoretical conclusions.

9:00

3aPAa4. Acoustics of ducted sources in motion. M. K. Myers (The George Washington Univ./JIAFS, MS 269, NASA Langley Res. Ctr., Hampton, VA 23681-2199, m.k.myers@larc.nasa.gov)

The radiation of sound into free space from sources enclosed in short ducts in subsonic forward motion has recently been of intense interest in connection with ducted fan aircraft engine noise technology. The current paper describes a boundary integral approach to calculating such fields which is applicable to arbitrary sources in circular ducts whose inner surfaces are lined with locally reacting absorbers. The theory is developed via a scattering formulation and leads to a system of two coupled singular boundary integral equations. For the case of a rigid inner duct surface, the system reduces to a single equation similar to that of unsteady subsonic lifting airfoil theory. The paper includes a description of the theoretical formulation and of a numerical solution of the governing integral equations. The numerical implementation is extremely economical to achieve, and its accuracy is affirmed by comparison with available results from alternate solutions obtained using CFD methods. Various results are presented to illustrate the effect of important parameters on the characteristics of the radiated sound.

9:20

3aPAa5. The effects of flanking transmission on sound attenuation in a finite-length lined duct, with mean flow. R. Kirby and A. Cummings (Faculty of Eng., Univ. of Hull, Hull HU6 7RX, UK, R.Kirby@eng.hull.ac.uk)

The acoustic performance of lined air-conditioning ducts is known to be compromised by the effects of flanking sound transmission. Two separate flanking paths have been identified; the first involves sound transmitted directly through the duct walls (sometimes termed radiation-by-pass) and the second involves the axial transmission of structural/acoustic waves along the duct walls. The attenuation of the internal sound field, particularly in relatively long ducts, is known to be limited by the effects of noise transmission caused by the formation of flanking paths. A model is described here which predicts the effect of both forms of flanking transmission on the attenuation of sound in a lined air-conditioning duct with mean flow in the central airway. Since most air-conditioning ductwork contains only a finite section of porous material, attenuation in both lined and unlined sections is included here. A finite-element eigenvalue solution is employed to couple the acoustic pressure field in the duct to the duct wall displacement. The principle of reciprocity is then used to model the effects of break-in. Finally, mode-matching techniques are employed to match the modal expansions across the discontinuity between the lined and unlined sections. [Financial support provided by the European Commission, BRITE/EURAM project FLODAC, Project No. BRPR CT97-0394.]

9:40

3aPAa6. Sound transmission in a slowly varying flow duct with lossless liner. Sjoerd W. Rienstra (Dept. of Math. & Computing Sci., Eindhoven Univ. of Technology, P.O. Box 513, 5600 MB Eindhoven, The Netherlands)

The explicit multiple-scales solution, presented in AIAA-No 98-2311, for modal sound transmission through slowly varying ducts with mean flow and acoustic lining, is extended to include the case of a (nominally) lossless liner ($Z=0$). Especially the hydrodynamic or vortical mode is examined since this contains, in cooperation with higher order modes, the possibility of sound production or absorption by transfer of acoustic energy to and from the vorticity layer.

10:00

3aPAa7. Scattering at localized absorbers in a lined duct wall. Fridolin P. Mechel (Landhausstrasse 12, D-71120 Grafenau, Germany)

Homogeneous absorbing duct linings usually are tuned for medium and high-frequency attenuation. If they were tuned to low frequencies also, their thickness would become large. A possibility to add low-frequency attenuation to a broadband attenuation at higher frequencies consists in the combination of localized Helmholtz resonators with a broadband lining. The scattering cross section of the resonator orifice is large enough to permit some axial spacing between resonators. A method will be presented to show how the scattering at localized resonator orifices in a lined duct wall can be computed. The sound field in the duct is synthesized with silencer modes. The resonator orifice is introduced into the modal analysis as an effective volume flow source. Its strength is evaluated from the boundary conditions. Numerical examples show the wanted low-frequency attenuation maxima by arrangements with only a little increase of the silencer length and lining thickness.

10:20–10:40 Break

Contributed Papers

10:40

3aPAa8. Nonlinear standing waves in the two-tube structure. Ke Liu and Dah-You Maa (Inst. of Acoust., Academia Sinica, P.O. Box 2712, Beijing 100080, PROC)

Nonlinear standing waves have been studied in a structure consisting of two lengths of tubing with different diameters. Preliminary theory of this structure is proposed. The measurement system of experiment is presented. A 100-W loudspeaker driver is used as a sound source to excite the larger tube of 45-mm diameter through a 10-mm hole near one end, which is closed. The properties of the output at the end of the smaller tube, as well as their relation to the intput were investigated, and a resonance diagram of the two-tube structure is completed. The experimental results agree well with the predicted values. At the end of the smaller tube of 13-mm diameter, a sound pressure level (SPL) of 176.5 dB has been obtained with low distortion. Emphases are placed on the analysis of fundamental SPL. It is possible to drive the structure directly with a modern high power loudspeaker to produce high sound intensity in a more extended space. Further research is in progress. [Work supported by the National Science Foundation of China.]

11:00

3aPAa9. Acoustic pulse reflectometry for the measurement of tubular structures. Thomas J. MacGillivray and Clive A. Greated (Dept. of Phys. and Astron., The Kings Bldg., Mayfield Rd., Edinburgh EH9 3JZ, Scotland, tm@ph.ed.ac.uk)

Acoustic pulse reflectometry is used in the reconstruction of bore profile and the calculation of input impedance for tubular objects with varying cross section. The technique, previously employed in the measurement of musical wind instruments, enables differences of the order 0.1 mm in internal radii to be detected. Experimental measurements made on small-scale tubular objects of varying complexity demonstrates the effectiveness of reflectometry for profiling such structures. Certain configurations for which the accuracy of the technique begins to break down are also apparent. Examination of the results allows the effective length and area of an object to be determined from the reconstructed profile. Input impedance curves evaluated for small radius stepped and single-branched tubes exhibit differences compared to the corresponding theoretical expressions. This requires consideration of the object dimensions and also of viscous and thermal effects. A procedure for detecting blockages within the structures is developed through examination of different object profiles. The reconstructed profile for a structure containing an obstruction appears altered in shape compared to the unblocked case. The size of the blockage and the axial position are not, however, distinguishable.

11:20

3aPAa10. Negative resistances in nonlinear lumped acoustic systems and IC-engine source data. Fredrik Albertson (MWL, KTH, Teknikringen 8, SE-100 44 Stockholm, Sweden)

Negative real parts of impedances can be found in IC-engine source characterization measurements. There is an obvious problem with the physical interpretation of negative resistances, and consequently there have been many questions about the validity of such results. This paper is an attempt to explain the origin of the mentioned negative acoustic resistances. To this end, a simple nonlinear lumped acoustic system, that is, a force-driven damped mass-spring system, is analyzed. Since this is a common case in acoustic measurements, linear analysis is performed in spite of the obvious nonlinear properties. It is shown that the degree of nonlinearity in the system is crucial to the values of the acoustic impedance. Furthermore, it is shown that it is possible to achieve negative resistances already in a simple lumped system. Finally, these results are also compared to simulated and measured IC-engine source impedances.

11:40

3aPAa11. Sound-speed determination in a fluid-filled elastic waveguide. James A. McConnell (Penn State Univ., Grad. Prog. in Acoust., P.O. Box 30, State College, PA 16804 and Acoustech Corp., State College, PA 16804, univibe@sabine.acs.psu.edu), Kevin J. Bastyr, and Gerald C. Lauchle (Penn State Univ., State College, PA 16804)

Theory and test methods are presented for determining the longitudinal sound speed inside a fluid-filled elastic waveguide. The waveguide is a vertically oriented open-ended column of water equipped with a moving coil driver. The elastic properties of the waveguide reduce the sound speed to the point where a passive anechoic termination can be used effectively. This facilitates a compact device that exhibits plane progressive waves for sensor calibration at low frequencies. Once the sound speed is determined, then the size of the device and usable bandwidth are known. The sound speed is determined through measurement of the longitudinal resonance frequencies associated with the free vibration case of a duct having ideal rigid and pressure-release boundary conditions. In practice, however, the moving coil driver presents an impedance boundary condition (e.g., not ideally rigid) that inadvertently couples the mechanical system of the

driver to the acoustic system of the waveguide. To circumvent this issue, frequency response measurements are made between a neutrally buoyant velocity sensor suspended in the fluid and an accelerometer mounted to the active face of the driver. In effect, the measurement decouples the two systems and provides the standing wave resonance frequencies of the duct having ideal boundary conditions.

12:00

3aPAa12. Sound propagation in a conical duct with flow. Rudolf N. Starobinski (Lab. d'Acoustique, URA 6613 CNRS, Univ. du Maine, av. O. Messiaen, BP 535, 72085 Le Mans, Cedex 9, France, starob@univ-lemans.fr)

The variations of acoustical exergy and acoustical mass velocity are used for a description of three-dimensional sound propagation in quasi one-dimensional moving medium in a conical duct of a different cross-sectional shape. Solution for the sound propagation in this system is represented by the solution for a matched slightly deformed conical waveguide without flow (reciprocity part of the propagation) corrected by nonreciprocity time delay that takes into account convection of the sound by flow. Equivalent circuit for a sound propagation in a conical duct is represented by two successive separate elements: reciprocity one, which describes a sound propagation in the matched waveguide, and a nonreciprocity part represented by the element of nonreciprocity delay. For the particular dependencies of the cross-sectional area against duct axis, the solution for propagating sound is found as two propagated noninteracted advancing and backward waves. The Green's functions and equivalent circuits for internal and external sound excitations are found as their decomposition by the eigenmodes of the matched waveguide.

Contributed Poster

This poster will be on display in the Poster Gallery from Thursday to Friday, 18–19 March. Author will be at the poster from 10:00 a.m. to 12:00 noon on Thursday, 18 March.

3aPAa13. A new acoustic conductor. Fathy Shenoda and Albeer Shenoda, Jr. (Dept. of Acoust., Natl. Inst. for Standards, Tersa St., El-Haram, El-Giza, Code 12211, P.O. Box 136 Giza, Egypt, abdo@tqc.nis.sci.eg)

A new acoustic conductor was designed and experimentally studied. This conductor consists of a perfectly rigid pipe of constant cross-section area and is treated at its side wall with a small gradually perforated area. This experimental study aimed to determine its behavior and to outline the design procedures for optimizing its performance. The parameters (reflection coefficient r, normalized acoustic resistance R, and reactance X, at the conductor inlet) characterize the matching performance of the conductor, and were measured for different configurations and at different conditions. The design parameters such as the length, the graduality factor with which the side-perforated area increases, the function with which the side-perforated area is changed and reaches a maximum width D_m at the end of the conductor, as well as the conductor cross-diameter, were separately studied in detail at different conditions. The conductor design is optimized at the conditions: The conductor terminates at a point where almost all the sound energy has been released. Within the effective frequency range, r, R, and X have the following values: $r=0.1$, $R=1$, and $X=0$. The extensive experimental study and the great number of measurements at different conditions lead to an empirical formula for the calculation of cut-off frequency f_c and optimum D_m.

WEDNESDAY MORNING, 17 MARCH 1999 ROOM MA005, 8:00 TO 11:20 A.M.

Session 3aPAb

Physical Acoustics: Nonlinear Motion of Bubbles and Drops II

R. Glynn Holt, Cochair
Department of Aerospace and Mechanical Engineering, Boston University, Boston, Massachusetts 02215, USA

Joachim Holzfuss, Cochair
Institut für Angewandte Physik, TU Darmstadt, Schlossgartenstrasse 7, D-64289 Darmstadt, Germany

Invited Papers

8:00

3aPAb1. The Rayleigh-like collapse of a conical bubble. Tim G. Leighton and Ben T. Cox (Inst. of Sound and Vib. Res., Univ. of Southampton, Southampton SO17 1BJ, UK, tgl@isvr.soton.ac.uk)

This paper describes an experimental investigation of the collapse of a conical bubble, with measurement of the liquid and bubble gas pressures, and sonoluminescence, generated during the collapse. A theoretical analysis, based on the 1917 formulation of Rayleigh, adequately predicts the pressures, and the time scales as measured by high-speed photography, within the limitations of both theory and measurement. One implication of this novel apparatus lies in the ability to control the inertia associated with the liquid without changing its other properties. The inertia is key to the dynamics of the type of bubble collapse which is associated with sonoluminescence and the emission of strong rebound pressures into the liquid. Another implication of this study is the ability to image the collapsing meniscus and the gas and, to a certain extent, place sensors within the gas of the collapsing bubble.

8:20

3aPAb2. Probing and stabilization of interfaces with acoustic radiation pressure: Application to bubbles and capillary bridges. David B. Thiessen, Mark J. Marr-Lyon, Philip L. Marston (Dept. of Phys., Washington State Univ., Pullman, WA 99164-2814), Thomas J. Asaki (Los Alamos Natl. Lab., Los Alamos, NM 87545), and Scot F. Morse (Naval Res. Lab., Washington, DC 20375)

Acoustic radiation pressure at interfaces can be used as a probe of dynamics and as a method of suppressing instability. Examples include the probing of the interfacial rheology of acoustically levitated bubbles in water in the presence of surfactants which are either insoluble [T. J. Asaki, D. B. Thiessen, and P. L. Marston, Phys. Rev. Lett. **75**, 2686–2689 and 4336 (1995)] or soluble [T. J. Asaki and P. L. Marston, J. Acoust. Soc. Am. **102**, 3372–3377 (1997)] in water. Modulated radiation pressure was also used to probe the dynamics of liquid bridges of oil surrounded by water [S. F. Morse, D. B. Thiessen, and P. L. Marston, Phys. Fluids **8**, 3–5 (1996)] and to suppress the breakup of cylindrical bridges having lengths significantly beyond the natural Rayleigh–Plateau limiting length [M. J. Marr-Lyon, D. B. Thiessen, and P. L. Marston, J. Fluid Mech. **351**, 345–357 (1997)]. In all of these examples the interfacial tension is significant for the normal modes of interest. Normal-mode frequencies can be significantly modified by using optical information for feedback control of the spatial distribution of the radiation pressure. [Work supported by the Office of Naval Research and by NASA.]

8:40

3aPAb3. Acoustic radiation forces on bubbles in real fluids. Alexander A. Doinikov (Inst. of Nuclear Problems, Byelorussian St. Univ., 11 Bobruiskaya St., Minsk 220050, Belarus, doinikov@inp.minsk.by)

Early theoretical studies on the acoustic radiation forces on gas bubbles have treated the surrounding medium as an ideal fluid devoid of viscosity and heat conduction, and for bubble–bubble interactions in addition with no compressibility. However, real fluids have all the above-mentioned properties and this fact may be very essential to the radiation forces. A more rigorous theory, allowing for the nonideality of the surrounding fluid, predicts a host of new exciting effects, such as the change of the sign of the force in a plane-traveling wave at high dissipation, long-range terms in the interbubble force which can cause the two bubbles to form a bound pair with a stable separation distance, etc. The purpose of this paper is to discuss such predictions.

Contributed Papers

9:00

3aPAb4. Cavitation bubbles' motions under ultrasound. Jean-Luc Laborde (EDF, Les Renardires ADEI, Rte. de Sens 77818, Moret-sur-Loing, Cedex, France, jean-luc.laborde@edfgdf.fr)

Propagation of power ultrasound (from 20 to 800 kHz) through a liquid initiates acoustic cavitation. Inceptions and germs grow into bubbles which collapse, possibly giving rise to extreme conditions of temperature and pressure (assessed to be up to 10 000 K and 500 atm). For instance, these conditions greatly enhance chemical reactions. A high-speed film shot at 500 fps clearly identifies stable and transient cavitation and shows bubble population phenomena. Clouds of bubbles grow up to ten times their emergence size during 15 ms, and move at velocity around 50 cm/s. Mathematical modeling is performed as a new approach to predict where active bubbles are and how intense cavitation is. A calculation based on fluid dynamics equations is undertaken, as CFD codes have shown great interest because they provide not only the pressure field but also velocity and temperature fields. Two phase flows (liquid-bubbles) could be modeled. Nonlinearities arising from the dissipation of the acoustic wave are computed and lead to the calculation of the acoustic streaming. This result gives a better knowledge of bubbles' behavior. The comparison with photographs, a high-speed film, and particle image velocity show good agreement with simulations.

9:20

3aPAb5. Interaction of driven delay-coupled bubbles. Stefan Luther (Drittes Physikalisches Institut, Univ. Göttingen, Bürgerstrasse 42-44, D-37073 Göttingen, Germany, luther@physik3.gwdg.de) and John S. Allen (Univ. of Virginia, Charlottesville, VA 22902)

A rigorous derivation of the governing equation of two spherical, coupled, compressible bubbles indicates a variable time delay coupling term [Fujikawa and Takahira, Acustica **61**, 188–199 (1986)]. However, the effects of this time delay were examined solely for free oscillations in that work. For acoustically driven bubbles, these time delay effects have been neglected in subsequent studies. This may be in part due to the computational complications involved in solving variable delay differential equations. In this study, delay effects are rigorously explored for acoustically forced bubbles. An equation for the overall energy balance of the system is derived and used to investigate novel Bjerknes Force effects. A direct comparison with nondelay formulations reveals important differences for certain parameter regimes. [Work supported by ''Graduiertenkolleg Strömungsinstabilität und Turbulenz.'']

9:40–10:00 Break

10:00

3aPAb6. Control of nonlinear bubble dynamics. Andrew J. Szeri and Matthew A. Wyczalkowski (Univ. of California, Dept. of Mech. Eng., Berkeley, CA 94720-1740, aszeri@me.berkeley.edu)

Bubbles, either free or encapsulated, are valuable as contrast agents in diagnostic ultrasound in medicine. In this capacity, the compressibility of microbubbles is exploited to increase the acoustic backscatter from internal vessels and cavities of interest after injection into the patient. The scattering cross section of the contrast agent is further increased by driving resonant radial pulsations of the microbubbles with the ultrasound field. Recent derivatives of this basic technique rely on nonlinear aspects of the bubble response to reduce clutter and thereby to extend imaging capability to new areas. Unlike the surrounding tissue, these nonlinear bubble oscillations have a backscatter signature at a different frequency than the forcing, and so are especially useful in distinguishing the area to be imaged. New control capabilities are described for changing the architecture of the bubble dynamics phase portrait and response diagram so as to enhance their utility in imaging applications. [Work supported by NSF.]

10:20

3aPAb7. Effects of shape oscillations on bubble dynamics and coalescence. Zaichun Feng (Dept. of Mech. Eng., MIT, Cambridge, MA 02139)

When a bubble is excited by an acoustic field, in addition to the volume oscillation, the bubble may deviate from the spherical shape and undergo shape oscillations. The shape oscillations can be directly caused by the anisotropic pressure or they can be caused by the energy transfer

from the volume mode through nonlinear modal couplings. The shape oscillations influence the bubble dynamics in many ways. First of all, shape oscillations can limit the volume responses of the bubble since the onset of shape oscillations can lead to the development of localized large curvature and hence the breakup of the bubble. Second, the resonance coupling between the volume mode and a shape mode can give rise to the occurrence of chaos even when the acoustic forcings are so weak that the bubble oscillates close to its equilibrium radius. Third, the coupling between two or more shape oscillation modes can lead to translational motions of the bubble centroid; this can indirectly affect the bubble coalescence in an acoustic field. Finally, the shape oscillations may influence the coalescence through modifying the short-range attractive forces between two neighboring bubbles.

10:40

3aPAb8. Bubble response to the amplitude modulation signal near the threshold of dynamical stability. Alexey O. Maksimov and Ekaterina V. Sosedko (Pacific Oceanological Inst., 43 Baltic St., Vladivostok, 690041, Russia, root%dan86@poi.marine.su)

There is a range of acoustic techniques for characterizing bubble populations within liquids [Leighton *et al.*, Ultrasonics **34**, 661–667 (1996)]. The linear resonant backscattering was the first detection technique. The great difference between the compressibility of gas in the bubble and surrounding liquid leads to the easy manifestation of nonlinear effects, the simplest of which is the presence of harmonics at $2\omega_p$, $3\omega_p$, etc., of the pure tone driving frequency ω_p in the scattering signal. However, bubble pulsation of finite amplitude results not only in the harmonics generation. The nonlinear resonance characterized by multistable oscillation states arising from the saddle-node bifurcations is a significant example. The emphasis of this study is to propose a technique for bubble sizing by using the ability of a bubble as a nonlinear oscillatory system to amplify weak signals near the threshold of dynamical stability. The analytical as well as numerical solutions have been derived for the nonlinear bubble response to the modulation driving pressure. The magnitude and the form of the acoustical signal reradiated near the threshold of dynamical stability are drastically different from the modulation of incident wave and enable the characterization of the bubble population in liquid.

11:00

3aPAb9. An acoustic levitation technique for measuring the rheology of foam near the order–disorder transition. R. Glynn Holt, Cory C. Clarke, and J. Gregory McDaniel (Dept. of Aerosp. and Mech. Eng., Boston Univ., 110 Cummington St., Boston, MA 02215, rgholt@bu.edu)

Understanding the rheological behavior of foams is important as a basic problem in fluid physics, and as a practical problem in many industries. Foams are tremendously important in a variety of applications. The most important quality of a foam in many of these applications is its response to imposed strain, or its rheological behavior. Yet there exists almost no experimental data on the rheological properties of real 3-D foams. This is due in large part to the earth-based requirements for contact containment, and to the fact that gravity-induced drainage quickly destroys all but the ''driest'' foams. A unique method to provide noncontact control and manipulation of foam samples, via acoustic levitation, is described. This levitation technique, coupled with low-gravity conditions, will enable investigation of dry (ordered) and wet (disordered) foams. The analysis which will allow determination of a foam's yield stress, effective bulk modulus, and effective bulk viscosity from the observed response of a foam sample to quasistatic, step function, and periodic acoustic and ambient pressure changes is outlined. Experimental results will be presented for foams experiencing small deformations. The results will be analyzed to determine if the foam may be modeled as a viscoelastic solid. [Work supported by NASA.]

WEDNESDAY MORNING, 17 MARCH 1999 ROOM MA041, 8:00 A.M. TO 12:20 P.M.

Session 3aPAc

Physical Acoustics: Periodic and Layered Media

Robert M. Keolian, Cochair
Physics Department, Naval Postgraduate School, Monterey, California 93943, USA

Antoni Sliwinski, Cochair
Institute of Experimental Physics, University of Gdansk, Wita Stwosza 57, 80-952 Gdansk, Poland

Contributed Papers

8:00

3aPAc1. Time-domain Floquet-wave Green's function for an infinite sequentially excited periodic line array of point radiators. Leopold B. Felsen (Dept. of Aerosp. and Mech. Eng., Boston Univ., 110 Cummington St., Boston, MA 02115, lbf@enga.bu.edu) and Filippo Capolino (Dept. of Info. Eng., Univ. of Siena, Italy)

A variety of new synthetic materials, especially those exploiting sonic or photonic bandgaps, are based on a background with strict or perturbed periodicity, which may be subjected to rapidly switched external modulation. This has motivated the present prototype study of the time domain Green's function for an infinite sequentially excited periodic line array of point radiators or scatterers. Such Green's functions, which parameterize TD Floquet wave (FW) dispersion, are the analytic building blocks for finite planar arrays with physical radiators. Various techniques are employed to develop exact expressions for the dispersive TDFW's synthesized by Poisson summation over the linearly time-delayed nondispersive impulsive point source radiators. These techniques include Fourier inversion of frequency domain FW's, TD spectral wavenumber decomposition and recombination, and use of complex space-time analytic signals. Each formulation furnishes different insights into propagating as well as evanescent TDFW spectra, and into TDFW dispersion. Some basic questions concerning causality and TDFW ''physical observability'' are posed and answered.

8:20

3aPAc2. Propagation features of evanescent acoustic waves. Adriano Alippi, Andrea Bettucci, Francis A. Farrelly, and Massimo Germano (Dept. of Energetics, Univ. of Rome ''La Sapienza,'' via Scarpa 14, 00161 Rome, Italy, alippi@uniroma1.it)

Evanescent waves are not true propagating waves, so questions regarding their traversal time or propagation direction are ill posed. However, physical phenomena related to the time delay of pulsed evanescent perturbations, or refraction effects through a discontinuity, can be easily put into evidence in acoustics by proper choice of acoustic modes and geometrical configuration. In this paper, lateral displacement and time delay through forbidden barriers of Lamb mode waves with contradirected phase and group velocities are studied. Low noise detection achieved by cutting off spurious mode generation and a common objection made toward experiments of this type is avoided. This objection states that the highest frequency components of the pulse travel faster and are less attenuated than the main carrier frequency of the packet, distorting the original pulse to such an extent as to render measurements unrelated to barrier traversal times. Elastic waves generated with piezoelectric transducers are injected into aluminum plates through wedge-shaped Lucite waveguides so as to generate the appropriate Lamb mode which traverses a forbidden region and is picked up after it with a similar setup of transducer and waveguide. Various configurations of wave barriers have been measured and possible theoretical interpretation is given.

8:40

3aPAc3. Experimental analysis of the propagation of elastic waves in a chain of spherical beads. M. de Billy and X. Jia (Groupe de Physique des Solides, Universités Paris 6 et 7, 2, place Jussieu, 75251 Paris Cedex 05, France, debilly@gps.jussieu.fr)

Granular materials are widely encountered in many domains such as soil mechanics, geophysics, and physics of condensed matter. Consequently, these media have been extensively analyzed in recent years [A. N. Bogdanov and A. T. Skvortsov, Sov. Phys. Acoust. **38**, 224–226 (1992) and C. Coste *et al.*, Phys. Rev. E **56**, 6104–6117 (1997)]. The present experimental study is concerned with the propagation of an elastic wave through a chain of spherical beads submitted to a static force. Two piezoelectric transducers are used for the generation and the detection of the trainwaves. A low-frequency signal is observed in the transmitted acoustic waves along the chain of beads. The central frequency ($25<f<200$ kHz) of this signal varies with the static force exerted on the beads and also with the diameter (d) of the spherical particles ($2<d<8$ mm). For a constant value of the static force, the amplitude of the signal is strongly affected by the material of the solid medium which support the acoustic wave (brass, steel, nylon). The increasing of the sound velocity with the applied force seems to verify the prediction based on the Hertzian contact.

9:00

3aPAc4. A closed formulation of sound fields in front of periodical absorbents. Dag Holmberg and Erling Nilsson (Dept. of Eng. Acoust., LTH, Lund Univ., P.O. Box 118, SE221 00 Lund, Sweden, Dag.Holmberg@kstr.lth.se)

Periodic resonant absorbers are known to give excessive back scattering for frequencies above a limit which is governed by the geometric proportions of the periodicity. One way to model this phenomenon is to transform the geometry into the wave number domain and solve the corresponding equation with respect to the pressure field. A drawback is that the equation matrix consists of an infinite (but relatively fast converging) set of harmonic components and therefore has to be truncated in order to be solved. However, it is possible to make use of the Poisson sum formula and obtain a closed formulation which can be solved in the wave domain without truncation. Furthermore, it is possible to transform the exact solution back to the spatial domain. This will yield an infinite series consisting of components which can be designated a physical interpretation. These components, i.e., partial pressures related to corresponding geometry, which constitute an exact solution, can then be truncated in a controlled and physical way.

9:20

3aPAc5. Sonic band structure and surface localized modes in a density-modulated system: An experimental and theoretical study. Christopher Carr (Dept. of Phys., Univ. of Davis, Davis, CA) and Roger Yu (Central Washington Univ., Ellensburg, WA 98926)

As a result of the Bloch theory, the eigenstates of an electron in a strictly periodic potential are extended and the eigenenergy levels form allowed energy bands separated by forbidden gaps. In the study reported here, a *finite* air-filled tube with *arbitrary* mass density modulation is considered which allows the inclusion of the effect of disorder. Since this theoretical model is finite, it was possible to make direct comparisons with the experiment. The baffled tube is excited with the sound source emitted at one end. The source can deliver short pulses as well as harmonic oscillations. Both normal modes analysis (NMA) and pulse analysis (PA) were used. The spectra obtained from both methods are compared with the theoretical prediction. For the tube with evenly spaced baffles, three passing frequency bands were found. More interestingly, a few ''surface'' localized resonant modes whose frequencies lie in the gaps were discovered. The wave functions of the surface modes are confined within a few sections of divided tube at both ends. It was found that the acoustic intensity of higher frequency bands is drastically lower than that of the lowest band, which suggests that the baffled tube can be used as a frequency filter.

9:40

3aPAc6. Multilayered Rayleigh waves in anisotropic periodically multilayered media: Comparison between theory and experiments using the acousto-optic technique. Catherine Potel, Jean-Francois de Belleval (Univ. Technol. Compiegne (UTC), LG2mS, UPRES ass. CNRS, BP 20529, 60205 Compiegne, France), Stefaan Devolder, Martine Wevers (Katholieke Univ. Leuven, Leuven, Belgium), and Oswald Leroy (Katholieke Univ. Leuven, Kortrijk, Belgium)

The propagation of surface waves, particularly Rayleigh waves, has become the subject of a large number of studies. As far as stratified media are concerned, many of the studies deal with an infinite substrate medium below the stratified or nonstratified medium, but, as far as infinite periodically stratified media are concerned, there is no complete work on leaky waves that behave as Rayleigh waves. By analogy with the behavior of the Rayleigh wave in isotropic media, the properties of what this group termed in previous papers ''multilayered Rayleigh wave'' in infinite anisotropic periodically multilayered media, were studied. These waves are a linear combination of three inhomogeneous Floquet waves and are dispersive. This theory was developed for plane waves. This paper aims to validate this theory by using an experimental acousto-optic technique linked to bounded beams. The experiments were carried out on a composite of carbon/epoxy layers. The coincidence of experimental and calculated dispersion curves of the multilayered Rayleigh modes was found to be quite good. [Work partially supported by the National Fund for Scientific Research and the Flemisch Institute for the Encouragement of the Scientific and Technological Research in Industry. Aerospatiale (France) has provided the characterized sample of carbon/epoxy composite.]

10:00–10:20 Break

10:20

3aPAc7. Modal waves in periodically multilayered fluid structures. Philippe Gatignol, Catherine Potel, and Jean-Francois de Belleval (Univ. Techn. Compiegne (UTC), LG2mS, UPRES ass. CNRS, BP 20529, 60205 Compiegne, France)

This paper aims to study the existence of modal waves and in particular of surface waves, in periodically multilayered fluid media. Generally speaking, these waves are propagation modes for which the acoustical energy propagates along the layers, whereas it remains bounded in a di-

rection perpendicular to the layers. Periodically multilayered media are here studied by the transfer matrix method. The calculus of eigenvalues of the transfer matrix for one period permits to distinguish between passing and stopping regions in the wave number/frequency plane. The transfer matrix for a finite number of periods can be calculated by using Tchebychef polynomials. The writing of the boundary conditions for a finite structure surrounded by vacuum leads to a factorized equation. Thus, two families of guided waves are obtained: the first one corresponds to structure modes which exist in passing regions only. The second one only depends on the period properties and corresponds to inhomogeneous Floquet waves. When the periodic structure is infinite, the modes of this second family coincide with surface waves.

10:40

3aPAc8. A theoretical investigation of sound transmission through a layered periodic structure in water. Aly H. A. Moustafa (Faculty of Electron. Eng., Dept. of Commun., Menoufla Univ., Menouf-32952, Egypt)

This paper presents a theoretical study of sonic passbands and stopbands that occur with a periodic one-dimensional structure of plates in water. The study uses the characteristic matrix method and considers a periodic structure of some materials that are characterized by a constant density and phase speed: perspex, aluminum, and steel. The computed results show the variation of the pressure transmission coefficient with frequency for various systems of plate configurations in water, and takes into account the attenuation of the plate material. The pattern of the results indicates clearly that sound propagation can be prohibited at certain frequencies while free propagation is allowed at others. The results compare very well with published data that are obtained using other methods.

11:00

3aPAc9. Modeling of inhomogeneous monochromatic plane wave at the interface between two arbitrary homogeneous anisotropic absorbent media. Bruno Roge, Patrick Lanceleur, and Jean-Francois de Belleval (UTC-LG2mS (UPRES A CNRS 6066), Centre de Recherches de Royallieu, BP 20.529, 60205 Compiegne Cedex, France)

This work aims to model the interaction of an inhomogeneous monochromatic oblique plane wave with a plane interface separating two semi-infinite homogeneous media. These media can be either isotropic or anisotropic, absorbent or not. A numerical method is proposed to generalize previously developed procedures, which were restricted to the case of incident homogeneous waves, interacting with absorbing materials. In this case the waves propagating are always inhomogeneous. Due to this inhomogeneity of the waves, the choice of compatible parameter for the incident wave is to be done on an energy criterion and not necessarily on a radiation one. The computation of all the parameters of all the involved waves makes several unexpected phenomena or behaviors to arise. For instance, by applying the study to the case of a water/nickel monocrystal interface, incident directions for which the energy flow vector is directed toward the transmission medium, whereas the slowness vector is directed toward the incident medium, are observed. The appearance of leaps in the reflection coefficient will then be explained by an orientation change of the slowness vector, which results from a forward/return of the energy flow vector through the interface.

11:20

3aPAc10. Micellar structures in layered oil/water surface systems studied with photoacoustics spectroscopy. Stanislaw J. Pogorzelski, Janusz Szurkowski, and Antoni Sliwinski (Inst. of Exp. Phys., Univ. of Gdansk, Wita Stwosza 57, 80-952, Gdansk, Poland)

The model layered system consisting of thin olive oil layers (ranging from 25 to 250 μm in thickness) spread on the water surface was studied using a photoacoustic method. The classical Rosenzweig–Gersho model assuming a one-dimensional heat flow in the sample was adopted as a depth profiling approach to interpret data in terms of the thermal diffusion length and thermal diffusivity. Distinctive changes in the PA signal phase and its amplitude discovered at the air/oil and oil/water interfaces, as well as at the depth of $9-13$ μm beneath the oil surface, point out the possibility of formation of organized adsorbed interfacial layers and micellar structures in a bulk oil phase of surfactants, if present in an oil medium at a certain concentration (above critical micellar concentration CMC) and temperature (Kraft point). Such organized structures have different thermodynamic parameters like specific heat or thermal conductivity that affect to a great extent the photoacoustic effect used in the depth profiling sensing.

11:40

3aPAc11. Time-of-flight measurements on high-frequency surface acoustic phonons in silicon. D. M. Photiadis (Naval Res. Lab., Washington, DC) and J. Ding (ThermaWave, Inc., San Francisco, CA)

Results from time-of-flight measurements of high-frequency surface acoustic phonons (50–500 GHz) in (001) silicon wafers at low temperatures are reported. Pulsed laser excitation is used for the generation of the high-frequency surface acoustic phonons and aluminum edge bolometers are used as detectors. The times defined by the fast initial response of the edge bolometer correspond to surface acoustic delays in silicon. Late time responses consistant with echoes from the back face of the wafer were also observed. These results and the accompanying analysis will be discussed.

12:00

3aPAc12. Surface acoustic waves in proton-exchanged lithium niobate and lithium tantalate. Daumantas Ciplys and Romualdas Rimeika (Vilnius Univ., Faculty of Phys., Lab. of Physical Acoust., Sauletekio 9, Vilnius 2054, Lithuania)

The use of surface acoustic waves in integrated optical devices seems to be very promising for applications in modern telecommunication and data processing technologies. The studies of surface acoustic wave propagation in lithium niobate and lithium tantalate with optical waveguides formed by the proton exchange technique are reported here. The influence of protonated layer parameters on the SAW propagation characteristics is investigated for various crystal cuts and waveguide fabrication conditions. The acoustic velocity and attenuation have been studied by the laser probe method. The effective electromechanical coupling coefficient of the protonated crystal surface has been measured by the method of thin metal film evaporation. Possibilities for controlling both the optical and acoustic properties of proton-exchanged waveguides by the post-exchange annealing have been studied. The results of experimental studies of SAW propagation parameters are compared with those of theoretical calculations performed for a layered structure, and the parameters of a protonated layer are evaluated. The light modulator based on the interaction of surface acoustic wave and guided optical modes is demonstrated.

Session 3aPPa

Psychological and Physiological Acoustics and Speech Communication: Localization and Speech Perception in Realistic Acoustic Environments

Ruth Y. Litovsky, Cochair
Department of Biomedical Engineering, Boston University, 44 Cummington Street, Boston, Massachusetts 02215, USA

Tammo Houtgast, Cochair
TNO Human Factors Research Institute, Kampweg 5, 3769 DE Soesterberg, The Netherlands

H. Steven Colburn, Cochair
Department of Biomedical Engineering, Boston University, 110 Cummington Street, Boston, Massachusetts 02215, USA

Chair's Introduction—7:55

Invited Papers

8:00

3aPPa1. Localization of sound in reverberant spaces. William M. Hartmann (Phys. and Astron., Michigan State Univ., East Lansing, MI 48824) and Brad Rakerd (Michigan State Univ., East Lansing, MI 48824)

Sound sources in the horizontal plane can be localized on the basis of interaural time differences (ITD) or interaural level differences (ILD). It will be argued that without the benefit of an onset transient, listeners can employ only the ILD to localize steady-state broadband sources in a typical reverberant environment. The ITD provides a useful cue only if the cross-correlation (CC) function is adequately large. At low frequencies, a CC peak near 0.1 is barely adequate, but in a reverberant room the physical CC peaks are often less than that. The physical CC peak increases with increasing noise band frequency, but the value of the CC peak that is required for localization increases faster. Therefore, ITD is not useful at any frequency. By contrast, a comparison of physical and psychoacoustical measurements shows that ILD is a useful cue. An optimized ILD model is able to account for human sound localization performance in a reverberant space for broadband and low-pass filtered noises, for both normal listeners and listeners with a high-frequency hearing loss. [Work supported by the NIDCD, Grant DC00181.]

8:20

3aPPa2. Localization of distracted speech and noise in reverberant and anechoic environments. Klaus Hartung and Jonas Braasch (Inst. of Commun. Acoust., Ruhr Univ., D-44780 Bochum, Germany, hartung@ika.ruhr-uni-bochum.de)

Eleven listeners were instructed to localize a test signal in the presence of a distractor sound in an anechoic environment and in a reverberant environment. The experiment was conducted in an auditory virtual environment using individually measured head-related transfer functions. A rectangular room ($6\times5\times3$ m) was created using the mirror-image method to simulate the reverberant environment. The distractor (noise burst, 500-ms duration, 20-ms $\cos^2$-ramp) was placed at 0, 30, or 90° azimuth. The signals, random noise bursts (200-ms duration, 20-ms $\cos^2$-ramp) or the German spoken word *''zuende''* were presented from 13 directions in the frontal hemisphere of the horizontal plane at different signal-to-noise ratios (S/N). For some S/N, the listeners were unable to discriminate between a number of directions of incidence of the test signal (median test). The *distinguishability of locations* (DOL) was introduced to measure the percentage of discriminated locations. The DOL is a function of the S/N, decreasing rapidly below a threshold of -12 dB in an anechoic environment. This threshold increased by about 5 dB under reverberant conditions. The reduced DOL was confirmed by a 2A-4IFC experiment. If a distractor were present in the anechoic environment, the perceived directions of the test signal were shifted significantly in the direction opposite to the distractor location for all distractor directions (sign test, $\alpha = 3D0.01$). [Work supported by DFG.]

8:40

3aPPa3. The precedence effect: Fusion and localization dominance. William A. Yost (Parmly Hearing Inst., Loyola Univ. of Chicago, 6525 N. Sheridan Rd., Chicago, IL 60626)

Fusion and localization dominance are two aspects of processing sounds in reverberant spaces. If a single sound source is perceived when a source and its reflections are presented then a perceptual fusion of the source and reflection has occurred. Localization dominance refers to the spatial location of a sound source and its reflections being dominated by the location of the source. Four listeners were presented a transient sound from one loudspeaker (source) in a sound-deadened room followed a few milliseconds later by the presentation of the transient at another loudspeaker (reflection). The listeners determined how many sound sources were detected (fusion) and the spatial location of these sources (localization dominance). The results will be discussed in terms of the temporal delay between the source and reflection (0.5 to 64 ms), the number of presentations of the source and reflection (1, 3, 6, 7, 9, 12), and three conditions of switching the source and reflection after the sixth presentation: no switch, the location of the source and the reflection were reversed (reversal switch), and the location of the source and reflection were moved in the same direction (lateral switch). [Work suported by NIDCD and AFOSR.]

9:00

3aPPa4. Physiological studies and neural mechanisms of echo suppression in the inferior colliculus of the cat. Ruth Y. Litovsky (Boston Univ., Dept. of Biomed. Eng., 44 Cummington St., Boston, MA 02215 and Eaton-Peabody Lab., Massachusetts Eye and Ear Infirmary), Bertrand Delgutte (Massachusetts Eye and Ear Infirmary, Boston, MA 02114), and Tom C. T. Yin (Univ. of Wisconsin, Madison, WI 53706)

Neurons in the inferior colliculus (IC) are sensitive to stimulus direction in free field and to individual directional cues, such as interaural disparities in time (ITD) and level (ILD). Our single-unit recordings in the IC of anesthetized cats explored neural mechanisms in the IC that might mediate echo suppression, using free-field and virtual space (VS) stimuli. Click pairs were used to simulate a sound source (lead) followed by a single reflection (lag) at delays of 1–100 ms. In both free field and VS, correlates of psychophysical echo suppression were found in the responses of most IC neurons. In many neurons, the suppression was directionally dependent in a way that could be linearly predicted from the response to the lead, with the most effective lead locations giving maximum suppression. Some neurons showed a decoupling between echo suppression and the directional response to the lead, suggesting that excitation and suppression are mediated by different neural mechanisms. Further decoupling was achieved by selectively holding constant some directional cues such as ITD and ILD in the VS stimuli. Results suggest that neural suppression in the IC depends on specific directional cues and is therefore a likely correlate of echo suppression in spatial hearing. [Work supported by NIH.]

9:20

3aPPa5. The cocktail party effect: Research and applications. Adelbert W. Bronkhorst (TNO Human Factors Res. Inst., P.O. Box 23, 3769 ZG Soesterberg, The Netherlands, bronkhorst@tm.tno.nl)

The ''cocktail party problem,'' defined in 1953 by Cherry [J. Acoust. Soc. Am. **25**, 975–979 (1953)] as ''how do we recognize what one person is saying when others are speaking at the same time'' has been the subject of a considerable number of studies in the last 45 years. Whereas Cherry already hypothesized that there are multiple effects that contribute to the ability to extract one speaker out of a babble, the term ''cocktail party effect'' has been claimed by only one of them: the influence of spatial separation of the voices. One important conclusion from past research on the cocktail party effect is that the truly binaural gain (the ''unmasking'') is, in general, relatively small (2–4 dB). The additional ''acoustic'' gain due to head shadow effects may be larger but depends strongly on the circumstances. In the present paper the research will be reviewed including recent evidence that much larger binaural gains may occur when the masker is ''informational'' in nature [Kidd *et al.*, J. Acoust. Soc. Am. **104**, 422–431 (1998)]. In addition, several applications based on the cocktail party effect, such as the use of a virtual auditory display for multiple-speaker communication, will be highlighted.

9:40

3aPPa6. Binaural hearing by listeners with hearing impairments. Monica L. Hawley, Ruth Y. Litovsky, and H. Steven Colburn (Hearing Res. Ctr. and Biomed. Eng., Boston Univ., 44 Cummington St., Boston, MA 02215, mlh@bu.edu)

The ability of listeners with hearing impairments to understand speech in the presence of competing speech sources is often compromised; however, the extent to which poor binaural hearing contributes to this compromise is not known. These studies are aimed at relating listeners' abilities to utilize binaural information in speech-based and non-speech-based tasks. In one set of measurements, speech intelligibility and localization of speech material were tested in the presence of one to three competing sources, placed at various spatial configurations. A second set of measurements tested the sensitivity to binaural information (i.e., MLD, ITD, and ILD discrimination). Listeners who obtained maximal binaural benefit in the speech intelligibility tasks generally showed good performance in all other tasks. Listeners who showed normal ITD/ILD discrimination could not always exploit that ability in more complicated tasks (MLD and speech-based tasks). Data were compared with the prediction of a model [Zurek, in *Acoustical Factors Affecting Hearing Aid Performance* (Allyn and Bacon, Boston, 1993)] which separates benefit of the ''better monaural ear'' and binaural interaction. Prediction was best when individuals MLDs were used to predict the binaural interaction term. Knowledge of the individual's binaural abilities may help clinicians choose an appropriate rehabilitative strategy. [Work supported by NIH.]

10:00–10:20 Break

10:20

3aPPa7. The ''cocktail-party effect'' viewed through the lens of psychophysics. Pierre L. Divenyi (Exp. Audiol. Res., V. A. Medical Ctr., Martinez, CA 94553)

In an attempt to understand the psychophysical processes underlying the ''cocktail-party effect''—a phenomenon whereby one speech signal is extracted from the ensemble of other speech signals distributed in space—it has been reduced to the psychophysical task of segregating two concurrent signals $X_1(t)$ and $X_2(t)$ differing with respect to various attributes. These attributes represent three orthogonal ''canonica'' dimensions—spatial location, temporal (low-frequency envelope AM) structure, and pitch, although the pitch dimension is split into spectral and virtual pitch components. In any segregation experiment, the two signals differ along at least two attributes; segregation is assumed when each signal is associated with the correct values on each dimension. At segregation threshold, there is a trade-off over a certain range, where an increased difference along one dimension leads to a reduced difference along another. Along each dimension, there is also a ''critical'' difference at which the trade-off no longer exists. When converted to speech parameter coordinates, these critical differences—for azimuthal, spectral, fundamental frequency, and modulation frequency separation—can provide psychophysical predictions for conditions under which a speech signal could be successfully recovered in a real-life cocktail-party situation. [Work supported by the National Institute on Aging and the VA.]

10:40

3aPPa8. Application of localization models to noise suppression in hearing aids. Volker Hohmann, Stephan Albani, and Johannes Nix (AG Medizinische Physik, Univ. of Oldenburg, Oldenburg, Germany)

One major problem of hearing-impaired people is the cocktail-party effect, i.e., the reduced ability to understand speech in noisy environments. Normal-hearing listeners use binaural information, i.e., interaural level and phase/time differences, in addition to monaural cues to localize sound sources in the environment. Based on the localization result and on the monaural cues, the listener performs a significant noise reduction by concentrating on one of the sources. Noise reduction algorithms have been proposed that try to imitate the binaural information processing in the hearing system by using two microphones at both ears and a central processor. This setup allows for the use of interaural parameters to estimate the direction of sound sources and to attenuate unwanted sound source directions. However, in noisy environments the binaural parameters become noisy as well, reducing the accuracy of the sound source estimation and therefore reducing the maximum performance of the noise reduction algorithm. In this presentation, a localization algorithm is introduced, which uses a statistical description of the binaural parameters in order to perform a robust estimation of sound source directions in noisy environments. Noise reduction schemes based on this localization algorithm are discussed.

Contributed Papers

11:00

3aPPa9. Speech perception in telephone situations under ambient noise conditions. Thomas Hempel, Sebastian Möller, Ute Jekosch (Inst. of Commun. Acoust., Ruhr Univ. Bochum, D-44780 Bochum, Germany, hempel@ika.ruhr-uni-bochum.de), Sabine Meunier, and Xavier Regal (Lab. de Mécanique et d'Acoust., CNRS, F-13402 Marseille, France)

In a telephone situation, the partners of a conversation generally experience ambient noise because they are located in acoustically realistic environments. The impact of the ambient noise on the quality of a telecommunication service is a double one: on the one hand, the noise deteriorates the acoustical speech signal either directly or via the sidetone path of a telephone handset, thus leading to lower intelligibility and overall quality. On the other hand, it distracts the listener's attention. Models which try to predict the effect of ambient noise for telephone network planning purposes in general only regard a diffuse room noise level. However, localization of possible ambient noise sources can help the listener to concentrate on the conversation rather than being distracted by the noise. A conversation test has been carried out in order to investigate the effect of ambient noise in both handset and hands-free telephone situations. Noise was either diffuse or localized at different positions relative to the listener. The test results are compared to intelligibility measures for masked speech given in literature. The investigation can help to quantify the impact of localized ambient noise and gives information to design realistic ambient noise environments for telephone or teleconferencing scenarios.

11:20

3aPPa10. Effects of aging on sound localization and speech understanding in realistic listening situations. Janet Koehnke and Joan Besing (U.S. Army Res. Lab., Human Res. and Eng. Directorate Bldg. 520, APG, MD, jkoehnke@arl.mil)

The ability to localize sound in quiet and noise and understand speech in noise was measured for four groups of subjects including adults under 50 years old and over 60 years old with normal hearing, and adults under 50 years old and over 60 years old with hearing loss. Performance was measured in anechoic and reverberant listening environments at two stimulus levels (25 dB SL and 70 dB SPL). Head-related transfer functions were used to create spatialized stimuli that were presented to subjects via earphones. Results indicate that performance on both tasks is affected by age and hearing loss. Localization errors are larger in older adults than younger adults with normal hearing, and larger in older adults with hearing loss than older adults with normal hearing. The intelligibility gain is smaller in older adults than younger adults with normal hearing, and smaller in older adults with hearing loss than older adults with normal hearing. Speech understanding in noise shows a large effect of reverberation, but localization is not affected by the same amount of reverberation. Overall, results suggest that in realistic environments these tasks are more difficult for older adults. [Work supported by the American Hearing Research Foundation.]

11:40

3aPPa11. Localization of distracted sound sources: Determining the role of binaural cues using unilaterally attenuated and interaurally uncorrelated signals. Jonas Braasch and Klaus Hartung (Inst. of Commun. Acoust., Ruhr Univ., D-44780 Bochum, Germany, braasch@ika.ruhr-uni-bochum.de)

Six listeners were instructed to localize manipulated random noise (200-ms duration, 20-ms $\cos^2$-ramp, 12 directions in the horizontal plane) in an auditory virtual environment using individual head-related transfer functions (HRTF). In the first condition, the left headphone channel was attenuated by 20 dB. In the second condition, an interaurally uncorrelated noise was used as the test signal by filtering two uncorrelated noises with the left and right HRTF. A second random noise was used as a distractor (500-ms duration, 20-ms $\cos^2$-ramp, 0° azimuth). The distractor was manipulated in the same way as the test signal. Four different signal-to-noise ratios (S/N): 0, −5, −7, and −10 dB (plus an unmasked condition) were tested. In condition 1, the additional level difference of 20 dB caused a lateral displacement of the auditory event in four listeners. This displacement decreased when the distractor was added. In condition 2 (uncorrelated noise), the listeners were able to estimate the left-right direction, but frequently showed front-back confusions. With decreasing S/N the perceived directions clustered at −90°, 0°, and 90° azimuth.

12:00

3aPPa12. Localization ability in the horizontal plane in adverse auditory environments. Nancy L. Vause (U.S. Army Res. Lab., Human Res. and Eng. Directorate, Aberdeen Proving Ground, MD 21005) and D. Wesley Grantham (Vanderbilt Univ. Medical Ctr., Nashville, TN 37212)

The purpose of this investigation was to examine the effects of adverse conditions on localization ability in the horizontal plane. The experiment was designed specifically to assess horizontal plane localization accuracy for a target signal presented in the adverse conditions of noise, headgear, and reverberation for two orientations. Eight normal hearing subjects participated in a source identification task in nine different experimental conditions of headgear, environment, and background noise for the frontal and lateral orientation. The results showed that (a) the effects of noise degraded localization performance in both the frontal and lateral orientations to a greater extent than reverberation or the combination of reverberation + noise; (b) subject performance was not significantly disrupted by reverberation in a quiet environment, but did slightly decrease when noise and reverberation were combined; however, performance in the lateral orientation improved in both quiet and noise conditions; and (c) localization accuracy declined when subjects wore protective headgear in all conditions for both orientations. [Work supported by NICDC and U.S. Army.]

Session 3aPPb

Psychological and Physiological Acoustics: Spectral Parameters (Poster Session)

Prudence Allen, Chair
School of Communication Sciences and Disorders, University of Western Ontario, 1500 Elborn College, London, Ontario N6G 1H1, Canada

Contributed Papers

All posters will be on display in the Poster Gallery from Monday to Wednesday, 15–17 March. Authors will be at their posters from 10:00 a.m. to 12:00 noon on Wednesday, 17 March.

3aPPb1. The lower limit of melodic pitch with filtered harmonic complexes. Daniel Pressnitzer, Roy D. Patterson, and Katrin Krumbholz (CNBH, Dept. of Physiol., Downing St., Cambridge CB2 3EG, UK, daniel.pressnitzer@mrc-cbu.cam.ac.uk)

Sounds with temporal regularities can evoke a variety of percepts: pitch, roughness, flutter, or rhythm, according to the frequency range of the regularity. However, only pitch supports the perception of melodies. In an effort to determine the lower limit of pitch, as opposed to flutter, etc., an experiment has been performed to study melody perception with very low notes, as a function of frequency region and phase. These bandpass-filtered harmonic complexes had cosine, alternating, or positive-Schroeder phase. Listeners had to detect differences between two successive four-note melodies that where built around a base pitch. The lowest base pitch at which listeners could perform the task depended on both frequency region and phase. When the combination tone region was masked by low-pass noise, the phase dependence was strongly reduced. The lower limit of pitch increased markedly with frequency region when the masking noise was present. The results are discussed with regard to time-domain models of pitch involving autocorrelograms or auditory images. These models suggest the presence of precise pitch cues in high-frequency regions which appear to be contradicted by the current data. [Work supported by the Fyssen Foundation and the UK MRC (G9703469).]

3aPPb2. Further examination of the relationship between overshoot and filtering. Elizabeth A. Strickland (AUS Dept., Purdue Univ., West Lafayette, IN 47907, estrick@purdue.edu)

In a previous experiment, threshold was measured for a brief duration probe positioned temporally at the onset of a broadband masker, with and without a broadband precursor, to determine the amount of overshoot. The probe level was then fixed 10 dB above the threshold levels determined in the overshoot experiment, and a notched-noise masker was varied in level to estimate filter shape, with and without a precursor. In general, filters were broader and the signal-to-noise ratio at threshold, k, was lower following a precursor, but there was not a clear relationship between the amount of change in the filters and overshoot. In the present study, filter shapes were measured with the probe level set at the threshold from the overshoot experiment, rather than 10 dB above. Results revealed that the change in k is in general closely related to the amount of overshoot (which would be expected) and also that there is at least some relationship between the change in filter width and the amount of overshoot. The study was also extended to look at possible filtering changes with decrease in overshoot, and to look at effects of overshoot from off-frequency precursors and maskers. [Work supported by NIH (NIDCD).]

3aPPb3. Frequency discrimination following linear frequency glide. Takuro Kayahara (Intelligent Modeling Lab., Univ. of Tokyo, 2-11-16 Yayoi, Bunkyo-ku, Tokyo 113-8656, Japan) and Takao Sato (Univ. of Tokyo, Tokyo 113-0033, Japan)

Difference limen for frequency (DLF) following linear frequency glide was measured using 2IFC procedure to investigate mechanisms underlying detection of frequency change in successive tones. In the experiment, a pair of 100-ms tone, one of which had fixed frequency of 1000 Hz, was presented. The interval between the two pulses was 200 ms and the order of pulses in each trial was randomized. An adapting tone preceded each pair by 200 ms and was either 200-ms linear frequency glide with frequency extent of 100 Hz (950–1050 Hz) or 200-ms stationary tone of 1000 Hz. In the result, when the glide preceded the pair of pulses, DLFs at 1000 Hz were significantly elevated irrespective of direction of glide compared to DLFs with no preceding tones. The stationary sine wave, however, had no effect on DLFs as several previous studies have reported. In sum, unidirectional continuous change of frequency disrupted a process of sampling and comparing frequencies from successive tones. These results indicate that the process of detecting continuous and successive change of frequency are at least partially mediated by a common mechanism.

3aPPb4. Notched-noise measures of frequency resolution in children: What acoustic cues are available at children's threshold levels? Prudence Allen and Louise Korpela (Univ. of Western Ontario, School of Commun. Sci. and Disord., Elborn College, London, ON N6G 1H1, Canada, pallen@julian.uwo.ca)

It has been suggested that young children's masked detection thresholds are obtained at signal-to-noise ratios for which the signals produce changes in multiple features of the masker [Allen *et al.*, J. Acoust. Soc. Am. (in press)]. In this study 500-, 2000-, and 4000-Hz tonal signals were added to flat- and notched-spectrum noise maskers at signal-to-noise ratios corresponding to children's threshold levels measured in a previous study of frequency resolution [Allen *et al.*, J. Speech Hear. Res. **32**, 317–324 (1989)]. The magnitudes of level, frequency, and periodicity cues were determined, assuming several degrees of frequency selective filtering. Results suggested that for all signal plus masker combinations, independent of frequency and masker spectrum, children's thresholds had been obtained at signal-to-noise ratios for which little or no frequency selectivity would have been required to produce potentially discriminable level differences [Jensen and Neff, Psychol. Sci. **4**, 1-4-107] of approximately 6 dB, which were often accompanied by average frequency and/or periodicity differences. Age-related changes in frequency selectivity therefore may not be required to explain children's higher masked detection thresholds as they are obtained at signal-to-noise ratios where multiple cues are present. [Work supported by NSERC.]

3aPPb5. Effects of practice on performance for different masking tasks. Roel Delahaye, Deb A. Fantini, and Ray Meddis (Dept. of Psych., Essex Univ., Wivenhoe Park, Colchester CO4 3SQ, UK)

The present study investigates the effects of long-term practice on masked signal detection with experienced listeners. The on-frequency masker (OFM) consists of a 700-Hz pure tone, which is sinusoidally amplitude-modulated at a 10-Hz rate. Similar flanking components can be placed at 300, 400, 500, 900, 1000, and 1100 Hz. The signal is composed of three, 50-ms, 700-Hz tone bursts that are placed in the dips of the OFM envelope. The flanking component envelope phases were either in phase (comodulated condition) or 180° out of phase (uncorrelated condition) with the OFM. In the reference condition only the OFM was present. Two subjects gained experience (20 h) before the first data collection session took place. After extended practice (40 h) a second session took place. The results of the first session show a release from masking in the comodulated condition with regard to the reference condition (CMR R-C) and the uncorrelated condition (CMR U-C). Results from the second session show that reference thresholds decrease more than the comodulated and uncorrelated thresholds. This resulted in a reduction or disappearance of CMR(R-C) but a preservation of CMR(U-C). Thus the amount of practice is inversely related to the magnitude of CMR(R-C), while CMR(U-C) is independent of practice.

3aPPb6. Simulations of spectral masking and the asymmetry of masking. Jesko L. Verhey and Torsten Dau (Graduiertenkolleg Psychoakustik and AG Medizinische Physik, Univ. Oldenburg, Germany)

Measurements and simulations of (i) notched-noise experiments and (ii) masking experiments where the signal and the masker have the same center frequency but different bandwidths, are presented. The simulations were performed with a model originally developed to describe effects of temporal masking and modulation detection [Dau *et al.*, J. Acoust. Soc. Am. **102**, 2892–2905 (1997)]. The model accounts well for notched-noise data which are mainly a consequence of the gammatone-filter parameters used in the peripheral filter stage of the model. The model also accounts for effects in notched-noise experiments with an asymmetric notch (''off-frequency listening''), which results from the decision stage that integrates signal information across frequency. A simple modulation-lowpass filter (energy integrator) would be sufficient to describe these experimental results. In contrast, the processing by a modulation filterbank is necessary to account for the conditions of ''asymmetry of masking'' in the second experiment.

3aPPb7. Spectral integration of auditory temporal information. David A. Eddins (Psychoacoust. Lab., Dept. of Speech and Hearing Sci., Indiana Univ., Bloomington, IN 47405)

Measures of temporal acuity reveal a remarkable ability to integrate temporal information across frequency throughout most of the audible spectrum. This apparent trading of spectral bandwidth and temporal resolution was investigated in three different experiments measuring amplitude-modulation detection, temporal gap detection, and intensity discrimination. Each experiment included six spectral conditions: a single band of noise 1600-Hz wide centered at 3000 Hz; a set of four noise bands 400-Hz wide having center frequencies separated by 1200 Hz (1200, 2400, 3600, 4800 Hz); and four conditions composed of only one of the four 400-Hz bands. The form of the modulation transfer functions did not depend upon total bandwidth or frequency region. Sensitivity to modulation was inversely related to total noise bandwidth. Temporal gap detection thresholds and intensity discrimination were strongly dependent upon total noise bandwidth but were independent of the spectral proximity and the center frequency of the noise bands. Analysis of the three experiments revealed that the inverse relation between intensity discrimination and noise bandwidth may be used to predict the variation in amplitude modulation and temporal gap detection thresholds with noise bandwidth.

3aPPb8. Direction discrimination for formant-frequency glides and modulation. Johannes Lyzenga and Robert P. Carlyon (MRC Cognition and Brain Sci. Unit, 15 Chaucer Rd., Cambridge CB2 2EF, UK)

The vowel properties that determine their classification are the positions of peaks in their frequency spectra: the formants. For normal-hearing subjects, the sensitivity of detecting linear glides in the positions of these formants and the ability to discriminate between the two possible directions of these glides as functions of their sizes, were measured. A frequency rove was used to prevent subjects from using the start and end points of the glides as cues. The same quantities were measured for a 5-Hz formant-frequency modulation. A three-interval, three-alternative forced-choice paradigm was used in all measurements. The stimuli were single-formant ''vowels'' generated for a number of different stimulus parameters, including fundamental, spectral slope, frequency region, and position of the formant relative to the harmonic spectrum. For most stimuli, sensitivity was approximately equal for detection (of glides and modulation) on the one hand, and direction discrimination on the other. Exceptions were found for a few ''formants'' that consisted of a single harmonic that only showed an amplitude change over the stimulus length. The detection of formant-frequency modulation can be disrupted by off-frequency modulated formants, and new data on this phenomenon for modulation-direction discrimination will be reported.

3aPPb9. Estimating the phase characteristic of the auditory system from masking by harmonic complexes. Jennifer J. Lentz and Marjorie R. Leek (Army Audiol. and Speech Ctr., Walter Reed Army Med. Ctr., Washington, DC 20307, jennifer_lentz@wramc1-amedd.army.mil)

As shown by several recent studies of positive and negative ''Schroeder-phase'' stimuli, masking by harmonic complexes is strongly affected by the temporal waveform of the masker [e.g., V. Summers and M. Leek, Hearing Res. **118**, 139–150 (1998)]. Differences in masking by the Schroeder waves provide a starting point for estimating the phase response of the auditory system. In this study, the gradient of phase change across masker bandwidth was varied by altering the Schroeder-phase algorithm. Depending on signal frequency (ranging from 500 to 4000 Hz), differences in masking could be 5–10 dB for phase gradients changing by only 10%. The phase gradient that resulted in a minimum amount of masking varied systematically with signal frequency, with low frequencies masked least effectively by waveforms with rapidly changing component phases, and high frequencies by waveforms with more shallow phase gradients. This relationship between phase gradient and signal frequency is taken to reflect the phase response of the auditory filter at that frequency. The phase gradients associated with minimal masking at each frequency can be used to construct a piecewise-estimate of the phase characteristic of the auditory system for individual listeners. [Work supported by NIH DC00626.]

3aPPb10. Unexpected dependency of psychoacoustical sharpness on the bandwidth of noise. Ulrich Haupt and Reinhard Weber (Dept. of Phys., Carl-von-Ossietzky Univ. of Oldenburg, D-26111 Oldenburg, Germany)

Based on semantic differential and scaling experiments, von Bismarck [Acustica **30**, 146–159 (1974)] proposed a model for psychoacoustical sharpness calculation, which later on was modified by Aures [Acustica **58**, 282–290 (1985)]. Categorical sharpness evaluation of sounds exhibited systematic deviations from calculated sharpness after Aures under special conditions. Sharpness ratings of bandpass noises with the same calculated sharpness decreased if the bandwidth ΔB of the noises increased [E. Kabot and R. Weber, DAGA '94, 1029–1032 (1994)]. The intent of the present study was to investigate this effect in detail. The stimuli to be assessed consisted of two sets of sounds containing tones and broadband noises ($\Delta B = 0.5$, 1, 2, and 5 Bark). All sounds in a set had equal calcu-

lated sharpness and were presented over headphones at the same loudness. Using a five-category scale, subjects evaluated each sound in two sessions, six times, in a random order. The results will be discussed against the background of new sharpness model calculations.

3aPPb11. Gap detection within and across perceptual channels. Andrew J. Oxenham (Dept. of Speech-Lang. Pathol. & Audiol. (133 FR), Northeastern Univ., 360 Huntington Ave., Boston, MA 02115)

The ability to detect gaps is degraded when the stimuli (markers) on either side of the gap have different power spectra. This may be due to peripheral frequency selectivity: when no transient is audible in the no-gap condition (e.g., when the markers have the same intensity and spectrum), listeners detect the transient introduced by the gap; when the markers fall into different auditory filters or are at different intensities, transients are audible regardless of the presence of a gap and listeners must perform a timing judgment. It has recently been suggested that changes in other, more central, perceptual dimensions, such as perceived location, may also affect gap detection. This study was designed to test whether a peripherally based model could also account for such data. Lateralization differences between the two broadband-noise markers were achieved using interaural time and intensity differences independently. Monaural gap detection with level differences between the markers was also tested. Results indicate that gap detection is poor only when level differences exist between the markers, independent of perceived location. Thus the data can in principle be accounted for by peripheral mechanisms. No evidence was found for the influence of higher perceptual channels. [Work supported by the NIDCD.]

3aPPb12. Acoustic weapons? Effects of very high sound levels. Jürgen Altmann (Experimentelle Physik III, Universität Dortmund/ Institut für Experimentalphysik III, Ruhr Universität Bochum, 44780 Bochum, Germany, Altmann@EP3.Ruhr-Uni-Bochum.DE)

Mainly in the context of so-called nonlethal weapons, acoustic weapons are under research and development in a few countries. Reliable information is scarce; allegations, mainly in the military press, have attributed drastic effects in particular to infrasound. Humans would suffer from disorientation and nausea up to vomiting and uncontrolled defecation, however without lasting damage. For damage to material, embrittlement of metals and even localized earthquakes have been mentioned. A literature review was done to investigate such claims and find out other effects of strong sound in the infrasound and low-frequency audio, high-frequency audio, and ultrasound ranges, as well as of blast waves. Whereas the infrasound allegations cannot be confirmed, marked nonauditory effects exist in the low audio range at levels above 150 dB. At higher frequencies and with blast waves, mainly in the auditory system is affected. With increasing level, annoyance, pain, and permanent damage ensue; protection is possible, however. Very strong blast waves can cause lung rupture and death. Because application scenarios range from protection of fixed installations via riot control to armed conflict, potential regulation should not be restricted to the law of warfare, and preventive limits will need to be detailed.

WEDNESDAY MORNING, 17 MARCH 1999 ROOM EB301, 9:00 A.M. TO 12:20 P.M.

Session 3aSA
International Workshop on Active Noise and Vibration Control

Structural Acoustics and Vibration: Active Control of Sound Radiation and Transmission

Peter Dean, Cochair
Lockheed Martin Missiles and Space Org., H1-33, B203, 3251 Hanover Street, Palo Alto, California 94304, USA

Paolo Gardonio, Cochair
Signal Processing and Control Group, ISVR, University of Southampton SO17 1BJ, UK

Invited Paper

9:00

3aSA1. Experiments on active control of sound radiation around double-wall resonance frequency. S. J. Pietrzko (EMPA—Swiss Federal Labs. for Mater. Testing and Res., CH-8600 Dübendorf, Switzerland, pietrzko@empa.ch)

The first part of this paper will be focused on identified modal shapes and sound power measurements of a double-wall panel in the low-frequency range around the double-wall resonance frequency. New experimental results show that for a double-wall panel with one laminated pane (asymmetric panel) around the predicted double-wall resonance frequency, there exist three natural frequencies, respectively three modes. One of these modes is highly complex and the other two are real. It is characteristic that at one of these real modes both planes of the panel move exactly in phase and at the second they move precisely out of phase. The second part of the paper will be focused on the design of control system to minimize the radiated sound power from the double-wall panel and efficiency of the proposed control. The radiation efficiency for each of the identified modes was estimated with goal to define the optimal position for the piezoactuators used to minimize the radiated sound power around the double-wall resonance frequency. Different control schemes will be presented. The efficiency of proposed control schemes will be compared and illustrated by means of laser scanned vibratory patterns of the panel.

9:20

3aSA2. Active control of harmonic and random sound transmission in a structural-acoustic system. M. J. Brennan and S. M. Kim (Inst. of Sound and Vib. Res., Univ. of Southampton, Southampton, Hampshire SO17 1BJ, UK, mjb@isvr.soton.ac.uk)

The active control of sound transmission in structural-acoustic coupled systems has been of interest in recent years. Two particular problems that have received attention are the active control of *harmonic* sound transmission into aircraft, and control of *random* noise transmission into the payload bay of space rockets. This paper describes an analytical and experimental investigation to compare the feedforward control of *harmonic* and *random* sound transmission into an acoustic cavity. A rectangular enclosure is considered that has five acoustically rigid walls and a flexible plate on the remaining side through which a plane acoustic wave is transmitted into the enclosure. The control systems are designed to reduce the acoustic potential energy inside the enclosure when the incident sound is either harmonic or random. Three control configurations, classified by the type of actuators, are investigated both theoretically and experimentally. They are the use of a structural actuator, the use of an acoustic source, and the simultaneous use of both structural *and* acoustic actuators. It is shown that the use of both actuators is desirable for the active control of *both* harmonic and random sound transmission into a coupled structural-acoustic system whose response is governed by plate and cavity controlled modes.

9:40

3aSA3. Near-field control of complex sources. Jiri Tichy (Grad. Prog. in Acoust., Penn State Univ., University Park, PA 16802)

The near-field of complex sources that are characterized by standing waves on their surface is modeled by baffled point sources. The near field is visualized by showing the spatial distributions of sound pressure, sound intensity, and energy density. The field maps provide essential information on the local energy flows. Several sound control schemes to minimize the total radiated sound power by placing small sources in the vicinity of the primary sources are analyzed and tested.

10:00

3aSA4. A comparison of active control strategies for the reduction of sound transmission through double panels. Paolo Gardonio and Stephen J. Elliott (Inst. of Sound and Vib. Res., Univ. of Southampton, Southampton, UK)

A theoretical study of the active isolation of air-borne and structure-borne sound transmission through a double panel system is presented. The reductions in the radiated sound are investigated for three different families of control approaches. The first and the second families are based on the minimization of total sound power radiation or the minimization of the weighted sum of the square values of the sound pressure at a set of positions between the two panels and the square values of the velocities at a set of positions of the radiating panel using either active mounts or/and control loudspeakers. The third family considers: first, the cancellation of out-of-plane velocities underneath the mounts using active mounts; second, the cancellation of sound pressure near each loudspeaker using loudspeakers; and third, the cancellation of both velocities and the sound pressure using both loudspeakers and mounts. The third family does not give good performances except at low frequencies. Alternatively, the minimization of weighted square values of plate velocities and cavity pressures gives good results which are comparable with those obtained with the optimal control approach of total sound power minimization. In general, the control loudspeakers give better control in all control approaches considered.

10:20–10:40 Break

10:40

3aSA5. Intensity error sensing in the active control of sound. Robert Koehler and Scott D. Snyder (Mech. Eng. Dept., Univ. of Adelaide, Adelaide, SA 5005, Australia)

In the active control of radiated sound fields, the use of intensity as an error signal has intuitive appeal, due to the fact that the measure is directly related to the sound power radiated from the source. To date, examinations of this proposition have been restricted largely to theoretical studies. This work to be presented here extends previously derived theoretical results, and presents experimental results from the use of intensity-based error measures in a practical adaptive active noise control system. It is found that while minimization of an acoustic pressure-based error signal does not guarantee a satisfactory global result, the use of an intensity-based error signal may not improve the situation. In fact, there are many instances where the use of a pressure-based error signal in the active noise control system may be preferable. This includes instances where the error signal is measured in the near field of the sound source, at locations where it was hoped that minimization of intensity-based error signals would deliver superior overall active control system performance.

11:00

3aSA6. Simulations of the feedback control of sound transmission through a plate using measured data. Thomas C. Sors and Stephen J. Elliott (Inst. of Sound and Vib. Res., Univ. of Southampton, Southampton, UK)

This paper describes a simulation of active structural acoustic control (ASAC) based on experimentally measured frequency response functions. An experimental arrangement consisting of a plate mounted between two rooms and equipped with integrated actuators and sensors is described. The aim of the experiment is to use these transducers mounted on the plate to reduce the transmission of an acoustic disturbance generated by a loudspeaker in one room to the other. Frequency response functions are measured from the loudspeaker and the actuators to the integrated sensors and also to a number of far-field error microphones. These measurements are used to predict the performance of various feedback controllers on the sound transmission. It is found that, provided there is only a small amount of delay inherent to the control process, significant reductions can be made for periodic disturbances and also some reductions can be made for broadband disturbances. [Work supported by the TNO Institute of Applied Physics, Delft, The Netherlands.]

11:20

3aSA7. Experiments on the active increase of sound transmission loss using distributed actuators. Kris Henrioulle and Paul Sas (Katholieke Univ. Leuven, Celestijnenlaan 300B, B-3001 Leuven, Belgium)

A series of experiments have been performed to improve actively the sound transmission loss through a single-panel partition in the low-frequency range. Two types of flat acoustic actuators, designed in the framework of the European project DAFNOR (distributed active foils for noise reduction), are tested. The first acoustic actuator is based on PVDF piezoelectric material, which induces a bending motion in the actuator. The second acoustic actuator is based on the electrostatic principle. The experimental setup consists of a single steel panel of size $300\times400\times1$ mm which is subject to a plane-wave acoustic excitation. The control system consists of the distributed acoustic actuator, which is placed near the steel panel. Various control strategies, which were previously simulated, are tested. The control actuator is driven by a controller which aims at reducing the acoustic energy at the radiating side. [The work reported herein was related to the EC Brite/Euram Research Project ''DAFNOR'' (under contract BRPR-CT96-0154). The project is supported by the Directorate-General for Science, Research and Development of the CEC.]

11:40

3aSA8. An experimental investigation of a novel active segmented partition for sound transmission control. Timothy W. Leishman[a] and Jiri Tichy (Grad. Prog. in Acoust., Penn State Univ., 217 Appl. Sci. Bldg., University Park, PA 16802, leishman@sabine.acs.psu.edu)

A unique dual diaphragm configuration for individual elements of active segmented partitions has recently been advanced as a practical, efficient means of controlling sound transmission. The configuration incorporates a useful combination of electro-mechano-acoustical actuation and segmentation, enabling effective global control of transmitting surface vibrations. In this work, experimental efforts are reported that explore important active and passive characteristics of such elements while adjoined in a full partition array. Each element is independently and stably controlled using a single-channel filtered-x adaptive controller (single reference input, single error input, single output). Acoustic pressure scans of element cavities and laser vibrometer scans of their transmitting surfaces affirm important properties of this partition construction that have been previously theorized. Other measurements demonstrate that the controlled transmission loss of the lightweight array lies uniformly between 55 and 60 dB over nearly all of the evaluated spectrum (30 to 300 Hz). Such extensive control is generally very difficult to realize over the lower audible frequency spectrum using an extended lightweight structure. Further measurements illustrate that this is comparable to the passive transmission loss of a much more massive benchmark partition of the same cross-sectional area, but constructed of thick, spaced layers of concrete and sand. [a]Currently at Crown International, 1718 W. Mishawaka Rd., Elkhart, IN 46515-1000.

12:00

3aSA9. A hybrid passive/active system for control of the noise radiated by a small generator. Maria Cuesta and Pedro Cobo (Instituto de Acustica, CSIC, Serrano 144, 28006 Madrid, Spain, iacpc24@fresno.csic.es)

The aim of this work was the design and implementation of a hybrid passive/active system to control the noise radiated by a small generator. The fundamental frequency of the periodic radiated noise depends on the electrical load plugged into the generator. Passive control is afforded by a rectangular enclosure with dimensions $1000\times710\times530$ mm^3. The wall panels of the enclosure (steel 1.5 mm thick) are lined with a 30-mm layer of sound absorbing material. Special attention is paid to technical aspects such as air refreshing and temperature inside the enclosure. The measured insertion loss is higher than 20 dB above 500 Hz. Low-frequency noise escapes the enclosure via intake and exhaust openings. Active control is applied to the exhaust noise. The reference signal is supplied by an accelerometer over the air filter case of the generator. A high-temperature loudspeaker is used as control source. The error signal is picked up by a cheap electric microphone. Since noise along the exhaust is too loud, the microphone sensitivity had to be reduced by taping its diaphragm. A commercial system is used to implement active noise control. [Work supported by CICYT, Project AMB97-1175-C03-01.]

WEDNESDAY MORNING, 17 MARCH 1999 ROOM H3010, 7:55 A.M. TO 12:20 P.M.

Session 3aSCa

Speech Communication: Psychoacoustic Methods in Speech Recognition I

Birger Kollmeier, Cochair
AG Medizinische Physik, Universität Oldenburg, Postfach 2503, D-26111 Oldenburg, Germany

Hynek Hermansky, Cochair
Oregon Graduate Institute of Science and Technology, Beaverton, Oregon 97006-8921, USA

Chair's Introduction—7:55

Invited Papers

8:00

3aSCa1. What can we learn from human processes of spoken language comprehension? Hiroya Fujisaki (Dept. of Appl. Electron., Sci. Univ. of Tokyo, 2641 Yamazaki, Noda, 278-8510 Japan, fujisaki@te.noda.sut.ac.jp)

Conventional approaches for automatic speech recognition and understanding are essentially bottom-up. Namely, they are based on the assumption that speech can be decomposed reliably into the smallest units, can be recognized by identifying these units first, and then by clustering them to find larger units and their interrelationships. It is thus taken for granted that speech recognition is the prerequisite to speech understanding. The human processes of spoken language comprehension, on the contrary, are rather holistic and do not necessarily require identification of every constituent unit. This is possible since the listener has the capability of constructing the expected message while listening, and of matching it against the input message on the basis of global features, without paying much attention to the details. In the author's view, the unit of human speech processing is considered to be not fixed, but variable in size depending on the context, situation, and knowledge. Likewise, the human processes of lexical access and parsing are considered to be quite different from those used in conventional systems for natural language processing. These issues will be discussed on the basis of studies by the author and his co-workers as well as by others.

8:20

3aSCa2. A psychoacoustical model of the auditory periphery as the front end for ASR. Jürgen Tchorz, Michael Kleinschmidt, and Birger Kollmeier (AG Medizinische Physik, Univ. Oldenburg, Oldenburg, Germany)

A psychoacoustical model of the auditory periphery was developed by Dau and others to predict human performance quantitatively in typical spectral and temporal masking experiments. Its main processing stages are basilar membrane filtering for spectral analysis, adaptive envelope compression in each frequency band which enhances changes in the input signal and suppresses steady-state portions, and low-pass filtering of envelope modulations. In the field of speech processing, the model was applied as the front end of an automatic speech recognition (ASR) system [J. Tchorz and B. Kollmeier, J. Acoust. Soc. Am. (submitted)]. Speaker-independent, isolated-digit recognition experiments in different types of noise were carried out to evaluate the robustness of the auditory-based ASR system in adverse conditions. Compared to a standard MFCC front end, the auditory-based preprocessing yielded significantly higher recognition rates in both additive and convolutive noise. Further experiments concentrated on the question, which of the processing stages of the psychoacoustically motivated model are essential for robust representation of speech? The results indicate that the adaptive compression stage and low-pass filtering of envelope modulations contribute most to robustness, whereas the spectral analysis part is less critical.

8:40–9:00 Discussion

9:00

3aSCa3. Automatic classification of the acoustical situation using amplitude-modulation spectrograms. Jürgen Tchorz and Birger Kollmeier (AG Medizinische Physik, Univ. Oldenburg, Oldenburg, Germany)

A fast and reliable classification of the acoustical situation is an important prerequisite for modern speech processing schemes. Noise suppression algorithms in digital hearing aids, for example, are strongly dependent on a proper noise level estimation. The classification algorithm which is presented is based on so-called amplitude-modulation spectrograms (AMS). It is motivated by neurophysiological findings in the auditory cortex in mammals. Its basic idea is that both spectral and temporal information of the signal is used to attain a separation between ''acoustical objects'' within the signal. Spectral information is gained by splitting the input signal into different frequency bands, temporal information is gained by analyzing amplitude modulations in each frequency band. Thus for each analysis frame of the input signal, a two-dimensional AMS pattern is created. Signals with similar spectral shape but different temporal properties are clearly distinct in the AMS representation. A neural network is trained on a large number of AMS patterns which were generated from speech and noise samples. After training, an automatic classification of speech and noise from ''unknown'' sources is performed with high accuracy. Furthermore, an estimate of the present signal-to-noise ratio is supplied for mixed input signals.

9:20

3aSCa4. Evaluation of PEMO in robust speech recognition. Klaus Kasper and Herbert Reininger (Inst. für Angewandte Physik, Goethe Univ., Robert-Mayer-Str. 2-4, 60054 Frankfurt, Main, Germany)

A major problem in speech recognition is the robustness of recognition performance against additive background noise and convolutive distortions due to changing transmission channels or varying microphone characteristics. One approach to overcome this problem is to apply PEMO [Dau, Püschel, and Kohlrausch, J. Acoust. Soc. Am. **99**, 3615–3622 (1996)] for extraction of noise robust feature vectors. The recognition performance achievable with PEMO in combination with a locally recurrent neural network (LRNN) or hidden Markov models (HMM) for feature scoring was evaluated in a task of speaker-independent word recognition. The robustness was tested and compared with that of other feature types by applying the speech recognition systems to speech signals disturbed by additive background noise and to speech signals recorded over telephone lines. It was found that only with LRNN it is possible to exploit the potential of PEMO, not with HMM. A detailed analysis of the interplay between PEMO features and the scoring techniques revealed that the long-term dependencies in the sequence PEMO features can only be captured by LRNN. Furthermore, LRNN discriminate between the distinct and sparse peaks of the PEMO speech representation—which are well maintained also in the case of noisy speech—and artifacts introduced by the additive or convolutive noise.

9:40–10:00 Discussion

10:00–10:20 Break

10:20

3aSCa5. Syllable-based speech recognition using auditorylike features. Steven Greenberg, Takayuki Arai, Brian Kingsbury, Nelson Morgan, Michael Shire, Rosaria Silipo, and Su-Lin Wu (International Computer Science Inst., 1947 Center St., Berkeley, CA 94704)

Classical models of speech recognition (both human and machine) assume that a detailed, short-term analysis of the signal is essential for accurate decoding of spoken language via a linear sequence of phonetic segments. This classical framework is incommensurate with quantitative acoustic/phonetic analyses of spontaneous discourse (e.g., the Switchboard corpus for American English). Such analyses indicate that the syllable, rather than the phone, is likely to serve as the representational interface between sound and meaning, providing a relatively stable representation of lexically relevant information across a wide range of speaking and acoustic conditions. The auditory basis of this syllabic representaion appears to be derived from the low-frequency (2–16 Hz) modulation spectrum, whose temporal properties correspond closely to the distribution of syllabic durations observed in spontaneous speech. Perceptual experiments confirm the importance of the modulation spectrum for understanding spoken language and demonstrate that

the intelligibility of speech is derived from both the amplitude and phase components of this spectral representation. Syllable-based automatic speech recognition systems, currently under development, have proven useful under various acoustic conditions representative of the real world (such as reverberation and background noise) when used in conjunction with more traditional, phone-based recognition systems.

10:40

3aSCa6. The profile of interaural decorrelation across frequency: A binaural representation of pitch and timbre. A. Quentin Summerfield (MRC Inst. of Hearing Res., Univ. of Nottingham, Nottingham, UK), John F. Culling (Univ. of Wales, Cardiff, UK), and Michael A. Akeroyd (Univ. of Nottingham, UK)

Tones can be detected in noise at lower signal-to-noise ratios (SNRs) when they possess different interaural timing to the noise. One account, equalization-cancellation (E-C), suggests that the left- and right-ear signals are adjusted in time and amplitude to maximize their similarity, and are then cancelled by subtraction. At low SNRs, E-C improves the SNR of the tone by cancelling the noise. E-C is also a method for measuring interaural decorrelation, because the remainder after subtraction is a measure of the extent to which the tone reduces the interaural correlation of the noise. Applying E-C independently in each frequency channel reveals the profile of interaural decorrelation across frequency induced by a complex signal in noise. The profile is a place representation akin to an excitation pattern. It has three properties. (i) It displays the spectrum of speech at low SNRs. (ii) Listeners can integrate it perceptually with the conventional profile of spectral amplitude. (iii) Its spectral structure is compatible with a subset of the dichotic pitches phenomena in which tonal percepts are induced by introducing interaural phase changes into broadband noises. Finally, the profile can be recast in a form compatible with temporal accounts of pitch and timbre based on autocorrelation.

11:00–11:20 Discussion

11:20

3aSCa7. Recognition of speech from temporal patterns. Sangita Sharma and Hynek Hermansky (Oregon Grad. Inst. of Sci. and Technol., Portland, OR, hynek@ece.ogi.ed)

Spectrum of short segments of speech signal is accepted as one of the prime acoustic correlates of phonetic quality and it forms the basis of most current feature representations of speech. However, the short-term spectral vectors are affected by coarticulation. The coarticulation can span time intervals of several phonemes. In spite of that, human speech perception is able to derive the identity of the individual underlying phoneme. This process does not seem to require successful decoding of neigboring phonemes [Allen, IEEE Trans. **AU-2**(4), 567–577 (1994)], but it may require information from a relatively large temporal span of the speech signal [Kozhevnikov and Chistovich, ''Speech: Articulation and Perception,'' Dept. of Commerce (1967)]. To allow for effective use of a syllable-level temporal information, a short-term spectrum-based vector is replaced as input to the classifier by rather long (about 1 s) vectors representing the time trajectory of critical-band spectral energy. Each temporal vector then spans many more than one phoneme. This technique forms the basis of a complete ASR system which is competitive with the current state-of-the-art speech recognition technology. [Work supported by the Department of Defense and by the National Science Foundation.]

11:40

3aSCa8. Some musings on systematic variability and speech recognition. Jordan Cohen (Ctr. for Commun. Res., Princeton, NJ 08502)

One of the major problems in speech recognition is the inability of trained models to generalize appropriately to channel variations, new speakers, or modified acoustics. The naive observer would believe that a multimillion-parameter system should be sufficient! The difficulty appears to be too many parameters rather than too few. For moderate-sized training corpora, systems learn all of the conditions in the training data rather than generalizing from the exemplars. (For instance, speech recognition algorithms will generally score the speech from a training speaker higher than that from a speaker who was excluded from the set.) One can force the issue by explicitly modeling systematic variation, and then ''normalizing'' at the front end or in the acoustic model. Two exemplars of this philosophy are Cepstral mean subtraction and vocal tract normalization [Frontiers in Speech Processing 94, LDC96s40, Linguistic Data Consortium (1995)]. In each case a single parameter from a very restrictive model is estimated, and accounting for the variability explicitly improves performance. Concrete examples of these situations are offered, and the impact of this work on future work in automatic speech recognition is discussed.

12:00–12:20 Discussion

Session 3aSCb

Speech Communication: Fluid Dynamic Models for Speech Production

Anders Lofqvist, Cochair
Haskins Laboratories, 270 Crown Street, New Haven, Connecticut 06511, USA

Christine H. Shadle, Cochair
Department of Electronics and Computer Science, University of Southampton, Highfield, Southampton SO17 1BJ, UK

Chair's Introduction—7:55

Invited Papers

8:00

3aSCb1. Fluid dynamic effects in speech. Michael Krane (CAIP Ctr., Rutgers Univ., Piscataway, NJ 08855, mkrane@caip.rutgers.edu)

A summary of fluid dynamic effects in speech are outlined using concepts from duct flow aerodynamics and aeroacoustics. A physical picture of fluid motion which produces both voiced and unvoiced sounds is presented, with emphasis on how movement of the acoustic medium affects both the generation and propagation of sound. Particular attention is given to the concept of vorticity (roughly, fluid particle rotational motion) as a means to characterize turbulent flow and as the means by which airflow produces or absorbs sound. First, it is shown how vorticity production by steady flow at the end of an open pipe may act as an absorber of sound, affecting the acoustic impedance of the open end. Unvoiced sound production is then discussed in terms of the formation of a jet by flow separation, the structure of jet vorticity, and how convection of jet vorticity through a nonuniform vocal tract produces sound. Order-of-magnitude estimates of these effects are presented. Finally, the role of these effects in voice production are detailed through a discussion of the modulation of glottal volume flow by movement of the glottal flow separation point and production of sound by the glottal jet.

8:20

3aSCb2. Turbulent glottal flow during phonation. Fariborz Alipour (Dept. of Speech Pathol. and Audiol., The Univ. of Iowa, Iowa City, IA 52242)

Human phonation is the flow-induced oscillation of the vocal folds, producing pulsatile jet through the glottis, which may become turbulent. This turbulent jet was investigated in an excised canine larynx model with simultaneous recordings of air particle velocity, subglottal pressure, airflow rate, and EGG signal for various conditions of phonation. Canine larynges were mounted on a plastic air tube and sustained oscillations were established and maintained by mechanically manipulating the cartilages to mimic the function of laryngeal muscles. The major control parameters were the airflow rate and the glottal adduction. The velocity was measured with a constant-temperature hot-wire anemometer system. To separate the turbulence from the periodic component of the velocity signal, the technique of phase shift averaging was employed. Results suggest that subglottal inlet flow to the larynx is pulsatile but mostly laminar, while the exiting jet is nonuniform and turbulent. The Reynolds number based on the mean glottal velocity and glottal hydraulic diameter varied between 1600 and 7000, the Strouhal number varied between 0.002 and 0.032, and the Womersley number ranged from 2.6 to 15.9. These results help define the conditions required for computational models of laryngeal flow. [This work was supported by NIDCD Grant No. DC03566-01.]

8:40

3aSCb3. A study of the supraglottal flow behavior during phonation. Xavier Pelorson, Coriandre Vilain (ICP/INPG, Univ. Stendhal, 46 av. F. Viallet, F-38031 Grenoble, France), and Avraham Hirschberg (Tech. Univ. Eindhoven, Eindhoven, The Netherlands)

Most physical models of phonation assume the formation of a free jet at the end of the glottis. The precise behavior of this jet is generally overlooked, assuming a symmetrical flow and a total dissipation of the kinetic energy past the glottis. However, asymmetry of the glottal flow (Coanda effect) and false folds effects (reattachment of the jet) have been observed on the basis of quasi-steady flow numerical simulations. In this paper the relevance of these effects on the basis of unsteady *in-vitro* measurements using pulsating flows through symmetrical models of the glottis is discussed. It is shown that asymmetry of the flow due to the Coanda effect is typical of steady flows but does not have time to be established during unsteady conditions. An extension of this study concerning effects of an asymmetry of the glottis will also be discussed. Concerning the effects of the false folds, many parameters have been studied such as the width of the false folds, and the distance between the true and the false folds. It is shown that for typical phonation configurations the possible effects of the false folds remain very weak. This might not be the case for pathological configurations.

9:00

3aSCb4. Models of frication: Advances and limitations. Christine H. Shadle (Dept. of Electron. and Computer Sci., Univ. of Southampton, Southampton SO17 1BJ, UK, chs@ecs.soton.ac.uk)

The increasing number of modeling studies of fricatives and frication in recent years is due at least partly to two major advances: increasing computational power makes it feasible to simulate the flow, and thus construct a more physically accurate model; improvements in vocal-tract imaging, particularly magnetic resonance imaging (MRI), allow capture of three-dimensional vocal-tract shape data, especially including small constrictions formed by soft tissue. However, the complexity of both techniques still tends to lead to incomplete models of frication, limited to static and/or highly simplified tract shapes. Further, the three-dimensional data are often used only to generate an area function, ignoring the cross-sectional shape data that can be crucial in defining aeroacoustic sources. Fricatives are not static, and some of their dynamic behavior, such as apparent modulation of the noise source in voiced fricatives, may be especially ill-served by quasistatic models. Dynamic MRI techniques can be used to acquire shape data with which to pursue dynamic models. Finally, the program VOAC will be discussed briefly (and in more detail elsewhere in this session) as an example of a way to use three-dimensional data and acoustic-flow interactions to enhance the model without unduly increasing computational, or conceptual, complexity.

9:20

3aSCb5. Computational aeroacoustics of subsonic jets for application to speech production. S. H. Frankel, W. Zhao, L. Mongeau (School of Mech. Eng., Purdue Univ., West Lafayette, IN 47907), and R. C. Scherer (Bowling Green State Univ., Bowling Green, OH 43403)

Computational aeroacoustics calculations, based on direct numerical simulations, were performed in order to predict the near-field and far-field sound radiated by a forced, round, unconfined, subsonic jet. The jet Mach number was around $Ma=0.4$, and the Reynolds number based on the jet velocity and diameter was approximately $Re=103$. The compressible Navier–Stokes equations were integrated using a high-order finite-difference scheme. A two-dimensional, axisymmetric, nonuniform grid was used. Both direct computations and acoustic analogies were used to compute the far-field sound. Of interest is the role of large-scale vortical flow structures and vortex pairing in the production of sound. The results were used to assess the validity and limitations of the computational approach through comparisons to previously published numerical results. The ultimate goal is to perform large eddy simulations of pulsating jets in a range of flow conditions more relevant to speech production, e.g., approximately $Ma=0.1$, $Re=105$, to establish the radiation efficiency and the physical origin of the aeroacoustic sources involved. [Work sponsored by NIH.]

9:40

3aSCb6. Synthesis of unvoiced speech sounds using an aeroacoustic source model. Michael Krane, Daniel Sinder, and James Flanagan (CAIP Ctr., Rutgers Univ., Piscataway, NJ 08855, mkrane@caip.rutgers.edu)

An aeroacoustics-based method for synthesizing unvoiced speech sounds is presented. The source model is that of Howe (1975) for sound generated by flow of vorticity through a nonuniform duct. In this formulation three quantities must be known: the potential flow velocity, which changes according to the duct shape, the vorticity, and the velocity induced by vorticity in the flow and its images in the duct walls. The potential flow velocity magnitude is found using a transmission-line representation of the vocal tract, and the direction is found using a panel method. A model for the generation and evolution of vorticity has been developed in which the vortex shedding frequency is a random variable, and the vortex convects at a constant speed and direction. The computational model was used to simulate three cases: (1) a jet flowing through a pipe constriction, (2) a fricative sound (/s/), and (3) a VCV combination (/a s a/). Simulation results are presented and compared to experimental data, in terms of spectra and listening tests.

10:00–10:20 Discussion

10:20–10:40 Break

Contributed Papers

10:40

3aSCb7. A computational study of glottal obliquity. Ronald C. Scherer (Dept. of Commun. Disord., Bowling Green State Univ., Bowling Green, OH 43403), Kenneth J. De Witt, Abdollah A. Afjeh, Chao Zhang (Univ. of Toledo, Toledo, OH 43606), and Steven H. Frankel (Purdue Univ., West Lafayette, IN 47907)

Glottal motion is not always symmetric during phonation. The cycle phase of one vocal fold may differ from that of the other, creating a dynamic glottal center line oblique to the tracheal center line. This condition is called ''obliquity'' of the glottis. Intraglottal pressures for a range of obliquity angles were obtained using a finite difference computational technique for steady flow in static geometries. As an example, for a uniform glottal duct, obliquity of 20 deg (one side convergent, the other divergent), subglottal pressure of 7.8 cm H_2O, and glottal diameter of 0.032 cm: (1) air pressures were significantly different between the two glottal walls (as large as approximately 24 pressures measured perpendicular to the tracheal axis, but less if measured perpendicular to the glottal duct, (2) pressure values were different in amount and even polarity from that expected for a uniform glottis with zero obliquity, and (3) there were significant pressure differences at glottal exit between the two sides. Aerodynamic equations for glottal flow need to be modified to account for obliquity. The computational pressure profiles will be compared to empirical results using a Plexiglas model (M5) of the larynx. [Work supported by NIH grant 1R01DC03577-01A1.]

11:00

3aSCb8. Estimating the nonacoustic fluctuating velocity amplitude from Cranen and Boves' vowel production data. Anna Barney (Faculty of Eng. and Appl. Sci., Univ. of Southampton, Southampton SO17 1BJ, UK)

In a dynamic mechanical model of the larynx and vocal tract [Barney *et al.*, J. Acoust. Soc. Am. (in press)], the fluctuating velocity field was shown to have contributions from an acoustic disturbance and also from nonacoustic flow associated with vortex transport along the model tract. Nonacoustic velocity fluctuations, interacting with changes in the tract area function, can constitute significant sources of sound; in the vocal tract these could occur at the lips, teeth, etc. However, such additional sources of sound are not generally included in models of voiced speech production. Cranen and Boves [J. Acoust. Soc. Am. **77**, 1543–1551 (1985)] obtained in-tract and radiated sound-pressure time histories from phonating subjects, from which they computed in-tract velocities. In this study the relative amplitudes of the acoustic and nonacoustic velocity fluctuations have also been estimated from their data. Though vocal tract area functions are not available, simple models of sound transmission and radiation allow an order-of-magnitude prediction of the contribution to the radiated sound associated with each part of the in-tract velocity field. Although these are preliminary investigations using a restricted data set, the evidence suggests that there is nonacoustic fluctuating flow within the vocal tract, capable of significant sound generation.

11:20

3aSCb9. A model of vocal-tract acoustics and aeroacoustics validated by flow experiments. Philip J. B. Jackson and Christine H. Shadle (Dept. of Electron. and Computer Sci., Univ. of Southampton, Southampton SO17 1BJ, UK, pjbj96r,chs@ecs.soton.ac.uk)

Modeling the acoustic response of the vocal tract is a complex task, both from the point of view of acquiring details of its internal geometry and of accounting for the acoustic-flow interactions. A **vo**cal-tract **ac**oustics program (VOAC) has been developed [P. Davies, R. McGowan, and C. Shadle, in *Vocal Fold Physics*, edited by I. Titze (Singular, San Diego, 1993), pp. 93–142], which uses a more realistic, aeroacoustic model of the vocal tract than classic electrical-analog representations. It accommodates area and hydraulic radius profiles, smooth and abrupt area changes, incorporating end corrections, side branches, and net fluid flows, including turbulence losses incurred through jet formation. Originally, VOAC was tested by comparing vowel formant frequencies (i) uttered by subjects, (ii) predicted using classic electrical analog, and (iii) predicted by VOAC. In this study, VOAC is further validated by comparing the predicted frequency response functions for a range of flow rates with measurements of the radiated sound from a series of mechanical models of unvoiced fricatives [C. Shadle, Ph.D. thesis, MIT-RLE Tech. Report 506 (1985)]. Results show VOAC is more accurate in predicting the complete spectrum at a range of flow rates. Finally, preliminary work is presented with VOAC used to simulate the sound generated at a sequence of stages during the release of a plosive.

11:40

3aSCb10. Vocal microtremor assessed by complex demodulation. Eugen Gallasch (Dept. of Physiol., Karl-Franzens Universität, Harrachgasse 21, 8010 Graz, Austria)

Vocal microtremor refers to small involuntary fluctuations of fundamental frequency (f_0) and sound intensity during attempted constant phonation. Physically such an utterance may be considered as a FM/AM process $x(t)$ with f_0 as carrier frequency (after filtering the acoustic signal around f_0 to eliminate its harmonics): $x(t)=a(t)*\cos(f_0 t+\phi(t))$ and $f(t)=d[\phi(t)]/dt$. To study the instantaneous changes of $f(t)$ and $a(t)$ as well as their mutual relationships, complex demodulation was applied. First, the complex analytic signal $y(t)$ was formed using the Hilbert operator **H**: $y(t)=x(t)+j\mathbf{H}[x(t)]=a(t)*\mathbf{e}^{j[f_0 t+\phi(t)]}$. Then demodulation was performed by multiplying $y(t)$ with the negative complex carrier, thus shifting the narrow-band spectral content around f_0 to zero: $z(t)=y(t)*\mathbf{e}^{-jf_0 t}=a(t)*\mathbf{e}^{j\phi(t)}$. At least the instantaneous quantities $a(t)$ and $f(t)$ could be recovered from $z(t)$. The analysis was implemented with MATLAB functions including procedures to estimate modulation indices and the cross-correlation coefficient of the demodulated signals. Both waveforms showed periodic as well as irregular patterns and were positively correlated (about 0.5), indicating physiological or mechanical coupling in the sound generating mechanisms. This analysis might be further useful to study musical vibrato as well as laryngeal and neurological disorders.

12:00

3aSCb11. Bifurcations at voice onset–offset. Jorge C. Lucero (Dept. Matematica, Univ. Brasilia, Brasilia DF 70910-900, Brazil, lucero@mat.unb.br)

Oscillation hysteresis is a common phenomenon in cases of flow-induced oscillation. In phonation, it is usually observed as different biomechanical configurations of the vocal fold system between voice onset and offset. From the perspective of the theory of nonlinear dynamical systems, the phenomenon may be described as a combination of a subcritical Hopf bifurcation at which an unstable limit cycle is generated from an equilibrium position of the vocal folds, and a saddle-node bifurcation between limit cycles at which the unstable limit cycle and a stable limit cycle coalesce and cancel each other [J. C. Lucero, J. Sound Vib. (in press)]. This description is investigated using a two-mass model of the vocal folds coupled to a two-tube approximation of the vocal tract. The purpose is to simulate the hysteresis in terms of voice output parameters as airflow, intensity, and fundamental frequency. The simulations show good agreement with available experimental measurements at voice onset–offset [e.g., L. L. Koenig and R. S. McGowan, J. Acoust. Soc. Am. **100**, 2689(A) (1996)]. Bifurcation diagrams are derived to illustrate and discuss the results. [Work supported by the CNPq (Brazil).]

Session 3aSP

Signal Processing in Acoustics and Engineering Acoustics: Binaural Technology I

Mahlon Burkhard, Cochair
Sonic Perceptions, Inc., 6964 Kensington Road, Brighton, Michigan 48116, USA

Jens Blauert, Cochair
Communication Acoustics, Ruhr-Universität Bochum, D-44780 Bochum, Germany

Chair's Introduction—7:55

Invited Papers

8:00

3aSP1. Sound localization with unilaterally degraded spectral cues. Frederic L. Wightman and Doris J. Kistler (Waisman Ctr., Univ. of Wisconsin, 1500 Highland Ave., Madison, WI 53705, Wightman@waisman.wisc.edu)

Two cues are thought to determine the apparent position of a sound, interaural time differences and the spectral patterning produced by the pinnae and upper body. The role of the spectral cues is the least well understood. One area of uncertainty is the extent to which cues from both ears are used. This study of the issue asked listeners to indicate the apparent positions of virtual sources synthesized from each listener's own head-related transfer functions (HRTFs). Four types of stimuli were intermingled during a run: (1) all cues preserved, (2) spectral cues degraded at the ear on the side contralateral to the source, (3) degraded cues on the same side as the source, and (4) cues degraded binaurally. Cues were degraded either by smoothing, which preserved the major interaural level cues, or by replacing the natural HRTF with a constant average spectrum, which perturbed the natural interaural level cues. The results suggest that degrading contralateral cues has only a minor effect, while degrading either ipsilateral or binaural spectral cues causes significant localization errors. Results from the two degradation conditions were the same, suggesting that interaural level differences are relatively unimportant localization cues. [Work supported by NIH, NASA, and ONR.]

8:20

3aSP2. Physical modeling of individual head-related transfer functions (HRTFs). Roland Sottek and Klaus Genuit (HEAD acoustics GmbH, Ebertstrae 30a, 52134 Herzogenrath, Germany, Roland.Sottek@head-acoustics.de)

A model of HRTFs was developed based on the Ph.D. thesis of Genuit. The two basic ideas are (1) HRTFs can be described by the influence of a few acoustically relevant objects; first the head was modeled by a sphere and the pinna with cavum conchae by two elliptical disks with an eccentric cylindrical cave (ear canal). (2) Individual variations of HRTFs correspond to variations of geometrical parameters (diameter of sphere, dimensions of disks and cave, . . .); the position of the ear canal entrance point is the most important parameter. Simulation results were compared to HRTFs measured with an artificial head of well-known geometry. In general, a good correspondence between calculated and measured HRTFs was found. The correlation is significantly higher if the influence of shoulder/torso is considered, too, modeled by an additional rigid sphere. Second, the shape of head and shoulder/torso was approximated with oblate respective prolate spheroids in order to get even better results. Sound field calculation were performed using numerical methods (boundary element method, source simulation technique) and analytical methods (solution of the wave equation, use of Huygens' integral formula). The interaction between the different reflecting and diffracting bodies was analyzed to validate a simplified model.

8:40

3aSP3. The relevance of the shoulder bounce to HRTFs considering head movements. Renato Pellegrini (Inst. für Kommunikationsakustik, Ruhr Univ. Bochum, Universitätsstr. 150, 44780 Bochum, Germany, pelleg@ika.ruhr-uni-bochum.de)

When measuring HRTF data for use in virtual auditory environments, individual HRTFs of subjects are commonly measured keeping the head in the front position vertical to the upper body. This measured data set is then used to simulate the direction of incidence of virtual sound sources. In real world situations, subjects normally tend to turn their heads only, instead of rotating with the whole upper body when focusing on a sound source. In virtual auditory environments this relative head-to-upper-body rotation is not accurately simulated. This error could theoretically deteriorate the perception of virtual sound sources. HRTF data sets were measured for different shoulder to head positions other than front, and psychoacoustical tests were made to give evidence to the importance of shoulder to head positioning. Timbral aspects and localization accuracy in static and dynamic situations were investigated by auditory testing. Results are discussed.

9:00

3aSP4. Determination of optimal HRTFs for binaural synthesis. Flemming Christensen, Henrik Moeller, Soeren K. Olesen, and Pauli Minnaar (Aalborg Univ., Fredrik Bajersvej 7B4, DK-9220 Aalborg OE, Denmark, acoustics@kom.auc.dk)

Earlier studies have shown that a carefully selected human substituting an artificial head can minimize the amount of localization errors for a group of people in a listening experiment, thus indicating that a set of head-related transfer functions (HRTFs) can be found, which to some extent fits a population. This study aims at exploring ways of designing such general sets of HRTFs suitable for larger populations. An effort is put into considering the importance of, e.g., different frequency regions of the transfer functions in order to focus on the most general characteristics and avoid focusing attention on highly individual features. The physical origin of the different parts of the HRTFs will be taken into consideration, and HRTF design methods using parameters derived through signal analysis will be studied.

9:20

3aSP5. The effects of source characteristics on the auditory localization of nearby sources. Douglas S. Brungart (Air Force Res. Lab., 2610 Seventh St., Wright–Patterson AFB, OH 45433-7901, brungart@falcon.al.wpafb.af.mil) and Nathaniel I. Durlach (MIT, Cambridge, MA 02139)

A series of recent experiments has examined the auditory localization of a nearby (<1 m) sound source under four conditions: (1) a fixed-amplitude condition where loudness-based distance cues were available; (2) a monaural condition where the contralateral ear was occluded by an ear-plug and muff; (3) a high-pass condition where the stimulus bandwidth was 3 Hz–15 kHz; (4) a low-pass condition where the stimulus bandwidth was 200 Hz–3 kHz. The results of these experiments were compared to those of a previous experiment that measured localization performance for a nearby broadband, random-amplitude source [Brungart *et al.*, J. Acoust. Soc. Am. **102**, 3140(A) (1997)]. Directional localization performance in each condition was consistent with the results of previous far-field localization experiments. Distance localization accuracy improved slightly in the fixed-amplitude condition, especially near the median plane, but was severely degraded in the monaural condition. Distance accuracy was also found to be highly dependent on the low-frequency energy of the stimulus: in the low-pass condition, distance accuracy was similar to that in the broadband condition, while in the high-pass condition, distance accuracy was significantly reduced. The results suggest that low-frequency interaural intensity differences are the dominant auditory distance cue in the near-field.

9:40

3aSP6. Role of two ears in upper hemisphere localization. Masayuki Morimoto (Environ. Acoust. Lab., Faculty of Eng., Kobe Univ., Nada, Kobe, 657-8501 Japan, mrmt@kobe-u.ac.jp)

It is well known that the elevation of a sound source is determined by spectral cues in the median plane, where the input signals to both ears are regarded as being identical. It is, however, still a problem how the elevation of a sound source is determined in any plane apart from the median plane, because the input signals to both ears are not identical. This paper investigates how the input signals to the left and right ears contribute to determine the elevation of a sound source at any position in the upper hemisphere. The localization tests regarding the elevation in five planes parallel to the median plane were performed. In the localization tests, pinna cavities of both or one of two ears were occluded. The results indicate that both ears play a role in determining the elevation of a sound source in any plane. Furthermore, they infer that the summation of spectral features of input signals to the left and right ears contributes to determine the elevation.

10:00–10:20 Break

10:20

3aSP7. Generation of binaural information using cross ambiguity functions. Michiaki Uchiyama and Mikio Tohyama (Kogakuin Univ., Bldg. 5-603, Nakano-machi 2665-1, Hachioji-shi, Tokyo, 192-0015 Japan)

This paper describes a method to generate binaural information. First of all, the accuracy of a conventional linear interpolation was examined by using signal-to-deviation ratio (SDR) and spectrum distortion. It was found that the accuracy of left and right direction HRTFs ($60-120°$) did not deteriorate despite the presence of a wide directional interval (SDR $\cong$ 23 dB). However, the accuracy of front and back direction HRTFs ($0--60°$ and $120-180°$) deteriorated as the interval broadened. For the shade-side ear's HRTFs, particularly, it was confirmed that the accuracy of linear interpolation deteriorated dramatically (SDR$\cong$8 dB). Therefore, a method was investigated for generating a shade-side ear's HRTF by using cross ambiguity functions (CAFs) whose model is related to dichotic listening. A shade-side HRTF could be generated with about a 10-dB SDR from a sunny-side HRTF, while the SDR becomes about 8 dB for a conventional linear interpolation estimation method. In this paper, the independence of HRTFs is also discussed, using the singular value decomposition from the point of view that it is possible to generate a new vector from a linear combination of vectors. In this article the accuracy of a linear interpolation from a base of HRTFs by SDR and spectrum distortion is examined.

10:40

3aSP8. Audition and the sense of presence in virtual environments. R. H. Gilkey, B. D. Simpson, S. K. Isabelle, A. J. Kordik (Dept. of Psych., Wright State Univ., Dayton, OH 45435), and J. M. Weisenberger (Ohio State Univ., Columbus, OH 43210)

Historical reports from suddenly deafened adults describing a sense of detachment from a world devoid of auditory input suggest that auditory cues may be crucial for achieving a sense of presence in virtual environments [R. H. Gilkey and J. M. Weisenberger, Presence **4**, 357–363 (1995)]. However, factors other than acoustic fidelity can affect the perceived quality of a virtual auditory display. For example, Simpson *et al.* [J. Acoust. Soc. Am. **100**, 2633(A) (1996)] showed that the sense of presence in virtual auditory environments was driven by characteristics of the real listening environment in which the virtual audio was heard. Specifically, when

the virtual auditory environment matches the real listening environment, the listening experience is particularly compelling. However, it was not clear whether auditory or visual experience with the real room mediated this effect. This paper describes attempts to separate the impact of auditory and visual information on presence by systematically manipulating these cues in synthesized environments. Implications for design of virtual environments and spatialized auditory displays are considered. [Work supported by AFOSR and Ohio Board of Regents.]

11:00

3aSP9. A series of experiments exploring the spatial separation of multiple talkers with 3-D audio technology. Richard L. McKinley, Mark A. Ericson, W. Todd Nelson (Air Force Res. Lab., 2610 Seventh St., Wright–Patterson AFB, OH 45433, rlmckinley@falcon.al.wpafb.af.mil), Robert S. Bolia (Veridian, Dayton, OH 45431), and Brian D. Simpson (Wright State Univ., Dayton, OH 45435)

Most auditory displays are monaural and do not take advantage of the capacity of the binaural system for spatial separation of multiple simultaneous talkers. A program of research has been developed at the Air Force Research Laboratory to investigate the enhanced communication effectiveness obtained with 3-D audio displays. Factors that are being manipulated include angular separation, the number of competing messages, and the sex of the target talker. Angular separation has been studied in both the horizontal and median planes, with between two and eight competing messages. The effect of duration of temporal overlap has also been explored. The goal of this research is to discover the maximum number of speech channels that a listener can effectively monitor, and whether this number is augmented by 3-D audio technology. Potential applications of 3-D audio technology for communications separation will be discussed.

11:20

3aSP10. Sound-image broadening by a single echo and its relation to the transient interaural cross-correlation function. Hirofumi Yanagawa (Chiba Inst. of Technol., 2-17-1 Tsudanuma, Narashino-shi, Chiba-ken 275-0016, Japan) and Takatoshi Okuno (Kogakuin Univ., Tokyo 192-0015, Japan)

The sounds reproduced by two loudspeakers often consist of a preceding sound and its echo when the listener's position is offset like the position of a driver when listening to a car stereo. Consequently, the sound image is broadened by the echo. In this article, the width of the sound image produced by the preceding sound and the echo under a loudness balance condition were examined. TRICC (the maximum value of the transient interaural cross-correlation function) was then applied to analyze such sound image broadening. In hearing experiments, a pair of noise bursts was used as a model of transient sound, such as speeches and musical sounds. A pointer noise (a pair of noises with correlation coefficients) was used to express the width of the sound image. The experiments showed that the width of the sound image increases as delay time between the preceding sound and the echo increases. When the delay time becomes longer than 10 ms, the width of the sound image corresponds to the value of the interaural correlation coefficients and not to the value of TRICC or IACC.

11:40

3aSP11. Applications of virtual auditory space in psychoacoustics and neurophysiology. Klaus Hartung (Inst. of Commun. Acoust., Ruhr Univ., D-44780 Bochum, Germany, hartung@ika.ruhr-uni-bochum.de), Susanne J. Sterbing (Dept. of Zool. a. Neurobiol., Ruhr Univ., D-44780 Bochum, Germany), Clifford H. Keller, and Terry T. Takahashi (Inst. of Neurosci., Univ. of Oregon, Eugene, OR 97403)

Virtual auditory space (VAS) refers to a technology where the source signal is convolved with filters called head-related transfer functions (HRTFs) and presented over headphones to recreate the signal at the eardrum that would have been received from a source in the free-field. VAS is a powerful tool because it allows the simulation of complex and realistic scenarios (e.g., echoes, reverberation, moving sources) that are impossible or too complicated for free-field setups, which often contain distortions caused by the setup itself (e.g., stereotactic bench, headholder). Crucial points of VAS are the measurement, equalization and interpolation of the HRTF. Different methods will be reviewed and the results of VAS and free-field stimulation for humans, guinea pigs, and barn owls will be compared. For barn owls, the amplitude spectra of virtual sounds were within ± 1 dB of amplitude spectra of free-field sounds measured near the eardrum. The neuronal responses to free-field and VAS presentations were nearly indistinguishable. For research with humans and guinea pigs, it was necessary to use the HRTF of each individual, whereas in the barn owl, only minor differences between the neuronal responses to the individual and nonindividual HRTF were observed. [Work supported by DFG, NIDCD, and NATO.]

12:00

3aSP12. The importance of binaural auralization for automotive industry. Klaus Genuit and Jens Poggenburg (HEAD acoustics GmbH, Ebertstrae 30a, 52134 Herzogenrath, Germany, klaus.genuit@head-acoustics.de)

In the automotive industry reliable information about the acoustical situation of a vehicle is necessary in an early stage of the development process. This enables the involved parties to work effectively on sound design and sound quality tasks. In this context, the so-called ''Binaural Hybrid Model'' has been developed. It is based on the determination of binaural transfer paths at vehicles using corresponding measurements. They are combined with airborne and structure-borne noise measurements at test rigs. Applied to vehicle interior noise caused by the engine, the influence of modified transfer paths, airborne radiation and/or input accelerations on the acoustical situation at the passenger's position can be simulated binaurally. This includes the consideration of the head orientation and the aurally equivalent reproduction of the interior sound. It enables the engineer to judge the resulting sound quality before a prototype is realized. The presented model considers airborne shares up to 12 kHz and structure-borne ones up to 2 kHz. An application for different vehicles with the same engine clarifies in which way relevant causes for customer complaints at one vehicle may be determined. The variation of single transfer paths and the resulting interior noise will be included.

Session 3aUWa

Underwater Acoustics: Scattering from Finite Structures Near Boundaries

John A. Fawcett, Cochair
Defence Research Establishment Atlantic, 9 Grove Street, P.O. Box 1012, Dartmouth, Nova Scotia B2Y 3Z7, Canada

Hans Georg Schneider, Cochair
Forschungesanstalt der Bundeswehr für Wasserschall und Geophysik, Klausdorfer Weg 2-24, D-24148 Kiel, Germany

Invited Papers

8:40

3aUWa1. Modeling scattering by objects near an interface. John A. Fawcett (Defence Res. Establishment Atlantic, P.O. Box 1012, Dartmouth, NS B2Y 3Z7, Canada)

For an object totally above or below an interface, the overall scattering from the object and the interface can be modeled as a series of multiple interactions [e.g., Hackman and Sammelmann, J. Acoust. Soc. Am. **84**, 1813–1825 (1988)]. The theory is outlined for a spherical or infinite cylindrical shell and the effects of the sediment sound speed and the source/receiver geometry on the backscattered time series are numerically investigated. The case of an object in a rough or range-dependent waveguide is also considered. Partial burial of an object is discussed. Some comparisons of modeled and experimental data (both in the spectral and temporal domains) are presented.

9:00

3aUWa2. Measurement of 3-D scattering from buried targets in very shallow water. Henrik Schmidt (MIT, Cambridge, MA 02139), Alain Maguer, Edoardo Bovio, and Warren Fox (SACLANT Undersea Res. Ctr., I-19138 La Spezia, Italy)

The objective of the GOATS'98 experiment was to determine the three-dimensional, spatial characteristics of seabed target scattering and reverberation in coastal environments with water depth less than 15 m. The experiment was carried out at Marciana Marina, Elba Island, in May 1998 in a joint effort between SACLANTCEN and MIT. Artificial targets were buried at various depths into the sandy bottom and insonified by a parametric source mounted on a 10-m tall tower which could be repositioned on a bottom-mounted rail under remote control. This arrangement allowed for insonifying the targets at a wide range of incident angles, including both the sub- and supercritical regimes. The scattering and reverberation were measured using a suite of fixed and mobile arrays. Specifically, an eight-element line array was mounted on an MIT Odyssey-II autonomous underwater vehicle (AUV) in a ''swordfish'' configuration. The AUV was launched from R/V ALLIANCE, anchored off-shore, to perform survey patterns in the target area, way-point navigated using a long baseline acoustic navigation network. During these surveys the parametric source would insonify the seabed at a high repetition rate, allowing for dense mapping of the 3-D scattering and reverberation. This paper reviews the experiment and the results, with particular emphasis on the versatility of using the new AUV technology for shallow-water target scattering measurements.

9:20

3aUWa3. Acoustic investigation of objects in shallow water using FEM and BEM. Otto von Estorff (Ocean Eng. II, TU Hamburg-Harburg, D-21071 Hamburg, Germany, estorff@tu-harburg.de)

The acoustic behavior of a submerged object is strongly influenced by the existence of reflecting boundaries, namely the water surface or the bottom. Only in some rare cases can it be assumed that the water region is ''infinite.'' The present paper is related to the investigation of underwater objects in shallow water by means of numerical methods. These must be able to take into account fluid/structure interaction effects as well as different boundary conditions. In the suggested methodology, displacement-based finite elements for the structure are coupled to acoustic boundary elements for the fluid medium. An underwater plate and a submerged cylinder will be investigated in different parametric studies. It will be shown how the boundaries (surface, bottom) can be taken into account, and in which cases the effect of boundaries could be neglected. Moreover, the required computational resources as well as the applicability of different methods will be discussed.

9:40

3aUWa4. A comparison of benchmark acoustic scattering solutions with tank experiments on buried and partially buried spheres. Raymond Lim (Coastal Systems Station, Dahlgren Div./Naval Surface Warfare Ctr., Code R22, 6703 W. Hwy. 98, Panama City, FL 32407-7001, lim@atcf.ncsc.navy.mil) and Harry J. Simpson (Naval Res. Lab., Washington, DC 20375-5350)

Predicting the scattering response of objects near boundaries is of growing interest in underwater acoustics, especially when these objects are buried. Standard propagation models suggest that burial in fast attenuating ocean bottoms can seriously retard efforts to find such objects with high-frequency imaging sonar because of the need to operate at close range to overcome loss in the backscattered signal strength, resulting in low search rates. However, recent observations of anomalous sound transmission at shallow grazing angles as well as anomalous long-range detections of buried objects call into question standard assumptions made in regard to the modeling of sound transmission through the water/sediment interface. The present work investigates the breakdown of these assumptions for the scattering problem by comparing laboratory measurements conducted in the NRL Shallow Water Laboratory with predictions of exact scattering solutions for simple targets at various degrees of burial. Scattering data collected recently for a 60-cm-diam. spherical steel shell is used in the investigation. A discussion of the agreement between theory and measurements, features of special interest, and the consequences to our understanding of the acoustics of buried objects is given. [Work supported by ONR.]

10:00

3aUWa5. Modeling scattering from objects near boundaries using infinite elements. David Burnett (SACLANT Undersea Res. Ctr., Viale San Bartolomeo 400, 19138 San Bartolomeo, La Spezia, Italy, burnett@saclantc.nato.int) and Richard Holford (Lucent Technologies, Bell Labs, Denville, NJ 07834)

There has been a rapidly growing interest in using infinite elements for modeling acoustic scattering and radiation from finite objects in unbounded regions. The paper will briefly review current infinite element technology, which is based on radial expansions in curvilinear coordinate systems. Although the radial expansions are derived for free-space conditions (4 pi steradians), the elements are also valid for half-spaces, using local hard, soft, or finite impedance conditions on the boundary. In this approach, wave propagation is modeled in only one half-space, with the boundary conditions on the interface approximating the effects of the other half-space, thereby enabling these types of infinite elements to model scattering from objects near, and on the illuminated side of, the boundary of a half-space. Theory and numerical results will be presented. A more general approach, which models wave propagation in both half-spaces, uses infinite elements in both half-spaces, with appropriate continuity conditions at the interface. This is the approach currently under investigation by the authors; their findings will conclude the paper.

10:20–10:40 Break

Contributed Papers

10:40

3aUWa6. Measurements of acoustic scattering from partially and completely buried thin-shelled targets. Warren L. J. Fox, Alain Maguer, Alessandra Tesei (NATO SACLANT Undersea Res. Ctr., Viale S. Bartolomeo 400, 19138 La Spezia, Italy), and Henrik Schmidt (MIT, Cambridge, MA 02139)

Conventional high-frequency imaging sonars become less effective in detecting and classifying bottom-laid targets when the targets become buried into seabottom sediments. Some recent work at the NATO SACLANT Undersea Research Centre has concentrated on investigating the use of lower-frequency sonars (2–16 kHz) in order to better exploit scattering features of buried targets that can aid in their detection and classification. Part of the recent GOATS'98 experiment performed near Elba Island, Italy, involved carefully controlled monostatic measurements of scattering by thin-shelled objects (spheres and cylinders) that were partially and completely buried in sand, as well as in free-field. Preliminary results are presented which show promising comparisons of the data to existing models. In addition to examining peak levels of the returns for detection purposes, special attention is paid to resonance effects (examined in the time and frequency domain), and the effect of burial on this part of the target response. Scholte–Stoneley and Lamb-type waves can be clearly identified in the backscattered signals. The issue of inverse scattering for classification purposes is also addressed. [Work supported in part by EC MAST Programme and ONR.]

11:00

3aUWa7. Target classification in shallow waters by time-frequency filtering. Nicole Gache and Patrick Chevret (CPE Lyon, LASSSO (LISA, EP92 CNRS), 43 Bd. du 11 Novembre 1918, BP 2077, Bat. 308, F 69616, Villeurbanne Cedex, France)

Efficient sonar target recognition must be based on a set of relevant parameters extracted from the echoes and directly related to the geometrical and mechanical properties of the target. Previous studies have shown that a wideband approach based either on simple spectral modeling or on time-frequency analysis is particularly suited to the understanding of echo formation mechanisms and to the classification in the free field (recognition rate as high as 96%). In shallow waters, the influence of the boundaries considerably reduces the performance of these methods due to the presence of several spurious echoes superimposed to the target echo components. Classification performance can be improved by using a method based on time-frequency filtering matched to a free-field reference target response. This method will be described and applied to experimental data issued from tank experiments. Several typical configurations have been first investigated: free-field, semi-infinite space for a set of targets (shells and solid targets of different shapes). It gives more than encouraging results, especially for the recognition of a spherical shell (about 100% of recognition). The method is now extended to a shallow-water configuration including seabed interaction.

11:20

3aUWa8. Numerical simulation of transient scattering from bodies and shells in a layered fluid–solid medium. Ilkka Karasalo (Dept. of Underwater Wave Propagation and Active Sonar, FOA, Stockholm, Sweden) and Johan Mattsson (Royal Inst. of Technol., Stockholm, Sweden)

Results from numerical simulation of transient scattering by 3-D objects immersed in seawater or buried in the bottom sediment are presented, and compared with data from a shallow-water experiment in the Baltic in which a bottom-penetrating parametric sonar was used for detection of submerged or buried objects. A range-independent fluid–solid model of the medium is used. The scatterers have smooth shape and are modeled as acoustically impenetrable or alternatively penetrable fluid-enclosed thin elastic shells. The dynamics of such shell-structured scatterers are described by Love's equations for thin shells. A recently developed numerical technique, based on a frequency-domain boundary integral equation (BIE) formulation of the scattering problem, is used to compute the scattered field. The Green's function of the layered medium is obtained by an adaptive transform integral method. The BIE is discretized by high-order B-splines, point collocation, and global numerical quadrature. The incident field may be excited by a point source, a point source array, or a plane wave. Scattering of transient fields is computed by Fourier synthesis of monofrequent field components. The composite simulation being highly parallelizable, a version for execution on workstation clusters under MPICH has been implemented, allowing for convenient handling of also computationally demanding broadband excitations.

11:40

3aUWa9. Sea experimental detection of an array of hollow spheres. R. Carbó and A. Molero (Instituto de Acústica, CSIC, Serrano 144, 28006 Madrid, Spain, iaccf31@fresno.csic.es)

A study of acoustic backscattering produced by a system of scatter arrays is reported. A simplified theoretical model has been developed to study the interference phenomenon due to the echo formation. This model establishes the relation between system geometry (target dimensions, scatter distance and depth) and sonar performances (directivity, pulse length, pulse repetition rate, wave length, and ship speed) getting a better system response. Target strength of a single scatter was defined at the laboratory, at an underwater tank with a dual-frequency side scan sonar working at 100 kHz. Different array geometries were placed in order to characterize minimum distance between scatters needed to discriminate them at the echogram. Experimental test has been realized at the sea with the same side scan sonar at 100- and 500-kHz frequency. Scatter arrays were placed at 15-m depth, were clearly located, and identified from a distance of 50 m. To identify the system two different arrays were placed: a short one with a reduced number of scatters, and a second one with a large amount of same scatters, with a total length of 48 m.

12:00

3aUWa10. Sound diffraction by an underwater topographical ridge. Ji-Xun Zhou, Xue-Zhen Zhang, and Yun S. Chase (School of Mech. Eng., Georgia Inst. of Technol., Atlanta, GA 30332-0405)

Scale model experiments have been conducted to study the diffraction of sound by an underwater convex surface with a very soft boundary (closed-cell foam material). The diffraction boundary can be well described as a locally reacting surface based on measured acoustic parameters (very low speed and density, and very high attenuation). The diffraction acoustic pressure (insertion loss) behind the ridge and along the diffraction surface were measured. Measured insertion losses were compared with the theory of matched asymptotic expansion (MAE), developed by Fock for electromagnetic waves and Pierce for acoustic waves. The experimental results are in good agreement with predictions from the MAE theory. This technique might be used to infer acoustic parameters for materials. It was found that the model of Delany and Bazley, which is widely used in architecture acoustics and outdoor sound propagation, may be inappropriate for the description of an underwater locally reacting impedance. [Work supported by ONR.]

Contributed Posters

These posters will be on display in the Poster Gallery from Thursday to Friday, 18–19 March. Authors will be at their posters from 10:00 a.m. to 12:00 noon on Wednesday, 17 March.

3aUWa11. Analysis of boundaries' effects in the evaluation of transient ultrasonic fields scattered by a rigid reflector. Khelladi Hassina and Djelouah Hakim (USTHB, Inst. d'Electron., Departement Instrumentation, BP32 El Alia 16111, Algeria)

One approach used to estimate the transient field scattered by a target with a known dimension and geometry is the convolution method. In the hypothesis of linear acoustic, and for a perfectly rigid reflector immersed in an isotropic, homogeneous, and lossless fluid, the detected acoustic pressure is expressed in the form of a time convolution between the radiator velocity profile and the transmit-receive impulse response. This last depends on the geometry of the transducer, the target, their relative position, and physical characteristics of the propagation medium. For that purpose, some simulations were done. The pressure waveform is explained in terms of the plane and edge waves. In order to determine the boundaries' effects on the detected pressure, targets of different size were used. The obtained results show that the edge waves were insignificant when large size targets are used.

3aUWa12. Sound scattering by moving inhomogeneity. Andrew G. Semenov and Vadim N. Alexeyev (N. N. Andreev Acoust. Inst., Russian Acad. of Sci., 4 Shvernik St., 117036 Moscow, Russia, bvp@acoins.msk.ru)

This report considers the propagation of sound in the vicinity of a rather general class of localized flows induced by the motion of spherically symmetric structures of the type of solid spheres and droplets or vortices in the liquid, say, ocean environment. Acoustic scattering from

such inhomogeneities, situated inside various flows, is analyzed with the aid of the M. J. Lighthill equation boundary value problem solution—both in the presence of vorticity and without it. The role of a moving body generating inhomogeneity as well as the role of the surface at which the tangential component of flow velocity could suffer a discontinuity are demonstrated in a most general form. Comparison of body and flow contribution to the observed scattered field is presented. The physical condition of flow presumably yields in a forward scattering direction—a situation of the type encountered in a conventional ocean tomography system, comprising a source–detector line, is proposed. The angular structure of the scattering amplitude and the frequency dependence of the scattered sound are evaluated.

WEDNESDAY MORNING, 17 MARCH 1999 ROOM H2053, 9:00 A.M. TO 12:00 NOON

Session 3aUWb

Underwater Acoustics and Acoustical Oceanography: Ultra Low Frequency (<1 Hz) Ocean Acoustics

Ralph A. Stephen, Cochair
Woods Hole Oceanographic Institute, Woods Hole, Massachusetts 02543, USA

Jean Paul Montagner, Cochair
Department Sismologie, Institut de Physique du Globe de Paris, 4 Place Jussieu, 75232 Paris 05, France

Invited Papers

9:00

3aUWb1. A review of ocean acoustics in the band 0.001–1.0 Hz. Ralph A. Stephen (Woods Hole Oceanogr. Inst., Woods Hole, MA 02543, rstephen@whoi.edu)

The first ultra-low frequency (ULF) (0.001–1 Hz) ambient acoustic noise measurements were made in the 1960s using the Columbia-Point Arena ocean-bottom seismic station. Interest in ULF acoustics was spurred in the mid-1980s by the development of the differential pressure gauge. Also in the mid-1980s the development of high dynamic range, broadband seismometers revolutionized whole earth seismometry. The Global Seismic Network (GSN) set as its goal the uniform distribution of 128 seismic stations over the surface of the globe, to provide high-quality data sets for whole earth tomography and other earth scale problems. To accomplish this goal requires about 20 permanent stations on the deep ocean floor. In the future, the acquisition of long time series of ULF acoustic noise in the deep ocean will become much more convenient and the opportunity will be given to exploit these data sets to study oceanographic and earth processes. The sources of ambient noise in this band include infra-gravity waves, swell interaction at coastlines, currents and turbulence near the seafloor, earthquakes, tsunamis, nonlinear interaction between ocean-surface waves, and air turbulence. Water column reverberations, Stoneley modes in sediment layers, and the effects of propagation from distant sources also modify the pressure spectra. [Work supported by NSF.]

9:20

3aUWb2. Ocean bottom seismic noise (1–10 000 s). Jean-Paul Montagner (Dept. Sismologie, IPG, 4 Pl. Jussieu, 75252 Paris, France, jepm@ccr.jussieu.fr)

There is now a good consensus in the geophysical scientific community of the necessity to install broadband seismic stations on the ocean bottom in order to improve our knowledge of the deep Earth dynamics. However, it is necessary to first investigate the level of seismic noise (0.01–10 000 s) and to compare it with the expected amplitude of seismic signal due to earthquakes. During the French pilot experiment SISMOBS/OFM (28 April–11 May 1992) in the Atlantic Ocean, two sets of Guralp CMG3 broadband seismometers were successfully installed and recovered. The first set, named OFP, was installed inside the ODP borehole 396B at 292 m below seafloor and the second one, named OFM, was installed on the sea bottom (semi-buried) close to the hole. A comparison of broadband seismic noise (1–3600 s) between OFP, OFM, and a typical continental GEOSCOPE seismic station SSB shows that the noise level of OFM is smaller (resp. larger) at periods longer than 20 s (resp. shorter than 2 s) than the one in the borehole and in SSB. The detection threshold is very low and makes it possible to get good records of teleseismic events as small as 5.4. These results were very encouraging since they demonstrate that in the future ocean bottom seismometers will provide very valuable information on earthquakes and Earth structure.

9:40

3aUWb3. Lessons from the Ocean Seismic Network Pilot Experiment. John A. Collins, Ken R. Peal, Ralph A. Stephen (Woods Hole Oceanogr. Inst., Woods Hole, MA 02543, jcollins@whoi.edu), Frank L. Vernon, John A. Orcutt, John A. Hildebrand, and Fred N. Spiess (Scripps Inst. of Oceanogr., La Jolla, CA 92093)

The basic goal of the Ocean Seismic Network Pilot Experiment (OSNPE) was to learn how to make reliable broadband (0.001–10 Hz) seismic measurements in the deep ocean. This objective addresses both the requirement for long-term, observatory-based measurements at a small number of carefully selected sites (i.e., the Ocean Seismic Network), and for portable arrays of broadband seismographs that can be deployed for about one year to study specific geological features. The OSNPE ran from February to June 1998. The site of the experiment was ODP Hole 843B (site OSN-1) located about 225 km southwest of Oahu, Hawaii. At the OSN-1

site, three broadband seismographs were deployed within 300 m of each other. The seismometers were (i) a Teledyne GeoTech KS54000 deployed in a borehole 240 m beneath the seafloor; (ii) a Guralp CMG-3T deployed on the seafloor; and (iii) a Guralp CMG-3T buried just beneath the seafloor. The latter two systems also carried long-period pressure sensors. Meteorological and oceanographic data were also recorded continuously throughout the experiment. The magnitude and direction of seafloor currents were recorded at the experiment site itself. Four NOAA/NDBC buoys in the vicinity of OSN-1 recorded wind speed, wave-height, and wave-direction. [Work supported by NSF.]

10:00

3aUWb4. Evaluation of teleseismic waveforms and detection thresholds from the OSN pilot experiment. Frank L. Vernon, John A. Orcutt, Gabi Laske, Fred N. Spiess (Scripps Inst. of Oceanogr., La Jolla, CA 92093, flvernon@ucsd.edu), John A. Collins, Ken R. Peal, Ralph A. Stephen, and Cecily J. Wolfe (Woods Hole Oceanogr. Inst., Woods Hole, MA 02543)

The first Ocean Seismic Network Pilot Experiment (OSNPE) took place from January to June of 1998. The site of the experiment was located about 225 km southwest of Oahu, Hawaii, where three broadband seismographs were deployed within 300 m of each other, (i) deployed in a borehole 240-m beneath the seafloor; (ii) on the seafloor; (iii) buried just beneath the seafloor. Each of the seafloor broadband seismograph stations also carried a Cox-Webb long-period, differential pressure gauge (DPG). The OSNPE ran concurrently with PELENET, a temporary deployment of five island broadband stations and SWELL, a temporary deployment of eight DPGs. Over 50 teleseismic earthquakes were observed. The broadband seismograms recorded during the OSNPE are coherent in the frequency band 0.01–0.1 Hz. At higher frequencies (0.1–3 Hz), there is considerably more variation between the borehole, buried, seafloor, and island sites. Careful examination of the waveforms shows significant differences in the frequencies above 0.1 Hz between the buried/surface broadband ocean bottom seismographs and the borehole seismograph. These variations appear to be associated with shear-wave reverberations and/or Stonely wave propagation within the sediment section. The teleseismic earthquakes permit a preliminary evaluation of the long period (0.01–0.07 Hz) detection thresholds.

10:20–10:40 Break

10:40

3aUWb5. GEOSTAR benthic observatory: Technological results. Hans W. Gerber (Technische Fachhochschule Berlin, Luxemburger Str., 10 D-13353 Berlin, Germany, hwgerber@tfh-berlin.de), Paolo Favali, Giuseppe Smriglio (Istituto Nazionale di Geofisica, 605 00143 Roma, Italy), Francesco Gasparoni (Tecnomare SpA, San Marco 3584 30124 Venezia, Italy), Jean Marvaldi, and Jean-Michel Coudeville (IFREMER, Plouzane, Brest, France)

GEOSTAR (GEophysical and Oceanographic STation for Abyssal Research) is a project funded by European Commission, MAST III. The aim of the project was the development of the first prototype of an innovative deep-sea benthic observatory capable of carrying out long-term scientific observations at abyssal depths (up to −4000 m). The prototype has been realized and tested successfully in Adriatic Sea in late summer 1998. GEOSTAR is made up of two main subsystems: Bottom Station and Mobile Docker. The Bottom Station includes the acquisition and power systems, all the scientific sensors and hosts the Communications. The Mobile Docker is a dedicated tool for surface-assisted deployment and recovery. GEOSTAR is characterized by a lightweight and modular frame, autonomous mission control capabilities, and multiple possibilities of interfacement with external devices. The Bottom Station is presently equipped with geophysical, geochemical, and oceanographic instruments (a triaxial seismometer, vectorial and scalar magnetometers, CTD, transmissometer, ADCP, and an electrochemical package), but it can easily host other sensors for different experiments. The observatory was deployed in the Adriatic Sea on 13 August 1998 and recovered on 2 September 1998. The observatory worked properly, recording 440 hours of scientific data. Data were processed, elaborated, and interpreted based on a multidisciplinary approach.

Contributed Papers

11:00

3aUWb6. Low-frequency dispersion computations by compound-matrix propagation. Sven Ivansson (FOA 640, Natl. Defence Res. Establishment, 17290 Stockholm, Sweden, sveni@sto.foa.se)

The basic propagating waveguide modes in underwater acoustics have lower cutoff frequencies. As the frequency is decreased below the cutoff frequency, the modal horizontal slowness typically becomes complex and tends to infinity while the modal wave number tends to a nonvanishing complex number. In certain laterally homogeneous fluid–solid media, there also exist slow $P-SV$ modes for which the horizontal slowness tends to infinity along the real axis while the horizontal wave number tends to zero as the frequency tends to zero. The flexural wave for an ice sheet on top of the ocean is a particular example. To investigate the low-frequency behavior of the modal horizontal slowness for these kinds of modes, computations of dispersion curves by propagator techniques are attempted for media composed of homogeneous fluid and solid layers. However, loss of numerical precision by cancellation effects appears for the needed elements of the solid-layer compound-matrix propagators. Guided by theoretical results for the asymptotic growth of these elements, cancellation-free expressions are derived. The harmful contributions causing loss of numerical precision at low frequencies are eliminated analytically. As an application of the new expressions, a numerical case study is performed. Improved results on low-frequency asymptotic expansions of the modal slownesses are obtained.

11:20

3aUWb7. On comparative contributions of natural ultra-low-frequency hydrodynamic wave fields to sound signals' variability on extended shallow-water traces. Andrew G. Semenov (N. N. Andreev Acoust. Inst., Russian Acad. of Sci., 4 Shvernik St., 117036 Moscow, Russia)

The ocean's ultra-low-frequency natural sound variability mechanism, related to sound interaction with extra slow hydrodynamic natural wave processes, gravitational surface, and internal wave, observed in the range of rad/s on long traces, is discussed. In the absence of natural internal waves, the ocean hydrodynamic field here is close to potential, so that its interaction with the sound field is minimal. Estimates are based on the model of ocean hydrodynamic waves representing the refraction index lattice for propagating sound modes. Small angle sound interaction with

weak enough surface waves lattice leads to additional mode phase transformation increasing with trace length. Interaction is shown to be especially substantial for low-frequency sound (of frequency less than 100–200 Hz) and very long traces (of length not less than 80–100 km) in a shallow ocean region, where it could be comparable to interaction observed due to internal waves. While for a given sound frequency value and short trace length, sound-hydrodynamic wave fields' interaction is determined exclusively by lattice refraction factor, for long enough traces, interaction is defined by refraction index and hydrodynamic wavelength product. This parameter variability for surface gravity waves in different ocean regions, based on generalized bottom pressure measurement data, is presented.

11:40

3aUWb8. Validation and application of an effective medium theory to heterogeneous anisotropic structures. Catherine Stamoulis (Dept. of EAPS, MIT, Cambridge, MA 02139 and Dept. of EPS, Harvard Univ., Cambridge, MA 02138), Dimitri Komatitsch (Harvard Univ., Cambridge, MA 02138), Thomas Jordan (MIT, Cambridge, MA 02139), and Jeroen Tromp (Harvard Univ., Cambridge, MA 02138)

The polarization anisotropy in the upper mantle requires inhomogeneities with small scale lengths. To represent heterogeneous anisotropic structures, such as ocean basins, Jordan *et al*. (1996) formulated stochastic models for small-scale heterogeneities, as samples of a random field of fourth-order hexagonally symmetric elasticity tensors C_{ijkl}. The random field has a characteristic horizontal wave number κ, independent of azimuth, and a characteristic vertical wave number $\eta\kappa$. The medium is therefore statistically transversely isotropic with horizontal heterogeneity scale $1/\kappa$, aspect ratio η, and self-affine scaling at high wave numbers specified by a fractal dimension D. The propagation of seismic waves with lengths $\gg 1/\kappa$ is described by five effective elastic constants, calculated to second order in the scattering by contracting the static fourth-order Green's strain tensor with the eighth-order variance tensor for C_{ijkl}. The validity of this self-consistent effective medium theory is tested by comparing the propagation characteristics that it predicts, as a function of range and frequency, with those measured from synthetic seismograms computed for realizations of the medium using a spectral element method [Komatitsch and Vilotte (1998)]. In particular, the theoretical, frequency-independent phase delays are compared with the frequency-dependent phase delays from the synthetic seismograms.

WEDNESDAY MORNING, 17 MARCH 1999 POSTER GALLERY, 8:00 TO 10:00 A.M.

Session 3aUWc

Underwater Acoustics: Transducers, Arrays and Instrumention (Poster Session)

Robert W. Farwell, Chair
Neptune Sciences, Inc., 150 Cleveland Avenue, Slidell, Louisiana 70458, USA

Contributed Papers

All posters will be on display in the Poster Gallery from Monday to Wednesday, 15–17 March. Authors will be at their posters from 8:00 a.m. to 10:00 a.m. on Wednesday, 17 March.

3aUWc1. Optoacoustic technique for remote control of underwater oceanographic instrumentation. Sergey V. Egerev (N. N. Andreev Inst. of Acoust., 4 Shvernika St., 117036, Moscow, Russia) and Andrey K. Morozov (Russian Acad. of Sci., Moscow, Russia)

A sound source excited through the irradiation of a water surface with a powerful laser pulse is called an optoacoustic (OA) source. This phenomenon makes possible the remote control of submerged oceanographic devices (buoys) directly from a flying vehicle equipped with a pulse laser. The principal factors are analyzed (i.e., reverberation, ambient noise, etc.) which influence the efficiency of OA digital data transfer. The gap between the two neighboring laser pulses is the only parameter of signal that allows the transmitting of data through this remote technique. This makes different versions of pulse-position modulation preferable. Algorithms for processing detected signals are described. The optoacoustic communication system was tested at the White Sea. A CO_2 laser on board a research vessel was used to launch an OA source. The acoustic signal level of about 10^5 Pa at a 1-m depth was achieved within the frequency band of up to 100 kHz. Test data messages at a rate of 2 bits per second for laser pulse repetition rate of about 0.5 Hz were transmitted along an experimental vessel-to-vessel 480-m line. The OA technique works well for devices submerged to depths of 2000 m and possibly more. [Work supported by RFBR.]

3aUWc2. Laser optoacoustic diagnostics of sea ice. Alexey O. Maksimov (Pacific Oceanological Inst., 43 Baltic St., Vladivostok, 690041, Russia, root%dan86@poi.marine.su)

The emphasis of the current study is the analysis of the mechanisms of generation and propagation of optoacoustical (OA) signals in the upper ocean for the winter season or Arctic sea, when the water surface is covered by ice sheet. Modulated or pulsed laser radiation, being absorbed in a layer of ice, results in the excitation of elastic perturbations, propagating on large distances over the surface and in the bulk of the ice canape and in the adjoining layer of liquid. Analytical expressions for the far-field acoustic field have been derived for the wavelengths of a laser source from decimal up to several microns. The diagram of directivity of acoustic radiation in liquid was computed for the frequency interval of modulation of laser intensity of 100 Hz to 15 kHz [A. O. Maksimov, Tech. Phys. Lett. **22**, 52–55 (1996)]. The particular attention was devoted to the description of radiation near the Mach angles of eigenmodes, propagating with veloci-

ties exceeding the sound speed in liquid. It happened that the interference pattern near the Mach angle is very informative for the diagnostics of physical parameters of the ice plate [A. O. Maksimov, Acoust. Phys. **43**, 577–582 (1997)].

3aUWc3. The ubiquitous FLEXBAR™ transducer element for low-frequency, broadband high-power sonar projector arrays. James W. Fitzgerald (The Kildare Corp., One Spar Yard Rd., New London, CT 06320, kildare@connix.com)

The piezoceramic FLEXBAR™, a modified free-free flexure bar, is a sonar projector element of extraordinary versatility and superior performance. It represents a cost-effective, mature transducer technology that is uniquely suitable for projectors of virtually any configuration; viz., planar, cylindrical, spherical, or conformal. Piezoceramic FLEXBAR™ projectors have been designed to operate at frequencies from ~250 Hz to ~5 kHz, with source levels and beam patterns only constrained by the available power and the allowable array envelope. In conjunction with pressure-equalizing oil-filled internal cavities, FLEXBAR™ projectors are operational to essentially any depth. For example, REFLEXDUCER™ model RFD-420/A, a cylindrical array comprised of 32 FLEXBAR™s, and incorporated into a housing 20 cm D×40 cm H, has the following performance characteristics: resonant frequency to $f_0 \cong 2000$ Hz; quality factor $Q_m \cong 3$; bandwidth B/W≅670 Hz (−3 dB); source level SL ≅210 dB//μPa/m; electric power in Pwr(e)≅12 500 W; acoustic power out Pwr(a)≅8125; electro-acoustic efficiency $\eta_{ea} \cong 65\%$. The unit, including an internal 1:5 step-up transformer with a tuned secondary, weights approximately 66 kg so that its effective acoustic power-to-weight ratio is ≅120 W/kg (≅55 W/lb). A conformal submarine-sail design is shown covering a bandwidth of 1–5 kHz at a source level of SL ≅245 dB//μPa/m, with steerable midband vertical beam patterns of θ_v ≅10 degrees (−3 dB) and steerable horizontal patterns of $\theta_h \cong 5$ degrees (−3 dB).

3aUWc4. PZT5 spherical hydrophone simulation using a coupled FE-BE method. Soon S. Jarng (Dept. of Control & Instrumentation, Chosun Univ., 375 Seoseok-Dong, Dong-Ku, Kwang-Ju, South Korea, ssjarng@soback.kornet21.net)

This paper describes the application of a coupled finite-element–boundary element method to obtain the steady-state response of a hydrophone. The particular structure considered is a flooded piezoelectric spherical shell. The hydrophone is three-dimensionally simulated to transduce an incident plane acoustic pressure onto the outer surface of the sonar spherical shell to electrical potentials on inner and outer surfaces of the shell. The acoustic field formed from the scattered sound pressure is also simulated. In addition, the displacement of the shell caused by the externally incident acoustic pressure is shown in temporal motion. The frequency response of the PZT5 spherical shell is also shown in comparison with theoretical expectation. The coupled FE-BE method is described in detail. [This study was granted by STEPI (Science & Technology Policy Institute) Korea, as 1998 international program of co-work of research between Korea and the United Kingdom. The FORTRAN program of the present work was run by a super computer (Cray C90) operated at SERI (now ETRI), Korea.]

3aUWc5. A linear constrained design method for minimizing the interference effect in linear and planar array. Joon-il Song, Koeng-Mo Sung (Appl. Acoust. Lab., Inst. of New Media and Commun., Seoul Natl. Univ., Kwanak-Ku, Seoul 151-742, Korea), and Jun-Seok Lim (Sejong Univ.)

In beamformer design, acoustic interaction effects experienced among the elements of an array will degrade its electroacoustic performance and change the beam patterns. An architectural modification has already been proposed as an effective measure for reducing this effect. Further reduction for interaction effects can be achieved by optimization techniques. This paper provides a new design method including the above constraints for linear or planar array. It is based on the solution of the linearly constrained least-squares problem and can be used in the arrays having arbitrary element locations. Results of computer simulations illustrating the performance of the beamformer are presented. [Work supported by UARC.]

3aUWc6. New sonar technologies using lower sound pressure levels. Kai Wicker and Egidius Arens (STN Atlas Elektronik GmbH, Sebaldsbrücker Heerstr. 235, D-28305 Bremen)

Depending on the conditions, modern active sonar equipment is capable of detecting targets up to distances of about 100 km. To reach this goal, high sound-pressure levels up to 220 dB or more are usually necessary. Simultaneously, this sound-pressure level dramatically increases the probability of being detected, which represents a tactical disadvantage. A second problem arose in the last few years. Sometimes it is assumed that there could be some influences on the marine environment due to the high sound intensities. A new active sonar method and its signal processing is proposed. It could also be applied for acoustical oceanography applications, e.g., seafloor classification. By maintaining very wide frequency ranges during very long time periods, the high sound-pressure level can be reduced drastically. This results in a low probability of being intercepted and also in a reduced influence on the environment. For a realization of this method, four main topics have to be investigated: (1) improved broadband transducers, (2) special designed signal types, (3) a new signal processing concept, and (4) detailed calculations of sound propagation taking into account the local sea and seafloor properties.

WEDNESDAY AFTERNOON, 17 MARCH 1999 ROOM H105, 2:00 TO 4:00 P.M.

Medals and Awards Plenary Session

James E. West, Cochair
President, Acoustical Society of America

Joachim Scheuren, Cochair
President, Deutsche Gesellschaft für Akustik

Deutsche Gesellschaft für Akustik

Lothar-Cremer-Preis

Helmholtz Medal

Acoustical Society of America

Presentation of Certificates to New Fellows of the Acoustical Society of America

Distinguished Service Citation to Elaine Moran

R. Bruce Lindsay Award to Paul E. Barbone

Helmholtz–Rayleigh Interdisciplinary Silver Medal to Jens P. Blauert

Honorary Fellowship to Leonid M. Brekhovskikh

Gold Medal to Henning E. von Gierke

Posters from various technical sessions remain on display in the Poster Gallery.

Session 3pAAa

Architectural Acoustics and Signal Processing in Acoustics: Verification of Auralization and Modeling Programs I

Michael Vorlaender, Cochair
Institut für Technische Akustik, Aachen University, D-52056 Aachen, Germany

Robert C. Coffeen, Cochair
Architectural Engineering, University of Kansas, Lawrence, Kansas 66045, USA

Chair's Introduction—4:15

Invited Papers

4:20

3pAAa1. Verification of prediction based on randomized tail-corrected cone-tracing and array modeling. Bengt-Inge L. Dalenbäck (CATT, Mariagatan 16A, SE-41471 Gothenburg, Sweden)

A new room acoustics prediction method, randomized tail-corrected cone-tracing (RTC), is described together with sample prediction/measurement comparisons. RTC is the result of ten years of experience using the image source model, ray- and cone-tracing, and combines elements of all three methods. RTC is a robust number-prediction method, including the effects of frequency-dependent diffuse reflection for both early and late reflections, as well as a method that creates echograms suitable for binaural post-processing and auralization. Further, a WIN32 DLL directivity interface (DDI) is described. The interface is general and is capable of arbitrary data-format translation and accurate distance-dependent high-resolution array modeling including beam steering. The array modeling is either made via a generic DDI module or via modules custom designed based on detailed manufacturer array specifications (transducer placement, directivity pattern, aim, weighting filter, and delay). Sample prediction/measurements comparisons are given for DSP-controlled column arrays under free-field conditions, in a large railway station and in a large church. It is demonstrated that the common fixed measurement distance 10-deg full space data is insufficient for modeling arrays both due to the limited angular resolution and because far-field conditions may not be reached until 30 m distance or beyond.

4:40

3pAAa2. Report on the second International Round Robin on Room Acoustical Computer Simulation. Ingolf Bork (Projekt 1.401 Physikalisch-Technische Bundesanstalt, D-38116 Braunschweig, Germany)

A Swedish concert hall with a volume of about 11 000 cubic meters served as a test object to compare the performance properties of room simulation software programs. In six octave bands and at 12 source–receiver combinations, nine acoustic parameters defined in ISO 3382 had to be calculated. In the first phase of this round robin only the geometry and a written description of the acoustically relevant properties were given, while in the second phase absorption and diffusion coefficients of the surfaces were prescribed for each octave band. The results obtained by the 16 participants from nine countries will be discussed and compared with measurements performed in the hall. The analysis of the discrepancies and the high variance of the calculated data show that the influence of the software user cannot be neglected and a high degree of practical experience in room acoustics is required to produce optimal results.

5:00

3pAAa3. Comparisons between computer simulations of room acoustical parameters and those measured in concert halls. Jens Holger Rindel (Norwegian Inst. of Bldg. Res., P.O. Box 123 Blindern, N-0314 Oslo, Norway), Hiroyoshi Shiokawa, Claus Lynge Christensen, and Anders Christian Gade (Tech. Univ. of Denmark, DK-2800 Lyngby, Denmark)

A number of European concert halls were surveyed in 1989. In this paper comparisons are made between measured room acoustical parameters and those obtained from computer simulations on concert halls using the ODEON program version 3.1. The key parameter compared with measured data is the reverberation time, and this is mainly used to adjust the absorption data of the surfaces in the computer model. But five additional parameters are calculated and compared with measured data as well. In order to determine the sensitivity of the computer model, comparisons are also made between the results obtained from computer simulations using models with a high geometrical fidelity and those from models with simplifications to geometry that are in better agreement with the laws of high-frequency modeling.

5:20

3pAAa4. Real time auralization with EASE 3.0. Wolfgang Ahnert (ADA Acoust. Design Ahnert, Gustav-Meyer-Allee 25, D-13355 Berlin, Germany, wahnert@ada-acousticdesign.de)

The new EASE 3.0 for Windows combines advanced features of the DOS-based system EASE 2.1 with the known ones of the Auralization package EARS 1.1. In case of the DOS-based system, one has to use additional hardware to convolve the calculated impulse responses with the head-related transfer functions and eventually with the dry tests signal. After calculation of the corresponding impulse response one can listen now in EASE 3.0 to the convolved binaural signal by use of just a normal sound card. Additionally, with a duplex sound card one can enter CD signals directly and, after a transient time of 50 ms to 2 s (depending on the computer parameters and the sample rate of the signal), one can obtain the auralized results. Another option allows one to calculate the direct sound sequence of used speaker signals in realtime also and then to use the auralization routine to check echo occurrence or correct localization of sound sources. The convolution algorithm used in EASE 3.0 is patent pending and was created in cooperation with LAKE/Australia. In a project still under construction, the measured results have been compared with auralization results obtained by physical scale model measurements. Both results will be demonstrated.

5:40

3pAAa5. Comparison of simulation and measured sound system performance in the German Reichstag Debate Hall, Berlin. Volker Loewer (IFB Rhein Main, Eleonorenstr. 11, D-65474 Bischofsheim, Germany, ifbrm@aol.com)

For the design of the new sound system for the Reichstag Debate Hall, Berlin, the ULYSSES computer aided acoustic design program has been used. The 3-D model of the room consisted of more than 1000 faces treated with different absorption in octave bands according to the architect's plans. Simulation of direct sound coverage, RT60, intelligibility, energy decay via ray-tracing, etc., was done to evaluate different solutions of the sound system designs and their interaction with room acoustics. It is intended to compare actual acoustic test results to simulated predictions and to discuss conformity and deviations. The software was also used to predict directivity balloons of the complex speaker arrays located in the debate hall. The balloons were derived from measured balloons of the single devices used in the arrays. Considering relative mechanical locations, acoustic centers, acoustic power, and delays, the predictions showed good conformity with polar measurements of a real cluster.

6:00

3pAAa6. A computer auralization and ''real world'' comparison using the computer programs EASE and EARS. Robert C. Coffeen (Architectural Eng., Marvin Hall, Univ. of Kansas, Lawrence, KS 66045) and Gabriel Caunt (Russ Berger Design Group, Inc., Dallas, TX 75244)

In order to compare a ''real world'' acoustic environment with a computer auralization of the same space, an Episcopal Church located in Prairie Village, Kansas (near Kansas City, Missouri) was selected as the ''real'' space. Anechoic speech and music recordings were reproduced in this space and recorded binaurally. The same anechoic recordings were introduced into a computer model of this room with auralizations produced by the computer programs EASE and EARS. The ''real world'' binaural recordings are compared with the computer-generated audio using both objective and subjective methods. The measured impulse response of the room and the computer-predicted impulse response are compared. Comparisons are also made between the measured and the predicted reverberation periods of the room.

WEDNESDAY AFTERNOON, 17 MARCH 1999 ROOM H1028, 4:35 TO 6:20 P.M.

Session 3pAAb

Architectural Acoustics: Sound Insulation and Subjective Annoyance

Jens Holger Rindel, Cochair
Norwegian Institute of Building Research, P.O. Box 123, Blindern, N-0314 Oslo, Norway

Angelo J. Campanella, Cochair
Campanella Associates, 3201 Ridgewood Drive, Columbus, Ohio 43026, USA

Chair's Introduction—4:35

Invited Papers

4:40

3pAAb1. On the utility of extending the low-frequency range of standards for sound isolation in buildings. Stephen J. Lind, Karl S. Pearsons, and Sanford A. Fidell (BBN Technol., 21128 Vanowen St., Canoga Park, CA 91303, slind@bbn.com)

Frequencies above 100 Hz are commonly considered in sound insulation computations as specified by ASTM E413 and ISO 717. This is appropriate for concerns about speech privacy in interior spaces. However, aircraft ground operations (including takeoff roll, engine run-ups, and thrust reverser deployment) may expose buildings near runways to appreciable amounts of energy at yet lower

frequencies. Several studies of low-frequency aircraft noise levels have recently been completed in the United States, and the U.S. Federal Aviation Administration is paying for architectural treatments to reduce low-frequency aircraft noise in residences near one airport. This paper describes the findings of a recent social survey of residential annoyance caused by low-frequency runway sideline noise, including noise in the 25 to 80 Hz one-third octave bands, and reviews other evidence about the role of low-frequency energy in sound isolation metrics.

5:00

3pAAb2. On subjective impact sound insulation classes. Per Hammer (Dept. of Eng. Acoust., Lund Univ., Box 118, 22100 Lund, Sweden, per.hammer@kstr.lth.se) and Erling Nilsson (Lund Univ., 22100 Lund, Sweden)

The possibility to divide impact sound annoyance into classes is investigated. The experiments, based on human perception, are done in a laboratory environment where various floor structures have been included to produce impact noise. These tests are correlated to studies pertained to real-life situations for tenants. The statistical tool to test the significant differences between the classes is Rou–Kupper. Real footsteps are used as a noise source. In addition, airborne sound insulation is treated in a similar manner, whereby one may conclude that there are some difficulties finding classes with statistical significant differences. [Work supported by the Swedish Council of Building Research.]

Contributed Papers

5:20

3pAAb3. Group subjective ratings of airborne sound insulation. John Bradley (IRC, Natl. Res. Council, Montreal Rd., Ottawa, ON K1A 0R6, Canada, john.bradley@nrc.ca)

This paper will compare various sound insulation measures as predictors of the grouped subjective ratings obtained from a field survey of 600 subjects and the airborne sound insulation of their 300 party walls. The subjects lived in both row housing and multi-floor apartment buildings in three different Canadian cities. The questionnaire first asked about general issues concerning the subjects building followed by more specific questions rating the sound insulation and the audibility of various noises. Sound transmission loss measurements were made in 1/3 octave bands from 100 to 4000 Hz. In addition to the standard ISO and ASTM single number ratings, 20 different single number sound isolation measures were calculated. Most were simple variations of the standard quantities. The standard STC rating (including the 8-dB rule) was one of the better predictors of most responses. Excluding the 8-dB rule decreased correlations with responses and especially those concerning hearing musical sounds. Several responses were best correlated with transmission loss values in the 160- and 200-Hz bands.

5:40

3pAAb4. Considerations about the influence of traffic noise in the design of new hospitals. Eduardo Bauzer Medeiros (Dept. de Engenharia Mecânica da UFMG, Av. Antônio Carlos 6627, 31270-901, Belo Horizonte–MG, Brazil, flugzbau@dedalus.lcc.ufmg.br) and Ivan de Azevedo Camelier (UBI, 6200, Covilhã, Portugal)

The main origin of noise disturbance in new hospitals located inside densely populated areas can usually be associated with vehicular traffic. However, the effect of this disturbance is often not fully appreciated. Compliance with standard legislation limits is often considered to be a satisfactory design criterion. In fact, even moderately higher noise levels can introduce physiological changes, which may have a decisive influence on the convalescence of a hospital patient. The present work associates some of the information which is available on the effects of patients subjected to different noise levels with considerations about hospital and the associated access roads design. Field measurements carried out in the vicinity of typical existing and planned hospitals are also described and associated with the local traffic conditions. Finally, a few practical guidelines are laid, considering a rest situation of a hospital under construction near an important access road. The objective is to establish a set of acoustic design guidelines for hospitals and the surrounding areas, particularly the road system, aiming at a more efficient convalescence period for the patients.

6:00

3pAAb5. Vibrations caused by construction work—Measurements and surveillance. Wolfgang Teuber and Ernst-Jo Voelker (Inst. for Acoust. and Bldg. Phys., Oberursel, Germany)

Numerous construction principles applied especially in underground engineering are the sources of vibrations. The measurement of vibrations and evaluation of the results are made based upon different criteria. These criteria are formed taking into consideration the influences upon people in the surrounding area, the risk of damage to buildings and the possibility of the malfunctioning of technical systems such as computers or laser equipment. Measurements were taken while several different construction methods were being applied. Short-term measurements are, for the most part, insufficient and must be completed by long-term research. Maximum acceptable values are defined in existing standards based on the influences of vibrations upon persons and upon various kinds of buildings. For technical equipment, stricter limits had to be defined. When the type and location of construction work changes, the application of an automatic monitoring system is advantageous. Such a system is described which was installed to survey computers with special hard disc drives. Existing measurement results allow for predictions and calculations to be made in order to determine the best method of construction. Some principles of building methods, measurements, and vibration monitoring are mentioned.

Session 3pAO

Acoustical Oceanography and Underwater Acoustics: Acoustic Tomography and Thermometry II

James F. Lynch, Chair
Woods Hole Oceanographic Institute, Bigelow 203, Woods Hole, Massachusetts 02543, USA

Invited Papers

4:20

3pAO1. Shallow-water tomography: Acoustic maps of the New England shelfbreak front. Ching-Sang Chiu (Dept. of Oceanogr., Naval Postgrad. School, Monterey, CA 93943), James F. Lynch, and Glen Gawarkiewicz (Woods Hole Oceanogr. Inst., Woods Hole, MA 02543)

In the summer of 1996, an integrated acoustic-oceanographic experiment was carried out in the Middle Atlantic Bight to study the dynamics of the shelfbreak front and the effects of the frontal variability on sound propagation. The experiment employed a suite of acoustic and oceanographic sensors, including several sources and two vertical hydrophone arrays (VLAs) straddling the shelfbreak front and a SeaSoar that provided several high-resolution, three-dimensional surveys of the frontal region. In this presentation, the results of an acoustic tomographic analysis of the frontal variability are reported. In deriving the tomographic maps, an adaptive beamformer was first used to detect, resolve, and track individual acoustic ray and modal arrivals from a 224- and a 400-Hz source on the slope to a vertical array on the shelf. A hybrid ray-mode inverse technique was then applied to the resolved arrivals to produce a time series of cross-frontal images of ocean temperature. The tomographic observations are interpreted together with the SeaSoar, ADCP, and thermistor data. [Work supported by ONR.]

4:40

3pAO2. Broadband geo-acoustic inversion in shallow water. Jean-Pierre Hermand (Environ. Res. Div. SACLANT Undersea Res. Ctr., viale San Bartolomeo 400, 19138 La Spezia, Italy, hermand@saclantc.nato.int)

The paper discusses an inversion method that allows the rapid determination of *in situ* geo-acoustic properties of the ocean bottom without resorting to large acoustic receiving apertures, synthetic or real. The method is based on broadband, waterborne measurements and modeling of the waveguide impulse response between a controlled source and a single hydrophone. Results from 1994–1997 experiments in Mediterranean shallow waters with single elements of vertical array and advanced drifting acoustic buoys are reviewed. Inversion of the bottom parameters is performed with an objective function that includes the processing gain of a model-based matched filter (MBMF) receiver relative to the conventional matched filter. The MBMF reference signals incorporate waveguide Green's functions for the known geometry and water column acoustic model, and hypothesized bottom geo-acoustic models. The inversion results demonstrated that—even for the fairly complex environmental conditions of the experiments—a single transmission of a broadband coded signal received at a single depth and a few hundred of forward modeling runs were sufficient to resolve the bottom features. These included the sound-speed profile, attenuation, density, and thickness of the top sediment layer, and sound speed and attenuation of the bottom. Exhaustive parameter search proved unequivocally the low-ambiguity and high-resolution properties of the MBMF-derived objective. The single-hydrophone bottom inverses closely agree with the ones obtained under the exact same conditions from matched-field processing of multitone pressure fields sampled on a vertical array. Both of these results agree with expectations from geophysical ground thrust.

Contributed Papers

5:00

3pAO3. Results for tomographic geoacoustic inversion on simulated multiarray data. A. Tolstoy (Integrated Performance Decisions, Inc., 8610 Battailles Ct., Annandale, VA 22003, atolstoy@ipdinc.com)

Only recently have broadband multiarray data been collected which are suitable for tomographic inversion for the estimation of shallow-water geoacoustic parameters. In particular, this unique data set was collected in the Haro Strait region off the west coast of Canada by N. R. Chapman and colleagues. These data have now been simulated and studied in preparation for the tomographic inversion of the actual data, a very difficult problem involving hundreds of parameters. Results to be discussed here concern these simulated data and recent successes in their inversion for the estimation of such properties as sediment sound-speeds and densities over a region where such parameters vary as a function of range, azimuth, and depth. [Work supported by ONR.]

5:20

3pAO4. Acoustic data preprocessing in the TOMOLAB/OCTOPUS project. Mauuary Didier and Bernard Faure (Laboratoire des images et signaux, INP, Grenoble, St. Martin d'heres, France, Didier.Mauuary@lis.inpg.fr)

This paper presents the acoustic data preprocessing task in the TOMOLAB graphic interface tool. TOMOLAB is a goal of the OCTOPUS project, under the MAST III program of the European Com-

munity. Data preprocessing consists in transforming raw tomographic data into compressed/correlated peaklike data. It is the first step before time delay estimation, time delay identification, and time delay inversion. The complete data processing must perform matched filtering, multisequence averaging, Doppler/phase compensation, and mooring motion correction. A synthetic view is given of several technical choices that integrate these tasks, jointly or successively. This work is based on internal studies and existing pieces of literature. The Hadamard transform, the Fourier matched filtering, fast Doppler processing, phase estimation/correction algorithm, delay shifting in the time or Fourier domain, data format and sampling are discussed. Efficient data processing has to account for the computing speed, the compression ratio, and achievable accuracy of delay estimation.

5:40

3pAO5. Matched-peak tomography. E. K. Skarsoulis (Inst. of Appl. and Computational Mathematics, FORTH, 71110 Heraklion, Crete, Greece)

A new approach is presented for the inversion of travel-time data in ocean acoustic tomography. Using model relations between sound-speed and arrival-time perturbations about a set of background states, arrival times and associated model errors are calculated on a fine grid of model states discretizing the parameter space. Each model state can explain (identify) a number of observed peaks in a particular reception laying within the uncertainty intervals of the corresponding predicted arrival times. The model states that explain the maximum number of observed peaks are considered as the more likely parametric descriptions of the reception; these model states can be described in terms of mean values and variances providing a statistical answer (matched-peak solution) to the inversion problem. An advantage of the proposed approach is that there is no need for initialization of the inversion procedure, i.e., no need for additional hydrographic information. Furthermore, the matched-peak solution for each reception is independent of the previous reception identification/inversion results. The method was applied to nine-month-long tomography data from the Thetis-2 experiment in the western Mediterranean sea. [Work partially supported by EU/MAST.]

6:00

3pAO6. On the simultaneous estimation of current and sound velocity structure in the ocean, using matched-field processing. Michael Taroudakis (Dept. of Mathematics, Univ. of Crete and Inst. of Appl. and Computational Mathematics, FORTH, P.O. Box 1527, 711 10 Heraklion, Crete, Greece, taroud@iacm.forth.gr) and Maria Markaki (Inst. of Appl. and Computational Mathematics, FORTH, 711 10 Heraklion, Crete, Greece)

A matched-field processing method for the simultaneous estimation of ocean current velocity structure and sound speed profiles, based on reciprocal transmissions of cw or broadband acoustic signals between two locations in the water column, is presented and discussed. For each transmission, a single source and a vertical array of hydrophones are used. The current velocity is introduced as an additional unknown in the inverse problem, through the concept of the ''effective sound speed,'' being the sum of the actual sound speed and the projection of the current velocity on a vertical plane, defined by the sound source and the receiver. The work is mainly focused on the study of the effect of variations of the current velocity on the various processors proposed for the matched-field inversions and on the inversion procedure itself, under the assumption that neither the actual position of the source receiver system nor the actual sound velocity structure are known. Using synthetic data, it is demonstrated that the results of inversion for the current velocity are reliable, under some limitations posed by the degree of uncertainty for the other unknown parameters. [Work supported by INTAS-RFBR.]

Contributed Posters

These posters will be on display in the Poster Gallery from Thursday to Friday, 18–19 March. Authors will be at their posters from 10:00 a.m. to 12:00 noon on Friday, 19 March.

3pAO7. The experimental demonstration of selective mode excitation in a shallow-water environment. James C. Preisig (Dept. of Appl. Ocean Phys. and Eng., Woods Hole Oceanogr. Inst., Woods Hole, MA 02543), John R. Buck (Univ. of Massachusetts, North Dartmouth, MA 02747), Mark Johnson (Woods Hole Oceanogr. Inst., Woods Hole, MA 02543), and Hu Dou (Univ. of Massachusetts, North Dartmouth, MA 02747)

The ability to selectively excite single acoustic modes in a shallow-water environment is demonstrated and analyzed. Using vertical source and receiving arrays and the feedback control techniques based on those in Buck *et al.* [IEEE J. Oceanic Eng. **22**, 281–291 (1997)], acoustic modes 1–3 were excited sequentially for periods up to 20 min with a fidelity of approximately 60 dB for mode 1 to 25 dB for mode 3. The filtering of the received signal used in the feedback loop by projection into the subspace spanned by the dominant system modes was found to significantly improve the system's performance. This result will be explained and analyzed. The requirement for phase stabilization of the sampled received signal is also presented. The ability demonstrated here for high fidelity selectively controlled modal content of a transmitted acoustic signal offers potential for new methods for acoustic tomography and for studying underwater acoustic propagation. [Work supported by ONR Ocean Acoustics.]

3pAO8. Model of acoustic monitoring of heat and mass transport in the Fram Strait. Konstantin A. Naugolnykh (Environ. Technol. Lab., Boulder, CO 80303), Ola M. Johannessen (Nansen Environ. and Remote Sensing Ctr., Bergen, Norway), Igor B. Esipov, Oleg B. Ovchinnikov, and Yuri I. Tuzhilkin (N. Andreyev Acoust. Inst., Moscow, 117036 Russia)

A computation model of acoustical monitoring of heat and mass transport in the Fram Strait is discussed. The method relies on the advections of small-scale inhomogeneities across the acoustic path and travel-time variations in the process of signal crossing of the Strait on a number of paths to infer the intervening of fine-scale variability and transverse current. Inhomogeneities of the current produce perturbations in the travel time of the sound, and the current can be sensed by generating a time-lagged cross correlation of the full acoustic field. Both the linear four-element transmission array and four-element receiving array with equally spaced elements were used for calculations. By combining the signals from each transmitter–receiver pair in different ways, a number of different path positions were probed and a profile of transverse current $U(r)$ along the propagation path r was retrieved, whereas the value of the travel-time variation is related with T—temperature change. The possibility of estimation of heat $Q \sim \int U(r)T(r)dr$ and mass $M \sim \int U(r)dr$ transport in the cross section is regarded. [Work supported by Environmental and Climate Programme of EC, Project PL970338.]

3pAO9. Internal wave inversions for one year of Pioneer–Hawaii ATOC transmissions. Kevin D. Heaney and the ATOC Group[a] (Sci. Applications Intl. Corp., 11803 Sorrento Valley Rd., San Diego, CA 92121)

The ATOC experiment transmitted 75-Hz signals from Pioneer Seamount off the coast of California to a vertical line array (VLA) off Hawaii. The combination of VLA and long-range propagation provides the opportunity to perform mode-based internal wave tomography. Each arrival is mode-filtered and the statistics of the mode arrivals are tabulated. These individual mode arrival time (centroid) and spread are then compared with calculated mode statistics from broadband PE modeling of the propagation path. In this manner a statistically robust inversion for the internal wave strength is performed. The weakness of the inversion is the sensitivity to the bottom scattering near the source. Results for one year of data will be presented for two different bottom types. The long-scale time series may indicate possible sources of internal waves in the ocean. Small time scale variations may be attributable to internal tides. [a] The ATOC Group: A. B. Baggeroer, D. Menememlis, and C. Wunsch (MIT); T. Birdsall, K. Metzger (Univ. of Michigan); C. Clark (Cornell Univ.); J. Colosi (WHOI); B. D. Corneulle, M. Dzieciuch, W. Munk, P. F. Worcester (SIO); D. Costa (Univ. of California, Santa Cruz, CA); B. D. Dushaw, B. M. Howe, J. A. Mercer, and R. C. Spindel (APL-U Wash.); A. M. G. Forbes (CSIRO, Hobart).

3pAO10. AMOC: Preliminary results. Hanne Sagen (NERSC, Edv. Griegsvei 3A, 5037 Solheimsviken, Norway, hanne.sagen@nrsc.no), Ola M. Johannessen, Halvor Hobaek, and Sigve Tjoetta (Univ. of Bergen, Bergen, Norway)

The scope of this presentation is to give preliminary results of the sensitivity study of sound propagation in the Arctic including the Fram Strait using propagation loss observations and existing acoustic propagation models. Special attention to the consequences for design of future acoustic monitoring concepts will be made. One of the important consequences of the preliminary results is the conflict between the optimum transmission frequency and the optimum frequency for retrieving information about the ice cover. If an experiment is designed to propagate over long distances at a relatively low frequency, then the reflection from a ''smooth'' ice cover is total and there will be no information about the ice thickness or internal properties of the ice cover. The attenuation due to the ice will be dominated by scattering from rough surface (large facets). So this type of experiment will give information about the averaged temperature through the travel times, while the ice information will be limited. Therefore two concepts have to be considered: one to measure ice parameters, which will need signals composed by appropriate frequencies, and another concept to measure averaged temperature, which needs low frequencies insensitive to ice cover.

3pAO11. Method of the main informative components for acoustic tomography. Alexander Ya. Kalyuzhnyi (Inst. of Hydromechanics, 8/4 Zhelyabov Str., Kiev, 252057, Ukraine) and Leonid G. Krasny (Ericsson, Inc., RTP, NC 27709)

Techniques for an ocean acoustic tomography are based on the representation of the sound-speed field (SSF) by an expansion of some orthogonal basis functions. It is usually assumed that the most efficient basis functions for the SSF expansion are so-called empirical orthogonal functions (EOF). Meanwhile, the experiments show that algorithms based on the EOF can be extremely sensitive to slight errors in the assumed signal and noise characteristics. A new improved algorithm for acoustic tomography will be presented which minimizes output statistical errors of the SSF estimation. The concept of this algorithm is to use eigenvectors of the Fisher information operator as the basis functions into the SSF expansion. The algorithm involves a quadratic inequality constrain on the SSF expansion coefficients to select the most informative components among all the eigenvectors. It is shown that it leads to a robust algorithm in which statistical errors do not accumulate. The performance of the proposed algorithm will be illustrated both for deterministic and random signals.

3pAO12. An ocean acoustic tomography experiment in the central Labrador Sea—First results. Detlef Kindler and Uwe Send (Inst. für Meereskunde, Univ. Kiel, Düsternbrooker Weg 20, D-24105 Kiel, Germany)

First results of an ongoing acoustic tomography experiment will be presented. Since August 1996 a mooring array consisting of four tomography transceivers (400 Hz), redeployed in the summers of 1997 and 1998, has been measuring acoustic travel times over distances of typically 170–300 km in the central Labrador Sea. The purpose of such measurements is to estimate time series of horizontally integrated properties like ocean heat content and vertical temperature stratification by inverting travel times into sound speeds and hence into heat contents and temperatures. These large-scale properties will be used to study the interannual variability of ocean heat budget and water masses formed in close connection to deep convection and the ensuing renewal of Labrador Sea Water (LSW) [R. A. Clarke and J. C. Gascard, J. Phys. Oceanogr. **13**, 1764–1778 (1983)]. The variability during winter results from destabilization of the water column near the ocean surface caused by atmospheric cooling, subsequent mixing down to 1000–2000 m, and the following restratification of the convection area. The investigations are focused on the upper 2000 m of the water column, which are well insonified by several trackable ray paths with enough acoustic energy to be processed. [Work supported by Deutsche Forschungsgemeinschaft.]

Session 3pEA

Engineering Acoustics and Underwater Acoustics: Recent Advances in Underwater Transducers II

Elizabeth A. McLaughlin, Cochair
Naval Undersea Warfare Center, Code 2131, Newport, Rhode Island 02841-1708, USA

Didier Boucher, Cochair
DCN Ingénierie Centre SUD, Sous-Direction Lutte Sous La Mer, BP 30, 83800 Toulon Naval, France

Contributed Papers

4:00

3pEA1. Application of the Tonpilz design for optimizing parameters of rod transducers. Boris Aronov (Acoust. Res. Lab., Dept. of Elec. and Computer Eng. and Ctr. for Marine Sci. and Tech., Univ. of Massachusetts, Dartmouth, North Dartmouth, MA 02747)

The optimum design of a rod transducer under various loading conditions and operating requirements is examined. It is often possible that the operational requirements can be met by using only a part of the rod volume with the electromechanical or piezoelectric element. The remaining sections of the rod can be replaced by passive materials or caps (i.e., a ''head'' and a ''tail'') while still maintaining the same input impedances and resonant frequency. Such a composite rod transducer made of active and passive materials having different length and cross-sectional areas is of the ''Tonpilz'' type. The proper choice of dimensions and materials for the caps will result in optimum transformation of mechanical (acoustical) loads and transducer performance. Both criteria of optimization, the rod transducer parameters and the procedure for determining properties of the caps that provides optimal loads, are discussed.

4:20

3pEA2. Large aperture 1-3 composite longitudinal resonator (tonpilz) transducer. Charles W. Allen, W. Jack Hughes, and David J. Van Tol (Appl. Res. Lab., Penn State Univ., P.O. Box 30, State College, PA 16804)

A large aperture underwater transducer utilizing 1-3 piezoelectric composite material that operates as a longitudinally resonant (tonpilz) device with a resonance frequency of 45 kHz has been fabricated and tested. The transducer consists of continuous plates of steel and aluminum that act as the rear and front masses, respectively, and a motor section of continuous 1-3 PZT-5H composite. The active radiating face (aluminum front mass) has dimensions of 6.3 in. (4.7 wavelengths) and 3.9 in. (2.9 wavelengths). Conventional transducers or arrays with radiating faces that have dimensions of over one wavelength require dicing or separate elements to reduce the effect of lateral modes in the components. The tonpilz transducer utilizing 1-3 composite material requires no dicing of any of its components, so fabrication of large aperture arrays that only require a single forward-looking narrow beam are greatly simplified. The measured acoustic responses versus frequency and angle demonstrate that there are no extraneous modes that affect the acoustic performance of the transducer and they compare well to theory for a one-dimensional longitudinal resonator. [Work sponsored by the Scripps Institution of Oceanography, University of California, San Diego.]

4:40

3pEA3. The development of a doubly curved acoustic array using injection molded 1-3 piezocomposite. Kim C. Benjamin, Stephen F. Oliver, Jose C. Arteiro (Naval Undersea Warfare Ctr. Div. Newport, 1176 Howell St., Newport, RI 02841, benjaminkc@code20nl.npt.nuwc.navy.mil), Russell S. Petrucci, and William J. Serwatka (Mater. Systems, Inc., Littleton, MA 01460)

The design, fabrication, and acoustic calibration of a doubly curved acoustic array for UUV oceanographic applications is presented. The sensor employs a unique piezoceramic thermoplastic composite which is conformable and capable of deep ocean operation. The composite consists of several small diameter (1.0 mm) PZT-5H rods regularly distributed in a two-dimensional lattice and aligned perpendicular to their diameter. The PZT-5H rods are encapsulated within a thermoplastic viscoelastic moldable epoxy matrix to form an active acoustic composite panel. The thermoplastic epoxy phase of the composite allows the panel to be shaped to a specific vehicle geometry. Low-profile (<1.0 mm) coaxial cable embedded within the composite panel provides addressing between the acoustic array elements and the processing electronics. [This work was supported by Code 80 of the Naval Undersea Warfare Center, Division Newport.]

5:00

3pEA4. Ultra-wide bandwidth backscattering measurements using a transparent flat PVDF sheet source. Scot F. Morse (Code 7136, Naval Res. Lab., Washington, DC 20375), Karen Gipson (Univ. of Puget Sound, Tacoma, WA 98416), Greg Kaduchak (Los Alamos Natl. Lab., Los Alamos, NM 87545), Kevin L. Williams (Univ. of Washington, Seattle, WA 98105), Brian T. Hefner, and Philip L. Marston (Washington State Univ., Pullman, WA 99164-2814)

A thin extended flat PVDF film surrounded by water is demonstrated to be suitable for exploring scattering responses of complicated targets over a range of frequencies from below 2 kHz to 1000 kHz. The target lies close to the source, and in the configuration normally used, the scattering passes through the source to a distant hydrophone. While initial experiments [Kaduchak *et al.*, J. Acoust. Soc. Am. **97**, 2644–2708 (1995)] explored the resonances of spherical shells for which analytical solutions are known, recent experiments have explored novel features in the responses of truncated tilted cylinders that are either hollow [Morse *et al.*, J. Acoust. Soc. Am. **103**, 785–794 (1998)] or solid [K. Gipson, Ph.D. thesis, Washington State Univ. (1998)]. The spectrum radiated by the sheet can be altered by using voltage-step, voltage-pulse, or weighted chirp excitations. An equivalent circuit model is useful for describing the radiated spectrum. Crisp tone bursts have also been produced and used to study the low-frequency resonances of a steel shell in Lake Union (Seattle). [Work supported in part by the Office of Naval Research and by APL.]

5:20

3pEA5. Mechanical properties of lead magnesium niobate/lead titanate ceramics. Elizabeth A. McLaughlin and Lynn Ewart (Naval Undersea Warfare Ctr., Code 2131, 1176 Howell St., Newport, RI 02841)

This research examines the mechanical properties of doped electrostrictive lead magnesium niobate / lead titanate (PMN-PT). While optimization of the electromechanical properties has been the focus of the materials development effort, mounting anecdotal evidence indicates that there are problems with the mechanical integrity of PMN-PT. Mechanical testing has been employed (1) to measure the flexural strength of doped PMN-PT and understand the causes of failure, and (2) to measure the compression strength of PMN-PT and identify the onset of microstructural damage. Navy type-III ceramic (PZT8) was measured as a benchmark. The average flexural strength of poled PZT8 was found to be 110 MPa. Average flexural strengths ranging from 44 to 60 MPa were measured for batches of barium- and lanthanum-doped PMN-PT. Fractography identified the causes of failure. Process modifications, by one vendor, have increased the flexural strength by 38%. The average compression strength of unpoled PZT8 was found to be 1040 MPa. An average compressive strength of 890 MPa was measured for barium-doped PMN-PT. Prior to failure, a ceramic develops microstructural damage at levels below the compression strength. Evidence of damage was found at stresses as low as one-third of the compressive strength. [Work supported by ONR and SPAWAR.]

5:40

3pEA6. Evidence of nonlinear losses in electrostrictive materials. Harold C. Robinson (Naval Undersea Warfare Ctr., Newport, RI 02841)

It has been well established that the equivalent piezoelectric properties used to model the large signal properties of electrostrictive materials such as lead magnesium niobate/lead titanate (PMN/PT) are functions of the operating conditions. Since these materials are nonlinear, DC bias field, AC drive field, prestress level, and temperature all affect the piezoelectric constants and the coupling factor. However, in transducer models based on equivalent circuits, the dielectric loss is represented as a constant under all of these conditions. Moreover, the dielectric loss tangent typically used in these models must either be inferred from transducer data or be measured under conditions (such as using an RLC meter) that do not represent the actual conditions of operation. This paper will present data, from both material and transducer measurements, suggesting that the losses in electrostrictive materials are strong functions of the temperature, drive field, and compressive prestress. Possible approaches to obtaining improved loss measures from material measurements will be discussed.

WEDNESDAY AFTERNOON, 17 MARCH 1999 ROOM H105, 4:20 TO 6:20 P.M.

Session 3pED

Education in Acoustics: Take Fives—Sharing Ideas for Teaching Acoustics

Uwe J. Hansen, Cochair
Department of Physics, Indiana University, Terre Haute, Indiana 47809, USA

Armin Kohlrausch, Cochair
IPO Center for Research on User-System Interaction, P.O. Box 513, NL-5600 MB Eindhoven, The Netherlands

Do you have a novel demonstration, a new laboratory experiment, a favorite video, a recorded sound example, or a new idea for teaching acoustics which you are willing to share with your colleagues? At this session a sign-up board will be provided for scheduling presentations. No abstracts are printed. Presenters are encouraged to have handouts to distribute. Multiple presentations are acceptable (not consecutively). Presentations are limited to 5 minutes. Keep them short! Keep them fun!

Session 3pMU

Musical Acoustics: Musical Instruments and Structural Acoustics II: Piano and Related Instruments

Isao Nakamura, Cochair
1-33-25 Kokuryo, Chofu, Tokyo 182-0022, Japan

Ingolf Bork, Cochair
Physikalische Technische Bundesanstalt, Bundesallee 100, D-38116 Braunschweig, Germany

Chair's Introduction—4:15

Invited Papers

4:20

3pMU1. Piano string excitation: The question of gravity influence on the sound spectra. Anatoli Stulov (Dept. of Mech. and Appl. Mathematics, Inst. of Cybernetics, Akadeemia tee 21, Tallinn, EE0026, Estonia)

The influence of gravity on the process of the grand piano hammer–string interaction was appreciated by D. E. Hall [J. Acoust. Soc. Am. **79**, 141–147 (1986)]. Using the reasonable physical assumptions, it was shown that the gravity influence is small and may not be taken into account. It is obvious, but it is important to know exactly what this influence is. The vibration spectra of different flexible strings excited by piano hammers in the gravity field and without gravity were analyzed here. Of course, the influence of gravity increases with the increasing of the contact time. Its depends on the hammer velocity; therefore, the string excitation by hammers with velocities less than 0.5 m/s was considered. It was shown that: the gravity influence is greater for the smooth hammers, and this influence is more essential for the middle range of notes; for the small velocities of hammers the gravity changes the mode energy levels of the primary harmonics up to 10 dB, if the hammer strikes only one string of the triple set; the gravity must be taken into account definitely, if the contact time is greater than 5 ms.

4:40

3pMU2. Experimental analysis of two-dimensional vibration of a piano string measured with an optical device. Hideyuki Tanaka, Keinosuke Nagai, and Koichi Mizutani (Inst. of Appl. Phys., Univ. of Tsukuba, Tsukuba Ibaraki, 305-8573 Japan)

It is well known that a piano string vibrates in the direction not only perpendicular to the soundboard but also parallel to it. The sound decays rapidly at first and then it decays slowly. A change in the predominant direction of vibration of the string from perpendicular to parallel contributes to the compound decay rate [G. Weinreich, Sci. Am. **240**, 118–127 (1979)]. In this paper, two-dimensional vibration of a piano string is measured with handmade equipment consisting of two phototransistors. Just after the string was struck with a hammer, it vibrates perpendicularly to the soundboard. Then it vibrates gradually in the direction parallel to the soundboard. As a result, a point of the string moves on an elliptic trajectory. It was found that the fundamental resonant frequency of the perpendicular vibration of the E1 string, for example, which is about 40 Hz, is 0.07 Hz lower than that of parallel vibration. This causes the change of rotating direction of the string every 7 s. The discrepancy of the resonant frequencies is also found in the vibration of the D♯1 string.

5:00

3pMU3. Damping of string motion, a significant parameter for sound quality. Klaus Wogram (Phys.-Techn. Bundesanstalt, Proj. 1.401, Bundesallee 100, D-38116 Braunschweig, Germany, klaus.wogram@ptb.de)

To improve the sound quality of pianos and upright pianos the piano maker mostly plans a change of the construction of the backs and the soundboard with its ribs, bridges, and back posts. Unfortunately he often disregards that all these efforts cannot be successful if the damping of the strings is insufficient. Its influence on the sound quality can be very much stronger than that of the soundboard. Guided by some examples, the importance of the dampers, their construction, their mass, and their position will be discussed. In addition the reduction of sound quality due to an insufficient damping of the not-speaking part of a string will be demonstrated.

5:20

3pMU4. The influence of inharmonicity on piano tuning. Taro Mori and Ingolf Bork (Physikalisch-Technische Bundesanstalt, Bundesallee 100, 38116 Braunschweig, Germany, taro.mori@ptb.de)

It is well known that octaves of piano sounds are stretched to more than a 2 : 1 ratio. One reason is that partials of piano tones are not exactly harmonic because of the flexural rigidity of the string. This inharmonicity is characterized by the coefficient B, which depends on the tension, length, Young's modulus, the area of cross section, and the radius of gyration of the string. Piano technicians are trained to tune the octave as ''beautifully'' as possible, but the inharmonicity of the string hinders perfect tuning without beat. For example, when the second partial of the lower sound and the first partial of the upper sound are tuned without beat, all other partial pairs show beats. On the other hand, since the timbre structure of partials is unique for each instrument, the tuned octaves of two different instruments may differ. Some piano sounds were simulated by additive synthesis with different octave, inharmonicity, and timbre in order to perform subjective hearing tests with some piano tuners. It could be shown that the tuned octave width depends not only on the coefficient B but also on the timbre. The influence of the sound board is also discussed.

5:40

3pMU5. Psychoacoustic model for calculating the sound quality of piano tones. Miriam N. Valenzuela (Inst. of Mech., Faculty of Aerosp. Technol., Univ. of the Federal Armed Forces, Munich, D-85577 Neubiberg, Germany, miriam.valenzuela@unibw-muenchen.de)

Assuming that only audible dissimilarities between different piano tones may lead to different quality judgments, experiments were conducted to determine the perceptual attributes listeners use to judge these dissimilarities. The psychoacoustic results showed that two major attributes contribute with over 90% to the explanation of the perceived dissimilarities: the psychoacoustic ''sharpness'' and a second attribute that was described with the scale ''open–closed.'' Both attributes depend on the specific loudness distribution of the sound signals and are defined as a weighted first moment of the critical-band rate distribution of specific loudness using different weighting functions. The weighting function used to calculate the second attribute emphasizes spectral components around 1 kHz. The model developed for calculating audible dissimilarities between piano tones showed a good agreement between psychoacoustically measured and calculated dissimilarities; the correlation was 0.90. The influence of the two attributes on sound quality judgments was verified by listening tests with appropriately modified piano sounds. The results showed that calculating the sound quality of musical instruments on the basis of their sound signals requires an aurally adequate signal processing. The model developed to calculate the sound quality of piano tones showed a good agreement between measured and calculated quality orders.

Contributed Paper

6:00

3pMU6. Stiffness of strings: Significance in musical acoustics. Edgar Lieber[a] (former member of ''Institut für Musikinstrumentenbau,'' D-08267 Zwota, Germany)

In a linear differential equation of a vibrating string there is a link representing stiffness of the string. In nonlinear theory, string stiffness has not yet been taken into consideration. The author has completed this by means of the Lagrange II method and presents essential results. The significance of string stiffness is different for the different groups of instruments. Pianos have remarkably stiff strings. This is inevitable and also necessary because stiffness participates essentially in forming vividness of sound. The well-known ''stretched octaves'' and also the typical tuning curve are caused by this. For plucked strings, stiffness forms character of sound, together with choice of plucking spot on string and with corpus. For bowed strings, it is preferable to have strings, with minor stiffness, because the interaction of bow/string is better. The effects of jitter and rippling (supplement of sound with statistic noise effects) are better formed by less stiff strings. For wound strings, minor stiffness is possible with cores of filament structure. Theory and examples will be discussed.

[a] Present address: Erich Ohser Str. 10, D-08525 Plauen, Germany.

WEDNESDAY AFTERNOON, 17 MARCH 1999 ROOM H107, 4:55 TO 6:20 P.M.

Session 3pNSa

Noise: Tribute to Henning von Gierke

Richard L. McKinley, Cochair
Armstrong Laboratories, AL/CFBA, 2160 7th Street, Wright–Patterson AFB, Ohio 45433-7901, USA

Alice H. Suter, Cochair
Alice Suter and Associates, 575 Dogwood Way, Ashland, Oregon 97520, USA

Chair's Introduction—4:55

Invited Papers

5:00

3pNSa1. Henning E. von Gierke: Mentor, colleague, and public policy leader. Alice H. Suter (Alice Suter and Assoc., 575 Dogwood Way, Ashland, OR 97520)

5:20

3pNSa2. Research pioneer in biomechanics, Henning E. von Gierke. Thomas J. Moore (Armstrong Laboratories, AL/CFBA, 2160 7th Street, Wright–Patterson AFB, OH 45433-7901)

5:40

3pNSa3. The major historical events in the relating of noise-induced hearing loss to noise exposure. Daniel L. Johnson (Interactive Acoustics, 4719 Mile High Dr., Provo, UT 84604)

One event was the recognition of ''boilermaker's disease.'' Another was some of the threshold shift studies during and after WWII that led to the BENOX report. After these developments, there were a series of key events and decisions that have led up to our current state of knowledge and procedures. How Henning von Gierke was influential in most of these and how his decisions have consistently proven to be correct will be demonstrated. For example, he contributed to the 1953 BENOX report, promoted the ''equal energy concept,'' conceived and patented the first noise dosimeter, oversaw the EPA ''levels'' and criteria documents, and was the chair of the working group that wrote the current international standard (ISO-R1999) that relates noise exposure to noise-induced hearing loss. He was also instrumental in supporting many key research issues such as fetal noise exposure, asymptotic temporary threshold shift, and the longitudinal hearing of children. Henning's perseverance and dedication has provided society with an answer to one of his favorite questions, ''how much noise is too much?''

6:00

3pNSa4. 50-year legacy of Henning E. von Gierke's scientific and engineering excellence. Richard L. McKinley (Armstrong Laboratories, AL/CFBA, 2160 7th Street, Wright–Patterson AFB, OH 45433-7901)

WEDNESDAY AFTERNOON, 17 MARCH 1999 ROOM H2032, 4:20 TO 6:20 P.M.

Session 3pNSb

Noise: Rotor Noise from Helicoptors and Propellers

Werner Dobrzynski, Cochair
DRL-Instiitut für Entwurfsaerodynamik, Lilienthalplatz 7, 38108 Braunschweig, Germany

Feri Farassat, Cochair
NASA Langley Research Center, Hampton, Virginia 23681-0001, USA

Invited Papers

4:20

3pNSb1. European helicopter rotor noise research—Highlights of recent projects. Wolf R. Splettstoesser (Deutsches Zentrum für Luft-und Raumfahrt e. V., Institut für Entwurfsaerodynamic, Lilienthal-platz 7, 38108 Branschweig, Germany, wolf.splettstoesser@dlr.de)

Significant advances in understanding, modeling, and controlling helicopter rotor noise have been made in the course of several major European rotor aeroacoustic research projects over the past years. The availability of the German–Dutch Wind Tunnel (DNW), in particular, has enabled research on relatively large main rotor models (up to typically 40% full scale). Here, the simultaneous application and use of blade-mounted absolute pressure sensors to study the very aeroacoustic source mechanisms, of advanced acoustic-data acquisition systems for the radiated noise, of non-intrusive flow visualization as well as flow and blade deflection measurement techniques to investigate the rotor wake and the blade dynamic response has provided much insight into the physics of rotor aeroacoustics, particularly into the rotor blade-vortex interaction (BVI) impulsive noise phenomenon. In efforts towards controlling BVI impulsive noise, in some research projects, active blade-root control techniques have been investigated to favorably affect the BVI geometry and thus minimize the impulsive noise radiation. Much of the experimental data acquired served as benchmark information to enhance the mathematical modeling of the rotor wake, the rotor airloads, and the noise radiation. In this lecture, several major European helicopter aeroacoustic research projects are discussed.

4:40

3pNSb2. Analysis and capability of a noncompact integration method for rotor noise prediction. J. Prieur (ONERA/Dept. of Numerical Simulation and Aeroacoustics, 29 avenue de la division Leclerc, 92322 Chatillon Cedex, France)

Rotor noise computations starting from CFD input data using either the Kirchhoff or the generalized Ffowcs Williams–Hawkings surface integral methods in unsteady conditions may be very lengthy. This is the case for directivity studies or noise level contour calculations for which a high number of observer locations is required. To overcome this drawback, a fast integration method has been designed. It starts from the emission time which avoids having to solve the retarded time equation and uses directly as integration grid the CFD rotating grid (*a priori* not adapted to acoustic calculations). This is made possible thanks to a noncompact treatment of each grid element. The method has already been successfully applied in a transonic rotor case using indifferently a subsonically or supersonically rotating CFD grid for the surface integration (G. Rahier and J. Prieur, 53rd Forum of the American Helicopter Society, 29 April–1 May 1997). The method is made more understandable based on a new and clearer justification and its possibilities of extension are discussed.

5:00

3pNSb3. Analysis of the excess noise of aircraft pusher propellers. Johan B. H. M. Schulten (Aeroacoustics Dept., Natl. Aerosp. Lab. NLR, P.O. Box 153, 8300 AD Emmeloord, The Netherlands, schulten@nlr.nl)

A pusher propeller configuration offers several advantages over the traditional tractor arrangement. For instance, the wing of a twin-engined aircraft is no longer exposed to the swirling and turbulent slipstream. This results in a much smoother wing inflow, a prerequisite for aerodynamic refinement. Acoustically, the more aft position of the propellers considerably reduces the noise impact on the fuselage, yielding the potential of a low cabin noise level. However, in general, the exterior noise of pusher propellers is augmented by the interaction with impinging wakes and exhaust jets. The present paper addresses the physical mechanism of this interaction by applying an unsteady lifting surface theory to the propeller blades. This requires the incident field to be resolved in circumferentially harmonic Fourier components. For each component the unsteady blade pressure distribution is computed as source input for an acoustic calculation. From sample computations for typical operating conditions it appears that the interaction substantially contributes to the total radiated noise of pusher propellers. The present method offers the possibility to investigate in detail the effect of alterations in blade design and flight conditions on tonal level and directivity.

5:20

3pNSb4. Recent developments in helicopter rotor noise prediction at NASA. Kenneth S. Brentner (NASA Langley Res. Ctr., Hampton, VA 23681-0001, k.s.brentner@larc.nasa.gov)

Significant progress has been made recently toward the efficient and robust prediction of helicopter high-speed impulsive noise. The far-field approximation to the Ffowcs Williams–Hawkings (FW–H) quadrupole has been augmented with a rigorous mathematical development. Two new quadrupole formulations—a retarded-time formulation known as Q1A and an emission-surface formulation known as Q2—have been developed and implemented for subsonic and supersonic source motion, respectively. A key numerical advantage of the far-field approximation is that volume integration of the source region surrounding the rotor blades is only performed once in a preprocessing stage. The resulting quadrupole noise computation is reduced to surface integration over the rotor disk in the vicinity of the blades. The solution-adaptive marching-cubes integration algorithm used for the emission-surface formulation will be described. Another recent advance in helicopter noise prediction is the use of the FW–H equation on a permeable integration surface surrounding the source region. This application of the FW–H equation has been shown to be both analytically and numerically superior to the Kirchhoff approach. Furthermore, numerical evidence is presented to demonstrate that the Kirchhoff method is inappropriate when a wake convects through the surface.

Contributed Papers

5:40

3pNSb5. Passive–active low-frequency vibroacoustical fault diagnosis method. Nadejda I. Bouraou (Dept. of Orientation and Navigation Systems, Natl. Tech. Univ. of Ukraine, 37 Peremogy pr., Kiev, 252056, Ukraine, nadya@burau.inec.kiev.ua), Leonid M. Gelman, and Pavel I. Marchuk (Natl. Tech. Univ. of Ukraine, Kiev, 252056, Ukraine)

The presented work is dedicated to the development of the new passive–active low-frequency automatic vibroacoustical early fault diagnosis method of helicopter engine units (compressor stages, turbine stages). The proposed method is based on signal processing of the rotating details of acoustic noise in the low-frequency range (0–25 kHz). There are two important characteristics of this method: (a) it uses a nonstationary narrow-band vibration excitation with variable central frequency, and (b) this excitation is provided by rotating rotor, and user of the method will vary the central frequency, and (b) this excitation is provided by rotating rotor, and user of the method will vary the central frequency of rotor rotation. The basis for using this method is the fact that, at the presence of fault (for example, fatigue crack) in testing details, parameters of arising free and forced oscillations change (nonzero spectral amplitudes of higher harmonics). The new analytical dependencies of testing object oscillation parameters from the relative crack size and parameters of nonstationary excitation are received. A multidimensional testing data vector for diagnostics and evaluation of faults is proposed and investigated.

6:00

3pNSb6. An advanced field measurement system for rotorcraft flight noise. James C. Yu and Kenneth D. Wright (NASA LaRC, MS 235, Hampton, VA 23681-0001)

A Langley-developed field acoustic measurement system has been extensively employed to support the NASA aircraft and rotorcraft flight noise research programs since the early 1980s. The system was first successfully used in the NASA Forward Flight Effects on Turbofan Noise program. Starting from the late 1980s, driven by the increased demand on expanded measurement capabilities for rotorcraft flight noise, an advanced field measurement system development program was initiated to support the rotorcraft flight noise measurement, reduction, and prediction. The paper reviews the three major stages of this extensive development program: the analog measurement system stage, the digital measurement system stage, and the digital remote acquisition and storage system stage. The data processing technology associated with these different stages of the system will be presented. The paper will discuss the research drivers for the measurement system development, the development strategy used to meet the system requirement, and lessons learned at each stage of the development. Discussion will also be given on the future rotorcraft flight noise measurement challenges and the advanced measurement systems required to meet these challenges.

Session 3pPA

Physical Acoustics: Duct Acoustics II

Walter Eversman, Cochair
Mechanical and Aerospace Engineering and Engineering Mechanics, University of Missouri, 202 Mechanical Engineering, Rolla, Missouri 65401, USA

Dirk Ronneberger, Cochair
Drittes Physikalisches Institut, University of Göttingen, Burgerstrasse 42-44, D-37073 Göttingen, Germany

Invited Papers

4:20

3pPA1. Interaction between resonators and fluid motion in ducts. Dirk Ronneberger (Drittes Physikalisches Institut der Universitaet Goettingen, Buergerstrasse 42-44, D-37073 Goettingen, Germany, ro@physik3.gwdg.de)

Each time one is confronted with unwanted narrow-band noise which propagates along a duct, it suggests itself to make use of resonators in the suppression of this noise. However, resonators may be highly sensitive to superimposed mean flow: Detuning and drastic decay of the quality factor is encountered in many cases, nevertheless, also the contrary may happen, namely the increase of the acoustic energy in the resonator. This may result in self-excited oscillations or in the amplification of the incident sound. The paper gives a review of these phenomena, and it will focus on the physical effects behind these phenomena. Simple models that are based on the governing physical effects have been developed and are compared to experimental results with different configurations of resonators in flow ducts. In the case of sound amplification the amplitude of the organized motion of the fluid may become very high so that the nonlinearity of the interaction with the mean flow becomes significant. The state of knowledge and the open questions in this respect will be addressed as well.

4:40

3pPA2. Active noise control by use of an aeroacoustic instability. Björn Lange and Dirk Ronneberger (III. Phys. Inst., Bürgerstr. 42-44, D-37073 Göttingen, Germany)

Ducts that are lined with a series of equally spaced cavities exhibit strong amplification of sound waves under specific flow conditions. The amplification is caused by an aeroacoustic instability wave traveling in the boundary layer of the lining. Since the effect is coupled with a drastic variation of the static pressure drop that depends on the amplitude of incident sound, the possibility is implied to efficiently generate high intensity sound at low frequencies: An incident sound wave with harmonically varying amplitude will cause a periodic modulation of the pressure drop and thus lead to the generation of sound at the modulation frequency. Based on these observations, an aeroacoustic loudspeaker has been designed combining a lined duct section as part of a flow channel and a conventional loudspeaker. The output power of the device amounts to up to 95 dB *re*: 1 pW/Hz at Ma=0.25 for frequencies ranging between 0 and 200 Hz—an observation of some significance with regard to the fact that traditional loudspeakers tend to be rather inefficient at low frequencies. As a feasibility test, the aeroacoustic loudspeaker is used as an actuator in an active noise control setup. High attenuation of low-frequency noise is achieved.

5:00

3pPA3. Computational aeroacoustics of ducts using parallel computers. Lyle N. Long (Dept. of Aerosp. Eng., Penn State Univ., 233 Hammond Bldg., University Park, PA 16802)

This paper will discuss recent attempts at using computational aeroacoustics (CAA) algorithms on parallel computers to solve duct propagation problems. The algorithms are higher-order accurate methods for solving the Euler and Navier–Stokes equations. As computer speed increases, more and more of the physics can be simulated. This talk will discuss the current status and trends of parallel supercomputers. While hardware trends allow us to solve more complicated problems, algorithm developments are also essential. This talk will address some new methods for solving aeroacoustics problems. Most of these new developments involve hybrid schemes that couple CAA methods with integral methods or traditional CFD codes with CAA codes. Since aeroacoustics problems involve length and time scales that are beyond computer power at the present time, clever schemes must be developed for using appropriate algorithms for the various physical phenomena. One very promising scheme [J. Comput. Phys. **133** (1997)] is the nonlinear disturbance equation (NLDE) method, which uses a traditional CFD code to predict the steady-state portion of the problem, and then a higher-order method to solve for the disturbances. The steady-state portion is included in the coefficients and source terms in the NLDE. [Work supported by NASA Langley.]

5:20

3pPA4. On the exact solution of the acoustic wave equation in a parabolic velocity profile in a hard-walled duct. L. M. B. C. Campos and J. M. G. S. Oliveira (Instituto Superior Técnico, 1096 Lisboa Codex, Portugal)

The exact solution of the acoustic wave equation in a parabolic shear flow profile is obtained; the only exact solution given in the literature [Goldstein and Rice (1963); Jones (1977), (1978); Scott (1979); Koutsoyannis (1980)] is for a linear velocity profile, and the solution for the exponential shear flow is given elsewhere [Campos and Serrão (1998)]. The wave equation has three singularities, like the Gaussian hypergeometric equation, but it is of an extended type, since the singularity at infinity is irregular (all three singularities of the Gaussian hypergeometric equation are regular). The other two singularities of the present equation are regular, and one lies at the axis of the duct, and the other at the dicritical layers, where the Doppler-shifted frequency vanishes. The critical layers do not exist (they lie outside the duct) for longitudinal wave vector antiparallel to the mean flow (case I), i.e., propagation upstream in a local frame of reference. In the opposite case of longitudinal wave vector parallel to the mean flow (case II) there are three subcases, depending on whether the Doppler-shifted frequency on the axis of the duct is: (case II A) positive, i.e., critical layers are at imaginary ''distance;'' (case II B) zero, i.e., the critical layer lies on the axis of the duct: (case II C) negative, i.e., two critical layers exist in the duct. In all cases (I, II A, II B, II C) it is possible to obtain the exact acoustic field over the whole flow region by expanding around the singularities and matching solutions. Since the acoustic wave equation in a shear flow does not lead to a Sturm–Liouville problem, the eigenfunctions need not be orthogonal or complete. There is a single set of natural frequencies and normal modes in cases I, II A, and II B, but not in case II C; in the latter case, where two critical layers lie in the flow, they may separate three sets of eigenvalues/eigenfunctions, in the regions between by the critical layers and the walls.

5:40

3pPA5. Experimental verification of a radial mode analysis technique using wall-flush mounted sensors. Lars Enghardt (DLR–Institut fuer Antriebstechnik, Abteilung Turbulenzforschung Berlin, Mueller-Breslau-Str. 8, 10623 Berlin, Germany, lars.enghardt@dlr.de), Yanchang Zhang (LUK GmbH & Co., 77815 Buehl, Germany), and Wolfgang Neise (DLR–Institut fuer Antriebstechnik, 10623 Berlin, Germany)

Sound fields in the inlet and outlet ducts of axial fans, compressors, and aircraft engines propagate as higher-order acoustical modes in a wide-frequency range. Decomposition of the sound field into azimuthal and radial modes permits direct conclusions on the sound generation processes and can lead to the identification of aerodynamic source areas. An established experimental method for assessing the sound field is to circumferentially traverse a radial microphone rake over 360 degrees, to measure the sound pressure in the duct at multiple circumferential and radial positions. On the inlet side of a turbo-machine this procedure cannot be employed because the wake of the rake would disturb the inlet flow conditions of the machine and alter its acoustic characteristics. Computer simulations have shown that the radial mode structure of the sound field can also be determined by measuring the sound pressure only at the inner duct wall, but at different axial locations. In this paper, experiments are described where the sound field in the outlet duct of an axial-flow fan is measured once with the conventional radial microphone rake and a second time with wall-flush mounted microphones. Subsequent radial mode analyses are carried out for both sets of measurement data to experimentally verify the new method.

Contributed Paper

6:00

3pPA6. Experimental study of acoustic impedance of a Helmholtz resonator submitted to a grazing flow. Slaheddine Frikha, Pierre Yves Hennion, and Samir Boukhari (Laboratoire de Mecanique Physique, UPMC CNRS, Upresa 7068, France, frikha@ccr.jussieu.fr)

Helmholtz resonators are usually used in ducts or in engines inlet and exhaust systems in order to reduce radiated noise. Their efficiency may be strongly affected since they are submitted to a fully turbulent grazing flow. An experimental analysis of a branched Helmholtz resonator composed by a circular neck and a circular cavity is presented here. An attempt is made to understand the evolution of entry impedance modification with respect to mean flow and the shear layer characteristics at the vicinity of the resonator aperture. An inverse method is used to identify the impedance of 25 resonators. This method presents the advantage that it is completely nonintrusive and does not require source control. The grazing flow modifies the orifice resistance and the effective neck length. A parametric study of these corrections is performed using experimental results obtained for a set of 25 resonators and a flow Mach number varying from 0 up to 0.25. The mean flow structure is also analyzed using a numerical model. The dimensions of the tested resonators are similar to those usually used in the exhaust and inlet systems of automotive engines. That leads to a new parametric model of these corrections more suitable to engine applications.

Contributed Poster

This poster will be on display in the Poster Gallery from Thursday to Friday, 18–19 March. Authors will be at their posters from 10:00 a.m. to 12:00 noon on Thursday, 18 March.

3pPA7. On the acoustic of inverse sinusoidal and catenoidal nozzles. L. M. B. C. Campos and F. J. P. Lau (Instituto Superior Técnico, 1096 Lisboa Codex, Portugal)

The acoustic wave equation, for quasi-one-dimensional propagation, along a duct of varying cross section, containing a low Mach number mean flow, is obtained using as variables either the potential or the velocity; the ray approximation, which holds only for wavelength short compared with the lengthscales or variation of cross section and mean flow velocity, is used as a factor to reduce the wave equation to a Schrödinger form. It is shown that the latter, reduced from, for the potential, is the most convenient to study the acoustics of catenoidal and sinusoidal nozzles; it is found that these inherit respectively the filtering properties of catenoidal horns, and transparency properties of sinusoidal horns. This approach also applies to the exponential nozzle whereas, for the Gaussian nozzle, the sound field can be expressed in terms of Hermite functions, using a semi-reduced form of the wave equations. The exact solutions of the nozzle wave equation, for the four families of ducts, are plotted as amplitude and phase versus distance, for several combinations of frequency and low Mach number. The nozzle families considered include the catenoidal in the sinusoidal and exponential and the first six eigenfunctions of Gaussian nozzles. The acoustics of inverse sinusoidal and catenoidal nozzles can also be studied, without use of the preceding transformations, via the solution of modified Mathieu equation.

WEDNESDAY AFTERNOON, 17 MARCH 1999 ROOM H106, 4:15 TO 6:20 P.M.

Session 3pPPa

Psychological and Physiological Acoustics: Perceptual Processing of Cross-Spectral Information

John F. Culling, Chair
School of Psychology, Cardiff University, Cardiff CF1 3YG, UK

Chair's Introduction—4:15

Invited Papers

4:20

3pPPa1. Matching formant frequencies of complex sounds on different fundamentals. C. J. Darwin and Pascal Dissard (Exp. Psych., Univ. of Sussex, Brighton, Sussex BN1 9QG, UK)

In order to explore the ability of listeners to match formant frequencies in periodic sounds that differ in their fundamental frequency ($F0$), listeners adjusted the frequency of one formant of periodically excited one- or two-formant sounds to match the timbre of a similar target sound that could have either the same or a different $F0$. Variability of matching (s.d. of matches within each listener) was low when matching sounds were on the same $F0$. Variability increased when matching sounds had different $F0$s. However, this increase was larger for sounds with resolved harmonics than for those with unresolved harmonics. This difference may reflect the perceptual cost of estimating the spectral envelope (and formant frequency) from the excitation pattern. [Work supported by EPSRC Grant No. GR/L03422.]

4:40

3pPPa2. A ''missing-data'' model of *F*0-invariance in vowel perception. Alain de Cheveigne (LLF, Univ. of Paris 7, 2 Pl. Jussieu, Paris, France)

In steady-state voiced speech production, the vocal tract transfer function is sampled at multiples of the fundamental frequency ($F0$). At high $F0$, sparse sampling causes two problems: (a) a gradual loss of information defining the spectral shape, and (b) $F0$-dependent distortion due to aliasing. If the shape of the spectral envelope contains lag-domain components (spatial frequencies) beyond the Nyquist limit, they are folded relative to the Nyquist limit and mixed with in-band components. The Nyquist limit ($T0/2$, where $T0=1/F0$) depends on the spacing between sampling points along the spectral envelope, and thus on $F0$. Distortion is thus $F0$-dependent, and all the more severe as $F0$ is high. Smoothing or interpolation are ineffective in dealing with this problem, and cannot produce an $F0$-invariant pattern. A solution is proposed based on the concept of ''missing feature theory,'' recently proposed for speech recognition. Pattern matching is limited to available data ($F0$-spaced sample points) using an $F0$-dependent weighting function. All other points are ignored. The model is proposed in two versions, one that operates on the short-term spectrum or excitation pattern, the other on the autocorrelation function. The model ensures $F0$-independent vowel identification, at the cost of an $F0$ estimate.

5:00

3pPPa3. Evidence of a dissociation between the mechanisms governing the perceptual grouping of spectral components and the computation of low pitch. Brian Roberts and Jeffrey M. Brunstrom (School of Psych., Univ. of Birmingham, Edgbaston, Birmingham B15 2TT, UK, b.roberts@bham.ac.uk)

The perceptual fusion of harmonically related partials is often assumed to result from the operation of a template mechanism that is responsible for computing low pitch. This dual-role hypothesis has been tested using frequency-shifted complexes. These sounds are inharmonic, but preserve a regular spectral pattern of equal component spacing. Stimuli had a nominal fundamental ($F0$) frequency of 200 Hz (roving range $\pm 20\%$), and were frequency shifted either by 25.0% or 37.5%. Three consecutive components (6–8) were removed and replaced with a sinusoidal probe, located at one of a set of regularly spaced positions spanning the gap. On any trial, subjects heard a complex tone followed by an adjustable pure tone in a continuous loop. Subjects were well able to match the pitch of the probe unless it corresponded with a position predicted by the spectral pattern of the complex. In contrast, hit rates were not depressed for probes positioned at integer multiples of the $F0$(s) corresponding to the low pitch(es) of the complex, which were predicted from previous data [Patterson, J. Acoust. Soc. Am. **53**, 1565–1572 (1973)]. The findings suggest that separate mechanisms are responsible for the computation of low pitch and for the perceptual grouping of partials.

5:20

3pPPa4. Auditory processing of coherent and incoherent frequency modulation. Robert P. Carlyon (MRC Cognition and Brain Sci. Unit, 15 Chaucer Rd., Cambridge CB2 2EF, England, bob.carlyon@mrc-cbu.cam.ac.uk)

When two elements of a visual array move coherently, there is a strong tendency to group them perceptually. This has prompted several authors to suggest that acoustic frequency components which undergo coherent FM should be perceptually fused, and that those which are modulated incoherently should be segregated. This paper will review the mounting body of evidence demonstrating that, once a number of co-varying cues are controlled for, the auditory system is insensitive to the difference between coherent and incoherent FM. Such cues include the greater inharmonicity, smaller swings in average frequency, and more salient distortion products which can occur with incoherent compared to coherent modulation. In addition, new evidence will be presented showing that listeners can be more sensitive to one form of incoherent FM than to another: Opposite-direction quasi-linear frequency sweeps imposed on two carriers are more detectable when the frequency of the lower component decreases and that of the higher component increases than vice versa. This occurs even though the frequency sweeps imposed on the individual components are equally detectable when those components are presented in isolation, and even though within-channel interactions are masked by noise.

Contributed Papers

5:40

3pPPa5. Searching for a time window for timbre: Dynamic spectral profiles. M. E. H. Schouten and W. J. M. Peeters (Res. Inst. for Lang. and Speech UiL-OTS, Utrecht Univ., Trans 10, 3512 JK Utrecht, The Netherlands, bert.schouten@let.uu.nl)

Subjects were asked to match resonance glides, of various durations and sweep widths around 1000 Hz, with two connected steady-state resonances whose frequencies could be controlled independently. The expectation was that short resonance glides (below 100 ms), would give rise to single, apparently stationary, perceptual events, so that the two matching steady-state patterns would not rise or fall. Long glides, on the other hand, were expected to be perceived as rising or falling and to be matched accordingly. It was hoped that this would provide a basis for an explanation of diphthongs as unitary percepts. The resonances formed part of dynamic spectral profiles and consisted of single formantlike peaks swept along the top of a spectral base, consisting of 25 harmonically or logarithmically spaced components from 200 to 5000 Hz. There was an effect of duration, although it interacted with sweep width. At durations shorter than about 120 ms, subjects placed the two steady profiles that they had to match with the dynamic profile, much closer together than with durations over 120 ms; however, this only occurred if sweep width was more than 600 Hz.

6:00

3pPPa6. A spectral layer model in speech and music perception. Werner A. Deutsch (Austrian Acad. of Sci., Liebiggasse 5, A-1010, Vienna, Austria, wad@kfs.oeaw.ac.at)

According to a model of the peripheral hearing system establishing a masking and overmasking paradigm, speech and music signals have been split into several spectral layers by means of spectral subtraction. Spectral components below the so-called psychoacoustical irrelevance threshold are eliminated in a first processing step. The resulting signal, which exhibits no noticeable difference to the unprocessed one, is fed into an overmasking procedure applying flattened hearing masking functions. This action implements a kind of a spectral peak detector device. Consequently, the discrimination between spectral peaks (auditory figure) and background components, especially in reverberant environments, is improved. As a result, different audible signal parts according to different spectral layers are obtained, separating spectral peaks and weaker spectral components. In a certain range, both parts of speech and music signals are equally intelligible. In music, leading voices can be extracted and separated from the orchestra sound. Recent research indicates that this type of figure-background discrimination based on the dynamic characteristics of the acoustic signal only can exhibit several perceptually relevant features in listeners with normal hearing as well as in subjects with sensineural hearing impairment.

Session 3pPPb

Psychological and Physiological Acoustics: Sound Quality

Gerhard Krump, Chair
Harman Audio Electronic Systems GmbH, Schlesische Strasse 135, D-94315 Straubing, Germany

Contributed Papers

4:20

3pPPb1. Interior car sound quality—Assessment of acceleration noises. Reinhard Weber (Dept. of Phys., Carl-von-Ossietzky Univ., D-26111 Oldenburg, Germany)

Investigation of booming noise effects was the reason for the present study. Interior noises of six different cars accelerating from 1500 to 6000 rpm at third gear (full load) were presented over headphones. Seventy normal-hearing subjects (approximately one-third males and two-thirds females) aged from 20 to 60 years (at least 15 subjects per decade) took part in two experiments. After an initial orientation phase, preference judgments were made using a paired comparison paradigm. In experiment 2, the noises were assessed on a bipolar categorical scale (*disagreeable/agreeable*) with nine subdivisions. Immediately after the experiments, an interview was conducted to learn about the subjects' impressions about the noises. The preference data were analyzed using MDPREF and compared to the categorical judgment data for different subsets of subjects. The results on subjective data will be presented, together with a correlation analysis on their relationship with a number of acoustical and psychoacoustical signal parameters (level, loudness, sharpness, fluctuation strength, roughness).

4:40

3pPPb2. The influence of sound quality on expected visual impression. Monica M. Söderholm (Electrolux Resesearch & Innovation, S-105 45 Stockholm, Sweden, monica.soderholm@notes.electrolux.se) and Daniel Västfjäll (Chalmers Univ. of Technology, S-412 96 Göteborg, Sweden)

Information from visual and auditory systems is often linked. One example of the cross-modal connection between sound and visual experience is different materials that easily can be identified by their sound quality. The purpose of this investigation was to analyze the anticipated visual impression of three vacuum cleaners when listening to the product. The participants in the listening test where asked to describe the visual impression of the vacuum cleaners and also how they thought the vacuum cleaner sounded like with own words. The 24 listeners were both female and male of different ages and the vacuum cleaners were judged live. Often something that is large, for instance, a truck compared to a car, does produce more sound. The experience that large products are louder than small products is an influence when listening to vacuum cleaners. The listeners expected a large vacuum cleaner when listening to a rather loud vacuum cleaner. There was a unanimous opinion among the participants that a loud vacuum cleaner was ugly, had a box shape, and was old. The vacuum cleaners that were described to have a nice sound were described as small and round with a nice design and nice colors.

5:00

3pPPb3. Comparison of two semantic-differential test methods. Etienne Parizet (Renault, 67 rue des bons raisins, 92508 Rueil-Malmaison Cedex 9, France, etienne.parizet@renault.com)

Two methods for conducting a multidimensional test were investigated. In the first and classical one, a sound (or a pair of sounds) is presented to the subject, who has to evaluate it (or compare the two sounds) for the various semantic parameters. In the second one, the test is repeated for each parameter (i.e., subjects must evaluate the whole set of sounds for the first parameter, then again for the second one, and so on). These two methods were compared on the basis of five diesel engine noises in small cars driving at idle. Sounds were compared in pairs for seven parameters (pleasant, loud, etc.). The characterization of sounds thus obtained was similar for the two methods. The second one proved to be more accurate (the accuracy is evaluated on the basis of repetition and triadic errors) and with a shorter duration than the first one, because listeners are concentrated on the selected sound parameter while hearing a new stimulus. Therefore, this method is recommended for conducting semantic differential tests.

5:20

3pPPb4. About perceptivity of narrow-band frequency response variations of loudspeakers. Gerhard Krump (Harman Audio Electron. Systems GmbH, Schlesische Str. 135, D-94315 Straubing, Germany, gkrump@harman.de)

Many loudspeakers show peaks and gaps at 1 kHz caused by the connection of the hard cone and soft surround, which produces interferences and complex vibrational modes. Great efforts are made by the speaker manufacturer to avoid this by changing the surround geometry and material, whereas primarily knowledge about the perceptive limits of the peaks and gaps in frequency response would be necessary. For this investigation line spectra with equal amplitudes and statistical phases between 1 Hz and 20 kHz were calculated by a personal computer. At 1 kHz spectral enhancements or gaps with a bandwidth of 1 Hz or of a half, one, or two critical bands were realized with five different critical band levels. Ten test persons had to compare the first line spectrum with equal amplitudes (anchor) with the second signal with spectral changes in a yes–no procedure presented by an earphone with free-field equalizer at a SPL of 70 dB. The just-noticeable changes in spectral envelope are different for enhancements and gaps and depend on the bandwidth and the critical band level of the variations. They can be explained with calculated masking patterns and literature data.

5:40

3pPPb5. Determination of hearing properties and their connection to psychoacoustical parameters. Kai Johannsen and Holger Prante (Inst. of Tech. Acoust., Einsteinufer 25, 10587 Berlin, Germany, johannsen@mach.ut.tu-berlin.de)

The sound quality of products is often evaluated in hearing experiments using the semantic differential and a subsequent factorial analysis. In this study the method is applied to determine basic hearing properties. In order to achieve optimal results of the hearing experiment, special interest has been taken in the choice of adjectives and sounds. This selection is based on the results of a previously conducted survey of sound attributes. The selected 25 sounds were recorded using an artificial head and presented binaurally to a jury of 20 adults with normal hearing. A factorial analysis of the ratings on 24 attribute scales produced six factors representing basic perceptive cognitive and emotional hearing dimensions. In a last step connections between these dimensions and psychoacoustical parameters calculated from the sounds were evaluated using an analysis of correlation. Although the results show high correlations between loudness, sharpness, and pitch strength and equivalent attributes, no such connections could be found for the psychoacoustical roughness and fluctuation strength. In order to find better-correlated parameters, other calculation methods for these properties are investigated.

6:00

3pPPb6. New approach in measuring auditory source width. Jörg Becker, Markus Sapp, and Frederik Görges (Inst. of Commun. Eng., Aachen Univ. of Technologie, 52056 Aachen, Germany)

Depending on the acoustical surrounding sound sources appear to be broadened. This spatial impression can be rated by a quantity called auditory source width. In this paper a new method for determining this auditory source width is presented. The system is based on the reproduction of an artificial head recording of the examined sound field mixed with a pair of virtual acoustic pointers. These pointers can be moved by test persons to fit the left and right border of the sound source whose ASW has to be rated. The acoustical pointers are implemented as digital signal generators followed by real-time HRTF filters, measured in azimuth steps of 2 deg and cross faded between the directions. Investigations on suitable temporal and spectral shapes of the pointer signals have been made to minimize the localization blur of the pointer. The HRTF measurements and the recordings were done with different artificial heads in order to examine their influence on the determined ASW. Furthermore the influence of different sound field reproduction systems—headphone and crosstalk cancellation—are examined.

WEDNESDAY AFTERNOON, 17 MARCH 1999 ROOM H2036, 4:20 TO 6:20 P.M.

Session 3pSA

Structural Acoustics and Vibration: Structural Vibrations

Jacek Jarzynski, Cochair
George W. Woodruff School of Mechanical Engineering, Georgia Institute of Technology, Atlanta, Georgia 30332-0405, USA

David Feit, Cochair
Carderock Division, Naval Surface Warfare Center, 9500 MacArthur Boulevard, West Bethesda, Maryland 20817, USA

Contributed Papers

4:20

3pSA1. Torsional waves in a viscoelastic layer. Qingchun Li and Jacek Jarzynski (The George W. Woodruff School of Mech. Eng., Georgia Inst. of Technol., Atlanta, GA 30332-0405, jacek.jarzynski@me.gatech.edu)

The objectives of this study are first to examine experimentally the propagation of torsional waves in a viscoelastic material, and second to use these data to determine the complex shear modulus of the material. The viscoelastic material used in this study is neoprene rubber. A magnetic drive is used to generate a transient, one-cycle, torsional wave in a brass rod, and this wave is transmitted into a layer of neoprene rubber bonded to the rod. A fiber-optic laser Doppler vibrometer is used as a noncontact probe to measure the torsional wave transmitted through the neoprene layer. The experimental data are compared with predictions from a theoretical model [D. P. Thomas, Int. J. Eng. Sci. **6**, 565–570 (1968)]. Also, the complex shear modulus is determined from a least-square fit of the theoretical model to the experimental data using the downhill Simplex method. Another application of torsional waves is to nondestructive testing of materials, particularly for testing the strength of adhesive bonds between layers. [Work supported by ONR.]

4:40

3pSA2. Estimates of dynamic strain and stress in pipes by measured average vibration velocity. Svante Finnveden (Dept. of Vehicle Eng., KTH, SE-100 44 Stockholm, Sweden, svantef@fkt.kth.se) and Roger Pinnington (Univ. of Southampton, Southampton SO17 1BJ, England)

A velocity method for estimating dynamic strain and stress in pipe structures is investigated. With this method predicted or measured spatial average vibration velocity and theoretically derived strain factors are used to estimate maximum strain. The nondimensional strain factor is defined as the maximum strain times the ratio of the sound velocity to the spatial rms vibration velocity. Measurements are made confirming that this is a descriptive number. Using a spectral finite-element method, numerical experiments are made varying the pipe parameters and considering all 16 possible homogeneous boundary conditions. While indicating possible limitations of the method when equipment is mounted on pipes, the experiments verify the theoretical results. The velocity method may become useful in engineering practice for assessments of fatigue life.

5:00

3pSA3. On the dynamic interaction of a pipe conveying fluid with an elastic resisting medium. Ventzeslav A. Dzhupanov, Peter A. Djondjorov, and Vassil M. Vassilev (Inst. of Mech., Bulgarian Acad. of Sci., Sofia, Bulgaria)

The problem of the dynamic stability of pipes conveying high-speed fluid and lying on an elastic foundation has been a subject of significant interest during the past 30 years due to the broad application of pipes as structural components in different technologies. The present study contributes to the solution of this problem, suggesting a new model of the foundation—an infinitely deep elastic stratum, whose width is equal to the length of the attached pipe. The material of the foundation is supposed to be a homogeneous and isotropic one. Its dynamic behavior is considered in the context of linear elasticity. The pipe vibration is governed by the usual Bernoulli–Navier–Mohr theory. An approximate solution of the respective mathematical problem is obtained applying Galerkin's method. As a result, the influence of the medium physical characteristics to the flutter dynamic stability of cantilevered pipes through the pair of acoustic velocities is examined.

5:20

3pSA4. Investigation at a top counter weight of a washing machine. Ulrich Heise (Noiselab, FHP Motors GmbH, Klingenbergplatz 1, 26133 Oldenburg, Germany) and Wolfgang Harbich (Noiselab, 13599 Berlin, Germany)

During the development of a new washing machine a problem came up in spite of the durability of the newly designed top counter weight. The top counter weight is necessary to balance the drum of the machine. The problem was caused by the dynamical behavior of the system. A modal analysis was made at the compensation weight in the machine. Several different modes and eigenvalues were detected. The disturbing mode was found. It was caused by the stiffness of the fastening and the mass of the weight. The top counter weight was fastened in the axial direction of the drum. The disturbing mode was eliminated due to the change of fastening from axial to radial fastening. The problem is now solved. Another point of view are the other eigenvalues of the weight. The size of the weight looks like a xylophone bar and, in the same manner, it can vibrate. These modes of the weight itself are not disturbing modes, because the excitation forces are too small in this area and at this frequency range for exciting the compensation weight.

5:40

3pSA5. A mixed use of finite element and geometrical techniques. Philippe Jean (Centre Scientifique et Technique du Bâtiment, 24 rue Joseph Fourier, 38400 St. Martin d'Hères, France)

The finite-element method is limited to either small geometries or to the low-frequency range, whereas geometrical approaches are best applied at medium and high frequencies, but do not take vibrating surfaces into account. When the vibrating boundaries of a volume are only a small part of the total boundary, it is worth combining the two methods. By using geometrical methods to compute a Green's function that includes all wave reflections on the surfaces of the volume, it is possible to restrict the integral representation of the pressure field to the vibrating surfaces. The surfaces to be meshed will be reduced to surfaces with known velocity fields. This approach offers a means of reducing computation times. It has been applied to large volumes corresponding to a room with a vibrating concrete wall and to a train with a vibrating window.

6:00

3pSA6. Irregular modes at the endshield of a heating system motor. Ulrich Heise (Noiselab, FHP Motors GmbH, Klingenbergplatz 1, 26133 Oldenburg, Germany)

Nowadays, more and more modern heating systems are not installed in separated rooms, so the expectation of noise comfort has been increased for the last years. A noise and vibration optimization was made at an electric motors b-sided endshield. Sometimes, the old endshield emitted airborne noise. This was caused by the structure-borne noise of the bearings together with a mode of the endshield. A modal analysis was made to detect the disturbing mode. The amazing thing of this test was that the (0,1) mode frequency has a higher resonance frequency as the (1,1) mode. Normally the (1,1) mode frequency has a 1.594 higher frequency than the (0,1) mode resonance [N. H. Fletcher and T. D. Rossing, *The Physics of Musical Instruments* (1991), pp. 69–71]. The b-sided bearings can make a mass coupling from the rotor to the endshield in radial direction, but not in this way in the axial direction. The (1,1) mode of the endshield had nearly the same structure-borne amplitude as the (0,1) mode, but the (1,1) mode does not transmit airborne noise. This depends on the mechanical dimensions of the (1,1) mode, because this mode is working with its dimensions on an acoustical short circuit on air.

Session 3pSC

Speech Communication: Psychoacoustic Methods in Speech Recognition II

Birger Kollmeier, Cochair
AG Medizinische Physik, Universität Oldenburg, Postfach 2503, D-26111 Oldenburg, Germany

Hynek Hermansky, Cochair
Oregon Graduate Institute of Science and Technology, Beaverton, Oregon 97006-8921, USA

Chair's Introduction—4:15

Contributed Papers

4:20

3pSC1. Application of a roughness model to pathological voices. Robert Reuter (Inst. Electron., Techn. Univ., Einsteinufer 17, D-10587 Berlin, Germany, rreuter@tubife1.ee.tu-berlin.de) and Hanspeter Herzel (Humboldt Univ., D-10115 Berlin, Germany)

Irregularities in voiced speech are often related to the intrinsic nonlinearities in the vibrations of the vocal folds. Desynchronization of vibratory modes can induce nonlinear phenomena such as subharmonics, biphonation (two independent pitches), and deterministic chaos. The resulting complex signals exhibit various amplitude and frequency modulations and are, therefore, perceived typically as rough voices. In clinical studies of pathological voices perceptive roughness scores are widely used. So far, however, no satisfactory correlation of ratings of roughness and acoustic parameters has been found. In this presentation a modified Aures model for the quantification of roughness is introduced. It is exemplified that subharmonics lead to high roughness scores whereas the roughness of biphonation depends strongly on the two frequencies. Finally, a set of 120 perceptually evaluated pathological voices is studied. It turns out that the roughness score obtained from the psychoacoustic model is stronger correlated to the ratings of phoniatricians than conventional perturbation measures such as jitter and shimmer.

4:40

3pSC2. How children recognize spoken words in speech recognition threshold assessment. Lebel Caroline (Institut Raymond-Dewar, 3600 Berri, Montreal, QC H2L 4G9, Canada) and Picard Michel (Universite de Montreal, Montreal, QC H3C 3J7, Canada)

The purpose of this study was to investigate the potential influence of language context effects on the speech recognition threshold (SRT) in children of different ages. To determine the respective contributions of audibility and linguistic factors to the SRT, the speech intelligibility index (SII), and indices *k* and *j* as proposed by Nittrouer and Boothroyd [J. Acoust. Soc. Am. **87**, 2705–2715 (1990)] were calculated for the following conditions: (1) SRT using an open-set response format; (2) SRT using a closed-set response format (dissimilar foils to increase predictability); and (3) SRT using test words at the beginning of a short sentence. Listeners were three groups of 24 normally hearing children in the first, third, and fifth grades, respectively. Results indicated that SII and factor *j* decreased significantly and factor *k* increased proportionally as a function of both lexical and sentence-level context effects in all groups. This suggests that audibility factors are less critical in the facilitating presence of language contexts. The largest effect was shown for lexical context effects with predictable outcome of decreased SRTs. These findings are compelling evidence of language context effects playing a significant role in school-age children required to recognize speech at barely audible levels.

5:00

3pSC3. Silicon cochlea: A digital VLSI implementation of a quantitative model of the auditory system. Matthias Brucke, Wofgang Nebel (Univ. of Oldenburg, Computer Sci. Dept., VLSI Group, 2611 Oldenburg, Germany), Alexander Schwarz, Bärbel Mertsching (Univ. of Hamburg, Hamburg, Germany), Martin Hansen, and Birger Kollmeier (Univ. of Oldenburg, Oldenburg, Germany)

In this paper a digital VLSI implementation of a quantitative model of the auditory system is presented, which includes several processing stages physiologically and psychoacoustically motivated by the function of the human ear. The model was successfully applied to a wide range of applications from psychoacoustical experiments to speech recognition. The hardware design is derived from a C/C++ notation of the algorithms using floating point arithmetics. One application of the model is used to determine the necessary internal precision of the computations for a transfer into a version suitable for a hardware implementation using fixpoint arithmetics. This application provides a very valid test bench since the significant speech processing features of the model are proofed by computing an objective speech quality measure. The processing scheme is divided into designs for two FPGAs and will be converted into ASICs in a later version. The implementation of the model as dedicated hardware provides efficient coprocessing power and allows implementations of complex auditory-based speech processing algorithms in real time because the chipset performs substantial parts of the necessary calculations.

5:20

3pSC4. Entropy rate based speech segmentation. Wolfgang Wokurek (Inst. of Natural Lang. Processing, Exp. Phonet., Stuttgart Univ., Azenbergstrasse 12, Stuttgart, 70174, Germany, wokurek@ims.uni-stuttgart.de)

The sequence of estimates of the speech signal's entropy rate is investigated as a potential basis for speech segmentation. Raising and falling edges of that entropy rate curve and its maxima and minima are considered as candidates for segment boundaries. These prominent points are compared to the phonetic segment boundaries and to acoustic landmarks [S. A. Liu, J. Acoust. Soc. Am. **100**, 3417–3430 (1996)]. The comparison is made using the ''Kiel corpus of read speech'' which is a phonetically manually labeled corpus of German utterances. The evaluation considers the entropy rate labels against the background of the phone segments. In particular the position and the count of the entropy rate labels within each phone are appraised. The average results are reported both as totals and broken down into phone classes and phones. The frame duration of the entropy rate estimation controls the smoothness of the curve and hence the label count per phone. A similar evaluation relates the entropy rate labels to the acoustic landmarks.

5:40–6:20 Discussion

Session 3pSP

Signal Processing in Acoustics and Engineering Acoustics: Binaural Technology II

Mahlon Burkhard, Cochair
Sonic Perceptions, Inc., 6964 Kennsington Road, Brighton, Michigan 48116, USA

Jens Blauert, Cochair
Communication Acoustics, Ruhr-Universität Bochum, D-44780 Bochum, Germany

Chair's Introduction—4:35

Contributed Papers

4:40

3pSP1. Implementation issues in the development of a real-time, Windows-based system to study spatial hearing. Joel D. Miller (Raytheon, NASA Ames Res. Ctr., M.S. 262-6, Moffett Field, CA 94035-1000, jdmiller@mail.arc.nasa.gov), Jonathan S. Abel (San Jose State Univ., NASA Ames Res. Ctr., Moffett Field, CA 94035-1000), and Elizabeth M. Wenzel (NASA Ames Res. Ctr., Moffett Field, CA 94035-1000)

As a tool to study spatial hearing, a customizable real-time 3-D-audio and virtual acoustic environment rendering system, Sound Laboratory (SLab), was developed. Design goals for this system included flexibility, extensibility, maintainability, and a fast development cycle per experiment. SLab is a Windows application composed of five distinct software layers: Application programming interface (API), 3D projection, signal flow translation, signal routing and processing, and digital signal processing library. The acoustic scene, including listener, source, and environment characteristics, is specified in the API layer and translated in the 3-D projection layer to geometric quantities, such as range and arrival angle, for each path rendered between the source and listener. The geometry and head-related transfer function coefficients are rendered using a set of parallel finite impulse response filters and delay lines built on Intel's Signal Processing Library. This rendering architecture provides the flexibility and the extensibility required for psychoacoustic experimentation, while the modular nature of the programming interface ensures maintainability and quick development of new experiments. The psychoacoustic parameters to be manipulated, the signal flow diagram, and the five software layers are discussed in detail, and various implementation issues are examined.

5:00

3pSP2. Computational model of an individual head-related transfer function using the BEM. Brian F. G. Katz[a] (Acoust. Dept., Penn State Univ., State College, PA 16801)

The head-related transfer function (HRTF), determined by the complex geometry of the pinnae and head, is the primary research and commercial tool for exploring and exploiting 3-D auralization and auditory localization. Research into the determining characteristics of the HRTF is difficult, as the anatomical variations between individuals are many. These variations make comparisons between individuals less than ideal for determining the relation between structure of the individual and components of the HRTF. This paper will discuss an investigation into the use of a geometrical model of an individual to calculate the HRTF. The calculation utilizes the boundary element method (BEM). As a tool, the use of a computer model allows for selected variations in the individual's anatomy and direct observation of the results, a difficult task in experimental measures. Previous work by the author discussed the variability in experimental measurement techniques of the HRTF. Comparisons are made between the model results and these HRTF measurements for the same individual. Some preliminary variations to the model and their effects are also discussed. Computational results show good agreement with the general trends of the measurements and the frequency limitations of the computation. [a] Currently at Artec Consultants, Inc., 114 W. 26th St., New York, NY 10001.

5:20

3pSP3. Auditory perception of reverberant surroundings. Jesper Sandvad (Waisman Ctr., Univ. of Wisconsin, Madison, WI and Acoust. Lab., Aalborg Univ., Denmark)

Three experiments on perception of reverberant surroundings were performed. In the first experiment, listeners were presented with binaural recordings of a speech signal and a set of photographs taken in different rooms, and were asked to point out where each recording was made. Most listeners performed very well in this task (average number of correct answers was 70%), showing that reverberation contains information on room properties that the listeners are able to extract. In the second experiment, listeners were asked to judge the relative size of different rooms by listening to the recorded signals. The results show substantial individual differences, with some listeners being close to veridical performance while others had only a few correct answers. A scaling analysis suggests that some listeners use the direct/reverberant energy ratio, while others use reverberation time as a cue for room size. In the third experiment, artificial reverberation generated by a geometric room model (including individual reflections) and from a stochastic model (controlling only energy measures) were compared with signals generated directly from measured room impulse responses. The results show comparable performance, suggesting that energy measures are the most important for assessing information on room parameters. [Work supported by ONR Grant No. N00014-96-1-0675.]

5:40

3pSP4. Comparison of wideband LMS, subband LMS, and a nonlinear entropic neural approach to adaptive noise cancellation for speech enhancement. P. W. Shields, M. Girolami, and D. R. Campbell (Dept. of Electron. Eng. and Phys., Univ. of Paisley, High St. Paisley, Renfrewshire PA1 2BE, Scotland, paul@diana22.pailsey.ac.uk)

An empirical comparison of three adaptive algorithms for speech enhancement in noisy reverberant conditions is presented. The subband least mean square (LMS) [E. Toner and D. R. Campbell, Speech Commun. **12**,

3p WED. PM

253–259 (1993)] and minimum entropy noise reduction schemes [M. Girolami, Electron. Lett. **33**(17), 1437–1438 (1997)] are compared with a reference wideband LMS approach [S. D. Stearns and R. A. David, *Signal Processing Algorithms* (Prentice–Hall, Englewood Cliffs, NJ, 1988)]. All three methods were applied to the enhancement of speech corrupted with speech-shaped noise. The schemes were tested using simulated anechoic and real-room reverberant ($T_{60}=0.3$ s) environments. The anechoic and real-room recordings were binaural including head shadow and diffraction effects. The subband LMS adaptive processing scheme uses the LMS adaptive noise cancellation algorithm in frequency-limited subbands. The inputs from each microphone are split into 16 contiguous subbands using a cochlear distribution according the function provided by Greenwood [J. Acoust. Soc. Am. **87**, 2592–2605 (1990)]. Each frequency-limited subband is processed using a LMS adaptive noise cancellation filter operating in an intermittent or continuous mode depending on input signal characteristics. The neural network approach is motivated by temporally sensitive hebbian super-synapses, which may form sparse representations based on commonly occurring spatio-temporal input patterns. The results for real-room signals demonstrate statistically equivalent performance of the subband LMS and wideband neural method, both of which prove superior to the wideband LMS algorithm.

6:00

3pSP5. Evaluation of the air particle velocity signal from the binaural pressure impulse response. Domenico Stanzial (CIARM-CNR c/o Cemoter Acoust. Dept., Via Canal Bianco 28, I-44044 Cassana, Ferrara, Italy) and Davide Bonsi (CIARM c/o Univ. of Ferrara, I-44100 Ferrara, Italy)

From the Lagrangian theory in linear acoustics one clearly infers that the generalized momenta of the sound field are the acoustic pressure and the three components of the air particle velocity. This means that only through the knowledge of the full set of these four quantities a complete physical identification of the sound field can be achieved. The binaural technology represents an important tool for this goal, since it offers a method for reconstructing the pressure sound field by means of a couple of pressure impulse responses measured in two close points. An additional improvement of the binaural signal processing can be obtained using the two pressure input signals for evaluating the velocity component along the direction determined by the measurement points. First the velocity impulse response component is evaluated by means of the Euler equation and then, by convolving this signal with the usual anechoic signal, the velocity is reconstructed. In this paper the rigorous mathematical procedure for accomplishing the above task is presented.

WEDNESDAY AFTERNOON, 17 MARCH 1999 ROOM H104, 4:40 TO 6:20 P.M.

Session 3pUWa

Underwater Acoustics: Sediment Acoustics

F. Michael Pestorius, Cochair
Applied Research Laboratories, University of Texas, Austin, Texas 78713-8029, USA

Nicholas G. Pace, Cochair
SACLANT Undersea Research Centre, Viale S. Bartolomeo 400, 19038 La Spezia, Italy

Contributed Papers

4:40

3pUWa1. Volume scattering realizations from ocean sediment sound-speed and density inhomogeneities. Kevin D. LePage (SACLANT Undersea Res. Ctr., Vl. S. Bartolomeo 400, 19138 La Spezia, Italy) and Henrik Schmidt (MIT, Cambridge, MA 02139)

Synthetic scattered field calculations can serve as a useful tool for evaluating the practicality of estimating bottom scattering properties from *in-situ* measurements. Here the temporal and angular characteristics of early time reverberation from volume inhomogeneity scatterers in the sub-bottom are investigated using perturbation theory in the framework of a spectral integral approach. In order to model realistic sediments more accurately, the theory treats the scattering from both sound-speed and density fluctuations in the presence of a background sound-speed gradient. To allow the simulation of realistic experimental geometries, the scattered field is propagated to various receivers through a general multilayered waveguide. Results show that there are several distinctive characteristics of the fields scattered by the different mechanisms which depend both on the scattering properties of the bottom and the unperturbed properties of the overall waveguide.

5:00

3pUWa2. In-sediment coherence measurements in a very shallow-water area. Joseph L. Lopes, Iris C. Paustian, and John S. Stroud (Coastal Systems Station, Naval Surface Warfare Ctr., Code R21, 6703 W. Hwy. 98, Panama City, FL 32407-7001)

A measurement was conducted in a very shallow-water (VSW) region to investigate acoustic propagation into a sandy bottom. The measurement utilized several acoustic sources and two identical hydrophone arrays. The sources were mounted onto a stationary sonar tower complete with horizontal pan and vertical tilt motors. Each hydrophone array consisted of four transducers that were buried via water-jetting methods approximately 10 m from the sonar tower. One array was situated such that the projected acoustic beam was parallel to the rippled structure associated with the sandy bottom, while the other was located where the transmitted beam was perpendicular to the rippled structure. Results of the in-sediment coherence data will be presented as functions of hydrophone burial depth and range in the frequency range between 30 and 150 kHz for the two buried arrays.

5:20

3pUWa3. Sediment critical angle estimation via *in situ* acoustic measurements. Alain Maguer, Warren L. J. Fox, Edoardo Bovio (NATO SACLANT Undersea Res. Ctr., Viale San Bartolomeo 400, 19138, La Spezia, Italy), and Henrik Schmidt (MIT, Cambridge, MA 02139)

The basic physics of sound penetration into ocean sediments is a current area of active research since a good understanding of this phenomenon is essential for designing sonar systems that can detect, localize, classify, and identify buried objects. The sound speed of the sediment is a crucial parameter since the ratio of sound speeds at the water–sediment interface determines the critical angle. Sediment sound speed is typically measured with core samples using high-frequency (100's of kHz) pulsed travel time measurements. Simulations using Biot theory and taking into account sediment permeability have shown that there may be a significant frequency dependence to sediment sound speed in the range 1–100 kHz. Here, sediment sound speed and critical angle estimation are investigated through the analysis of *in situ* acoustic measurements. Acoustic energy in the frequency range 2–16 kHz was directed toward a sandy seabottom, and a buried 14-element hydrophone array measured the incoming signals. The critical angle is estimated by analyzing both the variations of the penetration ratios and signal arrival times versus frequency, burial depth, and grazing angle. The influence of bottom roughness and sonar beamwidth on the penetration ratio is also investigated.

5:40

3pUWa4. Bulk viscidity model in acoustics of bubbly water-saturated soil. Isaac Shreiber (Inst. for Industrial Math., Hanachtom 4/24, 84311 Beer-Sheva, Israel, isaak@indigo.cs.bgu.ac.il)

Recent experimental studies of acoustic wave propagation in water-saturated soil showed that the shock wave structure in the medium is similar to acoustic waves in bubbly liquids; namely, shock waves in the medium have an oscillating profile and strong attenuation of amplitude. The main physical reasons preventing the generalization of bubbly liquid acoustics in this case are that bubble expansion in unlimited space differs from bubble expansion in porous media, and the most delicate moment of this generalization is how to define the mixture pressure, what the mixture pressure is, and how it corresponds to pressure in the bubbles and relates to bubble dynamics. The goal of this communication is to show how to generalize the bubbly liquid acoustics in the water–bubbles–sand case with the help of the cell-model approach. The cell model is used for the Rayleigh equation derivation for a single bubble dynamics in a porous medium, and the governing equations for nonlinear acoustic waves are derived. The obtained canonical equations can explain some experimental data of three-phase media acoustics.

6:00

3pUWa5. A mixed wave finite-element approach for solving Biot's poroelasticity equations in acoustics. Franck C. Sgard (LASH, DGCB URA CNRS 1652, ENTPE-Rue Maurice Audin, 69518 Vaulx-en-Velin Cedex, France, Franck.Sgard@entpe.fr), Noureddine Atalla, and Raymond Panneton (Univ. de Sherbrooke, QC J1K 2R1, Canada)

The use of finite-element models for solving Biot's poroelasticity equations often leads to large frequency-dependent systems. Recently, the authors have investigated the use of a selective modal analysis to decrease the size of large finite-element models involving poroelastic structures. The method used a dual real modal basis associated with the skeleton *in vacuo* and the fluid phase occupying the volume of the porous material to approximate the $\{U,p\}$ variables. However, this method converges poorly due to the importance of the damping brought in by the porous material. In this paper, an alternate reduction technique, based on a plane waves expansion method combined with a finite-element approach, is investigated in the case of a single porous layer. The theory behind the technique, together with numerical examples illustrating the performance of the approach, will be presented. [Work supported by Centre Jacques Cartier.]

WEDNESDAY AFTERNOON, 17 MARCH 1999 ROOM H2053, 4:20 TO 6:20 P.M.

3p WED. PM

Session 3pUWb

Underwater Acoustics: Scattering from Underwater Structures

George V. Frisk, Chair
Woods Hole Oceanographic Institute, Woods Hole, Massachusetts 02543, USA

Contributed Papers

4:20

3pUWb1. Influence of sound–structure interaction on backscattering amplitude in underwater acoustics. H. Peine (FWG, FB 331, Klausdorfer Weg 2-24, 24148 Kiel, Germany)

Sea-based backscattering experiments were carried out in the frequency range from Helmholtz numbers (ka) 10 to 30 with a model target. In order to improve target identification, focus here is on separating features related to sound structure interaction from those determined by the target's shape. At the frequencies under concern generally many overlapping vibration modes of the target are excited. Whereas with specially designed objects, like thin-walled hollow cylindrical or spherical shells, isolated resonance modes can be directly observed in the echo and assigned to surface waves, the model target used here resembles the complex structure of real obstacles. The structural responses measured by accelerometers attached inside the model are recorded simultaneously together with the backscattering amplitude allowing immediate comparison. Narrow-band swept sine and CW pulses were used. At each frequency the target was turned around a fixed axis with angle resolution better than 2 degrees. A novel spectral transfer function is tested modeling the frequency-dependent boundary impedance and therefore the envelope deformation of the scattered pulse due to interaction of the impinging wave with the target's interior. This model function has rather few parameters to be adjusted.

4:40

3pUWb2. A perturbation theory for scattering from targets near rough surface sediments: Numerical results. Garner C. Bishop and Judy Smith (Naval Undersea Warfare Ctr., Div. Newport, Newport, RI 02840)

A null field T-matrix perturbation theory developed for plane-wave scattering from a fluid loaded elastic spherical shell near a rough fluid elastic interface [J. Acoust. Soc. Am. **101**, 767–788 (1997)] is generalized to include scattering from spherical, spheroidal, and endcapped cylindrical targets near rough surface rigid, soft, fluid, and elastic sediments. Numerical results are obtained that demonstrate some of the effects of surface roughness on resonant and nonresonant target-boundary scattering.

5:00

3pUWb3. Localized modes of oscillating structures which lie on the bottom. Andrei Abramian (Inst. for Problems in Mech. Eng. RAS, Bolshoy pr. V. O. 61, 199178 St. Petersburg, Russia, abramian@hidro.ipme.ru)

The phenomenon of wave localization in hydroelastic systems leads to the strength concentration of radiation fields. The linear method considers the process of localization to be the formation of nonpropagation waves (trapped modes phenomenon). The presence of such waves in the total wave packet points to the existance of mixed natural spectrum of differential operators describing the behavior of hydroelastic systems. The problem of liquid and oscillating structure interaction caused by the trapped modes phenomenon has been solved (membranes, dies, plates and different liquid models). The areas of wave localization have been determined. These areas depend on both the parameters of oscillating structures and the liquid waveguide parameters (the linear dimensions of the channel filled with liquid; the height from the bottom to the liquid surface; the liquid density gradient according to the height, etc.). Necessary and sufficient conditions for the low-frequency trapped modes and the high-frequency trapped modes have been found. The wave localization in nonlinear elastic structures interacting with liquid has been studied. Cases of weak and strong nonlinearity have been investigated. It has been shown that the slightly decreasing tail is added to nonlinear localized modes depending on the frequency of linear localized modes. The tail is caused by the interaction of the mode's continuous spectrum and the localized modes.

5:20

3pUWb4. Trapping modes of oscillations in an infinitely long waveguide with submerged object in the form of a massive die. Dmitri Indeitsev (Inst. for Problems in Mech. Eng. RAS, Bolshoy pr. V.O. 61, St. Petersburg 199178, Russia, abramian@hidro.ipme.ru)

It is shown for an infinitely long waveguide—first in the form of a two-dimensional and then a three-dimensional channel—filled with an ideal compressible liquid with a free surface, that there can exist standing waves as well as traveling waves localized in the region of a dynamic submerged object—a massive die. The appearance of such waves is due to the presence of a mixed spectrum of characteristic frequencies of oscillation. In addition to the continuous spectrum, a point (discrete) spectrum distributed along the axis of the continuous spectrum is also present. A relation is found between the geometric parameters of the channel and the massive die for which this spectrum exists.

5:40

3pUWb5. Repulsion phenomena in the phase-velocity dispersion curves of circumferential waves on elastic cylindrical shells. Herbert Überall (Dept. of Phys., Catholic Univ., 6th and Michigan Ave. N.E., Washington, DC 20064), Gérard Maze, Fernand Léon, and Jean Ripoche (Univ. of Le Havre, 76610 Le Havre, France)

The complex eigenfrequencies of an evacuated, fluid-immersed infinite cylindrical shell, when plotted in the complex frequency plane, have been grouped into families corresponding to different types of circumferential waves. The real parts of these eigenfrequencies have been used to obtain dispersion curves versus frequency of the phase velocities of these circumferential waves, which are analogous to those of the Lamb waves on an elastic plate *in vacuo* labeled $A_0, A_1, \ldots$ and $S_0, S_1, \ldots$, but which contain an additional branch reminiscent of the fluid-borne Scholte–Stoneley wave. This branch forms together with the A_0-analog an interacting pair of dispersion curves which will be called A_{0+} (upper branch) and A_{0-} (lower branch). These exhibit a repulsion phenomenon near the ambient fluid sound speech analogous to that in perturbed, quasi-degenerate atomic levels. This is explained here by perturbation theory, showing that during repulsion the wave character gets exchanged so that at frequencies above the repulsion point A_{0+} is a flexural and A_{0-} a fluid-borne wave, and vice versa below the repulsion point.

6:00

3pUWb6. Localization in acoustic propagation in water with air cylinders. Zhen Ye and Emile Hoskinson (Dept. of Phys., Natl. Central Univ., Chungli, Taiwan, ROC)

Wave localization is the peculiar property of a scattering medium that completely blocks propagation, thus inducing a surprising phase transition, for example in optical or acoustic transparency or electrical conductivity. When localized, waves remain confined in space until dissipated. This property has been explained for randomly disordered scatterers. It is generally believed that disorder is an essential ingredient of localization, and in two dimensions (2D) waves are always localized with any amount of randomness. Here it is shown that waves are not always localized in 2D, but under proper conditions even periodic structures can achieve localization in the case of acoustic propagation through water containing an array of air cylinders. An essential component of localization in this case arises from the natural resonance and an amazing collective behavior of the cylinders. Exact numerical calculations reveal the unexpected result that localization is relatively independent of the precise location or organization of the scatterers. The results provide insight on 2D wave localization and offer an opportunity for further investigation of important questions about localization phenomena. [Work supported by NSC and NCU of ROC.]

Posters from various technical sessions remain on display in the Poster Gallery.

Session 3pAAa

Architectural Acoustics and Signal Processing in Acoustics: Verification of Auralization and Modeling Programs I

Michael Vorlaender, Cochair
Institut für Technische Akustik, Aachen University, D-52056 Aachen, Germany

Robert C. Coffeen, Cochair
Architectural Engineering, University of Kansas, Lawrence, Kansas 66045, USA

Chair's Introduction—4:15

Invited Papers

4:20

3pAAa1. Verification of prediction based on randomized tail-corrected cone-tracing and array modeling. Bengt-Inge L. Dalenbäck (CATT, Mariagatan 16A, SE-41471 Gothenburg, Sweden)

A new room acoustics prediction method, randomized tail-corrected cone-tracing (RTC), is described together with sample prediction/measurement comparisons. RTC is the result of ten years of experience using the image source model, ray- and cone-tracing, and combines elements of all three methods. RTC is a robust number-prediction method, including the effects of frequency-dependent diffuse reflection for both early and late reflections, as well as a method that creates echograms suitable for binaural post-processing and auralization. Further, a WIN32 DLL directivity interface (DDI) is described. The interface is general and is capable of arbitrary data-format translation and accurate distance-dependent high-resolution array modeling including beam steering. The array modeling is either made via a generic DDI module or via modules custom designed based on detailed manufacturer array specifications (transducer placement, directivity pattern, aim, weighting filter, and delay). Sample prediction/measurements comparisons are given for DSP-controlled column arrays under free-field conditions, in a large railway station and in a large church. It is demonstrated that the common fixed measurement distance 10-deg full space data is insufficient for modeling arrays both due to the limited angular resolution and because far-field conditions may not be reached until 30 m distance or beyond.

4:40

3pAAa2. Report on the second International Round Robin on Room Acoustical Computer Simulation. Ingolf Bork (Projekt 1.401 Physikalisch-Technische Bundesanstalt, D-38116 Braunschweig, Germany)

A Swedish concert hall with a volume of about 11 000 cubic meters served as a test object to compare the performance properties of room simulation software programs. In six octave bands and at 12 source–receiver combinations, nine acoustic parameters defined in ISO 3382 had to be calculated. In the first phase of this round robin only the geometry and a written description of the acoustically relevant properties were given, while in the second phase absorption and diffusion coefficients of the surfaces were prescribed for each octave band. The results obtained by the 16 participants from nine countries will be discussed and compared with measurements performed in the hall. The analysis of the discrepancies and the high variance of the calculated data show that the influence of the software user cannot be neglected and a high degree of practical experience in room acoustics is required to produce optimal results.

5:00

3pAAa3. Comparisons between computer simulations of room acoustical parameters and those measured in concert halls. Jens Holger Rindel (Norwegian Inst. of Bldg. Res., P.O. Box 123 Blindern, N-0314 Oslo, Norway), Hiroyoshi Shiokawa, Claus Lynge Christensen, and Anders Christian Gade (Tech. Univ. of Denmark, DK-2800 Lyngby, Denmark)

A number of European concert halls were surveyed in 1989. In this paper comparisons are made between measured room acoustical parameters and those obtained from computer simulations on concert halls using the ODEON program version 3.1. The key parameter compared with measured data is the reverberation time, and this is mainly used to adjust the absorption data of the surfaces in the computer model. But five additional parameters are calculated and compared with measured data as well. In order to determine the sensitivity of the computer model, comparisons are also made between the results obtained from computer simulations using models with a high geometrical fidelity and those from models with simplifications to geometry that are in better agreement with the laws of high-frequency modeling.

5:20

3pAAa4. Real time auralization with EASE 3.0. Wolfgang Ahnert (ADA Acoust. Design Ahnert, Gustav-Meyer-Allee 25, D-13355 Berlin, Germany, wahnert@ada-acousticdesign.de)

The new EASE 3.0 for Windows combines advanced features of the DOS-based system EASE 2.1 with the known ones of the Auralization package EARS 1.1. In case of the DOS-based system, one has to use additional hardware to convolve the calculated impulse responses with the head-related transfer functions and eventually with the dry tests signal. After calculation of the corresponding impulse response one can listen now in EASE 3.0 to the convolved binaural signal by use of just a normal sound card. Additionally, with a duplex sound card one can enter CD signals directly and, after a transient time of 50 ms to 2 s (depending on the computer parameters and the sample rate of the signal), one can obtain the auralized results. Another option allows one to calculate the direct sound sequence of used speaker signals in realtime also and then to use the auralization routine to check echo occurrence or correct localization of sound sources. The convolution algorithm used in EASE 3.0 is patent pending and was created in cooperation with LAKE/Australia. In a project still under construction, the measured results have been compared with auralization results obtained by physical scale model measurements. Both results will be demonstrated.

5:40

3pAAa5. Comparison of simulation and measured sound system performance in the German Reichstag Debate Hall, Berlin. Volker Loewer (IFB Rhein Main, Eleonorenstr. 11, D-65474 Bischofsheim, Germany, ifbrm@aol.com)

For the design of the new sound system for the Reichstag Debate Hall, Berlin, the ULYSSES computer aided acoustic design program has been used. The 3-D model of the room consisted of more than 1000 faces treated with different absorption in octave bands according to the architect's plans. Simulation of direct sound coverage, RT60, intelligibility, energy decay via ray-tracing, etc., was done to evaluate different solutions of the sound system designs and their interaction with room acoustics. It is intended to compare actual acoustic test results to simulated predictions and to discuss conformity and deviations. The software was also used to predict directivity balloons of the complex speaker arrays located in the debate hall. The balloons were derived from measured balloons of the single devices used in the arrays. Considering relative mechanical locations, acoustic centers, acoustic power, and delays, the predictions showed good conformity with polar measurements of a real cluster.

6:00

3pAAa6. A computer auralization and ''real world'' comparison using the computer programs EASE and EARS. Robert C. Coffeen (Architectural Eng., Marvin Hall, Univ. of Kansas, Lawrence, KS 66045) and Gabriel Caunt (Russ Berger Design Group, Inc., Dallas, TX 75244)

In order to compare a ''real world'' acoustic environment with a computer auralization of the same space, an Episcopal Church located in Prairie Village, Kansas (near Kansas City, Missouri) was selected as the ''real'' space. Anechoic speech and music recordings were reproduced in this space and recorded binaurally. The same anechoic recordings were introduced into a computer model of this room with auralizations produced by the computer programs EASE and EARS. The ''real world'' binaural recordings are compared with the computer-generated audio using both objective and subjective methods. The measured impulse response of the room and the computer-predicted impulse response are compared. Comparisons are also made between the measured and the predicted reverberation periods of the room.

WEDNESDAY AFTERNOON, 17 MARCH 1999 ROOM H1028, 4:35 TO 6:20 P.M.

Session 3pAAb

Architectural Acoustics: Sound Insulation and Subjective Annoyance

Jens Holger Rindel, Cochair
Norwegian Institute of Building Research, P.O. Box 123, Blindern, N-0314 Oslo, Norway

Angelo J. Campanella, Cochair
Campanella Associates, 3201 Ridgewood Drive, Columbus, Ohio 43026, USA

Chair's Introduction—4:35

Invited Papers

4:40

3pAAb1. On the utility of extending the low-frequency range of standards for sound isolation in buildings. Stephen J. Lind, Karl S. Pearsons, and Sanford A. Fidell (BBN Technol., 21128 Vanowen St., Canoga Park, CA 91303, slind@bbn.com)

Frequencies above 100 Hz are commonly considered in sound insulation computations as specified by ASTM E413 and ISO 717. This is appropriate for concerns about speech privacy in interior spaces. However, aircraft ground operations (including takeoff roll, engine run-ups, and thrust reverser deployment) may expose buildings near runways to appreciable amounts of energy at yet lower

frequencies. Several studies of low-frequency aircraft noise levels have recently been completed in the United States, and the U.S. Federal Aviation Administration is paying for architectural treatments to reduce low-frequency aircraft noise in residences near one airport. This paper describes the findings of a recent social survey of residential annoyance caused by low-frequency runway sideline noise, including noise in the 25 to 80 Hz one-third octave bands, and reviews other evidence about the role of low-frequency energy in sound isolation metrics.

5:00

3pAAb2. On subjective impact sound insulation classes. Per Hammer (Dept. of Eng. Acoust., Lund Univ., Box 118, 22100 Lund, Sweden, per.hammer@kstr.lth.se) and Erling Nilsson (Lund Univ., 22100 Lund, Sweden)

The possibility to divide impact sound annoyance into classes is investigated. The experiments, based on human perception, are done in a laboratory environment where various floor structures have been included to produce impact noise. These tests are correlated to studies pertained to real-life situations for tenants. The statistical tool to test the significant differences between the classes is Rou–Kupper. Real footsteps are used as a noise source. In addition, airborne sound insulation is treated in a similar manner, whereby one may conclude that there are some difficulties finding classes with statistical significant differences. [Work supported by the Swedish Council of Building Research.]

Contributed Papers

5:20

3pAAb3. Group subjective ratings of airborne sound insulation. John Bradley (IRC, Natl. Res. Council, Montreal Rd., Ottawa, ON K1A 0R6, Canada, john.bradley@nrc.ca)

This paper will compare various sound insulation measures as predictors of the grouped subjective ratings obtained from a field survey of 600 subjects and the airborne sound insulation of their 300 party walls. The subjects lived in both row housing and multi-floor apartment buildings in three different Canadian cities. The questionnaire first asked about general issues concerning the subjects building followed by more specific questions rating the sound insulation and the audibility of various noises. Sound transmission loss measurements were made in 1/3 octave bands from 100 to 4000 Hz. In addition to the standard ISO and ASTM single number ratings, 20 different single number sound isolation measures were calculated. Most were simple variations of the standard quantities. The standard STC rating (including the 8-dB rule) was one of the better predictors of most responses. Excluding the 8-dB rule decreased correlations with responses and especially those concerning hearing musical sounds. Several responses were best correlated with transmission loss values in the 160- and 200-Hz bands.

5:40

3pAAb4. Considerations about the influence of traffic noise in the design of new hospitals. Eduardo Bauzer Medeiros (Dept. de Engenharia Mecânica da UFMG, Av. Antônio Carlos 6627, 31270-901, Belo Horizonte–MG, Brazil, flugzbau@dedalus.lcc.ufmg.br) and Ivan de Azevedo Camelier (UBI, 6200, Covilhã, Portugal)

The main origin of noise disturbance in new hospitals located inside densely populated areas can usually be associated with vehicular traffic. However, the effect of this disturbance is often not fully appreciated. Compliance with standard legislation limits is often considered to be a satisfactory design criterion. In fact, even moderately higher noise levels can introduce physiological changes, which may have a decisive influence on the convalescence of a hospital patient. The present work associates some of the information which is available on the effects of patients subjected to different noise levels with considerations about hospital and the associated access roads design. Field measurements carried out in the vicinity of typical existing and planned hospitals are also described and associated with the local traffic conditions. Finally, a few practical guidelines are laid, considering a rest situation of a hospital under construction near an important access road. The objective is to establish a set of acoustic design guidelines for hospitals and the surrounding areas, particularly the road system, aiming at a more efficient convalescence period for the patients.

6:00

3pAAb5. Vibrations caused by construction work—Measurements and surveillance. Wolfgang Teuber and Ernst-Jo Voelker (Inst. for Acoust. and Bldg. Phys., Oberursel, Germany)

Numerous construction principles applied especially in underground engineering are the sources of vibrations. The measurement of vibrations and evaluation of the results are made based upon different criteria. These criteria are formed taking into consideration the influences upon people in the surrounding area, the risk of damage to buildings and the possibility of the malfunctioning of technical systems such as computers or laser equipment. Measurements were taken while several different construction methods were being applied. Short-term measurements are, for the most part, insufficient and must be completed by long-term research. Maximum acceptable values are defined in existing standards based on the influences of vibrations upon persons and upon various kinds of buildings. For technical equipment, stricter limits had to be defined. When the type and location of construction work changes, the application of an automatic monitoring system is advantageous. Such a system is described which was installed to survey computers with special hard disc drives. Existing measurement results allow for predictions and calculations to be made in order to determine the best method of construction. Some principles of building methods, measurements, and vibration monitoring are mentioned.

Session 3pAO

Acoustical Oceanography and Underwater Acoustics: Acoustic Tomography and Thermometry II

James F. Lynch, Chair
Woods Hole Oceanographic Institute, Bigelow 203, Woods Hole, Massachusetts 02543, USA

Invited Papers

4:20

3pAO1. Shallow-water tomography: Acoustic maps of the New England shelfbreak front. Ching-Sang Chiu (Dept. of Oceanogr., Naval Postgrad. School, Monterey, CA 93943), James F. Lynch, and Glen Gawarkiewicz (Woods Hole Oceanogr. Inst., Woods Hole, MA 02543)

In the summer of 1996, an integrated acoustic-oceanographic experiment was carried out in the Middle Atlantic Bight to study the dynamics of the shelfbreak front and the effects of the frontal variability on sound propagation. The experiment employed a suite of acoustic and oceanographic sensors, including several sources and two vertical hydrophone arrays (VLAs) straddling the shelfbreak front and a SeaSoar that provided several high-resolution, three-dimensional surveys of the frontal region. In this presentation, the results of an acoustic tomographic analysis of the frontal variability are reported. In deriving the tomographic maps, an adaptive beamformer was first used to detect, resolve, and track individual acoustic ray and modal arrivals from a 224- and a 400-Hz source on the slope to a vertical array on the shelf. A hybrid ray-mode inverse technique was then applied to the resolved arrivals to produce a time series of cross-frontal images of ocean temperature. The tomographic observations are interpreted together with the SeaSoar, ADCP, and thermistor data. [Work supported by ONR.]

4:40

3pAO2. Broadband geo-acoustic inversion in shallow water. Jean-Pierre Hermand (Environ. Res. Div. SACLANT Undersea Res. Ctr., viale San Bartolomeo 400, 19138 La Spezia, Italy, hermand@saclantc.nato.int)

The paper discusses an inversion method that allows the rapid determination of *in situ* geo-acoustic properties of the ocean bottom without resorting to large acoustic receiving apertures, synthetic or real. The method is based on broadband, waterborne measurements and modeling of the waveguide impulse response between a controlled source and a single hydrophone. Results from 1994–1997 experiments in Mediterranean shallow waters with single elements of vertical array and advanced drifting acoustic buoys are reviewed. Inversion of the bottom parameters is performed with an objective function that includes the processing gain of a model-based matched filter (MBMF) receiver relative to the conventional matched filter. The MBMF reference signals incorporate waveguide Green's functions for the known geometry and water column acoustic model, and hypothesized bottom geo-acoustic models. The inversion results demonstrated that—even for the fairly complex environmental conditions of the experiments—a single transmission of a broadband coded signal received at a single depth and a few hundred of forward modeling runs were sufficient to resolve the bottom features. These included the sound-speed profile, attenuation, density, and thickness of the top sediment layer, and sound speed and attenuation of the bottom. Exhaustive parameter search proved unequivocally the low-ambiguity and high-resolution properties of the MBMF-derived objective. The single-hydrophone bottom inverses closely agree with the ones obtained under the exact same conditions from matched-field processing of multitone pressure fields sampled on a vertical array. Both of these results agree with expectations from geophysical ground thrust.

Contributed Papers

5:00

3pAO3. Results for tomographic geoacoustic inversion on simulated multiarray data. A. Tolstoy (Integrated Performance Decisions, Inc., 8610 Battailles Ct., Annandale, VA 22003, atolstoy@ipdinc.com)

Only recently have broadband multiarray data been collected which are suitable for tomographic inversion for the estimation of shallow-water geoacoustic parameters. In particular, this unique data set was collected in the Haro Strait region off the west coast of Canada by N. R. Chapman and colleagues. These data have now been simulated and studied in preparation for the tomographic inversion of the actual data, a very difficult problem involving hundreds of parameters. Results to be discussed here concern these simulated data and recent successes in their inversion for the estimation of such properties as sediment sound-speeds and densities over a region where such parameters vary as a function of range, azimuth, and depth. [Work supported by ONR.]

5:20

3pAO4. Acoustic data preprocessing in the TOMOLAB/OCTOPUS project. Mauuary Didier and Bernard Faure (Laboratoire des images et signaux, INP, Grenoble, St. Martin d'heres, France, Didier.Mauuary@lis.inpg.fr)

This paper presents the acoustic data preprocessing task in the TOMOLAB graphic interface tool. TOMOLAB is a goal of the OCTOPUS project, under the MAST III program of the European Com-

munity. Data preprocessing consists in transforming raw tomographic data into compressed/correlated peaklike data. It is the first step before time delay estimation, time delay identification, and time delay inversion. The complete data processing must perform matched filtering, multisequence averaging, Doppler/phase compensation, and mooring motion correction. A synthetic view is given of several technical choices that integrate these tasks, jointly or successively. This work is based on internal studies and existing pieces of literature. The Hadamard transform, the Fourier matched filtering, fast Doppler processing, phase estimation/correction algorithm, delay shifting in the time or Fourier domain, data format and sampling are discussed. Efficient data processing has to account for the computing speed, the compression ratio, and achievable accuracy of delay estimation.

5:40

3pAO5. Matched-peak tomography. E. K. Skarsoulis (Inst. of Appl. and Computational Mathematics, FORTH, 71110 Heraklion, Crete, Greece)

A new approach is presented for the inversion of travel-time data in ocean acoustic tomography. Using model relations between sound-speed and arrival-time perturbations about a set of background states, arrival times and associated model errors are calculated on a fine grid of model states discretizing the parameter space. Each model state can explain (identify) a number of observed peaks in a particular reception laying within the uncertainty intervals of the corresponding predicted arrival times. The model states that explain the maximum number of observed peaks are considered as the more likely parametric descriptions of the reception; these model states can be described in terms of mean values and variances providing a statistical answer (matched-peak solution) to the inversion problem. An advantage of the proposed approach is that there is no need for initialization of the inversion procedure, i.e., no need for additional hydrographic information. Furthermore, the matched-peak solution for each reception is independent of the previous reception identification/inversion results. The method was applied to nine-month-long tomography data from the Thetis-2 experiment in the western Mediterranean sea. [Work partially supported by EU/MAST.]

6:00

3pAO6. On the simultaneous estimation of current and sound velocity structure in the ocean, using matched-field processing. Michael Taroudakis (Dept. of Mathematics, Univ. of Crete and Inst. of Appl. and Computational Mathematics, FORTH, P.O. Box 1527, 711 10 Heraklion, Crete, Greece, taroud@iacm.forth.gr) and Maria Markaki (Inst. of Appl. and Computational Mathematics, FORTH, 711 10 Heraklion, Crete, Greece)

A matched-field processing method for the simultaneous estimation of ocean current velocity structure and sound speed profiles, based on reciprocal transmissions of cw or broadband acoustic signals between two locations in the water column, is presented and discussed. For each transmission, a single source and a vertical array of hydrophones are used. The current velocity is introduced as an additional unknown in the inverse problem, through the concept of the ''effective sound speed,'' being the sum of the actual sound speed and the projection of the current velocity on a vertical plane, defined by the sound source and the receiver. The work is mainly focused on the study of the effect of variations of the current velocity on the various processors proposed for the matched-field inversions and on the inversion procedure itself, under the assumption that neither the actual position of the source receiver system nor the actual sound velocity structure are known. Using synthetic data, it is demonstrated that the results of inversion for the current velocity are reliable, under some limitations posed by the degree of uncertainty for the other unknown parameters. [Work supported by INTAS-RFBR.]

Contributed Posters

These posters will be on display in the Poster Gallery from Thursday to Friday, 18–19 March. Authors will be at their posters from 10:00 a.m. to 12:00 noon on Friday, 19 March.

3pAO7. The experimental demonstration of selective mode excitation in a shallow-water environment. James C. Preisig (Dept. of Appl. Ocean Phys. and Eng., Woods Hole Oceanogr. Inst., Woods Hole, MA 02543), John R. Buck (Univ. of Massachusetts, North Dartmouth, MA 02747), Mark Johnson (Woods Hole Oceanogr. Inst., Woods Hole, MA 02543), and Hu Dou (Univ. of Massachusetts, North Dartmouth, MA 02747)

The ability to selectively excite single acoustic modes in a shallow-water environment is demonstrated and analyzed. Using vertical source and receiving arrays and the feedback control techniques based on those in Buck *et al.* [IEEE J. Oceanic Eng. **22**, 281–291 (1997)], acoustic modes 1–3 were excited sequentially for periods up to 20 min with a fidelity of approximately 60 dB for mode 1 to 25 dB for mode 3. The filtering of the received signal used in the feedback loop by projection into the subspace spanned by the dominant system modes was found to significantly improve the system's performance. This result will be explained and analyzed. The requirement for phase stabilization of the sampled received signal is also presented. The ability demonstrated here for high fidelity selectively controlled modal content of a transmitted acoustic signal offers potential for new methods for acoustic tomography and for studying underwater acoustic propagation. [Work supported by ONR Ocean Acoustics.]

3pAO8. Model of acoustic monitoring of heat and mass transport in the Fram Strait. Konstantin A. Naugolnykh (Environ. Technol. Lab., Boulder, CO 80303), Ola M. Johannessen (Nansen Environ. and Remote Sensing Ctr., Bergen, Norway), Igor B. Esipov, Oleg B. Ovchinnikov, and Yuri I. Tuzhilkin (N. Andreyev Acoust. Inst., Moscow, 117036 Russia)

A computation model of acoustical monitoring of heat and mass transport in the Fram Strait is discussed. The method relies on the advections of small-scale inhomogeneities across the acoustic path and travel-time variations in the process of signal crossing of the Strait on a number of paths to infer the intervening of fine-scale variability and transverse current. Inhomogeneities of the current produce perturbations in the travel time of the sound, and the current can be sensed by generating a time-lagged cross correlation of the full acoustic field. Both the linear four-element transmission array and four-element receiving array with equally spaced elements were used for calculations. By combining the signals from each transmitter–receiver pair in different ways, a number of different path positions were probed and a profile of transverse current $U(r)$ along the propagation path r was retrieved, whereas the value of the travel-time variation is related with T—temperature change. The possibility of estimation of heat $Q \sim \int U(r)T(r)dr$ and mass $M \sim \int U(r)dr$ transport in the cross section is regarded. [Work supported by Environmental and Climate Programme of EC, Project PL970338.]

3pAO9. Internal wave inversions for one year of Pioneer–Hawaii ATOC transmissions. Kevin D. Heaney and the ATOC Group[a] (Sci. Applications Intl. Corp., 11803 Sorrento Valley Rd., San Diego, CA 92121)

The ATOC experiment transmitted 75-Hz signals from Pioneer Seamount off the coast of California to a vertical line array (VLA) off Hawaii. The combination of VLA and long-range propagation provides the opportunity to perform mode-based internal wave tomography. Each arrival is mode-filtered and the statistics of the mode arrivals are tabulated. These individual mode arrival time (centroid) and spread are then compared with calculated mode statistics from broadband PE modeling of the propagation path. In this manner a statistically robust inversion for the internal wave strength is performed. The weakness of the inversion is the sensitivity to the bottom scattering near the source. Results for one year of data will be presented for two different bottom types. The long-scale time series may indicate possible sources of internal waves in the ocean. Small time scale variations may be attributable to internal tides. [a] The ATOC Group: A. B. Baggeroer, D. Menememlis, and C. Wunsch (MIT); T. Birdsall, K. Metzger (Univ. of Michigan); C. Clark (Cornell Univ.); J. Colosi (WHOI); B. D. Corneulle, M. Dzieciuch, W. Munk, P. F. Worcester (SIO); D. Costa (Univ. of California, Santa Cruz, CA); B. D. Dushaw, B. M. Howe, J. A. Mercer, and R. C. Spindel (APL-U Wash.); A. M. G. Forbes (CSIRO, Hobart).

3pAO10. AMOC: Preliminary results. Hanne Sagen (NERSC, Edv. Griegsvei 3A, 5037 Solheimsviken, Norway, hanne.sagen@nrsc.no), Ola M. Johannessen, Halvor Hobaek, and Sigve Tjoetta (Univ. of Bergen, Bergen, Norway)

The scope of this presentation is to give preliminary results of the sensitivity study of sound propagation in the Arctic including the Fram Strait using propagation loss observations and existing acoustic propagation models. Special attention to the consequences for design of future acoustic monitoring concepts will be made. One of the important consequences of the preliminary results is the conflict between the optimum transmission frequency and the optimum frequency for retrieving information about the ice cover. If an experiment is designed to propagate over long distances at a relatively low frequency, then the reflection from a ''smooth'' ice cover is total and there will be no information about the ice thickness or internal properties of the ice cover. The attenuation due to the ice will be dominated by scattering from rough surface (large facets). So this type of experiment will give information about the averaged temperature through the travel times, while the ice information will be limited. Therefore two concepts have to be considered: one to measure ice parameters, which will need signals composed by appropriate frequencies, and another concept to measure averaged temperature, which needs low frequencies insensitive to ice cover.

3pAO11. Method of the main informative components for acoustic tomography. Alexander Ya. Kalyuzhnyi (Inst. of Hydromechanics, 8/4 Zhelyabov Str., Kiev, 252057, Ukraine) and Leonid G. Krasny (Ericsson, Inc., RTP, NC 27709)

Techniques for an ocean acoustic tomography are based on the representation of the sound-speed field (SSF) by an expansion of some orthogonal basis functions. It is usually assumed that the most efficient basis functions for the SSF expansion are so-called empirical orthogonal functions (EOF). Meanwhile, the experiments show that algorithms based on the EOF can be extremely sensitive to slight errors in the assumed signal and noise characteristics. A new improved algorithm for acoustic tomography will be presented which minimizes output statistical errors of the SSF estimation. The concept of this algorithm is to use eigenvectors of the Fisher information operator as the basis functions into the SSF expansion. The algorithm involves a quadratic inequality constrain on the SSF expansion coefficients to select the most informative components among all the eigenvectors. It is shown that it leads to a robust algorithm in which statistical errors do not accumulate. The performance of the proposed algorithm will be illustrated both for deterministic and random signals.

3pAO12. An ocean acoustic tomography experiment in the central Labrador Sea—First results. Detlef Kindler and Uwe Send (Inst. für Meereskunde, Univ. Kiel, Düsternbrooker Weg 20, D-24105 Kiel, Germany)

First results of an ongoing acoustic tomography experiment will be presented. Since August 1996 a mooring array consisting of four tomography transceivers (400 Hz), redeployed in the summers of 1997 and 1998, has been measuring acoustic travel times over distances of typically 170–300 km in the central Labrador Sea. The purpose of such measurements is to estimate time series of horizontally integrated properties like ocean heat content and vertical temperature stratification by inverting travel times into sound speeds and hence into heat contents and temperatures. These large-scale properties will be used to study the interannual variability of ocean heat budget and water masses formed in close connection to deep convection and the ensuing renewal of Labrador Sea Water (LSW) [R. A. Clarke and J. C. Gascard, J. Phys. Oceanogr. **13**, 1764–1778 (1983)]. The variability during winter results from destabilization of the water column near the ocean surface caused by atmospheric cooling, subsequent mixing down to 1000–2000 m, and the following restratification of the convection area. The investigations are focused on the upper 2000 m of the water column, which are well insonified by several trackable ray paths with enough acoustic energy to be processed. [Work supported by Deutsche Forschungsgemeinschaft.]

Session 3pEA

Engineering Acoustics and Underwater Acoustics: Recent Advances in Underwater Transducers II

Elizabeth A. McLaughlin, Cochair
Naval Undersea Warfare Center, Code 2131, Newport, Rhode Island 02841-1708, USA

Didier Boucher, Cochair
DCN Ingénierie Centre SUD, Sous-Direction Lutte Sous La Mer, BP 30, 83800 Toulon Naval, France

Contributed Papers

4:00

3pEA1. Application of the Tonpilz design for optimizing parameters of rod transducers. Boris Aronov (Acoust. Res. Lab., Dept. of Elec. and Computer Eng. and Ctr. for Marine Sci. and Tech., Univ. of Massachusetts, Dartmouth, North Dartmouth, MA 02747)

The optimum design of a rod transducer under various loading conditions and operating requirements is examined. It is often possible that the operational requirements can be met by using only a part of the rod volume with the electromechanical or piezoelectric element. The remaining sections of the rod can be replaced by passive materials or caps (i.e., a ''head'' and a ''tail'') while still maintaining the same input impedances and resonant frequency. Such a composite rod transducer made of active and passive materials having different length and cross-sectional areas is of the ''Tonpilz'' type. The proper choice of dimensions and materials for the caps will result in optimum transformation of mechanical (acoustical) loads and transducer performance. Both criteria of optimization, the rod transducer parameters and the procedure for determining properties of the caps that provides optimal loads, are discussed.

4:20

3pEA2. Large aperture 1-3 composite longitudinal resonator (tonpilz) transducer. Charles W. Allen, W. Jack Hughes, and David J. Van Tol (Appl. Res. Lab., Penn State Univ., P.O. Box 30, State College, PA 16804)

A large aperture underwater transducer utilizing 1-3 piezoelectric composite material that operates as a longitudinally resonant (tonpilz) device with a resonance frequency of 45 kHz has been fabricated and tested. The transducer consists of continuous plates of steel and aluminum that act as the rear and front masses, respectively, and a motor section of continuous 1-3 PZT-5H composite. The active radiating face (aluminum front mass) has dimensions of 6.3 in. (4.7 wavelengths) and 3.9 in. (2.9 wavelengths). Conventional transducers or arrays with radiating faces that have dimensions of over one wavelength require dicing or separate elements to reduce the effect of lateral modes in the components. The tonpilz transducer utilizing 1-3 composite material requires no dicing of any of its components, so fabrication of large aperture arrays that only require a single forward-looking narrow beam are greatly simplified. The measured acoustic responses versus frequency and angle demonstrate that there are no extraneous modes that affect the acoustic performance of the transducer and they compare well to theory for a one-dimensional longitudinal resonator. [Work sponsored by the Scripps Institution of Oceanography, University of California, San Diego.]

4:40

3pEA3. The development of a doubly curved acoustic array using injection molded 1-3 piezocomposite. Kim C. Benjamin, Stephen F. Oliver, Jose C. Arteiro (Naval Undersea Warfare Ctr. Div. Newport, 1176 Howell St., Newport, RI 02841, benjaminkc@code20nl.npt.nuwc.navy.mil), Russell S. Petrucci, and William J. Serwatka (Mater. Systems, Inc., Littleton, MA 01460)

The design, fabrication, and acoustic calibration of a doubly curved acoustic array for UUV oceanographic applications is presented. The sensor employs a unique piezoceramic thermoplastic composite which is conformable and capable of deep ocean operation. The composite consists of several small diameter (1.0 mm) PZT-5H rods regularly distributed in a two-dimensional lattice and aligned perpendicular to their diameter. The PZT-5H rods are encapsulated within a thermoplastic viscoelastic moldable epoxy matrix to form an active acoustic composite panel. The thermoplastic epoxy phase of the composite allows the panel to be shaped to a specific vehicle geometry. Low-profile (<1.0 mm) coaxial cable embedded within the composite panel provides addressing between the acoustic array elements and the processing electronics. [This work was supported by Code 80 of the Naval Undersea Warfare Center, Division Newport.]

5:00

3pEA4. Ultra-wide bandwidth backscattering measurements using a transparent flat PVDF sheet source. Scot F. Morse (Code 7136, Naval Res. Lab., Washington, DC 20375), Karen Gipson (Univ. of Puget Sound, Tacoma, WA 98416), Greg Kaduchak (Los Alamos Natl. Lab., Los Alamos, NM 87545), Kevin L. Williams (Univ. of Washington, Seattle, WA 98105), Brian T. Hefner, and Philip L. Marston (Washington State Univ., Pullman, WA 99164-2814)

A thin extended flat PVDF film surrounded by water is demonstrated to be suitable for exploring scattering responses of complicated targets over a range of frequencies from below 2 kHz to 1000 kHz. The target lies close to the source, and in the configuration normally used, the scattering passes through the source to a distant hydrophone. While initial experiments [Kaduchak *et al.*, J. Acoust. Soc. Am. **97**, 2644–2708 (1995)] explored the resonances of spherical shells for which analytical solutions are known, recent experiments have explored novel features in the responses of truncated tilted cylinders that are either hollow [Morse *et al.*, J. Acoust. Soc. Am. **103**, 785–794 (1998)] or solid [K. Gipson, Ph.D. thesis, Washington State Univ. (1998)]. The spectrum radiated by the sheet can be altered by using voltage-step, voltage-pulse, or weighted chirp excitations. An equivalent circuit model is useful for describing the radiated spectrum. Crisp tone bursts have also been produced and used to study the low-frequency resonances of a steel shell in Lake Union (Seattle). [Work supported in part by the Office of Naval Research and by APL.]

5:20

3pEA5. Mechanical properties of lead magnesium niobate/lead titanate ceramics. Elizabeth A. McLaughlin and Lynn Ewart (Naval Undersea Warfare Ctr., Code 2131, 1176 Howell St., Newport, RI 02841)

This research examines the mechanical properties of doped electrostrictive lead magnesium niobate / lead titanate (PMN-PT). While optimization of the electromechanical properties has been the focus of the materials development effort, mounting anecdotal evidence indicates that there are problems with the mechanical integrity of PMN-PT. Mechanical testing has been employed (1) to measure the flexural strength of doped PMN-PT and understand the causes of failure, and (2) to measure the compression strength of PMN-PT and identify the onset of microstructural damage. Navy type-III ceramic (PZT8) was measured as a benchmark. The average flexural strength of poled PZT8 was found to be 110 MPa. Average flexural strengths ranging from 44 to 60 MPa were measured for batches of barium- and lanthanum-doped PMN-PT. Fractography identified the causes of failure. Process modifications, by one vendor, have increased the flexural strength by 38%. The average compression strength of unpoled PZT8 was found to be 1040 MPa. An average compressive strength of 890 MPa was measured for barium-doped PMN-PT. Prior to failure, a ceramic develops microstructural damage at levels below the compression strength. Evidence of damage was found at stresses as low as one-third of the compressive strength. [Work supported by ONR and SPAWAR.]

5:40

3pEA6. Evidence of nonlinear losses in electrostrictive materials. Harold C. Robinson (Naval Undersea Warfare Ctr., Newport, RI 02841)

It has been well established that the equivalent piezoelectric properties used to model the large signal properties of electrostrictive materials such as lead magnesium niobate/lead titanate (PMN/PT) are functions of the operating conditions. Since these materials are nonlinear, DC bias field, AC drive field, prestress level, and temperature all affect the piezoelectric constants and the coupling factor. However, in transducer models based on equivalent circuits, the dielectric loss is represented as a constant under all of these conditions. Moreover, the dielectric loss tangent typically used in these models must either be inferred from transducer data or be measured under conditions (such as using an RLC meter) that do not represent the actual conditions of operation. This paper will present data, from both material and transducer measurements, suggesting that the losses in electrostrictive materials are strong functions of the temperature, drive field, and compressive prestress. Possible approaches to obtaining improved loss measures from material measurements will be discussed.

WEDNESDAY AFTERNOON, 17 MARCH 1999 ROOM H105, 4:20 TO 6:20 P.M.

Session 3pED

Education in Acoustics: Take Fives—Sharing Ideas for Teaching Acoustics

Uwe J. Hansen, Cochair
Department of Physics, Indiana University, Terre Haute, Indiana 47809, USA

Armin Kohlrausch, Cochair
IPO Center for Research on User-System Interaction, P.O. Box 513, NL-5600 MB Eindhoven, The Netherlands

Do you have a novel demonstration, a new laboratory experiment, a favorite video, a recorded sound example, or a new idea for teaching acoustics which you are willing to share with your colleagues? At this session a sign-up board will be provided for scheduling presentations. No abstracts are printed. Presenters are encouraged to have handouts to distribute. Multiple presentations are acceptable (not consecutively). Presentations are limited to 5 minutes. Keep them short! Keep them fun!

Session 3pMU

Musical Acoustics: Musical Instruments and Structural Acoustics II: Piano and Related Instruments

Isao Nakamura, Cochair
1-33-25 Kokuryo, Chofu, Tokyo 182-0022, Japan

Ingolf Bork, Cochair
Physikalische Technische Bundesanstalt, Bundesallee 100, D-38116 Braunschweig, Germany

Chair's Introduction—4:15

Invited Papers

4:20

3pMU1. Piano string excitation: The question of gravity influence on the sound spectra. Anatoli Stulov (Dept. of Mech. and Appl. Mathematics, Inst. of Cybernetics, Akadeemia tee 21, Tallinn, EE0026, Estonia)

The influence of gravity on the process of the grand piano hammer–string interaction was appreciated by D. E. Hall [J. Acoust. Soc. Am. **79**, 141–147 (1986)]. Using the reasonable physical assumptions, it was shown that the gravity influence is small and may not be taken into account. It is obvious, but it is important to know exactly what this influence is. The vibration spectra of different flexible strings excited by piano hammers in the gravity field and without gravity were analyzed here. Of course, the influence of gravity increases with the increasing of the contact time. Its depends on the hammer velocity; therefore, the string excitation by hammers with velocities less than 0.5 m/s was considered. It was shown that: the gravity influence is greater for the smooth hammers, and this influence is more essential for the middle range of notes; for the small velocities of hammers the gravity changes the mode energy levels of the primary harmonics up to 10 dB, if the hammer strikes only one string of the triple set; the gravity must be taken into account definitely, if the contact time is greater than 5 ms.

4:40

3pMU2. Experimental analysis of two-dimensional vibration of a piano string measured with an optical device. Hideyuki Tanaka, Keinosuke Nagai, and Koichi Mizutani (Inst. of Appl. Phys., Univ. of Tsukuba, Tsukuba Ibaraki, 305-8573 Japan)

It is well known that a piano string vibrates in the direction not only perpendicular to the soundboard but also parallel to it. The sound decays rapidly at first and then it decays slowly. A change in the predominant direction of vibration of the string from perpendicular to parallel contributes to the compound decay rate [G. Weinreich, Sci. Am. **240**, 118–127 (1979)]. In this paper, two-dimensional vibration of a piano string is measured with handmade equipment consisting of two phototransistors. Just after the string was struck with a hammer, it vibrates perpendicularly to the soundboard. Then it vibrates gradually in the direction parallel to the soundboard. As a result, a point of the string moves on an elliptic trajectory. It was found that the fundamental resonant frequency of the perpendicular vibration of the E1 string, for example, which is about 40 Hz, is 0.07 Hz lower than that of parallel vibration. This causes the change of rotating direction of the string every 7 s. The discrepancy of the resonant frequencies is also found in the vibration of the D♯1 string.

5:00

3pMU3. Damping of string motion, a significant parameter for sound quality. Klaus Wogram (Phys.-Techn. Bundesanstalt, Proj. 1.401, Bundesallee 100, D-38116 Braunschweig, Germany, klaus.wogram@ptb.de)

To improve the sound quality of pianos and upright pianos the piano maker mostly plans a change of the construction of the backs and the soundboard with its ribs, bridges, and back posts. Unfortunately he often disregards that all these efforts cannot be successful if the damping of the strings is insufficient. Its influence on the sound quality can be very much stronger than that of the soundboard. Guided by some examples, the importance of the dampers, their construction, their mass, and their position will be discussed. In addition the reduction of sound quality due to an insufficient damping of the not-speaking part of a string will be demonstrated.

5:20

3pMU4. The influence of inharmonicity on piano tuning. Taro Mori and Ingolf Bork (Physikalisch-Technische Bundesanstalt, Bundesallee 100, 38116 Braunschweig, Germany, taro.mori@ptb.de)

It is well known that octaves of piano sounds are stretched to more than a 2 : 1 ratio. One reason is that partials of piano tones are not exactly harmonic because of the flexural rigidity of the string. This inharmonicity is characterized by the coefficient B, which depends on the tension, length, Young's modulus, the area of cross section, and the radius of gyration of the string. Piano technicians are trained to tune the octave as ''beautifully'' as possible, but the inharmonicity of the string hinders perfect tuning without beat. For example, when the second partial of the lower sound and the first partial of the upper sound are tuned without beat, all other partial pairs show beats. On the other hand, since the timbre structure of partials is unique for each instrument, the tuned octaves of two different instruments may differ. Some piano sounds were simulated by additive synthesis with different octave, inharmonicity, and timbre in order to perform subjective hearing tests with some piano tuners. It could be shown that the tuned octave width depends not only on the coefficient B but also on the timbre. The influence of the sound board is also discussed.

5:40

3pMU5. Psychoacoustic model for calculating the sound quality of piano tones. Miriam N. Valenzuela (Inst. of Mech., Faculty of Aerosp. Technol., Univ. of the Federal Armed Forces, Munich, D-85577 Neubiberg, Germany, miriam.valenzuela@unibw-muenchen.de)

Assuming that only audible dissimilarities between different piano tones may lead to different quality judgments, experiments were conducted to determine the perceptual attributes listeners use to judge these dissimilarities. The psychoacoustic results showed that two major attributes contribute with over 90% to the explanation of the perceived dissimilarities: the psychoacoustic ''sharpness'' and a second attribute that was described with the scale ''open–closed.'' Both attributes depend on the specific loudness distribution of the sound signals and are defined as a weighted first moment of the critical-band rate distribution of specific loudness using different weighting functions. The weighting function used to calculate the second attribute emphasizes spectral components around 1 kHz. The model developed for calculating audible dissimilarities between piano tones showed a good agreement between psychoacoustically measured and calculated dissimilarities; the correlation was 0.90. The influence of the two attributes on sound quality judgments was verified by listening tests with appropriately modified piano sounds. The results showed that calculating the sound quality of musical instruments on the basis of their sound signals requires an aurally adequate signal processing. The model developed to calculate the sound quality of piano tones showed a good agreement between measured and calculated quality orders.

Contributed Paper

6:00

3pMU6. Stiffness of strings: Significance in musical acoustics. Edgar Lieber[a] (former member of ''Institut für Musikinstrumentenbau,'' D-08267 Zwota, Germany)

In a linear differential equation of a vibrating string there is a link representing stiffness of the string. In nonlinear theory, string stiffness has not yet been taken into consideration. The author has completed this by means of the Lagrange II method and presents essential results. The significance of string stiffness is different for the different groups of instruments. Pianos have remarkably stiff strings. This is inevitable and also necessary because stiffness participates essentially in forming vividness of sound. The well-known ''stretched octaves'' and also the typical tuning curve are caused by this. For plucked strings, stiffness forms character of sound, together with choice of plucking spot on string and with corpus. For bowed strings, it is preferable to have strings, with minor stiffness, because the interaction of bow/string is better. The effects of jitter and rippling (supplement of sound with statistic noise effects) are better formed by less stiff strings. For wound strings, minor stiffness is possible with cores of filament structure. Theory and examples will be discussed.

[a] Present address: Erich Ohser Str. 10, D-08525 Plauen, Germany.

WEDNESDAY AFTERNOON, 17 MARCH 1999 ROOM H107, 4:55 TO 6:20 P.M.

Session 3pNSa

Noise: Tribute to Henning von Gierke

Richard L. McKinley, Cochair
Armstrong Laboratories, AL/CFBA, 2160 7th Street, Wright–Patterson AFB, Ohio 45433-7901, USA

Alice H. Suter, Cochair
Alice Suter and Associates, 575 Dogwood Way, Ashland, Oregon 97520, USA

Chair's Introduction—4:55

Invited Papers

5:00

3pNSa1. Henning E. von Gierke: Mentor, colleague, and public policy leader. Alice H. Suter (Alice Suter and Assoc., 575 Dogwood Way, Ashland, OR 97520)

5:20

3pNSa2. Research pioneer in biomechanics, Henning E. von Gierke. Thomas J. Moore (Armstrong Laboratories, AL/CFBA, 2160 7th Street, Wright–Patterson AFB, OH 45433-7901)

5:40

3pNSa3. The major historical events in the relating of noise-induced hearing loss to noise exposure. Daniel L. Johnson (Interactive Acoustics, 4719 Mile High Dr., Provo, UT 84604)

One event was the recognition of ''boilermaker's disease.'' Another was some of the threshold shift studies during and after WWII that led to the BENOX report. After these developments, there were a series of key events and decisions that have led up to our current state of knowledge and procedures. How Henning von Gierke was influential in most of these and how his decisions have consistently proven to be correct will be demonstrated. For example, he contributed to the 1953 BENOX report, promoted the ''equal energy concept,'' conceived and patented the first noise dosimeter, oversaw the EPA ''levels'' and criteria documents, and was the chair of the working group that wrote the current international standard (ISO-R1999) that relates noise exposure to noise-induced hearing loss. He was also instrumental in supporting many key research issues such as fetal noise exposure, asymptotic temporary threshold shift, and the longitudinal hearing of children. Henning's perseverance and dedication has provided society with an answer to one of his favorite questions, ''how much noise is too much?''

6:00

3pNSa4. 50-year legacy of Henning E. von Gierke's scientific and engineering excellence. Richard L. McKinley (Armstrong Laboratories, AL/CFBA, 2160 7th Street, Wright–Patterson AFB, OH 45433-7901)

WEDNESDAY AFTERNOON, 17 MARCH 1999 ROOM H2032, 4:20 TO 6:20 P.M.

Session 3pNSb

Noise: Rotor Noise from Helicoptors and Propellers

Werner Dobrzynski, Cochair
DRL-Instiitut für Entwurfsaerodynamik, Lilienthalplatz 7, 38108 Braunschweig, Germany

Feri Farassat, Cochair
NASA Langley Research Center, Hampton, Virginia 23681-0001, USA

Invited Papers

4:20

3pNSb1. European helicopter rotor noise research—Highlights of recent projects. Wolf R. Splettstoesser (Deutsches Zentrum für Luft-und Raumfahrt e. V., Institut für Entwurfsaerodynamic, Lilienthal-platz 7, 38108 Branschweig, Germany, wolf.splettstoesser@dlr.de)

Significant advances in understanding, modeling, and controlling helicopter rotor noise have been made in the course of several major European rotor aeroacoustic research projects over the past years. The availability of the German–Dutch Wind Tunnel (DNW), in particular, has enabled research on relatively large main rotor models (up to typically 40% full scale). Here, the simultaneous application and use of blade-mounted absolute pressure sensors to study the very aeroacoustic source mechanisms, of advanced acoustic-data acquisition systems for the radiated noise, of non-intrusive flow visualization as well as flow and blade deflection measurement techniques to investigate the rotor wake and the blade dynamic response has provided much insight into the physics of rotor aeroacoustics, particularly into the rotor blade-vortex interaction (BVI) impulsive noise phenomenon. In efforts towards controlling BVI impulsive noise, in some research projects, active blade-root control techniques have been investigated to favorably affect the BVI geometry and thus minimize the impulsive noise radiation. Much of the experimental data acquired served as benchmark information to enhance the mathematical modeling of the rotor wake, the rotor airloads, and the noise radiation. In this lecture, several major European helicopter aeroacoustic research projects are discussed.

4:40

3pNSb2. Analysis and capability of a noncompact integration method for rotor noise prediction. J. Prieur (ONERA/Dept. of Numerical Simulation and Aeroacoustics, 29 avenue de la division Leclerc, 92322 Chatillon Cedex, France)

Rotor noise computations starting from CFD input data using either the Kirchhoff or the generalized Ffowcs Williams–Hawkings surface integral methods in unsteady conditions may be very lengthy. This is the case for directivity studies or noise level contour calculations for which a high number of observer locations is required. To overcome this drawback, a fast integration method has been designed. It starts from the emission time which avoids having to solve the retarded time equation and uses directly as integration grid the CFD rotating grid (*a priori* not adapted to acoustic calculations). This is made possible thanks to a noncompact treatment of each grid element. The method has already been successfully applied in a transonic rotor case using indifferently a subsonically or supersonically rotating CFD grid for the surface integration (G. Rahier and J. Prieur, 53rd Forum of the American Helicopter Society, 29 April–1 May 1997). The method is made more understandable based on a new and clearer justification and its possibilities of extension are discussed.

5:00

3pNSb3. Analysis of the excess noise of aircraft pusher propellers. Johan B. H. M. Schulten (Aeroacoustics Dept., Natl. Aerosp. Lab. NLR, P.O. Box 153, 8300 AD Emmeloord, The Netherlands, schulten@nlr.nl)

A pusher propeller configuration offers several advantages over the traditional tractor arrangement. For instance, the wing of a twin-engined aircraft is no longer exposed to the swirling and turbulent slipstream. This results in a much smoother wing inflow, a prerequisite for aerodynamic refinement. Acoustically, the more aft position of the propellers considerably reduces the noise impact on the fuselage, yielding the potential of a low cabin noise level. However, in general, the exterior noise of pusher propellers is augmented by the interaction with impinging wakes and exhaust jets. The present paper addresses the physical mechanism of this interaction by applying an unsteady lifting surface theory to the propeller blades. This requires the incident field to be resolved in circumferentially harmonic Fourier components. For each component the unsteady blade pressure distribution is computed as source input for an acoustic calculation. From sample computations for typical operating conditions it appears that the interaction substantially contributes to the total radiated noise of pusher propellers. The present method offers the possibility to investigate in detail the effect of alterations in blade design and flight conditions on tonal level and directivity.

5:20

3pNSb4. Recent developments in helicopter rotor noise prediction at NASA. Kenneth S. Brentner (NASA Langley Res. Ctr., Hampton, VA 23681-0001, k.s.brentner@larc.nasa.gov)

Significant progress has been made recently toward the efficient and robust prediction of helicopter high-speed impulsive noise. The far-field approximation to the Ffowcs Williams–Hawkings (FW–H) quadrupole has been augmented with a rigorous mathematical development. Two new quadrupole formulations—a retarded-time formulation known as Q1A and an emission-surface formulation known as Q2—have been developed and implemented for subsonic and supersonic source motion, respectively. A key numerical advantage of the far-field approximation is that volume integration of the source region surrounding the rotor blades is only performed once in a preprocessing stage. The resulting quadrupole noise computation is reduced to surface integration over the rotor disk in the vicinity of the blades. The solution-adaptive marching-cubes integration algorithm used for the emission-surface formulation will be described. Another recent advance in helicopter noise prediction is the use of the FW–H equation on a permeable integration surface surrounding the source region. This application of the FW–H equation has been shown to be both analytically and numerically superior to the Kirchhoff approach. Furthermore, numerical evidence is presented to demonstrate that the Kirchhoff method is inappropriate when a wake convects through the surface.

Contributed Papers

5:40

3pNSb5. Passive–active low-frequency vibroacoustical fault diagnosis method. Nadejda I. Bouraou (Dept. of Orientation and Navigation Systems, Natl. Tech. Univ. of Ukraine, 37 Peremogy pr., Kiev, 252056, Ukraine, nadya@burau.inec.kiev.ua), Leonid M. Gelman, and Pavel I. Marchuk (Natl. Tech. Univ. of Ukraine, Kiev, 252056, Ukraine)

The presented work is dedicated to the development of the new passive–active low-frequency automatic vibroacoustical early fault diagnosis method of helicopter engine units (compressor stages, turbine stages). The proposed method is based on signal processing of the rotating details of acoustic noise in the low-frequency range (0–25 kHz). There are two important characteristics of this method: (a) it uses a nonstationary narrow-band vibration excitation with variable central frequency, and (b) this excitation is provided by rotating rotor, and user of the method will vary the central frequency, and (b) this excitation is provided by rotating rotor, and user of the method will vary the central frequency of rotor rotation. The basis for using this method is the fact that, at the presence of fault (for example, fatigue crack) in testing details, parameters of arising free and forced oscillations change (nonzero spectral amplitudes of higher harmonics). The new analytical dependencies of testing object oscillation parameters from the relative crack size and parameters of nonstationary excitation are received. A multidimensional testing data vector for diagnostics and evaluation of faults is proposed and investigated.

6:00

3pNSb6. An advanced field measurement system for rotorcraft flight noise. James C. Yu and Kenneth D. Wright (NASA LaRC, MS 235, Hampton, VA 23681-0001)

A Langley-developed field acoustic measurement system has been extensively employed to support the NASA aircraft and rotorcraft flight noise research programs since the early 1980s. The system was first successfully used in the NASA Forward Flight Effects on Turbofan Noise program. Starting from the late 1980s, driven by the increased demand on expanded measurement capabilities for rotorcraft flight noise, an advanced field measurement system development program was initiated to support the rotorcraft flight noise measurement, reduction, and prediction. The paper reviews the three major stages of this extensive development program: the analog measurement system stage, the digital measurement system stage, and the digital remote acquisition and storage system stage. The data processing technology associated with these different stages of the system will be presented. The paper will discuss the research drivers for the measurement system development, the development strategy used to meet the system requirement, and lessons learned at each stage of the development. Discussion will also be given on the future rotorcraft flight noise measurement challenges and the advanced measurement systems required to meet these challenges.

Session 3pPA

Physical Acoustics: Duct Acoustics II

Walter Eversman, Cochair
Mechanical and Aerospace Engineering and Engineering Mechanics, University of Missouri, 202 Mechanical Engineering, Rolla, Missouri 65401, USA

Dirk Ronneberger, Cochair
Drittes Physikalisches Institut, University of Göttingen, Burgerstrasse 42-44, D-37073 Göttingen, Germany

Invited Papers

4:20

3pPA1. Interaction between resonators and fluid motion in ducts. Dirk Ronneberger (Drittes Physikalisches Institut der Universitaet Goettingen, Buergerstrasse 42-44, D-37073 Goettingen, Germany, ro@physik3.gwdg.de)

Each time one is confronted with unwanted narrow-band noise which propagates along a duct, it suggests itself to make use of resonators in the suppression of this noise. However, resonators may be highly sensitive to superimposed mean flow: Detuning and drastic decay of the quality factor is encountered in many cases, nevertheless, also the contrary may happen, namely the increase of the acoustic energy in the resonator. This may result in self-excited oscillations or in the amplification of the incident sound. The paper gives a review of these phenomena, and it will focus on the physical effects behind these phenomena. Simple models that are based on the governing physical effects have been developed and are compared to experimental results with different configurations of resonators in flow ducts. In the case of sound amplification the amplitude of the organized motion of the fluid may become very high so that the nonlinearity of the interaction with the mean flow becomes significant. The state of knowledge and the open questions in this respect will be addressed as well.

4:40

3pPA2. Active noise control by use of an aeroacoustic instability. Björn Lange and Dirk Ronneberger (III. Phys. Inst., Bürgerstr. 42-44, D-37073 Göttingen, Germany)

Ducts that are lined with a series of equally spaced cavities exhibit strong amplification of sound waves under specific flow conditions. The amplification is caused by an aeroacoustic instability wave traveling in the boundary layer of the lining. Since the effect is coupled with a drastic variation of the static pressure drop that depends on the amplitude of incident sound, the possibility is implied to efficiently generate high intensity sound at low frequencies: An incident sound wave with harmonically varying amplitude will cause a periodic modulation of the pressure drop and thus lead to the generation of sound at the modulation frequency. Based on these observations, an aeroacoustic loudspeaker has been designed combining a lined duct section as part of a flow channel and a conventional loudspeaker. The output power of the device amounts to up to 95 dB *re*: 1 pW/Hz at Ma=0.25 for frequencies ranging between 0 and 200 Hz—an observation of some significance with regard to the fact that traditional loudspeakers tend to be rather inefficient at low frequencies. As a feasibility test, the aeroacoustic loudspeaker is used as an actuator in an active noise control setup. High attenuation of low-frequency noise is achieved.

5:00

3pPA3. Computational aeroacoustics of ducts using parallel computers. Lyle N. Long (Dept. of Aerosp. Eng., Penn State Univ., 233 Hammond Bldg., University Park, PA 16802)

This paper will discuss recent attempts at using computational aeroacoustics (CAA) algorithms on parallel computers to solve duct propagation problems. The algorithms are higher-order accurate methods for solving the Euler and Navier–Stokes equations. As computer speed increases, more and more of the physics can be simulated. This talk will discuss the current status and trends of parallel supercomputers. While hardware trends allow us to solve more complicated problems, algorithm developments are also essential. This talk will address some new methods for solving aeroacoustics problems. Most of these new developments involve hybrid schemes that couple CAA methods with integral methods or traditional CFD codes with CAA codes. Since aeroacoustics problems involve length and time scales that are beyond computer power at the present time, clever schemes must be developed for using appropriate algorithms for the various physical phenomena. One very promising scheme [J. Comput. Phys. **133** (1997)] is the nonlinear disturbance equation (NLDE) method, which uses a traditional CFD code to predict the steady-state portion of the problem, and then a higher-order method to solve for the disturbances. The steady-state portion is included in the coefficients and source terms in the NLDE. [Work supported by NASA Langley.]

5:20

3pPA4. On the exact solution of the acoustic wave equation in a parabolic velocity profile in a hard-walled duct. L. M. B. C. Campos and J. M. G. S. Oliveira (Instituto Superior Técnico, 1096 Lisboa Codex, Portugal)

The exact solution of the acoustic wave equation in a parabolic shear flow profile is obtained; the only exact solution given in the literature [Goldstein and Rice (1963); Jones (1977), (1978); Scott (1979); Koutsoyannis (1980)] is for a linear velocity profile, and the solution for the exponential shear flow is given elsewhere [Campos and Serrão (1998)]. The wave equation has three singularities, like the Gaussian hypergeometric equation, but it is of an extended type, since the singularity at infinity is irregular (all three singularities of the Gaussian hypergeometric equation are regular). The other two singularities of the present equation are regular, and one lies at the axis of the duct, and the other at the dicritical layers, where the Doppler-shifted frequency vanishes. The critical layers do not exist (they lie outside the duct) for longitudinal wave vector antiparallel to the mean flow (case I), i.e., propagation upstream in a local frame of reference. In the opposite case of longitudinal wave vector parallel to the mean flow (case II) there are three subcases, depending on whether the Doppler-shifted frequency on the axis of the duct is: (case II A) positive, i.e., critical layers are at imaginary ''distance;'' (case II B) zero, i.e., the critical layer lies on the axis of the duct: (case II C) negative, i.e., two critical layers exist in the duct. In all cases (I, II A, II B, II C) it is possible to obtain the exact acoustic field over the whole flow region by expanding around the singularities and matching solutions. Since the acoustic wave equation in a shear flow does not lead to a Sturm–Liouville problem, the eigenfunctions need not be orthogonal or complete. There is a single set of natural frequencies and normal modes in cases I, II A, and II B, but not in case II C; in the latter case, where two critical layers lie in the flow, they may separate three sets of eigenvalues/eigenfunctions, in the regions between by the critical layers and the walls.

5:40

3pPA5. Experimental verification of a radial mode analysis technique using wall-flush mounted sensors. Lars Enghardt (DLR–Institut fuer Antriebstechnik, Abteilung Turbulenzforschung Berlin, Mueller-Breslau-Str. 8, 10623 Berlin, Germany, lars.enghardt@dlr.de), Yanchang Zhang (LUK GmbH & Co., 77815 Buehl, Germany), and Wolfgang Neise (DLR–Institut fuer Antriebstechnik, 10623 Berlin, Germany)

Sound fields in the inlet and outlet ducts of axial fans, compressors, and aircraft engines propagate as higher-order acoustical modes in a wide-frequency range. Decomposition of the sound field into azimuthal and radial modes permits direct conclusions on the sound generation processes and can lead to the identification of aerodynamic source areas. An established experimental method for assessing the sound field is to circumferentially traverse a radial microphone rake over 360 degrees, to measure the sound pressure in the duct at multiple circumferential and radial positions. On the inlet side of a turbo-machine this procedure cannot be employed because the wake of the rake would disturb the inlet flow conditions of the machine and alter its acoustic characteristics. Computer simulations have shown that the radial mode structure of the sound field can also be determined by measuring the sound pressure only at the inner duct wall, but at different axial locations. In this paper, experiments are described where the sound field in the outlet duct of an axial-flow fan is measured once with the conventional radial microphone rake and a second time with wall-flush mounted microphones. Subsequent radial mode analyses are carried out for both sets of measurement data to experimentally verify the new method.

Contributed Paper

6:00

3pPA6. Experimental study of acoustic impedance of a Helmholtz resonator submitted to a grazing flow. Slaheddine Frikha, Pierre Yves Hennion, and Samir Boukhari (Laboratoire de Mecanique Physique, UPMC CNRS, Upresa 7068, France, frikha@ccr.jussieu.fr)

Helmholtz resonators are usually used in ducts or in engines inlet and exhaust systems in order to reduce radiated noise. Their efficiency may be strongly affected since they are submitted to a fully turbulent grazing flow. An experimental analysis of a branched Helmholtz resonator composed by a circular neck and a circular cavity is presented here. An attempt is made to understand the evolution of entry impedance modification with respect to mean flow and the shear layer characteristics at the vicinity of the resonator aperture. An inverse method is used to identify the impedance of 25 resonators. This method presents the advantage that it is completely nonintrusive and does not require source control. The grazing flow modifies the orifice resistance and the effective neck length. A parametric study of these corrections is performed using experimental results obtained for a set of 25 resonators and a flow Mach number varying from 0 up to 0.25. The mean flow structure is also analyzed using a numerical model. The dimensions of the tested resonators are similar to those usually used in the exhaust and inlet systems of automotive engines. That leads to a new parametric model of these corrections more suitable to engine applications.

Contributed Poster

This poster will be on display in the Poster Gallery from Thursday to Friday, 18–19 March. Authors will be at their posters from 10:00 a.m. to 12:00 noon on Thursday, 18 March.

3pPA7. On the acoustic of inverse sinusoidal and catenoidal nozzles. L. M. B. C. Campos and F. J. P. Lau (Instituto Superior Técnico, 1096 Lisboa Codex, Portugal)

The acoustic wave equation, for quasi-one-dimensional propagation, along a duct of varying cross section, containing a low Mach number mean flow, is obtained using as variables either the potential or the velocity; the ray approximation, which holds only for wavelength short compared with the lengthscales or variation of cross section and mean flow velocity, is used as a factor to reduce the wave equation to a Schrödinger form. It is shown that the latter, reduced from, for the potential, is the most convenient to study the acoustics of catenoidal and sinusoidal nozzles; it is found that these inherit respectively the filtering properties of catenoidal horns, and transparency properties of sinusoidal horns. This approach also applies to the exponential nozzle whereas, for the Gaussian nozzle, the sound field can be expressed in terms of Hermite functions, using a semi-reduced form of the wave equations. The exact solutions of the nozzle wave equation, for the four families of ducts, are plotted as amplitude and phase versus distance, for several combinations of frequency and low Mach number. The nozzle families considered include the catenoidal in the sinusoidal and exponential and the first six eigenfunctions of Gaussian nozzles. The acoustics of inverse sinusoidal and catenoidal nozzles can also be studied, without use of the preceding transformations, via the solution of modified Mathieu equation.

WEDNESDAY AFTERNOON, 17 MARCH 1999 ROOM H106, 4:15 TO 6:20 P.M.

Session 3pPPa

Psychological and Physiological Acoustics: Perceptual Processing of Cross-Spectral Information

John F. Culling, Chair
School of Psychology, Cardiff University, Cardiff CF1 3YG, UK

Chair's Introduction—4:15

Invited Papers

4:20

3pPPa1. Matching formant frequencies of complex sounds on different fundamentals. C. J. Darwin and Pascal Dissard (Exp. Psych., Univ. of Sussex, Brighton, Sussex BN1 9QG, UK)

In order to explore the ability of listeners to match formant frequencies in periodic sounds that differ in their fundamental frequency ($F0$), listeners adjusted the frequency of one formant of periodically excited one- or two-formant sounds to match the timbre of a similar target sound that could have either the same or a different $F0$. Variability of matching (s.d. of matches within each listener) was low when matching sounds were on the same $F0$. Variability increased when matching sounds had different $F0$s. However, this increase was larger for sounds with resolved harmonics than for those with unresolved harmonics. This difference may reflect the perceptual cost of estimating the spectral envelope (and formant frequency) from the excitation pattern. [Work supported by EPSRC Grant No. GR/L03422.]

4:40

3pPPa2. A ''missing-data'' model of *F*0-invariance in vowel perception. Alain de Cheveigne (LLF, Univ. of Paris 7, 2 Pl. Jussieu, Paris, France)

In steady-state voiced speech production, the vocal tract transfer function is sampled at multiples of the fundamental frequency ($F0$). At high $F0$, sparse sampling causes two problems: (a) a gradual loss of information defining the spectral shape, and (b) $F0$-dependent distortion due to aliasing. If the shape of the spectral envelope contains lag-domain components (spatial frequencies) beyond the Nyquist limit, they are folded relative to the Nyquist limit and mixed with in-band components. The Nyquist limit ($T0/2$, where $T0=1/F0$) depends on the spacing between sampling points along the spectral envelope, and thus on $F0$. Distortion is thus $F0$-dependent, and all the more severe as $F0$ is high. Smoothing or interpolation are ineffective in dealing with this problem, and cannot produce an $F0$-invariant pattern. A solution is proposed based on the concept of ''missing feature theory,'' recently proposed for speech recognition. Pattern matching is limited to available data ($F0$-spaced sample points) using an $F0$-dependent weighting function. All other points are ignored. The model is proposed in two versions, one that operates on the short-term spectrum or excitation pattern, the other on the autocorrelation function. The model ensures $F0$-independent vowel identification, at the cost of an $F0$ estimate.

5:00

3pPPa3. Evidence of a dissociation between the mechanisms governing the perceptual grouping of spectral components and the computation of low pitch. Brian Roberts and Jeffrey M. Brunstrom (School of Psych., Univ. of Birmingham, Edgbaston, Birmingham B15 2TT, UK, b.roberts@bham.ac.uk)

The perceptual fusion of harmonically related partials is often assumed to result from the operation of a template mechanism that is responsible for computing low pitch. This dual-role hypothesis has been tested using frequency-shifted complexes. These sounds are inharmonic, but preserve a regular spectral pattern of equal component spacing. Stimuli had a nominal fundamental ($F0$) frequency of 200 Hz (roving range $\pm 20\%$), and were frequency shifted either by 25.0% or 37.5%. Three consecutive components (6–8) were removed and replaced with a sinusoidal probe, located at one of a set of regularly spaced positions spanning the gap. On any trial, subjects heard a complex tone followed by an adjustable pure tone in a continuous loop. Subjects were well able to match the pitch of the probe unless it corresponded with a position predicted by the spectral pattern of the complex. In contrast, hit rates were not depressed for probes positioned at integer multiples of the $F0$(s) corresponding to the low pitch(es) of the complex, which were predicted from previous data [Patterson, J. Acoust. Soc. Am. **53**, 1565–1572 (1973)]. The findings suggest that separate mechanisms are responsible for the computation of low pitch and for the perceptual grouping of partials.

5:20

3pPPa4. Auditory processing of coherent and incoherent frequency modulation. Robert P. Carlyon (MRC Cognition and Brain Sci. Unit, 15 Chaucer Rd., Cambridge CB2 2EF, England, bob.carlyon@mrc-cbu.cam.ac.uk)

When two elements of a visual array move coherently, there is a strong tendency to group them perceptually. This has prompted several authors to suggest that acoustic frequency components which undergo coherent FM should be perceptually fused, and that those which are modulated incoherently should be segregated. This paper will review the mounting body of evidence demonstrating that, once a number of co-varying cues are controlled for, the auditory system is insensitive to the difference between coherent and incoherent FM. Such cues include the greater inharmonicity, smaller swings in average frequency, and more salient distortion products which can occur with incoherent compared to coherent modulation. In addition, new evidence will be presented showing that listeners can be more sensitive to one form of incoherent FM than to another: Opposite-direction quasi-linear frequency sweeps imposed on two carriers are more detectable when the frequency of the lower component decreases and that of the higher component increases than vice versa. This occurs even though the frequency sweeps imposed on the individual components are equally detectable when those components are presented in isolation, and even though within-channel interactions are masked by noise.

Contributed Papers

5:40

3pPPa5. Searching for a time window for timbre: Dynamic spectral profiles. M. E. H. Schouten and W. J. M. Peeters (Res. Inst. for Lang. and Speech UiL-OTS, Utrecht Univ., Trans 10, 3512 JK Utrecht, The Netherlands, bert.schouten@let.uu.nl)

Subjects were asked to match resonance glides, of various durations and sweep widths around 1000 Hz, with two connected steady-state resonances whose frequencies could be controlled independently. The expectation was that short resonance glides (below 100 ms), would give rise to single, apparently stationary, perceptual events, so that the two matching steady-state patterns would not rise or fall. Long glides, on the other hand, were expected to be perceived as rising or falling and to be matched accordingly. It was hoped that this would provide a basis for an explanation of diphthongs as unitary percepts. The resonances formed part of dynamic spectral profiles and consisted of single formantlike peaks swept along the top of a spectral base, consisting of 25 harmonically or logarithmically spaced components from 200 to 5000 Hz. There was an effect of duration, although it interacted with sweep width. At durations shorter than about 120 ms, subjects placed the two steady profiles that they had to match with the dynamic profile, much closer together than with durations over 120 ms; however, this only occurred if sweep width was more than 600 Hz.

6:00

3pPPa6. A spectral layer model in speech and music perception. Werner A. Deutsch (Austrian Acad. of Sci., Liebiggasse 5, A-1010, Vienna, Austria, wad@kfs.oeaw.ac.at)

According to a model of the peripheral hearing system establishing a masking and overmasking paradigm, speech and music signals have been split into several spectral layers by means of spectral subtraction. Spectral components below the so-called psychoacoustical irrelevance threshold are eliminated in a first processing step. The resulting signal, which exhibits no noticeable difference to the unprocessed one, is fed into an overmasking procedure applying flattened hearing masking functions. This action implements a kind of a spectral peak detector device. Consequently, the discrimination between spectral peaks (auditory figure) and background components, especially in reverberant environments, is improved. As a result, different audible signal parts according to different spectral layers are obtained, separating spectral peaks and weaker spectral components. In a certain range, both parts of speech and music signals are equally intelligible. In music, leading voices can be extracted and separated from the orchestra sound. Recent research indicates that this type of figure-background discrimination based on the dynamic characteristics of the acoustic signal only can exhibit several perceptually relevant features in listeners with normal hearing as well as in subjects with sensineural hearing impairment.

Session 3pPPb

Psychological and Physiological Acoustics: Sound Quality

Gerhard Krump, Chair
Harman Audio Electronic Systems GmbH, Schlesische Strasse 135, D-94315 Straubing, Germany

Contributed Papers

4:20

3pPPb1. Interior car sound quality—Assessment of acceleration noises. Reinhard Weber (Dept. of Phys., Carl-von-Ossietzky Univ., D-26111 Oldenburg, Germany)

Investigation of booming noise effects was the reason for the present study. Interior noises of six different cars accelerating from 1500 to 6000 rpm at third gear (full load) were presented over headphones. Seventy normal-hearing subjects (approximately one-third males and two-thirds females) aged from 20 to 60 years (at least 15 subjects per decade) took part in two experiments. After an initial orientation phase, preference judgments were made using a paired comparison paradigm. In experiment 2, the noises were assessed on a bipolar categorical scale (*disagreeable/agreeable*) with nine subdivisions. Immediately after the experiments, an interview was conducted to learn about the subjects' impressions about the noises. The preference data were analyzed using MDPREF and compared to the categorical judgment data for different subsets of subjects. The results on subjective data will be presented, together with a correlation analysis on their relationship with a number of acoustical and psychoacoustical signal parameters (level, loudness, sharpness, fluctuation strength, roughness).

4:40

3pPPb2. The influence of sound quality on expected visual impression. Monica M. Söderholm (Electrolux Resesearch & Innovation, S-105 45 Stockholm, Sweden, monica.soderholm@notes.electrolux.se) and Daniel Västfjäll (Chalmers Univ. of Technology, S-412 96 Göteborg, Sweden)

Information from visual and auditory systems is often linked. One example of the cross-modal connection between sound and visual experience is different materials that easily can be identified by their sound quality. The purpose of this investigation was to analyze the anticipated visual impression of three vacuum cleaners when listening to the product. The participants in the listening test where asked to describe the visual impression of the vacuum cleaners and also how they thought the vacuum cleaner sounded like with own words. The 24 listeners were both female and male of different ages and the vacuum cleaners were judged live. Often something that is large, for instance, a truck compared to a car, does produce more sound. The experience that large products are louder than small products is an influence when listening to vacuum cleaners. The listeners expected a large vacuum cleaner when listening to a rather loud vacuum cleaner. There was a unanimous opinion among the participants that a loud vacuum cleaner was ugly, had a box shape, and was old. The vacuum cleaners that were described to have a nice sound were described as small and round with a nice design and nice colors.

5:00

3pPPb3. Comparison of two semantic-differential test methods. Etienne Parizet (Renault, 67 rue des bons raisins, 92508 Rueil-Malmaison Cedex 9, France, etienne.parizet@renault.com)

Two methods for conducting a multidimensional test were investigated. In the first and classical one, a sound (or a pair of sounds) is presented to the subject, who has to evaluate it (or compare the two sounds) for the various semantic parameters. In the second one, the test is repeated for each parameter (i.e., subjects must evaluate the whole set of sounds for the first parameter, then again for the second one, and so on). These two methods were compared on the basis of five diesel engine noises in small cars driving at idle. Sounds were compared in pairs for seven parameters (pleasant, loud, etc.). The characterization of sounds thus obtained was similar for the two methods. The second one proved to be more accurate (the accuracy is evaluated on the basis of repetition and triadic errors) and with a shorter duration than the first one, because listeners are concentrated on the selected sound parameter while hearing a new stimulus. Therefore, this method is recommended for conducting semantic differential tests.

5:20

3pPPb4. About perceptivity of narrow-band frequency response variations of loudspeakers. Gerhard Krump (Harman Audio Electron. Systems GmbH, Schlesische Str. 135, D-94315 Straubing, Germany, gkrump@harman.de)

Many loudspeakers show peaks and gaps at 1 kHz caused by the connection of the hard cone and soft surround, which produces interferences and complex vibrational modes. Great efforts are made by the speaker manufacturer to avoid this by changing the surround geometry and material, whereas primarily knowledge about the perceptive limits of the peaks and gaps in frequency response would be necessary. For this investigation line spectra with equal amplitudes and statistical phases between 1 Hz and 20 kHz were calculated by a personal computer. At 1 kHz spectral enhancements or gaps with a bandwidth of 1 Hz or of a half, one, or two critical bands were realized with five different critical band levels. Ten test persons had to compare the first line spectrum with equal amplitudes (anchor) with the second signal with spectral changes in a yes–no procedure presented by an earphone with free-field equalizer at a SPL of 70 dB. The just-noticeable changes in spectral envelope are different for enhancements and gaps and depend on the bandwidth and the critical band level of the variations. They can be explained with calculated masking patterns and literature data.

5:40

3pPPb5. Determination of hearing properties and their connection to psychoacoustical parameters. Kai Johannsen and Holger Prante (Inst. of Tech. Acoust., Einsteinufer 25, 10587 Berlin, Germany, johannsen@mach.ut.tu-berlin.de)

The sound quality of products is often evaluated in hearing experiments using the semantic differential and a subsequent factorial analysis. In this study the method is applied to determine basic hearing properties. In order to achieve optimal results of the hearing experiment, special interest has been taken in the choice of adjectives and sounds. This selection is based on the results of a previously conducted survey of sound attributes. The selected 25 sounds were recorded using an artificial head and presented binaurally to a jury of 20 adults with normal hearing. A factorial analysis of the ratings on 24 attribute scales produced six factors representing basic perceptive cognitive and emotional hearing dimensions. In a last step connections between these dimensions and psychoacoustical parameters calculated from the sounds were evaluated using an analysis of correlation. Although the results show high correlations between loudness, sharpness, and pitch strength and equivalent attributes, no such connections could be found for the psychoacoustical roughness and fluctuation strength. In order to find better-correlated parameters, other calculation methods for these properties are investigated.

6:00

3pPPb6. New approach in measuring auditory source width. Jörg Becker, Markus Sapp, and Frederik Görges (Inst. of Commun. Eng., Aachen Univ. of Technologie, 52056 Aachen, Germany)

Depending on the acoustical surrounding sound sources appear to be broadened. This spatial impression can be rated by a quantity called auditory source width. In this paper a new method for determining this auditory source width is presented. The system is based on the reproduction of an artificial head recording of the examined sound field mixed with a pair of virtual acoustic pointers. These pointers can be moved by test persons to fit the left and right border of the sound source whose ASW has to be rated. The acoustical pointers are implemented as digital signal generators followed by real-time HRTF filters, measured in azimuth steps of 2 deg and cross faded between the directions. Investigations on suitable temporal and spectral shapes of the pointer signals have been made to minimize the localization blur of the pointer. The HRTF measurements and the recordings were done with different artificial heads in order to examine their influence on the determined ASW. Furthermore the influence of different sound field reproduction systems—headphone and crosstalk cancellation—are examined.

WEDNESDAY AFTERNOON, 17 MARCH 1999 ROOM H2036, 4:20 TO 6:20 P.M.

Session 3pSA

Structural Acoustics and Vibration: Structural Vibrations

Jacek Jarzynski, Cochair
George W. Woodruff School of Mechanical Engineering, Georgia Institute of Technology, Atlanta, Georgia 30332-0405, USA

David Feit, Cochair
Carderock Division, Naval Surface Warfare Center, 9500 MacArthur Boulevard, West Bethesda, Maryland 20817, USA

Contributed Papers

4:20

3pSA1. Torsional waves in a viscoelastic layer. Qingchun Li and Jacek Jarzynski (The George W. Woodruff School of Mech. Eng., Georgia Inst. of Technol., Atlanta, GA 30332-0405, jacek.jarzynski@me.gatech.edu)

The objectives of this study are first to examine experimentally the propagation of torsional waves in a viscoelastic material, and second to use these data to determine the complex shear modulus of the material. The viscoelastic material used in this study is neoprene rubber. A magnetic drive is used to generate a transient, one-cycle, torsional wave in a brass rod, and this wave is transmitted into a layer of neoprene rubber bonded to the rod. A fiber-optic laser Doppler vibrometer is used as a noncontact probe to measure the torsional wave transmitted through the neoprene layer. The experimental data are compared with predictions from a theoretical model [D. P. Thomas, Int. J. Eng. Sci. **6**, 565–570 (1968)]. Also, the complex shear modulus is determined from a least-square fit of the theoretical model to the experimental data using the downhill Simplex method. Another application of torsional waves is to nondestructive testing of materials, particularly for testing the strength of adhesive bonds between layers. [Work supported by ONR.]

4:40

3pSA2. Estimates of dynamic strain and stress in pipes by measured average vibration velocity. Svante Finnveden (Dept. of Vehicle Eng., KTH, SE-100 44 Stockholm, Sweden, svantef@fkt.kth.se) and Roger Pinnington (Univ. of Southampton, Southampton SO17 1BJ, England)

A velocity method for estimating dynamic strain and stress in pipe structures is investigated. With this method predicted or measured spatial average vibration velocity and theoretically derived strain factors are used to estimate maximum strain. The nondimensional strain factor is defined as the maximum strain times the ratio of the sound velocity to the spatial rms vibration velocity. Measurements are made confirming that this is a descriptive number. Using a spectral finite-element method, numerical experiments are made varying the pipe parameters and considering all 16 possible homogeneous boundary conditions. While indicating possible limitations of the method when equipment is mounted on pipes, the experiments verify the theoretical results. The velocity method may become useful in engineering practice for assessments of fatigue life.

5:00

3pSA3. On the dynamic interaction of a pipe conveying fluid with an elastic resisting medium. Ventzeslav A. Dzhupanov, Peter A. Djondjorov, and Vassil M. Vassilev (Inst. of Mech., Bulgarian Acad. of Sci., Sofia, Bulgaria)

The problem of the dynamic stability of pipes conveying high-speed fluid and lying on an elastic foundation has been a subject of significant interest during the past 30 years due to the broad application of pipes as structural components in different technologies. The present study contributes to the solution of this problem, suggesting a new model of the foundation—an infinitely deep elastic stratum, whose width is equal to the length of the attached pipe. The material of the foundation is supposed to be a homogeneous and isotropic one. Its dynamic behavior is considered in the context of linear elasticity. The pipe vibration is governed by the usual Bernoulli–Navier–Mohr theory. An approximate solution of the respective mathematical problem is obtained applying Galerkin's method. As a result, the influence of the medium physical characteristics to the flutter dynamic stability of cantilevered pipes through the pair of acoustic velocities is examined.

5:20

3pSA4. Investigation at a top counter weight of a washing machine. Ulrich Heise (Noiselab, FHP Motors GmbH, Klingenbergplatz 1, 26133 Oldenburg, Germany) and Wolfgang Harbich (Noiselab, 13599 Berlin, Germany)

During the development of a new washing machine a problem came up in spite of the durability of the newly designed top counter weight. The top counter weight is necessary to balance the drum of the machine. The problem was caused by the dynamical behavior of the system. A modal analysis was made at the compensation weight in the machine. Several different modes and eigenvalues were detected. The disturbing mode was found. It was caused by the stiffness of the fastening and the mass of the weight. The top counter weight was fastened in the axial direction of the drum. The disturbing mode was eliminated due to the change of fastening from axial to radial fastening. The problem is now solved. Another point of view are the other eigenvalues of the weight. The size of the weight looks like a xylophone bar and, in the same manner, it can vibrate. These modes of the weight itself are not disturbing modes, because the excitation forces are too small in this area and at this frequency range for exciting the compensation weight.

5:40

3pSA5. A mixed use of finite element and geometrical techniques. Philippe Jean (Centre Scientifique et Technique du Bâtiment, 24 rue Joseph Fourier, 38400 St. Martin d'Hères, France)

The finite-element method is limited to either small geometries or to the low-frequency range, whereas geometrical approaches are best applied at medium and high frequencies, but do not take vibrating surfaces into account. When the vibrating boundaries of a volume are only a small part of the total boundary, it is worth combining the two methods. By using geometrical methods to compute a Green's function that includes all wave reflections on the surfaces of the volume, it is possible to restrict the integral representation of the pressure field to the vibrating surfaces. The surfaces to be meshed will be reduced to surfaces with known velocity fields. This approach offers a means of reducing computation times. It has been applied to large volumes corresponding to a room with a vibrating concrete wall and to a train with a vibrating window.

6:00

3pSA6. Irregular modes at the endshield of a heating system motor. Ulrich Heise (Noiselab, FHP Motors GmbH, Klingenbergplatz 1, 26133 Oldenburg, Germany)

Nowadays, more and more modern heating systems are not installed in separated rooms, so the expectation of noise comfort has been increased for the last years. A noise and vibration optimization was made at an electric motors b-sided endshield. Sometimes, the old endshield emitted airborne noise. This was caused by the structure-borne noise of the bearings together with a mode of the endshield. A modal analysis was made to detect the disturbing mode. The amazing thing of this test was that the (0,1) mode frequency has a higher resonance frequency as the (1,1) mode. Normally the (1,1) mode frequency has a 1.594 higher frequency than the (0,1) mode resonance [N. H. Fletcher and T. D. Rossing, *The Physics of Musical Instruments* (1991), pp. 69–71]. The b-sided bearings can make a mass coupling from the rotor to the endshield in radial direction, but not in this way in the axial direction. The (1,1) mode of the endshield had nearly the same structure-borne amplitude as the (0,1) mode, but the (1,1) mode does not transmit airborne noise. This depends on the mechanical dimensions of the (1,1) mode, because this mode is working with its dimensions on an acoustical short circuit on air.

Session 3pSC

Speech Communication: Psychoacoustic Methods in Speech Recognition II

Birger Kollmeier, Cochair
AG Medizinische Physik, Universität Oldenburg, Postfach 2503, D-26111 Oldenburg, Germany

Hynek Hermansky, Cochair
Oregon Graduate Institute of Science and Technology, Beaverton, Oregon 97006-8921, USA

Chair's Introduction—4:15

Contributed Papers

4:20

3pSC1. Application of a roughness model to pathological voices. Robert Reuter (Inst. Electron., Techn. Univ., Einsteinufer 17, D-10587 Berlin, Germany, rreuter@tubife1.ee.tu-berlin.de) and Hanspeter Herzel (Humboldt Univ., D-10115 Berlin, Germany)

Irregularities in voiced speech are often related to the intrinsic nonlinearities in the vibrations of the vocal folds. Desynchronization of vibratory modes can induce nonlinear phenomena such as subharmonics, biphonation (two independent pitches), and deterministic chaos. The resulting complex signals exhibit various amplitude and frequency modulations and are, therefore, perceived typically as rough voices. In clinical studies of pathological voices perceptive roughness scores are widely used. So far, however, no satisfactory correlation of ratings of roughness and acoustic parameters has been found. In this presentation a modified Aures model for the quantification of roughness is introduced. It is exemplified that subharmonics lead to high roughness scores whereas the roughness of biphonation depends strongly on the two frequencies. Finally, a set of 120 perceptually evaluated pathological voices is studied. It turns out that the roughness score obtained from the psychoacoustic model is stronger correlated to the ratings of phoniatricians than conventional perturbation measures such as jitter and shimmer.

4:40

3pSC2. How children recognize spoken words in speech recognition threshold assessment. Lebel Caroline (Institut Raymond-Dewar, 3600 Berri, Montreal, QC H2L 4G9, Canada) and Picard Michel (Universite de Montreal, Montreal, QC H3C 3J7, Canada)

The purpose of this study was to investigate the potential influence of language context effects on the speech recognition threshold (SRT) in children of different ages. To determine the respective contributions of audibility and linguistic factors to the SRT, the speech intelligibility index (SII), and indices *k* and *j* as proposed by Nittrouer and Boothroyd [J. Acoust. Soc. Am. **87**, 2705–2715 (1990)] were calculated for the following conditions: (1) SRT using an open-set response format; (2) SRT using a closed-set response format (dissimilar foils to increase predictability); and (3) SRT using test words at the beginning of a short sentence. Listeners were three groups of 24 normally hearing children in the first, third, and fifth grades, respectively. Results indicated that SII and factor *j* decreased significantly and factor *k* increased proportionally as a function of both lexical and sentence-level context effects in all groups. This suggests that audibility factors are less critical in the facilitating presence of language contexts. The largest effect was shown for lexical context effects with predictable outcome of decreased SRTs. These findings are compelling evidence of language context effects playing a significant role in school-age children required to recognize speech at barely audible levels.

5:00

3pSC3. Silicon cochlea: A digital VLSI implementation of a quantitative model of the auditory system. Matthias Brucke, Wofgang Nebel (Univ. of Oldenburg, Computer Sci. Dept., VLSI Group, 2611 Oldenburg, Germany), Alexander Schwarz, Bärbel Mertsching (Univ. of Hamburg, Hamburg, Germany), Martin Hansen, and Birger Kollmeier (Univ. of Oldenburg, Oldenburg, Germany)

In this paper a digital VLSI implementation of a quantitative model of the auditory system is presented, which includes several processing stages physiologically and psychoacoustically motivated by the function of the human ear. The model was successfully applied to a wide range of applications from psychoacoustical experiments to speech recognition. The hardware design is derived from a C/C++ notation of the algorithms using floating point arithmetics. One application of the model is used to determine the necessary internal precision of the computations for a transfer into a version suitable for a hardware implementation using fixpoint arithmetics. This application provides a very valid test bench since the significant speech processing features of the model are proofed by computing an objective speech quality measure. The processing scheme is divided into designs for two FPGAs and will be converted into ASICs in a later version. The implementation of the model as dedicated hardware provides efficient coprocessing power and allows implementations of complex auditory-based speech processing algorithms in real time because the chipset performs substantial parts of the necessary calculations.

5:20

3pSC4. Entropy rate based speech segmentation. Wolfgang Wokurek (Inst. of Natural Lang. Processing, Exp. Phonet., Stuttgart Univ., Azenbergstrasse 12, Stuttgart, 70174, Germany, wokurek@ims.uni-stuttgart.de)

The sequence of estimates of the speech signal's entropy rate is investigated as a potential basis for speech segmentation. Raising and falling edges of that entropy rate curve and its maxima and minima are considered as candidates for segment boundaries. These prominent points are compared to the phonetic segment boundaries and to acoustic landmarks [S. A. Liu, J. Acoust. Soc. Am. **100**, 3417–3430 (1996)]. The comparison is made using the ''Kiel corpus of read speech'' which is a phonetically manually labeled corpus of German utterances. The evaluation considers the entropy rate labels against the background of the phone segments. In particular the position and the count of the entropy rate labels within each phone are appraised. The average results are reported both as totals and broken down into phone classes and phones. The frame duration of the entropy rate estimation controls the smoothness of the curve and hence the label count per phone. A similar evaluation relates the entropy rate labels to the acoustic landmarks.

5:40–6:20 Discussion

Session 3pSP

Signal Processing in Acoustics and Engineering Acoustics: Binaural Technology II

Mahlon Burkhard, Cochair
Sonic Perceptions, Inc., 6964 Kennsington Road, Brighton, Michigan 48116, USA

Jens Blauert, Cochair
Communication Acoustics, Ruhr-Universität Bochum, D-44780 Bochum, Germany

Chair's Introduction—4:35

Contributed Papers

4:40

3pSP1. Implementation issues in the development of a real-time, Windows-based system to study spatial hearing. Joel D. Miller (Raytheon, NASA Ames Res. Ctr., M.S. 262-6, Moffett Field, CA 94035-1000, jdmiller@mail.arc.nasa.gov), Jonathan S. Abel (San Jose State Univ., NASA Ames Res. Ctr., Moffett Field, CA 94035-1000), and Elizabeth M. Wenzel (NASA Ames Res. Ctr., Moffett Field, CA 94035-1000)

As a tool to study spatial hearing, a customizable real-time 3-D-audio and virtual acoustic environment rendering system, Sound Laboratory (SLab), was developed. Design goals for this system included flexibility, extensibility, maintainability, and a fast development cycle per experiment. SLab is a Windows application composed of five distinct software layers: Application programming interface (API), 3D projection, signal flow translation, signal routing and processing, and digital signal processing library. The acoustic scene, including listener, source, and environment characteristics, is specified in the API layer and translated in the 3-D projection layer to geometric quantities, such as range and arrival angle, for each path rendered between the source and listener. The geometry and head-related transfer function coefficients are rendered using a set of parallel finite impulse response filters and delay lines built on Intel's Signal Processing Library. This rendering architecture provides the flexibility and the extensibility required for psychoacoustic experimentation, while the modular nature of the programming interface ensures maintainability and quick development of new experiments. The psychoacoustic parameters to be manipulated, the signal flow diagram, and the five software layers are discussed in detail, and various implementation issues are examined.

5:00

3pSP2. Computational model of an individual head-related transfer function using the BEM. Brian F. G. Katz[a] (Acoust. Dept., Penn State Univ., State College, PA 16801)

The head-related transfer function (HRTF), determined by the complex geometry of the pinnae and head, is the primary research and commercial tool for exploring and exploiting 3-D auralization and auditory localization. Research into the determining characteristics of the HRTF is difficult, as the anatomical variations between individuals are many. These variations make comparisons between individuals less than ideal for determining the relation between structure of the individual and components of the HRTF. This paper will discuss an investigation into the use of a geometrical model of an individual to calculate the HRTF. The calculation utilizes the boundary element method (BEM). As a tool, the use of a computer model allows for selected variations in the individual's anatomy and direct observation of the results, a difficult task in experimental measures. Previous work by the author discussed the variability in experimental measurement techniques of the HRTF. Comparisons are made between the model results and these HRTF measurements for the same individual. Some preliminary variations to the model and their effects are also discussed. Computational results show good agreement with the general trends of the measurements and the frequency limitations of the computation. [a] Currently at Artec Consultants, Inc., 114 W. 26th St., New York, NY 10001.

5:20

3pSP3. Auditory perception of reverberant surroundings. Jesper Sandvad (Waisman Ctr., Univ. of Wisconsin, Madison, WI and Acoust. Lab., Aalborg Univ., Denmark)

Three experiments on perception of reverberant surroundings were performed. In the first experiment, listeners were presented with binaural recordings of a speech signal and a set of photographs taken in different rooms, and were asked to point out where each recording was made. Most listeners performed very well in this task (average number of correct answers was 70%), showing that reverberation contains information on room properties that the listeners are able to extract. In the second experiment, listeners were asked to judge the relative size of different rooms by listening to the recorded signals. The results show substantial individual differences, with some listeners being close to veridical performance while others had only a few correct answers. A scaling analysis suggests that some listeners use the direct/reverberant energy ratio, while others use reverberation time as a cue for room size. In the third experiment, artificial reverberation generated by a geometric room model (including individual reflections) and from a stochastic model (controlling only energy measures) were compared with signals generated directly from measured room impulse responses. The results show comparable performance, suggesting that energy measures are the most important for assessing information on room parameters. [Work supported by ONR Grant No. N00014-96-1-0675.]

5:40

3pSP4. Comparison of wideband LMS, subband LMS, and a nonlinear entropic neural approach to adaptive noise cancellation for speech enhancement. P. W. Shields, M. Girolami, and D. R. Campbell (Dept. of Electron. Eng. and Phys., Univ. of Paisley, High St. Paisley, Renfrewshire PA1 2BE, Scotland, paul@diana22.pailsey.ac.uk)

An empirical comparison of three adaptive algorithms for speech enhancement in noisy reverberant conditions is presented. The subband least mean square (LMS) [E. Toner and D. R. Campbell, Speech Commun. **12**,

3p WED. PM

253–259 (1993)] and minimum entropy noise reduction schemes [M. Girolami, Electron. Lett. **33**(17), 1437–1438 (1997)] are compared with a reference wideband LMS approach [S. D. Stearns and R. A. David, *Signal Processing Algorithms* (Prentice–Hall, Englewood Cliffs, NJ, 1988)]. All three methods were applied to the enhancement of speech corrupted with speech-shaped noise. The schemes were tested using simulated anechoic and real-room reverberant ($T_{60}=0.3$ s) environments. The anechoic and real-room recordings were binaural including head shadow and diffraction effects. The subband LMS adaptive processing scheme uses the LMS adaptive noise cancellation algorithm in frequency-limited subbands. The inputs from each microphone are split into 16 contiguous subbands using a cochlear distribution according the function provided by Greenwood [J. Acoust. Soc. Am. **87**, 2592–2605 (1990)]. Each frequency-limited subband is processed using a LMS adaptive noise cancellation filter operating in an intermittent or continuous mode depending on input signal characteristics. The neural network approach is motivated by temporally sensitive hebbian super-synapses, which may form sparse representations based on commonly occurring spatio-temporal input patterns. The results for real-room signals demonstrate statistically equivalent performance of the subband LMS and wideband neural method, both of which prove superior to the wideband LMS algorithm.

6:00

3pSP5. Evaluation of the air particle velocity signal from the binaural pressure impulse response. Domenico Stanzial (CIARM-CNR c/o Cemoter Acoust. Dept., Via Canal Bianco 28, I-44044 Cassana, Ferrara, Italy) and Davide Bonsi (CIARM c/o Univ. of Ferrara, I-44100 Ferrara, Italy)

From the Lagrangian theory in linear acoustics one clearly infers that the generalized momenta of the sound field are the acoustic pressure and the three components of the air particle velocity. This means that only through the knowledge of the full set of these four quantities a complete physical identification of the sound field can be achieved. The binaural technology represents an important tool for this goal, since it offers a method for reconstructing the pressure sound field by means of a couple of pressure impulse responses measured in two close points. An additional improvement of the binaural signal processing can be obtained using the two pressure input signals for evaluating the velocity component along the direction determined by the measurement points. First the velocity impulse response component is evaluated by means of the Euler equation and then, by convolving this signal with the usual anechoic signal, the velocity is reconstructed. In this paper the rigorous mathematical procedure for accomplishing the above task is presented.

WEDNESDAY AFTERNOON, 17 MARCH 1999 ROOM H104, 4:40 TO 6:20 P.M.

Session 3pUWa

Underwater Acoustics: Sediment Acoustics

F. Michael Pestorius, Cochair
Applied Research Laboratories, University of Texas, Austin, Texas 78713-8029, USA

Nicholas G. Pace, Cochair
SACLANT Undersea Research Centre, Viale S. Bartolomeo 400, 19038 La Spezia, Italy

Contributed Papers

4:40

3pUWa1. Volume scattering realizations from ocean sediment sound-speed and density inhomogeneities. Kevin D. LePage (SACLANT Undersea Res. Ctr., Vl. S. Bartolomeo 400, 19138 La Spezia, Italy) and Henrik Schmidt (MIT, Cambridge, MA 02139)

Synthetic scattered field calculations can serve as a useful tool for evaluating the practicality of estimating bottom scattering properties from *in-situ* measurements. Here the temporal and angular characteristics of early time reverberation from volume inhomogeneity scatterers in the sub-bottom are investigated using perturbation theory in the framework of a spectral integral approach. In order to model realistic sediments more accurately, the theory treats the scattering from both sound-speed and density fluctuations in the presence of a background sound-speed gradient. To allow the simulation of realistic experimental geometries, the scattered field is propagated to various receivers through a general multilayered waveguide. Results show that there are several distinctive characteristics of the fields scattered by the different mechanisms which depend both on the scattering properties of the bottom and the unperturbed properties of the overall waveguide.

5:00

3pUWa2. In-sediment coherence measurements in a very shallow-water area. Joseph L. Lopes, Iris C. Paustian, and John S. Stroud (Coastal Systems Station, Naval Surface Warfare Ctr., Code R21, 6703 W. Hwy. 98, Panama City, FL 32407-7001)

A measurement was conducted in a very shallow-water (VSW) region to investigate acoustic propagation into a sandy bottom. The measurement utilized several acoustic sources and two identical hydrophone arrays. The sources were mounted onto a stationary sonar tower complete with horizontal pan and vertical tilt motors. Each hydrophone array consisted of four transducers that were buried via water-jetting methods approximately 10 m from the sonar tower. One array was situated such that the projected acoustic beam was parallel to the rippled structure associated with the sandy bottom, while the other was located where the transmitted beam was perpendicular to the rippled structure. Results of the in-sediment coherence data will be presented as functions of hydrophone burial depth and range in the frequency range between 30 and 150 kHz for the two buried arrays.

5:20

3pUWa3. Sediment critical angle estimation via *in situ* acoustic measurements. Alain Maguer, Warren L. J. Fox, Edoardo Bovio (NATO SACLANT Undersea Res. Ctr., Viale San Bartolomeo 400, 19138, La Spezia, Italy), and Henrik Schmidt (MIT, Cambridge, MA 02139)

The basic physics of sound penetration into ocean sediments is a current area of active research since a good understanding of this phenomenon is essential for designing sonar systems that can detect, localize, classify, and identify buried objects. The sound speed of the sediment is a crucial parameter since the ratio of sound speeds at the water–sediment interface determines the critical angle. Sediment sound speed is typically measured with core samples using high-frequency (100's of kHz) pulsed travel time measurements. Simulations using Biot theory and taking into account sediment permeability have shown that there may be a significant frequency dependence to sediment sound speed in the range 1–100 kHz. Here, sediment sound speed and critical angle estimation are investigated through the analysis of *in situ* acoustic measurements. Acoustic energy in the frequency range 2–16 kHz was directed toward a sandy seabottom, and a buried 14-element hydrophone array measured the incoming signals. The critical angle is estimated by analyzing both the variations of the penetration ratios and signal arrival times versus frequency, burial depth, and grazing angle. The influence of bottom roughness and sonar beamwidth on the penetration ratio is also investigated.

5:40

3pUWa4. Bulk viscidity model in acoustics of bubbly water-saturated soil. Isaac Shreiber (Inst. for Industrial Math., Hanachtom 4/24, 84311 Beer-Sheva, Israel, isaak@indigo.cs.bgu.ac.il)

Recent experimental studies of acoustic wave propagation in water-saturated soil showed that the shock wave structure in the medium is similar to acoustic waves in bubbly liquids; namely, shock waves in the medium have an oscillating profile and strong attenuation of amplitude. The main physical reasons preventing the generalization of bubbly liquid acoustics in this case are that bubble expansion in unlimited space differs from bubble expansion in porous media, and the most delicate moment of this generalization is how to define the mixture pressure, what the mixture pressure is, and how it corresponds to pressure in the bubbles and relates to bubble dynamics. The goal of this communication is to show how to generalize the bubbly liquid acoustics in the water–bubbles–sand case with the help of the cell-model approach. The cell model is used for the Rayleigh equation derivation for a single bubble dynamics in a porous medium, and the governing equations for nonlinear acoustic waves are derived. The obtained canonical equations can explain some experimental data of three-phase media acoustics.

6:00

3pUWa5. A mixed wave finite-element approach for solving Biot's poroelasticity equations in acoustics. Franck C. Sgard (LASH, DGCB URA CNRS 1652, ENTPE-Rue Maurice Audin, 69518 Vaulx-en-Velin Cedex, France, Franck.Sgard@entpe.fr), Noureddine Atalla, and Raymond Panneton (Univ. de Sherbrooke, QC J1K 2R1, Canada)

The use of finite-element models for solving Biot's poroelasticity equations often leads to large frequency-dependent systems. Recently, the authors have investigated the use of a selective modal analysis to decrease the size of large finite-element models involving poroelastic structures. The method used a dual real modal basis associated with the skeleton *in vacuo* and the fluid phase occupying the volume of the porous material to approximate the $\{U,p\}$ variables. However, this method converges poorly due to the importance of the damping brought in by the porous material. In this paper, an alternate reduction technique, based on a plane waves expansion method combined with a finite-element approach, is investigated in the case of a single porous layer. The theory behind the technique, together with numerical examples illustrating the performance of the approach, will be presented. [Work supported by Centre Jacques Cartier.]

WEDNESDAY AFTERNOON, 17 MARCH 1999 ROOM H2053, 4:20 TO 6:20 P.M.

3p WED. PM

Session 3pUWb

Underwater Acoustics: Scattering from Underwater Structures

George V. Frisk, Chair
Woods Hole Oceanographic Institute, Woods Hole, Massachusetts 02543, USA

Contributed Papers

4:20

3pUWb1. Influence of sound–structure interaction on backscattering amplitude in underwater acoustics. H. Peine (FWG, FB 331, Klausdorfer Weg 2-24, 24148 Kiel, Germany)

Sea-based backscattering experiments were carried out in the frequency range from Helmholtz numbers (ka) 10 to 30 with a model target. In order to improve target identification, focus here is on separating features related to sound structure interaction from those determined by the target's shape. At the frequencies under concern generally many overlapping vibration modes of the target are excited. Whereas with specially designed objects, like thin-walled hollow cylindrical or spherical shells, isolated resonance modes can be directly observed in the echo and assigned to surface waves, the model target used here resembles the complex structure of real obstacles. The structural responses measured by accelerometers attached inside the model are recorded simultaneously together with the backscattering amplitude allowing immediate comparison. Narrow-band swept sine and CW pulses were used. At each frequency the target was turned around a fixed axis with angle resolution better than 2 degrees. A novel spectral transfer function is tested modeling the frequency-dependent boundary impedance and therefore the envelope deformation of the scattered pulse due to interaction of the impinging wave with the target's interior. This model function has rather few parameters to be adjusted.

4:40

3pUWb2. A perturbation theory for scattering from targets near rough surface sediments: Numerical results. Garner C. Bishop and Judy Smith (Naval Undersea Warfare Ctr., Div. Newport, Newport, RI 02840)

A null field T-matrix perturbation theory developed for plane-wave scattering from a fluid loaded elastic spherical shell near a rough fluid elastic interface [J. Acoust. Soc. Am. **101**, 767–788 (1997)] is generalized to include scattering from spherical, spheroidal, and endcapped cylindrical targets near rough surface rigid, soft, fluid, and elastic sediments. Numerical results are obtained that demonstrate some of the effects of surface roughness on resonant and nonresonant target-boundary scattering.

5:00

3pUWb3. Localized modes of oscillating structures which lie on the bottom. Andrei Abramian (Inst. for Problems in Mech. Eng. RAS, Bolshoy pr. V. O. 61, 199178 St. Petersburg, Russia, abramian@hidro.ipme.ru)

The phenomenon of wave localization in hydroelastic systems leads to the strength concentration of radiation fields. The linear method considers the process of localization to be the formation of nonpropagation waves (trapped modes phenomenon). The presence of such waves in the total wave packet points to the existance of mixed natural spectrum of differential operators describing the behavior of hydroelastic systems. The problem of liquid and oscillating structure interaction caused by the trapped modes phenomenon has been solved (membranes, dies, plates and different liquid models). The areas of wave localization have been determined. These areas depend on both the parameters of oscillating structures and the liquid waveguide parameters (the linear dimensions of the channel filled with liquid; the height from the bottom to the liquid surface; the liquid density gradient according to the height, etc.). Necessary and sufficient conditions for the low-frequency trapped modes and the high-frequency trapped modes have been found. The wave localization in nonlinear elastic structures interacting with liquid has been studied. Cases of weak and strong nonlinearity have been investigated. It has been shown that the slightly decreasing tail is added to nonlinear localized modes depending on the frequency of linear localized modes. The tail is caused by the interaction of the mode's continuous spectrum and the localized modes.

5:20

3pUWb4. Trapping modes of oscillations in an infinitely long waveguide with submerged object in the form of a massive die. Dmitri Indeitsev (Inst. for Problems in Mech. Eng. RAS, Bolshoy pr. V.O. 61, St. Petersburg 199178, Russia, abramian@hidro.ipme.ru)

It is shown for an infinitely long waveguide—first in the form of a two-dimensional and then a three-dimensional channel—filled with an ideal compressible liquid with a free surface, that there can exist standing waves as well as traveling waves localized in the region of a dynamic submerged object—a massive die. The appearance of such waves is due to the presence of a mixed spectrum of characteristic frequencies of oscillation. In addition to the continuous spectrum, a point (discrete) spectrum distributed along the axis of the continuous spectrum is also present. A relation is found between the geometric parameters of the channel and the massive die for which this spectrum exists.

5:40

3pUWb5. Repulsion phenomena in the phase-velocity dispersion curves of circumferential waves on elastic cylindrical shells. Herbert Überall (Dept. of Phys., Catholic Univ., 6th and Michigan Ave. N.E., Washington, DC 20064), Gérard Maze, Fernand Léon, and Jean Ripoche (Univ. of Le Havre, 76610 Le Havre, France)

The complex eigenfrequencies of an evacuated, fluid-immersed infinite cylindrical shell, when plotted in the complex frequency plane, have been grouped into families corresponding to different types of circumferential waves. The real parts of these eigenfrequencies have been used to obtain dispersion curves versus frequency of the phase velocities of these circumferential waves, which are analogous to those of the Lamb waves on an elastic plate *in vacuo* labeled $A_0, A_1, \ldots$ and $S_0, S_1, \ldots$, but which contain an additional branch reminiscent of the fluid-borne Scholte–Stoneley wave. This branch forms together with the A_0-analog an interacting pair of dispersion curves which will be called A_{0+} (upper branch) and A_{0-} (lower branch). These exhibit a repulsion phenomenon near the ambient fluid sound speech analogous to that in perturbed, quasi-degenerate atomic levels. This is explained here by perturbation theory, showing that during repulsion the wave character gets exchanged so that at frequencies above the repulsion point A_{0+} is a flexural and A_{0-} a fluid-borne wave, and vice versa below the repulsion point.

6:00

3pUWb6. Localization in acoustic propagation in water with air cylinders. Zhen Ye and Emile Hoskinson (Dept. of Phys., Natl. Central Univ., Chungli, Taiwan, ROC)

Wave localization is the peculiar property of a scattering medium that completely blocks propagation, thus inducing a surprising phase transition, for example in optical or acoustic transparency or electrical conductivity. When localized, waves remain confined in space until dissipated. This property has been explained for randomly disordered scatterers. It is generally believed that disorder is an essential ingredient of localization, and in two dimensions (2D) waves are always localized with any amount of randomness. Here it is shown that waves are not always localized in 2D, but under proper conditions even periodic structures can achieve localization in the case of acoustic propagation through water containing an array of air cylinders. An essential component of localization in this case arises from the natural resonance and an amazing collective behavior of the cylinders. Exact numerical calculations reveal the unexpected result that localization is relatively independent of the precise location or organization of the scatterers. The results provide insight on 2D wave localization and offer an opportunity for further investigation of important questions about localization phenomena. [Work supported by NSC and NCU of ROC.]

Posters from various technical sessions remain on display in the Poster Gallery.

Posters from sessions which contain both lecture and poster presentations will be attended by the authors as listed below.

10:00–12:00

3aPAa13	Shenoda, Fathy	A new acoustic conductor
3pPA7	Campos, L. M. B. C.	On the acoustics of inverse sinusoidal and catenoidal nozzles
5pPAc13	Blum, Andreas	Acoustic determination of water distribution in unsaturated soil
5pPAc14	Lauriks, Walter	Surface waves above thin porous layers and periodic structures
5pPAc15	Roberts, Peter M.	Low-frequency acoustics stimulation of fluid flow in porous media
5pPAc16	Sohbi, Sahraoui	Damping modelization of acoustic foams at low frequency

11:00–12:20

4aED7	Foken, Wolfgang	Education of applied acoustics for students of automotive engineering
4aED8	Dutilleux, Pierre	Architecture and music: A laboratory
4pNSb11	Hempel, Thomas	Evaluation of interior car sound with a new specific semantic differential design
4pNSb12	Hellmann, Andreas	Motion perception and loudness judgements

Also, the following poster sessions are scheduled:
Poster Session 4aPPa
Poster Session 4aSCb

THURSDAY MORNING, 18 MARCH 1999 ROOM H3010, 7:55 TO 11:20 A.M.

Session 4aAAa

Architectural Acoustics and Signal Processing in Acoustics: Verification of Auralization and Modeling Programs II

Richard H. Campbell, Cochair
Bang Campbell Associates, P.O. Box 47, Woods Hole, Massachusetts 02543, USA

U. Peter Svensson, Cochair
Department of Applied Acoustics, Chalmers University of Technology, Sven Hultins Gath 8, S-41296 Gothenburg, Sweden

Chair's Introduction—7:55

Invited Papers

8:00

4aAAa1. Prediction of subjective properties of a sound field in a concert hall with tenth-scale model. Koji Ishida, Kiyoshi Sugino (Inst. of Technol., Tokyu Construction Co., Ltd., 3062-1 Tana Soneshita, Sagamihara, Kanagawa, 229-1124 Japan, k-ishida@hd.tokyu-cnst.co.jp), and Hideki Tachibana (Univ. of Tokyo, Tokyo, 106-8558 Japan)

This paper discusses a scale model experiment for room acoustic design of the Yokohama Minatomirai Concert Hall which was opened in June 1998. Priority was given to subjective evaluation in the acoustical design process. To this end a measure to improve S/N ratio of the impulse response and filtering procedure for cancellation of the influence of sound source were investigated. Binaural impulse responses measured with different boundary conditions of the hall were convolved with dry sources, and simulated sounds were compared subjectively. The examination of the auralization reflected on interior design. Comparison of subjective and objective properties with full scale and scale model has been carried out in order to verify auralization using scale model experiment. Good agreement on both evaluations was obtained.

8:20

4aAAa2. The geometric room model as a surround-sound auralization resource. Michael Thomas Driscoll, Eric L. Reuter, and Richard H. Campbell (Elec. and Computer Eng. Dept., Worcester Polytechnic Inst., 100 Institute Rd., Worcester, MA 01609)

A large church near the WPI campus was chosen as an experimental site for its splendid acoustics as reported by musicians who perform there. The church was modeled using the CATT-Acoustic software, and the resulting computed acoustic parameters compared favorably with MLSSA measurements taken in the church. A brass choir was recorded in the church using a surround-sound multitrack microphone technique. The brass players were also recorded as individuals with acoustic isolation between the instruments. Each layer's actual position in the church during the recording session was defined in the model as a CATT source with its associated

directivity pattern, and positioned in the church CATT model. Impulse reponses were computed from each source location to a set of CATT receivers which duplicated the surround-sound microphone array. The isolated brass instrument recordings were then convolved with these impulse responses and auralized to a surround-sound mix. The auralized version and the actual recorded version were compared for authenticity by a panel of listeners.

Contributed Papers

8:40

4aAAa3. Realization of an auralization software based on echograms calculated by a sound ray technique. Dominique A. Archambeau (Dept. of Appl. Acoust. and Lighting, Univ. of Liege, 10 Grande Traverse, 4000 Liege 1, Belgium, D.Archambeau@ulg.ac.be)

Among the different auralization implementations yet devised, a completely computerized auralization technique, in which the acoustics of the room to be treated is simulated by a sound ray tracing algorithm, was realized. The major difficulty closely linked with this process was to convert the set of temporal energy distributions (one per frequency band), issued from the ray tracing software, into pressure echograms or impulse responses, so that the phase information had to be reintroduced. The various stages were conducted according to an earlier investigation of this problem [R. Heinz, *Entwicklung und beurteilung von computergestützten methoden zur binauralen raumsimulation* (Verlag Shaker, Aachen, 1994)]. Several methods able to derive the binaural room impulse responses from the corresponding monaural impulse response were then studied. These binaural impulse responses were next convolved with any vocal or musical anechoic signal yielding the signal as it could be heard or auralized in the real room. The convolutions were conducted in the frequency domain using the fast Fourier transform algorithm. This auralization program was finally tested on various acoustical spaces and a subjective study was then carried out to compare real sound signals and the corresponding auralized ones.

9:00

4aAAa4. A new client-server system for auralization. Christoph Moldrzyk and Bernard Metzler (TU Berlin, FSP-PV/PRZ, Sekr. MA 073, Strasse des 17. Juni 136, 10623 Berlin, Germany, aural@prz.tu-berlin.de)

A system for parallel calculation of sound fields was developed. The system will provide for remote, concurrent access via Internet. A remote user will be offered the opportunity to upload three-dimensional room geometries onto the server. The room impulse response will be retransmitted after its calculation. It will locally be convoluted with appropriate dry sounds. Parallel computing—depending on the number of available processing engines—will allow speeding up the calculation several times compared with existing solutions. The service offered can be used at any location depending on Internet availability. Additionally, the server system comprises a data archive of acoustic measurements and architectural information (geometries, materials, etc). Integrating it into Internet services will establish a unique opportunity for the user—while planning rooms at the desk or any location—to get online information about the physical behavior of his/her intended design. Many users may use the system simultaneously with different requirement profiles. The proposed approach also allows for real-time convolution on the server if the user–server connectivity offers appropriate bandwith. The Internet Resource Reservation Protocol RSVP will be employed to reserve sufficient bandwith. Assuming adequate network behavior, real-time performance could be guaranteed.

9:20

4aAAa5. Considerations for including surface scattering in room-acoustics auralization. Rendell R. Torres and Mendel Kleiner (Chalmers Rm., Acoust. Group, Dept. of Appl. Acoust., Chalmers Univ. of Tech., SE-41296, Gothenburg, Sweden, rendell@ta.chalmers.se)

Recent research in auralization has centered on including wave-theoretical aspects that are unaccounted for by well-developed but frequency-limited geometrical models [Dalenbäck *et al.*, J. Audio Eng. Soc. **42**(10) (1994)]. For example, inclusion of edge diffraction (or edge scattering) has been shown (via scale-model measurements and listening tests) to contribute audibly to the early part of the room impulse response [Torres and Kleiner, Proc. 16th Intl. Congress on Acoust. (1998)]. Modeling room *surface* scattering requires consideration of at least two main concerns: (1) characteristics of typical room surfaces and (2) types of numerical models most suitable for reasonable speed and accuracy. Typical room surfaces (e.g., in concert halls) can have a periodic nature at one wave number-scale and a statistical nature at another. This suggests use of a multiscale, multiple-scattering description possibly based on a combination of perturbation models, ''boss'' models, variational models, or higher-order Kirchhoff theory. It may also require simplified surface-descriptors like those used for random rough surfaces. The second main concern influences the form of the model (e.g., time-domain versus frequency-domain formulations, chosen surface parameters) and its usefulness for auralization programs. Possible models are discussed with their respective applicability to room acoustics auralization. [Work supported by Johnsons Stiftelse and Teknikbrostiftelsen.]

9:40

4aAAa6. Acoustical modeling and auralization as a design tool for concert hall renovation. Bennett Brooks (Brooks Acoust. Corp., 27 Hartford Turnpike, Vernon, CT 06066, bbrooks@brooks-acoustics.com)

A 400-seat university concert hall was modeled using the CATT-Acoustic software system. Good agreement was found between objective measurements and model predictions for the original hall. Also, the subjective quality of the auralized model was judged by music faculty to be an accurate representation of the original hall. These results provided confidence in the model as a design tool for hall renovations. Design decisions were made based on objective parameters, such as early reflection density, and the subjective quality of the sound for a series of model configurations. The final design was largely realized and the renovated hall has been well received by both faculty and community. Sound samples illustrating auralized design options will be presented.

10:00–10:20 Break

10:20

4aAAa7. Use of bidirectional reflectance distribution function in a particle tracing method. Jean-François Dindart (LaBRI 351 crs de la Libération, 33405 Talence Cedex, France, dindart@labri.u-bordeaux.fr), Jean-Jacques Embrechts[a] (Liège Univ., Liège 1, Belgium), and Catherine Sémidor (ERIAC, Ecole d'architecture et de paysage de Bordeaux, 33405 Talence Cedex, France)

A previous article (DAFX98, Barcelone) described the particle tracing method, which can be viewed as an efficient alternative to distributed ray-tracing. This method is intended to offer a more accurate simulation of sound reflection than the classical ones. The reflection model in the particle tracing method is based on the bidirectional reflectance distribution function (brdf) which describes the directional distribution of reflected sound. As all mathematical framework, this function can be implemented in different ways. A model derived from physical acoustics and described in a recent paper by Embrechts (ASA/ICA Seattle 98) is used. Comparisons of computed and measured results are used to validate the method in a simple rectangular classroom of the Ecole d'architecture et de paysage de Bordeaux. The reflection parameters' effects are made predominant in these experiments. The room acoustics parameters of this classroom are measured with different treatments of one wall (concerning its sound reflective properties). The reflective properties of the walls are also modelized with the Embrechts model and the room-acoustics criteria are computed in the same configurations. The validation on this simple room is finally discussed on the basis of the computed and measured results.
[a] National Fund for Scientific Research.

10:40

4aAAa8. A simulation package for room acoustics with an open interface. Guido Bartsch (Inst. for Technol. Acoust., Templergraben 55, 52056 Aachen, Germany)

The solution of complex acoustic problems of the low-frequency sound field presupposes the numeric implementation of the wave equation. Especially for the calculation of sound fields in a finite volume (interior problem), the method of the finite elements (FEM) can be applied. The software market gives the acoustic engineer many different commercial simulation packages, which have no or only a limited user interface for user extensions. This was the reason to create the simulation module called WaveSolve^{3D}. Due to its high portable structure WaveSolve^{3D} can be used on all current and future computer generations, and thereby permits the running of the application on the hardware with the best computing power. In the context of this paper some simulation results computed by WaveSolve^{3D} will be presented. Verification can be achieved by comparison with analytical results in simple enclosures or with measurement results for more complex rooms. The work is part of a project which intends to extend the frequency range in room acoustical computer simulation.

11:00

4aAAa9. Evaluation and modeling of small rooms. Eva Arato-Borsi, Tamas Poth (Hungarian Radio, Tech. Dept., 1800 Budapest, Brody S. 5-7, Hungary, borsinear@muszak.radio.hu), and Andor Furjes (Tech. Univ. of Budapest, 1111 Budapest, Hungary)

The objective characterization of the sound field in a small room with parameters relating to the subjective side needs great experimental efforts. Well-controlled sound is important and critical in reference listening rooms and recording rooms. These are small rooms in the acoustic sense. In order to find new objective parameters for room acoustical evaluation of these spaces, several subjective tests were carried out. In the paper, the results of the listening tests are given. The new objective parameters derived from measured impulse responses are presented. A series of modeling has been carried out by using various geometrical approaches, and the predicted room responses were compared to actual measurements. Because neither purely geometrical room acoustics algorithms nor traditional finite-element techniques can be used effectively, new investigations are needed. The goal of these investigations is to find a high- and medium-frequency modeling algorithm that predicts the most important sound field parameters accurately enough.

THURSDAY MORNING, 18 MARCH 1999 ROOM H1028, 7:55 A.M. TO 12:20 P.M.

Session 4aAAb

Architectural Acoustics: Development and Verification of Prediction Methods in Building Acoustics

Trevor R. T. Nightingale, Cochair
Institute for Research in Construction, National Research Council, Building M27, Montreal Road, Ottawa, Ontario K1A OR6, Canada

Eddy Gerretsen, Cochair
TNO Institute of Applied Physics, P.O. Box 155, NL-2600 Delft, The Netherlands

Chair's Introduction—7:55

Invited Papers

8:00

4aAAb1. Intercomparison test of sound insulation measurement in test facilities. I. A. Schmitz, A. Meier, and G. Raabe (Physikalisch-Technische Bundesanstalt, Bundesallee 100, 38023 Braunschweig, Germany, Alfred.Schmitz@ptb.de)

The implementation of ISO 140 harmonized at the European level requires for the determination of the characteristic values of building elements that the airborne sound insulation of partitions be measured in test facilities with suppressed flanking transmission. When heavy separating elements are under test, it is also important to take the energy dissipation of the test facility itself into account, as these factors considerably influence the sound insulation measured. Additional measurements of the total loss factor inform about the energy dissipation and may be used to convert sound reduction indices obtained under different test facility conditions. However, in the past two years measuring techniques and experience of loss factor determination have developed to such an extent that reliable results can be obtained now. Moreover, in Germany all test facilities with flanking transmission are to be converted into facilities without flanking transmission. This is why a government-financed intercomparison was carried out, which was aimed at determining the new situation of the German test facilities by measuring the sound insulation of the same solid wall. In addition to the sound insulation, the total loss factors of the partition were measured. The first part of this paper reports on the background, the way of proceeding, and the methods of measurement used for the intercomparison, as well as on the results obtained in a preliminary study at PTB.

8:20

4aAAb2. Intercomparison test of sound insulation measurement in test facilities. II. A. Meier, A. Schmitz, and G. Raabe (Physikalisch-Technische Bundesanstalt, Bundesallee 100, 38023 Braunschweig, Germany, Andreas.Meier@ptb.de)

In the second part of this paper, the results obtained in the principal test are presented and the differences between the sound insulation found in the individual testing facilities discussed. It is moreover shown, if the total loss factor allows the sound reduction indices to be converted, thus a uniform assessment of heavy, solid building elements on all test facilities is achieved. On the basis of these results it will be investigated whether the theoretical approaches of the prediction methods (e.g., ISO 12354) are sufficient for the conversion of the sound insulation of building elements.

8:40

4aAAb3. Verification of using SEA to model differing laboratory conditions. Sean Smith (Acoust. Dept., Istituto Elettrotecnico Nazionale Galileo Ferraris, Strada delle Cacce 91, Torino 10135, Italy, smith@ac.ien.it) and Roberto Pompoli (Univ. of Ferrara, Ferrara 44100, Italy)

In the Inter-comparison of European Laboratory Measurements of Airborne Sound Insulation of Walls under the EC Measurement and Testing Programme 1990–1994 a significant difference, of up to 12 dB, was found in the reproducibility results for the participating 21 laboratories. This difference was associated only with specimen 1, the double leaf lightweight plasterboard wall. This paper presents possible reasons for the large reproducibility values for this wall using experimental evidence and theoretical models, statistical energy analysis (SEA). While the calculation of the sound reduction index (R) does take into account the different test wall areas and reverberation times of the respective laboratories involved, some factors which may prove significant to the measured R values are not. This paper discusses a variety of factors which may affect the resultant R values. It is suggested that the principle factor which may effect the results of this test program for the double wall is the material used for the border of the test opening in the various laboratories, which connects both leaves of the double wall. The SEA can be used to model approximately the various laboratory conditions. When comparing the measured and SEA predicted reproducibility results there is good agreement.

9:00

4aAAb4. Predicting sound transmission through perforated brick walls using SEA. Marco Fringuellino and Sean Smith (Acoust. Dept., Istituto Elettrotecnico Nazionale Galileo Ferraris, 91 Strada Delle Cacce, Torino 10135, Italy, fringue@ac.ien.it)

The use of perforated bricks or blocks is the most common form of wall construction found in Central and Southern Europe. However, very few theoretical models have been developed for the purpose of predicting sound transmission through these walls or analyzing their behavior. In this paper statistical energy analysis (SEA) is adopted to predict the sound reduction index (R) for these type of walls for comparison with measured data. Due to the enormous variations in brick types used within these countries, measurements were carried out on walls with varying sizes of perforations, density, volume, and surface treatments. For the purpose of this paper special attention is given to the effect on the sound transmission due to the perforations and the effect of additional plastered layers. It was found that SEA can be used as an approximate prediction technique. However, due to the extreme cellular nature in the majority of these types of brick and lack of sufficient modal overlap, within the building acoustic frequencies under study, only very simple SEA models could be adopted. Further theoretical models must be developed outside of the SEA framework to provide sufficient analysis of the behavior for the majority of these multi-component structures.

9:20

4aAAb5. Predicting the sound reduction of building elements from material data. Eddy Gerretsen (TNO Inst. of Appl. Phys., P.O. Box 155, NL-2600 AD Delft, The Netherlands, gerretsen@tpd.tno.nl)

The airborne and impact sound reduction of building elements are important quantities to compare the acoustic performance of products and to use as input for prediction models for the acoustic performance of buildings. Besides the excising measurement methods, it can be very useful to have also calculation models to predict these quantities for various types of elements from data on the design and materials used. Such models provide a quick and easy way to estimate the effect of changes in an element and to check for anomalies in measurement results. For homogeneous elements a calculation model is given in an annex to EN 12354-1. That model will be discussed and possible extensions to layered, stiffened, or double elements will be presented. For more or less homogeneous elements, various so-called mass-law predictions are in use. Some of these will be discussed in relation to the theoretical mass-law which can be deduced from the mentioned model.

9:40

4aAAb6. Measurement of K_{ij} with free-standing masonry walls. Carl P. Hopkins (Acoust. Ctr., BRE, Watford WD2 7JR, UK)

Measurements have been carried out to determine K_{ij} values for masonry blockwork wall elements in the laboratory. Structural coupling measurements in the laboratory required investigation of the energy flow on the test construction in conjunction with the laboratory as well as determination of the coupling/material parameters. Experimental work was carried out on full-size masonry wall elements that were free-standing upon a concrete floor base. Measurement procedures used to determine K_{ij} were based upon proposals made by CEN/TC126/WG6. The intended use of the measurements was to investigate structural coupling between masonry walls for the generic T-junction with two different junction connection details, interleaved blocks and butted and tied blockwork. To compare the two different types of junction connection, an H-block construction was used that consisted of a single separating wall element with four flanking elements. When the modal overlap determined from measurements was less than unity, the general trend was that the laboratory measurements overestimated K_{ij} in comparison to values quoted in prEN12354-1.

10:00–10:20 Break

10:20

4aAAb7. Vibration response of building elements in wood frame constructions when excited along an edge. T. R. T. Nightingale and R. E. Halliwell (Natl. Res. Council Canada, Inst. for Res. in Construction, Ottawa, ON K1A 0R6, Canada)

When predicting the apparent sound insulation in wood frame buildings it is necessary to obtain accurate measures of both the junction attenuation and any attenuation of the structure-borne sound in the surfaces connected to the junction. Most walls and floors in wood frame constructions can be viewed as being rib-stiffened plates and as such they can not be treated as homogeneous and isotropic. The framing members, joists in the floor and studs in the wall, may break the surface into a series of smaller subpanels. Measured velocity data are presented to show that if structure-borne energy is propagating at right angles to the framing members,

then the vibration response of the surface will not be uniform and there will be a strong gradient in the energy density. More energy is stored near the source. It is also shown that a gradient exists for the case where the direction of propagation is parallel to the framing members. In both cases internal losses are insufficient to account for the gradient. This has several important implications, as it may bias measures of junction attenuation and framed surfaces may have to receive special treatment in prediction models. These issues will also be discussed.

10:40

4aAAb8. Structure-borne sound transmission at floor/joist connections in wood frame buildings. Ivan Bosmans and Trevor R. T. Nightingale (Natl. Res. Council Canada, Inst. for Res. in Construction, Montreal Rd., Ottawa, ON K1A 0R6, Canada)

The overall sound transmission in wood frame buildings is largely affected by flanking transmission involving the structural members of the building. Due to the inhomogeneous and anisotropic nature of the building components, as well as the difficulty of modeling the structural connections, theoretical predictions of flanking transmission are characterized by a considerable uncertainty. This paper investigates structure-borne sound transmission at plate/beam junctions which are typical of floors in wood frame buildings. The aim of this study is to gain a better insight into the dynamic behavior of the floor assembly and to improve the accuracy of the theoretical predictions of vibrational energy flow through floors. For this purpose, measurements are carried out on a small floor section for various coupling conditions of the joists. By varying the number of fasteners used to attach the joist to the plate, frequency ranges are identified where the junction behaves as a line connection or as a series of local connections. The experimental results are compared to theoretical predictions using statistical energy analysis, where coupling loss factors are calculated based on the wave approach for semi-infinite plates.

11:00

4aAAb9. Evaluation of prEN 12354 parts 1 and 2 for Nordic dwelling houses. Dan B. Pedersen (DELTA Acoustics and Vibration, Kongsvang Alle 33, DK-8000 Aarhus C, Denmark)

Standardized prediction models for airborne and impact sound insulation in buildings are described in prEN 12354 parts 1 and 2. These models have been evaluated by comparing the predicted and measured sound insulation for common building constructions used in Nordic dwelling houses. In total, more than 200 comparisons were carried out under a project sponsored by Nordtest. Results from laboratory measurements can be used as input data for the prediction models. However, it is often possible to calculate such input data. The standard includes informative annexes on calculation of, e.g., the sound reduction index for monolithic elements, the vibration reduction index for junctions, etc. Both the annexes and alternative calculation principles have been evaluated. Calculations based on a few modifications of the informative annexes are recommended for application of the standard in the Nordic countries. Finally, acoustical input data are proposed for some types of construction like lightweight double-leaf walls, floor coverings, etc.

Contributed Papers

11:20

4aAAb10. Application of CEN prediction models to German building situations. Heinrich A. Metzen (Gruenzweig + Hartmann AG, Dept. LM-B, P.O. Box 1240, D-68521 Ladenburg, Germany)

The calculation models for airborne and impact sound transmission specified in the European standards EN 12354-1 and -2 were applied to a number of common German building situations. Most of the buildings investigated were constructed from heavy elements made of brick or concrete. The measured results for the various situations were taken from qualification tests carried out by German acoustical laboratories or consultants. The calculations were performed by use of the new, commercially available software program BASTIAN, which enables, besides the calculation of airborne and impact sound transmission, the calculation of sound transmission across facades from the outside. Input data not delivered within the BASTIAN database has been estimated. Special interest was focused on the influence of element area and assumed structural reverberation time *in situ* on the calculated final result.

11:40

4aAAb11. Vertical flanking sound transmission loss by timber-framed-glass facades. Rolf Schumacher and Bernd Sass (Inst. für Fenstertechnik, Rosenheim, Germany)

The results of measurements both of the airborne and the structure-borne flanking sound transmission by timber-framed-glass facades are reported following the new European drafts standards for flanking transmission of lightweight partitions in the laboratory [document of CEN/TC 126-N 284 . . . 286 (1989)]. Several practical types of junctions of these facades to a massive concrete wall/ceiling have been investigated by airborne and structure-borne excitation to discuss the question, if this junction resp. the vibration reduction index K_{ij} has a substantial influence on the transmission loss of the junction or not. The results, especially by using the vibrational excitation method, show effects of a structural absorption decrease along the length of the element, the differences in the structural reverberation time T_s due to the different materials of the single elements of the facade, and the description of the overall transmission loss as an additional combination of the detailed parts of the element. Comparison with the mathematical model of overall sound transmission between adjoining rooms in a building due to prEN 12354-1:1996 with and without junction loss will be discussed. [Work supported by DGfH and NABau.]

12:00

4aAAb12. About the sound insulation of windows. Bernd Sass, Rolf Schumacher, and Hans Froelich (Inst. für Fenstertechnik, Rosenheim, Germany)

The results of statistical research and measurements of the airborne sound transmission loss of windows of any kind of frame material (aluminium, wood, PVC, . . .), glass types, and window dimensions are reported to revise the well-known table 40 in the German standards DIN 4109, Beiblatt 1 (issue 1989). A new table will be presented with a strong connection of the sound reduction index R of both the glass and the frame material and of the frame-to-pane-ratio, or, better to say, the dependence of the sound reduction from the dimensions of the window resp. the glass pane. Proposals are given as to correction terms to respect these substantial influences for the predictional work in practice. [Work supported by DIBt and Bundesverband Fenster & Fassade.]

Contributed Posters

These posters will be on display in the Poster Gallery from Monday to Wednesday, 15–17 March. Authors will be at their posters from 10:00 a.m. to 12:00 noon on Wednesday, 17 March.

4aAAb13. Noise transmission through a finite plate: Physical approach. Valery A. Masyukov (Inst. for Problems in Mech., Russian Acad. of Sci., prospekt Vernadskogo 101/1, Moscow 117526, Russia, masyuk@ipmnet.ru)

The problem of forced sound transmission through a thin elastic plate of finite size, placed in an infinite rigid baffle, is considered on a basis of the following simple approximation of radiation coefficient as a function of angle of incidence: the secant (as for an infinite plate)—below and at some angle called diffractional and a constant (as for a small plate)—at higher angles. The constant depends only on Helmholtz number and is easily obtained in a 2-D approximation. Simple analytical expressions are deduced for the transmission coefficient allowing not only for the finite plate size but also for a lack of near-grazing incident waves in the noise angular spectrum. These expressions are in excellent agreement with complicated 3-D computations fulfilled earlier. A clear physical explanation is given for the well-known underestimation of transmission loss (TL) of real panels by the infinite-plate diffuse-field theory both below and at coincidence. At coincidence, the lack of near-grazing waves and averaging over 1/3 octave band are shown to be responsible for the discrepancy. The obtained formulas can be used for easy calculation of TL for real plates in a full audio range.

4aAAb14. Prediction equations of isolating systems: Gypsum panels. Manuel Recuero (Departamento de Ingenieria Mecánica y Fabricación, Universidad Politécnica de Madrid, Ctra. Valencia Km. 7, 28031 Madrid, Spain, mrecuero@diac.upm.es), Constantino Gil, and Antonio Minguez Antonio (Universidad Politécnica de Madrid, 28031 Madrid, Spain)

Several prediction equations of acoustic noise isolation are presented and applied to gypsum structures of one, two, and three plates, with different thickness. On the other hand, acoustic noise isolation for simple, double, and triple gypsum panels is measured in transmission loss chambers officially recognized. The experimental results obtained are compared with the values obtained with the prediction equations in order to evaluate the error. The measurements are done in 1/3-octave bands as the ISO 140-3 proposes, using B&K equipment. It has also measured the panel vibrations with accelerometers with acoustic intensity techniques in order to explain several panel behaviors. Taking into account the former results, some prediction equations have been obtained versus mass and frequency, for values below 50 kg/m^2 so the measuring process can be done easily.

THURSDAY MORNING, 18 MARCH 1999 ROOM MA001, 8:00 TO 10:20 A.M.

Session 4aABa

Animal Bioacoustics: Acoustics of Terrestrial Animals

Ann E. Bowles, Cochair
Hubbs-Sea World Research Institute, 2595 Ingraham Street, San Diego, California 92109, USA

Hermann Wagner, Cochair
Institut für Biologie II, RWTH Aachen, Kopernikusstrasse 16, D-52074 Aachen, Germany

Contributed Papers

8:00

4aABa1. Spotted Owl reactions to helicopter and chain saw noise. David Delaney, Larry Pater (U.S. Army Construction Eng. Res. Labs., Champaign, IL), Teryl Grubb (U.S. Forest Service, Flagstaff, AZ), M. Hildegard Reiser (Holloman AFB, NM), and Paul Beier (Northern Arizona Univ., Flagstaff, AZ)

Noise impacts on Mexican Spotted Owls (MSO) were documented during the 1995 non-nesting and the 1996 nesting seasons. Members of the MSO population in the Lincoln National Forest, NM, were exposed to typical helicopter and chain saw noise stimuli. The noise stimuli were presented at a variety of controlled levels and distances. Proximate behavioral responses, nesting success, and nesting productivity were observed and documented. The data were sufficient to establish response threshold distances and noise levels for both types of noise. No spotted owl flushes were recorded when the noise stimulus was >105 m distant, regardless of stimulus type. As stimulus distance decreased, spotted owl flush frequency was shown to increase. In terms of A-weighted noise level, the response threshold for helicopter noise was found to be 92 dB SEL and 46 dB LEQ for chain saws. [Work supported by U.S. Air Force.]

8:20

4aABa2. Mechanisms of auditory distance perception in passerine birds. Marc Naguib (Freie Univ. Berlin, Inst. fuer Verhaltensbiologie, Haderslebener Str. 9, D-12163 Berlin, Germany, mnaguib@zedat.fu-berlin.de)

Use of auditory cues to assess the distance of signaling conspecifics (called ranging) is a difficult, albeit important, perceptual task in animals and humans. Cues are provided by the changes in a signal (degradation) that accumulate with increasing propagation distance. This contribution focuses on mechanisms of ranging and on its accuracy in two passerine birds species. Playback of tape-recorded songs presented to territorial Carolina wrens (*Thryothorus ludovicianus*) in the field showed that subjects used reverberation, the relative intensities of high frequencies, and the amplitude of conspecific song as auditory distance cues. Use of several cues could increase the accuracy of ranging by pooling information derived in different ways. Thus further experiments addressed specifically the accuracy of ranging in chaffinches (*Fringilla coelebs*). Playbacks with digitally degraded songs (in a virtual forest) suggest that distance perception involves uncertainties. The results will be discussed with regard to the

perceptual processing of acoustic signals and in light of problems caused by the variation of acoustic properties of the environment. [Work supported by Sigma-Xi Grants-in-Aid of Research, the Chapman Memorial Fund of the American Museum of Natural History, and the University of North Carolina at Chapel Hill.]

8:40

4aABa3. Acoustic structure of chorus howling in wolves and consequences for sound propagation. Karl-Heinz Frommolt (Humboldt Univ., Inst. of Biol., Invalidenstr. 43, D-10 099 Berlin, Germany)

The acoustic features of chorus howling of three captive Grey wolf packs (*Canis lupus lupus*) were described. Two components could be found: a part with nearly no frequency modulations (A part) and a part with deep frequency modulations (B part). Sound energy in the A part is concentrated around 400 Hz, whereas in the B part, maximum amplitudes could be measured in the region between 800 and 1200 Hz. Complex acoustic interactions of the vocalizing animals could be observed during the A part. These interactions include matching of dominant frequency and nearly synchronous onset. It is proposed that the B part would be more effective in sound propagation in respect to environment-caused excess attenuation.

9:00

4aABa4. The harmonics-to-noise ratio applied to dog barks. Tobias Riede, Guenter Tembrock (Inst. fuer Biologie, Humboldt Univ. Berlin, Invalidenstrasse 43, 10115 Berlin, Germany, TobiasRiede@rz.hu-berlin.de), Hanspeter Herzel (Humboldt Univ. Berlin, 10115 Berlin, Germany), and Leo Brunnberg (Freie Univ. Berlin, 14163 Berlin, Germany)

In this paper a parameter is introduced to animal bioacoustics which is commonly used in human phoniatrics—the harmonics-to-noise ratio (HNR). It is a ratio of the acoustic energy of the harmonic components to that of the noise. Barks of domestic dogs are short, loud, and broadband utterances. The rationale for this method is that the acoustic wave of a barking call is characterized by the ratio of harmonic and noise components. Fifty barks from each of ten adult dogs (dachshound) uttered during a mild threat were considered. The HNR is estimated as follows: a 50-ms time segment from the middle of the call is Fourier transformed (sampling frequency 30 kHz, 512-point Hanning window). A ten-point moving average curve was calculated from the spectrum. The maximum difference between the spectrum and the moving average is used as HNR. Two test persons were asked to arrange the barks of the ten dogs according to their personal perception of hoarseness. The measured HNR agrees perfectly with the perceived ordering. In one dog's barks the HNR were measured twice to test the robustness of the procedure. A paired t-test showed no significant differences between the two samples. This exemplifies that the relatively simple HNR is valuable in animal bioacoustics.

9:20

4aABa5. Otoacoustic emissions and their neuronal correlates in the Mongolian gerbil. Michael Faulstich and Manfred Koessl (Zoologisches Inst. der LMU, Luisenstr. 14, 80333 Muenchen, Germany)

Though distortion product otoacoustic emissions (DPOAE) are widely used in hearing research, some fundamental properties of their generation and transmission are still unclear. To investigate the properties of the generation and propagation of DPOAE, as well as the degree of their neuronal encoding in the auditory system, DPOAE in the ear canal and the corresponding neuronal representation of cochlear distortions in the AVCN of the gerbil have been measured simultaneously. Additionally, the group delay for the $2f1$-$f2$ DPOAE was measured for frequencies between 1 and 60 kHz. It was found that for frequencies above 2 kHz, forward and reverse sound transmission via the middle ear are comparable and that DPOAE are encoded practically unattenuated in the AVCN. For frequencies below 2 kHz, a loss of DPOAE amplitude of up to 40 dB compared to the intracochlear level could be observed, most likely stemming from high-pass filtering by the middle ear during reemission. For frequencies above 2 kHz, the group delay decreased with increasing frequency, but additionally, an atypical decrease of the group delay for frequencies below 2 kHz was found. This may indicate a change of the character of nonlinear cochlear mechanics for low frequencies represented in the cochlear apex.

9:40

4aABa6. Aversion-related changes in the call structure of Squirrel monkey vocalizations. Kurt Hammerschmidt and Claudia Fichtel (Dept. of Neurobiology, German Primate Ctr. (DPZ), D-37077 Göttingen, Germany)

It is generally assumed that the variation in primate calls is, to a certain extent, correlated with the internal state of a caller. However, it remains difficult to describe this relationship because it is difficult to get reliable information of the internal state of a caller. Therefore, the vocalizations given by Squirrel monkeys were analyzed in a self-stimulation study done by Uwe Jürgens (1978). In this study it was measured how certain intracerebral stimulations were experienced by the subject. The Squirrel monkeys were in a cage with two compartments. Presence in one compartment was followed by a stimulation, whereas presence in the other compartment was stimulus free. As the animals were free to move from one compartment to the other, they could decide whether they wanted to avoid the stimulus or not. The multiparametric analysis revealed significant correlations between call parameters and the degree of aversion. Whereas single call types showed partly different parameter correlations, a shift in call pitch was found for all call types. In other words, the more intense the aversion was, the higher the frequency parameters (e.g., peak frequency or frequency range) were.

10:00

4aABa7. Vocalization analysis during the castration of pigs. Gunther Marx (Inst. for Animal Sci. and Animal Behavior Mariensee (FAL), D-31535 Neustadt, Germany, marx@tzv.fal.de), Eberhardt von Borell, Thomas Horn, and Jens Thielebein (Martin-Luther Univ., Halle-Wittenberg, D-06108 Halle, Germany)

Castration is usually carried out on young male pigs by surgical means to prevent boar taint in older males. The specific structure of vocalizations of piglets may provide some information on the extent of pain experienced by the animal. A total of 96 piglets from 24 litters out of a commercial herd were allotted to four different treatments between the age of d 7 and 19: (a) castration without anesthesia [C], (b) castration with local anesthesia [CA], (c) fixation without anesthesia [F], (d) fixation with local anesthesia [FA]. Vocalizations were recorded with a calibrated microphone (B&K4133) and a DAT recorder (SONY-TCD-D8). Analysis was done with Entropics Signal Processing System (ESPS5.0) software on a workstation (SGI Indy) and provides a multiparametric description of call characteristics. Plasma catecholamines were analyzed from plasma taken immediately after each treatment. Call structure within vocalizations of castrated piglets [C] changed during periods of tearing and cutting of the spermatic cord (call energy: 92.030.41 vs 88.750.31 dB before tearing; $p<0.01$). CA treatment reduced peak levels (CA: 95.090.65 vs C: 99.350.35 dB; $P<0.01$). Correlations between call structure and physiological stress parameters indicate that these behavioral characteristics are useful for measuring stress by means of a noninvasive method. Several parameters from numerical analysis of calls were found to be sensitive to stressful treatments during castration.

Session 4aABb

Animal Bioacoustics: Acoustics of Echolocating Animals

Paul Nachtigall, Cochair
Hawaii Institute of Marine Biology, P.O. Box 1106, Kailua, Hawaii 96734

Hans-Urich Schnitzler, Cochair
Animal Physiology, University of Tuebingen, Auf der Morgenstelle 28, 72076 Tuebingen, Germany

Invited Papers

10:40

4aABb1. Do echolocating bats use the acoustic flow field? Annette Denzinger and Hans-Ulrich Schnitzler (Animal Physiol., Univ. of Tuebingen, 72076 Tuebingen, Germany)

In transfer flight, CF bats continuously emit signals consisting of a long CF and a short terminal FM (tFM) component. So far, the CF component is only discussed in the context of the perception of fluttering insects. However, changes in the relative movement between the bat and the targets it passes create systematic changes in the amplitude and frequency of the echoes. These changes represent an acoustic flow field containing spatial information. To establish whether CF bats evaluate flow-field information, the echolocation and flight behavior of *Pteronotus parnellii* and *Rhinolophus ferrumequinum* was studied when flying on known flight paths in the field. In undisturbed flight, signals with a prominent CF and a weak tFM component were emitted (CF mode), well suited for analyzing the available flow-field information. An obstacle introduced directly into the flight path caused an evasive flight maneuver and a distinct change in echolocation behavior indicated mainly by more prominent tFM components allowing a better target localization. New data suggest that bats avoid obstacles positioned aside of the flight path without leaving the CF mode. It is assumed that information encoded in the CF component (possibly flow-field information) is sufficient to guide the bat on known flight paths and around newly appearing lateral targets.

11:00

4aABb2. Auditory scene analysis for perceptually guided behavior in the echolocating bat. Cynthia F. Moss (Dept. of Psychol., Univ. of Maryland, College Park, MD 20742)

The echolocating bat actively probes its environment with ultrasonic vocal signals and builds a three-dimensional (3-D) auditory scene from information carried by the returning echoes. The bat's sonar receiver computes the azimuth and elevation of a sonar target from the intensity, timing, and spectrum of sonar echoes at the two ears. It estimates target distance from the time delay between each sound transmission and returning echo. Rapidly processing spatial-acoustic information, the bat's perceptual system analyzes the 3-D auditory scene to support spatially guided behaviors in a dynamic environment. Psychophysical data from two-choice phantom target discrimination tasks suggest that the bat integrates and segregates echo streams along the delay axis. These findings, together with the results of laboratory insect capture experiments, show that echo delay information is used to guide and coordinate a complex set of adaptive motor behaviors. Measures of neutral spatial selectivity in the bat superior colliculus (SC) also suggest the importance of echo-delay processing for spatially guided behavior. Spatial tuning of SC neurons may be important to the bat's acoustic orienting behavior, since changes in its head aim, pinna position, flight behavior, and vocal production patterns are closely coupled to the 3-D location of a target.

11:20

4aABb3. Auditory categories for the perception of echo spectra in bats. Sabine Schmidt (Zoologisches Inst. der LMU, Luisenstr. 14, 80333 Muenchen, Germany, sabi@zi.biologie.uni-muenchen.de)

Bats obtain an auditory representation of their environment by sonar. The categories relevant for the perception of echo spectra by *Megaderma lyra*, a species using multiharmonic sonar calls, were studied in a series of 2-AFC experiments with complex tones. First, the bats classified complex tones on the basis of absolute pitch rather than by their relative pitch. Absolute pitch, combined with a long lasting memory representation of echo spectra, may form the basis of an acoustical library for object identification. Second, evidence was provided for the spontaneous perception of a collective pitch at the fundamental of the complex tones, as well as for the use of a vowellike quality based on the broadband spectral composition of the complex tones. In addition, the bats could be trained to concentrate on the spectral pitch of a single component in complex spectra. Collective pitch, vowel timbre, and spectral pitch perception may all be vital for acoustical orientation in this ground gleaning bat which has to sort out multiple echoes. The collective pitch of the echo allows one to relate each echo to its respective call. The timbre and the spectral pitches of sonar call echoes carry information about object structure. [Work supported by SFB 204.]

11:40

4aABb4. Does echolocation wavelength restrict bats' choice of prey? Robert D. Houston, Arjan M. Boonman, and Gareth Jones (School of Biological Sci., Univ. of Bristol, Woodland Rd., Bristol BS8 1UG, UK, Arjan.Boonman@bristol.ac.uk)

The size range of insects encountered by bats that use narrowband echolocation signals (FM-CF or quasi-CF) extends to sizes much smaller than the wavelengths used by these bat species. It was hypothesized that the expected Rayleigh scattering sets a lower limit on the size of prey which can be detected. To test the Rayleigh scattering theory empirically, insects were ensonified with pure-tone pulses ranging from 20 to 85 kHz and their target strengths were measured. The target strength of the smaller insects was frequency-dependent within the frequency range used by aerial-hawking bats. The target strength diminished sharply as the wing length to wavelength ratio decreased below unity. A model was developed to predict maximum detection distances, which lead to an estimate of the optimum frequency to be used for detecting each insect size. In a dietary analysis, it was found that the bat species using the shortest wavelengths took the smallest insects. The minimum prey size detectable by each bat species was predicted. The longest wavelength bats (*Vespertilio murinus, Nyctalus noctula*) took smaller prey than were estimated. The diets of the shorter wavelength bats agreed with predictions of the model. [Work supported by BBSRC.]

Contributed Paper

12:00

4aABb5. The role of selection in marine mammal biosonar: Why pinnipeds don't echolocate. Ronald J. Schusterman, David Kastak (Long Marine Lab., Univ. of California, 100 Shaffer Rd., Santa Cruz, CA 95060, rjschust@cats.ucsc.edu), and David Levenson (Scripps Inst. of Oceanogr., Univ. of California, La Jolla, CA 92093)

Pinnipeds inhabit dark and sometimes murky water, as do dolphins; however, they have not evolved sonar. Why? What factors resulted in pinnipeds evolving a different Umwelt from echolocating dolphins, even though at a superficial level, it seems that similar environmental pressures should select for similar Umwelts? Pinnipeds don't echolocate, because, unlike aquatic dolphins, pinnipeds are truly amphibious. Thus the hearing of seals and sea lions is adapted for sound detection at the low- and mid-range frequencies both in water and air, while dolphins are specialized to hear, localize, and differentiate aspects of high-frequency sounds only in water. Pinnipeds are adapted to combine a variety of sensory cues with spatial memory in order to navigate, forage, detect predators, and communicate under water. Some pinnipeds rely heavily on their vibrissae to forage benthically, while others are specialized in terms of visual sensitivity. Experiments have shown that an elephant seal can become completely dark-adapted in the time it takes ($\sim$5 min) to dive from the bright surface to foraging depths of 500 m. Clearly, the ''apparent'' selective pressures that would give rise to echolocation in pinnipeds have not been in operation, presumably because pinnipeds perform many reproductive activities on land or ice. [Work suported by ONR.]

THURSDAY MORNING, 18 MARCH 1999 ROOM H1058, 8:00 A.M. TO 12:20 P.M.

Session 4aAO

Acoustical Oceanography: Acoustic Seafloor Classification I

Larry Mayer, Cochair
Ocean Mapping Group, Department of Geodesy and Geomatics Engineering, University of New Brunswick, Frederickson, New Brunswick E3B 5A3, Canada

Eric Pouliquen, Cochair
SACLANT Undersea Research Centre, Viale San Bartolomeo 400, 19138 La Spezia, Italy

Invited Papers

8:00

4aAO1. A theoretical and experimental examination of seabed discrimination using the first and second backscatter from an echo sounder. Gary J. Heald (DERA (Bincleaves), Weymouth, Dorset, UK), Nicholas G. Pace, and Cathy M. Dyer (Univ. of Bath, Claverton Down, Bath, UK)

At normal incidence it is possible to detect a second echo from the seabed in addition to the first echo that is traditionally used by echo sounders. It can be shown that the second backscatter contains information about the seabed that is not contained in the first backscatter. The second echo requires treatment as a bistatic, on axis, geometry in order to understand the mechanisms that provide new information. The effective range of the source is three times the water depth, whereas the receiver is at the water surface for the case where the transducer is at the water surface. The bistatic geometry means that the receiver may be in the near field of the scattering from the seabed. This would mean that the second echo is sensitive to changes in the reflection coefficient of the sediment. Modeling the water surface roughness is achieved by expanding the beamwidth of the source to a level that is representative of the spreading at such an interface. Data from controlled tank experiments over a range of sediment types and water surface conditions are presented. Time-series data from an ocean experiment have been analyzed and show good agreement with ground truth data.

8:20

4aAO2. Variability in the acoustic response from natural shallow-water marine sediments. Douglas N. Lambert (Naval Res. Lab., Code 7431, Stennis Space Center, MS 39529) and Richard W. Faas (Univ. of Southern Mississippi, Stennis Space Center, MS 39529)

The large variation in sediment acoustic response observed between soft clays and sands provides a satisfactory means to estimate sediment properties remotely using acoustic techniques. However, the accuracy of these predictions is limited by variations in sediment properties, both horizontally and vertically on a scale of centimeters to meters, within a given sediment volume, and sets the accuracy limits or ''error bars'' for prediction of sediment properties. In order to quantify these limits, a series of measurements of acoustic response were made at six sites off Gulfport, MS in sediments ranging from sands to muds. A broadband transducer with an 8° constant beamwidth was mounted on a trolley suspended from an I-beam connected to a pair of legs at each end of the beam. This ''swingset'' was lowered to the seafloor with the transducer mounted at normal incidence and at an altitude of 3.0 m. Measurements were made at both 30 and 50 kHz at each of eight positions 0.3-m apart along the beam. Results suggest greater variability occurs in the vertical direction (6–24 dB) than in the horizontal direction (6–18 dB).

8:40

4aAO3. Seafloor characterization using a low-frequency multibeam echo sounder: Ambiguities in backscattering strength interpretation. Xavier Lurton (Laboratoire d'Acoustique Sous-Marine, IFREMER, BP 70, 29280 Plouzané, France) and Laurent Guillon (Université du Maine, 72085 Le Mans Cedex 9, France)

This paper presents the seafloor characterization difficulties and methodological requirements met when dealing with apparent discordances between acoustical data and geological observations. The poor spatial resolution of low-frequency multibeam echo sounders used for deep-water seafloor mapping precludes access to small-scale feature descriptors (spectral, or non-Rayleigh statistics); only average angular backscattering strength (BS) measurements are then available. However, since a given acoustical response may ambiguously represent various geological realities, precise modeling of angular BS accounting for seafloor inner structure and properties is crucial. Oriented medium-scale roughness of the interface may cause level biases, observed as azimuth-dependent BS variations. More noticeably, sound penetration inside the sediment volume may affect strongly the overall response; this is modeled through an equivalent input backscattering strength from buried layers, accounting for propagation phenomena inside sediment stacks. Only confrontation with both accurate sediment coring, *in situ* geotechnical measurements, and thorough investigations of the geological context may remove these interpretation ambiguities: such a situation is presented and discussed for a difficult experimental case from a deep-sea fan area, where a sandy zone shows lower BS levels than the surrounding clay areas. An interpretation is proposed, based upon the acoustical properties of nonconsolidated sands.

9:00

4aAO4. Textural analysis of sidescan sonar imagery and generic seafloor characterization. Philippe Blondel (Southampton Oceanogr. Ctr., European Way, Southampton SO14 3ZH, UK, pbo@soc.soton.ac.uk)

Sidescan sonar imagery is a primordial component of geophysical and environmental surveys of the seafloor. Most of the data are still interpreted visually and qualitatively by experts. The method presented here uses textural analysis, and supplements the interpreter with reliable quantitative results. Indices are derived from grey-level co-occurrence matrices, whose mathematical expressions have been adapted to the specifics of sidescan sonar imagery. The indices measure the different properties of the acoustic textures and correlate them with the characteristics of the seafloor. This technique, called TexAn, has been extensively ground-truthed in complex midocean ridge terrains, using submersible and ROV observations, and *in situ* sampling. The frequencies used so far range from 6.5 to 500 kHz; all applications have been validated and ground-checked. Current applications are mainly concerned with the geology of midocean ridges, continental margins, and coastal waters. The technique has also been demonstrated for the detection of mines and subsurface structures. Being hardware-independent, TexAn enables quantitative assessments of sidescan sonar imagery, at all stages of processing and in all conditions. Another advantage of TexAn is the detection of details hitherto invisible to the human eye, however experienced.

9:20

4aAO5. Optimized echo-envelope matching for acoustic sediment classification with high-frequency single-beam sonars. Daniel D. Sternlicht and Christian P. de Moustier (Marine Physical Lab., Scripps Inst. of Oceanogr., 9500 Gilman Dr., La Jolla, CA 92093-0205)

To extract geoacoustic parameters from the envelope shape of bottom backscattered echoes measured with single-beam high-frequency echosounders, it is advantageous to compare the measured average echo magnitude with an echo envelope model that incorporates bottom scattering theory and sediment properties measured at spatial scales commensurate with acoustic wavelength. With a fully calibrated sonar system, iterative comparisons between model and data yield sediment properties such as grain size, roughness, and volume scattering statistics. Results are presented for a two-phase optimization approach to echo-envelope matching: first the sediment type is established by iterating on the reflection coefficient to match the peak echo amplitude and to establish a general fit with generic values for the remaining geoacoustic parameters, then a three-parameter global optimization is performed using a combination of simulated annealing and downhill simplex searches over the allowable range of roughness spectral strength, volume scattering cross section, and a constrained range of reflection and bottom absorption coefficients which are correlated with mean grain size. Bottom echo envelopes collected at 33 and 93 kHz, over substrates ranging from clay to sand, yield solutions for grain size and geoacoustic properties which are consistent with ground-truth measurements. [Work supported by ONR N00014-94-1-0121.]

9:40

4aAO6. Recent advances in acoustic sediment classification. Michael Richardson, Warren Wood, Wolfgang Jans, Peter Fleischer, Keven Briggs, Dawn Lavoie, Dan Lott, Doug Lambert, Dennis Lindwall, Don Walter (Marine Geosciences Div., Naval Res. Lab., Stennis Space Center, MS 39529), Sean Griffin (OMNI Technologies, Kenner, LA 70065), and Eric Smith (Univ. of Texas, Austin, TX 78731-80)

Most acoustic techniques used to classify seafloor sediments rely on operator experience and require extensive ground-truth data to calibrate system predictions. Recent developments in transducer design, inversion and deconvolution techniques, and sensor motion composition should improve the reliability and accuracy of normal-incidence, seafloor classification techniques. This presentation provides an introduction to papers that describe the application of these techniques to normal-incidence acoustic returns collected from a variety of siliciclastic and carbonate sediments in coastal waters surrounding Florida and the Bahamas. Site locations and descriptions, sediment characteristics based on *in situ* and laboratory measurements, and a description of the acoustic measurement techniques are given. In addition, 3-D visualization techniques that provide near real-time presentation of results are described. Profiles of sediment acoustic impedance, compressional wave attenuation, seafloor roughness, and volume heterogeneity are directly determined from acoustic returns and physical constraints. Other properties such as sediment type, grain size, porosity, and shear strength are predicted on the basis of empirical relationships relating acoustic impedance and/or attenuation to sediment physical properties. Comparisons of predicted and measured sediment properties are given and the ping-to-ping variability inherent in acoustic returns is discussed. [Work supported by ONR.]

10:00–10:20 Break

Contributed Papers

10:20

4aAO7. Inversion of short-range bistatic scatter for seabed properties. Nicholas G. Pace (SACLANT Undersea Res. Ctr., Via Bartolomeo 400, La Spezia, Italy, pace@saclantc.nato.int)

Measurements of bistatic acoustic seabed scatter obtained from an AUV operated off the coast of Elba are reported and interpreted in terms of seabed properties. A directional transmitter operating alternatively at 8 and 16 kHz was located at the rear end of an AUV and a line array of receivers was located on an extension from the nose. The AUV was fully instrumented and was programed to follow routes consisting of 5-m radius circles with straight-line connections at a height above the seabed of approximately 3 m.

10:40

4aAO8. Sediment geoacoustic properties determined from local and spatially integrated measurements of interface waves. Thomas K. Berger, Thomas R. Hahn, and Michael J. Buckingham (Marine Physical Lab., Scripps Inst. of Oceanogr., Univ. of California, San Diego, 9500 Gilman Dr., La Jolla, CA 92093-0238, tberger@ucsd.edu)

In Aug./Sept. 1998, as part of a sediment classification exercise at a site near Panama City, Florida and coordinated by NRL, Stennis, a vertical hydrophone array was deployed at mid-water depth to measure the velocity and directionality of interface waves. An airgun, 20-m deep on the seabed and at a range of approximately 1 km, excited head waves, and the received signal was used to invert for the sound speed using two methods: first, by comparing the arrival times of the water wave with those of the interface wave, and second, by considering the critical angle computed from the vertical directionality of the received signal as found from a cross correlation of signals from the hydrophones at known separations. The first method gives an average of the sound speed integrated along the path length, while the second method establishes the sediment properties near the array. The array was allowed to drift, giving measurements along various paths and at different local positions. By comparing the local and averaged properties of the sediment, the heterogeneity was established and the spatial variation determined more completely than could be achieved by either purely averaged or local measurements alone. [Work supported by ONR.]

11:00

4aAO9. Model-based seafloor identification with parametric sonar data: Experimental results. Andrea Caiti (Dept. of Electron. Systems and Automation, Univ. of Pisa, Pisa, Italy), Oddbjorn Bergem, Eric Pouliquen, and Enzo Michelozzi (SACLANT Undersea Res. Ctr., La Spezia, Italy)

A method is proposed to estimate the geoacoustic parameters of the uppermost seafloor strata using normal-incidence backscattered acoustic data obtained with a parametric sonar in the 4–12 kHz frequency range. A model-based identification approach has been pursued. The time-domain backscattering model BORIS [Bergem *et al.*, SACLANTCEN Memorandum SM-328 (1997)] has been selected as a forward model. A specific wavelet transform has been defined in order to obtain a significant measure of the discrepancy between data and model predictions in the wavelet-transformed domain. This discrepancy is minimized as a function of the bottom parameters. The technique has been tested on experimental data gathered in different locations in order to assess its perfomance on different bottom types. Identification results have been compared with independent ground truth collected by core analysis and video camera inspection. The comparison shows excellent agreement between acoustically determined parameters and ground truth. [This work has been partially supported by European Union, Contract No. MAS3-CT95-046, project ISACS.]

11:20

4aAO10. Sub-band imaging and mapping for seabed characterization using a wideband synthetic aperture bathymetry prototype. Jacques Chatillon (CPE Lyon, LASSSO (LISA, EP92 CNRS), 43 Bd. du 11 Novembre 1918, BP 2077, Bat. 308, F 69616, Villeurbanne Cedex, France)

Seabed was surveyed by means of two side-scan arrays. Echo processing was based on synthetic aperture technique and cross correlation for providing high-resolution maps. The paper deals with some results obtained by means of this sonar with several processing techniques. The use of synthetic aperture processing leads to sonar images with a constant resolution; the bathymetry processing permits the retrieval of the elevation of the resolution cells in order to reconstruct the relief of the seabed. The use of wide band signals (6–12 kHz) has allowed the development of time-domain algorithms for processing high-resolution images and maps. Additional information on the seabed was extracted from the spectral signatures of the echoes. First, splitting the global bandwidth into several

sub-bands permitted the evaluation of the sound penetration into the sediment. This led to several images of the same area with additional spectral information. Second, the bathymetry was used in order to compensate the influence of the grazing angle on the echo spectrum. This processing gives the spectral coloration of the bottom echoes directly, and leads to an efficient method for seabed characterization and classification.

11:40

4aAO11. Estimating the ocean bottom properties from multifrequency data. Ling Xiao, Renhe Zhang, and Zaixiao Gong (Natl. Lab. of Acoust., Inst. of Acoust., Chinese Acad. of Sci., Beijing 100080, PROC)

The inversion for the ocean bottom properties can be divided into two parts: constructing the cost function and the search strategy. In this paper, a cost function based on the multifrequency signal is given. The cost function is robust to the error caused by the range measurement. A controlled exhausted search method, named the box division algorithm (BDA), is adopted for the search strategy. BDA is a reliable search method with high efficiency. A numerical result is given for the benchmark inversion problem. An inversion test for real data is also presented. All the tests show that BDA and the cost function can play a robust role in the inversion for the ocean bottom properties. [Work supported by NSF of China.]

12:00

4aAO12. Seismic depth imaging and remote sensing of rock properties. Natalia A. Sidorovskaia and Emmitt S. Lockard (Landmark Graphics Corp., A Halliburton Co., 1100 Poydras St., Ste. 1300, New Orleans, LA 70163, nsidorovskaia@lgc.com)

An inversion of time-domain seismic data to the depth domain is used to enhance the structural signatures of complex geological features. Currently available algorithms for building three-dimensional depth-velocity models are overviewed. It is shown that the accuracy of the numerical model is sensitive to several important factors. First, the quality of the numerical model depends upon the amount of well control incorporated into the inversion algorithm. Second, velocity dispersion in seismic data may be an important parameter for predicting bottom elastic properties, such as porosity, permeability, fluid saturation, etc. The scattering and intrinsic attenuation of the acoustic signal by the Biot and the squirt-flow mechanisms at the macroscopic and microscopic levels for elastic geological structures are reviewed. A new numerical approach based on the scattering from aggregates of fluid-filled elastic objects is also introduced. Currently available numerical models, taking some aspects of elastic scattering into account, and their further development are discussed. The results indicate the first step in remote sensing of complex anisotropic geologic features from broadband seismic data.

THURSDAY MORNING, 18 MARCH 1999 ROOM MA144, 8:20 TO 11:40 A.M.

Session 4aBB

Biomedical Ultrasound/Bioresponse to Vibration: Modeling and Imaging

E. Carr Everbach, Cochair
Engineering Department, Swarthmore College, 500 College Avenue, Swarthmore, Pennsylvania 19081-1397, USA

T. Douglas Mast, Cochair
Applied Research Laboratory, Pennsylvania State University, University Park, Pennsylvania 16801, USA

Contributed Papers

8:20

4aBB1. Time-domain numerical solution of the KZK equation for modeling sound beams radiated by rectangular sources. Michalakis A. Averkiou (ATL Ultrasound, P.O. Box 3003, Bothell, WA 98041-3003) and Vera A. Khokhlova (Moscow State Univ., Moscow 119899, Russia)

A time-domain numerical solution of the KZK equation for modeling finite-amplitude sound beams radiated by rectangular sources similar to those used in diagnostic ultrasound is presented. The KZK equation accounts for the effects of diffraction within the parabolic approximation, nonlinearity, and thermoviscous absorption, on the propagation of sound beams. The algorithm is based on that used by Lee and Hamilton [J. Acoust. Soc. Am. **97**, 906–917 (1995)] to model circular sources. The diffraction integral has the form of a two-dimensional diffusion equation. The implicit backward finite difference (IBFD) scheme adapted for two dimensions is used in the near field, where the solution tends to be oscillatory. For the remainder of the field, the alternate direction implicit (ADI) method is used for higher accuracy with larger steps than those used in IBFD. The simulation model may be used to predict the FDA regulatory measurements of medical diagnostic scanners.

8:40

4aBB2. On the use of a modified optical flow algorithm for the correction of axial strain estimates in ultrasonic elastography in medical diagnosis. Andreas Lorenz, Helmut Ermert (Institut fuer Hochfrequenztechnik, Ruhr Univ., 44780 Bochum, Germany), Miguel Garcia-Schuermann, Hans-Joerg Sommerfeld, Theodor Senge (Ruhr Univ. Bochum, 44627 Herne, Germany), and Stathis Philippou (Ruhr Univ. Bochum, 44781 Bochum, Germany)

Tumors of the prostate exhibit a significant mechanical hardness in comparison to the surrounding tissue. However, they often can not be reliably detected in the *B*-mode image. For this reason, digital palpation of the prostate is still a major tool in tumor diagnostics. Ultrasonic elastography estimates the tissue elasticity from an image series recorded under increasing axial tissue compression applied by the transrectal probe. As a new imaging modality, it promises to support conventional prostate screening methods. Usually, time delays from two corresponding *A*-lines are estimated by cross-correlation methods applied to the acquired rf data set assuming a uniform axial compression. However, in clinical *in vivo* data, especially in data which were acquired with a sector scanner, significant lateral motion of the tissue which deteriorates the elasticity estimate was observed. A method is presented which uses a modified ''optical

flow'' algorithm to determine the global two-dimensional motion of the imaged object. This information is used to correct the corresponding *A*-lines according to the encountered lateral deformation. It is shown that this method is able to improve the strain estimates on data with low signal-to-noise conditions. Images of phantoms and clinical *in vivo* data are presented. [Work supported by DFG Grant ER 94/20-1.]

9:00

4aBB3. 3D compounding of B-scan ultrasound images. Jochen F. Krücker, Charles R. Meyer, Theresa A. Tuthill, Gerald L. LeCarpentier, J. Brian Fowlkes, and Paul L. Carson (Dept. of Radiol., Univ. of Michigan Med. Ctr., 200 Zina Pitcher Pl., Ann Arbor, MI 48109-0553)

Ultrasound imaging compounded from different look directions can significantly decrease speckle noise and increase structural contrast. In addition, current limits on the field of view from small aperture scanheads can be overcome by combining two or more sets of partially overlapping 3D scan volumes into one super-volume by spatially coregistering the overlapping portions. The purpose of this study was to demonstrate both of these compound imaging enhancements. A 1.5-D linear array was used to obtain overlapping ultrasound volumes in phantoms and test subjects, reconstructed from at least 60 parallel B-scan planes for each volume. In the cases where independent look directions were required, either the transducer was tilted or the scan direction was changed. In all cases, the overlapping volumes were coregistered using an automated procedure based on a mutual information (MI) metric. The algorithm accounts for different look directions and/or tissue motion by geometrically transforming one volume set such that the MI of its overlap with the other is maximized, which leads to good structural overlap. The accuracy and stability of the MI algorithm demonstrate the feasibility of both compounding methods, offering increased lesion contrast and 3D fields of view larger than those from any currently available ultrasound imaging systems.

9:20

4aBB4. Modeling of noise generation by turbulence in a larger human blood vessel. Andriy O. Borisyuk (Inst. of Tech. Acoust., Dept. of Elec. Eng., Dresden Univ. of Technol., Mommenstr. 13, D-01062 Dresden, Germany, borisyuk@eakaw2.et.tu-dresden.de)

An acoustic model of a larger human blood vessel is developed in order to study noise field in the human chest produced by flow of blood. The model accounts for the basic features of the generation and propagation of noise in the body, and permits consideration of a simple stenotic narrowing in vessel. The low Mach number turbulent wall pressure model of Chase is used to describe random sources in the vessel. The solution obtained relates the mean statistical characteristics of the noise field in the thorax to the parameters of the vessel and the blood flow, and reflects the influence of the body tissue on the sound transmission from the source (wall pressure fluctuations) to a receiver resting on the skin. The numerical analysis of the solution reveals the characteristic signs of the presence of a stenotic narrowing in the vessel. These are increase of the noise levels and production of the new frequency components determinable by the mean flow velocity in and the diameter of the constriction. [Work supported by the Alexander von Humboldt Foundation.]

9:40

4aBB5. Ultrasonic examinations of the forward and reflected waves in human arteries. Tadeusz Powalowski, Zbigniew Trawinski (Ultrasonic Dept., Inst. of Fundamental Technolog. Res., Polish Acad. of Sci. ul. Swietokrzyska 21, 00-049 Warsaw, Poland), Arnold Hoeks (Maastricht Univ., 6200 MD Maastricht, The Netherlands), and Marcel Rutten (Eindhoven Univ. of Technol., 5600 MB Eindhoven, The Netherlands)

A new method of noninvasive examinations of the forward and reflected (backward-traveling) pressure waves in human arteries is presented. The study concerned the effect of an artery stenosis on the value of the reflection coefficient modulus and the time delay of the reflected wave relative to the forward wave. The investigations were carried out in the common carotid artery of a healthy person and of a person with 60% stenosis of the internal carotid artery. The instantaneous value of the blood pressure in the common carotid artery was determined from ultrasonic measurement of the instantaneous artery diameter and from the systolic and diastolic blood pressures measured by cuff in the brachial artery. The coefficient of wave reflection was calculated on the basis of noninvasive ultrasonic investigations of the characteristic and input impedance in the common carotid artery. The results of the examinations indicate that a vessel stenosis causes an increase in the value of the reflection coefficient modulus and a decrease in the time delay between the reflected and forward pressure waves at the measurement point just proximal the stenosis. This observation can be of significance for noninvasive diagnosing of atherosclerosis of arterial vessels.

10:00

4aBB6. Ultrasound diagnostic of the blood vessels' random neoplasm distributed in focus sphere limited environs. E. I. Oboznenko (Dept. of Electron., NTUU Kiev Polytechnic Inst., Kiev 252056, Ukraine)

The scattering of ultrasonic waves in the cylindrical volume, formed with a height of $ct/2$ (c—sound velocity, t—probe duration) and a focused beam of R radius in the vicinity of the focal zone is examined. There are N vessels of different diameter and random orientation of stream velocity relative to the beam axis. In the case of random blood vessels orientation, the average Doppler echo-signal frequency also will be random f. The estimation of coherent and noncoherent pressure in echo signal is reduced to statistical averaging for discrete scatters—blood vessels. The probability characteristics of the average effective surface of the vessels scattering with the different rules of wave's incidence angle in the opposite direction (uniform laws, Gaussian laws, etc.) are determined. It was shown that with uniform law of the vessels' orientation angle's distribution, the Doppler frequency is approximately equal to: $\langle f \rangle = f_0(1-2\langle M \rangle)$, but taking into account the random vessel orientation it will be: $f = f_0(1+2\langle M \rangle \cos\langle Q_{\text{inc}} \rangle)$, where $\langle M \rangle$ is the average Marh's number, and a $\langle Q_{\text{inc}} \rangle$ is the average wave's angle of incidence. The proposed method serves for classification of the vessel's neoplasm formation in cancer diagnostics.

10:20–10:40 Break

10:40

4aBB7. Passive thermoacoustic tomography—A new kind of acoustic imaging for material testing and medicine. Victor I. Passechnik, Andrej A. Anosov, and Konstantin M. Bograchev (ELDIS IRE RAS, Starosadskiy per., 8, 101 000, Moscow, Russia, passechn@bfhome.msk.ru)

Passive thermoacoustic tomography is a method for reconstructing temperature distributions inside objects, using the intensity of ultrasonic thermal acoustic radiation emitted from within the object. Methods for the reconstruction of 2-D and 3-D temperature distributions were analyzed by computer simulation. The standard error of reconstruction did not exceed 0.25 K (for about 300 measurements and fluctuation error of every measurement 0.1 K). The physical experiments for temperature reconstruction were carried out using a glycerin phantom with a heated area at a depth of 16 mm. The radiation was measured in one plane with angles of 0 and 45 degrees to the phantom border. The 2-D internal temperature distribution in this plane was reconstructed with a standard error of 0.4 K. The 1-D temperature transversal distribution was studied in a human hand immersed in water, the radiation being measured from both sides of the hand. The reconstructed distribution was approximated by a cubic parabola with an error of less than 0.5 K. Application of correlation properties of thermal acoustical radiation is discussed as well. [Work supported by Russian Basic Research Foundation Grant No. 98-01-00100.]

11:00

4aBB8. Wavelet imaging of temporomandibular joint in motion for real-time diagnosing system. Waldemar Lis, Marek Moszynski, and Roman Salamon (Acoust. Dept., Tech. Univ. of Gdansk, Narutowicza 11/12, 80-952 Gdansk, Poland, marmo@pg.gda.pl)

The new inexpensive method of diagnosing the temporomandibular joint by analyzing acoustic emission signals generated by the joint in motion was presented previously [W. Lis *et al.*, ''Application of processed acoustic emission data for investigation of temporomandibular joint pathology,'' Proc. of 47th ICB Seminar on Ultrasound in Biomeasurements, Diagnostics and Therapy (1998)]. Moreover, the advantages of wavelet techniques over classical Fourier analysis were observed for this case. The time-frequency imaging of such signals has clear anatomic interpretation of pathological diseases. The paper presents the adaptation of discrete wavelet transform (DWT) for analysis of signals acquired from the temporomandibular joint in a real-time system. Additionally, it is shown that common PC hardware is sufficient for collecting data and real-time display. Specially designed software for acquisition and analysis of acoustic emission of this joint was developed and results of its use are presented. The software package was equipped in small database for managing the measurements of clinical cases.

11:20

4aBB9. Pulse waveform design using time reversal for cardiac ultrasound imaging. T. M. Maniatis, Konstantina S. Nikita (Dept. of Elec. and Computer Eng., Natl. Tech. Univ. of Athens, 15773 Zografou Cambus, 9 Iroon Polytechniou St., Zografou, Athens, Greece), Stergios Stergiopoulos (Defence and Civil Inst. of Environ. Medicine, North York M3M 3B9, Canada), and Nikoloas K. Uzunoglu (Natl. Tech. Univ. of Athens, Athens, Greece)

The time-reversal method is being used to design pulse waveform signals for cardiac ultrasound imaging. The objective is to remove the impact of the dominant scatterers of the human body located between the sensors and the heart's near region. The proposed pulse waveform design method has been evaluated with numerical experiments that simulate the acoustical scattering effects of generic cardiac ultrasound imaging operations. Moreover, it is shown that the time-reversal method, when it is being applied on a portion of the received signal, provides a direct real-time assessment of the dominant scatterers' relevant transfer function.

THURSDAY MORNING, 18 MARCH 1999 ROOM H112, 7:55 A.M. TO 12:20 P.M.

Session 4aEA

Engineering Acoustics and Signal Processing in Acoustics: Digital Signal Processing for Hearing Aids I

Stephen C. Thompson, Cochair
Knowles Electronics, Inc., 1151 Maplewood Drive, Itasca, Illinois 60564, USA

Wolfgang H. Doering, Cochair
Department of Otorhinolaryngology, Audiology Section, University of Technology, RWTH Aachen, Pauwelsstrasse 3, D-52074 Aachen, Germany

Chair's Introduction—7:55

Invited Papers

8:00

4aEA1. Digital signal processing in hearing aids. Jeremy Agnew (Starkey Labs., Inc., 1110 Elkton Dr. Unit E, Colorado Springs, CO 80907)

For individuals with a hearing impairment, digital signal processing offers the promise of implementing previously unavailable methods of manipulating sound to compensate for hearing loss. However, hearing aids also present a complex technical challenge for the incorporation of DSP technology. Modern hearing aids are powered by zinc-air cells, since this chemistry produces one of the highest energy densities of all battery technologies and results in the most power for the smallest size. However, the use of these cells places severe limitations on the DSP technology that may be incorporated into a hearing aid. The available operating voltage is 1.25 V and, in order to provide an acceptable battery lifetime for the consumer, the available current drain is severely limited. An additional design challenge is that the entire DSP hearing aid must fit into the human ear. This presentation will focus on the complexity of achieving DSP technology in hearing aids within these electronic and mechanical limitations. General discussion will focus on circuitry necessary to achieve DSP in a hearing aid and on the various considerations and limitations that must be taken into account when making design decisions.

8:20

4aEA2. Noise reduction algorithms for digital hearing instruments. Volkmar Hamacher and Inga Holube (Siemens Audiologische Technik GmbH, Erlangen, Germany, volkmar.hamacher@med.siemens.de)

One of the main problems for hearing instrument users is the reduction of speech intelligibility in noisy and/or reverberant environment. To compensate for this disadvantage, noise reduction algorithms preceding or integrated in the hearing instruments' signal processing are required. New generations of powerful digital hearing instruments enable the implementation of sophisticated algorithms, which have been partly applied in other communication devices. These algorithms offered promising benefit in previous

laboratory studies with hearing instrument users. This paper presents a survey of noise reduction strategies implemented in current hearing instruments and new algorithms applicable in future devices will be given. The algorithms can be divided into different classes concerning their approach in noise reduction. One class of algorithms uses the signal from one microphone and reduces the noise by analysis of the signal characteristics. Another class of noise reduction techniques uses several microphones and exploits spatial information about the sound field to improve the signal-to-noise ratio. Restrictions for the different algorithms are the computational effort and the preconditions to the interfering noise field. The expected benefit for hearing instrument users in typical everyday life hearing situations will be discussed.

8:40

4aEA3. Noise reduction strategies employing interaural parameters. Thomas Wittkop, Volker Hohmann, and Birger Kollmeier (AG Medizinische Physik, Univ. of Oldenburg, Oldenburg, Germany)

The binaural noise reduction algorithm for hearing aids employing directional filtering and dereverberation introduced by Peissig [J. Peissig, V. Hohmann, and B. Kollmeier, DAGA '92, 1049–1052 (1992)] was already studied and developed further in the past [T. Wittkop and V. Hohmann, DAGA '97, 246–247 (1997)]. In this paper, a new noise reduction algorithm will be described which is based in part on the above-mentioned algorithm and was developed with particular respect to the sound quality of the processed signal. An additional stage of processing is introduced which is able to attenuate a single lateral jammer sound source while preserving high signal quality in simple acoustical environments. Moreover, a decision unit is introduced and described which is used to rate the complexity of the acoustical environment and to switch off processing stages automatically if the environment does not match the prerequisites for a particular processing stage, i.e., if the processing is assumed to deteriorate the signal rather than to give any benefit. Measurements of quality judgments employing paired comparisons will be described and the results will be discussed and compared to former results obtained with the old algorithm.

9:00

4aEA4. Combination of monaural and binaural noise suppression algorithms and its use for the hearing impaired. Mark Marzinzik, Thomas Wittkop, and Birger Kollmeier (AG Medizinische Physik, Universität Oldenburg, D-26111 Oldenburg, Germany, mark@medi.physik.uni-oldenburg.de)

A single-channel noise suppression algorithm based on the Ephraim–Malah suppression scheme [Y. Ephraim and D. Malah, IEEE Trans. Acoust. Speech Signal Process. **32**, 1109–1121 (1984)] was tested with hearing-impaired subjects for different noise conditions. Significant benefits could be demonstrated for hearing-impaired subjects regarding reductions in listener fatigue and in the mental effort needed to listen to speech in noise over longer periods of time. However, an improvement of speech reception thresholds measured with the Göttingen sentence test could not be shown. Hence, a combination of the single-channel noise suppression scheme with the directional filter binaural noise reduction algorithm [T. Wittkop and V. Hohmann, this conference] is investigated. While the directional filter is assumed to suppress distinct noise sources, as, for example, jammer talkers that are not located in the desired direction, the monaural noise suppression algorithm reduces the diffuse stationary noise floor. Different combination strategies are being studied and evaluated with hearing-impaired subjects with regard to speech intelligibility, ease of listening, and subjective quality. The benefits as well as the shortcomings of the combined noise suppression algorithms for hearing-impaired subjects will be described and discussed. Implications for future developments will be drawn.

9:20

4aEA5. Signal processing algorithms for an open-platform DSP hearing aid. Brent W. Edwards (ReSound Corp., 220 Saginaw Dr., Redwood City, CA 94063, bedwards@resound.com), John Melanson (AudioLogic, Boulder, CO 80301), and Nikolai Bisgaard (Danavox, Taastrup, DK-2630 Denmark)

The development of DSP chips that meet the small-size and low-power constraints of hearing aids has increased the signal processing capabilities of such devices tremendously. Processing schemes that would be difficult, if not impossible, to implement on an analog chip can easily be implemented digitally. These signal processing algorithms for hearing aids can be classified into one of three categories: those intended to restore impaired hearing to normal, those designed to improve speech intelligibility in noisy situations, and those that improve the functionality of the device. The signal processing algorithms for an open-platform, or software-based, DSP hearing aid will be discussed, with an emphasis on features that are unique to this device. These include FFT-based multiband compression, active feedback cancellation, and digitally processed multi-microphone directionality. The perceptual benefits associated with each algorithm will be provided.

9:40

4aEA6. Acceptable delays in hearing aids and implications for feedback cancellation. S. Laugesen, K. V. Hansen (Oticon Res. Ctr., Eriksholm, Kongevejen 243, DK-3070 Snekkersten, Denmark), and J. Hellgren (Linköping Univ., Sweden)

The advent of digital hearing aids has made it possible to realize a vast range of advanced signal processing algorithms. Undoubtedly, some candidate algorithms will involve comprehensive throughput delays. This applies, for instance, to all algorithms that are based on the discrete Fourier transform, due to the inherent block processing. The results of a literature study on the potential audible effects of delays in hearing aids will be presented in an outline. The rather restrictive limitations on throughput delay that appear from this study have consequences for many attractive hearing aid applications of digital signal processing. As an example, digital feedback cancellation without additive probe noise is considered. Such a system is based on adaptive identification of the

feedback path, found only by means of the excitation provided by the external input signal to the hearing aid. Since the external input signal appears both as reference and disturbance in the adaptive system identification, the estimate of the feedback path becomes erroneous when the external input signal contains significant amounts of autocorrelation. It is shown that the only effective remedy to this problem is to increase the throughput delay of the hearing aid.

10:00–10:20 Break

Contributed Papers

10:20

4aEA7. Real-time combined compression and linear gain processing for digital hearing aids. Juan Carlos Tejero-Calado (Univ. of Malaga, Campus de Teatinos—Complejo Tecnologico, 29080 Malaga, Spain), Janet Rutledge, and Peggy Nelson (Univ. of Maryland School of Medicine, Baltimore, MD 21201)

Amplitude compression processing is used to reduce amplitude-level variations of speech to fit reduced dynamic ranges of hard-of-hearing (HoH) listeners. However, compression processing results in spectral smearing due in part to reduced peak-to-valley ratios. HoH listeners have difficulty detecting important spectral peaks in speech [Nelson and Revoile, 1998]. Thus spectral smearing due to compression processing may have unwanted negative effects on speech understanding. Presented here is a real-time processing algorithm based on a sinusoidal speech model that preserves the important spectral peaks through hybrid compression and linear gain processing. Primary spectral peaks are identified in 7.5-ms analysis frames using 30-ms Hamming windows. A 256-pt FFT is used for speech sampled at 8.013 kHz. The stimuli are divided into frequency bands surrounding the spectral peaks, and the desired compression ratio for each frequency band is applied [Tejero-Calado *et al.*, 1998]. For speech synthesis, an inverse FFT and overlap-add method is used with a triangular window that is double the analysis frame length. The algorithm is currently implemented using a TMS320C30 EVM. The resulting processed speech has good sound quality, compressed amplitude, and preserved spectral contrast. Preliminary tests indicate that HoH listeners benefit from the processing algorithm over conventionally amplified speech signals.

10:40

4aEA8. Electrical compensation of the microphone sensitivities in a dual microphone directional hearing aid. Stephen C. Thompson (Knowles Electronics, Inc., 1151 Maplewood Dr., Itasca, IL 60564)

Hearing aids with directional sensitivity have shown enhanced user satisfaction for their improved performance in noisy environments. One way to achieve the directional response patterns is to use two omnidirectional microphones with the necessary beamforming electronics to form a beam with the desired directionality. Proper operation of the beamforming circuitry requires that the frequency-dependent sensitivities of the two microphones be accurately matched, or corrected, in both magnitude and phase. This paper presents a method of electrically compensating the response of the two microphones to provide an accurate match for beamforming without the need for special sorting of the pairs for matched response. The circuit is suitable for field recalibration if aging causes the sensitivities to vary, and can also be implemented as an adaptive circuit to update the compensation parameters with time for any slow drift with time.

11:00

4aEA9. Acoustic feedback reduction in hearing aids—A feasibility study. Mariano Roccasalva-Firenze and Boaz Rafaely (Inst. of Sound and Vib. Res., Univ. of Southampton, Highfield, Southampton S017 1BJ, UK, br@isvr.soton.ac.uk)

Acoustic feedback in hearing aids occurs when the receiver of the hearing aid produces an acoustic signal that leaks to the microphone and causes oscillations and instability, limiting the hearing aid gain. The problem is worse in vented hearing aids, which are commonly used to reduce the unnatural feeling caused by the ear occlusion. Common solutions to the feedback problem are low-pass filtering for analog hearing aids, and adaptive feedback cancellation for digital hearing aids. Hearing aids are commonly designed primarily to compensate for the hearing loss, and therefore often suffer from feedback instability. In this work it is shown that the hearing aid can perform better if both the feedback problem and the required compensation are considered in the hearing aid design. An experiment was performed to study the hearing aid feedback mechanism in both an ear simulator and in human ears under various conditions. Then hearing aid filters that minimize the feedback problem for the human-ear data, while providing maximum gain for hearing loss compensation, were computed. The filter design problem was formulated as a convex optimization problem and solved using sequential quadratic programming. Results of the feedback path measurements and the hearing aid filters will be presented.

11:20

4aEA10. A four-microphone noise reduction system for hearing aids. Martin Kompis, Peter Feuz (Univ. Clinic of ENT, Head and Neck Surgery, Inselspital, 3010 Berne, Switzerland, martin.kompis@insel.ch), Gregory Valentini, and Marco Pelizzone (Cantonal Univ. Hospital, 1211 Geneva, Switzerland)

A novel four-microphone noise reduction scheme for conventional hearing aids and cochlear implants is investigated. The acoustic field is sampled with a total of four microphones. Two microphones are mounted on either side of the head in behind-the-ear hearing aid housings. Each pair of microphones forms a fixed beamformer, and the outputs of the two devices are post-processed by an adaptive beamforming scheme. The adaptive beamformer is programmed to further enhance target signals emitted in the front of the listener while suppressing noise arriving from other directions. The system has been implemented in real time on a custom-built portable digital signal processing system. The output of the system can be used to drive headphones or the audio input of a number of conventional hearing aids and cochlear implant speech processors. The four-microphone noise reduction system has been evaluated in two different acoustic environments with speech recognition tests conducted on four normal-hearing listeners. Preliminary results indicate an improved directional pattern and significantly enhanced speech recognition in noise, when compared to either a fixed or an adaptive beamformer by itself. In a moderately reverberant room, signal-to-noise advantages of up to 17 dB were observed. [Work supported by the Josephine-Clark Foundation.]

11:40

4aEA11. Modeling of acoustics of hearing aid earmold systems. Grzegorz Szwoch and Bozena Kostek (Tech. Univ. of Gdansk, WETI, Sound Eng. Dept., PL-80-952 Gdansk, Poland, kid@sound.eti.pg.gda.pl)

The earmold system of hearing aids guides an amplified and compressed sound into the ear canal. The description of the propagation of acoustical waves in this system is complex because of the fact that the auditory tube is not straight and the eardrum does not form a perfectly flat end. In more advanced hearing aids, the earmolds are acoustically fitted, according to the patient's needs. However, this is done experimentally during the fitting process. Modeling of earmolds with irregular shapes can be based on the approach widely used in speech acoustic and in digital sound synthesis, namely the physical modeling of acoustical waveguides.

The elaborated model uses fragments of tubes of different diameters and lengths. The difference in acoustic impedance at the boundaries of each two fragments is described by the reflection coefficient. The acoustic wave propagation is modeled using a pair of delays. The model enables the finding of a spectral response characteristic of a hearing aid earmold system in the process of its matching to the patients needs. The details of the proposed approach and some results will be presented in the paper. [Work supported by KBN, Poland, Grant No. 8 T 11E 03415.]

12:00

4aEA12. A high performance wearable signal processor system for the evaluation of digital hearing aid algorithms. Uwe Rass and Gerhard H. Steeger (FH Nuernberg, FB NF, Wassertorstr. 10, D-90489 Nuernberg, Germany, Gerhard.Steeger@fh-nuernberg.de)

Today's commercially available digital hearing aids contain specialized hardware to keep the power consumption low. These specialized processors are not able to run arbitrary signal processing strategies. However, new audiological algorithms have to be assessed in the everyday acoustical environment of the hearing impaired before developing specialized hardware. Therefore, flexible experimental hearing aids, which include general purpose signal processors, are needed for R&D purposes. Such a system has been developed, based on the high performance signal processor Motorola DSP56303. The wearable signal processor units also include high-quality stereo analog-to-digital (ADC) and digital-to-analog (DAC) converters with 20-bit word length each. The available dynamic range exceeds 90 dB. The input and output gain can be adjusted by digital potentiometers. The housing of the device is small enough to carry the experimental hearing aid in a pocket (dimensions $150\times80\times25$ mm). Software tools have been developed to ease the development of new algorithms. A set of configurable modules implements all hardware-dependent software routines and gives easy access to the peripherals and interfaces. A comfortable fitting interface allows easy control of the signal processing unit from a PC, even by assistant personnel. Thus the unit is best suited for use in interdisciplinary research projects.

Session 4aED

Education in Acoustics: Demonstrations in Acoustics Education

Sally G. Revoile, Cochair
(University of Maryland, Baltimore, Maryland), Sea Island, Georgia 31561, USA

P. K. Raju, Cochair
Department of Mechanical Engineering, Auburn University, Ross 201, Auburn, Alabama 36849, USA

Lothar Gaul, Cochair
Institut für Mechanik, Universität Stuttgart, Pfaffenwaldring 9, 70550 Stuttgart, Germany

Chair's Introduction—8:35

Contributed Papers

8:40

4aED1. A computer-based lung sound simulator. Martin Kompis (Univ. Clinic of ENT, Head and Neck Surgery, Inselspital, 3010 Bern, Switzerland, martin.kompis@insel.ch), Oliver Schwarz, Mathias Becher, and Ulrich Burri (Univ. of Appl. Sci., 2501 Biel-Bienne, Switzerland)

A novel lung sound simulator for teaching and research purposes is presented. While heart sound simulators have been used for many years in medical schools and schools of nursing, first algorithms for the simulation of lung sounds have become available only recently [M. Kompis and E. Russi, Med. Biol. Eng. Comput. **35**, 231–238 (1997)], and no practically useful device has been presented up to now. The newly developed lung sound simulator requires no specialized hardware except for a personal computer, a standard sound card, and loudspeakers which are able to reproduce the predominately low-frequency sounds. Normal, bronchial, and tracheal respiratory sounds can be simulated, and continuous and discontinuous adventitious lung sounds, as well as heart sounds, can be added. The attributes of these sounds, such as, e.g., loudness, duration, and pitch, are controlled by the user. Changes in the simulation parameters can be made effective almost immediately. Simulated sounds can be saved for later use, and recordings of real lung sounds can be reproduced from within the lung sound simulator program, allowing direct comparison between real and simulated sounds. Simulation parameters can be stored and libraries of simulated lung sounds can be created.

9:00

4aED2. Measurement and visualization of vibroacoustic fields caused by impact on solid surfaces. Vygantas Augutis and Darius Gailius (Varpo 10-12, Kaunas 3028, Lithuania, dagail@tef.ktu.lt)

The system for measuring and visualization of vibroacoustic fields, and observation of propagation of acoustic waves of various types on solids surfaces was developed. It is possible to reconstruct the measured vibration or compute modes of vibration (movie, animation) and determine types of acoustic waves and their speeds from the measured data arrays. The vibroacoustic fields of some objects were measured (glass block, steel block, rod, pipe, etc.) in a frequency range from 1 kHz to 10 MHz. The amplitudes of vibrations range from 10 to 2000 nm. Different devices for reception and actuation of vibrations were developed and used: piezoelectric, electromagnetic, microphones, etc. The results of the investigation are presented in CD-ROM (conditions of measurement, animated vibrations, modes).

9:20

4aED3. Speech and hearing demonstrations in MATLAB. Martin P. Cooke and Guy J. Brown (Dept. of Computer Sci., Univ. of Sheffield, Regent Court, 211 Portobello St., Sheffield, UK, m.cooke@dcs.shef.ac.uk)

Education can be greatly enhanced by the provision of tools which allow students to interact with, explore, and manipulate key elements of the phenomena under study. Such facilities are even more important in

areas such as the perception, production, and recognition of sounds, whose subject matter is difficult to convey by words or pictures alone. Consequently, a collection of software applications has been developed, each adopting either an ''experiment-replication'' or a ''white box'' paradigm. The first category includes demonstrations of audiometric testing, perceptual separation of concurrent vowels, perception of alternating two-tone stimuli, and auditory induction. In the ''white box'' paradigm, students interact with the parameters of an algorithm or model, such as endpoint detection of speech, cepstral analysis, and models of peripheral auditory function. The applications are written in MATLAB, which provides a high-level interface to signal processing tools, graphical user interface components, and sound handling functions. As part of an ongoing action research study, the value of this work is being assessed against our learning objectives for final-year undergraduate and masters-level courses in speech and hearing technology. [Work supported by EU ELSNET Language Engineering Training Showcase.]

9:40

4aED4. Hydrodynamic analog of a thermoacoustic device. Robert M. Keolian (Grad. Prog. in Acoust. and Appl. Res. Lab., Penn State Univ., P.O. Box 30, State College, PA 16804-0030, bonzo@sabine.acs.psu.edu)

An apparatus that oscillates one medium past another is used to demonstrate the principles of a thermoacoustic device. By analogy, heat pumping is represented by the flow of water uphill. Temperature is represented by the water height. The two oscillating media are sheets of Lexan Thermoclear plastic (GE Plastics). Water fills the hollows within the plastic sheet and participates in the so-called bucket brigade, which transports water in this demonstration, or heat in an actual thermoacoustic device. [Work supported by the ONR.]

10:00–10:20 Break

10:20

4aED5. A learning program in psychoacoustics with interactive computer-based listening experiments. Martina Kremer and Detlef Krahe (Univ. of Wuppertal, Fuhlrottstrasse 10, 42097 Wuppertal, Germany, krahe@uni-wuppertal.de)

The processing of dynamic sound files in psychoacoustic listening experiments and learning software will be demonstrated by the multimedial learning software called ''Audite.'' In the field of psychoacoustics, the computer can be used as a universal medium to combine high-quality listening experiments with the presentation of multimedia learning software. They can be generated off-line, depending on the parameter input of the customer. Problems occur if the software should be presented online in the Internet. In this case, only low-quality sound files can be generated interactively. Further, the possibilities of the multimedia representation are reduced so the realization of reasonable didactic structures becomes more difficult, too. By the development of new program structures, the implementation of dynamic and high-quality sound files generated at the run time is realized. In addition, the insertion of improved script languages allows the representation of system-independent multimedia information and the realization of improved interactivity by the customer.

10:40

4aED6. WWW-based acoustics education—Considerations and implementation. Martti A. Rahkila and Matti A. Karjalainen (Helsinki Univ. of Technol., Lab. of Acoust. and Audio Signal Processing, P.O. Box 3000, FIN-02015 HUT, Finland, Martti.Rahkila@hut.fi)

The World Wide Web, WWW, is without a doubt one of the most interesting environments for computer-based education, acoustics being one of the areas of teaching. Technically, the WWW is a moderately simple system and it provides platform independence, easy operation for users, and easy use of multimedia information for content providers. But when it comes to WWW-based education, things just aren't so simple anymore. At the Helsinki University of Technology Acoustics Laboratory, computer-based acoustics education has been a research interest for several years now. This paper considers various aspects of WWW-based acoustics education from the point of view of content design and user interaction, not forgetting usability issues or learning evaluation questions either. The goal is to explore the possibilities of the WWW technology and find the most suitable ways of providing self-study, interactive education material of acoustics and audio signal processing. Moreover, the paper discusses implementation details of interactivity, user control, and evaluation. Acoustics and sound-related topics such as on-line processing and network audio problematics have been included. An example technical solution, a ''User Agent''-style architecture, is presented along with a tutorial level sample application.

Contributed Posters

These posters will be on display in the Poster Gallery from Thursday to Friday, 18–19 March. Authors will be at their posters from 11:00 a.m. to 12:20 p.m. on Thursday, 18 March.

4aED7. Education of applied acoustics for students of automotive engineering. Wolfgang Foken (Westsächsische Hochschule Zwickau (FH), Kraftfahrzeugtechnik, Postfach 201037, D-08012 Zwickau, Germany, wolfgang.foken@fh.zwickau.de)

Every year 120 students of automotive engineering are enrolled at the University of Applied Sciences in Zwickau (Germany). It is extremely necessary to give them an overview knowledge in the field of applied acoustics. The aim of this paper is to present some methodical aspects of these lessons. Practical tutorials are an essential part of these lessons. Exemplary, the tutorial ''Indoor noise of the passenger compartment'' is selected. For example, the task is to scan the indoor sound field with a 2-D microphone array and to compare the obtained modes with results from FEM/BEM calculations. The students become familiar with practical measuring methods, with the spectral analysis equipment, and, last but not least, with the application of numerical methods in acoustics. For students of automotive engineering having somehow an ''emotional'' relationship to the object ''car'' it is always useful to provide a lot of practical appli-

cations. The theoretical fundamentals should be trained; however, the lessons must not be overloaded with theoretical treatises. This way it is possible to make the students sensitive to problems of acoustics.

4aED8. Architecture and music: A laboratory. Pierre Dutilleux (ZKM|Inst. for Music and Acoust., Karlsruhe, Germany) and Christian Müller-Tomfelde (GMD-IPSI, Darmstadt, Germany)

A museum exhibit gives the visitors an opportunity to experience the relation between sounds and performance space. A catalog of dry recorded sounds is available, as well as two categories of performance spaces: The so-called complex shapes (i.e., concert hall, roman theater, living room, natural echo) and the so-called basic shapes (i.e., free field, tube, cube, sphere). The visitor is free to combine any sound with any space. A computer processes the sounds as if they were heard in the selected space. The impulse responses of the complex shapes have been measured and a room simulator (Spatialisateur) has been programmed to imitate these spaces. The basic shapes are imitated using simpler algorithms. The resonances of the sphere are distributed according to the roots of the first derivative of the Bessel functions. The room selection is such that most people can recognize or identify a space after listening to a few sounds. Visitors, musicians, and even acousticians can learn intuitively how a piece of music sounds in one place or in another. Music students are fascinated to hear how a room can modify the sound of their instrument. The basic shapes allow the demonstration of modal acoustics.

THURSDAY MORNING, 18 MARCH 1999 ROOM MA004, 7:55 A.M. TO 12:20 P.M.

Session 4aMU

Musical Acoustics: Quality of Musical Instruments and Human Voice

René Caussé, Cochair
IRCAM, 1 Place Igor Stravinsky, F-75004 Paris, France

Johan E. F. Sundberg, Cochair
Royal Institute of Technology, KTH, Speech, Music, Hearing, Box 70014, 100 44 Stockholm, Sweden

Chair's Introduction—7:55

Invited Papers

8:00

4aMU1. Some aspects on fairly objective results of subjective tests. Klaus Wogram (Phys.-Techn. Bundesanstalt, Proj. 1.401, Bundesallee 100, D-38116 Braunschweig, Germany, klaus.wogram@ptb.de)

When performing tests with playing subjects on musical instruments it is neccessary to regard that the musicians judge under the influence of prejudices and the appearence of the instrument under test. This obviously affects the results which are no longer generally accepted. To avoid those difficulties the PTB has developed a method which delivers mostly reproducible results for the compared instruments. The aim of this method is to create a psychological situation in which the subject is no longer interested to identify the manufactor and the type or model of the specimen, but will concentrate strictly on the musical parameters like tone color, response, intonation, and others.

8:20

4aMU2. Vocal qualities that singers can control but often limit. Ingo R. Titze (Dept. of Speech Pathol. and Audiol. and The Natl. Ctr. for Voice & Speech, Univ. of Iowa, Iowa City, IA 52242)

In singing, there is sometimes a conflict between maximizing the size and consistency of the voice and maximizing the number of distinct qualities that can be utilized. Most vocalists can voluntarily change vocal register (from chest to fry, falsetto, and in some cases whistle), vocal ring (from resonant to fluty), vocal tightness (from normal to breathy or pressed), and vocal roughness. But classical singers, for whom electronic amplification is often not an option, limit the use of the full scope of these qualities. Falsetto register which involves only part of the vocal fold in vibration, is used sparingly because it doesn't balance with chest voice in terms of loudness. The same can be said for breathy voice, produced with a wider glottis. Some vocal qualities are not used because they are spectrally unbalanced, and rough voice is often rejected because it suggests lack of refinement and harmonic purity. With amplification, many of the restrictions on vocal quality are removed. [Work supported by Grant No. P60 DC00976 from the National Institute on Deafness and Other Communication Disorders.]

8:40

4aMU3. Assessment of musical instrument quality criteria: The notion of ''openness'' for a trumpet. Rene Causse, Camille Begnis, and Nicolas Misdariis (IRCAM-1, place Igor Stravinsky, F-75004 Paris, France, causse@ircam.fr)

Judgment of musical instrument quality is a complex process that implies criteria relating to the nature of the sound produced (accuracy, timbre, . . .) but also sensations closely linked to the contact between the instrument and the musician (ease of playing, . . .). From this viewpoint, a set of trumpets was studied [Causse *et al.* (1995)]: from playing tests carried out by professional trumpet players, attempts were made, on the one hand, to define subjective factors they used in their judgments and, on the other hand, to

correlate these factors with geometrical or acoustical parameters. This preliminary study led to three notions implied in this judgment process, among which was the sound volume, and to propose, for each of them, a significant physical interpretation. Following this study, the sound volume, which is an important component of the trumpet player's vocabulary and which seems to be associated with a broader notion of openness, was focused on. Different possible interpretations of openness, through a questionnaire, followed by an experimental procedure (playing and hearing tests), were explored. In addition, complementary measurements were done in order to propose a more precise physical interpretation. The first results obtained from the second study will be presented and discussed.

9:00

4aMU4. Diagnosis and therapy for brasses. Methods of measurement, evaluation, and improvement of the acoustical quality of brass wind instruments. Gregor J. Widholm (Inst. fuer Wiener Klangstil, Univ. fuer Music and Performing Arts in Vienna, Vienna, Austria)

The operation of brass wind instruments and the relationship between their mechanical parameters and acoustical properties are more or less well understood. Problems may arise if one attempts to compare, e.g., measured intonation or response with the judgment of professional players. It can be seen that brass instruments have a measurable objective intonation quality and may have two or more different subjective qualities because of the fact that instrument and player are parts of a closed control loop. Methods are described to obtain objective quality parameters, taking into account the player's contribution. An example is the dependency of intonation values on the played dynamic level. In the second part of the paper, recently developed software tools for researchers and instrument makers are presented. While in the past most emphasis was put on diagnosis only, today's increased processing power allows one to focus on therapy tools based on optimization algorithms. Computer optimization requires a description of the instrument shape which is automatically modified in order to improve the instrument quality, as indicated in a user-defined target function. Obtaining the shape of an instrument is difficult unless bore reconstruction from measured input impedance can be performed. Results of current research are presented.

9:20

4aMU5. Violin quality and bridge mobility. Erik V. Jansson (Speech, music and hearing, KTH, Stockholm, SE-100 44, Sweden)

In the measured bridge-mobility curves of a Stradivarius violin, two sharp prominent peaks were found at approximately 450 and 550 Hz, and a broad rounded hill with a maximum at approximately 2.5 kHz. The labeling P1 and P2 is suggested for the peaks in honor of Frederick Saunders (principal peak P) and BH, bridge hill for the 2.5-kHz hill. The P2 maximum is the highest, the BH the second highest, and the P1 the lowest. Measured bridge-mobility of soloist quality violins [E. V. Jansson, Acust. Acta Acust. **83**, 337–341 (1997)] and measured radiation of Italian violins [H. Duennwald, Acustica **51**, 281–287 (1982)] show similar features. The similarity indicates that the bridge-mobility predicts the sound reaching the listener's ear well. A strong P1 and especially a strong P2 should be an indicator of a full tone. Balanced with the BH hill, it indicates the quality of a good violin. [Work supported by KTH, Swedish Natural Science Research Council, Swedish Institute, and Wenner-Gren Center Foundations for Scientific Research.]

9:40

4aMU6. Quality aspects of violin bows. Anders Askenfelt (Dept. of Speech, Music and Hearing, Royal Inst. of Technol., S-10044 Stockholm, Sweden, andersa@speech.kth.se) and Knut Guettler (Norwegian State Acad. of Music, N-0302 Oslo, Norway)

The string player's test of a bow includes four major aspects: (1) the bow should be ''well balanced'' with an appropriate total weight; (2) the bow should have a good grip of the string over the entire length of the bow stroke; (3) the ''timbre of the bow'' should be pleasing; and (4) the bow should bounce easily in advanced bowing patterns like rapid spiccato and ricochet. A poor bow will: fatigue the player by demanding too much physical effort (in particular in string crossings); tend to lose the grip of the string when approaching the tip; disguise the tonal quality of a fine instrument; and be sluggish and scratchy in rapid bouncing sequences. Some plausible physical properties which govern these four quality aspects will be presented, focusing on the last, the bouncing bow. [Work supported by School of Electrical Engineering, Royal Institute of Technology, Stockholm.]

10:00–10:20 Break

10:20

4aMU7. Tone quality and important modal properties of the guitar. Howard A. K. Wright (Dept. of Phys. and Astron., Edinburgh Univ., Edinburgh EH9 3JZ, UK, Howard.Wright@ed.ac.uk)

The main function of a string instrument's body is to convert string vibrations into radiated sound that is detected by the listener. The coupling between string and body modes determines the vibrational response of the instrument to a plucking/bowing force applied to the string, and therefore has a crucial influence on the instrument's sound. The nature of this coupling depends on the body's modal properties as detected at the bridge. An interesting question arises: how do changes to the body modes affect the perceived tone quality of the instrument? The use of numerical models permits independent control of an instrument's modal properties. By performing psychoacoustical tests with sounds synthesized from these models one can examine the effect on perceived tone of changes to individual body modes. In relation to the guitar, this approach has shown that mode shapes, and, in particular, the positions of nodal lines in relation to the bridge, have a powerful influence on tone quality. This paper reviews the current understanding of the links between the guitar's modal properties and its sound, and highlights the need for further numerical and psychoacoustical work as a means of extending our knowledge in this area.

10:40

4aMU8. Acoustic quality of musical instruments and categorization. Michele Castellengo, Charles Besnainou (Laboratoire d'Acoustique Musicale, CNRS-UPMC-Min. Cult., 11 Rue de Lourmel, 75015 Paris, France, castel@ccr.jussieu.fr), and Daniele Dubois (CNRS-INaLF, LCPE, 1 Rue Maurice Arnoux, 92120 Montrouge, France)

The qualitative evaluation of high vintage musical instruments gives rise to several theoretical as well as technical questions. Depending on the experts, either instrument makers trained in various technologies or variously skilled and styled interpreters, the judgments rely on different criteria, regarding the object itself, its manipulations, as well as acoustic or aesthetic properties of the sounds it produces. Various experiments were run with classical guitars (Montchalin, 1993), harpsichords (Guyot, Castellengo, and Dumoulin, 1997), and violin bows (Saint-Loubry and Besnainou, 1997). The judgments were processed in free categorization tasks of musical (listened or performed) sequences, followed by verbal comments on the partitions realized. The analysis of the psychological judgments of similarity and difference, and the linguistic processing of the verbal comments, led to the identification of the relevance of various perceptual modalities (not only acoustic but also kinaesthetic, haptic, and even visual) as well as symbolic associations constructed through experience and training. Physical correlates of the psychologically relevant parameters were transformed by sound synthesis. These experiments allow further theoretical and practical conclusions.

Contributed Papers

11:00

4aMU9. On the effect of phase relations for the perception of pitch and timbre of bass tones. Alexander Galembo (Dept. of Psych., Queen's Univ., Kingston, ON K7L 3N6, Canada), Anders Askenfelt (Royal Inst. of Technol., SE-10044, Stockholm, Sweden), and Lola L. Cuddy (Queen's Univ., Kingston, ON K7L 3N6, Canada)

In contrast to the old classic statement that the human ear is insensitive to phase relations, many results have been published by psychoacousticians that demonstrate the influence of phase on timbre and pitch perception in experimental situations. The experiments usually involve artificial complex tones consisting of high order (unresolvable) harmonics restricted to a specific region of fundamental frequencies. A musically important question is whether or not the effects of phase on pitch and timbre perception are sufficiently strong to be relevant to discussions of the tone quality of real musical instruments. Acoustical analyses and tests of perception in the bass range, where temporal processes are thought to be prominent, provide promising means of studying such effects. Experiments with phase relations in bass tones will be presented. The examples range from harmonic steady multicomponent tones with flat spectrum to inharmonic tones with pianolike spectral dynamics. The results presented have implications for psychoacoustical demonstrations and for a batter understanding of the tone quality of musical instruments, in particular the piano.

11:20

4aMU10. Objective and subjective evaluation of performance precision in piano chords. Jan Tro (NTNU, Acoust., O. S. Bragstads plass 2, N-7034 Trondheim, Norway, tro@tele.ntnu.no)

Analysis of timing precision and dynamic patterns in piano performances using sound recordings may not become a trivial task due to the influence of the recording technique, the room acoustics, and the need for a well-defined attack position for single tone events. During the last ten years the use of standardized registration and transmission of musical performance events makes it a lot easier to do performance analyses even if the present commercially available tools (MIDIized acoustical pianos) still are questioned concerning reliability and reproducibility. This paper discusses the use of a MIDIized piano for multiple recordings of piano performances by several professional artists. The results are based on statistical analyses of both precision and dynamics variation among the performers and deviation for each performer. Subjective listening tests have been used for evaluating musical variables on a subjective quality scale. [B. Repp, ''Individual Differences in Shaping a Musical Phrase,'' 5th ICMPC, Seoul (1998); J. Tro, ''Micro Dynamics Deviation as a Measure of Musical Quality in Piano Performances?,'' 5th ICMPC, Seoul (1998).]

11:40

4aMU11. The effect of crook profile on the perceived playing properties of the bassoon. David B. Sharp (Dept. of Environ. and Mech. Eng., Open Univ., Milton Keynes MK7 6AA, UK), Howard A. K. Wright (Edinburgh Univ., Edinburgh EH9 3JZ, UK), and William Ring (T. W. Howarth and Co. Ltd., Worthing BN11 1TH, UK)

Previous measurements [Sharp *et al.*, Proc. Intl. Symp. on Musical Acoustics, 209–214 (1998)] have shown a difference between the profiles of bassoon crooks manufactured in the first half of this century and those manufactured in the second half. Although all the measured crooks have approximately the same initial and final radii, earlier crooks (manufactured by Heckel) typically have a wider bore in the midsection than crooks made more recently (both by Heckel and other manufacturers). Bassoonists have claimed that older Heckel crooks have more desirable playing characteristics than more modern crooks. Psychoacoustical tests were performed to investigate this claim, and to determine whether listeners can distinguish between sounds produced using different crooks. In the tests, players were recorded performing individual notes, scales, and a musical passage on a reference bassoon using a variety of crooks. The crooks were concealed from the players to prevent visual identification. The performers were then questioned about the playing qualities of the crooks. Pairs of sounds produced using different crooks were presented over headphones and listeners were asked to make judgments on the timbres of the sounds. Results from the tests are discussed with reference to the crook profile measurements.

12:00

4aMU12. A common origin for vocal accuracy and melodic expectancy: Vocal constraints. Frank A. Russo and Lola L. Cuddy (Dept. of Psych., Queen's Univ., Kingston, ON K7L 3N6, Canada, russof@psyc.queensu.ca)

Participants were assigned to one of four groups (no music training, instrumental training, vocal training, and semiprofessional vocalists). Participants were asked to sing 16 three-note melodic sequences previously calibrated by listeners for the degree to which the third note fulfilled the perceptual expectancy established by the first two notes [L. L. Cuddy and C. A. Lunney, Percept. Psychophys. **57**, 451–462 (1995)]. The current study assessed the sung accuracy of the entire three-note sequence with three measures ($F0$ tracking, expert judgment, and self-judgment). All measures revealed that, on average, semiprofessionals were most accurate and musically untrained participants the least accurate. The pattern of accuracy across the 16 sequences, however, was consistent across all groups; intersubject correlations were generally high and significant. Moreover, accuracy measures obtained from each group corresponded to the degree of fulfillment of perceptual expectancy. Two possible accounts of the findings are discussed. Vocal accuracy may reflect perceptual expectancy. Alternatively, vocal accuracy and perceptual expectancy may both reflect a common origin, that of vocal constraints. The latter account has been articulated as the motor theory of melodic perception [F. A. Russo and L. L. Cuddy, Conf. Musical Cognition & Behavior, Rome (1998)].

Session 4aNSa

Noise: Transportation Noise and Its Effects on People

Barbara Griefahn, Cochair
Institute für Arbeitsphysiologie, Ardeystrasse 67, D-44139 Dortmund, Germany

Louis C. Sutherland, Cochair
27803 Longhill Drive, Rancho Palos Verdes, California 90275-3508, USA

Invited Papers

8:00

4aNSa1. Sleep disturbances caused by road traffic noise. Evy Ohrstrom (Dept. of Environ. Medicine, Goteborg Univ., Box 414, SE 405 30 Goteborg, Sweden, evv.ohrstrom@envmed.gu.se)

In the last 15–20 years, there has been an increased use of new and less expensive methods, e.g., body motility techniques (awakenings, arousal), and questionnaires (perceived sleep quality, aftereffects) in studies of noise-induced sleep disturbances, both in laboratory settings and large-scale field studies. Studies on road traffic noise indicate that L_{Amax} levels of 45 dB may increase the time to fall asleep by 7 to 15 min. Recent studies show an acute increase in number of body movements irrespective of L_{Amax} levels from road traffic noise and there is a significant increase of number of awakenings above 55 L_{Amax} in the average population. Noise-sensitive groups react at 5 dB lower levels. Aftereffects of noise-disturbed sleep (reduced perceived sleep quality and increased tiredness or sleepiness during the day) have been found among the average population after acute and chronic exposure to road traffic noise at L_{Amax} levels around 50 dB. Noise-induced sleep disturbances may also lead to lower psycho-social well-being. More research effort is needed, e.g., on effects of critial groups and situations, various types of environmental noise, effects on daily activities, effects of countermeasures against noise, and on predictive indicators of sleep disturbances for presumed health effects.

8:20

4aNSa2. U.S. field research on nighttime sleep disturbance. Lawrence S. Finegold (U.S. Air Force Res. Lab., Wright–Patterson AFB, OH 45433)

This paper provides a review of field research on nighttime sleep disturbance in residential communities conducted primarily in the U.S. over the past decade. It compares the methodology for studying sleep disturbance which has evolved during this series of research projects with the research approach used historically in Europe and elsewhere. A new dose–response relationship is offered, based on a meta-analysis of a database developed from field research around civilian airports and military airbases. This paper presents the details of this database meta-analysis. The new sleep disturbance prediction curve is recommended as an update to the interim curve adopted by the U.S. Federal Interagency Committee on Noise (FICON) in 1992. At that time, there was a lack of consensus in both U.S. and European scientific communities concerning whether both laboratory and field research data should be used in the development of a new prediction curve. The new curve is based solely on field study data and a ''percent awakened'' as an objective measure of sleep disturbance. Thus, it should more accurately predict sleep disturbance in residential environments than the previous FICON curve. It is hoped that additional research will validate this new curve and further investigate habituation in newly exposed communities.

Contributed Papers

8:40

4aNSa3. An interdisciplinary study on railway and road traffic noise: Behavioral results. Barbara Griefahn, Carola Deppe, Rudolf Moog, Peter Mehnert (Institut fuer Arbeitsphysiologie, Ardeystr. 67, D-44139 Dortmund, Germany), Ulrich Moehler (Moehler + Partner, Schwanthalerstr. 79, D-80336 Muenchen, Germany), Anke Schuemer-Kohrs (Elberfeldstr. 32, D-58095 Hagen, Germany), and Rudolf Schuemer (FernUniversitaet/ZIFF, D-58084 Hagen, Germany)

Mainly, laboratory studies revealed traffic noise as a dominant environmental cause of sleep disturbances. They are less suitable to reflect situational or individual factors. In many countries noise pollution is limited at the legally defined night hours. Hence, the aim was to estimate the influence of timing of sleep determined by working hours, preferences of sleeping times related to individual factors like eveningness, age, gender, etc. During 10 nights, the sleep of 377 apparently healthy people was indicated by actimetry and sleep logs and related to the individual outdoor noise levels emitted either by railway or by road traffic. As expected, indicators of sleep were found to depend on timing of sleep and on individual variables as age, morning–eveningness, etc., whereas none of the various parameters of noise revealed significant relations to sleep disorders. However, source-related outdoor noise did not meet the real situation indoors. The impact of railway/road traffic noise on sleep at home cannot be judged yet, but has to be answered, because sleeping times were not covered in 50% of the cases by the legally defined night. Moreover, work flexibility is expected to increase as well as traffic density during the night.

9:00

4aNSa4. Methods of determination of acoustic data in field studies. Manfred Liepert, Ulrich Moehler (Moehler + Partner, Schwanthalerstr. 79, D-80336 Muenchen, Germany), Rudolf Schuemer (FernUniversitaet/ZIFF, D-58084 Hagen, Germany), and Barbara Griefahn (Institut fuer Arbeitsphysiologie, Ardeystr. 67, D-44139 Dortmund, Germany)

An interdisciplinary field study examining the annoyance by rail and road traffic noise with special regard to sleep disturbance was carried out. The noise induced responses were determined by questionnaires and

physiological measurement of sleep disturbance. For subjects taking part in the physiological examination, acoustical measurements have been taken inside and outside the bedroom. The individual noise levels for all subjects have been calculated using the German standards RLS90 and Schall03. As input variables (such as number and speed of passing trains or vehicles) for these calculations on one hand measured data and on the other hand official data have been used. Whereas the measured data deliver reliable information about the traffic during the physiological measurements, the official data mostly refer to maximum (e.g., speed) or average values. Furthermore, the noise levels have been calculated for different measurement points. Thus, together with the measured noise levels a variety of subject individual level values have been collected. The selection of these noise levels and the effect on the noise response relationship shall be discussed. Special regard will be taken on indoor and outdoor levels and the aspects of measurement and calculation and its input data.

9:20

4aNSa5. An interdisciplinary study on railway and road traffic noise: Acoustical results. Ulrich Moehler, Manfred Liepert (Moehler + Partner, Schwanthalerstr. 79, D-80336 Muenchen, Germany), Rudolf Schuemer (FernUniversitaet/ZIFF, D-58084 Hagen, Germany), and Barbara Griefahn (Institut fuer Arbeitsphysiologie, Ardeystr. 67, D-44139 Dortmund, Germany)

Former studies have discovered differences in annoyance reactions determined by questionnaire between railway and road traffic noise. The night time disturbance reactions caused by road traffic noise showed greater scores at the same noise levels than those caused by railway noise. Therefore an interdisciplinary study examining questioned annoyance reactions (day and night time reactions) and also measuring sleep disturbance was conducted. In eight areas—four areas with predominant road traffic noise and four areas with predominant railway noise—acoustical, psychological, and physiological data were gathered. Acoustical indices for both sources were calculated for all subjects using German standards. For subjects taking part in the physiological examination, acoustical measurements indoor and outdoor the bedroom have beeen taken in 10 nights per area. The physiological measurements of sleep disturbance have been taken by actimetry. The acoustical measurements show typical differences between railway and road traffic noise. Several acoustical indices have been calculated from the measured data and corelated to both psychological and physiological data. There is high correlation between the acoustical and psychological variables for both sources whereas the correlation between acoustical and physiological data is very low (see also Schreckenberg *et al.* and Griefahn *et al.*).

9:40

4aNSa6. An interdisciplinary study on railway and road traffic noise: Annoyance differences. Dirk Schreckenberg (ZEUS GmbH, Universitaetsstr. 142, D-44799 Hagen, Germany), Anke Schuemer-Kohrs (Elberfeldstr. 32, D-58095 Hagen, Germany), Rudolf Schuemer (Fern Univ. / ZIFF, D-58084 Hagen, Germany), Barbara Griefahn (Inst. fuer Arbeitsphysiologie, D-44139 Dortmund, Germany), and Ulrich Moehler (Moehler + Partner, D-80336 Muenchen, Germany)

An interdisciplinary study was made to compare the annoyance responses to railway noise and to road traffic noise. Acoustical measurements were taken in eight areas to assess the noise levels caused by railway and road traffic noise. Road traffic noise was predominant in four of the eight areas and railway noise in the other four areas. A total of 1600 residents were interviewed. The data allow the individuals' annoyance responses to be related to the individual noise levels for each of the two sources. Some preliminary results of the not yet completed study with regard to the relative annoyance by the two sources are described. The general annoyance (24 h, by day *and* at night) is less for railway than for road traffic noise at equal noise levels. Also, the disturbances at night attributed to railway noise are less than those attributed to road traffic noise. In the daytime, the difference in the disturbance between railway and road traffic noise depends on the disturbance aspect considered: With regard to communication, there is a greater annoyance attributed to railway than to road traffic noise. With regard to outdoor recreation, road traffic noise is more disturbing than railway noise.

10:00–10:20 Break

10:20

4aNSa7. Measuring retrospective annoyance in field studies: Prerequisites, procedures, and problems. Rainer Guski, Ute Felscher-Suhr (Dept. Psych., Ruhr Universitaet Bochum, D-44780 Bochum, Germany, Rainer.Guski@Ruhr-Uni-Bochum.De), and Rudolf Schuemer (Fernuniversitaet Hagen, Germany)

The definition and measurement of annoyance varies between studies. This paper is concerned mainly with measurement topics, e.g., graphical versus magnitude estimations or verbal scales; the effect of mentioning frames of reference with respect to (a) exposure time, (b) exposure area, or (c) range of possible degrees of annoyance/exposure. With verbal response scales, the number of response steps varies between 2 and 7; some studies simply provide for categorical judgments, others provide for nearly equidistant verbal steps—in order to allow for parametric treatments of data. In this context, an international study is reported which intended to gain comparable response scales for different languages. The decision criteria used for selecting 5 steps on the total range between the lowest and the highest possible degree of annoyance are discussed, and the use of certain verbal modifiers in English, German, and French are proposed. Together with instructions for mentioning the frames of reference, these modifiers should be able to get comparable annoyance scores in field studies.

10:40

4aNSa8. The psychological cost of aircraft noise for children. Sylvia V. Mackensen (Inst. for Med. Psychol., Univ. of Munich, Munich, Germany), Monika Bullinger (Univ. of Hamburg, Hamburg, Germany), Markus Meis (Univ. of Oldenburg, Oldenburg, Germany), Gary W. Evans (Cornell Univ., Ithaca, NY), and Staffan Hygge (Royal Inst. of Technol., Gävle, Sweden)

Psychological effects of aircraft noise exposure on children have only recently been addressed in the literature. The current study took advantage of a natural experiment by the opening of a new airport, exposing formerly nonexposed children to low aircraft noise. In this prospective longitudinal investigation, which employed nonexposed control groups, effects of aircraft noise prior to inauguration of the new airport, as well as effects of chronic noise and its reduction at the old airport, were studied in children aged 9 to 13 years. The psychological health of children was investigated with a standarized quality of life scale as well as with a motivational measure. In addition, a self-report noise annoyance scale was used. In the 393 children studied at the new airport over three time points, results showed a significant decrease of total quality of life 18 months after aircraft noise exposure, as well as a motivational deficit in the new airport area. In the old airport, parallel impairments were present before the airport relocation but subsided thereafter. These findings are in accord with reports of impaired psychological health after noise exposure and indicate the relevance of monitoring psychological parameters as a function of environmental stressors among children.

11:00

4aNSa9. Noise annoyance assessment around Paris airports. Jerome Defrance (CSTB, 24 rue Joseph Fourier, F-38400 Saint-Martin-d'Heres, France, j.defrance@cstb.fr), Jean-Marc Abramowitch, and Ferit Bonfil (ACOUSTB, F-38400 Saint-Martin-d'Heres, France)

Within the context of the French Noise and Sound Annoyance Survey ordered by the General Direction of Civil Aviation (DGAC) and the French Environment Ministry, a complete noise impact study concerning Paris-Charles-de-Gaulle and Paris-Orly airports is carried out. On the one hand, a survey of noise annoyance due to aircraft activity around these airports is led through a sounding out of opinion. On the other hand and later on, a complete campaign of 24-hours-a-day measurement of air traffic is carried out around the same previous zones on a total of 36 fixed receiver points. The aim of this work is to establish the correlation between the annoyance perceived by the local residents and the physical characterization of noise expressed through different exposure-to-the-noise indexes which exist at the moment. The results of this survey bring some technical elements able to validate the choice of the future exposure index(es) used in France for the setting up of Noise Annoyance Maps and Noise Exposure Maps around airports.

11:20

4aNSa10. Sound propagation prediction with emphasis on planning needs. Matias Ringheim (Kilde Akustikk a/s, P.O. Box 229, N5701 Voss, Norway)

Significant research efforts are directed toward understanding various aspects of outdoor sound propagation. Some of the results can be used when creating noise prediction methods for planning purposes. From a planning point of view, it is necessary to use prediction algorithms and noise descriptors which are relevant in terms of community disturbance and annoyance. Our knowledge of community noise response is largely based on social surveys, and the results are mainly related to fairly simple noise descriptors. There is often a striking contrast between the available knowledge relating to human response, and the detailed nature of sound propagation studies. There is a clear need for prediction improvements, but not necessarily in directions that seem to dominate present research. For planning purposes, it is appropriate to use the noise impact foundation to identify potential prediction improvements and related research topics. The consequences of this point of view will be discussed.

THURSDAY MORNING, 18 MARCH 1999 ROOM H2032, 7:55 TO 11:20 A.M.

Session 4aNSb

Noise: Noise Emission from Machinery I

Angelo J. Campanella, Cochair
Campanella Associates, 3201 Ridgewood Drive, Columbus, Ohio 43026, USA

Hans G. Jonasson, Cochair
SP Swedish National Testing and Research Institute, Box 857, SE-50115 Borås, Sweden

Chair's Introduction—7:55

Invited Papers

8:00

4aNSb1. Noise emission—A part of the risk assessment concerning the safety of machinery. H. Lazarus and P. Kurtz (Federal Inst. for Occupational Safety and Health, Dortmund, Germany)

ISO/IEC guide 51 describes safety aspects in products, processes, and services. EN 292/EN 414/EN 1050 describe the safety of machinery: concepts, general principles of design, and the risk assessment. For specific machinery groups standards on ISO or CEN level describe safety aspects, technical data or test methods. Problems with the implementation of noise into these standards are discussed because the reduction of emission of machinery (noise, vibration, toxic agents) has, until now, obviously been neglected, as it seems, due to the unsuitable approach of classical risk reduction. Therefore the European Machinery-Directive requires (i) a reduction of risks to the lowest possible level (ii) and the information of the user about existing residual risk. Thus machinery standards to reduce noise-emission must comprise (1) specified measuring procedures (yet existing to a large extent) including representative operating conditions for emission measurements, (2) collected emission values for each type of machinery in order to derive the state of the art, and (3) examples for noise reduction by design. Exemplary C-standards will be presented.

8:20

4aNSb2. A review of current strategies and criteria for low-frequency noise control from combustion turbines. Robert A. Putnam (Siemens Westinghouse, 4400 Alafaya Trail, Orlando, FL 32708, putnamra @ notes.westinghouse.com), Roland Hetzel, and Johannes van de Logt (Siemens KWU, 91058 Erlangen, Germany)

The environmental noise impact on neighboring communities from power generation installations containing large industrial combustion turbines is often dependent upon the level of low-frequency sound emission. Compliance with commonly specified C-weighted far-field criteria can be a particular challenge. An improved knowledge of the low-frequency sound emissions from the combustion turbine exhaust is required, as well as a design approach which accounts for the possible need for future corrective measures. Such design strategies will be defined and described together with the results of actual case histories of successful installations.

8:40

4aNSb3. Noise emission measurements *in situ*—A comparison between different methods. Hans G. Jonasson (SP Swedish Natl. Testing and Res. Inst., Box 857, SE-501 15 Bors, Sweden, hans.jonasson@sp.se)

Within the frame of a European project within the research program Standards, Measurements and Testing, different methods for the determination of emission sound pressure levels and sound power levels have been tested. The different methods have been ISO/DIS 3747, ISO 9614-2, the ISO 11200 series, that is ISO 11201, 11202 and 11204, and a new method, ISO ''11205,'' using the sound intensity level to approximate the emission sound pressure level. Comparison measurements have been made on several different machines *in situ* using eight different measurement teams on each machine/test site combination. The results indicate that ISO 11202 tends to overestimate the emission sound pressure level in relation to ISO 11201, that ISO 11204-4 has a limited field of application, that ''11205'' tends to underestimate the emission sound pressure level, in particular for large machines with noise emitting parts far from each other, that ISO/DIS 3747 works very well, and that ISO 9614-2 tends to underestimate the sound power level in relation to ISO 3741. The results are discussed and possible improvements to the different standards are proposed.

9:00

4aNSb4. Strategy for locating the reference sound source and microphones when determining sound power *in situ*. A theoretical investigation for the revision of ISO 3747. Jean R. Jacques (I.N.R.S., Mission Normalisation, 75680 Paris Cedex 14, France, jacquesj@inrs.fr)

A present challenge in industrial acoustics is the accurate determination of the sound power of large machines in ordinary workrooms. Such a method is being worked out as the revised ISO 3747 standard. It is a comparison method with sound pressure measurements at a limited number of microphone positions in the reverberant field. The accuracy of the method was studied using a high-performance ray-tracing computer model for the propagation of sound in industrial halls. All parameters influencing the accuracy of the method have been considered: room size and wall absorption, dimensions and shape of the machine, source distribution (one single point source or a distribution of point sources over the machine volume), omnidirectional and directional machines, position of the reference sound source with respect to the machine (on top or to the side), and microphone positions. Results analysis shows that sound power can be determined with grade 2 of accuracy even for large directional machines operating in moderately reverberant workrooms provided a specific methodology is used for locating the reference sound source and the microphones based on a zoning of the room. A criterion for validating a microphone position based on the excess of sound pressure level is proposed.

9:20

4aNSb5. Sound power determination by using sound intensity scanning procedure—Adequate sound-field indicators and criteria limiting the measurement uncertainty. Gerhard Hübner, Yumei Gao-Sollinger, and Volker Wittstock (Univ. Stuttgart, ITSM, Pfaffenwaldring 6, D-70550 Stuttgart, Germany)

The uncertainty of sound-source sound power determined by an intensity scanning method depends on the one hand on several measurement parameters such as scanning speed, integration time, density of scanning pattern paths, measurement equipment quality, and on the other hand, on the sound field quality having met under the actual *in situ* measurement conditions. In order to guarantee certain limits for the measurement uncertainties, it is necessary to adjust the measurement parameters to the actual specific conditions for the sound field under test. In the past (see ISO 9614-1) this adjustment was carried out with success by first determining certain indicators describing the actual sound field situation numerically and using the indicators together with relevant criteria in order to check the initially chosen measurement parameters in respect to the given uncertainty limits. At present, an international standard for a relevant scanning precision method (ISO 9614-3) is in preparation. Thereby, adequate indicators and criteria are in discussion worldwide. By an extensive measurement program carried out under well-defined laboratory conditions, and on machines *in situ* completed by theoretical investigations, certain proposals result that are relevant for the new standard, which will be presented in the paper.

9:40

4aNSb6. Remarks about the local environmental correction for determination of the emission sound-pressure level. Gustav A. Sehrndt (Consultant, Kapuzinerstr. 8, D-50737 Cologne, Germany) and Karlheinz Biehn (BAuA, Federal Inst. for Occupational Safety and Health, D-44149 Dortmund, Germany)

One of the standards for the determination of the emission sound-pressure level (ESPL) uses a local environmental correction $K3$ which takes into account both the average sound-pressure level (VSPL) on a measuring surface and an average environmental indicator $K2$ [ISO 11204, ANSI S12.43]. $K2$ may be determined either by estimation of the absorption area or by measurements with a reference sound source (RSS); these include also determination of the VSPL. $K3$ is most important for sources with distinct directivity. To investigate bias and errors of $K3$ for these sources, a few model machines and source-room configurations have been used. On illuminated microphone positions, results show standard deviations of repeatability for the ESPL of the same order of magnitude as these for the VSPL. In the shadow of sound, bias and errors will sum up and are amplified by the characteristics of the $K3$ calculation method. [Work supported by BauA.]

10:00–10:20 Break

10:20

4aNSb7. Determination of the airborne sound power radiated by structure-borne sound sources of arbitrary shape—First step of extension of the direct finite-element method to three-dimensional sources. Gerhard Hübner and André Gerlach (Universität Stuttgart, ITSM, Pfaffenwaldring 6, D-70550 Stuttgart, Germany, gerlach@itsm.uni-stuttgart.de)

The direct-finite-element method (DFEM) is an algorithm for calculation and measurement of airborne sound power radiated by structure-borne sources. Using a structure-borne source parameter directly means redundant intermediate sound field information such as sound pressure and sound intensity are not necessary. Previous investigation showed that for plane structure-borne sound sources, the DFEM can be derived from the Rayleigh description of sound radiation exactly. This paper deals with the extension of the DFEM for three-dimensional structure-borne sound sources. For these sound sources the DFEM algorithm as already used for plane structure-borne sound sources must be supplemented by a net of imaginary counter sources in order to meet the boundary condition of the arbitrarily shaped vibrating body. This supplement is described and discussed using some examples. Finally, measurement results are presented which are in good conformity with the theoretical results of the modified DFEM.

10:40

4aNSb8. Noise as indicator of instability in centrifugal pumps. Mirko Čudina (Faculty of Mech. Eng., Univ. of Ljubljana, Aškorčova 6, 1000 Ljubljana, Slovenia)

The total emitted noise from the pumping set is generated partially by the pump, partially by the electric motor and partially by the cooling fan, and has four characteristic noise origins: aerodynamic, hydrodynamic, mechanical, and electromagnetic. Emitted noise level of a centrifugal pump depends on its size and the operating conditions (speed and load). At the design point of operation (Q_{des}) and without cavitation the hydrodynamical and aerodynamical noise in form of the rotational noise due to the rotational frequency and blade passing frequency are predominant noise sources. At the off-design operating condition the dominant noise sources within the pumping set without cavitation of the pump is nonrotational noise due to the rotating stall and surge, at $Q < Q_{\mathrm{des}}$, and due to the laminar boundary layer vortex shedding, at $Q > Q_{\mathrm{des}}$. When the cavitation within the pump occurs the nonrotational noise predominates within the entire range of operating conditions. The onset of the stall, surge, and cavitation in the centrifugal pump cause instability of a pumping system. Special attention was given to the state of pump operation when the instability due to the stall or surge and cavitation simultaneously occurs, and to the noise generated thereof.

11:00

4aNSb9. The description of noise emission from machinery for use in software programs for noise prediction. W. Probst (ACCON GmbH, Graefelfinger Str. 133 A, 81375 Munich, Germany)

Noise prediction deals with the calculation of noise levels at workplaces from the emission values of machines. In such a calculation, the dimensions of machines, the source distribution on the machine surface, and the directivity of radiation have to be taken into account if the workplace is not far away. Unfortunately, methods of measuring emission values with enveloping surface or with the comparison method do not give all this information, which is necessary to make such a calculation. As a good approximation for many cases, the machine itself is simulated by a rigid body with many point sources on its surface. This is a similar method as is used to calculate the radiation from buildings (E DIN EN 12354-4) with some additional rules. For the future, a direct conversion from measured sound pressure or intensity levels to the source distribution data for a machine should be developed.

Session 4aPAa

Physical Acoustics and Engineering Acoustics: Numerical Methods for Computing Sound Radiation and Scattering I

Gary H. Koopmann, Cochair
Department of Mechanical Engineering, Pennsylvania State University, 157 Hammond Building, University Park, Pennsylvania 16802, USA

Martin Ochmann, Cochair
Technische Fachhochschule Berlin, Fachbereich Mathematik und Physik/Fernstudien Institut, Luxemburgerstrasse 10, D-13353 Berlin, Germany

Invited Papers

8:00

4aPAa1. Application of the surface variational principle in coupled fluid-structure interaction analysis. Kenneth A. Cunefare (Georgia Inst. of Technol., School of Mech. Eng., Atlanta, GA 30332-0405)

The surface variational principle (SVP) provides a unique tool for the investigation of coupled fluid-structure interactions, particularly on axisymmetric structures. The implementation of the SVP considered here uses basis functions that span the entire wetted surface of an object of interest. If the same or similar basis functions are used to model the structural dynamic response, the result is an analysis tool that can provide detailed insight into the coupling of fluid and structural motion across a broad range of scales. Further, since the method is grounded on a Ritz-expansion and a variational approach, the convergence behavior of the method is known and may be used to assess the accuracy of the results. In this manner, the SVP has been used to investigate the influence of feature representation within structural acoustic models, to investigate the feasibility of bounding the structural response to a perturbation in structural detail, and to investigate the controlling mechanisms for the coupling of exterior sound fields to interior fields through finite elastic cylinders. This paper introduces the coupled SVP method, reviews the advantages and disadvantages of the numerical implementation of the SVP, and presents some of the insights this method has provided.

8:20

4aPAa2. Energy source superposition technique for solving two-dimensional acoustic problems. David W. Herrin and Andrew F. Seybert (Dept. of Mech. Eng., Univ. of Kentucky, 521 CRMS Bldg., Lexington, KY 40506-0108, dwherr01@engr.uky.edu)

An energy source superposition technique has been developed to determine sound energy and intensity. Using this method, the intensity along the boundary is approximated by superimposing energy sources placed outside the acoustic domain. The unknown amplitudes of these sources are found using a linear least squares, then these energy sources may be superimposed to approximate the sound energy. Several tests were performed to evaluate the approach. First, it was demonstrated that the energy sources could be superimposed if the interference pattern between propagating waves was neglected. This was demonstrated for plane waves, cylindrical waves, and spherical waves. Two-dimensional energy results were then compared for the few cases where a closed form solution could be obtained like the pulsating cylinder and the one-dimensional duct. Finally, results were compared to acoustic boundary element solutions with good agreement. [Work supported by the University of Kentucky Center for Computational Sciences.]

8:40

4aPAa3. An impedance coating formulation for a coupled structural acoustics code. Ian C. Mathews (Dept. of Aeronautics, Imperial College, Prince Consort Rd., London SW7 2BY, UK, i.mathews@ic.ac.uk) and Richard A. Jeans (BlueWater Res., London N1 2NA, UK)

In the automotive and aerospace industries as well as the underwater acoustics defense applications the addition of coatings to modify the response of the vibrating structure is commonplace. The surface of the structure is therefore separated from the surrounding fluid by this coating. Traditionally, the coating is modeled using continuum or thick-shell-type finite elements. Difficulties arise if the Poisson ratio for such a coating is close to one-half. In the approach presented in this paper, it is proposed to model the behavior of these coatings by a 2×2 coupling matrix relating the normal velocity and pressure on each side of the coating. The impedance relationships developed for such coatings are local, complex, and maybe frequency dependent. A second approach for modeling a coating is also detailed and validated. In this approach the coating is assumed to behave on any point on the surface as an infinite plane layer of compressible fluid. For this approach to be valid, the thickness of the coating must be negligible with respect to the acoustic wavelength in the exterior fluid. The analytical solutions developed for validating both proposed methods will also be derived in this paper.

9:00

4aPAa4. Numerical computation of underwater sound scattering from a complex elastic object. Anton M. Homm (Forschungsanstalt der Bundeswehr für Wasserschall und Geophysik, Klausdorfer Weg 2-24, 241848 Kiel, Germany, AntonHomm%BWB@bwb.org)

There are numerous analytical approaches for the calculation of sound scattering from cylinderlike structures. However, limitations exist in the complexity of objects, which can be handed that way. In this case numerical methods are necessary to compute the acoustical response of the model. The investigated structure consists of two cylinders of different radii connected by a conical section. The ends are covered by hemispherical caps. An axisymmetric finite-element code (SARA2d) has been used to calculate the response of the target, due to an incident plane wave. Semi-infinite elements are implemented at the boundary of the acoustic fluid to take care of the Sommerfeld radiation condition. In the covered frequency range, which comprised Helmholtz numbers up to $ka \sim 13$, specular and elastic properties of the target contribute to the scattered signal. The calculations were performed during a one year research stay at the Naval Undersea Warfare Center (NUWC) in Newport, Rhode Island, USA. Additionally an attempt has been made to compare parts of the results with boundary element methods (SYSNOISE) and coupled FEM/BEM (ANSYS/SYSNOISE). For the coupled calculations only three-dimensional methods have been available, hence those results are restricted to relatively low Helmholtz numbers.

9:20

4aPAa5. Leaky wave scattering contributions for tilted thick cylindrical shells in water above the coincidence frequency: Ray theory and computational models. Florian J. Blonigen and Philip L. Marston (Dept. of Phys., Washington State Univ., Pullman, WA 99164-2814)

Scattering measurements [Morse, Marston, and Kaduchak, J. Acoust. Soc. Am. **103**, 785–795 (1998)] and sonar images [Kaduchak, Wassmuth, and Loeffler, J. Acoust. Soc. Am. **100**, 64–71 (1996)] demonstrate that above the coincidence frequency, the responses of tilted cylindrical shells associated with leaky antisymmetric Lamb waves can give major contributions to the scattering of sound. Thin-shell dynamics is not applicable for the modeling of the shell's response and an approximate ray formulation has been developed for situations where exact solutions are unavailable. Relevant contributions include meridional [P. L. Marston, J. Acoust. Soc. Am. **102**, 358–369 (1997)] as well as helical [P. L. Marston, J. Acoust. Soc. Am. **102**, 1628–1638 (1997)] leaky rays. The present research emphasizes computational tests for situations where helical antisymmetric Lamb wave contributions are important. These include situations where contributions from the broad meridional ray enhancement interfere with helical ray contributions. The results are helpful for interpreting features of the scattering. [Work supported by the Office of Naval Research.]

Contributed Papers

9:40

4aPAa6. Model and experiments of multiple acoustical scattering from small obstacles. Martin Schickert (MFPA Weimar, Amalienstr. 13, D-99423 Weimar, Germany) and Helmut Ermert (Ruhr Univ. Bochum, D-44780 Bochum, Germany)

A self-consistent model is presented to calculate acoustical scattering of waves from many discrete obstacles, including multiple scattering. The model provides a formulation for incorporating single scattering Green's functions into a multiple scattering solution using auxiliary sources. Geometry and material parameters of the scatterers in the ensemble may be different, and are arbitrary as long as each single scattering solution is known. In restricting the number of auxiliary sources the model is approximate, yet it is empirically shown to work in a quantitative manner for scatterers of ka up to about one, where k is the wave number of the background medium and a is half of the cross section of a scatterer. To ease experimental verification, a two-dimensional setup is considered where obstacles are circular cylinders of infinite length. The model is tested against experimental data gathered from ultrasonic experiments in a water tank. Ensembles of two to ten strong scattering cylinders were used, their radius being chosen such that $ka = 3D$ 0.5 at the mean frequency of the transducers. Numerical and experimental results are compared in time and frequency domain and show quantitative agreement in all investigated arrangements. Results of a numerical experiment including 50 different cylinders are also shown.

10:00–10:20 Break

10:20

4aPAa7. Computational methods and experimental measurements of scattered ultrasonics transient fields. Khelladi Hassina and Djelouah Hakim (Inst. d'Electron., Departement Instrumentation, U.S.T.H.B, BP. 32 El Alia 16111, Alger, Algeria)

The aim of this study is to find the transient acoustic field scattered by a target with a known dimension and geometry. The target is a rigid reflector immersed in an isotropic, homogeneous, and lossless fluid. For that purpose, the presented model takes into account not only the impulse response of the insonified medium, but also that of all the elements which constitute the electroacoustic line. The main elements of the latter are a transmitter-receiver system and an ultrasonic probe modeled by its electroacoustic and acoustoelectric impulse responses. In the hypothesis of a linear, invariant, and causal measurement line, the detected pressure is expressed in the form of a time convolution between the impulse response of all the elements which compose the electroacoustic line and the impulse response of the medium. This last depends on the geometry of transducer, target, their relative position, and the propagation medium. A signal processing method of the experimental data is developed in order to evaluate the global impulse response system. The results of this process will then be used to obtain, by simulation, the effective pressure signal. Some experimental results are presented to show the good agreement with the theoretical model proposed.

10:40

4aPAa8. A time-domain numerical model for the acoustic scattering from rigid or elastic targets. Ahmed El-Ghaouty, Bertrand Dubus (IEMN, Dept. ISEN, UMR CNRS 9929, 41 boulevard Vauban, 59046 Lille Cedex, France, dubus@isen.fr), and Antoine Lavie (Universite d'Artois, 62400 Bethune, France)

In order to predict the backscattered echoes from immersed targets, a numerical model based on the space–time Helmholtz–Kirchhoff integral formulation (HKIF) is developed in the EQI code. Two different schemes are implemented for the space–time discretization: a classical finite-element discretization in space and finite difference discretization in time (FEM/FDM) and a space–time finite-element discretization (FEM/FEM). The computed results are provided for the test case of a rigid sphere. Two well-known spurious effects of the discretized HKIF are described: (i) the existence of an instability which grows exponentially as time progresses and (ii) the inaccuracy of the results in the shadow zone. The origin of these effects and the relative performance of the FEM/FDM and FEM/FEM methods are discussed. Finally, the coupling with a finite-element structural model (ATILA code) and its effect on the instability are also presented.

11:00

4aPAa9. Resonant scattering phenomenon by in-plane periodic cracks. Eugene J. Danicki (Polish Acad. of Sci. (IPPT), 00-049 Warsaw, Poland) and Donna C. Hurley (Natl. Inst. of Standards and Technol., Boulder, CO 80303)

Two isotropic elastic halfspaces, with periodic domains of perfect bonding and with perfect disbonds (cracks) in between, are considered. In such a system, a free-interface vibration may exist, the frequency of which depends on the crack period and width. This vibration occurs when a bulk wave is scattered by the cracks. There is a deep drop in the transmission coefficient of the wave through the interface, and a corresponding rise in the reflection coefficient, dependent on frequency and the propagation direction of the incident wave. Steel and aluminium halfspaces are considered in each of three combinations, with either perfect or sliding contact between cracks. Numerical results are obtained by extending an existing theory [E. Danicki, J. Acoust. Soc. Am. **100**, 2942–2948 (1994)] to account for near-normal incidence. This phenomenon is important for understanding the operation of comb transducers, which may be used for the ultrasonic investigation of materials. Analysis of the interface wave can aid in optimization of the comb material and its groove-to-period relative width, for either solid or sliding contact between the comb and the sample.

11:20

4aPAa10. An approach to calculating spatial impulse response of curved transducers: Linear arrays with cylindrically curved surfaces. Ping Wu and Tadeusz Stepinski (Uppsala Univ., Dept. of Mater. Sci. Signals and Systems, Box 528, S-751 20 Uppsala, Sweden)

The spatial impulse response method (SIRM) is a powerful tool to calculate transient fields that has been applied extensively to planar sources with both uniform and nonuniform excitations as well as to spherically and axisymmetrically curved transducers. Yet, it seems that the SIRM has not found application to other curved transducers, like linear arrays with cylindrically curved, focusing surfaces, which are commonly used in nondestructive testing and medical imaging. This paper is intended to propose an approach for the calculation of the spatial impulse response of such linear arrays. The approach starts from a general form of the expression for spatial impulse response, which is a double surface integral, and finally gives a single integral after coordinate transformation. The single integral is numerically calculated. The approach is generally applicable. Spatial impulse responses of a linear array with a cylindrically concave surface are presented, and analyzed in comparison with that of the corresponding linear array with planar surface.

11:40

4aPAa11. Radiation of a sphere near reflecting planes. Vladimir B. Yashkin (Lab. of Structural Acoust., Mech. Eng. Res. Inst., M. Kharitonievsky 4, Moscow 101830, Russian Federation, vya@geocities.com)

A numerical solution by the equivalent sources method to the radiation problem for a sphere in fluid near a rigid plane, in a wedge, and in a corner, is presented and discussed. Distributed circular equivalent sources are used. Dependencies of the radiation impedance and power flow on the geometry parameters are analyzed. It is shown that finite dimensions of the radiator lead to an increase in radiation power flow more than an order of magnitude compared to its value in the free space.

12:00

4aPAa12. Ultrasonic field analysis by numerical quadruple integration with repeated trapezoidal rule. Tohru Imamura (Natl. Res. Lab. of Metrology, 1-1-4, Umezono, Tsukuba, Ibaraki 305-8563, Japan, imam@nrlm.go.jp)

To compute the ultrasonic field by the square flat transducers, numerical quadruple integration is being carried out with repeated trapezoidal rule. The medium of ultrasonic propagation is supposed to be isotropic and nonabsorptive. Only the longitudinal wave is being treated, which follows the Huygens principle. The sound pressure, the particle velocity, and the specific acoustic impedance, which is the quotient of the sound pressure by the particle velocity, are all obtained. Using the repeated trapezoidal rule with automatic interval halving, how results are converged is investigated. The computed resuls are surveyed numerically for each single, double, triple, and quadruple integration. These results are used for the higher-fold numerical multiple integrations. By this method, the effect of tilt for the receiving square flat transducer to the similar transmitting transducer is obtained, which seems very difficult to analyze by using the axial symmetry of the ultrasonic field [T. Imamura, J. Acoust. Soc. Am. **103**, 3041(A) (1998)].

Session 4aPAb

Physical Acoustics: Measurement and Evaluation of Ultrasound I

R. C. Chivers, Cochair
6 Louis Fields, Guildford GU3 3JG, UK

Rainer Reibold, Cochair
Physikalisch-Technische Bundesanstalt, Bundesalle 10, D-38116 Braunschweig, Germany

Invited Papers

8:00

4aPAb1. Hydrophone calibration at the UK National Physical Laboratory: From primary standards to dissemination. Bajram Zeqiri (Ctr. for Mech. and Acoust. Metrology, Natl. Phys. Lab., Queens Rd., Teddington, Middlesex TW11 0LW, UK, bajram.zeqiri@npl.co.uk)

Ultrasonic hydrophones continue to play a pivotal role in assessing the safety of medical ultrasonic equipment. International and national standards require measurements of the acoustic fields generated by this type of equipment to be made using hydrophones of specified properties such as bandwidth, spatial resolution, etc. A critical property of the hydrophone is the absolute calibration of its receive sensitivity and its ultimate traceability to national standards of measurement. At NPL, the primary standard laser interferometer has been in operation for over 10 years, providing this traceability for the majority of hydrophones currently used worldwide. This presentation will give an outline description of the interferometer, describing how the primary standard is disseminated to the user community through secondary standard hydrophones using a nonlinear intercomparison method. A number of key results related to the long-term stability of reference hydrophones will be presented. The paper will then concentrate on recent developments in the application of the interferometer which have sought to increase its working frequency range up to 60 MHz.

8:20

4aPAb2. Ultrasonic power measurement by means of radiation force. K. Beissner (Physikalisch-Technische Bundesanstalt, D-38116 Braunschweig, Germany)

The time-average acoustic power emitted by an ultrasonic source transducer is one of the key values characterizing the strength of ultrasonic fields. According to both fundamental IEC Standards dealing with the acoustic output of medical devices, namely that of diagnostic devices (IEC 61157) and that of therapeutic devices (IEC 61689), the ultrasonic power is to be measured and declared. The measurement method considered to be the most reliable one and recommended in IEC 61161 is that using a radiation force balance. In the present paper, various radiation force balance designs are discussed and compared. It is shown that the correctness of the results depends mainly on the acoustic properties of the target. One way of checking the performance of the radiation force balance is to use a translation stage with a computer-controlled step motor, which allows high-resolution variation of the transducer/target distance. The results of international intercomparisons of ultrasonic power measurements using continuous-wave reference transducers as well as a commercial, pulsed diagnostic instrument are presented and discussed.

8:40

4aPAb3. Thermoacoustic sensors. Burkhard Fay and Hans-Peter Reimann (Physikalisch-Technische Bundesanstalt, D-38116 Braunschweig, Germany)

The two procedures mainly used for determining ultrasonic power—the sound radiation force method and the planar scanning technique—are complicated, and require a relatively expensive measuring setup. These procedures are therefore unsuitable for the routine inspection of ultrasonic equipment used in medical and technical applications. In contrast to these procedures, the thermoacoustic sensor is well-suited for this purpose. It is of simple design, small in dimension, and its application requires only relatively

inexpensive equipment. The ultrasonic power is determined from the heat produced by the ultrasonic signal in a suitable absorbing material. A disadvantage of this first sensor type is that the power of the ultrasonic signal can be determined only if its amplitude spectrum is known. The new thermoacoustic sensor allows the power of ultrasonic signals to be determined even if their amplitude spectra are unknown. When this sensor type is used, the ultrasonic signal first travels a short distance in a weakly absorbing propagation medium before it enters the absorber, where its energy is completely transformed into heat. In this case, the ultrasonic power is determined from the frequency-independent temperature gradient originating in the weakly absorbing propagation medium immediately in front of the absorber.

9:00

4aPAb4. Fiber-tip sensors for ultrasonic measurement. Christian Koch, Volker Wilkens, and Walter Molkenstruck (Lab. 1.43, Physikalisch-Technische Bundesanstalt, PF 3345, D-38023 Braunschweig, Germany)

Modern trends in the application of ultrasound, such as the increasing use of high-frequency fields and high power pulses, constantly increase the demands for resolution and robustness of ultrasonic sensors. An alternative to customary measurement techniques consists of using the tips of optical fibers as sensor elements. Because of the small outer diameter of an optical fiber and the optical principle of measurement, fiber-tip sensors combine high spatial resolution with wide bandwidth; in addition, they are robust components. After classification of the kinds of fiber-tip sensors, a brief introduction to the principle of operation of displacement and pressure detection is given. The acoustic properties of the sensors are discussed on the basis of transfer functions obtained by calibration measurements up to 50 MHz. Shock-wave detection is the usual application of fiber-tip sensors, and experimental results of an investigation of an electromagnetic lithotripter are presented. If the fiber tip is, however, covered with dielectric coatings, the detection of ultrasound generated by focused piston transducers is possible, and this technique opens up new fields of application for fiber-optic sensing.

9:20

4aPAb5. Two-dimensional hydrophone arrays: Measurement methods for the new millenium. A. M. Hurrell (Precision Acoust. Ltd., Poundbury House, Dorchester, Dorset DT1 2PG, UK, pa@acoustics.co.uk) and F. A. Duck (Royal United Hospital, Bath BA1 3NG, UK)

As the boundaries of knowledge of ultrasound systems are extended, the limitations of current measurement systems are exposed. To meet the challenge posed by ever more demanding standards of measurement, Precision Acoustics has designed and manufactured an innovative two-dimensional hydrophone array—the Acoustic Imager. Calibration data for the Acoustic Imager is presented, and it has been shown to have a higher sensitivity than a polymer probe or membrane type hydrophones of the same diameter (0.2 mm). This is achieved while maintaining a frequency response flat enough to meet the requirements of an IEC866 class A device over the frequency range 1–20 MHz. The experimental results presented, from the characterization of both linear and nonlinear ultrasonic fields, demonstrate the advantages of hydrophone arrays for ultrasonic field measurements (e.g., reduced scan times, minimization of phase errors). Demonstrative examples are also provided to display the data postprocessing capabilities of the Acoustic Imager in the assessment of the acoustic parameters used to describe medical ultrasound fields.

9:40–10:00 Break

10:00

4aPAb6. An international comparison of transducer surface vibration distribution determination. M. A. Bangash (Dept. of Phys., Univ. of Surrey, Guildford GU2 5XH, UK), W. Molkenstruck, R. Reibold (PTB, Bundesallee100, 38116 Braunschweig, Germany), and R. C. Chivers (6 Louis Fields, Guildford GU3 3JG, UK)

A lack of knowledge of the detailed behavior of the actual transducers used in a particular application can provide an indeterminate limitation on the sensitivity or the accuracy of the measurements being made. In principle, knowledge of the distribution of the surface vibration of the transducer permits the irradiating field at any point in the region of interest to be determined. Previous reports of surface vibration distribution determination have suffered from a lack of verification. The present work reports measurements made on four transducers (two with ceramic elements and two with PVdF elements of an approximate diameter of 10 mm at frequencies between 2.25 and 3.0 MHz) using two independent techniques. Measurements were made of the fields in transverse planes at four different distances from each transducer. The PTB measurements employed optical diffraction tomography while those from Guildford used scanned miniature (0.25- or 0.5-mm-diam PVdF) hydrophones to measure both amplitude and phase. Excellent agreement was found between the measurements from the two techniques, including absolute pressure levels, confirming that the vibration distribution of a transmitting transducer can be reliably determined although it requires great technical care and, at present, is time consuming.

10:20

4aPAb7. Toepler, Mach, and Wood: The visualization of sound. Robert T. Beyer (Dept. of Phys., Brown Univ., Providence, RI 01912)

The 19th Century saw great strides in making sound visible. A major pioneer was August Toepler (1836–1912). Toepler studied the so-called singing flame. To make periodic fluctuations visible, he interposed a rotating disc with slits between the flame and the viewing telescope. In so doing, he developed the idea of the stroboscope, which ultimately became a common device. In a second experiment, Toepler focused the image of a spark source; he then covered the image with an opaque screen. If the rays of light passed through a region with a differing index of refraction, the rays would be bent and thus miss the opaque covering. Toepler called this method *schlieren beobachtung*, or striae observation. The American, R. W. Wood, popularized this second technique. Examples will be shown. Even before Wood, Ernst Mach (1836–1916) applied Toepler's method to the study of shock waves. Examples will also be shown here.

10:40

4aPAb8. Wideband calibration of PVDF hydrophones by an electromagnetic hydrophone using theoretical spectra of overtones. Leszek Filipczynski, Tamara Kujawska, and Janusz Wojcik (Ultrasonic Dept., Inst. of Fundamental Technolog. Res., Polish Acad. of Sci., Swietokrzyska 21, 00-049 Warsaw, Poland)

PVDF hydrophones are limited in their frequency band, thus distorting measured pulses. For nonlinear effects, caused by propagation of ultrasonic pulses with finite amplitudes, the frequency characteristics are of particular importance. One can correct those distortions knowing the sensitivity characteristics of the hydrophone. To find the sensitivity of the PVDF hydrophone, focused pressure pulses were at first measured by themselves and compared with those measured by the electromagnetic hydrophone (EMH) at low source pressure (linear propagation conditions). So due to the narrow frequency band, one avoided frequency distortions in the EMH, where the absolute pressure was obtained from only two measurements: electrical and magnetic. To discover the sensitivity frequency characteristics, a wideband pulse spectrum of overtones (at known high source pressure) was obtained. Multiplying the theoretical spectrum by the expected sensitivity characteristics, to match theoretical and measured spectra, one obtained the true frequency characteristics. Finally, the averaging effect occurring on the surface of the sensitive electrode of the PVDF hydrophone was computed and eliminated, to obtain the sensitivity for the incident plane wave. For determination of theoretical pressure pulses and their spectra, a special numerical code was elaborated, based on numerical solutions of the nonlinear wave propagation.

11:00

4aPAb9. Optical measurement of wide bandwidth ultrasound fields. Todd A. Pitts and James F. Greenleaf (Ultrasound Res. Lab., Mayo Clinic and Foundation, 200 First St. SW, Rochester, MN 55905)

A technique for measuring instantaneous three-dimensional pressure in a wideband ultrasound pulse is presented. A collimated laser pulse impinges on the ultrasound field, and the optical intensity in a diffraction plane subsequent to this scattering event is imaged onto a CCD camera and stored. Timing is controlled precisely, allowing the acousto-optic interaction to occur at the same point in the temporal evolution of the sound field each time the experiment is performed. After interaction with the ultrasound pulse, the optical phase is approximately proportional to the ray sum of instantaneous pressure in the pulse (taken in the direction of optical propagation). Optical phase immediately subsequent to passage through the ultrasound pulse is computed from recorded optical intensity via a phase retrieval algorithm. The experiment is performed at several angles as the ultrasound transducer is rotated about an axis normal to the optical axis of the imaging system. Tomographic reconstruction algorithms are applied to the retrieved optical phase data, computing pressure at *all* points in the ultrasound pulse. The resulting pulse may be propagated forward or backward in time under a source-free model. Reconstructions of the field from a 2.5-MHz array transducer compare well with hydrophone measurements.

11:20

4aPAb10. Methods of beam divergence corrections on broadband direct contact ultrasonic technique. Silvio E. Kruger, Jacques Charlier (Service de Metallurgie Physique/ULB 50, Av. F. Roosevelt, CP194/3 Brussels, B-1050 Belgium, skruger@ulb.ac.be), and Joao M. A. Rebello (LABOEND/COPPE/UFRJ CP68505 Rio de Janeiro, Brazil CEP21945-970)

The separation of intrinsic attenuation and velocity parameters from extrinsic factors is a complex task in nondestructive ultrasonic characterization of materials. The effect of the ultrasonic beam divergence due to finite source is discussed both theoretically and experimentally in this work. The objective is to evaluate different techniques of attenuation and velocity measurements with beam divergence corrections on direct contact configuration. Both amplitude and phase spectra for signals generated and detected by commercial NDE broadband transducers are to be corrected. The effectiveness of each technique is evaluated with different transducers and sample geometry. The results show that a smaller effective transducer diameter than the nominal must be assumed in theoretical corrections [P. H. Rogers and A. L. Van Buren, J. Acoust. Soc. Am. **55**, 724–728 (1974)] and that the experimental determination of calibration correction for a particular transducer by a reference sample can be a good alternative.

11:40

4aPAb11. Characterization of ultrasonic contact transducers using a Michelson interferometer. Donna C. Hurley and Terence P. Lerch (Natl. Inst. of Standards & Technol., Boulder, CO 80303, hurley@boulder.nist.gov)

Accurate measurements of velocity, attenuation, and other ultrasonic properties of materials involve diffraction corrections that can significantly alter the measured values. Although diffraction calculations require knowledge of the transducer's effective radius, this parameter is difficult to determine precisely for contact transducers. Here, an experimental method to quantitatively characterize longitudinal contact transducers is presented. Narrowband (toneburst) electronics excite the transducer, and a Michelson interferometer measures the out-of-plane displacements on the sample's opposite side. With a resolution of approximately 10 μm, this optical technique allows transverse spatial scans of the displacement field to be obtained. Furthermore, the on-axis position may be located with the interferometer and the transducer excitation frequency varied. The frequency dependence of the on-axis amplitude is measured using a sample whose thickness is approximately half the nearfield distance at the transducer's center frequency. The shape of the transverse scans and the observed minimum in the frequency dependence permit the transducer's effective radius to be calculated. Measurements are presented for transducers in the 1- to 10-MHz range with nominal radii between 2.5 and 6.4 mm. The results are compared to a numerical diffraction model to evaluate the accuracy and precision of this approach.

Session 4aPAc

Physical Acoustics: Elastic Properties of Materials I: Methods

Heinz Jürgen Fröhlich, Cochair
Paul-Drude Institut für Festkörper-Elektronik, Hausvogteiplatz 5-7, D-10117 Berlin, Germany

Jan D. Achenbach, Cochair
Center for Quality Engineering and Failure Prevention, Northwestern University, 2137 North Sheridan Road, Evanston, Illinois 60208-3020, USA

Invited Papers

8:00

4aPAc1. Quantitative measurements of solid and fluid properties with near-field acoustics. Bernard Cretin, Pascal Vairac, and Raphael Patois (Laboratoire de Physique et Metrologie des Oscillateurs du CNRS, 32 Ave. de l'Observatoire, 25044 Besancon Cedex, France, bcretin@univ-fcomte.fr)

Local measurement of the elastic or viscoelastic properties of solids and fluids has been widely investigated with far-field acoustics e.g., (determination of resonance frequencies and damping, interference between different waves or modes). However, actual techniques need high operating frequencies to shorten the wavelength. Conversely, the proposed method is based on near-field acoustics: a subwavelength acoustic source interacts with the investigated medium within a short distance related to the radius of the source. The resonance frequency of a cantilever is used to measure the interaction between this small vibrating source and the investigated medium. For the characterization of solids, this device is a part of the scanning microdeformation microscope (SMM) that is a kind of ac contact force microscope. For the characterization of fluids, the vibrating tip is replaced by a small sphere. Standard operating frequency of the resonator is 20–30 kHz. The paper presents both theoretical and experimental aspects of the electromechanical resonator, the vibrating element (the tip with radius in the 0.5 to 10-mm range for the investigation of solid samples and the sphere having a 100- to 500-mm diameter for the investigation of fluids), and the interaction. Main features, advantages, and limitations of the presented method will be discussed.

8:20

4aPAc2. Elastic and viscoelastic characterization by Brillouin spectroscopy. Fioretto Daniele (INFM and Dipartimento di Fisica, Universita' di Perugia, via Pascoli, I-06100 Perugia, Italy)

Brillouin light scattering has been widely used in the last years to investigate the elastic and viscoelastic properties of both films and bulk samples. This has been possible thanks to the development of a new class of high-contrast Fabry–Perot interferometers, which permit the detection of the weak light signal scattered by surface and bulk phonons. A brief review on measurements performed in metallic, semiconductor and organic thin films is reported and connections between experimental data and physical parameters of the medium are discussed. The results of the viscoelastic characterization of supercooled liquids are also reported, giving information on the dynamics of disordered systems close to the glass transition.

Contributed Papers

8:40

4aPAc3. Influence of the deposition conditions on the elastic properties of chemical vapor deposited (CVD) diamond films studied by laser ultrasonics. Kris Van de Rostyne, Christ Glorieux, Weimin Gao, Walter Lauriks, Jan Thoen (Lab. voor Akoestiek en Thermische Fysica, Katholieke Univ. Leuven, Leuven, Belgium), and Milos Nesladek (Limburgs Univ., Centrum, Belgium)

One of the aims in optimizing the deposition of CVD diamond is to increase the stiffness. Laser ultrasonics offers a useful tool to nondestructively investigate elastic parameters of materials. A colored liquid–transparent free-standing film configuration allowed the excitation and detection of pseudo-Lamb waves in order to simultaneously determine the longitudinal (v_L) and transverse (v_T) acoustic velocity of the film. The absorption of pulsed laser light by the colored liquid served as an efficient conversion mechanism of optical energy into elastic energy. The excited waves were detected with a wide bandwidth photodeflection setup. Several free-standing films, deposited under different conditions, were investigated.

9:00

4aPAc4. Measurement of elastic properties of GaAs with laser-generated surface acoustic waves. C. M. Flannery, E. Chilla, and H.-J. Fröhlich (Paul Drude Inst. für Festkörperelektronik, Hausvogteiplatz 5–7, D-10117 Berlin, Germany)

Surface acoustic wave (SAW) velocities were measured as a function of angle on both GaAs (001) and GaAs (111) crystal cuts. Surface acoustic wave packets were generated by a pulsed nitrogen laser beam focused into a line shape on the sample surface. The SAWs were detected by a PVDF foil with steel wedge transducer at different propagating distances. The system was automated to measure SAW velocity at a range of angles, and thus produces a velocity-angle (or slowness) curve. From the slowness curve the three independent elastic constants may be derived. The SAW velocity measurement setup is presented and aspects of the propagation of SAW modes for different cuts and angles are discussed. The accuracy of the elastic constants derived from SAW measurements on both cuts is examined, and other detected acoustic wave modes are discussed with regard to their origin and suitability for elastic constant measurement.

9:20

4aPAc5. Behavior of the LSAW loss in multi-layer systems. Paul Wallner, Werner Ruile, and Robert Weigel (Siemens AG, Corporate Technol., ZT KM1, 81730 Munich, Germany, pwallner@physik.tu-muenchen.de)

Compared with common SAW, the leaky SAW shows attenuation even if material-dependent loss types like viscosity, dielectric damping, or airloading are neglected. In fact, this typically LSAW loss is caused by a pure bulk wave emission into the piezoelectric substrate. For the search of low-loss crystal cuts it is important that this kind of loss strongly depends on the crystal cut. Only such crystal cuts are important for technical use where this leaky loss shows a minimum. Moreover, former investigations confirmed that an additional metal layer on the piezoelectric substrate can shift the minimum loss to other crystal cut angles, e.g., the shift from 36rotYX to 42rotYX $LiTaO_3$ with 10% Al. New computations show that this behavior can be understood as a general effect: The shift depends on the material constants of layer and substrate. In multi-layer structures all the material constants influence the angle of minimum propagation loss. A distinct angle of minimum can be reached by using a distinct ratio of the layers. This means, if the ratio differs from 10% Al or the aluminum layer is covered with a second layer, the minimum of propagation loss due to bulk wave emission is shifted away from 42rotYX $LiTaO_3$.

9:40–10:00 Break

10:00

4aPAc6. Characterization of elastic materials by resonance acoustic spectroscopy. F. Honarvar (Dept. of Mech. Eng., K. N. Toosi Univ. of Technol., P.O. Box 16765-3381, Tehran, Iran), A. N. Sinclair, and Y. Fan (Univ. of Toronto, Toronto, ON M5S 3G8, Canada)

Application of resonance acoustic spectroscopy (RAS) for characterization of various properties of elastic materials is discussed in this paper. Resonances are indicators of the elastic properties of the material such as density and elastic constants. They can also signal any perturbation in layer thickness and interfacial contact of a multilayered rod. Using a novel technique, called material characterization by RAS (MCRAS), the elastic constants of isotropic materials are measured to within 0.3%. MCRAS is compared with other techniques for determining elastic constants, and is observed to be simple, quick, and applicable in cases where other techniques fail to work. Characterization of elastic properties of nonisotropic materials is also considered, and experimental results on continuous-fiber metal matrix composite wires are presented. It is also demonstrated how RAS can be used for measurement of cladding thickness and detection of cladding delamination in coated rods. Experimental results are also presented on using RAS for gauging the extent of nonisotropy and approximate grain size of transversely isotropic materials.

10:20

4aPAc7. Thermoacoustic testing on thermal protection systems. Gerhard Bayerdörfer (Industrieanlagen-Betriebsgesellschaft mbH, Postfach 1212, D-85521 Ottobrunn, Germany)

The IABG has designed and built a thermoacoustic facility capable of producing surface temperatures up to 1300 °C at sound pressure levels up to 160 dB. The purpose of this facility is to simulate aerothermal environments as encountered during the mission of space planes. The thermal protection systems (TPSs) of space planes are very susceptible to fatigue under these environments and therefore need extensive qualification testing before being used in operational missions. After reviewing the design aspects of the facility with a description of the selected components, a number of typical applications are presented such as tests in a progressive wave tube as well as tests in a reverberation chamber. In both cases difficulties arise in measuring the dynamic pressures acting on the test specimens under the extreme thermal environment. The paper therefore includes a discussion of possible measuring techniques for temperature and vibration control.

10:40

4aPAc8. Evaluation technique for spectra of complex Young's moduli. H. G. Bossemeyer (Inst. A for Mech., Univ. of Stuttgart, Stuttgart, Germany and Forschungsanstalt der Bundeswehr für Wasserschall und Geophysik, Klausdorfer Weg 2-24, 24148 Kiel, Germany)

For a proper design of acoustic absorbers, detailed information about temperature- and frequency-dependent elastic moduli of absorber materials is essential. Dynamic Young's modulus data depicted in a complex plane determine whether a material is thermo-rheological simple or not. However, even if all data points fit well to a single curve, suggesting simple behavior, severe systematic errors can be involved. A new evaluation technique which relies on well-known visco-elastic material models is introduced to detect systematic errors and to obtain more reliable modulus spectra.

11:00

4aPAc9. The nonlinear mesoscopic elasticity class of materials. Paul A. Johnson (EES-4, MS D443, Los Alamos Natl. Lab., Los Alamos, NM 87545, paj@lanl.gov) and Robert A. Guyer (Univ. of Massachusetts, Amherst, MA 01002)

It is becoming clear that the elastic properties of rock are shared by numerous other materials (sand, soil, some ceramics, concrete, etc.). These materials have one or more of the following properties in common: strong nonlinearity, hysteresis in stress–strain relation, and discrete memory. Primarily, it is the material's compliance, the mesoscopic linkages between the rigid components, that give these materials their unusual elastic properties. It can be said that these materials have *nonlinear mesoscopic elasticity* and encompass a broad class of materials. Materials with nonlinear mesoscopic elasticity stand in contrast to liquids and crystalline solids whose elasticity is due to contributions of atomic level forces, i.e., materials with *atomic elasticity*. Atomic elastic materials are well described by the traditional (Landau) theory of elasticity; however, mesoscopic elastic materials are not. Mesoscopic materials are well described by the P–M (Preisach–Mayergoyz) model of nonlinear elasticity developed by Guyer and McCall. A sequence of experiments on numerous materials illustrates the evidence of nonlinear mesoscopic elastic behavior. In experimental analysis a surprising discovery was made: *damaged atomic elastic materials behave as mesoscopic elastic materials*. It is significant that the nonlinear mechanism(s) in mesoscopic elastic materials remains a mystery.

11:20

4aPAc10. Elastic nonlinearity and damage detection in quasibrittle materials using single mode nonlinear resonant ultrasound spectroscopy (SIMONRUS). Koen Van Den Abeele (Lab. of Building Phys., Catholic Univ. Leuven, Celestijnenlaan 131, 3001 Heverlee, Belgium)

A promising tool for NDT of quasibrittle materials has been developed and applied in the field of damage detection. The technique focuses on the acoustic nonlinear response of the material's resonance modes when driven at small wave amplitudes. A diagnostic method was constructed to quantify the acoustic nonlinearity of homogenous and isotropic samples in bench-top resonance experiments. The analysis of the data is supported by a phenomenological model based on the Preisach model of hysteresis. Six material parameters—two linear and four nonlinear—can be extracted from a simple set of amplitude-dependent resonance experiments, and completely define the material state of the sample. The characterization procedure is applied to damage detection in slate plates. Linear and nonlinear parameters were measured for progressive fatigue induced by cyclic mechanical loading. A rapid increase of the nonlinear parameters was observed early in the loading process and only a small to modest variation of the linear parameters. Near failure, the nonlinear coefficient deduced from the softening of the modulus increased by a factor of 1000. Similar observations were made when analyzing the second and third harmonics. Presently, linear and nonlinear behavior of slate exposed to natural and accelerated hygrothermal aging is being monitored.

11:40

4aPAc11. Nonlinear slow dynamics and memory in rocks. James A. TenCate, Eric Smith (Earth and Environ. Sci., Los Alamos Natl. Lab., Los Alamos, NM 87545, tencate@lanl.gov), and Robert A. Guyer (Los Alamos Natl. Lab., Los Alamos, NM 87545 and Univ. of Massachusetts, Amherst, MA)

Longitudinal resonance experiments on thin bars of sandstone reveal that their nonlinear behavior is richly diverse; they exhibit *nonlinear mesoscopic elasticity*. Resonance experiments show that, as a function of increasing drive level, resonance frequencies shift downward, curve-shape changes, and harmonics and slow dynamics appear. Slow dynamics [Geophys Res. Lett. **23**, 3019–3022 (1996)] refers to the following: a large strain applied to a rock (''conditioning'') reduces its modulus (i.e., it behaves like a softer spring); if the strain is applied for several minutes, the rock will remain ''soft'' even after the strain is removed. The rock eventually recovers to its initial stiffness although the recovery may take minutes to hours. In order to explore the mechanisms of nonlinear response, including slow dynamics, experiments were performed to study the processes of conditioning and recovery. It was found that the two processes appear to be asymmetric. Conditioning takes place quickly; recovery takes place in two stages. After the conditioning strain is removed, the rock's modulus quickly recovers to *nearly* the same stiffness. However, the final stage of recovery (i.e., completely back to its original state) takes minutes to hours, depending on the length of time the conditioning strain was applied.

THURSDAY MORNING, 18 MARCH 1999 ROOM MA043, 7:55 A.M. TO 12:00 NOON

Session 4aPAd

Physical Acoustics: Shock Waves in Liquids

Wolfgang Eisenmenger, Cochair
1 Physikalisches Institut, Universität Stuttgart, Pfaffenwaldring 57, D-70550 Stuttgart, Germany

David T. Blackstock, Cochair
Applied Research Laboratories, University of Texas, P.O. Box 8029, Austin, Texas 78713-8029, USA

Chair's Introduction—7:55

Invited Papers

8:00

4aPAd1. Shock wave characteristics in liquids and extracorporal lithotripsy. Wolfgang Eisenmenger (1. Phys. Inst., Univ. Stuttgart, Pfaffenwaldring 57, D-70550 Stuttgart, Germany)

Reliable determinations of shock wave parameters such as risetime, pulse width, and positive and negative pressure amplitudes are prerequisites for a study and comparison of different stone destruction mechanisms in lithotripsy. In comparing stone destruction mechanisms, it is found that the fiber-optic probe hydrophone is ideally suited for reliable shock-wave measurements, especially also in the negative pulse range. Different stone destruction mechanisms as a direct action of the shock wave penetrating into the stone, the sound soft reflection, i.e., the Hopkinson effect, the importance of cavitation, and finally the action of evanescent waves in the stone caused by the passing pressure wave in the liquid are discussed in their dependence on shock wave parameters. The results are compared with experiment.

8:20

4aPAd2. Numerical simulation of ultrasonic shock wave propagation in lossy liquids obeying a frequency power law. Eckard Steiger and Siegfried Ginter (Institut fuer Hoechstfrequenztechnik und Elektronik/Akustik, Universitaet Karlsruhe, Kaiserstrasse 12, D-76128 Karlsruhe, Germany, Eckard.Steiger@etec.uni-karlsruhe.de)

Ultrasonic shock waves are applied for several noninvasive therapies like extracorporal lithotripsy. In order to design and to optimize therapeutical devices it is essential to predict accurately the shockwave propagation through the arrangement transducer/coupling medium/human tissue. An explicit high-order FDTD-discretization of a set of nonlinear acoustic equations has been shown to model the lithotripter pulse propagation in water in a quality that beats all other known methods. To consider attenuation caused by tissue structures, realistic broadband models of soft tissue attenuation are provided by frequency power laws that include strong dispersion. In this contribution a new method to include these frequency power laws into the explicit FDTD model is presented. It is based on a causal continuous time domain formulation of the attenuation law which contains a Riemann–Liouville derivative operator of fractional order. This operator is discretized by using a quadrature formula. The resulting FDTD algorithm is verified. It turns out to be an efficient tool to compute the dispersive and attenuating effects of soft tissue on the propagation of high-intensity ultrasonic pulses and shock waves. Exemplary nonlinear dispersive propagation of a lithotripter pulse through tissue is simulated.

8:40

4aPAd3. Shock waves in reactive bubbly systems. V. K. Kedrinskii (Lavrentyev Inst. of Hydrodynamics, Novosibirsk, 630090, Russia)

Shock wave propagation in a reactive bubbly system results in the formation of a quasi-stationary self-sustaining wave regime which is known as a bubbly detonation wave [Hasegawa, Fujiwara, 1982]. This paper presents experimental and numerical results of the features of formation of the wave regime mentioned and includes (1) data on a shock wave/single bubble and shock/shock interactions, (2) an analysis of a bubbly cavitation role in initiating detonation of liquid High Explosives, and (3) analysis of the explosive processes arising when storage containers containing pressure-liquified gases or a combustible liquid are suddenly depressurized. The results of numerical analysis of bubbly detonation as a physical model of a hot-spot mechanism responsible for explosive processes in liquid media and the possibility of its application to the problem of acoustical analogies of laser systems are considered.

9:00

4aPAd4. Shock waves from cavitation bubbles. Werner Lauterborn, Thomas Kurz, Cordt Schenke, Claus-Dieter Ohl, Reinhard Geisler, and Olgert Lindau (Drittes Phys. Inst., Univ. Göttingen, Bürgerstr. 42-44, D-37073 Göttingen, Germany)

Cavitation bubbles are produced in water by focused laser light with pulse durations in the 100-fs and 10-ns range. Special attention is paid to the shock waves during breakdown and first collapse of the bubble or bubbles generated. The special focusing properties of femtosecond pulses lead to cylindrical shock waves from elongated breakdown channels and to more complicated shock wave patterns in the pre-breakdown region. Bubble collapse leads to spherical outgoing shock waves in the case of spherical shrinking of the bubble and to a sequence of distinct shock waves in the case of aspherical shrinking. The shock waves are made visible with shadowgraph techniques, including femtosecond pulses for illumination, and are measured with a fiberoptic hydrophone. [Work supported by the Deutsche Forschungsgemeinschaft.]

9:20

4aPAd5. Phase-conjugated ultrasonic beams of finite amplitude. A. P. Brysev, F. V. Bunkin, L. M. Krutyansky, V. L. Preobrazhensky, A. D. Stakhovsky (General Phys. Inst., Russian Acad. of Sci., Vavilov St. 38, Moscow 117942, Russia), Yu. V. Pyl'nov (Inst. of Radioengineering, Electron., and Automation, Moscow 117454, Russia), K. B. Cunningham, S. J. Younghouse, and M. F. Hamilton (Univ. of Texas, Austin, TX 78712-1063)

Generation of intense, phase-conjugated ultrasonic beams by a single active magnetic element in a supercritical parametric mode has been demonstrated experimentally and theoretically. Specifically, phase conjugation with amplification greater than 80 dB, producing intensities of several hundred W/cm^2 at MHz frequencies, is accomplished via parametric electromagnetic pumping of magnetoelastic solids. Reversal of the sound field incident on the conjugator has been confirmed by observation of the self-targeting of beams on scattering sites in water [Usp. Fiz. Nauk **168**, 877–890 (1998) (in Russian)]. The large amplification provided by the conjugator leads to nonlinear distortion and shock formation in the conjugate field. These nonlinear effects are studied experimentally with measurements based on light diffraction for conjugated beams in water having intensities of 2 W/cm^2 and frequencies near 5 MHz. Numerical simulations corresponding to experimental conditions take into account absorption, diffraction, nonlinearity, and the finite size of the conjugator. The simulations reveal the presence of shocks, yet accurate reversal of the incident field despite the strong waveform distortion [Phys. Acoust. (in press (1998)]. Potential applications of this technololgy are discussed. [Work supported by RFBR (Grants 96-02-17301, 98-02-16761), CRDF (Project RE1-270), and ONR.]

Contributed Papers

9:40

4aPAd6. Acoustic time-reversal experiments in the nonlinear regime. Mickaël Tanter, Jean-Louis Thomas, François Coulouvrat,[a] and Mathias Fink (Lab. Ondes et Acoust., ESPCI, Univ. Paris 7, CNRS UMR 7587, 10 rue Vauquelin 75231 Paris Cedex 05, France, michael.tanter@espci.fr)

Until now, time-reversal mirrors (TRM) were only used in a low power regime for which nonlinearities can be neglected. Here, their behavior is investigated in a higher power regime compelling nonlinearities to be taken into account. If one considers the acoustic wave equation in a weakly nonlinear medium, the time-reversal invariance holds. Thus, Burger's equation is invariant when time and direction of propagation are simultaneously reversed. In a nonlinear medium, the shape of a sinusoid changes continuously during propagation as energy is transferred to harmonics. The inverse process would take place after reflection on a TRM. This property holds as long as the shock distance is not reached, otherwise the shock discontinuity implies an irreversible change of the entropy and the time-reversal invariance is broken. These results are confirmed by a finite differences simulation of Burger's equation. However, experiments are very difficult to carry out because of the limited bandwidth of transducers. Nevertheless, for 1-D problems and an antisymmetric wave packet, a time reversal is equivalent to a reflection on a pressure release interface. This trick has been used to conduct an experiment giving qualitative good agreements with the simulation. [a] Also at Lab. de Modélisation en Mécanique, Univ. Paris VI, CNRS UMR 7607, 4 place jussieu, F75252 Paris Cedex 05, France.

10:00–10:20 Break

10:20

4aPAd7. Nonlinear profiles and spectra transformation in going from vibrating piston to traveling wave. Valeri G. Andreev and Oleg V. Rudenko (Dept. of Acoust., Phys. Faculty, Moscow State Univ., 119899, Moscow, Russia, andreev@na.phys.msu.su)

The effects of nonlinear relation between the radiating surface motion law and the traveling wave profile are studied. These effects are significant in the neighbor of the source for the vibration velocities compared with a sound speed. The source was modeled as a nonlinear vibrating system, namely, as a piston excited by external force and loaded by the medium. The temporal profiles and harmonics amplitudes of waves radiated by the piston at harmonic, wide-band (pulsed) and noise excitation are calculated. The effects of dynamic (regular) and stochastic wave generation are compared, and characteristic features of spectral transformation for these two cases are analyzed. Special attention is paid to the difference between the boundary nonlinear phenomena considered here and bulk effects due to nonlinear elastic properties of a medium. A possibility of observing such phenomena for the radiation of high intensity waves into the bubbly liquid is discussed. [Work supported by CRDF and RFBR.]

10:40

4aPAd8. Nonlinear phenomena in resonator caused by finite displacement of vibrating piston. Oleg V. Rudenko and Andrey V. Shanin (Faculty of Phys., Moscow State Univ., Moscow, Leninskie Gory, 119899, Russia)

Design of high-Q resonators demands reducing of all types of energy loss. When linear losses are eliminated, the nonlinear absorption due to shock-wave formation becomes significant. Such methods as using frequency-dependent reflecting boundaries (providing phase shifts between harmonics), using a selective absorbent for second harmonic, and design of resonators with complicated geometrical shape are known for damping of the shock formation process. The new type of nonlinear distortion of a wave profile is studied. This phenomenon appears in linear media and is caused by finite displacement of boundary. The magnitude of the effect depends on the ratio of two small parameters: Mach number and Q^{-1}, and therefore, it can be significant even for small pumping. The effect of moving the boundary is accumulative in time and is of the same order as effect of volume nonlinearity. The temporal profiles of nonlinear vibrations at harmonic pumping are calculated. The optimum law of piston movement providing the maximum energy accumulation in a resonator is suggested. The nonstationary problem is solved. New mathematical models based on functional equations are proposed. This model has a discrete character and requires some specific approaches, unlike the models for volume nonlinearity. [Work supported by INTAS-RFBR European grant.]

11:00

4aPAd9. Nonlinear waves in closed tubes. Michal Bednařík (CTU-FEE, 16627 Prague, Czech Republic, bednarik@feld.cvut.cz)

The purpose of this investigation was to choose a suitable model equation for description of finite amplitude waves in closed tubes filled with air. The boundary layer effects were also taken into account. Unfortunately, a general analytic solution of the used model equations has not been known, consequently it was necessary to find a numerical method for solution of these equations. When a standing wave is driven to high amplitude in an acoustic resonator, nonlinear effects couple energy from low- to high-frequency modes, ultimately resulting in shock wave formation and heightened dissipation. Therefore this work was focused on study of suppressing the energy transfer into harmonics that represents a parasitic loss. This suppressing of the energy transfer enables store energy in the form of an acoustic standing wave in a resonant cavity more effectively.

11:20

4aPAd10. Multi-frequency plane, nonlinear, and dissipative waves for arbitrary distances. Claes M. Hedberg (Dept. of Mech. Eng., Univ. of Karlskrona-Ronneby, 371 79 Karlskrona, Sweden, claes.hedberg@ima.hk-r.se)

A solution for multi-frequency plane waves propagating through a dissipative and nonlinear medium is presented. It originates from the well-known Mendousse solution, a ratio between Bessel function series, for a pure sinusiodal wave. The solution is exact. The only limitation, which is inherited from the Mendousse solution, is the slow convergence of the series when the nonlinearity is very large compared to the dissipation. Otherwise, any frequencies, amplitudes, and phases can be introduced in the original wave and the solution is valid for any propagated distance. Results for some multi-frequency signals are presented.

11:40

4aPAd11. Double-strand cellular DNA damage by lithotripter generated shock waves. A. Kochański, J. Mejnartowicz, A. Latos-Bieleńska (Chair and Dept. of Medical Genetics, Univ. of Medical Sci., Poznań, Poland), J. Etienne, and L. Filipczyński (Polish Acad. of Sci., Warsaw, Poland)

During the last years the biological effects of exposure to SWL have been intensively investigated. In contrast to the other studies the lithotripsy effects on cellular DNA have been rather poorly analyzed so far. In the present study the influence of the therapeutic level energy (18- and 20-kV) shock waves on the cellular DNA was analyzed. These levels of energy correspond to 16 and 30 MPa, respectively. The DNA was analyzed by the classical agarose electrophoresis approach. In contrast to the previously published data, the present results of the DNA analysis strongly suggest the double-strand DNA damage by shock waves generated by the lithotripter. This kind of double-strand DNA damage precludes the cell survival. Therefore, the used methods may be a useful approach in monitoring the biological processes in which the biological tissue is exposed to shock waves generated by a lithotripter.

THURSDAY MORNING, 18 MARCH 1999 POSTER GALLERY, 8:00 TO 10:00 A.M.

Session 4aPPa

Psychological and Physiological Acoustics: Models and Sound Quality (Poster Session)

Lutz Wiegrebe, Chair

CNBH, Physiological Laboratories, Cambridge University, Downing Street, Cambridge CB2 3E6, UK

Contributed Papers

All posters will be on display in the Poster Gallery from Thursday to Friday, 18–19 March. Authors will be at their posters from 8:00 a.m. to 10:00 a.m. on Thursday, 18 March.

4aPPa1. Modeling masking patterns for sinusoidal and narrow-band noise maskers. Ralph P. Derleth, Torsten Dau, and Birger Kollmeier (Graduiertenkolleg Psychoakustik und AG Medizinische Physik, Univ. Oldenburg, Germany)

In a recent paper by Moore, Alcántara, and Dau [J. Acoust. Soc. Am. **104**, 1023–1038 (1998)] masking patterns for sinusoidal and narrow-band noise were presented. Data were collected for all four masker-signal combinations. The same subjects participated in the different experimental conditions and the same experimental procedure was used in each case. Despite the influence of combination products, a strong influence of temporal fluctuations on the masking patterns for sinusoidal maskers was found for masker-signal frequency separations up to a few hundred Hz. The present study shows model predictions obtained with the modulation-filterbank model [Dau *et al.*, J. Acoust. Soc. Am. **102**, 2892–2905 (1997)]. This model is able to use envelope fluctuations, for example, beats, as a detection cue, but it does not contain a nonlinear peripheral filter stage. Thus the model predictions offer the possibility to separate

between effects caused by temporal effects like beating and those caused by combination products. As in the experimental data of Moore *et al.*, less masking was found for the tone-on-tone masking condition than for the tone-in-noise masking condition, for tone-masker frequency separations lower than 250 Hz. The asymmetry of masking between the signal-tone masker-noise condition and the signal-noise masker-tone condition can also be accounted for quantitatively by the model.

4aPPa2. Frequency selectivity in amplitude-modulation processing. Stephan Ewert and Torsten Dau (Carl von Ossietzky Univ. Oldenburg, AG Medizinische Physik, D-26111 Oldenburg, Germany)

Effects of frequency selectivity in the audiofrequency domain are well established and associated with the existence of independent frequency channels (critical bands). Several studies suggested a comparable spectral decomposition in the modulation-frequency domain. However, in these studies the bandwidth and the shape of the postulated channels were derived only indirectly and for a restricted range of low-frequency modulations. A principal problem in modulation masking experiments is the restricted dynamic range of the modulation depth available to detect the test modulation. Particularly, in conditions with a stochastic carrier and a stochastic masker-modulation, two basic factors limit resolution: The amplitude statistics of the bandlimited masker-modulation noise and the intrinsic envelope fluctuations of the carrier noise. The present study offers an optimized experimental condition for the derivation of modulation-filter shapes. A direct approach to obtain the modulation-filter shape is presented and modulation-tuning curves are derived up to modulation rates of 100–160 Hz for different spectral positions of the carrier. In addition, across-frequency effects in modulation masking with the probe and the masker separated by about two octaves are examined. The experimental results are compared with threshold estimates based on the integrated modulation power in a hypothetical modulation filter.

4aPPa3. On the apparent source width (ASW) for bandpass noises related to the IACC and the width of the interaural cross-correlation function (W_{IACC}). Shin-ichi Sato and Yoichi Ando (Grad. School of Sci. and Technol., Kobe Univ., Rokkodai, Nada, Kobe, 657-8501, Japan, 944d909n@kobe-u.ac.jp)

It has been shown that the ASW for 1/3 octave band noises and music signal can be described as functions of the IACC and the W_{IACC}, which is defined as the time interval of the interaural cross-correlation function within 10% of the maximum [Sato and Ando, J. Acoust. Soc. Am. **100**, 2592(A) (1996); **102**, 3188(A) (1997)]. In this study, it is examined whether or not the ASW for bandpass noises with different bandwidth Δf also can be calculated with the IACC and the W_{IACC}. In order to control the W_{IACC}, the bandwidth of the bandpass noises of 500 Hz center frequency was changed in the range of 1/3–3 octave. Results of the scale values of ASW obtained by the paired comparison method are compared with calculated ASW. [Work supported by the Grant-in-Aid for Scientific Research JSPS.]

4aPPa4. Parameter estimation of the passive cochlear model. Emilios K. Dimitriadis (Bioeng. and Physical Sci. Prog., ORS, 13 South Dr., Bldg. 13/3N17, NIH, Bethesda, MD 20892, dimitria@helix.nih.gov) and Richard S. Chadwick (NIH, Bethesda, MD 20892)

Two critical issues in every cochlear modeling effort are the choice of model dimensionality and the corresponding model parameters of the passive system. The cochlea is often represented by an axial array of single or multiple degree-of-freedom lumped parameter systems, which are axially coupled via the fluid–structure interaction. For most cases, precise anatomical data for the axial distribution of model parameters are lacking and one has to make educated guesses as to their values. The problem is more complicated with multiple degree-of-freedom models, where it is not clear which parts of the structure should be lumped together to constitute the different degrees of freedom. In this work, one-, two-, and three-degree-of-freedom systems are compared and contrasted in their ability to predict passive, *in situ* measured responses. Following that, an effort is made to apply parameter estimation techniques that will result in models which optimally predict passive *in situ* data. The estimation methods are based on least-squares fitting of recorded frequency response data, but the relatively large number of parameters requires that a number of auxiliary conditions be established based on our partial knowledge of anatomy and physiology. Issues are discussed and recent results presented and contrasted among the different models.

4aPPa5. Time constants of pitch processing arising from auditory filtering. Lutz Wiegrebe, Hans S. Hirsch, Roy D. Patterson (CNBH, The Physiological Labs., Cambridge Univ., Cambridge, UK), and Hugo Fastl (Technische Univ., Muenchen, Germany)

This study uses rippled noise and ''AABB'' noise [Wiegrebe *et al.*, J. Acoust. Soc. Am. **104**, 2307–2313 (1998)] to investigate time constants associated with pitch processing in the auditory system. RN and AABB have identical long-term spectra and autocorrelations but they differ in their temporal dynamics. Previously, it was shown that, when the pitch of the stimuli is below about 350 Hz, listeners could discriminate broadband AABB from RN based on a pitch-strength difference. Here, the effect of frequency passband on the RN-AABB discrimination was investigated. In each 1-kHz band, discrimination performance decreased with decreasing delay (32–4 ms). As the center frequency increased from 0.5 to 4 kHz, the rate of decrease became smaller such that discrimination was still significant in the highest band with the shortest delay. Further experiments suggest that the RN-AABB discrimination and its frequency effects are based on pitch-strength differences. Auditory simulations suggest that integration of pitch information occurs in two stages comprising a short, frequency-dependent time constant of auditory filtering and a long, yet undetermined neural time constant separated by a nonlinear transformation, i.e., half-wave rectification. [Supported by the Medical Research Council, the ''Prof. Dr. Ing. Erich Mueller-Stiftung'' and the ''Deutsche Forschungsgemeinschaft.'']

4aPPa6. Do ears really just perform frequency analysis of crackle sound? Eckard Blumschein (Dept. of Electron. Eng., Guericke Univ., PSF 4120, D-39016 Magdeburg, Germany; blumschein@et.uni-magdeburg.de)

Experience concerning measurement and interpretation of a special crackle sound which relates to the quality of so-called short arc welding is summarized. There are salient elements in it, which sound different when time is reversed. Other observations also gave rise to put into question the adequacy of traditional, purely spectral processing of acoustical signals. Further evidence has been collected in order to substantiate general needs for a better understanding of how audition might really work, and to justify the search for an approach that could overcome the well-known imperfections of spectrograms. Considerations start with interpretation of data given on response of basilar membrane to clicks by Recio *et al.* (1998) and on branched, more apical recorded click latencies in Cai's (1992) thesis. Gammachirp-like behavior of basilar membrane has been considered a superposition of coupled oscillations. The branched latencies were found to fit a conjectured exact relationship to 1/CF surprisingly well. It does not result from the velocity of the traveling wave, but the way around; the latter is merely an epiphenomenon. These findings back an

idea that latencies provide an accurate second coding, in addition to place. So, the cochlea itself may act as a delay line, being requisite for autocorrelation-based models of temporal perception.

4aPPa7. Relevant psychoacoustic parameters in assessments on wind turbine noise. Christoph Eichenlaub and Reinhard Weber (Dept. of Phys., Carl-von-Ossietzky Univ., D-26111 Oldenburg, Germany)

Subjective judgments on wind turbine noise were to determine noise quality parameters which are related to the unpleasantness of noise immissions. In a pre-test paired comparisons of wind turbine noises using headphone presentations showed the superiority of head related recordings compared to single microphone recordings. Loudness contributed mostly to the unpleasantness and masked the contribution of other noise quality parameters. Hence in the main experiment artificial head recordings from a representative set of ten wind turbines were equalized in loudness and judged after their unpleasantness in a complete paired comparison trial by 22 subjects. Insufficient reliability and consistency led to an exclusion of 9 subjects. From the BTL-scaled answers of 13 subjects a factor analysis provided two factors ($F1$: 71%/$F2$: 12% of total variance). Means and percentiles of the unweighted, A-, B-, and C-weighted SPL, loudness, roughness, sharpness, fluctuation strength, tonality and impulsiveness were calculated and answers of 11 subjects with high and moderate loads on factor 1 showed significant correlation coefficients with tonality measures ($r = 0.8$ to 0.83). The answers of subjects with high loads on factor 2 significantly correlated with fluctuation strength. No further noise quality parameters turned out to be relevant.

4aPPa8. Categorical assessments on fluctuation strength of synthesized sounds. Imke Raubold and Reinhard Weber (Dept. of Phys., Carl-von-Ossietzky-Univ., D-26111 Oldenburg, Germany)

Results on category scaled fluctuation strength of different kinds of synthesized signals are presented. Fluctuation can become a major aspect of sound quality, and the intent of the study was to investigate the relationship between ratio-scaled data in literature [e.g., Zwicker and Fastl, *Psychoacoustics* (Springer-Verlag, New York, 1991)] and categorical judgments. Signals used comprise AM or FM tones with different carrier frequencies (0.25, 0.5, 1, 2, 4, 8 kHz) as well as modulated noises. Modulation frequencies vary from 0.25 to 32 Hz in octave steps. The whole set of 66 stimuli each lasting for 6 s was divided into three sequences presented over headphones in a sound-proof cabin. As in previous roughness assessments [Daniel and Weber, Acustica **83**, 113–123 (1997)] judgments were made using an ''analog'' category scale consisting of five categories (*not -, a little -, medium -, rather -,* and *very fluctuating*) which are combined with a continuous scale to overcome limited resolution of the categories. It turns out that the concept of *fluctuation* is interpreted differently by subjects, especially by ''naives'' and already trained ''experts.'' The consequences for the different kinds of noises will be discussed as well as the relationship to ratio-scaled data.

4aPPa9. Validation of objective assessment methods for tonal noise from wind farms. Holger Ostendorf and Reinhard Weber (FB Physik, Univ. Oldenburg, D-26111 Oldenburg, Germany)

The perceived impact of wind farm noise depends not only on the overall level of noise emitted, but also on the character of the noise. In particular, the presence of tonal components increases the subjective annoyance. Procedures for the detection of tonal components in the environmental noise and for the assessment of the annoyance due to these components have been proposed in national standards and legislation, e.g., German norm DIN 45681 (draft), Joint Nordic Method. To validate tonality calculation procedures, noises from a representative sample of nine wind turbines of German wind farm sites were recorded by means of a dummy head at the emission measuring point nearby the turbines. Together with a set of five synthesized pink noises with tonal components of different strengths, ten selected wind turbine noises were randomly presented at equal loudness over headphones. Sixteen subjects had to assess categorically the tonality of each noise, which occurred six times in two sessions. The resulting subjective answers showing high inter- and intraindividual agreement could serve as an excellent validation basis for eight selected tonality calculation procedures. It will be shown that the prominence ratio-based methods are the best in modeling subjective tonality assessments.

4aPPa10. Response to low-frequency HVAC noise. Broner Norm (Vipac Engineers & Scientists, Melbourne, 3207, Australia) and Patricia Davies (Purdue Univ., West Lafayette, IN 47907-1077)

With the increasing use of variable air volume systems in building air-conditioning, there has been an increased occurrence of low-frequency and rumble noise problems. ASHRAE is currently funding a research program to determine the relationship between low-frequency HVAC noise and comfort in occupied spaces. A pilot psycho-acoustic study was conducted using up to nine subjects. Twelve noise stimuli representing various HVAC sounds were utilised and subjects assigned an annoyance and loudness rating using the absolute magnitude estimation technique. The results showed that for noise stimuli dominated by low-frequency energy, the annoyance was more severe than the loudness, rather than equal as has been generally assumed. The main study is currently underway and some of the results will be discussed. The subjective rating responses were correlated with the dB SPL and other noise metrics and Sound Quality metrics. The results have implications with respect to assessment of low-frequency noise in buildings and possibly to the external environment.

4aPPa11. Psychat—A program for psychoacoustical tests. Matthias Scholz (Ackerwand 21, Weimar 99423, Germany, Scho.Co@t-online.de), Vincent Rioux, Daniel Västfjäll, and Mendel Kleiner (Chalmers Univ. of Technol., S-41279 Gothenburg, Sweden)

Sound quality investigations require flexible sound and graphic handling, available on usual personal computers. Psychat is a program designed to fulfill requirements of flexible sound quality testing. The core idea of this program is to offer a fully modular system manipulating objects like audio-players, functions that present visual stimuli or other I/O devices and adaptive descriptor scales. With the help of a graphical editor test leaders can create their own test configuration. Several tests can be linked to a whole project and can be saved as templates and used in other projects. Standard sound quality experiments and more complex tests can be created without programming skills. The principle of modularity allows growing functionality, keeping compatibility, and adapting the system to the users needs. The program collects raw data, includes some basic statistical methods, and offers possibilities to export data in a number of formats.

Session 4aPPb

Psychological and Physiological Acoustics: Central Auditory Processing

Beverly A. Wright, Chair
Audiology and Hearing Sciences Program, Northwestern University, 2299 North Campus Drive, Evanston, Illinois 60208-3550, USA

Contributed Papers

8:00

4aPPb1. Sensory dissonance of two-tone complexes. Andrzej Rakowski and Andrzej Miskiewicz (Music Acoust. Lab., Fryderyk Chopin Acad. of Music, Okolnik 2, 00-368 Warszawa, Poland)

Sensory dissonance, a basically unpleasant auditory sensation related to amplitude or frequency modulation of sound, is an element of a broader concept of musical dissonance. The present study was carried out to determine the magnitude of sensory dissonance produced by beats in two-tone complexes. The method of absolute magnitude estimation was employed for scaling. The measurements were obtained for tone frequencies ranging from 32 to 4000 Hz and beat frequencies ranging from 2 to 2000 Hz. The results show that at beat frequencies higher than 20 Hz, sensory dissonance is equivalent to roughness. The beat frequency at which the maximum of roughness and of sensory dissonance is observed increases with the frequency of the low tone in a complex, ranging from 20 for a 32-Hz tone to about 100 for a 4000-Hz tone. At beat frequencies lower than 20 Hz, sensory dissonance is produced by audible fluctuations of loudness. The effect of loudness fluctuations on sensory dissonance is most pronounced in the range of lowest audible frequencies.

8:20

4aPPb2. Perceptual consequences of spectro-temporal smearing in the wavelet coding of speech. Nicolle H. van Schijndel, Tammo Houtgast, and Joost M. Festen (Dept. of Otolaryngol., Univ. Hospital VU, P.O. Box 7057, 1007 MB Amsterdam, The Netherlands, NH.vanSchijndel@azvu.nl)

In this study, speech is spectro-temporally smeared, i.e., the contrasts in the spectral and/or temporal domain are reduced. This spread-of-excitation type of manipulation is embedded in a spectro-temporal analysis and resynthesis scheme. In order to perform a perceptually relevant analysis, wavelet coding with a Gaussian wavelet of 1/4 octave is used. The detectability of smearing and the effect on intelligibility are measured for normal-hearing and hearing-impaired listeners. Smearing is imposed concentrating on the spectral domain (related to upward and downward spread of masking), concentrating on the temporal domain (related to forward and backward masking), and considering the spectral and temporal domain in combination (spectro-temporal spread of excitation). Mechanisms underlying the just-noticeable degree of smearing, and the intelligibility of smeared speech will be addressed. The results may provide insight into the sharpness of the internal spectro-temporal representation of the auditory system and its effect on speech intelligibility. Comparing normal-hearing and hearing-impaired listeners, the role of a reduced sharpness in auditory spectro-temporal coding as a possible explanation for degraded speech intelligibility will be discussed. [Work supported by the Netherlands Organization for Scientific Research (NWO).]

8:40

4aPPb3. The Indiana Test of Auditory Memory and Processing Rate (ITAMPR). Charles S. Watson, David A. Eddins, and Gary R. Kidd (Dept. of Speech and Hearing Sci., Indiana Univ., Bloomington, IN 47401)

The Indiana Test of Auditory Memory and Processing Rate (ITAMPR) is designed to measure children's abilities to identify sequences of speech elements. Subtests determine whether identification performance is primarily limited by the rate at which the stimuli are presented or by the number of stimuli in a sequence. Stimuli consist of 80-ms syllables, /ba/ and /da/, produced using a Klatt synthesizer. Listeners respond by repeating the sequence that they heard. The first subtest determines the fastest rate at which three-syllable sequences can be correctly identified, with rate manipulated by reducing the inter-syllable intervals. The second subtest determines the largest number of syllables that can be correctly repeated, using an intersyllable interval of 400 ms. A third subtest intentionally covaries number of syllables and rate of presentation, to determine the combined effects of these two variables. ITAMPR data are reported for approximately 330 normal-hearing children who were entering first grade, but were otherwise unselected. Lack of significant associations between rate and memory thresholds and several measures of language development suggests that auditory temporal processing and auditory memory, as measured by the ITAMPR, are not primary factors in language skills or disorders. [Work supported by Indiana University and the Benton County School Corporation.]

9:00

4aPPb4. Comparisons between but not within sounds are impaired in stroke victims with unilateral neglect. Rhodri Cusack, Robert P. Carlyon, and Ian H. Robertson (MRC-CBU, 15 Chaucer Rd., Cambridge CB2 2EF, UK, rhodri.cusack@mrc-cbu.cam.ac.uk)

Neglect is characterized by impaired performance on visual tasks in which competing stimuli are presented and patients show little or no awareness of stimuli further towards the left. Described here is a previously unreported deficit in making comparisons between sequentially presented sounds. In experiment 1, ability to lateralize a narrow-band noise with an ITD was compared to performance on a 3IFC ITD discrimination task using similar sounds. Patients performed similarly to age-matched controls on the one-interval task, but were highly impaired on the three-interval task. This might be due to a temporal attention disorder, or to a problem tracking sounds at different spatial locations. In experiment 2, performance was tested on a nonspatial, 2IFC frequency discrimination task. Patients were again severely impaired relative to age-matched controls. This could not be explained by differences in peripheral frequency discrimination (measured using a one-interval FM detection task). These findings are unlikely to be a general effect of task difficulty, as (1) a control group with frontal lesions performed very similarly to the age-matched normals and (2) 3IFC tasks are usually considered to be easier than yes–no tasks. They indicate a specific impairment in attending to sequential sounds.

9:20

4aPPb5. Influence of condition variation on learning in auditory backward masking. Beverly A. Wright, Matthew B. Fitzgerald (Audiol. and Hearing Sci. Prog., 2299 N. Campus Dr., Northwestern Univ., Evanston, IL 60208-3550), Paul A. Johnston, and Miriam D. Reid (Univ. of California, San Francisco, CA 94143-0732)

The influence of condition variation on learning rate in an auditory backward-masking task was assessed by measuring pure-tone detection thresholds in 24 different trial blocks in five groups of eight normal-hearing adults assigned to different conditions midway in the testing sequence. Thresholds for a tonal signal (10 ms, 1000 Hz) presented immediately before a noise masker (300 ms, 200–1800 Hz, 40 dB SPL spectrum level) were evaluated in blocks 1–9 and 19–24. The decrease in threshold observed between the means of blocks 1–3 and blocks 19–24 depended upon the condition tested in blocks 10–18. Mean threshold decreased by nearly 20 dB for listeners who detected a backward-masked tone presented in a temporal gap between two maskers, by around 15 dB for listeners who detected a backward-masked tone at a higher frequency or a forward-masked tone, and by around 12 dB for listeners who did the standard backward-masking task or who rested for 20 min. This information may be useful for the development of interventions for elderly persons and children with language impairment who have been observed to have excessive auditory backward masking. [Work supported by NIDCD and the McDonnell-Pew Program in Cognitive Neuroscience.]

9:40

4aPPb6. Computational audition: Auditory perceptual organization and systematic music theory. Uwe Seifert, Lueder Schmidt, and Eichert Randolph (Inst. of Musicology, Univ. of Hamburg, Neue Rabenstr. 13, 20354 Hamburg, Germany)

The term ''computational audition'' encompasses top-down and bottom-up approaches in hearing, speech, and music. As an information processing approach, the main task is to relate auditory funtion (i.e.,perceptual processes and representational structures) to structure (i.e., neural circuits). It is argued that there are two main (Gestalt) problems in computational audition: (a) the well-known constancy problems in auditory perception as exemplified in Bekesy (1969, 1974) and (b) the correspondence problem in sequential integration which is the main grouping problem in temporal pattern perception. These problems are best attacked from functional psychophysics and a neuroethological point of view in terms of intercausal nets [Wirkungsgefuege; Mittelstaedt (1969); Bischof (1995)]: Connected functional input–output relations are interpreted as causal relations. Therefore, a research strategy for auditory image formation [Yost (1992)] which may allow connecting signal and information processing approaches is proposed. This functional psychophysical approach to computational audition in connection with neuroethology in research on music perception is called systematic music theory. Computational audition may offer the possibility for a ''theory of music'' in the sense of Hermann von Helmholtz and Carl Stumpf which is related to a biologically rooted theory of hearing.

THURSDAY MORNING, 18 MARCH 1999 ROOM H104, 10:15 A.M. TO 12:20 P.M.

Session 4aPPc

Psychological and Physiological Acoustics, Speech Communication, and Musical Acoustics: Honoring the Contributions of Reinier Plomp

Tammo Houtgast, Cochair
TNO Human Factors Research Institute, Box 23, 3769 ZG Soesterberg, The Netherlands

Robert V. Shannon, Cochair
House Ear Institute, 2100 West Third Street, Los Angeles, California 90057, USA

Chair's Introduction—10:15

Invited Papers

10:20

4aPPc1. On the tones that make music. Adrianus J. M. Houtsma (IPO, P.O. Box 513, 5600 MB Eindhoven, The Netherlands)

Advances in musical acoustics, music psychology, architectural acoustics, and electroacoustics during the past few decades have all contributed to our present understanding of the complex processes involved in making, listening to, and enjoying music. Psychoacoustics has made contributions by exploring basic relationships between tones, tone combinations, and tone sequences on the one hand, and sensations of loudness, pitch, timbre, consonance, dissonance, and rhythm on the other. Statistical analyses of musical intervals used in certain compositions, for instance, show a clear relationship with auditory critical bandwidth. Musical instruments typically used for playing lead voices or complex harmonies are found to have lower partials with an exact or nearly exact harmonic relationship so that they can convey clear and unambiguous pitch sensations. Even spatial effects have been used by composers since the Renaissance to the present day. Such effects don't always lead to the intended results, however, because of the often unpredictable acoustic behavior of listening spaces. Reinier Plomp has made significant contributions to our present understanding of these problems. The title of this presentation is, in fact, the subtitle of an auditory demonstration CD recently issued by him in The Netherlands.

10:40

4aPPc2. Honoring the contributions of Reinier Plomp in psychoacoustics. Brian C. J. Moore (Dept. of Exp. Psych., Univ. of Cambridge, Cambridge CB2 3EB, England)

Reinier Plomp has had a huge impact on the field of psychoacoustics of a period of 40 years. Many of this papers have become regarded as ''classical.'' His studies on the ''science of science'' led to the conclusion that the number of published papers cited more than 25 times is a good indicator of an author's scientific impact. Seven out of the first ten of Plomp's publications (and 27 in total) satisfy this criterion, which is a remarkable achievement. This lecture briefly reviews some of the most highly cited of Plomp's papers,

concentrating on temporal integration at threshold, the rate of decay of auditory sensation, the ability to ''hear out'' partials in complex tones, the perception of the pitch of complex tones, and tonal consonance and the critical bandwidth. Many of the concepts introduced in these papers were novel at the time, but are now widely accepted. His data have stood the test of time. I, and many others, are grateful to him for the clarity of his writing, the breadth of his conception, his ability to identify key problems, and his role as ''Promoter'' of many fine Ph.D. students.

11:00

4aPPc3. Contributions of spectral resolution to speech recognition in noise. Robert V. Shannon and Qian-Jie Fu (House Ear Inst., 2100 W. Third St., Los Angeles, CA 90057)

Plomp's model of the speech recognition threshold (SRT) provides a remarkably good description for normal-hearing and hearing-impaired listeners. According to the model, an attenuation factor (A) and a distortion factor (D) can account for the changes in SRT with increasing noise levels. In a recent series of studies, phoneme recognition under conditions of reduced spectral representation and varying signal-to-noise conditions has been measured in both normal-hearing listeners and cochlear implant listeners. Plomp's basic frameworks were adapted to account for these new data. Results from normal-hearing listeners showed that the reduction in spectral resolution and other spectral manipulations could be well quantified in terms of the D factor. The performance of the best cochlear implant user was similar to that of normal-hearing subjects listening to a similar level of spectral reduction, indicating that the D factor in the spectral domain alone could be used to account for the performance in noise of these cochlear implant users. However, some of the cochlear implant listeners had poorer performance than processor-matched normal-hearing subjects, suggesting that the distortion factor in the amplitude domain, such as distorted loudness growth introduced by acoustic-to-electric amplitude mapping, should also be considered. [Work supported by NIH.]

11:20

4aPPc4. Speech perception: Ideas and concepts initiated by Reinier Plomp. Tammo Houtgast (TNO Human Factors Res. Inst., P.O. Box 23, 3769 ZG Soesterberg, The Netherlands)

In the late 1960s, a central issue in the research group on speech and hearing at TNO, headed by Reinier Plomp, was the relation between the perceptual and physical characteristics of sound. One impressive example concerned the research on vowel sounds, conducted together with Louis Pols. By adapting novel approaches for studying supra-threshold phenomena (triadic comparison of stimuli, Kruskal's multi-dimensional scaling technique), the perceptual differences among vowel sounds could be visualized in a two- or three-dimensional representation of vowel points. This representation appeared to be in excellent agreement with a physical configuration of the vowel points, based on one-third-octave band analysis of the vowel sounds. It is conceptually only a small step from these isolated steady-state vowels, corresponding to points in a multi-dimensional space, to running speech resulting in a trace within that space. The spectral distances between successive points in such a speech trace reflect the rate-of-change in the speech signal as perceived by a listener. This framework of thinking, i.e., the perceptual relevance of projecting speech in the spectral domain, did lay at the roots of our later work on the development of objective measures for quantifying speech intelligibility.

11:40

4aPPc5. Fifty years in (psycho)acoustics: Some conclusions. Reinier Plomp (Straatweg 220, 3621 BZ, Breukelen, The Netherlands)

The exceptional honor of this session gives me the opportunity to introduce some questions usually not discussed in conferences papers. My point of departure is that the function of our hearing is to inform us as reliably as possible about the world of sounds around us. It is the task of hearing research to find the laws involved. In carrying out this task, we are permanently confronted with several temptations. Their common origin is the scientific rule to keep the number of variables as small as possible. In this way, parts get more attention than structure. Hence, many essential aspects of everyday sounds had to wait surprisingly long before they got proper scientific attention. Some examples will be discussed under the following headings: (1) the temptation to study the perception of isolated sound elements such as single tones and vowels rather than the dynamic spectrotemporal patterns of connected speech; (2) the temptation to consider hearing primarily as ''designed'' for perceiving sounds from a single source rather than from two or more simultaneous sound sources; (3) the temptation to restrict our attention to the auditory parameters of sounds rather than including cognition as an essential complementary part of hearing.

Session 4aSAa

Structural Acoustics and Vibration: Smart Materials I

Vasundara V. Varadan, Cochair
Department of Engineering Science and Mechanics, Pennsylvania State University, 149 Hammond Building, University Park, Pennsylvania 16802, USA

Ulrich Gabbert, Cochair
Institute of Mechanics, University of Magdeburg, Universitaetsplatz 2, D-39106 Magdeburg, Germany

Chair's Introduction—7:55

Invited Papers

8:00

4aSAa1. Numerical simulation and optimization of smart piezoelectric structures. Ulrich Gabbert and Christian-Toralf Weber (Univ. of Magdeburg, Inst. of Mech., Universitaetsplatz 2, D-39106 Magdeburg, Germany, ulrich.gabbert@mb.uni-magdeburg.de)

In this paper an overview about a finite-element-based simulation tool for smart structures is given, which includes also optimization procedures (e.g., for sensor/actuator placement) as well as control strategies. The focus of the paper is on piezoelectric materials (wafers and fibers) as active components, which are controlled by electric fields and consequently, the coupled electro-thermo-mechanical field equations have to be solved. The element library contains 1-D, 2-D, and 3-D multifield finite elements as well as special layered elements to simulate thin-walled structures with different layers of passive and active materials based on a layerwise constant shear angle theory. A substructure/superelement technique can be used in static as well as dynamic applications. In the optimization of actuator distributions a discrete-continuous optimization procedure will be presented, where the actuator positions at the structure are described by dicrete 0-1 variables, and the control parameters are included as continuous variables. Mathematical solution algorithms for nonlinear, mixed optimization problems are used to solve the optimization problem. Test examples (e.g., active vibration damping to reduce noise radiation) and comparisons with experimetal results will be presented to discuss the quality of the finite-element simulation and optimization tool.

8:20

4aSAa2. Annihilation of beam vibrations by shaped piezoelectric actuators: Coupled theory. Hans Irschik, Michael Krommer, and Uwe Pichler (Johannes Kepler Univ. of Linz, Div. of Tech. Mech., Altenbergerstrasse 69, A-4040 Linz, Austria, irschik@mechatronik.uni-linz.ac.at)

Flexural vibrations of smart beams are studied in this paper. Layers made of piezoelectric material are used to perform a distributed actuation of the beam. Special emphasis is given to the following actuator shaping problem: A spatial shape function of the distributed actuator is sought such that vibrations induced by external forces are completely annihilated. The formulation is restricted to forces with a given spatial distribution and an arbitrary time evolution of their intensity. The scope is to derive a class of easy to obtain analytic solutions of this inverse problem. Actuator equations are used in the present contribution which take into account the interaction of mechanical and electrical fields. Extending the preliminary results, the above actuator shaping problem is solved in the context of these coupled equations. Beams with different boundary conditions are considered. Shape functions responsible for nonuniqueness of the shaping problem are also considered. These nilpotent solutions may be added to the above derived solution of the actuator problem without producing any additional vibrations. The presented analytic results are validated by means of coupled finite-element calculations.

8:40

4aSAa3. Closed-loop finite-element modeling of smart structures—An overview. Vasundara V. Varadan, Young-hun Lim, Senthil V. Gopinathan, and Vijay K. Varadan (Penn State Univ., 149 Hammond Bldg., University Park, PA 16802, vvvesm@engr.psu.edu)

Smart structures incorporate sensors, actuators, and control electronics that permit the structure to tailor its response to changes in the environment in an optimal fashion. The sensors and actuators are constructed using functional materials such as piezoelectric materials. Finite-element modeling has been successfully used to model these complex structures. More recently, closed-loop numerical simulation of the tailored response of a smart structure has become possible by combining the finite-element equations of the sensor response to applied dynamical loads to the input voltage or current to the actuators via a control algorithm. Optimization of

sensor/actuator placement as well as optimization of the control gains will be discussed. Applications to control of cabin noise are studied. Constrained layer damping, incorporating active passive damping, can also be simulated. The talk will present an overview of the approach in relation to others in the extant literature.

9:00

4aSAa4. Komornik's feedback stabilization: An experimental realization. Frederic Bourquin, Michel Joly (Laboratoire des matriaux et des structures du gnie civil, UMR113 LCPC/CNRS, Champs sur Marne, France), and Manuel Collet (Ple. Universitaire Lonard de Vinci, DER Calcul scientifique, La Defense, France)

Most active control strategies applied in mechanical engineering are, in fact, active damping or suboptimal stabilization implemented with the help of new transducers. Indeed, it is very difficult to apply real optimal active control feedback on a distributed structure like a beam, plate, or shell. The infinite number of degrees of freedom puts forward the intrinsic problems of exact controllability and observability. The physical properties corresponding to their results are the observation of spill-over and the lack of efficiency of many experimental devices. An original solution to obtain a prescribed energy decay is to use aversion of Komornik's feedback. Although it is a pure product of mathematical developments, Komornik's algorithm can be implemented on line on a real structure. This method should really prove of interest in mechanical engineering. After a short overview of Komornik's feedback, this paper presents the experimental characteristics of this control strategy. By comparing with data associated with alternative control strategies like DVF or IFF, some specific properties of Komornik's method can be shown. Indeed, the real efficiency of this feedback and a large capability of eliminating modal spill-over instabilities is emphasized. As a conclusion, the principles for potential experimental developments on large-scale structures are introduced.

9:20

4aSAa5. Active fiber composite actuators for reducing acoustic radiation from cylindrical shells. Donald McDowell, Jr., Stephen Plunkett, Gregory Goddu (Naval Undersea Warfare Ctr., Newport, RI), and Aaron Bent (Continuum Control Corp., Cambridge, MA 02141)

Active fiber composites were developed to provide a mechanically robust method for large-area, orthotropic actuation and sensing in active structures. This presentation will describe the application of active fiber composite actuators to the reduction of acoustic radiation from a cylindrical shell by active control. The composite actuation layer is formed by small diameter piezoelectric fibers that are unidirectionally aligned and imbedded in a resin matrix system. A separate, etched, interdigital electrode layer makes the electrical connections. By nature of its structure, an active fiber composite actuator or sensor allows use of the primary piezoelectric effect in the plane of the composite. Active fiber composites are inherently tolerant of damage and can be conformed to a wide range of structural shapes. To control acoustic radiation from a cylindrical shell, active fiber composite actuators are used to generate a strain field that counteracts the strain associated with acoustically efficient shell motions. Optimal placement of the actuators is determined using numerical models verified by an experimental characterization of the shell dynamics. The control signal applied to the actuator is determined, in real time, using adaptive control. Error sensing methods using accelerometers or active fiber composite sensors were considered. [Work supported by DARPA.]

9:40

4aSAa6. Variational formulations for the vibration of a micropolar piezoelectric body. Silvia G. Ciumasu and Dumitru Vieru (Theoret. Mech. Dept., Tech. Univ. ''Gh. Asachi'' Iasi, Bd. Copou, nr. 22, 6600, Romania, sciumasu@sb.tuiasi.ro)

This work is a continuation of the previous study ''Polarization gradient in micropolar piezoelectricity,'' which was presented at The 5th International Conference on Integral Methods in Science and Engineering, IMSE'98, 10–13 August 1998, Michigan Tech, Houghton, MI. The present paper is concerned with the variational formulation for the free vibration of a micropolar piezoelectric body. These variational principles can be considered as generalizations of the corresponding variational formulations in classical piezoelectricity. It is shown that there exist types of variational formulations depending on the internal energy, electric enthalpy, mechanical enthalpy, and enthalpy, respectively.

10:00–10:20 Break

10:20

4aSAa7. Active noise reduction for steel bridges. Arthur P. Berkhoff, Fred G. de Beer, Karel N. H. Looijmans, Michiel W. R. M. van Overbeek, and Niek J. Doelman (TNO Inst. of Appl. Phys., P.O. Box 155, 2600AD Delft, The Netherlands, berkhoff@tpd.tno.nl)

Experimental and computational results are given for active control systems minimizing sound radiation from steel bridges for trains. The performance of the active systems with respect to noise reduction, convergence, stability, and actuator requirements is described. At frequencies above approximately 300 Hz passive means can be used to reduce the radiation of noise from railway track. At lower frequencies, however, passive means to reduce acoustic radiation are not possible due to various reasons. Additionally, the

main source of acoustic radiation at low frequencies is the steel bridge instead of the railway track. Therefore, the active noise control system for the steel bridge is based on the active isolation of track vibration by minimizing the mean-squared force between the steel bridge and the support for the rails. This is accomplished by controlling the distance between the rail supports and steel bridge with piezoelectric stack actuators. Transfer functions, load impedances, and actuator characteristics obtained from finite-element analysis and measurements lead to noise level reductions of 10 to 20 dB, depending on the control strategy and the available computational resources of the real-time implementation.

10:40

4aSAa8. Wavelets transform in oscillation and optimal feedback control of smart cantilever thin-walled beams. Victor Florin Poterasu (Tech. Univ., Bdul. Copou 22, Iasi, 6600 Romania, poterasu@sb.tuiasi.ro) and Liviu L. Librescu (Virginia Polytechnic Inst. and State Univ., Blacksburg, VA 24061-0219)

Based on the recent results obtained by Na and Librescu concerning the dynamic response characteristics of thin-walled cantilever beams made by smart materials subjected to transient loadings, this paper proposes to use the technique of wavelets transforms. As smart materials, the piezoelectric elements in the optimal feedback control of adaptive structures are considered and the oscillations are induced by the action of the blast loading. Wavelets provide a new tool for analysis, control, and identification of localized phenomena and vibrations. Instead of seeking to break down a signal into its harmonics, which are global functions that go forever, the signal is broken down into a series of local basis functions called wavelets. Each wavelet is located in a different place on the time axis. Several families of wavelet functions were studied. Haar, Meyer, Mallat, Daubechies, and Newland are in pattern recognition, image processing, turbulence, etc. This paper uses the Haar wavelets in order to perform the optimal control law with input voltage constraint and input power consumption. The influence of the inclusion of the excitations in the quadratic performance criterion of size and location of piezoactuator patches on the dynamic response of thin-walled beams subjected to blast pulses are studied.

Contributed Papers

11:00

4aSAa9. Love waves in nonclassical micropolar piezoelectricity. Dumitru Vieru and Silvia G. Ciumasu (Theoret. Mech. Dept., Tech. Univ. ''Gh. Asachi'' Iasi, Bd. Copou, nr. 22, 6600, Romania, sciumasu@sb.tuiasi.ro)

The basic equations of the linear theory of the micropolar piezoelectricity with polarization gradient have been derived in the paper ''Polarization gradient in micropolar piezoelectricity,'' presented at IMSE'98, 10–13 August 1998, Michigan Tech, Houghton, MI. In the case of the two-dimensional problem, the fundamental system of differential equations is split up into two independent systems. The second type of the two-dimensional problem is considered. In this paper, electromechanical-lycoupled Love waves are studied in the case of propagation along an isotropic, micropolar, dielectric layer attached to an isotropic, purely micropolar half-space.

11:20

4aSAa10. A coupled finite-element–normal modes expansion method to model Lamb waves generated with integrated transducers in composite plates. Emmanuel Moulin, Jamal Assaad, Christophe Delebarre (IEMN, UMR CNRS 9929, OAE Dept., Univ. de Valenciennes et du Hainaut Cambrésis, le Mont Houy, BP 311, 59304 Valenciennes Cedex, France), and Daniel Balageas (ONERA, 92322 Chatillon Cedex, France)

The use of miniaturized piezoelectric transducers integrated to a host composite material could enable the development of an on-line ultrasound health monitoring system for composite structures. Preliminary testing has already demonstrated the suitability and practical feasibility of this kind of integrated system, but a better control of these features now seems to be necessary. And especially, since the exploited ultrasonic vibration modes for plate-shaped structures are Lamb waves, the generation of desired Lamb modes should be mastered. Therefore, an original modeling approach has been developed, in order to help to design and optimize these ''smart materials.'' This modeling technique aims at determining the amplitude of each Lamb mode excited in a composite plate with surface-bonded or bulk-embedded piezoelectric elements. It consists of a coupling of the numerical finite-element method (FEM) and the normal modes expansion method. Indeed, a limited finite-element mesh of the transducer and its close vicinity is built. Then the numerically computed mechanical field is introduced as a forcing function into the normal modes' equations. In addition, the adequacy and accuracy of this modeling method have been experimentally demonstrated by using composite specimens containing small integrated piezoelectric elements.

11:40

4aSAa11. Active noise and vibration control for turboprop aircraft. Thomas Rohde, Ingo U. Borchers, Sigurd Häusler (Daimler Benz Aerospace, Dornier GmbH, Vibroacoustics Dept., D-88039 Friedrichshafen, Germany), and Michael Möser (Technische Universität Berlin, D-10587 Berlin, Germany)

Interior noise in modern turboprop aircraft is a serious problem as it is directly related to passenger comfort, crew performance, and aircraft weight. For turboprop aircraft the most important noise sources are the propellers generating intense low-frequency noise which is, in general, difficult to reduce by passive measures. Therefore, extensive work has been conducted on active noise control using loudspeakers as secondary sources and microphones as error sensors. In addition, new control techniques have been investigated applying structural actuators for controlling the structural fuselage modes coupling to the critical acoustical modes. The present paper demonstrates the feasibility of using the new structural actuator technique in turboprop aircraft. Multiple piezoceramics have been attached to the structure of the Acoustic Test Cell (ATC) based on the Dornier 328 turboprop aircraft. The ceramics are driven according to a theoretical optimization process based on measured transfer functions. Noise reduction for the first three BPFs has been calculated and measured for different piezo configurations. The achieved results are compared and discussed. It is shown that the new technique of active vibration control is a powerful tool not only to control vibrations but also to significantly reduce the interior noise levels in modern turboprop aircraft.

Session 4aSAb
International Workshop on Active Noise and Vibration Control

Structural Acoustics and Vibration: Active Noise Control in Enclosures

Leonardo Lecce, Cochair
Instituto de Piogretto Velivolli, University de Napoli, Via Claudio 21, 80125 Napoli, Italy

Paul J. Remington, Cochair
BBN Systems and Technologies, 70 Fawcett Street, Cambridge, Massachusetts 02138, USA

Invited Papers

8:00

4aSAb1. Developments in active control of aircraft interior noise—Directions for tonal and broadband noise sources. Richard J. Silcox (Structural Acoust. Branch, NASA Langley Res. Ctr., M.S. 463, Hampton, VA 23681-0001, r.j.silcox@larc.nasa.gov)

Aircraft interior noise is a continuing problem for a wide range of aircraft types. Interior noise levels in general aviation aircraft make communication difficult, significantly impact pilot endurance, and are considered important to the reemergence of this class of aircraft. For passengers in propeller-powered commuter aircraft, conversation is difficult at best and becomes oppressive on the passengers for long periods. It is also regarded as one reason for the replacement of propeller commuter aircraft by the emerging regional jet. In business jets, the passengers are often interested in conducting meetings during flights. This calls for low SPL and SIL for which the aircraft incurs both space and weight penalties. Large commercial aircraft pay a significant weight penalty for current interior noise levels considered acceptable. With the drive for more weight-effective airframes, the challenge becomes even more difficult. This paper will show some current efforts to develop more efficient active control technologies for both tonal noise sources and broadband noise sources. These will include improvements in controller technologies, actuator implementation, optimization of transducer topology, improved coupling to the noise source, and integration of the active technology with conventional passive technology.

8:20

4aSAb2. Active noise and vibration control for a high-speed railcar: Rolling rig measurements. Rolf Schirmacher (Müller-BBM GmbH, Robert-Koch-Straße 11, D-82152 Planegg, Germany, schi@mbbm.de), Georg Hölzl (Deutsche Bahn AG, D-80939 München, Germany), and Joachim Scheuren (Müller-BBM GmbH, D-82152 Planegg, Germany)

The feasibility of active noise and vibration control (ANVC) of the low-frequency interior noise (around 100 Hz in the case presented) of a high-speed railcar is studied. The car chosen for this study is the first generation of the German Intercity Express (ICE) trains. Based on the design of the car, the bogie, and the bogie/car body interface, an active control system combining some aspects of active vibration isolation and active structural acoustic control was proposed and studied by model experiments and simulations [Schirmacher *et al.*, Proc. Active **97**, 557–564]. Based on these results, an active system with four actuators fitting into the secondary suspension was installed at one bogie, and the whole railcar was tested at the rolling rig of Deutsche Bahn in Munich. Test drives on the rig cover speeds up to 250 km/h with and without railway line track simulation. For wheel harmonics in the critical frequency range, global sound-level reductions of more than 12 dB have been achieved in the whole passenger compartment, with peaks of more than 20 dB at single passenger seats. For dominant wheel harmonics, global reductions of 6–8 dB can be expected, averaged over the whole passenger compartment.

8:40

4aSAb3. Two unique approaches for actively controlling the interior acoustic response of a cylindrical aircraft enclosure using active constrained layer damping and end actuation. Peter C. Herdic,[a] Brian H. Houston (Naval Res. Lab., Code 7136, Washington, DC 20375), and Amr M. Baz (Univ. of Maryland, College Park, MD 20742)

Experimental results are reported involving the use of 12 active constrained layer damping (ACLD) patches instrumented on a fuselage section under radial point excitation. ACLD utilizes an active piezo film constraining layer over a viscoelastic layer to increase damping and apply restoring moments. Results reported to date showed that performance was achieved both in the reduction of the interior acoustic response and of the structural vibratory response. A more detailed analysis is reported here of the uncontrolled/controlled structural acoustics derived from high spatially sampled surface velocity and interior pressure measurements. A second control approach is reported where interior acoustic levels are reduced by control of the efficient end cap coupling to the interior by placing control actuators on each end. Analytic and numeric models are used to identify three dominate interior acoustic mechanisms: (1) a forced response on the interior by purely structural modes, (2) purely normal acoustic cavity modes, and (3) mixed structural/acoustic modes. Numeric control ''experiments'' are reported where both interior acoustic minimization and end-constraint control

laws are employed. Good performance was found and discussion will involve the effectiveness of the control laws on each of these mechanisms. [Work supported in part by NASA, Langley.] [a] Also SFA, Inc.

9:00

4aSAb4. The reduction of structure-borne road noise by active noise and vibration control. Paul Sas (Katholieke Univ. Leuven, Dept. of Mech. Eng., Celestijnenlaan 300B, B-3001 Heverlee, Belgium) and Wouter Dehandschutter (Lernout & Hauspie Speech Products, B-1780 Wemmel, Belgium)

In this work, the feasibility of active structural and acoustic control of structure-borne rolling noise in a passenger car is demonstrated. A full vibroacoustical analysis of the demonstrator vehicle was carried out, in order to characterize fully the on-road behavior (coherence analysis, operational force analysis, and transfer path analysis), as well as to derive the necessary input/output models. The results of these analyses have been used as input for the actuator design and the control configuration determination (reference signals, actuator number and location, feedback signal determination). Different control configurations have been investigated and tested by means of numerical simulations and laboratory tests. Two control configurations, each using a different kind of control source, have been retained: a structural acoustic control system which works with six inertial shakers positioned at the main vibration transmission paths of the car suspension, and an antinoise system with four loudspeakers inside the cabin. A new inertial actuator based on the moving coil work principle has been designed and realized. A broadband control system based on an adaptive feedforward control system using six reference signals, 6/4 actuators (ASAC/ANC), and four error signals has been implemented and tested in the demonstrator car.

Contributed Papers

9:20

4aSAb5. Active noise control in aircraft cabins. Colin F. Ross (Ultra Electron. Ltd., Noise & Vib. Systems, 1 Cambridge Business Park, Cowley Rd., Cambridge CB4 4WZ, England, Colin.Ross@ultranvs.co.uk)

There is significant interest from the aircraft industry to reduce the noise and vibration levels in aircraft cabins. In the last 5 years, active noise and vibration control systems have been introduced and have been shown to have transformed the environment of turboprop aircraft. These systems have provided significant reductions in cabin noise and vibration and further improvements are being sought. Tonal noise control was the most important objective and also the easiest to implement. Further improvements in the reduction of propeller and engine tones can be achieved, but the focus is beginning to shift to the control of broadband noise. This paper will review the performance of current systems and identify the areas where improvement will be required to meet the industrial objective. It will also review the available technology and identify the areas which are most likely to be successful with the practical constraints of an aircraft environment.

9:40

4aSAb6. Adaptive road noise cancellation for a midclass estate car. Uwe Letens (Daimler-Benz AG, Stuttgart, Germany, Uwe.Letens@PCD.Daimler-Benz.com), Gregor Koners (Daimler-Benz AG, Stuttgart, Germany), and Timothy J. Saunders (Lotus Eng., Norwich, UK)

It is well known that estate cars (in the US called ''station wagon'') tend to be sensitive to low-frequency vibration input caused by the stochastic macrostructure of the road surface. This may result in a strong low-frequency acoustic excitation within the passenger cabin which is subjectively felt to be uncomfortable. As a feasibility study an ANC system has been installed into an experimental car. The aim was to show the potential for a reduction of the unpleasant noise. To begin, an investigation of the vibrational behavior of the chassis was performed. Within the critical frequency range there were only a few dominant principal components that could be extracted. As primary sensors for a feedforward ANC system accelerometers have been mounted at positions on the axles, giving a maximum of multiple coherence coupled with the cabin noise. A PC-based data acquisition and processing system has been used to set up the ANC system which feeds loudspeakers as secondary sources for cancellation in the cabin. Adaption is maintained by error microphones installed into the headliner of the cabin. The resultant reduction of the road noise provides a considerable enhancement in the noise comfort of the estate car.

10:00–10:20 Break

10:20

4aSAb7. Active noise control experiences on a GT high-speed car. Antonio Sollo, Antonio Paonessa (Alenia Aerospace, Aeronautic Div., Viale dell'Aeronautica-80038 Pomigliano d'Arco, Naples, Italy), Leonardo Lecce, and Massimo Viscardi (Univ. of Naples ''Federico II,'' 80125 Naples, Italy)

The presentation will show some results of an extensive experimental work aimed at the reduction of the engine noise inside the binnacle of a GT high-speed car. The car is completely made by carbon fiber and the engine is rigidly attached to the body and for this reason the vibrations of the engine are directly transmitted inside the binnacle, thus producing very high noise levels in all the oeprating conditions. Preliminary laboratory experiments were made by simulating the noise in the cavity by means of different loudspeakers and a first configuration of the ANC system was optimized. This last included some speaking panels driven by several piezoceramic patches elastically suspended from the roof. The laboratory results were encouraging, and the measured noise reductions were sensible even if the simulated primary field was scaled down due to the nonlinear behavior of the speaking panels at high driving voltages. The second step of the work consisted in optimizing a second configuration of the ANC system which was using two control microphones for each seat and two loudspeakers for each seat, located near passenger heads. The control unit was capable of following seven different engine orders and thus following the rapid changes of the noise field. The results were impressive and very good noise reductions have been measured on the road at different operative conditions (both stabilized and in acceleration).

10:40

4aSAb8. Active control of enclosed sound fields via impedance changes. Marie-Annick Galland, Olivier Lacour (LMFA, Ecole Centrale de Lyon, BP 163, 69131 Ecully Cedex, France), and Denis Thenail (LMS Numerical Technologies, Leuven, Belgium)

The potentialities of active strategies based on boundary condition control are investigated for globally reducing the noise in cavities. Two active systems previously developed [Furstoss, Thenail, and Galland, J. Sound Vib. **203**, 219–236 (1997)] are exploited in order to assign the most suited wall impedance for noise reduction: the first is referred to as ''direct'' control and permits precise realizations for harmonic excitations, the second is a hybrid passive/active feedback control well suited for random noise treatments. Experimental analysis and numerical developments are conducted on a rectangular three-dimensional cavity closed by a simply supported elastic plate. Noise is generated by an external load applied to the plate. Different impedance values are successively assigned, and their effect is estimated on the global sound-level reduction. Attention is also given to plate vibration changes, which may occur. Different typical behaviors of the plate-cavity system are first investigated for harmonic excitations. The hybrid control system appears to be a good compromise for all cases, and shows promising behavior when dealing with broadband excitations.

11:00

4aSAb9. Active noise control procedures in a generic composite helicopter cabin. Frank Simon and Simone Pauzin (ONERA/CERT-BP 4025, 2, avenue Edouard Belin, 31055 Toulouse Cedex 4, France, Franck.Simon@onecert.fr)

Composite materials are used more and more in the helicopter domain, instead of metal structures, which leads toward a degradation of the acoustic comfort in the cabin because of the decreasing mass and low performances of composites. So, active control procedures can be used in addition to passive treatments. The paper deals with the feasibility of active noise control procedures in order to reduce the radiated noise generated in a composite helicopter cabin, through the mechanical deck. A generic composite fuselage is excited by four shakers to simulate the noise produced by the four gear box fastenings. Four decorrelated random signals are generated to produce forces equal to about 1 N into the 500–3000 Hz band. Modal analysis and structural intensity measurements are achieved on the mechanical deck, and pressure fields are acquired in two parallel planes. Moreover, theoretical acoustic modes of the cavity are computed with a FEM model. These different data allow one to analyze the structural behavior of the mechanical desk and the structure–cavity coupling. Four piezoelectric actuators, located in front of the excitations, are controlled by feedforward algorithms to reduce the pressure fields with different types of error sensors and cost functions.

11:20

4aSAb10. An active approach to interior noise reduction for a modern electrical locomotive. M. Viscardi, M. Fontana (Active Srl., Piazza Garibaldi, 3, 80142 Napoli, Italy), A. Vecchio (Università di Napoli ''Federico II,'' 80125 Napoli, Italy), B. Mocerino (Ansaldo Trasporti, 80100 Napoli, Italy), and L. Lecce (Università di Napoli ''Federico II,'' 80175 Napoli, Italy)

The present work deals with the noise measurement and characterization inside the cabin of an electric locomotive and the first results of an active control approach aimed at noise suppression to improve the acoustic comfort of drivers during the service. Characterization of each single source contributing to the measured overall level has at first been performed on an experimental basis, through a set of microphones located inside the cabin and directly near the main sources at the engine cooler fan, the air conditioning system, and also, during travel, on the exteriors to measure the airborne and the rail–wheels contact noise. During this stage the engine cooler fan has been identified as the main source strongly contributing to increase the noise level in the cabin. First experimental activities have so been planned and performed to assess an active noise control system reducing the annoyance on this last source. Technical reasons have pushed to prefer a system directly working on the acoustic interior more than at the noise source, mainly based on loudspeakers and microphones distributed in the cabin. By the use of active digital filters some of the tonal peaks presented in the noise spectra were so suppressed in the range 0–1000 Hz, producing an overall noise reduction in the band of 5 dB for both seats.

11:40

4aSAb11. A multichannel active system for control of the booming inside a van. Teresa Bravo, Pedro Cobo (Instituto de Acustica, CSIC. Serrano 144, 28006 Madrid, Spain, iacpc24@fresno.csic.es), and Juan Manuel Martin (Nissan European Technol., Ctr.-Espaa (NECT-E), 08040 Barcelona, Spain)

The van under study presents a problem of booming when the engine periodic noise excites some low-frequency modes of the cabin. The aim of this work is the design and implementation of a multichannel active system to alleviate this problem. First, a reference signal is searched correlated with the noise measured by a microphone in the driver head position. The best reference signal is the longitudinal vibration picked up by an accelerometer under the differential group. Then, the acoustic field inside the van is modeled by the normal modes theory. Optimization by simulated annealing allows one to find the best locations for six loudspeakers and six microphones. Finally, the multichannel active noise control is implemented by using a commercial system. Measurements of noise reduction have been carried out in the semianechoic room at NECT-E under usual driving conditions (third gear, slow acceleration). [Work supported by CICYT, Project AMB97-1175-C03-01.]

Session 4aSCa

Speech Communication: Parameters of *F*0 Contours

Bernd Möbius, Cochair
Bell Labs, Lucent Technologies, 600 Mountain Avenue, Murray Hill, New Jersey 07974-0636, USA

Thomas Portele, Cochair
IKP, University of Bonn, Poppelsdorfer Allee 47, 53115 Bonn, Germany

Chair's Introduction—10:15

Invited Papers

10:20

4aSCa1. Modeling the alignment of fundamental frequency contours. Jan P. H. van Santen and Bernd Möbius (Bell Labs, Lucent Technologies, 600 Mountain Ave., Rm. 2D-431, Murray Hill, NJ 07974)

Segmental factors can cause large temporal changes in local fundamental frequency (F_0) movements associated with accented syllables (''accent curves''), but these changes are often not phonologically or perceptually significant. Yet, other factors can cause temporal changes that are smaller but nevertheless significant. A model is proposed according to which accent curves are (phonologically, perceptually) equivalent when they are generated from a common accent curve template using a common set of alignment rules. These alignment rules specify where the points making up the template are to be placed on the time axis, based on the durations of the segments in the syllable sequence with which the accent curve is associated. This model is shown to provide a detailed and accurate account of alignment of accent curves over a wide range of segmental configurations. The model is embedded in a superpositional framework, in which accent curves, segmental perturbation curves, and phrase curves are combined to account for complicated surface F_0 contours. Height of accent curves is determined via a multiplicative model from factors related to prominence and position in the phrase.

10:40

4aSCa2. Measuring perceptual equality. Thomas Portele (IKP, Univ. of Bonn, Bonn, Germany)

When performing *F*0 stylizations and parametrizations in order to establish the essential parts of an *F*0 contour, it is necessary to assess the similarity between original and stylized contours. The most reliable method is a perceptual assessment, which means in its most severe form that no differences are perceptible between original and resynthesized versions. Such tests have a number of possible influences (resynthesis quality, auditory storage, whether or not perceptible diffences are included), and they are tedious and time-consuming, as will be exemplified by results obtained in the evaluation of this maximum-based description. Computational comparisons, on the other hand, are unable to mirror human perception, because it is well known that small differences in the acoustic domain may be perceived while larger differences may pass unnoticed. The mean difference, as measured by some researchers, is problematic, because the goal of stylization is to abstract away from unimportant features. A successful stylization is perceptually equal to the original but has a large mean difference caused by successful abstraction. The current limited knowledge of pitch perception and interpretation requires perceptual tests to evaluate stylization quality.

11:00–11:20 Discussion

11:20

4aSCa3. Comparing two different principles of parametric F_0 modeling. Gregor Möhler (Inst. of Natural Lang. Processing, Univ. of Stuttgart, Azenbergstr. 12, 70174 Stuttgart, Germany)

A number of data-based approaches to intonation modeling represent F_0 movements using continuous parameters [P. Taylor, Proc. ESCA/IEEE Workshop on Speech Synthesis, Monhonk, NY (1994), pp. 175–178; G. Möhler, Ph.D. Thesis, University of Stuttgart, Stuttgart, Germany, 1998]. This is contradictory to most intonation theories, which suggest that intonation can be modeled with a set of distinct phonological entities that are phonetically realized as F_0 movements (e.g., J. Pierrehumbert, Ph.D. Thesis, MIT, Cambridge, MA, 1980). This principle has rarely been incorporated into data-based intonation modeling. In this study two data-based intonation models are compared following the two principles described above. The models are trained on the male speaker of the German news corpus. The first approach uses an F_0 parametrization with six continuous parametric intonation event (PaIntE) parameters. These parameters are derived by approximating the F_0 curve with an appropriate model function. In the second model, a vector quantization (VQ) is applied to the PaIntE parametrization, resulting in a number of distinct F_0 shapes. CART trees are used for predicting both the PaIntE parameters and the VQ code words from a set of features derived from the respective utterance. The intonation quality was assessed and it was found that the VQ model has advantages over the PaIntE model, because the curve as a whole can be predicted, rather than individual parameters. Furthermore, phonetic analysis can be based on the basic shapes represented in the code book.

11:40

4aSCa4. Analysis and synthesis of *F*0 contours by linear prediction coding. Joachim J. Mersdorf and Kai U. Schmidt (Inst. of Commun. Acoust., Ruhr Univ. 44780, Bochum, Germany)

At present, there is still a lack in integrated methods for automatic analysis, coding, prediction, and generation of *F*0 contours. The use of linear prediction coding could be a first step in that direction [Mersdorf *et al.*, ESCA Tutorial and Research Workshop on Intonation: Theory, Models and Applications, 235–238 (1997)]. The approach allows an automatic extraction of different parameters (e.g., accents) from intonation contours by means of appropriately simplified residual functions using rectangles. Such a signal approximation can be regarded as an excitation signal for prosodic accents and sentence mode. In that source-filter approach [cf. H. Fujisaki, in *The Production of Speech* (Springer-Verlag, New York, 1983), pp. 39–55] the resulting filter coefficients can be interpreted either as physiological parameters or as individual features in the intonation shape. The method was developed for both prosodic data analysis and acoustical contour resynthesis. Its structure is easy to describe and allows a very simple editing and modifying by shifting position, length, and height of typical rectangles. Furthermore, accents can be detected automatically at positions where the sign of the approximated rectangles changes. Perceptual evaluation indicated that the approximated and resynthesized *F*0 contours sound very natural.

12:00–12:20 Discussion

THURSDAY MORNING, 18 MARCH 1999 POSTER GALLERY, 8:00 A.M. TO 12:00 NOON

Session 4aSCb

Speech Communication: Potpourri of Speech Production, Speech Disorders, Auditory Feedback and Other Fascinating Topics (Poster Session)

Joseph S. Perkell, Chair
Research Laboratory of Electronics, Massachusetts Institute of Technology, 50 Vassar Street, Cambridge, Massachusetts 02139, USA

Contributed Papers

All posters will be on display in the Poster Gallery from Thursday to Friday, 18–19 March. All authors will be at their posters on Thursday 18 March. Contributors of odd-numbered papers will be at their posters from 8:00 a.m. to 10:00 a.m. and authors of even-numbered papers will be at their posters from 10:00 a.m. to 12:00 noon.

4aSCb1. The effect of reduced tonal space in Parkinsonian speech on the perception of Cantonese tones. Patrick C. M. Wong and Randy L. Diehl (Dept. of Psych., Univ. of Texas, Austin, TX 78712, pcmwong@ccwf.cc.utexas.edu)

Wong and Diehl [J. Acoust. Soc. Am. **104** (1998)] showed that subjects' perception of Cantonese level tones involves the assessment of the distance between the extreme fundamental frequency (*F*0) values in the carrier sentence and the *F*0 of the target syllable (''the extreme-target distance''). Listeners were best able to identify the tone when this distance was relatively large. This is true regardless of whether the carrier sentence is in English or Cantonese. However, only synthesized speech stimuli were used in that study. The present study used Parkinsonian speech stimuli. Because the speech of Parkinson's Disease (PD) patients is monotonal, it naturally forms a reduced tonal space (the ratio between the speaker's highest speaking *F*0 to the lowest), and thus the extreme-target distance should also be reduced. The results of the study confirmed the Wong and Diehl findings with natural PD speech, and showed that in addition to the extreme-target distance, the tonal space among the target tones themselves also affects tone perception; the smaller the tonal space, the worse the perception. Relation between misperception and tonal contours will also be discussed. [Work supported by NIDCD.]

4aSCb2. Comparing materials for the evaluation of symptom severity in the read speech of spasmodic dysphonia patients. Masanobu Kumada (Haskins Labs., 270 Crown St., New Haven, CT 06511 and Dept. of Physiol. I, Natl. Defense Med. College, Tokorozawa, Japan, kumada@haskins.yale.edu), Fredericka Bell-Berti (St. John's Univ., Jamaica, NY and Haskins Labs.), and Douglas N. Honorof (Yale Univ., New Haven, CT and Haskins Labs.)

Reliability and validity of evaluation methods for assessing the degree of severity of spasmodic dysphonia (SD) symptoms have become a matter of concern for voice specialists. With the syllable method [M. Kumada *et al.* (1997)], overall degree of severity is represented by the proportion of impaired syllables. This method has shown promise for English, though it appears to work better for evaluating prose read aloud than for evaluating the recitation of sequences of cardinal numbers, because inappropriate pauses are more easily identified in prose. The present study aims to compare types of English prose according to their tendencies to reveal SD symptoms. Specifically, audio recordings of seven patients reading Fairbanks Rainbow Passage are evaluated by five voice professionals, as are audio recordings by the same patients of sentences in which tempo is expected to be highly predictable and thus, by hypothesis, potentially more stable for purposes of cross-speaker comparison. These sentences are constructed entirely of stressed monosyllables. If the phonatory dysfunction observed correlates with disturbances to so-called stress-timing patterns

[K. L. Pike, *Intonation of American English* (Ann Arbor, 1945)], sequences of stressed monosyllables would be expected to be especially useful in the evaluation of SD.

4aSCb3. Perceptual rating and acoustic analysis of tracheo-esophageal voice. Joost M. Festen and Irma M. Verdonck (Dept. of Otolaryngol., Univ. Hospital VU, P.O. Box 7057, 1007 MB Amsterdam, The Netherlands, jm.festen@azvu.nl)

Perceptual analysis of tracheo-esophageal (TE) voice shows a large variability among listeners and is time consuming. Therefore, an acoustic analysis procedure has been developed that can handle these often very irregular signals. The analysis is based on moderate, comfortable, and strong phonations of a sustained vowel /a/ and includes sound-pressure level, fundamental frequency, frequency stability, spectral shape, and other measures. As an evaluation of the acoustic analysis an experiment was conducted to collect perceptual ratings for the same phonations. Ratings were given by naive listeners on scales like pitch, noisiness, strength, and deviance. Relations between the acoustic parameters and the perceptual evaluation will be discussed.

4aSCb4. Assessment of BOTOX effects on adductor spasmodic dysphonia using LTAS-guided analysis. Eugene H. Buder, Michael P. Cannito (School of Audiol. and Speech-Lang. Pathol., The Univ. of Memphis, 807 Jefferson Ave., Memphis, TN 38105, ehbuder@memphis.edu), Merlin Taylor (Univ. of Mississipi, University, MS), Gayle E. Woodson (Univ. of Tennessee–Memphis, Memphis, TN), and Thomas Murry (Univ. of Pittsburgh, Pittsburgh, PA)

Connected speech samples from 17 women with adductor spasmodic dysphonia before and one month after unilateral botulinum toxin (BOTOX) injection of the thyroarytenoid muscle were analyzed using long-term averaged spectra (LTAS). Respiratory noises were removed prior to analysis but consonants were not. Prior LTAS research on this disorder before and after unilateral recurrent laryngeal nerve resection [K. Izdebski, Acta Otolaryngol. **97**, 373–378 (1984)] predicts similar strengthening of lower-frequency harmonics and weakening of upper-frequency harmonics following chemodenervation using BOTOX. Pre- to post-treatment differences between standardized spectral magnitudes in LTAS frequency bins below 5 kHz revealed these effects for BOTOX treatment. Repeated measures ANOVA indicated a significant treatment-by-frequency band interaction (p less than 0.001). Discriminant analysis yielded 79% overall classification success for pre/post treatment conditions using only four frequency bands of approximately 250 Hz width, one in the $f0$ region and three in the 1–3 kHz region. These results support the hypothesized treatment effect. Furthermore, the LTAS-based discriminations motivated case-by-case analyses of harmonic magnitude measures. For example, examinations of relative magnitudes of first harmonics and formant-excited harmonic groups further our understanding of differing treatment effects on individual voices. [Work supported by NIH.]

4aSCb5. Linear and nonlinear responses to speech rate in left and right temporal cortex. Richard Wise, Dale Bailey, Alex Leff (MRC Cyclotron Unit, Hammersmith Hospital, London W12 0NN, UK, richard@wren.rpms.ac.uk), and Sophie Scott (MRC CBU, Cambridge CB2 2EF, UK)

Aspects of speech processing in the temporal lobes were investigated in a functional neuroimaging study using a parametric design, where the rate of hearing single words was varied. A previous study distinguished regions in left and right temporal cortex where activity varied linearly with rate (up to 90 wpm) from a single region, in the left posterior temporal cortex, where activity was maximal at 10 wpm [Price *et al.*, Neurosci. Lett. **146**, 179–82 (1992)]. A fMRI study of left and right primary auditory cortex (PAC) and posterior dorsolateral temporal cortex [Dhankhar *et al.*, J. Neurophysiol. **77**(1), 476–483 (1997)] showed a decline in activity at rates above 90 wpm. In the current PET study, speech rate was varied up to 180 wpm, and the consequent curves in activity were investigated for the shape of the consequent nonlinearity in activity. These curves are described and related to hypothesized hemisphere specialization in speech processing. This result raises important issues about the responsiveness of the auditory system in relation to the rate at which it can process speech input.

4aSCb6. A functional neuroimaging comparison of the neural processing of speech and signal correlated noise. Sophie Scott (MRC CBU, 15 Chaucer Rd., Cambridge CB2 2EF, UK), Richard Wise (Hammersmith Hospital, London W12 0NN, UK), Cath Mummery, and John Ashburner (Inst. of Neurology, London WC1N 3BG, UK)

Functional neuroimaging affords unique insights into the neural activity of intact human brains. In previous studies, presenting speech to subjects without an explicit task demand (so-called ''passive'' listening) produced strong activations in bilateral dorsolateral temporal cortex (DLTC) that is both extensive and symmetrical [Wise *et al.*, Brain **114**, 1803–1817 (1991)]. Thus such results support the hypothesis that the DLTC of both hemispheres is involved in the acoustic and phonological processing of speech. This is contradictory to conventional understanding that the left temporal lobe, particularly Wernicke's area, is responsible for speech identification and recognition. A study using positron emission tomography was performed which aims to contrast speech processing with a similarly complex signal; speech- and signal-correlated noise analog were presented in a listening task. Correlations specific to speech stimuli were located symmetrically in anterior regions of both superior temporal sulci. The only asymmetry waas a left-lateralized response to speech in the posterior superior temporal sulcus, corresponding closely to structural asymmetry on the subjects' magnetic resonance images. These results are discussed in relation to the role of the right hemisphere in recovery of speech comprehension after left hemisphere-damage.

4aSCb7. Brain function in spasmodic dysphonia: A functional MRI study. Masanobu Kumada (Haskins Labs., 270 Crown St., New Haven, CT 06511 and Dept. of Physiol. I, Natl. Defense Med. College, Tokorozawa, Japan, kumada@haskins.yale.edu), Einar Mencl, Kenneth R. Pugh (Yale Univ. School of Medicine, New Haven, CT and Haskins Labs.), R. Todd Constable (Yale Univ. School of Medicine, New Haven, CT), Fredericka Bell-Berti (St. Johns Univ., Jamaica, NY and Haskins Labs.), Douglas N. Honorof (Yale Univ., New Haven, CT and Haskins Labs.), and Vincent L. Gracco (Haskins Labs.)

The symptoms of spasmodic dysphonia (SD) are caused by the hyperadduction or hyperabduction of the vocal folds, but its mechanism is unknown. The purpose of this study is to locate dysfunctional regions in the brains of SD patients by functional MRI (fMRI) and to identify the mechanism of this disorder. The extrapyramidal system works normally as a stabilizer of muscle activities. This hypothesis is that its dysfunction (especially in the basal ganglia and brainstem) causes instability of the activity of the vocalis muscle which induces symptoms (voice break, etc.). The data for four normal subjects have been obtained, and sessions for four SD patients are planned. The tasks are: isolated phonations of /a/ in chest register (Ch); isolated phonations of /a/ in falsetto register (Fa); and breathing naturally for baseline (Br). Subjects phonate in Ch and Fa to visual cues given every 2 s. Each scan consists of nine 20-second blocks of tasks (2 Chs, 2 Fas, 5 Brs), and is repeated four times with counterbalanced task order. Imaginary phonation scans for Ch and Fa, in which subjects just imagine phonation without actually setting the vocal cords into vibration, are also repeated four times.

4aSCb8. Attention to auditory feedback during sentence production by speakers with and without stuttering. Dragana Barac-Cikoja (Gallaudet Univ., Washington, DC and NIDCD, Bethesda, MD), Shrita Squire, and Christy L. Ludlow (NIDCD, Bethesda, MD)

As participants repeated a target sentence, their speech was processed in real time and fed back through the headphones either (a) unaltered, (b) spectrally altered to simulate alien origin, or (c) replaced by a recording of the target sentence triggered by the participant's speech. White noise from bone conduction maskers, in addition to the speech from the headphones, masked air-conducted speech. Gaps 100-ms long were randomly inserted in speech feedback to participants as they uttered each sentence. Detection accuracy was compared across a group of fluent speakers and a group of people with mild to moderate stuttering. Error rates for each of the three feedback conditions were calculated across six repetitions of the five target sentences. While the incidence of errors was higher in the group with stuttering, the pattern of errors was the same for both groups: misses (undetected gaps) prevailed in the unaltered feedback condition; and false alarms (incorrect gap identifications) predominated under alien feedback conditions (i.e., the spectrally altered and the replaced speech). The role of voice familiarity in speech monitoring will be discussed.

4aSCb9. Effect of target source and dynamics on voice *F*0 stability in the presence of auditory feedback pitch perturbations. Theresa Burnett and Charles Larson (Dept. of Commun. Sci. and Disord., Northwestern Univ., 2299 N. Campus Dr., Evanston, IL 60208)

The quickness with which a motor system recovers from an unanticipated perturbation is an indication of its stability. This principle was examined with regard to the voice *F*0 control system and auditory feedback. Trained singers sang a steady note or an upward glissando, either from memory or by tracking a synthesized tone. At an unanticipated time during phonation, the singers' auditory feedback pitch was ''flattened'' by 1 semitone for a period of 100 ms, creating an effect similar to that which would be heard during a production error. All singers produced voice *F*0 changes in response to the auditory perturbations, and many of these voice *F*0 changes were oscillatory in nature. The number of oscillations and the speed with which they were dampened were measured and compared across the different types of vocal productions (steady note versus glissando) and across the different target sources (pitch memory versus synthesized tone). Results indicate that voice pitch stability varies with the nature of the target.

4aSCb10. Rapid changes in speech parameters with a change in auditory stimulation from a cochlear implant. Joseph Perkell (M.I.T.-R.L.E., Rm. 36-591, 50 Vassar St., Cambridge, MA 02139, perkell@speech.mit.edu), Lekisha Jackson (Anderson Consulting, Houston, TX), Majid Zandipour, Jennell Vick, Harlan Lane, and Melanie Matthies (M.I.T.-R.L.E., Cambridge, MA 02139)

To investigate the speed of speech production changes in response to a change in hearing, the speech processors of two cochlear implant users were switched on and off a number of times in a single experimental session for each subject. The subjects repeated short utterances (''a said,'' ''a shed,'' ''a sad,'' and ''a shad'') many times in semi-random order. The transitions between hearing (on) and nonhearing (off) states were timed to occur between utterances, and the number of utterances between transitions was varied to minimize subject anticipation of the change. Using transition times as line-up points, values of median and skewness of sibilant spectra and vowel *F*1, *F*2, duration, and SPL were each averaged over repetitions of each utterance and compared across the on–off and off–on transitions. Vowel SPL and duration had changed by the first utterance following the transition, indicating that the subjects were using subtle aspects of the processor output to detect its state even in the absence of overt sound input. Changes in spectral median and skewness and *F*1 and *F*2 were less immediate, more varied, and differed between the two subjects. The paradigm is currently being refined to further investigate this issue. [Work supported by NIH.]

4aSCb11. A longitudinal investigation of formant frequency development in childrens' speech production. Bruce L. Smith, Mary Kay Kenney, and Jana Sobecks (Dept. of Commun. Sci. and Disord., Northwestern Univ., 2299 N. Campus Dr., Evanston, IL 60208-3570)

While cross-sectional/group investigations provide important findings about the development of speech production, such studies do not furnish details regarding the development of individual children across time. However, such information is necessary for understanding childrens' speech production development more thoroughly and for evaluating, from a somewhat different perspective, ideas that have been proposed on the basis of cross-sectional findings. In the present study, four subjects were recorded at approximately one-year intervals for four to six years as they produced about 20 repetitions (per session) of each of several target stimuli; three of the children were approximately $1\frac{1}{2}$ years old at the onset of the study, and the other was about 4 years of age. Measurements of *F*1 and *F*2 for three different vowels for all four children showed some patterns supporting the general notion that formant frequencies tend to decrease with increased age. However, there were also a number of instances in which a particular child's formant frequency values showed little or no change across the entire 4–6 years. These longitudinal data suggest that childrens' formant frequency values do not necessarily decrease in a consistent fashion with increases in age and physical size.

4aSCb12. Acoustical correlates of near-term suicidal risk. Aslı Özdaş, Richard G. Shiavi, D. Mitchell Wilkes (Dept. of Elec. Eng., Vanderbilt Univ., Box 1824, Station B, Nashville, TN 37235), Marilyn K. Silverman, and Stephen E. Silverman (Vanderbilt Univ., Nashville, TN 37235)

In the course of many years of clinical work in emergency rooms and office consultation with suicidal patients, clinicians have often successfully predicted suicidality based on the vocal patterns of the patients, independent of the content. Vocal sound and clinical substance reciprocally augmented each other in determining the near-term risk [M. K. Silverman and S. E. Silverman, ''From sound to silence: A preliminary investigation of the use of vocal parameters in the prediction of near-term suicidal risk,'' submitted to J. Med. Psychotheraphy]. Vocal patterns heard as representing a ''hollow,'' ''toneless'' sound were designated unanimously as the most compelling feature in suicidal voices. Motivated by qualitative descriptions of experienced clinicians, a quantitative study was carried out that investigated the acoustic correlates of near-term risk. The audio tapes selected for this research were suicide notes left on tapes donated by survivors, recordings of several patients who had been hospitalized, and recordings of 911 suicide in progress calls. This research is concerned with realistic speech data encountered in real-life situations due to the inability to study suicidal behavior in any kind of controlled setting. To compensate for spectral variability introduced by different recording environments, robustness techniques such as long-term mean removal and frequency warping were utilized. The relative significance of resonant frequencies and frequency bands in terms of their ability to predict the near-term suicidal risk was evaluated. Preliminary results suggest that the frequency spectrum patterns of the suicidal voice may have utility in the assessment of near-term risk.

4aSCb13. Classroom acoustics and vocal efficiency. David Canning (City Univ., London EC1V OHB, UK, d.canning@btinternet.com), Allen Hirson (City Univ., London EC1V OHB, UK), and Paul Arnold (Manchester Univ., Manchester, UK)

The modern school classroom predicated upon the premise that effective vocal communication can take place. Such communication depends upon intact processes of speech production and reception. Numerous studies have demonstrated the inadequate acoustic conditions of classrooms and the impact of this situation on the reception of speech. A smaller number of studies indicate high levels of vocal damage within the teaching profession. This study examines the vocal efficiency of teachers in classrooms before and after acoustic treatments of the teaching space. The paper will present acoustic measurements of the teaching voice with and

without amplification and in acoustically treated and untreated classrooms. The impact of both physical and electro-acoustic modifications will be presented. [The authors gratefully acknowledge the support of Luton Unitary Education Authority's Service for the Hearing Impaired, facilities of the Speech Acoustics Laboratory at City University, and the support of BioAcoustics Ltd. UK.]

4aSCb14. Cross-modal integration in speech and nonspeech tasks. Janet M. Weisenberger and Sandra M. Kreidler (Speech and Hearing Sci., Ohio State Univ., Columbus, OH 43210, jan+@osu.edu)

Studies of audiovisual speech perception show that both modalities contribute to the speech perception process. One salient example of this is the McGurk effect, in which visual /ga/ and auditory /ba/ might produce the fused percept of /da/. The present study investigated whether similar multimodal integration occurs for tactile–visual presentation via tactile speech perception devices, and whether these integration effects are specific to speech, or can also occur for nonspeech stimuli. The first experiment tested visual, auditory, tactile, and multimodal presentation of speech and nonspeech stimuli. Results indicated McGurk-type integration effects for both audiovisual and tactile–visual speech tokens, as well as some evidence of similar effects for nonspeech stimuli. Overall levels of tactile–visual integration were lower than audiovisual levels, possibly because of minimal subject training with the tactile aid. A second experiment provided two months of tactile aid training prior to integration testing. Preliminary results show an increase in McGurk-type integration for tactile–visual presentation. Overall findings suggest that the integration process is not restricted to audiovisual presentation. [Work supported by NIH.]

4aSCb15. Contribution of articulatory kinematics to visual perception of stop consonants. Michael D. Hall (Psych. Dept., Univ. of Nevada Las Vegas, 4505 Maryland Pkwy., Box 455030, Las Vegas, NV 89154-5030, hallm@nevada.edu), Jordan Green, Christopher A. Moore, and Patricia K. Kuhl (Univ. of Washington, Seattle, WA 98195)

Little is known about visual cues that are critical to the accurate categorization, and perceived quality, of individual phonemes. The current study provided a preliminary evaluation of the relationship between orofacial movements and visual perception of phonemes distinguished by place of articulation. A female talker produced VCV utterances for /b/, /d/, and /g/ consonants; a natural range of variation was obtained by producing each consonant in several vowel contexts. Peak displacement, peak closing velocity, and peak opening velocity were measured from the upper lip, lower lip, and jaw. Observers identified place and rated the perceived quality, or goodness, of each token as an example of the consonant category (1=poor,7=good). As expected, observers identified bilabials with near-perfect accuracy, whereas they often confused alveolars and velars. More importantly, kinematic variation affected category goodness, particularly for /b/. Linear regression analyses indicated that goodness ratings within the /b/ category were highly correlated with lower lip and jaw displacement. In fact, articulatory displacement predicted these goodness ratings more effectively than did vowel context. Implications for understanding visual place cues are discussed. [Work supported by NICHD.]

4aSCb16. Research on the acoustic features of stutterer's voices for the purposes of computer animation. Elżbieta Smołka (Inst. of Phys., Maria Curie-Skłodowska Univ., pl. Marii Curie-Skłodowskiej 1, 20-031 Lublin, Poland)

This paper deals with computerized visual echo, by means of which an animated image of lips speaking in chorus with the stutterer is provided. The computer animation is based on identifying the acoustic features of the Polish vowels. Only two parameters and identifying map could be made and with its help the area of each vowel occurrence could be determined. Then every area was assigned the characteristic image of lips that is typical of articulation of the vowel connected with this area. Three identifying maps are needed–for male voices, female voices, and children's voices. They were elaborated on the basis of examination of 30 correct speaking people. Attempts were made at identifying vowels uttered by 12 stutterers on the basis of maps created earlier. For the stutterer's voices the results of identification range around 70%. However, too small a group was examined to draw definite conclusions. Therefore, similar investigation will be continued, so as to finally confirm the applicability of computerized visual echo to stutterer's therapy.

4aSCb17. Instrumental speech-quality measures: New insights, ideas, and results. Ulrich Heute (LNS/TF/CAU Kiel, Kasiserstr. 2, D-24143 Kiel, Germany, uh@techfak.uni-kiel.de)

Two bases for instrumental quality measurements in speech transmission are well known: comparison between (i) distorted and undistorted signals and (ii) distortion and undistorted signal. Revisiting an approach on the latter basis, combined with a quality-attribute matching [U. Halka and U. Heute, Speech Commun. **11**, 15–30 (1992)], the drawbacks of long-term system characterization, too many degrees of freedom, and, especially, this basis itself are addressed. The first basis and several psychoacoustically motivated variants are then discussed. Thorough investigations of applicability and negligibility of psychoacoustical knowledge show that *good* modeling is indeed useful [M. Hauenstein, DSP Research Series, No. 10, Shaker-Verlag Aachen (1997) (in German)], in contrast to earlier statements, despite the extra computations needed. Returning to the idea of separating certain system characteristics (like linear distortions or frequency shifts) as partially done in the first quoted work, a completely different consideration turns out to be valuable: Instead of adding them as parts of the (possibly nonlinearly) combined distortions, their determination may be used to remove them from the measure as (partially) insignificant effects [J. Berger, DSP Research Series, No. 13, Shaker-Verlag Aachen (1998) (in German)]. New measures derived from these thoughts are presented and compared to other methods.

4aSCb18. Influence of the direction of a single reflection on speech intelligibility. Marc Brüggen (Inst. of Commun. Acoust., Ruhr Univ. Bochum, 44780 Bochum, Germany, brueggen@ika.ruhr-uni-bochum.de)

Speech intelligibility in a complex environment such as a room is affected not only by competing sound sources but also by reflections off walls, the ceiling, or the floor. In this context, the benefit of early reflections for intelligibility in rooms has been demonstrated principally. In which way the auditory system achieves this improvement is still a matter of discussion. Therefore, a speech comprehensibility test was performed in a simulated scenario. Each stimulus consists of a speech target sound that emanates from a 45° azimuth direction and competes with a noise source at −45° azimuth. Both are in the horizontal plane. The speech target is accompanied by a single reflection adjusted in time-delay and level relative to the primary sound to be beneficial for intelligibility [e.g., Nabelek and Robinette, J. Acoust. Soc. Am. **63**, 187–194 (1978)]. During the tests, the variable under investigation was the direction of the reflection. Speech comprehensibility was measured with an open response paradigm utilizing meaningless one-syllable words as speech material. The direction-dependent results indicate an interaction of influences in accordance with earlier findings.

4aSCb19. The adaptive modified rhyme test. Jan Zera (Dept. of Acoust. and Electromagnetic Hazards, Central Inst. for Labour Protection, Czerniakowska 16, 00-701 Warsaw, Poland, jazer@ciop.waw.pl)

This paper discusses an application of the adaptive maximum-likelihood procedure (MLP) [Watson and Pelli, Percept. Psychophys. **33**, 113–120 (1983)] to speech intelligibility measurements conducted with the modified rhyme test (MRT) [House *et al.*, J. Acoust. Soc. Am. **37**, 158–166 (1965)]. The MLP procedure allows the experimenter to preset

the target intelligibility at any value and determine the corresponding speech-to-noise (S/N) ratio. This makes it an efficient tool for estimating the change in the S/N ratio required to maintain identical intelligibility in different noise conditions of the communication channel. The MLP-MRT was tested on a group of 12 listeners. The S/N ratio corresponding to intelligibilities of 50%, 70%, and 88% was determined in five test runs of 30 items each. Subsequently, the S/N ratios estimated by the adaptive procedure were verified by measuring the intelligibility scores by a nonadaptive method. Results showed that intelligibility scores obtained by the nonadaptive method differed by less than 5% from the intelligibility preset in the adaptive procedure. [Part of the work was done as a collaborative project between NRC and the Defence and Civil Institute of Environmental Medicine, during the author's stay with the Acoustics and Signal Processing Group, NRC, Ottawa, Canada.]

4aSCb20. Method for the development of sentence materials for efficient measurement of the speech reception threshold. Niek J. Versfeld and Laura Daalder (Univ. Hospital VU, P.O. Box 7057, 1007 MB Amsterdam, The Netherlands, N.J.Versfeld@AMC.UVA.nl)

Due to technological advancements, modern hearing aids may have many adjustable parameters, multiple memories, and the ability to house all sorts of signal-processing algorithms. To enable a systematic evaluation of the speech intelligibility for a variety of hearing-aid settings, large sets of speech materials are required. This paper reports on the creation and evaluation of a set of 1272 sentences uttered by two male and two female speakers. Two subsets were formed (one for a male speaker and one for a female speaker) to enable efficient measurement of the speech reception threshold in stationary speech-shaped noise. Each subset consists of 39 lists, each comprising 13 sentences. The properties of the new subsets are comparable to the existing sets that are used in clinical practice. [Work supported by the Heinsius Houbolt foundation.]

4aSCb21. Spectrographic analysis of stuttering episodes. Wiesława Kuniszyk-Jóźkowiak and Waldemar Suszyński (Inst. of Phys., Maria Curie-Skłodowska Univ., pl. Marii Curie-Skłodowskiej, 20-031 Lublin, Poland)

Changes in time of frequencies and formant levels were measured in disturbed phoneme articulation. Ten stutterers read the same text in two situations: with simultaneous auditory feedback (SAF) and delayed auditory feedback (DAF). Words chosen for the analyses were ones uttered nonfluently with SAF and fluently with DAF. Frequency characteristics of the phonemes uttered nonfluently and realized fluently were made using computer procedures. These characteristics were analyzed in time intervals of 10 ms. Time evolutions of frequencies and formant levels were made in the cases of fluent and nonfluent articulation of the same phonemes. Results for the stutterers were compared with the ones for fluent speakers in identical utterances. The analysis of time evolution of formant allowed for a description of the vocal tract dynamics in the moments of stuttering. Studying the behavior of these formants in the conditions of forced fluency, that is, with DAF, afforded for anticipating the possible changes in the dynamics of the vocal tract leading to proper pronunciation. The significance of the measures of the parameters was shown for diagnosing and treatment of stuttering.

4aSCb22. The learning of tactile syllables as reflected by blink rate and skin conductance variations. Thomas Arnhold and Hans Georg Piroth (Inst. for Phonet. and Speech Commun., Munich Univ., Schellingstr 3, D-80799 Munich, Germany, piroth@phonetik.uni-muenchen.de)

In a series of experiments the learning of tactile speech has been investigated. The experiment to be reported was concerned with the role of physiological measures in interpreting perceptual stimulus processing. Five untrained participants underwent seven sessions of an identification test on six tactile syllables. The electrocutaneous stimuli representing three fortis and three lenis fricatives followed by a schwa were constructed as dynamical patterns and delivered to the left forearm (place of articulation from labial to velar: distal to proximal stimulation, fortis patterns moving faster than lenis patterns). Correct and incorrect answers as well as skin conductance reactions (SCR) and eye blinks were registered. For statistical analysis SCR-peak amplitudes and blink rate (BR) were calculated from stimulus onset to end of interstimulus interval. A MANOVA on SCR and blink rate shows significantly decreasing SCRs and increasing BRs over sessions. BR is higher in the case of correct identification. On the other hand, SCRs reveal a main effect of the stimulus factor based on higher amplitudes for front (distal) consonant equivalents. BRs (increasing with learning) are interpreted as reflecting cognitive activity, whereas SCRs (habituating over sessions) seem to represent orienting behavior.

Session 4aSP

Signal Processing in Acoustics: Acoustic Signal Processing for Systems with 2D/3D Sensor Arrays I

Stergios Stergiopoulos, Cochair
Defence and Civil Institute of Environmental Medicine, P.O. Box 2000, North York, Ontario M3M 3B9, Canada

Deiter Kraus, Cochair
STN ATLAS Elektronik GmbH, Naval Division, System Analysis and Signal Processing Group, MME6, Sebaldsbrücker Heestrasse 235, 28305 Bremen, Germany

Chair's Introduction—7:55

Invited Papers

8:00

4aSP1. A review of modern ultrasonic diagnostic systems. John M. Reid (School of Biomed. Eng., Sci., and Health Systems, Drexel Univ., 32nd St. and Chestnut St., Philadelphia, PA 19104)

Modern ultrasonic imaging systems used in medical diagnosis have taken full advantage of digital technology, to the limits set by the fundamental acoustic properties of tissue. These properties set the penetration and resolution that is obtainable. The architecture of these systems now resembles that of a computer, since software control and data manipulation are essential parts of the imaging process. Many types of image processing are now done during the image formation and display process. New types of imaging use the Doppler and nonlinear effects to advantage. Many of these advances depend not only on the older types of video image memories, but also on direct storage of the rf data. Although the details of operation are proprietary information, the general structure of these systems is known. A knowledge of the hardware and software operation could assist in further efforts at image enhancement.

8:20

4aSP2. Requirements to signal processing for visualizing surfaces from three-dimensional ultrasound data sets. Georgios Sakas (Fraunhofer Inst. of Computer Graphics (FhG-IGD), Rundeturmstr. 6, D-64283 Darmstadt, Darmstadt, Germany)

Three-dimensional ultrasound can be regarded as the generalization of the traditional 2-D technique with the aim to provide a ''tomographic'' acquisition of the body interior, and moreover, to visualize surfaces of internal organs and pathology, such as fetuses, bone, liver, vessels, skin, brain, but also cysts, tumors, etc. The first requirement for visualizing a surface is obviously the ability of a system to provide mostly clear, sharply defined, high contrast surfaces of internal interfaces between tissue types. The presence of speckle (e.g., parenchyma within liver, amniotic fluid, etc.) greatly reduces the ability of presenting surfaces. ''Ideal'' surfaces from the visualization point of view have a small width (i.e., narrow transition zone between different tissues), are smooth, high contrast, continuous, gapless, and show the same gradient and average intensity. Although these requirements can hardly be fulfilled all at once, one wishes/expects that selective image processing can help overcome several of these difficulties. Numerous examples of this group's previous works demonstrating all 3-D surface visualization drawbacks listed above, together with some image-processing-based improvement techniques proposed so far, will be presented.

8:40

4aSP3. Exploitation and usage of signal evaluating concepts of nature—Ultrasonic data acquisition and neural network signal processing. Thomas Fritsch (BRAIN, Leitenweg 8a, 97286 Sommerhausen-Winterhausen, Germany), Miroslaw Wrobel (Silesian Tech. Univ., Gliwice, Poland),[a] Eckard Glaser (SUNY, Buffalo, NY), and Janet Grassmann (Stanford Univ., Stanford, CA)

The objective of the work is the mapping of the main features of data acquisition and neural signal processing concepts, which can be found in nature like the biosonar of bats and dolphins, to technical applications like medical ultrasound or material testing. A first attempt in this direction was the exploitation of higher harmonics of an emitted ultrasound wave for the measurement of very weak signals by an acousto-optical Mach-Zehnder- and Sagnac-Interferometer. A second ongoing work is the analysis of a frequency-modulated signal by neural network signal processing methods for the purpose of medical ultrasound application. The first promising results give rise to the hope of further technical applications. [a] Former address. Currently with BRAIN.

9:00

4aSP4. Multidimensional adaptive beamforming for integrated active-passive sonar and medical imaging applications. Stergios Stergiopoulos (Defence and Civil Inst. of Environ. Medicine, P.O. Box 2000, North York M3M 3B9, Canada)

The present investigation introduces an adaptive beamforming scheme that separates the computationally intensive multidimensional beamforming into two simple modules, which are line and circular array beamformers. This approach minimizes the number of degrees of freedom associated with the adaptation process and provides near instantaneous convergence, which is essential for integrated active-passive sonar and medical ultrasound imaging applications. The proposed adaptive processing concept has been implemented in an integrated active-passive real-time sonar deploying a cylindrical array. Preliminary efforts include also the appli-

cation of a line array adaptive beamformer in medical ultrasound imaging systems. Real data results from the adaptive and conventional beamforming outputs of the cylindrical array sonar system and the line array of the ultrasound system demonstrate the superior performance of the adaptive beamformer in suppressing the reverberation and cluttering effects in active sonar and medical ultrasound applications. Moreover, for passive sonar applications, the adaptive processing provides substantially improved angular resolution performance as compared with that of the conventional beamformer. Both these two performance improvements for a line and a cylindrical array sonar are of particular importance for mine hunting operations.

9:20

4aSP5. Matched-field imaging of laser ultrasound using a novel correlation cancelling approach. James V. Candy, Robert Huber, David H. Chambers, and Graham H. Thomas (Lawrence Livermore Natl. Lab., P.O. Box 808, Livermore, CA 94551, candy1@llnl.gov)

Matched-field imaging (MFI), which has evolved from various underwater acoustic applications, provides a solution to the inverse problem through forward modeling. In terms of investigating parts for flaws during nondestructive evaluation (NDE), the matched-field approach offers a reasonable technique for imaging provided the necessary preprocessing and parameter estimation can be accomplished. In this paper the results of controlled NDE experiments are described which are aimed at detecting a well-defined flaw in an aluminum part. By heating with a pulsed laser an ultrasonic wave is generated and received by a synthetic array of interferometers. It is demonstrated how these displacement measurements coupled to MFI can be used to detect the flaw. Preprocessing is accomplished by a correlation cancelling scheme designed to separate correlated (reference) from uncorrelated (flaw) measurements. The reference signals are generated by using a known flawless part of the same dimensions and material. The canceller then provides the ''optimal'' separation removing the wash, etc., and leaving just information about the flaw. Further basic processing is accomplished (filtering, etc.) and the underlying arrivals and velocities are estimated using a semblance processor providing a set of parameters required for MFI. The results of this approach applied to experimental data are promising.

9:40

4aSP6. Application of the continuous wavelet transform to the angular location of jet aircraft. Brian G. Ferguson and Kam W. Lo (Defence Sci. and Technol. Organisation, P.O. Box 44, Pyrmont 2009, Australia)

For a fast moving source and widely spaced sensors, the passive wideband cross-correlation method for time delay estimation requires compensation for the relative time scaling between the received signals, otherwise the time delay estimates will be in error. Passive wideband cross correlation with differential Doppler compensation is equivalent to evaluating the continuous wavelet transform, which is an operation that transforms a function (represented by the output waveform of one sensor) by integrating it with time-scaled and time-delayed versions of some kernel function (represented by the output waveform of the other sensor). When the signal-to-noise ratio is high, the coordinates of the wavelet transformed global maximum provide reliable estimates of both the time delay and the ratio of the time scales of the signals received by the two sensors. The wavelet transform is used to process real acoustic data recorded from an orthogonal configuration of three microphones during the low altitude transit of a jet aircraft. The resulting time delay estimates are used to calculate the variation with time of the azimuth and elevation angles of the aircraft during its transit.

10:00–10:20 Break

Contributed Papers

10:20

4aSP7. Neural network-based spatial filtration algorithm for a 2-D microphone array. Andrzej Czyzewski and Jacek Lasecki (Tech. Univ. of Gdansk, WETI, Sound Eng. Dept., PL-80-952 Gdansk, Poland, andrzej@sound.eti.pg.gda.pl)

In order to process acoustic signals obtained from a 2-D microphone array, a neural network-based system was developed. The neural network provides a nonlinear filtration of acoustic signals transformed into the frequency domain. The neural network was trained in such a way that it is performing a spatial filtration of sounds arriving to microphones from various directions. It was trained in acoustically diversified rooms with phonemes edited from speech which were played back by loudspeakers placed at various angles in relation to the microphones. A standard error back-propagation algorithm (EBPA) was used in the supervised training procedures. The desired amplification was defined for each sound pattern. As a result, some sharp directivity characteristics were obtained. The results demonstrate that such a spatial filter ensures a substantial increase in the signal-to-noise ratio and a significant improvement in the intelligibility of speech obscured by background noise and by undesired signals coming from various directions. A comparison between the results obtained using the neural network algorithm and results obtained using some standard beamformer algorithms was also made. The developed algorithm details and results of spatial filtration based on the neural network approach are demonstrated. [Work supported by KBN, Poland, Grant No. 8 T 11E 03415.]

10:40

4aSP8. Error analysis concerning the directional resolution of space-apart four-microphone probes. H. Odjijdja (Technische Univ. Berlin, Einsteinufer 25, D-10587 Berlin, Germany) and P. Krämer (GeBRA Gesellschaft für Bau- und Raumakustik mbH, D-10555 Berlin, Germany)

For room acoustical measurements, the direction of incident sound waves and reflections is of great interest. With space-apart four-microphone probes, the direction can be evaluated by analyzing the differences in propagation time of discrete reflection patterns. The microphone positions can have different spatial arrangements (Cartesian, tetrahedron). The directional resolution depends highly on the exactness of the evaluated propagation time between the microphones. Important factors influencing the calculation of the propagation time are the sound velocity and the distances between the single microphones. Starting from the assumption of constant tolerances of these factors, the error analysis of the directional resolution has been carried out for several kinds of spatial microphone arrangements. The calculation is based on a simple model (plane wave propagation) as well as on a more general attempt (consider-

ing the exact location of the source). The actual resolution is dependent on the incident direction. Nevertheless, the magnitude of the error considering all directions is nearly the same for the investigated arrangements.

11:00

4aSP9. Software for estimation and processing simulation of microphone line arrays. Christos Sevastiadis (Dept. of Elec. and Comput. Eng., Aristotle Univ. of Thessaloniki, Univ. Campus, Thessaloniki, 540 06, Greece), Christodoulos C. Chamzas (Cultural and Educational Technol. Inst., Xanthi, 671 00, Greece), George M. Kalliris, and George V. Papanikolaou (Aristotle Univ. of Thessaloniki, Thessaloniki, Greece)

Software for estimation and processing simulation of microphone line arrays was developed, based on the fundamentals of sensor array theory and the basic concepts governing the array beamforming. Periodical, nonperiodical, and logarithmic microphone line arrays can be designed in a convenient way. Spatial structures, directivity patterns, and other properties of the microphone arrays are shown and examined diagrammatically. Optimization of the microphone array directivity index through the entire audio spectrum, using the logarithmic design and the apropriate filters, is shown as well. All properties can be easily examined and dynamically changed via a useful user interface. The designed microphone arrays can also be simulated using sound recordings of a single microphone or WAV files in PCM format. The program's output is an audio processing simulation of the acoustic field which can be accessed through WAV file registering. This stand-alone, fully adjustable simulation software can be a user-friendly tool in understanding the basic concepts of the microphone array design theory.

11:20

4aSP10. Evaluation of various infrasonic array detectors. Eugene Smart (HQ AFTAC/TT, 1030 S. Hwy. A1A, PAFB, FL 32925-3002, paseador@rayleigh.tt.aftac.gov)

Several signal detectors are evaluated for infrasonic array data: (a) power detector that reviews a suite of array beams; if the mean square excursion in the window exceeds that of a longer preceding interval by an arbitrary threshold factor, a detection is declared. (b) Time domain F-detector, similar to the power detector, except that F is the detection criterion; F is proportional to the estimated S/N ratio. (c) $f-k$ detector, similar to the time domain F-detector, except that it operates in the frequency–wave number domain. (d) Closure detector: cross-correlation lag times minus delay times of the best-fitting plane wave approach zero when a plane wave is present. Statistical distributions of waveform characteristics critical for signal detection are measured in a large, representative set of infrasonic data covering all hours of the day, four seasons of the year, and various geographic locations. The measurements are required for modeling detector performance: (a) The power detector uses data preceding the detection window to estimate the expected mean square excursion in the window itself, assuming continuity. The statistical distribution of such estimates is measured. (b) The mean-square excursion in a randomly chosen time window varies from channel to channel in real data. The statistical distribution of such variation is measured.

11:40

4aSP11. A statistical analysis of acoustical detection and tracking of small jet aircraft. Roy Adams (U.S. Army Space and Missile Defense Command, Adv. System Concepts Div. (SMDC-TC-PS), P.O. Box 1500, Huntsville, AL 35807), D. Keith Wilson, and Nassy Srour (U.S. Army Res. Lab., Adelphi, MD 20783)

Ground-based networks of acoustical arrays can be used to track the location of moving ground vehicles and flying aircraft. In this paper, a method is proposed for simulating the statistical accuracy of location estimates derived from array networks. The method is based on combining Cramer–Rao lower bounds for the bearing accuracy of the individual arrays, by using a general stochastic inverse formulation. Environmental phenomena associated with acoustic propagation, such as refraction by wind and temperature gradients, ground interactions, terrain masking, and signal coherence degradation by turbulence, are included in the calculations. Issues unique to sources moving at high subsonic Mach numbers, such as source radiation patterns and propagation delays, are discussed. The statistical analysis is compared to measurements made at Fort Bliss (Texas) on a small, jet-powered drone aircraft flying at 1000 feet above ground level. Differences between radar (truth) and acoustical tracking data are compared to the simulation-based predictions.

12:00

4aSP12. Multidimensional array signal processing with multidimensional matrix operations. Oleg A. Rogozovskyi (Signal Theory Group, Ruhr Univ. Bochum, Universitaetstr. 150 IC 6/34, D-44780, Bochum, Germany, rog@sth.ruhr-uni-bochum.de)

Digital processing of multidimensional (m-D) array signals requires an adequate description. Such descriptions could be made by using multidimensional matrices. Associating m-D matrices with multilineal forms, one could derive a set of algebraic operations. Most important of them for the signal processing is the m-D convoluted multiplication. It is shown that, making use of the m-D matrix operations, one can save a computational load. It could be three times less for multiplication by processing of the 3-D data matrix. A spatio-temporal processing with a time processing on the first stage (e.g., by Fourier transform) brings some advantages. If the signals are wide band, short time, or nonstationary (e.g., from array with position distortions or from moving one), such processing on the first stage could be noneffective. Constraints on signal and array parameters for this case are derived. If this constraint is not fulfilled, first stage time processing must be replaced by a spatial one. For sonar, radar, and image applications that could be beamformers and focusing algorithms. For both variants of the spatio-temporal processing, log-likelihood algorithms for 1-D, 2-D, and 3-D arrays are derived. Postprocessing algorithms with high resolution and parameter tracing by m-D matrix description are obtained also.

Session 4aUW

Underwater Acoustics: Rough Surface Scattering, Bubbles and Noise

Darrell R. Jackson, Chair
Applied Physics Laboratory, University of Washington, Seattle, Washington 98105, USA

Contributed Papers

9:20

4aUW1. A new, semiempirical model for predicting bistatic surface backscattering strengths. Roger Gauss (Naval Res. Lab., Washington, DC 20375-5350, roger.gauss@nrl.navy.mil) and Joseph Fialkowski (Planning Systems, Inc., McLean, VA 22102-3304)

A Lloyd-mirror model of bubble-cloud scattering, along with perturbation theory for the rough air–sea interface, have been used as a basis for generating a new algorithm for predicting the strength of acoustic backscatter from the ocean surface. Multiparameter curve fits of the model to acoustic data from the Critical Sea Test program (1988–1996) and other at-sea experiments have been used to derive a new, semiempirical description of the dependence of surface backscattering strength on the incident and scattered grazing angles, the acoustic frequency, and environmental descriptors. The model represents an advance on previous algorithms (Chapman–Harris, Ogden–Nicholas–Erskine) in several ways: (1) a much improved, physics-based description of the grazing-angle dependence, applicable to arbitrarily low grazing angles; (2) a much improved description of low-to-moderate sea-state bubble scattering; (3) can handle vertically bistatic geometries; and (4) is applicable to a broader range of frequencies (50 to 5000 Hz). [Work supported by ONR.]

9:40

4aUW2. Time-dependent scattering from bubble clouds: Implications for the use of acoustic pulses. James W. Clarke, Tim G. Leighton (Inst. of Sound and Vib. Res., Univ. of Southampton, Highfield, Southampton SO17 1BJ, UK, jwlc@isvr.soton.ac.uk), Gary J. Heald, and Hugh A. Dumbrell (Defence Evaluation Res. Agency, Weymouth, Dorset DT4 8UR, UK)

A theoretical model has been developed to investigate the ring-up times, or time taken to reach steady-state oscillation, of gas bubbles in fresh water. The model utilizes numerical solutions of the Herring–Keller bubble model and damping values after Prosperetti's 1977 analysis to calculate the extinction cross-sectional area of a bubble as a function of time in response to a continuous harmonic sound field. The model has also been extended to determine the extinction cross-section area of multiple bubbles of varying population distributions assuming no bubble–bubble interactions. The results have shown that the ring-up time of a bubble is dependent on its closeness to resonance and the driving pressure amplitude. Investigation of various bubble populations has shown that the ring-up time of the resonant bubbles may be masked by the presence of large off-resonant bubbles and that high-amplitude sound fields enhance this effect. The implications of these findings for the use of acoustic pulses are explored. [Work supported by DERA.]

10:00

4aUW3. A time-domain path integral method for analyzing reflections from a rough sea surface. S. E. Forsythe, Jean C. Piquette (Naval Undersea Warfare Ctr., 1176 Howell Rd., Newport, RI 02841, forsythese@code20nl.npt.nuwc.navy.mil), Mohsen Badiey (Univ. of Delaware, Newark, DE 19716), and J. Simmen (Office of Naval Res., Arlington, VA 22217)

Recently, experimental data were gathered for broadband (500 Hz–20 kHz) sound transmissions in shallow water over a period of seven days. The processed data form a good approximation to the impulse response of the environment, including direct signal paths, surface interactions, and bottom interactions, from a source to both local and remote receivers. Since the signals resulting from a single interaction with the ocean surface can be cleanly separated from other arrivals, these signals become a rich source of information about surface wave motion and thus about the state of the sea. To analyze the effects of surface waves (surface wave height, period, wave number, wave direction) on the received signal, including frequency dependence, a tool for efficiently calculating broadband response of a rough sea is needed. Instead of solving for the wave field at many frequencies and synthesizing the result into a broadband response using Fourier techniques, a direct computation of the response uses raylike techniques to sum over all significant paths in the time domain. For some problems, this technique is much more efficient than frequency-domain approaches such as PE or wave number integration, while providing the low-frequency accuracy that is only approximated by ray theory approaches. [Work supported by ONR.]

10:20–10:40 Break

10:40

4aUW4. Surf zone breaking wave air entrainment and noise generation. Ming-Yang Su (Naval Res. Lab., Code 7332, Stennis Space Center, MS 39529) and Joel C. Wesson (Neptune Sci., Inc., Slidell, LA 70458)

During two field experiments conducted at CERC (Coastal Engineering Research Center) at Duck, NC in 1997 and 1998, NRL made simultaneous measurements of air void fraction and sound intensity due to wave breaking across the surf zone under various weather conditions with or without wind forcing. The void fraction sensors, wave pressure gauges, and hydrophones were deployed by two distinctly different methods. The first method used a new and unique swinging-bar which has the top end attached to a surface float, with its bottom end attached to a universal joint anchored in the sandy bottom. The second method used the CERC Sensor Insertion System (SIS), to place the instruments in the water at various points and depths along the 600-m-long pier at the facility. This paper presents the characteristics and statistics of the spatial and temporal variations of these void fraction measurements associated with surface wave profiles, and power spectra and time-frequency spectra of sound intensity under wave breaking. The corresponding relationship between the void fraction variation and sound intensity shall also be presented.

11:00

4aUW5. Acoustic measurements of air entrainment by a plunging free water jet. Thomas R. Hahn, Thomas K. Berger, and Michael J. Buckingham (Marine Physical Lab., Scripps Inst. of Oceanogr., Univ. of California, San Diego, 9500 Gilman Dr., La Jolla, CA 92093-0238, thahn@ucsd.edu)

Low-frequency acoustic emissions of a free plunging water jet were studied to determine the volumetric rate of gas transfer across the pool surface. At the studied jet velocities, up to 10 m/s, air bubbles are entrained at the interface and form well-defined bubble clouds penetrating up to 20 cm into the pool. The resulting biphasic region of the submerged jet was found to be an efficient acoustic resonator. The radiated sound field was recorded with hydrophones close to the region of the submerged jet

and strong resonances were found below 1 kHz. The frequencies of the lowest modes were measured for a given jet diameter as a function of the jet velocity. The observed acoustic eigenfrequencies are unique functions of the jet velocity and the gas flux, independent of the details of the gas entrainment. This functional dependence was investigated both experimentally and theoretically, allowing an inversion of the acoustic data for the air flux across the interface as a function of the jet velocity. Reference measurements of the air flux were made to calibrate the inversions. Using this technique, measurements of the air flux were made for a variety of jet diameters, lengths, and velocities. [Work supported by ONR.]

11:20

4aUW6. The influence of marine surface films on underwater sound. Stanislaw Pogorzelski (Inst. of Exp. Phys., Univ. of Gdansk, Wita Stwosza 57, 80-952 Gdansk, Poland, fizsp@paula.univ.gda.pl)

Essential characteristics of wind-generated ambient noise at sea depend on a few aerodynamic parameters of the sea surface–atmosphere interaction process. The film smoothing effect attributed to a reduction of the friction velocity and wind wave growth rate is shown, for model marine films, to be expressed in the corresponding changes of the sound-level intensity versus wind speed and frequency characteristics. Naturally generated ambient noise in the ocean is also created by breaking waves, resonating gas bubbles, spray, precipitation, or solid impacts, and has particular features. The spectrum of rain shows a peak at 13–15 kHz with the spectral level SL, in dB, linearly dependent on the log rain rate. The effect of a monomolecular film covering the surface exposed to splashing water droplets, uniformly distributed, and modeled as incoherently radiating dipoles, is evaluated assuming the Marangoni damping mechanism of surface disturbances by a viscoelastic film. The result is a pronounced reduction of SL beneath the film by 10 log K, 3–20 dB, for realistic systems, where the damping ratio K is a complex function expressed by the surface activity, elasticity, concentration, and diffusional coefficient of surfactants composing the film.

11:40

4aUW7. Under-ice noise resulting from thermally induced fracturing of the arctic ice pack: Theory and a test case application. Peter J. Stein, James K. Lewis, and James C. Parinella (Scientific Solutions, Inc., 18 Clinton Dr., Hollis, NH 03049)

A theory is presented relating thermally induced fracturing of pack ice to under-ice noise. The thermomechanics of pack ice relates thermally induced strain rates to stresses within various layers of the floe. Paradigms are used to specify the relative quantity of fracturing and stress relief as the ice tensile yield strength ice is exceeded. The thermomechanics is complemented by an acoustic model that relates the number of fracture events to acoustic levels at arbitrary frequency and depth below the ice. This theory assumes each fracture acts as a monopole source, the fractures are evenly distributed horizontally, and the energy of each fracture propagates through the ice and water as elastic waves in a stratified media. Noise from fracturing occurring over the top 40 cm of a 160-cm-thick floe will propagate over distances of ~100 km. However, noise from fracturing occurring in the lower 100 cm of the floe will only propagate ~10 km. The theories were used to develop a numerical model for predicting under-ice noise for a given thermal forcing. The model was used to simulate stresses in a multiyear floe and under-ice noise levels. Model-predicted ice stresses and under-ice noise compare well with observed stresses and noise.

Contributed Posters

These posters will be on display in the Poster Gallery from Wednesday to Friday, 17–19 March. Authors will be at their posters from 10:00 a.m. to 12:00 noon on Friday, 19 March.

4aUW8. The modeling of acoustic wave scattering on fractal seabed surface. Zbigniew Lubniewski and Andrzej Stepnowski (Tech. Univ. of Gdansk, Acoust. Dept., ul. Narutowicza 11/12, 80-952 Gdansk, Poland, lubniew@eti.pg.gda.pl)

The one-dimensional model of a plane wave scattering on a corrugated seabed surface was analyzed in order to investigate the process of transferring the fractal structure of the bottom surface onto bottom scattering impulse response. The investigation evaluates the adequacy of the fractal dimension of a bottom impulse response as a descriptive parameter of a bottom type. The Kirchhoff approximation was used in the model. Several types of sea bottom surfaces with different fractal dimensions were used in modeling and the relation between fractal dimension of a bottom surface and fractal dimension of its impulse response was found.

4aUW9. Wave scattering in underwater acoustics. Francoise Schmitt, Franck Daout, and Emmanuel Siohan (Ecole navale Batiment des laboratoires, 29 240 Brest naval, France)

In underwater acoustics it is necessary to take into account the wave scattering by the seafloor. For example, on sonar pictures the speckle noise proceeds from the constructive and destructive interferences between allthe waves reflected by the elementary scatterers. The origins of this phenomenon are seafloor roughness and its acoustic properties, wave incidence, frequency, multiples reflections, the dimensions of the insonified surface, etc. The aim of this study is to characterize the scattering of waves exclusively from the roughness. Thus a hypothesis of perfectly reflecting surface is taken. Moreover, specific-geometry periodic surfaces are considered to take into account the multiple reflections and the shadow area easily. Finally it is supposed that the roughness and the wavelength are of the same size. The models to describe the scattered field are based on Kirchhoff's theory and on Fraunhoffer's diffraction theory. Some experiences in the acoustic tank yield good agreement between theoretical and experimental results. They show that the orientation and the area of the insonified and observed surfaces are parameters for the scattering angles and for the relative scattered amplitudes.

4aUW10. The effect of grease ice formation on ambient noise. Ola M. Johannessen and Hanne Sagen (NERSC, Edv. Griegsvei 3A, 5037 Solheimsviken, Norway and Geophysical Inst., Univ. of Bergen, Bergen, Norway, hanne.sagen@nrsc.no)

During cooling, a very thin visco-elastic film of ice, grease ice, can be formed over large areas of the marginal ice zone. This thin layer of ice has been observed to dampen out the shorter surface waves, which in turn reduces the ambient noise level. Ambient noise recordings made by a bottom-mounted buoy and sonobuoys during SIZEX 92 showed that grease ice causes a 9-dB stronger reduction close to the seafloor than in recordings made 18 m below sea surface. The topic of this presentation is to show why the grease ice causes a stronger dampening of the ambient noise close to the sea floor than close to the surface. The major result of the study is that the wave dampening effect of the grease ice accounts only for around half the reduction of the ambient noise. The other half is caused by a creation or enhancement of a surface duct prior to the grease ice formation which causes sound above around 100 Hz to be trapped close to the surface. These results illustrate how ambient noise characteristics are shaped partly by the noise-generating processes and partly by propagation effects.

4aUW11. Scattering and reflection of sound by random rough surfaces. Guy Rabau (CNRS LMA, 31 Chemin Joseph Aiguier, 13402 Marseille Cedex 20, France, RABAU@alphalma.cnrs-mrs.fr)

The classical underwater acoustical models for shallow or deep water configuration (Lambert's law, facet's model, etc.) generally use a simple approximation to take into account the real nature of the bottom (and, in particular, the roughness of the surface). When the wavelength and the dimensions of the roughness are equivalent (1 kHz$<$frequency $<$5 kHz), it is difficult to validate these models through lack of calibrated measures. In this paper, the influence of a rough and inhomogeneous bottom on the propagation is shown. Therefore, on different types of rough or/and inhomogeneous bottoms, the diffusion diagram generated by an incident plane wave was measured. The experiment was done on a 1 to 100 scale with a 250-kHz source. Original synthetic materials were used to simulate the sea bottom. Besides the interest of the experimental setup, this paper reports comparisons between results from theoretical model and experimental results, and it describes the limits of the theoretical model and its defects. In particular, it describes the impact of the scattering in shallow or deep water propagation due to the rough and inhomogeneous bottom.

Meeting of the Standards Committee Plenary Group (PL)

Organization of Standards Committee Plenary Group Meeting

- **S1 ACOUSTICS**—U.S. Technical Advisory Group (TAG) for *IEC/TC 29* Electroacoustics and *ISO/TC 43* Acoustics
- **S2 MECHANICAL VIBRATION AND SHOCK**—U. S. Technical Advisory Group (TAG) for ISO/TC 108 Mechanical Vibrational and Shock and Subcommittees SC1, SC2, SC3, SC5, and SC6
- **S3 BIOACOUSTICS**—U.S. Technical Advisory Group (TAG) for *ISO/TC 43 Acoustics, IEC/TC 29* Electroacoustics, and *ISO/TC 108/SC4* Human Exposure to Mechanical Vibration and Shock
- **S12 NOISE**—U.S. Technical Advisory Group (TAG) for *ISO/TC 43/SC1* Noise and *ISO/TC 94/SC12* Hearing Protection

Discussion at the Standards Committee Plenary Group meeting will consist of national (U.S.) and international items relevant to all S Committees, plus a general review of the international standardization (U.S. TAG) activities.

The meeting of the Standards Committee Plenary Group will precede the meetings of the Accredited Standards Committees to take place sequentially on the same day as follows: S12, S3, S1, S2.

The U.S. Technical Advisory Group (TAG) Chairs for the various international Technical Committees and Subcommittees under ISO and IEC, which are parallel to S1, S2, S3, and S12 are given below.

Details of the four S Committees are also listed.

U.S. TAG Chair/Vice Chair	TC or SC	U.S. Technical Advisory Group (TAG)
ISO		
P. D. Schomer, Chair H. E. von Gierke, Vice Chair	**ISO/TC 43** Acoustics	S1 and S3
P. D. Schomer, Chair H. E. von Gierke, Vice Chair	**ISO/TC 43/SC1** Noise	S12
D. D. Reynolds, Chair	**ISO/TC 108/SC4** Human Exposure to Mechanical Vibration and Shock	S3
D. J. Evans, Chair	**ISO/TC 108** Mechanical Vibration and Shock	S2
R. H. Mehta, Chair K. Won, Vice Chair	**ISO/TC 108/SC1** Balancing, including Balancing Machines	S2
A. F. Kilcullen, Chair	**ISO/TC 108/SC2** Measurement and Evaluation of Mechanical Vibration and Shock as Applied to Machines, Vehicles and Structures	S2
B. E. Douglas, Chair	**ISO/TC 108/SC3** Use and Calibration of Vibration and Shock Measuring Instruments	S2
D. J. Vendittis, Chair	**ISO/TC 108/SC5** Condition Monitoring and Diagnostics of Machines	S2
G. Booth, Chair	**ISO/TC 108/SC6** Vibration and Shock Generating Systems	S2
IEC		
V. Nedzelnitsky, U.S. TA	**IEC/TC 29** Electroacoustics	S1 and S3

ACCREDITED STANDARDS COMMITTEES (ASC)

S1 on Acoustics
J. P. Seiler, Chair
G. S. K. Wong, Vice Chair

S2 on Mechanical Vibration and Shock
D.J. Evans, Chair

S3 on Bioacoustics
L. S. Finegold, Chair
R. F. Burkard, Vice Chair

S12 on Noise
P. D. Schomer, Chair
B. M. Brooks, Vice Chair

Posters from various technical sessions remain on display in the Poster Gallery.

Posters from sessions which contain both lecture and poster presentations will be attended by the authors as listed below.

2:00–4:00

3pNSb12	Murphy, William J.	Four protectors in search of a rating system
3pNSb13	Zannin, Paulo H. T.	Effects of cup, cushion, headband force, and foam lining on the attenuation of earmuffs
5pNSa10	Lelong, Joel	Effect of the acceleration on vehicle noise emission

4:40–6:20

4pNSd8	Baumann, Uwe	Characteristics of MRI acoustic notice in functional and high resolution imaging of the auditory pathways
4pNSd9	Bezvesilna, Olena N.	Adaptive decision method for acoustical turbomachinery diagnostics
4pNSd10	Engel, Zbigniew	Investigations of sound insulation of partitions used for integrated enclosures

5:20–6:20

4pPAb10	Poggi, Sylvain	Laser Doppler anemometry applied to airborne acoustics: Influence of the signal processing parameters
4pPAb11	Urbanczyk, Marian	Acoustoelectric effect in gas sensor of the SAW type
4pPAb12	Opilski, Aleksander	Optional SAW sensor for low nitrogen dioxide concentration

Also the following poster sessions are scheduled:
Poster Session 4pPPb

Session 4pAA

Architectural Acoustics: Building Acoustics I: Airborne and Impact Sound Transmission and Classroom Acoustics

Sten Ljunggren, Cochair
Department of Building Technology, KTH, Brinellvägen 34, S-100 44 Stockholm, Sweden

Alfred C. C. Warnock, Cochair
National Research Council, Building M39, Montreal Road, Ottawa, Ontario K1A OR6, Canada

Chair's Introduction—12:55

Invited Paper

1:00

4pAA1. The influence of identical room dimensions on the sound insulation at low frequencies. Wolfgang Kropp and Tor Kihlman (Dept. of Appl. Acoust., Chalmers Univ. of Technol., SE-41296 Gothenburg, Sweden, wk@ta.chalmers.se)

At low frequencies the sound insulation between rooms is only valid for the specific case under consideration as shown in works by different authors. The expression ''low frequencies'' implies a frequency range where the rooms' dimensions are comparable with the wavelength of sound in the rooms (i.e., normally below about 250 Hz for normal rooms). Both theoretical studies as well as experimental studies in the laboratory show that there is a substantial decrease of the sound insulation when the dimensions of the sending and receiving rooms coincide. The question arises if this decrease of the sound insulation can also be observed for the sound insulation of partitions in the field. The results are often biased by other effects such as flanking transmission or smaller differences in the fabrication of the partitions. By means of statistical studies field measurements are analyzed to show the influence of the room dimensions on the sound insulation in the field. To avoid the deterioration of the sound insulation, changes in the dimensions would be required which do not allow for symmetrical building designs as it is often preferred in practice.

Contributed Papers

1:20

4pAA2. Sound transmission loss of double-glazed window panes—an empirical approach. Siegfried Koch (Fraunhofer-Institut fuer Bauphysik, Nobelstr. 12, D-70569 Stuttgart, Germany, koch@ibp.fhg.de)

There are only a few contributions to the theory of sound transmission loss (STL) of double-glazed window panes, e.g., by M. Rehfeld *et al.* (1996). The situation is nearly the same with the empirical approach of reducing data from laboratory measurements to a simple formula, as done by K. Goesele (1977). Goesele inferred a result in terms of the single-number rating according to ISO 717 based on many laboratory STL measurements as described in DIN 52210 and ISO 140. In particular, measurements of air-filled double-glazed window panes had been used. Meanwhile, the gas fillings changed, because the thermal insulation of the window panes had to be increased. In the last five years a large number of STL measurements of double-glazed window panes with different dimensions (pane thicknesses, gap between the panes) and gas fillings have been carried out at the Fraunhofer-Institut fuer Bauphysik. From these measurements some typical behaviors of STL versus frequency belonging to specific pane configurations could be derived. This should allow an approximate prediction of the STL for given physical dimensions of double-glazed window panes.

Posters from various technical sessions remain on display in the Poster Gallery.

Posters from sessions which contain both lecture and poster presentations will be attended by the authors as listed below.

2:00–4:00

3pNSb12	Murphy, William J.	Four protectors in search of a rating system
3pNSb13	Zannin, Paulo H. T.	Effects of cup, cushion, headband force, and foam lining on the attenuation of earmuffs
5pNSa10	Lelong, Joel	Effect of the acceleration on vehicle noise emission

4:40–6:20

4pNSd8	Baumann, Uwe	Characteristics of MRI acoustic notice in functional and high resolution imaging of the auditory pathways
4pNSd9	Bezvesilna, Olena N.	Adaptive decision method for acoustical turbomachinery diagnostics
4pNSd10	Engel, Zbigniew	Investigations of sound insulation of partitions used for integrated enclosures

5:20–6:20

4pPAb10	Poggi, Sylvain	Laser Doppler anemometry applied to airborne acoustics: Influence of the signal processing parameters
4pPAb11	Urbanczyk, Marian	Acoustoelectric effect in gas sensor of the SAW type
4pPAb12	Opilski, Aleksander	Optional SAW sensor for low nitrogen dioxide concentration

Also the following poster sessions are scheduled:
Poster Session 4pPPb

Session 4pAA

Architectural Acoustics: Building Acoustics I: Airborne and Impact Sound Transmission and Classroom Acoustics

Sten Ljunggren, Cochair
Department of Building Technology, KTH, Brinellvägen 34, S-100 44 Stockholm, Sweden

Alfred C. C. Warnock, Cochair
National Research Council, Building M39, Montreal Road, Ottawa, Ontario K1A OR6, Canada

Chair's Introduction—12:55

Invited Paper

1:00

4pAA1. The influence of identical room dimensions on the sound insulation at low frequencies. Wolfgang Kropp and Tor Kihlman (Dept. of Appl. Acoust., Chalmers Univ. of Technol., SE-41296 Gothenburg, Sweden, wk@ta.chalmers.se)

At low frequencies the sound insulation between rooms is only valid for the specific case under consideration as shown in works by different authors. The expression ''low frequencies'' implies a frequency range where the rooms' dimensions are comparable with the wavelength of sound in the rooms (i.e., normally below about 250 Hz for normal rooms). Both theoretical studies as well as experimental studies in the laboratory show that there is a substantial decrease of the sound insulation when the dimensions of the sending and receiving rooms coincide. The question arises if this decrease of the sound insulation can also be observed for the sound insulation of partitions in the field. The results are often biased by other effects such as flanking transmission or smaller differences in the fabrication of the partitions. By means of statistical studies field measurements are analyzed to show the influence of the room dimensions on the sound insulation in the field. To avoid the deterioration of the sound insulation, changes in the dimensions would be required which do not allow for symmetrical building designs as it is often preferred in practice.

Contributed Papers

1:20

4pAA2. Sound transmission loss of double-glazed window panes—an empirical approach. Siegfried Koch (Fraunhofer-Institut fuer Bauphysik, Nobelstr. 12, D-70569 Stuttgart, Germany, koch@ibp.fhg.de)

There are only a few contributions to the theory of sound transmission loss (STL) of double-glazed window panes, e.g., by M. Rehfeld *et al.* (1996). The situation is nearly the same with the empirical approach of reducing data from laboratory measurements to a simple formula, as done by K. Goesele (1977). Goesele inferred a result in terms of the single-number rating according to ISO 717 based on many laboratory STL measurements as described in DIN 52210 and ISO 140. In particular, measurements of air-filled double-glazed window panes had been used. Meanwhile, the gas fillings changed, because the thermal insulation of the window panes had to be increased. In the last five years a large number of STL measurements of double-glazed window panes with different dimensions (pane thicknesses, gap between the panes) and gas fillings have been carried out at the Fraunhofer-Institut fuer Bauphysik. From these measurements some typical behaviors of STL versus frequency belonging to specific pane configurations could be derived. This should allow an approximate prediction of the STL for given physical dimensions of double-glazed window panes.

1:40

4pAA3. Sound level differences in shafts—Measurements in the IAB laboratory. Andreas Kurz, Knut Schroeter, and Wolfgang Teuber (Inst. for Acoust. and Bldg. Phys., Kiesweg 22, 61440 Oberursel, Germany)

The sound isolation between rooms can be lowered by the implementation of additional sound paths, e.g., by sound transmission via shafts. Above all, this applies to shafts which have openings to the adjacent rooms. With a normal metal duct and with certain outlets, the sound isolation was measured when a sound dampener was additionally implemented into the duct. The openings of the outlets were changed, then the level difference and the isolation index were measured. The construction of the test facility will be described.

2:00

4pAA4. Noise propagation in open-plan space with barriers. Marilda Duboc (Dept. of Mech. Eng./COPPE, Federal Univ. of Rio de Janeiro, Prédio do Centro de Tecnologia, Bloco A., Decania, Ilha do Fundão, RJ, Brasil, duboc@ct.ufrj.br) and Jules G. Slama (Federal Univ. of Rio de Janeiro, Ilha do Fundáo–RJ, Brasil)

Open-plan spaces have, in general, the distance between the floor and the ceiling much smaller to the other dimensions. This feature permits modeling sound propagation using the image source method, considering only reflection on the ceiling and the floor, which are represented by two infinite parallel planes. This paper presents some results of a computation simulation developed to represent this model. The computation program calculates the sound pressure level and the insertion loss in an open-plan space in the presence of a barrier and of a belt of absorbing material placed to the ceiling over the barrier and permits simulation of the conditions of a test method specific of open-plan spaces, the ASTM-Designation E 1111 (Standard Test Method for Measuring the Interzone Attenuation of Ceiling Systems). The results show the existence of points of weak insertion loss in the shadow zone and that a belt of absorbing material on the ceiling permits the increase of the barrier efficiency. For validation of the computation method, a comparison was made with a Kuttruff model [H. Hatanaka *et al.*, Inter-Noise (July 1995), pp. 743–746], for the simple case without barrier and belt of absorbing material. The results have presented a good agreement.

2:20

4pAA5. An algorithm for auralization of airborne sound insulation. Rainer Thaden (Inst. of Technolog. Acoust., RWTH Aachen Templergraben, 55 52056 Aachen, Germany, rth@akustik.rwth-aachen.de)

On the basis of a prediction model for airborne sound insulation (EN 12354-1), a signal processing tool was developed for auralization of indoor and outdoor noise in receiving rooms. For this purpose the direct transmission and four flanking paths were taken into account according to their one-third octave band data. These energy components were addressed to specific field situations in the receiving room with specific delays and directions. The directions of the five transmission paths as well as the reverberation tail were treated binaurally. A large number of building elements can be simulated with nine different hearing rooms. The algorithm was implemented in C (and partly in Assembler). Typical processing time for generation of a 20-s audio file is approximately 10 s on a Pentium II with 233 MHz. Typical time signals, frequency responses, and some sound examples will be presented illustrating this algorithm. This work was done in cooperation with the PTB and supported by Gruenzweig and Hartmann AG.

2:40

4pAA6. Low-frequency impact sound transmission through floor systems. Alf Warnock (Natl. Res. Council, M59, Montreal Rd., Ottawa, ON K1A 0R6, Canada, alf.warnock@nrc.ca)

An extensive series of measurements of airborne and impact sound insulation on joist floors of various types was recently completed at NRC. About 190 floors with different joist types, subfloors, ceiling types, ceiling support systems, and type and thickness of sound absorber were constructed and sound insulation measured to frequencies lower than required by standards. The joist types comprised solid wood, wood trusses, I-joists, and steel joists. Glass, rock, and cellulose fiber sound-absorbing materials were used. Three concrete slabs were included in the series and a few of the joist floors had concrete toppings installed. Impact devices used on the floors included the standard ISO/ASTM E492 tapping machine, a walker, a JIS 1419 tire impactor, and two experimental rubber balls. The impact measurements provide an extensive, consistent set for examining alternative impact tests and possible modifications to standard tests using the ISO tapping machine. Correlations among the sound levels from the different impactors show that levels from the ISO tapping machine correlate well with those from a walker at low frequencies although the spectra are quite different in shape. The data and the prospects for a new test method and rating system will be discussed.

3:00

4pAA7. The use of agglomerated cork as an underlay for improvement of impact sound insulation in buildings. Antonio Carvalho, Constantinos Vafiadis (Acoust. Lab., Dept. of Civil Eng., College of Eng., Univ. of Porto, R. Bragas, P-4099 Porto Codex, Portugal, carvalho@fe.up.pt), and Hugo Borrego (Corticeira Amorim Industria, P-4536 Mozelos VFR, Portugal)

The cork-oak is only abundant in the Western part of the Mediterranean and is an important feature of Portuguese landscape and heritage. Portugal has about 30% of the world's cork-oak trees and accounts for more than half of the world's cork production. Agglomerated cork has natural cork granules (the by-products from the production of other cork products) as its base material. The project goal was to test and characterize the use of agglomerated cork as underlay to increase the impact sound insulation. Eight different cork agglomerate products were tested to assess their impact sound insulation quality when used as underlays with four different floor coverings (linoleum, ceramic tile, and two types of wood parquet). The measurements were made on-site (with flanking transmissions) on a coffered concrete floor without a fastened ceiling and according to International, Portuguese, and American standards (ISO-140/6 and 717, NP-669 and 2073, and ASTM-E989 and 1007). The results show that the use of this underlay improves the weighted index (Ln, w, or IIC) for each respective reference floor up to 19 (for ceramic tiles), 20 (thin parquet), 21 (linoleum), and 26 dB (thick parquet). Prediction formulas, determined by statistical analysis, are also presented.

3:20

4pAA8. Sound irradiation from walls when excited by impact sound from fresh and waste water lines. Knut Schroeter and Wolfgang Teuber (Inst. for Acoust. and Bldg. Phys., Oberursel, Germany)

The noise produced by fresh and waste water lines is usually transmitted into neighboring walls and into rooms which should be protected. Impact sound leads to sound velocity levels which can be measured on the wall. With the help of irradiation coefficients, airborne noise levels can be calculated taking the light and heavy walls of two IAB test rooms into consideration. To vary the transmission of structure-borne sound, different pipe clamps with insulated thimbles were used. The measurement will be compared with earlier results in these test facilities. Comparisons with *in situ* measurements will also be made

3:40–4:00 Break

4:00

4pAA9. Speech intelligibility in simulated classroom sound fields. John Bradley (IRC, Natl. Res. Council, Montreal Rd., Ottawa, ON K1A 0R6, Canada, john.bradley@nrc.ca)

Speech intelligibility in classrooms is determined by both speech/noise ratios and room acoustics factors. Using a rhyme test, speech intelligibility scores were obtained in sound fields simulated using an electroacoustic system in an anechoic room. The 16 sound fields consisted of the combi-

nations of four levels of speech/noise ratio and four levels of a room acoustics measure giving an even distribution over all conditions likely to occur in realistic situations. The results were used to test the validity of acoustical measures that reflect the combined influence of speech/noise and room acoustics factors such as the speech transmission index, the Alcons measure, and useful/detrimental sound ratios. They were also used to investigate improved acoustical measures for speech in rooms and to evaluate the importance of speech/noise ratios relative to room acoustics factors.

4:20

4pAA10. Speech intelligibility in primary school classrooms. David J. MacKenzie (Heriot-Watt Univ., Dept. of Bldg. Eng. and Surveying, Riccarton, Edinburgh EH14 4AS, UK, D.J.MacKenzie@hw.ac.uk)

Recent research has highlighted the growing problem of noise levels in classrooms. The speech intelligibility of 60 occupied primary school classrooms has recently been investigated: high noise levels, long reverberation times, and poor classroom design are but some of the problems encountered. The recommended %ALcons should be 5%, whereas in some modern classrooms the value was 100%. The shape of the classroom, as well as the materials used, can lead to locations within the classroom where the quality of speech heard can be poor. Measurements were carried out in classrooms before and after acoustic treatment: the speech intelligibility in treated classrooms improved noticeably. Throughout the research project children have been involved with the majority of the measurements, with their opinion being sought and listened to. The results have been used to tackle problems of poor acoustics in local schools and also in the appraisal of two new academic buildings to be constructed in Edinburgh. These buildings are for the education of children who are either hearing impaired or have a language difficulty. The design of the buildings has been carefully considered as well as the materials being used and the correct criteria for classroom acoustics.

4:40

4pAA11. Background noise levels in classrooms. Gary W. Siebein, Martin A. Gold, Mitchell Lehde, and John Ashby (Architecture Technol. Res. Ctr., P.O. Box 115702, Univ. of Florida, Gainesville, FL 32611-5702)

Field measurements of background noise levels produced by air-conditioning systems were taken in a sample of 47 elementary school classrooms. Noise levels were grouped by air-conditioning system type and resulting noise criterion (NC) levels. Eight computer models of classrooms were constructed with varying combinations of absorbent materials on the surfaces of the rooms. A sound source was configured to approximate the normal speaking voice of a teacher in the room. RASTI measures were estimated for six seating locations in each room for background noise levels from 0 dB to NC- 55 in 5-NC point increments. RASTI values remained above 0.8 in seven of the eight rooms at NC levels of 32 and below. RASTI levels decreased to 0.50 and less in all eight rooms at levels of NC- 45. The one exception to this was the room constructed with a gypsum board ceiling, vinyl tile floor, and gypsum board walls. Even with no background noise, RASTI values in this room never exceeded 0.60. Background noise levels of NC 32 or less appear to be necessary in most typical classrooms to maintain reasonable RASTI values. Very few of the actual classrooms visited achieved these noise levels.

5:00

4pAA12. Good acoustics: A target for the new School of Architecture. Elvira B. Viveiros (Dept. of Architecture, Federal Univ. of Santa Catarina, Florianopolis, Brazil, 88040-900)

A competition for a new building for the School of Architecture is being commissioned in Florianopolis, Brazil. The project involves classrooms for theoretical classes, ateliers, library, auditorium, laboratories, staff offices, and support rooms. It consists of a 6000-sq.-m building. The site faces a noisy road, which is bound to become even noisier as the whole area develops. The provisional existing building already presents inadequacies, as for instance lecturers have complained they need to stop talking while a lorry passes along. The paper presents the proposed solutions to acclimate the new school to its environment, as well as the project details to provide good acoustic quality for the different rooms. For instance, taking into account particularities of this kind of school, absorption mechanisms play simultaneous roles in the classrooms. As the projects being developed by the students need to be hung up for oral presentation, wooden panels were planned for the side walls. Acting as vibrating membranes, the reverberation time is adequate, whilst the panels hold the posters for presentations. Solutions to avoid noise break-in are also shown.

Contributed Posters

These posters will be on display from Monday to Wednesday, 15–17 March. Authors will be at their posters from 10:00 a.m. to 12:00 noon on Wednesday, 17 March.

4pAA13. System development to reduce floor impact sound in apartment houses. Jaehee Jang, Byunghun Lim (SK R&D Center, SK Bldg. 192-18, Chongro-Gu, Seoul, Korea, jhjang@cosmos.skec.co.kr), and Sangwoo Lee (Kyunggi Univ., Seoul, Korea)

The floating floors used to reduce floor impact sound in European countries are not as compatible with Korean style floors because every residential floor in Korea is heated up by the floor heating method. In this case, considering the floor heat radiation effect, the cement screen is constructed to be about 40 to 50 mm thick. So constructing the low-density damping materials, such as glasswool, under the cement screen over 20 mm definitely makes some cracks. To prevent this kind of floor crack and to improve the impact insulation performance, the floating floor system using a plastic pallet and rubber was developed. The developed plastic pallet is 30 cm wide $\times 60$ cm deep $\times 4$ cm high and is designed to array on a concrete slab; above this plastic pallet, a 2-cm thick thermal insulator is constructed. On this, the insulator heating coil is installed, and finally the 4-cm-thick cement screen is constructed over that. The test results of impact insulation performance for the developed system show good improvement, about 15 dBa between before and after installation of the system.

4pAA14. Additional improvement of airborne and impact sound insulation of ceilings in prefabricated standard house-buildings. Eberhard Küstner, Peter S. Krämer, Jürgen Scholze, and Ernst Sonntag (GEBRA Gesellschaft für Bau- und Raumakustik mbH, Agricolastr. 26, D-10555 Berlin, Germany, kraemer_gebra@compuserve.com)

Earlier studies for the improvement on airborne and impact noise insulation of ceilings in prefabricated standard house-buildings has been continued by the support of the German Ministery of Building. The investigated slab blocks were erected in 1987 in Potsdam. The raw ceilings made of solid concrete have a thickness of 140 mm. These realized ceilings have a weighted airborne sound insulation of $R'_w = 49$ dB and a normalized impact-sound pressure level of $L'_{n,w} = 77$ dB (averaged over nine measurements). A selection of floating floor materials were built in and measured: dry laser constructions (with plaster and compound cement slabs), asphalt applied by melting, and anhydrite layers. The aim of the project was to fulfill the requirements ($R'_w = 54$ dB, $L'_{n,w} = 53$ dB) of German Standard DIN 4109 from 1989, minimizing construction height and cost. Based on earlier studies (Scholze, DAGA '94) all floating floors with a height larger than 45 mm (asphalt floor 40 mm) have been im-

proved to reach the requirements of DIN 4109. Using mineral wool as sound insulation material below the floating floor gave results up to $R'_w = 56$ dB (maximum value) and $L'_{n,w} = 48$ dB.

4pAA15. Towards a classification of acoustic comfort. A case study of a university classroom. Fausto Rodriguez-Manzo (Universidad Autonoma Metropolitana-Azcapotzalco CyAD, Av. San Pablo 180, Col. Reynosa Tamaulipas, Azcapotzalco D. F., CP 02200, Mexico, rfme@hp9000a1.uam.mx)

When it comes to speaking about acoustic comfort, one is generally dealing with a concept implying high levels of subjectivity. Hence, it becomes difficult to distinguish precisely the borderline between comfort and acoustical annoyance for an activity in a given space. Acoustical classification tools such as noise rating, noise criteria, preferred noise criteria, room criteria, balanced noise criteria, sound transmission class, and impact insulation class have proved to be partially useful in establishing averages of comfort in rooms, regardless of the spectral quality, which is intimately related to the acoustic quality of the room, and in turn related to the architectural comfort of the environment. This paper deals with the problem of correlating the quantitative aspects of acoustical measurements with elements of subjective perception. An accurate rating of the subjective acceptability of noise by polling the students, together with a simultaneous measurement of physical parameters, would result in a more realistic measure of acoustic comfort. Thus, the design of a method to correlate these parameters for the particular case of a university classroom is presented.

THURSDAY AFTERNOON, 18 MARCH 1999 ROOM MA001, 2:00 TO 6:00 P.M.

Session 4pAB

Animal Bioacoustics: Acoustics of Echolocating Animals II

Cynthia F. Moss, Cochair
Department of Psychology, University of Maryland, College Park, Maryland 20742, USA

Gianni Pavan, Cochair
Centro Interdisciplinare di Bioacustica e Ricerche Ambientali, Universita di Pavia, Via Taramelli 24, 27100 Pavia, Italy

Invited Papers

2:00

4pAB1. Discrimination of phantom targets by an Atlantic bottlenose dolphin (*Tursiops truncatus*). Roland Aubauer (Inst. of Zoology II, Univ. of Erlangen, Staudtstrasse 5, 91058 Erlangen, Germany, raubauer@biologie.uni-erlangen.de), Whitlow W. L. Au, Jeff L. Pawloski, Deborah A. Pawloski, and Paul E. Nachtigall (Hawaii Inst. of Marine Biol., Univ. of Hawaii, Kailua, HI 96734)

The ability to make fine distinctions in properties of targets is one of the outstanding characteristics of the dolphin sonar system. Behavioral experiments with these animals can reveal target echo features that can be used to model the biological sonar in order to evolve technical systems with equivalent capabilities. A phantom echo generator was developed in order to obtain programmable control over echo parameters in the time and frequency domains. Dolphin sounds are recorded with a hydrophone, transformed into the desired phantom echoes, and played back with a projector hydrophone. The signal transformation is based on the acoustic impulse response of a target and is executed on a DSP system in real time. In the first experiment the capability of a dolphin to discriminate between acoustically simulated phantom replicas of targets and their real equivalents was tested. Phantom replicas were presented in a probe technique during a materials discrimination experiment. The animal accepted the phantom echoes and classified them in the same way as it classified real targets.

2:20

4pAB2. The transmission beam pattern and echolocation signal of the harbor porpoise (*Phocoena phocoena*). Whitlow W. L. Au (Hawaii Inst. of Marine Biol., P.O. Box 1106, Kailua, HI 96734, au@nosc.mil), Ronald A. Kastelein, H. Tineke Rippe, and Nicole Schooneman (Harderwijk Marine Mammal Park, The Netherlands)

The transmission beam pattern of an echolocating harbor porpoise (*Phocoena phocoena*) was measured in both the vertical and horizontal planes. An array of seven Brüel & Kjaer 8103 hydrophones connected to an amplifier-line driver module and a Racal Store-7 instrumentation tape recorder which was operated at 30 ips (76 cm/s). The porpoise was trained to station in a hoop and echolocate a cylindrical target located at a range between 7 and 9 m while the array was located 2 m in front of the hoop. The beam in the vertical plane was pointed forward with a 3-dB beamwidth of approximately 19 degrees and the beamwidth in the horizontal plane was approximately 16°. The individual hydrophones in both the vertical and horizontal arrays measured signals that were similar in shape throughout the 40-degree span of the array. The porpoise emitted clicks with interclick intervals that were greater than the round trip travel time between the animal and the target by 20 to 35 ms. Histogram of source level, peak frequency, and bandwidth are also presented. The average source level, peak frequency, and bandwidth were 157 dB, 128 kHz, and 16 kHz, respectively.

2:40

4pAB3. Sperm whale clicks and the Norris/Harvey theory of click generation. Bertel Møhl (Dept. of Zoophysiology, Bldg. 131, Univ. of Aarhus, Aarhus, Denmark, bertel.moehl@biology.aau.dk)

In Odontocetes, sounds are generated within the melon, a structure homologous with the nose of terrestrial mammals. In sperm whales this nose is hypertrophied, accounting for about 1/3 of the length or weight of adults. A sound-generating function has been ascribed to this organ complex [K. S. Norris and G. W. Harvey, in NASA Spec. Publ. 262, edited by S. R. Galler *et al.* (1972), pp. 397–417]. A sound generator weighing upward of 10 tonnes and with a cross section of 2 m is expected to generate high level, directional sounds. This prediction is not supported by the published data for sperm whale clicks (SL's of 180 dB re: 1 μPa; little, if any, directionality). Such data, if truly characterizing sperm whale clicks, does not support the Norris/Harvey theory. To increase the amount of data, a hydrophone array, suspended from three platforms separated by 1 km and linked by radio, was deployed at the slope of the continental shelf off Andenes, Norway, in the summers of 1997 and 1998. The SL's above 210 dB re: 1 μPa were recorded. Also, SL differences exceeding 20 dB for the same click at different directions were seen. Thus, previously published properties of sperm whale clicks underestimate maximum capabilities of the sound generator and therefore cannot falsify the Norris/Harvey theory. [Work supported by the Danish National Research Foundation.]

3:00

4pAB4. Insights into the acoustic behavior of sperm whales. Gianni Pavan (Centro Interdisciplinare di Bioacustica e Ricerche Ambientali, Universita' di Pavia, Via Taramelli 24, 27100 Pavia, Italy, gpavan@telnetwork.it)

Sperm whales are still mysterious creatures. Other than to communicate, it is very likely they use sounds to navigate, to orientate, to avoid obstacles, and to find food in obscure ocean depths. Their regular clicking may serve for both communication and long-range echolocation, while codas and other patterned click sequences may serve mostly for social communication. It is known that sperm whales dive deep to search for food, probably squid and giant squid. However, to date nobody has been able to see a sperm whale detecting and capturing prey. Recordings made with towed arrays while pursuing underwater animals at close range have revealed sounds possibly used for echolocation. Accelerated click series may serve for detection and interception of prey. The patterning of clicks closely resembles the echolocation trains of dolphins, and it is very likely that sperm whales search for food in a very similar way. Bioacoustics and new technologies, such as time-depth recorders, ''crittercams,'' and satellite-based telemetry devices may offer new and valuable insights in understanding their behavior, their survival strategies, and their relationships in the food chain. Understanding these aspects is required to define and to tune conservation strategies to offer them a chance to survive.

Contributed Papers

3:20

4pAB5. Acoustic censusing of sperm whales at Kaikoura, New Zealand—An inexpensive method to count clicks and whales automatically. Olaf Jaeke (Bremer Str. 59, D-21073 Hamburg, Germany, olaf.jaeke@t-online.de) and Stephen Dawson (Univ. of Otago, Dunedin, NZ)

Special DSP software was developed to automatically count sperm whale clicks recorded along acoustic transects, and to facilitate the calibration of these counts through automated and interactive analyses of dive cycle and range experiments. Minimum pulse width and maximum interpulse interval are used as criteria for automated click detection. In addition to these criteria, interclick intervals and click amplitudes can be used for the tracing of clicks during interactive analyses. Interactive analysis of a dive of a single whale recorded under almost ideal conditions gave the following results: The mean of all interclick intervals measured within bouts of regular clicks was 0.801 s ($n=2203$ intervals, cv 27.5%), the reciprocal of which corresponds to c. 1.25 clicks per second. Including 10 s between fluke-up and the first click recorded, silences between bouts of regular clicks, and a silence between the last regular click detected and two surface clicks found 3:37 min after the last regular click, the average click rate over a dive time of 42:23 min is 0.88 per second ($n=2244$ clicks). In several dive cycles analyzed, interclick intervals were found to oscillate periodically during bouts of regular clicks. These oscillations correlated with click amplitude.

3:40

4pAB6. Specific food-related calling in dolphins. Kebkal G. Konstantin (9, Epronovskaya, 335024 Sevastopol, Ukraine, kostya@fb10.tu-berlin.de)

The results of acoustical observation of feeding behavior of bottlenose dolphins demonstrated the high degree of correlation between feeding events and very specific food signals related to every feeding act. In the paper, the features of such signals are described. They consist of specific click trains (recognizable as ''creaks'' or ''squeaks''). Working normally for echolocation, in this case, however, the use of such click series for echolocation is physically impossible. Whether the food signals serve as an anaesthetization of a prey or merely as emotional signals is not clear. The fact is that they are in any case produced before and also shortly after the moment of catching a prey, and their intensities are high enough to provide their reliable detection even in a dolphin's back fin area. The food signals consist of some distinctive parts: (1) the stage of gaining a click's repetition rate and their power, (2) the sector with a short gap of acoustic activity, and (3) the part of highest repetition rate of low powerful clicks. Parameters of every such signal's sector may somewhat vary for different individuals staying, however, stable enough to be mathematically modeled and separated from any other click trains not related to feeding events.

4:00–4:20 Break

4:20

4pAB7. The Larynx–Melon–Vestibular Lips (LMVL) model of the dolphin sonar. II. The melon beam former. James W. Fitzgerald (The Kildare Corp., 1 Spar Yard Rd., New London, CT 06320)

The LMVL model of the dolphin sonar is based on the following system components: (1) the *Larynx*, controlled by the palatopharyngeal sphincter and operating as a ''sawtooth'' relaxation oscillator, is the source of the echolocation pulses (the so-called ''clicks''), and its acoustic output is coupled to the melon through the impedance matching nasal ducts; (2) the *Melon*, because of its low sound velocity, acts as a ''slow waveguide'' to form the observed forward-looking beam patterns; and (3) the residual air in the nasopharyngeal cavity acts as an air-pressure reservoir to energize relaxation oscillations of the *Vestibular Lips*, resulting in the lip-modulated tonal phonations (the so-called ''whistles'') that radiate through the corresponding vestibular sac. The larynx sawtooth generator has been treated previously [J. W. Fitzgerald, Part I Oceans '94, Vol. I, pp.

271–276 (Sept. 1994)]. The measured sound velocity in the melon decreases with temperature from $v \cong 1.39 \times 10^5$ cm/s @10 °C to $v \cong 1.28 \times 10^5$ cm/s @40 °C. Melonlike acoustic slow waveguides, with intermediate sound velocities, yielded average pulse beamwidths of $\theta_1 \cong 11.5°$ (−3 dB) and $\theta_2 \cong 20.0°$ (−10 dB). This compares to accepted average values from measurements on live dolphins of $\theta_1 \cong 10.0°$ (−3 dB) and $\theta_2 \cong 21.8°$ (−10 dB) [W. Au, *The Sonar of Dolphins* (Springer-Verlag, New York, 1993), p. 105]. These preliminary measurements of melonlike acoustic slow waveguides, and the dissertation of Part I of this series, support the LMVL model of the dolphin sonar.

4:40

4pAB8. A plausible mechanism of acoustic click production in the dolphin. Nikolai A. Dubrovsky and Lyudmila R. Giro (Andreyev Acoust. Inst., Shvernika Ul. #4, 117036 Moscow, Russia)

A mechanism of click production has been studied. Three steps were considered: experiments with *Tursiops truncatus*, calculations to determine the source position, and physical and mathematical models for simulation of a physical mechanism of click production. It was found that the acoustic source is situated in close proximity of the right nasal plug. A physical model of a nasal passage was composed of a rubber tube open on one end and connected to a pressurized gas container on the other. A rubber ring was put on the underwater part of the tube, which blocked the air passage at small access pressure. By varying this pressure of the elastic properties of the tube and the ring, one can put the model in a self-oscillation mode of vibrations. The displacement curve (DC) of the ring has a triangle shape and duration of about 700 mks. There were three noticeable acoustic pressure clicks with duration of 50–80 mks, phase-locked to pronounced changes in the DC. A mathematical model was developed to explain the origin of clicks and their locking to the bends of DC. The characteristics of clicks formed by the models are similar to the clicks of the dolphin.

5:00

4pAB9. Time resolution of the dolphin's auditory system: Better than 20 microseconds? Gennadi L. Zaslavski (Univ. Authority for Appl. Res. and Industrial Development, Tel-Aviv 61392, Israel)

The time resolution of the dolphin's sonar estimated as a minimum interval between echo highlights at which the dolphin is still capable of distinguishing the targets, ranges from 10 to around 300 microseconds. The problem, however, is that the target echo highlights are highly correlated and produce regularly spaced ripples in the amplitude spectrum. It is not clear whether the dolphins discriminated between a target's echo in the time or frequency domain. Unless special measures are taken to eliminate this equivocalness, the experimental results can be equally accounted for discrimination cues in either domain. Different techniques were used to eliminate frequency discrimination cues that could be used by a dolphin. The double clicks that were designed differed in interpulse interval despite their long-term amplitude spectra being identical, and the highly correlated double clicks were replaced with the uncorrelated noise double pulses [G. Zaslavskiy, Proc. I.O.A. **19**, Pt. 9]. The dolphin's auditory system time resolution was found to be 25 to 30 microseconds. In this presentation the new measurement of the dolphin's time resolution of 17 to 25 microseconds will be discussed. The time resolution was estimated as a minimum delay of the click from onset of the noise or tone pulse just detectable by the dolphin.

5:20

4pAB10. Improved signal processing techniques for measurement of the interpulse interval (IPI) of sperm whale clicks. Thomas J. Hayward (Naval Res. Lab., Washington, DC 20375) and G. Pavan (Univ. degli Studi di Pavia, 27100 Pavia, Italy)

Improved signal processing techniques are described for estimating the interpulse interval (IPI) associated with the multiple pulses in a sperm whale click. These pulses are believed to result from repeated reflections of the original pulse within the spermaceti organ in the whale's head. Previous estimates of the IPI have been based on time series correlation or on computation of the cepstrum of the received waveform [J. Goold, J. Acoust. Soc. Am. **100**, 3431–3441 (1997)]. The present work describes real-time computation and display of the spectrogram and cepstrogram (time-cepstral distribution) [G. Pavan, Proc. IOA **19**(9) (1997)] and examines the benefits of the simultaneous display of this information for field analysis and for browsing long recordings to identify sperm whale clicks. In addition, a detailed model of the spectral modulation associated with the multiple pulses is developed and leads to improved estimation of the IPI. Examples are presented that indicate the method may be more robust with respect to additive noise and the effects of surface reflection than the cepstrum-based approaches. [Work of the first author supported by ONR. Work of the second author supported by the University of Pavia, Italy, the Italian Ministry of the Environment, and by the Italian Navy.]

5:40

4pAB11. Why do whales communicate at the frequencies they do? Lessons from underwater acoustic signal processing. Kevin D. Heaney (Sci. Applications Intl. Corp., 11803 Sorrento Valley Rd., San Diego, CA 92121) and Chris Clark (Cornell Univ., Ithaca, NY)

The combination of frequency-dependent attenuation of acoustic energy and the ambient noise field of the deep ocean provides a window of opportunity for acoustic communication ranging from 10 to 1000 Hz. Why do pelagic whale species choose to use center frequencies between 20 and 50 Hz rather than higher frequencies in the window of opportunity? It is not a size limitation, because similar size whales which reside nearby in shallow water have center frequencies of propagation from 400 to 700 Hz. Experience in underwater signal processing has shown that internal wave scattering can be significant for acoustic frequencies above 50 Hz. Here the postulate is presented that deep-water whales (blues and fins) have chosen to send acoustical signals at 20 Hz to minimize internal wave scattering of their acoustic energy. The implications to range of detection will be made from a signal processing point of view and the impact that this would have on marine mammal biology will also be presented. Similar arguments, though based on different physics, will be employed to discuss the shallow-water whales' (bowhead, humpback, gray) choice of 400 Hz.

Session 4pAO

Acoustical Oceanography: Acoustic Seafloor Classification II

Larry Mayer, Cochair
Ocean Mapping Group, Department of Geodesy and Geomatics Engineering, University of New Brunswick, Fredericton, New Brunswick E3B 5A3, Canada

Eric Pouliquen, Cochair
SACLANT Undersea Research Centre, Viale San Bartolomeo 400, 19138 La Spezia, Italy

Contributed Papers

2:20

4pAO1. Aspects of near-real time acoustic sediment characterization. Wolfgang Jans (Naval Res. Lab., Stennis Space Center, MS 39529-5004 and Federal Armed Forces Underwater Acoust. and Marine Geophys. Inst. (FWG), Klausdorfer Weg 2-24, 24148 Kiel, Germany), Warren T. Wood (Naval Res. Lab., Stennis Space Center, MS 39529-5004), and Eric Smith (Univ. of Texas, Austin, TX 78731-8029)

Quantitative near normal incidence acoustic measurements were made with a calibrated, broadband, narrow-beam echo sounder at a variety of natural sediment sites along the Florida coast. The measured reflectivity of the water–sediment interface along track lines was converted into a map-view image, using recently developed interpolation and visualization software. The computed reflectivity was then compared to sediment samples and visual observations recovered from the same area. The measurements demonstrated that areas of different bottom type within a site could be clearly distinguished using acoustic techniques. At some sites, conventional expectations that softer sediments show a lower reflectivity than harder sediments were fulfilled. However, at other sites, the expectation superficially appears to be violated presumably due to the influence of bottom roughness. The presence of turtle grass also reduces reflectivity. To gain an understanding of these findings, histograms of the received echo signal and frequency spectra for different areas have been compared. The rapid 2.5-D visualization of bottom reflectivity and bathymetry has been shown to provide improved capability for near-real time decisions in seafloor investigations. [Work supported by ONR and BWB.]

2:40

4pAO2. Comparison of seafloor character as measured by calibrated vertical-incidence profiler and sidescan sonar. Peter Fleischer (Code 7431, Naval Res. Lab., Stennis Space Center, MS 39529), Wolfgang Jans (Naval Res. Lab. and Federal Armed Forces Underwater Acoust. and Marine Geophys. Inst. (FWG), 24148 Kiel, Germany), and Warren T. Wood (Naval Res. Lab., Stennis Space Center, MS 39529)

Sidescan sonar backscatter from a variety of continental shelf bottom types reveals considerable divergence from vertical-incidence reflection coefficients. Acoustic data are from a 300-kHz sidescan sonar and a calibrated, constant beam width, 10–50 kHz vertical incidence profiler, and are supported by extensive physical, geoacoustic, textural, and morphologic measurements. Bottom types include a wide range of quartzose and carbonate sands and silts, seagrass, coral heads, coral reef, and hardbottoms. The two systems show notable divergences over seagrass and carbonate hardbottoms, which produced low normal-incidence reflection coefficients but high backscatter from sidescan sonar, and smooth, packed sands, which gave high normal-incidence reflection coefficients but low sidescan backscatter. The divergences appear to be caused by bottom roughness. Narrow-beam, vertical incidence systems are subject to signal loss from out-of-beam scattering over rough bottoms, whereas roughness increases backscatter at the low grazing angles over which the sidescan system operates. Although both systems will accurately map bottom character, there is no direct correspondence betwen the two vis-à-vis bottom type. Therefore, to extend seafloor classification from vertical incidence profiling into an areal approach with sidescan sonar requires more than simple lateral extrapolation. [Work supported by ONR.]

3:00

4pAO3. Effects of differing sediment types and structures on normal incident acoustic reflections. Warren T. Wood (Naval Res. Lab., Stennis Space Center, MS 39529), Wolfgang Jans (Naval Res. Lab. and Federal Armed Forces Underwater Acoust. and Marine Geophys. Res. Inst. (FWG), 24148 Kiel, Germany), and Eric Smith (Univ. of Texas, Austin, TX 78731-8029)

Data acquired during a recent survey of coastal Florida and the Bahamas have provided an opportunity to correlate normal and near normal incidence acoustic returns with distinguishing seafloor sediment characteristics. These include physical property measurements (both *in situ* and laboratory) as well as bottom textural measurements derived from diver observations and from video and stereo photography. Measurements were made with a calibrated 1–3 piezocomposite transducer, which offered a very narrow (~8 deg) beam width over the 10–50-kHz transmitted chirp. In addition, a roll and pitch sensor mounted on the transducer and 0–5 deg ship motion allowed for a monostatic backscatter experiment. This resulted in quatitative measurements of reflectivity versus angle over a relatively broad frequency band. Interestingly, the measured reflection coefficients were significantly lower (especially at high frequencies) and exhibited a greater range in values than those obtained in laboratory tank measurements with a flat, level interface. Also, the range of reflectivity at any fixed angle and anchor location was greater than the systematic dependence on angle. This suggests that very slight ship motion combined with either bottom roughness or discrete scatterers is responsible for the variable reflectivity. [Work supported by ONR.]

3:20

4pAO4. *In situ*, laboratory, and modeled permeability of unconsolidated sands. Dawn L. Lavoie (Code 7431, Naval Res. Lab., Stennis Space Center, MS 39529), Allen Reed (Univ. of Southern Mississippi, Stennis Space Center, MS 39529), and Keven Briggs (Naval Res. Lab., Stennis Space Center, MS 39529)

Bulk physical sediment properties, especially permeability, are required to predict sediment geoacoustic and geotechnical behavior. Of the variables controlling permeability in surficial sediments, pore space distribution is probably the most significant. The objective is to quantify the relationship between sediment microfabric and sediment flow properties. Relatively undisturbed samples were collected by divers from the upper 25 cm of seafloor from several locations on the Florida shelf and near Bimini in the Bahamas. The undisturbed sediment microfabric was maintained by impregnating the samples using a polyester resin. Sediment microfabric was examined using petrographic and scanning electron microscopes. Representative images were scanned and analyzed using Image Tool and Image Tool Plug Ins. Using erosion-dilation analysis, the 2D imaged pores and pore network were defined and quantified. CT images were used to determine sediment isotropy and to generate 3D structural images, which were used as input to effective medium theory to predict single-phase flow within the sediment. The modeling results are compared to laboratory-measured permeability from the same samples, and with permeability measured *in situ* using a falling head permeameter. [This work was supported by the Naval Research Laboratory.]

3:40

4pAO5. Subsurface classification of shallow gassy river sediments using broadband seismic data. Stephen F. Bloomer, N. Ross Chapman (School of Earth and Ocean Sci., Univ. of Victoria, P.O. Box 3055, Victoria, BC V8W 3P6, Canada), William T. Collins (Quester Tangent Corp., Sydney, BC V8L 5Y8, Canada), and Peter G. Simpkin (INRS-Océanologie, Rimouski, QC G5L 3A1, Canada)

Acoustic seabed classification from sonar data has generally focused on attributes of the return echo from the seafloor. For many shallow-water engineering applications, such as dredging, detailed knowledge of the shallow sub-bottom is also required. Consequently, acoustic classification of the sub-bottom is also often essential. In 1995, a shallow-water, high-resolution seismic predredging survey was conducted on the St. Lawrence River in water depths of 10–15 m using the IKB SEISTEC high-resolution profiler, which has a bandwidth of 1–12 kHz and subsurface penetration in excess of 10 m. In these river sediments, it was found that shallow gas had a controlling effect on the appearance of the seismic sections in some places. The shallow gas could often be identified as a curtain in which there are no acoustic returns below a strong subsurface reflector with a phase reversal relative to the seafloor reflection. The frequency dependency of the ratio of the signal amplitude between the seafloor and sub-bottom reflectors may also be diagnostic of gas reflectors in that, instead of attenuation, resonances may occur. Using the spectral-ratio method, the attenuation between successive reflectors characteristic of the sediment between the reflectors can be determined. Results of classifying subsurface sediments between distinct reflectors from this survey will be presented.

4:00

4pAO6. Acoustic inversion for Biot parameters in water-saturated sand. Nicholas P. Chotiros (Appl. Res. Labs., Univ. of Texas, P.O. Box 8029, Austin, TX 78713-8029)

Using an inversion of Biot's theory, based on the formulation by Stoll, operative values of grain bulk modulus and the frame bulk and shear moduli of water-saturated sand may be extracted from measurements of compressional and shear wave speeds and reflection loss. The inversion process is nonlinear, but in practice it is well behaved and converges quite rapidly to unique values. The term grain bulk modulus, as defined in the formulation by Stoll, is not necessarily identical to the bulk modulus of the grain material, as is often assumed. Examples of the inversion will be given, and the significance of the operative values of the grain bulk modulus will be discussed. [Work supported by Office of Naval Research: Ocean Acoustics.]

4:20–4:40 Break

4:40

4pAO7. Acoustic classification of a shell-covered seafloor. Timothy K. Stanton (Dept. of Appl. Ocean Phys. and Eng., Woods Hole Oceanogr. Inst., Woods Hole, MA 02543-1053)

Acoustic scattering by the seafloor is sometimes influenced, if not dominated, by the presence of discrete volumetric objects such as shells. Classification of a shell-covered seafloor requires understanding of the acoustic scattering properties of the shells. A series of measurements of target strength of a type of benthic shelled animal and associated scattering modeling have recently been completed. In addition, a simple formula has been derived that expresses the area scattering strength of the seafloor in terms of the reduced target strength (RTS) of the discrete scatterers and their packing factor (where RTS is the target strength normalized by the size of the scatterers). The formula shows that, to first order, the backscattering at high acoustic frequencies by a dense layer of shells (or other discrete bodies such as rocks) depends principally upon material properties of the objects and packing factor, and is independent of size and acoustic frequency. There are reasonable comparisons between scattering data from shell-covered sections of seafloor and predictions using this formula and the measurements/modeling of shell target strength. The functional dependence of this and other seafloor scattering formulas upon shell and shell-bed characteristics are discussed to assess one's ability to classify a shell-covered seafloor. [Work supported by ONR.]

5:00

4pAO8. Scaling regimes in incoherent surface-reflected and in-sediment sound fields. Eric Smith (Appl. Res. Labs., Univ. of Texas, Austin, TX 78713-8029), Michael D. Richardson, Warren T. Wood (Naval Res. Lab., Stennis Space Center, MS 39529-5004), and Wolfgang Jans (Naval Res. Lab. and Federal Armed Forces Underwater Acoust. and Marine Geophys. Inst. (FWG), Klausdorfer Weg 2-24, 24148 Kiel, Germany)

A suite of collocated measurements of broadband in-sediment acoustic propagation and surface reflection was made at nine sites on the Florida shelf and in the Gulf of Mexico, between 16 August and 6 September 1998. Closely spaced in-sediment transmission measurements, and populations of narrow-beam echo soundings, provided ensembles from which mean and incoherent components of propagating and reflected sound fields were derived. The two components contain mutually independent information about the effective bulk properties and heterogeneity of the medium. Attenuation of the direct arrival through the sediment depends on both intrinsic absorption and scattering from heterogeneities. Temporal decay of the incoherent ''coda'' at a point, not described by homogeneous effective-medium theory, requires scattering to maintain sound energy in a region. Incoherent coda in the surface reflection can be generated either from multiple scattering near the surface, or random reflection within the sediment bulk. Scaling regimes of both kinds of attenuation will be demonstrated and compared, between in-sediment propagation and surface reflection, and among different sites. As a control, scaling of the coda decay constant will also be compared to results of reflection from sand in an indoor tank, from which stratification and surface roughness were removed. [Work supported by ONR.]

5:20

4pAO9. Seabottom roughness study using a hydrosweep–multibeam system. Bishwajit Chakraborty, Vijay N. Kodagali (Natl. Inst. of Oceanogr., Dona Paula, Goa: 403 004, India, bishwajt@csnio.ren.nic.in), and Hans W. Schenke (Alfred Wegener Inst. for Polar and Marine Res., 27515 Bremerhaven, Germany)

Seabottom profiling using a multibeam echosounder is a well-known method to acquire a high-resolution and high-density data set for bathymetric mapping of survey area. The use of multibeam echosounder backscatter signals for bottom roughness characterization is a modern technique. Here, the model results of seabottom backscatter data using a hydrosweep-multibeam system, from some of the geologically well-known areas of Southern Oceans, are presented. Using the capabilities of multibeam systems, angular backscatter strengths are determined employing various corrections. Different bottom backscattering modeling techniques like the composite roughness [Jackson *et al.*, J. Acoust. Soc. Am. **79**, 1410–1422 (1986)] and two-layer Helmholtz–Kirchhoff model [Talukdar *et al.*, J. Acoust. Soc. Am. **97**, 1545–1558 (1995)] for estimation of bottom roughness is applied. Various seabottom parameters like root-mean-square (rms) relief height, correlation lengths, attenuation coefficients, and layer thickness using the two-layer Helmholtz–Kirchhoff model are calculated. The interface roughness parameters, i.e., slope and intercept values, and volume roughness parameters are computed using the composite roughness theory for the same geological areas.

5:40

4pAO10. The comparison of inverse filtering techniques applied together with fractal analysis in the sea bottom recognition. Zbigniew Lubniewski, Marek Moszynski, and Andrzej Stepnowski (Tech. Univ. of Gdansk, Acoust. Dept., ul. Narutowicza 11/12, 80-952 Gdansk, Poland, lubniew@eti.pg.gda.pl)

The results of the combined approach using fractal analysis and inverse filtering methods applied to sea-bottom-type recognition are presented. The single-beam one-frequency echosounder was used in described investigations. The bottom-scattering impulse response was used to extract descriptive parameters of a seabed type. Both direct methods, including windowed SVD, regularization and wavelet analysis, as well as iterative techniques like maximum entropy, and expectation, maximization, and smoothing (EMS) were investigated. The data were acquired from acoustics surveys on Lake Washington and Liberty Bay. The results were compared and discussed especially in the context of excessive smoothing of the extracted fractal features by applied newly developed inverse techniques.

6:00

4pAO11. Seafloor scattering: Modeling and analysis of classification clues. Anatoliy N. Ivakin (Andreev Acoust. Inst., Shvernika 4, Moscow 117036, Russia, aniva@glasnet.ru)

Possibilities of scattering data inversion for various seabed properties are analyzed using recently developed models of acoustic bottom interaction. Different scattering mechanisms are considered giving the main contributions to total bottom scattering which are due to different types of medium irregularities: volume inhomogeneities of the sediment medium and roughness of its surface and internal interfaces. High-frequency model of scattering corresponds to sufficiently strong absorption and small penetration into the sediment such that the influence of seabed stratification is negligible. At lower frequencies, a layered seabed scattering model considers also refraction and interference effects due to sediment stratification as well as effects of elastic scattering and reflection from the basement supporting both compressional and shear waves. Frequency-angular dependencies of the scattering strength for both monostatic and bistatic cases are calculated and analyzed for various seabed types. Distinctive features are discussed which can be used as classification clues for determination of various parameters of the seafloor. Additional clues are revealed from an analysis of the spatial correlation function of the scattered field that can be used for distinguishing and/or separating the volume and roughness components of scattering.

Contributed Posters

These posters will be on display from Thursday to Friday, 18–19 March. Authors will be at their posters from 10:00 a.m. to 12:00 noon on Friday, 19 March.

4pAO12. Generalized additive models for classifying sea-bottom types. Patrick Schneider (Instituto de Ciencias del Mar, Barcelona, Spain) and John Hedgepeth (BioSonics, Inc., Seattle, WA)

One encounters many types of sea-bottom, a continuous spectrum of all kinds of transitions between one category and another, not just clear-cut categories. A number of parameters, which the BioSonics Visual Bottom Typer extracts from the data, are looked at as a continuum, from one bottom type to another. As generalized additive models (GAMs) are nonlinear regression models, they can be useful to find relating functions for some of the parameters, significant for different bottom characteristics. The advantage of the GAMs is that if there should be a linear relation between two parameters, they are also able to reveal this, because a linear model is included as one special case in a GAM. Also, there can be problems with GAMs: There may not be a single transition from, e.g., soft/muddy to hard/rocky, but different kinds of bottom types can be connected in arbitrary ways; building a library from known bottoms, as has previously been done, might be the easiest and most practicable way.

4pAO13. Bottom layers' structure influence on ocean shelf water low-frequency source sound field numerical modeling. Andrew G. Semenov, Alexander M. Derzjavin, and Oleg V. Kudryavtzev (N. N. Andreev Acoust. Inst., Russian Acad. of Sci., 4 Shvernik St., 117036 Moscow, Russia)

The low-frequency vector wave field modeling method for the prediction of fields in layered inhomogeneous ocean and the ocean bottom environment is proposed. The method is especially stable to vertically cut media multiple arbitrary thickness layers. Based on integral presentation of 2-D cylindrically symmetric source wave fields in elastic media, the method accounts for all wave types involved. Inhomogeneous media in the problem are cut in N horizontally homogeneous layers, for which 4 $(N-1)$ equations were derived, accounting for conditions on both layers boundaries. Equation factors found by the Schmidt global matrix method are introduced in Fourier–Bessel integral expressions for local field parameters. Expressions were calculated numerically to obtain values of

acoustic pressure and elastic stress, vertical and horizontal particle velocity component in liquid and elastic media, respectively. Deviations fromexact solutions expressed in modeling stability losses were obliged mainly to layers' excessive thickness choice. A simple enough ''benchmark'' problem solution, where results for the conventional and the proposed method were compared to the exact solution, demonstrates method advan-tages. Point source of frequency 0.01–10.0 Hz, situated in a water-layer field model is presented. The influence of the bottom elastic layers' structure on model parameters is demonstrated. The geological–acoustic bottom model depending on frequency is proposed.

THURSDAY AFTERNOON, 18 MARCH 1999 ROOM MA043, 2:00 TO 6:20 P.M.

Session 4pBB

Biomedical Ultrasound/Bioresponse to Vibration: Lithotripsy

Robin L. Cleveland, Cochair
Department of Aerospace and Mechanical Engineering, Boston University, Boston, Massachusetts 02215, USA

Michael Delius, Cochair
Institute for Surgical Research, University of Munich, Klinikum Grosshadern, D-81366 Munich, Germany

Invited Papers

2:00

4pBB1. Effect of increased ambient pressure on lithotripsy-induced cavitation in bulk fluid and at solid surfaces. Michael R. Bailey (Appl. Phys. Lab., College of Ocean and Fishery Sci., Univ. of Washington, 1013 NE 40th St., Seattle, WA 98105), Robin O. Cleveland (Boston Univ., Boston, MA 02215), Oleg A. Sapozhnikov (M. V. Lomonosov Moscow State Univ., Moscow 119899, Russia), James A. McAteer, James C. Williams, Jr. (Indiana School of Medicine, Indianapolis, IN 46202-5120), and Lawrence A. Crum (Univ. of Washington, Seattle, WA 98105)

By reducing cell damage but maintaining stone comminution, overpressure (OP)—increased hydrostatic pressure—offers the promise of safer more effective shock wave lithotripsy (SWL) [Delius, UMB **23**, 611–617]. A current hypothesis is that stones offer cavitation sites—sites of violent bubble activity—when the cavitation nuclei in a free field have been dissolved into the fluid by overpressure. Cavitation around solid bodies and in a free field with and without overpressure is investigated. High-speed photography and dual passive cavitation detection (PCD) were used to measure the temporal and spatial extent of cavitation in a 10-cm^3 plastic chamber that minimally altered the shock wave. In a free field at OP=0 atm, cavitation bubbles formed and collapsed in 280 ± 20 μs. The time of collapse t^c was halved at OP=1 atm, and cavitation activity was not detectable at OP=3 atm. With a stone present, a bubble $\sim$10 times larger than free-field bubbles grew on the surface of the stone and collapsed after 440 ± 50 μs. With overpressure t_c shortened cavitation was still measurable ($t_c=80\pm12$ μs at OP=3 atm). Results were similar with human kidney stones, artificial cement stones, and an aluminum plate, and support the caviation hypothesis. [Work supported by NIH DK43881, FIRCA, and CRDF.]

2:20

4pBB2. Clinical evaluation of cavitation thresholds in patients undergoing lithotripsy. Andrew J. Coleman, Prashant K. Verma (Dept. of Med. Phys., St. Thomas' Hospital, Lambeth Palace Rd., London, UK), and Mark D. Cahill (Univ. of Bath, Claverton Down, Bath, UK)

Thirty patients undergoing extracorporeal lithotripsy for renal and uteretic stone disease were included in a study of cavitation thresholds. A passive, focused hydrophone was used to detect the 1-MHz component of the broadband noise emmission from bubbles generated at depth in tissue close to the focus of a Stortz Monolith SL20 lithotripter. A theoretical model was used to obtain predictions of the peak negative pressure at the focus of the lithotripter at output settings corresponding to those used clinically. A detectable cavitation threshold was identified in 18 patients. As the output level of the lithotripter is reduced, multiple bubble collapses cease to be detected below a well-defined threshold which is similar in all patients. There is also some evidence that this threshold is dependent on the previous exposure history of the tissue. [Work supported by MRC.]

2:40

4pBB3. Relationship of shock wave lithotripsy (SWL)-induced lesion size to renal hemodynamics at differing SWL parameters. Andrew P. Evan (Dept. of Anatomy, Indiana Univ., School of Medicine, MS 208, 635 Barnhill Dr., Indianapolis, IN 46202), Lynn R. Willis, Bret A. Connors, Philip Blomgren, and James E. Lingeman (Methodist Hospital, Inc., Indianapolis, IN)

The present study was designed to determine the relationship between lesion size and hemodynamic changes by altering the kV level, shock number, and pre-treatment status of the kidney. Six-week old pigs were divided into groups based on treatment protocol: 12, 18, and 24 kV at 2000 shocks, 24 kV at 8000 shocks, pyelonephritis 24 kV at 2000 shocks and sham. Following anesthesia each pig was prepared for clearance determinations of glomerular filtration rate, renal plasma flow, and PAH extraction. The lower pole of one kidney was treated with an unmodified HM3 lithotripter except the sham group. Renal function was measured 1 h before and 1 and 4 h after SWL followed by renoval of both kidneys for morphological analysis. Lesion size increased as kV ($0.27\pm0.1\%$, $2.28\pm0.3\%$, $6.1\pm1.7\%$, respectively) and shock number ($6.1\pm1.7\%$, $13.6\pm1.4\%$) increased. Renal hemodynamic changes oc-

curred independent of lesion size. Pyelonephritis potentiated the hemodynamic changes seen with 2000 shocks and therefore, more closely mimicked 8000 shocks. Thus two separate mechanisms may be responsible for vascular and tubular injury induced by SWL, and that pre-existing renal disease may potentiate the lesion induced by a clinical dose of SWL. [Work supported by NIH Grant No. PO1 DK43881.]

3:00

4pBB4. Controlled and forced collapse of inertial cavitation bubbles during SWL. Pei Zhong and Xufeng Xi (Dept. of Mech. Eng. and Mater. Sci., Duke Univ., Box 90300, Durham, NC 27708)

The dynamics of inertial cavitation induced by current clinical lithotripters is uncontrolled. Recently, it has been shown [Zhong *et al.*, J. Urol. **158**, 2323–2328 (1997)] that a second shock wave generated in a few hundred microseconds following the standard lithotripter pulse can be used to control and force the collapse of cavitation bubbles toward the target stones, leading to increased stone comminution. Different approaches of generating the second shock wave have been tested, including combination of two EH generators and modification of ellipsoidal reflectors. To provide a unit that can be combined with clinical EH lithotripters, a piezoelectric annular array (PEAA) generator was designed and fabricated. This PEAA generator consists of eight 50-mm PZT4 elements of 200-kHz resonant frequency, which produce a peak compressive pressure of ~ 8 MPa with a -6-dB beam diameter of 5 mm. A fiber-optic link was used to trigger the release of the PEAA generator (jitter less than 10 μs). The combined shock-wave generator, with optimal time delay between the release of the lithotripter and the second pulses, was found to increase stone fragmentation *in vitro* by 48% to 67%, as compared to the standard lithotripter. [Work supported by NIH RO1 DK 52985.]

3:20

4pBB5. Shock wave–inertial microbubble interaction. Pei Zhong, Xufeng Xi, Songlin Zhu (Dept. of Mech. Eng. and Mater. Sci., Duke Univ., Box 90300, Durham, NC 27708, pz1@me1.egr.duke.edu), and Haifan Lin (Duke Univ., Durham, NC 27710)

To produce *in situ* shock wave–inertial microbubble interaction, an annular ellipsoidal reflector, confocal but 15 mm shorter in major axis than the ellipsoidal reflector of a XL-1 lithotripter, was fabricated and combined with the XL-1 reflector. With this modification, a small portion of the spark-generated spherical shock wave is reflected and diffracted by the annular reflector, producing a weak shock wave approximately 8.5 μs in front of the lithotripter pulse. This preceding shock wave ($-0.96 < P < -1.91$ MPa at 25 kV) induces inertial microbubbles, which expand to a maximum size of 100 to 200 μm before being collapsed *in situ* by the ensuing lithotripter pulse. High-speed shadowgraph imaging and passive cavitation detection have revealed strong secondary shock wave emission immediately following the propagating lithotripter shock front and microjet formation along the wave propagation direction, features that are absent from the standard lithotripter pulses. With optimal pulse combination, membrane permeabilization of mouse lymphoid cells produced by the modified shock waves is substantially enhanced (up to 91%) at low dosage (<50 shocks), and cell injury is significantly increased (up to 50%) at high dosage (>100 shocks), compared to standard lithotripter pulses. [Work supported by NIH R21 HL60327.]

3:40

4pBB6. Transfer of an exact number of molecules into cells by shock waves. M. Delius and G. Adams (Inst. for Surgical Res., Univ. of Munich, Klinikum Grosshadern, 81366 Munich, Germany, delius@icf.med.uni-muenchen.de)

Shock wave application to cells *in vitro* causes a transient increase of the permeability of the cell membrane which does not lead to cell death. The transfer of molecules into the cytosol was quantified with florescein dextrans by flow cytometry. It was much higher than the uptake by endocytosis. It did not change over the next hours; there was no efflux. It depended linearly on the dextran concentration in the medium. In addition, transfer of a low number of dextran molecules of high molecular weight was equal to a high number of low weight. In conclusion, shock wave transfer reflects directly the amount of fluid transferred. It is in the femtoliter range. The number of molecules acoustically transferred by a certain fluid volume into a cell depends on their concentration in the medium. The protein gelonin was used to transfer different numbers of molecules into the cytosol and to assess the cell proliferation. Acoustic transfer of a single molecule or of any other defined number of molecules into the cell is a simple method to assess dose-response effects. It might be widely applied in disciplines such as physiology, biochemistry, and drug design.

4:00

4pBB7. Aspects of pressure pulse lithotripter measurements. Friedrich Ueberle (Dornier Medtech, Industriestrasse 15, 82110 Germering, Germany)

Although pressure pulse waves have been used as the standard treatment of kidney stones (ESWL) for the last 15 years, the relevance of their different physical parameters is not fully understood. The new approach of tissue treatment for pain reduction (ESWA, ESWT) raises even more questions. In 1998, the IEC document 61846 ''Ultrasonic-pressure pulse lithotripters—Characteristics of fields'' was internationally accepted. It contains the descriptions of all the parameters which may be measured, as well as the different hydrophone types which may be used. Additional work was done, e.g., by the FDA and in the ''German society for shockwave lithotripsy'' (DGS) to define a standard set of pressure pulse data, measured according to the IEC standard. The standard parameters may be measured using different hydrophone types and using either (only) the positive parts of the waves or the complete wave, including rarefaction parts for the calculation of energy parameters. Choosing a hydrophone capable of serving the demands of lifetime, signal confidence (including time parameters and rarefaction pressure), as well as cost efficacy is the most delicate task. Various aspects necessary for the interpretation of standard parameters measured using different hydrophones will be discussed.

Contributed Papers

4:40

4pBB8. *In vivo* modeling of the HM3 lithotripter. Robin O. Cleveland (Dept. of Aerosp. and Mech. Eng., Boston Univ., Boston, MA 02215)

A computer model for the propagation of shock waves in the HM3 lithotripter has recently been developed using the KZK equation [Averkiou and Cleveland, J. Acoust. Soc. Am., submitted]. The model has been extended to account for propagation through inhomogeneous tissue. The tissue was modeled as a layered medium with properties varying in the direction of acoustic propagation. Tissue absorption was modeled as consisting of four relaxation processes which provided an excellent fit to empirical absorption characteristics. Results were compared to waveforms measured in pigs [Cleveland *et al.*, Ultrasound Med. Biol. **24**, 293–306 (1998)]. Measured and calculated waveforms were in good agreement, including the rise time of the shock. However, at the focus measured, peak pressure was less than calculated numerically. It is supposed that small-scale arbitrary inhomogeneities, that the model does not account for, produced aberration effects that lead to the reduction in measured amplitude. The model predicted large negative pressures in the perirenal fat where cavitation events have been detected. [Work supported by NIH PO1-DK43881.]

5:00

4pBB9. Renal vasoconstriction caused by SWL to one pole of one kidney may attenuate the injury caused by subsequent SWL to the other pole of that kidney. Lynn R. Willis (Dept. of Pharmacology and Toxicology, Indiana Univ., School of Medicine, MS A528, 635 Barnhill Dr., Indianapolis, IN 46202), Andrew P. Evan, Bret A. Connors, Philip Blomgren, and James E. Lingeman (Methodist-Clarian Hospital, Inc., Indianapolis, IN)

These experiments examined the size of the renal lesions produced by SWL after 2000 shocks applied first to one pole and then immediately to the other pole of the same kidney. Anesthetized, 6-week-old pigs received 2000 shock waves at 24 kV (Dornier HM3) first to the lower pole and then to the upper pole of the same kidney (4000 shocks in all). Bilateral measurements of renal blood flow (RBF) were obtained 1 h before and 1 and 4 h after SWL. Lesion sizes in each pole were determined by serial sectioning and digital photography. SWL successively to lower and then upper poles in each of two pigs caused marked bilateral renal vasoconstriction (reduction of RBF). In one pig, the upper-pole lesion was only about 5% the size of the initial lower-pole lesion. In the second pig, the lesions in the upper and lower poles were of similar sizes. In both pigs, the combined lesion sizes after 4000 shocks (6.81% and 5.72%, respectively) were nearly the same as the size of lesions produced by a single application of 2000 shocks to only one pole (6.1 ± 1.7). The data suggest that renal vasoconstriction limits the renal injury caused by SWL.

5:20

4pBB10. Shot-to-shot variability of acoustic axis of a spark-source lithotripter. Oleg A. Sapozhnikov (Dept. of Acoust., Phys. Faculty, Moscow State Univ., Moscow 119899, Russia, olegs@na.phys.msu.su), Michael R. Bailey, and Lawrence A. Crum (Univ. of Washington, Seattle, WA 98105)

The shot-to-shot spatial variability of acoustic and cavitation fields of a spark-source lithotripter was investigated. Spark jitter, variation in the arc strength and location is cited for lack of repeatability in laboratory experiments and is thought to contribute to the success of the Dornier HM3 in comminuting kidney stones, which tend to move during treatment. Transverse variability of the acoustic focus was assessed by measuring the location of the shock wave (SW) induced fountain. The water bath was lowered and a small cup half-filled with ink and having a gridded paper roof was placed at the level of the focus. An ink drop created by the fountain was recorded on the paper. Drop diameter varied from 0–12 mm, location of its center varied by about 1 mm. The extent and location of the cavitation field was measured by high-speed camera. The cavitation cluster was 1×10 cm at its largest extent but bubbles collapsed in a narrow 1–2 mm line. The location of the line was repeatable to within 2 mm. The results indicated that spark jitter affected SW amplitude but had little effect on the location of the acoustic axis. [Work supported by NIH (DK 43881), CRDF and RFBR.]

5:40

4pBB11. Use of two pulses to localize and intensify cavitation in lithotripsy. Dahlia L. Sokolov, Michael R. Bailey, and Lawrence A. Crum (Appl. Phys. Lab., College of Ocean and Fishery Sci., Univ. of Washington, 1013 NE 40th St., Seattle, WA 98105)

A single electrohydraulic lithotripter pulse excites a cigar-shaped cavitation field that plays a role in both stone comminution and tissue damage during kidney stone treatment. The diameter and length of such a field (in water) are approximately 1 and 10 cm, respectively, and the lifetime is ~ 500 μs. A second, time-delayed pulse can be used to suppress cavitation during growth. As a result, by using two lithotripters facing each other and firing simultaneously, a cavitation field can be created for which the lithotripsy pulses sum coherently at the center to enhance cavitation and counteract each other off-center to suppress cavitation. The result is an intense and localized cavitation field, contained entirely by a cylinder of diameter ~ 3 and length ~ 4 cm, and having a lifetime twice that of a single-pulse field. When produced *in vivo*, such a localized cavitation field may increase the rate of stone comminution while mitigating damage to surrounding tissue. Experiments were undertaken *in vitro* with a Dornier HM3 experimental lithotripter, using a Kodak EktaPro 4540 digital high-speed motion analyzer for data acquisition. [Work supported by NIH PO1 DK43881.]

6:00

4pBB12. Generation of a very high pressure pulse at the surface of a sandwiched piezoelectric material. Jean-Pierre Sferruzza and Dominique Cathignol (INSERM Unite 281, 151 Cours Albert Thomas, 69424 Lyon Cedex 03, France, cathignol@lyon151.inserm.fr)

New clinical concepts in lithotripsy demand small size shock heads. Reduction of piezoelectric shock head is only possible if accompanied by a corresponding increase of the pressure generated at the surface of each transducer, so that the total pressure at the focus remains the same. Because the pressure generated by a transducer is proportional to the electric field applied between its two electrodes, a higher pressure could be generated by using greater electric fields. Nowadays, the value of the usual fields is no more than 2 kV/mm and the generated pressure at the surface is about 10 bars. Unfortunately, higher pulsed fields applied on the transducer lead to breaking phenomena. For the first time, a proposal is presented to increase the pressure using sandwiched transducers, which are a combination of several stacked transducers excited at such times that the pressure waves generated by each one are fully added at the interface transducer–propagating medium. This new and patented technique has been successfully tested. More than 30 bars were obtained with a two-layer transducer each 5-mm thick, and working under an 8-kV excitation voltage. Using this new elementary transducer a piezoelectric shock head of only 20-cm diameter is expected.

Session 4pEAa

Engineering Acoustics and Signal Processing in Acoustics: Digital Signal Processing for Hearing Aids II

Roger T. Richards, Cochair
Naval Undersea Warfare Center, 1176 Howell Street, Newport, Rhode Island 02841, USA

Juergen Peissig, Cochair
Sennheiser electronic, 30900 Wennebostel, Germany

Contributed Papers

2:00

4pEAa1. Acoustical analysis on the performance of digital hearing aids. Yingyong Qi and Andrew Dittberner (Univ. of Arizona, P.O. Box 210071, Tucson, AZ 85721, yqi@u.arizona.edu)

The acoustic spectral distances were computed for phonemes, /p/, /t/, and /k/ recorded under a variety of recording conditions, which include: a low (50 dB SPL) and high (80 dB SPL) signal level, a quiet and noisy listening environment, and no processing and processing by three different signal-processing algorithms of a hearing aid. All recordings were obtained using a Zwislocki coupler inside the Knowles Manikin for Acoustic Research. The purpose of this study was to determine whether the acoustic distance between confusable phonemes can be used to evaluate the performance of speech-processing algorithms used in nonlinear, digital hearing aids. The acoustic distance was the rms amplitude difference in the short-term spectra between any two speech segments after they were optimally aligned in time. It was hypothesized that: (1) There would be a significant reduction of acoustic distance among the selected phonemes when speech signals were filtered to simulate a given hearing loss configuration. (2) The use of a hearing aid would significantly alleviate the reduction of acoustic distance among these phonemes. Results, in general, were supportive to these hypotheses. It is, therefore, feasible to assess the information-processing function of a nonlinear, digital hearing aid using an instrument-based approach.

2:20

4pEAa2. Clinical trials of a hybrid adaptive beamformer (HAB) for improved speech understanding in noise. G. L. Gibian, Walter Koroljow, Andy LaRow, Scott Shaw (Planning Systems, Inc., 7923 Jones Branch Dr., McLean, VA 22102), Peggy Nelson, and LaGuinn Sherlock (Univ. of Maryland School of Medicine, Baltimore, MD 21201)

A wearable, hybrid adaptive beamformer (HAB) device has been developed using a four-microphone array and a combination of adaptive and fixed-weight beamforming. The HAB is being evaluated with hard-of-hearing (HoH) listeners in a variety of environments. Pilot tests used HINT test sentences and noise from separate loudspeakers (106-deg angle) in an audiological booth (AI-weighted direct-to-reverberant ratio 9.1 dB). Measured sentence reception thresholds (SRTs) indicated that the HAB provided 14.5, 16.1, and 12.8 dB improvement over the single microphone for two normal-hearing and one HoH listener. Results will be reported for ongoing objective and subjective testing of elderly listeners with mild to moderate hearing losses. Subjects are fitted monaurally with a commercially available behind-the-ear hearing aid with a dual microphone array following the NAL-R fitting algorithm. Comparisons are made between listeners' SRTs in noise, using: (a) conventional single-microphone, (b) dual microphone, and (c) four-microphone HAB devices. HINT sentences are presented with single and dual noise sources at two arrival angles in three room environments: (a) sound booth, (b) favorable environment, and (c) noisy/reverberant environment. Listeners rate the three hearing aid systems and indicate their preference in paired comparison testing. SRTs, ratings, and preference judgments will be reported. [Work supported by NIH.]

2:40

4pEAa3. Qualitative and quantitative results from a speech enhancement scheme assessed by hearing-impaired subjects. P. W. Shields and D. R. Campbell (Dept. of Electron. Eng. and Phys., Univ. of Paisley, High St. Paisley, Renfrewshire PA1 2BE, Scotland, paul@diana22.pailsey.ac.uk)

A multi-microphone sub-band adaptive system for binaural preprocessing of speech signals for potential processing in future hearing aids has been investigated. Results are presented from both quantitative and qualitative assessments of the performance of the processing scheme as recorded from hearing-impaired subjects. The quantitative assessment is based on intelligibility testing of the algorithm using real-room recordings, $T_{60}=0.3$ s, with multi-talker babble as the unwanted noise source. This evaluation has been conducted by using the four-alternative auditory feature test developed by Foster and Haggard [J. Br. Audiol. **21**, 165–174 (1987)]. A corresponding mean opinion score on speech quality from each test subject provides the qualitative analysis. A response time measure was included with the qualitative measure. The processing scheme uses the least mean squares (LMS) [S. D. Sterns and R. A. David, *Signal Processing Algorithms* (Prentice–Hall, Englewood Cliffs, NJ, 1988)] adaptive noise cancellation algorithm in frequency-limited subbands. The inputs from each microphone are split into 16 contiguous subbands using a cochlear distribution according the function provided by Greenwood [J. Acoust. Soc. Am. **87**, 2592–2605 (1990)]. Each frequency-limited subband is processed using a LMS adaptive noise cancellation filter operating in an intermittent or continuous mode depending on input signal characteristics. The results show a statistically significant and practically valuable improvement in both intelligibility and perceived speech quality using the proposed scheme.

3:00

4pEAa4. Array technology for binaural hearing aid applications. Ivo L. D. M. Merks, Marinus M. Boone, and A. J. Berkhout (Lab. of Acoust. Imaging and Sound Control, Delft Univ. of Technol., Lorentzweg 1, 2628 CJ Delft, The Netherlands, ivo@akst.tn.tudelft.nl)

An increasing number of people have great difficulties in understanding speech in noisy environments. These difficulties can be resolved with a directional microphone array which attenuates the background noise while it transmits the desired signals unaltered to the hearing aid. A highly directional endfire array has been developed containing only four omnidirectional microphones which are integrated into the arm of a pair of spectacles. Two endfire arrays, one per ear, devise a binaural hearing aid which further increases the speech intelligibility and also enables localization. The arrays realize maximum directivity with a least-squares optimization of the array processing which also takes into account the diffraction effects due to the presence of the head. The microphone signals are pro-

cessed with FIR filters to obtain maximum control over both the amplitude and phase of the transfer functions of the filters, thereby achieving maximum directivity. The microphone array attenuates the background noise of a diffuse sound field from 5 dB at 500 Hz to 10 dB at 4 kHz. The improvement in speech reception threshold (SRT) of 16 normal hearing and 26 hearing-impaired subjects will be measured and presented in this paper.

3:20

4pEAa5. Headphones as near-field electromagnetic radiators and probable health impairing objects. Florian M. Koenig (Ultrasone Electroacoustics GmbH, Schellenbergstrasse 7, D-82110 Germering, Germany, ultrasone@t-online.de)

The progress in electroacoustics offers a miniaturized, head-related sound source to produce spatial auditory events [F. M. Koenig, AES Preprint No. 4495 (1997)]. These objects, so-called headphones, are working as dynamic (electromagnetic) or electrostatic transducers. Irrespective of this exists knowledge by epidemic studies about low-frequency electromagnetic fields and their health-impairing effects on biological organisms worldwide. A well-known result is the ''TCO ('95) environmental labeling of displays'' or radiation reduced computer monitors and screens. Independent efforts point out that the TCO idea should be valid also for other electronical consumer products like halogen headlights, clock radios, or housing machines. Is it necessary to add the near-field reinforcing headphone? First measurements over 23 headphones gave the answer, Yes [F. M. Koenig, 24. DAGA (1998), in preparation]. Using a pink noise C-weighted signal by a usual SPL of 70 dB reveals that the majority of customary headphones generate an electromagnetic field emission at the human head, which crosses the border level of the TCO'95 or German recommendation for the housing area [VDE-DIN No. 0848, part 4A1/11/90]. Continued investigations underline this earlier result. The steps' contrary high-field dispositions will also be shown.

THURSDAY AFTERNOON, 18 MARCH 1999 ROOM H112, 3:55 TO 6:00 P.M.

Session 4pEAb

Engineering Acoustics and Noise: Implications of Recent Standards

Victor Nedzelnitsky, Cochair
National Institute for Standards and Technology, Sound Building (233), Gaithersburg, Maryland 20899-0001, USA

Dieter P. A. Gottlob, Cochair
Federal Environmental Agency, Bismarckplatz 1, D-14193 Berlin, Germany

Chair's Introduction—3:55

Invited Papers

4:00

4pEAb1. The role of international and European standardization in relation to European directives. Leif Nielsen (DS, ISO/TC43&CEN/TC211 secr, Kollegievej 6, DK-2900 Charlottenlund, Denmark, len@ds.dk)

There are three different types of relations between standards and EU directives: (1) Self-contained directives: Basically such directives do not call for standards. However, though standards do not contain noise limits, many standardized measurement methods exist, and much work has been initiated in order to avoid conflicting measurement methods in directives and standards. (2) ''Reference to standards:'' Such directives may, e.g., contain noise limits, and measurement methods are given by direct reference to specific standards which may be international or European. (3) ''New approach:'' This is the most modern way of using standards in relation to directives. Such directives contain only so-called ''essential requirements'' leaving the technical content to be fulfilled by standards. Standards in this context are required by the EU Commission to be European standards prepared by CEN. The most well-known example is the machinery safety directive. This has lead to the preparation of some 400 safety standards containing noise paragraphs. The EU commission has just started preparing a directive on external noise. Many standardization activities are also going on in this area. At the moment it is not known which type of directive is intended and which role the international and European standardization work will have.

4:20

4pEAb2. Strategy policy of ISO/TC43 ''Acoustics.'' Klaus Brinkmann (Physikalisch-Technische Bundesanstalt, Bundesallee 100, D-38116 Braunschweig, Germany, klaus.brinkmann@ptb.de)

The scope of ISO Technical Committee 43 ''Acoustics,'' together with its Subcommittees ''Noise'' and ''Building Acoustics'' comprises standardization in the whole field of acoustics, i.e., the measurement of sound, its generation, transmission, and reception as well as its effects on Man and the environment. Close liaison is maintained with related international and regional standardization committees, especially IEC/TC 29, which is responsible for electroacoustic standards. ISO standards elaborated by TC 43 are equally addressed to a variety of parties, such as industry, regulatory authorities, trade and consumer groups, research institutes, testing laboratories and consulting engineers, health and safety inspectors, audiologists, and communication experts. Representatives of these groups from 24 different countries contribute actively to its work. More than 120 standards have been published so far and the present

program of work includes nearly 80 projects for new or revised standards. In the past few years, major emphasis was laid on the measurement of machinery noise and the measurement and rating of sound insulation in buildings and of building products, both in the context of recent regional legislation. Fields like environmental noise, transport noise, noise prediction, and simplified measurement methods for building acoustics are considered to be future priority areas.

4:40

4pEAb3. New trends in standards indicate need for more interlaboratory comparisons and data. Victor Nedzelnitsky (Natl. Inst. of Standards and Technol. (NIST), Sound Bldg. 233, Rm. A147, Gaithersburg, MD 20899-0001, vnedzel@nist.gov)

Current trends in standards development now place, and will continue to place, significantly increased demands on laboratories around the world. Shorter IEC/ISO procedural deadlines and the increasing pace and complexity of standards development require that more work be accomplished in less time. Several trends account for the increasing complexity of measuring instrument standards from IEC TC 29 electroacoustics. One trend is the breadth and rapidity of technological developments in transducers and modern analog/digital electronics. Other trends involve the inclusion in standards of more information regarding uncertainties, test methods, procedures, and EMC (electromagnetic compatibility). This information is needed because these IEC standards are being used to support development of OIML recommendations in legal metrology, as well as national and regional standards and regulations in many countries. The need to produce correct statements regarding measurement uncertainties, methods, and procedures greatly increases the need to acquire extensive, reliable data, especially from interlaboratory comparisons, both for the preparation of new standards, and for the necessary periodic revision of existing ones. Finding resources to meet this need is an important challenge for the field of acoustics. Activities begun in BIPM and other organizations will provide data for primary (but not necessarily secondary) acoustical metrology.

5:00

4pEAb4. The implementation of ISO/IEC guide 25 for acoustical standards at NRC Canada. George S. K. Wong and Lixue Wu (Acoustical Standards, Inst. for Natl. Measurement Standards, Natl. Res. Council, Ottawa, ON K1A 0R6, Canada)

Since the publication of ISO/IEC Guide 25, national acoustical measurement laboratories are under pressure to follow the recommendation of the Guide to update the calibration procedures to ensure confidence in the calibration services offered. The uses of the Guide (currently under revision as DIS 17025: General requirements for the competence of testing and calibration laboratories) promote cooperation between laboratories, acceptance of measured data in industries and in the harmonization of standards and procedures. In the international scene, the acceptance of calibration and test results between countries will ease the removal of nontariff barriers to trade. This presentation provides a brief discussion on the requirements and the strategy used to enhance the acoustical standards program at the National Research Council.

5:20

4pEAb5. Hot new topics in ASA/ANSI standardization. Paul Schomer (Schomer & Assoc., 2117 Robert Dr., Champaign, IL 61821)

The ASA Committee on Standards has many new work efforts underway. As chairman of the ANSI S12 committee (noise), this author is primarily versed in the hot new noise standards being developed. Hence, this paper will concentrate on noise standards. (The S12 committee can be considered the counterpart to ISO TC 43/SC 1 and concentrates on noise.) Several new efforts are underway in S-12, including (1) classroom acoustics, (2) room noise criteria, (3) model community noise ordinances, (4) community noise assessment, (5) consumer product noise labeling, and (6) *in situ* hearing protector measurements. In addition, there is a new effort in the S-3 committee (bioacoustics) dealing with warning signal definitions. Clearly, these new topics depart from many of the traditional standards topics such as measurement of workplace machinery noise or office and business equipment noise. Rather, these new work efforts concentrate on criteria development, measures to assess response to noise in various settings, or various human interactions with sound, etc. Several of these topics, such as community noise assessment, noise labeling, or hearing protector measurement, relate to ongoing international efforts. This paper will briefly describe the goals, progress, key contacts, and schedules for these work efforts.

Contributed Paper

5:40

4pEAb6. A simple three-dimensional (3-D) sound intensity probe. Erik Druyvesteyn, Hans-Elias de Bree (Univ. of Twente, P.O. Box 217, 7500 AE Enschede, The Netherlands, w.f.Druyvesteyn@el.utwente.nl), and Bert Roozen (Philips Res./CFT Labs., 5656 AA Eindhoven, The Netherlands)

An important property of sound intensity measurements is that the free-field properties of a sound source can be determined, although the source is positioned in a reverberant environment. The standard intensity probe consists of two closely spaced, accurately matched pressure microphones (p-p probe). A 3-D intensity probe consists of three pairs of matched microphones. The necessity of accurate matching makes such a probe large, complicated, and expensive. As an alternative for the p-p probe a p-u probe has been published [104th AES Convention Amsterdam; preprint 4651], where the particle velocity (u) is determined using the Microflown. It consists of two heated wires, 40 mm apart. The temperature difference of both wires is linearly dependent with the particle velocity (u) and can be measured accurately. A 3-D intensity probe will be reported consisting of one (pressure) microphone and three particle velocity sensors placed orthogonal for the velocity vector (u) determination. Experiments have been performed in an anechoic and a reverberation room. It was found that the free-field properties of a sound source, as determined from experimental results in the reverberation room, coincide with the experimental results in the anechoic room, showing that this 3-D intensity probe works satisfactorily.

Session 4pMU

Musical Acoustics: Mapping Multiple Physical and Perceptual Attributes to Musical Structures

Roger A. Kendall, Cochair
Department of Systematic Musicology, UCLA, Box 951657, Los Angeles, California 90095-1657, USA

Stephen E. McAdams, Cochair
Laboratoire de Psychologie Experimentale (CNRS), 28 rue Serpente, F-75006 Paris, France

Chair's Introduction—1:55

Invited Papers

2:00

4pMU1. Timbral effect of parameter interchange between musical instrument types. James W. Beauchamp (School of Music and Dept. of Elec. and Comput. Eng., Univ. of Illinois at Urbana–Champaign, 2136 Music Bldg., 1114 W. Nevada, Urbana, IL 61801)

One method of studying the perceptual importances of physical parameters is to generate stimuli involving parameter interchange between instrument types. A new method of doing this models each instrument in terms of excitation and filter, derived from spectral analysis data, and includes independent temporal controls for fundamental frequency, spectral centroid, and amplitude. When temporal parameters are interchanged between instrument models, hybrid sounds result where it is possible to recognize perceptual aspects of both original instruments. When a parameter is inserted into a new environment, its value toward suggesting a particular instrument type may be enhanced. This paper explores conditions under which interchanged parameters may evoke particular instrument responses as opposed to simply merging with the new environment. Such salient parameters may assist in efforts to classify automatically instrument types.

2:20

4pMU2. Multidimensional scaling of musical timbre constrained by physical parameters. Stephen McAdams (Laboratoire de Psychologie Experimentale (CNRS), 28 rue Serpente, F-75006 Paris, France and IRCAM, 1 place Igor Stravinsky, F-75004 Paris, France, smc@ircam.fr) and Suzanne Winsberg (IRCAM, F-75004 Paris, France)

A new multidimensional scaling technique [S. Winsberg and G. De Soete, Br. J. Math. Stat. Psychol. **50**, 55–72 (1997)] is applied to the analysis of dissimilarity judgments on musical timbres in both group and individual data. This technique constrains the resulting spatial model such that the order of items along a given perceptual dimension preserves their order along a previously established physical dimension. The fit between perceptual and physical dimensions is achieved with spline functions and yields what may be interpreted as the auditory transform of the physical dimension needed to obtain the perceptual one. A reanalysis of ten timbre spaces from the literature shows that this kind of model does not work as well on group data as it does on individual data due to differences in the nature of underlying dimensions and in the form of the auditory transforms for different listeners. Further, an analysis of individual data sheds light on the reasons why higher dimensions in published timbre spaces are so often difficult to interpret.

2:40

4pMU3. Multidimensional acoustical and psychoacoustical aspects of inharmonic plate and bar tones of real and resynthesized instruments. Edward C. Carterette and Roger A. Kendall (Music Percept. and Acoust. Lab., Dept. of Ethnomusicology, Univ. of California, Los Angeles, 405 Hilgard Ave., Los Angeles, CA 90095)

Following a brief review of the mathematics of inharmonic plates and bars, the acoustics and comparative psychoacoustics of the tones of Indonesian bars and plates are considered. Tones were derived from real instruments of the UCLA Department of Ethnomusicology's Javanese and Balinese gamelans, and from resynthesis of spectral analyses of instrumental tones. The comparative psychoacoustics of the tones was assessed by a number of methods, including JNDs, ratings by MDS similarity-scaling, and verbal-attribute magnitude estimation. Several methods were used to converge on the general perceptual and cognitive properties of the tones. Illustrative findings are: It was shown (1) that Indonesian gamelan makers can and do tune their metallophones in stretched octaves. Their stretchings (1.02 to 1.05 times the normal octave) were fit by a mathematical model which was derived from the data of many gamelans. (2) That the perceptual dimensions of Indonesian and Balinese gongs were interpreted as pitch, ombak (beating), and volume. These dimensions can be mapped to frequency, amplitude modulation, and spectral envelope. It was concluded that gong makers can modify the plates to achieve desired physical properties and correlated perceptual dimensions. One important finding is that the relative positions of two close axially symmetrical modes control the ombak rate.

3:00

4pMU4. Memory for melodies, poetry, faces, and other complicated things. W. Jay Dowling (Univ. of Texas at Dallas, Richardson, TX 75083-0688)

For over 100 years it has been a well-known ''fact'' of research on memory that after something is memorized, it is gradually forgotten over time. This is largely true of the relatively impoverished and meaningless materials that memory researchers have typically relied upon. As early as 1913, Ballard showed that poetry can be recalled better and better following memorization (''hypermnesia''), and recent work by Erdelyi and others supports those results. Hypermnesia in recognition, however, has proved elusive. The present experiments demonstrate hypermnesia in recognition memory for unfamiliar folktunes. The complexity and meaningfulness of stimuli such as melodies, poetry, and perhaps faces evoke memory processes that lead to improvement rather than decay over the early span of time following acquisition.

3:20

4pMU5. What makes singing expressive? Johan Sundberg (Voice Res. Ctr., Speech Music Hearing, KTH Stockholm, Sweden)

Answers to this question are sought in two experiments analyzing performances of songs from the classical Lieder repertoire as sung by professional baritone singers. In one experiment, two versions of the same excerpts were compared; in one the singer attempted first to sing with as little expression as possible, and then as in a concert. In another experiment, a professional singer performed a Lied with a prerecorded piano accompaniment provided over earphones (a) with the original text of the poem and (b) replacing the text syllables with the syllable [mV:]. The significance to expressiveness of observed differences is evaluated by synthesis experiments. The results suggest that expressivity contains information on musical structure, facilitates categorization of tones, and adds an emotional coloring. Expressivity is communicated by means of a code involving meaningful modulation of various parameters such as tempo, pitch, loudness, and vibrato extent. It also includes certain characteristic patterns such as ascending glides to target pitches, and smoothing or sharpening of loudness and pitch contours.

3:40–4:00 Break

4:00

4pMU6. Vibrato and portamento, hypotheses and tests. Peter Desain (Music Mind Machine Project, NICI/KUN, Nijmegen, The Netherlands)

As Seashore already pointed out, continuous aspects in music performance, which happen during and in between notes, can be a relevant means for expression. These modulations, like vibrato and portamento, are very consistently controlled and seem to exhibit striking regularities. However, there are many conflicting hypotheses in the literature about these regularities, especially concerning the relation between vibrato and global tempo. To investigate these more systematically, experiments were conducted in which different instruments perform the same piece at different tempi. The results, relating vibrato rate, extent, and phase to tempo and timing will be presented. Apart from understanding the process of music performance better, they may be applied in the design of synthesizers and software for the music studio.

4:20

4pMU7. Acoustical specification and musical meaning. Eric F. Clarke (Univ. of Sheffield, Sheffield S10 2TN, UK)

Musical meaning has commonly been regarded as only very distantly related to music's acoustical surface. This paper proposes that there is actually a rather close relationship between the two—that musical meaning is specified with considerable immediacy in sound. An important aspect of the meaning of an everyday sound in the environment is its source, and this same principle can be interestingly extended to music if the notion of ''source'' is generalized somewhat to encompass more than just physical/instrumental origin. Following a brief introduction to the theory of ecological acoustics on which such a claim is based, and an illustration of its application to everyday environmental sounds, a number of musical examples will be used to illustrate the diverse aspects of musical meaning that are specified in musical sound, ranging from states of the performing body to the cultural allegiances of musical genres.

4:40

4pMU8. Cross-modal integration: Synchronization of auditory and visual components in simple and complex media. Scott D. Lipscomb (Inst. for Music Res., Div. of Music, Univ. of Texas, 6900 N. Loop 1604 West, San Antonio, TX 78249)

Recently, there has been a significant amount of interest in the perceptual interaction between auditory and visual (A–V) systems in multimodal contexts. Both psychologists and musicians are beginning to investigate the manner in which a stimulus perceived in one sensory modality may affect the cognitive processing of a stimulus in a separate modality. Beginning in the 1950s, a series of psychophysical investigations revealed cross-modal influences using extremely simple stimuli. Most studies incorporating more complex stimuli have focused on the referential aspect of musical sound, i.e., the ''cognitive congruency'' of the music and the visual images. The present study will specifically investigate the alignment of accents (i.e., salient events) in the auditory domain with those in the visual domain, and the effect of this alignment on subject perception of the A–V composite. The author will report on three experiments utilizing varying levels of stimulus complexity: single-object animations, animations by Norman McLaren, and motion picture excerpts. A–V alignment was manipulated as the independent variable with subject ratings of effectiveness as the dependent variable. A revised model of film music perception will be presented, proposing a dynamic relationship between stimulus complexity and significance of AV synchronization in the determination of subject ratings.

5:00

4pMU9. Music serves as a vehicle in multimedia contexts. Annabel J. Cohen (Dept. of Psych., Univ. of Prince Edward Island, Charlottetown, PE C1A 4P3, Canada)

The vast amount of information in multimedia presentations ought to place inordinate demands on perceptual and cognitive systems. Yet there seems to be a superfluity of resources for processing music in the midst of processing information from visual and verbal sources. Research of the author and others reveals the remarkable ability of listeners to accomplish three kinds of musical processing in multimedia contexts: picking up cross-modal structural similarities, generating meanings and associations, and establishing cross-modal linkages in memory. Emphasizing principles of structural congruence and semantic association [S. E. Marshall and A. J. Cohen, Music Perc. **6**, 95–112 (1988)], a framework is described for examining these musical processes in the context of simultaneous visual and verbal input streams [A. J. Cohen, Proc. 5th International Conf. on Music Perc. and Cog. (1998), pp. 13–20]. The present paper highlights how music *transports* different types of information (e.g., acoustic, temporal-structural, semantic). These different types of information carried by the music can be selectively exploited to accomplish such functions as masking, focusing attention, disambiguation, reminiscence, suspension of disbelief, and creation of aesthetic experience. [Work supported by SSHRC.]

5:20

4pMU10. Identification and qualification of instrumental sound sources: Elaboration. Catherine Sémidor, Léonie Couthon, and Aline Barlet (ERIAC Ecole d'architecture et de paysage de Bordeaux, Domaine de Raba, 33405 Talence Cedex, France, catherine.semidor@bordeaux.archi.fr)

From multitrack anechoic recordings of orchestral, or other musical instruments, a quantitative analysis of musical instruments' power and directivity was conducted [Semidor and Couthon, ICA98]. A qualitative study is now proposed to complete the knowledge about the perceived sound of these same instruments by listeners. The following elements are examined: (1) the ''recognizing threshold'' of instrumental sources, from a directivity point of view. Particularly, studying the differentiation difference between sources of the same family, or sources with a pronounced directivity and others. (2) The subjective ''qualification'' of sources in function of directivity, that is the influence of the quantity of information on directivity, on the qualification of the source. (3) Correlation of those results with the quantitative study conducted before. Are the main objective parameters noticed in a subjective point of view? This study is conducted in a first approach in laboratory conditions. Its main applications are sound recording, sound reinforcement, measurement, and simulation in room acoustics. It is well known that taking into account sound sources' characteristics permits the improvement of a room's design in order to increase the audience comfort.

Contributed Papers

5:40

4pMU11. Amplification of the difference tones $(f2-f1)$. Pierre Dutilleux (ZKM|Inst. for Music and Acoust., Karlsruhe, Germany)

Difference tones have been known by composers and performers for a long time. Nevertheless, these tones are still difficult to use in a musical context because their appearance is fairly unpredictable. A cello player, Michael Bach, has developed a sophisticated playing technique to produce these tones. Unfortunately the public was not aware of it because it could not here them as well as the player did. Evidence of the presence of the difference tones in the acoustic signal has been found in some cases. In most cases these tones develop in the head of the listeners only at fairly high sound-pressure levels. In order to control the amount of difference tones in a musical sound, a processing method has been developed that artificially produces the difference tones. The squared and filtered instantaneous envelope of the acoustic signal delivers them. These tones can then be mixed to the original sounds as needed and the public can perceive the difference tones even at moderate sound-pressure levels. The system was implemented and performed well during concerts. With a celletto (cello without any sounding box) it is possible to hear only difference tones.

6:00

4pMU12. Parsing complex rhythmic structures: The contribution of spectral and temporal dimensions of timbre. Punita G. Singh (Sound Sense Consultancy Services, 20-A Aurangzeb Rd., New Delhi 110011, India, pgsingh@hotmail.com)

Perceptual parsing of sequences with multiple possible metric interpretations was studied. Sequences of 12 complex tones were used as stimuli, with either no deliberate accents provided, or physical accents introduced by changing timbre at positions implying a triple, quadruple, or multiple meter (i.e., both triple and quadruple simultaneously). Subjects reported if they perceived a triple meter, quadruple meter, ambiguous meter, or no meter. The number of harmonics (2, 4, or 8) or the locus of three harmonics were the spectral variables used to mark timbre accents. Steepness of rise and decay time ($95+5$ ms versus $5+95$ ms) was the temporal variable used. These attributes served well as accent markers for sequences with unambiguous meters. However, listeners were generally unable to parse sequences where multiple meters were provided by the same timbre cue. For sequences where multiple meters were provided by contrasting timbres, listeners generally picked the metrical structure implied by spectrally richer or brighter timbres comprising more or higher harmonics. Temporal envelope slope was not effective in facilitating parsing of meters.

Session 4pNSa

Noise: Military Aircraft Noise

Bernard F. Berry, Cochair
National Physical Laboratory, Teddington TW11 0LW, UK

Lawrence S. Finegold, Cochair
U.S. Air Force Research Laboratory, Wright–Patterson AFB, Ohio 45433, USA

Chair's Introduction—1:55

Invited Papers

2:00

4pNSa1. A review of recent military aviation noise programs. Eric Stusnick (Wyle Labs., 2001 Jefferson Davis Hwy., Ste. 701, Arlington, VA 22202, estusnic@arl.wylelabs.com)

This presentation reviews recent studies that have been carried out by Wyle Laboratories on noise from military aircraft operations. Four different areas of research will be described—modeling, measurements, psychoacoustics, and noise control. The discussion of subsonic aircraft noise models includes NOISEMAP, ROUTEMAP, MR_NMAP, and the Rotorcraft Noise Model, while that of supersonic noise models includes CORBOOM, BOOMAP3, and PCBOOM. The discussion of aircraft noise measurements includes sonic boom monitoring, military training route measurements, NOISENET, potential damage to unconventional structures by sonic boom, and rotorcraft noise measurements. The psychoacoustic discussion includes the development of the onset rate correction for high-speed, low-flying military jet overflights and community response to sonic booms. The discussion of aircraft noise control will describe the use of active noise control to reduce noise from hush houses and static jet engine runups.

2:20

4pNSa2. U.S. Air Force research on military aircraft noise and its effects. Lawrence S. Finegold, Robert A. Lee, and Richard L. McKinley (U.S. Air Force Res. Lab., Wright–Patterson AFB, OH 45433, LFinegold@falcon.al.wpafb.af.mil)

For over half a decade, the U.S. Air Force (USAF) has been conducting a program of research on military aircraft noise and its effects. This paper provides a brief overview of some of the major projects implemented at Wright-Patterson Air Force Base in the past decade on noise measurement and monitoring, noise propagation modeling, and the effects of noise on humans, animals, and structures. It also includes both sonic boom research and subsonic aircraft overflight noise. Several international collaborative efforts have been conducted with NATO partners on both fixed-wing aircraft and helicopter overflight noise. In addition to the community noise portion of this program, the USAF has also conducted research on the auditory effects of military occupational noise exposure, development of hearing protection devices, and the development of three-dimensional audio information presentation. Although time limits preclude a comprehensive review of the extensive USAF program, highlights of some of the most interesting and important projects will be provided.

2:40

4pNSa3. Adjustment factors for assessing long-term aircraft and other noise environments. Paul Schomer (Schomer & Assoc., 2117 Robert Dr., Champaign, IL 61821)

LEQ and DNL are commonly used to assess the long-term noise environments around airports, roads, etc. Frequently, the measure used is the long-term (e.g., yearly average) DNL or long-term daytime LEQ, etc. Schultz and others have related the long-term DNL or LEQ to community response as measured by the percent of a community that is highly annoyed. These relations exhibit a large scatter to the data. It is possible for a specific community to exhibit many times the percent highly annoyed predicted by these ''standard'' relationships. Some have suggested adjustments to LEQ or DNL to better explain community response and reduce the scatter in the relations between DNL and percent highly annoyed. These adjustments include ''busy day,'' a ''nave'' community (not familiar with the sound), a ''quiet rural setting,'' and the presence of ''rattles.'' This paper uses experimental data, case histories, and logic, to examine the efficacy of these adjustments.

3:00

4pNSa4. Modeling of military aircraft noise in support of environmental impact mitigation. Neil M. Standen (Jacques Whitford Environment Ltd., 2781 Lancaster Rd., Ottawa, ON K1B 1A7, Canada) and Gary W. Humphries (Dept. of Natl. Defence, Ottawa, ON K1A 0K2, Canada)

The Military Training Area in Labrador, Canada is used by NATO Alliance air forces of the United Kingdom, Germany, and the Netherlands, and is managed by the Canadian Department of National Defence (DND). Protection of the natural environment is a major consideration in the management of the training area. This paper describes a computer-based noise propagation model that will be used to support environmental management. The paper demonstrates its use in planning flying training sorties to mitigate short-

term environmental impacts, and also its use in assessing environmental effects of the flying activity over the longer term. The model enables DND to maximize the extent of the range available for flight training by accurately calculating noise levels on the ground, and hence the degree and method of noise impact mitigation that is appropriate. The noise propagation model is used in conjunction with other computer-based tools for flight track modeling, terrain modeling, and specifying locations of noise-sensitive areas (typically wildlife habitats which may change in location during the training period). Other projects are aimed at investigating and evaluating acceptable levels of noise impact, in terms of consequences on wildlife viability in these habitats.

3:20

4pNSa5. The theoretical and practical aspects of producing source data for helicopter noise modeling. R. J. Weston and R. Beaman (RAF Inst. of Health, RAF Halton, Aylesbury, Bucks HP22 5P6 UK)

Accurate source data are the key to future developments in noise modeling. With the increasing need to model helicopter noise, suitable source data will be required. For helicopters, the directivity of the noise source is an essential component of the model. This paper reviews a system for determining helicopter directivity together with a discussion of future developments. An overview of an international helicopter noise measurement trial conducted in June 1998 to determine directivity will be presented along with some of the data.

3:40–4:00 Break

4:00

4pNSa6. Military aircraft noise and health—Methodological issues in research. Ian H. Flindell (Inst. of Sound and Vib. Res., Univ. of Southampton, Southampton SO17 1BJ, UK)

The possibility of long-term health effects associated with prolonged exposure to military low-altitude flying (MLAF) noise in designated training areas in the UK remains an area of public concern. Definitive research in this area is difficult for many reasons. In addition to the general problems which apply to all noise and health research; of defining the effects of variables of interest; of estimating individual exposure; of independently identifying susceptible individuals; and of controlling for confounding factors, the generally low levels of MLAF noise exposure (measured as outdoors LAeq) and the wide variability of training schedules to meet varying tactical requirements create further difficulties. MLAF events are often irregular, infrequent, and may have higher maximum levels and higher onset rates than other types of environmental noise. What are the theoretical reasons why these factors should contribute to increased risks of health effects? Acoustic startle effects and associated physiological responses can equally be interpreted either as signs of healthy reactivity or as precursors of disease. MLAF events can contribute to acute annoyance at the time that they occur, but the possible mechanisms for noise-related annoyance to contribute to longer term morbidity through some vague and unspecified stress hypothesis are obscure.

4:20

4pNSa7. The response of the acoustic reflex to noise from low-flying military aircraft. Geoff Kerry, Claire Lomax, Peter D. Wheeler (Univ. of Salford, Salford M5 4WT, UK), and David J. James (Royal Air Force Innsworth, Gloucester GL3 1EZ, UK)

Noise from low-flying military jet aircraft is often characterized as loud and sudden. Some researchers have suggested that the rise time of noise from such operations might be faster than the response time of the acoustic reflex, reducing protection to the inner ear. Recordings of Tornado GR1 overflights have been applied to simple models of the middle ear taken from the literature to estimate the likely response of the acoustic reflex and the attenuation of noise transmitted to the inner ear. Results indicate the reflex will provide some degree of protection to this type of noise, and that the rate of rise of the stimulus influences both the speed of the reflex response and the attenuation at a specific time. This procedure is complicated and relies on certain assumptions being made. Another approach is considered which uses complex computer models of the human ear, which allow simulation of a range of conditions together with the possibility of defining the cochlear response. Both approaches are presented, and the direction of future work toward defining a descriptor for the assessment of possible noise-induced auditory effects is discussed.

4:40

4pNSa8. Military aircraft jet overflights and children's hearing—Allegations, issues, and measurement uncertainties. Peter D. Wheeler and Nikki Matkovits (Univ. of Salford, Salford M5 4WT, UK)

The scientific literature of the past 20 years contains several references to the use of high-frequency audiometry for investigating susceptibility to, and early diagnosis of, noise-induced hearing loss. More recently, the measurement of high-frequency hearing acuity in children has been cited as an important tool in the identification and attribution of noise-induced hearing loss from alleged exposure to transient noise sources such as low-flying military jet aircraft. The enormous range of hearing thresholds found above 8 kHz, even in young adults, has been reported by many researchers. Measurement uncertainties in the range 8–16 kHz can be substantial, and detection judgments at such frequencies for inexperienced subjects represent a further source of variance. This study aims to quantify the uncertainties associated with high-frequency audiometric measurements on children and adults in order to inform the interprtation of existing data and assist in the design of new studies. The outcome will be reported and taken into account in a review of the conclusions of recent published work involving high-frequency audiometry for the measurement of children's hearing in areas subjected to low-altitude military jet overflights.

5:00

4pNSa9. Presenting noise information to community decision-makers. David T. Dubbink (Noise Management Inst., 864 Osos St., Ste. D, San Luis Obispo, CA 93401)

Resolving community noise problems requires not only accurate data about noise impacts, but also demands an effective means of communicating this information to decision-makers. The Interactive Sound Information System (ISIS) is a ''new media'' package designed to explain and demystify the complex metrics used to describe noise impacts. Central to the ISIS package is the idea that ''real'' noise examples, shaped to reflect local situations, are the very best way to build an understanding of noise management issues. The system has been used effectively by governmental agencies and noise management specialists as a means of delivering information that is both understandable and technically accurate. The United States Air Force, in association with the FAA, has supported development of an expanded version of the program that incorporates state-of-the-art multimedia technology. The new version of the program is designed for a wide audience, and its operation does not demand technical expertise. It uses the 3-D viewing capabilities of the Virtual Reality Modeling Language (VRML). The updated software is built on the Java platform, giving the package both modularity and Internet capabilities. The program links to airport and highway noise prediction models.

THURSDAY AFTERNOON, 18 MARCH 1999 ROOM H1028, 1:55 TO 5:40 P.M.

Session 4pNSb

Noise and Psychological and Physiological Acoustics: Product Sound Quality

Dennis Walton, Cochair
Abbott Laboratories, P.O. Box 152020, Irving, Texas 75015-2020, USA

Armin Kohlrausch, Cochair
IPO Center for Research on User-System Interaction, P.O. Box 513, NL-5600 MB, Eindhoven, The Netherlands

Chair's Introduction—1:55

Invited Papers

2:00

4pNSb1. The perception of product sound quality. Ute Jekosch (Inst. of Commun. Acoust., Ruhr Universität Bochum, D-44780 Bochum, Germany, jekosch@ika.ruhr-uni-bochum.de)

There are different methods and methodologies available to assess the quality of sounds. Generally, instrumental and auditory assessment can be distinguished. For instrumental assessment, physical data are collected and analyzed, and a sound quality value is computed in the end. Auditory assessment methods use human listeners who judge on the quality of a perceived sound. Experts very often face the fact that instrumental and auditory quality values are not in accordance with each other. This holds especially for the case where instrumental methods are used to predict how a human listener will perceive the quality of a sound. It is the task of sound quality assessment research to abridge the gap between predicted and experienced sound quality. There are different approaches to reach this goal. The talk concentrates on one specific aspect, namely on the function of sounds. Sounds convey a meaning. The meaning is assigned to them by the listener. The relation between form and content is either arbitrary or fixed. Instrumental and auditory sound quality assessment have to consider these aspects: An appropriate assessment of sound quality has to include the aspects of the acoustic/auditory form, the listener, and the meaning he/she assigns to the auditory event.

2:20

4pNSb2. Development of a noise criterion for laboratory medical instrumentation. William H. Muto (Abbott Labs., P.O. Box 152020, Irving, TX 75015-2020)

Over the past two decades, medical laboratory instrumentation has undergone a major transformation in terms of its functionality, sophistication, and degree of automation. A common complaint among laboratory professionals using these instruments has been that laboratory noise levels have increased, and that certain instruments are especially noisy. The goal for this project was to establish an instrument noise criterion that would serve as a standard for the company's future generations of instruments. The ideal standard in

this context would eliminate or greatly reduce customer complaints due to noise without significantly increasing development and manufacturing costs. After surveying various noise criteria and after preliminary investigatory studies, a variation of balanced noised criteria curves (NCB), proposed by Beranek (1989), was adopted as the basis for the standard. The current presentation will provide: (1) a description of the adopted noise criteria, (2) practical considerations for use in the current context, (3) measurement methods and tools used, and (4) a summary of progress to date regarding the use and utility of the adopted noise criteria.

2:40

4pNSb3. Adequacy of product sound: Design–develop test; is it so simple? Michiel A. A. Schallig (Oliemolenstraat 5, Drachten, The Netherlands)

Philips DAP B.V. is a major producer of consumer household appliances. Electric shavers and vacuum cleaners are examples of the products that are produced. Consumer satisfaction is of paramount importance for the company. This is obvious for the functional aspects of the appliance, but satisfaction goes beyond functionality. Design, price, ergonomics, and sound are a few aspects which can contribute to the desired level of satisfaction. To achieve this delicate balance within such different constraints is a difficult process. Control of the sound production of appliances is something that has to be tackled from the start of the development, but becomes increasingly difficult. Especially ''softer'' constraints like ''sound quality'' blurr the development process. Despite the difficulties, these softer aspects are considered more and more important. In the real development processes, however, it is, for example, very difficult to get good measurement data of human perception. Often this is done by panel research, but this is a very slow process and depends heavily on the availability of the correct panels. This is one of the many problem aspects that are related to developing appliances with a ''quality sound.'' Some real world experiences, observations, and problems on the road to adequate sounds are described.

3:00

4pNSb4. Combined application of computer simulation and sound quality in the design of a home appliance. Brandon D. Tinianow (Johns Manville Tech. Ctr., 10100 West Ute Ave., Littleton, CO 80127, tinianow@jm.com) and Benjamin Cimerman (Vibro-Acoust. Sci., Inc., Los Angeles, CA 90010)

Computer-generated simulation tools are commonly used for acoustical product design, but often for spectral levels only. Sound quality, as expressed in sones and phons, quantifies sound as perceived psychologically by a listener, but possesses no predictive capability. In this study, both methods were combined to improve an appliance's performance in terms of noise. Using intensity mapping, noise paths contributing most to user annoyance were identified. A computer model of the appliance was then created using the widely recognized statistical energy analysis method. This model was employed to simulate design modifications targeting the paths identified as most critical by the sound quality study. Design modifications were implemented in a hardware prototype of the appliance as suggested by the model and this re-designed appliance was again subjected to the sound quality assessment. Results show that the appliance's performance was significantly improved.

Contributed Papers

3:20

4pNSb5. Three-dimensional localization and characterization of acoustical sources in a truck cabin. Patrick Dubail and Manell E. Zakharia (CPE Lyon, LASSSO (LISA, EP92 CNRS), 43 Bd. du 11 Novembre 1918, BP 2077, Bat. 308, F 69616, Villeurbanne Cedex, France)

In the framework of acoustic comfort, an accurate localization (in range and angles) of the sources transmitting noise to the driver was investigated. The aim of such a localization is to act on the predominant sources in priority (in a given frequency range). The sources were either vibrating ones corresponding to the excitation point, or fictive ones corresponding to complex propagation and multiple reflections on the cabin elements. An experiment has been conducted on a real cabin with a single point of excitation. The mechanical excitation was achieved via a shaker; frequency-modulated signals have been used that cover a very wide frequency range (0.03 to 15 kHz). Both active and digital corrections were used. Two crossed line arrays of 112 microphones were used for the reception, all the signals were digitized and processed later on. Standard wideband beamforming and beam steering were used on both arrays (in the time domain). For every frequency (or frequency range), the 3D localization (horizontal and vertical angle, time) of sources was achieved. The major sources (15 to 20) were isolated using the radon transform. A fine analysis was achieved in order to provide, in addition to their 3-D localization, their spectral content.

3:40

4pNSb6. Exploration of associated imaginations on sound perception (AISP): A method for helping people to describe and to evaluate their sound perceptions. Petra Muckel, Leo Ensel, and Brigitte Schulte-Fortkamp (Dept. of Psych. (A6), Univ. of Oldenburg, D-26 111 Oldenburg, Germany)

A qualitative method especially developed for helping people to describe and evaluate their sound perceptions will be presented: The development of this method for ''Exploration of Associated Imaginations on Sound Perception'' (AISP) took place in a project about interior car sounds and possesses relationships with CIS (categorical scaling intermittent and subsequent thinking aloud) by Schulte-Fortkamp. Its starting points are the subjects' spontaneous imaginations and memories when they are going to listen. Focused on the effects of sounds, the design of AISP encourages people to describe their perception of sounds by telling their spontaneous associations, e.g., imaginations, memories, and embedded sensations and feelings in their own words and fashion. In an interview aided by a questionnaire, the subject evaluates sounds in leading his/her attention to his/her own imaginations, memories, and feelings while listening. These imaginations function as a context and biographical background for the subject's feelings; they make it easier to find words for the description of the sound perception, especially for the emotional effects of sounds. The purpose is to learn about descriptions of sounds and their possible emotional effects by associated imaginations and feelings.

4:00–4:20 Break

4:20

4pNSb7. A semantic differential design especially developed for the evaluation of interior car sounds. Nicolas Chouard (Dept. of Acoust., Univ. of Oldenburg, D-26111 Oldenburg, Germany, nicolas@aku.physik.uni-oldenburg.de) and Thomas Hempel (Univ. of Bochum, D-44780 Bochum, Germany)

The use of semantic-differential (SD) procedure allows sound designers to compare interior car sounds on the basis of polarity profiles. In order to get representative information, SD designs have to be based on car-sound-specific verbal spaces. Due to the peculiarities of languages and conceptions of car culture in different countries, it is, moreover, not sufficient to use translated lists as they are available in the literature. In this contribution, the development of a representative verbal space for German subjects is presented. Two different approaches are used which are finally combined in order to get an intermediate list of adjective pairs. A representative and usable set of adjective pairs is established by reducing this list on the basis of SD tests with car sounds presented at the same loudness. The different steps and drawbacks in the development of the SD design are described and discussed. The components as well as the underlying dimensions of the verbal space are presented.

4:40

4pNSb8. A system for natural reproduction of sound and vibration. Hermann Remmers (ITAP GmbH, Carl-von-Ossietzky Str. 9-11, D-26129 Oldenburg, Germany, remmers@itap.de), Carsten Reckhardt, and Michael Bellmann (Univ. of Oldenburg, D-26111 Oldenburg, Germany)

For the psychoacoustical evaluation of sound, usually artificial head recordings are reproduced with headphones or loudspeakers. Interior aircraft or car noise, however, contains high sound and vibration energy components below 20 Hz. If these spectral components are not reproduced, subjects often complain about an unnatural hearing impression. In this paper, a reproduction system is presented that extends the audio bandwidth down to 2 Hz. For presenting vibration signals, the subject's chair (e.g., aircraft or car seat) is mounted on an exciter system. The three-dimensional vibration signal spans the frequency range from 6 to 80 Hz. A report is given on psychoacoustic experiments and results with this sound and vibration reproduction system.

5:00

4pNSb9. Affective judgment of aircraft sound quality. Daniel Västfjäll (Chalmers Rm. Acoust. Group, Dept. of Appl. Acoust., Chalmers Univ. of Technol., SE-412 96 Göteborg, Sweden), Àrni Ingvarsson (Saab AB, SE-581 88 Linköping, Sweden), and Mendel Kleiner (Chalmers Univ. of Technol., SE-412 96 Göteborg, Sweden)

Emotion is an important feature of the description and evaluation of sound quality, but this fact has often been treated as a ''nuisance variable'' in sound quality. The objective of this study was to investigate sound quality descriptors of aircraft sounds. The approach to descriptors in this case originated from the need for consideration of emotion in sound quality research. Thirty-two participants ($n=32$) rated eight recorded sounds from turboprop aircraft binaurally replayed over headphones. Subjects rated 21 descriptors designed to capture the subjective dimensions of aircraft sounds. The descriptors were commonly used sound quality adjectives, which have emotional/affective connotation. The principal component analysis resulted in two main components. The first factor was interpreted as pleasantness and the second factor as stimuli intensity. These results indicate that affective descriptors can model perception of aircraft sound, i.e., emotional evaluation is important to aircraft sound quality. This study indicates that both description and judgment/decisions about sounds can be based on emotions. One approach to understand and improve sound quality modeling is to investigate the subjective emotional impression of sounds. [Work supported by NFFP Grant No. 232.]

5:20

4pNSb10. Sound quality design for high-speed trains' indoor noise: Psychoacoustic evaluation of tonal components. Christine Huth, Hugo Fastl (Inst. of Man-Machine-Commun., Tech. Univ. München, Arcisstr. 21, D-80333 München, Germany), Ulrich Widmann (Müller BBM, Planegg), and Georg Hölzl (Deutsch Bahn AG, BT 512)

For the specification of the sound quality inside future high-speed trains, tonal components produced by the motors or corrugated rails can play an important role. Therefore, in psychoacoustic experiments, the dominance of tonal components at 630 or 1250 Hz was assessed. For an increase of the corresponding $\frac{1}{3}$-oct band by 20 dB, a clear tonal character is audible which is only half as pronounced for an increase of 12.5 dB at 630 Hz or 10 dB at 1250 Hz. In line with the expectation, no tonal quality is perceived, if the $\frac{1}{3}$-oct band in question is not enhanced. However, a decrease of sound energy in a $\frac{1}{3}$-oct band by 20 dB can also produce a faint tonal sensation with a magnitude of about $\frac{1}{10}$ of the tonal sensation produced by an increase of 20 dB. The results obtained with stimuli simulating the sound quality inside high-speed trains are in good agreement with data from basic psychoacoustic experiments. Therefore, it is expected that sound quality evaluation of high-speed trains indoor noise can profit from a multitude of psychoacoustic data available.

Contributed Posters

These posters will be on display in the Poster Gallery from Thursday to Friday, 18–19 March. Authors will be at their posters from 10:00 a.m. to 12:00 noon on Thursday, 18 March.

4pNSb11. Evaluation of interior car sound with a new specific semantic differential design. Thomas Hempel (Inst. of Commun. Acoust., Univ. of Bochum, D-44780 Bochum, Germany, hempel@ika.ruhr-uni-bochum.de) and Nicolas Chouard (Univ. of Oldenburg, D-26111 Oldenburg, Germany)

In an accompanying contribution [see Chouard and Hempel, ''A semantic differential design especially developed for the evaluation of interior car sounds''] the development of a semantic differential design based on a verbal space adapted to the description of interior car sounds was presented. In this contribution, this is used in semantic differential tests in order to characterize the interior car sound of eight different cars presented at the same loudness. Results of polarity profiles as well as factor analysis and cluster analysis on the set of cars are presented. Advantages and drawbacks of the method are discussed from the point of view of the experimenter.

4pNSb12. Motion perception and loudness judgments. Andreas Hellmann (Univ. Oldenburg, Dept. of Psych., D-26111 Oldenburg, Germany, hellmann@psychologie.uni-oldenburg.de)

Besides its acoustic properties, many other nonacoustic properties have been shown to influence the judgments of loudness, noisiness, and noise effects of sounding events. In the environment, one finds moving as well as nonmoving sound sources. The sound emitted may be either constant or dynamic. In an experiment, the effect of the perceived motion of

a sound source or sound event on loudness judgments was investigated. Sounds were presented which were ambiguous and could be perceived both as moving and as nonmoving events. In different experimental conditions, the same sound stimuli were presented and introduced as moving or nonmoving events. The subjects judged the loudness of the events. At the end of the experiment, it was reported whether they had perceived the sound events as moving, nonmoving, or both. The results show an effect of perceived motion on judged loudness: Loudness judgments are higher if the sound events are perceived as moving than if they are perceived as nonmoving.

Session 4pNSc

Noise: Urban Acoustics

Jean-Dominique Polack, Cochair
Laboratoire d'Acoustique Musicale, University Paris VI, Case 161, 75252 Paris, Cedex 05, France

Roger Wayson, Cochair
Civil and Environmental Engineering Department, University of Central Florida, P.O. Box 162450, Orlando, Florida 32816, USA

Chair's Introduction—1:55

Invited Papers

2:00

4pNSc1. A cognitive approach of urban soundscapes. Daniele Dubois and Sophie David (LCPE, ENS, 1, rue Maurice Arnoux, 92120 Montrouge, France, dubois@idf.ext.jussieu.fr)

The presented cognitive approach of noises in urban environments focuses on meaning and as such integrates linguistic, psychological, and acoustic conceptualizations and methodologies. It deals with the acoustic phenomena that are perceived, conceived, and said as relevant by the subjects. The productivity of this approach has been evaluated in two research programs. Experiments combining linguistic and psychological analyses showed that urban soundscapes include a complex combination of unpleasant and pleasant noises. The identity of the source and the temporal and spatial contexts of occurrence of the noises are present in subjects' cognitive representation and influence their perception. Experiments on alarm signals showed that contextual contraints influence the perceptual thresholds of the signals, their identification, and their efficiency (contrasting signals as such with nonmeaningful noises). In conclusion, such a ''situated'' cognitive (and pluridisciplinary) approach allows (i) at a theoretical level, to identify the roles of top down (high level) constraints on low-level perceptual processing and (ii) at a methodological level, it suggests to first design procedures to identify the meaningful categories of sounds and their properties at linguistic and psychological levels before describing them in physical dimensions and experimentally manipulating them in psychophysical paradigms.

2:20

4pNSc2. An intersensory approach to urban analysis and design. Marie-Christine Couic and Jean-Jacques Deletre (Ctr. de Recherche sur l'Espace Sonore et l'Environnement Urbain, Cresson, Ecole d'Architecture de Grenoble, BP 2636, 38036 Grenoble Cedex 2, France)

Cresson laboratory's research on sound in urban space led to the development of a theorical model called ''sonic effect'' that takes into account not only the physical and space aspects of the sound but also the user's perception. With this model, some interactions between senses were observed that have been analyzed from an intersensory standpoint. The first step of the method is to register on tape the feeling of candidates when walking through a selected area of the city. This raw material is then analyzed by dedicated software that extracts a few classes where expressions are closed from a semantic standpoint. These classes correspond to specific areas and overlap in transition zones where intersensory perception is expected. Physical measurements (sonic, thermodynamic, luminous) confirm these locations. Further analysis is then performed to reveal dynamic schemes of interaction. The evolution of the relationship between the most salient urban objects and the user is examined in order to consider the evolution between expression (description, evocation, . . .), motion, and senses. A limited number of protocols was found when meeting an object, but the articulation between the main components of intersensory perception (expression, motion, and senses) is still being analyzed. [Work supported by CNRS/PIR-VILLES.]

2:40

4pNSc3. Fractal modeling of diffusive urban configurations. Philippe Woloszyn (Cerma Lab., UMR CNRS 1663, Ecole d'Architecture, rue Massenet, F-44300 Nantes, France, woloszyn@cerma.archi.fr)

This contribution is based upon the environmental specificities of the urban built form and it is part of the Research Programme *CNRS-Interdisciplinary Programmes for Towns* ''Towards an Urban Sonic Ambience Simulator.'' Its purpose is to develop an acoustic model based upon fractal measurements of urban interfaces, to be applied for sound simulations. The fractal technique

exposed here for modeling the complexity of urban forms quantifies discrete morphologies of the town with an automatic capture procedure based on Minkowski's operators. In order to model the complexity of urban streets, the *dilution measurement* is given for a collection of urban surfaces with *fractal indicators* to evaluate the spectral diffuseness for every element. The implementation of the diffusive acoustic model will then be performed using finite-element software, composing the diffusive surfaces collection as a complex equivalent urban configuration. The final comparison with the results of on-site experimentations will give a spectral approach of the diffusion coefficient for the urban configuration. In the near future, the technique described in this paper aims at allowing the spectral control of the acoustical parameters by connecting a fractal morphological evaluation and a qualification of the acoustical phenomenon, modeled as a diffusive process.

3:00

4pNSc4. The University of Central Florida Rail Noise Model. Roger L. Wayson and John M. MacDonald (Univ. of Central Florida, Civil and Environ. Eng. Dept., P.O. Box 162450, Orlando, FL 32816-2450, wayson@pegasus.cc.ucf.edu)

The Railway Noise Model (RNM) is a point source simulation model using a Windows-based program written in Visual Basic. Locomotives and rail cars are input by the laser using a graphical interface. The interface allows spreadsheet-type format or the user may use the mouse to drag and drop railroad tracks and barriers and to place receivers. The model has the ability to model heavy rail and light rail locomotives and rail cars. The user can observe defined trains moving along the railroad tracks to check input. L_{eq} sound levels are calculated and reported during the simulation and then tabulated at the conclusion of simulation. The algorithms of the RNM follow the U.S. Federal Transit Authority Noise and Vibration Impact Assessment (DOT-T-95-16) guidelines. The Railway Noise Model uses L_{max} passby levels from REMEL curves to compute sound levels. The RNM simulates a 24-h period of rail traffic and computes L_{dn}, L_{max}, SEL, and L_{eq} levels at the receivers. Testing has shown that the RNM results match those of the FTA promulgated spreadsheet. The RNM is capable of modeling complex geometries and conditions not available in the FTA spreadsheet and supports all noise sources available in the spreadsheet.

3:20

4pNSc5. The University of Central Florida Community Noise Model. Roger L. Wayson and John M. MacDonald (Univ. of Central Florida, Civil and Environ. Eng. Dept., P.O. Box 162450, Orlando, FL 32816-2450, wayson@pegasus.cc.ucf.edu)

The Community Noise Model (CNM) is a true simulation model written in Visual Basic allowing modeling of motor vehicles. User input is simplified by permitting spreadsheet input or graphical input using a mouse. Due to its simulation nature, the model handles interrupted flow traffic much better than conventional line source models. The model begins by using reference energy mean emission levels (REMELS) from a quite extensive measurement program. Propagation characteristics (geometric spreading, ground effects, atmospheric absorption, diffraction, etc.) are calculated at user-specified time step and energy is summed at user-defined locations. Using the acoustic energy summations, the model reports Leq, Lmax, and statistical levels. Traffic parameters are also reported. Validation has been performed as well as comparison to other established models and will be presented. The CNM performed quite well and at intersections outperformed other models when comparisons were done to measured data.

Contributed Papers

3:40

4pNSc6. Noise abatement in urban areas. A. A. F. M. Beeks, M. G. Dittrich, and P. P. Kooijman (TNO Inst. of Appl. Phys., P.O. Box 155, 2600 AD Delft, The Netherlands)

Two studies on noise abatement in urban areas, performed for the Dutch Ministerie of Transport (SSZ program), are presented. The first is a feasibility study on noise reduction of a range of vehicles. Buses and lorries were found to have comparable noise levels, whereas delivery vans and taxis were found to be much quieter. Specific noise sources can be high. More stringent (European) regulation or governmental stimulation measures are required. A survey was held amongst 396 inhabitants in two cities. Most noise disturbance was shown to be caused by buses (low-frequency acceleration noise). The second study was on noise disturbance during goods delivery to shops. This was initiated after the extension of business hours and the introduction of stricter regulations (60 dB peak limit). Current measured peak A-weighted noise levels at 7.5 m were found to vary between 60 and 95 dB. The study concluded that noise control measures for most sources are technically achievable within three years. Initial estimates indicate 10%–20% higher investment on vehicles and handling equipment. Lorry diesel engine noise is about 15 dB too high. Well-designed quiet electric traction systems are a quieter alternative.

4:00–4:20 Break

4:20

4pNSc7. Urban noise survey for the city of Porto Alegre, Brazil. Miguel A. Sattler (Univ. Federal do Rio Grande do Sul, Dept. de Engenharia Civil, Av. Osvaldo Aranha, 99-3o andar, Porto Alegre, RS, Brazil, CEP 90035-190)

This paper presents the methods and results of a simplified traffic noise survey for the city of Porto Alegre, the southmost capital city in Brazil. Noise measurement data and hourly vehicle flow data were used. Both were obtained at 6 p.m. Values from 560 sites were considered, making possible the construction of a simplified traffic noise map, built upon Leq values. The work, which tries to identify, for the stated time, the impact of noise on the population, in terms of the magnitude of the population exposed to different noise levels, has shown that 90% of the population included in the sample is exposed to A-weighted noise levels exceeding 65 dB.

4:40

4pNSc8. Planning and designing of developments against noise impacts—Hong Kong experience. Chee Kwan Lee and Kwok Keung Lau (Environ. Protection Dept., The Government of the HKSAR of the PROC, 46/F Revenue Tower, Hong Kong, cklee@epd.gov.hk)

In the next 15 years, there will be a rapid population growth in Hong Kong anticipated to be about 1.5 million people. It is a challenge for the Government of Hong Kong Special Administrative Region to find adequate land and to provide sufficient infrastructures to accommodate the increasing population while at the same time to keep up the environmental qualities. Owning to high demand for residential development, infrastructures, and other necessary facilities, it is not always possible to rely solely on buffer distance provided between noise-sensitive developments and noisy highways to avoid noise problems even for a piece of virgin land. To tackle the problems, due consideration needs to be given to minimize the potential noise impacts at the earliest planning stage when studying the alignments of highways. This paper presents the application of the above approaches in the planning of a 500 ha site.

5:00

4pNSc9. Local ordinance targeted to low-frequency noise. Bennett Brooks (Brooks Acoust. Corp., 27 Hartford Turnpike, Vernon, CT 06066, bbrooks@brooks-acoustics.com)

The local authorities of a suburban town wanted to control the low-frequency noise emissions due to the musical entertainment at night clubs and taverns. Complaints from residents about booming bass guitar and drum sounds had to be balanced with the need for tavern owners to conduct business reasonably. It was recognized that the existing town code, which placed limits on A-weighted noise levels at property boundaries, was not an effective means to control low-frequency noise emissions. A revised ordinance was developed to address this issue, which now places additional limits on the allowable noise levels in specific octave bands. In particular, this includes the low-frequency (bass) octave bands. The octave band limits were selected such that the summation of band levels equals the A-weighted overall noise limit.

5:20

4pNSc10. Collection data of noise emissions from building construction sites. Stefan Becker and Edelbert Schaffert (BeSB GmbH Berlin, Undinestr. 43, 12203 Berlin, Germany)

Until now, construction noise has mainly been looked at in terms of machinery. Several publications deal with the noise emission of construction machinery such as excavators, saws, etc. Government noise limits are normally given as average levels for daytime or night time. Thus (especially during the construction of the walls) noise predictions cannot be made on the basis of information of single tools only. Therefore a new study was initiated by the German Umweltbundesamt to collect data describing the total noise emission during the construction of buildings. The integrated approach has to be used, especially during the construction of the walls, because of the variety of simultaneous working processes. The study will determine the average sound-power level, information on sound impulses, and time information during each construction phase depending on the method used (e.g., prefabricated or cast concrete). The emission data have been obtained from measurements at several construction sites, observation of the construction works, and discussions with construction-site managers.

5:40

4pNSc11. Models for acoustic sources in urban areas. David Gaulin and Michel Bérengier (Laboratoire Central des Ponts et Chaussées, Ctr. de Nantes, Rte. de Bouaye, BP 19, 44340 Bouguenais, France, Michel.Berengier@lcpc.fr)

Due to the large increase of populations in urban areas and the impact of sound phenomena on their life, the control of noise in cities is now of great importance. To predict acoustic fields for various urban situations, several theoretical approaches are currently under development. One of these is based on the diffusion theory [J. Picaut *et al.*, Acust. Acta Acust. **83**(4), 614–621 (1997)]. Whatever the model used, good predictions will be obtained only if the acoustic sources are accurately modeled. Those sources, classified following a qualitative approach, can be issued from traffic (cars, trucks, buses, motorcycles, etc.) but can also have human components (children in a school-yard, people in a market place, on a pedestrian street, . . .). The aim of this research concerns the modeling of each kind of source. The main parameters retained are the height, the directivity pattern, the sound power frequency spectrum, and the time history. The modeling techniques are based on statistical analysis and inverse fitting procedures on experimental data carried out over a large sample inside each source category. Afterwards, source characteristics will be introduced in the diffusion model and results will be compared with experiments performed on scale models and real urban situations.

6:00

4pNSc12. Sound field modeling in streets by a diffusion equation. Judicaël Picaut (Lab. Central des Ponts et Chaussées, Ctr. de Nantes, BP 19, 44340 Bouguenais, France, Judicael.Picaut@lcpc.fr) and Laurent Simon (Inst. d'Acoust. et de Mécanique, 72017 Le Mans Cedex 9, France)

By considering that surface irregularities of building facades are sufficient to produce diffusion in streets, the diffuse sound field modeling by the mathematical theory of diffusion is used to predict sound propagation and reverberation in rectangular streets. This modeling was first developed to predict the sound field in rooms with diffusely reflecting boundaries [J. Picaut, J.-D. Polack, and L. Simon, Acust. Acta Acust. **83**(4), 614–621 (1997)]. In this paper, the modeling is applied to urban acoustics without significant modification. A 3-D diffusion equation is derived for the sound energy density and solved for time-varying sources and in steady state. A diffusion coefficient is introduced to characterize the degree of diffusion of the street, and an exchange coefficient depending on the absorption coefficient is used to take the wall absorption into account. When the diffusion coefficient is chosen correctly, predicted reverberation times and sound attenuation are in accordance with experimental data obtained in a scale model of a street. With new developments, by introducing in the model, for example, intersections, moving sources, meteorological effects . . . , this original modeling should be in the future, a simple solution to predict the noise impact in large urban areas.

Session 4pNSd

Noise: Noise Emission From Machinery II

Hans G. Jonasson, Cochair
SP Swedish National Testing and Research Institute, Box 857, SE-50115 Borås, Sweden

Angelo Campanella, Cochair
3201 Ridgewood Drive, Columbus, Ohio 43026, USA

Chair's Introduction—1:55

Invited Papers

2:00

4pNSd1. A new hybrid approach, for estimating *in situ* the acoustic power radiated from vibrating structures. J. Nicolas, O. Beslin, and O. Foin (Mech. Eng. Dept., G.A.U.S. (Groupe d'Acoustique et Vibrations de l'Univ. de Sherbrooke), Univ. de Sherbrooke, Sherbrooke, QC J1K 2R1, Canada)

Measuring *in situ*, the acoustic power radiated by a vibrating panel with classical intensity techniques, is not always possible because of the influence of other surrounding sources. This is a major difficulty during the characterization in vehicles' noise problems. In this paper, a new experimental–numerical hybrid approach is presented which permits the evaluation *in situ*, of minimum and maximum indicators for the acoustic power intrinsically radiated by a particular panel situated in a more complex system. This is a two-step method: (i) the *in situ* vibration field of the panel is measured using a laser scan or an accelerometers array. (ii) Two indicators of the acoustic power are calculated. A minimum indicator is obtained by calculating the acoustic power radiated by the panel vibration field as if it were in free space (unbaffled vibration field). A maximum indicator is calculated considering a baffled vibration field (half free space). Interestingly enough, the measured data are projected in a base of trigonometric functions which allow quick calculations for a large frequency span. Then, precomputed baffled and unbaffled radiation impedances are used to calculate the radiated power. Comparisons between exact and estimated radiated powers are presented and discussed.

2:20

4pNSd2. Localization of noise sources inside machines by using a scaled dummy head. Helene Illaire and Jens Blomqvist (Dept. of Appl. Acoust., Chalmers Univ. of Technol., SE-41296 Gothenburg, Sweden, jens@ta.chalmers.se)

This study presents the use of the fine spatial resolution of the human auditory system to localize sound sources in small enclosures, by means of a 1:10 scale dummy-head and subsequent real-time frequency scaling. This method has been applied to the localization of rattle sources in the gearbox of a truck. After investigation of cues necessary for localization in the horizontal plane in a reverberant environment, a dummy-head of a scale of 1:10 has been designed. The dummy-head reproduces the general shape of the human head but the pinnae are not found necessary for inclusion for this investigation at low frequencies. To preserve the ability to localize, the frequency content of the recorded signal is scaled by the same factor as the dummy-head, i.e., it is divided by a factor of 10. Therefore, a frequency divider system has been developed to divide the frequency in real-time by 10 and uses a time-expansion method. The design of the system and the problems encountered are presented, together with the results obtained.

2:40

4pNSd3. Order tracking of diesel engines with a Kalman filter. Krystof Kryniski and Ulf Carlsson (MWL, KTH, Stockholm S 100 44, Sweden, kk@FKT.KTH.SE)

Order tracking analysis is one of the techniques used to monitor the performance of diesel engines. The objectives are to separate vibration into terms corresponding to the rotational speed and its multiples and then to monitor the changes over the revolution of a crankshaft. A Kalman filter provides the technique of isolating each of the components that are synchronous to the shaft rotation. By filtering the signal in the time domain it has also the capabilities to follow any variation of the rotational speed. Thus, the Kalman filter, if properly designed, can provide a tool for testing not only steady engine operation but can also be used to analyze both the engine acceleration and declarations under different loads. The paper discusses first, the process of monitor the frequency components locked up to the rotational speed with high resolution. Then, it shows how to reconstruct the synchronous components, in terms of amplitude and phase, to produce the vibration patter over the crankshaft revolution.

3:00

4pNSd4. Characterization of I. C. engines as a linear acoustic source using internal measurements. Slaheddine Frikha, Samir Boukhari (Laboratoire de Mecanique Physique, UPMC, CNRS Upresa 7068, France, frikha@ccr.jussieu.fr), Xavier Mouton (Renault, Guyancourt, France), and Arnauld Vitel (PSA, La Garenne, France)

Nowadays, faced with international competition, the vehicle constructors are constrained to reduce their studies' periods and costs. The knowledge of engine acoustic properties as a source exciting its inlet and exhaust pipes is required to perform predictive computations. Present here is a new method allowing engine source characterization as an acoustic pressure source having finite impedance that consists of fitting the engine nonlinear behavior by an equivalent linear one. It is based on a multi-charges approach. Internal pressures at a few points of a set of silencers are used to identify the pressure and the velocity at the outlet of the catalytic converter. The main future of the method is its ability to characterize the engine at realistic functioning conditions. In particular, the inverse model does not include a tail pipe radiation model, so the back pressure may be imposed to a realistic one. That reduces the effects of nonlinearity of the engine and increases the accuracy of the identified source. The internal pressure data are obtained by real measurement since a prototype of the engine exists. Otherwise, they can be computed which allows beginning the design of the exhaust system at an early stage of engine designing.

3:20

4pNSd5. Experimental study of rasping noise in internal combustion engine exhaust systems. Mondher Ayadi, Slaheddine Frikha, Pierre Yves Hennion (Laboratoire de Mecanique Physique, UPMC, CNRS URESA, 7068 Paris, France, ayadi@ccr.jussieu.fr), and Jean Michel Coulon (Arvin Exhaust System, Preston, UK)

The abnormal noise, known as rasping noise by several exhaust muffler designers, is a metallic intermittent noise which irritates the ear and has an adverse effect on vehicle marketability. It occurs in small cars having no more than two boxes in their exhaust systems. This phenomenon is highly noticed during a rapid acceleration or deceleration in cold conditions. However, it is sharply attenuated when the exhaust system is warmed up. An experimental study has been undertaken. Several exhaust systems, ranging from a simple pipe to a complete exhaust line, are tested. Pressure measurements in the line are performed by piezoelectric transducers. The tail pipe noise measurements are performed by a microphone. It has been observed that, unlike the usual exhaust noise that contains essentially second and fourth orders, the perception of the so-called rasping noise is associated with high-frequency components in the signal and needs higher-order analysis to be fully characterized. The experiments also show the steepening of the waves when rasping noise is listened. The high axial temperature gradient causes an increasing of that effect and probably a generation of shock waves which excite the main muffler and cause the metallic noise.

3:40

4pNSd6. Power output of a machine operating near elastic structures. Tatiana M. Tomilina, Michael P. Korotkov, and Vladimir B. Yashkin (Lab. of Structural Acoust., Mech. Eng. Res. Inst., M. Kharitonievsky 4, Moscow 101830, Russian Federation, tatiana@cgrsmx.iki.rssi.ru)

For predicting the noise levels produced by machinery, techniques, like SEA, based on the energy balance equations in which the radiation power of each noise source (machine) is used as an input parameter, are often employed. Usually, the standard value of the power measured in the free space is taken and it is assumed independent of acoustic environment. In the present work, it is shown experimentally and in computer simulation examples that the power output of an extended noise source operating near an elastic structure can differ significantly (several orders of magnitude) from its standard value. Possible corrections for the energy techniques are discussed.

4:00

4pNSd7. Development of a high-frequency precision anechoic test facility. John Duda, Martin Hirschorn (Industrial Acoustics Co., 1160 Commerce Ave., Bronx, NY 10462), Mark Gilbert, and Guy Torio (Shur Brothers, Evanston, IL 60602)

Although anechoic wedges with absorption coefficients of 0.99 as tested in typical impedance tubes meet ISO inverse square-law standards, they may not be satisfactory for anechoic rooms used for measurements of microphone response characteristics. Due to size restrictions, impedance tube tests are limited to frequencies below about 250 Hz and there is no standard method to test wedges for absorption at higher frequencies. This paper describes how pulse signal and reverberation room tests were employed to rank the high-frequency performance of three types of anechoic wedges considered for a microphone test facility: Standard patented Metadyne ™ (perforated metal) wedges—conventional fiberglass wedges and an improved high performance Metadyne wedge system. The results of laboratory tests and tests conducted in anechoic rooms are presented. In all cases the preferred system, high-performance Metadyne wedges, is shown to meet the stringent acoustic absorption requirements needed for this application. The paper indicates the need for new standards for laboratory testing of anechoic wedges at high frequencies and an alternate method to inverse square-law tests for evaluating anechoic room performance such as stepped frequency sweep tests. Such a new standard will be proposed in the presentation.

These posters will be on display in the Poster Gallery from Thursday to Friday, 18–19 March. Authors will be at their posters from 4:40 p.m. to 6:20 p.m. on Thursday, 18 March.

4pNSd8. Characteristics of MRI acoustic noise in functional and high-resolution imaging of the auditory pathways. Uwe Baumann (Dept. of Audiol., Ludwig-Maximilians-Universität, Marchionini-Str. 15, 81377 München, Germany) and Lorenz Jäger (Ludwig-Maximilians-Universität, 81377 München, Germany)

The acoustic noise generated by magnetic resonance image (MRI) systems causes problems for the measurement of funtional responses to acoustic stimuli. The time structure and spectral composition of the MRI noise depends mainly on the sequence of gradient switching. As a rule of thumb, faster switching produces more intense noise than slower switching. Functional and high-resolution MRI of the auditory pathways require fast switching sequences to ensure high place and time resolution. To investigate the characteristics of the MRI noise, five different sequences (EPI-fMRI, 3D-MPRAGE, 3D-CISS, 2D-FLASH, EPI-DIFF) were recorded on a 1.5-T device (Siemens Vision) at the position of subject head and also 1.2 m outside the MRI opening to estimate artifacts caused by direct induction into the microphone (B & K 4165). The measured peak SPL inside the MRI varied between 101 and 130 dB depending on the sequence, but a comparison with the results outside the MRI cabinet (87–100 dB SPL peak) revealed for the 3D-CISS and EPI-DIFF sequence an influence of direct induction with an amount up to 20 dB. An ear-related spectral analysis and a virtual pitch calculation was performed to estimate the amount of tonality of each sequence.

4pNSd9. Adaptive decision method for acoustical turbomachinery diagnostics. Olena N. Bezvesilna (Dept. of Devices, Natl. Tech. Univ. of Ukraine, 37, Peremogy pr., Kiev, 252056, Ukraine) and Leonid M. Gelman (National Tech. Univ. of Ukraine, Kiev, 252056, Ukraine)

Acoustical turbomachinery diagnostics is advisable to do automatically and complexly using simultaneously different methods. The mentioned diagnostics is condition monitoring diagnostics. Such diagnostics is necessary to do at all operation regimes of turbomachinery and therefore with changes of interfering data of turbomachinery and of environment condition in which diagnostics is carried out. However, in the presence of variable interfering data, optimum properties of decision methods are not realized. In addition, features used for diagnostics are usually statistically dependent. To provide diagnostics in the mentioned conditions it is necessary to apply the adaptive approach. A new automatic adaptive sequential method for acoustical turbomachinery diagnostics is proposed and developed for: (a) presence of variable interfering data; (b) changes in the space of these data limits of erroneous test probabilities; (c) availability of statistical dependencies between features. A new procedure to account for the statistical dependencies between features is proposed and developed. Acoustical diagnostics of the gas-turbine engine based on noise emission is presented. [Work supported by the MacArthur Foundation.]

4pNSd10. Investigations of sound insulation of partitions used for integrated enclosures. Zbigniew Engel and Jan Sikora (Dept. of Mech. and Vibroacoustics, Univ. of Mining and Metallurgy, al. Mickiewicza 30, 30-059 Krakow, Poland, engel@uci.agh.edu.pl)

Integrated enclosures, rarely applied in practice, are useful in the reduction of the excessive noisiness of machines and equipment. They are especially important for the machinery requiring constant and direct operation and maintenance, for which the application of other enclosures (e.g., fully closed) is inadmissible. Results of the sound insulation investigations of new types of partitions designed for the construction of integrated enclosure elements have been presented in the paper. Several specimens of partitions, which, according to their acoustic properties belong either to single (homogeneous and heterogeneous) or to multiple partitions (consisting of single, mixed and layered ones), were prepared for experiments. Double partitions with air cavities either empty or filled with sound absorptive materials, rigid, elastic, or granular absorbers (damping the airborne and material sound levels), appeared to be the main solution. The best partitions were used in the prototype of the integrated enclosure constructed for the engine lathe testing. The mechanical noise level of the lathe was reduced by 15 dB. The sound-insulating performance of the prototype has shown that the construction of integrated enclosures can be utilized in designing the new machines characterized by the lower acoustic activity—in comparison with the present standards.

Session 4pPAa

Physical Acoustics and Engineering Acoustics: Numerical Methods for Computing Sound Radiation and Scattering II

Martin Ochmann, Cochair
Technische Fachhochschule Berlin, Fachbereich Mathematik und Physik/Fernstudien Institut, Luxemburgerstrasse 10, D-13353 Berlin, Germany

Gary H. Koopmann, Cochair
Department of Mechanical Engineering, Pennsylvania State University, 157 Hammond Building, University Park, Pennsylvania 16802, USA

Invited Papers

2:00

4pPAa1. Application of wavelet decomposition (space-wave number) to sound radiation 1D. M. Martinet, N. Hamzaoui, and J. L. Guyader (Laboratoire Vib. Acoustique de L'INSA de Lyon, 20 avenue A. Einstein, 69621 Villeurbanne Cedex, France)

The purpose of this presentation is to study the contribution of a multiresolution analysis based on a decomposition in wavelets, so as to predict the acoustic radiation of a vibrating structure. In order to analyze the sensitiveness of different parameters of this approach, it is suggested that it be applied to the radiation of a heterogeneous beam in flexion. After an analysis of the radiation associated with different forms of wavelets, the displacement field of the beam is decomposed on a wavelet basis, and its radiation will be then computed and faced with a result stemming from a classical technique. First, the interest, researched by this approach, is linked to the reduction of the number of points of mesh of the vibratory field of the beam, and second, to a physics analysis giving way to access to the spatial localization of the radiated parts. The formulation of the one-dimensional problem, the physics concepts of the multiresolution analysis, and a confrontation with a bibliographic reference, analyzing the advantages and the drawbacks of this approach, are thus presented here.

2:20

4pPAa2. BEM and the use of explicit frequency-dependent matrices—A study on computing wave scattering and radiation. Steffen Marburg (Institut für Festkörpermechanik, Technische Univ., D-01062 Dresden, Germany, marburg@mfm.mw.tu-dresden.de)

The use of explicit frequency-dependent matrices as in finite-element methods has not really been established in boundary element methods yet. The particular integral method (PIM) that may be applied to construct explicit frequency-dependent matrices has already been tested for the solution of interior problems in structural acoustics. However, a formulation for the exterior problem using PIM has not been published. In this paper, the author will discuss ways to apply the PIM to compute wave scattering and sound radiation.

2:40

4pPAa3. A surface element formulation of the equivalent source method. U. Peter Svensson (Dept. of Appl. Acoust., Chalmers Univ. of Tech., SE-41296 Gothenburg, Sweden), Mayumi Nakano, Kimihiro Sakagami, and Masayuki Morimoto (Kobe Univ., Kobe 657-8501, Japan)

A time-domain formulation of the equivalent source method which uses planar surface elements is presented. The boundary condition of a closed surface can be fulfilled using monopole elements for boundary conditions specifying the normal velocity, the sound pressure, or the local impedance. By interpreting the equivalent sources as double layers of free-field radiating monopoles with a uniform source signal over the element, the impulse response matrix is easy to find via the Rayleigh integral. The problem of determining the source signals of these equivalent sources involves the inversion of a single real-valued matrix as shown in Kropp and Svensson [Acustica **81**, 528–543 (1995)], and the matrix is very sparse. The relation to the boundary element method is discussed, and as an example, the sound radiation from a kettledrum is presented. By using a Green's function technique, any vibration pattern can be synthesized using post-processing. Interpolation can be used to study the far-field radiation of vibration patterns that are more complicated than the element mesh can resolve.

3:00

4pPAa4. Two surface element formulations in the time domain for the calculation of sound fields in cavities with varying boundary conditions. Wolfgang Kropp and U. Peter Svensson (Dept. of Appl. Acoust., Chalmers Univ. of Technol., SE-41296 Gothenburg, Sweden)

Two different surface element formulations are presented which apply the equivalent source method in the time domain. The first method uses planar surface elements. The boundary condition of the cavity surface in the form of a prescribed impedance is fulfilled by using monopole elements (i.e., layers of free-field radiating monopoles with a uniform signal over the element). The second

method is based on the Kirchhoff–Helmholtz integral. While the traditional boundary element technique uses the free-field Green's functions, here a set of specialized Green's functions is applied which is adapted to the cavity geometry. This set of functions fulfills the boundary conditions for the cavity with rigid walls. In this way the Kirchhoff–Helmholtz integral is simplified substantially and only areas of the surface with nonrigid boundary conditions have to be included in the calculations. Advantages and disadvantages of both formulations are highlighted, and results from both methods are compared for rooms of different complexity.

3:20

4pPAa5. Using the equivalent sources method (SUP) for multibody radiation problem. Tatiana M. Tomilina (Lab. of Structural Acoust., Mech. Eng. Res. Inst., M. Kharitonievsky 4, Moscow 101830, Russian Federation, tatiana@cgrsmx.iki.rssi.ru)

The radiation problem for a finite body vibrating in a fluid near rigid scatterers and for elastic structures is discussed. It is shown that the ESM is the most appropriate method for treating the problem. Formulation of the boundary conditions on the surfaces of elastic scatterers is the key point of the method here. New results of computer simulation and laboratory experiment concerning the energetics of sound radiation are presented. The comparison of two modifications of the ESM is considered in this paper: one modification is based on the Rayleigh multipole expansion and the other uses the equivalent sources of the monopole type.

3:40

4pPAa6. Efficient boundary element calculations using thin-plate acoustic elements. John B. Fahnline (Appl. Res. Lab., 16 Appl. Sci. Bldg., University Park, PA 16802, jbf@wt.arl.psu.edu) and Gary H. Koopmann (Ctr. for Acoust. and Vib., University Park, PA 16802)

Thin-plate elements are commonly used to represent structural components whose thicknesses are much smaller than the structural wavelength. This simplifies the analysis, because otherwise several elements are required to represent correctly the strain distribution through the thickness, leading to much larger models. Thin-plate elements also have advantages when they are used in acoustic boundary element calculations. By using dipole sources at the midline of the elements to generate the basis functions for the acoustic analysis, the boundary condition can be enforced such that the opposite sides of the plate are forced to move together. The surface velocity boundary condition then only has to be enforced over one side of the elements (even though both sides are in contact with the acoustic medium). Mechanical radiation impedance calculations can also be simplified because the dipole source basis functions create the same pressure field on opposite sides of the plate elements and thus impart no force to the structure. The only exception is for ''self-element'' terms, where the dipole sources create equal, but opposite, surface pressures. Several example problems are used to validate the calculations, including a vibrating strip, a transversely oscillating disk, and a cantilever plate.

Contributed Papers

4:00

4pPAa7. Finite-element methods applied to the propagation of acoustic wave along immersed wedges. A. C. Hladky-Hennion, P. Langlet, R. Bossut (IEMN, département ISEN, 41 boulevard Vauban, 59046 Lille Cedex, France), and M. de Billy (Université Paris 7, 75251 Paris Cedex 05, France)

Immersed in water, wedges can generate either propagating or radiating acoustic guided waves according to the value of the apex angle. The propagation of such waves is analyzed with the help of two methods based on finite-element methods: a time analysis [A. C. Hladky-Hennion *et al.*, J. Acoust. Soc. Am. **104**, 64–71 (1998)] and a modal analysis for which an original numerical technique is suggested to describe the radiating (or supersonic) modes. The finite-element results obtained with the two methods for brass and duraluminum wedges are compared to the experimental measurements. A good agreement is observed for either subsonic or supersonic regions.

4:20–4:40 Break

4:40

4pPAa8. A combined finite-element, boundary integral, and spherical harmonic hybrid technique for computing multiple-body sound radiation. John B. BlottmanIII and Anthony J. Kalinowski (Naval Undersea Warfare Ctr. Div. Newport, 1176 Howell St., Newport, RI 02841-1708, blottman-john-b@code21.npt.nuwc.navy.mil)

Transducer interactions within an array are known to affect the array performance and the life expectancy of the transducers. The ability to predict array performance is required for large close-packed arrays of acoustic transducers. In these cases, traditional full finite-element methods prove costly. A combined multiple acoustic scattering model that is based on spherical harmonic functions and a finite-element-based description of an elastic body of arbitrary geometry is formulated to predict the performance of an array of acoustic transducers. The finite-element model produces the dynamic system matrix. A boundary integral equation relates surface pressure and velocity. Boundary elements are partitioned for the case of the surface of an arbitrary body circumscribed by a spherical surface to provide an implicit transfer of surface pressures to spherical fluid pressures and particle velocities. These quantities are then transformed in terms of spherical harmonics. The resulting series is combined with the spherical harmonic representation of the fluid using the addition theorem for multiple scatters. The technique has been exercised to evaluate an array of piezoelastic shells, driven by an electrical potential. Results compare well to those of a coupled finite-element–boundary-element method. [Work sponsored by the Office of Naval Research.]

5:00

4pPAa9. A reflection free boundary condition for propagation in uniform flow using mapped infinite wave envelope elements. Walter Eversman (Mech. and Aerosp. Eng. and Eng. Mech., Univ. of Missouri—Rolla, Rolla, MO 65401, eversman@umr.edu)

A new reflection free boundary condition based on mapped infinite wave envelope elements is developed for finite-element modeling of acoustic radiation in a uniformly moving medium. These elements are useful for obtaining closure for computations on an infinite domain in which a radiating body is immersed in a moving medium which is essentially undisturbed outside of the near field. The application described is for harmonic excitation which leads to a model independent of time. An additional result of this study shows that the mapped wave envelope elements provide a boundary condition equivalent to stiffness, mass, and damping matrices appended to the inner mesh. By choosing the transition between the standard FEM mesh and the mapped WE as a surface of constant phase, the mass matrix is caused to vanish identically. This has implications for transient FEM modeling of acoustic radiation. A demonstration of the characteristics of the mapped WE elements is given in the

context of acoustic radiation from a turbofan inlet for which benchmark results are known. It is found that for similar computational cost mapped infinite wave envelope elements are superior to conventional wave envelope elements for time-independent formulations.

5:20

4pPAa10. How reliable is the method of comparative sources? Kai-Ulrich Machens[a] (Inst. of Tech. Acoust., Tech. Univ. of Berlin, Berlin, Germany, kamachen@gfn.daimler-benz.com)

Radiation and scattering from vibrating bodies can be expressed by a source system that is placed inside the radiator and whose source strengths are determined appropriately. The method of comparative sources (MCS) provides an estimate of these source strengths from the near-field data. The MCS is reviewed by applying it to cylinders with elliptical cross section. This geometry is suitable to check the method for two reasons. First, it is general enough to demonstrate methodical difficulties which arise from its spatially varying field impedances as a result of different surface curvatures. On the other hand, it is not too complicated to allow analytical treatment by Mathieu functions. Therefore, it is possible to generate exact solutions of the sound field from different, more and less efficiently radiating velocity distributions. These solutions are compared to results obtained by the MCS, in which various source systems and different weighting functions are used. This way, it is demonstrated that the relative error in the surface velocity approximation generally is not proportional to the error in the radiated sound power. Moreover, it is shown that certain weighting functions may be advantageous and that it is more difficult to predict inefficient than efficient radiators by this method. [a] Now at Daimler-Benz Group, ATG Research and Technology.

5:40

4pPAa11. Designing electrodynamic loudspeakers by using a new computer modeling scheme. Martin Rausch, Reinhard Lerch, Manfred Kaltenbacher, Hermann Landes (Dept. of Elec. Measurement Technol., Univ. of Linz, Altenbergerstr. 69, A-4040 Linz, Austria, Martin.Rausch@jk.uni-linz.ac.at), Gerhard Krump, and Leonhard Kreitmeier (Harman Audio Electron. Systems GmbH, D-94315 Straubing, Germany)

A new technique for the computer modeling of fluid-loaded magneto-mechanical transducers is presented. This numerical technique is based on a finite-element method (FEM) and allows the precise calculation of the magnetic, mechanical, and acoustic fields, including their couplings. Further on, nonlinear effects in the mechanical and magnetic behavior are considered. Therewith, the complex dynamic behavior of electrodynamic loudspeakers was studied and, furthermore, an appropriate computer-aided engineering (CAE) environment has been established. This CAE tool allows an optimization of critical parameters, for example: The validity of the computer simulations is verified with the help of appropriate measurements. The calculated and measured values for eigenfrequencies, axial pressure responses, and electrical input impedances are in excellent agreement. The applicability of the presented calculation scheme with respect to the computer-aided design of moving coil drivers is demonstrated by reporting several practical applications, which are of great interest for loudspeaker manufacturers. In the present paper, the elimination of response dips at intermediate frequencies, the calculation of polar responses, and the examination of the so-called jump-out excursion, are presented.

6:00

4pPAa12. Acoustic photo- and cinematography based on interference transformation. Gerd K. Heinz, Thanh T. Nguyen, and Dirk Duebler (Gesellschaft zur Foerderung angewandter Informatik e.V., D-12484 Berlin, Rudower Chaussee 5, Germany)

A time-domain technique is introduced to localize far and moving acoustic objects (compare URL http://www.gfai.de/www_open/perspg/heinz.htm). The algorithm is called ''Heinz Interference Transformation'' (HIT) [Heinz *et al.*: ''Time pattern, data addressing, coding and topographic maps between multiple connected neural fields—a physical approach to neural superimposition and interference,'' BioNet'96, Berlin, ISBN 3-00-001107-2]. HIT reproduces mirrored (optical) projections just as nonmirrored reconstructions of different sources depend on the direction of time axis. Based on time-domain calculations, the introduced method reproduces an approximation for different source points in a grid matrix, arranged in an virtual space or array or field in physical dimensions of the measured scene. It is possible to reconstruct acoustic single-time events to cinematographies (movies). Maximum image rate is the sample frequency of time functions. Independent of the integration interval, it is possible to reconstruct in cinematographies the wave field or movies. Properties of HIT, influence of time functions' properties and channel number, different algorithmical tasks, relations between time and space, aliasing and reconstruction parameters are discussed as examples. [Work supported by German BMWi, Marktvorbereitende Industrieforschung.]

Invited Poster

This poster will be on display in the Poster Gallery from Thursday to Friday, 18–19 March. Authors will be at their posters from 10:00 a.m. to 12:00 noon on Friday, 19 March.

4pPAa13. Some aspects of the scattering calculation using the source simulation technique. Paulo Henrique T. Zannin (Dept. Engenharia Mecanica, Univ. Fed. Parana, Centro Politecnico, Curitiba, PR 81531-990, Brazil)

In this work the source simulation technique was used to calculate the scattering of a plane wave by a cylinder with radial or elliptical transversal section. Numerical simulations have shown that: (1) the shape of the auxiliary surface, (2) the number of sources, and (3) the way the sources are distributed are the most relevant parameters to ensure an accurate solution for the problem. In the case of the single-layer method, sources should not be positioned close to the surface or to the center of the body, because the problem becomes ill-conditioned. The auxiliary surface and the scatterer should be as similar as possible in order to minimize the boundary error. With respect to the number of sources (N), there are two opposite effects: (1) if (N) is too small, the sound field is not reproduced accurately, (2) if (N) is too large, computing time increases and solution accuracy decreases. The method breaks down when excitation frequency coincides with the eigenfrequencies—a narrow range of frequencies—of the space formed by the auxiliary surface. As the auxiliary surface is frequently represented by simple surfaces (cylinder, sphere), one can easily calculate the eigenfrequencies, and therefore avoid them.

Contributed Poster

This posters will be on display in the Poster Gallery from Thursday to Friday, 18–19 March. Authors will be at their posters from 10:00 a.m. to 12:00 noon on Friday, 19 March.

4pPAa14. Numerical modeling of axisymmetric sources in infinite baffle. Bronislaw Zoltogorski, Andrzej Dobrucki, and Cecylia Szmal (Wroclaw Univ. of Technol., Inst. of Telecommunications and Acoust., Wybrzeze Wyspianskiego 27, 50-370 Wroclaw, Poland, brz@zakus.ita.pwr.wroc.pl)

According to standards, characteristics of loudspeakers should be measured in an anechoic room with the use of sufficiently great rigid baffle. To achieve accordance of numerical calculations to results of measurements, the numerical algorithms for a source in an infinite baffle are needed. In the paper three boundary integral methods—the Huygens–Rayleigh (HR) integral method, the Kirchhoff–Helmholtz (KH) integral method, and the simple-source density (SSD) method—are explored for the sources of revolution with optional surface velocity distributions and shapes of cross sections (cone, flat piston, dome). It was shown that solution of the boundary-value problem for the KH and SSD methods exists and is unique for all frequencies. The HR method is numerically the simplest and is free of existence/uniqueness problems but is theoretically founded for a flat piston only, whereas for sources of other shapes it gives erroneous results. The problem of inclusion of an infinite baffle into the numerical model is easy to overcoming for the SSD method because an auxiliary source-density function rapidly decreases out of source and only a small fragment of the baffle influences the final result. For the KH method that question is more difficult because pressure on the baffle surface does not decrease sufficiently fast. The improved KH method that overcomes this deficiency is described.

THURSDAY AFTERNOON, 18 MARCH 1999 ROOM MA041, 2:00 TO 6:20 P.M.

Session 4pPAb

Physical Acoustics: Measurement and Evaluation of Ultrasound II

Rainer Reibold, Cochair
Physikalish-Technische Bundesanstalt, Bundesalle 100, D-38116 Braunschweig, Germany

R. C. Chivers, Cochair
6 Louis Fields, Guildford GU3 3JG, UK

Contributed Papers

2:00

4pPAb1. Calibration of contact transducers by means of thermoacoustic sensors. Michael Glinka (Physikalisch-Technische Bundesanstalt, Labor 1.43, Bundesallee 100, 38116, Braunschweig, Germany)

The utilization of the *thermoacoustic effect* for measuring the absolute value of acoustic power by means of thermoacoustic sensors is discussed. The sensor's response to the incident acoustic power is measured as the temperature increase T. This temperature increase is computed by the differential equation describing the sensor, which contains only the sensor's material constants: density ρ, specific heat capacity c_w, and conductivity Λ_w,

$$\frac{\partial T}{\partial t} = \frac{\Lambda_w}{\rho c_w}\nabla^2 T + \frac{1}{\rho c_w}\cdot W. \tag{1}$$

It is shown how the distribution of heat sources W (caused by the absorbed ultrasonic field) can be optimized for the realization of thermoacoustic sensors adapted to experimental situations. A discussion of different types of sensors will show that the complex transfer functions are restricted by the material constants. It is shown how the solutions of (1) presented can be used to improve the dynamic performance. Experimental results obtained by the use of different sensors and contact transducers (calibrated by the reciprocity method) are compared with respective solutions of the parabolic heat flow equation (1).

2:20

4pPAb2. Improvement of the lateral resolution of finite-size hydrophones. Tarek Boutkedjirt and Rainer Reibold (Physikalisch-Technische Bundesanstalt, D-38116 Braunschweig, Germany)

In recent years, there has been an increasing number of ultrasound applications which utilize frequencies well above 10 MHz. Piezoelectric hydrophones are commonly used for the characterization of the respective fields. With the exception of specially designed laboratory devices, limits are set to the hydrophones currently available due to their finite size. Instead of measuring the acoustic pressure at a point, these devices furnish a value integrated over the sensitive aperture. The adverse averaging effect is particularly prominent in the Fresnel zone of the sound field and at frequencies above 10 MHz, where the aperture dimensions are of the order of several acoustic wavelengths in water. This problem can be solved by numerically deconvolving the aperture function from the observed response of the finite-size receiver. The efficiency of the deconvolution process is shown for both numerical simulations and experimental investigations. Special regard is paid to the methods of noise reduction by means of averaging, smoothing, and filtering.

2:40

4pPAb3. The use of the finite-element method to analyze the influence of depolarization by structuring to the performance of 2D arrays. Daniel Schmitt, Peter K. Weber (Dept. of Ultrasound, FH-IBMT, Ensheimerstr. 48, D-66386 St. Ingbert, Germany, peterw@ibmt.fhg.de), Roger W. Whatmore, and Chris Goat (Cranfield Univ., Cranfield, UK)

3-D ultrasonic imaging can be achieved by steering conventional single-element scanners (pseudo 3-D imaging). The use of 2-D arrays offers a wide range of possibilities for electronic focusing and steering, which will lead beyond the limitations of pseudo 3-D imaging. Measurements of single-array elements have shown that the method of structuring, like dicing, and its process parameters, leads to a decreased coupling factor. This will result in a loss of efficiency and bandwidth. Because this effect can be reduced by repolarizing the array, one can assume a depolarization of a certain depth along the cutting edge of the material. It is very difficult to determine the degree of depolarization and the depth of this dead zone. Using simple geometric models with good aspect ratio and a completely depolarized death zone, the influence of its depth on the coupling factor can be determined. These presumptions are not valid for most 2-D arrays in ultrasonic imaging. Their complex geometry and parameter combinations can be analyzed by the finite-element method. Results obtained from finite-element simulations that are in good agreement with the measurements will be presented and compared with other methods.

3:00

4pPAb4. Investigation of effective geometrical parameters for a pulse-echo linear array with cylindrically curved, focusing surface. Ping Wu and Tadeusz Stepinski (Uppsala Univ., Dept. of Mater. Sci. Signals and Systems, Box 528, S-751 20 Uppsala, Sweden)

Linear arrays with cylindrically curved, focusing surfaces working in pulse-echo mode are currently being used for applications in nondestructive testing. Such commercial arrays are usually specified with nominal geometrical parameters (GPs), such as width, length, and radius of curvature (focal length), which, when used in the conventional piston source model, may result in an inaccurate prediction of the actual radiated field. Like a spherical focused transducer which has been extensively investigated for determining its effective GPs, a linear array with cylindrically curved, focusing surface has its effective GPs which allow the piston source model to provide a more realistic prediction of the actual radiated field. The goal of this paper is to investigate effective GPs for such a linear array used in pulse-echo mode. The effective GPs are determined by comparing the fields predicted by the extended angular spectrum approach (ASA), which is applicable to curved transducers, with the measured fields. Pulse-echo fields from the array were measured in water using a pointlike scatterer, and calculated using both nominal and effective GPs in the extended ASA. The results show that effective GPs do permit the piston source model to yield a more precise prediction of the measured fields.

3:20

4pPAb5. Characterization of an ultrasound system. Steinar Vervik and Magne Vestrheim (Dept. of Phys., Univ. of Bergen, N-5007 Bergen, Norway)

Frequency responses of an ultrasound system consisting of sender electronics, sender transducer, air as coupling medium, receiver transducer, and receiver electronics are measured and theoretically regenerated in the range 170 to 270 kHz. Magnitude and phase of the sender and receiver sensitivities are estimated by utilizing the reciprocity principle in combination with models and measurements of the transducer–transducer coupling function and the frequency response and loading effects of the electronics. Voltage-to-particle velocity frequency responses and electrical input admittances of the transducers are theoretically regenerated by the use of experimental modal analysis methods. The sound speed and absorption coefficient are estimated with diffraction corrections through spectral analysis methods. Simulated and measured waveforms are compared. Using time-frequency analysis, mode effects are studied and the waveforms and delays are related to the different functional blocks of the system. Differences between the measured and simulated transit times are found to be of the order of 10 ns in the range considered. The results are of interest in the analyses of zero-flow performance of ultrasound flow meters, in, for example, the study of signal detection criteria and in analyses of delays caused by nonfluid parts of the measurement system.

3:40

4pPAb6. A unified linear system approach to ultrasonic radiation from a baffled transducer. Kathy J. Hays-Stang (Univ. of Texas at Arlington, Arlington, TX)

An acoustic disturbance can be viewed as a waveform in space and time, or by the temporal or spatial frequency content of the acoustic disturbance. For each waveform and frequency viewpoint, the individual Green's function for acoustic radiation from a baffled transducer is available in the literature. The unified approach allows the Green's function for any given viewpoint to be transformed appropriately to obtain the Green's function for a desired viewpoint (personal conversations with the late Bill D. Cook). Given a Green's function for the acoustic radiation in a linear acoustic system, and the impulse responses of the other system components, the output can be determined for a given input. Choice of the most advantageous radiation impulse response/transfer function can reduce calculation time or provide physical insight for a problem of interest.

4:00

4pPAb7. Application of a fiber-optical probe hydrophone for *in vivo* measurements of therapeutical ultrasound. Thomas Dreyer, Rainer E. Riedlinger (Inst. fuer Hoechstfrequenztechnik u. Elektronik/Akustik, Univ. Karlsruhe, D-76128 Karlsruhe, Germany, Thomas.Dreyer@etec.uni-karlsruhe.de), Johannes Zenk, and Heinrich Iro (Univ. des Saarlandes, D-66421 Homburg, Germany)

Knowledge of sound fields used in therapeutical applications with focused strong ultrasonic pulses *in vivo* is of great importance to the user and researcher. In this study the ultrasonic field of an experimental high energy pulsed ultrasound (HEPUS) device for tumor treatment is investigated. Using HEPUS, the mechanism of acute tissue destruction is based mainly on cavitation effects in the focal region. A self-focusing piezoelectric transducer generates the applied pressure signal which is a high-amplitude sinusoidal burst with a duration of about 12 μs. These burst signals differ significantly from those in lithotripsy, but have similar amplitudes. A fiber-optical probe hydrophone provides the possibility of minimal invasive pressure measurements *in vivo* because of its small sensor diameter. During insonification in rabbits, the focal sound pressures and spatial pressure distributions were recorded in the liver and the back muscle *in vivo*. The fiber tip of the hydrophone was placed directly in the tissue by puncturing, using a cannula. The results obtained are compared with *in vitro* measurements. They are discussed regarding the influence of attenuation and nonlinear propagation in tissue. Additionally, an error estimation for the pressure measurement *in vivo* is presented. [Work supported by Wilhelm Sanders Stiftung Gz. 89.030.2.]

4:20–4:40 Break

4:40

4pPAb8. Fiber-optic dielectric multilayer hydrophone for ultrasound detection. Volker Wilkens and Christian Koch (Lab. 1.43, Physikalisch-Technische Bundesanstalt, PF 3345, D-38023 Braunschweig, Germany)

Fiber-tip sensors have proved to be useful for the investigation of ultrasonic signals since they, in principle, overcome some limitations of common piezoelectric hydrophones. A high damage threshold of the sensor is obtained, measurements are not disturbed by electromagnetic influences, and a high temporal and lateral resolution is possible. An optical hydrophone is presented that comprises a fiber tip coated with a dielectric multilayer system of the Fabry–Perot type. The acoustic pressure measurement using the sensor is based on the elastic deformation of the layer system by an incident ultrasonic wave and the detection of the induced change of the optical reflectance. Measurement results obtained by sensors with different layer numbers providing different sensitivities are shown, and the variation of the sensor characteristics depending on the size and shape of the fiber tip is investigated. The appearance of optical loss modulations caused by the stimulation of flexural waves in the fiber in certain measurement configurations is discussed. Several sensor designs are considered to improve the performance of the system in different fields of application, for instance the characterization of lithotripter shock waves, the investigation of cavitation phenomena, and the detection of ultrasound cw signals.

5:00

4pPAb9. Ultrasound cleaning of microfilters. Jens Hald, Irina Bjørnø (UltraTech ApS, Måløv Byvej 229, DK-2760, Måløv, Denmark), and Leif Bjørnø (Tech. Univ. of Denmark, DK-2800 Lyngby, Denmark)

The aim of the present work is to develop, design, and manufacture a high-power ultrasound transducer module to be used for preventing the blocking of plastic-based microfilters by organic materials, and possibly to prolong the lifetime of the filters in industry using the cavitation on the surface of the filter. A numerical, FE- and BE-based model for calculation of the response of ultrasonic transducers of various geometries formed the basis for the design of such transducers. During laboratory experiments frequency and output power have been varied in order to find the optimal transducer design suitable for cleaning of microfilters without damaging the filter structure. The filter surface was studied using an optical microscope before and after the experiment. When high-power ultrasound (max. 75 W/cm^2) was applied to the surface of some microfilters, no visible damage was found, while others filters were damaged. The results of the laboratory experiments formed background for the final design of an ultrasound transducer module for use by foodstuff filtration plants. [This work was financed by the EU Project WAMBIO PL96-3257 (FAIR Programme).]

Contributed Posters

These posters will be on display in the Poster Gallery from Thursday to Friday, 18–19 March. Authors will be at their posters from 5:20 p.m. to 6:20 p.m. on Thursday, 18 March.

4pPAb10. Laser Doppler anemometry applied to airborne acoustics: Influence of the signal processing parameters. Sylvain Poggi, Bruno Gazengel, Jean-Christophe Valière, and Anne-Marie Bruneau (IAM, Laboratoire d'Acoustique de l'Université du Maine, UMR CNRS 6613, Av. Olivier Messiaen, F-72085 Le Mans Cedex 9, France)

Laser Doppler anemometry (LDA) is widely used for fluid mechanics but may also provide measurements of the acoustic particle velocity. The validation of its use in acoustics, which is being achieved, requires knowledge of the appropriate data processing parameters. In order to understand their effects, an experiment is conducted in which LDA measures structural velocities. In this experiment, the velocity of a shaker tip measured by LDA is compared with the velocity measured by a laser vibrometer. The LDA signal is a sinusoidal frequency modulation whose instantaneous frequency is proportional to the measured velocity. LDA-measured velocities are estimated using either spectrum analysis or time-frequency analysis. These comparisons point out three major results. Even if the velocity is small, which corresponds to a narrow bandwidth of the measured signal, oversampling should be preferred. Time windows should be chosen as short as possible despite the poor estimation of the instantaneous frequency. These first two results lead to a precise temporal description of the measured velocity but a rough one in the amplitude domain. However, the *a priori* knowledge of the excitation signal frequency enables the precise estimation of the velocity amplitude by means of a least-square method.

4pPAb11. Acoustoelectric effect in gas sensor of the SAW type. Marian Urbanczyk and Aleksander Opilski (Inst. of Phys., Tech. Univ. of Silesia, ul. B. Krzywoustego 2, 44-100 Gliwice, Poland)

The initial value of the electric conductivity of the sensorial layer determines the working point of the sensor and is of essential importance with respect to the sensitivity of the sensor, because it determines the value of the acoustoelectric effect in that system. Basing on measurements it has been found that the electric conductivity of a lead phthalocyanine layer placed in an NO_2 atmosphere increases. This effect becomes higher as the temperature rises. In a SAW sensor the effect of the electric potential of a surface wave with a sensorial layer occurs in a high-frequency field. It has been found that the conductivity of lead phthalocyanine layers depends on the frequency to an extremely high degree. If compared with direct-current measurements, the alternating-current conductivity is greater by about two orders; its frequency being equal to the frequency of the propagated surface wave applied (43 MHz). Practically, the value of the conductivity of semiconducting layers at higher frequencies makes possible the occurrence of an acoustoelectric effect in the sensor.

4pPAb12. SAW sensor for low nitrogen dioxide concentration. Aleksander Opilski, Marian Urbanczyk, and Wiesaw Jakubik (Inst. of Phys., Tech. Univ. of Silesia, ul. B. Krzywoustego 2, 44-100 Gliwice, Poland)

The devolopment of a technique concerning macromolecular compounds has made it possible to get thin layers that change their physicochemical properties as a result of their interaction with the ambient atmosphere. Changes of the physical properties of specially prepared chemically sensitive layers influence the conditions of the propagation of an acoustic surface wave arranged in the layered system piezoelectric waveguide layer of the compound. Particularly, if the mass and electric conductivity of the chemically sensitive layer changed, the velocity of propagation of the acoustic wave changes. The presented paper includes a short review of the SAW gas sensor field and some experimental results for the detection of a low concentration of nitrogen dioxide in the air.

Session 4pPAc

Physical Acoustics: Elastic Properties of Materials II: Special Materials

Jan D. Achenbach, Cochair
Center for Quality Engineering and Failure Prevention, Northwestern University, 2137 North Sheridan Road, Evanston, Illinois 60208-3020, USA

Heinz-Jürgen Fröhlich, Cochair
Paul-Drude Institut für Festkörper-Elektronik, Hausvogteiplatz 5-7, D-10117 Berlin, Germany

Invited Papers

2:00

4pPAc1. Effects of grain size and shape on ultrasonic attenuation and backscattering. R. B. Thompson (Ctr. for Nondestruct. Eval., Iowa State Univ., Appl. Sci. Complex II, 1915 Scholl Rd., Ames, IA 50011)

The influence of scattering from gain boundaries on the attenuation and backscattering of ultrasonic waves in polycrystals is a classical problem which has received considerable attention. However, the great majority of the effort has considered equiaxed grains. Extensions to polycrystals with elongated grains and multiple dimension scales will be presented. Experimental results will be reported for aluminum and titanium polycrystals, including a number of cases in which the directions of high attenuation exhibit low backscattering and vice versa. Although these observations were initially found to be surprising, significant progress has been made towards an understanding. The status of diagnostic experiments and theoretical efforts to explain these observations will be summarized. Implications of the results in the design of improved nondestructive techniques to detect flaws and characterize microstructure, including progress towards *in situ* techniques to monitor recrystallization will be discussed. [Portions of this work supported by the United States DOE, NSF, and the FAA.]

2:20

4pPAc2. Ultrasonic study of multi-ply composites. S. I. Rokhlin (Ohio State Univ., Nondestruct. Eval. Prog., Edison Joining Technol. Ctr., 1248 Arthur E. Adams Dr., Columbus, OH 43221)

Multi-ply composites are studied ultrasonically using transmission and reflection spectroscopy and time-resolved line focus acoustic microscopy. For quasi-isotropic multi-ply composites, the ultrasonic response does not exhibit isotropic behavior as, for example, is observed in mechanical tests. The amplitudes of the ultrasonic obliquely transmitted/reflected signals depend on the sample orientation relative to the incident plane as well as top ply orientation and ply sequence. In addition to the plane-wave study, the applicability of the time-resolved line focus acoustic microscopy for determination of elastic constants of composites is discussed and the results are compared to data obtained by the self-reference double-through-transmission ultrasonic bulk wave method. A theoretical model to predict ultrasonic wave propagation in the multi-ply anisotropic structure is described. The efficiency and performance of the transfer and global matrix methods are compared. The theoretical results are compared with experiment and used to interpret the complicated wave behavior in this material.

2:40

4pPAc3. Integration of modeling and acoustic microscopy measurements for multiple layered coatings. J. D. Achenbach and Z. Guo (Northwestern Univ., Ctr. for Quality Eng. and Failure Prevention, 2137 Sheridan Rd., Evanston, IL 60208, achenbach@nwu.edu)

The determination of material constants of multiple-layered coatings by line-focus acoustic microscopy requires a combination of the $V(z)$ measurement technique with a well-founded and accurate measurement model. This paper is concerned with the determination of the material constants of a two-layered ZrC/ZrN coating on a stainless steel substrate, as well as with an evaluation of the bond quality of the interfaces in-between the layers. A $V(z)$ measurement model, which accounts for bond-quality variations, is developed by combining a derived spectrum of reflection coefficients with acoustic microscopy considerations. Material constants are determined by systematically minimizing the differences between measured results, obtained by line-focus acoustic microscopy, and results simulated with the measurement model. Sensitivity of the technique and accuracy of the results are briefly discussed.

3:00

4pPAc4. Review of the method of reduced variables for the dynamic mechanical properties of viscoelastic materials. Bruce Hartmann and Gilbert F. Lee (Carderock Div. Naval Surface Warfare Ctr., West Bethesda, MD 20817-5700, hartmann@dt.navy.mil)

Under certain conditions, a change in temperature is equivalent to a change in frequency for dynamic mechanical measurements in viscoelastic materials. This property allows one to extend the effective frequency range of the measurements by shifting isotherms along the log frequency axis using the method of reduced variables, also known as time–temperature superposition. The most commonly used analytical equations describing the required shift are the WLF equation and the Arrhenius equation, but shifting can be implemented without the necessity of an analytical representation. This review will consider the physical basis for this property, known as thermorheological simplicity, the limitations of its applicability, and the advantages and disadvantages of various shifting procedures. Techniques that have been used include shifting the real part of the modulus, the imaginary part of the modulus, the loss factor, and the use of complex compliance rather than complex modulus. Other important issues are the choice of reference temperature and the use of a vertical shift in addition to a horizontal shift. [Work supported by the Carderock Division of the Naval Surface Warface Center's In-house Laboratory Independent Research Program sponsored by the Office of Naval Research.]

3:20

4pPAc5. Ultrasonic anomalies in betaine phosphate/betaine phosphite mixed crystals. Juras Banys, Vytautas Samulionis (Faculty of Phys., Vilnius Univ., Sauletekio 9, Vilnius 2040, Lithuania, juras.banys@ff.vu.lt), Georg Voelkel (Univ. Leipzig, Leipzig D-04103, Germany), and A. Kloepperpieper (Univ. des Saarlandes, D-66123, Sarrbruecken, Germany)

Measurements of the longitudinal ultrasonic velocity and the attenuation along the x, y, and z axes have been carried out in deuterated betaine phosphite (DBPI) single crystals in the vicinity of the ferroelectric and antiferrodistortive phase transitions. For ultrasonic modes propagating along the x and z axes the critical slowing down has been observed, but along the y axis critical slowing down was absent for both phase transitions. Regardless of the weakness of elastic anomalies at ferroelectric phase transition the ultrasonic behavior in DBPI can be explained by the Landau–Khalatnikov theory for uniaxial ferroelectrics. The ultrasonic behavior at the antiferrodistortive phase transition indicates that this phase transition is very close to the tricritical one. The relaxation time of the order parameter in the vicinity of the transition to the antiferodistortive phase for DBPI crystal was estimated. Similar results have been obtained for the mixed crystals betaine phosphate/betaine phosphite in the region of the antiferrodistortive phase transition. The temperature behavior of the ultrasound velocity and attenuation indicates the existence of the ionic conductivity in these cystals. It should be noted that conductivity phenomena is highly anisotropic in these crystals.

3:40–4:00 Break

4:00

4pPAc6. Ultrasonic absorption in concrete. Joseph A. Turner (Dept. of Eng. Mech., W317.4 Nebraska Hall, Univ. of Nebraska–Lincoln, Lincoln, NE 68588-0526, jat@unlinfo.unl.edu)

The propagation of ultrasound in concrete is greatly affected by the heterogeneous composition. An ultrasonic plane wave will attenuate as it propagates. Part of this attenuation is due to scattering effects which result from the aggregate. Another component of the attenuation is due to true dissipation from viscoelastic effects. Total attenuation has been previously proposed as a materials characterization parameter, although the distinction between scattering attenuation and dissipation is often not made. Experimental results are presented which should help separate these effects. Absorption measurements were made on a number of specimens with differing aggregate composition and water–cement ratio. The absorption is shown to be independent of the nature of the aggregate, as expected. In addition, the absorption is shown to be dependent upon the water–cement ratio and thus is related to the strength. Frequency dependence of absorption is also discussed. It is anticipated that ultrasonic absorption may be a useful parameter for characterizing concrete material properties. [Work supported by the Nebraska Research Initiative and Layman Fund.]

4:20

4pPAc7. Elastic wave propagation and scattering in heterogeneous, anisotropic media: Textured polycrystalline materials. Joseph A. Turner (Dept. of Eng. Mech., W317.4 Nebraska Hall, Univ. of Nebraska–Lincoln, Lincoln, NE 68588-0526, jat@unlinfo.unl.edu)

The propagation of elastic waves through heterogeneous anisotropic media is considered. Appropriate ensemble averaging of the elastic wave equation leads to the Dyson equation which governs the mean response of the field. The Dyson equation is given here in terms of anisotropic elastic Green's dyads for the medium with and without heterogeneities. The solution of the Dyson equation for the mean response is given for heterogeneities that are weak. The formalism is further specified for the case of equiaxed cubic polycrystalline metals with a single aligned axis. The Green's dyads in this case are those for a transversely isotropic medium. Simple expressions for the attenuations of the shear horizontal, quasicompressional, and quasishear waves are given in terms of integrations on the unit circle. The derived expressions are limited to frequencies below the geometric optics limit, but give the attenuations in a direct manner. Comparisons with previous results are also discussed. It is anticipated that a similar approach is necessary for the study of wave propagation in complex anisotropic materials such as fiber-reinforced composites. In addition, the results are applicable to diffuse ultrasonic inspection of textured polycrystalline media.

4:40

4pPAc8. Elastic modules modification and phonon focusing in zinc oxide. Uladzimir V. Zubrytski (Inst. of Phys., Natl. Belarus Acad. of Sci., 68 Scaryna Ave., Minsk 220072, Belarus)

Despite the direct observations of the acoustic waves focusing in different solids [J. P. Wolfe, Phys. Today **48**, 34–40 (1995)], the properties of the phonons' propagation and possibility of these control have not been studied in hexagonal media. To check this statement [U. V. Zubrytski, Z. Tekhn. Fiz. **67**, 59–64 (1997)] and obtain striking demonstrations of drastic changes in the phonon focusing patterns at elastic properties, modification of such solids' phonon focusing is simulated in zinc oxide grown by the hydrothermal method, in the vapor state at and without doping with lithium, and magnetron sputtering, in this paper. Simulation shows that elastic modules modification within the accuracy of available experimental data causes both sharp increasing of the intensities and defocusing of the individual phonon modes. Quantitative dependences of the effect have been established for bulk acoustic waves in the samples investigated. The findings allow one to elaborate not only the equilibrium but the dynamic method to control selectively both intensities and angular distributions of the acoustic energy fluxes in the crystals and thin layers as well. Besides, the elastic constants recovering from the measuring of the focusing factor can be realized. [Work partially supported by the Belarusian Republican Foundation for Fundamental Research.]

5:00

4pPAc9. Picosecond ultrasonics in gold nanoparticles. Arnaud Devos (IEMN, Dept. ISEN, 41 Bd. Vauban, 59046 Lille, France), Bernard Perrin, and Jean Claude Jeannet (Univ. Pierre et Marie Curie, CNRS, 75252 Paris Cedex 05, France)

Pump–probe optical techniques with femtosecond laser sources can be used to provide information about the acoustical properties of very thin films. With this so-called ''picosecond ultrasonics technique,'' echoes shorter than 10 ps can be time-resolved in films whose thicknesses are

larger than a few tens of nm; for smaller thicknesses, the acoustic excitation induces very high frequency acoustic resonances ranging from 0.1 up to 2.5 THz. In this work, the results of a picosecond ultrasonics experiment performed on gold colloids which represent an example of nanostructures is presented. The samples studied were of three types: solutions (gold particles dispersed in water), gels (gold particles embedded in a polymer matrix), and a film of particles attached on a polymer monolayer. The particle size was between 5 and 20 nanometers. In all the samples, oscillations in the transmitted probe beam which are ascribed to the vibrational mode of the sphere were observed. A second oscillation with a much longer period is also reported in the solution and gels cases. [Work supported by CNRS.]

5:20

4pPAc10. Ultrasonic waves birefringence in wood-based composite panels. Voichita Bucur (Université ''Henri Poincaré'' Nancy I, BP 239, F-54506 Vandoeuvre, France, bucur@lermab.u-nancy.fr) and Simone Garros (Ctr. de Recherches Forestières Nancy, F-54280 Champenoux, France)

The aim of this research is to study the ultrasonic waves birefringence in three wood-based composite panels, chipboards, oriented strandboards, and medium-density fiberboards, for the characterization of their global elastic and structural properties. Shear waves of 1 MHz were used to study the ultrasonic birefringence and to determine the shear terms of the stiffness matrix. As a complement for anisotropic behavior panel study, longitudinal waves of the same frequency were used to determine the corresponding terms of the stiffness matrix. Shear wave birefringence is the highest in the transversal anisotropic plane of the panels. Textural anisotropy was observed at the scale of the skin and core. Data related to the local characterization of the skin and core of the panels by x-ray microdensitometric technique revealed that, generally, the profile of the panel is symmetric and the skin density is higher than the core density. The nondestructive estimation of the birefringence of ultrasonic waves is a useful tool for further evaluation of panel performance related to their structural integrity and bond performance.

5:40

4pPAc11. Investigation of dissipative effects in a poroelastic layer coated plate. Stephane Rigobert, Franck Sgard (Lab. des sciences de l'habitat, DGCB, URA CNRS 1652, Ecole Nationale des Travaux publics de l'Etat, 2 rue Maurice Audin, 69518 Vaulx-en-Velin, France), and Noureddine Atalla (Univ. de Sherbrooke, QC J1K 2R1, Canada)

Nowadays, porous media are widely used in multilayered structures for noise control applications in such fields as aeronautics, automobiles, building acoustics, and environmental acoustics. Recently, a finite-element model based on pressure-deplacement formulation of Biot's poroelasticity theory has been extensively used to predict the acoustical and structural reponse of a multilayer structure. For practical applications, such models may lead to large frequency-dependent matrices and thus require huge computational ressources. The goal of this work is to solve the problem in the particular case of a poroelastic layer attached to an elastic plate. The idea is to develop a plate finite element which acounts for the behavior of the elastic plate and the porous solid phase. The fluid phase of the porous medium will be taken into account using equivalent fluid finite elements. In this paper, the assumptions and numerical results justifying the proposed simplifications will be discussed. In particular, the relative importance of the different dissipation mechanisms in the plate-porous system will be numerically assessed. These results constitute guidelines for considering the relevant dissipation phenomena in the simplified finite-element model of the system.

THURSDAY AFTERNOON, 18 MARCH 1999 ROOM H107, 2:00 TO 4:00 P.M.

Session 4pPPa

Psychological and Physiological Acoustics: Hearing Impairment, Hearing Instruments and Cochlear Implants

Astrid van Wieringen, Chair
Laboratory Experimentele ORL, KU Leuven, Kapucijnenvoer 33, 3000 Leuven, Belgium

Contributed Papers

2:00

4pPPa1. Contribution of reduced audibility to subnormal localization performance in hearing-impaired listeners. S. Theo Goverts, Tammo Houtgast, and Sophia E. Kramer (Dept. of Otorhinolaryngology/Audiol. Hospital, Vrije Universiteit, P.O. Box 7057, 1007 MB Amsterdam, The Netherlands, st.goverts@azvu.nl)

After speech reception, sound localization seems to be the second-most important hearing problem associated with auditory impairment. Recently a laboratory test on localization was developed which provides good resemblance to localization tasks in daily life. Subjects are presented with everyday sounds (about 1.5 s each) from eight evenly distributed directions. Only on the target sound (a telephone), presented randomly in time, were listeners required to indicate the azimuth of presentation. Data from 40 hearing-impaired listeners show a large variability in performance ranging from near normal to very poor. Aspects of hearing that may contribute to a subnormal performance are reduced audibility, incomplete or noisy spectro-temporal coding in the auditory periphery, or inadequate binaural processing. As a first step towards understanding the reduced performance for hearing-impaired listeners, results will be discussed on a localization test for normal-hearing listeners with noise-masked audiograms that match the audiograms for categories of hearing-impaired listeners. Results will be compared to previous findings on the role of audibility and spectro-temporal coding in the precedence effect.

2:20

4pPPa2. Method of measuring and preventing unstable feedback in hearing aids. Shawn X. Gao and Sigfrid D. Soli (House Ear Inst., Los Angeles, CA 90057)

Acoustic feedback is a practical problem that can limit the performance and benefit of any hearing aid. In the past, there have been no clinical available methods for accurately predicting the frequencies and gains that will cause unstable feedback for a particular hearing aid in an

individual's ear. The proposed method uses a typical clinical real-ear probe microphone system to acquire the real-ear aided responses by placing the hearing aid in the ear canal and setting the hearing aid gain to two different known settings. The Open Loop Transfer Function (OLTF) of the hearing aid can be derived based on the acquired aided signals. Once the OLTF of the hearing aid is known, potentially unstable frequencies are identified and maximum hearing aid gain and maximum hearing aid insertion gain are determined. The measurement allows the dispenser to modify the desired hearing aid response at only the frequencies that will cause unstable feedback. It consequently eliminates the trial and error method and prevents over-adjustment of the hearing aid. A description of theory and measurement procedure will be provided, as well as examples of its use on KEMAR and hearing-impaired individuals.

2:40

4pPPa3. Artificial noise signals with speechlike spectral and temporal properties for hearing instrument assessment. Wouter A. Dreschler (Dept. of Exp. and Clinical Audiol., Academic Medical Ctr., P.O. Box 22660, NL-1100 DD, Amsterdam, The Netherlands, w.a.dreschler@amc.uva.nl), Hans Verschuure (Erasmus Univ., Rotterdam, The Netherlands), Carl Ludvigson, and Soren Westermann (Topholm & Westermann, DK-3500 Vaerlose, Denmark)

The introduction of different forms of nonlinear amplification and noise-reduction algorithms calls for more intelligent ways to specify the properties of hearing instruments. Traditional specifications no longer reflect important characteristics of hearing instruments. Also, for the psychophysical evaluation in a laboratory setting, well-defined noises are necessary; aided speech perception will be largely determined by the properties of the speech signal and the concurrent background noise. The field of hearing instrument specification and evaluation has become a complex area in which traditional tools have lost their relevance. There is a strong need for a new approach based on new test signals that are broadband and dynamic. Standardized broadband noises are required for comparative measurements in different hearing instruments. Based on these notions a working group of the International Collegium of Rehabilitative Audiology (ICRA) started a consensus process to design well-defined artificial noise signals that can become a standard for hearing instrument assessment, both for technical measurements and for applications in the clinical and psychophysical evaluation. This paper reports about the design criteria, the actual realization, and some examples of applications in the measurement of digital signal processing hearing instruments.

3:00

4pPPa4. Gap detection thresholds of Laura cochlear implant users for complex patterns of stimulation. Astrid van Wieringen and Jan Wouters (Lab. Experimentele ORL, KULeuven, Kapucijnenvoer 33, 3000 Leuven, Belgium)

The ability to detect silent intervals on single and multiple electrode pairs was examined for different types of speechlike stimulus configurations in four postlingually deafened Laura cochlear implantees. Gap detection thresholds were determined in function of stimulus complexity, spectral disparity within and across the markers bounding the gap, stimulus asymmetry (cf. consonant–vowel versus vowel–consonant patterns), and pulse rate. All stimuli were roving in duration from 200 to 600 ms to ensure that subjects could not use overall duration as a cue. In addition, all the experimental conditions were balanced in loudness. Preliminary results have shown that stimulation of single electrode pairs yields smaller gap detection thresholds than stimulation of multiple electrode pairs, and that gap detection thresholds on multiple electrode pairs increase as the distance between the electrodes increases. Subsequent measurements illustrate that gap detection thresholds across multiple electrode pairs can decrease substantially after sufficient training, and that the spectral composition of the stimulus only affects gap detection when the spectral disparity occurs across, not within, markers. These findings, together with others concerning stimulus asymmetry and pulse rate, are of fundamental importance to understand the biophysical limitations of electrical stimulation related to the coding of sound by the auditory system.

3:20

4pPPa5. Two-microphone noise reduction for the LAURA cochlear implant. Jeff Vanden Berghe and Jan Wouters (Lab. Experimentele ORL, KULeuven, Kapucijnenvoer 33, 3000 Leuven, Belgium)

An adaptive noise cancellation scheme based on two-stage adaptive filtering has been developed for a two-microphone configuration in one hearing aid. This strategy has been tested with hearing-impaired listeners and yields a significant improvement of the speech reception threshold in background noise, as measured with sentences and two-syllable words [J. Vanden Berghe and J. Wouters, J. Acoust. Soc. Am. **103**, 3621–3626 (1998)]. As the effect of background sounds is even more severe for cochlear implant (CI) users than for the hearing impaired in general, this strategy was tested with four LAURA CI users. The system was implemented in real time on Audallion, a portable DSP-platform for hearing aids (Audiologic-Resound-Danavox Digital Alliance), and used as a preprocessor for the input to the CI speech processor. Speech intelligibility data in noise were obtained with and without this two-microphone noise reduction algorithm. The data indicate a similar effect for CIs as for hearing-impaired and normal-hearing people. For all subjects, measurement of the SRT for the two-stage adaptive filtering strategy shows an improvement of more than 10 dB in SNR when compared to the unprocessed condition. An analysis of variance indicates this improvement to be highly significant.

3:40

4pPPa6. Efficiency of a medical treatment of the acoustic trauma following impulse noise exposure in the guinea pig. Pascal Magnan, Christine d'Aldin, and Armand L. Dancer (French–German Res. Inst. of Saint-Louis, 5 rue du Général Cassagnou, BP 34, F-68301 Saint-Louis Cedex, France, dancer@newel.net)

Most of the patients suffering from acute acoustic trauma have been exposed to impulse noises. Temporary or permanent threshold shift (TTS or PTS) can be observed after such an exposure. They are correlated to structural and functional modifications of the peripheral auditory system and particularly of the sensory hair cells. Studies performed in guinea pig exposed to continuous noise have shown a positive effect of corticotherapy and oxygenotherapy (the treatments are given immediately after the end of the exposure). The aim of this paper is to assess the efficiency of those treatments in the guinea pig exposed to impulse noises; i.e., 20 pistol rounds of 157-dB peak pressure (at a 5-s interval). Threshold shifts (electrocochleography) and distortion products are measured for 15 days and are compared with histological observations (scanning electron microscopy). The results allow one to understand better the cochlear mechanisms of damages and to assess the efficiency of the classical treatments of the acoustic trauma following impulse noise exposures.

Session 4pPPb

Psychological and Physiological Acoustics: Human Factors (Poster Session)

Volker Hohmann, Chair
AG Medizinsche Physik, Universität Oldenburg, D-26111 Oldenburg, Germany

Contributed Papers

All posters will be on display from Thursday to Friday, 18–19 March. Contributors will be at their posters from 4:00 p.m. to 6:00 p.m. on Thursday, 18 March.

4pPPb1. The detection of complex submarine signals: A study of the linear frequency modulation criterium. François Santon and Agnes Tozza (LMA–CNRS, 31 Ch J. Aiguier, 13402 Marseille Cedex 20, France, santon@lma cnrs-mrs.fr)

The objective of this work is to know, in the context of submarine detection, what is the effect of a linear frequency modulation on the detection of glissando's signals. Indeed, this frequency modulation is often present in submarine signals, whether of biological or mechanical origin. Different types of glissandos are considered, increasing, increasing–decreasing, increasing with plateau, and decreasing. Differences have not been noted between the detection thresholds for the first three types of signals. In general, the detection threshold is very close to the maximum frequency of the signals threshold. In the case of a decreasing glissando, it can be noticed that the detection threshold is lower by a few dB than the threshold of the signal's highest frequency.

4pPPb2. Construction of a minimal set of sound parameters for multidimensional tests. Etienne Parizet (Renault, 67 rue des bons raisins, 92508 Rueil-Malmaison Cedex 9, France) and Valery Nosulenko (Anvie, Paris, France)

In a multidimensional test, the selection of sound parameters may be difficult, because these parameters must not be numerous while describing the whole perception and have to be understood unambiguously by naive listeners. The method of free verbalizations [E. Samoylenko, S. McAdams, and V. Nosulenko, Int. J. Psych. **31**(6), 255–278 (1996)] allows the construction of a minimal set of parameters. A minimal set of seven parameters was built for diesel engine idle noise. These parameters were then used for a semantic differential test, with other listeners and no sound training session. It was checked that the characterizations of sounds thus obtained for each parameter were very close to those given by the first test using free verbalizations. That means that the parameters were well understood by listeners and that all semantic ambiguities were avoided. Such a parameter set can be used for routine tests in the same sound context.

4pPPb3. Sound and vibration at low frequencies. Michael A. Bellmann, Carsten Reckhardt, Volker Mellert (Physik Akustik, Carl v. Ossietzky Univ. Oldenburg, D-26111, Germany), and Hermann Remmers (Inst. für Technische und Angewandte Physik GmbH, Oldenburg D-26111, Germany)

Equal-loudness-level contours are assumed to reflect the frequency sensitivity of the auditory system. Studies on equal-loudness-level contours show considerable differences even when the same measurement method is used. Recent studies [Gabriel *et al.*, DAGA 96; Reckhardt *et al.*, DAGA 97] report on the influence of measurement method, threshold, and choice of test tone level. In this study, an adaptive 2-AFC method [Reckhardt *et al.*, DAGA 97; Verhey *et al.*, DAGA 97] is used for measuring equal-loudness level contours in the frequency range of 16 to 160 Hz at 60 phon. The data are measured in a pressure chamber for 12 normal-hearing subjects. Results are higher than the standard curve specified in ISO 226. In a study of Reckhardt *et al.* it is shown that the inter-individual variance is decreased by taking the individual threshold of hearing into account. The results from low-frequency measurements support this finding. In addition, this study investigates the influence of vibration on loudness perception. Equal-loudness-level contours are measured in the presence of distinct vibration levels above vibration threshold in a frequency range of 10 to 80 Hz.

4pPPb4. Development and evaluation of an adaptive loudness scaling procedure. Thomas Brand and Volker Hohmann (AG Medizinische Physik, Universität Oldenburg, D-26111 Oldenburg, Germany, tom@medi.physik.uni-oldenburg.de)

Loudness scaling procedures are used in the diagnostics of hearing impairment to assess the recruitment phenomenon, i.e., the pathological growth of loudness. In these procedures, acoustical stimuli at different levels are presented to the subject and the task is to rate the perceived loudness on a category scale. The aim of this study is the development and evaluation of an adaptive loudness scaling procedure in which the level of the next stimulus is calculated on the basis of the previous trials. Based on empirical results from normal-hearing and hearing-impaired listeners, the procedure was optimized in order to yield minimal test–retest deviations and minimal biases due to range and context effects at minimum measuring time. To achieve these aims, different settings of the following parameters were tested: Number of response alternatives, track length, initial level, adaptive procedure, and parametrization of the loudness function. The best setting was shown to yield an equal distribution of stimulus levels in the full dynamic range of the individual subject with a minimum number of ''inaudible'' and ''too loud'' presentations. For each categorial loudness the corresponding stimulus level is estimated with a standard deviation of about 5 dB.

4pPPb5. Factors influencing the subjective rating of tonal components in noise. Matthias Vormann (Carl von Ossietzky Universität Oldenburg, Fachbereich Physik Arbeitsgruppe Akustik, Carl von Ossietzky Strasse 9-11, D-26111 Oldenburg, Germany, matthias@aku.physik.uni-oldenburg.de) and Jesko L. Verhey (Carl von Ossietzky Universität Oldenburg, D-26111 Oldenburg, Germany)

If environmental or artificial noises contain tonal components, they are more annoying than noises without tonal components. Therefore the German norm, DIN 45681 (draft): ''Detection of tonal components of noise and determination of a tone adjustment for the assessment of noise immi-

sions'' was proposed to quantify this increased annoyance. Within this definition the effects of the tonal components are reduced to the increasing annoyance of the signals. In the literature no satisfying data exists about the subjective ratings of tonal components in noises (in German called ''Tonhaltigkeit''). For this reason the present study investigates the influence of selected physical parameters on subjective ratings of the ''Tonhaltigkeit.'' An adaptive procedure is used to adjust the hearing impression ''Tonhaltigkeit'' of different noises to a reference signal consisting of a single sinusoidal.

4pPPb6. Effects of a neoprene wetsuit hood on low-frequency underwater hearing thresholds. John R. SimsII, David M. Fothergill, and Michael D. Curley (Naval Submarine Medical Res. Lab., Box 900, Groton, CT 06349-5900)

In an effort to create guidelines for exposure to low-frequency underwater sound, it is necessary to obtain population data on the minimal detectable sound-pressure level at these frequencies. Underwater hearing thresholds were obtained from 15 male and 5 female recreational SCUBA divers with and without a 3-mm wetsuit hood. Dives were conducted at a 1-m depth in a large quiet anechoic pool. A J13 transducer was located 4 m directly below the subject. Thresholds were determined using two-interval forced-choice with a 0.71 probability of positive response at convergence. A 1-s pure tone was presented with a 20-ms rise and fall at 100, 200, 250, 300, 400, and 500 Hz. Results indicate there was no difference in thresholds between male and female divers. Without a wetsuit hood, mean thresholds decreased from 99 dB (s.d. 6 dB) re: 0.000 001 Pa at 100 Hz to 85 dB (s.d. 10 dB) at 500 Hz. Thresholds were statistically similar at 100 to 300 Hz with and without the wetsuit hood, but were significantly increased at 400 and 500 Hz with the hood ($p<0.001$). In conclusion, a wetsuit hood attenuates frequencies at 400 Hz and above by approximately 10 dB. [Work supported by CNO, N-87.]

4pPPb7. Estimates of the instantaneous versus overall loudness of noise emissions. Thomas Filippou and Hugo Fastl (Inst. of Man-Machine-Commun., Tech. Univ. Muenchen, Arcisstr. 21, D-80333 Muenchen, Germany)

Usually when comparing the relations between instantaneous and overall loudness judgments of noise emmissions, the overall loudness is *larger* than the average of the instantaneous loudness judgments. Obviously, the prominent parts of a noise emmission play a crucial part in overall loudness judgment. Two models were proposed to describe the overall loudness on the basis of the instantaneous loudness judgments [Fastl, DAGA 97]. The merits of the different models in predicting the overall loudness of noise emissions with a different number of events were studied. For emissions with 2 up to 11 events within 15 min, a simple percentile of the instantaneous loudness judgments cannot predict overall loudness. However, when the events are prolonged by an exponential decay with 30-s time constant, the judgment of overall loudness can be predicted with an average accuracy of 6%.

4pPPb8. On the use of auditory information in human movement control. Andreas Hellmann and Rainer Guski (Univ. Bochum, Dept. of Psych., D-44780 Bochum, Germany, hellmann@psychologie.uni-oldenburg.de)

A human acting and moving in the environment often produces sounds, which are related to his or her body movements. Movement control requires the continuous use of perceptual information about the ongoing movement. It was investigated whether humans can and do use sound produced by their movements as auditory information for the control of their movements. In the experiments the movements or tasks required from the subjects were varied, as well as the available auditory and visual information. The success in the movement tasks was measured. The results obtained so far show that auditory information is used for movement control by the subjects, especially with complicated movements.

4pPPb9. Short and medium motor responses to auditory pitch shift: Latency measurements of the professional musician's audio-motor loop for intonation. Dietrich Parlitz and Marc Bangert (Inst. for Musicphysiol. and Performing Arts Medicine, Univ. for Music and Theatre, D-30175 Hannover, Germany, parlitz@hmt-hannover.de)

For the singer's voice, as well as for many musical instruments, like strings or brass, a precise intonation relies on a quick and adaptive fine-tuning mechanism, i.e., a motor response correcting for deviations of the produced tone due to mechanical properties of the body and instrument as well as due to environmental parameters. The aim of the procedure is either to be in tune with an internal representation of the correct pitch or to be in harmony with accompanying instruments or singers. In an experimental setup with a real-time audio pitch shifter and an infrared-based motion analysis system, this unique ability of musicians can be studied systematically. In a group of (a) expert viola players, (b) expert trombone players, and (c) professional singers, the distribution of pitch-shift-reaction-times (PSRTs) is measured (1) in a solo-player/singer situation and (2) in an ensemble/choir situation. Results are compared to recent studies with nonmusicians [T. A. Burnett *et al.*, J. Acoust. Soc. Am. **103**, 3153–3161 (1998)]. Similarities to other orientation reactions like saccadic eye-movements and to the rapid pitch-correcting mechanisms in the echo-locating system of the bat are discussed.

Session 4pSAa

Structural Acoustics and Vibration: Smart Materials II

Sabih I. Hayek, Cochair
Department of Engineering Science and Mechanics, Pennsylvania State University, 227 Hammond Building, University Park, Pennsylvania 16802, USA

Hans Irschik, Cochair
Division of Technical Mechanics, Johannes Kepler University, Altenbergerstrasse 69, A-4040 Linz, Austria

Chair's Introduction—1:55

Invited Papers

2:00

4pSAa1. Zonal and global control of structural intensity in an infinite elastic plate. Sabih I. Hayek, Jungyun Won (Active Vib. Control Lab., Dept. of Eng. Sci. and Mech., Penn State Univ., University Park, PA 16802, hesm@engr.psu.edu), and Giman Kim[a)] (Kumoh Natl. Univ. of Technol., Kumi, Kyungbuk, 703-701, Korea)

In a previous paper, the active control of active structural intensity (SI) in an infinite elastic plate was discussed. The plate is excited by mechanical noise sources, which generate a vector active SI field in the plate. A colocated point force and a point moment actuator at an arbitrary location on the plate were used. An algorithm was developed to minimize the active SI at a reference point on the plate. The control strategy was aimed at minimization of only the SI at a reference point. In this paper, the active control of SI in a desired zone or a large global area of the plate is explored through the use of multiple controllers spread over the plate. Furthermore, the cost function to be minimized also includes the required power injected by the controllers. Thus the minimization algorithm minimizes both the total SI in a zone as well as the total injected power by the controllers. The influence of the number and type of controllers, and the location of these controllers relative to the source region for the minimization of both the total SI in a region and the input mechanical power of these controllers, is explored. [a)] Currently Visiting Scholar at Penn State Univ.

2:20

4pSAa2. A comparison between active and semi-active global vibration control of structures. Michael J. Brennan and Jedol Dayou (Inst. of Sound and Vib. Res., Univ. of Southampton, Southampton, Hampshire SO17 1BJ, UK, mjb@isvr.soton.ac.uk)

Semi-active devices, such as tunable vibration neutralizers, have been used for a number of years to control structural vibration at the point where the device is attached to the structure. More recently there has been some work on the use of these devices to control the global vibration of a structure and hence the radiated sound. In parallel with this, research has been conducted on the active control of sound radiation from structures. Because there are a number of advantages in using semi-active rather than fully active control in terms of cost and complexity, it is important to be able to quantify the benefits of each strategy on the global control of vibration. The aim of this paper, therefore, is to compare the effectiveness of the two control strategies by focusing on a simple structure such as a beam. Simulations will be presented to show that, provided the dynamic behavior of the structure and the semi-active device are known, then a semi-active device can be appropriately positioned so that it will perform almost as well as the fully active system. Moreover, it will be shown that a simple local control strategy can be employed provided that the device is positioned correctly.

2:40

4pSAa3. Compact, inexpensive, analog robust controller modules for cabin noise control. Vasundara V. Varadan, Ramanathan Sreenivasan, Woosuk Chang, and Vijay K. Varadan (Penn State Univ., 149 Hammond Bldg., University Park, PA 16802, vvvesm@engr.psu.edu)

Control of noise in an enclosure when the noise source is exterior to the enclosure has applications to rooms, automobiles, helicopters, airplanes, and other vehicles. Reducing the interior noise to acceptable levels is necessary for safety and comfort. One approach to control of interior noise is through vibration suppression of the trim panels that often line the interior of such enclosures. It is ultimately these trim panels that reradiate the noise to the interior. In order to actively control the vibrations of the trim panels, using discrete piezoelectric sensors and actuators, control electronics are needed. Adaptive digital control, while being efficient and powerful, also requires the presence of a computer and DSP boards. There may also be frequency limitations posed by the speed of available DSP boards. An alternative approach is to design compact and inexpensive analog controller units, which also offers the possibility of having such controllers designed as ASIC chips. To demonstrate the efficacy of this approach, results will be presented for the control of noise in a cabin with multiple trim panels when excited by broadband noise from the exterior using MEMS vibration sensors and PZT actuators.

Contributed Papers

3:00

4pSAa4. Active control of acoustic and structural intensities of a submerged elastic plate. Matthias Fischer and Sabih I. Hayek (Active Vib. Control Lab., Dept. of Eng. Sci. and Mech., 227 Hammond Bldg., Penn State Univ., University Park, PA 16802)

In this paper, the active control of active structural intensity (SI) and the resultant radiated active acoustic intensity (AI) in a coupled structure-fluid system is explored. The system consists of an infinite elastic plate submerged in an infinite heavy acoustic medium. The plate is excited to vibration by mechanical noise sources, which generate a vector-active SI field in the plate and a vector AI field in the coupled acoustic medium. Due to heavy fluid loading, the flexural waves in the plate are strongly coupled to the acoustic waves. A line-force and line-moment actuators, which are located at arbitrary locations on the plate, are used for control. The mechanical noise source and control actuators interact not only by their mutual flexural impedance through the elastic plate, they also interact through an acoustic path as well. The control algorithm is aimed at minimizing both SI and AI. The cost function to be minimized consists of a weighted sum of the SI and AI in the far field of the mechanical source region. The influence of the location of these controllers relative to the source region and the relative weighting given to SI versus AI in the cost function is explored.

3:20

4pSAa5. Direct adaptive predictive control using gradient descent. Kenneth Eure, Jer-Nan Juang, and Richard Silcox (NASA Langley Res. Ctr., Hampton, VA 23681, j.juang@LaRC.NASA.Gov)

Predictive control has been successfully used for the regulation of plate vibrations. Past implementations of predictive control have included both feedforward and feedback algorithms. These algorithms may be used as a nonadaptive or an adaptive control method as long as conditional updating is employed or a sufficient level of dither is added to the control signals in order to maintain input and output data coherence for system identification. For large-order systems with many input and outputs, the adaptation rate is severely limited due to the computational burden. The direct adaptive controller presented in this paper uses a gradient descent method to directly determine the predictive control parameters for the feedback regulator. The key features of this control scheme include the use of leakage to prevent drifting of the identified parameters in the presence of closed loop data. The initial information needed by the control scheme is an estimate of the plant order and an estimate of the plant pulse response from input/output data. Because this scheme is adaptive, the controller poses robustness against errors in the estimate of the plant's pulse response which allows the time-varying characteristics of the plant to be regulated.

THURSDAY AFTERNOON, 18 MARCH 1999 ROOM EB301, 2:00 TO 5:40 P.M.

Session 4pSAb
International Workshop on Active Noise and Vibration Control

Structural Acoustics and Vibration: Other Applications of Active Control

Nick Doelman, Cochair
TNO, Stieltjesweg 1, P.O. Box 155, 2600 AD Delft, The Netherlands

Kam Ng, Cochair
Office of Naval Research, 800 North Quincy Street, Arlington, Virginia 22217-5000, USA

Invited Paper

2:00

4pSAb1. Unsteady dynamics and control of marine thrusters. Ralf Bachmayer and Louis Whitcomb (Dept. of Mech. Eng., Johns Hopkins Univ., 123 Latrobe Hall, 3400 N. Charles St., Baltimore, MD 21218)

This paper reports advances in the unsteady dynamical modeling and control of marine thrusters. First, recent advances in finite-dimensional nonlinear dynamical modeling of marine thrusters are reviewed [Healey *et al.*, IEEE J. Oceanic Eng. **20**(4), 354–361 (1995); Bacmayer *et al.*, IEEE/MTS Oceans'98]. Second, a novel nonlinear model-based control algorithm is presented. Third, the performance of the nonlinear model-based control algorithm is evaluated in comparison with conventional and previously reported thrust control algorithms [Whitcomb and Yoerger, IEEE/MTS Oceans'95 **2**, 1019–1028 (1995)]. [Work supported by NSF and ONR.]

Contributed Papers

2:20

4pSAb2. Active noise reduction in an ear terminal. Georg E. Ottesen (SINTEF Telecom and Informatics, N-7034 Trondheim, Norway)

An active ear terminal is being designed to obtain both hearing protection and radio communication in adverse environments. Passive damping is sufficient for high frequencies, but low frequencies must be damped by active methods. Even when low-frequency noise is not harmful to the hearing, it heavily increases the effort of communication. Active noise reduction may use the signal from an outer microphone, or from an inner microphone. Active noise reduction obtained by these two microphone positions are simulated and discussed. Analog and digital filters are considered. The time delay budget of the active system is drawn up. Time delays should be minimized to obtain the best performance of the active noise reduction system. The physical system of transducers with their acoustic surroundings contains time delays which cannot be compensated

by filtering. These time delays can be determined from the transfer functions of the system. The physical design of the ear terminal is performed with a view to reduce these delays. The signal prosessing delay adds to the delay of the physical system. The total delay determines the upper frequency limit of the active noise reduction system.

2:40

4pSAb3. The Plymouth Prowler, active noise control exhaust system. Part I: Noise reduction. J. Clay Shipps (Tenneco Automotive, Inc., 1025 W. Nursery Rd., Ste. 102, Linthicum, MD 21090)

An active noise control exhaust system or electronic exhaust system was developed for the Plymouth Prowler to demonstrate the ability to reduce backpressure greatly while also significantly reducing the exhaust noise. An electronic exhaust system is typically composed of passive and active elements. One of the major advantages of electronic exhaust systems is that most of the flow restrictions in the passive elements can be removed; this is reponsible for the backpressure reduction. Reduced backpressure typically results in a 3% to 6% horsepower gain at the rated engine speed of the vehicle and increases torque over most of the engine speed range. The electronic exhaust system also has the capability of greatly reducing the exhaust noise. The active elements can produce antinoise at very high levels such that, when combined with the unwanted exhaust noise, an overall decrease in the radiated tailpipe noise occurs. This allows the vehicle to meet the legal passby requirements with significant margin while maintaining appropraite sound quality characteristics. This paper will describe the system developed for the Prowler and the resulting performance gains.

3:00

4pSAb4. The Plymouth Prowler, active noise control exhaust system. Part II: Noise shaping. Timothy E. Meeks and J. Clay Shipps (Tenneco Automotive, Inc., 1025 W. Nursery Rd., Ste. 102, Linthicum, MD 21090)

An active noise control exhaust system or electronic exhaust system was developed for the Plymouth Prowler to demonstrate the ability to reduce exhaust backpressure greatly while creating a legal sports car sound for the vehicle. One of the major advantages of electronic exhaust systems is that flow restrictions in the passive elements can be removed, consequently decreasing the total backpressure. This backpressure reduction typically results in a 3% to 6% horsepower gain at the rated engine speed of the vehicle and also increases torque at most engine speeds. The electronic exhaust system also has the capability of shaping the exhaust noise. The active elements can produce antinoise at very high levels such that, when combined with the unwanted exhaust noise, there is a significant reduction of selected harmonics. The software which processes the antinoise can be programmed to use engine speed information to determine which harmonics will comprise the resulting waveform. This control varies the vehicle's sound quality characteristics while meeting passby noise requirements. This paper will describe the system developed for the Prowler and the resulting performance gains and sound quality enhancements.

3:20

4pSAb5. Design considerations for a low-impedance loudspeaker in active noise control exhaust systems. Steven P. Kahn (Tenneco Automotive, Inc., 1025 W. Nursery Rd., Ste. 102, Linthicum, MD 21090)

To meet the needs of automotive original equipment customers, a low-impedance loudspeaker has been designed for active noise control exhaust systems that reduces system cost, decreases overall weight, eliminates complexity, and improves reliability. The current design practice is to convert the 12-V dc supply of the car battery to 36 V dc. This supply voltage is used in conjunction with a switching amplifier to drive the noise canceling loudspeaker. By utilizing a low-impedance loudspeaker, the 12-V dc supply from the battery can be fed directly to the amplifier, thereby eliminating the dc–dc converter completely. This approach also simplifies the cable harness and reduces the number of connectors. To develop a low-impedance loudspeaker that allows the realization of these advantages, one must consider the following: output level, electrical damping, frequency bandwidth, power handling, and manufacturability. The interaction and trade-offs between these issues must be understood and optimized. Test results between the current configuration and the new approach will also be presented.

3:40–4:00 Break

4:00

4pSAb6. Contemplations about the numeric transposition of the generalized Kirchhoff integral with the intention of active noise reduction. Mattias Trimpop (Institut fuer Laermschutz, Arnheimer Str. 107, D-40489 Duesseldorf, Germany) and Detlef Krahe (Bergische Universitaet Wuppertal, D-42097 Wuppertal, Germany)

The method of feedback is often used for reduction of noise in defined areas because feedback is able to compensate chances of the transfer function. However, the feedback system cannot work in some special cases, e.g., in single events or impulse noise no preceded signals parts are existing and usable for prediction. Therefore, the feedforward system has to be used in these cases and the prediction is realized by acquisition of the sound wave before it reaches the interesting point of immission. After the presentation of the one-dimensional feedforward system presented in the last year, now the two- and three-dimensional cases and their mathematical treatments will be discussed. For that purpose acoustic wave fields will be analyzed by the generalized Kirchhoff integral and minimized using sound sources in a defined wave field area. Further, the expected problems in the practical application of the numerical solution will be discussed.

4:20

4pSAb7. Self-adaptive absorber of underwater sound with electrorheological fluid. Dieter Guicking, Patrick Michaelis, and Helge Neumann (Drittes Physikalisches Institut, Universitaet Goettingen, Buergerstr. 42-44, 37073 Goettingen, Germany, guicking@physik3.gwdg.de)

Laboratory experiments have been made on an adaptive-passive absorber of underwater sound with viscous flow in ERF (electrorheological fluid) as absorption mechanism. The absorber model is of the velocity transformation type where a thin fluid layer is confined between an inertial back mass and a piston. Axial vibration of the piston by the incident sound wave causes a strong radial fluid oscillation and thereby enhances the sound absorption. With ERF as fluid, the reflection coefficient depends on the gap width and the field strength. In the present setup the gap width can be varied by a stepper motor. A two-parameter feedback control strategy employing a genetic algorithm has been developed to adjust the gap width and the field strength to minimize the reflectivity as measured by the two-microphone method in an impedance tube. The optimum of 10% to 20% reflection is reached within a few generations of adaptation.

4:40

4pSAb8. Active noise within the generating/pumping groups of a large hydroelectric plant. Leonardo Lecce, Massimo Viscardi, Bruno Maja, Vincenzo Limone, Mario D'Ischia (Dipartimento Progettazione Aeronautica, Università di Napoli ''Federico II,'' Via Claudio, 21, 80125 Napoli, Italy), and Francesco Di Maso (ENEL (National Agency for Elec. Energy), Naples, Italy)

This work is related to a feasibility study for the implementation of an active noise control system to reduce the hydraulic turbomachine's noise in the Presenzano power plant. Previous studies showed that interested turbines are low frequencies noise sources, generating pure tones at 150 and 200 Hz (third and fourth harmonics of the turbine's BPF). At these frequencies passive noise control systems are ineffective in front of relevant costs and an active approach was so decided to be tested. In accordance with a classical architecture, the preliminary system was composed of four error microphones, four secondary noise sources, and a digital controller implementing an adaptive digital filter. Main performed activities could be identified through four successive steps: (i) analysis of the

turbomachine's generated primary field levels and space distribution, (ii) secondary sources generated noise field measurement, ten different loudspeakers locations were investigated at this stage; (iii) sensor and actuator locations' optimization by the use of a genetic algorithm's procedure, and (iv) active noise control tests. A mean reduction of 15 dB at 150 Hz and 7.5 dB at 200 Hz was measured at the error sensors during these tests, revealing the good opportunities of such an approach but also the opportune improvement to pass at a practical implementation.

5:00

4pSAb9. Sound reflex compensation in active noise control. Zbigniew Ogonowski (Inst. of Automatic Control, Silesian Tech. Univ., ul. Akademicka 16, PL-44-101 Gliwice, Poland, zogonowski@ia.polsl.gliwice.pl)

Creation of a zone of quiet in an enclosure by using active noise control (ANC) methods causes problems with additional noise generated by a reflection of secondary sound. The paper presents a new method of the reflected sound compensation. The idea is to augment the main ANC controller with an auto-feedback controller (AFC). No additional measurement is needed because AFC is fed back with the main controller output. Increase of delay time of the successive reflection assures nonanticipation of the compensation. AFC corrects an activation of the secondary source of sound to cancel the reflected secondary sound generated by the main controller. AFC synthesis uses a mathematical model of the reflection. A specially designed method of the model identification using multisinusoidal excitation is described in the paper. Usually, geometry of the enclosure is constant, thus stationarity of the model is assured. The choice of the model structure implying stability issues is discussed in the paper. Stability of the AFC loop depends also on the reflection delay time. A special stabilizing design method is presented in the paper. An illustrative example of the method application is described.

5:20

4pSAb10. Active volume sound absorber. Alexander A. Mazanikov (Dept. of Appl. Mathematics, Murmansk State Tech. Univ., MGTU, Sportivnaia St., 13, Murmansk, 183010, Russia, Alexander.Mazanikov@mstu.edu.ru)

The absorbtion cross section (ACS) of a passive volume sound absorber asymptotically equals its geometric cross section. On the other hand, the ACS of an active absorber principally could be arbitrarily large. However, the increase of the ACS results in a rapid growth of the near acoustic fields. This puts restrictions on the practically achievable values of the ACS. The talk presents the results of a simulation of sound field levels generated by active absorbers of spherical shape and different wave sizes in response to incident plane waves. It is shown that near the absorber the level of the sound field increases as compared to the passive absorber of the same size. In the far zone the field of the active absorber corresponds to the field of the passive absorber with larger geometric scale. It is demonstrated that sound energy is absorbed rather on the back side of the absorber then on its front face (with respect to the direction of incident wave).

THURSDAY AFTERNOON, 18 MARCH 1999 ROOM H1012, 2:00 TO 6:20 P.M.

Session 4pSCa

Speech Communication: Parameters of *F*0

Bernd Möbius, Cochair
Lucent Technologies, 600 Mountain Avenue, Murray Hill, New Jersey 07974-0636, USA

Thomas Portele, Cochair
IKP, University of Bonn, Bonn, Germany

Contributed Papers

2:00

4pSCa1. Comparing the naturalness of several approaches for generating *F*0 contours in German text-to-speech systems. Hansjrg Mixdorff and Dieter Mehnert (TU Dresden, Mommsenstr. 13, 01062 Dresden, Germany, mixdorff@teles.de)

Generating near-to-natural $F0$ contours is an important issue in text-to-speech synthesis and contributes vastly to the quality of synthetic speech. In earlier studies by the authors, a model of German intonation was developed that is based on the quantitative Fujisaki model. A typical $F0$ contour is described as a sequence of major rises and falls, which are modeled by onsets and offsets of accent commands connected to accented syllables. The current paper addresses perception experiments comparing the intonational naturalness of a Fujisaki-model-based TTS and four other German TTS systems with comparably high segmental quality. Natural speech samples were used as a reference. Three of the TTS systems had PSOLA, and one LPC segmentals. Two types of experiments were conducted with 20 subjects: (1) a pair comparison of 15 isolated sentences, (2) a ranking test based on a news passage of about 15 sec produced with each of the systems. Preliminary results from experiment (1) show, that on a naturalness scale from 0 to 5, the natural speech samples reach a maximum score of 4.5, with values of 2.8 for the best synthesis, the LPC-based one. The system with Fujisaki-model-based intonation leads the group of PSOLA systems, which is closely clustered at a mean of 2.4.

2:20

4pSCa2. Quantifying correlations in pitch- and amplitude contours. Hans-Peter Herzel (Inst. Theor. Biol., Humboldt Univ., Invalidenstr. 43, D-10115 Berlin, Germany, h.herzel@biologie.hu-berlin.de) and Robert Reuter (Inst. Electron. Techn. Univ., Berlin, Germany)

Nonlinear phenomena such as subharmonics, biphonation, or deterministic chaos induce characteristic patterns in pitch and amplitude contours. A novel measure of correlations in contours termed MAC (mean average correlation) is introduced. For uncorrelated and weakly correlated noise, the expectation values and standard deviations of MAC are calculated. It is shown that trend elimination induces spurious correlations. Moreover, simulations of the circle map are analyzed and high values of MAC for subharmonic and chaotic data are found. Examples are presented of severely rough voices and excised larynx data and correlations are

quantified in the corresponding contours by MAC. Finally, the connection between perceived voice quality and MAC is studied with the aid of 120 perceptually evaluated voices. [Work supported by the Deutsche Forschungsgemeinschaft.]

2:40

4pSCa3. Influences of various factors upon parameters of the command–response model for fundamental frequency contour generation. Sumio Ohno, Yoshikazu Hara, and Hiroya Fujisaki (Dept. of Appl. Electron., Sci. Univ. of Tokyo, 2641 Yamazaki, Noda, 278-8510 Japan, ohno@te.noda.sut.ac.jp)

The command–response model by Fujisaki and his co-workers formulates the generation process of the fundamental frequency contour (henceforth $F0$ contour) in terms of a set of input commands carrying linguistic and paralinguistic information and the mechanisms that respond to these commands. The parameters of the mechanisms are time constant of the phrase control mechanism (α), that of the accent control mechanism (β), and the baseline frequency (Fb). The present study investigates the influences of speech rate, speaking style, and individual difference on these parameters as well as their variability. The speech material consisted of recordings of a short story by six native speakers of Japanese at three speech rates (slow, normal, and fast) and in two speaking styles (reading and conversational). The parameters were extracted by the method of analysis-by-synthesis, and the results were analyzed statistically. The analysis indicated that utterance-to-utterance variations are quite small in all three parameters for a given rate, style, and speaker. Among the three parameters, only α showed a small but systematic tendency to increase with the speech rate, while differences in speaking style did not affect these parameters. Individual differences were quite small in α and β, while Fb varied from speaker to speaker.

3:00

4pSCa4. Application of the command–response model to the analysis, interpretation, and synthesis of fundamental frequency contours of speech of various languages. Hiroya Fujisaki and Sumio Ohno (Dept. of Appl. Electron., Sci. Univ. of Tokyo, 2641 Yamazaki, Noda, 278-8510 Japan, fujisaki@te.noda.sut.ac.jp)

A command–response model has been presented by Fujisaki and his co-workers initially for the process of generation of the fundamental frequency contour (henceforth $F0$ contour) of the common Japanese. It consists of a set of input commands carrying linguistic and paralinguistic information, and the mechanisms that respond to these commands to generate both phrase and accent components, which, together with a baseline value, constitute the actual $F0$ contour. Subsequent works have shown that the model is applicable also to $F0$ contours of some other dialects of Japanese as well as of other languages including Chinese, English, German, Greek, Spanish, and Swedish. It has been argued, however, that the model may not be able to generate certain contour types that are not found in Japanese but are commonly used in other languages [e.g., P. Tayler, Speech Commun. **15**, 183]. This paper shows how these contour types can actually be generated by the same mechanisms, with certain language-specific timing, polarity and magnitude of the input commands, all within the framework of syntactic and prosodic constraints of each language. The results will be demonstrated by resynthesized speech, and testify the validity and usefulness of the model for multilingual text-to-speech synthesis.

3:20

4pSCa5. Iconic prosody and information in spontaneous oral narrative. Guillermo Andrés Toledo (CIRAL, Fac. Lettres, Univ. Laval, Québec, QC G1K 7P4, Canada and LIS-CONICET, Argentina)

The information interchange on cognitive categories of the mental representation of referents (concepts) interrelated with prosodic marking (levels of phonological prominence) have been studied. Speakers actualize a limited amount of information inactivating backwards. These cognitive processes appear in three states of the referents: activation, semi-activation, and inactivation. In activation, a concept would be focalized in actual stream of consciousness. In semi-activation, the information is situated in a peripheral zone of consciousness: the concept was already activated. In inactivation, the concept would be activated in the hearer's conscience for the first time. These states were analyzed through data extracted from spontaneous narrative discourses obtained from an Argentinean Spanish speaker. The iconicity of prosodic prominences, a correlation between the phonetic encoding and the mental status of information weight, was explored acoustically. Measurements were made through $F0$ data normalized by a logarithmic z-score transformation calculated in the highest value of an item classified among one of the three states. Findings were similar to previous research on semi-spontaneous materials [G. Toledo, 16th International Congress on Acoustics, 4aSC1]: lower prominences were the marking of activation and semi-activation, and higher prominences were the feature of inactivation, i.e., a degree of prosodic iconicity.

3:40–4:00 Break

4:00

4pSCa6. A phonological interpretation of the ''Gussenhoven–Rietveld Effect.'' Stefanie Jannedy and Mary E. Beckman (Dept. of Linguist., Ohio State Univ., Columbus, OH 43210)

Dutch listeners rate the perceived prominence of the second fundamental frequency ($F0$) peak (P2) to increase as the first peak (P1) increases and decreases in $F0$ while P2 is held constant. This Gussenhoven–Rietveld effect was replicated with English listeners [Ladd *et al.* (1994)]. They interpret the positive correlation between the frequency of P1 and the perceived prominence of P2 as a function of the pitch range. Gussenhoven and Rietveld (1997) attribute this effect to parsing P1 and P2 as occurring in a single phrase, signaled by the intonation contour between the peaks. It is proposed that listeners parse the intonation phrase internal $F0$ peaks as relational to each other and as good or bad instances of phonological accent categories: An $F0$ contour with a lower P1 and a higher P2 can be interpreted as an $H^*\ L+H^*$ sequence, with the realization of the $L+H^*$ as not prominent for this category. A flat-shaped $F0$ contour with P1 and P2 roughly equal can be interpreted as an H^* accent on both peaks. A higher P1 interpolating onto a lower P2 can be interpreted as a rather prominent instance of a downstepped H^* accent on P2. This explanation assumes a phonological interpretation of intonation contours.

4:20

4pSCa7. Changes of voice parameters and melody patterns during the first year of life in human twins. Kathleen Wermke (Inst. of Anthropology, Humboldt Univ. Berlin, Medical Faculty Charité, Tucholskystr. 2, 10117 Berlin, Germany, kathleen.wermke@charite.de), Werner Mende (Berlin-Brandenburg Acad. of Sci., Berlin, Germany), Hanno Borschberg, and Roland Ruppert (Maternity Hospital, Chemnitz, Germany)

The study analyzed changes of cry characteristics of twins using spectrograms, fundamental frequency contours (melody), and several indicators of microvariability of the fundamental frequency ($F0$) calculated with the aid of a KAY Elemetrics CSL Model 4305. Subjects were 15 identical and 15 fraternal healthy twin pairs, whose spontaneous utterances were recorded every 6 weeks over the first year of life. Developmental changes of $F0$, jitter, perturbation quotient, degree of voiceless, degree of subharmonic components as well as the evolution of complex melody patterns were analyzed. Correlations of the voice data with anthropometric data (weight, length, head circumference) and obstetrical factors (time of gestation, presentation, birth modus) were calculated to consider influences by growth discordance or different birth histories. As identical twins have a much greater congenital synchronization of development, universals of prespeech evolution are more convincingly expressed in these pairs (lower intrapair differences). A statistically significant higher intrapair concordance in identical twins was found for the mean $F0$ within the first week

of life, for the mean $F0$ and jitter in the period within 5–8 months of life, and for certain melody patterns. For other parameters, significant intrapair differences between identical and fraternal twins were not found.

4:40

4pSCa8. On the waveforms and spectra of glottal flow models. Boris Doval and Christophe R. d'Alessandro (LIMSI-CNRS, BP133, F91403 Orsay, France, doval@limsi.fr)

Several glottal flow models have been proposed for speech analysis and synthesis (e.g., LF, Rosenberg, R++, and Klatt). All these models do not use the same number of parameters, or the same name for similar parameters, and it appears difficult to compare their merits. Then, a unified framework for studying the time and frequency domain properties of glottal flow models is proposed. It is shown that all the models can be represented by a common set of five time-domain parameters: three scale parameters ($T0$, peak amplitude, open quotient), a shape parameter (asymmetry quotient), and a closure continuity parameter. A generating function is computed for each model by normalization of the model with respect to scale parameters and closure continuity parameter. The specific features of each model are represented in its generating function. The spectrum of generating functions is low pass, and its derivative can be characterized by a spectral maximum, coined ''glottal formant.'' The closure continuity parameter corresponds to a spectral tilt component. The scale parameters are interpreted using scaling properties of the Fourier transform. Then, the glottal flow spectra can be characterized by two breakpoints. Frequencies of these breakpoints can be computed analytically for each model parameter setting.

5:00

4pSCa9. Analysis of pitch accent categories in Welsh. Nicholas J. Kibre (Univ. of California, Santa Barbara, CA)

This paper describes the results of a study of pitch accent categories in Welsh, and their distribution in natural speech. In addition to these descriptive findings, it describes the development of a data-driven approach to intonation. To be useful for the analysis of natural speech, an intonational model must provide means for determining an unambiguous phonological representation for any observed speech token. One approach which will be addressed is the Tilt Model [K. Dusterhoff and A. Black, ESCA Workshop on Intonation (1997); P. Taylor, ICSLP (1998)], amended as necessary to account for the accent patterns of Welsh. This will be compared with an alternative of using statistical methods, particularly factor analysis, to determine the underlying descriptive dimensions of pitch accents in the language. The resulting model will be applied to a corpus of spoken Welsh utterances, and initial findings on the distribution of accent types will be reported.

5:20

4pSCa10. Empirical eigenfunctions obtained from high-speed imaging of the vocal folds. David A. Berry, Ingo R. Titze (Dept. of Speech Pathol. and Audiol., Univ. of Iowa, Iowa City, IA 52242), and Hanspeter Herzel (Humbold Univ., Berlin, Germany)

Previously, the method of empirical eigenfunctions has been used to interpret both periodic and aperiodic oscillations from a finite-element model of vocal fold vibration. For a typical case of periodic vibrations from the model, it was shown that two eigenfunctions explained 98% of the variance of the nodal trajectories. Furthermore, the extracted eigenfunctions were qualitatively similar to analytic normal modes computed from a linear continuum model. Even for complex aperiodic oscillations, 85% of the variance could be explained by just three eigenfunctions. The method of empirical eigenfunctions is now applied to quantitative observations of vocal fold movement obtained from excised canine larynx experiments. With the aid of a high-speed imaging system (the Kodak EktaPro 4540), both periodic and aperiodic oscillations were captured. The newly calculated eigenfunctions will be presented, and contrasted with those obtained previously from finite element simulations. Hints of low dimensionality and mechanisms of irregular oscillation will be discussed. [Work supported by NIH, Grant No. R29 DC03072.]

5:40

4pSCa11. A design of laryngeal structures for a physiological articulatory model. Chao-Min Wu (ATR Human Information Processing Res. Labs., 2-2 Hikaridai, Seika-cho, Soraku-gun, Kyoto, 619-02 Japan), Jianwu Dang (ATR Human Information Processing Res. Labs., Kyoto, 619-02 Japan and Univ. of Waterloo, Waterloo, ON N2L 3G1, Canada), and Kiyoshi Honda (ATR Human Information Processing Res. Labs., Kyoto, 619-02 Japan)

A model of the hyoid–larynx complex is designed and incorporated into a physiological articulatory model. The previously reported articulatory model [Dang and Honda, Proc. ICSLP98] consists of the tongue, mandible, hyoid bone, and vocal tract wall. The aim of this work is to include the laryngeal structures to simulate the tongue–larynx interaction which is observed in natural speech. The framework of laryngeal structures is composed of the thyroid, cricoid, and arytenoid cartilages, which are connected by muscles, ligaments, and joints. The form and geometry of the cartilages are extracted from volumetric MR images of a male speaker and represented in a quasi-3D shape. They are modeled to yield joint rotation and translation as well as vertical movements. The ligaments and muscles are represented by mass points with viscoelastic springs, and the cartilages are composed by springs with an extremely large stiffness. Laryngeal factors of F0 control such as cricothyroid rotation and laryngeal vertical movement are demonstrated in the simulation, and plausible dynamic behaviors of the tongue–larynx interaction are observed. The performance of the model is tested by comparison of acoustic output from the model with recorded speech.

6:00–6:20 Discussion

Session 4pSCb

Speech Communication and Psychological and Physiological Acoustics: Models of Speech Processing in the Auditory Pathway

Steven Greenberg, Cochair
International Computer Science Institute, 1947 Center Street, Berkeley, California 94704, USA

Roy D. Patterson, Cochair
Centre for the Neural Basis of Hearing, Physiology Department, Cambridge University, Cambridge CB2 3EG, UK

Chair's Introduction—1:55

Invited Papers

2:00

4pSCb1. Time-interval information in the auditory representation of speech sounds. Roy D. Patterson (Ctr. for the Neural Basis of Hearing, Physiol. Dept., Cambridge Univ., Cambridge CB2 3EG, UK)

In the auditory system, the primary fibers that encode mechanical motion of the basilar partition are phase-locked to that motion, and this information is preserved, to varying degrees, up to the inferior colliculus. It is known that this timing-interval information is used in localization, and it is probably also used to separate sources from diffuse background noise. The time intervals are on the order of milliseconds, and so traditional speech preprocessors (like MFCC systems) with frames on the order of 15 ms, remove the time-interval information from the representation. The performance of these systems deteriorates badly when the speaker is in a noisy environment. This suggests that time-interval processing will eventually need to be integrated into speech recognition systems if they are to achieve the kind of noise resistance characteristic of human speech recognition. An auditory image model (AIM) will be presented that is designed to stabilize repeating time-interval patterns like those produced by voiced speech, and results from experiments where AIM has been used as a preprocessor for automatic speech recognition. [Work supported by UK MRC (G9703469).]

2:20

4pSCb2. On temporal smoothing and speech perception. Oded Ghitza (Bell Labs., Lucent Technologies, 700 Mountain Ave., Murray Hill, NJ 07974)

Neurophysiological and psychophysical studies provide evidence for the existence of temporal integration mechanisms in the auditory system. These may be viewed as low-pass filters, parametrized by their cutoff frequencies. It is of interest to specify these cutoffs, particularly for tasks germane to the effect of temporal smoothing on speech quality, within the context of speech-coding strategies (e.g., what is the smallest number of bits with which to represent temporally smoothed speech that is perceptually indistinguishable from the original?). In order to answer such questions, speech-processing rules have been derived so as to create synthetic speech capable of generating model auditory-nerve (AN) firing patterns temporally smoothed in a manner commensurate with that observed in neurophysiological studies of the AN (e.g., at low characteristic frequencies, neural discharges of AN fibers are phase locked to the underlying driving critical-band signal, i.e., synchrony is maintained; at high CFs, temporal information is preserved by the instantaneous average rate of the neural firing pattern, which is related to the temporal envelope of the underlying driving signal). This presentation describes the processing rules and the results of psychophysical experiments performed to measure the cutoff frequencies of these filters within the context of speech quality.

2:40

4pSCb3. Modeling speech intelligibility and quality on the basis of the ''effective'' signal processing in the auditory system. Birger Kollmeier, Matthias Wesselkamp,[a] Martin Hansen,[b] and Torsten Dau (AG Medizinische Physik, Universität Oldenburg, Germany)

A model of the ''effective'' signal processing performed by the auditory system is applied to the quantitative assessment of speech intelligibility (cf., Kollmeier *et al.*, Proc. ICA 95, III, 81–84). It consists of a gamma one filterbank followed by envelope extraction, nonlinear adaptation circuits, and subsequent modulation low-pass filtering in each filter channel before being fed into a cross-correlation-type detector or pattern recognizer. The model is capable of predicting the speech intelligibility of both normal and hearing-impaired listeners under a wide range of signal-to-noise ratios, as well as the perceived quality of speech signals whose spectro-temporal properties are systematically degraded. The degradations are generated with a modulated noise reference unit either in a band-specific, time-independent way or in a broadband, temporally varying way. These intelligibility and quality assessment data can be used to deduce the components of the model most germane to the processing of speech, as well as provide information about how to enhance and extend the model for better predictive performance. [a]Now at Siemens Audiologische Technik, Erlangen, Germany. b)Now at Widex Hearing Aids, Vaerloese, Denmark.

3:00

4pSCb4. Periodotopic organization in the ICC of gerbils: A 2-deoxyglucose study. Gerald Langner and S. Braun (Neuroacoust., Zoological Inst., Tech. Univ. of Darmstadt, Schnittspahnstr. 3, D-64287, Darmstadt, Germany)

Periodicity is an important property of many acoustic signals. In the central inferior colliculus (ICC) of the auditory brainstem pathway, frequency and periodicity information converge on a tonotopically organized network. Electrophysiological investigations demonstrate a marked degradation of temporal information in the ICC pertaining to the envelope of spectrally complex signals relative to that observed at the level of the auditory periphery. The temporal information appears to be transformed into a rate-place code and is represented topographically in an orientation orthogonal to the spectral frequency (tonotopic) axis. Additional evidence for orthogonal orientation of frequency and periodicity is derived from a magnetoencephalographic (MEG) study of human auditory cortex and from optical recordings in cat auditory cortex. 2-deoxyglucose labeling was used to investigate the topographic organization of frequency and periodicity information in the ICC of the Mongolian gerbil. The results of this study provide additional evidence for such topographic orthogonality, as well as for convergent information flow, suggesting that neurons in the ICC project to a specific subpopulation of cells in the low-frequency area of the auditory cortex that integrate information across separate periodotopically organized frequency bands.

3:20–3:40 Discussion

3:40–4:00 Break

4:00

4pSCb5. The representation of spectrally dynamic signals in primary auditory cortex. Shihab Shamma (Dept. of Elec. Eng., Univ. of Maryland, College Park, MD 20742)

Natural sounds, including speech, are traditionally characterized by their patterns of pitch, timbre, loudness, and modulation, all of which are closely related to the instantaneous spectrum of these signals. The central auditory system has developed elegant mechanisms to encode this spectro-temporal information. Thus, at the level of the primary auditory cortex (AI), the dynamic spectrum is repeatedly represented over a wide range of spectral and temporal resolutions. This multi-scale representation is derived from response patterns of cells selective to such parameters as local bandwidth, asymmetry of spectral peaks, and onset/offset transition rates. Physiological experiments measured the spectral and dynamic properties of neurons in AI using linear system analysis. One set of experiments used broadband signals with sinusoidally modulated spectral envelopes (''ripples''). Varying the density (or frequency), amplitude, phase, and velocity of the ripple pattern in a systematic fashion was used to derive a ripple transfer function. From this function it is possible to derive a spectro-temporal (impulse) response function via an inverse Fourier transform. A separate technique computed the neuronal impulse response (via reverse correlation) using signals with random and dynamic spectral characteristics. This presentation summarizes the application of these two analytical techniques to characterizing AI neuronal responses and discusses the scientific and technical implications of these multi-scale, cortical representations.

4:20

4pSCb6. Representation of consonant–vowel syllables in mammalian auditory cortex: Effects of background noise and speaking rate. Christoph E. Schreiner, Sarah Wong, Ben Bonham, Steve Cheung, and Purvis Bedenbaugh (Coleman Lab., W. M. Keck Ctr. for Integrative Neurosci. and Sloan Ctr. for Theoretical Neurobiology Univ. of California, San Francisco, CA 94143-0732)

The representation of synthetic and naturally spoken consonant–vowel (CV) syllables was investigated in the auditory cortex of the cat and the squirrel monkey. Spatially discrete and temporally synchronized patterns of neuronal activation are systematically distributed across the tonotopic axis. This activation pattern is largely determined by the dynamics of the signal's spectro-temporal envelope (such as the energy modulation associated with plosive consonants and the onset of voicing). The spatio-temporal activity is strongly influenced by sound pressure level, resulting in significant changes in neuronal response strength and distribution (analogous to those associated with sinusoidal signals). In contrast, background noise has a much smaller impact on the excitation pattern, except at levels sufficiently high as to cause extensive suppression of overall activity. Varying the speaking rate (i.e., shortening vocalic durations and the interval separating CV syllables) was systematically investigated. Forward masking and adaptation affect the magnitude, latency, and spatial distribution of neuronal activity for both slow and rapid speaking rates. These effects are differentially distributed across cortical fields. [Work supported by grants from NINDS and NSF.]

4:40

4pSCb7. Magnetoencephalographic evidence for temporal representations in human auditory cortex. David E. Poeppel (Dept. of Linguist., Univ. of Maryland, 1401 Marie Mount Hall, College Park, MD 20742), Timmothy P. L. Roberts (Univ. of California, San Francisco, CA 94143), and Steven Greenberg (Intl. Computer Sci. Inst., Berkeley, CA 94704)

It is generally assumed that the auditory representation of speech is derived primarily from the spatial distribution of activity across the tonotopically organized neuronal axis. Such temporal parameters as spike synchronization, interspike interval, and neuronal oscillations are also regarded as potential complements to the classical tonotopic representation of the speech spectrum. The present study used magnetoencephalography (MEG) to investigate the temporal behavior of large neuronal ensembles in human auditory cortex. Experimental stimuli were sinusoidal and square-wave signals, sinusoidally amplitude-modulated tones, and synthetic vowels. The results indicate the presence of a systematic representation of the signal spectrum and pitch derived from the latency pattern of the major auditory-evoked neuromagnetic field. The magnitude of latency differential to signals of variable frequency and pitch can be as large as 25 ms. This ''tono-chronic'' analysis may offer an alternative encoding mechanism for pitch and spectral information that plays an important role in the perception of complex signals such as speech. [Research supported by the James S. McDonnell Foundation and the National Science Foundation.]

5:00

4pSCb8. An oscillatory correlation framework for the separation of speech from interfering sounds. Guy J. Brown (Dept. of Comput. Sci., Univ. of Sheffield, Regent Court, 211 Portobello St., Sheffield S1 4DP, UK, g.brown@dcs.shef.ac.uk) and DeLiang L. Wang (The Ohio State Univ., Columbus, OH 43210-1277)

Speech is seldom heard in isolation—usually, a mixture of sounds reaches our ears. Hence, the auditory system is faced with a scene analysis problem—it must group together spectral components that are likely to have arisen from the same environmental source. At the neurobiological level the auditory system also faces a binding problem—it must construct meaningful wholes from features that are represented in separate neural structures. Models of auditory function based on the theory of oscillatory correlation offer a potential solution to the scene analysis and binding problems. According to this theory, perceptual streams are represented by populations of neural oscillators, such that oscillators belonging to the same stream are synchronized (phase locked with zero phase lag), and are desynchronized from oscillators belonging to different streams. A neural oscillator model of auditory function has been developed, capable of segregating speech from interfering sound sources. The core of the model is a two-layer neural oscillator network, in which lateral connections among oscillators encode harmonicity as well as proximity in time and frequency. A variant of this model is able to account for the sharing of acoustic evidence among streams, as would occur in ''duplex'' perception of speech.

5:20

4pSCb9. Implications of a sensory-motor theory for the representation and segregation of speech. Neil Todd (Dept. of Psychol., Oxford Rd., Manchester Univ., Manchester M13 9PL, UK)

Discussed is a computational model which attempts to simulate the principal brain structures involved in sensory-motor sequencing, including auditory cortex, posterior parietal cortex, cerebellum, motor cortex, and the motor output system. A particular focus in this presentation is on the auditory cortical component responsible for computing a 3-D spatio-temporal power spectrum of the auditory image flow [N. Todd, Proc. 16th ICA (1998)], which captures information topographically on three levels, roughly corresponding to timbre, pitch, and rhythm, and reflects the temporal resolution of the cochlea, inferior colliculus, and auditory cortex, respectively. By considering the spatio-temporal orientations of cortical receptive fields (RFs), it is possible to delineate a set of stationary and moving primitive features upon which the higher-order constructs of pitch and timbre are built. A separate model population of secondary auditory cortical neurons, which receive inputs from the population of primary RFs, provides a potential means of accounting for a number of important phonological and melodic processes. Implications of this model are discussed for the development of new algorithms for the representation and segregation of speech via self-organization of primary and secondary RFs by means of the principle of information maximization.

5:40–6:00 Discussion

THURSDAY AFTERNOON, 18 MARCH 1999 ROOM H111, 1:55 TO 6:20 P.M.

Session 4pSP

Signal Processing in Acoustics: Acoustic Signal Processing for Systems with 2D/3D Sensor Arrays II

Stergios Stergiopoulos, Cochair
Defence and Civil Institute of Environmental Medicine, P.O. Box 2000, North York, Ontario M3M 3B9, Canada

Dieter Kraus, Cochair
STN ATLAS Elecktronik GmbH, Naval Division, System Analysis and Signal Processing Group, MME6, Sebaldsbrücker Heestrasse 235, 28305 Bremen, Germany

Chair's Introduction—1:55

Invited Papers

2:00

4pSP1. Robust matched-field processing in underwater acoustics. Newell O. Booth (Space and Naval Warfare Systems Ctr., Code D881, San Diego, CA 92152-5000)

During the last decade, underwater acoustic matched-field processing (MFP) has been shown to be a robust and powerful means of extracting information related to the propagation of sound and the location of acoustic sources in the ocean. Using large arrays of acoustic receivers, broadband sources of acoustic energy, and physically accurate propagation models, MFP techniques have been used to detect, localize, and track acoustic sources. It is also possible to estimate the array shape as well as oceanographic parameters which affect acoustic propagation. Using a broad definition of matched-field processing, this paper reviews its application to underwater acoustics and acoustical oceanography. Physical phenomena which contribute to the successful application of MFP are discussed, along with other phenomena which have contributed great simplifications.

2:20

4pSP2. Phase conjugation and matched-field processing. W. A. Kuperman, W. S. Hodgkiss, H. C. Song, Aaron Thode (Marine Physical Lab., Scripps Inst. of Oceanogr., La Jolla, CA 92093-0701), T. Akal, and C. Ferla (SACLANT Undersea Res. Ctr., La Spezia, Italy)

Matched-field processing (MFP) can be implemented with a backpropagation algorithm. The method requires the same knowledge of the environment as the conventional MFP replica search approach. Rather than use numerical backpropagation, the phase conjugation (PC) approach (also referred to as a time-reversal mirror) uses physical sources at each receiver position to backpropagate the phase-conjugated data on the receive array. The acoustic field then focuses at the position of the original radiating source that is the same position of the main lobe of the analogous MFP ambiguity surface. No *a priori* environmental information is required. Two experiments implementing PC in the ocean have been successfully conducted in 1996 and 1997. These experiments and the physics of PC provide new insight into MFP.

2:40

4pSP3. Optimized image processing for multi-beam/multi-aspect sidescan sonar application. Ursula Hoelscher-Hoebing and Dieter Kraus (STN ATLAS Elektronik GmbH, Sebaldsbruecker Heerstrasse 235, D-28305 Bremen, Germany, hoelscher.u@stn-atlas.de)

In the development of future sonor systems, computer-aided classification (CAC) becomes increasingly important. Adequate processing of the multidimensional image data is one important component in a multi-beam/multi-aspect sidescan sonar CAC system. Because the target strength of an object varies with aspect angle, the sonar echo and its representation in a sidescan image is rather random. To make sure that a maximum echo strength is gained, in multi-beam/multi-aspect sidescan sonars overlapping bottom areas are insonified by temporal successive pings, giving the echoes of the target under different aspect angles. Taking advantage of the multi-aspect echo structure in the images of successive pings, they are fused to one sidescan image. Existing image fusion algorithms now require an operator to set threshold values distinguishing target and shadow zones from bottom reverberation zones. An unsupervised method is proposed here for segmentation and optimal fusion of multidimensional images. Its basic steps are image segmentation by means of the EM algorithm; clustering of image segments applying the Markov random field approach; and fusion of successive pings images following a minimum/mean/maximum strategy according to the results of image segmentation and clustering.

3:00

4pSP4. Signal processing algorithm for sound source localization with discretionarily distributed multiple receiving sensors. Nai-chyuan Yen (CLY Assoc., 2109 Rampart Dr., Alexandria, VA 22309-1537, CLY-yen@juno.com)

The deployment of strategically placed multiple receiving sensors has many practical ways to detect, localize, and classify a sound source in situations such as monitoring an isolated street disturbance in an urban environment with posted microphones or identifying a submerged object in the ocean with air-dropped sonobuoys. A simple processsing algorithm based on signals received from multiple sensors is derived from the information contained in the cross-spectrum matrix formed from the receiving sensors. Using the magnitude distribution of eigenvalues across the frequency bandwidth as the indication for the strength of signal excess in the frequency domain, their corresponding eigenvectors provide the required complex number weightings to select the related coherence components of the signal. By examining the phase angle data from each sensor's weighting factor, a set of simultaneous algebra equations can be formulated to estimate the location of the sound source. The computation procedure of this approach is uncomplicated in comparison with the traditional triangulation method. Furthermore, the additional accompanied computed eigenvalues can be utilized for the characterization of the detected sound source, thereby establishing its identification reference. Simulated examples are used to test out the effectiveness of this multiple sensor sound source evaluation methodology at various operational scenarios.

3:20

4pSP5. Optimal amplitude shading for arrays of irregularly spaced or non-coplanar elements. Timothy C. Gallaudet and Christian P. de Moustier (Marine Physical Lab., Scripps Inst. of Oceanogr., 9500 Gilman Dr., La Jolla, CA 92093-0205)

The majority of optimal amplitude shading methods for arrays of irregularly spaced or non-coplanar elements rely on numerical optimizations and iterative techniques to compute the desired weighting function because analytic solutions generally do not exist. Optimality is meant here in the Dolph–Chebyshev sense to provide the narrowest mainlobe width for a given sidelobe level. A simpler and more efficient technique to compute the shading weights for arbitrary line array shapes or element spacings is presented and it is shown that it is sufficient to sample the optimal Dolph–Chebyshev window, computed for a uniform line array of equivalent aperture length, at the element position of the nonuniform array. Examples are given for narrow-band plane-wave beamforming with curved arrays in which phase compensation is achieved by projecting the elements on a line tangent to the array. For the same mainlobe width, the resulting peak sidelobe levels are within 3 dB of a 30-dB Dolph–Chebyshev weighted uniform line array of equal aperture length and number of elements. Results are presented for computer simulations and for data collected at sea with the Toroidal Volume Search Sonar by the Coastal Systems Station, Panama City, Florida. [Work sponsored by ONR-NRL (Contract No. N00014-96-1-G913).]

3:40

4pSP6. Localization of the sources using blind identification of signal subspace. Bendjama Ammar and Bourennane Salah (S. D. E. M., URA, CNRS 2053, B. P. 52, Quartier Grossetti, 20250 Corte, France)

To find the direction of arrival (DOA) of N sources impinging on an array of M sensors, actual fourth-order direction-finding methods try to solve an N-dimensional problem from the statistics of the data. Current narrow-band array processing techniques are based on the second-order statistics of the received signals. In many situations, the received signals are non-Gaussian, so that they contain valuable statistical information in their moments of order greater than two. In these circumstances, it makes sense to develop array processing techniques which are designed to use their higher-order information. Of particular interest are the algorithms based on higher-order cumulants, which are asymptotically insensitive to Gaussian noise: it is thus neither necessary to know, to model, or to estimate the noise covariance, which is a reasonable assumption in many practical situations. In this paper, an approach of direction finding is proposed, based on the first step of blind identification of source steering. As a second step, the direction-finding concept is now possible due to the development, these last years, of several blind source separation methods which allow the blind identification of source-steering vectors.

4:00–4:20 Break

4:20

4pSP7. Blind source separation by convex optimization to resolution enhancement. Kenbu Teramoto and Noriko Mori (Dept. of Information Sci., Saga Univ., Saga, 8408502 Japan)

In the current blind source separation (BSS) one tries to separate statistically independent unknown source signals from their linear mixtures without explicit knowledge of the mixing coefficients. However, in the case that the sources radiate statistically dependent signals, difficulties exist in separating sources. In such cases, it is important to utilize the nonlinear convex constraints. In this paper, a convex optimization method for BSS and parameter estimation of unknown components in the signal transfer function is proposed. This technique relies upon seeking the unique KKT (Karush–Kuhn–Tucker) point of the augmented Lagrange function which is defined over the direct product of source object space and observed signal space. Utilizing prior knowledge about spatial characteristics of the point spread function and short-time statistical characteristics of noise concurrently, the proposed algorithm can converge to the reliable solution on the contrary to the independent component analysis (ICA) exhibiting oscillations. Applying the proposed method to a 3-D sparse aperture holographic sonar which has a limited number of transducers distributed sparsely, the novel method yields features that reduce the artifacts caused by under-sampled data and achieve higher resolution with higher convergence rate to the optimal solution than that of ICA.

4:40

4pSP8. Forward/backward first-order statistics algorithm for the estimation of DOA in a multipath environment. Joon-il Song, Han-Su Kim, Koeng-Mo Sung (Appl. Acoust. Lab, Inst. of New Media and Commun., Seoul Natl. Univ., Kwanak-Ku, Seoul 151-742, Korea), and Jun-Seok Lim (Sejong Univ.)

Many kinds of direction of arrival (DOA) estimation methods in the coherent environments have been studied for many decades. Most of them use spatial smoothing to tackle the coherent environments. An alternative method was proposed by Pillai which used first-order statistics on each sensor datum [S. U. Pillai, *Array Signal Processing* (Springer-Verlag, New York, 1989)]. The method handled the complex numbered input data with additional symmetric array so that it needed two times as many sensors as it needed in the case of the real numbered input data. In this paper a DOA estimation method using forward/backward first-order statistics is proposed which can handle the complex numbered input data without additional sensors. [Work supported by UARC.]

5:00

4pSP9. Robust Kalman-based DOA estimator with variable fading memory. Han-Su Kim, Koeng-Mo Sung (School of Elec. Eng., Seoul Natl. Univ., Seoul, Korea), and Jun-Seok Lim (Sejong Univ.)

In this paper, VFM (variable fading memory) is introduced to the robust Kalman-based DOA (direction of arrival) estimator [Han-Su Kim and Koeng-Mo Sung, Proc. 16th ICA/135th ASA **1**, 1327–1328 (1998)] for DOA estimation of uncorrelated narrow-band plane waves under the impulsive noise environment. To introduce VFM properly into the Kalman filter, the proposed algorithm is derived from a modified least-squares criterion with VFM for DOA estimation. Since the derived VFM can be adaptively calculated with respect to the estimation error, the proposed algorithm has the effectiveness to the impulsive noise in stationary or nonstationary situations. The introduction of VFM enables the time-varying DOA to be estimated properly and prevents the estimated error caused by the impulsive outlier from propagating into future time instants, adaptively decreasing the importance of past observations. The proposed method can make the small perturbation to the parameters using the Huber function, named M-estimation, and adaptively reduce the estimation error propagation caused by past observations of the impulsive noise using VFF. Compared to the conventional Kalman algorithms, simulations show that the proposed algorithm is robuster than any other conventional Kalman algorithms to the impulsive noise.

5:20

4pSP10. Frequency-angle selectivity under conditions of 3-D antenna motion. Igor I. Gorban and Sergey P. Volkovetsky (Inst. of Math. Machines and Systems, 42 Ave. Acad. Glushkov, Kiev, Ukraine, 252187, gorban@immsp.kiev.ua)

Common estimation of frequency-angle signal parameters under conditions of complicated 3-D antenna motions with angle rotations around the space axes is researched. A program package for modeling has been developed. The package calculates Fisher informative matrix and Cramer–Rao estimates of frequency-angle signal parameters. Research showed that (1) frequency-angle selectivity essentially depends on parameters of motion. Common estimates may be essentially better for systems with complicatedly moving antennas than for systems with static antennas or antennas moving with constant velocity; (2) a constant component of velocity makes the common estimates of frequency-angle signal parameters worse and variable components make them better; (3) angle selectivity is mainly determined not by size of array, as for static antenna, but by sizes of area where there is antenna motion (especially periodical motion); (4) in conditions of complicated antenna motion, increasing of angle selectivity takes place even if frequencies of the signal or Doppler's shift are unknown; (5) by correctly taking into consideration complicated antenna motion, there is often a real possibility to increase common frequency-angle selectivity of the systems.

5:40

4pSP11. Estimation of time-varying signal parameters via VFM Kalman filtering. Sang-Wook Lee (School of Elec. Eng., Seoul Natl. Univ., Seoul 151-742, Korea, lsw@acoustics.snu.ac.kr), Jun-Seok Lim (Sejong Univ.), Byung-Doo Jun, and Koeng-Mo Sung (Seoul Natl. Univ., Seoul 151-742, Korea)

This paper proposes a VFM (variable fading memory) Kalman filtering and applies it to the parameter estimation for time-varying signal. By adaptively calculating fading memory, the proposed algorithm does not require any fixed predetermined fading memory when estimating a time-

varying signal. The time-varying signal parameter estimation performance is evaluated by computer simulations for two cases, one of which is the chirp signal whose frequency varies linearly with time and the other is the chirp signal with an impulsive outlier.

6:00

4pSP12. Coupling criteria for arrays in a channel. Charles F. Gaumond (Acoust. Div., Naval Res. Lab., 4555 Overlook Ave. SW, Washington, DC 20375)

In this paper, an analogy is made and developed between a linear array of receivers with far-field sources in an unbounded, homogeneous medium and an arbitrary array of receivers with arbitrarily placed sources in a channel. The transfer function of a signal transmitted through a channel is the well-studied transmission loss (TL). The singular value decomposition (SVD) is performed on the transfer function between sources and receivers. The three components of the SVD are related to various factors in the case of the linear array in an unbounded, homogeneous medium. The case of a translationally invariant channel described using modes is considered. This modal description is also related to the three components of the SVD. The sum of the eigenvalues of the SVD is proposed as a single number which quantitatively describes the amount of coupling between an arbitrary array and the sound channel, assuming that the distribution of sources spans the propagating modes. This single number can then be used to assess the ability of various array configurations to sample the sound channel. [Work supported by ONR.]

THURSDAY AFTERNOON, 18 MARCH 1999 ROOM H2053, 2:00 TO 6:20 P.M.

Session 4pUW

Underwater Acoustics: Shallow Water

Alexandra Tolstoy, Cochair
Integrated Performance Decisions, Inc., 8610 Battailles Court, Annandale, Virginia 22003, USA

Finn B. Jensen, Cochair
SACLANT Undersea Research Centre, Viale San Bartolomeo 400, 19138 La Spezia, Italy

Contributed Papers

2:00

4pUW1. High-resolution modal mapping in a complex shallow-water environment. Kyle M. Becker (MIT/WHOI Joint Prog. in Oceanogr. and Oceanogr. Eng., Woods Hole Oceanogr. Inst., Woods Hole, MA 02543) and George V. Frisk (Woods Hole Oceanogr. Inst., Woods Hole, MA 02543)

During March 1997, a modal mapping experiment (MOMAX) was conducted to measure the spatial variability of low-frequency sound propagation in shallow water [G. V. Frisk *et al.*, J. Acoust. Soc. Am. **103**, 3028(A) (1998)]. The fields created by cw sources in the frequency range 50–300 Hz were measured using an array of freely drifting hydrophone buoys equipped with GPS navigation. The resulting data consist of complex pressure mapped onto a high-resolution geospatial grid. Based on the tenets of normal mode theory, the wave number content of the field was extracted using a high-resolution implementation of the Hankel tranform technique [K. M. Becker *et al.*, J. Acoust. Soc. Am. **103**, 3029(A) (1998)]. Neglecting horizontal refraction, the resulting spectra can be mapped onto a corresponding spatial grid. Several modal maps are presented for various source/receiver configurations and frequencies with emphasis placed on the variablility of the wave numbers in space. These modal maps can then be used as the basis for inferring the local geoacoustic properties of spatially varying shallow-water waveguides. [Work supported by ONR.]

2:20

4pUW2. Broadband inversion of shallow-water range-dependent acoustic data using a genetic algorithm. Dick G. Simons and Mirjam Snellen (TNO Phys. and Electron Lab., Underwater Acoust. Group, Oude Waalsdorperweg 63, 2509 JG The Hague, The Netherlands)

In October 1997, shallow-water experiments were carried out on the Bank of Adventure southwest of Sicily. The purpose of this trial was to obtain acoustic data in range-dependent environments for testing and further developing matched-field inversion methods to determine geoacoustic properties of the sea floor. On one track of the experiments, an acoustic source was towed over a sloping bottom with a water depth varying from 100 m at the vertical receiving array to 75 m at the end of the 7-km track. The array comprises 64 hydrophones and covered the central 62 m of the water column. At several source-receiver ranges, the source (towed below the thermocline) transmitted a multitone signal in the band 50–300 Hz. Detailed sound-speed profiling of the water column and seismic profiling of the bottom were performed along the track. Broadband inversion of the acoustic data was done using a genetic algorithm as the global search method. The forward model uses standard adiabatic mode theory. Inversion results are shown for different geoacoustic models with different complexity concerning sediment layering. The bottom parameters obtained agree well with the results of the seismic analysis and its geological interpretation.

2:40

4pUW3. Analysis of modal dispersion in the Middle Atlantic Bight. John E. Laliberte, Gopu R. Potty, and James H. Miller (Dept. of Ocean Eng., Univ. of Rhode Island, Narragansett, RI 02882)

Ocean environmental acoustic experiments were conducted on the Middle Atlantic Bight during the August 1996 Shelf Break Primer Experiment. Broadband acoustic sources, SUS charges, were dropped across and along the shelf in depths ranging from 85 to 350 m. The experimental data were collected at two veritical hydrophone arrays situated at the top of the shelf. The acoustic signal received was analyzed using a Morlet wavelet. This wavelet analysis enabled time and frequency characteristics to be extracted. Scalograms, representations of the energy distribution in the time-frequency plane, were used to assess the modal dispersion. The group speeds for modes 1–4 at frequencies 15–240 Hz were estimated using the wavelet scalogram. The mode dispersion was dependent upon the bathymetry, depth, and range features of the shelf. A normal mode code was used to compare the observed dispersions with theory. In addition, the influence of the bathymetry, depth, and range features were analyzed for their impact on the modal dispersion. [Work supported by ONR.]

3:00

4pUW4. Effects of the time-varying ocean on broadband propagation in shallow water. Peter L. Nielsen, Francesco Bini-Verona, and Finn B. Jensen (SACLANTCEN, Viale S. Bartolomeo 400, 19138 La Spezia, Italy, nielsen@saclantc.nato.int)

Prediction of underwater sound propagation is generally performed by assuming a time-invariant ocean. In May 1997 SACLANTCEN conducted an experiment south of Elba in the Mediterranean Sea with the aim of investigating the time-dependent effects of the ocean on sound propagation in shallow water. Broadband LFM signals (300 Hz to 7.5 kHz) were transmitted every 1 min for 36 h over a fixed 15-km propagation path. Extensive measurements of the environmental parameters were done during the transmissions in order to perform a meaningful correlation between the time-varying environmental and acoustic data. Previous analysis of the low-frequency part of the acoustic data [Jensen *et al.*, J. Acoust. Soc. Am. **103**, 2856(A) (1998)] show high stability in the first 6 h of propagation, but at longer transmitting time and higher frequencies a strong variability in the received acoustic signals is seen. The main features in the time-varying environmental parameters causing fluctuations in the acoustic signals are identified. These features are then used in a numerical propagation model in order to assess to what degree it is possible to predict the time dependence of the received acoustic data in this particular shallow-water area. [This work was supported by the EC under the MAST-III project PROSIM, Contract No. MAS3-CT95-0008.]

3:20

4pUW5. The influence of internal waves on signal fluctuation in the Yellow Sea. Zhenge Sun, Renhe Zhang, and Jin Yan (Natl. Lab. of Acoust., Chinese Acad. of Sci., P.O. Box 2712, Beijing, 100080, PROC, szg@farad.ioa.ac.cn)

This paper studies the signal fluctuation due to the tide and internal waves in the Yellow Sea. The spread of internal waves appears to be the fluctuation of the thermocline in summer time. As a result, the characteristics of normal modes including their wave numbers and group velocities vary with this fluctuation. This leads to the signal fluctuations since the receiving signals are actually the interference results of arriving modes. The influence of internal waves on normal modes and signal fluctuation was examined in an experiment in the Yellow Sea in 1998. In the experiment, an ADCP and thermistor chain were used to observe the internal waves, while a vertical array with 32 hydrophones was used to receive CW and FM acoustic signals. The CW signals provided the measurement of amplitude fluctuation at several frequencies from 450 to 650 Hz. The FM signals were used to get the mode arriving structure by means of pulse compression and mode filtering technique. The variation of mode group delay between the 3800-Hz signal and the 450-650 Hz signal was also measured.

3:40

4pUW6. Acoustic intensity and phase variability caused by time-evolving internal wave fields. Steven Finette, Marshall Orr, Altan Turgut, Stephen Wolf, Bruce Pasewark (Acoust. Div., Naval Res. Lab., Washington, DC 20375, finette@wave.nrl.navy.mil), and John Apel (Global Ocean Assoc., Silver Spring, MD 20908)

Relationships between time-evolving internal wave fields in a shallow-water environment and both acoustic intensity and phase variability are explored through a computer simulation model developed from experimental data acquired on the continental shelf off the New Jersey coast [Apel *et al.*, IEEE J. Ocean. Eng. **22**, 465–500 (1997)]. From an analysis of SWARM (Shallow Water Acoustics in a Random Media) data, single realizations of the acoustic field are computed at an array located approximately 42 km from sources emitting at 224 and 400 Hz. Using a wide-angle parabolic equation, the acoustic field is computed in 1-min intervals over a 12-h time window during which both spatially diffuse and spatially localized internal wave fields propagate through the water column. Results include time-evolving modal power and scintillation indices, and can be interpreted in terms of mode coupling. The ability to locate a source using phase-coherent techniques such as matched field processing will also be addressed. [Work supported by ONR.]

4:00–4:20 Break

4:20

4pUW7. Characterizations of the internal waves and their effects on sound propagation in the central area of the Yellow Sea. Jin Yan, Renhe Zhang, and Zhenge Sun (Natl. Lab. of Acoust., Chinese Acad. of Sci., Beijing 100080, PROC, yanjin68@hotmail.com)

In the late summer of 1996, a joint China–USA experiment was performed in the central area of the Yellow Sea. The analysis of the data from thermistor string and CTD reveals that (1) there was intense internal wave activity in the experimental area, and the isotherm displacement induced by internal waves could be as large as 8 m; (2) the power spectrum of the vertical displacement had a significant peak near the M2 tide frequency, and was approximately proportional to $\omega^{-3/2}$; and (3) the internal wave field was dominated by first-order modes. Based on the observed properties of the internal waves, a model of the induced sound-speed distribution is developed, and computer simulations are conducted for cw and wide-band signal propagation by using the PE method. Numerical results are presented for comparison with the experimental data. [Work supported by NNSF of China and ONR of USA.]

4:40

4pUW8. Temporal coherence of broadband acoustic signals in the presence of internal waves in shallow water. T. C. Yang and K. Yoo (Naval Res. Lab., Washington, DC 20375)

Ocean medium fluctuations reduce the temporal coherence of acoustic signals. At low (e.g., 500 Hz) frequencies, temporal coherence limits the time duration of a replica field used for matched-field source localization in a random ocean. At mid (e.g., 10 kHz) frequencies, temporal coherence of the acoustic signal dictates the update rate for the channel equalizer for a phase coherent communication scheme. In this paper, the temporal coherence of broadband acoustic signals is studied at low- and mid-frequencies in a shallow-water environment which includes both the linear and nonlinear (solitary) internal waves. The internal wave model is constructed based on the measured (average) sound-speed profile and sound-speed variance collected during the SWARM-95 experiment. A broadband pseudorandom (PRN) signal is used at low- and midfrequencies. The signals are propagated using a PE model through the internal wave perturbed sound-speed profiles which evolve in time according to the internal wave equation of motion. Temporal coherence at 400 Hz is shown to agree with experimental observations based on the SWARM-95 measurements. Implications for midfrequency communications will be discussed. [This work is supported by the Office of Naval Research.]

5:00

4pUW9. A look at the modal phase structure function in shallow water. Brian J. Sperry (MIT/WHOI Joint Prog. in Oceanogr. and Ocean Eng., Woods Hole Oceanogr. Inst., Woods Hole, MA 02543) and Jim Lynch (Woods Hole Oceanogr. Inst., Woods Hole, MA 02543)

Experimental and theoretical work in shallow-water acoustic propagation has invariably encountered the complexities of the shallow-water environment. A useful measure of the propagation complexity for array processing is the ''modal phase structure function.'' The modal phase structure function makes it possible to study how environmental fluctuations affect point-to-point phase differences, quantities which are directly related to modal coherences. A method has been developed, using perturbation theory, that directly relates the modal phase structure function to the environmental sound-speed correlation function. Despite its relative

simplicity, this method can address fully coupled mode range dependence, as well as anisotropy in the environmental correlation function. The phase structure function may be applied to time and frequency coherence problems as well. Another strength of the technique is that contributions from various processes, such as mesoscale and finescale variability, interface roughness and geoacoustic variability, may be separated out under reasonable assumptions. Early calculations show good agreement with experimental results. [Work supported by ONR.]

5:20

4pUW10. Sound vertical coherence in shallow water with a thermocline. Renhe Zhang and Fenghua Li (Natl. Lab. of Acoust., Inst. of Acoust., Chinese Acad. of Sci., Beijing 100 080, PROC zrh@canna.ioa.ac.cn)

A China–U.S. cooperative experiment was conducted in the Far Yellow Sea with a thermocline in August 1996. The explosive sources were discharged either above the thermocline or below the thermocline. The pulsed signals were received by a vertical array spanning the whole water column, and the shortest separation between two hydrophones is 2 meters. The vertical correlation of the received data is analyzed in this paper. Experimental data show that vertical coherence has different depth structure for different source, frequency, and range, and it is also shown that the relationships between the coherence and the frequency and between the coherence and the range are different for different source and receiver. It is found in the experimental data that the vertical coherence is not reciprocal. Numerical results and theoretical explanations of these relationships are also given in this paper. [Work supported by NSF of China and ONR of the U.S.]

5:40

4pUW11. Mode diffusion and pulse broadening in shallow-water acoustic propagation. Robert I. Odom (Appl. Phys. Lab., Univ. of Washington, 1013 NE 40th St., Seattle, WA 98105)

An acoustic signal propagating in a range-dependent shallow-water waveguide is scattered and attenuated as a result of interaction with medium heterogeneities. An initial signal pulse consisting of a few modes will spread in time linearly with propagation distance as energy is redistributed among available modes due to mode coupling. Over longer propagation distances in a random waveguide, modal energy reaches equilibrium, and the average modal energy becomes constant. (The modes are, of course, subject to geometric spreading, intrinsic attenuation, and radiation losses, but it is assumed that all modes are equally affected so that, locally, the energy per mode is a constant.) Energy propagates at a velocity that is an average of the group velocities for individual modes. The pulse width grows mores slowly now as the square root of the propagation distance, rather than linearly. This transition to square-root broadening in randomly perturbed multimode fiber optic waveguides is well known and observed. Employing a diffusion equation for the modal acoustic energy in a random shallow-water waveguide with an elastic bottom, heterogeneity-induced pulse broadening is investigated for realistic environmental properties. [Work supported by ONR.]

6:00

4pUW12. Effects of internal waves and bores on acoustic transmissions in the Strait of Gibraltar. Christopher O. Tiemann, Peter F. Worcester, Bruce D. Cornuelle (Scripps Inst. of Oceanogr., Univ. of California at San Diego, La Jolla, CA 92093, ctiemann@ucsd.edu), and Uwe Send (Univ. of Kiel, 24105 Kiel, Germany)

The Strait of Gibraltar Acoustic Monitoring Experiment was conducted in April 1996 to determine the feasibility of using acoustic methods to make routine, rapidly repeated transport measurements in the Strait of Gibraltar, as well as to explore the acoustic scattering caused by the unique internal wave field in the Strait. The acoustic data from high-frequency (2 kHz) reciprocal transmissions across the Strait are unique in that they clearly isolate the acoustic effects of passing internal bores without the added complexity of surface and bottom interactions. Although the acoustic scattering caused by each passing internal bore is different, some common characteristics can be identified. The challenge is to explain these acoustic observations in terms of the physical processes occurring. Acoustic propagation models through range- and time-dependent sound-speed fields representing the Strait and perturbed by internal bore models are being used to understand these observations and to determine to what aspects of the bore the acoustics are most sensitive.

Contributed Posters

These posters will be on display in the Poster Gallery from Wednesday to Friday, 17–19 March. Authors will be at their posters from 10:00 a.m. to 12:00 noon on Friday, 19 March.

4pUW13. High-frequency acoustic propagation measurements in coastal areas. Joseph L. Lopes, Iris C. Paustian, Kerry W. Commander, and John S. Stroud (Coastal Systems Station, Naval Surface Warfare Ctr., Code R21, 6703 West Hwy. 98, Panama City, FL 32407-7001)

A measurement was conducted in a very shallow-water (VSW)/surf zone (SZ) region to investigate acoustic propagation and coherence in coastal areas. The measurement utilized several acoustic sources and hydrophones. The sources were mounted onto a stationary sonar deployed in the VSW. The sonar tower was equipped with a horizontal pan and vertical tilt motors. The hydrophones were attached to steel pipes that were water-jetted into the sediment such that the hydrophones were located in the SZ near the midpoint of the water column. The acoustic frequencies varied from approximately 30 to 800 kHz. Data were acquired by directing the acoustic sources (located in the VSW) toward the free-field hydrophones. The data were analyzed using coherence techniques. Results of this acoustic measurement will be reported.

4pUW14. Normal mode propagating through rapid range-dependent shallow water. Fenghua Li and Renhe Zhang (Natl. Lab. of Acoust., Inst. of Acoust., Chinese Acad. of Sci., Beijing 100 080, PROC, zrh@canna.ioa.ac.cn)

When the normal modes propagate through the range-independent shallow water, the different normal modes are separated into different wave packets in the time domain because of the different group velocities. If the normal modes propagate through some kinds of shallow water which are rapidly range-dependent due to the bottom or the fluctuation in the water column, etc., coupling between different-order modes will happen. And even the same normal mode at the receiver will be divided into two or more wave packets in the time domain, each packet representing the energy coupled from the different normal mode at the source to that mode at the receiver. Those divisions provide a lot of useful information about the rapid range-dependent environment. The divisions of one normal mode are calculated by a coupled mode code which is developed based on BDRM theory, and are also used to estimate the simulated rapid range-dependent environment in this paper. [Work supported by NSF of China.]

4pUW15. Analysis of active hydroacoustic system's parameters versus conditions of sound propagation in inland water. Jacek Gawrysiak (Tech. Univ. of Gdansk, Narutowicza str 11/12, 80-952 Gdansk, Poland)

The paper contains the numerical calculations of a dependence between the shape of the sound velocity profiles in inland water and sonar parameters such as: directional pattern, range, signal-to-noise ratio, and so on.

4pUW16. On the horizontal structure of a field in separate modes radiated by a parametric antenna in axially nonuniform acoustic waveguides. Sergei Gurbatov, Sergei Egorychev, Vasily Kurin, Nikolai Pronchatov-Rubtsov, and Leonid Kustov (Dept. of Radiophys., Nizhny Novgorod Univ., 23 Gagarin Ave., Nizhny Novgorod, 603600, Russia, gurb@rf.unn.runnet.ru)

The results of laboratory experiments on propagation of low-frequency acoustic waves produced by a parametric antenna in a few-mode waveguide with a linear depth variation along propagation direction are described. Mode structure of the radiated field and the characteristics of eigenwaves forming an acoustic field in waveguides of different types, which model shelf areas of the world oceans, are obtained. The study of the horizontal structure of separate normal waves was carried out by allocation of mode pulses due to the intermode dispersion. Also, the revealing of mode contents of radiated field was carried out by Fourier analysis of the signal received by evenly moving along the propagation route acoustic probe. The different Doppler frequency shifts of eigenmodes allows the resolution of each normal mode. It is shown experimentally that the azimuth structure of separate modes is transformed in the process of sound propagation to an area of smaller waveguide depths. For a particular mode, the direction at which mode radiation reaches a maximum value changes due to decreases in a waveguide depth when the number of normal waves evidently decreases. Experimental data obtained are confirmed by the results of numerical simulations. [Work supported by RFBR Grant No. 98-02-16402 and INTAS-RFBR Grant No. 95-IN-RU-0723.]

4pUW17. Effect of seismic waves on the acoustic field interference structure in the shallow sea. Elena Borodina (Inst. of Appl. Phys., 46 Ulyanov Str., Nizhny Novgorod, 603600, Russia), Sergei Egorychev, Vasily Kurin, Nikolai Pronchatov-Rubtsov (Nizhny Novgorod Univ., Nizhny Novgorod, 603600, Russia, nikvas@rf.unn.runnet.ru), and Yury Petukhov (Radiophysical Res. Inst., Nizhny Novgorod, 603600, Russia)

The influence of lateral waves on forming of the acoustic field space-frequency interference structure in a shallow sea was investigated theoretically and experimentally. Within the scope of the simple model of shallow sea as a fluid layer of thickness H on an elastic half-space, the analytical frequency and horizontal range dependencies of amplitudes of compressional and shear lateral waves were derived. Numerical simulation was carried out for natural and laboratory experiment conditions. The numerical results showed the resonant character of frequency dependencies of compressional and shear wave amplitudes, with abrupt narrow maximums at critical frequencies of leak and propagating modes, respectively. It was shown also, that below the critical frequency of the first mode the interference structure is formed mainly by the fundamental mode and the shear wave, which substantially exceeds the compressional one; besides, the shear wave amplitude is almost two times less than the zero mode at distances of about 10 H. Thus it was proved that at ranges up to 200 H realized at both natural and laboratory experiment conditions, only the shear wave significantly influences forming of the space-frequency interference field structure in a shallow sea. [Work supported by RFBR Grant No. 98-02-16402, CCPE Grant No. 95-0-8.1-34.]

Posters from various technical sessions remain on display in the Poster Gallery.

Posters from sessions which contain both lecture and poster presentations will be attended by the authors as listed below.

10:00–12:00

3pAO7	Preisig, James C.	The experimental demonstration of selective mode excitation in a shallow water environment
3pAO8	Naugolnykh, Konstantin A.	Model of acoustic monitoring of heat and mass transport in Fram Strait
3pAO9	Heaney, Kevin D.	Internal wave inversions for 1 year of Pioneer-Hawaii ATOC transmissions
3pAO10	Sagen, Hanne	AMOC: Preliminary results
3pAO11	Kalyuzhnyi, Alexander Ya.	Method of the main informative components for acoustic tomography
3pAO12	Kindler, Detlef	An ocean acoustic tomography experiment in the Central Labrador Sea-first results
4aUW8	Lubniewski, Zbigniew	The modeling of acoustic wave scattering on fractal seabed surface
4aUW9	Schmitt, Francoise	Wave scattering in underwater acoustics
4aUW10	Johannessen, Ola M.	The effect of grease ice formation on ambient noise
4aUW11	Rabu, Guy	Scattering and reflexion of sound by random rough surfaces
4pAO12	Schneider, Patrick	Generalized additive models for classifying sea-bottom types
4pAO13	Semenov, Andrew G.	Bottom layers structure influence on ocean shelf water low frequency source sound field numerical modeling
4pPAa13	Zannin, Paulo H. T.	(Invited) Some aspects of scattering calculation using the source simulation technique
4pPAa14	Zoltogorski, Bronislaw	Numerical modeling of axisymmetric sources in infinite baffle
4pUW13	Lopes, Joseph L.	High frequency acoustic propagation measurements in coastal areas
4pUW14	Li, Fenghua	Normal mode propagating rapid range-dependent shallow water
4pUW15	Gawrysiak, Jacek	Analysis of active hydroacoustic systems parameters versus conditions of sound propagation in inland water
4pUW16	Gurbatov, Sergei	On the horizontal structure of a field in separate modes radiated by a parametric antenna in axially nonuniform acoustic waveguides
4pUW17	Borodina, Elena	Effect of seismic waves on the acoustic field interference structure in the shallow sea
5pSAb8	St. Deus, Dr.	Test of various sound transducer systems for the use in ANC-systems and several applications of the ANC-system NANCY®.

Also, the following poster sessions are scheduled:

Poster Session 5aAB

Poster Session 5aMUb (in room Ma141)

Poster Session 5aPPb

Poster Session 5aPPc

Session 5aAA

Architectural Acoustics: Building Acoustics II: Reverberation, Absorption, and Scattering

Alfred C. C. Warnock, Cochair
National Research Council, Bldg. M39, Montreal Road, Ottawa, Ontario K1A OR6, Canada

Sten Ljunggren, Cochair
Department of Building Technology, KTH, Brinellvägen 34, S-100 44 Stockholm, Sweden

Chair's Introduction—7:55

Contributed Papers

8:00

5aAA1. The anecoicity phenomenon in a live room. Higini Arau (Estudi Acustica. H. Arau. Trav. de Dalt, 118 Barcelona 08024, Spain)

The radius of reverberation must be obtained by iteration of the following equation: $Q/r^2=312(T/V)e^{-0.04r/T}$. The phenomena of the anecoicity are noticed when the radius of the reverberation does not exist because the sound direct curve never intercepts the sound reverberant curve; because of that the sound reverberant field is not a constant, as it was assumed in the classical formulation. In this case it is known [M. Barron and L. J. Lee, J. Acoust. Soc. Am. **84**, 618–628 (1988)] that the reverberant function is dependent on the distance through an exponential function. Therefore a minimum distance of reverberation will exist among both curves, which are very near. This distance is obtained by finding the minimum of the function: $e^{0.04r/T}/r^2=312T/QV$. This minimum distance is $r_{\min}=50T$. Also, a minimum directivity factor of the source is determined, including $r_{\min}$: $Q_m=105\,561.5209T^3/V$. This $Q[m]$ expresses the minimum directivity factor, for a determinated T and V, that must have the sound source because the sound direct field never intercepts the reverberant sound field. With this it will be possible to establish a direct dialog source-receptor without the liveness of the room being damaged.

8:20

5aAA2. Orthogonal acoustical factors of sound fields in a bamboo forest. Hiroyuki Sakai (Grad. School of Sci. and Technol., Kobe Univ., Rokkodai, Nada, Kobe, 657-8501, Japan), Shozo Shibata (Kyoto Univ., Sakyo, Kyoto, 606-8224 Japan), and Yoichi Ando (Kobe Univ., Rokkodai, Nada, Kobe, 657-8501 Japan)

In order to discuss acoustical quality of sound fields in a bamboo forest, acoustical measurements were conducted for orthogonal acoustical factors of a sound field. Results at a distance of 40 m from the source show that the IACC was 0.16 at 2 kHz. This value is smaller than that in the forest previously investigated [Sakai, Sato, and Ando, J. Acoust. Soc. Am. **104**, 1491–1497 (1998)]. The measured subsequent reverberation time T_{sub} was about 1.5 s in the frequency range above 1 kHz. For a certain music source with a higher frequency component, therefore, it is found that sound fields in the bamboo forest have excellent acoustic properties.

8:40

5aAA3. A refined room acoustical simulation algorithm based on free path distribution. Oliver Schmitz (Inst. of Tech. Acoust., Tech. Univ. Aachen, Templergraben 55, 52056 Aachen, Germany, osc@akustik.rwth-aachen.de)

Eyring's or Sabine's formula gives good results in rooms with a diffuse field. However, when long, flat, or coupled rooms, for example, are investigated, these formulas do not describe the decay correctly. The error has its reason in the assumption of an exponential decay with just one exponential coefficient calculated from the mean free path length and an averaged absorption coefficient. A new approach to calculate decay curves and reverberation time, already introduced by Vorländer [''A fast room acoustical algorithm based on free path distribution'' ICA 98] has been further refined. This method uses statistical results obtained by a short ray-tracing simulation. Free path length and absorption coefficient are statistically recorded for each reflection during this simulation. The recorded data represent the geometry of the room under investigation. In the next step several processes, each defined by an exponential function, are generated using this information, which are superposed to give a better approximation for the decay curve of the room. Some additional steps must be introduced to these processes to give reasonable results. This lecture will present the refined algorithm and some results.

9:00

5aAA4. Performing room surfaces' effects on the acoustical condition distributions. Aye Erdem Aknesil (Yildiz Tech. Univ., Faculty of Architecture, Yildiz-Besikta, Istanbul, Turkey)

To obtain suitable acoustic conditions for the important rooms from the room acoustics point of view, some parameters have to be evaluated. For example, reaching the acceptable reverberation time limits, not the place of surfaces but the total absorbtion, has an important role according to the size of surfaces and absorbability. On the other hand, while designing the first reflections or avoiding the constitution of acoustical defects like echo, the place of the suitable surfaces is important. When considering the importance of the distribution of acoustical conditions, the question is posed of how the surface affects this matter. In line with this observation, the aim of this study is to find the effects of the surfaces according their ratios.

9:20

5aAA5. Reverberation in rectangular long enclosures with diffusely reflecting boundaries. Jian Kang (The Martin Ctr., Cambridge Univ., 6 Chaucer Rd., Cambridge CB2 2EB, UK, jk10021@hermes.cam.ac.uk)

Based on the technique of radiosity, a computer model has been developed for calculating acoustic indices in rectangular enclosures with diffusely reflecting boundaries. The model divides every boundary into a number of patches and replaces patches and receivers with nodes in a network. The energy moving between nodes depends on the form factor between pairs of patches. For a cube, there is good agreement between the model result and classical theories, which can be regarded as a validation of the model. Computations for long enclosures show that (1) with the increase of source–receiver distance the RT30 increases continuously and the early decay time (EDT) increases rapidly until it reaches maximum and then decreases slowly—correspondingly, the decay curves are concave in the near field and then become convex. (2) Air absorption has greater effect on both reverberation and sound attenuation along the length than that with geometrically reflecting boundaries [J. Kang, Acust./acta

acust. **82**, 509–516 (1996)]. (3) With a constant cross-sectional size, reverberation time reaches a maximum as the aspect ratio tends to 1. (4) With a given amount of absorption, reverbation can vary considerably with various absorption distributions in a cross section. [Work supported by Lloyd Foundation.]

9:40

5aAA6. The genetic algorithms for the optimization of distributed loudspeaker systems. Corinne Fillol and Claude P. Legros (LAUTM, Universite Toulouse le Mirail, 31058 Toulouse Cedex, France, legros@univ-tlse2.fr)

In reverberant and highly noisy environments, public address systems are often used in order to improve the speech intelligibility. Nevertheless, a number of common problems are generally encountered with such installations. Too many distributed loudspeaker systems suffer an inappropriate utilization of loudspeakers which leads to an excessive excitation of reverberant field and a poor audience coverage decreasing the intelligibility. Two rules of thumb have been well formulated to optimize uniformity of audience coverage, but both of them did not take in account the emission of the loudspeaker in its acoustic environment. Too many sound systems, in factories and public spaces, are therefore ineffective and do not respect the safety standards. Nowadays, it is possible to predict the acoustic performance and to simulate the radiation of a sound system in space by the means of geometric approach. The utilization of such a program with natural algorithms allows the optimization of the positioning and the number of loudspeakers by considering the acoustic characteristics of the room and sources. The performance of this method is applied in the case of choosing a best configuration from 16 possible loudspeaker locations in a classroom in order to obtain an optimum speech intelligibility and allow a smaller cost of renovation.

10:00–10:20 Break

10:20

5aAA7. A Helmholtz resonator with elongated orifice. Rolf T. Randeberg, Ulf R. Kristiansen, and Tor E. Vigran (Acoust. Group, Norwegian Univ. of Sci. and Technol., N-7034 Trondheim, Norway, randeber@tele.ntnu.no)

For panel absorbers there is an increasing trend toward a design not utilizing fibrous components. For the distributed Helmholtz type of resonator absorbers, the challenge is to increase the natural losses, making the absorbers reasonably broadbanded. In this paper a new type of distributed resonators is investigated. Using a double-plate construction, the resonator necks have been substantially elongated in the lateral direction, while their widths have been kept small. Thus the viscous losses in the resonator necks have been increased compared to traditional resonators. Measurements are compared with a theoretical model using analytic solutions for the slit impedances, the end corrections, and the resistance of the inner and outer surfaces. For the volume between the plates, a finite-difference approach is used. The results show a high dependency on the plate separation, and to attain high absorption over a broad frequency range, this separation should be on the order of one boundary layer.

10:40

5aAA8. A seamless absorbing ceiling with a smooth surface: Álvaro. Daniel E. Commins (commins acoustics workshop, 15 rue Laurence, F-75020 Paris, France and 350 Fifth Ave., New York, NY 10118, comminsacoustics@compuserve.com) and Frank H. Wilhelmi (Wilhelmi Werke A. G., D-35633 Lahnau, Germany)

The use of absorbing ceilings is generalized. Contemporary architecture, in many cases, does not relish the use of ''classical'' absorbing ceilings of the perforated or slit type. Some manufacturers have developed smooth absorbing ceilings that can cover large areas without seams. Until today, the finish of these ceilings was unacceptable wherever a perfectly smooth surface was required. Improving on existing technology has led to a new type of ceiling: its surface is quite similar to a stucco or plasterboard finish, but its absorption coefficient is of the order of 0.5 over the full frequency range. The quality of the finished surface depends on the material itself and the quality of construction. Examples will be shown. In addition, this new type of ceiling has been mixed with other materials such as stucco, wood, fiberglass, and even loudspeakers. It has been shown in a full-size test model that it is possible to apply the same finish to all these materials, thus making the transition between the various components invisible. The absorptive and reflective parts of a wall or ceiling become undistinguishable. This ceiling has been named Álvaro since it was developed with the active input of Architect Álvaro Siza.

11:00

5aAA9. Effect of plate vibration on sound absorption of the micro-perforated elastic plate. Manabu Tanaka (Bldg. Res. Corp., Osaka, 5650873 Japan, czu14202@nifty.ne.jp) and Daiji Takahashi (Kyoto Univ., Kyoto, 6068317 Japan)

Perforated plates have long been used as sound absorbers, and many studies have been done on their acoustic characteristics. In these studies, the effect of plate vibration caused by the incident sound wave is neglected. This is reasonable for the perforated plate of ordinal design [D. Takahashi, Appl. Acoust. **51** (1997)]. However, if the ratio of perforation decreases, e.g., in case of the micro-perforated plate, the effect of plate vibration is considered to be distinct, because the flow resistance of the plate is relatively large in this case. In this study, a new theoretical model for predicting the acoustic characteristics of the micro-perforated elastic plate (MPEP) is presented. This model includes the effect of plate vibration caused by the pressure difference between both surfaces of the plate. Numerical experiments are also carried out with this model. From the results, it may be said that the plate vibration occurs when the surface porosity of the perforated plate is roughly under 1%. This model can be applied to the perforated plates of any flow resistance, i.e., from the ordinarily perforated plate to nonperforated plate throughout.

11:20

5aAA10. Simplified calculus to estimate the acoustical absorption of nonplanar materials. Jaime Pfretzschner, Francisco Simon, Rosa M. Rodriguez, and Carlos de la Colina (Inst. de Acustica (CSIC), Serrano 144, 28006 Madrid, Spain)

The absorption curve, in function of the frequency, in hard-backed layers of granular materials, shows undesirable series of maxima and minima related to the layer deep. In order to increase the efficiency of these absorbing materials, it is necessary to smooth their frequency response curve. It is obvious that one of the easiest solutions consists of modifying the layer surface with selected profiles (e.g., wedges). For these situations, a simplified method of analytical calculus for the valuation of the absorption, in function of the frequency, has been developed. The validity of the theoretical approximations has been checked against experimental measurements in different test samples by means of a standing wave tube. Additionally, the application of this study to the design of absorbent acoustic noise screens, against traffic noise, made with recycled rubber crumbs of tires, is also presented. [Work supported by a LIFE project.]

11:40

5aAA11. Reflection and diffraction in room-acoustic modeling. Jan Baan and Diemer de Vries (Lab. of Acoust. Imaging and Sound Control, Delft Univ. of Technol., Delft, The Netherlands)

Many programs for room-acoustic modeling are based on the mirror image source concept. This way, only specular reflections are taken into account such that the resulting wave field is incomplete. Nonspecular reflections, or diffraction phenomena, can be added using an algorithm based on Pierce's theory. Then, the true wave field is significantly better approximated. However, comparison of both results reveals that, averaged over time and space, the energy is equal in both cases: the added diffraction field so strongly interferes with (i.e., is so strongly correlated with) the specular reflections that no energy is added. This intuitively surprising

result can be argued with a thought experiment. In this context, taking into account that acoustic perception is described with energetic criteria (clarity, definition, lateral energy fraction, etc.), it should be critically reconsidered as to how far the physically incomplete mirror image source programs are adequate for the prediction of the global acoustic quality of a hall.

12:00

5aAA12. Absorption and scattering characteristics of a modified Schroeder diffuser. Antti Jarvinen, Lauri Savioja (Lab. of Acoust. and Audio Signal Processing, Helsinki Univ. of Technol., P.O. Box 3000, FIN-02015 HUT, Finland, Antti.Jarvinen@hut.fi), and Kaarina Melkas (Nokia Res. Ctr., FIN-33721 Tampere, Finland)

The modified Schroeder diffuser was presented in an earlier study [A. Jarvinen *et al.*, J. Acoust. Soc. Am. **103**, 3065(A) (1998)]. Results from the simulations with various numerical techniques were also reported. The developed structure is simpler than the traditional Schroeder diffusers and the total volume of the diffuser is utilized. The acoustical properties of the structure are studied further and optimized for different applications. Three-dimensional numerical simulations using boundary and finite-element methods and finite-difference time domain method are used and results are verified with scattering and absorption measurements. In addition to the previous study, simulations include structural coupling. This opens up new possibilities for adjusting the structure for different purposes such as broadband absorber. The low-frequency absorption effect [H. Kuttruff, Appl. Acoust. **42**, 215–231 (1994)] can be taken into account by including the acoustical properties of the materials into calculations. Furthermore, this type of construction is applicable as a modular acoustic panel. The advantages of the modified diffuser construction are shown in comparison to traditional designs with similar acoustic characteristics.

Contributed Posters

These posters will be on display in the Poster Gallery from Monday to Wednesday, 15–17 March. Authors will be at their posters from 10:00 a.m. to 12:00 noon on Wednesday, 17 March.

5aAA13. High-frequency asymptotics and random matrix theory in reverberant rooms. Olivier Legrand and Fabrice Mortessagne (Laboratoire de Physique de la Matière Condensée, UMR CNRS-UNSA 6622, Parc Valrose, 06108 Nice Cedex 2, France)

It is now recognized that in the low-frequency range below Schroeder's cutoff a modal approach of the spectral fluctuations in a reverberant room is appropriate. Indeed, in his experimental study of the modal frequencies in a reverberation room, Davy [J. L. Davy, Proc. Inter-Noise, 159–164 (1990)] confirmed that the level repulsion is in good accord with the predictions of the Wigner–Dyson's random matrix Theory (RMT). In *Quantum Chaology* many works have tried to understand the link between the observed spectral statistics of wave cavities which are known to be chaotic in the limit of rays and the statistics of eigenvalues of random matrices. Here this matter is addressed in the context of room acoustics by considering an asymptotic representation of the response in chaotic rooms in terms of periodic rays. Various results are established concerning universal aspects of the spectral fluctuations recovering predictions of RMT both in the moderate and large modal overlap regimes [O. Legrand and F. Mortessagne, Acustica–acta acustica **82** (Suppl. 1), S150 (1996)]. The results are illustrated in a two-dimensional chaotic enclosure using a semiclassical Green's function formalism [F. Mortessagne and O. Legrand, Acustica–acta acustica **82** (Suppl. 1), S152 (1996)].

5aAA14. Mode counts for rooms and waveguides. Christopher L. Morfey, Matthew C. M. Wright, and Seong-Ho Yoon (Inst. of Sound and Vib. Res., Univ. of Southampton, Southampton SO17 1BJ, UK)

The density of modes in a room (3D) or waveguide cross section (2D) is known to be approximated at high frequencies by expressions involving room volume and surface area, or (in 2D) the area and perimeter of the waveguide cross section. Deviations of the actual mode count from the smoothed approximation are studied numerically and analytically, for simple shapes: rectangular (2D and 3D), and annular (2D). Periodic clustering of eigenvalues, associated with cyclic rays [R. Balian and C. Bloch, Ann. Phys. **69**, 76–160 (1972)], is demonstrated at high frequencies. Expressions are given for estimating the standard deviation of 2D and 3D mode counts from their smoothed values, in a finite frequency band, when one dimension is much smaller than the others.

5aAA15. An extension of the transfer function method described in ASTM E 1050-90 for its use in semianechoic conditions. Miguel Angel Picard Lopez, Pedro Solana Quiros, and Javier Fermin Urchueguia Schoelzel (Dept. de Fisica Aplicada, Univ. Politecnica de Valencia, Camino de Vera 14, 46022 Valencia, Spain)

The wave tube described in the above standard requires a rigid end characterized by a very high impedance, ensuring the correctness of the measurement of the sample-specific acoustic impedance. This method can also be employed for the measurement of other characteristic parameters associated with fibrous materials, more specifically, its dynamic flow impedance. If the rigid end is removed and the tube is enlarged with a piece containing absorbing material, the tube termination impedance is obtained when measuring without the probe. This impedance is affected by the tube modal response, which is a function of the tube's length. If a fine slice of the sample (as compared to the wave length inside the tube) is then used, and again an impedance measurement is performed, the values obtained are in phase with the first measurement (without sample) and differ by the amount of the dynamic flow impedance of the sample. Measurements have been performed with Rockwool samples of different densities giving good results, as shown in a recent J. Sound Vib. paper. The advantage of this method is that measurements can be done with a nonideal end, as its effects are taken into account in the evaluation procedure.

5aAA16. Toward a global *in situ* method for materials acoustic impedance assessment at very low frequencies using evolution strategy. Guillaume J. A. Dutilleux (Lab. des Sci. de l'Habitat, Ecole Nationale des Travaux Publics de l'Etat, rue Maurice Audin, 69518 Vaulx-en-Velin, France) and U. R. Kristiansen (NTNU, 7034 Gloeshaugen, Norway)

As the current *in situ* absorption measurement methods are both local and based on time-domain processing, the time-frequency uncertainty relationship limits their ability to measure at low frequencies, leaving the building engineer with an uncovered frequency range. The complementary approach proposed here is to work in the frequency domain instead and to consider the measurement problem as an inverse and optimization one. A critical assumption for practicality is that very few measurement points should be necessary to define the pressure field without ambiguity. As the optimization problem is clearly not local, a global algorithm is necessary in combination with a forward model of the room giving the pressure field from the boundary conditions. A numerical study is given concerning a

2-D rectangular room modeled by the finite-difference method. Each wall has a specific impedance. An evolution strategy is used as a global optimization tool, both alone and in combination with a local search method, to find the boundary conditions of an imaginary room. Good results are obtained over the 100–250-Hz frequency range, with only as many measurement points as unknown variables.

5aAA17. Sound-absorption properties of suspended ceilings with plastic foils. Ivan Bosmans, Walter Lauriks, Geert Lombaert, Joris Mermans, and Gerrit Vermeir (Lab. voor Akoestiek en Thermische Fysica, Katholieke Univ. Leuven, Leuven, Belgium)

Suspended ceilings using plastic foils can be used as wall or ceiling finishing systems. The cavity behind the foil (plenum) is used for hiding technical appliances. Without sound-absorbing material in the plenum, the absorption coefficient of the suspended ceiling can be very low, and even with absorbing material in the cavity, the presence of the membrane can seriously degrade the acoustic performance. The sound-absorption properties of suspended ceilings using a plastic impervious membrane are investigated theoretically and experimentally. The sound absorption coefficient has been modeled using a general model for the acoustic transmission and absorption of a multilayered structure. Measurements have been performed in a reverberant room using different sound-absorbing materials in the cavity. Due to the impervious foil, the structure behaves as a resonant system. The different physical mechanisms of these resonances will be highlighted and simple equations to estimate the resonance frequencies are put forward. Under certain conditions, the absorption coefficient can become *exactly* one, but at other frequencies the sound absorption can be quite low, unless sufficient sound-absorbing material is provided in the cavity. Using a perforated membrane increases the sound absorption drastically.

Session 5aAB

Animal Bioacoustics: Animal Bioacoustics Poster Session

Ronald J. Schusterman, Cochair
Long Marine Laboratory, University of California, 100 Shaffer Road, Santa Cruz, California 95060, USA

Nikolai A. Dubrovsky, Cochair
Andreyev Acoustics Institute, 4 Shvernika Street, 117036 Moscow, Russia

Contributed Papers

All posters will be on display from Wednesday to Friday, 17–19 March. To allow contributors an opportunity to see other posters, contributors of odd-numbered papers will be at their posters from 8:00 a.m. to 10:00 a.m. and contributors of even-numbered papers will be at their posters from 10:00 a.m. to 12:00 noon on Friday, 19 March.

5aAB1. Positioning accuracy of a large-aperture hydrophone array for sperm whale research. Magnus Wahlberg (Inst. of Coastal Res., Natl. Board of Fisheries, Nya Varvet 31, 426 71 Va Frölunda, Sweden, magwah@dd.chalmers.se)

Source positioning accuracy of a large-aperture (1 km) hydrophone array was investigated, using 2-D and 3-D algorithms. The array was used for positioning and SL determination of sperm whales off the coast of Northern Norway during the summers of 1997 and 1998 (see Møhl, this volume). Positioning accuracy is dependent on mainly four factors: (1) positioning accuracy of the hydrophones, (2) variation in sound velocity of the medium, (3) inaccuracies in the measurements of the time-of-arrival differences, and (4) choice of algorithm (errors associated with geometric over-simplification). Errors introduced by the factors (1) and (3) had small effects compared with errors introduced by the factors (2) and (4). The total estimated error varied considerably in different areas covered by the array and for different array configurations. Sound velocity showed only modest variation with depth, except for a -0.2-m/s per meter gradient in the 0–100-m depth interval caused by summer heating of the surface water. For a sound source close to the surface, this sound velocity gradient causes a shadow zone starting some hundred meters from the source. Such a shadow zone may lead to underestimates of source level estimates from 2-D algorithms. [Work supported by the Danish National Research Foundation.]

5aAB2. Analysis of the sound emissions of captive bottlenose dolphins (*Tursiops truncatus*). Inês Mello (CAPS, Instituto Superior Técnico, Av. Rovisco Pais, 1096 Lisboa Codex, Portugal, ines_mello@hotmail.com), Cristina Brito (Projecto Delfim, 1100 Lisboa, Portugal), and Manuel E. dos Santos (Unidade de Investigação de Eco-Etologia, 1100 Lisboa, Portugal)

Bottlenose dolphins (*Tursiops truncatus*) produce a great variety of sounds, including whistles, echolocation clicks, and other pulsed sounds. The behavior and the sound emissions of eight bottlenose dolphins were studied in a dolphinarium (Zoomarine, Albufeira, Portugal). Acoustic recordings were made with a B&K 8103 hydrophone and a Sony TCD-D10 Pro DAT recorder. Systematic behavioral observations were conducted (including show behaviors) simultaneously with acoustic recordings. Whistles were the most abundant signal type ($n=4238$) and several frequency modulation profiles were found to be repeatedly produced. Echolocation click trains and other pulsed signals were also produced. Whistle production throughout the day showed statistical concordance among 4 days of systematic sampling. Highest levels of whistle production occurred in interactions among the dolphins and in interactions between the dolphins and their trainers. The clicks and other pulsed sounds, more frequent in resting and swimming, showed a similar occurrence cycle

throughout the day. Performances of conditioned behaviors (during shows) were associated with decreased levels of whistles and increased levels of click trains and other pulsed sounds.

5aAB3. Directional hearing or binaural phenomenon? Gennadi L. Zaslavski (Univ. Authority for Appl. Res. and Industrial Development, Tel-Aviv 61392, Israel)

Binaural phenomenon is known to be responsible for sound localization in humans. A similar mechanism is thought to provide the dolphin with the ability to localize targets and sound source. At the same time, the dolphin possesses quite good directional hearing, let alone very directional click transmission, which is absent in humans. The directional hearing in the dolphin, at least in the horizontal plane, appears to be consistent with two ears' reception. Does it signify that the binaural phenomenon coexists in dolphins with directional hearing? As far as humans are concerned, the spatial hearing does not involve any substantial hearing directionality. The directionality seems to negate the main advantage of the binaural hearing, that is instantaneous determination of a sound source direction, and complicate the use of binaural cues. It was found that the lesser intensity of high-frequency clicks the smaller an angle between their sources should be for the dolphin to hear them simultaneously. The directivity pattern of the dolphin's auditory system was measured as a dependence of the threshold angle between the sources on the click's intensity. At high frequencies, the dolphin's auditory system performed as a directional system rather than an omnidirectional binaural system known for humans.

5aAB4. Localization of sounds from a paired source in the dolphin and fur seal. Gennadi L. Zaslavski (Univ. Authority for Appl. Res. and Industrial Development, Tel-Aviv 61392, Israel)

There is a notion that the dolphin's spatial hearing operates similarly to that of humans, even though the dolphin's ability to localize a source in the vertical plane is practically the same as in the horizontal one. Binaural phenomena are used to explain localization in the dolphin; however, there are no interaural differences in the vertical plane. Given the dolphin's very short echolocation click and high time resolution, one would find it difficult to describe the dolphin's hearing in terms of binaural phenomenon. The dolphin's sonar system performs as a monaural rather than a binaural system [G. Zaslavskiy and V. Ryabov, in *Marine Mammal Sensory System* (1991)]. In fact, very directional sonar click transmission and reception seem to account well for the dolphin's spatial hearing. In the present study, the way in which dolphins and fur seals respond to a sum of the signals from two sources will be discussed. There are different hearing phenomena in the human associated with the binaural perception of the sound coming from two different directions. Some of these phenomena were found in the fur seal but none of them was present in the dolphin.

5aAB5. Range accuracy: One more peculiarity of the dolphin's sonar. Gennadi L. Zaslavski (Univ. Authority for Appl. Res. and Industrial Development, Tel-Aviv 61392, Israel)

In order to measure range accuracy in the dolphin, a range difference discrimination experiment should be performed. However, when two targets are presented at different distances simultaneously, even at an angle as big as 40–60=B0, one dolphin's click can cause echoes from both targets. As a result, the targets can be distinguished by the difference in the echo arrival time without measuring the target distance. The best way to prevent the dolphin from simultaneous targets insonifying by each click turned out to be successive submerging of the targets in water at different distances from the dolphin. Nevertheless, it proved to be impossible to force the dolphin to measure the distance from itself to the targets. Two dolphins solved the task by measuring the time interval between the target echo and echo from a reference object; that could be the pool walls or even a nylon net. There was no consistent change in the threshold range difference with the targets' range, whereas it regularly decreased when the targets were moved closer to the reference object. The dolphins preferred to measure the relative target position even if the reference object was at a much greater distance than the targets.

5aAB6. Perception of harmonic complexes in budgerigars (*Melopsittacus undulatus*). Micheal L. Dent, Robert J. Dooling (Dept. of Psych., Univ. of Maryland, College Park, MD 20742), and Marjorie R. Leek (Walter Reed Army Medical Ctr., Washington, DC 20307)

Many studies have shown that birds have auditory spectral resolving powers similar to mammals, but it has long been thought that they are superior in analyzing temporal information. To investigate the ability of budgerigars to process rapid temporal cues within complex waveforms, birds were required to discriminate among harmonic complexes with identical long-term spectra, but with temporal waveforms that differed in envelope shape or fine structure. Using operant conditioning procedures, birds were trained to discriminate a highly peaked waveform, created with all components starting in cosine phase, from waveforms with a random selection of phase for each component, creating a flatter envelope shape. In a second experiment, birds discriminated between harmonic complexes that were identical in both spectrum and waveform envelope, but that differed in the fine structure within fundamental periods. In both experiments, birds could easily discriminate among waveforms with fundamental frequencies up to 800 Hz, with some decrement in performance at higher frequencies. Humans are unable to perform similar tasks for frequencies higher than about 300 Hz, suggesting that time processing of complex sounds in the avian auditory system may preserve information presented at rates at least three times the limits shown for humans. [Work supported by NIH DC00198.]

5aAB7. Frequency discrimination and advertisement call in the aquatic clawed frog, *xenopus l. laevis*: Qualifications for interindividual recognition. Andreas Elepfandt (Inst. Biologie, Humboldt Univ., Invalidenstr. 43, 10115 Berlin, Germany)

The acuity of frequency discrimination was tested in the clawed frog, *xenopus l. laevis* by means of conditioning. *xenopus* is completely aquatic and communicates acoustically on the bottom of ponds. For conditioning, a tank was built in which pure tones could be presented to the animal. The paradigm was discrimination of water surface waves contingent upon the underwater tone presented simultaneously, i.e., distinguishing a wave presented with tone A from a wave with tone B. Frequency discrimination was best in the range 1600–2000 Hz, where relative discrimination up to 2% was found. This range matches the range of the dominant frequency in the frog's advertisement call. Whereas there is considerable variation between individuals, the dominant frequency of a given individual is very constant, varying by less than 10–20 Hz even when the hormonal status of the animal or the temperature of the water is changed. Thus the animals can distinguish between calling males on the basis of the dominant frequency. In the field, males establish territories whose location may remain constant for weeks up to years, so that stable neighbor relationships are formed. In such a situation, recognition of the neighbor's call may be advantageous.

5aAB8. Acoustic attraction of the parasitoid fly *Ormia ochracea* to the song of its host. Nathalie Ramsauer and Daniel Robert (Inst. for Zoology, Univ. of Zurich, Winterthurerstr. 190, CH-8057 Zurich, Switzerland, drobert@zool.unizh.ch)

The parasitoid fly *O. ochracea* locates its cricket host by acoustically detecting its calling song. The phonotactic abilities of the fly's auditory system were investigated behaviorally. Phonotaxis was investigated in a large (w 2.5×14.5×h 3 m), sound-proofed, flight cage equipped with loudspeakers. Simulated cricket calls with different carrier frequencies including the standard song (4.8 kHz, 45 pps, 13-ms pulse length) were played back to attract the flies. Behavioral threshold curves were estab-

lished by varying the sound pressure level (SPL) for songs with different frequencies (3.5 to 6.0 kHz). Threshold was determined when phonotaxis failed to occur but was validated only if the fly subsequently reacted to the next higher SPL in the intensity series. Between 4.5 and 5.2 kHz, thresholds were observed to be around 40 dB (re: 20 Pa; i.e., at 4.8 kHz: 38.3 dB, s.d.=3.0 dB, $n=5$ animals). The sensitivity of phonotaxis to the level of masking noise was also tested by masking songs of different frequencies with varying noise levels. Noise-threshold curves show the behavior to be least affected by noise at 4.8 kHz, where successful phonotaxis to a 60-dB SPL song occurs up to a masking noise level of 45.3 dB SPL. However, at the frequency of best physiological threshold (5.0 kHz), masking occurs at 39.0 dB SPL. [Work supported by the Swiss Science Foundation.]

5aAB9. Sound-induced cuticular vibrations in the atympanate bladder grasshopper *Bullacris membracioides*. Daniel Robert (Inst. for Zoology, Univ. of Zurich, Winterthurerstr. 190, CH-8057 Zurich, Switzerland, drobert@zool.unizh.ch), Moira J. van Staaden (Bowling Green State Univ., Bowling Green, OH 43403), and Heiner Roemer (Inst. for Zoology, Karl-Franzens-Univ., Graz, A-8010, Austria)

In terrestrial animals, detection of sound waves over long distances conventionally requires the presence of tympanal ears. Although it lacks tympana, the South African bladder grasshopper Bullacris membracioides (Orthoptera, Pneumoridae) is endowed with an acute sense of hearing. Long-range acoustical communication is mediated by duets in which the males loud song (1.7 kHz, 98 dB SPL at 1 m) is answered by the females milder reply (at 4 kHz, 60 dB SPL), allowing the male to locate her. Males present a conspicuously inflated abdomen that constitutes a resonant sound radiator. Both males and females harbor six pairs of mechanosensory organs attached to the wall of abdominal segments A1–A6 that are involved in sound reception [M. van Staaden and H. Roemer, Nature **394**, 773]. Using microscanning laser vibrometry to investigate the mechanics of atympanate hearing, sound-induced vibrations were shown to differ between male and female in their deflection shapes and amplitudes. Male cuticular vibrations culminate at 1.7 kHz, confirming the resonant nature of their abdominal wall. In both sexes, vibrations at the points of sensory insertions indicate that conventional tympana do not constitute a necessary condition for highly sensitive auditory function. [Work supported by the Austrian and the Swiss Science Foundations.]

5aAB10. Anatomy and biomechanics of interaural coupling in a sarcophagid fly. Daniel Robert (Inst. for Zoology, Univ. of Zuerich, Winterthurerstr. 190, CH-8057 Zuerich, Switzerland, drobert@zool.unizh.ch), Ronald N. Miles (Binghamton Univ., Binghamton, NY), and Ronald R. Hoy (Cornell Univ., Ithaca, NY)

In flies, the sense of hearing is related to the parasitic life-style. First reported in the parasitoid family Tachinidae, tympanal hearing is used to acoustically locate singing hosts. Here, the auditory anatomy and biomechanics of another family of parasitoid, the Sarcophagidae, is presented. These small auditory organs are located on the ventral prosternum and in several respects conform to the general Bauplan of a dipteran ear. However, the structural organization of their auditory periphery—the tympanal complex—is quite different: it is conspicuously lacking the central pivoting sclerite that constitutes the key element for directional sensitivity by mechanical coupling found in tachinids [Robert *et al.*, J. Comp. Physiol. **179**, 29–44 (1996)]. Based on scanning laser vibrometry, deflection shape analysis shows that, in response to sound, the tympana vibrate asymmetrically but with deflection modes clearly different from those observed in tachinids. The tympanal complex does not oscillate about a fixed central fulcrum, but sways about one of its relatively immobile ends. Interaural coupling is proposed to be caused by he anisotropic tympanal structure. This data suggests the presence of an alternative mechanism for directional hearing in this fly. [Work supported by NIH, NSF, and the Swiss Science Foundation.]

5aAB11. Sound localization in shallow waters in the clawed frog *Xenopus l. laevis*. Sebastian Tuschick (Inst. Biologie, Humboldt Universität zu Berlin, Invalidenstr. 43, 10115 Berlin, Germany, sebastian.tuschick@rz.hu-berlin.de)

Sound localization in waters by small animals like *Xenopus* was considered impossible due to the following physical facts: (i) The sound is not attenuated by going around the animal's head, thus preventing interaural intensity difference. (ii) In water sound propagates five times faster than in air, yielding too little interaural time difference for detection. Tests showed, however, that *Xenopus* can locate underwater sound. To investigate the biophysical mechanisms of sound localization in *Xenopus*, tympanic vibration was measured with laser vibrometrics. The measurements were conducted in an artificial pond (6×9 m^2, 1 m deep) that was especially constructed for analysis of underwater sound. To produce equal sound from any direction relative to the animal, a platform was built which could be rotated with the animal while sound was broadcast from a constant position. Initial experiments show a higher amplitude of tympanic vibration if sound is applied from the ipsilateral side compared to the contralateral side. The highest tympanic responses were observed between 1.6 and 2.1 kHz, the dominant frequency of the *Xenopus* advertisement call. Thus, obviously special biophysical adaptations of the ear enable *Xenopus* to localize underwater sound.

5aAB12. Sound propagation in natural environments. Evelyn B. Glaser (Zool. Inst., J. W. Goethe Univ., Siesmayerstr. 70, 60323 Frankfurt am Main, Germany, e.glaser@zoology.uni-frankfurt.de)

The basic model of acoustic communication in animals is one of transmitters, receivers, and a transmitting pathway in between. The acoustic features of each component involved determine the acoustic behavior of animals in natural environments. The aim of this work is to describe the alteration of sounds propagating through a natural habitat by measurements and modeling. Birdsongs and various artificial sounds are broadcast and recorded at five distances at different habitats (temperate meadow and desert). The sounds are designed to match several acoustical characteristics of birdsongs. The signals of two microphones are recorded simultaneously with a DAT-recorder and analyzed off-line. The transfer functions between the referenced loudspeaker output and the respective recording inputs are then computed. The resulting distinct patterns for the power-spectra depend on the spatial arrangements of the transmitter and the receivers and the acoustic impedance of the transmitting pathway. Important spatial features are the horizontal and vertical distance between transmitter and receiver and their distance to the surface. The amplification and damping of the sounds can be explained by the interference of the directly transmitted and the reflected wave. The measured and the computed spectral patterns show a high degree of similarity.

5aAB13. Mosquito bioacoustics: Microscanning laser vibrometry of sound-induced antennal vibrations. Martin C. Goepfert and Daniel Robert (Inst. for Zoology, Univ. of Zurich, Winterthurerstr. 190, CH-8057 Zurich, Switzerland, mgoepfer@zool.unizh.ch)

The acoustically oriented mate-finding behavior of mosquitoes is a classic acoustic near-field detection and communication system. Male mosquitoes are attracted by the female flight sound, and previous studies [H. Tischner and A. Schief, Zool. Anz. Suppl. **18**, 453–460 (1955)] indicated that the male antenna enters resonance in response to these sounds. Microscanning laser vibrometry was used to document the biomechanics of antennal sound detection in *Aedes aegypti*. Measurements confirm that the antenna acts as a velocity receiver with the antennal shaft rocking about its socket in a rodlike manner. The frequency response of the male antenna, revealed by white-noise analysis, shows maximum velocities around 500 Hz corresponding to the dominant frequency emitted by flying conspecific females. The female antenna, however, is not tuned to the male flight sounds, suggesting that only males use incident sounds for mate detection. The function of sound-induced antennal vibrations in females remains unclear. Further comparative analysis focusing on the di-

rectionality of the antennal response and sound emission will be presented. [Work supported by the Deutscher Akademischer Austauschdienst and the Swiss Science Foundation.]

5aAB14. The detection of conspecific and heterospecific calls in noise by birds. Bernard Lohr, Timothy F. Wright, and Robert J. Dooling (Dept. of Psych., Univ. of Maryland, College Park, MD 20742)

Little is known about the effects of noise on the ability of birds to detect vocal communication signals. To address this question, an operant conditioning procedure was used to test two species of birds, budgerigars (*Melopsittacus undulatus*) and zebra finches (*Taeniopygia guttata*), for their ability to detect conspecific and heterospecific calls in noise. Calls from three species, budgerigars, zebra finches, and canaries (*Serinus canaria*), served as test stimuli. In general, budgerigars showed lower thresholds (better detection abilities) across all call types than zebra finches. Both zebra finches and budgerigars showed a similar pattern of threshold changes for call types from different species. Calls of budgerigars were the easiest to detect, followed by canary calls, and finally zebra finch calls. Call bandwidth, which increases across species from budgerigars, to canaries, to zebra finches, may influence the pattern observed in thresholds. Low-frequency, band-passed noise simulating anthropogenic noise sources resulted in considerably less masking than broadband white noise. Generally, these results conform to the power spectrum model of auditory function. [Work supported in part by the Comparative and Evolutionary Biology of Hearing at the University of Maryland, NIDCD Grant No. DC00198 to R.J.D., the SERDP program, and the U.S. Army Construction Engineering Research Laboratories.]

FRIDAY MORNING, 19 MARCH 1999 ROOM H1058, 8:00 TO 11:00 A.M.

Session 5aAO

Acoustical Oceanography: Coastal Pollution Research and Monitoring

John R. Proni, Cochair
U.S. Department of Commerce, NOAA/AOML/OAD, 4301 Rickenbacker Causeway, Miami, Florida 33149, USA

Manell E. Zakharia, Cochair
CPE Lyon, LASSO (LISA, EP92, CNRS), 43 Boulevard du 11 Novembre 1918, BP 2077, Batiment 308, 69616 Villeurbanne, Cedex, France

Invited Papers

8:00

5aAO1. Acoustical measurements in marine environmental monitoring and research in the United States. Roland E. Ferry (U.S. Environ. Protection Agency, Region 4, 61 Forsyth St. SW, Atlanta, GA 30303)

Acoustical measurements play an important role in marine environmental monitoring and research in the United States. Acoustics is employed by a variety of government agencies with environmental roles and responsibilities, including the U.S. Environmental Protection Agency, National Oceanic and Atmospheric Administration, U.S. Geological Survey, U.S. Army Corps. of Engineers, and the Department of the Interior. The U.S. Environmental Protection Agency (U.S. EPA) has specific coastal regulatory responsibilities mandated by the Clean Water Act and the Marine Protection, Research and Sanctuaries Act of 1972, to limit impacts to the marine environment as a result of wastewater discharges and the disposal of dredged material. To accomplish these tasks, the U.S. EPA and responsible parties use acoustics to gather ambient oceanographic data needed to make environmentally sound decisions regarding ocean outfall and dredged material disposal site placement. Acoustics is also used to assess dredged material and wastewater plume fields to determine the fate and transport of pollutants. In addition, acoustics is used in post-disposal surveys to monitor dredged material impacts to nearby marine communities. Acoustical measurements with real-time data transmission have been successfully used to monitor oceanographic conditions near an ocean disposal site for daily management of disposal activities.

8:20

5aAO2. Acoustics tools for ocean pollution research and monitoring in the MAST program. Gilles Ollier (EC/DG XII/MAST, Rue de la Loi 200, B1049, Brussels, Belgium, Gilles.Ollier@dg12.cec.be)

The monitoring of ocean pollution as well as coastal waters monitoring and management is a growing interest of the European Commission (EC). Among several methods, acoustical measurements remain the preferred one for insight observations. In the framework of the MAST program (Marine Science and Technology, Directorate General for Research, DGXII), the EC has supported several programs dealing either with the understanding of physical phenomena and the development of new acoustic instruments or with the development of integrated systems (and mainly survey ROVs) where the acoustics plays an important role for sediment characterization. Among others, the following projects will be presented: TRIDISMA (three-dimensional sediment transport measurement by acoustics), MAUVE (miniaturized and reconfigurable instrument for multipurpose survey with a mini autonomous underwater vehicle; includes a multifunction acoustical unit for the survey of coastal waters), ARAMIS (advanced ROV package for automatic mobile inspection of sediments; includes bathymetric sonar, obstacle avoidance sonar and vertical sounder), and BIOSONAR [sonar technology for monitoring and assessment of benthic communities; acoustic determination of bottom type (sand, eelgrass, mussels, . . .)]. The paper will review the past research activity of the EC-funded projects in pollution monitoring and will show the emphasis of the fifth framework program in this area.

8:40

5aAO3. On the use of active low-frequency sonar systems for the monitoring of littoral environment. Dominique Morisset (Groupe d'Etudes Sous-Marine de l'Atlantique, DGA/DCE/GESMA, BP 42, F29240, Brest Naval, France)

The aim of conventional low-frequency sonar systems is either to detect and classify targets (containers, fish schools, submarines, divers, mines, . . .) or to communicate between two or more underwater geographical locations (communication, tomography). The increase of both military and civilian interest in shallow-water areas (typically from the shelf break to the shore), requires a better understanding of the effects of oceanographic environment on acoustic propagation and reverberation. Unfortunately, the available environmental information concerning bottom characteristics, sound-speed variability (in databases or charts), is often inaccurate and unreliable and, most of the time, it does not cover very wide areas. Hence, in order to get a comprehensive environmental knowledge during operations and to improve performance prediction, low-frequency sonar systems are now equipped with environment assessment functionality. Experimental results concerning the impact of shallow-water environment on sonar signals will be presented. Two major aspects will be investigated: the impact of both sound-speed profile variability and bottom heterogeneity. The optimization of low-frequency sonar design and its use for the assessment and the monitoring of littoral environment (i.e., acoustic data inversion) will then be discussed.

9:00

5aAO4. A hybrid model for echo prediction in coastal waters. Patrick Chevret (CPE Lyon, LASSSO (LISA, EP92 CNRS), 43 Bd. du 11 Novembre 1918, BP 2077, Bat. 308, F 69616, Villeurbanne Cedex, France)

Echo prediction in coastal waters is a complex task due to the fact that a very wide range of scales is involved in the propagation and the scattering phenomena. The model developed is based on a separate formulation of the propagation and the scattering aspects and a coupling procedure. The propagation modeling is performed using a high-order parabolic operator; it is used from the source to the vicinity of the target. At this step, the field is decomposed in a set of plane waves that are scattered by the target (decomposition on the target mode). The reflected plane waves are then propagated back to the receiver. This global approach can be considered, somehow, as an ''exact one,'' nevertheless it is limited to simple shapes and is very time consuming. A simplified formulation has been developed in parallel that avoids the coupling problem by computing separately the medium and the target response. The free-field echo of the target (monostatic response) can be either a numerical or an experimental one. The final echo is obtained by the convolution of both responses. Both model's performances are compared (computation time, accuracy, . . .).

9:20

5aAO5. Detecting, mapping, sampling, and analyzing oceanic suspended particulate matter: Methods complementary to acoustic detection of environmentally sensitive ocean outfall and dumped materials. Terry A. Nelsen and John R. Proni (NOAA, AOML, Ocean Acoust. Div., 4301 Rickenbacker Cswy., Miami, FL 33149, proni@aoml.noaa.gov)

Natural systems such as lakes, rivers, and oceans can be described by dissolved and particulate components. Particulate sources in coastal oceanic environments include natural materials from seaward riverine and estuarine flows and anthropogenic sources such as ocean dumping and outfalls. Plumes of suspended particulate matter (SPM) can be natural (lithogenic and biogenic), anthropogenic, and any mixture of these. Because SPM can range from environmentally neutral (i.e., lithogenic and biogenic) to hazardous (heavy metals, bacteria, . . .), detecting, tracking, sampling, and sourcing SPM plumes can be beneficial for the environment and human health. Acoustic methods have proven successful in detecting and mapping oceanic SPM over large spatial areas but are limited in resolving internal fine structure, estimating relative contributions of merged plumes from various sources (e.g., river outflow versus dumping), and differentiating between introduced and *in situ* SPM. To complement acoustics, CTD/optical/water survey tools have been employed for guided sampling of plumes. Water samples for total suspended matter (TSM) and particle size distributions have proven useful both to calibrate acoustic measurements and provide insight into signatures provided by particle size distributions. Signatures, determined by factor and component analyses, allow mapping of SPM components as well as estimating their dilution and long-termed budgets.

9:40

5aAO6. Measurements of near-bed current flow and suspended sediments using acoustics. Peter D. Thorne (Proudman Oceanogr. Lab., Bidston Observatory, Birkenhead, Merseyside L43 7RA, UK)

In recent years the development of: (i) multifrequency acoustic backscatter systems to measure suspended sediment particle size and concentration, (ii) coherent Doppler and correlation techniques to evaluate flow, and (iii) high-frequency scanning systems to obtain bed microtopography, have significantly advanced the capability to examine the fundamental processes of sediment entrainment and deposition. The outcome from these observations is beginning to make an important contribution to the understanding of the basic mechanisms of sediment transport. In this report, highlights of acoustic measurements of sediment processes collected in both the marine environment and in the laboratory are presented. The particular attribute of acoustics to nonintrusively provide high temporal and spatial resolution profiles of intrawave, and turbulence processes are particularly focused upon, and the scientific output from contemporary studies discussed. [Work supported by the coastal protection division of MAFF through the CAMELOT program, NERC, and the EC contract TRIDISMA, MAS3-CT95-0017.]

10:00–10:20 Break

10:20

5aAO7. Measurements of the spherical reflection coefficient at grazing sound incidence above sediment. Henning Harms, Rainer Matuschek, and Volker Mellert (Dept. of Phys., Univ. Oldenburg, D-26111 Oldenburg, Germany, rm@aku.physik.uni-oldenburg.de)

Liquid undissolved fluid pollutants covering the sea bottom, in general, form a thin layer of a few cm, which cannot be detected acoustically by normal sound incidence due to the small difference of impedance compared to water. Such layers, however, can strongly affect the spherical reflection coefficient at grazing sound incidence. Using broadband chirp signals, the interference pattern at the receiving hydrophone is found to provide information on the physical properties of the sediment surface and its coating. Laboratory measurements in a small water tank with flat and rippled sand sediments coated by various different chemical substances revealed a systematic dependence of the measured excess attenuation function (EAF) on the acoustic impedance of the chemical, the layer thickness and the grazing angle of the incident sound. Results of numerical modeling performed with a fast field program (FFLAGS) show good agreement with the measurement results. In order to prove the applicability of the new detection method, measurements in shallow water will be presented. [Work supported by BMBF.]

10:40

5aAO8. Recent advances in coastal ocean pollution research and monitoring. John R. Proni and Terry A. Nelson (NOAA, AOML, Ocean Acoust. Div., 4301 Rickenbacker Cswy., Miami, FL 33149)

Design of both real-time studies of oceanic discharges of potential pollutants such as sewage effluent, and long-term monitoring of same, are complicated by a number of factors. These factors include lack of knowledge of the space and time distribution of the discharge plume, proper placement sites for sample gathering, and lack of knowledge of the space-time distribution of ''interfering'' plumes (plumes from sources other than the discharge plume under study). Progress has been made in the development of ''integrated sensor suites'' which produce data with substantial synergistic benefits. Ocean acoustics plays a key role in integrated sensor suite data unification. In a recent study in the coastal waters off San Juan, Puerto Rico, the ability of acoustics systems to view essentially the complete oceanic water enabled a connection to be made between salinity, temperature, and turbidity measurements gathered in the upper 5 m in the water column to a specific port of a sewage effluent diffuser. Having established the ''connectivity'' of the distal field measurement to a specific port, a dilution value at the distal point could confidently be calculated. This example is but one of many of the synergies available from utilization of multiple sensor suites unified through acoustics.

FRIDAY MORNING, 19 MARCH 1999 ROOM MA001, 7:55 A.M. TO 12:20 P.M.

Session 5aBB

Biomedical Ultrasound/Bioresponse to Vibration: Safety Guidelines for Diagnostic Ultrasound

Francis A. Duck, Cochair
Department of Medical Physics, Royal United Hospital, Bath BA1 3NG, UK

Wesley L. Nyborg, Cochair
Department of Physics, University of Vermont, Burlington, Vermont 05405, USA

Chair's Introduction—7:55

Invited Papers

8:00

5aBB1. European Committee for Medical Ultrasound Safety (ECMUS): Tasks and activities. Hans-Dieter Rott (Inst. for Human Genetics, Univ. of Erlangen-Nuremberg, Schwabachanlage 10, D-91054 Erlangen, Germany, hdrott@humgenet.uni-erlangen.de)

The European Committee for Medical Ultrasound Safety (ECMUS, ''The Watchdogs'') is an interdisciplinary group of European scientists who are permanently engaged in monitoring the safety of diagnostic ultrasound. The task of the Watchdog Group is to inform the members of the European Federation of Ultrasound in Medicine and Biology (EFSUMB) about potential risks of ultrasound and to give advice for its appropriate use. The group meets at least once a year. Its activities include literature reviews, publication of tutorial articles and guidelines, organization of EFSUMB Congress safety sessions, and preparation and publication of a safety statement which is regularly reconfirmed or amended. The Watchdogs can be contacted through the EFSUMB office in London [http://www.efsumb.org/ecmus.htm] or directly to any of the members who are prepared to comment on any question concerning safety issues of medical ultrasound. The present Watchdog members are: Prof. Philippe Arbeille, Physicist in Tours, France; Prof. Ulrich Cobet, Biophysicist in Halle, Germany; Dr. Francis Duck, Physicist in Bath, UK; Prof. Karel Marsál, Obstetrician Gynecologist in Lund, Sweden; Prof. Hans-Dieter Rott, Human Geneticist in Erlangen, Germany; and Dr. Kjell Salvesen, Obstetrician and Epidemiologist in Trondheim, Norway.

8:20

5aBB2. Temperature elevation generated by ultrasound in soft-tissue, bone, and transcranial phantoms. Junru Wu (Dept. of Phys., Univ. of Vermont, Burlington, VT 05405)

Ultrasound imaging has been widely used in medicine and many new procedures are being developed to obtain images of regions in a human body once considered beyond the reach of ultrasound. To address the safety issue related to the thermal effects of ultrasound, the American Institute of Ultrasound in Medicine and the National Electrical Manufacturers Association have developed simple equations to calculate thermal indices (TI) that indicate the worst-case temperature elevations for various clinical situations. To experimentally verify the equations, soft-tissue, bone, and transcranial phantoms were constructed. The measured results of temperature rise in the phantoms generated by diagnostic ultrasound were compared with various thermal indices. In general, TI underestimated temperature rise *in situ*. The disparity can be attributed to transducer surface heating.

8:40

5aBB3. Thermal test objects and the measurement of temperature rise produced by diagnostic ultrasound. A. Shaw, N. M. Pay, and R. C. Preston (Natl. Phys. Lab., Teddington, Middlesex TW11 0LW, UK, AS@npl.co.uk)

Although the AIUM/NEMA TI (or thermal index) values are now widely used as an indicator of the heating potential of diagnostic ultrasound fields, they are open to criticism on a number of grounds. As an alternative to the TI approach, substantial effort at NPL has gone into developing both reference thermal sensors and tissue mimicking materials for use in thermal test objects (TTOs) to actually measure the temperature rise produced by diagnostic exposure under standardized conditions. In a major project for the UK Department of Health, 20 pulsed Doppler fields have been measured with both soft tissue and soft tissue/bone TTOs under worst case and AIUM-equivalent derated conditions. Results were compared with calculated TIs, with NPL predictions of temperature rise and, when available, with the scanner's on-screen TI value. Under worst case conditions, up to 3 °C was measured in soft tissue mimic and up to 10 °C in bone mimic; AIUM-equivalent measurements were generally three to five times lower. Calculated TI values were generally intermediate between AIUM-equivalent and worst case values. This presentation will briefly describe the design and performance of the TTOs and discuss the comparison with other methods and the significance of the findings.

9:00

5aBB4. ICRU Report 61: Providing reference data for tissue properties. Andrew C. Fairhead (Dept. of Biomed. Phys. and Bio-Eng., Aberdeen Royal Hospitals, Foresterhill, Aberdeen AB25 2ZD, UK, a.fairhead@biomed.abdn.ac.uk)

The recently published ICRU Report 61, entitled ''Tissue Substitutes, Phantoms and Computational Modelling in Medical Ultrasound,'' will be described. As well as reviewing current practice, it specifies *requirements* of the materials and techniques used to make ultrasound phantoms for various purposes. It also covers that aspect of computational modeling concerned with thermal disometry, because the ''body models'' used in this activity have a similar purpose to phantoms used for measuring temperature rise. Both must simulate the part of the body of interest, to a sufficient accuracy for the intended purpose. This involves designing tissue substitutes or simulations with certain values of acoustic and thermal properties, to within a certain tolerance. If thermal measurements and computations are to be reproducible within and between organizations, these values and tolerances must be agreed. At the moment, reference data from tissues are sparse. The report suggests suitable values for a selection of tissues. In the presentation, the need for more data and the problems associated with obtaining them will be emphasized.

9:20

5aBB5. Fundamentals of the Mechanical Index and caveats in its application. Christy K. Holland (Dept. of Radiol., Univ. of Cincinnati, 234 Goodman St., Cincinnati, OH 45267-0742, Christy.Holland@uc.edu) and Robert E. Apfel (Yale Univ., New Haven, CT)

The Mechanical Index, MI, resulted from theoretical considerations of the short-pulse acoustic threshold for inertial cavitation in water populated with microbubbles of all sizes [R. E. Apfel and C. K. Holland, Ultrasound Med. Biol. **17**, 179–185 (1991)]. The assumption, therefore, is that if one does not reach the threshold MI, 0.7, then the probability for inertial cavitation is negligible. The question arises: Can the utility of the MI be extended to situations in which the threshold MI is exceeded, thereby allowing for some estimate of the quantification of a potential bioeffect due to microcavitation? Also, can MI be extended to situations in which pulses are, unlike the original formulation, not short? *In vitro* experiments over a broad frequency range in which the nuclei content is controlled have not been reported. However, lung damage from 1- to 6-MHz pulsed diagnostic ultrasound has been assessed *in vivo* in the mouse, neonatal mouse, rat, rabbit, pig, neonatal pig, and monkey. The damage observed may be mediated by inertial cavitation, yet no such causal relationship has been established to date. The possible consequences of gas body activation associated with aerated lung tissue and intestinal gas pockets represent specific instances of cavitation considerations relevant to clinical practice. In this review, the MI will be evaluated as a gauge for potential bioeffects from diagnostic scanners capable of operating at high output levels.

9:40

5aBB6. Ultrasonically induced vascular damage to the mouse intestine. Douglas L. Miller (Dept. of Radiol., 3315 Kresge III, Univ. of Michigan, 200 Zina Pitcher Pl., Ann Arbor, MI 48109-0553, douglm@umich.edu) and Richard A. Gies (Battelle Pacific Northwest Natl. Lab., Richland, WA)

The mouse intestine represents a valuable model system for evaluating exposure indices and safety guidelines for medical ultrasound. After anesthetized hairless mice are exposed to ultrasound in a 37 °C degassed water bath, three types of vascular damage may be observed in the intestines: hyperemia, which appears to be due to heating, hemorrhage into the lumen, which apparently results

from cavitation activity, and petechiae in the wall of the intestine, which apparently may be caused either by heating or by gas body activation. Continuous-wave exposure tends to yield thermal effects, while lithotripter shock waves induce nonthermal hemorrhages. The petechiae are greatly enhanced when gas bodies from ultrasound contrast agents are introduced into the circulation. The thermal effects require temperature elevations in excess of about 5 °C for several minutes and may be related to the thermal index. The nonthermal effects require pressure amplitudes in excess of about 1.23 MPa for petechiae and 2.4 MPa for hemorrhages with 10-μs pulses at 1 MHz and may be related to the mechanical index. However, the cavitational effects appear to depend more strongly on ultrasonic frequency from 0.4–2.4 MHz than is indicated by the mechanical index. [Work supported by NIH CA 42947.]

10:00–10:20 Break

Contributed Papers

10:20

5aBB7. Thermal safety considerations for diagnostic ultrasound. Morton W. Miller (Dept. of Obstetrics and Gynecology, Univ. of Rochester Medical Ctr., 601 Elmwood Ave., Box 668, Rochester, NY 14642) and Wesley L. Nyborg (Univ. of Vermont, Burlington, VT 05405)

As the output of diagnostic ultrasound equipment increased during the past decade, so did the potential for producing significant temperature elevation. The introduction of equipment features for real-time display of an estimated upper limit to the temperature rise is proving helpful to informed users. In obstetrical applications it is particularly important to know whether teratological effects could be produced under the operating conditions being used. While there is an extensive body of literature on defects produced in progeny of laboratory animals exposed to heat during pregnancy, its specific relevancy to clinical ultrasound situations is unclear. Most exposures were done by placing pregnant animals in heated chambers. Although the temperature of the medium (air or water) surrounding the animal was maintained constant during the time of an experiment, the temperature rise experienced by the fetus increased during most or all of that time. In contrast, when an ultrasound beam is focused on fetal bone, it is expected that the temperature will rise to its steady-state value relatively rapidly. An approach based on reaction rate theory is proposed as an approximate method for relating effects of the two kinds of exposures.

10:40

5aBB8. Mechanical index: The influence of nonlinear propagation in water and tissue. Mark D. Cahill and Victor F. Humphrey (Dept. of Phys., Univ. of Bath, Bath BA2 7AY, UK)

Safety indices for diagnostic ultrasonic scanners are calculated from measurements made in water, which are derated to account for the attenuation of tissues. Shock waves are expected to form more readily in water than in tissue, because of water's lower intrinsic attenuation. The resulting increase in the attenuation of high-amplitude waves leads to the possibility that amplitudes might be underestimated from water-based measurements. By considering idealized models of scanners involving a rectangular source with two focal planes, the effect of such nonlinear propagation on the mechanical index has been investigated. As expected, it was found that the mechanical index is greatly reduced from that which would be predicted by a linear extrapolation from low-amplitude measurements. However, under most circumstances considered, the reduction of the analogous index in tissue was commensurate with that in water, partly because of the weaker frequency dependence of attenuation in tissue, which promotes the formation of shocks. The evaluation of mechanical index at the location of peak-derated intensity did, however, result in an underestimation of the peak negative pressure by about 10%, and even greater errors resulted when the gain and operating frequency were raised.

11:00

5aBB9. Boundaries to effective acoustic output regulation from acoustic saturation. Francis A. Duck and Hazel C. Starritt (Dept. of Medical Phys., Royal United Hospital, Bath BA1 3NG, UK, f.duck@bath.ac.uk)

Acoustic saturation limits the pressure amplitude which may be reached at any position in an ultrasonic beam. The saturation pressure, p_{sat}, is a function of acoustic frequency, distance from the source, and the acoustic nonlinearity parameter. It is independent of the source pressure. An approximate expression has been used [Naugol'nykh and Romanenko, Sov. Phys. Acoust. **5**, 191–195 (1959)] to predict p_{sat} at the focus of spherically focused medical diagnostic beams in a lossless medium. p_{sat} typically lies in the range 1–10 MPa, lower values being associated with higher frequencies and longer focal depths. Mechanical index and spatial-peak intensities are also subject to saturation effects, being calculated from acoustic pressure. A significant range of conditions exist for which acoustic saturation prevents MI, and derated I(spta) and I(sppa), from exceeding the regulatory limits set by the Food and Drug Administration in the USA. Action limits set by IEC 61157 are sufficiently low to be unaffected in the majority of cases. It is concluded that the existence of acoustic saturation presents a strong argument to review present procedures for regulating acoustic output from diagnostic ultrasound equipment.

11:20

5aBB10. Review on the viability of mammalian cells in ultrasonic standing wave fields. Otto Doblhoff-Dier, Theo Gaida (Inst. for Appl. Microbiology, Univ. of Agricultural Sci., Nussdorfer Lände 11, A-1190 Vienna, AT Austria, doblhoff@edv2.boku.ac.at), Wolfgang Burger, Felix Trampler, Martin Gröschl, Ewald Benes (Vienna Univ. of Technol., A-1040 Vienna, AT Austria), James M. Piret, and Steven M. Woodside (Univ. of British Columbia, Vancouver, BC V6T 1Z3, Canada)

Ultrasonic standing waves have been used in a number of applications for the separation of suspended particles, such as the separation of animal cells in fermentation processes. This technology has led to the development of high cell density, continuous perfusion fermentation systems with

increased volumetric productivity. The ultrasonic separation device additionally can be used for controllable selective retention of viable cells and selective removal of cell debris. A key issue with this technology is the question if the ultrasound fields applied can be stressful to animal cells growing in suspension, thereby decreasing cell viability or impeding metabolic functions. This issue is also of interest to regulatory bodies concerned with quality assurance and quality control of pharmaceuticals derived from animal cell culture. Available data concerning cell viability, productivity, and metabolic activities will be reviewed and put into perspective to regulatory and fermentation technological concerns, such as product identity and purity, biological activity, consequences for subsequent protein purification procedures, long-term continuous production strategies, etc. [Work supported in part by the European Commission, Contract No. ERBFMRXCT970156.]

11:40–12:20
Discussion of the Future Direction of Safety Standards by W. Nyborg and F. Duck

FRIDAY MORNING, 19 MARCH 1999 ROOM H112, 7:55 TO 9:40 A.M.

Session 5aEA

Engineering Acoustics: SAW Devices

Harold C. Robinson, Cochair
Naval Undersea Warfare Center, 1176 Howell Street, Newport, Rhode Island 02841-1708, USA

Daniel Hauden, Cochair
LPMO-CNRS, 32 Avenue de l'Observatoire, F-25044 Besançon, Cedex, France

Chair's Introduction—7:55

Invited Papers

8:00

5aEA1. Surface acoustic waves and devices—A brief overview. Harold C. Robinson (Naval Undersea Warfare Ctr. Div., Newport, RI 02841)

This paper will provide a basic introduction to surface acoustic waves and devices. Surface acoustic waves have been employed in a broad spectrum of devices, from filters and oscillators used in communications, to chemical and biosensors. This tutorial will detail the fundamentally important properties of surface acoustic waves which make them useful in devices. The principal methods of generating them will be discussed. A broad overview of their areas of application, as well as the types of devices which are possible using them, will be given.

8:20

5aEA2. Surface acoustic wave sensors for the detection of gases and for biological applications. Manfred von Schikfus (Institut für Angewandte Physik, Universitaet Heidelberg, Albert-Ueberle-Strasse 3-5, 69120 Heidelberg, Germany)

The presence of organic or inorganic chemical species can be detected by their reaction with a suitable reagent. In acoustic sensors where the sensor reagent is immobilized on the device, the associated mass increase is detected by a change of the propagation characteristics of an acoustic wave. Acoustic surface wave (SAW) devices promise an advantage over the commonly used quartz oscillators because of their inherent higher sensitivity associated with their high operating frequency of up to several hundred MHz. Until now SAW devices have not found widespread application, mainly because of handling difficulties associated with the necessity to mount these devices on sockets and to connect them electrically with bonding wires. In this contribution, techniques will be presented to overcome problems associated with the operation of SAW sensors in aggressive liquids or in gases at elevated temperatures. A new type of SAW device has been developed in which no ohmic electrical contacts are required. Instead, electrical connection between the device and the electronic circuitry is achieved by inductive coupling. In this way, operation and preparation of the devices is considerably eased. Data will be presented on immunosensing in buffer solutions, and on gas sensing at temperatures up to 500 °C.

8:40

5aEA3. Radio-frequency surface acoustic wave filters for mobile communications systems. Ulrike Rösler, Werner Ruile, and Clemens C. W. Ruppel (Corporate Technol., Siemens AG, ZT KM 1, 81730 Munich, Germany, ulrike.roesler@mchp.siemens.de)

Surface acoustic wave (SAW) filters are small, rugged, crystal stable, and can be fabricated with high reproducibility. SAW filters play a key role in the rapidly growing market of mobile communication systems and are used for channel filtering as well as for RF filtering. For today's communications systems novel types of SAW filters are being developed in order to meet the stringent requirements with respect to low insertion loss, high relative bandwidths, good stopband rejection properties, and power durability. Most SAW RF filters are fabricated on cuts of $LiTaO_3$ and $LiNbO_3$. To obtain very low loss filters precise knowledge of the wave propagation and loss mechanisms is a prerequisite. Using advanced analysis tools, substrate-cut-metallization combinations can be

chosen for minimized propagation losses. To enhance power durability of SAW filters both substrate-metallization combination as well as the design have to be optimized. Two different filter techniques are used for SAW RF filters. The working principles of double mode structure (DMS) filters and ladder-type filters, both using resonances to minimize the lengths of the structures and the required chip size, will be described. As examples, RF filters for GSM and PCN, diplexer for GSM, and duplexers for cordless phones will be presented.

Contributed Papers

9:00

5aEA4. Measurements of elastic properties of polymeric humidity-sensitive films at different temperatures. Cinzia Caliendo and Enrico Verona (Istituto di Acustica ''O. M. Corbino,'' CNR, Via del Fosso del Cavaliere 100, 00133 Roma, Italy, Caliendo@idac.cnr.rm.it)

Chemically sorbent polymeric films are commonly coated on acoustic wave devices to realize gas or vapor sensors. Temperature variations, as well as analyte adsorption, lead to softening of the film, producing a perturbation in the acoustic wave/film interaction. To achieve a high level of sensor's performance, the chemically sensitive coating has to be characterized in terms of acoustic parameters temperature and frequency dependence. An acoustic wave device has been used as a probe of the storage and loss moduli of a thin viscoelastic film over a range of temperature (20 °C−150 °C) and of frequency (factor of more than 20). Using an equivalent circuit model of the acoustic wave/thin viscoelastic film interaction, the overmentioned moduli have been deduced as a function of temperature from the experimental data for Poly(bis-tributhylphosphine-Ni-diethynylbiphenyl), Ni-DEBP, coated acoustic device, previously tested as a sensitive layer for relative humidity detection.

9:20

5aEA5. Humidity sensing properties of uncoated and coated SAW delay lines. V. I. Anisimkin (Russian Acad. of Sci., Inst. of Radioengineering and Electron., Moscow), A. Bonfiglio, C. Caliendo, E. Verona (CNR-Istituto di Acustica, 100-00133, Roma, Italy), and M. Penza (PASTIS-CNRSM, Brindisi, Italy)

The relative changes in the SAW propagation velocity $\Delta v/v$ were measured as a function of the relative humidity (RH) at the normal conditions. The results of the measurements were compared for different bar substrates (AT,x-, ST,x-, yx-SiO_2, yz-, 128° y,x-$LiNbO_3$) and different coatings deposited on these substrates (polyvinyl alcohol, Pd, $Pd_{0.99}Ni_{0.01}$, $Pd_{0.97}Ni_{0.03}$). In accordance with theoretical predictions [V. I. Anisimkin and E. Verona, IEEE Trans. Ultrason. Ferroelectr. Freq. Control **45**(5), 1–8 (1998)], the behavior of the $\Delta v/v(RH)$ curves for a given coating was found to be dependent on the material of substrate and its crystallographic orientation. The magnitudes $\Delta v/v$ for uncoated SiO_2 were two to ten times larger than those were for uncoated SiO_2. The coating of the substrates by polyvinyl alcohol and Pd increased sensitivity of SAW towards humidity by 30 to 100 times, providing large response $\Delta v/v \approx 100$ ppm even at small RH≈1%. The threshold concentration for the coated SAW devices was estimated as RH≈0.01%.

FRIDAY MORNING, 19 MARCH 1999 ROOM MA144, 8:00 TO 10:00 A.M.

Session 5aMUa

Musical Acoustics: General Topics in Musical Acoustics I

James W. Beauchamp, Cochair
School of Music and Department of Electrical and Computer Engineering, University of Illinois at Urbana-Champaign, Urbana, Illinois 61801, USA

Helmut Fleischer, Cochair
Institute of Mechanics, Faculty of Aerospace Technology, University of the Federal Armed Forces, D-85577 Neubiberg, Germany

Contributed Papers

8:00

5aMUa1. Sound power of musical instruments measured with sound intensity in a practice room. Tadeusz Fidecki (Music Acoust. Lab., Chopin Acad. of Music, Okolnik 2, 00-368 Warszawa, Poland, fidecki@chopin.edu.pl)

The data on sound power of musical instruments published by various authors demonstrate considerable spread. In most studies, sound pressure was used for the determination of sound power. In the present study sound power was determined from sound intensity. The discrete point method with 10 measurement points on a hemisphere and 80 to 300 points on rectangular surfaces was used for the evaluation of sound power. The measurements were carried out for three instruments: the bassoon, the upright piano, and the snare drum. The instruments were played by professional musicians in a typical practice room. The music samples played on the bassoon and on the piano were scales and excerpts of music. The samples played on the snare drum were rhythmic sequences and tremolo sounds. The results demonstrate that sound intensity is a reliable method for the estimation of sound power level of musical instruments played in a small practice room. The paper discusses the influence of the measurement method, the test room acoustics, the playing technique, the choice of music sample, and the player's stability on the uncertainty of measurement. [This work was supported by Grant No. 7-T07B-043-10 from the State Committee for Scientific Research.]

5a FRI. AM

8:20

5aMUa2. Data-driven modeling of acoustical instruments. Bernd Schoner, Charles Cooper, Christopher L. Douglas, Edward S. BoydenIII, and Neil A. Gershenfeld (Phys. and Media Group, MIT Media Lab, 20 Ames St., Cambridge, MA 02139, schoner@media.mit.edu)

Comprehensive digital analysis and synthesis of musical instruments using direct observations of their physical behavior have been developed and implemented for the violin. In a training session, control input data from unobtrusive bow and finger sensors is recorded simultaneously with the violin's audio output. These signals are used to train a cluster-weighted probabilistic prediction model that reproduces the nonlinear relationship between the control inputs and the target audio output data. Cluster-weighted modeling was developed to apply previous results from linear systems theory and time-series approximation theory in the broader context of a globally complex and nonlinear model. The presented sound synthesis engine makes use of familiar sound synthesis techniques, but extends them with a complex input/output framework that naturally incorporates dynamic control. The final system predicts audio data based on new control data. While a violinist plays the interface device (a silent violin), the computer model reproduces the sound of the original violin. Recent work has extended the system of sensors and algorithms to model string vibration dynamics as well as the radiated sound.

8:40

5aMUa3. Application of linear prediction coding and additive synthesis in computer music. Magdalena Klapper (Dept. of Computer Sci., Univ. of Mining and Metallurgy, Cracow, Poland)

The contemporary computer technique gives a composer quite new possibilities for sound creation. The interference into the sound structure and modification of it, through the mediation of computer, allows one to obtain a new aesthetic value. The paper presents involvement of two methods of signal processing: additive synthesis and linear prediction coding, to obtain an amazing musical effect. Both of the methods were used in two stages: analysis and resynthesis. The stage of analysis allows for the description of a sound by a certain group of information about its structure. Modification of these parameters allows the changes to be made to the sound structure. Employing the analysis methods to the sounds they are not dedicated to may also give an effect of far sound structure modification. It may be given as an example analyzing nonharmonic sounds with a heterodyne filter, or lpc analysis of fast changing sounds. In these cases the sound structure modification results from loss of data during analysis. A wide range of possibilities of sound creation, made accessible by the contemporary computer technique, is a difficult challenge for imagination and a unique aesthetic of a composer.

9:00

5aMUa4. Sounds that are not what they sound: The unrecognizability of piano sounds transformed due to string preparations. Alexandra Hettergott (Koflergasse 19/9, A-1120 Vienna, Austria)

Three different performances of John Cage's, *Sonatas and Interludes for Prepared Piano* (1946–1948), each of which is a recent CD recording, were analyzed in relation to a common notational model. Though following the same lines regarding the preparations of the grand piano by means of screws, bolts, nuts, rubber, and/or plastic, applied to the double and triple piano strings, realizations of the same piece may differ from one another in almost all musical parameters: not only in aspects of tempo and dynamics, but also with respect to the respective spectral distribution, as pitch strength and tone color, and also in the perceived pitches themselves. The course of a tone sequence in one performance perceptually may completely be changed relating to the other. Cage's preparations, though detailed up to a certain point, thus allow one to take interpretative liberties. The performances were compared referring to both their spectral and temporal characteristics, each of them yielding a completely different sound quality. Differences and factorial common facts will be shown in multi-component features derived from; in addition, several sound examples will be given.

9:20

5aMUa5. Measurements of arm motion, timing, and striking force in a simple drumming task. Sofia Dahl (Dept. of Speech, Music and Hearing, Royal Inst. of Technol. (KTH), SE-100 44 Stockholm, Sweden, sofia@speech.kth.se) and Virgil P. Stokes (Karolinska Inst., Stockholm, Sweden)

How does the percussionist's playing technique and feedback from the instrument influence the performance with respect to timing and striking force? In an attempt to answer this question the motion of the right arm and drumstick, and the timing and striking force in a simple repeated drumming task were measured for three professional percussionists and one amateur. The task consisted of single strokes with interleaved accents played at three different tempi and at three dynamic levels. Three striking tools (drumsticks, mallets, and brushes) and three different types of striking surfaces were used. Differences between the players' performances under the different experimental conditions will be reported. [Work supported by the Bank of Sweden Tercentenary Foundation.]

9:40

5aMUa6. A tale of three violins: Comparison of radiation mechanisms measured with near-field acoustic holography. Lily M. Wang and Courtney B. Burroughs (Grad. Prog. in Acoust., Penn State Univ., P.O. Box 30, State College, PA 16804)

Complex pressure measurements have been made on multiple planes surrounding three violins, while bowed with a mechanical bowing apparatus: a Scherl & Roth student instrument, Hutchins' SUS295, and a Hutchins' mezzo-violin. The data are used with a multiplanar near-field acoustic holography (NAH) algorithm to reconstruct the surrounding radiated sound fields of each instrument, including pressure and intensity from the surface extending out to the far field. Areas of significant radiation on each violin are identified, compared, and related to structural differences between the instruments. [Work supported by NSF Graduate Research Fellowship, Lucent Technologies/Bell Laboratories GRPW Grant, and AAUW Selected Professions Dissertation Fellowship.]

Session 5aMUb

Musical Acoustics: General Topics in Musical Acoustics II (Poster Session)

James W. Beauchamp, Cochair
School of Music and Department of Electrical and Computer Engineering, University of Illinois at Urbana-Champaign, Urbana, Illinois 61801, USA

Helmut Fleischer, Cochair
Institute of Mechanics, Faculty of Aerospace Technology, University of the Federal Armed Forces, D-85577 Neubiberg, Germany

Contributed Papers

All posters will be on display on Friday, 19 March from 9:40 a.m. to 12:20 p.m. in Room MA141. To allow contributors an opportunity to see other posters, contributors of odd-numbered papers will be at their posters from 9:40 a.m. to 11:00 a.m. and contributors of even-numbered papers will be at their posters from 11:00 a.m. to 12:20 p.m.

5aMUb1. Method for time-domain localization of stochastic noise in quasiperiodic signals. Knut Guettler (Norwegian State Acad. of Music, P. B. 5190 Majorstua, 0302 Oslo, Norway, knut.guettler@samson.nmh.no)

In order to establish knowledge on the sources of noise in nearly periodic signals, it is essential to apply methods that give the best possible resolution in the time domain. Of particular importance is this kind of analysis when attempting to synthesize low-pitched bowed string instruments, where most of the noise appears in pulses. The present method isolates the noise from the signal without the use of any nonrectangular window or zero padding. This can conveniently be done by combining FFT with the Bluestein filter [L. I. Bluestein, Nerem Record, 218–219 (1968)], which allows the number of elements under analysis to be arbitrarily chosen as an exact integer product of the signal period. The suggested method minimizes leakage to neighboring elements when returning to the time domain after the deterministic/stochastic signal separation, thus providing a very reliable separation between the two signal components in both domains. Sound examples will be given for several instruments.

5aMUb2. The acoustic analysis of reinforced harmonics. Michael E. Edgerton, Diane Bless, Susan Thibeault, Margaret Fagerholm (The Univ. of Wisconsin, Waisman Ctr. #469, 1500 Highland Ave., Madison, WI 53705-2280, edgerton@waisman.wisc.edu), and Brad Story (The Denver Ctr. for the Performing Arts, Denver, CO 80204)

The relationship between articulation and harmonic reinforcement among five overtone singers was mapped from analyses of acoustic signals and radiographic data, with much variation found. A dominant feature of reinforced harmonics (R.H.) is the isolation of one harmonic while attenuating its neighboring harmonics. This is achieved by laying regions of high pressure (formants) over the framework of the harmonic series. These formants are manipulated to reduce the bandwidth which boosts the selected harmonic and dampens adjacent harmonics. LPC Fourier analyses contrasting normal speech to R.H. production demonstrated that bandwidth narrowed significantly (at 3 dB down) from 150 to 20 Hz, while center bandwidth (and selected harmonic) during R.H. increased amplitude by 34 dB, and damping of adjacent harmonics decreased amplitude by 30 dB. Next, bandwidth was measured by applying an artificial larynx to two subjects who showed bandwidth narrowing from 258 to 18 Hz; center bandwidth frequency increased by 12 dB and damping of adjacent harmonics by 14 dB. Last, R.H. production was modeled using a resynthesis program to allow manipulation of formant frequencies, amplitudes, and bandwidths of normal phonation to achieve R.H., while R.H. production was manipulated to attain normallike phonation.

5aMUb3. Time relations between harmonics of violin tones in dependence on playing techniques. Petr Volný, Jan Štěpánek, and Václav Syrový (Musical Acoust. Dept., Acad. of Performing Arts, Malostranské nám. 13, 118 00 Praha 1, Czech Republic, VOLNY@H.AMU.CZ)

Particular violin tones were played by a professional violin player in an anechoic room. The tones from the whole violin range, played nonvibrato using selected bowing techniques (naturale, sul ponticello, sul tasto) and dynamics of playing (p, mf, f), were recorded. The analysis based on the short-time Fourier transform was used to compute the time courses of amplitudes and frequencies of separated harmonics from the SPL recordings of the tones. The time characteristics of the time envelopes of the whole tone and his harmonics were calculated in the next step. For example, attack time, decay time, and relative starting time were studied. The influence of playing techniques, dynamics, and tone pitch on these time characteristics was described.

5aMUb4. Harmonic and unharmonic components of violin tones in dependence on playing techniques. Ondřej Moravec, Jan Štěpánek, and Václav Syrový (Musical Acoust. Dept., Acad. of Performing Arts, Malostranské nám. 13, 118 00 Praha 1, Czech Republic, MORAVEC@H.AMU.CZ)

Properties of harmonic and unharmonic spectral components of violin tones played nonvibrato using different bowing techniques (naturale, sul ponticello, sul tasto) and dynamics of playing (p, mf, f) were studied by means of suitable analytical methods. The tones from the whole violin range were recorded in an anechoic room. The shape of the spectral envelope, harmonicity, and amplitude relations among harmonic components were observed. Unharmonic components were investigated in three frequency bands separated by fundamental frequency of the tone and by the frequency of the highest ''well pronounced'' harmonic. Specific analytical tools and describing quantities were used in each part of the spectrum. The dependence of the spectrum on playing techniques, dynamics, and tone pitch was discussed.

5aMUb5. Comparison of five perceptual timbre spaces of violin tones of different pitches. Jan Štěpánek, Zdeněk Otčenášek (Musical Acoust. Dept., Acad. of Performing Arts, Malostranské nám. 13, 118 00 Praha 1, Czech Republic, STEPANEK@H.AMU.CZ), and Alois Melka (AKUSTIKA, 166 29 Praha 6, Czech Republic)

Violin timbre was studied for five tone pitches (H3, F #4, C5, G5, D6). A set of violin tones played on different instruments was recorded in an anechoic room. The recordings were subsequently manipulated to weaken an influence of tone transient parts on the perception. Two pair listening tests in headphones were performed for each pitch: timbre dissimilarity scaling test and spontaneous verbal description of timbre dissimilarities. A perceptual timbre space was constructed from the results of dissimilarity scaling test for each pitch using the multidimensional scaling method. Projections of verbal descriptions into the perceptual spaces enabled their external interpretation. Some perceptual attributes and pairs of attributes of violin timbre were established (''narrow,'' ''rustle,'' ''soft''–''sharp,'' ''dark''–''bright,'' ''clear''–''blurred'') based on correlation analysis of word occurrence frequencies on individual tones and on comparison of word projection coordinates in perceptual spaces. Comparing the results for five studied pitches it was possible to pronounce the hypothesis of salient violin timbre dimensions.

5aMUb6. Diagnosing dead spots of electric guitars and basses by measuring the mechanical conductance. Helmut Fleischer (Inst. of Mech., Faculty of Aerosp. Technol., Univ. of the Federal Armed Forces Munich, D-85577 Neubiberg, Germany, Helmut.Fleischer@rz.unibw-muenchen.de)

The ''sustain'' of the string signal is considered as a quality attribute of an electric plucked instrument. In musical practice, distinct locations are observed on the fretbroad where a string decays faster than at adjacent frets. Such ''dead spots'' originate from the fact that the string may cause the neck to vibrate. Energy flows from the string to the neck with the consequence that the string vibration decays irregularly fast. Experiments were performed with the aim of finding a measuring approach for the diagnosis of dead spots in terms of the vibration willingness of the neck. Various parameters (decay rate, surface velocity, admittance) were ascertained for a series of electric guitars and basses. Special care was taken to ensure comparable and ''natural'' boundary conditions. Measuring the mechanical conductance (i.e., the real part of the point admittance) on the neck with the instrument held in normal playing position proved a straightforward and reliable method for the diagnosis of dead spots. The measuring procedure and instrumentation will be presented. Typical results will be given in a compact 3-D representation (conductance versus frequency for each fret), evaluated and related as well to the decay rates as to the vibrations of the instrument body.

5aMUb7. Directivity of the violin radiation. Zdeněk Otčenášek and Václav Syrový (Musical Acoust. Dept., Acad. of Performing Arts, Malostranské nám. 13, 118 00 Praha 1, Czech Republic, OTCENASEK@H.AMU.CZ)

The sound of a violin played by a person in an anechoic room was recorded simultaneously by 16 microphones lying in a circle with the violin in the middle (the angle among the microphone positions was 22.5 degrees). To create the sound radiation pattern for the individual frequencies, the levels of harmonics were specified in the spectrum obtained from the SPL recordings on the microphones in the given geometrical layout. Next, the violin was excited artificially, by the personal presence of the same player, in the same position as being played by a person. The manner of recording remains unchanged. The constant exciting independent of the frequency enabled the comparison of the directivities of the radiation for different frequencies. Consider the results obtained from both ways of violin exciting, a wide range of angles was searched in which the radiation is stable enough even in the sense of listening to tones recorded when the violin was played by a person.

5aMUb8. Recent results on ''unison quality,'' or finding objective and quantitative criteria to decide that a piano is perfectly tuned. Rene E. Causse, Eric Marandas (IRCAM, 1 place Igor Stravinsky, 75004 Paris, France), and Olivier Thomas (TELECOM, 75634 Paris Cedex 13, France)

The difference in tuning (mistuning) between the three strings of a unison group is the parameter used by the tuner to adjust for each note the double decay of the sound, characteristic of piano tones, generally from the notes F1 to C5. However, in the case of important irregularities in hammer stricking, increasing the mistuning to adjust the double decay (slope and relative level of each decay) is not sufficient and only the proper adjustment of the regularity of the action of the hammer would lead to a better temporal evolution of the sound [Causse *et al.*, Proc. ISMA'98]. To further explore what tuners call ''unison quality,'' which means finding objective and qualitative criteria to decide that a piano is well tuned, the double-decay of the first partials of notes of a piano with different ''unison qualities'' and different hammer stricking irregularities was measured. In parallel, a simple simulation was refined of the vibration of a unison group of strings where excitation irregularities were simulated by varying the initial displacements and velocities of the strings. In this presentation, results of simple listening tests done with piano tuners will be presented.

5aMUb9. Space-induced distortion of starting transient of musical sound. Hrvoje Domitrovic, Mladen Maletic, and Sinisa Fajt (Faculty of Elec. Eng. and Computing, Dept. of Electroacoustics, Unska 3, HR-10000 Zagreb, Croatia, hrvoje.domitrovic@fer.hr)

Musical sound can be defined as complex sound that begins with a starting transient followed by a (more or less) steady sound and ends with a decaying sound. After that, continuous movement from one frequency to the another follows. The rate of change of loudness for partial tones that are greater than a certain threshold and their relative starting times are different for miscellaneous musical instruments. Recognition of a particular musical instrument depends upon short starting and ending transients. Relative starting time of the starting transient's partial is limited by the rate of change of loudness that is greater than 600 dB/s. The envelope of all rates of change defines the maximum rate of change for loudness levels and partials that dominates in a certain time interval. The beginning transient is the complex phenomena, assessed with early sound and rate and synchronized with the rise of loudness and dominant partial tone in the observed time interval. The just-noticeable threshold of rates of loudness change for partial tones for various musical instruments in different acoustically treated spaces was measured and described in this paper.

5aMUb10. Jazz drummers' swing ratio in relation to tempo. Anders Friberg and Andreas Sundstroem (Royal Inst. of Technol., Dept. of Speech, Music and Hearing, Drottning Kristinas vg 31, SE-100 44 Stockholm, Sweden, andersf@speech.kth.se)

It is common in jazz to perform consecutive eighth notes as long–short patterns. Drummers' performances on the ride cymbal of these long–short patterns were measured on excerpts taken from commercial recordings. It was found that the ratio between the long and the short note (swing ratio) varied substantially with tempo. At slow tempi the swing ratio was as high as 3.5:1, while at fast tempo it reached 1:1. The absolute duration of the short note, however, was found to be constant (about 100 ms) for medium to fast tempi. This suggests the existence of a limit on tone duration and also that the short note may function as an up-beat to the following note. A similar relation between swing ratio and tempo was also observed in a production experiment where listeners adjusted the swing ratio of a computer-generated performance.

5aMUb11. Emotions in the singing voice: Acoustic cues for joy, fear, anger, and sadness. Esther J. Langeheinecke, Hans-Ulrich Schnitzler (Animal Physiol., Univ. of Tuebingen, 72076 Tuebingen, Germany), Monika Hischer-Buhrmester, and Klaus-Ernst Behne (Inst. fuer Musikpaedagogische Forschung, Hochschule fuer Musik und Theater Hannover, 30175 Hannover, Germany)

Singers can vocally express their emotional interpretation of a musical piece. The analysis of melodies performed by trained sopranos in four labeled affective states, revealed differences in time, amplitude, spectral, and frequency parameters. The tempo was 40% slower in samples expressing sadness, while other modifications of rhythm showed no emotion-specific patterns. Complex amplitude modulations within a tone were reduced to two parameters: the maximum amplitude and its position. In joy and anger, that maximum amplitude was higher and appeared earlier within a tone. Sound-pressure levels were significantly lower in fear and sadness. The energy distribution in the spectrum, which is reflecting timbre, did not show any differences in the lower harmonics, but the peak amplitude of the singer's formant (clustering of third to fifth harmonic) was significantly higher in joy and anger. The extent of the vibrato, a characteristic feature for the voice of a trained singer, and the variations of the extent depended on the emotional expression. The linear average of the vibrato note's undulating frequency as an approximation for the perceived pitch differed up to 5 to 10 Hz between emotions, with a tendency to lower frequencies in sadness.

5aMUb12. Effect of timing variations on the categorical perception of musical rhythm patterns. George Papadelis (School of Musical Studies, Faculty of Fine Arts, Univ. of Thessaloniki, Thessaloniki 54006, Greece, papadeli@mus.auth.gr) and George Papanikolaou (Aristotle Univ. of Thessaloniki, Thessaloniki 54006, Greece)

Musical rhythm patterns are mainly characterized by durational relationships between their different time levels. As written rhythmic values imply, these relationships are graphically represented by simple integer ratios and that fact reflects a basic criterion for their perceptual encoding into discrete perceptual categories. Temporal analysis of any musical performance reveals that deviations from accurate metronomic timing is a very common practice among musicians and these deviations are perceived either as musical expressivity, or just as inaccurate performance of rhythm. The degree of deviation also affects the categorization of a certain rhythmic pattern. In the present study, a mapping of the perceptual space between adjacent rhythm categories was attempted, through a systematic timing variation of simple rhythm patterns, as well as the investigation of the *perceptual magnet effect* [P. Iverson and P. Kuhl, J. Acoust. Soc. Am. **97**, 553–562 (1995)] at various musical tempi. Sixteen musicians participated in identification, goodness rating, and discrimination tasks. The relative strength of the prototype within each category was determined, as well as the change in the position of category boundaries in different tempi. Discrimination graphs were finally plotted and comparisons were performed between the positions of discriminability peaks and the related category boundaries.

5aMUb13. Simulation of vacuum-tube amplifiers. Markus Sapp, Jörg Becker, and Claas Brouër (Inst. of Commun. Eng., Aachen Univ. of Technologie, 52056 Aachen, Germany)

Vacuum tube amplifiers are said to add ''warmth'' to an audio signal. They are used for subtle signal modifications as well as soft sounding distortions. But since most signal processing for musical recordings is performed in the digital domain, algorithms for a digital simulation of the desired effects produced by tube amplifiers would be useful. In the work presented here two approaches are followed. The first is based on the simulation of the characteristic transfer curves (waveshaping) combined with a frequency response correction. In the second, more complex one, the complete electronic circuit is simulated using an analog behavioral model of the vacuum tube. The output signals of the simulations are compared to the output of a real vacuum tube preamplifier analytically as well as within listening tests. The computational cost for a real-time implementation of the different algorithms is set into relation to the simulation results.

5aMUb14. Polarity of noise and musical tone in a phenomenological point of view. Jürgen Vogt and Elmar Lampson (Inst. for the Studium Fundamentale, Univ. Witten/Herdecke, Alfred-Herrhausen-Str. 50, D-58448 Witten, Germany)

In direct observation, noise and musical tone are polar phenomena. Think of the noise of a falling coin: usually nobody will listen to the quality of this sound but he will immediately think of a falling coin. To perceive a musical tone, inward experience has to be accepted. Although this experience seems to be subjective, a musical tone has an unequivocal and universal quality, whereas noise is diffused and chaotic. Starting from this polarity, an arrangement of the phenomena between noise and tone is deduced. There are two paths: (1) By reduction of the chaotic features of noise, the modes of vibration become simpler. In the end, simple tones are heard or can be ''filtered'' out by attention. (2) Some or all modes of vibration can lock in the harmonic frequencies as a universal law. The first path is called composition: for a sound which is classified near one of the poles, the significance of the other pole is decreased. The second is called intensification (according to J. W. Goethe's *Farbenlehre*): a harmonic sound still has multimode features and sounds characteristic. Simultaneously the tone becomes richer. [Work supported by the Anthroposophische Gesellschaft in Deutschland e.V.]

5aMUb15. Physico-acoustical properties of emission affected resonance spruce wood. Emil Rajcan and Stanislav Urgela (Dept. of Phys. and Appl. Mech., Tech. Univ. in Zvolen SK-960 53 Zvolen, Slovakia, emil@vsld.tuzvo.sk)

High-quality resonant spruce wood for violin top plate and wood from traditional Slovak resonant spruce locality with various degrees of emission damage were studied experimentally. The modal analysis was done on quarter-cut spruce plates of wedge shape typical for violin making. Acoustical resonance and holographic interferometry were used to measure the relevant physico-acoustical characteristics. These characteristics (density, Young's modulus, and acoustical constant) were obtained by using the bending beam vibration mode (2,0). The obtained results showed that the sorting of resonant spruce wood for violin based on empirical experiences has a physico-acoustical reason, and actual industrial emissions have not significant influence on relevant physico-acoustical characteristics of investigated resonant spruce wood.

Session 5aNSa

Noise: Power Plant Noise

Joachim Gilg, Cochair
Muller BBM, GmbH, Robert Koch Strasse 11, D-82152 Planegg, Germany

Frank H. Brittain, Cochair
Bechtel Corporation, 50 Beale Street, San Francisco, California 94105, USA

Chair's Introduction—7:55

Invited Papers

8:00

5aNSa1. Prospects for active noise control in power plants. Glenn E. Warnaka (Appl. Acoust. Res., L.L.C., 2120 Old Gatesburg Rd., State College, PA 16803) and Bruce E. Walker (Hersh Acoustical Engineering, Inc., Westlake Village, CA 91361)

Active noise control has been applied in power plants to suppress noise from a variety of sources. Applications have included combustion fans, large exhaust stacks, emergency diesel generators, dust collectors, high temperature exhausts, etc. Active noise control systems have been used to control the noise from fan blade passage frequencies, turbine blade frequencies, and other similar noises. In addition, tests have been successful in suppressing random noise, especially at low frequencies. Active noise control has also been used to extend high-frequency attenuation beyond the usual frequency range by using the active noise control systems to spoil the symmetry of the duct and so prevent cross-mode formation. In other cases, active noise control has been coupled with known elements of passive noise control to achieve synergistic results. Active noise control sources can be protected from difficult environments such as high-flow velocities, weather, and high temperatures by using waveguides or Helmholtz resonators between the active sources and point of attack in the environment. This paper presents a view of future developments in active noise control that can be realized by the extension of current active noise control methods to new and challenging applications.

8:30

5aNSa2. Modern methods for attenuation in ductwork and silencers. F. P. Mechel (Landhausstrasse 12, D-71120 Grafenau, Germany)

Silencers in power plant ductwork should find a good compromise between the (generally rather high) needed sound transmission loss and the static flow pressure loss induced by them. The annual costs of the electric power consumption created by a silencer may exceed the costs of investment. Modern design possibilities will be displayed. All of them can be computed with the instrument of mode analysis. On the classical background, that attenuation is concentrated in broadband silencers with straight, homogeneous linings, the following improvements will be illustrated with examples. First, because a broadband silencer needs thick linings for low frequencies and small free duct width for high frequencies, both increasing the static pressure loss, subdivide the silencer in sections for different frequency subbands, with stepping lining thicknesses and duct widths. It will be indicated how such steps can be computed Second, insert the necks of Helmholtz resonators between lining sections designed for medium and high frequencies. The resonator volumes are behind the lining sections. The increase in silencer length is very small; the increase in thickness is small, because the main extension of the resonator volumes is in the duct direction. Such resonators may be designed for an efficient low-frequency additional attenuation. Third, duct elbows with their static pressure losses exist anyhow in most ductworks. They can be designed as very efficient high-frequency silencers, thus permitting to avoid the narrow lining spacings in the silencer. Criteria for good corner silencers will be illustrated. Fourth, most silencers in a ductwork begin and end with a conical duct transition. If they are rigid, their combined effects are small. If, however, they are suitably lined, they can produce remarkable additional attenuation.

9:00

5aNSa3. Turbine exhaust noise radiated by stack walls and tops. Walter F. L. Reinicke (Müller—BBM GmbH, Planegg, Germany)

Rapid progress in noise abatement of plants enforced by the German environmental legislation caused the reduction of, among others, the stack noise due to ventilators and combustion machines of power plants whereas flow noise inside and traffic noise outside the stack remained unchanged. This paper refers to investigations supported by the German Umweltbundesamt in 1981 when power plants were equipped with flue gas desulfurization units. The goal was to calculate the sound transmission in steps: Reflection of

sound power induced to the stack, attenuation in the series of wide tubes, directivity of radiation from the opening with hot gas flow, and influence of wind on directivity. This holds also for combustion turbines (CT) where the influence of gas temperature on the directivity index and of the coupling with wind is stronger. Measurements of this effect at real turbines, however, failed, and there are only a few results of sound attenuation in the stack tube of CT combined with HRSG at lower temperatures. Typical ratios of sound power radiated by the wall and the opening of stacks will be presented on the basis of measured and calculated transmission loss data of steel tube walls.

9:30

5aNSa4. Limiting technology for combustion turbine power plants—how quiet can we make them? Frank Brittain (Bechtel Corp., 50 Beale St., San Francisco, CA 94105), Norbert Kirschfink (Hamon and CIE S. A., Brussels, Belgium), and David Parzych (Power Acoust., Inc., Orlando, FL 32828)

There is a demand for ever quieter combustion turbine power plants. As the community noise limit goes down, the cost and impact of the noise controls on the design increase. At some point, the noise controls significantly affect the size of the plant and the cooling device (cooling tower or air-cooled condenser). This is caused, in part, by silencer self-noise and because the octave bands controlling the A-weighted noise level decrease to include the 31.5-Hz band. While meeting almost any noise limit is considered technically feasible, the cost and impact on the design can become excessive. Several low-noise limits that have been met by several existing plants are reviewed. A specific combined-cycle power plant is used to investigate the impact of lowering noise limits. An indoor plant is used, because adequately controlling the multitude of sources for an outdoor plant is not considered feasible. The noise controls that are expected to be needed to meet various A-weighted noise limits are identified. Limits at which costs for these become excessive or start affecting the size of the plant and cooling device are estimated. While no cost estimates are provided, several definitions of excessive are made.

10:00–10:10 Break

10:10

5aNSa5. Feasibility of meeting a limit of 85 dB everywhere inside a power plant. Ulrich Scholz (ABB Turbo Systems, Thermal Machinery Lab., Dept. of Acoust., CH-5401 Baden, ulrich.scholz@chtus.mail.abb.com)

In recent years the importance of acoustics in the construction of industrial plants has greatly increased. According to many regulations an employee may not be exposed to an 8-h time-weighted average A-weighted sound level of more than 85 dB. The requirement 85 dB at any point is easy to check, even for a nonacoustician. Therefore, a SPL of 85 dB became a standard value in areas with no permanent working places, such as in noisy areas of power plants. Acoustic design in a power station must be handled thoroughly, consistently, and competently. To achieve an optimum solution the plant must be treated as a whole. Knowledge is needed of the processes within power station systems, the components, and their acoustic characteristics, as well as of architectural acoustics, and thermoacoustics. The redevelopment of the cogeneration power station ''Berlin Mitte'' is used to illustrate the acoustic engineering for a project with stringent indoor requirements. The approach used, noise reductions needed, and noise controls selected are reviewed. The requirement of a level of 85 dB in the near field was achieved. One special highlight was the steam turbine by-pass system, for which the standard design causes 98–108 dB.

Contributed Papers

10:40

5aNSa6. Noise control as a revenue enhancer. Bennett Brooks (Brooks Acoust. Corp., 27 Hartford Turnpike, Vernon, CT 06066, bbrooks@brooks-acoustics.com)

A small (1.6-MW) power plant was designed to a very strict noise specification. As the various noise sources in plant design iterations were reduced in level, the engine coolers emerged as important noise sources. Noise design requirements dictated that the cooler fan tip speed be significantly reduced. Cooling requirements led to a necessary increase in fan diameter and thus general size of the cooler tube bundles and support structure, at greater acquisition cost. However, the slower fans required smaller electric drive motors. The reduced parasitic load of the smaller motors enabled the plant to export more electric power for revenue. The added investment in quiet fans was recouped in 13 months of operation.

11:00

5aNSa7. How to accurately distinguish between industrial and traffic noise—New statistical methods for the acquisition and evaluation of data. Sergio C. Martinez (TÜV Rheinland, Am Grauen Stein, D-51105 Köln, Germany)

Statistical methods are used to analyze long-time data series and to distinguish between industrial and traffic noise. Different approaches must be observed for the interpretation of measured data and for the relative influence of noise sources: linear or energetical superposition, and addition or product of mathematical probabilities. Consistent results are available with these methods. Numerical simulations furthermore reduce possible errors. Data series at additional emmission points are used to obtain re-

dundant parameters in the given environmental conditions. Numerical calculations are presented on the problem of linear or energetical superposition and the application of them on two real-life-scenarios. The progress in the application of these methods [S. C. Martinez, Fortschritte der Akustik DAGA **95**, 77–85 (1995)] will be demonstrated. Special emphasis will be put on some possible errors in the application of the guideline VDI 3723 (application of statistical methods for the description of variating ambient noise levels).

Contributed Poster

This poster will be on display in the Poster Gallery from Thursday to Friday, 18–19 March. Author will be at the poster from 2:00 p.m. to 4:00 p.m. on Friday, 19 March.

5aNSa8. Measurement methodology for sound power levels of industrial noise sources. Willy Bruyninckx, Luc Kelders, Walter Lauriks, and Jan Thoen (Laboratorium voor Akoestiek en Thermische Fysica, Katholieke Univ. Leuven, Leuven, Belgium)

For the purpose of noise impact evaluation of industrial noise sources, one often needs reliable values of the sound power level L_{RW} of an entire plant or large parts of it, where one quite often has to do with a large number of distributed noise sources. A methodology will be presented which is based on sound-pressure level measurements at a sufficiently large number of points distributed around a plant, resulting in noise contour maps allowing the calculation of L_{RW}. The method has been compared with other approaches in a well-controlled free field setting of a simple combination of noise sources.

FRIDAY MORNING, 19 MARCH 1999 ROOM H2013, 8:00 A.M. TO 12:00 NOON

Session 5aNSb

Noise: Road Traffic Noise I

Steven Heinrich, Cochair
TUEV Automotive GmbH, Kaiserstrasse 100, 52134 Herzogenrath-Kohlscheidt, Germany

Richard F. Schumaker, Cochair
General Motors N.A. Proving Ground, MC483-356-006, Milford, Michigan 48380, USA

Invited Papers

8:00

5aNSb1. Reduction of road traffic noise: The legislature's point of view. Reiner Stenschke and Michael Jaecker (Umweltbundesamt, Postfach 330022, D-14191 Berlin, Germany)

Measures to improve motor-vehicle technology play an important role in the reduction of road traffic noise. Therefore, appropriate noise control regulations must ensure that all possibilities for reducing noise levels through technical vehicle-related measures are exploited. An important basis for achieving this is the introduction of a test method for motor vehicle type approval that depicts the driving and operating modes occurring in real traffic as closely as possible, so as to ensure that future noise limit value reductions will influence noise emissions in real traffic more effectively than has been the case to date. Furthermore, there is the need for a separate noise emission regulation for tires that ensures that tires introduced to the market satisfy ambitious noise criteria. In addition, it must be ensured that low-noise road surfaces are used when road surface renewal work is carried out on noisy streets in particular. An essential requirement for reducing road traffic noise is that noise control regulations are complied with by all vehicles throughout their lifetimes. To this end, a concept for improving the efficiency of compliance monitoring must be developed. The contribution will present available results and report on planned activities in this field.

8:20

5aNSb2. How to reduce tire/road noise: Chances and limits. Frank Gauterin (Continental AG, Jaedekamp 30, D-30419 Hannover, Germany, gauterin@conti.de)

Tire/road noise is an important sound source for traffic noise. Measures for tire/road noise reduction are reviewed and discussed concerning chances and limits for a traffic noise reduction. Vehicle layout, tire construction, road specification, and legal requirements are taken into account.

8:40

5aNSb3. A spatial analysis of topographic and vegetation factors affecting the propagation of highway traffic noise. John C. Bennett (Dept. of Geography, San Diego State Univ., 5500 Campanile Dr., San Diego, CA 92182-4493, jbennett@rohan.sdsu)

This paper presents the results of a spatial analysis of measured noise levels with environmental factors derived from a geographic information system (GIS). The more traditional methods used by the Federal Highway Administration (FHWA, 1978 and 1982) are range limited and not suitable for large-scale topographic variation near a freeway noise source. Over 30 field measurements of noise levels were collected along a freeway in San Diego County that included a heterogeneous landscape of mesas and valleys. A digital elevation model and a vegetation map of the study area have been incorporated into a GIS to evaluate a suite of environmental factors. Topographic features limit the line-of-sight analysis traditionally used in the past and new variables of landscape ''ensonification'' and slope configuration are shown to bridge part of that gap in this study.

9:00

5aNSb4. Prediction of traffic noise control by forests using a three-dimensional GFPE model. Nicolas Barriere and Yannick Gabillet (Ctr. Scientifique et Technique du Batiment, 24 rue J. Fourrier, 38400 St. Martin d'Heres, France, barriere@cstb.fr)

To predict outdoor sound propagation through forests, multiple natural effects have to be taken into account such as ground effects and meteorology that vary along the path of propagation as well as horizontal trunk scattering effect. It is of great interest, for engineering applications, to know the weight of the different effects. A previous work with a two-dimensional model has shown the interest of an infinite forest band [N. Barriere and Y. Gabillet, Proceedings of Euro-noise 98, Munich]. The prediction method is based on a theory for fast calculation of the parabolic equation [K. E. Gilbert, J. Acoust. Soc. Am. **94**, 2343–2352 (1993)], and has recently been developed at the CSTB for a three-dimensional sound propagation. This method allows prediction of noise attenuation due to a forest band of finite length with its corresponding, ground, meteorological, and scattering effects. Results show the great interest of forests on traffic noise control.

9:20

5aNSb5. A numerical method to predict sound propagation for realistic road environments. Benoît Gauvreau and Michel C. Bérengier (Laboratoire Central des Ponts et Chaussées, Ctr. de Nantes, Rte. de Bouaye, BP 19, 44340 Bouguenais, France, Michel.Berengier@lcpc.fr)

When dealing with traffic noise propagation over large distances, models assuming flat and homogeneous grounds and homogeneous atmosphere are not sufficient to have an accurate prediction. A first improvement was obtained by many authors who worked on new theoretical approaches individually dealing with the influence of mixed grounds, stratified atmosphere, noise barriers, etc. on sound propagation. Thus, many models were built. In order to predict sound pressure levels for complex conditions representative of realistic traffic noise situations, a model based on the resolution of the wave equation through a parabolic approximation has been developed. The problem is numerically solved for various conditions including mixed grounds, upward and downward refracting turbulent atmospheres, and the presence of noise barriers producing a variation of the sound celerity profile along the propagation path between the source and the receiver, over several hundred metres. The numerical approach is based on the split-step Padé technique mainly developed and recently improved by the acoustic group of the Ecole Centrale in Lyon, France [Chevret *et al.*, J. Acoust. Soc. Am. **100**, 3587–3599 (1996)]. Interesting comparative results with other theoretical approaches and experimental data have been obtained and will be widely developed in the paper.

9:40–10:00 Break

10:00

5aNSb6. Simnoise: A new low-traffic-flow road noise estimation by a statistical approach. Gaetano Licitra, Mauro Cerchiai, and Silvia Canessa (A. R. P. A. T. (Environ. Protection Agency of Tuscany), Dept. of Livorno—Environ. Phys., Via Marradi No. 114, I-57126 Livorno, Italy, fisica@luda.it)

Road noise models usually limit the possibility of sound-level prediction with low vehicular fluxes, especially during the night period, because they provide urban traffic noise with a minimum number of some hundreds of vehicles per hour. In order to predict sound levels in urban areas for both night and day periods and to plan corrective actions, a model that can be applied in case of very low traffic flows (even lower than 50 vehicles for hour) is proposed here. This model uses a Monte Carlo method based on a dependent Poissonian vehicle distribution, a spatial Gaussian one with respect to the lane center, and a Cauchy distribution for velocities. These are estimated using the English Road Research Laboratory model, calibrated using only geometrical site description and vehicular fluxes informations, based on 75 measurement points in a speed range between 20 and 60 km/h, for almost 230 hourly night L_{eq} levels. The prevision values resulted in good agreement with actual values with an error depending on the entries. For the range between 10–2000 vehicles, an error was observed of about 1–2 dB on the actual value.

10:20

5aNSb7. A theoretical tire model based on the general field equations. Krister Larsson and Wolfgang Kropp (Dept. of Appl. Acoust., Chalmers Univ. of Technol., S-412 96 Goteborg, Sweden)

Most of the models for the structure-borne sound behavior of tires are designed for the low-frequency range (i.e., below 300–400 Hz) and often contain the geometrical details of the tire. Above this frequency range the curvature of the tire can be omitted while the internal structure (i.e., multilayers of steel and rubber) increases in importance. For this higher-frequency range, a model has been developed based on the general field equations. The model consists of a double-layered thick plate, representing the tire belt, which is prestressed due to the internal pressure in the tire. An elastic bedding supports the plate, in order to take into account the compression of the air inside the tire cavity and also to take into account the influence of the side walls on the belt. Both the radial and the tangential motions in the belt are included, since the model is based on the general field equations. The model also incorporates the effect of the local deformation of the soft rubber surface. Results from the model are compared with results from other models from the literature and with measurements.

10:40

5aNSb8. Modeling of traffic noise pollution with neural networks. A. I. El Mallawany (Housing & Bldg. Res. Ctr. Dokki, P.O. Box 1770, Cairo, Egypt, hbrc@idsc1.gov.eg), M. I. Abdallah (Zagazig Univ., Zagazig, Egypt), and M. Abd El Gawad (Housing & Bldg. Res. Ctr. Dokki, Cairo, Egypt)

A neural-network-based model for evaluating and predicting the mean energy and the noise pollution level of the traffic noise in the city of Cairo is developed. A comparison between the different prediction models was carried out, and the neural model was shown to be associated with minimum error. In conclusion, the neural model can be used to make systematic predictions of noise level, and provide planners with some suitable means for formulating legal regulations for urban noise pollution.

11:00

5aNSb9. A simulation model for urban traffic noise. A. Di Giulio (Dept. of Mech. Eng., Politecnico di Milano, Piazza Leonardo da Vinci 32, 20133 Milano, Italy, augusto.digiulio@polimi.it), F. Mancosu (Pirelli SpA), C. Nucci, and L. Zocchi (Politecnico di Milano, Milano, Italy)

Urban traffic noise is studied by a simulation model whose main features are the following: effects of traffic lights, speed limit, possibility of vehicles overtaking, and driving styles. In the model there is a basic assumption about driver's behavior (''follow the leader''), considering the case of straight and level road with two lanes for every carriageway, and two traffic lights. Three driving styles are considered: A (''quiet driver''): change of gear at 60% of engine speed corresponding to maximum torque, B (''normal driver''): at 80%, C (''fast driver''): at 100%. The behavior rules provide for: keeping of safety distance, overtaking if there are vehicles at different speeds, deceleration and stop at traffic lights with red, synchronization of two traffic lights, if requested. From the kinematic side, the model was validated by comparison with acceleration distribution of a real vehicle's flow, while the acoustic one was by the comparison with noise levels measured along urban streets. The simulation model lets one take into account the following factors concerning the traffic noise emission: main noise sources of vehicle (tires, engine, intake and exhaust system), traffic flow and maximum speed allowed, traffic mix as regards different driving styles.

11:20

5aNSb10. Sound field studies of truck tires. E.-U. Saemann (Continental A. G., Jaedekamp 30, D-30419 Hannover, Germany, saemann@conti.de), J. Hald, and A. Schuhmacher (Bruel & Kjaer A/S, Skodsborgvej 305, DK-2850 Naerum, Denmark)

To understand the noise source mechanism of tire/road noise better than in the past, it is essential to look at the complete sound field of a tire. In the technique of spatial transformation of sound fields (STSF), the Helmholtz integral equation is combined with the acoustical near-field holography. Thus it is possible to analyze the noise source in great detail and to calculate the sound in the far field. A drawback of the acoustical holography is that only planar views of the sound field can be calculated. One method to overcome this limitation is to combine the measurement results of STSF with the inverse boundary element method. By modeling the surface of the tire with boundary elements, the velocities on each element can be identified. First results will be presented. Comparing the sound field of a standing tire excited by a shaker with the sound field of a tire on a drum, it is possible to extract the part of the sound field that is caused by the geometry on the tire only.

11:40

5aNSb11. Low noise road surfaces in the Federal Republic of Germany. State of the art. Siegfried Ullrich (Bundesanstalt für Straßenwesen, PF 100150, D-51401 Bergisch Gladbach, Germany)

The texture of road surfaces influences the rolling noise of cars and trucks. High texture depths cause high noises by the incitation of tire tread vibrations. Low depths favor the generation of aerodynamic noise sources in the tire tread, for example, air pumping. This type of noise can be suppressed by open surfaces on wearing courses with high void contents. As coatings with low diameter gritting material on worn concrete showed, air pumping noises can also be reduced on closed road surfaces. But trials on gussasphalt turned out to be not very successful thus far. The greater part of the rolling noise on such surfaces is apparently caused by a waviness with wavelengths between 3 and 6 cm, which could be caused by the embedment of chippings. A similar reason seems to be responsible for the limited noise reduction on concrete surfaces with burlap finishings. Measurements at a 5.5-m-diam internal drum with sandpaper surfaces and different grittings on asphalt concrete allows the hope that the rolling noise of car tires can be reduced by several decibels, if road surfaces are gritted by small diameter stones from a small fraction without oversizes.

FRIDAY MORNING, 19 MARCH 1999 ROOM MA004, 8:00 TO 10:00 A.M.

Session 5aPAa

Physical Acoustics: Radiation and Relaxation

D. Keith Wilson, Cochair
U.S. Army Research Laboratory, 2800 Powder Mill Road, Adelphi, Maryland 20783, USA

Leif Bjørnø, Cochair
Department of Industrial Acoustics, Building 425, Technical University of Denmark, DK-2800 Lyngby, Denmark

Contributed Papers

8:00

5aPAa1. Analytic expressions for the far-field transition distance for localized waves. David Chambers (Lawrence Livermore Natl. Lab., P.O. Box 808 L-372, Livermore, CA 94551, chambers2@llnl.gov) and Arthur Gautesen (Iowa State Univ., Ames, IA 50011)

Expressions estimating the distance to the near-field/far-field transition point are obtained for the problem of a localized wave emitted from a circular aperture. These expressions are based on bounding the error between the exact diffraction integral and its far-field approximation. The resulting formulas involve integrals over the normal velocity distribution within the aperture. They can be evaluated for both narrow- and broadband pulses. For the special case of a single frequency with uniform spatial weighting, the predicted transition distance is the standard Rayleigh range. The expressions are evaluated for a number of localized waves and compared with numerical simulations of the full fields on axis.

8:20

5aPAa2. Moment method calculation of radiation from a cylindrical tube with an infinite flange. Noam Amir, Chaim Matzner (Commun. Eng. Dept., Ctr. for Technol. Education, Holon, 52 Golomb, Holon 58102, Israel, noamoto@wine.cteh.ac.il), and Samuel Shtrikman (Weizmann Inst. of Sci., Rehovot 76100, Israel)

This work addresses the calculation of acoustic radiation from a cylindrical tube with an infinite flange, using the moment method. Expressions for the acoustic variables are presented in three separate regions: inside the tube, outside the tube, and on the boundary between them. Examination of the velocity field on this boundary shows that a singularity is present at the corner where the tube and flange meet. A set of basis functions is then developed, which can model this singularity efficiently, resulting in a solution that converges very rapidly. This is demonstrated by a comparison to a solution of the same problem, using the normal modes of the tube as basis functions. The present results are compared with those for the radiation from an unflanged tube, as given in the classic paper by Lewin and Schwinger.

8:40

5aPAa3. Acoustic performance of finite-length apertures using finite-element analysis. Richard Lyons (Dept. of Civil and Bldg. Eng., Loughborough Univ., Loughborough LE11 3TU, UK, r.lyons@lboro.ac.uk.), Patrick C. Macey (PAFEC Ltd., Nottingham NG8 6PE, UK), and Jane L. Horner (Loughborough Univ., Loughborough LE11 3TU, UK)

There is a wide range of published literature covering ducts of infinite or semi-infinite length and to a lesser extent there are studies on apertures having restricted dimensions. The work presented in this paper is taken from recent research into the characterization of acoustic devices in finite-length apertures, which may need to allow for a flow of fluid. Results of a finite-element solution for a short duct between two half spaces are presented, along with a closed-form solution [K. H. Jun and H. J. Eom, J. Acoust. Soc. Am. **98**, 2324–2327 (1995)] as a validation of the finite-element method. Further results of more complicated aperture geometry, which are not easily amenable to such forms of solution, have also been investigated and are presented.

9:00

5aPAa4. Influence of the frequency-range broadening for the value of the acoustic vibrational relaxation time. Bogumil B. J. Linde (Inst. of Exp. Phys., Univ. of Gdansk, Wita Stwosza 57, 80-952 Gdansk, Poland, fizbl@univ.gda.pl) and Nikolaj B. Lezhnev (Acad. of Sci. of Turkmenistan, Gogola 15, 74-000 Ashgabat, Turkmenistan)

This paper deals with the many acoustical investigations, provided by some scientists (Rapuano *et al.*), in two liquid compounds: benzene C_6H_6 and carbon disulfide CS_2. These compounds are typical liquids where one can observe the acoustical relaxation combined with Kneser processes—energy transfer between translational and vibrational degrees of freedom. Acoustical values, a characteristic of the compounds, were different in many papers and the goal was to try to explain these discrepancies and show how it is possible to avoid these mistakes. The main problem in experimentally determining the relaxation time from the dependence of absorption and frequencies was the narrow frequency range.

9:20

5aPAa5. Universal local state equation for description of exponential and resonant relaxation at sound-wave propagation. German A. Maksimov and Vladimir A. Larichev (Dept. of High Density Energy Phys., Moscow Eng. Phys. Inst., Kashirskoe sh. 31, Moscow, 115409, Russia, maximov@dpt39.mephi.ru)

The generalization of the thermodynamic theory of internal parameters [L. I. Mandelshtam and M. A. Leontovich, Sov. Phys JETP **7**, 438–444 (1937)], which leads to a description of medium response in terms of exponential relaxations, is presented in the report for the case of resonant relaxations. The basis of this generalization is an alternative formulation of Onsager's principle of kinetic coefficient symmetry for values of different symmetry at time inversion. Using this fact, the generalized local linear state equation is derived for medium holding in the vicinity of thermodynamic equilibrium. It is shown that the developed state equation is an exhaustive one for the description of linear response of medium in the framework of local models. The variety of dispersive and dissipative properties, which is described by the generalized state equation, is demonstrated for the case of the single process of resonant relaxation. It is shown that all the existing local models of linear response of medium are the particular cases of the generalized state equation. [Work supported by ISTC in Moscow.]

9:40

5aPAa6. Propagation of a short acoustic pulse in a medium with two relaxation processes. Exact solution. German A. Maksimov and Vladimir A. Larichev (Dept. of High Density Energy Phys., Moscow Eng. Phys. Inst., Kashirskoe sh. 31, Moscow, 115409, Russia, maximov@dpt39.mephi.ru)

Shape distortion of a short acoustic pulse during its propagation through relaxation media is an important source of information about relaxation time's spectrum (RTS). The basic relations for pulse acoustic diagnostics were developed in the work [G. A. Maksimov, Acoust. Phys. **42**, 541–550 (1996)] by using known exact solutions as well as asymptotic analysis. Only two exact solutions for short-pulse distortion due to relaxation are known at present. They are the solution for single relaxation process [J. A. Morriso, Q. Appl. Math. **14**, 153–169 (1956); J. D. Achenbach and C. C. Chao, J. Mech. Phys. Solids. **10**, 245–252 (1962)] and the solution for the distributed spectrum being proportional to inverted relaxation time [S. Z. Dunin and G. A. Maximov, Izv. ANSSSR Appl. Math. Mech. **54**, 480–484 (1990) (in Russian)] . The new analytical representation of Green's function for pulse propagating in media with two relaxation processes is obtained. This representation consists of three parts, which describe acoustic precursor as well as high- and low-frequency components of pulse body. The high-frequency component can be written in an invariant form that is fair for arbitrary RTS. The low-frequency component has more complicated dependence on parameters of RTS. The analysis of this dependence is made and analytical expressions are obtained. The usefulness of these expressions is confirmed by comparison with results of direct numerical calculations.

Session 5aPAb

Physical Acoustics: Acoustic Remote Sensing of the Atmosphere I

D. Keith Wilson, Cochair
U.S. Army Research Laboratory, 2800 Powder Mill Road, Adelphi, Maryland 20783-1197, USA

Volker Mellert, Cochair
Physics Department, University of Oldenburg, D-26111 Oldenburg, Germany

Chair's Introduction—10:15

Invited Papers

10:20

5aPAb1. Current progress and problems in atmospheric acoustics. Margarita A. Kallistratova (Obukhov Inst. of Atmospheric Phys., 3 Pyzhevsky, Moscow 109017, Russia, margo@omega.ifaran.ru)

The problems of basic and applied research in the area of atmospheric acoustics are elucidated. Main results are reviewed from the theoretical and experimental investigations of audible and infrasonic wave propagation in the atmosphere which were carried out during the last few decades. The role of the acoustic techniques in studying the structure and dynamics of meteorological fields is discussed. The data are given on a practical use of echo sounders (SODARs) and the systems of radio acoustic sounding (RASS) in monitoring the atmospheric boundary layer parameters. Some other practical applications of the acoustic methods in the atmosphere are considered. A number of problems are formulated, whose solution is necessary for a further advancement of atmospheric acoustics and for the use of the acoustic techniques in studying the lower and middle atmosphere. [Work supported by INTAS through Grant No. 96-1869 and RFBR through Grant No. 96-05-65741.]

11:00

5aPAb2. Scattering of sound in a stratified moving atmosphere. V. E. Ostashev, G. H. Goedecke, and R. C. Wood (Dept. of Phys., Box 30001, New Mexico State Univ., Las Cruces, NM 88003-8001)

An equation derived recently for the sound-scattering cross section per unit volume in a stratified moving atmosphere is presented. The dependence of the temperature and wind velocity contributions to the cross section on the scattering angle is studied in detail analytically and numerically for different stratifications of temperature and wind velocity. Such studies are important for acoustic sounding of the atmosphere by sodars since the equation for the sound scattering cross section is a theoretical basis for this remote sensing technique. It is shown that both temperature and wind velocity fluctuations contribute to the backscattering signal if the wind velocity is not zero at the height of scattering. This means that a signal received by a monostatic sodar is a linear combination of the structure parameters of both temperature and wind velocity fluctuations, while it has previously been assumed that this signal is proportional only to the structure parameter of temperature fluctuations. The new results obtained should be taken into account in existing techniques of acoustic remote sensing of the atmosphere. [This material is based upon work supported by the U.S. Army Research Office under Contract Nos. DAAG55-98-1-0463 and DAAG55-97-1-0178.]

11:20

5aPAb3. Advances in acoustic remote sensing of the atmosphere at the IAO SBaa RAS. Nikolai P. Krasnenko (Inst. of Atmospheric Optics, 1, Akademicheskii av., Tomsk 634055, Russia, aa zuev@iao.tomsk.su)

Advances in acoustic remote sensing of the atmosphere made at the Institute of Atmospheric Optics of the Siberian Branch of the Russian Academy of Sciences (Tomsk, Russia) for a 24-year period are considered. Sodars developed at the IAO are described. Results of theoretical analysis of methods for acoustic sounding of the atmosphere are presented including the interaction of the acoustic radiation with the atmosphere, optimization of the sodar parameters, and accuracy of sodar measurements of the atmospheric parameters. The emphasis is on investigations of the effect of acoustic refraction on the sodar operation as well as on search for new information capabilities in acoustic sounding. Results of investigations of the parameters of the atmospheric boundary layer above dry land and ocean and airports with the sodars developed at the IAO are given. Sodar-derived data are compared with the results of lidar sensing and ballon and radiozonde measurements of the atmospheric parameters.

11:40

5aPAb4. On acoustic sounding of large-scale turbulence in the middle atmosphere. Sergey N. Kulichkov (Inst. of Atmos. Phys., Russian Acad. of Sci., Pyzevsky 3, Moscow 109017, Russia)

The possibilities of the bistatic acoustic method to measure sound turbulence with vertical and horizontal scales equal to 10–1000 m and 1–100 km correspondingly in the middle atmosphere ($z = 20-80$ km) are discussed. More then 60 surface explosions with yields of 20–70 tons realized in different seasons during 1989–1991 were used as sources of the initial acoustic pulses. The receivers were placed at distances of 300 and 310 km toward the West and the North from the sources, respectively. Infrasound signals scattered

from large-scale turbulence in the middle atmosphere and recorded on the ground surface in the geometric shadow of explosions were analyzed. The theoretical approach was based on the theory of Fresnel reflection of sound from anisotropic acoustic refractive index irregularities in the approximation of a local-layered structure. It was found that intense turbulence exists in the middle atmosphere during all seasons, with the maximum in July. Vertical gradients of the effective sound velocity in the middle atmosphere are characterized by great values, which earlier were observed only in the atmospheric boundary layer. Samples of the profiles of those obtained for different seasons are presented.

12:00

5aPAb5. Dislocations in the wave front of acoustic waves propagating through thermal turbulent fields. Ph. Blanc-Benon and D. Juvé (Ecole Centrale de Lyon, LMFA UMR CNRS 5509, BP 163 69131 Ecully Cedex, France, phbb@ec-lyon.fr)

Acoustic waves traversing a turbulent medium develop random changes in phase and amplitude. Here the wavefront distortions of a spherical wave that traverses a medium exhibiting temperature fluctuations are investigated under well controlled laboratory conditions. A heated grid in air is placed horizontally in a large anechoic room and the mixing of the free convected plumes above the grid generates an homogeneous isotropic thermal turbulent field. By varying the frequency of the ultrasonic source and the distance of propagation, all the regimes from weak scattering to strong scattering can be explored. The presentation will concentrate on the measurements of phase variations along a linear array of microphones. Measurements of these phase differences demonstrate the limitation of the Rytov's method for remote sensing techniques due to the existence of phase jumps between neighboring elements of the array. Numerical simulations based on a wide-angle parabolic equation are used to explain these rapid phase variations in terms of random caustics and phase dislocations.

FRIDAY MORNING, 19 MARCH 1999 ROOM MA005, 8:00 TO 11:40 A.M.

Session 5aPAc

Physical Acoustics: Elastic Properties of Materials III: Piezoelectrics, Plates, and Shells

Heinz-Jürgen Fröhlich, Cochair
Paul-Drude Institut fur Festkörper Elektronik, Hausvogteiplatz 5-7, D-10117 Berlin, Germany

Jan D. Achenbach, Cochair
Center for Quality Engineering and Failure Prevention, Northwestern University, 2137 North Sheridan Road, Evanston, Illinois 60208-3020, USA

Contributed Papers

8:00

5aPAc1. Acoustoelectric sensing and actuating of physicochemical processes by SAW. R. Giriuniene and E. Garshka (Dept. of Phys., Vilnius Univ., 2054 Vilnius, Lithuania)

The purpose of the paper is to present the studies of the influence of SAW in cw mode on catalyst properties of semiconductive catalyst surface and of the peculiarities of the control of chemical processes on this surface with the help of the SAW. Also, the studies of this structure when the surface of the semiconductor is covered with ion-selective membrane and the gap is filled with electrolyte are presented. It is found that SAW in pulse mode presents a very effective tool for monitoring catalytic and sorption processes on this surface and in the electrolyte itself. It allows the determination of a nature and limited stage of the reaction. The change of acoustoelectric parameters reflects the electronic processes which take place on the catalyst surface during the reaction. The activation energy of the processes on the real surface of the catalyst is determined by acousto-electric method too. The acousto-electrocatalytic effect is investigated. It is found that SAW in cw mode changes the catalyic activity on the semi-conductive catalyst surface and in some cases the catalytic selectivity of the surface.

8:20

5aPAc2. Piezoelectric interfacial waves in directions of vanishing slowness curvature. Eugene J. Danicki (Polish Acad. of Sci. (IPPT), 21 Swietokrzyska Str., Warsaw 00-049, Poland)

Piezoelectric interfacial waves can propagate in a piezoelectric body along the conducting plane embedded in it (that is, at the bonding of two metallized pieces of a crystal); its velocity is close to one of the shear bulk waves. The wave-field penetration depth depends on the shear wave slowness curvature. At investigated propagation directions of vanishing curvature, the wave decays at about two or more wavelengths. There are only a handful of such points in investigated crystals: 12 distinct ones in quartz and 6 in lithium niobate. They are analyzed applying Stroh formalism (the case of fourfold defective matrix), and using the recently developed ''papal'' approximation to the planar harmonic Green's function. In almost all cases, the approximation evaluated at a given wave number is accurate enough for application in a sufficiently wide wave number domain. This is beneficial for physical interpretation of numerical results. (The method can also be adopted for analysis of Rayleigh and pseudo surface waves in anisotropic crystals.) Possible applications of the investigated waves include: (a) low-temperature investigations of materials or superconducting layers (propagating inside the crystal, the wave is well protected from an adverse environment), (b) validation of material constants, and (c) in surface acoustic wave devices.

8:40

5aPAc3. Application of the piezoelectric implant method to study the frost phase in frozen porous media. Stephane Pouyez and Robert Hazebrouck (L.A.M.H 1230 rue de l'Universite 62400, Bethune, France, hazebrouck@univ-artois.fr)

This work describes the adaptation of the piezoelectric implant method for frozen porous media. This technique has been successfully used for monitoring cement setting [S. Pouyez and R. Hazebrouck, Biot Conference on Poromechanics (1998)]. Earlier results have shown that, for porous media, the electrical impedance resonance peak of the implant can be calculated by Biot's theory. The slow wave has a predominant contribution to the piezoelectric disc response. Experiments in glass beads embedded in water monitored in a temperature range of $[-20, 10\ ^\circ\mathrm{C}]$ are presented. Results are in good agreement with those obtained by using the transmission of longitudinal waves. The implant method is very sensitive and free of any problem caused by the mechanical contact occurring in most existing methods using ultrasonic velocities measurement. Thus in the vicinity of 0 °C and for positive values of the temperature, the proposed method allows one to follow the slow reheating of the sample while ultrasonic measurement becomes less efficient because of the attenuation. The implant remains in the sample, so the frost and defrost cycles for heterogeneous materials in civial engineering can be monitored with this method. The implant method also might be of interest for the study of frozen soils.

9:00

5aPAc4. The energy velocity of attenuating guided ultrasonic waves in plates. Arnaud Bernard, Marc Deschamps (Laboratoire Mecanique Physique, Univ. Bordeaux 1, 351 Cours de la Liberation, 33405 Talence Cedex, France), and Mike Lowe (Imperial College, Exhibition Rd., London SW7 2BX, UK)

The understanding of the propagation characteristics of guided waves is fundamental to their exploitation in nondestructive evaluation (NDE) techniques. Long-range testing methods often rely on the detection of the arrival of a wave packet which is understood to travel at the group velocity of the wave mode, and which is easily calculated. However, although in practice the group velocity is a perfectly adequate measure of the energy velocity of the wave packet, it is strictly correct only when the wave mode is lossless. The paper will examine the nature of the energy propagation vectors within a plate and the energy velocity of Lamb waves. Both elastic plates with lossless modes and plates with attenuation will be considered, the latter leading to differences between the group velocity and the energy velocity. Experimental results will be presented as validation, using a plate with material damping under conditions where the difference between group velocity and energy velocity is significant.

9:20

5aPAc5. Guided waves' propagation in an elastic plate of linearly varying thickness. Arnaud Guillet, Mounsif Ech Cherif El Kettani, and Francine Luppe (LAUE, UPRESA 6068 Pl. R. Schuman, 76610 Le Havre, France)

Experimental studies of guided waves propagating in an elastic plate of linearly decreasing thickness are presented. The plate is embedded in water, and the mode's excitation is achieved by means of an ultrasonic beam at a given incident angle. Measurements are done either with a receiving transducer or with a laser interferometer. In the first case, the amplitude of the leaking wave and its reemission angle are measured, while, in the second case, the normal acoustic displacement at the surface of the plate is obtained. Use of the surface wave analysis method then provides the dispersion curves of the propagating waves. For plates of small thickness slopes (one or two degrees), the interface waves are shown to behave mostly as generalized Lamb waves which adapt continuously to the varying thickness as they propagate. Evidence of waves propagating backward before having reached the plate end is shown. Mode's conversions also occur, giving rise to intermodes' branches in the dispersion plane.

9:40–10:00 Break

10:00

5aPAc6. Transmission-line modeling (TLM) of an elastic wave propagation in two dimensions. Y. Kagawa, T. Fujitani, and T. Tsuchiya (Dept. of Elec. Eng., Okayama Univ., Okayama, 700-8530 Japan)

Transmission-line matrix modeling (TLM) provides a simulation approach to the wave propagation for which the Huygens' principle is discretely realized on computer. The TLM modeling is primarily developed for the electromagnetic wave propagation simulation in time domain and its application has been widely practiced. The application to acoustic field problems is the easy extension as it is of scalar field, while the elastic wave is of vectorial field like the electromagnetic wave so that a special TLM node must be developed. The formulation of the elastic wave problems are well established, which can be expressed in terms of the two separate potential waves. The two waves can independently be present, whereas is experienced in seismic wave observation, the elastic wave consists of the longitudinal and shear waves. They, however, couple at the boundaries to satisfy the boundary condition at which mode conversion is said to take place. The present paper proposes the two potential wave approach. The two scalar waves using simple regular TLM nodes are simulated to propagate independently under the boundary conditions which should properly be devised. The expression is discussed for a two-dimensional homogeneous elastic field and some examples are demonstrated, compared with the solutions of another approach, such as the finite difference.

10:20

5aPAc7. Direct measurement of dynamic elastic constants of a disc. Francisco J. Nieves, Francisco Gascón (Dept. Física Aplicada, Univ. Sevilla, E.T.S. de Arquitectura, Reina Mercedes 2, ES-41012 Sevilla, Spain, fjnpavon@cica.es), and Ana Bayón (Univ. Politécnica Madrid, ES-41012 Sevilla, Spain)

In two preceding papers [F. J. Nieves, F. Gascón, and A. Bayón, J. Acoust. Soc. Am. **104**, 176–180 (1998); J. Acoust. Soc. Am. (to be published)], the possibility of measuring the two dynamic elastic constants by excitation of axisymmetric vibration of an isotropic cylinder, whose length L equals its diameter D, and by means of the detection of the two lowest natural frequencies, one symmetric and another antisymmetric, has been demonstrated. The variational method and the Ritz procedure with polynomies are followed to calculate numerically the two lowest nondimensional frequencies for a disc with $L/D=0.1$ and the result is antisymmetric. The quotient between both nondimensional frequencies is a function only of the Poisson ratio and it is single-valuated. Then the measurement of these frequencies allows the calculation of that elastic constant. The quotient dependence on the Poisson ratio is strong and almost linear, which implies a much better sensibility than it was for $L/D=1$. Moreover, one of the calculated frequencies, the disc diameter, and the material density permit the calculation of the shear modulus. The theory is checked with a laboratory experiment on a stainless steel disc of 5 cm in diameter.

10:40

5aPAc8. Investigation of thin film shear modulus from spatially resolved measurement of Love wave velocity. G. Behme, E. Chilla, and H.-J. Froehlich (Paul Drude Inst., Hausvogteiplatz 5-7, 10117 Berlin, Germany, behme@pdi-berlin.de)

The investigation of transversely polarized surface acoustic waves (SAWs) is strongly hindered by their missing out-of-plane oscillation component because commonly applied measurement techniques are based on access to that component. Nevertheless, these waves are very interesting for accurate extraction of thin film elastic properties as well as for SAW devices and sensor applications. In this contribution we report a new development of spatially resolved SAW analysis. The scanning acoustic force microscope (SAFM) has been extended in its sensitivity to in-plane polarized waves. A nonlinear mechanism could be found that couples the

in-plane surface oscillations to torsional cantilever vibrations. This mechanism is used to transfer the rf SAW signals to kHz frequencies and to measure the SAW phase velocity. The new technique has been applied to study the Love wave propagation in the layered system fused silica on ST-cut quartz. The phase velocity could be derived from measurements of the phase shift along a propagation distance in the micron range. The obtained velocities show a clear spatial variation at elastic changes within the investigated surface. This is used to investigate the shear modulus of the layer material by numerically solving the inverse problem of SAW propagation.

11:00

5aPAc9. Vibration response of perforated thin plates. Pascal Allemon, Robert Hazebrouck (LAMH, Univ. d'Artois, Equipe acoust., 1230 rue de l'Universite, 62400 Bethune Cedex, France, pallemon@club-internet.fr), Florin Breaban, and Andre Deffontaine (IUT, 62408 Bethune Cedex, France)

The vibration behavior of perforated metal thin plates is studied here. In order to highlight specific phenomena, a rather simple experiment has been researched. While covering a large range of frequencies, a sinusoidally varying point force has been applied to a free boundary circular plate at its midpoint. In that case, the plate vibrations obtained are of an axial symmetry type; for that geometry the first symmetrical modes only are excited. The driving-point mechanical impedance is measured. For a plane stress problem, the perforated plate vibration response is evaluated by assimilating perforated plates to equivalent solid thin plates whose effective elastic constants are determined with the help of Meijers' theory [Ph.D. thesis, University of Delft, Holland, 1967]. First of all, the numerical simulation is validated by comparing theoretical impedance results to those obtained experimentally. Then, the use of double exposure holographic laser interferometry permits one to verify that modes observed on photographs correspond in general to theoretical ones. Initially developed for the study of perforated plate static behavior, that theory can certainly be used for the dynamic study of various geometry perforated plates.

11:20

5aPAc10. An acoustic wave's transmission through an elastic cylindrical shell and investigation of its parameters. Igor L. Oboznenko, Elena I. Oboznenko, and Victor Samonenko (NTUU Kiev Polytech. Inst., Kiev 252056, Ukraine)

The method of elastic parameter's estimation of cylindrical shells and surroundings is proposed. The method is based on measurement of the transmitted wave by the calibrated ultrasonic hydrophone inside of the elastic shell. Metallic, plastic, rubber, and blood shells are discussed. It has been demonstrated that acoustical pressure inside the shell, for frequencies lower than the frequency of mechanical resonance, does not depend on the frequency, but rather depends on mechanical parameters like Young's modulus, Poisson coefficient, density, and geometry (median radius and thickness) of the shell. Irradiation in various wave reference angles in relation to normal is applied for determination of the shell and those resonances also are different (10–1000 times in frequency). Transmitted waves have been calculated for both the elastic plate model and elastic shell models of different geometry. The pass wave field significantly depends upon shell material. Its resonances also are different (10–1000 times in frequency). It has been demonstrated that up to 60% higher accuracy in calculations of the pressure of transmitted waves can be achieved when the exact solution is used in comparison with the approximate solution for the elastic plate model. There is a good correlation between computational and experimental results.

Contributed Posters

These posters will be on display in the Poster Gallery from Thursday to Friday, 18–19 March. Authors will be at their posters from 2:00 p.m. to 4:00 p.m. on Friday, 19 March.

5aPAc11. Inline process monitoring of thermosets by ultrasonic measurements in a compression mould. M. Rath, G. Hinrichsen (Tech. Univ. of Berlin, Inst. of Nonmetallic Mater., Polymer Phys., Englische Strasse 20, 10587 Berlin, Germany), J. Döring, and W. Stark (Federal Inst. for Mater. Res. and Testing, 12200 Berlin, Germany)

Moulding compounds are heterogeneous materials and consist of granules or pellets, usually mixed with a special resin-hardener combination, reinforcing agents, accelerators, lubricants, pigments, and other additives ready for manufacturing. Thermosetting moulding compounds are defined as raw materials manufacturing plastic parts under the influence of pressure and heat, mainly by compression, transfer, and injection moulding. Current research addresses ultrasonic quality sensor utilization for inline cure monitoring, to control and analyze compression moulding. A ''smart'' process control would require the measurement of elastic moduli and viscosity during cure. In this research, an ultrasonic impulse-transmission method is used to directly monitor changes in the mechanical properties of moulding compounds throughout the cure cycle. Measurements were performed during the processing using transducers which were designed to operate at elevated temperatures and pressures in a compression mould. Measurements of ultrasound velocity and change of attenuation coefficient of longitudinal and shear waves were made throughout the process cycle. Use was made of the ultrasonic measurements to monitor the influence of various parameters on the manufacturing process, such as filler concentration, humidity content, artificial weathering at elevated temperatures, and hardener concentration. [Work supported by Deutsche Forschungsgemeinschaft (DFG).]

5aPAc12. Accurate noncontact measurement of elastic properties of ceramics using acoustic microsopy and laser ultrasonics. C. M. Flannery (Paul-Drude Inst. für Festkörperelektronik, Hausvogteiplatz 5–7, D-10117 Berlin, Germany) and G. M. Crean (Natl. Microelectronics Res. Ctr., Univ. College, Cork, Ireland)

Accurate measurement of elastic properties of advanced materials is of considerable importance for the further development of such materials and their applications. For many materials, data for elastic properties are not available or are unreliable. Noncontact, nondestructive techniques are of particular interest as being suitable for process control and hostile environments. Acoustic microscopy and laser ultrasonic techniques can measure bulk acoustic wave velocities (longitudinal and shear), from which elastic properties may be extracted, but there are many problems with measuring shear wave velocity with acoustic microscopy and with generating and detecting bulk acoustic wave modes using laser ultrasonics. In this work, a dual-probe beam laser interferometer setup is used to measure the velocity of laser-generated surface acoustic waves on materials; these results are combined with measurements of longitudinal velocity obtained with a standard 50-MHz point-focus-beam acoustic microscope. The technique is illustrated and applied to a set of ceramic samples (silicon nitride, silicon carbide, alumina, zirconia). Results are compared to available data and it is shown that elastic properties of isotropic materials (Young's modulus, Poisson's ratio) can be measured by this noncontact, nondestructive method to accuracies of 1% or better. This compares very well to other noncontact measurement methods.

5aPAc13. Some dynamic properties of the nonhomogeneous thermoelastic prestressed media. Valery V. Kalinchuk, Tatyana I. Belyankova, Yury E. Puzanoff, and Irina A. Zaitseva (Res. Inst. of Mech. and Appl. Mathematics, Rostov State Univ., Rostov-on-Don, 344090, Russia, kalin@gis.rnd.runnet.ru)

The problem of steady-state harmonic oscillations is considered for a nonhomogeneous thermoelastic prestressed medium. The mechanical parameters of this medium are considered to be arbitrary, sufficiently smooth functions of one of the coordinates (depth). The oscillations are realized under the action of the load or the rigid stamp oscillated on the medium's surface. Two models of a nonhomogeneous thermoelastic medium are investigated: a nonhomogeneous layer of finite thickness on the undeformed foundation and a nonhomogeneous layer on the surface of the homogeneous half-space. This investigation is based on the numeric construction of the Green's function of the medium and the analysis of this function's properties. The different types of changing with the depth of the numerical parameters of the layer's material have been considered. The maximal changing of the parameters is located near the upper or lower bound of the layer. [Work supported by RFFI.]

5aPAc14. On the investigation of the stressed state of the elastic and piezoelectric bodies. Valery V. Kalinchuk, Tatyana I. Belyankova, Yury E. Puzanoff, and Irina A. Zaitseva (Res. Inst. of Mech. and Appl. Mathematics, Rostov State Univ., Rostov-on-Don, 344090, Russia, kalin@gis.rnd.runnet.ru)

The solutions of the set of dynamic problems on the oscillations of the electroelastic prestressed medium is the basis of the detailed analysis of the influence of the initial stressed state's type and initial stress's value to the structure of the surface wave field and to the resonance phenomena arising from the interaction between the medium and the external concentrated elements. The initial stressed state is considered to be homogeneous or changing with the depth. It has been defined by the parameters of the external concentrated elements under which the initial stress's influence to the dynamics is maximal. The high efficiency of using the resonance phenomena for the nondestructive control of stressed state's character and the initial (residual) stress's value has been established. [Work supported by RFFI.]

FRIDAY MORNING, 19 MARCH 1999 ROOM H1028, 8:00 A.M. TO 12:20 P.M.

Session 5aPPa

Psychological and Physiological Acoustics: Binaural Hearing—Models, Movement and Measures

Leslie R. Bernstein, Chair
Department of Surgery, University of Connecticut Health Center, 263 Farmington Avenue, Farmington, Connecticut 06030, USA

Contributed Papers

8:00

5aPPa1. The normalized correlation: Accounting for NoSπ thresholds with Gaussian and ''low-noise'' masking noise. Leslie R. Bernstein (Surgical Res. Ctr., Dept. of Surgery (Otolaryngol.) and Ctr. for Neurological Sci., Univ. of Connecticut Health Ctr., Farmington, CT 06030), Steven van de Par (IPO, 5600 MB Eindhoven, The Netherlands and Univ. of Connecticut Health Ctr., Farmington, CT 06030), and Constantine Trahiotis (Univ. of Connecticut Health Ctr., Farmington, CT 06030)

Recently, both Eddins and Barber [J. Acoust. Soc. Am. **103**, 2578–2589 (1998)] and Hall *et al.* [J. Acoust. Soc. Am. **103**, 2573–2577 (1998)] demonstrated that ''low-noise'' noise produced more masking of antiphasic tones than did Gaussian noise. Eddins and Barber could not account for this finding by considering changes in the normalized interaural correlation produced by adding antiphasic signals to the diotic maskers. They calculated the normalized correlation subsequent to half-wave, square-law rectification and low-pass filtering. That approach was used successfully by Bernstein and Trahiotis [J. Acoust. Soc. Am. **100**, 3774–3784 (1996)] to account for binaural detection performance as a function of frequency. In this presentation, it will be shown that one can account quantitatively for thresholds obtained with ''low-noise'' noise and with Gaussian noise by incorporating a stage of compression prior to rectification and low-pass filtering. The compressive function employed produces effects similar to those measured along the basilar membrane. Adding compression allows one to account quantitatively for the low-noise-noise and Gaussian-noise thresholds while maintaining a highly successful quantitative account of

the Bernstein and Trahiotis data. Thus the normalized correlation remains a very useful metric that accounts for a wide variety of binaural detection data. [Work supported by NIH-DC-02103 and NIH-DC-00234.]

8:20

5aPPa2. Should normalization be included in cross-correlation-based models of binaural processing? Steven van de Par (IPO, Ctr. for Res. on User-System Interaction, P.O. Box 513, 5600 MB Eindhoven, The Netherlands and Surgical Res. Ctr., Dept. of Surgery (Otolaryngol.) and Ctr. for Neurological Sci., Univ. of Connecticut Health Ctr., Farmington, CT 06030), Constantine Trahiotis, and Leslie R. Bernstein (Univ. of Connecticut Health Ctr., Farmington, CT 06030)

It is generally accepted that cross-correlation-based models of binaural information processing provide excellent qualitative and quantitative accounts of data obtained in a wide variety of experimental contexts. These contexts include binaural detection, lateralization, localization, and the perception of pitch mediated by strictly binaural cues. The purpose of this research was to investigate the application of ''normalization'' as part of the computation of indices of interaural correlation. Such indices have often been utilized to account for binaural detection data but the normalization, to our knowledge, has neither been explicitly studied nor evaluated on its own merits. Normalization ensures that the value of correlation obtained with identical inputs will be $+1$ (or for polarity-opposite inputs, -1). Nevertheless, normalization, as a stage of processing, is not overtly included in modern cross-correlation-function-based models. In this presentation logical arguments and new data regarding the need to include normalization within cross-correlation-based models of binaural detection/discrimination are provided. The new data were obtained while roving the overall levels of the stimuli in a binaural detection task. The data indicate that, to account for binaural detection, an extremely rapid and accurate stage of normalization must be included in cross-correlation-based models. [Work supported by NIH-DC-02103 and NIH-DC-00234.]

8:40

5aPPa3. Dichotic perception of AM and FM signals. E. Ozimek, J. Konieczny, and A. Wicher (Inst. of Acoust., Adam Mickiewicz Univ., ul. Matejki 48/49, Poznań, Poland)

The study deals with the binaurally perceived modulation depth (m_p) of amplitude-modulated signals (Exp. I) and binaurally perceived frequency deviation (Δf_p) of frequency-modulated signals (Exp. II), for their diotic and dichotic perception. Various combinations of modulation depth (m) and frequency deviation (Δf) at the left and right ear were used. It was found that when the interaural difference in modulation depth ($\Delta m = m_l - m_r$) or interaural difference in frequency deviation ($\Delta\Delta f = \Delta f_l - \Delta f_r$) were equal to zero (i.e., diotic perception), the binaurally perceived modulation depth or binaurally perceived frequency deviation were the same as those in monaural perception. For sufficiently small Δm or $\Delta\Delta f$, the perceived modulation depth, or frequency deviation, approximated the mean of the magnitudes presented to the left and the right ear. However, for large interaural differences in Δm or $\Delta\Delta f$, the binaurally perceived quantities were lower than their arithmetic means, and showed nonlinear trends. Comparison of the perceived modulation depths determined in the experiment and those calculated under the assumption of the linear summation of AM signals from the left and the right ear are also discussed.

9:00

5aPPa4. Interaction in the perceived lateralization of two sounds having different interaural time differences. Makio Kashino (NTT Basic Res. Labs., Atsugi, Kanagawa, 243-0198, Japan, kashino@av-hp.brl.ntt.co.jp)

Perceived lateralization of a 0.25-s, 500-Hz test tone was measured in the presence of a 1-s, 1/3-oct band noise centered at 500 Hz. The interaural time difference (ITD) of the noise was fixed at zero, and that of the test tone was varied trial by trial in the range of -500 to 500 μs (negative sign meaning that the left channel signal leads). The test tone started at various temporal positions between 1.25 s before the onset of the noise and 1.25 s after the offset of the noise. Subjects indicated perceived lateral position of each test tone on a left–right axis. It was found that perceived lateralization of test tones presented before the noise was approximately a linear function of ITD. On the other hand, that of test tones presented concurrently with the noise was shifted away from the noise, depending on the ITD relationship between the tone and noise. This contrast effect remained even 1.25 s after the offset of the noise, replicating the previous finding of localization aftereffect [M. Kashino and S. Nishida, J. Acoust. Soc. Am. **103**, 3597–3604 (1998)]. These results suggest rapid gain control of ITD-selective units, probably due to inhibitory mutual interactions.

9:20

5aPPa5. Virtual auditory localization in noise. Mark A. Ericson, W. Todd Nelson (Air Force Res. Lab., 2610 Seventh St., Wright–Patterson AFB, OH 45433, mericson@falcon.al.wpafb.af.mil), and Robert S. Bolia (Veridian, Dayton, OH 45431)

Interfering sounds have different interaural cross correlations (IACCs) depending on the location and environment in which they are produced. IACCs, in addition to signal bandwidth and signal-to-noise ratio, influence localization acuity. Most localization experiments use stimuli presented in the free-field without maskers or with one directional masker [Good and Gilkey, J. Acoust. Soc. Am. **99**, 1108–1117 (1996)]. Hirsh [J. Acoust. Soc. Am. **22**, 196–200 (1950)] and Mershon and Lin [Ergonomics **30**, 1161–1173 (1987)] have measured auditory localization in reverberant environments. However, in these studies the signals and masker(s) were presented in the reverberant environment. No studies have addressed the effects of diffuse noise on auditory localization over headphones. The current study examines the effect of band passing a directional noise signal presented over headphones masked by noises of different interaural cross correlations. The signal-to-noise ratio is varied from $+10$ to -10 dB, and the signal is low-pass filtered at 1.6, 4, 8, and 15 kHz. Findings from this study have implications for models of binaural hearing and the design of directional audio displays.

9:40

5aPPa6. Investigating the precedence effect with a virtual auditory environment. Thomas Djelani (Inst. of Commun. Acoust., Ruhr Universitaet Bochum, D-44780 Bochum, Germany, djelani@aea.ruhr-uni-bochum.de)

Due to the precedence effect humans are capable of localizing sound in reverberant environments. Despite the importance of this effect its mechanism is not completely understood yet. Especially the question of how the precedence effect is controlled by higher levels of the auditory system is still open. A new approach for further investigations of the precedence effect is the use of a real-time virtual auditory-environment system (SCAT-Lab), which allows one to create and auralize virtual rooms. The subjects listen to the presented scenarios via headphones using individual head-related transfer functions (HRTFs). The SCAT-Lab uses a head tracker to measure the listeners head position and orientation and modifies the HRTFs accordingly. The system offers a high degree of flexibility in creating realistic and complex scenarios for psychoacoustic experiments. For example, it can be used to set up the Clifton effect experiment [J. Acoust. Soc. Am. **82**, 1834 (1987)] just by moving one wall in a virtual room. The evaluation of the SCAT-Lab system for precedence effect experiments has been performed to test the possibilities and limits given by this new tool for further psychoacoustic experiments.

10:00–10:20 Break

10:20

5aPPa7. Binaural room scanning—A new tool for acoustic and psychoacoustic research. Philip Mackensen, Uwe Felderhof, Günther Theile (Inst. für Rundfunktechnik, D-80939 München, Germany), Ulrich Horbach, and Renato Pellegrini (Studer, CH-8105 Regensdorf, Germany)

A new technology called ''*binaural room scanning*'' (BRS) is introduced, allowing real-time virtual loudspeaker reproduction in any virtual room. It is based on a special convolution algorithm for auralization and on the involvement of spontaneous head movements by means of a head-

tracking system. A complete set of relevant dummy head HRTFs is measured for each loudspeaker and the resulting response in the original room. The data are stored and used for convolution. Thus the BRS system does not apply room synthesis methods (e.g., ray-tracing), but, in contrast, enables accurate virtual binaural listening in a real (cloned) loudspeaker reproduction room. Since natural head movements are realizable in the simulated sound field, it offers new possibilities in the application of listening tests, not only in the area of room acoustics and loudspeaker reproduction, but also for psychoacoustic research. Examples will be reported.

10:40

5aPPa8. Minimum audible movement angle in vertical, horizontal, and oblique planes: Effects of velocity and frequency content. D. Wesley Grantham and Benjamin W. Y. Hornsby (Dept. of Hearing and Speech Sci., Vanderbilt Bill Wilkerson Ctr. for Otolaryngol. and Commun. Sci., Vanderbilt Univ. Med. School, 1114 19th Ave. S., Nashville, TN 37212)

Minimum audible movement angles (MAMAs) were measured employing a pseudo-virtual method of stimulus presentation. All stimuli were digitally recorded through KEMAR's two ears while he was positioned in an anechoic chamber with moving loudspeakers presenting sounds in one of seven planes: frontal horizontal, lateral horizontal, median sagittal, lateral vertical, or one of three different oblique planes. These recorded binaural stimuli were subsequently played through insert earphones to subjects seated in a darkened sound-insulated room. Subjects had to say on each trial whether a single moving sound moved ''left'' or ''right'' (''up'' or ''down;'' ''front'' or ''back''). With velocity held constant during a run (from 0 to 180°/s), stimulus duration was varied adaptively to track the MAMA threshold. Stimuli were Gaussian noise bursts that were either wideband, 4-kHz low-passed, or 4-kHz high-passed. Results will be discussed in terms of human sensitivity at low and high frequencies to dynamic information provided primarily by (1) changing interaural difference cues (frontal horizontal plane); (2) changing spectral cues (median vertical plane); and (3) combinations of changing interaural and spectral cues. [Work supported by NIDCD.]

11:00

5aPPa9. Marking the starting and ending points of auditory apparent motion: Effect of timing, spatial separation, and azimuth. Thomas Z. Strybel and Diane L. Guettler (Dept. of Psych., California State Univ. Long Beach, Long Beach, CA 90840)

Participants identified the path of auditory apparent motion (AAM), produced by the appropriate timing (burst duration and stimulus onset asynchrony, SOA) of two successive noise bursts (high-pass A-weighted noise at 55 dB). Three burst duration/SOA combinations were tested: 100/50 ms, 400/100 ms, and 400/600 ms. The first two combinations produce AAM; the last was a nonmoving control. The stimulus sequence was presented through two loudspeakers selected from a horizontal array so as to produce two spatial separations (16 and 33°) and three midpoint locations (-23, 0, and 23° azimuth). The actual starting and ending locations were jittered around each midpoint. Participants faced a large cloth screen having a grid pattern and were instructed to identify the cells corresponding to the starting and ending points of the stimulus sequence. At timing values producing motion, the path of motion was displaced in the direction of the motion with the greatest direction effect occurring at 100/50 ms. However, the midpoint between the loudspeakers also affected the path of AAM. At -22° azimuth, the path was displaced toward the left, regardless of motion direction. At 22° azimuth the path was displaced toward the right. This midpoint effect was obtained only at timing values producing AAM.

11:20

5aPPa10. Changes in perceived velocity following adaptation to simulated auditory motion. Hisashi Uematsu and Makio Kashino (NTT Basic Res. Labs., 3-1, Morinosato-Wakamiya, Atsugi, Kanagawa, 243-0198 Japan, hisashi@av-hp.brl.ntt.co.jp)

To investigate whether adaptation to auditory motion can cause changes in perceived velocity, measurements of perceived velocity were conducted for apparently moving stimuli produced by varying only interaural time differences (ITDs). Following adaptation to a 10-s 500-Hz tone, a 500-Hz test tone was presented, followed by a 250-Hz standard tone. The velocity (ITD change rate) of the adapter tone was chosen from the range of 300 to 2400 μs/s, and that of the standard tone was fixed at 300 μs/s. Subjects judged which of the test and standard tones was perceived as moving faster. The constant method was used to obtain the velocity of the test tone judged to be equal to that of the standard tone. It was found that the perceived velocity of the test tone following adaptation was slower than the physical value by up to 70 μs/s. Adaptation did not affect the perceived direction of the test tone in the present velocity range of the adapting and test tones. These results indicate that adaptation to auditory motion cannot only produce countermotion of a physically stationary sound, as has been reported, but also cause changes in perceived velocity of a moving sound. Theoretical implications will be discussed.

11:40

5aPPa11. Effects of the spatial distribution of competing sounds on speech reception thresholds. John F. Culling, Monica L. Hawley, and Ruth Y. Litovsky (Hearing Res. Ctr. and Dept. of Biomed. Eng., 44 Cummington St., Boston Univ., Boston, MA 02215, cullingj@cf.ac.uk)

The experiment tested whether listeners can suppress competing sound from several different locations simultaneously. Speech reception thresholds were measured adaptively in anechoic virtual auditory spaces with a target voice directly ahead and competing sounds in four spatial configurations. Three concurrent competing sounds were distributed on the horizontal plane among consecutively numbered positions at 30-degree intervals, position 4 being directly ahead, 1 far left, and 7 far right. The competitor configurations were 444, 367, 567, and 777. Four types of competing sound were used: speech (same voice), reversed speech, speech-shaped noise, and speech-modulated, speech-shaped noise. The patterns of results across spatial configurations were similar for each type of competitor, although binaural advantage (777 vs 444) was 2–3 dB greater for speech competitors than for noise. Speech gave thresholds 3 dB higher than reversed speech throughout, suggesting linguistic interference effects. Most notably, however, 567 and 777 always gave similar thresholds (7–10 dB lower than 444). The multiple source locations of 567 produce a sound field with relatively low interaural coherence, but binaural unmasking experiments indicate that masking release demands maskers of high within-channel interaural coherence. Multiple competing sources on both sides (367) were more difficult to suppress. [Work supported by MRC and NIH.]

12:00

5aPPa12. Audiometry for binaural hearing. Juerg M. Stettbacher (Swiss Federal Inst. of Technol. (ETH), Zurich and Signal and Information Processing Lab, CH-8092 Zurich, Switzerland, stettbac@isi.ee.ethz.ch)

As traditional audiometry is based on very artificial conditions, the results in many cases do not coincide with practical experience in everyday life. The accuracy of the so-called useful hearing loss in legal cases has been questioned many times. A new procedure is therefore proposed. It is based on real acoustic free-field situations reproduced over a loudspeaker array. The sound field is controlled by using digital signal processing. The kinds of measurements and stimuli have been derived from a model of cognitive hearing. Different measurement types consider different aspects of natural hearing. An assessment model helps to combine the results from various measurements to a single index. It directly describes the useful hearing loss with respect to everyday hearing. It is not intended to serve as a diagnostic tool, but as a useful and accurate measure in legal or insurance cases. Results from first experiments will be presented.

Session 5aPPb

Psychological and Physiological Acoustics: Hearing Impairment I (Poster Session)

M. Patrick Feeney, Chair
School of Hearing and Speech Science, Ohio University, Lindley Hall, Room 218, Athens, Ohio 45701-2979, USA

Contributed Papers

All posters will be on display in the Poster Gallery from Thursday to Friday, 18–19 March. Authors will be at their posters from 8:00 a.m. to 10:00 a.m. on Friday, 19 March.

5aPPb1. A comparison of power-based and admittance measures of the acoustic reflex threshold. M. Patrick Feeney, Kristen L. Smith (Ohio Univ., School of Hearing and Speech Sci., Lindley Hall Rm. 218, Athens, OH 45701, feeney@ohiou.edu), and Douglas H. Keefe (Boys Town Natl. Res. Hospital, Omaha, NE 68131)

Contralateral acoustic reflex thresholds obtained using a standard clinical admittance system with a 220-Hz probe tone were compared to those obtained using a frequency-domain-based system for calculating wideband middle ear acoustic impedance and energy reflectance (ZR) [D. H. Keefe *et al.*, J. Acoust. Soc. Am. **91**, 470–485 (1992)]. A white noise activator presented through an ER-3A insert phone was used to elicit the contralateral reflex in ten normal-hearing young subjects. The probe signal, a 40-ms wideband chirp, was presented through an ER-10C microphone system for the ZR measures. The microphone signal was then digitized and stored for data analysis. Measurements of reflex-induced changes in the power absorbed by the middle ear and in wideband admittance were then derived to estimate reflex thresholds. An analysis of variance revealed that the average reflex threshold was about 16 dB lower for the power-based and wideband admittance measures than for the clinical measure ($p<0.001$). However, the two ZR measures were not significantly different from each other. These results have implications for reducing the level of sound exposure during clinical acoustic reflex testing, and for obtaining reflex thresholds that may be beyond system limits for standard clinical systems. [Work supported by OURC.]

5aPPb2. Performance of children on the Multisyllabic Lexical Neighborhood Test as a function of the number of channels of stimulation. Michael Dorman (Dept. of Speech and Hearing Sci., Arizona State Univ., Tempe, AZ 85287-0102, mdorman@imap2.asu.edu), Philip Loizou (Univ. of Arkansas, Little Rock, AR), Mario Svirsky, and Karen Kirk (Univ. of Indiana School of Medicine, Indianapolis, IN)

When monosyllabic words are processed in the manner of cochlear implant signal processors and are presented to adult, normal-hearing listeners for identification, 4 channels of stimulation allow mean scores of 48% correct, 6 channels allow 71% correct, 8 channels allow 87% correct, and 12 channels allow 89% correct. When patients fit with cochlear implants are tested with the same material, only 7% of the patients achieve scores in the range of scores for normals with 8 channels, 28% achieve scores in the range of 6 or more channels, 61% achieve scores in the range of scores for 4 or more channels and 39% achieve scores below that of normals with 4 channels. The aim of the research to be reported was to collect, for both normal-hearing children and children with cochlear implants, scores on the Multisyllabic Lexical Neighborhood Test. The results will provide a window on the effective channels of stimulation delivered to children who use cochlear implants with 8–20 physical channels of stimulation.

5aPPb3. Temporal jitter disrupts speech intelligibility: Simulations of auditory aging. M. Kathleen Pichora-Fuller (School of Audiol. and Speech Sci., Univ. of British Columbia, 5804 Fairview Ave., Vancouver, BC V6T 1Z3, Canada, kpf@audiospeech.ubc.ca), Bruce A. Schneider (Univ. of Toronto, Mississauga, ON L5L 1C6, Canada), and Hollis Pass (Univ. of Britsh Columbia, Vancouver, BC V6T 1Z3, Canada)

Declines in auditory temporal processing have been observed in aging adults and may partially account for their difficulty in understanding spoken language. To mimic age-related loss of synchrony, sentences were temporally jittered. Intact and jittered SPIN sentences were presented in background babble, and sentence–final word recognition was measured in young listeners with normal hearing. If $x(t)$ is the input signal, the internal representation of the signal, $y(t)$, is assumed to be a time-delayed version of the input with the time delay, d, varying over time as $y(t)=x[t-d(t)]$. The first factor contributing to the jitter is the range of delays that might occur over time, modeled as the rms value of a band-limited noise. The second factor is the rate at which delays change, modeled as the bandpass of a band-limited noise. Word recognition was unchanged when the second factor dominated the jitter (rms=0.05 ms, BW=500 Hz), reduced slightly (10%) when the first factor dominated (rms=0.25 ms, BW=100 Hz), and reduced greatly (50%) when both factors contributed to the jitter (rms=0.25 ms, BW=500 Hz). This work is a first attempt to simulate temporal aspects of auditory aging.

5aPPb4. Rupture pressures of membranes in the ear. Magne Kringlebotn (Dept. of Phys., Norwegian Univ. of Science and Technol., N-7034 Trondheim, Norway)

The rupture pressure differences across the tympanic membrane, the round window membrane, and Reissner's membrane, as well as the force and corresponding pressure at the stapes footplate that causes the annular ligament to rupture, have all been measured in cadaver ears from Norwegian cattle. Reported mean rupture pressures are 0.41 atm for the tympanic membrane, larger than 2 atm for the found window membrane, 0.048 atm for Reissner's membrane, and 30 atm for the oval window annular ligament. The latter pressure corresponds to 0.68-kg force applied to the footplate, having a mean area of 2.25 square mm. The ruptures of the tympanic membrane in cattle appeared without exception as small tears in the pars flaccida, quite opposite to human ears where ruptures in this area are very rare. The weakness of the pars flaccida is probably the reason for a lower rupture pressure for the tympanic membrane in cattle than in man. The rupture pressure of the tympanic membrane has also been measured in a few ears from fox.

5aPPb5. Prediction of post-operative profits in cochlear implanted people using electrical stimulation test results. Henryk Skarzynski, Andrzej Czyzewski, and Bozena Kostek (Inst. of Physiol. and Pathol. of Hearing, ul. Pstrowskiego 1, 01-943 Warsaw, Poland)

There are few techniques adequate for assessing the remaining sensitivity of a hearing nerve in deaf people or those with a severe hearing loss. The procedures developed at the Institute of Physiology and Pathology of Hearing in Warsaw allow the determination of some vital characteristics of the hearing sense that help to make decisions regarding the cochlear implantation. The post-operative profits evaluation is also very important in the case of cochlea implanted persons. Apart from standard preexamination procedures, a test based on the electrical stimulation via the external auditory canal filled with saline can be performed. In order to evaluate the test results, both the dynamics range defined by the auditory threshold and the uncomfortable loudness level and the time difference limen test are considered. However, usually the results of electrical stimulation tests are highly diversified, depending on a patient's age and condition, thus there was a need to create a database allowing one to find and to study the correlation between obtained test results and patients' ability to receive and understand sounds. In this way, the interpretation of the electrical stimulation test results for the new diagnosed cases was made more reliable. [Work supported by KBN, Poland, Grant No. 4 P05C 082 12.]

5aPPb6. The impact of placement of noise sources on directional hearing aid benefit. Todd Ricketts (Purdue Univ., West Lafayette, IN, toddr@purdue.edu)

The impact of the number and position of noise sources on measured directional hearing aid benefit was investigated. Directional benefit was quantified as the difference between hearing-in-noise test (HINT) signal-to-noise ratios for omnidirectional and directional hearing aid conditions. Noise environments included a single noise source placed at 180-degree azimuth, and three different five source arrays. All noise sources were uncorrelated and simulated noise only in the rear hemisphere, or noise surrounding the listener. Binaurally fit subjects listened through three different commercial hearing aids with significantly different polar directivity patterns. Testing was completed in two different reverberant environments with average reverberation times of 642 and 1456 ms. The relative level of hearing aid benefit differed significantly depending on the specific noise array used. Results revealed that the pattern of directional benefit across the noise environments could generally be predicted from differences in the hearing aids average polar directivity patterns. The directional benefit across hearing aid types revealed a similar pattern in both reverberant environments, though less benefit was generally obtained in the more reverberant environment in agreement with previous investigations of directional hearing aids. These results suggest that some previous investigations of directional benefit may need reevaluation.

FRIDAY MORNING, 19 MARCH 1999 POSTER GALLERY, 10:00 A.M. TO 12:00 NOON

Session 5aPPc

Psychological and Physiological Acoustics: Hearing Impairment II (Poster Session)

Oliver Wegner, Chair
AG Medizinische Physik, Universität Oldenburg, D-26111 Oldenburg, Germany

Contributed Papers

All posters will be on display in the Poster Gallery from Thursday to Friday, 18–19 March. Authors will be at their posters from 10:00 a.m. to 12:00 noon on Friday, 19 March.

5aPPc1. Communication problems in noisy workplaces for normal hearing and hearing-impaired employees. Bas A. Franck, Wouter A. Dreschler (Dept. of Exp. Audiol., Academic Medical Ctr., P.O. Box 22660, NL-1100 DD, Amsterdam, The Netherlands, b.a.franck@amc.uva.nl), Alexandra D. Pastoors, and Juergen Kiessling (Justus-Liebig Univ., D-35385 Giessen, Germany)

Although much is known about hearing impairment, there is a real lack in knowledge about the relation between unfavorable listening conditions and the individual hearing capacities of normal-hearing and hearing-impaired listeners. Moreover, occupational communication problems are hardly exploited. Therefore, a suitable questionnaire has been developed that is based on studies of Gatehouse (1994), Kapteyn and Kramer (1997), and Boermans (1997). The questionnaire was completed by four different subgroups that cover hearing-impaired subjects with and without hearing aids and normal-hearing subjects that work in soft or loud background noise. It appears that most hearing-impaired employees mainly suffer from speech-related soft noises, especially in communicative tasks. Loud noises are annoying for all subgroups, whereas reverberation causes only problems in high noise levels. Localization and identification appear to be strongly related and are only problematic for a subset of the hearing-impaired subjects, without hearing aids. Interindividual differences between subjects suggest a need for flexible communication devices. These devices should combine functions of selective amplification, protection, recognition of warning sounds, and reduction of noise and reverberation. [Work supported by TAP.]

5aPPc2. Effects of selective serotonin reuptake inhibitors on auditory processing. K. Gopal, D. M. Daly, R. G. Daniloff, and L. Pennartz (Speech and Hearing Sci., Univ. of North Texas, Denton, TX 76203 and Hugin, Box 210855, Dallas, TX 75211-0855)

In mammalian auditory systems, serotonergic and cholinergic systems modulate inhibition of GABA-ergic interneurons. Auditory processing has been evaluated in a patient who suffered withdrawn depression, lethargy, hypersensitivity to touch/pressure, light, and sound (but not taste/smell), and difficulty understanding speech. Treatment with fluvoxamine and fluoxetine, selective serotonin reuptake inhibitors, reversibly alleviated complaints. A sibling is similarly afflicted. Testing while medicated and at least 15 days after voluntary withdrawal (unmedicated; symptomatic without depression) revealed pure tone, SRT, word discrimination scores, tympanograms, and acoustic reflex thresholds within normal limits. Medicated

SCAN-A results were normal; unmedicated results were disordered. Unmedicated, both otoacoustic emissions and ABR waves I, III, and V, were significantly larger, bilaterally. Central processing and vigilance were evaluated with sets of sparse acoustic stimuli. While medicated, responses to stimuli at each ear revealed well-defined transitions ($p<0.0001$) over 90 min. Vowels were homogeneous with controls; **/ge/je/**, **/be/we/**, and **/be/de/ge/** were markedly shorter and consistently differed from normals ($p<0.0001$; the /*de*/ of **/be/de/ge/** covered approximately 200 Hz). During unmedicated testing, responses to **/ge/je/** began at medicated levels but approached chance levels over 10 min; responses to **/be/we/** were consistent (and aberrant) throughout.

5aPPc3. The changing loudness aftereffect following adaptation to visual motion-in-depth. Norimichi Kitagawa (Dept. of Psych., Tokyo Metropolitan Univ., 1-1 Minami Osawa, Hachioji, Tokyo, Japan)

After exposure to a sound increasing or decreasing in level, a steady sound is perceived as changing loudness in the opposite direction. This study shows that this auditory aftereffect of changing loudness results from adaptation to a visual motion-in-depth, too. A visual adapting stimulus was a square of fixed size which changes in retinal disparity, so that it appears to move toward or away from the subject. The increasing or decreasing 1000-Hz tone was used as an auditory adaptation stimulus. The magnitude of the aftereffect was measured after adaptation to each of the following conditions: (a) auditory stimulus only; (b) auditory and visual stimuli in the same direction (increasing and moving toward, or vice versa); (c) auditory and visual stimuli in the opposite direction (increasing and moving away from, or vice versa); and (d) visual stimulus only. The aftereffect was observed in any of these conditions, and even in condition (d). The magnitude of the aftereffect reached the maximum in condition (b). The aftereffect in condition (c) was almost the same as that caused in condition (a). These results suggest that the mechanism processing the change in level in auditory system responds to the visual motion-in-depth.

5aPPc4. Classification of the acoustic environments using a psychoacoustic model. Melanie Ostendorf and Volker Hohmann (Graduiertenkolleg Psychoakustik and AG Medizinische Physik, Univ. Oldenburg, Germany)

Complex digital hearing aid algorithms employ different signal processing stages, e.g., noise reduction and loudness control. Most of these stages are suitable only for special acoustic environments or need different parameter sets for different environments to assure optimum rehabilitation success. Future ''intelligent'' digital hearing aids should therefore incorporate a model of the acoustic environment to adapt the signal processing to the acoustic environment. In particular, the presence of a speech signal and of different types of ambient noise should be detectable. In this study, the perception model introduced by Dau *et al.* [J. Acoust. Soc. Am. **102**, 2829–2919 (1996)], which was originally developed to model different psychoacoustical tasks, e.g., forward masking and modulation detection is used as a preprocessor for this type of classification algorithms. This approach seems promising, as the model includes a modulation frequency analysis which was shown to be a good estimator of speech activity [Ostendorf, Fortschritte der Akustik DAGA 98, Zürich]. First results on the classification accuracy using this model are presented.

5aPPc5. On the relationship between auditory evoked potentials and psychophysical loudness. Oliver Wegner (Graduiertenkolleg 'Psychoakustik', Carl-von-Ossietzky-Universität, Oldenburg, Germany), Torsten Dau, and Birger Kollmeier (Carl-von-Ossietzky-Universität, Oldenburg, Germany)

This study examines the question of whether the neurophysiological events reflected by the auditory evoked potentials are similar to the events underlying loudness perception. Recent studies showed that, at brainstem level, loudness does not seem to be directly related to the potential amplitude (wave V). This is the case for the loudness growth function for tone pulses [J. K. Nousak and D. R. Stapells, ''Loudness and the ABR/MBR in noise-masked normal-hearing subjects,'' ARO meeting, p. 39 (1998)] as well as for loudness summation obtained with optimized chirp stimuli [Wegner *et al.*, ''Untersuchungen zu Lautheitskorrelaten in akustisch evozierten Potentialen,'' DAGA 98, Zürich (in press)]. In both conditions, the results obtained with early evoked potentials suggest a higher compression as that normally derived from psychophysical data and as reflected in common loudness models. This study presents brainstem and cortical potentials evoked by bandlimited stimuli of equal loudness. The role of the synchronization, stimulation rate, and temporal integration at both processing levels is discussed.

5aPPc6. Conductive hearing losses caused by static pressure differences in the ear. Magne Kringlebotn (Dept. of Phys., Norwegian Univ. of Science and Technol., N-7034 Trondheim, Norway)

The frequency characteristics of sound transmission loss in the ear have been measured as a function of the static pressure difference across the tympanic membrane as well as the static pressure difference between the inner ear fluids and the middle ear. The measurements have been performed on cadaver ears from Norwegian cattle. On average, for an increasing static overpressure in the ear canal up to 10 cm of water in magnitude, the transmission loss below 1 kHz increases rapidly to about 13 dB for positive overpressures and to about 9 dB for negative, and then more slowly to about 28 and 26 dB at 60 cm of water. At higher frequencies the transmission losses become smaller, but are markedly different for positive and negative overpressures in the ear canal. The sound transmission in the ear is little influenced by a pressure increase in the inner ear fluids.

Session 5aSAa

Structural Acoustics and Vibration: Vibrations of Complex Structures

John J. McCoy, Cochair
School of Engineering, Catholic University of America, Washington, DC 20064, USA

Yuri I. Bobrovnitskii, Cochair
Laboratory of Structural Acoustics, Mechanical Engineering Research Institute, M. Kharitonievsky 4, Moscow 101830, Russia

Contributed Papers

8:20

5aSAa1. Determination of Young's modulus and internal friction coefficient from flexural wave in thin bars. Qiushuang Guo and David A. Brown (Acoust. Res. Lab., Dept. of Elec. and Computer Eng. and Ctr. for Marine Sci. and Technol., UMass—Dartmouth, North Dartmouth, MA 02747, dbrown@umassd.edu)

The flexural wave equation including internal friction and the correction due to rotatory inertia and shear deflection for thin bars is solved. The system response of the forced-free bar excited in flexural vibrations is obtained. Corrections for rotatory inertia and shear deflection have to be included for a best fit. The numerical factor representing the correction effect of shear deflection is smaller than previous results which means that shear deflection has a greater correction contribution than previously thought. At low-frequency range, the Young's modulus obtained from flexural modes is different from that from longitudinal modes. This may suggest that more correction effects need to be included for the flexural system. [Work supported by the Ph.D. Program and the Strategic Environtechnology Partnership (STEP) through the Advanced Technology Center at the University of Massachusetts Dartmouth.]

8:40

5aSAa2. Vibration analysis of rotating Euler beam. Kuo Mo Hsiao (Dept. of Mech. Eng., Natl. Chiao Tung Univ., Hsinchu, Taiwan, ROC)

The objective of this paper is to derive an exact expression for linear vibration equations of a rotating Euler beam, and investigate the effect of Coriolis and centrifugal force on the natural frequency of the rotating beam. Consider a uniform Euler beam rigidly mounted on the periphery of a rigid hub, which rotates about the hub axis fixed in space at a constant angular speed. The deformational displacements of the beam are defined in a rotating rectangular Cartesian coordinate system which is rigidly tied to the hub. The vibration of the beam is measured from the position of the steady-state axial deformation, and only infinitesimal free vibration is considered. The equations of motion for the rotating Euler beam are derived by the d'Alembert principle and the virtual work principle. In order to capture all inertia effect and coupling between extensional and flexural deformation, the consistent linearization of the fully geometrically nonlinear beam theory is used in the derivation. A method based on the power series solution is proposed to solve the natural frequency. Numerical examples are studied for the natural frequency of rotating beams with different angular velocity and setting angle.

9:00

5aSAa3. Statistical energy analysis of two spring-coupled oscillators. Svante Finnveden (Dept. of Vehicle Eng., KTH, 100 44 Stockholm, Sweden, svantef@fkt.kth.se)

The response of two spring-coupled oscillators is investigated to develop our understanding of the weak coupling assumption in the modal approach to statistical energy analysis (SEA). The oscillators have stochastic uncoupled resonance frequencies that are normal distributed. For this case, the SEA coupling power proportionality holds for the ensemble average response, even for single frequency excitation, provided that a suitable definition of modal energy is adopted. It is seen that strength of coupling, from an ensemble point of view, is defined by the nondimensional ''interaction strength.'' This quantity may, for multi-modal systems, be interpreted as the ratio of the SEA conductivety to the product of the modal overlaps in each element, in which case the strength of the coupling measure agrees with the one that previously was found to govern the ensemble-averaged energies in one-dimensional wave guide systems.

9:20

5aSAa4. A clamped beam, images solution. Jonas Brunskog (Dept. of Eng. Acoust., LTH, Lund Univ., P.O. Box 118, SE-221 00 Lund, Sweden, Jonas.Brunskog@kstr.lth.se)

The method of images is a well-known idea in theoretical physics, but not often used in structural acoustics. When considering the problem of obtaining Green's function for a general bounded domain, the reflection is described by an image source, and position and sign of the image is chosen to fulfill the boundary conditions. The Green's function can then be found as the superposition of the free Green's function for the two sources. Consider now a finite beam, clamped at the boundaries and driven by a point force. In order to make use of periodicity, expand the region along the x axis. To the original force an infinite number of image sources were added. The image expansion is even, and the clamped boundaries convert to simply supported edges. The reforcing supports are introduced in the equation as infinite sums. The system is now infinite, implying Fourier transforms to be used on the spatial coordinate. The transformed displacement and inverse transform are solved for formally. The support forces are related to the beam displacement, so that the yet-unknown reaction forces are solved for. The resulting infinite sums are given explicitly using the Poisson sum formula and the contour integration.

9:40–10:00 Break

10:00

5aSAa5. Modal overlap and dissipation effects in a fuzzy structure containing a continuous master element. Michael V. Drexel and Jerry H. Ginsberg (G. W. Woodruff School of Mech. Eng., Georgia Inst. of Technol., Atlanta, GA 30332-0405, jerry.ginsberg@me.gatech.edu)

This work was prompted by a study by Strasberg [J. Acoust. Soc. Am. **102**, 3130(A) (1997)] in which a large suspended mass had numerous small spring–mass–damper systems attached to it. The system parameters in his model were selected such that the isolated natural frequency of each attached system was close to the natural frequency of the isolated master structure. Strasberg found when an impulse excitation is applied to the master structure, the critical issue is the bandwidth of the isolated attached systems in comparison to the spacing between the natural frequencies of

those systems. Modal overlap, which corresponds to bandwidths that exceed the spacing of those frequencies, was shown to lead to an impulse response that decays exponentially. In contrast, light damping leads to an impulse response that consists of a sequence of exponentially decaying pulses, due to delayed energy return from the subsystems. The present work explores these issues for continuous systems by replacing the one-degree-of-freedom master structure with a cantilevered beam. The system parameters are selected to match Strasberg's model, with the suspended subsystems placed randomly along the beam. The beam displacement is represented as a Ritz series whose basis functions are cantilever beam modes. The coupled equations are solved by a state–space eigenmode analysis that yields a simple closed-form representation of the response in terms of the complex eigenmode properties. The continuous fuzzy structure is shown not to display the transfer of energy between the master structure and the substructures exhibited by the discrete fuzzy structure, apparently because the attachment points move asynchronously due to the spatial dependence of the beam's displacement.

10:20

5aSAa6. Reflection and transmission at an attachment half-space. John J. McCoy (Catholic Univ. of America, Washingon, DC 20064)

The reflection and transmission at the connection of an attachment half-space to a core half-space that contains a source of mechanical energy and one or more scatterers is considered. Both the attachment and core half-spaces have property measures that are invariant with distance from the connection plane, but may vary with position in planes parallel to the connection plane. At issue is the construction of a reflection operator that both applies at the connection plane and is expressed in terms of operators that separately describe the responses of the half-spaces at the connection plane, i.e., of impedance operators that can be written for the half-spaces in isolation. A successful construction is achieved for a connection that spans the entire connection plane. For this scenario, the construction achieved is easily identified as a generalization of a ''nonreflecting boundary condition,'' in that the reflection operator obtains no reflection for any incident field, if the impedance operators for the two half-spaces are the same. The achieved construction is next demonstrated to *not* apply for a connection that spans only a finite portion of the connection plane, i.e., an aperture. For this second scenario, pressure release conditions apply for both half-spaces at points on the connection plane that are outside the aperture. The reason for the failure is the impedance operators that apply in the context of a full-plane connection are not uniquely described for a connection that applies to a finite aperture. That is, mobility operators that can be identified with the DtN map obtained on factoring a two-way description of the fields in the half-spaces into separated one-way descriptions, are uniquely defined regardless of the connection region. However, the inverse of this mobility operator requires connection across the entire plane. The implication of this demonstration for more complex experimental scenarios in both propagation modeling and structural acoustics is discussed.

10:40

5aSAa7. Localized modes of long floating structures. Dmitri Azalinov (Inst. for Problems in Mech. Eng. RAS, Bolshoy pr. V. O. 61, St. Petersburg 199178, Russia, azalinov@hidro.ipme.ru)

The paper is devoted to the problem of fluid–structure interaction. Nowadays the problems of construction and maintenance of buoyant air stations arouse large interest. As a rule, a buoyant air station is a long plate of defined width and it locates near a shore at a small depth. It means that for the construction of a mathematical model one can use the equations of the thin plate oscillations on shallow water. It is shown in what frequency ranges the propagation of bending-gravitation waves is possible. Apart from cutoff frequencies a real spectrum of eigenfrequencies and conditions of its existence have been determined. The presence of such frequences makes possible phenomena of wave localization in area of the plate and its resonance. The localization of a standing wave type occurs in one of the directions, at the same time the wave propagation occurs in the perpendicular direction. The eigenmode is symmetrical and has maximum in the middle of the plate. The parameters of a plate–liquid system have been determined, when these effects can be possible. These problems have been solved with a combination of analytical and computer approaches.

11:00

5aSAa8. Elastic wave scattering on a rod-like inclusion. Nikolai A. Lavrov (Inst. for Problems of Mech. Eng. of Russian Acad. of Sci., Bolshoi Prospect 61, St. Petersburg, 199178, Russia, lavrov@euler.ipme.ru)

Wave propagation in an infinite (or semi-infinite) elastic solid containing a thin curvilinear rod-like inclusion (or liquid-filled cavity) is under consideration. The materials of the inclusion and the medium are isotropic, homogeneous, and linearly elastic. They differ in mass density, Young's modulus, and Poisson's ratio. The transversal size of the inclusion is much smaller than the large linear size which is assumed to be comparable with the incident wavelength. Numerical implementation of the direct methods (FEM, BEM, FDM, and their combinations) is connected with the principal difficulty caused by the degeneration of the region (presence of a small geometrical parameter). To overcome this obstacle an asymptotic decomposition is carried out. The original problem is reduced to two problems of decreased dimension. The first one is governed by the integral equation over the rod axis and describes the spatial dynamic effects of the process. The second one is 2-D problem of elastostatics. It is governed by the system of integral equations over the cross section and describes the deformation of it. The deflection of the cylindrical inclusion and the stress concentration are calculated in the case of the normal incidence.

11:20

5aSAa9. A boundary controller for realistic double-panel partitions; Feasibility and experimental validity. B. Jemai, Mohammed N. Ichchou, and L. Lezequel (Laboratoire de mecanique des solides, 36, avenue de Guy de colongue 69009, Ecully, France, jemai@ec.lyon.fr)

The double-panel partitions are often used in noise control engineering because of their high attenuation capacity of noise. In the literature, simply supported panels with thick fluid cavities are considered to investigate the physical phenomena governing the vibro-acoustic behavior. In this study, a realistic partition is considered. It is a set of two flat rectangular and glass panels and three rubber bands and a frame. The panels are fixed to each other and to the frame using the rubber bands as separators at the edges. A numerical model taking into account possible motion of the panel's boundaries and the fluid–structure interaction is developed. The influences of the rubber stiffness and the panel's mass-to-stiffness ratio and the fluid cavity thickness on the pumping mode are considered. The study shows that a double-panel partition where rubber band rigidity is higher than the equivalent rigidity of the fluid cavity is not interesting because it behaves as a single panel. However, the partition with lower rubber rigidity provides higher attenuation in all the frequency domain except near the mass–air–mass mode where an active structural control is shown possible by partial piezoelectric sheets at the panel's boundaries. A comparison with an experimental study is proposed in this work.

11:40

5aSAa10. Combined damping treatments. A. Nikiforov (Krylov Shipbuilding Research Inst., 196158, Moskovskoe Shosse 44, St. Petersburg, Russia, krylspb@sovam.com)

At present, to decrease a vibration of engineering structures three main types of damping treatments are used: (i) layer of hard viscoelastic plastic with sublayer of hard light plastic; (ii) layer of soft viscoelastic plastic or rubber, constrained by thin hard layer; and (iii) layer of thickness viscoelastic material. All these treatments ensure effective vibration damping at a limited frequency range. Structures of combined damping treatments uniting properties of some of the above-mentioned ones are proposed. Damping effectiveness of proposed treatments is essential at more wide frequency range. Formulas to estimate the loss factor of combined treatment are given. Measured loss factor of one of the proposed treatments is shown. Data of an experiment and an estimation are close to each other.

12:00

5aSAa11. On the acoustical properties of cylindrical shells and pipe sleeves. D. Gužas (Lithuanian Agricultural Acad., Vilnius 2007, Lithuania)

Acoustical properties of cylindrical shells and pipes differ greatly from plane sound insulation properties. Sometimes opposite results are achieved, especially at low frequencies. The report presents these differences and causes that have been proved theoretically. The sound permeability through sleeves has not been fully investigated as yet. Here analysis and comments of the works performed are presented.

FRIDAY MORNING, 19 MARCH 1999 ROOM EB301, 9:00 TO 11:00 A.M.

Session 5aSAb
International Workshop on Active Noise and Vibration Control

Structural Acoustics and Vibration: Active Control in Aircraft Engines

Rudolf Maier, Cochair
Daimler Benz Forschung und Technik, Postfach 80 04 65, 81663 Muenchen, Germany

Ricardo Burdisso, Cochair
Vibration and Acoustics Laboratories, Virginia Polytechnic and State University, Blacksburg, Virginia 24061, USA

Invited Papers

9:00

5aSAb1. An overview of the fan active noise control effort at NASA, Lewis. Lawrence J. Heidelberg (NASA, Lewis Res. Ctr., 21000 Brookpark Rd., Cleveland, OH 44135, l.j.heidelberg@lerc.nasa.gov)

NASA, Lewis began an effort, several years ago, in the area of fan tone active noise control. This effort was part of the Advanced Subsonic Transport Program. The effort consists of two parts: (1) building a test facility (the active noise control fan) to allow proof of concept testing, and (2) a contract effort to bring several concepts to the test phase. This paper will describe the test facilty and its unique capabilities such as a continuously rotating rake to measure the complete modal structure of the fan tones. Concepts tested will be described and the test results will be briefly discussed. All the concepts involve modal control. The concepts range from a single wall actuator array to control a single radial mode order, to multiple orders in both inlet and exhaust ducts using active vanes. In addition, a hybrid system (active+passive elements) and active treatment system will be presented. The performance of these systems will be discussed in terms of mode and tone total power reduction.

9:20

5aSAb2. Application of active control techniques to the turbomachine fan noise reduction. J. Julliard, Ch. Lozachmeur, and D. Berge (SNECMA, Site de Villaroche, 77550 Moissy-Cramayel, France)

Fan noise is a dominant source in future high-bypass engines with a lower and more extended frequency signature. The reduced efficiency of passive liners with thinner and shorter nacelles leading to a more severe noise legislation requires work on active technologies in order to reduce even better the fan noise radiation (especially tones) in the near and far fields. This paper deals with active noise control (ANC) applied to the reduction of fan tones. The described investigation is an experimental study performed on a fan model installed in an anechoic chamber. Error sensors are successively located in the near-field radiation and flush mounted in the forward and aft duct fan. Loudspeakers are used as actuators to generate a secondary acoustic field. A moving antenna in the far field measures the noise radiation and the zones of silence. A new multi-channel controller, highly efficient in terms of frequency and channel number, is used. Transfer functions between actuator and sensors are analyzed and numerical simulation calculations are achieved for optimization of the number and location of error sensors and actuators. Fundamental tone of the fan is controlled with reductions up to 10–15 dB.

9:40

5aSAb3. A modal concept for active noise control in circular or annular ducts. Yanchang Zhang,[a] Lars Enghardt, and Wolfgang Neise (DLR-Inst. fuer Antriebstechnik, Abteilung Turbulenzforschung Berlin, Mueller-Breslau-Strasse 8, 10623 Berlin, Germany)

A new active noise control strategy is presented which is aimed at reducing circumferential as well as radial acoustic modes in circular and/or annular ducts as used, for example, in aircraft engines. The azimuthal mode structure of the duct sound field is measured by using circumferentially spaced sensors in several axial planes which are mounted flush with the inner duct wall. No attempt is made to control the entire primary sound field, but only the dominant azimuthal modes which are propagational in the duct. With this procedure, the number of control variables is greatly reduced. The radial modes are reduced in an indirect way, i.e., the exact radial mode structure of the primary sound field in the duct need not be known for this purpose. [a]Now with LUK GmbH & Co., Industriestrasse 3, 77815 Buehl, Germany.

10:00

5aSAb4. Active flow control using MEMS actuators to reduce fan noise. Jinwei Feng, Nikhil Rao, Ricardo A. Burdisso, and Wing F. Ng (Vib. and Acoust. Labs., Mech. Eng. Dept., Virginia Tech, Blacksburg, VA 24061-0238)

Active flow control is employed for wake filling in the upstream guide vanes of a fan stage to reduce the unsteady pressure on the downstream rotor blades. Micro-electro-mechanical systems (MEMS)-based micro-valves are used to control precisely the amount of blowing air used to energize the low velocity wake fluid coming off the trailing edge of the stationary blades. A multichannel feedback proportional-integral-and-derivative controller is used to provide the control signals to the microvalves to optimize the blowing air needed to obtain uniform wake filling along the span of the guide vanes. An experiment is conducted using a small-scale turbofan simulator in an anechoic chamber to monitor the fan noise reduction due to wake filling. The error signals used for the controller were the pressure differences between a Pitot probe placed in the freestream flow and Pitot probes placed in the wakes of the guide vanes. Results indicate noise reduction of 10 dB at the blade-passing frequency tone and 2–5 dB at the harmonics. In addition, the controller is able to track the change in flow conditions due to transients of the turbofan simulator speed, thus demonstrating the successful implementation of the active flow control to minimize fan noise. [Work supported by AFSOR and NASA.]

10:20

5aSAb5. Active cancellation of rotor/stator interaction tones in turbofan engines. Bruce E. Walker, Alan S. Hersh (Hersh Acoust. Eng., Inc., 780 Lakefield Rd., Unit G, Westlake Village, CA 91361, haebew@iswest.com), Lawrence J. Heidelberg (NASA Lewis Res. Ctr., Cleveland, OH), and Michael E. Spencer (Signal Processing Solutions, Redondo Beach, CA)

Rotor/stator-generated aerodynamic noise in turbofan engines, HVAC axial fans, and other turbomachinery is often dominated by blade passage harmonics produced by dipole sound sources. Radiation toward the inlet and exhaust depends upon the effective orientation of the dipole sources relative to the propagation angles of the excited modes. Absorption of this tonal noise using passive treatment is often compromised because of a lack of knowledge of the relative phases and amplitudes of the propagating modes. A modal-based active cancellation system has been developed for global suppression of rotor/stator interaction tones. Axially spaced annuli of controlled wall-mounted actuators are located immediately upstream and downstream of the hubs and tips of stator vanes. Wall-mounted error microphone arrays are located in the inlet nacelle and exhaust duct. Actuator drive vectors are determined in an adaptive-quadrature control algorithm that seeks to minimize total radiated noise. The concept was initially developed and tested on a 24-in. axial fan facility and then extended and demonstrated on the 48-in. Active Noise Control Fan facility at NASA Lewis Research Center. Simultaneous suppression of modes (4,0) and (4,1) of 8–17 dB toward the inlet and 3–11 dB toward the exhaust was achieved at the second blade-passage harmonic.

Contributed Paper

10:40

5aSAb6. Comparison of two algorithms for modal active control of fan noise in a duct. Laurent Tardy, Eric Gonneau, and Jean-Pierre Guilhot (Lab. d'Acoust. de Metrologie et d'Instrumentation, 38 rue des 36 Ponts, F31400 Toulouse, France)

The reduction of fan noise in circular ducts has been realized using active control. Preliminary modal decomposition has allowed the determination of preponderant acoustical modes. The comparison of two methods has been executed both in simulation and experimentation. First, the x-filtered LMS algorithm has been tested. The second algorithm, based on a harmonic controller specially adapted for tonal noise, was composed of multiple in-phase and quadrature weights; it only needs two complex coefficients per frequency and per mode. Simulations have been first performed to evaluate filter lengths and step sizes. In an initial experiment, the fundamental has been reduced by 15 dB thanks to a SISO environment acting on the (1,0) mode. Then, with a MIMO controller, the (0,0) and the (1,0) modes could have been cancelled simultaneously at the fundamental frequency and the first harmonic. The test bed is composed of an axial fan whose fundamental frequency is 2150 Hz and a 0.1-m-diam duct; the actuators and sensors are, respectively, crowns of four loudspeakers and four error microphones mounted on the wall. With regard to these experimental results, both control methods have been compared, looking at efficiency, stability, and speed, in accordance with computational complexity.

Session 5aSCa

Speech Communication: New Spectral Analysis Techniques for Speech

James L. Hieronymus, Cochair
Bell Laboratories, 600 Mountain Avenue, Murray Hill, New Jersey 07934, USA

Louis Pols, Cochair
Institute of Phonetic Sciences, University of Amsterdam, Herengracht 338, 1016 CG Amsterdam, The Netherlands

H. Timothy Bunnell, Cochair
Speech Research Laboratory, Alfred I. DuPont Hospital for Children, 1600 Rockland Road, Wilmington, Delaware 19803, USA

Frederic Bimbot, Cochair
IRISA, Universitáire de Beaulieu, 35042 Rennes, Cedex, France

Chair's Introduction—7:55

Invited Papers

8:00

5aSCa1. Wavelets for speech processing. Shubha Kadambe (HRL Labs., 3011 Malibu Canyon Rd., Malibu, CA 90265, skadambe@isl.hrl.hac.com)

This presentation is focused on the application of wavelets for speech. Wavelet analysis was recently introduced to the signal and image processing community. Since then it has been applied to various problems. Robustness is an issue in the case of speech-based systems. Wavelet analysis seems to be one answer for this problem. In this lecture, an overview of what are wavelets and why wavelets are used for speech processing is given. Wavelet-based speech applications such as phoneme recognition and low bit-rate speech compression are discussed. Experimental results are provided to demonstrate the usefulness of wavelet analysis for speech applications.

8:20

5aSCa2. Analysis of voiced speech using harmonic models. Yannis Stylianou (AT&T Labs. Res., 180 Park Ave., Florham Park, NJ 07932-0971)

It is very common to consider voiced speech as a periodic or quasiperiodic signal. Therefore, harmonic models are usually proposed for the modeling of this part of speech. This paper focuses on the harmonic analysis of speech. Three models are presented and compared. The first model is the simplest among the three models and it supposes that the speech signal is a stationary signal. The second model does not make the hypothesis of the stationarity of the speech signal; however, it is an harmonic model. The third model does not consider speech as a stationary signal, and even though the fact that it uses the fundamental frequency as the basic frequency of the signal, it is not an harmonic model. The analysis presented here has as a goal to clarify the harmonic analysis of speech signals. From an application point of view, the first simple model seems to be quite good for low bit rate speech coding. The other two models are more complicated and they need more parameters to represent the speech signal. However, these models are more efficient in modeling the speech signal and they give us more insight about speech that can be used on applications like speech analysis and synthesis.

8:40

5aSCa3. Data-driven speech analysis for ASR. Hynek Hermansky (Oregon Grad. Inst. of Sci. and Technol., Portland, OR 97006-8921, hynek@ece.ogi.edu)

A typical large vocabulary automatic speech recognition (ASR) system consists of three main components: (1) the feature extraction, (2) the pattern classification, and (3) the language modeling. Replacing hardwired prior knowledge in the pattern classification and language modeling modules by the knowledge derived from the data turned out to be one of most significant advances in ASR research in the past two decades. However, the speech analysis module so far resisted the recent data-oriented revolution and is typically built on textbook knowledge of speech production and perception. Since it is believed that speech was optimized by millenia of human evolution to fit properties of human speech perception, deriving the speech processing knowledge from speech data may make some sense. The work describes some attempts in this direction. The linear discriminant analysis is used to learn about structure of speech signal to derive optimized spectral basis functions and filters (replacing conventional cosines of the cepstral analysis and conventional delta filters for deriving dynamic features) in processing the time-frequency plane of the speech signal. [Work supported by the Department of Defense and by the National Science Foundation.]

9:00–9:20 Discussion

Contributed Papers

9:20

5aSCa4. Crime-detection automatic speaker verification and identification (CASVI) system. Igor I. Gorban, Nick I. Gorban, and Anatoly V. Klimenko (Inst. of Math. Machines and Systems, 42 Ave. Acad. Glushkov, Kiev, Ukraine, 252187, gorban@immsp.kiev.ua)

The crime-detection automatic speaker verification and identification (CASVI) system, using a new spectral and cepstral analysis technique, is described. Robust speaker recognition algorithms, the operation modes, the control windows, the testing methodology, and the testing results of the system are presented. Research of the system has shown it can efficiently work with strongly corrupted utterances, while the corruption of the utterances being compared may be considerably different. For any utterances, permissible frequency distortions are 35 dB in the operating band and the permissible signal-to-noise ratio of additive noise is 12 dB. In these conditions, the CASVI system using 12-s speech utterances demonstrates the possibility to verify and identify persons on the level of 90% of correct acceptance when the false-alarm rate is 10%. The verification and identification time by the system takes some minutes. The CASVI system does not require high qualification of an expert. The system has a very simple interface that allows working in full automatic mode and forming reports without any special schooling. The CASVI system is a software product installed on a Pentium-based PC running with Windows 95.

9:40

5aSCa5. Revisiting analysis by synthesis. Timothy Bunnell and Silvio Eberhardt (Speech Res. Lab., duPont Hospital for Children and Univ. of Delaware, 1600 Rockland Rd., Wilmington, DE 19803, bunnell@asel.udel.edu)

Analysis by synthesis (AbS)—analyzing a speech signal by determining parameters for its synthesis—has been visited by investigators for several decades, but this approach has not resulted in commonly used speech acoustic analysis tools. The most prominent reasons for this are the substantial computational demands of AbS and the availability of fast analysis methods like LPC that are ''good enough'' in most cases. However, the availability of substantially more powerful, yet inexpensive, computers and the need for analysis methods that work well in all cases prompted this revisit to the use of AbS. To that end, an AbS program was developed that performs a pitch synchronous fit of formant synthesis parameters to acoustic speech signals. This program, called GASP, uses the Levenberg–Marquardt method to adjust synthesis parameters to achieve an accurate approximation to the input speech spectrum for each analysis epoch. At present, GASP fits five formants and one antiresonance along with corresponding bandwidths and two source parameters (amplitude and spectral slope). The talk will illustrate advantages and some disadvantages of the GASP approach, and describe an extension of GASP that incorporates temporal as well as spectral constraints on parameter fitting. [Work supported by Nemours Research Programs and NIH.]

10:00

5aSCa6. Speech visualization with auditory contours. Peter Daniel (Neutrik Cortex Instruments, Erzb.-Buchberger-Allee 14, D-93051 Regensburg, Germany, daniel@neutrik-cortex.de), Harald Mundt (Appl. Tech. Univ. Regensburg, D-93049 Regensburg, Germany), and Matthias Vormann (C. v. O. Univ. Oldenburg, D-26111 Oldenburg, Germany)

Speech perception is based on several steps of abstraction or contourization. In analogy to primary visual spatial contours Terhardt introduced the spectral pitch as the primary auditory spatial contour for further complex perceptions like phonemes, syllables, and sentences. Spectral pitch can be derived from the part-tone time-pattern (PTTP) as proposed by Heinbach [Acustica **67**, 242–256 (1988)]. The PTTP can be seen as a physical equivalent of the spectral pitch contour. It consists of spectral maxima extracted from a spectrum analysis with time and frequency resolution according to the human ear. By resynthesis it can be shown that the PTTP contains all relevant information of the original signal. In addition one can edit and modify the PTTP of speech in a controlled way and auralize the changes through resynthesis. Further applications like the analysis of $F0$ contours, separation into voiced and unvoiced parts, virtual pitch analysis and segregation of simultaneous signals will be discussed.

10:20–10:40 Break

10:40

5aSCa7. Spectral analysis of esophageal speech. Jinlin Lu, Satoshi Nakamura, and Kiyohiro Shikano (Grad. School of Information Sci., Nara Inst. of Sci. and Technol., Nara, Japan)

Esophageal speech is widely used by larynegetomized people. The purpose of this paper is to show the spectral characteristics of esophageal speech and to investigate the effect of the spectral component in the higher-frequency region from the viewpoint of speech quality. In order to obtain accurate spectral characteristics of esophageal speech which is perturbed both in period and amplitude, the STRAIGHT method [Kawahara *et al*., ICASSP-97, 1303–1306 (1997)] was used partly, and some other processes were added into it. The results from sustained Japanese five vowels, which were produced by seven esophageal and seven normal adult speakers, indicate that (1) spectral tilt of each of the esophageal vowels is larger than that of the normal vowels, (2) the energies in the higher-frequency region of esophageal speech are systematically larger than those of the normal speech. A paired comparison approach was used to evaluate the resynthesized speech which is obtained from a synthesizer based on an RK-source model [Klatt *et al*., J. Acoust. Soc. Am **87**, 820–857 (1990)] and the original prosodical parameters. When the energy in the higher-frequency region was attenuated at some values, then the resynthesized speech was preferred more by the listeners.

11:00

5aSCa8. Comparing alternate representations of acoustic properties in vowel perception. Terrance M. Nearey, Michael Kiefte (Dept. of Linguist., Univ. of Alberta, Edmonton, AB T6G 2E7, Canada), and James H. Hillenbrand (Western Michigan Univ., Kalamazoo, MI 49008)

Hillenbrand and Nearey [submitted; see J. Acoust. Soc. Am. **100**, 2688(A) (1996)] have shown that listeners' identification of vowels can be well predicted using a two-target, formant-based feature set. However, their analysis also suggests that other factors affect the perception of vowels in natural /hVd/ syllables. Various methods have been proposed for the representation of acoustic cues to vowel quality. This work will compare several alternate methods of characterizing short-time spectra, including cosine series [Zahorian and Jagharghi, J. Acoust. Soc. Am. **94**, 1966–1982 (1993)] and Gaussian mixtures [Zolfaghari and Robinson, Proc. 4th Intl. Conf. Spoken Lang. Proc., 1229–1332 (1996)], as well as more traditional envelope-peak (formant) based analyses. Alternate methods of sampling or summarizing time-series of such parametric representations will also be explored. To what extent can other representations improve predictions of listeners' behavior? Using cross-validation techniques, alternative methods will be evaluated on the acoustic and perceptual data of Hillenbrand *et al.* [J. Acoust. Soc. Am. **97**, 3099–3111 (1995)] based on more than 1500 /hVd/ syllables, as well as on perceptual data for vowels resynthesized from measurements of the subset of those stimuli studied by Hillenbrand and Nearey (1996).

11:20–11:40 Discussion

Session 5aSCb

Speech Communication: Speech Production Issues

Douglas H. Whalen, Chair
Haskins Laboratories, 270 Crown Street, New Haven, Connecticut 06511, USA

Contributed Papers

8:00

5aSCb1. Maximum likelihood methodology applied to empirically described probability distributions of speech movement data. H. Betty Kollia (Dept. of Logotherapy, TEI Patras, Patra, 26334, Greece) and Jay Jorgenson (Oklahoma State Univ., Stillwater, OK 74078)

In previous work [J. Acoust. Soc. Am. **102**, 3164–3165(A) (1997)] an analysis of speech production data [from Kollia *et al.*, J. Acoust. Soc. Am. **98**, 1313–1327 (1995)] was initiated using Maximum Likelihood methodology in order to introduce a more realistic description of the behavior of the articulators. In this way the kinematic measures are described via natural probability distributions determined by the data set itself. These results show much smaller confidence intervals when the possible values of these parameters are described as lying in a bounded range (versus a normal distribution) with a diminishing likelihood of observing a data point farther from (than closer to) the mean. In this study the data are used to estimate the probability distributions (one for each value of the independent variable). The methodology employed, the family of probabilty distributions described by the data (one family for velocity-displacement data and another family for displacement-displacement data), and the resulting statistical analysis via maximum Likelihood methodology are reported on. Finally, the entire analysis is described in terms of what can be viewed as stochastic linear regression analysis with general error terms and the method for further analysis of error terms for comparable data. [Work supported by NSF.]

8:20

5aSCb2. Emphasized versus unemphasized /aJ/: Jaw, tongue, and formants. Donna Erickson (Ctr. for Cognit. Sci., Ohio State Univ., Columbus, OH 43210, erickson@shs.ohio-state.edu), Osamu Fujimura (Ohio State Univ., Columbus, OH 43210), and Jianwu Dang (ATR, Human Information Processing Res. Labs, Kyoto, 619-02 Japan)

This study documents the relation between formants and jaw/tongue dorsum position in the context of emphasized–unemphasized monosyllabic words with the vowel /aJ/ in read speech. Articulatory and acoustic data were obtained by x-ray microbeam at the University of Wisconsin (courtesy, J. Westbury) from three American English speakers for about 300 words per speaker. Emphasized as opposed to unemphasized words are characterized by higher $F1$, lower $F2$, and lower jaw and tongue dorsum. Preliminary analysis of one speaker using a one-way ANOVA indicates the differences are statistically significant. For one speaker for emphasized vowels, an increase of lowering minima by 2 and 3 mm, respectively, for jaw and dorsum results in a 100-Hz change in $F1$ and $F2$ each. The biomechanical mechanism relating dorsum position to jaw position will be discussed, in conjunction with the recent C/D-model interpretation of jaw movement and durational change as the consequence of syllable magnitude control [O. Fujimura, B. Pardo, and D. Erickson, ESCA (1998)]. [Work supported by NSF SBR-951199B and ATR/HIP, Kyoto, Japan.]

8:40

5aSCb3. Control of oral closure in stop consonants with different closure durations. Anders Lofqvist (Haskins Labs., 270 Crown St., New Haven, CT 06511, lofquist@haskins.yale.edu)

This study examined lip and tongue kinematics in the production of stop consonants that differ in the duration of the oral closure. The linguistic material consisted of Swedish words that contained either a short vowel followed by a long stop, or a long vowel followed by a short stop. Articulatory movements were recorded using a magnetometer system. The average closure duration for the long stops was 100–150 ms, about twice the closure duration for the short stops. Preliminary results for one subject suggest that the lip closure for the long stop was produced with an upward movement trajectory of the lower lip that reached a higher position during the closure than the trajectory for the stop with a short oral closure. As a result, there was more mechanical interaction between the upper and lower lips, with the lower lip pushing the upper lip upward. For stops articulated with the tongue, the tongue moved along a longer path during the stop closure for the long than for the short stops. The average velocity of the tongue movement during the stop closure was lower for the long than for the short stops. [Work supported by NIH.]

9:00

5aSCb4. Coarticulation of tongue and jaw movements in speech. Vincent L. Gracco (Haskins Labs., 270 Crown St., New Haven, CT), Douglas M. Shiller, and David J. Ostry (McGill Univ., Montreal, QC H3A 1B1, Canada)

Coarticulatory patterns in speech movements arise from the interaction of neural control signals with mechanical and geometrical properties of vocal tract structures. By determining those aspects of the biomechanical system that are compensated for in neural signals, it can be learned what the nervous system ''knows'' abouts its own dynamics. Previous work has shown that coarticulatory patterns in jaw movement may arise as a consequence of muscle properties and dynamics rather than characteristics of the neural code [Ostry, Gribble, and Gracco, J. Neurosci. (1996)]. This finding suggests that the nervous system may take limited account of orofacial dynamics in planning speech movements. However, in the case of interarticulator coarticulation, mechanical interaction among articulators may necessitate a more complex pattern of control. As a first step in assessing the characteristics of control signals that underlie interarticulator patterning, kinematic patterns of coarticulation in the tongue and jaw are reported on. Patterns of individual articulator motion as well as interarticulator spatial and temporal relationships will be described. [Research supported by National Institute of Deafness and Other Communication Disorders Grant No. DC-00594, NSERC (Canada), and FCAR (Quebec).]

9:20

5aSCb5. Effects of lip protrusion on measurements of lip aperture. D. H. Whalen, Bryan Gick, and Anders Lofqvist (Haskins Labs., 270 Crown St., New Haven, CT 06511, whalen@haskins.yale.edu)

Lip movement during speech has been measured by many techniques. One common class of methods uses one marker for each lip, usually located midsagittally at the vermilion border. However, equating the distance between markers with the distance between the lips is problematic. Westbury and Hashi [J. Phonet. **25**, 405–419 (1997)] found that compression of the lips during stop closure precluded using a single value for the minimum distance when the lips were together. Thus lip trajectories alone cannot determine the point of closure nor estimate lip aperture during vowels. The present experiment used video images collected simultaneously from front and side views of phonemes varying in lip shape (three vowels, two fricatives). The distance between the vermilion borders (i.e., typical marker locations) was about 3 mm larger than the actual aperture for /u/ relative to /a/ and /i/ and for the palatal fricative relative to /s/. This difference correlated best with the degree of upper lip protrusion. Outward curling of the lips, bringing the inner margins closer during rounding, seems the likeliest explanation. Predicting the actual aperture from marker locations must consider both the vertical separation and the degree of protrusion. [Work supported by NIH Grant No. DC-02717.]

9:40

5aSCb6. No role for syllables in English speech production. Niels O. Schiller (Cognit. Neuropsych. Lab., Dept. of Psych., Harvard Univ., Cambridge, MA 02138)

Four experiments investigating the role of the syllable in English speech production are reported. In experiment 1, pictures had to be named. Pictures were preceded by visually masked primes that corresponded to the first syllable (CV or CVC) of the picture name or were one segment shorter or longer than its first syllable. Naming latencies were shortest in the CVC priming condition independent of the syllabic structure of the target. Experiment 2 replicated this effect with words. In experiment 3, all words could be grouped into pairs and overlapped in the first three letters while being different in syllable structure (e.g., se.cret–sec.tion). The same result as in the previous two experiments was obtained. Experiment 4 was added to show that the size of the priming effect increased with longer prime exposure duration. The results contradict the syllable priming hypothesis but are in line with the segmental overlap hypothesis.

10:00–10:20 Break

10:20

5aSCb7. Two kinematic models of the human tongue from MRI data. Edward Davis (Dept. of Mech. Eng., Johns Hopkins Univ., Charles and 34th St., Baltimore, MD 21218, Ned@jhu.edu), Maureen Stone (Univ. of Maryland Med. School, Baltimore, MD 21201), and Andrew Douglas (Johns Hopkins Univ., Baltimore, MD 21218)

Two models of tongue motion were developed and applied to tagged cine MRI data of the human tongue during movement from the consonants /k/ and /s/ to the vowels /i/, /a/, and /u/, in three sagittal slices (L, M, R). The first model, a global kinematic model, utilized surface edges of the tongue perimeter observed within the images. The model focused on decomposing tongue surface movements into the following mechanical deformations: rigid-body motions (translation and rotation) and homogeneous stretch and shear. The global model indicated that coarticulatory effects occurred in both vowels and consonants. Deformation was greatest from /k/ to /a/, and was composed primarily of horizontal expansion, vertical compression, and vertical lowering. Asymmetries were observed in the deformation patterns. The second model, a local kinematic model based on the motion of approximately 40 tag intersection points within the tongue, utilized the same low-order polynomial basis functions that are applied in finite-element analysis, within a finite number of small discreet regions. Specifically, the local model quantified the principal strains within discrete regions inside the tongue during consonant–vowel deformations. The local model was able to illuminate detail of local muscle activity within an individual syllable.

10:40

5aSCb8. Integration of three-dimensional and pressure sensitive palatography for speech production study. Masahiko Wakumoto (ATR Human Information Processing Res. Labs., 2-2 Hikari-dai, Seika-cho, Soraku-gun, Kyoto 619-0288, Japan and 1st Dept. of OMF Surgery, School of Dentistry, Showa Univ., Tokyo, 145-8515 Japan, mwakumo@hip.atr.co.jp), Shinobu Masaki, Kiyoshi Honda (ATR Human Information Processing Res. Labs., Kyoto 619-0288, Japan), Naoki Kusakawa (ATR Intl., Kyoto 619-0288, Japan), and Toshikazu Ohue (Nitta Co. Ltd., Nara 639-1085, Japan)

Tongue-palate contact patterns during speech production have been measured by electropalatography (EPG). A conventional EPG system produces only a flat contact pattern, and does not provide data for either the three-dimensional aspect nor tightness of tongue-palate contact. This paper describes work integrating two recently developed palatography techniques, i.e., three-dimensional electropalatography (3D-EPG) [M. Wakumoto and S. Masaki, J. Acoust. Soc. Am. **102**, 3166(A) (1997)], and pressure sensitive palatography (PSPG) [M. Wakumoto *et al.*, Proceedings of ICSLP98]. The former displays the electrode pattern on a realistic palatal shape, and the latter measures contact pressure by a thin sheet sensor array. The two systems are combined using the following procedures: (1) individual palatal shape and contact patterns in the 3D field during consonant production are acquired by 3D-EPG, (2) dynamic tongue-palatal contact pressure during the same consonant production at the same contact area is monitored by PSPG. A preliminary experiment revealed contact pressure differences between voiceless and voiced consonants ([t] > [d]) while the contact area for these consonants were almost identical. This result suggests that the combined method can usefully augment the study of tongue-palate contact during consonant closures.

11:00

5aSCb9. Tongue–jaw trade-offs and naturally occurring perturbation. Christian Kroos, Anja Geumann, and Philip Hoole (Inst. fuer Phonetik, Munich Univ., Schellingstr. 3, D-80799 Munich, Germany, kroos@phonetik.uni-muenchen.de)

Experimentally induced perturbation of speech shows that articulatory resources are flexibly marshalled to achieve phonetically defined goals. Are such key principles of motor control observable in unconstrained speech? Two sources of natural perturbation were considered: coarticulation and loud speech. Alveolar consonants were investigated. The expectation was that V-to-C coarticulation and different loudnesses would cause consonantal jaw position to vary. Would the tongue use compensation to keep vocal tract constriction relatively constant? Would trade-off patterns vary over consonants sharing place of articulation but differing in manner? One preliminary hypothesis, motivated by pilot experiments, was that trade-offs would be most apparent in acoustically sensitive sounds such as sibilants. This was not confirmed. Jaw position was so precise for sibilants that no lingual compensation was required. Probably the teeth function here as an active articulator. Nevertheless, clear patterns in overall magnitude of variability in the alveolar consonants were observed. For both jaw and tongue, variability increased from fricatives via stops to the lateral (and nasal). Within the tongue these sound-specific effects were more pronounced for tongue-back than tongue-tip. Even such simple facts await a coherent explanation. To this end, discussion will focus on the acoustic properties of these sounds. [Work supported by DFG Ti69/31.]

11:20

5aSCb10. Maintenance of adaptive strategies to oral-articulatory perturbations. Shari R. Baum (School of Commun. Sci. & Disord., McGill Univ., 1266 Pine Ave. W., Montreal, QC H3G 1A8, Canada) and David H. McFarland (Univ. de Montreal, Montreal, QC, Canada)

The present investigation examined whether speakers would adapt to a palatal perturbation in [s] production subsequent to focused practice, and whether the compensatory motor programs developed would be immediately available after a short period of rest. The fricative [s] was produced in three vowel contexts [si sa su] with and without a specially designed artificial palate in place at three time intervals: at the onset of the experiment, after a one-hour period of [s]-intensive practice with the palate in place, one hour later after a period of rest without the palate in place. Recordings of [š] under normal speaking conditions were also made at each time interval to examine any potential carryover effects. Preliminary analyses revealed that centroid frequencies of the [s] productions were significantly lower in the perturbed condition relative to normal upon first insertion of the palate. After the practice period, centroids in the two conditions more nearly approximated one another. However, after a rest period, speakers' fricative productions were again impaired by the presence of the artificial palate. Results are discussed in relation to the development and retention of adaptive articulatory programs in speech motor control. [Work supported by NSERC.]

11:40

5aSCb11. Adjustments in kinematic parameters of bilabial articulatory gestures during repeated oral readings of the same passage. Ludo Max (Lab. for Speech Physiol. and Motor Control, Dept. of Speech-Lang. Pathol. and Audiol., Seton Hall Univ., South Orange, NJ 07079, maxludo@shu.edu)

Repetitive practice of nonspeech motor acts typically results in behavioral, kinematic, and kinetic changes that reflect underlying neuromotor adjustments (motor learning). The effects of repetitive performance on the organization of speech movements, however, are less well understood. Yet, knowledge of such effects could (1) contribute to important theoretical notions in speech motor control, (2) reveal methodological concerns with currently used research paradigms, and (3) provide additional theoretical and clinical insights into speech disorders that are positively affected by repetitive practice. The present study therefore investigated the effects of repeated oral readings of a single passage on kinematic parameters of bilabial articulatory gestures (only closing gestures are discussed here). Seven adults, all normal speakers, performed five readings of a 200-word passage containing five instances of each of three target words. Movements of the lips and jaw were transduced with a strain gauge system whereas articulation rate was determined acoustically. All subjects increased articulation rate from reading 1 to reading 5. Kinematic adjustments were more consistently found (across subjects and target words) for a derived signal representing lip aperture than for movements of the individual articulators. Preliminary analyses suggest that some adjustments may be mediated by phonetic context and/or syllable stress.

12:00

5aSCb12. Simulation of token-to-token variability in vowel production. Christine R. Mooshammer (ZAS, Jaegerstr. 10/11, 10117 Berlin, Germany, timo@zas.gwz-berlin.de), Pascal Perrier (ICP, INPG, 38031 Grenoble Cedex, France), and Yohan Payan (TIMC, IMAG, Grenoble, France)

It has been suggested [Perkell and Nelson, *Speech Motor Control* (1982), pp. 187–204] that the patterns of articulatory variability observed over several repetitions of a same vowel could be explained by perceptual requirements. To further assess this hypothesis, the patterns of articulatory variability generated by the addition of noise to the motor control inputs to the tongue are studied. A 2-D biomechanical tongue model [Payan and Perrier, Speech Commun. **22**, 185–205 (1997)] was used, where muscular forces are generated according to Feldman's equilibrium point hypothesis. Target motor commands were determined for /i, y, a, e, o, u/ and noise was then added to these commands. For each vowel, ten repetitions of /əVə/ sequences were simulated. The generated patterns of variability were characterized by computing two-sigma dispersion ellipses around the target tongue position. A comparison was carried out with data collected on a native speaker of German with an electromagnetometer (EMA, Carstens AG). Simulated and collected data depict noticeable differences in orientation and size of the ellipses. This suggests that the token-to-token variability is not likely to be explained by a random inaccuracy of the motor inputs to the tongue. [Work supported by German Research Council Grant No. GWZ 4/3-1 and CNRS.]

FRIDAY MORNING, 19 MARCH 1999 ROOM H107, 7:55 A.M. TO 12:20 P.M.

Session 5aSPa

Signal Processing in Acoustics: Acoustics in Multimedia

Henrik Moller, Cochair
Acoustics Laboratory, Aalborg University, Fredrik Bajers Vej 7 B4, DK-9220 Aalborg Ø, Denmark

David I. Havelock, Cochair
Microstructural Sciences, National Research Council, M36 Montreal Road, Ottawa, Ontario K1A OR6, Canada

Chair's Introduction—7:55

Invited Papers

8:00

5aSPa1. MM and the music world. Phil Ramone (N2K, Inc., 55 Broad St., New York, NY 10004)

Creating music for the new and old media, for example: DVD standard, downloading, compression, and watermarking. The future of music production minus picture or a full bandwidth audio with high-quality pictures, including documentary. In general, the new frontierlike canvas of 1999 into the new millenium.

8:20

5aSPa2. Cognitive theories of musical meaning. Roger A. Kendall and Edward C. Carterette (Music Percept. and Acoust. Lab., Depts. of Ethnomusicology and Psych., Univ. of California, Los Angeles, CA 90095)

In this age of computer-based multimedia, it is useful to have a theoretical basis for combining audio and visual elements. Leonard Meyer (1956) discussed three primary types of musical meaning: referentialism, the arbitrary association of a musical event with a meaning outside of the music itself; formalism, the meanings in music arising from explicit knowledge about the formal structure of music; expressionism, meanings that arise from the tensions and releases embodied within the music itself. A similar model is suggested by Charles Peirce: index, parallel to Meyer's ''referentialism;'' icon, in which musical patterns suggest connections to nonmusical frames of reference; symbol, similar to Meyer's ''expressionism.'' It is clear that for either iconic or indexical meaning to be communicated, one must first apprehend the syntactical, ''embodied meaning.'' Therefore, the tripartite taxonomical categories outlined above are not discrete and orthogonal. It is best to conceive of musical meaning as existing along a continuum from areferential (syntactical) to referential. Since the visual frame of reference can also be mapped onto this continuum, a useful model for the interaction of audio and visual elements in film, dance, and animation arises. Audio-visual examples will illustrate the dynamic unfolding of meanings suggested by the model.

8:40

5aSPa3. Fully immersive audio environments—musical, aesthetical, and computational considerations. David G. Malham (Dept. of Music, Univ. of York, York YO10 5DD, England, dgm2@york.ac.uk)

Before the development of the telephone and the phonograph, all audio experiences were essentially three-dimensional. Composers and musicians had to accept the limitations of human performers and the acoustics in which they played. The development in the nineteenth century of the technological means necessary to provide performances of music which were remote in either time or space from the original was accommpanied by an almost complete removal of this three-dimensional aspect. Engineers and musicians have been searching ever since for ways of restoring the balance. Progress in this endeavor has been rapid in the last two decades, so much so that composers, musicians, and sonic artists now have a wide range of techniques at their disposal for manipulating the spatial elements in their compositions. This paper looks at various aspects of the technologies involved and the implications their availability has for composers and sonic artists working in the medium. This is presented within the context of a historical perspective. Special consideration is given to technologies which are intended to allow presentation to audiences, rather than, for instance, the more typical virtual reality systems which is concerned with smaller numbers of individuals.

9:00

5aSPa4. A novel computing structure for 3-D audio rendering with multiple sources. Jiashu Chen (Lucent Technologies, Inc., Rm. 1E-234, 200 Laurel Ave., Middleton, NJ 07748)

A novel computing structure has been implemented for efficient 3-D audio production. Head-related transfer function (HRTF) on a sphere is represented as a linearly weighted combination of M eigenfunctions (EFs). Each EF is a function of frequency (or time) and each weight (of M) is a function of azimuth and evaluation. With this representation the 3-D positioned binaural signals of any single sound source can be obtained by first multiplying the dry signal with M weights and then convolving them with M EFs. Proper delay corresponding to ITD is introduced into binaural signals for the listener. Similarly, multiple sound source 3-D positioning is achieved by weighting each source with its corresponding weights and by filtering them with the same set of EFs. For every source added only one more set of weight has to be used to multiply the source without increasing the time-consuming EF filtering. It results in an order of magnitude or more MIPS saving compared with direct convolution, especially when the number of sources is large. This computing structure also offers scalability, graceful degradation, and other additional advantages.

9:20

5aSPa5. Challenges facing 3-D audio display design for multimedia. Durand Begault (SJSU/Human Factors Res. and Technol. Div., NASA Ames Res. Ctr., Moffett Field, CA 94035, db@eos.arc.nasa.gov)

The challenges facing successful multimedia presentation depend largely on the expectations of the designer and end user for a given application. Perceptual limitations for distance, elevation, and azimuth sound source simulation differ significantly between headphone and cross-talk cancellation loudspeaker listening and therefore must be considered. Simulation of an environmental context is desirable but the quality depends on processing resources and control over interaction with the host acoustical environment. While techniques such as data reduction of head-related transfer functions have been used widely to improve simulation fidelity, another approach involves determining thresholds for environmental acoustic events. Psychoacoustic studies relevant to this approach are reviewed in consideration of multimedia applications. [Work supported by San Jose State University–NASA Ames Research Center Cooperative Grant NC 2-327.]

9:40

5aSPa6. Interactive acoustic modeling of complex environments. Thomas Funkhouser (Computer Sci. Dept., Princeton Univ., Princeton, NJ 08544), Ingrid Carlbom, Gary Elko, Gopal Pingali, Mohan Sondhi, and James West (Bell Labs., Murray Hill, NJ)

A primary challenge in acoustic modeling is computation of reverberation paths from sound sources fast enough for real-time auralization. This talk describes a system that uses precomputed spatial subdivision and ''beam tree'' data structures to enable real-time acoustic modeling and auralization in interactive virtual environments. The spatial subdivision is a partition of 3-D space into convex polyhedral regions (cells) represented as a cell adjacency graph. A beam-tracing algorithm recursively traces pyramidal beams through the spatial subdivision to construct a beam tree data structure representing the regions of space reachable by each potential sequence of transmission and specular reflection events at cell boundaries. From these precomputed data structures, high-

order specular reflection and transmission paths can be computed at interactive rates to spatialize fixed sound sources in real-time as the user moves through a virtual environment. Unlike previous acoustic modeling work, this beam-tracing method: (1) supports evaluation of reverberation paths at interactive rates, (2) scales to compute high-order reflections and large environments, and (3) extends naturally to compute paths of diffraction and diffuse reflection efficiently. A system based on this method is being used to develop interactive applications in which a user experiences a virtual environment immersively via simultaneous auralization and visualization.

10:00–10:20 Break

10:20

5aSPa7. Multichannel sub-band inverse filtering for room dereverberation. Hong Wang (Res. Dept., PictureTel Corp., 100 Minuteman Rd., Andover, MA 01810)

Room dereverberation is difficult because the impulse responses are long, nonminimum phase and change significantly with time and source/receiver positions. The problem was approached in two steps: (1) Explore the possibility of inverse filtering when a training signal is available; (2) blindly estimate impulse responses from reverberant signals and then perform inverse filtering. It is found that by dividing the signals into a large number of sub-bands, the impulse responses of many of the sub-bands become invertible. The invertibility of each sub-band depends on the zero distribution of the full band impulse response. When multiple microphones are used, full band dereverberation is achieved by selecting the best microphone in each sub-band and reconstructing the full band signal from dereverberated sub-band signals. An almost perfectly recovered reverberant speech of RT$=0.85$ s, when the training signal is used, will be demonstrated. For the second step, reverberant signals from multiple sensors are divided into sub-bands. In each sub-band, the ratio of impulse responses from two sensors is estimated by the least-mean-square estimation. Pade approximation is used to estimate each individual impulse response. The sub-band signals are then inverse-filtered and combined to form a full band dereverberated signal.

10:40

5aSPa8. Echo cancellation for multimedia applications. M. Mohan Sondhi (Bell Labs, Lucent Technologies, 600 Mountain Ave., Murray Hill, NJ 07974)

In any attempt at creating natural audio-visual communication between two remote locations, acoustic echoes are generated due to the coupling between the loudspeakers and microphones in each conference room. If ignored, these echoes can completely disrupt audio communication. Teleconferencing systems today use single-channel (monophonic) speech communication. In order to recreate a natural ''presence'' in the remote location, multichannel (stereo) communication is desirable, and will no doubt be the preferred future mode of teleconferencing between two spatially separated groups of participants. A third type of conference is a desktop conference between several locations. In such applications the remote participants are displayed on a screen, and synthesized stereo may be used to simulate sound coming from the direction of each of them. The talk will discuss the characteristics of echoes in all such situations, and the solutions currently available to deal with them. The solutions can also be useful for eliminating disturbances other than echoes, e.g., the sound from a car's stereo system picked up by the transmitter of a hands-free telephone.

Contributed Papers

11:00

5aSPa9. Contribution of sound spatialization to audio-visual quality in videoconferencing. N. Chateau (France Telecom/CNET, 2, Ave. Pierre-Marzin, F-22307 Lannion, France)

Two experiments were conducted to evaluate the contribution of sound spatialization to audio-visual quality in videoconferencing. The first experiment aimed at measuring the threshold of perception of a spatial mismatch between a sound and a related image. Twenty-four subjects had to judge whether the sound of videoconference samples emanated or not from the same direction in the horizontal plane as the related image. The actual spatial discrepancies ranged from 0 to 25 by 5° steps and the sound had three distinct bandwidths (300–3400, 100–7000, 100–15 000 Hz). In a second experiment, subjects had to judge the audio-visual quality of the same stimuli on a five-point categorical scale (ACR). Results of the first experiment indicate that the 75% threshold of perceived spatial mismatch is reached between 5 and 10° and is independent of sound bandwidth. Results of the second experiment show that audio-visual quality is influenced by sound bandwidth [$F(2,46)=110.94$, $p<0.001$], the angular separation [$F(5,115)=48.64$, $p<0.001$], and the interaction between these two factors [$F(10,230)=10.55$, $p<0.001$]. Combination of the results of the two experiments highlight that for a given bandwidth, perceived audio-visual quality is linearly dependent (Pearson's $r^2>0.84$) of perceived spatial audio-visual coherence.

11:20

5aSPa10. Multimedia database of musical instrument sounds. Bozena Kostek and Piotr Suchomski (Tech. Univ. of Gdansk, Sound Eng. Dept., Pl-80-952 Gdansk, Poland)

The presented study addresses the broad problem of automatic recognition of musical instrument sounds. Many applications of the algorithms dealing with these tasks may be foreseen. Nowadays, with the rapid growth of electronic libraries and databases such as those found on the Internet, the possible application may be to search a musical database for the sounds of chosen instruments or for musical tunes. For the purpose of the experiments that deal with instrument sound recognition, a multimedia database of musical instrument sounds was engineered. It encompasses: basic information on musical instruments, including playing techniques, description of parameters extracted from sound, images, sound samples within the instrument musical scale, exemplary musical phrases played by a given instrument, time- and frequency-domain representation of sounds for the whole instrument musical scale, and tables containing the sound parameter values. The database makes it possible to create various kinds of charts and printed reports for all parameters, enables SQL-based queries, and shows a collection of linked HTML pages. The engineered multimedia database was used in musical instrument timbres and musical phrases recognition experiments conducted by one of the authors, employing some computational intelligence methods as neural networks, fuzzy logic, and rough sets.

11:40

5aSPa11. Vibration characteristics of microphone membranes. Holger Pastille (Inst. f. Tech. Acoust., Tech. Univ. Berlin, Einsteinufer 25, D-10587 Berlin, Germany, hp@stones.com)

Using laser scanners, the vibration pictures of the condenser microphone diaphragms were taken. In order to be monofrequent, the microphone was in an impedance tube. Standard microphones were used. The behavior of the vibrations can be well observed in the animated pictures. Besides the fundamental component, the nonlinear parts are also of special interest. Coherence between the sound-pressure level and the distortion of the microphone cap is seen. Seen also is the motion of the diaphragm itself. Results are shown for two studio microphones and a measuring microphone, each for three selected sound-pressure levels.

12:00

5aSPa12. Development of a multiprocessor system (HUGO) for acoustic applications. Jochen Kleber (Inst. of Tech. Acoust., Univ. of Aachen, Templergraben 55, 52056 Aachen, Germany, jkl@akustik.rwth-aachen.de)

For research in acoustics, audio signals must often be subjected to a complex processing. For listening tests, a real-time processing becomes desired in practice, in order to be able to switch between different situations. A free programmable device was implemented with up to eight channels with analogous and digital inputs and outputs. On four DSP's with a computing power of in total 160 MIPS, applications can be implemented. During design of hardware and software, it was considered to highest audio quality. In future this device can be used for other interesting developments, such as multichannel front ends with an A/D dynamics of 125 dB. In the paper, two applications will be presented more closely: crosstalk cancellation and binaural mixing console.

FRIDAY MORNING, 19 MARCH 1999 ROOM H111, 10:00 A.M. TO 12:20 P.M.

Session 5aSPb

Signal Processing in Acoustics and Engineering Acoustics: General Signal Processing in Acoustics

Kim C. Benjamin, Chair
Naval Undersea Warfare Center, 1176 Howell Street, Newport, Rhode Island 02841, USA

Contributed Papers

10:00

5aSPb1. Practical aspects of analyzing cyclostationary noise emitted by real acoustic sources. Karel Vokurka (Dept. of Phys., Tech. Univ. of Liberec, Hálkova 6, CZ-461 17 Liberec, Czech Republic, karel.vokurka@vslib.cz)

In previous presentations [K. Vokurka, J. Acoust. Soc. Am. **101**, 3045(A) (1997); **103**, 2819(A) (1998)] it was shown that time-frequency statistical characteristics of noise and vibration measured on reciprocating machinery yield information which can be conveniently used, e.g., in quality control or for diagnostic purposes. A basic assumption in developing suitable signal processing algorithms was that the number of samples in each period of cyclostationarity of the analyzed noise or vibration was exactly the same. However, this assumption is only seldom fulfilled by real acoustic noise or vibration. Hence, a suitable preprocessing technique must be applied to the measured signal. This technique may be either signal resampling, or external control of a sampling interval using multiple tachopulses, frequency multipliers, etc. In the paper, advantages and disadvantages of these techniques are discussed from the point of view of different types of measured acoustic noise or vibration signals, their possible phase modulations, and of the computed time-frequency statistical characteristics. [Work supported by the Grant Agency of the Czech Republic and by the European Commission.]

10:20

5aSPb2. Measurement of loudspeaker parameters by inverse nonlinear control. W. Klippel (Klippel GmbH, Aussiger Str. 3, 01277 Dresden, Germany, klippel-gmbh@t-online.de)

Nonlinear loudspeaker models have been developed to predict and explain the generation of nonlinear distortions in the reproduced sound at large amplitudes. These models require additional nonlinear parameters such as the force factor, stiffness of the mechanical suspension, and voice-coil inductance depending on the instantaneous excursion of the voice-coil. These parameters have to be measured dynamically since static approaches have shown to produce inaccuracies in describing the dynamic behavior of the loudspeaker due to hystereses and creep effects. The identification of the optimal model parameters can be accomplished by using an adaptive nonlinear system provided with the known input signal and an output signal measured on the speaker. An inverse nonlinear identification by using a nonlinear controller connected to the loudspeaker input has advantages over direct loudspeaker modeling in respect to robustness, convergence speed, and stability. Results of practical loudspeaker measurement are presented and discussed in respect to quality assessment of loudspeakers in the large-signal domain.

10:40

5aSPb3. Automatic classification of wideband acoustic signals. Alain Dufaux, Laurent Besacier, Michael Ansorge, and Fausto Pellandini (Inst. of Microtechnol., Univ. of Neuchtel, Rue A.-L. Breguet 2, CH-2000 Neuchtel, Switzerland)

Until now, very few contributions were published in the field of wideband acoustic signal recognition, especially for handling impulsive noise signals such as glass breaking, detonations, or door slams, as encountered in security applications, where the signals are highly nonstationary and composed of higher frequency components. This paper shows how the audio alarm recognition problem can efficiently be tackled using either pattern recognition methods relying on Bayes classifiers, or on artificial neural networks (ANN). After extraction of filterbank coefficients in the acoustic analysis module, typical feature vectors are achieved from the concatenation of k consecutive signal frames, in order to exploit dynamic temporal information. The redundancy induced by this dynamic modeling requires a reduction of the feature space dimension, performed with a conventional principal component analysis. The performance of both systems is evaluated experimentally (7000 tests) for the classification of three types of noise events (glass breaking, door slams, and stationary noises). The score of correct classification reaches 99% for the statistical approach,

and 98% for the ANN-based system. It is further noticed that errors do not occur on the same signal files for both methods. Thus robustness enhancement can be reasonably expected, when using hybrid methods or fusion strategies.

11:00

5aSPb4. Algorithms for modeling nonlinear geometric distortion of vinyl records. Robert Henke and Eva Wilk (Hochschule fuer Film und Fernsehen, Studiengang Ton, Karl-Marx-Str. 33-34, D-14482 Potsdam, Germany)

Classical vinyl records have a characteristic sound that is distinct from an ideal digital system and is often described as warm, mellow, or ''analog.'' Responsible for this sound is the sum of linear and nonlinear distortions which occur during recording and playback of the record. The distortions are due to mechanical and electrical nonlinearities. One main source of nonlinear distortion lies in the discrepancy between the cutter's shape and that of the playback stylus: The cutter is a sharp tool while the playback stylus has a ball-like shape to distribute the tracking force over a wider area. This leads to a slightly different movement of the playback stylus in comparison to the recorded groove, yielding so-called ''geometric distortions.'' The mechanical, i.e., geometrical nature of this phenomenon, makes it possible to find accurate mathematical descriptions. This approach was used to develop a model for the real-time simulation of the typical sound of a vinyl record. The developed tool allows the simulation of the ''vinyl sound'' and can basically be used to create—and control—a wide range of nonlinear distortion which can vary from a slight enhancement of a given signal to new effects of sound design.

11:20

5aSPb5. Ultrasonic reflection tomography: Signal processing and resolution. P. Lasaygues, J. P. Lefebvre, and S. Mensah (CNRS-LMA 31, chemin Joseph Aiguier 13402 Marseille Cedex 20, France)

Medical imaging is, with nondestructive testing of materials, the main application of ultrasonic reflection tomography (URT). This method results from an inverse born approximation (IBA). URT allows perturbations (theoretically small) of a reference medium to be visualized. One is then concerned with a Fourier synthesis problem and the first step is to correctly cover the frequency space of the object by an adequate spatial and frequency scanning. In practice, the frequency bandwidth of the used ultrasonic pulses is limited by the transducers, leading to a poor coverage of the object's spectrum and to a relatively poor resolution of images. Low and high frequencies are restored by a Papoulis deconvolution method that presents advantage not to modify the spectral content of the signal within its frequency band. The resolution enhancement procedure was first tested on academic targets (wire), and on test targets (square aluminum and triangular PVC rods), showing the possibility to obtain high-resolution images with low-frequency transducers. Finally, we compare the resolution given by a 250-kHz transducer to the one obtained, with a classical technique, by a 2,5 MHz transducer. The overall dimension of test objects is in that case less than the wavelength.

11:40

5aSPb6. Application of ultrasound reflection tomography for nondestructive evaluation of objects with a complex geometry. Rymantas J. Kažys, Liudas Mažeika, and Elena Jasiūnienė (Ultrasound Res. Ctr., Kaunas Univ. of Technol., Studentų str. 50, LT-3031, Kaunas, Lithuania, ulab@tef.ktu.lt)

In the case of solid objects with complex geometry, conventional ultrasound tomography techniques tend not to be efficient enough. The objective of the paper is the development and experimental verification of an ultrasound tomography approach suitable for objects with non-flat boundaries. The reconstructed images in ultrasound reflection tomography usually are imperfect because of ultrasound wavefront curvature, which is significantly affected by wave refraction and mode conversion phenomena at the boundaries. In order to achieve better resolution of reconstructed images in the ultrasound reflection tomography, the curvature of the wavefronts has to be known and taken into account performing backprojection. Ultrasonic wavefronts were reconstructed from measured ultrasonic wave parameters. Obtained results were taken into account performing backprojection in the ultrasound refection tomography. When the curvature of the wavefront is known, the shape and the size of the defects can be reconstructed with greater accuracy. In order to determine accuracy of the proposed method, computer simulations and experimental measurements have been carried out and sources of possible errors were detected. From the results presented it can be seen that the method proposed increases accuracy of the ultrasonic reflection tomography.

12:00

5aSPb7. Low-pass filter for the DFT process and its application to impulse response of sound-field and ultrasonic B-mode echo simulator. Tjundewo Lawu and Mitsuhiro Ueda (Dept. of Intl. Development Eng., Tokyo Inst. of Technol., 2-12-1 O-okayama, Meguro-ku, Tokyo, 152-8552 Japan)

Convolution and correlation are closely related operations that are basic to many areas of signal processing. To obtain the frequency component of the signals using discrete Fourier transform (DFT), the continuous signals must first be sampled. A low-pass antialiasing filter which is simple to implement is proposed. The low-pass filter has equally good frequency response characteristics and can be used to eliminate possible aliasing effects by ensuring that the signal to be sampled is limited in the spectral content. The impulse response of the sound field was calculated by using the proposed low-pass antialiasing filter and compared with the rigorous solution to verify the realizability of the filter. The filter was also applied to construct the ultrasonic B-mode image of a 3-D phantom model.

Session 5aUWa

Underwater Acoustics: Wave Propagation: Session in Honor of Leonid M. Brekhovskikh II

Peter N. Mikhalevsky, Cochair
SAIC, 1710 Goodridge Drive, McLean, Virginia 22102, USA

Nikolai Dubrovsky, Cochair
N. N. Andreyev Acosutics Institute, 4 Shvernika Street, 117036 Moscow, Russia

Contributed Papers

8:00

5aUWa1. Signal coherence and energy effects of propagating internal solitary wave packets. Timothy F. Duda and James C. Preisig (Appl. Ocean Phys. and Eng. Dept., MS 11, Woods Hole Oceanogr. Inst., Woods Hole, MA 02543)

Order-400 Hz sound propagated through continental-shelf internal solitary wave packets is shown by simulation to fluctuate strongly via mode coupling. The coupling is controlled by the modal input conditions, wave and packet dimensions, and the ambient sound-speed profile. In the case of a moving packet, relative modal phase changes dominate over the others, changing the coupling and controlling signal fluctuations. The phasing within the packet varies over minutes in a moving packet, causing fluctuations with comparable time scales. The directionality of energy flux between high-order acoustic modes and (less attenuated) low-order modes determines a gain factor for distantly detected signals. A significant finding is that a packet near a source will amplify low-order modes if the source favors high-order modes, giving amplification at distant ranges. Conversely, a packet far from a source can energize otherwise quiet higher modes. Intermittency in the coupling means that signal energy fluctuations and modal diversity fluctuations at a distant receiver are complementary, with energy fluctuations suggesting a source-region packet and mode fluctuations suggesting a receiver-region packet. In addition to the monochromatic results described above, the effects on pulses (broadband signals) will be compared with experimental observations. [Work supported by ONR Ocean Acoustics.]

8:20

5aUWa2. The two domains in envelope spectrum of ocean ambient noise. A. V. Furduev (Andreev Acoustics Inst., ul. Shvernika 4, Moscow, 117036 Russia)

Analyzing level fluctuations of the natural ambient underwater noise shows that the spectrum of the envelope usually consists of two frequency domains of different physical nature. The low-frequency domain is governed by variations in wind speed, that is, variations in surface density of the source power. The high-frequency domain is related to rough-surface sound scattering. The boundary between the domains correspond to frequencies of 0.05–0.1 Hz. Experiments have shown that both cross-frequency noise correlation and correlation between the noise and wind speed fluctuations are high if only frequencies lower than 0.1 Hz are retained in the spectrum, these correlations being low for unfiltered noise. Thus, if there is no ship-traffic noise, the frequency correlation coefficient remains to be 0.6–0.8 within 0.1–10 kHz if the high-frequency domain is cut off and it is close to zero in disjoint filtering bands for unfiltered noise. The experimental data are discussed and interpreted with the use of the noise model allowing for space–time parameters of the wind speed.

8:40

5aUWa3. Sensitivity analysis of the acoustic field in shallow water to environmental parameters. Lianghao Guo and Zaixiao Gong (Natl. Lab of Acoust., Inst. of Acoust., Chinese Acad. of Sci., Beijing 100080, PROC)

Environmental parameters, such as sound-speed profile and bottom structure, have very important effects on the acoustic propagation in shallow water. In this paper, some detailed simulations are presented for a typical shallow water with a thermocline. The simulated properties include the coherent and incoherent transmission loss, averaged energy loss, group velocity, phase of the acoustic field, and the multipath arrival structure. The concerned environmental parameters include surface speed, thermocline depth and thickness, water depth, bottom structure, and its geoacoustic parameters. The results show that the coherent transmission loss and the phase of the acoustic field are sensitive to the environmental parameters, while the other properties are relatively stable. Theoretical explanations of these results are also given. Both the sensibility and the relative stability can be utilized. Through reasonable cost function design, the former can be used to invert the geoacoustic parameters of the bottom, while the latter can be used to localize distant targets. Finally, the geoacoustic parameter inversion for a complicated bottom is given by using the real data from a vertical line array. With the obtained bottom parameters, experimental transmission loss is well explained.

9:00

5aUWa4. Role of acoustics in oceanographic monitoring of the Arctic ocean. Konstantin D. Sabinin (N. N. Andreyev Acoust. Inst., 4 Shvernik St., Moscow, 117036, Russia)

Acoustic soundings of the Arctic ocean (AO) along some tracks in crucial regions of the ocean can provide satisfactory information for the monitoring of the most important oceanographic features of the AO waters, namely, the heat content of the Atlantic water layer in the AO and the upper ocean salinity. Optimal location of the acoustic tracks for monitoring of the heat content space-time variability is discussed. It is shown that the remote sensing of the upper ocean salinity by acoustic tomography (acoustic halinometry) is quite possible since changes in the sound speed in the upper AO are due to changes in salinity, while temperature here is nearly always close to the freezing point. The results of the acoustic halinometry numerical modeling are demonstrated using oceanographic data obtained in the Amundsen Basin of the AO. The effect of a combination of different *in situ* and remote sensing measurements for monitoring of the salinity flux through the Bering Strait is discussed. [Work supported by RFFR and CRDF.]

9:20

5aUWa5. On the adiabaticity of acoustic propagation through nongradual ocean structures. E. C. Shang, Y. Y. Wang (CIRES, Univ. of Colorado/NOAA/ETL, Boulder, CO 80303), and T. F. Gao (Inst. of Acoust., Academia Sinica, Beijing, PROC)

The adiabaticity of acoustic propagation is attractive for acoustic field description, data interpretation, and inverse scheme consideration. It is well known that, in general, the adiabaticity can be held for *gradual* medium, and the criteria of adiabaticity have been given by Milder (1969), Brekhovskikh (1973), and Brekhovskikh and Lysanov (1982), respectively. In this paper, the adiabaticity of acoustic propagation through nongradual ocean structures is investigated both theoretically and numerically. Here, the term nongradual means that the scale of the ocean structure M is smaller than the modal interference distance D_{mn} between mode ''m'' and mode ''n.'' Two examples of the nongradual ocean structures are discussed: (1) polar frontal zone with a width of about 2 km, and (2) internal solitons in shallow water with a width about 0.8 km. Comments on the criteria given by Milder and Brekhovskikh will be addressed. [Work supported by ONR and NOAA.]

9:40

5aUWa6. Wave propagation in the ocean with fine structure stratification. Remir F. Shvachko (N. N. Andreyev Acoust. Inst., 117036 Moscow, Russia, bvp@asu.acoins.msk.su)

The highly anisotropic fine-structure inhomogeneities may be interpreted as being irregular (stochastic) in depth and regular (deterministic) in horizontal coordinate. These properties lead to the Bragg sound scattering, and hence to sound penetration into the shadow zones, prereverberation, and stochastic channeling. In other words, due to various effects of sound reradiation by the inhomogeneities, the sound penetrates into (spatial, temporal, angular) domains that are forbidden by the geometrical acoustics. Sound fields in the shadow zones carry information on the ocean fine structure stratification and thereby may be used in tomography experiments. The phenomenon of insonifying the shadow zone over a 10-m-thick microchannel was confirmed experimentally at a frequency of several kHz, up to distances of about 25 km. Because any convergence zone gives rise to volume-scattered signals that penetrate into the next shadow zone, the second-zone signal may have the same order of magnitude as the multiply bottom-reflected ones, the volume-scattered signals predominating within the third zone. The developed models for the leakages caused by the subsurface and fine-structure channels and by fine-structure scattering agree well with the experimental data obtained in different ocean regions.

10:00–10:20 Break

10:20

5aUWa7. Coupling to SH as a loss mechanism in shallow-water acoustic propagation. Darin J. Soukup (Geophys. Prog., Box 351650, Univ. of Washington, Seattle, WA 98195), Robert I. Odom (Univ. of Washington, Seattle, WA 98105), and Jeffrey Park (Yale Univ., New Haven, CT 06520-8109)

Since horizontally polarized shear waves (SH) are polarized normal to the propagation and polarization direction of a bottom interacting shallow-water acoustic signal, they are generally not considered as a loss mechanism. However, most marine sediments are anisotropic to some degree as a result of the bedding process with a symmetry axis normal to the bedding planes. Particle motions of compressional (P), vertically polarized shear waves (SV), and SH waves are no longer independent. Dispersion calculations show that the quasi-P-SV and quasi-SH mode branches attract and repel as the symmetry axis is rotated. For certain ranges of the symmetry axis angle, the phase velocities of the quasi-P-SV and quasi-SH approach each other. Coupled-mode computations have been performed, which indicate that energy can be efficiently redistributed among modes with both P-SV and SH components in the bottom. The coupling is induced by range dependence in the waveguide, and energy is distributed among all propagating modes. This is in contrast to propagation in TI and isotropic bottoms for which the range-dependent mode coupling is more strongly nearest neighbor. Loss to the quasi-SH should be considered when modeling propagation in shallow water with an anisotropic bottom. [Work supported by ONR.]

10:40

5aUWa8. An energy-conserving one-way coupled mode propagation model. Ahmad T. Abawi (SPAWAR Systems Ctr., San Diego, CA 92130-5001, abawi@spawar.navy.mil)

The equations of motion are used to derive a coupled mode model for wave propagation in a range-dependent waveguide. Traditionally in ocean acoustics the wave equation has been used to derive these equations. The use of the equations of motion has three major advantages over the use of the wave equation: (1) It results in coupled mode equations that are first order, (2) the resulting coupling coefficients are anti-Hermitian, which guarantees energy conservation, and (3) simple expressions can be derived for the coupling coefficients in terms of local modes and their vertical derivatives. In contrast, the coupled mode equations derived from the wave equation are second order. Also, simple expressions for the coupling coefficients are hard to obtain because they involve second derivatives of the modes with respect to range. This model is applied to the ASA benchmark problem [J. Acoust. Soc. Am. **87**, 1499–1510 (1990)]. The results show excellent agreement with those obtained from other well-known range-dependent models.

11:00

5aUWa9. Numerical simulation of time domain ocean acoustic propagation. Cedric Boisson and Joel Piraux (CNRS-LMA, 31 chemin Joseph Aiguier, F-13009 Marseille, France, boisson@alphalma.cnrs-mrs.fr)

The time domain parabolic equation is studied for ocean acoustic long-range propagation, including wide-angle propagation, without involving Fourier synthesis. Instead of solving the wave equation with boundary conditions in the whole ocean domain, the governing equations are written in a moving coordinate system. Since the studied frame is moving with acoustic perturbations, dependent variables evolve more gradually, which increases time integration accuracy. The number of space points and thus CPU time are greatly reduced because the pulse occupies a narrow range window. Numerical tests were made to study first the headwave problem by handling discontinuities of sound speed and density at a layer interface. Media with continuously variable celerity profile were also studied: there was a particular interest in studying wave propagation in media with multiple deep sound channels. Results were compared with those worked out with other codes based on Bessel–Fourier analysis (SPARC developed by M. B. Porter), requiring much CPU time. An excellent agreement was observed. The originality of the interactive program developed is to display a movie of wave propagation. It is an efficient tool to solve the direct problem and consider the inverse problem.

11:20

5aUWa10. Energy-conserving and reciprocal solutions for higher-order parabolic equations. Dmitry Yu. Mikhin (P. P. Shirshov Oceanology Inst. of the Russian Acad. of Sci., Nakhimovskii prospect, 36, Moscow 117218, Russia, dmitry@rav.sio.rssi.ru)

Conservation of sound energy in nonabsorbing media and acoustical reciprocity in stationary fluids at rest are the fundamental properties of the acoustic field. Preserving these properties in parabolic approximations is essential for accurate modeling of sound propagation in shallow-water environments. Recently Godin proposed a family of wide-angle parabolic equations (PE's) for motionless fluid which are energy conserving, reciprocal, and allow improved description of mode coupling without adversely affecting phase accuracy. For moving media, a generalized Claerbout PE was also derived. Its solutions preserve the acoustic energy in the absence of dissipation and satisfy the flow-reversal theorem (FRT), which is an extension of reciprocity principle to moving media. The report presents a

numerical scheme for solving the proposed PE's. The algorithm preserves the conservational properties of the original (pseudo-)differential equations. Implicit finite-difference solutions satisfy discrete analogs of the energy conservation law and FRT. The developed computer model is applied to simulate acoustic tomography of oceanic currents. Inversion follows the method of matched nonreciprocity tomography. Flow reconstruction in range-dependent coastal environments is analyzed under the presence of small-scale uncertainties in bottom topography. [Work supported by CRDF, INTAS, and RBRF.]

11:40

5aUWa11. Sound-propagation modeling with the enhanced ray theory in four dimensions. Nikolay E. Maltsev (MVM Intl., 370-2601 Ridelle Ave., Toronto, ON M6B 4B4, Canada)

Sound-propagation models, based on the ray theory, have existed for decades. Conceptional flaws in the standard ray theory, such as singularities on caustics and nonlinear boundary value problem for the rays, connecting source, and receiver, limit the scope of ray theory applications. In a recent report [N. E. Maltsev, Proc. of 16 ICA and 135 ASA Mtg. **3**, 1935–1936 (1998)], the new approach, or enhanced ray theory (ERT), was presented, free from the defects of the standard ray theory, mentioned above. The 4D (three space dimensions plus time) ERT code was developed for the desktop computer. ERT code uses triangulation of the 3D environment by simplexes, for the approximation of the refraction coefficients of the liquid and solid parts of the media, parametrization of rays and wave fronts in barycentric coordinates, inside these simplexes, differential equations for eigenrays, and differential equations for wave fronts. Examples of ERT model predictions in the 3D environment for single-frequency and impulse sources, and comparisons with SAFARI code for benchmark problems are presented.

12:00

5aUWa12. On the adiabatic normal modes in the 3-D inhomogeneous waveguide. Oleg A. Godin (School of Earth and Ocean Sci., Univ. of Victoria, P.O. Box 3055, Victoria, BC V8W 3P6, Canada, ogodin@uvic.ca)

Several distinct formulations of the adiabatic approximation have been proposed in the literature on modal propagation in the 3-D, range-dependent waveguide. These formulations predict the same phase but differ in the adiabatic mode amplitude and, hence, in their reciprocity and energy-conserving properties. These formulations, including those due to L. M. Brekhovskikh and O. A. Godin [*Acoustics of Layered Media. 2. Point Sources and Bounded Beams* (Springer-Verlag, Berlin, 1992), p. 253] and M. B. Porter [J. Acoust. Soc. Am. **96**, 1918–1921 (1994)], are compared with respect to their accuracy and domain of validity assuming small and smooth variation of mode propagation constants characteristic of underwater acoustic waveguides. Perturbation theory for horizontal (modal) rays and dynamic ray tracing are used in the analysis. A new approximate expression for the adiabatic mode amplitude in 3-D problems is derived that requires environmental information only along source–receiver radial and possess higher accuracy than previous formulations. The domain of validity of the result is determined in terms of horizontal gradients of environmental parameters. Mode phase corrections due to horizontal ray curvature are evaluated. Implications on applicability of the uncoupled azimuth approximation for sound propagation modeling in a horizontally inhomogeneous ocean are discussed. [Work supported by NSERC.]

Contributed Posters

These posters will be on display in the Poster Gallery from Thursday to Friday, 18–19 March. Authors will be at their posters from 2:00 p.m. to 4:00 p.m. on Friday, 19 March.

5aUWa13. Internal wave imprint in the oceanic ambient noise. Alexandr V. Furduev and Andrey N. Serebryany (N. N. Andreyev Acoust. Inst., 117036 Moscow, Russia, bvp@asu.acoins.msk.su)

Investigations of dependencies between the characteristics of ambient noise field and different types of hydrophysical inhomogeneities in the ocean had revealed the possibility of realization of passive acoustic tomography methods (without transmitting signal and only on the basis of a noise field). Internal gravity waves are one of such inhomogeneities. They are manifested in the ambient noise field by modulation of noise level due to variation of sound-speed profile and by noise of ''suloy'' created on the sea surface by intense internal waves. The results of complex field experiments on synchronous measurements of internal waves and ambient noises are presented and analyzed. The observations were carried out near the Mascarene Ridge in the Indian Ocean, the region of generation of large-amplitude internal waves. The interrelation between fluctuations of noise field (received by vertical array of hydrophones) and vertical displacements of thermocline caused by internal waves had confirmed the possibility of practical realization of the acoustical system for internal wave observation. It was shown that amplitudes, periods, number of modes and directions of internal wave propagation can be determined on the basis of measuring of noise fluctuations. [Work supported by Russian Foundation for Basic Research.]

5aUWa14. Ocean monitoring by using underwater sound channel as a feedback loop. A. V. Furduev (Andreev Acoustics Inst., ul. Shvernika 4, Moscow, 117036 Russia)

A method is proposed to monitor variability of the medium parameters on an acoustic path. The method has been tested for temperature and current monitoring in the Black Sea. The technique is based on the regenerative scheme with a positive feedback. A specific feature of the method is that the medium to be studied forms a part of the measuring instrument, this approach leading to self-matching to a frequency of the interference maximum and thereby requiring lower acoustic power than that in other methods. The measurements have confirmed an accuracy of 1 sm/s in current monitoring. Two modes of monitoring have been tested: (1) a self-excitation mode when information on the variability is carried by the frequency, the spectrum of frequency deviations characterizing the physical nature of the variability; (2) a regeneration mode when the received ambient noise is reradiated from a distant point, this mode yielding higher contrast of the interference spectrum and allowing the delays between rays to be estimated, the interference variability characterizing processes on the path. The proposed method is promising for short paths, harbors, and straits to monitor heat- and mass-exchange processes, fish migrations, ship traffic, or ice drift.

Session 5aUWb

Underwater Acoustics and Signal Processing in Acoustics: Underwater Communication and Signal Processing

Chris Jones, Cochair
Applied Physics Laboratory, University of Washington, Seattle, Washington 98105, USA

Alain Maguer, Cochair
NATO SACLANT Undersea Research Centre, Viale San Bartolomeo 400, 19038 La Spezia, Italy

Contributed Papers

8:40

5aUWb1. First results from an acoustic-communication transmission model using 3D Gaussian beams and quadrature detection. Paul A. Baxley, Homer Bucker, and Joseph Rice (Space and Naval Warfare Systems Ctr., San Diego, Acoust. Branch, Code D881, San Diego, CA 92152-5001)

Analysis of shallow-water, acoustic-communication channels must account for the joint phenomena of multipath spread and Doppler spread. A physics-based, numerical propagation model is being developed to reproduce these effects via the combined use of three-dimensional Gaussian beams and quadrature detection for finite-duration tones. Closely spaced microbeams are traced in three spatial dimensions to properly incorporate out-of-plane boundary effects from rough boundaries and a sloping seafloor. Refraction, absorption, reflection, scattering, and Doppler-shifts influence the individual beams according to our best understanding of these physical processes. At an arbitrarily located quadrature-detector receiver, signal contributions are accumulated with coherent treatment of the travel-time, phase, and Doppler shifts associated with each microbeam. This approach supports the analysis of the spatio-temporal dispersion associated with the significant multipath arrivals. Fluctuation and coherence statistics may be analyzed via the specification of source/receiver motion or time-varying boundaries. Simulations of the quadrature response for measured shallow-water channels (<200 m) near San Diego, California will be presented. For these first case studies, sea-surface roughness is neglected, but scattering from a rough bottom is considered and Doppler spread is assumed to arise solely from source/receiver motion. [Work supported by the SPAWARSYSCEN San Diego Independent Research Program.]

9:00

5aUWb2. Examination of time-reversal acoustics and applications to underwater communications. Antonio A. M. Abrantes, Kevin B. Smith, and Andres Larraza (Dept. of Phys., Naval Postgrad. School, Monterey, CA 93943, kevin@physics.nps.navy.mil)

Recent experimental work [Roux *et al.*, Appl. Phys. Lett. **70**, 1811–1813 (1997); Kuperman *et al.*, J. Acoust. Soc. Am. **103**, 25–40 (1998)] has shown that the novel technique of time-reversal acoustics (TRA) can be applied in shallow-water environments to focus energy back at a source location from a transmitted signal received at a distant receiver array. This refocusing produces a local intensification of the field as well as a convergence of the signal in time. These two aspects of TRA techniques suggest it may be a viable approach for use in underwater communication systems. Because TRA techniques rely on the reconvergence of multipath information into focused arrivals at the original source locations, the influence of multipath spreading is removed. The energy transmitted is then enhanced by the focusing, thereby increasing the SNR. Specifically of interest in this study will be an analysis of how well the signal can be refocused in typical shallow-water environments and what type of data transfer rates can be achieved using TRA on realistic systems. [Work supported by ONR.]

9:20

5aUWb3. Characterization of the underwater channel for acoustic communications. Gerard Loubet and Bernard Faure (Laboratoire des Images et des Signaux, INPGrenoble, D. U., 38402 St. Martin d'Heres Cedex, France, Gerard.Loubet@lis.inpg.fr)

In recent years, acoustic underwater (AUW) communications have known a huge increase in research and development due to the growing needs of wireless transmission systems. While mobile radio channels fit well within the model of Rayleigh fading, this model is often used for the design of communication systems. However, many experimentations carried out by our laboratory (LIS ex CEPHAG) with the French Navy or within European Community MAST projects (LORACOM and PARACOM) have shown that this model do not fit for AUW transmissions. The AUW channel is well modeled, using ray tracing, by great deterministic propagation paths (macro-multipath) associated with random fluctuations (micro-multipaths). Experimental results will be presented. The slow variations of the deterministic part may be due to internal waves, the little, fast variations of the received energy by appearance or disappearance of micro-paths. A random channel modeling developed for LORACOM project (Contract No. MAS2-CTG4-0080) agrees with this behavior. Different AUW medium characterizations depending on the channel geometry (shallow or deep water communications), on the frequencies (between 1 and 10 kHz), and on the range (1 to 100 km) will be discussed. Spatial coherence results will also be presented.

9:40

5aUWb4. Telesonar channel estimation and adaptation. Joseph Rice, Richard Shockley (Space and Naval Warfare Systems Ctr., San Diego, CA), Dale Green (Datasonics, Inc., Cataumet, MA), John Proakis, and Milica Stojanovic (Northeastern Univ., Boston, MA)

Sound is the best form of energy for broadcasting communication signals in the ocean. However, the physical channel is impaired by non-white noise, frequency-selective absorption, a refractive medium, a sloping seafloor, a dynamic sea-surface, and scattering at the boundaries. Temporal variability of these influences and motion of the link terminals introduce fluctuations in the received signal and noise fields. These oceanographic and geometric factors produce measurable effects on underwater acoustic communication systems. The relevant direct measures of these channel effects include multipath spreading, Doppler shifts and spreading, coherence time, and noise statistics. Measuring and understanding these effects support optimization of both modulation and demodulation parameters. Such channel adaptation strategies enhance quality of service for the communication link. Theory, simulation, and ocean experiment illustrate link improvements. [Work funded by ONR 32, the SSC-SD Independent Research Program, and the Navy SBIR Program.]

10:00

5aUWb5. Channel characterization using FSK wave forms. Vincent K. McDonald, Jr., Joseph Rice (SPAWARSYSCEN, San Diego, CA 92152), and Dale Green (Datasonic, Inc., Cataumet, MA 02534)

Automatic characterization of underwater acoustic communication channels can support connectivity over a wide range of operational ocean environments. With quantitative measures of the prevailing channel, adaptive modems may optimize the modulation and initialize the demodulation equalizer. A novel channel-estimation technique involving noncoherent processing of received FSK wave forms has been described recently by Green and Rice (Proc. IEEE Oceans'98) and Rice and Green (Proc. MTS Ocean Community Conference, 1998). This technique uses received handshake signals to measure temporal and spectral spreading and signal excess directly, and to estimate coherence parameters. This effort will focus on applying this channel-estimation technique to received and autonomously recorded 8–13 kHz MFSK signals using shallow horizontal channels. [Work supported by ONR 32 and SPAWARSYSCEN.]

10:20–10:40 Break

10:40

5aUWb6. Improved reliability and data rates for AUV acoustic communications. Daniel Kilfoyle (MIT, Woods Hole Oceanograph. Inst., Joint Prog. in Oceanograph. Eng., Dept. of Elec. Eng., 406 Sippewissett Rd., Falmouth, MA 02540, dkilfoyle@whoi.edu)

The availability of parallel channels in a point-to-point communication system may be exploited to increase data rate and reliability, without additional power, beyond that possible with a single channel. The severe power and bandwidth constraints imposed on an autonomous underwater vehicle acoustic telemetry link motivate the use of spatial modulation techniques to achieve these benefits, particularly for missions requiring real time sensor data transmission. Theoretical performance improvements for coherent modulation schemes yielding the equivalent of 6 dB or greater signal-to-noise ratio gain are shown. Experimental results from an underwater range near the Bahama Islands are given. Inclusion of a modest horizontal line array on the vehicle and a remote transceiver on the surface are the sole additional requirements beyond a conventional telemetry system.

11:00

5aUWb7. Statistics-governed channel simulation. Dale Green (Datasonics, Inc., Cataumet, MA 02534) and Joseph Rice (SPAWAR, San Diego, CA)

A numerical channel simulator suitable for real-time, laboratory testing of undersea acoustic communication systems and governed by specified statistics for signal dispersion, coherence, and noise is presented. This work is motivated by a desire to understand the important parameters of nonstationary underwater acoustic channels and to explore the corresponding quality of service achievable within the constraints of those channel parameters. The simulator implements temporal variation (i.e., time coherence of both signals and interference) in either of two essentially equivalent ways: either as a Markov process, according to user-specified decorrelation time, or as realizations of spectral spreading. The quadrature response and underlying channel characteristics obtained from a physics-based model initiate and statistically govern the simulator. An important extension to the initializing statistics is inclusion of spectral spreading for individual macropaths, rather than the relatively gross spectral spreading formerly employed. Last, the simulator superposes recorded or simulated nonwhite, nonstationary channel noise, including co-channel network MAI (multiple-access interference) and jammers. Note that the interface between the physics-based model and the statistics-based real-time simulator is natural and well-defined. Thus any appropriate physics-based model or measured ocean channel statistics may be used to initialize the real-time simulator. [Work supported by ONR 32, the SSC-SD Independent Research Program, and the Navy SBIR Program.]

11:20

5aUWb8. Information theoretic/chaotic sonar signal processing. Azizul H. Quazi and Richard A. Katz (Naval Undersea Warfare Ctr., Signal and Information Processing, Code 3124, 1176 Howell St., Newport, RI 02841, quaziah@npt.nuwc.navy.mil)

Dynamical systems generate complex signals. Very often, traditional sonar signal processing in both the time domain and frequency domain are not adequate enough to characterize the complex dynamics of underwater sources that generate, radiate and/or reflect sonar signals. Recent advances in signal processing are aimed at capitalizing on the inherent complexities in a signal structure by applying information theoretic/chaotic processing analysis tools to reveal signal dynamics, otherwise unseen when traditional (linear) signal processing methods are applied. Here examples are presented of periodicities (i.e., limit cycles), quasi-periodicites (2-torus and n-torus motion) and nonperiodic (chaotic) motion as applied to signals-of-interest in underwater acoustic applications. It is demonstrated how nonlinear diagnostic tools, when appropriately applied to underwater acoustic time series measurements, can be used for extracting new information about system dynamics.

11:40

5aUWb9. Colored-noise performance of the order-truncate-average-ratio (OTAR) filter. Jeffrey H. Shapiro (MIT, 77 Massachusetts Ave., Cambridge, MA 02139-4307, jhs@mitrlevm.mit.edu) and Thomas J. Green, Jr. (MIT, Lincoln Lab., Lexington, MA 02420-9185)

Spectrogram background normalization for narrow-band passive acoustic detection systems has a long history. This presentation addresses a more complicated scenario in which broadband background whitening is still desired, with simultaneous preservation of intermediate-bandwidth spectral features and suppression of narrow-band interference. Toward this end, a nonlinear processor—the order-truncate-average-ratio (OTAR) spectral filter—is presented and analyzed. While much is known about order statistics, closed-form expressions for the mean and covariance of the output of this filter appear to be unattainable. However, for white Gaussian noise-input time-series with no spectral averaging (conditionally exponential spectral statistics), approximate expressions for the output mean and covariance have been derived. Moreover, for scenarios employing spectral averaging on colored Gaussian noise-input time-series, expressions for the output mean have been derived. All of these analytical results agree well with simulation of the OTAR filter. The analysis has been applied to evaluate an appropriate transfer function for the filter and to illustrate a number of other interesting properties. [Work supported by SPAWAR, under Air Force Contract F19628-95-C-0002.]

12:00

5aUWb10. Maximum *a posteriori* probability background estimation. Thomas J. Green, Jr., William H. Payne, Jr., Vivian E. Titus, and Eric J. Van Allen (MIT Lincoln Lab., 244 Wood St., Lexington, MA 02420-9185, tjgreen@LL.mit.edu)

Signal detection in acoustic data is complicated by a structured, nonuniform background that obscures signal characteristics. Consequently, efforts to estimate and whiten the background can yield significant improvements in downstream performance. In fact, the structure of the Neyman–Pearson optimal signal detector includes an explicit background whitening step. Linear estimators suffer from the difficulty of distinguishing between signal and background in the region of interest. Consequently, signal contamination can cause substantial errors in background estimates that reduce signal detectibility via subsequent algorithms and analysis. A nonlinear estimator has been developed that exploits models of both the measured data and the presumed scene and maximum *a posteriori* prob-

ability (MAP) theory to produce a background estimate. The data model is guided by the measurement physics and the scene model is based on a Markov random field assumption. Both models are augmented to accommodate anomalies. In this seminar the MAP estimator is described, along with practical issues associated with algorithm initialization, simulated performance with both white and colored-noise inputs, and real data examples. [Work supported by SPAWAR, under Air Force Contract F19628-95-C-0002.]

Contributed Posters

These posters will be on display in the Poster Gallery from Thursday to Friday, 18–19 March. Authors will be at their posters from 2:00 p.m. to 4:00 p.m. on Friday, 19 March.

5aUWb11. Identification of the radiating sources in underwater acoustics. Bourennane Salah and Bendjama Ammar (URA CNRS 2053, Quartier Grossetti 20250, Corte, France)

In the context of the narrow-band or wideband array processing problem, in this paper a robust algorithm is developed to improve the accuracy of the estimation of the direction of arrival of the sources. It is well known that when the noise cross-spectral matrix is unknown, these estimates may be grossly inaccurate. The band noise spectral matrix, the classical noise model, is used. By means of a linear operator and an iterative algorithm for estimating the spatial correlation length, a new estimator for the direction of arrival of the sources is developed. The proposed algorithm is based upon a particular partition of the received signal vector which leads one to obtain an approximation of the noise subspace matrix without eigendecomposition. Then using both a propagation operator and non-eigenvector algorithm to estimate the projection matrix, a new robust algorithm is developed for the source characterization problem in the presence of noise with an unknown cross-spectral matrix. It will be shown that the performance of bearing estimation algorithms improves substantially when this robust algorithm is used. Experimental data results are presented for the band noise spectral matrix.

5aUWb12. Three-dimensional auditory display of passive sonar data. Suzanne Richardson (Schlumberger, 8311 North FM 620 Rd., Austin, TX 78726, srichard@austin.apc.slb.com) and Charles Loeffler (Univ. of Texas, Austin, TX 78758)

Submarine sonar operators typically use visual and monaural audio outputs to locate obstacles, ships, and animals in the surrounding ocean. Recently, the effectiveness of using 3-D, rather than monaural, sonar audio outputs was investigated. A multi-channel signal processing system has been developed that converts sonar signals collected by elements of a hydrophone array into binaural signals for the left and right ears, which provide accurate 3-D aural imaging of an underwater acoustical environment. An operator who listens to the binaural signals via stereo headphones will perceive that he is immersed in the underwater acoustical environment. The system incorporates two banks of FIR filters (one for the left ear and one for the right ear) to process the sonar data. The FIR filters simultaneously beamform the hydrophone data and filter the data with head-related transfer functions in order to create binaural signals that provide 3-D sound. [Work supported by Applied Research Laboratories: U. T. Internal Research and Development.]

FRIDAY AFTERNOON, 19 MARCH 1999 POSTER GALLERY, 12:00 TO 6:20 P.M.

Posters from various technical sessions remain on display in the Poster Gallery.

Posters from sessions which contain both lecture and poster presentations will be attended by the authors as listed below.

2:00–4:00

5aNSa8	Bruyninckx, Willy	Measurement methodology for sound power levels of industrial noise sources
5aPAc11	Rath, M.	Inline process monitoring of thermosets by ultrasonic measurements in a compression mould
5aPAc12	Flannery, C. M.	Accurate noncontact measurement of elastic properties of ceramics using acoustic microscopy and laser ultrasonics
5aPAc13	Kalinchuk, Valery V.	Some dynamic properties of non-homogeneous thermoelastic pre-stressed media
5aPAc14	Kalinchuk, Valery V.	On the investigation of the stressed state of the elastic and piezoelectric bodies
5aUWa13	Furduev, Alexandr	Internal wave imprint in the oceanic ambient noise
5aUWa14	Furduev, A. V.	Ocean monitoring by using underwater sound channel as a feedback loop
5aUWb11	Salah, Bourennane	Identification of the radiating sources in underwater acoustics
5aUWb12	Richardson, Suzanne	3-D auditory display of passive sonar data

Also, the following poster sessions are scheduled:
Poster Session 5pPPb
Poster Session 5pSCa
Poster Session 5pSCb

ability (MAP) theory to produce a background estimate. The data model is guided by the measurement physics and the scene model is based on a Markov random field assumption. Both models are augmented to accommodate anomalies. In this seminar the MAP estimator is described, along with practical issues associated with algorithm initialization, simulated performance with both white and colored-noise inputs, and real data examples. [Work supported by SPAWAR, under Air Force Contract F19628-95-C-0002.]

Contributed Posters

These posters will be on display in the Poster Gallery from Thursday to Friday, 18–19 March. Authors will be at their posters from 2:00 p.m. to 4:00 p.m. on Friday, 19 March.

5aUWb11. Identification of the radiating sources in underwater acoustics. Bourennane Salah and Bendjama Ammar (URA CNRS 2053, Quartier Grossetti 20250, Corte, France)

In the context of the narrow-band or wideband array processing problem, in this paper a robust algorithm is developed to improve the accuracy of the estimation of the direction of arrival of the sources. It is well known that when the noise cross-spectral matrix is unknown, these estimates may be grossly inaccurate. The band noise spectral matrix, the classical noise model, is used. By means of a linear operator and an iterative algorithm for estimating the spatial correlation length, a new estimator for the direction of arrival of the sources is developed. The proposed algorithm is based upon a particular partition of the received signal vector which leads one to obtain an approximation of the noise subspace matrix without eigendecomposition. Then using both a propagation operator and non-eigenvector algorithm to estimate the projection matrix, a new robust algorithm is developed for the source characterization problem in the presence of noise with an unknown cross-spectral matrix. It will be shown that the performance of bearing estimation algorithms improves substantially when this robust algorithm is used. Experimental data results are presented for the band noise spectral matrix.

5aUWb12. Three-dimensional auditory display of passive sonar data. Suzanne Richardson (Schlumberger, 8311 North FM 620 Rd., Austin, TX 78726, srichard@austin.apc.slb.com) and Charles Loeffler (Univ. of Texas, Austin, TX 78758)

Submarine sonar operators typically use visual and monaural audio outputs to locate obstacles, ships, and animals in the surrounding ocean. Recently, the effectiveness of using 3-D, rather than monaural, sonar audio outputs was investigated. A multi-channel signal processing system has been developed that converts sonar signals collected by elements of a hydrophone array into binaural signals for the left and right ears, which provide accurate 3-D aural imaging of an underwater acoustical environment. An operator who listens to the binaural signals via stereo headphones will perceive that he is immersed in the underwater acoustical environment. The system incorporates two banks of FIR filters (one for the left ear and one for the right ear) to process the sonar data. The FIR filters simultaneously beamform the hydrophone data and filter the data with head-related transfer functions in order to create binaural signals that provide 3-D sound. [Work supported by Applied Research Laboratories: U. T. Internal Research and Development.]

FRIDAY AFTERNOON, 19 MARCH 1999 POSTER GALLERY, 12:00 TO 6:20 P.M.

Posters from various technical sessions remain on display in the Poster Gallery.

Posters from sessions which contain both lecture and poster presentations will be attended by the authors as listed below.

2:00–4:00

5aNSa8	Bruyninckx, Willy	Measurement methodology for sound power levels of industrial noise sources
5aPAc11	Rath, M.	Inline process monitoring of thermosets by ultrasonic measurements in a compression mould
5aPAc12	Flannery, C. M.	Accurate noncontact measurement of elastic properties of ceramics using acoustic microscopy and laser ultrasonics
5aPAc13	Kalinchuk, Valery V.	Some dynamic properties of non-homogeneous thermoelastic pre-stressed media
5aPAc14	Kalinchuk, Valery V.	On the investigation of the stressed state of the elastic and piezoelectric bodies
5aUWa13	Furduev, Alexandr	Internal wave imprint in the oceanic ambient noise
5aUWa14	Furduev, A. V.	Ocean monitoring by using underwater sound channel as a feedback loop
5aUWb11	Salah, Bourennane	Identification of the radiating sources in underwater acoustics
5aUWb12	Richardson, Suzanne	3-D auditory display of passive sonar data

Also, the following poster sessions are scheduled:
Poster Session 5pPPb
Poster Session 5pSCa
Poster Session 5pSCb

Session 5pAA

Architectural Acoustics: Building Acoustics III: Acoustical Measurements

K. Heinrich Kuttruff, Cochair
Institute of Technical Acoustics, Technical University of Aachen, D-52063 Aachen, Germany

Angelo Campanella, Cochair
Campanella Associates, 3201 Ridgewood Drive, Columbus, Ohio 43026, USA

Chair's Introduction—1:55

Contributed Papers

2:00

5pAA1. A system for measuring the directional parameters of room acoustics. Hiroyuki Okubo, Masamichi Otani, Ryo Ikezawa, and Setsu Komiyama (Japan Broadcasting Corp. (NHK), 1-10-11 Kinuta, Setagaya-ku, Tokyo, 157-8510 Japan)

A new system for measuring the directional parameters of room acoustics has been developed. The system consists of five omni-directional microphones, audio interfaces, DSPs (digital signal processors), and control software. This software synthesizes the directional pattern of the microphones, and calculates the directional parameters automatically. The lateral component (LC), front- to-back ratio (FBR), and left-to-right ratio (LRR) of directional room impulse responses are easy to measure with this system. The system was used to take measurements in two halls. The first hall was a concert hall, with the measurements of impulse responses taken at 72 points. The second was a multipurpose hall, the shape of which could be altered three ways (for concerts, conventions, and exhibitions), and the measurements were taken at 12 points for each shape. The total of 108 data points from the four room shapes represents the range of room types. The directional parameters are sensitive to room shape, wall materials, and the positions of seats. These data may also be useful for studies on the correspondence between the objective description and subjective evaluation of the acoustical quality of rooms.

2:20

5pAA2. Frequency response measurement with composed audio test signal. Mladen Maletic, Hrvoje Domitrovic, and Ivan Djurek (Faculty of Elec. Eng. and Computing, Dept. of Electroacoustics, Unska 3, HR-10000 Zagreb, Croatia, mladen.maletic@fer.hr)

The composed audio test signal (CATS) is formed by mixing three mutually independent composed saw signals (CSSs). The CSS sequences are a special type of pseudorandom signal. The CATS closely follows the characteristics of natural signals, and its behavior is controlled by the well-defined and configurable parameters. The amplitude probability density function of the CATS follows Gaussian distribution. Furthermore, second and third CSS sequences are generated using the perturbated parameters of the first one. Pseudorandom noise can have a spectrum and amplitude distribution similar to that of white noise. The CATS methods employ efficient cross correlation between input and output to recover the periodic impulse response (PIR) of the system being measured. The PIR can be considered as the impulse response only if the CATSs period equals or exceeds the duration of the system impulse response. The frequency response can then be found by taking the discrete Fourier transform of the impulse response. The CATS can be used as a test signal with two-channel analyzers. The averaged cross spectrum is divided by the averaged autospectrum of the input channel to obtain the frequency response.

2:40

5pAA3. Fluctuation of room acoustical parameters on small spatial intervals. Diemer de Vries and Jan Baan (Lab. of Acoust. Imaging and Sound Control, Delft Univ. of Technol., Delft, The Netherlands)

The Delft Acoustics group has introduced array technology in room acoustic measurement practice: instead of at a limited number of ''representative'' places, impulse responses are measured along an array of closely sampled microphone positions. By displaying the responses as a visual entity, the wave character of the sound field is clearly revealed. The data form a base for further processing, enabling the separation and analyzing of the different wave-field components. The sound fields in several concert halls have been measured this way. From impulse responses recorded with 0.05-m spatial separation, the common room acoustical parameters have been determined. It appears that, even between the ten positions in front of one and the same seat, unexpected fluctuations occur, e.g., when measured in octave bands, the clarity index varies over 1 dB on this interval, the lateral energy fraction 0.2 (i.e., between 0.1 and 0.3). For the broadband versions, these variations are approximately halved, still being significant. These results explain why the predictive value of these parameters for the perceptual quality of the acoustics on a (group of) seat(s) is limited. Instead of at one point, the values at several adjacent points should be considered.

3:00

5pAA4. Influence of time variance on room impulse response measurement. Fumiaki Satoh (Dept. of Architecture, Chiba Inst. of Technol., Tsudanuma 2-17-1, Narashino-shi, Chiba, 275-0016 Japan), Yoshito Hidaka (Tohwa Univ., Chikushigaoka 1-1-1, Minami-ku, Fukuoka-shi, Fukuoka, 815-8510 Japan), and Hideki Tachibana (Tokyo Univ., Roppongi 7-22-1, Minato-ku, Tokyo, 106-8558 Japan)

The measurement of room impulse response is made under the assumption that the sound propagation system is time invariant. Actually, however, the air in a room is usually moving and the temperature is changing to a greater or lesser extent. In order to examine the influence of such time variance on the measurement of room impulse response, experimental investigations were performed in a reverberation room in which the air was excited by fans and in a concert hall in which the air-conditioning system was operated. Impulse response measurements were performed by the maximum-length sequence (MLS) method and the sweep pulse (SP) method and these results were compared. From the results, it has been found that the reverberation decay tends to become steeper by repeating the impulse response measurement to get high signal-to-noise ratio and the SP method is more robust than the MLS method against the influence of time variance of the atmospheric condition in a room.

3:20

5pAA5. Time variances with MLS technique: Theoretical considerations concerning rotating microphones in building acoustics. Wieland Weise and Alfred Schmitz (Appl. Acoust., Physikalisch-Technische Bundesanstalt, Bundesallee 100, 38116 Braunschweig, Germany)

For some time now, the technique of maximum length sequence (MLS) measurement has been successfully applied in building acoustics. Rotating microphones which are otherwise useful, especially for the determination of sound reduction, cannot be used here because the time invariance of the system would be violated. The measurement errors arising when rotating microphones are used in experiments were already investigated previously. However, in view of the future process of standardization of measuring techniques in building acoustics, theoretical understanding is necessary. Theoretical analyses are presented which exhibit the deviations of the measurements. Emphasis is placed on the differences arising when a synchronous or asynchronous relation between microphone round trip time and MLS period is chosen.

3:40–4:00 Break

4:00

5pAA6. Measurements of anechoic room characteristics. Miroslava A. Milosevic and Dejan G. Ciric (Faculty of Electron. Eng., Univ. of Nis, Nis, Yugoslavia)

A simple measurement system with a computer as the main unit is developed for the measurements of the characteristics of an anechoic room, such as measurements of the sound-pressure decay in space, the sound-pressure decay in time, and the sound insulation. The measurements are performed in two steps. The room response signals are first recorded and stored in the PC memory. Then, these signals are processed by designed software depending on the type of measurement. The departure of sound-pressure decay in space from the ideal characteristic is observed. The sound-pressure decay in time is obtained by the integrated-impulse method using the maximum-length sequence technique. The sound insulation is measured only for a specially designed door between the anechoic and the control room because of its insulation, which is rather low in regard to the other parts of an anechoic room. The measurements performed in the anechoic room of the Faculty of Electronic Engineering in Nis have shown that the departure of sound-pressure decay in space from the ideal characteristic is rather below the limit of 1 dB in frequency range from 50 Hz upward. The door sound insulation is above 55 dB.

4:20

5pAA7. An Internet-oriented system for acoustic measurements of sound fields. Masatugu Sakurai, Shinichi Aizawa (Yoshimasa Electronic, Inc., 1-58-10, Yoyogi, Sibuya, Tokyo, 151-0053 Japan, info@ymec.co.jp), and Yoichi Ando (Kobe Univ., Nada, Kobe, 657-8501 Japan)

A new diagnostic system was developed, based on the model of the auditory-brain system. The system, including the AD and DA converters, works on the PC for Windows, thus there is no need for special additional devices. Further, the system is available on the Internet, where a user can obtain further information about the system, and utilize it easily in practice by downloading a demonstration program. After obtaining the binaural impulse responses, four orthogonal factors, including the SPL, the initial time delay gap between the direct sound and the first reflection, the subsequent reverberation time, and the IACC are analyzed. Then, these factors may be used for the calculation of the scale values of both global and individual subjective preference. In addition, two more factors, τ_{IACC} and W_{IACC}, in the interaural cross-correlation function are figured out for evaluating the image shift or balance of sound fields and the apparent source width (ASW), respectively. Also, the effective duration of ACF, τ_e, and fine structures of autocorrelation function of sound signals, including the value of first maximum, ϕ_1, and its delay time, τ_1, are analyzed. This system may be utilized for automatic control of sound fields by electroacoustic systems also.

Contributed Posters

These posters will be on display from Monday to Wednesday, 15–17 March. Authors will be at their posters from 10:00 a.m. to 12:00 noon on Wednesday, 17 March.

5pAA8. Four-microphone-array measurements combined with geometrical room acoustic simulation technique. Jörg Becker, Markus Sapp (Inst. of Commun. Eng., Aachen Univ. of Technologie, 52056 Aachen, Germany), and Oliver Schmitz (Aachen Univ. of Technologie, 52056 Aachen, Germany)

For a revision of the acoustics of enclosures it is important to analyze the existing acoustical mechanisms. Therefore, measurement of room impulse response functions is a usual standard. The temporal progression of the incident sound can be determined from these impulse responses. Single number quantities can be evaluated, too. However, the knowledge of the direction of the first reflection is also of prime importance. Computer simulation of the room acoustic is a powerful tool to evaluate these directions but it is only reasonable if the geometry of the room is well known. Often it is difficult to get detailed information of the geometry, especially if there are curved walls. This paper focuses on the evaluation of spatial information of sound fields with a four-microphone-array measurement system and the post-processing with algorithms taken from geometrical room acoustic simulation. With multidimensional sound field analysis it is possible to get the direction of the important reflections. Virtual sound sources can be calculated. With a back tracing algorithm the history of higher-order reflections can be determined or the geometry of the room model and the results of computer simulation can be verified by a comparison of measured and calculated VSS.

5pAA9. On the accuracy of the assessment of room acoustical parameters using MLS technique and ray-tracing simulation. Marcio Henrique de Avelar Gomes and Samir Nagi Yousri Gerges (Universidade Federal de Santa Catarina-Depto. de Eng. Mecanica-Laboratorio de Vibracoes e Acustica-cx. postal 476-Florianopolis, SC 88040 900, Brazil, avelar@gva.ufsc.br)

Advances in psychoacoustics through the years have made it possible to evaluate the acoustical quality of a room, based on several numerical parameters that have been developed. Even though there is not total agreement about which parameters are truly important, some of them are accepted by most of the acousticians. Most of these parameters can be determined from the impulse responses of a room. This work presents a comparison between results simulated using a commercial ray-tracing computer program, and measured with one of the most modern techniques of measuring impulse responses, which uses a maximum length sequence (MLS) as the driving signal. Limitations concerning the use of the measuring technique, and the ray-tracing program, as well, are analyzed and discussed.

Session 5pBB

Biomedical Ultrasound/Bioresponse to Vibration: Low Intensity/Low Frequency Ultrasound

E. Carr Everbach, Cochair
Engineering Department, Swarthmore College, 500 College Avenue, Swarthmore, Pennsylvania 19081-1397, USA

Gail ter Haar, Cochair
Physics Department, Royal Marsden Hospital, Sutton, Surrey SM2 5PT, UK

Chair's Introduction—2:15

Invited Papers

2:20

5pBB1. Therapeutic ultrasound—An historical overview. Gail ter Haar (Phys. Dept., Royal Marsden Hospital, Sutton, Surrey SM2 5PT, UK)

Ultrasound was used with therapeutic intent long before its potential as an imaging modality was contemplated. Initially it was thought of as acting solely through its heating ability, but more recently there has been scientifically convincing evidence that beneficial effects can be induced in the absence of biologically relevant bulk temperature rise, thus indicating that nonthermal mechanisms may also play a part in ultrasound treatments. Apart from the high-intensity, surgical uses (operating at peak intensities around 2 kW cm^{-2}), ultrasound has been applied amongst other things to promote wound healing, to stimulate bone repair, to accelerate healing in tendon injuries, and as a thrombolytic agent. The majority of therapeutic ultrasound techniques operate at intensities of 500 mW cm^{-2} or less (spatially averaged intensities). It is interesting to compare the different techniques and modes of delivery in an attempt to understand the mechanisms of action that produce beneficial biological effects.

2:40

5pBB2. Enhancement of fibrinolysis by low-intensity c.w. ultrasound. Charles W. Francis, Valentina Suchkova (Vascular Medicine Unit, Univ. of Rochester Med. Ctr., Rochester, NY 14642), and E. Carr Everbach (Swarthmore College, Swarthmore, PA 19081)

Continuous-wave ultrasound at intensities below 4 W/cm^2 (SATA) and frequencies around 1 MHz has been shown to accelerate enzymatic fibrinolysis *in vitro* and in some animal models. The mechanism for this ultrasound accelerated thrombolysis (UAT) is unknown, although heating is unlikely. Hyperbaric studies have shown that approximately half of the acceleration is removed with overpressures of 3 atm or more, implicating cavitational mechanisms as dominant contributors to UAT, if not the sole ones. Detection of bubbles and cavitational activity in UAT via passive and active detectors corroborates this view. Recent studies using 40-kHz cw ultrasound at intensities as low as 0.25 W/cm^2 show promise for eventual clinical applications, including insonification through bone without significant heating. [Work supported by NIH.]

Contributed Papers

3:00

5pBB3. Ultrasonic-induced phase transitions of micrometer-size droplets. Oliver D. Kripfgans, J. Brian Fowlkes, and Paul L. Carson (Univ. of Michigan, Dept. of Radiol., Kresge III R3315, Ann Arbor, MI 48109-0553, oliver.kripfgans@umich.edu)

Droplets for various applications were generated by mixing albumin (bovine) with saline and a low boiling point liquid (dodecaflouropentane). The resulting emulsion contains small droplets with a lower size range on the order of a few micrometers. The type of mixing process was found to determine the range of droplet sizes. The albumin, as a surface active agent, is assumed to build a shell around the droplets and prevents coalescence, since mixtures without albumin did not produce stable droplets. Increases in temperature of the resting host fluid showed that droplets could be superheated well above their natural boiling point. It is assumed that this property is caused by an increase in pressure within the droplet due to surface tension. The superheated state could be overcome by the application of ultrasonic pulses and/or hydrodynamical action (flow). The presence of ultrasound contrast agents allowed ultrasonic-induced phase transitions at the natural boiling point. Droplets producing bubbles for transpulmonary applications have been studied previously. The interest here was primarily in larger bubbles for therapeutic applications and to serve as point beacons for aberration correction. [Work supported in part by PHS Grant No. R01 HL54201 from the National Heart, Lung and Blood Institute.]

3:20

5pBB4. Ultrasonic technique for the investigation of structural properties of biological fluids. Algirdas Voleišis, Rymantas J. Kažys, Liudas Mažeika, Reimondas Šliteris, and Birutė Voleišienė (Ultrasound Res. Ctr., Kaunas Univ. of Technol., Studentų str. 50, LT-3031, Kaunas, Lithuania, ulab@tef.ktu.lt)

Biological fluids are specific objects for acoustical investigation due to the wide spectra of relaxation processes, especially nonstationary fluids such as blood during its coagulation process. The proposed method combines measurement of ultrasound attenuation over a frequency range and, ultrasound velocity dispersion being negligible, precise measurement of velocity variations at fixed frequency. In the dynamic spectroscopy method the wideband ultrasonic signal transmitted through the media is digitized with a sample rate of 200 MHz, averaged, and processed by a PC. Ultrasound absorption frequency dependency with intervals of 1 min is determined from amplitude spectra. Using small volume (1 ml) cell with

multiple reflections, in the range of 2–17-MHz, diffraction corrections and ultrasonic attenuation were determined in low-absorptive standard liquid, conservative, and native coagulating blood. The clot formation process in the native blood is also monitored at frequencies 5 or 10 MHz using the time-of-flight method with the acquisition of the results. In the cell of 0.2 ml volume sensitivity of 0.2 ns is achieved. Cell parameters and influence of the pulse bandwidth are analyzed. According to the ultrasound velocity variations, four typical blood coagulation phases were observed during 30 min, less expressed being the first phase (0–2 min).

3:40

5pBB5. Are there gas cavities in red blood cells? Dmitry A. Selivanovsky, Igor N. Didenkulov, and Olga V. Kostina (Inst. of Appl. Phys., 46 Ulyanov St., Nizhny Novgorod, 603600, Russia)

Many of marine single-cell organisms (phytoplankton) have gas cavities which allow them to keep their life cycle. Existence of gas cavities can essentially have an influence on acoustic and mechanical properties of cells. It seems reasonable to suppose that such cavities can also exist in erythrocites, life cycle of which is related to gas exchange. The present work was aimed on measurements of acoustomechanical properties of human red blood cells to reveal their gas cavities. The velocities of erythrocite sedimentation (VES) in natural conditions and under compression/decompression were measured. The VES was found to increase considerably under or after compression/decompression. The effect was observed both for blood from healthy and sick people. Special microscope observations of sedimentation process allowed findings that compression/decompression changes the natural orientation of erythrocites: after compression/decompression their main planes become vertical instead of horizontal for natural conditions. Such a phenomenon can be explained with the model of the red blood cell as a body with gas cavity. A compression/decompression changes the balance between centers of gravity and buoyancy making cells rotate and consequently to decrease the viscous force. [Work supported in part by RFBR, Russia.]

4:00

5pBB6. The acoustic system for investigation of the temporomandibular joint pathology. Waldemar Lis, Roman Salamon, and Jozef Zienkiewicz (Dept. of Acoust., Tech. Univ. of Gdansk, 80-952 ul. G. Narutowicza, 11/12 Poland, wall@eti.pg.gda.pl)

The temporomandibular joint is the most complicated joint from the anatomic standpoint. Diagnosing it is still a problem to be solved. Modern top quality devices do not provide a complete solution—the barrier here is the high price of a single examination. For this reason, new, cheap methods of diagnosing the temporomandibular joint are being sought. One of these methods is diagnosing on the basis of passive listening for acoustic signals emitted by the joint in motion. This paper presents the application of the FFT and wavelet method for the purpose of examining the acoustic signal analysis of the temporomandibular joint. The advantages and disadvantages of both methods, the Fourier method and wavelet method, are discussed. Finally, the results obtained by the Fourier analysis in time window and by a wavelet method are presented and compared.

4:20

5pBB7. The velocity of ultrasound propagation through brain tissue at low ultrasound frequencies. Igor Zoric (Faculty of Mining and Petroleum Eng., Pirottijeva 6, HR 10000 Zagreb, Croatia, izoric@rudar.rgn.hr), Bojan Ivancevic, and Kristian Jambrosic (Faculty of Electrotechnic Eng. and Computing, HR 10000 Zagreb, Croatia)

The acoustic properties of the brain tissue have been in the focus of much scientific research. These properties determine the possibilities of the application and development of the ultrasound methods, as well as the development of the equipment used by the neurosurgeon during the resection of the brain tissue. The results of the measurements of these acoustic properties done at megahertz frequency range have been published. Although the velocity of ultrasound wave propagation does not directly influence the distribution of the ultrasound field within the cranium, it enables the determination of the specific resistance, which has an important role in the distribution of the ultrasound field within the cranium. Using the published results and the conditions of the measurements that have been done, the velocity of ultrasound propagation for the frequency range at which cavitation ultrasonic surgical aspirators work has been estimated. After that the measurement of the velocity of the propagation has been done at the frequency of 24 kHz. The values of both the estimated and the measured velocities of the ultrasound propagation prove the validity of the assumptions on which the estimation is based on.

4:40

5pBB8. Modification of chamber resonance through active mass control. James S. Martin and Peter H. Rogers (Georgia Inst. of Technol., School of Mech. Eng., Atlanta, GA 30332-0405)

A traveling wave chamber was constructed for the controlled insonification of rodents in order to test the physiological effects of intense underwater low-frequency sound. In initial testing, this chamber exhibited a sharp resonance in the band of interest. This resonance was found to be dictated by the mass of the piston driver and the stiffness of the chamber's contents. The presence of the resonance significantly reduced the operational bandwidth of the chamber. Conventional approaches to shifting the resonance out of the band of interest by directly altering piston mass and/or armature stiffness were found to be impossible. An open-loop active control system was devised which utilized piston-mounted accelerometers and summed their output with the drive signal prior to a power amplifier. Since the driver is well characterized as a force transducer, the result of this control scheme is that the piston mimics a significantly lighter structure with no reduction in the actual piston mass. The operational bandwidth of the chamber was increased with a minimum of additional hardware and negligible additional power consumption. Loop gain can be limited by stability limits imposed by the phase response of the power amplifier. This scheme may also have applications in transducer design.

Session 5pEA

Engineering Acoustics: General

P. K. Raju, Cochair
Department of Mechanical Engineering, Auburn University, Auburn, Alabama 36849-5341, USA

Marinus M. Boone, Cochair
Laboratory of Acoustic Imaging and Sound Control, TU Delft University of Technology, P.O. Box 5046, 2600 GA Delft, The Netherlands

Chair's Introduction—1:55

Contributed Papers

2:00

5pEA1. Using tubephones for wideband auditory stimulation in brain research. Matti Airas, Antti Jarvinen (Lab. of Acoust. and Audio Signal Processing, Helsinki Univ. of Technol., P.O. Box 3000, FIN-02015 HUT, Finland), and Esa Piirila (Sample Rate Systems Oy, Tampere, Finland)

This study was motivated by the need for a high-quality auditory stimulation system for brain research purposes. Magnetic imaging techniques such as functional magnetic resonance imaging (fMRI) and magnetoencephalography (MEG) prevent the use of typical headphones. In fMRI, a high magnetic field does not allow placing magnetic materials inside the imaging system. In MEG, the extremely weak magnetic fields present in the human brain are measured and any magnetic material in the magnetically shielded room would corrupt the results. In these cases, one possible solution is to place electromagnetic transducers outside of the measurement room. Sound has then to be transmitted to the patient's ears by tubes which produce a highly distorted response. It is shown that by combining acoustical design with analog and digital equalization, wideband flat frequency response is achieved. The design and construction of the apparatus are described and problems like the effect of nonlinear distortion of the transducers are discussed. Practical applications of the system are shown and other possible constructions are compared with the implemented one.

2:20

5pEA2. A parametrized model of psychoacoustical roughness for objective vehicle noise quality evaluation. Robert Hoeldrich and Martin Pflueger (Joanneum Res., Schiestattgasse 14/b, A-8010 Graz, Austria)

In the assessment of vehicle interior noise quality, sound characteristics caused by modulation play an important role because they contribute significantly to the perceived annoyance. The proposed parameterized model for the sensation of psychoacoustical roughness was developed as part of a research program with the aim of establishing an on-board analysis system for vehicle interior noise quality based on objective sound parameters. The roughness model can be adjusted by model parameters to calculate versions of roughness, thereby accentuating different psychoacoustical assumptions. The model is based on the excitation-time pattern of the interior car sound which is recorded using an artificial head system. From the excitation-time pattern, a set of specific roughness parameters in overlapping critical bands is obtained utilizing different weighting functions for the envelope spectrum in each band and various correlation methods between adjacent bands. The specific roughness parameters in critical bands are superimposed in several ways, resulting in a set of modulation parameters. The model was successfully tested not only in predicting roughness assessments, as reported in a companion paper, but it also proved to result in one valid objective parameter for the description of vehicle interior noise quality.

2:40

5pEA3. Psychoacoustic measurement of roughness of vehicle interior noise. Martin Pflueger, Robert Hoeldrich (Joanneum Res., Schiestattgasse 14/b, A-8010 Graz, Austria), Franz Brandl, and Werner Biermayer (AVL List GmbH, A-8020 Graz, Austria)

In analyzing vehicle interior noise there exists hardly any correlation between the subjective impressions of test persons and available roughness parameters. It has become necessary to develop a new roughness model for these sounds and to set up a subjective database as a basis for the analytical description of interior noise quality. This paper focuses on psychoacoustical experiments for the assessment of roughness by using different methods and different kinds of vehicle interior sounds. The analysis of the results shows that small experimental manipulations lead to a large variety of different results. The different meanings of the word roughness have to be taken into account. Each person has his or her own interpretation of roughness differing between the phenomena of roughness, *r*-roughness, rumble, fluctuation strength, etc. Another important point is the reduction of accidental influences of psychoacoustical parameters, like, for example, the influence of loudness on the perception of roughness. By using a special headphone–subwoofer playback system in the laboratory, it is possible to achieve ratings comparable with field experiments. As reported in a companion paper, a new generalized psychoacoustical model of modulation parameters was successfully tested with the obtained roughness rankings.

3:00

5pEA4. RPG diffusers used for noise screening applications. Franco G. M. Bertellino, Luca Stantero, and Antonio Massacesi (Microbel s.r.l., via Livorno, 60, Torino, Italy, microbel@envipark.com)

The paper deals with the performances of noise barriers designed using the reflecting phase grating diffuser theory, which is based on the interference produced by slots of different depths. Usually such structures are used to improve sound diffusion in recording rooms, but they can be suitable also to reduce highway and railway noise for their capability of scattering sounds. A theoretical approach has been used to project their shape using a self-developed VB application, able to predict the scattered sound distribution as well. The theoretical results have been verified with a physical scale model in an anechoic room: insertion losses in several configurations have been measured, together with intensity measurements of the scattered acoustic field. Experimental results seem to match quite well those obtained using the simulation program.

3:20

5pEA5. Multi-purpose apparatus for evaluation of noise transmitted through air ducts. Antonino Di Bella and Roberto Zecchin (Dipartimento di Fisica Tecnica, Univ. of Padova, Via Venezia 1, I-35131 Padova, Italy, labacus@iftpd1.iftpd.unipd.it)

The noise generated in HVAC systems by fans or air turbulence is propagated along ducts and, through duct walls, can be irradiated in rooms; moreover duct lines can easily transmit the sound produced in noisy environments from one room to another, vanishing the sound insulation of walls which they are passing through. The knowledge of sound insulating properties of duct walls is fundamental for a good system design, including unitary attenuators and active noise control devices. In this work a multi-purpose apparatus for evaluation of noise transmitted through air ducts in a reverberant room is presented. This apparatus allows one to measure, with the same equipment, the sound power level emitted from a short length ducts specimen in a reverberant room, as well as linear sound attenuation and break-in and break-out transmission loss. A further application of the same apparatus is the measurement of sound insulation and normal incidence impedance of small plane elements of isotropic or composite materials.

3:40

5pEA6. Annoyance of the induction machine noise radiation. Cüneyt Öztürk and Aydýn Bahadýr (Türk Elektrik Endüstrisi AP, R&D Dept. Davutpapa, Litros Yolu, Topkapý, 34020, Istanbul, Turkey, cozturk@tee.com.tr)

Designing and developing products to enhance the favorable and diminish the undesirable features of their sounds are the prime concerns of noise control engineers. Development of new products that might be based on the understanding of the physics of sound, how sound is perceived by the listeners, and how special features of sound determine our reactions are all significant issues of noise engineering. Noise problems of the induction machines mostly arise during the early stages of design and development. The main energy source in an electric motor is the magnetic field. Maxwell stresses act on the inner stator surface bore, giving rise to spectral distribution over the stator as a function of time. These forces excite the stator's lamination and housing, which have distributed mass and damping. This study describes the noise radiation characteristics of the induction machine with special emphasis on the annoyance issue that varies behind the declared emission values and gains increasing significance with customer consciousness and competition in the market.

4:00–4:20 Break

4:20

5pEA7. A numerical and experimental investigation into the effects of cavity geometry on the production of cavity tones. Brenda Henderson and Homayun Navaz (Kettering Univ., 1700 W. Third Ave., Flint, MI 48504)

The effect of the leading and trailing edge geometries on the production of tones associated with the flow of low-speed subsonic air over a cavity were investigated experimentally and numerically. The leading edge geometries considered in the study included an overhang (simulating car door gaps) and an overhang with delta tabs such as used to control jet noise. The trailing edge geometries used in the investigations included sloped and rounded impingement regions. The numerical results documented the periodic fluctuations of the transverse velocity, pressure, and density of the shear layer and the resulting cavity pressures. The periodic vortex behavior in the cavity mouth and impingement region was also studied numerically to predict possible configurations for sound suppression. Experimental investigations of the cavity sound-pressure levels were used to determine the validity of the numerical simulations and the predicted cavity configurations for sound suppression.

4:40

5pEA8. Hybrid discrete vortex method (DVM)/boundary element method (BEM) calculations for cavity acoustics. Ronald J. Epstein (Phantom Works, The Boeing Co., P.O. Box 516, MC S1067126, St. Louis, MO 63166-0516), Anthony Leonard (California Inst. of Technol., Pasadena, CA 91125), and Alan B. Cain (Phantom Works, The Boeing Co., St. Louis, MO 63166-0516)

A hybrid computational methodology has been developed for cavity acoustics applications. The method utilizes a discrete vortex method coupled to an acoustic boundary element calculation. The discrete vortex method uses a Lagrangian evolution in time and space of a field of Gaussian distributed vortex blobs to simulate a two-dimensional, time-dependent, vorticity dominated shear layer. The method yields accurate and fast unsteady solutions to the time-dependent nonlinear flow equations. The cavity acoustics is modeled using acoustic boundary elements which are distributed on the surface of the cavity geometry. The vortex simulation of the shear layer is coupled to the boundary element calculation through Neumann boundary conditions imposed on the cavity surface. The hybrid method simulates a shear layer interacting with a cavity at low Mach number. In example calculations, acoustic radiation and far-field directivity patterns are calculated for the two-dimensional cavity/shear layer system.

5:00

5pEA9. Sound power measurements at low frequencies. Albert Schaffner (Austrian Workers Compensation Board, Adalbert Stifter Str. 65, 1200 Vienna, Austria, albert.schaffner@auva.sozvers.at)

The sound power level of a sound source is usually determined by sound intensity or sound-pressure measurements either in a free-field environment or in enclosures. Although these measurements provide good comparable results for the middle- and high-frequency range, there are large discrepancies at low frequencies. Using the sound intensity method as reference, it can be shown that these discrepancies are systematic. In the case of measuring sound pressure in a free field, they are due to the near-field error depending on the distance of the measurement surface to the source. Measuring sound pressure in enclosures—especially in rooms with hard walls—interference effects cause a change in the sound power output of the source, depending on the distance of the source to the room boundaries. The effects described above have been investigated theoretically and the results have been confirmed by accurate measurements.

5:20

5pEA10. Beams of sound: A low-distortion airborne parametric array. F. Joseph Pompei (MIT Media Lab, Cambridge, MA 02139)

An improved airborne parametric array, which uses audio preprocessing and wideband transducers to significantly reduce distortion, is described and demonstrated. The airborne parametric array has been previously shown [Yoneyama *et al.*, J. Acoust. Soc. Am. **73**, 1532–1536 (1983)] to produce highly directional audible sound from the nonlinear self-demodulation of a modulated ultrasonic beam. The resulting audible sound contained a high degree of distortion (up to 50% THD), which is a result of using pure AM modulation and narrow-band transducers. By preprocessing the audio signal and employing wideband transducers, the distortion is shown to be reduced to only 5%, while still maintaining a 3° beamwidth.

5:40

5pEA11. Noise problems of the induction motors. Cüneyt Öztürk (Türk Elektrik Endüstrisi AP, R&D Dept., Davutpapa, Litros Yolu, Topkapý 34020, Istanbul, cozturk@tee.com.tr)

The audible noise produced by electrical machines is developed depending on the various energy sources that generally appear during the rotation of the rotor. Usually the main energy source in the electrical machines is the magnetic field. Maxwell stresses act on the stator core, armature, and stator laminations, and generally exhibit spectral distribution as a function of time. These forces may provide excitation on the mechanical resonances of the machine's mechanical system that have a distributed mass, stiffness, and damping. The force waves and their possible contribution to overall machine noise can be predicted by analysis of the electrical design, which can be optimized to reduce their effect. Careful analysis and design are required, with perhaps additional magnetic core material to keep flux levels low, and air gap large, without compromising good performance. Behind the features of the magnetic and mechanical structure, the aerodynamic features and excitations provided by the air circulation and the movement can also gain significance when the similar interaction appears with the machine structure. Interaction might be amplified during the coincidence of the mechanical resonances and the provided excitation on similar frequencies.

6:00

5pEA12. The powerful role of the Commanders Decision Aid (CDS) software and acoustic sensor to increasing ground combat vehicle survivability. Ronald M. Yannone (Sanders, a Lockheed Martin Co., 95 Canal St., Nashua, NH 03060)

With the proliferation of diverse anti-tank guided missiles and top attack munitions, ground combat vehicles require the use of multispectral sensors. The issues that arise by adding sensors to these vehicles are the additional cost, size, weight, and power required. Even more critical is the ability of the sensor to provide timely, high-confidence, low-false alarm rate threat detection and classification information to the crew. Amidst a heavy signal clutter battlefield and multiple sensors aboard the vehicle, the concerns are information overload for the crew, being detected by enemy sensors, and quickly depleting limited countermeasure assets by responding to false alarms. The use of infrared and laser warning receivers (IRW, LWR) has been assessed to be very beneficial toward this aim, but not sufficient. Operations analysis has shown that with the addition of an acoustic sensor and decision aid software, crew survivability increases dramatically with low cost. The paper reviews the ground combat vehicle problem space, the data, the complementary data the IRW, LWR, and acoustic sensors provide, and how the Commander's Decision Aid (CDA) software performs multispectral/multisensor fusion, threat classification, threat prioritization, countermeasures response management, and countermeasures effectiveness assessment via various scenario descriptions.

FRIDAY AFTERNOON, 19 MARCH 1999 ROOM H2013, 2:00 TO 5:20 P.M.

Session 5pNSa

Noise: Road Traffic Noise II

Richard F. Schumaker, Cochair
General Motors N.A. Proving Ground, MC 483-356-006 Milford, Michigan 48380, USA

Steven Heinrich, Cochair
TUEV Automotive GmbH, Kaiserstrasse 100, 52134 Herzogenrath-Kohlscheidt, Germany

Invited Papers

2:00

5pNSa1. Perception and meaning of warning signals in urban contexts. Corsin Vogel, Jean-Dominique Polack, Michele Castellengo (Laboratoire d'Acoustique Musicale, CNRS-UPMC-Min. Cult., 11 rue de Lourmel, F-75015 Paris, France, vogel@ccr.jussieu.fr), and Daniele Dubois (CNRS-INaLF, LCPE, 1 rue Maurice Arnoux, F-92120 Montrouge, France)

Perception of warning signals in urban context points out the question of their efficiency with regard to the citizens. Efficiency of warning signals can be described in terms of their meaning for persons who are concerned with. Indeed, subjects can adequately react to the signals only if these latter are identified, that is, only if the signals make sense to the subjects. Therefore, information about mental representations of citizens exposed to warning signals is necessary. An experiment was realized involving 15 signals mixed with two different urban contexts: steady traffic noise and public park ambience. Results show that the two contextual constraints influence the perceptual thresholds of the warning signals as well as their identification. Warning signals can be classified with respect to their different meanings in different urban contexts. Especially, it appeared that signals having an identical semantic description nevertheless may present very different acoustical properties. The classes of signals obtained with the psychological description are a way to determine new acoustical features related to the meaning of warning signals, and so to their efficiency.

2:20

5pNSa2. Application and extension of acoustic holography techniques for tire noise investigations. Fulop Augusztinovicz, Jssnos Gransst, Ferenc Mssrki (Tech. Univ. of Budapest, Dept. of Telecommunications, Sztoczek u. 2., H-1111 Budapest, Hungary, fulop@hit.bme), Wim Hendricx, and Herman Van der Auweraer (LMS Intl., B-3001 Leuven, Belgium)

Acoustic holography (AH) is a powerful measurement tool for the investigation of complex sound radiation problems. Enabling detailed source investigations based on noncontact measurements, it is especially useful for the investigation of rotating noise sources such as automotive tires. Nevertheless, conventional AH techniques are burdened by the constraint that the source is assumed to be planar. Based on a detailed measurement series which was performed on a laboratory roller bench, the radiation of a test tire was

investigated by means of AH. It was found that even though valuable information could be obtained, the most important forward and backward radiation of the tire is difficult to tackle in this way. Another approach of the radiation analysis is offered by developing an inverse BEM method. Different implementations of the method have been worked out and tested, based mainly on the SYSNOISE and MATLAB software packages. The technique is applied to experimental tire mock-ups as well as to real-life tire measurements. The practical application and inherent limitations of the technique are also discussed.

2:40

5pNSa3. Measurements of the acoustic absorption coefficient of double-layer asphalts: Analysis of variability. David Casini, Cesare Fagotti, Andrea Poggi, and Simone Secchi (A.R.P.A.T.–Regional Agency for the Environ. Protection of Tuscany, Via San Salvi, 12, 50135, Florence, Italy, arpat.fisica@fi.nettuno.i)

The measurements of the acoustic absorption coefficient were carried out on two kinds of double-layer asphalt located in an urban environment. Three different methods of analysis were used: pseudorandom MLS signal, intensimetry, and Kundt's tube. The measurements with MLS signal were done with a loudspeaker 3-m high and a 1/2-in. microphone 1.5 m above the asphalt. The absorption coefficient has been obtained by the deconvolution of the MLS signal. In the analysis with the Kundt's tube, the transfer function method was used on an asphalt core sample (10-cm diameter) extracted ''*in situ*.'' Two layers, respectively, 2.5 and 5 cm thick, with different granulometry, composed the first asphalt analyzed. In the second asphalt, the superior layer has a larger granulometry. All the results obtained with the different measurement techniques point out a major absorption peak around 630 Hz and a secondary peak around 2000 Hz, for the first asphalt, and 500 and 4000 Hz for the second asphalt. The measurements point out a large variability of the results obtained in different sections of the road. Variation with asphalt's composition and measurement uncertainty is analyzed.

3:00

5pNSa4. Assessment of impact noise determined by binary traffic systems. Miguel A. Sattler (Univ. Federal do Rio Grande do Sul, Dept. de Engenharia Civil, Av. Osvaldo Aranha, 99-3o andar, Porto Alegre, RS, Brazil, CEP 90035-190)

The environmental impact resulting from proposed solutions to solve problems related to the fast growth of Brazilian cities is rarely properly assessed. That is the case of urban traffic noise. There has been a significant growth of vehicles in the last years. In the face of the lack of resources by the public sector to provide adequate public transport for the population, traffic has been increasing considerably year after year. One of the alternatives attempted by the Secretary of Transport of the city of Porto Alegre, south of Brazil, to reduce traffic jams, is to implement an increasing number of binary traffic systems, by using two single-way roads instead of one two-way road. This has increased noise in previously quiet areas of the city. The present paper presents measured values of the resulting noise impact of such measures, considering noise levels before and after the introduction of one of these binary traffic systems.

3:20

5pNSa5. Preventative medical limits for chronic traffic noise exposure. Christian Maschke (Robert Koch-Inst., Federal Inst. for Infectious and Noninfectious Diseases, Section: Environ. Medicine, 12101 Berlin, Germany), Karl Hecht, and Hans-Ulrich Balzer (Inst. for Stress Res. (ISF), 10115 Berlin, Germany)

Because of an expert's report on the medical effects of noise on healthy adults, permissible values for mainly traffic noise have been estimated by the standard of knowledge. If the permissible values are exceeded, then preventative medical action is necessary. Below this value the probability of noise-induced health hazards is essentially zero. The effect due to noise as a health hazard is, besides the mechanical damage of the inner ear, a psycho-physiological deregulation which can be either indirectly due to the annoyance or directly caused by stress of the vegatative-hormonal system. Therefore, different permissible values for annoyance, the stress on the vegetative-hormonal system, and for the loss of hearing are suggested, for both continuous and maximum noise levels. In addition, the deregulation depends on the time of the acoustic exposure because the sensitivity to noise follows a 24-h cycle (circadian rhythm). It is therefore necessary to give personal permissible limits for the evening noise and the nocturnal noise.

3:40–4:00 Break

4:00

5pNSa6. Standardization in the field of traffic noise—An overview of current projects. Ulrich Schober (DIN Deutsches Institut für Normung, D-10772 Berlin, Germany, schober@nals.din.de)

Standardization of vehicle noise measurement procedures is an important instrument for achieving comparable and reproducible measurement results and therefore to provide means for minimizing traffic noise in the long run. In the International Organization for Standardization Technical Committee ISO/TC 43 ''Acoustics'' and other ISO/TCs many standards about noise emission measurements on all kinds of vehicles including aircraft, and about tire/road noise effects and road surface characteristics are currently under preparation in several working groups. Some standards are under revision to bring them in line with the advances in vehicle technology, other standards are prepared due to the needs from vehicle manufacturers and environmental protection representatives. The lecture presents ongoing developments in important projects and emphasizes their joint aspects and differences. Examples: (i) Revision of ISO 362 about noise measurement on accelerating cars and motorcycles which is important for type testing. (ii) Project about measurement of tire noise. (iii) Project about the influence of road surfaces on traffic noise to facilitate acoustical characterization of road surfaces (ISO 11819 series). (iv) Revision of ISO 3891 about aircraft noise. (v) Projects about noise emission measurements on vessels (revision of ISO 2922) and small recreational craft (new ISO 14509). (vi) Revision of ISO 3095 about noise emission of railbound vehicles.

4:20

5pNSa7. Cadastre of the acoustic characteristics of the whole road network of the Brussels region. Jean-Pierre Clairbois, Peter Houtave (Acoustical Technologies, Av. Brugmann 215, B-1050 Brussels, Belgium), Andreas Koellmann (TUV-Automotive, D-52134 Herzogenrath, Germany), and Gerhard Mosdzianowski (B-4721 Kelmis, Belgium)

The Brussels Institute of the Environment (IBGE-BIM) took the initiative to start a global study assembling elements of its future noise planning. Road surface noise is an important element of these. A strong methodology has been decided in order to get an exhaustive database of the whole road network of the Brussels region (1800 km). The idea is to get an interactive tool in order to control the actual conditions of the road surfaces and their influence on the global road traffic noise, and also to be able to look at the different possible improvement scenarios. Establishing this database required not only to visit every road of the network, but also to assemble all relevant data for estimating the road and traffic conditions. The methodology and tools used for the work, the results, and a statistical analysis of the database are presented. This work has been completed by noise measurements (CPB and trailer methods) of the nine different kinds of road surfaces used in the Brussels region. A strategy of action is suggested and the maintenance of the database is started so that the evolution of the network can be continuously considered within the noise planning. [Work supported by IBGE-BIM.]

4:40

5pNSa8. Modeling the propagation of traffic noise in topographically modified atmospheric environments. Dietrich Heimann (DLR, Institut für Physik der Atmosphäre, Oberpfaffenhofen, D-822234 Wessling, Germany, d.heimann@dlr.de)

A meteorological mesoscale model is used to simulate the time-dependent distribution of temperature and the corresponding development of autochthonous slope-wind systems in a narrow two-dimensional valley during the course of a cloud-free day. Further simulations consider the topographical modification of allochthonous airflow across the valley. A numerical sound particle model was designed to cope with both the uneven terrain and the inhomogeneous meteorological environment. The acoustical model takes up the simulated meteorological fields and calculates the propagation of noise which originates from a steady source (road or railway) in the valley. The coupled modeling system ensures consistency of topography, meteorological parameters, and the sound field. The temporal behavior of the sound-pressure level across the valley is examined. The results show remarkable, meteorologically induced variations of the sound level during the course of a cloud-free day. In addition, it is shown how the location of a planned traffic way can be optimized with respect to minimum noise impact in the valley [D. Heimann and G. Gross, Appl. Acoust. (in press)].

5:00

5pNSa9. The effect of road features on the traffic noise—Prediction and measurement. Wolfgang Foken (Westsächisische Hochschule Zwickau (FH), Kraftfahrzeugtechnik, Postfach 201037, D-08012 Zwickau, Germany, wolfgang.foken@fh-zwickau.de)

In order to calculate the noise level from road traffic, prediction methods are used in most countries, for instance the ''RLS90'' (''Guideline for Noise Control at Roads'') is the relevant calculating method in Germany. The initial situation is always the amount of cars, the percentage of trucks, and their velocities. In addition, features of the road are required, for example, the road pavement, the gradient, and the existence of traffic lights. They are considered to be surcharges. The aim of this paper is the critical evaluation of these road features and the comparison with measured data. The paper shows that traffic lights generally do not cause an increase of the noise level. It was noted that the surcharge for traffic lights depends on the traffic density and the percentage of trucks. Therefore, a general usage of the ''RLS90'' surcharge for traffic lights is questionable. The German ''RLS90'' often underestimates the effect of the road pavement. Measurements also indicate the necessity of defining the surcharge for the road pavement as a continuous function of the velocity. The surcharge for the road gradient does not depend on the velocity but a reliance on the percentage of trucks is assumed.

Contributed Poster

This poster will be on display in the Poster Gallery from Thursday to Friday, 18–19 March. The author will be at the poster from 2:00 p.m. to 4:00 p.m. on Thursday, 18 March.

5pNSa10. Effect of the acceleration on vehicle noise emission. Joel Lelong and Roger Michelet (Dept. MMA, Inrets, 25 av. F. Mitterrand, Case 24 69675, Bron Cedex, France)

In urban areas, traffic noise, considered as one of the most important public nuisances, is generated by stop–go traffic. Irregular urban traffic is directly linked to traffic regulation devices, which are the cause of frequent accelerations/decelerations of vehicles, depending on driving behavior. In order to predict sound levels at the time of conception, traffic regulation devices, measurements of acceleration passby noise, are necessary. Urban streets are synonymous with complex acoustical environments (presence of reverberant obstacles and multiple sources of noise): carrying out of *in situ* vehicle noise emissions measurements is impossible. Measuring vehicles' noise emissions on test tracks can overcome this difficulty, therefore resulting in a better understanding of the acceleration effect on vehicle noise emission. The method described in this paper is based on simultaneous measurements of kinematical data (speeds, accelerations), mechanical parameters (gear ratio, engine speed), and acoustical levels ($L_{A\,max}$). First results obtained on cars show significant differences between acceleration levels and cruise levels obtained at same speeds. The level of increase depends on the acceleration value, the gear ratio, and the engine speed. These first results have been compared to existing published results. [Work supported by French Research Program on Ground Transportation (PREDIT).]

Session 5pNSb

Noise: Future Noise Policy in Europe

Tjeert ten Wolde, Cochair
European Commission, Rue de la Loi 200, B-1049 Brussels, Belgium

Paul D. Schomer, Cochair
USA CERL, P.O. Box 9005, Champaign, Illinois 61826-9005, USA

Invited Papers

2:00

5pNSb1. The new noise policy of the European Union. Tjeert ten Wolde (European Commission, Rue de la Loi 200 (TRMF 1/68), B-1049 Bruxelles, Belgium, Tjeert.Tenwolde@dg11.cec.be)

In 1996 the European Commission published a so-called Green Paper in which proposals were done for a future EU policy on environmental noise. More than 450 institutions and individuals commented and on the basis of these the European Commission concluded that there is more than sufficient support for most of the proposals and started the process of the further development of the policy. Central elements in the policy are the harmonization of the noise indicators and the assessment methods in the European Union, the introduction of noise mapping and action plans for cities and member states, and information of the public and periodical EU action plans. Target setting will probably remain the responsibility of the Member States or local authorities. It is the aim that the coherence and quality of the EU policy on noise sources will improve. In 1998 working groups started with the development of indicators, dose-effect relationships, computation and measurement methods, mapping procedures, and guidelines for abatement plans. An overview of their tasks and their progress shall be presented. In parallel the development of a first Directive for environmental noise began. The progress with this process shall also be reported.

2:20

5pNSb2. A European noise indicator. Martin van den Berg (Ministry of Environment, Noise Directorate IPC 635, pbox 30945, 2500 GX Den Haag, The Netherlands)

The European Commission installed five working groups with tasks to advise the Commission on a future European noise policy. The first working group, chaired by the author, was required to advise on European noise indicator. From research that was carried by INRETS [study related to the preparation of a communication on a future EC noise policy, LEN Report nr 9420 Lyon (1994)] it was clear that a large variety exists in noise indicators and calculation methods, which makes it difficult to compare efficiency of abatement measures. According to the time schedule the working group is to produce its final report in February 1999. In the presentation the conclusions of the working group will be discussed.

2:40

5pNSb3. EU's future noise policy: Progress report of WG Dose/Effect. Jacques Lambert (INRETS, Case 24, 69675 Bron Cedex, France, lambert@inrets.fr)

In order to assist the preparation of the EU's future noise policy, WG 2 (Dose/Effect) has launched a work program that will: provide dose/effect relationships for annoyance, sleep disturbance, speech interference (and other effects if necessary), provide proposals for noise indices, define needs on dose/effect research and play an active role in the initiation and coordination of that research, make proposals for the dissemination of information to the public and to authorities (national, local and regional), and make a proposal for the setting of targets by authorities making use of harmonised dose/effect relationships. An inventory of existing material is now available as well as an identification of research needs (March 1999). A position paper will be delivered to the European Commission by 2002. It will focus on thresholds and dose-effect relationships related to transportation noise (road, rail, and aircraft), industrial noise, entertainment and recreational noise, on the setting of targets for the point of view of health effects, and dissemination of gathered information.

3:00

5pNSb4. Harmonization of computational and measurement methods for noise exposure in the European Union. Dieter P. A. Gottlob (Federal Environ. Agency, Bismarckplatz 1, D-14193 Berlin, Germany, d.u.gottlob@t-online.de)

In the framework of the new European noise policy, the European Commission has created working groups to assist in the preparation of this policy. The members are appointed by the Commission on the recommendation of the member states, local authorities, and various organizations. Working group 3 (WG 3) is dealing with the harmonization of calculation and measurement procedures for noise assessment, mapping, planning, and noise abatement. Calculation methods shall be elaborated for road, rail, aircraft, outdoor machinery, and industry. They shall be suited for calculating the long-term noise exposure as well as single events, especially from air and rail traffic. Additionally, they shall be developed for a variety of geometrical and weather conditions which occur in the member states. At the Copenhagen Conference (September 1998), WG 3 started working and discussed the work program

with experts from various countries. It was decided that emission data and transmission models should be separated. Emission measurement procedures should be provided, and the propagation models currently in use should be improved, especially in their physical representation. In the next months an action plan will be elaborated. In this paper the current state of the discussions will be presented.

3:20

5pNSb5. A progress report on E. C. proposed noise mapping. John Hinton (Environ. Services Dept., Birmingham City Council, England, bham.acoustics@dial.pipex.com)

As an integral part of the development of a framework directive for the assessment and reduction of environmental noise, the European Commission has set up five working groups on the perception of noise. Working Group 4 (W.G.4) is investigating noise mapping techniques and is required to produce a position paper for the E. C. giving guidelines for effective noise mapping. It is now widely accepted that the provisions of mapping information is essential to a process designed to reduce exposure of citizens throughout Europe to unacceptable levels of environmental noise. This will be achieved by providing the public and politicians with information on the scale of the problems that are faced and by providing decision makers at local, regional, national, and European level with the information they require to develop action plans for noise reduction. Mapping will also provide a means of monitoring the implementation and effectiveness of such plans. W.G.4 held its first meeting just prior to the Invitational Conference on the European Unions Future Noise Policy held in Copenhagen in early September 1998. The paper will provide a progress report of W.G.4.

3:40–4:00 Break

4:00

5pNSb6. A new EU directive concerning the noise emission by equipment used outdoors. Volker K. P. Irmer (Umweltbundesamt, Berlin, Germany)

The Green Paper ''Future Noise Policy'' [COM(96) 540 final] identifies noise in the environment as one of the main environmental problems in Europe. It emphasizes the continuing need for legislative measures at the Community level concerning noise emission from various sources. In February 1998, the Commission adopted a proposal for a European Parliament and Council Directive on the approximation of the laws of the member states relating to the noise emission by equipment used outdoors [COM(1998) 46 final, published in OJ No. C 124, 22.04.1998, p. 1]. It intends to simplify legislation, to contribute to the smooth functioning of the internal market, and to protect the health and well-being of citizens by reducing the overall noise exposure. The proposal covers 55 types of equipment, all of which are to be marked with the guaranteed noise-emission level; in addition, noise limits are laid down for 19 types of equipment (13 already covered by existing directives, 6 new ones). Noise limits are laid down in two stages (the first one eliminating most noisy equipment, the second one taking into account advanced technology). The requirements of the proposal are explained and the progress made in the Council and European Parliament is reported.

4:20

5pNSb7. The action programme of UIC and CER (Community of European Railways) ''abatement of railway noise emissions from goods trains.'' Peter Hübner (Deputy Director Way and Works, President of UIC-Task Force Noise & Vib., Swiss Federal Railways, Mittelstrasse 43, CH-3030 Berne, Switzerland marianne.mb.binggeli@sbb.ch)

Although rail transport has a low environmental impact overall, noise from goods trains remains a major problem. Research has identified that wheel roughness is the critical factor and that composite materials will deliver adequate braking with less damage to the wheel surface than existing iron brake blocks. Accordingly the UIC/CER has made a formal commitment to fit composite blocks to existing wagons, as well as to all new wagons. Existing wheels cannot cope with the thermal stress from composite blocks. Fitting new wheels only when the old are worn out will be cost neutral, but will take 15–20 years. Premature wheel replacement will involve additional cost, but will deliver the benefits in 5 years. This can be achieved with financial assistance from E.U. member-states, who will thereby avoid unnecessary outlay on noise barriers. At the same time proposals for a E.U. noise creation standard should reflect the performance achieved by the modified wagons. The railways propose a voluntary environmental agreement with the E.U.

Contributed Paper

4:40

5pNSb8. Characterization of quiet areas: Subjective evaluation and sound-level indices. Dick B. Botteldooren, Saskia Decloedt, and Jürgen Bruyneel (Dept. of Information Technol., Univ. of Gent, St. Pietersnieuwstraat 41, 9000 Gent, Belgium)

In densely populated regions, a government may decide to conserve quiet areas within reach of the average population. To characterize such areas, long-term exposure measures and typical limits have to be decided upon. Since the main goal of the silent area is to provide repose for Man, a subjective evaluation of silence may also be envisaged. In this paper, subjective evaluation of silence and sound-level measurements obtained in two related, but independent studies of open area are compared. Thorough statistical analyses lead to the conclusion that statistical noise levels with larger index (L_{A95} to L_{A50}) are best suited to predict subjective silence. Critical levels are obtained. They lead to over 80% correct classification for both studies. Reported disturbance, on the other hand, seems correlated to events, but does not have a strong influence on the global rating of silence.

Session 5pPAa

Physical Acoustics: Acoustic Remote Sensing of the Atmosphere II

D. Keith Wilson, Cochair
U.S. Army Research Laboratory, 2800 Powder Mill Road, Adelphi, Maryland 20783, USA

Volker Mellert, Cochair
Physics Department, University of Oldenburg, D-26111 Oldenburg, Germany

Invited Papers

2:00

5pPAa1. Acoustic tomography as a remote sensing method inside the atmospheric surface layer. Astrid Ziemann, Klaus Arnold, and Armin Raabe (Universität Leipzig, Institut für Meteorologie, Stephanstr. 3, D-04103 Leipzig, Germany, ziemann@rz.uni-leipzig.de)

Acoustic travel time tomography will be applied on the atmosphere to directly provide spatially averaged values of meteorological quantities (temperature and wind field) which are needed for the evaluation of numerical models as well as to complete *in situ* point measurements and conventional studies of the atmospheric surface layer over natural surfaces. Sound waves propagate through the atmosphere with different sound velocities according to the distribution of air temperature and wind vector and become, therefore, an information carrier about the medium properties. In the presented study acoustic travel time data were measured between sources and receivers placed around an array of 200×260 m^2 as initial values for the tomographic reconstruction. Thereby, a frequently applied procedure of ray tomography, the simultaneous iterative reconstruction technique, characterized by simple handling and small computational requirements, was used. Additionally, a special system of equations for the isolation of the temperature and wind influence on the sound speed was solved. To estimate the sound ray propagation and to simulate acoustic travel times during various meteorological conditions a ray tracing model based on a modified version of Snell's law corresponding to the influence of wind vector will be introduced.

2:20

5pPAa2. Opto-acoustic sounding of the atmospheric parameters. Lyudmila G. Shamanaeva (Inst. of Atmospheric Optics of the SB RAS, 1, Akademicheskii Ave., Tomsk 634055, Russia, zuev@iao.tomsk.su)

Experimental investigations of sound pulse generation accompanying the propagation of high-power pulsed laser radiation in the atmosphere were started at the IAO SB RAS in 1986. Based on these investigations, new opto-acoustic methods of sounding of the atmospheric temperature, wind velocity, relative humidity, and number density of micron fraction of atmospheric aerosols were suggested. A source of the acoustic signal in an opto-acoustic sounding system is a discrete laser spark made by focusing a CO_2 laser beam into the atmosphere at distances up to 500 m. The number density of coarsely dispersed aerosols was determined from the number of pulses in the acoustic signal generated by the discrete laser spark. Results of opto-acoustic measurements of the number density of coarsely dispersed aerosols agree well with the microphysical model of aerosol atmosphere for Western Siberia. A threshold laser energy density resulting in the origin of local plasma formations is about $6-10$ J/cm^2. For lower laser energy densities, the acoustic radiation is generated due to laser-induced thermal expansion of the propagation medium. The measurable parameters are the effective laser beam radius, the coefficient of laser radiation absorption, and the total laser beam energy.

2:40

5pPAa3. Radio acoustic sounding of the planetary boundary layer. Gerhard Peters (Meteorological Inst., Hamburg Univ., Bundesstrasse 55, D20146 Hamburg, Germany)

Refractive index variations of the atmosphere caused by sound waves are used as tracers for radar waves in order to determine the sound velocity and thus the (virtual) temperature remotely. This combined usage of acoustic and electromagnetic waves—called ''radio acoustic sounding system (RASS)''—has gained considerable interest, as sensitive radar wind profilers have been used for one decade in atmospheric research and monitoring. The RASS function can easily be added to radar wind profilers with the help of sound sources at the radar site. Due to the sound attenuation, the range of most systems is limited to the typical depth of the planetary boundary layer, which is particularly important for the exchange of mass, energy, and momentum between atmosphere and surface. Due to refinements of the signal analysis, a measurement accuracy comparable to conventional *in situ* sensors has recently been achieved. In contrast to *in situ* measurements, RASS has the great advantage to provide continous and simultaneous data from many altitudes. RASS cannot only deliver accurate temperature profiles but also profiles of the mean wind and of high-frequency fluctuations of the vertical wind component. Currently a RASS-based method is being developed for high-resolution horizontal wind measurements.

3:00

5pPAa4. The application of SODAR and RASS configurations in operational meteorology. D. Engelbart (Deutscher Wetterdienst, Meteorol. Observatorium, D-15864 Lindenberg, Germany, engelbart@mol.dwd.d400.de)

In operational meteorology, the recent improvements in scale resolution as well as physical parametrizations of numerical weather prediction models imply the demand of improvements in its measured data base, i.e., in measuring systems. Compared with the classical aerological sounding by radiosondes, supplying data of meteorological standard parameters twice per day, active remote-sensing systems like SODAR and RASS are able to increase both time resolution and vertical resolution considerably depending on system configuration. By using pure acoustical sounding a SODAR allows the derivation of vertical profiles of the 3-D wind vector, whereas integrated systems like SODAR and RASS or windprofiler and RASS are able to supply temperature profiles as well. A crucial point regarding assimilation of operationally measured data into numerical models is described by data quality. A second general point is focused on the availability of remotely sensed data. Generally, in operational meteorology acoustic remote sensing may aid in three major tasks, i.e., data supply of operational numerical models, improvement of physical parametrizations by supplying validation data and monitoring of complex parameters, e.g., boundary-layer height. As an example for model validation the presentation finally will show some results of SODAR- and RASS-derived flux profiles in comparison to high-resolution model results.

3:20

5pPAa5. Acoustic sounding of fog and rain. Sergei V. Shamanaeva and Lyudmila G. Shamanaeva (Inst. of Atmospheric Optics of the SB RAS, 1, Akademicheskii Ave., Tomsk 634055, Russia, zuev@iao.tomsk.su)

The coefficients and phase functions of sound scattering by a single rigid spherical particle whose parameter Mie changes in a wide range have been calculated with the use of exact formulas of the Mie scattering theory. Analytical expressions are given for the dependence of sound attenuation on the parameters of fog and rain and acoustic frequency. The acoustic scattering cross section of a single particle has been derived. New methods of acoustic sounding of fog and rain have been suggested and theoretically analyzed. Experimental data on the transformation of raindrop size distribution have been obtained by processing of raw spectra of acoustic signals recorded in rain for 20 s and 1, 2, 3, 5, and 25 min with cw bistatic sodars operating at frequencies of 5 and 40 kHz. The bimodal character of the raindrop size spectra was established. The position of the second maximum in the raindrop size spectrum was shifted with time toward larger raindrop sizes, from 0.3 to 1 mm. The estimated rain intensity varied from 0.5 to 1.9 mm per hour. The obtained results demonstrate that high-frequency cw bistatic sodars are very promising for measurements of fog and rain.

3:40

5pPAa6. Acoustic pulse sounding of the atmospheric boundary layer. Igor P. Chunchuzov (Obukhov Inst. of Atmos. Phys., Russian Acad. of Sci., Pyzhevskii 3, Moscow 109017, Russia)

The method of acoustic pulse sounding of the atmospheric boundary layer is used to study spatial coherence and frequency spectra of the pulse travel time fluctuations between the pulse source and the triangular set of receivers 2.5 km apart from each other. The wind speed fluctuations were measured up to 200–300 m with the use of SODAR and the anemometers placed on the mast of 56-m height. The maximum coherence between the wind speed and pulse travel time fluctuations was obtained for the period of 8 min. This period is thought to be associated with the ducted internal waves in the troposphere. The use of the pulse sounding for the acoustic tomography of the atmospheric boundary layer is proposed.

4:00–4:20 Break

Contributed Papers

4:20

5pPAa7. Acoustic investigation of a vorticity filament using time-reversal mirrors. Sébastien Manneville, Agnès Maurel, Mathias Fink (Lab. Ondes et Acoust., E.S.P.C.I., Univ. Paris VII, URA CNRS 1503-10 rue Vauquelin, 75005 Paris, France, sebastien.manneville@espci.fr), Frédéric Bottausci, Philippe Petitjeans, and Eduardo Weisfred (E.S.P.C.I., URA CNRS 75005 Paris, France)

A new experiment of a filamentary vortex in water characterized by ultrasound is presented. The flow is generated by two corotating discs in an infinite medium, and suction can be applied at the center of the discs. Acoustic time reversal mirrors [see Roux *et al.*, ASA Proc. 1433 (1998)] provide dynamical, nonintrusive, and global measurements of the vortex characteristics. Three different regimes are observed depending on the control parameters (distance between the discs, rotation frequency of the discs, and suction flow rate): (1) a regime of stable, stationary vortex where the velocity profile is compared to the Burgers model and scaling laws are investigated when varying the control parameters, (2) a regime of intermittency with cycles of vortex breakdowns, and (3) a domain where the vortex never shows up.

4:40

5pPAa8. Investigation of the effects of acoustic refraction on Doppler measurements caused by wind- and temperature profiles. Annette Schomburg, Detlef Englich, and Volker Mellert (Dept. of Phys., Acoust., C.v.O., Univ. of Oldenburg, 26111 Oldenburg, Germany)

The subject of this investigation is the errors appearing in Doppler SODAR measurements due to wind and temperature profiles. Usually the wind velocity is calculated from the measured Doppler shift under the assumption of straight line propagation. Wind and temperature profiles cause a deviation of the rays from the straight path which is given by the choice of geometry between transmitting antenna, receiving microphone and scattering volume. The appearing errors in the magnitude of the Doppler shift because of the displacement of the scattering volume, changes of scattering angle, and scattering vector have been investigated. Results from simulations, where the exact position of the scatterer, as well as the ray deformation, has been taken into account, show that upwind and downwind errors are symmetrical. This leads to a new method of measuring wind profiles. Outdoor measurements performed with a new SODAR configuration will be presented. Four receivers allow a construction in which each receiver pair builds a plane to measure down- and upwind components. The resulting two wind profiles describe the horizontal wind

component. With a fifth receiver near the source, the vertical component should be measurable, so that the complete wind vector and even the temperature profile could be determined.

5:00

5pPAa9. Sodar-derived vertical profiles of the parameters of atmospheric turbulence. Lyudmila G. Shamanaeva and Aleksandr Ya. Bogushevich (Inst. of Atmospheric Optics of the SB RAS, 1, Akademicheskii Ave., Tomsk 634055, Russia, zuev@iao.tomsk.su)

The vertical profiles of the structural characteristics of temperature and wind velocity fields and longitudinal and transverse structure functions of the wind velocity field measured with the Zvuk-2 three-channel Doppler sodar are presented for altitudes of 75–535 m above the ground with a 20-m altitude resolution. The sodar operated at a frequency of 1700 Hz, its pulse repetition period was 10.5 s, and its pulse length was 150 ms. One transceiving antenna was pointed vertically and two others were tilted at angles of 20 degrees from the vertical in orthogonal planes. Backscattered signal power was additionally measured. Sodar data were interpreted using the iterative algorithm considering the excess turbulent attenuation of a sodar signal. Sodar-derived structural characteristics were compared with simultaneous measurements by an ultrasonic anemometer/thermometer. The structure functions of the wind velocity field were calculated from long series of observations of vertical profiles of the wind velocity vector. At night when the wind shear was observed the longitudinal structure functions below it were strongly suppressed, whereas above the wind shear they sharply increased. Under conditions of daytime convection the structure functions first increased with the separation between the observation points and then saturated.

5:20

5pPAa10. The Radar-RASS spaced-antenna windprofiler, a tool to measure atmospheric turbulence. Lutz Hirsch (Max-Planck-Inst. for Meteorol., Bundesstr. 55, 20146 Hamburg, Germany, hirsch@dkrz.de)

Recently a Radar-RASS spaced-antenna wind profiling system with four receiving antennas has been developed. The system was designed to use the RASS-signal for radar-interferometry measurements of high-resolution time-series of the 3-D wind vector. The use of the deterministic RASS-backscatter signal which is insensitive to clutter interferences from the ground or elevated targets makes this system a useful tool for turbulence observation in the atmospheric boundary layer. The well-known problem of overestimating the horizontal velocity using simple correlation algorithms, caused by decaying refraction pattern, had to be addressed carefully. Multiple published approaches to find the correct horizontal velocity in the frequency domain using power and cross spectra as well as in the time-domain using correlation-functions were compared to each other. Based on these comparisons the implementation of the most suitable algorithm for the present system together with problems like noise suppression or system constants estimation will be discussed. Results of field measurements will be presented and the performance of the system to derive high-resolution time series of the 3-D wind vector will be demonstrated. Average quantities will be compared with the results of a SODAR operated next to the RASS.

5:40

5pPAa11. Experimental method of acoustic tomography of the atmospheric surface layer. Klaus Arnold, Astrid Ziemann, and Armin Raabe (Institut für Meteorologie, Universität Leipzig, Stephanstr. 3, 3-04103 Leipzig, Germany, arnold@rz.uni-leipzig.de)

Acoustic tomography is proposed as a technique for remote monitoring of near surface temperature and wind fields. An experimental method is presented which provides area-averaged values of the demanded meteorological parameters. In this study travel time tomography was used by measuring the travel time of a signal at a defined propagation path. In such a system a number of sources simultaneously transmit an acoustic signal (sine oscillation) which is detected at a number of receivers. The travel time of each signal was estimated by cross correlation between the received and the transmitted signal. Each peak of the cross correlation is associated with a separate ray path and the delay time corresponds to the travel time of the transmitted signal. The travel time data were inverted to obtain estimates of the meteorological parameters. A field experiment was carried out in autumn 1997 at the test site Melpitz near Leipzig to provide the input data for the tomographic reconstruction. Six sources and four receivers were positioned at an array of 200×260 m^2. Derivations of area-averaged values result from inversion of the single values of travel time for all ray paths.

FRIDAY AFTERNOON, 19 MARCH 1999 ROOM MA042, 1:55 TO 5:20 P.M.

Session 5pPAb

Physical Acoustics: Sonochemistry

J. Reisse, Cochair
Sciences Appliquées, Université Libre de Bruxelles, Av. F. D. Roosevelt 50, B1015 Bruxelles, Belgium

Kenneth S. Suslick, Cochair
Department of Chemistry, University of Illinois, 600 South Mathews Avenue, Urbana, Illinois 61801, USA

Chair's Introduction—1:55

Invited Papers

2:00

5pPAb1. Sonochemical synthesis of new materials. Kenneth S. Suslick, Gennady Dantsin, Arash Ekhtiarzadeh, and Arul Dhas (Univ. of Illinois, 600 S. Mathews Ave., Urbana, IL 61801, ksuslick@uiuc.edu)

High-intensity ultrasound has found new applications in the synthesis of unusual inorganic materials. The chemical effects of ultrasound originate from acoustic cavitation, which produces local transient conditions of ~5000 K, ~500 atm, with heating and cooling rates that exceed 1×10^{10} K/s. In cold liquids, ultrasound is able to drive reactions that normally occur only under extreme

conditions. Examples include intercalation, activation of liquid–solid reactions, and synthesis of amorphous and nanophase materials. The sonochemical syntheses of nanophase metals, alloys, metal carbides, supported heterogeneous catalysts, and nano-colloids derives from the sonochemical decomposition of volatile organometallic precursors during cavitation, which produces clusters a few nm in diameter. Such nanostructured solids are active heterogeneous catalysts for various reactions. Most recently, we have discovered a new synthesis of nanometer-sized MoS_2 and of transition metal colloids of iron, cobalt, and iron–cobalt alloy colloids. Sonication of molybdenum hexacarbonyl in the presence of sulfur produces a novel morphology of MoS_2 with extremely high activity for catalytic hydrodesulfurization of thiophene. Stabilized iron, cobalt, and alloy colloids have also been prepared that are amorphous as initially prepared with particle sizes ~5 nm as determined by TEM. Magnetic studies show that the colloids are superparamagnetic and function as useful ferrofluids.

2:20

5pPAb2. On the frequency effect and the solvent effect in sonochemistry. Kristin Bartik, Nicolas Segebarth, Juliana Vandercammen, and Jacques Reisse (Lab. de Chimie Organique E.P., Univ. Libre de Bruxelles, 50 av. F. D. Roosevelt, 1050 Bruxelles, Belgium)

The frequency effect in sonochemistry remains an open question. On the basis of data reported in the literature it seems that sonochemistry in water is faster in the high-frequency range (between 500 kHz and 1 MHz) than in the low-frequency range (between 20 and 100 kHz). This work is devoted to the study of the frequency effect in various solvents. The study of a frequency effect is far from trivial. Indeed, a systematic study would require that all the other parameters of the system be kept constant. This condition is never fully fulfilled. Heat dissipation and electrical energy consumption were used to characterize the ultrasound intensity even if criticisms can be formulated against these very indirect methods of measuring the ultrasound intensity. Various sonochemical reactions were studied. The frequency change (with all that it encompasses) clearly has an effect, and this effect is different in water, organic solvents, and emulsions. An interpretation of these observations will be proposed.

2:40

5pPAb3. Production of free radicals in ultrasound fields. Gareth J. Price (Dept. of Chemistry, Univ. of Bath, Bath BA2 7AY, UK, g.j.price@bath.ac.uk)

It is well known that a major consequence of cavitational collapse in liquids is the production of highly reactive chemical species such as free radicals. These can be used to perform useful chemistry, although in some cases they can be undesirable byproducts of a reaction. A series of trapping techniques to study radical formation in organic and aqueous systems has been developed. These include the use of UV/visible, fluorescence, and electron spin resonance spectroscopies. The paper will describe the methods and give some results to demonstrate the effects of varying the experimental conditions on radical formation. Examples will be taken from synthetic chemistry, from polymerization reactions, and from aqueous solutions (including biomedical ultrasound sources) to illustrate the factors of importance and the implications of the results for these processes.

3:00

5pPAb4. Sonolysis of nitrophenol and nitrophenyl acetate in aqueous solution. C. von Sonntag, A. Tauber, and H.-P. Schuchmann (Max-Planck-Institut für Strahlenchemie, P.O. Box 101365, D-45413 Mülheim, Germany, vonsonnt@mpi-muelheim.mpg.de)

The dual aspects of aqueous sonochemistry can be nicely demonstrated by the use of nitrophenol as a substrate. The nature and sonolytic yield of the products depends drastically on the state of dissociation of this substrate (pK_a 7.1). At pH 4, the undissociated compound, being hydrophobic, is enriched in the boundary layer of the cavitational bubble and develops a partial pressure within the bubble, in contrast to the situation at pH 10 where the phenolate anion exists. Accordingly, at pH 4 the degradation is gas-phase pyrolytic, but at pH 10 it occurs in the aqueous phase induced by OH radicals. There has been a debate as to whether thermohydrolysis of substrates such as 4-nitrophenyl acetate, which has been thought to proceed in a layer of ''supercritical'' water surrounding the collapsing cavitational bubble, plays a role in their aqueous-solution sonolysis. New results, especially the absence of nitrophenol formation, indicate that this is not the case. This, as well as the formation of considerable amounts of OH-radical-induced and ''deep pyrolysis'' products clearly shows that the 4-nitrophenyl acetate system is incapable of specifically probing any domain of supercriticality.

3:20

5pPAb5. Sonoluminescence from water–ethylene glycol mixtures. Melanie Bradley, Muthupandian Ashokkumar, and Franz Grieser (Adv. Minerals Products Res. Ctr., School of Chemistry, Univ. of Melbourne, Parkville, 3052 Australia)

The emission obtained from air-saturated ethylene glycol–water mixtures has been examined using 3-ms pulses of 500-kHz ultrasound. In pure ethylene glycol at 24 °C the intensity of the signal obtained is about eight times weaker than that in pure water. At 50/50 vol.% the signals are comparable to pure water. Addition of aliphatic alcohols to a 50/50 vol.% solution quenches the signal, and the more hydrophobic the alcohol, the greater the effect. Addition of the anionic surfactant sodium dodecylsulfate enhances the signal at low concentration (1–2 mM). As the percentage of ethylene glycol in the mixture increases, the extent of the alcohol quenching and the surfactant enhancement is diminished. The effect of the additives can be explained in terms of their absorption at the solution/bubble interface and their role in controling bubble-bubble coalescence. In addition for the case of alcohol quenching, it is postulated that evaporation into the bubble also occurs and the presence of this alcohol in the core of the bubble interferes with the processes that produce sonoluminescence. This latter conclusion is similar to what we have previously raised for sonoluminescence quenching in water by alcohols [Ashokkumar *et al.*, J. Phys. Chem. **101**, 10845–10850 (1997)].

5pPAb6. Bridging the gap between single- and multibubble sonoluminescence. Thomas J. Matula (Appl. Phys. Lab., Univ. of Washington, 1013 NE 40th St., Seattle, WA 98105)

Sonoluminescence from a single bubble (SBSL) is related to sonoluminescence from a cavitation field (MBSL) by a commonality of cause (acoustic cavitation) and effect (light emission). However, questions remain as to the extent of this association. Furthermore, detailed comparisons are difficult due to the dissimilar approaches used in generating, and conditions amenable to, sonoluminescence from a single bubble versus a cavitation field. Previous comparisons of the spectral and temporal characteristics of the light emission have been limited by the sparse quantity of available data [T. J. Matula and R. A. Roy, ''Comparisons of sonoluminescence from single-bubbles and cavitation fields: Bridging the gap,'' Ultrasonics Sonochemistry **4**, 61–64 (1996)]. Further comparison studies are currently underway in order to establish whether or not a more direct relationship exists between MBSL and SBSL. These studies include a near-IR spectral comparison, a comparison of the effects of doping with small quantities of impurities, and a comparison of the effects of an overpressure on the light intensity. An increased understanding of the relationship between these two phenomena should be extremely useful to sonochemistry researchers. [Work supported by DOE-EM.]

4:00–4:20 Break

Contributed Papers

4:20

5pPAb7. Ultrasonic generator with frequency modulation used in sonochemistry. Mircea Alexandru Sarbu, Elek Demeter (Res. Inst. for Electron. Machines, Bd. Tudor Vladimirescu 45, 79623 Bucharest, Romania, sarbuma@pcnet.pcnet.ro), Mircea Vinatoru (Inst. of Organic Chemistry, 71141 Bucharest, 15-254, Romania), and Adrian Daniel Constantinescu (Res. Inst. for Electrotechnics, Splaiul Unirii 313, 74204 Bucharest, Romania)

The electronic generator includes an oscillator and a power stage working in tandem. It is supplied with an unfiltered rectified tension voltage. The signal applied to the transducer is completely modulated in amplitude, having a modulation sinusoidal frequency of 100 Hz. The adaptation transfer of power is realized by a voltage transformer, in this case the rate of voltages being 3.2. The input power was halved by a separate connection, at which one gets 0.707 of the maximum tension voltage. The output signal of the oscillator is frequency modulated with a white noise signal, the resulting signal having a frequency deviation less than 10% of the oscillation frequency. Frequency modulation by a white noise signal generates a broadband signal, very useful for the improvement of the efficiency of the chemical reaction. The carried experiments proved that the use of half of the transmitted power led to interesting results, too. So, for the case of the Weissler reaction of potassium iodine decomposition, at the same time of sonification there was practically a double concentration of the obtained substance, iodine, for the case of half of the power generator.

4:40

5pPAb8. Effect of crosslinking on dynamic mechanical properties of polyurethanes. Jeffry J. Fedderly, Gilbert F. Lee, and John D. Lee (Carderock Div. Naval Surface Warfare Ctr., West Bethesda, MD 20817-5700, leejd@dt.navy.mil)

The dynamic mechanical properties of five polyurethane compositions of varying crosslink density were measured using a resonance technique. The five crosslinked polyurethanes are the reaction products of 4,4′-diphenylmethane diisocyanate and various polypropylene glycol diol/triol blends. Crosslink density was controlled by varying the ratio of diol to triol. The dynamic mechanical data was fit to the Havriliak-Negami dispersion relation. The most significant effect of increased crosslinking was to increase the low-frequency modulus. A slight increase in relaxation time was observed as crosslink density was increased over the given range, which approximately correlates with the modest change in glass transition temperature seen in this series. Values for the high-frequency modulus and asymmetry of the dispersion were not effected by crosslink density. Comparisons are also made with the sound absorption height and width limits predicted for uncrosslinked polymers [Hartmann *et al.*, J. Acoust. Soc. Am. **101**, 2008–2011 (1997)]. [Work supported by the Carderock Division of the Naval Surface Warfare Center's In-house Laboratory Independent Research Program sponsored by the Office of Naval Research.]

5:00

5pPAb9. Kinetics of halogenated organic compounds degradation by ultrasound. Hui-Ming Hung, A. J. Colussi, and M. R. Hoffmann (W. M. Keck Labs., California Inst. of Technol., Pasadena, CA 91125)

The kinetics of degradation of CH_2Cl_2, $CHCl_3$, CCl_4, C_2Cl_4, C_2Cl_6, CH_3CCl_3, and $CHCl_2CH_2Cl$ as induced by ultrasonic irradiation in Ar-saturated solution at frequencies of 205, 358, 618, and 1078 kHz were investigated. Optimal degradation rates were obtained at 618 kHz. At the same frequency, the degradation rate constants for the chlorinated hydrocarbons increases with their Henry's law constants due to the enhanced rectified diffusion. A quantitative analysis of rectified diffusion from Eller–Flynn's model within the framework of recently developed sonochemical observations is able to account for the experimental results [T. G. Leighton, *The Acoustic Bubble* (Academic, New York, 1994), pp. 379–438]. The model predicts a sonochemical reaction efficiency of about 20% for these halogenated hydrocarbons. [Work supported by ONR and Argonne National Laboratory.]

Session 5pPAc

Physical Acoustics: Porous Media

James M. Sabatier, Cochair
National Center for Physical Acoustics, University of Mississippi, University, Mississippi 38677, USA

Walter Lauriks, Cochair
Department Natuurkunde, Katholieke University Leuven, Physics Department, Celestijnenlaan 200D, B-3001 Leuven, Belgium

Contributed Papers

2:00

5pPAc1. Coupled-phase model for the acoustical properties of granular materials. Keith Attenborough and Olga Umnova (Dept. of Mech. Eng., Faculty of Technol., The Open Univ., Milton Keynes, MK7 6AA, UK, O.V.Umnova@open.ac.uk)

The external flow approach has been used to predict acoustical properties of granular materials, assuming the constituent particles are identical and spherical. Analytical expressions for steady-state permeability, high-frequency limit of tortuosity, and characteristic viscous dimension have been derived using the Kuwabara cell model to allow for hydrodynamic interactions between the particles. Good agreement between theoretical and experimental [E. Charlaix, A. P. Kushnick, and J. P. Stokes, Phys. Rev. Lett. **61**, 1595–1598 (1988)] results has been demonstrated for stacked glass beads. A new similarity relationship between complex density and compressibility has been derived. It is analogous to that obtained earlier for materials with straight cylindrical pores [M. R. Stinson and Y. Champoux, J. Acoust. Soc. Am. **91**, 685–695 (1992)]. In addition to hydrodynamic interactions between particles, thermal interactions have been considered using the ''mirror approximation'' [Y. Hemar and N. Hermann, J. Phys. II France **7**, 637–647 (1997)]. The characteristic impedance of the stacked glass beads layer has been calculated using this relationship and is shown to be in good agreement with measured values and the predictions of pore-based models. [Work supported by EPSRC.]

2:20

5pPAc2. Physics of acoustic-to-seismic coupling and detection of buried objects. James M. Sabatier and Ning Xiang (Natl. Ctr. for Physical Acoust., Univ. of Mississippi, University, MS 38677, sabatier@olemiss.edu)

Airborne acoustic waves coupled into the surface of the ground excite Biot type I and II compressional and shear waves. If a mine-like target or other inhomogeneity is present below the surface, the ground surface vibrational velocity will show distinct changes due to reflection and scattering of these waves. Sound waves with a wavelength comparable to the object size are suitable for recognizing geometrical shapes of targets, while true wave-like acoustic scattering phenomena can be observed with a shorter acoustic wavelength. In this paper, a review of porous material physics relevant to mine detection will be presented. Recent development in the acoustic technology for mine detection will be reported. Taking advantage of a noncontact measurement technique, the surface vibrational velocity is detected with a laser Doppler vibrometer. [This work is supported by U.S. Army Communications-Electronics Command.]

2:40

5pPAc3. Prediction and measurement of the transmission coefficients of transversely isotropic porous plates. Achour Aknine and Bernard Castagnède (I.A.M., Univ. du Maine, Ave. Olivier Messiaen, 72085 Le Mans Cedex 9, France, aknine@laum.univ-lemans.fr)

The prediction of the transmission coefficients is based on the Biot theory of elastic waves propagation in fluid-saturated porous solids. An elastic wave impinging upon an interface between a fluid and a fluid-saturated anisotropic porous solid can generate two compressional waves (one fast and one slow) and two shear waves (one horizontal and one vertical) in the porous medium. The motion in the porous plate results in coupled differential equations involving separate displacements in the skeleton and the saturating fluid. The wave speeds of the propagation modes in the porous medium were determined by seeking the solution of the equations of motion as plane acoustical waves. The transmission coefficients were finally obtained from boundary conditions at the interfaces between the fluid and the porous plate. They were experimentally determined, in the case of a porous corundum ceramic plate immersed in water, by using an ultrasonic immersion technique. The agreement between the predicted and measured transmission coefficients versus the angle of incidence for this plate is acceptable and has been achieved using adjustable and fitted parameters.

3:00

5pPAc4. About Biot's theory and the acoustic propagation in aerogels. Luc Forest, Vincent Gibiat (Lab. Ondes et Acoust., URA CNRS 1503, ESPCI, 10 rue Vauquelin, 75231 Paris Cedex 05, France, luc.forest@espci.fr), and Thierry Woignier (Univ. Montpellier II, 34095 Montpellier Cedex 05, France)

Although aerogels are now well known for their very particular acoustical behavior (very low speed of sound, very low acoustical impedance), no theoretical model has been proposed to describe both velocity and absorption. Since aerogels are porous media constituted by an amorphous silica skeletal and air-filled pores, it seems interesting to study the possible application of the current reference theory of propagation in elastic porous media, developed in the 1950s by Biot. Biot has proposed a semiphenomenological theory in which the average motion of both solid and fluid parts is studied separately. Then he introduces in Lagrange's equations the energies of two interpenetrating ''effective media,'' considering each phase, solid and fluid, as homogeneous. Viscous losses are taken into account from Poiseuille's model. The prediction concerning the velocities in the ultrasonic range are shown accurate and a simple rheological model derived from this theory is defined. Concerning the attenuation, theoretical results and experimental data are carefully compared in the frequency range (0.8–8 MHz). A qualitative agreement for the low-density samples is obtained and it will be shown that the agreement could become quantitative if a dynamic permeability higher than the static one is taken into account.

3:20

5pPAc5. Influence of static pressure on ultrasound propagation in plastic foams. Christophe Ayrault, Alexei Moussatov, and Bernard Castagnède (LAUM, UMR CNRS 6613, IAM, av. O. Messiaen 72085 Le Mans Cedex 9, France)

The present study deals with the response of an air-saturated porous absorbing material (plastic foams) to external static pressure variation in air. Dynamics of two essential characteristics—acoustical index of refraction and transmission coefficient—are presented both analytically and experimentally. It is shown that the squared index of refraction and the logarithm of transmission coefficient depend linearly on inverse square root of pressure. The standard Johnson–Allard equivalent fluid model for porous media has been utilized. Experimental data in the pressure range from 0.2 to 5 bar at 70 and 84 kHz agree well with the model and thus provide background to a method allowing one to determine experimentally some constitutive parameters of the model. Oncoming research will define the limits of the suggested method. Some of the limits might be due to skeleton vibrations which are seldom observed in air. Promising results are obtained in tests performed with highly damping foams. Increased pressure improves the air-transducer coupling and reduces effective attenuation. It was not possible to characterize such foams earlier by ultrasonics. In addition, it does not affect scattering losses in media, thus providing an opportunity for separating scattering contribution from other losses.

3:40

5pPAc6. Propagation of an ultrasonic impulse in porous media having a rigid frame. Zine el Abidine Fellah, Achour Aknine, Bernard Castagnède, and Claude Depollier (Lab. Acoust., Univ. du Maine, 72085 Le Mans Cedex 9, France)

The sound propagation in porous materials having a rigid frame filled by air, is well described by the equivalent fluid model where the interactions between fluid and structure are taken into account in the dynamic tortuosity $\alpha(\omega)$ and in the dynamic compressibility $\beta(\omega)$ defined by the basic equations

$$\rho\alpha(\omega)\frac{\partial\langle\mathbf{v}\rangle}{\partial t}=-\nabla\langle p\rangle, \quad \frac{\beta(\omega)}{K_a}\frac{\partial\langle p\rangle}{\partial t}=-\nabla\langle\mathbf{v}\rangle.$$

In the domain of the low-frequency approximation, the behavior of these response factors leads to a wave equation with a dissipative term due to the viscous effects. For high frequencies, a porous material becomes a dispersive medium in which the phase and group velocities are functions of frequency; in such a material a transient pulse changes its shape by spreading. A theoretical model of the sound propagation in a dispersive porous material is presented. This problem is posed in the time domain for an ultrasonic pulse in a slab of porous material. A method is proposed for computing the sound field in the medium. This allows one to deduce the transmission and reflection coefficients which are dependent only on the physical parameters of the medium (but not of the incident wave), which is important for inverse problems. The spreading of the transient pulse is calculated for various porous media and compared to experimental data.

4:00–4:20 Break

4:20

5pPAc7. Calorimetric measurements of losses in mineral wool. Jonas Brunskog, Dag Holmberg (Dept. of Eng. Acoust., LTH, Lund Univ., P.O. Box 118, SE-221 00 Lund, Sweden), and Lars Wadsoe (Lund Univ., SE-221 00 Lund, Sweden)

Measurements of the heat generated in mineral wool during a steady-state single-frequency dynamic process are presented. A microcalorimeter is used to register the heat. The calorimeter consists of a heat sink, i.e., a large water container held at constant temperature, a measurement volume, and a temperature gradient sensor in between. The temperature gradient is then related to the heat flux. The sensitivity of the equipment is on the order of 1 microwatt. A small rod is connected to a shaker outside the calorimeter and to a mineral wool specimen in the other end. The dissipated energy in mineral wool can then be measured during a steady-state single-frequency dynamic process. In order to obtain a value of the reversible energy, one can also measure the acceleration and the voltage to the shaker. Dry friction will cause measurement errors, but if a measurement without any sample is performed, this can partly be compensated for. The heat flux can be related to the dissipation in the mineral wool.

4:40

5pPAc8. Anisotropy and sound propagation in glass wool. Viggo Tarnow (DTU, AKP, Bygning 358, DK 2800 Lyngby, Denmark)

Sound propagation in glass wool is studied theoretically and experimentally. Theoretical computation of attenuation and phase velocity for plane, harmonic waves will be presented. Glass wool is a highly anisotropic material, and sound waves propagating in different directions in the material will be considered. The computations are based on the geometry of the glass wool that is decribed by the density of fibers and their diameters. The air drags viscously on the fibers, and movements of the fiber skeleton are important at low frequencies. Propagation of elastic waves in the skeleton is computed by regarding it as a continuous medium described by its elastic moduli and mass density. The computed attenuation of sound waves, for frequencies 50–5000 Hz, will be compared with experimental results for glass wool with fiber diameters of 6.8 micrometers, mass density of 15 and 30 kg/m^3, and elastic moduli of 2000 and 16 000 Pa (sound wave vector perpendicular to fibers).

5:00

5pPAc9. Measurement of ground impedance—Test of method. Hans G. Jonasson and Mikael Oegren (SP Swedish Natl. Testing and Res. Inst., Box 857, SE-501 15 Bors, Sweden, hans.jonasson@sp.se)

Within the frame of a Nordtest project, a method to measure the acoustic impedance of ground has been tested. The Nordtest method has been tested by four different measurement teams, each carrying out four measurements on each of four different test sites. The results show good agreement between the different measurement teams. The measurement uncertainty is less than or equal to one ground class. The proposed Nordtest method, which has much in common with a similar standard under preparation by ANSI, is based on the following: A loudspeaker generating pink noise is used. The measurements are carried out in octave bands. The ground is divided into 12 different classes. For each class the level difference has been calculated theoretically using a specified ground impedance model based on the flow resistivity. The class assigned to a certain ground surface is the one yielding the smallest difference between measured and calculated data. The result reported is the ground class. Different indicators are used to assess the quality of the measurement.

5:20

5pPAc10. The bulk acoustic properties of a porous medium, derived from a single impedance test. Alan Cummings (School of Eng., Univ. of Hull, Hull HU6 7RX, UK, a.cummings@edm.hull.ac.uk)

In the majority of engineering applications, porous sound absorbing media may be treated as equivalent fluids, with vibration of the solid skeleton being neglected. Most measurement techniques for the bulk acoustic properties of such media (e.g., complex characteristic impedance and propagation constant) involve tests on large samples of material, rather complex series of tests on smaller single samples, or surface impedance tests on two small samples of differing thicknesses. Recently, however, a least-squares method [C. Braccesi and A. Bracciali, Appl. Acoust. **54**, 59–70 (1998)] was employed to find values of the structure factor and flow resistivity, in a two-parameter model, from a single surface impedance curve. Though the technique proved successful, the two-parameter model is less accurate over a wide frequency range that the well-known empirical curve fitting method of Delany and Bazley. In the present paper, a least-squares method is described for determining the eight empirical

parameters in the Delany and Bazley method from a single surface impedance curve. Examples of its application are given, and it is demonstrated that it gives a better fit to measured data than the two-parameter model.

5:40

5pPAc11. Determination of porous material data via two-port measurements. Mats Abom (ABB Corp. Research, 721 78 Vaesteras, Sweden, mats.abom@secrc.abb.se)

The classical model used to describe porous materials of fibrous type is the so-called equivalent fluid model. For typical fibrous materials this model is valid except for low frequencies where solid frame vibrations become important. Since porous materials are widely used in dissipative silencers, the trend for better and better modeling requires a good knowledge of acoustic data for such materials. This means that a complete characterization is necessary to provide input data for, e.g., FEM or BEM codes. As known from theory, this is possible by specifying the complex wave number (Ka) and complex characteristic impedance (Za) for a propagating plane wave. Of course, for a nonisotropic material, these data must be measured in more than one direction. The standard technique to determine Ka and Za is to use a standing wave tube and measure the complex impedance for two samples of different thickness. In this paper an alternative approach is suggested based on the measurement of the acoustic two-port for a single sample mounted in a duct with plane wave propagation. The paper describes the development of such a two-port test rig and discusses the advantages compared to earlier used techniques.

6:00

5pPAc12. Acoustic signal attenuation, velocity, and filtering by beach sand, with different water content. Hasson M. Tavossi and Bernhard R. Tittmann (Penn State Univ., Dept. of Eng. Sci. and Mech., 227 Hammond Bldg., University Park, PA 16802)

The high-intensity acoustic pulses, transmitted by a piezoelectric transducer of center frequency 40 kHz, are sent through a beach sand medium and received, at up to 35-cm depth, by an identical receiver transducer. The received acoustic signals are then amplified and analyzed on computer. Experimental data are collected at different depth and water content of pore spaces between the grains. Experimental results show that sound arrival velocity decreases from 197 m/s for humid sand, to 120 m/s for partially water-saturated sand with air bubbles, which are always present. Acoustic signal attenuation increased by a factor of ten, from humid to partially water-saturated sand. The peak frequencies in FFT of the transmitted acoustic signal and its speed are dependent on compactness of the medium. The peak spectral amplitude is close to 9.7 kHz for humid sand and 7.5 kHz, for sand partially saturated with water. Experimental data on wave dispersion, phase velocity, and attenuation versus frequency, up to 24 kHz, are obtained. Latest results and tentative theoretical interpretation of experimental data, including porosity and grain size distribution, will be presented.

Contributed Posters

These posters will be on display from Thursday to Friday, 18–19 March. Authors will be at their posters from 10:00 a.m. to 12:00 noon on Thursday, 18 March.

5pPAc13. Acoustic determination of water distribution in unsaturated soil. Andreas Blum, Ivo Flammer, and Peter Germann (Geographical Inst., Univ. of Bern, Hallerstr. 12, CH-3012 Bern, Germany, blum@giub.unibe.ch)

Sending acoustic pulses through soil columns, one obtains information on the soil's elasticity characteristics and therefore on its state of humidity. In this laboratory water flow was investigated through $30\times30\times100$-cm^3 columns of undisturbed and unsaturated soil. The initial peak of the sound wave arriving at the detector is assumed to be ballistically transmitted through the soil. Its frequency is 10 kHz, thus a spatial resolution of about 6 cm is expected. The present aim is to obtain spatial and temporal information about the soil water distribution by a tomography technique. On this poster acoustic absorption and propagation time measurements during water infiltration are presented. The data are compared with conventional soil humidity measurements by time domain reflectometry.

5pPAc14. Surface waves above thin porous layers and periodic structures. Walter Lauriks, Luc Kelders (Lab. voor Akoestiek en Thermische Fysica, Dept. Natuurkunde, Katholieke Univ. Leuven, Celestijnenlaan 200D, B-3001 Leuven, Belgium), and Jean François Allard (Univ. du Maine, UMR CNRS 6613, 72085 Le Mans Cedex 9, France)

Airborne surface waves above thin air-saturated porous layers and periodic structures have been studied in the low-ultrasonic frequency domain. These waves were observed performing two different kinds of experiments. Because surface waves are related to a pole in the reflection coefficient, we adapted a setup based on near-field acoustical holography to the frequency range of interest. In this way, it was possible to measure the reflection coefficient of the porous layer as a function of the angle of incidence. The existence of a surface wave was observed for different layer thickness. Second, the velocity of the inhomogeneous waves has been determined directly by time-of-flight measurements of ultrasonic bursts, by phase velocity measurements with a sine signal, and from interference patterns of standing waves. The results are compared to predictions using several models. The reflection coefficient above the reticulated polyurethane foams was predicted by an equivalent fluid model, the frame being motionless at the frequencies considered here. For the calculations of the velocity above rectangular- and triangular-groove gratings, we adapted models developed for electromagnetic waves above these structures to acoustics.

5pPAc15. Low-frequency acoustic stimulation of fluid flow in porous media. Peter M. Roberts and Arvind Sharma (Los Alamos Natl. Lab., Group EES-4, MS-D443, Los Alamos, NM 87545, proberts@lanl.gov)

Historical Russian and U.S. research has indicated that acoustic or elastic (seismic) waves transmitted into oil reservoirs at frequencies of 1–500 Hz can increase oil production rates. Results from prior field tests on reservoir formations and laboratory experiments on porous rock samples have been largely inconclusive. The underlying physical mechanisms are still speculative. Comprehensive experimental laboratory and theoretical data on the interactions between acoustic waves and fluid flow in porous media are required before the phenomenon can be exploited reliably for enhanced oil recovery or other applications such as groundwater remediation. A specialized laboratory facility was constructed to characterize effects that low-frequency stress oscillations have on permeability and two-phase fluid flow in cylindrical rock and sand samples. Applied mechanical axial stress, axial and radial strains, permeability changes, fluid production rates, and dynamic elastic moduli are all measured during excitation of the samples. Positive results were observed for enhanced permeability, mobilization of trapped immiscible fluid phases, and increased production rates for sandstone-brine-decane and sand-water-trichloroethylene systems. These results will be presented along with discussions of possible physical mechanisms involved. [Work supported by the U.S. Department of Energy, Office of Fossil Energy.]

5pPAc16. Damping modelization of acoustic foams at low frequency. Sahraoui Sohbi and Mariez Emmanuel (Lab. d'Acoust. de l'Univ. du Maine, UMR CNRS 6613, 72085 Le Mans, Cedex 9, France)

The polymeric foams are commonly used as sound absorbing materials. These foams can exhibit at low frequency a resonant vibration of skeleton where the fluid damping is important. The two-phase material dynamic behavior is then described by the Biot equations. This paper examines the elasticity of air-filled PU foams through their microstructure. The foam is modeled by an elastic bars periodic network. It is shown that the orientation distribution in the space of the bars and their geometry control the macroscopic properties and the anisotropy. The study of the solid-phase deformation was based on a model developed for isotropic foams [W. E. Warren and A. M. Kraynik, J. Appl. Mech. **55**, 341–346 (1988)]. An approximative evaluation of the permeability was derived from results obtained for regular arrays of parallel solid cylinders [J. E. Drummond and M. I. Tahir, Int. Multiphase Flow **10**, 515–540 (1984)]. The objective of this investigation is to achieve the stress/strain and permeability tensors in the particular case of axisymmetric foams.

FRIDAY AFTERNOON, 19 MARCH 1999 ROOM MA043, 2:00 TO 5:40 P.M.

Session 5pPAd

Physical Acoustics and Noise: Outdoor Sound

Robin L. Cleveland, Cochair
Department of Aerospace and Mechanical Engineering, Boston University, Boston, Massachusetts 02215, USA

Keith Attenborough, Cochair
Faculty of Technology, The Open University, Milton Keynes MK7 6AA, UK

Contributed Papers

2:00

5pPAd1. The eigenray method for rapidly estimating refraction effects in a linear profile atmosphere. Michael J. White (Appl. Res. Assoc., 5941 S. Middlefield Rd., Littleton, CO 80123)

Eigenray solutions to sound propagation in an atmosphere with a linear sound-speed profile offer a convenient technique to estimate the effects of refraction. Eigenrays represent the trajectories of wave fronts that depart from the source and reach a given receiver. In a linear profile, the rays are arcs of circles, and over flat ground with perfect reflection, the paths can be constructed from a series of hops. Improvements to the eigenray technique are proposed that match the exact solution for pressure and phase in the unbounded linear profile. For reflection, the choice of a correct branch in the expression for divergence is necessary so that adjacent receivers with different numbers of eigenrays report the same pressure. Extension of the technique to lend estimates for some more complex situations is straightforward, although it fails to offer an advantage near caustics and focal regions.

2:20

5pPAd2. Atmospheric sound propagation: Application to the case of aircraft landing and take off. Cora Cremezi (ADP Laboratoire, Bat 631, Orly Sud 103, 94396 Orly Aerogare Cedex, France, LaboADP@compuserve.com) and Claude P. Legros (LAUTM, Universite Toulouse-Le Mirail, 5 allee Antonio Machado, 31058 Toulouse Cedex, France)

Atmospheric sound propagation has been studied for a long time in the case of source and receiver close to the ground. In the case of an elevated source, studies are scarce and influence of the different propagation effects has not been studied in detail. As transport noises become more and more of a great concern, and among other, aircraft noise around airports, it is necessary to study what phenomena really happen. In aeronautics, this knowledge could initiate new thoughts about noise indices. This study is characterized by a great number of parameters (meteorology, source characteristics, atmosphere) and the main difficulties lie in difficult meteorological condition knowledge and aircraft flight condition uncertainties. A simple ray tracing has shown creation of shadow areas, caustics, and source height influence on propagation, according to meteorological profiles. Then, a more complete propagation model based on a parabolic equation method has been developed. It takes into account aircraft movements, considering an infinite number of fixed sources to represent the flyover. The model and some preliminary results are presented while an experimentation is going on to validate it better. Once validated, it should allow the estimation of noise level probabilities according to meteorological probabilities.

2:40

5pPAd3. Long-range acoustic propagation in the nocturnal boundary layer. Xiao Di and Kenneth E. Gilbert (Appl. Res. Lab. and the Grad. Prog. in Acoust., Penn State Univ., P.O. Box 30, State College, PA 16804)

It is a common observation that sound travels to long distances in the nocturnal boundary layer (NBL). For such long-range propagation, the cumulative effects of turbulence can be significant even though NBL turbulence is generally much weaker than typical daytime turbulence. In this paper a 3D version is used of the Green's function parabolic equation (GF-PE) to investigate the effects of turbulence on average levels and cross-range correlation in the NBL at distances of up to 10 km. A comparison is made between 2D and 3D predictions for 50 and 100 Hz. In addition, the cross-range coherence is computed at various ranges for the two frequencies. The implications for beamforming on horizontal arrays in the NBL are discussed. [Work supported by the Defense Advanced Research Projects Agency (DARPA).]

3:00

5pPAd4. Calculation of sound reduction by a thick noise barrier in downwind conditions. Jens Forssén (Dept. of Appl. Acoust., Chalmers Univ. of Technol., S-41296, Göteborg, Sweden, jf@ta.chalmers.se)

The downwind propagating sound field from a monopole source is solved by applying a Hankel transform in a stratified medium, according to the method by Rasmussen. The influence of the noise barrier is calculated using the equivalent source method with ring sources of zero order placed inside the fictious surface of the barrier. At the surface the boundary condition is fulfilled by choosing the correct amplitudes of the equivalent sources. The total field is then calculated as the sum of contributions propagated downwind from both the original source and the equivalent sources.

3:20

5pPAd5. Acoustic scintillations induced by atmospheric turbulence, as imaged with a large planar vertical microphone array. D. Keith Wilson, Calandra R. Tate (U.S. Army Res. Lab., 2800 Powder Mill Rd., Adelphi, MD 20783), David C. Swanson, and Karl M. Reichard (Penn State Univ., P.O. Box 30, State College, PA 16804)

A planar vertical array of 32 microphones (eight elements in the vertical direction, and four in the horizontal; overall dimensions approximately 6 by 3 m) was constructed on agricultural land near the Pennsylvania State University. Several data sets having 20-min duration were collected, for atmospheric states including windy daytime conditions and still nighttime conditions. The received signals due to a source 770 m distant from the array were processed to form a time-varying virtual image of the source. During the daytime, the source image undergoes dramatic scintillations and fluctuations in its apparent position. The nighttime image is quite stable, and the vertical dependence of the microphone signals suggests that the sound energy propagates as well-defined modes. Cross coherence between the microphones, as a function of vertical and horizontal separation, is also discussed.

3:40–4:00 Break

4:00

5pPAd6. Sound propagation near the ground in a turbulent atmosphere. V. E. Ostashev and G. H. Goedecke (Dept. of Phys., Box 30001, New Mexico State Univ., Las Cruces, NM 88003-8001)

For many geometries of sound propagation in an atmosphere, the sound-pressure field is a sum of the direct wave from the source to the receiver and that reflected from the ground. The resulting field is significantly affected by atmospheric turbulence. A theory is presented that gives an analytical formula for the mean-square sound pressure in an anisotropic turbulent atmosphere with temperature and wind velocity fluctuations. This formula contains a ''turbulence'' factor T which describes the reduction of interference maxima and minima due to atmospheric turbulence. For the important particular case of isotropic turbulence, T is expressed in terms of the coherence function of the direct wave from the source to the receiver. The turbulence factor T and the mean-square sound pressure are calculated and compared for Kolmogorov, Gaussian, and von Karman spectra of temperature and wind velocity fluctuations. Furthermore, the relative contributions to the mean-square sound pressure due to temperature and wind velocity fluctuations are compared. [This material is based upon work supported by the U.S. Army Research Office under Contract No. DAA G55-98-1-0463.]

4:20

5pPAd7. The high-power acoustical warning systems. Branko Somek, Sinisa Fajt, and Hrvoje Domitrovic (Faculty of E. E. and Computing, Dept. of Electroacoustics, Unska 3, HR-10000 Zagreb, Croatia, branko.somek@fer.hr)

The high-power acoustical warning and informing systems are necessary for various aims. Mostly these systems work in open space, particularly in urban areas (towns, villages, river valleys). The useful coverage depends upon used transducers-emitters and installed electrical power. Almost all such systems have omnidirectional coverage, i.e., equal acoustical energy is radiated in all directions. The environmental conditions (air temperature and humidity, strength and direction of wind, etc.) and miscellaneous barriers (buildings, land configuration, trees) have an influence on the sound propagation for warning and informing systems. The other important point is that these systems are also used for spoken messages, not only for alarm. The computer simulation was done which takes all these parameters into account, and enables calculation of needed acoustical and electrical parameters.

4:40

5pPAd8. Infrasound detector design for recording sonic booms and events of CTBT interest. Hein Haak (Royal Netherlands Meteorological Inst., Dept. of Seismology, P.O. Box 201, 3730 AE De Bilt, The Netherlands) and Läslo Evers (Royal Netherlands Meteorological Inst., Dept. of Seismology, P.O. Box 201, 3730 AE De Bilt, The Netherlands)

The Royal Netherlands Meteorological Institute (KNMI) is involved in a project concerning the detection of nuclear explosions and sonic booms. The main area of research and development is concerned with the infrasonic instruments. This includes the pressure sensor, electronics, and the noise-reducers. An optimal array-layout is necessary, next to a suitable instrument, to succesfully record infrasonic events. Therefore, the theoretical design of the array and practical implementation at Deelen are of main concern for the acquisitional part of the project. Once data are recorded, the data processing and interpretation has to be done. An on-line data analyses tool was developed to distinguish an infrasonic event from noise and other useless signals. The instruments are based on the Validyne Differential Pressure devices. To create an instrument sensitive in the 0.01–100 Hz frequency range, several constructional efforts were made p.e. acoustic capillary, backing volume, and signal inlet volume. The signal inlet volume is coupled to a noise-reducer, porous hoses or pipes. The symmetrical layout of the hoses/pipes guarantees an improvement in signal-to-noise ratio through spatial integration. The array of 16 microbarographs has an apeture of 2 km. Array techniques, i.e., slowness analyses, were applied to determine the most optimal layout.

5:00

5pPAd9. Wind induced infrasound in the atmosphere. Jin Lai Xie (Computer Information and Network Ctr., The Chinese Acad. of Sci., Beijing, PROC 100080) and Zhao Hua Xie (The Chinese Acad. of Sci., Beijing, PROC 100080)

Characteristics of atmosphere infrasound noise field have been studied by measuring and analyzing the infrasound noise field in the atmosphere. A set of space correlation radii of noise corresponding to wind speed 4 m/s has been obtained, which can be taken as the tentative basis for an acoustical array design. At the same time, the wind speed-pressure relation curves have been measured and calculated, and the antijamming ability of the array receiving infrasonic signals and noise-reducing tube is obtained. The following conclusions can be obtained from the present calculations, waveform diagrams, and the field measurements: (1) The spatial correlation radii of the noise caused by the wind are small. (2) The measured curves for wind noise are in accordance with Bernoulli theorem basically. (3) The correlation detection is advantageously available for antinoise. (4) The different averaging duration of the wind noise will cause different results. (5) The main source of natural noise background on ground is the aerodynamic noise produced by local surface wind. The main period lies within 1 to 100 s.

5:20

5pPAd10. Snell's law of refraction and sound rays for a moving medium. D. Hohenwarter and F. Jelinek (Inst. of Technol., Dept. for Res. and Testing, Vienna, Austria)

Fermat's principle of least time is used to calculate a new law of refraction for a stratified medium moving horizontally with different temperatures in each layer. This new law of refraction includes velocity of sound, wind speed, and the angle between the vectorial sum of sound velocity and the wind speed. This new equation is compared with the usual approximations for the different refraction laws of a moving medium occasionally mentioned in literature as ''Snell's law for a moving media.'' The sound rays in a moving thermically stratified medium are refracted more or less (dependent on either upwind or downwind sound propagation), then calculated according to the ''Snell's law.'' For upward-oriented sound rays and a moderate thermical stratification with high wind speeds,

the difference in the angle of refraction between the new refraction law and the usual approximation is roughly 3 degrees and neglectable for grazing incidence. The sound ray trajectories expressed as analytical equations for a constant sound velocity combined with a wind speed profile proportional to height; the results are shown in a figure. Furthermore, the sound ray trajectories for a linear sound speed profile combined with a linear height-dependent wind speed profile are calculated and shown graphically.

FRIDAY AFTERNOON, 19 MARCH 1999 ROOM H1028, 2:00 TO 6:20 P.M.

Session 5pPPa

Psychological and Physiological Acoustics: Pitch, Loudness and Frequency Effects

Robert L. Carlyon, Chair
MRC Cognition and Brain Sciences Unit, 15 Chaucer Street, Cambridge CB2 2EF, UK

Contributed Papers

2:00

5pPPa1. Adaptation to a two-component amplitude modulator. Hideki Iwasawa (NTT Adv. Technol., Atsugi, Kanagawa, 243-0198, Japan, iwasawa@av-hp.brl.ntt.co.jp) and Makio Kashino (NTT Basic Res. Labs., Atsugi, Kanagawa, 243-0198, Japan)

Threshold shifts of amplitude modulation (AM) detection caused by adaptation to single- and two-component amplitude modulators were determined. The single-component modulator was sinusoid at either 4, 17, or 21 Hz. The two-component modulator was a complex of sinusoids at 17 and 21 Hz. The carrier was sinusoid at 1000 Hz for both adapting and test tones. Five adults with normal hearing participated in the 6-day experiment. Adaptation to modulators elevated thresholds of AM detection of the same and nearby frequencies relative to the unmodulated-adaptor or no-adapting conditions. In contrast to the findings in modulation detection interference (MDI), where the low-frequency beat of a masker with a two-component modulator interfered with detection of AM at the beat frequency [S. Sheft and W. A. Yost, J. Acoust. Soc. Am. **102**, 1106–1112 (1997)], the two-component amplitude modulator did not affect the threshold for detecting AM at the beat frequency. The present results suggest that envelopes are not detected as such, but resolved into components, and that the mechanism responsible for AM adaptation is earlier in processing level than that involved in MDI.

2:20

5pPPa2. A privileged perceptual status for rising intensity tones. John G. Neuhoff (Dept. of Psych., Lafayette College, Easton, PA 18042-1781)

Recent cross-modal matching experiments have shown that listeners reliably overestimate the change of rising level tones relative to equivalent falling level tones [J. G. Neuhoff, Nature **395** (6698), 123–124 (1998)]. In a natural listening environment this overestimation could provide a selective advantage, because rising intensity can signal source movement toward an organism. In the present work, listeners heard equivalent rising and falling level tones, and in a three-alternative forced-choice task, indicated which sound demonstrated the greatest change in loudness, or whether the amount of loudness change was the same. If one sound was judged to change more than the other, listeners indicated the magnitude of disparity in loudness change between the two sounds. Results indicate a privileged perceptual status for rising intensity tones, and a greater perceptual disparity between rising and falling intensity tones as overall level increases. These results suggest an asymmetry in the neural coding of tonal rising and falling intensity sweeps, and may be indicative of localization priorities in a natural listening environment.

2:40

5pPPa3. Effects of instantaneous phase shifts and gap duration on pitch of unresolved complex tones. Louise J. White (Lab. of Exp. Psych., Univ. of Sussex, Falmer, Brighton BN1 9QG, UK, louisew@biols.susx.ac.uk) and Christopher J. Plack (Univ. of Essex, Colchester CO4 3SQ, UK)

Introducing a phase change between two short bursts of a sinusoid can produce a pitch shift which corresponds to a shift in the peak of the long-term spectrum [I. V. Nabalek, Acustica **82**, 531–539 (1996)]. The present experiment examined this effect with a complex tone consisting of unresolved harmonics where the phase change was applied to the envelope of the complex. The hypothesis that a long-term pitch mechanism sensitive to envelope phase is reset in response to a discontinuity in the stimulus was tested: The stimulus was an unresolved complex tone consisting of the harmonics of a 250-Hz $F0$ filtered between 5500 and 7500 Hz. Two 20-ms bursts separated by short gaps were presented; the starting phase of the first burst, the phase between the bursts, and the duration of the gap were varied. A pitch-matching paradigm was used. If the gap between the bursts causes the mechanism to reset, the resetting hypothesis predicts that a phase manipulation of the second burst will not alter the pitch of the complex. Pitch shifts were obtained which do not support a resetting hypothesis, but rather a mechanism in which the mean pulse rate is used to determine pitch.

3:00

5pPPa4. Fundamental frequency discrimination: Influence of lateralized temporal fringes. Hedwig Gockel, Robert P. Carlyon (MRC Cognition and Brain Sci. Unit, 15 Chaucer Rd., Cambridge CB2 2EF, UK), and Christophe Micheyl (UPRESA CNRS 5020, Hopital E. Herriot, 69437 Lyon Cedex 03, France)

Fundamental frequency ($F0$) discrimination can be impaired substantially by the presence of another complex (the ''fringe'') immediately before and after the target complex. This has been attributed to listeners over-integrating information about the fringe $F0$ when estimating the target $F0$. It has been shown [C. Micheyl and R. P. Carlyon, J. Acoust. Soc. Am. (in press)] that for the impairment to occur (i) target and fringes have to be in the same frequency region; (ii) if all harmonics of target and fringes are unresolved then they may differ in $F0$; otherwise, they have to be similar. The present experiments investigated the effect of lateralized fringes. In a 2I-2AFC adaptive procedure, difference limens for $F0$ for a 100-ms harmonic target complex were measured in the presence and absence of 200-ms harmonic fringes. The nominal $F0$ was 88 or 250 Hz. Stimuli were bandpass-filtered between 125 and 625, 1375 and 1875, or 3900 and 5400 Hz. The target was presented monaurally, while the fringes were monaural (ipsilateral or contralateral) or binaural (diotic or dichotic, lateralized by ILD or ITD). Results showed reduced effects of fringes

localized away from the target, the exact size depending on the resolvability of the components and their specific lateralization. [Work supported by Wellcome Trust.]

3:20

5pPPa5. Competition between space and time in the auditory system. Robert P. Carlyon (MRC Cognition and Brain Sci. Unit, 15 Chaucer Rd., Cambridge CB2 2EF, England, bob.carlyon@mrc-cbu.cam.ac.uk) and Laurent Demany (Univ. Bordeaux 2, F-33076 Bordeaux Cedex, France)

Listeners were presented with a dichotic 1-s bandpass-filtered (3900–5300 Hz) pulse train at a rate of Fr Hz in one ear and 2Fr in the other, against a noise background. Each pulse in the Fr train was simultaneous with a pulse in the other ear. Listeners adjusted the ILD of a bandpass-filtered noise to match the perceived location of one pulse train, and then adjusted the rate of a diotic train, presented at that ILD, to match its perceived rate or pitch. At low rates (e.g., Fr=1 Hz) they heard pulses alternating between the midline and the ear receiving the 2Fr train, with the perceived rate in each location approximately equal to Fr. At high rates (e.g., Fr=100 Hz) they heard a pitch of Fr in one ear and 2Fr in the other. At intermediate rates ($12<\mathrm{Fr}<50$ Hz) a duplex region occurred, whereby the Fr train was heard close to the midline but where the 2Fr train was perceived at its ''correct'' rate. This duplex region, combined with other results, argues against simple schemes in which binaural localisation occurs either entirely ''before'' or ''after'' sequential binding processes.

3:40

5pPPa6. Forgetting pitch and loudness. Sylvain Clément, Laurent Demany, and Catherine Semal (Lab. de Neurophysiologie, UMR CNRS 5543, Univ. Bordeaux 2, 146 rue Leo-Saignat, 33076 Bordeaux, France)

Short-term memory for pitch and loudness was investigated in discrimination experiments using a 2I-2AFC paradigm with feedback. The two stimuli presented in each trial were separated by a variable delay (D); they consisted of pure tones, a series of resolved harmonics, or series of unresolved harmonics mixed with lowpass noise. A roving procedure was employed in order to minimize the influence of context coding [N. I. Durlach and L. D. Braida, J. Acoust. Soc. Am. **46**, 372–383 (1969)]. During an initial training phase, frequency and intensity discrimination thresholds [$P(C)=0.80$] were measured with an adaptive staircase method while D was fixed at 0.5 s. The corresponding physical differences (in cents or dB) were then constantly presented at four values of D: 0.5, 2, 5, and 10 s. In the case of intensity discrimination, d' markedly decreased when D increased from 0.5 to 2 s, but was not further reduced when D was longer. In the case of frequency discrimination, the decline of d' as a function of D was significantly less abrupt. Similar decline functions were observed for 50- and 500-ms pure tones. These results support the idea that pitch and loudness are processed in separate modules of auditory memory.

4:00–4:20 Break

4:20

5pPPa7. Loudness recalibration and complex tones. Dan Mapes-Riordan and William A. Yost (Parmly Hearing Inst., Loyola Univ. of Chicago, 6525 N. Sheridan Rd., Chicago, IL 60626, dmapes@luc.edu)

Loudness recalibration occurs when a loud (recalibration) tone at frequency $f1$ precedes quieter test tones at frequencies $f1$ and $f2$. Previous experiments [Mapes-Riordan and Yost, J. Acoust. Soc. Am. **101**, 3170(A) (1997)] have shown that the recalibration tone can decrease the loudness of the test tone at $f1$ by more than 6 dB. The current experiments addressed loudness recalibration when the test signal and/or recalibration signal was harmonic complex tones. In the first experiment an adaptive tracking procedure measured the equal loudness point between a harmonic complex and a pure tone. In the recalibration conditions, the loudness comparisons were preceded by a recalibration signal consisting of various combinations of frequencies contained in the harmonic complex, or by a pure tone corresponding to the pitch of the missing fundamental. In the second experiment, listeners were asked to adjust the level of a single harmonic ($f3$) in a harmonic complex ($f1-f5$) until it was heard as a separate tone in conditions with and without a recalibration tone at $f3$. The results of these experiments will be discussed in terms of the loci of loudness recalibration relative to perceptual stream formation. [Work supported by a NIDCD Program Project Grant.]

4:40

5pPPa8. Is the auditory filter optimal? Bruce A. Schneider (Univ. of Toronto, Toronto, ON L5L 1C6, Canada)

Gabor [J. I. E. E. London **93**, 429–457 (1946)] showed that a narrowband filter, with a Gaussian impulse-response envelope, provided the optimal compromise between good temporal resolution and good spectral resolution. The impulse-response function of this optimal Gaussian filter, however, begins before the impulse is applied, and, therefore, is not physically realizable in the auditory domain. A variety of physically realizable impulse response functions were examined to determine which one came closest to the optimal compromise achieved by the Gaussian filter. It is shown that a filter, whose impulse response function is either a gamma function or a generalized Rayleigh function, comes closest to being optimal. Moreover, these two filter types provide good fits to the data from notched-noise experiments.

5:00

5pPPa9. Adaptive psychophysics based on unforced-choice tasks. Christian Kaernbach (Inst. für Allgemeine Psych., Univ. Leipzig, Seeburgstr. 14-20, 04 103 Leipzig, Germany)

Perceptual thresholds are usually measured by means of adaptive staircase procedures. The latter are commonly combined with forced-choice tasks in order to avoid problems arising from unstable criteria in yes/no tasks. The present study suggests the use of ''unforced-choice'' tasks, when the observer is given an additional response alternative, ''don't know.'' Simulations and experimental data are presented which demonstrate that if combined with an appropriate adaptive rule, the unforced-choice paradigm can be at least as efficient as forced-choice tasks, if not superior.

5:20

5pPPa10. Correlations between speech processing and auditory functions at 1 kHz. Ingrid M. Noordhoek, Tammo Houtgast, and Joost M. Festen (Dept. of Otolaryngol., Univ. Hospital VU, P.O. Box 7057, 1007 MB Amsterdam, The Netherlands, im.noordhoek@azvu.nl)

Even when all relevant speech information is presented above threshold, intelligibility may still be reduced for hearing-impaired listeners. An attempt is made to relate impaired speech processing to a deterioration of specific auditory functions. Performance of hearing-impaired listeners is measured on psychoacoustic tests concerning temporal and spectral resolution, frequency and intensity discrimination, and temporal and spectral integration. All auditory functions are measured at 1 kHz. Speech reception is measured with the SR*B*T test (speech reception *bandwidth* threshold). This test determines the minimum width of a speech band with a center frequency of 1 kHz required for 50% intelligibility. A wider-than-normal SR*B*T can simply be the consequence of inaudibility of part of the speech signal. To account for this possibility, each SR*B*T is converted to an SII (speech intelligibility index, the new articulation index). This SII may be interpreted as the proportion of the total speech information required by the listener for 50% intelligibility. An elevated SII is considered an indication of impaired processing of suprathreshold speech. This may be caused by the deterioration of specific auditory functions. Relations between the performance on psychoacoustic tests and the (elevated) SII will be examined. [Work supported by the Foundation ''Heinsius-Houbolt Fonds.'']

5:40

5pPPa11. Further studies of auditory decruitment and a visual analog. Georges Canévet, Xavier Regal, Olivier Sauvage (CNRS-LMA, 13402 Marseille Cedex 20, France), Robert Teghtsoonian, and Martha Teghtsoonian (Smith College, Northampton, MA)

A tone continuously decreasing in amplitude from moderate to weak levels will, at any point in the sweep, have a loudness increasingly lower than an equally intense tone presented alone. This accelerated loss in loudness has been called decruitment [Canévet and Scharf, J. Acoust. Soc. Am. **88**, 2136 (1990)] and interpreted in part as an adaptation effect. For a 1-kHz tone, the amount of decruitment increases with the duration of the sweep and becomes asymptotic at about 20 s; a phenomenon similar to decruitment can be observed for circles continuously shrinking in size [Teghtsoonian *et al.*, P & P, 1998, submitted]. Further studies, in which tone frequency and sensation level are varied, show that (a) at 4 kHz, the degree of decruitment increases with sweep duration for a longer period (over 50 s) and achieves a higher value than obtained with a 1-kHz tone, and (b) sensation level has little effect on either measure. These findings for loudness are not easily interpreted in terms of simple adaptation but may be consistent with a form of adaptation characterized as ''medium-term.'' A study confirming the accelerated shrinkage of a continuously decreasing circle is also reported and the problem this creates for adaptation-based interpretations of loudness decruitment is noted.

6:00

5pPPa12. Effect of time distribution of energy on loudness evaluation. Sabine Meunier (Lab. de Mécanique et d'Acoustique–CNRS, 13402 Marseille Cedex 20, France), Patrick Susini (Inst. de Recherche et Coordination Acoustique/Musique, Marseille, France), and Xavier Regal (Lab. de Mécanique et d'Acoustique–CNRS, 13402 Marseille Cedex 20, France)

Most work on loudness have been done on stationary sounds. However, environmental sounds are usually temporally variable, and memory effects could be important in loudness evaluation of long-lasting dynamic sounds. The loudness of one-minute sounds containing a local dominating peak of energy was measured. The sounds differed only by the temporal position of the peak. The influence of peak location on the global loudness judgment was evaluated. The global loudness was first evaluated using magnitude estimation. Contrary to expectations, mean estimations were the same for all sounds regardless of peak distribution. In a second experiment, subjects had to judge the loudness, using cross-modal matching. They matched the size of a circle on a computer screen with the loudness of the sound. At the end of the signal, a global estimation was also made using the same cross-modal matching paradigm. This global estimation was made either just after the sound or after a pause of one minute. During the pause, the subject had to perform a distracting task. Relations between global and continuous judgments are discussed. The study can help to design a model of the loudness of temporally variable sounds.

FRIDAY AFTERNOON, 19 MARCH 1999 POSTER GALLERY, 2:00 TO 4:00 P.M.

Session 5pPPb

Psychological and Physiological Acoustics: Binaural Processing, Cocktail Party Effects and Localization (Poster Session)

Kourosh Saberi, Chair
Beckman Laboratory, Caltech, Pasadena, California 91125, USA

Contributed Papers

Posters will be on display from Thursday to Friday, 18–19 March. Authors will be at their posters from 2:00 p.m. to 4:00 p.m. on Friday, 19 March.

5pPPb1. Spectral integration in binaural processing. Kourosh Saberi, Yoshifumi Takahashi, and Haleh Farahbod (Div. of Biol., Caltech, Pasadena, CA 91125)

Results are reported from human psychophysical and animal neurobehavioral experiments that examined the ability of the binaural system to integrate information across frequency channels. The psychophysical experiments measured the lateralization of low-frequency (<1200 Hz) multitone complexes as a function of number of components (five or fewer) and frequency spacing between these components (25 to 400 Hz). A pointing task was used to match the perceived lateral position of a broadband noise burst to that of the complex. The complex contained a fixed interaural delay of 1500 μs leading to the left, and the pointer's perceived lateral position was adjusted by varying its interaural level difference. Parallel neurophysiological experiments were conducted in the optic tectum (superior colliculus) of the barn owl, using narrow-band dichotic noise bursts and multitone stimuli; the localization behavior of the owl in response to these same stimuli was also measured. Results show complex patterns of responses with implications for models of frequency interaction in the binaural system. Linear multiplicative or additive models customarily used in cross-correlation analysis do not explain the entire data set. [Work supported by NIH.]

5pPPb2. A cocktail party effect in the median plane? Robert S. Bolia (Veridian, 5200 Springfield St., Dayton, OH 45431, rbolia@falcon.al.wpafb.af.mil), Mark A. Ericson, W. Todd Nelson, Richard L. McKinley (Air Force Res. Lab., Wright–Patterson AFB, OH 45433-7901), and Brian D. Simpson (Wright State Univ., Dayton, OH 45435)

Recent research has been conducted on the effects of spatialized audio on a listener's ability to detect and identify a target speech signal when presented among nontarget speech signals in the horizontal plane [W. T. Nelson *et al.*, Proceedings of the 1998 IMAGE Conference (1998), pp. 159–166]. However, the existence of a ''cocktail party effect'' in the median plane has not been addressed. The purpose of the present investigation was to determine whether or not the spatial separation of multiple simultaneous speech sources in the median plane leads to improved detec-

tion and intelligibility. Independent variables include the number and angular separation of the speech signals, the sex of the target talker, and the presence or absence of head motion cues. All speech signals—phrases from a modified Coordinate Response Measure [T. J. Moore, AGARD Conference Proceedings 311: Aural Communication in Aviation (1981), pp. 2.1–2.6]—were digitally filtered via nonindividualized HRTFs and presented over headphones. Results will be compared with those obtained in the horizontal plane. Inplications for the design of auditory displays will be discussed.

5pPPb3. Perceptual learning in the discrimination of interaural time differences. Takayuki Kawashima (Dept. of Psych., Div. of Humanities and Sociology, Univ. of Tokyo, 7-3-1, Hongo, Bunkyo-ku, Tokyo, 113-0033 Japan, lh76038@hongo.ecc.u-tokyo.ac.jp), Makio Kashino (NTT Basic Res. Labs., Atsugi, Kanagawa, 243-01 Japan), and Takao Sato (Univ. of Tokyo, Bunkyo-ku, Tokyo, 113-0033 Japan)

Experiments were conducted to clarify whether spatial resolution improves with practice. Four adult subjects were involved in measuring a discrimination threshold in interaural time difference (ITD) discrimination tasks. The threshold was measured using adaptive, 2-alternative, forced-choice procedure. The subjects were pretested with 500-Hz pure tones which have ± 300 (plus meaning that the right channel signal leads) or 0 μs ITDs. Then two subjects were repeatedly tested for 9 days (about 80 min per day) at 300 μs ITD and the others at -300 μs ITD, with feedback to their responses. Following the practice period they were tested at ± 300 and 0 μs ITDs again (post-test). At the trained ITDs, the spatial resolution improved throughout practice period, and the threshold declined from 81 to 39 μs on average between pretest and post-test. At untrained ITDs, on the other hand, the resolution did not improve between two tests. The improvement was maintained even 74 days after the post-test. These results suggest that the spatial resolution based on ITD improves with practice, and the improvement occurs locally in a certain ITD region, at least within 300 μs around the trained ITD.

5pPPb4. Measuring the role of masker-correlation uncertainty in binaural masking experiments. Armin Kohlrausch and Jeroen Breebaart (IPO-Ctr. for Res. on User-System Interaction, P.O. Box 513, NL-5600 MB Eindhoven, The Netherlands)

Masked thresholds of a 500-Hz sinusoid were measured in an NρSπ condition for both running and frozen-noise maskers using a 3IFC procedure. The nominal masker correlation varied between 0.64 and 1, and the bandwidth of the masker was either 10, 100, or 1000 Hz. The running-noise thresholds were expected to be higher than the frozen-noise thresholds because of interaural correlation uncertainty of the masker intervals for running-noise conditions. Since this correlation uncertainty decreases with increasing masker bandwidth, differences between running- and frozen-noise conditions should decrease with increasing bandwidth for interaural correlations smaller than $+1$. For an interaural correlation close to $+1$, no difference between frozen-noise and running-noise thresholds is expected for all values of the masker bandwidth. These expectations are supported by the experimental data. For the 10-Hz running-noise condition, the thresholds can be accounted for in terms of interaural correlation uncertainty. For the frozen-noise conditions and both the 100- and 1000-Hz running-noise conditions, it is likely that the limits of accuracy of the internal representation determine the detection thresholds. [Work supported by the Dutch Organisation for Scientific Research (NWO).]

5pPPb5. Modeling the role of masker-correlation uncertainty in binaural masking experiments. Jeroen Breebaart and Armin Kohlrausch (IPO-Ctr. for Res. on User-System Interaction, P.O. Box 513, NL-5600 MB Eindhoven, The Netherlands)

Recently, a new approach to modeling binaural interaction was described [Breebaart *et al.*, J. Acoust. Soc. Am. **103**, 2844–2845 (1998)]. This model is based on a subtractive mechanism and is sensitive to interaural time differences as well as interaural intensity differences. In order to extend this model to masking data for partially correlated noise maskers, the following experimental findings have to be considered. (a) For broadband maskers with correlations < 0.95, the power ratio between signal and masker difference intensity (i.e., masker intensity at the output of the subtractive mechanism) is constant. (b) In broadband conditions, frozen- and running-noise maskers lead to the same thresholds, indicating that masker correlation uncertainty does not influence detectability of the signal. (c) For narrow-band running-noise maskers, the masker correlation uncertainty is the dominant factor to explain signal thresholds. Result (a) can be implemented by applying a logarithmic compression to the output of the substractive mechanism and adding an internal noise with a constant rms value. With this modification, the model is capable of describing the differences between frozen- and running-noise maskers as listed under (b) and (c). [Work supported by the Dutch Organisation for Scientific Research (NWO).]

5pPPb6. *A priori* knowledge of the sound source spectrum in median plane localization. Kazuhiro Iida (AVC Res. Lab., Matsushita Comm. Ind., 600 Saedo, Tsuzuki, Yokohama, 224-8539 Japan, kiida@adl.mci.mei.co.jp) and Masayuki Morimoto (Kobe Univ., Nada, Kobe, 657-8501 Japan)

The previous papers [e.g., J. Hebrank and D. Wright, J. Acoust. Soc. Am. **56**, 935–938 (1974); F. L. Wightman and D. C. Kistler, J. Acoust. Soc. Am. **101**, 1050–1063 (1997)] indicated that the median plane localization mechanism requires *a priori* knowledge of the source spectrum. Listeners, however, localize a sound image accurately for various sound sources on the median plane, such as music, voice, and noise. Since these sources differ from each other in spectrum, it is inferred that listeners have acquired the knowledge of the source spectrum for each sound source. This paper clarifies whether *a priori* knowledge of the sound source spectrum is classified by the kinds of source or not in the median plane localization mechanism.

5pPPb7. Analysis of different pointing methods in localization experiments of sound sources. Christoph Pörschmann and Thomas Djelani (Inst. of Commun. Acoust., Ruhr-Universität Bochum, 44780 Bochum, Germany, poersch@ika.ruhr-uni-bochum.de)

Sound localization experiments are described which aim to analyze and compare different pointing methods for sound-source localization in virtual and real environments. In the first experiment, subjects indicated the perceived direction of sound incidence by pointing directly to the source with their hands. In the second experiment, the direction was indicated using the GELP (Gods eye localization pointing) technique, i.e., by pointing at a spherical model of the auditory space. In the third experiment, a head-pointing task was applied, that is to say the direction of localization was indicated by turning the head toward the direction of the source. All the localization tests were carried out in a virtual auditory environment. Individually measured HRTFs were used for the auralization; the stimuli (pulsed white noise) were presented via headphones. The subjects were allowed to perform small head movements in order to improve the localization capability. The results of the experiments are discussed. The systematic errors that occur when using the different pointing methods are analyzed. It is shown that the localization blur averaged over all the directions is smaller using the GELP technique, while the blur for the front directions is smaller when the subjects point directly to the source.

5pPPb8. Localization experiments with saccadic responses in virtual auditory environments. Heike Heuermann-Mehmood and Hans Colonius (Inst. fuer Kognitionsforschung, FB 5-A6, C. v. Ossietzky, Univ. Oldenburg, 26111 Oldenburg, Germany)

In this study, subjects had to localize sound sources in free-field listening conditions and in virtual environments. Under virtual listening conditions, three auditory displays with distinct degrees of individualization were used. In contrast to previous studies using verbal reports or pointing

techniques, the participants indicated the perceived location of a sound source by turning their eyes toward it. Localization performance under virtual conditions was comparable to free-field conditions for all subjects, at least if individual HRTFs were used. In general, judgments turned out to be more accurate than in previous studies, especially with regard to dispersion of single judgments. This may be due to a close link between the auditory and the oculomotor system, leading to a quasiautomatic saccade toward an auditory stimulus, even without a corresponding visual target.

FRIDAY AFTERNOON, 19 MARCH 1999 ROOM H2036, 2:00 TO 6:20 P.M.

Session 5pSAa

Structural Acoustics and Vibration: Structural Vibration, Radiation and Scattering II

Donald B. Bliss, Cochair
Department of Mechanical Engineering, Duke University, Hudson Hall Science Drive, Durham, North Carolina 27708, USA

Victor T. Grinchenko, Cochair
Institute of Hydromechanics, Hydrodynamic Acoustics, Zhelyabov Str. 8/4, 252057 Kiev, Ukraine

Contributed Papers

2:00

5pSAa1. The modulation direct field radius: Model. Sven Lindblad and Karl-Ola Lundberg (Dept. of Eng. Acoust., LTH Lund Univ., P.O. Box 118, SE-22100 Lund, Sweden, sven.lindblad@kstr.lth.se)

When experimentally estimating reverberant field parameters, it is important to be positioned outside the ''direct field.'' In an often used model the total energy density is considered to be a sum of two terms, associated with the direct field and the reverberant field, respectively. The first term is diminishing with increasing source–receiver distance, while the second is receiver position independent. At a certain distance the magnitudes of the two terms are equal. In an extended model which allows fluctuating input power, the modulation direct field radius is monotonically increasing with the modulation frequency. As the modulation frequency goes to zero, the radius diminishes to the usual steady-state direct field radius. The reason is that the reverberant field smears out the modulation, especially above a certain modulation frequency, while the modulation in the direct field is maintained. Damping is often estimated by measuring decay times when a constant input power is suddenly switched off. The modulating signal is then one unit step. The magnitude spectrum of such a signal, though falling, has components at all frequencies. The implication of this is that no sufficiently large measuring source–receiver distance exists, using this method.

2:20

5pSAa2. Eigenforms and eigenfrequency spectrum of finite elastic cylinder. Victor T. Grinchenko (Inst. of Hydromechanics, 8/4 Zhelyabova St., 252057 Kiev, Ukraine, vgr@ihm.kiev.ua)

The reflection of elastic waves from free boundaries is accompanied by the effects of transformation of longitudinal waves to transverse ones and vice versa. The transformation is the physical basis for interesting and practically important peculiarities in eigenfrequency spectrum and characteristics of eigenforms. The cases of finite cylinder ($R<L$) and circular plate ($R>L$) are considered to illustrate these peculiarities. The main idea of the boundary problem solution method is described. The method provides a way to get the eigenmode characteristics accurately in a wide-frequency range. The general conclusion of the study is that it is not possible to give a qualitative explanation of the eigenfrequency spectrum and eigenform properties in the scope of the concept of standing waves with respect to propagating ones in long elastic cylinder and infinite layer. The special propagating evanescent waves are important in the eigenmode forming process. The influence of this kind of wave results, for example, in occurrence of eigenfrequencies value, which increases when dimensions of the cylinder increase. Specific features of corresponding eigenforms are discussed. Comparison of the numerical and experimental data is presented.

2:40

5pSAa3. Acoustic pressure radiated by a vibrating body in the high-frequency domain. Eric Landel, Patrick Blanc (Principia R. D., Zone Portuaire de Brgaillon, F-83507 LA Seyne/Mer, France), and Thierry Loyau (INRS, F-54501 Vandoeuvre, France)

To develop methods of predicting radiated noise that can be used in design offices, it is essential to formulate hypotheses to simplify the general problem. The expression of the acoustic presssure autospectrum for quasiplane surfaces in far field is used, obtained from the Green's function, which depends on: the Green's function, the cross-spectral density function of the normal acceleration on the body. The spatial distribution of the vibrational field on the vibrating body is, in an industrial context, very difficult to obtain, as it would require too many measurement points. It is therefore necessary to approximate it, and to this end it is assumed that: the vibrating body can be approximated by a combination of elementary surfaces; these surfaces are thin plates; the energy of each mode is uniformly distributed in a given frequency band. Once the vibrational field has been characterized in this way, it is possible to deduce the acoustic radiated pressure. A number of validation tests were carried out, which demonstrated close agreement between the computed and experimental data in the two following cases: a baffle plate and a box.

3:00

5pSAa4. Finite panel sound radiation through an absorbent layer. Ennes Sarradj (TU Dresden, Inst. fuer Technische Akustik, 01062 Dresden, Germany, sarradj@eakis1.et.tu-dresden.de)

It is often required to predict the sound radiated from a vibration through an absorbent layer (trim). Statistical energy analysis may be applied in such a case. The required radiation coupling loss factor is estimated from the radiation efficiency. To get the radiation efficiency for the trimmed panel, that of the panel (into air, without trim) is combined with the transmission loss of the absorbent layer to give a corrected radiation efficiency. Although this procedure is quite straightforward, it may produce poor results. An alternative and more accurate procedure for the estimation of the radiation efficiency is presented. The absorbent layer is fully considered in the calculation, which is done using a wave number integration technique. The results from both methods show remarkable differences.

3:20

5pSAa5. Low-frequency ($ka<10$) monostatic scattering and elastic wave generation produced by end insonification of homogeneous, finite rods ($l/a=8$). Timothy J. Yoder (SFA, Inc., Largo, MD), Joseph A. Bucaro, and Brian H. Houston (Naval Res. Lab., Washington, DC)

A parametric study of the low-frequency ($ka<10$) monostatic scattering and elastic wave generation produced by end insonification of homogeneous, finite rods ($l/a=8$) as a function of their material parameters (density, Young's modulus, and Poisson's raito) is presented. The monostatic scattering and surface displacement are calculated via finite/boundary elements (verified through experiments performed by Laboratory for Structural Acoustics at NRL) as a function of the rod's material parameters. These parameters are slowly varied to show the acoustic transitions that occur between rods composed of different materials. One backscattering feature is of particular interest because its amplitude is large and it only occurs for certain materials. The appearance (and disappearance) of this highlight can be used for material identification and is explained by the behavior of the fluid-loaded longitudinal wave dispersion characteristics of the rod. The dispersion characteristics are calculated [P. B. Nagy, J. Acoust. Soc. Am. **98**, 454–457 (1995)] and compared to the dispersion found by transforming the surface displacement calculated via finite/boundary elements. This comparison identifies the elastic waves generated on the fluid-loaded rod and is ultimately used to identify the cause of the large backscattering feature.

3:40

5pSAa6. The modulation direct field radius: Experiments. Karl-Ola Lundberg and Sven Lindblad (Eng. Acoust., LTH, Lund Univ., P.O. Box 118, SE-221 00 Lund Sweden, karl-ola.lundberg@kstr.lth.se)

The modulation transfer function, CMTF, of a linear system can be derived by post processing the impulse-response by band-pass filtering and squaring followed by a Fourier transform. Experiments were carried out in a reverberation chamber of $5.6\times6.4\times6.1$ m. The source was a small loudspeaker with an approximately omnidirectional radiation. The impulse-responses were measured on axis by means of a microphone along a straight line at 16 different source-receiver distances in the range 0.4–4 m. The corresponding free-field impulse-response was measured in a nonechoic chamber, also on axis at the distance 1.00 m. The postprocessing was performed computationally. The direct field contribution in the reverberation chamber impulse-responses was excluded by subtracting the response by the adjusted free-field impulse-response. The adjustment consisted of amplitude scaling and left or right shifting, depending on the actual source–receiver distance. The CMTFs were computed for the adjusted impulse-response and for the adjusted free-field impulse-response. For a selected modulation frequency, the magnitudes of the two derived CMTFs were equal at a certain source–receiver distance, here named modulation direct field radius. The results agree very well with the proposed model.

4:00–4:20 Break

4:20

5pSAa7. Broadband 3-D high spatial density structural response measurements of a pair of framed air-loaded cylinders of differing internal complexity. Joseph F. Vignola (Naval Res. Lab., Washington, DC 20375-5000 and SFA, Landover, MD 20785), Douglas M. Photiadis, and Brian H. Houston (Naval Res. Lab., Washington, DC 20375-5000)

The presence of internal structure can greatly alter the acoustic behavior of elastic structures. The effect of a large number of internal oscillators on the vibrational response of an air-loaded framed cylindrical shell has been examined experimentally. This examination included the construction of two shells of the same design, one of which has 880 attached oscillators. Spatially dense (200 axial points by 80 azimuthal $=16\,000$ points) 3-D laser Doppler vibrometer measurements have been collected for both of these structures for the case of broadband radial point excitation. Comparisons made between these two visually identical structures reveal dramatic differences. These include a modification of the participation factors between the three displacement polarizations and strong spatial confinement of the vibration response due to complexity. These results are presented together with a discussion of mechanisms which may account for these observations. [Work sponsored by ONR.]

4:40

5pSAa8. Measurements of the condition of compliant coatings for prediction of acoustic performance. John W. Doane (GTRI/SEAL, Georgia Tech, M/S 0405, Atlanta, GA 30332, john.doane@gtri.gatech.edu) and Jacek Jarzynski (Georgia Tech, Atlanta, GA 30332)

The goal of this work was to develop a system and analysis procedure for measuring the material properties of a viscoelastic polymer slab. This is accomplished by exciting a transient acoustic wave in the slab which has been bonded to a steel plate and observing the wave's propagation along the surface of the slab. This propagation is modeled numerically and an iterative analysis process yields the properties of interest. The system is a scanning laser Doppler vibrometer which is capable of measuring the particle velocity on the surface of a reflective target. The scanning feature allows for data to be taken rapidly at a number of locations via a computer-driven algorithm which also digitizes and stores the data for post-processing analysis. There are two numerical models developed for this problem, one based on geometrical ray acoustics and the other based on inverse Fourier and Hankel transform methods. The ray model is developed to give a quicker and relatively simpler way of investigating the physics of the problem whilst the inverse transform method gives a more robust and detailed method for analyzing the peculiarities of the problem.

5:00

5pSAa9. Analysis of structure-borne sound transmission using spatial statistical distributions. Ross A. Fulford (Inst. fuer Technische Akustik, Einsteinufer 25, 10587 Berlin, Germany, fulf0637@mach.ut.tu-berlin.de)

For a source of vibration, i.e., a machine, connected to a receiving structure, i.e., a floor, the vibrational power transmitted is dependent upon the dynamic characteristics of both the source and receiver. If the source and receiver are connected at N points and with M components of motion, the exact character of each structure can only be quantified using $(MN)^2$ frequency-dependent terms. Most often this leads to an analysis involving a vast amount of data. Upon recognition of such, together with an understanding that the terms have inherent variations, an approximate analysis method is suggested in which the precise nature of the structure's spatial response is disregarded and instead considered as a probabilistic distribution. With the approach, not only is the amount of data required significantly reduced but, moreover, the precision with which it has to be procured is also relieved. Application is demonstrated alongside work in progress with respect to practical implementation.

5:20

5pSAa10. The influence of sound radiation on vibration of mechanical structures. Andrzej B. Dobrucki and Bronislaw Zoltogorski (Wroclaw Univ. of Technol., Inst. of Telecommunications and Acoust., Wybrzeze Wyspianskiego 27, 50-370 Wroclaw, Poland)

Two methods of inclusion of coupling between the vibrating structure and produced acoustic field are discussed. The first iterative method consists of calculation of successive corrections of exciting nodal forces caused by sound pressure and solving the FEM equation of the structure. It has been proved that near the resonances of the structure this method can be nonconvergent. The second method consists of calculation of the generalized complex stiffness matrix of the sound field on the surface of the structure and including it into the stiffness matrix of the structure. The resulting stiffness matrix is a full matrix, and the algorithm for solving the FEM equation system is time consuming. It has been shown that near resonances of the structure, the global mechanical power provided to the radiating structure decreases in comparison to the power provided to the

nonradiating structure. Near the antiresonant frequencies, the power provided to the structure with included radiation is greater. On this basis, a simple method of calculation of mechanoacoustical efficiency near the resonances and antiresonances of the structure is derived. The considerations are useful for calculation of efficiency of electroacoustical transducers. The results of calculation for vibrating and radiating shells of revolution are given.

5:40

5pSAa11. Acoustic emission model for a thin circular plate with large deflections. Nicolae Enescu, Mihai Bugaru, and Mihai V. Predoi (Catedra de Mecanica, Universitatea Politehnica Bucuresti, Splaiul Independentei 313, Bucharest, Romania)

This paper presents a model for the acoustic emission of a circular plate, in the domain of large deflections. The thin circular plate is considered homogeneous, isotropic, and fixed on the boundaries. In the hypothesis of large displacements, the nonlinear von-Karman dynamic model was adopted. The external action is periodic and axisymmetric. An approximate analytical method was developed, based on the Kantorovich method and the asymptotic method, to compute the dynamic response of the plate. Starting from the characteristic parameters of the nonlinear vibrations of the plate, a model of acoustic emitter based on the Rayleigh formulation was developed, to obtain the acoustical pressure and the spatial directivity characteristic. Experimental tests were developed in an anechoic chamber, in order to confirm the model. The physical model of the plate consists of a circular frame having a high rigidity and a brass plate of 0.2-mm width. In the transverse direction, passing through the mass center of the plate, it acts as an excitatory device and the acoustic emission of the plate is analyzed. In this way, the natural frequencies of the plate and the spatial directivity characteristic have been determined and a satisfactory agreement with the theoretical results has been found.

6:00

5pSAa12. The acoustic power radiated by a circular plate hanged articulately. W. J. Rdzanek (Inst. of Phys., Pedagogical Univ. of Rzeszów, Rejtana 16a, 35-311 Rzeszów, Poland)

Radiation of the acoustic wave by vibrating planar circular plate, hanged articulately into a planar rigid infinite baffle is considered. Axially symmetric, harmonic in time vibrations are investigated. Frequency characteristics of radiated real power are determined. There is achieved the comparative analysis of the real power in the case of articulated hanging of the plate and radiated power by a plate with a rigidly fixed edge.

FRIDAY AFTERNOON, 19 MARCH 1999 ROOM EB301, 2:00 TO 4:20 P.M.

Session 5pSAb
International Workshop on Active Noise and Vibration Control

Structural Acoustics and Vibration: Transducers for Active Noise and Vibration Control

Geoff Leventhall, Cochair
Consultant in Noise, Vibration and Acoustics, 150 Cradocks Avenue, Ashtead, Surrey KT21 1NL, UK

L. Eric Cross, Cochair
Electrical Engineering, Pennsylvania State University, 187 Materials Research Laboratory, University Park, Pennsylvania 16802-4800, USA

Invited Papers

2:00

5pSAb1. Novel electrostrictive poly(vinylidene fluoride-trifluoroethylene) copolymer actuators. Q. M. Zhang, Vivek Bharti, Z-Y. Cheng (Mater. Res. Lab., Penn State Univ., University Park, PA 16802), T. Romotowski, Frank Tito (Naval Undersea Warfare Ctr., Newport, RI 02841), and R. Y. Ting (Univ. of Central Florida, Orlando, FL 32816)

Electroactive materials for applications in active noise and vibration control should possess a high displacement capability, high reliability, and be easily fabricated to conform to complicated surfaces and shapes. Apparently, almost all the current available materials cannot meet these requirements. It was discovered recently that a massive electrostriction (strain level $\sim 5\%$) can be achieved in specially treated P(VDF-TrFE) copolymers [Q. M. Zhang, Vivek Bharti, and X. Zhao, Science **280**, 2101 (1998)]. More significantly, because of the high elastic modulus, the material also exhibits high elastic energy and power density, an order of magnitude higher than those from the conventional piezoceramic and magnetostrictive materials. In addition to the large longitudinal strain, the transverse strain can be tuned over a broad range by varying the processing and irradiation conditions, from near zero in unstretched samples to more than the longitudinal strain in stretched samples. In this paper, the electromechanical properties of this class of material and the performance under different external conditions will be presented. The results on the unimorph and multilayer actuator performance fabricated using the new electrostrictive polymers with different electrode materials will also be presented. [Work supported by ONR.]

2:20

5pSAb2. Cymbal-based actuator panels. Thomas R. Howarth and James F. Tressler (Naval Res. Lab., Washington, DC 20375-5350, howarth@nrl.navy.mil)

The cymbal flextensional element has been configured into a ''1-3'' piezocomposite-type arrangement between two stiff plates to produce a thin packaged actuator device for active noise and vibration control. This presentation will discuss the activities at the Naval Research Laboratory in developing the cymbal-based actuators from the basic element design to useful device applications. This paper

will discuss the effects of spacing, element geometries, and material selections with respect to operating frequency bands and displacement profiles. Results of measured in-air immitance and laser Doppler vibrometry LDV) will be presented to discuss the output profiles. Results of a program for integrating the panels into high force applications will be described and shown. [This research was supported by the Office of Naval Research Code 321SS.]

Contributed Papers

2:40

5pSAb3. Estimate of the radiated acoustical power using strain sensing. Helmut Berger (Inst. for Telecommun. and Electroacoust., Darmstadt Univ. of Technol., Merckstrasse 25, 64283 Darmstadt, Germany)

In common active structural acoustic control systems, the acoustical feedback signal is obtained from error microphones placed in the far field of the vibrating structure. Using strain sensors on the surface, the need for far-field acoustic sensors is eliminated, which is advantageous in practical applications where no microphones can be used. An estimate of the radiated acoustic power from a vibrating plate by the use of on-plate PVDF sensors is discussed. Since the number and the location of the sensors directly affect the quality of the radiation information, the influence of various sensor arrangements is investigated. For this purpose, a clamped rectangular plate is considered which is excited at four discrete frequencies in such a way that four modes contribute effectively to sound radiation. Since the vibrational behavior is well known, the required number of PVDF sensors may be reduced, which speeds up the computation of the radiated acoustic power during the adaptation process. It will be shown that the analytical results agree well with experimental data.

3:00

5pSAb4. A new piezoelectric active noise reduction earplug. Raoul Bauer, Pascal J. F. Hamery, Pierrick Lotton,[a] and Armand L. Dancer (French–German Res. Inst. of Saint-Louis, 5 rue du général Cassagnou, BP 34, 68301 Saint-Louis Cedex, France, dancer@nucleus.fr)

This paper describes the electroacoustic components of a new active noise reduction (ANR) earplug device. Compared to a helmet, an earplug offers a better passive attenuation at low frequencies. Moreover, reducing dimensions of the acoustic cavity minimizes problems of resonance and acoustic delays, and allows active attenuation at higher frequencies (up to about 2 kHz). However, the microphone and the loudspeaker which are inserted into the earplug yield specific requirements (dimensions, output pressure, ...). The microphone used is a commercially available Electret. The loudspeaker is specially designed for this application. It consists of a cylindrical piezoelectric ceramic loaded with a thin fluid air. This laterally radiating loudspeaker provides a high-volume flow compared to its dimensions. Prototypes with ceramics of different properties have been tested. A classic model of equivalent circuit based on electromechanical analogies has been adapted to describe their behavior. Theoretical and experimental frequency responses of the earplug in cavities, artificial and real ears will be presented. Lastly, several examples of simulation of the active attenuation that can be obtained with the earplug together with a numerical ANR filter designed by ISL will be mentioned. [a] Also at Laboratoire d'Acoustique de l'Université du Maine, Avenue Olivier Messiaen 72085 Le Mans Cedex 9, France.

3:20

5pSAb5. Robust design of a sensorless bass-enhanced moving-coil ANC actuator. Mingsian R. Bai and Kwangmor Chu (Dept. of Mech. Eng., Natl. Chiao-Tung Univ., 1001 Ta-Hsueh Rd., Hsin-Chu 30050, Taiwan, ROC, msbai@cc.nctu.edu.tw)

Loudspeakers have been employed by far as the major ANC actuators. However, the responses of moving-coil loudspeakers are generally poor in low-frequency range because the diaphragms are unable to produce sufficient volume velocity. To alleviate the problem, this study focuses on enhancing the low-frequency performance of loudspeakers by means of modern control techniques. Both magnitude and phase of the frequency response are optimally compensated. A self-sensing velocity observer is utilized for producing the cone velocity signal required by the controller. Feedback H_∞ robust control and feedforward H_2 model matching control are employed to simultaneously achieve robust stabilization and tracking performance. The proposed controller is implemented using a combined digital signal processor and operational amplifier circuitry.

3:40

5pSAb6. Magnetostrictive actuation and digital variable structure control for active noise and vibration cancellation. R. D. Greenough, R. J. Smith (Dept. of Phys., Univ. of Hull, Hull HU6 7RX, UK), A. J. Wilkinson, and A. G. Jenner (Univ. of Hull, Hull HU6 7RX, UK)

Magnetostrictive actuators are ideally suited to active suppression of noise and vibration because of their low-frequency response, low-voltage operation, and high-load-bearing capability. In developing a system for active control, it was recognized that a strategy was important to contend with the nonlinear, hysterectic, and load-dependent behavior of the actuators. Consequently, digital variable structure control (DVSC) was selected, a method which has been successfully implemented in the laboratory and is now being employed and developed for practical applications. It has been demonstrated that with DVSC and a controller sample rate of 4 kHz, 32 dB of cancellation can be achieved at ~ 5 Hz. However, recent developments have increased the sample rate to ~ 8 kHz. Operation of the controller hardware with a simulated load has shown it capable of cancelling a vibration level of $0.001 g_2/\mathrm{Hz}_{0.5}$ up to 150 Hz. Experiments with the uprated controller have achieved cancellation levels of 40 dB in practice. In servo mode, the controller clearly demonstrates its ability to contend with the nonlinear properties of magnetorestrictive actuators working under load. The system is presently being investigated for use in, for example, aircraft structures and industrial machines.

4:00

5pSAb7. Piezo actuators for active vibration control and isolation—principles and practical experiences. Rolf Schirmacher (Müller-BBM GmbH, Robert-Koch-Straße 11, D-82152 Planegg, Germany, schi@mbbm.de)

Piezoelectric actuators based on PZT ceramics are a widely used drive system and are also often used for active noise and vibration control applications. They offer high static and dynamic forces, are very stiff, allow high-frequency dynamic applications, and contain no moving parts. But they also have severe disadvantages: They are very sensitive to bending moments and pulling forces and have to be driven by electrical fields of some kV/mm to obtain displacements of about 1%. The actuators have a high capacitance, which is a challenge for the power amplifiers, and the material exhibits hysteresis which shows up as nonlinearities. Based on these restrictions, different concepts for the application of piezo actuators for active vibration control and isolation systems are presented, and mechanical as well as electrical aspects are discussed. For a real life application, it was decided to use one of the concepts at an experimental stage. The design of this actuator system will be presented. Experimental results and experiences will be shown, including test stand results of the entire active vibration control system. The main problem proved to be with the nonlinearities of the actuator response, which are prohibitive for at least some applications.

Contributed Poster

This poster will be on display in the Poster Gallery from Thursday to Friday, 18–19 March. Author will be at the poster from 10:00 a.m. to 12:00 noon on Friday, 19 March.

5pSAb8. Test of various sound transducer systems for the use in ANC-systems and several applications of the ANC-system NANCY®. Dr. St. Deus and W. Schatz (ABS GmbH, Wildenbruchstraße 15, 07745 Jena, Germany)

With the introduction of ANC technologies, sound transducers have been increasingly applied in industrial fields. as well. In most cases, sound generators are set up through loudspeaker systems known from audio applications. Thus they are constructed to satisfy requirements of volume and quality (frequency response, distortion factor) while playing speech and music. This is different than applications of ANC systems in industrial environments. The following features are mainly required: (1) production of high sound pressure, especially for low frequencies (down to 30 Hz and less); (2) resistance against high temperatures (up to 700 °C) and aggressive environments (high environment pressure or vacuum); (3) compact design; (4) long operating life (min. 1 year); and (5) directional effect (preferably unidirectional, sound downward). Currently, criteria as above are increasingly determining further developments of sound transducer systems. With respect to that, various sound transducer systems were tested in a lab channel with the ANC system NANCY®. The results are stated here. In addition several examples of use of the ANC system NANCY® are presented.

FRIDAY AFTERNOON, 19 MARCH 1999 POSTER GALLERY, 2:00 TO 6:00 P.M.

Session 5pSCa

Speech Communication: Speech Perception and Recognition (Poster Session)

James M. Hillenbrand, Chair
Speech Pathology and Audiology, Western Michgian University, Kalamazoo, Michgian 49008, USA

Contributed Papers

Posters will be on display in the Poster Gallery from Thursday to Friday, 18–19 March. Authors will be at their posters on Friday, 19 March. To allow contributors an opportunity to see other posters, contributors of odd-numbered papers will be at their posters from 2:00 p.m. to 4:00 p.m. and contributors of even-numbered papers will be at their posters from 4:00 p.m. to 6:00 p.m.

5pSCa1. Vowel recognition from harmonic spectra. James M. Hillenbrand (Speech Pathol. and Audiol., Western Michigan Univ., Kalamazoo, MI 49008), Robert A. Houde (RIT Res. Corp., Rochester, NY 14623), Terrance M. Nearey (Univ. of Alberta, Edmonton, AB 26G 2E7, Canada), and Michael J. Clark (Western Michigan Univ., Kalamazoo, MI 49008)

Vowel classification methods based on either formant representations or overall spectral shape nearly always begin with the calculation of a smoothed, pitch-independent spectrum. In this report, a method is described for the classification of vowels directly from high-resolution spectra that retain harmonics of the voice source. Recordings were made of ten sustained vowels spoken by 20 men and 20 women. Smoothed spectral-shape templates for each of the vowels from a random half of the talkers were constructed as the average of the normalized spectra of like vowels spoken by different talkers. The key steps in the normalization procedure consist of: (1) removal of spectral tilt by the subtraction of a running average of spectral amplitudes, (2) dynamic range compression of the tilt-adjusted spectrum, and (3) smoothing across frequency. High-resolution harmonic spectra from the remaining half of the talkers were then classified by computing the bin-for-bin difference between the harmonic spectrum and each of the smoothed spectral-shape templates.

5pSCa2. To be nasalized, or not to be nasalized. Ho-hsien Pan (Dept. of Foreign Lang. and Lit., Natl. Chiao Tung Univ., Hsinchu, Taiwan, 30005, ROC)

Vowel nasalization is a common process found in languages with or without phonemic contrasts between oral and nasal vowels. In English, there are no phonemic distinctions between oral and nasal vowels. Oral vowels are nasalized when followed by nasals. In Bengali and Hindi, where there are phonemic distinctions between oral and nasal vowels, oral vowels are nasalized when followed by nasals [Ferguson and Chowdhury (1960)]. In Taiwanese, which is a language with phonemic nasal and oral vowels, the presence and absence of nasality in the vowel nucleus is the major cue to lexical identification of words such as /saŋ−|bi˧/ [saŋ˧] ''send rice,'' /saŋ−mi˧/[saŋ˧m̃i˧] ''send things'' [Pan (1997)]. Thus the nasalization of Taiwanese oral vowels, which is a process based on the

''ease of articulation'' principle, would impose difficulties for lexical identification. This study used both nasal airflow and acoustical data to investigate whether Taiwanese oral vowels are nasalized when both preceded and followed by nasals in words such as /tsin-˧gɔŋ˧/ [tsin˧ŋɔŋ˧] ''very silly.'' The results showed that Taiwanese vowels are not nasalized when positioned between nasals. It is proposed that lexical identification interacts with phonetic process and prevents the vowel nasalization from occurring. [Work supported by NSC, Taiwan.]

5pSCa3. Voiced–unvoiced classification for recognition of stop consonants. Mahesh Krishnamoorthy, DongSuk Yuk, Krishna Dayanidhi, Samir Chennoukh, Daniel Sinder, and James Flanagan (CAIP Ctr., Rutgers Univ., 96 Frelinghuysen Rd., Piscataway, NJ 08854)

Significant error in stop consonant recognition is caused by the confusion between voiced stop consonants and their unvoiced counterparts. The recognition is based on HMM's which use 12 MFCC's and energy with their time derivatives. The voicing state is the distinctive feature of homorganic stop consonants. According to recognition error-rate analysis, it seems that the cepstral feature does not accurately represent the voicing state of the modeled phone. For this purpose, a voiced–unvoiced classifier in conjunction with HMM's is proposed to improve the recognition of stop consonants. The recognition is done in two passes. In the first pass, a phone recognizer uses well-trained HMM's to identify a stop consonant. This pass provides the recognized stop consonant in addition to the log probability. In the second pass, the voiced–unvoiced classifier checks if the voicing state of the phone segment matches with its phonetic description. In the case of mismatch and low probability of recognition, the voiced (unvoiced) consonant is swapped with its corresponding unvoiced (voiced) counterpart. Recognition results are presented in terms of error rate, using different techniques of voiced–unvoiced classification. This method reduces the recognition error rate of stop consonants. [Research supported by DARPA Contract Nos. DABT63-93-C-0037, N66001-96-C-8510, and NSF Contract No. IRI-9618854.]

5pSCa4. Speech segmentation and the use of sequential phonological constraints. Crouzet Olivier and Bacri Nicole (Laboratoire de Psychologie Experimentale, Universite Paris 5, CNRS URA 316, 28 rue Serpente, 75006 Paris, France, crouzet@psycho.univ-paris5.fr)

Previous experiments [Crouzet (1997); Vroomen and De Gelder (forthcoming)] led to the claim that constraints on legal and illegal consonant clusters may help to segment the speech signal. Two paradigms (word spotting and phoneme monitoring in nonwords) are contrasted in order to get a better understanding of (1) whether the previous results were actually linked to early phonological processes, to lexical competitions, or to distributional constraints and (2) whether the legality status of consonant clusters should be understood as the application of an abstract phonological knowledge on an already deciphered phonemic string or as a disruption of a speech rhythm that would increase the perceptual prominence of sound sequences and that could consequently take place before phonemic coding has been accomplished. The results of the word spotting experiment allows the argument that the effect should be interpreted in terms of phonological constraints. However, in the phoneme monitoring experiment, the reversed effect was observed. This fact could lead to the rejection of the speech rhythm disruption hypothesis. The phoneme monitoring task could not be relevant yet to investigate this issue and the use of another paradigm (speech perception in noise) that would be more appropriate is proposed.

5pSCa5. Burst spectra and place of articulation in read speech. Richard S. McGowan (Sensimetrics Corp., 48 Grove St., Somerville, MA 02144)

The burst spectra of voiceless stop releases are examined with a set of wide-band filters. These spectra are selected from one male speaker and one female speaker of American English, each reading from a list of 100 sentences. A set of rules is proposed for inferring place-of-articulation based on filter amplitudes obtained from a training set of utterances. The formulation of these rules is aided by segregating the data according to speaker and according to the second formant frequency at voice onset of the following vowel. This work is part of a project to infer articulatory movement from speech acoustics. [Work supported by the NIH through Grant No. DC-01247.]

5pSCa6. Does ''one hundred fifty-five'' mean 155 or 100,55 or 100,50,5? Corine Bickley (Res. Lab. of Electron., MIT, Rm. 36-579, Cambridge, MA 02139) and Lennart Nord (KTH, Stockholm, Sweden)

The goal of this study is to determine what are the acoustic cues, if any, that differentiate the spoken phrase that means 155 from one that means 100,55 or others for 150,5 or 1,155 or 100,50,5. The motivation for this study comes from an issue that arose in designing a speech-user interface—that is, a user interface controlled by a user's speech via a speech recognizer. Users of a speech-user interface for programs that require numerical input (engineering design systems, accounting packages, etc.) need to speak sequences of numbers such as 100,50,5 (for example, to specify a three-dimensional coordinate location) as well as 100,55 (for a two-dimensional coordinate location). In this study, speakers produced utterances of one-, two-, and three-number sequences in two languages: Swedish and English. These productions were analyzed acoustically in terms of fundamental frequency, syllable duration, and amplitude. Listeners identified for each production whether the speaker intended to specify one, two, or three numbers, and which numbers. The results of the acoustic analyses will be presented and discussed with respect to the listener judgments. [Work supported in part by EC-TIDE Grant No. ENABL DE 3206.]

5pSCa7. The acoustic front-end of the FUL speech recognition system. Henning Reetz and Aditi Lahiri (Dept. of Linguist., Univ. of Konstanz, 78462 Konstanz, Germany, henning.reetz@uni-konstanz.de)

The featurally underspecified lexicon (FUL) speech recognition system converts the incoming speech signal into hierarchically organized monovalent phonological features in an early processing stage without identifying segments. After this conversion, only the presence of these features is used to access items from a 100 000 word dictionary which contains featural, segmental, morphological, and semantic information. The extraction of these features from the acoustic signal is based on standard LPC analysis for vowels, semi-vowels, and liquids, and from spectral shapes of DFT spectra for other sounds. Acoustic criteria for these features are only broadly specified to allow a wide range of speaker and dialectal variation. Most features are generated online from the signal without any further delay other than the width of the spectral windows. Only the feature [abrupt] uses some contextual temporal information.

5pSCa8. Inventory of the used ''phonetic elements.'' Shahla Sehhati (FSP-PV, Res. Ctr. for Network Technologies and Multi Media Applications Board, TUBKOM Tech. Univ. Berlin, TU Berlin, Sekr. MA 073 Straße des 17. Juni 136, D-10623 Berlin, Germany, shahla@prz.tu-berlin.de)

The extracted library of the phonetic elements for the speech synthesis based on phoneme cluster is extended additionally with the particularly selected elements. The auditive controlling observation and the experience by cluster segmentation have shown that the speech quality is improved by some critical phonetic combinations with the possibility of integration of

the important allophone variants in the library. This paper describes the reduction of a great number of these elements into an available limited quantity and the investigation of the effectivity of extending the library with selected allophones. Generally, the criteria for the selection of combined or hybrid basic elements for speech synthesis are one of the most interesting and challenging workfields. The subjective test results confirm that, in many cases, the addition of selected allophones optimizes further the quality of the library. With earlier results [Sh. Sehhati, Erstellen von Lautelementebibliotheken under Verwendung von Phonemclustern auf der Grundlage des LPC-Sprachsyntheseverfahrens.dissertation, TU Berlin (1975)]. References: [L. Mackensen, *Deutsches Wörterbuch* (Südwest Verlag, München, 1967); Th. Siebs, *Deutsche Aussprache, Reine und gemäßigte Hochlautung mit Aussprache Wörterbuch* (de Gruyter, Berlin, 1969)].

5pSCa9. Production and perception of acoustic cues to gender and individual talker identity. Jo-Anne Bachorowski (Dept. of Psych., Wilson Hall, Vanderbilt Univ., Nashville, TN 37240, j.a.bachorowski@vanderbilt.edu) and Michael Owren (Cornell Univ., Ithaca, NY 14853)

Although listeners routinely identify both gender and individual identity of talkers from their speech, explanations of these abilities remain problematic. Integrating source-filter theory with knowledge regarding variation in vocal production-related anatomy, predictions concerning gender and talker indexical cueing were tested using ''point,'' /e/, and schwa vowels that were extracted from the naturally produced speech of 40 male and 40 female talkers. Very high rates of gender classification were obtained using $F0$ and an estimate of vocal tract length, the two measures that best reflect sexual dimorphism in vocal-production-related anatomy. In contrast, individual talker classification depends primarily on the various cues associated with vocal tract filtering. Ongoing perceptual studies are being conducted to evaluate the perceptual importance of these findings to listeners. [Work supported by NSF.]

5pSCa10. The time course of lexical involvement in phonetic categorization. James M. McQueen (Max-Planck-Inst. for Psycholinguist., Wundtlaan 1, 6525 XD Nijmegen, The Netherlands), Dennis Norris (MRC Cognition and Brain Sci. Unit, Cambridge CB2 2EF, UK), and Anne Cutler (Max-Planck-Inst. for Psycholinguist., 6525 XD Nijmegen, The Netherlands)

Two experiments in Dutch examined how the influence of lexical knowledge on phonetic decisions changes over time. A [f]–[s] continuum (edited natural speech) was placed in initial position in monosyllables to make word–nonword and nonword–word continua: *flauw* (dull)–*slauw* and *flaap–slaap* (sleep). Syllable-final continua were made in the same way: *maf* (silly)–*mas* and *jaf–jas* (coat). Materials were low-pass filtered at 3 kHz. In experiment 1 there was a significant lexical effect for both initial and final fricatives: throughout the continua there were more [f] responses in the word–nonword than in the nonword–word continua. Lexical involvement was strongest in the listeners' fastest responses but disappeared in their slowest responses, both for the final fricatives (in line with previous findings) and the initial fricatives (contradicting earlier studies showing the strongest effects in the slowest responses). Experiment 2 tested whether listeners would still use lexical knowledge in their fastest responses under severe time pressure. They were asked to respond before a tone, presented 500 ms after fricative offset. The results replicated experiment 1. Lexical knowledge appears to be used in phonetic decision-making only within a limited time frame.

5pSCa11. Use of temporal envelope cues for the recognition of words and phonologically significant contrasts. Liat Kishon-Rabin and Michal Nir-Dankner (Commun. Disord. Dept., Sackler School of Medicine, Tel-Aviv Univ., Ramat-Aviv, Israel, lrabin@ccsg.tau.ac.il)

The goals of this study were: (1) measure the recognition of words and speech pattern contrasts using temporal cues only, and (2) to evaluate the effect of training on the ability to perceive segmental, suprasegmental, and phoneme information from the speech waveform only. Fifteen subjects, 20–40 years of age, with normal hearing, were tested before and after extensive training. Test stimuli consisted of: (a) eight segmental and two suprasegmental contrasts of the SPAC test using a binary forced-choice paradigm, and (b) monosyllabic words from the isophonemic AB word lists presented in open set. Spectral information was eliminated by multiplying the speech waveform with white noise using commercially available array processing software. Testing and training were under computer control. Preliminary results suggest that: (1) intonation and stress are perceived well using temporal information only, (2) manner is perceived better than either place or voicing contrasts, (3) training improves the perception of speech using temporal cues only, and (4) there is a strong correlation between speech pattern contrasts as measured in open and closed set paradigms. The findings will be discussed in relation to the relative importance of the stimuli's spectral and temporal cues and their relevance to clinical data of individuals with profound hearing loss.

5pSCa12. On the link between acoustic cue distributions and categorization dependencies. Roel Smits (Max Planck Inst. for Psycholinguist., Wundtlaan 1, 6525 XD Nijmegen, The Netherlands, Roel.Smits@mpi.nl)

The HICAT model of hierarchical categorization [R. Smits, J. Acoust. Soc. Am. **103**, 2980(A) (1998)] explicitly models dependencies in four-alternative forced-choice categorizations involving two binary distinctions. A philosophy has been developed which predicts which dependencies are likely to occur for a given pair of phonetic distinctions on the basis of the acoustic distributions of relevant cues in natural utterances. It is argued that, because speech perception happens under severe time pressure, listeners try to minimize categorization complexity while maximizing categorization accuracy. For certain phonetic distinctions, the cue distributions allow listeners to use simple, independent categorization strategies while still performing close to optimally. Severe coarticulation, however, necessitates a more complex strategy involving categorization dependencies which reflect dependendencies in the cue distributions. This philosophy was tested experimentally. Spectral locations of fricative and vowel resonances in syllables /si, sy, Si, Sy/ were measured on a large set of naturally spoken tokens. Based on the resulting distributions it was predicted that listeners' fricative categorization will be dependent on the vowel categorization. Next, a categorization experiment was run using a two-dimensional fricative-vowel continuum. The dependencies inferred from the categorization data using the HICAT model will be compared to the predictions.

Session 5pSCb

Speech Communication: Consonants and Vowels (Poster Session)

Carol Espy-Wilson, Chair
ECE Department, Boston University, 8 St. Mary's Street, Boston, Massachusetts 02215, USA

Contributed Papers

All posters will be on display in the Poster Gallery from Thursday to Friday, 18–19 March. Authors will be at their posters on Friday, 19 March. To allow contributors an opportunity to see other posters, contributors of odd-numbered papers will be at their posters from 2:00 p.m. to 4:00 p.m. and contributors of even-numbered papers will be at their posters from 4:00 p.m. to 6:00 p.m.

5pSCb1. Variation in the pronunciation of German ''ein_.'' Peter M. Janker, Bernd Pompino-Marschall, and Seadet Zeynalowa (Ctr. for General Linguist., Berlin, Germany)

Pronunciation variation of German ''ein_'' is examined (unstressed indefinite article ''ein,'' ''einen,'' as well as stressed instances of ''ein_,'' i.e., the numeral or as part of a compound) based on a larger corpus of read and spontaneous speech according to segmental variation (elisions, assimilations, etc.) and acoustic features (segmental durations, extent of formant transitions, etc.). Second, the results of a combined electropalatographical/electromagnetic-articulographical study are presented. Two male subjects uttered the items ''ein'' and ''einen'' embedded in test sentences at normal, slow, and fast speech rate. Electropalatographically tongue palate contacts for the nasal segments (duration, center of gravity of contact area) were analyzed. The EMA measurements of movement from the diphthong to nasal (or from diphthong to nasal to schwa to nasal) were done with a sensor coil mounted 1 cm behind the tip of the tongue and another one mounted on a strip of elastic foil glued to the EPG palate for sensoring velar movement. Articulatory analysis revealed quite complex gestural reductions for bisyllabic ''einen:'' Even for items without schwa elision (only at a slow rate) there is no velar closing movement for the schwa.

5pSCb2. Taiwanese prenasalized stops and poststopped nasals. Hohsien Pan (Dept. of Foreign Lang. and Lit., Natl. Chiao Tung Univ., Hsinchu, Taiwan, 30050, ROC)

Prenasalized stops and poststopped nasals were classified into a category of ''nasal+stop'' segments in Chinese [Chan (1987)]. In Taiwanese, which is a member of the Chinese language family, initial prenasalized stops b,g [$^{m}\circ$b,^{ŋg}] would change into homorganic nasals [m,ŋ] when preceded by nasals. Moreover,strong energy attacks can be observed at the release of oral closures for b,g [m,ŋ] [Pan(1994)]. This raises the issue of whether Taiwanese prenasalized stops alternate with post stopped nasals. This study investigated the alternation between prenasalized stops and post stopped nasals in Taiwanese by using nasal airflow, oral airflow, and acoustical data. Preliminary results showed that when prenasalized stops changed into nasals, there was energy damping before the release of oral closure, and rise of acoustical energy at the release of oral closure. Though not environmentally conditioned, post stopped nasals [$^{m}\circ$b,^{ŋ}g] were free variations of homorganic prenasalized stops [m^{p},$ŋ^{k}$]. [Work supported by NSC, Taiwan.]

5pSCb3. Do harmonic consonant clusters in Georgian have only one release? Priscilla C. McCoy (Phonology Lab., Univ. of California, Berkeley, CA 94720)

It has been claimed that in Georgian, a language in the Kartvelian or South Caucasian family of languages, harmonic consonant clusters have a single release. To examine this claim, different constituencies and orderings of harmonic consonant clusters and nonharmonic consonant clusters were recorded and analyzed in order to (1) assess the phonetic reality of the initial claim; and (2) compare durations of cluster releases and whole cluster segments in nonharmonic environments to those, if any, exhibited in harmonic environments. Preliminary results of the relative distribution of release durations across these two groups illustrate an interesting division of release and cluster duration figures and (2) show a possible positive correlation of a sonority hierarchy [G. N. Clements, ''The role of the sonority cycle in core syllabification,'' in *Between the Grammar and Physics of Speech*, edited by J. Kingston and M. E. Beckman, Papers in Laboratory Phonology 1 (Cambridge U.P., Cambridge, 1990)]. This also builds on previous work on Georgian consonants and their relationship to a sonority hierarchy by McCoy [1995]. The implications for consonant clusters and Georgian phonology are investigated, which in turn suggests some phonological priorities in Georgian.

5pSCb4. Effect of frequency modulation of *F*0 on the accuracy of formant frequency matches. Pascal Dissard and Chris J. Darwin (Lab. of Exp. Psych., Univ. of Sussex, Brighton, Sussex BN1 9QG, UK)

Listeners adjusted the formant frequency of a one-formant complex sound to match the timbre of a similar fixed sound (formant frequency =1100 or 1200 Hz). On each trial the two sounds' fundamental frequencies (*F*0) were in the ratio 1 : 1.13. In half the blocks the sounds were on low fundamentals (80 and 90.4 Hz), giving unresolved harmonics in the region of the formant peak; in the other half of the blocks the *F*0 was high (221.2 and 250 Hz), giving resolved harmonics near the formant peak. Orthogonal to this manipulation the *F*0 was either unmodulated for both sounds, or had a frequency modulation (FM) of 6 Hz and 3% depth. Data from seven listeners showed that, with no FM, matches are more variable within each listener for sounds with resolved than for sounds with unresolved harmonics, but that this difference disappears with FM. The result provides evidence that frequency modulating *F*0 improves listeners' ability to estimate a formant frequency that is cued by resolved harmonics. [Work supported by EPSRC Grant No. GR/L03422.]

5pSCb5. Articulatory discriminability of vowels: Articulator and corpus effects. Philip Hoole (Inst. fuer Phonetik, Munich Univ., Schellingstr. 3, D-80799 Munich, Germany, hoole@phonetik.uni-muenchen.de)

The principal aim of this work was to compare the potency of different sources of articulatory information for differentiating the vowels of German in discriminant analyses. The secondary aim was to determine whether results depended on the corpus analyzed. Articulatory data (electromagnetic articulography; seven speakers) was available for tongue, lower-lip, and jaw position. Three corpora were compared. The first two used highly controlled nonsense-word material but differed in speech rate (normal versus fast). The third corpus embedded the vowels in a wide variety of real words and sentences. Using as a baseline the classification accuracy obtained with tongue-position data only, the increase in accuracy was about 9% with jaw data, 14% with lip data, and 17% with both jaw and lip. A further noticeable improvement (23% re. baseline) resulted from adding in velocity or acceleration data. Classification patterns were remarkably similar over the three corpora; the real-word corpus was simply, but consistently, about 10% worse than the ''nonsense-normal'' corpus, with ''nonsense-fast'' in between. Results will be related to the structure of the German vowel system. Corpus effects on articulatory behavior will be further discussed by comparing PARAFAC factor analysis of tongue configuration for the nonsense versus the real corpora. [Work supported by DFG Ti69/29.]

5pSCb6. Perceptual consequences of unintended epenthetic stops. Natasha Warner and Andrea Weber (Max Planck Inst. for Psycholinguist., Nijmegen, The Netherlands)

In many languages, historically an epenthetic stop has appeared between a nasal and a fricative or a nasal and another stop, as /p/ in English ''empty'' (from earlier ''œmtig''). Ohala [Phonetica **52**, 160–170 (1995), and in press] proposes an articulatory explanation for epenthesis involving listener misperceptions. Ohala predicts that epenthetic stops will match the place of articulation of the preceding nasal. The current study investigates listeners' perception of epenthetic stops. A speaker produced nonsense words ending in nasal stop sequences, such as /flg@mk, tuloʏp/ from orthographic representation. Thus the speaker did not intend to produce epenthetic stops [(floʕmpk, tuloʏkp)]. Listeners monitored for /p/ or /k/. Listeners perceived a /p/ significantly more often after labial nasals (more /p/ responses to /mk/ final words than to /nk/ and /rhookn k/ final words, $p<0.0001$), and perceived /k/ significantly more often after velar nasals (more /k/ responses to /loʏp/ final words than to /mp/ and /np/ final words, $p<0.0001$). Tokens with epenthetic stop bursts (acoustic analysis) received the most responses. These results provide experimental verification of the proposed articulatory and perceptual origins of epenthetic stops: listeners perceive stops the speaker did not intend, predominantly in environments where the articulatory explanation predicts epenthetic stops to occur.

5pSCb7. The relevance of *F*4 in distinguishing between different articulatory configurations of American English /r/. Carol Y. Espy-Wilson and Suzanne Boyce (Boston Univ., ECE Dept., 8 St. Mary's St., Boston, MA 02215)

American English /r/ is often cited as a segment exemplifying a many-to-one articulatory to acoustic relationship. Articulatory data show a continuum of vocal tract configurations for /r/, ranging from ''retroflexed'' to ''bunched,'' all involving three constrictions: (1) in the pharynx, (2) along the palate, and (3) at the lips. Researchers have noted, however, that all of these configurations result in similar acoustic profiles, at least for $F1$, $F2$, and $F3$. In this study, acoustic and articulatory data were used to investigate the mechanisms which determine the shape of the $F4$ trajectory for /r/. Articulatory positioning data and simultaneous acoustic data were collected from five subjects who said the phrase ''Say warav for me.'' The Electromagnetic Midsagittal Articulometer (EMMA) system was used to record the positions of three points on the tongue. Preliminary analysis based on the y position of the front, mid, and back transducers suggests that the behavior of $F4$ changes with different /r/ configurations and that the frequency of $F4$ is based on the length of the cavity between the palatal and pharyngeal constrictions.

5pSCb8. Vowel-dependent VOT variation: An experimental study. Steve S. Chang, John J. Ohala, Gunnar Hansson, Benjamin James (UC Berkeley, 1203 Dwinelle Hall, Berkeley, CA 94720, changs@socrates.berkeley.edu), Julie Lewis, Lily Liaw, Margaret Urban, Alan Yu (UC Berkeley), and Kenneth Van Bik (UC Berkeley)

That the VOT of voiceless stops is typically longer before high, close vowels and shorter before low, open ones is well documented. The hypothesis was tested that high vowels engender longer VOT because they offer greater resistance to the air escaping from the mouth (thereby delaying the transglottal pressure differential required for voicing). A correlation was sought between oral pressure decay (OPD) and VOT. Acoustic and aerodynamic data were collected from a male native speaker of American English uttering 12 nonsense words of the type atí, atà in isolation ten times. Pressure data was sampled by inserting a tube into the subject's pharyngeal cavity via the nose. The VOT was measured from the release of the burst to the onset of the first periodic cycle. The OPD was defined as the time required for oral pressure to decrease from the peak to a fixed low threshold. The OPD and VOT measurements displayed a significant, linear correlation, indicating that VOT and vowel height are indeed mechanically linked. Moreover, tokens with voiceless stops preceding sonorants, e.g., atwà, akjà, yielded the longest VOTs since sonorants have narrower constrictions, resulting in longer OPDs.

5pSCb9. The perception of German syllabic [n]. Bernd Pompino-Marschall and Peter M. Janker (Ctr. for General Linguist., Berlin, Germany)

Perception of syllabic [n] was studied using different inflectional forms of the German indefinite article, i.e., ''ein'' (nom. sing. masc.) versus ''einen'' (acc. sing. masc.). Inspection of a larger corpus of spoken German revealed that the most frequent pronunciation of ''einen'' is the allegro form with only a lengthened—not literally bisyllabic—[n]. Identification tests were run with manipulated items of a naturally spoken ''einen.'' The original utterance consisted of a glottalized [a] segment of 68-, a diphthong of 65-, and a [n] of 49-ms duration produced at a fundamental frequency of about 200 Hz by a female speaker. The duration of the diphthong and the nasal were varied in five steps of approximately 10 ms by doubling/cutting pairs of individual pitch periods. A second set of 25 stimuli was produced by cutting the initial glottalized segment. Analyses of variance revealed highly significant effects of nasal duration and glottalization independent of diphthong duration: Longer nasal segments as well as the presence of glottalization resulted in an increase in ''einen'' responses. The identification seems to be independent of rate of articulation but not of general speaking rate when the test items are embedded in larger utterances.

5pSCb10. Loudness and prominence in front vowels. Frank G. Gooding (Dept. of Linguist., Univ. of Wales, Bangor LL57 2DG, UK)

The perception of the high front vowels such as [i] is known to be dominated by the upper formant (UF) region, as is shown by the fact that [i] can be elicited by a single formant positioned there [P. Delattre *et al.*, Word **8**, 195–210 (1952)]. The basis of this dominance remains unclear, however, and is investigated by the present study. The simplest explanation would be that the UF region dominates $F1$ in terms of peak or total loudness. However, this is not reflected in current auditory models [e.g., B. Moore and B. Glasberg, Acustica **82**, 335–345 (1996)]. The representations of [i]-like vowels produced by this model, for instance, whether expressed as dB, phons, or sones, all show $F1$ strongly dominating the UF region in terms of excitation level or loudness. Two possible explanations

for this discrepancy come to mind: first, that the model is inaccurate; or second, that the perceptual dominance reflects mechanisms more central to the modeled excitation patterns. In the first case, the inaccuracy is likely to lie in the equal loudness data used by the model. An experiment was designed to test between these possibilities. Two formant versions of [i] and other front vowels were presented to subjects, who could control the amplitude of $F2$. The $F2$ threshold and equal loudness point was determined for each subject. Results indicate that the equal loudness point of $F2$ occurs at an intensity far below, and hence reflects a sensitivity far greater, than that predicted by the model. This implies that central mechanisms are not required to explain the perceptual dominance, and that the equal loudness data probably needs to be revised.

5pSCb11. Adults' perception and production of the English vowel /i/. Elaina Frieda[a] (Bussenstr. 32, 70184 Stuttgart, Germany, emfrieda@netscape.net)

The present experiment examined the link between the perception and production of the English vowel /i/. Thirty-five male subjects produced the vowel /i/ in the following two conditions: first, subjects produced ''casual'' or citation speech; second, subjects produced exaggerated (hyperarticulated) speech. Subjects then completed a perceptual experiment employing a method of adjustment procedure which enabled them to select their own preferred or ideal exemplar for /i/. Subjects' vowel productions were measured with LPC analysis for the following parameters: $F0$, $F1$, $F2$, and duration. The perceptual data were averaged for each subject to determine their preferred $F1$ and $F2$ dimensions. Comparing the two speech samples yielded predicted results in that the hyperarticulated speech was more extreme and fronted within the vowel space than the citation speech. Analyses also revealed a negative correlation between subjects' citation speech and their perceptual data, reflecting a tendency for the perceptual data to be higher and more fronted in the vowel space than citation speech. The production data were converted to bark difference scores for $F1-F0$ (vowel height) and $F2-F1$ (front–back dimension). These values were compared to subjects' perceptual data and demonstrated that the hyperarticulated speech was more similar to the perceptual data than citation speech. [a] Formerly at Dept. of Psych., Univ. of Alabama, Birmingham, AL.

5pSCb12. Reflection patterns and coloration of vowels. Anthony J. Watkins (Dept. of Psych., Univ. of Reading, Reading RG6 6AL, UK, syswatkn@reading.ac.uk)

When sounds are played in a room, the direct sound is accompanied by later-arriving reflections. If the reflections arrive within about 50 ms they are not heard separately, but seem to be perceptually incorporated with the direct sound. In addition, the reflection pattern can have a filtering effect, which can change the sound's spectral envelope, and which might be heard as a change in timbre or ''coloration.'' Thus, colored reflected sounds tend to follow after an uncolored direct sound. It has been suggested that the reflections' coloration is perceptually suppressed under these circumstances. The present experiment was designed to test this idea. Brief, 20-ms reflection patterns were designed that ''colored'' vowels' spectral envelopes and which followed after a direct sound in ''two-part filters.'' Coloration was measured by changes in listeners' identifications of vowels that are played through these filters. This was compared with the coloration in a condition with reversed two-part filters where the reflection pattern was caused to precede the direct sound. There should be more coloration in the reversed condition if there is normally suppression of coloration from later-arriving reflections. However, coloration was no greater in the reversed condition even though the reflections' perceptual effects were substantial.

5pSCb13. Help or hindrance: How violation of different assimilation rules affects spoken-language processing. Andrea Weber (Max-Planck-Inst. for Psycholinguist., P.O. Box 310, 6500 AH Nijmegen, The Netherlands, andrea.weber@mpi.nl)

Recent phoneme detection studies showed that spoken-language processing is inhibited by violation of obligatory assimilation [e.g., Otake *et al.* (1996)]. A phoneme detection experiment was designed to replicate this effect with German fricative assimilation. German fricative assimilation is progressive and applies within syllables. The velar fricative [x] occurs after back vowels, the palatal fricative [ç] after front vowels. In contrast to previous findings, listeners detected [x] *faster* when violation occurred. A second experiment explored whether these results are due to the tested assimilation applying within syllables, whereas earlier experiments tested assimilation across syllables. Again, listeners detected [x] *faster* when the assimilation rule was violated across a syllable boundary. The discrepancy with the earlier results might be due to the German fricative assimilation rule being progressive, while earlier experiments tested regressive assimilation. A third experiment tested German place assimilation for nasals. Regressive place assimilation in German is obligatory within syllables. A velar stop /k/ specifies the place for the preceding nasal /ŋ/. This time listeners detected the target phoneme /k/ *more slowly* when the assimilation was violated. The results show that whereas violation of regressive assimilation inhibits processing, violation of progressive assimilation speeds up processing.

5pSCb14. Perceptual properties of English fricatives. Allard Jongman, Michelle Spence, Yue Wang, Brian Kim, and Diana Schenck (Cornell Phonet. Lab., Dept. of Modern Lang., Cornell Univ., Ithaca, NY 14853)

A series of experiments was conducted to determine the properties that contribute to fricative perception. Listeners' identification of English fricatives based on fricative-vowel syllables and on isolated fricative noise portions reveals the perceptual salience of each fricative and the extent to which fricative-to-vowel transitions contribute to identification. Two further experiments specifically address perception of the nonsibilant fricatives, which, it has been claimed, may be based more on semantic or facial factors. One experiment investigates how a semantically matching or mismatching precursor affects perception of minimal pairs (e.g., fin-thin). A second experiment determines the extent to which auditory and/or visual information each contribute to fricative perception. Moreover, regression of these perceptual data on acoustic measurements, including noise duration, amplitude, relative amplitude, spectral peak location, spectral moments, and locus equations [see Jongman *et al.*, J. Acoust. Soc. Am. **103**, 3086A (1998)], indicates which acoustic properties play a significant role in fricative perception. [Work supported by NIH.]

5pSCb15. Influence of frequency range in the perceptual recognition of fricatives. Sergio Feijóo, Santiago Fernández, and Ramón Balsa (Departamento de Física Aplicada, Universidad de Santiago de Compostela, 15706 Santiago, Spain, fasergio@usc.es)

The objective of this paper is to study the importance of various frequency bands for the identification of fricatives. Tokens were CV syllables formed by the combination of the Galician fricatives /θ,f,s,ʃ/ and the vowels /a,e,i,o,u/ which were pronounced in Hyperspeech form by a man and a woman. Tokens were sampled at 32 kHz and low-pass filtered with cutoff frequencies of 11, 8, 5.5, 4, and 3 kHz. Thus, the total number of tokens was $240=4$ fricatives$\times 5$ vowels$\times 2$ sexes$\times 6$ frequencies. Thirty-seven listeners carried out the perceptual experiments in two conditions: (1) whole fricative noise plus 100 ms of the following vowel, and (2) whole fricative noise. The results of the perceptual experiments show that as the cutoff frequency is lowered, (a) /s/ tends to be recognized as /θ/ in both conditions; (b) the fricative noise of /θ/ tends to be recognized as /f/, and (c) recognition of /f/ and /ʃ/ is affected to a lesser extent. Results

suggest the importance of low-frequency energy in the characterization of /f/ and /ʃ/. Acoustic analysis is being carried out to determine if the identification of the filtered fricatives can be explained by relations among the spectral bands.

5pSCb16. Phonetic priming of features in a naming task. Tobey L. Doeleman (Cornell Phonet. Lab., Dept. of Linguist., Cornell Univ., Ithaca, NY 14853, tld5@cornell.edu)

The role of features in speech perception is investigated in a series of priming experiments in which subjects named CV syllables consisting of the English consonants [p, b, t, d, f, v, s, z] followed by the vowel [a]. Natural tokens were used to create sixty-four prime-target pairs which varied critically the number of features the consonants shared (0–3). The pairs were further classified into 8 stimulus sets based on the feature relationship: unrelated, identity, shared manner and voicing, manner and place, voicing and place, manner only, voicing only, and place only. Patterns of reaction times and accuracy data for the naming task are compared for the different stimulus sets. The same 64 pairs were blocked according to the voicing, place, or manner feature of the target, and presented to three subsequent groups of subjects who were thus given information about a particular feature. Results are discussed with reference to previous findings from a series of gating experiments (using the same stimulus set manipuluation) which found that subjects given place information had significantly higher scores in a consonant identification task than subjects given manner information [T. L. Doeleman, J. Acoust. Soc. Am. **101**, 3111(A) (1997)].

5pSCb17. Top-down influences on phonetic processing as a function of aging. Jeffrey Boyczuk and Shari Baum (McGill Univ., School of Commun. Sci. and Disord., 1266 Pine Ave. W., Montreal, QC H3G 1A8, Canada, jboycz@po-box.mcgill.ca)

A phonetic identification experiment was conducted in order to assess the extent to which lexical information influenced low-level speech perception processes in three different age groups of subjects (20–29 years, 60–69 years, and 70–79 years). Subjects were required to label syllable-initial, bilabial stop consonants which varied in voice onset time (VOT) as either /b/ or /p/. Following Ganong [J.E.P.: H.P.P. **6**, 110–125 (1980)], a pair of VOT continua with opposing lexical biases was created: one continuum ranged from the word /bʊk/ to the nonword /pʊk/ while the other continuum ranged from the nonword /bʊ t/ to the word /pʊt/. VOT values for the syllable-initial /b/–/p/ phoneme were the same at corresponding steps in the two continua. Results indicated a significant influence of lexical status on phonetic identifications for all age groups. Furthermore, a significant difference in the location of the phonetic crossover boundary was observed, with older subjects showing longer VOT values than young subjects. While findings suggest that top-down processing is still a prevalent part of phonetic perception in elderly individuals, it appears that aging may bring changes in the values of the acoustic parameters used to define phonetic categories. [Work supported by McGill University.]

5pSCb18. Speaking rate effects on vowel identification in natural sentence contexts. Adam M. Berman, Jonathan S. Neville, and Terry L. Gottfried (Dept. of Psych., Lawrence Univ., Appleton, WI 54912)

Previous research [T. L. Gottfried, J. L. Miller, and P. E. Payton, Phonetica **47**, 155–172 (1990)] has indicated for synthetic speech that vowel identification changes according to the speaking rate of the sentence context, even when the vowel contrast is specified experimentally only by spectral differences. This study tests listeners' identification of /i/ vs /ɪ / in stimulus continua created by altering formant values and durations of the target syllables ''beat'' and ''bit'' in naturally produced sentences. These targets were spoken in two sentence frames, one spoken at a moderate rate of speech and the other compressed to twice the speaking rate. Longer syllable durations significantly shifted the boundary of the spectral continuum, so that there were more ''beat'' responses as compared to shorter durations. However, unlike what was found for synthetic vowel series, there was no significant effect of sentence rate on the number of ''beat'' responses. Reasons for this different outcome, and the relevance of these findings for theories of rate normalization, are discussed. [Work supported by Lawrence University Faculty Grant.]

5pSCb19. Perceptual vowel spaces derived by computer game. James D. Miller, Arnold F. Heidbreder, and Nicole N. Wyzinski (Central Inst. for the Deaf, 818 S. Euclid Ave., Saint Louis, MO 63110, jdm@cid.wustl.edu)

A same–different task embedded in a computer game is used to obtain latencies of responses to vowel pairs. The ''player'' responds as fast as possible when the sounds in a pair are different and is not to respond when they are the same. The game concept and computer program were originally developed by K. Manabe and R. Dooling of the University of Maryland. Vowel sounds /i,ae,a,u/ were synthesized with interformant valley depths of 9, 18, 36, and 99 dB. All vowels were equalized in loudness based on balances made by four normally hearing listeners. Five listeners, two with normal hearing, two hearing-aid users, and one cochlear-implant user were tested four times, once at each valley depth. The logarithmic mean latencies for each different pair were taken as similarity measures for multidimensional scaling (mds). Average latencies decreased with increasing valley depths. For the two normally hearing listeners and one of the hearing-aid users, the perceptual vowel spaces derived by mds looked like the vowel equilateral, and the intervowel distances correlated highly with distances in Millers Auditory Perceptual Space. For one hearing-aid and the cochlear-implant user the vowel spaces were abnormal in appearance. Individual results will be presented.